

39th International Free-Electron Laser Conference

FEL19

Hamburg, Germany

26-30 August 2019

Universität Hamburg, Main building



Proceedings







2019 Young Scientist FEL Award

Chao Feng (SARI)
Joe Duris (SLAC)

Prize Committee

Zhirong Huang (Chair, SLAC)

2019 FEL Prize

Enrico Allaria (Sincrotrone Trieste)
Alex Lumpkin (Argonne/Fermilab)
Gennady Stupakov (SLAC)

Conference Organization

Local Organizing Committee

Conference Chairs: Winfried Decking (DESY) & Harald Sinn (European XFEL)
Administrative Chairs: Matthias Kreuzeder & Katharina Kuszka
Conference Secretariat: Christel Övermann & Katrin Lando
Computing Services: Carsten Kluth
Proceedings: Michaela Marx & Ruth Rudolph
Student Grants: Jörg Roszbach
Poster Sessions: Thomas Wamsat
Presentation Manager: Riko Wichmann
Speaker Preparation: Oliver Koschig
Lab Visits: Dirk Nölle & Rolf Treusch
Auxiliary support: Rebecca Jones-Krueger, Hannah Gerth

International Executive Committee

I. Ben-Zvi, BNL & Stony Brook University
M.-E. Couprie, Synchrotron SOLEIL
W. Decking (**Chair**), DESY
A. Friedman, Ariel University
J.N. Galayda, SLAC
L. Giannessi, ENEA & ELETTRA-Sincrotrone Trieste
H. Hama, Tohoku University
H-S. Kan, PAL/POSTECH
K.-J. Kim, ANL & The University of Chicago
V.N. Litvinenko, Stony Brook University & BNL
E.J. Minehara, JAEA & WERC
D.C. Nguyen, Los Alamos National Laboratory
S. Reiche, PSI
J. Roszbach, DESY & Hamburg University
O.A. Shevchenko, BINP
H. Tanaka, RIKEN Spring-8
A.F.G van der Meer, FELIX Facility, Radboud University
R.P. Walker (**Secretary**), Diamond Light Source
Y.K. Wu, Duke University
Z.T. Zhao, SINAP

JACoW Editorial Team

Ivan Andrian (Elettra-Sincrotrone Trieste, Italy)
Dong-Eon Kim (PAL/POSTECH, Korea)
Natalia Juszka (CERN, Switzerland)
Michaela Marx (DESY, **Editor-in-Chief**)
Raphael Müller (GSI, Germany)
John Poole (Pioneer Editor and founding member of JACoW, UK)
Ruth Rudolph (DESY, Germany)
Volker RW Schaa (GSI, Germany)
Jens Völker (HZB, Germany)

Conference Organization

Scientific Program Committee

Stephen Benson, Thomas Jefferson National Accelerator Facility
Simona Bettoni, Paul Scherrer Institut
Sandra Biedron, University of New Mexico and Element Aero
John Byrd, Argonne National Laboratory
Bruce Carlsten, Los Alamos National Laboratory
Francesca Curbis, MAX IV Laboratory and Physics Department, Lund University
Giovanni De Ninno, Elettra Sincrotrone Trieste
Simone Di Mitri, Elettra Sincrotrone Trieste
Yuantao Ding, SLAC National Accelerator Laboratory
Bruno Diviacco, Elettra Sincrotrone Trieste
David Dunning, Science and Technology Facilities Council
Massimo Ferrario, INFN - Laboratori Nazionali di Frascati
Gianluca Geloni (**Chair**), European X-Ray Free-Electron Laser Facility
Avraham Gover, Tel Aviv University
Jan Grünert, European X-Ray Free-Electron Laser Facility
Ryoichi Hajima, National Institutes for Quantum and Radiological Science and Technology
Jang-Hui Han, Pohang Accelerator Laboratory
Toru Hara, RIKEN Spring-8 Center
Rasmus Ischebeck, Paul Scherrer Institut
Young Uk Jeong, Korea Atomic Energy Research Institute
Heung-Sik Kang, Pohang Accelerator Laboratory
Marie Labat, Synchrotron SOLEIL
Alex H. Lumpkin, Fermi National Accelerator Laboratory
Atoosa Meseck, Helmholtz-Zentrum Berlin
Hideaki Ohgaki, Institute of Advanced Energy, Kyoto University
Eduard Prat, Paul Scherrer Institut
Jia Qika, University of Science and Technology of China
Daniel Ratner, SLAC National Accelerator Laboratory
Steve Russell, Los Alamos National Laboratory
Fernando Sannibale, Lawrence Berkeley National Laboratory
Evgeny Schneidmiller, Deutsches Elektronen-Synchrotron
Siegfried Schreiber (**Chair**), Deutsches Elektronen-Synchrotron
Svitozar Serkez, European X-Ray Free-Electron Laser Facility
Oleg Shevchenko, Budker Institute of Nuclear Physics
Frank Stephan, Deutsches Elektronen-Synchrotron
Takashi Tanaka, RIKEN Spring-8 Center
Dong Wang, Shanghai Institute of Applied Physics, Chinese Academy of Sciences
Sverker Werin, MAX IV Laboratory and Physics Department, Lund University
Ying K. Wu, Duke University
Juhao Wu, SLAC National Accelerator Laboratory
Alexander Zholents, Argonne National Laboratory

FEL Prize Committee

Zhirong Huang (**Chair**), SLAC
Bruce Carlsten, LANL
Marie Emmanuelle Couprie, SOLEIL
Hiroyuki Hama, Tohoku University
Mikhail Yurkov, DESY

Contents

Preface	i
FEL Award Winners	iii
Committees	iv
Contents	vi
Papers	1
MOA01 – Riding the FEL Instability (Dedicated to Alberto Renieri)	1
MOA02 – First Lasing of a Free Electron Laser in the Soft X-Ray Spectral Range with Echo Enabled Harmonic Generation	7
MOA03 – First Lasing at the CAEP THz FEL Facility	11
MOA07 – Commissioning and First Lasing of the FELiChem: A New IR and THz FEL Oscillator in China	15
MOC01 – Regenerative Amplifier FEL - from IR to X-Rays	20
TUA01 – Parallel Operation of SASE1 and SASE3 at the European XFEL	25
TUA04 – Harmonic Lasing Experiment at the European XFEL	29
TUB01 – Echo-Enabled Harmonic Generation Lasing of the FERMI FEL in the Soft X-Ray Spectral Region	33
TUP001 – Extension of the PITZ Facility for a Proof-of-Principle Experiment on THz SASE FEL	38
TUP002 – Progress in Preparing a Proof-of-Principle Experiment for THz SASE FEL at PITZ	41
TUP003 – Design of a Magnetic Bunch Compressor for the THz SASE FEL Proof-of-Principle Experiment at PITZ	45
TUP004 – A Superradiant THz Undulator Source for XFELs	48
TUP006 – The FHI FEL Upgrade Design	52
TUP007 – Experience with the Superradiant THz User Facility Driven by a Quasi-CW SRF Accelerator at ELBE	56
TUP008 – Concept of High-Power CW IR-THz Source for the Radiation Source Elbe Upgrade	59
TUP009 – Integration of an XFELo at the European XFEL Facility	62
TUP012 – Smith-Purcell Radiation Emitted by Pico-second Electron Bunches from a 30 keV Photo-Electron Gun	66
TUP014 – Crossed-Undulator Configuration for Variable Polarized THz Source	69
TUP015 – Design of High-Repetition Terahertz Super-Radiation Based on CAEP THz FEL Superconducting Beam-line	73
TUP017 – Terahertz FEL Simulation in PAL XFEL	77
TUP018 – Superradiant Emission of Electron Bunches Based on Cherenkov Excitation of Surface Waves in 1D and 2D Periodical Lattices: Theory and Experiments	80
TUP019 – Regime of Multi-Stage Non-Resonant Trapping in Free Electron Lasers	83
TUP020 – Terahertz Free Electron Maser Based on Excitation of a Talbot-Type Super-Mode in an Oversized Microwave System	87
TUP021 – Development of Powerful Long-Pulse Terahertz Band FELs Based on Linear Induction Accelerators	91
TUP023 – Analytical and Numerical Comparison of Different Approaches to the Description of SASE in High Gain FELs	94
TUP024 – Electronic Modulation of the FEL-Oscillator Radiation Power Driven by ERL	98
TUP025 – Current Status of Free Electron Laser @ TARLA	102
TUP026 – Unaveraged Simulation of a Regenerative Amplifier Free Electron Laser	106
TUP027 – Modelling Crystal Misalignments for the X-ray FEL Oscillator	110
TUP028 – Power Variations of an X-ray FEL Oscillator in Saturation	114
TUP032 – Regenerative Amplification for a Hard X-Ray Free-Electron Laser	118
TUP033 – Q-Switching of X-Ray Optical Cavities by Using Boron Doped Buried Layer Under a Surface of a Diamond Crystal	122
TUP035 – Sensitivity of LCLS Self-Seeded Pedestal Emission to Laser Heater Strength	126
TUP036 – A Waveguide-Based High Efficiency Super-Radiant FEL Operating in the THz Regime	127
TUP037 – Optimization of the Transverse Gradient Undulator (TGU) for Application in a Storage Ring Based XFELo	131
TUP038 – Axial Symmetry in Spontaneous Undulator Radiation for XFELo Two-Bunch Experiment	134
TUP041 – X-cos SCILAB Model for Simulation of Intensity and Gain of Planar Undulator Radiation	138
TUP042 – Analysis of Undulator Radiations With Asymmetric Beam and Non-Periodic Magnetic Field	141
TUP047 – An Analysis of Optimal Initial Detuning for Maximum Energy-Extraction Efficiency	145
TUP049 – Simulating Shot-Noise of 'Real' Electron Bunches	149
TUP050 – Comparison Between, and Validation Against an Experiment of, a Slowly-varying Envelope Approximation Code and a Particle-in-Cell Simulation Code for Free-Electron Lasers	153
TUP051 – Plasma Accelerator Driven Coherent Spontaneous Emission	157

TUP053 – An Investigation of Possible Non-Standard Photon Statistics in a Free-Electron Laser I: Experiment . . .	161
TUP054 – An Investigation of Possible Non-Standard Photon Statistics in a Free-Electron Laser II: Theory . . .	165
TUP055 – Two-Color Operation of FLASH2 Undulator	168
TUP056 – Feasibility Studies of the 100 keV Undulator Line of the European XFEL	172
TUP057 – Analysis of Parameter Space of Soft X-Ray Free Electron Laser at the European XFEL Driven by High and Low Energy Electron Beam	176
TUP058 – First Characterization of the Photon Beam at the European XFEL in July, 2017	180
TUP059 – Influence of Energy Chirp in the Electron Beam and Undulator Tapering on Spatial Properties of the Radiation From Seeded and SASE FEL	184
TUP060 – An Advanced Compression Option for the European XFEL	187
TUP061 – Super-X: Simulations for Extremely Hard X-Ray Generation With Short Period Superconducting Undulators for the European XFEL	191
TUP062 – Two Colors at the SASE3 Line of the European XFEL: Project Scope and First Measurements . . .	195
TUP063 – Physical Design and FEL Performance Study for FEL-III Beamline of SHINE	199
TUP064 – Effect on FEL Gain Curve Using Phase Shifters	203
TUP065 – Optimization of a Coherent Undulator Beamline for New Advanced Synchrotron Light Source in Korea	206
TUP066 – Start-to-End Simulations for the Soft X-Ray FEL at the MAX IV Laboratory	210
TUP067 – Advanced Concepts in the Design for the Soft X-Ray FEL at MAX IV	214
TUP072 – Orbital Angular Momentum from SASE	218
TUP073 – High-Repetition-Rate Seeding Schemes Using a Resonator-Amplifier Setup	222
TUP074 – FLASH Upgrade for Seeding	226
TUP076 – Seeding R&D at sFLASH	230
TUP077 – Study of a Seeded Oscillator-Amplifier FEL	234
TUP078 – Impact of Electron Beam Energy Chirp on Seeded FELs	238
TUP079 – Status of the Hard X-Ray Self-Seeding Setup at the European XFEL	242
TUP080 – Harmonic Off-Axis Seeding at the DELTA Short-Pulse Source	246
TUP083 – Energy Spread Impact on HHG and EEHG FEL Pulse Energy	250
TUP087 – Start-to-end Simulations of the Reflection Hard X-Ray Self-Seeding at the SHINE Project	254
TUP088 – Numerical Simulations for Generating Fully Coherent Soft X-Ray Free Electron Lasers With Ultra-Short Wavelength	258
TUP090 – Considerations on Implementing EEHG with a Strong Linear Chirp	262
TUP091 – Start-to-End Simulation of the NSRRC Seeded VUV FEL	266
TUP092 – XFEL Third Harmonic Statistics Measurement at LCLS	269
TUD02 – Application of Infrared FEL Oscillators for Producing Isolated Attosecond X-Ray Pulses via High-Harmonic Generation in Rare Gases	272
TUD03 – Fine and Hyperfine Structure of FEL Emission Spectra	276
TUD04 – Cavity-Based Free-Electron Laser Research and Development: A Joint Argonne National Laboratory and SLAC National Laboratory Collaboration	282
TUT01 – Superradiance and Stimulated-Superradiant Emission of Bunched Electron Beams	288
WEA01 – Overview of CW RF Guns for Short Wavelength FELs	290
WEA04 – Growing and Characterization of Cs ₂ Te Photocathodes with Different Thicknesses at INFN LASA . . .	297
WEB01 – Identification and Mitigation of Smoke-Ring Effects in Scintillator-Based Electron Beam Images at the European XFEL	301
WEB02 – Wire-Scanners with Sub-Micrometer Resolution: Developments and Measurements	307
WEB03 – Application of Machine Learning to Beam Diagnostics	311
WEB04 – Few-Femtosecond Facility-Wide Synchronization of the European XFEL	318
WEP003 – Balanced Optical-Microwave Phase Detector for 800-nm Pulsed Lasers with Sub-Femtosecond Resolution	322
WEP004 – Timing Stability Comparison Study of RF Synthesis Techniques	325
WEP006 – A PolariX TDS for the FLASH2 Beamline	328
WEP007 – Usage of the MicroTCA.4 Electronics Platform for Femtosecond Synchronization Systems	332
WEP008 – Multi-Beamline Operation at the European XFEL	335
WEP009 – Long Term Stability and Slow Feedback Performance at the European XFEL	339
WEP010 – Femtosecond Laser-to-RF Synchronization and RF Reference Distribution at the European XFEL . .	343
WEP011 – Longitudinal Intra-Train Beam-Based Feedback at FLASH	346
WEP012 – THz Spectroscopy with MHz Repetition Rates for Bunch Profile Reconstructions at European XFEL	350

WEP013 – Fast Kicker System for European XFEL Beam Distribution	353
WEP014 – Long Pulse Kicker for European XFEL Beam Distribution	357
WEP015 – Electro-Optical Bunch Length Detection at the European XFEL	360
WEP016 – Precise Laser-to-RF Synchronization of Photocathode Lasers	364
WEP019 – Concept of a Novel High-Bandwidth Arrival Time Monitor for Very Low Charges as a Part of the All-Optical Synchronization Systems at XFEL and FLASH	368
WEP024 – 1.3 GHz Solid State Power Amplifier for the Buncher in CTFEL Facility	371
WEP026 – Preliminary Geometry Optimization of a 3.5-Cell SRF Gun Cavity at ELBE Based on Beam Dynamics	374
WEP027 – A Fast and Accurate Method to Shim Undulator Using Multi-Objective GA	378
WEP030 – All-Fiber Photonic, Ultralow-Noise, Robust Optical and Microwave Signal Generators for FELs and UED	382
WEP031 – Timing Synchronization Activities for Drift-Free Operation of Ultrafast Electron Diffraction System at KAERI	385
WEP034 – Characterization of FEL Spectra Using Specific Figures of Merit	388
WEP035 – NIR Spectrometer for Bunch-Resolved, Non-Destructive Studies of Microbunching at European XFEL	392
WEP036 – The PolariX-TDS Project: Bead-Pull Measurements and High-Power Test on the Prototype	396
WEP037 – RF Jitter and Electron Beam Stability in the SwissFEL Linac	400
WEP038 – Commissioning and Stability Studies of the SwissFEL Bunch-Separation System	404
WEP041 – Feasibility of Single-Shot Microbunching Diagnostics for a Pre-Bunched Beam at 266 nm	408
WEP042 – Observations of Short-Range Wakefield Effects in TESLA-Type Superconducting RF Cavities	412
WEP043 – Multi-Energy Operation Analysis in a Superconducting Linac Based on off-Frequency Detune Method	416
WEP045 – Status of the Klystrons for the European XFEL after Commissioning and First User Operation Phase	420
WEP046 – The European XFEL Photocathode Laser	423
WEP047 – Update on the Photocathode Lifetime at FLASH and European XFEL	427
WEP048 – FLASH Photoinjector Laser Systems	430
WEP049 – RF Power Waveguide Distribution for the RF Gun of the European XFEL at DESY	434
WEP050 – Status of Chirped Pulse Laser Shaping for the PITZ Photoinjector	437
WEP051 – PITZ Experimental Optimization for the Aimed Cathode Gradient of a Superconducting CW RF Gun	440
WEP052 – Simulation Studies on the Saturated Emission at PITZ	444
WEP053 – Development of a Multialkali Antimonide Photocathode at INFN LASA	448
WEP054 – Beam Dynamics Optimization of a Normal-Conducting Gun Based CW Injector for the European XFEL	452
WEP055 – Multiphysics Analysis of a CW VHF Gun for European XFEL	456
WEP056 – Engineering Design of Low-Emittance DC-SRF Photocathode Injector	460
WEP057 – Performance Optimization of Low-Emittance DC-SRF Injector Using Cs ₂ Te Photocathode	463
WEP058 – Drive Laser Temporal Shaping Techniques for Shanghai Soft X-Ray Free Electron Laser	466
WEP059 – Characterizing a Coherent Electron Source Extracted From a Cold Atom Trap	469
WEP062 – Test of Cs ₂ Te Thickness on Cathode Performance at PITZ	473
WEP063 – The Preliminary Study of a Pre-Bunched Terahertz Free Electron Laser by a Velocity Bunching Scheme	477
WEP064 – Performance of S-Band Photocathode RF Gun With Coaxial Coupler	481
WEP067 – Development and Commissioning of a Flip Coil System for Measuring Field Integrals	484
WEP070 – Influence of Radiation Exposure on the FEL Performance at FLASH	488
WEP072 – Expected Radiation Properties of the Harmonic Afterburner at FLASH2	492
WEP073 – Experience With MCP-Based Photon Detector at FLASH2	495
WEP076 – A Superconducting Undulator With Variable Polarization Direction for the European FEL	499
WEP079 – Effect of Heat Load on Cryo-Cooled Monochromators at the European X-Ray Free-Electron Laser: Simulations and First Experimental Observations	502
WEP080 – ROSA: Reconstruction of Spectrogram Autocorrelation for Self-Amplified Spontaneous Emission Free-Electron Lasers	506
WEP081 – Design and Development of High-Speed Data Acquisition System and Online Data Processing with a Heterogeneous FPGA/GPU Architecture	510
WEP085 – Field Integral Measurements of DAVV Undulators and Future Measurement Plan	513
WEP086 – Capabilities of Terahertz Super-Radiance from Electron Bunches Moving in Micro-Undulators	517
WEP089 – Pulse Energy Measurement at the SXFEL	521
WEP092 – Spare Undulator Production for PAL-XFEL HX1 Beamline	524
WEP093 – Radiation Damage Monitoring at PAL-XFEL	528
WEP094 – Variable-Period Variable-Pole Number Hybrid Undulator Design for Novosibirsk THz FEL	531
WEP095 – The Athos Soft X-Ray Beamlines at SwissFEL	535

WEP097 – Operational Model of the Athos Undulator Beamline	538
WEP098 – Advanced Operational Models of the Apple X Undulator	541
WEP100 – Conceptual Design of a Permanent Magnet Undulator for Fast Pulse-to-Pulse Polarization Switching in an FEL	545
WEP101 – Linear Polarisation via a Delta Afterburner for the CompactLight Facility	549
WEP103 – A Plasma Attenuator for Soft X-Rays in LCLS-II	553
WEP104 – A High-Power, High-Repetition Rate THz Source for LCLS-II Pump-Probe Experiments	556
WEP107 – Polarizing Afterburner for the LCLS-II Undulator Line	560
WED01 – Experience with Short-Period, Small Gap Undulators at the SwissFEL Aramis Beamline	564
WED02 – Absorbed Radiation Doses on the European XFEL Undulator Systems During Early User Experiments	569
THA04 – Ultrafast Magnetisation Dynamics at the Low-Fluence Limit Supported by External Magnetic Fields . .	574
THB02 – Understanding 1D to 3D Coherent Synchrotron Radiation Effects	578
THB04 – Longitudinal Phase Space Study on Injector Beam of High Repetition Rate X-Ray FEL	584
THP001 – Steffen Hard-Edge Model for Quadrupoles with Extended Fringe-Fields at the European XFEL . . .	588
THP002 – Beam Based Alignment in all Undulator Beamlines at European XFEL	592
THP003 – Arbitrary Order Perturbation Theory for a Time-Discrete Model of Micro-Bunching Driven by Longitudinal Space Charge	596
THP007 – Frequency-Detuning Dependent Transient Coaxial RF Coupler Kick	599
THP008 – Design of a Multi-Cell SRF Reduced-Beta Cavity for the Acceleration of Low Energy Electron Beams	603
THP009 – Space Charge Field Beam Dynamics Simulations for the THz SASE FEL at PITZ	606
THP010 – Simple and Robust Free Electron Laser Doubler	609
THP011 – Experimental Benchmarking of Wakefields at the FERMI FEL Linac and Undulator Line	613
THP012 – Compact FEL-Driven Inverse Compton Scattering Gamma-Ray Source	617
THP013 – User Operation of Sub-Picosecond THz Coherent Transition Radiation Parasitic to a VUV FEL . . .	621
THP015 – The X-Band Linear Compression System in Dalian Coherent Light Source	625
THP016 – Study of Microbunching Instability in SHINE Linac	629
THP018 – Transverse Deflecting Structure Dynamics for Time-Resolved Machine Studies of Shine	632
THP020 – Microbunching Enhancement by Adiabatic Trapping	635
THP022 – A General Optimization Method for High Harmonic Generation Beamline	638
THP024 – Spontaneous Coherent Radiation of Stabilized Dense Electron Bunches	643
THP027 – Simulation and Optimization of the Transport Beamline for the NovoFEL RF Gun	647
THP030 – An Updated Design of the NSRRC Seeded VUV Free Electron Laser Test Facility	651
THP031 – Simulation and Optimization of Injector System for the Pre-bunched THz FEL	654
THP033 – XFEL Isochronous Chicanes: Feasibility Study	658
THP035 – Beam Shaping for High-Repetition-Rate X-Ray FELs	661
THP036 – Microbunch Rotation for Hard X-Ray Beam Multiplexing	665
THP037 – A Novel One-Dimensional Model for CSR Wakefields	669
THP041 – Interaction of Powerful Electro-Magnetic Fields With Bragg Reflectors	673
THP044 – The Simulation Study for Single and Multi Turn ERL Based EUV FEL	677
THP047 – Laser-Driven Compact Free Electron Laser Development at ELI-Beamlines	680
THP048 – Progress Towards Laser Plasma Electron Based Free Electron Laser on COXINEL	684
THP049 – A Versatile THz Source for High-Repetition Rate XFELs	688
THP051 – Generating Trains of Attosecond Pulses with a Free-Electron Laser	692
THP054 – Nanosecond Pulse Enhancement in Narrow Linewidth Cavity for Steady-State Microbunching	697
THP055 – A Storage Ring Design for Steady-State Microbunching to Generate Coherent EUV Light Source . .	700
THP060 – Development of RF-Undulators and Powering Sources for Compact Efficient Compton FEL-Scatrons	704
THP061 – Bayesian Optimisation for Fast and Safe Parameter Tuning of SwissFEL	707
THP065 – Multi-Objective FEL Design Optimisation Using Genetic Algorithms	711
THP066 – XARA: X-Band Accelerator for Research and Applications	715
THP068 – LCLS-II Extruded Aluminum Undulator Vacuum Chambers — New Approaches to an Improved Aper- ture Surface Finish	719
THP069 – Observations on Microbunching of Electrons in Laser-Driven Plasma Accelerators and Free-Electron Lasers	722
THP071 – Progress in High Power High Brightness Double Bunch Self-Seeding at LCLS-II	726
THP073 – Status Update for the High Gain High Efficiency TESSA-266 Experiment	730
THP074 – FLASH: The Pioneering XUV and Soft X-Ray FEL User Facility	734

THP078 – Status of the CompactLight Design Study	738
THP079 – Status and Perspectives of the FERMI FEL Facility (2019)	742
THP081 – PoIFEL — New Facility in Poland	746
THP084 – Status of the Soft X-Ray Laser (SXL) Project at MAX IV Laboratory	749
THP085 – Status of Athos, the Soft X-Ray FEL Line of SwissFEL	753
THP086 – Operation Modes of the SwissFEL Soft X-Ray Beamline Athos	757
THD03 – FEL Optimization: From Model-Free to Model-Dependent Approaches and ML Prospects	762
FRA01 – FEL Operation at the European XFEL Facility	766
FRA02 – LCLS-II - Status and Upgrades	772
FRA03 – FLASH - Status and Upgrades	776
Appendices	781
List of Authors	781
Institutes List	793
Participants List	808

RIDING THE FEL INSTABILITY (DEDICATED TO ALBERTO RENIERI)

G. Dattoli*, ENEA - Frascati Research Center, Frascati, Rome, Italy
C. Pellegrini†, UCLA, Physics & Astronomy, Los Angeles, CA, USA

Abstract

The Free Electron Laser (*FEL*) transforms the kinetic energy of electrons into coherent light. The underlying mechanism occurs through the *FEL* instability, leading to the growth of coherent radiation from noise, characterizing all the generators of coherent radiation from free electrons (Gyrotrons, *CARM* ...). The *FEL* instability shares many features with other instabilities occurring in Plasmas and electron beams, sometimes competing with them. In this paper we give a short description of these analogies, their relevant physical roots and comment on the importance and role of their interplay.

FEL INSTABILITY

The *FEL*, in its modern conception, started in 1976 with the amplification of a CO_2 laser, co-propagating with an electron beam in an undulator magnet [1]. The experiment confirmed what Madey had predicted few years before [2], namely that the electron beam may be induced to lose power, thus enhancing the laser intensity. The *FEL* small signal gain curve was carefully examined, along with the kinematical conditions under which the laser beam can be amplified or depleted, thus revealing an, albeit inefficient, electron beam acceleration. The following year, an *FEL* oscillator [3] showed that, under appropriate conditions, the amplification mechanism was sufficient to sustain the laser oscillation in the *IR* and drive the system to complete saturation.

The original conception of *FEL* [2] was a quantum treatment of a process called “stimulated bremsstrahlung” by Madey. The dynamical behavior of *FEL* was successively clarified by Colson [4–6] who showed that all the relevant physics can be described by a classical model based on the use of a pendulum like equation, coupled to those giving the laser field evolution. Many discussions arose at the time, regarding the nature of the *FEL* itself [7], compared to population inversion devices. However smart the answer was, it could not circumvent the pragmatic observation that the *FEL* is a tool that steals power from a relativistic e-beam, transforming it into coherent “laser-like” power.

The question now becomes what “laser like” means and whether it is true that the *FEL* light is fully coherent. The theoretical treatment developed by Bambini and Renieri [8–12] used means from analytical mechanics to describe the *FEL* problem in terms of a non relativistic

Hamiltonian, leading to the pendulum equation and opening the way to the investigation of the *FEL* quantum coherence properties [7, 8]. This is the gross picture before the eighties. It became slowly clear that the *FEL* phenomenology had not to be dissimilar from the Physics of travelling wave tubes. The analogy between *FEL* and other generators of light by other free electron devices (Klystron, Gyrotron, *CARM*, ...) was pointed out in [13] (see also ref. [7] for a more recent discussion. For a comparison with conventional laser sources, see [14]).

The common feature emerging from the relevant theoretical picture was that the optical field growth is associated with a dispersion relation leading to a third (or fourth) order *ODE* [15–17]. The roots of the associated characteristic polynomial fix the condition for the onset and rise of the electromagnetic field. Within this context the field grows as the result of the *FEL* instability, with a rise time or gain length, given by the “fast growing” root.

The breakthrough in this direction came from [18] where a new operating condition for the *FEL* was foreseen, thus paving the way for the fourth generation synchrotron radiation devices, the *X-Ray FELs*, characterized by very high brightness, power and by extremely short pulse duration. A proposal to build an *X-Ray FEL* using a 15 GeV electron beam from the *SLAC* linac [19] led to the design and construction of *LCLS* and other similar systems in Europe and Asia. *X-Ray FELs* give for the first time the possibility of exploring matter with X-rays at the angstrom-femto-second space and time scale characteristic of atomic systems, thus opening a new window on the exploration of matter and its dynamical processes.

We have pointed out that the *FEL* small signal dynamics is the result of an instability, the further interplay with the e-beam produces a heating, determining the increase of the energy spread, which eventually induces saturation [20]. This is a complex mechanism, associated with Landau damping, and will be further discussed in the next sections of the paper.

STORAGE RING FEL, RENIERI LIMIT AND SAW-TOOTH INSTABILITY

In the previous section we have mentioned that the *FEL* growth is the result of an instability, counteracted by the self induced beam energy spread. Many *FEL* oscillators have been proposed and operated in the past [21–28] in an electron storage ring, with the intent of providing

* giuseppe.dattoli@enea.it
† pellegrini@physics.ucla.edu

radiation in the *IR* to *UV* with relatively large average power.

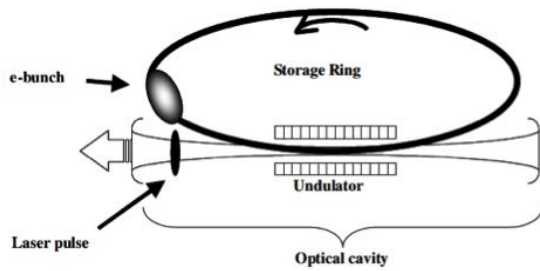


Figure 1: *FEL* Storage Ring Oscillator: the electron and a synchronous laser bunch overlap after any ring turn.

The relevant dynamics can be illustrated by the following steps (see Fig. 1):

- The electron beam is circulated many times inside the optical cavity, synchronized to the radiation pulse. At each interaction, it transfers energy to the radiation and increases its own energy spread.
- The *FEL* intensity increase continues until the induced energy spread reduces the gain below the cavity losses. The threshold energy spread determining the laser switching off is of the order of

$$\langle \Delta E \rangle \leq \frac{E}{4N} \quad (1)$$

whit N number of undulator periods.

- The laser process stops and radiation in the storage ring reduces the energy spread. After a damping time τ_s , when the beam original condition have been restored by the ordinary damping mechanisms, the laser process starts again. The average laser power is therefore given by

$$P_L \leq \frac{1}{4N}, \quad \frac{E}{\tau_s} = \frac{1}{4N} P_s \quad (2)$$

This is the Renieri limit [29, 30] and states that the laser power of a storage ring *FEL* does not exceed a fraction of the power P_s lost in the whole machine via synchrotron radiation. It has been confirmed by the theory, simulation and experiment [31, 32]. It is a very important contribution to the Physics of *FEL*'s operating in a storage ring.

However the *FEL* instability and radiation damping are not the only physical mechanisms at work in a storage ring, which is a complex environment. Electrons move inside the vacuum chamber, where various instrumentation items and *RF* cavities are present. The interaction of the electron with these devices generates additional electromagnetic fields, called "wake-fields". They interact with the beam and can induce further instabilities. One of them is the saw-tooth

instability, manifesting itself through an anomalous increase of the beam energy spread and bunch length. The literature in the field is quite impressive (see ref. [33–43] for a partial list), where authoritative account (analytical and numerical) of the relevant phenomenology have been presented. The anomalous energy spread increase can limit the *FEL* power below the value foreseen by the Renieri theory.

We report below an outline of the relevant theoretical studies.

- Understanding of the relevant phenomenology, development of scaling relations aimed at clarifying the existence of a threshold current above which an anomalous spread appears (Kheil-Schnell, Boussard, ...).
- Mode coupling and instability (Sacherer, Laclare, ...).
- Fokker-Planck analysis and turbulent mode coupling (Renieri).
- Integral equation treatment (Wang, Krinsky, Pellegrini, ...) which provided the analytical basis for the Boussard criterion.

With the advent of *FEL* the question was raised about the interplay between microwave and *FEL* instabilities. It was noted that they induced qualitatively analogous behavior on the beam energy spread, characterized by a fast blow up and then by a damping. The understanding of such an interplay occurred using arguments not dissimilar from those leading to the Renieri limit and goes as it follows.

The Boussard criterion states the existence of a threshold beam current (I_{th}) above which the energy spread exceeds the natural value, the parameter $\delta^2 = \frac{I}{I_{th}}$ can be used to fix the associated amount of energy spread increase with respect to the natural counterpart $\sigma_A^2 = \delta^2 \sigma_0^2$. If the *FEL* induced energy spread exceeds σ_A , the instability can be switched off (see Figs. 2-3) and the corresponding *FEL* threshold intensity is [44–46]

$$P^* \approx \chi \frac{P_s}{4N}, \quad \chi = 1.673 \frac{\delta^{\frac{2}{3}} - 1}{g_0} \mu^2, \quad \mu = 4N \sigma_0 \quad (3)$$

where g_0 is the small signal gain coefficient.

The *SR-FEL* dynamics has displayed so many interesting complex phenomenon, with implications going well beyond the mere generation of coherent radiation. The non linear effects in accelerators and the associated instabilities make the study of the relevant dynamics very much interesting. The study of the competition of different instabilities has opened an entire new world. We learned how they may contribute to control each other, we understood how the *FEL* may contribute to the regulation of saw-tooth, head tail [47] instabilities, Touscheck beam lifetime ... The relevant studies dynamics taught us how the whole system (in

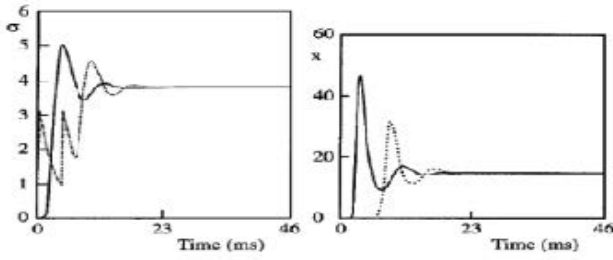


Figure 2: Induced energy spread in storage ring *FEL* without (solid line) and with (dash line) saw tooth instability. Same for the laser intensity.

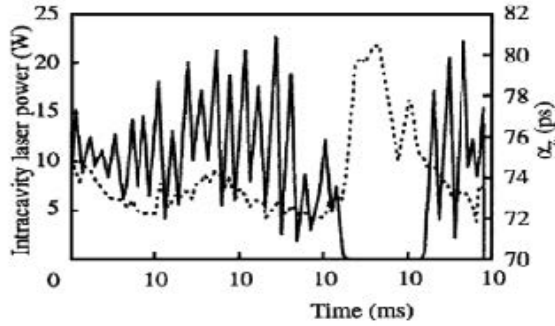


Figure 3: Experimental results (SUPERACO) solid line induced energy spread *FEL* on (solid) Saw-tooth contribution (dash), when *FEL* is off the saw tooth contribution blows up.

Storage Rings and other accelerator as well) should be considered from a unitary point of view, and within this context the *FEL* appears as one of the intrinsic feedback mechanisms contributing to the electron-beam equilibrium with the accelerator environment [48]. Alberto Renieri has been a pioneering and decisive contributor to these studies.

CONCLUDING COMMENTS

In the previous sections we insisted on regarding the *FEL* as the result of an instability, we have commented on the role of control acted on the accelerator environment by its competition with other types of instabilities, hence the title of this paper. The importance of the seminal ideas put forward in the previous comments reflects in more recent researches [49, 50] foreseeing the use of a Storage Ring to drive a short wavelength *SASE FEL* operation. The role of laser heater in suppressing or mitigating the coherent synchrotron instability [51, 52] can be framed within the same context.

Let us however go back to the *FEL* power growth and to its route to saturation. The small signal *FEL* dynamics is ruled by a Volterra integro-differential equation with a gain memory kernel reported below [53]

$$\frac{d}{d\tau}a = i\pi g_0 \int_0^\tau \tau' e^{-i\nu\tau'} a(\tau - \tau') d\tau'. \quad (4)$$

It can be reduced to the third order *ODE*

$$(\hat{D}_\tau^3 + 2i\nu\hat{D}_\tau^2 - \nu^2\hat{D}_\tau) a(\tau) = i\pi g_0 a(\tau), \quad a|_{\tau=0} = a_0, \quad \hat{D}_\tau a|_{\tau=0} = 0, \quad \hat{D}_\tau^2 a|_{\tau=0} = 0. \quad (5)$$

Its solution depends on the characteristic third order polynomial. The explicit form of the dimensionless field amplitude writes [54]

$$a(\tau) = \frac{a_0}{3(\nu + p + q)} e^{-\frac{2}{3}i\nu\tau} \cdot \left\{ (-\nu + p + q) e^{-\frac{i}{3}(p+q)\tau} + 2(2\nu + p + q) e^{\frac{i}{6}(p+q)\tau} \cdot \left[\cosh\left(\frac{\sqrt{3}}{6}(p-q)\tau\right) + i\frac{\sqrt{3}\nu}{p-q} \sinh\left(\frac{\sqrt{3}}{6}(p-q)\tau\right) \right] \right\},$$

$$p = \left[\frac{1}{2} (r + \sqrt{d}) \right]^{\frac{1}{3}}, \quad q = \left[\frac{1}{2} (r - \sqrt{d}) \right]^{\frac{1}{3}},$$

$$r = 27\pi g_0 - 2\nu^3, \quad d = 27\pi g_0(27\pi g_0 - 4\nu^3),$$

$$\tau = \frac{Nz}{\lambda_u}, \quad \nu \equiv \text{detuning parameter}. \quad (6)$$

The fast growing term is contained in the contributions associated with the hyperbolic functions. A practical issue is that of embedding the above formulae to get a simple relation yielding either the power growth $P(z)$ (including the saturation) and the induced energy spread $\sigma_i(z)$ along the undulator coordinate z (Fig. 4)

$$P_1(z) = P_0 \frac{A(z)}{1 + \frac{P_0}{P_{F,1}} (A(z) - 1)},$$

$$A(z) = \frac{1}{9} \left[3 + 2 \cosh\left(\frac{z}{L_g}\right) + 4 \cos\left(\frac{\sqrt{3}}{2} \frac{z}{L_g}\right) \cosh\left(\frac{z}{2L_g}\right) \right],$$

$$P_0 \equiv \text{Input seed power}, \quad L_g \equiv \text{Gain length},$$

$$P_F = \sqrt{2} \rho P_E, \quad \rho \equiv \text{Fel Pierce parameter},$$

$$P_E \equiv e\text{-beam power} \quad (7)$$

and

$$\sigma_i(z) = 3C \sqrt{\frac{A(z)}{1 + 9B(A(z) - 1)}}, \quad C = \frac{1}{2} \sqrt{\frac{\rho P_0}{P_E}}, \quad (8)$$

$$B \approx \frac{1.24}{9} \frac{P_0}{P_F}, \quad \sigma_{i,F} \approx \frac{C}{\sqrt{B}} \approx 1.6 \rho.$$

The derivation of the previous relations can be framed within different analytical models, Ginzburg-Landau, asymptotic solution of pendulum field equations, wise combination of numerical and scaling relations [55].

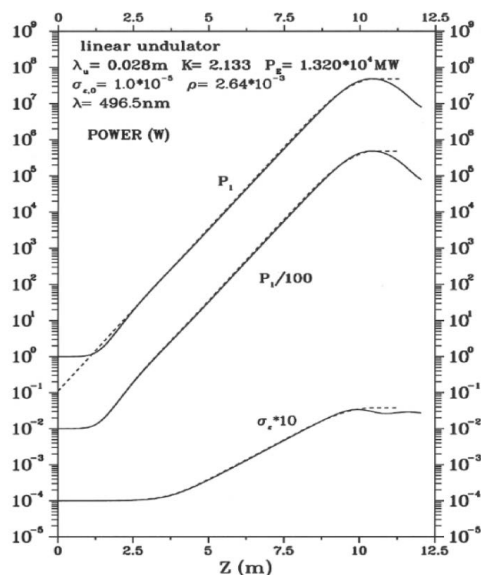


Figure 4: Power and energy spread evolution.
Upper curves - continuous line: 1-D simulation, dashed line fast growing root only.
Middle curves - continuous line: 1-D simulation, dashed line: Eq. (7).
Lower curves - continuous line: 1-D simulation, dashed line: Eq. (8).

Whatever the procedure is, they represent the result of a non common ability of combining physical intuition and analytical means to provide results of practical interest. Alberto mastered all these aspects and left an important lesson for all of us as man and scientist.

Aa a final comment we like to mention other two distinguished members of the “ENEA-Frascati-FEL school”: Franco Ciocci and Amalia Torre, they passed away on the eve of last year, their work, their contributions and their smiling presences will remain forever with us.

ACKNOWLEDGEMENTS

The Authors express their sincere appreciation to Drs. Marie Emmanuelle Couprie and Silvia Licciardi for the help offered during the compilation of the paper.

REFERENCES

- [1] L.R. Elias, J.M.J. Madey, H.A. Schwettman, T.I. Smith, “Observation of Stimulated Emission of Radiation by Relativistic Electrons in a Spatially Periodic Transverse Magnetic Field”, *Phys. Rev. Lett.*, 36, 717, 1976. doi:10.1103/PhysRevLett.36.717
- [2] J.M.J. Madey, “Stimulated Emission of Bremsstrahlung in a Periodic Magnetic Field”, *J. Appl. Phys.* 42,1906, 1971. D. Marcuse, *Principle of Quantum Optics*, Academic Press New York, 1980. doi:10.1063/1.1660466
- [3] D.A.G. Deacon *et al.*, “First Operation of a Free-Electron Laser”, *Phys. Rev. Lett.*, 38, 892, 1977. doi:10.1103/PhysRevLett.38.892
- [4] W.B. Colson, “One-body electron dynamics in a free electron laser”, *Phys. Lett.* 64A, pp. 190–192, 1977. doi:10.1016/0375-9601(77)90712-5
- [5] W.B. Colson, “The nonlinear wave equation for higher harmonics in free-electron lasers”, *IEEE J. Quantum Electron.*, QE-17, pp. 1417–1427, 1981. doi:10.1109/JQE.1981.1071273
- [6] W.B. Colson, “Classical free electron laser theory”, in *Laser Handbook*, W.B. Colson, C. Pellegrini, A. Renieri (Eds.), vol. VI, North Holland, Amsterdam, 1990.
- [7] G. Dattoli, E. Di Palma, S. Pagnutti and E. Sabia, “Free Electron coherent sources: From microwave to X-rays”, *Phys. Rep.*, 739, pp. 1–51, 2018. doi:10.1016/j.physrep.2018.02.005
- [8] A. Bambini, A. Renieri, “The free electron laser: A single-particle classical model”, *Lett. Nuovo Cim.*, 21, 399, 1978. doi:10.1007/BF02762613
- [9] A. Bambini, A. Renieri A, S. Stenholm, “Classical theory of the free-electron laser in a moving frame”, *Phys. Rev. A*, 19, 2013, 1979. doi:10.1103/PhysRevA.19.2013
- [10] A. Renieri *et al.*, “Experimental and theoretical aspects of the free electron laser”, in *Laser Handbook*, M.S. Bass, L. Stith (Eds.), vol. IV, North-Holland, Amsterdam, 1985.
- [11] A. Renieri *et al.*, “Quantum theory of free electron laser”, in *Laser Handbook*, W.B. Colson, C. Pellegrini, A. Renieri (Eds.), vol. VI, North Holland, 1990.
- [12] F. Ciocci, G. Dattoli, A. Renieri, A. Torre, “About the mathematical aspects of the FEL and their relationship to quantum optics”, *Phys. Rep.*, vol. 141, 1, pp. 1–50, 1986. doi:10.1016/0370-1573(86)90106-7
- [13] V.L. Bratman, N.S. Ginzburg, M.I. Petelin, “Common properties of free electron lasers”, *Opt. Commun.*, vol 30, 3, pp. 409–412, 1979. doi:10.1016/0030-4018(79)90382-1
- [14] G. Dattoli, M. Del Franco, M. Labat, P.L. Ottaviani and S. Pagnutti, “Introduction to the Physics of Free Electron Laser and Comparison with Conventional Laser Sources”, in *Free Electron Lasers*, Sandor Varro, IntechOpen. doi:10.5772/35429
- [15] M.I. Petelin, “On the theory of ultrarelativistic cyclotron self-resonance masers”, *Radiophysics and Quantum Electronics*, vol. 17, 6, pp. 902–908, 1974. doi:10.1007/BF01038662
- [16] G. Nusinovich, *Introduction to the Physics of Gyrotrons*, The Johns Hopkins University Press, 2004.
- [17] E. Di Palma, E. Sabia, G. Dattoli, S. Licciardi, I. Spassovsky, “Cyclotron auto resonance maser and free electron laser devices: A unified point of view”, *J. Plasma Phys.*, 83, 2017. doi:10.1017/S0022377816001239
- [18] R. Bonifacio, C. Pellegrini, L. M. Narducci, “Collective instabilities and high-gain regime in a free electron laser”, *Opt. Commun.*, 50, pp. 373–378, 1984. doi:10.1016/0030-4018(84)90105-6
- [19] C. Pellegrini, “A 4 to 0.1 nm Fel Based on the SLAC Linac”, in *Proc. Workshop IV Generation Light Sources*, C. Cornacchia and H. Winick eds, SSRL/SLAC Rep. 92/02, pp. 364–375, 1992.

- [20] C. Pellegrini, A. Marinelli, and S. Reiche, “The physics of x-ray free-electron lasers”, *Rev. Mod. Phys.* 88, 015006, 2016. doi:10.1103/RevModPhys.88.015006
- [21] M.E. Couprie *et al.*, “Operation of the super-ACO, FEL in the UV range at 800 MeV”, *Euro. Lett.*, 21, 9, pp. 909–914, 1993. doi:10.1209/0295-5075/21/9/006
- [22] M.E. Couprie *et al.*, “Temporal dynamics of storage ring free electron lasers”, *Phys. Rev. E*, 53, 2, pp. 1871–1889, 1996. doi:10.1103/PhysRevE.53.1871
- [23] Kulipanov G.N., *et al.*, “The VEPP-3 storage-ring optical klystron: Lasing in the visible and ultraviolet regions” *Nucl. Instr. Meth. A* 296, 1-3 (1990). doi:10.1016/0168-9002(90)91179-F
- [24] M.E. Couprie *et al.*, “The results of lasing linewidth narrowing on VEPP-3 storage ring optical klystron”, *Nucl. Instr. Meth. A*, 304, pp. 47–52, 1991. doi:10.1016/0168-9002(91)90818-B
- [25] H. Hama *et al.*, “Observation of micro-macro temporal structure and saturation mechanism on the UVSOR free electron laser”, *Nucl. Instr. Meth. Phys. Res. A: Accelerators, Spectrometers, Detectors and Associated Equipment*, vol. 358, pp. 365–368, 1995. doi:10.1016/0168-9002(94)01513-9
- [26] T. Yamazaki T. *et al.*, “First lasing of the NIJI-IV storage-ring free-electron laser”, *Nucl. Instr. Meth. Phys. Res. A*, vol. 331, pp. 27-33, 1993. doi:10.1016/0168-9002(93)90008-6
- [27] M. Billardon *et al.*, “First Operation of a Storage-Ring Free-Electron Laser”, *Phys. Rev. Lett.*, 51, 1652, 1983. doi:10.1103/PhysRevLett.51.1652
- [28] K. Yamada *et al.*, “Visible oscillation of storage-ring free electron laser on TERAS”, *Nucl. Instr. Meth. Phys. Res. A*, vol. 318, pp. 33–37, 1992. doi:10.1016/0168-9002(92)91019-6
- [29] A. Renieri, “Storage ring operation of the free-electron laser: The amplifier”, *Nuov. Cim. B*, 59, pp. 160–178, 1979. doi:10.1007/BF02739308
- [30] G. Dattoli, A. Renieri, “Storage ring operation of the free-electron laser: The oscillator”, *Nuovo Cim. B*, 59, pp. 1–39, 1980. doi:10.1007/BF02739044
- [31] P. Elleaume, “Macro-temporal structure of storage ring free electron lasers”, *J. Physique*, vol. 45, pp. 997–1001, 1984. doi:10.1051/jphys:01984004506099700
- [32] P. Elleaume, “Microtemporal and spectral structure of storage ring free-electron lasers”, *IEEE J. Quantum Electron.*, vol. 21, pp. 1012–1022, 1985. doi:10.1109/JQE.1985.1072746
- [33] V.K. Neil and A.M. Sessler, “Longitudinal resistive instabilities of intense coasting beams in particle accelerators”, *Rev. Sci. Instrum.*, 36, 429, 1965. doi:10.1063/1.1719594
- [34] E. Keil and W. Schnell, “Concerning Longitudinal Stability”, CERN, ISR tech. rep. CERN-ISR-TH-RF-69-48, 1969.
- [35] D. Boussard, “Observation of microwave longitudinal instabilities”, CERN, CPS tech. rep. CERN-LabII-RF-INT-75-2, 1975.
- [36] F. Sacherer, “A longitudinal stability criterion for bunched beams”, *IEEE Trans. Nucl. Sci.*, 20, 825, 1973. doi:10.1109/TNS.1973.4327254
- [37] F. Sacherer, “Bunch lengthening and microwave instability”, *IEEE Trans. Nucl. Sci.*, 24, p. 1393, 1977. doi:10.1109/TNS.1977.4328955
- [38] T. Suzuki, Y. Chin, and K. Satoh, “Mode coupling theory and bunch lengthening in SPEAR II”, *Particle Accel.*, 13, p. 179, 1983.
- [39] A. Renieri, “Turbulence and Bunch Lengthening in Electron-Positron Storage Rings”, LNF Internal note 76/11(R), 1976.
- [40] K. Oide and K. Yokoya, “Longitudinal single-bunch instability in electron storage rings”, *Phys. Rev. Lett.*, KEK Preprint 90-10, 1990, <http://cds.cern.ch/record/208816/files/kek-preprint-90-10.pdf>
- [41] Y. Cai, “Linear theory of microwave instability in electron storage rings”, *Phys. Rev. ST Accel. Beams*, 14, 061002, 2011. doi:10.1103/PhysRevSTAB.14.061002
- [42] J.L. Laclare, “High current single bunch transverse instabilities at the ESRF: a new approach”, CERN accelerator school, pp. 264, 1985.
- [43] J.M. Wang and C. Pellegrini, “On the Condition for a Single Bunch High Frequency Fast Blow-Up”, in Newman W.S. (eds) 11th International Conference on High-Energy Accelerators. *Experientia Supplementum*, vol 40. Birkhäuser, Basel, 1980. doi:10.1007/978-3-0348-5540-2_72
- [44] G. Dattoli, L. Giannessi, P.L. Ottaviani, A. Renieri, “A model for the saturation of a storage ring free electron laser”, *Nucl. Instrum. Meth. A*, vol. 365, pp. 559–563, 1995. doi:10.1016/0168-9002(95)00507-2
- [45] R. Bartolini, G. Dattoli, L. Mezi and A. Renieri, “Suppression of the Sawtooth Instability in a Storage Ring by Free-Electron Laser: An Example of Nonlinear Stabilization by Noise”, *Phys. Rev. Lett.*, 87, 134801, 2001. doi:10.1103/PhysRevLett.87.134801
- [46] G. Dattoli *et al.*, “Storage-ring free-electron-laser dynamics and head-tail instability”, *Phys. Rev. E*, 58, 6570, 1998. doi:10.1103/PhysRevE.58.6570
For the head tail instability see:
- [47] C. Pellegrini, “On a new instability in electron-positron storage rings. (the head-tail effect)”, *Nuov. Cim. A*, 64, pp. 447–473, 1969. doi:10.1007/BF02754905
- [48] A. Renieri *et al.*, “Saturation and electron-beam lifetime in a storage ring free-electron laser”, *Phys. Rev. E*, vol. 69, pp. 036501, 2004. doi:10.1103/PhysRevE.69.036501
- [49] Z. Huang, K. Bane, Y. Cai, A. Chao, R. Hettel and C. Pellegrini, “Steady State Analysis of Short-wavelength, High-gain FELs in a Large Storage Ring”, in *International Workshop on Frontiers in FEL Physics and Related Topics*, Elba Island, Italy, September 8–14, 2007.
- [50] G. Dattoli, E. Di Palma, A. Petralia and J.V. Rau, “SASE FEL Storage Ring”, *IEEE J-QE*, 48, pp. 1259–1264, 2012. doi:10.1109/JQE.2012.2208733
- [51] E.L. Saldin, E.A. Schneidmiller, and M.V. Yurkov, “Klystron instability of a relativistic electron beam in a bunch compressor”, *Nucl. Instr. Meth. Phys. Res. A: Accelerators, Spectrometers, Detectors and Associated Equipment*, vol. 490, pp. 1–8, 2002. doi:10.1016/S0168-9002(02)00905-1

- [52] T. Shaftan and Z. Huang, “Experimental characterization of a space charge induced modulation in high-brightness electron beam”, *Phys. Rev. Accel. Beams*, 7, 080702, 2004. doi:10.1103/PhysRevSTAB.7.080702
- [53] G. Dattoli, A. Marino, A. Renieri, F. Romanelli, “Progress in the Hamiltonian picture of the free-electron laser”, *IEEE-JQE*, 17, pp. 1371–1387, 1981. doi:10.1109/JQE.1981.1071268
- [54] G. Dattoli, A. Renieri, A. Torre, *Lectures on Free Electron Laser theory and related topics*, World Scientific, 1993. doi:10.1142/1334 It should be noted that the same result was obtained by the late Professor H. Fang in an unpublished paper written before (1990).
- [55] G. Dattoli, A. Doria, E. Sabia and M. Artioli, *Charged Beam Dynamics, Particle Accelerators and Free Electron Lasers*, IOP Expanding Physics, Institute of Physics Publishing, 2017.

FIRST LASING OF A FREE ELECTRON LASER IN THE SOFT X-RAY SPECTRAL RANGE WITH ECHO ENABLED HARMONIC GENERATION

E. Allaria*, A. Abrami, L. Badano, M. Bossi, F. Capotondi, D. Castronovo, M. Cautero, P. Cinquegrana, I. Cudin, M. B. Danailov, A. Demidovich, S. Di Mitri, B. Diviacco, S. Grulja, W.M. Fawley, M. Ferianis, L. Foglia, G. Gaio, F. Giacuzzo, L. Giannessi, F. Iazzourene, G. Kurdi, M. Lonza, N. Mahne, M. Malvestuto, M. Manfreda, C. Masciovecchio, N.S. Mirian, I. Nikolov, G. Penco, E. Principi, L. Raimondi, P. R. Ribic, R. Sauro, C. Scafuri, P. Sigalotti, S. Spampinati, C. Spezzani, L. Sturari, M. Svandrik, M. Trovo, M. Veronese, D. Vivoda, M. Zaccaria, D. Zangrando, M. Zangrando, Elettra – Sincrotrone Trieste SCpA, Basovizza
D. Garzella, CEA, Gif-sur-Yvette
P. Miotti, CNR-IFN, Padova
M. Coreno, CNR-ISM, Trieste and Elettra – Sincrotrone Trieste SCpA, Basovizza
V. Grattoni, DESY, Hamburg
G. De Ninno, Elettra – Sincrotrone Trieste SCpA, Basovizza and University of Nova Gorica, Nova Gorica
N. Bruchon, Elettra – Sincrotrone Trieste SCpA, Basovizza and University of Trieste, Trieste
T. Tanikawa, EuXFEL, Schenefeld
G. Penn, LBNL, Berkeley, California
F. Frassetto, L. Poletto, LUXOR, Padova
M.A. Pop, MAX IV Laboratory, Lund
H.H. Braun, E. Ferrari, E. Prat, S. Reiche, PSI, Villigen
E. Roussel, PhLAM/CERCLA, Villeneuve d'Ascq Cedex
C. Feng, SARI-CAS, Pudong, Shanghai
E. Hemsing, SLAC, Menlo Park, California
M.E. Couprie, A. Ghaith, SOLEIL, Gif-sur-Yvette
D. Xiang, Shanghai Jiao Tong University, Shanghai

Abstract

We report on the successful operation of a Free Electron Laser (FEL) in the Echo Enabled Harmonic Generation (EEHG) scheme at the FERMI facility at Sincrotrone Trieste. The experiment required a modification of the FEL-2 undulator line which, in normal operation, uses two stages of high-gain harmonic generation separated by a delay line. In addition to a new seed laser, the dispersion in the delay-line was increased, the second stage modulator changed and a new manipulator installed in the delay-line chicane hosting additional diagnostic components. With this modified setup we have demonstrated the first evidence of strong exponential gain in a free electron laser operated in EEHG mode at wavelengths as short as 5 nm.

INTRODUCTION

With two FEL lines the FERMI user facility [1] is providing powerful radiation in the spectral range from 100 nm to 4 nm characterized by high degree of longitudinal and transverse coherence. Both FEL lines rely on the use of an external seed laser to initialize the coherent

emission process. FEL-1 [2], optimized for the long wavelength spectral range (100 nm – 20 nm), is based on a single stage, high gain harmonic generation (HG) scheme [3], while FEL-2 [4] operates at a shorter spectral range (20 nm – 4 nm) thanks to a double stage HG process employing a fresh bunch scheme (HG-FB) [5].

In the recent years, scientists have started exploiting the capability of FERMI of producing fully coherent pulses performing experiments not possible with other sources. Due to FERMI's strong coherence, techniques such as four wave mixing [6], coherent control [7], are now available for scientific users in the EUV- soft x-ray spectral range.

Because longitudinal coherence has become an important distinguishing parameter for FERMI with respect to other FEL sources, studies for possible future upgrades have been driven by the goal of extending its capabilities for coherence control toward even shorter wavelengths [8]. As a first step toward this direction an experiment has been organized at FERMI in 2018 to experimentally validate the benefits predicted by theory for the recently proposed seeding scheme EEHG [9].

We report here on the successful operation of the EEHG FEL at FERMI [10]. We first present the experimental setup pointing out the modifications done to some

* e-mail: enrico.allaria@elettra.eu

of the existing FEL-2 hardware necessary for EEHG implementation. Then we give results showing the clear evidence of strong exponential gain initiated by coherent, narrow-band EEHG bunching in the XUV spectral range.

EXPERIMENTAL SETUP

The FEL-2 line at FERMI was temporarily modified to allow EEHG seeding. This process required the installation of a new modulator for the second stage of FEL-2, a new seed laser line delivering up to 50 μJ pulses at 264 nm, an increased dispersion in the magnetic chicane and several new diagnostics. Figure 1 shows the layout of the FEL-2 undulator line for the standard operational mode (HGFG-FB) and for the EEHG.

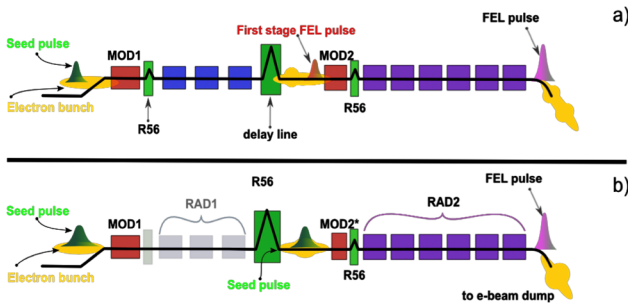


Figure 1: a) Nominal layout of FEL-2 for HGFG-FB. b) Modified layout used for the EEHG experiment.

These modifications took into account the temporary scope of the experiment (i.e., a six month period). The standard operating mode of FEL-2 in HGFG-FB was restored within few weeks following the end of the EEHG experiment.

New Second Modulator

In order to allow the resonant interaction of the electron beam with an UV seed laser, the second modulator (MOD2) had to be replaced by one with a longer period (MOD2*). The modification of an existing Elettra undulator provided a system with the required characteristics, as summarized in Table 1.

Table 1: MOD2* Parameters

Parameter	Value	Units
Length	1.5	m
Magnetic period	113	mm
Maximum k	12	
Peak field	1.2	T

MOD2* was installed in April 2018 and removed in September 2018 at the end of the EEHG experiment.

Large Magnetic Chicane

EEHG relies on the use of a large dispersion ($R56$ of a few mm) in the first chicane. The existing delay-line magnetic chicane (Fig.1) was upgraded to produce the larger $R56$ necessary to produce bunching at harmonics higher than 40 at 1.5 GeV electron beam energy. Thanks to an increase of the magnet separation together with an upgrade of the power supply that allowed increasing the

maximum current from 500A to 750A, the first $R56$ could be increased up to more than 2 mm for a 1.3 GeV beam.

Second Seed Laser

EEHG needs two seed lasers interacting with the same (longitudinal) portion of the electron beam in the two modulators. As a first seed laser we used the existing seed laser of FEL-2 which is based on the third harmonic generation of a Ti:Sa laser. The second seed laser was provided by a second Ti:Sa laser that normally is provided to FERMI users for pump and probe experiments [11]. This infrared laser has been converted to the UV on a dedicated optical table installed close to the delay line chicane. A special, in-vacuum mirror installed in a manipulator allowed injecting this second seed laser to the electron beam axis from the center of the delay-line chicane.

For both seed lasers the central wavelength was 264 nm, and the pulse length was in the range 100 – 120 fs (FWHM). In both cases the energy per pulse could be adjusted depending on the requirements in the range 0 – 50 μJ .

A description for the second seed laser injection system and the dedicated diagnostic installed can be found in Ref. [12].

RESULTS

During the period of the experiment the electron beam energy was progressively increased from 0.9 GeV to 1.5 GeV. Due to the limit in the maximum dispersion available from the first chicane, most of the studies were performed at 1.35 GeV [13]. At this energy it is possible to operate the final radiator at wavelengths as short as 7 and 5 nm with sufficient gain and the $R56$ of the first chicane can be increased up to the value needed to efficiently operate the EEHG at the harmonics ($H=35, 45$) required for these wavelengths.

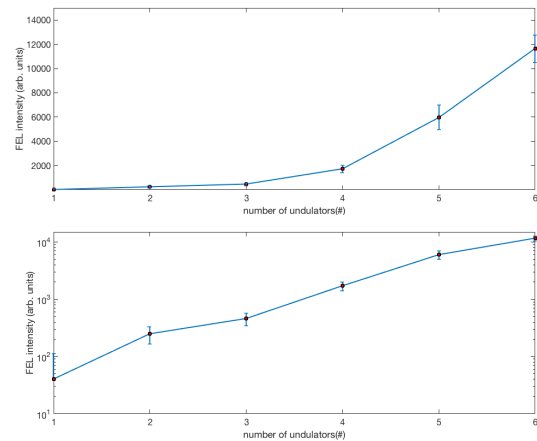


Figure 2: Measured gain curve of EEHG at H35 in linear scale (upper graph) and logarithmic scale (lower graph).

Clear indication of FEL amplification in the final radiator was measured for various harmonics and wavelengths (Fig.2). An optimal amplification of the FEL radiation along the six undulators of the FEL-2 radiator required an accurate alignment of the electron beam trajectory.

Once the standard EEHG parameters were optimized, the most important parameter for maximizing the FEL intensity was the definition of a straight trajectory for the electron beam in the radiator and the corresponding alignment of this trajectory with pointing of the two seed lasers. Given the significant gain along the radiator and the energy transfer from the electrons to the radiation field tapering of the undulator strength K can be important in maximizing the FEL power and preserving the FEL spectral quality. Figure 3 shows how the spectral quality was not degraded during the FEL amplification.

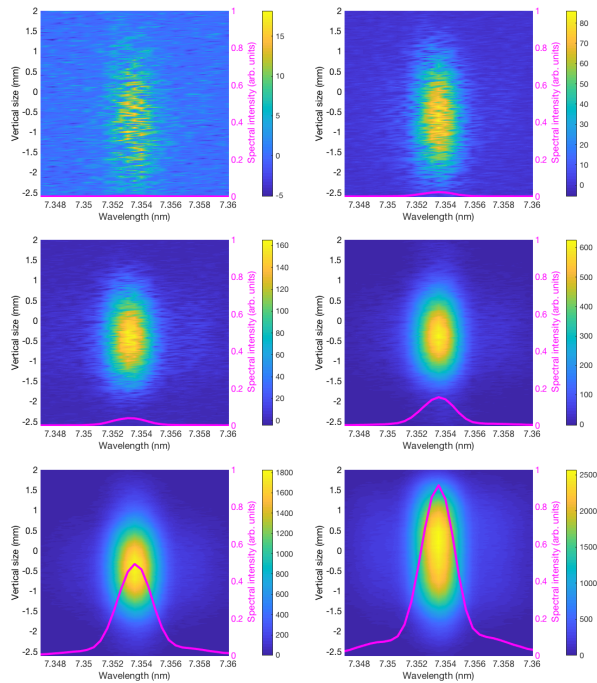


Figure 3: Evolution of the FEL spectrum along the amplification occurring in the radiator.

The sensitivity of EEHG to the induced energy spread controlled with the laser heater was also studied with details given in a separate contribution [14].

Initial operation at 0.9 GeV was quite important for fast commissioning of the new systems. As a result the first EEHG signal at 14 nm ($H = 18$) was easily obtained and optimized (Fig. 4).

Studies at 0.9 GeV were also important for direct comparison of the two seeding schemes EEHG and HGFG-FB. At this 14-nm wavelength it is indeed possible to operate the FEL in HGFG-FB mode within the modified setup. These comparative studies have shown the reduced sensitivity of EEHG to electron beam phase space distortions as compared to HGFG-FB [15].

For all the harmonics studied during the EEHG experiment it has been possible to optimize the FEL to a condition characterized by very narrow and clean spectra. Two such examples of these narrow spectra are reported in Figure 4.

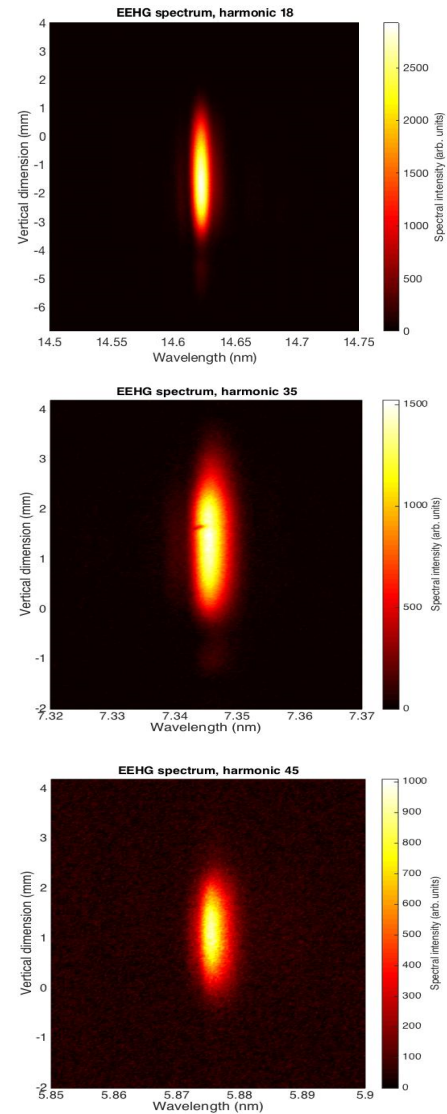


Figure 4: 2D images of the FEL spectrum as measured by PRESTO [16] for the EEHG operated at harmonic 18 a), 35 b), and 45 c).

CONCLUSIONS

We have successfully operated FERMI's FEL-2 in EEHG mode down to 5-nm wavelengths showing large exponential gain and high quality spectra. These results confirm the benefits for the EEHG scheme predicted by theory with respect to other seeding techniques.

ACKNOWLEDGEMENTS

We would like to thank G. Stupakov, S. Bettoni, D. Ratner, G. Marcus, F. Bencivenga, E. Pedersoli, M. Sacchi, C. Callegari, Z. Huang, T. Raubenheimer, and A. Zholents for useful discussions. We acknowledge continuous support of R. Godnig, R. Bracco, R. Visintini, and the FERMI - Elettra operator group during the course of the experiment. This work was in part supported by the Director, Office of Science, Office of Basic Energy Sciences, of the U.S. Department of Energy under Contract Nos.

DE-AC02-76SF00515 and DE-AC02-05CH11231 and award No. 2017-SLAC-100382. DG was supported by an Outgoing CEA fellowship from the CEA-Enhanced Eurotalents program, co-funded by FP7 Marie-Sklódowska-Curie COFUND program (Grant Agreement 600382).

REFERENCES

- [1] E. Allaria *et al.*, “The FERMI free-electron lasers” *Journal of Synchrotron Radiation* **22**, 485 (2015). pp 485-491. doi:10.1107/S1600577515005366
- [2] E. Allaria *et al.*, “Highly coherent and stable pulses from the FERMI seeded free-electron laser in the extreme ultraviolet”, *Nat. Photon.* **6**, 699 (2012). doi: 10.1038/nphoton.2012.233
- [3] L.H. Yu *et al.*, “First Ultraviolet High-Gain Harmonic-Generation Free-Electron Laser”, *Phys. Rev. Lett.* **91**, (2003). Doi: 10.1103/PhysRevLett.91.074801
- [4] E. Allaria *et al.*, “Two-stage seeded soft-X-ray free-electron laser”, *Nat. Photon.* **7**, 913 (2013). Doi: 10.1038/nphoton.2013.277
- [5] I. Ben-Zvi, K.M. Yang, L.H. Yu, “The “fresh-bunch” technique in FELs”, *Nucl. Inst. & Meth. A* **318**, 726 (1992). Doi: 10.1016/0168-9002(92)91147-2
- [6] L. Foglia *et al.*, “First Evidence of Purely Extreme-Ultraviolet Four-Wave Mixing”, *Phys. Rev. Lett.* **120**, 263901 (2018). Doi: 10.1103/PhysRevLett.120.263901
- [7] K.C. Prince *et al.*, “Coherent control with a short-wavelength free-electron laser” *Nat. Photon.* **10**, 176 (2016). Doi: 0.1038/nphoton.2016.13
- [8] L. Giannessi *et al.*, “Status and Perspectives of the FERMI FEL Facility (2019)”, presented at the 39th Int. Free Electron Laser Conf. (FEL'19), Hamburg, Germany, Aug. 2019, paper THP079.
- [9] G. Stupakov, “Using the beam-echo effect for generation of short-wavelength radiation” *Phys. Rev. Lett.* **102**, 074801 (2009). Doi: 10.1103/PhysRevLett.102.074801
- [10] P.R. Rebernik *et al.*, “Coherent soft X-ray pulses from an echo-enabled harmonic generation free-electron laser”, *Nat. Photon.* **13**, 555 (2019). Doi: 10.1038/s41566-019-0427-1
- [11] M. Danailov *et al.*, “Towards jitter-free pump-probe measurements at seeded free electron laser facilities”, *Optics Express* **22**, 12869 (2014). Doi: 10.1364/OE.22.012869
- [12] E. Allaria *et al.*, “Amplified Emission of a Soft-X Ray Free-Electron Laser Based on Echo-Enabled Harmonic Generation”, in *Proc. 10th Int. Particle Accelerator Conf. (IPAC'19)*, Melbourne, Australia, May 2019, pp. 2230-2232. doi:10.18429/JACoW-IPAC2019-WEXXPLM1
- [13] P. Rebernik Ribic, “Echo-Enabled Harmonic Generation Lasing of the FERMI FEL in the Soft X-Ray Spectral Region”, presented at the 39th Int. Free Electron Laser Conf. (FEL'19), Hamburg, Germany, Aug. 2019, paper TUB01, this conference.
- [14] S. Spampinati, E. Allaria, L. Giannessi, and P. Rebernik Ribic, “Energy Spread Impact on HGHG and EEHG FEL Pulse Energy”, presented at the 39th Int. Free Electron Laser Conf. (FEL'19), Hamburg, Germany, Aug. 2019, paper TUP083, this conference.
- [15] G. Penco *et al.*, “Experimental Characterization of the Electron Energy Chirp Impact on the FEL Operating in Echo-Enabled Harmonic Generation Mode”, presented at the 10th Int. Particle Accelerator Conf. (IPAC'19), Melbourne, Australia, May 2019, paper TUPRB034, unpublished.
- [16] M. Zangrando *et al.*, “Recent results of PADReS, the Photon Analysis Delivery and REduction System, from the FERMI FEL commissioning and user operations” *Journal of Synchrotron Radiation* **22**, 565 (2015). doi:10.1107/S1600577515004580

FIRST LASING AT THE CAEP THz FEL FACILITY*

P. Li, D. Wu[†], M. Li, K. Zhou, L. G. Yan, J. X. Wang, Y. Xu, Q. Pan, D. X. Xiao,
X. Luo, H. B. Wang, X. M. Shen, P. Zhang, L. J. Shan, T. H. He, J. Liu, Y. Liu
Institute of Applied Electronics, China Academy of Engineering Physics, Mianyang, China

Abstract

China Academy of Engineering Physics terahertz free electron laser (CAEP THz FEL, CTFEL) is the first THz FEL user facility in China, which was an oscillator type FEL. This THz FEL facility consists of a GaAs photocathode high-voltage DC gun, a superconducting RF linac, a planar undulator and a quasi-concentric optical resonator. The terahertz laser's frequency is continuous adjustable from 0.7 THz to 4.2 THz. The average power is more than 10 W and the micro-pulse power is more than 0.3 MW. In this paper, the specific parameters and operation status of CTFEL are presented. Finally, some user experiments are introduced briefly.

INTRODUCTION

Terahertz (THz) radiation is an electromagnetic wave with a frequency range of 0.1 to 10 THz. It is between microwave and infrared light and has very unique properties such as transient, low energy, penetration, and broadband. It has caused widespread concern in recent years. Free electron laser (FEL) can be the most powerful tool as terahertz power source. It has many advantages, such as monochrome, high-power, linear-polarization, continuously tunable frequency. Many FEL facilities, such as ELBE in Germany [1], FELIX in Holland [2], UCSB in the USA [3] and NovoFEL in Russia [4], have played important roles in the THz sciences. In the near future, of the 20 FEL facilities planned to be built in the whole world, there will be at least 8 ones operating in the THz range [5].

CAEP THz FEL (CTFEL) is the first THz FEL user facility in China [6, 7], which is an oscillator type FEL, see Figure 1. This THz FEL facility consists of a GaAs photocathode high-voltage DC gun, a 1.3 GHz superconducting RF linac [8, 9], a planar undulator and a quasi-concentric optical resonator. The repetition of CTFEL is 54.167 MHz, which means the average current can be up to 5 mA. The effective accelerator field gradient is about 10 MV/m.

CTFEL has achieved the saturation radiation in August, 2017[10] after two year's commissioning. The terahertz wave frequency is now continuously adjustable from 0.7 THz to 4.2 THz. The average power is above 10 W and the micro-pulse power is more than 0.5 MW. In this paper, the components of this facility and some of its applications are introduced. Also an upgrade plan is proposed.

* Work supported by National Natural Science Foundation of China with grant (11575264, 11605190 and 11805192), Innovation Foundation of CAEP with grant (CX2019036, CX2019037)

[†] wudai04@163.com

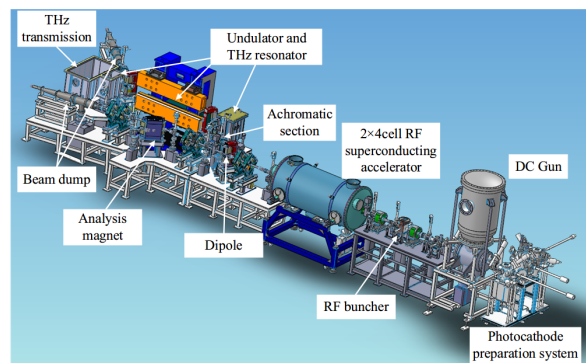


Figure 1: The Layout of the CTFEL Facility.

FACILITY COMPONENTS

Overview

Figure 2 shows the block diagram of the CTFEL facility, in which you can see more details. The 532nm continuous mode-locked driving laser is incident on the photocathode of the gallium arsenide semiconductor. The electrons are laterally focused by a solenoid, longitudinally bunched through the buncher, then enters the superconducting cavity, where electrons are finally accelerated to 7~8 MeV. The accelerated electrons are transported through the achromatic section into the undulator to generate THz spontaneous radiation. The radiation resonates in the THz optical cavity and reaches saturation. Saturated THz light is coupled out through the small hole in downstream mirror, and the output terahertz light is transmitted to the user's laboratory for user experiments.

The electron beam parameters are summarized in Table 1. The accelerator is designed to operate in both CW and macro-pulse mode. It is now working in macro-pulse mode with the duty cycle >10%. In the near future, the CW operation will be reached after the machine fast protection system is installed.

Table 1: Electron Beam Parameters

Parameters	Design goal	Unit
Bunch charge	10~100	pC
Micro-pulse repetition	54.167	MHz
Macro-pulse repetition	1~20	Hz
Duty cycle	$10^{-5} \sim 1$	
Average current	1~5	mA
Kinetic energy	6~8	MeV
Normalized emittance	<8	μm
Micropulse length (RMS)	1.5~3	ps
Energy spread	~ 0.2	%

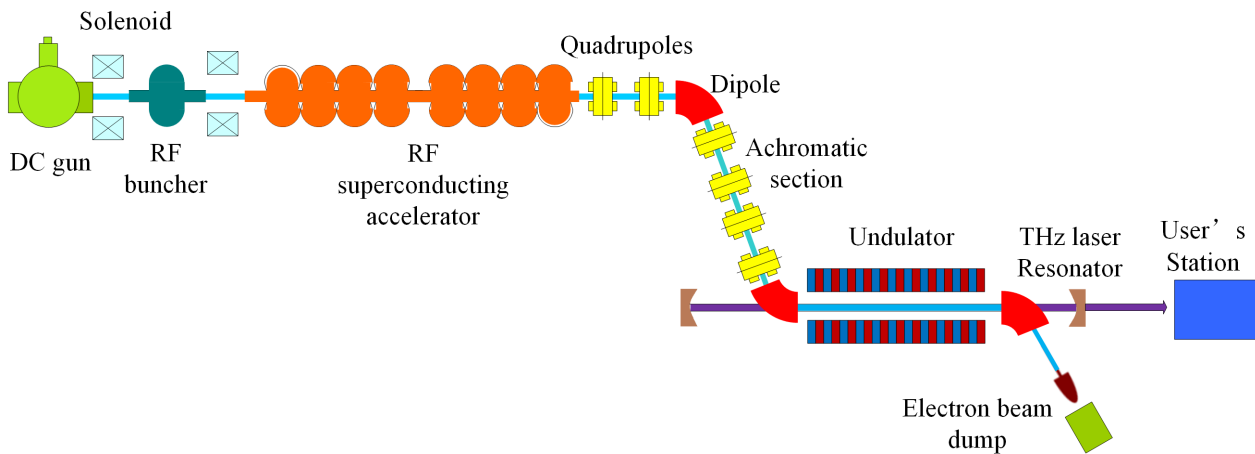


Figure 2: Block diagram of the CTFEL facility.

High-Voltage DC Electron Source

Figure 3 shows the system of the high-voltage DC electron source, which consists of a photocathode preparation chamber, a load-lock system, a drive laser, a high-voltage DC gun and some beam elements such as three solenoids and an RF buncher. The DC gun has a four-way type with a radial dimension of $\Phi 500$ mm to reduce the field strength of the electrode surface. The high-voltage insulator uses a charge-discharge-type ceramic insulator to improve the stability of the working field. The cathode support rod and the ground potential are added. By a series of technical improvement such as baking and NEG, the vacuum in the working state can be maintained at 3×10^{-9} Pa, and the electron beam kinetic energy at the exit of the electron gun is about 200~350 keV, which is currently working at 320 keV.

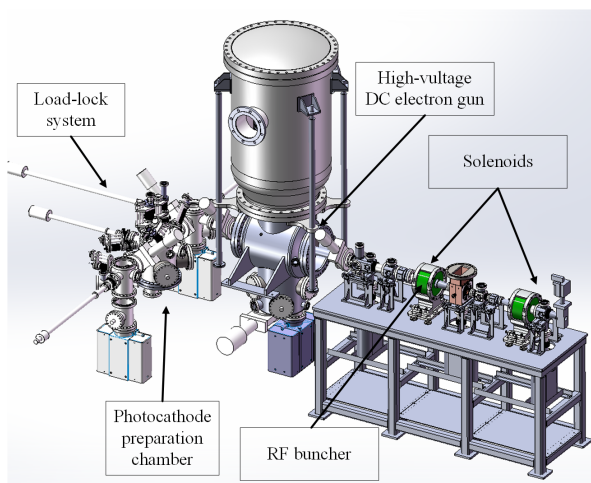


Figure 3: The high-voltage DC electron source.

RF Superconducting Accelerator

Owing to the advantages of superconducting RF technology in CW mode operation, a 2×4 -cell superconducting linac module has been adopted to accelerate electron beams

from the DC-gun up to an energy of 6~8 MeV. With the goal of 5 mA, 54.17 MHz CW beams, the components have been designed accounting for higher-order modes (HOMs), beam loading and cryogenic issues. The phase stability of the low-level RF control system is 0.1° , and the amplitude stability is better than 0.05%. After the acceleration, the normalized emittance of the beam is less than 8 mm-mrad, and the relative energy spread is less than 0.2%.

THz Resonator and Transmission

The THz wave is generated and resonates in the undulator and the THz optical cavity system. The two cavity mirrors form a quasi-concentric optical resonator with a Cavity length 2.769 m and a Mirror curvature 1.85 m. The Waveguide between optical cavity has a size of 14mm \times 28 mm. The terahertz laser power is then extracted by a hole of 2.4 mm in diameter on the downstream mirror, and then goes through a diamond window to transmit to the user's lab. The THz transmission system is shown in Figure 4.

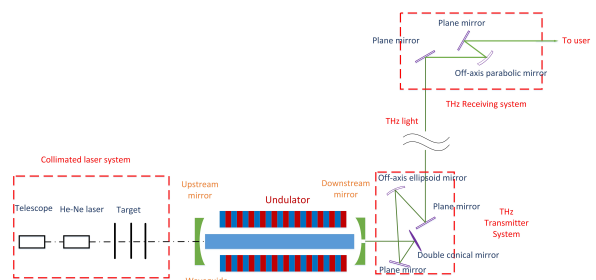


Figure 4: The THz resonator and Transmission system.

THz LASER

Table 2 shows the main parameters of the CTFEL THz laser measured in user lab. CTFEL Terahertz average power is measured by a TK absolute energy meter. The spectrum is measured by a Fourier spectrometer (Bruker VERTEX 80V), see Figure 5, also the micro-pulse length. The frequency is adjusted by both the undulator gap and the electron

energy. The THz beam transverse profile is captured by a pyroelectric array camera "Pyrocam IIIHR". The beam fulfill the transverse Gaussian distribution. The minimum beam size around the focal point is estimated as less than 1 mm in radius.

Table 2: THz Laser Parameters

Parameters	Value	Unit
Tunable frequency range	0.7~4.2	THz
Spectral FWHM	2~3	%
Macro-pulse average power	>10	W
Macro-pulse repetition	1~20	Hz
Macro-pulse length	0.3~2	ms
Micro-pulse RMS length	400~500	fs
Micro-pulse interval	18.5	ns
Micro-pulse power	>0.3	MW
Minimum transverse radius	<1	mm
Polarization	Horizontal	

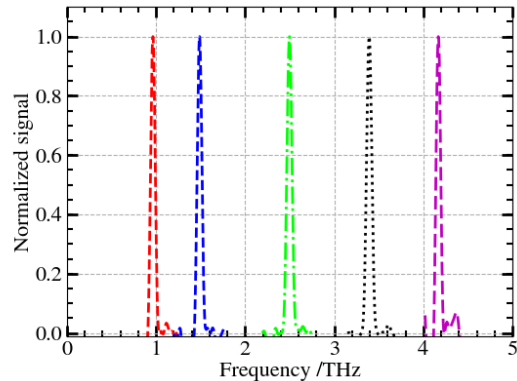


Figure 5: The THz frequency measurement.

After the completion of CTFEL, it played an important role in the field of terahertz in China. Several user experiments have been carried out on the CTFEL device. The optical rotation of molybdenum disulfide MoS₂ was studied. The optical rotation effect of single-layer MoS₂ on linearly polarized THz light was observed for the first time. The "picosecond THz pump-picosecond detection" platform was built to obtain the nonlinear THz dynamics of the GaSb sample. The graphene THz detector and the GaN detector were calibrated, by which the micropulse of CTFEL was detected. The decomposition reaction of pyrophosphate (PPi) catalyzed by alkaline phosphatase was studied, and the effect of "activation" on the enzyme was observed. The effects of terahertz on bacterial growth and physiological status of mice were studied. It was found that the growth of E. coli was affected and the protein expression level changed.

UPGRADE PLAN

Although CTFEL has played a great role in terahertz science, its frequency band is still not too wild to meet the

needs of scientific research. An upgrade plan is proposed, showing in Figure 6. After the upgrade, the electron beam energy will be up to 50MeV, and the radiation frequency will be 0.1THz~150THz, covering the entire terahertz and infrared bands. In the mean time the ERL technology is applied in this project, which will increase the efficiency of the entire device. CTFEL will become an important high average power long-wavelength FEL source in the world in the near future.

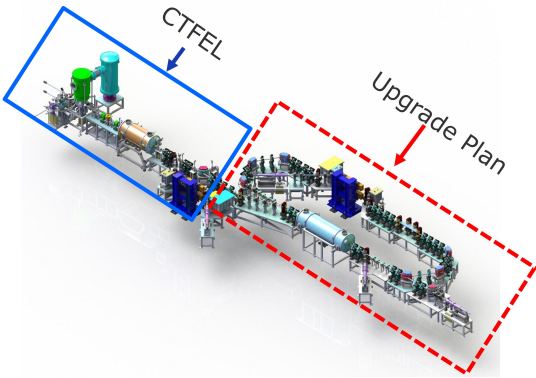


Figure 6: CTFEL upgrade plan.

SUMMARY

In this paper CTFEL facility has briefly introduced, which is the first THz free electron laser oscillator in China. This facility mainly consists of a high-brightness high-voltage DC electron source, a CW RF superconducting accelerator and a undulator-optical-cavity system. The terahertz frequency of CTFEL is continuously adjustable from 0.7 THz to 4.2 THz. The average power is more than 10 W and the micro-pulse power is above 0.3 MW. CTFEL is an user facility, and will be upgraded in the near future, which will greatly promote the development of the THz science and its applications on material science, chemistry science, biomedical science and many other Frontier science in general.

REFERENCES

[1] F. Gabriel *et al.*, "The rossendorf radiation source ELBE and its FEL projects," *Nuclear Instruments and Methods in Physics Research Section B: Beam Interactions with Materials and Atoms*, vol. 161, pp. 1143–1147, 2000.

[2] D. Oepts, A. van der Meer, and P. van Amersfoort, "The free-electron-laser user facility FELIX," *Infrared Physics & Technology*, vol. 36, no. 1, pp. 297–308, 1995.

[3] G. Ramian, "The new UCSB free-electron lasers," *Nuclear Instruments and Methods in Physics Research Section A: Accelerators, Spectrometers, Detectors and Associated Equipment*, vol. 318, no. 1-3, pp. 225–229, 1992.

[4] G. Kulipanov *et al.*, "Research highlights from the Novosibirsk 400 w average power THz FEL," *Terahertz Sci. Technol* vol. 1, no. 2, pp. 107–125, 2008.

- [5] K. Cohn, J. Blau, W. Colson, J. Ng, and M. Price, “Free electron laser in 2015,” in *Proceedings of FEL2015*, Daejeon, Korea, 2015, pp. 625–629. doi: 10.18429/JACoW-FEL2015-WEP016.
- [6] Y. H. Dou, X. J. Shu, and Y. Z. Wang, “3D-simulations of transverse optical modes of the free electron laser resonator with hole output coupling,” *Communications in Computational Physics*, vol. 1, no. 5, pp. 920–929, 2006.
- [7] P. Li, Y. Jiao, W. Bai, H. B. Wang, X. H. Cui, and X. K. Li, “Start-to-end simulation of CAEP FEL-THz beamline,” *High Power Laser and Particle Beams*, vol. 26, pp. 213–217, 2014.
- [8] X. Luo *et al.*, “Design and fabrication of the 2×4-cell superconducting linac module for the free-electron laser,” *Nucl. Instr. Meth. A*, vol. 871, pp. 30–34, 2017.
- [9] K. Zhou *et al.*, “Progress of the 2x4-Cell Superconducting Accelerator for the CAEP THz-FEL Facility,” in *Proc. of International Conference on RF Superconductivity (SRF’17)*, Lanzhou, China, July 17-21, 2017, doi:10.18429/JACoW-SRF2017-MOPB037.
- [10] D. Wu *et al.*, “First Lasing of the CAEP THz FEL Facility Driven by a Superconducting Accelerator,” in *Proc. 9th International Particle Accelerator Conference (IPAC’18)*, Vancouver, BC, Canada, April 29-May 4, 2018, (Vancouver, BC, Canada), doi: 10.18429/JACoW-IPAC2018-TUPMF044.

COMMISSIONING AND FIRST LASING OF THE FELiChEM: A NEW IR AND THz FEL OSCILLATOR IN CHINA*

Heting Li[†] and Qika Jia on behalf of the FELiChEM team
National Synchrotron Radiation Laboratory (NSRL)
University of Science and Technology of China, Hefei, China

Abstract

A new infrared FEL named FELiChEM aiming at the energy chemistry has been constructed and commissioned at NSRL in Hefei. It consists of two FEL oscillators driven by one normal-conducting S-band linac with maximum beam energy of 60 MeV. The two oscillators generate the mid-infrared and far-infrared lasers covering the spectral range of 2.5-50 μm and 40-200 μm , respectively. First lasing was achieved at a wavelength of 15 μm with an electron energy of 35 MeV. Till now, we have observed the FEL signal from 3.5 μm to 30 μm and achieved the maximum micropulse energy up to 27 μJ at 15 μm .

INTRODUCTION OF FELICHEM

Under the financial support of Natural Science Foundation of China, the project “Tunable Infrared Laser for Fundamental of Energy Chemistry” (FELiChEM) was started in 2015. It is a dedicated experimental facility aiming at energy chemistry research [1, 2]. The core device is a free electron laser (FEL) consisting of two oscillators driven by one normal-conducting S-band linac with maximum electron energy of 60 MeV.

Figure 1 shows the schematic layout of FELiChEM. Both the accelerator hall and the experimental hall are existed buildings and we were allowed to design the facility with this constriction. The electron accelerator is located in a 12m \times 16m semi-underground tunnel, as shown by the photo of Fig. 2. Two branches connected with the linac are the two oscillators. The branch using the electron beam bended from the end of the first accelerating tube is the far-infrared oscillator which generates the 40-200 μm FEL, while another one called the mid-infrared oscillator generates the 2.5-40 μm FEL. The output FEL pulses from the

Table 1: Design Target of FELiChEM

Parameter	Specification
Covering spectrum	2.5 ~ 200 μm
MIR FEL oscillators	2.5 ~ 50 μm
FIR FEL oscillators	40 ~ 200 μm
Macro-pulse length	5 ~ 10 μs
Repetition of macro-pulse	10/20 Hz
Macro-pulse energy	~100 mJ
Micro-pulse length	1 ~ 5 ps
Micro-pulse energy	~ 50 μJ
Bandwidth	0.3 ~ 3 %

two oscillators share one beam line and are transported to the experimental hall, where the stations for FEL diagnostics, photo dissociation, photo excitation and photo detection are in one line. The total length of the beam line is about 36 m.

The users of these stations have brought out their requirements on the IR-FEL performance, as summarized in Table 1. In addition, some users have extra requirements, for example, the photo excitation and dissociation stations hope that the peak and average power of IR-FEL can be as high as possible. The design of the oscillator and the electron accelerator has been introduced in the Ref. [1-3].

Due to the delay of the civil construction, the installation of the accelerator was delayed by more than one year and was finished in June, 2018. Then in the next month we started the commissioning of the linac. Unfortunately, after two month the high-repetition grid pulser of the electron gun was broken suddenly and we had no choice but to wait it reworking. In May 2019, we restarted the commissioning, and observed the spontaneous radiation at the 15 μm wavelength in 9, June. On the same day, the first lasing up to 1 μJ per micropulse was detected at the same wavelength.

Next, we will briefly introduce the facility and the commissioning status, and then the first lasing results.

ELECTRON ACCELERATOR

The electron accelerator mainly consists of: an 80 kV electron gun, a 476 MHz subharmonic standing wave pre-buncher, a 2856 MHz fundamental frequency traveling wave buncher, two 2856 MHz fundamental frequency traveling wave accelerating tubes separated by a magnetic compressor (chicane). Besides, a set of solenoid focusing coils are used from the gun exit to the end of the first accelerating tube.

The triode gun is driven by a grid pulser with the repetition frequency that can be switched in 476/238/119/59.5/29.5 MHz. For the operation safety of the grid pulser, we have turned down the high voltage from 100 kV to 80 kV,

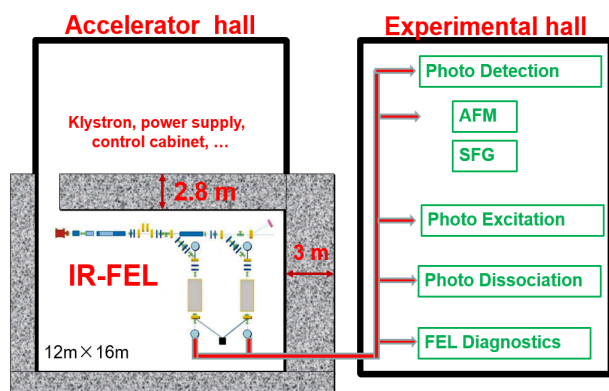


Figure 1: Schematic layout of FELiChEM.

* Work supported by National Natural Science Foundation of China (21327901).

[†]Email address: lihetng@ustc.edu.cn



Figure 2: Photo of the accelerator and FEL oscillators in the semi-underground tunnel.

and re-optimized the following parameter setting of the linac. The pre-buncher works at a gap voltage of 34 kV and can compress the bunch by more than 20 times. The buncher shares the power with the first 2-meter accelerating tube from one klystron. Its input power is optimized at 5 MW and the rms bunch length can be compressed to 4.5 ps. After the second accelerating tube, the maximum beam energy can reach 60 MeV. The magnetic chicane is designed as an optional operation condition, which will be used in the future for enhancing the FEL performance.

Table 2: Summary of Electron Beam Parameters

Parameter	Target	Achieved
Electron Energy /MeV	15-60	25-60
Energy spread /keV	<240	<200@35MeV; <240@60MeV;
Bunch charge /nC	1.0	~1.2
Normalized rms transverse emittance / mm.mrad	<30	40~50
Micro-pulse rms length /ps	1-5	~4.5
Micro-bunch rep. rate /MHz	476/238/ 119/59.5/ 29.75	119/59.5 /29.75
Macro-bunch length / μ s	5-10	1-6
Macro-pulse rep. rate /Hz	1-20	1-10

Seeing Table 2, we do not achieve the target value for several parameters. Currently, we cannot obtain the beam energy below 25 MeV due to a small problem with the power splitting between the buncher and the first accelerating tube, and this will be solved soon. The microbunch repetition rate, the macrobunch length and repetition rate are increased step by step because the beam loading effect at different beam current is also different so that we need to optimize the linac parameters carefully, especially the parameter setting of the LLRF feedforward. The measured beam emittance is much larger than the design value. The

reason for this problem is that a part of the mechanical support for the solenoid around the buncher was magnetized by the magnetic field of the solenoid. We plan to replace this part in the next machine shutdown.

FEL OSCILLATORS

FELiChEM includes two oscillators covering the spectral range of 2.5-50 μ m and 40-200 μ m, respectively. Each oscillator consists of two important components: undulator and optical cavity. Their basic parameters are listed in Table 3 and detailed design can be found in Ref. [1].

Table 3: Summary of Oscillator Parameters

	Parameter	specification
MIR undulator	Period /mm	46
	Period number	50
	Undulator parameter K	0.5-3.2
MIR cavity	Cavity length /m	5.04
	Reyleigh length /m	0.78
	Reflectivity	99%
	Diameter of mirrors /mm	50
FIR undulator	Diameter of coupling holes /mm	1.0/1.5/2.5/3.5
	Period /mm	56
	Period number	40
	Undulator parameter K	0.5-3.3
FIR cavity	Cavity length /m	5.04
	Reyleigh length /m	0.78
	Reflectivity	99%
	Diameter of mirrors /mm	80
	Diameter of coupling holes /mm	1.0/2.0/4.0

In each oscillator, two spherical mirrors with Copper base and Gold coatings are used to form a symmetrical optical cavity. A planar permanent magnet undulator manufactured by KYMA is placed in the centre of the two optical cavities so that we have enough available space for beam transport and diagnostic on the two sides. The IR radiation is outcoupled from the downstream cavity, which contains multiple mirrors with different outcoupling hole sizes and mechanical conditioner for switching mirrors.

In the MIR oscillator, to achieve the target radiation intensity and cover the spectral range of 2.5-50 μm , we use the 2.3-m-long undulator with a period length of 46 mm. Considering the optical size on the mirror for the FEL wavelength below 5 μm , the Rayleigh length of the cavity was optimized equal to one third of the undulator length. Based on the electron beam parameters given in Table. 2, the small signal gain is up to higher than 100% for most of the working region of the FEL wavelength. However, in the two sides of the wavelength region, it is still not high enough. We have carried out the time-dependent three-dimension simulation using the code *genesis* [4] combining with the code *OPC* [5]. As presented in Ref. [1, 2], the results show that the macropulse energy exceeds 100 mJ except for the wavelength shorter than 4 μm .

In the FIR oscillator, a 2.24-m-long undulator with a period length of 56 mm was used and the Rayleigh length of the cavity was selected equal to half of the undulator length. However, due to the serious diffraction effect of the long wavelength FEL, we need to add a waveguide to reduce the diffraction loss in the FIR oscillator. A planar waveguide with the height of $b=10$ mm is used inside the undulator chamber. We have calculated the small signal gain for the FIR-FEL by replacing the Gaussian mode of the optical beam by the fundamental waveguide mode, and the results show that the waveguide enhances the small signal gain by more than two times. In addition, according to the operation experience of CLIO and FELIX [6, 7], “spectral gap” may appear in this waveguide FEL. Considering this problem for FELiChEM, we have developed the simulation code for simulating overmoded waveguide FEL based on Genesis [8]. At present, we are working on accurately simulating the transport of the optical beam from the outer of the waveguide into the inner.

In our design of the FEL oscillator, one thing worth pointing out is the optimization of the important and complicated relations between the key parameters of the oscillator, including the cavity length L_c , the curvature radius of mirrors R_c , the stable factor of the resonator cavity g , the Rayleigh length Z_R , the optical beam size at the waist ω_0 and on the mirror ω_M , the far-field divergence angle θ_f , the angular tolerance requirement for the mirrors θ_m , and so on. Here, as different from other reference, we write the expressions of θ_f and θ_m as [9]

$$\theta_f = \frac{\lambda_s}{\pi\omega_0}, \quad \theta_m = \theta_f(1 + g). \quad (1)$$

Here, λ_s is the FEL wavelength.

For the overall optimization, we plot these relations in one figure using dimensionless qualities, as shown in Fig. 3 [9]. From Fig. 3, one can find that the larger curvature radius of the mirror corresponds to longer Rayleigh length and larger tolerance to angular misalignment, but also to a smaller light spot on the mirrors, consequently higher power density on the mirrors and higher outcoupling rate. There is a trade-off between the smaller diffraction loss, the larger tolerance to the angular misalignment and the

lower power density on the mirrors. Normally, the FEL oscillator is optimized close to a concentric resonator. For a near-concentric resonator, one can write $g \approx -1+x$, $x \ll 1$, so it has $\theta_m = \theta_f \cdot x \ll \theta_f$. For our MIR oscillator, we take the ratio of the curvature radius of the mirrors to the resonator length as $R_c/L_c = 2.756/5.04 = 0.547$. Then from Fig. 3, we have $Z_R = 0.15 L_c = 0.77 = L_u/3$, $\omega_0/\omega_M = 1/3.41$, $\theta_m/\theta_f = 0.172$, $g = -0.8278$.

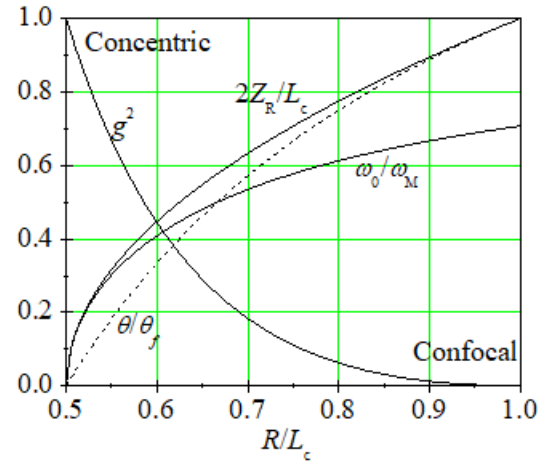


Figure 3: Overall optimization of several important relations between the key parameters of an FEL oscillator [9].

FIRST LASING RESULTS

In the end of May 2019, we started the commissioning of the linac. Then in Jun. 9, we started to detect the spontaneous radiation with a liquid-nitrogen cooled MCT (HgCdTe) detector whose working region is from 2-16 μm . Due to the strong space radiation dose inside the accelerator tunnel, we had to detect the IR signal in the experimental hall at the photo dissociation station (see Fig. 1) which is about 20 m far away from the outcoupling mirror. From the outcoupling hole, the IR light had to pass through a diamond window mounted under Brewster angle, and be reflected by two parabolic mirrors and five flat mirrors, then pass through a CsI window and arrive at the detector. We considered to lase at 15 μm with a comparatively high gain even for relatively low beam quality and optical transport loss.

To achieve first lasing the undulator parameter was set to $K = 2.02$. The electron energy was adjusted to 35 MeV at a current of 40 mA and a macropulse length of 6 μs . The former corresponds to a bunch charge of 1.2 nC at a repetition rate of 29.75 MHz. The electron beam was aligned to the cavity axis by monitoring the electrons with 3 Beryllium OTR view screens that can be moved into the electron beam path within the undulator vacuum chamber.

To detect the undulator spontaneous radiation, the downstream mirror was lifted up from the cavity axis. After a carefully scan of the position of the MCT detector at the light-emitting window, soon we observed the signal of the IR spontaneous radiation. Then we put down the outcoupling mirror with a 1.5 mm diameter hole into the cavity

axis and expected to detect the undulator spontaneous radiation outcoupled from the hole. The pitch and yaw angles of both cavity mirrors were aligned with a precision of about 0.15 mrad using a red laser. As we wished, the signal from the hole was observed. Next, we began to scan the cavity length in the step of two wavelength, and very soon, we found the intensity of the IR signal grew rapidly until the detector was saturated. A pyroelectricity probe was placed in front of the light-emitting window to replace the MCT detector, and obtained the FEL signal with the micro-pulse energy higher than 1 μ J. Figure 4 shows the photo of the light spot of the first lasing at 15 μ m detected by pyroelectricity camera, and Fig. 5 shows the measured FEL intensity together with the beam current at different positions.

Subsequently, the detuning curve of the 15 μ m FEL was measured and given in Fig. 6. One can see that lasing was observed over a cavity length scan range of 200 μ m. Till now, we have observed the FEL signal from 3.5 μ m to 30 μ m with a gap at 20 μ m. According to the design, the optical beam size of 20 μ m FEL inside the undulator is smaller than the vacuum chamber so that it should not be the “spectral gap” as in a waveguide FEL. Further studies will be carried on.

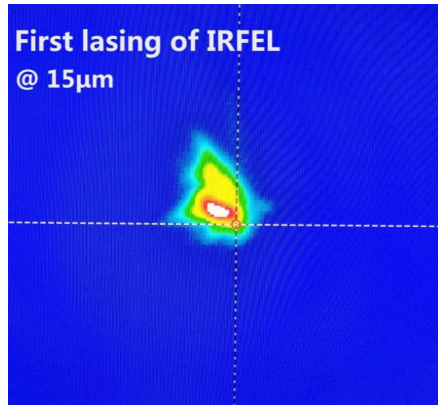


Figure 4: The photo of the light spot of the first lasing at 15 μ m detected by pyroelectricity camera.

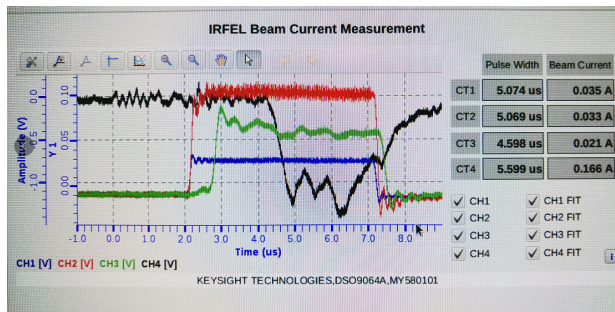


Figure 5: The measured electron beam current and FEL intensity. CT1: blue line, beam current at the exit of electron gun, 0.035 A corresponding to 1.2 nC per microbunch; CT2: red line, beam current at the exit of linac; CT3: green line, beam current before entering the beam dump; CT4: black line, FEL intensity detected at the photo dissociation station.

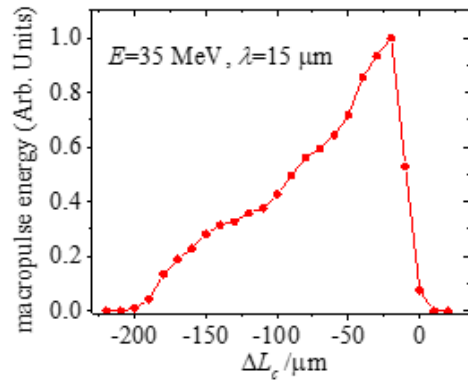


Figure 6: The measured detuning curve of the 15 μ m FEL.

SUMMARY AND OUTLOOK

A new infrared FEL has been commissioned at the NSRL in Hefei. It will be dedicated for energy chemistry research. The oscillator FEL is operated with 15 – 60 MeV electrons from a normal-conducting S-band linac equipped with a gridded thermionic gun, and consists of two oscillators covering the spectral range of 2.5-50 μ m and 40-200 μ m, respectively. First lasing was observed at a wavelength of 15 μ m with an electron energy of 35 MeV from the MIR oscillator. Till now, we have detected the FEL signal from 3.5 μ m to 30 μ m with a gap at 20 μ m and achieved the maximum micropulse energy up to 27 μ J at 15 μ m.

In the near future, we will firstly commission the machine working at the microbunch repetition rate of 119/238/476 MHz, then increase the macrobunch length to 10 μ s and raise the macrobunch repetition rate to 20 Hz. Meanwhile, we will do what we can do to improve the stability of the FEL pulses. After these works, we will provide the users the MIR FEL for commissioning of the end-stations, and at the same time, we will commission the FIR oscillator in timesharing mode.

REFERENCES

- [1] Heting Li *et al.*, “Design of FELiChEM, the first infrared free-electron laser user facility in China”, *Chinese Phys C*, vol. 41, pp. 018102, 2017.
- [2] Heting Li *et al.*, “Design of the mid-infrared FEL oscillator in China”, in *Proc. FEL’15*, paper TUP028, pp. 427-429.
- [3] Zhigang He *et al.*, “Linac design of the IR-FEL project in China”, in *Proc. FEL’15*, paper MOP010, pp. 46-48.
- [4] S. Reiche, “GENESIS 1.3: a fully 3D time-dependent FEL simulation code”, *Nucl. Instrum. Methods Phys. Res., Sect. A*, vol. 429, no. 1-3, pp. 243-248, Jun. 1999.
doi:10.1016/S0168-9002(99)00114-X
- [5] P. J. M. van der Slot, H. P. Freund, W. H. Miner Jr., S.V. Benson, M. Shinn, and K.-J. Boller, “Time-Dependent, Three-Dimensional Simulation of Free-Electron-Laser Oscillators”, *Phys. Rev. Lett.*, vol. 102, pp. 244802, 2009.
doi:10.1103/PhysRevLett.102.244802
- [6] Ruslan Chulkov, Vitaliy Goryashko, Denis D. Arslanov, *et al.*, “Multimode dynamics in a short-pulse THz free electron laser”, *Phys. Rev. ST Accel. Beams*, vol. 17, pp. 050703, 2014.
doi:10.1103/PhysRevSTAB.17.050703

- [7] J.-M. Ortega, J.-P. Berthet, F. Glotin, and R. Prazeres, “Evidence for competition modes in a partially guided far-infrared free-electron laser”, *Phys. Rev. ST Accel. Beams*, vol. 17, pp. 100701, 2014.
doi:10.1103/PhysRevSTAB.17.100701
- [8] Weiwei Li *et al.*, “Numerical Method for Free Electron Laser using an Overmoded Rectangular Waveguide”, arXiv: 1806.00162
- [9] Qika Jia, “Parameter design considerations for an oscillator IR-FEL”, *Chinese Physic C*, vol. 41, pp. 018101, 2017.
doi:10.1088/1674-1137/41/1/018101

REGENERATIVE AMPLIFIER FEL – FROM IR TO X-RAYS

D. C. Nguyen†, P. M. Anisimov, C. E. Buechler, Q. R. Marksteiner, R. L. Sheffield
Los Alamos National Laboratory, Los Alamos, New Mexico, USA

Abstract

The Regenerative Amplifier FEL (RAFEL) feeds back a small fraction of the radiation exiting a high-gain undulator as the seed for the next pass, and achieves narrow linewidth and saturation in a few passes. For the IR RAFEL, we used an optical cavity with annular mirrors to reinject ~10% of the IR radiation back into a two-meter undulator [1]. We theorized the RAFEL output transformed from an annular beam to an on-axis beam due to optical guiding at high power [2]. A number of researchers have proposed RAFEL and XFEL to achieve full temporal coherence in VUV and X-ray FELs [3-8]. For the XFEL, symmetric Bragg backscattering off high-quality diamond crystals can provide very high reflectivity for the XFEL cavity [7-9]. The required reflectivity for a RAFEL feedback cavity is much lower than the XFEL. We show that 6% feedback is sufficient for the X-ray RAFEL at 9.8 keV to saturate and achieve 0.5-eV bandwidth. We discuss options to out-couple more than ~50% of the RAFEL intra-cavity power and discuss challenges associated with X-ray absorption in the out-coupler.

INTRODUCTION

With the successful commissioning of the European XFEL and the on-going construction of the LCLS-II superconducting linac XFEL at SLAC, a fully coherent X-ray free-electron laser delivering transform-limited X-ray pulses with unprecedented brilliance is a real possibility in the near future. Full temporal coherence can be achieved with either an XFEL or an X-ray RAFEL, both of which will require an optical cavity consisting of low-loss, high-quality Bragg mirrors [10]. The XFEL requirements for are more stringent: Bragg crystals with 99% reflectivity forming a long optical cavity with μm dimension accuracy and nanoradian angular stability, in addition to the relatively long and high charge electron bunches at MHz bunch repetition rate. Numerical simulations predict the X-ray pulses inside an XFEL optical cavity will need to recirculate a few hundred passes before they reach steady-state and achieve narrow linewidth [9]. In contrast, the RAFEL requires 2-3 passes in a lower-Q feedback cavity (lower reflectivity) and less stringent angular stability compared to the XFEL. The RAFEL has been demonstrated in the infrared by our group [1] and proposed by a number of researchers for the VUV and X-ray regions as a means to generate fully coherent short-wavelength FELs [3-8].

The RAFEL design shares a number of features of the XFEL such as improved longitudinal coherence and pulse-to-pulse stability over SASE. There are however a few important differences between RAFEL and XFEL.

First and foremost is the amount of optical feedback in each pass; in RAFEL, the optical feedback is typically a few percent of radiation power in the previous pass, whereas XFEL requires feedback fraction greater than 90%. Thus, while the intra-cavity power of the XFEL is several times the output power, the RAFEL output power is almost the same as the power exiting the undulator. The small optical feedback in RAFEL significantly relaxes the reflectivity requirements for the cavity mirrors. The second difference is the single-pass gain; the RAFEL single-pass gain is high, on the order of 10^2 to 10^3 , compared to the XFEL single-pass gain of ~2X. The higher gains reduce the number of passes for RAFEL to reach saturation and achieve spectral narrowing. The third difference is the output spectral width; the XFEL can achieve a very narrow linewidth (a few meV) whereas the RAFEL output has a spectral width of a single SASE spectral peak, which is approximately the Fourier transform of the X-ray pulse width (about the same as the electron bunch length).

We present experimental results of the IR RAFEL and numerical simulations of a fully coherent RAFEL at 9.8 keV with spectral linewidth of ~0.5 eV (5×10^{-5} relative). We show candidates for the low-loss Bragg reflectors for different X-ray energies, discuss a number of options to out-couple the intra-cavity power and present the results of Genesis FEL simulation for the 9.8-keV RAFEL.

INFRARED RAFEL

The infrared RAFEL was experimentally demonstrated at 16 μm at LANL in 1997. The feedback cavity for this demonstration is shown in Fig. 1. The electron beam entered the cavity from the left through the smaller annular mirror and exit on the right. Approximately two-third of the intra-cavity power was coupled out through the large annular mirror. A summary of the IR RAFEL parameters is shown in Table 1.

Table 1: Summary of IR RAFEL Parameters

Parameter	Symbol	Value
Beam energy	E_b	16.7 MeV
Peak current	I_p	270 A
Bunch length	l_c	5 mm
Undulator period	λ_u	2 cm
Undulator parameter	K_{rms}	0.92
Undulator length	L_u	2 m (1 m taper)
FEL wavelength	λ	16.3 μm
3D gain length	L_G	0.125 m

† dcnguyen@lanl.gov

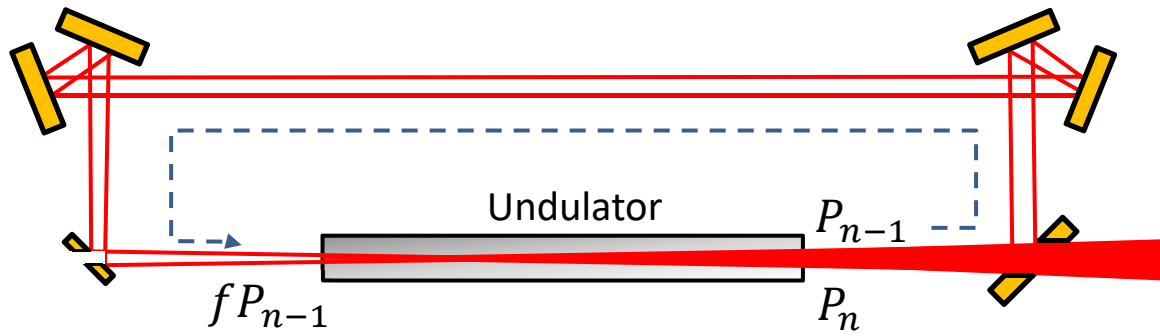


Figure 1: Schematic of the IR RAFEL. The optical feedback cavity consists of six copper mirrors, two flat annular mirrors and two pairs of curved mirrors. The electron beam travels from the left through the two annular mirrors and the undulator.

The pairs of mirrors at the top of Fig. 1 form two off-axis paraboids; one paraboid collimates the diverging IR beam and the other focuses the IR beam to a small waist at a location about 2 gain lengths inside the undulator. The first annular mirror on the left has a 5-mm diameter hole to allow most of electron beam to pass through and enter the undulator. The second annular mirror on the right has a 14-mm diameter hole to allow the electron and two-third of the FEL power to exit. We estimate only 10% of the IR beam is reinjected into the undulator. Two sets of IR pulses circulate in the feedback cavity that has a roundtrip time of 18.46 ns, twice the electron bunch separation of 9.32 ns. The RAFEL power at the end of the n^{th} pass is given by

$$P_n = (f P_{n-1}) \frac{1}{9} e^{\frac{L_u}{L_G}}$$

where f is the feedback fraction, L_u is the undulator length and L_G is the 3D gain length. Fig. 2 shows the optical power build-up from noise to saturation. The net gain per pass is about 1.5X. From the cavity ring-down (Fig. 3), we deduce a cavity loss per pass of ~66%. Thus, we estimate the RAFEL has a large-signal gain of 4.5X. The calculated small-signal gain is much higher, about 330X per pass.

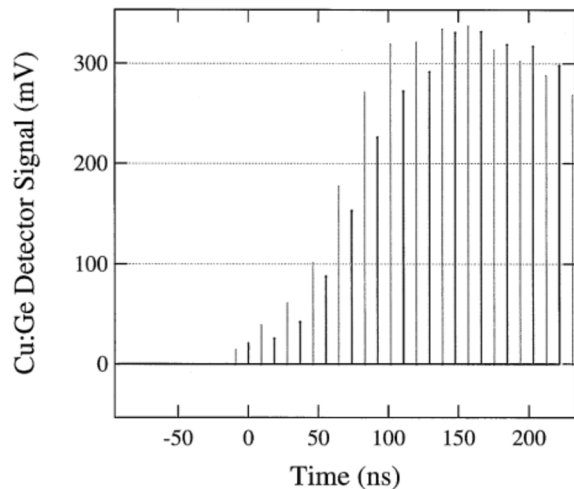


Figure 2: Optical energy build-up in the IR RAFEL. Two sets of IR pulses (dark and gray) exist inside the ring cavity with round-trip time twice the electron bunch spacing.

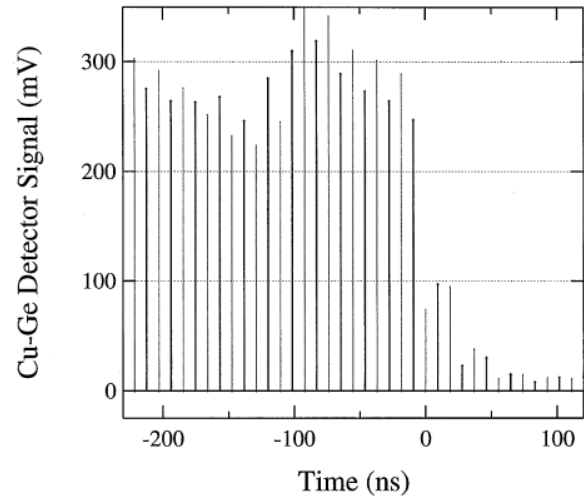


Figure 3: Ring-down of the IR RAFEL energy. The pulse energy decreases to one-third its initial value in one pass.

We measured the output energy of ~1,000 micropulses versus detuning from the synchronous cavity length. The cavity length detuning FWHM is 1 mm (Fig. 4), approximately the electron bunch length (5 mm) divided by the number of passes (~6) for the FEL pulse to saturate.

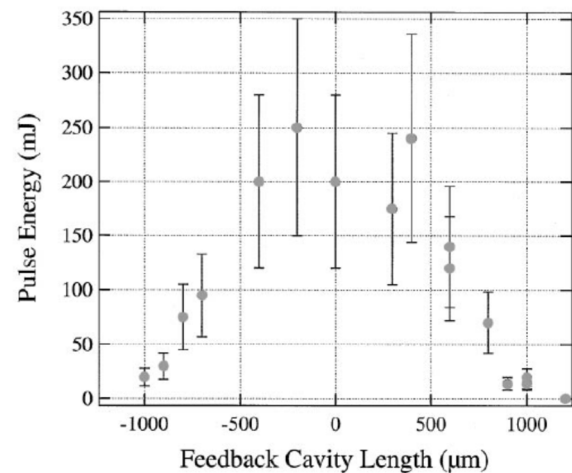


Figure 4: Cavity detuning length of the IR RAFEL.

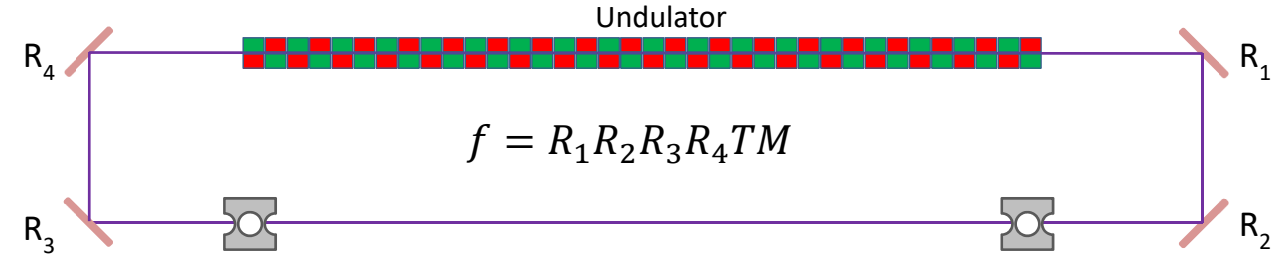


Figure 7: Schematic of an X-ray RAFEL. The feedback fraction f is the product of the four mirror reflectivity (R_1 through R_4), the combined transmission T of the two compound refractive lenses (CRL) and the spectral power fraction selected by the Bragg mirrors M within the cavity angular acceptance as defined by the radiation mode over the CRL separation.

X-RAY RAFEL GENESIS SIMULATIONS

We performed time-dependent FEL simulations using the Genesis 1.3 FEL simulation code [12]. The parameters for the electron beam and RAFEL optical feedback are summarized in Table 3.

Table 3: Summary of X-ray RAFEL Parameters

Parameter	Symbol	Value
Beam energy	E_b	10.5 GeV
Peak current	I_p	2.5 kA
Bunch length	l_e	2.4 μm
Bunch charge	q	20 pC
Norm. rms emittance	ε_n	0.2 μm
rms energy spread	δE_b	1.05 MeV
Undulator period	λ_u	2.6 cm
Undulator parameter	K_{rms}	1.76
Undulator length	L_u	3.38 m
# of undulators	N_u	7
FEL wavelength	λ	1.261 \AA
FEL gain parameter	ρ	0.001
3D gain length	L_G	1.37 m

The number of undulators used in these simulations (seven) is chosen such that the SASE radiation has a well-defined transverse mode and the SASE power is sufficiently high so that only 6% feedback ($f = 0.06$) within the spectral and angular width of the cavity mirrors far exceeds the start-up noise. The cavity angular width is defined by

$$\Delta\theta \sim \frac{w_r}{L}$$

where w_r is the radiation mode $1/e^2$ radius on the CRL and L is the distance between the CRLs.

Figure 8 show the semi-log plots of SASE power (blue), RAFEL power in Pass 2 (orange), Pass 3 (yellow), Pass 4 (green) and Pass 5 (purple). The SASE power is simulated with more than seven undulators to show the saturated SASE power; however, only seven undulators are used in the simulations of SASE power with the narrow spectral

filter. The RAFEL power growth curves show lethargy and synchrotron oscillation typical of coherent amplification.

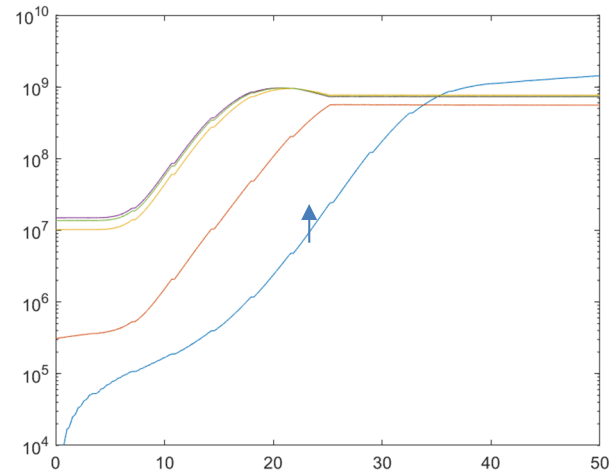


Figure 8: Semi-log plots of SASE (blue), pass 2 (orange), pass 3 (yellow), pass 4 (green) and pass 5 (purple). The SASE simulation is stopped at the 7th undulator (arrow).

Figure 9 plots the SASE and filter spectra on a linear scale, showing only 6% of the power within a SASE spectral spike (orange) is used as the coherent seed for Pass 2.

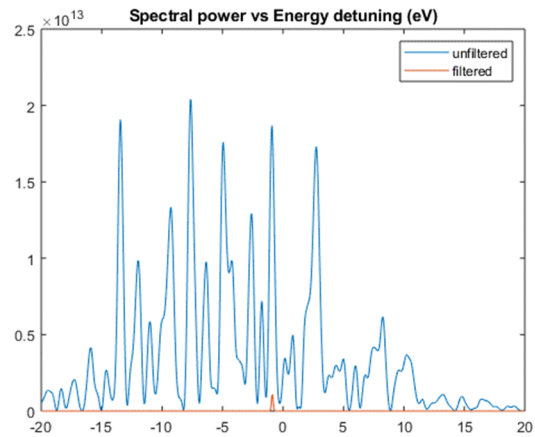


Figure 9: SASE and filtered signal on a linear scale. The Gaussian-shaped filter selects only 6% of the spectral power within a single SASE spike as the coherent seed for amplification in Pass 2.

In Fig. 10, we show the RAFEL spectrum at the end of the 7th undulator on the linear (10a) and log (10b) scales. The spectral width of the RAFEL peak in Pass 5 is 0.5 eV, wider than the spectral width of the filter (0.15 eV). The RAFEL spectral width is determined by the Fourier transform of the short electron bunch and not by the Bragg spectral width. An interesting result is the suppression of SASE by two orders of magnitude in Pass 5 relative to Pass 1 (SASE only, no RAFEL). Since the RAFEL spectral power is enhanced by three orders of magnitude, the ratio of RAFEL to SASE in Pass 5 is five orders of magnitude.

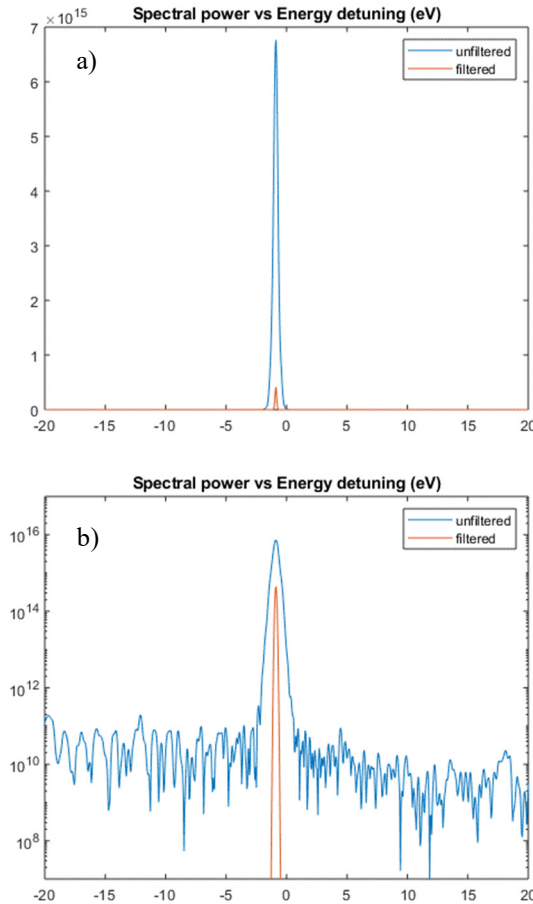


Figure 10: Plots of spectral power in Pass 5 versus energy detuning in eV on linear (a) and log (b) scale.

CONCLUSION

We have shown that the RAFEL with 45° diamond Bragg reflectors is a feasible approach to a fully coherent X-ray FEL with narrow linewidth. The spectral linewidth of a 9.83-keV X-ray RAFEL at saturation in Pass 5 is 0.5 eV, corresponding to 5×10^{-5} relative linewidth. Genesis simulations show that the X-ray RAFEL can saturate in two passes with only 6% feedback within the SASE spectral peak. While the total RAFEL power is slightly lower than the total SASE power, the RAFEL spectral brightness is three orders of magnitude higher than SASE. We observe a factor of 100X reduction in the SASE spectral power

when RAFEL is lasing, and thus the contrast between the coherent RAFEL spectral peak to the SASE background is five orders of magnitude.

ACKNOWLEDGEMENTS

We thank Yuri Shvyd'ko, Gabriel Marcus, Zhirong Huang, Ryan Lindberg, Tor Raubenheimer and Dilling Zhu for many helpful discussions and suggestions.

REFERENCES

- [1] D. C. Nguyen et al., "First Lasing of the Regenerative Amplifier FEL," *Nucl. Instr. Meth. Phys. Res. A*, vol. 429, p. 125, 1999.
DOI:10.1016/S0168-9002(99)00090-X
- [2] J. C. Goldstein, D. C. Nguyen and R. L. Sheffield, "Theoretical study of the design and performance of a high-gain, high-extraction-efficiency FEL oscillator," *Nucl. Instr. Meth. Phys. Res. A*, vol. 393, p. 137, 1997.
DOI:10.1016/S0168-9002(97)00445-2
- [3] B. Faatz et al., "Regenerative FEL amplifier at the TESLA test facility at DESY," *Nucl. Instr. Meth. Phys. Res. A*, vol. 429, p. 424, 1999.
DOI:10.1016/S0168-9002(99)00123-0
- [4] Z. Huang and R. D. Ruth, "Fully Coherent X-Ray Pulses from a Regenerative-Amplifier Free-Electron Laser," *Phys. Rev. Lett.* vol. 96, p. 144801, 2006.
DOI:10.1103/PhysRevLett.96.144801
- [5] B. W. J. McNeil et al., "A design for the generation of temporally-coherent radiation pulses in the VUV and beyond by a self-seeding high-gain free electron laser amplifier," *New Journal of Physics*, vol. 9, p. 239, 2007.
DOI:10.1088/1367-2630/9/7/239
- [6] G. Marcus et al., "X-Ray Regenerative Amplifier Free-Electron Laser Concepts For LCLS-II," in *Proc. 38th Int. Free-Electron Laser Conf.*, Santa Fe, New Mexico, USA, August 2017, paper MOP061, DOI:10.18429/JACoW-FEL2017-MOP061
- [7] K.-J. Kim, Y. V. Shvyd'ko, and S. Reiche, "A Proposal for an X-Ray Free-Electron Laser Oscillator with an Energy-Recovery Linac," *Phys. Rev. Lett.* vol. 100, p. 244802, 2008.
DOI:10.1103/PhysRevLett.100.244802
- [8] K.-J. Kim and Y. V. Shvyd'ko, "Tunable Optical Cavity for an X-ray Free-electron-laser Oscillator," *Phys. Rev. ST Accel. Beams*, vol. 12, p. 030703, 2009.
DOI:10.1103/PhysRevSTAB.12.030703
- [9] R. R. Lindberg et al., "Performance of the X-ray Free-Electron Laser Oscillator with Crystal Cavity," *Phys. Rev. ST Accel. Beams*, vol. 14, p. 010701, 2011.
DOI:10.1103/PhysRevSTAB.14.010701
- [10] T. Kolodzie et al., "Diamond Drumhead Crystals for X-ray Optics Applications," *J. Applied Crystallography*, vol. 49, pp. 1240-1244, 2016.
DOI:10.1107/S1600576716009171
- [11] Y. Shvyd'ko and R. Lindberg, "Spatiotemporal response of crystals in x-ray Bragg diffraction," *Phys. Rev. ST Accel. Beams*, vol. 15, p. 100702, 2012.
DOI:10.1103/PhysRevSTAB.15.100702
- [12] H. P. Freund, P. Van der Slot, Yu. Shvyd'ko, "An X-Ray Regenerative Amplifier Free-Electron Laser Using Diamond Pinhole Mirrors," arXiv:1905.06279 (2019)

PARALLEL OPERATION OF SASE1 AND SASE3 AT THE EUROPEAN XFEL

S. Liu[†], F. Brinker, W. Decking, L. Fröhlich, R. Kammering, D. Nölle, F. Obier, M. Scholz,
E. Schneidmiller, T. Wilksen, M. Yurkov, DESY, Hamburg, Germany

R. Boll, N. Gerasimova, T. Mazza, M. Meyer, A. Scherz, H. Sinn, EuXFEL, Schenefeld, Germany

Abstract

At the European XFEL a hard X-Ray SASE FEL (SASE1) and a soft X-Ray SASE FEL (SASE3) share in series the same electron beamline. This configuration couples the operation conditions for both undulators and their subsequent user experiments in terms of SASE intensity and background. We report on our experience in parallel operation and discuss the solutions that enable the operation of both undulators as independently as possible.

INTRODUCTION

The European XFEL is in operation since 2017. It is based on superconducting accelerator technology and serves three undulator beamlines simultaneously [1]. The three beamlines are named as SASE1, SASE2 and SASE3. SASE1 and SASE2 are hard X-Ray beamlines (3-25 keV) and SASE3 is a soft X-Ray beamline (0.25-3 keV). The first lasing of SASE1 beamline was achieved in May 2017 [2], followed by the first lasing of SASE3 in February 2018 and the first lasing of SASE2 in May 2018 [3]. After that the three beamlines are operated in parallel [4, 5].

The layout of the three beamlines is shown in Fig. 1. One can see that SASE1 and SASE3 are located in series in the same electron beamline. This configuration couples the operation conditions for both undulators and their subsequent user experiments in terms of SASE intensity and background.

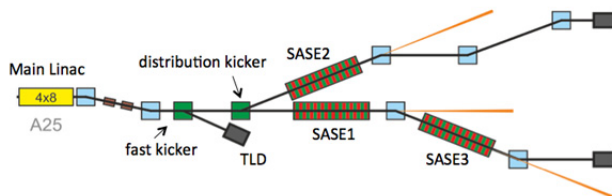


Figure 1: Layout of the three undulator beamlines at the European XFEL starts from the last cryomodule of the main linac.

Coupling Between SASE1 and SASE3 Beamlines

Two different techniques, an afterburner and "fresh bunch", are used to operate SASE1-SASE3 beamline. Spent electron from SASE1 is used to generate radiation in SASE3 in the afterburner configuration [1]. FEL process in SASE1 induces energy spread in the electron beam which is proportional to the radiation pulse energy. As a result, SASE3 and SASE1 performance are coupled such that increase of the radiation pulse energy in SASE1 leads to degradation of SASE3 output. The calculated

minimum operational wavelength of SASE3 versus operating wavelength of SASE1 is shown in Fig. 2 (left) (for 14 GeV and 250 pC electron beam case) [6]. Operation of SASE3 in saturation is only possible for the wavelengths above the curves¹. However, FEL efficiency visibly falls down as it is illustrated with measured pulse energy coupling between SASE1 and SASE3 shown in Fig. 2 (right). Electron energy is 14 GeV and bunch charge is 250 pC in this experiment. SASE1 and SASE3 operate at the wavelength of 0.13 nm and 1.4 nm, respectively.

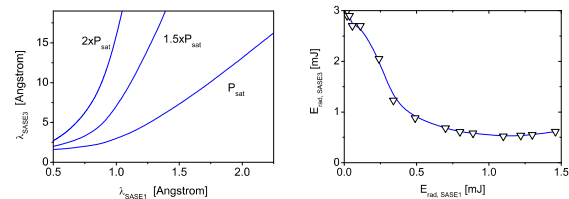


Figure 2: Calculated wavelength coupling (left) and measured pulse energy coupling (right) between SASE1 and SASE3 beamlines when operating SASE3 as a succession of SASE1 for 14 GeV and 250 pC electron beam case.

Mitigate Coupling with Betatron Switcher

In order to mitigate the coupling between SASE1 and SASE3, the betatron switcher technique (also called "fresh bunch" technique) was introduced [7, 8]. Using the fast kicker (4.5 MHz) in front of SASE1 [9], one can give a kick to the SASE3 bunches and generate a betatron oscillation for these bunches in SASE1. This kick is then compensated by a corrector (or a quadrupole kick) in front of SASE3, which also generates a betatron oscillation for the SASE1 bunches in the SASE3 beamline.

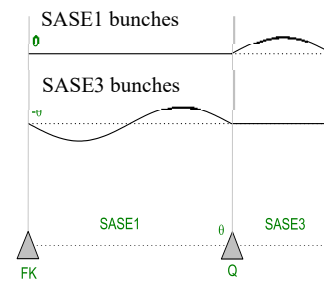


Figure 3: Betatron switcher used to suppress SASE3 bunches lasing in SASE1 and SASE1 bunches lasing in SASE3.

In this way, lasing of SASE3 bunches in SASE1 beamline and SASE1 bunches in SASE3 beamline are suppressed. The scheme of this technique is shown in Fig. 3. Dedicated simulations to study the performance of this

[†]shan.liu@desy.de

scheme are presented in [10]. In the following, we will present the experimental performance of the betatron switcher.

PERFORMANCE OF BETATRON SWITCHER

The betatron switcher was demonstrated at the European XFEL in May 2018. Figure 4 shows an example of the SASE pulse energy output from the XGM monitor [11] during the operation with the betatron switcher mode. In this example, the first 50 bunches are SASE1 bunches and the last 5 bunches are SASE3 bunches. In Fig. 4 (bottom) one can see the calculated suppression factor²: lasing of SASE3 bunches in SASE1 beamline is suppressed by around factor 200 and lasing of SASE1 bunches in SASE3 beamline is suppressed by around factor 100. The suppression of SASE3 bunches in the SASE1 beamline is more effective, because the hard X-ray beamline is more sensitive to the orbit distortion than the soft X-ray beamline.

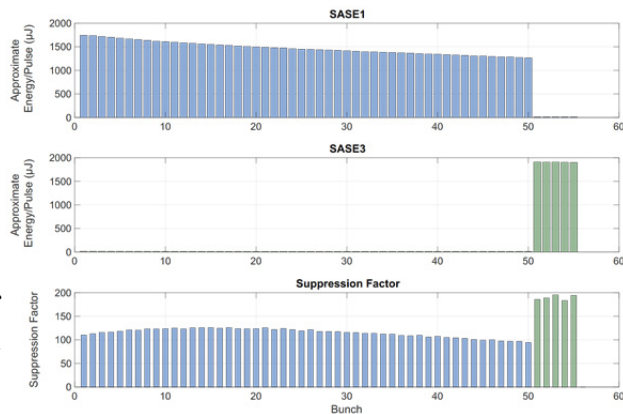


Figure 4: SASE pulse energy in SASE1 (top) and SASE3 beamline (middle) and suppression factor (bottom) as a function of bunch number.

Residual Lasing

Since the vacuum chamber in the undulator section is relatively small, the maximum kick (i.e. the maximum oscillation amplitude) that can be generated is limited by the beam losses in both beamlines. Meanwhile, SASE1 beamline is more sensitive to beam losses than SASE3 beamline, because it has more undulator cells and it operates with smaller undulator gaps.

Due to the limited oscillation amplitude, SASE1 bunches can still reach the same saturation level as SASE3 bunches, although the saturation length is much longer. Therefore, residual lasing of SASE1 bunches in SASE3 can still be observed by the SASE3 users. The background level from the residual lasing of SASE1 bunches highly depends on the ratio of number of bunches between SASE1 and SASE3 and the operation photon energy in the SASE3 beamline. Typically the background

varies from 1% to 10% of the total pulse energy.

An additional fast kicker is installed in front of the SASE3 beamline during 2019 summer shutdown, which will help to increase the amplitude of betatron oscillations for SASE1 bunches in SASE3 beamline (without changing the oscillation amplitude in SASE1 beamline)³.

Further Techniques to Suppress Residual Lasing

There are several ways to suppress residual lasing in combination with the betatron switcher.

Since the saturation length of the kicked SASE1 bunches are much longer than the SASE3 bunches, one can open the undulator cells beyond the saturation point of SASE3 bunches. Besides, one can also add aggressive quadratic taper starting from the saturation of SASE3 bunches.

Another way is to use different compression settings by applying different RF flat tops for SASE1 and SASE3 bunches. Adding stronger compression for SASE3 bunches result in larger peak currents, which consequently leads to shorter gain lengths for SASE3 bunches.

OTHER TYPES OF BACKGROUND OBSERVED IN SASE3

Except for residual lasing, the SASE3 users have also observed other types of backgrounds. The backgrounds range from optical to XUV. The backgrounds in these ranges can affect the photon detectors and damage the user samples when x-ray beam is focused for single shot imaging experiments.

Optical Background

Background in the optical light range has been observed on a YAG screen in the SQS instrument and wavefront sensor. By using an Al filter one can reduce the background on the imager. However, when the ratio of SASE1/SASE3 bunches is increased, imagers can not be used even with Al filters (see Fig. 5).

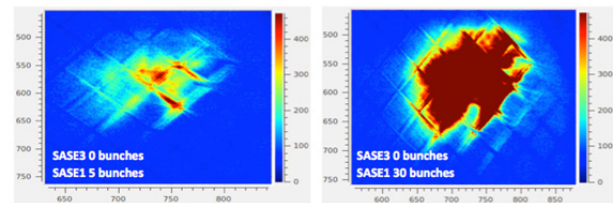


Figure 5: Optical background observed on a YAG screen in the SQS instrument with an Al filter inserted upstream in the beamline for the operation with 5 (left) and 30 (right) SASE1 bunches. The quadratic pattern that is visible stems from a grid structure imprinted on the YAG screen.

XUV Background

Background in the XUV range (few tens of eV) has

² One should keep in mind that due to the limited dynamic range of the XGM monitor, the actual suppression factors should be higher than the values shown here.

³ However, the maximum oscillation amplitude is still limited to 2 mm both by the kicker strength (with 14 GeV electron beam) and for safety reasons.

been verified by introducing small amounts of nitrogen in the gas absorber, as well as by inserting thin diamond filters, which remove some contributions. However attenuation strongly depends on the photon energy. Background in this range can ionize the samples, which affect especially the electron and ion spectroscopy experiments.

One example of the ionization of atomic beam by the background from SASE1 bunches is shown in Fig. 6. This effect is observed even when the SASE3 undulators are open as shown in Fig. 6 (right).

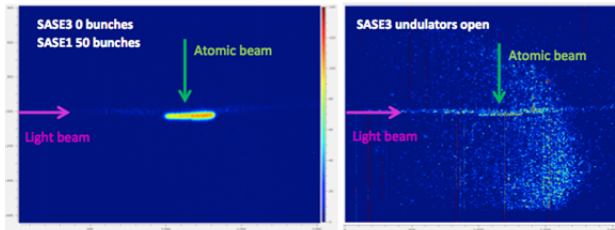


Figure 6: XUV background observed on velocity map imaging (VMI) spectrometer at the SQS instrument.

Optical Afterburner Effect

The background from optical to XUV range can be explained by the optical afterburner effect reported in [12]. Energy modulations, induced by SASE process on the scale of coherence time, can be converted into density modulations (in the range from VUV to FIR, depending on the configurations) in a dispersive element (can be chicane, arc or simply dump dipole), then the modulated beam radiates (can be CSR, edge radiation or a dedicated undulator) in the corresponding wavelength range (from VUV to FIR) [13].

Since there is a significant momentum compaction factor ($R56=110$ um) in the arc between SASE1 and SASE3, the density modulations induced by the arc can radiate in different ways as mentioned above. The background observed when the SASE3 undulators were open (see Fig. 6 (right)) is most probably due to edge radiation as explained in [14]. One can control the modulation scale by changing $R56$ and cancel this effect by either modify the arc or install a chicane (behind or in front of the arc).

On the other hand, this effect can be used for SASE1 pulse duration measurements or for SASE3 pump-probe experiments. Such measurements have already been demonstrated at FLASH [15].

FLEXIBLE OPERATION MODES

To help coping with the background issues, different operation modes were introduced together with the operation of the betatron switcher.

Typical 10 Hz Mode

The typical operation mode at the European XFEL delivers bunches to all SASEs within a train at 10 Hz repetition rate (see Fig. 7 (top)) and the SASE1 and SASE3 bunches are in sequence. This mode works for experi-

⁴ The slow detector has better transverse resolution than the fast detector and it is needed for some experiments.

ments exploiting pulse-resolved large-area detectors, and detectors for electron and ion Time of Flight (ToF) spectroscopy. However, the slower detectors⁴ cannot separate the SASE1 background from the SASE3 bunches and may record corrupted data. In addition fixed experimental targets are constantly exposed to the SASE1 background, which can cause sample heating or even damage the samples in single shot diffraction experiments.

5 Hz Mode

5 Hz mode (see Fig. 7 (middle)) is used to separate the SASE1 and SASE3 bunches into two sequential trains. In this way, one can work with the slow detectors with the help of a train picker (optical chopper), which enables full separation of the two SASEs, and the SASE1 background can be stopped before reaching the samples at SASE3 instruments. Therefore, this mode is needed for single shot imaging, pulson-demand experiments and radiation sensitive samples.

Interleaved Mode

Since not all the experiments require high repetition rates, interleaved mode (see Fig. 7 (bottom)) with SASE1 and SASE3 within a train is a good option for lower repetition rate (below 2.25 MHz) experiments. In this mode, both experiments can benefit from the long pulse window and double their data rate.

Other Modes

Besides the above-mentioned modes, the bunch pattern server and the timing system also allow different combinations of modes, and the users can define their own bunch pattern and repetition rate according to their needs [5].

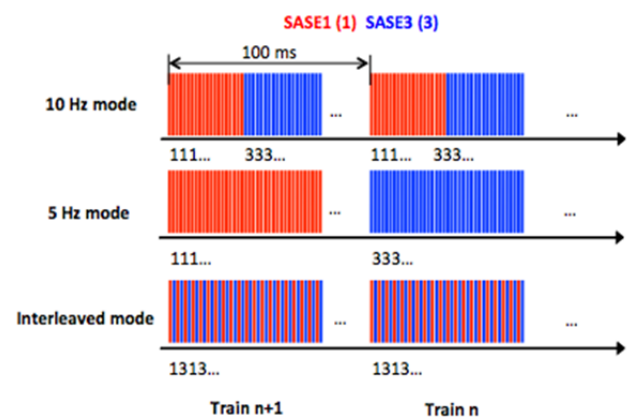


Figure 7: Example of operation modes for parallel operation of SASE1 and SASE3. SASE1 bunches are marked in red and SASE3 bunches are in blue.

SUMMARY AND FUTURE PLANS

In this paper we first presented the coupling between SASE1 and SASE3 operation, when they use the same electron beam. Decoupling has been achieved using the betatron switcher technique, which suppresses lasing of SASE3 bunches in SASE1 beamline and vice versa by generating betatron oscillations for different bunches. We

showed that residual lasing of SASE1 bunches in SASE3 can still be observed due to the limited oscillation amplitude in the present setup. Different ways to further suppress the residual lasing were introduced including the use of different undulator configurations in SASE3 and the use of different compression setting for SASE1 and SASE3 bunches.

Except for the residual lasing, background from optical to XUV range was also observed. This can be explained by the optical afterburner effect and might be cancelled by modifying the arc between SASE1 and SASE3 beam-line.

In the end, we introduced different operation modes, which we established in the parallel operation of SASE1 and SASE3 and explained how we can adapt these modes to different user requirements.

The experience we have learned in the parallel operation of SASE1 and SASE3 will help us to design the future undulator beamlines. Design studies for the two empty tunnels SASE4 and SASE5 downstream of SASE2 (see Fig. 1) are ongoing [16-18]. Besides, R&D towards doubling FEL beamlines with a 2nd fan is also in progress.

ACCKNOWLEDGEMENTS

The author would like to thank all the colleagues, who have contributed to the operation of the European XFEL, and the colleagues from SASE3 instruments (SCS and SQS), who helped to distinguish different backgrounds.

REFERENCES

[1] M. Altarelli, R. Brinkmann *et al.*, “XFEL: The European X-Ray Free-Electron Laser Technical Design Report”, DESY, Hamburg, Germany, DESY 2006-097, 2006.

[2] H. Weise and W. Decking, “Commissioning and First Lasing of the European XFEL”, in *Proc. 38th Int. Free Electron Laser Conf. (FEL'17)*, Santa Fe, NM, USA, Aug. 2017, pp. 9-13, doi:10.18429/JACoW-FEL2017-MOC03

[3] M. Scholz, “First Lasing at the SASE2 and SASE3 FELs of European XFEL”, presented at the 39th Int. Free Electron Laser Conf. (FEL'19), Hamburg, Germany, Aug. 2019, paper MOA04.

[4] D. Noelle, “FEL Operation at the European XFEL Facility”, presented at the 39th Int. Free Electron Laser Conf. (FEL'19), Hamburg, Germany, Aug. 2019, paper FRA01.

[5] L. Froehlich *et al.*, “Multi-Beamline Operation at the European XFEL”, presented at the 39th Int. Free Electron Laser Conf. (FEL'19), Hamburg, Germany, Aug. 2019, paper WEP008.

[6] E. Schneidmiller and M. V. Yurkov, “An Overview of the Radiation Properties of the European XFEL”, in *Proc. 36th Int. Free Electron Laser Conf. (FEL'14)*, Basel, Switzerland, Aug. 2014, paper MOP066, pp. 204-209.

[7] R. Brinkmann, E. Schneidmiller, and M. V. Yurkov, “Betatron Switcher for a Multi-Color Operation of an X-Ray FEL”, in *Proc. 32nd Int. Free Electron Laser Conf. (FEL'10)*, Malmö, Sweden, Aug. 2010, paper MOPC07, pp. 127-130.

[8] R. Brinkmann, E. A. Schneidmiller and M. V. Yurkov, “Possible operation of the European XFEL with ultra-low emittance beams”, *Nucl. Instrum. and Methods A*, 616(1), pp. 81-87, 2010.

[9] F. Obier, W. Decking, M. Huening, and J. Wortmann, “Fast Kicker System for European XFEL Beam Distribution”, presented at the 39th Int. Free Electron Laser Conf. (FEL'19), Hamburg, Germany, Aug. 2019, paper WEP013.

[10] A. Sargsyan, V. Sahakyan, and W. Decking, “Parallel Operation of SASE1 and SASE3 Undulator Sections of European XFEL”, in *Proc. 8th Int. Particle Accelerator Conf. (IPAC'17)*, Copenhagen, Denmark, May 2017, pp. 2554-2556, doi:10.18429/JACoW-IPAC2017-WEPAB001

[11] J. Grünert *et al.*, “Pulse Resolved Photon Diagnostics at MHz Repetition Rates”, presented at the 39th Int. Free Electron Laser Conf. (FEL'19), Hamburg, Germany, Aug. 2019, paper WED03.

[12] E. L. Saldin, E. A. Schneidmiller and M. V. Yurkov, “Optical afterburner for an x-ray free electron laser as a tool for pump-probe experiments”, *Physical Review Special Topics-Accelerators and Beams*, 13.3 (2010): 030701.

[13] E. A. Schneidmiller, “Optical afterburner effect in SASE1/3 line”, presented in the joint R&D meeting, DESY, Hamburg, Germany, July 2019.

[14] G. Geloni, V. Kocharyan, E. Saldin, E. Schneidmiller and M. Yurkov, “Theory of edge radiation. Part I: Foundations and basic applications”, *Nucl. Instrum. and Methods A*, 605(3), pp. 409-429, 2009.

[15] S. Duesterer *et al.*, “Development of experimental techniques for the characterization of ultrashort photon pulses of extreme ultraviolet free-electron lasers”, *Physical Review Special Topics-Accelerators and Beams*, 17.12 (2014): 120702.

[16] E. Schneidmiller *et al.*, “Feasibility Studies of the 100 keV Undulator Line of the European XFEL”, presented at the 39th Int. Free Electron Laser Conf. (FEL'19), Hamburg, Germany, Aug. 2019, paper TUP056.

[17] E. Schneidmiller and M. V. Yurkov, “Analysis of Parameter Space of Soft X-Ray Free Electron Laser at the European XFEL Driven by High and Low Energy Electron Beam”, presented at the 39th Int. Free Electron Laser Conf. (FEL'19), Hamburg, Germany, Aug. 2019, paper TUP057.

[18] S. Serkez *et al.*, “Super-X: Simulations for Extremely Hard X-Ray Generation with Short Period Superconducting Undulators for the European XFEL”, presented at the 39th Int. Free Electron Laser Conf. (FEL'19), Hamburg, Germany, Aug. 2019, paper TUP061.

HARMONIC LASING EXPERIMENT AT THE EUROPEAN XFEL

E.A. Schneidmiller*, F. Brinker, W. Decking, M. Guetg, S. Liu, D. Noelle,
M. Scholz, M.V. Yurkov, and I. Zagorodnov,
DESY, Hamburg, Germany
N. Gerasimova, G. Geloni, J. Gruenert, J. Laksman, Y. Li, J. Liu, S. Karabekyan, N. Kujala,
Th. Maltezopoulos, I. Petrov, L. Samoylova, S. Serkez, H. Sinn, and F. Wolff-Fabris
European XFEL GmbH, Schenefeld, Germany

Abstract

Harmonic lasing is an opportunity to extend the photon energy range of existing and planned X-ray FEL user facilities. Contrary to nonlinear harmonic generation, harmonic lasing can provide a much more intense, stable, and narrow-band FEL beam. Another interesting application is Harmonic Lasing Self-Seeding (HLSS) that allows to improve the longitudinal coherence and spectral power of a Self-Amplified Spontaneous Emission (SASE) FEL. This concept was successfully tested at FLASH in the range of 4.5 - 15 nm and at PAL XFEL at 1 nm. In this contribution we present recent results from the European XFEL where we successfully demonstrated operation of HLSS FEL at 5.9 Angstrom and 2.8 Angstrom, in the latter case obtaining both 3rd and 5th harmonic lasing.

INTRODUCTION

Successful operation of X-ray free electron lasers (FELs) down to the Angstrom regime opens up new horizons for photon science. Even shorter wavelengths are requested by the scientific community.

One of the most promising ways to extend the photon energy range of high-gain X-ray FELs is to use harmonic lasing, which is the FEL instability at an odd harmonic of the planar undulator [1–5] developing independently from the lasing at the fundamental. Contrary to the nonlinear harmonic generation (which is driven by the fundamental in the vicinity of saturation), harmonic lasing can provide much more intense, stable, and narrow-band radiation.

Another interesting option, proposed in [5], is the possibility to improve spectral brightness of an X-ray FEL by the combined lasing on a harmonic in the first part of the undulator (with an increased undulator parameter K) and on the fundamental in the second part of the undulator. Later this concept was named Harmonic Lasing Self-Seeded FEL (HLSS FEL) [6].

Harmonic lasing was initially proposed for FEL oscillators [7] and was tested experimentally in infrared and visible wavelength ranges. It was, however, not demonstrated in high-gain FELs and at a short wavelength until the successful experiments [8] at the second branch of the soft X-ray FEL user facility FLASH [9, 10] where the HLSS FEL operated in the wavelength range between 4.5 nm and 15 nm. Later, the same operation mode was tested at PAL XFEL at 1 nm [11].

In this paper we report on recent results from the European XFEL [12] where we successfully demonstrated operation of HLSS scheme at 5.9 Angstrom and at 2.8 Angstrom. Moreover, we observed for the first time the fifth harmonic lasing in a high-gain FEL.

HARMONIC LASING

Harmonic lasing in single-pass high-gain FELs [1–5] is the amplification process in a planar undulator of higher odd harmonics developing independently of each other (and of the fundamental) in the exponential gain regime. The most attractive feature of the saturated harmonic lasing is that the spectral brightness (or brilliance) of harmonics is comparable to that of the fundamental [5]. Indeed, a good estimate for the saturation efficiency is $\lambda_w / (hL_{\text{sat},h})$, where λ_w is the undulator period, h is harmonic number, and $L_{\text{sat},h}$ is the saturation length of a harmonic. At the same time, relative rms bandwidth has the same scaling. So, the reduction of power is compensated by the bandwidth reduction and the spectral power remains the same.

Although known theoretically for a long time [1–4], harmonic lasing in high-gain FELs was not considered for practical applications in X-ray FELs. The situation was changed after publication of ref. [5] where it was concluded that the harmonic lasing in X-ray FELs is much more robust than usually thought, and can be effectively used in the existing and future X-ray FELs. In particular, the European XFEL [13] can greatly outperform the specifications in terms of the highest possible photon energy: it can reach 60-100 keV range for the third harmonic lasing. It was also shown [14] that one can keep sub-Angstrom range of operation of the European XFEL after CW upgrade of the accelerator with a reduction of electron energy from 17.5 GeV to 7 GeV. Another application of harmonic lasing is a possible upgrade of FLASH with the aim to increase the photon energy up to 1 keV [15].

HARMONIC LASING SELF-SEEDED FEL

A poor longitudinal coherence of SASE FELs stimulated efforts for its improvement. Since an external seeding seems to be difficult to realize in X-ray regime, a so called self-seeding has been proposed [16, 17]. There are alternative approaches for reducing bandwidth and increasing spectral brightness of X-ray FELs without using optical elements. One of them was proposed in [5], it is based on the combined lasing on a harmonic in the first part of the undulator (with

* evgeny.schneidmiller@desy.de

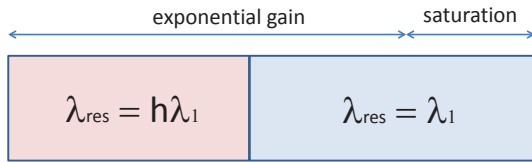


Figure 1: Conceptual scheme of a harmonic lasing self-seeded FEL.

increased undulator parameter K) and on the fundamental in the second part. In this way the second part of the undulator is seeded by a narrow-band signal generated via a harmonic lasing in the first part. This concept was named HLSS FEL [6].

Typically, gap-tunable undulators are planned to be used in X-ray FEL facilities. If the maximal undulator parameter K is sufficiently large, the concept of harmonic lasing self-seeded FEL can be applied (see Fig. 1). An undulator is divided into two parts by setting two different undulator parameters such that the first part is tuned to a h -th subharmonic of the second part which is tuned to a wavelength of interest λ_l . Harmonic lasing occurs in the exponential gain regime in the first part of the undulator. The fundamental in the first part stays well below saturation. In the second part of the undulator the fundamental is resonant to the wavelength previously amplified as the harmonic. The amplification process proceeds in the fundamental up to saturation. In this case the bandwidth is defined by the harmonic lasing but the saturation power is still as high as in the reference case of lasing at the fundamental in the whole undulator, i.e. the spectral brightness increases.

The enhancement factor of the coherence length (or bandwidth reduction factor) that one obtains in HLSS FEL in comparison with a reference case of lasing in SASE FEL mode in the whole undulator, reads [6]:

$$R \simeq h \frac{\sqrt{L_w^{(1)} L_{\text{sat},h}}}{L_{\text{sat},1}} \quad (1)$$

Here h is harmonic number, $L_{\text{sat},1}$ is the saturation length in the reference case of the fundamental lasing with the lower K -value, $L_w^{(1)}$ is the length of the first part of the undulator, and $L_{\text{sat},h}$ is the saturation length of harmonic lasing.

Despite the bandwidth reduction factor (1) is significantly smaller than that of self-seeding schemes using optical elements [16, 17], the HLSS FEL scheme is very simple and robust, and it does not require any additional installations, i.e. it can always be used in existing or planned gap-tunable undulators with a sufficiently large range of accessible K -value.

EXPERIMENT AT THE EUROPEAN XFEL

The European XFEL is a X-ray FEL user facility, based on superconducting accelerator [12]. It provides ultimately bright photon beams for user experiments since 2017. Two

hard X-ray undulators (SASE1 and SASE2) and one soft X-ray undulator (SASE3) are presently in operation [18]. Harmonic lasing experiments were performed in the SASE3 undulator on April 19 and on August 2-3, 2019.

The electron beam energy in both cases was 14 GeV and the bunch charge was 250 pC. SASE3 undulator consists of twenty one 5 m long undulator segments plus intersections containing quadrupoles and phase shifters between the segments [19]. The undulator has a period of 6.8 cm and the K -values can be changed between 4 and 9 in the specified working range. Note that in order to observe HLSS effect with the 5th harmonic we had to work outside of this standard range (K was set to 3.2).

In April we aimed at the 3rd harmonic lasing at 2.1 keV. The experiment was performed as follows. As a preparation step, we defined the number of undulator segments to be tuned to the third subharmonic of 2.1 keV radiation that was our target photon energy. We set the undulator K value to 8.74 and lased at 700 eV on the fundamental. As it is described above, in the first part of the undulator we have to avoid the nonlinear harmonic generation what means that we have to stay three or more orders of magnitude below saturation. We have found that five undulator segments satisfy this condition.

Then we set the undulator K -value to 4.91 and had a normal SASE operation at 2.1 keV (wavelength 5.9 Angstrom). We choose twelve undulator segments to stay at the onset of saturation. The pulse energy was measured at 700 μJ with X-ray gas monitor (XGM) detector [20, 21]. In the same way as it was done in the earlier experiments at FLASH [8], we closed gaps of first five undulator segments one by one such that the undulator K became 8.74, and the resonance photon energy was 700 eV (wavelength 17.7 Angstrom). In other words, we moved to the configuration, shown on Fig. 1, with $h = 3$, five segments in the first part of the undulator and seven segments in the second part. As soon as K in each of the first five segments deviates from the original

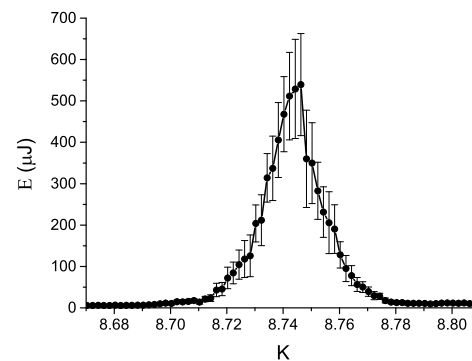


Figure 2: Scan of the K -value of the first part of the undulator consisting of five undulator segments, tuned to 700 eV. Mean pulse energy and its standard deviation are measured after the second part of the undulator tuned to 2.1 keV. FEL operates in "5+7 segments HLSS" mode.

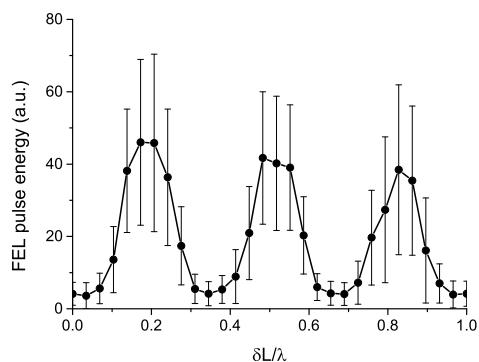


Figure 3: Synchronous scan of phase shifters after first four undulator segments. FEL pulse energy is measured after the second part of the undulator tuned to 2.1 keV. Mean pulse energy and its standard deviation are plotted versus a delay measured in units of the fundamental wavelength in the first part (tuned to 700 eV). FEL operates in "5+6 segments HLSS" mode.

value of 4.91, we observe a strong reduction of pulse energy, measured with an XGM. However, when K approaches the value of 8.74, the pulse energy almost recovers.

We performed a scan of the K -value of the first part of the undulator, tuned to 700 eV, and measured pulse energy after the second part, tuned to 2.1 keV. The result is presented in Fig. 2 where one can see a sharp resonance. Taking into account the above mentioned fact that lasing on the fundamental at 700 eV was too weak to produce nonlinear harmonics, we can conclude that we have the 3rd harmonic lasing in the first part of the undulator at 2.1 keV that continues as lasing on the fundamental in the second part.

An independent confirmation of harmonic lasing is the result of a scan of phase shifters in the first part of the undulator, presented in Fig. 3. For this scan, we used six undulator segments in the second part in order to increase sensitivity of the system by reducing saturation effects. We performed synchronous scan of phase shifters between the first five undulator segments over a range in which the fundamental radiation at $\lambda = 17.7$ Angstrom slips over the electron beam by a single cycle. If we seeded the second part of the undulator by the nonlinear harmonic generation in the first part, the phase shifter scan would result in a single cycle. However, one can clearly see three cycles in Fig. 3 which proves that we had harmonic lasing.

The purpose of HLSS scheme is to increase FEL coherence time and to reduce bandwidth. From formula (1) we estimate the coherence enhancement factor $R \approx 2$ for our experimental conditions. An increase of the coherence time results in a corresponding reduction of the number of longitudinal modes with respect to the SASE case. In the frequency domain we should then observe a reduction of the average number of spikes in single-shot spectra. In an ideal case, we could also expect a reduction of the average bandwidth by a factor of two, to the level of 0.1% FWHM. Unfortunately, a

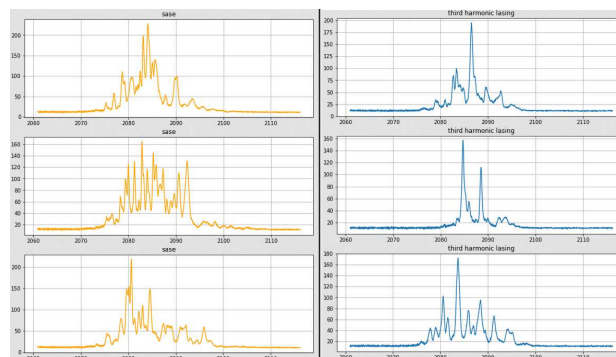


Figure 4: Single-shot spectra for SASE (left column) and HLSS (right column). Plots show spectral intensity (in arbitrary units) versus photon energy (in eV). HLSS operates in "5+7 segments" configuration.

reduction of the average bandwidth was not possible in our case since the bandwidth is strongly affected by the energy chirp of the electron bunches.

To measure spectra, the SASE3 monochromator [22] was used in spectrometer mode: the spectral distribution of the soft X-rays was converted into visible light in a YAG:Ce crystal located in the focal plane of the monochromator and was recorded by a CCD. To resolve spikes in single shot spectra, we recorded the spectra in 3rd diffraction order with a 50 l/mm grating.

We took a series of spectra for HLSS configuration (five segments at 700 eV and seven segments at 2.1 keV) as well as for standard SASE with twelve segments at 2.1 keV. As expected, the average spectrum width was dominated by the chirp and was the same in both cases, 0.6% FWHM. However, we could clearly observe a reduction of number of spikes in spectra. This is illustrated by Fig. 4 where one can see three representative shots for each configuration.

On August 2-3, 2019 we went to 4.5 keV lasing on the fundamental (2.8 Angstrom) and then tested HLSS scheme on the 3rd harmonic by setting first five segments to 1.5 keV. After that we set these segments to 900 eV and obtained HLSS operation with the 5th harmonic seeding. In both cases the fundamental in the first part of the undulator was well below saturation, so that there were no nonlinear harmonics. This was confirmed by phase shifter scans as described above (see Fig. 3). In particular, in the case of the 5th harmonic lasing we saw five cycles instead of one at 900 eV. We also did K -scans of the first five segments that showed a narrow resonance. These results will be published elsewhere.

Finally, we conclude that Harmonic Lasing Self-Seeded FEL was successfully operated at the European XFEL in the Angstrom regime with the 3rd and the 5th harmonics.

REFERENCES

- [1] J.B. Murphy, C. Pellegrini and R. Bonifacio, "Collective instability of a free electron laser including space charge and harmonics", *Opt. Commun.*, vol. 53, p. 197, 1985. doi: 10.1016/0030-4018(85)90331-1

- [2] R. Bonifacio, L. De Salvo, and P. Pierini, "Large harmonic bunching in a high-gain free-electron laser", *Nucl. Instr. Meth. A*, vol. 293, p. 627, 1990. doi:10.1016/0168-9002(90)90334-3
- [3] Z. Huang and K. Kim, "Three-dimensional analysis of harmonic generation in high-gain free-electron lasers", *Phys. Rev. E*, vol. 62, p. 7295, 2000. doi:10.1103/PhysRevE.62.7295
- [4] B.W.J. McNeil, G.R.M. Robb, M.W. Poole, and N.R. Thompson, "Harmonic lasing in a free-electron-laser amplifier", *Phys. Rev. Lett.* vol. 96, p. 084801, 2006. doi:10.1103/PhysRevLett.96.084801
- [5] E.A. Schneidmiller and M.V. Yurkov, "Harmonic lasing in x-ray free electron lasers", *Phys. Rev. ST-AB*, vol. 15, p. 080702, 2012. doi:10.1103/PhysRevSTAB.15.080702
- [6] E.A. Schneidmiller and M.V. Yurkov, "Harmonic Lasing Self-Seeded FEL", in *Proc. FEL'13*, New York, NY, USA, Aug. 2013, paper WEPSo78, pp. 700–703.
- [7] W.B. Colson, "The nonlinear wave equation for higher harmonics in free-electron lasers", *IEEE J. Quantum Electron.*, vol. 17, p. 1417, 1981. doi:10.1109/JQE.1981.1071273
- [8] E.A. Schneidmiller *et al.*, "First operation of a harmonic lasing self-seeded free electron laser", *Phys. Rev. ST-AB*, vol. 20, p. 020705, 2017. doi:10.1103/PhysRevAccelBeams.20.020705
- [9] W. Ackermann *et al.*, "Operation of a free-electron laser from the extreme ultraviolet to the water window", *Nature Photonics*, vol. 1, p. 336, 2007. doi:10.1038/nphoton.2007.76
- [10] B. Faatz *et al.*, "Simultaneous operation of two soft x-ray free-electron lasers driven by one linear accelerator", *New Journal of Physics*, vol. 18, p. 062002, 2016. doi:10.1088/1367-2630/18/6/062002
- [11] I. Nam *et al.*, "Soft X-ray harmonic lasing self-seeded free electron laser at Pohang Accelerator Laboratory X-ray free electron laser", *Applied Phys. Lett.*, vol. 112, p. 213506, 2018. doi:10.1063/1.5030443
- [12] W. Decking, H. Weise, "Commissioning of the European XFEL Accelerator", in *Proc. IPAC'17*, Copenhagen, Denmark, May 2017, pp. 1–6. doi:10.18429/JACoW-IPAC2017-MOXAA1
- [13] M. Altarelli *et al.* (Eds.), "XFEL: The European X-Ray Free-Electron Laser. Technical Design Report", Preprint DESY 2006-097, DESY, Hamburg, 2006.
- [14] R. Brinkmann, E.A. Schneidmiller, J. Sekutowicz and M.V. Yurkov, "Prospects for CW and LP operation of the European XFEL in hard X-ray regime", *Nucl. Instrum. and Methods A*, vol. 768, p. 20, 2014. doi:10.1016/j.nima.2014.09.039
- [15] E.A. Schneidmiller and M.V. Yurkov, "A possible upgrade of FLASH for harmonic lasing down to 1.3 nm", *Nucl. Instrum. and Methods A*, vol. 717, p. 37, 2013. doi:10.1016/j.nima.2013.04.008
- [16] J. Feldhaus *et al.*, "Possible application of X-ray optical elements for reducing the spectral bandwidth of an X-ray SASE FEL", *Optics. Comm.*, vol. 140, p. 341, 1997. doi:10.1016/S0030-4018(97)00163-6
- [17] G. Geloni, V. Kocharyan and E.L. Saldin, "A novel self-seeding scheme for hard X-ray FELs", *Journal of Modern Optics*, vol. 58, p. 1391, 2011. doi:10.1080/09500340.2011.586473
- [18] W. Decking *et al.*, "Status of the European XFEL", in *Proc. IPAC'19*, Melbourne, Australia, May 2019, pp. 1721–1723. doi:10.18429/JACoW-IPAC2019-TUPRB020
- [19] S. Abeghyan *et al.*, "First operation of the SASE1 undulator system of the European X-ray Free-Electron Laser", *J. Synchrotron Rad.* vol. 26, p. 302, 2019. doi:10.1107/S1600577518017125
- [20] A.A. Sorokin *et al.*, "X-ray gas monitors for free-electron lasers", submitted to *J. Synchrotron Rad.*, vol. 26, 2019.
- [21] T. Maltezopoulos *et al.*, "Operation of X-ray gas monitors at the European XFEL", submitted to *J. Synchrotron Rad.*, vol. 26, 2019.
- [22] N.Gerasimova, "Performance of the SASE3 monochromator equipped with a provisional short grating. Variable line spacing grating specifications", Technical Report, 2018. doi:10.22003/XFEL.EU-TR-2018-001

ECHO-ENABLED HARMONIC GENERATION LASING OF THE FERMI FEL IN THE SOFT X-RAY SPECTRAL REGION

P. R. Ribič^{†,1}, Elettra-Sincrotrone Trieste, Area Science Park, Trieste, Italy

¹also at University of Nova Gorica, Nova Gorica, Slovenia, on behalf of the EEHG collaboration*

Abstract

The layout of the FERMI FEL-2 undulator line, normally operated in the two-stage high-gain harmonic generation (HGHG) configuration, was temporarily modified to allow running the FEL in the echo-enabled harmonic generation (EEHG) mode. The EEHG setup produced stable, intense, and nearly fully coherent pulses at wavelengths as short as 5.9 nm (~211 eV). Comparing the performance to the two-stage HGHG showed that EEHG gives significantly better spectra in terms of the central wavelength stability and bandwidth, especially at high harmonics, where electron-beam imperfections start to play a significant role. Observation of stable, narrow-band, coherent emission down to 2.6 nm (~474 eV) indicates the possibility to extend the lasing region to even shorter wavelengths.

INTRODUCTION

The FERMI free-electron laser (FEL) in Trieste, Italy is an externally seeded FEL facility consisting of two undulator lines that provide users with laser-like pulses in the entire extreme-ultraviolet (EUV) spectral region. The FEL-1 line is based on a single high-gain harmonic generation (HGHG) stage [1], where an ultraviolet (~264 nm) seed laser is used to trigger the amplification process at a high harmonic h of the seed, producing nearly fully coherent pulses in the range from 100 nm to 20 nm [2]. To reach shorter wavelengths, the FEL-2 line employs a two-stage HGHG cascade based on the fresh-bunch (FB) approach [3], generating output in the range from 20 nm to 4 nm [4]. The high degree of (longitudinal) coherence at FERMI allows performing experiments previously not possible in the EUV, such as, e.g., four wave-mixing [5], and coherent control [6].

Experience has shown, however, that at the shortest wavelengths available at the FEL-2 line, the sensitivity to the shape of the electron-beam (e-beam) phase space becomes critical and may severely affect the FEL radiation in terms of longitudinal coherence, pulse energy, and shot-to-shot stability. In addition, the two-stage HGHG cascade employed at FEL-2 cannot cover the whole harmonic range, as the final harmonic number is a product between the harmonic numbers of the individual stages. Last, but not least, the two-stage setup uses a relatively large portion of the e-beam to accommodate the double seeding process, which makes the implementation of double-pulse operation somewhat difficult.

Recent experiments [7-11] have suggested that the drawbacks of the two-stage HGHG could be overcome by

using a seeding technique called echo-enabled harmonic generation (EEHG), where the e-beam phase space is shaped with two seed lasers to enable FEL emission at high harmonics [12]. The method is intrinsically much less sensitive to the initial e-beam imperfections, making it a strong candidate for producing highly stable, nearly fully coherent, and intense FEL pulses, down to soft x-ray wavelengths.

Here, we demonstrate the first EEHG lasing at wavelengths as short as 5.9 nm at the (modified) FEL-2 line at FERMI [13]. We show that EEHG gives significantly better spectra in terms of the central wavelength stability and bandwidth, as compared to the two-stage HGHG cascade. The observation of stable, narrow-band emission down to 2.6 nm indicates the possibility to extend the lasing region to shorter wavelengths.

EXPERIMENT

The implementation of the EEHG seeding scheme at FERMI required modifying the FEL-2 line. The technical details are given in Ref. [14]. In summary, a second seed laser line required by EEHG and delivering up to 50 μ J per pulse at 264 nm was setup; the second stage modulator of FEL-2 was replaced by a new one, allowing resonant interaction at 264 nm; the dispersion of the magnetic chicane normally used for the FB approach was increased to be suitable as the first (strong) chicane for EEHG; new e-beam and laser diagnostics were installed to allow overlapping the e-beam and the second seed laser.

In EEHG, the output wavenumber k_E is given by $k_E = nk_1 + mk_2$, where n and m are non-zero integers and $k_{1,2} = 2\pi/\lambda_{1,2}$ are the wavenumbers of the two seed lasers operating at wavelengths λ_1 and λ_2 [12]. In our experiment, the two seed lasers had the same wavelength, $\lambda_1 = \lambda_2$, so $k_E = (n + m)k_1$, or $\lambda_E = \lambda_1/h$, where $h = n + m$ is the harmonic number and λ_E is the EEHG output wavelength. Most of the measurements were performed in the $n = -1$ configuration to maximize the signal [12], but we have also observed output at $n = -2, -3$, and $n = -4$. The latter option was employed at high harmonics due to the limitations of our setup (limited first dispersion and limited second seed power).

To optimize the EEHG output at a specific harmonic h , the first (strong dispersion) $R_{56}^{(1)}$ was fixed (to typically around 2 mm, depending on the e-beam energy) and the strength of the second dispersion section $R_{56}^{(2)}$ was set according to $R_{56}^{(2)} \approx \frac{|n|}{h} R_{56}^{(1)}$ [12]. All of the parameters (second dispersion and both seed laser intensities) were iteratively tuned to maximize emission.

[†] primoz.rebernik@elettra.eu

RESULTS

Figure 1 demonstrates exponential gain (lasing) of the FERMI FEL operated in the EEHG configuration at 7.3 nm, i.e., $h = 36$ of the (second) seed laser. The e-beam energy was set to 1.31 GeV. The dispersion of the first (strong) chicane was fixed at 2.38 mm, while that of the weaker (second) chicane was set to 62 μm to optimize the output in the $n = -1$ tune. The measured gain length of ~ 1.9 m matches relatively well the one obtained from GENESIS simulations [15] using experimentally determined e-beam and seed laser parameters. To compare the experimental and simulated gain lengths, the measured pulse energies were multiplied by a factor of two. The discrepancy between the measured and simulated values are probably associated with a degradation of the transmission efficiency of the beamline optics and detectors.

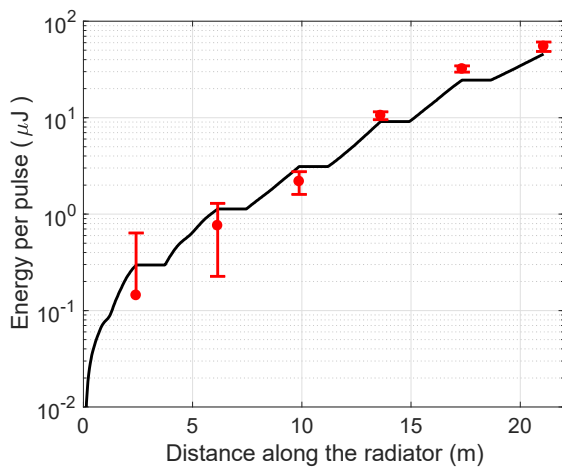


Figure 1: Measured (red circles) and simulated (black line) EEHG gain curve at 7.3 nm. See text for details.

Figure 2 shows a series of single shot spectra demonstrating the high spectral quality and stability of the FERMI FEL operated in the EEHG mode at 5.9 and 7.3 nm. A detailed analysis of 1000 consecutive shots shows a Gaussian-like shape in both cases with a relative central wavelength stability of $\sim 7 \times 10^{-5}$, and 16% and 25% RMS intensity fluctuations at 7.3 nm and 5.9 nm, respectively. We chose the minimum width containing 76% of the pulse energy ($\sigma_{76\%}$) as a measure of the spectral bandwidth. This puts more weight on the tails of the spectrum and accounts for spectral features that can come from e-beam imperfections and laser phase errors. The measured average $\sigma_{76\%}$ at 7.3 nm is 3.0×10^{-3} nm, giving a relative bandwidth of $\sim 4 \times 10^{-4}$. This is approximately $1.5 \times$ the $\sigma_{76\%}$ of a transform-limited pulse calculated from the EEHG bunching [12]. Such deviations can probably be assigned to a residual linear frequency chirp on the second seed laser and possible spectral broadening due to e-beam instabilities. At 5.9 nm, the measured average $\sigma_{76\%}$ is 2.4×10^{-3} nm, and is around $1.8 \times$ the value obtained from theory. These increased deviations from the calculated bandwidth, compared to 7.3 nm, are due to

significant sideband structures in the spectra shown in the bottom panel of Fig. 2, and are attributed to a higher sensitivity of the output to e-beam instabilities at shorter wavelengths. Additional measurements (not presented here) show a correlation between the position and intensity of the spectral sidebands and e-beam compression, confirming that spectral degradation is related to the e-beam and not laser phase errors.

Even though the second stage modulator of the FEL-2 line was replaced with a longer period one, this still allowed operating FERMI in the two-stage cascade configuration down to a wavelength of ~ 8 nm. Therefore, it was possible to directly compare the performances of the two schemes employing the same e-beam (at an e-beam energy of 0.9 GeV). To move from the EEHG to the two-stage cascade configuration, the mirror used for insertion of the second seed laser beam was extracted.

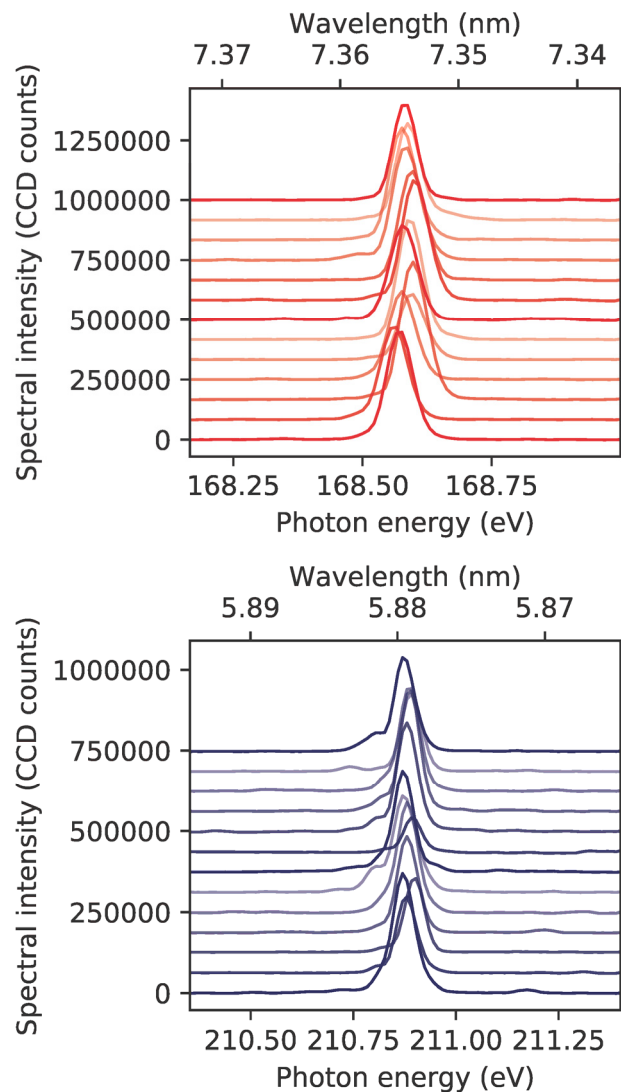


Figure 2: Single-shot spectra randomly chosen in a sequence of 1000 consecutive shots at 7.3 nm (top panel) and 5.9 nm (bottom panel) in the $n = -1$ configuration.

Figure 3 compares the output of the FERMI FEL operated in the EEHG and the two-stage cascade configura-

tions. While EEHG exhibits clean and narrow, quasi-Gaussian spectra with low fluctuations of the central wavelength, the spectra of the two-stage HGHH cascade are characterized by significant irregularities and relatively high fluctuations of the central wavelength. The expected better performance of EEHG is a consequence of a much lower sensitivity of the scheme to initial e-beam imperfections compared to HGHH [16].

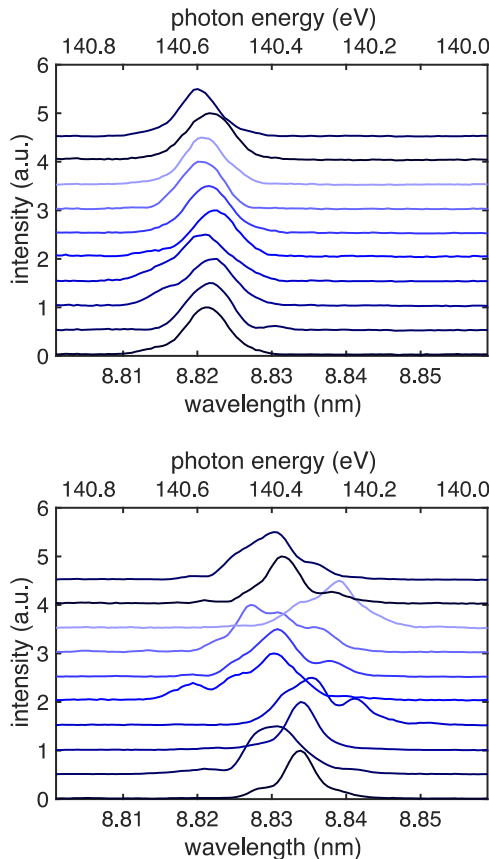


Figure 3: Consecutive single-shot spectra of the FERMI FEL operated in the EEHG (top) and two-stage cascade (bottom) configurations.

In an attempt to reach even shorter wavelengths with EEHG, we increased the e-beam energy up to 1.5 GeV. Due to the limitations of our setup (i.e., limited dispersive strength of the first chicane, limited second seed power), we had to operate EEHG in the $n = -4$ configuration, which resulted in reduced bunching. Furthermore, because of decreased gain at <4 nm, the output was considerably weaker compared to the one at 5.9 and 7.3 nm and was mainly due to coherent emission. Nevertheless, using an in-vacuum CCD to directly detect the soft X-ray photons diffracted by the spectrometer grating allowed us to measure the signal down to wavelengths as short as 2.6 nm, as shown in the bottom panel of Fig. 4.

CONCLUSION

We reported the first EEHG lasing in the soft x-ray spectral region (below 10 nm) at the modified FEL-2 line

of the FERMI FEL. The output at 7.3 nm is characterized by clean, quasi single-line spectra and pulse energies on the order of tens of μJ . At 8.8 nm, the EEHG setup clearly outperformed the two-stage cascade configuration in the investigated parameter space in terms of spectral purity and stability. It should be noted, however, that the two-stage cascade still provided higher energies per pulse compared to EEHG. The reason is that the maximum bunching achievable with EEHG was lower compared to the two-stage cascade. EEHG therefore strongly relied on the exponential gain, which required careful alignment of the e-beam trajectory along the whole undulator line, while for HGHH, the conditions could be significantly relaxed.

By optimizing the EEHG parameters we could observe coherent emission down to wavelengths as short as 2.6 nm. These observations establish EEHG as a strong candidate for producing highly stable, nearly fully coherent, and intense FEL pulses in the soft x-ray spectral region. More details on the experiment can be found in Ref. [13] and Ref. [14].

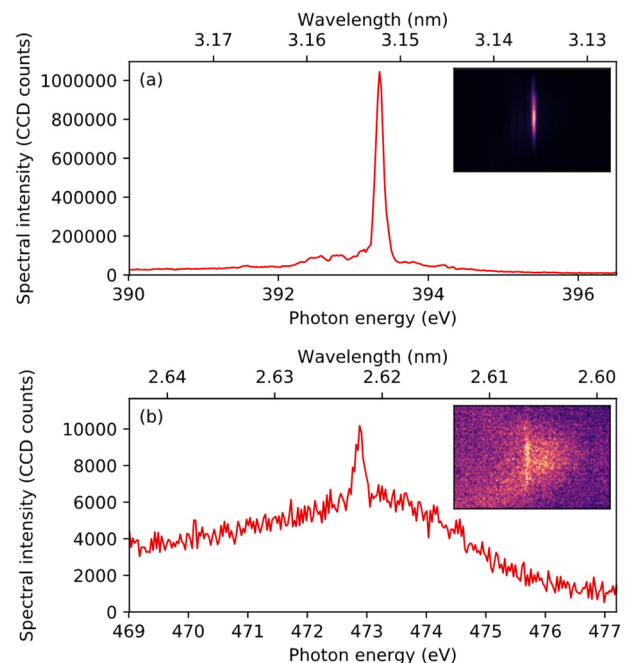


Figure 4: Coherent EEHG emission at 3.1 nm (top) and 2.6 nm (bottom).

ACKNOWLEDGEMENTS

We would like to thank G. Stupakov, S. Bettoni, D. Ratner, G. Marcus, F. Bencivenga, E. Pedersoli, M. Sacchi, C. Callegari, Z. Huang, T. Raubenheimer, and A. Zholents for useful discussions. We acknowledge continuous support of R. Godnig, R. Bracco, R. Visintini, and the FERMI - Elettra operator group during the course of the experiment. This work was in part supported by the Director, Office of Science, Office of Basic Energy Sciences, of the U.S. Department of Energy under Contract

Nos. DE-AC02-76SF00515 and DE-AC02-05CH11231 and award No. 2017-SLAC-100382. DG was supported by an Outgoing CEA fellowship from the CEA-Enhanced Eurotalents program, co-funded by FP7 Marie-Sklódowska-Curie COFUND program (Grant Agreement 600382).

REFERENCES

- [1] L. H. Yu, “Generation of intense UV radiation by subharmonically seeded single-pass free-electron lasers”, *Phys. Rev. A*, vol. 44, pp. 5178-5193, 1991.
doi:10.1103/PhysRevA.44.5178
- [2] E. Allaria *et al.*, “Highly coherent and stable pulses from the FERMI seeded free-electron laser in the extreme ultraviolet”, *Nat. Photon.*, vol. 6, pp. 699-704, 2012.
doi:10.1038/nphoton.2012.233
- [3] L.-H. Yu, I. Ben-Zvi, “High-gain harmonic generation of soft X-rays with the ‘fresh bunch’ technique”. *Nucl. Instrum. Methods Phys. Res. A*, vol. 393, pp. 96-99, 1997.
doi:10.1016/S0168-9002(97)00435-X
- [4] E. Allaria *et al.*, “Two-stage seeded soft-X-ray free-electron laser”, *Nat. Photon.*, vol. 7, pp. 913-918, 2013.
doi:10.1038/nphoton.2013.277
- [5] F. Bencivenga *et al.*, “Four-wave mixing experiments with extreme ultraviolet transient gratings”, *Nature*, vol. 520, pp. 205-208, 2015. doi.:10.1038/nature14341
- [6] K. C. Prince *et al.*, “Coherent control with a short-wavelength free-electron laser”, *Nat. Photon.*, vol. 10, pp. 176-179, 2016. 10.1038/nphoton.2016.13
- [7] D. Xiang *et al.*, “Demonstration of the echo-enabled harmonic generation technique for short-wavelength seeded free electron lasers”, *Phys. Rev. Lett.*, vol. 105, p. 114801, 2010. doi:10.1103/PhysRevLett.105.114801
- [8] Z. T. Zhao *et al.*, “First lasing of an echo-enabled harmonic generation free-electron laser”, *Nat. Photon.*, vol. 6, pp. 360-363, 2012. doi: 10.1038/nphoton.2012.105
- [9] D. Xiang *et al.*, “Evidence of high harmonics from echo-enabled harmonic generation for seeding X-ray free electron lasers”, *Phys. Rev. Lett.*, vol. 108, p. 24802, 2012.
doi:10.1103/PhysRevLett.108.024802
- [10] E. Hemsing *et al.*, “Highly coherent vacuum ultraviolet radiation at the 15th harmonic with echo-enabled harmonic generation technique”, *Phys. Rev. Spec. Top. Accel. Beams*, vol. 17, p. 70702, 2014.
doi:10.1103/PhysRevSTAB.17.070702
- [11] E. Hemsing *et al.*, “Echo-enabled harmonics up to the 75th order from precisely tailored electron beams”, *Nat. Photon.*, vol. 10, pp. 512-515, 2016.
doi:10.1038/nphoton.2016.101
- [12] D. Xiang, G. Stupakov, “Echo-enabled harmonic generation free electron laser”, *Phys. Rev. Spec. Top. Accel. Beams*, vol. 12, p. 30702, 2009.
doi:10.1103/PhysRevSTAB.12.030702
- [13] P. R. Ribič *et al.*, “Coherent soft X-ray pulses from an echo-enabled harmonic generation free-electron laser”, *Nat. Photon.*, vol. 13, pp. 555-561, 2019.
doi:10.1038/s41566-019-0427-1
- [14] E. Allaria *et al.*, “First lasing of a free electron laser in the soft x-ray spectral range with echo enabled harmonic generation”, presented at the FEL’19, Hamburg, Germany, Aug. 2019, paper MOA02, this conference.
- [15] S. Reiche, “GENESIS 1.3: a fully 3D time-dependent FEL simulation code”, *Nucl. Instrum. Methods Phys. Res. A*, vol. 429, pp. 243-248, 1999.
doi:10.1016/S0168-9002(99)00114-X
- [16] G. Penn, “Stable, coherent free-electron laser pulses using echo-enabled harmonic generation”. *Phys. Rev. Spec. Top. Accel. Beams*, vol. 17, p. 110707, 2014.
doi:10.1103/PhysRevSTAB.17.110707

*THE EEHG COLLABORATION

P. R. Ribič¹, A. Abrami, L. Badano, M. Bossi, F. Capotondi, D. Castronovo, M. Cautero, P. Cinquegrana, I. Cudin, M. B. Danailov, G. De Nino¹, A. Demidovich, S. Di Mitri, B. Diviacco, W. M. Fawley, M. Ferianis, L. Foglia, G. Gaio, D. Garzella², F. Giacuzzo, L. Giannessi³, S. Grulja, F. Iazzourene, G. Kurdi, M. Lonza, N. Mahne⁴, M. Malvestuto, M. Manfreda, C. Masciovecchio, N. S. Mirian, I. P. Nikolov, G. M. Penco, E. Principi, L. Raimondi, R. Sauro, C. Scafuri, P. Sigalotti, S. Spampinati, C. Spezzani, L. Sturari, M. Svandrlik, M. Trovó, M. Veronese, D. Vivoda, M. Zaccaria, D. Zangrando, M. Zangrando⁴, E. M. Allaria, Elettra-Sincrotrone Trieste, Area Science Park, Trieste, Italy

¹also at University of Nova Gorica, Nova Gorica, Slovenia

²also at CEA/DRF/LIDYL, Université Paris-Saclay, Saclay, France

³also at ENEA C.R. Frascati, Frascati, Italy

⁴also at Istituto Officina dei Materiali, Consiglio Nazionale delle Ricerche, Basovizza, Italy

H.-H. Braun, E. Ferrari, E. Prat, S. Reiche, Paul Scherrer Institut, Villigen PSI, Switzerland
N. Bruchon, Department of Engineering and Architecture, Università degli Studi di Trieste, Trieste, Italy

M. Coreno, ISM-CNR, Istituto di Struttura della Materia, LD2 Unit, Trieste, Italy
M. E. Couprie, A. Ghaith, Synchrotron SOLEIL, L'Orme des Merisiers, Saint-Aubin, Gif-sur-Yvette, France

C. Feng, Shanghai Advanced Research Institute, Chinese Academy of Sciences, Shanghai, China
F. Frassetto, P. Miotti, L. Poletto, Institute for Photonics and Nanotechnologies CNR-IFN, Padova, Italy

V. Graton, Deutsches Elektronen-Synchrotron DESY, Hamburg, Germany

E. Hemsing, SLAC National Accelerator Laboratory, Menlo Park, CA, USA

G. Penn, Lawrence Berkeley National Laboratory, Berkeley, CA, USA

M. Pop, MAX-IV, Lund University, Lund, Sweden

E. Roussel, Université Lille, CNRS, UMR 8523 - PhLAM - Physique des Lasers Atomes et Molécules, Lille, France

T. Tanikawa, European XFEL, Schenefeld, Germany

D. Xiang, Key Laboratory for Laser Plasmas (Ministry of Education), School of Physics and Astronomy, Shanghai Jiao Tong University, Shanghai, China

EXTENSION OF THE PITZ FACILITY FOR A PROOF-OF-PRINCIPLE EXPERIMENT ON THz SASE FEL

P. Boonpornprasert*, G. Georgiev, G. Koss, M. Krasilnikov, X.K. Li, F. Müller, A. Oppelt, S. Philipp, H. Shaker, F. Stephan, T. Weilbach, DESY, Zeuthen, Germany
Z. Amirkhanyan, CANDLE, Yerevan, Armenia

Abstract

The Photo Injector Test Facility at DESY in Zeuthen (PITZ) has been proposed as a suitable facility for research and development of an accelerator-based THz source prototype for pump-probe experiments at the European XFEL. A proof-of-principle experiment to generate THz SASE FEL radiation by using an LCLS-I undulator driven by an electron bunch from the PITZ accelerator has been planned and studied. The undulator is foreseen to be installed downstream from the current PITZ accelerator, and an extension of the accelerator tunnel is necessary. Radiation shielding for the extended tunnel was designed, and construction works are finished. Design of the extended beamline is ongoing, not only for this experiment but also for other possible experiments. Components for the extended beamline, including magnets for beam transport, a chicane bunch compressor, electron beam diagnostics devices, and THz radiation diagnostics devices have been studied. An overview of these works will be presented in this paper.

INTRODUCTION

The European XFEL has planned to perform pump-probe experiments by using its x-ray pulses and THz pulses. To provide the THz pulses, THz generation using laser-based and accelerator-based sources has been considered and studied [1]. For the accelerator-based sources, an interesting idea is to generate THz pulses using a Self-Amplified Spontaneous Emission (SASE) FEL driven by electron bunches from a "PITZ-like" accelerator. Preliminary simulations in [2] show that the SASE FEL can produce pulse energies up to 1 mJ with a spectrum bandwidth of 2-3 % at a wavelength of 100 μm .

Based on the above idea, PITZ has been considered as an ideal machine for the development of such a THz source. Proof-of-principle experiments to generate THz SASE FEL radiation by using an LCLS-I undulator driven by an electron bunch from the PITZ accelerator has been planned and studied. Preliminary Start-to-End (S2E) simulations based on a model beamline were performed [3, 4], yielding a THz pulse energy of about 0.5 mJ at a wavelength of 100 μm .

In order to demonstrate such SASE FEL generation experimentally, installation of the LCLS-I undulator downstream from the current PITZ accelerator has been planned. Figure 1 shows a schematic layout of the PITZ facility. There are two tunnels, the main tunnel and the tunnel annex, separated by a concrete wall with a thickness of 1.5 m. The undulator

is foreseen to be installed in the tunnel annex. Therefore, an extension of the existing beamline to connect with the undulator is required.

This paper describes a proposed configuration of the beamline extension and radiation shielding improvement for the tunnel annex. Note that the configuration has not been fully optimized. Studies towards a final design and construction are ongoing.

TUNNEL EXTENSION AND RADIATION SHIELDING IMPROVEMENT

We plan to transport the electron beam from the main tunnel through an aperture inside the wall to the undulator in the tunnel annex, as shown in Fig. 1. Since the electron beam will be blocked by a beam dump in the tunnel annex, the radiation shielding of this tunnel has to be improved.

The FLUKA simulation package [5] was used to calculate produced radiation dose rates and design appropriate radiation shielding for the tunnel annex. The design goal was to limit the dose rates outside the accelerator area to less than 3 $\mu\text{Sv/h}$ during beam operations. The radiation protection wall and the movable door made of barite concrete (density of $>3.4 \text{ t/m}^3$) were realized as the appropriate shielding. Construction of the radiation shielding was already finished, as shown in Fig 2.

THE EXTENSION BEAMLINE

The layout of the extension beamline is surrounded by the red dashed box in Fig. 1. Main components of the extended beamline are a chicane bunch compressor, collimators, a switchyard, the LCLS-I undulator, and beam dump sections.

The *chicane bunch compressor* consists of four magnets (D1-D4) with a negative R56 of -0.17 m. Its total length is 3.56 m and it is designed to deflect the electron beam vertically. Design consideration of the chicane is presented in [6].

Vertical and horizontal collimators are used to remove unwanted parts of the beam. Each collimator is a metal sheet with various apertures. The collimator station is located in the main tunnel before the wall. It consists of horizontal and vertical actuators supplied with the collimators. Each collimator can be used individually or simultaneously with the other one.

The *Switchyard* is a dipole magnet located directly after the wall in the tunnel annex. It is used as a horizontal steerer magnet in the current configuration. However, there are possible plans to add other beamlines in the tunnel annex

* prach.boonpornprasert@desy.de

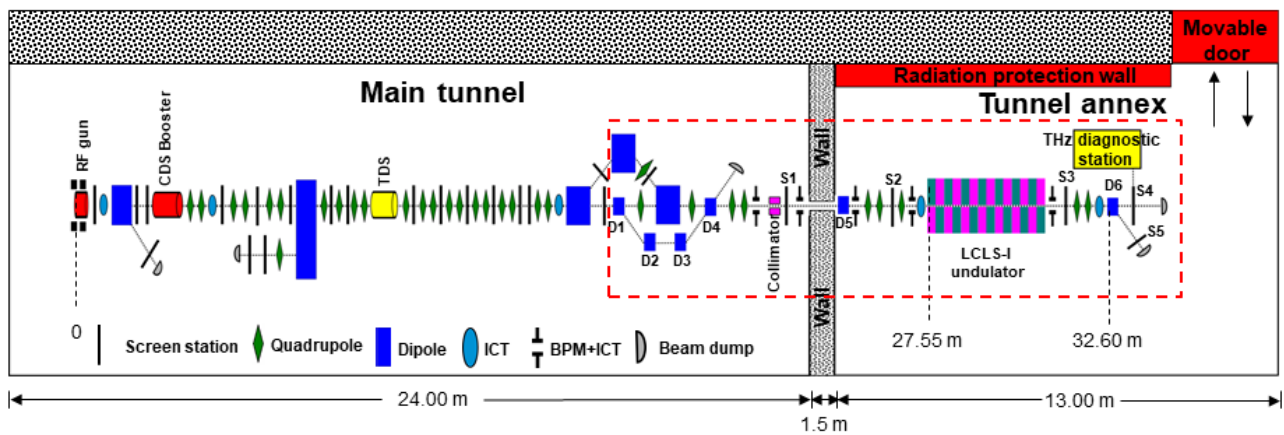


Figure 1: The layout of PITZ beamline including the proposed extension for the THz SASE FEL proof-of-principle experiments (surrounded by a red dashed box).



Figure 2: The radiation protection wall and the movable door in the tunnel annex.

for different experiments, and the switchyard can be used as the first dipole magnet of doglegs.

The LCLS-I undulator is a planar undulator with a fixed gap, so it has a constant K-value of 3.49. The undulator has 112 periods with a period length of 30 mm. More details about the undulator can be found in [7].

Beam dump sections are planned to be installed in three different locations, as shown in Fig. 1. The first beam dump is installed next to D4 in order to dump the beam in the main tunnel. The second beam dump is installed next to the screen S4, and the third beam dump is installed next to the screen S5.

The following is a list of all magnets used in this configuration

- six dipole magnets - four magnets are used for the chicane, one magnet is used for the switchyard, and one magnet is used for the beam dump section in the tunnel annex.
- nine quadrupole magnets.
- At least five steerer magnets - Type and install location of each steerer magnet are under consideration.
- the LCLS-I undulator.

FEL PERFORMANCE

S2E simulations based on the configuration in Fig. 1 are presented in [8]. Electron beams were optimized and transported to the undulator entrance by using the ASTRA code [9]. Then, the optimized beams were used as inputs for Genesis 1.3 [10] for the calculation of THz SASE radiations. Table 1 shows parameters of the optimized beam at the undulator entrance, and the output FEL radiation when a long flattop photocathode laser (FWHM~21.5 ps) was used in the ASTRA code.

Table 1: Parameters of the Optimized Beam at the Undulator Entrance and the Simulated FEL Radiation

Parameter	Value	Unit
<i>Simulated electron beam:</i>		
Bunch charge	4.0	nC
Momentum	17.0	MeV/c
Energy spread	0.4%	
Peak current	180.6	A
Beam emittance	4.3/4.9	mm mrad
<i>Simulated FEL radiation:</i>		
Pulse energy	493.1±108.8	μJ
Pulse power	52.7±11.8	MW
Center wavelength	101.8±0.7	μm
Spectrum width	2.0±0.4	μm

ELECTRON BEAM DIAGNOSTICS

Screen stations with YAG screens are used for transverse beam position and transverse size measurements. We plan to install five screen stations in the extension beamline including:

- S1 is used for observation of the beam after the collimator.
- S2 is used for observation of the beam before the undulator.

- S3 is used for observation of the beam after the undulator and is equipped with a THz mirror to deflect the THz radiation to the THz diagnostic station. Since the electron beam impinges on the THz mirror, transition radiation is generated. Therefore, the radiation that transport to the THz diagnostic station is a mixture between the radiation from the undulator and the transition radiation.
- S4 has a similar purpose to S3. It is used for observation of the beam and is also equipped with a THz mirror to deflect the THz radiation to the THz diagnostic station. Since the electron beam is already deflected away by D6 and therefore no transition radiation generated from the THz mirror.
- S5 is used for observation of the beam before the beam dump.

Beam Position Monitors (BPMs) are used for beam transverse position measurements. They can be used to measure and correct the beam trajectories. At least five BPMs are planned to be installed in the extension beamline.

Integrating current transformers (ICTs) used for charge measurements are planned to be installed at two locations, before the undulator, and before D6.

THz RADIATION DIAGNOSTICS

The THz radiation diagnostics system will be setup on a trolley. Therefore, it is convenient to move and use at both screen stations, S3 and S4. There are two THz radiation detectors foreseen to be used in the diagnostic system, a pyroelectric detector used for measurements of the radiation pulse energy and a THz camera used for measurements of the transverse distribution.

With different optical configurations, this diagnostics system can be used to measure various properties of the THz radiation including total pulse energy, polarization, transverse distribution, and spectral distribution.

CONCLUSIONS

Extension of the PITZ beamline into the tunnel annex for the THz SASE FEL proof-of-principle experiment is under study. Radiation shielding of the tunnel annex was improved by adding a radiation protection wall and a movable door. A preliminary layout of the extended PITZ beamline is proposed and described. S2E simulations of SASE FEL using this layout were performed and reported in [8]. Further research on the design configuration of the beamline and construction plan is ongoing.

ACKNOWLEDGEMENTS

The authors would like to thank colleagues at PITZ for many useful comments and discussions.

REFERENCES

- [1] P. Zalden *et al.*, "Terahertz Science at European XFEL", European XFEL, Schenefeld, Germany, Rep. XFEL.EU TN-2018-001-01.0, 2018.
- [2] E. Schneidmiller, M. Yurkov, M. Krasilnikov, and F. Stephan, "Tunable IR/THz source for pump probe experiment at European XFEL", in *Proc. 34th Int. Free-Electron Laser Conf.(FEL'12)*, Nara, Japan, Aug. 2012, paper WEPD55, pp. 503-506.
- [3] M.Krasilnikov *et al.*, "Start-to-End Simulations of THz SASE FEL Proof-of-Principle Experiment at PITZ", in *Proc. 13th Int. Computational Accelerator Physics Conf. (ICAP'18)*, Key West, FL, USA, Oct. 2018, paper TUPAF23, pp. 246-252. doi:10.18429/JACoW-ICAP2018-TUPAF23
- [4] X.K. Li *et al.*, "Design Studies of a Proof-of-Principle Experiment on SASE FEL at PITZ", in *Proc. 10th Int. Particle Accelerator Conf. (IPAC'19)*, Melbourne, Australia, May 2019, paper TUPRB018, pp. 1713-1716. doi:10.18429/JACoW-IPAC2019-TUPRB018
- [5] T.T. Böhlen *et al.*, "The FLUKA Code: Developments and Challenges for High Energy and Medical Applications", *Nuclear Data Sheets*, vol. 120, pp. 211-214, 2014.
- [6] H. Shaker *et al.*, "Design of a Magnetic Bunch Compressor for the THz SASE FEL Proof-of-Principle Experiment at PITZ", presented at the 39th Int. Free-Electron Laser Conf. (FEL'19), Hamburg, Germany, Aug. 2019, paper TUP003, this conference.
- [7] J. Arthur *et al.*, "Linac Coherent Light Source (LCLS) Conceptual Design Report", SLAC, Menlo Park, CA, USA, Rep. SLAC-R-593, 2002.
- [8] X.K. Li *et al.*, "Progress in Preparing a Proof-of-Principle Experiment for THz SASE FEL at PITZ", presented at the 39th Int. Free-Electron Laser Conf. (FEL'19), Hamburg, Germany, Aug. 2019, paper TUP002, this conference.
- [9] K. Flöttmann, ASTRA particle tracking code, <http://www.desy.de/~mpyf10>
- [10] S. Reiche, GENESIS 1.3 code, <http://genesis.web.psi.ch>

PROGRESS IN PREPARING A PROOF-OF-PRINCIPLE EXPERIMENT FOR THz SASE FEL AT PITZ*

X.-K. Li[†], M. Krasilnikov, P. Boonpornprasert, H. Shaker, Y. Chen, G. Georgiev, J. Good, M. Gross, P. Huang, I. Isaev, C. Koschitzki, S. Lal, O. Lishilin, G. Loisch, D. Melkumyan, R. Niemczyk, A. Oppelt, H. Qian, G. Shu, F. Stephan, G. Vashchenko, DESY, Zeuthen, Germany

Abstract

A proof-of-principle experiment for a THz SASE FEL is undergoing preparation at the Photo Injector Test facility at DESY in Zeuthen (PITZ), as a prototype THz source for pump-probe experiments at the European XFEL, which could potentially provide up to mJ/pulse THz radiation while maintaining the identical pulse train structure as the XFEL pulses. In the proof-of-principle experiment, LCLS-I undulators will be installed to generate SASE radiation in the THz range of 3-5 THz from electron bunches of 16-22 MeV/c. One key design is to obtain the peak current of nearly 200 A from the heavily charged bunches of a few nC. In this paper, we report our simulation results on the optimization of the space charge dominated beam in the photo injector and the following transport line with two cathode laser setups. Experimental results based on a short Gaussian laser will also be discussed.

INTRODUCTION

At the European X-ray free-electron laser facility (EuXFEL) pump-probe experiments play important roles in many research frontiers in biology, chemistry and condensed matters, etc. Among them are the THz-pump X-ray-probe experiments, where a THz pulse is used to excite a sample and the following X-ray pulse is used to detect its reactions [1]. In order to provide the THz pump source, several proposals are under consideration. In one proposal the high-energy electron beam will be re-used to drive a THz undulator [2], as already demonstrated at FLASH [3]. Another idea is to put an independent PITZ-like photo-injector near the user hall to drive a THz undulator [4], which is currently undergoing a proof-of-principle experiment at PITZ. The expected advantages include: 1) Due to the low beam energy, the accelerator needs no big beam dump and can be installed close to user experiments so that no long THz beamline has to be built; 2) The PITZ-like accelerator with identical bunch train structure as the XFEL pulses could support all the EuXFEL end stations with THz pulses, provided that a switchyard for the THz pulses is built. Previous studies [4–7] have showed that milli-joule level THz pulses could be generated from 4 nC electron bunches with 200 A peak current in Apple-II or similar undulators through the SASE process. For the proof-of-principle experiment, the existing PITZ beamline is to be extended with LCLS-I undulators installed in the tunnel annex. In this paper, we will report the current status of this project, including start-to-end simulation studies

based on a regularly operating Gaussian cathode laser and on a longitudinally shaped flattop laser. It will be shown that similar peak current can be achieved from both laser setups and the resulting radiation energies are close to 1 mJ. For Gaussian laser pulses, experiments have been carried out to demonstrate the production of a few nC bunch charge and the possibility of matching the heavily charged bunch to the undulator.

START-TO-END SIMULATIONS

The photo-injector at PITZ consists of an L-band photocathode RF gun, solenoids for emittance compensation, an L-band booster cavity and many correction and focusing magnets, with a total beamline length of 22 m [8]. In the start-to-end simulations, we first optimize the photo-injector and then design the transport line until the proposed undulator entrance. The radiation from the optimized beams is finally evaluated with Genesis 1.3 [9]. At PITZ, two cathode laser setups are available: a short Gaussian laser (FWHM=6~7 ps) which is in stable operation and a long flattop laser (FWHM~22 ps) which can be realized by longitudinal pulse shaping with bi-diffracting crystals before the laser is amplified [8]. Although both lasers are Gaussian transversely, it is also possible to produce approximately uniform transverse distributions by overfilling a tunable beam shaping aperture (BSA). For the THz project, both lasers are under consideration. For the Gaussian laser, relatively small bunch charge of 2.5 nC is employed to avoid emission saturation, as shown later. In the presence of the long flattop laser, the bunch charge of 4 nC is taken.

Optimization of the Injector

In the optimization we took the highest achievable gun gradient of 60 MV/m into account to reduce the space charge effects during emission. With this gradient, the highest beam momentum downstream the booster is about 22 MeV/c, which corresponds to a radiation wavelength of 60 μm in the LCLS-I undulator. In this paper, we consider a nominal wavelength of 100 μm (3 THz in frequency) with a beam momentum of 17 MeV/c.

Since the beam emittance is not critical for FELs in the THz range, the optimization is focused on the peak current and the energy spread [5], as a higher peak current helps to improve the FEL gain and a smaller energy spread simplifies beam transport and also leads to higher FEL gain. With the particle tracking code Astra [10], the laser spot size, the accelerating phases in the gun and in the booster and the solenoid current were searched by the differential-evolution

* Work supported by the European XFEL GmbH

[†] xiangkun.li@desy.de

(DE) algorithm [11] in a manner that the beam energy spread was minimized at the undulator center while the beam emittance was relatively small (~ 4 mm mrad). The simulations stopped at $z = 20$ m. From the optimization results, the peak current at $z = 20$ m has been analyzed against the input parameters. It is found that the peak current (I_{peak}) strongly depends on the laser spot size (BSA), as shown in Fig. 1. For both laser setups, the peak current increases with the spot size. Smaller BSA means higher charge density and stronger space charge forces, which lengthens the beam when the beam energy is still small before entering the booster cavity, as shown later in Fig. 3. Meanwhile, higher peak currents can be obtained from the flattop laser since more charge is involved.

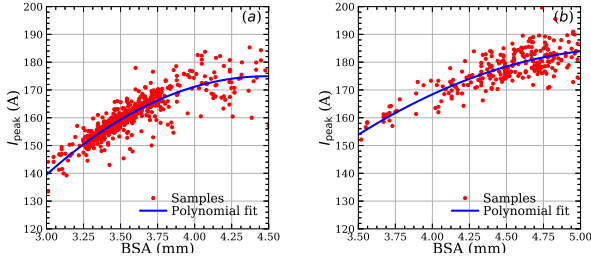


Figure 1: Dependence of peak current on laser spot size (BSA) for (a) the Gaussian and (b) the flattop laser.

Another important input parameter is the booster phase (ϕ_{booster}), which is related to the correlated energy spread ($\sigma_E^{\text{corr}} = \langle E_k z \rangle / \sigma_z$) in Fig. 2. By accelerating the beam off-crest, the longitudinal phase space is chirped so that the tail has higher kinetic energy than the head has at the booster exit ($\sigma_E^{\text{corr}} < 0$). In the following drift the beam energy spread reduces gradually due to the space charge forces. The difference in initial bunch profile and charge resulted in different optimal booster phases for the two lasers, that is, around -30 degrees for the Gaussian laser and is around -20 degrees for the flattop laser.

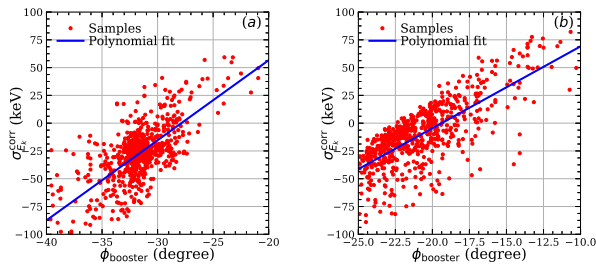


Figure 2: Dependence of correlated energy spread on the booster phase for (a) the Gaussian and (b) the flattop laser.

Beam Transport and Matching

From the above optimization results, two cases with relatively high peak current (~ 170 A) have been selected for further transport to the undulator. The drift length between the booster and the undulator is more than 20 m. Besides, the LCLS-I undulator has a strong magnetic field (1.28 T)

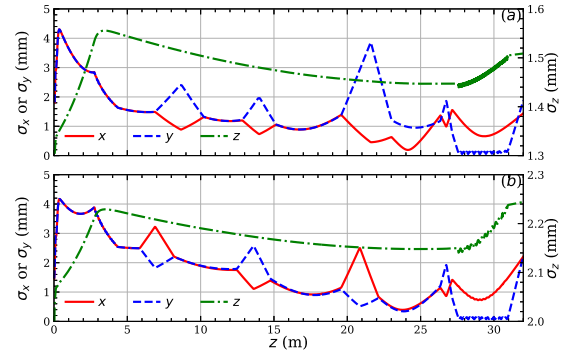


Figure 3: Beam transport for (a) the Gaussian and (b) the flattop laser.

and very small vacuum chamber (5×11 mm), which strictly defines the transverse phase spaces of the beam at the undulator entrance [7]. Considering these facts, two quadrupole magnet triplets have been chosen from the PITZ beamline to deliver the beam to the undulator and another two to match the beam into it. Fig. 3 shows the evolutions of the optimized RMS beam size for both laser setups, where the location of triplets can be found by changes in the beam size. The optimized longitudinal profiles at the undulator entrance are shown in Fig. 4 together with the slice emittance. The peak current is around 175-180 A for both setups. Note that the peak current has increased during the transport for the beam being compressed by ballistic bunching. Since the Gaussian laser is shorter, the resulting current profile is narrower. Other beam parameters at the undulator entrance are compared in Table 1.

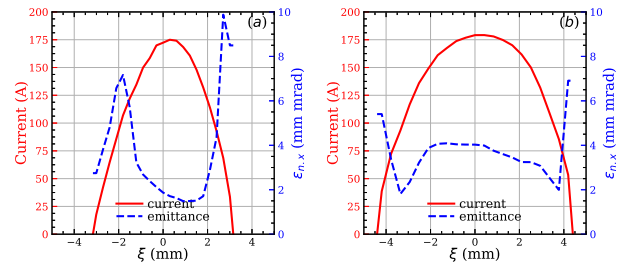


Figure 4: Current profile and slice emittance of the optimized beam at the undulator entrance for (a) the Gaussian and (b) the flattop laser.

Table 1: Simulated Beam Parameters at Undulator Entrance

Parameter	Gaussian	Flattop	Unit
Laser FWHM	6	22	ps
Laser spot diameter	4.0	4.5	mm
Bunch charge	2.5	4.0	nC
Momentum	17	17	MeV/c
Energy spread	0.2	0.4	%
Peak current	175	179	A
Beam emittance	4.1/3.9	4.3/4.9	mm mrad

THz Radiation Generation

The optimized beams were then treated as inputs for Genesis 1.3 [9] for the calculation of THz SASE radiation. The undulator has 113 periods with a period of 30 mm and a peak magnetic field of 1.28 T. For statistics, 100 runs were performed with various initial seeds for shot noise. The pulse energies (E) along the undulator are given in Fig. 5, where the gray lines are individual simulations and the black ones are the averaged results. The spectra (λ_s) of the pulses are shown in Fig. 6. The main properties of the THz pulses from both setups are compared in Table 2. As expected, higher THz pulse energies are obtained from the flattop laser setup because it has more charge.

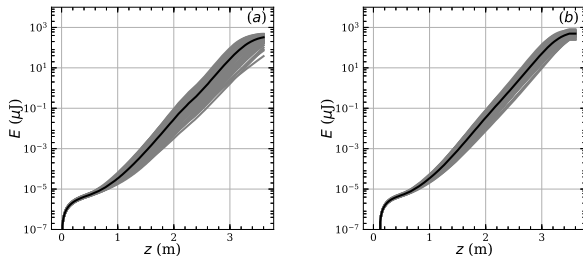


Figure 5: THz pulse energy along the undulator for (a) the Gaussian and (b) the flattop laser.

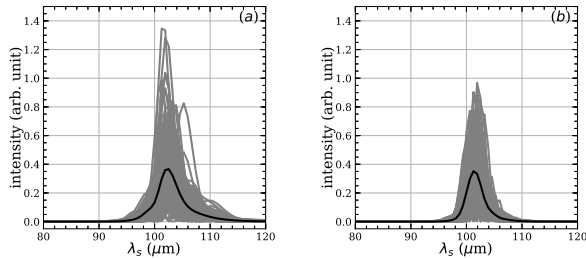


Figure 6: THz pulse spectra for (a) the Gaussian and (b) the flattop laser.

Table 2: Simulated THz SASE Radiation Parameters

Parameter	Gaussian	Flattop	Unit
Pulse energy	323±99	493±109	μJ
Pulse power	97±30	53±12	MW
RMS arrival time jitter	3.3	1.5	ps
Center wavelength	103±1.1	102±0.7	μm
RMS spectrum width	3.6±1.0	2.0±0.4	μm

EXPERIMENTAL STUDIES

As the preparation of the extension beamline is in progress, experimental studies have been performed in the existing beamline, focused on the production, characterization and matching of an electron bunch of a few nC. Since the Gaussian laser was in operation for other parallel activities at PITZ, it was used. To generate high bunch charge, the laser

energy has been scanned with BSA diameter varying from 3.0 to 4.5 mm. The emission curves are given in Fig. 7 (a). For these large BSAs, more than 4 nC has been measured. However, only 2.5 nC with a BSA size of 4.0 mm was considered in the following experiments in order to avoid strong saturated emission (deviation of the extracted bunch charge from linear fit).

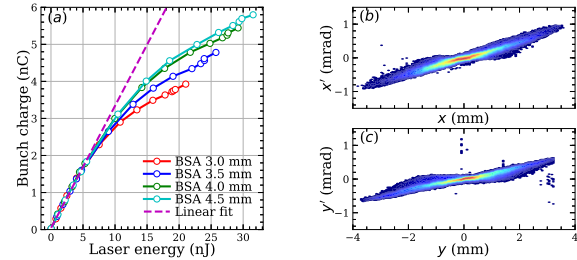


Figure 7: (a) Emission curves and transverse phase spaces in (b) horizontal plane and (c) vertical plane.

The solenoid current was scanned for minimizing the transverse beam emittance measured by the slit-scan method [8]. The phase spaces for the lowest emittance are shown in Fig. 7 (b) and (c), giving 4.0 and 3.8 mm mrad in horizontal and vertical planes, respectively. The emittance is comparable with the optimization (~ 4 mm mrad).

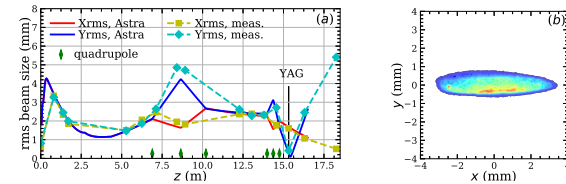


Figure 8: (a) Transport and matching of the electron beam from simulation and measurement and (b) transverse distribution at the matching screen (YAG in (a)).

To safely transport the beam through the undulator vacuum chamber, a flat electron beam which focuses both horizontally and vertically is needed. The matching has been demonstrated in the existing beamline with two quadrupole triplets, as shown in Fig. 8. Next, the flattop laser will be involved for investigating the possibilities of producing, transporting and matching even more charge to the undulator.

CONCLUSION

An accelerator based THz SASE FEL is currently under construction at PITZ as a proof-of-principle experiment for pump-probe experiments at European XFEL. In this paper, the start-to-end simulations were presented, with two different laser setups being considered and compared, both yielding a THz pulse energy close to 1 mJ. Experimentally, we have verified the capability of producing a few nC bunch charge from the photocathode RF gun with the Gaussian laser. The beam quality was comparable to simulation results and the beam matching was demonstrated in the existing beamline. Next, experiments will be carried out with more bunch charge from a long flattop laser.

REFERENCES

- [1] P. Zalden *et al.*, “Terahertz Science at European XFEL”, XFEL.EU TN-2018-001-01.0, 2018.
- [2] T. Tanikawa *et al.*, “Superradiant Undulator Radiation for Selective THz Control Experiments at XFELs”, arXiv preprint arXiv:1803.05323, 2018.
- [3] K. Tiedtke *et al.*, “The soft x-ray free-electron laser FLASH at DESY: beamlines, diagnostics and end-stations”, *New journal of physics* 11.2, 2009, 023029. doi:10.1088/1367-2630/11/2/023029
- [4] M. Krasilnikov, F. Stephan, E. Schneidmiller, and M. V. Yurkov, “Tunable IR/THz Source for Pump Probe Experiments at the European XFEL”, in *Proc. FEL'12*, Nara, Japan, Aug. 2012, paper WEPD55, pp. 503–506.
- [5] P. Boonpornprasert *et al.*, “Start-to-End Simulations for IR/THz Undulator Radiation at PITZ”, in *Proc. FEL'14*, Basel, Switzerland, Aug. 2014, paper MOP055, pp. 153–158.
- [6] P. Boonpornprasert, M. Krasilnikov, and F. Stephan, “Calculations for a THz SASE FEL Based on the Measured Electron Beam Parameters at PITZ”, in *Proc. FEL'17*, Santa Fe, NM, USA, Aug. 2017, pp. 419–421. doi:10.18429/JACoW-FEL2017-WEP004
- [7] M. Krasilnikov, P. Boonpornprasert, H.-D. Nuhn, E. Schneidmiller, F. Stephan, and M. V. Yurkov, “Start-to-End Simulations of THz SASE FEL Proof-of-Principle Experiment at PITZ”, in *Proc. ICAP'18*, Key West, Florida, USA, Oct. 2018, pp. 246–252. doi:10.18429/JACoW-ICAP2018-TUPAF23
- [8] M. Krasilnikov *et al.*, “Experimentally minimized beam emittance from an L-band photoinjector”, *Phys. Rev. ST Accel. Beams* 15, Oct. 2012, 100701. doi.org/10.1103/PhysRevSTAB.15.100701
- [9] S. Reiche, GENESIS 1.3 code, <http://genesis.web.psi.ch/>.
- [10] K. Flottmann, ASTRA particle tracking code, <http://www.desy.de/~mpyf10/>.
- [11] R. Storn and K. Price, “Differential evolution - a simple and efficient heuristic for global optimization over continuous spaces”, *Journal of global optimization* 11, 1997, 341–359.

DESIGN OF A MAGNETIC BUNCH COMPRESSOR FOR THE THz SASE FEL PROOF-OF-PRINCIPLE EXPERIMENT AT PITZ*

H. Shaker[†], P. Boonpornprasert, G. Georgiev, G. Koss, M. Krasilnikov, X. Li, A. Lueangaramwong, F. Mueller, A. Oppelt, S. Philipp, F. Stephan, G. Vashchenko, T. Weilbach
DESY, Zeuthen, Germany

Abstract

For pump-probe experiments at the European XFEL, a THz source is required to produce intense THz pulses at the same repetition rate as the X-ray pulses from XFEL. Therefore, an accelerator-based THz source with identical electron source as European XFEL was suggested [1] and proof-of-principle experiments utilizing an LCLS I undulator will be performed at the Photo Injector Test Facility at DESY in Zeuthen (PITZ). The main idea is to use a 4nC beam for maximizing the SASE radiation but also to allow different radiation regimes, a magnetic bunch compressor can be used. This helps e.g. to reduce the saturation length inside the undulator and also to study super-radiant THz radiation. In this paper a design of a chicane type magnetic bunch compressor re-using HERA corrector magnets is presented.

INTRODUCTION

To demonstrate an accelerator-based tunable THz source for pump-and-probe experiments at the European XFEL, a proof of principle study is started at the Photo-Injector Test Facility at DESY in Zeuthen site (PITZ) [1-8]. This experiment will be done by using the electron beam produced at PITZ and by using LCLS-I undulators inside the existing accelerator tunnel extension. Since PITZ and European XFEL electron sources are identical, the X-ray and THz radiation can be produced with identical bunch train structure. This means for every X-ray pulse a corresponding THz pulse can be provided for the pump-and-probe experiments.

With nominal 4 nC bunch charge, 200 A peak current and 16-25 MeV, this experiment wants to demonstrate a near one milli-joule pulse energy radiation in the frequency range of 3-15 THz based on the SASE mechanism. To have flexibility to work with lower charges and shorter initial bunches a magnetic bunch compressor is required. By beam compressing, we will have shorter bunch length with higher peak current. This effect reduces the saturation length inside the undulator and also opens the door for coherent or super-radiant radiation studies [9]. In this paper, a design for a chicane-type magnetic bunch compressor will be presented. This bunch compressor will be installed in the main PITZ tunnel and since PITZ is a multi-purpose machine minimum beamline modification is desirable. To take advantages of available components, we will re-use corrector magnets from earlier HERA machine at DESY to assemble the bunch compressor. Figure 1 shows the end-

section of the PITZ beamline in the main tunnel. In this figure, you can see the vertical chicane and the rotated beam dump which will be added to the current beamline. We considered both the desired bunch compressing magnitude and available spaces in the beamline to find an optimum design.

R_{56} is a main parameter of the bunch compressor and can be expressed in the first order by $R_{56} = \Delta z / \delta$, where Δz is the difference between output and input bunch lengths and δ is the relative energy spread. Inside a chicane type bunch compressor without any quadrupoles the higher energy particles travels less distance then it has negative R_{56} . This means we need a positive energy chirp for bunch compressing. The positive energy chirp can be produced by changing the booster phase. The acceptable maximum relative energy spread can be calculated based on 1-D FEL theory. Based on this theory the relative energy spread should be less than the Pirece parameter (ρ) [10]:

$$(1) \quad \left\{ \begin{array}{l} \rho = \left[\frac{I}{\gamma^3 I_A} \frac{\lambda_u^2}{2\pi\sigma_x\sigma_y} \frac{(K \times [JJ])^2}{32\pi} \right]^{1/3} \\ [JJ] = J_0(\xi) - J_1(\xi), \xi = \frac{K^2}{2(2+K^2)} \\ I_A \approx 17kA \end{array} \right.$$

For the LCLS-I undulator, the undulator K parameter is 3.49 and its periodic length (λ_u) is 3 cm. For the rms beam size (σ_x and σ_y) of about 1 mm and peak current (I) of 200 A, the Pierece parameter is equal to 0.015 and 0.01 for the beam energy of 16 MeV and 25 MeV, respectively. To cover the full energy range, the maximum 1% energy chirp is selected for our design. Using equation (1), R_{56} would be about -0.18m for maximum 6ps compression from the bunch center for each side. This means for a relative short bunch we can compress a bunch to sub-picosecond level. R_{56} is only dependent to the first drift length (L_1), dipole length (L_d) and the deflecting angle (θ) and it can be calculated roughly using this equation [11]:

$$(2) \quad R_{56} \approx -\theta^2 (2 \times L_1 + 4/3 \times L_d)$$

To install the bunch compressor, there are two free spaces available at the end of PITZ beamline, one between 1st and 3rd dipole in Second High Energy Dispersive Arm (HEDA2) and another one between the 3rd HEDA2's dipole and the tunnel wall. But both spaces are not enough alone to fit the bunch compressor. Therefore we decided to use a vertical setup which helps us to use both spaces without any need to remove the HEDA2 dipoles. Based on this setup, the minimum acceptable angle for the chicane is 16.77° to not hit the 3rd dipole of HEDA2.

* Work supported by the European XFEL

[†] hamed.shaker@desy.de

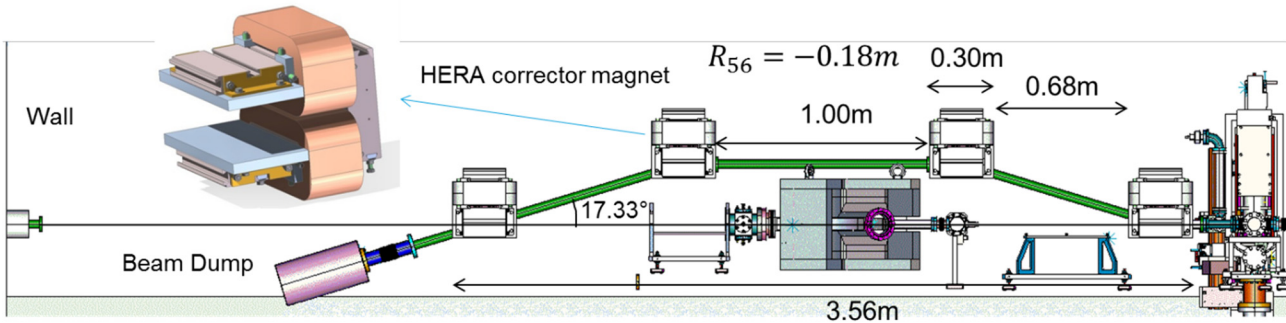


Figure 1: End-section of PITZ beamline in the main tunnel including the vertical chicane and the rotated beam dump.

CHICANE CONFIGURATION

As mentioned previously, the available HERA corrector magnets will be used to build this bunch compressor. They are rectangular dipoles with a pole length of 30cm, a gap of 5cm and maximum magnetic field of 0.155T. Figure 2 and Table 1 show the layout and parameters of the HERA corrector magnet, respectively. As you can see in Figure 1 and by considering the dipole pole lengths, the maximum available projected drift between two first dipoles is 0.68m. To find the chicane angle for our desired $R_{56}=-0.18\text{m}$, which was calculated in the last section, we used the MADX code [12]. We found $\theta=17.33^\circ$ which is larger than our threshold (16.77°).

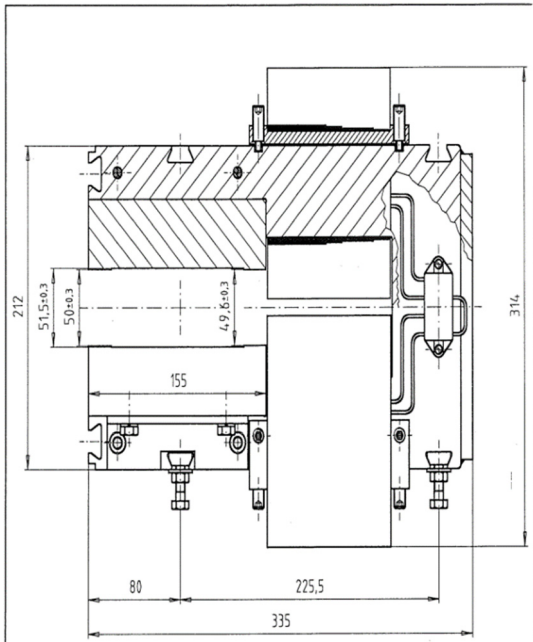


Figure 2: Layout of a HERA corrector magnet (CH Type).

Table 1: HERA Corrector Magnet Specifications

Parameter	Specification
Pole Shape	Rectangular
Pole length	300 mm
Pole Gap	50±0.3 mm
Maximum field at 2.4A	0.155 T

BUNCH COMPRESSION

For low charges, we used the CSRtrack code [13] to study the bunch compression of our designed chicane.

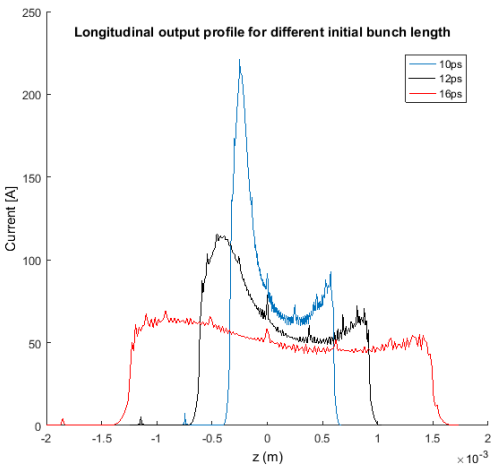


Figure 3: Simulated bunch compression for different initial bunch length using the CSRtrack code. The tail is on the left side.

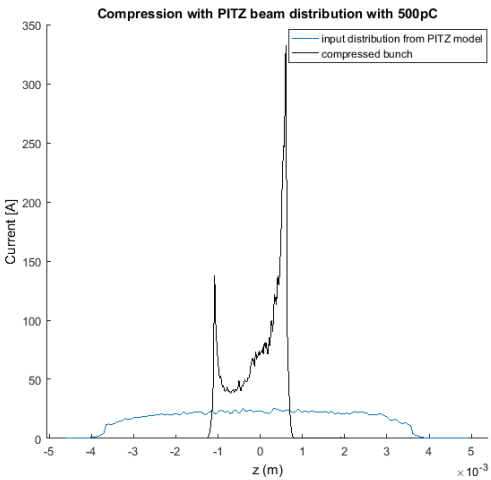


Figure 4: Simulated bunch compression of the PITZ beam distribution with 500 pC bunch charge and 17 MeV mean energy using CSRtrack code. The tail is on the left side.

Firstly, as input for the chicane, different simple particle distributions with a flat-top longitudinal profile, 30A peak current, 20.5MeV energy and various bunch lengths were constructed. Figure 3 shows the chicane's output distributions. For relative long bunches the compression is more uniform but when we use shorter bunches, we see a peak at the tail of the bunch. For the 10ps case this peak is shorter than 0.8ps. As a second step, a PITZ beam distribution produced by ASTRA [14] was used as the input. The initial bunch length was about 24ps and the total charge was 500pC. The peak current was about 22A and the energy was 17MeV. Figure 4 shows the input and output profiles. The bunch was compressed with two peaks in both ends and each peak has about 0.3ps FWHM which makes it ideal for super-radiant radiation study. In general word, a peak at the tail has an interesting effect. It can stimulate the seeding for the rest of the bunch. We haven't considered the effect of dipole fringe fields but since our compression factor is usually below 10, dipole's fringe field effects can be ignored.

OTHER CONSIDERATIONS

One screen station will be installed in the second drift of the bunch compressor for beam diagnostic, energy collimation and transverse modulation for seeding [15]. We also want to install a THz CTR radiation detector station after the chicane to measure the bunch length. Another station is also considered to be installed after the third dipole to measure synchrotron radiation which can be used to measure the bunch length. The maximum transverse beam size is 6 mm (~ 2 mm rms) which means both 36 mm and 63 mm standard size vacuum beam-pipe can be used for the beam transportation inside the chicane.

CONCLUSION

A bunch compressor is a very useful tool to generate and study different kind of THz radiation. Further study with higher bunch charges in the nC range is needed in order to see if it is possible to compress such high bunch charges without big beam distortion.

REFERENCES

- [1] E.A. Schneidmiller, M.V. Yurkov, M. Krasilnikov, F. Stephan, "Tunable IR/THz Source for Pump Probe Experiments at the European XFEL," in *Proc. FEL'12*, Nara, Japan, Aug. 2012, paper WEPD55.
- [2] P. Boonpornprasert *et al.*, "Extension of the PITZ Facility for a Proof-of-Principle Experiment on THz SASE FEL", presented at the 39th Int. Free Electron Laser Conf. (FEL'19), Hamburg, Germany, Aug. 2019, paper TUP001.
- [3] X. Li *et al.*, "Progress in Preparing a Proof-of-Principle Experiment for THz SASE FEL at PITZ", presented at the FEL'19, Hamburg, Germany, Aug. 2019, paper TUP002.
- [4] X. Li *et al.*, "Design Studies of a Proof-of-Principle Experiment on THz SASE FEL at PITZ", in *Proc. IPAC'19*, Melbourne, Australia, May 2019, pp. 1713-1716.
doi:10.18429/JACoW-IPAC2019-TUPRB018
- [5] P. Boonpornprasert *et al.*, "Experimental Optimization and Characterization of Electron Beams for Generating IR/THz SASE FEL Radiation with PITZ", in *Proc. IPAC'17*, Copenhagen, Denmark, May 2017, pp. 2650-2653.
doi:10.18429/JACoW-IPAC2017-WEPAB033
- [6] P. Boonpornprasert *et al.*, "Calculations for a THz SASE FEL Based on the Measured Electron Beam Parameters at PITZ", FEL17, NM, US, Aug. 2017.
doi:10.18429/JACoW-FEL2017-WEP004
- [7] P. Boonpornprasert, M. Krasilnikov, F. Stephan, and B. Marchetti, "Numerical Simulations of a Sub-THz Coherent Transition Radiation Source at PITZ", in *Proc. FEL'15*, Daejeon, Korea, Aug. 2015, paper MOP033, pp. 97-100.
- [8] P. Boonpornprasert *et al.*, "Start-to-End Simulations for IR/THz Undulator Radiation at PITZ", in *Proc. FEL'14*, Basel, Switzerland, Aug. 2014, paper MOP055, pp. 153-158.
- [9] N. Stojanovic *et al.*, "Accelerator- and laser-based sources of high-field terahertz pulses", *Journal of Physics B: Atomic, Molecular and Optical Physics*, Volume 46, Number 19, September 2013.
- [10] M. Venturini, "Basics on FEL physics; undulators; high-level machine-design parameters", USPAS, Rutgers University, June 2015.
- [11] D. Nguyen *et al.*, "RF Linac for High-Gain FEL Bunch Compression", USPAS, Los Alamos National Laboratory, June 2014.
- [12] MAD-Methodical Accelerator Design,
<http://madx.web.cern.ch/madx/>.
- [13] M. Dohlus, CSRtrack code,
<http://www.desy.de/xfel-beam/csrtrack/>.
- [14] K. Floettmann. ASTRA code,
<https://www.desy.de/~mpyflo/>.
- [15] X. Zhu *et al.*, "Theoretical and numerical analyses of a slit-masked chicane for modulated bunch generation", *Journal of Instrumentation*, vol. 10, Oct. 2015.

A SUPERRADIANT THz UNDULATOR SOURCE FOR XFELS

T. Tanikawa*, S. Karabekyan, S. Serkez, G. Geloni, European XFEL, Schenefeld, Germany
S. Kovalev, Helmholtz-Zentrum Dresden-Rossendorf (HZDR), Dresden, Germany
S. Casalbuoni, Karlsruhe Institute of Technology, Karlsruhe, Germany

V. B. Asgekar, S.P. Pune University, Pune, India

M. Gensch¹, Technische Universität Berlin, Berlin, Germany

¹also at German Aerospace Center (DRL), Berlin, Germany

Abstract

The European XFEL has successfully achieved first lasing in 2017 and meanwhile three SASE FEL beamlines are in operation. An increasing number of users has great interest in a specific type of two-color pump-probe experiments in which high-field THz pulses are employed to drive nonlinear processes and dynamics in matter selectively. Here, we propose to use a 10-period superconducting THz undulator to provide intense, narrowband light pulses tunable in wide range between 3 and 100 THz. The exploitation of superconducting technology allows us to meet the challenge of generating such low photon energy radiation despite the very high electron beam energy at the European XFEL. In this paper, we will present the latest developments concerning THz undulator design and the expected THz pulse properties for the case of the European XFEL.

CONCEPT AND MOTIVATIONS

X-ray Free-Electron Lasers are currently the extremely bright and tunable sources of ultrashort X-ray pulses available for basic scientific research. Among many possible uses, the ultrahigh brightness and the ultrashort duration of these pulses can be exploited in a “pump-probe” configuration, to probe non-equilibrium states of a matter sample that can be excited by previous interaction with terahertz radiation. Since the latest generation XFELs under early operation stages or construction, such as the European XFEL [1] and the LCLS-II [2] are based on superconducting technology, THz pulses are also required in CW or burst mode with repetition rates of between 100 kHz and 4.5 MHz. The generation of high-field THz pulses at such high duty-cycle by means of femtosecond lasers does not allow achieving the required parameters in terms of pulse energy and narrow-bandwidth; therefore, a superradiant THz undulator emerges as one promising solution. In this paper, we describe the technological feasibility for implementing a few-period superradiant THz undulator that fits the particular case of the electron linac of the European XFEL.

THz UNDULATOR PARAMETERS

The main challenge in the construction of a THz undulator for the production of superradiant THz pulses at the European XFEL is the very high-energy of the electron beam, nominally in the range from 8.5 to 17.5 GeV. In fact, the

resonance condition on-axis for the first harmonic reads:

$$\lambda = \lambda_U \frac{1 + K^2/2}{2\gamma^2}, \quad (1)$$

and

$$K = 93.66B[T]\lambda_U[m] \quad (2)$$

with λ the fundamental wavelength, λ_U the undulator period, γ the Lorentz factor, K the undulator parameter, and B the magnetic field. We will limit our considerations to fundamental frequencies higher than 3 THz, corresponding to about $\lambda = 100 \mu\text{m}$, and assuming an electron beam energy fixed throughout the paper of 17.5 GeV. If we now fix $\lambda_U = 1 \text{ m}$, we find that in order to reach a minimal frequency of about 3 THz a value $K = 685$ is needed, corresponding to a maximum field on axis $B \approx 7.3 \text{ T}$, which is feasible to reach using a well-proven NbTi technology.

The total pulse energy generated by a single electron bunch W_{bunch} while passing through any kind of radiator depends on the bunch length and follows the relation

$$W_{\text{bunch}} = N_e [1 + (N_e - 1)|\bar{F}(\nu)|^2] W_0 \quad (3)$$

where N_e is the number of electrons in the bunch, W_0 the pulse energy emitted by a single electron and $\bar{F}(\nu)$ the bunch form factor. In order to sustain FEL lasing at X-ray wavelengths, very high peak currents must be achieved (in the order of several kilo amperes for the European XFEL), and hence it is needed to strongly compress the electron bunch in the first place. Therefore, it makes sense to exploit the spent XFEL electron beam for generating superradiant THz pulses, because the form factor until high THz frequency is available. The level of compression depends on the charge, with bunches of lower charge being compressed more to obtain the same peak-current level. In Fig. 1, the nominal electron current profiles, calculated using start-to-end simulation for the European XFEL with different charges [3], are reported. In Fig. 2 we show the pulse energy that can be obtained at different fundamental frequencies (by changing the K parameter of the THz undulator) for several nominal electron bunch charges using 10 % bandpass filter with boxcar line function. From Fig. 2 we can see a competition between the N_e^2 dependence of the pulse energy, which favors high charges, and the form factor dependence on the frequency, which favors low charges (at the same peak current, needed to sustain the previous FEL process). As expected, the highest electron charge considered here, 500 pC, yields the best

* takanori.tanikawa@xfel.eu

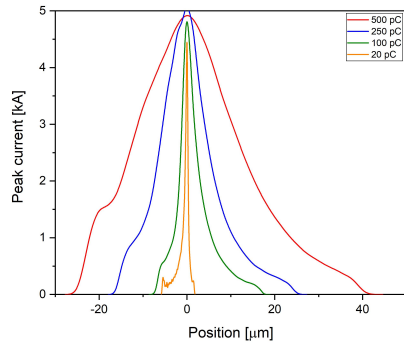


Figure 1: S2E simulated electron current profiles for different charges at the European XFEL.

results, in terms of energy per pulse, in the lowest frequency range, between 3 and 6 THz with expected energies above 100 μJ . A charge of 250 pC appears optimal in the range between 6 and 15 THz, with energies above 30 μJ . Finally, the lower charge of 100 pC is suitable for frequencies starting from 15 THz. Our proposed undulator is expected to obtain energies above 10 μJ up to frequencies of about 30 THz. For frequencies higher than that value, the yield remains around the 10 μJ level up to frequencies of about 50 THz. Finally, note that the yield of the lowest nominal charge of 20 pC always falls below that of the 100 pC. We note that the choice of charges is forcefully linked to the operation mode of the considered XFEL, so that operational restrictions might apply. It should also be remarked that angular filtering can be used, instead of spectral filtering.

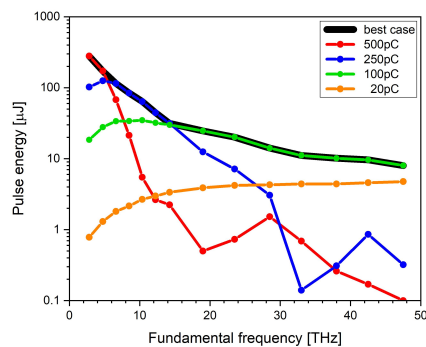


Figure 2: Tunability of the THz undulator fundamental: pulse energy at different fundamental frequencies for several electron bunch charges using a 10 % bandpass filter.

As just mentioned, it is important to look at the expected beam size at the fundamental frequency inside the undulator. This is critical to understand the minimum gap acceptable in the undulator design, under the assumption that we accept the full transverse size at the longest fundamental wavelength. We will consider the case for the fundamental at 3 THz at electron energy of 17.5 GeV. In order to study the transverse size of the THz source we used two approaches, analytical

and numerical. Analytical formulas are available for the field of the radiation source at resonance, in the middle of the undulator, and at any position in free space, after the undulator, even in the near zone [4]. The numerical computations are done using wave-front propagation codes [5]. The results of back-propagation at different distances and the calculation of the FWHM are shown in Fig. 3 left where we also plot a comparison with the analytical expressions, and in Fig. 3 right the result of back-propagation at the virtual source.

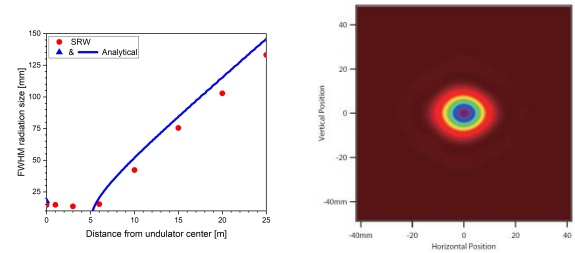


Figure 3: Radiation beam size evolution from the undulator center for a fundamental of 3 THz with an electron beam energy of 17.5 GeV. Blue triangles: analytical expectations in the undulator center, at $z = 0$ and after the undulator exit at 3 THz. Red circles: results from wave-front propagation simulations at 3 THz. SRW back propagation at the source for a fundamental of 3 THz.

In Fig. 4 we report the frequency in THz of the first harmonic on axis produced by an undulator with different period lengths, ranging from 0.6 to 1.5 m, as a function of the peak field on axis B, for 17.5 GeV, the maximum nominal electron beam energy of the European XFEL.

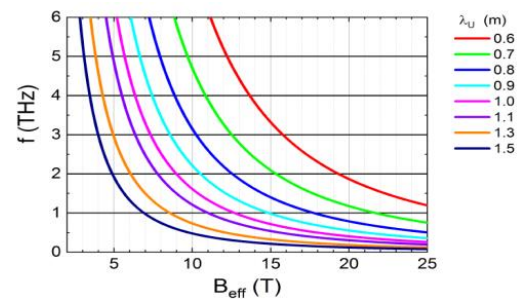


Figure 4: Frequency of the first harmonic on axis produced by an undulator with different period lengths, as a function of the effective field on axis B, for 17.5 GeV electron beam energy.

In order to reach 3 THz as the minimum value for the frequency of the first harmonic, for magnetic peak fields below 10 T the period length of the undulator should be longer than 0.9 m. To have some margin, and to keep the period length as short as possible we focus on a period length of 1 m.

Undulators are realized with different technologies [6]. The most widely used is the permanent magnet technology. Alternatively, it is possible to use electromagnets wound with

copper conductors or with superconductors. If the engineering current density needed to produce the desired magnetic peak field on axis is below 10 A/mm², electromagnets using copper as a conductor can be used.

Above this limit of the engineering current density, the ohmic losses become untreatable. For the same period length and vacuum gap, especially for long period lengths, superconducting undulators can produce higher magnetic peak fields on axis than the permanent magnet ones [7]. We consider a NbTi based THz superconducting undulator working at liquid helium temperature (4 K), feasible for the European XFEL. NbTi operates up to magnetic fields on the conductor of about 10 T [8]. The simulation for the magnetic field profile of a 10 periods undulator model from Fig. 5 with the code Radia [9] has been performed using the engineering current densities of 115 A/mm² in the outer coils, and 55 A/mm² in the inner coils. The on-axis effective magnetic field of 7.3 T allows reaching the minimum value of 3 THz for the frequency of the first harmonic.

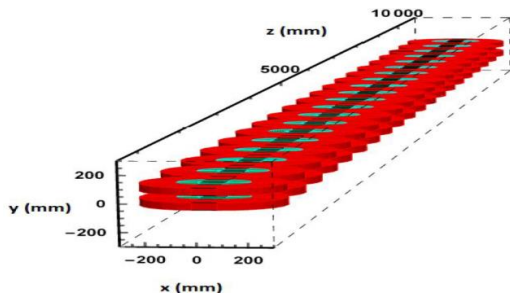


Figure 5: Ten periods of the THz undulator model simulated with the code Radia. Green parts show the inner coils and red parts show the outer coils.

THz TRANSPORT LINE

As concerns the feasibility of the transport of the generated THz pulses to the experimental end stations, we assume that the THz undulator would be positioned just in front of the electron beam dump as is the case at the prototype device at the XUV FEL FLASH. Experience at FLASH shows that Kepler telescopes of a length of 12 m allow transport and refocusing without diffraction losses [10] down to frequencies of 3 THz. A distance of 290 m, as needed in the case of the XTD4 tunnel at the European XFEL, would then require 24 Kepler-telescopes and a total of 48 mirrors (of which 32 would be focusing optics and 16 would be planar mirrors). The main loss will be due to the actual reflectivity. At FLASH and TELBE gold-coated aluminum or copper optics are employed, with the gold coating being a layer of about 200 nm, substantially thicker than the skin depth at these frequencies. Then the reflectivity of the optics can be as high as 99 % resulting in a reflectivity loss of 36 % for the mere transport to the experimental end stations. Additionally, there potentially will be losses in the window separating the accelerator vacuum from the experiment vacuum, which are in the few 10 % range, depending on the choice of mate-

rial. Therefore roughly 50 % of the generated pulse energies are received at the experiments.

CONCLUSION

In this paper, we explored the possibility of using the spent electron beam at the European XFEL to produce high-field THz pulses by means of a superconducting undulator. We show that current superconducting technology allows for the construction of such device with 10-periods with fundamental frequency starting from 3 THz using a 17.5 GeV electron beam. Lower frequencies can be obtained by using lower nominal electron energy points. Owing to the quality of XFEL electron beams, one can generate narrow-band, frequency-tunable THz pulses with the frequency range of 30 down to 3 THz and corresponding pulse energies range of 10 to 280 μJ (see Table 1). Furthermore, mJ-level pulse energies are achievable when the full bandwidth between 1 and 100 THz is utilized. The repetition rate naturally follows that of the European XFEL. Moreover, the THz transport line, albeit several hundred meters long, is feasible and can be hosted in the tunnels designed for the X-ray transport. For more details regarding this study, see [11].

Table 1: Maximum pulse energy (total, up to 100 THz and around the fundamental frequency with 10 % bandpass filter) at different values of the fundamental and corresponding electron charge (see Fig. 3).

Fundamental frequency [THz]	Tot. pulse energy [μJ]	Fund. pulse energy [μJ]	Electron charge [pC]
3	3450	279	500
5	2600	172	500
7	1540	115	250
9	1340	84	250
10	1180	64	250
12	1050	45	250
14	955	31	250
19	441	25	100
24	388	20	100
29	345	14	100
33	311	11	100
38	285	10	100
43	263	10	100
48	245	8	100

REFERENCES

- [1] M. Altarelli *et al.*, “The European X-ray free-electron laser facility in Hamburg”, *Nucl. Instrum. Meth. B*, vol. 269, p. 2845, 2011. doi:10.1016/j.nimb.2011.04.034
- [2] J. N. Galayda, J. N. Galayda, “The New LCLS-II Project : Status and Challenges”, in *Proc. LINAC’14*, Geneva, Switzerland, Aug.-Sep. 2014, paper TUIOA04, pp. 404–408.
- [3] I. Zagorodnov, DESY MPY Start-to-End Simulations, <http://www.desy.de/felbeam/s2e/xfel.html>

- [4] G. Geloni *et al.*, "Fourier treatment of near-field synchrotron radiation theory", *Opt. Commun.*, vol. 276, p. 167, 2007. doi:10.1016/j.optcom.2007.03.051
- [5] O. Chubar and P. Elleaume, "Accurate and Efficient Computation of Synchrotron Radiation in the Near Field Region", in *Proc. EPAC'98*, Stockholm, Sweden, Jun. 1998, paper THP01G, pp. 1177-1179.
- [6] J. Clarke, *The Science and Technology of Undulators and Wigglers*, Oxford University Press, 2004.
- [7] S. Casalbuoni *et al.*, "Test of Short Mockups for Optimization of Superconducting Undulator Coils", *IEEE Trans. Appl. Supercond.*, vol. 24, p. 4101905, 2014. doi:10.1109/TASC.2013.2295921
- [8] <https://nationalmaglab.org/magnet-development/applied-superconductivity-center/plots>
- [9] O. Chubar *et al.*, "A three-dimensional magnetostatics computer code for insertion devices", *J. Synchrotron Radiat.*, vol. 5, p. 481, 1998. doi:10.1107/S0909049597013502
- [10] M. Gensch *et al.*, "New infrared undulator beamline at FLASH", *J. Infrared Phys. & Tech.*, vol. 51, p. 423, 2008. doi:10.1016/j.infrared.2007.12.032
- [11] T. Tanikawa *et al.*, "A superradiant THz undulator source for XFELS", *J. Inst.*, vol. 14, paper P05024, 2019. doi:10.1088/1748-0221/14/05/p05024

THE FHI FEL UPGRADE DESIGN

W. Schöllkopf, S. Gewinner, A.M.M. Todd¹, W.B. Colson¹, M. De Pas, D. Dowell¹, S.C. Gottschalk¹, H. Junkes, J.W. Rathke¹, T.J. Schultheiss¹, L.M. Young¹, G. von Helden, and G. Meijer
Fritz-Haber-Institut der Max-Planck-Gesellschaft, Berlin, Germany

Abstract

Since coming on-line in November 2013, the Fritz-Haber-Institut (FHI) der Max-Planck-Gesellschaft (MPG) Free-Electron Laser (FEL) has provided intense, tunable infrared radiation to FHI user groups. It has enabled experiments in diverse fields ranging from bio-molecular spectroscopy to studies of clusters and nanoparticles, nonlinear solid-state spectroscopy, and surface science, resulting in more than 55 peer-reviewed publications so far. A significant upgrade to the original FHI FEL has been funded and is presented here.

A second short Rayleigh range undulator FEL beamline is being added. It will permit lasing from $< 5 \mu\text{m}$ to $> 160 \mu\text{m}$. Additionally, a 500 MHz kicker cavity will permit simultaneous two-colour operation of the FEL from both FEL beamlines over an optical range of 5 to 50 microns by deflecting alternate 1 GHz pulses into each of the two undulators. We describe the upgraded FHI FEL physics and engineering design and present the plans for two-colour FEL operations by the end of 2020.

FEL LAYOUT & DESIGN PARAMETERS

The layout of the original and proposed FHI FEL Upgrade beamlines is shown in Fig. 1. The existing design consists of the accelerator section, the MIR beamline and a diagnostic beamline. The design performance parameters and physics design [1], the engineering design [2], first lasing [3], and subsequent user performance [4] for the existing FEL have been described.

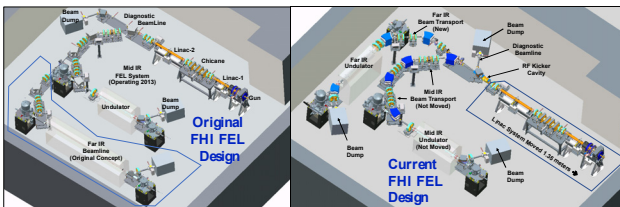


Figure 1: Original (left) and Current (right) FHI MIR and FIR FEL Designs.

The FEL consists of a 50 MeV accelerator driven by a gridded thermionic gun with a beam transport system that feeds two undulators and a diagnostic beamline. The first normal-conducting 2.998 GHz linac accelerates the electron bunches to a nominal energy of 20 MeV, while the second one accelerates or decelerates the electrons to deliver any final energy between 15 and 50 MeV. A chicane between the structures allows for adjustment of the bunch length as required. Originally, the Mid-IR and Far-IR

undulators were planned to be parallel to each other directed 180 degrees from the accelerator axis [Refs. 1, 2]. However, we have now selected a single achromat for the Far-IR FEL which is now at 90 degrees to the accelerator axis. The accelerator section has been moved back 1.35 m to allow insertion of an RF kicker cavity, and the diagnostic beamline has been relocated. The principal subject of this paper is the design and fabrication of the Far-IR beamline and FEL, and the changes in configuration from the original design that we have adopted.

MID-IR FEL PERFORMANCE

The generated IR radiation forms ps-long micro-pulses at a pulse repetition rate of 1 GHz. Up to 10,000 consecutive micro-pulses form a pulse train, referred to as the macro-pulse that are repeated at a rate of 10 Hz. Figure 2 shows tuning curves of the macro-pulse energies for 6 different electron energies ranging from 18 to 44 MeV. For any given electron energy, the IR wavelength can be tuned continuously by a factor of 2 to 3 by changing the undulator gap. The data plotted in Fig. 2 has been observed for a relatively narrow FEL line spectrum with $\Delta\lambda / \lambda \sim 0.4$, where λ is the central wavelength and $\Delta\lambda$ denotes the full width at half maximum (FWHM) of the spectral distribution that is monitored with a grating spectrometer. Best performance in terms of macro-pulse energy is found for $\lambda \sim 7.5 \mu\text{m}$. Even more pulse energy (and pulse peak power) can be achieved by fine adjustment of the FEL cavity length (5.4 m nominal length) at the cost of an increased spectral line width. The latter corresponds to shorter mid-IR radiation pulses. This way, pulses as short as 500 fs can be generated.

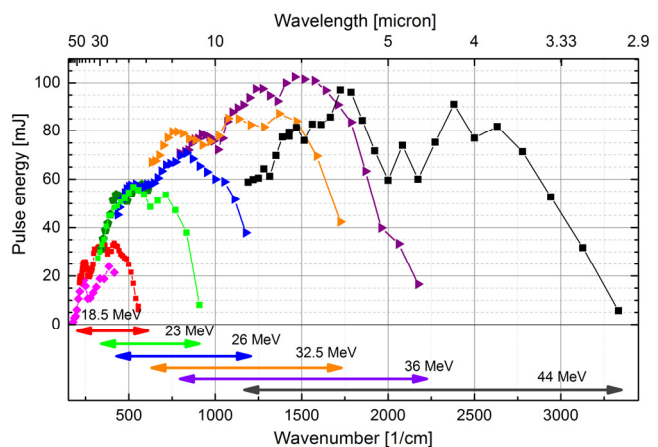


Figure 2: Macro-pulse energy measured at the FHI FEL Mid-IR system which has been in user operation since 2013. Each curve is measured by an undulator gap scan for the electron energies indicated at the bottom.

¹ Consultants to the Fritz-Haber-Institut

FAR-IR BEAMLINE DESIGN

In addition to completing a Far-IR beamline capable of generating wavelengths greater than 150 μm , a key feature of the revised FHI FEL upgrade was a desire for simultaneous two-colour operation across the 3 μm to > 150 μm range. Users insisted that both beamlines be capable of operating simultaneously at the same 5 to 50 μm . Pulse picking requirements forced the two optical cavities to be the same length. We have chosen a short Rayleigh range Far-IR undulator that is not a waveguide, which we believe should resolve the wavelength holes observed on Flare [5].

In order to do this, we will separate the existing system after the linacs, leaving the Mid-IR arc in place. The electron gun, sub-harmonic buncher, linacs and chicane will be moved back 1.35 m to allow the insertion of a 500 MHz RF kicker cavity powered by a 65 kW solid-state amplifier.

Initial beam dynamics analysis revealed that emittance growth along the long back leg of the original Far-IR beamline was unacceptable. This realization occurred at the final design review setting a furious redesign effort in motion. Fortunately, we were quickly able to find a solution with excellent performance by instituting a bypass line and single achromat on the Far-IR beamline, as shown in Fig. 1. This design is not completely achromatic and isochronous, but is sufficiently close that performance is not negatively impacted. An additional benefit is a large reduction in parts count and hence, all-important cost. The diagnostic beamline has had to be relocated, but is still capable of performing the required measurements in the new location.

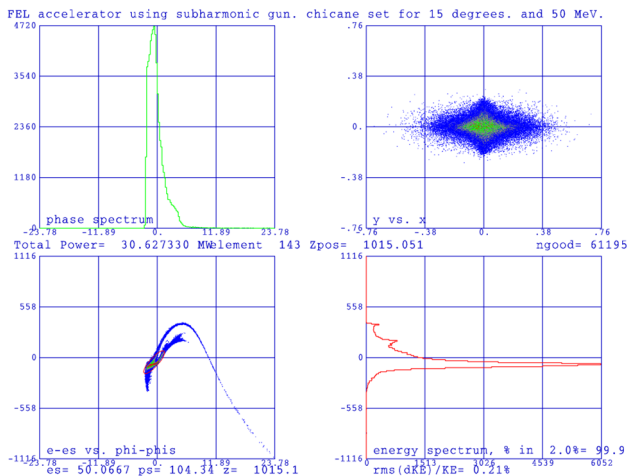


Figure 3: 50 MeV end-to-end TStep simulation at the exit of the Far-IR achromat.

Figure 3 shows the phase space after the Far-IR achromat for a 50 MeV electron beam with the chicane set for 15 degrees. The resultant rms energy spread of 0.21% and the FWHM bunch length of 2.5 ps were used in the FEL physics simulations described below.

Figure 4 shows an 18 MeV Trace3D simulation from the exit of linac 2 (left) to the Far-IR beam dump (right). The horizontal (blue) and vertical (red) $5\epsilon_{\text{rms}}$ beam envelopes can be seen to be well matched into the undulator (elements 54 and 55). The dispersion (gold) is well controlled at entry

to the undulator. K_{rms} is 2.15 for this case yielding a radiation wavelength of 150 μm .

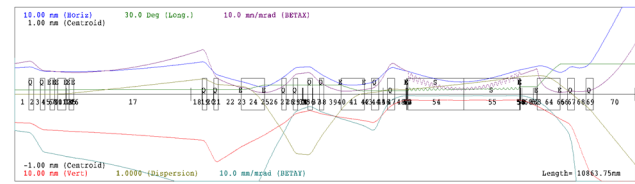


Figure 4: Trace3D simulation of the Far-IR beamline from the linac 2 exit (left) to the beam dump (right).

A key component of the update engineering design, shown in Fig. 5, is the new 500 MHz kicker cavity which operates in a dipole mode using the electric field between the vanes to deflect the beam. The cavity is capable of deflecting the 50 MeV electron beam through ± 2 degrees. It is surrounded by two small 2 degree rectangular dipole magnets. For two-color operation, the beam is alternatively bent -1, -2, -1 \Rightarrow -4 degrees by the dipole-kicker-dipole combination into the Far-IR line and -1, +2, -1 \Rightarrow 0 degrees for the Mid-IR beamline. For single-color operation, the kicker is not used and the dipoles are off for the Mid-IR and at -2, -2 \Rightarrow -4 for the Far-IR. A more detailed view of this region showing the kicker beam box and dipoles is shown in Fig. 6.

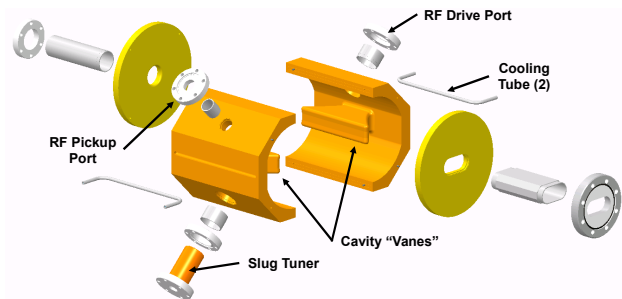


Figure 5: Exploded view of the 500 MHz RF kicker cavity showing the vanes.

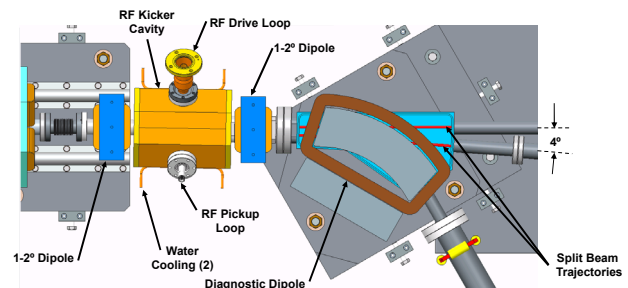


Figure 6: Detail of the RF kicker region

FEL PHYSICS DESIGN

No significant change is anticipated in the performance of the Mid-IR beamline. The anticipated performance of the Far-IR beamline will deliver 2.5 ps pulses at 50 MeV with bunch charge of 200 pC. This is sufficient to deliver the 5 μm radiation demanded by users. Shorter bunches

should be possible with more aggressive chicane settings and hence increased IR power.

At long wavelengths, the optical mode is wide due to increased diffraction, and requires a relatively large resonator mirror diameter of 7.2 cm. The outer radius of the gold mirrors is designed to control the optical mode shape with 96% of the power in the fundamental mode. Hole out-coupling is used on the downstream mirror. This unique FIR FEL open resonator design enables continuous tunability over the largest wavelength range of any laser of any kind.

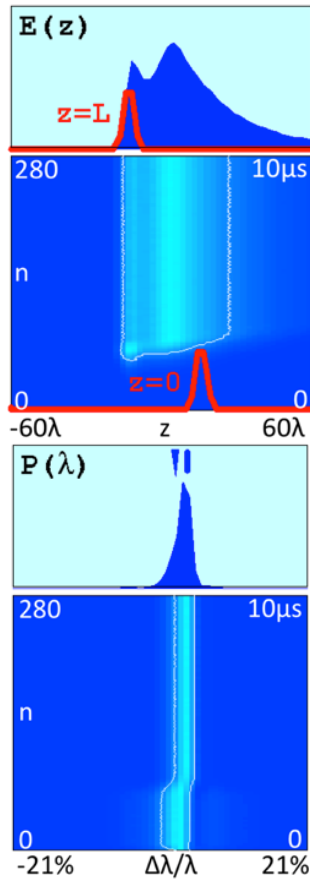


Figure 7: Final, steady-state optical pulse shape $E(z)$ (blue-top left) for 120λ , with the electron pulse (red) superimposed at $z = L$. The relative positions at $z = 0$ (bottom left) shows the electron pulse a full 30λ ahead of the optical pulse. The intensity (bottom left) and spectral (bottom right) evolution of the optical pulse shape (light blue) is shown over the $n = 280$ amplification passes of the $10\mu s$ macropulse. The final optical spectrum $P(\lambda)$ has an $\sim 2.5\%$ width (top right).

The slippage distance of the optical pulse is more than six times longer than the short 2.5 ps (FWHM) long electron pulse, but provides sufficient single-pass gain to reach saturation in strong optical fields in $2.4\mu s$. Figure 7 shows the final steady-state optical pulse and spectrum.

FAR-IR UNDULATOR DESIGN

The parameters for the Far-IR undulator have been selected. The period is 68 mm , there are 30 spectrally active periods and the minimum gap is 3.2 cm , corresponding to a root-mean-square (*rms*) undulator parameter $K_{\text{rms}} \sim 2.29$. The Far-IR FEL cavity will be 5.4 m long, as is the existing Mid-IR cavity. However, the former will have a smaller Rayleigh range of just $1/3$.

Because of the diameter of the long wavelength optical modes, the 6.5 cm gap of the dipoles at each end of the undulator is very large to avoid mode scrapping, and thus these beam boxes provide a significant engineering challenge.

STATUS OF FAR-IR FABRICATION

We have already begun the fabrication process for the FHI FEL Upgrade. Tenders have been issued for the dipole magnets, kicker cavity, and solid-state-amplifier. Diagnostics, steerers, quadrupole magnets, magnet power supplies, and other components have been issued and the first components are already beginning to be delivered. We anticipate having all critical components in hand by summer 2020. The goal is to complete all upgrade activities by the end of 2020.

UPGRADES TO THE MIR-BEAMLINE

In the process of developing the FHI FEL upgrade design, and partially due to the analysis of the upgrade, we have uncovered a number of deficiencies in the existing system that have been remedied. These include movement and reorientation of the achromat dipole magnets based upon vault location surveys. We have also adjusted the tuning of the linac 1 bunching cavity. This resulted in shorter bunches, a nearly 3-fold increase in the optical power delivered to 400 mJ per macropulse, and reduced vault radiation levels that allow operation at higher PRF. New bipolar relay circuitry will eliminate hysteresis effects in the rarely-used chicane dipoles, allowing the achievement of higher undulator peak current. Similarly, an improved RF arc protection system and higher gun voltage (40 kV with a target of 45 kV) have already extended operations towards 50 MeV and should enable extension of the macropulse length beyond the typical value of $10\mu s$.

CONCLUSIONS

The physics design for the FHI FEL has been completed and the engineering design is ongoing. Major tenders have been issued and POs are being let for many other key systems. The plan is to start installation of all ex-vault components ahead of user shutdown. Two-colour operation is scheduled to be available before the end of 2020.

REFERENCES

- [1] H. P. Bluem *et al.*, "The Fritz Haber Institute THz FEL Status," in *Proc. FEL'10*, Malmo, Sweden, August 2010, paper MOPA09.
- [2] A. M. M. Todd *et al.*, "Commissioning Status of the Fritz Haber Institute THz FEL," in *Proc. IPAC'11*, San Sebastian, Spain, September 2011, paper THPC106.

- [3] W. Schöllkopf *et al.*, “First Lasing of the IR FEL at the Fritz-Haber-Institut Berlin,” in *Proc. FEL’12*, Nara, Japan, August 2012, paper MOOB01.
- [4] W. Schöllkopf *et al.*, “The new IR and THz FEL Facility at the Fritz Haber Institute in Berlin,” *Advances in X-ray Free-Electron Lasers Instrumentation III*, Sandra G. Biedron, Editor, *Proc. of SPIE*, vol. 9512, 95121L (2015).
doi:10.1117/12.2182284
- [5] D. Arslanov, R. Jongma, L. van der Meer *et al.*, “Scanning Problems of FLARE, a THz-FEL with a waveguide,” in *Proc. FEL’14*, Basel, Switzerland, August 2014, paper TUP065.

EXPERIENCE WITH THE SUPERRADIANT THz USER FACILITY DRIVEN BY A QUASI-CW SRF ACCELERATOR AT ELBE

M. Bawatna†, Helmholtz-Zentrum Dresden-Rossendorf (HZDR), Dresden, Germany
B. Green, Magnet Science & Technology, Tallahassee, FL, USA

Abstract

Instabilities in beam and bunch parameters, such as bunch charge, beam energy or changes in the phase or amplitude of the accelerating field in the RF cavities can be the source of noise in the various secondary sources driven by the electron beam. Bunch charge fluctuations lead to intensity instabilities in the superradiant THz sources. The primary electron beam driving the light sources has a maximum energy of 40 MeV and a maximum current of 1.6 mA. Depending on the mode of operation required, there are two available injectors in use at ELBE. The first is the thermionic injector, which is used for regular operating modes and supports repetition rates up to 13 MHz and bunch charges up to 100 pC. The second is the SRF photocathode injector, which is used for experiments that may require lower emittance or higher bunch charges of up to 1 nC. It has a maximum repetition rate of 13 MHz, which can be adjusted to lower rates if desired, also including different macro pulse modes of operation. In this contribution, we will present our work in the pulse-resolved intensity measurement that allows for correction of intensity instabilities.

INTRODUCTION

The Electron Linac for beams with high Brilliance and low Emittance (ELBE) superconducting radiofrequency (SRF) accelerator [1] is a facility at the Helmholtz Zentrum Dresden Rossendorf (HZDR). At the ELBE user facility, there are two available electron injectors in use [1,2] as in Fig. 1. The thermionic injector, which supports repetition rates up to 13 MHz and bunch charges up to 100 pC, and the Super Radio Frequency (SRF) photo-cathode injector, which is used for experiments that may require lower emittance or higher bunch charges of up to 1 nC. Moreover, the SRF injector at ELBE also has a maximum repetition rate of 13 MHz with different macro pulse modes of operation. The required properties of the electron bunches (form, charge, position) afford electron beam diagnostics that exceeds presently available solutions at ELBE. Here we discuss ideas of suitable electron bunch diagnostic techniques amongst which novel single-shot electro-optic techniques for online monitoring of electron bunch form and arrival time in a new THz lab, equipped with state of the art spectrometers and laser systems.

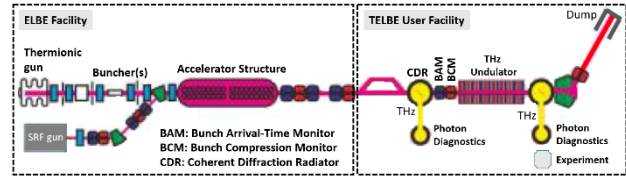


Figure 1: ELBE accelerator beamlines for THz radiation production.

The superradiant THz sources at ELBE accelerator (TELBE) THz facility is performing ultra-fast pump-probe experiments by providing a unique combination of high pulse energies and high repetition rates. In this type of experiment, the electric or magnetic field in the THz pump pulse acts as the excitation of dynamics in the matter. This dynamic in turn is then probed by ultra-short (light) pulses, typically with the sub THz cycle resolution as in [3].

In this paper, we will present the pulse-resolved intensity monitor at TELBE.

The paper is organized as follows: the first section introduces the requirements for the pulse-resolved intensity monitor at TELBE. The second section presents the methods and material used, as well as the intensity instability measurements. After summarizing the results, foreseeable future development and upgrades are discussed.

TERAHERTZ RADIATION DETECTION AT TELBE

Detecting THz radiation can sometimes be problematic because it occupies a position in the electromagnetic spectrum between optical and microwave wavelengths.

There are many different approaches to detecting THz, utilizing a variety of physical phenomena. The ability to detect THz is critical to our work at TELBE user facility, as this is a necessary prerequisite to using it in meaningful experiments and diagnostic setups.

It is crucial to be able to see the intensity of single pulses, to get a reliable measurement of the average power, and to analyze the beam profile. Some experiments require information on the longitudinal (in the time domain) shape of individual pulses or even their actual waveform. The following sections present the pyroelectric THz detection scheme utilized at TELBE to characterize the TELBE THz radiation.

Pyroelectric Detectors

The pyroelectric effect is a phenomenon that occurs when so-called pyroelectric materials change temperature. Changes in temperature cause a change of the electrical polarization, which induces a voltage across the material.

† m.bawatna@hzdr.de

This voltage then gradually decreases due to leakage current, either through the material itself or through an outside path. Pyroelectric materials can, therefore, be used to detect radiation from the THz to x-ray range by measuring the voltage across them. Any change in voltage is caused by heat being deposited in the material by a light pulse. Thus, the appearance of a detected light pulse is two spikes in voltage, of opposite polarity. The first spike appears when the material is warmed by the light pulse, the second spike is caused when the material cools back to its original temperature after the pulse has passed, while a continuous radiation beam would not lead to a detectable signal.

Front end electronics have been developed at DESY that take these two pulses and output them as a single pulse to make analyzing the detected pulses easier [4]. Fig. 2 shows the signal measured by the pyroelectric detector at TELBE user facility. Pyrodetectors work at room temperature and can be operated at repetition rates in the 100 kHz regime. This type of detector has been most frequently used at TELBE to date because it allows the pulse to pulse intensity detection at the typical operating repetition rate of 100 kHz. It is also easy to convert the signal to a quantitative measure of the pulse energy because the intensity response is linear. There are a few significant problems, though, with this type of detector.

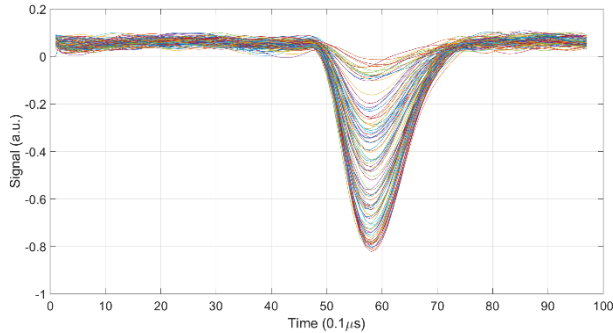


Figure 2: Signal measured by the pyroelectric detector that shows the intensity fluctuation for 10000 THz pulses.

The frequencies of interest in THz are generally difficult to absorb with the standard materials used in pyroelectric detectors. These materials can be transparent to some frequencies in the THz range, which of course make it difficult to detect them. Any frequencies that pass through the absorber material are not measured in the detector, leading to lower readings than the actual beam power. There is also a problem with linearity at high intensities. The unique fast detectors that were developed at DESY have a linear response up to a signal value of 1 V, so it is essential to limit incoming intensity so that the signal is less than 1 V in order to stay in the linear regime. Besides the base noise level is high ($\mu 50$ mV). This leads to a large error bar in the few 10% ranges in single pulse intensity measurements. Finally, pyroelectric detectors are too slow to resolve the actual pulse duration.

PULSE-RESOLVED INTENSITY MONITOR AT TELBE

One of the challenges at TELBE is to account for changes in the intensity of the THz pulses. Intensity measurements can be performed alongside the experiment, as shown in Fig. 3. A wire grid polarizer is used as a beam splitter, and a small portion of the THz beam acting as a pump excitation is diverted into a purpose-built pyroelectric detector as in [5]. The most important factors for choosing the specific pyroelectric detector, developed at DESY for the TELBE intensity monitor, are its sufficiently high speed and robustness in. These pyroelectric detectors have a relatively high noise floor of 50 mV. One must also be careful not to put too much intensity onto the detector. If the intensity is too high, the detector no longer has a linear response.

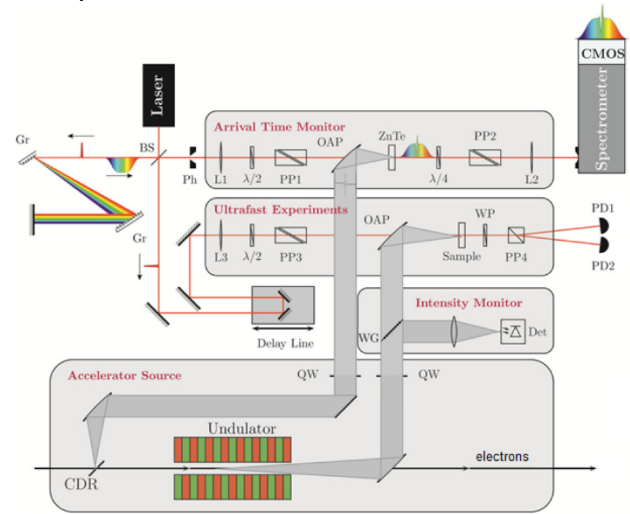


Figure 3: Schematic diagram of the developed pulse-resolved diagnostic at the TELBE facility, combining a 30 fs (FWHM) resolution arrival-time monitor with a pulse intensity monitor.

In this specific case, the linear regime is when the output signal remains below 1 volt. Combined with the noise floor of 50 mV, this results in a relatively poor S/N ratio. The intensity fluctuations and the spectral content for 10000 THz pulses are shown in Fig. 4 and Fig. 5 respectively, taken over 1 second. Major frequencies are marked. A detailed discussion of the observed intensity instabilities will be presented in a full article. Such an analysis can help in identifying the origin of different instabilities.

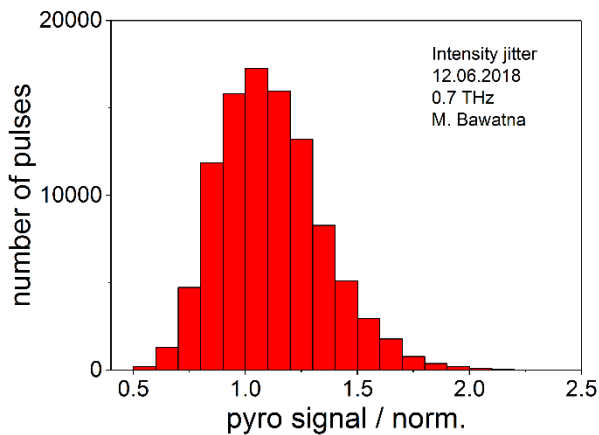


Figure 4: Histogram of the change in the intensity of pulses from the TELBE undulator.

These instabilities can come from any number of sources, from fluctuations in the bunch charge to beam position instabilities to electronic noise in the detection setup.

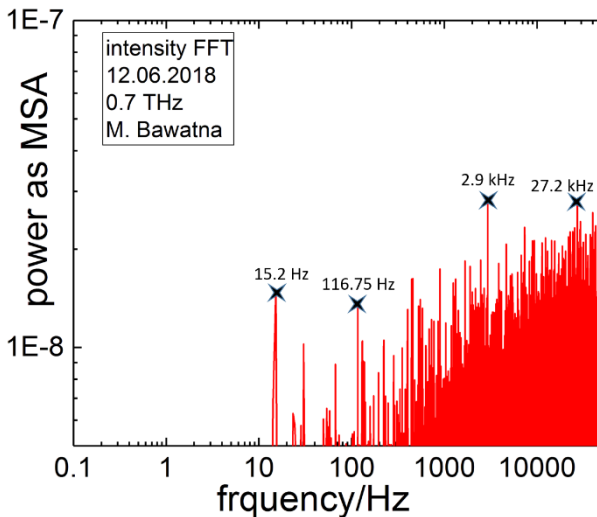


Figure 5: Spectrum of the fluctuations in the beam intensity of the undulator pulses tuned at a 700 GHz, taken over 1 second.

The evaluation of including the pulse-resolved intensity measurement to the data analysis was done on the Electro-optic sampling setup as shown in Fig. 3, which is most commonly used to measure the time-domain form of THz pulses. This effect is quasi-simultaneous and can be used to detect signals on femtosecond timescales.

Data was taken after tuning the undulator at 700 GHz, with a repetition rate of 100 kHz, the beam energy was 24 MeV and a bunch charge was 70 pC. Fig. 6 shows the effect of intensity fluctuation on the Fourier transform of the signal measured by the electro-optic sampling setup shown in Fig. 3.

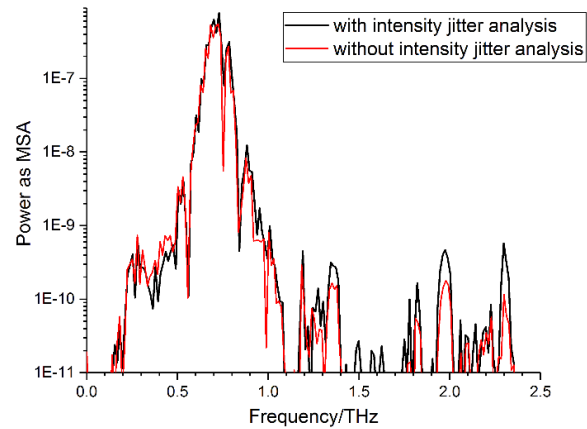


Figure 6: Fourier transform of the signal measured by electro-optic sampling at 700 GHz tune with including the pulse-resolved intensity measurement into the data analysis.

CONCLUSION AND FUTURE WORK

In this paper, the determination of the pulse-resolved intensity fluctuations serves to correct for them in experimental data. Moreover, these instabilities in pulse energy can be harnessed to provide a pulse-energy-resolved measurement utilizing the intensity fluctuations as a fast modulation of the pulse intensity. The pulse-resolved intensity measurement is still under development and evaluation. The results will be presented in a full article.

REFERENCES

- [1] J. Teichert *et al.*, "Results of beam parameter measurement of the ELBE electron accelerator after commissioning", *Nucl. Instr. Meth. Phys. Res. A*, 507:354, 2003. doi:10.1016/S0168-9002(03)00918-5
- [2] J. Teichert *et al.*, "Experiences with the SRF Gun II for User Operation at the ELBE Radiation Source," in *Proc. 9th Int. Particle Accelerator Conf. (IPAC'18)*, Vancouver, Canada, Apr.-May 2018, paper THPMF040. doi:10.18429/JACoW-IPAC2018-THPMF040
- [3] S. Kovalev *et al.*, "Probing ultra-fast processes with the high dynamic range at 4th-generation light sources: Arrival time and intensity binning at unprecedented repetition rates", *Structural Dynamics*, vol. 4, no. 2, p. 024301, 2017. doi:10.1063/1.4978042
- [4] S. Wesch *et al.*, "A multi-channel THz and infrared spectrometer for femtosecond electron bunch diagnostics by single-shot spectroscopy of coherent radiation", *Nucl. Instr. Meth. Phys. Res. A*, 665:40, 2012. doi:10.1016/j.nima.2011.11.037
- [5] B. Green, "Superradiant Terahertz Sources and their Applications in Accelerator Diagnostics and Ultra-fast Science," Ph.D. dissertation, Fakultät für Physik, Karlsruher Institutes für Technologie (KIT), 2017. doi:10.5445/IR/1000070730

CONCEPT OF HIGH-POWER CW IR-THz SOURCE FOR THE RADIATION SOURCE ELBE UPGRADE

P. Evtushenko[†], U. Lehnert, P. Michel, T. Cowan,
Helmholtz-Zentrum Dresden-Rossendorf, Dresden, Germany

Abstract

The Radiation Source ELBE at Helmholtz-Zentrum Dresden-Rossendorf (HZDR) is a user facility based on a 1 mA - 40 MeV CW SRF LINAC. Presently HZDR is considering upgrade options for the ELBE or its replacement with a new CW, SRF LINAC-based user facility. A part of the user requirements is the capability to generate IR and THz pulse in the frequency range from 0.1 through 30 THz, with pulse energies in the range from 100 μ J through a few mJ, at the repetition rate between 100 kHz and 1 MHz. This corresponds to the pulse energy increase, dependent on the wavelength, by a factor from 100 through 1000. In this contribution, we outline key aspects of a concept, which would allow to achieve such parameters. These aspects are: 1 - use of a beam with longitudinal density modulation and bunching factor of about 0.5 at the fundamental frequency; 2 - achieving the density modulation through the mechanism similar to the one used in optical klystron (OK); 3 - generating the necessary for the modulation optical beam by an FEL oscillator, and 4 - using two electron injectors. First injector would provide a beam for the FEL oscillator. Second high charge injector would provide the beam for the high pulse energy generation for users. All-in-all the concept of the new radiation source is very similar to an OK, but operating with two beams simultaneously.

INTRODUCTION

To achieve the very high pulse energies of few hundred μ J, at the above-mentioned repetition rates a new configuration of the photon source is proposed. To our knowledge other existing electron beam-based photon generation schemes cannot provide the required combination of the high pulse energy and repetition rate. In the scheme proposed here an electron beam with a longitudinally modulated density will be used to generate coherent undulator radiation. It is suggested to achieve the necessary longitudinal density modulation of the electron beam with the help of a scheme similar to the one used in Optical Klystron FEL OK [1]. Operation of such a photon source will require the seeding, i.e., energy modulating optical beam, tunable, essentially, in the whole frequency range of the source - 0.1 to 30 THz, with sufficiently high peak power. With suggest, that such sources can be realized as an FEL oscillator. Moreover, it is proposed that the intra-cavity optical pulse of the oscillator should be used for the energy modulation of the electron beam. This will allow to significantly relax the requirements on the oscillator and on the electron beam, required to drive it. The required FEL oscillator can be operated with the electron beam

with the bunch charge less than 100 pC. To keep the optical resonator length easily manageable, the oscillator can be operated with the bunch frequency of about 10 MHz. The combination of the 100 pC bunch charge and the repetition rate of the 10 MHz would require a CW accelerator system with average current of about 1 mA, which is comfortably within the ELBE's accelerator system capability.

To satisfy the requirements of the high IR-THz pulse energy, the beam with the bunch charge significantly higher, than the 100 pC necessary for the seeding oscillator, will necessary. It is suggested to operate such beam with the bunch charge approximately 10 times higher, i.e., at 1 nC, or higher, when allowed by electron gun technology. For higher reliability, easier tuning and optimization of such a radiation source, it is proposed that the 100 pC beam and 1 nC beam should be generated by two separate electron sources. The repetition rate of high bunch charge beam can be as high as 1 MHz. The minimal repetition frequency of the high charge beam can be arbitrary low, with the only condition that it must be a sub-harmonic of the repetition frequency of the beam in the FEL oscillator-modulator.

The undulator based source will provide a relatively narrowband - multicycle radiation pulses. In parallel to such a source, the new facility would also have a broadband few-cycle THz sources. These sources will be based either on a coherent diffraction radiation CDR, coherent synchrotron radiation (CSR) or coherent edge radiation (CER) from a dipole magnet. To provide high pulse energy this source would be operated by the beam from the high bunch charge electron gun. The continuous pulse train, from the high bunch charge electron gun, can be split into few beams with the help of an RF separator. The different beams, downstream of the RF separator would be used to drive different sources simultaneously.

SUPERRADIANT UNDULATOR WITH STRONGLY COMPRESSED BUNCH

The intensity of coherent undulator radiation, as of any other coherent radiation mechanism, can be expressed as $I_c(\omega) = I_0(\omega) N_e^2 |f_b(\omega)|^2$, where $I_0(\omega)$ is the undulator radiation intensity from a single electron, N_e is the number of the electrons in the bunch, and $f_b(\omega)$ is the Fourier transform of the longitudinal bunch distribution also called bunching factor. Since the coherent radiation intensity dependence on the bunch charge is quadratic, a part of the new facility design direction is to use the bunch charge as high as practical for a CW accelerator system.

To understand the concept proposed here and our design choices, it is helpful to consider, first, the coherent

[†]P.Evtushenko@hzdr.de

undulator radiation output from a strongly compressed bunch. It can be shown that the maximum spectral brightness of the undulator radiation is achieved at first harmonic $n = 1$ and with the undulator parameter $K = 1$ [2, 3]. Figure 1 shows the calculated pulse energy from an undulator assuming, $n = 1$ (first harmonic), $K = 1$, undulator period $\lambda_u = 30$ cm, and number of undulator period $N_u = 17$. The calculation also assumes bunch charge of 1 nC. Four cases are shown in Fig. 1. First case, shown as black line, corresponds to the completely longitudinally coherent radiation, i.e., $f_b(\omega) = 1$, which is the upper limit of the undulator radiation intensity for the particular undulator with the bunch charge of 1 nC. Another two cases assume Gaussian longitudinal bunch distribution. To show the effect of the RMS bunch length on the coherent undulator radiation intensity, calculations made for bunch length of 0.2 ps and 1 ps RMS are shown by blue and green lines correspondently. To maximize the possible pulse energy, it is assumed, that the beam energy is adjusted for each wavelength such that the undulator parameter K is always equals to 1, which make this set of calculations optimistic. The bunch length of 0.2 ps is chosen for this example because estimations suggest that this could be the limit of bunch compression for a 1 nC bunch, when it is accelerated to the energy of 50 MeV and longitudinally compressed including removal of the linac's RF curvature to the second order. The calculations summarized in the Fig. 1 demonstrate that even in a somewhat optimistic case, a conventional coherent undulator source driven by a short bunch could provide pulses energies around 100 μ J only in the frequency range from 0.2 THz to about 1.5 THz.

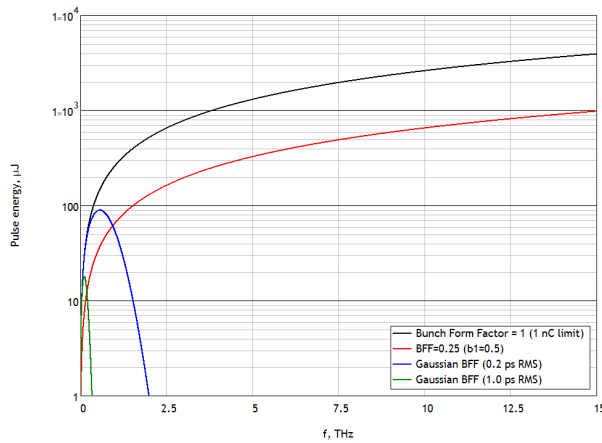


Figure 1: Coherent undulator radiation intensity.

LONGITUDINAL BEAM MODULATION

The main reason for the lower pulse energy of the coherent undulator source at frequencies higher than ~ 1.5 THz is the small longitudinal form factor of the bunch. One way to overcome the limitations of the bunching factor given by bunch compression is to use longitudinally modulated, with the periodicity of the desired radiation wavelength, beam. We argue, that with the requirement of the pulse repetition rate between 100 kHz and 1 MHz, the most suitable way to modulate the beam

longitudinally on the scale from 10 μ m through 250 μ m is to use the mechanisms used in an OK or a laser heater. There, the longitudinal density modulation is obtained via the two-step process. First, the electron beam energy is modulated by co-propagating the electron beam together with an optical beam in an undulator. The mean beam energy, the wavelength of the external optical beam, the undulator period and its K parameter are arranged to satisfy the FEL resonant condition. This leads to the net energy exchange between the external optical mode and the electron beam with periodicity of the optical mode. In the second step, the energy modulated beam is passed through a beam transport section with longitudinal dispersion. This results in the modulation of the longitudinal density of the electron beam again with the periodicity of the external optical mode. The detailed description of this process can be found in [4] and its references. Here we only summarize results and list most relevant parameters. Linear 1D theory of the micro-bunching instability predicts the growth of the slice energy spread to ~ 50 keV for the 1 nC bunch when it is accelerated to 50 MeV. For the robustness of the concept, for now, we assume that the slice energy spread could grow to 200 keV. We also assume the capability to induce the energy modulation amplitude 3 times larger than the slice energy spread. Under such condition the bunching factor of ~ 0.5 at first harmonic can be achieved. The energy change of an electron co-propagating with an optical mode in undulator is given by, $\Delta E_m = -e \cdot \mathcal{E}_{h\omega} \cdot K \cdot L_{mod} \cos(\varphi) / 2\gamma$, where e is the electron charge, $\mathcal{E}_{h\omega}$ is the amplitude of the modulating optical mode electrical field, L_{mod} is the length of the undulator-modulator, and φ is the phase of the optical mode corresponding to the longitudinal position of the electron. Assuming $L_{mod} = 1$ m and maximum beam energy of 50 MeV we get the required amplitude of the optical mode to be ~ 40 MV/m. Assuming radius of the mode of 1.5 mm, and 1 ps pulse length, the mode with the amplitude of 40 MV/m would correspond to pulse energy of $E_p = (\mathcal{E}_{h\omega}^2 c \epsilon_0 \pi r^2 \Delta t) / 2$ about 15 μ J.

FEL OSCILLATOR AS ENERGY MODULATOR

FEL modelling based on the set of Dattoli's analytical formulas [5], aided by empirical correction factors introduced by S. Benson [6], predicts that a very high performance FEL oscillator could provide the necessary amplitude of the optical mode in the outcoupled pulse.

On the other hand, an FEL oscillator can easily provide the necessary electrical field amplitude, when its intra-cavity optical pulse is used. In this case the outcoupling from the resonator can be minimized, so that only a very small fraction of the intra-cavity power, necessary for the FEL system monitoring and diagnostics, is outcoupled. The FEL oscillator modelling, which assumes the use of an undulator with period of 100 mm and 40 periods, and an electron beam parameters as presently used at ELBE: bunch charge of 77 pC, the RMS pulse length of 0.5 ps, longitudinal emittance of 50 keV·ps, and transverse

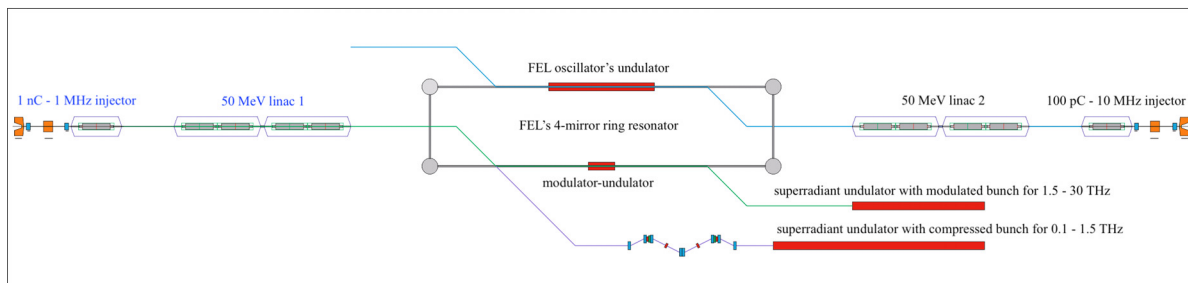


Figure 2: Layout option of the two-beam optical klystron IR-THz source utilizing two separate electron sources and two separate linacs for 1 nC beam with repetition rate of 1 MHz and 100 pC beam with the repetition rate of 10 MHz.

normalized emittance in both planes of 10 mm-mrad, and Rayleigh length of the optical resonator of 1 m, show that for any wavelength, in the required range, the intra-cavity pulse can provide electrical fields of, at least, five times higher than the required one.

The optical resonator of the oscillator can be implemented as a ring resonator. On the ring resonator two different undulators would be installed. A longer undulator would be used with the low charge - high repetition rate beam to generate and maintain the optical beam. The shorter undulator installed on the return pass of the resonator would be used for the energy modulation of the high charge. The two electron beams would be transported in two separate, completely independent beamlines. The advantage of such configuration is that it adds two additional degrees of freedom to the system. One is the freedom to choose the modulator-undulator length. Another is the freedom to choose the transverse size of the optical mode in the modulator-undulator. While the modulator length can be chosen only once, the transverse size of the mode can be made adjustable in a completed system. This can be accomplished either by deformable mirrors, or using sets of exchangeable optics. Adjusting the transverse beam mode size would allow to adjust and control the modulation amplitude without any changes to the oscillator. It is reasonable to expect that the high bunch charge beam will have larger transverse emittance than the beam used to drive the oscillator, therefore its size, when matched to an undulator will be different as well. Then for an optimal interaction with the optical beam the transverse size of the optical beam might need to be adjusted.

POSSIBLE SYSTEM LAYOUTS

Two layouts of the accelerator system can be considered. In both cases two electron sources are needed: one for the high bunch charge 1 nC beam at 1 MHz for the radiation generation, another for 100 pC beam at 10 MHz to drive the FEL oscillator. The use of ELBE linac modules with accelerating gradient of 12.5 MV/m is assumed, such that two modules can accelerate beam to 50 MeV. One possibility would be to use a single linac where the two beams are propagating in opposite directions during acceleration. The length of the LINAC section with adjacent beam optics systems can be made sufficiently short, so that the 1 MHz beam and 10 MHz beams, do not meet. The advantage of such configuration is cost saving on the

SRF linac and the LHe cryo plant. Another layout option, shown in Fig. 2, uses two separate linacs. Such layout would have substantially simpler beam optics, and would allow much easier ways to organize multi-user operation. The injector and linac 2, shown on the right, are used to drive the FEL oscillator, which would be used for energy modulation of the high bunch charge, or for FEL user experiments similarly to present ELBE's FELs. The beam from injector and linac 1, shown on the left, could be used either with its maximum repetition rate of 1 MHz, or its fraction, to drive the superradiant undulator with modulated beam. In a similar fashion, this beam would be also used, after a strong non-linear compression, for with the second superradiant undulator for generation in the frequency range 0.1 through 1.5 THz. It would be possible to use both undulator sources simultaneously with repetition rate of up to 500 kHz. Since the bottom undulator source does not require energy modulation it is possible to use it and the FEL oscillator for independent user experiments at the same time. Besides the IR-THz sources it is foreseen to have electron beam driven positron source used for material research. This source also requires high bunch charge with a repetition rate not higher than 1 MHz, therefore with be using the 1 nC-1MHz injector and linac. It will be possible to use this source simultaneously with superradiant undulators at repetition rate of few hundred kHz, splitting the 1 MHz beam with the help of RF beam separators.

REFERENCES

- [1] N.A. Vinokurov, A.N. Skrinksky, Preprint INP 77-59, Novosibirsk, 1977.
- [2] D.F. Alferov *et al.*, "Undulator radiation", in *Zh. Tekhn. Fiz.*, vol. 43, p. 2126, 1973; translated from *Sov. Phys. Tech. Phys.* 18, p. 1336, 1974.
- [3] S. Krinsky, "An undulator for the 700 MeV VUV-ring of the National Synchrotron Light Source", in *Nuclear Instruments and Methods*, vol. 172, pp. 73-76, 1980. doi:10.1016/0029-554X(80)90611-4
- [4] L. H. Yu, "Generation of intense uv radiation by subharmonically seeded single-pass free-electron lasers", in *Phys. Rev. A*, vol. 44, no. 8, pp. 5178-5193, 1991. doi.org/10.1103/PhysRevA.44.5178
- [5] G. Dattoli, A. Renieri, A. Torre, *Lectures on the free electron lasers theory and related topics*, Singapore: World Scientific Publishing Co. Pte. Ltd., 1993.
- [6] S. Benson, private communication.

INTEGRATION OF AN XFELO AT THE EUROPEAN XFEL FACILITY*

P. Rauer[†], I. Bahns, W. Hillert, J. Rossbach, Universität Hamburg, Hamburg, Germany
W. Decking, Deutsches Elektronen Synchrotron (DESY), Hamburg, Germany
Harald Sinn, European XFEL GmbH, Schenefeld, Germany

Abstract

An X-ray free-electron laser oscillator (XFELO) is a fourth generation X-ray source promising radiation with full three dimensional coherence, nearly constant pulse to pulse stability and more than an order of magnitude higher peak brilliance compared to SASE FELs. Proposed by *Kim et al.* in 2008[1] an XFELO follows the concept of circulating the light in an optical cavity - as known from FEL oscillators in longer wavelength regimes - but uses Bragg reflecting crystals instead of classical mirrors. With the new European X-ray free-electron laser (XFEL) facility recently gone into operation, the realization of an XFELO with radiation in the Angstrom regime seems feasible. Though, the high thermal load of the radiation on the cavity crystals, the high sensibility of the Bragg-reflection on reflection angle and crystal temperature as well as the very demanding tolerances of the at least 60 m long optical resonator path pose challenges which need to be considered. In this work these problems shall be summarized and results regarding the possible integration of an XFELO at the European XFEL facility will be presented.

INTRODUCTION

Current hard X-ray free-electron laser (FEL) facilities all use the self-amplified spontaneous emission (SASE) scheme for operation. While these sources produce very brilliant femtosecond X-ray pulses with excellent transverse coherence, they suffer from a lack of longitudinal coherence. A promising approach for reaching full longitudinal coherence in the hard X-ray regime proposed by *Kim et al.* in 2008 [1] is the X-ray free-electron-laser oscillator (XFELO). This scheme is based on using an undulator very short compared to state of the art hard X-ray SASE sources and a highly reflective cavity based on very pure diamond crystals serving as Bragg reflectors. As these Bragg reflectors also act as spectral filters an XFELO promises a spectral bandwidth in the order of the crystals bandwidth ($\Delta\lambda/\lambda_c \approx 10^{-5} - 10^{-7}$) and therefore orders of magnitude better than SASE-FELs. Furthermore, as the radiation field is built up over many cavity round trips, very low shot-to-shot fluctuations can be expected, even making the XFELO a promising candidate for X-ray quantum optics (XQO) [2]. With the recently commissioned European XFEL the realization of an XFELO becomes in reach. This is due to the facility's excellent electron beam properties and especially due to its very high bunch repetition rate of up to 4.5 MHz in pulsed-mode [3] which enables resonator lengths of only 33 m.

As will be evident from the following section, given the beam properties of the European XFEL the single pass gain exceeds a simple low gain oscillator, i.e. the case as discussed in the original proposition by *Kim et al.* in 2008. This comes with some advantages such as lower demands on the mechanical tolerances, but also with some disadvantages as will be discussed later.

A major issue one needs to address when dealing with an XFELO is the effect of the light-matter interaction between the X-ray field and the Bragg reflectors. This is due to the high requirements for the angular and spatial stability [4, 5] as well as the necessity of very stable Bragg conditions. In the following simulations excluding and including the effect of heating on the XFELO stability will be shown indicating a high relevance of appropriately handling heating effects.

XFELO WITHOUT HEAT LOAD

The simulations of an X-ray oscillator shown in this paper are all based on a combination of the established FEL code *Genesis1.3*[6] and a self written three dimensional wave-front propagation code which first transforms the radiation from the time into the frequency domain and then propagates each two dimensional frequency slice based on the *Fourier Optics* approach[7, 8]. The reflection of the radiation with the Bragg mirrors (in all three reciprocal dimensions) is currently evaluated based on the approximate two-beam dynamical diffraction theory¹.

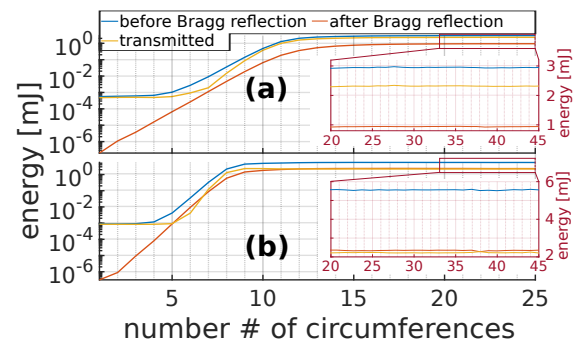


Figure 1: The pulse energy in logscale vs. number of circumferences after the undulator (blue), directly before reentering the undulator (red) and of the forward transmitted pulse (orange) for (a) 250 pC and (b) 500 pC electron bunches. The inset show the saturated energy curve in linear scale and extends the abscissa.

Figure 1 shows the simulation results based on a very simple two diamond mirror XFELO backscattering configuration² with one focusing lens. For out-coupling the downstream

¹ It will soon be extended by the more general n-beam diffraction theory.
² As such backscattering geometry induces multiple beam diffraction - not included in the simulations - an actually realized XFELO would be based on a more complex mirror setup.

* Work supported by BMBF (FKZ 05K16GU4)

[†] patrick.rauer@desy.de

Table 1: Important Parameters Used for Simulation With the Slice Specific Parameters Given for the Slice with the Peak Current

	bunch charge	beam energy	energy spread	energy chirp	bunch length	peak current	norm. slice emittance	und. parameter
	q [pC]	E_B [GeV]	σ_E [MeV]	ΔE [MeV]	t_B [fs]	I_A [kA]	$\epsilon_{(x,y)}$ [mm mrad]	K_{Und}
(a)	250	14.5	0.5	17	24	5.05	(0.324,0.289)	2.8784
(b)	500	14.5	0.5	12	42	4.91	(0.364,0.338)	2.8685
und. length	avg. beta	Bragg wavelength	resonator length	focal length	angular jitter	t -jitter	mirror tilt	cavity loss factor
L_U [m]	$\tilde{\beta}_{(x=y)}$ [m]	λ_c [Å]	L_{Cav} [m]	f_{Lense} [m]	$\tilde{\sigma}_k$ [nrad]	$\tilde{\sigma}_t$ [fs]	$\Delta\Theta$ [nrad]	R_{Cav}
20	25	1.3698	33.31	33.31	100	30	100	0.2

mirror is taken as only $t_{C1} = 42 \mu\text{m}$ thick having a transmission of 2.5 % at the resonant wavelength while the upstream one is taken as $t_{C2} = 150 \mu\text{m}$. The simulations were calculated for realistic electron beam distributions produced by Igor Zagorodnov *et al.*[9] which were projected and parametrized to the longitudinal dimension with every slice of time containing information derived from the transverse dimensions. Additionally important error sources such as angular and timing jitter of the e-beam and mirror tilt are included. Other errors such as absorption in the idealized lenses are taken into account by using a cavity loss factor R_{Cav} describing the fraction of these losses compared to the total reflected energy. Table 1 displays important parameters of the electron distributions, the magnitude of the errors as well as other significant parameters related to the XFEL oscillators such as the undulator parameter K , the central reflection wavelength λ_c , and parameters related to the optical cavity configuration.

As Fig. 1 shows both the (a) 250 pC and the (b) 500 pC electron bunches saturate to quite high photon energies in the millijoule range in only few passes while having a bandwidth of only $\sigma_f \approx 10^{-5}$ and furthermore showing a very high stability on the energy range as can be seen from the inset. Still, there are some things to note. First, the (b) 500 pC case shows with $\mathcal{G} \approx 9$ a severely higher peak single pass gain \mathcal{G} than the (a) 250 pC case with $\mathcal{G} \approx 3.5$, while for a SASE-FEL one would rather expect a comparable gain but saturation at roughly twice the pulse energy. The reason for that is the width of the electron bunches. As the temporal width of the reflected pulse is, due to the small spectral reflection bandwidth, roughly on the order of $t_R \approx 60$ fs the 500 pC electron beam has more overlap with the reflected and stretched seed and therefore also gets a higher gain. Another peculiar fact to note is the high transmitted energy which is $E_{trans}^{500\text{pC}} = 2.22(1)$ mJ for the (b) 500 pC and even higher $E_{trans}^{250\text{pC}} = 2.32(1)$ mJ for the (a) 250 pC bunches and therefore strongly exceeding the transmitted fraction of only a few percent noted before. The reason is the same as for the difference in gain. As due to the Fourier limit a 24 fs or a 42 fs long electron pulse will always generate a spectral width greater than the reflection bandwidth of the regarded (3 3 3)-diamond reflex, the spectral tails which are outside of this bandwidth will get transmitted width nearly 100 % as shown in Figs. 2(a) and 2(b). As the single pass gain for the regarded parameters is much higher than for a classical low gain FEL oscillator there is a considerable fraction of energy in these tails which leads to high transmitted energy but also

a higher spectral width and quite peculiar spectral shape of the transmitted pulse. Also the energy jitter of the transmitted pulse is, with roughly a fraction of 10^{-2} , lower than for a SASE-FEL but higher than at a conventional FEL Oscillator(FELO) which averages the pulse energy over hundreds of round trips.

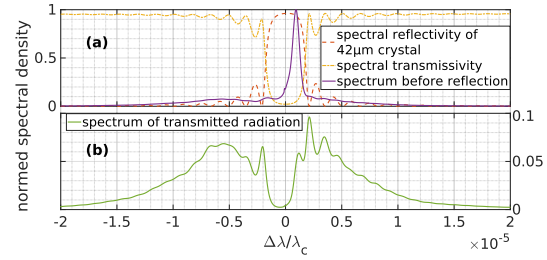


Figure 2: The spectra of the (a) saturated radiation pulse after the undulator before reflection and (b) the out coupled radiation of the 250 pC electron bunch. The majority of the transmitted energy lies in the tails of the incoming radiation outside the reflection bandwidth.

INFLUENCE OF HEAT LOAD

As can be seen from the results presented in Fig. 1 the pulse energy in a saturated XFEL can reach up to several millijoule. Even when taking into account a more conservative estimate of some hundreds of microjoule it is evident that at a rate of at some MHz this will lead to a considerable heat load on the crystal as was already shown by Zemella *et al.*[10]. Approximating the resonant wavelength λ_c with Bragg's law $\lambda_c \propto a_{lat}(T)$ being proportional to the lattice parameter $a_{lat}(T)$ one sees that it is very sensitive to the thermal expansion and therefore to the heat load. It has already been discussed[10] and shown[11] that cooling the crystal to 50 K or 100 K can ease this effect due to the reduced thermal expansion and the much increased thermal conductivity and would be of utter importance for XFEL operation. As was discussed by Maag *et al.* in 2017[11] the very high phonon mean free path l_{mfp} in diamond reaching up to the mm-range at low T introduces effects which are not incorporated in the diffusive Fourier's law and effectively lower the scalar thermal conductivity κ_C , especially when one conservatively assumes purely diffusive scattering at the boundaries. In this work this is incorporated assuming radial symmetry and purely diffusive scattering by using an effective anisotropic thermal conductivity [12–14]

$$\tilde{\kappa}_C^{\text{eff}}(T) = \kappa_C^{\text{bulk}}(T) \cdot \left(\left[1 + 4/3 \cdot l_{mfp}^{\text{bulk}}(T)/t_C \right]^{-1} \left[1 + 3/8 \cdot l_{mfp}^{\text{bulk}}(T)/t_C \right]^{-1} \right)$$

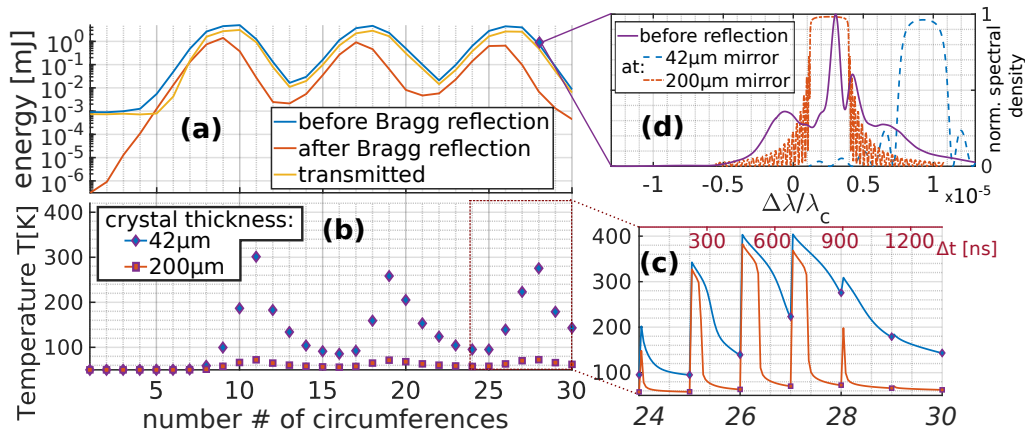


Figure 3: Simulation results of the 500 pC electron bunch with parameters denoted in table 1 but including the influence of the heat load on the crystal temperature. (a) shows the energy vs the number of circumferences clearly exhibiting strong oscillatory features. (b) shows the crystal surface temperature at the center of the incoming beam at the arrival of the next pulse important for the reflection while (c) shows the actual temperature progression also in between the pulses exemplary for the last few passes. Figure (d) shows the spectrum of the radiation after the undulator at the exemplary circumference #28 where the energy peaks and the strongly shifted reflection curves.

with the first dimension being the cross plane and the second dimension the in plane (radial) thermal conductivity.

Figure 3 shows the results for the parameters of the 500 pC electron beam from table 1 but this time including the influence of heat load which was simulated using the FEM-software *COMSOL Multiphysics*®. Despite starting from $T_{crys} = 50$ K Fig. 3(a) shows a strong effect on the energy curve. While showing peak energies comparable to or, for the transmitted beam with $E_{trans}^{500pC} = 3.1$ mJ, even slightly higher than the case without heat load, the energy drops significantly after the peak and show a oscillatory behavior. These particular features can be explained by looking at the temperature T at the photon pulse arrival time displayed in 3(b) and the exemplary spectrum shown in 3(d) for the 28th circumference. The first thing to note is that the energy does not mainly drop due to the overall shift of the reflection curves with respect to the base resonant wavelength λ_c but due to the larger shift of the thin out-coupling diamond with respect to the thick diamond's reflection curve. This leads to a combined reflectivity of only few %. As can be seen from the temperature curves the thin diamond heats significantly more than the thick diamond which is not only due to the effective thermal conductivity reduction discussed above but also due to the smaller volume where the heat can diffuse to. This is also evident from looking at Fig. 3(c) exhibiting much slower thermal diffusion in the thin diamond after circumference #27 even though starting at nearly the same peak temperature. This points out that the entire crystal volume close to the interaction area with the X-ray pulse is at an elevated temperature reducing the temperature gradient ∇T and therefore thermal diffusion.

The reason for the flatness of the peaks is mainly due the high gain of $\mathcal{G} \approx 9$ compensating reflection losses caused by the resonant wavelength shifts. That allows the heat to build up over - in this case - around three round trips until it leads to the situation depicted in Fig. 3(d) having reflection losses which cannot be compensated by the gain anymore.

Then it takes another some five round trips with low incoming radiation energy for the heat to dissipate in the crystal and the two reflection curves reach enough overlap to allow effective pass-to-pass gain greater than zero.

DISCUSSION AND OUTLOOK

Based on the results shown in **XFEL WITHOUT HEAT LOAD** which were obtained by using realistic electron beams optimized for standard SASE operation with strong chirp and critical error sources such as angular beam jitter and mirror tilt the realization of an XFEL seems very feasible at the European XFEL. Even assuming higher cavity losses one would still reach an out-coupled beam with a brilliance higher than any available SASE source while showing a very good shot to shot stability. Unfortunately this view changes when taking into account the effect of heat load on the crystal temperature as shown in the previous section. This still allows high peak brilliance but the out-coupled beam would show severe shot to shot jitter. Nonetheless there are some possibilities to handle the effect. The simplest would be to lower the single pass gain leading to reduced saturation energies and bringing the XFEL more closely to the operation of a conventional FEL. Another possibility is to use a thicker out-coupling mirror reducing the strong shift of the reflection curves with respect to each other. This would be possible due to the short electron bunches producing spectra wider than the diamond reflection width. This comes with the cost of an out-coupled radiation more subject to shot to shot jitter in the electron parameters but which is mostly compensated by the strong single mode coherent seeding.

Finally, tests at the European XFEL are considered.

ACKNOWLEDGEMENTS

This research was supported in part through the Maxwell computational resources operated at Deutsches Elektronen-Synchrotron (DESY), Hamburg, Germany.

REFERENCES

- [1] K.-J. Kim, Y. Shvyd'ko, and S. Reiche, "A proposal for an x-ray free-electron laser oscillator with an energy-recovery linac," *Physical Review Letters*, vol. 100, no. 24, Jun. 2008. doi: 10.1103/physrevlett.100.244802.
- [2] B. Adams and K.-J. Kim, "X-ray comb generation from nuclear-resonance-stabilized x-ray free-electron laser oscillator for fundamental physics and precision metrology," *Physical Review Special Topics - Accelerators and Beams*, vol. 18, no. 3, Mar. 2015. doi: 10.1103/physrevstab.18.030711
- [3] *European XFEL*, http://www.xfel.eu/overview/facts_and_figures/
- [4] S. Stoupin, F. Lenkszus, R. Laird, K. Goetze, K.-J. Kim, and Y. Shvyd'ko, "Nanoradian angular stabilization of x-ray optical components," *Review of Scientific Instruments*, vol. 81, no. 5, p. 055 108, 2010. doi: <http://dx.doi.org/10.1063/1.3428722>
- [5] C. Maag, J. Zemella, and G. J. Rossbach, "Numerical studies of the influence of the electron bunch arrival time jitter on the gain process of an xfel-oscillator for the european xfel," in *Proc. of FEL2015, Daejeon, Korea*, paper TUP032, 2015, pp. 436–438.
- [6] S. Reiche, *Genesis 1.3*, <http://genesis.web.psi.ch/>
- [7] O. Chubar, M.-E. Couprie, M. Labat, G. Lambert, F. Polack, and O. Tcherbakoff, "Time-dependent FEL wavefront propagation calculations: Fourier optics approach," *Nuclear Instruments and Methods in Physics Research Section A: Accelerators, Spectrometers, Detectors and Associated Equipment*, vol. 593, no. 1-2, pp. 30–34, Aug. 2008. doi: 10.1016/j.nima.2008.04.058
- [8] J. D. Schmidt, *Numerical Simulation of Optical Wave Propagation With Examples in MATLAB*, ser. SPIE Press Monograph. SPIE Press, 2010, vol. Vol. PM199, ISBN: 978-0-8194-8326-3
- [9] I. Zagorodnov, "Start2end simulation fel beam xfel," 2014, <http://www.desy.de/fel-beam/s2e/xfel.html>
- [10] J. Zemella, J. Rossbach, C. Maag, M. Tolkiehn, and H. Sinn, "Numerical simulations of an XFEL for the European XFEL driven by a spent beam," in *Proc. of FEL2012, Nara, Japan*, paper WEPD29, 2012, pp. 429–433, ISBN: 978-3-95450-123-6.
- [11] C. Maag, I. Bahns, J. Rossbach, and P. Thiessen, "An experimental setup for probing the thermal properties of diamond regarding its use in an xfelo," in *Proc. of FEL2017, Santa Fe, USA*, paper MOP064, 2017, pp. 200–203. doi: 10.18429/JACoW-FEL2017-MOP064
- [12] A. Majumdar, "Microscale heat conduction in dielectric thin films," *Journal of Heat Transfer*, vol. 115, no. 1, p. 7, 1993. doi: 10.1115/1.2910673
- [13] J. Maassen and M. Lundstrom, "Steady-state heat transport: Ballistic-to-diffusive with fourier's law," *Journal of Applied Physics*, vol. 117, no. 3, p. 035 104, 2015. doi: 10.1063/1.4905590
- [14] J. Kaiser, T. Feng, J. Maassen, X. Wang, X. Ruan, and M. Lundstrom, "Thermal transport at the nanoscale: A fourier's law vs. phonon boltzmann equation study," *Journal of Applied Physics*, vol. 121, no. 4, p. 044 302, Jan. 2017. doi: 10.1063/1.4974872

SMITH-PURCELL RADIATION EMITTED BY PICO-SECOND ELECTRON BUNCHES FROM A 30 KeV PHOTO-ELECTRON GUN

M. R. Asakawa*, S. Yamaguchi

Department of Pure and Applied Physics, Kansai University, Osaka, Japan

Abstract

A compact radiation source based on the combination of Smith-Purcell radiation and the coherent radiation emitted by the short electron beam is being developed. A photo-electron gun driven by 100 fs laser generated short pulse electron beam with a charge of 300 pC at the space-charge limitation operation. To evaluate the pulsewidth of the photo-electron beam, we developed a method based on the envelope equation. In this method, the pulsewidth was evaluated by the comparison of the measured beam radius and calculated beam radius. The result showed that while the pulsewidth increased with the beam charge, it remained shorter than 3.3 ps even at the maximum charge operation. With this electron beam, experiments to generate Smith-Purcell radiation was performed. Nonlinear dependence of the radiation energy on the charge was observed and this result indicated the occurrence of the collective radiation process.

PULSEWIDTH LENGTHENING OF PHOTO-ELECTRON BEAM

The electron gun consists of a cathode electrode held at -30 keV and a grounded anode electrode. The photo-emission surface of tungsten, 19 mm in diameter, was irradiated by a frequency-tripled Ti:sapphire laser. The pulsewidth of the laser pulse was measured to be 92 fs. The incident angle was set to be 60 degree to the normal and the ellipsoidal laser spot had an area of $1.5 \times 3 \text{ mm}^2$. The irradiation energy onto the cathode was varied from 20 to 260 μJ . Further irradiance led to the unfavorable plasma formation which caused to short-circuit. The spacing between the electrodes were 10 mm. The anode electrode was a metallic disk, 14 mm in diameter, 2 mm in thickness, and had a pinhole with a diameter of 2 mm at the center. The electron passed through this pinhole moved forward to a phosphor screen located at 83 mm from the pinhole. The beam diameter was estimated from the fluorescent image and the beam charge was also measured at the phosphor screen. The pressure of the electron gun was maintained below $5 \times 10^{-7} \text{ Pa}$ for all experiments [1].

By irradiating a 220 μJ laser pulse, the photo-electron gun reached to the space-charge limitation [2] and electron beam with a charge of 300 pC emerged from the cathode electrode. Roughly estimated current density at the cathode surface exceeded to 20 kA/cm^2 , which is 700 times as dense as Child-Langmuir limitation current density. Figure 1 shows the dependence of the beam diameter on the beam charge at the phosphor plate. The maximum charge of the electron beam which passed through the pinhole was measured to be

11.6 pC when the electron gun reached at the space charge limitation operation. It is seen that the diameter increased with the beam charge up to the charge of 4 pC and remained almost constant for larger charge. This result indicates that the electron beam with the charge greater than 5 pC may increase its pulsewidth to relax the repulsive self-field.

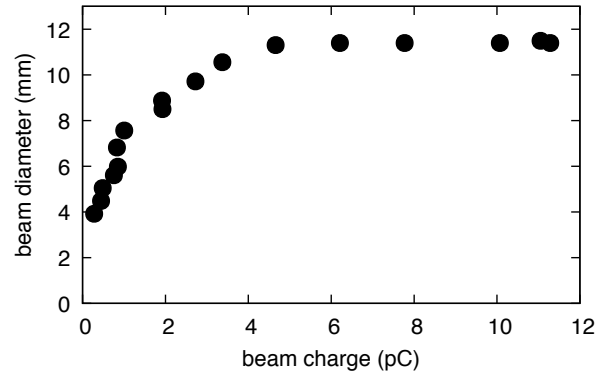


Figure 1: Dependence of the beam diameter on the beam charge.

To estimate the pulsewidth of the beam charge from the dependence of the beam radius on the beam charge shown in Figure 1, we developed a method based on the envelope equation [3]

$$\frac{d^2 r}{dz^2} - \frac{K}{r} - \frac{\epsilon}{r^3} = 0, \quad (1)$$

where r denotes the radius of the electron beam moving along z -axis with a perviance K and an emittance ϵ . The emittance ϵ of the photo-electron beam emerged from a metallic cathode with a work function ϕ by irradiation of photons with a energy of $h\nu$ is given by

$$\epsilon = \gamma \beta \pi r \sqrt{\frac{2(h\nu - \phi)}{3mc}}, \quad (2)$$

where γ and β are the Lorentz factor and the normalized velocity of the electron beam, respectively. In our case, $\phi = 4.5 \text{ eV}$ and $h\nu = 4.66 \text{ eV}$. The perviance K for the electron beam with an initial radius r_0 , an initial current density j_0 at the pinhole and a normalized pulsewidth τ is defined as

$$K = \alpha(\tau) \frac{ej_0 r_0}{2\epsilon_0 m (\gamma \beta c)^3}, \quad (3)$$

Here $\alpha(\tau)$ is the ratio of the transverse electric field produced by a short-pulse electron beam with a pulsewidth T to that produced by a DC electron beam, and the normalized pulsewidth τ is defined as

$$\tau = \frac{c \beta T}{r} \quad (4)$$

* asakawa@kansai-u.ac.jp

Different from the DC electron beam, the short-pulse electron beam produce the electric field not only on its cylindrical side-surface but also on its both base surfaces. According to Gauss' law, thus, the transverse electric field of the short-pulse beam is weaker than that of DC beam. Parameter $\alpha(\tau)$ is introduced to take account this effect. From numerical calculations of the electric fields produced by the cylindrically distributed charges whose τ (= height/radius) range from 10^{-3} to 1, we obtain an empirical formula

$$\alpha(\tau) = 0.78\tau^{0.59}. \quad (5)$$

A particle in cell type numerical simulation stated that the pulsewidth of the electron beam lengthened significantly near the cathode electrode and remained constant after the beam passed through the pinhole. With the assumption that the pulsewidth remained unchanged during the propagation in the 83 mm-long field free drift space, the initial current density j_0 is evaluated by a charge Q measured at the phosphor plate and a pulsewidth T which functions as a calculation parameter

$$j_0 = \frac{Q}{\pi r_0^2 T}. \quad (6)$$

Here the pinhole radius $r_0 = 1$ mm. The estimation of the pulsewidth was carried out in the following steps.

- measure the beam charge Q_{exp} and beam radius r_{exp} at the phosphor plate.
- by using eq. (1), calculate radii r_{cal} of beams after the propagation through the 83 mm-long drift space with a charge of Q_{exp} and various pulsewidth T .
- find the best T with which r_{cal} agrees well with r_{exp} .

Figure 2 shows the dependence of the estimated pulsewidth on the beam charge. It is seen that the pulsewidth increases rapidly as the charge exceeds 5 pC and, even with the maximum charge, the pulsewidth remains less than 3.3 ps. Corresponding longitudinal spatial length of the electron beam is $0.33c \times 3.3\text{ps} = 0.327$ mm, here 0.33 is the normalized velocity of 30 kV electron. The photo-electron beam was short enough to excite the coherent millimeter-wave.

GENERATION OF COHERENT SMITH-PURCELL RADIATION USING SHORT-PULSE ELECTRON BEAM

The electron beam whose longitudinal length is shorter than the radiation wavelength can generate coherent radiation. We performed the experiment to generate the coherent Smith-Purcell radiation with the photo-electron beam. A metallic grating with a period of 2 mm was assembled just behind the pinhole so that the electron beam may graze the grating surface. Experimental setup is shown in Figure 3 and details of the grating are listed in table 1. With this grating, the resonance wavelength of the Smith-Purcell radiation is to be 4.1 mm for an observation angle of 10 degree

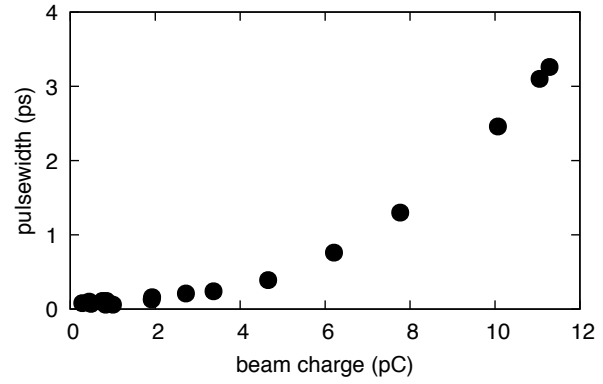


Figure 2: Dependence of the pulsewidth on the beam charge.

and is 12 times longer than the longitudinal beam length of the electron beam at the maximum charge. The radiation was outcoupled through a single-crystalline quartz window into the air and the radiation energy was measured using a bolometer. In this case, the movable phosphor plate served as a charge collector to measure the charge of the beam which had passed through the grating.

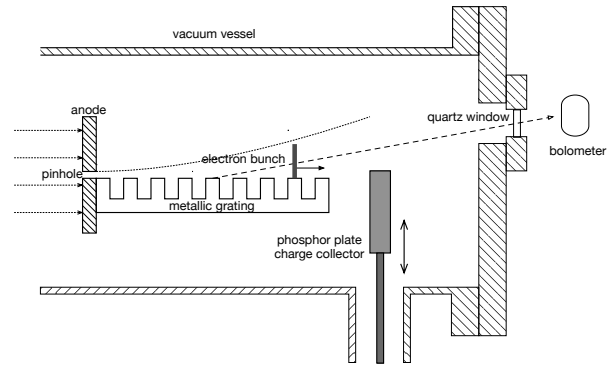


Figure 3: Experimental setup.

Table 1: Grating Parameters

period	2 mm
depth	4 mm
number of periods	20
width	5 mm

Figure 4 shows the dependence of the radiation energy on the beam charge. Due to the increase in the beam radius during the propagation along the grating surface, the half of the electron beam was scraped off, so the maximum charge was limited to 7.9 pC in this experiment. The radiation energy was proportional to 1.6th power of the charge. This nonlinear dependence is the evidence of the collective behavior of the short electron beam [4].

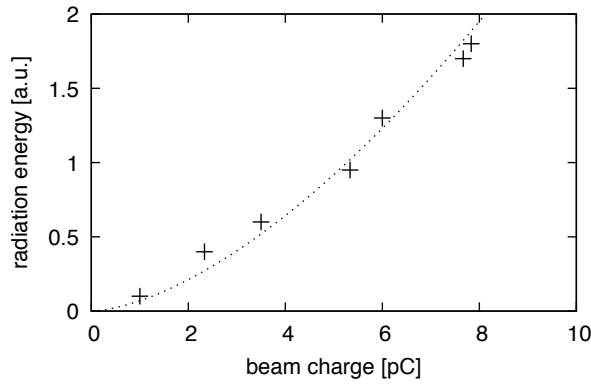


Figure 4: Dependence of the radiation energy on the beam charge. Dashed line indicates $\propto Q^{1.6}$ curve.

In an ideal situation, however, quadratic dependency should be observed. First the weaker dependency observed in the experiment may be linked to the increase in the longitudinal length of the electron beam with the beam charge. Radiation field produced by a pack of N electrons lying in the longitudinal length of $c\beta T$ is approximately expressed as

$$NE_0 \left[1 - \frac{1}{6} \left(\frac{\pi c \beta T}{\lambda} \right)^3 \right], \quad (7)$$

where E_0 is the radiation field produced by single electron and λ is the wavelength of the radiation. In the experiments $\pi c \beta T / \lambda$ is 1/4 at most, thus the second term involving the pulsewidth lengthening effect is negligible. The other cause that should be consider may be the fact that number of electrons contributing to produce Smith-Purcell radiation is not proportional to the beam charge. Because the surface wave from which Smith-Purcell radiation originates is evanescent, only the electrons moving vicinity of the grating surface contribute to excite the surface wave. The damping length of the surface wave $\frac{1}{\alpha}$ is related to the wavenumber of the surface wave k , the wavenumber of the grating κ and the plasma frequency of the electron beam ω_p as [4, 5]

$$\alpha^2 = (k + \kappa)^2 - \frac{\omega^2}{c^2} + \frac{\omega_p^2}{c^2}. \quad (8)$$

For this experiment, $\frac{1}{\alpha} \approx 0.4$ mm. Only electrons within 0.4 mm from the grating surface, thus, contribute to the radiation process. As shown in Figure 1, the beam diameter rapidly increased from 4 mm to 11 mm as the charge increase from 0.1 pC to 4 pC. Thus the cross-sectional charge density was not proportional to the charge and rather remained constant for low charge range. We attribute the weaker dependency to this effect.

Further experiments are now under way. A terahertz time-domain spectroscopy system had been installed to measure the time-trace of the electric field of the radiation. Also combined metallic slit arrays are being developed to demonstrate the efficient outcoupling of the energy of the evanescent surface wave [6].

REFERENCES

- [1] M. R. Asakawa, *et al.*, “Electron Guns for Free-Electron Lasers”, *IEEEJ Trans. on Fundamental and Materials*, 134, 2014, pp. 22-25. doi:10.1541/ieejfms.134.22
- [2] H. Yamamoto, *et al.*, “Space-Charge Limitation of a Femtosecond Photoinjector”, *Int. J. Opt.*, vol. 2011, Article ID 714265, pp. 1-5. doi:10.1155/2011/714265
- [3] *The Physics of Charged-Particle Beams 2nd edition*, J. D. Lawson, Oxford Science Publications, 1988, pp. 173.
- [4] D. Li, *et al.*, “Super-radiant Smith-Purcell radiation from periodic line charges”, *Nucl. Instrum. Methods Phys. Res., Sect. A*, vol.674, 2012, pp. 20-23. doi:10.1016/j.nima.2012.01.039
- [5] H. L. Andrews, C. A. Brau, “Gain of a Smith-Purcell free-electron laser”, *Phys. Rev. Spec. Top. Accel Beams*, 7, 2004, 070701. doi:10.1103/PhysRevSTAB.7.070701
- [6] D. Li, *et al.*, “Terahertz Radiation from Combined Metallic Slit Arrays”, *Scientific Reports*, 9, 2019, 6804. doi:10.1038/s41598-019-43072-2

CROSSED-UNDULATOR CONFIGURATION FOR VARIABLE POLARIZED THz SOURCE

H. Saito, H. Hama, S. Kashiwagi, T. Muto, K. Nanbu, N. Morita, H. Yamada
Research Center for Electron Photon Science, Tohoku University, Sendai, Japan

Abstract

A variable polarized THz source employing a crossed-undulator configuration has been developed at Research Center for Electron Photon Science (ELPH), Tohoku University. An initial experiment will be demonstrated shortly using newly constructed compact planar undulators at a femtosecond short-bunch facility, t-ACTS, in ELPH. The undulators have equivalent parameters such as the period length of 8 cm and the number of periods is 7, but the field directions are crossed each other perpendicularly. The resonant frequency of 1.94 THz for the beam energy of 22 MeV. Magnetic field measurements have been already performed. The measured field strength distributions of the two undulators were mostly identical to each other. A beam transport line of variable R56 triple bend lattice intersecting the crossed-undulator configuration has been studied for phase control of interference between two radiations (namely the phase shifter). According to a tentative design of the phase shifter beam line, the degree of circular polarization may exceed 0.9 for the fundamental frequency of 1.94 THz in a narrow cone of angular spread of 2 mrad.

INTRODUCTION

Polarization control using the crossed-undulator configuration proposed by M. B. Moiseev et al. and K.-J. Kim [1, 2] was firstly demonstrated by J. Bahrtdt et al. on a synchrotron radiation source BESSY-1 in 1990 [3]. The crossed-undulator configuration consists with two planar undulators with magnetic fields perpendicular to each other separated by an electromagnetic modulator (we call “the phase shifter line”). The phase shifter had brought variable delay time and then the phase difference between two radiation waves was able to vary from 0 to 2π . Since a monochromator was used the two waves is coherently superposed and then any states of polarization from linear to circular in both helicities can be produced. A great advantage in this method is that first helicity switching is enable owing to small change of beam pass length in the phase shifter line, meanwhile changing magnetic field helicity in the identical helical undulator takes some considerable time even using electromagnetic undulator. In studies for handedness (chirality) in materials, the first helicity switching is pretty important because signal-to-noise ratio of circular dichroism experiment is usually very poor.

Circular dichroism spectroscopy using longer wavelength electromagnetic radiations is valuable for the studies of structural analysis of biomolecules such as proteins, nucleic acids. Since polarization control using optical elements for the solid-state/laser based THz sources is

well established yet, it would be worth to consider the first helicity switching of circular polarization for accelerator-based THz source. In this sense, without monochromators, direct superposition of coherent THz radiations from the crossed-undulator configuration is a state-of-the-art solution for the biomolecular circular dichroism.

In this article, a current status of development of the variable polarized THz source at ELPH, Tohoku University.

THz CROSSED-UNDULATOR CONFIGURATION

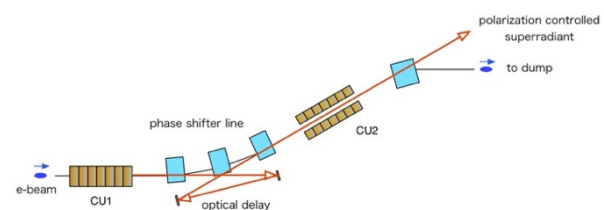


Figure 1: Crossed-undulator configuration. Path length difference between the beam and THz superradiance has to be varied in the phase shifter line. Since the e-beam transport matrix element of R_{56} should be variable for compensation of bunch lengthening due to momentum dispersion, the optical delay is controlled so as to satisfy the radiation phase difference from 0 to 2π .

Conceptual layout of the crossed-undulator configuration is shown in Fig. 1. The lower energy beam causes bunch lengthening in itself because of finite energy spread. In addition, R_{56} inside of the undulator has to be taken into account as well. So careful consideration of the phase shifter line is indispensable. At present, we have a tentative design of triple-bend beam achromat transport with small bending angle, which is better than a chicane type line. The study regarding the phase shifter beam line will be reported elsewhere [4].

Femtosecond Short-Bunch Facility, t-ACTS

At the t-ACTS (test Accelerator as Coherent THz Source) facility [5], Tohoku University, the short-pulse electron beam is stably produced via velocity bunching scheme in a traveling wave accelerating structure [6]. A specially designed independently tunable cells thermionic RF gun (ITC-RF gun) is employed to manipulate the longitudinal phase space of the beam extracted from LaB₆ cathode. The beam filtered in an alpha magnet accelerated in a 3 m S-band linac. The usual bunch length of a micro-pulse deduced from CTR spectrum measured by a Mi-

chelson interferometer is 80 ~ 100 fs [7]. Macropulse duration is able to vary from 1 to 2 μ s, so that it contains 3000 ~ 5000 micropulses (typical charge is ~ 2 pC/bunch). We have already observed 3 THz undulator super-radiance successfully. Although the maximum beam energy is 50 MeV, velocity bunching mode provides an energy of 22 MeV due to off-crest acceleration.

Crossed-Undulator

Table 1: Undulator Parameters

Magnet array	Halbach type
Block dimension	70 mm x 23 mm x 20 mm
Period length	80 mm
Number of periods	7
Magnet material	NdFeB
Residual magnetic field	1.22 T
Gap	33 mm
Peak magnetic field	0.471 T
K value	3.52

In order to demonstrate a proof-of-principle experiment, fixed-gap planar undulators for the crossed-undulator configuration were designed, in which one is for horizontal deflection (CU1) and the other is vertical one (CU2). The undulator parameters are given in Table 1. The fundamental frequency has been chosen to be ~ 2 THz because taking the bunch length and beam energy of the t-ACTS linac into account the coherent radiation around such frequencies is easily generated with no troublesome machine tuning. The number of periods is only 7 for both undulators because available space in the t-ACTS facility is limited and the first step of this study would be a proof-of-principle experiment.

For the low energy electron beam, undulator focusing powers in perpendicular direction to the deflecting plane is often disturb the quality of the radiation and the expected optics of beam transport for the experiment. The focusing power per unit length is calculated as $k = \frac{1}{2} \left(\frac{B_0}{B\rho} \right)^2$, where B_0 and $B\rho$ are the undulator peak magnetic field and the beam rigidity and obtained to be 20.6 m⁻² for the beam energy of 22 MeV that is considerably large and then not able to ignored. Phase advance of the betatron motion along the whole undulator length is approximately π . In addition, the oscillating amplitude in the particle trajectory is not so small that another focusing power in the deflecting plane arises as well. Particle tracking simulation with a 3 D magnetic field calculation [8] was performed to evaluate the focusing powers and find matching conditions so as to make a beam waist at the centre of undulator for both planes. Deduced focusing powers in the plane perpendicular to the deflecting plane and the deflecting plane are 22.2 m⁻² (this is consistent with the theoretical value) and -1.2m⁻², respectively. The matching conditions of Twiss parameter (β , α) for the non-deflecting plane and the deflecting plane were obtained to be (2.4 m, 2.6) and (2.8 m, 1.8), respectively for

an entrance position of 1 m upstream of the undulator centre. Simulated trajectory of particles in the non-deflecting plane is shown in Fig. 2 for instance.

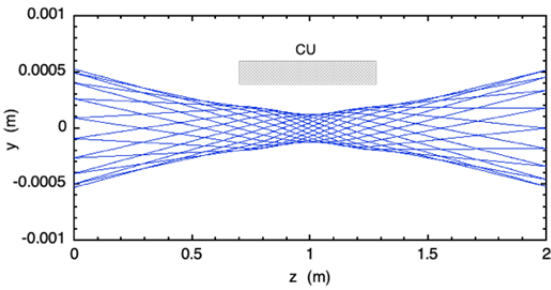


Figure 2: Symmetric beam trajectory satisfying a matched condition in the non-deflecting plane.

The undulators were manufactured and fabricated already at a Japanese industry, NEOMAX engineering Co., Ltd. Measured magnetic fields of CU1 and CU2 are denoted in Fig. 3 together with calculated one using RADIA [9] with the residual field of 1.221 T. Those field distributions are well agreed. Since the target wavelength is longer, accuracy of the field characteristics such as phase error is not critical.

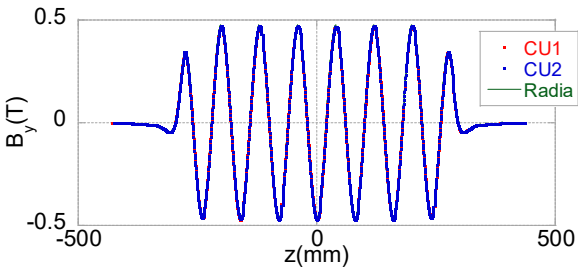


Figure 3: Measured magnetic fields in the direction perpendicular to deflecting planes of both CU1 and CU2. RADIA calculation is also plotted.

R₅₆ IN THE UNDULATOR

Quality of coherent radiation from CU2 is really important for complete control of the polarization. As one notices, there seems to be some obstacles should be considered. If the 6-dimensional phase space of the beam is preserved, two radiations would be successfully composed. Coherent synchrotron radiation (CSR) would affect the transverse phase space in bending transport lines. The CSR effect is, however, able to reduce by choosing small bending angle. In this crossed-undulator configuration, a serious issue is bunch lengthening caused during passing through undulator because of lower beam energy. In order to design the phase shifter line introducing proper R₅₆ that compensates that in the undulator, accurate estimation of path length difference in the undulator is required.

Using the first order approximation, the path length difference ΔL of a particle having a relative energy deviation δ is calculated as

$$\Delta L = R_{56} \delta = c \beta_0 t_0 \left(\frac{1}{\gamma_0} - \alpha_c \right) \delta, \quad (1)$$

where the subscript 0 denotes the reference particle. The momentum compaction factor α_c is calculated as

$$\alpha_c = \frac{1}{L_0} \int_0^{L_0} \frac{\eta}{\rho} ds \quad (2)$$

It should be noted that even in a drift space R_{56} is not vanished and negligible. Figure 4 shows the path length dependence of R_{56} calculated by a tracking simulation using the realistic magnetic field. As one can see R_{56} is rapidly increasing than the drift space because of the dispersion function in the undulator, and bunch lengthening in the undulator is approximately 20 μm for the 1 % energy spread that is comparable to the initial bunch length. In addition, bunch lengthening in the drift space is significant as well. Consequently, the beam optics for the phase shifter line has to be carefully designed.

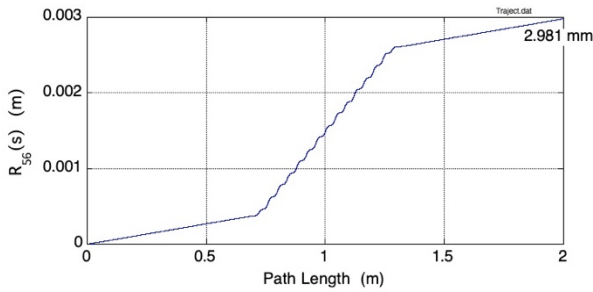


Figure 4: R_{56} variation along the beam line include the undulator. Straight lines at both sides are in drift spaces.

DEGREE OF CIRCULAR POLARIZATION

Polarization properties of the radiation is well-expressed by using Stokes parameters S_{1-3} [10]. Degree of Circular polarization ($DoCP$) is expressed as $DoCP = S_3/S_0$ ($= +1$: right hand, $= -1$ left hand). Assuming complete sinusoidal electric field of the undulator radiation with angular dependence of the resonant wavelength as

$$\lambda(\theta) = \frac{\lambda_u}{2\gamma^2} \left(1 + \frac{K^2}{2} + \gamma^2 \theta^2 \right), \quad (3)$$

After some maths angular dependence of $DoCP$ is deduced to be

$$DoCP(\theta) = \sin \left[\pi \frac{4k(\cos\theta - 1) \pm \zeta}{2\zeta + \theta^2} \right] \times \left[1 - \frac{4k(\cos\theta - 1) \pm \zeta}{N_u(2\zeta + \theta^2)} \right], \quad (4)$$

where $\zeta = \frac{1}{2\gamma^2} \left(1 + \frac{K^2}{2} \right)$ and N_u is the number of periods of the undulator. A symbol $k = \ell/\lambda_u$ and ℓ is the distance between centres of two undulators. Equation (4) is expressed for which the on-axis phase difference between two undulator radiations is tuned to a complete circular polarization. Figure 5 shows expected angular depend-

ence of $DoCP$ for the case of the undulator parameters in Table 1 with a beam energy of = 22 MeV and the distance is 2.6 m. Higher $DoCP$ might be obtained at solid angle within ~ 2 mrad. It should be noted that the calculation is for single-particle case. Although effects of transverse beam emittance is not estimated yet, the normalized beam emittance of the t-ACTS linac (~ 5 mm.mrad) is so smaller than diffraction limit of THz radiation that the effects would be limited.

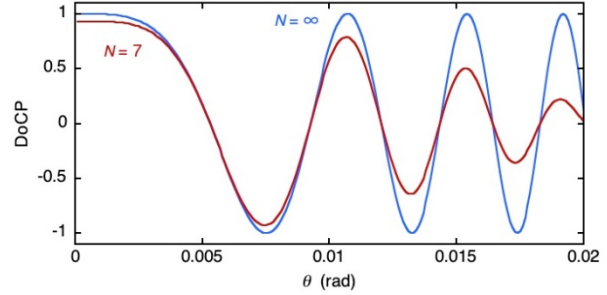


Figure 5: Calculated $DoCP$ according to Eq. (4).

CONCLUSION

A variable polarized THz light source using a crossed-undulator configuration has been developed at Tohoku University. Currently preparation including hardware for a proof-of-principle experiment at t-ACTS facility is underway. The measured magnetic fields of undulators are in good agreement with each other. Fundamental frequency and angular spread of the radiation are estimated to be 1.9 THz and 17 mrad (HWHM), respectively. A phase shifter has been under designing work by considering bunch lengthening in whole system geometry and the undulator. Assuming the sinusoidal radiation fields, degree of circular polarization larger than 0.9 would be obtained in the solid angle of 2 mrad. Detailed study is still under way.

ACKNOWLEDGEMENT

This work was supported by JSPS KAKENHI Grant Number JP17H01070 and JP15K13401.

REFERENCES

- [1] M. B. Moiseev, M. M. Nikitin, and N. I. Fedesov, "Change in the kind of polarization of undulator radiation", *Sov. Phys. J.*, 21, 332 (1987).
doi:10.1007/BF00894728
- [2] K-J. Kim, "Polarization characteristics of synchrotron radiation sources and a new two undulator system", *Nucl. Inst. and Meth.*, 222, 11 (1984).
doi:10.1016/0167-5087(84)90497-6
- [3] J. Bahrdrdt, A. Gaupp, W. Gudat, M. Mast, K. Molter, W. B. Peatman, M. Scheer, Th. Schroeter, and Ch. Wang, "Circularly polarized synchrotron radiation from the crossed undulator at BESSY", *Rev. of Sci. Instr.*, 63, 339 (1992).
doi:10.1063/1.1142750
- [4] N. Morita *et al.*, presented at Annual meeting of Japanese Particle Accelerator Society, Kyoto, August, 2019.

- [5] H. Hama, M. Kawai, S. Kashiwagi, F. Hinode, F. Miyahara, K. Nanbu, T. Muto, Y. Tanaka, X. Li, and N.-Y. Huang, "Test-accelerators as coherent terahertz source program (t-ACTS) at Tohoku University", *Energy Procedia*, vol. 9, 391 (2011).
doi:10.1016/j.egypro.2011.09.042
- [6] L. Serafini and M. Ferrario, "Velocity bunching in photo-injectors", *AIP Conf. Proc.*, 581, 87, (2001).
doi:10.1063/1.1401564
- [7] H. Hama, T. Abe, S. Kashiwagi, F. Hinode, T. Muto, K. Nanbu, K. Takahashi, I. Nagasawa, K. Kanomata, H. Saito and Y. Saito, "Demonstration of Coherent Radiation Generation up to 3 THz from Femtosecond Electron Pulses", *J. Opt. Photonics Eng.*, 2:004 (2017).
- [8] H. Hama, private computer code, SUZUCHAN v12, (2011).
- [9] O. Chubar *et al.*, "A three-dimensional magnetostatics computer code for insertion devices", *J. Synchrotron Rad.*, vol. 5, 481, (1998).
doi:10.1107/S0909049597013502
- [10] N. M. Garcia, I. d. Erasquin, C. Edminston and V. Gruev, "Surface normal reconstruction using circularly polarized light", *Opt. Express*, Vol. 23, No. 11, 14391, (20125).
doi:10.1364/OE.23.014391

DESIGN OF HIGH-REPETITION TERAHERTZ SUPER-RADIATION BASED ON CAEP THz FEL SUPERCONDUCTING BEAMLINE*

D. Wu, K. Zhou, L. G. Yan, P. Li[†], J. X. Wang, L. B. Li, Q. Pan, D. X. Xiao,
X. Luo, H. B. Wang, X. M. Shen, P. Zhang, L. J. Shan, T. H. He, M. Li

Institute of Applied Electronics, China Academy of Engineering Physics, Mianyang, 621900, China

Abstract

China Academy of Engineering Physics terahertz free electron laser (CAEP THz FEL, CTFEL) is the first THz FEL oscillator in China. CTFEL spectrum covers from 0.7 THz to 4.2 THz. However, there are still many applications requiring lower frequency. The super-radiation of the ultra-short electron beam bunches could generate ultra-fast, carrier-envelope-phase-stable, and high-field terahertz. The coherent diffraction/transition radiation (CDR/CTR) and coherent undulator radiation (CUR) can be also synchronized naturally. In this paper, the dynamic and the design of the super-radiation are introduced. The main parameters of the CDR/CTR and CUR are also discussed. A multi-color pump-probe system based on super-radiation is also proposed.

INTRODUCTION

CAEP THz FEL (CTFEL) facility is the first high average THz source based on FEL in China [1, 2], which is driven by a DC gun with a GaAs photocathode [3, 4] and two 4-cell 1.3 GHz super-conducting radio frequency (SRF) accelerator [5, 6]. The repetition rate of CTFEL is 54.167 MHz, one over twenty-four of 1.3 GHz. The effective accelerating field gradient is about 10 MV/m.

CTFEL has achieved the stimulated saturation in August, 2017[7, 8]. The terahertz frequency is continuously adjustable from 0.7 THz to 4.2 THz.

The upgrade of CTFEL is to broaden its spectrum and improve its power. There are many applications on condensed matter physics in the spectrum from 0.1 THz to 1.5 THz, such as control of antiferromagnetic spin waves[9], resonant and nonresonant over matters[10], magnetic order [11], the 2D materials[12], and so on. So, it is important to cover the lower frequency domain, and afford a high-repetition, carrier-envelope-phase-stable THz source.

When the electron beam bunch is compressed to less than 1 ps, et, less than the wavelength of THz wave, the terahertz coherent radiation will be generated as transition radiation, diffraction radiation, synchrotron radiation, or undulator radiation, which are often called as super-radiation. In this paper, a beamline is design based on CTFEL to generate a multi-color THz beams with Coherent Diffraction/Transition Radiation (CDR/CTR) and Coherent Undulator Radiation

(CUR). The repetition can reach up to 54 MHz, and the pulse energy is more than 0.1 μ J.

BEAMLINE DESIGN

Figure 1 shows the layout of the CTFEL facility. High average power high-brightness electron beam is emitted from the high-voltage DC gun equipped with a GaAs photocathode. The beam is then energized by a 2 \times 4-cell RF superconducting accelerator and gain kinetic energy from 6 MeV to 8 MeV. Passing through an achromatic section, the beam then goes into the undulator magnet field and generates spontaneous radiation. The radiation resonates in the THz optical cavity and reaches saturations.

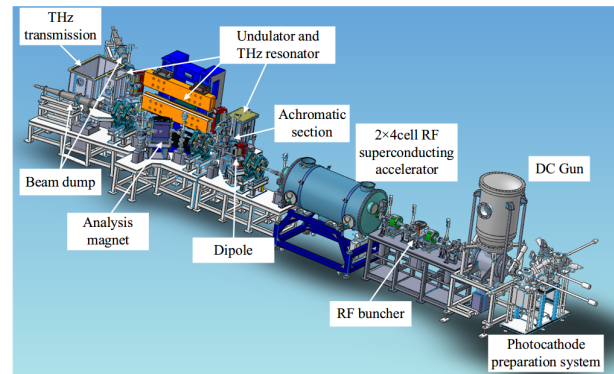


Figure 1: The layout of CTFEL facility.

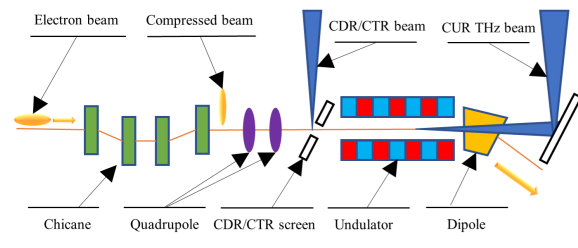


Figure 2: Schematic diagram of the super-radiation beam line.

When the electron pass straight downstream the SRF cavity, it can be used to generate the super-radiation. The schematic is shown on Fig. 2. The chirped bunch firstly passed through a chicane to be compressed, and then a screen with a hole to generate CDR beam (or CTR beam without a hole), then a short undulator to generate CUR beam.

* Work supported by National Natural Science Foundation of China with grant (11575264, 11605190 and 11805192), Innovation Foundation of CAEP with grant (CX2019036, CX2019037)

[†] burnlife@sina.com

DYNAMIC SIMULATION

There are two ways to achieve ultra-fast electron beam, by velocity bunching or by chicane. Figure 3 (a) shows the ultra-fast beam's longitudinal phase space compressed by velocity bunching. The undulator is located 12 m downstream of the cathode. The velocity bunching keeps the longitudinal rms length of the beam less than 200 fs within 1 m (as shown in Fig. 3 (b)), which is enough to place a CTR/CDR target and 10-period short undulator. The energy spread is wider than the requirement of free electron laser but it has less effect on super-radiation. One of the superconducting cavity is used to be as a buncher, so the energy of the electron beam is a little low, as shown in Fig. 3 (c). The kinetic energy is about 5.2 MeV, which will reduce the width of CDR/CTR spectrum.

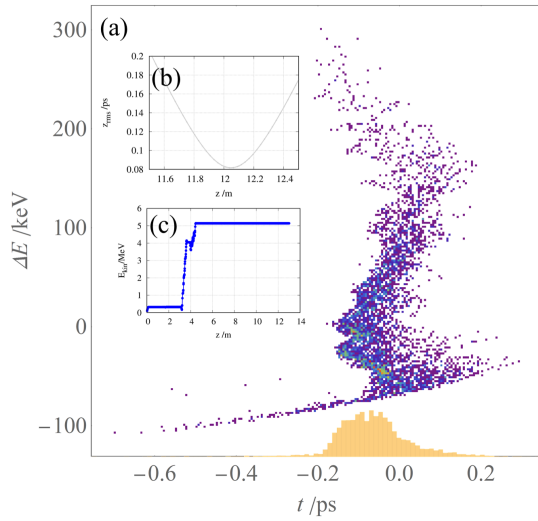


Figure 3: Longitudinal phase space of the electron beam compressed by velocity bunching.

When the chicane is on, the longitudinal distribution grows wider than the velocity bunching because of the coherent synchrotron radiation (CSR), as shown in Fig. 4 (a). However, the length increases much slower after the longitudinal focal point, as shown in Fig. 4 (b). And the energy of the electron beam could be larger than 7 MeV to generate a broader spectrum.

SUPER-RADIATION CALCULATION

When an electron beam generate a coherent radiation, its energy spectrum can be described as:

$$U(\omega) = U_e(\omega)[1 + N(N-1)F(\omega)], \quad (1)$$

where U_e is the spectrum generated by a single electron, it differs from the radiation type, such as undulator radiation (UR), diffraction radiation (DR) or transition radiation (TR), and so on; N is the electron number, and $F(\omega)$ is called the form factor. Ignoring the horizontal effects, the form factor

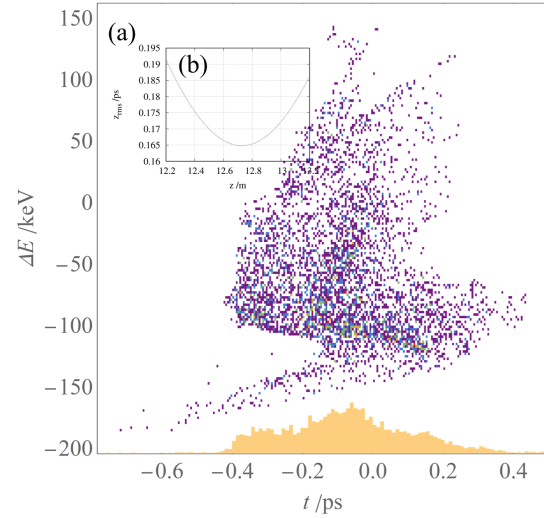


Figure 4: Longitudinal phase space of the electron beam compressed by a chicane.

can be written as:

$$F(\omega) = \left| \int_{-\infty}^{\infty} \rho_{long}(t) \exp(-i\omega t) dt \right|^2, \quad (2)$$

where $\rho_{long}(t)$ is the longitudinal distribution of the beam.

When the diffraction radiation happens, the single electron spectrum $U_{e,DR}$ is[13]:

$$\frac{d^2 U_{e,DR}}{d\omega d\Omega} = \frac{e^2}{4\pi^3 \epsilon_0 c} \frac{\beta^2 \sin^2 \theta}{(1 - \beta^2 \cos^2 \theta)^2} T(\theta, \omega), \quad (3)$$

where

$$T(\theta, \omega) = [T_b(\theta, \omega) - T_a(\theta, \omega)]^2,$$

$d^2 U_e / (d\omega d\Omega)$ is the radiation energy distribution of DR when a single electron passes into an infinite metal radiator, e is the electron charge, ϵ_0 is the vacuum dielectric constant, c is the speed of light in vacuum, and β is the relativistic speed of the electron. T is the form factor of the radiator, $T_b(\theta, \omega)$ is determined by the radius of the aperture b and $T_a(\theta, \omega)$ by the entire radiator a , ω is the frequency, θ is the observation angle relative to direction of the beam, Ω is the solid angle of radiation. When b equals to 0, the DR becomes TR.

Considering only the fundamental mode of the undulator radiation, the single electron spectrum $U_{e,UR}$ is:

$$\frac{d^2 U_{m,UR}}{d\Omega d\omega} = \frac{e^2 \gamma^2 K^2}{4\pi \epsilon_0 c (1 + K^2/2)^2} \cdot M_u(\omega) \cdot |JJ|^2, \quad (4)$$

where

$$M_u(\omega) = \frac{\sin^2(\pi N_u (\omega - \omega_1) / \omega_1)}{\sin^2(\pi (\omega - \omega_1) / \omega_1)},$$

$$JJ = J_0 \left(\frac{K^2}{4 + 2K^2} \right) - J_1 \left(\frac{K^2}{4 + 2K^2} \right),$$

J is bessel function, and $K = 0.934 \cdot B_0[\text{T}] \cdot \lambda_u[\text{cm}]$ is called *undulator parameter*, $\lambda_1 = \frac{\lambda_u}{2\gamma^2} (1 + K^2/2)$, is the center wavelength of the fundamental mode, N_u is the period number of the undulator.

Considering a bunch charge of 100 pC, an RMS bunch length of 200 fs, an undulator period of 5 cm, and an undulator period number of 10, the different radiation energy spectrum can be calculated. The results are shown in Fig. 5. The super-radiation will be ultrafast, high-energy, and high-repetition. The pulse energy is mostly more than 100 nJ, and the peak power is more than 25 kW. The peak power of CTR is more than 1 MW. When the CTR radiation is focus within a diameter of 1 mm, the peak electronic field would be about 0.5 MV/cm.

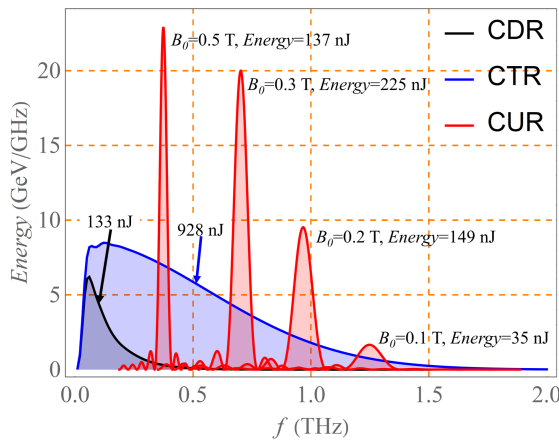


Figure 5: The radiation energy spectrum with different radiation types.

Simulations using the SPECTRA code [14] were performed with these parameters and the result is presented in Fig. 6. The peak frequencies of radiation under different magnetic fields are consistent with the theoretical calculations, but with wider bandwidth. The reason is because the off-axis frequency is not the same as the frequency on the axis, and is included in simulation.

MULTI-COLOR PUMP-PROBE DESIGN

To build a multi-color pump-probe system, it is important to make sure the synchronization between the pump and the probe. Because the CDR/CTR and CUR are generated by the same beam bunch, they are synchronized naturally. The jitter is mostly caused by the trajectory difference between micro-pulses. In addition, the drive laser itself and THz induced by the ultra-fast laser can be the pump beam, too. The multi-color pump-probe system is shown in Fig. 7.

SUMMARY

This paper has briefly introduced a super-radiation system based on the CAEP THz FEL facility. The coherent diffraction/transition radiation (CDR/CTR) and coherent undulator radiation (CUR) can be synchronized naturally. And these

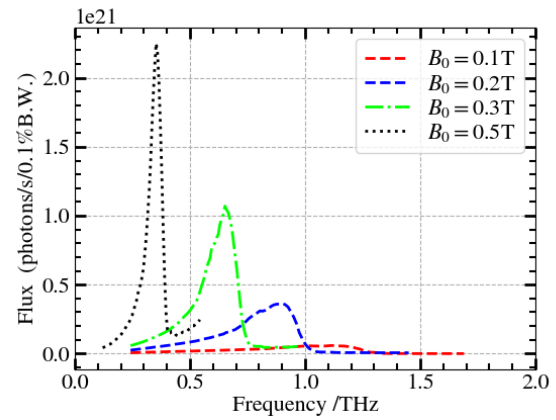


Figure 6: The super-radiation spectrum calculated by SPECTRA.

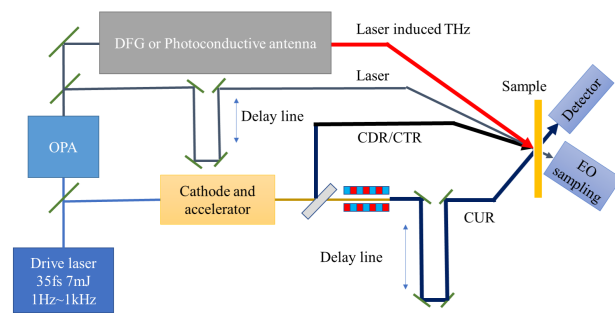


Figure 7: Schematic diagram of multi-color pump probe system.

super-radiation source can be ultra-fast with high repetition and CEP stable. The simulation and calculation indicate that the radiation duration can be less than 200fs rms, and the pulse energy can reach almost 1 μJ , which makes the peak field be about 0.5 MV/cm. Combined with the drive laser, OPA system and laser induced THz, a multi-color pump-probe system can be established, which will greatly expand the application of CTFEL facility.

REFERENCES

- [1] Y.-H. Dou, X.-J. Shu, and Y.-Z. Wang, "3d-simulations of transverse optical modes of the free electron laser resonator with hole output coupling," *Communications in Computational Physics*, vol. 1, no. 5, pp. 920–929, 2006.
- [2] P. Li, Y. Jiao, W. Bai, H. B. Wang, X. H. Cui, and X. K. Li, "Start-to-End Simulation of CAEP FEL-THz beamline," *High Power Laser and Particle Beams*, vol. 26, pp. 213–217, 2014.
- [3] H. Wang, K. Li, M. Li, D. Wu, D. Xiao, and X. Yang, "A GaAs photoemission DC gun for CAEP high-average-power THz FEL," *Proceedings of FEL 2014*, 318–321, paper TUA03, 2014.
- [4] D. Wu *et al.*, "Studies on factors affecting the life-time of high average current GaAs photocathode," in *Proceedings of SAP2014*, Lanzhou, China, 2014, 12–15, paper WEAMH6.

- [5] X. Luo *et al.*, “Design and fabrication of the 2x4-cell superconducting linac module for the free-electron laser,” *Nuclear Instruments and Methods in Physics Research Section A: Accelerators, Spectrometers, Detectors and Associated Equipment*, vol. 871, pp. 30–34, 2017, ISSN: 0168-9002. doi: 10.1016/j.nima.2017.06.058
- [6] K. Zhou *et al.*, “Progress of the 2x4-cell superconducting accelerator for the CAEP THz-FEL facility,” in *Proceedings of the 18th International Conference on RF Superconductivity*, Lanzhou China, Jul. 2017. doi: 10.18429/JACoW-SRF2017-MOPB037
- [7] M. Li *et al.*, “First lasing of CAEP THz free electron laser,” *High Power Laser Particle Beams*, vol. 29, no. 10, p. 1, 2017.
- [8] M. Li *et al.*, “Experimental study on the stimulated saturation of terahertz free electron laser,” *Acta Physica Sinica*, vol. 67, no. 8, p. 84 102, 2018.
- [9] T. Kampfrath *et al.*, “Coherent terahertz control of antiferromagnetic spin waves,” *Nature Photonics*, vol. 5, no. 1, p. 31, 2011. doi: 10.1038/nphoton.2010.259
- [10] T. Kampfrath, K. Tanaka, and K. A. Nelson, “Resonant and nonresonant control over matter and light by intense terahertz transients,” *Nature Photonics*, vol. 7, no. 9, p. 680, 2013. doi: 10.1038/nphoton.2013.184
- [11] S. Kovalev *et al.*, “Selective THz control of magnetic order: new opportunities from superradiant undulator sources,” *Journal of Physics D: Applied Physics*, vol. 51, no. 11, p. 114 007, 2018. doi: 10.1088/1361-6463/aaac75
- [12] H. A. Hafez *et al.*, “Extremely efficient terahertz high-harmonic generation in graphene by hot dirac fermions,” *Nature*, vol. 561, no. 7724, p. 507, 2018. doi: 10.1038/s41586-018-0508-1
- [13] S. Casalbuoni, B. Schmidt, P. Schmüser, and B. Steffen, “Far-infrared transition and diffraction radiation,” DESY, Tech. Rep., 2005.
- [14] T. Tanaka and H. Kitamura, “SPECTRA: a synchrotron radiation calculation code,” *Journal of Synchrotron Radiation*, vol. 8, no. 6, pp. 1221–1228, 2001. doi: 10.1107/S090904950101425X

TERAHERTZ FEL SIMULATION IN PAL XFEL

J. H. Ko, H.-S. Kang, Pohang Accelerator Laboratory, Pohang, Republic of Korea

Abstract

Terahertz radiation is being used in various fields such as imaging, diagnosis, inspection, etc. For the Terahertz research, the Pohang accelerator laboratory (PAL) is planning to make a terahertz free electron laser based on self-amplified spontaneous emission (SASE). Using free electron laser method, we will be able to conduct the THz-pump x-ray probe experiment. For the terahertz free electron laser, we conducted the simulation study on the accelerator with e-beam energy below 40 MeV, using a photo-cathode RF gun, one s-band accelerator and one undulator shorter than 4 meters.

INTRODUCTION

In Pohang accelerator laboratory, we have a plan to make a THz FEL facility to conduct the THz pump X-ray probe experiment and other experiments of using THz radiation. For this purpose, a demanded condition of THz radiation is an intensity over 100 μJ , a various frequency range (5 to 20 THz) and a spectrum under 5%. To make a THz FEL facility which is satisfied with these conditions, we conduct the Accelerator simulation and FEL simulation using ASTRA and SIMPLEX [1, 2]. We conduct the ASTRA simulation for designing a photo-cathode RF gun, an S-band accelerator, accelerator solenoids, and two quadrupole magnet triplets. We conduct the SIMPLEX simulation using the result of ASTRA simulation. The simulation parameters are listed in Table 1 and 2, and the structure of the THz FEL accelerator is shown in Figure 1.

Table 1: Electron Beam Parameter

Electron beam	
Electron beam energy	25 MeV to 35 MeV
Electron beam charge	4 nC
RMS electron bunch length	1.8 mm
Peak current	265 A
Horizontal Emittance	4 mm-mrad
Vertical Emittance	5 mm-mrad
Energy spread	0.001

Table 2: Undulator Parameter

Undulator	
Type	Planar
Period	3.5 cm
K	1.6 to 3.321
Magnetic field	0.7 T to 1.016 T
Length	4 m
Gap	9 mm

ACCELERATOR SIMULATION

The wavelength of terahertz radiation is much longer than the wavelength of x-ray or UV radiation. Accordingly, the electron bunch length of the THz FEL is allowed to be as long as 1.8 mm. To make a THz FEL radiation, we need high peak current. To satisfy these conditions, we need a high electron charge over 4 nC.

The wavelength of the FEL radiation is calculated by the below equation.

$$\lambda = \frac{\lambda_u}{2\gamma^2} \left(1 + \frac{K^2}{2} \right)$$

λ is an FEL wavelength, λ_u is a period length of the undulator, $K=93.4 \cdot \lambda_u B_{peak}$. Using this equation, we can get the electron beam energy when the radiation frequency is in the THz range. When the undulator period length is 3.5 cm, the magnetic field of the undulator is under 1.016 T, undulator gap is 9 mm, and electron beam energy in 25 MeV to 35 MeV, the available range of the THz radiation wavelength is 5 THz to 30 THz. We make a specific electron beam condition using the ASTRA, which satisfies the electron beam parameter. The ASTRA simulation results are shown in Figure 2, 3, 4, and 5.

To generate a high charge electron beam, we should use a larger laser beam size in the input condition and control the gun solenoid condition. Using quadrupole triplets, we can match the electron beam between accelerator and undulator.

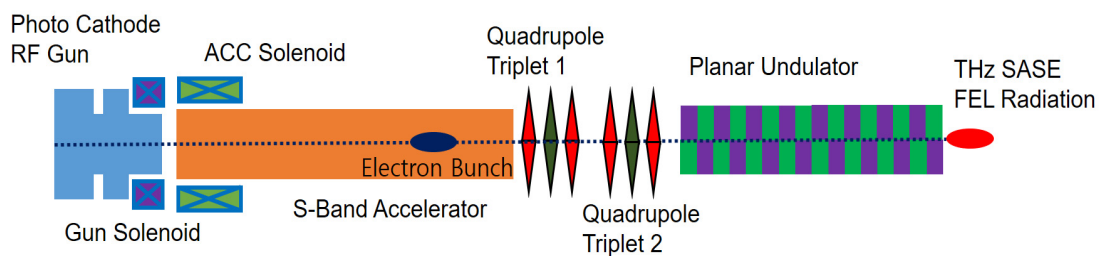


Figure 1: Schematic structure of THz FEL facility in PAL XFEL.

When the electron beam energy is in a few tens of MeV range, the vertical focusing of the undulator is so high that the vertical electron beam size grows too much in the undulator. To overcome this, we need to make a very small vertical beam size at the undulator start position ($z = 10.3$ m) and we make a focal position of the horizontal beam at the middle of the undulator ($z = 12.3$ m).

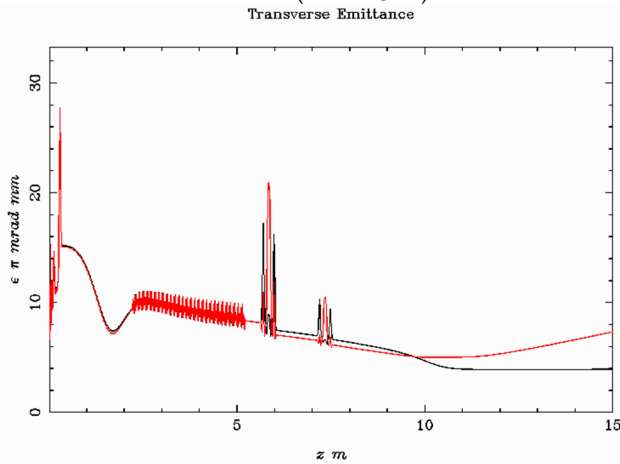


Figure 2: Transverse emittance of electron beam. Transverse emittance of the electron beam has controlled by the B field strength of the gun solenoid.

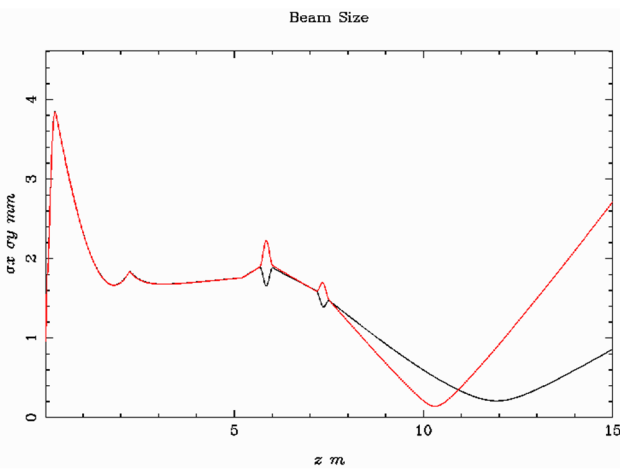


Figure 3: RMS electron beam size.

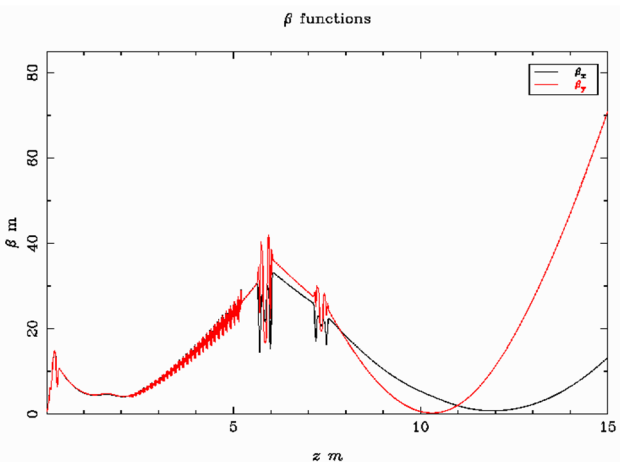


Figure 4: Beta function.

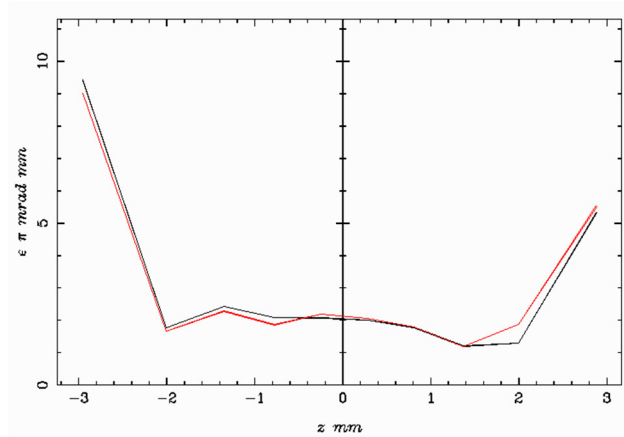


Figure 5: Slice emittance at the $z=10.3$ m.

The emittance is vertically 5 mm-mrad and horizontally 4 mm-mrad at the entering position of the undulator but the slice emittance of the electron bunch is much smaller than the result. The slice emittance of the electron beam centre is nearly 2 mm-mrad at the entering position of the undulator.

FEL SIMULATION

Using the result of the ASTRA simulation, we conduct the FEL simulation by using the SIMPLEX code [2]. We choose the same undulator installed in the PAL-XFEL soft x-ray line and reduce the undulator length to 4 m. Undulator parameters are shown in Table 2. After selecting the undulator parameter, we input the initial electron beam parameter at the undulator entrance. We use the result of the beta function and alpha function of ASTRA simulation at $z = 10.3$ m. The result of SIMPLEX simulation is shown in Figure 6,7,8, and 9.

Figure 6, 7, 8, and 9 show the FEL energy of each undulator and the electron beam condition. In our plan, we control the photon energy by changing the electron beam energy and undulator K . K is adjusted by the gap distance. The K value of 3.321 is the maximum K value of the undulator. The THz FEL range is 12.16 THz to 26.47 THz when the electron energy is 35 MeV and 6.17 THz to 17.77 THz when the electron energy is 25 MeV. The output FEL energies are over 300 μ J.

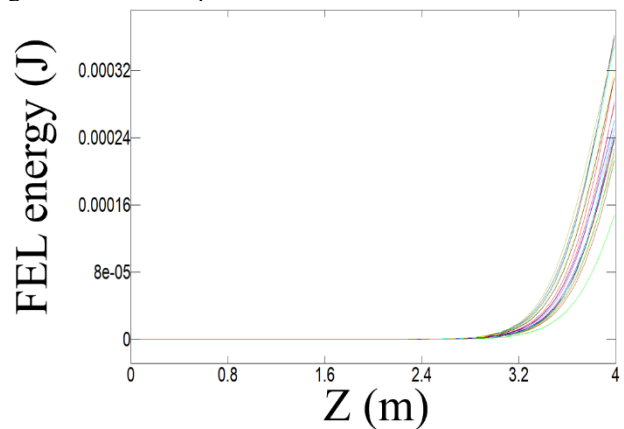


Figure 6: FEL energy of 35 MeV, K2.0, 26.47 THz.

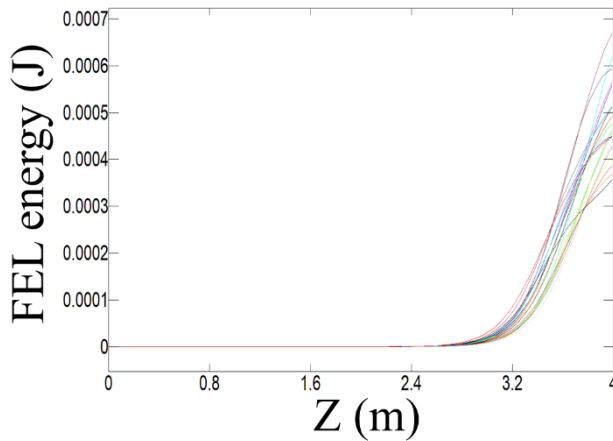


Figure 7: FEL energy of 25 MeV, K 1.6, 17.77 THz.

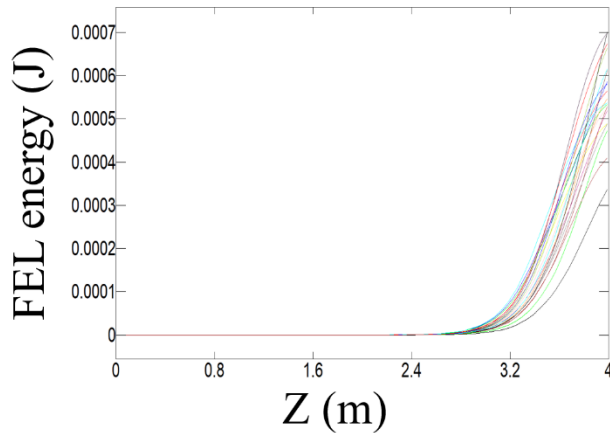


Figure 8: FEL energy of 35 MeV K 3.321, 12.16 THz.

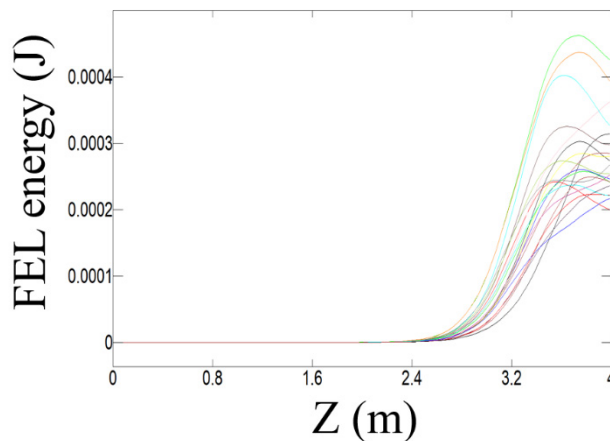


Figure 9: FEL energy of 25 MeV, K 3.321, 6.17 THz.

Figure 10 shows the spectrum of FEL. In Figure 10 (a), the 26.47 THz has the spectrum bandwidth of 2.2 % in FWHM, in (b) the 17.77 THz has the spectrum bandwidth of 2.7 % in FWHM, in (c) the 12.16 THz has the spectrum bandwidth of 3.0 % in FWHM, and in (d) the 6.17 THz has the spectrum bandwidth of 4.1 % in FWHM.

These results show the FEL photon energy can tune from 6.17 to 26.47 THz, the FEL intensity is over 300 μ J, and the spectrum bandwidth is under 5 %.

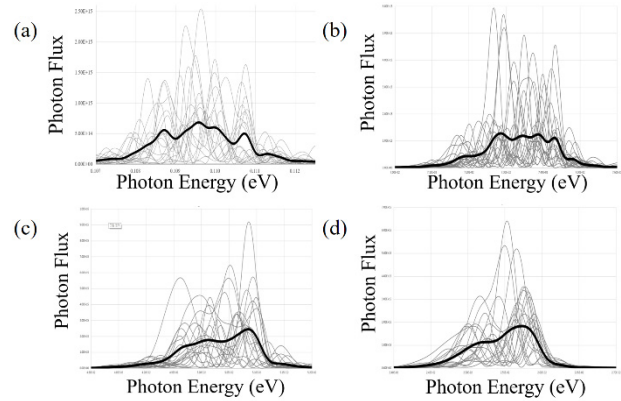


Figure 10: FEL spectrum of (a) 35 MeV, K 2.0, 26.47 THz, bandwidth 0.605 THz (b) 25 MeV, K 1.6, 17.77 THz, bandwidth 0.484 THz (c) 35 MeV K 3.321, 12.16 THz, bandwidth 0.362 THz (d) 25 MeV, K 3.321, 6.17 THz, bandwidth 0.254 THz.

CONCLUSION

In Pohang Accelerator Laboratory, we have a plan to construct a THz FEL facility. For this purpose, we conduct the FEL simulation and Accelerator simulation using ASTRA code and SIMPLEX code. Using this result, we determine the undulator length under 4 m. In the FEL simulation, the important parameter is the vertical focusing strength of the undulator. To overcome the vertical focusing strength, we make a very small vertical beam size using two quadrupole triplets. In this condition, the simulation's result shows the FEL energy over 300 μ J and spectrum bandwidth under 5 % with various THz FEL frequency. In the future, we will conduct the more specific simulation of matching of accelerator and undulator and search for the better THz FEL energy condition and a wide photon energy range.

ACKNOWLEDGEMENTS

This research was supported by Basic Science Research Program through the National Research Foundation of Korea (NRF) funded by the Ministry of Education (Grant No. 2019R111A1A01059813).

This research was supported by the Ministry of Science and ICT of Korea and partly by the Basic Science Research Program (Grant No. 2017R1A2B4007274) through the National Research Foundation of Korea (NRF) funded by the Ministry of Science and ICT of Korea.

REFERENCES

- [1] K. Flöttmann, "ASTRA: A Space Charge Tracking Algorithm", http://www.desy.de/~mpyflo/Astra_manual/Astra-Manual_V3.2.pdf
- [2] T. Tanaka, "SIMPLEX: Simulator and Postprocessor for free electron Laser EXperiments," *J. of Synchrotron Radiat.*, vol. 22, pp. 1319–1326, 2015.
doi: 10.1107/S1600577515012850

SUPERRADIANT EMISSION OF ELECTRON BUNCHES BASED ON CHERENKOV EXCITATION OF SURFACE WAVES IN 1D AND 2D PERIODICAL LATTICES: THEORY AND EXPERIMENTS*

A.M. Malkin[†], N.S. Ginzburg¹, I.V. Zheleznov, V.Yu. Zaslavsky¹, A.S. Sergeev, I.V. Zotova,
Institute of Applied Physics RAS, Nizhny Novgorod, Russia
M.I. Yalandin, Institute of Electrophysics, Ekaterinburg, Russia
¹also at Nizhny Novgorod State University, Nizhny Novgorod, Russia

Abstract

We report of the experiments on Cherenkov generation of 150 ps superradiance pulses with a central frequency of 0.14 THz, and an extremely high peak power up to 70 MW. In order to generate spatially coherent radiation in shorter wavelength ranges (including THz band) in strongly oversized waveguiding systems, we propose a slow wave structure with double periodic corrugation (2D SWS). Using quasi-optical theory and PIC simulations, we demonstrate the applicability of such 2D SWS and its advantages against traditional 1D SWS. Proof-of-principle experiments on observation G-band Cherenkov superradiance in 2D SWS are currently in progress.

INTRODUCTION

In recent years, significant progress was achieved in generation of high-power ultrashort microwave pulses based on superradiance (SR) of electron bunches extended in the wavelength scale. In this process, coherent emission from the entire volume of the bunch occurs due to the development of microbunching and slippage of the wave with respect to electrons.

The SR pulses with the highest peak power were obtained for the Cherenkov mechanism when electrons interact with the backward wave propagating in slow-wave structures (SWS). In the Ka-band, peak power exceeding 1 GW was obtained [1, 2]. In these experiments, an electron bunch interacts with a synchronous spatial harmonic of the lowest TM-polarized volume mode of periodically corrugated waveguide with an oversize factor $D/\lambda \approx 1$ (D is the mean diameter and λ is the radiation wavelength). However, in the shorter wavelength bands, the use of single-mode SWS is becoming more complicated due to strict requirements for transportation of the high-current electron beams and increase of the Ohmic losses.

Advancement of vacuum electronic devices into sub-THz and THz frequency ranges calls for oversized beam-wave interaction space due to the fact that the dimensions of the beam guiding systems can not be reduced lower than the millimeter scale. Thus, in order to provide coherent THz radiation from the spatially extended beams, excitation of surface modes existing in 1D and 2D corrugated systems appears to be attractive [3-6].

In this paper, we present recent results of theoretical and experimental studies of SR emission based on excitation of surface waves by extended bunches. Using oversized 1D slow-wave structures allows for a significant increase of total current and, correspondingly, the output radiation power. Based on SR of electron bunches in a cylindrical corrugated waveguide, 150 ps short-pulse SR emission with a central frequency of 0.14 THz, and an extremely high peak power reaching 50-70 MW were obtained in the joint effort by the Institute of Electrophysics RAS and IAP RAS.

Further increase of the frequency or of the aimed radiation power requires the increase of the transverse dimensions of the interaction space, which, in turn, leads to the loss of the mode control over the azimuthal coordinate. The problem of mode synchronization over this coordinate can be solved by using the SWS with 2D corrugation. Proof-of-principle experiments are in progress based on the RADAN accelerator. We present here the results of 3D numerical simulation of Cherenkov SR emission in the 3mm wavelength range in an oversized cylindrical waveguide with 2D corrugation of the wall. A SR pulse with a duration of 0.5 ns and an output power of ~ 70 MW was obtained.

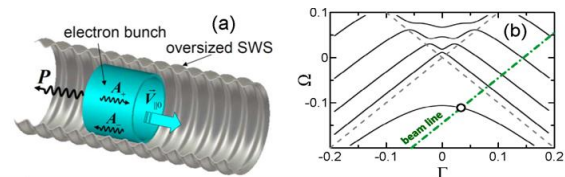


Figure 1: a) Scheme of SR pulse generation with excitation of a surface wave in an oversized periodically corrugated waveguide. b) Dispersion characteristics of the corrugated waveguide and an electron beam.

SIMULATION AND EXPERIMENTS ON GENERATION OF SURFACE-WAVE SR PULSES IN 1D LATTICES

Cherenkov SR of electron bunch exciting the surface wave in an oversized 1D corrugated cylindrical waveguide (Fig. 1a) can be considered within quasi-optical approach [3]. In this case the radiation field near a shallow corrugation is presented as a sum of two counter-propagating TM polarized wavebeams:

$$H_{\varphi} = \text{Re}(A_+(z, r, t)e^{i\omega t - ikz} + A_-(z, r, t)e^{i\omega t + ikz}), \quad (1)$$

* Work supported by RFBR grant No. 17-08-01072 and the Program of Presidium RAS No.10 (0035-2018-0022).

[†] malkin@appl.sci.nnov.ru

propagation and mutual coupling of which is described by two non-uniform parabolic equations:

$$\begin{aligned} \frac{\partial A_+}{\partial z} + \frac{\partial A_+}{c \partial t} + \frac{i}{2k} \frac{\partial}{\partial r} \left(\frac{1}{r} \frac{\partial (r A_+)}{\partial r} \right) &= i \alpha \delta(r - r_0) A_- + \\ &+ \frac{i I_0}{\omega S_b} f(z - v_0 t) \frac{\partial}{\partial r} (\psi(r) J), \quad (2) \\ - \frac{\partial A_-}{\partial z} + \frac{\partial A_-}{c \partial t} + \frac{i}{2k} \frac{\partial}{\partial r} \left(\frac{1}{r} \frac{\partial (r A_-)}{\partial r} \right) &= i \alpha \delta(r - r_0) A_+, \end{aligned}$$

The amplitude of the RF current J is found from the electron motion equations. Synchronous interaction of electrons with forward partial waves leads to development of self-bunching and formation of powerful SR pulse.

Simulations show that the most optimal conditions for SR emission correspond to excitation of the backward surface wave near the Bragg frequency (π - regime, Fig.1b). For parameters of an electron bunch formed by an accelerator RADAN (electron energy of 300 keV, a total current of 2 kA, a bunch duration of 500 ps) and a corrugated waveguide with the mean radius of 3.75 mm, corrugation period of 0.825 mm, and corrugation depth of 0.36 mm the operating frequency in the resonant point is of 0.14 THz ($D/\lambda \approx 3.5$). In this case the power of generated SR pulse emitted in $-z$ direction achieves ~ 200 MW for pulse duration of ~ 200 ps (Fig. 2a). As it is seen in Fig. 2b the instant spatial structure of the partial wave corresponds to formation of the evanescent surface wave with the field amplitude exponentially decaying from the corrugation.

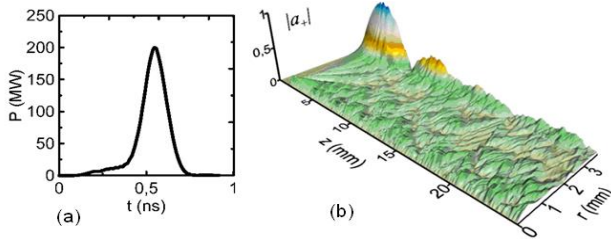


Figure 2: SR emission with excitation of the backward surface wave: a) generated SR pulse, b) structure of the forward partial wave.

Based on the theoretical analysis, experiments on observation of the sub-terahertz SR pulse generation were carried out in IEP RAS (Ekaterinburg). Photo of the experimental set-up is shown in Fig. 3a,b. A typical oscilloscope trace of generated SR pulses with a duration of about 150 ps and a rise time of 100 ps reconstructed in the “power-time” coordinates is presented in Fig. 3c. Frequency measurements using a set of cut-off waveguide filters show that the pulse spectrum has a central frequency in the interval 0.13-0.15 THz. The peak power of generated SR pulses was estimated by integrating the detector signal over the directional pattern and achieved of 50-70 MW, that strongly exceeds the value obtained in the previous sub-terahertz experiments [4] with single-mode waveguides.

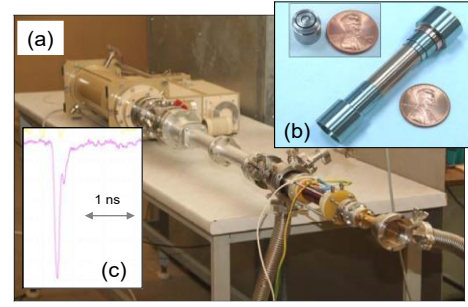


Figure 3: Photo of the experimental set-up (a), corrugated waveguide and coaxial reflector (b) used for observation of SR with excitation of a surface wave. (c) Oscilloscope trace of the 0.14 THz SR pulse with duration of 150 ps and peak power up to 70 MW.

SIMULATION OF HIGH-POWER CHERENKOV SR PULSE GENERATION IN 2D SLOW-WAVE STRUCTURES

However, at larger oversize factors, the transverse mode selection problem arises, that leads to deformation of the radiation pattern of a Cherenkov SR generator. A promising method to solve this problem in highly oversized systems is based on using slow wave structures in the form of cylindrical waveguide with two-dimensional corrugation of its walls, 2D SWS [5,6]. Similar structures were proposed [7] for transverse synchronization of radiation and provision of distributed feedback (DFB) in free electron masers (FEM) based on sheet [8] or tubular [9] electron beams. Due to formation of azimuthal wave fluxes, such structures ensure synchronization of the radiation of a tubular electronic bunch of large diameter. The distinguishing feature of Cherenkov devices exploiting 2D DFB is that in this case, unlike FEM, the 2D structures can play the role of SWS and of a synchronizer simultaneously. Recent experiments [6] at IAP RAS based on the SATURN accelerator has proven the viability of surface wave oscillators with 2D SWS operating in steady state oscillation regime.

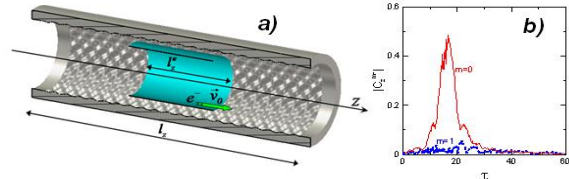


Figure 4: Simulations of 90 GHz SR pulse generation with excitation of azimuthally symmetric surface wave in a cylindrical 2D SWS: a) geometry of the interaction space; b) temporal dependence of the amplitudes $|\hat{C}_z^m|$ of modes with different azimuthal indices (in the framework of a quasi-optical approach).

In order to demonstrate the effectiveness of the proposed approaches we carried out the simulations of SR pulse generation in 3-mm wavelength band (90 GHz) with parameters of experiment to be conducted at the Institute of Electrophysics. We assumed that the surface

wave is excited by a hollow cylindrical electron bunch with electron energy of 300 keV, the total current of 2 kA, a bunch duration of 1 ns, the mean injection radius of 7.5 mm, and the beam width of 0.2 mm. These parameters can be obtained using high-current accelerators, namely RADAN accelerator [3]. Interaction takes place in 2D SWS with mean diameter $D = 17.2$ mm, period of corrugation 2.7 mm and corrugation depth 1.1 mm (Fig.4a). For the chosen radiation frequency, the oversized factor is of $D/\lambda \approx 5.7$. The total length of SWS was 6 cm.

First simulations were carried out based on the quasi-optical theory developed in [10]. In the frame of this approach the electromagnetic field near the 2D corrugated surface is presented as a sum of four components (compare to Eq.(1)), two of them propagate in longitudinal $\pm z$ directions and two others in azimuthal directions. Evolution of all components is described by a set of coupled parabolic equations. This set is complemented by the averaged motion equations for electrons and also by the corresponding boundary conditions. The results of simulations are presented in Fig. 4b. As it is seen, the radiated field includes mainly the azimuthally symmetric harmonic $m=0$ at almost all stages of the SR pulse formation. In fact, it is provided by the presence of azimuthal wave fluxes in the 2D periodic structure which leads to synchronization of radiation from different parts of the electron bunch during the SR pulse formation. As a result, the amplitude and phase distributions are close to azimuthal symmetry.

Conclusions obtained in the framework of the averaged quasi-optical approach are confirmed by the results of PIC modeling using the CST PIC code. Figure 5 presents the results of PIC modeling for the parameters of the 2D SWS and an electron bunch mentioned above. One can see that at the central frequency of about 90 GHz, peak output power of SR pulses reaches 70 MW for the pulse duration of ~ 0.5 ns with azimuthally symmetric output pattern. The surface wave is formed by the modes with radial indices $n = 1, 2$, and 3, while the amplitudes of asymmetric modes (e.g., $TM_{1,1}$) are negligibly small. It should be noted that use of a 2D SWS ensures the formation of a reproducible azimuthally symmetric structure of the output radiation even at certain deviations of the relativistic tubular bunch axis from the waveguide axis.

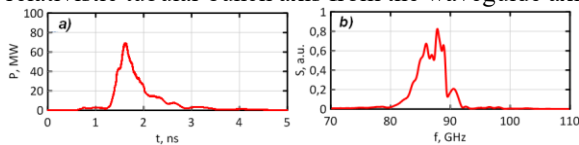


Figure 5: 3D simulations of 90 GHz SR pulse generator with 2D SWS: a) temporal dependence of the output radiation power; b) the spectrum of the output signal.

Thus, the results of our model analysis demonstrate good prospects of using the regime of surface-wave excitation in highly oversized 2D corrugated SWS for the generation of SR pulses in the millimeter waveband. It

should be noted that, similarly to SR in single-mode waveguides, optimization of the profile of 2D corrugation would provide a significant increase in the peak power of output radiation at fixed energy characteristics of the electron bunch. It is also of interest to analyze the possibility of using 2D periodic SWS for SR pulses generation in the short-wavelength part of the millimeter band. Experimental investigations in this direction are currently planned on the basis of the RADAN electron accelerators.

REFERENCES

- [1] S.D. Korovin *et al.*, "Generation of Cherenkov superradiance pulses with a peak power exceeding the power of the driving short electron beam", *Phys.Rev.E*, vol. 74, p. 016501, 2006, doi:10.1103/PhysRevE.74.016501
- [2] N.S. Ginzburg *et al.*, "Generation of Electromagnetic Fields of Extremely High Intensity by Coherent Summation of Cherenkov Superradiance Pulses", *Phys. Rev. Lett.*, vol. 115, p. 114802, 2015, doi:10.1103/PhysRevLett.115.114802
- [3] N.S. Ginzburg *et al.*, "Generation of Sub-Terahertz Superradiance Pulses Based on Excitation of a Surface Wave by Relativistic Electron Bunches Moving in Oversized Corrugated Waveguides", *Phys. Rev. Lett.*, vol. 117, p. 204801, 2016, doi:10.1103/PhysRevLett.117.204801
- [4] M.I. Yalandin *et al.*, "Generation of powerful subnanosecond microwave pulses in the range of 38–150 GHz", *IEEE Trans. on Plasma Sci.* vol.28, no.5, p. 1615, November 2000, doi:10.1109/27.901243.
- [5] N.S. Ginzburg *et al.*, "Powerful surface-wave oscillators with two-dimensional periodic structures", *Appl. Phys. Lett.*, vol. 100, p. 143510, 2012, doi:10.1063/1.3701580.
- [6] N.S. Ginzburg *et al.*, "Theoretical and experimental studies of relativistic oversized Ka-band surface-wave oscillator based on 2D periodical corrugated structure", *Phys. Rev. AB.*, vol. 21, p. 080701, 2018, doi:10.1103/PhysRevAccelBeams.21.080701.
- [7] N.S.Ginzburg *et al.*, "Dynamics of free-electron lasers with two-dimensional distributed feedback", *Opt. Comm.*, vol. 112, p. 151, 1994, doi:10.1016/0030-4018(94)00442-0.
- [8] A.V.Arzhannikov *et al.*, "Using Two-Dimensional Distributed Feedback for Synchronization of Radiation from Two Parallel-Sheet Electron Beams in a Free-Electron Maser", *Phys. Rev. Lett.*, vol. 117, p. 114801, 2016, doi:10.1103/PhysRevLett.117.114801.
- [9] I.V.Konoplev *et al.*, "Experimental and theoretical studies of a coaxial free-electron maser based on two-dimensional distributed feedback", *Phys. Rev E*, vol. 76, p. 056406, 2007, doi:10.1103/PhysRevE.76.056406.
- [10] N.S. Ginzburg *et al.*, "Generation of high-power Cherenkov superradiance pulses using 2D periodic slow-wave structures based on oversized cylindrical waveguides.", *Tech. Phys. Lett.*, vol. 43, p. 756, 2017, doi:10.1134/S1063785017080193

REGIME OF MULTI-STAGE NON-RESONANT TRAPPING IN FREE ELECTRON LASERS*

A. V. Savilov[†], I.V. Bandurkin, Yu. S. Oparina, N. Yu. Peskov, Institute of Applied Physics, Nizhny Novgorod, Russian Federation

Abstract

We describe three works united by the idea of the non-resonant regime providing an effective trapping in a beam with a great energy spread. (I) Operability of this regime was demonstrated in the high-efficient 0.8 MeV Ka-band FEM-amplifier. (II) In short-wavelength FELs the multi-stage trapping in several consecutive sections can be organized. We describe efficiency enhancement and improving the frequency wave spectrum in multi-stage SASE and super-radiant FELs. (III) The multi-stage amplification of a single-frequency wave signal can provide cooling of the electron bunch.

NON-RESONANT AND MULTI-STAGE TRAPPING

A key problem in realization of free-electron lasers (FELs) is a small efficiency at the saturated stage of the electron-wave interaction. The averaged radiation loss in the relativistic Lorentz-factor is determined by the so-called FEL parameter, $\Delta\gamma_{\text{rad}}/\gamma_0 \sim \rho$, which is typically $\rho \sim 10^{-3}$ for X-ray FELs [1]. A similar condition limits the admissible energy spread in the electron bunch, $\Delta\gamma_{\text{spread}}/\gamma_0 \sim \rho$. A known way to increase the efficiency is the use of trapping and adiabatic deceleration of electrons in a tapered undulator. Due to tapering, the energy $\gamma_{\text{res}}(z)$ corresponding to the exact electron-wave resonance decreases slowly with the axial coordinate (Fig. 1 a). A fraction of electrons is trapped by the radiated wave, and energies of these particles decrease together with γ_{res} . In principle, it is possible to exceed limitation $\Delta\gamma_{\text{rad}}/\gamma_0 \sim \rho$ in this scheme, but it is difficult to provide trapping of a significant fraction of the beam, if the limitation $\Delta\gamma_{\text{spread}}/\gamma_0 \sim \rho$ is not fulfilled. This is because only electrons being close to the resonance with the wave at the beginning of the interaction can be trapped.

The regime of non-resonant trapping [2, 3] can provide an effective trapping in a beam with a great energy spread. In this regime, the wiggler is profiled in such a way that the electron beam is out of resonance with the operating wave at the beginning of the wiggler, and different electron fractions gradually get into synchronism as the wiggler's period decreases (Fig. 1 b).

Recently, the regime of multi-stage trapping was proposed for FELs and for other types of electron devices [4].

In the multi-stage system, the non-resonant trapping is provided several times in several consecutive sections (Fig. 1 c). In each section only a relatively small fraction of the beam is trapped and pass their energy to the wave. However, repetition of this process from section to section involves in the electron-wave interaction almost all particles of the electron beam.

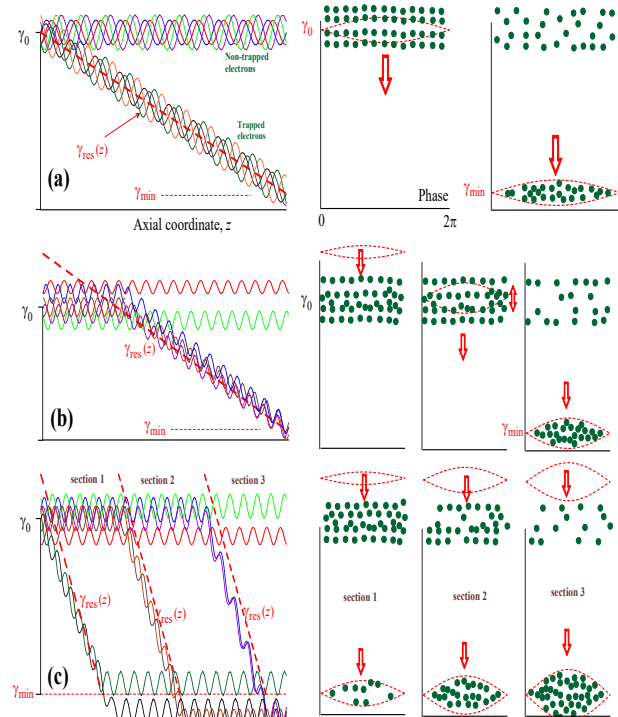


Figure 1: (a) Traditional regime of trapping. (b) Regime of non-resonant trapping. (c) Regime of the multi-stage non-resonant trapping.

KA-BAND FEM-AMPLIFIER

The regime of non-resonant trapping has been developed and experimentally demonstrated in Ka-band. In this regime, the wiggler is profiled in such a way that the electron beam is out of resonance with the operating wave at the beginning of the wiggler, and different electron fractions gradually get into synchronism as the wiggler's period decreases.

Examination of this regime in the FEM-amplifier was performed in collaboration between JINR (Dubna) and IAP RAS (N. Novgorod) at the experimental facilities of the linear induction accelerator LIU-3000 [5, 6]. Simulation of the FEM was carried out for the parameters close to the experimental conditions. The regime of a reversed guide magnetic field [7, 8] was chosen; this regime provides a high quality of formation of the helical electron beam in the smoothly up-tapered wiggler.

* Work supported by the RFBR (grants 18-02-40009, 18-02-00765) and by the IAP RAS Project 0035-2019-0001

[†] savilov@appl.sci-nnov.ru.

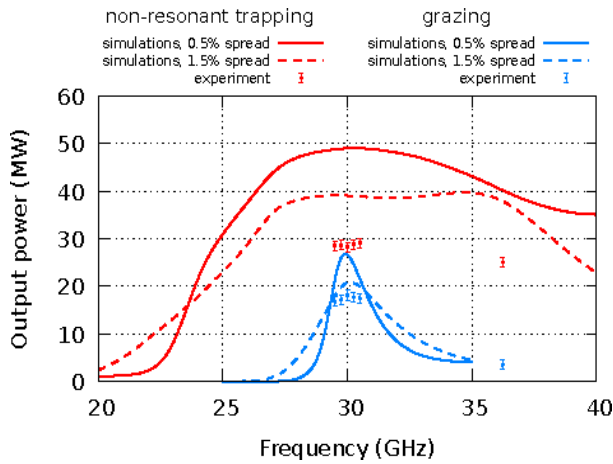


Figure 2: Simulations of the FEM-amplifier: output power versus the frequency for the non-resonant trapping regime (red lines) and grazing regime (blue lines). Experimental results (the output powers measured in the examined regimes) are shown by dots of corresponding colours.

Simulations of the FEM-amplifier were performed in the frame of the model described in [9, 10]. Simulations show (Fig. 2) that the amplification gain is almost independent of the axial velocity spread up to $\Delta\beta/\beta \approx 1.5\%$, which confirms the low sensitivity of the proposed scheme to the spread. For comparison, the more traditional regime of the grazing of dispersion characteristics, which is also capable of providing a relatively wide gain band in an FEM amplifier was studied using a wiggler with a regular winding. In this regime, the axial velocity of the particles is close to the group velocity of the operating wave. Optimization at a central frequency of 30 GHz leads to an output power of 25 MW (a gain of ~ 35 dB) and a gain band of about ± 1 GHz, which is significantly worse as compared to the regime of trapping.

Experiments on FEM amplifiers were based on a 0.8 MeV / 200 A / 200 ns / 1 pulse/s electron beam. Two feeding magnetrons were used: the first one, tunable in the range 29.5–30.5 GHz, and the second one, operating at a frequency of 36.4 GHz. The output power of both magnetrons was attenuated to the same level of 10 kW. In the first experiments, the grazing regime utilizing a regular helical wiggler with a period of 6 cm was studied. As a result, an output radiation power of ~ 17 MW in 170–200 ns RF pulses was achieved. This power was observed in the whole frequency band of the first magnetron. However, the power decreased down to 3–4 MW, when the second 36.4 GHz magnetron was utilized.

To provide the operation of the FEM amplifier in the non-resonant trapping regime, a helical wiggler of the same length (about 1.5 m) with period profiled from 7.2 cm to 4 cm, was designed. Steady amplification was observed with an output power being noticeably higher than that obtained in the grazing regime. The maximum power amounted to 25–28 MW in 150–200 ns pulses, which had almost the same duration as the beam pulse. It is important that this power level was obtained using both of the driving magnetrons. The parameters of the system were the same when

using different feeding sources, which may serve as a kind of modelling of the “instantaneous” amplification band. A comparison of the results obtained in various regimes of the FEM is summarized in Fig. 2. The output power of the FEM in the non-resonant trapping regime exceeds the maximum power obtained in the grazing regime by 1.5 times in the 30 GHz region, and almost an order of magnitude at a frequency of about 36 GHz.

NON-RESONANT AND MULTI-STAGE TRAPPING

In work [4], the regime of multi-stage trapping was studied for the simplest model of amplification of a single-frequency signal. In this work we show that at definite conditions this regime can be realized in the super-radiant regime and in the SASE regime of FELs (Figs. 3 a and b, respectively). The both regimes represent amplification of initial multi-frequency noise modulation in the operating electron bunch. Figure 4 illustrates sectioned process of amplification of a noise wave signal by a short e-bunch in the regime of the super-radiant FEL. The first section is not tapered, $\gamma_{\text{res}} = \text{const}$, and the efficiency reaches the saturation in this stage. The use of three tapered sections increases the electron efficiency by an order of magnitude. At the end of the 3rd section, the change in electron energy is approximately the half of the change in the tapered resonant energy, $\langle \gamma_0 - \gamma \rangle \approx 0.75(\gamma_0 - \gamma_{\text{res}})$. This means that $\sim 75\%$ of electrons effectively take part in the electron-wave interaction process.

Figure 5 illustrates sectioned SASE FEL process. The first section is not tapered, $\gamma_{\text{res}} = \text{const}$, and its length corresponds to the saturations of the change in the averaged electron energy, $\langle \gamma_0 - \gamma \rangle$. The use of four tapered sections increases the electron efficiency by a factor ≈ 25 . At the end of the 5th section, the change in electron energy is approximately the half of the change in the tapered resonant energy, $\langle \gamma_0 - \gamma \rangle \approx 0.5(\gamma_0 - \gamma_{\text{res}})$. This means that $\sim 50\%$ of electrons effectively take part in the electron-wave interaction process. It is important also that the process of the multi-stage electron-wave interaction improves the spectrum of the amplified wave signal.

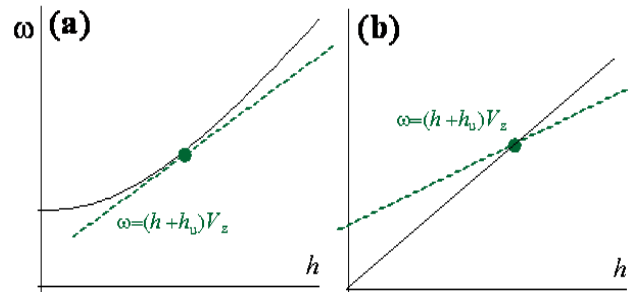


Figure 3: Dispersion diagrams in the regime of super-radiation of a wave packet propagating in a waveguide with a group velocity being equal to the electron velocity (a), as well as in the regime of the SASE amplification of a wave packet propagating in the free space with the speed of light (b).

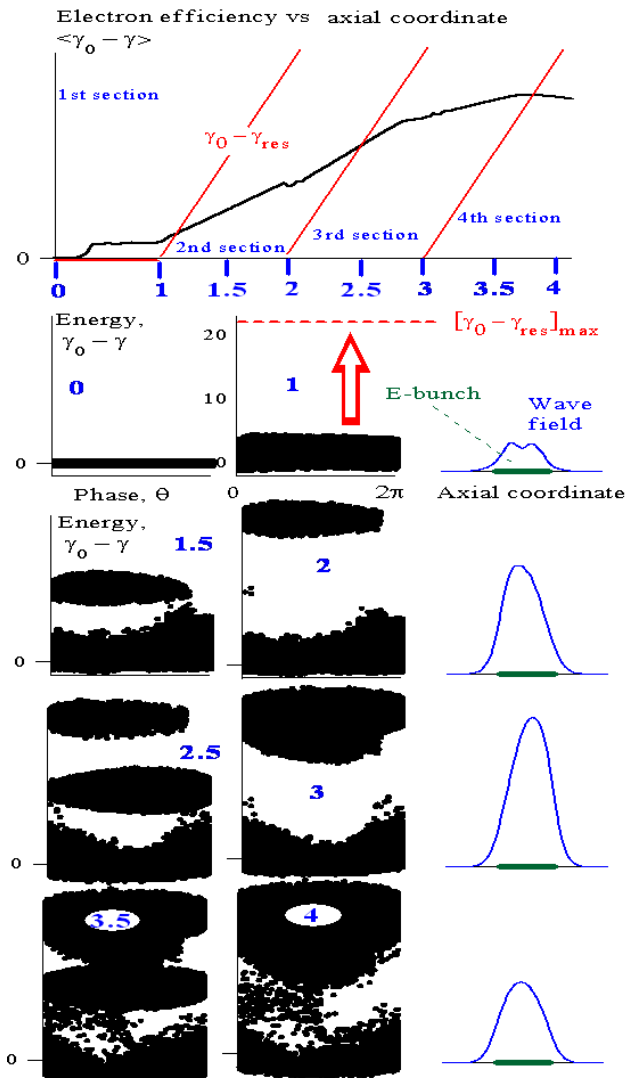


Figure 4: Multi-stage super-radiant process. Averaged change in electron energy versus the axial coordinate, profiling of the resonance energy, distributions of electrons on the energy-phase planes in various parts of the operating region, and distributions of the wave amplitude along the axial coordinate.

MULTI-STAGE BEAM COOLING

A different way to use the regime of multi-stage trapping is to provide cooling of the electron bunch. In this regime, the electron bunch moves along a cyclic trajectory. At each period of the motion, it passes through an electron-wave interaction system and amplifies there a single-frequency rf-wave signal (Fig. 6). A weak electron-wave interaction is specially provided, so that the initial energy spread in the electron beam is big in the scale of the electron-wave interaction. The tapering of every section is provided such that the resonant energy, $\gamma_{\text{res}}(z)$, decreases from maximal initial electron energy down to the minimal one, $\gamma_{\text{max}} \rightarrow \gamma_{\text{min}}$. Thus, on the phase plane the “bucket” (corresponding to the resonant electron-wave interaction) at each stage passes the entire electron layer. In this multi-stage process, amplification of the wave leads to the decrease in the energy

spread. This can be used for improving of the quality of the operating electron bunched in FELs. If this is true, then this method of the cooling amplification can be an important application of sub-THz relativistic electronics technique.

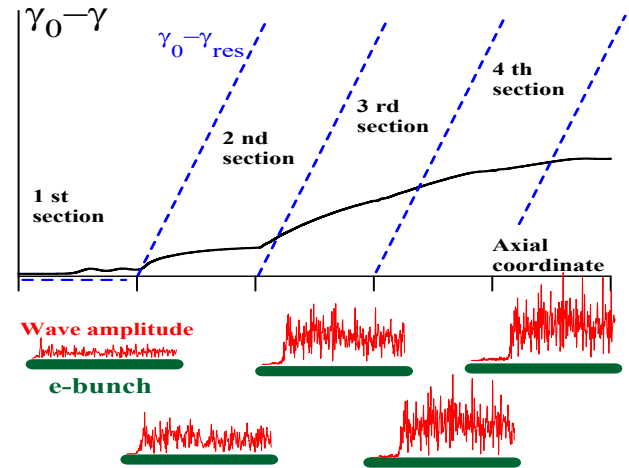


Figure 5: Multi-stage SASE process. Averaged change in electron energy versus the axial coordinate, profiling of the resonance energy, and distributions of the wave amplitude along the axial coordinate inside the electron bunch at outputs of the 1st ... 5th sections.

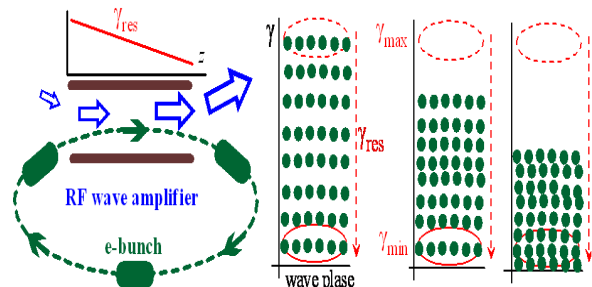


Figure 6: Multi-stage cooling of the electron beam.

REFERENCES

- [1] C. Pellegrini, A. Marinelli, S. Reichel, “The physics of x-ray free-electron lasers,” *Rev. Mod. Phys.*, vol. 88, p. 015006, 2016. doi:10.1103/RevModPhys.88.015006
- [2] A. V. Savilov, “Cyclotron resonance maser with a tapered magnetic field in the regime of “nonresonant” trapping of the electron beam,” *Phys. Rev. E*, vol. 64, p. 066501, 2001. doi:10.1103/PhysRevE.64.066501
- [3] A. V. Savilov, I. V. Bandurkin, N. Yu. Peskov, “Regime of non-resonant trapping in a FEM,” *Nucl. Instr. Meth. Phys. Res. A*, vol. 507, p. 158, 2003. doi:10.1016/S0168-9002(03)00862-3
- [4] S. V. Kuzikov, A. V. Savilov “Regime of “multi-stage” trapping in electron masers”, *Phys. Plasmas*, vol. 25, p.113114, 2018. doi:10.1063/1.5049880
- [5] N. S. Ginzburg, A. A. Kaminsky, A. K. Kaminsky, N. Yu. Peskov, S. N. Sedykh, A. P. Sergeev, A. S. Sergeev, “High-efficiency single-mode Free-Electron Maser oscillator based on a Bragg resonator with step of phase of corrugation,” *Phys. Rev. Lett.*, vol. 84, p. 3574, 2000. doi:10.1103/PhysRevLett.84.3574

- TUP019

TERAHERTZ FREE ELECTRON MASER BASED ON EXCITATION OF A TALBOT-TYPE SUPER-MODE IN AN OVERSIZED MICROWAVE SYSTEM *

A. V. Savilov[†], Yu.S. Oparina, N.Yu. Peskov,
Institute of Applied Physics, Nizhny Novgorod, Russian Federation

Abstract

We propose an electron maser operating in the THz frequency range and based on the excitation of not a fixed transverse mode of the operating cavity but of a supermode formed by a fixed set of the transverse modes. This allows selective excitation of a THz operating wave in an oversized microwave system fed by a high-current relativistic electron beam.

INTRODUCTION

A natural problem arising in the case of realization of a THz electron oscillator with a high-current relativistic electron beam is an inevitable use of an oversized microwave system, which characteristic transverse size significantly exceeds the wavelength of the operating wave [1,2]. In this situation, it becomes difficult (and even just impossible starting from a certain limit) to provide selective excitation of a chosen transverse mode of the operating cavity. First of all, the selectivity of the feedback is a serious problem. A typical configuration of the electron-wave interaction region in an auto-oscillator is a piece of a waveguide terminated at the input/output ends by two mirrors providing the feedback; for instance, Bragg-type mirrors can be used to provide effective reflection of far-from-cut-off waves (Fig. 1a). Naturally, in the case of a far-from-cut-off wave excited in an oversized waveguide, it is difficult to create a reflector providing reflection of only one transverse mode [2]. Second, it is difficult to ensure the single-mode electron-wave interaction in an oversized system, as in these situations many transverse modes are close to resonance with electrons [3].

In this work, we propose a different concept of selective excitation of a THz operating wave in a high-power relativistic electron maser with an oversized microwave system fed by a high-current relativistic electron beam. Our basic idea is to give up working in a fixed transverse mode. Instead, we propose to work in a supermode, which is formed by a fixed spectrum of several transverse modes of an oversized waveguide (Fig. 1 b). The spectrum of the partial transverse modes is determined by both electronic and electrodynamic factors. First, effective interaction between the supermode formed by these partial modes and the electron beam should be provided. This means that in the middle part of the waveguide the supermode field should have a maximum at the point of injection of the electron beam into the transverse cross-section of the

waveguide. Second, the supermode should possess a high Q-factor. Therefore, at the input/output ends of the waveguide, the transverse structure of the supermode should be very specific; namely, the field should be present only close to the mirrors to provide almost complete reflection of the supermode back to the cavity (Fig. 1b).

To organize such a super-mode, we propose a simple approach, which is based on the use of Talbot's effect [1,4,5], namely, periodic reproduction of the transverse structure of a multi-mode wave field in an oversized waveguide. We propose to use this approach to fix a high-Q operating supermode in a simple microwave system consisting of a waveguide terminated by two simple mirrors (Fig. 1 b). On the basis of a multi-mode set of self-consistent equations of the electron-wave interaction we demonstrate the possibility of selective self-excitation of the supermode. The "proper" transverse-axial structure of the high-Q supermode is formed at the small-signal stage of the gain guiding during several trips of the wave over the cavity. In fact, this effect (formation of a high-Q supermode by a set of several partial transverse modes) is analogous to the effect of mode locking known in the physics of quantum lasers [6].

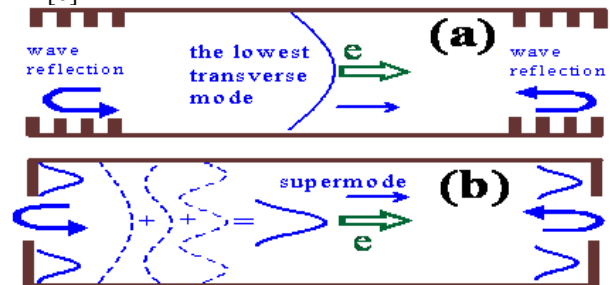


Figure 1: (a) Traditional scheme of excitation of a far-from-cutoff travelling wave in the cavity formed by a piece of waveguide with two input/output mirrors (Bragg-type mirrors are shown as an example). (b) Excitation of a supermode formed by a set of several transverse modes.

THE SIMPLEST 2-D MODEL: DEMONSTRATION OF THE BASIC IDEA

Let us consider a waveguide with a characteristic transverse size much bigger than the wavelength of the operating wave, $D \gg \lambda$ (Fig. 2). Any symmetrical transverse distribution of the wave field in this waveguide is reproduced $E(x, z + L) = E(x, z)$ with the period $L = D^2 / \lambda$. This phenomenon of repetition of the transverse wave structure is well known in the literature as the Talbot effect [4] and widely used for designing various microwave systems [1,5].

* Work supported by supported by the Russian Science Foundation, Project # 19-12-00212.

[†] email address savilov@appl.sci-nnov.ru.

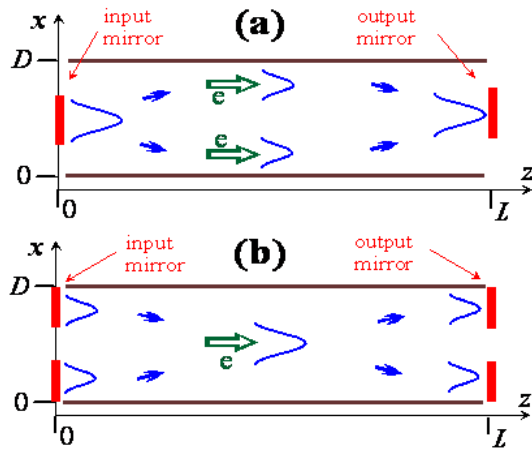


Figure 2: Two configurations of Talbot-type cavities. (a) The supermode field is focused in the center of the cross-section in the regions of the input/output mirrors and interacts with a tubular electron beam. (b) The supermode field is focused in the center of the waveguide cross-section in the middle of the waveguide, $z=L/2$, and interacts with a close-to-axis electron beam.

We propose to use the Talbot effect as a way to create an oversized microwave system of an electron maser that provides a high Q-factor for a supermode forming several transverse modes. Let us imagine that at the input of the cavity the field of this supermode is concentrated in a quite narrow section close to the center of the waveguide cross section (Fig. 2 a). If the length of the waveguide corresponds to Talbot's effect, then this transverse profile of the total wave field is reproduced at the output. This wave field can be completely reflected by a simple output mirror that has a metal surface only about the non-zero field area of the supermode. The counter propagation of the reflected wave back to the input mirror is completely analogous to the direct propagation of the supermode. Therefore, the input mirror, which is similar to the output one, completely reflects the counter wave into the forward wave and, thus, closes the feedback circuit.

Another scheme of a Talbot-type cavity can be formed by "shifting" the scheme shown in Fig. 2 a along the z-axis by half the Talbot length, $L/2$. In this case, the supermode forms two wave beams at the input and the output of the cavity (Fig. 2 b). In the middle of the cavity, these two beams are transformed into one beam located in the middle of the cavity cross-section. Again, the electron beam injected in the center of the cross section is easily separated from the input/output mirrors placed near the walls of the waveguide.

On the basis of a multi-mode set of self-consistent equations of the electron-wave interaction we demonstrate the possibility of the selective self-excitation of the supermode. As the first step, we use the simplest planar 2-D model (Fig. 2 b) with equidistant spectrum of transverse modes. The excitation process starts with small random noises in the electron beam. After the first trip of the wave packet through the cavity, several modes being close to the

resonance with electrons are excited with different amplitudes and phases (Fig. 3 a). The biggest amplitude belongs to the transverse mode with $n=3$, as this mode is the closest to the resonance. As a result, the transverse structure of the wave field in the point before the output mirror is close to the structure of this mode with $n=3$. Naturally, the output mirror is almost transparent for this wave field, and about 2/3 of the wave power escapes from the cavity. However, the situation changes radically at the next several trips of the wave, when the

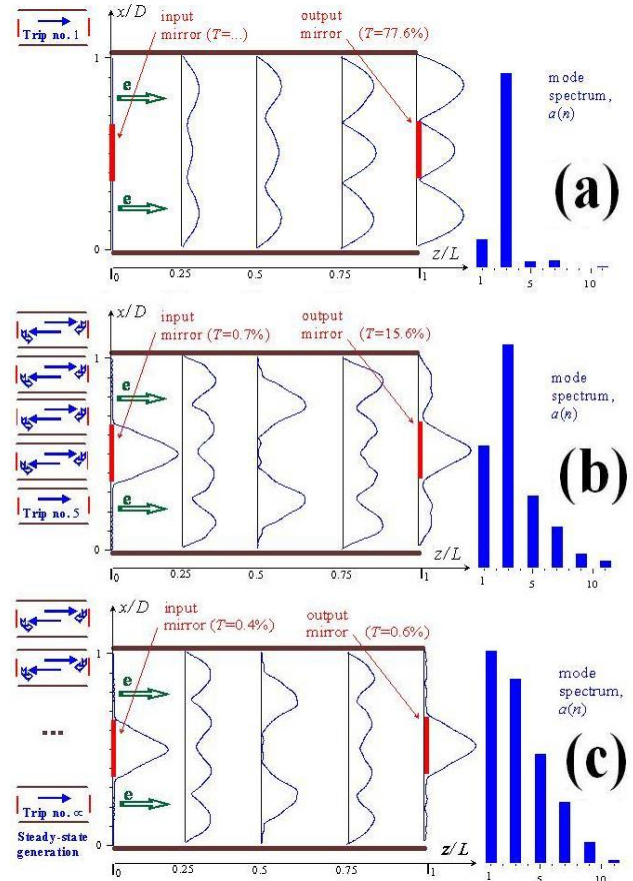


Figure 3: Evolution of the spatial-temporal structure of the RF wave excited in the Talbot-type cavity. Transverse structures of the wave field in different cross-sections of the cavity and spectra of the excited transverse modes in the small-signal regime of the auto-oscillator excitation after the first (a), fifth (b), as well as at the steady-state regime of the stable operation (c).

transverse structure of a high-Q supermode is established (Figs. 3 b). In the small-signal regime of the electron-wave interaction, we see the supermode formed by a set of mainly five symmetrical transverse modes. The input mirror reflects this supermode almost perfectly (the power transition coefficient is under 1%). As for the output mirror, in the small-signal regime it reflects only about 85% of the power of this supermode back to the cavity. This is due to the effect of the electron-wave interaction on both the spectrum of the excited partial modes and their axial

structure; this disturbs slightly the ideal Talbot's reproduction of the transverse structure of the total field.

The supermode structure stays constant during the small-signal stage of the excitation of this auto-oscillator. The transition to a nonlinear regime of the stable steady-state generation leads to a slight change in the structure of the supermode due to the reduced influence of the electron-wave interaction. As a result, the Talbot's reproduction of the transverse structure of the supermode field is almost perfect, and the power transition factor of the output mirror is reduced from 15% (in the small-signal regime) down to 0.6% (Fig. 3 c). Thus, a very high-Q supermode is excited; the total losses of the power of the supermode at the input/output mirrors are about 1%. One more result is that in the steady-state regime the mode with $n=3$ closest to the resonance ceases to be dominant. This means that the spectrum of the supermode in the steady-state regime is determined basically by the parameters of the microwave system. The predictability of the spectrum of partial transverse modes of the waveguide forming the supermode is an important factor from the point of view of organization of the radiation output from the cavity.

HIGH-POWER THz FEL

We have used this approach for a design of a THz Free-Electron Maser fed by a relativistic high-current electron beam. We study the possibility to use a relativistic electron beam produced from modern high-current accelerator (5-10 MeV / 2-10 kA / 200 ns) to excite a Talbot-type supermode at frequencies close to 2 THz. For a 7 MeV beam considered in simulations, the undulator period of 6 cm corresponds to the electron-wave resonance in the required frequency range.

In this design, we have modified the supermode configuration shown in Fig. 1 a. Namely, it is possible to reduce twice the cavity length by using the output mirror providing the almost total reflection of the wave packet (Fig. 4). The Talbot's effect takes place for the equidistant spectrum of the transverse modes. In a waveguide with circular cross section, the spectrum is close-to-equidistant only for quite high transverse modes, and the "halved" Talbot's supermode is formed by these modes at the cavity length $L = 2R^2 / \lambda$.

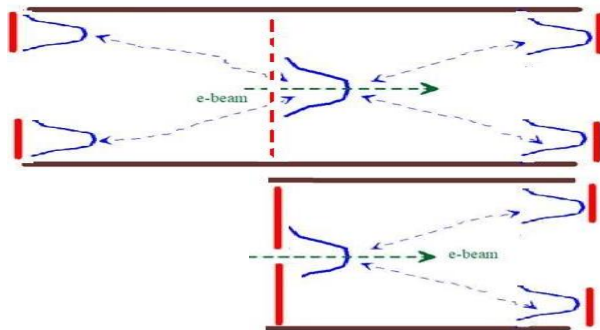


Figure 4: Transition from the Talbot-type cavity shown in Fig. 2 b to the "halved" cavity.

Naturally, the use of high operating transverse modes results in a weak electron-wave interaction. However, we have found that at a slightly shorter length, $L = 1.9R^2 / \lambda$, the "halved" Talbot's effect approximately takes place for a supermode formed basically by low ($TE_{1,n}$ $n=1, \dots, 7$) transverse modes.

In simulations (Fig. 5), we used this supermode in a cavity with the radius ~ 1 cm and the length ~ 1 m. The parameters of the system is chosen so that the closest-to-resonance transverse mode is $TE_{1,4}$. The supermode possesses a quite low diffraction Q-factor, so that $\sim 50\%$ of the supermode field passes the output mirror and forms the output radiation. The calculated efficiency of this FEM is at the level of 4-6% at electron currents 2-4 kA; this corresponds to the output power 0.6-1.7 GW at the frequency close to 2 THz.

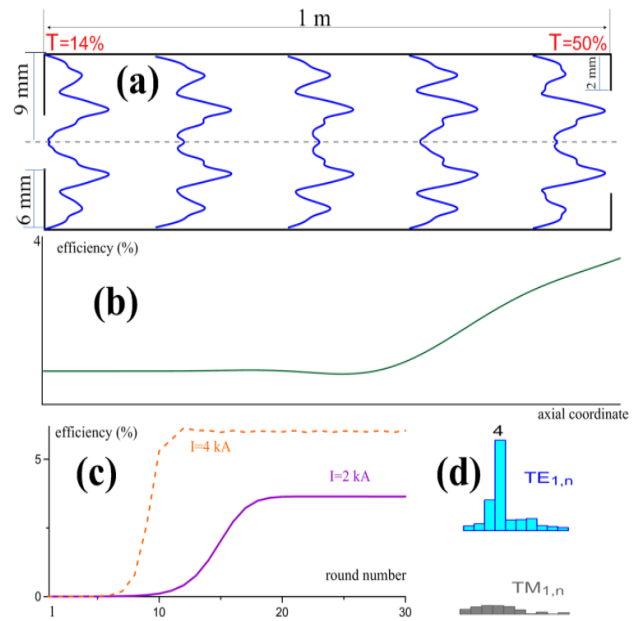


Figure 5: Relativistic high-current 2 THz FEM. (a) Operating cavity and transverse structures of the super-mode in various cross-sections of the cavity. (b) electron efficiency versus the axial coordinate in the steady-state regime. (c) Electron efficiency versus the wave trip number at electron currents 2 kA and 4 kA. (d) Spectrum of the supermode at the output of the cavity.

REFERENCES

- [1] W.H. Urbanus et al, "High-power electrostatic free-electron maser as a future source for fusion plasma heating: Experiments in the short-pulse regime", *Phys. Rev. E*, vol. 59, pp. 6058-6063, 1999. DOI:10.1103/physreve.59.6058
- [2] S. Ceccuzzi et al, "Traditional vs. advanced Bragg reflectors for oversized circular waveguide", *Fusion Eng. and Design*, vol. 123, pp. 477-480, 2017.
- [3] V.L. Bratman et al, "Simulations of the build-up of transverse and longitudinal structures of the microwave field in the Fusion FEM", *Nucl. Instr. Meth. Phys. Res. A*, vol. 407, pp. 40-44, 1998. DOI: 10.1016/S0168-9002(97)01364-8

DEVELOPMENT OF POWERFUL LONG-PULSE TERAHERTZ BAND FELS BASED ON LINEAR INDUCTION ACCELERATORS*

V.Yu. Zaslavsky[†], N.S. Ginzburg¹, A.M. Malkin, N.Yu. Peskov¹, A.S. Sergeev,
Institute of Applied Physics RAS, Nizhny Novgorod, Russia
A.V. Arzhannikov, E.S. Sandalov, S.L. Sinitsky, D.I. Skovorodin, A.A. Starostenko,
Budker Institute of Nuclear Physics, Novosibirsk, Russia
¹also at Nizhny Novgorod State University, Nizhny Novgorod, Russia

Abstract

The paper is devoted to development of high-power long-pulse THz-band FELs based on the new generation of linear induction accelerators elaborated recently at Budker Institute (Novosibirsk). These accelerators generate microsecond electron beams with a current at kA-level and an energy of 2 to 5 MeV (with a possibility to increase the electrons energy up to 20 MeV). Based on this beam, we initiated a new project of multi-MW long-pulse FEL operating in the frequency range of 1 to 10 THz using a wiggler period of 3 to 6 cm. For this FEL oscillator, we propose a planar two-mirror resonator comprising highly selective advanced Bragg reflectors. Alternately, electrodynamic system for oscillators of this type can use hybrid two-mirror resonator consisting of an upstream advanced Bragg reflector and a downstream weakly reflecting conventional Bragg reflector. Simulations demonstrate that the advanced Bragg reflector based on coupling of propagating and quasi-cutoff waves ensures the mode control at the values of the gap between the corrugated plates forming such a resonator of up to 20 wavelengths. Simulations of the FEL driven by electron beam generated by the LIA-2 in the frame of both averaged approach and 3D PIC code demonstrate that the THz radiation power can reach the level of 10 to 20 MW.

INTRODUCTION

Distributed feedback based on periodic Bragg structures is widely used in classical and quantum generators of coherent radiation. Correspondingly, the frequency band of oscillators with this feedback mechanism covers the millimeter and optical (infrared) bands [1–3]. Use of Bragg mirrors in X-ray lasers was discussed in multiple works (for example, [4]). In the present paper, we show that the advanced Bragg structures can be efficiently used in terahertz free-electron lasers. In addition to the compatibility with the transport channels of intense electron beams, the advantage of the proposed structures is the spatial coherence of radiation at large values of the oversize factor of the interaction region with respect to both transverse coordinates.

Scheme of a planar FEL under consideration is shown in Fig. 1. A feature of this scheme is the use of Bragg

mirrors coupling the longitudinal and transverse (with respect to the velocity of the particles) wavebeams.

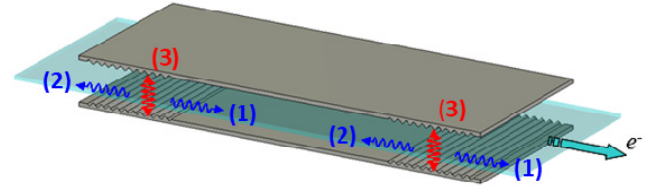


Figure 1: Scheme of FEL with two-mirror advanced Bragg resonator. Arrows (1), (2) indicate propagating of paraxial waves, (3) – quasi-cutoff feedback wave.

TUNABLE TERAHERTZ BRAGG REFLECTORS BASED ON COUPLING OF PROPAGATING AND CUTOFF WAVES

Bragg reflectors in the form of corrugated waveguide sections were proposed in [2] and are widely used currently as elements of electrodynamic systems in relativistic masers [3]. An obvious advantage of such systems is the compatibility with transportation of a high-current relativistic electron beam. Similarly to their optical prototypes, conventional variants of Bragg structures provide coupling and mutual scattering of the two counter-propagating paraxial waves. In the experiments on generation of radiation in the long wavelength part of the millimeter wavelength band, usual diameter of such cavities is restricted by size of several wavelengths.

In order to advance the relativistic masers into the sub-millimeter wavelength band, an increase in the oversize parameter of the cavities is required. However, this leads to a dramatic reduction in selectivity of the resonators composed from conventional Bragg structures due to overlapping of the reflection zones for different waveguide modes. Besides, a significant drop of the absolute values of the reflection coefficient of such structures takes place.

This problem can be solved using advanced Bragg structures based on coupling of propagating and quasi-cutoff waves. Similarly to sub-millimeter wave gyrotrons, the inclusion of the cutoff wave into the feedback loop leads to mode spectrum purification because the frequency interval between the cutoff waveguide modes is much higher than that between the paraxial waves. As a result, an advanced Bragg structures can be efficiently used as a narrow band reflector in the long-pulse THz-band FELs.

*This work was supported by the Russian Scientific Foundation (RSCF), grant No. 19-12-00212 and the Program of Presidium RAS No.10 (0035-2018-0022).

[†] zas-vladislav@appl.sci-nnov.ru

A planar advanced Bragg reflector is formed by two metal plates with a sinusoidal corrugation [5]. Under the Bragg resonance conditions, this structure provides coupling of two counter-propagating waves via excitation of a cutoff mode. As a result, advanced Bragg structures possess a narrow-band reflection zone near the cutoff frequency of the quasi-cutoff mode. It is important to note that the period of an advanced Bragg structure is approximately two times longer than the period of a conventional one, which is obviously beneficial in short-wavelength bands in terms of the manufacturing process. Another advantage of the advanced Bragg structure is the tunability of the reflection zone. At moderate values of the transverse size, variation of the distance between the plates is accompanied by a relatively wide shift of the reflection zone following the change in the cutoff frequency. At the same time, the reflection coefficient has rather small change for structures with optimal geometry.

Simulations of the advanced Bragg reflector (Fig. 2a) were carried out using the 3D code *CST MICROWAVE STUDIO*. The advanced Bragg reflector was composed of two parallel copper plates with a length of 20 cm, the period and depth of corrugation were 0.3 mm and 15 μ m, correspondingly. Such structure provides resonance coupling of the propagating TEM waves and the quasi-cutoff mode of TM_{40} -type at the gap of 6 mm.

The result of the simulation of an advanced Bragg structure is shown in Fig. 2a. At such a large oversize parameter it sustains the reflectivity at the high level (power reflection more than 90%). For comparison, the properties of a conventional Bragg reflector of the same dimensions were studied (see Fig. 2b).

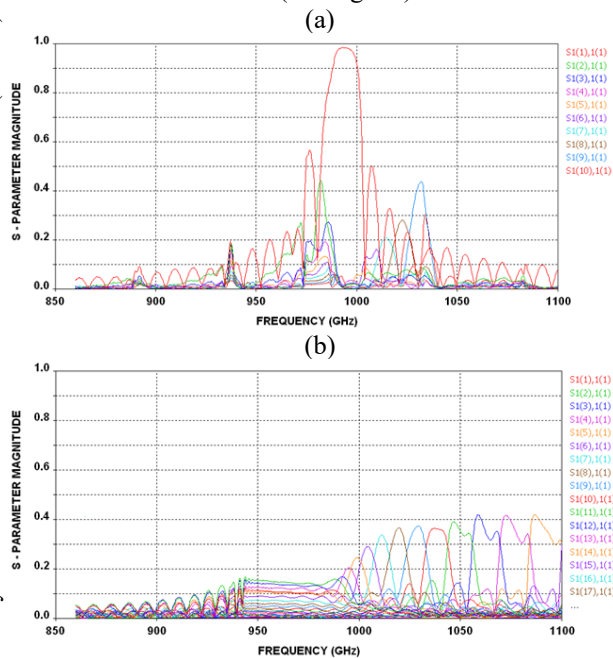


Figure 2: 3D simulations of Bragg resonators at THz-band using *CST MICROWAVE STUDIO* software. (a) Advanced Bragg reflector, (b) conventional Bragg reflector.

PROJECT OF POWERFUL BRAGG FEL FOR THz-BAND

The basis of the project is powerful induction linac elaborated recently at BINP RAS (the LIA-2 accelerator) [6]. This accelerator generates an electron beam with a current at kA-level and energy of 2 - 5 MeV (with the possibility to increase electrons energy up to 20 MeV).

Based on this beam, we initiated a new project of multi-MW long-pulse THz FEL. In fact, the use of the beam with specified particles energy allows for a realization of the FEL in the range of 1 - 10 THz using the wiggler with a period of 3 to 6 cm. For the realized beam current of ~ 1 - 2 kA, the radiation power is estimated on the level of 10 - 100 MW even while the electron efficiency remains rather low, about 1 to 0.1% (which, obviously, would decrease with increase of the radiation frequency).

Results of simulation of the FEL driven by a 5 MeV / 1 kA electron beam generated by the LIA - 2 are presented in Fig. 3. This beam is focused by the guide magnetic field of ~ 0.15 T (in reversed configuration) and operating transverse electron velocities in the beam are pumped by the wiggler having 4 cm spatial period. For this FEL-oscillator we consider two-mirror resonator consisting of advanced Bragg reflectors of planar geometry (see Fig.1).

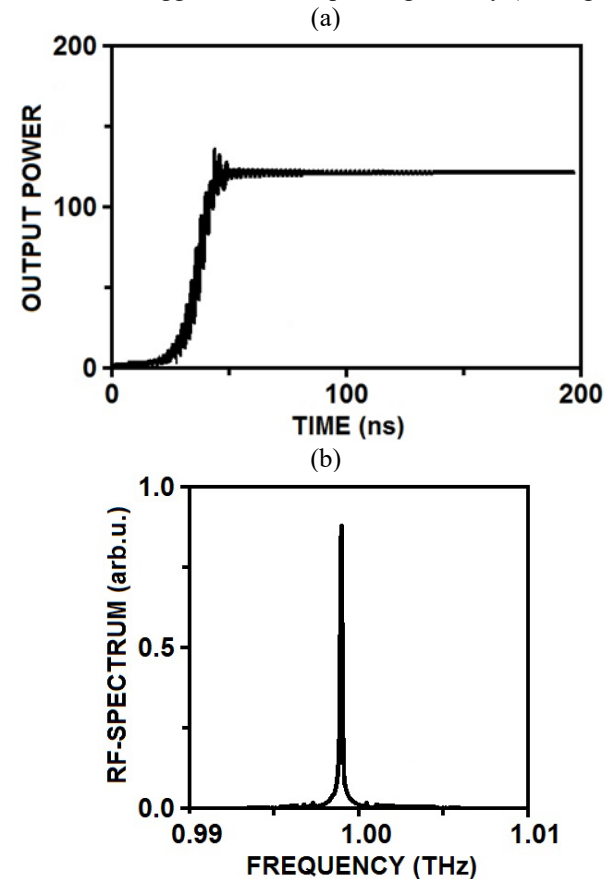


Figure 3: Results of simulations of FEL – oscillator in the frame of averaged theory. (a) Establishment of stationary narrow-band oscillation regime, (b) radiation spectrum.

Simulations demonstrated that Bragg structures of such type possess high reflectivity and ensure selectivity of the resonator for the transverse size (gap) up to 20 wavelengths. This size is sufficient for usage with the intense relativistic electron beams. For operation at 1 THz, we designed the resonator with a 6 mm gap and the Bragg structures 20 cm (up-stream) and 10 cm (down-stream) long having corrugation of the 0.3 mm period and 10 – 15 μm depth, a regular section of 50 -70 cm long between them. According to the simulations, under designed parameters the electron efficiency could reach 2 to 3% and the output power is 50 to 100 MW. The Ohmic losses in this case do not exceed 25 - 30% of the radiated power.

In summary, a novel concept of high-power THz-band Bragg FEL was developed. Original feature of this concept (in comparison with the others for now operating THz FEL) is the possibility to use electron beams with high-current (kA-level) and long-pulse (hundreds ns) duration. Such beams would allow achieving record levels of the radiation power of 10 - 100 MW and pulse energy up to 10 J for the THz-band. Operability of key components of electrodynamic system for such FEL, namely, the advanced Bragg resonators, was demonstrated in the proof-of-principle experiments in terahertz band at the oversize parameter of $\varnothing/\lambda \sim 7$.

REFERENCES

- [1] H. Kogelnik *et al.*, “Coupled-Wave Theory of Distributed Feedback Lasers”, *J. Appl. Phys.*, vol. 43, p. 2327, 1972. doi: 10.1063/1.1661499
- [2] V. L. Bratman *et al.*, “FEL's with Bragg reflection resonators: Cyclotron autoresonance masers versus ubitrons”, *IEEE J. Quantum. Electr.*, vol. 19, p. 282, 1983. doi: 10.1109/JQE.1983.1071840
- [3] A. V. Arzhannikov *et al.*, “Using Two-Dimensional Distributed Feedback for Synchronization of Radiation from Two Parallel-Sheet Electron Beams in a Free-Electron Maser”, *Phys. Rev. Lett.*, vol. 117, p. 114801, 2016. doi:10.1103/PhysRevLett.117.114801
- [4] K.-J. Kim *et al.*, “A Proposal for an X-Ray Free-Electron Laser Oscillator with an Energy-Recovery Linac”, *Phys. Rev. Lett.*, vol. 100, p. 244802, 2008. doi: 10.1103/PhysRevLett.100.244802
- [5] N. S. Ginzburg *et al.*, “Powerful terahertz free electron lasers with hybrid Bragg reflectors”, *Phys. Rev. ST Accel Beams*, vol 14, p. 042001, 2011. doi: 10.1103/PhysRevSTAB.14.042001
- [6] P. V. Logachev *et.al.*, “LIU-2 linear induction accelerator”, *Instruments and Experimental Techniques*, vol. 56, no. 6, p. 672, 2013. doi:10.1134/S0020441213060195

ANALYTICAL AND NUMERICAL COMPARISON OF DIFFERENT APPROACHES TO THE DESCRIPTION OF SASE IN HIGH GAIN FELs

O.A. Shevchenko[†], N.A. Vinokurov¹, Budker Institute of Nuclear Physics, Novosibirsk, Russia
¹also at Novosibirsk State University Novosibirsk, Russia

Abstract

Correlation function theory which has been developed recently gives rigorous statistical description of the SASE FEL operation. It directly deals with the values averaged over many shots. There are two other approaches which are based either on Vlasov equation or on direct solution of particle motion equations. Both of them perform calculations for some particular initial conditions. After that one can either consider the result as a “typical” sample, or repeat calculations for other initial conditions and then average the results. To check the validity of these three approaches it might be interesting to compare them with each other. In this paper we present the results of such comparison obtained for the 1-D FEL model. We show that two-particle correlation function approximation is equivalent to the quasilinear approximation for the Vlasov equation approach. These two approximations are in a good agreement with the results of direct solution of particle motion equations at linear and early saturation stages. To obtain this agreement at strong saturation, high order harmonics in Vlasov equation have to be taken into account, which corresponds to taking into account of three and more particle correlations in the correlation function approach.

INTRODUCTION

SASE FELs are widely used now as bright sources of coherent radiation in X-ray region [1]. Radiation of such FELs is a result of initial inhomogeneity of particle density, and therefore its parameters fluctuate significantly from shot to shot and within one pulse. To determine these parameters in a single shot one has to solve particle motion equations together with Maxwell equations. For a real shot it is not possible not only because of large number of particles but also because of unknown initial conditions. However, parameters averaged over many shots can be found by standard methods of statistical mechanics. Recently the correlation function theory, which deals with such parameters, was developed based on BBGKY chain of equations. Detailed description of this theory for general case is given elsewhere [2]. In this paper we shall consider simple 1-D case where the theory can be verified by comparing with other approaches based on direct solution of motion equations and solution of Vlasov equation for random smoothed density distribution in one-particle phase space.

BASIC EQUATIONS AND NUMERICAL SOLUTION ALGORITHM

The 1-D approximation is widely used in the FEL

[†] O.A.Shevchenko@inp.nsk.su

theory [3]. Despite the fact that it does not have rigorous foundation, it gives a good qualitative description of the physical processes taking place in single pass FEL.

Equations of Motion

Interaction of two particles in FEL occurs mainly through radiation. Knowing the particle trajectory one can calculate its radiation field and formally substitute it to the motion equations. But, unlike the case of the Coulomb interaction, the resulting set of equations will contain retardation. Fortunately some approximations relevant to FEL radiation field allow to eliminate retardation by special choice of independent variable and to obtain a set of ordinary differential equations. In 1-D case the resulting set of equations can be written in the following simple form:

$$\frac{dz^{(k)}}{d\theta} = 1 + 2\Delta^{(k)}; \quad \frac{d\Delta^{(k)}}{d\theta} = \frac{1}{N_\lambda} \sum_{z^{(l)} < z^{(k)}} \Phi(z^{(k)}, z^{(l)}) \cdot (1)$$

where $z^{(k)}$ and $\Delta^{(k)}$ - longitudinal coordinate and relative energy deviation of the k -th particle, N_λ - number of particles per radiation wavelength, $\theta = 2\gamma_{\parallel}^2(t - z)$ - special “time” variable (see [2] for details). Particular form of interaction “force” $\Phi(z^{(k)}, z^{(l)})$ depends on the used approximation. Further we shall restrict our consideration to the model of charged sheets. In this model $\Phi(z^{(k)}, z^{(l)}) = -8\rho^3 \cos(z^{(k)} - z^{(l)})$, ρ - Pierce parameter. For the numerical solution of (1) it is also convenient to make substitution $z^{(k)} = \theta + \tilde{z}^{(k)}$. The resulting set of equations is given below:

$$\frac{d\tilde{z}^{(k)}}{d\theta} = 2\Delta^{(k)}; \quad \frac{d\Delta^{(k)}}{d\theta} = -\frac{1}{N_\lambda} 8\rho^3 \operatorname{Re}\left(e^{i\tilde{z}^{(k)}} S^{(k)}\right). \quad (2)$$

$S^{(k)} = \sum_{z^{(l)} < z^{(k)}} e^{-i\tilde{z}^{(l)}}$ where . The set of equations (2) can be easily solved numerically using any simple difference scheme. The only difficulty is the large number of particles. One also needs to remember that to obtain averaged values the system has to be solved many times with “random” initial conditions. Calculation of the value $S^{(k)}$ can be simplified substantially if one sorts particles at each integration step so, that $\tilde{z}^{(l)} < \tilde{z}^{(k)}$ if $l < k$. In this case $S^{(k)} = S^{(k-1)} + e^{-i\tilde{z}^{(k-1)}}$. The order of particle arrangement

after each integration step is not violated very much and almost any sorting algorithm is efficient in this case.

Vlasov Equation and Quasilinear Approximation

The Vlasov equation for the considered model can be easily obtained directly from the motion equations (1):

$$\left(\frac{\partial}{\partial \theta} + (1 + 2\Delta)\frac{\partial}{\partial z}\right)f(z, \Delta, \theta) = -\frac{\partial}{\partial \Delta}f(z, \Delta, \theta) \int_0^z \Phi(z-z')f(z', \Delta', \theta)d\Delta'dz' \quad (3)$$

It is convenient to introduce the slow varying amplitudes of distribution function $\tilde{f}^{(n)}(z, \Delta, \theta)$ which we shall call harmonics. For numerical solution it also convenient to consider amplitudes $\tilde{f}^{(n)}(z, \Delta, \theta)$ be periodic in θ with some period T :

$$f(z, \Delta, \theta) = \tilde{f}^{(0)}(z, \Delta, \theta) + 2\text{Re}\left(\sum_n \tilde{f}^{(n)}(z, \Delta, \theta)e^{in(\theta-\theta_0)}\right) \quad (4)$$

$$\tilde{f}^{(n)}(z, \Delta, \theta) = \sum_\nu f_\nu^{(n)}(z, \Delta)e^{-in\theta} \quad \nu_m = (2\pi/T) \cdot m$$

For the coasting beam in this model one has to use the following initial condition: $f_\nu^{(0)}(0, \Delta) = 0$ at all $\nu \neq 0$. Value of T is determined from the condition that the bunch length corresponding to one period has to be larger than two slippage lengths in the whole undulator.

Substituting (4) and explicit expression of $\Phi(z-z')$ into (3) we obtain the following set of equations:

$$\left((1 + 2\Delta)\frac{\partial}{\partial z} - i\nu\right)f_\nu^{(0)}(z, \Delta) = \frac{\partial}{\partial \Delta} \sum_{\nu'} \left(A_{\nu'}(z)f_{\nu-\nu'}^{(1)*}(z, \Delta) + A_{\nu'}^*(z)f_{\nu+\nu'}^{(1)}(z, \Delta)\right)$$

$$\left((1 + 2\Delta)\frac{\partial}{\partial z} + i(2n\Delta - \nu)\right)\tilde{f}_\nu^{(n)}(z, \Delta) = \frac{\partial}{\partial \Delta} \sum_{\nu'} \left(A_{\nu'}(z)f_{\nu-\nu'}^{(n-1)}(z, \Delta) + A_{\nu'}^*(z)f_{\nu+\nu'}^{(n+1)}(z, \Delta)\right) \quad (5)$$

$$A_\nu(z) = 4\rho^3 \int_0^z \int f_\nu^{(1)}(z', \Delta')d\Delta'dz'$$

This system can be solved numerically using explicate difference scheme. It should be noted here that $f_\nu^{(n)}(z, \Delta)$ are random functions and to get averaged values this system has to be solved multiple times with different initial conditions.

One also can simplify (6) by using so called quasilinear approximation [4]. In this approximation we assume that saturation takes place due to the growth of the energy

spread only. We neglect all high order harmonics $f_\nu^{(n)}(z, \Delta)$ at $n > 1$ as well as $f_\nu^{(0)}(z, \Delta)$ at $\nu \neq 0$.

Correlation Function Equation

The set of equations for the two-particle correlation function for the case of coasting beam is given bellow:

$$(1 + 2\Delta_1)\frac{\partial}{\partial z_1}F(1) = -\int d\{2\}\Phi(1, 2)\frac{\partial}{\partial \Delta_1}G(1, 2)$$

$$\left((1 + 2\Delta_1)\frac{\partial}{\partial z_1} + (1 + 2\Delta_2)\frac{\partial}{\partial z_2}\right)G(1, 2) + \int \left(\frac{\partial F(1)}{\partial \Delta_1}\Phi(1, 3)G(2, 3) + \frac{\partial F(2)}{\partial \Delta_2}\Phi(2, 3)G(1, 3)\right)d\{3\} =$$

$$= -\frac{1}{N_{\lambda_w}}\left(\Phi(1, 2)\frac{\partial}{\partial \Delta_1} + \Phi(2, 1)\frac{\partial}{\partial \Delta_2}\right)F(1)F(2) \quad (6)$$

To calculated current and radiation spectral distributions one needs to know two-time correlation function which obeys the following equation:

$$\left(\frac{\partial}{\partial \theta_1} + (1 + 2\Delta_1)\frac{\partial}{\partial z_1}\right)G_2(1, 2; \theta_1 - \theta_2) = -\frac{\partial F(1, \theta_1)}{\partial \Delta_1} \int \Phi(1, 3)G_2(3, 2; \theta_1 - \theta_2)d\{3\}$$

It has to be solved with the initial condition $G_2(1, 2, 0) = G(1, 2)$. It also makes sense to introduce slow varying amplitudes or harmonics of the correlation function the following way:

$$G(z_1, \Delta_1; z_2, \Delta_2) = G^{(0)}(z_1, \Delta_1; z_2, \Delta_2) + \sum_{n>0} \left(\tilde{G}^{(n)}(z_1, \Delta_1; z_2, \Delta_2)e^{in(z_1-z_2)} + \kappa.c.\right) \quad (7)$$

By substituting (7) into (6) one can show that high order harmonics are not exited if only two-particle correlation function is taken into account.

For the high order harmonics to appear one needs to take into account many particles correlations. They may play important role at saturation if its mechanism is not quasilinear. In this case one has to consider three and more particles correlations.

RESULTS OF SIMULATIONS

In simulations we used the following set of parameters: $\rho = \sigma_e = 9 \cdot 10^{-4}$ - Pearce parameter and energy spread, $N_\lambda = 500$ - number of particles per radiation wavelength, $N_w = 2000$ - number of undulator periods. The bunch length in the case of direct solution of particle motion equations was 4000 of radiation wavelengths. Therefore, the total number of particles was $2 \cdot 10^6$. Averaging was

done over 2000 sets of initial conditions. In quasilinear simulations averaging was done over $2 \cdot 10^4$ sets. When harmonics were taken into account (0, 2nd and 3^d) we used 1300 sets as simulation was rather slow.

Corresponding Quantities for Comparison

To compare simulation results obtained from three approaches we need to find corresponding quantities which can be matched. If $\tilde{z}^{(k)}(\theta)$ and $\Delta^{(k)}(\theta)$ are solutions of particle motion equations (2) then the bunching factor can be found from the expression:

$$B(z, \theta) = \left\langle e^{i\tilde{z}^{(k)}(\theta)} \right\rangle \Big|_{z - \tilde{z}^{(k)}(\theta) < \pi}$$

Analog of the two-time correlation function, integrated by energies in this case will be $\langle B(z_1, \theta_1) B^*(z_2, \theta_2) \rangle \approx C(z_1, z_2, \theta_1 - \theta_2)$ (valid for long bunch). Here averaging is done over initial conditions,

We shall use the following quantities for comparison - square of the bunching factor

$$\begin{aligned} |b(z)|^2 &= \int G(z, \Delta_1, z, \Delta_2) d\Delta_1 d\Delta_2 \approx \\ &\approx C(z, z, 0) \approx \int \sum_{\nu} \langle f_{\nu}^{(1)}(z, \Delta_1) f_{\nu}^{(1)*}(z, \Delta_2) \rangle d\Delta_1 d\Delta_2 \end{aligned}$$

and current spectral density

$$\begin{aligned} J_{\nu}(z) &= \int G_2(z, \Delta_1, z, \Delta_2, \tau) e^{i(1+\nu)\tau} d\Delta_1 d\Delta_2 d\tau \approx \\ &\approx \int C(z, z, \tau) e^{i\nu\tau} d\tau \approx T \int \langle f_{\nu}^{(1)}(z, \Delta_1) f_{\nu}^{(1)*}(z, \Delta_2) \rangle d\Delta_1 d\Delta_2 \end{aligned}$$

Comparison of Different Approaches

The results of comparison are presented in Fig. 1 and Fig. 2.

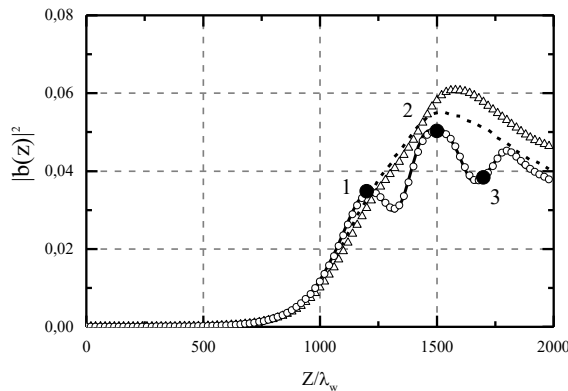


Figure 1: Dependence of bunching factor on beam position in undulator. Solid line - correlation function theory, circles - Vlasov equation in quasilinear approximation, dashed line - direct solution of motion equations, triangles - Vlasov equation with high order harmonics

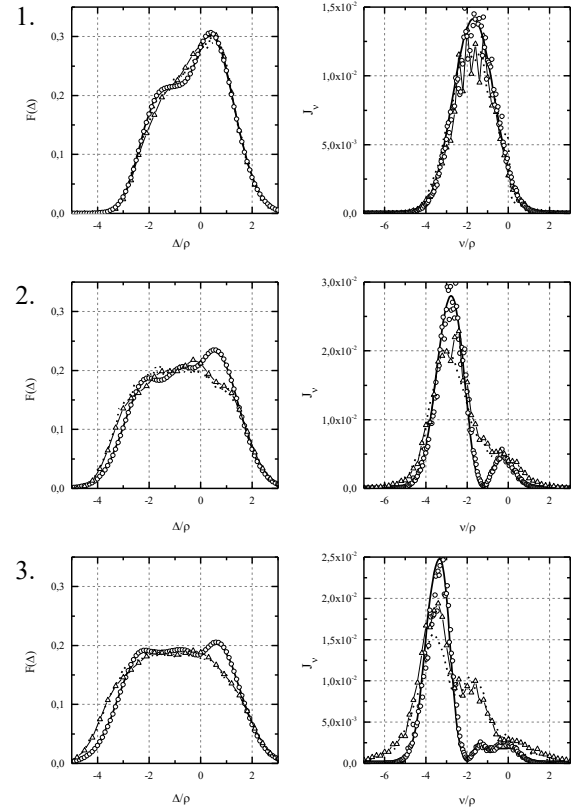


Figure 2: Energy distribution and current spectrum at different points in undulator shown in Fig. 1. Legend is the same as in Fig.1.

It worth noting that perfect agreement of the correlation function theory with quasilinear approximation is not surprising. Value $\tilde{g}(1;2) = \sum_{\nu} f_{\nu}^{(1)}(z_1, \Delta_1) f_{\nu}^{(1)*}(z_2, \Delta_2)$

corresponds to $\tilde{G}^{(1)}(1;2)$. It obeys exactly the same equation without the RHS. term responsible for shot noise. And for the three-particle correlation function $H(1,2,3) = \tilde{H}_0(1,2,3) e^{i(z_3 - z_2)} + \tilde{H}_2(1,2,3) e^{i(2z_1 - z_2 - z_3)} + \dots$ one can find the following corresponding values composed of zero and high order harmonics:

$$\begin{aligned} \tilde{h}_0(1,2,3) &= \sum_{\nu} \sum_{\nu' \neq \nu} \left(f_{\nu-\nu'}^{(0)}(z_1, \Delta_1) f_{\nu}^{(1)*}(z_2, \Delta_2) f_{\nu'}^{(1)}(z_3, \Delta_3) \right) \\ \tilde{h}_2(1,2,3) &= \sum_{\nu} \sum_{\nu'} \left(f_{\nu+\nu'}^{(2)}(z_1, \Delta_1) f_{\nu}^{(1)*}(z_2, \Delta_2) f_{\nu'}^{(1)*}(z_3, \Delta_3) \right) \end{aligned}$$

which means that appearance of high order harmonics is related to many-particle correlations.

CONCLUSION

Direct solution of motion equations showed that at deep saturation stage high order harmonics in Vlasov equation have to be taken into account. In correlation function theory these harmonics are related to many-particle correlations. Neglecting of these correlations in BBGKY chain is equivalent to quasilinear approximation.

REFERENCES

- [1] C. Pellegrini Phys. Scr., 91, 014004 (2016)
doi: 10.1088/1402-4896/aa5281
- [2] O.A. Shevchenko and N.A. Vinokurov, Proc. of FEL2009, Liverpool, UK, (2009), paper MOOA02, pp. 8-14.
- [3] K.-J. Kim, Nucl. Instrum. Methods Phys. Res., Sect. A250, 396 (1986), *doi: 10.1016/0168-9002(86)90916-2*
- [4] N. A. Vinokurov, Z. Huang, O. A. Shevchenko, and K.-J. Kim, "Quasilinear Theory of High-Gain FEL Saturation" Nucl. Instrum. Methods Phys. Res., Sect. A 475, 74(2001).
doi: 10.1016/S0168-9002(01)01525-X

ELECTRONIC MODULATION OF THE FEL-OSCILLATOR RADIATION POWER DRIVEN BY ERL

O. A. Shevchenko[†], S. V. Tararyshkin, Ya. V. Getmanov¹, S. S. Serednyakov¹, E. V. Bykov, Budker
Institute of Nuclear Physics, Novosibirsk, Russia,
A. Melnikov¹, M. Fedin, S. Veber¹, International Tomography Center SB RAS, Novosibirsk, Russia,
¹also at Novosibirsk State University, Novosibirsk, Russia

Abstract

FEL oscillators usually operate in CW mode and produce periodic train of radiation pulses but some user experiments require modulation of radiation power. Conventional way to obtain this modulation is using of mechanical shutters but it cannot provide very short switching time and may lead to decreasing of the radiation beam quality. Another way could be based on the electron beam current modulation but it cannot be used in the ERL. We propose a simple way of fast control of the FEL lasing which is based on periodic phase shift of electron bunches with respect to radiation stored in optical cavity. The phase shift required to suppress lasing is relatively small and it does not change significantly repetition rate. This approach has been realized at NovoFEL facility. It allows to generate radiation macropulses of desirable length down to several microseconds (limited by quality factor of optical cavity and FEL gain) which can be synchronized with external trigger. We present detailed description of electronic power modulation scheme and discuss the results of experiments.

INTRODUCTION

Novosibirsk Free Electron Laser (NovoFEL) facility comprises three FELs, which use energy recovery linac (ERL) as a source of electrons [1]. All three FELs are FEL oscillators. They operate in CW mode and produce periodic train of radiation pulses. Energy recovery allows to achieve very high averaged current of the electron beam which results in high average power of radiation. There are applications where this power is really needed [2] but most often it has to be attenuated. In some experiments users want to have large peak power and to avoid overheating of their samples at that [3]. This demand can be fulfilled by modulation of FEL radiation. For this purpose one can think of mechanical shutter but this shutter cannot be done to be fast enough and it also disturbs transverse profile of radiation.

Ideal solution of this problem would be to instantly turn on and off the FEL lasing process. For the single pass FEL based on linear accelerator the lasing can be controlled by the beam injection [4]. In ERL, injection is required to operate in CW mode; it is not possible to switch it on and off instantly. Particularly, for the case of NovoFEL accelerator, beam loading effects in the accelerating structure are very significant because of high average current: fast switching of the current leads to transient effects resulting in beam loss. Instead of that, more “delicate” approach should be developed that keeps the electron beam current almost constant, but efficiently suppresses the lasing in FEL. In this

work we developed and implemented at NovoFEL the approach that allows to generate the THz macropulses at any repetition rate and almost any individual length from several seconds and down to several microseconds (the minimal pulse duration is determined by growing up and decay time of lasting which depends on the FEL gain and the quality factor of the optical cavity). This regime has been examined at all three FELs by generation of macropulses with tens of microseconds duration. Possible applications of the electronic modulation of THz radiation are discussed in this paper.

IMPLEMENTATION OF ELECTRONIC POWER MODULATION

In FEL oscillator lasing is possible only when radiation and electron bunches come to undulator simultaneously. In other words electron bunch repetition rate has to be almost equal to the round-trip frequency of the optical cavity (usually acceptable detuning does not exceed 10^{-4}). Changing repetition rate by about 1% will certainly stop lasing, at the same time corresponding variation of the average beam current is not significant and can be easily tolerated by the accelerating structure of ERL. Bunch repetition rate is determined by the frequency of the master oscillator which signal is also used as an input for RF generators. This frequency cannot be changed very fast. Fortunately there is another approach which results in the change of repetition rate and in the termination of lasing.

If injection of one electron bunch is delayed by, e.g., one period of the RF accelerating field it almost does not influence on beam dynamics in accelerator but this bunch comes to undulator in wrong time and does not interact with THz wave, which stops its amplification and leads to fast decay of radiation power. To prevent the formation of new THz wave, injection phase has to be shifted periodically, which actually leads to the small decreasing of the repetition rate.

Implementation Scheme

The scheme of practical implementation of the injection phase shifting is shown in Fig. 1. Injection is triggered by trigger signal modulator, which counts the pulses coming from the master clock. Pulses come with the repetition rate equal to RF accelerating field frequency 180.4 MHz. The simplest algorithm of the trigger signal modulator operation is the following: it bites N-1 successive pulses out of the 180.4 MHz pulse sequence and then triggers injection with the next Nth pulse (for the 1st FEL N = 32, for the 2nd FEL N = 24 and for the 3^d FEL N = 48). In normal regime

[†] email address O.A.Shevchenko@inp.nsk.su

(CW) the phase shifter is switched off, while in power modulation mode it is on. The phase shifter operation algorithm is the following: it periodically bites each K^{th} pulse out of the 180.4 MHz pulse sequence which results in the shift of injection phase by one RF period. The smaller values of K used, the better suppression of FEL lasing is achieved. On the other hand, K should be large enough to avoid influence on accelerator operation. It was shown experimentally that $K = 100$ is sufficient to suppress FEL lasing completely without influencing the accelerator operation.

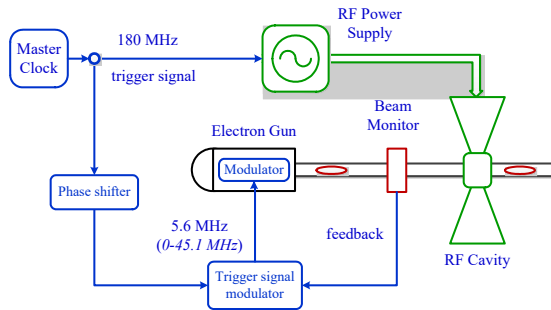


Figure 1: Layout of the injection phase shifting system.

Resulting Time Structure of FEL Radiation

A typical example of time dependence of the first FEL radiation is shown in Figure 2. In the normal operation regime (CW) this structure is a continuous train of short radiation pulses (50-100 ps), which follow each other with the frequency of ~ 5.6 MHz determined by the optical cavity length.

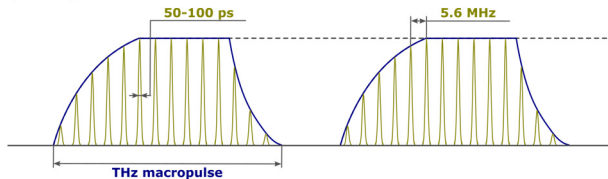


Figure 2: Schematic view of NovoFEL radiation macropulses. The length of the individual THz pulse and their repetition rate are shown for 1st FEL.

When NovoFEL operates in the power modulation mode, the laser radiation consists of macropulses with minimal duration about 10 μs and arbitrary repetition rate which is controlled by user. Each macropulse contains tens of individual THz radiation pulses and its fronts depend on the FEL gain (pulse raise) and the quality factor of the optical cavity (pulse decay). The characteristic rise and decay time is about 2 μs .

There are two regimes of the phase shifter control. In the first fully digital regime user sets duration of time intervals during which the shifter is turned on and off. In this regime one gets periodic train of radiation macropulses. In the second regime the shifter is normally turned on, so that the lasing is suppressed. It is turned off by external triggering signal for the digitally set time duration. In this regime one can get single macropulses, which can be synchronized with user equipment.

RESULTS AND DISCUSSIONS

Generation of Macropulses at NovoFEL

In order to demonstrate the possibilities of electronic modulation system (EMS), we recorded the THz macropulses with different pulse length at all three FELs of NovoFEL, which correspond to different energy ranges of available radiation. Macropulses of THz radiation with different length in the range of 10 μs to 40 μs obtained at 130 μm wavelength (1st FEL) are shown in Fig.3. Pulses with duration of more than 400 μs are also available, but they do not have any direct practical implementations except for the aim of keeping a stable average power over a long period of time in CW experiments (see below).

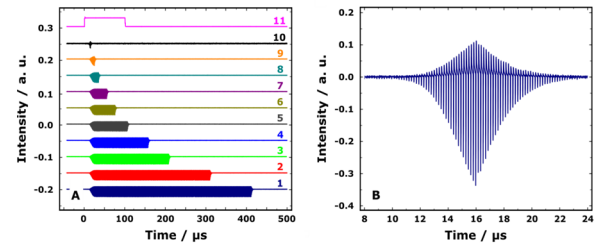


Figure 3: (A) Macropulses of THz (130 μm) radiation. Durations are (1) 400 μs ; (2) 300 μs ; (3) 200 μs ; (4) 150 μs ; (5) 100 μs ; (6) 70 μs ; (7) 50 μs ; (8) 30 μs ; (9) 20 μs ; (10) 10 μs (multiplied by 10); (11) trigger signal. Each subsequent pulse is vertically shifted; (B) Macropulse with 10 μs duration. The individual pulses of THz radiation with the frequency of 5.6 MHz are clearly visible.

Fig. 3 (B) shows the rising and falling edges of the shortest obtained macropulse. The time resolution of the detector used at the first FEL (Fig. 3 B) is enough to see the fine structure of THz macropulse, which consists of the series of short individual pulses at electron beam repetition rate.

Measurement of the FEL Parameters

From the analysis of THz macropulse edges one can obtain characteristic rise and decay time and calculate FEL gain and round-trip losses in optical cavity. An example of such calculation is shown in Fig. 4 and Fig. 5.

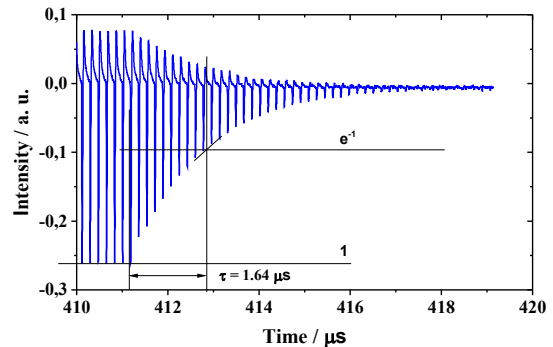


Figure 4: Calculation of losses for the first FEL optical cavity. Characteristic decay time is 1.64 μs , round-trip losses are 10.3 %.

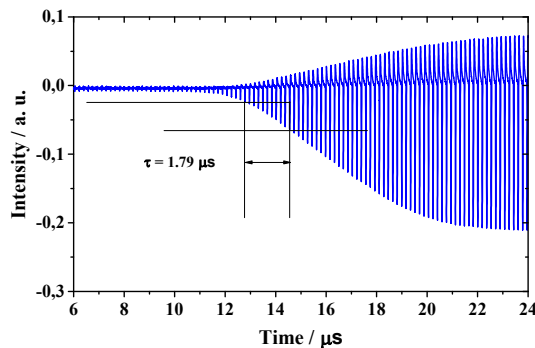


Figure 5: Gain calculation for the first FEL. Characteristic rise time is 1.79 μs , gain exceeds losses by 9.5 %.

Obtained parameters are in reasonable agreement with previously made calculations [5].

POSSIBLE APPLICATIONS OF ELECTRONIC MODULATION OF THZ RADIATION AT NOVOFEL

Electronic modulation system at NovoFEL provides unique possibilities for controlling and tuning average power of THz radiation and repetition rate of THz macropulses directly on the user stations. The possible applications of EMS used in experiments with THz radiation include the following options: (i) controlling of average THz power over the long time period; (ii) formation of short macropulses with highest peak power available; (iii) lock-in detection.

Control of the Average THz Power in CW Experiments

In order to precisely measure the influence of CW THz radiation on different objects it is crucial to have a stable average THz power over a long period of time (hours), which due to working principles of NovoFEL is quite challenging task. Indeed, the generation of THz radiation is determined by fine tuning of a number of different parameters that are sensitive to the long time stability of electron beam, heating of optical resonators and other parts, etc. In turn, using EMS the desired power can be achieved by measuring the average power in real time and then automatically adjusting the number of electron beam pulses with shifted frequency that suppress lasing. For optimal performance, the working average power should be approximately two times lower than the peak power available at the moment in order to have an amplification reserve.

Reduction of the average power may be also very useful for adjustment of the accelerator as it allows to reduce beam losses at the recuperation stage.

Formation of Short High-power THz Macropulses

In addition to studying the cumulative effects of THz on various objects, EMS allows one to routinely perform time resolved experiments with a time resolution determined by the shortest available THz macropulse. As it can be seen

from Fig. 3, 10 μs THz pulses are reachable with typical amplification coefficients of the optical resonators of NovoFEL. Apart from resolution in time, the use of macropulses decreases the average THz power of NovoFEL, but keeps its peak value. Such a control of radiation power is important in practically every experiment, because of a possibility to irreversible damage the sample under study. It should also be noted that the impact of individual THz pulses on the sample in the microsecond macropulse can be investigated, which further extend the temporary resolution of the experiment.

Lock-in Detection

EMS can be used in experiments utilizing lock-in detection schemes where the modulation of THz power at certain frequency is required. The repetition rate of THz macropulses, which is set by frequency generator directly at the user stations, can be used for lock-in detection of the modulated signal. Since NovoFEL can be operated in CW mode, there is no low frequency limit for macropulse repetition rate. The upper limit is mainly determined by the rise and decay times of the FEL optical resonator and corresponds to 10-50 kHz. The advantage of using lock-in detection scheme offered by EMS is a possible increase in the signal to noise ratio of measured values.

CONCLUSION

In this work an approach for the creation of THz macropulses at any repetition rate and almost any individual pulse length were developed and implemented at NovoFEL. Suggested radiation electronic modulation system is based on periodic shift of the phase of electron bunch injection. Such a shift suppresses lasing and forms macropulses from quasi-continuous radiation of NovoFEL. The system is directly embedded into the electronic infrastructure of NovoFEL and can be triggered directly on user stations. For users such electronic modulation system provides a unique possibility, e.g., to control the average power of THz radiation over a long period of time or to create macropulses with as short as 10 μs duration.

In order to characterize EMS, series of macropulses with different durations from 10 to 400 μs were measured for three available frequency ranges. Using the rising and falling edges of typical macropulses the calculations of the gain and total losses were done. Obtained characteristics are in a good agreement with the data obtained earlier.

ACKNOWLEDGEMENTS

Experiments with FEL macropulse parameters measurements were funded by Russian Science Foundation, grant number 17-13-01412.

REFERENCES

- [1] O. A. Shevchenko *et al.*, "The Novosibirsk Free Electron Laser – unique source of terahertz and infrared coherent radiation" *Phys. Procedia* 2016, 84, 13-18. doi: 10.1016/j.phpro.2016.11.004

- [2] V. V. Kubarev, "Dynamics Of The THz Optical Discharge" presented at the 39th International Conference on Infrared, Millimeter, and Terahertz waves (IRMMW-THz), 14-19 Sept. 2014, 2014; pp 1-2.
doi:0.1109/IRMMW-THz.2014.6956280
- [3] S. L. Veber *et al.*, "X-band EPR setup with THz light excitation of Novosibirsk Free Electron Laser: Goals, means, useful extras." *J. Magn. Reson.* 2018, 288, 11-22.
doi: 10.1016/j.jmr.2018.01.009
- [4] A. Marinelli, D. Ratner, A. A. Lutman *et al.*, "High-intensity double-pulse X-ray free-electron laser" *Nat. Commun.* 2015, 6, 6369. doi:10.1038/ncomms7369
- [5] V. V. Kubarev, "Calculation, optimisation, and measurements of optical resonator parameters of the Novosibirsk terahertz free-electron laser" *Quantum Elec.* 2009, 39, 235-240.
doi:10.1070/QE2009v039n03ABEH013896

CURRENT STATUS OF FREE ELECTRON LASER @ TARLA *

A. Aksoy[†], Ç. Kaya, Ö. Karşı, B. Koç, Ö. F. Elçim

Institute of Accelerator Technologies, Ankara University, Ankara, Turkey

Abstract

Turkish Accelerator and Radiation Laboratory (TARLA), which is supported by the Presidency Strategy and Budget Directorate of Turkey, aims to be a state-of-art research instrument for light source users in Turkey. Two superconducting accelerating modules of TARLA will drive two different planar undulator magnets with periods of 110 mm (U110) and 35 mm (U35) in order to generate high brightness Continuous Wave (CW) Free Electron Laser (FEL) tunable in between 5-350 μm . Additionally, the linacs will drive a Bremsstrahlung radiation station to generate polarized gamma radiation. Main components of TARLA, such as injector, superconducting accelerating modules and cryoplant are under commissioning, currently. In this study, we present the current status of the facility as well as expected FEL performance.

INTRODUCTION

TARLA has been proposed as the first accelerator based FEL user facility in Turkey. The facility which has been commissioning is located at Institute of Accelerator Technologies in Golbasi Campus of Ankara University, which is about 15 km south of the capital city of Turkey, Ankara. The first priority of the facility is to make the country understood that the accelerator technology is the only tool for the solution of challenges of the new science. High brightness, tunable and powerful FEL beam will be generated between 5-350 μm by two planar undulators in a period of 35 mm and 110 mm, respectively. Furthermore, 5-30 MeV Bremsstrahlung radiation will be produced for fixed target and astro-physics experiments [1, 2]. The schematic view of the facility is given in Fig. 1.

FACILITY DESCRIPTION

TARLA accelerator design consists of two sections called injector and main accelerating section. Main accelerating section consists of two superconducting RF (SRF) modules will be installed following the high power low energy injector section. Each module has two superconducting Nb cavities operating at frequency of 1.3 GHz and temperature of 1.8 K (super-liquid helium). The cavities that have maximum accelerating gradient of up to 15 MV/m at continuous wave (CW) mode will allow beam to be accelerated up to 50 MeV. The high power beam operating at quasi-CW mode will be employed to generate radiation and secondary particles in a wide energy range to a diverse user community. Main electron beam parameters of TARLA are given in Table 1.

Table 1: TARLA Main Electron Beam Parameters

Parameter	Unit	Value
Beam Energy	MeV	15 - 40
Max. Average Beam Current	mA	1.5
Max. Bunch Charge	pC	120
Horizontal Emittance	mm.mrad	<15
Vertical Emittance	mm.mrad	<12
Longitudinal Emittance	keV.ps	<85
Bunch Length	ps	0.4 - 6
Bunch Repetition Rate	MHz	0.001-104
Macro Pulse Duration	μs	50 - CW
Macro Pulse Repetition Rate	Hz	1 - CW

Injector

The injector fed by a grid modulated thermionic triode DC electron gun, consists of two buncher cavities operating at 260 MHz and 1.3 GHz, several focusing magnets and diagnostic tools. The electron current is extracted from a tungsten dispenser cathode with a modulated grid voltage yielding bunches with 600 ps initial FWHM length. The bunches will first be compressed in the drift following the energy modulation obtained in the subharmonic buncher (SHB) in order to get into the linear phase range of the second buncher. The following 1.3 GHz fundamental buncher (FB) then introduces enough energy chirp to generate longitudinal (temporal) waist inside the first cell of the first SC cavity via ballistic bunching. Following successful commissioning of electron gun, the injector section has been tested at present.

Accelerator

TARLA main acceleration unit is composed of two similar superconducting linear accelerator modules mounted in a common vessel and constitute so called cryomodules [3], and a bunch compressor section between them. A cryomodule has two TESLA RF cavities [4] with an accelerating gradient of 10 MV/m at CW mode, for each cavity. The beam will further be accelerated to 40 MeV by main accelerating section. The (fixed R_{56}) bunch compressor between the cryomodules will allow highly stable beam by magnetic insertions. The electron beam will reach the required energy by the second cryomodule while reducing the energy spread [5]. Once the electron beam will arrive to the expected energy, it will send either to FEL hall or Bremsstrahlung hall. The parameters of TARLA cryomodule is given with Table 2.

The cryostat and mechanical tuning systems of cryomodules are originated by ELBE project [6]. The tuning system of the cryomodules has been modified slightly by mounting piezo-actuators on lever arms to have better RF performance for pulsed RF operations. The resolution and the speed of

* Work supported by Strategy and Budget Department of Turkey with Grand No: 2006K-120470

[†] avniaksoy@ankara.edu.tr

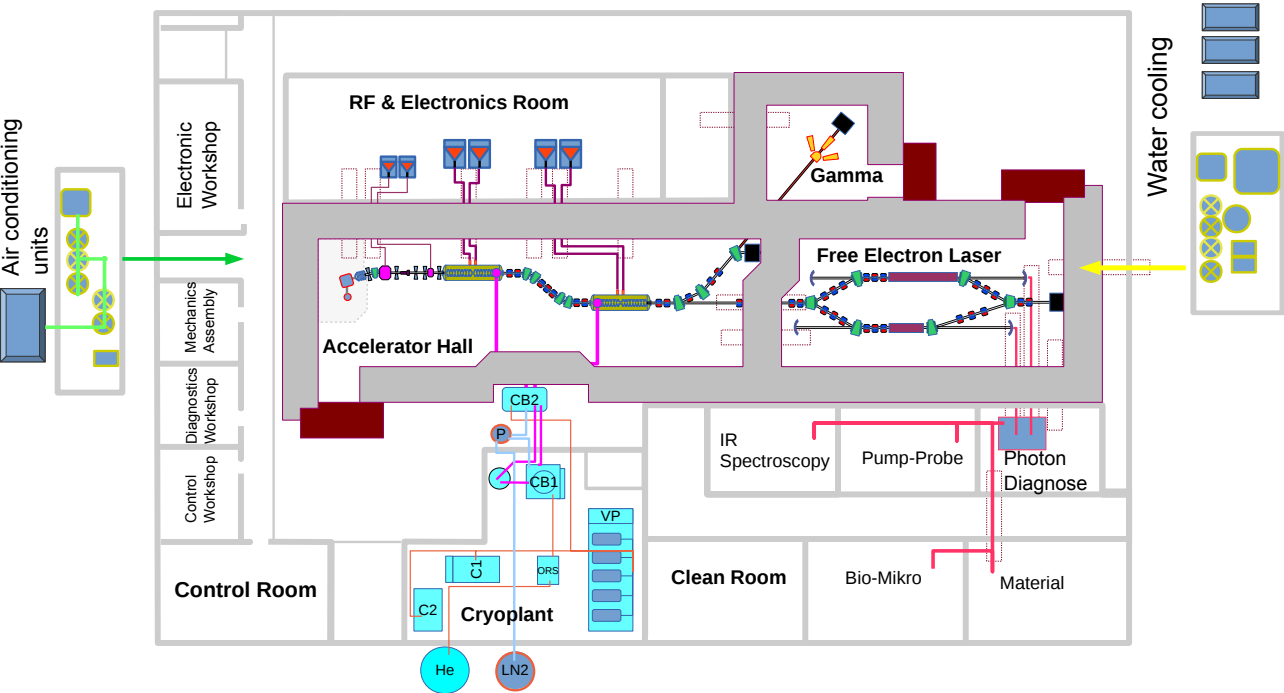


Figure 1: Layout of TARLA facility.

Table 2: TARLA CM Parameters

Parameter	Unit
Frequency @1.8 K (MHz)	1300 ± 0.05 MHz
Tuning Range (kHz)	120 kHz
Ext. Q of Input Couplers	(1.2 ± 0.2) × 10 ⁷
Ext Q of HOM Couplers	> 5 × 10 ¹¹
Accelerating Voltage/CM (MV)	> 20
Cryogenic Losses @ Max. Grad. (W)	< 75
Coupler Power @ CW (kW)	≥15
Tunning Resolution	1 Hz
Tunning Speed	1 kHz

tunning has been improved from 10 Hz - 5 Hz/ms to 1 Hz - 1 kHz. The cryomodules have been manufactured by Research Instruments GmbH [7]. Each cavity has been tested on its own under XFEL manufacturing conditions and assembled into the helium vessel, after that they were vertically tested at DESY in 2016. Fig. 2 shows the gradient values of TARLA cavities under vertical tests [8]. They were delivered after successful tests results such as coupler and leak tests etc. at the end of 2017.

Helium Plant

TARLA cryogenic system has a capable of 1.8 K superfluid helium at ±0.2 mbar pressure stability. The system allows to provide 4K, 2K and 1.8 K superfluid helium by a compressor station, two cold boxes, a dewar and varm vacuum pumps. TARLA helium plant has been manufactured and delivered by Air Liquide Advanced Technologies [9] in 2016. The main concern of the plant is to provide 16 mbar pressure stability at sub-atmospheric pressure. TARLA he-

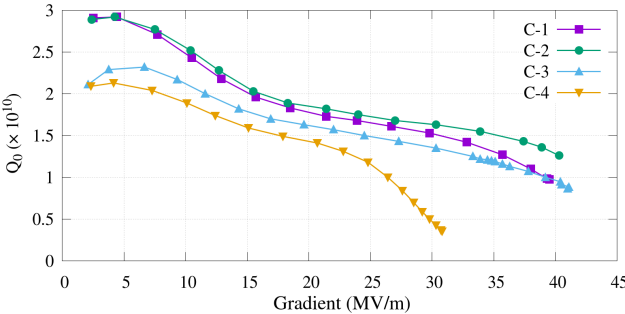


Figure 2: Vertical tests of TARLA cavities.

lium plant has been performed for a long time operation with test caps instead of TARLA cryomodules. The measurement results show that the pressure is as high stable as while the test caps under a heat load equal to the full heat loss of the cryomodules.

FREE ELECTRON LASER

Two FEL beamlines are planned to cover a broad range of infrared region. Since the users prefer to have long infrared waves, we extend to more than far infrared region to middle. Two optical resonators housing two different NbFe hybrid undulators with periods of $\lambda_{U110} = 110$ mm and $\lambda_{U35} = 35$ mm will be utilized to have between 5-350 μ m FEL. Figure 3 shows possible observable wavelength range for beam energy vs. undulator strengths. Expected FEL parameters are obtained from calculations are listed in Table 3.

In order to estimate the performance of TARLA FEL several simulation tools are investigated during desing study. For instance, in order to simulate the light-beam interaction within the undulator and the propagation of the light outside

Table 3: Some Resonator and Expected FEL Parameters

Parameter	U35	U110
Wavelength (μm)	3.5-34.	24.-390.
Period Length (mm)	35.	110.
No of Poles (#)	52	24
Length (m)	1.47	2.6
Undulator Strength (min-max)	0.39-1.	1.3-2.5
Max. Peak Power (MW)	10	5
Max. Average Power (W)	0.1 - 100	0.1-90
Max. Pulse Energy (μJ)	10	8
Pulse Length (ps)	1 - 10	1 - 10

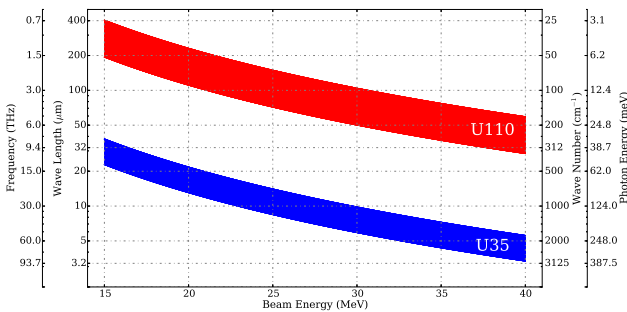


Figure 3: The wavelength range with respect to beam energy and undulator strength for U35 and U110.

the undulator for U35 in which the optical field propagates in free space, we have used GENESIS and Optical Propagation Code (OPC) codes in parallel [10]. Following Figures 4-7 summarizes the simulation results for maximum and minimum obtainable wavelengths from U35.

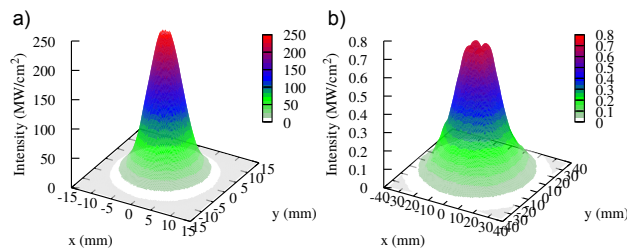


Figure 4: Intra-cavity power intensity of FEL a) for 3.5 μm b) for 32 μm .

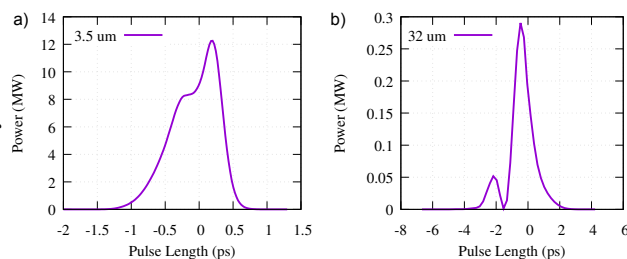


Figure 5: Power vs pulse length of FEL a) for 3.5 μm b) for 32 μm .

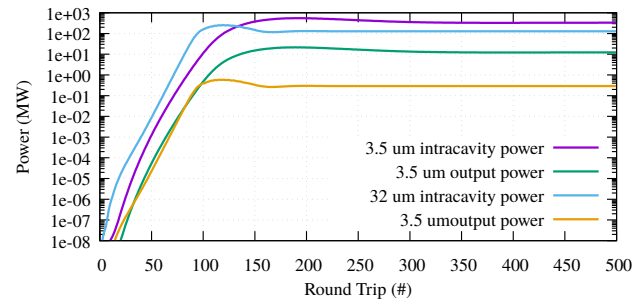


Figure 6: Power vs round trip of FEL for 3.5 μm & 32 μm .

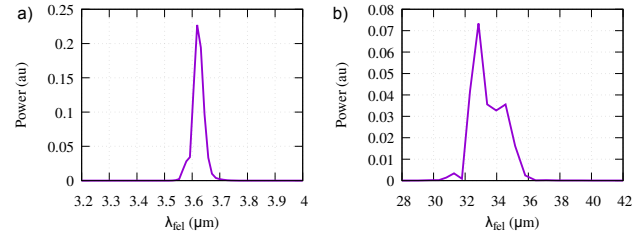


Figure 7: Spectrum of FEL for 3.5 μm & 32 μm .

For the FEL generated by U110 will have longer wavelengths thus the natural diffraction of the light becomes so large. In order to guide the electromagnetic wave a waveguide will be employed for this FEL beamline. In parallel to the optical resonator design, we investigate simulation tools to take into account the effect of waveguide propagation inside the undulator.

CONCLUSION

TARLA thermionic electron gun and injector line are in operation, currently [11]. The helium cryoplant has been commissioned and pressure stability by test cups has been promising. The long time operation tests of buncher RF amplifiers are ongoing for phase stabilization to prevent the beam energy spread. The leak tests of cryomodels are successfully completed at site. The integrated tests of helium plant and cryomodels will be performed as soon as possible, that will be a common time schedule of both companies. After achieving the integrated commissioning of helium plant and cryomodel tests, we are planning that the first cryomodel at 1st quarter of 2020 and the second is at end of the same year, in full operation.

As of the experimental infrastructure, TARLA has already provide a conventional near infrared laser source to the users since 2018. The first FEL lasing we expected to be achieved in 2022 and provide the users at the same year. Besides becoming the first accelerator based light source facility, TARLA also is an aware of being a pioneer facility that constructs an accelerator facility using its own resources in the country. TARLA facility will serve a variety of opportunities to the researchers in basic and applied science especially the ones who need high power laser in middle and far infrared region. Experimental stations for laser diagnostic, Pump-Probe, IR spectroscopy, have been equipping with the machine side synchronously.

REFERENCES

- [1] A. Aksoy and O. Karsli, "The technical design report of turkish accelerator and radiation laboratory in ankara," Tech. Rep., 2015.
- [2] A. Aksoy, Ö. Karşlı, and Ö. Yavaş, "The turkish accelerator complex ir fel project," *Infrared Physics & Technology*, vol. 51, no. 5, pp. 378–381, 2008.
doi:10.1016/j.infrared.2007.12.027
- [3] J. Teichert *et al.*, "Rf status of superconducting module development suitable for cw operation: Elbe cryostats," *Nucl. Instr. and Meth A*, vol. 557, no. 1, pp. 239 – 242, 2006.
doi:10.1016/j.nima.2005.10.077
- [4] B. Aune *et al.*, "Superconducting tesla cavities," *PRST-AB*, vol. 3, p. 092001, Sep 2000.
doi:10.1103/PhysRevSTAB.3.092001
- [5] A. Aksoy *et al.*, "Current status of turkish accelerator and radiation laboratory in ankara: the tarla facility," *Canadian Journal of Physics*, vol. 96, no. 7, pp. 837–842, 2018.
doi:10.1139/cjp-2017-0750
- [6] F. Gabriel *et al.*, "The rossendorf radiation source elbe and its fel projects," *Nucl. Inst. and Meth B*, vol. 161-163, pp. 1143 – 1147, 2000.
doi:10.1016/S0168-583X(99)00909-X
- [7] "RI Research Instruments, Research Instruments website," <https://research-instruments.de>, accessed: 08-December-2018.
- [8] A. Aksoy, O. Karşlı, Ç. Kaya, B. Koç, and O. Elçim, "Current Status of Turkish Accelerator and Radiation Laboratory," in *IPAC'19*, 2019, paper TUPMP048, pp. 1359–1361.
doi:10.18429/JACoW-IPAC2019-TUPMP048
- [9] "A.L.A.T. Air Liquide Advanced Tehnologies, Air Liquide Advanced Tehnologies website," <https://advancedtech.airliquide.com>, accessed: 23-May-2019.
- [10] J. G. Karssenbergh, K.-J. Boller, J. W. J. Verschuur, I. Volokhine, and P. J. M. van der Slot, "FEL-Oscillator Simulations with Genesis 1.3", in *Proc. FEL'06*, Berlin, Germany, Aug.-Sep. 2006, paper TUPPH037, pp. 407-410.
- [11] C. Kaya *et al.*, "Beam Diagnostics E-GUN Test Stand at TARLA", in *Proc. IPAC'14*, Dresden, Germany, Jun. 2014, pp. 704-706.
doi:10.18429/JACoW-IPAC2014-M0PRI045

UNAVERAGED SIMULATION OF A REGENERATIVE AMPLIFIER FREE ELECTRON LASER

P. Pongchalee, B.W.J. McNeil
SUPA, Department of Physics, University of Strathclyde, Glasgow, UK
also at Cockcroft Institute, Warrington, WA4 4AD, UK

Abstract

A regenerative amplifier free-electron laser (RAFEL) design and simulation requires the modelling of both the electron-light interaction in the FEL undulator and the optical propagation within the cavity. An unaveraged 3D simulation was used to model the FEL interaction within the undulator using the Puffin code. This allows a broadband, high temporal-resolution of the FEL interaction. The Optical Propagation Code (OPC) was used to model the optical beam propagation within the cavity and diagnostics at the cavity mirrors. This paper presents the optical field conversion method between Puffin and the OPC codes and demonstrates the full model via a VUV-RAFEL simulation.

INTRODUCTION

When using an oscillator FEL at shorter wavelengths, such as UV and X-ray, the optical components used to create the cavity will be a limiting factor due to the absorption of the optical materials at shorter wavelengths, or due to a lack of tunability via e.g. Bragg reflections. The RAFEL uses the high-gain undulator and a *small* amount of feedback to obtain the system saturation. Hence, the RAFEL can use low reflectivity mirrors for the optical cavity and operate into the short wavelength regime [1]. An overview of RAFEL operation over a wide range of parameters in the 1D limit is given in [2].

Several 3D FEL codes, such as Genesis 1.3 [3], are used to model the FEL interaction based on the Slowly Varying Envelope Approximation (SVEA). However, Puffin [4] is an unaveraged FEL code without the SVEA approximation and does not use undulator period averaging of the electron trajectories. The resultant radiation field retains the fast-oscillating term and allows the modelling of broadband (few cycle radiation field) and more complex electron dynamics. This paper describes how the modelling of such behaviour can be achieved in a RAFEL.

Previously, Genesis 1.3 was used with the Optical Propagation Code (OPC) [5], to simulate a RAFEL in the VUV-FEL by running both codes sequentially [6]. OPC includes 3D mirror reflection and free-space propagation through the optical path of the cavity. OPC is used here to model the optical propagation inside the RAFEL cavity while the FEL interaction inside the undulator is modelled using Puffin.

This paper first describes the translation of the input/output optical field files between Puffin and OPC necessary for linking the two codes. A RAFEL design operating in the VUV at 100 nm is then described. The optical cavity was designed to satisfy the cavity stability condition and match the undulator length and the electron beam repetition rate.

FORMAT CONVERSION

The Puffin field data consists of 4D array data set in the HDF5 format with the dimension of $(2, n_z, n_y, n_x)$, which is the two sets of 3D field data in space separated by the polarised orientation (x-polarized and y-polarized field). The n_z represents the data in the direction corresponding to the propagation of the field. For one-wavelength long data simulation, the output field from Puffin is a single period oscillation, as shown the example of the transverse Gaussian field in Figure 1.

The OPC field is described in two files. The first is the field data in the format of binary data in the Genesis ‘.dfl’ field file format. Each point of data contains 8 bytes (64-bit) of binary data that represents the floating number, which can be dumped into a 1D array. The size of the product of the number of grid points in x and y etc, is contained in the second OPC parameter file containing the gridpoint parameters, number of slices in z etc. The transverse optical field profile data consists of two components of the complex number – real and imaginary parts, which interleave in the array by odd and even indices of the 1D data array. For the temporal information in the OPC data, the number of slices sets as the additional axis of the array corresponding to the z -direction of the optical propagation.

The Python conversion script starts by considering the envelope of the optical field from the analytical function, which includes real and imaginary parts of the sinusoidal function. For a simple plane wave, the real-valued radiation field that would be obtained from Puffin is written in Eq. (1)

$$A_{puffin}(\mathbf{r}, t) = A_0(\mathbf{r}, t) \cos(kz - \omega t + \phi(\mathbf{r}, t)) \quad (1)$$

where A_{puffin} is the scaled radiation field with the amplitude of A_0 , k is the radiation wave number, ω is the angular frequency of the radiation wave, and $\phi(\mathbf{r}, t)$ is the phase of the field. The analytic signal will be used to translate the real-value field from Puffin into the complex representation of OPC field format using the Hilbert transform [7], which has the effect of shifting the phase of the original signal by $-\pi/2$. The Hilbert transform (denoted by a ‘hat’) of the original Puffin field can then be written in Eq. (2) as:

$$\hat{A}_{puffin}(\mathbf{r}, t) = A_0(\mathbf{r}, t) \sin(kz - \omega t + \phi(\mathbf{r}, t)) \quad (2)$$

The envelope itself can be constructed from the modulus of the analytic signal composing with the original field and its Hilbert transform, which corresponds to the OPC field format, which is written in the complex notation in Eq. (3).

$$\begin{aligned}\tilde{A}_{opc}(\mathbf{r}, t) &= A_{puffin}(\mathbf{r}, t) + i\hat{A}_{puffin}(\mathbf{r}, t) \\ &= A_0(\mathbf{r}, t) \exp[i(kz - \omega t + \phi(\mathbf{r}, t))]\end{aligned}\quad (3)$$

In this way, $A_{puffin}(\mathbf{r}, t) = \text{Re}(\tilde{A}_{opc}(\mathbf{r}, t))$. Hence, the real-value Puffin field data at each grid point will be transferred directly to the real part grid points of the OPC data and the phase-shifted part of the Puffin field, via its Hilbert transform, will be used as the imaginary part of the OPC field. The example of the conversion process is shown in Fig. 1.

For the backward conversion from OPC into Puffin, the process simply extracts the real part of the OPC data file and assumes the number of grid points etc in the OPC parameter has not changed. The script converts to HDF5 format.

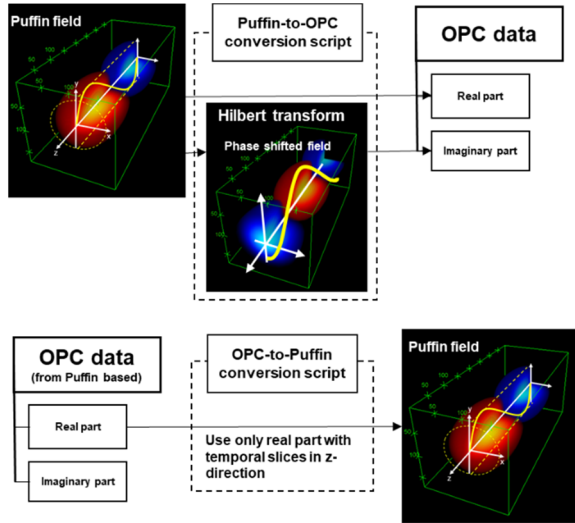


Figure 1: The form of the Puffin output field and the conversion method into the OPC field format. Top: Puffin-to-OPC and Bottom: OPC-to-Puffin format conversion.

DESIGN PARAMETERS

100 nm Wavelength FEL

The VUV RAFEL simulations are for a 100 nm wavelength. All parameters are taken from CLARA conceptual design report [8], with an electron energy of 250 MeV and peak current 400 mA. The undulator length for RAFEL operation, using only one-third of the SASE saturation undulators consists of five 1.25m modules comprised of 29 undulator periods of $\lambda_u = 27.5$ mm and a gap between modules of ~ 0.45 m for quadrupole focussing etc.

Optical Cavity

The RAFEL system required a small feedback optical cavity. The cavity length is set to 17.5 m to match the 8.5

MHz bunch repetition rate. The optical cavity design takes the output field at the undulator exit and must propagate it to the undulator entrance to seed a new incoming electron pulse. The radiation field is focussed to the undulator entrance to maximise the overlap between the radiation field and electron beam. The layout of the undulator with the optical cavity is shown in Fig. 2. The first mirror of radius of curvature 12.32 m (so that its focal length is $12.32/2 = 6.16$ m) has been placed 8.0 m away from the undulator exit with a 2.0 mm diameter out-coupling hole. The second mirror at the undulator entrance has a radius of curvature of 9.98 m, i.e. a stable resonator. The RAFEL operation should then reach saturation within a few cavity round-trips [6].

The system is designed to use mirrors with the reflectivity in a range of 20% to 40% to cover a sufficiently broad range of wavelengths around 100 nm. The relatively high reflectance at these wavelengths can be obtained from using Boron films deposited coating [9].

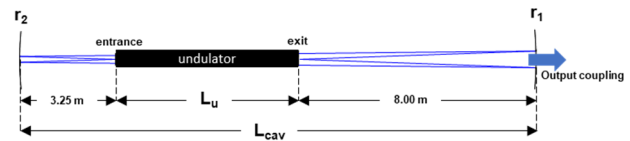


Figure 2: Schematic of the RAFEL used in the simulation. The blue line shows the ray-tracing of the propagating optical beam inside the cavity.

EXAMPLE SIMULATION

To test the simulation set up, a simple setup uses a single wavelength in a periodic mode of the Puffin simulation. This is equivalent to the steady-state approximation. The simulation starts in the first pass using the shot noise of electron beam, the main input of the system and the undulator lattice files required by Puffin. The radiation field output from the first pass at the undulator exit is then converted from Puffin format to OPC format as described above. The grid size of two codes must be matched at the beginning of the simulation setup. The OPC main input file contains all of the optical path and the optical elements, i.e. mirrors. The converted field then propagates using OPC through the optical cavity system via free-space propagation and the two mirrors - the first mirror has a hole out-coupling and the second mirror reflects the light to the undulator entrance. The propagated field at the undulator entrance is then converted from OPC field format into Puffin format and used as the radiation seeding in the next pass via the Puffin main input file. The process runs sequentially, as shown in Fig. 3.

The simulation output of the optical field at different points through the cavity is shown in Fig. 4. The integration of using Puffin and OPC still contains the fast-oscillating term of the radiation field that shows the resulting wavefront of the propagating fields. The diverging beam at the undulator exit due to diffraction and the converging beam at the reflective mirrors can be seen.

The RAFEL operation can be analysed via the input seeding from the optical cavity at the undulator entrance

and the output field after passing through an FEL undulator at the exit. The result shows there is sufficient optical feed-back to achieve saturated RAFEL operation a mirror reflectivity of 20% for both mirrors and an upstream mirror hole out-coupling of 2.0mm. The RAFEL system saturates at around five round-trips as seen from the power output of Fig. 5.

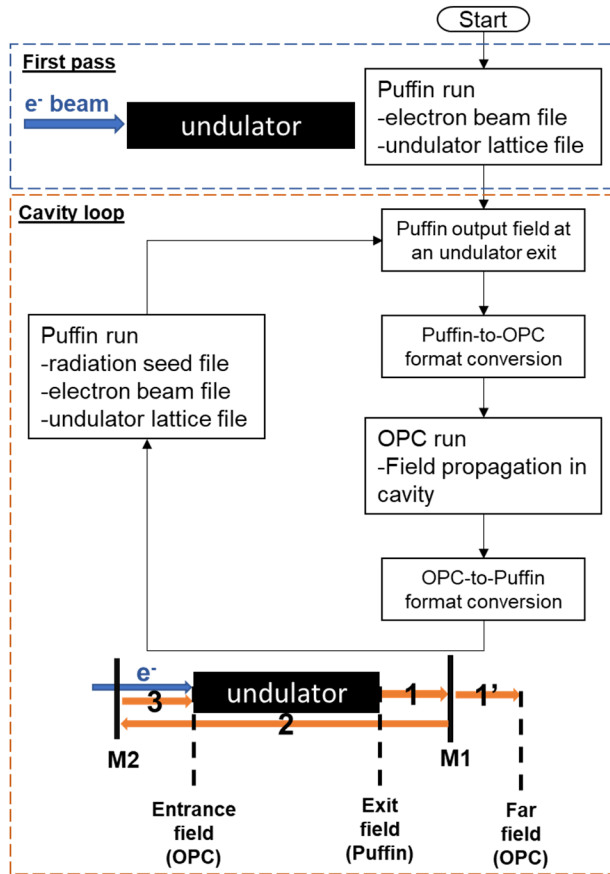


Figure 3: The diagram shows the flow chart of the RAFEL simulation, including the first pass, conversion script, and the cavity loop which is a simple Bash shell script. (1) The first propagation using OPC from the undulator exit to mirror-1 (M1) with a hole out-coupling and the far-field diagnostic point (1'). (2) The second propagation from a reflected optical beam at M1 to mirror-2 (M2). (3) The third propagation from M2 to the undulator entrance as the next loop radiation seeding.

CONCLUSION

The Puffin and OPC simulation codes have been developed for use together for FEL oscillator simulations. Conversion scripts were developed to enable radiation field transfer between the two codes. And demonstrated with a steady state, single wavelength periodic mode model of a VUV-RAFEL design. This will enable the development of FEL modelling of potential ultra short-pulse, broadband simulations in the future.

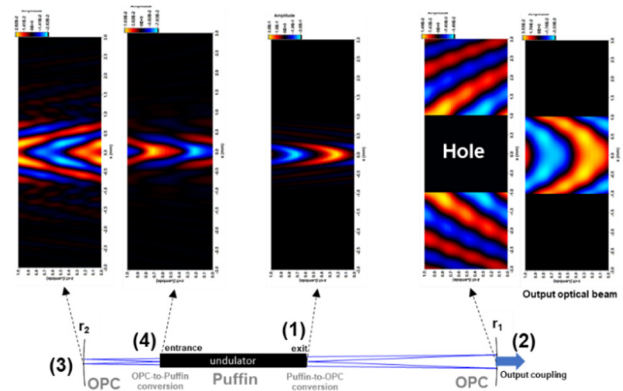


Figure 4: The schematic shows the optical beam of one-wavelength (periodic-mode) at the difference diagnostic positions of the RAFEL system. The Red and Blue colours show the positive and negative values of the electric field, respectively. Point (1) is the diverging optical beam at the undulator exit propagates to (2) at the mirror-1 with a hole out-coupling. Part of the beam is then reflected back as a converging beam to the mirror-2 at point (3), and then focused to point (4) at the undulator entrance.

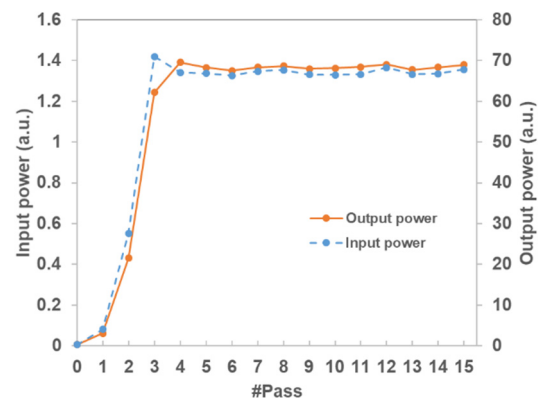


Figure 5: The input and output power at the undulator entrance and exit, respectively. The plot shows the system saturation at around five round-trips of propagation.

REFERENCES

- [1] B. W. J. McNeil, "A simple model of the free-electron-laser oscillator from low into high gain," *Nuclear Instruments and Methods in Physics Research Section A: Accelerators, Spectrometers, Detectors and Associated Equipment*, vol. 296, no. 1-3, pp. 388-393, 1990.
- [2] D. J. Dunning, B. W. J. McNeil, and N. R. Thompson, "Short wavelength regenerative amplifier free electron lasers," *Nuclear Instruments and Methods in Physics Research Section A: Accelerators, Spectrometers, Detectors and Associated Equipment*, vol. 593, no. 1-2, pp. 116-119, 2008.
- [3] S. Reiche, "GENESIS 1.3: a fully 3D time-dependent FEL simulation code," *Nuclear Instruments and Methods in Physics Research Section A: Accelerators, Spectrometers, Detectors and Associated Equipment*, vol. 429, no. 1-3, pp. 243-248, 1999.

- [4] L. T. Campbell, and B. W. J. McNeil, "Puffin: A three dimensional, unaveraged free electron laser simulation code," *Physics of Plasmas*, vol. 19, no. 9, pp. 093119, 2012.
- [5] P. J. M. van der Slot, and K. J. Boller, "Recent Updates to the Optical Propagation Code OPC."
- [6] B. W. J. McNeil, N. R. Thompson, D. J. Dunning, J. G. Karssenberg, P. J. M. van der Slot, and K. J. Boller, "A design for the generation of temporally-coherent radiation pulses in the VUV and beyond by a self-seeding high-gain free electron laser amplifier," *New journal of physics*, vol. 9, no. 7, pp. 239, 2007.
- [7] N. E. Huang, *Hilbert-Huang transform and its applications*, World Scientific, 2014.
- [8] J. A. Clarke, D. Angal-Kalinin, N. Bliss, R. Buckley, S. Buckley, R. Cash, P. Corlett, L. Cowie, G. Cox, and G. P. Diakun, "CLARA conceptual design report," *Journal of instrumentation*, vol. 9, no. 05, pp. T05001, 2014.
- [9] M. Vidal-Dasilva, M. Fernández-Perea, J. A. Méndez, J. A. Aznárez, and J. I. Larruquert, "Electron-beam deposited boron coatings for the extreme ultraviolet," *Applied optics*, vol. 47, no. 16, pp. 2926-2930, 2008.

MODELLING CRYSTAL MISALIGNMENTS FOR THE X-RAY FEL OSCILLATOR*

R. R. Lindberg[†], Argonne National Laboratory, Lemont, IL 60439 USA

Abstract

The X-ray FEL oscillator has the potential to be a revolutionary new light source providing unprecedented stability in a narrow bandwidth [1]. However, a detailed understanding of cavity tolerance and stability has only begun, and there are presently no suitable simulation tools. To address this issue, we have developed a fast FEL oscillator code that discretizes the field using a Gauss-Hermite mode expansion of the oscillator cavity. Errors in crystal alignment result in a mixing of the modes that is easily modeled with a loss and coupling matrix. We show first results from our code, including the effects of static and time-varying crystal misalignments.

INTRODUCTION

The x-ray FEL oscillator [1,2], in which the output from a low-gain FEL is returned to interact with subsequent electron bunches by an x-ray cavity built of Bragg crystals and focusing elements, has garnered much interest over the past decade. In this paper we will focus on how the output of a single frequency component can be affected by crystal tilts, as this will provide the first look into what tolerances we require for the crystal optics.

XFELO CAVITY MODES

We expand the transverse profile using the Gauss-Hermite modes defined by the optical cavity. Along x we write

$$E(x; z) = \sum_{\ell} \frac{\mathcal{E}_{\ell}(z) \exp\left[-\frac{x^2(1+iz/z_R)}{4\sigma_x^2(1+z^2/z_R^2)}\right]}{\sqrt{2^{\ell} \ell! \sigma_x (1+z^2/z_R^2)^{1/2}}} \quad (1)$$

$$\times H_{\ell}\left[\frac{x/\sigma_x}{\sqrt{2(1+z^2/z_R^2)}}\right] e^{-i(\ell+1/2)\text{atan}(z/z_R)} \\ = \sum_{\ell} \mathcal{E}_{\ell}(z) M_{\ell}(x; z), \quad (2)$$

where M_{ℓ} is the mode shape of the ℓ^{th} Gauss-Hermite mode that is defined in terms of the rms width σ_x and the Rayleigh range $z_R = \sigma_x/\sigma_{x'} = 2k_1\sigma_x^2$ for a paraxial field with carrier wavevector $k_1 = 2\pi/\lambda_1$; a similar expansion holds in y . Ignoring slippage, the FEL field equation is then

$$\frac{d}{dz} \mathcal{E}_{\ell,m} = -\frac{ek_1 K[\text{JJ}]}{4\gamma_0 \epsilon_0} \sum_j e^{-i\theta_j} M_{\ell}(x_j) M_m(y_j), \quad (3)$$

where the sum is over all particles in the FEL slice, γ_0 is the reference energy, the ponderomotive phase $\theta_j(z) = (k_1 + k_u)z - ck_1 t_j(z)$ for a particle with time t_j moving in an

electromagnetic wave with wavenumber $k_1 = 2\pi/\lambda_1$ and undulator wavenumber $k_u = 2\pi/\lambda_u$, e and ϵ_0 are the electric charge and permittivity of free space, and $[\text{JJ}]$ is the Bessel function factor for an undulator with deflection parameter K . The equations of motion for the phase θ_j and the scaled particle energy difference $\eta_j = (\gamma_j - \gamma_0)/\gamma_0$ are

$$\frac{d\theta_j}{dz} = 2k_u \eta_j - \frac{k_1}{2} (\mathbf{p}_j^2 + K^2 k_u^2 \mathbf{x}_j^2 / 2\gamma^2) \quad (4)$$

$$\frac{d\eta_j}{dz} = \frac{eK[\text{JJ}]}{2mc^2 \gamma_0^2} \sum_{\ell,m} \mathcal{E}_{\ell,m} e^{i\theta_j} M_{\ell}(x_j) M_m(y_j) + c.c., \quad (5)$$

where transverse position and angle are \mathbf{x}_j and \mathbf{x}'_j .

Upon exiting the undulator, the field is returned to the undulator beginning by the x-ray cavity. For a perfectly aligned cavity this results in some loss for each mode \mathcal{E}_{ℓ} , but imperfections and misalignments result in mode coupling and effective loss in the fundamental Gaussian mode.

At lowest order misalignments act to shift the optical axis by a position and angle at each pass that can be found by tracking a ray through the system. The result is that the optical axis becomes offset in position by $\mathbf{X}_d = (X_d, Y_d)$, and in angle by $\boldsymbol{\Theta}_d = (\theta, \psi)$. Then, the displaced field at the beginning of the undulator for pass $n+1$ is related to the field at the end of the undulator from pass n via

$$E^{(n+1)}(\mathbf{x}; 0) = (1 - \alpha) e^{ik(x - \mathbf{X}_d) \cdot \boldsymbol{\Theta}_d} \times E^{(n)}(\mathbf{x} - \mathbf{X}_d; L_u), \quad (6)$$

where α is the amplitude loss due to imperfect reflectivity. To transform this into a relationship between mode expansion coefficients, we need to project the displaced field onto the Gauss-Hermite basis. We will do this explicitly for the x -direction only, as expressions for y are essentially the same. We insert the expansion (1)-(2), multiply by the mode $M_{\ell}(x)$, and integrate over x to obtain

$$\mathcal{E}_{\ell}^{(n+1)}(0) = (1 - \alpha) \int dx e^{ik\theta(x - X_d)} M_{\ell}(x) \times \sum_{\ell'} M_{\ell'}(x - X_d) \mathcal{E}_{\ell'}^{(n)}(L_u). \quad (7)$$

$$= (1 - \alpha) \sum_{\ell'} \mathcal{P}_{\ell, \ell'}(\theta, X_d) \mathcal{E}_{\ell'}^{(n)}(L_u), \quad (8)$$

where we have defined the projection operator \mathcal{P} as shown. It turns out that this integral can be done in terms of the associated Laguerre polynomial $L_n^m(x)$; if $\ell \geq \ell'$ we have

$$\mathcal{P}_{\ell, \ell'} = \sqrt{\ell'!/\ell!} e^{-ik_1 X_d \theta/2} e^{-[(X_d/\sigma_x)^2 + (\theta/\sigma_{x'})^2]/8} \times \left(\frac{X_d + iz_R \theta}{\sqrt{2}\sigma_x}\right)^{\ell - \ell'} L_{\ell'}^{\ell - \ell'}\left(\frac{X_d^2 + z_R^2 \theta^2}{4\sigma_x^2}\right), \quad (9)$$

* Work supported by U.S. Dept. of Energy Office of Sciences under Contract No. DE-AC02-06CH11357.

[†] lindberg@anl.gov

Table 1: XFEL Parameters for Simulations

Name	Symbol	Value
Energy	$\gamma_0 mc^2$	7 GeV
Energy spread	σ_γ/γ_0	2×10^{-4}
Normalized emittance	ε_n	0.2 mm · mrad
Peak current	I	10 A
Undulator periods	N_u	3000
Undulator length	L_u	53 m
Rayleigh range	Z_R	10 m

while the expression for $\ell' > \ell$ can be obtained by exchanging ℓ and ℓ' and setting $X_d \rightarrow -X_d$ in the second line of (9). The code consists of solving the FEL equations (3)-(5), followed by applying the cavity misalignment operation (8) with \mathcal{P} defined in (9).

RESULTS

The FEL gain can be represented as a matrix \mathcal{G} that joins the field coefficient $\mathcal{E}_\ell^{(n)}(0)$ at the beginning of the n^{th} pass to that at the end of the undulator in the following manner:

$$\mathcal{E}_\ell^{(n)}(L_u) = \sum_{\ell'} \mathcal{G}_{\ell,\ell'} \mathcal{E}_{\ell'}^{(n)}(0). \quad (10)$$

In the linear gain regime \mathcal{G} is independent of \mathcal{E} , while in general it is found by solving the FEL equations (3)-(5). Our first test of the code was to compare the the gain matrix with that of the theory in [3]. The test example assumed an XFEL with nominal gain $\mathcal{G}_{00} \approx 0.184 + 0.075i$, and we found agreement to better than 10% for both the real and imaginary parts of the 5×5 submatrix joining the five lowest order Gauss-Hermite modes. To go further, we write out the complete mapping from pass to pass as

$$\mathcal{E}^{(n+1)} = (1 - \alpha)\mathcal{P}(\Theta_d, X_d)(\mathbb{1} + \mathcal{G})\mathcal{E}^{(n)}. \quad (11)$$

If we subtract $\mathcal{E}^{(n)}$ from both sides and approximate $\mathcal{E}^{(n+1)} - \mathcal{E}^{(n)} \approx d\mathcal{E}^{(n)}/dn \rightarrow \Lambda\mathcal{E}$ as is appropriate for a low gain system in the linear gain regime, we can rewrite (11) as the following linear matrix system

$$\Lambda\mathcal{E} = [(1 - \alpha)\mathcal{P}(\Theta_d, X_d)(\mathbb{1} + \mathcal{G}) - \mathbb{1}]\mathcal{E}, \quad (12)$$

where Λ is a complex growth rate (eigenvalue). We solved this for various optical axis displacements and compared the results to simulations in Fig. 1. For these and the following simulations we use the XFEL parameters suggested in [4] and listed in Table 1, although subsequent work has shown that significantly higher gains can be achieved (see, e.g., [5]); here the nominal power gain $2\Re(\mathcal{G}_{00}) \approx 0.36$, the losses $2\alpha = 0.2$, while the displacement $X_d/\sigma_r = 0.1$ corresponds to a crystal tilt of about 20 nrad (the scaled angular offset $\theta/\sigma_{r'} \approx 0.1X_d/\sigma_r$ is small).

Next, we'll want to look at how misalignments affect saturated output of an XFEL. We begin by considering static misalignments for the same parameters as in Table 1. From

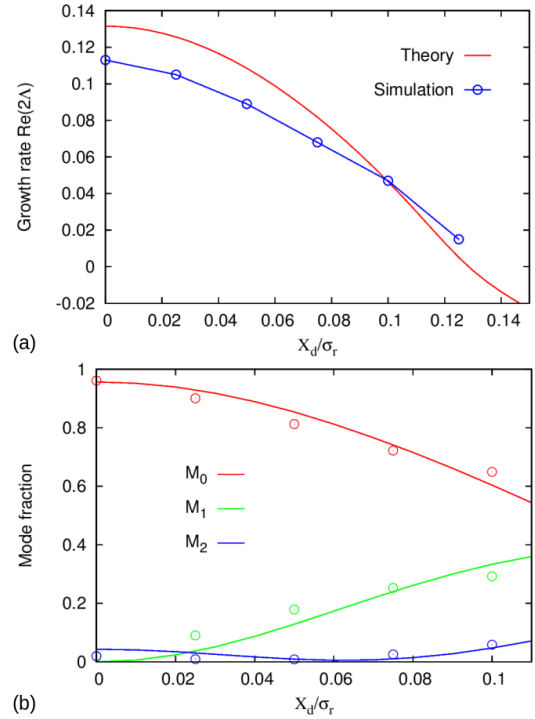


Figure 1: Comparison of theory (solid lines) and simulation (points) for the growth rate (a) and mode content (b) of an XFEL that has a static misalignment leading to a displaced optical axis of X_d/σ_r . Parameters are from Table 1.

Fig. 1 we find that the gain will vanish and the output will be near zero when the crystal misalignments result in a displacement $X_d \approx 0.15\sigma_r$. Thus, we chose $0 \leq X_d \leq 0.1\sigma_r$, which roughly corresponds to varying the crystal misalignment between 0 and 20 nrad. We plot the results of the static misalignment in Fig. 2(a). We find that as the net linear gain 2Λ decreases from about 0.12 for perfect alignment to 0.04 when $X_d = 0.1\sigma_r$, the output power reduces from 1.2 MW to ~ 0.23 MW. Note that at the low end only about 62% of this power is contained in the Gaussian mode, while $\sim 30\%$ is in antisymmetric modes.

In practice the crystal tilts will vary with time. From general physical principles we expect variations that are much slower than the cavity ring-down time will directly imprint themselves upon the output, while fluctuations that occur over much faster time-scales will be averaged over; in other words, in the former case the output power will vary as a function of time such that its value matches that predicted by the steady-state results in Fig. 1, while in the latter case the output should be relatively constant but at a somewhat lower value. We plot results from these two extreme cases in Fig. 2(b) and (c). Panel (b) plots the power as a function of pass number when the crystal tilt oscillates with a period $T = 400$, which is much longer than 2π times the ring-down time $2\pi/\alpha \sim 60$. In this case the output power is approximately given by

$$P_{\text{out}} \approx P_{\text{ideal}} \cos^2(2\pi n/T) + P_{X_d} \sin^2(2\pi n/T), \quad (13)$$

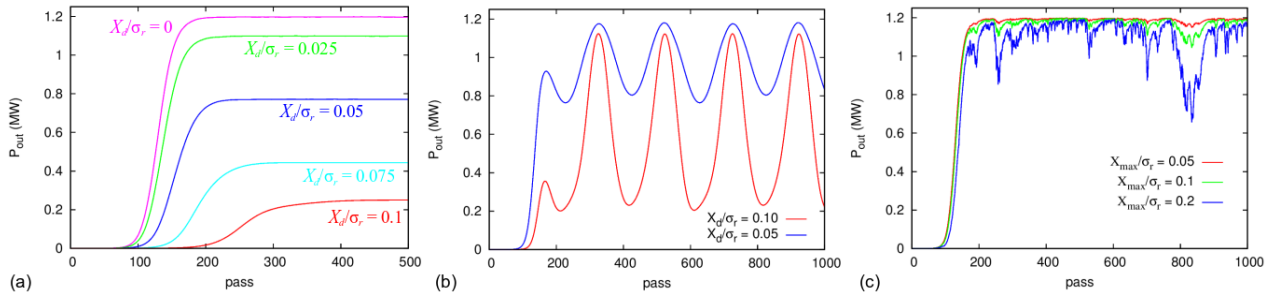


Figure 2: Power output as a function of pass number for cavity misalignments leading to a displaced optical axis of X_d/σ_r . Panel (a) plots steady-state output for static misalignments, while (b) plots the output for slow variations given by $X_d \cos(2\pi n/T)$ for $T = 400$, for which the output oscillates with half the period $T/2$ and the maxima and minima are roughly defined by the static predictions in panel (a). Panel (c) plots the output for random variations on a pass-to-pass basis, where the same pseudo-random sequence is used but with different maximum amplitudes X_{\max} .

and the power oscillates with a period $T/2$ between the value its ideal value P_{ideal} and that with the maximal tilt P_{X_d} .

In the other extreme we can imagine a crystal tilt that fluctuates randomly from pass-to-pass. We show three such cases in Fig. 2(c), where we assign the optical axis displacement at any pass the value rX_{\max} , with r a random number between -1 and 1 . We see that the rms (maximum) power fluctuations are less than 4% (10%) up to value of $X_d = 0.1\sigma_r$, while even $X_d = 0.2\sigma_r$ produces useful output whose rms variations are $\lesssim 10\%$. The general features of each plot are quite similar (e.g., the dip in power near pass 800) because we chose the same pseudo-random sequence for all cases. Interestingly, the mean output power does not significantly change for the random variations chosen.

Finally, we would like to understand how power fluctuations occurring at a variety of time scales affect the output. As a first step, we consider sinusoidal perturbations that have different periods. This will provide some insight into how fluctuations characterized by a particular power spectrum will degrade performance. We show the results of this first study in Fig. 3. Panel (a) shows the output fluctuations for an optical axis displacement of $X_d \cos(2\pi n/T)$ with $X_d = 0.1\sigma_r$ and various perturbation periods T , while (b) plot the same thing for $X_d = 0.1\sigma_r$. Both cases essentially follow Eq. (13) when the period of variation $T \geq 200 \gg 2\pi/\alpha = 60$. As the period approaches the cavity ring-down, $T = 100$ and 50 , the output still oscillates with a period of approximately $T/2$, but with a smaller amplitude of the oscillation: the maximum output power is less than P_{ideal} and the minimum power is greater than P_{X_d} . Finally, for variations at the fastest scale $T = 20$, which is about one-third the cavity ring-down time, the power variations are quite small; panel (a) shows rms fluctuations of 1.3% when $X_d = 0.1\sigma_r$, while the power variations in panel (b) where $X_d = 0.5\sigma_r$ are $\sim 0.4\%$. Both of these results are consistent with the random fluctuations of Fig. 2(c).

CONCLUSIONS

We have developed a code that simulates the FEL oscillator by representing the field as a sum of its cavity modes.

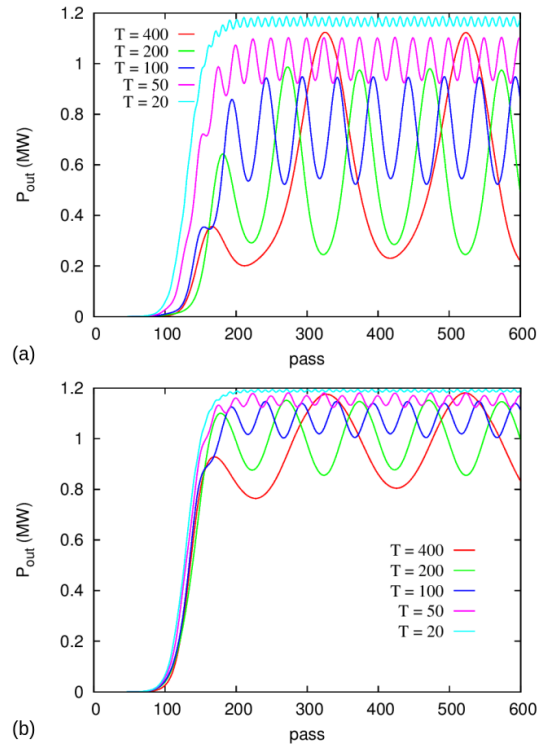


Figure 3: Saturated FEL output for an oscillating optical axis displacement of $X_d \cos(2\pi n/T)$, where $X_d = 0.1\sigma_r$ in panel (a), and $X_d = 0.05\sigma_r$ in panel (b).

When the FEL gain is low the field is well-represented by a few low-order modes, and the code is very efficient. Adding imperfections of the cavity can be done in a straightforward manner, and we have illustrated this by examining how the XFEL output varies with a variety of fluctuating crystal misalignments. The results here have been for a single cavity configuration, and future work will be to do similar tests when the FEL gain is higher, and for cavities that are designed to balance the requirements of FEL gain with the desire to have a system that is more robust to various cavity fluctuations and imperfections.

REFERENCES

- [1] K.-J. Kim, Y. Shvyd'ko, and S. Reiche, "A Proposal for an X-Ray FEL Oscillator with an Energy-Recovery Linac," *Phys. Rev. Lett.* **100**, 244802, 2008.
- [2] R. Colella and A. Luccio, "Proposal for a free electron laser in the X-ray region," *Opt. Comm.* **50**, 41, 1984.
- [3] G.-T. Park, "Performance-limiting factors for x-ray free-electron laser oscillator as a highly coherent, high spectral purity x-ray source," PhD thesis, U. Chicago, 2012.
- [4] R. R. Lindberg, K.-J. Kim, Yu. Shvyd'ko, and W. M. Fawley, "Performance of the x-ray free-electron laser oscillator with crystal cavity," *Phys. Rev. ST-AB* **14**, 010701, 2011.
- [5] W. Qin, *et al.*, "Start-to-end simulations of for an X-ray FEL oscillatot at the LCLS-II and LCLS-II-HE," in *Proc. FEL 2017*, pp. 247, 2017.

POWER VARIATIONS OF AN X-RAY FEL OSCILLATOR IN SATURATION*

R. R. Lindberg[†] and K.-J. Kim¹, Argonne National Laboratory, Lemont, IL, USA
¹also at University of Chicago, Chicago, IL, USA

Abstract

Basic FEL theory predicts that the fractional power fluctuations of an ideal oscillator in steady state should be given by the ratio of the spontaneous power in the oscillator bandwidth to that stored in the cavity at saturation. For the X-ray FEL oscillator with its narrow bandwidth Bragg crystal mirrors, this ratio is typically a few parts per million, but some simulations have shown evidence of power oscillations on the percent level. We show that this is not related to the well-known sideband instability, but rather is purely numerical and can be eliminated by changing the particle loading. We then briefly discuss to what extent variations in electron beam arrival time may degrade the power stability.

INTRODUCTION

The x-ray FEL oscillation (XFEL) has the potential to be an intense source of narrow-bandwidth x-rays that is also incredibly stable [1, 2]; theory predicts that the fractional pulse-to-pulse energy stability could approach the 10^{-5} to 10^{-6} level. We investigate ways in which this stability might be disturbed, showing that the sideband instability will not be an issue, that certain power fluctuations observed in simulation are purely numerical, and the extent to which electron arrival time jitter affects FEL output.

SIDEBAND INSTABILITY

Ideally, an FEL oscillator at saturation should operate like standard atomic lasers, outputting steady-state pulses of radiation whose energy is approximately constant and whose spectral content can approach the Fourier limit. On the other hand, there are many potential causes for variations in the saturated output power of an FEL oscillator. These include fluctuations in the cavity and/or electron beam properties, short-pulse effects that arise when the distance that the radiation of central wavelength λ_1 slips ahead of an electron after N_u undulator periods becomes comparable to the electron beam duration σ_e , and instabilities. Perhaps the best-known instability is the sideband or trapped particle instability, in which particle motion in the ponderomotive bucket during a single pass can lead to large variations in output power and multi-modal spectral output.

We can understand the physics of the sideband instability using the arguments of [3]: we consider a perturbation of the radiation power like that shown in Fig. 1(a), where the power $P_1 \sim P_{\text{sat}} = (I/e)\gamma mc^2/2N_u$, with I the electron beam current, γ the Lorentz factor, and e , m , and c the electron

charge, mass, and the speed of light. If the width of region 1 equals the synchrotron period in region 1 $\sim \lambda_1(P_{\text{sat}}/P_1)^{1/4} \sim N_u\lambda_1$, then in the first half of the undulator the particles in region 1 make one-half a synchrotron oscillation and lose the energy $\sim \gamma mc^2(P_1/P_{\text{sat}})^{1/4}/2N_u$ to the field. In the second half of the undulator where these particles are in the absorptive phase, the field has slipped ahead by a distance $N_u\lambda_1/2$ and the particles extract energy from the wave in region 2. On the other hand, if we consider the particles initially in region 2 we find that since the power and hence the synchrotron frequency is initially smaller, they do not make a full half-rotation in the bucket after half the undulator length. Thus, they lose less energy to region 2 than is given to region 1, and extract less energy from region 3 than particles initially in region 1 take from region 2. The net effect is that the perturbation is amplified, so that in general the FEL oscillator in saturation is unstable to the growth of sidebands at frequencies $\omega_1 \pm \omega_s \sim (2\pi c/\lambda_1)(1 \pm 1/N_u)$.

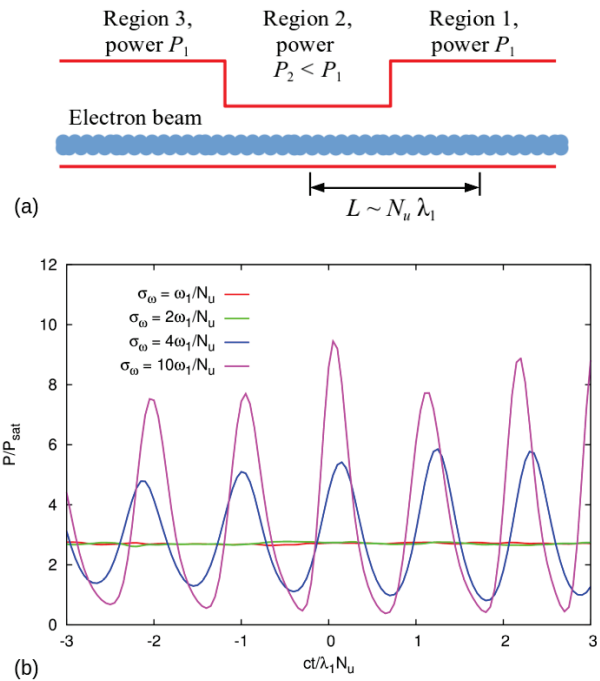


Figure 1: (a) Illustration of a perturbation that would be amplified by the sideband instability. (b) Saturated output power for various mirror bandwidths σ_ω that are of order the synchrotron frequency at saturation ω_1/N_u .

Since the instability amplifies the sidebands at normalized frequency difference $\pm 1/N_u$, we expect that it can be suppressed in oscillators that have narrow-bandwidth reflective mirrors. For example, the x-ray FEL oscillator [1, 2]

* Supported by U.S. Dept. of Energy Office of Sciences under Contract No. DE-AC02-06CH11357 and from the DOE ADRP grant #29545.

[†] lindberg@anl.gov

(XFEL) uses Bragg crystal mirrors whose reflective bandwidths are less than a few times 10^{-6} , which is much smaller than the normalized synchrotron frequency $1/N_u \gtrsim 3 \times 10^{-4}$, and we expect that the XFEL is largely immune to the sideband instability. To investigate this further, we ran a number of extended 1D simulations as described in [4], in which we (artificially) varied the bandwidth of the crystal mirror. For this study we assume that the reflectivity is Gaussian with width σ_ω , so that it acts on the field in frequency space via the multiplication by $\sqrt{R}e^{-\omega^2/4\sigma_\omega^2}$, where the reflectivity R is chosen to be 0.85.

We summarize the results of this study in Fig. 1(b), where we plot the power in saturation scaled by $P_{\text{sat}} = (I/e)\gamma mc^2/2N_u$ as a function of time normalized by the characteristic synchrotron period $\lambda_1 N_u/c$ for four different mirror bandwidths σ_ω . The plot shows that the sideband instability, with its characteristic power peaks length $\sim N_u \lambda_1$, is active when the mirror bandwidth is larger than about twice the synchrotron frequency, $\sigma_\omega \gtrsim 2\omega_1/N_u$, and otherwise plays no role on the saturated dynamics. Although this precise value of σ_ω that is required will depend upon the cavity power P , which in turn depends upon the cavity gain and loss, this dependence is weak ($\sim P^{1/4}$), and will not affect an XFEL that has $\sigma_\omega/(\omega_1/N_u) \lesssim 10^{-2}$.

SIMULATIONS OF STEADY STATE OPERATION

In the previous section we showed that the sideband instability does not plague an XFEL because of the spectral filtering provided the Bragg crystal mirrors. Hence, we expect that the steady-state power fluctuations can in principle approach the theoretical limit given by the spontaneous radiation power emitted into the narrow Bragg bandwidth. Nevertheless, some XFEL simulations have shown evidence of a long-wavelength power oscillation in saturation. We show an example in Fig. 2; (a) demonstrates the characteristic exponential growth and saturation after ~ 200 passes, while panel (b) plots the same thing on a linear scale, showing clear evidence in the stored energy about its mean of approximately 18 μJ . We have found that these oscillations can be correlated with periodic variations of the radiation phase that in this case occur with a period $\sim 4 \times 130$ passes. Since the FEL gain should not depend upon the radiation phase initially random particles, we suspect that the oscillations have a numerical rather than physical origin. In fact, we have found that they are due to the way in which the macroparticle phases are initialized.

The standard macroparticle loading scheme [5,6] carefully chooses the initial particle phases $\theta_j = (k_1 + k_u)z - ck_1 t_j$ to correctly simulate the shot noise with a small number of particles (here t_j is the particle time when it reaches location z in the undulator, while $k_1 = 2\pi/\lambda_1$ and $k_u = 2\pi/\lambda_u$). To do this in the presence of non-zero energy spread and emittance, the loading scheme divides the total number of particles within any slice N_{slice} into N_{slice}/N_b “beamlets”

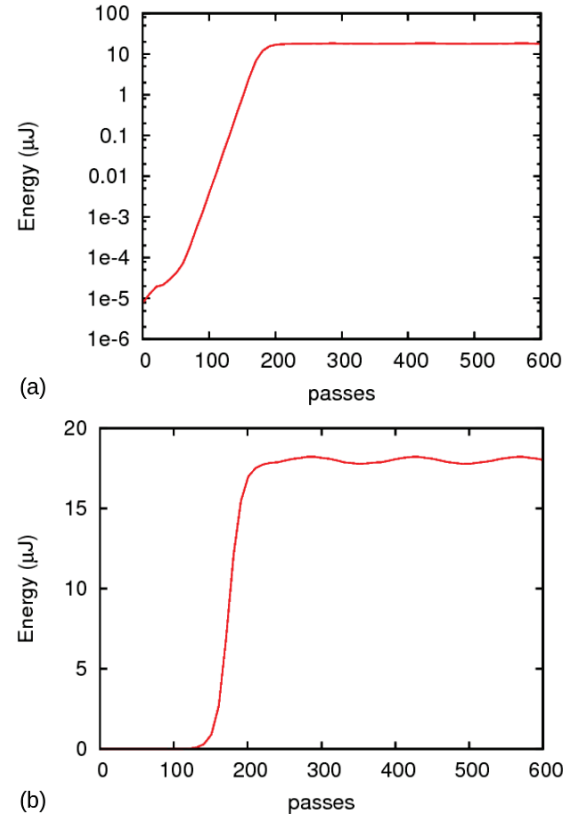


Figure 2: (a) Exponential growth of the XFEL cavity energy and subsequent saturation at pass ~ 200 . (b) Same graph on a linear scale, which shows clear evidence power oscillations whose period is 120 passes.

with N_b particles, and initializes the phase according to

$$\theta_{j|n,\ell} = \frac{2\pi}{N_b} \left(n + \frac{N_b^2}{N_{\text{slice}}} \ell \right) + (2\delta)r_{n,\ell}, \quad (1)$$

where $1 \leq n \leq N_b$ labels the particles within a beamlet, $1 \leq \ell \leq N_{\text{slice}}/N_b$ identifies the beamlet, $r_{n,\ell}$ is a random number between 0 and 1, and $\delta \approx \sqrt{3N_{\text{slice}}/N_{\text{real}}}$ sets the initial simulation bunching statistics to match that of a electron beam that has $N_{\text{real}} \gg N_{\text{slice}}$ randomly distributed electrons; the macroparticles within a beamlet have an identical energy and transverse coordinates, which insures that the shot noise statistics is maintained even as the phase changes due to energy spread and emittance.

If the energy oscillations seen in Fig. 2 are physical, they should not depend upon the particle loading. Figure 3 tests this by varying both the number of macroparticles per slice and the number per beamlet: panel (a) uses $N_{\text{slice}} = 2048$, (b) has $N_{\text{slice}} = 4096$, while (c) uses $N_{\text{slice}} = 8192$, and we clearly see that the oscillation amplitude decreases with the number of macroparticles. More interestingly, Figure 3(a)-(b) both show that the oscillation amplitude decreases at fixed N_{slice} as the number of particles per beam N_b is increased, and furthermore that this increases the energy oscillation frequency. Further investigation shows that this latter effect

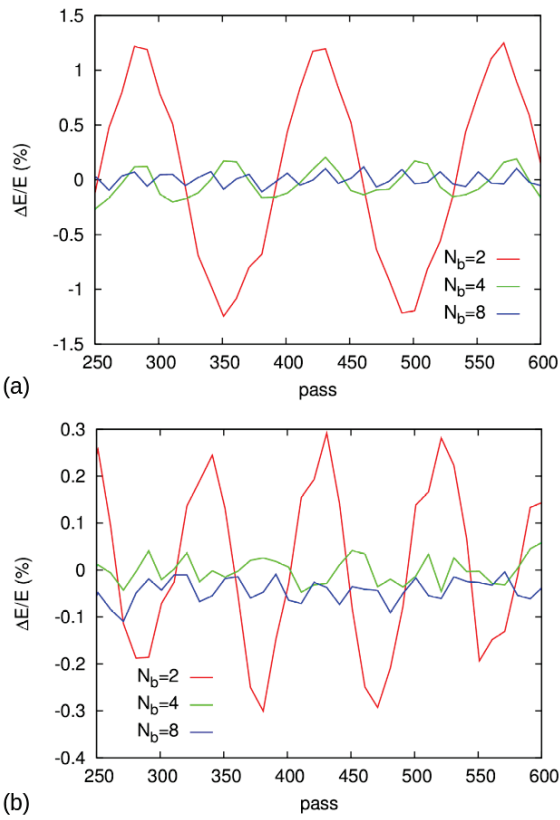


Figure 3: XFELO cavity power after saturation for (a) 2048 macroparticles/slice and (b) 4096 macroparticles/slice. The red, green, and blue lines indicate the number of particles per beamlet as described in the text, which shows that the power oscillations are numerical artifacts that depend upon the initial loading.

is related to the linear increase in the radiation phase with pass number. Since the gain depends weakly on the initial relative phase between the electrons and the field, the gain oscillates as the phase increases. Inspection of the loading Eq. (1) indicates that for $\delta \ll 1$ the phase difference between particles and field that corresponds to a local maximum (or minimum) in the gain is when the phase changes by $2\pi/N_b$; hence, it is periodic at twice the frequency, and the period of the gain oscillation is roughly $2N_b$ times smaller than period of the phase change. Figure 3 clearly shows the halving of the oscillation period as N_b is doubled from 2 to 4 (red and green lines); the blue line with $N_b = 8$ also follows this trend, although the precise frequency is more difficult to discern.

VARIATIONS IN ELECTRON BEAM ARRIVAL TIME

Finally, we close by presenting some simulation results regarding how variations in the electron-beam arrival time affects FEL output. Previous work [4] has shown that reasonable XFELO gain can be maintained in the presence static timing errors whose magnitude is $\lesssim 15$ fs for the parameters listed in Table 1. The net linear gain here is about 15%, and

Table 1: XFELO Parameters for Simulations

Name	Symbol	Value
Energy	$\gamma_0 mc^2$	7 GeV
Energy spread	σ_γ/γ_0	2×10^{-4}
Normalized emittance	ε_n	0.2 mm · mrad
Peak current	I	10 A
Bunch length	σ_t	1 ps
Undulator periods	N_u	3000
Undulator length	L_u	53 m
Rayleigh range	Z_R	10 m

we have found that the saturated energy decreases by about 30% when the timing error $\Delta T = 10$ fs $= \sigma_t/100$. Furthermore, if the arrival time varies slowly over many passes then the cavity energy at any instant will approximately equal that of its corresponding steady-state value. In this case we expect that feedback can be usefully applied to reduce any variations.

Figure 4 considers the other extreme in which the arrival time jitter fluctuates randomly from pass to pass. Here, we assume that the arrival time is uniformly distributed between $-\Delta t$ and Δt , and Fig. 4 shows that the stored cavity energy has very small fluctuations when $\Delta T \lesssim 10$ fs $= \sigma_t/100$, while the fluctuations increase to the several percent level if $\Delta T = 50$ fs. Finally, we see that the XFELO gain is maintained and the energy fluctuations are manageable even in the presence of arrive time jitter $\sim \sigma_t/10 = 100$ fs.

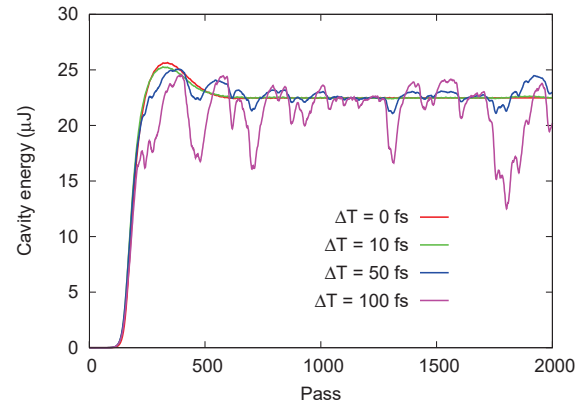


Figure 4: Stored XFELO energy for various random jitter in the arrival time, which is assumed to be a uniformly distributed random number between $-\Delta T$ and ΔT .

CONCLUSIONS

We have shown that the narrow bandwidth Bragg crystal mirrors of an XFELO effectively suppress the sideband instability. Additionally, we have found that certain particle loading schemes can lead to spurious energy fluctuations in the XFELO output, and indicated how one might avoid these. Finally we showed that the XFELO output is not strongly affected by arrival time jitter that is $\lesssim 10\%$ of the bunch length.

REFERENCES

- [1] K.-J. Kim, Y. Shvyd'ko, and S. Reiche, "A Proposal for an X-Ray Free-Electron Laser Oscillator with an Energy-Recovery Linac", *Phys. Rev. Lett.*, vol. 100, p. 244802, Jun. 2008, doi:10.1103/PhysRevLett.100.244802
- [2] R. Colella and A. Luccio, "Proposal for a free electron laser in the X-ray region", *Opt. Commun.*, vol. 50, p. 41-44, May 1984, doi:10.1016/0030-4018(84)90009-9
- [3] R. W. Warren, J. C. Goldstein, and B. E. Newnam, "Spiking mode operation for a uniform-period wiggler." *Nucl. Instrum. Methods Res. Sec. A*, vol. 250, p. 19-25, Sep. 1986, doi:10.1016/0168-9002(86)90854-5
- [4] R. R. Lindberg and K.-J. Kim, "Mode growth and competition in the x-ray free-electron laser oscillator start-up from noise", *Phys. Rev. ST-AB*, vol. 12, p. 070702, Jul. 2009, doi:10.1103/PhysRevSTAB.12.070702
- [5] C. Penman and B. W. J. McNeil, "Simulation of input electron noise in the free-electron laser", *Opt. Commun.*, vol. 90, p. 82, Aug. 1992, doi:10.1016/0030-4018(92)90333-M
- [6] W. M. Fawley, "Algorithm for loading shot noise microbunching in multidimensional, free-electron laser simulations", *Phys. Rev. ST Accel. Beams*, vol. 5, p. 070701, Jul 2002, doi:10.1103/PhysRevSTAB.5.070701

REGENERATIVE AMPLIFICATION FOR A HARD X-RAY FREE-ELECTRON LASER

G. Marcus, Y. Ding, Y. Feng, A. Halavanau, Z. Huang, J. Krzywinski, J. MacArthur, R. Margraf, T. Raubenheimer, D. Zhu, SLAC National Accelerator Laboratory, Menlo Park, CA 94025, USA
V. Fiadonu, Santa Clara University, Santa Clara, CA 95053, USA

Abstract

An X-ray regenerative amplifier FEL (XRAFEL) utilizes an X-ray crystal cavity to provide optical feedback to the entrance of a high-gain undulator. An XRAFEL system leverages gain-guiding in the undulator to reduce the cavity alignment tolerances and targets the production of longitudinally coherent and high peak power and brightness X-ray pulses that could significantly enhance the performance of a standard single-pass SASE amplifier. The successful implementation of an X-ray cavity in the XRAFEL scheme requires the demonstration of X-ray optical components that can either satisfy large output coupling constraints or passively output a large fraction of the amplified coherent radiation. Here, we present new schemes to either actively Q-switch a diamond Bragg crystal through lattice constant manipulation or passively output couple a large fraction of the stored cavity radiation through controlled FEL microbunch rotation. A beamline design study, cavity stability analysis, and optimization will be presented illustrating the performance of potential XRAFEL configurations at LCLS-II/-HE using high-fidelity simulations.

INTRODUCTION

The production of longitudinally coherent radiation from single-pass self-amplified spontaneous emission (SASE) FEL amplifiers has been the subject of continued interest. Cavity-based X-ray FELs (CBXFELs) [1] such as the X-ray free-electron laser oscillator (XFEL) [2] and the X-ray regenerative amplifier free-electron laser (XRAFEL) [3, 4] have seen renewed interest as a means of producing and preserving longitudinally coherent hard X-ray (HXR) FEL pulses. While the XFEL and XRAFEL schemes share a common infrastructure (a high-brightness, high repetition rate electron beam, an undulator, and an X-ray cavity) they target very different but complementary FEL performance characteristics (see, for example, [1] and references therein). The XFEL relies on a low-loss cavity supporting a low-gain FEL while the XRAFEL leverages a high-gain FEL interaction. Consequently, the requirements on the cavity for a XRAFEL are relatively relaxed. The science that is enhanced and/or enabled by these two concepts are therefore very different. Here, we focus on the practical elements and performance characteristics of an XRAFEL implementation of a CBXFEL at the LCLS-II facility.

The LCLS-II [5, 6] and the LCLS-II-HE upgrade [7, 8] will be capable of delivering high-brightness electron beams to the HXR undulator at repetition rates as high as ~ 1 MHz, making realistic X-ray cavity geometries and footprints fea-

sible. Significant cavity component development and evaluation has been undertaken by the team at Argonne National Lab in the context of the XFEL. They have shown that high quality diamond Bragg crystals have record-high reflectivities [9], ultra-low thermal expansion and high thermal diffusivity [10], and high mechanical and radiation hardness [11]. These properties make diamond an excellent candidate for the XRAFEL.

The flexibility of the high-gain XRAFEL system, however, allows for the investigation of strongly tapered undulators for high conversion efficiency of electrical to optical power. Efficient undulator tapering relies on stable, high power, and longitudinally coherent seed pulses [12, 13], which a RAFL would excel at delivering. In this regard, diamond optics present a challenge because of their ultra-high reflectivities, making it difficult to extract a large fraction of the stored X-ray pulse energy. Here, we briefly present two methods that may be used to output couple a significant fraction of the stored cavity X-ray power. One method, cavity Q-switching, relies on a manipulation of the cavity optics while the second method, microbunch rotation and off-axis lasing, manipulates the gain medium itself (the electron bunch). We also explore the consequence of the Q-switching concept on the design of the cavity and the performance of the scheme.

RADIATION OUTPUT COUPLING METHODS

Various output coupling methods have been explored within the context of an XRAFEL implementation at the LCLS-II facility. These include both active and passive methods that require manipulation of either the cavity optical components or the gain medium itself. We briefly present two concepts below.

Transient Thermal Expansion of Diamond Lattice Constant

Transient thermal expansion of the diamond lattice constant can be achieved through short-pulsed optical laser excitation. The lattice spacing, therefore, can be manipulated to satisfy or not satisfy the Bragg reflection condition on demand - the cavity can be actively 'Q-switched'. The thermal transport time scale of absorbed energy out of the primary absorbed region on the crystal is 10's of ns due to the high thermal conductivity of diamond, which is sufficiently short compared to a typical roundtrip time in the cavity ($\sim 1\mu\text{s}$ for LCLS-II). Since all of the cavity power is dumped through this process, the effective repetition rate of the XRAFEL is lowered from ~ 1 MHz to $\sim 10 - 50$ kHz, and depends on

the number of passes needed for the XRFEL to reach a steady-state saturated condition from start up. However, it opens the possibility of producing and dumping high *peak* power and fully coherent FEL pulses.

Initial simulations including a time-dependent heat analysis of the diamond crystal surface has shown that it is extremely difficult to get a uniform temperature profile to a depth of an extinction length ($\sim 5\mu\text{m}$ for the parameters studied here). A novel technique has been explored to enable a more uniform temperature profile. This technique leverages a boron doped buried layer under the surface of the diamond to increase the absorption of light in the infrared part of the spectrum. A program has been initiated to experimentally investigate this technique. More detail can be found in [14].

Off-axis Lasing Through Controlled Microbunch Rotation

The microbunches in an electron beam can be rotated in a defocusing quadrupole or in a quadrupole triplet, which can then radiate off-axis in a re-pointed undulator [15, 16]. This scheme opens the possibility of passively output coupling radiation from an XRFEL cavity through gain medium manipulation. The off-axis radiation can either bypass the post-undulator diamond crystal with a strong enough kick or can possibly fall outside the diamond rocking curve and therefore be transmitted. The on-axis radiation can be recirculated and used to seed the next electron bunch. In this way, the nominal ~ 1 MHz repetition rate of the LCLS-II can be maintained while the XRFEL produces high *average* power.

The quadrupole triplet scheme was tested at LCLS where HXR microbunch rotation greater than 5 microradian at a 9.5 keV photon energy was experimentally demonstrated. The quadrupoles of the LCLS undulator FODO lattice were used to perform the microbunch rotation (see Figure 1c). During this shift, roughly $850\mu\text{J}$ pulse energy was split evenly between two spots (see Figure 1a). Various rotation angles were also explored (see Figure 1b). More details on this scheme can be found in [17].

XRFEL CAVITY DESIGN

We begin with the assumption that the X-ray cavity will adopt, as an initial implementation, a rectangular geometry (see Figure 2a). Two compound refractive lenses provide focusing, and when symmetrically placed within the cavity, provide radiation waists at the locations marked w_1 and w_2 . This particular geometry is being explored because it fits into the LCLS undulator hall, works for both the XFEL and XRFEL schemes, is being studied as part of the CBXFEL project [1], and can be upgraded to a tunable geometry [18]. The equivalent unfolded optical lattice of the cavity is shown in Figure 2b. Gaussian beam ABCD optics provides a suitable framework with which to analyze the system [19]. Within this framework, one can find the complex Gaussian ‘eigen- q ’ of the system, which defines the self-reproducing mode that is self-consistent upon round

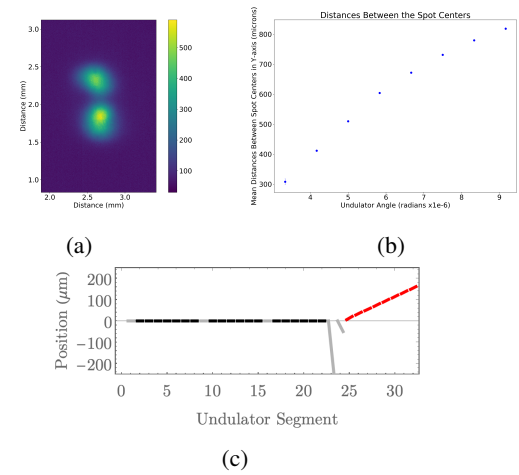


Figure 1: (a) Two transverse spots with equal energy on the post-undulator direct imager. (b) Spot separation on the direct imager as a function of the undulator pointing. (c) LCLS undulator configuration for microbunch rotation at a particular angle.

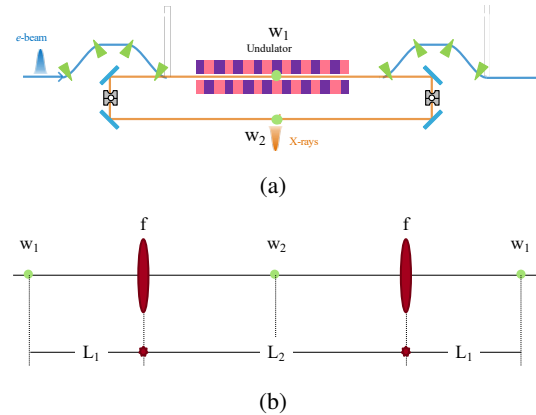


Figure 2: (a) Mockup of the rectangular cavity. (b) Unfolded equivalent optical lattice.

trip propagation:

$$q_o = \frac{Aq_i + B}{Cq_i + D} = q_i. \quad (1)$$

Here, q_i and q_o are the initial and propagated complex beam parameters, respectively, and depend on the ABCD matrix elements of the optical system. This equation has two solutions:

$$\frac{1}{q_{a,b}} = \frac{D - A}{2B} \mp \frac{1}{B} \sqrt{m^2 - 1}, \quad (2)$$

where $m = (A + D)/2$. The m parameter determines the stability of the cavity both in the context of stable or unstable periodic focusing systems and in terms of the self-consistent eigensolutions, $q_{a,b}$ being stable against small perturbations. A stable cavity will have $-1 < m < 1$ while the period of oscillation (either geometrically or perturbatively) is given by $\theta = \cos^{-1}(m)$.

The strategy for choosing L_1, L_2 and f is as follows. First, the w_1 that is equivalent to the guided mode solution in the high gain FEL is solved for under the constraints that $2L_1 + L_2 = L_{cav}$ for a stable cavity and that all matrix elements (A, B, C, D) are real. One advantage of the high gain XRA FEL is that it can tolerate significant radiation losses in the cavity. It is possible for the radiation to make multiple round trips in the cavity before interacting with a following fresh electron beam. Depending on the electron beam repetition rate and the total cavity length (L_{cav}), L_2 can be chosen such that the the period of perturbation oscillation, θ , matches the period of radiation-beam interaction. Another advantage of choosing w_1 to be the guided mode solution is that the radiation at the entrance of the undulator after propagating through the cavity is larger than this solution and is slightly converging. The larger field size makes the XRA FEL slightly less susceptible to lateral and angular displacements (errors) and the seed field intensity nominally increases as the radiation approaches the waist. This is advantageous for strong undulator tapering. Finally, the high-gain XRA FEL system can gain guide laterally or angularly displaced seed radiation back to the undulator axis and can significantly correct mirror angular displacement errors.

CAVITY STABILITY ANALYSIS

After performing the above design optimization, a root sum square (RSS) statistical tolerancing analysis, similar to what has been performed in [1], can be performed for the XRA FEL given the cavity parameters L_1, L_2, f . Here, it is assumed that the cavity wraps the entire undulator, has a total cavity length $L_{cav} \sim 323$ m, and supports three round trips of the X-ray pulse before interacting with a following fresh electron bunch (assuming 100 pC charge electron bunch parameters for an LCLS-II-HE scenario, the parameters of which can be found in [7]). These initial estimates project a mirror angular error tolerance of $\sigma_m \sim 70$ nrad.

Gain guiding, however, is not currently captured in the analytical tolerancing analysis. Here, we present preliminary results of time-independent GENESIS [20] simulations for the case presented above for the production of 9.8 keV photons. The electron bunch length for this scenario is similar to the Fourier-limited pulse length associated with diamond (400) crystal plane reflectivity making the single-frequency simulations a reasonable approximation. Figure 3 shows the results of ~ 150 simulations where the angular errors of the four cavity mirrors were assumed to be independent and normally distributed with RMS errors of $\sigma_m = 0.35 \mu\text{rad}$ (top row) and $\sigma_m = 0.5 \mu\text{rad}$ (bottom row). Each simulation included modeling the diamond mirror net efficiencies assuming the output coupling crystal was Q-switched using the technique described above and propagating the radiation fields through the cavity using standard Fourier optics techniques. The 3-pass roundtrip efficiency in this case was $\sim 5\%$. Without any mirror errors, the saturated power of the radiation after the 30th interaction with the electron beam is ~ 4 GW. Figures 3b and 3d indicate that roughly 4% and

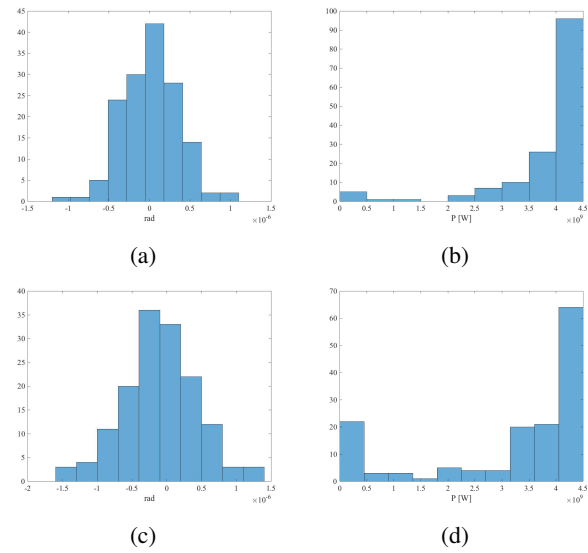


Figure 3: (a) Histogram of M1 errors for $\sigma_m = 0.35 \mu\text{rad}$. (b) Histogram of final power after 30 interactions of the radiation with the electron beam in the cavity for $\sigma_m = 0.35 \mu\text{rad}$. (c) Histogram of M1 errors for $\sigma_m = 0.5 \mu\text{rad}$. (d) Histogram of final power after 30 interactions of the radiation with the electron beam in the cavity for $\sigma_m = 0.5 \mu\text{rad}$.

25% of the final power levels do not reach an appreciable level of 1 GW. Note that a $\sigma_m = 0.35 \mu\text{rad}$ mirror error is 5 times the analytic estimate. A further reduction in the mirror error in simulation will result in less low-power shots.

DISCUSSION

An XRA FEL implementation at LCLS-II-HE offers a compelling pathway for the production fully coherent high average and peak power hard X-ray FEL pulses. A number of options exist for output coupling a large fraction of the stored cavity power, only two of which were presented here. These schemes include both active and passive methods and rely on both cavity optics as well as gain medium manipulations. Gain guiding in the high-gain FEL process relaxes the alignment and stability requirements of the cavity optomechanical systems.

ACKNOWLEDGEMENTS

We thank K.-J. Kim, Y. Shvyd'ko, R. Lindberg and D. Shu for many helpful and insightful discussions. This work was supported by U.S. Department of Energy Contract No. DE-AC02-76SF00515 and the Laboratory Directed Research and Development program at SLAC National Accelerator Laboratory.

REFERENCES

- [1] G. Marcus *et al.*, "Cavity-based free-electron laser research and development: a joint Argonne national laboratory and SLAC national laboratory collaboration", presented at FEL'19, Hamburg, 2019, paper TUD04, this conference.

- [2] K.-J. Kim, Y. Shvyd'ko, and Sven Reiche, "A proposal for an x-ray free-electron laser oscillator with an energy-recovery linac" *Phys. Rev. Lett.* vol. 100, pp. 244802, 2008, doi:10.1103/PhysRevLett.100.244802
- [3] Z. Huang and R.D. Ruth, "Fully coherent x-ray pulses from a regenerative-amplifier free-electron laser", *Phys. Rev. Lett.* vol. 96, pp. 144801, 2006, doi:10.1103/PhysRevLett.96.144801
- [4] G. Marcus *et al.*, "X-ray regenerative amplifier free-electron laser concepts for LCLS-II", in *Proc. 38th Int. Free-Electron Laser Conf.*, New Mexico, 2017, doi:10.18429/JACoW-FEL2017-MOP061
- [5] T.O. Raubenheimer, ed., "LCLS-II final design report", SLAC, Menlo Park, CA, LCLSII-1.1-DR-0251-R0, 2015.
- [6] T.O. Raubenheimer, "Technical challenges of the LCLS-II CW x-ray FEL", in *Proc. 6th Int. Particle Accelerator Conf.*, Virginia, USA, 2015, doi:10.18429/JACoW-IPAC2015-WEYC1
- [7] T.O. Raubenheimer, ed., "LCLS-II-HE conceptual design report", SLAC, Menlo Park, CA, LCLSIIHE-1.1-DR-0001-R0, 2018.
- [8] T.O. Raubenheimer, "The LCLS-II-HE, a high energy upgrade of the LCLS-II", *60th ICFA Advanced Beam Dynamics Workshop on Future Light Sources*, Shanghai, China, 2018, doi:10.18429/JACoW-FLS2018-MOP1WA02
- [9] Yuri Shvyd'ko *et al.*, "Near-100% Bragg reflectivity of x-rays", *Nat. Phot.* 5, pp. 539, 2011, doi:10.1038/nphoton.2011.197
- [10] S. Stoupin, Y. Shvyd'ko, "Thermal expansion of diamond at low temperatures", *Phys. Rev. Lett.* vol. 104, pp. 085901, 2010, doi:10.1103/PhysRevLett.104.085901
- [11] T. Kolodziej *et al.*, "High Bragg reflectivity of diamond crystals exposed to multi-kW mm² x-ray beams", *J. of Synch. Rad.*, vol. 25, pp. 1022, 2018, doi:10.1107/S1600577518007695
- [12] C. Emma *et al.*, "High efficiency, multiterawatt x-ray free electron lasers", *Phys. Rev. Accel. and Beams*, vol. 19, pp. 020705, 2016, doi:10.1103/PhysRevAccelBeams.19.020705
- [13] J. Duris, A. Murokh and P. Musumeci, "Tapering enhanced stimulated superradiant amplification", *New J. of Phys.*, vol. 17, pp. 063036 2015, doi:10.1103/PhysRevAccelBeams.21.080705
- [14] J. Krzywinski *et al.*, "Q-Switching of X-Ray Optical Cavities With a Boron Doped Buried Layer Under the Surface of a Diamond Crystal", presented at FEL'19, Hamburg, 2019, paper TUP033, this conference.
- [15] J. MacArthur *et al.*, "Microbunch rotation and coherent undulator radiation from a kicked electron beam", *Phys. Rev. X*, vol. 8, pp. 041036, 2018, doi:10.1103/PhysRevX.8.041036
- [16] J. MacArthur *et al.*, "Microbunch rotation and coherent undulator radiation from a kicked electron beam", presented at FEL'19, Hamburg, 2019, paper MOD02, this conference.
- [17] R. Margraf *et al.*, "Microbunch rotation for hard x-ray beam multiplexing", presented at FEL'19, Hamburg, 2019, paper THP036, this conference.
- [18] Yuri Shvyd'ko, "Feasibility of x-ray cavities for free electron laser oscillators", *ICFA Beam Dynamics Newsletter*, No. 60, 2013.
- [19] A. Siegman, *Lasers*, University Science Books, 1986.
- [20] S. Reiche, "GENESIS 1.3: a fully 3D time-dependent FEL simulation code", *Nucl. Instr. Meth. Phys. Res. Sec. A*, vol. 429, pp. 243, 1999, doi:10.1016/S0168-9002(99)00114-X

Q-SWITCHING OF X-RAY OPTICAL CAVITIES BY USING BORON DOPED BURIED LAYER UNDER A SURFACE OF A DIAMOND CRYSTAL

J. Krzywinski, D. Zhu, G. Marcus, Y. Feng, A. Halavanau, J. MacArthur, Z. Huang
 SLAC National Accelerator Laboratory, Stanford University, Menlo Park CA, USA
 A. Kissas, Santa Clara University, Santa Clara CA, USA

Abstract

Improvement of the longitudinal coherence of X-ray Free Electron Lasers has been the subject of many recent investigations. The XFEL oscillator (XFEL) and Regenerative Amplifier Free-Electron Laser (RAFEL) schemes offer pathways to fully coherent, high brightness X-ray radiations. The XFEL and RAFEL both consist of a high repetition rate electron beam, an undulator, and an X-ray crystal cavity to provide optical feedback. The X-ray cavity will be based on diamond crystals in order to manage a high thermal load. We are investigating a 'Q switching' mechanism that involves the use of a 'Bragg switch' to control the X-ray pulse energy built-up and outcoupling inside the X-ray cavity. In particular, one can use an optical laser to manipulate the diamond crystal lattice constant to control the crystal reflectivity and transmission. It has been shown that a 9 MeV focused boron beam can create a buried layer, approximately 5 microns below surface, with a boron concentration up to 10^{21} atoms/cm³, with localized and enhanced optical absorption. Here, we present simulations showing that absorbing laser pulses by a buried layer under the crystal surface would allow creating a transient temperature profile which would be well suited for the 'Q switching' scheme.

INTRODUCTION

The brightness of x-ray sources has been increased one to ten billion times by x-ray free-electron lasers (XFELs) that generate high intensity coherent photon pulses at wavelengths from nanometers to less than one angstrom and a duration of a few to 100 femtoseconds [1]. For the first time XFELs allow for experimental exploration of the structure and dynamics of atomic and molecular systems at the angstrom-femtosecond space and time scale. This have created a plethora of new opportunities for scientific research in physics, chemistry, biology, material science and high energy density physics [1, 2]. A characteristic feature of single-pass SASE FELs, however, is the poor longitudinal coherence, which results from the initial amplification of incoherent radiation shot-noise [1]. Improvement of the longitudinal coherence is of great practical importance and has been the subject of many recent investigations. With high repetition rate machines, such as European XFEL [3], and LCLS-II [4] coming online soon, an XFEL oscillator (XFEL) [5, 6] or Regenerative Amplifier Free-Electron Laser (RAFEL) [7, 8] offers a pathway to the production of stable, fully coherent, high brightness, and high average power X-ray radiation. These so-called cavity-based X-ray free-electron lasers (CBXFELs) consist of a high repetition

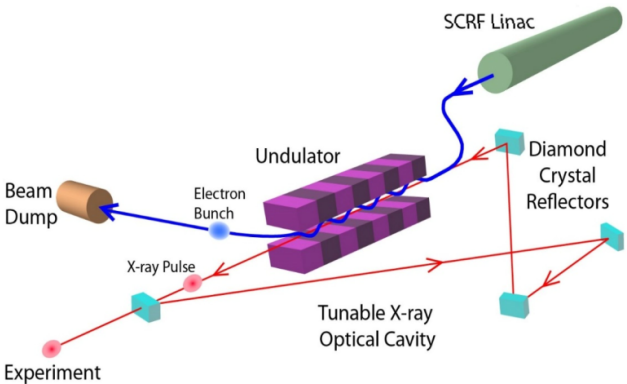


Figure 1: Schematic illustration of an X-ray cavity for XFEL or RAFEL. Four crystals form a closed X-ray cavity via Bragg reflection [9].

rate electron beam, a short undulator, and an x-ray crystal cavity (in the case of hard X-rays) to provide optical feedback (Fig. 1).

Q-SWITCHING OF X-RAY OPTICAL CAVITIES

Like optical laser cavities, outcoupling optics and mechanisms is one of the essential components, which can come in the form of a partial reflector or cavity 'dumper'. We are investigating the viability of a 'Q switching' mechanism that involves the use of a 'Bragg switch' to dump the x-ray pulse energy built-up inside an x-ray cavity [10, 11]. The idea of Bragg switching by a controlled lattice deformation using piezoelectric excitation, generation of optical and acoustic phonons or picosecond thermal excitations has been proposed and demonstrated at synchrotron sources by several authors [10–18]. However, the construction of an x-ray cavity around a high repetition rate XFEL will require using materials that can manage high thermal load. Single crystal diamond is a good candidate as it has superb thermal and mechanical properties and, because it is a low Z material, X-ray energy deposition per volume is much less than other candidates such as silicon crystal [19]. Therefore techniques that have been already proposed cannot be applied directly here as our choice of materials is limited to low Z materials and the XRAFEL cavity output-coupling techniques needs further studies.

In this work we investigate the use of optical laser to manipulate the crystal lattice constant in such a way that the crystal reflectivity/transmission can be controlled by the relative timing of the optical laser excitation and the

arrival of the x-ray pulse, as well as laser power. Unlike the previous work [18] that reported a picosecond scale response time, here the goal is to make use of a much longer time window, and find the optimal parameters for minimizing impact on the reflected x-ray wavefront, so that the beam can be re-circulated back to the entrance of the undulator and deliver the highest possible seed power. The key for the optimization of the CBXFEL performance using this ‘Q switch’ scheme is to find the best way of controlling the temporal-temperature profile close to the crystal’s surface, as well as keeping the spatial-temperature profile uniform over the x-ray beam footprint.

As an example, we present here investigation of transient thermal excitation of the diamond lattice constant achieved through short pulse optical laser excitations. The lattice spacing, therefore, can be manipulated to satisfy or not satisfy the Bragg reflection condition at desired times. The thermal transport time scale of absorbed energy out of the primary absorption region in the crystal is 10’s of ns due to the high thermal conductivity of diamond. This is significantly shorter time scale compared to the projected pulse repetition rate of the superconducting LINAC driven sources at 1-5 MHz, which enables the possibility for pulse to pulse control of the crystal reflectivity in order to realize a ‘Q switch’ for the cavity.

While the most obvious route was to use an optical laser pulse to switch the pre-aligned crystal away from the Bragg condition, in order to render the whole crystal non-reflecting which dumps the cavity power-buildup, lattice constant would need to be changed throughout the crystal thickness. As the time scale of switching in this case will be partially governed by the thickness of the crystal, thin diamond crystal plates with thickness on the order of the crystal reflection extinction depth will need to be used. This will introduce further challenges in crystal fabrication, mounting, and cooling. An alternative approach, as illustrated in Figure 2, allows the use of thicker crystals. In this rectangular cavity setup, we maintain all crystals except for the out-coupling crystal at an elevated temperature T_1 and aligned to Bragg condition at 90° . Instead of using a laser pulse to switch the crystal *off*, we propose to use the synchronized laser pulse train to maintain the surface temperature to match the other crystals, while the rest of the outcoupling crystal stays at a lower temperature T_2 . The temperature and lattice constant distribution when the x-ray arrives at the out-coupling crystal can be controlled both by the power and the timing of the laser pulse, in order to achieve best reflectivity and minimum wavefront distortion for the closed cavity configuration shown in Fig. 2(a). When one wants to dump the cavity, the heated region can be turned *off* by changing the laser parameters (power, timing) for the corresponding laser pulse. The x-ray pulse returned to the outcoupling crystal can therefore transmit through as shown in Fig. 2(b) with a very small absorption loss. With this scheme, a high quality thick crystal can be used, while still allow fast switching time scale.

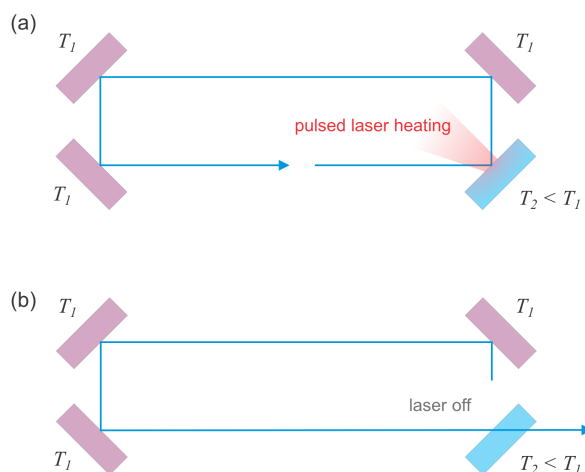


Figure 2: (a) Configuration of the closed cavity. The lower right crystal is kept at lower temperature. A synchronized laser pulse is used to control the surface temperature and lattice constant to meet the Bragg condition. (b) configuration of an open cavity with the laser switched OFF. The lower right crystal at lower temperature would thus become transparent to the ‘resonant’ wavelength.

One challenge to achieve high reflectivity of the outcoupling crystal is to establish a transient uniform temperature profile over the depth of the extinction length of $\sim 5 \mu\text{m}$ (assuming 9.8 keV photons using the (400) reflecting planes at a 45° Bragg angle). Initial simulations including a time-dependent thermal transport analysis of the diamond crystal assuming energy deposition directly on the surface using near-band-gap UV wavelength has shown that it is rather difficult, as shown in Figure 3 (top). Here we propose a novel scheme to enable a more uniform temperature profile. It has been shown [20] that by using 9 MeV focused boron beam one can create a buried layer, approximately 5 microns below surface, with a boron concentration up to 10^{21} atoms/cm³. Such concentration levels should be sufficient to absorb infrared laser pulses [21] and would allow improved control of a desired temperature profile close to the surface. The compatibility with an IR instead of UV pulse also simplifies significantly the laser setup requirement. The time dependent temperature profile from the absorbed IR light at the depth of the implanted boron in a diamond crystal is shown in Figure 3 (bottom) and it indicates that a uniform temperature profile can be obtained. A collaboration with colleagues at Universidad Autonoma de Madrid to use the CMAM microbeam line to perform boron ion implantation has been initiated. In the first phase of this investigation, HPHT type IIa diamond crystals will be characterized both before and after boron ion implantation to ensure a high diamond crystal quality can be sustained. Experimental measurements are planned for FY20. A second phase of the investigation includes testing the Bragg switching concept with these implanted diamonds in a time-resolved experiment, and later in a 20-m-round-trip cold cavity at the LCLS using the XPP

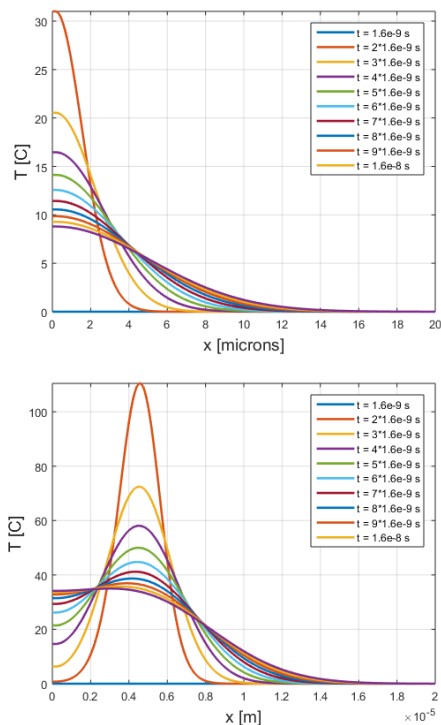


Figure 3: Time dependent thermal profile into the crystal from surface heating (top) and time dependent thermal profile into the crystal of a boron doped diamond (bottom).

experimental hutch [22]. Time domain thermal mechanical modeling will also be performed considering potential future average and impulsive thermal loading, for Q-switch optimization.

DIAMOND CRYSTAL CHARACTERIZATION

White beam topography can be used as an initial characterization, e.g. at the Advanced Photon Source (APS) at Argonne National Lab. At the BM-1 beamline white beam topography setup, a collimated polychromatic synchrotron X-ray pulse is sent onto the diamond crystal sample and multiple Laue reflections are captured on the X-ray film downstream. The film is then developed and digitized for analysis. White beam topography, while not providing enough information about the reflection surface, is a very fast and efficient technique to quickly locate the primary defects such as inclusions, dislocations and stacking faults within the diamond crystals, which usually appear as brighter features on the image due to their broader wavelength acceptance and sometimes multiple re-scattering of the X-rays. To quantitatively determine the potential locations for the boron ion deposition, we calculate the RMS variance map of the obtained white beam topography images.

We apply a circular mask, with a size corresponding to about 3σ of the X-ray beam size, and scan it across, retaining the values of mean and variance of integral intensity. In addition, we determine the areas connected by $<5\%$ difference

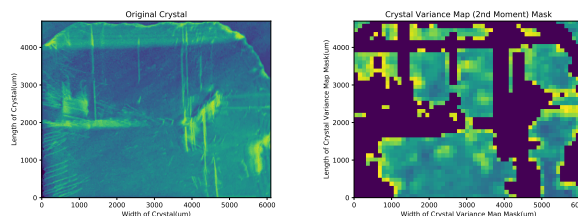


Figure 4: Left: white beam topograph of a type IIa diamond crystal. Right: variance maps with masked potential doping areas

in variance with the neighboring points. As a result, we produce a crystal map of the areas, concurring both for doping and possible CBXFEL tests [23]. The variance as a function of position on the crystal is then plotted in color in Fig. 4. We note that spatial resolution and non-linear gain of the film is an important limiting factor for higher quality topographs. Therefore, we will use the resulting variance maps as a guidance for ion deposition, while rely on monochromatic beam topography for crystal quality assurance. The results of these studies will be reported elsewhere.

Ideally monochromatic beam rocking curve analysis to be performed before and after the ion deposition to access the impact of the implantation to crystal surface by evaluating the rocking curve height and width in a spatially resolved way. In addition, the angular variation in the rocking curve center is a reflection of the residual mechanical strain of the crystal lattice. This angular variation must be minimized to preserve the transverse coherence of the reflected beam in an oscillator application, in addition to achieving high reflectivity. We believe both white beam and monochromatic beam topography measurements are important to fully characterize the diamond samples in order to identify the best region on the highest quality diamond crystals for CBXFEL applications.

ACKNOWLEDGEMENTS

Authors would like to thank Y. Shvydko and P. Pradhan (ANL) for their help with white beam topography measurements at APS. This work was supported by U.S. Department of Energy Contract No. DE-AC02-76SF00515 and the Laboratory Directed Research and Development program at SLAC National Accelerator Laboratory.

REFERENCES

- [1] C. Pellegrini, "X-ray free-electron lasers: from dreams to reality," *Physica Scripta*, vol. 2016, 2017. doi:10.1088/1402-4896/aa5281
- [2] C. Bostedt, *et al.*, "Linac coherent light source: the first five years," *Rev. Mod. Phys.*, vol. 88, pp. 015007, 2016. doi:10.1103/RevModPhys.88.015007
- [3] M. Altarelli, *et al.*, "The european x-Ray free-electron laser," Hamburg, Germany, DESY 2006-097, 2007.

- [4] R. W. Schoenlein, *et al.*, “The linac coherent light source: recent developments and future plans,” *Applied Sciences* vol. 7, pp. 850, 2017. doi:10.3390/app7080850
- [5] K.-J. Kim, Y. Shvyd’ko, and S. Reiche, “A proposal for an x-ray free-electron laser oscillator with an energy-recovery linac,” *Phys. Rev. Lett.*, vol. 100, pp. 244802, 2008. doi:10.1103/PhysRevLett.100.244802
- [6] K.-J. Kim *et al.*, “Progress towards an x-ray FEL oscillator,” presented at 37th Int. Free-Electron Laser Conf., Daejeon, Korea, 2015, WEB03, unpublished.
- [7] Z. Huang and R. Ruth, “Fully coherent x-ray pulses from regenerative-amplifier free electron laser,” *Phys. Rev. Lett.*, vol. 96, pp. 144801, 2006. doi:10.1103/PhysRevLett.96.144801
- [8] G. Marcus *et al.*, “X-ray Regenerative Amplifier Free-Electron Laser Concepts for LCLS-II”, in *Proc. 38th Int. Free Electron Laser Conf. (FEL’17)*, Santa Fe, NM, USA, Aug. 2017, pp. 192–195. doi:10.18429/JACoW-FEL2017-MOP061
- [9] Bernhard Adams *et al.*, “Scientific opportunities with an x-ray free-electron laser oscillator,” arXiv:1903.09317, 2019.
- [10] D.S. Allam, “A piezoelectric beam chopper,” *J. Phys. E: Sci. Instrum.*, vol. 3, pp. 1022, 1970. doi:10.1088/0022-3735/3/12/426
- [11] A. Grigoriev *et al.*, “Subnanosecond piezoelectric x-ray switch,” *App. Phys. Lett.*, vol. 89, pp. 021109, 2006. doi:10.1063/1.2219342
- [12] E. Zolotoyabko *et al.*, “Control of synchrotron x-ray diffraction by means of standing acoustic waves,” *Rev. Sci. Instr.*, vol. 75, pp. 699, 2004. doi:10.1063/1.1645652
- [13] P.H. Bucksbaum *et al.*, “The phonon Bragg switch: a proposal to generate sub-picosecond X-ray pulses,” *Solid State Communications*, vol. 111, pp. 535, 1999. doi:10.1016/S0038-1098(99)00235-5
- [14] J.M.H. Sheppard, *et al.*, “Simulations of the phonon Bragg switch in GaAs,” *Solid State Communications*, vol. 136, pp. 181, 2005. doi:10.1016/j.ssc.2005.05.056
- [15] P. Gaal, *et al.*, “Ultrafast switching of hard X-rays,” *J. Synch. Rad.*, vol. 21, pp. 380, 2014. doi:10.1107/S1600577513031949
- [16] M. Sander, *et al.*, “Characterization of an ultrafast Bragg-Switch for shortening hard x-ray pulses,” *J. Appl. Phys.*, vol. 120, pp. 193101, 2016. doi:10.1063/1.4967835
- [17] H. A. Navirian *et al.*, “Shortening x-ray pulses for pump-probe experiments at synchrotrons,” *J. Appl. Phys.*, vol. 109, pp. 126104, 2011. doi:10.1063/1.3601057
- [18] M. Sander, *et al.*, “Demonstration of a picosecond Bragg switch for hard X-rays in a synchrotron-based pump-probe experiment,” *J. Synch. Rad.*, vol. 26, pp. 1253, 2019. doi:10.1107/S1600577519005356
- [19] Y. Shvyd’ko, V. Blank, and S. Terentyev, “Diamond x-ray optics: transparent, resilient, high-resolution, and wavefront preserving,” *MRS Bulletin*, vol. 42, pp. 437, 2017. doi:10.1557/mrs.2017.119
- [20] M. D. Ynsa *et al.*, “Study of the effects of focused high-energy boron ion implantation in diamond,” *Nucl. Instr. Meth. Phys. Res. Sec. B*, vol. 404, pp.207, 2017. doi:10.1016/j.nimb.2017.01.052
- [21] E. Bustarret *et al.*, “Optical conductivity studies in heavily Boron-doped diamond,” *Phys. Stat. Sol. (a)*, vol. 186, 2001. doi:10.1002/1521-396X(200108)186:2<303::AID-PSSA303>3.0.CO;2-5
- [22] M. Chollet *et al.*, “The x-ray pump-probe instrument at the linac coherent light source,” *J. Synch. Rad.*, vol. 22, pp. 503, 2015. doi:10.1107/S1600577515005135
- [23] G. Marcus *et al.*, “Cavity-based free-electron laser research and development: a joint Argonne National Laboratory and SLAC National Laboratory collaboration,” presented at 39th Int. Free-Electron Laser Conf., Hamburg, 2019, TUD04, this conference.

SENSITIVITY OF LCLS SELF-SEEDED PEDESTAL EMISSION TO LASER HEATER STRENGTH

G. Marcus, D. Bohler, Y. Ding, W. M. Fawley, Y. Feng, E. Hemsing,
Z. Huang, J. Krzywinski, A. Lutman, D. Ratner
Menlo Park, CA 94025, USA

Abstract

Measurements of the soft X-ray, self-seeding spectrum at the LCLS free-electron laser generally display a pedestal-like distribution around the central seeded wavelength that degrades the spectral purity. We have investigated the detailed experimental characteristics of this pedestal and found that it is comprised of two separate components: (1) normal SASE whose total strength is nominally insensitive to energy detuning and laser heater (LH) strength; (2) sideband-like emission whose strength positively correlates with that of the amplified seed and negatively with energy detuning and LH strength. We believe this latter, non-SASE component arises from comparatively long wavelength amplitude and phase modulations of the main seeded radiation line. Its shot-to-shot variability and LH sensitivity suggests an origin connected to growth of the longitudinal microbunching instability on the electron beam. Here, we present experimental results taken over a number of shifts that illustrate the above mentioned characteristics.

INTRODUCTION

This work was recently accepted for publication in *Physical Review Accelerator and Beams* [1].

REFERENCES

- [1] G. Marcus *et al.*, “Experimental observations of seed growth and accompanying pedestal contamination in a self-seeded, soft x-ray free-electron laser,” *Phys. Rev. Accel. and Beams*, vol. 22, pp. 080702, 2019. doi:10.1103/PhysRevAccelBeams.22.080702

A WAVEGUIDE-BASED HIGH EFFICIENCY SUPERRADIANT FEL OPERATING IN THE THz REGIME *

P. Musumeci[†], A. Fisher, UCLA Department of Physics and Astronomy, Los Angeles, CA, USA
B. Van Der Geer, Pulsar Physics

E. A. Nanni, E. C. Snively, SLAC National Accelerator Laboratory, Menlo Park, CA, USA
A. Gover, Tel Aviv University, Tel Aviv, Israel

Abstract

In this paper we describe a novel self-consistent 3D simulation approach for a waveguide FEL operating in the zero-slippage regime to generate high power THz radiation. In this interaction regime, the phase and group velocity of the radiation are matched to the relativistic beam traveling in the undulator achieving long interaction lengths. Our numerical approach is based on expanding the existing 3D particle tracking code GPT (General Particle Tracer) to follow the interaction of the particles in the beam with the electromagnetic field modes of the waveguide. We present two separate studies: one for a case which was benchmarked with experimental results and another one for a test case where, using a longer undulator and larger bunch charge, a sizable fraction of the input beam energy can be extracted and converted to THz radiation. The model presented here is an important step in the development of the zero-slippage FEL scheme as a source for high average and peak power THz radiation.

INTRODUCTION

Free-Electron Laser radiation sources have long been an attractive solution to generate large amounts of electromagnetic radiation in spectral ranges where solid-state based devices are less effective including THz, extreme UV, soft and hard X-rays[1]. The THz range is particularly interesting for an FEL due to the fact that only relatively modest energy (\sim few up to tens of MeV) electron beams are required in order to match the resonance condition for efficient interaction in an undulator magnet.

In the THz range, fueled by the recent developments in laser-based generation of nearly single-cycle radiation pulses[2], much interest has been diverted towards broad bandwidth THz applications, for example in the study of non-linear response in materials. On the other hand, most THz FEL operate with fairly long electron beams and target the generation of narrowband THz radiation [3,4]. This is due to the intrinsic bandwidth of the FEL associated with the slippage effects which limits the number of undulator periods over which a strong interaction can be maintained.

Following earlier work on wave-guided FEL[5,6], we recently revisited a strong coupling scheme for electrons and electromagnetic wave co-propagating in an undulator,

based on the zero-slippage interaction where the group velocity of the radiation in a waveguide is matched to the electron beam axial velocity [7]. This scheme has the potential for broadband interaction (see Fig. 1), extended interaction lengths and high efficiency energy conversion.

Two sets of experiments were completed using the same setup at UCLA Pegasus Laboratory. In the first one, we used a laser-generated THz pulse to impart energy modulation on an electron beam to show THz-based beam compression. In the second one, raising the charge of the e-beam we showed THz amplification and generation. [8,9]. In the design and analysis of the results for these experiments, an interesting issue we had to face was the lack of adequate simulation tools to model this interaction. Standard wide-spread use FEL codes such as GENESIS or GINGER typically employ the slice-model and suffer from limitations related to period-averaging and slowly varying envelope approximation which fail to capture the dispersion dominated radiation evolution and the broad bandwidth of the interaction in a waveguide FEL.

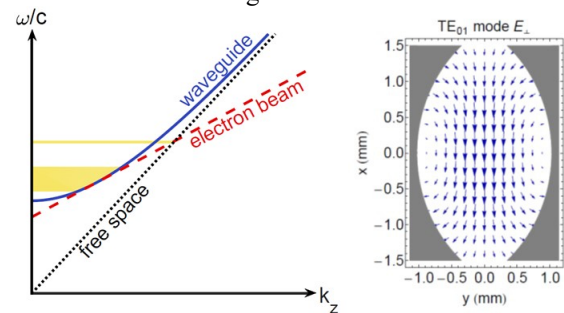


Figure 1: Left) Schematics of the waveguide coupling scheme. Strong interaction occurs where phase synchronicity between the radiation and the electron occurs. In the free space case, this intersection is limited to a single point. In the waveguide an entire range of frequencies can interact with the beam (due to the tangential crossing). Right) Spatial profile of the TE₀₁ fundamental curved parallel plate waveguide mode which dominates the interaction.

In order to understand our experiments we used a mixture of a GPT module [10] to follow the particle evolution assuming a frozen-field approximation (radiation fields propagating unperturbed by the presence of the e-beam), and a 1D self-consistent modal-decomposition based FEL simulation wafEL [9] where the full dispersion relation for the waveguide was used. In this paper we combine the two approaches and use GPT to calculate the spectrum of the radiation along the undulator. We will first describe the

* Work mainly supported by DOE grant DE-SC0009914 and NSF grant PHY-1734215.

[†] musumeci@physics.ucla.edu

approach and use it to validate the simulation in the cases already benchmarked with experimental results. We will then explore the scientific opportunities outlined at the end of [9] to use this scheme for the generation of high power THz radiation.

DESCRIPTION OF THE CODE

The frequency-domain modal decomposition is a natural solution to describe the evolution of the field in our system as it allows complete freedom in setting the dispersion relation for the different modes. This solution provided the basis of the UCLA waffEL code, which on the other hand had the strong limitation of one dimensional particle dynamics and completely neglected the effects of emittance and undulator focusing.

While exploring various methods to extend the simulations to three spatial dimensions, it was pointed out that more than a decade ago GPT developed an element suitable to simulate the interaction of the beam with free-space resonator modes [11,12]. It then became a natural solution to extend this model to calculate the interaction with the curved parallel plate waveguide modes.

The transverse and longitudinal wavenumbers for the modes in a curved parallel plate waveguide with radius R and separation b are

$$k_{mn} = \frac{1}{b} \left(n\pi + (2m+1) \tan^{-1} \frac{b}{\sqrt{2Rb-b^2}} \right)$$

$$k_z(\omega) = \sqrt{(\omega/c)^2 - k_{mn}^2}$$

The TM (TE) mode profiles can be derived from the expression for the electric (magnetic) longitudinal field which can be written [13]

$$\Phi_{mn} = \frac{e^{\frac{\beta_{mn}^2 x^2}{\alpha_{mn}(y)}}}{\sqrt[4]{\alpha_{mn}(y)}} He_m \left(\frac{2\beta_{mn}x}{\sqrt{\alpha_{mn}(y)}} \right) (\cos) \left[k_{mn}y + \frac{2\beta_{mn}^4 y x^2}{k_{mn}\alpha_{mn}(y)} - \left(m + \frac{1}{2} \right) \tan^{-1} \frac{2\beta_{mn}^2 y}{k_{mn}} \right] e^{\pm i k_z z}$$

where He_m are the Hermite polynomials of order m and

$$\alpha_{mn}(y) = 1 + 4 \frac{\beta_{mn}^4 y^2}{k_{mn}^2} \quad \text{and} \quad \beta_{mn} = \sqrt{\frac{k_{mn}}{\sqrt{2Rb-b^2}}}$$

The transverse E-field complex amplitudes for each mode are then given by

$$\mathbf{T}_{(x,y)}(x,y)e^{\pm i k_z z} = \frac{-i}{k_{mn}^2} \left(k_z \frac{\partial E_z}{\partial(x,y)} \mp \omega \mu_0 \frac{\partial H_z}{\partial(y,x)} \right)$$

Just like in waffEL and any other frequency based FEL code, we model the electric field as a sum over different modes:

$$\mathbf{E}(\mathbf{r}, t) = \text{Re} \sum_j c_j \mathbf{T}_j(x, y) e^{-i(k_j z - \omega_j t)} \quad (1)$$

where we limited the description to forward propagating modes (no backward wave interactions), index j runs both over the different frequencies ω_j and the different mode numbers (m, n) and the longitudinal wavenumber is $k_j =$

$k_{z,m,n}(\omega_j)$. The complex coefficients c_j encode the spectral content of the radiation field as it evolves along the interaction. The spectral interval between the different frequencies ΔN is the simulated bandwidth $(f_{\max} - f_{\min})$ divided by the number of modes N_{freq} and normalized by the frequency resolution $2L/c$ where L is the interaction length.

There are two different equivalent ways to derive the equations for the evolution of the mode (amplitude and phase). One option is to start from Maxwell equations, substitute Eq. (1) and project the source term onto the mode basis. Alternatively, we can also observe that energy conservation implies that the energy given by a mode to any one particle needs to be removed from the energy in that mode. This second view is completely equivalent, and offers an intuitive approach to the calculation of the evolution of the mode profile.

$$\frac{dW_j}{dt} = -\Delta N \sum_i Q_i \mathbf{v}_i \cdot \mathbf{E}_j(\mathbf{r}_i, t) \quad (2)$$

where the sum is over all macroparticles of charge Q_i and velocity \mathbf{v}_i and $W_j = \frac{1}{2} \epsilon_0 |c_j|^2 V$ is the energy of the mode j integrated over the frequency interval ΔN . $V \sim L\pi b^2/3$ is the mode volume and is related to the normalization factor of the mode basis $T_j(x, y)$.

Starting from Eq. (2) we can derive the differential equations for the real and imaginary parts of the amplitude coefficients for each mode j . For the interaction with the TE modes (no E_z) at each time step we will have

$$\frac{dc_j}{dt} = - \sum_i \frac{Q_i}{\epsilon_0 V} \left(v_{x,i} T_{x,j}(x_i, y_i) + v_{y,i} T_{y,j}(x_i, y_i) \right) e^{-i(k_j z_i - \omega_j t)}$$

where (x_i, y_i, z_i) represent the instantaneous particle positions. The complex initial conditions $c_{0,j}$ can be specified externally if the initial electric field is known. For example, a simple initial gaussian spectrum pulse with no spectral phase can be initialized.

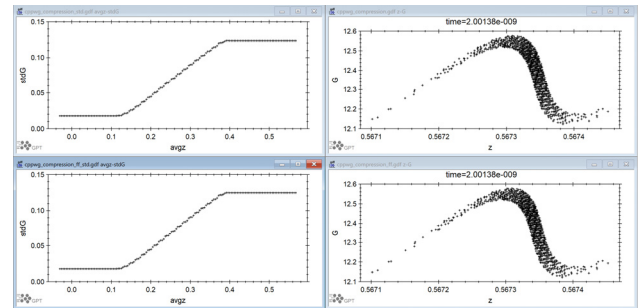


Figure 2: Comparison between GPT results from cppwg01mf.c and code benchmarked with experimental results. Left) Energy spread vs. z . Right) Longitudinal phase space.

Frozen-field approximation

By neglecting the back action of the particles on the fields, we can study the evolution of the beam distribution

in the so-called frozen field approximation. We use a simple THz amplification case for this comparison similar to what presented in [9], but without any undulator tapering.

The results of this comparison are excellent as shown in Fig. 2 where we simulate the first of the UCLA experiments and show the phase space of the beam and the evolution of the energy spread along the undulator. The parameters for this simulations are given in the first column in Table 1.

Table 1: Parameters Used in the Simulation

Parameter	PEGASUS	THz FEL
Beam energy	6.3 MeV	8.8 MeV
Bunch charge	0-8 pC	200 pC
Beam energy spread	0.5 %	0.5 %
RMS Bunch length	200 fs	2 ps
THz central frequency	0.84 THz	0.8 THz
Seed energy	1 uJ	1 uJ
Undulator period	3 cm	3.6 cm
Undulator magnetic field	0.45 T	0.6 T
Waveguide spacing	2.06 mm	2.4 mm
Waveguide radius	2.0 mm	2.0 mm

Self-Consistent Solution

We then move on to simulate the behavior of the system self-consistently (*i.e.* allowing for feedback of the beam on the radiation). The case we consider has similar parameters as described in [9], with an injected peak electron beam current of 20 Amp and a long (60 cm) untapered undulator. We compare in Fig.3 the results of the 1D and 3D simulations. In the 1D wafFEL simulation, one of the main issues is the estimate of the overlap integral between the electron beam distribution and the mode profile which enters in the coupling factor. This is the main reason for the difference in the output energy.

The output options have been maintained similar to the original GPT module and we can look at the field profile as a function of time (oversampled in a time-window consistent with N_{freq}), or in the frequency domain at the evolution of amplitude and phase of each mode. The code runs fast on a high-end quad-core laptop processor taking 5 mins to push 10000 particles for the undulator length with $N_{freq} = 51$ frequency modes. Computation time is expected to scale linearly with number of particles and number of modes.

FUTURE OUTLOOK

There are two main outcomes of the work presented in this paper. First we will continue working on modal decomposition with GPT as this tool offers a unique opportunity to study in detail cases where standard FEL codes can only reach using approximations. For example in this

case we can use real undulator field maps and no period-averaging approximation is needed to follow the beam dynamics. For simulation starting with unbunched beam and very low signal, it will be important to implement a quiet-start algorithm. In wafFEL this was done using a charge-weight. This is easily extendable to GPT, but further tests and benchmarks will be required to assess how to implement it in 3D. Longitudinal space charge (not at the wavelength scale, but at the bunch length scale) and beam rearranging between the slices is also naturally taken into account in this model. The use of supercomputers can enable for a large number of modes to be simulated.

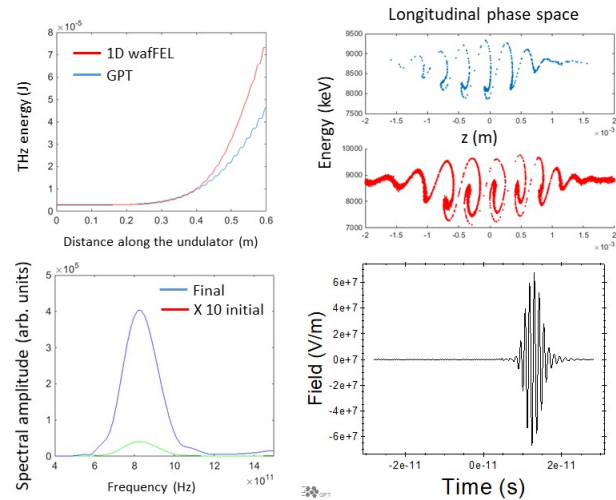


Figure 3: Top left) Comparison of THz energy vs. undulator distance between wafFEL and GPT for parameter set given in second column of Table 1. Top right) Output longitudinal phase spaces. Bottom left) Initial and final spectral amplitudes in GPT. Bottom right) Final THz electric field pulse profile vs. time in GPT.

At this regard one interesting possibility that we will be pursuing is to take advantage of source-dependent expansion (SDE) initially proposed by Sprangle in the '80s [14] to limit the number of modes required to describe the radiation. Especially in cases where a strong seed is used (such as in TESSA amplifiers [15]), the mode will be described for the entire interaction with a gaussian profile with changing waist and radius of curvature. By following how the radiation waist and curvature evolve, it is possible to limit the numbers of modes required to be solved.

The other direction is to directly exploit the outcome of the paper to study high efficiency THz FELs. Starting with higher energy electron beams or higher brightness electron beams and strongly tapering the undulator (or the waveguides) can enable large efficiency. Further studies are certainly required, but the goal of achieving 10 uJ at 10 THz within 10 % bandwidth seems within the reach of a super-radiant tapering-enhanced THz FEL.

REFERENCES

- [1] R. Bonifacio, C. Pellegrini, L. M. Narducci. "Collective instabilities and high-gain regime free electron laser." *AIP Conference Proceedings*, vol. 118, 236 (1984). doi:10.1063/1.34640
- [2] C. P. Hauri *et al.* "Strong-field single-cycle THz pulses generated in an organic crystal." *Applied Physics Letters*, vol. 99 (2011): 161116. doi:10.1063/1.3655331
- [3] G. P. Gallerano, and S. Biedron. "Overview of terahertz radiation sources." in *Proceedings of the 2004 FEL Conference*, vol. 1, 2004, paper FRBIS02.
- [4] G. Ramian, "The new UCSB free-electron lasers." *Nucl. Inst. Meth. Phys. Res. Sec. A*, vol. 318, 1-3 (1992), 225-229. doi:10.1016/0168-9002(92)91056-F
- [5] A. Doria, G. P. Gallerano, A. Renieri, "Kinematic and dynamic properties of a waveguide FEL", *Opt. Commun.*, vol. 80, 5-6 (1991), pp. 417-424. doi:10.1016/0030-4018(91)90434-F
- [6] F. Ciocci, G. Dattoli, L. Giannessi and A. Torre, "Inhomogeneous broadening effects in a waveguide free-electron laser." *IEEE journal of quantum electronics*, vol. 30, no. 1 (1994): 180-184. doi: 10.1109/3.272078
- [7] E. Curry *et al.* "THz-driven zero-slippage IFEL scheme for phase space manipulation." *New Journal of Physics*, vol. 18, no. 11 (2016): 113045. doi:10.1088/1367-2630/18/11/113045
- [8] E. Curry, *et al.* "Meter-scale terahertz-driven acceleration of a relativistic beam." *Physical Review Letters*, vol. 120, (2018), 094801. doi:10.1103/PhysRevLett.120.094801
- [9] E. C. Snively *et al.* "Broadband THz amplification and superradiant spontaneous emission in a guided FEL." *Optics Express*, vol. 27.15, (2019), pp 20221-20230. doi:10.1364/OE.27.020221
- [10] Pulsar Physics, General Particle Tracer, <http://www.pulsar.nl>
- [11] M. J. de Loos, C. A. J. van der Geer, S. B. van der Geer, "3D Multi-Frequency FEL Simulations with the General Particle Tracer Code", in *Proc. EPAC 2002*, Paris, France, paper TUPRI079, pp. 849-851.
- [12] S. B. van der Geer, M. J. de Loos, "The General Particle Tracer Code", Phd Thesis TU Eindhoven 2002, ISBN 90-386-1739-9
- [13] T. Nakahara, N. Kurauchi. "Guided beam waves between parallel concave reflectors." *IEEE Transactions on Microwave Theory and Techniques*, vol. 15, no. 2 (1967): 66-71. doi:10.1109/TMTT.1967.1126379
- [14] P. Sprangle, A. Ting, C. M. Tang. "Analysis of radiation focusing and steering in the free-electron laser by use of a source-dependent expansion technique." *Physical Review A*, vol. 36.6 (1987): pp. 2773-2781. doi:10.1103/physreva.36.2773
- [15] J. Duris, A. Murokh, P. Musumeci, "Tapering enhanced stimulated superradiant amplification," *New Journal of Physics*, vol. 17.6 (2015), pp. 063036. doi:10.1088/1367-2630/17/6/063036

OPTIMIZATION OF THE TRANSVERSE GRADIENT UNDULATOR (TGU) FOR APPLICATION IN A STORAGE RING BASED XFEL*

Y. S. Li[†], University of Chicago, IL, USA

R. R. Lindberg and K.-J. Kim, Argonne National Laboratory, IL, USA

Abstract

The stringent energy spread requirement of the XFEL poses a challenge for its application in storage rings. One way to overcome this is by using a transverse gradient undulator (TGU) [1]. The TGU gain formula was discussed previously [2,3]. In this paper, we begin by reviewing the analytical 3D gain formula derived from the gain convolution formula. Following that, we apply numerical optimization to investigate the optimal beam and field parameters for maximal TGU gain. We found that a small emittance ratio (i.e. “flat beam” configuration) has a strong positive impact on TGU gain, as well as other patterns in the optimal parameters.

THEORY

An in-depth exploration of TGU physics can be found in [2]. Here, we provide an essential summary. A TGU scheme has two key ingredients. First, we introduce dispersion upstream of the TGU that correlates electron position and energy, i.e.

$$y = y_0 + D\eta, \quad (1)$$

where D is the dispersion strength and y_0, η are the initial vertical electron position and relative energy deviation respectively. (We assume here that the TGU acts in the y -direction.) Secondly, the TGU introduces a linear dependence in K on transverse displacement, i.e. $K(y) \approx (1 + \alpha y)K_0$, where K_0 is the on-resonance undulator parameter and α is the TGU magnetic gradient. Then, we can cancel out the energy spread by requiring

$$\alpha D = (2 + K_0^2)/K_0^2 \quad (2)$$

The TGU is only effective if $D\sigma_\eta \gg \sigma_y$, i.e. if beam size is primarily dominated by dispersion.

The 3D gain formula in this scenario is derived to be

$$G = \frac{G_0}{4\pi} \int_{-1/2}^{1/2} dz ds \frac{i(z-s)}{\sqrt{\mathfrak{D}_x \mathfrak{D}_y}} \exp \left[-2ix(z-s) - \frac{2\tilde{\sigma}_\eta^2(z-s)^2}{1 + \Gamma^2} - \left(\frac{\Gamma}{1 + \Gamma^2} \frac{\tilde{\sigma}_\eta}{\tilde{\beta}_y} \right)^2 \frac{(z^2 - s^2)^2}{2} \frac{\mathfrak{D}_y}{\mathfrak{D}_x} \right], \quad (3)$$

where

$$\Gamma = \frac{D\sigma_\eta}{\sigma_y}, \quad x = \pi N_u \Delta\nu, \quad (4)$$

$$\tilde{\sigma}_\eta = 2\pi N_u \sigma_\eta, \quad \tilde{\beta}_y = \beta_y / L_u, \quad (5)$$

$$\frac{G_0}{4\pi} = 4\pi\gamma_r \frac{I}{I_A} \frac{K_0^2 [JJ]^2}{(1 + K_0^2/2)^2} N_u^3 \lambda_1^2, \quad (6)$$

and $\sigma_{x,y}$ are the RMS electron beam sizes, L_u, N_u are the undulator length and number of undulator periods respectively, $\Delta\nu \equiv (1 - \lambda/\lambda_1)$ is the detuning factor based on resonant FEL wavelength λ_1 , σ_η is the relative energy spread, $\beta_{x,y}$ is the respective betatron function, γ_r is the resonant Lorentz factor, I is the beam current, $I_A \approx 17$ kA is the Alfvén current, $[JJ] \equiv J_0[K_0^2/(4 + 2K_0^2)] - J_1[K_0^2/(4 + 2K_0^2)]$ is the Bessel factor, and

$$\mathfrak{D}_{x,y} = \Sigma_{x,y}^2 + sz L_u^2 \Sigma_{\phi x,y}^2 - iL_u(z-s) \left[\frac{1}{4k} + k \Sigma_{\phi x,y}^2 \Sigma_{x,y}^2 \right], \quad (7)$$

$$\mathfrak{D}_y = \Sigma_y^2 + sz L_u^2 \Sigma_{\phi y}^2 - iL_u(z-s) \left[\frac{1}{4k} + k \Sigma_{\phi y}^2 \Sigma_y^2 \right], \quad (8)$$

$$\Sigma_y^2 = \sigma_y^2 + \sigma_{ry}^2 + D^2 \sigma_\eta^2, \quad (9)$$

$$\Sigma_x^2 = \sigma_x^2 + \sigma_{rx}^2, \quad (10)$$

$$\Sigma_{\phi x,y}^2 = \sigma_{px,y}^2 + \sigma_{\phi x,y}^2. \quad (11)$$

Here, $\sigma_{px,py}$ are the RMS electron beam divergences, $\sigma_{rx,ry}$ are the RMS radiation beam sizes, and $\sigma_{\phi x,\phi y}$ are the RMS radiation beam divergences.

In the context of a storage ring, there is a further constraint on the transverse emittances, namely $\epsilon_x + \epsilon_y = \epsilon_{x,0}$, with $\epsilon_{x,0}$ being the natural electron beam emittance [4]. We define the coupling constant k_c such that

$$\epsilon_x = \frac{\epsilon_{x,0}}{1 + k_c}, \quad \epsilon_y = \frac{k_c \epsilon_{x,0}}{1 + k_c}. \quad (12)$$

Modern storage rings are capable of operating in both round ($k_c = 1$) and flat ($k_c \ll 1$) beam configurations. Therefore, the coupling constant will be an important parameter in our investigation.

NUMERICAL OPTIMIZATION

We wish to optimize gain, as given by Eq. 3, with respect to electron and radiation beam parameters. In each optimization run, we fixed $\{\epsilon_{x,0}, \sigma_\eta\}$ and scan over k_c ranging from 0.001 to 1. At each value of k_c , the optimal parameters

* This work is supported by U.S. Dept. of Energy, Office of Science, Office of Basic Energy Sciences, under Contract No. DE-AC02-06CH11357, and U.S. National Science Foundation under Award No. PHY-1549132, the Center for Bright Beams.

[†] ysli@uchicago.edu

Table 1: Hypothetical Storage Ring Parameters (derived from PETRA-IV) [5]

Name	Symbol	Value
Electron beam		
Rel. gamma	γ_r	1.166×10^4
Beam current	I	40 A
Output radiation		
Res. energy	$\hbar\omega_1$	14.4 keV
Rad. emittance	ϵ_r	6.85 pm
Undulator		
Undulator period	λ_u	1.5 cm
Number of periods	N_u	2000
Undulator parameter	K_0	1.06

were found via the hill climber algorithm [6]. There are six “core” parameters which form our search space: the beta functions β_x, β_y which determine electron beam size, the Rayleigh ranges Z_{Rx}, Z_{Ry} which determine radiation beam size, the dimensionless TGU factor Γ characterizing the strength of the TGU, and finally the dimensionless detuning $x = \pi N_u \Delta\nu$.

From the six core parameters we also investigate several “derived” parameters: radiation beam aspect ratio $\alpha_{\text{rad}} \equiv |E_y|^2 / |E_x|^2$, dispersion D , and TGU magnetic gradient α , all of which may be practical values of interest. All other machine parameters are typical of a 4th generation light sources such as PETRA-IV or APS-U. Refer to Table 1.

Simulation Considerations

We explored a number of different optimization algorithms, including gradient descent, simulated annealing and simple hill climber. Ultimately, we chose the hill climber algorithm due to its simplicity and the (empirically observed) convex nature of the objective function. Provided reasonable starting parameters, a simple hill climber algorithm converged relatively quickly and reliably.

We also imposed the constraint $Z_{Rx} = \beta_x$ to simplify the search space. While they are in principle independent parameters, we found in practice that their optimal values are often equal. This result is unsurprising since we expect the largest gain when the radiation mode shape overlaps that of the electron beam [3].

RESULTS

Varying Natural Emittance

Figure 1 (top) shows the optimal gain with respect to k_c for fixed $\sigma_\eta = 0.15\%$ and different values of $\epsilon_{x,0}$. There are two key observations. First, with smaller k_c (i.e. flatter electron beam), gain increases dramatically, by up to an order of magnitude. Secondly, gain also increases with decreasing $\epsilon_{x,0}$ (perhaps unsurprisingly). In this case, the highest gain was obtained when $\epsilon_{x,0} = \epsilon_r = 6.85$ pm. Figure 2 shows the optimal beta functions. With smaller k_c , the optimal

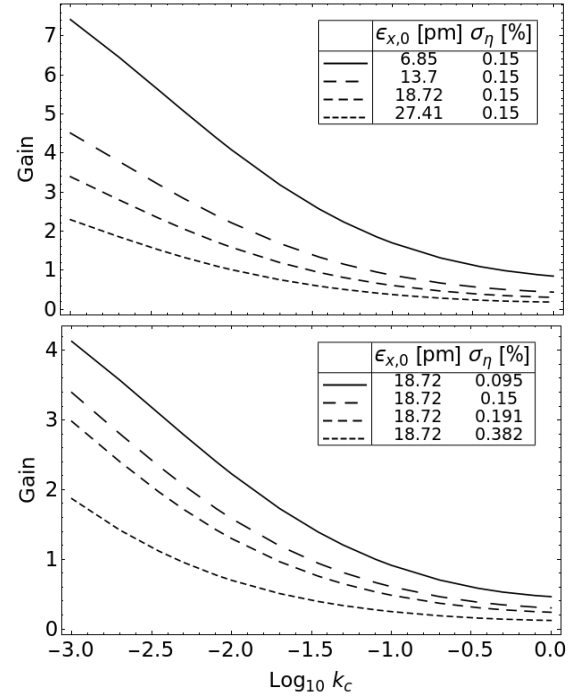


Figure 1: Optimal gain vs k_c for varying $\epsilon_{x,0}$ (top) and σ_η (bottom).

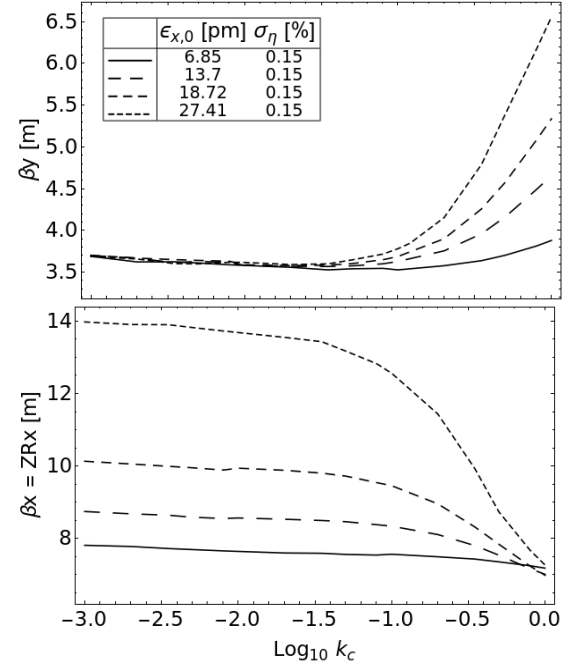


Figure 2: Optimal β_y (top) and β_x (bottom) vs k_c for varying $\epsilon_{x,0}$.

β_y decreases and so does its sensitivity to $\epsilon_{x,0}$. In fact, for $\log_{10} k_c \lesssim -1.5$, the optimal β_y is apparently independent of $\epsilon_{x,0}$. The opposite behavior is observed in β_x . We attribute this behavior to the constraint $\epsilon_x + \epsilon_y = \epsilon_{x,0}$, whence decreasing k_c decreases ϵ_y and increases ϵ_x simultaneously. Thus changing $\epsilon_{x,0}$ affects a particular direction less if its

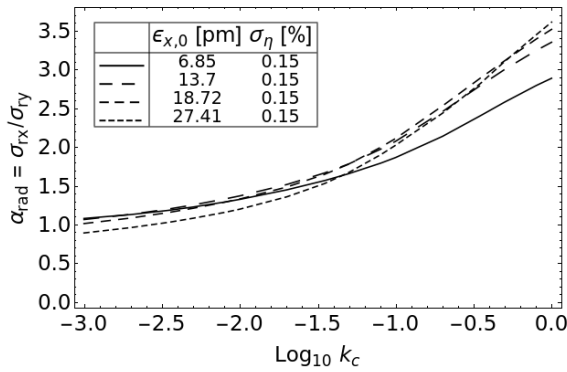


Figure 3: Optimal beam aspect ratio α_{rad} vs k_c for varying $\epsilon_{x,0}$.

“share” of the natural emittance is smaller. In addition, if we decrease $\epsilon_{x,0}$ such that it is comparable to ϵ_r , the optimal $\beta_{x,y}$ becomes relatively independent of k_c .

Figure 3 shows the optimal radiation beam aspect ratio. Interestingly, with smaller k_c the optimal aspect ratio tends to 1. In other words, the optimal radiation mode shape is approximately round.

Varying Energy Spread

Figure 1 (bottom) shows the optimal gain for different σ_η . In addition to observations made in the previous subsection, we also see that smaller σ_η leads to higher gain, as expected.

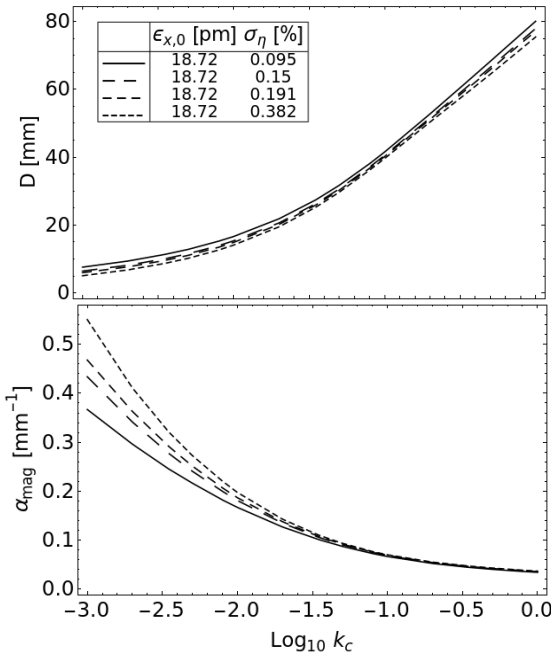


Figure 4: Optimal dispersion (top) and magnetic gradient (bottom) vs k_c for varying σ_η .

Interestingly, most optimal parameters are relatively independent of σ_η . These include the beta functions, beam dispersion D and TGU magnetic gradient α (Figure 4).

CONCLUSION

The results clearly indicate that a flat-beam configuration (i.e. $k_c \ll 1$) greatly enhances gain in a TGU-enabled storage ring. This is easily satisfied in a storage ring, where the vertical emittance contribution primarily comes from magnet misalignments or coupling [4]. Typical values of k_c in modern storage rings can approach $\sim 10^2$ or smaller. From Figure 1, we see that large gain (often greater than 1) can be achieved in this regime, even with generously large $\epsilon_{x,0}$ and σ_η .

There are also several empirical observations to be made regarding optimal beam and machine parameters. First, for small k_c , the optimal β_y becomes independent of $\epsilon_{x,0}$ and σ_η (Figure 2). Second, for small k_c , the output radiation tends towards an aspect ratio of unity (Figure 3). This could prove useful in applications where a round radiation mode is desired. It is unclear at the moment whether this behavior is truly asymptotic, and how it could be explained from an analytical standpoint. Finally, we observed that σ_η does not significantly impact any of the optimal parameters within the range tested. At first glance, this is surprising given that σ_η shows up prominently in the numerators of the latter two terms in the exponent of Equation 3. However, it is also “hidden” in the definitions of Γ and \mathfrak{D}_y , belying its complicated role in the gain equation.

ACKNOWLEDGEMENTS

This work is supported by U.S. Dept. of Energy, Office of Science, Office of Basic Energy Sciences, under Contract No. DE-AC02-06CH11357, and U.S. National Science Foundation under Award No. PHY-1549132, the Center for Bright Beams.

REFERENCES

- [1] T.I. Smith *et al.*, “Reducing the sensitivity of a free-electron laser to electron energy”, *J. Appl. Phys.*, vol. 50, p. 4580, 1979, doi:10.1063/1.326564
- [2] R. R. Lindberg *et al.*, “Transverse gradient undulators for a storage ring X-ray FEL oscillator”, in *Proc. FEL 2013*, New York, USA, paper THOBNO02, p. 740, 2013.
- [3] K.-J. Kim, Z. Huang and R. R. Lindberg, “Synchrotron Radiation and Free-Electron Lasers”, *Cambridge University Press*, April 2017, doi:10.1017/9781316677377
- [4] H. Wiedemann, “Particle Accelerator Physics”, 2015 (Springer), doi:10.1007/978-3-319-18317-6
- [5] C. G. Schroer *et al.*, “PETRA IV: the ultralow-emittance source project at DESY”, *J. Synch. Rad.*, vol. 25, p. 1277–1290, Sep. 2018, doi:10.1107/S1600577518008858
- [6] S. J. Russell and P. Norvig, *Artificial Intelligence: A Modern Approach*, 2003 (Prentice Hall), ISBN 0130803022

AXIAL SYMMETRY IN SPONTANEOUS UNDULATOR RADIATION FOR XFELO TWO-BUNCH EXPERIMENT*

Y. S. Li[†], University of Chicago, IL, USA

R. R. Lindberg and K.-J. Kim, Argonne National Laboratory, IL, USA

Abstract

A well known discrepancy exists between 2D and 3D FEL simulation codes with respect to the radiation field intensity prior to the exponential gain regime [1]. This can be qualitatively explained by the fact that the 3D field representation preserves many more modes than does the axisymmetric field solved for by a 2D code. In this paper, we seek to develop an analytical model that quantifies this difference. We begin by expanding the spontaneous undulator radiation field as a multipole series, whose lowest order mode is axisymmetric. This allows us to calculate the difference in predicted intensity. Next, we confirm these results with numerical calculation and existing FEL codes GINGER and GENESIS. Finally, we discuss the implications of this study with respect to the XFELO two-bunch experiment to be conducted at LCLS-II.

INTRODUCTION

The x-ray FEL oscillator (XFELO) has the potential to be a new source of bright x-rays with unprecedented spectral purity [2–4]. Over the last decade, there have been separate experiments demonstrating the necessary technologies to meet the stringent operational demands of the XFELO: diamond Bragg crystal reflectors with high reflectivity [5], low thermal conductivity [6], and sufficient resilience to high-intensity x-rays [7]; availability of suitable compound refractive mirrors [8]; feedback system for the stabilization of x-ray components [9]. The next logical step is a holistic experiment integrating these technologies together into a proof-of-concept for the XFELO.

To this end, a collaboration between Argonne and SLAC has recently proposed a cavity-based XFELO (CBXFELO) experiment to be performed at the hard x-ray line at LCLS-II [10, 11]. The goal is to test whether we can sufficiently stabilize a large-scale x-ray cavity so as to observe FEL gain. Specifically, we plan to send two electron bunches separated longitudinally by about 2 ns into an undulator, such that the first bunch generates spontaneous undulator radiation (SUR) that is then returned by the x-ray cavity to be amplified by the second bunch. Doing this requires coordinating a number of engineering and physics efforts.

This paper is focused on one aspect of the physics – the symmetry of SUR and its impact on subsequent gain. This is important to our numerical modelling process, specifically

in comparing 2D vs 3D FEL codes. To clarify, 2D codes, such as GINGER [12], assumes cylindrical symmetry in the electric field, such that there is only one transverse dimension. 3D codes, such as GENESIS [13], preserve the full two dimensional transverse space, but at the cost of significantly larger computational complexity. Previous literature [14] have shown that 2D and 3D codes agree well in the exponential gain and nonlinear saturation regime, for both high-gain FELs and low-gain oscillators. This is because axisymmetric modes typically experience the largest FEL gain, so that they eventually overwhelm all other transverse modes.

On the other hand, this situation does not apply early in the gain process, where the two-bunch CBXFELO experiment is expected to operate. In this case, we expect significantly lower field intensity predicted from a 2D code vs the 3D version. Understanding and quantifying this difference is an important step in the numerical modeling process, which in the bigger picture, will allow us to better predict and optimize the number of photons measurable in the experimental setup.

THEORY

We begin by investigating the degree to which SUR can be described by an axisymmetric mode most suitable for amplification. Consider the SUR from a collection of electrons: any single electron j with 6D coordinates $(t_j, \eta_j, \mathbf{x}_j, \mathbf{x}'_j)$ contributes the field [14]

$$\mathcal{E}_{\nu,j}(\vec{\phi}) = e^{i\omega t_j} e^{-ik\vec{\phi}\cdot\vec{\mathbf{x}}_j} \int_0^{L_u} dz e^{i(\Delta\nu-2\eta_j)k_u z} \times e^{\frac{1}{2}ik(\vec{\phi}-\vec{\mathbf{x}}'_j)^2(z-L_u/2)}, \quad (1)$$

where for simplicity we neglect constant prefactors in this discussion. The field in (1) is in frequency-angular representation, with $\nu \equiv \omega/\omega_1$ being the scaled frequency relative to the resonant FEL frequency $\omega_1 = 2\pi c/\lambda_1$, and $\vec{\phi}$ being the 2D angular coordinate. Furthermore, let $\Delta\nu \equiv \nu - 1$ be the detuning and L_u be the undulator length.

Next, we write in polar coordinates $\vec{\phi} \equiv (\phi, \psi)$, where ϕ, ψ are the magnitude and phase of the angle vector respectively. Using the Jacobi-Anger identity, we perform a multipole expansion to obtain

$$\mathcal{E}_{\nu,j}(\phi, \psi) = e^{i\omega t_j} \sum_{n=-\infty}^{\infty} \int_{-L_u/2}^{L_u/2} dz i^n e^{in(\psi-\theta(z))} \times J_n(k\phi|\vec{\mathbf{x}}_j + z\vec{\mathbf{x}}'_j|) e^{ik(\phi^2+\vec{\mathbf{x}}'^2_j)z/2} \times e^{ik_u(\Delta\nu-2\eta_j)(z-L_u/2)}. \quad (2)$$

* This work is supported by U.S. Dept. of Energy, Office of Science, Office of Basic Energy Sciences, under Contract No. DE-AC02-06CH11357, and U.S. National Science Foundation under Award No. PHY-1549132, the Center for Bright Beams.

[†] ysli@uchicago.edu

The $n = 0$ term in this expansion yields the axisymmetric component of the SUR. We denote that by

$$\mathcal{E}^S(\phi) \equiv e^{i\omega t_j} \int_{-L_u/2}^{L_u/2} dz J_0(k\phi|\vec{x}_j + z\vec{x}'_j|) \times e^{ik(\phi^2 + \vec{x}'_j{}^2)z/2} e^{ik_u(\Delta\nu - 2\eta_j)(z + L_u/2)}. \quad (3)$$

Vanishing angular divergence

In the case of an electron beam with vanishing (or negligible) angular divergence, i.e., $\vec{x}'_j = 0$ for all electrons, we are able to simplify Eq. (3) into a more tractable form. Assume for simplicity that $\Delta\nu = \eta = 0$, and that the beam is round with a Gaussian spatial profile:

$$f(r) = \frac{1}{\sigma_x^2} e^{-r^2/2\sigma_x^2}, \quad (4)$$

where σ_x is the electron beam size. We define [14]

$$\sigma_{r'} = \sqrt{\lambda_1/2L_u}, \quad \sigma_r = \sqrt{2\lambda_1 L_u}/4\pi, \quad (5)$$

to be the natural angular divergence and beam size of the SUR respectively. Notice that $\sigma_{r'}\sigma_r = \lambda_1/4\pi \equiv \epsilon_r$, the emittance of the radiation beam. Now let us rescale the radial angular coordinate accordingly

$$\tilde{\phi} \equiv \frac{\phi}{\sqrt{2}\sigma_{r'}}, \quad (6)$$

such that full radial angular flux (integrated over angular phase ψ) is found to be

$$\begin{aligned} \mathcal{F}(\tilde{\phi}) &= \frac{\sin^2(\pi\tilde{\phi}^2/2)}{(\pi\tilde{\phi}^2/2)^2} \sum_{n=-\infty}^{\infty} I_n\left(\frac{\tilde{\phi}^2}{2\sigma^2}\right) e^{-\tilde{\phi}^2/2\sigma^2} \\ &= \frac{\sin^2(\pi\tilde{\phi}^2/2)}{(\pi\tilde{\phi}^2/2)^2}, \end{aligned} \quad (7)$$

where $\sigma \equiv \sigma_r/\sigma_x$, i.e., the ratio of natural radiation beam size to electron beam size. The symmetric radial angular flux, on the other hand, is

$$\mathcal{F}^S(\tilde{\phi}) = \frac{\sin^2(\pi\tilde{\phi}^2/2)}{(\pi\tilde{\phi}^2/2)^2} I_0\left(\frac{\tilde{\phi}^2}{2\sigma^2}\right) e^{-\tilde{\phi}^2/2\sigma^2}. \quad (8)$$

Figure 1 shows the plot of \mathcal{F} and \mathcal{F}^S with different σ . With decreasing σ , e.g. increasing electron beam size at fixed radiation beam size, the symmetric flux becomes narrower and represents a smaller portion of the full SUR angular spectrum.

NUMERICAL RESULTS

For a general electron beam, Equation 3 is difficult to solve analytically. We resort to numerical integration combined with random sampling of the desired electron distribution. Figure 2 shows the angular spectrum for a beam with parameters similar to the CBXFEL experiment. Here, $\sigma_x = 5.8\sigma_r$ and $\sigma_{x'} = 0.989\sigma_{r'}$. Compared to the case of vanishing

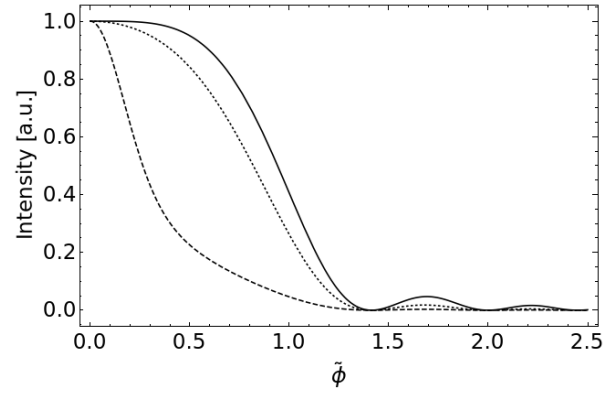


Figure 1: Angular flux for all modes (solid line), and symmetric mode only with $\sigma = 0.2$ (dashed) and $\sigma = 1$ (dotted).

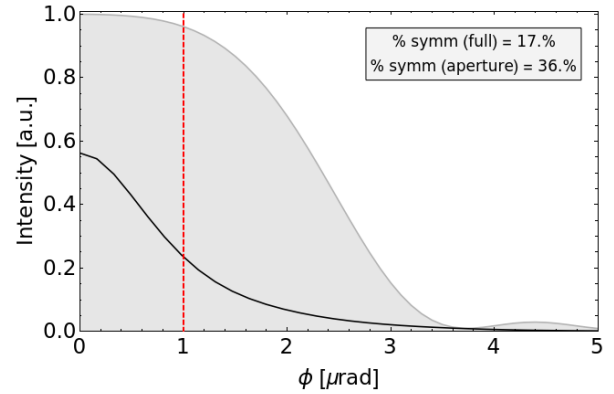


Figure 2: Angular flux with CBXFEL experimental parameters. Depicted are the full flux (gray background), and symmetric flux only (black). The total integrated flux ratio of the symmetric mode to all modes is about 17% over all angles, or 36% if we introduce an aperture of 1 μrad (indicated by dotted red line).

angular divergence, the inclusion of a finite divergence effectively reduces the “height” of the symmetric flux $\mathcal{F}^S(0)$ and results in a longer “tail” at larger angles.

Over repeated runs, the total integrated power of the symmetric mode comprises approximately 17% of that of all modes. If we introduce an aperture of 1 μrad however, we are able to improve this ratio to about 36%. A large ratio is crucial for the second pass in the XFEL experiment, since we expect only the symmetric part of the SUR to experience significant gain.

Comparison with FEL Codes

In the vanishing angular divergence case, we checked Eq. (3) with 2D FEL code GINGER and obtained good agreement. See Figure 3. The result from GINGER was averaged over multiple shots. In addition to Fig. 3, we also obtained good agreement for $\sigma_x \approx 2, 4$ and $8\sigma_r$ (not pictured).

With the inclusion of CBXFEL experiment parameters, it is not straightforward to perform a direct comparison between theory and FEL code. This is because the experimental setup involves electron beam focusing and undulator gaps,

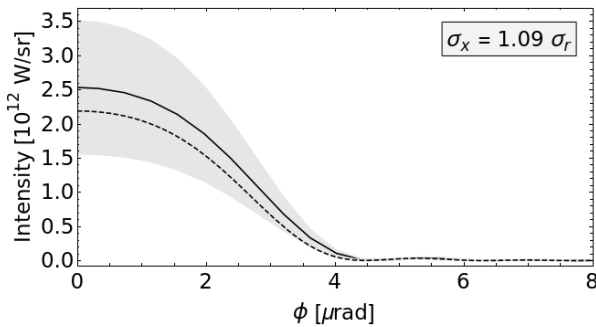


Figure 3: Comparison of angular flux between Eq. (8) (dashed) and 2D FEL code GINGER (solid) shows good agreement. Gray band shows 1σ of the shot-to-shot variation in GINGER. We set $\sigma_x \approx 1.1\sigma_r$.

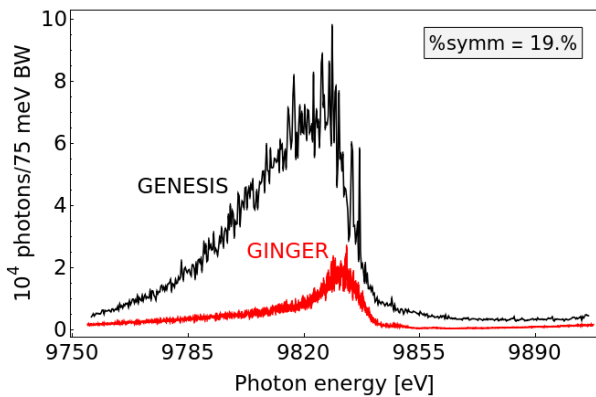


Figure 4: Spectral photon flux predicted by GINGER vs. GENESIS for CBXFEL parameters. Total integrated power ratio between GINGER and GENESIS is about 19%, which agrees well with theory.

which contradicts the assumption of no focusing and single undulator in deriving Eq. (3). However, we are able to directly compare the results of GINGER vs. GENESIS in terms of predicted photon flux. Should the discrepancy between 2D and 3D code be accurately described by Eqs. (2) and (3), the ratio of predicted flux should approach roughly 1/5 as seen in the previous section (Fig. 2). We found this to be indeed the case (Fig. 4).

CONCLUSION

We have introduced analytical expressions representing the symmetric and non-symmetric modes of SUR, confirmed its accuracy with existing FEL codes, as well as demonstrated its ability to account for the difference between 2D and 3D FEL codes (before exponential gain regime). This will allow us to more confidently utilize both codes and provides a better basis for quantitative comparison.

The next step would be to investigate the gain in the radiation pulse after the second bunch. A potential complication comes from the cavity mirrors. Ironically, the pristine reflectivity of the diamond crystals, by its very nature, restricts the number of photons we are able to out-couple from the cavity. Therefore, the gain needs to be significant stronger than the

background SUR from the second pass and other sources of measurement noise. Since gain only occurs in the narrow frequency and angular bandwidth of the mirrors, we believe that a physical aperture could potentially restrict the phase space to allow the gain to dominate. This is supported by Fig. 2. By introducing a $1\mu\text{rad}$ aperture, we were able to improve the symmetric flux ratio to over one third. We hope to confirm this result with further, more detailed numerical calculation, taking into account the precise reflectivity curve of the diamond crystal.

ACKNOWLEDGEMENTS

We would like to thank Gabriel Marcus (SLAC) for his advice on using GENESIS. The FEL code GENESIS is written and maintained by Sven Reiche (PSI), while the code GINGER is created by William M. Fawley (SLAC). Funding for this project is provided in part by U.S. DOE, Office of Science, Office of BES, under Contract No. DE-AC02-06CH11357 and in part by the U.S. National Science Foundation under Award No. PHY-1549132, the Center for Bright Beams.

REFERENCES

- [1] Z. Huang and K.-J. Kim, "Review of X-ray free-electron laser theory," *Phys. Rev. STAB*, vol. 10, p. 034801, 2007. doi:10.1103/PhysRevSTAB.10.034801
- [2] K.-J. Kim, Y. Shvyd'ko, and S. Reiche, "A proposal for an X-ray free-electron laser with an energy-recovery linac," *Phys. Rev. Lett.*, vol. 100, p. 244802, 2008. doi:10.1103/PhysRevLett.100.244802
- [3] R. R. Lindberg, K.-J. Kim, Y. Shvyd'ko, and W. M. Fawley, "Performance of the X-ray free-electron laser with crystal Cavity," *Phys. Rev. STAB*, vol. 14, p. 010701, 2011. doi:10.1103/PhysRevSTAB.14.010701
- [4] W. Qin *et al.*, "Start-to-End Simulations for an X-Ray FEL Oscillator at the LCLS-II and LCLS-II-HE", in *Proc. 38th Int. Free Electron Laser Conf. (FEL'17)*, Santa Fe, NM, USA, Aug. 2017, pp. 247–250. doi:10.18429/JACoW-FEL2017-TUC05
- [5] Y. Shvyd'ko, S. Stoupin, V. Blank, and S. Terentyev, "Near 100% Bragg Reflectivity of X-rays," *Nature Photonics*, vol. 5, p. 539, 2011. doi:10.1038/nphoton.2011.197
- [6] S. Stoupin, and Y. Shvyd'ko, "Ultraprecise studies of the thermal expansion coefficient of diamond using backscattering x-ray diffraction," *Phys. Rev. B*, vol. 83, p.104102, 2011. doi:10.1103/PhysRevB.83.104102
- [7] T. Kolodziej *et al.*, "High Bragg reflectivity of diamond crystals exposed to multi-kW/mm X-ray beams," *Journal of Synchrotron Radiation*, vol. 25, no. 4, p. 1022, 2018. doi:10.1107/S1600577518007695
- [8] T. Kolodziej *et al.*, "Efficiency and coherence preservation studies of Be refractive lenses for XFEL application," *Journal of Synchrotron Radiation*, vol. 25, no. 2, p. 354, 2018. doi:10.1107/S160057751701699X
- [9] S. Stoupin *et al.*, "Nanoradian angular stabilization of x-ray optical components," *Rev. Sci. Instrum.*, vol. 81, p. 055108, 2010. doi:10.1063/1.3428722

- [10] K.-J. Kim *et al.*, “Test of an X-ray cavity using double bunches from the LCLS-II Cu-Linac,” in *Proc. IPAC 2019*, p. 1887, 2019. doi:10.18429/JACoW-IPAC2019-TUPRB096
- [11] G. Marcus *et al.*, “Cavity-Based Free-Electron Laser Research and Development: A Joint Argonne National Laboratory and SLAC National Laboratory Collaboration”, presented at the 39th Int. Free Electron Laser Conf. (FEL’19), Hamburg, Germany, Aug. 2019, paper TUD04.
- [12] GINGER code and documentation made available through private comm. with author W. Fawley (SLAC).
- [13] GENESIS version 2 code and documentation available at genesis.web.psi.ch.
- [14] K.-J. Kim, Z. Huang and R. R. Lindberg, *Synchrotron Lasers and Free-Electron Lasers*, 2017 (Cambridge University Press).

XCOS SCILAB MODEL FOR SIMULATION OF INTENSITY AND GAIN OF PLANAR UNDULATOR RADIATION

H. Jeevakhan, National Institute of Technical Teachers' Training and Research, Bhopal, India
G. Mishra, Physics Department, Devi Ahilya University, Indore, India

Abstract

Scilab Xcos based model has been designed to simulate the intensity and gain of planar undulator radiation. Numerical approach has been used to determine the trajectories of an electron along 'x' and 'z' directions, traversing through a planar undulator. The present paper describes the technical details of the different blocks, parameters and possibility of combined model used for trajectories and intensity. Simulation results are compared with the previous conventional syntax based codes.

INTRODUCTION

Free electron laser (FEL), attosecond pulses can be used in attosecond interferometry to explain the nature of materials [1-2], design of Q-bits [3] and in other cutting age multidisciplinary researches. FEL is coherent light source generated due to passage of relativistic electron beam through a periodic magnetic structure in presence of resonating electromagnetic radiation. Trajectory of electron beam in undulator, Intensity of out coming radiation and the transfer of energy from electron beam to radiation i.e. overall gain in FEL system are the parameters of interest in FEL technology and applications. Simulation software's are used to calculate the intensity and gain of real FEL system before actual experimentation.

Scilab is an open source software with numerous applications in engineering and research[4]. Scilab Xcos based simulation models for analytical solutions of electron trajectory equations have been presented with some limitations by H Jeevakhan *et al.* [5]. An improved analytical Xcos Model has been used to find the trajectory of the electron moving in the Harmonic undulator and variation of magnetic field along the axis of undulator [6]. This paper has also presented a model to find trajectory by second integral of the undulator magnetic field profile given by real measurements.

In the present paper, Scilab Xcos model has been presented based on numerical approach for trajectory of electron along undulator along 'x' and 'z' direction. The intensity of the out coming spontaneous radiation can also be simultaneously calculated by numerical method, by using this same model. The gain can further be simulated by employing Madey's Theorem for a given FEL system. The results are also compared with the previous program results based on Fortran.

PLANAR UNDULATOR FIELD

For present simulation, planar undulator magnetic field is considered and is given by [7-8]:

$$B = [0, a_0 B_0 (\sin k_u z), 0] \quad (1)$$

Where, $k_u = \frac{2\pi}{\lambda_u}$ and where k_u is undulator wave number, λ_u is undulator wave length, B_0 is peak magnetic field.

The equation of motion of relativistic free electron moving in undulator field is given by

$$ma = -\frac{e}{c} [\vec{v} \times \vec{B}] \quad (2)$$

For numerical calculation, the acceleration along 'x' and 'z' direction can be written as

$$m\ddot{x} = \frac{K}{\gamma} \Omega_u v_z \sin(\Omega_u \beta_*) t \quad (3)$$

$$m\ddot{z} = \frac{K}{\gamma} \Omega_u v_x \sin(\Omega_u \beta_*) t \quad (4)$$

The component of β along x' and 'z' direction can be evaluated analytically as,

$$\beta_x = -\frac{K}{\gamma} [\cos(\Omega_u t)] \quad (5)$$

$$\beta_z = \beta_* - \frac{K^2}{4\gamma^2} [\cos(2\Omega_u t)] \quad (6)$$

corresponding initial values read as,

$$\beta_{x=0} = -\frac{K}{\gamma} \quad (7)$$

$$\beta_{z=0} = -\frac{K^2}{4\gamma^2} \quad (8)$$

Where $\beta_* = 1 - \frac{1}{2\gamma^2} \left(1 + \frac{K^2}{2}\right)$, γ is relativistic parameter, $K = \frac{a_0 e B_0}{\Omega_u m_0 c}$ is the undulator parameter, m_0 is rest mass of electron, and $\Omega_u = k_u c$

The Intensity of radiation can be evaluated from Lienard - Wiechart integral [9],

$$\frac{d^2 I}{d\omega d\Omega} = \frac{e^2 \omega^2}{4\pi^2 c} \left| \int_{-\infty}^{\infty} \{\hat{n} \times (\hat{n} \times \hat{\beta})\} \exp \left[i\omega \left(t - \frac{z}{c} \right) \right] dt \right|^2 \quad (9)$$

For Numerical simulation of Intensity along the axis the Eq. (9) can be re written as

$$\frac{d^2 I}{d\omega d\Omega} = \frac{e^2 \omega^2}{4\pi^2 c} \left| \int_0^T \{\widehat{\beta}_x\} \exp \left[i\omega \left(t - \frac{z}{c} \right) \right] dt \right|^2 \quad (10)$$

SIMULATION MODEL AND RESULTS

The model design based on numerical analysis is given in Fig. 1. It is based on execution of equations. Single execution of this model in Xcos window gives the numerical simulation of trajectory along 'x' and 'z' direction for a particular value of ' ω '. Intensity and gain can be calculated by running the model on console for various values of ' ω '. The present model comprises of three sections.

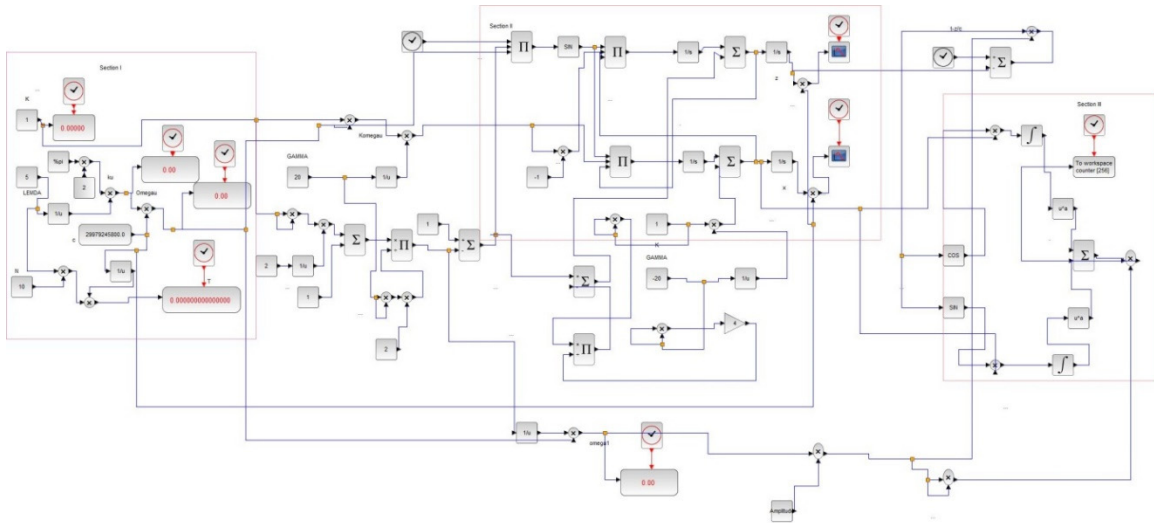


Figure 1: Simulation model for Trajectory and Intensity at particular value of ' ω ' (Numerical Method).

Section I

This section consists of the desired primary parameters, natural constants and secondary parameters used in simulation and tabulated in Table 1. The primary parameters such as undulator wavelength undulator parameter, number of undulator period and relativistic factors are fixed to tune the wave length of out coming radiation.

Table 1: Parameters Used for Simulation

Primary Parameter	Symbol	Values
Undulator parameter	K	1
Number of Undulator periods	N	10
Undulator wavelength	λ	5cm
Relativistic parameter	γ	20

The values of natural constants are taken in CGS units. The magnitude of the secondary parameters (Table 2) depends on the values of the primary parameters and utilized in further simulation process. The Total time for traversing of electron 'T' in undulator will decides the final integration time and steps of integration.

Table 2: Secondary Parameters for Simulation

Secondary Parameters	Symbol	Values
Total time for traverse of electron in undulator	T	1.66782×10^{-9} s
Undulator wave number	k_u	1.26 cm^{-1}
Undulator frequency	Ω_u	$3.76 \times 10^{10} \text{ s}^{-1}$
Radiation frequency	ω	$2.009 \times 10^{13} \text{ rad/s}$

Section II

In section II, Eqs. (3) and (4) is executed and represents numerical model for velocity and trajectory along 'x' and 'z' direction. As in numerical computation, the output of one equation has to be feeded to the input of other for further calculations. Equations (3) and (6) & Eqs. (4) and (5) are interdependent. In conventional programming loop

is used for such calculations. In present case, it is done by giving feed back of the output of one block to the input of other and vice versa, as shown in Fig. 1.

The integration block is used for integration of Eqs. (3) and (4) & Eqs. (7) and (8) are used for initial values of Eqs. (5) and (6) respectively. The results of trajectory calculated along 'x' and 'z' directions is presented in the Fig. 2. This figure also displays the result obtained from the Fortran code based on Runge-kutta method.

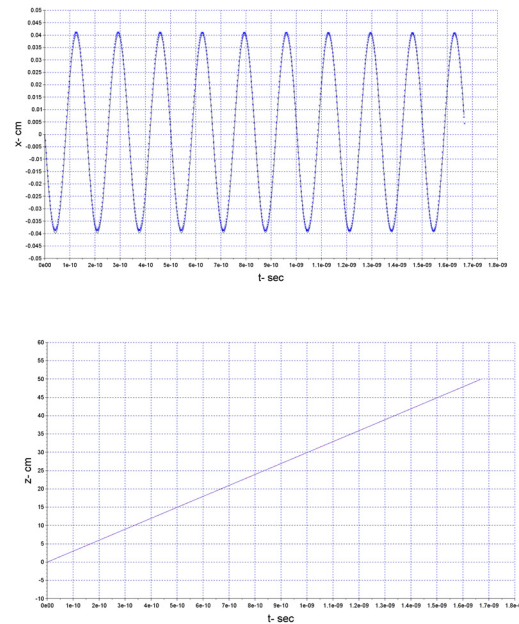


Figure 2: Trajectory of electron along 'x' and 'z' in Planar undulator (Numerical calculation).

Section III

This section, finally executes Eq. (10) and represents the Numerical model for on axis radiation intensity calculation. The value 'z' and the ' β_x ' is required for the calculation of intensity at particular value of " ω ". The solver kind used for simulation is RK45- Rungekutta 4(5).

The complete model has to be simulated for different values of ' ω '. To calculate the intensity for different values of ' ω ' separate code written on console.

The model designed on Xcos window has been called and executed for different values of ' ω ' as per requirement, by using the 'set context' feature available in simulation tab in menu bar of Xcos window. The FEL gain is simulated by applying the derivative command on the intensity data results from present model, as per Madey's Theorem. The intensity and gain curve for present simulation is displayed in Figs. 3 and 4 respectively. The Intensity graph also displays the result obtained from the Fortran code for Eq. (10).

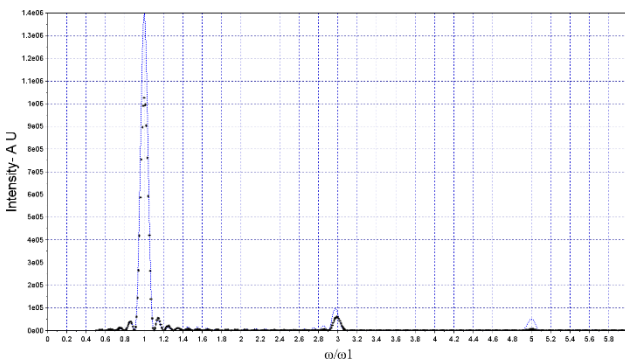


Figure 3: Simulation results for Intensity for various value of ' ω ' given by Model in Fig. 1.

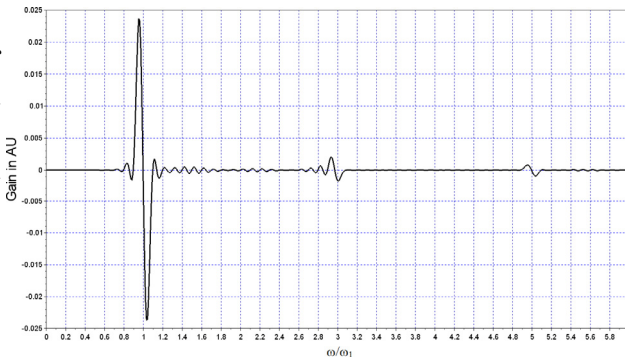


Figure 4: Simulation results for Gain for various value of ' ω '.

CONCLUSION

In the present paper Scilab Xcos based model has been designed and utilised for simulation of electron trajectories, Intensity and gain by applying algorithm of numerical method. In present simulation, Xcos and Console window has been simultaneously used for intensity calculations. The Xcos model does not require a separate plot command for trajectory plot, however intensity and gain is plotted from separate command in console window. The present work can be extended as a numerical model for trajectory, intensity and gain for FEL system having constant magnetic field component. The GUI model for present simulation is also a future scope of work.

REFERENCES

- [1] J.D. Koralek *et al.*, "Generation and characterization of ultrathin free-flowing liquid sheets", *Nat. Commun.*, vol. 9, pp. 1353, 2018. doi:10.1038/s41467-018-03696-w
- [2] S. Usenko *et al.*, "Attosecond interferometry with self-amplified spontaneous emission of a free-electron laser", *Nat. Commun.*, vol. 8, pp. 15626, 2017. doi: 10.1038/ncomms15626
- [3] O. Reinhardt *et al.*, "Free Electron Qubits", Conference: *CLEO: QELS Fundamental Science*. doi:10.1364/CLEO_QELS.2019.FF1F.66
- [4] SCILAB, <https://www.scilab.org/>
- [5] H. Jeevakhan and Sanjeet Kumar, "Simulation of Electron Trajectories in Undulator with SCILAB", InPAC 2018 proceedings, Jan 2018, ID 267.
- [6] H. Jeevakhan, S. Kumar, and G. Mishra, "Analysis of Electron Trajectories in Harmonic Undulator with SCILAB's Model Based Design Codes", in *Proc. FLS'18*, Shanghai, China, Mar. 2018, pp. 93-97. doi:10.18429/JACoW-FLS2018-WEA2WD03
- [7] G. Dattoli *et al.*, *Lectures on FEL Theory and Related Topics*, World Scientific, Singapore, 1993. doi:10.1038/s41467-018-03696-w
- [8] G. Mishra, Mona Gehlot, and Jeevakhan Hussain, "Bi-harmonic free electron laser gain with variably polarizing undulator", *J. Mod. Opt.*, vol. 56, p. 667, 2009. doi:10.1142/1334
- [9] J. D. Jackson, *Classical Electrodynamics*, Wiley, New York, 1975.

ANALYSIS OF UNDULATOR RADIATIONS WITH ASYMMETRIC BEAM AND NON-PERIODIC MAGNETIC FIELD

H. Jeevakhan, National Institute of Technical Teachers' Training and Research, Bhopal, India
G. Mishra, Physics Department, Devi Ahilya University, Indore, India

Abstract

Harmonic Undulator radiations at third harmonics with non periodic constant magnetic field has been analysed. Symmetric and asymmetric electron beam with homogeneous spread has been used to present viable solution for the resonance shift inherited in undulator with constant magnetic field. The out coming radiation, recovers shifts in resonance and regain its intensity with asymmetric electron beam and harmonic field.

INTRODUCTION

Free electron lasers [FEL] generation is a cutting edge technology and has large numbers of research applications [1]. Tunability and brilliance at lasing wave length in FEL are key parameters for number of applications. Lasing wavelength of FEL depends upon the value of undulator parameter, undulator wavelength and relativistic parameter of electron beam used. Recent works in FEL theory has emphasised the effect on non periodic magnetic field i.e. constant magnetic field component along or perpendicular or in both directions of the periodic magnetic field of planar undulator on the out coming undulator radiations. Quality of electron beam is also major concern in analysis of output undulator radiation. Partial compensation on the divergence of undulator radiation has been demonstrated by imposing weak constant magnetic component in the analytical form and all the major sources of homogeneous and inhomogeneous broadening have been accounted for the characteristics of the electrons beam by K. Zhukovsky [2]. The constant non-periodic magnetic constituents are studied to compensate the divergence of the electronic beam [3]. Dattoli *et al* has initially reported the effect on undulator radiation given by planar undulator with constant magnetic field component [4]. The later studies focus on higher harmonics generation by addition of additional harmonic field [5].

Harmonic planar undulator consists additional harmonic field along with sinusoidal planar magnetic field, uses modest electron beam energy and to increase the efficiency of FELs [6-9]. H jeevakhan et al have presented semi analytical results for the effect of perpendicular constant magnetic field on the gain of harmonic undulator at higher harmonics [10]. In the present paper we have analysed harmonic undulator with perpendicular non periodic magnetic field with asymmetric electron beam with energy spread and having shifted mean energy. The Harmonic field compensate the intensity loss and the asymmetric electron beam brings the undulator radiation back to resonance.

UNDULATOR FIELD

Planar undulator sinusoidal magnetic field encompass with a perpendicular constant magnetic field in present analysis and is given by

$$H = [H_0\kappa, b_0H_0(\sin k_p + \Delta \sin k_l)z, 0] \quad (1)$$

Where, $k_p = \frac{2\pi}{\lambda_p}$ and $k_l = \frac{2\pi}{\lambda_l}$ where k_p and k_l are undulator and harmonic undulator wave number respectively, λ_p is undulator wave length and $\lambda_l = l\lambda_p$, l is harmonic integer, H_0 is peak magnetic field, $\Delta = \frac{b_1}{b_0}$, b_0 and b_1 controls the amplitude of main undulator field and additional harmonic field and κ is the magnitude of constant non periodic magnetic field. The harmonic undulator can be designed by introducing shims in regular interval as per the design of harmonic undulator as shown in Fig. 1. The spacing between shims decides it, as 3rd or 5th harmonic undulator similarly as the harmonic number ' l ' decides in Eq. (1).

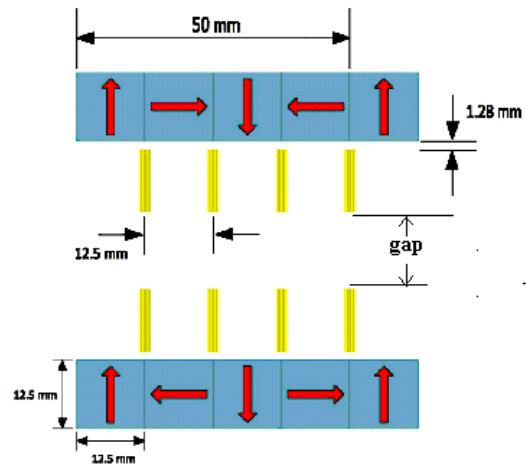


Figure 1: Schematic of one Period of harmonic Undulator($l=3$).

The velocity of electron traversing through undulator is derived by using Lorentz force equation:

$$\frac{dv}{dt} = -\frac{e}{\gamma mc} (\vec{v} \times \vec{H}) \quad (2)$$

This gives

$$\begin{aligned} \beta_x &= -\frac{\kappa}{\gamma} \left[\cos(\Omega_p) + \Delta \frac{\cos(l\Omega_p)}{l} \right] t \\ \beta_y &= -\frac{\kappa}{\gamma} \kappa \Omega_p t \end{aligned} \quad (3)$$

$$\beta_z = \beta^* - \frac{K^2}{2\gamma^2} \left[\left\{ \frac{1}{2} \cos(2\Omega_p) + \frac{1}{2} \left(\frac{\Delta}{l} \right)^2 \cos(2l\Omega_p) + \left(\frac{\Delta}{l} \right) \cos(1 \pm l)\Omega_p \right\} t + (\kappa\Omega_p t)^2 \right] \quad (4)$$

Where m and m_0 are relativistic and rest mass of electron respectively and value of m is governed by the relativistic parameter γ , $K = \frac{b_0 e H_0}{\Omega_p m_0 c}$ is the undulator parameter and $\beta^* = 1 - \frac{1}{2\gamma^2} \left[1 + \frac{K^2 + K_1^2}{2} \right]$ with $K_1 = \frac{\Delta K}{l}$ and $\Omega_p = k_p c$. The solution of Eq. 4 gives the electron trajectory along z direction,

$$\frac{z}{c} = \beta^* t - \frac{K^2}{8\gamma^2 \Omega_p} \sin(2\Omega_p t) - \frac{K_1^2}{8\gamma^2 l \Omega_p} \sin(2l\Omega_p t) - \frac{KK_1}{2\gamma^2 (1 \pm l) \Omega_p} \sin(1 \pm l) \Omega_p t - \frac{K^2 \kappa^2 \Omega_p^2 t^3}{6\gamma^2} \quad (5)$$

The spectral properties of radiation can be evaluated from Lienard - Wiechart integral [11],

$$\frac{d^2 I}{d\omega d\Omega} = \frac{e^2 \omega^2}{4\pi^2 c} \left| \int_{-\infty}^{\infty} \{ \hat{n} \times (\hat{n} \times \hat{\beta}) \} \exp \left[i\omega \left(t - \frac{z}{c} \right) \right] dt \right| \quad (6)$$

when integrated over undulator length, $T = \frac{2N\pi}{\Omega_u}$ and ω is the emission frequency with variables as

$$\xi_1 = -\frac{\omega K^2}{8\gamma^2 \Omega_p}, \quad \xi_2 = -\frac{\omega K_1^2}{8\gamma^2 l \Omega_p} \text{ and } \xi_{3,4} = -\frac{\omega K K_1 \kappa}{2\gamma^2 (1 \pm l) \Omega_p}$$

The brightness expression read as

$$\frac{d^2 I}{d\omega d\Omega} = \frac{e^2 \omega^2}{4\pi^2 c} \left(\frac{K}{\gamma} \right)^2 \left[\left| i \int_0^T dt \left\{ \cos(\Omega_p t) + \frac{\Delta}{l} \cos(l\Omega_p t) \right\} \exp i(\vartheta t + \varphi t^3) J_m(0, \xi_1) J_n(0, \xi_2) J_p(\xi_3) J_q(\xi_4) \right|^2 + \left| \int_0^T dt \{ \kappa \Omega_u t \} \exp i(\vartheta t + \varphi t^3) J_m(0, \xi_1) J_n(0, \xi_2) J_p(\xi_3) J_q(\xi_4) \right|^2 \right] \quad (7)$$

Where,

$$\vartheta = \frac{\omega}{\omega_1} - \{ m - nl - p(1-l) - q(1+l) \} \Omega_p$$

$$\varphi = \frac{\omega K^2 \kappa^2 \Omega_p^2}{6\gamma^2}$$

And Eq. (7) can be further reduced to

$$\frac{d^2 I}{d\omega d\Omega} = \frac{e^2 \omega^2 T^2}{4\pi^2 c} \left\{ |I_x|^2 S(\vartheta, \varphi) + |I_y|^2 S'(\vartheta, \varphi) \right\} \quad (8)$$

With

$$I_x = \frac{K}{2\gamma} \left[\{ J_{m+1}(0, \xi_1) + J_{m-1}(0, \xi_1) \} J_n(0, \xi_2) J_p(\xi_3) J_q(\xi_4) + \frac{\Delta}{h} \{ J_{n+1}(0, \xi_2) + J_{n-1}(0, \xi_2) \} J_m(0, \xi_1) J_p(\xi_3) J_q(\xi_4) \right]$$

$$I_y = \frac{2i\pi K \kappa N}{\gamma}$$

$$S(\vartheta, \varphi) = \left| \int_0^1 e^{(\vartheta' \tau + \varphi' \tau^3)} d\tau \right|^2$$

$$S'(\vartheta, \varphi) = \frac{\partial S(\vartheta, \varphi)}{\partial \vartheta} = \left| \int_0^1 \tau e^{(\vartheta' \tau + \varphi' \tau^3)} d\tau \right|^2$$

$\vartheta' = \vartheta T$, $\varphi' = \varphi T^3$ and $\tau = t/T$ is unit interaction time.

EFFECT OF ENERGY SPREAD

To introduce energy spread in the electron beam, the line shape functions $S(\vartheta, \varphi)$ and $S'(\vartheta, \varphi)$ in Eq. 8 will be modified as

$$S(\vartheta + \delta\vartheta, \varphi) = \int_{-\infty}^{\infty} S(\vartheta, \varphi) f(\mathcal{E}) d\mathcal{E} \quad (9)$$

$$S'(\vartheta + \delta\vartheta, \varphi) = \int_{-\infty}^{\infty} S'(\vartheta, \varphi) f(\mathcal{E}) d\mathcal{E} \quad (10)$$

Where, $f(\mathcal{E})$ represents Gaussian type energy distribution [12]. Eq. (8) can be solved to get modified line shape function for the values as $m = 1, 3, 5, \dots$, with $\mu = 4N\sigma$

For Non symmetric electron beam

$$S(\vartheta + \delta\vartheta, \varphi) = \int_0^1 \exp i \left\{ (\vartheta' + 4\pi m N \varepsilon_1) \tau - \frac{m^2 \pi^2 \mu^2 \tau^2}{2} + \varphi' \tau^3 \right\} d\tau \quad (11)$$

$$S'(\vartheta + \delta\vartheta, \varphi) = \int_0^1 \tau \exp i \left\{ (\vartheta' + 4\pi m N \varepsilon_1) \tau - \frac{m^2 \pi^2 \mu^2 \tau^2}{2} + \varphi' \tau^3 \right\} d\tau \quad (12)$$

ε_1 is mean energy spread, σ is the r.m.s relative energy spread

For symmetric electron beam i.e. $\varepsilon_1 = 0$, then Eq. (11) and (12) can be re written as

$$S(\vartheta + \delta\vartheta, \varphi) = \int_0^1 \exp i \left\{ (\vartheta') \tau - \frac{m^2 \pi^2 \mu^2 \tau^2}{2} + \varphi' \tau^3 \right\} d\tau \quad (13)$$

$$S'(\vartheta + \delta\vartheta, \varphi) = \int_0^1 \tau \exp i \left\{ (\vartheta') \tau - \frac{m^2 \pi^2 \mu^2 \tau^2}{2} + \varphi' \tau^3 \right\} d\tau \quad (14)$$

RESULTS AND DISCUSSION

Equation (8) reads the intensity of spontaneous radiations extracting from harmonic planar undulator with non periodic magnetic field specified by the value of κ . The line shape functions $S(\vartheta, \varphi)$, $S'(\vartheta, \varphi)$ in Eq. (8) from asymmetric electron beam is given by Eqs. (11) and (12) and for symmetric electron beam is given by Eqs. (13) and (14). In earlier reported works [4,5,10] the second term in Eq. (8) consisting I_y has been neglected due to diminishing value of κ . In our analysis we have included the second term in numerical integration and its effect on the line shape function. The parameters used for simulation are listed in Table 1.

Table 1: Simulation Parameters

S. No	Parameters	Value
1.	Undulator parameter	$K=1$
2.	Electron beam relativistic parameter	$\gamma = 100$
3.	Undulator wavelength	$\lambda_u=5$ cm
4.	Addition periodic harmonic field number	$l = 3$
5.	Energy spread parameter	$\mu = 0.01$
6.	Harmonic field parameter	$K_1=0$

Figure 2 illustrates the intensity distribution of radiations by symmetric electron beam at third harmonic in arbitrary units with selection of parameters given in Table 1 and different values of κ . The line shape functions $S(\vartheta, \varphi)$ and $S'(\vartheta, \varphi)$ are read from Eqs. (13) and (14) respectively. There is a shift in resonance and reduction in intensity with effect of non periodic constant field contribution. At $\kappa=0.00012$ there is distortion of Gaussian line shape function. In Fig. 2 the shift in resonance at third harmonic in terms of normalised frequency (ω/ω_1) is 0.0069 for value of $\kappa=0.00008$. The shift in resonance at third harmonic is more as compare to previous reported works [5,10]. For same simulation parameters it was shown that for the same value of $\kappa=0.00008$ the resonance shift is 0.0045 and the intensity reduction is nearly 12 % whereas in present case the intensity reduction is 6.2 %, as the second term in Eq. (8) is included in analysis along with energy spread.

In Fig. 3 we have presented a solution to bring back the radiation at resonance. The electron beam has been given a shift in the mean energy position and an asymmetric electron beam is used for analysis. All the parameters are kept same as used in Fig. 1 and for constant magnetic field $\kappa=0.00008$ the mean energy spread ε_1 has been

varied. As the mean energy parameter changes the peak of intensity of radiation shifted in opposite direction. The radiation regains its original position for $\varepsilon_1 = 0.0017$ with slight intensity degradation.

In Fig. 3, it has been also illustrated that shift in resonance has been compensated with asymmetric electron beam with non zero value of $\varepsilon_1 = 0.0017$. The intensity degradation mainly occurs due to energy spread in the electron beam, can be accommodated by additional harmonic field.

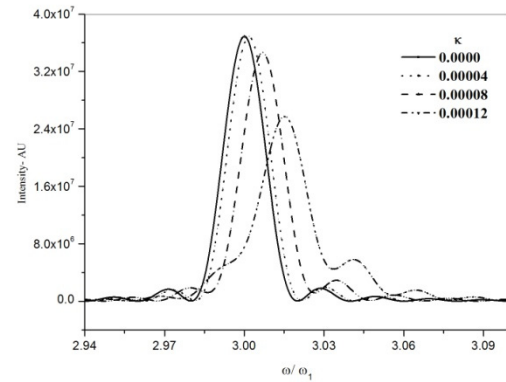


Figure 2: Frequency Spectrum at third harmonic with parameter given in Table 1 varying constant magnetic field parameter κ from 0 to 12×10^{-5} .

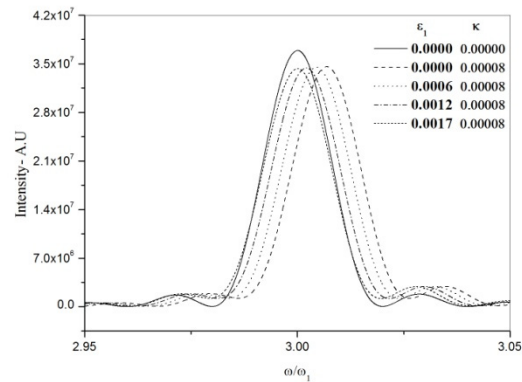


Figure 3: Frequency Spectrum at third harmonics with parameters same given in Table 1, $\kappa = 8 \times 10^{-5}$ and varying ε_1 from 0 to 17×10^{-4} .

The harmonic field enhances intensity and compensate the loss by energy spread parameter μ and due to constant magnetic field. The effect of energy spread with variation of energy spread parameter $\mu=0.01$ on the intensity at third harmonics with constant magnetic field as $\kappa = 0.00008$ and variation harmonic field parameter as $K_1 = 0.0$ to 0.075 is shown in Fig. 3 and keeping all the remaining parameter as given in Table 1.

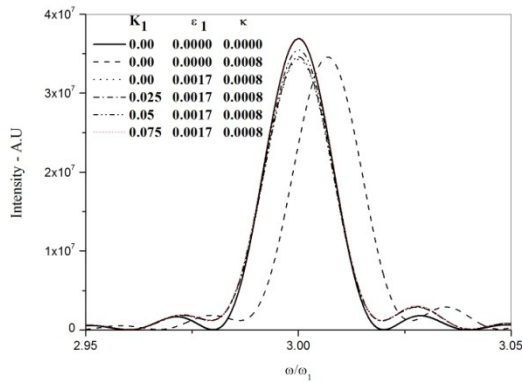


Figure 4: Frequency spectrum at third harmonics with varying harmonic field amplitude as $K_1=0$ and 0.075 , $\kappa=0.00008$, $\varepsilon_1 = 0.0017$ and rest parameters same as in Fig. 1

As a particular case intensity reduction by $\mu=0.01$ and $\kappa = 0.00008$ can be compensated by additional harmonic field $K_1 = 0.075$ and shift in resonance is compensated by the selection of $\varepsilon_1 = 0.0017$ as manifested in Fig. 4.

In conclusion, there is as an intensity enhancement at third harmonics due to additional harmonic field where as shift in resonance remains unaltered in previous reported results. The present analysis gives solution both for intensity enhancement along with resonance shift of radiation simultaneously. The harmonic field can be generated by the addition of shims in the planar undulator structure. The constant magnetic field inherently present due to earth's magnetic field or error in the design of the undulator modifies spectrum of which can be compensated by using asymmetric electron beam.

REFERENCES

- [1] R. Brinkmann, "The European XFEL Project", in *Proc. FEL'06*, Berlin, Germany, Aug.-Sep. 2006, paper MOBAU03, pp. 24-28.
- [2] K. Zhukovsky, "High harmonic generation in the undulators for free electron lasers", *Optics Communications*, vol. 353, pp. 35-41, 2015.
doi: 10.1016/j.optcom.2015.04.079.
- [3] K. Zhukovsky, "Emission and tuning of harmonics in a planar two-frequency undulator with account for broadening", *Laser and Particle Beams*, vol. 34, pp. 447-456, 2016. doi: 10.1017/S0263034616000264
- [4] G. Dattoli *et al.*, "Undulator radiation in a periodic magnetic field with a constant component", *Journal of Applied Physics*, vol. 104, p.124507, 2008.
doi: 10.1063/1.3039094
- [5] H. Jeevakhan, G. Mishra, "Harmonic undulator radiations with constant magnetic field", *Optics Communications*, vol. 335, pp. 126-128, 2015.
doi:10.1016/j.optcom.2014.09.028
- [6] R. W. Warren and N. Piovela, "Compound wiggler to lase on a selected harmonic", *Nuclear Instruments and Methods in Physics A*, vol. 304, p. 696, 1991.
doi: 10.1016/0168-9002(91)90958-S
- [7] G. Mishra, Mona Gehlot, Jeevakhan Hussain, "Bi-harmonic free electron laser gain with variably polarizing undulator", *Journal of Modern Optics*, vol. 56, p. 667, 2009. doi: 10.1080/09500340902745393
- [8] G. Mishra, Mona Gehlot, Jeeva Khan Hussain, "Spectral properties of bi-harmonic undulator radiation", *Nuclear Instruments and Methods in Phys. Res. A*, vol. 603, p. 495, 2009. doi:10.1016/j.nima.2009.02.009
- [9] J. Hussain, V. Gupta, and G. Mishra, "Harmonic Undulator Radiation and FEL Gain with Two-Peak Electron Beam Energy Distribution", in *Proc. FEL'09*, Liverpool, UK, Aug. 2009, paper MOPC17, pp. 75-78.
- [10] H. Jeevakhan, P. K. Purohit, and G. Mishra, "Influence of Horizontal Constant Magnetic Field on Harmonic Undulator Radiations and Gain", in *Proc. FEL'15*, Daejeon, Korea, Aug. 2015, paper MOP004, pp. 34-37.
- [11] J. D. Jackson, *Classical Electrodynamics*, Wiley, New York, 1975.
- [12] G. Dattoli *et al.*, *Lectures on FEL Theory and Related Topics*, World Scientific, Singapore, 1993.

AN ANALYSIS OF OPTIMAL INITIAL DETUNING FOR MAXIMUM ENERGY-EXTRACTION EFFICIENCY*

Qika Jia[†], National Synchrotron Radiation Laboratory,
University of Science and Technology of China, Hefei, Anhui, China

Abstract

For low gain free electron laser (FEL), the phase space evolutions of trapped electrons in the phase bucket are analyzed through calculating their synchrotron oscillation periods, which vary with the initial detuning and initial phase. The optimal initial detuning for the maximum energy-extraction efficiency and the corresponding saturation length are given. The analysis demonstrated that for the low gain case the gain of the strong optical field is about a quarter of that of the weak optical field (small signal gain), and the saturation power larger than that of high gain FEL can be achieved in the resonator of oscillator FEL.

INTRODUCTION

In free-electron laser (FEL), the phase of the electron in the combined radiation optical field and the undulator magnetic field plays a crucial role in the interaction between the optical field and the electron. The evolution of electron distribution in the phase space strongly affects the FEL performance [1, 2].

Usually, the electron phase space evolution has been studied with numerical simulations (e.g. [3-5]), an analytical solution for the phase space evolution of electrons in a self-amplified spontaneous emission (SASE) FEL was given in [6]. In this paper, I present an analysis of electron phase space evolution for low gain FEL based on calculation of the synchrotron oscillation period for different electrons, and study the relations of initial detuning with the energy-extraction efficiency and saturation power.

THE EQUATIONS OF PHASE SPACE EVOLUTION

The energy exchange between the optical field and the electron beam depends on the phase of the electron in the optical field plus the undulator magnetic field: $\phi = (k_s + k_u)z - \omega t$, where k_s , k_u are the corresponding wave numbers of the optical field and the undulator magnetic field. For the resonant electron its phase is fixed, namely it has $\phi' = 0$. Therefore the phase velocity of the electron ϕ' describe the resonance offset of the electron, so it is called the detuning parameter. The detuning parameter can be expressed as the relative energy deviation from the resonant energy

$$\phi' = 2k_u(\gamma - \gamma_r) / \gamma_r \quad (1)$$

where γ is the normalized energy of the electrons, γ_r is the resonant energy. From above phase equation and the energy equation of the electron, the FEL pendulum equation can be obtained (for convenience, denoting $\psi = \phi + \varphi_s + \pi/2$, φ_s is the phase of the radiation field) [2]:

$$\psi'' = -\Omega^2 \sin \psi \quad (2)$$

where $\Omega = \sqrt{2k_u k_s a_u a_s f_c} / \gamma$, $a_s = eE_s / (mc^2 k_s)$ and $a_u = eB_u / (mc^2 k_u)$ are dimensionless vector potential of the *rms* radiation optical field E_s and undulator magnetic field B_u , respectively; f_c is the undulator coupling factor: for circularly polarized helical undulator $f_c = 1$; for linearly polarized planar undulator it is a difference of the two Bessel function $f_c = J_0(\xi) - J_1(\xi)$, $\xi = a_u^2 / 2(1 + a_u^2)$.

The evolution of electron longitudinal dynamics can be described with the motion of electrons in the phase space (ψ, ψ') . There are two classes of electron trajectory in the phase space: the bounded and the unbounded. The separatrix is the boundary separating the two of them. The region enclosed by the separatrix is called the ponderomotive bucket. The maximum value of ψ' along the separatrix gives the half-height of the bucket: $\psi'_m = 2\Omega$. As the optical field intensity increase, the bucket separatrix expands, more electrons can be trapped.

For low gain case, such as amplification of the light at each pass through the undulator in oscillator FEL, the Ω can be regarded as a constant, and the change of φ_s can be neglected, (thus the bucket can be regarded as invariant), then from the pendulum equation, one can get the first integral

$$\psi'^2 / 2 - \Omega^2 \cos \psi = U \quad (3)$$

where U is a constant determined by the initial conditions.

As a trapped electron undergoes one complete orbit in the ponderomotive bucket, it travels down the undulator by a distance called synchrotron oscillation period L_{sy} . To extract the energy from the electrons to the optical field, the electrons initially are injected in the top of the bucket, i.e. the initial energy of electron beam is larger than the resonant energy. The interaction saturates after the electrons have executed approximately half of an oscillation in the ponderomotive well. At this point, the most of electrons are located in the bottom of the ponderomotive bucket.

For the phase near zero $\psi \approx 0$, the pendulum equation (Eq. (2)) can be approximately written as

$$\psi'' \approx -\Omega^2 \psi$$

So the electrons near the $\psi = 0$ make a simple harmonic vibration in the phase space, the corresponding period of the synchrotron oscillation is $L_{sy0} = 2\pi / \Omega$. Therefore Ω is the wave number of the synchrotron oscillation for the zero

* Work supported by the National Nature Science Foundation of China under Grant No. 11675178, and National Key Research and Development Program of China No. 2016YFA0401901.

[†] jiaqk@ustc.edu.cn

phase electrons.

The synchrotron oscillation period for the general trapped electrons can be given from the second integral of Eq. (2)

$$L_{sy} / L_{sy0} = K(\chi^2) \pi / 2 \quad (4)$$

here K is Elliptic function of the first kind, $\chi^2 = (1 + U / \Omega^2) / 2$. The synchrotron oscillation period varies with the initial detuning and initial phase (Fig. 1).

Let $x = \psi$ and $y = \psi' / 2\Omega$ be the detuning parameter normalized with the the half-height of the bucket, Eq. (3) become as

$$y^2 + \sin^2(x/2) = \chi^2 \quad (5)$$

We consider the electrons initially been monoenergetic and uniformly distributed in phase. For the trapped electrons in the phase bucket, they rotate clockwise along the closed

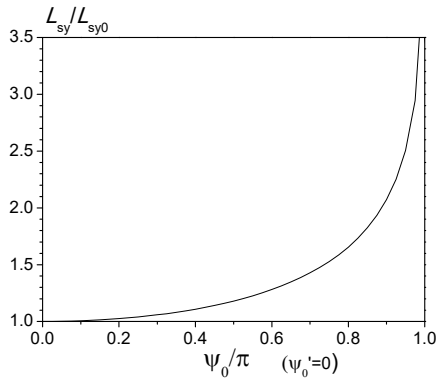


Figure 1: The synchrotron oscillation period with the initial phase (resonance case).

trajectories with different synchrotron oscillation periods determined by initial detuning and initial phase (Eq. (4)).

For the i th electron, we have

$$x_i / y_i = \tan \theta_i \quad (6)$$

where

$$\theta_i = 2\pi z / L_{syi} + \theta_{i0}, \quad \theta_{i0} = \tan^{-1}(x_{i0} / y_{i0})$$

and L_{syi} is the synchrotron oscillation period of the i th electron with the initial phase x_{i0} and the initial detuning y_{i0} .

It has $y_{i0} = y_0$ (monoenergetic), and $|x_{i0}| \leq x_{0m}$, $x_{0m} = 2\arccos(y_0)$ is the maximum initial phase of the trapped electrons (see Fig. 2).

The motion of the trapped electrons in the phase bucket can be obtained by numerically solving Eqs. (4-6).

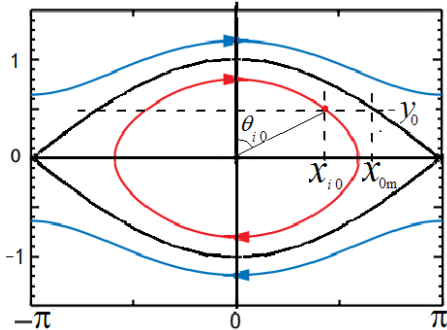


Figure 2: The phase space parameters.

THE OPTIMAL INITIAL DETUNING

In FEL process, the electrons interact with the optical field, the energy transference from the electron beam to the optical field occurred and it make the optical field be amplified. The energy-extraction efficiency can be calculated according to

$$\eta(z, y_0) = \frac{\langle \delta\gamma \rangle}{\gamma} = f_t \frac{\langle \delta\psi' \rangle_{tr}}{2k_u} = \frac{x_{0m}}{\pi} \frac{\Omega}{k_u} (y_0 - \langle y \rangle) \quad (7)$$

where $\delta\gamma$ is the electron energy losses, $\langle \rangle$ represent the average over all electrons, of which the averaged energy variation of the untrapped electrons can approximately be zero, $\langle \rangle_{tr}$ represent the average over all the trapped electrons, f_t is the trapping fraction. The last step in the above equation is obtained for the initial uniformly distributed electron beam $f_t = x_{0m} / \pi$ and with mono initial detuning y_0 .

To get a net gain a positive initial detuning is taken, i.e. the initial energy of the electron beam is larger than the resonant energy.

One can see that the larger initial detuning, the larger energy can be extracted from the trapped electrons, but the smaller will be the trapping fraction. Therefore there is an optimal initial detuning for the largest energy-extraction efficiency.

Using Eqs.4-7, for a given initial detuning we calculate the variation of the energy-extraction efficiency with the distance of electron traveled in the undulator, and get the maximum energy-extraction efficiency and the corresponding interaction length, i.e., the saturation length Z_s . Then for different initial detuning, we give the corresponding variation of the maximum energy-extraction efficiency and the saturation length (Fig. 3, Fig. 4).

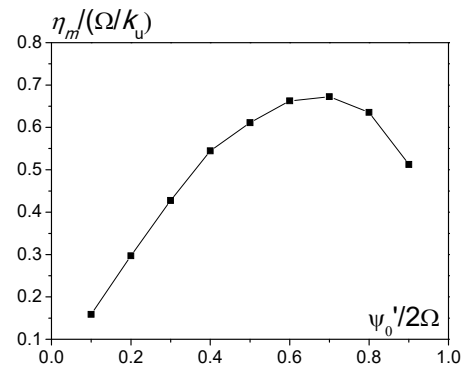


Figure 3: The maximum energy-extraction efficiency with the initial detuning.

From Figure 3 it is shown that there is an optimal initial detuning as analyzed previous, while the saturation length Z_s increases with increasing the initial detuning (Fig. 4). The optimal initial detuning is $\psi_0' / 2\Omega = 0.7$, which gives the largest energy-extraction efficiency $\eta_m = 0.67 * \Omega / k_u$, the corresponding saturation length is $Z_s = 0.7 L_{sy0}$ (Fig. 4), it is larger than the qualitative estimate of $L_{sy0} / 2$.

For free-electron laser oscillators, the optical field

develops from the spontaneous radiation, initially in the phase space the most of electrons are outside of the phase bucket. As the optical field intensity increase with the multi-pass gain, the phase bucket grow larger, the trapped portion of the electron bunch become larger. Then at saturation one can change the value of the electron beam detuning at entrance of the undulator to get the larger energy extraction efficiency. This has been proven already in the simulation and experiment [7], in which the energy extraction efficiency is increased by around 50% through ramping the beam energy postsaturation. The simulation results of [7] show that the energy extraction $\Delta\gamma$ increased from 0.0552 to 0.0882, the increase by 60%, when the initial energy is changed from 0.0406 to 0.0795. The corresponding variation of the initial detuning $\psi_o' / 2\Omega$ is about from 0.24 to 0.44, then from our study here (Fig. 3) it gives the change of the energy extraction efficiency about from 0.35 to 0.57, the increase by 63%, agree with the results of [7]. In addition, according to our analysis (see Fig. 3) the energy extraction efficiency can be further increased by optimizing the initial detuning.

From the relationship of the optical field gain to the energy-extraction of the electron beam, we can calculate the corresponding gain:

$$g / (2k_u \rho L)^3 = -\langle \Delta\gamma \rangle (L_{sy0} / \pi L)^3 \quad (8)$$

where ρ is the FEL parameter, $(2\gamma\rho)^3 = 2\pi r_e n_e a_u^2 f_c^2 / k_u^2$, r_e is the classical electron radius and n_e is the peak electron density; L is the length of the undulator. With $L=Z_s$ and the optimal parameters values previous given, Eq. (8) gives 0.063 for the gain of the strong optical field, it is about a quarter of the gain for the weak optical field: $0.27(2k_u L \rho)^3$ (the small signal gain). The numerical simulations in [2] consistent with this point.

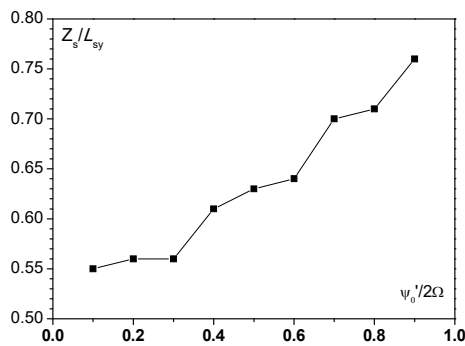


Figure 4: Varying of the saturation length with the initial detuning.

The optical field power has the relationship with the synchrotron oscillation period of the zero-phase electron as follow:

$$P = 36(\pi L_g / L_{sy0})^4 \rho P_e \quad (9)$$

where P_e is the power of the electron beam, $L_g = 1 / (2\sqrt{3}k_u \rho)$ is the optical power gain length.

Corresponding the largest energy- extraction efficiency previous given, the saturation power is

$$P_s \approx (5L_g / L)^4 \rho P_e \quad (10)$$

For low gain FEL, it has $L < 3L_g$ [8], therefore the saturation power in the resonator of oscillator FEL can be larger than that of high gain FEL (for SASE : $P_s \sim \rho P_e$). The “low gain” refers to the gain of each single pass amplification, but the whole gain for multipass amplification is high.

For the optimal initial detuning, the evolution of the bunching factor can be exhibited (Fig. 5), which is given by

$$\tilde{b} = (\psi_{0m} \sum e^{-i\psi_i} / N_t - \sin \psi_{0m}) / \pi \quad (11)$$

where N_t is the number of the trapped electrons. We assume that no bunching occurred for the untrapped electrons. From Fig. 5, we can see that the bunching factor evolve cyclically according to the synchrotron oscillation. It firstly increase and reach the maximum at about $0.3L_{sy0}$, afterward they reduce and down to the minimum at about the saturation ($Z=0.7L_{sy0}$). These are different from that in the high gain case, in which the bunching factor are maximum at saturation [5].

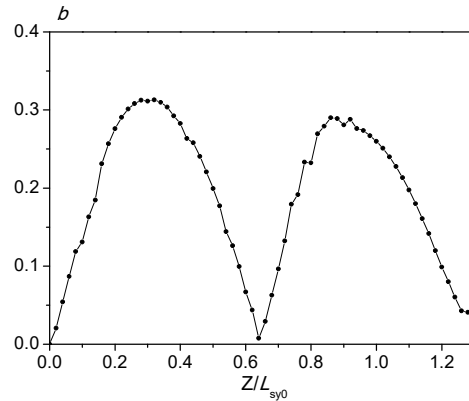


Figure 5: Varying of the bunching factor.

SUMMARY

In this paper, we analyzed the evolution of the electron distribution in the phase space. We give the phase motion of the trapped electrons in the phase bucket for low gain FEL by calculation of their synchrotron oscillation periods which are determined by initial detuning and initial phase. Then using normalized parameters, we give the optimal initial detuning for the largest energy-extraction efficiency to be $\psi_o' / 2\Omega = 0.7$ and the corresponding saturation length to be $L_s = 0.7L_{sy0}$. We exhibited that the bunching factor are minimum at about saturation. Our analysis demonstrated that for the low gain case the gain of the strong optical field is about a quarter of that of the weak optical field (i.e. the small signal gain), and for oscillator FEL the saturation power larger than that of SASE can be achieved in the resonator.

SIMULATING SHOT-NOISE OF ‘REAL’ ELECTRON BUNCHES

P. Traczykowski^{1,2,3}, L.T. Campbell^{1,2,3}, B.W.J. McNeil^{1,2}

¹SUPA, Department of Physics, University of Strathclyde, Glasgow, G4 0NG

²Cockcroft Institute, Warrington, WA4 4AD, UK

³ASTeC, STFC Daresbury Laboratory, Warrington, WA4 4AD, UK

Abstract

An algorithm and numerical code for the up-sampling of a system of particles, from a smaller to a larger number, is described. The method introduces a Poissonian ‘shot-noise’ to the up-sampled distribution, typical of the noise statistics arising in a bunch of particles generated by a particle accelerator. The algorithm is applied on a phase-space distribution of relatively few simulation particles representing an electron beam generated by particle accelerator modelling software, for subsequent injection into an Free Electron Laser (FEL) amplifier which is used here to describe the model. A much larger number of particles is usually required to model the FEL lasing process than is required in the simulation models of the electron beam accelerators that drive it. A numerical code developed from the algorithm was then used to generate electron bunches for injection into the unaveraged 3D FEL simulation code, Puffin. Results show good qualitative and quantitative agreement with analytical theory. The program and user manual are available at [1].

INTRODUCTION

When modelling a Free Electron Laser (FEL) [2], the number of simulation particles used to model the acceleration stages often needs to be increased before simulation of the FEL itself. This is mainly due to the fine longitudinal electron bunching structures at the FEL radiation wavelength that need to be modelled. Such fine detail is unlikely to be required when modelling the accelerator stages before the FEL. The data from the accelerator stages usually have a relatively sparse ‘*macroparticle*’ distribution in phase space, and do not model the Poissonian noise statistics of a real electron distribution. Here, a method is described which breaks up this sparse phase-space distribution of macroparticles into a greater number of ‘*microparticles*’, each representing fewer electrons, to give a more dense phase-space distribution that is suitable for injection into an FEL simulation code such as Puffin [3], used here as the target code to demonstrate the methods used. The method ensures that the microparticle distribution has the correct Poissonian shot-noise statistics of a real electron beam [4]. This is necessary to simulate the spontaneous light generation which arises from the shot-noise and acts as the seed field from which shorter wavelength amplifier FELs start up in the Self Amplified Spontaneous Emission mode of operation [2].

DENSITY DISTRIBUTION FUNCTIONS

The method first uses the macroparticles of the accelerator modelling stage to create a discrete charge histogram of bin

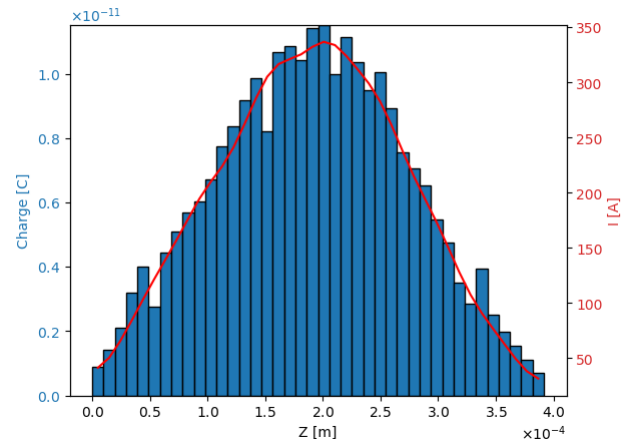


Figure 1: Sample electron density profile along the z -axis. The plot shows the original binned histogram of the macroparticle charge and the interpolated data. The original beam is sampled over 50 bins and then smoothed using the *Python SciPy* `scipy.ndimage.gaussian` filter [5].

width Δz_h along the longitudinal z -axis of beam propagation at a given time (e.g. on entering the FEL). A continuous, optionally smoothed, longitudinal charge distribution function $f_z(z)$, so the beam current $I(z) \approx c f_z(z)$ for the relativistic beams assumed here, is then created by interpolating from this histogram. This charge density function is then used to apply the correct charge $f_z(z)\Delta z_s$, to each longitudinal slice of microparticles of width Δz_s , where usually $\Delta z_h > \Delta z_s$. A transverse, optionally smoothed, charge density function $f_\perp(x, y, z)$ is then created for each longitudinal slice using a similar 2-D histogram-interpolation method. Here the z -dependence of $f_\perp(x, y, z)$ will be in integer units of the slice width Δz_s . The longitudinal density function and the transverse density function can then be interpolated to create a continuous 3-D charge density function, $f(x, y, z) = f_z(z)f_\perp(x, y, z)$. This function is significantly smoother than a discrete charge distribution of the initial, often relatively sparse, macroparticle distribution and allows for a less noisy, more realistic, distribution of microparticles for input into the FEL modelling software. The new set of microparticles is created in each longitudinal slice via a 2-D Cumulative Distribution Function (CDF) approach in the transverse plane – in this case we will call it Joint Distribution Function (JDF) [6]. The effects of Poissonian shot-noise are then added to each microparticle using the method of [4]. The microparticle distributions so generated can then model complex electron beam phase spaces. The longitudinal charge histogram and the corresponding current

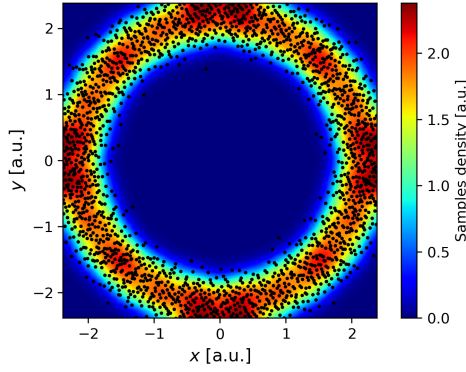


Figure 2: An example of a electron density map of a hollow beam in the transverse (x, y) plane. The initial 150 macroparticles (not shown) were first binned over 50×50 histogram grid. A Gaussian smoothing of factor of 1.5 times this grid spacing was used to obtain the transverse density function, here plotted over 500×500 points in a colour density map. The black dots are 2000 microparticles created using the JDF method.

evaluated from the charge distribution function, is shown in the example of Fig. 1. The electron beam parameters are similar to a beam generated in designs for the CLARA FEL test facility [7] and are: $I_{pk}=395$ A, $\epsilon_n=0.3$ mm mrad, $\tilde{\gamma}=475$, $\sigma_\gamma=0.04$, $\sigma_t=273$ fs and $Q=250$ pC.

MICROPARTICLE GENERATION

The joint probability distribution function approach described above for the transverse plane maintains all of the transverse electron beam structure which can occur across a beam. Projection of charge onto the x and y axes, so that $f_\perp(x, y, z) = f(x, z) \times f(y, z)$, would remove more complex transverse beam structures that may occur in real electron beams. An example of a more complex transverse structure that requires the use of a JDF is a hollow electron beam in the transverse plane. Fig. 2 demonstrates the use of the JDF in the transverse cross-section of such a beam, maintaining the hollow beam structure.

MOMENTUM DISTRIBUTION

Following the generation of the microparticles, the momentum of the macroparticles is mapped onto new microparticle set. The Python *SciPy* library [5] allows this via its *griddata* module. *griddata* interpolates the values of the macroparticle momenta onto the new microparticles using either nearest neighbour or a linear interpolation. This method of using JDF for creating new microparticle positions, and *griddata* for momentum, has proven to be efficient and sufficiently accurate.

NOISE APPLICATION

Shot-noise is applied to the microparticles only along the longitudinal z -axis as described in [4]. The shot-noise is

applied via each microparticle's charge weight and its mean position in the z -axis. For example, if the distribution had N_λ microparticles per resonant wavelength λ_r , then the mean distance between each would be λ_r/N_λ . The noise is applied to position of the microparticle by altering its position so that $z \rightarrow z + \delta z$, where:

$$\delta z = \frac{\lambda_r}{N_\lambda \sqrt{N_e}} Rnd, \quad (1)$$

where N_e is the microparticle charge weight (i.e. the number of electrons it represents) and Rnd is random number in the range ± 0.5 . This value is calculated and applied individually to each microparticle. A random Poisson noise is then applied to the microparticle charge weight.

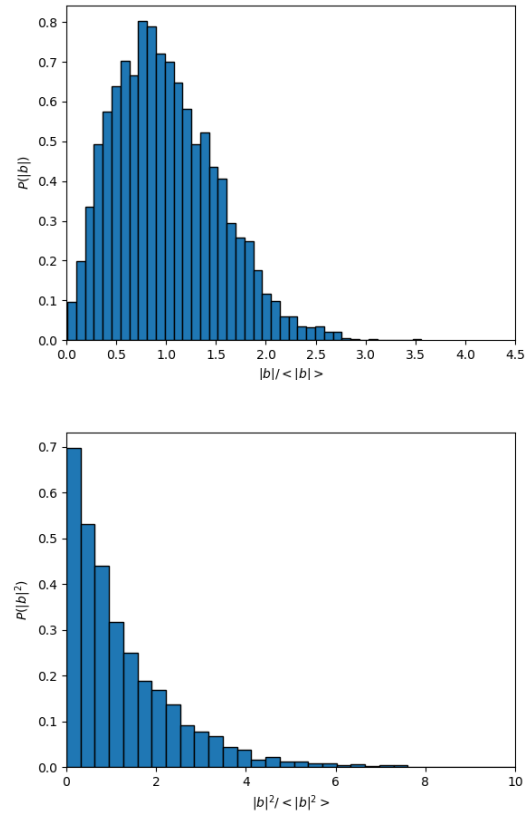


Figure 3: Microparticle probability distribution after JDF is applied showing top $P(|b|)$ (Rayleigh distribution function) and bottom $P(|b|^2)$ (negative exponential distribution function) in good agreement with the results of [4].

The results were tested by analysing the bunching statistics shown on Fig.3 and other beam statistics presented on Fig. 4. Additional test was performed to verify the bunching behaviour in absence of FEL interactions in simulation software Puffin where a flat top current was first generated with a sparse resolution and next the described up-sampling procedure was used to generate the new set of particles. The newly generated particles were then used as input file while

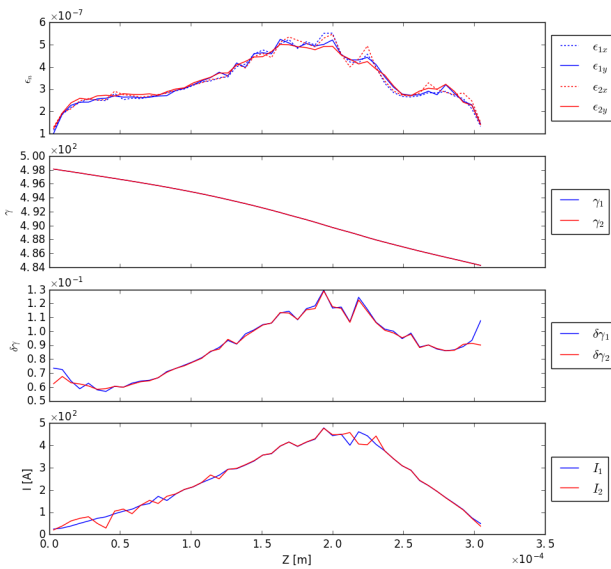


Figure 4: The plots show from the top: the normalised emittance ϵ_n ; local Lorentz factor γ , local spread in the Lorentz factor δ_γ and current I for both the macroparticle beam (blue) and, after JDF is applied, the microparticle beam (red).

FEL interactions were turned off to allow the electron bunch propagate through undulator. The analytic model described in [4] was used to set the outer boundaries for the bunching parameters and slice of one wave length from the middle of the beam was selected for comparison. The expected result was that in absence of FEL interactions the beam will propagate through undulator and the bunching value in the selected slice will not exceed the boundaries set by analytic model. The results of the numerical experiment are shown on Fig. 5. The bunching statistics show good agreement with the model of [4].

COMPARISON OF DATA

In changing from the macroparticle to microparticle distribution, the macroscopic beam parameters, such as current, energy spread, emittance etc, should remain essentially unchanged. In this example the source was electron bunch generated by the ASTRA [8] software for a CLARA FEL [7] simulation. Fig. 4 plots beam parameters as calculated for both the macroparticle distribution at the output from ASTRA and the microparticle distribution following application of the JDF method as described above. Note that, as expected, the plots obtained for the microparticle distribution are a little smoother than the original macroparticle distribution. This is due to much more dense microparticle density along the z -axis. Further smoothing can be applied as described above.

CONCLUSION

The JDF method of up-sampling a system of macroparticles into a greater number of microparticles that have the

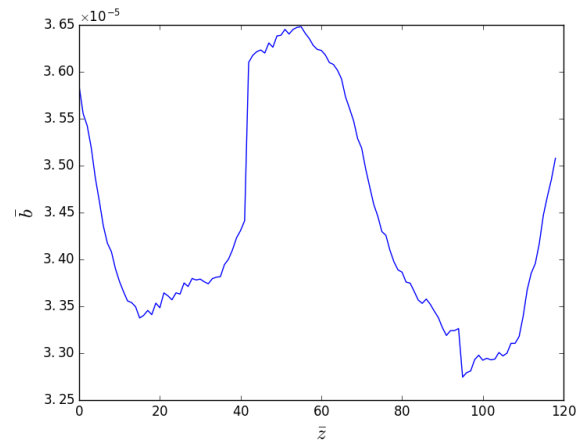


Figure 5: Bunching in electron beam propagating through the undulator with FEL interactions turned off. The \bar{b} predicted by theory [4] for this configuration is 3.97×10^{-5} and $\sigma_{|b|}$ is 2.077×10^{-5} . As one can observe the results from numerical model of noise presented in this paper keeps within the limit predicted by the theoretical model.

equivalent shot-noise statistics as a system of electrons, is shown to give good agreement with the original macroparticle of energy spread, energy, emittance and current. The new microparticle beam also agrees with theoretical values for the bunching statistics. The JDF processed microparticle beam is more realistic than the initial macroparticle beam. The JDF method is computationally efficient and easy applicable in most computer programming languages - here Python was used. It has been successfully applied in a start-to-end type simulation of CLARA FEL using Puffin software. The output data was compared in [9] with the same simulation using Genesis 1.3 [10] and gave very good agreement.

ACKNOWLEDGMENTS

We gratefully acknowledge support of: The Science and Technology Facilities Council Agreement Number 4163192 Release #3; STFC's ASTeC department for HPC access, using the STFC Hartree Centre; and John von Neumann Institute for Computing on JUROPA at Jülich Supercomputing Centre under project HHH20.

REFERENCES

- [1] <https://github.com/UKFELs/JDF>
- [2] Brian W.J. McNeil and Neil R. Thompson, "X-ray free-electron lasers, *Nature Photon.*, vol. 4, 814 (2010). doi:10.1038/nphoton.2010.239
- [3] L.T. Campbell and B.W.J. McNeil, "Puffin: A three dimensional, unaveraged free electron laser simulation code", *Phys. Plasmas* **19**, 093119 (2012). doi:10.1063/1.4752743
- [4] B.W.J. McNeil, M.W. Poole and G.R.M. Robb, *Physical Review Special Topics - Accelerators and Beams* Vol 6, 070701 (2003), doi:10.1103/PhysRevSTAB.6.070701

- [5] E. Jones, E. Oliphant, P. Peterson, *et al.*, SciPy: Open Source Scientific Tools for Python, 2001 - , <http://www.scipy.org/>
- [6] E. W. Weisstein, “Joint Distribution Function,” <http://mathworld.wolfram.com/JointDistributionFunction.html>
- [7] J.A. Clarke *et al.*, “CLARA conceptual design report” Journal Of Instrumentation, vol. 9, T05001 (2014). doi:10.1088/1748-0221/9/05/t05001
- [8] K. Floettmann, “ASTRA - A space charge tracking algorithm,” <http://www.desy.de/mpyflo>
- [9] D.J. Dunning *et al.*, “Start-to-End Simulations of the CLARA FEL Test Facility”, in *Proc. 9th Int. Particle Accelerator Conf. (IPAC’18)*, Vancouver, Canada, Apr.-May 2018, pp. 4430–4433. doi:10.18429/JACoW-IPAC2018-THPMK060
- [10] S. Reiche, “GENESIS 1.3: a fully 3D time-dependent FEL simulation code”, *Nucl. Instr. Meth. Phys. Res. Sect. A*, vol. 429, p. 243, 1999. doi:10.1016/S0168-9002(99)00114-X

COMPARISON BETWEEN, AND VALIDATION AGAINST AN EXPERIMENT OF, A SLOWLY-VARYING ENVELOPE APPROXIMATION CODE AND A PARTICLE-IN-CELL SIMULATION CODE FOR FREE-ELECTRON LASERS

L.T. Campbell^{1,3}, H.P. Freund⁴, J.R. Henderson^{1,3}, B.W.J. McNeil^{1,2},
P. Traczykowski^{1,2,3} and P. J. M. van der Slot⁵

¹SUPA, Department of Physics, University of Strathclyde, Glasgow, G4 0NG

²Cockcroft Institute, Warrington, WA4 4AD, UK

³ASTeC, STFC Daresbury Laboratory, Warrington, WA4 4AD, UK

⁴University of New Mexico, Albuquerque, New Mexico, 87131 United States of America

⁵Mesa+ Institute for Nanotechnology, University of Twente, Enschede, The Netherlands

Abstract

Free-electron lasers (FELs) operate at wavelengths down to hard x-rays, and are either seeded or start from noise. There is increasing interest in x-ray FELs that rely on Self-Amplified Spontaneous Emission (SASE), and this involves increasing simulation activity in the design, optimization, and characterization of these x-ray FELs. Most of the simulation codes in use rely on the Slowly-Varying Envelope Approximation (SVEA) in which Maxwell's equations are averaged over the fast time scale resulting in relatively small computational requirements. While the SVEA codes are generally successful, the predictions of these codes sometimes differ in various aspects of the FEL interaction. In contrast, Particle-in-Cell (PiC) simulation codes do not average Maxwell's equations and are considered to be a more complete model of the underlying physics. Unfortunately, they require much longer run times than SVEA codes and have not been validated by comparison with experiment as often as the SVEA codes. In order to remedy this, and to resolve issues that arise due to different predictions between the SVEA codes, we present a comparison between one SVEA code (MINERVA) and a PiC simulation code (PUFFIN) with the experimental measurements obtained at the SPARC SASE FEL experiment at ENEA Frascati. The results show good agreement between the two codes and between the codes and the experiment. Since the formulations of the two codes share no common elements, this validates both formulations and demonstrates the capability to model the FEL interaction from the start of the undulator through the undulator and into deep saturation.

INTRODUCTION

While free-electron lasers (FELs) have been intensively studied since the 1970s, new developments and concepts keep the field fresh. Intensive work is ongoing into new FEL-based light sources that probe ever shorter wavelengths with a variety of configurations. There presently exists a large variety of FELs ranging from long-wavelength oscillators using partial wave guiding to ultraviolet and hard x-ray FELs that are either seeded or starting from noise (SASE). As these

new light sources come on-line, interest will grow in shorter pulses, new spectral ranges and higher photon fluxes. The increasing activity in the design and construction of FEL light sources is associated with increasing simulation activity to design, optimize, and characterize these FELs. Most of the FEL simulation codes in use at the present time can be categorized as either SVEA or PiC simulations. In the SVEA, the optical field is represented by a slowly-varying amplitude and phase in addition to a rapid sinusoidal oscillation. The field equations are then averaged over the rapid sinusoidal time scale and, thereby, reduced to equations describing the evolution of the slowly-varying amplitude and phase. Within the context of the SVEA, FEL simulation codes fall into two main categories where the particle trajectories are found by first averaging the trajectories over an undulator period (the so-called wiggler-averaged-orbit approximation), or by the direct integration of the Newton-Lorentz equations. There is a further distinction between the SVEA codes based upon the optical field representation, and codes have been written using either a grid-based field solver or a superposition of optical modes. Simulation codes using the wiggler-averaged-orbit analysis in conjunction with a grid-based field solver include (but are not limited to) GINGER [1], GENESIS [2], and FAST [3]. In contrast, SVEA codes that integrate the Newton-Lorentz equations in conjunction with a Gaussian mode superposition for the optical fields include MEDUSA [4] and MINERVA [5]. One common feature of all the SVEA codes, however, is the way in which time-dependence is treated. The fast time scale average results in a breakdown of the optical pulse into temporal slices each of which is a single wave period in duration. The optical slices slip ahead of the electron slices at the rate of one wavelength per undulator period. As a result, the SVEA codes integrate each electron and optical slice from $z \rightarrow z + \Delta z$ and then allow the optical slice to slip ahead of the electron slices. These codes have been extremely successful in modeling FELs; however, their predictions are not always identical for all aspects of the FEL interaction. In contrast, PiC codes do not average Maxwell's equations and are considered to represent a more fundamental model of the physics of FELs.

A PiC code makes no average over the rapid sinusoidal oscillation and integrates the Newton-Lorentz equations for the particles. As a result, PiC codes require substantially more computational resources than SVEA codes and are not so commonly in use and have not been as extensively validated against experiments as have the SVEA codes. At the present time, the primary PiC code for FEL simulations is PUFFIN [6, 7]. In view of this, we undertake in this paper to present a comparison of one SVEA code (MINERVA) and a PiC code (PUFFIN) with experimental measurements. The properties/capabilities of these codes have been presented in the literature and will not be discussed here other than to emphasize that while MINERVA applies the SVEA it does not average the Newton-Lorentz equations over the undulator period. As such, both PUFFIN and MINERVA integrate the particle trajectories in the full magnetostatic and electromagnetic field representations. Other than this, the two codes share no common elements. In particular, the particle loading algorithms used to treat start-up from noise are different. MINERVA uses an adaptation of the algorithm described by Fawley [1] while PUFFIN uses an algorithm developed by McNeil et al. [8]. Our purpose in this paper is to compare the simulation results obtained by the two codes and to "validate" the codes by comparison with experimental measurements taken in a SASE FEL. To this end, comparisons between PUFFIN and MINERVA and between the two codes and experimental measurements at the "Sorgente Pulsata ed Amplificata di Radiazione Coerente" (SPARC) experiment which is a SASE FEL located at ENEA Frascati [9] are presented in following sections. The best estimate for the experimental parameters of SPARC are summarized in Table 1.

Table 1: Parameters of the SPARC FEL Experiment

Electron beam	
Energy	151.9 MeV
Bunch charge and duration	450 pC, 12.67 ps
ϵ_x, ϵ_y	2.5, 2.9 mm-mrad
RMS Energy spread	0.02%
σ_x, σ_y	132, 75 μm
α_x, α_y	0.938, -0.705
Undulators and quadrupoles	
Period and length	2.8 cm, 77 Periods
Amplitude and K_{rms}	7.8796 kG, 1.457
Gap Length	0.40 m
Quadrupole length	5.3 cm
Quadrupoles field gradient	0.9 kG/cm

A parabolic temporal bunch profile was used in MINERVA while PUFFIN employed a Gaussian temporal profile. The experiment employed six undulators for an overall length

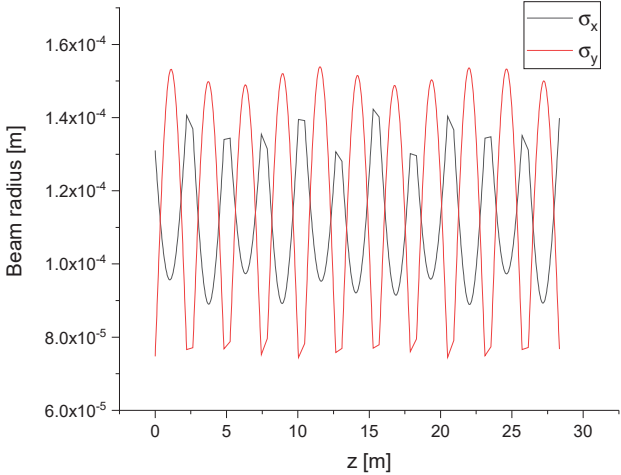


Figure 1: PUFFIN simulation propagation of the beam propagation through the undulator/quadrupole lattice.

of about 15 meters, but this was too short to reach saturation given the bunch charge. In order to compare the codes in the saturated regime, we extended the undulator/FODO lattice to include 11 undulators. As a result, the experimental data is used to anchor the validation of the codes in the start-up and exponential growth regions, while the code results are compared for the initial start-up, exponential growth and deep saturation regimes. The quadrupole orientations were fixed and did not alternate. The electron beam was matched into the undulator/focusing lattice. The resonance occurred at a wavelength of 491.5 nm. The pulse energies were measured in the gaps after each undulator segments by opening the gap, thereby detuning the FEL interaction, in the further downstream undulators [9]. The simulated propagation of the beam through the undulator/quadrupole lattice is shown in Fig. 1, where we plot the beam envelope in x and y versus position as determined by PUFFIN. The MINERVA propagation results were similar. Observe that the beam is well-confined over the 28 meters of the extended lattice with an average beam size of approximately 115 μm .

A comparison of the evolution of the pulse energy as found in MINERVA and PUFFIN, and as measured in the experiment, is shown in Fig. 2 where the MINERVA simulation is indicated by the blue line and the PUFFIN simulation is indicated by the green line. The measured pulse energies for a sequence of shots are indicated by the red markers where the error bars indicate the standard deviation over a sequence of shots. Observe that the agreement between the two codes, and between the codes and the measured pulse energies, are excellent over the entire range of the experiment.

We remark that the exponential growth region starts in the second undulator and that the start-up region is encompassed in the first undulator segment. The experimental measurements indicate that the pulse energy after the first undulator falls into the range of about 8.4×10^{-12} through 1.74×10^{-11} J while MINERVA yields a pulse energy of 2.52×10^{-11} J and PUFFIN yields 4.02×10^{-11} J. The simulation results are in relatively close agreement with the experiment and

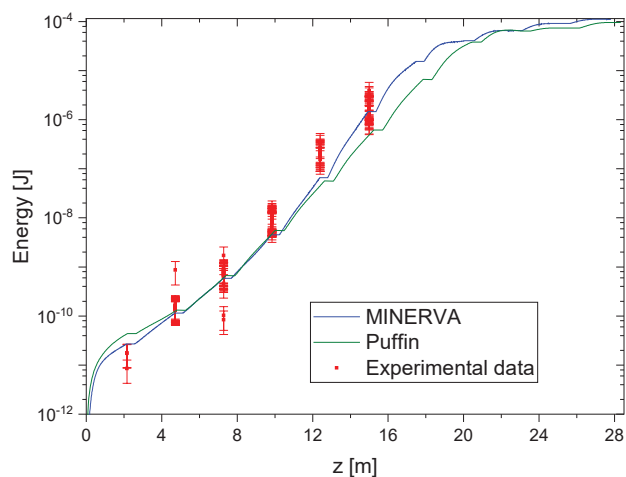


Figure 2: Comparison of simulation results with PUFFIN and MINERVA and the measured pulse energies versus distance through the undulator (data courtesy of L. Giannessi).

with each other, although PUFFIN exhibits slightly higher start-up noise than MINERVA. This agreement is an important observation since the particle loading algorithms in the two codes share no commonality. Apart from differences that might derive from the parabolic versus Gaussian temporal profiles and the different particle loading algorithms, another source of the difference in the slightly higher start-up noise in PUFFIN is the fact that PUFFIN naturally includes a wider initial spectral range than MINERVA. The exponential growth region starts in the second undulator and the two codes are in excellent agreement with each other and with the experimental measurements out to the end of the sixth undulator. These results are in substantial agreement with the parameterization developed by Ming Xie [10]. Using a β -function of about 2 m, we find that the Pierce parameter $\rho \approx 2.88 \times 10^{-3}$ and that this parameterization predicts a gain length of 0.67 m, and a saturation distance of 18.1 m (including the additional 3.2 m represented by the gaps between the undulators). This is in reasonable agreement with the simulations which indicate that saturation occurs after between about 18-20 meters of undulator/FODO line. Finally, the predictions of the two codes in the saturation regime after about 20 m are also in remarkable agreement. After 28 m of undulator/FODO lattice PUFFIN predicts a pulse energy of 90 μ J while MINERVA predicts 111 μ J which constitutes a difference of about 18%.

The larger initial spectral linewidth excited in the start-up region exhibited by PUFFIN is shown more clearly in Fig. 3 which presents a comparison between the evolution of the relative linewidth as determined from PUFFIN and MINERVA and by measurement. It is clear that PUFFIN predicts a significantly wider initial spectrum than MINERVA. This is consistent with the wider bandwidth modelled by PUFFIN and the fact that, unlike MINERVA, it models the generation of the wider bandwidth coherent spontaneous emission. Exponential gain due to the resonant FEL interaction starts in the second undulator and this is expected to rapidly over-

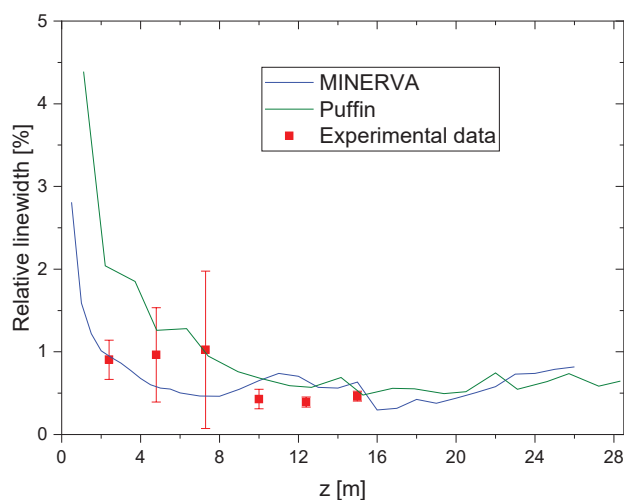


Figure 3: Comparison of the measured relative linewidth in red (data courtesy of L. Giannessi) with that found in the simulations (blue for MINERVA and green for PUFFIN).

come any incoherent synchrotron radiation from the start-up region in the first undulator. In view of this, the PUFFIN results converge rapidly to that found by MINERVA and to the measured linewidths after the second undulator. Note, however, that the measured linewidth after the first undulator seems to be in better agreement with the MINERVA result, but this may be due to the bandwidth of the detector. Agreement between the simulations and the measured linewidth is within about 35% after 15 m. As shown in the figure, the predicted linewidths are in substantial agreement with the experimental measurements, and good agreement between the codes is found over the entire range of integration through the saturated regime.

SUMMARY AND CONCLUSION

In this paper, describe a comparison between simulation codes based on the SVEA formulation (MINERVA) and a PiC formulation (PUFFIN). The two codes have simulated the SPARC SASE FEL at ENEA Frascati. Good agreement has been found both between the two codes and between the codes and the experiment, thereby validating both formulations. This is significant because these two formulations have virtually no elements in common, and we can conclude from this that they both faithfully describe the physics underlying FELs. In particular, the agreement between the codes and the experimental measurements regarding the start-up regime in the SPARC FEL validates the different particle loading algorithms in both codes. One limitation of the SVEA models derives from the fast time scale average which means that these codes cannot treat ultra-short pulse production. This limitation is not present in PiC codes; hence, the validation of PUFFIN implies that it may be a useful model for future ultra-short.

ACKNOWLEDGMENTS

The authors would like to thank: The Argonne Leadership Computing Facility - a DOE Office of Science User Facility supported under contract DE-AC02-06CH11357; The University of New Mexico Center for Advanced Research Computing, supported in part by the National Science Foundation, for providing high performance computing resources used for this work; Science and Technology Facilities Council (Agreement No. 4163192 Release #3); ARCHIE-WeSt HPC, EPSRC grant EP/K000586/1; John von Neumann Institute for Computing (NIC) on JUROPA at Jülich Supercomputing Centre (JSC), project HHH20. The authors acknowledge helpful discussions with L. Giannessi.

REFERENCES

- [1] W. Fawley, "Algorithm for loading shot noise microbunching in multidimensional, free-electron laser simulation codes", *Phys. Rev. ST Accel. Beams* 5, 070701 (2002), doi:org/10.1103/PhysRevSTAB.5.070701
- [2] S. Reiche, "GENESIS 1.3: a fully 3D time-dependent FEL simulation code", *Nucl. Instrum. Methods Phys. Res. A* 429, 243 (1999). doi:10.1016/S0168-9002(99)00114-X
- [3] E.L. Saldin, E.A. Schneidmiller, and M. Yurkov, "FAST: a three-dimensional time-dependent FEL simulation code", *Nucl. Instrum. Methods Phys. Res. A* 429, 233 (1999). doi:10.1016/S0168-9002(99)00110-2
- [4] H.P. Freund, S.G. Biedron, and S.V. Milton, "Nonlinear harmonic generation in free-electron lasers", *IEEE J. Quantum Electron* 26, 275 (2000). doi:10.1109/3.825873
- [5] H.P. Freund, P.J.M. van der Slot, D. Grimminck, I. Setya, and P. Falgari, "Three-dimensional, time-dependent simulation of free-electron lasers with planar, helical, and elliptical undulators", *New J. Phys.* 19, 023020 (2017). doi:10.1088/1367-2630/aa59f1
- [6] L.T. Campbell and B.W.J. McNeil, "Puffin: A three dimensional, unaveraged free electron laser simulation code", *Phys. Plasmas* 19, 093119 (2012). doi:10.1063/1.4752743
- [7] L.T. Campbell, J.D.A. Smith, and P. Traczykowski, "An Updated Description of the FEL Simulation Code Puffin", in *Proc. 9th Int. Particle Accelerator Conf. (IPAC'18)*, Vancouver, Canada, Apr.-May 2018, pp. 4579-4582. doi:10.18429/JaCoW-IPAC2018-THPMK112
- [8] B.W.J. McNeil, M.W. Poole, and G.R.M. Robb, "Unified model of electron beam shot noise and coherent spontaneous emission in the helical wiggler free electron laser", *Phys. Rev. ST Accel. Beams* 6, 070701 (2003), doi:10.1103/PhysRevSTAB.6.070701
- [9] L. Giannessi *et al.*, "Self-amplified spontaneous emission for a single pass free-electron laser", *Phys. Rev. ST Accel. Beams* 14, 060712 (2011), doi:10.1103/PhysRevSTAB.14.060712
- [10] M. Xie, "Design optimization for an x-ray free electron laser driven by the SLAC linac", in *Proc. IEEE 1995 Particle Accelerator Conference*, Vol. 183, IEEE Cat. No. 95CH35843 (1995).

PLASMA ACCELERATOR DRIVEN COHERENT SPONTANEOUS EMISSION

B.M. Alotaibi^{1,2}, R. Altujiri^{1,2}, A. F. Habib^{2,3}, B. Hidding^{2,3}, B.W.J. McNeil^{2,3}, P. Traczykowski^{2,3}

¹Physics Department, Faculty of Science,

Princess Nourah Bint Abdulrahman University, Riyadh, KSA

²SUPA, Department of Physics, University of Strathclyde, Glasgow, UK

³Cockcroft Institute, Warrington, UK

Abstract

Plasma accelerators [1] are a potentially important source of high energy, low emittance electron beams with high peak currents and generated within a relatively short distance. While novel plasma photocathodes [2] may offer improvement to the normalised emittance and brightness of electron beams compared to Radio Frequency-driven accelerators, a challenge is the energy spread and chirp of the beams, which can make FEL operation impossible. In this paper it is shown that such an energy-chirped beam, with a dynamically evolving current profile due to ballistic bunching, can generate significant coherent radiation output via the process of Coherent Spontaneous Emission (CSE) [3]. While this CSE is seen to cause some FEL-induced electron bunching at the radiation wavelength, the dynamic evolution of the energy chirped pulse dampens out any high-gain FEL interaction.

INTRODUCTION

Significant effort have been dedicated to demonstrating a plasma-based accelerator driven FEL [4–6]. However, next to stability challenges, the inherent by-product of plasma-based accelerators is a relatively large slice energy spread ($\sigma_\gamma/\gamma > \rho$) and a correlated energy spread (‘chirp’) when compared with RF linacs. In this paper, the dynamics of the electron bunch from a plasma photocathode [2], which can have an inherent negative energy chirp, is explored. One effect, which to the authors knowledge has not been modelled before with such a PWFA plasma photocathode-generated energy chirped beam, is to induce the generation of Coherent Spontaneous Emission (CSE) [3, 7]. CSE arises when the electron pulse has significant *current* gradients over a resonant radiation wavelength. It is shown that for the electron beam parameters used here, such current gradients can be realised when the energy chirped beam undergoes spatial dispersive compression in its propagation direction due to the correlated energy spread [3, 7]. By dominating any normal spontaneous emission, it has been shown in 1D simulations that CSE can also self-seed the FEL interaction in a process called Self Amplified Coherent Spontaneous Emission (SACSE) [8]. The CSE was also shown in 1D to help mitigate the effects of a homogeneous electron energy spread in beams without an energy chirp, significantly reducing the start-up time and enhancing the generation of high intensity, short, superradiant radiation pulses from a poor-quality electron pulse [9].

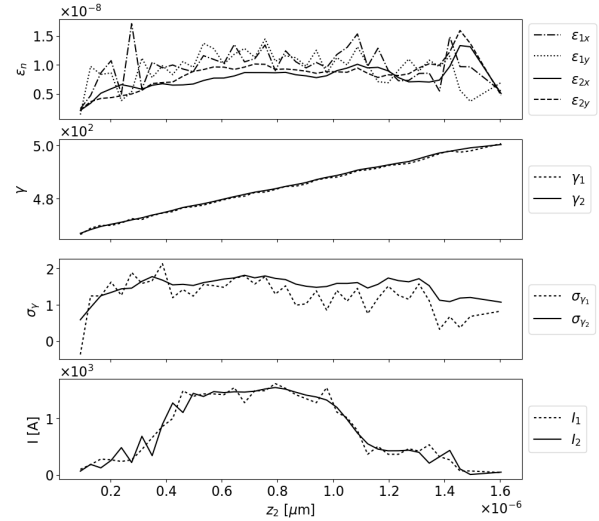


Figure 1: From top, the electron beam normalised emittance ϵ_n , localised Lorentz factor γ , RMS energy spread σ_γ and current I , as a function of window position $z_2 = (ct - z)$ of the beam. In this window, travelling at speed c along the z -axis of the undulator, the head of the electron bunch is on the left, the tail on the right, and the beam will propagate to larger values of z_2 as the beam propagates through the undulator. The dashed plots (index 1) show the original macroparticle beam from the VSim simulation and the solid plots (index 2) show the beam following smoothing and up-sampling to a greater number of microparticles with the correct shot-noise statistics.

ELECTRON BUNCH SIMULATION

A macroparticle distribution is taken from a VSim simulation of a PWFA. These macroparticles have too sparse a phase-space distribution for an accurate FEL simulation as there are too few macroparticles per resonant wavelength and they have unrealistic shot-noise statistics. These macroparticles are converted into a suitable distribution of *microparticles* using the scripts [10] and [11]. The relevant bunch parameters of a microparticle beam are compared to the original beam of macroparticles in Fig. 1. The microparticle distribution has had the correct shot-noise statistics applied as described in [12]. It is seen that the electron beam has a negative longitudinal energy chirp, which is the result of the beam acceleration in the electric field of the nonlinear plasma wave.

UNAVERAGED FEL SIMULATION

The unaveraged 3D FEL simulation code Puffin was used [13, 14] as it is able to model both macroscopic electron beam changes due to the electron beam energy chirp and any CSE and SACSE that may arise. The Ming Xie formalism of [15, 16] was used to chose the planar undulator period λ_u and undulator parameter a_u . The estimated beam parameters of the unchirped beam of Fig. 1 are: $I_{pk} = 1500$ A, $\epsilon_{xy} = 0.01$ mm mrad, $\gamma = 486$, $\sigma_\gamma = 0.3\%$, $Q = 3.6$ pC.

The undulator parameters selected for simulations were $\lambda_u = 0.015$ m and $a_u = 1.0$. The resulting radiation wavelength is $\lambda_r \approx 67$ nm and the FEL parameter at peak current is $\rho = 0.021$. Given that the average slice energy spread is $\sigma_\gamma/\gamma \approx 3 \times 10^{-3}$ the energy spread condition for FEL lasing of $\sigma_\gamma/\gamma \lesssim \rho$ is well satisfied in the absence of an energy chirp. The steady state, Self Amplified Spontaneous Emission (SASE) saturation length is then approximated as $L_{sat} \approx 1.4$ m and saturation power $P_{sat} \approx 2.2$ GW. The electron bunch does not, however, conform to the steady-state approximation as it is only ~ 6 cooperation lengths long, where the cooperation length $l_c = \lambda_r/4\pi\rho$ [17]. This relatively short electron pulse length will result in the output of short, single pulses, at saturation. This type of short pulse operation is in the weak superradiant regime of FEL operation [17] and also results in reduced saturation powers from that of the steady-state, Ming Xie approximation above. The Puffin simulation uses the energy chirped electron bunch distribution output from the PWFA as shown in Fig. 1. The beam of microparticles was matched to the natural focusing channel of the undulator lattice chosen for the simulation as above using the method of [18]. It is seen from the parameters of the chirped pulse, plotted in Fig. 1, that the electron pulse generated by the PWFA has a length of $l_e \approx 24\lambda_r \approx 6l_c$ and has a negative energy chirp in z (positive energy chirp in z_2). During propagation through the undulator, dispersion will cause this short, energy chirped electron bunch to self-compress longitudinally due to rotation in longitudinal phase space, which is significant at these relatively low energies, and it may even ‘flip over’ in longitudinal phase space [3]. During this process, the electron bunch length may approach that of the resonant wavelength ($l_e \sim \lambda_r$) and consequently would be expected to radiate significant CSE. In what follows the CSE generation due to energy chirped bunch shortening and any FEL processes were modelled self-consistently. The FEL interaction may also amplify CSE in addition to the spontaneous emission due to electron beam shot-noise in the SACSE [8]. As with SASE, given the large energy chirp here, any SACSE process would be expected to be significantly affected. The electron bunch length is plotted as a function of position through the undulator in Fig. 2, and is seen to shorten and flip over before lengthening again.

The energy of the radiation pulse as a function of distance through the undulator emitted by the chirped bunch is shown in Fig. 3 both with and without the FEL interaction included in the simulation. The FEL interaction is ‘switched off’ in the

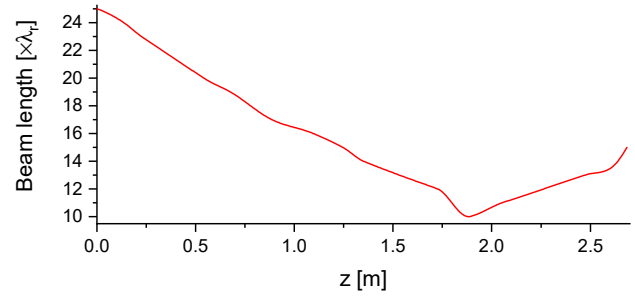


Figure 2: The full electron bunch length in units of resonant wavelength. The initial energy chirp at $z = 0$ m is seen to cause the electron pulse to compress and then will decompress longitudinally.

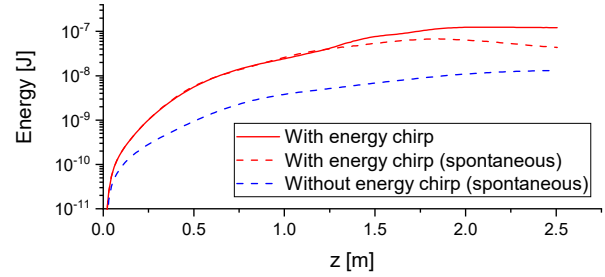


Figure 3: Radiation energy as a function of distance z through the undulator. Two of the plots (red) are for the chirped pulse including (solid) the FEL interaction and (dashed) without the FEL interaction. The case without energy chirp or FEL interaction (blue dashed) gives an energy growth with a quasi-linear dependence with z , corresponding to shot-noise spontaneous emission without significant CSE contribution.

Puffin simulation by artificially de-coupling the electrons from the radiation field. Also shown is the spontaneous emission with the energy chirp artificially removed from the electron bunch. The corresponding average bunching parameters $|\bar{b}|$, for both the chirped and un-chirped electron pulses are shown in Fig. 4.

The radiation pulse ‘instantaneous’ power (i.e. unaveraged over a radiation wavelength [13]) and electron bunching parameter $|b|$ at saturation, is shown in Fig. 5 as a function of local position z_2 . It is seen from the Fig. 2 that the elec-

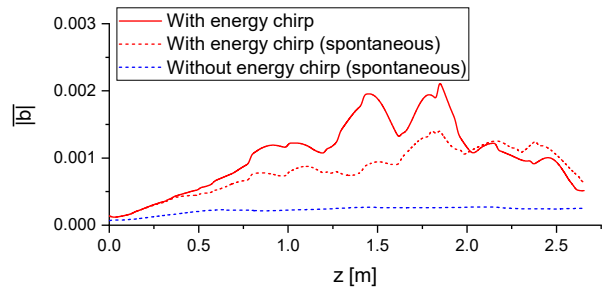


Figure 4: Average bunching parameter evolution for the electron pulse as a function of distance through the undulator both with (solid red) and without (dashed red) the FEL interaction. Also shown is the average bunching for the case of no energy chirp (dashed blue).

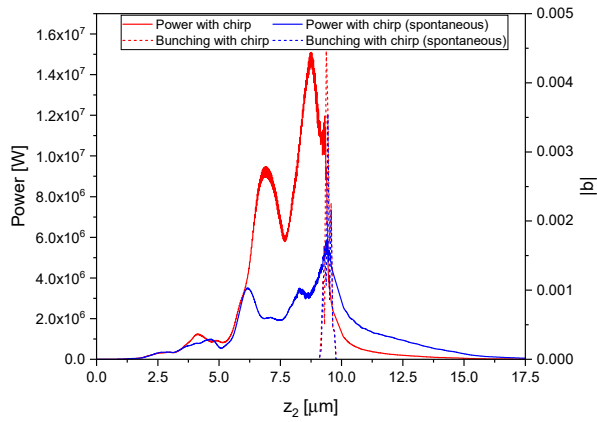


Figure 5: The radiation power profile (solid red) and the electron bunching parameter (dashed red) as a function of $z_2 = (ct - z)$ at $z = z_{sat} = 1.95$ m through the undulator for the energy chirped case and corresponding case for the FEL interaction ‘switched off’ (solid blue and dashed blue).

tron energy chirp causes the electron bunch to longitudinally compress in phase space and shorten as it propagates through the undulator. At saturation, $z = 1.95$ m, the electron bunch is only ~ 10 resonant radiation wavelengths long. When the FEL interaction is switched off, the electrons then only emit spontaneous emission due to both shot-noise and CSE. Figure 3 shows that the energy growth is not exponential but is proportional to $\sim z^2$, more consistent with CSE [3]. That the radiation energy emitted in the absence of the FEL interaction is similar to that with the FEL interaction, confirms that the emission in both cases arise mainly from CSE. In the absence of any energy chirp or FEL interaction, there is no shortening of the electron pulse and the CSE emission is greatly reduced. The energy growth is then quasi-linear with distance z through the undulator, consistent with incoherent spontaneous emission due to shot-noise only.

The evolution of the mean electron bunching parameter $|\bar{b}|$ of Fig. 4 increases quasi-linearly with distance through the undulator until $z \approx 1.2$ m. This is in broad agreement with the increased bunching due to the dispersive shortening of the electron pulse which causes significant current gradients with respect to the radiation wavelength. It is this type of bunching which drives the Coherent Spontaneous Emission [3] and which may act as a self-generated seed field which can be amplified as SACSE [8,9]. Also plotted is the electron bunching of the electron pulse in the absence of any energy chirp. As described above, there is no shortening of the electron pulse and the bunching remains approximately constant and at a much smaller value, mainly due to shot-noise, than when the pulse shortens and significant current gradients occur at the radiation wavelength scale. The differences of the radiation emission and electron bunching, between the spontaneous-only case, when the FEL interaction is switched off, and that where the FEL interaction is included in the simulation, can be attributed to a small additional bunching due to SACSE. Some small periodic bunching about the radiation wavelength $\lambda_r \approx 67$ nm due to SACSE, can be seen in the evolution of the electron phase-

space through the undulator. The lack of any significant FEL gain is consistent with the work of [19] where for negative values of their chirp parameter \hat{a} , here $\hat{a} \approx -2$ at $z = 0$ m, FEL power output is greatly reduced from that expected from an un-chirped beam. So while some increased bunching is evident due to the FEL interaction between radiation and electrons, it is not operating in the collective, high-gain mode, significantly reducing the power emitted. Following the minimum of its length, the electron bunch continues to disperse as it propagates through the undulator, flipping over in phase space and indeed re-absorbing some of the emitted radiation and is consistent with that of previous simplified models [3]. Figure 5 (red) plots both the radiation power and electron bunching as a function of local position at saturation. It is seen that the electron pulse bunching, corresponding to the electron pulse at saturation of Fig. 2, is within a small local interval around $z \sim 9.5$ μm. The radiation pulse power for $z_2 < 9.5$ μm has propagated ahead of the electron bunch and is propagating in vacuum.

Figure 5 show results for both simulations with the FEL interaction switched on (red) and off (blue). The radiation is then that due to spontaneous radiation from shot-noise and CSE only. The difference in the power emitted between the two is then due to the FEL interaction as observed from the additional electron bunching of Figs. 4 and 2. The modest increase in output power demonstrates that the FEL is not, however, operating in the high-gain regime.

CONCLUSION

Using a start-to-end approach, PWFA driven FEL operation was studied numerically using an unaveraged 3D model. The PWFA electron pulse output had a significant quasi-linear energy chirp. This chirp causes the electron pulse to shorten as it propagates through the undulator and emit significant CSE power. This CSE was seen to drive the electrons to give some weak periodic bunching at the resonant radiation wavelength, but not to enter into a collective, high-gain regime where analysis in the steady-state regime (no pulse effects) predicts output powers approximately two orders of magnitude greater. The dynamic shortening of the electron pulse and subsequent emission of CSE as it propagates through the undulator is an effect that is not normally modelled in FEL simulations. Methods to remove the electron beam energy chirp are the subject of on-going research and, if possible, are expected to allow the high gain FEL interaction to develop and output short coherent pulses of high power radiation.

ACKNOWLEDGMENTS

The authors wish to thank (i) KAUST Supercomputing Laboratory (KSL) Thuwal, Saudi Arabia, (ii) STFC's ASTeC, using the STFC HPC Hartree Centre, (iii) The Science and Technology Facilities Council Agreement Number 4163192 Release #3, (iv) and the John von Neumann Institute for Computing on JUROPA at Jülich Supercomputing Centre, under project HHH20.

REFERENCES

- [1] E. Esary *et al.*, “Physics of laser-driven plasma-based electron accelerators”, *Rev. Mod. Phys.*, vol. 81, pp. 1229, 2009. doi:10.1103/RevModPhys.81.1229
- [2] B. Hidding *et al.*, “Ultracold Electron Bunch Generation via Plasma Photocathode Emission and Acceleration in a Beam-Driven Plasma Blowout”, *Phys. Rev. Lett.*, vol. 108, pp. 035001, 2012. doi:10.1103/PhysRevLett.108.035001
- [3] L. T. Campbell and B. W. J. McNeil, “Puffin: A Three Dimensional, Unaveraged Free Electron Laser Simulation Code”, in *Proc. FEL'12*, Nara, Japan, Aug. 2012, paper MOPD12, pp. 73–76.
- [4] M. Pittman, S. Ferré, J.P. Rousseau, L. Notebaert, J.P. Chambaret, and G. Chériaux, “Design and characterization of a near-diffraction-limited femtosecond 100-TW 10-Hz high-intensity laser system”, *Appl. Phys. B*, vol. 74, pp. 529–535, Apr. 2002. doi:10.1007/s003400200838
- [5] Z. Huang, Y. Ding, and C.B. Schroeder, “Compact X-ray Free-Electron Laser from a Laser-Plasma Accelerator Using a Transverse-Gradient Undulator”, *Phys. Rev. Lett.*, vol. 109, pp. 204801, Nov. 2012. doi:10.1103/PhysRevLett.109.204801
- [6] H.P. Schlenvoigt *et al.*, “A compact synchrotron radiation source driven by a laser-plasma wakefield accelerator”, *Nat. Phys.*, vol. 4, pp. 130–133, 2008. doi:10.1038/nphys811
- [7] J. Henderson, L.T. Campbell, and B.W.J. McNeil, “Chirped and Modulated Electron Pulse Free Electron Laser Techniques”, in *Proc. FEL'14*, Basel, Switzerland, Aug. 2014, paper MOC04, pp. 303–309.
- [8] B.W.J. McNeil, G.R.M. Robb, D.A. Jaroszynski, “Self-amplification of coherent spontaneous emission in the free electron laser”, *Opt. Commun.*, vol. 165, pp. 65–70, 1999. doi:10.1016/S0030-4018(99)00222-9
- [9] B.W.J. McNeil, G.R.M. Robb, D.A. Jaroszynski, “SACSE in a FEL amplifier with energy spread”, *Nucl. Inst. Meth. Phys. Res. A*, vol. 445, pp. 72–76, 2000. doi:10.1016/S0168-9002(00)00116-9
- [10] <https://github.com/UKFELS/FXFEL>
- [11] <https://github.com/UKFELS/JDF>
- [12] B.W.J. McNeil, M.W. Poole, G.R.M. Robb, “Unified model of electron beam shot noise and coherent spontaneous emission in the helical wiggler free electron laser”, *Phys. Rev. ST Accel. Beams.*, vol. 6, pp. 070701, 2003. doi:10.1103/PhysRevSTAB.6.070701
- [13] L.T. Campbell and B.W.J. McNeil, “Puffin: A three dimensional, unaveraged free electron laser simulation code”, *Phys. Plasmas.*, vol. 19, pp. 093119, 2012. doi:10.1063/1.4752743
- [14] L.T. Campbell, B.W.J. McNeil, P.T. Traczykowski, and J.D.A. Smith, “An Updated Description of the FEL Simulation Code Puffin”, in *Proc. IPAC'18*, Vancouver, Canada, Apr.-May 2018, pp. 4579–4582. doi:10.18429/JACoW-IPAC2018-THPMK112
- [15] M. Xie, “Design Optimization for an X-Ray Free Electron Laser Driven by SLAC Linac”, *Proc. the Particle Accelerator Conference 1995 (Geneva)* in *Proc. PAC'95*, Dallas, TX, USA, May 1995, paper TPG10, pp. 183–185.
- [16] M. Xie, “Exact and variational solutions of 3D eigenmodes in high gain FELs”, *Nucl. Instrum. and Methods Phys. Res. A*, vol. 445, pp. 59–66, 2000. doi:10.1016/S0168-9002(00)00114-5
- [17] R. Bonifacio, B.W.J. McNeil, and P. Pierini, “Superradiance in the high-gain free-electron laser”, *Phys. Rev. A*, vol. 40, pp. 4467–4475, 1989. doi:10.1103/PhysRevA.40.4467
- [18] <https://github.com/UKFELS/Paraffin>
- [19] E.L. Saldin, E.A. Schneidmiller, and M.V. Yurkov, “Self-amplified spontaneous emission FEL with energy-chirped electron beam and its application for generation of attosecond x-ray pulses”, *Phys. Rev. Special Topics Accel. Beams.*, vol. 9, pp. 050702, 2006. doi:10.1103/PhysRevSTAB.9.050702

AN INVESTIGATION OF POSSIBLE NON-STANDARD PHOTON STATISTICS IN A FREE-ELECTRON LASER I: EXPERIMENT

Jeong-Wan Park*, University of Hawaii at Manoa, Honolulu, U.S.
Kwang-Je Kim¹, Ryan Lindberg, Argonne National Laboratory, Lemont, U.S.
¹also at University of Chicago, Chicago, U.S.

Abstract

It was reported that the photon statistics of the seventh coherent spontaneous harmonic radiation of the MARK III FEL was sub-Poissonian [1], which concludes that Fano factor F (the ratio of photon number variance to the average photon number) is less than unity. Whether FEL light exhibits such non-standard behavior is an important issue; if it does, our understanding of the FEL needs to be radically modified. In this paper, we re-examine the analyses of experimental data in Ref. [1]. We find that the observed value of F could be explained within the standard FEL theory if one combines the detector dead time effect with photon clustering arising from the FEL gain. We propose an improved experiment for a more definitive measurement of the FEL photon statistics.

INTRODUCTION

In an experiment performed some time ago by Chen and Madey [1], it was reported that the photon statistics of the seventh coherent spontaneous harmonic radiation (CSHR) of the MARK III infrared (IR) free-electron laser (FEL) was sub-Poissonian—neither Poissonian as expected from a coherent FEL output nor chaotic as expected from an incoherent radiation source. If FEL light exhibits such non-standard behavior, our understanding of the FEL needs to be radically modified. In this paper we present a re-examination of the data analysis by Chen and Madey. In the companion paper [2], we study theoretical basis for the non-standard FEL photon statistics.

SET-UP OF THE EXPERIMENT

The Chen-Madey experiment was made at the MARK III FEL [3] operating at a fundamental IR wavelength of 2.68 μm ; further parameters are presented in Table 1. The photon counting measurements used the seventh harmonic at 382 nm where high efficiency photo-multiplier tubes (PMTs) are available, since a poor efficiency PMT typically emphasizes the statistics of the measurement itself, resulting in a Poisson distribution irrespective of the statistics of the source [1, 4]. In classical terms, the coherent spontaneous harmonic radiation (CSHR) is produced by the nonlinear components of the wobble motion in the undulator, and enhanced by the seventh harmonic component of the electron current that occurs as the fundamental mode approaches the oscillator saturation [1].

* jwpark@hawaii.edu

Table 1: MARK III FEL Specification

Parameters	Value	Unit
K (undulator parameter)	1.13	
λ_u (undulator period)	2.3	cm
λ_1 (fundamental mode wavelength)	2.68	μm
Macropulse length	2	μs
Macropulse repetition rate	15	Hz
Micropulse length	2	ps
Micropulse repetition rate	2.856	GHz
Average electron beam energy	43.5	MeV
Energy spread (FWHM)	0.4%	
Peak micropulse current	30	A

The set-up of Chen-Madey experiment is shown in Fig. 1. The output FEL light from the cavity passed through an aperture and then a lens before it reached a dichroic beam splitter that transmitted the fundamental mode and reflected the CSHR. The beam line for the CSHR consisted of a monochromator, an adjustable slit, a fast, high quantum efficiency PMT, and an amplifier. The CSHR was brought to a focus at the adjustable slit and monochromator combination; the former was used to adjust the count rate, while the latter selected the 7th harmonic. Since the slit was at the focal plane of the lens, its size defined the effective optical mode waist of the measured seventh CSHR photons.

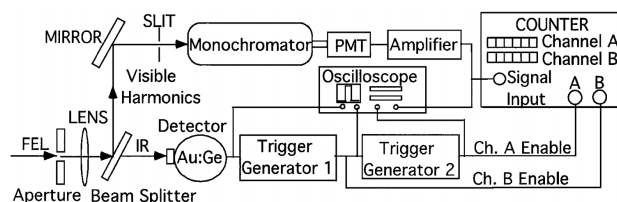


Figure 1: Diagram of photon counting experiment of the seventh CSHR from Mark III FEL [1].

Measurements of the CSHR were triggered by the signal of the IR fundamental which is measured by a fast Au:Ge IR detector. A start signal was sent to the counter by trigger generator 1 when the amplitude of the IR detector reaches a pre-set voltage, followed by an end signal after 80 ns. During the 80 ns time window the counter records the number of 7th harmonic pulses from the PMT along channel B. In addition, trigger generator 2 enables channel A of the counter to record the number of background photons.

The linac delivered about 230 electron bunches within each 80 ns observation window which corresponds to about 6

cavity round-trip times. There are on average 19.5 radiation pulses at the fundamental circulating in the cavity while the macropulse is on. The wholly classical fluctuations of these bunches is diminished to the extent that each group of 230 bunches can be considered as the indistinguishable members of an ensemble. Emission into the seventh harmonic is low, so that on average the PMT measures ≤ 3 photons during any single 80 ns time window.

The goal of the measurement was the Fano factor F , defined by the ratio of the photon number variance to its mean,

$$F = \langle (\delta n)^2 \rangle / \langle n \rangle. \quad (1)$$

Poisson statistics has $F = 1$, $F > 1$ is super-Poissonian, while $F < 1$ signifies a sub-Poissonian source that cannot be described by classical means.

DEAD TIME OF THE COUNTER AND OBSERVED PHOTON STATISTICS

The dead time is the recovery time of a counter during which it cannot react to any photoelectron pulse. It is well-known that the dead time reduces the measured Fano factor when it becomes comparable to the inverse of the average count rate. This can be understood by considering the extreme case where the count rate is much larger than the inverse of the dead time. In this case the counter measures a photon right after every time it recovers, the count rate become uniform and equal to the inverse of the dead time, and the variance approaches zero ($F \rightarrow 0$). Hence, the reduction of the measured Fano factor for a fixed dead time becomes more significant as the count rate increases.

Furthermore, the degree to which dead time affects the measured F at a fixed count rate will also depend upon the details of the emission process. For example, photon clustering during the observation window results in an additional reduction of measured Fano factor below that of Poisson source with a constant emission rate [5]. Such photon clustering may occur in the Chen-Madey experiment if the emission probability of the CSHR increases due to FEL gain. Hence, one must consider the possibility that nonlinear bunching at the seventh harmonic could increase the CSHR during the measurement time window, which in turn would suppress F beyond that predicted from dead time alone.

RESULT OF THE EXPERIMENT

The result of Chen-Madey experiment is shown in Fig. 2. The dashed line for the theoretical dead time-modified-Poisson-radiation (DTMPR) assumes a Poisson source with 6.3 ns dead time, which was obtained from separate measurements of a LED source. The solid line fit to the observed Fano factor of the unattenuated seventh CSHR is noticeably lower than the DTMPR as shown in Fig. 2. For this reason, Chen and Madey claimed to have observed sub-Poissonian statistics in the FEL seventh CSHR (the attenuated results of Fig. 2 are irrelevant here).

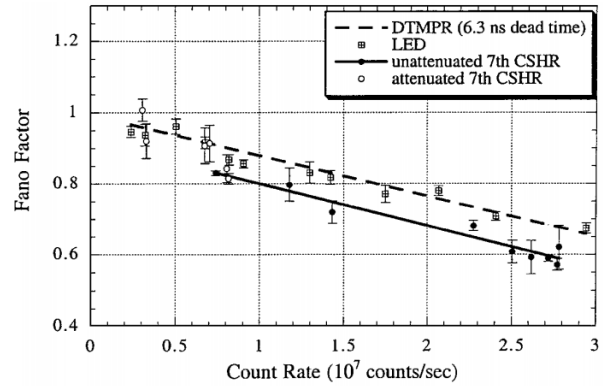


Figure 2: Result of the Chen-Madey experiment [1].

Chen and Madey also measured the auto-correlation function of the PMT voltage defined by [6]

$$G(\tau) \equiv T^{-1} \int_0^T dt V(t)V(t+\tau). \quad (2)$$

They expected that any photon clustering due to FEL gain would result in an enhancement of the auto-correlation function at the cavity round-trip time. Instead, the auto-correlation function displayed a local minimum at the cavity round-trip time, and Chen and Madey concluded that photon clustering could not be present. However, even if the emission is a random Poisson process with intensity increasing at each cavity round-trip, the number of photons within the observation window (normally two or three) is too little to reveal the increase faithfully through the auto-correlation function. This has been verified by our simulations, implying that their auto-correlation function study cannot rule out photon clustering within the observation window.

SIMULATION OF THE PHOTON STATISTICS

As mentioned in the previous section, the influence of photon clustering on the measured Fano factor should be studied in more detail before definite conclusions regarding the F at the source can be made. Since the Mark III FEL is no longer available to repeat the experiment, we have simulated Chen-Madey experiment using GINGER [7], and used the predicted output power at the seventh harmonic to set the (potentially time-varying) Poisson rate for the CSHR. Hence, we ignored the chaotic light nature of any given pulse, which should be an appropriate assumption since there is on average 0.05 photons within a coherence length.

The steps of the simulation are:

1. Use GINGER to determine the FEL power in the fundamental and seventh harmonic as a function of the pass number.
2. Determine the starting time (pass number) of the 80 ns time window by using the experimentally measured ratio of the power in the fundamental at the start to that in saturation.

Table 2: Possibility That the Data Can Be Explained by the Standard FEL Thoery, Depending on the Starting Cavity Round-Trip Number of the Observation Window. NP: Non-Paralyzable Daed Time, P: Paralyzable Dead Time. ○: Consistent, △: Approximately Consistent, ×: Inconsistent.

Starting number	54		55		56		57		58		59		60		61		64	
Dead time type	NP	P	NP	P	NP	P	NP	P	NP	P	NP	P	NP	P	NP	P	NP	P
Fano factor	×	×	×	×	○	○	○	○	○	○	×	△	×	×	×	×	×	×
Auto-correlation	×		×		×		×		△		○		○		○		○	

- Determine the seventh harmonic power during the 80 ns window determined in step 2 to set the emission probability, and simulate the measurement including dead time.

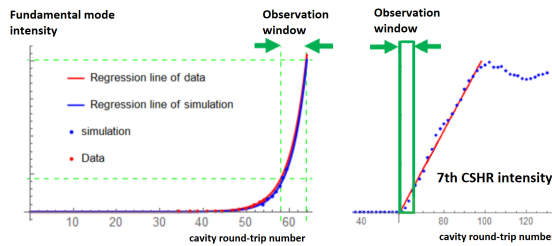


Figure 3: Simulated radiation field intensity.

The procedure of step 2 is shown in the left-hand plot of Fig. 3, where we show that the best best fit of the experiment to simulation implies that the observation window begins at GINGER round trip number 58. The right-hand plot of Fig. 3 shows the GINGER prediction of the 7th harmonic intensity profile during the same 80 ns.

In Fig. 4 we show the Fano factors of the 7th harmonic CSHR data obtained by Chen and Madey and the simulated Fano factors for two different dead time models, *paralyzable* and *non-paralyzable*. In the non-paralyzable (NP) model the counter is rendered “dead” for one dead time after a count, while in the paralyzable (P) model any photon that arrives when the counter is dead is not counted and extends the dead time by another unit; real counters typically live between these two extremes. It is seen that simulated Fano factors are consistent with the measured one. Hence, we have found by clustering the photons towards the end of the measurement window, the FEL gain could reduce F in a manner that is consistent with the measurement.

Still there are a number of uncertainties and sources for error in our procedure. For example, identifying the start of the time window is complicated by the fact that only the lower limit of the fundamental mode intensity in saturation is available from the published Chen-Madey data. Furthermore, the simulated intensity of the fundamental mode may differ somewhat from that measured due to uncertainties in the oscillator parameters, and we have found that errors in power by a factor of two would change the starting point of the observation window by ± 3 cavity round-trips.

For these reasons we compared both the Fano factor F and auto-correlation function $G(\tau)$ derived from measurements to those predicted by our simulations assuming several dif-

ferent starting pass numbers and two different models of the dead time. We summarize this comparison in Table 2, where we find that there is a range of parameters and models for which our simulations are consistent with the data.

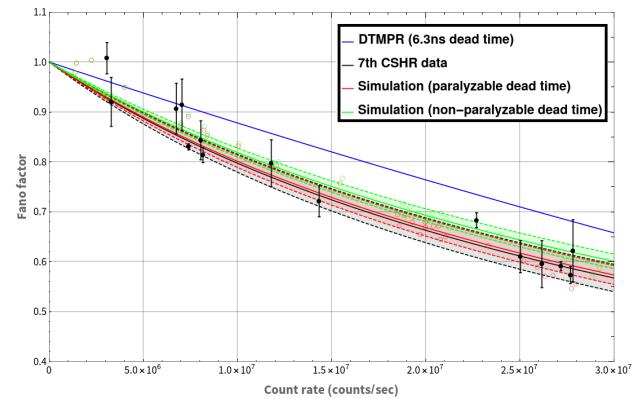


Figure 4: The simulated Fano factor for the found observation window starting at the 58 cavity round-trip. The shaded areas are the 3- σ bands, and the error bar represents one standard deviation.

A PROPOSED IMPROVED EXPERIMENT

The main difference between Chen-Madey analysis and our study is in the degree of the photon clustering within the observation window. In an improved experiment, the degree of photon clustering can be monitored by recording PMT traces over many ensembles. Furthermore, since the photon statistics will depend on the quantum efficiency significantly only if the Fano factor is not close to the unity, photon count at different efficiencies can be performed. With an FEL operating in the visible light regime, the photon statistics at the fundamental mode can also be measured.

CONCLUSION

According to our simulation of the Fano factor of Chen-Madey experiment, the reduced Fano factor observed in the experiment could also be explained with the standard theory if one combines the detector dead time effect with photon clustering arising from FEL gain. Considering the significance of the claim of sub-Poissonian FEL light made by Chen and Madey, an improved re-measurement may be useful.

ACKNOWLEDGEMENT

Work supported by U.S. DOE, Office of Science, Office of BES, under Award No. DE-SC0018428.

REFERENCES

- [1] T. Chen and J. M. Madey, "Observation of Sub-Poisson Fluctuations in the Intensity of the Seventh Coherent Spontaneous Harmonic Emitted by a rf Linac Free-Electron Laser", *Phys. Rev. Lett.*, vol. 86, p. 5906, Jun 2001. doi:10.1103/PhysRevLett.86.5906
- [2] J.-W. Park, K.-J. Kim, and R. R. Lindberg, "An Investigation of Possible Non-Standard Photon Statistics in a Free-Electron Laser II: Theory", presented at the FEL'19, Hamburg, Germany, Aug. 2019, paper TUP054, this conference.
- [3] G. A. Barnett, J. M. J. Madey, C. B. McKee, K. D. Straub, and E. B. Szarmes, "The Mark III IR FEL: improvements in performance and operation", *Nucl. Instrum. Methods Phys. Res., Sect. A*, vol. 375, p. 97, Jun 1996. doi:10.1016/0168-9002(95)01324-5
- [4] M. S. Fox, *Quantum Optics: An Introduction*, 1st ed. (Oxford University Press, 2006). ISBN:9780198566731.
- [5] G. Vannucci and M. C. Teich, "Dead-time-modified photo-count mean and variance for chaotic radiation", *J. Opt. Soc. Am.*, Vol. 71, p. 164, Feb 1981. doi:10.1364/josa.71.000164
- [6] J. A. Gubner, *Probability and Random Processes for Electrical and Computer Engineers*, 1st ed. (Cambridge University Press, 2006). doi:10.1017/cbo9780511813610
- [7] W. M. Fawley, *A User Manual for GINGER and its Post-Processor XPLOTGIN*, (Office of Scientific and Technical Information, 2002). doi:10.2172/792978

AN INVESTIGATION OF POSSIBLE NON-STANDARD PHOTON STATISTICS IN A FREE-ELECTRON LASER II: THEORY

Jeong-Wan Park*, University of Hawaii at Manoa, Honolulu, U.S.
Kwang-Je Kim¹, Ryan Lindberg, Argonne National Laboratory, Lemont, U.S.
¹also at University of Chicago, Chicago, U.S.

Abstract

In this paper we explore whether we can at present find a theoretical basis for non-standard, sub-Poissonian photon statistics in the coherent spontaneous harmonic radiation of an FEL as was claimed to have been measured with the Mark III FEL [1]. We develop a one dimensional quantum FEL oscillator model of the harmonic radiation in the linear gain regime to calculate the photon statistics. According to our study, it seems unlikely that the photon statistics for an FEL oscillator starting from the noise could be sub-Poissonian.

INTRODUCTION

This is the second, theoretical part of our study into possible non-standard, sub-Poissonian photon statistics for harmonic emission from an FEL. The motivation is an experiment by Chen and Madey [1], which claimed to have observed sub-Poissonian statistics at the seventh harmonic during the linear gain regime of the MARK III FEL oscillator. In our first paper we take a critical look at the experiment [2]; here, we revisit the standard theory of FEL photon statistics of the fundamental mode starting from the noise, and then develop the simplest quantum extension of the classical theory of harmonic radiation production as driven by the fundamental mode. We include the cavity loss with a beam splitter model, and compute the photon statistics of the harmonic modes. We show that the statistics cannot be sub-Poissonian for any initial state of the electrons.

A MODEL OF LIGHT EMITTED BY RANDOMLY DISTRIBUTED ELECTRONS

First, we revisit the photon statistics of undulator radiation when there is no significant bunching in the electron beam. The variance of the number of photons for coherent wave trains emitted by randomly distributed electrons (Fig. 1) is given by [3, 4]:

$$\langle(\delta n)^2\rangle = \langle(\delta n)^2\rangle_Q + \langle(\delta n)^2\rangle_C; \quad (1)$$

$\langle(\delta n)^2\rangle_Q$ is the portion of variance originating from quantum mechanics, whereas $\langle(\delta n)^2\rangle_C$ arises from classical fluctuation of the electrons [5]. Consequently, the Fano factor $F = \frac{\langle(\delta n)^2\rangle}{\langle n \rangle}$ of the photon statistics can also be decomposed into the quantum and classical portions:

$$F = F_Q + F_C. \quad (2)$$

When the mode number $M = t_p/\tau_{coh} \gg 1$ (t_p is the pulse length and τ_{coh} is the coherence time) one can write [4, 5]

$$F_Q = \frac{\langle(\delta n)^2\rangle_Q}{\langle n \rangle} = 1, \quad F_C = \frac{\langle n \rangle}{M}. \quad (3)$$

Thus, in this case $F > 1$ and the photon statistics is super-Poissonian.

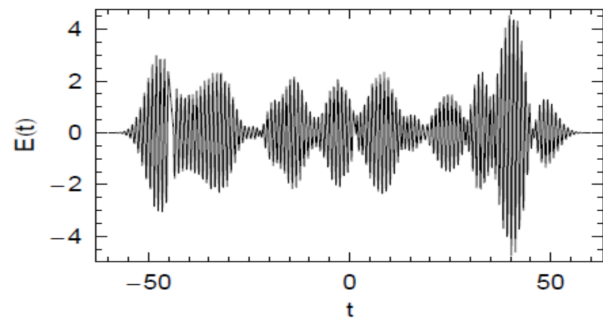


Figure 1: A sum of coherent wave trains emitted by randomly distributed electrons [5].

PHOTON STATISTICS OF THE FUNDAMENTAL MODE

A one Dimensional Quantum FEL Model

To investigate the photon statistics, we shall develop a quantum model of the FEL oscillator starting from the noise. In this model we will only consider one frequency mode of the field, since in the linear gain regime the FEL acts as a linear amplifier and all frequency components are independent [6]. When energy spread can be neglected the evolution of the electric field operator as the pass number n increases becomes [5, 7]

$$a_{1,n+1} = g a_{1,n} + \mathcal{F}_n; \quad (4)$$

the first subscript of field operator a represents the harmonic number, the second denotes the cavity round-trip number, and $|g|^2$ is the gain per cavity round-trip. An explicit expression for g is:

$$g \equiv \frac{1}{3} \sum_{\alpha} e^{-i\mu_{\alpha} 2k_u \rho L_u}, \quad (5)$$

where μ_{α} are the three roots of $(\mu - \frac{\Delta\nu}{2\rho})(\mu^2 - \frac{q^2}{4}) = 1$, $\Delta\nu = \frac{\omega - \omega_1}{\omega_1}$, ω_1 is the fundamental mode's angular frequency, $q = \frac{\hbar\omega_1}{\gamma\gamma_r mc^2}$ is the ratio of the characteristic photon energy to

* jwpark@hawaii.edu

the energy bandwidth of the FEL (also called the quantum FEL parameter), and γ_r is the resonant Lorentz factor of the electron, L_u is the undulator length, k_u is the undulator's wave number, and ρ is the FEL Pierce parameter. We assume that the electron beam is fresh at the beginning of each pass, and its operator at the end of the n^{th} pass is

$$\mathcal{F}_n = -i \sum_{\alpha} \Upsilon_{\alpha} e^{-i\mu_{\alpha} 2k_u \rho L_u} \mathcal{B}_{n_0} - i \sum_{\alpha} \frac{\Upsilon_{\alpha}}{\mu_{\alpha}} e^{-i\mu_{\alpha} 2k_u \rho L_u} \mathcal{P}_{n_0}, \quad (6)$$

where $\Upsilon_{\alpha} \equiv \frac{\mu_{\alpha}}{(\mu_{\alpha} - \mu_{\beta})(\mu_{\alpha} - \mu_{\gamma})}$, and \mathcal{B}_{n_0} and \mathcal{P}_{n_0} are the initial bunching and collective momentum of the electron beam, respectively.

Photon Statistics

We incorporate cavity loss using the beam splitter model [8, 9], in which the finite reflectivity $\sqrt{\eta_h}$ at harmonic h is modeled by the division of the signal into the “output” portion $\sqrt{\eta_h} e^{i\phi_{1,n}} a_{1,n}$ and the “unused” part $\sqrt{1-\eta_h} e^{i\phi_{1,u,n}} a_{1,u,n}$. Here, $\phi_{1,n}$ and $\phi_{1,u,n}$ are the phase shift for the output field and unused field, respectively, and each of these two fields separately satisfy the commutation relation $[a, a^{\dagger}]$ but commute with each other. Then, we have the quantum iterative relation

$$a_{1,n+1} = g\sqrt{\eta_1} e^{i\phi_{1,n}} a_{1,n} + \mathcal{F}_n + g\sqrt{1-\eta_1} e^{i\phi_{1,u,n}} a_{1,u,n}. \quad (7)$$

Note that the commutation relation $[a_{1,n}, a_{1,n}^{\dagger}] = 1$ is preserved. Solving the recursion relation, we obtain

$$a_{1,n} = (g\sqrt{\eta_1})^{n-1} e^{i\Phi_1} a_{1,1} + \sum_{j=1}^{n-1} (g\sqrt{\eta_1})^{n-j-1} e^{i\Phi_{j+1}} \times [\mathcal{F}_j + g\sqrt{1-\eta_1} e^{i\phi_{1,u,j}} a_{1,u,j}] \quad (8)$$

where $\Phi_j = \sum_{k=j}^{n-1} \phi_{1,k}$. The first two moments of the photon number operator become:

$$\langle n \rangle_{1,n} = \sum_{j,k=1}^{n-1} (|g|\sqrt{\eta_1})^{2(n-1)-(j+k)} \langle \mathcal{F}_{n_j}^{\dagger} \mathcal{F}_{n_k} \rangle \quad (9)$$

$$\langle n^2 \rangle_{1,n} = \frac{(|g|^2 \eta_1)^{n-1} (|g|^2 - 1) - |g|^2 (1 - \eta_1)}{|g|^2 \eta_1 - 1} \langle n \rangle_{1,n} + \sum_{j,k,l,m=1}^{n-1} (|g|\sqrt{\eta_1})^{4(n-1)-(j+k+l+m)} \times \langle \mathcal{F}_{n_j}^{\dagger} \mathcal{F}_{n_k}^{\dagger} \mathcal{F}_{n_l} \mathcal{F}_{n_m} \rangle, \quad (10)$$

where $\mathcal{F}_{n_j} \equiv e^{i[\Phi_{j+1} - j \text{Arg}(g)]} \mathcal{F}_j$. One can show that the Fano factor of the fundamental after the n^{th} cavity round-trip, $F_{1,n}$, satisfies

$$F_{1,n} = \frac{(|g|^2 \eta_1)^{n-1} - 1}{|g|^2 \eta_1 - 1} + \frac{\langle (\delta \mathfrak{A}_n)^2 \rangle}{\langle n \rangle_n} + 1 \geq 1, \quad (11)$$

provided $|g|^2 \geq 1$. Therefore, the photon statistics is not sub-Poissonian for any initial state of the electrons. For completeness, we also include the expression for the Hermitian operator \mathfrak{A}_n :

$$\mathfrak{A}_n = \sum_{j,k=1}^{n-1} (|g|\sqrt{\eta_1})^{2(n-1)-(j+k)} \mathcal{F}_{n_j}^{\dagger} \mathcal{F}_{n_k}^{\dagger}. \quad (12)$$

Statistics for the Minimum Noise Electron State

The Fano factor can be explicitly computed if the initial electrons are in the minimum noise state $|\Psi\rangle$, defined as that which is annihilated by the Hermitian conjugate of electron beam operator:

$$\mathcal{F}_n^{\dagger} |\Psi\rangle = 0. \quad (13)$$

Using Eqs. (9), (11), and (12), we compute the Fano factor to be

$$F_{1,n} = 1 + \langle n_1 \rangle_n, \quad (14)$$

which is the same as that of chaotic light.

In the classical regime when $q \ll 1$, as applies to the Chen-Madey experiment, the phase operator of the j^{th} electron prior to the FEL interaction can be decomposed as

$$\Theta_{j_0} = \theta_j^c + \tilde{\Theta}_j, \quad (15)$$

where θ_j^c is a c-number denoting the initial classical position while $\tilde{\Theta}_j$ is the quantum correction that will be treated as a small quantity.

The minimum noise state's wave function of the j^{th} electron in $\tilde{\theta}$ space is a Gaussian function centered about its classical position θ_j^c with RMS width equal to \sqrt{q} [5]. Although the corresponding wave function's width in the position space is much less than the radiation wavelength, as θ_j^c is randomly distributed, the electrons' radiation can still be regarded as coherent wave trains emitted by randomly distributed electrons. This may explain why Eqn. (14) is in accordance with Eqn. (3).

Comparison to Existing Literature

Banacloche [10] showed that the radiation is chaotic during the linear gain regime of the high-gain FEL starting from the noise, if the electrons are initially in momentum eigenstates prior to the FEL interaction. In his analysis, he attributed the random phase distribution of the initial electrons to the infinite width of the wave function in the position space, and found the same Fano factor as that for spontaneous emission, Eqn. (3). Interestingly, this result is the same as what was just derived for electrons initially being described by the minimum noise state.

Gjaja and Bhattacharjee [11] studied whether fluctuation of the field variable in phase with the output field can be reduced below the symmetrical vacuum fluctuation's quantum limit, in the linear gain regime of a FEL starting from the noise. A field with such reduced fluctuation is named amplitude-squeezed radiation. They found that in a high-gain FEL, regardless of the initial state of the electrons,

amplitude-squeezed radiation cannot be emitted. For a low-gain FEL, if the electrons are not entangled initially, and the initial wave functions of all electrons have the same width in position and also in momentum, they found that the amplitude-squeezed radiation cannot be emitted either. However, they discovered that some initially entangled state of the electrons can result in the amplitude-squeezed radiation, which is interestingly not accompanied by the sub-Poissonian photon statistics according to Eqn. (11).

THE HARMONIC MODE'S PHOTON STATISTICS

Our quantum theory for the generation of non-linear higher harmonic modes is based upon the simplest quantum extension of the classical theory. For a harmonic mode h that is dominantly-driven by the fundamental mode we have

$$a_{h,n+1} = a_{h,n} + k_h a_{1,n}^h. \quad (16)$$

We promote the classical fields to quantum operators to obtain the corresponding iterative relation. Including the cavity loss with the beam splitter model we find that

$$\begin{aligned} a_{h,n+1} = & \sqrt{\eta_h} e^{i\phi_{h,n}} a_{h,n} + k_h a_{1,n}^h \\ & + \sqrt{1 - \eta_h} e^{i\phi_{h,u,n}} a_{h,u,n}. \end{aligned} \quad (17)$$

In terms of the initial values $a_{h,n}$ therefore becomes

$$\begin{aligned} a_{h,n} = & \sqrt{\eta_h}^{n-1} e^{i\Phi_{h,1}} a_{h,1} + \sum_{j=1}^{n-1} \sqrt{\eta_h}^{n-j-1} e^{i\Phi_{h,j+1}} \\ & \times \left(k_h a_{1,j}^h + \sqrt{1 - \eta_h} e^{i\phi_{h,u,j}} a_{h,u,j} \right), \end{aligned} \quad (18)$$

where, as before, $\Phi_{h,j} = \sum_{k=j}^{n-1} \phi_{h,k}$. Consequently, the first two moments of the photon statistics become:

$$\langle n_h \rangle_n = |k_h|^2 \sum_{j,k=1}^{n-1} \sqrt{\eta_h}^{2(n-1)-(j+k)} \langle a_{1,n_j}^{\dagger h} a_{1,n_k}^h \rangle, \quad (19)$$

$$\begin{aligned} \langle n_h^2 \rangle_n = & \langle n_h \rangle_n + \sum_{j,k,l,m=1}^{n-1} \sqrt{\eta_h}^{4(n-1)-(j+k+l+m)} \\ & \times |k_h|^4 \langle a_{1,n_j}^{\dagger h} a_{1,n_k}^h a_{1,n_l}^{\dagger h} a_{1,n_m}^h \rangle, \end{aligned} \quad (20)$$

where $a'_{1,n_j} \equiv a_{1,j} e^{i\Phi_{h,j+1}/h}$. In a similar way to what we did before, the Fano factor of the harmonic mode after the n^{th} cavity round-trip, $F_{h,n}$, satisfies

$$F_{h,n} = \frac{\langle (\delta \mathcal{C}_{h,n})^2 \rangle}{\langle n_h \rangle_n} + 1 \geq 1, \quad (21)$$

and the photon statistics is not sub-Poissonian for any initial state of the electrons. The Hermitian operator $\mathcal{C}_{h,n}$ is:

$$\mathcal{C}_{h,n} = |k_h|^2 \sum_{j,k=1}^{n-1} \sqrt{\eta_h}^{2(n-1)-(j+k)} a_{1,n_j}^{\dagger h} a_{1,n_k}^h. \quad (22)$$

CONCLUSION

We have theoretically investigated the FEL photon statistics using the standard theory. It does not seem probable that the photon statistics in the linear gain regime of the FEL starting from the noise is sub-Poissonian, regardless of the harmonic number or the initial state of the electrons. Therefore if a sub-Poissonian FEL light is experimentally observed contradicting our finding, a theory beyond the standard one may be necessary to explain the observation.

ACKNOWLEDGEMENT

Work supported by U.S. DOE, Office of Science, Office of BES, under Award No. DE-SC0018428.

REFERENCES

- [1] T. Chen and J. M. Madey, "Observation of Sub-Poisson Fluctuations in the Intensity of the Seventh Coherent Spontaneous Harmonic Emitted by a rf Linac Free-Electron Laser", *Phys. Rev. Lett.*, vol. 86, p. 5906, Jun 2001. doi:10.1103/PhysRevLett.86.5906
- [2] J.-W. Park, K.-J. Kim, and R. R. Lindberg, "An Investigation of Possible Non-Standard Photon Statistics in a Free-Electron Laser I: Experiment", presented at the FEL'19, Hamburg, Germany, Aug. 2019, paper TUP053.
- [3] J. Goodman, *Statistical Optics*, 1st ed. (Wiley-Interscience, 2000), ISBN:9780471399162.
- [4] R. Loudon, *The Quantum Theory of Light*, 3rd ed. (Oxford University Press, 2000), ISBN:9780198566731.
- [5] K.-J. Kim, Z. Huang, and R. R. Lindberg, *Synchrotron Radiation and Free-Electron Lasers*, 1st ed. (Cambridge University Press, 2017). doi:10.1017/9781316677377
- [6] W. Becker and J. K. McIver, "Photon statistics of the free-electron-laser startup", *Phys. Rev. A*, vpl. 28, p. 1838, Sep 1983. doi:10.1103/PhysRevA.28.1838
- [7] R. Bonifacio, N. Piovella, G. R. M. Robb, and A. Schiavi, "Quantum regime of free electron lasers starting from noise", *Phys. Rev. ST Accel. Beams*, vol. 9, p. 090701, Sep 2006. doi:10.1103/PhysRevSTAB.9.090701
- [8] M. S. Fox, *Quantum Optics: An Introduction*, 1st ed. (Oxford University Press, 2006), ISBN:9780198566731.
- [9] H. Bachor and T. Ralph, *A Guide to Experiments in Quantum Optics*, 2nd ed. (Wiley-VCH, 2004). doi:10.1002/9783527619238
- [10] J. Gea-Banacloche, "Quantum theory of the free-electron laser: Large gain, saturation, and photon statistics", *Phys. Rev. A*, vol. 31, p. 1607, Mar 1985. doi:10.1103/PhysRevA.31.1607
- [11] I. Gjaja and A. Bhattacharjee, "Generation of squeezed radiation from a free-electron laser", *Phys. Rev. A*, vol. 36, pp. 5486–5489, Dec 1987. doi:10.1103/PhysRevA.36.5486

TWO-COLOR OPERATION OF FLASH2 UNDULATOR

E.A. Schneidmiller*, M. Braune, B. Faatz, F. Jastrow, M. Kuhlmann,
A. Sorokin, K. Tiedtke, and M.V. Yurkov
DESY, Hamburg, Germany

Abstract

FLASH is the first soft X-ray FEL user facility, routinely providing brilliant photon beams for users since 2005. The second undulator branch of this facility, FLASH2, is gap-tunable which allows to test and use advanced lasing concepts. In particular, we tested recently a two-color mode of operation based on the alternation of tunes of the undulator segments (every other segment is tuned to the second wavelength). This scheme is advantageous in comparison with a subsequent generation of two colors in two consecutive sections of the undulator line. First, source positions of the two FEL beams are close to each other which makes it easier to handle them. Second, the amplification is more efficient in this configuration since the segments with respectively "wrong" wavelength still act as bunchers. We developed methods for online intensity measurements of the two colors simultaneously that require a combination of two detectors. We present some examples of such measurements in the XUV and soft X-ray regimes.

INTRODUCTION

Two-color lasing is a popular operation mode of X-ray FEL user facilities. A possible way to generate two colors in a gap-tunable undulator, operating in SASE regime, is to split the undulator into two sections, and set different K-values in each of these sections. An additional useful element for X-ray pump, X-ray probe experiments could be a chicane between the two sections to control a time delay between the pulses of two different colors. One can use the same electron bunch (parts of the same bunch) for lasing in the two sections of the undulator [1]. In this case the beam quality is partially spoiled in the first section (that typically operates at the onset of saturation), and one has to compromise intensities of two colors. As an alternative, one can use fresh-bunch technique based on the principle of the betatron switcher [2]. A practical realization of this principle was done in a way that the head and the tail of the bunch lase in two different sections of the undulator [3,4].

One of the issues with these sectioned-undulators schemes (or, split undulators) is a significant spatial separation of effective source positions of the two X-ray beams. This separation can make it difficult to efficiently focus both beams on a sample. As an alternative, one can consider two-color lasing in the undulator with the alternation of tunes of single undulator segments enabling close positions of source points. This scheme was realized at LCLS for small separation of tunes (about 1%) and was described in [5] as the gain-modulated FEL.

* evgeny.schneidmiller@desy.de

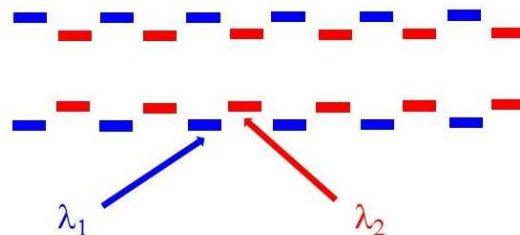


Figure 1: Conceptual scheme of two-color lasing with the alternation of undulator tunes.

We tested the two-color mode with the alternation of undulator tunes at FLASH [6,7] in the regime of a large separation of tunes (several tens percents), and present the main results in this paper.

TWO-COLOR LASING WITH THE ALTERNATION OF UNDULATOR TUNES

The principle of operation of the described two-color scheme is simple. Let us consider the gap-tunable undulator of the FLASH2 branch of the soft X-ray free electron laser facility FLASH [7]. The undulator consists of twelve 2.5 m long segments, maximum K-value is 2.7. For generation of two colors, all odd segments are tuned to wavelength λ_1 , and even segments to λ_2 (see Fig. 1). With respect to the amplification of the electromagnetic wave with the wavelength λ_1 , the FEL process is disrupted as soon as the electron beam leaves λ_1 segment and enters a "wrong" segment tuned to λ_2 . However, energy modulations in the electron bunch, accumulated due to the interaction with the electromagnetic field in the λ_1 segment, continue to get converted into density modulations (bunching) in the λ_2 segment due to its longitudinal dispersion. Thus, in the next λ_1 segment the beam with an enhanced bunching quickly radiates a stronger field than the one coming from the previous λ_1 segment (which in addition is diffracted), and the FEL process continues with higher amplitudes. In some sense the mechanism is similar to that of the multi-stage (or distributed) optical klystron [8–11]. In this qualitative description we do not consider effects of longitudinal velocity spread due to the energy spread and emittance of the electron beam. According to our estimates, these effects were practically negligible in our experiments.

The longitudinal dispersion of an undulator segment is characterized by a transfer matrix element $R_{56} = 2N_w\lambda$, where N_w is the number of undulator periods per segment and λ is the resonance wavelength. If $\lambda_1 < \lambda_2$, the FEL gain is, obviously, weaker for λ_1 in the corresponding λ_1

segments. However, the R_{56} in λ_2 segments is stronger and gives a larger addition to the final gain at λ_1 wavelength. Thus, the total gain in the linear regime can be comparable even if λ_1 is significantly shorter than λ_2 . In principle, the number of segments does not have to be the same for λ_1 and λ_2 , and we also tried 7 + 5 configuration. But typically 6 + 6 case was better in the sense of reaching comparable intensities.

If the undulator line is sufficiently long, nonlinear effects start to play a role in the last segments. In this case the amplification processes at both wavelengths are not independent anymore, and they start to compete in terms of modification of longitudinal phase space of the electron beam. As a result, the radiation power is somewhat smaller compared to standard single-color lasing in saturation regime. However, it can still be sufficient for many experiments.

SIMULTANEOUS MEASUREMENTS OF TWO COLORS

As it was mentioned, two colors are not generated independently, so that one can not measure their intensities by turning off one color and measuring the other one (and vice versa). Moreover, in case of user experiments one should have online nondisruptive measurements. Thus, one of the goals of our studies was to develop methods for such measurements. It is obvious that we can find pulse energies of each of the X-ray beams as soon as we have two linear detectors. In this case we have a system of two linear equations with two unknowns, and should be able to easily retrieve pulse energies at λ_1 and λ_2 .

We have four of such detectors available in the FLASH2 tunnel and experimental hall: two gas monitor detectors (GMDs) for measurements of absolute pulse energy [12], the online photoionization spectrometer (OPIS) for non-invasive wavelength measurements [13], and micro-channel plate (MCP) detector for pulse energy measurements with a large dynamic range [14]. Note that in the following we refer to ensemble averaged pulse energies throughout the text.

As an example, let us consider the measurement we did with the tunnel GMD and OPIS. Note that both devices are placed in the tunnel next to each other, and there are no transmission effects that can be different for two X-ray beams. In the time-of-flight spectra of the OPIS, relative intensities of the two X-ray colors can be determined since the signals of the respective photoelectrons are separated in arrival time due to different kinetic energies. From these signal intensities a ratio of number of photons of the two wavelengths can be evaluated. Thus, we have the first linear equation:

$$N_2 = pN_1, \quad (1)$$

where N_1 and N_2 are unknown average photon numbers, and p is the measured coefficient. If the tunnel GMD is set to the measurements of pulse energy at λ_1 , it will show spurious pulse energy $\tilde{\mathcal{E}}_{gmd}$ when the second color is present:

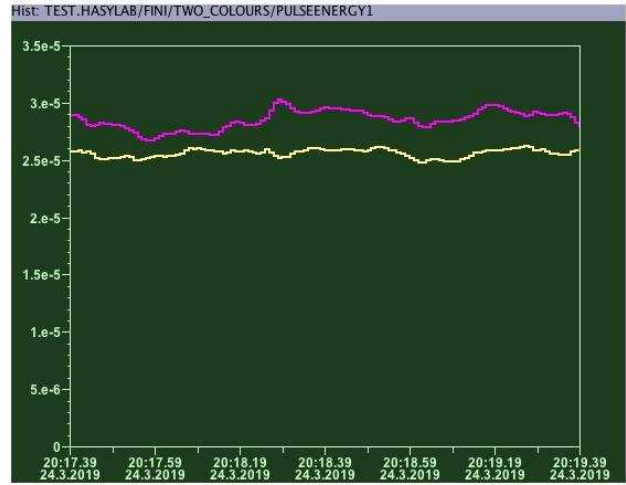


Figure 2: Online measurement of FEL intensities in two-color mode with two gas monitor detectors. Pulse energies in Joules are shown for 7 nm (yellow) and for 10 nm (pink) versus real time.

$$\tilde{\mathcal{E}}_{gmd} = \hbar\omega_1 \left(N_1 + N_2 \frac{\sigma_2\gamma_2}{\sigma_1\gamma_1} \right). \quad (2)$$

Here $\sigma_{1,2}$ are the photoionization cross sections and $\gamma_{1,2}$ are the mean charges for a given gas and the two photon energies (see, e.g. [15]), $\omega_1 = 2\pi c/\lambda_1$. Solving Eqs. (1) and (2) for N_1 and N_2 , we get the final result for the actual pulse energies $\mathcal{E}_1 = \hbar\omega_1 N_1$ and $\mathcal{E}_2 = \hbar\omega_2 N_2$:

$$\mathcal{E}_1 = \frac{\tilde{\mathcal{E}}_{gmd}}{1 + p \frac{\sigma_2\gamma_2}{\sigma_1\gamma_1}}, \quad \mathcal{E}_2 = p\mathcal{E}_1 \frac{\omega_2}{\omega_1}. \quad (3)$$

In a similar way one can get simple expressions for the combination of the MCP-based detector and the tunnel GMD. The MCP detector can be cross-calibrated with the GMD at a certain wavelength, say λ_1 . When two X-ray beams are present, it shows a linear combination of two actual pulse energies: $\tilde{\mathcal{E}}_{mcp} = \mathcal{E}_1 + s\mathcal{E}_2$. It is interesting to note that in the wavelength range of our experiments we had $s \approx 1$. Combining this equation with Eq. (2), we obtain the actual pulse energies.

Finally, we did the measurements with two GMDs, one in the tunnel and one in the experimental hall. They have to be filled with different gases, then Eq. (2) can be also used for the second GMD but with the different constants σ and γ . Moreover, we should correct the photon numbers N_1 and N_2 in that equation for the beamline transmission that has to be measured once for each wavelength individually. Then we have again the system of two equations from which we obtain actual pulse energies. The two-color measurement with two GMDs is now integrated into GMD server and can be used online for tuning and monitoring of this operation mode at FLASH2 (see Fig. 2).

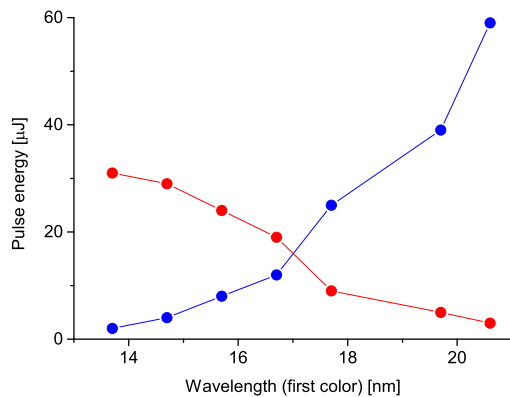


Figure 3: Pulse energies of two XUV beams measured with the GMD+OPIS method. The first color (odd undulator segments) is scanned between 13.7 nm and 20.6 nm (shown in blue). The second color (even segments) stays tuned at 22.6 nm (shown in red).

SOME EXPERIMENTAL RESULTS

In this Section we present some results related to the two-color operation in the FLASH2 undulator branch. On January 23, 2019 we demonstrated two-color lasing in XUV regime. Accelerator energy was 760 MeV, bunch charge was 0.3 nC. Wavelengths were measured with the OPIS and with a wide-spectral-range XUV spectrometer [16], both spectrometers showed the same results within 0.1 nm. Pulse energies were measured with the help of OPIS and the tunnel GMD as described in the previous Section. We explored the wavelength range from 13 nm to 27 nm, pulse energies were between a few microjoules and several tens microjoules. We also studied a possibility of scanning one wavelength while the other stayed constant, and present here an example of such a scan (see Fig. 3). The undulator was in 6 + 6 configuration: the even segments were kept tuned to $\lambda_2 = 22.6$ nm, while the odd segments were scanned in the range of λ_1 between 13.7 nm and 20.6 nm. One can see from Fig. 3 that wavelength scan in a wide range is possible but the two colors are not generated independently. When we increase λ_1 , pulse energy at this wavelength increases significantly at the expense of the pulse energy reduction at a fixed λ_2 .

On March 24, 2019 we could run FLASH accelerator at 1235 MeV (close to the maximum energy) with a bunch charge of 0.3 nC. We were able to operate in soft X-ray regime and to find the shortest wavelengths at which we could operate FLASH2 undulator in two-color mode with reasonable intensities of both X-ray beams. We used a significant frequency separation, and could get, for example, about 30 μ J at 7 nm and at 10 nm wavelengths simultaneously (see Fig. 2). We could reduce wavelengths to 6 nm and 9 nm with pulse energies being at the level of a few microjoules. For simultaneous lasing at 7 nm and 10 nm we could measure a part of the FEL gain curve (see Fig. 4) using three methods described in the previous Section. In

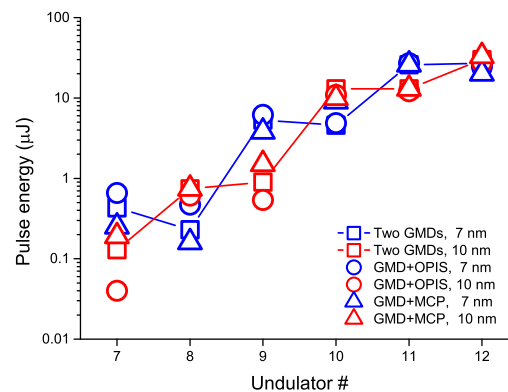


Figure 4: Gain curve of two-color lasing. Pulse energies at 7 nm (blue) and at 10 nm (red) versus the undulator segment number. Measurements were done with three methods: two GMDs (squares), GMD+OPIS (circles), and GMD+MCP (triangles).

general, the three methods showed a reasonable agreement at high intensity level, when the FEL operated in nonlinear regime and the intensities were relatively stable.

In conclusion, we were able to successfully demonstrate two-color lasing with the alternation of undulator tunes at FLASH. The methods for simultaneous measurement of two colors were developed, operational limits in terms of wavelengths and pulse energies were determined. Two-color mode can be offered to users of FLASH2.

REFERENCES

- [1] T. Hara et al., “Two-colour hard X-ray free-electron laser with wide tunability”, *Nature Commun.* **4**(2013)2919. doi: 10.1038/ncomms3919
- [2] “Possible operation of the European XFEL with ultra-low emittance beams”, R. Brinkmann, E.A. Schneidmiller, M.V. Yurkov, *Nucl. Instrum. and Methods A* **616**(2010)81. doi:10.1016/j.nima.2010.02.121
- [3] A.A. Lutman et al., “Fresh-slice multicolour X-ray free-electron lasers”, *Nature Photonics* **10**(2016)745. doi:10.1038/nphoton.2016.201
- [4] M.W. Guetg et al., “Dispersion-Based Fresh-Slice Scheme for Free-Electron Lasers”, *Phys. Rev. Lett.* **120**, 264802 (2018). doi:10.1103/PhysRevLett.120.264802
- [5] A. Marinelli et al., “Multicolor Operation and Spectral Control in a Gain-Modulated X-Ray Free-Electron Laser”, *Phys. Rev. Lett.* **111**, 134801 (2013). doi:10.1103/PhysRevLett.111.134801
- [6] W. Ackermann et al., “Operation of a free-electron laser from the extreme ultraviolet to the water window”, *Nature Photonics* **1**(2007)336. doi: 10.1038/nphoton.2007.76
- [7] B. Faatz et al., “Simultaneous operation of two soft x-ray free-electron lasers driven by one linear accelerator”, *New Journal of Physics*, **18**(2016)062002. doi:10.1088/1367-2630/18/6/062002

- [8] N. A. Vinokurov and A. N. Skrinsky, Preprint of INP 77-59, Novosibirsk, 1977. S1600577519005174
- [9] V. Litvinenko, “Storage ring FELs and the prospects”, *Nucl. Instrum. and Methods A*, vol. 304, pp. 463, 1991. doi:10.1016/0168-9002(91)90817-A
- [10] E.L. Saldin, E.A. Schneidmiller, M.V. Yurkov, “The Free Electron Laser Klystron Amplifier Concept”, in *Proceedings of the 2004 Free Electron Laser Conference*, Trieste, Italy, 2004, paper MOPOS16, p. 143.
- [11] Y. Ding *et al.*, “Optical klystron enhancement to self-amplified spontaneous emission free electron lasers”, *Phys. Rev. ST-AB* **9**(2006)070702. doi:10.1103/PhysRevSTAB.9.070702
- [12] A.A. Sorokin *et al.*, “An X-ray gas monitor for free-electron lasers”, *J. Synchrotron Rad.* **26**(2019)1092. doi:10.1107/
- [13] M. Braune *et al.*, “Non-invasive online wavelength measurements at FLASH2 and present benchmark”, *J. Synchrotron Rad.* **25**(2018)3. doi:10.1107/S16005775170138
- [14] O. I. Brovko *et al.*, “Experience With MCP-Based Photon Detector at FLASH2”, presented at the 39th Int. Free Electron Laser Conf. (FEL’19), Hamburg, Germany, Aug. 2019, paper WEP073.
- [15] K. Tiedtke *et al.*, “Gas detectors for x-ray lasers”, *Journal of Applied Physics* **103**(2008)094511. doi:10.1063/1.2913328
- [16] T. Tanikawa *et al.*, “First observation of SASE radiation using the compact wide-spectral-range XUV spectrometer at FLASH2”, *Nucl. Instrum. and Meth. A* **830**, 170-175 (2016). doi:10.1016/j.nima.2016.05.088

FEASIBILITY STUDIES OF THE 100 keV UNDULATOR LINE OF THE EUROPEAN XFEL

E.A. Schneidmiller*, V. Balandin, W. Decking, M. Dohlus, N. Golubeva,
D. Noelle, M.V. Yurkov, I. Zagorodnov
DESY, Hamburg, Germany

G. Geloni, Y. Li, S. Molodtsov, J. Pflueger, S. Serkez, H. Sinn, T. Tanikawa, S. Tomin
European XFEL GmbH, Schenefeld, Germany

Abstract

The European XFEL is a multi-user X-ray FEL facility based on superconducting linear accelerator. Presently, three undulators (SASE1, SASE2, SASE3) deliver high-brightness soft- and hard- X-ray beams for users. There are two empty undulator tunnels that were originally designed to operate with spontaneous radiators. We consider instead a possible installation of two FEL undulators. One of them (SASE4) is proposed for the operation in ultrahard X-ray regime, up to the photon energy of 100 keV. In this contribution we present the results of the first feasibility studies of this option.

INTRODUCTION

The European XFEL is a X-ray FEL user facility, based on superconducting accelerator [1]. It provides ultimately bright photon beams for user experiments since 2017. Two hard X-ray undulators (SASE1 and SASE2) and one soft X-ray undulator (SASE3) are presently in operation [2], see Fig. 1. There are two empty undulator tunnels that were originally designed [3] to host the undulators U1 and U2 (see Fig. 1) to be used for generation of spontaneous undulator radiation in the range 20-90 keV.

Recently, design studies have been initiated aiming at conceptual and technical designs of FEL undulator lines instead of spontaneous radiators in the empty tunnels. One of the options, requested by the user community, is an undulator capable of generation of powerful X-ray radiation in the ultrahard photon energy range, up to 100 keV. Realization of such an option would rely on the unique features of the European XFEL among other facilities of such kind, namely the highest electron energy (17.5 GeV) and the longest tunnels. Note that the idea of using a SASE undulator for lasing up to 90 keV instead of spontaneous radiators in one of the empty tunnels was suggested and illustrated with numerical simulations in [4]. In this paper we perform extended considerations of this option.

UNDULATOR LENGTH AND LOCATION

The hard and ultrahard X-ray undulator can be located in the tunnel XTD3 (place for U1 in Fig. 1) or in XTD5 (place for U2). The planned lengths for the installation of the spontaneous radiators is 120 m in XTD3 and 140 m in XTD5. It would be desirable to have a larger length for

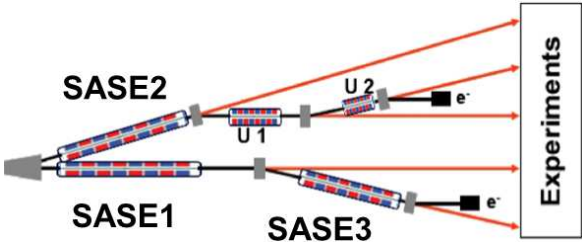


Figure 1: Layout of undulator tunnels of the European XFEL

SASE4 if it is supposed to lase up to 100 keV, and one can consider alterations to the tunnel infrastructure and electron lattice. In particular, a more aggressive bending can be considered at the end of XTD3, thus making about 200 m in this tunnel available for the installation of the SASE4 undulator. Also, we discuss an installation of a bypass line (as an alternative to the fresh bunch technique [4]) to avoid beam quality deterioration in SASE2 undulator (see below).

EXPECTED PROPERTIES OF THE ELECTRON BEAM

Electron beams with a high peak current, low emittance and energy spread are required for operation of short-wavelength FELs. This is especially important when we discuss a challenging range of photon energies, up to 100 keV. We performed start-to-end simulations of the beam dynamics in the European XFEL accelerator (tools and methods are described in [5]), and present here the results for 100 pC bunches, accelerated to 17.5 GeV and transported to the SASE2 undulator. The current, emittance, uncorrelated energy spread are presented in Fig. 2 as functions of a position along the bunch length. One can see that slice parameters in the bunch core are good: peak current is 5 kA, slice emittance is below 0.3 mm mrad, and uncorrelated energy spread is below 1 MeV. The latter parameter can degrade if the bunches are transported through SASE2 undulator, it can increase up to 3 MeV due to the quantum diffusion [6] if SASE2 operates with fully closed gap. To fully decouple operation of SASE2 and SASE4, it would be desirable to consider a bypass line (also wakefield effects would be strongly reduced then).

We also consider an advanced compression, namely eSASE [7]. In that case, we compress the beam relatively weakly in bunch compressors (to 1-2 kA) thus avoiding strong CSR effects during compression and transport. Then

* evgeny.schneidmiller@desy.de

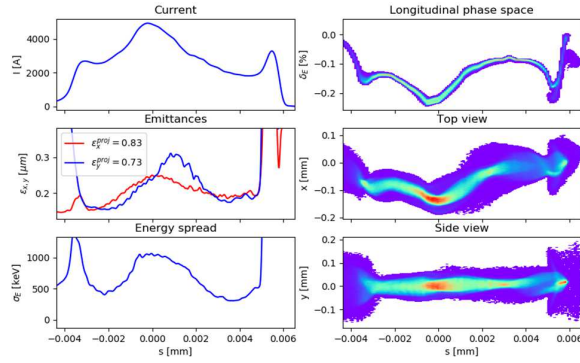


Figure 2: The results of start-to-end simulations for the bunch charge of 100 pC. Left column: current, slice emittance (horizontal in red, vertical in blue) and uncorrelated energy spread versus the position along the bunch length. Left column: longitudinal phase space, top view and side view of the bunch.

we can obtain a high peak current in front of SASE4 as follows: we modulate the beam by a laser in a wiggler and get high-current spikes in a compact chicane. First simulation results are encouraging [8].

LIMITATION ON THE PHOTON ENERGY

A fundamental limit on a shortest wavelength of a SASE FEL is given by the growth of uncorrelated energy spread due to quantum fluctuations of the undulator radiation [6, 9]. The shortest wavelength can be estimated as [10]:

$$\lambda_{\min}^q [\text{Å}] \simeq \frac{4 \epsilon_n [\mu\text{m}]}{I^{3/5} [\text{kA}] L_w^{2/5} [\text{m}]} \quad (1)$$

Here I is the peak current, ϵ_n is the rms normalized emittance, L_w is the undulator length. It is assumed that electron energy and undulator parameters can be freely chosen and are optimized. Let us estimate the limit for the following parameters: $I = 5 \text{ kA}$, $\epsilon_n = 0.3 \text{ mm mrad}$, $L_w = 175 \text{ m}$. According to (1) we get $\lambda_{\min}^q \simeq 0.06$, and the corresponding photon energy is about 200 keV.

UNDULATOR TECHNOLOGY

To be specific, we will assume that the magnetic length of SASE4 undulator can be as large as that of SASE1 and SASE2 undulators [11], namely 175 m. All the calculations below are done for the beam energy of 17.5 GeV, include quantum diffusion in SASE4 undulator, and assume the following slice parameters of the lasing core of electron bunch at the entrance of SASE4: peak current 5 kA, normalized slice emittance 0.3 mm mrad, and uncorrelated energy spread 1 MeV. It follows from formulas of ref. [10] that the shortest achievable FEL wavelength is simply proportional to an undulator period for these parameters. Thus, it is worth considering short-period undulators such as in-vacuum or superconducting ones. On the other hand, we should not exclude from consideration the standard out-of-vacuum undulators with longer periods and advanced lasing options.

Apart from giving a possibility to reach high photon energy, SASE4 undulator should have a significant tunability range because it will be one of the five undulators simultaneously providing X-ray beams for users. Let us briefly consider three different scenarios using the properties of undulators summarized in [12].

In-Vacuum Undulator

The technology of in-vacuum (IV) undulators is relatively well developed and used at other XFEL facilities (SACLA, Swiss FEL). Let us consider as an example the undulator period of 22 mm and the gap of 5 mm. For the above mentioned parameter set we find that the tunability range would be 40 - 100 keV.

Superconducting Undulator

A few meters long superconducting (SC) undulators are installed and successfully operated at storage ring based light sources, but substantial R&D is required towards building a long string of undulators of an excellent quality for X-ray FELs. The main advantage of SC undulators is a possibility to combine a short period and a strong magnetic field, resulting in a large K-value. For example, for a period of 25 mm and the pole gap of 7 mm (beam stay-clear gap is 5 mm), the maximum K-value is about 5.5. Then, for our parameter set, the tunability range of such an undulator would be 7 - 90 keV. An interesting technical option could be the period doubling that would allow to further reduce the period length while increasing the tunability. More details on SASE4 performance with a superconducting undulator can be found in [13].

Standard out-of-Vacuum Undulator

This is the most cheap and reliable technology. Let us consider an undulator with the period of 35 mm and the gap of 7.5 mm. The tunability range would be 8 - 60 keV on the fundamental, and the upper limit can be extended to 85 keV with harmonic lasing [14]. In case of a higher quality of the electron beam, the highest photon energy can be above 100 keV.

As an option, one can consider a combination of two undulators with different periods in the same way as it was proposed for FLASH upgrade [15]. For example, an undulator with a period of 40 mm and magnetic length of 100 m can be followed by a 75 m long section with the period of 30 mm. With the gap of 10 mm, this configuration would provide the same tunability range as the undulator with the period of 35 mm and the gap of 7.5 mm, considered before. Note that the gap might be a critical issue for an XFEL based on the superconducting accelerator with a high average beam power.

Let us finally note that the large tunability in case of the last two options is a very attractive feature. It supports the operation of multi-user facility with the same electron energy most of the time and may let serve two user stations operating at 7 - 25 keV and 25 - 100 keV with a possible day/night switching.

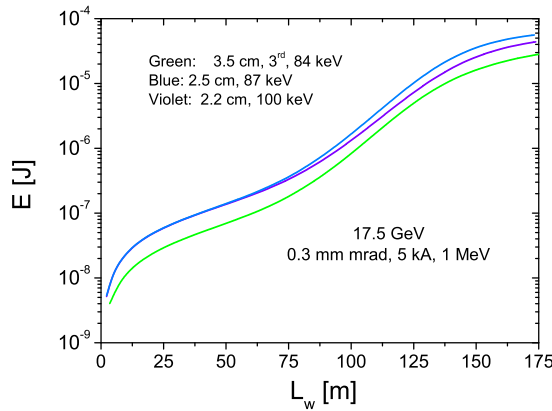


Figure 3: FEL pulse energies versus undulator length for the three undulator cases: superconducting (blue), in-vacuum (violet), and standard out-of-vacuum with the 3rd harmonic lasing (green).

EXPECTED PROPERTIES OF THE RADIATION

We performed numerical simulations with the code FAST [16] for three sets of undulator parameters from the previous Section and photon energies approaching 100 keV. Pulse energies versus undulator length are shown in Fig. 3, they are in the range of several tens of microjoules what corresponds to about 10^9 photons per pulse. Divergence of the FEL radiation for these photon energies is about $0.3 \mu\text{rad}$ (FWHM), and the intrinsic bandwidth ranges between 10^{-4} and 3×10^{-4} (FWHM). Actual bandwidth might be influenced by an energy chirp (but an installation of a dechirper can help keep it small).

The transverse coherence depends on the ratio of a geometric emittance to the wavelength [17] and is expected to be relatively poor for photon energies about 100 keV. If the normalized emittance is 0.3 mm mrad , the degree of transverse coherence (see the definition in [17]) can be estimated at the level of 20% using the results of ref. [17] (see Fig. 4).

Radiation properties can be improved in case of using eSASE based compression scheme that might allow for compression to a higher peak current while preserving slice emittance of the lasing spikes. In this case the number of photons per pulse can be increased to the level of 10^{10} for the photon energies about 100 keV, and the transverse coherence can be also improved.

ADVANCED LASING CONCEPTS

High energy photons can be produced by nonlinear harmonic generation mechanism but with low intensity, large fluctuations and a strong background on the fundamental. One can consider, instead some advanced schemes eliminating these problems. Harmonic lasing was already mentioned as an opportunity to extend the photon energy range of SASE4, it can provide high-brightness photon beams [14].

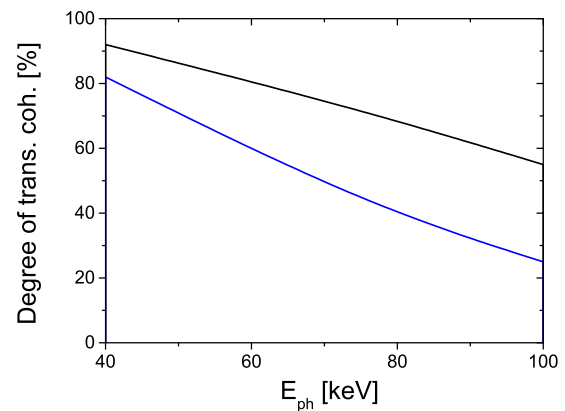


Figure 4: Expected degree of transverse coherence (see the definition in [17]) of SASE FEL radiation as a function of photon energy. Blue line: normalized emittance is 0.3 mm mrad . Black line: normalized emittance is 0.2 mm mrad . Electron beam energy is 17.5 GeV . Estimates were done using the results of Ref. [17].

Recent experimental developments [18–20] confirm a validity of this concept in X-ray regime. Another option is the reverse tapering of the main undulator plus an afterburner [21] where an efficient background-free generation of harmonics is possible as it was shown in recent experiments [22]. One can also consider cascaded frequency multiplication [23,24] that might be especially efficient when several compact chicanes are installed as parts of the undulator system. The operation of the single-stage multiplication scheme, the frequency doubler, was demonstrated experimentally [25,26]. One or more of these methods could complement standard SASE FEL operation on the fundamental, and this would be especially desirable in the case of using the standard undulator technology.

SUMMARY AND OUTLOOK

We can conclude that 100 keV lasing at the European XFEL seems to be feasible. Final choice of the photon energy range, possible length and location of the undulator, choice of the undulator technology will be a result of an iterative process that includes in particular user requirements, financial and technological aspects.

REFERENCES

- [1] W. Decking and H. Weise, “Commissioning of the European XFEL Accelerator”, in *Proc. 8th Int. Particle Accelerator Conf. (IPAC’17)*, Copenhagen, Denmark, May 2017, pp. 1–6. doi:10.18429/JACoW-IPAC2017-MOXA1
- [2] W. Decking *et al.*, “Status of the European XFEL”, in *Proc. 10th Int. Particle Accelerator Conf. (IPAC’19)*, Melbourne, Australia, May 2019, pp. 1721–1723. doi:10.18429/JACoW-IPAC2019-TUPRB020
- [3] M. Altarelli *et al.* (Eds.), *XFEL: The European X-Ray Free-Electron Laser. Technical Design Report*, Preprint

- DESY 2006-097, DESY, Hamburg, 2006 (see also <http://xfel.desy.de>). doi:10.3204/DESY_06-097
- [4] R. Brinkmann, E.A. Schneidmiller and M.V. Yurkov, "Possible operation of the European XFEL with ultra-low emittance beams", *Nucl. Instrum. and Methods*, vol. 616, section, p. 81, 2010. doi:10.1016/j.nima.2010.02.121
- [5] I. Zagorodnov, M. Dohlus, and S. Tomin, "Accelerator beam dynamics at the European X-ray Free Electron Laser", *Phys. Rev. Accel. Beams*, vol. 22, p. 024401, Feb 2019. doi:10.1103/PhysRevAccelBeams.22.024401
- [6] E. Saldin, E. Schneidmiller and M. Yurkov, "Calculation of energy diffusion in an electron beam due to quantum fluctuations of undulator radiation", *Nuclear Instruments and Methods in Physics Research*, vol. 381, Issues 2–3, Nov 1996, pp. 545–547. doi:10.1016/S0168-9002(96)00708-5
- [7] A. Zholents and W. Fawley, "Proposal for Intense Attosecond Radiation from an X-Ray Free-Electron Laser", *Phys. Rev. Lett.*, vol. 92, p. 224801, published 4 June 2004. doi:10.1103/PhysRevLett.92.224801
- [8] I. Zagorodnov et al., "An advanced compression option for the European XFEL", FEL' 19, Hamburg, Germany, paper TUP060, this conference.
- [9] J. Rossbach, E. Saldin, E. Schneidmiller and M. Yurkov, "Interdependence of parameters of an X-ray FEL", *Nucl. Instrum. and Methods*, vol. 374, Issue 3, Jun 1996, pp. 401–407. doi:10.1016/0168-9002(96)00189-1
- [10] E. Saldin, E. Schneidmiller, M. Yurkov, "Design formulas for short-wavelength FELs", *Opt. Commun.*, vol. 235, Issues 4–6, May 2004, pp. 415–420. doi:10.1016/j.optcom.2004.02.071
- [11] S. Abeghyan et al., "First operation of the SASE1 undulator system of the European X-ray Free-Electron Laser", *J. Synchrotron Rad.*, vol. 26, pp 302–310, Mar 2019. doi:10.1107/S1600577518017125
- [12] E. Gluskin, presentation at APS meeting, Aug. 2012
- [13] S. Serkez et al., "Super-X: Simulations for Extremely Hard X-Ray Generation With Short Period Superconducting Undulators for the European XFEL", FEL' 19, Hamburg, Germany, paper TUP061, this conference.
- [14] E.A. Schneidmiller and M.V. Yurkov, "Harmonic lasing in x-ray free electron lasers", *Phys. Rev. ST Accel. Beams*, vol. 15, p. 080702, August 2012. doi:10.1103/PhysRevSTAB.15.080702
- [15] E. Schneidmiller et al., "A Concept for Upgrade of FLASH2 Undulator Line", in *Proc. 10th Int. Particle Accelerator Conf. (IPAC'19)*, Melbourne, Australia, May 2019, pp. 1736–1739. doi:10.18429/JACoW-IPAC2019-TUPRB024
- [16] E. Saldin, E. Schneidmiller, M. Yurkov, "FAST: a three-dimensional time-dependent FEL simulation code", *Nucl. Instrum. and Methods A429(1999)233*, vol. 429, Issues 1–3, June 1999, pp. 233–237. doi:10.1016/S0168-9002(99)00110-2
- [17] E. Saldin, E. Schneidmiller, M. Yurkov, "Coherence properties of the radiation from X-ray free electron laser", *Opt. Commun.*, vol. 281, Issue 5, March 2008, pp. 1179–1188. doi:10.1016/j.optcom.2007.10.044
- [18] E.A. Schneidmiller et al., "First operation of a harmonic lasing self-seeded free electron laser", *Phys. Rev. Accel. Beams*, vol. 20, p. 020705, February 2017. doi:10.1103/PhysRevAccelBeams.20.020705
- [19] I. Nam et al., "Soft X-ray harmonic lasing self-seeded free electron laser at Pohang Accelerator Laboratory X-ray free electron laser", *Applied Phys. Lett.*, vol. 112, p. 213506, 2018. doi:10.1063/1.5030443
- [20] E.A. Schneidmiller et al., "Harmonic lasing of the European XFEL in the Angstrom regime", FEL' 19, Hamburg, Germany, paper TUA04, this conference.
- [21] E.A. Schneidmiller and M.V. Yurkov, "Obtaining high degree of circular polarization at x-ray free electron lasers via a reverse undulator taper", *Phys. Rev. ST Accel. Beams*, vol. 16, p. 110702, Nov 2013. doi:10.1103/PhysRevSTAB.16.110702
- [22] E. Schneidmiller and M. V. Yurkov, "Reverse Undulator Tapering for Polarization Control and Background-Free Harmonic Production in XFELs: Results from FLASH", in *Proc. 38th Int. Free Electron Laser Conf. (FEL'17)*, Santa Fe, NM, USA, Aug. 2017, pp. 106–108. doi:10.18429/JACoW-FEL2017-MOP032
- [23] R. Bonifacio, L. De Salvo, and P. Pierini, "Large harmonic bunching in a high-gain free-electron laser", *Nucl. Instrum. and Methods*, vol. 293, Issue 3, August 1990, Pages 627–629. doi:10.1016/0168-9002(90)90334-3
- [24] J. Feldhaus et al., "Efficient frequency doubler for the soft X-ray SASE FEL at the TESLA Test Facility", *Nucl. Instrum. and Methods*, vol. 528, Issues 1–2, 1 August 2004, pp. 471–475. doi:10.1016/j.nima.2004.04.134
- [25] H.-D. Nuhn et al., "Characterization of Second Harmonic Afterburner Radiation at the LCLS", in *Proc. 32nd Int. Free Electron Laser Conf. (FEL'10)*, Malmö, Sweden, Aug. 2010, paper THOC12, pp. 690–695.
- [26] M. Kuhlmann, E. Schneidmiller, and M. V. Yurkov, "Frequency Doubling Mode of Operation of Free Electron Laser FLASH2", in *Proc. 38th Int. Free Electron Laser Conf. (FEL'17)*, Santa Fe, NM, USA, Aug. 2017, pp. 117–120. doi:10.18429/JACoW-FEL2017-MOP036

ANALYSIS OF PARAMETER SPACE OF SOFT X-RAY FREE ELECTRON LASER AT THE EUROPEAN XFEL DRIVEN BY HIGH AND LOW ENERGY ELECTRON BEAM

E.A. Schneidmiller, M.V. Yurkov, DESY, Hamburg, Germany

Abstract

Three undulator beamlines: SASE1 and SASE2 (hard X-ray), and SASE3 (soft X-ray) are in operation at the European XFEL serving six user instruments. Next stages of the facility development are installation of two undulator beamlines in empty tunnels SASE4 and SASE5 as middle term upgrade, and extension of the facility with the second fan of undulators as long term upgrade. Construction of soft X-ray beamlines is considered in both upgrade scenario. In the case of SASE4/SASE5 electron beam with energies 8.5 GeV - 17.5 GeV will be used in order to provide simultaneous operation of new undulator beamlines with existing SASE1-SASE3. One of the scenarios for a second fan of undulators involves using of low energy (2.5 GeV) electron beam. In this paper we analyze parameter space of soft X-ray SASE FELs driven by high energy and low energy electron beam, compare output characteristics, and discuss potential advantages and disadvantages.

INTRODUCTION

Start-up configuration of the European XFEL includes two hard X-ray SASE FELs, SASE1 and SASE2, and one soft X-ray SASE FEL, SASE3 serving six user instruments [1]. All undulators are planar, variable gap devices. SASE1 and SASE2 are equipped with identical undulators with 4 cm period length. SASE3 undulator has similar mechanical design, but the period length is 6.8 cm. Radiation wavelength at fixed electron energy is changed by means of changing the undulator gap. Trusted tunability ranges of undulators are limited to $\lambda_{\max}/\lambda_{\min} = 3.6$ for SASE1/SASE2 and 4.5 for SASE3 which is not sufficient for covering all user experiments at one fixed electron energy. By the time, five operating points of the electron beam energy have been fixed (8.5, 11.5, 14, 16.5, and 17.5 GeV) providing most flexible way for simultaneous operation of users at all three beamlines. Full wavelength range covered by start-up configuration spans from 0.05 nm to 5.1 nm.

Start-up of the facility operation proceeded smoothly: all three SASE radiators produce x-ray radiation with parameters close to design values, and all six user stations serve user experiments [2, 3]. Middle term plans of the facility development assume installation of two more SASE FEL beamlines in empty tunnels and construction of four user instruments [1]. Strategic extension of the facility assumes installation of new undulator beamlines and user stations doubling user capacity. Here an option of low energy beamline has been considered when electron beam at the energy of 2.5 GeV is extracted from accelerator and is transported via bypass electron beamline to the undulator for generation

of soft X-ray radiation. Upgrade of the the accelerator to CW mode of operation is also included in a long term R&D program [4].

Next generation X-ray FELs should provide wide capabilities for performing user experiments:

- wide tunability range;
- control of the radiation pulse duration;
- coherence control: temporal and spatial;
- polarization control: linear, circular, elliptical;
- wide capabilities for pump-probe experiments involving FEL radiation (fundamental harmonic, higher harmonics, independent colors), laser and accelerator based radiation sources;
- control of the photon flux up to ultimate level.

Not all of these features are implemented in the start-up configuration of the European XFEL. In this paper we discuss possible potential development of soft-Xray/VUV FEL beamline with extended wavelength range and extended user capabilities. We consider two options: high energy option, 8.5 GeV - 17.5 GeV, and low energy, 2.5 GeV option. Our study shows that high energy option has evident advantages in terms of peak radiation power, pulse energy, photon flux, and transverse coherence. Additionally, operation at higher charges and higher electron energies holds potential for generation of the radiation pulse energies on a sub-Joule level [5]. High energy option can be realized on a middle term time scale using present infrastructure of the European XFEL which foresees installation of two more undulators and four user instruments.

HIGH ELECTRON ENERGY: 8.5 - 17.5 GeV

First step of our study is an overview of parameter space aiming extension of the operating range in the direction of longer wavelengths. The only mean to do this is to increase the undulator period. Figure 1 shows contour plot of the maximum wavelength as function of the undulator period and electron beam energy. We find that undulator with period length 10 to 12 cm provides maximum wavelength of 25 - 45 nm at the electron energy of 8.5 GeV. Operation at the electron energy of 17.5 GeV with an open undulator gap will allow to reach radiation wavelengths below 1 nm.

Plot in Fig. 2 illustrates main parameters of SASE FEL for the case of 11 cm undulator period length. Numerical example is calculated for electron bunch with baseline parameters: bunch charge 250 pC, peak current 5 kA, rms normalized emittance 0.6 mm-mrad, rms energy spread 2.5 MeV [6]. Blue, black and red colors refer to the radiation wavelength, saturation length, and radiation pulse energy in the saturation regime. Solid lines show values of the parameters for closed

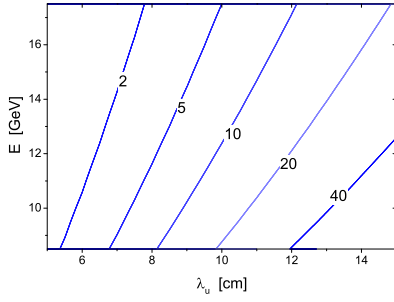


Figure 1: Maximum radiation wavelength as function of the electron energy and undulator period.

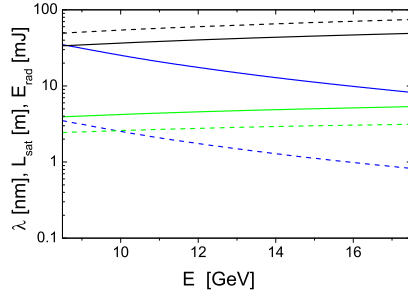


Figure 2: Radiation wavelength (blue), saturation length (black), and radiation pulse energy in the saturation (green) versus electron energy. Solid lines and dashed lines correspond to closed and open undulator gap, respectively. Undulator period is equal to 11 cm. Bunch charge is 250 pC [6]. Simulations are performed with code FAST [7].

undulator gap, and dashed lines represent values for open undulator. Undulator parameter changes from 13.2 (closed gap) to 4.1 (open gap), and wavelength tunability range at fixed energy is $\lambda_{\max}/\lambda_{\min} = 10$. We see that parameters of the SASE FEL change very slowly in the whole wavelength range spanning from 0.8 nm to 35 nm. When SASE FEL operates at closed undulator gap, saturation length changes from 34 m at 8.5 GeV to 49 m at 17.5 GeV, and radiation pulse energy is increased from 4 to 5.3 mJ. Operation at open gap leads to increase of the saturation length by a factor 1.5, and radiation pulse energy falls by a factor 1.6. Such a slow dependence of output characteristics is consequence of small value of the diffraction parameter. In the case under study diffraction parameter is in the range $B = 0.07 - 0.1$ for closed gap, and $B = 0.7 - 1$ for open gap. This feature explains so slow change of output characteristics. Indeed, when energy spread and betatron oscillation effects are negligible, operation of the FEL amplifier is described by the diffraction parameter $B = 2\Gamma\sigma^2\omega/c$ with the gain parameter Γ [8]:

$$\Gamma = \left[\frac{I}{I_A} \frac{16\pi^2 K^2 A_J^2}{(1 + K^2)\lambda_w^2 \gamma} \right]^{1/2},$$

Efficiency of an FEL amplifier in saturation is universal function of the only diffraction parameter B :

$$\eta \approx \bar{\rho} \quad \text{for } B < 1,$$

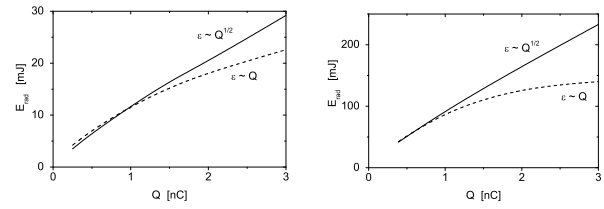


Figure 3: Energy in the radiation pulse versus bunch charge for SASE3 at the European XFEL. Left plot: FEL operates in the saturation regime. Right plot: operation with tapered parameters for the undulator length of 100 meters. Electron energy is 17.5 GeV, radiation wavelength is 1.6 nm. Solid and dashed lines correspond to the emittance scaling as $q^{1/2}$, and q , respectively.

$$\eta \approx \bar{\rho}/B^{1/3} \quad \text{for } B > 1,$$

where 3D FEL parameter $\bar{\rho} = \lambda_w \Gamma / (4\pi)$. FEL gain length scales as $1/B^{1/3}$ for $B > 1$, and changes slowly (in fact logarithmically with B) at small values of diffraction parameter. For large value of the undulator parameter K and small values of diffraction parameter B , the gain parameter scales as $\Gamma \propto 1/\gamma^{1/2}$. As a result, saturation length scales as $L_{\text{sat}} \propto \gamma^{1/2}$, and radiation pulse energy in saturation scales as:

$$E_{\text{rad}} \approx \bar{\rho} \times N_e \times \gamma \times m_e c^2 \propto N_e \times \gamma^{1/2} \times I^{1/2},$$

which explains relevant dependencies shown in Fig. 2.

We should note that FEL efficiency can be increased with application of undulator tapering. In the case of diffraction limited beam one can gain a factor up to 10 in efficiency with respect to saturation value. Also, European XFEL holds potential to operate with high charge bunches, up to 5 nC. As a result, very high radiation pulse energies can be achieved as we reported earlier in ref. [5], see Fig. 3.

LOW ELECTRON ENERGY: 2.5 GeV

This option has been analyzed at the design stage of the project [9]. It is assumed to extract electron beam after the last bunch compression stage. Then electron beam is transported via bypass beamline to the undulator and produces radiation. We fix electron energy to 2.5 GeV for this option. The only remaining parameter for optimization is undulator period. In the same way as it has been done in the previous section, we derive dependencies for the wavelength range, saturation length, and radiation pulse energy in the saturation (see Fig. 4).

Let us compare low energy option with high energy option. Saturation length at the radiation wavelength of 1 nm is 40 meters for the low energy option with 3 cm undulator period length, and 70 meters for high energy option with 11 cm undulator period length. However, practical characteristics of the low energy options significantly below those provided by high energy option. Indeed, we see that operation at fixed energy of the electron beam significantly shrinks available

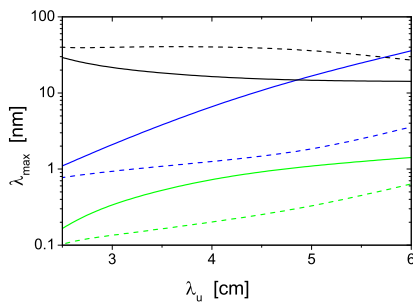


Figure 4: Radiation wavelength (blue), saturation length (black), and radiation pulse energy in the saturation (green) versus undulator period length. Solid lines and dashed lines correspond to closed and open undulator gap, respectively. Bunch charge is 250 pC [6]. Energy of electrons is 2.5 GeV. Simulations are performed with code FAST [7].

wavelength range. For high energy option we combine both means for the wavelength change: undulator gap and electron energy change. Helpful factor was also large K value of the long period undulator. For low energy option undulator K value falls down with undulator period, and tunability range shrinks drastically for shorter undulator periods. Energy in the radiation pulse is by an order of magnitude below that of high energy option. This happens due to two reasons: lower electron energy and operation of FEL process above diffraction limit. The value of the diffraction parameter B is about 30 when operating at the radiation wavelength around 1 nm. Mode degeneration effect can take place in this case reducing transverse coherence and pointing stability of the radiation [10].

DISCUSSION

An option of SASE FEL with long period undulator driven by high energy electron beam can be attractive option for perspective extension of the European XFEL on a middle term period: existing tunnels and infrastructure ideally fit for installation of such undulator. Essential feature of this undulator beamline is extended wavelength range. Use of variable polarization devices (e.g., of APPLE type) solves the problem of polarization control. Installation of a long undulator will be very useful for extension of user capabilities. Longer undulator can be used for generation of two or more independent colors [11, 12]. Installation of chicanes in the beamline will allow to control timing of different colors and organize relevant pump-probe experiments. Several harmonics can be generated as well [13, 14]. Implementation of Harmonic Lasing Self Seeding (HLSS) will allow to control longitudinal coherence [13]. This scheme essentially exploits high undulator K value. Application of the undulator tapering in combination with high charges will allow to generate very powerful radiation with pulse energies on a sub-Joule level [5]. External seeding can be also implemented for longer wavelengths when the effect of the noise growth in frequency multiplication schemes is on a low level [15].

ACKNOWLEDGMENTS

Results presented in this paper have been discussed at the meetings devoted to revision of parameter space and discussion of potential extensions of the European XFEL. We are grateful to our colleagues from DESY and European XFEL for fruitful collaboration during this work: M. Altarelli, C. Bressler, R. Brinkmann, W. Decking, R. Feidenhans'l, G. Geloni, N. Gerasimova, J. Grünert, T. Limberg, A. Madsen, A. Mancuso, M. Meyer, S. Molodtsov, J. Pflueger, L. Samoylova, A. Schwarz, S. Serkez, H. Sinn, T. Tschentscher, and H. Weise. We thank our colleagues from the Beam Dynamics Group for providing us with parameters of the electron beam: M. Dohlus, G. Feng, I. Zagorodnov. We are grateful to M. Krasilnikov and F. Stephan for fruitful collaboration on high charge option. We thank R. Brinkmann for fruitful collaboration and support of our work.

REFERENCES

- [1] M Altarelli *et al.* (Eds.), "The European X-ray free-electron laser. Technical design report.", Preprint DESY, 2006-097, DESY, Hamburg, 2007.
- [2] W. Decking *et al.*, "First operation of a MHz-repetition-rate Hard X-Ray Free-Electron Laser driven by a superconducting linear accelerator", submitted to publication.
- [3] V. Balandin *et al.*, "First characterization of the photon beam at the European XFEL in July, 2017", presented at FEL'19, Hamburg, Germany, 2019, paper TUP058, this conference.
- [4] R. Brinkmann *et al.*, "Prospects for CW and LP operation of the European XFEL in hard X-ray regime", *Nucl. Instrum. and Methods A*, vol. 768, p. 20, 2014. doi:10.1016/j.nima.2014.09.039
- [5] E.A. Schneidmiller and M.V. Yurkov, "Photon beam properties at the European XFEL", Preprint DESY 11-152, DESY, Hamburg, 2011.
- [6] W. Decking, T. Limberg, XFEL.EU Technical Note 1-22 (2013) XFEL.EU TN-2013-004-01, European XFEL, Hamburg, 2013.
- [7] E.L. Saldin, E.A. Schneidmiller and M.V. Yurkov, "FAST: a three-dimensional time-dependent FEL simulation code", *Nucl. Instrum. and Methods A*, vol. 429, p. 233, 1999. doi: 10.1016/S0168-9002(99)00110-2
- [8] E.L. Saldin, E.A. Schneidmiller and M.V. Yurkov, *The Physics of Free Electron Lasers*, Springer Verlag, Berlin, 1999. doi:10.1007/978-3-662-04066-9
- [9] E.L. Saldin, E.A. Schneidmiller and M.V. Yurkov, "The Potential for Extending the Spectral Range Accessible to the European X-ray Free Electron Laser in the Direction of Longer Wavelengths", Preprint TTF FEL 2004-05, DESY, Hamburg, 2004.
- [10] E.A. Schneidmiller and M.V. Yurkov, "Coherence properties of the radiation from FLASH", *J. Mod. Optics*, vol. 63, p. 239, 2015, doi:10.1080/09500340.2015.1066456
- [11] R. Brinkmann, E. Schneidmiller, M. Yurkov, "Possible operation of the European XFEL with ultra-low emittance beams", *Nucl. Instr. Meth. A*, vol. 616, p. 81, 2010. doi: 10.1016/j.nima.2010.02.121

- [12] A. Lutman *et al.*, “Fresh-slice multicolour X-ray free-electron lasers”, *Nature Photonics*, vol. 10, p. 745, 2016. doi:10.1038/nphoton.2016.201
- [13] E. L. Saldin, E.A. Schneidmiller, M.V. Yurkov, “Properties of the third harmonic of the radiation from self-amplified spontaneous emission free electron laser”, *Phys. Rev. ST Accel. Beams*, vol. 9, p. 030702, 2006. doi:10.1103/PhysRevSTAB.9.030702
- [14] M. Kuhlmann *et al.*, “Frequency doubler and two-color mode of operation at free electron laser FLASH2”, *Proc. SPIE*, vol. 10237, 1023710, 2017. doi:10.1117/12.2265584
- [15] E.L. Saldin, E.A. Schneidmiller and M.V. Yurkov, “Study of a noise degradation of amplification process in a multistage HGHG FEL”, *Opt. Commun.*, vol. 202, p. 169, 2002. doi:10.1016/S0030-4018(02)01091-X

FIRST CHARACTERIZATION OF THE PHOTON BEAM AT THE EUROPEAN XFEL IN JULY, 2017

V. Balandin, B. Beutner, F. Brinker, W. Decking, M. Dohlus, L. Fröhlich, U. Jastrow, R. Kammering, T. Limberg, D. Noelle, M. Scholz, A. Sorokin, K. Tiedtke, M.V. Yurkov, I. Zagorodnov, DESY, Hamburg, Germany
U. Boesenberg, W. Freund, J. Grünert, A. Koch, N. Kujala, J. Liu, T. Maltezopoulos, M. Messerschmidt, I. Petrov, L. Samoylova, H. Sinn, European XFEL, Germany

Abstract

This report presents the first characterization of the photon beam properties from SASE1 FEL at the European XFEL. Development of the amplification process has been traced from the level of the radiation pulse energy in sub- μJ level (beginning of high gain linear regime) up to mJ level (saturation regime). Experimental method is based on the analysis of single shot photon beam images allowing to derive spatial properties of the FEL radiation mode. An important conclusion is that experimental results demonstrate reasonable agreement with baseline parameters. Developed techniques of the photon beam characterization also provided solid base for identification of the problems and means for improving SASE FEL tuning and operation.

INTRODUCTION

First light from the European XFEL [1] has been detected on May 3rd, 2017 at the photon energy of 1.3 keV and electron beam energy of 6.4 GeV [2]. Start-up phase of the European XFEL included a lot of tasks performed in parallel such as gradual increase of electron energy, tests of hardware, electron beam diagnostics, electron beam formation system, electron beam optics, test and tuning of the undulator, commissioning of photon beam diagnostics and photon beam transport system. Two months after the event of the "first light", operation of all systems improved significantly, and detected radiation pulse energies reached design values in a mJ range. First characterization of the photon beam has been performed in July 2017, a month before an official starting date of user experiments (September 1st, 2017). Energy of the electron beam was 13.5 GeV, bunch charge was 500 pC, radiation wavelength 0.15 nm. Two photon diagnostic systems (FEL imager and X-ray gas monitor (XGM) detector) were available at that time which was sufficient for basic characterization of the radiation. This allowed us to measure the gain curve and trace evolution of the FEL radiation mode along significant part of the amplification regime, from almost beginning of the high gain exponential regime to saturation. Analysis of the FEL radiation modes have shown that in the whole range of the radiation pulse energies (from μJ to mJ level) they are surprisingly close to those predicted ten years ago at the design stage of the project [3]. Measured properties of the electron beam in the accelerator were also in agreement with design parameters [2, 4]. Thus, both results of the electron beam and photon beam measurements provide strong argument in

favor of conclusion that physical parameters of the machine are close to design values.

It turned out that analysis of the spatial properties of FEL radiation modes demonstrated to be a powerful tool for characterization physical parameters of SASE FEL process. As an extension of this experimental method we plan to implement correlations of FEL images with machine parameters which will allow to apply statistical techniques for determination of important parameters of SASE FEL such as gain length, saturation length, coherence time, radiation pulse duration, number of radiation modes in the pulse (longitudinal and transverse), degree of transverse coherence [5–8].

EXPERIMENTAL RESULTS

Measurements have been performed at the North branch of the European XFEL, SASE1 FEL. It is equipped with planar, variable gap undulator with 4 cm period length. It consists of 35 modules, each of 5 meter long. Machine operated at the energy of 13.5 GeV, bunch charge 500 pC, and the radiation wavelength was 0.15 nm. Special efforts have been taken for tuning machine to design parameters of the electron beam [2, 4].

By the time of described experiment only two photon diagnostics tools were in operation: FEL imager and XGM detector [9–13]. FEL imager is equipped with scintillating Ce:YAG screen and a scientific CMOS camera, and is located at a distance of 230 meters downstream the undulator end. XGM detector, located at 185 m behind the undulator, is cal-

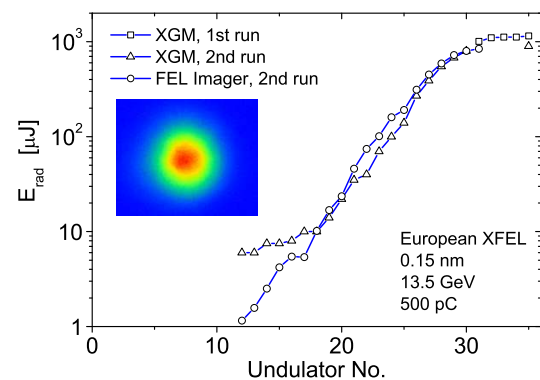


Figure 1: Gain curve of the European XFEL. The inset shows a single photon beam image. Electron energy is 13.5 GeV, bunch charge is 500 pC, radiation wavelength is 0.15 nm.

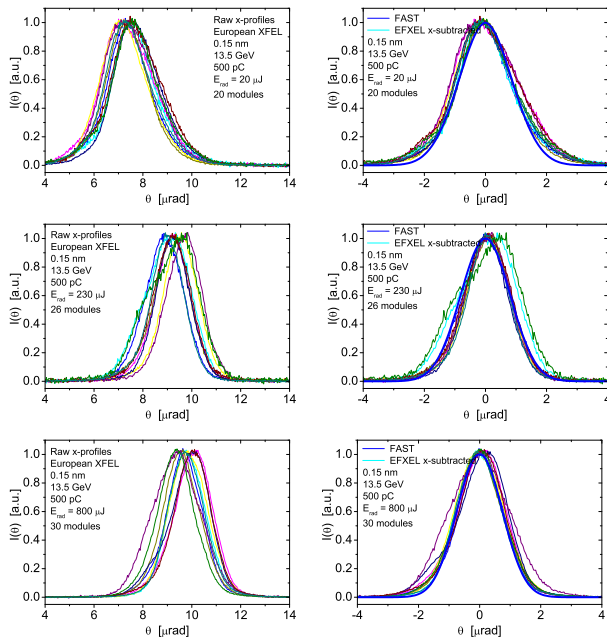


Figure 2: Single shot transverse profiles of the radiation pulses. Thin colored lines show 10 shots of the European XFEL. Left column: raw results. Right column: spatial jitter is subtracted. Bold blue lines on the right hand side are numerical simulations with code FAST [14] for baseline parameters of the electron beam [4]. Average radiation energy in the pulse is 20 μJ (upper row), 230 μJ (middle row), and 800 μJ (bottom row).

ibrated ionization chamber allowing precise measurements of average radiation energy over several pulse trains. XGM is also capable to resolve the shot-to-shot pulse energies at 4.5 MHz repetition rate within trains. However, at pulse energies below 50 μJ the XGM sensitivity is not sufficient to perform absolute measurements, but relative changes can be monitored down to the low level of spontaneous radiation of a single undulator segments.

Machine operated with one bunch per train with macropulse repetition rate 10 Hz, and FEL imager is used for single shot measurements of the photon beam images. Radiation pulse energy is derived by means of calculating the integrated intensity. XGM signal is used for calibration of FEL imager in the trusted dynamic range. A set of solid attenuators is used to keep x-ray flux on a scintillator at a level preventing saturation effects. Also, sCMOS camera is equipped with a set of neutral filters for controlling light intensity coming from scintillator.

Experimental procedure is organized in the following way. We tune SASE FEL to maximum signal at full undulator length (35 undulator modules). Then, keeping fixed all machine parameters, we gradually open undulator sections from the downstream end and record XGM readings and about 200 photon beam images at each step. Plots in Fig. 1 show experimental results for the gain curve. Both results are shown here, XGM and FEL imager. With FEL imager we can detect

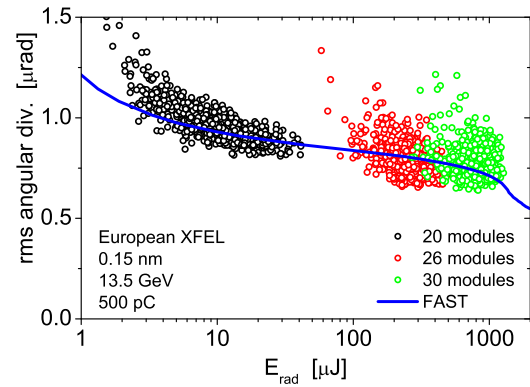


Figure 3: Dependence of the FWHM angular divergence on the radiation pulse energy. Bold blue line shows results of numerical simulations with code FAST [14] for baseline parameters of the electron beam [4]. Full radiation profiles are shown in Fig. 2.

lower, by about an order of magnitude, radiation intensities. The measured gain curve clearly demonstrates a stage of exponential amplification and a saturation regime after 25th module. Measurements at the radiation energies below a fraction of μJ suffer from high noise and background, so amplification process in 1/3rd of the undulator length could not be traced.

Analysis of the photon beam images allows to derive single shot angular distributions of the radiation intensity shown in Fig. 2. Plots in the left column show raw results. Strong pointing jitter takes place which is caused by sporadic electron beam orbit jitter. Subtraction of the spatial jitter allows us to select pure FEL radiation mode (see right column of Fig. 2) and trace its evolution along significant part of the amplification regime, from almost beginning of the high gain exponential regime to saturation (from μJ to mJ level). Bold grey curves on these plots show FEL mode calculated with code FAST [14] for design parameters of the electron beam [3]. Surprisingly good agreement takes place. Angular divergence of the FEL radiation is not a constant value, but it changes in the amplification process. SASE FEL radiation has wider cone at small radiation energies (beginning of the amplification). Then it passes plateau in the high gain exponential regime, and finally shrinks in the nonlinear regime. Signature of this physical behavior is clearly demonstrated when we plot angular divergence as a function of the energy in the radiation pulse. Blue line in Fig. 3 presents simulations with code FAST for baseline parameters, and circles are the results of measurements. Good agreement with predictions for baseline parameters takes place in the whole range. As we already mentioned in the introduction, measured electron parameters were also close to design values. These observations are strong arguments in favor of the statement that physical parameters of the machine are close to design parameters.

Contour plots in Fig. 4 allow to trace SASE FEL parameters in saturation versus emittance and peak current. Base-

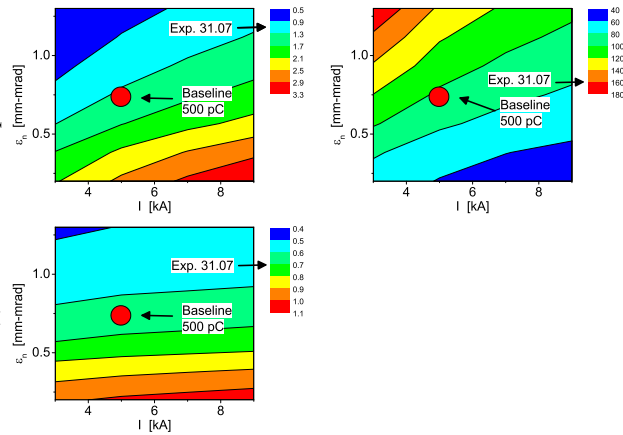


Figure 4: Overview of SASE1 saturation parameters in emittance - peak current parameter space. Calculations are performed with code FAST [14]. Top left: average energy in the radiation pulse (mJ). Top right: saturation length (meters). Bottom left: FWHM angular divergence of the radiation (μrad). Red circles denote operating point with baseline parameters [4]. Arrows directed to scale bars show measured parameters.

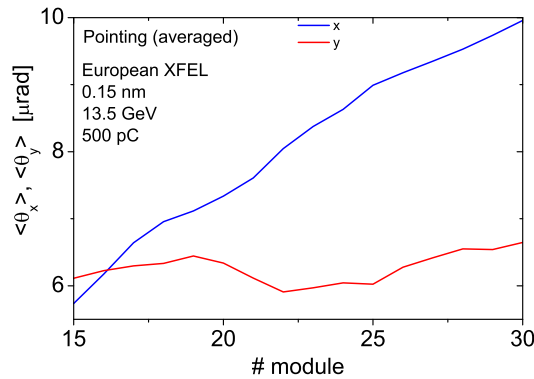


Figure 5: Drift of the photon beam angular pointing along the undulator measured in the experiment.

line parameters are shown as red points on the plots. We see that there is good agreement between measured and design parameters for the values of the radiation pulse, while there is pretty big overhead in the saturation length of about 70%. Note that stability of the machine operation during experiment was far from ideal, and has been disturbed by many sporadic jitters of orbit and beam formation system. In particular, jitter of electron orbit resulted in 30% of the photon beam pointing jitter. Lack of tuning experience also took place, and one of the problems was found during post processing of photon beam images. Figure 5 shows drift of the photon beam angular pointing as function of the undulator length. Since angle is derivative of the transverse displacement of the trajectory, we find that trajectory of the electron beam in the last 15 modules is nearly parabolic with maximum deviation in the end of about 180 μm. Such a strong deviation of the orbit from a straight line results in much

longer saturation length. Also, a problematic region has been identified with large local trajectory kick. So, analysis of the amplification process with screens provides us reliable way for controlling electron beam trajectory imperfections.

DISCUSSION

In this paper we described the first photon beam characterization from the European XFEL. By now similar studies are performed on a regular basis to check physical parameter space and stability of the machine operation. General result of these studies is that physical parameter space of SASE FEL is close to baseline parameters when special efforts are applied for control of the electron beam parameters. Stability of machine operation and quality of tuning improved significantly such that there is only some 20% overhead of the saturation length [2]. However, we still observe that the fluctuation of the radiation pulse energy is mainly driven by jittering accelerators parameters. The nature and source of jittering is under study, and we believe that proper tuning of all systems of the superconducting accelerator will allow reducing fluctuations to the level of fundamental fluctuations as it has been demonstrated at FLASH [5–8].

REFERENCES

- [1] M Altarelli *et al.* (Eds.), Preprint DESY 2006-097, DESY, Hamburg (2007).
- [2] W. Decking *et al.*, “First operation of a MHz-repetition-rate Hard X-Ray Free-Electron Laser driven by a superconducting linear accelerator”, submitted for publication.
- [3] E.A. Schneidmiller and M.V. Yurkov, Preprint DESY 11-152, DESY, Hamburg (2011).
- [4] W. Decking, T. Limberg, XFEL.EU Technical Note 1-22 (2013) XFEL.EU TN-2013-004-01, European XFEL, Hamburg (2013).
- [5] C. Behrens *et al.*, “Constraints on photon pulse duration from longitudinal electron beam diagnostics at a soft x-ray free-electron laser”, *Phys. Rev. ST AB* 15, 030707 (2012). doi: 10.1103/PhysRevSTAB.15.030707
- [6] E. Schneidmiller and M. V. Yurkov, “Application of Statistical Methods for Measurements of the Coherence Properties of the Radiation from SASE FEL”, in *Proc. 7th Int. Particle Accelerator Conf. (IPAC’16)*, Busan, Korea, May 2016, pp. 738–740. doi:10.18429/JACoW-IPAC2016-MOPOW013
- [7] E.A. Schneidmiller and M.V. Yurkov, CERN Yellow Reports: School Proceedings, Vol. 1, 539-596 (2018). doi: 10.23730/CYRSP-2018-001.539
- [8] O. I. Brovko *et al.*, “Experience With MCP-Based Photon Detector at FLASH2”, presented at the 39th Int. Free Electron Laser Conf. (FEL’19), Hamburg, Germany, Aug. 2019, paper WEP073.
- [9] A. Koch *et al.*, “Design and initial characterisation of X-ray beam diagnostic imagers for the European XFEL”, in *Proc. SPIE* 9512, 95121R-1 (2015). doi:10.1117/12.2182463
- [10] J. Grünert *et al.*, “X-ray photon diagnostics devices for the European XFEL”, in *Proc. SPIE*, 8504, X-Ray Free-Electron Lasers: Beam Diagnostics, Beamline Instrumentation, and Applications, 85040R (2012). doi:10.1117/12.929710

- [11] J. Grünert *et al.*, “X-ray photon diagnostics at the European XFEL”, *J. Synchrotron Rad.* 26, 000-000. [XQ5005] (2019). doi:10.1107/S1600577519006611 1107/S1600577519005174
- [12] T. Maltezopoulos *et al.*, “Commissioning of a photoelectron spectrometer for soft X-ray photon diagnostics at the European XFEL”, *J. Synchrotron Rad.* 26, 1045-1051. (2019). doi:10.1107/S1600577519003552
- [13] A.A. Sorokin *et al.*, “An X-ray gas monitor for free-electron lasers”, *J. Synchrotron Rad* 26, 1092-1100 (2019). doi:10.1016/S0168-9002(99)00110-2
- [14] E.L. Saldin, E.A. Schneidmiller and M.V. Yurkov, “FAST: a three-dimensional time-dependent FEL simulation code”, *Nucl. Instrum. and Methods A* 429, 233 (1999). doi:10.1016/S0168-9002(99)00110-2

INFLUENCE OF ENERGY CHIRP IN THE ELECTRON BEAM AND UNDULATOR TAPERING ON SPATIAL PROPERTIES OF THE RADIATION FROM SEEDED AND SASE FEL

E.A. Schneidmiller, M.V. Yurkov, DESY, Hamburg, Germany

Abstract

In this report we present analysis of the spatial properties of the radiation from an FEL amplifier for the case of energy chirp in the electron beam and undulator tapering. Two configurations, seeded FEL amplifier, and SASE FEL are under consideration. Studies are performed with numerical simulations using time-dependent FEL simulation code FAST. Evolution of the amplification process is traced along the undulator. It is shown that spatial properties of the radiation may be significantly distorted by the effect of energy chirp in the electron beam and undulator tapering.

INTRODUCTION

FEL amplification process is sensitive to the detuning from the FEL resonance. Energy chirp in the electron beam and undulator tapering are responsible for the change of the resonance condition. Undulator tapering is widely used in practical devices. Well known examples are post-saturation undulator tapering for radiation power increase, reverse undulator tapering for effective operation of afterburners, and application of linear undulator tapering for compensation of energy chirp effect [1–3]. These are essentially one dimensional effects [3–5]. Detuning effects significantly influence on the spatial properties of the radiation from FEL amplifier [6]. It has been shown in [7] in the framework of 3D FEL theory that effects of energy chirp and undulator tapering will result in an increase of the angular divergence and decrease of the degree of transverse coherence of the radiation from SASE FEL.

In this paper we trace evolution of amplification process in an FEL amplifier from start-up to the deep nonlinear regime. The case of linear frequency detuning (along undulator or along electron bunch) is under study. We compare two configurations: seeded FEL amplifier, and SASE FEL. We found that for positive linear detuning there is optimum value of chirp (tapering rate) when maximum output radiation power is achieved. Increase of the detuning in the positive direction leads to significant increase of the angular divergence of the radiation. On the other hand, radiation power significantly drop when increasing strength of the detuning in the negative direction (the power of the effect is similar to that given by 1D approximation). Stronger negative tapering results in shrinking of the angular divergence of the radiation.

BASIC DEFINITIONS

Detuning from the FEL resonance is defined as:

$$C = \frac{2\pi}{\lambda_w} - \frac{\pi(1 + K^2)}{\lambda\gamma^2},$$

where λ_w is undulator period, λ is radiation wavelength, K is rms value of the undulator parameter, γ is Lorentz factor. Figure of merit of the detuning effect on the FEL performance is detuning parameter $\hat{C} = C/\Gamma$ with the gain parameter Γ given by [6]:

$$\Gamma = \left[\frac{I}{I_A} \frac{16\pi^2 K^2 A_{JJ}^2}{(1 + K^2) \lambda_w^2 \gamma} \right]^{1/2}.$$

3D FEL parameter relates to the FEL gain parameter as $\bar{\rho} = \lambda_w \Gamma / (4\pi)$.

For the linear law of the undulator tapering the detuning parameter is

$$\hat{C}(\hat{z}) = \beta \hat{z}, \quad \beta = -\frac{\lambda_w}{4\pi \bar{\rho}^2} \frac{K_0}{1 + K_0^2} \frac{dK}{dz}.$$

Here longitudinal coordinate is normalized as $\hat{z} = \Gamma z$, and K_0 refers to the initial value of the undulator parameter.

The chirp parameter α is the figure of merit for an effect on FEL amplification process of the energy chirp along the electron bunch:

$$\alpha = -\frac{d\gamma}{dt} \frac{1}{\gamma \omega \bar{\rho}^2},$$

where $\omega = 2\pi c/\lambda$.

There is a symmetry between the linear energy chirp and the undulator tapering [3]. Indeed, if we look at the radiation field acting on some test electron from an electron behind it, this field was emitted at a retarded time. In the first case a radiating electron has a detuning due to an energy offset, in the second case it has the same detuning because undulator parameters were different at a retarded time. The effect of the energy chirp is compensated by the undulator tapering when

$$\frac{1}{H_{w0}} \frac{dH_w}{dz} = -\frac{1}{2} \frac{(1 + K_0^2)^2}{K_0^2} \frac{1}{\gamma_0^3} \frac{d\gamma}{cdt}.$$

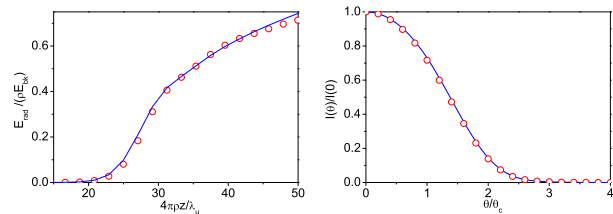


Figure 1: Equivalence of energy chirp and undulator tapering. Left: Average radiation pulse energy along undulator. Right: Average angular divergence in the far zone in the saturation. Solid curve: $\alpha = 0.07$, $\beta = 0$. Circles: $\alpha = 0$, $\beta = 0.035$.

FEL PERFORMANCE

In the following we illustrate operation of the FEL amplifier with linear chirp (tapering) using numerical simulations with code FAST [8]. To be specific, we used baseline parameters of the electron beam at the European XFEL: charge 20 pC, rms pulse duration 1.2 fs, normalized rms emittance 0.32 mm-mrad, rms energy spread 4.1 MeV [9, 10]. Undulator period is 4 cm, and energy of electrons is 8.5 GeV, radiation wavelength is 0.62 nm. The value of diffraction parameter is equal to 5 for this parameter set. Output results are presented in normalized form, and can be scaled to a wider range of the physical parameters.

We start with demonstration of compensation of the energy chirp by the undulator tapering [3]. We see from Fig. 1 that compensation takes place for both values, energy in the radiation pulse and angular divergence of the radiation. Some small difference is connected with not sufficient statistics.

Taking into account equivalence of linear energy chirp and undulator tapering, we present results only for wide range of the energy chirp values covering the whole range of practical interest. We trace amplification process along the undulator up to deep nonlinear regime and compare characteristics of SASE FEL and seeded FEL. Different color codes on the plots correspond to different values of the energy chirp parameter α . Color codes are: black for $\alpha = 0$, red for $\alpha = 0.025$, green for $\alpha = 0.07$, blue for $\alpha = 0.15$, turquoise for $\alpha = 0.2$, brown for $\alpha = -0.025$, violet for $\alpha = -0.05$. To help visual identification of the sign of the energy chirp, we use solid curve type for positive, and dashed curve type for negative values of α . Plots on the left and the right hand side refer to SASE FEL and seeded FEL, respectively.

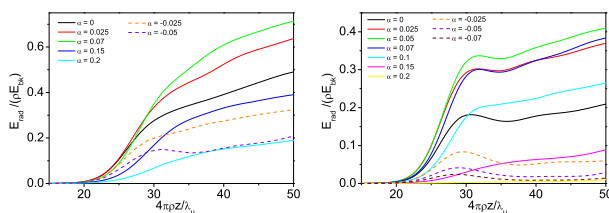


Figure 2: Energy in the radiation pulse along the undulator for different values of the energy chirp parameter α . Left plot: SASE FEL. Right plot: seeded FEL.

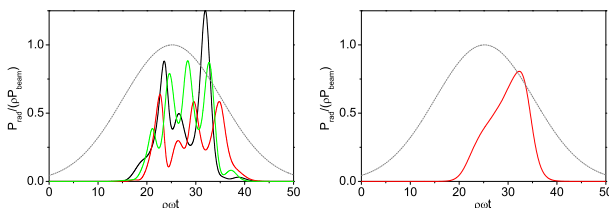


Figure 3: Temporal profile of the radiation pulse in the saturation regime. $\alpha = 0.07$. Left plot: three shots from SASE FEL. Right plot: seeded FEL. Grey line shows axial profile of the electron bunch.

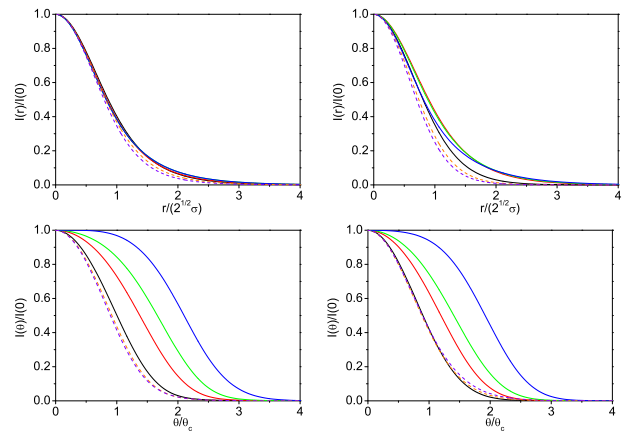


Figure 4: Average distribution of the radiation intensity in the near zone (top row) and in the far zone (bottom row) in the saturation for different values of the energy chirp parameter α . Left column: SASE FEL. Right column: seeded FEL.

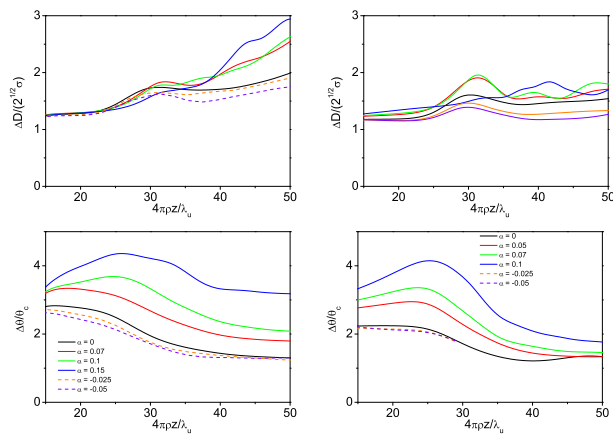


Figure 5: Evolution along the undulator of FWHM spot size of the radiation in the near zone (top row) and FWHM angular divergence of the radiation in the far zone (bottom row) different values of the energy chirp parameter α . Left column: SASE FEL. Right column: seeded FEL.

Overview of the results shows that both, SASE and seeded FEL exhibit pretty similar performance. Figure 2 shows evolution of the FEL efficiency along the undulator. Longitudinal coordinate is normalized to the gain parameter as $\tilde{z} = \Gamma z$, and FEL efficiency is defined as $\tilde{\eta} = E_{rad} / (\tilde{\rho} E_{bk})$, where $E_{bk} = N_e \gamma mc^2$ is kinetic energy of the electron bunch. We find that FEL efficiency rapidly decreases for negative values of the energy chirp. Situation is different for positive values of α . First, efficiency grows with α , reaches maximum value at $\alpha \approx 0.07$, and then starts to drop. Figure 3 shows temporal profile of the radiation pulse in the saturation regime for $\alpha = 0.07$ corresponding to maximum FEL efficiency. Time is normalize as $\tilde{p} \omega t$.

Plots in Fig. 4 present intensity distributions of the radiation in the near and far zone in the saturation. We see that angular divergence of the radiation shrinks for negative values of α , and gradually expands for positive values. Plots

in Fig. 5 trace relevant FWHM values along the undulator. Spot size in the near zone and angular divergence of the radiation in the far zone are always wider for the case of SASE FEL which is a signature of the degradation of transverse coherence for the frequency chirped SASE FEL [7]. However, by the time we can not put a number for the drop of the degree of transverse coherence, more comprehensive study is required.

REFERENCES

- [1] N.M. Kroll, P.L. Morton, and M.N. Rosenbluth, "Free-electron lasers with variable parameter wigglers", *IEEE J. Quantum Electron.*, vol. 17, p. 1436, 1981. <https://doi.org/10.1109/JQE.1981.1071285>
- [2] E.A. Schneidmiller, M.V. Yurkov, "Obtaining high degree of circular polarization at x-ray free electron lasers via a reverse undulator taper", *Phys. Rev. ST Accel. Beams*, vol. 16, p. 110702, 2013. doi:10.1103/PhysRevSTAB.16.110702
- [3] E.L. Saldin, E.A. Schneidmiller, M.V. Yurkov, "Self-amplified spontaneous emission FEL with energy-chirped electron beam and its application for generation of attosecond x-ray pulses", *Phys. Rev. ST Accel. Beams*, vol. 9, p.050702, 2006. doi:10.1103/PhysRevSTAB.9.050702
- [4] S. Krinsky and Z. Huang, "Frequency chirped self-amplified spontaneous-emission free-electron lasers", *Phys. Rev. ST Accel. Beams*, vol. 6, p. 050702, 2003. doi.org/10.1103/PhysRevSTAB.6.050702
- [5] Z. Huang and G. Stupakov, "Free electron lasers with slowly varying beam and undulator parameters", *Phys. Rev. ST Accel. Beams*, vol. 8, p. 040702, 2005. doi.org/10.1103/PhysRevSTAB.8.040702
- [6] E.L. Saldin, E.A. Schneidmiller, M.V. Yurkov, *The Physics of Free Electron Lasers*, Springer-Verlag, Berlin, 1999.
- [7] Z. Huang, Y. T. Ding, and J. Wu, "Three-Dimensional Analysis of Frequency-Chirped FELs", in *Proc. 32nd Int. Free Electron Laser Conf. (FEL'10)*, Malmö, Sweden, Aug. 2010, paper MOPB28, pp. 91–94.
- [8] E.L. Saldin, E.A. Schneidmiller, and M.V. Yurkov, "FAST: a three-dimensional time-dependent FEL simulation code", *Nucl. Instrum. and Methods A*, vol. 429, p. 233, 1999. doi:10.1016/S0168-9002(99)00110-2
- [9] M Altarelli *et al.* (Eds.), "The European X-Ray Free-Electron Laser Technical Design Report", Preprint DESY 2006-097, DESY, Hamburg, 2007.
- [10] W. Decking, T. Limberg, "European XFEL Post-TDR Description", Technical Note XFEL.EU TN-2013-004-01, European XFEL, Hamburg, 2013.

AN ADVANCED COMPRESSION OPTION FOR THE EUROPEAN XFEL

I. Zagorodnov, M. Dohlus, E.A. Schneidmiller, M.V. Yurkov
Deutsches Elektronen-Synchrotron, Hamburg, Germany

Abstract

An advanced compression scheme which allows to obtain a high peak current while preserving the low slice emittance is considered. The beam is compressed weakly in the bunch compressors and the current is increased by ESASE setup at the entrance of the undulator line. It is shown by numerical studies that such approach allows to reduce harmful collective effects in the bunch compressors and in the transport line. Simulations of FEL physics confirm the possibility to obtain a high level of SASE radiation at the ultra-hard photon energy level of 100 keV.

INTRODUCTION

The European XFEL provides SASE photon beams for user operation since 2017 [1]. Currently it has three photon lines (SASE1, SASE2, SASE3, see Fig. 1) and should reach the photon energy of 25 keV [2].

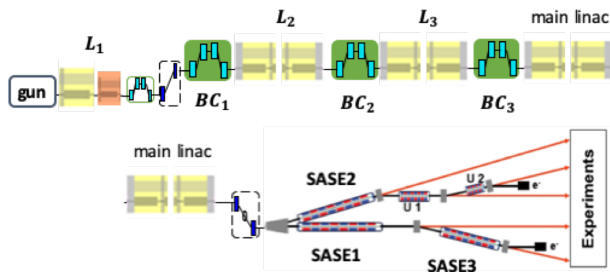


Figure 1: The European XFEL layout.

There is a possibility to use one of free tunnels (U1 or U2, see Fig. 1) for the ultrahard x-ray undulator line to produce the SASE photons with energy of 100 keV [3]. We study two possible scenarios: standard compression to 5 kA and an advanced compression with ESASE setup [4] up to 10 kA. The latter compression scheme allows to reduce the collective effects and to obtain a better electron slice parameters and to reach a higher level of SASE energy per electron bunch.

ACCELERATOR BEAM DYNAMICS

We have done numerical modeling of the accelerator beam dynamics up to the entrance of SASE2 undulator line. We have not included the effect of the last arc from SASE2 to U1 tunnel. The electron bunch with charge of 100 pC has been compressed to 2 and 5 kA. In the choice of the working points we have followed the approach of paper [5] and have used two codes: Ocelot [6] and Krack3 [7].

The tracking of particles in Ocelot is done in the same way as, for example, in Elegant [8]. Quadrupoles, dipoles, sextupoles, RF cavities and other lattice elements are modeled by linear and second order maps. The focusing effect of RF cavities is taken into account according to the

Rosenzweig-Serafini model. The space charge forces are calculated by solving the three-dimensional Poisson equation in the bunch frame. The CSR module uses a fast ‘projected’ one-dimensional method [9]. The wakefields and the incoherent synchrotron radiation (ISR) effects are included.

Beam Dynamics in Linac

Table 1: Compression Parameters

Parameter	5 kA	2 kA
energies $E_1/E_2/E_3$, MeV	130 / 700 / 2400	
R_{56}^1/R_{56}^2 , mm	56 / 52	
compression factors C_1/C_2	3.5 / 28	
R_{56}^3 , mm	55	37
total compression C_3	862	340
Z'_3 , 1/m		0
Z''_3 , 1/m/m	600	300

In standard operation we compress the electron bunch to the peak current of 5 kA and accelerate it to 17.5 GeV. The parameters of the longitudinal beam dynamics are listed in Table 1. The positive value of the second derivative of the inverse compression function Z_3 allows to reduce the compression strength in the bunch head [5]. To suppress the microbunching instability the energy spread in the bunch was increased in the laser heater, which is installed before the injector dogleg. The power of the laser is chosen to have at the linac end the rms slice energy spread of 1 MeV. The results of the simulation are shown in Fig. 2. The bunch has relatively small slice emittance: 0.2 μm in the horizontal plane and 0.3 μm in the vertical plane. The projected emittances are listed in Fig. 2 as well. The larger slice emittance in the y-plane is due to CSR effects in the vertically oriented bunch compressors. The larger horizontal projected emittance and the ‘‘banana’’ shape of the bunch in x-plane are due to not compensated CSR effects in the switchyard arc before SASE2 undulator line.

In order to suppress the self-fields and to improve the bunch properties we consider an another compression scenario: to compress the same bunch to 2 kA current in the linac and to 10 kA current in ESASE setup in the vicinity of the undulator line. The main parameters are listed in Table 1. The power of the heater is chosen to have after main linac the rms slice energy spread of 0.65 MeV. The results of the simulation for the bunch before ESASE setup are shown in Fig. 3. The bunch has slice emittance of 0.2 μm in both planes. The projected emittances in both planes are by factor 2 smaller than in the former case. Nevertheless, we see a larger projected emittance in the horizontal plane due to CSR impact in the arc before SASE2 undulator line.

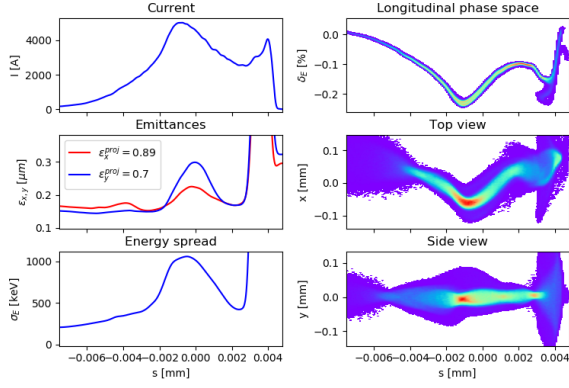


Figure 2: Electron beam properties at SASE2 entrance for the beam compressed to 5 kA.

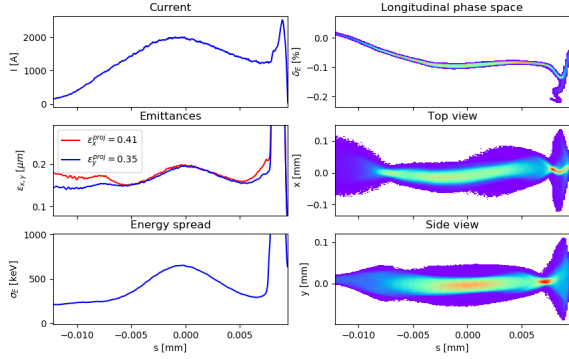


Figure 3: Electron beam properties at SASE2 entrance for the beam compressed to 2 kA.

Beam Dynamics in ESASE Setup

Table 2: ESASE Setup Parameters

Parameter	
modulator period λ_w , m	0.7
chicane magnet field strength, T	0.25
chicane magnet length, m	1
chicane parameter R_{56} , mm	0.78
laser power P_L , GW	8
laser spot size w_0 , mm	0.65

Figure 4 shows the layout and the optics of ESASE setup. The main parameters of the setup are listed in Table 2. The bunch from Fig. 3 is tracked with Ocelot taking into account the incoherent and the coherent synchrotron radiation effects.

The electron beam passes two periods of the wiggler with period λ_w of 0.7 m. At the same time a laser pulse with wave length λ of 800 nm propagates through the wiggler collinearly with the electrons and impose energy modulations. The wiggler parameter K is equal to 73.2 and the maximal deviation of the reference electron from the orbit $r_{max} = K/(\gamma k_w)$ is 0.24 mm. The transverse rms beam size is equal to 25 μm . Hence, taking into account r_{max} , we choose the laser spot size to be 0.65 mm. It gives the

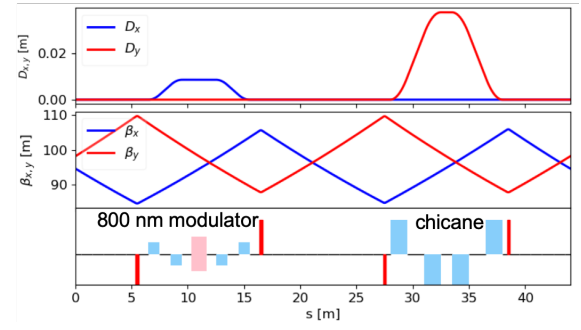


Figure 4: Layout and optics of ESASE setup.

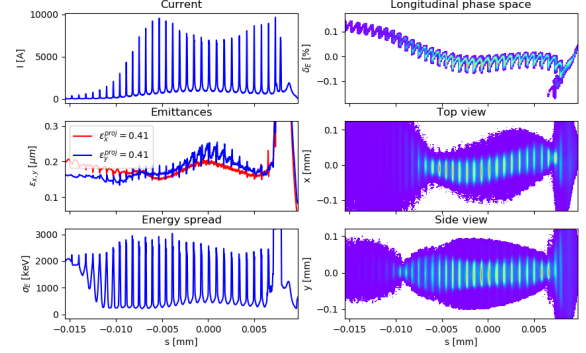


Figure 5: Electron beam properties after ESASE setup.

relatively large Rayleigh length of 1.7 m which is larger than the wiggler length L_w of 1.4 m.

The amplitude of the energy change in the wiggler can be found as

$$\Delta E = \sqrt{\frac{P_L}{P_A}} \frac{2KL_w mc^2}{\gamma w_0} \left(J_0 \left(\frac{K^2}{4 + 2K^2} \right) - J_1 \left(\frac{K^2}{4 + 2K^2} \right) \right),$$

where $\gamma = E_b/(mc^2)$, $P_A = I_A mc^2/e$, I_A is Alfven current. The laser pulse has a peak power P_L of 8 GW, which gives the energy modulation amplitude ΔE equal to 3.14 MeV.

Next the electron beam passes through the dispersive magnetic chicane. In order to produce the maximal microbunching the chicane parameter R_{56} has to be chosen near to the value $R_{56}^0 = E_b/(\Delta E k)$ which is equal to 0.7 mm. To compensate the effect of self-fields it is adjusted to 0.78 mm.

After the chicane we have enhancement of the electron peak current and the slice energy spread by approximately factor $C = \Delta E/\sigma_E$ which in this case is equal to 4.8.

Figure 5 shows the electron beam parameters after ESASE setup. We see the enhancement of the current from 2 kA to 10 kA. Simultaneously the energy spread at the position of the current spikes increases to 3 MeV. The slice and the projected emittances in the deflection plane of the chicane increase slightly due to CSR impact.

RADIATION PROPERTIES AT 100 keV

The technology of in-vacuum undulators is well developed and used at other facilities. We consider SASE4 undulator with undulator period of 22 mm and the active length of

175 m. The SASE4 undulator could be installed in U1 tunnel (see Fig. 1). For the time being in our analysis we consider SASE2 tunnel. This position takes into account the impact of the switchyard arc.

The simulations are done with three-dimensional code ALICE [10] for the photon energy of 100 keV. We have used the real number of the electrons and have included the energy losses and quantum fluctuations due to synchrotron radiation in the undulator. To compensate the energy loss and to increase the energy in the photon pulses we have used a non-linear taper for the rms undulator parameter:

$$K = K_0 - 1.5 \cdot 10^{-5} z[m] - 1.3 \cdot 10^{-6} (z[m] - 90)^2 H(z[m] - 90),$$

where $K_0 = 0.567393$ and $H(\cdot)$ is the Heaviside function.

The left plot in Fig. 6 shows the energy in the photon pulse along the SASE4 undulator beam line. The red solid line corresponds to the bunch with the peak current of 5 kA shown in Fig. 2. At the end of the undulator line it reaches the SASE energy of 40 μ J. The SASE power along the pulse for one shot is shown in red on the right plot in Fig. 6. The lasing part is relatively narrow due to the optics and the orbit mismatch along the electron bunch.

The blue solid line on the left plot in Fig. 6 corresponds to the bunch after ESASE setup with the peak current of 10 kA shown in Fig. 5. At the end of the undulator line it reaches the SASE energy of 110 μ J. The SASE power along the pulse for one shot is shown in blue in Fig. 7. Due to the transverse shifts of the slices seen in Fig. 5 we have not managed to bring all current spikes to the same level of lasing power.

To estimate the impact of the synchrotron radiation in the switchyard arc to SASE2 undulator we have additionally considered the case when SASE4 undulator has the position in the SASE1 tunnel (see Fig. 1). The corresponding results are shown by dashed curves on the left plot in Fig. 6. The beam with the peak current of 5 kA produces the photon pulses with energy of 50 μ J. It is only small increase compared to the former case for SASE2 tunnel. The beam with the peak current of 10 kA, formed by ESASE setup, produces the photon pulses with total energy of 180 μ J. It gives factor 2 difference to the former case for SASE2 tunnel.

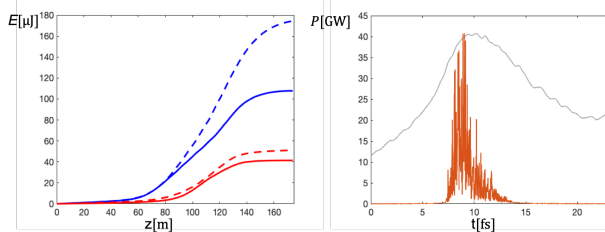


Figure 6: The left plot shows the SASE energy along SASE4 undulator. The red curves presents the results for nominal compression to 5 kA. The blue curves show the results for eSASE setup. The solid lines present the results for SASE2 tunnel. The dashed lines show the results for SASE1 tunnel. The right plot presents the SASE power for the 5kA beam in SASE2 tunnel.

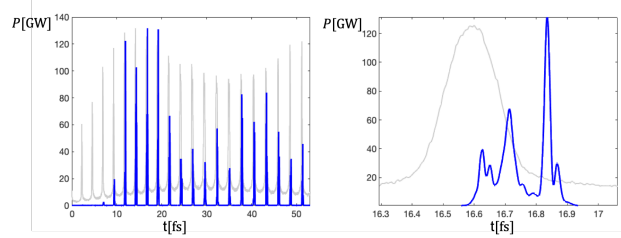


Figure 7: Photon power with eSASE setup for SASE2 tunnel. The gray curves show the current profile.

MICROBUNCHING AND CSR ISSUES

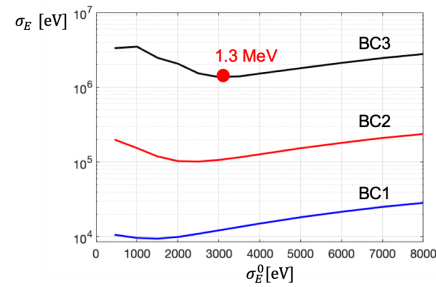


Figure 8: The slice energy spread due to microbunching for the bunch with the peak current of 2 kA vs. the initial energy spread after the laser heater.

In the simulations presented above we have been optimistic and took quite small values for the final slice energy spread. In the simulations we have used $5 \cdot 10^6$ macroparticles and could not resolve the parasitic microbunching effects in the linac. For this reason we have done a devoted study of the minimal energy spread after the linac for the case when we take into account the microbunching due to the space charge forces. In our study we have used the periodic Poisson solver [11] and the real number of electrons in the slice. We have varied initial energy σ_E^0 at the position of the laser heater and have analyzed the energy spread after the bunch compressors. The results for the charge of 100 pC compressed to the peak current of 2 kA are shown in Fig. 8. We see that the estimation of the minimal slice energy spread is equal to 1.3 MeV. It is two times larger as the energy spread of 0.65 MeV used in the simulations of the previous sections. For the beam with the peak current of 5 kA our estimation is even more pessimistic. With the current optics and the compression scenario we will have more than 4.5 MeV of the slice energy spread [12]. We are looking now for possible solutions to reduce the microbunching.

The analytical estimation gives 0.2 MeV slice energy spread from the ISR. However, the impact of the CSR on the bunch properties is considerable. As it can be seen from Fig. 6 we need to suppress the CSR effects in the switchyard arc to SASE2 and are looking now for possible solutions as well [13, 14].

REFERENCES

- [1] H. Weise and W. Decking, “Commissioning and First Lasing of the European XFEL”, in *Proc. FEL’17*, Santa Fe, NM, USA, Aug. 2017, pp. 9–13. doi:10.18429/JACoW-FEL2017-MOC03
- [2] E.A. Schneidmiller and M.V. Yurkov, “Photon beam properties at the European XFEL”, DESY Report No. DESY 11-152, XFEL.EU TR-2011-006, 2011.
- [3] E. Schneidmiller *et al.*, “Considerations for the Ultrahard X-ray Undulator Line of the European XFEL”, in *Proc. IPAC’19*, Melbourne, Australia, May 2019, pp. 1732–1735. doi:10.18429/JACoW-IPAC2019-TUPRB023
- [4] A.A. Zholents, “Method of an enhanced self-amplified spontaneous emission for x-ray free electron lasers”, *Phys. Rev. ST Accel. Beams*, vol. 8, pp. 040701, 2005. doi:10.1103/PhysRevSTAB.8.040701
- [5] I. Zagorodnov, M. Dohlus, and S. Tomin, “Accelerator beam dynamics at the European X-ray Free Electron Laser”, *Phys. Rev. Accel. Beams*, vol. 22, pp. 024401, 2019. doi:10.1103/PhysRevAccelBeams.22.024401
- [6] S. I. Tomin, I. V. Agapov, M. Dohlus, and I. Zagorodnov, “OCELOT as a Framework for Beam Dynamics Simulations of X-Ray Sources”, in *Proc. IPAC’17*, Copenhagen, Denmark, May 2017, pp. 2642–2645. doi:10.18429/JACoW-IPAC2017-WEPAB031
- [7] M. Dohlus, *Krack 3 User Guide*, DESY, 2018.
- [8] M. Borland, *User’s Manual for Elegant*, APS-ANL, Chicago, IL, 2017.
- [9] E.L. Saldin, E.A. Schneidmiller, and M.V. Yurkov, “Radiative interaction of electrons in a bunch moving in an undulator”, *Nucl. Instrum. Methods Phys. Res. A*, vol. 417, no. 1, pp. 158-168, 1998. doi:10.1016/S0168-9002(98)00623-8
- [10] I. Zagorodnov, “Numerical Modeling of Collective Effects in Free Electron Laser”, in *Proc. ICAP’12*, Rostock-Warnemunde, Germany, Aug. 2012, paper TUAC11, pp. 81–85.
- [11] M. Dohlus and Ch. Henning, “Periodic Poisson model for beam dynamics simulation”, *Phys. Rev. Accel. Beams*, vol. 19, pp. 034401, 2016. doi:10.1103/PhysRevAccelBeams.19.034401
- [12] M. Dohlus, “3D simulation of microbunching due to space charge effects”, talk at S2E meeting, DESY, 2019. www.desy.de/fel-beam/s2e/talks.html#a2019.04.16
- [13] S. Di Mitri *et al.*, “Cancellation of Coherent Synchrotron Radiation Kicks with Optics Balance”, *Phys. Rev. Lett.* vol. 110, pp. 014801, 2013. doi:10.1103/PhysRevLett.110.014801
- [14] T. Hara *et al.*, “High peak current operation of x-ray free-electron laser multiple beam lines by suppressing coherent synchrotron radiation effects”, *Phys. Rev. Accel. Beams*, vol. 21, pp. 040701, 2018. doi:10.1103/PhysRevAccelBeams.21.040701

SUPER-X: SIMULATIONS FOR EXTREMELY HARD X-RAY GENERATION WITH SHORT PERIOD SUPERCONDUCTING UNDULATORS FOR THE EUROPEAN XFEL

S. Serkez*, G. Geloni, S. Karabekyan, Y. Li, T. Tanikawa,
S. Tomin, F. Wolff-Fabris, European XFEL, Schenefeld, Germany
S. Casalbuoni, KIT, Karlsruhe, Germany
C. Boffo†, Bilfinger Noell, Würzburg, Germany
M. Dohlus, E. Schneidmiller, M. Yurkov, I. Zagorodnov, DESY, Hamburg, Germany
A. Trebushinin, BINP, Novosibirsk, Russia

Abstract

The European XFEL is a high-repetition multi-user facility with nominal photon energy range covering almost 3 orders of magnitude: 250 eV - 25 keV. In this work we explore the possibility to extend the photon energy range of the facility up to 100 keV via combination of superconducting undulator technology, period doubling and harmonic lasing, thus allowing for excellent tunability. To this purpose, we propose a dedicated FEL line, discuss its overall concept and provide analytical and numerical estimations of its expected performance.

INTRODUCTION

The European XFEL first lased in 2017 [1] and can currently sustain simultaneous operation of three separate FEL lines, SASE1, SASE2 and SASE3 [2]. One distinctive trait of the facility is its high-energy, superconducting linear accelerator reaching up to 17.5 GeV and up to 27000 pulses per second distributed in 10 macrotrains with an intra-train repetition rate up to 4.5 MHz. In the mid-term, two novel FEL lines will be installed in two already available empty tunnels [3] and possibly, in the longer term, a second fan of FEL tunnels will be excavated [4]. The high electron energy strongly hints at the possibility of generating extremely hard X-ray pulses well beyond the nominal 25 keV with an ad-hoc superconducting FEL undulator line that we call Super-X. In this paper we explore Super-X up to the 100 keV range. We assume -from the very beginning- the use of a nominal electron beam as is, from start-to-end simulations, at the entrance of the SASE1 undulator, i.e. not spoiled by collective interactions or wakes during the transport to different undulator lines. Superconducting undulators (SCU) can produce, with respect to permanent magnet ones, for the same period length and vacuum gap a higher peak field on axis. This allows to increase the photon energy range as well as the flux. Superconducting technology allows period doubling using a single magnetic structure. Period doubling further increases the photon energy tunability [5–8]. Although other technical realizations of super-hard X-ray FEL lines have been positively assessed [9], Super-X is an appealing option for reaching lasing at ultra-high photon energies with a large

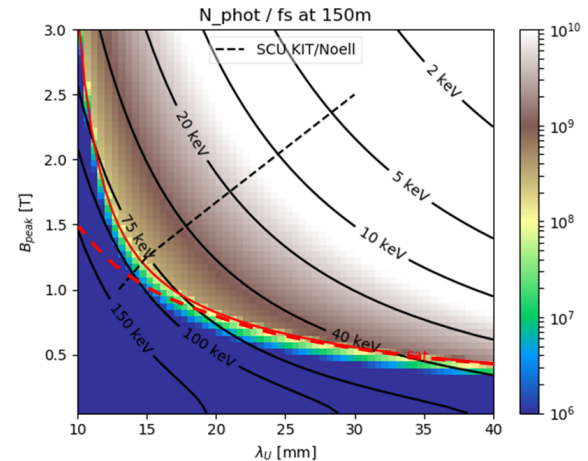


Figure 1: Estimated performance of a SCU XFEL line. The black dotted line shows the state-of-the-art magnetic field achievable for a 5 mm vacuum gap. The red solid and dashed lines refer to FEL saturation, the dashed line excluding quantum fluctuations effects.

tunability range considering SASE and additional advanced FEL schemes discussed in this contribution.

ANALYTICAL ESTIMATIONS

We envision a SCU system with a geometrical length of 150 m, which fits conservatively the empty tunnels currently available at the European XFEL [3], and a filling factor of about 80%. In order to study the relevant parameter space we parametrized the 3D gain length according to [10, 11], which provide two alternative methods to estimate the FEL performance. We fixed, as just described, a total setup length of 150 m, assumed a flat-top electron beam with a current of 5 kA, an energy of 17.5 GeV, a normalized slice emittance of 0.4 mm mrad, an rms energy spread of 1 MeV and average betatron functions around 30 m. Using [10, 11] we estimated the number of photons per femtosecond duration of the electron bunch as a function of on-axis peak magnetic field and undulator period, for different photon energies. We validated our estimations with time-dependent FEL simulations performed with Genesis [12] and Simplex [13]. Results are shown in Fig. 1. The black dotted line refers to the maximum magnetic field in reach of state-of-the-art SCU assuming a

* svitozar.serkez@xfel.eu

† Current address: Fermilab, Battavia, Illinois, USA

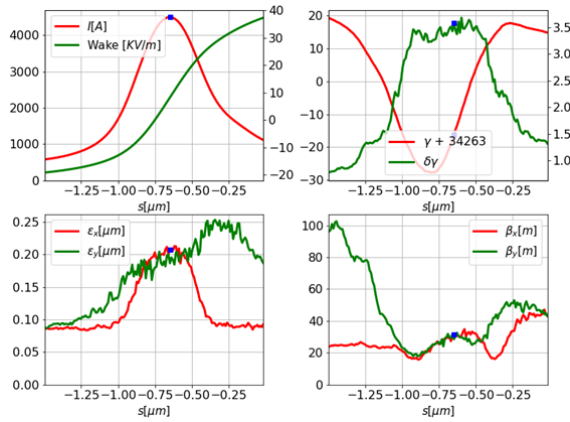


Figure 2: Simulated 20 pC nominal electron bunch at the entrance of SASE1.

vacuum gap of 5 mm [5], and defines the minimum achievable photon energy. The crossing of the continuous red line with the continuous black lines (which specify a certain photon energy) shows the period length at which saturation can be achieved for the setup considered here. When quantum diffusion of energy spread is ignored, see [14], the red dashed line must be used instead. This preliminary analysis shows that an acceptable number of photons of about 10^9 per femtosecond length of the radiation pulse can be reached for periods between 15 mm and 20 mm, at photon energies in the 100 keV range near saturation.

SIMULATIONS

We followed up analytical estimations with more detailed FEL simulations.

For the electron beam we used both simplified models and start-to-end simulations. The radiation output depends considerably on the electron beam quality. In Fig. 2 we show an example of a start-to-end simulation for the electron beam performed for a 20 pC bunch, where the emittance is smallest, at the entrance of SASE1. Compared to the model beam considered in the previous section, here the normalized emittance is decreased from 0.4 mm mrad to 0.2 mm mrad.

We assumed an undulator period of 18 mm. The impact of random undulator field errors was included by adding, every half period, random deviations from the design field with a relative rms of 0.15%, corresponding to the half of those measured in the KIT-Noell undulator operating in the KIT synchrotron [15] and corrected the field integrals. Such tolerance reduction allows one to obtain radiation power levels comparable to those of an ideal undulator (Fig. 3). Otherwise, field errors can be efficiently dealt with by compensating the added path with phase shifters. Figure 4 shows the Wigner distribution function and its marginals (power and spectral profiles). The total photon yield is of about $9 \cdot 10^8$ photons.

Here we assumed a 5 mm vacuum gap, and the presence of resistive wakes alters the Wigner distribution significantly. In first approximation, because of wakes, different parts

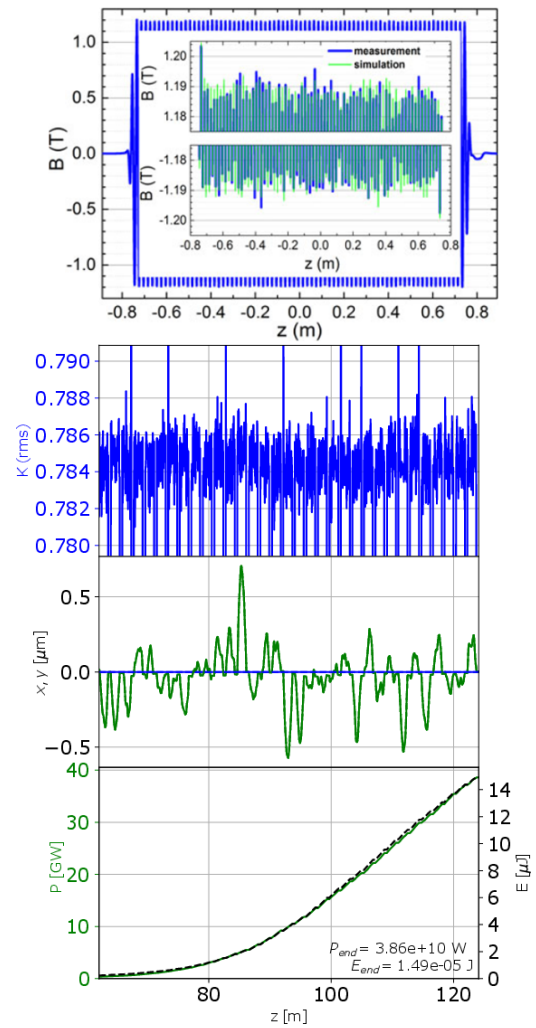


Figure 3: Top subplot: measured magnetic field errors of the existing U20 undulator (reproduced from reference [15] under the Creative Commons Attribution License (CCBY) 4.0 license). Bottom subplot: undulator K value calculated period-wise assuming half the RMS value of the measured errors, electron beam trajectory in such undulator and radiation power growth.

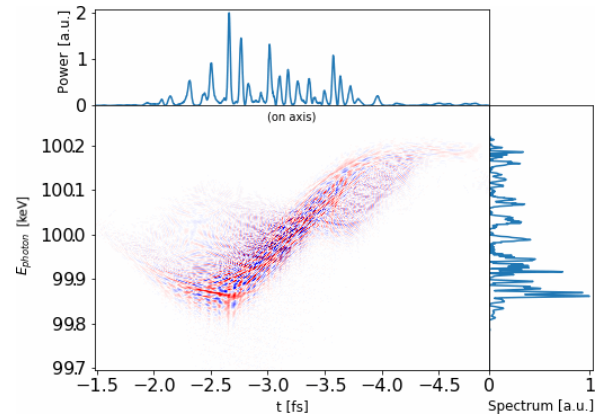


Figure 4: Wigner distribution and its marginals for the start-to-end electron bunch in Fig. 2. Resistive undulator wakes and field errors are included in the simulations (see text).

of the electron beam loose energy at different rates, e.g. wakes are responsible for a change in the electron beam chirp along the undulator. However, only one energy loss rate can be compensated via linear undulator tapering. In this way, longitudinal wakefields limit the maximum duration of the lasing window and their effect cannot be ignored. The combined effects of initial electron energy chirp and resistive wakes "tilt" the Wigner distribution, thus increasing the spectral bandwidth.

Finally, transverse coherence was found to deteriorate considerably, down to a degree of about 60%. This value strongly depends on the electron beam characteristics. For example, an increase in emittance from 0.2 mm mrad to 0.4 mm mrad would yield a further decrease of the degree of coherence to about 20%.

SPECIAL MODES OF OPERATION

One peculiar option of SCUs is the possibility of doubling the period, by changing the current direction in a subset of the windings [16]. This allows for switching between e.g. 18 mm and 36 mm using the same magnetic structure. By this, the spectral reach of the SCU is substantially increased, see Fig. 1 and allows for tuning the setup between a few keV and around 100 keV. Such large tunability range will enable advanced lasing schemes and can be also beneficial to facilities designed to operate a single undulator line for diverse experiments. Period doubling would also enable self-seeding operation at high energies. One may, in fact, seed at around 15 keV using the doubled period and subsequently tune part of the radiator at a higher harmonic.

If the European XFEL will enable CW operation [17, 18], the maximum electron beam energy will be decreased, possibly down to 7.8 GeV. Then, the SCU line could allow reaching photon energies between 10 keV to 20 keV with a period of 18 mm, and between 2 keV and 10 keV with the doubled 36 mm period.

Finally, the implementation of an SCU line would allow, for a particular choice of undulator period around 20 mm, to take better advantage of Harmonic Lasing (HL) [19]. Figure 5 shows the ratio of the gain lengths of HL at the 3rd harmonic (assuming the HL undulator period λ_u as a free parameter) and of a 20 mm period SCU operating at fundamental. 3D effects and quantum fluctuations are taken into account. One can see that a 40 mm period undulator, lasing with optimised 3rd harmonic cannot compete with the 20 mm SCU operating at the fundamental, moreover the HL method applied to the SCU, i.e. at 20 mm period, can clearly bring an advantage.

CONCLUSIONS

We discussed the concept of Super-X, a dedicated ultra hard X-ray SCU FEL line for the European XFEL. The use of SCUs allows for wide photon energy tunability: in particular, exploiting the period doubling option, one could continuously reach the range spanning from a few keV up to around 100 keV. Moreover, in case a CW mode of op-

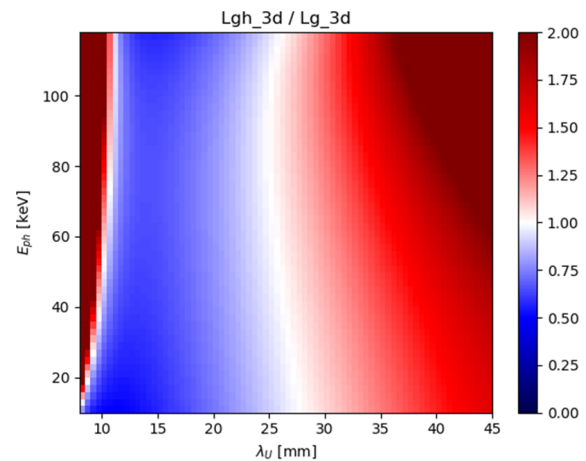


Figure 5: Ratio of the gain length for the HL setup to that of a 20 mm-period SCU operating at fundamental.

eration would be enabled at the European XFEL, SCUs could be the only way to reach into the 20 keV range. Here we estimated the expected performance of a 150 m-long FEL line for the European XFEL, with the help of known parametrizations [10, 11] benchmarked with Genesis and Simplex. Around 100 keV, a European XFEL-class, fresh electron bunch would yield around 10^9 photons per femtosecond with low transverse coherence. At those photon energies the photon beam characteristics were found to strongly depend on the electron beam characteristics and on the photon energy itself. Electron beam energy chirps and resistive undulator wakefields are expected to substantially modify the FEL beam Wigner distribution effectively yielding an increase in the radiation bandwidth. Random period-wise field errors can be efficiently dealt with by correcting the field integrals and compensating the added path with phase shifters. Moreover, the use of harmonic lasing becomes beneficial around a choice of 20 mm period, while period doubling would allow self-seeding at a subharmonic of the target photon energy (for example, self-seeding at 15 keV with a target energy of 30 keV).

REFERENCES

- [1] H. Weise and W. Decking, "Commissioning and First Lasing of the European XFEL", in *Proc. 38th Int. Free Electron Laser Conf. (FEL'17)*, Santa Fe, NM, USA, Aug. 2017, pp. 9–13; doi:10.18429/JACoW-FEL2017-MOC03
- [2] D. Noelle, "FEL Operation at the European XFEL Facility", presented at the 39th Int. Free Electron Laser Conf. (FEL'19), Hamburg, Germany, Aug. 2019, paper FRA01.
- [3] "Shaping the Future of the European XFEL: Options for the SASE4/5 Tunnels", workshop held in December 2019, Schenefeld, Germany, slides available at <https://indico.desy.de/indico/event/21806/>.
- [4] M. Altarelli *et al.* Ed., "The European X-Ray Free-Electron Laser – Technical Design Report", DESY, Hamburg, Germany, Rep. DESY 2006-097, July 2007.
- [5] M. Turenne, C. Boffo, and S. Casalbuoni, private communication

- [6] J. Bahrtdt and E. Gluskin, “Cryogenic permanent magnet and superconducting undulators”, *Nucl. Instrum. Methods Phys. Res., Sect. A*, vol. 907, pp. 149–168, Nov. 2018.
- [7] S. Casalbuoni *et al.*, “Superconducting Undulators: From Development towards a Commercial Product”, *Synchr. Radiat. News*, vol. 31, no. 3, pp. 24–28, May 2018.
- [8] R. Dejus, M. Jaski, and S. H. Kim, “On-axis brilliance and power of in-vacuum undulators for the Advanced Photon Source”, ANL/APS/LS-314, Argonne, IL, USA, Nov. 2009. doi:10.2172/969637.
- [9] E. Schneidmiller *et al.*, “Feasibility Studies of the 100 keV Undulator Line of the European XFEL”, presented at the 39th Int. Free Electron Laser Conf. (FEL’19), Hamburg, Germany, Aug. 2019, paper TUP056.
- [10] M. Xie, “Exact and variational solutions of 3D eigenmodes in high gain FELs”, *Nucl. Instrum. Methods Phys. Res., Sect. A*, vol. 445, pp. 59–66, 2000.
- [11] E. L. Saldin, E. A. Schneidmiller, and M. V. Yurkov, “Design formulas for short-wavelength FELs”, *Opt. Commun.*, vol. 235, no. 4–6, pp. 415–420, May 2004.
- [12] S. Reiche, “GENESIS 1.3 – A Fully 3D Time Dependent FEL Simulation Code”, in NIM Proceedings of the 20th International FEL Conference (FEL98), Williamsburg, VA, USA, 1998.
- [13] T. Tanaka, “SIMPLEX: simulator and postprocessor for free-electron laser experiments”, *J. Synchrotron Radiat.*, vol. 22, no. 5, pp.1319-1326, 2015. doi:10.1107/S1600577515012850.
- [14] J. Rossbach *et al.*, “Fundamental limitations of an X-ray FEL operation due to quantum fluctuations of undulator radiation”, *Nucl. Instrum. Methods Phys. Res., Sect. A*, vol. 393, no. 1–3, pp. 152–156, 1997.
- [15] S. Casalbuoni *et al.*, “Magnetic Field Measurements of Full-Scale Conduction-Cooled Superconducting-Undulator-Coils”, *IEEE Trans. Appl. Supercond.*, vol. 28, no. 3, pp. 4100704, 2018.
- [16] S. Casalbuoni *et al.*, “Superconducting Undulator Coils with Period Length Doubling”, in *Proc. 10th Int. Particle Accelerator Conf. (IPAC’19)*, Melbourne, Australia, May 2019, TUPGW017, accepted for publication on IOP. doi:10.18429/JACoW-IPAC2019-TUPGW017
- [17] J. Sekutowicz *et al.*, “Research and development towards duty factor upgrade of the European X-Ray Free Electron Laser linac”, *Phys. Rev. Spec. Top. Accel Beams*, vol. 18, no. 5, pp. 1–9, 2015.
- [18] R. Brinkmann *et al.*, “Prospects for CW and LP operation of the European XFEL in hard X-ray regime”, *Nucl. Instrum. Methods Phys. Res., Sect. A*, vol. 768, pp. 20–25, Mar. 2014.
- [19] E. A. Schneidmiller and M. V. Yurkov, “Harmonic lasing in x-ray free electron lasers”, *Phys. Rev. Spec. Top. Accel Beams*, vol. 15, no. 8, p. 080702, Aug. 2012.

TWO COLORS AT THE SASE3 LINE OF THE EUROPEAN XFEL: PROJECT SCOPE AND FIRST MEASUREMENTS

S. Serkez*, G. Geloni, N. Gerasimova, J. Grünert, S. Karabekyan, A. Koch, J. Laksman, Th. Maltezopoulos, T. Mazza, M. Meyer, S. Tomin, European XFEL, Schenefeld, Germany
W. Decking, L. Froehlich, V. Kocharyan, Y. Kot, E. Saldin, E. Schneidmiller, M. Scholz, M. Yurkov, I. Zagorodnov, DESY, Hamburg, Germany
M. Huttula, University of Oulu, Finland
E. Kukk, University of Turku, Turku, Finland

Abstract

The European XFEL is a high-repetition rate facility that generates high-power SASE radiation pulses in three beam-lines. A joint upgrade project, with Finnish universities, to equip the SASE3 beamline with a chicane has been recently approved to generate two SASE pulses with different photon energies and temporal separation. In this work we report the status of the project, its expected performance, and recent experimental results. Additionally, we discuss methods to diagnose the properties of the generated radiation.

INTRODUCTION AND PROJECT SCOPE

Funding has been recently granted by the Academy of Finland, with co-funding by the European XFEL, for constructing a device at the SASE3 undulator of the European XFEL. This will add two-color capability with tunable delay, and enable pump-probe experiments at the SASE3 endstations. A similar scheme is already enabled at SASE2, owing to the presence of the Hard X-ray Self-Seeding chicanes. The proposed setup relies on the simplest method available at date for generating two closely separated pulses of different colors at XFELs as suggested in [1] and experimentally proven in [2, 3]. The scheme is illustrated in Fig. 1, where the baseline SASE3 soft X-ray undulator is split into two independently radiating parts, $U1$ and $U2$, by a magnetic chicane. The chicane introduces a tunable delay and washes out the electron microbunching from $U1$, which is important if the color separation, in energy, is smaller than the FEL amplification bandwidth. One must ensure that the electron beam quality at the entrance of $U2$ is still good enough to sustain the FEL process, which limits the power that can be extracted below the saturation level. The photon energy separation between the two pulses can theoretically span across the entire range made available by the undulator system. In the case of SASE3 at the electron energy of 8.5 GeV, this range roughly spans between 240 eV and 1 keV. At 14 GeV – between 650 eV and 2.9 keV. For 17.5 GeV – between 1.02 keV and 3 keV. However, the impact of the FEL process on the electron beam quality depends on the photon energy, so that the first pulse to be produced should be at the highest energy.

A dedicated chicane will allow for a maximum delay of about 2.3 ps, see [4]. The minimum delay between pump

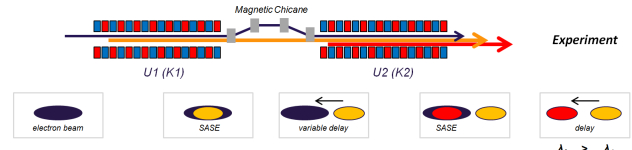


Figure 1: Simplest 2-color scheme relying on a single magnetic chicane.

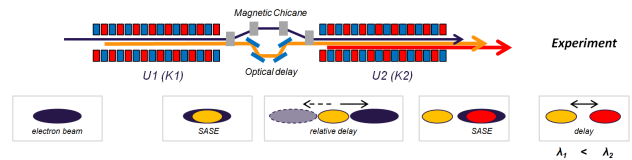


Figure 2: Solving the zero-crossing problem by implementing an optical delay line.

and probe radiation pulses is not zero. The electron beam is naturally overtaken by the radiation emitted in $U1$, as it moves slower than the speed of light in $U2$. The delay between pump and probe FEL pulses is thus larger than zero even when chicane is switched off and is in the order of 1 μ m (3fs).

Optical Chicane and Possible Further Upgrades

The magnetic chicane can only increase the delay between the FEL pulses, and its construction and commissioning constitutes only the first phase of the two-color project at SASE3. In fact, in order to enable a zero-delay and even a negative one, two possible solutions can be considered. The first, which constitutes the second phase of the project, consists in the introduction of an optical delay line to retard the radiation emitted in the first undulator with respect to the electron beam and, therefore, to compensate or overcompensate the radiation slippage, Fig. 2. A more detailed concept for the chicane with an optical delay line was developed in [4], see Fig. 3. It will allow for a negative delay of up to 100 fs, thus enabling zero-crossing and subsequent scan until 2.3 ps. Further investigation on the actual implementation of the scheme is being conducted.

An alternative solution can be found in electron beam manipulations enabling fresh slice lasing, which may be achieved by means of a “dechirper module”, or other techniques inducing a kick in part of the electron beam [5]. In this way, the trajectory of electrons vary as a function of the

* svitozar.serkez@xfel.eu

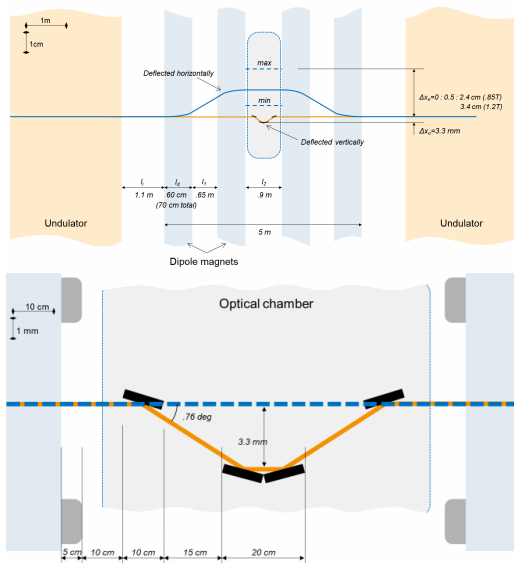


Figure 3: Concept of chicane and optical delay line.

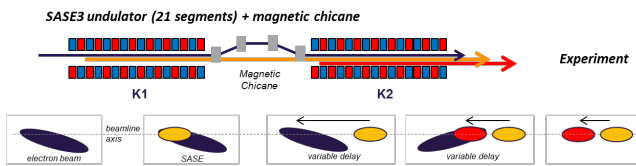


Figure 4: Solving the zero-crossing problem by implementing a fresh slice technique.

longitudinal position in the beam. One can obtain that in $U1$ the electron beam emits radiation from a short lasing window at the tail, while in $U2$ the lasing window is located in the head of the beam. If the distance between the two lasing windows is larger than the expected radiation slippage, both positive and negative pump-probe delays will be achievable, see Fig. 4.

SIMULATIONS

Simulations were performed for the baseline case in Fig. 1 as well as for the fresh bunch option. For the baseline case, we assumed a nominal 20 pC electron bunch from start-to-end electron simulations (4.5 kA current, normalized emittance $\epsilon_n = 0.2$ mm mrad, 1.3 MeV rms energy spread [6]), see [7], which gives the shortest radiation pulse duration. The electron energy was 8.5 GeV, which allows reaching the lowest photon energy (250 eV). $U1$ was set to lase at 630 eV, with 5 active segments, and $U2$ was set to lase at 250 eV with 7 active segments. The output at the exit of $U1$ and $U2$, respectively, is shown in Fig. 5. The simulated mean energy per pulse is 50 μ J for $U1$ at 630 eV, corresponding to 5×10^{11} photons per pulse, and 70 μ J for $U2$, corresponding to 1.5×10^{12} photons per pulse.

The presence of two separate sources, inside $U1$ and $U2$, complicates the focusing at the sample. However, it was shown in [7] that KB mirrors can be tuned to image a virtual

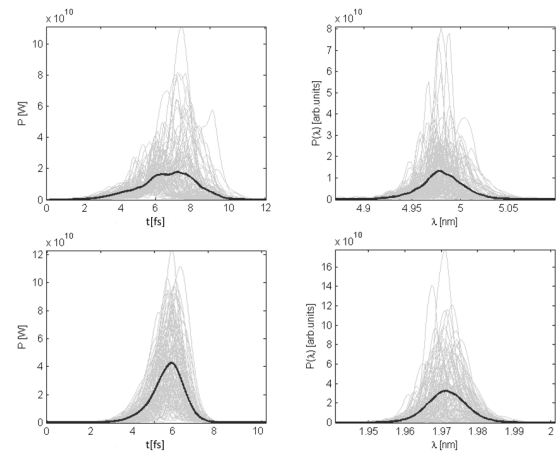


Figure 5: Simulated temporal duration and spectra at the exit of $U1$ and $U2$, according to the setup in Fig. 1. Grey lines refer to single shots, black lines are the ensemble average.

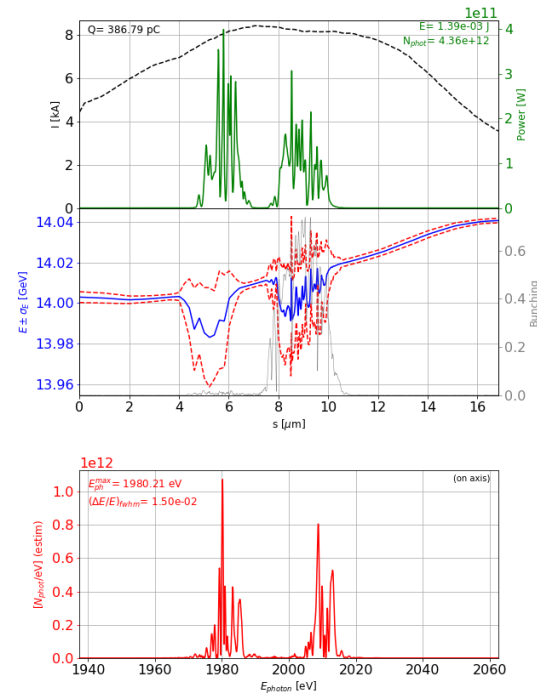


Figure 6: Simulated temporal duration (top) and spectrum (bottom) at the exit of the setup in Fig. 4. Grey lines refer to single shots, black lines are the ensemble average. The electron beam deterioration within the lasing windows is evident from the middle plot.

source in between the two, leading to a fluence in the order of 10^{18} ph/cm² per pulse on the sample.

Simulations for the fresh-slice option were run, instead, with a 500 pC start-to-end nominal bunch (5 kA current, normalized emittance $\epsilon_n = 0.45$ mm mrad, 0.5 MeV rms energy spread [6]), in order to ensure enough length to accommodate two separate lasing windows. In this case, both pulses evolve up to saturation, see Fig. 6.

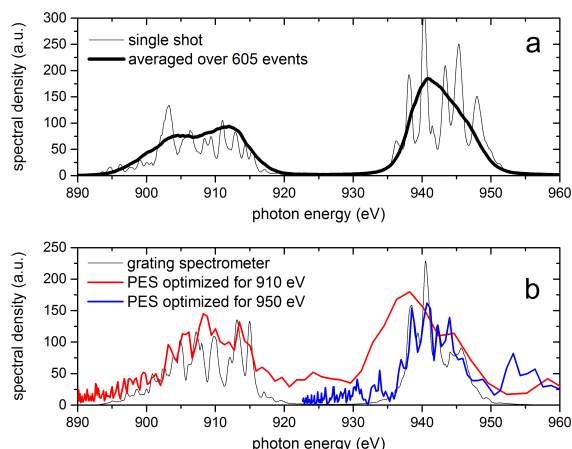


Figure 7: Experimental demonstration of two-color lasing: (a) single shot (thin line) and averaged over 605 events (thick line) spectral distribution measured with grating spectrometer; (b) single shot spectra measured with grating spectrometer (black line), with PES optimized for 910 eV (red line) and with PES optimized for 950 eV (blue line).

FIRST MEASUREMENTS AND DIAGNOSTICS

First tests on the expected performance of the system in Fig. 1 have been performed at the European XFEL without the chicane, which is expected to be installed in 2020. The SASE3 undulators were divided into two parts consisting of 9 segments for $U1$ and 11 segments for $U2$, and tuned to different photon energies, ranging from about 700 eV to about 1 keV, and selected in such a way that the two spectra did not overlap. The electron beam energy and charge were 14 GeV, and 250 pC respectively. Typical pulse energies were above the 350 μ J-range for each of the two colors.

Figure 7a shows the spectrum for the case of 950 eV emitted in $U1$ and 910 eV emitted in $U2$ with average pulse energy about 600 μ J in each color, thin and thick lines correspond to single shot spectrum and the ensemble average of 605 events respectively. The spectra were measured using grating soft X-ray spectrometer which comprises the SASE3 monochromator beamline [8] operating in spectrometer mode [9]. The grating spectrometer, although providing high resolution up to $5 \cdot 10^3$ and thus allowing to characterize spectrum with high accuracy, is an invasive device with a limited spectral window which does not allow to detect two pulses simultaneously in case they are largely separated in photon energy.

To provide non-invasive shot-to-shot diagnostics in multi-bunch mode in terms of each color intensity and spectrum, the gas-based Time-Of-Flight (TOF) Photo-Electron Spectrometer (PES) [10] can be used during user experiments. The PES device consists of 16 eTOF drift-tubes, located around the interaction region with a target gas and partitioned into four groups (one per quadrant) with independent control of the retardation voltage. The latter allows to independently optimize their photon energy resolution. When FEL operates in single color mode, each PES can be cross-

calibrated in terms of pulse energy to the X-ray Gas Monitor (XGM) device [11]. The XGM, being capable to measure absolute intensity, is not capable to distinguish the photon energies, so that PES is to be used as a diagnostic tool for two-color experiments. To achieve higher detection precision, for each color we add the signal from several PES detectors. We found the XGM/PES pulse energy correlation coefficient to be 0.93 from which we estimate a pulse energy error of 7%. The single shot PES spectra acquired during 2-color operation are presented in Fig. 7b. The red curve shows the output of PES quadrant optimized for 910 eV, and the blue curve – of optimized for 950 eV. Although the optimized PES resolution is too low to resolve SASE spectrum structure, it is capable of providing the bandwidth estimation for each photon energy.

SCIENTIFIC RELEVANCE

The two-color operation mode enables a large number of scientific applications based on a pump-probe excitation scheme of molecules, doped clusters or nanoparticles with two individually controllable X-ray pulses. As an example, one can enable atomic site-specific excitation or ionization in molecules at the SQS scientific instrument of the European XFEL [12]. This is achieved by tuning the pump wavelength to match the energy of a specific resonant excitation from an atomic core or inner-valence orbital, or by choosing an energy just above the binding energy of a certain atomic orbital. A typical case where such site-selectivity is applicable would be organic compounds containing heavy element(s), sulphur or phosphorus atoms. The probe can then be tuned independently to react with another atomic site in the molecule or, for example, to enhance its sensitivity to the presence of a particular fragment or isomer created as the result of the pump pulse. Furthermore, the variable time delay between the pump and the probe allows real-time insight into the dynamics of the pump-induced processes, such as the relatively slow nuclear rearrangement and dissociation, or the faster electronic motion. As an example, the case of chloriodoethane was presented in [7], where the charge transfer from the chlorine to iodine atomic site can be monitored by a suitable choice of the two wavelengths.

CONCLUSION

We reported on the status of the European XFEL two-color project at SASE3. We discussed different implementations, from the simplest setup just based on the installation a single magnetic chicane, to more advanced allowing for delay zero-crossing. We also presented simulations for different cases and preliminary measurements of temporally superimposed two-color pulses without the chicane.

ACKNOWLEDGEMENTS

The Academy of Finland is acknowledged for funding the instrumentation of the two-color project at the European XFEL.

REFERENCES

- [1] G. Geloni, V. Kocharyan, and E. Saldin, "Scheme for femtosecond-resolution pump-probe experiments at XFELs with two-color ten GW-level X-ray pulses", DESY 10-004, 2010. <https://arxiv.org/abs/1001.3510>.
- [2] A. A. Lutman *et al.*, "Experimental Demonstration of Femtosecond Two-Color X-Ray Free-Electron Lasers", *Phys. Rev. Lett.*, vol. 110, p. 134801, 2013. doi:10.1103/PhysRevLett.110.134801.
- [3] T. Hara *et al.*, "Two-colour hard X-ray free-electron laser with wide tunability", *Nat. Comm.*, vol. 4, p. 2919, 2013. doi:10.1038/ncomms3919.
- [4] S. Serkez, "Two colors at SASE3: Chicane design choice for the 2CPP Finnish-EuXFEL collaboration project", Internal Design Document, 2018.
- [5] A. Lutman *et al.*, "Fresh-slice multicolour X-ray free-electron lasers", *Nat. Phot.*, vol 10, pp. 745-750, 2016. doi:10.1038/nphoton.2016.201
- [6] I. Zagorodnov, DESY MPY Start-to-End Simulations page, <http://www.desy.de/fel-beam/s2e/xfel.html>
- [7] G. Geloni *et al.*, "Opportunities for Two-color Experiments at the SASE3 undulator line of the European XFEL", DESY 17-068, 2017. <https://arxiv.org/abs/1706.00423>.
- [8] H. Sinn *et al.*, "Technical Design Report: X-Ray Optics and Beam Transport", XFEL.EU TR-2012-006, 2012. doi:10.3204/XFEL.EU/TR-2012-006
- [9] N. Gerasimova, "Performance of the SASE3 monochromatized equipped with provisional short grating", XFEL.EU TR-2018-001, 2018. doi:10.22003/XFEL.EU-TR-2018-001
- [10] J. Laksman *et al.*, "Commissioning of a photoelectron spectrometer for soft X-ray photon diagnostics at European XFEL", *J. Synchrotron Rad.*, vol. 26, p. 1010-1016, 2019. doi:10.1107/S1600577519003552
- [11] Th. Maltezopoulos *et al.*, "Operation of X-ray gas monitors at the European XFEL", *J. Synchrotron Rad.*, vol. 26, p. 1045-1051, 2019. doi:10.1107/S1600577519003795
- [12] T. Mazza, H. Zhang, and M. Meyer, "Scientific Instrument SQS", Tech. Des. Rep., December 2012. doi:10.3204/XFEL.EU/TR-2012-007.

PHYSICAL DESIGN AND FEL PERFORMANCE STUDY FOR FEL-III BEAMLINE OF SHINE

N.S. Huang^{*}, Shanghai Institute of Applied Physics, Chinese Academy of Sciences, Shanghai, China
also at University of Chinese Academy of Sciences, Beijing, China

H.X. Deng[†], B. Liu, D. Wang,

Shanghai Advanced Research Institute, Chinese Academy of Sciences, Shanghai, China

Abstract

The first hard X-ray free electron laser (XFEL) facility in China, the Shanghai High-Repetition-Rate XFEL and Extreme Light Facility (SHINE), is under construction, which allows for generating X-ray pulses in the photon energy range from 3 keV to 25 keV. To produce X-ray pulses with photon energy up to 25 keV, FEL-III undulator line of SHINE employs superconducting undulators. However, the smaller gap of the superconducting undulator poses serious wakefield effect reducing the FEL power, compared to the normal planar undulator. For a setup design optimization, the design and performance of the FEL-III undulator line are presented using start-to-end beam simulations at self-amplified spontaneous emission (SASE) and self-seeding mode. The wakefield impact on FEL performance is then investigated. A linear undulator tapering technique is adopted for recovering the FEL power to the non-wakefield level.

INTRODUCTION

Advanced high brightness X-ray light sources, X-ray free electron lasers (XFELs), bring significant opportunities to many fields for scientific exploring. The Shanghai High-Repetition-Rate XFEL and Extreme Light Facility (SHINE) is the first hard X-ray FEL facility in China [1], that will be fed by a superconducting linac at a high repetition rate, up to 1 MHz, and is being designed under a multi undulator line collaboration to generate X-ray of photon energy range from 3 keV to 25 keV. One of the undulator lines, FEL-III, will cover the spectral range between 10 keV and 25 keV. Reaching such wide spectral range requires high tunability of undulator parameter owing to the resonance condition of the FEL process. Superconducting undulator with a short period length is probably a better choice. However, the designed FEL performance is degrading due to resistive wall wakefield effects along the superconducting undulator line, which is more serious compared to normal conducting one.

Thus, it is necessary to investigate the wakefield impact on FEL performance of FEL-III, e.g., the pulse energy and FEL bandwidth. While various advanced FEL concepts are being explored for SHINE, this paper presents the detailed FEL simulations in only the self-amplified spontaneous emission (SASE) and self-seeding case for start-to-end electron beam coming from the superconducting linac. The basic

parameters are listed in Table 1. The slice parameters of the start-to-end electron beam are illustrated in Fig. 1. The core of the bunch has relatively flat energy with a current of 1500 A, slice energy spread 0.8 MeV and slice emittance of 0.2 mm-mrad. The generations of 15 keV X-ray pulse based on a 8 GeV electron beam are performed. The FEL simulations were carried out by the time-dependent mode of GENESIS [2]. The interaction between X-ray pulse and crystal is calculated by BRIGHT [3].

Table 1: Normal Electron Beam and Undulator Parameters

Parameter	Value	Unit
Electron beam energy	8	GeV
Slice energy spread	0.8	MeV
Total charge	100	pC
Photon energy	15	keV
Undulator period length	16	mm
Undulator segment length	4	m
Break length	1	m
Total length	200	m

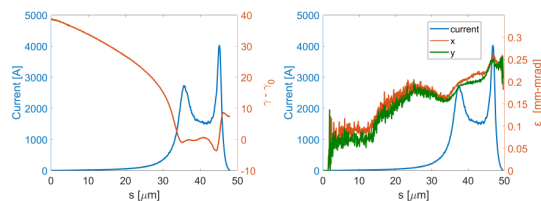


Figure 1: Slice energy (left), x (red) and y (green) slice emittance (right) of the start-to-end electron beam.

FEL PERFORMANCE

According to the project targets, several different operating modes have been explored for the different undulator line of SHINE. These modes include, but are not limited to, SASE, self-seeding [4], echo-enabled harmonic generation (EEHG) [5] and cascading schemes. FEL-III beamline is envisioned to operate from 10-25 keV in the SASE and self-seeding mode using the superconducting undulator. To estimate the capacity of FEL-III, we begin with the start-to-end simulation results without wakefield effects at 15 keV photon energy for SASE and self-seeding mode.

Fig. 2 illustrates the SASE performance of 15 keV output. The final pulse energy is about 380 μJ, corresponding to

^{*} huangnanshun@sinap.ac.cn

[†] denghaixiao@zjlab.org.cn

1.6×10^{11} X-ray photons. The peak power exceeds 20 GW at the flat profile of peak current 1500 A. At the exit of the undulator, the full width at half maximum (FWHM) bandwidth equals to nearly 40 eV, while the FWHM temporal duration is around 50 fs. The low transverse emittance of start-to-end electron beam generates a short saturation length. Thus, there is significant room to explore post-saturation tapering for higher pulse energy and spectral brightness.

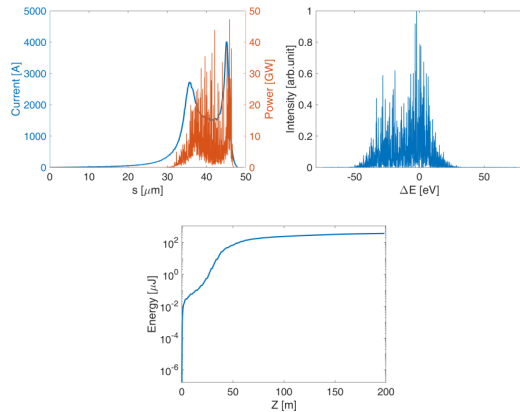


Figure 2: The radiation properties from FEL-III at photon energy of 15 keV: power along the FEL pulses (top left), spectra (top right) and pulse energy growth along the undulator (bottom).

The temporal coherence of SASE FEL can be improved with self-seeding scheme. An "8 cells + 32 cells" scheme with single crystal has been chosen in this simulation, in which 8 upstream undulator segments are used for SASE growth, and 32 downstream undulator segments serve as an FEL amplifier of the seeding. The simulation results are shown in Fig. 3.

The top left plot in Fig. 3 illustrates the gain curve of two undulator sections. The FEL pulse amplifies to just over $10 \mu\text{J}$ in the first stage of amplification where single SASE spikes typically reach 3 GW. The monochromatized radiation had an average power of about 5 MW after the crystal filter function was applied, seen in the top right plot in Fig. 3, which is much larger than the shot noise power of refreshed electron beam. Most SASE power transmits through the crystal and becomes the background noise without interaction between delayed electron beam in the second stage. The final pulse energy exceeds $350 \mu\text{J}$, corresponding to 1.4×10^{11} X-ray photons. At the exit of the undulator, the spectrum bandwidth equals to nearly 0.35 eV (FWHM). A room to explore post-saturation tapering can be seen again.

WAKEFIELD IMPACT ON FEL PERFORMANCE

In order to achieve a 25 keV FEL photon energy with 8 GeV beam energy, a superconductive undulator with 16 mm period length and gap 4 mm is chosen. One of the critical issues of the superconductive undulator is the smaller

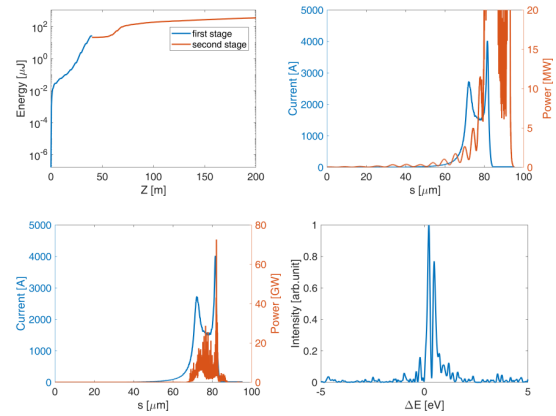


Figure 3: The self-seeding performance of FEL-III. The pulse energy gain curve (top left), the filtered pulse (top right), power along the FEL pulses (bottom left) and its spectra (bottom right) is shown. The flat part of the current profile covers a monochromatic seed generated by filtering of the diamond crystal (400).

operation gap, which is mainly related to the wakefield effect. Based on our previous wakefield study of the SXFEL facility [6, 7], an analytical formula is used to calculate the wakefield generated in the resistive wall. If a slice energy change on the order of the FEL Pierce parameter occurs due to the resistive wall wakefield, the FEL performance could be impacted. The slice energy change over the bunch length with the current can be seen in Fig. 4. The max beam energy losses due to the resistive wall wakefield are 190 keV/m from the theory. Then, the wakefield energy loss is imported timely and locally on the electron beam in GENESIS.

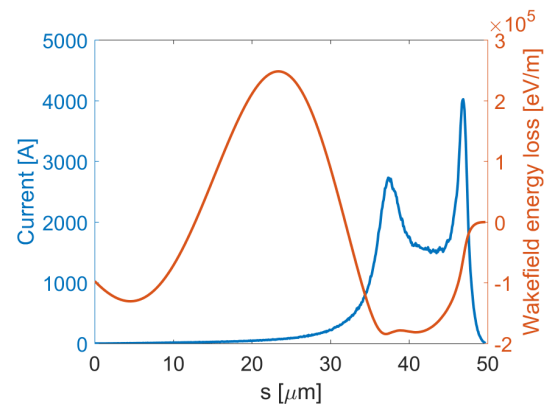


Figure 4: The peak current (blue) and the wakefield energy loss (red) along the bunch coordinate are shown.

The SASE performance is affected by the wakefield significantly. Fig. 5 illustrates the FEL power evolution along undulator (top left), final electron beam energy distribution (top right), FEL temporal profile (bottom left) and output spectrum (bottom right). It can be seen that wakefield will produce a non-linear energy modulation along the undulator. In the absence of the wakefield-induced energy loss (Fig. 2),

the 15 keV FEL can finally achieve 380 μJ pulse energy with a peak power of approximately 20 GW. However, when the wakefield is considered (Fig. 5), the FEL pulse energy drops to 60 μJ and the spectrum degrades and broadens. The results show that the pulse energy of the final 15 keV FEL pulse will be degraded by a factor of 6 with a gradual beam energy loss of 38 MeV along the whole undulator section.

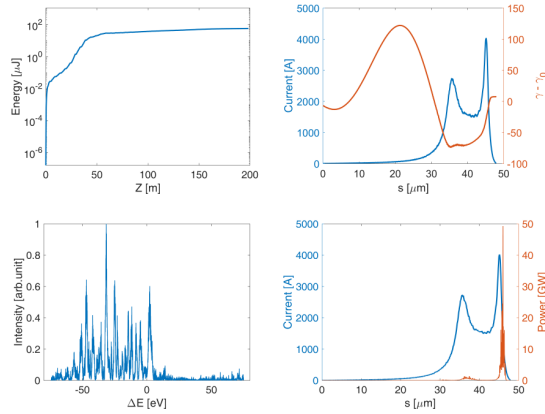


Figure 5: The pulse energy growth along undulator (top left), final energy distribution (top right), power along FEL pulse (bottom left) and spectrum (bottom right) is shown. After 200 m undulator line, a large energy modulation caused wakefield can be seen in energy distribution. The energy loss of electron beam results in resonant condition detune terminating the FEL process and degrading FEL pulse energy.

UNDULATOR TAPERING

The FEL pulse energy reduction caused by the continuous beam energy loss can be compensated by gradually tapering the undulator. In this section, a linear taper of SHINE undulator is adopted to bring pulse energy back to the level without wakefield effect. Besides the conventional linear taper, there are significant spaces to explore the undulator taper to reach a very high brightness. But a complicated algorithm for tapering optimization is beyond the scope of what we can address in this paper.

Fig. 6 shows the start-to-end simulation results of SASE and self-seeding mode with an undulator taper coefficient of 0.7% on whole 200 m undulator line. The SASE results reach 390 μJ pulse energy which returns to the level without wakefield. Due to the resonant energy detune caused by tapering effect, the radiation power from the peak of current 4000 A is smaller than the result without wakefield. The self-seeding mode can generate 360 μJ pulse corresponding 1.5×10^{11} photons per pulse with narrower bandwidth (FWHM) of 0.17 eV. The first tapered undulator part in self-seeding mode causes a lower SASE background resulting in a richer signal-to-noise ratio.

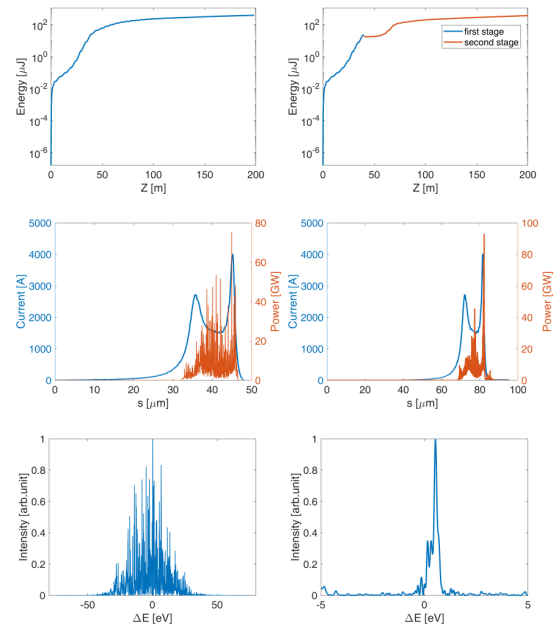


Figure 6: Left curves show the SASE results, and right curves show self-seeding results. Pulse energy along undulator (top), power along FEL pulse (center) and related spectrum (bottom) are shown. With a linear 0.7% tapering along whole 200 m undulator, the radiation could recover to the level without wakefield impact.

CONCLUSION

We performed the start-to-end simulations for SASE and self-seeding mode at the FEL-III of SHINE. In the case of SASE, about 1.6×10^{11} photons per pulse with 40 eV bandwidth can be generated. With a self-seeding scheme, the output at 15 keV is 1.4×10^{11} photons per pulse with 0.35 eV spectral bandwidth, corresponding to 4×10^{14} photons/s/meV spectral flux. In the start-to-end SASE simulation with the wakefield effects, the total beam energy loss of 38 MeV along the undulator line causes serious degradation of FEL performance: the pulse energy drops to 60 μJ from original 380 μJ . The FEL performance loss caused by wakefield can be compensated with a linear undulator taper of 0.7%. Besides, there are significant spaces to explore the undulator taper to reach a very high brightness. More in-depth studies will be done in future.

ACKNOWLEDGEMENTS

This work was partially supported by the National Key Research and Development Program of China (2018YFE0103100, 2016YFA0401900) and the National Natural Science Foundation of China (11935020, 11775293).

REFERENCES

- [1] C. Feng and H.-X. Deng, "Review of fully coherent free-electron lasers", *Nuclear Science and Techniques*, vol. 29, p.160, 2018. doi:10.1007/s41365-018-0490-1

- [2] S. Reiche, “GENESIS 1.3: a fully 3D time-dependent FEL simulation code”, *Nuclear Instruments and Methods in Physics Research Section A: Accelerators, Spectrometers, Detectors and Associated Equipment*, vol. 429, pp. 243–248, 1999. doi:10.1016/S0168-9002(99)00114-X
- [3] N.-S. Huang, K. Li, and H.-X. Deng, “BRIGHT: the three-dimensional X-ray crystal Bragg diffraction code”, *Nuclear Science and Techniques*, vol. 30, p. 39, 2019. doi:10.1007/s41365-019-0559-5
- [4] J. Amann *et al.*, “Demonstration of self-seeding in a hard-X-ray free-electron laser”, *Nature Photonics*, vol. 6, p. 693, 2012. doi:10.1038/nphoton.2012.180
- [5] G. Stupakov, “Using the Beam-Echo Effect for Generation of Short-Wavelength Radiation”, *Physical Review Letters*, vol. 102, p. 074 801, 2009. doi:10.1103/PhysRevLett.102.074801
- [6] M. Song, K. Li, C. Feng, H. Deng, B. Liu, and D. Wang, “Wake-field issue and its impact on x-ray photon pulse in the sxfel test facility”, *Nuclear Instruments and Methods in Physics Research Section A: Accelerators, Spectrometers, Detectors and Associated Equipment*, vol. 822, pp. 71–76, 2016. doi:10.1016/j.nima.2016.03.089
- [7] M.-H. Song, C. Feng, D.-Z. Huang, H.-X. Deng, B. Liu, and D. Wang, “Wakefields studies for the sxfel user facility”, *Nuclear Science and Techniques*, vol. 28, no. 7, p. 90, May 2017. arXiv:1611.00883

EFFECT ON FEL GAIN CURVE USING PHASE SHIFTERS

Myung-Hoon Cho *, Chi-Hyung Shim, Gyu-Jin Kim, H. Yang, and Heung-Sik Kang
PAL, Pohang, Korea

Abstract

Phase matching between FEL and electron beam should be precisely controlled for FEL amplification. Phase shifters located between undulators performs the phase matching. An electron beam can be controlled to be in the in- or out-phase by setting the phase shifters from the phase shifter scan. In this article, we show effects of FEL gain curve by setting the in- and out-phase of electron beam. We address reasons of the reduction of FEL intensity in the out-phase condition dividing the linear and saturation FEL amplification regimes. In the linear regime the gain curve is shifted, and in the saturation regime the electron loss occurs during the undulator tapering. Our results show agreements with experiments performed at PAL-XFEL.

INTRODUCTION

Most x-ray free-electron laser (XFEL) facility requires segmented undulators with drift sections. Drift sections include quadrupoles for beam focus, beam path correctors, diagnostics, and beam phase shifters [1,2]. While an electron beam travels drift sections, the electron beam phase can be mismatched to the generated X-ray. This phase mismatch can lead to a reduction of XFEL intensity, therefore the phase matching can be an import optimization process.

Enhancement of FEL efficiency by matching phase can be understood by so-called ‘phase jump’ at the saturation region [3,4]. The key idea is setting a dominant electron beam phase zero so called ‘synchronous phase’ before entering the next undulator. To investigate effects on the FEL gain curve, two cases of the phase-matched condition (the in-phase) and 180° off-set condition from the in-phase condition (the out-phase) are considered.

THEORY AND SIMULATION

We show optimization of FEL and FEL gain curve by the phase shifters. To understand the changes of FEL gain curve, we develop a linear theory for the linear region and use KMR analysis [4,5] for the saturation region, those are compared with FEL simulations.

Linear Regime

If we ignore the time dependent terms, 1D FEL equations are given as [6]

$$\frac{d\theta}{dz} = \hat{\eta} \quad (1.a)$$

$$\frac{d\hat{\eta}}{dz} = ae^{i\theta} + a^*e^{-i\theta} \quad (1.b)$$

$$\frac{da}{dz} = -\langle e^{-i\theta} \rangle_{slice} \quad (1.c)$$

Here, $\theta \equiv (k + k_u)z - \omega t$ is the electron phase, $\eta \equiv (\gamma - \gamma_0)/\gamma_0$ is the energy deviation ratio to γ_0 , and a is the slowly varying electric field envelope. The equations are normalized by $\hat{z} = 2k_u \rho z$, $\hat{\eta} = \eta/\rho$, and $a = eK[JJ]E/4\gamma_0^2 k_u mc^2 \rho^2$, where $[JJ]$ is the harmonic factor, and ρ is the FEL parameter. Introducing the collective variables : the bunching factor $b = \langle e^{-i\theta} \rangle_{slice}$ and the collective momentum $P = \langle \hat{\eta} e^{-i\theta} \rangle_{slice}$, Eq. (1) is rewritten by ignoring the non-linear terms : $dP/d\hat{z} = a + a^* \langle e^{-i2\theta} \rangle - i\langle \hat{\eta}^2 e^{-i\theta} \rangle \approx a$

$$\frac{da}{d\hat{z}} = -b \quad (2.a)$$

$$\frac{db}{d\hat{z}} = -iP \quad (2.b)$$

$$\frac{dP}{d\hat{z}} = a \quad (2.c)$$

Eq. (2) is the linearized FEL equation, which can be summarized to be an third-order differential equation

$$\frac{d^3 a}{d\hat{z}^3} = ia \quad (3)$$

The general solution of Eq.(3) can be obtained as

$$a(\hat{z}) = \frac{1}{3} \sum_{l=1}^3 \left[a(\hat{z}_0) - i \frac{b(\hat{z}_0)}{\mu_l} - i\mu_l P(\hat{z}_0) \right] e^{-i\mu_l \hat{z}} \quad (4)$$

, where μ_l indicates three radiation modes : a simple propagator $\mu_1 = 1$, a damper $\mu_2 = -(1 + \sqrt{3}i)/2$, and a grower $\mu_3 = (-1 + \sqrt{3}i)/2$. Assuming the electron beam in the in-phase, the initial conditions at $\hat{z}_0 = 0$ are $a(0) = C_1 + C_2 + C_3$, $b(0) = \mu_1 C_1 + \mu_2 C_2 + \mu_3 C_3$, and $P(0) = i(\mu_1^2 C_1 + \mu_2^2 C_2 + \mu_3^2 C_3)$. Considering a SASE condition of $a(0) = P(0) = 0$ with initial bunching factor of $b(0) = b_0$, a grower mode becomes dominant, then Eq.(4) is simplified to be

$$a_{in}(\hat{z}) \cong \frac{i-\sqrt{3}}{6} b_0 e^{\frac{\sqrt{3}+i}{2} \hat{z}} \quad (5)$$

To calculate the changed gain curve at the out-phase, we simply set the phase replacing θ by $\theta + \pi$. Eq. (1) is then reformulated to be the linearized equations which is reduced to a single third-order differential equation same as Eq. (3). Therefore, the expression of the solution is identical to the in-phase solution of Eq. (4) except of the initial conditions. according to the phase shifter position $\hat{z}_0 \neq 0$. The initial conditions at $\hat{z} = \hat{z}_0$ can be defined obtained using Eq. (5):

$$a(\hat{z}_0) = -\frac{1}{3} b_0 e^{i(\frac{\hat{z}_0}{2} - \frac{\pi}{6})} e^{\frac{\sqrt{3}}{2} \hat{z}_0} \quad (6.a)$$

* mh0309@postech.ac.kr

$$b(\hat{z}_0) = -\frac{da}{d\hat{z}}\bigg|_{\hat{z}_0} = \frac{1}{3}b_0e^{i\frac{\hat{z}_0}{2}}e^{\frac{\sqrt{3}}{2}\hat{z}_0} \quad (6.b)$$

$$P(\hat{z}_0) = i\frac{db}{d\hat{z}}\bigg|_{\hat{z}_0} = \frac{i}{3}b_0e^{i(\frac{\hat{z}_0}{2}+\frac{\pi}{6})}e^{\frac{\sqrt{3}}{2}\hat{z}_0} \quad (6.c)$$

The solution of the out-phase equation then is derived as

$$a_{out}(z) = \frac{1}{9}b_0e^{\frac{\sqrt{3}+i}{2}\hat{z}_0}\left[(\sqrt{3}+i)e^{-i(\hat{z}-\hat{z}_0)} + ie^{\frac{-\sqrt{3}+i}{2}(\hat{z}-\hat{z}_0)} + \frac{\sqrt{3}-i}{2}e^{\frac{\sqrt{3}+i}{2}(\hat{z}-\hat{z}_0)}\right] \quad (7)$$

Note that these expressions are available for $\hat{z} \geq \hat{z}_0$. Eq. (7) agrees well with the 1D static simulation as shown in Fig. 1.

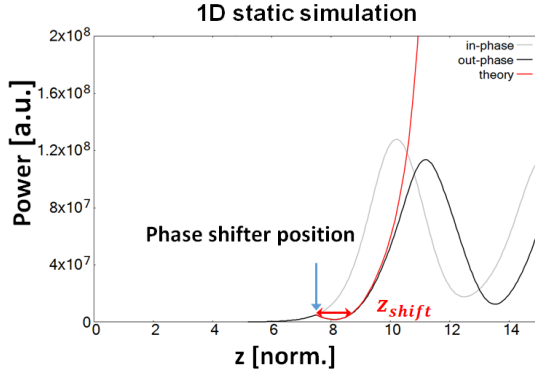


Figure 1: FEL gain curves of the in-phase and the out-phase. The phase is shifted at $\hat{z}_0 = 7.5$. The shifting distance is $\Delta\hat{z} = 1.27$ agreeing with the expectation.

After $\hat{z} = \hat{z}_0$, the FEL gain curve is modulated for a distance where three modes of propagator, damper, and grower are accompanied. However, the grower is dominant being farther from the phase shifter, this resembles the phase shifter shifts the gain curve. To obtain the shifting distance we further modify Eq. (7) by assuming $\hat{z} \gg \hat{z}_0$, which becomes

$$|a_{out}(\hat{z})|^2 \approx \frac{b_0^2}{9}e^{\sqrt{3}(\hat{z}-1.27)} \quad (8)$$

Eq.(8) shows the gain curve shift is shifted about **1.27** from the in-phase gain curve.

Saturation Regime

As the electron beam enters the saturation region, electrons are bunched locally. A dominant FEL amplification or diminishment is determined by the bunched electrons. To express electrons' trajectory in the phase space, the equations of motion of Eq. (1.a) and (1.b) are rewritten as

$$\frac{d\psi}{d\hat{z}} = \hat{\eta}, \quad \frac{d\hat{\eta}}{d\hat{z}} = -a_0 \sin \psi \quad (9)$$

whose Hamiltonian is

$$H = \frac{1}{2}\hat{\eta}^2 + a_0(1 - \cos \psi) \quad (10)$$

, where $a_0 \equiv |a|/2$, $\psi \equiv \theta + \phi + \pi/2$, and $a = |a|e^{i\phi}$. The separatrix can then be defined for the trajectory of

$H_{sep} = H(\psi = \pm\pi, \hat{\eta} = 0)$. The separatrix function is expressed as

$$\hat{\eta}(\psi) = \pm 2\sqrt{a_0} \cos \frac{\psi}{2} \quad (11)$$

When electrons locate in the separatrix or 'phase bucket', the electrons participate in FEL process. In the phase space undulator taper normally shifts down the phase bucket and the phase shifter moves the electrons to the right or left.

To study FEL gain curve by a phase shifter depending on a different longitudinal position, we conduct 1D static FEL simulation. 20 segmented undulator modules are prepared and each undulator module is composed of 5 m undulator and 1 m drift section. To prevent confusion, we test only one phase shifter, therefore, the out-phase condition is selected for just one undulator module and all others are the in-phase. Figure 2 summarizes results of two phase shifters at 30 m and 41 m. The out-phase condition reduces the FEL gain curve, which is because of the electron loss from the phase bucket (red lines). FEL amplification is fully suppressed at deep saturation region as shown in Fig. 2 (c), that means the phase bucket loses electrons significantly. This addresses FEL optimization using phase shifters is very important at saturation region especially when the electron beam is well bunched.

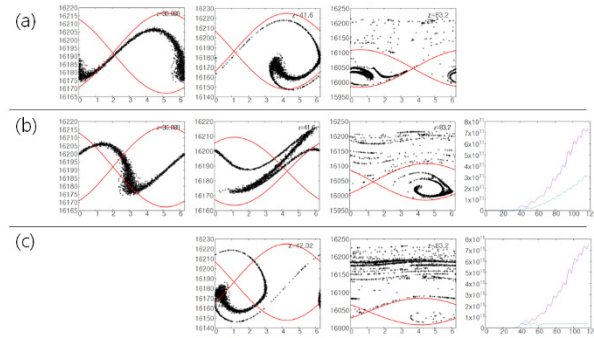


Figure 2: Comparisons of FEL gain curves with the electron phase distribution. (a) The reference without phase shifters. With the phase shifters (b) at 30 m, (c) at 41 m in the out-phase condition. The red line in the phase distribution is the phase bucket following Eq. (11).

EXPERIMENT

Normally the phase shifter is a compact magnetic chicane which elongates the electron beam path. Pohang Accelerator Laboratory X-ray Free Electron Laser (PAL-XFEL) operates the phase shifter made up of permanent magnets [1]. In the operation, the phase scan is performed by changing the gap of magnets (phase shifter gap), which retards the electron beam phase. Phase matching is done by finding the phase shifter gap producing the optimal FEL intensity. In Fig. 3 (a), the installed phase shifter between undulator modules is shown, and Fig. 3 (b) shows an example of the phase shifter scan.

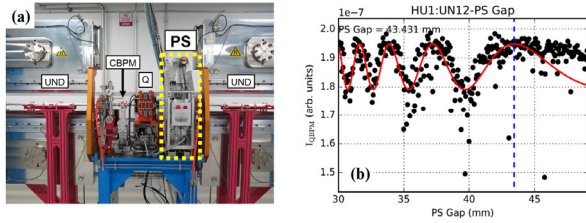


Figure 3: (a) Intersection between undulator (UND) modules. Cavity beam position monitor (CBPM), quadrupole (Q) and phase shifter (PS) has been installed. (b) Measured FEL intensity according to the gap of phase shifter. Fitting by sine function is drawn as the red solid line and the optimal phase is determined by setting PS gap (blue dashed line).

During the FEL optimization all phase shifters are set to be the maximum FEL intensity, so the electron beam can be set in the in-phase condition. To see the gain curve change, one phase shifter is set to be the out-phase condition by selecting the minimum FEL intensity from the phase shifter gap scan. Comparisons of the in- and out-phase conditions are shown in Fig. 4. Targeted experiment conditions are 5 keV FEL energy with the undulator parameter $K=1.87$, the undulator period 26 mm, and the electron beam charge 200 pC.

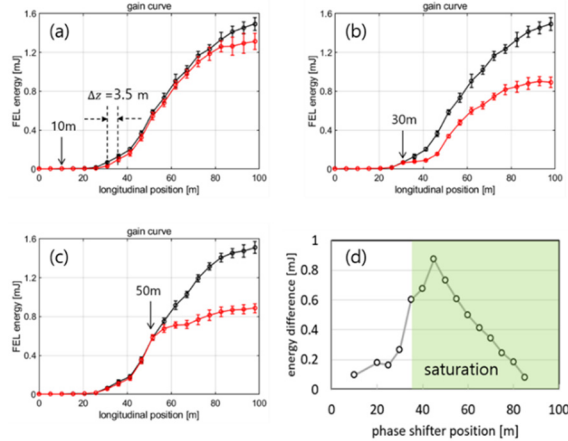


Figure 4: Gain curve comparison between the in- and out-phase conditions. One phase shifter is set for the out-phase at (a) 10 m, (b) 30 m, and (c) 50 m. (d) FEL energy difference between the in- and out-phase from the phase shifter scan.

Fig. 4 lists three phase shifters of the in- and out-phase conditions. From the FEL gain curve (black line), the saturation starts around $z=30$ m. In Fig. 4 (a) at $z=10$ m, the phase shifter shifts the gain curve around 3.5 m, which is 1.2 in normalized unit and it is comparable to the theoretical value of 1.27. However after the saturation the gain curve is similar to the reference. The gain curve is reduced significantly around the end of the linear regime as shown in Fig. 4 (b). When the phase shifter is located in deep saturation region as shown in Fig. 4 (c), the FEL amplification is suppressed. These FEL reductions are reproduced by the

simulation results of Fig. 2. Therefore the phase shifter scan is efficient and important for the saturation region.

CONCLUSION

We studied the in- and out-phase effect on the FEL gain curve. FEL intensity difference between the in- and out-phase conditions increases as entering the saturation region. FEL reduction by the out-phase condition is separated in the linear and saturation regimes. In the linear regime the gain curve is simply shifted. In the saturation regime electrons are lost from the phase bucket which operates FEL process. From this analysis the phase shifter scan is more efficient for the saturation region and the undulator tapering.

ACKNOWLEDGEMENTS

This research was supported by the Ministry of Science and ICT of Korea and partly by the Basic Science Research Program (Grant No. 2017R1A2B4007274) through the National Research Foundation of Korea (NRF) funded by the Ministry of Science and ICT of Korea.

REFERENCES

- [1] H.-G. Lee *et al.*, “Design and Fabrication of Prototype Phase Shifter for PAL XFEL”, in *Proc. IPAC'13*, Shanghai, China, May 2013, paper THPME027, pp. 3564-3566.
- [2] H.-S. Kang and H. Loos, “X-ray free electron laser tuning for variable-gap undulators”, *Phys. Rev. Accel. Beams* vol. 22, p. 060703, 2019.
doi:10.1103/PhysRevAccelBeams.22.060703
- [3] A. A. Varfolomeev, T. V. Yarovoi, and P. V. Bousine, “Possible enhancement of SASE FEL output field intensity induced by local phase jump”, *Nucl. Instruments Methods Phys. Res. Sect. A Accel. Spectrometers, Detect. Assoc. Equip.*, vol. 407, p. 296, 1998.
doi:10.1016/S0168-9002(98)00038-2
- [4] A. Mak, F. Curbis, and S. Werin, “Phase jump method for efficiency enhancement in free-electron lasers”, *Phys. Rev. Accel. Beams*, vol. 20, p. 060703, 2017.
doi:10.1103/PhysRevAccelBeams.20.060703
- [5] N. M. Kroll, P. L. Morton, and M. N. Rosenbluth, “Free-electron lasers with variable parameter wigglers”, *IEEE J. Quantum Electron.*, vol. 17, p. 1436, 1981.
doi:10.1109/JQE.1981.1071285
- [6] Kwang-Je Kim, Zhirong Huang, and Ryan Lindberg, *Synchrotron Radiation and Free-Electron Lasers*, Cambridge University Press, 2017.

OPTIMIZATION OF A COHERENT UNDULATOR BEAMLINE FOR NEW ADVANCED SYNCHROTRON LIGHT SOURCE IN KOREA

Inggyo Jeong^{1,2,*}, Yujong Kim^{1,2,†}, Seunghyun Lee², Jaeyong Lee², Pikad Buaphad^{1,2},
Youngwoo Joo^{1,2}, Hyeri Lee^{1,2}, and Moonyoung Han²

¹Dept. of Accelerator and Nuclear Fusion Physical Engineering, UST, Daejeon, 34113, Korea

²Future Accelerator R&D Team, Nuclear Data Center, KAERI, Daejeon, 34057, Korea

Abstract

Recently, the demand for a new advanced synchrotron light source in Korea is rapidly growing. Six local governments in Korea would like to host the new synchrotron light source project in their own provinces. The new advanced synchrotron light source will be the Diffraction-Limited Storage Ring (DLSR), which is based on the Multi-Bend Achromat (MBA) lattice. For the new synchrotron light source, we would like to build a special 60-m long coherent undulator beamline, which can deliver high-intensity coherent radiation at the hard X-ray region. To design the coherent undulator beamline, we have performed numerous beam dynamics simulations with GENESIS and SIMPLEX codes. In this paper, we report design concepts and those simulation results for the coherent undulator beamline.

INTRODUCTION

PLS-II, the third generation light source at Pohang in Korea, has been well utilized so far. Since the recent annual growth of PLS-II users is about 600, and its total users are about 7,000 in 2018, PLS-II is close to facility saturation, and the demand for a new advanced synchrotron light source is growing. In addition, due to the suddenly changing international situation between Korea and Japan, Korean government is planning to develop and produce advanced materials in Korea. To do this, the Korean government is also considering to build new advanced synchrotron light sources and has already allocated \$1.2M budget to design a new advanced synchrotron light source in 2020.

Currently, several studies have been conducted for a new advanced synchrotron light source in Korea, and one of them is ongoing by Future Accelerator R&D Team in Korea Atomic Energy Research Institute (KAERI). The blueprint of the new advanced synchrotron light source in Korea is shown in Fig. 1, which consists of three parts; a CW SRF injection linac, a small UV & soft X-ray storage ring [1], and a main Diffraction-Limited Storage Ring (DLSR) with a Multi-Bend Achromat (MBA) lattice [2]. As shown in Fig. 2, we would like to use long drift spaces between the superperiods for coherent beamlines with many undulators. By injecting high quality electron beam from the injector linac continuously, the 60-m undulator beamline in the main storage ring can generate coherent high-brightness X-rays during the tens-of-turn operation mode. In this study, we

present the design concepts and the simulation results of the coherent undulator beamline to generate hard X-ray at a wavelength of 0.1 nm with the Self-Amplified Spontaneous Emission Free Electron Laser (SASE FEL) concept [3, 4]. The beam dynamics and the radiation along the beamline are simulated with GENESIS and SIMPLEX codes [5, 6].

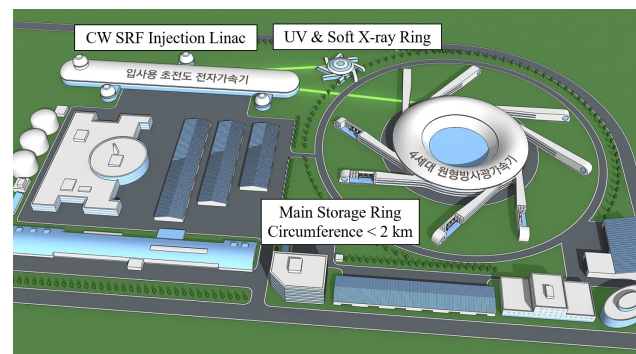


Figure 1: The blueprint of a new advanced synchrotron light source in Korea. The large round building on the right is the MBA-based main storage ring [2].

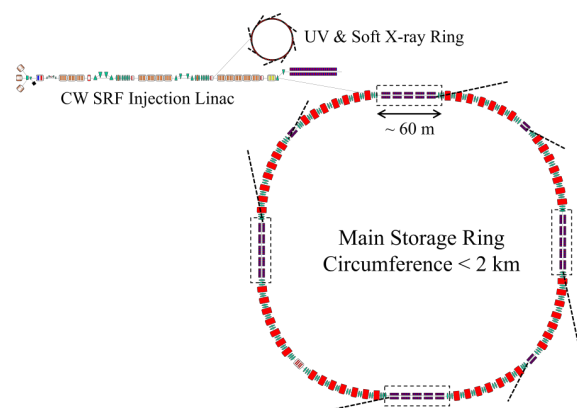


Figure 2: The layout of the new advanced synchrotron light source in Korea. Boxed sections are the coherent undulator beamlines [2].

DESIGN OF UNDULATOR BEAMLINE

Design Parameters

Although the design of the accelerator is ongoing, several key properties of the accelerator are already determined. The energy of the electron beam under consideration is 6 GeV for

* jungingyo@gmail.com

† yjkim@kaeri.re.kr

the main storage ring with 60-m long drift spaces between the superperiods. The maximum four coherent undulator beamlines can be installed at those drift spaces to deliver high intensity coherent hard X-rays.

Table 1: Design Parameters for the Coherent Undulator Beamline and Test Electron Bunch

Parameter	Value	Unit
Energy of Electron Beam E	6.0	GeV
Photon Wavelength λ_{ph}	0.1	nm
Undulator Period λ_u	15	mm
Undulator Parameter K	1.295	–
Undulator Module Length	3.96	m
Quadrupole Length (QF, QD)	0.18	m
Length of FODO Lattice	9.0	m
Number of Undulator Modules	10	–
Average β -function $\bar{\beta}_{x,y}$	15	m
Normalized Slice Emittance (rms) $\epsilon_{n,s}$	0.3	μm
Single Bunch Charge Q	200	pC
Bunch Length (rms) σ_z	9.0	μm
Peak Current I_{peak}	2.7	kA
Slice Relative Energy Spread (rms) $\sigma_{\delta,s}$	0.01	%

Design parameters for the coherent undulator beamline are summarized in Table 1. To achieve the saturation of the SASE FEL power at 0.1 nm within 60 m, numerous parameters of undulator and electron beam are optimized. The resonant wavelength of planar undulator is give by

$$\lambda_{ph} = \frac{\lambda_u}{2\gamma^2} \left(1 + \frac{K^2}{2} \right), \quad (1)$$

where λ_{ph} is the resonant photon wavelength, λ_u is the undulator period, γ is the energy of electron beam in units of electron rest mass energy, and K is the undulator strength parameter [4]. To get sub-nm photon wavelength, λ_u is set as 15 mm. From Eq. (1), K is calculated as 1.295. Those parameters can be achieved by using the in-vacuum undulator (IVU), which has already been installed at various synchrotron light sources [7, 8].

As shown in Fig. 3, β -functions and a layout of a single FODO lattice of the coherent undulator beamline are optimized with SIMPLEX code [6]. The FODO lattice consists of a focusing quadrupole, a defocusing quadrupole, and two undulator modules. Average β -functions are 15 m for both $\bar{\beta}_x$ and $\bar{\beta}_y$.

We set parameters of the test electron bunch for the coherent undulator beamline by using those of SwissFEL because energy of the electron beam (6 GeV) is close to that of SwissFEL (5.8 GeV) [7]. The single bunch charge Q of 200 pC with a uniform normalized slice emittance $\epsilon_{n,s}$ of 0.3 μm is distributed in Gaussian form in the longitudinal direction. The rms bunch length σ_z is 9.0 μm , and the peak current I_{peak} is about 2.7 kA.

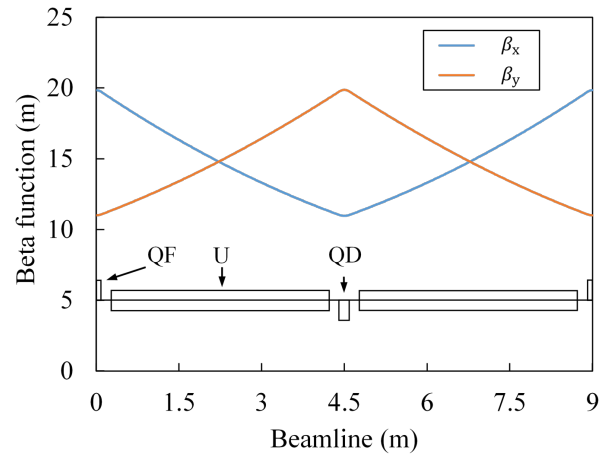


Figure 3: β -functions and a layout of the FODO lattice for the coherent undulator beamline.

Parameter Verification

Before the simulation, theoretical verification of the parameters is required to achieve the exponential growth of the radiation power within 60 m. For the verification, Pierce parameter ρ is defined as a following:

$$\rho = \left[\frac{1}{16} \frac{I_{peak}}{I_A} \frac{K^2 [JJ]^2}{\gamma^2 \epsilon_{n,s} \bar{\beta}_{x,y} k_u^2} \right]^{1/3} \quad (2)$$

Here, the Bessel function factor $[JJ] = [J_0(\xi) - J_1(\xi)]$ with $\xi = K^2/(4 + 2K^2)$, the Alfvén current $I_A \approx 17$ kA, and $k_u = 2\pi/\lambda_u$ [4]. With the parameters from Table 1, ρ is given by 4.887×10^{-4} .

To obtain the saturation of the SASE FEL power within the coherent undulator beamline, the saturation length L_{sat} should be shorter than 60 m. Typically, L_{sat} of SASE FEL [3] is given by

$$L_{sat} \approx 20L_G, \quad (3)$$

where the one-dimensional (1D) power gain length L_G [4] is given by

$$L_G = \frac{\lambda_u}{4\pi\sqrt{3}\rho}. \quad (4)$$

From the design parameters, calculated L_G is 1.41 m, and L_{sat} is about 28.2 m, which is shorter than the 60-m drift section.

There are two other requirements for the SASE FEL saturation within 60 m. The slice relative energy spread $\sigma_{\delta,s}$ of the electron must be smaller than the Pierce parameter ρ ;

$$\sigma_{\delta,s} < \rho. \quad (5)$$

Also, the normalized slice emittance $\epsilon_{n,s}$ should satisfy a following condition;

$$\epsilon_{n,s} < \frac{\lambda_{ph}}{4\pi} \frac{\gamma \bar{\beta}_{x,y}}{L_G}. \quad (6)$$

The design parameters in Table 1 are good to satisfy both two conditions in Eqs. (5) and (6).

SIMULATION OF UNDULATOR BEAMLINE

Table 2: Simulation Results of the Coherent Undulator Beamline

Parameter	Value	Unit
Photon Wavelength λ_{ph}	0.1	nm
Photon Energy E_{ph}	12.4	keV
Saturation Length	36	m
Bandwidth (rms)	0.138	%
Pulse Length (rms)	5.56	μ m
Pulse Duration (rms)	18.5	fs
Radiation Power at Saturation	1.8	GW

To test the performance of the coherent undulator beamline, GENESIS code is used [5]. The main results of the simulation are summarized in Table 2, and the radiation power at the center of the single bunch along the coherent undulator beamline is shown in Fig. 4. Each line represents the radiation power with a different random seed. The radiation power is saturated around 36 m, corresponding to 8 undulator modules or 4 FODO lattices. The radiation power of core part in the single bunch is 1.8 GW at the saturation.

Note that the test electron bunch is ideal with uniform normalized slice parameters. Therefore the saturation length can be increased if we use a real 3D beam distribution. After the linac design, a new optimization with a realistic 3D electron beam distribution will be conducted.

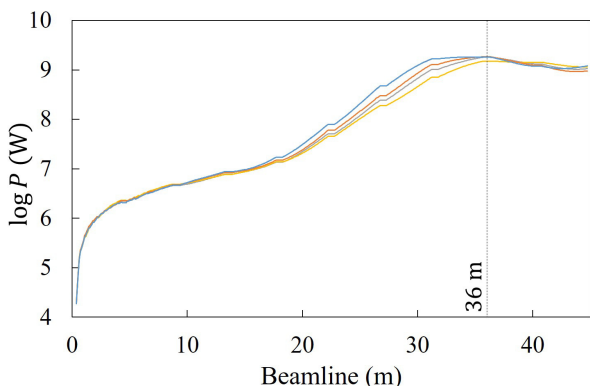


Figure 4: Radiation power of core part in the bunch along the coherent undulator beamline.

The single-shot radiation spectrum at the saturation length of 36 m is shown in Fig. 5. The bandwidth is 0.138% with respect to 12.4 keV. To reduce the bandwidth of the coherent beamline, tapering will be applied. We are also considering applying the self-seeding technology to get a narrower bandwidth and a higher intensity [9].

CONCLUSION

In this paper, by using the SASE FEL concept, we have designed the coherent undulator beamline for a new advanced

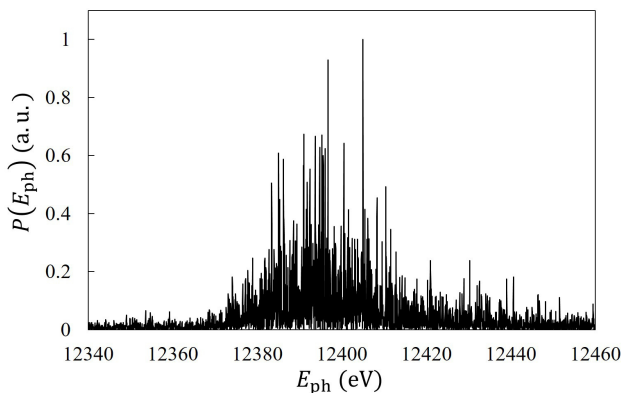


Figure 5: Radiation spectrum at 36 m.

synchrotron light source in Korea. Parameters of the electron beam and the coherent undulator beamline are determined to satisfy the SASE FEL lasing conditions for the hard X-rays at 0.1 nm. With the calculated parameters and GENESIS simulations, it was confirmed that the saturation of the SASE FEL power can be achieved within 60 m for an energy of 6 GeV electron beam.

For the next step, optimization with a realistic 3D electron beam distribution will be carried out in the near future. With the bunch, tapering will be applied to get a higher radiation power and a narrower bandwidth. Temporal structure is also an important property of coherent radiation. By applying the self-seeding technology, it can be possible to produce attosecond long hard X-rays with our design.

In addition, more deep research on beam quality degradation in the synchrotron is required. In our design, an electron bunch will be dumped after tens of turns because synchrotron radiation and other sources may increase the slice energy spread, which can destroy coherent FEL lasing. Therefore, optimization of our design and detailed operation conditions including the maximum circulation number of an electron bunch in the synchrotron should be studied further.

REFERENCES

- [1] J. Y. Lee *et al.*, “Design of 1.5 GeV Compact Storage Ring for the EUV and Soft X-rays”, in *Proc. IPAC’19*, pp. 1028–1030, 2019. doi:10.18429/JACoW-IPAC2019-MOPTS079
- [2] Y. Kim, “A New 4th Generation Synchrotron Light Source in Korea”, Project white paper, 2019.
- [3] P. Schmüser *et al.*, “Self-Amplified Spontaneous Emission,” in *Ultraviolet and soft X-ray free-electron lasers*, Vol. 229, Springer Science & Business Media, pp. 104–105, 2008.
- [4] Z. Huang and K.-J. Kim, “Review of X-ray Free-electron Laser Theory,” *PRST-AB*, Vol. 10, pp. 034801, 2007. doi:10.1103/PhysRevSTAB.10.034801
- [5] S. Reiche, “GENESIS 1.3: a fully 3D time-dependent FEL simulation code,” *Nucl. Instr. & Meth. A*, Vol. 429, pp. 243–248, 1999. doi:10.1016/S0168-9002(99)00114-X

- [6] T. Tanaka, “SIMPLEX: simulator and postprocessor for free-electron laser experiments,” *J. Synchrotron Radiat.*, Vol. 22, pp. 1319–1326, 2015.
doi:10.1107/S1600577515012850
- [7] R. Ganter *et al.*, “SwissFEL - Conceptual Design Report”, PSI, Villigen, Switzerland, PSI-10-04, 2010.
- [8] T. Shintake, “SPRING-8 Compact SASE Source”, in *Proc. LINAC'06*, paper FR1002, pp. 813–816, 2006.
- [9] S. Reiche, “Overview of Seeding Methods for FELs”, in *IPAC'13*, paper WEZB102, pp. 2063–2067, 2013.

START-TO-END SIMULATIONS FOR THE SOFT X-RAY FEL AT THE MAX IV LABORATORY

W. Qin*, F. Curbis, M. Pop, S. Werin, Lund University and MAX IV Laboratory, Lund, Sweden
J. Andersson, L. Isaksson, M. Kotur, E. Mansten, S. Thorin, MAX IV Laboratory, Lund, Sweden

Abstract

A Soft X-ray FEL (the SXL) using the existing 3 GeV linac at the MAX IV Laboratory is currently in the design phase. In this contribution, start-to-end simulations, including the photo-injector simulations using ASTRA, the linac simulations using ELEGANT and the FEL simulations using GENESIS, are presented for 100 pC and 10 pC operation modes. The features of the electron beam from the MAX IV linac and their impact on the FEL performance are discussed.

INTRODUCTION

A Soft X-ray FEL (the SXL) [1] at the MAX IV Laboratory is currently in conceptual design phase. The SXL utilizes the existing 100 Hz, 3 GeV linac [2] and the photocathode injector [3,4] at MAX IV to generate high brightness electron beams to drive radiation ranging from 1 nm to 5 nm. Considering the features of the 3 GeV beam from the existing linac, phase I of the SXL would be mostly operating in SASE mode using beam parameters that do not require major modification of the existing linac. With improvement of the beam quality, especially removal of the beam chirp, more advanced schemes are foreseen in phase II.

The layout of the SXL FEL is sketched in Figure 1. There are two injectors, one based on a thermionic RF gun to produce beams for the 1.5 GeV and 3 GeV ring injection, the other based on a photocathode RF gun to produce high brightness beams for the Short Pulse Facility (SPF) [5] and the SXL. After the injector, the electron beam is accelerated in the S-band linac and compressed by two double-achromat bunch compressors. The 3 GeV electron beam is then matched and sent into the undulator line, which consists of 3 m long, 40 mm period, APPLE-X undulator modules. The overall undulator line length is not fully defined yet. Empty sections before the main undulator and in the middle of the undulator are reserved for possible advanced schemes such as external seeding or self-seeding. Small chicanes could be added in the undulator break sections to delay the electron beam for possible coherence improvement schemes and high power schemes. The X-ray pulses are transported through the photon diagnostic section and then to the experimental stations.

In this paper, we present start-to-end particle tracking results from the photocathode gun to the end of the undulator line. The particle tracking is conducted in three stages. The injector is simulated with ASTRA [6] from the cathode to approximately 100 MeV. At the end of the first linac, ELEGANT [7] is used to model the downstream acceleration to 3 GeV and two-stage bunch compressions, including

wakefields and CSR effect. The ELEGANT output distribution is sent into GENESIS [8] to simulate the generation of FEL pulses. 2M macro-particles are used in the simulations. Simulation details for the three stages are described in the following sections.

INJECTOR SIMULATION

The designed SXL injector is optimized based on the currently operating 10 Hz MAX IV injector, consisting of a 1.6 cell S-band BNL/SLAC type RF gun with a copper cathode, an emittance compensation solenoid, a 5.2 m long S-band linac, a drive laser system and relevant diagnostics. Standard operation of the designed injector generates 100 pC electron beam with 100 Hz repetition rate. Another operation mode aims at generating 10 pC electron beams with lower emittance and shorter pulse duration. To generate 100 pC charge, a 263 nm laser pulse with plateau temporal distribution and cut-gaussian transverse distribution is illuminated on the copper cathode, with 7.6 ps temporal duration and 0.24 mm transverse rms size. The maximum field is 100 MV/m and the gun phase is 25 degrees. Figure 2 shows the electron beam slice parameters and longitudinal phase space at the injector exit for the 100 pC case. An electron beam with about 18 A current, 6 ps FWHM duration and slice emittance lower than 0.4 μm is obtained. By adjusting the laser diameter and gun settings, a 10 pC electron beam with 11 A current, 1 ps FWHM duration and 0.2 μm slice emittance is obtained.

Further optimization of the gun and injector setup is ongoing. More parameters are included and advanced algorithm like MOGA is deployed in the optimization procedure. Comparing ASTRA results with full space charge code Impact-T [9] is also ongoing. A gun test stand has been setup at MAX IV as a useful platform to test the performance of the SXL gun.

LINAC SIMULATION

The MAX IV linac consists of 39 normal conducting S-band accelerating sections. Bunch compression is accomplished with two double-achromat type bunch compressors at 260 MeV and 3 GeV. The bunch compressors have positive R56 and positive T566, thus linearizing the longitudinal phase space without the help of a prior harmonic cavity. The linearization effect can also be tweaked using sextupoles in the bunch compressors. The second bunch compressor is also used as a beam distributor for the SPF and a diagnostic beamline. Figure 3 shows the electron beam slice parameters and longitudinal phase space at the exit of the linac for the 100 pC case. After the two-stage compression, the

* weilun.qin@sljus.lu.se

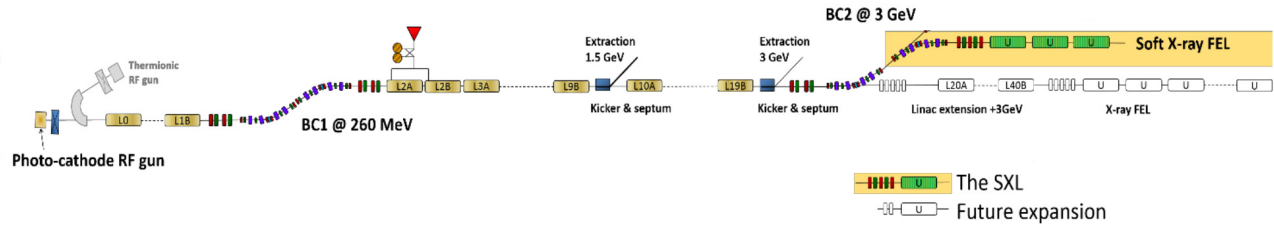


Figure 1: Layout of the SXL FEL.

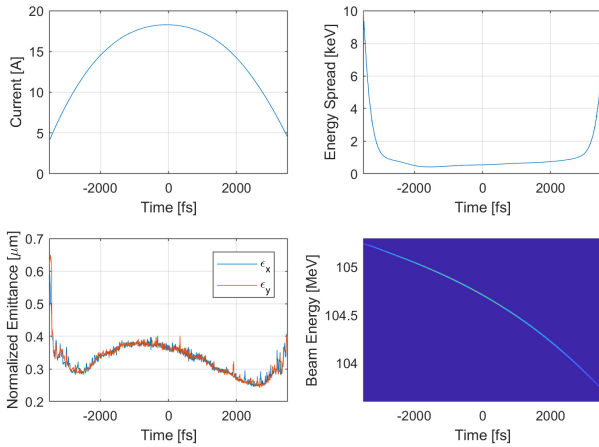


Figure 2: Electron beam slice parameters and longitudinal phase space at the injector exit (before BC1) for 100 pC charge. Bunch head is to the left.

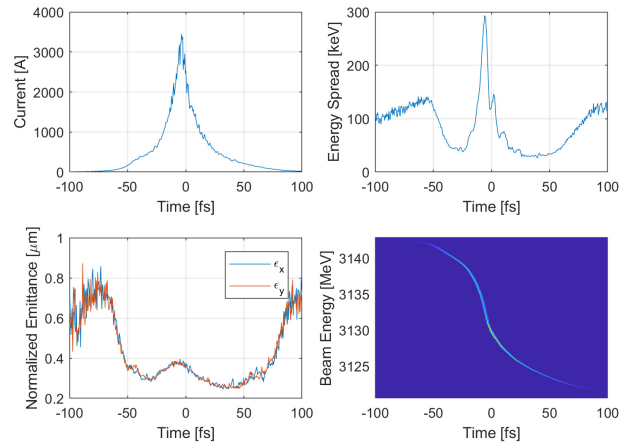


Figure 3: Electron beam slice parameters and longitudinal phase space at the linac exit (after BC2) for 100 pC charge. Bunch head is to the left.

electron beam is compressed to about 15 fs FWHM with a 3.5 kA narrow current peak. The slice energy spread is about 0.3 MeV. The slice emittance is well preserved in the acceleration and compression. A residual energy chirp is presented in the longitudinal phase space, with about 0.5 MeV/fs in the core part. Figure 4 shows the electron beam slice parameters and longitudinal phase space at the exit of the linac for the 10 pC case. The slice emittance in this case is increased to about 0.4 μm in x plane while it is kept below 0.3 μm in y plane. The residual chirp in the longitudinal phase space is increased to about 1 MeV/fs.

Removing the residual positive chirp as shown in Figure 3 with the current setup of the linac is not easy to realize. There are considerations of configuring the second bunch compressor to zero R56 or negative R56 with additional magnets. Overcompressing the beam and cancelling the residual chirp using wakefields is another possible configuration, while initial simulations show that this might require an increase in bunch charge to provide enough wakefields. Initial simulations on the jitter and tolerance of the linac are ongoing.

FEL SIMULATION

The simulation parameters for the high charge mode (1A) and low charge mode (1B) of the SXL are shown in Table

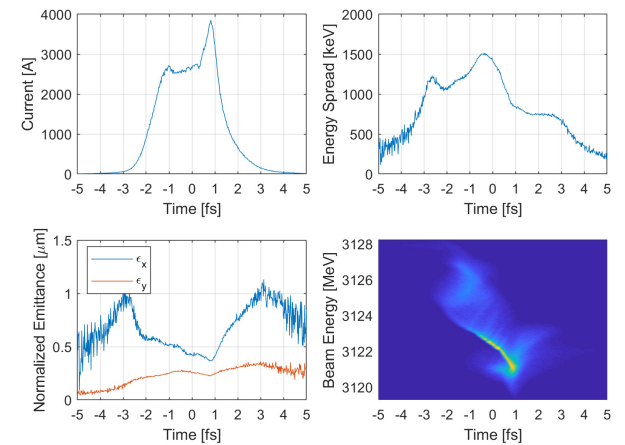


Figure 4: Electron beam slice parameters and longitudinal phase space at the linac exit (after BC2) for 10 pC charge. Bunch head is to the left.

1. The APPLE-X type undulator allows for full polarization control while the simulations here are for linear polarized light. The undulator module is 3 m long with 40 mm period. The undulator strength K can be tuned between 1.2 and 3.9 to generate radiation from 1 nm and 5 nm at a fixed 3 GeV beam energy.

Table 1: SXL FEL Simulation Parameters

Parameters	1A	1B	Unit
Q_b	100	10	pC
E_b	3	3	GeV
$\sigma_{E,slice}$	0.3	1.5	MeV
dE/dt	0.5	1	MeV/fs
$\varepsilon_{n,slice}$	0.35/0.35	0.4/0.25	μm
I_{pk}	3.5	3.5	kA
λ_u	40	40	mm
K	1.2-3.9	1.2-3.9	
L_{module}	3	3	m
L_{break}	0.76	0.76	m
$\langle\beta\rangle$	8	8	m
λ_s	1-5	1-5	nm

After BC2, the electron beam distribution from ELEGANT is matched and sent into GENESIS for FEL simulation. Twenty GENESIS runs with different random numbers are conducted for each case. Figure 5 and 6 show the GENESIS simulation results for both high charge (1A) and low charge (1B) at 1 nm. For the 100 pC case, maximum average bunching is reached after 11 modules, producing FEL pulses with 160 μJ pulse energy and 15 fs duration. Due to the residual beam chirp, the FEL bandwidth is broadened to about 0.6%. For the 10 pC case, owing to the lower slice emittance, the FEL saturates after 8 modules. The 10 pC electron beam has about 3 fs FWHM duration, while the FEL output has 0.8 fs FWHM duration. This is because the radiation from the high current peak in the bunch tail is dominating in the FEL process and slips ahead to the bunch head. Since the electron beam duration is comparable to the slippage length, the temporal profile is almost one single spike, providing good longitudinal coherence. Although the beam chirp in the 10 pC case is higher than that in the 100 pC case, the FEL bandwidth is even narrower due to the short electron pulse duration. It is worth mentioning that, for both of the two cases, the chromatic effects in the linac are not fully optimized, causing increase of projected emittance. With further optimization of the chromatic effects, the FEL pulse energy can be further improved.

In the FEL simulation in this paper, undulator wakefields and taper are not yet included. Wakefields from the undulator vacuum chamber will further introduce an energy chirp in the beam phase space and an average energy loss to the beam. The wake induced energy chirp is relatively small compared with the residual chirp in the beam, thus has no significant impact on the FEL performance. The average energy loss can be compensated by an linear undulator taper. Post-saturation taper can further increase the pulse energy, especially for longer wavelengths.

SUMMARY

In this paper, we have presented start-to-end simulation results for the SXL FEL. Using the photocathode injector and

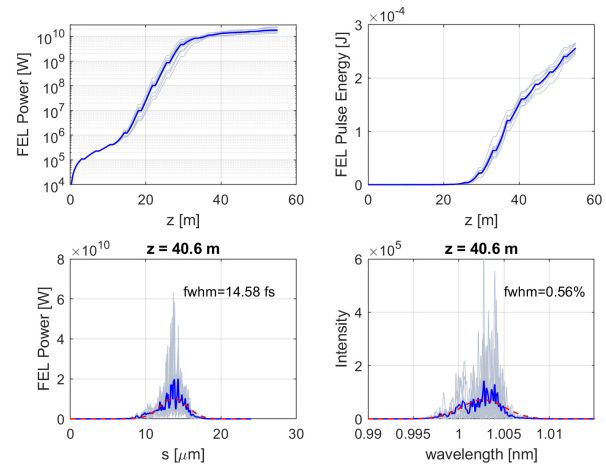


Figure 5: GENESIS simulation results for the 100 pC case (1A) at 1 nm. Each grey line corresponds to one shot simulation and the blue line corresponds to the average of all the 20 shots.

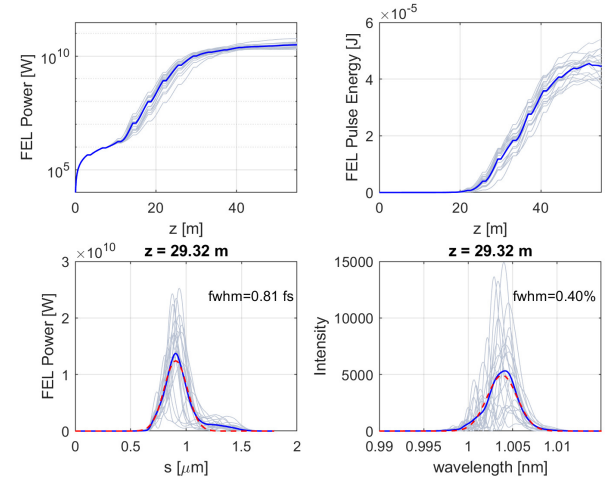


Figure 6: GENESIS simulation results for the 10 pC case (1B) at 1 nm. Each grey line corresponds to one shot simulation and the blue line corresponds to the average of all the 20 shots.

the 3 GeV linac at MAX IV, high brightness electron beams are generated and used to produce FEL pulses ranging from 1 nm to 5 nm. Large positive energy chirp is presented in the electron beam longitudinal phase space. For baseline SASE operation, simulation results show that the chirped beam is sufficient to drive an FEL with good performance. FEL pulses with a few femtosecond or even subfemtosecond pulse duration can be generated. Simulations including undulator wakefields and tapering are ongoing.

ACKNOWLEDGEMENTS

This work is supported by Knut and Alice Wallenberg foundation.

REFERENCES

- [1] S. Werin *et al.*, “The Soft X-Ray Laser Project at MAX IV”, in *Proc. 8th Int. Particle Accelerator Conf. (IPAC’17)*, Copenhagen, Denmark, May 2017, pp. 2760–2762. doi:10.18429/JACoW-IPAC2017-WEPAB077
- [2] S. Thorin *et al.*, “The MAX IV Linac”, in *Proc. 27th Linear Accelerator Conf. (LINAC’14)*, Geneva, Switzerland, Aug.-Sep. 2014, paper TUIOA03, pp. 400–403.
- [3] J. Andersson *et al.*, “Initial Commissioning Results of the MAX IV Injector”, in *Proc. 37th Int. Free Electron Laser Conf. (FEL’15)*, Daejeon, Korea, Aug. 2015, paper TUP036, pp. 448–451.
- [4] J. Andersson *et al.*, “The Pre-Injector and Photocathode Gun Design for the MAX IV SXL”, in *Proc. 10th Int. Particle Accelerator Conf. (IPAC’19)*, Melbourne, Australia, May 2019, pp. 2064–2066. doi:10.18429/JACoW-IPAC2019-TUPTS061
- [5] S. Werin, S. Thorin, M. Eriksson, and J. Larsson, “Short pulse facility for MAX-lab,” *Nucl. Instruments Methods Phys. Res. Sect. A Accel. Spectrometers, Detect. Assoc. Equip.*, vol. 601, no. 1–2, pp. 98–107, Mar. 2009.
doi:10.1016/j.nima.2008.12.106
- [6] K. Flöttmann, “ASTRA: A space charge tracking algorithm,” *Manual, Version*, vol. 3, p. 2014, 2011.
- [7] M. Borland, “Elegant: A flexible SDDS-compliant code for accelerator simulation,” Argonne National Lab., IL (US), 2000.
- [8] S. Reiche, “GENESIS 1.3: a fully 3D time-dependent FEL simulation code,” *Nucl. Instruments Methods Phys. Res. Sect. A Accel. Spectrometers, Detect. Assoc. Equip.*, vol. 429, no. 1–3, pp. 243–248, 1999.
doi:10.1016/S0168-9002(99)00114-X
- [9] J. Qiang, S. Lidia, R. D. Ryne, and C. Limborg-Deprey, “Three-dimensional quasistatic model for high brightness beam dynamics simulation,” *Phys. Rev. Spec. Top. - Accel. Beams*, vol. 9, no. 4, p. 44204, Apr. 2006.
doi:10.1103/PhysRevSTAB.9.044204

ADVANCED CONCEPTS IN THE DESIGN FOR THE SOFT X-RAY FEL AT MAX IV

W. Qin*, F. Curbis, M. Pop, S. Werin
Lund University and MAX IV Laboratory, Lund, Sweden

Abstract

A Soft X-ray FEL (the SXL) is currently being designed at the MAX IV Laboratory. In the work to adapt the FEL to the scientific cases several advanced options are being studied for coherence enhancement, generation of short pulses and two-color pulses. We will discuss the current status and initial results of the schemes studied, especially regarding the FEL performance with the features of the MAX IV linac, including a positive energy chirp.

INTRODUCTION

A Soft X-ray FEL (the SXL) [1] at the MAX IV Laboratory is currently in conceptual design phase. Phase I of the SXL will be based on realistic chirped electron beam from the existing 3 GeV linac [2]. The baseline is SASE FEL operating with 100 pC and 10 pC charge. To meet the increasing demand of various features of the FEL pulses, such as ultra-short pulses, two-color pulses, coherence improvement as well as high flux pulses, advanced FEL schemes need to be employed. The SXL is based on 3 m long, 40 mm period APPLE-X undulator with strength K tuning range from 1.2 to 3.9. The length of the whole undulator line is not yet fully defined but should be enough to bring the shortest wavelength to saturation. To allow possible implementation of advanced schemes, a few sections are reserved, as sketched in Figure 1. Prior to the undulator line, one section is reserved for modulator and chicane modules for external seeding methods such as the Echo-Enabled Harmonic Generation (EEHG) [3, 4], or attosecond pulse generation methods such as the XLEAP [5]. In the middle of the undulator line one section is reserved for split undulator based two-color FEL pulse generation as well as monochromator based self-seeding [6]. Space for small delay chicanes in each undulator break section is reserved for schemes such as high-brightness SASE [7] and high power short pulse generation. In this paper we present preliminary advanced concepts for the design of the SXL as well as example simulations for the schemes that are relatively straightforward to implement. FEL simulations are conducted using 3D FEL code GENESIS [8].

SHORT PULSE GENERATION

Ultra-short pulse is crucial for probing ultra-fast dynamics as it defines the resolution in time. Typical operation of FELs provides pulses with a few tens of femtosecond duration, close to the length of the electron beam. While for ultra-fast applications, FEL pulses down to a few fem-

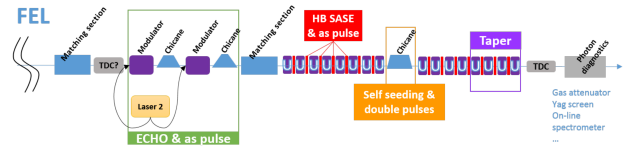


Figure 1: Schematic layout showing the implementation of various FEL schemes.

tosecond or even subfemtosecond are required. To generate ultra-short FEL pulses, common methods are selecting an ultra-short region of the electron beam to lase or shortening the electron beam itself. To select an ultra-short region, one can use a slotted foil [9] or a modulation laser [10] in the laser heater section, one can also enhance the beam current of a local region using a few-cycle laser [11], another method is transversely tilting the electron beam [12] to create good interaction region in the beam. One way to shorten the electron beam is to start with lower bunch charge, which produces a shorter beam with lower emittance from the beginning and allows higher compression factor [13]. Selecting an ultra-short region usually requires additional hardware, while low charge method is straightforward to implement, despite it produces less pulse energy. In the current design of the SXL, the low charge method is considered as a standard way to produce ultra-short pulses and thus one of the two baseline operation modes.

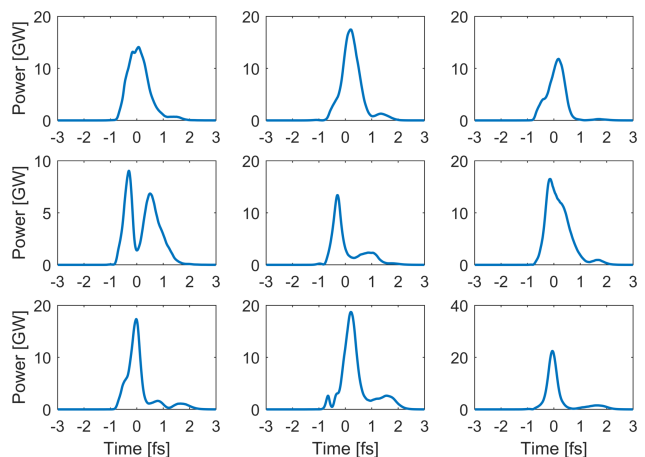


Figure 2: 9-shot simulated temporal profiles for the 10 pC mode of the SXL. The resonant wavelength is 1 nm.

Start-to-end simulations have been conducted for the low charge operation mode of the SXL. Beam parameters and phase space before the undulator can be found in Ref. [14]. The 10 pC electron beam is compressed to about 3.5 kA after two double-achromat compressions. Figure 2 shows

* weilun.qin@sljus.lu.se

9-shot FEL temporal distributions for the low charge case at 1 nm. Ultra-short FEL pulses with an average (over 20 shots) of 0.8 fs FWHM duration, 15 μJ pulse energy is obtained. Since the bunch length is comparable to the slippage length, almost one single spike is generated, giving good longitudinal coherence.

For low charge operation at longer wavelength such as 5 nm, the FEL pulse slips out of the electron bunch quickly, causing the FEL to saturate. Figure 3 shows the power growth along the undulator for 5 nm radiation, which saturates around 20 m. The inset plot shows the temporal profile around power saturation position. The averaged temporal profile over 20 shots gives about 1.5 fs FWHM duration, corresponding to about 80 μJ average pulse energy.

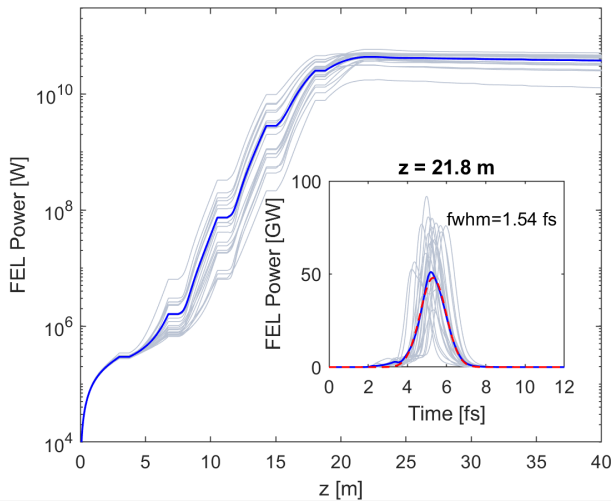


Figure 3: Simulated power growth along the undulator for 5 nm radiation. The inset plot shows corresponding temporal profile around saturation.

TWO-COLOR PULSE GENERATION

Two-color two-pulse FEL provides the ability to do X-ray pump X-ray probe experiments with natural synchronization. According to the resonant condition, generating two-color FEL requires either two distinct beam energies, two undulator K values or two undulator periods. Various methods have been proven the capability to produce two-color FEL pulses. The split undulator method [15] splits the undulator line into two sections with two distinct K values. The wavelength separation of the two FEL pulses can be varied over a large range with the help of gap tunable undulators. A magnet chicane is placed between the two sections to tune the delay between the two pulses. This method is highly flexible in wavelength separation and delay control but lacks efficiency since the beam quality is reduced in the first section due to the lasing process. Fresh-slice technique [16] has been developed to improve the efficiency of the split undulator method. Twin bunch method [17], which generates two electron bunches from the injector and accelerates them to different energies, is highly efficient since it requires only half of the undulator

length compared with the split undulator method. However, the twin bunch method is limited in tunability due to the correlation between the energy separation and delay of the two electron bunches. Among the scientific applications of two color pulses, large wavelength separation has drawn increasing interest in the user community. Generation of such pulses favors the split undulator method owing to its flexibility in wavelength separation.

For the SXL, both the split undulator method and the twin bunch method are considered. There has already been some experiments at MAX IV about generating twin bunches from the injector. While the twin bunch method requires start-to-end simulations to figure out what wavelength separation range it can cover, the split undulator method has more flexibility and defines the longest undulator length given a pair of target wavelengths. Here, in this paper, we show a widely separated two-color FEL example aiming at 250 eV and 500 eV. The electron beam is assumed to be 100 pC, 3 GeV without energy chirp, other parameters are 2.5 kA peak current, 0.5 μm normalized emittance and 0.3 MeV energy spread. The first undulator section consists of 7 undulator modules, tuned to 500 eV ($K=2.56$). The second undulator section consists of 8 undulator modules, tuned to 250 eV ($K=3.9$). A chicane section is assumed to control the delay between the two colors and smear out the microbunching from the first undulator section. The delay between the two pulses is assumed to be 50 fs in this simulation. Figure 4 shows GENESIS simulated pulse energy growth along the undulator. Both pulses are close to saturation and produce above 100 μJ pulse energy. The saturation length for the second color is longer than a fresh electron beam due to the increased energy spread from the FEL process in the first section.

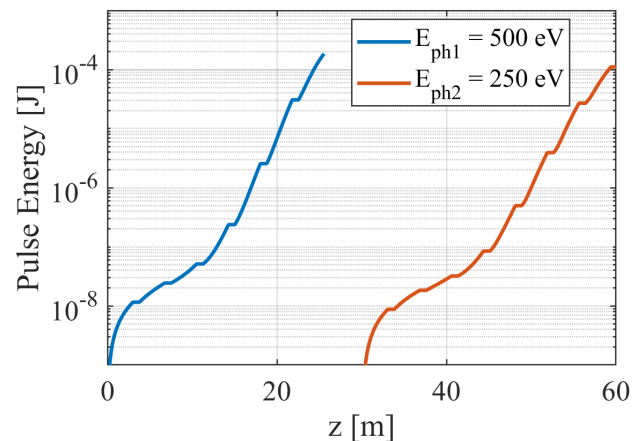


Figure 4: Pulse energy growth along the undulator for two-color generation at 500 eV and 250 eV.

Like the SASE FEL case, an energy chirp would broaden the spectrum while almost not affect the saturation length. The positive energy chirp would even slightly increase the saturation pulse energy due to detuning effect. With the split undulator method, it may not be able to let both pulses saturate with a given length of undulator line in the case

where higher photon energies are required. For higher photon energy with small wavelength separation, the twin bunch method would be appropriate. Another possible way to improve the efficiency of the split undulator method and bring both pulses to saturate could be using the beam chirp to create a transverse tilt in the beam and enable the fresh-slice technique.

HIGH-BRIGHTNESS SASE

Since SASE FEL starts from shot noise of the electron beam and the FEL pulse only slips over a small fraction of the whole electron beam, the FEL pulse has spiky temporal profile and spectrum, giving poor longitudinal coherence. There are numerous ways to improve the longitudinal coherence. With recent progress in external seeding, the HHG or the EEHG method may reach the long wavelength end of the SXL operation range. Soft X-ray self-seeding based on monochromator can cover the full operation range but has limitation on undulator length needed and stability. Another way to improve the longitudinal coherence is the high-brightness SASE scheme which introduces extra delays between the FEL pulse and the electron beam, thus increasing the coherence length. The delays can be introduced via small magnet chicanes in the undulator break sections.

For the SXL, the delay chicanes could be placed in the 0.76 m long break sections, providing delays up to a few femtosecond. Since the R56 of the small chicanes are not zero, the electron beam also experiences an extra rotation in longitudinal phase space. In initial theory of the high-brightness SASE, no R56 is included and the amount of chicane delays are gradually increasing with the position. R56 from small chicanes would cause the electron beam to overbunch quickly in the exponential growth stage of FEL and limit the saturation pulse energy. As is pointed out in Ref. [18], undulator module length also affects the narrowest bandwidth that high-brightness SASE can achieve. Shorter undulator module is favorable since it allows to apply the delay more frequently.

In this paper, we show preliminary simulation results of the high-brightness SASE for the SXL. The electron beam is assumed to be the same unchirped beam as the two-color case. The delay sequence is assumed to be a decreasing geometric sequence. GENESIS version 4 is used to scan the first delay and the ratio between two consecutive delays. Figure 5 shows temporal profiles and spectra for SASE with 3 m undulator (top row), high-brightness SASE with 3 m undulator (middle row) and high-brightness SASE with 2 m undulator (bottom row). The SASE case is plotted at 40 m, while the other two are plotted at 30 m. Due to the optical klystron effect from the delay chicanes, the bunching process in the high brightness scheme is accelerated and the FEL saturates faster than the SASE case. It can be seen that with 3 m long undulator, the averaged bandwidth is reduced to about half of the SASE case, while with 2 m long undulator, the averaged bandwidth can be further reduced to 4×10^{-4} , giving 6 times bandwidth reduce. It should be

noted that a large energy chirp would significantly affect the effect of the high-brightness SASE scheme. As in Ref. [14], start-to-end simulations show, the SASE spectrum is twice large compared with the unchirped case. Studies using the chirped start-to-end electron beam in the high-brightness scheme are ongoing.

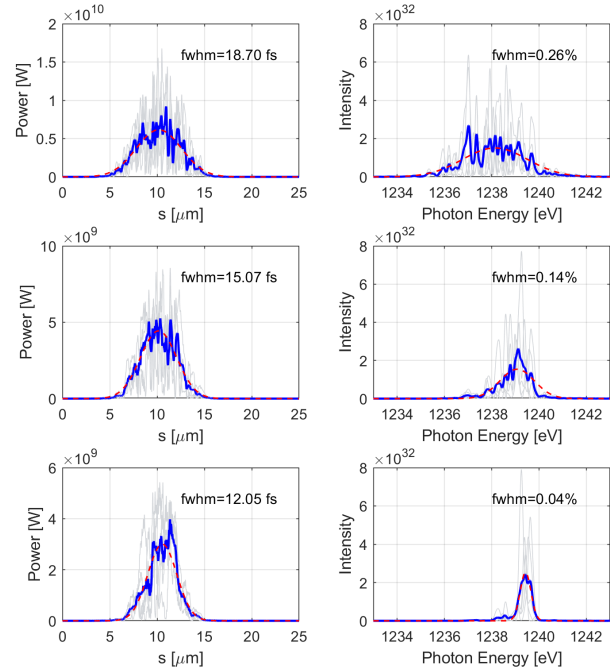


Figure 5: Temporal profiles and spectra for SASE with 3 m undulator (top row), high-brightness SASE with 3 m undulator (middle row) and high-brightness SASE with 2 m undulator (bottom row). The simulation is based on unchirped electron beam. Five GENESIS runs are conducted for each case and the blue line indicates the average over the five shots.

CONCLUSION

We have presented a few advanced concepts in the design of the SXL, along with preliminary simulations using chirped start-to-end simulated 3 GeV beam or ideal unchirped beam. Low charge operation for short pulse generation as well as two-color two-pulse generation using split undulator method can accommodate to the chirped beam. Both the energy chirp and undulator module length are limiting the performance of the high-brightness SASE scheme. More detailed studies are ongoing to characterize the chirp influence on the advanced schemes. Studies on other schemes, like XLEAP, twin bunch, self-seeding and external seeding, are also ongoing.

ACKNOWLEDGEMENTS

This work is supported by Knut and Alice Wallenberg foundation.

REFERENCES

- [1] S. Werin *et al.*, “The Soft X-Ray Laser Project at MAX IV”, in *Proc. 8th Int. Particle Accelerator Conf. (IPAC’17)*, Copenhagen, Denmark, May 2017, pp. 2760–2762, doi:10.18429/JACoW-IPAC2017-WEPAB077
- [2] S. Thorin *et al.*, “The MAX IV Linac”, in *Proc. 27th Linear Accelerator Conf. (LINAC’14)*, Geneva, Switzerland, Aug.-Sep. 2014, paper TUIOA03, pp. 400–403.
- [3] G. Stupakov, “Using the Beam-Echo Effect for Generation of Short-Wavelength Radiation”, *Phys. Rev. Lett.*, vol. 102, no. 7, 2009, doi:10.1103/PhysRevLett.102.074801
- [4] D. Xiang and G. Stupakov, “Echo-enabled harmonic generation free electron laser”, *Phys. Rev. Spec. Top. - Accel. Beams*, vol. 12, no. 3, 2009, doi:10.1103/PhysRevSTAB.12.030702
- [5] J. P. MacArthur, J. P. Duris, Z. Huang, and A. Marinelli, “High Power Sub-Femtosecond X-Ray Pulse Study for the LCLS”, in *Proc. 8th Int. Particle Accelerator Conf. (IPAC’17)*, Copenhagen, Denmark, May 2017, pp. 2848–2850, doi:10.18429/JACoW-IPAC2017-WEPAB118
- [6] D. Ratner *et al.*, “Experimental demonstration of a soft x-ray self-seeded free-electron laser”, *Phys. Rev. Lett.*, vol. 114, no. 5, 2015, doi:10.1103/PhysRevLett.114.054801
- [7] B. W. J. McNeil, N. R. Thompson, and D. J. Dunning, “Transform-limited x-ray pulse generation from a high-brightness self-amplified spontaneous-emission free-electron laser”, *Phys. Rev. Lett.*, vol. 110, no. 13, 2013, doi:10.1103/PhysRevLett.110.134802
- [8] S. Reiche, “GENESIS 1.3: a fully 3D time-dependent FEL simulation code”, *Nucl. Instruments Methods Phys. Res. Sect. A Accel. Spectrometers, Detect. Assoc. Equip.*, vol. 429, no. 1–3, pp. 243–248, 1999, doi:10.1016/S0168-9002(99)00114-X
- [9] P. Emma *et al.*, “Femtosecond and Subfemtosecond X-Ray Pulses from a Self-Amplified Spontaneous-Emission-Based Free-Electron Laser”, *Phys. Rev. Lett.*, vol. 92, no. 7, 2004, doi:10.1103/PhysRevLett.92.074801
- [10] A. Marinelli *et al.*, “Optical Shaping of X-Ray Free-Electron Lasers”, *Phys. Rev. Lett.*, vol. 116, no. 25, 2016, doi:10.1103/PhysRevLett.116.254801
- [11] A. A. Zholents, “Method of an enhanced self-amplified spontaneous emission for x-ray free electron lasers”, *Phys. Rev. Spec. Top. - Accel. Beams*, vol. 8, no. 4, pp. 8–13, 2005, doi:10.1103/PhysRevSTAB.8.040701
- [12] E. Prat, F. Löhl, and S. Reiche, “Efficient generation of short and high-power x-ray free-electron-laser pulses based on superradiance with a transversely tilted beam”, *Phys. Rev. Spec. Top. - Accel. Beams*, vol. 18, no. 10, 2015, doi:10.1103/PhysRevSTAB.18.100701
- [13] Y. Ding *et al.*, “Measurements and Simulations of Ultralow Emittance and Ultrashort Electron Beams in the Linac Coherent Light Source”, *Phys. Rev. Lett.*, vol. 102, no. 25, 2009, doi:10.1103/PhysRevLett.102.254801
- [14] W. Qin *et al.*, “Start-to-end simulations for the Soft X-ray FEL at the MAX IV Laboratory”, in *Proc. 39th Int. Free Electron Laser Conf. (FEL’19)*, Hamburg, Germany, Aug. 2019, paper TUP066, this conference.
- [15] A. A. Lutman *et al.*, “Experimental Demonstration of Femtosecond Two-Color X-Ray Free-Electron Lasers”, *Phys. Rev. Lett.*, vol. 110, no. 13, p. 134801, Mar. 2013, doi:10.1103/PhysRevLett.110.134801
- [16] A. A. Lutman *et al.*, “Fresh-slice multicolour X-ray free-electron lasers”, *Nat. Photonics*, vol. 10, no. 11, pp. 745–750, Nov. 2016, doi:10.1038/nphoton.2016.201
- [17] A. Marinelli *et al.*, “High-intensity double-pulse X-ray free-electron laser”, *Nat. Commun.*, vol. 6, no. 1, p. 6369, May 2015, doi:10.1038/ncomms7369
- [18] E. Prat, M. Calvi, R. Ganter, S. Reiche, T. Schietinger, and T. Schmidt, “Undulator beamline optimization with integrated chicanes for X-ray free-electron-laser facilities”, *J. Synchrotron Rad.*, vol. 23, pp. 861–868, 2016, doi:10.1107/S1600577516007165

ORBITAL ANGULAR MOMENTUM FROM SASE

J. Morgan^{1,2}, B.W.J. McNeil^{1,2}, B.D. Muratori^{2,3}, P. Williams^{2,3}, A. Wolski^{2,4}

¹SUPA, Department of Physics, University of Strathclyde, Glasgow

²Cockcroft Institute, Warrington, UK

³ASTeC, STFC Daresbury Laboratory, Warrington, UK

⁴University of Liverpool, Liverpool, UK

Abstract

To reach very short wavelengths and high intensities of light, free-electron lasers, FELs, are used which produce radiation from amplified noise in an electron beam. In this SASE regime, mode competition dictates that the dominant transverse mode of the radiation will be Gaussian. A method is proposed to suppress the Gaussian mode via phase shifts which allows higher order Laguerre-Gaussian modes to be amplified. These modes are of interest as they carry orbital angular momentum, OAM. Techniques for generating OAM radiation with a FEL have been proposed previously, however, this is the first look at altering mode competition in order to get a dominant OAM mode starting from the initial shot noise in the electron beam.

INTRODUCTION

Recently, much attention has been paid to light which carries OAM. This light has helical phase-fronts characterized by $e^{il\phi}$, where ϕ is the azimuthal coordinate and l is an integer number named the topological charge. The magnitude of l gives the number of intertwined helices in the phase front and the sign of l gives the handedness of these helices. Conventional methods for generating OAM light require downstream optics which convert the radiation from a standard laser [1]. This has its limitations. The optical elements' damage threshold limits the brightness and wavelength of light which is transmitted and constraints arise from the lasers themselves. In contrast, in the FEL, the phase structure of light can be controlled through the manipulation of the electrons themselves and offers the benefit of having a wide range of wavelengths accessible.

Previous work has shown that OAM can be produced in a FEL through a variety of methods. Recently, OAM radiation has been produced at FERMI through harmonic lasing schemes involving helical undulators as well as using a spiral zone plate to convert the radiation downstream from normal FEL output [2]. Another method from Hemsing and colleagues creates OAM radiation by first bunching electrons into a helix through second harmonic interaction with a helical undulator. [3].

The current methods for producing OAM radiation in a FEL have their limitations. The intensity of light from harmonic lasing schemes is less than that at the fundamental frequency [2]. Other methods rely on seeding the FEL either with an OAM seed laser for amplification or with a pre-bunched electron beam. When a FEL is seeded in this way, the output is restricted by the quality of seeds available. This

causes difficulty at very short wavelengths as a seed may not be available at the required wavelength and the intensity of the seed must be large to overcome the initial shot noise in the beam. It would be useful, instead, for the initial seed for amplification to come from the shot noise in the electron beam itself. This work looks at the feasibility of just this, generating OAM through suppression of the Gaussian mode.

THEORY

Electrons enter the undulator with random phases due to shot noise in the electron gun. In the self-amplified-spontaneous emission (SASE) mode of operation, the initial amplitude due to the noise acts as a seed for the FEL interaction and is amplified. The incoherence of the electrons is mimicked by the radiation they produce. This radiation can be described by a superposition of the orthogonal Laguerre-Gaussian beams, $LG_{pl}(\phi, \hat{r})$,

$$E(\phi, \hat{r}) = \sum_{l=-\infty}^{\infty} \sum_{p=0}^{\infty} a_{pl} LG_{pl}(\phi, \hat{r}), \quad (1)$$

where a_{pl} is the initial mode amplitude. The Laguerre-Gaussian, LG, modes are chosen as they provide a convenient mode basis and are often used in the study of OAM beams. These modes are written in terms of their OAM index l and the radial mode index p . The fundamental Gaussian mode is found when $p = l = 0$.

All of the modes will have a contribution from the initial electron density. However, due to their transverse profile, the higher order modes have longer gain lengths [4] with the shortest gain length belonging to the Gaussian mode. The Gaussian mode, therefore, dominates FEL interaction, suppressing the higher order modes, leading to the Gaussian mode of operation typical of a FEL. Here we demonstrate that suppressing the Gaussian mode will lead to the amplification of the higher order modes.

Suppression of the Gaussian Mode

It is possible to disrupt the interaction between electrons and radiation through a relative phase shift. A longitudinal delay of the electrons which shifts the electron phase relative to the fundamental wavelength by $\Delta\theta$ will shift the electrons relative to the n th harmonic by $n\Delta\theta$. It has been demonstrated that the exponential gain of the fundamental wavelength can be suppressed when $\Delta\theta$ is a non-integer multiple of 2π and can increase the power in higher harmonics [5]. Instead of considering the higher harmonics of

the radiation, this work looks at the higher order transverse modes at the fundamental wavelength.

Examination of the transverse phase profile of the Laguerre-Gaussian modes indicates that a rotational shift, $\Delta\phi_r$, of the electron beam about the longitudinal axis results in a relative phase shift between the electrons and the transverse modes of $l\Delta\phi_r$. The total phase change, $\Delta\Psi_l$, between the electrons and the different l modes from the combination of longitudinal and rotational shifts is, therefore,

$$\Delta\Psi_l = \Delta\theta + l\Delta\phi_r \quad (2)$$

Eq. 2 describes how, through careful selection of $\Delta\theta$ and $\Delta\phi_r$, different relative phase changes between the electrons and the OAM modes can be achieved. If successive repetition of the shifts causes the exponential gain of the Gaussian mode to be disrupted - such that the gain length of the Gaussian mode is longer than of the higher order modes - then a dominant OAM mode will self-select for amplification.

RESULTS

Initial Results

The FEL is modeled using the FEL simulation code Puffin [6]. Presented first, is the result of rotating the electrons along the longitudinal axis according to the rotation matrix,

$$R(\phi_r) = \begin{bmatrix} \cos \phi_r & 0 & -\sin \phi_r & 0 \\ 0 & \cos \phi_r & 0 & -\sin \phi_r \\ \sin \phi_r & 0 & \cos \phi_r & 0 \\ 0 & \sin \phi_r & 0 & \cos \phi_r \end{bmatrix} \quad (3)$$

which acts on the phase space vector constructed from the variables (x, p_x, y, p_y) , where x and y are the transverse coordinates, and p_x and p_y are the conjugate of momenta. The rotation is applied - along with a longitudinal shift - between undulator modules each around a gain length long. In order to alter mode competition to select for a LG_{01} mode, the shift pairs are chosen so that $\Delta\Psi_1 = 2\pi$. The set-up utilizes three alternating pairs of shifts, the longitudinal shifts, $\Delta\theta = \pi/2, \pi$ and $3\pi/2$ and the corresponding rotational shifts $\Delta\phi_r = 3\pi/2, \pi$ and $\pi/2$ respectively. These sections are repeated until the end of the undulator lattice.

The results of this set-up are displayed in Fig.1. Decomposition of the power into the different Laguerre-Gaussian modes demonstrates that suppressing the competing transverse modes means the LG_{01} mode dominates the interaction. This causes the LG_{01} mode to grow over an order of magnitude above the Gaussian mode. Also included in the figure is the bunching factor of the different helical modes calculated using [7],

$$b_l = \langle \exp(i\theta_j - il\phi) \rangle, \quad (4)$$

where the brackets indicate the ensemble average over the whole electron beam. The b_1 factor has exponential growth as the electrons propagate through the undulator while the bunching factors for the competing modes b_0 and b_{-1} grow

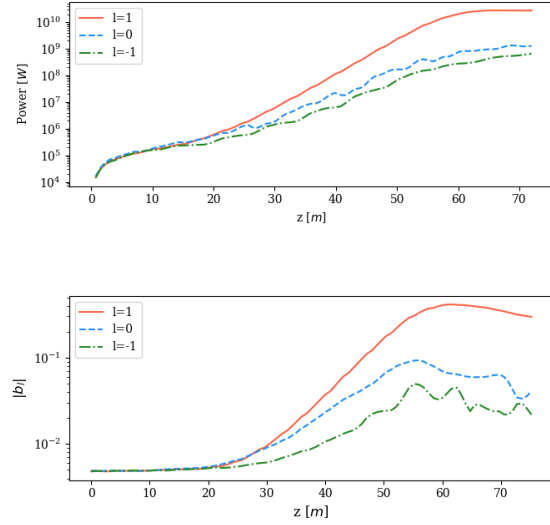


Figure 1: Time-averaged power decomposition of the fundamental frequency into Laguerre-Gaussian modes (top) and mean helical microbunching factor (bottom) when the phase shifts $\Delta\theta = \pi$, $\Delta\phi_r = \pi$; $\Delta\theta = 3\pi/2$, $\Delta\phi_r = \pi/2$; and $\Delta\theta = \pi/2$, $\Delta\phi_r = 3\pi/2$ are applied between undulator modules. This results in the most power being contained in the LG_{01} mode.

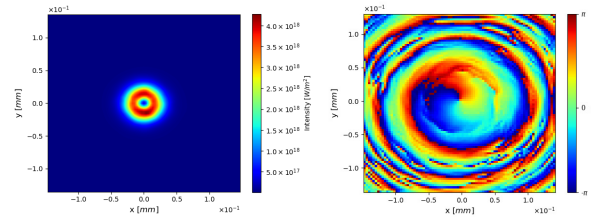


Figure 2: Intensity (left) and phase (right) at $z = 55.28$ m when the phase shifts $\Delta\theta = \pi$, $\Delta\phi_r = \pi$; $\Delta\theta = 3\pi/2$, $\Delta\phi_r = \pi/2$; and $\Delta\theta = \pi/2$, $\Delta\phi_r = 3\pi/2$ are applied between undulator modules.

at a slower rate. This set has not been optimized and further disruption of the Gaussian mode may be possible. Further evidence of the OAM mode is provided in Fig. 2 which shows a snapshot of the phase and intensity of radiation near saturation. The phase of the radiation has a transverse profile typical to the LG_{01} mode and the intensity is the expected doughnut structure of OAM modes.

How to Rotate an Electron Beam

The results presented above use a point transform to rotate the electron beam. Investigated here is a physical method to achieve such a transform. A beamline for rotating a beam through an arbitrary angle around the longitudinal axis can be constructed from a set of quadrupoles with appropriate tilt angles around that axis. The design that we present here is based on that of Talman [8], who used a similar system

for achieving a "Möbius" transformation in a storage ring. The rotation matrix described by (3) can be created from,

$$\tilde{M}\left(\frac{\phi_r}{2} + \frac{\pi}{4}\right)\tilde{M}\left(-\frac{\pi}{4}\right) = R(\phi_r) \quad (5)$$

The matrices \tilde{M} are defined as,

$$\tilde{M}(\theta) = R(\theta)MR^{-1}(\theta) \quad (6)$$

where:

$$M = \begin{bmatrix} \cos \mu & \beta \sin \mu & 0 & 0 \\ -\frac{1}{\beta} \sin \mu & \cos \mu & 0 & 0 \\ 0 & 0 & -\cos \mu & -\beta \sin \mu \\ 0 & 0 & \frac{1}{\beta} \sin \mu & -\cos \mu \end{bmatrix} \quad (7)$$

represents a phase advance through angles μ and $\mu + \pi$ in the transverse and horizontal spaces, respectively. The required transformation M can be achieved using a set of 5 quadrupoles arranged symmetrically:

$$M = Q_1 D_A Q_2 D_B Q_3 D_B Q_2 D_A Q_1 \quad (8)$$

where Q_n is the transfer matrix for a quadrupole of focusing strength $k_1 L_n$ and $D_{A(B)}$ is the transfer matrix for a drift of length $L_{A(B)}$. A transformation $\tilde{M}(\theta)$ can be constructed using the same set of quadrupole magnets, but with each set of quadrupoles tilted by an angle, θ , around the longitudinal axis.

Using the thin-lens approximation for the quadrupole magnets, the matrix M in (8) can be expressed in terms of the quadrupole strengths and drift lengths. Equation (7) then provides a set of constraints from which the quadrupole strengths and drift lengths can be found for a given μ and β . Not all values of μ and β admit physical solutions. However, a solution can be found for $\mu = \pi/2$, in which case the required focusing strengths are,

$$k_1 L_1 = \frac{L_B \xi}{L_A^2 - L_B^2} \quad k_1 L_2 = -k_1 L_3 = \frac{\xi}{L_B} \quad (9)$$

and the drift length L_B is given by:

$$L_B = \frac{2}{3} \left(\eta + \frac{1}{2} + \frac{1}{\eta} \right) L_A \quad (10)$$

The quantities ξ and η are defined as:

$$\xi^2 = 1 + \frac{L_B}{L_A} \quad \eta^3 = \frac{27}{16} \frac{\beta^2}{L_A^2} \left(1 + \sqrt{1 - \frac{32}{27} \frac{L_A^2}{\beta^2}} \right) - 1 \quad (11)$$

A system to rotate a beam with the transfer matrix (3), can be constructed from two sets of five quadrupoles, with each set having the same drift length and quadrupole strength. In the first set, the quadrupoles are tilted by an angle $\phi_r/2 + \pi/4$ around the longitudinal axis, where ϕ_r is the desired rotation angle in the beam; in the second set, the quadrupoles are tilted by an angle $-\pi/4$. To change the beam rotation angle

requires changing the tilt angle of the first 5 quadrupoles: this may be done either mechanically or by constructing each magnet so as to resemble octupole magnets but with the current in the coils arranged to allow an arbitrary superposition of normal and skew quadrupole fields. A rotation of the field is then achieved by changing the ratio of normal to skew quadrupole field strengths.

An example of a rotation system has $L_A = 0.35 \text{ m}$, $\mu = \pi/2$ and $\beta = 1 \text{ m}$, the overall rotational beamline length is approximately 5 m and the maximum quadrupole strength is 2.53 m^{-1} . In practice, the length of the beamline is likely to increase when physical lengths are used for quadrupoles. Since there is no drift on either side of the set of five quadrupoles, the adjacent quadrupoles in the first and second sets may be combined into a single quadrupole.

DISCUSSION

Initial trials of the rotation system have been unsuccessful. The first issue concerns the total length of the rotation beamline. If the radiation diffracts too much between undulator modules, the interaction between the electrons and the radiation field is diminished and the Gaussian mode is not suppressed. This may not be a significant concern when the radiation wavelength is short and diffraction is low. There are also practical concerns due to the added length of the FEL, as the undulator line more than doubles in length due to the added shifts.

The second issue arising comes from the change in the longitudinal phase (z) position for different electrons. Variations in the transverse components of momentum change the z component of momentum p_z . Since the electrons will have different transverse momentum, depending on their distance from the beam radius, this causes a different longitudinal momentum variation for different electrons and leads to a debunching of the electron beam. Further work will examine if this debunching effect can be reduced.

CONCLUSION

The feasibility of generating light with OAM in a FEL from amplified shot noise in an electron beam is investigated. Trials in which a rotation of the electron beam is used to manipulate the relative phases between the electrons and the different OAM modes showed that suppressing a Gaussian mode will allow growth in the higher order $|l| = 1$ modes. However, although physical realisation of the transform matrix (3) has been demonstrated, the resulting transverse momentum changes debunched the electron beam. Further work is needed to design a system which could be implemented.

ACKNOWLEDGEMENTS

We gratefully acknowledge the support of STFC's ASTeC department for HPC access. Using the STFC Hartree Centre; The Science and Technology Facilities Council Agreement Number 4163192 Release #3; and the John von Neumann Institute for Computing (NIC) on JUROPA at Jülich Supercomputing Centre (JSC), under project HHH20.

REFERENCES

- [1] A. M. Yao and M. J. Padgett, "Orbital angular momentum: origins, behavior and applications," *Adv. Opt. Photon.*, vol. 3, no. 2, pp. 161-204, 2011. doi:10.1364/AOP.3.000161
- [2] P. R. Ribič *et al.*, "Extreme-ultraviolet vortices from a free-electron laser," *Phys. Rev. X.*, vol. 7, no. 3, p. 031036, 2017. doi:10.1103/PhysRevX.7.031036
- [3] E. Hemsing *et al.*, "Helical electron-beam microbunching by harmonic coupling in a helical undulator," *Phys. Rev. Lett.*, vol. 102, no. 17, p. 174801, 2009. doi:10.1103/PhysRevLett.102.174801
- [4] E. Hemsing, A. Gover, and J. Rosenzweig, "Virtual dielectric waveguide mode description of a high-gain free-electron laser.ii. modeling and numerical simulations," *Phys. Rev. A.*, vol. 77, no. 6, p. 063831, 2008. doi:10.1103/PhysRevA.77.063831
- [5] B. W. J. McNeil, M. W. Poole, and G. R. M. Robb, "Inducing Strong Density Modulation with Small Energy Dispersion in Particle Beams and the Harmonic Amplifier Free Electron Laser", in *Proc. PAC'05*, Knoxville, TN, USA, May 2005, paper RPPT021, pp. 1718-1720.
- [6] L. Campbell and B. McNeil, "Puffin: A three dimensional,unaveraged free electron laser simulation code," *Phys. Plasmas*, vol. 19, no. 9, p. 093119, 2012. doi:10.1063/1.4752743
- [7] E. Hemsing, A. Marinelli, and J. Rosenzweig, "Generating optical orbital angular momentum in a high-gain free-electronlaser at the first harmonic," *Phys. Rev. Lett.*, vol. 106, no. 16, p. 164803, 2011. doi:10.1103/PhysRevLett.106.164803
- [8] R. Talman, "A proposed möbius accelerator," *Phys. Rev. Lett.*, vol. 74, no. 9, p. 1590, 1995. doi:10.1103/PhysRevLett.74.1590

HIGH-REPETITION-RATE SEEDING SCHEMES USING A RESONATOR-AMPLIFIER SETUP

S. Ackermann*, B. Faatz, V. Grattoni, C. Lechner, G. Paraskaki, DESY, Hamburg, Germany
G. Geloni, S. Serkez, T. Tanikawa, EuXFEL, Schenefeld, Germany
W. Hillert, University of Hamburg, Hamburg, Germany

Abstract

The spectral and temporal properties of Free-Electron Lasers (FEL) operating on the basis of self-amplified spontaneous emission (SASE) suffer from the stochastic behavior of the start-up process that fluctuates on a bunch-to-bunch basis. Several so-called "seeding"-techniques using external radiation fields to overcome this limitation have been proposed and demonstrated. The external seed is usually generated by high-power laser systems, which are not yet available with a sufficient laser pulse energy at the high repetition rates of superconducting FEL facilities. In this contribution we discuss several seeding schemes that lower the requirements for the used laser systems, enabling seeded operation at high repetition rates by the means of a resonator-amplifier setup.

INTRODUCTION

Recently, more and more FEL facilities worldwide have been built to meet the risen number of photon scientists' experiments. The first of those facilities is FLASH, the Free-Electron Laser in Hamburg [1, 2]. Many facilities use the self-amplification by stimulated emission of radiation (SASE) principle, which suffers from poor temporal and spectral properties due to the stochastic behavior of the start-up process.

Several seeding techniques [3] have been experimentally studied, from the direct-seeding approach, e.g. using High-Harmonic Generation (HHG) [4] to phase-space manipulation techniques like High-Gain Harmonic Generation (HGHG) [5–7] or Echo-Enabled Harmonic Generation (EEHG) [8, 9] using external laser fields, which are currently limited in target wavelength and repetition rate. For FLASH, the future use of these techniques is currently under study [10, 11] as well as for the European X-Ray Free-Electron Laser (EuXFEL) [12].

In contrast to the aforementioned laser-based seeding schemes, methods like active spectral filtering of SASE radiation allow for amplification of radiation without the need of an external seed laser, thus they are working at any wavelength or repetition rate and are not in the scope of this contribution.

Motivation

Most of the seeding techniques rely on the availability of laser systems with high power, short wavelengths, and high peak intensities. For the typical burst repetition rates

of free-electron lasers driven by superconducting linear accelerators - 4.5 MHz at EuXFEL or 1.003 MHz at FLASH - and depending on the power needed, such laser systems are not easily available. A reduction in the repetition rate of the photon burst is sometimes not desired, as for the usual diluted samples a large number of FEL pulses is needed to get sufficient statistics. Some photon science experiments however only use a fraction of this repetition rate like time-of-flight measurements with typical timescales of several μ s.

In the past, resonators at low-gain FELs have been investigated using time-independent simulation codes [13–16]. Recently, also some studies taking advantage of time-dependent and three-dimensional simulation codes have been performed [17]. The idea of building an optical cavity around an undulator at FLASH has also already been studied [18].

The usage of a resonator-amplifier setup for a seeded FEL is a promising approach to reach short wavelengths at the high repetition-rates of superconducting linear accelerators - reaching the water window at around 4 nm using HGHG seeding and 1 nm using EEHG.

First simulations relying upon a resonator setup to drive an High-Gain Harmonic-Generation seeded FEL operating at the 10th harmonic for operating parameters in the FLASH parameter range are currently being conducted, showing promising results [19].

BASIC SETUP

An electron bunch generates radiation, either directly seeded or by the spontaneous undulator radiation, in an undulator called modulator. This modulator can consist of several undulator modules. Its main purpose is to imprint an energy modulation onto the electron bunch. The radiation is reflected by mirrors, then stretched and slightly monochromatized by a grating, and focused in the modulator again where it is overlapped with the next electron bunch. This set of hardware components is called resonator and can be seen in Fig.1. Eventually, after several fresh bunches, an equilibrium state will be reached where the radiation losses over a round trip are compensated by the generation of radiation in the modulator. The electron bunches can then be used in the different seeding schemes exploiting their beneficial longitudinal electron density distribution.

* sven.ackermann@desy.de

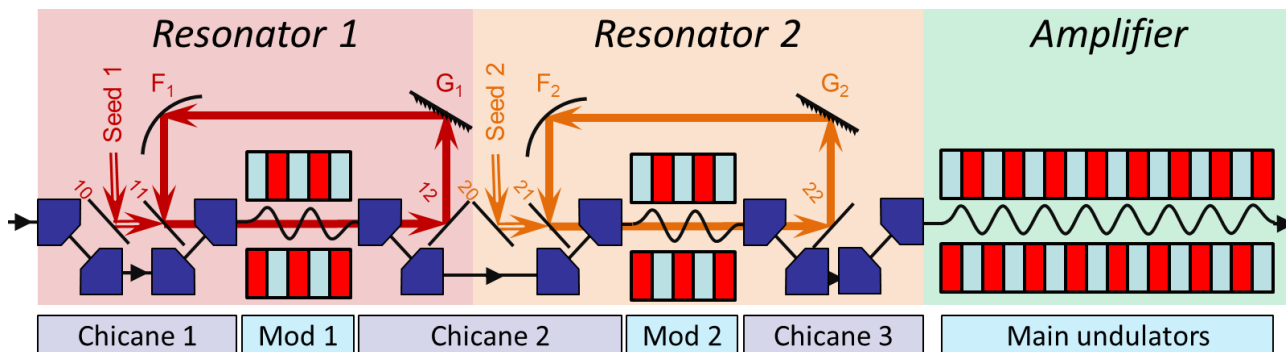


Figure 1: Resonator-amplifier setup. Each resonator consists of a small undulator, called modulator, two plain mirrors M_{11} and M_{12} (M_{21} , M_{22}), a grating G_1 (G_2) and a focusing element F_1 (F_2). In addition, through one element M_{01} (M_{02}) an external seed can be coupled into the optical cavity. The complete resonator is then enclosed by two chicanes to bend the electron beam around the optical elements on the modulator axis and to convert the energy modulation introduced in the modulator into a longitudinal electron density distribution. In the shown configuration both resonators share the second chicane. The resonators are followed by the amplifier, which is also used as the main undulator if the FEL is driven in SASE mode. The sketch does not reflect any scales. Also, the position of the optical components is only for demonstrative purposes.

HIGH REPETITION RATES IN BURST MODE

The following section focuses on several seeding schemes that are currently under study for the use with a resonator-amplifier FEL setup.

High-Gain Harmonic Generation

The most simple HGHG seeding approach exploiting the resonator-amplifier setup contains only one resonator. A seed beam can be coupled into the resonator for the first electron bunch. Two chicanes enclose the optical cavity to guide the electron beam around the needed optical components in the setup. By setting the second chicane to the correct values, the energy modulation in the seeded bunches is transformed into a longitudinal density modulation which enhances the bunching on the corresponding, shorter wavelength. For the FLASH case, the wavelength aimed at is around 4 nm.

Echo-Enabled Harmonic Generation

For EEHG, one needs two resonators and two chicanes. Each modulator is now enclosed by its own optical cavity. This allows for the two seed laser pulses to be specifically made for the requirements in the respective modulator. However, it adds complexity to the setup. If the mirrors of the optical cavity downstream the seed incoupling mirrors can be retracted, this setup also allows for classical EEHG and single-stage HGHG.

Of course one could think of using just one optical cavity and installing a delay stage in the chicane between the two resonators. In this path, attenuators can be installed to change the intensity of the seed in the second modulator. However, this also reduces the intensity of the seed reaching the first resonator again, reduces flexibility and limits the operation parameters in a way such that the energy reaching the second modulator is always lower than in the first.

For hard X-ray FELs, wavelengths of below 1 nm might be reachable.

TECHNICAL CONSIDERATIONS

The path length in the optical cavity must allow for a round-trip time that corresponds to an exact multiple of the FEL burst repetition rate. For the FLASH, which operates at 1.003 MHz this mean the optical cavity needs to have a length of about 150 m. Here, in an actual experiment one has to consider basically two points.

1. While it is possible to have several round trips in the optical cavity, this also means that the losses in the optical cavity will accumulate. On the other hand, the footprint of the setup will be reduced by a factor equal to the number of round trips, making it less prone to thermal conditions of the environment.

2. A longer optical cavity reduces the number of mirrors to be passed by the radiation, enhancing the overall intensity that is overlapped with the following bunch, and reducing thermal stress on the optical components, e.g. by a larger beam size.

Seed Source

Although the resonator-amplifier setup can work in a completely unseeded manner, providing an external seed might improve the operation of this system. In the UV range, several laser options are available to drive the resonator-amplifier setup at the macro pulse repetition rate of 10 Hz.

For short wavelengths at high repetition rates one needs special seed sources paired with a self-sustaining radiation generation so that the seed source itself does not need to supply the high repetition rate the FEL will lase at.

One of such choices can be a laser system providing radiation at the third harmonic of a near infrared laser system. Such systems offer a broad tuning range, also in terms of

wavelength, which means that using techniques that produce harmonics of these wavelength will provide gapless spectra. For short wavelength, one would like to reduce the harmonics needed. This can be done using an HHG source, which is available at 10 Hz and 62.3 nm with pulse powers of about 130 MW [20].

Further Considerations

For even shorter wavelength, one can use the frequency doubling technique [21] in addition to the seeding. If the beam line is equipped with variable gap undulators, one sets the final undulators to a harmonic wavelength of the target wavelength of the seeded FEL and produce radiation on that harmonic. By this, one is capable of reducing the harmonic number needed for the seeding, thus loosens the requirements for optical cavity and electron beam.

Some users want lower repetition rates. For example, usual time-of-flight measurements are performed on time scales in the frequency range of 100 kHz. In the future, this repetition rate requirements might be met by high-power lasers systems that are currently being developed. Of course, lower repetition rates could be mitigated by allowing a larger number of round trips.

Another idea that does not rely on a high rep-rate laser is to actually seed with the full rep-rate and prevent a number of bunches from lasing, so that the FEL radiation comes in rep-rates suited for the experiment. Possible ways of preventing lasing are to kick the bunch onto a non-lasing trajectory through the undulator, which can require a modification of the beam pipe, or even building up a complete bypass beam line. Continuous wave operating (CW) mode is connected to the previous concepts as the repetition rates are lower than in the burst mode operation. In the optimal case, this scenario is the same as for lower repetition rates with the exception of the necessity of a kicker system.

SUMMARY AND OUTLOOK

In this paper, we presented the approach of using a resonator-amplifier setup for seeding at the high repetition rates of Free-Electron Lasers driven by superconducting accelerators. We discussed the principle use of this technique for schemes like High-Gain Harmonic Generation or Echo-Enabled Harmonic Generation together with the option to use frequency doubling. We discussed the possibility to get continuous spectra from existing seed laser options.

In the future, further optimization studies have to be performed on the material for the used mirrors and gratings, used laser systems, and focal properties of the optical components used. In parallel, one has to show within which tolerances the system can be operated in terms of geometry (such as optical cavity length), arrival time jitter, bunch charge, and bunch length. From the technical side, one has to think of ways to stabilize the geometry of the setup over the long distances of several hundreds of meters.

Since the round trip photon beam will get longer every round trip due to the presence of the grating, one will get

longer photon pulses from the seeded region of the electron bunch. In order to keep the photon pulses in the resonator short and thus maintain the temporal stability of the arrival time, a time-compensating monochromator has to be studied. This device should keep the pulse length short while still working as a monochromator. This would allow to keep a longer electron bunch and stabilize the arrival time of the photon pulse. Such devices are also foreseen to be used in the photon beam treatment at FLASH [22].

REFERENCES

- [1] J. Rossbach *et al.*, "10 Years of Pioneering X-ray Science at the Free-Electron Laser FLASH at DESY", *Physics Reports* 808, 2019. doi:10.1016/j.physrep.2019.02.002
- [2] W. Ackermann *et al.*, "Operation of a Free Electron Laser in the Wavelength Range from the Extreme Ultraviolet to the Water Window", *Nature Photonics* 1, 336–342, 2007. doi:10.1038/nphoton.2007.76
- [3] S. Reiche, "Overview of Seeding Methods for FELs", in *Proc. 4th Int. Particle Accelerator Conf.*, Shanghai, China, 2013, pp. 2063–2067, paper WEZB102.
- [4] S. Ackermann *et al.*, "Generation of Coherent 19- and 38-nm Radiation at a Free-Electron Laser Directly Seeded at 38 nm", *Phys. Rev. Lett.* 111, 114801, 2013. doi:10.1103/PhysRevLett.111.114801
- [5] K. Hacker *et al.*, "First Lasing of an HHG Seeded FEL at FLASH" in *Proc. Intern. FEL 2015 Conf.*, Daejeon, Korea, pp. 646–649, paper WEP030.
- [6] L.H. Yu, J. Wu, "Theory of High Gain Harmonic Generation: An Analytical Estimate", *Nucl. Instrum. Meth.* A483, 2002, 493. doi:10.1016/S0168-9002(02)00368-6
- [7] C. Lechner *et al.*, "Seeding R&D at sFLASH", presented at 39th Intern. FEL 2019 Conf., Hamburg, Germany, paper TUP076, this conference,
- [8] P. Ribič, "Coherent Soft X-ray pulses from an Echo-Enabled Harmonic Generation Free-Electron Laser", *Nature Photonics*, May 2019. doi:10.1038/s41566-019-0427-1
- [9] E. Allaria, "First Lasing of a Free Electron Laser in the Soft X-Ray Spectral Range with Echo Enabled Harmonic Generation", presented at the 39th Intern. FEL 2019 Conf., Hamburg, Germany, paper MOA02, this conference.
- [10] V. Grattoni *et al.*, "FLASH Upgrade for Seeding", presented at the 39th Intern. FEL 2019 Conf. Hamburg, Germany, paper TUP074, this conference.
- [11] G. Paraskaki *et al.*, "Impact of Electron Beam Energy Chirp on Seeded FELs", presented at the 39th Proc. Intern. FEL 2019 Conf. Hamburg, Germany, paper TUP078, this conference.
- [12] T. Takanori *et al.*, "Feasibility Study of an External-Laser Seeding for the European XFEL", presented at the 39th Proc. Intern. FEL 2019 Conf. Hamburg, Germany, paper TUP005, this conference.
- [13] G. Dattoli *et al.*, "MOPA Optical Klystron FELs and Coherent Harmonic Generation", *Nucl. Instrum. Meth.* A507, 2003, pp. 26–30. doi:10.1016/B978-0-444-51417-2.50013-4

- [14] G. Dattoli *et al.*, "Oscillator-Amplifier Free Electron Laser Devices with Stable Output Power", *Journal of Applied Physics* 95(6):3211–3216, 2004. doi:10.1063/1.1645649
- [15] G. Dattoli, *et al.*, "The Tandem FEL Dynamic Behavior.", *IEEE Journal of Quantum Electronics*, 31:1584 – 1590, 09 1995. doi:10.1109/3.400416
- [16] G. Penco *et al.*, "Optical Klystron Enhancement to Self Amplified Spontaneous Emission at FERMI", *Photonics*, 4:15, 03 2017. doi:10.3390/photonics4010015
- [17] H. P. Freund *et al.*, "Three-dimensional, Time-dependent Simulation of a Regenerative Amplifier Free-Electron Laser", *Phys. Rev. ST Accel. Beams*, 16:010707, 2013. doi:10.1103/PhysRevSTAB.16.010707
- [18] B. Faatz *et al.*, "Regenerative FEL Amplifier at the TESLA Test Facility at DESY", *Nucl.Instrum. and Methods A*429, 1999, 424-428. doi:10.1016/S0168-9002(99)00123-0
- [19] G. Paraskaki *et al.*, "Study of a Seeded Oscillator-Amplifier", presented at the 39th Proc. Intern. FEL 2019 Conf. Hamburg, Germany, paper TUP077, this conference.
- [20] E. Takahashi *et al.*, "Generation of 10-mJ Coherent Extreme-Ultraviolet Light by Use of High-Order Harmonics", *Opt. Lett.* 27, 1920–2, 2002. doi:10.1364/OL.27.001920
- [21] J. Feldhaus *et al.*, "Efficient Frequency Doubler for the Soft X-ray SASE FEL at the TESLA Test Facility", *Nucl. Instrum. Meth. A*528, 2004, 471-475. doi:10.1016/j.nima.2004.04.134
- [22] N. Gerasimova *et al.*, "The Monochromator Beamline at FLASH: Performance, Capabilities and Upgrade Plans", *Journal of Modern Optics* 58, 1480-1485, 2011. doi:10.1080/09500340.2011.588344

FLASH UPGRADE FOR SEEDING *

V. Grattoni[†], B. Faatz, G. Paraskaki, S. Ackermann, C. Lechner, J. Zemella,
M. M. Kazemi, T. Lang, DESY, Hamburg, Germany
W. Hillert, University of Hamburg, Hamburg, Germany

Abstract

An upgrade for FLASH, the SASE FEL in Hamburg, is planned after 2020 aiming at fulfilling user requirements like fully coherent, variable polarization, and multi-colour pulses. In this proceeding, we focus on the FLASH1 beamline that will be operated in seeded mode at a high repetition rate. In particular, we will present and discuss the proposed seeding schemes for delivering FEL radiation with wavelengths from 60 down to 4 nm.

INTRODUCTION

FLASH is the free-electron laser in DESY, Hamburg [1]. It has three beamlines: FLASH1, FLASH2 and FLASH-Forward, and the maximum number of bunches per second for user experiments is 5000 shared amongst the beamlines thanks to the long flat top of the RF-Voltages enabled by the TESLA cavities. The various beamlines can share the produced bunches, in fact, simultaneous operation between FLASH1 and either FLASH2 or FLASHForward is possible [2] thanks to a kicker septum placed in front of the FLASH2 beamline. Also, seeding techniques are studied at sFLASH that is placed upstream of the FLASH1 undulator. The current status of the sFLASH project is discussed in [3]. At the moment the HGHG seeded radiation is operated at 10 Hz, which corresponds to the repetition rate of the current seed laser so that the potential of FLASH is only partially exploited. In addition, the radiation is not accessible by the users of the FLASH1 experimental hall. But, using the FLASH1 undulator as radiator for seeding is not a solution, because the transport of the bunched electron beam from the second sFLASH chicane to the undulator is challenging and saturation is reached before the end of the undulator [4]. The foreseen FLASH upgrade [5] is going to dedicate FLASH1 as a seeding beamline for user delivery at wavelengths spanning from 60 down to 4 nm and increase the repetition rate for seeding operation to 100 kHz in a first stage, and then to 1 MHz by the implementation of an innovative seed laser scheme.

In this contribution, the main details of the seeding upgrade and preliminary start-to-end simulation results are presented.

FLASH UPGRADE OVERVIEW

The upgrade plans of the FLASH facility are described in Ref. [5]. It includes a laser heater, an energy increase

from 1.25 to 1.35 GeV and a redesign of the bunch compressors [6]. A modification of FLASH2 is planned to allow for more advanced FEL schemes like multi-colour and attosecond pulses [7]. As mentioned in the introduction, FLASH1 will be devoted to seeding, delivering FEL radiation with a wavelengths between 60 and 4 nm. Figure 1 shows a scheme of the designed FLASH1 beamline. It consists of two modulators and one radiator, the first modulator is followed by a magnetic chicane with maximum longitudinal dispersion of 25 mm, enabling EEHG operation at the $n=-1$ working point even at the shortest wavelength (4 nm). A second chicane is installed before the radiator, with a foreseen maximum dispersion of 300 μ m and it will be used as bunching chicane for both EEHG and HGHG. The current FLASH1 fixed gap undulators are going to be replaced by variable gap helical undulators. The detailed undulator parameter are going to be presented in the next section. So far, fixed gap undulators in FLASH1 has limited FLASH2 operation, as for every wavelength change it is also necessary to change the electron beam energy. With this upgrade, the machine will be operated at two fixed electron beam energies: 750 MeV and 1.35 GeV to reach all design wavelengths. This will significantly ease wavelength changes. Three seed laser options are under study for FLASH1: two are in the ultra-violet (UV) range and one in the visible in the range 413-480 nm. The UV seed laser in one case is the result of a cascaded process with final wavelength range 294-327 nm, in the other case it is the third harmonic of the seed source resulting in the range 230-300 nm, but it has a much lower energy. For this reason, in this and previous studies (see [8]) only the VIS option and the UV option in the range 294-327 nm are studied.

UNDULATOR PARAMETERS AND TUNABILITY

The undulators foreseen for the radiator section are APPLE III type with variable polarization and gap (with minimum gap 8 mm). The undulator has a period λ_u of 33 mm, and a total length of 2.5 m. This undulator enables wavelengths from 60 to 20 nm within the e-beam energy of 750 MeV and wavelengths from 20 to 4 nm at 1.35 GeV. For the external seeding schemes, also seed laser tunability should be considered. The UV seed laser gives a continuous tunability starting from FEL wavelengths of 36.4 nm and shorter, but for longer wavelengths there are gaps as shown in fig. 2. While the VIS seed gives a continuous tunability for the whole FEL wavelength range of interest. Up to the 12th harmonic FEL radiation will be generated using the HGHG scheme by enabling only one of the two modulators and seed lasers. In fact, this harmonic is the lowest one rou-

* Work supported by the Federal Ministry of Education and Research of Germany within FSP-302 under FKZ 05K13GU4, 05K13PE3, and 05K16PEA and the German Research Foundation within GrK 1355.
[†] vanessa.grattoni@desy.de

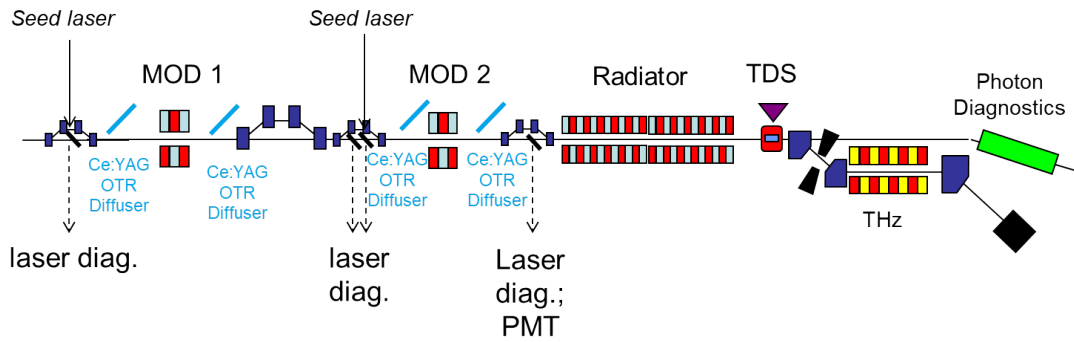


Figure 1: Proposed FLASH1 seeding beamline and fundamental diagnostics.

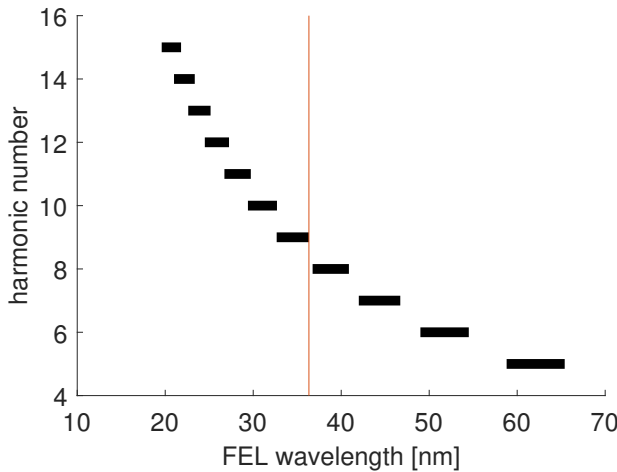


Figure 2: Tunability of the seeded FEL for the seed laser wavelength tuning range 294 – 327 nm and an e-beam energy of 750 MeV. For wavelengths shorter than 36.4 nm (left side of the red line), continuous, gap-free tunability is achieved.

tinely produced at FERMI [9] in the FEL1 beamline. EEHG scheme will be applied to enable shorter wavelengths down to 4 nm. This scheme has been recently successfully shown at FERMI [10].

Modulator Parameters

The modulator is planar and will have an undulator period λ_u of 82.6 mm, the length considered so far is 2.478 m. The minimum gap will depend on the seed laser type (UV or VIS) that will be chosen. Knowing the seed laser wavelengths, it is possible to estimate the needed undulator strengths and thus gaps needed in the two cases: UV seed and VIS seed. In table 1 the calculated gaps for the e-beam energy E_0 of 1.35 GeV, where the gaps are smaller, are given. For the UV

Table 1: Gaps needed for the different seed laser and electron beam energies options.

seed type	E_0	gap
UV	1.35 GeV	18-19 mm
VIS	1.35 GeV	14-15 mm

case the minimum gap is larger compared to the VIS case. These gap values should not be a limitation for the diameter of the vacuum pipe.

SIMULATION RESULTS

FEL simulations were performed using GENESIS 4 [11]. The advantage in using this code is that the particles are not constrained in one slice for all the simulation, but they can move freely from one slice to another consecutive one. This aspect is essential for the EEHG where the first chicane has usually high dispersion, thus the longitudinal particle displacement exceeds several slices. Initial tolerance studies on the seed lasers for the two different seed laser options UV and VIS have been presented for the most challenging FEL target wavelength 4 nm in [8] and are compared with the theory estimation given in [12]. At the moment, CSR studies for these two options are under investigation. The recently achieved results with a start-to-end (S2E) simulation are presented and they are compared with simulation results obtained using an ideal gaussian beam defined with the same parameters presented in table 2. For the S2E simulation, a particle distribution file from ELEGANT [13] is dumped before the first modulator of the seeding beamline. The beam used for the FEL simulation has been described in [6], for which space charge (SC), incoherent (ISR) and coherent synchrotron radiation (CSR) effects are taken into consideration. The main beam properties are summarised in table 2. Once

Table 2: Main parameters of the beam simulated in [6]. I_{peak} shows the peak current, and $\epsilon_{p,(x,y)}$ are the transverse projected emittances.

E_0	σ_E	I_{peak}	charge	$\epsilon_{p,x}$	$\epsilon_{p,y}$
1.35 GeV	75 keV	500 A	250 pC	0.5 μ m	0.4 μ m

the sdds distribution file from ELEGANT is converted in hdf5 format, it is possible to load it to GENESIS 4 and track it along the seeding beamline using the "one for one" simulation mode. For this initial test, a UV seed laser at 300 nm is used, and the radiator is tuned to the thirty-second harmonic of the seed laser. The parameters for EEHG has been decided by maximising the Stupakov bunching formula [14].

Content from this work may be used under the terms of the CC BY 3.0 licence (© 2019). Any distribution of this work must maintain attribution to the author(s), title of the work, publisher, and DOI

Table 3: Parameters for EEHG seeding. The harmonic number is given by the sum of n and m , $A_{1,2} = \Delta E_{1,2}/\sigma_E$, where ΔE is the energy modulation transferred from the seed laser to the electron beam and σ_E is the energy spread of the electron beam. $R_{56}^{(1),(2)}$ is the dispersion strength of the chicane, where $^{(1)}$ and $^{(2)}$ indicate respectively the first and the second chicane.

harmonic	n	m	A_1	A_2	$R_{56}^{(1)}$	$R_{56}^{(2)}$
32	-1	33	4.6	5.3	5.974 mm	185 μ m

Table 3 shows the main EEHG parameters used for the simulation. The expected FEL saturation power is derived with the Ming-Xie formulas, adapted for pre-bunched beam [15] using the parameters presented in Table 2. The FEL saturation power results to be 1.13 GW and it is achieved after 9.9 m of undulator active length. The Pierce parameter is calculated to be 0.0017 and the gain length 1.12 m. So, with the radiator described in the previous section, we expect to achieve FEL saturation after four undulator modules. The result without including ISR and CSR in the seeding section are shown in figs. 3 to 5. In these figures "S2E beam" represents the simulation done using the beam coming from the ELEGANT simulation and "ideal beam" the simulation done using an ideal beam.

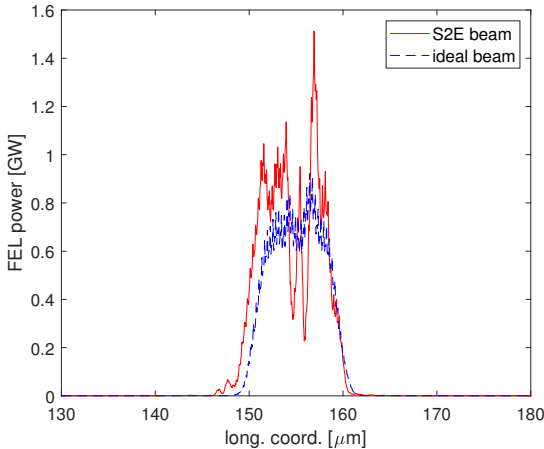


Figure 3: FEL power profile after 10 meters from the start of the radiator section.

FEL power at 10 m achieves the estimated saturation value and fluctuations could be associated to the statistics of the simulations. The spectra are shown in fig. 5. They are compatible except a tiny peak on the left of the main peak of the S2E beam, that might come from the e-beam imperfections.

CONCLUSION AND OUTLOOK

The envisioned FLASH1 beamline for the FLASH2020+ upgrade has been presented. The FEL performance has been introduced using a beam coming from linac simulations where SC, CSR and ISR has been included, showing that

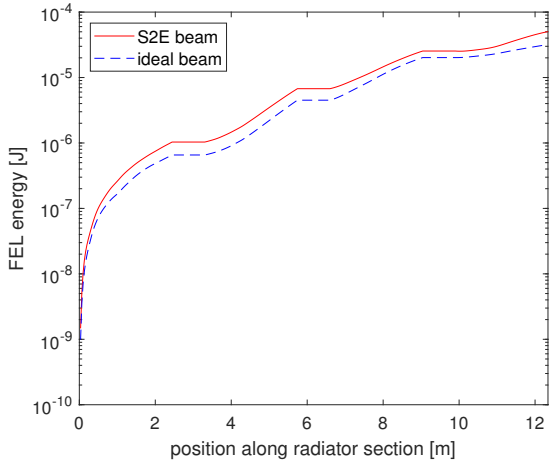


Figure 4: FEL gain curve along the radiator in logarithmic scale, both maximum and mean FEL power are shown.

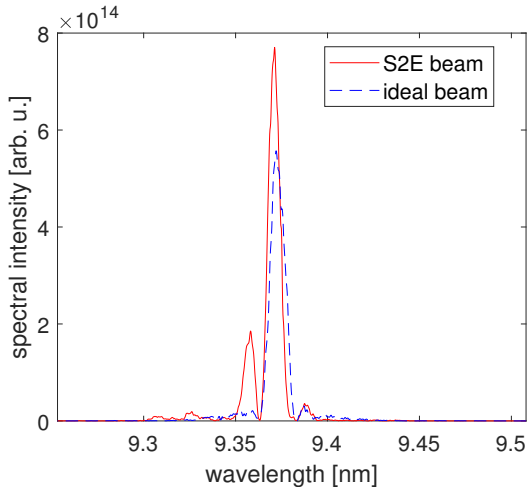


Figure 5: FEL spectrum profile after 10 meters from the start of the radiator section.

with a realistic beam it is possible to radiate seeded radiation. Next step will be to improve the quality of the radiation pulse obtained in terms of longitudinal coherence. Also, studies on the wakefield effects in the radiator section to evaluate the optimal vacuum system that preserves the EEHG process are planned. Furthermore, there are ongoing studies to characterise the impact of CSR effects from the two EEHG chicanes.

ACKNOWLEDGEMENTS

The authors would like to thank S. Reiche for his support with the new version of GENESIS. S. Schreiber for scientific discussion and the FLASH2020+ competence team for supporting the project.

REFERENCES

[1] W. Ackermann *et al.*, "Operation of a free-electron laser from the extreme ultraviolet to the water window", *Nature Photon-*

- ics 1,336 (2007). doi:10.1038/nphoton.2007.76
- [2] B. Faatz *et al.*, “Simultaneous operation of two soft x-ray free-electron lasers driven by one linear accelerator”, *New Journal of physics*, 18, 062002 (2016). doi:10.1088/1367-2630/18/6/062002
- [3] C. Lechner *et al.*, “Status of the sFLASH Experiment”, in *Proc. 9th Int. Particle Accelerator Conf. (IPAC'18)*, Van-couver, Canada, Apr.-May 2018, pp. 1471–1473. doi:10.18429/JACoW-IPAC2018-TUPMF085
- [4] V. Grattoni *et al.*, “An Option to Generate Seeded FEL Ra-diation for FLASH1”, in *Proc. 9th Int. Particle Accelerator Conf. (IPAC'18)*, Vancouver, Canada, Apr.-May 2018, pp. 1448–1451. doi:10.18429/JACoW-IPAC2018-TUPMF079
- [5] M. Vogt, K. Honkavaara, J. Rönsch-Schulenburg, S. Schreiber, and J. Zemella, “Upgrade Plans for FLASH for the Years After 2020”, in *Proc. 10th Int. Particle Accelerator Conf. (IPAC'19)*, Melbourne, Australia, May 2019, pp. 1748–1751. doi:10.18429/JACoW-IPAC2019-TUPRB027
- [6] J. Zemella and M. Vogt, “Optics & Compression Schemes for a Possible FLASH Upgrade”, in *Proc. 10th Int. Particle Accelerator Conf. (IPAC'19)*, Melbourne, Australia, May 2019, pp. 1744–1747. doi:10.18429/JACoW-IPAC2019-TUPRB026
- [7] E. Schneidmiller *et al.*, “A Concept for Upgrade of FLASH2 Undulator Line”, in *Proc. 10th Int. Particle Accelerator Conf. (IPAC'19)*, Melbourne, Australia, May 2019, pp. 1736–1739. doi:10.18429/JACoW-IPAC2019-TUPRB024
- [8] V. Grattoni *et al.*, “Simulation Studies for a EEHG seeded FEL in the XUV”, in *Proc. 10th Int. Particle Accelerator Conf. (IPAC'19)*, Melbourne, Australia, May 2019, pp. 1705–1708. doi:10.18429/JACoW-IPAC2019-TUPRB013
- [9] E. Allaria *et al.*, “Tunability experiments at the FERMI@Elettra free-electron laser”, *New J. Phys.* 14, 113009 (2012). doi:10.1088/1367-2630/14/11/113009
- [10] P.R. Ribic *et al.*, “Coherent soft x-ray pulses from an echo-enabled harmonic generation free-electron laser” *Nature Photonics*, 13, 555–561 (2019). doi:10.1038/s41566-019-0427-1
- [11] S. Reiche <https://github.com/svenreiche/Genesis-1.3>
- [12] E. Hemsing, B. Garcia, Z. Huang, T. Raubenheimer, and D. Xiang “Sensitivity of echo enabled harmonic generation to sinusoidal electron beam energy structure”, *Phys. Rev. Accel. Beams* 20, 060702 (2017). doi:10.1103/PhysRevAccelBeams.20.060702
- [13] M. Borland “User’s Manual for elegant” APS LS-231 (1993).
- [14] D. Xiang and G. Stupakov, “Echo-enabled harmonic generation free electron laser”, *Phys. Rev. ST Accel. Beams*, 12, 030702 (2009). doi:10.1103/PhysRevSTAB.12.030702
- [15] L. Giannessi, “Seeding and Harmonic Generation in Free-Electron Lasers.” In: Jaeschke E., Khan S., Schneider J., Hastings J. (eds), “Synchrotron Light Sources and Free-Electron Lasers.”, Springer, Cham (2016).

SEEDING R&D AT sFLASH*

C. Lechner[†], S. Ackermann, R. W. Assmann, B. Faatz, V. Grattoni,
I. Hartl, S. D. Hartwell, R. Ivanov, M. M. Kazemi, T. Laarmann, T. Lang, G. Paraskaki,
A. Przystawik, J. Zheng, DESY, Hamburg, Germany
S. Khan, DELTA, TU Dortmund University, Dortmund, Germany
A. Azima, H. Biss, M. Drescher, W. Hillert,
V. Miltchev, J. Rossbach, University of Hamburg, Hamburg, Germany

Abstract

Free-electron lasers (FELs) based on the self-amplified spontaneous emission (SASE) principle generate photon pulses with typically poor longitudinal coherence. FEL seeding techniques greatly improve longitudinal coherence by initiating FEL amplification in a controlled way using coherent light pulses. The sFLASH experiment installed at the FEL user facility FLASH at DESY in Hamburg is dedicated to the study of external seeding techniques. In this paper, the layout of the sFLASH seeding experiment is presented and an overview of recent developments is given.

INTRODUCTION

The exponential amplification process in soft and hard x-ray free-electron lasers (FELs) is typically initiated by spontaneous undulator radiation generated by the high-brightness electron bunches at the beginning of the undulator. This stochastic start-up of FELs based on the self-amplified spontaneous emission (SASE) principle results in poor longitudinal coherence.

In the seeded mode of operation, the FEL amplification process is initiated by coherent light pulses generated in an external source. At sFLASH, the high-gain harmonic generation (HG) [1] seeding scheme is employed.

The seeding experiment sFLASH is installed in the FLASH1 beamline of the FEL user facility FLASH [2], which has been in user operation since 2005 [3], now delivering SASE FEL radiation down to 4.1 nm [4]. The superconducting linear accelerator of the FLASH facility can generate a maximum of 5000 electron bunches per second for user experiments, which can be distributed between the beamlines FLASH1 and FLASH2 or the plasma wakefield acceleration experiment FLASHForward [5] using a flat-top kicker and a Lambertson DC septum [2], enabling flexible parallel operation of the beamlines [6–8].

THE sFLASH EXPERIMENT

The essential components of the seeding experiment sFLASH are shown in Fig. 1, their parameters are listed in Tab. 1. The electron bunches arriving from the energy collimation section of the FLASH1 electron beamline can interact with ultraviolet seed pulses in two electromagnetic

Table 1: Experimental Parameters

parameter	value
modulators	
period length	200 mm
number of periods	5
maximum K value	10.8
radiator	
number of modules	3 / 1
length of module	2 m / 4 m
period length	31.4 mm / 33 mm
maximum K value	2.72 / 3.03
chicanes	
R_{56} of C_1 (for HG)	0 μ m
R_{56} of C_2 (for HG)	<150 μ m
electron bunches	
beam energy	680 – 700 MeV
typ. peak current	0.6 kA
bunch charge	0.4 nC
bunch duration	>500 fs (fwhm)
seed laser pulses	
UV wavelength (seed 1/2)	269 nm/270 nm
UV pulse energy	0.40 – 0.50 mJ
approx. UV pulse duration	100 – 400 fs (fwhm)
approx. NIR pulse duration	40 – 50 fs (fwhm)

wigglers [9] (M_1 and M_2 in Fig. 1). After each of these so-called modulators, a four-dipole chicane is installed (C_1 and C_2). For HG-seeded FEL operation, modulator M_2 and chicane C_2 are used. The seeded electron bunches then enter the 10-meter-long variable-gap radiator system [10] where FEL emission at the desired harmonic takes place. After extraction from the electron beamline, the generated light pulses are either transported to the in-tunnel photon diagnostics (photon energy detectors; Ce:YAG fluorescence screens; spectrometer with $\lambda/\Delta\lambda \approx 500$) or to a photon diagnostics laboratory outside of the accelerator tunnel. There, the seeded FEL pulses can be analyzed in a THz streaking [11] setup by overlapping them with the THz field from a source driven by the seed laser system. At a second beamline in the photon diagnostics laboratory, a reflective extreme ultraviolet (XUV) pulse shaper [12] is currently being set up.

The longitudinal phase-space distribution of the electron bunches is diagnosed by virtue of a transverse-deflecting

* Work supported by Federal Ministry of Education and Research of Germany under contract No. 05K13GU4, 05K13PE3, and 05K16PEA.
[†] christoph.lechner@desy.de

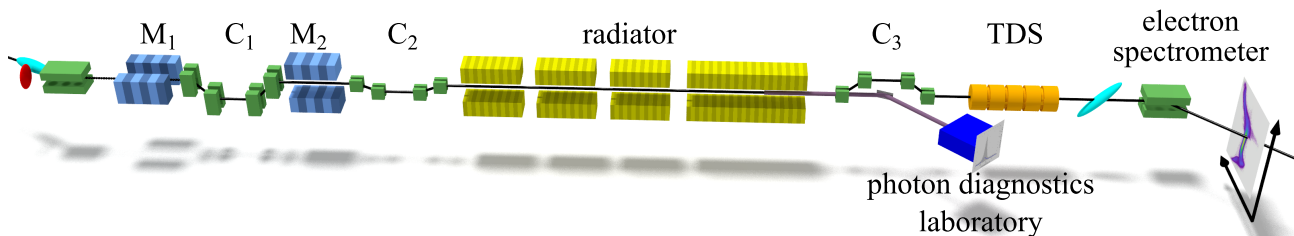


Figure 1: Schematic layout of the sFLASH seeding experiment. The electron beam travels from left to right. See text for further details.

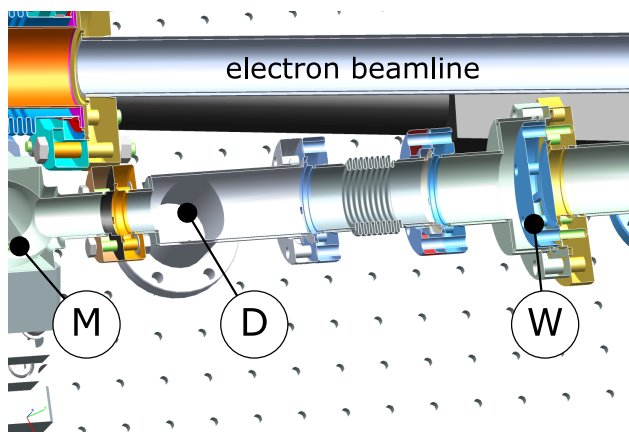


Figure 2: Cross-section of the upgraded sFLASH laser injection beamline. The electron beam travels from left to right in the electron beamline. The second dipole of the FLASH1 energy collimator dogleg is to the right of the shown beam-line section. The laser beam is directed onto the electron beam axis in the modulator by the final transport mirror (M) before it is transmitted through the vacuum window (W), which is the interface between laser transport vacuum (on the left side) and accelerator vacuum (on the right side) [13].

structure (TDS) in combination with a dipole spectrometer. The signatures of the laser-electron interaction are routinely used to control the sub-picosecond laser-electron timing, but measured longitudinal phase-space distributions were also used to study the lasing of the seeded FEL [14].

A dedicated near-infrared (NIR) Ti:sapphire laser system (central wavelength 810 nm, FWHM bandwidth ~ 35 nm) in a laboratory adjacent to the accelerator tunnel drives a third-harmonic generation (THG) process in one (for HHG) or two (for development of EEHG, see below) ultraviolet seed sources. The relative timing as well as the energy of the two seed pulses can be independently controlled. Finally, the seed pulses of orthogonal polarization are combined spatially in a thin-film polarizer before they are injected into the evacuated transport beamline to the interaction regions in the modulators. The maximum ultraviolet seed pulse energy at the entrance window to the evacuated transport beamline is in the range of 0.40 mJ – 0.50 mJ.

Seed Laser Injection

The sFLASH seed laser injection beamline was upgraded during the FLASH shutdown in June/July 2019. Figure 2 shows the newly installed section of this beamline. Up to now, the thin vacuum window (made from crystalline quartz) separating the accelerator vacuum from the vacuum of the transport beamline was before the final transport mirror (which directs the laser pulses onto the electron beam axis in the modulator) and the two screen stations used to diagnose the seed laser beam. The vacuum window is now installed after the final mirror, resulting in several improvements: Firstly, all optical components of the seed laser transport system are no longer in accelerator vacuum, making them readily accessible for maintenance. Secondly, the seed laser radiation can be extracted for (online) diagnostic purposes between the last mirror and the interaction region. The installation of additional seed laser diagnostics (at position (D) in Fig. 2) is currently being prepared. In the course of this upgrade, the vacuum chambers containing the seed injection and focusing system [15] originally installed for the experiments that demonstrated direct-HHG seeding at 38 nm [16, 17] were removed.

Laser-electron interaction was already achieved with the upgraded hardware. Seeded FEL operation at the sFLASH experiment is to be re-commissioned in fall 2019.

Upgrade Plans for the First Chicane

The advanced seeding scheme echo-enabled harmonic generation (EEHG) [18] enables the efficient generation of bunching at high harmonics. Compared to HHG seeding, EEHG adds less energy spread to the electron beam and imperfections of the electron beam have reduced impact on the parameters of the generated photons (see [19] for a simulation study for HHG). EEHG-seeded FEL operation was recently demonstrated at the seeded FEL user facility FERMI at wavelengths down to 5.9 nm (harmonic 45 of the 264-nm seed laser) [20].

At high harmonics, this promising seeding scheme calls for a significant overshearing of the longitudinal phase-space distribution of the incoming electron beam in the first modulator-chicane section. However, the accessible R_{56} range of the currently installed first chicane (C_1 in Fig. 1) is limited both by the first field integral of the chicane dipoles as well as the inner diameter of the vacuum chamber, restricting

the accessible parameter space [21, 22]. To overcome these limitations, an upgrade of the first sFLASH chicane was engineered and is being prepared. This upgrade comprising a flat vacuum chamber and new dipole magnets aims at longitudinal dispersions of about 6 millimeters at an electron beam energy of 700 MeV.

SUMMARY AND OUTLOOK

The seeding experiment sFLASH is installed at the FEL user facility FLASH. Recently, HGHG-seeded FEL operation was mainly performed at the 7th and 8th harmonic of the ultraviolet seed laser. In summer 2019, the seed laser injection beamline was upgraded enabling development of seed laser diagnostics techniques which is important in view of the envisioned FLASH2020+ upgrades [23, 24]. The laser-electron interaction was recommissioned and we plan to re-establish seeded FEL operation in fall 2019. Currently, an upgrade of the first chicane is being prepared, lifting present restrictions of the parameter space of EEHG seeding.

ACKNOWLEDGEMENTS

Without the help from many groups at DESY, the preparation and commissioning of all components of the seeding experiment would not have been conceivable. Their support is gratefully acknowledged.

REFERENCES

- [1] L.H. Yu, "Generation of intense uv radiation by subharmonically seeded single-pass free-electron lasers", *Phys. Rev. A* 44, pp. 5178–5193, 1991. doi:10.1103/PhysRevA.44.5178
- [2] J. Rönsch-Schulenburg, K. Honkavaara, S. Schreiber, R. Treusch, and M. Vogt, "FLASH - Status and Upgrades", presented at the 39th Int. Free Electron Laser Conf. (FEL'19), Hamburg, Germany, Aug. 2019, paper FRA03, this conference.
- [3] K. Honkavaara and S. Schreiber, "FLASH: The Pioneering XUV and Soft X-Ray FEL User Facility", presented at the 39th Int. Free Electron Laser Conf. (FEL'19), Hamburg, Germany, Aug. 2019, paper THP074, this conference.
- [4] S. Schreiber, "First Lasing in the Water Window with 4.1 nm at FLASH", in *Proc. 33rd Int. Free Electron Laser Conf. (FEL'11)*, Shanghai, China, Aug. 2011, paper TUOB12, pp. 164–165.
- [5] R. D'Arcy *et al.*, "FLASHForward: plasma wakefield accelerator science for high-average-power applications", in *Philosophical Transactions of the Royal Society A*, vol. 377, p. 20180392, 2019. doi:10.1098/rsta.2018.0392
- [6] B. Faatz *et al.*, "Simultaneous operation of two soft x-ray free-electron lasers driven by one linear accelerator", *New J. Physics*, vol. 18, p. 062002, 2016. doi:10.1088/1367-2630/18/6/062002
- [7] J. Rönsch-Schulenburg *et al.*, "Experience with Multi-Beam and Multi-Beamline FEL-Operation", in *Proc. 8th Int. Particle Accelerator Conf. (IPAC'17)*, Copenhagen, Denmark, May 2017, paper WEPAB021, pp. 2621–2624. doi:10.18429/JACoW-IPAC2017-WEPAB021
- [8] T. Plath *et al.*, "Free-electron laser multiplex driven by a superconducting linear accelerator", *J. Synchrotron Radiation*, vol. 23, p. 1070, 2016. doi:10.1107/S1600577516009620
- [9] G. Angelova *et al.*, "The Optical Replica Synthesizer in FLASH", in *Proc. 29th Int. Free Electron Laser Conf. (FEL'07)*, Novosibirsk, Russia, Aug. 2007, paper WEPH039, pp. 438–440.
- [10] M. Tischer *et al.*, "Undulators of the sFLASH Experiment", in *Proc. 1st Int. Particle Accelerator Conf. (IPAC'10)*, Kyoto, Japan, May 2010, paper WEPD014, pp. 3114–3116.
- [11] A. Azima *et al.*, "Direct measurement of the pulse duration and frequency chirp of seeded XUV free electron laser pulses", *New J. Phys* vol. 20, p. 013010, 2018. doi:10.1088/1367-2630/aa9b4c
- [12] L.L. Lazzarino *et al.*, "Shaping femtosecond laser pulses at short wavelength with grazing-incidence optics", *Opt. Express* vol. 27, issue 9, pp. 13479–13491, 2019. doi:10.1364/OE.27.013479
- [13] mechanical engineering: S. Schneider, DESY.
- [14] T. Plath *et al.*, "Mapping few-femtosecond slices of ultra-relativistic electron bunches", *Sci. Rep.* vol. 7, p. 2431, 2017. doi:10.1038/s41598-017-02184-3
- [15] J. Bödewadt, E. Hass, and J. Rossbach, "Commissioning Results of the Photon-Electron Diagnostic Unit at sFLASH", in *Proc. 10th European Workshop on Beam Diagnostics and Instrumentation for Particle Accelerators (DIPAC'11)*, Hamburg, Germany, May 2011, paper MOPD54, pp. 173–175.
- [16] S. Ackermann *et al.*, "Generation of Coherent 19- and 38-nm Radiation at a Free-Electron Laser Directly Seeded at 38 nm", *Phys. Rev. Lett.* 111, 114801, 2013. doi:10.1103/PhysRevLett.111.114801
- [17] C. Lechner *et al.*, "First Direct Seeding at 38nm", in *Proc. 34th Int. Free Electron Laser Conf. (FEL'12)*, Nara, Japan, Aug. 2012, paper TUOAI01, pp. 197–199.
- [18] G. Stupakov, "Using the Beam-Echo Effect for Generation of Short-Wavelength Radiation", *Phys. Rev. Lett* 102, p. 074801 (2009). doi:10.1103/PhysRevLett.102.074801
- [19] G. Paraskaki *et al.*, "Impact of Electron Beam Energy Chirp on Seeded FELs", presented at the 39th Int. Free Electron Laser Conf. (FEL'19), Hamburg, Germany, Aug. 2019, paper TUP078, this conference.
- [20] P.R. Ribič *et al.*, "Coherent soft X-ray pulses from an echo-enabled harmonic generation free-electron laser", in *Nat. Photonics*, 13, pp. 555–561, 2019. doi:10.1038/s41566-019-0427-1
- [21] J. Bödewadt *et al.*, "Parameter Optimization for Operation of sFLASH With Echo-Enabled Harmonic Generation", in *Proc. 8th Intl. Particle Accelerator Conf. (IPAC'17)*, Copenhagen, Denmark, May 2017, paper WEPAB015, pp. 2592–2595. doi:10.18429/JACoW-IPAC2017-WEPAB015
- [22] H. Biss, "Conceptual Design of a Chicane Upgrade for EEHG Seeding at sFLASH", Master's thesis, University of Hamburg, Germany, 2019.
- [23] M. Vogt, K. Honkavaara, J. Rönsch-Schulenburg, S. Schreiber, and J. Zemella, "Upgrade Plans for FLASH for the Years After 2020", in *Proc. 10th Int. Particle Accelerator Conf. (IPAC'19)*, Melbourne, Australia, May 2019, pp. 1748–1751. doi:10.18429/JACoW-IPAC2019-TUPRB027

- [24] V. Grattoni *et al.*, “FLASH Upgrade for Seeding”, presented at the 39th Int. Free Electron Laser Conf. (FEL’19), Hamburg,

Germany, Aug. 2019, paper TUP074, this conference.

STUDY OF A SEEDED OSCILLATOR-AMPLIFIER

G. Paraskaki*, S. Ackermann, B. Faatz, V. Grattoni, C. Lechner, M. Mehrjoo, DESY, Hamburg
G. Geloni, S. Serkez, T. Tanikawa, EuXFEL, Schenefeld
W. Hillert, University of Hamburg, Hamburg

Abstract

In recent years, there is interest of the Free-Electron Laser (FEL) community in external-seeding techniques such as the Echo-Enabled Harmonic Generation (EEHG) and the High-Gain Harmonic Generation (HHHG). With these techniques, pulses of an improved temporal coherence are generated, but at the same time, they are limited by the repetition rates that seed lasers can currently offer with the required pulse energies. A big challenge is to combine the advantages of seeding schemes with high repetition rates. For this purpose, we study a combination of an oscillator-amplifier. The modulator in the oscillator is used at a long wavelength to modulate the electron beam and an amplifier is operated to extract the FEL radiation of the desired harmonic. This way we can use a seed laser of 10 Hz in a burst mode and a resonator to feedback the radiation at repetition rates of superconducting accelerators instead of using an external seed at these high-repetition rates. In this contribution, we present simulation results of a seeded oscillator-amplifier FEL in an HHHG scheme.

INTRODUCTION

For over ten years, SASE FELs have been delivering radiation to users in XUV and X-ray wavelength range [1]. Wavelengths from 100 nm down to below 0.1 nm have been achieved with 100 to several thousand pulses per second. In more recent years, several user facilities have improved the radiation properties by using different seeding schemes, mostly external seeding [2–4] and self-seeding at shorter wavelengths [5]. The next development that is planned is to go towards continuous wave (CW)-operation with superconducting accelerator technology, thus increasing the number of pulses per second to a million [6, 7]. A big challenge is to improve the radiation properties at high repetition rates and at short wavelengths simultaneously. Present schemes that use an external laser are investigating the possibility to work with superconducting machines such as FLASH and XFEL which could reach repetition rates of 1 MHz and 4.5 MHz respectively.

A system of an oscillator-amplifier has been studied in the past [8–11] and more recently as a high-gain oscillator with time-dependent three-dimensional simulations [12, 13]. The system was successfully studied up to the third harmonic of the initial frequency and, in all cases, the process was starting by amplifying the initial shot noise. It should be noted that since the initial studies the mirror and laser technology have been improved and at the same time, the simulation codes

have been further developed allowing a more systematic and detailed study.

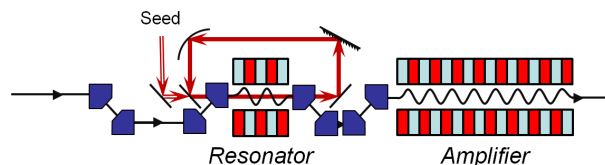


Figure 1: A possible design for the implementation of an HHHG seeded Oscillator-Amplifier.

THE LAYOUT

High-Gain Harmonic Generation [14] is a seeding scheme that is normally realized in a single-stage. In this process, the electron beam energy is modulated with a seed laser in the modulator, which is an undulator tuned to be resonant with the frequency of the seed laser. The energy modulation is converted into a density modulation in a dispersive section of a longitudinal dispersion R_{56} . After achieving the required density modulation for the desired harmonic of the seed laser, the electrons enter the radiator which is tuned to be resonant with the chosen harmonic of the seed laser. This scheme is aiming at fully coherent FEL radiation.

The layout under study is shown in Fig. 1. The process of a seeded oscillator-based HHHG, which will be referred to as a "multi-pass HHHG" in this contribution, is following the same principles of a "single-pass HHHG". The electron and the laser beam interact along the modulator to achieve energy modulation. Even though the energy modulation required can be achieved in a short distance, such as 2 gain lengths [14], in this case we use a longer undulator to achieve higher gain and compensate for the cavity losses. The radiation generated in one pass along the modulator is following the optical elements of the cavity and is redirected back to the beginning of the modulator for the next pass. The length of the cavity must be such that the roundtrip time of the radiation after travelling one time within the cavity is synchronised with the bunch separation. The cavity can in principle consist of simple transportation mirrors. Additionally, a monochromator (grating) and a focusing mirror can be added. Diagnostics could also be installed along this photon beamline for further control. The electron beam, after leaving the modulator, is guided to the next section through the bunching chicane. Finally, it generates radiation at a harmonic of the modulator wavelength in the amplifier.

In our studied cases, the FEL process starts with a seed laser of 300 nm or 50 nm. For the ultraviolet (UV) seed laser, a regular seed laser could be used to initiate the process,

* georgia.paraskaki@desy.de

while for the 50 nm an HHG source can be chosen [15]. The target harmonic for the simulations presented is the 10th, therefore, the output wavelengths are 30 nm and 5 nm for the 300 nm and 50 nm seed laser, respectively.

SIMULATIONS

All simulations are performed with Genesis 1.3 version 4 in a time-dependent mode [16]. The simulation parameters are presented in Table 1. The field manipulation is done with Ocelot [17]. For the simulations, a fresh electron bunch is used along with an input seed laser for the first pass. At the end of the modulator, the field distribution is saved and the electron bunch continues in Genesis and travels in the chicane and later in the amplifier. The manipulated field file is loaded into Genesis for the next pass in the modulator in which it overlaps with a fresh bunch. Ocelot can be used, among other functions, to implement the slippage effect, monochromatize, focus, propagate and diagnose the field in each pass. In the simulations presented here, the field is only shifted longitudinally to simulate the slippage effect and its amplitude is reduced to include the intracavity losses.

Table 1: Simulation Parameters

Electron beam		
Energy	750 MeV	1350 MeV
Unc. energy spread	120 keV	120 keV
Peak current	1 kA (Flat-top)	1 kA (Flat-top)
Seed laser		
Wavelength	300 nm	50 nm
Input power	10 MW	80 MW
Chicane		
R_{56}	-32 μm	-12 μm

Results at 300 nm Modulator and 30 nm Amplifier

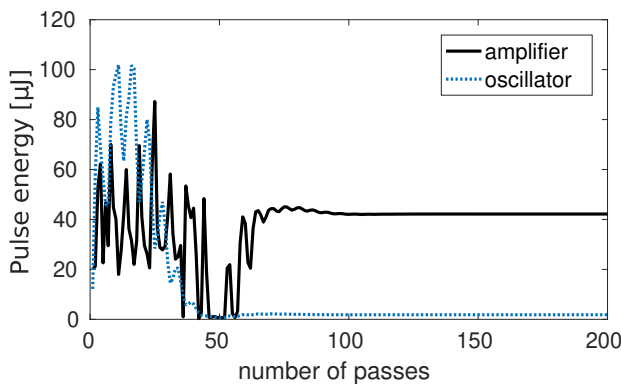


Figure 2: Multi-pass HHG with a 300 nm-wavelength seed laser with a target final wavelength of 30 nm. Comparison of pulse energy evolution at the end of the modulator and at the amplifier as a number of passes.

The simulations start with a 300 nm-wavelength seed laser of 10 MW peak power which is used only for the first pass. The electron beam energy is 750 MeV and we have assumed resonator losses of 43% per roundtrip. In Fig. 2 we see the pulse energy at the end of the modulator and the end of a 10.3 m long amplifier for 200 passes. One can see that for the first 70 passes the energy follows some oscillations before it finally stabilizes and then, the optimized R_{56} enables a clean output spectrum as can be seen in Fig. 3a. The start-up process is currently under study. The calculated FWHM spectra bandwidth is $3.8 \cdot 10^{-3}$ for a final 10 fs FWHM photon pulse.

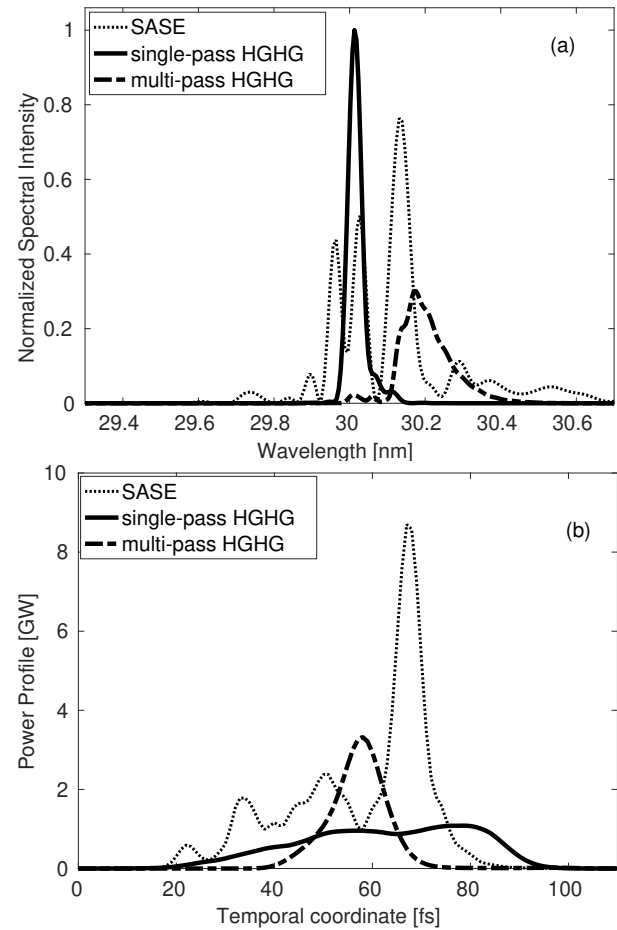


Figure 3: (a) Spectra comparison for a target wavelength of 30 nm with the same initial parameters and lattice. In (b) we compare the output power profile for the same cases.

Based on the calculated energy modulation and bunching induced at the end of the chicane after stabilization, we have performed a single-pass HHG simulation. The initial parameters are the same and one can see the calculated spectrum of the simulated single-pass HHG in Fig. 3a. The calculated FWHM bandwidth in this case is $1.2 \cdot 10^{-3}$ for a final 47 fs FWHM pulse. It should be noted that the radiation pulse in the oscillator is getting shorter due to the slippage effect until it stabilizes. This shortening of the pulse duration is leading to the bandwidth broadening in the

frequency domain. Finally, in the same figure, we present the optimized SASE spectrum simulated with a 2.5 kA peak current electron bunch and at optimal position along the amplifier. In Fig. 3b we show the final power profiles in the amplifier. For the multi-pass HGHG simulation, we observe that the peak power exceeds 3 GW, but the pulse duration is considerably shorter even though the process starts with the same seed laser duration as the single-pass HGHG.

Results at 50 nm Modulator and 5 nm Amplifier

For this working point, a 50 nm-wavelength seed laser of 80 MW peak power is used for the first pass and an electron beam energy of 1350 MeV. The system is studied for 200 passes. In this case, the gain length is longer and therefore the amplification per pass is lower, the tolerances are tighter for the bunching and a dispersive section of a lower longitudinal dispersion is required. In addition, the losses in the cavity at this wavelength are higher. In this preliminary study, we assume 50% roundtrip losses.

In Fig. 4 we see the pulse energy at the end of the modulator and the end of a 20 m long amplifier. The energy at the oscillator, and therefore at the amplifier, is stabilized after roughly 80 passes. Finally, in Fig. 5a we see the output spectrum at the 159th pass. The calculated FWHM bandwidth is $1.1 \cdot 10^{-3}$ for an 8 fs final radiation pulse duration. Even though the peak pulse power exceeds 2 GW as it is shown in Fig. 5b, the energy remains on average at $19.9 \mu\text{J}$ because of the pulse shortening in the cavity and hence, in the amplifier.

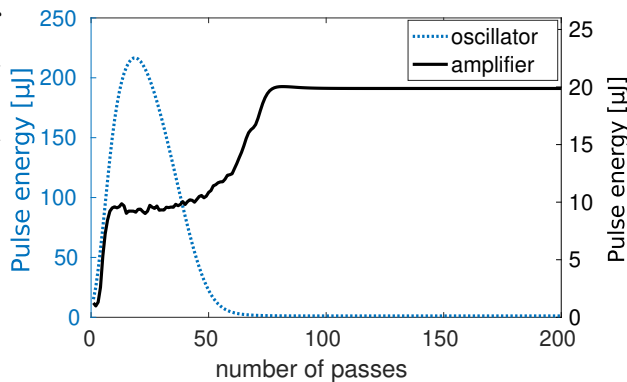


Figure 4: Multi-pass HGHG with a 50 nm-wavelength seed laser with target final wavelength of 5 nm. Comparison of pulse energy evolution at the end of the modulator and at the amplifier as a number of passes.

In addition, we show in Fig. 5a the final spectrum for a single-pass HGHG optimized for the modulation amplitude achieved in the multi-pass HGHG after stabilization and the same initial electron beam parameters. The calculated FWHM bandwidth in this case is $1.48 \cdot 10^{-4}$ for a final 75 fs pulse. Similar to the 30 nm case, we see that the short pulses in the cavity are leading to a broadening of the bandwidth. Finally, the optimized SASE spectrum is shown in the same figure for an electron bunch of 2.5 kA peak current at saturation, for completeness.

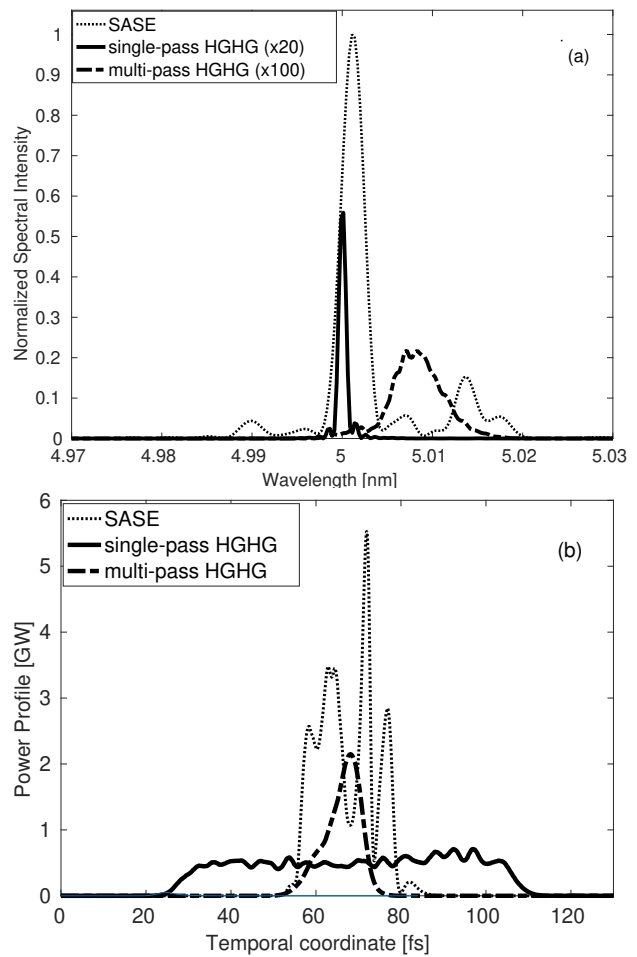


Figure 5: (a) Spectra comparison for a target wavelength of 5 nm for a SASE, a single-pass, and a multi-pass HGHG. Notice that the spectra of HGHG have been rescaled. In (b) we compare the output power profile for the same cases.

OUTLOOK

In this contribution, we showed simulation results for a multi-pass HGHG with target wavelengths of 30 nm and 5 nm. Further studies on the startup process and on the control of the field in the resonator are underway. These include the study of the focusing effect, the impact of monochromatization and the control of the duration of the radiation pulses in the resonator. This optimization aims at the improvement of the start-up process to reach a stationary state after a few passes and the improvement of the spectral properties. In addition, for the 5 nm case, a study of the same layout for higher losses is planned. Finally, the study of a multi-pass EEHG is foreseen. Further options and considerations on alternative layouts can be found in [18].

ACKNOWLEDGMENTS

I would like to thank Mykola Veremchuk for adding a Genesis 4 radiation field writing procedure to OCELOT.

REFERENCES

- [1] P. J. Neyman, J. Blau, K. R. W. B. Colson, S. C. Gottschalk, and A. M. M. Todd, “Free Electron Lasers in 2017”, in *Proc. 38th Int. Free Electron Laser Conf. (FEL'17)*, Santa Fe, NM, USA, Aug. 2017, paper MOP066, pp. 204–209. doi:10.18429/JACoW-FEL2017-MOP066
- [2] P. Ribič *et al.*, “Coherent Soft X-ray pulses from an Echo-Enabled Harmonic Generation Free-Electron Laser”, *Nature Photonics*, vol. 13, p. 555–561, 2019. doi:10.1038/s41566-019-0427-1
- [3] Chao Feng *et al.*, “Coherent extreme ultraviolet free-electron laser with echo-enabled harmonic generation”, *Phys. Rev. Accel. Beams*, vol. 22, p. 050703, 2019. doi:10.1103/PhysRevAccelBeams.22.050703
- [4] K. E. Hacker *et al.*, “First Lasing of an HGHG Seeded FEL at FLASH”, in *Proc. 37th Int. Free Electron Laser Conf. (FEL'15)*, Daejeon, Korea, Aug. 2015, paper WEP030, pp. 646–649.
- [5] J. Amann *et al.*, “Demonstration of self-seeding in a hard-x-ray free-electron laser”, *Nature Photonics*, vol. 6, pp. 693–698, 2012. doi:10.1038/nphoton.2012.180
- [6] J. N. Galayda, “The New LCLS-II Project : Status and Challenges”, in *Proc. 27th Linear Accelerator Conf. (LINAC'14)*, Geneva, Switzerland, Aug.-Sep. 2014, paper TUIOA04, pp. 404–408.
- [7] Z. T. Zhao, D. Wang, Z. H. Yang, and L. Yin, “SCLF: An 8-GeV CW SCRF Linac-Based X-Ray FEL Facility in Shanghai”, in *Proc. 38th Int. Free Electron Laser Conf. (FEL'17)*, Santa Fe, NM, USA, Aug. 2017, pp. 182–184. doi:10.18429/JACoW-FEL2017-MOP055
- [8] G. Dattoli, L. Giannessi, and P.L. Ottaviani. “MOPA optical klystron FELs and coherent harmonic generation”, *Nuclear Instruments and Methods in Physics Research Section A: Accelerators, Spectrometers, Detectors and Associated Equipment*, vol. 507, pp. 26–30, 2003. doi:10.1016/S0168-9002(03)00828-3
- [9] G. Dattoli, L. Giannessi, and P. L. Ottaviani, “Oscillator-amplifier free electron laser devices with stable output power”, *Journal of Applied Physics*, vol. 95(6), pp. 3211–3216, 2004. <https://doi.org/10.1063/1.1645649>
- [10] G. Dattoli, B. Faatz, L. Giannessi, and P.L. Ottaviani, “The tandem FEL dynamic behavior”, *IEEE Journal of Quantum Electronics*, vol. 31, p. 1584–1590, 1995. doi:10.1109/3.400416
- [11] B. Faatz *et al.*, “Regenerative FEL amplifier at the TESLA test facility at DESY”, *Nuclear Instruments and Methods in Physics Research Section A: Accelerators, Spectrometers, Detectors and Associated Equipment*, vol. 429(1-3), pp. 424–428, 1999. doi:10.1016/S0168-9002(99)00123-0
- [12] G. Penco *et al.* “Optical Klystron Enhancement to Self-Amplified Spontaneous Emission at FERMI”, *Nature Photonics*, vol. 4, p. 15, 2017. doi:10.3390/photonics4010015
- [13] H. P. Freund, D. C. Nguyen, P. A. Sprangle, and P. J. M. van der Slot, “Three-dimensional, time-dependent simulation of a regenerative amplifier free-electron laser”, *Phys. Rev. ST Accel. Beams*, vol. 16, p. 010707, Jan 2013. doi:10.1103/PhysRevSTAB.16.010707
- [14] Li Hua Yu, Juhao Wu, “Theory of high gain harmonic generation: an analytical estimate”, *Nuclear Instruments and Methods in Physics Research Section A: Accelerators, Spectrometers, Detectors and Associated Equipment*, vol. 483, p. 493–498, 2002. doi:10.1016/S0168-9002(02)00368-6
- [15] E. Takahashi *et al.*, “Generation of 10-mJ Coherent Extreme-Ultraviolet Light by Use of High-Order Harmonics”, *Opt.Lett.*, vol. 27, p. 1920, 2002. doi:10.1364/OL.27.001920
- [16] S. Reiche, “GENESIS 1.3: a fully 3D Time-Dependent FEL Simulation Code”, *Nucl. Instrum. and Methods Phys. Res. A*, vol. 429, p. 243, 1999, doi:10.1016/S0168-9002(99)00114-X
- [17] S. Serkez, S. Tomin, “OCELOT: a versatile computational tool for light sources”, 2016–present; <https://github.com/ocelot-collab/ocelot>
- [18] S. Ackermann *et al.*, “High Repetition-Rate Seeding Schemes Using a Resonator-Amplifier Setup”, presented at the 39th Int. Free Electron Laser Conf. (FEL'19), Hamburg, Germany, Aug. 2019, paper TUP073, this conference.

IMPACT OF ELECTRON BEAM ENERGY CHIRP ON SEEDED FELS

G. Paraskaki*, S. Ackermann, B. Faatz, V. Grattoni,
C. Lechner, J. Zemella, DESY, Hamburg, Germany
W. Hillert, University of Hamburg, Hamburg, Germany

Abstract

Seeded FELs enable the generation of fully coherent, transform-limited and high brightness FEL pulses, as the start-up process is driven by an external coherent light pulse. During the design process of such FELs, it is important to choose carefully the electron beam parameters to guarantee high performance. One of those parameters is the electron beam energy chirp. In this contribution, we show simulation results and we discuss how the electron beam energy chirp affects the final spectrum.

INTRODUCTION

It is a quite common choice to study seeding techniques with an electron beam that has a relatively constant current, as far as this can be realistic, and is unchirped with a temporally constant energy. An energy chirp would possibly degrade the performance of the FEL since it might affect the density modulation efficiency and in addition, it shifts the central wavelength of the output radiation [1]. At the same time, in SASE FELs, it has been shown that a slightly positive chirp may be beneficial [2]. In seeded FELs, the energy chirp has already been proposed as a method to distinguish the signal of Echo-Enabled Harmonic Generation (EEHG) from High-gain Harmonic Generation (HG) for low harmonics [3], and as a method to produce two-color lasing as well [4]. In addition, it can be used as an FEL-chirp control technique [5, 6], since there is a correlation between the energy of the electron beam and the frequency of the FEL pulse that is defined through the resonance condition. Finally, the performance of EEHG with a chirped electron beam has been evaluated [7] for future designs.

In this contribution, we study the impact of a linear electron beam energy chirp of variable amplitude and sign on the HG-seeded FEL. More specifically, the wavelength shift and the impact on intensity and bandwidth are discussed and presented with simulation results. The optimum working points are determined and their stability is compared under an electron beam energy jitter and timing jitter study.

IMPACT ON HG

Wavelength Shift

The essential components for HG are a modulator in which the seed laser interacts with the electron beam and induces electron beam energy modulation, a dispersive section in which the energy modulation is converted into density modulation and a radiator that is resonant with the wavelength of the wanted harmonic of the seed laser [8]. For

a better understanding of the effect of an energy chirp on the dispersive section that is used for the creation of density modulation in HG, it is useful to recall the process of bunch compressors. Bunch compressors (BCs) are sections with longitudinal dispersion R_{56} that are used to compress an electron beam temporally, usually to achieve a higher peak current and shorter FEL pulses. For an effective compression, the electron beam needs to travel in the dispersive section with, for instance, a linear energy chirp $h = \frac{dE}{ds} \frac{1}{E}$. This can be expressed mathematically as:

$$\delta = \delta_0 + hs_i + h's_i^2 + O(s^3),$$

where δ is the relative energy offset, δ_0 represents the uncorrelated energy offset, s_i is the initial longitudinal intrabunch coordinate within the bunch and $h' = \frac{d^2E}{ds^2} \frac{1}{E}$. A chirp with a positive sign represents an electron bunch with a head of higher energy and a tail of lower energy. In this contribution, we restrict ourselves to a linear energy chirp h . An electron of an energy offset δ would exit a BC of a longitudinal dispersion R_{56} with a new longitudinal coordinate [9]:

$$s_f = s_i + R_{56}\delta = s_i(1 + hR_{56}) + R_{56}\delta_0.$$

Therefore, after differentiating, we get the linear compression factor:

$$C_{BC} = \frac{ds_i}{ds_f} = (1 + h \cdot R_{56})^{-1}. \quad (1)$$

In the case of HG, the dispersive section converts the energy modulation to density modulation by forming microbunches with a longitudinal periodicity that is equal to the wavelength of the seed laser. However, if the electron beam is chirped, the periodicity will be affected by the compression/decompression that takes place due to Eq. (1). This is illustrated schematically in Fig. 1. The compression factor of the wavelength of the FEL radiation would be [10]:

$$C_{HGHG} = \frac{\lambda_{HGHG}}{\lambda'_{HGHG}} = (1 + H \cdot B)^{-1}, \quad (2)$$

where $H \cdot B \propto h \cdot R_{56}$ [10]. This result is analogous to the derived formula of Eq. (1) for bunch compression.

* georgia.paraskaki@desy.de

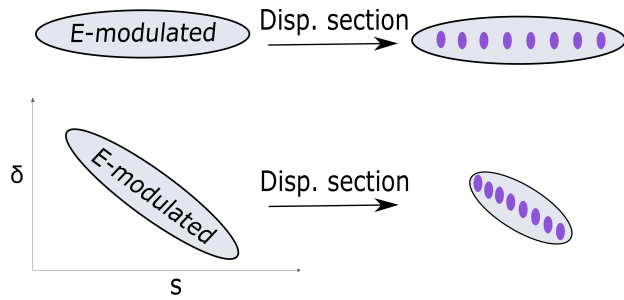


Figure 1: Impact of a dispersive section on the longitudinal phase space distribution of an energy modulated electron beam. In both cases, microbunches are formed. However, when the energy-modulated electron beam is chirped, the distance between the microbunches is altered.

SIMULATION RESULTS

sFLASH [11] is an experiment at FLASH in Hamburg and it is dedicated to seeding development study. The simulations were performed with Genesis 1.3 [12] version 4 in a time-dependent mode using typical sFLASH parameters, shown in Table 1.

Table 1: Simulation Parameters

Electron beam	
Energy	685 MeV
Uncorrelated energy spread	50 keV
Peak current	500 A (Gaussian)
Bunch length	60 μm (rms)
Seed laser	
Wavelength	266 nm
Peak Power	40 MW (Gaussian)
Laser pulse length	20 μm (rms)

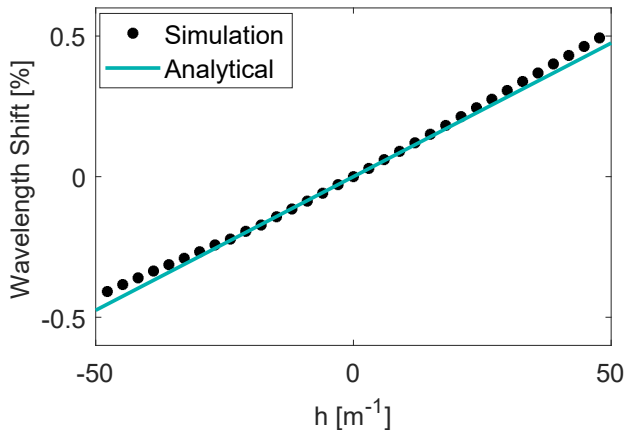


Figure 2: Impact of a linear energy chirp on the central wavelength of the output FEL spectrum of HGFG.

In Fig. 2 the effect of a linear energy chirp on the the final wavelength is shown. The simulated results of the final FEL spectrum are compared to the analytical estimation (Eq.2).

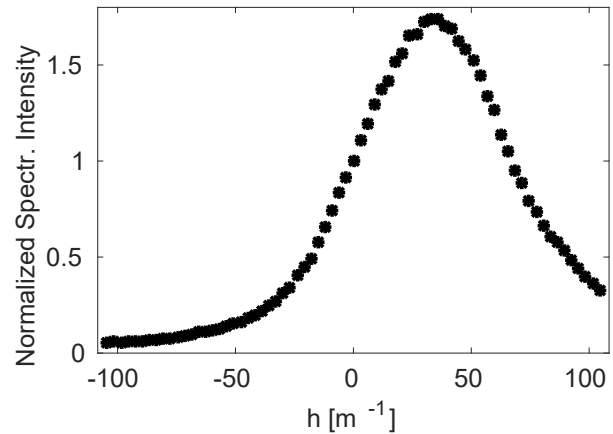


Figure 3: Impact of the electron beam energy chirp on the peak spectral intensity of the output spectrum. The intensity is normalized to the one of the unchirped electron beam. The $h = 0 \text{ m}^{-1}$ is defined with the resonance condition.

According to Fig. 3, a peak spectral intensity is reached for a positive chirp of 33 m^{-1} . However, one should notice that the peak spectral intensity can be optimized by optimizing the undulator parameter K of the radiator for each chirp to achieve optimal performance. In the simulations presented in this paper, we have used the undulator parameter calculated with the resonance condition for the nominal energy. Unlike the wavelength shift, the behaviour of the intensity is not symmetric for different signs of chirps, with a clear preference in positive chirps.

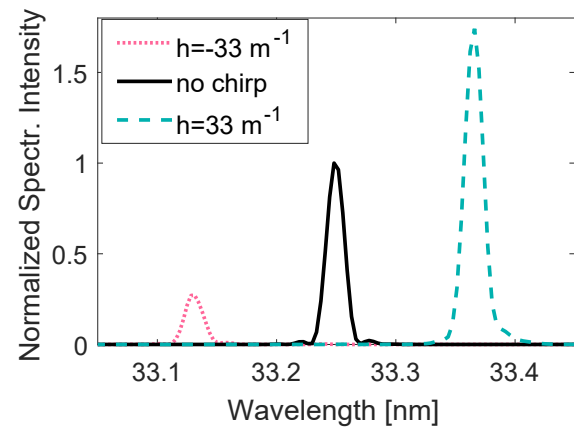


Figure 4: Impact of an initial electron beam energy chirp on the output spectrum in comparison with the spectrum generated with an unchirped electron beam. The intensity is normalized to the one of the unchirped electron beam.

For selected chirps out of this scan, the output spectra are shown in Fig. 4. The calculated bandwidth is not varying significantly, with the positive-chirped electron beam having

less than 1% broader bandwidth and the negative-chirped electron beam having roughly 7.7% broader bandwidth than the unchirped case. The FWHM bandwidth of unchirped electron beam is $4.41 \cdot 10^{-4}$. In the same figure, one can see the wavelength shift as well.

Jitter Study

Additional simulations were performed to investigate whether the performance of chirped electron beams is sensitive to electron beam energy jitter and timing jitter between the seed laser and the electron beam. For the simulations we assumed a maximum timing offset of ± 100 fs and a maximum beam energy offset of $\pm 0.2\%$. The working points which are studied and compared are 1) with an unchirped electron beam and 2) with a chirp of 33 m^{-1} .

Timing jitter In Fig. 5 the timing jitter sensitivity of the two different working points is shown. It is concluded that an electron beam with an energy chirp leads to a peak spectral intensity which is more stable to timing jitter within a small range of jitter (± 20 fs). However, for larger deviations (more than ± 50 fs) the unchirped electron beam is affected less by the jitter. In both cases, we have optimal performance for the nominal case in which the peak current of the electron beam overlaps longitudinally with the peak power of the seed laser in the middle of the modulator. Finally, we notice that both curves are asymmetric; the unchirped electron beam has a better performance in terms of peak spectral intensity when the seed laser is falling behind, than when it is ahead compared to the nominal case. The chirped electron beam leads to increased spectral intensity for positive timing offset, which means that the seed laser is energy-modulating a part of the electron beam that has higher than the nominal energy.

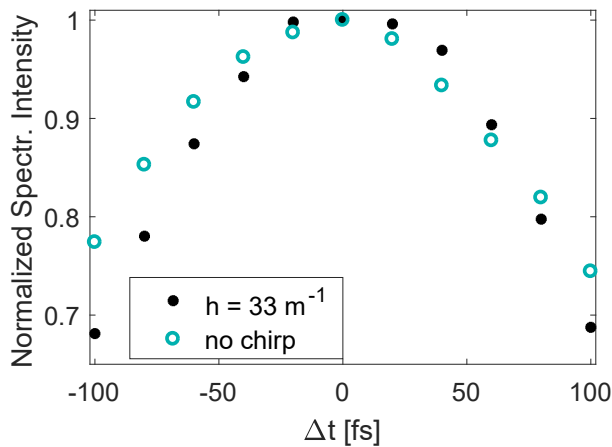


Figure 5: Impact of timing jitter on the intensity of the output spectrum for a chirped and an unchirped electron beam. We assume that for $\Delta t = 0$ the peak current of the electron beam overlaps with the peak power of the seed laser in the middle of the modulator. The intensity is normalized the maximum intensity for each chirp.

Electron beam energy jitter The energy jitter was simulated as a constant additional term applied to all particles over the electron bunch (see Fig. 6). Similarly to the timing jitter, for small deviations the chirped electron beam seems to be more stable and for larger deviations, the unchirped electron beam is lead to considerably lower performance. It should be noted that by fine-tuning the undulator parameter of the radiator one can optimize each working point, therefore we are only interested in the stability of these working points.

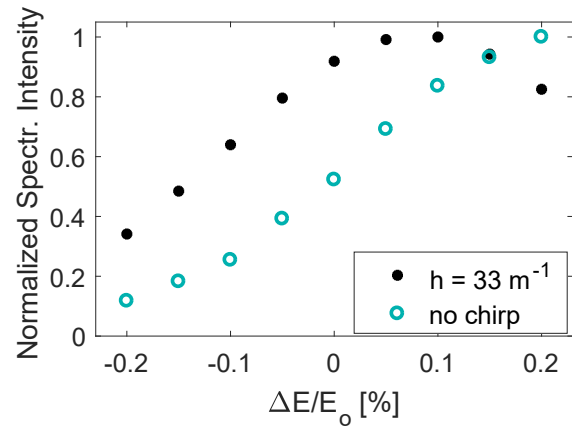


Figure 6: Impact of energy jitter on the peak intensity of the output spectrum for a chirped and an unchirped electron beam. We assume that for $\Delta E/E_0 = 0$ the energy is the nominal one. The intensity is normalized to the maximum one for each chirp.

DISCUSSION

It was shown that the effect of energy chirp for HGHG is mainly imprinted as a wavelength shift and as an intensity increase/decrease, while the impact on the bandwidth is negligible on the selected spectra studied. It was observed in the simulations that the optimum intensity is appearing for a chirp $h = 33 \text{ m}^{-1}$ with which one can gain in peak spectral intensity. A fine tuning of the resonant wavelength of the radiator can increase the performance of the working points simulated here. The timing jitter and the electron beam energy jitter study showed that the chirped electron beam that was studied offers more stability in the output spectrum for small jitter ranges in terms of peak spectral intensity. However, one should take into account that this advantage is coming with a shifted in wavelength spectrum. It is concluded that given the needs and the goals of an HGHG experiment one can use chirped electron beams as well without sacrificing the performance of the FEL if the wavelength shift can be tolerated. Finally, for the simulated setup a positive chirp is preferable.

ACKNOWLEDGMENTS

I would like to thank Sven Reiche for his support on issues regarding Genesis 4.

REFERENCES

- [1] Guanglei Wang, Chao Feng, Haixiao Deng, Tong Zhang, and Dong Wang, “Beam energy chirp effects in seeded free-electron lasers”, *Nuclear Instruments and Methods in Physics Research Section A Accelerators Spectrometers Detectors and Associated Equipment*, vol. 753, pp. 56–60, 2014. doi:10.1016/j.nima.2014.03.015
- [2] E. L. Saldin, E. A. Schneidmiller, and M. V. Yurkov, “Self-amplified spontaneous emission FEL with energy-chirped electron beam and its application for generation of attosecond x-ray pulses”, *Phys. Rev. ST Accel. Beams*, vol. 9, p. 050702, 2006. doi:10.1103/PhysRevSTAB.9.050702
- [3] Z. T. Zhao *et al.*, “First lasing of an echo-enabled harmonic generation free-electron laser”, *Nature Photonics*, vol. 6, p. 360–363, 2012. doi:10.1038/nphoton.2012.105
- [4] B. W. Garcia *et al.*, “Echo-Enabled Harmonic Generation Results with Energy Chirp”, in *Proc. 38th Int. Free Electron Laser Conf. (FEL’17)*, Santa Fe, NM, USA, Aug. 2017, pp. 64–67. doi:10.18429/JACoW-FEL2017-MOP017
- [5] V. Grattoni *et al.*, “Control of FEL Radiation Properties by Tailoring the Seed Pulses”, in *Proc. 9th Int. Particle Accelerator Conf. (IPAC’18)*, Vancouver, Canada, Apr.-May 2018, pp. 1444–1447. doi:10.18429/JACoW-IPAC2018-TUPMF078
- [6] J. Wu *et al.*, “Interplay of the Chirps and Chirped Pulse Compression in a High-Gain Seeded Free-Electron Laser”, *J. Opt. Soc. Am. B*, vol. 24, no. 3, p. 484, 2007. doi:10.1364/JOSAB.24.000484
- [7] M. A. Pop and S. Werin, “Considerations on Implementing EEHG with a Strong Linear Chirp”, in *Proc. 10th Int. Particle Accelerator Conf. (IPAC’19)*, Melbourne, Australia, May 2019, pp. 1830–1832. doi:10.18429/JACoW-IPAC2019-TUPRB071
- [8] Li Hua Yu *et al.*, “First ultraviolet high-gain harmonic-generation free-electron laser”, *Physical Review Letters*, vol. 91, p. 074801, 2003. doi:10.1103/PhysRevLett.91.074801
- [9] Yipeng Sun, Paul Emma, Tor Raubenheimer, and Juhao Wu, “X-band rf driven free electron laser driver with optics linearization”, *Physical Review Special Topics - Accelerators and Beams*, vol. 17, p. 074801, 2014. doi:10.1103/PhysRevSTAB.17.110703
- [10] C. Feng, D. Wang, and Z. T. Zhao, “Study of the Energy Chirp Effects on Seeded FEL Schemes at SDUV-FEL”, in *Proc. 3rd Int. Particle Accelerator Conf. (IPAC’12)*, New Orleans, LA, USA, May 2012, paper TUPPP056, pp. 1724–1726.
- [11] C. Lechner *et al.*, “Status of the sFLASH Experiment”, in *Proc. 9th Int. Particle Accelerator Conf. (IPAC’18)*, Vancouver, Canada, Apr.-May 2018, pp. 1471–1473. doi:10.18429/JACoW-IPAC2018-TUPMF085
- [12] S. Reiche, “GENESIS 1.3: a fully 3D Time-Dependent FEL Simulation Code”, *Nucl. Instrum. and Methods Phys. Res. A*, vol. 429, p. 243, 1999. doi:10.1016/S0168-9002(99)00114-X

STATUS OF THE HARD X-RAY SELF-SEEDING SETUP AT THE EUROPEAN XFEL

G. Geloni, X. Dong, S. Karabekyan, D. La Civita, L. Samoylova, S. Serkez, R. Shayduk,
 H. Sinn, V. Sleziona, M. Vannoni, M. Yakopov, European XFEL, Schenefeld, Germany
 J. Anton, S. Kearney and D. Shu, ANL, Argonne, Illinois, United States

W. Decking, V. Kocharyan, S. Liu, E. Negodin, E. Saldin, T. Wohlenberg, DESY, Hamburg, Germany
 V. D. Blank, S. Terentiev, TISNCM, Troitsk, Russia

Abstract

A Hard X-Ray Self-Seeding (HXRSS) setup will be soon commissioned at the European XFEL. It relies on a two-chicanes scheme to deal, in particular, with the high pulse repetition rate of the facility. In this contribution we review the physics choices made at the design stage and the expected performance of the setup. We will also focus on the description of the hardware installations made at the SASE2 line of the European XFEL.

INTRODUCTION AND SETUP

Single crystal monochromator Hard X-ray Self-Seeding (HXRSS) [1, 2] allows for an increased spectral density and longitudinal coherence at hard X-ray SASE FELs by means of active spectral filtering. This capability is now being enabled at the European XFEL, where the compatibility with the high-repetition rate in burst mode is important and heat-loading of the crystals needs to be dealt with. This issue can be mitigated with the introduction of a two-chicane HXRSS setup, Fig. 1. As shown in [3], and reviewed here, a two-chicane solution allows for an increased Signal-to-Noise Ratio (SNR), the signal being the seeded FEL pulse, and the noise being, in this case, the underlying shot-noise amplification. The natural exploitation of this increased ratio is for decreasing the crystals heat loading, while keeping the seed signal large enough for the setup to work. One should consider that there are two sources of heat-load on the crystals: one is related to radiation around the undulator resonant frequency (both SASE and seeded signals), which tends to heat-up the crystal as illustrated in Fig. 2, while the second one is related to the broadband spontaneous emission. One always needs to confront with the spontaneous radiation (SR) heat-load, which is always present and is nearly independent of the fundamental tune. However, a higher

SNR of the 2-stage self-seeding can be used to decrease the FEL power level needed at the crystal position, and therefore the crystal heat-load caused by FEL radiation. Since the heat-load due to both FEL and SR heavily depends on the wavelength, the relative importance of the two contributions also depends on the wavelength.

In this paper we will first discuss simulation results relying on start-to-end simulations of the electron beam that drives the FEL process. We stress that a comparison between the simulated electron beam properties and those achieved in reality is important. First, to precisely foresee the actual performance of the HXRSS setup at the European XFEL and, second, to optimize performance by changing the electron beam properties. This, however, will require an ad-hoc experimental measurements campaign and is beyond the scope of this work.

Further on, based on simulations we will show the nominal performance of the HXRSS setup designed for the European XFEL, which is expected to operate from below 5 keV (theoretically down to 3 keV, with probable limitations due to heat-loading) up to 14.4 keV (and above, if one considers the option of tuning part of the radiator to a harmonic of the fundamental [4]). Finally, we will discuss the hardware implementation of the setup at the European XFEL.

SIMULATIONS

We first consider an upper target for seeding of a photon energy of 14.4 keV, to be generated at the SASE2 undulator at the European XFEL. SASE2 consists of 35 segments of 5 m magnetic length each, with a period of 40 mm, and we assume a 100 pC beam optimized for seeding, as described in [3]. The 14.4 keV energy point is the most demanding in terms of electron beam quality and necessary undulator length, and its analysis allows to optimize the chicane

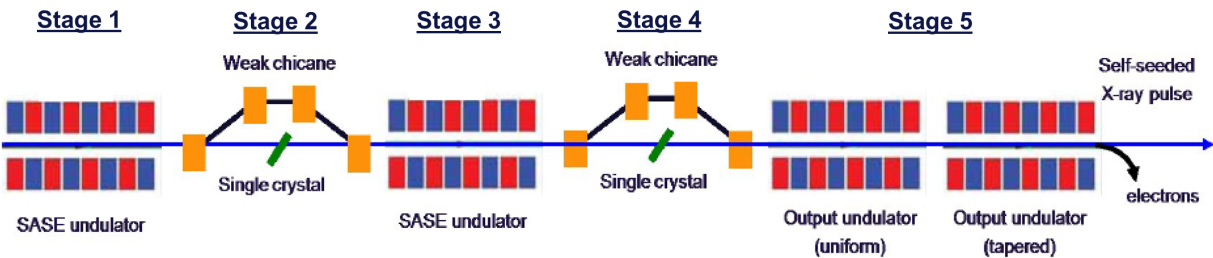


Figure 1: Sketch of the two-chicane HXRSS at the European XFEL.

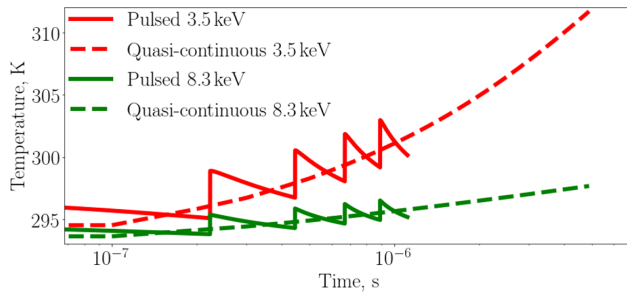


Figure 2: Calculations of peak temperatures at 3.5 keV for the case of 3 μ J FEL incident power level, using impulsive heating model and treating each pulse in the train individually. Dashed lines correspond to the quasi-continuous case.

placement in the overall setup. We proceeded by optimizing the output of a double-chicane HXRSS setup at saturation in the case when the two undulator stages preceding the magnetic chicanes are formed by 7 undulator segments (we call this case “7+7”), by 8 undulator segments (we call this case “8+8”) and by 9 undulator segments (we call this case “9+9”). For these simulations we used 100 μ m thick diamond crystals and a symmetric C400 reflection. In Fig. 3 we

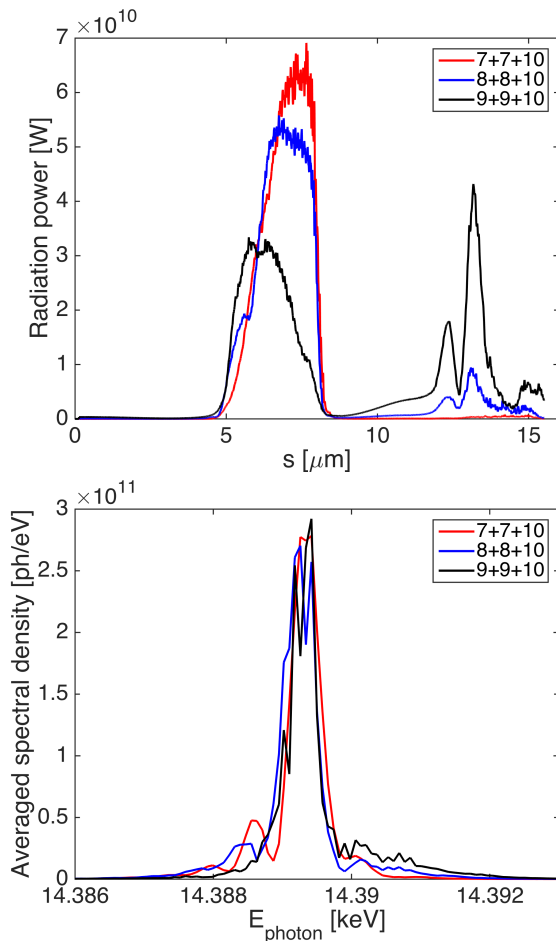


Figure 3: Radiation power (upper plot) and averaged spectral density (lower plot) at saturation after 10 undulators, for different configurations “7 + 7”, “8 + 8” and “9 + 9”. All plots are the results of an ensemble average over 10 events.

plot the radiation power and the averaged spectral density at the exit of the self-seeding setup at saturation, i.e. after the two seeding chicanes followed by 10 undulator segments for the three cases “7 + 7”, “8 + 8” and “9 + 9”. All plots refer to an ensemble average over 10 events. The “7 + 7” option is characterized by the highest radiation power, and in the “8 + 8” and “9 + 9” scenarios, the pre-pulses from the third stage are large compared to the final twice-filtered pulse. Moreover, looking at the spatially-averaged spectral density one sees that the maximum value is comparable in all cases. The conclusion from this analysis is that the “7 + 7” case is the best performing one: by increasing the length of the first undulator part the signal can be increased at the expenses of a larger incident power on the crystal, and of a larger impact on the electron beam quality. As we increase the length of the setups from 7 + 7 to 9 + 9 the SNR increases but the electron beam quality deteriorates, and the output flux decreases (while a large pre-pulse appears). An analysis of detrimental effects due to energy spread and emittance beyond the nominal level [3] shows that the 7 + 7 setup should perform within about 80% of the nominal level for emittance increases up to 40% (from a nominal value below 0.4 mm mrad) and energy spread increase of about 500% (from a nominal value of about 2 MeV). In order to account for deviations from the nominal FEL performance, we suggested to add one extra segment in each undulator part, and to configure the double-chicane HXRSS setup at the European XFEL as in the “8+8” configuration, at least during the commissioning period.

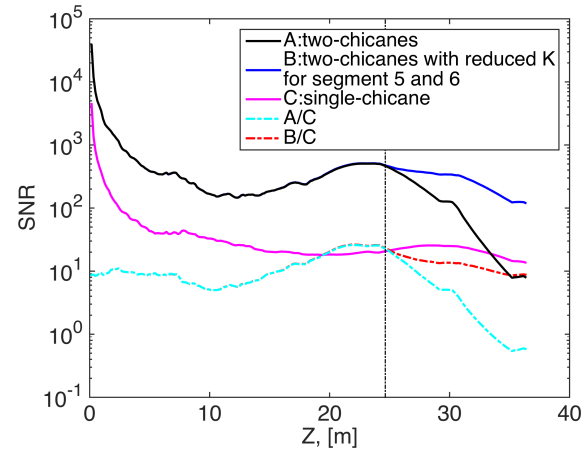


Figure 4: Signal-to-noise ratio at low photon energy (3.5 keV) for a 4 + 4 two-chicane setup, compared to the case of a single-chicane setup, with and without retuning of the undulator parameter. The vertical line indicates the point where K is changed, see text.

Analysis of a low photon-energy point around 3.5 keV [3] showed that a 4 + 4 setup is best at these energies, and may yield an estimated spectral flux of $6 \cdot 10^{10}$ ph/eV per pulse around saturation, corresponding to a peak power of about 50 GW. Studying the low photon-energy point also allowed us to compare the evolution of the SNR of the two-chicane setup to that of a one-chicane setup, see Fig. 4, where the

SNR is calculated out of an ensemble of ten pulses. Curve (A) corresponds to the two-chicane case and curve (C) to the single-chicane setup. The ratio (A/C) along the final undulator is also shown. The SNR ratio (A/C) remains almost constant (about a factor 10) up to saturation. Note that the large values around 10^4 for the (A) curve at the beginning of the amplification process in Fig. 4 are due to a numerical effect: at the beginning of the radiator, when one starts from shot noise, there is no radiation at the very beginning of the amplification process. Finally, after saturation, the SNR ratio (A/C) drops due to the fact that the single-chicane setup saturates further downstream compared to the two-chicane setup, due to the lower seed level. One can, of course, change the value of the K undulator parameter in the two-chicane setup to keep up with the change of electron energy (B). Even a simple reduction of the value of K (without an optimized tapering profile, whose study is outside of the scope of this contribution) is enough to keep the SNR almost constant beyond the saturation point, see Fig. 14 (B and B/C), see [3] for more details.

HARDWARE INSTALLATION

The chicane design, based on H-type magnets, allows for a maximum delay of about 450 fs up to an energy of 11 GeV, and of about 180 fs for 17.5 GeV, Fig. 5, in order to provide the possibility for multi-color experiments with tunable delay, owing to the variable-gap undulators of the European XFEL. The power supply allows for steps of about 0.1 fs, thus enabling the possibility of autocorrelation measurements. The two chicanes were installed in the SASE2 tunnel during the 2018/2019 winter shutdown.

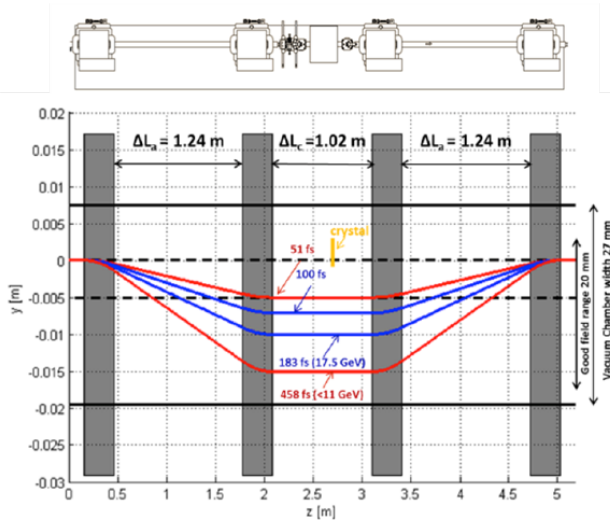


Figure 5: Sketch of the self-seeding chicane.

The vacuum chamber is sketched in Fig. 6, right. It is equipped with two windows, one at 45 degrees and one at 90 degrees with respect to the horizontal plane, in order, respectively, to observe the crystal and -via a YAG screen- to detect various crystal reflections. A monochromator consists of a flange with a main goniometer stage for pitching the

crystal, as well as X, Y and tip-tilt stages to insert the crystal and controlling the roll¹ angle Fig. 6, left. A crystal holder with two slots, Fig. 7 is mounted on the crystal positioning system. C100 and C111 cut crystals are currently lodged in the slots of both monochromators.

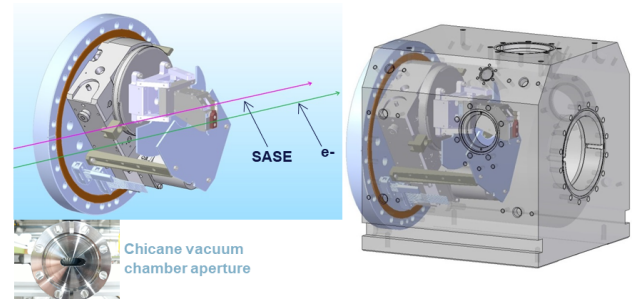


Figure 6: Monochromator flange and vacuum chamber.

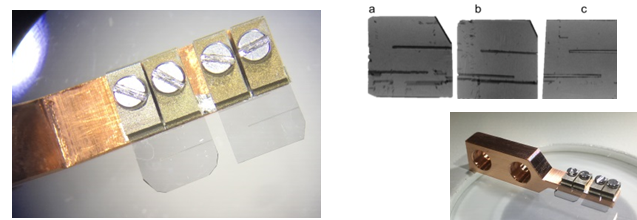


Figure 7: Crystal holder with two slots and several diamond crystals.

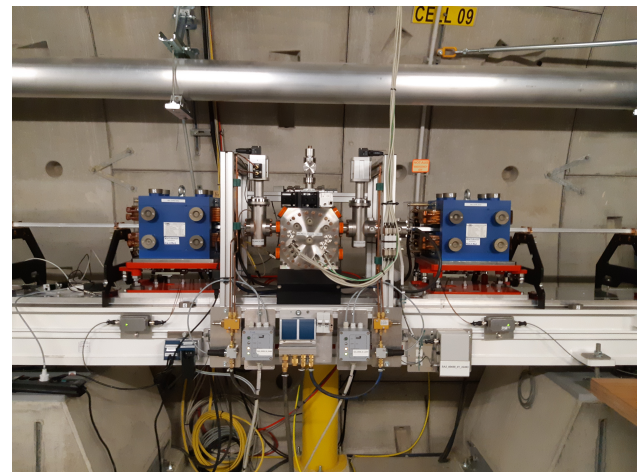


Figure 8: One of the two setups installed in the SASE2 tunnel. The beam direction is from right to left.

The monochromators were installed in Summer 2019. One of the two chicanes setup is pictured in Fig. 8.

CONCLUSIONS

A Hard X-Ray Self-Seeding (HXRSS) setup has been installed and will soon be commissioned at the European XFEL. The availability of high repetition rate X-ray pulses poses novel challenges in the setup development, compared to the choices made at other facilities, mainly crystal heat-loading and radiation-damage issues. However, high-repetition rate is expected to allow for unprecedented output

¹ Also called yaw e.g. at the LCLS, due to a different naming convention.

characteristics. From simulations, a two-chicane HXRSS setup, installed in a “8+8” configuration, was found to be optimal for the European XFEL. In this paper we discussed design and choices peculiar to the European XFEL, and we reviewed the hardware installations currently in place. Commissioning of the setup, where the HIREX spectrometer [5] will help finding the seeded signal, is expected to take place in Autumn 2019.

REFERENCES

- [1] G. Geloni, V. Kocharyan, and E. Saldin, “A novel self-seeding scheme for hard X-ray FELs”, *J. Mod. Opt.*, vol. 58, pp. 1391, Jun. 2011. doi:10.1080/09500340.2011.586473
- [2] J. Amann *et al.*, “Demonstration of self-seeding in a hard-X-ray free-electron laser”, *Nature Photonics*, vol. 6, pp. 693–698, Aug. 2012. doi:10.1038/nphoton.2012.180
- [3] S. Liu *et al.*, “Preparing for high-repetition rate hard x-ray self-seeding at the European X-ray Free Electron Laser: Challenges and opportunities”, *Phys. Rev. Accel. Beams*, vol. 22, pp. 060704, Jun. 2019. doi:10.1103/PhysRevAccelBeams.22.060704
- [4] G. Geloni, V. Kocharyan, and E. Saldin, “Extension of self-seeding to hard X-rays >10 keV as a way to increase user access at the European XFEL”, DESY 11-224, 2011. arxiv:1111.5766
- [5] N.G. Kujala *et al.*, “The High Resolution Hard X-Ray Single Shot Spectrometer (HIREX Spectrometer) Installation and Commissioning in SASE2 Beamline of the European XFEL”, presented at the FEL’19, Hamburg, Germany, Aug. 2019, paper WEP074, this conference.

HARMONIC OFF-AXIS SEEDING AT THE DELTA SHORT-PULSE SOURCE*

A. Meyer auf der Heide[†], B. Büsing, S. Khan, D. Krieg, C. Mai

Center for Synchrotron Radiation (DELTA), TU Dortmund, Dortmund, Germany

Abstract

At the 1.5-GeV synchrotron light source DELTA operated by the TU Dortmund University, a short-pulse source employs the coherent harmonic generation (CHG) scheme. Here, a laser pulse interacts with a stored electron bunch forming a microbunching structure to generate ultrashort synchrotron light pulses at harmonics of the laser wavelength. As an upgrade of the short-pulse facility, the echo-enabled harmonic generation (EEHG) scheme will be implemented, which requires a second laser-electron interaction to yield much higher harmonics compared to CHG. In a study towards twofold laser seeding, the possibility of seeding at undulator harmonics with a crossing angle between laser and electron beam was investigated.

THE DELTA SHORT-PULSE SOURCE

At DELTA, a 1.5-GeV synchrotron light source operated by the TU Dortmund University, a short-pulse source employs the coherent harmonic generation (CHG) scheme to generate ultrashort pulses in the vacuum ultraviolet (VUV) regime [1]. As depicted in Fig. 1 (top), the concept [2] is based on an interaction between an electron bunch and a co-propagating external ultrashort laser pulse in an undulator (modulator) which results in a sinusoidal modulation of the electron energy. In a following magnetic chicane, the energy modulation leads to a density distribution with the periodicity of the laser wavelength. While preserving the duration of the laser pulse, this microbunching structure gives rise to coherent emission in a second undulator (radiator) tuned to a harmonic of the laser wavelength.

In a planned upgrade, a more sophisticated seeding scheme known as echo-enabled harmonic generation (EEHG) [3] will be implemented at the DELTA short-pulse source [4]. This scheme comprises two laser-electron interactions in undulators (modulators), each followed by a magnetic chicane, as well as a third undulator (radiator). As shown in Fig. 1 (bottom), the strong chicane after the first energy modulation leads to stripes of small energy spread in longitudinal phase space. The second modulation and chicane converts the stripes to a density distribution with narrow structures resulting in the coherent emission of higher laser harmonics compared to the CHG scheme.

In addition to coherently emitted VUV pulses, the energy-dependent path length along the storage ring causes a longitudinal displacement of the modulated electrons leaving a sub-ps dip in the temporal charge distribution. Like an

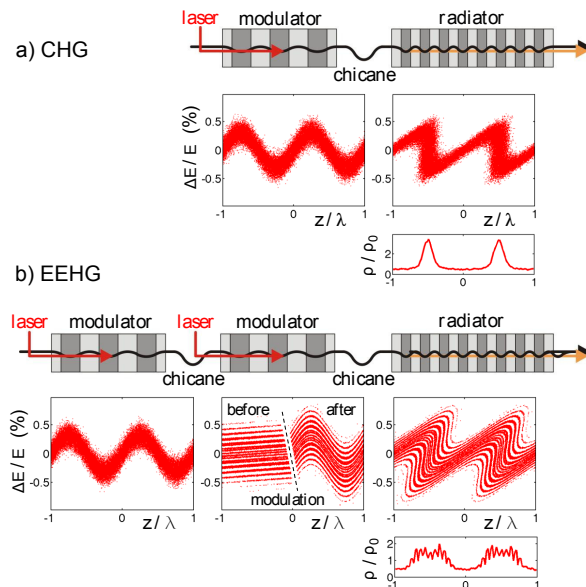


Figure 1: Top: Setup for CHG, corresponding longitudinal phase space distributions (energy deviation vs. longitudinal position) and final longitudinal electron density. Bottom: Setup for EEHG and corresponding distributions.

equally short bunch, the dip gives rise to coherent emission of THz radiation, which is detected at a dedicated beam-line [5] and provides information on the quality of the laser-electron interaction. Temporal modulation of the seed pulse allows to control the THz spectrum, e.g., a periodically modulated laser pulse leads to narrowband emission [6, 7]. Currently, CHG is performed by seeding with 50-fs pulses from a Ti:sapphire laser system at a wavelength of either 800 or 400 nm and a repetition rate of 1 kHz. Experiments are usually performed with a single bunch in the storage ring at a maximum current of 20 mA and a revolution frequency of 2.6 MHz. Modulator and radiator are parts of an electromagnetic undulator with 250 mm period length and 7 periods each. Three rewired undulator periods between them are used as a chicane.

LASER ELECTRON INTERACTION

The change ΔE of the electron energy in the electric field $\vec{E}_L = (E_L, 0, 0)$ of the laser pulse with horizontal polarization is given by

$$\Delta E = -e \int \vec{E}_L \cdot \vec{v} dt = -e \int E_L \cdot v_x dt, \quad (1)$$

where v_x is the horizontal component of the electron velocity \vec{v} in a planar undulator. The key for an optimum energy

* Work supported by the BMBF (05K16PEA, 05K16PEB), MERCUR (Pr-2014-0047), DFG (INST 212/236-1 FUGG) and the state of NRW.

[†] arne.meyeraufderheide@tu-dortmund.de

transfer over all undulator periods is the condition, that the electron lags behind one laser wavelength λ_L per undulator period λ_U . Since the same condition holds for spontaneous emission at the fundamental undulator wavelength, the undulator is usually tuned to the laser wavelength.

Another way to describe the laser-electron interaction is an interference between the laser pulse with energy E_L and the spontaneous undulator radiation with energy E_R . Assuming spectral overlap between the two radiation fields, the change of the electron energy is given by [8]

$$\Delta E = 2\sqrt{E_L E_R \frac{\Delta\omega_L}{\Delta\omega_R}} \cos \phi, \quad (2)$$

where $\Delta\omega_L/\Delta\omega_R$ is the bandwidth ratio between laser and undulator radiation and ϕ is the ponderomotive phase of the electron in the laser field. In essence, a laser-induced energy modulation requires overlap of the laser field with spontaneous undulator radiation coinciding in wavelength, emission angle, and polarization.

OFF-AXIS SEEDING

Usually, seeding with the laser path being collinear with the electron beam axis in the modulator yields the optimum energy modulation. However, seeding with a crossing angle between the laser and electron path can be useful under certain circumstances.

One example is seeding with two laser pulses in the same straight section, which is the case in the EEHG scheme but also in seeding with multiple harmonics to create a sawtooth-shaped energy modulation [9, 10] or in a two-wavelength scheme to generate attosecond X-ray pulses [11]. Bringing two laser pulses onto a common axis requires one of the pulses to pass through a mirror reflecting the other pulse. The mirror passage degrading the laser pulse quality can be avoided by introducing a crossing angle.

Another example is a modulator with insufficient period length λ_U and field parameter K to reach the laser wavelength for a given electron beam with Lorentz factor γ . Since the spontaneous undulator wavelength is given by

$$\lambda_R = \frac{\lambda_U}{2\gamma^2} \left(1 + \frac{K^2}{2} + \theta^2 \gamma^2 \right), \quad (3)$$

a nonzero angle θ of the laser beam with respect to the undulator axis allows to match undulator and laser wavelength if $\lambda_R < \lambda_L$ at $\theta = 0$.

Yet another example is energy modulation with tilted laser wavefronts to achieve a higher bunching factor in seeding schemes like CHG [12, 13]. An additional motivation to investigate off-axis seeding at DELTA is to experimentally test the statement underlying Eq. (2) that energy modulation scales with the intensity of spontaneous undulator radiation overlapping with the laser field. The code SPECTRA [14] was used to calculate the spatial and spectral distribution of radiation emitted by the modulator.

Seeding at the Fundamental Undulator Wavelength

In first experiments, variation of the laser-electron crossing angle was investigated with fundamental radiation of the modulator tuned close to the laser wavelength [15]. For each angle, a scan of the undulator wavelength was performed to find the optimum modulation indicated by the THz signal. As Fig. 2 shows, the results (blue) are consistent with a modulator wavelength being blue-shifted by $\lambda_U \theta^2 / 2$ such that the undulator radiation matches a fixed laser wavelength of 795 nm at emission angle θ . Furthermore, it was found that the emission angle of CHG radiation follows roughly half the value of the crossing angle, which was attributed to the curvature of the seed laser wavefronts.

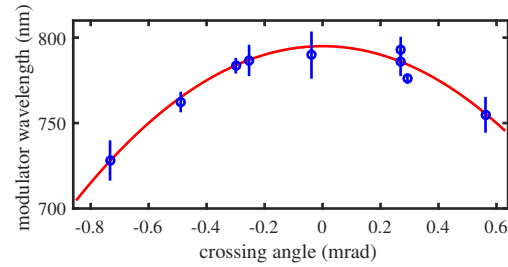


Figure 2: On-axis wavelength of the modulator tuned for maximum THz signal for different laser-electron crossing angles [15]. Red curve: Expectation for $\lambda_L = 795$ nm.

Seeding at the Second Undulator Harmonic

Recent seeding experiments were performed with the off-axis second harmonic of the modulator matching the seed wavelength [4]. Here, a crossing angle is required since the second harmonic of an undulator has zero on-axis intensity. The setup at DELTA allows the modulator to be tuned close to 800 nm while the laser pulses are frequency-doubled to a wavelength of 400 nm. The calculated angular distribution of 400-nm emission for an undulator tuned to 775 nm in the left part of Fig. 3 shows red-shifted radiation of the second undulator harmonic. For a realistic estimate of the spatial overlap, the laser divergence has to be taken into account. The right part of Fig. 3 shows a convolution of the undula-

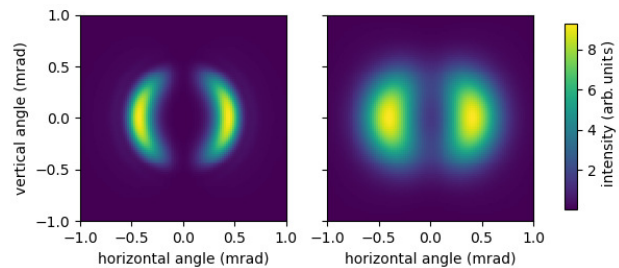


Figure 3: Left: Angular distribution of 400-nm radiation from an undulator tuned to 775 nm (left) as calculated with SPECTRA [14]. Right: Convolution with a 2-dimensional Gaussian includes the effect of laser beam divergence [4].

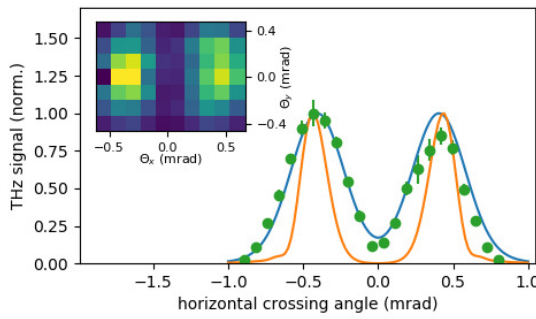


Figure 4: Normalized THz signal (dots) under variation of the horizontal crossing angle at zero vertical angle together with SPECTRA calculations without (orange) and including (blue) the laser divergence (see Fig. 3). Inset: THz signal under coarse variation of the horizontal and vertical crossing angles $\theta_{x,y}$ [4].

tor radiation with a 2-dimensional Gaussian representing a divergence of 0.15 mrad (rms).

In the experiment, the zero laser-electron crossing angle was found by tuning the modulator to the seed wavelength of 400 nm and maximizing the energy modulation indicated by coherent THz emission. Tuning the undulator to just below 800 nm and varying the crossing angle by moving the electron beam axis results in the THz signals shown in Fig. 4. In a coarse 2-dimensional scan (inset), the acquired THz signals resemble the expected distribution according to the SPECTRA calculation. A finer scan of the horizontal crossing angle matches the calculation if the laser divergence is included (green curve). A small observed asymmetry in the THz signal may result from unwanted vertical displacement due to nonlinearities of the beam position monitors since the electron beam is moved by several millimeters.

Seeding with Vertical Polarization

The second harmonic of a strong planar undulator ($K > 1$) with a horizontal midplane has a vertically polarized radiation component. This is due to the longitudinal motion of the electrons at twice the frequency of the horizontal motion, leading to a figure-8 trajectory in a frame moving with average velocity. Seen from a vertical elevation, the longi-

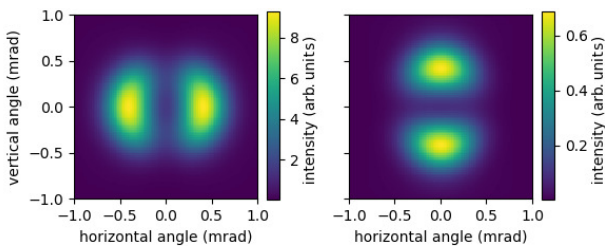


Figure 5: Angular distributions of 400-nm emission with horizontal (left) and vertical (right) polarization from a horizontal planar undulator tuned to 775 nm. In both figures, the effect of laser beam divergence is included. Note the different intensity scales.

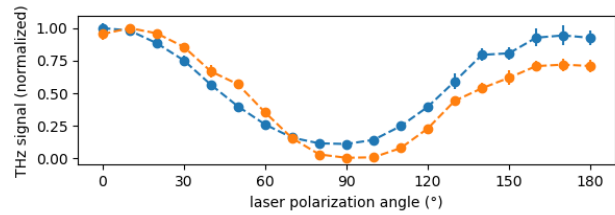


Figure 6: Scans of the laser polarization at crossing angles chosen for maximum horizontally polarized (orange) and maximum vertically polarized emission (blue).

tudinal motion appears to have a vertical orientation. As shown in the SPECTRA calculations (Fig. 5), horizontally polarized emission is mainly in the midplane while vertically polarized light is emitted with much lower intensity above and below the midplane. Nevertheless, a nonzero energy modulation is expected from seeding with vertically polarized laser pulses at a vertical crossing angle even though the electrons perform only horizontal motion in the planar undulator.

In the experiment, the polarization angle of the seed pulses was varied using a half-wave plate while recording the THz signal. The results are presented in Fig. 6 for two crossing angles at the maximum of horizontally and vertically polarized emission, respectively. In both cases, horizontally polarized seed pulses (polarization angles 0° or 180°) result in the highest THz signal. However, for vertically polarized seed pulses (90°) the THz signal drops to nearly zero at a horizontal crossing angle (orange dots) while a significant signal (more than 10% of the maximum) persists at a vertical crossing angle (blue dots). In this case, the electric field of vertically polarized light has a component parallel to the undulator axis which, according to Eq. (1), changes the electron energy. The undulator is tuned such that an electron lags behind the laser field by about 800 nm per undulator period and experiences two 400-nm cycles. The longitudinal electron velocity also performs two cycles per undulator period and is thus in resonance with the 400-nm laser field. Depending on its ponderomotive phase, energy gain/loss of an electron at maximum longitudinal velocity exceeds the energy loss/gain at minimum velocity.

CONCLUSION

Successful off-axis seeding has been demonstrated giving further insight into the laser-electron interaction process and confirming the notion that the energy exchange scales with the intensity of spontaneous undulator radiation having spatial and spectral overlap with the seed pulse. Further calculations and experiments with off-axis seeding are necessary to investigate its potential for a future EEHG setup.

ACKNOWLEDGEMENTS

We are pleased to thank our colleagues at DELTA and the TU Dortmund University. The continuous support from other institutes, particularly from DESY Hamburg, HZB Berlin, and KIT Karlsruhe is gratefully acknowledged.

REFERENCES

- [1] S. Khan *et al.*, "Coherent Harmonic Generation at DELTA: A New Facility for Ultrashort Pulses in the VUV and THz Regime", *Sync. Rad. News* 24(5), 2011, pp. 18-23. doi:10.1080/08940886.2011.618092
- [2] R. Coisson and F. De Martini, "Free-electron coherent relativistic scatterer for UV-generation", in *Physics of Quantum Electronics* 9, edited by S. F. Jacobs *et al.*, USA: Addison Wesley, 1982, p. 939.
- [3] G. Stupakov, "Beam Echo Effect for Generation of Short-Wavelength Radiation", in *Proc. 31st Free Electron Laser Conf.*, Liverpool, United Kingdom, 2009, paper MOOB01, pp. 15-22.
- [4] A. Meyer auf der Heide *et al.*, "The DELTA Short-Pulse Source: Upgrade Plans from CHG to EEHG", in *Proc. Int. Part. Accel. Conf.*, Melbourne, Australia, 2019, pp. 1457-1460. doi:10.18429/JACoW-IPAC2019-TUPGW025
- [5] M. Höner *et al.*, "A Dedicated THz Beamline at DELTA", in *Proc. 2nd Int. Part. Accel. Conf.*, San Sebastián, Spain, 2011, paper THPC015, pp. 2939-2941.
- [6] P. Ungelenk *et al.*, "Continuously tunable narrowband pulses in the THz gap from laser-modulated electron bunches in a storage ring", *Phys. Rev. Accel. Beams* 20, 2017, p. 020706. doi:10.1103/PhysRevAccelBeams.20.020706
- [7] C. Mai *et al.*, "Pulse Shaping Methods for Laser-Induced Generation of THz Radiation at the DELTA Storage Ring", in *Proc. Int. Part. Accel. Conf.*, Melbourne, Australia, 2019, pp. 1453-1455. doi:10.18429/JACoW-IPAC2019-TUPGW024
- [8] A. A. Zholents and M. S. Zolotarev, "Femtosecond X-Ray Pulses of Synchrotron Radiation", *Phys. Rev. Lett.* 76, 1996, pp. 912-915. doi:10.1103/PhysRevLett.76.912
- [9] G. Stupakov and M. S. Zolotarev, "Using Laser Harmonics to Increase Bunching Factor in EEHG", in *Proc. 33rd Free-Electron Laser Conf.*, Shanghai, China, 2011, paper MOPB19, pp. 45-48.
- [10] D. Ratner and A. Chao, "Seeded Radiation Sources with Saw-tooth Waveforms", in *Proc. 33rd Free-Electron Laser Conf.*, Shanghai, China, 2011, paper MOPB21, pp. 53-56.
- [11] A. A. Zholents and G. Penn, "Obtaining attosecond x-ray pulses using a self-amplified spontaneous emission free electron laser", *Phys. Rev. ST Accel. Beams* 8, 2005, p. 050704. doi:10.1103/PhysRevSTAB.8.050704
- [12] C. Feng, T. Zhang, H. Deng, Z. T. Zhao, "Three-dimensional manipulation of electron beam phase space of seeding soft x-ray free-electron lasers", *Phys. Rev. ST - Accel. Beams* 17, 2014, p. 070701. doi:10.1103/PhysRevSTAB.17.070701
- [13] S. Khan, "Enhancing coherent harmonic generation using tilted laser wavefronts" in *Proc. 36th Free-Electron Laser Conf.*, Basel, Switzerland, 2014, paper MOP084, pp. 248-251.
- [14] T. Tanaka and H. Kitamura, "SPECTRA: a synchrotron radiation calculation code", *J. Synchrotron Rad.* 8, 2001, pp. 1221-1228. doi:10.1107/S090904950101425X
- [15] S. Khan *et al.*, "Characterization and Optimization of Ultrashort and Coherent VUV Pulses at the DELTA Storage Ring", in *Proc. Int. Part. Accel. Conf.*, Richmond, USA, 2015, pp. 1452-1455. doi:10.18429/JACoW-IPAC2015-TUPWA022

ENERGY SPREAD IMPACT ON HGHG AND EEHG FEL PULSE ENERGY

S. Spampinati[†], E. Allaria, L. Giannessi¹, P. Rebernik Ribic²,
Elettra - Sincrotrone Trieste S.C.p.A., Basovizza, Trieste
¹also at ENEA C.R. Frascati, Rome, Italy
²also at University of Nova Gorica, Nova Gorica, Slovenia

Abstract

VUV and X-ray free electron lasers (FELs) require a very bright electron beam. Seeded FEL harmonic generation is particularly sensible to energy spread and slice energy spread can limit the highest harmonic conversion factor at which coherent radiation can be produced. Different cascade schemes can have different sensibility to the slice energy spread. At FERMI we have evaluated the impact of the slice energy spread on the performance of high gain harmonic generation (HGHG) and of echo enable harmonic generation (EEHG) by measuring the FEL pulse energy as function of the electron beam slice energy spread. The measurements were done at different harmonics. The slice energy spread was varied through the laser heater located in the linac that drives FERMI.

INTRODUCTION

Facility based on X-ray and VUV free electron lasers (FELs) [1-7] permits to perform a wide class of experiments in physics and chemistry with implications in other fields such as biology.

Most of the existing FEL facilities [1, 2, 4-7] rely on the Self Amplified Spontaneous Emission requiring a very bright electron beam characterized by high density in the 6-dimensional phase space implying high current, low transverse emittance and low energy spread [8]. Sensitivity to the energy spread is enhanced for seeded FELs [3]. The high current required by the FEL is obtained compressing the beam in one or more magnetic chicanes. Several collective effects can develop in the linac and in the bunch compressors spoiling the final beam quality and particular techniques have to be used to counteract these effects. Longitudinal microbunching instabilities MBI is one of the most relevant collective effect that can spoil the electron beam quality and the FEL performance [9].

To counteract MBI, linacs used to drive FELs are usually equipped with a laser heater located in the injector [10-12]. The laser heater consists of a short undulator located in a magnetic chicane where an external infrared laser pulse interacts with the electron beam. The increased energy spread can be adjusted to the right level to smear the density modulation in the bunch compressor and then dumping the MBI. Control of MBI and energy spread is particularly important for those seeded schemes based on frequency up conversion mechanisms used to produce highly coherent radiation at an harmonic of the seed.

In High gain harmonic generation (HGHG) [13, 14] an

external laser is used to modulate the electron beam energy in a first undulator. This periodic energy modulation at the seed laser wavelength is then converted to current modulation, containing components at the harmonics of the seed. The bunched beam is then injected in a second undulator, tuned at one of the harmonics of the seed, where the coherent emission starts and is amplified by the FEL process. In order to produce a significant bunching the induced energy modulation has to overcome the natural slice energy spread of the beam, at the same time the final energy spread has to be small enough to allow FEL amplification. This makes the scheme very sensitive to energy spread and limit the maximum number of harmonic conversion to slightly more than 10.

A new seeded mechanism call echo enable harmonic generation (EEHG) was proposed [15, 16] and demonstrated on test facilities [17-19]. Recently EEHG has been extended in the soft x-ray down to 5nm in a series of tests done at FERMI [20].

In this work we report measurements performed during the EEHG experiment at FERMI aimed at evaluating the impact of the slice energy spread on the performance of EEHG. The experiment rely on measurements of the FEL pulse energy as function of the electron beam slice energy spread. The measurements were done at different harmonics. In several cases the behaviour of EEHG as a function of the slice energy spread has been compared with similar measurements done with the same beam using the HGHG scheme. The slice energy spread was varied through the laser heater and the FEL properties were characterized using few different kind of detectors.

HGHG AND EEHG AT FERMI

The FERMI user facility is based upon two externally seeded FELs and covers the extreme ultraviolet (FEL-1) [3] and soft x-ray (FEL-2) [17]. Figure 1a shows the layout of FEL-2 line. FEL-2 is composed of two stage each one working according to the HGHG scheme described above. The seed of the first stage is provided by an external seed while the output of the first stage is used as seed for the second stage. The electron beam coming from the first stage is delayed by a magnetic chicane before entering in the second stage. The electron beam modulation in the second modulator and the FEL emission in the second stage occur now in a fresh part of the electron beam. Figure 1b shows EEHG scheme implemented in FEL-2 line [20]. The first dispersive section is switched off and the undulator segments of the first radiator are opened at a large gap to provide an almost null field on the axis. In the first modulator, the e-beam energy is modulated by the interaction with the first seed laser, as in HGHG. The

[†] simone.spampinati@elettra.eu

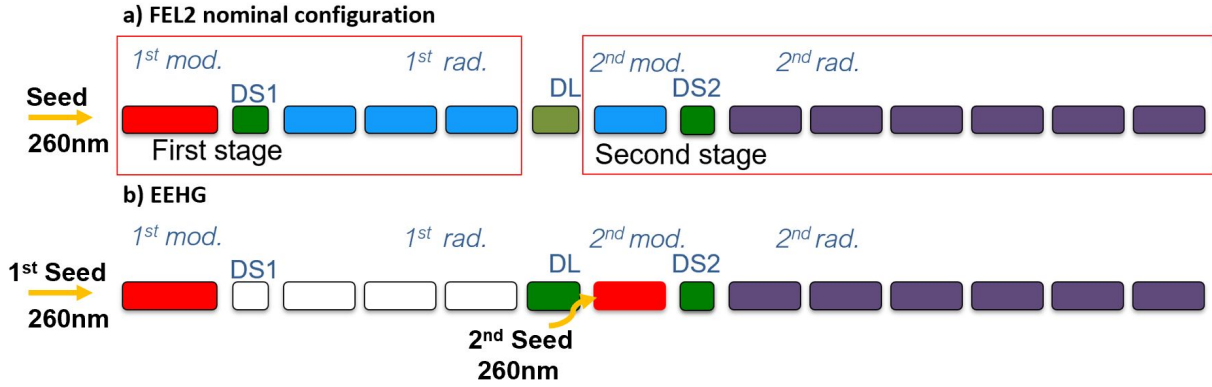


Figure 1: a) nominal layout of FEL-2. b) EEHG implemented at FERMI.

current of the magnetic delay line is increased to provide a sufficiently high dispersion ($r56 \sim 2$ mm). After passing through this strong dispersive section, the portion of the longitudinal e-beam phase space that interacted with the seed is strongly modified resulting in a series of stripes characterized by a reduced energy spread. The beam goes to a single stage of HGHG where the seed is provided by a second UV laser. Both seeds in this case interact with the same part of the beam. Due to the reduced slice energy in each stripe, it is possible to produce a significant bunching with a single stage at very high harmonics of the seed using a moderate energy modulation provided in the second modulator.

As a result of the preparation of phase space before entering the second modulator, EEHG is expected to tolerate larger energy spread. Particularly in EEHG the slice energy spread is expected to have a smaller impact in the degradation of the harmonic bunching with respect to HGHG. The bunching at the harmonic a_E can be expressed, following the notation in [18] as:

$$(1) \quad b_{n,m} = e^{-\frac{\xi_E^2}{2}} J_n(-\xi_E A_1) J_m(-a_E A_2 B_2)$$

where the normalized laser modulations are $A_{1,2} = \frac{\Delta E_{1,2}}{\sigma_E}$

and the normalized dispersion are $B_{1,2} = \frac{KR_{56}^{1,2}}{E}$.

σ_E is the slice energy spread, and E is the beam energy. The EEHG scaling factor has been defined as $\xi_E = nB_1 + a_E B_2$. In our case both seed laser have the same k vector and the harmonic number is $a_E = n + m$.

During the EEHG experiments done at FERMI we had the possibility to verify the minor sensitivity of EEHG to energy spread with respect to HGHG. Figure 2 shows the behaviour of FEL intensity, both in HGHG and EEHG, as a function of the energy of the laser that drive the laser heater.

Figure 2a shows the FEL pulse energy at 14.7nm, corresponding to the 18th harmonic of the seed (e-beam energy 0.9 GeV), as function of the laser heater energy. The red curve is referred to the HGHG. As previously demonstrated a very small level of heating is enough to suppress the microbunching and to improve the FEL performances in the HGHG setup. Increasing the LH energy above the optimum value, needed to suppress the microbunching,

drops the FEL power because the increased energy spread and the reduced bunching efficiency. The blue curve shows the behaviour of the EEHG tuned at the same wavelength. We can see that the optimum FEL energy is obtained for a greater value of the laser energy compared to the HGHG case. Our current explanation of this effect is related to the bigger dispersion of the delay line used for EEHG that increases the microbunching gain and consequently more heating from the laser heater is required to suppress MBI and optimize the energy spread at the second dispersion section where the harmonic bunching is produced. Then the FEL remain constant even increasing the laser heater energy by a big factor. Figure 2b shows the same measurement done with the FEL tuned at 8.6 nm corresponding to the 30th harmonic of the seed (e-beam energy 1.1 GeV). In this case the power of EEHG starts to decrease for a laser heater energy double respect to the optimum value. At higher electron beam energy (and lower R56 on the first chicane) the MBI is reduced and hence the optimum for the LH intensity is lower.

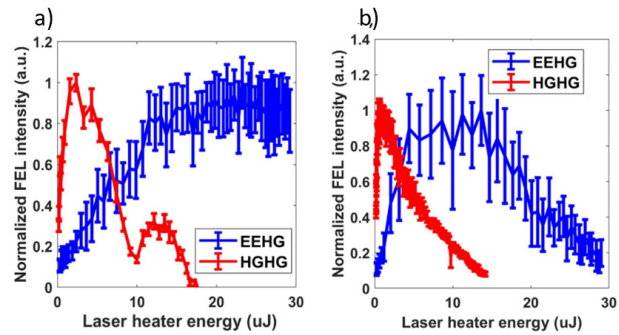


Figure 2: a) FEL energy vs laser heater energy at harmonic 18th. b) FEL energy vs laser heater energy at harmonic 30th.

We can see that the optimum FEL energy is obtained for a greater value of the laser energy in the case of the lower harmonic. The measurements at the 18th harmonic were taken with an electron beam of 0.9GeV and 1.1GeV respectively for the 18th and 30th harmonic. Probably the electron beam was affected by a stronger microbunching at lower energy requiring more energy spread by the laser

heater. From the theoretical equation for energy spread provided by the laser heater [10] and from experimental measurement with the deflector we have that the minimum energy spread that optimize the FEL emission is 240 keV at H18 and 200 keV at H30.

Figure 2 shows that the sensitivity to the energy spread increases with the harmonic number both in the HGHG configuration and in EEHG. This behaviour is expected and can be derived from the equations for the harmonic bunching. In Fig. 3 we plot the EEHG bunching obtained from eq. (1) as function of the energy spread at the two harmonics.

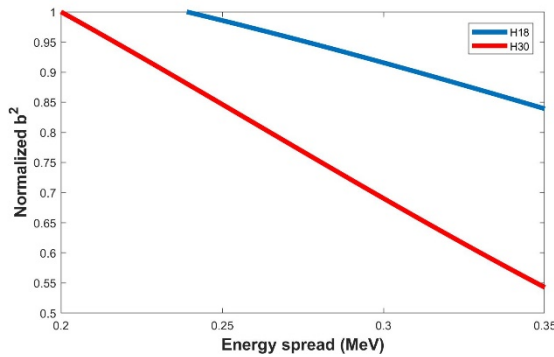


Figure 3: Theoretical normalized square of the bunching calculated for H18 and H30.

The measurements reported in Fig. 2 were taken with all the parameters optimized to have the maximum pulse energy. It is possible to further reduce the sensitivity of EEHG to the energy spread tweaking the value of the second energy dispersive section. Indeed, from eq. 1 it is possible to show that ξ_E governs the formation of the bunching and is always convenient to minimize $|\xi_E|$ and to have a value of n small and negative.

For small value of $|\xi_E|$ the ratio of the dispersions is approximately equal to the harmonic number $a_E \approx \frac{nB_1}{B_2}$ and the effect of the energy spread on the bunching is reduced. From the exponential term in eq. 1 we can see that there is no impact of the energy spread on the bunching for $|\xi_E| = 0$. However, this case the bunching is 0. The bunching and his sensitivity to energy spread grow increasing the value of $|\xi_E|$ towards his optimum value. We have studied the different sensitivity of the FEL energy to the energy spread for different value of $|\xi_E|$. During the experiment we fixed the value of R_{56}^1 and we hanged the value of $|\xi_E|$ by changing the value of R_{56}^2 . The measurements were repeated for several harmonic of the seed laser. The results reported in Fig. 4 and Fig. 5 are referred to the 30th harmonic of the seed.

Figure 4 shows the FEL energy as function of the value of the R_{56}^2 (blue curve) with the expected behaviour of the bunching. The three points indicate the value of R_{56}^2 for which we took the measurement reported in Fig. 5. The green curve shows the scaling function as function of the value of the of R_{56}^2 .

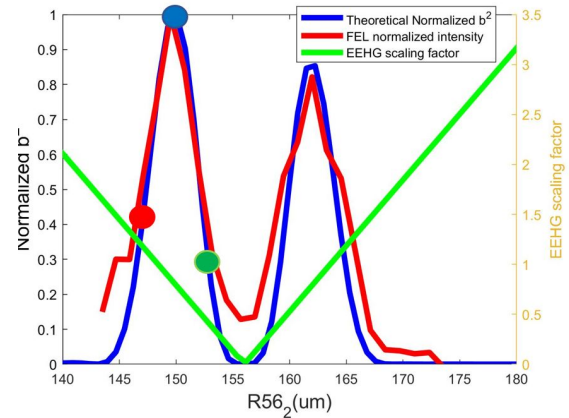


Figure 4: Normalized theoretical square bunching (blue), measured normalized FEL intensity (red) and) EEHG scaling factor (green) vs R_{56} of the second dispersion section.

Figure 5a shows the FEL energy as function of the laser heater energy for the three values, indicated by three dots in Fig. 4, of R_{56} of the second chicane around the left peak of the blue and red curves in Fig. 4. Figure 5b shows the expected behaviour of the bunching vs the energy spread for the three same values of R_{56} . The expected behaviour of the sensitivity to the energy spread as function of the EEHG scaling function is confirmed.

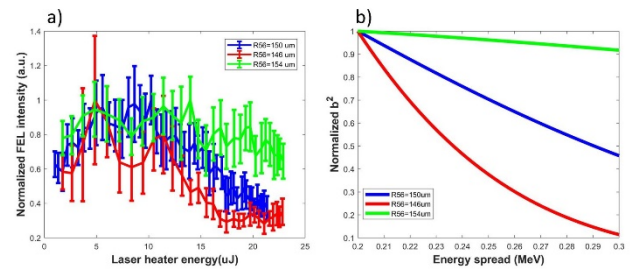


Figure 5: a) FEL intensity vs. laser heater energy. b) Theoretical b^2 vs. energy spread.

CONCLUSIONS

We have evaluated the impact of the slice energy spread on the performance of high gain harmonic generation (HGHE) and of echo enable harmonic generation (EEHG) by measuring the FEL pulse energy as function of the electron beam slice energy spread. EEHG confirms to be less effected by the slice energy respect to HGHE.

REFERENCES

- [1] W. Ackermann *et al.*, “Operation of a free-electron laser from the extreme ultraviolet to the water window”, *Nat. Photon.* vol. 1, 336–342 (2007). doi:10.1038/nphoton.2007.76
- [2] P. Emma *et al.*, “First lasing and operation of an angstrom-wavelength free-electron laser.” *Nat. Photon.*, vol. 4, 641–647 (2010). doi:10.1038/nphoton.2010.176

- [3] E. Allaria *et al.*, “Highly coherent and stable pulses from the FERMI seeded free-electron laser in the extreme ultra-violet”, *Nat. Photon.*, vol. 6, 699 (2012). doi:10.1038/nphoton.2012.233
- [4] T. Ishikawa *et al.*, “A compact X-ray free-electron laser emitting in the sub-angstrom region”, *Nat. Photon.*, vol. 6, 540–544 (2012). doi:10.1038/nphoton.2012.141
- [5] E. Allaria *et al.*, “Two-stage seeded soft-X-ray free-electron laser”, *Nat. Photon.*, vol. 7, 913 (2013). doi:10.1038/nphoton.2013.277
- [6] H.-S. Kang *et al.*, “Hard X-ray free-electron laser with femtosecond-scale timing jitter”. *Nat. Photon.*, vol. 11, 708–713 (2017). doi:10.1038/s41566-017-0029-8
- [7] SwissFEL, <https://www.psi.ch/en/swissfel/about-swissfel>
- [8] S. Di Mitri, “On the Importance of Electron Beam Brightness in High Gain Free Electron Lasers”, *Photonics*, vol. 2, 317–341 (2015). doi:10.3390/photonics2020317
- [9] E. Saldin, E. A. Schneidmiller, M. V. Yurkov, “Klystron instability of a relativistic electron beam in a bunch compressor”, *Nucl. Instrum. Methods Phys. Res. Sect. A.*, vol. 490, 1–2 (2002). doi: 10.1016/S0168-9002(02)00905-1
- [10] Z. Huang *et al.*, “Measurements of the linac coherent light source laser heater and its impact on the x-ray free-electron laser performance”, *Phys. Rev. Spec. Top. - Accel. Beams*, vol. 17, 13, 020703 (2010). doi:10.1103/PhysRevSTAB.13.020703
- [11] S. Spampinati, *et al.*, “Laser heater commissioning at an externally seeded free-electron laser”, *Phys. Rev. Spec. Top. - Accel. Beams*, vol. 17, 120705 (2014). doi:10.1103/PhysRevSTAB.17.120705
- [12] E. Ferrari, *et al.*, “Impact of Non-Gaussian Electron Energy Heating upon the Performance of a Seeded Free-Electron Laser”, *Phys. Rev. Lett.*, vol. 112, 114802. (2014). doi:10.1103/PhysRevLett.112.114802
- [13] L. H. Yu, “Generation of intense UV radiation by subharmonically seeded single-pass free-electron lasers”. *Phys. Rev. A*, vol. 44, 5178–5193 (1991). doi:10.1103/physreva.44.5178
- [14] L. H. Yu *et al.*, “High-Gain Harmonic-Generation Free-Electron Laser”, *Science*, vol. 289 (2000), 932–934. doi:10.1126/science.289.5481.932
- [15] G. Stupakov, “Using the Beam-Echo Effect for Generation of Short-Wavelength Radiation”, *Phys. Rev. Lett.*, vol. 102 (2009), 074801. doi:10.1103/PhysRevLett.102.074801
- [16] D. Xiang, G. Stupakov, “Echo-enabled harmonic generation free electron laser”, *Phys. Rev. Spec. Top.- Accel. Beams*, vol. 12, 30702 (2009). doi:10.1103/PhysRevSTAB.12.030702
- [17] D. Xiang *et al.*, “Demonstration of the Echo-Enabled Harmonic Generation Technique for Short-Wavelength Seeded Free Electron Lasers”, *Phys. Rev. Lett.*, vol. 105, 114801 (2010). doi:10.1103/PhysRevLett.105.114801
- [18] Z. T. Zhao *et al.*, “First lasing of an echo-enabled harmonic generation free-electron laser”, *Nat. Photon.*, vol. 6, 360–363 (2012). doi:10.1038/nphoton.2012.105
- [19] E. Hemsing *et al.*, “Echo-enabled harmonics up to the 75th order from precisely tailored electron beams” *Nat. Photon.*, vol. 10, 512–515 (2016). doi:10.1038/nphoton.2016.101
- [20] E. Allaria, “First Lasing of a Free Electron Laser in the Soft X-Ray Spectral Range with Echo Enabled Harmonic Generation”, presented at the FEL’19, Hamburg, Germany, (2019), paper MOA02, this conference.

START-TO-END SIMULATIONS OF THE REFLECTION HARD X-RAY SELF-SEEDING AT THE SHINE PROJECT *

Tao Liu[†], Chao Feng, Xiaohao Dong

Shanghai Advanced Research Institute, Chinese Academy of Sciences, Shanghai 201210, China

Abstract

The Shanghai high repetition rate XFEL and extreme light Facility (SHINE) project is designed to produce fully coherent X-ray photons covering the photon energy from 3 keV to 25 keV. We have reported our FEL proposal and schemes in the hard X-ray regime which is self-seeding based on the crystal monochromator previously. Comparing to the transmission self-seeding scheme, the reflection one has several advantages and might be the base proposal. Start-to-end (S2E) simulations from the beam generation by Astra, the linac accelerating by Elegant to the FEL simulation by Genesis are performed. In this manuscript, the FEL simulations based on the S2E beam will be presented mainly. The results demonstrate the feasibility of the reflection hard X-ray self-seeding at the SHINE project.

INTRODUCTION

Hard X-ray self-seeding FEL scheme based on a crystal monochromator was proposed and has been demonstrated that it is a practicable method to generate a fully coherent hard X-ray pulse. Currently, transmission and reflection modes are considered each FEL facility worldwide. The transmission mode [1] has been adopted more popular, such as LCLS [2], PAL-XFEL and European XFEL. The reflection mode is also feasible which has been used and demonstrated successfully at SACLA [3].

Both of the line FEL-1 and FEL-3 at SHINE will work on hard X-ray self-seeding FEL schemes for covering 5-15 keV (nominal 3-25 keV). In the previous papers [4,5], the transmission case and the reflection case have been proposed and discussed, where both of the advantages and disadvantages were presented and compared. In some degree, the reflection case shows a higher monochromatic efficiency, a lower heat-loading, better signal-to-noise ratio and higher pulse energy.

In this manuscript, we will present a start-to-end simulation results. The tracked electron beam generated by Astra [6], and accelerated and transported by Elegant [7], is used for generation of hard X-ray FEL by Genesis [8] with typical photon energy of 12.4 keV at the line FEL-1, where SASE, single-stage self-seeding and two-stage self-seeding configurations are carried out.

REFLECTION SELF-SEEDING

As shown in Fig. 1, the layout of a two-stage reflection self-seeding scheme is presented here. Adopting two-stage

scheme, one can decrease the heat-loading on the crystal, enhance the monochromaticity, and correct the beam offset of the s-polarized reflection.

The magnetic field centre of the second undulator section will be adjusted according to the beam offset. The second monochromator with opposite direction can make the trajectory back to the initial one. However, this method does not work on the gap-fixed undulator.

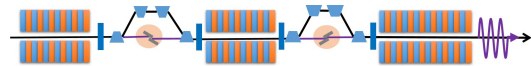


Figure 1: Layout of the two-stage reflection hard X-ray self-seeding scheme at the SHINE.

The basic double-crystal monochromator is shown in Fig. 2, where the layout consists of a channel-cut crystal and a beam stopper. The beam stopper is pressed against the right edge of the forward crystal which is used to block the SASE pulse transmitting the crystal. Refer to the normal monochromator of the beam line, smaller Bragg angle is used for higher energy photon. Typically, the C111 symmetric diamond crystal can cover 5-15 keV energy photons in the range of 11.6-37 degree Bragg angles. The channel-cut gap D is assumed as 100 μm . For the 12.4 keV photon, the Bragg angle of C111 is 14.1 degree and then the induced time delay is 162 fs and the transverse offset is 194 μm .

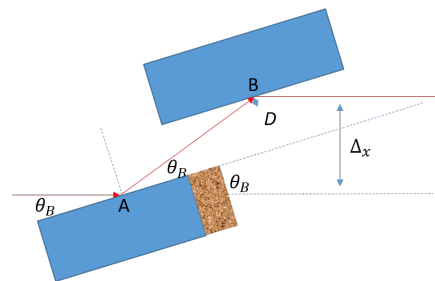


Figure 2: Reflection monochromator with double-crystal for self-seeding.

LINAC AND BEAM PARAMETERS

The schematic layout of the SHINE is shown in Fig. 3, which includes a 8 GeV accelerator and three FEL lines. In the baseline of the SHINE, an 100 MeV electron beam with 100 pC charge is generated in the photon-injector section and accelerated to 8 GeV at the exit of the linac. The peak current is more than 1500 A, the rms normalized slice emittance is less than 0.5 mm-mrad and the rms slice energy spread is less than 0.01%.

* Work supported by the National Natural Science Foundation of China Grant No. 11605277

[†] liutao@sinap.ac.cn; liutao@zjlab.org.cn

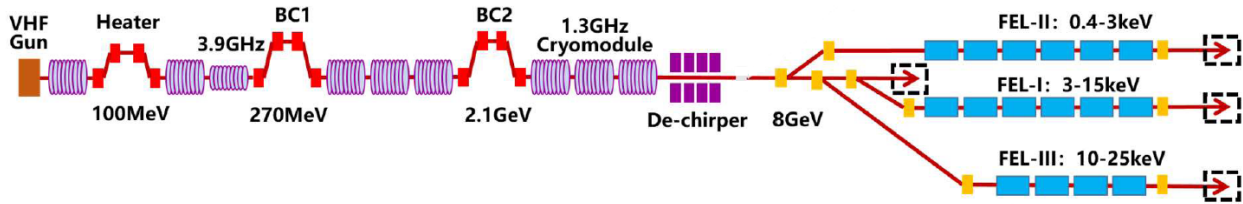


Figure 3: Schematic layout of SHINE.

Considering the 12.4 keV photon generated in the line FEL-1, the beam will be transport through the switchyard and matched at the entrance of the line FEL-1. Currently the S2E beam has been tracked from RF gun to the entrance of undulator using Astra and Elegant. Figure 4 shows the tracked beam properties.

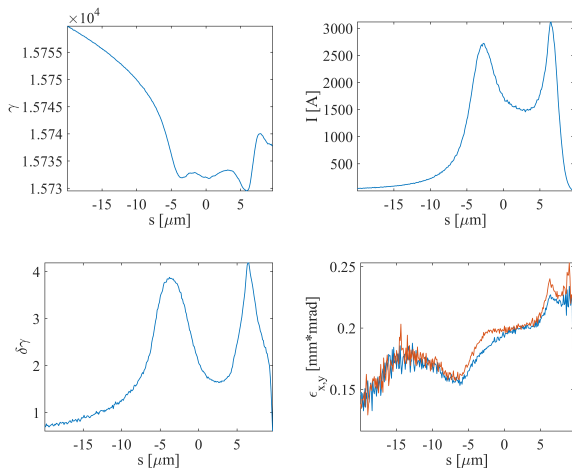


Figure 4: Sliced parameters of the tracked beam: Top-left: the sliced relative energy distribution. Top-right: the current profile. Bottom-left: the sliced relative energy spread. Bottom-right: the normalized emittance of x (blue) and y (red). Beam tail is at the left side of s coordinate axis.

The beam envelope of $s = 0$ position is matched for FEL radiation. Beam energy is 8039 MeV, peak current is 1730 A, both emittances of x and y are 0.2 mm·mrad and energy spread is 0.013%. Calculated by Xie's Model [9], the optimal Twiss parameters are $\beta_x = 18.05$, $\beta_y = 7.64$, $\alpha_x = -1.56$ and $\alpha_y = 0.67$. The matched results are shown in Fig. 5. It is noted that the mismatch and offset of the beam exist, that will impact on the radiation pulse performance.

FEL SIMULATIONS

The line FEL-1 has 43 undulator modules, where each module is a 4-m-long permanent magnet planar hybrid structure with 152 periods of $\lambda_u = 26$ mm and an adjustable magnetic gap. For such long undulator section, it can be used for SASE FEL well. We replaced the 7th module and the 13th module as the reflection monochromators for self-seeding schemes. Two-monochromator adoption is order

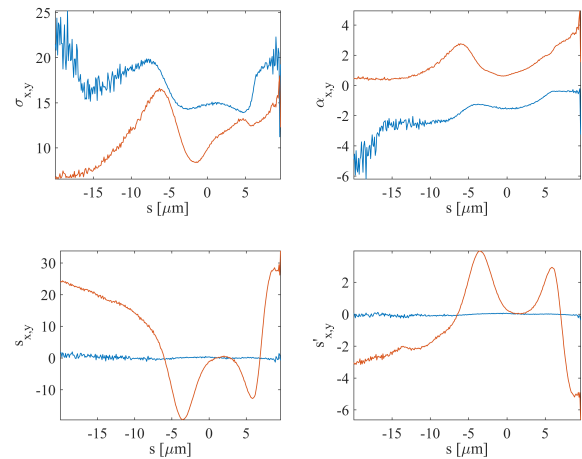


Figure 5: Twiss parameters of x (blue) and y (red) of the electron beam: Top-left: the sliced beam size. Top-right: the sliced $\alpha_{x,y}$. Bottom-left: the sliced transverse offsets. Bottom-right: the angular deviation. Beam tail is at the left side of s coordinate axis.

to decrease the heat-loading, improve the monochromaticity further and eliminate the sideband. Here both SASE and self-seeding FEL S2E simulations are carried out in the following.

SASE

Figure 6 presents the 12.4 keV SASE FEL performance in which undulator tapering is considered. It is noted that the exponential gain performs and stops at about 70 m with $\sim 130 \mu\text{J}$ (saturation). Due to undulator tapering, the FEL pulse energy increases continuously and is up to $1300 \mu\text{J}$ and the peak power is 80 GW with bandwidth FWHM of 0.15% at the exit of the undulator section.

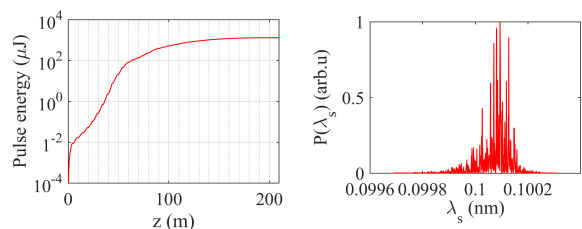


Figure 6: SASE. Beam tail is at the left side of s coordinate axis.

Self-seeding

For the self-seeding scheme, both single-stage case and two-stage case are presented here. In order to decrease the heat-loading of the crystal, the first monochromator is placed at the 7th undulator module. Before the monochromator, the SASE pulse energy is about $0.3 \mu\text{J}$ shown in Fig. 7.

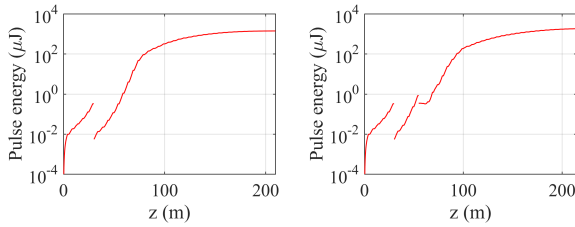


Figure 7: Pulse energy growth along the undulator for self-seeding schemes. Left: Single-stage self-seeding. Right: Two-stage self-seeding.

Figure 8 shows the single-stage self-seeding spectra evolution in both of the time and frequency domains. Before the monochromator, the SASE pulse with 10s MeV peak power, $0.3 \mu\text{J}$ pulse energy and FWHM 0.5% bandwidth is generated. The monochromatization process is simulated by XOP [10]. A fully coherent radiation pulse with FWHM $6\text{e-}5$ bandwidth and 0.3 MeV peak power is filtered out from the SASE pulse. In the seeding section downstream, the

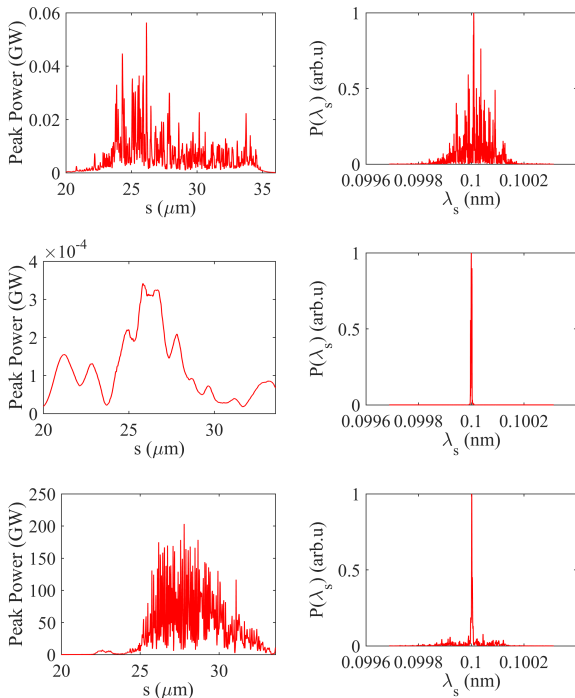


Figure 8: Spectra in the time domain and frequency domain for the single stage self-seeding. Top: Spectra before the monochromator. Middle: Spectra after the monochromator. Bottom: Final spectra after the single-stage self-seeding with tapered undulator.

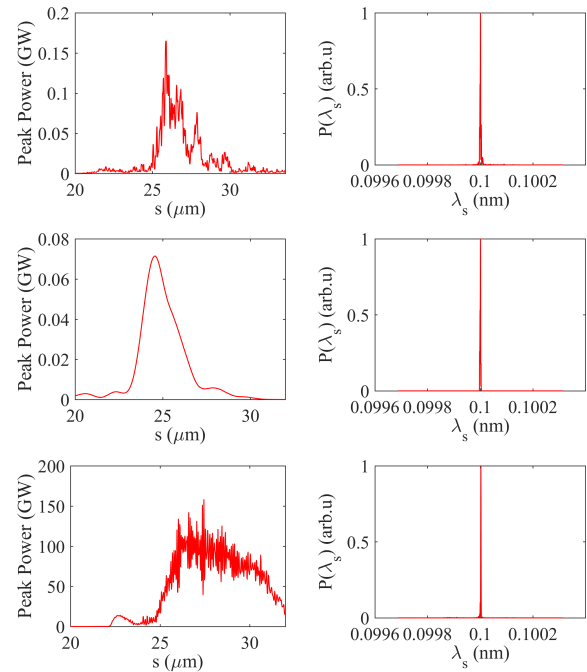


Figure 9: Spectra in the time domain and frequency domain for the two-stage self-seeding. Top: Spectra after the first self-seeding stage and before the second monochromator. Middle: Spectra after the second monochromator. Bottom: Final spectra after the two-stage self-seeding with tapered undulator.

pure radiation is high than the noise power of the beam, and will be amplified as the seed laser. Due to the long distance undulator section, tapering is also adopted and the final peak power is about 150 GW and the pulse energy is $1300 \mu\text{J}$. The bandwidth is less than $1\text{e-}4$, but the sideband is considerable.

Figure 9 shows the two-stage self-seeding spectra evolution in both of the time and frequency domains. Firstly, we still use the same SASE section and the following monochromator as the single-stage case as shown in the top and middle of Fig. 8. After a 5 undulator modules section, the seeded FEL peak power is 100 MW , the pulse energy is $0.6 \mu\text{J}$ and sideband starts appearing. At this time, the second monochromator works and a pure FEL pulse is filtered out with 70 MW peak power much higher than the beam noise. Similarly, the 70 MW seed laser is amplified to saturation quickly and further increases by tapering. The final peak power is 100 GW and the pulse energy is $1800 \mu\text{J}$. The spectra is still fully coherent with the bandwidth FWHM of $6\text{e-}5$ and the sideband is invisible. It is illustrated that the result is much better is the single-stage case.

CONCLUSION

The S2E simulation presents the SASE, single-stage self-seeding and two-stage self-seeding results of 12.4 keV photon. For the SHINE project, the two-stage reflection self-seeding is feasible to generate fully coherent hard X-ray. Next step, we will design the reflection monochromator and test the photon energy range at the synchrotron radiation facility.

ACKNOWLEDGEMENTS

The authors would like to thank for Bo Liu, Haixiao Deng and Dong Wang for helpful discussions and useful comments.

REFERENCES

- [1] G. Geloni, V. Kocharyan, and E. L. Saldin, “A novel selfseeding scheme for hard x-ray FELs”, *Journal of Modern Optics*, vol. 58, no. 16, p. 1391, 2011. doi:10.1080/09500340.2011.586473
- [2] J. Amann *et al.*, “Demonstration of self-seeding in a hard-X-ray free-electron laser”, *Nature Photonics*, vol. 6, p. 693, 2012. doi:10.1038/nphoton.2012.180
- [3] I. Inoue *et al.*, “Generation of narrow-band X-ray free-electron laser via reflection self-seeding”, *Nature Photonics*, vol. 13, p. 319, 2019. doi:10.1038/s41566-019-0365-y
- [4] T. Liu *et al.*, “Optimization for the two-stage hard X-ray self-seeding scheme at the SCLF”, in *Proc. IPAC’18*, Vancouver, BC, Canada, May. 2018, paper THPMK070, pp. 4460–4463. doi:10.18429/JACoW-IPAC2018-THPMK070
- [5] T. Liu *et al.*, “Proposal of the reflection hard X-ray self-seeding at the SHINE project”, in *Proc. IPAC’19*, Melbourne, Australia, May 2019, pp. 1792–1794. doi:10.18429/JACoW-IPAC2019-TUPRB047
- [6] K. Flöttmann, *Astra - A Space Charge Tracking Algorithm*, <http://www.desy.de/~mpyf10>, 2000.
- [7] M. Borland, *User’s Manual for Elegant*, APS-ANL, Chicago, IL, 2017.
- [8] S. Reiche, “GENESIS 1.3: a fully 3D time-dependent FEL simulation code”, *Nucl. Instrum. Methods Phys. Res. A*, vol. 429, no. 1-3, p. 243, 1999. doi:10.1016/S0168-9002(99)00114-X
- [9] M. Xie, “Design optimization for an X-ray free electron laser driven by SLAC linac”, in *Proc. PAC’95*, Dallas, TX, USA, May 1995, paper TPG10, pp. 183–195.
- [10] ESRF, X-ray Oriented Programs Software Package, <https://www.aps.anl.gov/Science/Scientific-Software/XOP>

NUMERICAL SIMULATIONS FOR GENERATING FULLY COHERENT SOFT X-RAY FREE ELECTRON LASERS WITH ULTRA-SHORT WAVELENGTH

K. S. Zhou[†], H. X. Deng, B. Liu, D. Wang,

Shanghai Advanced Research Institute, Chinese Academy of Sciences, Shanghai, China

Abstract

For the fully coherent, ultra-short and high power soft x-rays are becoming key instruments in many different research fields, such as biology, chemistry or physics. However, it's hard to generate this kind of advanced light source by the conventional lasers, especially for the soft x-rays with ultra-short wavelength because of no suitable reflectors. The external seeded free electron laser (FEL) is considered as one feasible method. Here, we give an example to generate highly temporal coherent soft x-rays with the wavelength 1nm by the two-stage cascaded schemes. The external seeded scheme EEHG is used as the first-stage while the HGHG scheme is used as the second-stage.

INTRODUCTION

The SASE scheme, external seeded scheme and self-seeding scheme are three important methods for the high-gain free electron lasers (FEL). The SASE scheme is now the main method to generate X-ray FEL which has been successfully used in many facilities [1, 2, 3], however, the SASE scheme use the local shot noise of the electron beam which will cause a few spikes in the output spectrum. The external seeded scheme use the fully coherent conventional laser as the seed to modulate the electron beam, if the power of the seed laser are large enough to suppress the shot noise of the electron beam, the output radiation pulse will be fully coherent in principle [4, 5]. Self-seeding scheme is another way to generate the fully coherent radiation pulse, this scheme uses crystals to filter the radiation pulse from the upstream sections to get monochromatic seeding pulse for the downstream sections, however, the output radiation power and central wavelength may have larger shot-to-shot fluctuations than SASE scheme according to the experiment [6].

China will build a high-repetition rate of 1MHz FEL facility (SHINE) based on superconducting LINAC technology. According to the requirements of the users, three beam lines will be built at the first time (FEL-I, FEL-II and FEL-III), one of them (FEL-II) is designed to generate highly temporal coherent soft x-rays with the central wavelength 1nm.

To generate this kind of advanced light source, the two-stage cascaded EEHG/HGGH scheme with fresh bunch technology is chosen as the baseline for FEL-II, it is comprised of two stages while the First-stage is EEHG and the second stage is HGHG. The principle of HGHG was proved in 1990s [7] and it is currently adopted in FERMI

FEL user facility. EEHG scheme can work at high harmonics of seeding lasers which is successfully demonstrated by NLCTA, SDUV and FERMI recently [8, 9, 10, 11].

LAYOUT AND DESCRIPTION

The layout of the two-stage cascaded EEHG/HGGH scheme for FEL-II is shown in Figure 1.

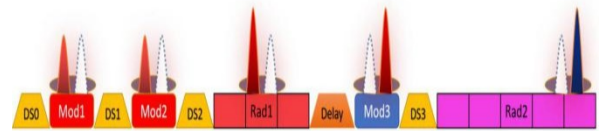


Figure 1: The layout of the two-stage cascaded scheme.

The first-stage EEHG is designed to generate 5nm fully coherent soft x-rays, the up-conversion harmonic number is 54 of 270nm seeding lasers, it has two modulators, two dispersion sections, and a long radiator. Then, the electron beam is delayed to interact with the radiation pulse from the first-stage, and the up-conversion harmonic number for the second-stage HGHH is 5, the second stage HGHH is comprised of one modulator, one dispersion section and a lone radiator. Finally, the highly temporal coherent 1nm soft x-ray is generated by the second long radiator.

The parameters of electron bunch from the output of LINAC for start-to-end simulations are given in Figure 2.

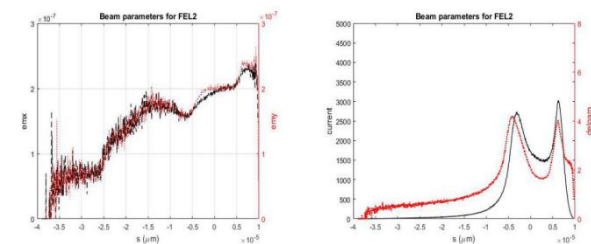


Figure 2: The emittance of x/y (left). The current and energy spread of electron bunch (right).

From Figure 2, one can find that the emittance for both sides x and y is lower than 0.3mm*mrad of the electron beam according to the first version from LINAC, and the peak current of the electron beam is larger than 1500A, besides, the energy of the electron beam is about 8GeV.

The lattice of the two-stage cascaded EEHG/HGGH scheme is given in Figure 3 based on the particle tracing program Elegant.

[†] zhokaishang@sinap.ac.cn

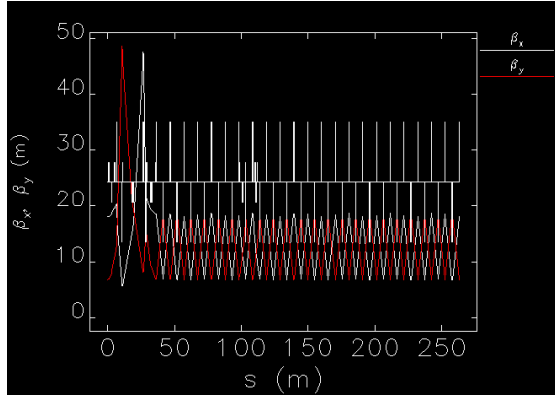


Figure 3: The lattice of two-stage cascaded EEHG/HGHG scheme.

Table 1: Length of the Different Parts of FEL-II

Element	Value	Unit
The first-stage EEHG		
DS0	5	m
Mod1	2.88	m
Mod2	1.44	m
DS1	15.3	m
DS2	7.2	m
Rad1	50	m
Delay chicane	5	m
The second-stage HGHG		
Mod3	5	m
DS3	5	m
Rad2	140	m

The length of the different element is shown in Table 1. For the first-stage EEHG, the up-conversion harmonic number is 54, in order to get large enough bunching factor at the specified harmonic to suppress the shot noise of the electron beam and minimize the ISR effect causing by the two dispersion sections in EEHG scheme, we have choose the parameters $A_1 = 9$, $A_2 = 6$ (in units of the initial energy spread) and $n = -3$ (this parameter coming from the EEHG bunching factor b_{nm}) [12], the modulation deep for Mod1 and Mod2 is introduced by two seeding lasers, the parameters of them are listed in Table 2.

Table 2: The Main Parameters of Seed Laser

Seed laser		
Title	value	unit
Wavelength	~270	nm
Peak power1	18	GW
Peak power2	30	GW
Pulse length (FWHM)	~20	fs
Rayleigh length	~3.52	m

Table 2 shows that the peak power of the two seeding lasers is about 18GW and 30GW, respectively. However, the requirements of peak power can be lower if we increase the length of the two modulators, besides, the pulse length also can be longer than 20fs which depends on the input length of the electron bunch.

To optimize the maximum bunching factor at 54th seeding lasers, we have scanned the strength of two dispersion sections which is shown in Figure 4.

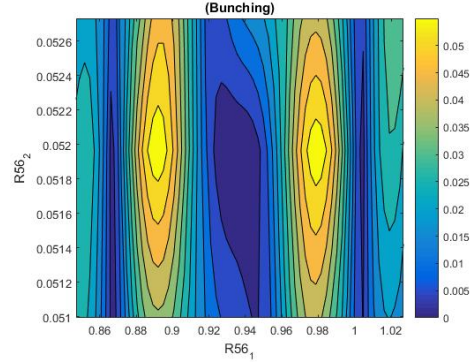


Figure 4: The optimized bunching factor for the first-stage EEHG.

Figure 4 shows that the ideal bunching factor at 54th harmonic of seeding lasers is 0.06, the corresponding strength of the two dispersion sections is $R56_1 \approx 0.9mm$ and $R56_2 \approx 50\mu m$, respectively.

The parameters of the undulators in the different sections of FEL-II are listed in Table 3.

Table 3: Parameters of Undulators in Different Sections

Undulators		
Element	Strength of K	Length of λ_u
Mod1	33.3	24cm
Mod2	33.3	24cm
Mod3	8.4	6.8cm
Rad1	8.4	6.8cm
Rad2	3.5	6.8cm

The S2E simulation is performed by Genesis [13], the evolution of the EEHG phase space and the output bunching factor for the first-stage EEHG is shown in Figure 5.

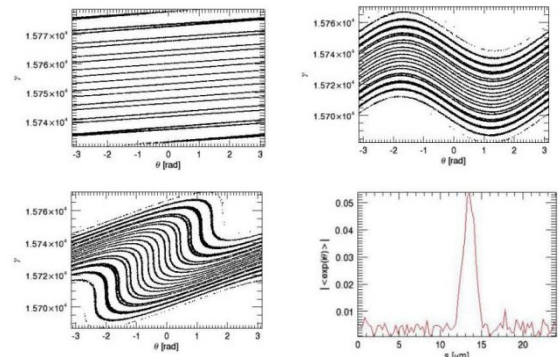


Figure 5: The evolution of EEHG phase space and bunching factor.

From Figure 5 one can find that the bunching factor is about 0.05, the radiation power and spectrum of the first-stage is given in Figure 6.

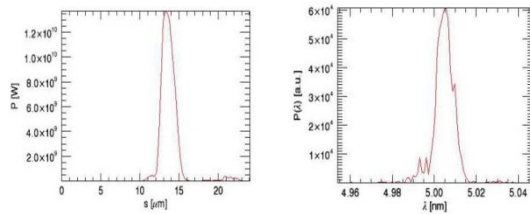


Figure 6: The output radiation power and spectrum from the first-stage EEHG.

Figure 6 shows that the output 5nm radiation power is about 12GW which is far away from saturation (about 25GW), however, it is enough to modulate the electron beam in second-stage, besides, the radiation power can be controlled by opening the gap of height variable undulators, after that, the radiation pulse is delayed to modulate a part of electron beam which is close to the head part, the HHG bunching factor of the second-stage is given in Figure 7.

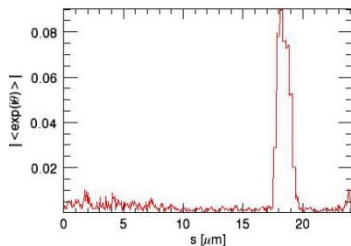


Figure 7: The bunching factor of the second-stage HHG.

From Figure 7, we can find that the fifth harmonic bunching factor of the second-stage HHG is about 0.08, and then the density modulated electron beam is sent to a long radiator to generate 1nm highly temporal coherent soft x-rays. The radiation power and spectrum of the second-stage is shown in Figure 8.

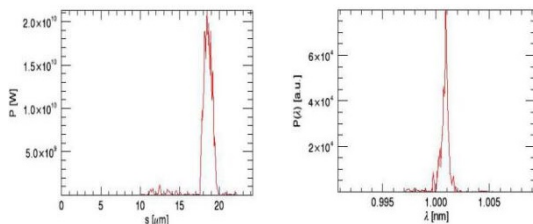


Figure 8: The radiation power and spectrum from the second-stage.

From Figure 8, one can find that the power of the 1nm highly temporal coherent radiation pulse is about 20GW.

CONCLUSION

The two-stage cascaded EEHG/HHG scheme is recognized as a method to generate highly temporal coherent soft x-rays with ultra-short wavelength. In this paper, this scheme is designed to generate 1nm soft x-rays, and it is

proved to work well at ultra-high harmonics of seeding lasers by the S2E simulation.

However, other effects may hinder the ability of this scheme to obtain this kind of soft x-rays with ultra-short wavelength and highly temporal coherence, such as IBS, CSR/ISR, MBI and phase error of the seeding lasers [14, 15, 16, 17], all these effects need to be carefully considered in the future optimization.

ACKNOWLEDGEMENTS

The authors would like to thank Chao Feng, and Tao Liu for helpful discussions and useful comments.

REFERENCES

- [1] P. Emma *et al.*, "First lasing and operation of an ångstrom-wavelength free-electron laser", *Nature Photonics*, vol. 4, 641 (2010), doi:10.1038/nphoton.2010.176
- [2] T. Ishikawa *et al.*, "A compact X-ray free-electron laser emitting in the sub-ångstrom region", *Nature Photonics*, vol. 6, 540 (2012), doi:10.1038/nphoton.2012.141
- [3] H. S. Kang *et al.*, "Hard X-ray free-electron laser with femtosecond-scale timing jitter", *Nature Photonics*, vol. 11, 708–713 (2017), doi:10.1038/s41566-017-0029-8
- [4] L. H. Yu, "Generation of intense uv radiation by subharmonically seeded single-pass free-electron lasers", *Phys. Rev. A*, vol. 44, 5178 (1991), doi:10.1103/physreva.44.5178
- [5] G. Stupakov, "Using the Beam-Echo Effect for Generation of Short-Wavelength Radiation", *Phys. Rev. Lett.*, vol. 102, 074801 (2009), doi:10.1103/PhysRevLett.102.074801
- [6] J. Amann *et al.*, "Demonstration of self-seeding in a hard-X-ray free-electron laser", *Nature Photonics*, vol. 6, 693 (2012), doi:10.1038/nphoton.2012.180
- [7] L.-H. Yu *et al.*, "High-Gain Harmonic-Generation Free-Electron Laser", *Science*, vol. 289, issue 5481, pp. 932–934, doi:10.1126/science.289.5481.932
- [8] D. Xiang *et al.*, "Demonstration of the Echo-Enabled Harmonic Generation Technique for Short-Wavelength Seeded Free Electron Lasers", *Phys. Rev. Lett.*, vol. 105 (2010) 114801, doi:10.1103/PhysRevLett.105.114801
- [9] Z. T. Zhao *et al.*, "First lasing of an echo-enabled harmonic generation free-electron laser", *Nature Photonics*, vol. 6, (2012) 360, doi:10.1038/nphoton.2012.105
- [10] E. Hemsing *et al.*, "Echo-enabled harmonics up to the 75th order from precisely tailored electron beams", *Nature Photonics*, vol. 10, 512–515 (2016), doi:10.1038/nphoton.2016.101
- [11] P. R. Ribič *et al.*, "Coherent soft X-ray pulses from an echo-enabled harmonic generation free-electron laser", *Nature Photonics*, vol. 13 (2019) 555, doi:10.1038/s41566-019-0427-1
- [12] K. Zhou, C. Feng, and D. Wang, "Feasibility study of generating ultra-high harmonic radiation with a single stage echo-enabled harmonic generation scheme", *Nucl. Instr. Meth. A*, vol. 834, 30 (2016), doi:10.1016/j.nima.2016.07.021

- [13] S. Reiche, GENESIS 1.3: a fully 3D time-dependent FEL simulation code, *Nucl. Instr. Meth. A*, 429, 243 (1999).
doi:10.1016/S0168-9002(99)00114-X
- [14] A. Piwinski, in *Proc. 9th Int. Conf. on High Energy Accelerators*, SLAC Stanford, 1974, p. 405.
- [15] Z. Huang, K. Kim, “Formulas for coherent synchrotron radiation microbunching in a bunch compressor chicane”, *Phys. Rev. ST Accel. Beams*, vol. 5, 074401 (2002),
doi:10.1103/PhysRevSTAB.5.129903
- [16] D. Ratner, A. Fry, G. Stupakov, and W. White, “Laser phase errors in seeded free electron lasers”, *Phys. Rev. ST Accel. Beams*, vol. 15, 030702 (2012),
doi:10.1103/PhysRevSTAB.15.030702
- [17] E. Hemsing *et al.*, “Seeding Experiments and Seeding Options for LCLS II”, in *Proc. 38th Int. Free Electron Laser Conf. (FEL'17)*, Santa Fe, NM, USA, Aug. 2017, pp. 219-224,
doi:10.18429/JACoW-FEL2017-TUB01

CONSIDERATIONS ON IMPLEMENTING EEHG WITH A STRONG LINEAR CHIRP

Mihai Pop*, Sverker Werin, Francesca Curbis, Weilun Quin
Physics department, Lund University, Lund, Sweden

ABSTRACT

Due to the stochastic nature of SASE radiation its longitudinal coherence is limited to a small fraction of the electron bunch. By pre-bunching the electrons before entering a radiator, the FEL radiation is ensured to have the same initial phase all through the bunch. Echo enabled harmonic generation (EEHG) is a technique that, by cleverly using two modulators and two dispersive sections, creates microbunches of electrons at a high harmonic of the seed laser used in the modulators. In this paper we will present some of the challenges of using this technique in combination with a strongly chirped beam and indicate a few ways to overcome said challenges.

INTRODUCTION

In a recent experiment [1], EEHG has been shown to be suitable as a high harmonic generation scheme with evidence of coherent radiation up to the 100th harmonic of a 260 nm UV laser.

The motivation for this work partly emerges in the wake of a bigger project to build a soft X-Ray FEL laser at MAX-IV the design would have account a large energy chirp of the electron beam at the Linac exit.

The scope of this paper is to have a better understanding of the effects of a strong linear chirp on the EEHG concept, not to give a definitive answer on using EEHG as a seeding method for SXL. For starters it is worth going through the classic EEHG process as proposed in [2].

The electron beam is modulated by having it co-propagate with a high intensity laser (Seed 1), in what is usually a strong insertion device Figure 1 Modulator 1. For long undulators with narrow gain bandwidth it is possible to have different modulation levels for different parts of the electron beam as electrons get off-resonance energies.

A strong dispersive section(in our case Chicane 1) folds the energy modulation of the electron bunch creating a fine structure of equally spaced energy slices. If the electron beam has a chirp, this element will either compress or de-compress the electron bunch depending on the combination of the chirp and dispersion sign.

To convert the fine energy separation into longitudinal bunching, a classic scheme involving a modulator (Figure 1

Modulator 2) and a weak dispersive section is used (Figure 1 Chicane 2).

In our analysis we use scaled notations as in [3] to have a feeling for the general phenomena rather than particular cases.

- **Scaled chirp** $Ch = \frac{\lambda_{mod1} Chirp [eV/m]}{2\pi\sigma_e}$. We can think of it as how many σ_e will the energy increase in one wavelength along the bunch.
- **Scaled Amplitude** $A_i = \frac{E-E_0}{\sigma_e}$. This parameter may be understood as the beam energy modulation amplitude in units of energy spread.
- **Scaled dispersion strength** $B_i = \frac{2\pi R56_i \cdot \sigma_e}{\lambda_{mod1} E_0}$. where $R56[m]$, is the normal momentum compaction factor. It is useful to think about B_i as the number of λ_{mod1} a particle with energy deviation of $1 \sigma_e$ is shifted w.r.t. a particle with reference energy.

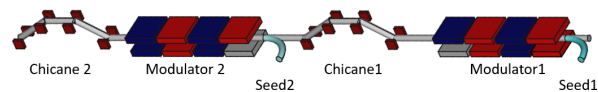


Figure 1: Layout of the EEHG scheme depicting the first modulator Modulator 1, the first dispersive section, in our case a chicane (Chicane 1), the second modulator Modulator 2, the second dispersive section, Chicane 2.

FEL SIMULATIONS

Common Settings

Simulations were carried out on LUNARC [4] using the FEL simulation code Genesis1.3 V4.3.1 with the *one4one* control parameter on, meaning that each electron is simulated as an individual particle. The layout used in simulations is similar to the one depicted in Figure 1. And it comprises of two identical modulators and two chicanes with positive momentum compaction $R56 > 0$. A summary of the electron beam and lattice parameters is shown in Table 1.

All the simulations are based on the matching presented in Figure 2. The radiator is tuned to 5 nm and for the EEHG simulations the seed has the wavelength of 260 nm or 248 eV. As a test case we use a SASE run with 0.23 scaled (0.5 MeV/fs) energy chirp using the same radiator.

*mihai.pop@maxiv.lu.se

Table 1: Lattice and Beam Parameters

Beam parameters			
γ	5871		
σ_E/E	1e-4		
Δl_{bunch}	80 μm		
Modulators	Period [m]	Length [m]	A_i
Modulator 1	0.25	2	3
Modulator 2	0.25	2	3
Chicanes	Length [m]	B_i	R_{56} [mm]
Chicane 1	3	18.15	24
Chicane 2	1	0.35	0.1
Radiator	period [m]	Length [m]	
Rad	0.04	4	

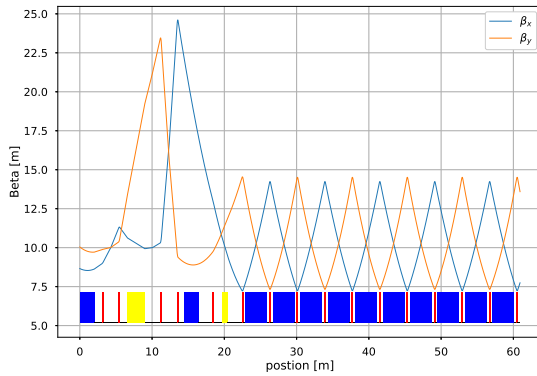


Figure 2: Beta function matching.

Chirp Sign Effects on Bunching

As discussed in the introduction, certain combinations of chirp and dispersive section sign lead either to a compression or a de-compression of the bunch. We used a series of chirps $\pm 0.23 \pm 0.1 \pm 0.05$ and 0, in scaled units, to highlight how the FEL radiation quality depends on the chirp. Among these, the -0.05 and -0.1 chirp are the only ones that get compressed (the final bunch length is shorter than the initial). Even though -0.23 has negative chirp it is over-compressed to over 3 times its initial size. This can be easily checked using $\frac{\Delta l}{l} = Ch(B1 + B2)$ bunch lengthening formula in [3]. The -0.05 case has a more extreme compression of about 3 times, which will have effects on the gain curve and the spectrum.

In Figure 3 the phase space of three different types of chirp is plotted. We highlight three phenomena that occur due to the chirp in the electron beam as it passes through the ECHO scheme.

1. In Figure 3 d), the peak current value is 25 % higher for the negative chirp than for the positive one.

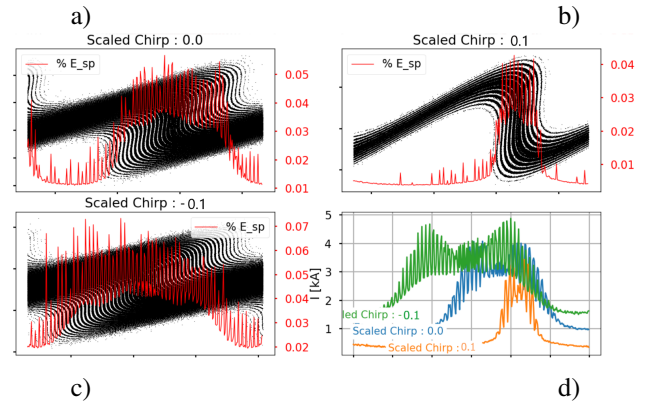


Figure 3: Figure plotting the electron beam phase space, slice energy spread and current profile at the entrance of the radiator. Phase space and slice energy spread for a) No chirp, b) scaled chirp of 0.1, c) scaled chirp of -0.1. d) current profile for the three chirp cases.

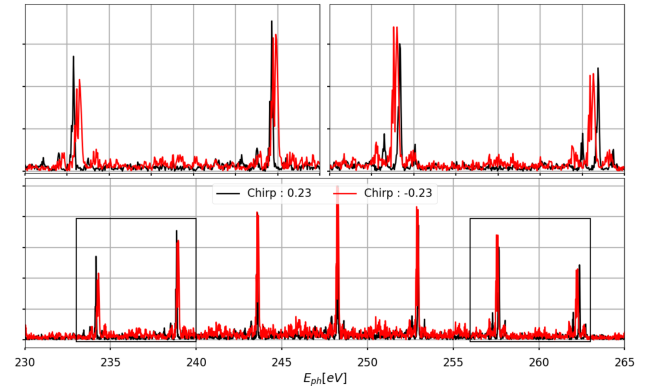


Figure 4: Spectra after 2 undulator periods (bottom). Zoom in left square (upper left), zoom in right square (upper right) for chirped beams with 0.23 (black) and -0.23 (red) scaled chirps.

2. The slice energy spread is almost two times higher for negative than for positive chirp, as one would expect from a compression scheme. Comparing to the initial 0.01% energy spread we see that all EEHG cases have a number of times higher values for this parameter.
3. Within one period of the seed laser Figure 3 a), b) and c), and by extension in the entirety of the bunch, the proportion of the beam that is modulated is 4 times as high for the negative as for the positive chirp. This effect is largely due to the energy spread relative to the modulation amplitude in Modulator 2.

A more subtle effect is related to the side-bands in the EEHG spectrum. We can use the spontaneous radiation generated by the particles a few periods into the radiator to get some information about electron bunching at various wavelengths. In Figure 4 we look at the spectrum of this radiation to observe the effect of the chirp on the spacing between high peak current regions, manifesting in the

spectrum. A larger distance in time domain will translate to a smaller separation in the frequency domain. After Chicane 1 the -0.23 chirp case will have a stronger chirp than the 0.23 case therefore the modulations induced in modulator 2 will be spread out more by Chicane 2 and hence the side-bands separation will be smaller. Indeed analyzing the top left and top right plots of Figure 4 we see that the side-bands of 0.23 chirp are always further apart from the central peak.

Power Output

Looking at the Gain curves in Figure 5 it is plain to see that the FEL process favors the negatively chirped cases with the shortest saturation length of 11 m for -0.05 scaled chirp, which also has the highest pulse energy of 1.5 mJ. We attribute these values to its high compression and thus peak current. The saturation length of chirps 0.23 and -0.23 is longer than SASE indicating that the current profile has been stretched to the point that it doubled the initial gain length.

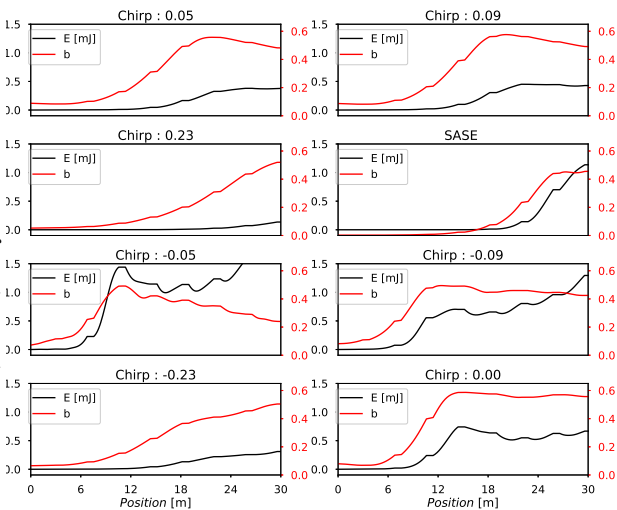


Figure 5: Pulse energy (black plot line) and bunching (red plot line) for different chirps in the electron beam along the radiator.

Spectra

We begin our spectral analysis looking at Figure 6 where the spectra of different chirp cases are plotted. As a first observation we find that the spectra of all the EEHG have a FWHM below 0.05% except the -0.05 case which is 0.2%, five times as wide. By looking at the phase space at the exit of Chicane 1 for this specific chirp, Figure 7, we can see that there are different chirps along the beam detail that does not appear in the other cases. We suspect this generates bunching at slightly different wavelengths that creates this broadening but further investigation is needed.

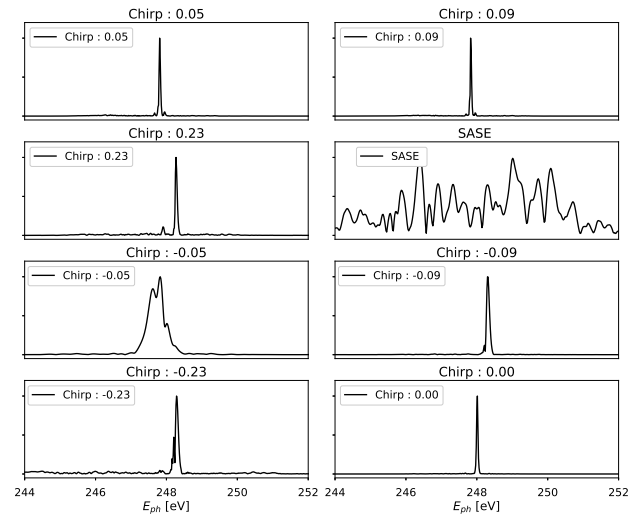


Figure 6: Spectra for different chirps and SASE at saturation (black) and after two undulator periods (red).

Negatively chirped shots have, in general, broader spectra, this may be due to the fact that in Chicane 1 they pass through a phase of over bunching that increases the energy spread, and the -0.05 is an extreme case of that. Out of the EEHG shots the 0 chirp has the narrowest spectra.

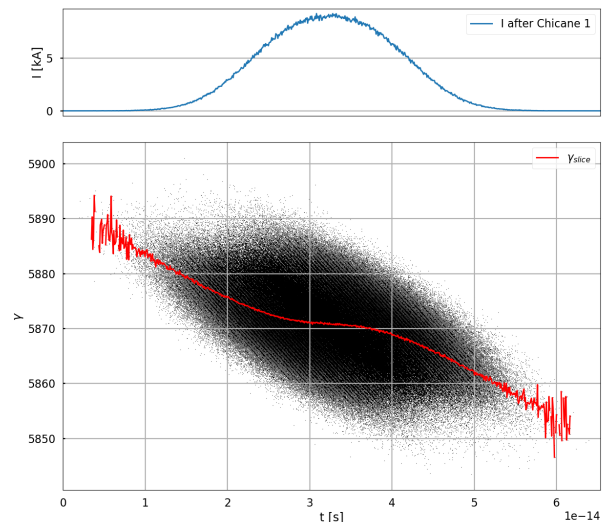


Figure 7: Phase space for -0.05 scaled chirp with slice energy along the bunch at the exit of chicane 1.

CONCLUSIONS

We have studied the chirp influence on EEHG FEL and shown that there is a strong dependency of the FEL radiation quality with the chirp for a given EEHG configuration. In our simulations we still found that 0 chirp is preferable but there are also advantages of certain combinations of chirp and chicane strength. Further work is needed to properly evaluate the over-compressing cases or possibly integrate the bunch compression as part of the EEHG scheme.

REFERENCES

- [1] P. Rebernik Ribič and e. a. Abrami, “Coherent soft X-ray pulses from an echo-enabled harmonic generation free-electron laser”, *Nature Photonics*, pp. 1–8, 2019.
doi:10.1038/s41566-019-0427-1
- [2] D. Xiang and G. Stupakov, “Echo-enabled harmonic generation free electron laser”, *Physical Review Special Topics - Accelerators and Beams*, vol. 12, no. 3, pp. 1–10, 2009.
doi:10.1103/PhysRevSTAB.12.030702
- [3] G. S. Z. Huang, D.F. Ratner and D. Xiang, “Effects of Energy Chirp on Echo-enabled Harmonic Generation Free Electron Lasers”, *Proc. of International Free Electron Laser Conference (FEL'09)*, Liverpool, UK, August 23-28, 2009, paper MOPC45.
- [4] SNIC, “The computations/simulations/ were performed on resources provided by the swedish national infrastructure for computing (snic) at [lunarc (aurora)]ie9 for windows phone 7: Adobe flash, demos and development”, <https://www.snic.se/>

START-TO-END SIMULATION OF THE NSRRC SEEDED VUV FEL

S. Y. Teng¹, C. H. Chen², W. K. Lau², A. P. Lee²
¹Department of Physics, NTHU, Hsinchu, Taiwan
²NSRRC, Hsinchu, Taiwan

Abstract

A free electron laser (FEL) driven by a high brightness electron linac system has been proposed to generate ultra-short intense coherent radiation in the vacuum ultraviolet region. It is a third harmonic high-gain high harmonic generation (HGHG) FEL for generation of VUV radiation with wavelength at 66.7 nm from a 20 mm period length helical undulator. A 200 nm seed laser is used for beam energy modulation in a 10-periods helical undulator of 24 mm period length. A small chicane is placed between the two undulators to optimize power growth in the radiator. In this study, we perform start-to-end simulation to foresee the operational performance of the test facility and preliminary results are presented.

INTRODUCTION

The VUV FEL is a third harmonic HGHG FEL seeded by a 200 nm laser. The beam energy modulator is a 10-periods helical undulator with 24 mm period length. The radiator is also a helical undulator but of 20 mm period length which allows generation of high power coherent radiation at 66.7 nm wavelength [1]. Schematics of the NSRRC seeded VUV FEL is shown in Fig.1. The FEL is driven by a linac system that delivers a 100 pC, ~250 MeV high brightness electron beam. It is worth noting that a dogleg bunch compressor with linearization optics is used [2]. In this study, we perform simulation of beam dynamics in the proposed system starting from photoinjector cathode to FEL output. Space charge tracking in the photoinjector is done by GPT code [3], tracking of particles in the bunch compressor and linac systems is done by ELEGANT [4] and 3D time-dependent simulation of high gain FEL using GENESIS [5]. Data transfer between these two codes is done with SDDS [4].

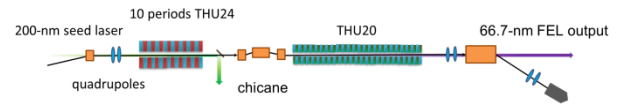


Figure 1: Schematics of the NSRRC third harmonic HGHG FEL.

Simulated drive beam properties by GPT and ELEGANT such as electron distribution in longitudinal phase space and beam current profile are summarized in the next section. The third section shows preliminary GENESIS simulation results of FEL interactions in modulator and radiator. The last section is the conclusions and summarized the direction for future study.

DRIVE BEAM

The bunch compressor designed for the driver is a double dog-leg configuration that provides a first order longitudinal dispersion function (i.e. R_{56}) and linearization optics for correction of nonlinearity introduced into the beam due to rf curvature. Bunch length or the peak current under various operation conditions can be adjusted by tuning R_{56} . It can be realized by changing the longitudinal positions of the outside dipoles of the dogleg compressor and by adjusting the quadrupoles and sextupoles. After bunch compression, the beam is accelerated to designed energy by two rf linac sections. In this simulation study, beam energy is at 263 MeV.

Electron Distribution in Longitudinal Phase Space

There is a residual energy chirp left after bunch compression. The beam is actually slightly over-compressed and the chirp is of ~42 keV/mm. This is tentatively corrected by a 1 m corrugated pipe dechirper structure [2]. Electron distribution of the dechirpered beam in longitudinal phase space at linac system exit is showed in Figure 2. Sliced energy spread in this case can be as low as 0.05%. In order to save tunnel space, dechirper using rectangular dielectric-lined waveguide is recently under study.

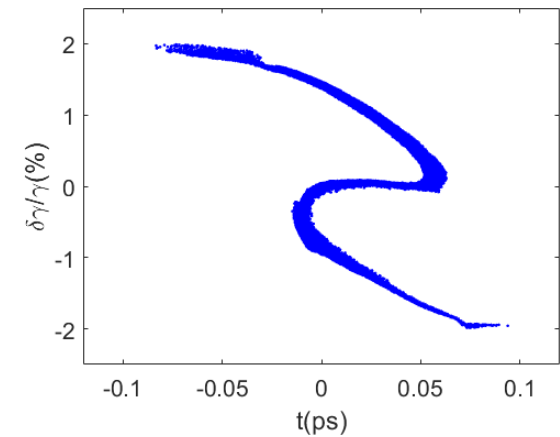


Figure 2: Electron distribution of the compressed beam in longitudinal phase space at linac system exit. Residual beam energy chirp is compensated by a 1 m corrugated pipe dechirper.

Beam Current Profile

After the dogleg bunch compressor, the 100 pC beam is compressed into 51 fs in duration so that the beam current profile is roughly uniform in the middle part. Fig. 3 shows

the current profile at linac system exit. Nominal peak current is about 800 A at the bunch centre.

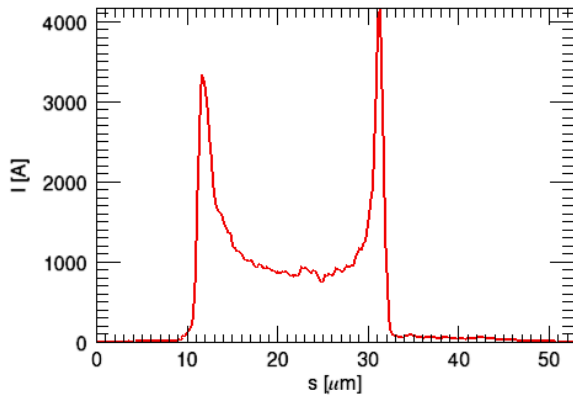


Figure 3: Beam current profile of the compressed beam at the exit of the drive linac.

HGHG FEL SIMULATION

3D time-dependent simulation of HGHG FEL is divided into two parts. First, we calculate beam energy modulation by the 200 nm seed laser in THU24 undulator. The second part is the beam-wave interaction in the radiator but with a small chicane placed upstream. The drive beam data from ELEGANT is converted from SDDS format to ASCII data format by the SDDS code for FEL simulation with GENESIS. A pair of quadrupoles has been used to minimize betatron oscillations in the radiator (see Fig. 1).

Beam Energy Modulation

The seed laser is coupled into the first helical undulator (i.e. THU24) for beam energy modulation. While betatron oscillation in THU20 is minimized by optimizing beam size at its entrance, beam size at THU24 entrance is at $\sim 300 \mu\text{m}$. Seed laser spot size is set at about three times of the beam size at modulator entrance (i.e. Rayleigh length equals to 20 m). In this context, an energy modulator of 0.14% can be achieved for laser power at 300 MW. Figure 4 depicts the distribution of the energy modulated beam in longitudinal phase space after the THU24 helical undulator.

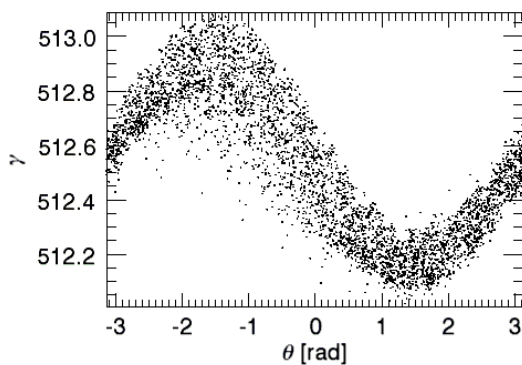


Figure 4: Distribution of the energy modulated beam in longitudinal phase space after the THU24.

Dispersive Section

The purpose of the dispersive section is to provide necessary microbunching at 200 nm spacing so that coherent harmonic undulator radiation can be generated in roughly the first two gain length. Such coherent is acted as the seed for high gain FEL interaction in the radiator [6]. The dispersive section is a simple four-dipole chicane. Strength of the dipole magnets are optimized for fastest power growth in the radiator. It is found that at 0.1 T dipole strength, the saturation length of the 66.7 nm radiation is the shortest.

Power Growth in Radiator

The VUV radiation is saturated at about 3.5 m with an output power of 240 MW. This result is in good agreement with the prediction of saturated output power by Xie's fitting formula [7]. Radiation power growth along beam axis is shown in Fig. 5. In the first few gain length, the prebunched electron beam by laser-beam interaction in the modulator THU24 radiates coherently at third harmonics of the seed laser. Coherent undulator radiation power at 1.5 m undulator length is about 15 MW. As microbunching (at 66.7 nm spacing) in THU20 becomes significant, the VUV radiation grows exponentially and saturates at ~ 3.5 m.

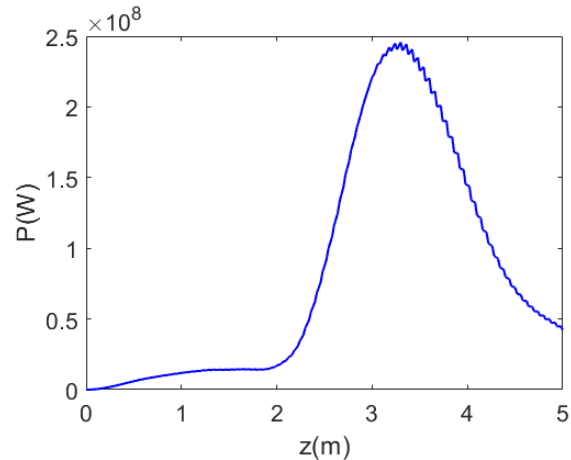


Figure 5: Evolution of VUV radiation in THU20 helical undulator.

Table 1: HGHG FEL Parameters at 66.7 nm Operation

Modulator period [mm]	24
Modulator parameter K	1.84
Modulator length [m]	0.24
Seed laser Rayleigh range [m]	20
Seed power [MW]	300
Radiator period [mm]	20
Radiator parameter K	0.867
Radiator output power [MW]	240
Electron beam energy [MeV]	263
RMS beam size [μm]	260
Normalized emittance [mm-mrad]	3
Peak current [A]	800
Beam modulation [%]	0.14
Magnet strength of 4-dipole chicane [T]	0.1

CONCLUSION

In this start-to-end simulation study, we obtained a distribution of ~ 800 A, 51 fs compressed electron beam from GPT/ELEGANT simulation and transfer the output data to GENESIS at input and simulated the beam-wave interactions in modulator and radiator of a third harmonic HGFG FEL. Saturated output power of 240 MW can be obtained at 66.7 nm wavelength. A set of preliminary operational parameters is listed in Table 1. The properties of the drive beam from the high brightness linac system as well as the FEL interaction are by no means optimized. Further optimization of operational parameters is absolutely necessary. Further, the effects of undulator and laser field errors have to be investigated for engineering design. It has to be pointed out that the effect of coherent synchrotron radiation (CSR) occurred in the small chicane is neglected. We believe that it is insignificant for such a low energy beam and the chicane field strength is relatively weak.

More sophisticated seeding schemes such as EEHG [8] and energy-cooled HGFG [9] are obviously topics for future studies.

ACKNOWLEDGEMENTS

The authors thank Drs. Alex Chao and Juhao Wu for helpful discussions on the FEL physics and GENESIS simulation skill.

REFERENCES

- [1] W. K. Lau *et al.*, “An updated design of the NSRRC seeded VUV free electron laser test facility”, presented in the *39th Int. Free-Electron Laser Conf. (FEL'19)*, Hamburg, Germany, Aug. 2019, THP030, this conference.
- [2] W. K. Lau *et al.*, “Design of a dogleg bunch compressor with tuneable first-order longitudinal dispersion”, in *Proc. 38th Int. Free-Electron Laser Conf. (FEL'17)*, Santa Fe, USA, Aug. 2017, pp. 305-307.
doi.org/10.18429/JACoW-FEL2017-TUP031
- [3] Generic Particle Tracer, <https://www.pulsar.nsl/>
- [4] M. Borland, *User's Manual for elegant*, APS Light Source Note, LS-287, Sep. 2001.
- [5] S. Reiche, GENESIS, <http://genesis.web.psi.ch/>
- [6] L. H. Yu and J. Wu, “Theory of high gain harmonic generation: an analytical estimate”, *Nucl. Instr. Meth. A* 483 (2000), pp.493-498.
doi:10.1016/S0168-9002(02)00368-6
- [7] M. Xie, “Exact and variational solution of 3D eigenmodes in high gain FELs”, *Nucl. Instr. Meth. A* 445 (2000), pp. 59-66.
doi:10.1016/S0168-9002(00)00114-5
- [8] D. Xiang and G. Stupakov, “Echo-enabled harmonic generation free electron laser”, *Phys. Rev. ST Accel. Beams*, vol. 12, (2009), p. 030702.
doi:10.1103/PhysRevSTAB.12.030702
- [9] H. Deng and C. Feng, “Using off-resonance laser modulation for beam-energy-spread cooling in generation of short-wavelength radiation”, *Phys. Rev. Lett.* vol. 111 (2013), 084801.
doi:10.1103/PhysRevLett.111.084801

XFEL THIRD HARMONIC STATISTICS MEASUREMENT AT LCLS

A. Halavanau, E. Hemsing, A. Lutman, C. Emma, G. Marcus, C. Pellegrini,
SLAC National Accelerator Laboratory, Stanford University, Menlo Park, USA

Abstract

We investigate the statistical properties of the 6 keV third harmonic XFEL radiation at 2 keV fundamental photon energy at LCLS. We performed third harmonic self-seeding in the hard X-ray self-seeding chicane and characterized the attained non-linear third harmonic spectrum. We compare theoretical predictions with experimental results.

INTRODUCTION

Third harmonic XFEL generation is often considered to be very useful for tripling the photon frequency in planar undulators. The odd harmonic wavelength on axis is given by

$$\lambda = \frac{\lambda_u}{2h\gamma^2} (1 + K^2/2). \quad (1)$$

where λ is the fundamental FEL radiation wavelength, λ_u is the undulator period with magnetic parameter K , $h = 3, 5, 7$ is the odd harmonic number. Initially, harmonics are evolving independently from the fundamental in the linear regime [1,2]. Very quickly, the linear regime is altered by the nonlinear bunching at the fundamental frequency, entering the nonlinear harmonic generation (NHG) regime [1–4]. Thus, most of the XFEL third harmonic power is generated in NHG regime, and is estimated to be a few percent level of the fundamental XFEL power [5].

It was shown, however, that harmonic power can be drastically increased by disrupting the fundamental, but letting third harmonic bunching continue to develop linearly. It can be done in numerous ways, e.g. introducing phase shifters to disrupt the fundamental, and/or by using frequency filters [2,3]. This process, known as “harmonic lasing”, allows accessing high photon energies at much higher power level at existing XFEL facilities. It has been previously considered for LCLS-II operations in detail in [6]. Recently, harmonic lasing has been performed at DESY [3] and at Pohang Accelerator Laboratory [7] in EUV regime.

EXPERIMENTAL SETUP

In this proceeding, we study the possibility of using the LCLS hard X-ray self-seeding (HXRSS) chicane Diamond crystal as a frequency filter in an HXR harmonic lasing setup. The first experimental results were reported in [8]. Since the original LCLS HXR beamline did not have variable gap and phase-shifters, experimental demonstration of the harmonic lasing was challenging and it will be done when the new LCLS-II HXR undulator is available. Here we focus on analyzing recorded data for the NHG and third harmonic self-seeding processes.

Our experimental setup, presented in Fig. 1, generated 2 keV photons at fundamental in U1-U15 undulator section,

Table 1: LCLS HXR Beamline Parameters During the Measurements

Parameter	Units	Value
Pulse duration	fs	80
Pulse energy (xtal)	μJ	80
Fundamental	keV	2
Third harmonic	keV	6
Gain length	m	4.1
Beam current	kA	1800
Energy spread	MeV	2.0
Emittance (proj.)	μm	0.8

and thereby produced 6 keV photons at the third harmonic. The LCLS pulse intensity was reduced by retracting first 3 undulators, to ensure a safe level of X-ray pulse energy absorbed by the diamond crystal. The generated non-linear third harmonic field was overlapped with the electron beam downstream of the HXRSS chicane, where the bunching at fundamental was removed. The Diamond crystal, while strongly absorbing the fundamental photon energy, propagated 6 keV photons with about 60 % attenuation. The LCLS HXR beamline experimental parameters are grouped in Table 1.

We registered the fundamental pulse energy with the gas intensity monitor and third harmonic spectra with a spectrometer. The data was then accumulated to provide spectral sums for the statistical analysis.

STATISTICAL PROPERTIES OF THE THIRD HARMONIC RADIATION

To derive the statistical properties of XFEL radiation at the fundamental frequency, we consider a chaotic ensemble of fully polarized sources [9]. It can be shown that a single mode probability density obeys negative exponential law:

$$p_1(I) = \frac{1}{\langle I \rangle} \exp\left(-\frac{I}{\langle I \rangle}\right). \quad (2)$$

Here I is the instantaneous single mode radiation intensity and $\langle I \rangle$ is its time average. Iteratively integrating using a convolution rule $p_2(W) = \int_0^W p_1(W-x)p_1(x)dx$, one



Figure 1: Experimental layout of XFEL third harmonic studies at LCLS.

quickly arrives to a well-known formula often referred to as “Gamma” statistics

$$p_M(W) = \frac{M^M}{\Gamma(M)} \left(\frac{W}{\langle W \rangle} \right)^{M-1} \frac{1}{\langle W \rangle} \exp \left(-M \frac{W}{\langle W \rangle} \right), \quad (3)$$

where M has the physical meaning of number of modes in XFEL pulse. In the linear regime, higher harmonics are expected to follow the same probability law, with a different number of modes M [4].

In the nonlinear regime, for h -th odd harmonic radiation, one should take into account the h -th power scaling, therefore we transform $p_1(W) \rightarrow p_1^{(h)}(z)$ with $z = W^h$ [10]. Then the single mode probability density is given by

$$p_1^{(h)}(z) = \frac{1}{h\langle W \rangle} z^{(1-h)/h} \exp \left(-\frac{z^{1/h}}{\langle W \rangle} \right), \quad (4)$$

with $\int_0^\infty p_1^{(h)}(z) dz = 1$. Convoluting with itself, we arrive to:

$$p_2^{(h)}(z) = \frac{1}{h^2 \langle W \rangle^2} \int_0^z [z'(z-z')]^{(1-h)/h} \times \exp \left(-\frac{z'^{1/h} + (z-z')^{1/h}}{\langle W \rangle} \right) dz' \quad (5)$$

Due to the difference in prefactor and in the exponential in Eq. (4), the integral in Eq. (5) becomes fundamentally different. Notice that any positive odd number h in $(1-h)/h$ yields a negative fraction, therefore the integrand in Eq. (5) has branching points at 0, z . Integrating Eq. (5) for $h = 3$ and two and more modes in closed form becomes cumbersome and does not match with the “Gamma” law given by Eq. (3). Instead, S -fold mode convolutions can be integrated numerically to an arbitrary precision, ensuring the condition $\int_0^\infty p_S^{(3)}(z) dz = 1$ for any given number of third harmonic modes S .

COMPARISON WITH EXPERIMENTAL SPECTRA

To perform further investigation of the derived statistics, we analyze recorded spectra (see Fig. 2) and its statistics. Figure 3 displays numerically evaluated nonlinear third harmonic statistics for a different number of third harmonic modes S . For asymptotics analysis we plotted “Gamma” statistics that approximately matches the $p_S^{(3)}(z)$ alongside. Very interestingly, $p_S^{(3)}(z)$ asymptotically follows “Gamma” statistics with the relation for the number of modes $S/M_{fit} \approx 34$. We also provide a comparison of semi-analytically calculated probability density function with the measured experimental spectral sums in Fig. 3. Figure 3 also displays the fitted M in $p_S^{(3)}(z)$. Notice that initially S is large due to all modes of the nonlinear third harmonic passed through the filtering crystal. It is then slightly reduced between U17 and U22, and then increases downstream of U22. Overall, the derived statistics corroborates with the measurements to a very good extent.

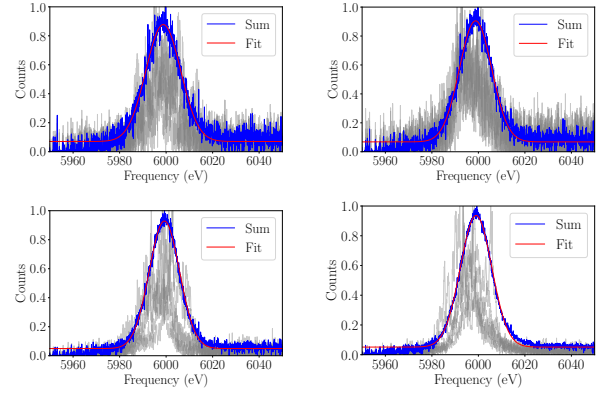


Figure 2: Shot-to-shot (gray) and cumulative spectra (blue) of the third harmonic at (left to right, top to bottom) U18, U20, U22 and U26 location.

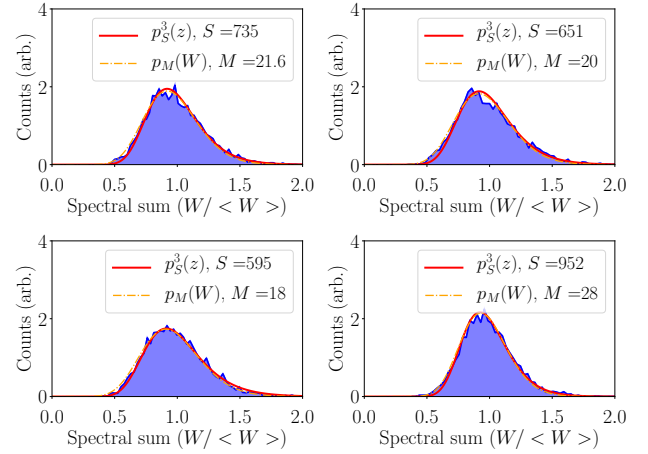


Figure 3: Histograms of spectral sums of the third harmonic radiation at (left to right, top to bottom) U18, U20, U22 and U26 location.

COMPARISON WITH STATISTICS OF THE FUNDAMENTAL

An interesting comparison can be drawn from the fundamental statistics of the XFEL pulse, recorded by the gas intensity monitor. We will use RMS fluctuations given by

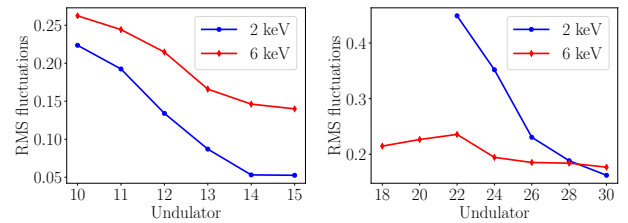


Figure 4: RMS fluctuations of the fundamental (2 keV) and third harmonic (6 keV) radiation intensity as a function of LCLS HXR undulator number.

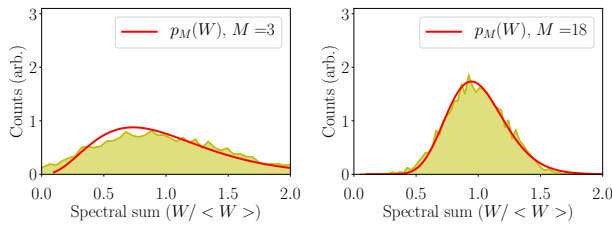


Figure 5: Statistics of the fundamental 2 keV radiation intensity at U22 (left) and U26 (right) location.

the following relation

$$\sqrt{\frac{\sigma_W^2}{W^2}} = \frac{1}{\sqrt{M}}, \quad (6)$$

where W is the intensity, σ_W^2 is the intensity variance, and M is approximately the number of Poisson modes given by (2). Ref. [4] gives an estimate of non-linear third harmonic RMS fluctuations to be 4 times more noisy (see Eq. (B10) in [4]). This estimate is provided for the case of the exponential SASE regime of the fundamental. In our experiment, we first drove 2 keV fundamental photon energy close to saturation, in order to generate large number photons at 6 keV [8].

Comparison of RMS intensity fluctuations is presented in Fig. 4. We observe the discrepancy of about factor of 2 with theoretically predicted value, possibly attributed to the noise in gas intensity monitor that was used to record the fundamental. Additionally being close to saturation in fundamental photon energy alters the assumptions of Ref. [4]. The direct measurement of the third harmonic statistics in various regimes require additional preparation of the detector hardware and will be performed separately.

We provide a comparison between fundamental and third harmonic RMS fluctuations in Fig. 4. As expected, the non-linear third harmonic has more fluctuations than fundamental; see Fig. 4, left. When going to the case of self-seeding, fundamental starts to develop around U22, and the “Gamma” statistics emerge as seen in Fig. 5. Thus, XFEL radiation field enters an interesting regime, where the statistical RMS fluctuations of both fundamental and third harmonic are equal.

SUMMARY AND CONCLUSIONS

In summary, we have analyzed recorded spectra for XFEL fundamental 2 keV and third harmonic 6 keV photon energy. We derived semi-analytical model for the third harmonic statistics and observed an agreement between the data and our model. We demonstrate that non-linear third harmonic statistics in case of large number of modes asymptotically follows the “Gamma” and eventually Gaussian statistics.

Existing LCLS-II HXRSS chicane infrastructure can be used for future third harmonic self-seeding and harmonic lasing experiments. We present here a special case when both fundamental and third harmonic attain the same level of statistical fluctuations in the process of third harmonic self-seeding.

We note that combining our setup with the new variable gap LCLS-II HXR undulator and phase-shifters will significantly enhance harmonic lasing process at HXR photon energy. The results of these studies will be reported elsewhere.

ACKNOWLEDGEMENTS

This work was supported by the U.S. Department of Energy Contract No. DE-AC02-76SF00515 and award no. 2017-SLAC-100382. Authors would like to thank Z. Huang for the valuable suggestions throughout the research. A.H. is grateful to E. Schneidmiller for many discussions on this topic during IPAC19 conference.

REFERENCES

- [1] R. Bonifacio, L. De Salvo Souza, P. Pierini, and E. T. Scharlemann. *NIM:A*, 296:787–790, (1990). doi:10.1016/0168-9002(90)91307-W
- [2] B. W. J. McNeil, G. R. M. Robb, M. W. Poole, and N. R. Thompson. *Phys. Rev. Lett.*, 96:084801, (2006). doi:10.1103/PhysRevLett.96.084801
- [3] E. A. Schneidmiller and M. V. Yurkov. *Phys. Rev. ST Accel. Beams*, 15:080702, (2012). dpo:10.1103/PhysRevSTAB.15.080702 [Erratum: *Phys. Rev. ST Accel. Beams*, 15:119901, (2012)]. doi:10.1103/PhysRevSTAB.15.119901
- [4] Z. Huang and K.-J. Kim. *Phys. Rev. E*, 62:7295–7308, (2000). doi:10.1103/PhysRevE.62.7295
- [5] D. Ratner, *et al*, *Phys. Rev. ST Accel. Beams*, 14:060701, 2011. doi:10.1103/PhysRevSTAB.14.060701
- [6] G. Marcus, Y. Ding, Z. Huang, T. Raubenheimer, G. Penn, “Harmonic lasing options for LCLS-II”, *Report No. SLAC-PUB-16081*, (2014).
- [7] I. Nam, C.-K. Min, C. Kim, H. Yang, G. Kim, H. Heo, S. Kwon, S. H. Park, and H.-S. Kang. *Applied Physics Letters*, 112(21):213506, (2018). doi:10.1063/1.5030443
- [8] C. Emma, *et al*, In *Proc. of IPAC2019 Melbourne, Australia, May 19-24, 2019*, page TUPRB091, 2019. doi:10.18429/JACoW-IPAC2019-TUPRB091
- [9] J.W. Goodman. *Statistical Optics*. Wiley Series in Pure and Applied Optics. Wiley, (2000).
- [10] E.L. Saldin, E.A. Schneidmiller, and M.V. Yurkov. *Optics Communications*, 212(4), pp. 377–390, 2002. doi:10.1016/S0030-4018(02)02008-4

APPLICATION OF INFRARED FEL OSCILLATORS FOR PRODUCING ISOLATED ATTOSECOND X-RAY PULSES VIA HIGH-HARMONIC GENERATION IN RARE GASES

R. Hajima*, R. Nagai, K. Kawase,

National Institutes for Quantum and Radiological Science and Technology, Tokai, Ibaraki, Japan

H. Ohgaki, H. Zen,

Kyoto University, Uji, Kyoto, Japan

Y. Hayakawa, T. Sakai, Y. Sumitomo,

Nihon University, Funabashi, Chiba, Japan

M. Shimada, T. Miyajima,

High Energy Accelerator Research Organization, Tsukuba, Ibaraki, Japan

Abstract

High harmonic generation (HHG) in rare gases is now becoming a common technology to produce attosecond pulses in VUV wavelengths. So far HHG sources have been realized by femtosecond solid-state lasers, not FELs. We propose a FEL-driven HHG source to explore attosecond pulses at photon energies above 1 keV with a MHz-repetition, which is difficult with solid-state lasers. A research program has been funded to establish technologies for the FEL-HHG, which covers generation and characterization of few-cycle IR pulses in a FEL oscillator, stacking of FEL pulses in an external cavity, and a seed laser for stabilization of carrier-envelope phase in a FEL oscillator. In this paper, we present the scheme of FEL-HHG and the status of the research program.

INTRODUCTION

Recent development of solid-state laser technologies has realized a generation of isolated attosecond pulses in ultraviolet and X-ray wavelengths via high harmonic generation (HHG) in rare gas and solid-state targets [1]. As such attosecond photon sources are routinely available in laboratories, attosecond science is becoming an active research field, in which ultrafast dynamics in atoms and molecules is investigated in detail.

Combination of HHG and a free-electron laser (FEL) was examined at a SASE FEL, where a UV pulse from HHG was used as a seed laser to stabilize the shot-to-shot variation in spectrum and energy of the FEL pulses [2]. The experiment can be called HHG-seeded FEL or HHG-FEL. To the contrary, an optical pulse generated from an infrared FEL can be used, in principle, to drive HHG, that is FEL-HHG [3]. However, such an experiment has never been considered seriously.

In the present paper, we describe a research project towards the FEL-HHG to generate attosecond VUV and X-ray pulses from an infrared FEL oscillator.

FEL-HHG

Advantage of FEL-HHG

There are several trends in the development of HHG photon sources. One of the major trends is increasing the photon energy (or decreasing the photon wavelength) available in HHG photon sources. The highest photon energy so far demonstrated is a generation of a bright supercontinuum that spans from the ultraviolet to more than 1.6 keV [4]. The experiment utilized a mid-infrared laser pulse, a wavelength of $\lambda = 3.9 \mu\text{m}$, as a driver of HHG. Theoretical and experimental studies revealed that the HHG cut-off energy scales as $\lambda^{1.7}$ in the phase-matched condition [4]. Pushing the cut-off energy above 1.6 keV has not realized mainly due to the lack of mid-infrared laser pulses satisfying conditions for HHG, wavelength, pulse energy, pulse duration, and repetition. Thanks to wavelength tunability and high-repetition availability, a FEL oscillator is a potential driver of HHG photon sources complementary to conventional solid-state femtosecond lasers.

Few-Cycle Pulse Generation

Generation of isolated attosecond pulses from HHG is available in several schemes [5]. The simplest one is utilizing carrier-envelope-phase-stable (CEP-stable) few-cycle pulses as a driver of HHG.

In a FEL oscillator, few-cycle lasing has been studied experimentally and theoretically. In normal conducting linac FELs, few-cycle lasing was observed in a transient regime before the onset of saturation, when the FEL oscillator was operated at a small negative detuning of the cavity length [6]. This lasing behavior was analytically studied in the context of supermode theory and recognized as a multisupermode regime that occurs in the limit where all the supermodes converge toward a unique degenerate supermode [7]. After the onset of saturation, the lasing shifts to a chaotic regime and a few-cycle solitary pulse is no longer available.

Another type of few-cycle lasing appears in a FEL oscillator operated with a long macro pulse from a superconducting linac [8]. This steady-state few-cycle lasing is accompanied by high extraction efficiency and occurs at the condition of a

* hajima.ryoichi@qst.go.jp

perfectly synchronized cavity, or zero detuning length, with high-gain and small-loss parameters [9]. We consider this lasing can be applied for driving a HHG photon source.

Stabilization of Carrier-Envelope Phase

In the generation of isolated attosecond pulses from few-cycle laser pulses, photon yield and cut-off energy depend on carrier-envelope phase (CEP) [10]. Therefore, CEP-stable laser pulses are necessary for a practical use of isolated attosecond pulses from HHG photon sources. In solid-state lasers, generation of CEP-stable few-cycle pulses is now a well-established technology.

However, CEP stabilization in FEL oscillators has never been demonstrated because the evolution of FEL pulses is initiated by the shot noise. In the steady-state few-cycle lasing at the perfectly synchronized cavity, the leading part of the optical pulse contains incoherent shot noise with random amplitude and phase. The amplitude and phase in the entire FEL pulse are governed by the interaction between the electrons and the radiation initiated by the shot noise in the leading part. Consequently, the carrier frequency and phase of the FEL pulses are not stabilized.

We propose that the above shot-noise-induced fluctuation can be completely stabilized by an external CEP-stable seed laser to lock the phase and amplitude of the leading part of the FEL pulse [11]. Simulations including the seed laser pulse show that a CEP-stable few-cycle FEL pulse can be generated at a FEL oscillator and the jitter of CEP is small enough with a realistic accelerator parameters.

PROPOSED CONFIGURATION OF FEL-HHG

Figure 1 shows a schematic view of the proposed FEL-HHG. The FEL wavelength should be determined from the requirements of attosecond pulse generation in HHG. For a generation of attosecond pulses whose wavelength covers from VUV to X-ray above 1 keV, we assume the FEL wavelength of 2-6 μm from the scaling law of HHG cut-off energy. A superconducting linac is adopted to deliver a CW pulse train to the FEL-HHG.

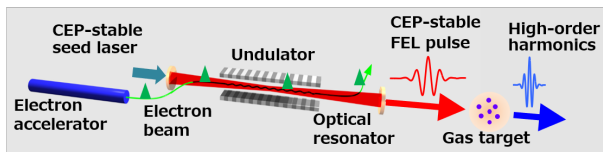


Figure 1: Schematic view of high-harmonics generation driven by an infrared FEL oscillator (FEL-HHG).

Example sets of FEL-HHG parameters are listed in Table 1, where the FEL wavelength is 2 μm and 6 μm and the parameters are chosen so that FEL pulse energy is 0.5 mJ. We consider such FEL oscillators can be constructed with existing technologies: a photo-cathode electron gun [12] and superconducting RF cavities [13].

Table 1: Example Parameters of FEL Oscillators for FEL-HHG

	(A)	(B)
Electron beam energy (MeV)	85	50
bunch charge (pC)	60	100
norm. emittance (x/y) (mm-mrad)	12/12	12/12
bunch length (ps)	0.27	0.4
peak current (A)	220	250
bunch repetition (MHz)	10	10
undulator		
undulator parameter (rms)	1.34	1.25
pitch (cm)	4.0	4.5
number of periods	80	40
FEL		
wavelength (μm)	2	6
Rayleigh length (m)	0.92	0.52
FEL parameter, ρ	0.0030	0.0052
cavity loss	6%	4%

RESEARCH PROGRAM

Overview of the Program

A 10-year research program (2018-2027) has been funded to establish basic technologies for the FEL-HHG. In the program, we are conducting research and development towards the FEL-HHG at two FEL facilities, KU-FEL at Kyoto University and LEBRA-FEL at Nihon University, both of which are infrared FEL oscillators driven by normal conducting linear accelerators. These facilities of normal conducting FELs can be exploited for basic technologies development and a following proof-of-concept experiment of FEL-HHG, whereas FEL-HHG for a full-scale application of attosecond VUV and X-ray pulses should be realized by a superconducting linac FEL oscillator.

The research subjects to be conducted are (1) generation and characterization of few-cycle mid-infrared pulses from FEL oscillators, (2) enhancement of FEL pulse energy by an external optical cavity, (3) scheme for CEP stabilization of FEL pulses including the development of a mid-infrared seed laser. We plan to explore these subjects in the first 6 years, 2018-2023, and proceed to an experimental demonstration of the FEL-HHG at one of two facilities. A seed laser for the CEP stabilization and a HHG gas target will be developed at National Institutes for Quantum and Radiological Science and Technology (QST).

In the following sections, we describe the status of our research program at each laboratory.

KU-FEL

KU-FEL at Kyoto University is operated to provide FEL pulses from 3.4 to 26 μm for user experiments [14]. We recently achieved lasing with high-extraction efficiency at the perfectly synchronized cavity length at KU-FEL and a

numerical simulation reproducing the experimental result suggests a generation of a few-cycle FEL pulse [15]. For realizing such lasing within a limited macro pulse duration, 8 μs , at KU-FEL, we applied dynamic cavity desynchronization (DCD), in which RF phase for the klystron input signal was modulated to change the electron bunch interval during a macro pulse [16]. We optimized parameters for the DCD, timing and depth of the modulation, to maximize the extraction efficiency. A measurement of spent electron beam energy indicated a FEL extraction efficiency of 5% at the end of a macro pulse as shown in Fig.2. In this experiment, electron beam energy was 27 MeV, bunch charge was 40 pC, and FEL wavelength was 11.6 μm .

In our research program, we plan to study a scaling law of FEL extraction efficiency and pulse duration with respect to the FEL gain and the cavity round-trip loss. Previous studies show that efficiency is a function of the cavity round-trip loss normalized to the FEL small gain integrated over the slippage distance [17].

The FEL lasing of 5% extraction efficiency was realized with 40-pC electron bunches from a 4.5-cell RF gun operated at a thermionic cathode mode. The bunch charge can be increased to 120 pC by changing the gun operation to a photo-cathode mode [18]. A drive laser for the photo-cathode operation is now ready and FEL lasing with 120-pC bunches will be soon carried out.

The FEL cavity of KU-FEL is equipped with two gold-coated copper mirrors, one of which has an on-axis small hole for out coupling. In order to reduce the cavity loss, the mirrors will be replaced by dielectric mirrors. After the replacement, we expect the cavity loss can be reduced from 3% with the hole-coupling to 1% with a dielectric mirror. Inverse square root of the normalized cavity loss, $1/\sqrt{\alpha}$, for FEL lasing at 10 μm can be varied from 13 (with thermionic cathode and metal mirrors) to 38 (with photo-cathode and dielectric mirrors), which is beyond the JAERI-FEL parameter to demonstrate extraction efficiency of 9%, $1/\sqrt{\alpha} = 27$ [9]. For the further increasing of FEL pulse energy, we also plan to install a new 1.6-cell RF gun to provide a train of 1-nC bunches.

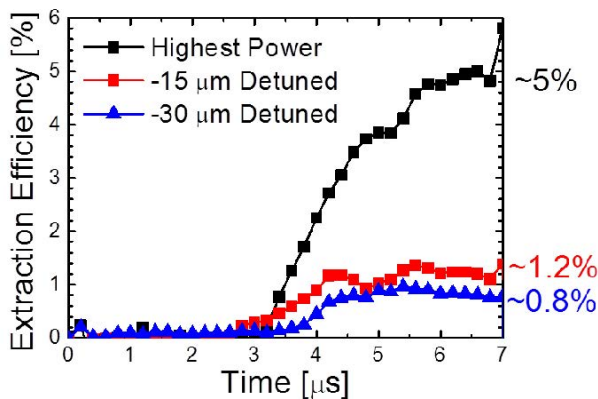


Figure 2: Temporal evolution of extraction efficiency under the relative cavity length of 0, -15 and -30 μm . [15]

LEBRA-FEL

The FEL oscillator at LEBRA covers 0.827-6.1 μm with a macro-pulse of 20 μs [19]. We plan to explore FEL pulse stacking in an external optical cavity utilizing advantage of the relatively long macro pulse.

Stacking laser pulses in an external cavity is a common technology to enhance the energy of pulses from a mode-locked laser for HHG [20] and other applications [21]. Generation of high-harmonics from a gas target is possible either using stored pulses in an external cavity or using a laser pulse dumped from a cavity. Such cavity dump can be done with semiconductor photo switches.

An experiment of FEL pulse stacking was conducted at the superconducting linac FEL at Stanford. They demonstrated accumulation of micropulses with more than 75 times the energy of the incident FEL pulses [22]. The Stanford FEL was operated at a quasi-CW mode and the external cavity could work in the steady-state mode, in which the injected pulse energy was balanced with the cavity loss. In normal-conducting-linac FELs, pulse stacking in the transient mode is suitable for maximizing the stored pulse energy [23]. In LEBRA-FEL, we will optimize the external cavity to realize FEL pulses for HHG experiments.

For the pulse stacking experiment, we set up an external cavity at an experimental room of LEBRA-FEL. The cavity is a bow-tie shape and the frequency of the cavity is chosen at 44 MHz, double of the FEL cavity frequency. The cavity length must be controlled precisely to stack successive pulses coherently. The FEL pulse train of 20 μs is, however, not long enough to tune the cavity length. Thus, we use a fiber laser oscillator for the cavity tuning. As a preliminary tuning of the cavity, we injected laser pulses from the fiber oscillator and confirmed multiple recirculation of injected laser pulses in the cavity (Fig. 3). Further tuning of the external cavity is in progress.

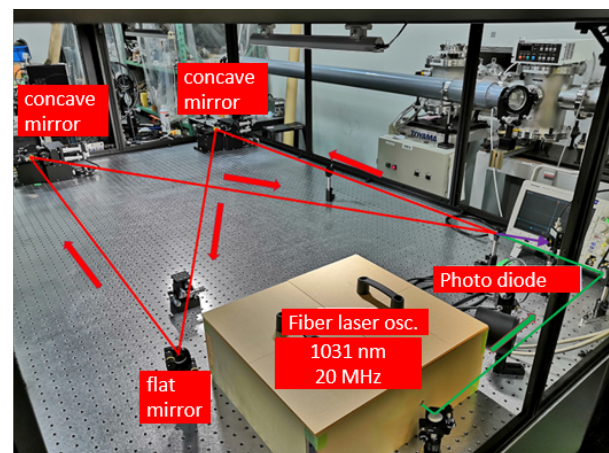


Figure 3: The external cavity for the FEL pulse stacking experiment at LEBRA-FEL.

In parallel with the experimental work, we are making simulation studies to predict a performance of the pulse stacking with optimized cavity parameters, transmittance

of the input coupler and recirculation path length. In the simulations, we use a 3-dimensional FEL code, GENESIS, coupled with a wave propagation code to calculate iterative interaction of a FEL pulse and electron bunches [24].

QST

A seed laser for the CEP-stabilization in a FEL oscillator must provide CEP-stable laser pulses with a moderate pulse energy, ~ 1 nJ. In addition, the laser pulse should be synchronized to the electron bunch repetition. Since generation of such laser pulses below $3 \mu\text{m}$ is well-established, we focus our efforts on the development of seed lasers at wavelength longer than $3 \mu\text{m}$. We design a laser system comprising a mode-locked fiber oscillator and a 30-W class fiber amplifier followed by a difference frequency generation between the light pulse of the fiber laser and its wavelength shifting. Figure 4 shows a fiber oscillator developed as the first stage of the laser system. The oscillator produces laser pulses at a repetition rate of 23.5 MHz and an average power of 150-300 mW. The second stage of the system, a 30-W amplifier, is now under fabrication.

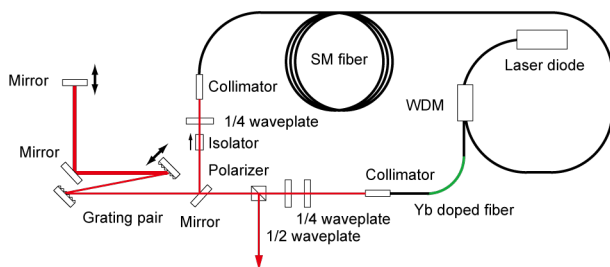


Figure 4: Schematic drawing of a fiber oscillator developed for a mid-IR seed laser. Output laser pulses are delivered to an amplifier followed by a difference frequency generation.

SUMMARY

We have proposed an attosecond photon source based on high-harmonic generation driven by mid-infrared FEL oscillators (FEL-HHG). The FEL-HHG is able to provide attosecond VUV and X-ray pulses with a MHz repetition. A research program has been funded for developing basic technologies for the FEL-HHG and realizing a proof-of-concept experiment of the FEL-HHG. In this research program, two FEL facility, KU-FEL and LEBRA-FEL, are exploited as platforms for the technology development.

ACKNOWLEDGEMENTS

This work was supported by MEXT Quantum Leap Flagship Program (MEXT Q-LEAP) Grant Number JP-MXS0118070271. The authors thank Xiao-Min Tong, Jiro Itatani, Nobuhisa Ishii and Keisuke Nagashima for helpful discussion.

REFERENCES

[1] F. Krausz and M. Ivanov, *Rev. Mod. Phys.* 81, 163 (2009). doi:10.1103/RevModPhys.81.163

[2] T. Togashi *et al.*, *Optics Express* 19, 317-324 (2011). doi:10.1364/OE.19.000317

[3] M. Tecimer, *Phys. Rev. ST-AB* 15, 020703 (2012). doi:10.1103/PhysRevSTAB.15.020703

[4] T. Popmintchev *et al.*, *Science* 336, 1287-1291 (2012). doi:10.1126/science.1218497

[5] M. Chini, K. Zhao and Z. Chang, *Nature Photonics* 8, 178-186 (2014). doi:10.1038/nphoton.2013.362

[6] G.M.H. Knippels *et al.*, *Phys. Rev. Lett.* 75, 1755 (1995). doi:10.1103/PhysRevLett.75.1755

[7] P. Chaix, N. Piovella, G. Gregoire, *Phys. Rev. E* 59, 1136 (1999). doi:10.1103/PhysRevE.59.1136

[8] R. Hajima and R. Nagai, *Phys. Rev. Lett.* 91, 024801 (2003). doi:10.1103/PhysRevLett.91.024801

[9] N. Nishimori *et al.*, *Nucl. Instr. Meth. A* 483, 134-137 (2002). doi:10.1016/S0168-9002(02)00298-X

[10] N. Ishii *et al.*, *Nature Comm.* 5, 3331 (2014). doi:10.1038/ncomms4331

[11] R. Hajima and R. Nagai, *Phys. Rev. Lett.* 119, 204802 (2017). doi:10.1103/PhysRevLett.119.204802

[12] N. Nishimori *et al.*, *Phys. Rev. Accel. Beams* 22, 053402 (2019). doi:10.1103/PhysRevAccelBeams.22.053402

[13] H. Sakai *et al.*, *Phys. Rev. Accel. Beams* 22, 022002 (2019). doi:10.1103/PhysRevAccelBeams.22.022002

[14] H. Zen *et al.*, *Physics Procedia* 84, 2016, pp. 47-53. doi:10.1016/j.phpro.2016.11.009

[15] H. Zen *et al.*, "Measurement of Extraction Efficiency of Kyoto University Free Electron Laser", in *Proc. 15th Annual Meeting of Particle Accelerator Society of Japan*, Nagaoka, Japan, Aug. 7-10, 2018, pp. 162-166 (in Japanese). https://www.pas.jp/web_publish/pasj2018/proceedings/PDF/FROL/FROL03.pdf

[16] R.J. Bakker *et al.*, *Phys. Rev. E* 48, R3256(R) (1993). doi:10.1103/PhysRevE.48.R3256

[17] N. Piovella *et al.*, *Phys. Rev. E* 52, 5470 (1995). doi:10.1103/PhysRevE.52.5470

[18] H. Zen *et al.*, in *Proc. IPAC'16*, 754-756, (2016). doi:10.18429/JACoW-IPAC2016-MOP0W018

[19] K. Hayakawa *et al.*, "Operation of Near-infrared FEL at Nihon University", in *Proc. FEL'07*, Novosibirsk, Russia, Aug. 2007, paper MOPPH046, pp. 114-117. <http://JACoW.org/f07/papers/MOPPH046.pdf>

[20] H. Carstens *et al.*, *Optica* 3, 366 (2016). doi:10.1364/OPTICA.3.000366

[21] T. Akagi *et al.*, *Phys. Rev. Accel. Beams* 19, 114701 (2016). doi:10.1103/PhysRevAccelBeams.19.114701

[22] T.I. Smith, P. Haar, H.A. Schwettman, *Nucl. Instr. Meth.* A393, 245-251 (1997). doi:10.1016/S0168-9002(97)00486-5

[23] P. Niknejadi *et al.*, *Phys. Rev. Acc. Beams* 22, 04704 (2019). doi:10.1103/PhysRevAccelBeams.22.04704

[24] Y. Sumitomo *et al.*, in *Proc. IPAC'19*, 1778-2781 (2019). doi:10.18429/JACoW-IPAC2019-TUPRB041

FINE AND HYPERFINE STRUCTURE OF FEL EMISSION SPECTRA

V.V. Kubarev[†], Ya.V. Getmanov, O.A. Shevchenko

Budker Institute of Nuclear Physics, Novosibirsk, Russian Federation

Y.U. Jeong, S.Y. Bae, Korea Atomic Energy Research Institute, Daejeon, Republic of Korea

Abstract

This paper presents the results of experimental investigations of the fine and hyperfine spectral structures of the Novosibirsk free-electron laser (NovoFEL) and the compact free-electron laser of the Korea Atomic Energy Research Institute (KAERI FEL) by means of the optimal instruments, resonance Fabry-Perot interferometers. The very high coherence of the NovoFEL spectrum was measured in regimes with one pulse circulating inside its optical resonator (the coherence length is 7 km, and the relative width of the hyperfine structure lines is $2 \cdot 10^{-8}$) and with total absence of coherence between two circulating pulses, i.e. the fine structure.

Sixty pulses circulate simultaneously inside the KAERI FEL optical resonator, and the measured coherence length on average covers ten pulses (the coherence length is 1 m; the relative width of the fine structure lines is 10^{-4}).

INTRODUCTION

The spectrum of FEL radiation depends on its coherence. Practically all FELs radiate some sequence of short pulses, which are produced by pulse/pulses circulating inside the optical resonator and periodically fed by the electron beam. The spectral contour of the FEL radiation is determined by the intra-pulse coherence, which depends on fast radiation instabilities and their suppression. For example, two different types of fast side-band instabilities were observed in the terahertz NovoFEL. The instabilities, studied in works [1-3], can be fully suppressed due to detuning between the electron and light repetition frequencies. In such a stabilized regime, the contour of the NovoFEL laser line has a Gaussian form with a width equal to the Fourier-transform limit.

A fine structure of FEL radiation can appear in systems with many pulses inside an optical resonator due to certain coherence between the pulses, which is usually some technical feature of the FEL facility. It is clear that in common case, intra-cavity light pulses are physically independent because they neither overlap nor interfere with one another. However, on the other hand, the main feature of any laser is the tendency to generate coherent radiation. Such tendency can be realized if intra-cavity light pulses are linked with one another by means of electron beam, when the electron pulse density has a spike or front shorter than the radiation half wavelength. A fine structure of FEL radiation caused by coherency of intra-cavity pulses was observed earlier on the INEA [4], FELIX [5], and FLARE [6] FELs. In the paper we describe such effect on the KAERI FEL and its absence on the NovoFEL.

Finally, a hyperfine structure of FEL emission spectrum (optical resonator modes) is *a priori* present in all FELs with an optical resonator. In the simplest case of one radiation pulse inside an optical resonator, the output train of FEL light pulses is radiation of one and the same intra-cavity pulse, which is periodically partly outcoupled and coherently refreshed by the electron beam. It is clear that coherency of output pulses can be very high as coherency of radiation of any stationary laser. It depends on slow fluctuations in the active medium because the physical limit of quantum fluctuations, determined by the ratio of spontaneous and stimulated emissions (Schawlow-Townes limit), is very high. Thus, the subject of this investigation is the real value of hyperfine coherency or the average number of output coherent pulses. In the work, the value was exactly measured for the terahertz NovoFEL.

FEL FACILITIES

Compact KAERI FEL

A detailed description of the KAERI FEL is presented in papers [7-9]. The acceleration system of the installation includes the 6- to 7-MeV microtron with a current of 40 to 50 mA in a macropulse 5 to 6 μ s long consisting of 2.8-GHz micropulses, as well as the electron-optical beam-line with bending magnets and quadrupole lenses. This beam-line connects the acceleration system with the radiation-source one. The radiation-source system includes the 2-m 80-pole planar electromagnetic undulator with a magnetic field of 4.5 to 6.8 kG and the optical resonator. A detailed description of the optical resonator and its optimization is given in [9].

The laser generation by the KAERI FEL takes place in the wavelength range of 110 to 160 μ m. The macropulse and micropulse radiation power is 50 to 100 W and ~ 0.5 to 1 kW, respectively. The micropulse duration is about of 30 ps. The repetition frequency of macropulses is 1 Hz in the typical operation regime. The contour spectrum of the laser radiation is the main fundamental mode with FWHM = 1-2 % and a moderate admixture of two side-band modes with a total spectrum base width of 2-3 % [8].

The optical resonator of the KAERI FEL is a hybrid resonator open in the horizontal x direction. It has a Gauss-beam field distribution, set by the horizontal curvature of its mirrors. In the transverse vertical y direction, it is a planar waveguide resonator with an operational TE_1 mode formed by the waveguide parallel metallic surfaces, slid apart to a distance of 2 mm. In the KAERI FEL, the repetition frequency of electron bunches is fixed equal to the magnetron frequency of the microtron RF system (2.8 GHz). The radiation of the optical resonator is output through a circular hole with a diameter 0.75 mm in one of

[†] V.V.Kubarev@inp.nsk.su

its identical cylindrical mirrors ($R_x = 3000$ mm, $R_y = \infty$). The resonator length is $L_0 = 2781$ mm; the undulator length is 2000 mm; the horizontal size of the mirrors is 30 mm.

The KAERI FEL radiation is transported by the vacuum beam-line of open type to the user hall, where these experiments were carried out.

Terahertz NovoFEL

The Novosibirsk FEL facility is based on the multiturn energy recovery linac (ERL) [10,11]. The ERL can operate in three modes, providing electron beam for three different FELs. The whole facility can be treated as three different ERLs (one-turn, two-turn, and four-turn), which use the same injector and the same linac. The one-turn ERL is placed vertically. It works for the terahertz NovoFEL, the undulator of which is installed on the concrete floor.

Depending on the number of turns, the maximum final electron energy can be 12, 22, or 42 MeV. The electron energy in the terahertz NovoFEL is 12 MeV. The bunch length in the one-turn ERL is about 100 ps. The maximum average current achieved in the one-turn ERL is 30 mA, which is still the world's record for ERLs.

One essential difference of the Novosibirsk ERL as compared with other facilities is the use of low-frequency non-superconducting 180.4 MHz RF cavities. On the one hand, this makes the linac bigger, but on the other hand, this allows increasing the transverse and longitudinal acceptances, which in turn enables operation with longer electron bunches with large transversal and longitudinal emittances. Moreover, there are no beam break-up instabilities on the Novosibirsk ERL, and the average beam current is now limited by the electron gun power.

The first stage FEL includes two electromagnetic undulators 3.5 meter long with a period of 12 cm, a phase shifter, and an optical cavity. The chosen undulator pole shape provides equal electron beam focusing in the vertical and horizontal directions. The phase shifter is installed between the undulators; it is used for phasing of the radiation of the two undulators.

The optical cavity of the terahertz NovoFEL is of the open type; it is composed of two copper mirrors covered by gold [12,13]. The curvature radius of the mirrors is 15 m. The distance between the mirrors is 26.589 m, which corresponds to a round-trip frequency (and a resonance electron repetition rate) of 5.64 MHz. The radiation is out-coupled into the beam-line through the circular 8-mm hole in the mirror center. The open-type optical beam-line was filled with dry nitrogen at atmosphere pressure. A CVD-diamond window separated the optical beamline from the vacuum chamber of the optical resonator.

The laser system of the first stage FEL generates coherent radiation tunable in the range of 80-240 μ m as a continuous train of 30-120 ps pulses with a repetition rate of 5.6, 11.2, and 22.4 MHz (the number of pulses inside the optical resonator is 1, 2, and 4). The maximum average output power is 0.5 kW; the peak power is more than 1 MW. The contour laser line in a stabilized regime has a 0.3%-

width Gaussian form, which is equal to the Fourier-transform limit.

INSTRUMENTS AND METHODS

Resonance Fabry-Perot Interferometer (FPI). Two Operation Modes of FPI.

Optical setups for our spectral investigations are shown in Fig. 1. In both schemes, FEL radiation (I) is input into beam-forming system (II), after which the beam size decreases to the optimal value and the beam wavefront becomes plane. Then follows the main part of the devices: resonance Fabry-Perot interferometers (III). Radiation passed through the FPIs was measured by detector system (IV).

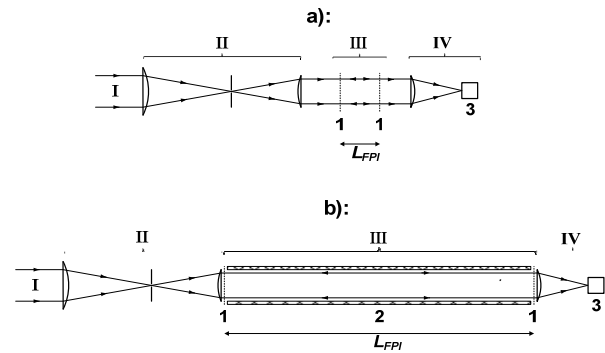


Figure 1: Optical schemes of devices used for measuring fine and hyperfine structures of KAERI FEL (a) and NovoFEL (b) spectra: I – radiated FEL beams, II – lens beam compressors and wavefront correctors, III – mesh resonance Fabry-Perot interferometers, IV – detector systems; 1 – electroformed metallic meshes, 2 – hollow dielectric waveguide (glass tube), 3 – different detectors. The length of Fabry-Perot interferometer L_{FPI} is the distance between the meshes.

An important feature of the FPIs is their resonance length L_{FPI} [14]. It should be noted that in the classical theory of FPI, continuous waves (CW radiation) circulating in a device always interfere with one another. With some simple modifications, this theory can be applied to pulse-periodical radiation of FEL only when $L_{FPI} = \Lambda/(2n)$ or $L_{FPI} = (\Lambda/2) \cdot m$, where Λ is the distance between pulses and n and m are integers. In the first case, it is necessary to take into account additional loss of radiation in the FPI; in the second case, only sets of pulses divided by the distance $\Lambda \cdot m$ are analysed. When an FPI has a non-resonance length, as in work [4], its efficiency fall dramatically (pulses inside the FPI do not overlap fully) and interpretation of the experimental results is practically impossible without special simulation.

The typical operation mode of FPI setups is the frequency-domain mode, when the transmitted radiation power is slowly measured as a function of ΔL_{FPI} (small variation of L_{FPI} near its resonance value). Sometimes the time-domain mode of FPI operation (the NovoFEL case) is

very useful, when a rather fast detector measures the transmitted power as a function of time (3 on Fig. 1b) at a constant resonance length L_{FPI} .

In the fine mode of the KAERI FEL experiment, an FPI with $L_{FPI-1} = 53.6$ mm ($m=1$) was used (Fig. 1a). We also checked the measured data of the FPI using a device with the double length $L_{FPI-2} = 107.2$ mm ($m=2$). In both FPIs, electroformed Ni meshes with square symmetry and 30- μ m period were used as mirrors. A step-motor translation stage was changing the distance between the mirrors; a commercial pyroelectric detector was measuring the transmitted power.

For the hyperfine mode of the KAERI FEL experiment we prepared a high resolution FPI with $L_{FPI-3} = 536$ mm ($m=10$) and Ni meshes with a 20- μ m period. However, the transmittance of such device was small, and therefore we had to apply a liquid He-cooled detector. Unfortunately, the production of liquid He in the South Korea stopped, and this experiment was remitted for future.

Fine and hyperfine spectral experiments on the NovoFEL require FPIs with much higher resolution. Thus, an ultra-long vacuum waveguide FPI was created (Fig. 1b). Its length is equal to 2658.9 mm, which is ten times less than the NovoFEL optical resonator length. Actually, it is a modified (lengthened) optical resonator of our universal gas laser [15-17], which was used earlier in many technological experiment on the NovoFEL facility [3]. The EH₁₁ waveguide operating mode of the FPI makes it possible to have a plane wave-front at a long distance, and the vacuum medium allows avoiding atmosphere absorption. The length of the FPI can be fixed or vary with the temperature of hollow invar rods, in which a thermo-stabilized liquid was circulating. A 10-period scanning of a NovoFEL fine structure takes about 10 minutes. In the slow frequency-domain working mode, a lock-in commercial pyroelectric detector system was applied. When the FPI worked in the fast time-domain mode, the FPI length was fixed near the resonance value due to the stable temperature of the invar rods. In this case, a self-made Schottky diode detector [18] was recording the transmitted power oscillograms.

EXPERIMENTAL RESULTS

Fine Structure of the KAERI FEL Spectrum

The fine mode structure of the KAERI FEL spectrum at a wavelength of 117 μ m is shown in Fig. 2. We used two FPIs with the lengths $L_{FPI-1} = 53.6$ mm ($m=1$) and $L_{FPI-2} = 107.2$ mm ($m=2$). For the first device, $2L_{FPI-1} = \Lambda$, and for second, $2L_{FPI-2} = 2\Lambda$, where Λ is the distance between pulses. Thus, in the first FPI, all pulses will interfere. In the second one, two sets of pulses shifted by one pulse (for example, sets of conventional even and odd pulses) will interfere independently. We can see in Fig. 2 that the fine mode structures corresponded to the pulse frequencies. We used FPI-2 to confirm the experimental results of FPI-1 because the calculated instrumental function of FPI-1 was only two times narrower than the measured mode. In both experiments, we had the same result: the fine mode width

of 0.29 GHz. It is easy to show [14] that the average number of coherent pulses N_c is equal to the fineness of the FPI interferogram ε multiplied by the number m . So, in our experiment we have $N_c = \varepsilon_1 \cdot 1 \approx 10$ or $N_c = \varepsilon_2 \cdot 2 \approx 10$. In the KAERI FEL optical resonator, 60 pulses circulate simultaneously, and thus the coherency covers only 1/6 part of all the pulses.

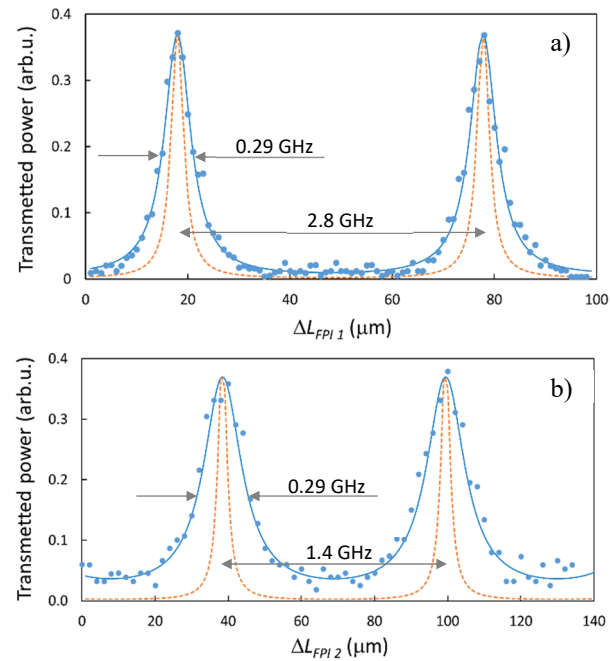


Figure 2: Fine structure of KAERI FEL radiation spectrum at central wavelength of 117 μ m (2.6 THz) measured by Fabry-Perot interferometers with lengths $L_{FPI-1} = 53.6$ mm (a) and $L_{FPI-2} = 107.2$ mm (b). Dots: experimental points, blue solid lines: best fitting to experimental points. Dashed orange lines: instrumental functions of interferometers.

The obtained results can have the following explanation. The KAERI FEL definitely has a feature (spike or front) in electron pulses that are shorter than the radiation half-wavelength, which can synchronize all light pulses. Actually, only part of the light pulses are synchronized because of accumulation of phase shift caused by the electron pulse frequency jitter. In our case, the jitter for a time period of order of the laser generation rise time (0.2-0.5 μ s) is substantial. We were not able to measure such jitter. But the experimental value of the parameter for a longer time period ($\delta f/f = \pm 250$ kHz/2.8 GHz $\approx \pm 10^{-4}$) gives a calculated number of coherent pulses, which corresponds to the experimentally observed one $N_c \approx 10$.

We also measured the power of fine modes in a wider spectral range. Figure 3 presents the relative powers of 11 central fine modes, like those shown in Fig. 2. We can see slow decrease in these modes relative to the maximum mode for $\Delta L_{FPI-1} = 117$ μ m; it corresponds to the contour laser line of the KAERI FEL. This classical behaviour of the fine structure differs from the results of the FLARE experiment [6], where a large unintelligible difference in the powers of close fine modes was observed.

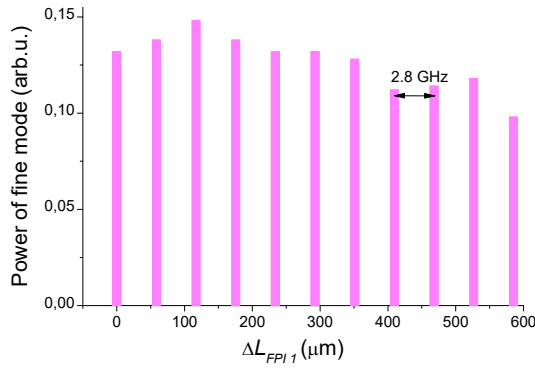


Figure 3: Relative powers of 11 central fine modes of the KAERI FEL.

Hyperfine Structure of the KAERI FEL Spectrum

Though no hyperfine structure of the KAERI FEL is measured in the experiment, it would be useful to make some remarks. The first is the *a priori* presence of a structure, because the KAERI FEL works in a quasi-stationary regime, which is formed by its optical resonator. Therefore the observed fine structure (Fig. 2) is actually only the averaged contour lines for the hyperfine structure with the period $\Delta\nu_{\text{hf}} = c/2L_0 = 54$ MHz, where c is the light velocity and L_0 is the optical resonator length. The fineness of the structure cannot be smaller than the passive quality factor of the optical resonator (≈ 10), but it can be much larger (the quality factor of the active laser resonator).

The second remark is about the technical possibility of increasing the fine coherency up to 60 pulses. In this case, the fine and hyperfine coherencies transform (degenerate) into a common coherency, which will be characterized by very narrow lines (like lines of hyperfine structure) and a high frequency of 2.8 GHz (like the frequency of fine structure). Such spectrum of the KAERI FEL radiation can be very useful for spectroscopy applications.

Fine Structure of the NovoFEL Spectrum

A low pulse frequency regime of the NovoFEL operation makes fine coherency impossible. Actually, the pulse frequency jitter would be $\delta f/f \leq \lambda/2\Lambda = \lambda m/2L_0 = 5 \cdot 10^{-6}$, where $\lambda = 0.15$ mm, $m = 2$, and $L_0 = 26589$ mm. The real jitter of the NovoFEL pulse frequency is probably an order of magnitude larger. Thus, two-pulse and four-pulse regimes of the NovoFEL will give the same hyperfine spectral structures as in a one-pulse regime because the pulses inside the optical resonator are practically independent and equivalent. This was confirmed in our experiments, in which absolutely the same normalized spectra were observed.

Hyperfine Structure of the NovoFEL Spectrum

For the study of hyperfine structure of the NovoFEL our special ultra-long resonance FPI (Fig.1b) was used. The main problem of such slow measurements in the frequency domain consisted in obtaining a very stable single-mode regime for a long time (~ 10 -15 min for a 10-period inter-

ferogram). We should note that it was needed only for obtaining a good multi-period interferogram because the best time of the NovoFEL fine coherency was only 25 μ s. One of the best examples of such interferogram is shown in Fig. 4. Unlike lower-resolution spectra of the KAERI FEL, here the FPI instrumental function is much wider than the hyperfine lines measured. Moreover, in such measurement we can obtain only the low estimate of the hyperfine coherency. For example, the measured spectrum in Fig. 4 practically coincides with the instrumental function. Nevertheless, when we take a line width of 10^{-7} , we have a visible difference in the contrast of the spectrum. Thus, the low estimate of the hyperfine monochromaticity here is $\delta\nu/\nu \leq 5 \cdot 10^{-8}$.

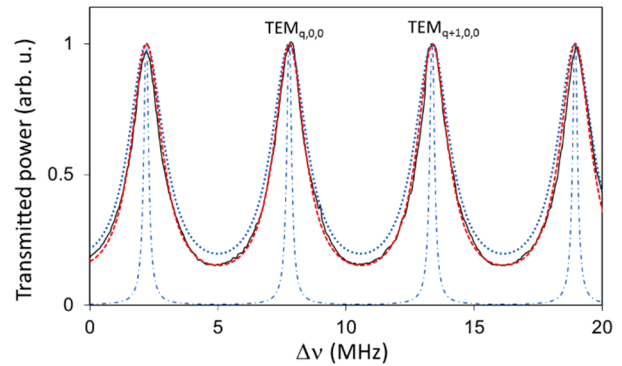


Figure 4: Hyperfine structure of THz NovoFEL radiation at central wavelength of 164 μ m (1.83 THz). Solid black line: measured NovoFEL radiation, dashed red line: instrumental function of ultra-long waveguide vacuum FPI with 30- μ m nickel meshes, blue dotted line: spectrum appreciably differing from experimental one as a result of convolution of laser line with relative spectral width of 10^{-7} (blue chain line) and instrumental function.

Replacement of the present 30- μ m nickel FPI meshes with 12- μ m gold meshes can provide four-fold narrowing of the instrumental function, but that is not sufficient. Therefore, we used a principally other time-domain method for exact measuring a NovoFEL hyperfine structure.

In the time-domain method, a two-pulse 11.2-MHz regime of the NovoFEL is used. The main idea of the method is going from the frequency domain to the time domain, where hard-to-measure narrow spectral lines transform into easy-to-measure long time intervals. It is also important that two phase-independent systems of pulses in the 11.2-MHz regime will effectively interfere inside the resonance FPI. Thus, in the output of the FPI we will have a beating signal. The signal maxima will be at the times when the radiation fields of the interfering pulses coincide; the minima will occur when the fields are opposite (Fig. 5b). The minimum beating period (T_{min} in Fig. 5b) will be observed for an opposite phase change in the two systems of pulses. Thus, this value T_{min} will also be the time of coherency (a 180-degree phase change) in each 5.6-MHz system of pulses or time of NovoFEL hyperfine coherency. We measured many oscillograms, like shown in Fig. 5b, to find

the minimum value of the beating period. As a result, the following parameters were obtained: the hyperfine coherency time $T_{min} = 25 \mu\text{s}$, the average number of NovoFEL coherent output pulses in the one-pulse 5.6-MHz regime is 140, the coherency length is 7 km, and the monochromaticity of the hyperfine comb-structure of the NovoFEL radiation is $2.2 \cdot 10^{-8}$.

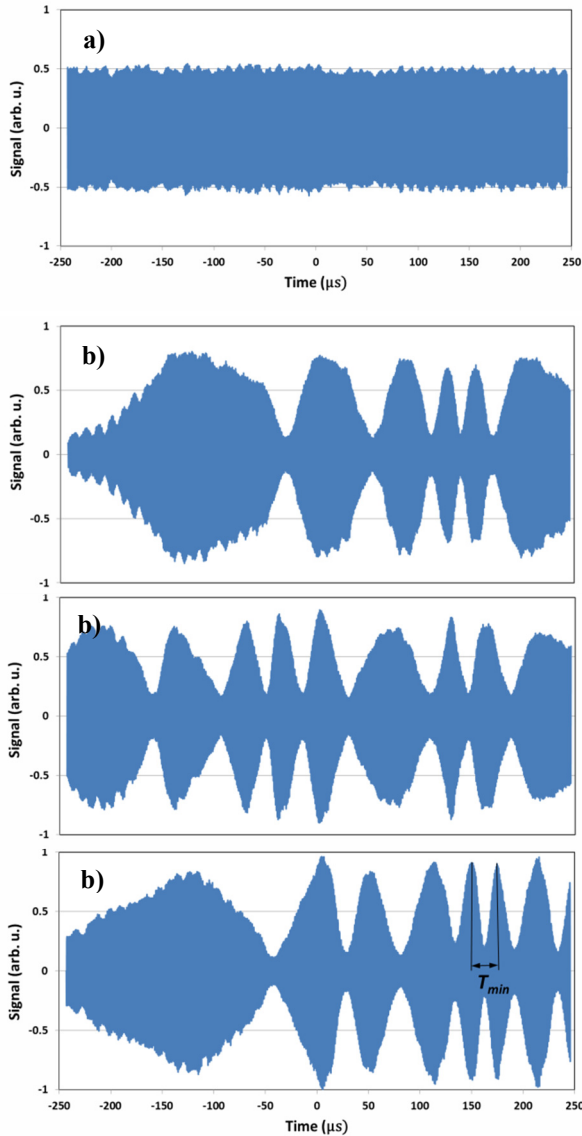


Figure 5: Power signals of Schottky diode detector (3 in Figure 1b, integration time of 100 ns) (a) for 5.6-MHz NovoFEL regime with single pulse in optical resonator and (b) for 11.2-MHz NovoFEL regime with two pulses in optical resonator. T_{min} is minimum modulation period. All signals were measured at the resonance FPI length, when its transmittance is maximal.

CONCLUSION

In the experimental investigation, the fine mode structure of the KAERI FEL radiation with a line monochromaticity of 10^{-4} was found. We are going to measure a hyperfine structure of the laser in the near future.

The hyperfine structure of the NovoFEL with a line monochromaticity of $2.2 \cdot 10^{-8}$ was measured. There is no fine mode structure or coherency between different pulses inside the optical resonator.

Knowing the real structure of FEL radiation is important for different user spectroscopic methods developed on the facilities.

ACKNOWLEDGEMENTS

The study was supported by a grant of the Russian Science Foundation (project No 19-73-20060).

REFERENCES

- [1] V.V. Kubarev, *et al.*, "Modulation instability, three mode regimes and harmonic generation at the Novosibirsk terahertz free electron laser", *Nuclear Instruments & Methods in Nuclear Research*, vol. A603, pp. 25-27, 2009. doi:10.1016/j.nima.2008.12.122
- [2] V.V. Kubarev, "Detailed observation of modulation instability on THz NovoFEL", *Proc. IRMMW-THz-2012*, Wollongong, Australia, Sept. 23-28, 2012, paper Fri-A-4-2. doi:10.1109/IRMMW-THz.2012.6380437
- [3] V.V. Kubarev, "Optical system, diagnostics, and experiments on terahertz and infrared free electron lasers", Doctoral thesis, Budker Institute of Nuclear Physics, Novosibirsk, Russia, 2016. http://www.inp.nsk.su/images/diss/Kubarev_diss.pdf
- [4] G.P. Gallerano, A. Doria, E. Giovenale, and G. Messina, "Coherence effects in FEL radiation generated by shot electron bunches", *Nuclear Instruments & Methods in Nuclear Research*, vol. A358, pp. 78-81, 1995. doi:10.1016/0168-9002(94)01578-3
- [5] H.H. Weits and D. Oepts, "Coherent Spontaneous Emission and Spontaneous Phase Locking in a Free-Electron Laser", *IEEE Journal of Quantum Electronics*, vol. 35, pp. 15-25, 1999. doi:10.1109/3.737614
- [6] M. Ozerov *et al.*, "A THz spectrometer combining the free electron laser FLARE with 33 T magnetic fields", *Appl. Phys. Lett.*, vol. 110, pp. 094106-(1-4), 2017. doi:10.1063/1.4977862
- [7] Y.U. Jeong *et al.*, "First lasing of the KAERI compact far-infrared free-electron laser driven by magnetron-based microtron", *Nuclear Instruments & Methods in Nuclear Research*, vol. A475, pp. 47-50, 2001. doi:10.1016/S0168-9002(01)01533-9
- [8] Y.U. Jeong *et al.*, "Upgrade of a compact FIR FEL driven by magnetron-based microtron for the wavelength range of 100-300 μm ", *Nuclear Instruments & Methods in Nuclear Research*, vol. A507, pp. 125-128, 2003. doi:10.1016/S0168-9002(03)00854-4
- [9] V. Kubarev and Y.U. Jeong, "Comprehensive analytical optimization of the hybrid optical resonator of the KAERI compact terahertz free-electron laser", *Nuclear Instruments & Methods in Nuclear Research*, vol. A930, pp. 173-179, 2019. doi:10.1016/j.nima.2019.03.097
- [10] G.N. Kulipanov *et al.*, "Novosibirsk free electron laser – facility description and recent experiments", *IEEE Transaction on Terahertz Science and Technology*, vol. 5(5), pp. 798-809, 2015. doi:10.1109/TTHz.2015.2453121
- [11] O.A. Shevchenko *et al.*, "Novosibirsk free electron laser: Recent achievements and future prospects", *Radiophysics*

- and *Quantum Electronics*, vol. 59, pp. 605-612, 2017. doi:10.1007/s11141-017-9727-9
- [12] V.V. Kubarev, B.Z. Persov, N.A. Vinokurov, and A.V. Davidov, "Optical resonator of powerful free-electron laser", *Nuclear Instruments & Methods in Nuclear Research*, vol. A528, pp. 199-202, 2004. doi:10.1016/j.nima.2004.04.046
- [13] V.V. Kubarev, "Calculation, optimization, and measurements of optical resonator parameters of the Novosibirsk terahertz free-electron laser", *Quantum Electronics*, vol. 39, pp. 235-240, 2009. doi:10.1070/QE2009V039N03ABEH013896
- [14] V.V. Kubarev, "Resonance Fabry-Perot interferometers as optimal devices for investigation of fine and hyperfine free-electron laser emission spectra", submitted for publication.
- [15] V.V. Kubarev, E.A. Kurenskii, "Very-low-noise H₂O laser with rf pumping", *Quantum Electronics*, vol. 25, pp. 1141-1145, 1995. doi:10.1070/qe1995v025n12abeh000551
- [16] V.V. Kubarev, and E. A. Kurenskii, "Ultralow-noise high-power DCN laser with rf pumping", *Quantum Electronics*, vol. 26, pp. 303-306, 1996. doi:10.1070/qe1996v026n04abeh000655
- [17] V.V. Kubarev, "Xenon as an effective buffer gas in submillimetre lasers based on vibrational-rotational transition", *Quantum Electronics*, vol. 26, pp. 191-192, 1996. doi:10.1070/QE1996v026n03ABEH000623
- [18] V.V. Kubarev, G.M. Kazakevich, Y.U. Jeong, and B.J. Lee, "Quasi-optical highly sensitive Schottky-barrier detector for a wide-band FIR FEL", *Nuclear Instruments & Methods in Nuclear Research A*, vol. 507, pp. 523-526, 2003. doi:10.1016/S0168-9002(03)00911-2

CAVITY-BASED FREE-ELECTRON LASER RESEARCH AND DEVELOPMENT: A JOINT ARGONNE NATIONAL LABORATORY AND SLAC NATIONAL LABORATORY COLLABORATION

G. Marcus, F.-J. Decker, G. L. Gassner, A. Halavanau, J. Hastings, Z. Huang, Y. Liu, J. MacArthur,
R. Margraf, T. Raubenheimer, A. Sakdinawat, T. Tan, D. Zhu, SLAC National Accelerator
Laboratory, Menlo Park, CA 94025, USA

J. W. J. Anton, L. Assoufid, K. Goetze, W. Jansma, S. Kearney, K.-J. Kim, R. Lindberg, A. Miceli, X. Shi, D. Shu,
Y. Shvyd'ko, J. P. Sullivan, M. White, Argonne National Laboratory, Argonne, IL 60439, USA
B. Lantz, Stanford University, Stanford, CA 94305, USA

Abstract

One solution for producing longitudinally coherent FEL pulses is to store and recirculate the output of an amplifier in an X-ray cavity so that the X-ray pulse can interact with following fresh electron bunches over many passes. The X-ray FEL oscillator (XFEL) and the X-ray regenerative amplifier FEL (XRAFL) concepts use this technique and rely on the same fundamental ingredients to realize their full capability. Both schemes require a high repetition rate electron beam, an undulator to provide FEL gain, and an X-ray cavity to recirculate and monochromatize the radiation. The shared infrastructure, complementary performance characteristics, and potentially transformative FEL properties of the XFEL and XRAFL have brought together a joint Argonne National Laboratory (ANL) and SLAC National Laboratory (SLAC) collaboration aimed at enabling these schemes at LCLS-II. We present plans to install a rectangular X-ray cavity in the LCLS-II undulator hall and perform experiments employing 2-bunch copper RF linac accelerated electron beams. This includes performing cavity ring-down measurements and 2-pass gain measurements for both the low-gain XFEL and the high-gain XRAFL schemes.

INTRODUCTION

The incontrovertible success of the world's first hard X-ray free-electron laser (XFEL), LCLS [1], has led to a significant increase in the global FEL capacity. Additional facilities in Japan, Germany, Switzerland, Korea and China are either planned or are currently operating. These light sources, based primarily on Self-Amplified Spontaneous Emission (SASE) [2], are capable of producing extremely bright, transversely coherent, ultra-short X-ray pulses that have opened the door to new regimes of photon science [3, 4]. They have revolutionized the study of chemistry, physics, biology, and many other related fields of science and technology. Single-pass SASE FEL amplifiers, however, suffer from poor longitudinal coherence due to the stochastic nature of the start-up process. The improvement of the FEL longitudinal coherence and the ability to trade off peak power, average power, pulse duration, and bandwidth is of great practical importance [5].

Longitudinal coherence can be obtained by seeding an FEL amplifier with narrow bandwidth radiation well above

the effective shot noise power in the electron beam. Examples of this include self-seeding [6, 7], which has been successfully implemented at LCLS in both the hard [8] and soft [9] X-ray spectral regions. Variations on this concept are also being studied [10, 11]. Self-seeding, however, nominally suffers from low seed power in an attempt to preserve the electron beam properties important for lasing and is fundamentally still dependent on the noisy SASE process leading to large (potentially 100%) seed power fluctuations.

Another leading candidate for obtaining longitudinal coherence leverages an X-ray cavity to monochromatize and store a fraction of a recirculating X-ray pulse so that it can interact with following fresh electron bunches over many passes. These so-called cavity-based X-ray free-electron lasers (CBXFELs) include the X-ray free-electron laser oscillator (XFEL) [12] and the X-ray regenerative amplifier free-electron laser (XRAFL) [13]. In the past, these concepts were not feasible at X-ray FEL facilities because of the lack of high-reflectivity X-ray cavity mirrors and because of the limited repetition rate of the normal conducting technologies responsible for the production and acceleration of the electron bunches delivered to the undulator. The progress in achieving high-reflectivity diamond crystal mirrors in the hard x-ray regime [14–16] and in superconducting technology adopted by LCLS-II [17, 18] and LCLS-II-HE [19], however, will be capable of supporting steady-state repetition rates up to ~ 1 MHz, making the footprint of the recirculating optical cavity reasonable.

The XFEL and XRAFL concepts rely on the same fundamental ingredients to realize their full capability. Each scheme requires a high repetition rate electron beam, an undulator to provide FEL gain, and an X-ray optical cavity to recirculate and monochromatize the X-ray radiation. While the XFEL and XRAFL schemes share a common infrastructure, they target different but complementary FEL performance characteristics. The XFEL relies on a low-loss cavity supporting a low-gain FEL for ultra-narrow bandwidth while the XRAFL leverages a high-gain FEL interaction that can support much larger radiation output coupling.

As an example of the difference between the two CBXFEL schemes, Table 1 shows a semi-qualitative comparison of operational characteristics while Table 2 shows the typical hard X-ray (HXR) performance characteristics that are ex-

pected for SASE, XRA FEL, and XFEL at LCLS-II/-HE.

Table 1: Semi-Qualitative Comparison Between the XRA FEL and XFEL Schemes

	XRA FEL	XFEL
Gain & output coupling	High	Low
Necessary cavity roundtrip efficiency	$\sim 1\%$	$\sim 85\%$
Passes to saturation	$\sim 10^3$	$\sim 100^3$
Repetition rate	Q-switched (~ 10 -50 kHz), CW (\sim MHz)	CW (\sim MHz)

The XFEL can produce temporally long and coherent pulses with extremely stable and ultra-narrow bandwidths that ultimately result in X-rays that are roughly three orders of magnitude higher in average brightness than that of SASE at LCLS-II/-HE. The XRA FEL system, conversely, aims at the production of longitudinally coherent but shorter FEL pulses that can result in both high average and peak brightness (Q-switched) X-rays.

The shared infrastructure, complementary performance characteristics, and transformative FEL properties of the two CBXFEL schemes has brought together a joint ANL/SLAC collaboration aimed at enabling these schemes at LCLS-II and the LCLS-II-HE upgrade. The primary objective of this collaboration is the construction of a rectangular X-ray cavity around the first seven LCLS-II HXR undulator sections (see Figure 1a), allowing for the investigation of crucial aspects related to CBXFEL physics using a pair of electron bunches (sub μ s separation) from the SLAC copper (Cu) RF linac. The experimental program includes two-pass gain measurements as well as cavity ring-down measurements for both the low-gain XFEL and the high-gain XRA FEL schemes. We envision this as a three-year project with the possibility for schedule contingency of an extra year driven largely by the LCLS-II commissioning and downtime schedules. Future studies using electron bunches from the high repetition rate accelerator will be possible after appropriate cavity upgrades are made.

EXPERIMENTAL SETUP

Figure 1a shows a mockup (top view) of a potential rectangular X-ray cavity in the LCLS-II undulator hall while Figure 1b shows a cartoon version with the electron and photon paths noted. Four motion stacks will form the basis of the optical cavity that in turn will mount four HPHT-IIa diamond crystal plates in strain free holders. The first two crystal plates reflect the X-ray pulse into and out of the undulator line using the (400) Bragg reflection and will be located in the middle of the four-dipole electron beam delay chicanes that bracket the seven undulator sections. Two additional crystals reflect the X-ray pulse back to the electron path in the undulator. To control the transverse

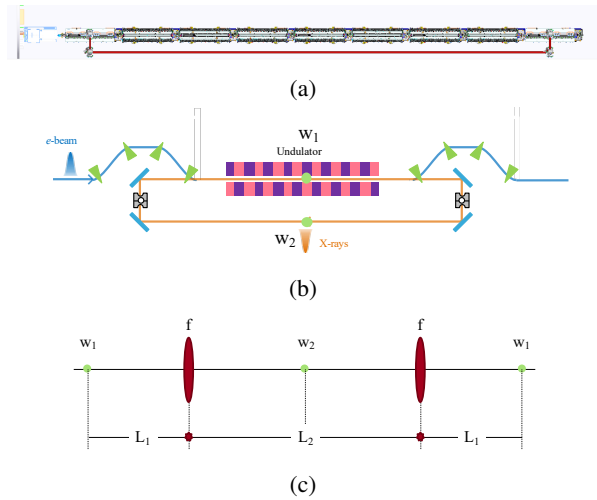


Figure 1: (a) Top view of the rectangular cavity as envisioned. From left to right in the undulator beamline: TDUND, chicane and optics chamber, 7 HXR undulators, chicane and optics chamber. The solid red line illustrates the X-ray cavity return line. Not shown are two CRLs on the short ends of the rectangle (see (b) below). (b) Cartoon of the CBXFEL concept showing the paths of the electrons and photons. (c) Equivalent unfolded optical lattice of the X-ray cavity in (b) above.

cavity mode, two paraboloidal compound refractive lenses (CRLs) made of Beryllium [20–22] will be placed symmetrically in the short arms of the rectangle. The motion stacks will include nanoradian-level-resolution positioning stages. The diamonds deployed in this cavity will be cut parallel to the (100) crystal surface, where the bulk of previous R&D has been performed, and high-quality diamond samples can be fabricated by multiple vendors (see [23] for a recent review). A long-range laser interferometer system, along with additional X-ray diagnostics, will be used for alignment, characterization, and stabilization of the cavity. A non-destructive in-situ diagnostic line will include high-resolution measurements of the X-ray transverse profile. The XFEL/XRA FEL cavity design will include sufficient diagnostics to enable the required precision angular alignment to be accomplished [24].

TOLERANCES OF THE X-RAY CAVITY

Figure 1c shows the equivalent unfolded optical lattice of the X-ray cavity in Figure 1b including focusing elements provided by compound refractive lenses (CRLs). This symmetric system has a waist at two locations, w_1 and w_2 as noted in the figure. The coupling between the electron beam and the X-rays is typically optimized in the low-gain XFEL scenario when the radiation waist is in the middle of the undulator, as it is here, and when $Z_R \approx \langle \beta \rangle$, where Z_R is the X-ray pulse Rayleigh length and $\langle \beta \rangle$ is the average beta function of the electron beam in the undulator. Table 3 shows the undulator and cavity parameters for the proposed experimental setup. An electron beam energy of ~ 10.3 GeV

Table 2: Projected HXR Performance Characteristics at the High Repetition Rate LCLS-II/-HE from SASE, XRA FEL, and XFEL

	SASE	XRA FEL	XFEL
Peak Power	~10 GW	~50 GW	~100 MW
Average power	~100 W (at 1 MHz)	10 W (at 10 kHz)	20 W (at 1 MHz)
Spectral bandwidth	~10 eV	~0.1 eV	~1 meV
Pulse length	~ 1 – 100 fs	~ 20 fs	~ 1 ps
Stability	Poor	Excellent	Excellent
Longitudinal coherence	Poor	Excellent	Excellent
Transverse mode	Defined by gain-guiding	Defined by gain-guiding	Defined by the optical cavity

Table 3: Major Undulator and Cavity Parameters

Parameter	Value	Unit
Undulator		
Period	2.6	cm
Number of segments	7	-
Periods per segment	130	-
Length	28	m
K	2.44	-
Cavity		
Crystal material	C*(400)	-
Bragg angle	45	degree
Photon energy	9.83	keV
Wavelength	1.26	Angstrom
Bragg width (energy)	75	meV
Bragg width (angle)	8	μrad
Total length	~66	m

is needed to support the gain of 9.83 keV photons in the LCLS-II HXR undulator. This, in turn, yields an $\langle \beta \rangle \approx 22$ m for a matched electron bunch in the strong focusing undulator FODO lattice and a matched waist size $w_1 \approx 30 \mu\text{m}$. Commercially available beryllium CRLs with a focal length of 28.4 m (at a 9.83 keV photon energy) produce a waist size of $w_1 \approx 32 \mu\text{m}$, which is close to the matched solution.

As an initial approximation, if the error in mirror angles are independent and random, a statistical tolerancing analysis using the Root Sum Square (RSS) method can be performed to estimate the required stability of the motion stacks. In this method, the total error in displacement at the undulator entrance after propagation through the optical cavity can be

written as

$$\Delta_{tot} = c_1 \theta_{m1} + c_2 \theta_{m2} + c_3 \theta_{m3} + c_4 \theta_{m4}, \quad (1)$$

where the c_i are functions of the optical cavity parameters (drift lengths, focal lengths, etc.) and the θ_{mi} are the individual mirror angular errors. The total RMS error in the displacement, assuming independent and equal magnitude mirror errors ($\sigma_{mi} = \sigma_m$), can then be found by propagation in the usual sense as

$$\sigma_{tot} = \sqrt{(c_1^2 + c_2^2 + c_3^2 + c_4^2) \sigma_m^2}. \quad (2)$$

Setting the tolerance as $\pm TOL = \pm 3 \sigma_{tot}$, one can then find the mirror RMS fluctuations that results in an unlikely $3 \sigma_{tot}$ ($\sim 0.27\%$ chance) event to occur. If the tolerance is set such that the trajectory deviation is one half the RMS electron beam size at the entrance to the undulator ($TOL = \sigma_e/2$), the RMS fluctuation in the mirror angles must be less than ~ 55 nrad. This is routinely realized in precision x-ray optics mechanisms. These tolerances should be relaxed for the XRA FEL due to gain-guiding of the radiation during high-gain amplification.

The use of this statistical tolerancing method is somewhat questionable given the small number of independent sources of error (there are only four mirrors). Therefore, both the high and low gain two-pass systems are being evaluated with time-dependent and three-dimensional FEL simulations using genesis [25] and Fourier optics propagation of the resulting fields through the optical cavity.

TWO-BUNCH CURF ELECTRON BEAM DYNAMICS

The high-brightness electron beams from the CuRF linac have been successfully supporting the high-gain SASE FEL for the past 10 years at LCLS and are well characterized [26]. Beam shaping is employed to ensure a uniform longitudinal phase space (LPS) at the entrance to the undulator [27]. An example of two typical electron beam LPS's is shown in

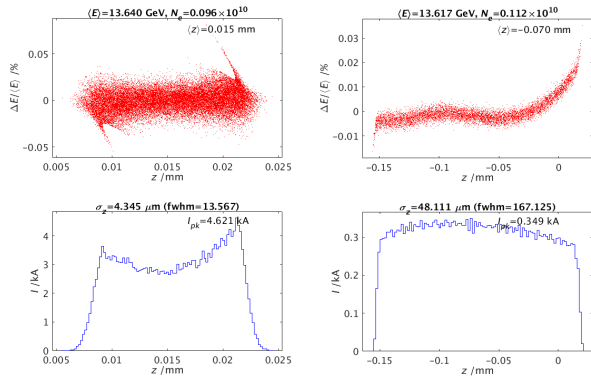


Figure 2: Typical longitudinal phase space (top) and current profile (bottom) of a high peak current (left) and low peak current (right) high-brightness electron beam at the entrance to the HXR undulator from the CuRF linac (LiTrack simulations).

Figure 2. Here, LiTrack [28] simulations show that a ~ 150 pC charge electron beam that is ~ 50 fs long can have a peak current of ~ 3 kA, an RMS energy spread of 1.5 MeV, and a slice emittance of ~ 0.6 mm-mrad (left). Electron beams similar to this are deployed in regular operation. Low peak current solutions are also possible. LiTrack simulations show that a 180 pC charge electron beam that is ~ 300 fs long in the core can have a peak current of ~ 300 A, a slice RMS energy spread in the core of ~ 150 keV, and a slice-emittance of ~ 0.5 mm-mrad (right). These solutions should be more than sufficient to demonstrate both low and high two-pass gain.

Two-bunch operation using the CuRF linac has been demonstrated in the past [29] for various relative delays between the two electron bunches ranging from a few ns to ~ 210 ns. Two bunches are generated by two independent lasers impinging on the photoinjector cathode. Their relative charge difference can be controlled to about the 1% level, their individual time separation can be adjusted with a precision of 0.07 ps, and their RMS temporal separation jitter can be controlled to less than 17 fs [30,31]. In order to control and remove the energy difference between the two bunches, one can introduce a small phase difference in the second section of the CuRF linac.

The optical cavity in the undulator hall will have a round trip length of ~ 66 m requiring a relative delay between the electron beams of ~ 220 ns. Two-bunch spacing of 210 ns (600 RF wavelengths) for the high peak current scenario has been achieved in the past. The FEL performance in this case nearly achieved twice the single bunch performance.

Ideally, the electron bunches need to be spatially and angularly aligned in the undulator to within a fraction of the electron bunch transverse size over the length of the undulator. Addressing this alignment requires additional R&D and infrastructure. In the past, the demonstrated two-bunch mode of operation typically provided two different electron beam energies at the entrance of the undulator to produce FEL photons at two different photon energies. This

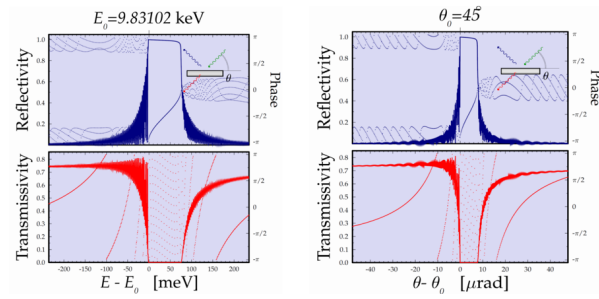


Figure 3: Bragg reflectivity of diamond crystals in the (400) reflection as a function of the photon energy and angular deviation ($E_0 = 9.83$ keV, $\theta_0 = 45^\circ$).

enabled the use of dispersion bumps to control the relative alignment of the electron bunch trajectories to within 5-10% of the transverse size. This technique will not be possible for two bunches of equal energy. In addition, transverse long range wakefields, introduced by the first bunch and acting on the second bunch, have to be compensated to ensure closed orbits in the undulators. Therefore, four ultra-fast strip-line kickers will be installed in the LTU to independently control the four transverse coordinates (x , x' , y , y') of each electron bunch.

TWO-PASS GAIN MEASUREMENTS

As previously mentioned, a rectangular X-ray cavity will be constructed around the first seven sections of the LCLS-II HXR undulator, formed by four diamond crystals (see Figure 1 above). A rectangular cavity configuration, rather than a tunable zig-zag geometry [32], is adopted here based on the limited transverse space available in the undulator hall. The photon energy and corresponding wavelength, determined from the required 45° Bragg angle and the symmetric (400) diamond crystal reflection plane, are 9.83 keV and 1.26 Å, respectively. The Bragg reflection curves as a function of photon energy and angular deviation from 45° are shown in Figure 3. The two-pass gain measurements that will be made as part of this experimental program and that utilize the infrastructure mentioned above will proceed as follows. The normal conducting SLAC photoinjector and accelerator will produce two electron bunches that are spaced by ~ 220 ns, which is set by the cavity round-trip time. The first electron bunch produces radiation that is monochromatized and returned to the entrance of the undulator so that it can interact with the following electron bunch. This experiment will test the key enabling aspects of any CBXFEL - the operation of an X-ray cavity that can store an X-ray pulse produced by an electron bunch and that the pulse can be amplified by another electron bunch. Performance estimates for both the low-gain and high-gain systems are discussed below. These estimates are based on the undulator and cavity parameters listed in Table 3 and the electron bunch parameters mentioned above.

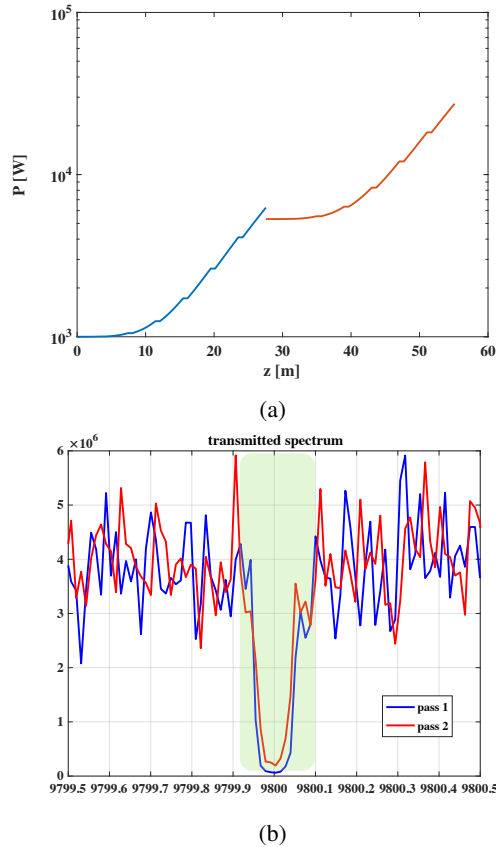


Figure 4: (a) Single-frequency (time-independent) simulations showing the two-pass gain for the low-gain XFEL scenario. (b) View of the average transmitted spectrum over 25 time-dependent simulations near the resonant photon energy. The spectral region of interest is highlighted in green.

Low-Gain (XFEL) Measurements

Previous estimates have predicted that the number of photons produced by the first bunch, monochromatized, and deflected into the cavity, is $N_\gamma = 5.8 \times 10^4$ and that the maximum intensity gain should be at least a factor of two [24]. Additional studies have since been performed using detailed genesis simulations. Figure 4a shows the results of relatively simple time-independent simulations showing two-pass gain. In this case, the results of the single-frequency simulation are simply fed back into the simulation of the second pass while the expected cavity roundtrip efficiency is used to scale the pulse power. The propagation of the radiation wavefront through the cavity has been ignored. The second pass gain is found to be ~ 5 at the optimal detuning.

Figure 4b shows the transmitted spectrum of passes 1 and 2 averaged over 25 shots for time-dependent simulations. In this case, the reflection curves of Figure 3 are used to filter the first pass radiation both in photon energy and angle. The output coupling diamond crystal in this case is assumed to be $20\mu\text{m}$ thick and manufactured using a drumhead technique [33]. The full three-dimensional radiation field is propagated through the cavity using Fourier optics techniques. The gain

of the second pass relative to the first pass in the spectral region of interest is ~ 3.15 and agrees remarkably well with the single-frequency results. There were no cavity errors in this case. Future work will include cavity mirror angular errors and will be used to compare against the analytical results presented above and to define the tolerances on the angular stability of the cavity optical system.

High-Gain (XRFEL) System

A similar numerical analysis of the high-gain system was also performed. For brevity, the figures are not shown here. Time-independent simulations predict that the second pass gain through the system will be ~ 85 while time-dependent simulations including propagation of the three-dimensional fields through the cavity show the gain of the second pass over the first in the spectral region of interest to be ~ 100 .

DISCUSSION

The successful implementation of a CBXFEL configuration is predicated on a high repetition rate electron beam and a high precision X-ray cavity. LCLS-II and the LCLS-II-HE upgrade will be capable of delivering electron bunch repetition rates as high as ~ 1 MHz to the HXR undulator. It has been established that diamond crystals have the requisite properties to handle the high average and peak thermal load of the stored cavity X-ray power for both the XFEL and XRFEL concepts. Beam dynamics modeling and options for X-ray cavity output coupling for an XFEL and XRFEL are under active investigation and development. However, an FEL-scale optical cavity in the HXR spectral range has yet to be demonstrated. The project presented here addresses the joint ANL/SLAC collaboration strategy by conducting targeted R&D on the X-ray cavity infrastructure, exploring the physics of the XFEL and XRFEL schemes with real experiments, and demonstrating the necessary performance tolerances needed to realize a full-scale CBXFEL implementation.

ACKNOWLEDGEMENTS

This work was supported by U.S. Department of Energy Contract No. DE-AC02-76SF00515.

REFERENCES

- [1] P. Emma, *et al.*, "First lasing and operation of an angstrom-wavelength free-electron laser," *Nat. Phot.*, vol. 4, pp. 641, 2010. doi:10.1038/nphoton.2010.176
- [2] R. Bonifacio, C. Pellegrini, and L. M. Narducci, "Collective instabilities and high-gain regime in a free electron laser," *Opt. Comm.*, vol. 50, pp. 373, 1984. doi:10.1016/0030-4018(84)90105-6
- [3] C. Bostedt, *et al.*, "Ultra-fast and ultra-intense x-ray sciences: first results from the Linac Coherent Light Source free-electron laser," *J. of Phys. B: Atomic, Molecular and Optical Physics*, vol. 46, pp. 164003, 2013. doi:10.1088/0953-4075/46/16/164003

- [4] Christoph Bostedt, *et al.*, “Linac Coherent Light Source: the first five years,” *Rev. of Mod. Phys.*, vol. 88, pp. 015007, 2016. doi:10.1103/RevModPhys.88.015007
- [5] R. W. Schoenlein, *et al.*, “New science opportunities enabled by LCLS-II x-ray lasers,” SLAC, Menlo Park, CA, SLAC-R-1053, 2015.
- [6] J. Feldhaus, *et al.*, “Possible application of X-ray optical elements for reducing the spectral bandwidth of an X-ray SASE FEL,” *Opt. Comm.*, vol. 140, pp. 341, 1997. doi:10.1016/S0030-4018(97)00163-6
- [7] G. Geloni, V. Kocharyanb and E. Saldin, “A novel self-seeding scheme for hard x-ray FELs,” *J. of Mod. Opt.*, vol. 58, pp. 1391, 2011. doi:10.1080/09500340.2011.586473
- [8] J. Amann *et al.*, “Demonstration of self-seeding in a hard-X-ray free-electron laser,” *Nat. Phot.*, vol. 6, pp. 693, 2012. doi:10.1038/nphoton.2012.180
- [9] D. Ratner *et al.*, “Experimental demonstration of a soft x-ray self-seeded free-electron laser,” *Phys. Rev. Lett.*, vol. 114, pp. 054801, 2015. doi:10.1103/PhysRevLett.114.054801
- [10] A. Halavanau, *et al.*, “High Power and Brightness Double Bunch LCLS-II,” presented at 39th Int. Free-Electron Laser Conf., Hamburg, 2019, THP071.
- [11] I. Inoue, *et al.*, “Generation of narrow-band x-ray free-electron laser via reflection self-seeding,” *Nat. Phot.*, 13, pp. 319, 2019. doi:10.1038/s41566-019-0365-y
- [12] K.-J. Kim, Y. Shvyd’ko, and Sven Reiche, “A proposal for an x-ray free-electron laser oscillator with an energy-recovery linac,” *Phys. Rev. Lett.* vol. 100, pp. 244802, 2008. doi:10.1103/PhysRevLett.100.244802
- [13] Z. Huang and R.D. Ruth, “Fully coherent x-ray pulses from a regenerative-amplifier free-electron laser,” *Phys. Rev. Lett.* vol. 96, pp. 144801, 2006. doi:10.1103/PhysRevLett.96.144801
- [14] Yu. Shvyd’ko, *et al.*, “High-reflectivity high-resolution x-ray crystal optics with diamonds,” *Nat. Phys.*, 6, pp. 196, 2010. doi:10.1038/nphys1506
- [15] Yuri Shvyd’ko, *et al.*, “Near-100% Bragg reflectivity of x-rays,” *Nat. Phot.* 5, pp. 539, 2011. doi:10.1038/nphoton.2011.197
- [16] T. Kolodziej, *et al.*, “High Bragg reflectivity of diamond crystals exposed to multi-kW mm² x-ray beams,” *J. of Synch. Rad.*, vol. 25, pp. 1022, 2018. doi:10.1107/S1600577518007695
- [17] T.O. Raubenheimer, ed., “LCLS-II final design report,” SLAC, Menlo Park, CA, LCLSII-1.1-DR-0251-R0, 2015.
- [18] T.O. Raubenheimer, “Technical challenges of the LCLS-II CW x-ray FEL,” in *Proc. 6th Int. Particle Accelerator Conf.*, Virginia, USA, 2015. doi:10.18429/JACoW-IPAC2015-WEYC1
- [19] T.O. Raubenheimer, “The LCLS-II-HE, a high energy upgrade of the LCLS-II,” 60th *ICFA Advanced Beam Dynamics Workshop on Future Light Sources*, Shanghai, China, 2018. doi:10.18429/JACoW-FLS2018-MOP1WA02
- [20] A. Snigirev, *et al.*, “A compound refractive lens for focusing high-energy x-rays,” *Nature*, 384, pp. 49-51, 1996. doi:10.1038/384049a0
- [21] B. Lengeler, *et al.*, “Imaging by parabolic refractive lenses in the hard x-ray range,” *J. Synchrotron Rad.*, 6, pp. 1153, 1999. doi:10.1107/S0909049599009747
- [22] T. Kolodziej, *et al.*, “Efficiency and coherence preservation studies of Be refractive lenses for XFEL application,” *J. Synchrotron Rad.*, 25, pp. 354 2018. doi:10.1107/S160057751701699X
- [23] Yu. Shvyd’ko, *et al.*, “Diamond x-ray optics: transparent, resilient, high-resolution, and wavefront preserving,” *MRS Bulletin*, 42, pp. 437, 2017. doi:10.1557/mrs.2017.119
- [24] K.-J. Kim, *et al.*, “Test of an x-ray cavity using double-bunches from the LCLS Cu-linac,” *Proc. of the 10th Int. Particle Accelerator Conf.*, Melbourne, 2019, TUPRB096. doi:10.18429/JACoW-IPAC2019-TUPRB096
- [25] S. Reiche, “GENESIS 1.3: a fully 3D time-dependent FEL simulation code,” *Nucl. Instr. Meth. Phys. Res. Sec. A*, vol. 429, pp. 243, 1999. doi:10.1016/S0168-9002(99)00114-X
- [26] C. Behrens, *et al.*, “Few-femtosecond time-resolved measurements of X-ray free-electron lasers,” *Nat. Comm.*, vol. 5, pp. 3762, 2014. doi:10.1038/ncomms4762
- [27] Y. Ding, *et al.*, “Beam shaping to improve the free-electron laser performance at the Linac Coherent Light Source,” *Phys. Rev. Accel. and Beams*, vol. 19, pp. 100703, 2016. doi:10.1103/PhysRevAccelBeams.19.100703
- [28] K. Bane and P. Emma, “LiTrack: a fast longitudinal phase space tracking code with graphical user interface,” in *Proc. of the 21st Particle Accelerator Conf.*, Knoxville, TN, 2005, FPAT091.
- [29] F.-J. Decker, *et al.*, “A Demonstration of Multi-Bunch Operation in the LCLS,” in *Proc. of the 32nd Int. Free-Electron Laser Conf.*, Malmö, Sweden, 2010, WEPB33.
- [30] F.-J. Decker, *et al.*, “Recent developments and plans for two bunch operation with up to 1 μ s separation at LCLS,” SLAC, Menlo Park, CA, SLAC-PUB-17128, 2018.
- [31] F.-J. Decker, private communication, 2019.
- [32] K.-J. Kim and Y. Shvyd’ko, “Tunable optical cavity for an x-ray free-electron-laser oscillator,” *Phys. Rev. ST Accel. Beams.*, vol. 12, pp. 030703, 2009. doi:10.1103/PhysRevSTAB.12.030703
- [33] Tomasz Kolodziej, *et al.*, “Diamond drumhead crystals for x-ray optics applications,” *J. of Appl. Cryst.*, vol. 49, pp. 1240, 2016. doi:10.1107/S1600576716009171

SUPERRADIANT AND STIMULATED-SUPERRADIANT EMISSION OF BUNCHED ELECTRON BEAMS

A. Gover, Tel-Aviv University, Tel-Aviv, Israel

R. Iancu, Tel-Aviv University, Tel-Aviv and Shenkar College, Ramat-Gan, Israel

Friedman, Ariel University, Ariel, Israel

C. Emma, N. Sudar, P. Musumeci and C. Pellegrini, UCLA, Los Angeles, CA, USA

Abstract

We outline the fundamental processes of coherent radiation emission from a bunched charged particles beam [1]. In contrast to spontaneous emission of radiation from a random electron beam that is proportional to the number of particles N , a pre-bunched electron beam emits spontaneously coherent radiation proportional to N^2 through the process of (spontaneous) superradiance (SP-SR) (in the sense of Dicke's [2]). The SP-SR emission of a bunched electron beam can be even further enhanced by a process of stimulated-superradiance (ST-SR) in the presence of a seed injected radiation field. These coherent radiation emission processes are presented in term of a radiation mode expansion model, applied to general free electron radiation schemes: Optical-Klystron, HGHG, EEHG, and coherent THz sources based on synchrotron radiation, undulator radiation or Smith-Purcell radiation. The general model of coherent spontaneous emission is also extended to the nonlinear regime - Tapering Enhanced Stimulated Superradiance (TESSA) [3], and related to the tapered wiggler section of seed-injected FELs. In X-Ray FELs, these processes are convoluted with other effects, but they are guidelines for strategies of wiggler tapering efficiency enhancement.

MANUSCRIPTS

This tutorial lecture is based on a recently published review article [1] that details the physics and state of the art of research on the subject of superradiant emission of bunched electron beams, and particularly pre-bunched beam FEL. The readers are referred to this article for detailed presentation. Here is a short summary of the contents and conclusions of the tutorial lecture.

The fundamental coherent radiation emission processes from a bunched charged particles beam were outlined. In contrast to spontaneous emission of radiation from a random electron beam that is proportional to the number of particles, a pre-bunched electron beam can emit spontaneously coherent radiation proportional to the number of particles—squared, through the process of (spontaneous) superradiance (SP-SR) (in the sense of Dicke's [2]), as shown in Fig. 1.

In the presence of a seed-injected radiation field, the coherent SP-SR emission of a bunched electron beam can be even further enhanced by a process of stimulated superradiance – ST-SR.

In this review, these fundamental coherent radiation emission processes were considered for both single bunch and periodically bunched beams in a model of radiation

mode expansion. The general model of coherent spontaneous emission was extended to the nonlinear regime, particularly for undulator (wiggler) interaction, where an exceedingly efficient radiative energy extraction process has been identified [3]: “Tapering-Enhanced Stimulated-Superradiant Amplification” (TESSA) (see Fig. 2).

Processes of SP-SR and TESSA take place also in tapered wiggler seed-injected free-electron lasers (FELs). In such FELs, operating in the x-ray regime, these processes are convoluted with other effects. However, these fundamental emission concepts are still useful guidelines for the strategy of wiggler tapering efficiency and power enhancement.

Based on this model, previous theories and experiments were reviewed on coherent radiation sources based on SP-SR (coherent undulator radiation, synchrotron radiation, Smith-Purcell radiation, transition radiation etc.) in the THz regime, and other on-going works on tapered wiggler efficiency-enhancement concepts in all optical frequency regimes up to UV and x rays.

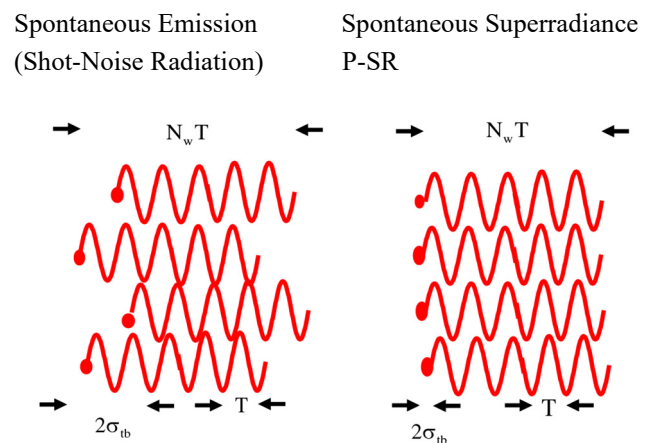


Figure 1: Coherent (right) vs. Random (left) superposition of radiation wavepackets.

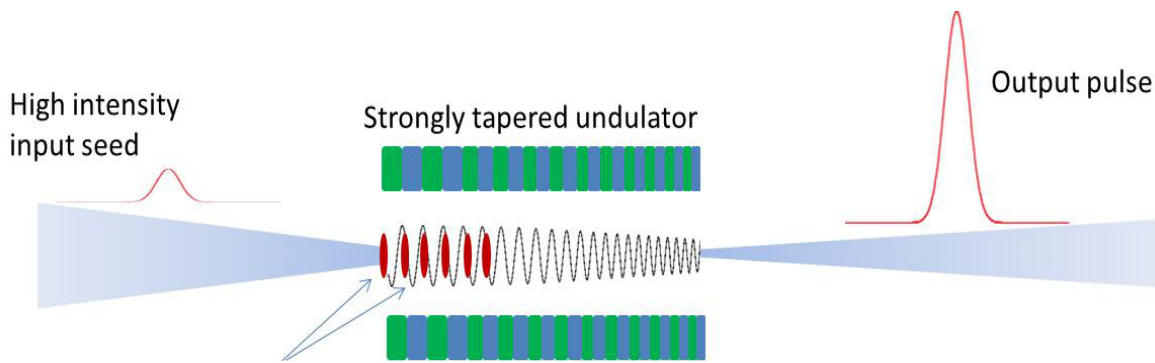


Figure 2: Tapering Enhanced Stimulated Superradiant Amplification - TESSA.

CONCLUSION

1. Fundamental radiation emission processes of bunched beam at zero order:
-Spontaneous Superradiance (SP-SR) $\propto n^2, z^2$
-Stimulated Superradiance (ST-SR) $\propto n, z, E(0)$
2. A. Model of periodical tightly bunched e-beam interaction with a single radiation mode in the nonlinear regime was used to describe:
-SR and ST-SR in a uniform wiggler.
-Tapering Enhanced Superradiance (TES),
-Tapering Enhance Stimulated Superradiance Amplification (TESSA) and Oscillation (TESSO).
3. Presented self-interaction of a bunched beam in a uniform wiggler and seedless TESSA concepts.
4. Reviewed application of THz superradiant sources based on SR emission by sub-picosec bunches.
5. Reviewed applications of TESSA, TESSO in the THz to UV frequencies range.
6. Related to optimization of tapering strategy in the tapered wiggler section of X-Ray FELs.

ACKNOWLEDGEMENTS

This research was supported in part by a grant from the United State-Israel Binational Science Foundation (BSF), Jerusalem, Israel, the Israel Science Foundation (ISF), and the German-Israeli Project Cooperation (DIP)

REFERENCES

- [1] A. Gover, R. Iancu, A. Friedman, C. Emma, N. Sudar, P. Musumeci and C. Pellegrini, "Superradiant and stimulated-superradiant emission of bunched electron beams", *Review of Modern Physics*, vol. 91, no. 3, p. 035003, 2019.
doi:10.1103/RevModPhys.91.035003
- [2] R. H. Dicke, "Coherence in Spontaneous Radiation Processes", *Phys. Rev.*, vol. 93, p. 99, 1954.
doi:10.1103/PhysRev.93.99
- [3] N. Sudar *et al.*, "High Efficiency Energy Extraction from a Relativistic Electron Beam in a Strongly Tapered Undulator", *Phys. Rev. Lett.*, vol. 117, p. 174801, 2016.
doi:10.1103/PhysRevLett.117.174801

OVERVIEW OF CW RF GUNS FOR SHORT WAVELENGTH FELs

H. Qian*, Deutsches Elektronen Synchrotron, Zeuthen, Germany
E. Vogel†, Deutsches Elektronen Synchrotron, Hamburg, Germany

Abstract

Hard X-ray FELs (XFELs) operating with pulsed RF provides unprecedented peak brilliance for scientific research. Operating the accelerators with CW RF improves the flexibility w.r.t. the available time structure for experiments and opens the next frontier of average brilliance. One of the challenges of CW XFELs is the electron source, which requires both the CW operation and the highest possible beam quality allowing lasing at shortest wavelengths. With a given linac energy, higher beam brightness results in shorter X-ray wavelength. As the injector defines the lower limit of the electron beam brightness of the complete accelerator, R&D is devoted to CW photoinjector improvements since decades. In this contribution, the worldwide development status of CW RF guns, both normal conducting and superconducting, is reviewed.

INTRODUCTION

Short wavelength free electron lasers (FEL) in the X-ray regime have seen great success in the last decades, such as FLASH, LCLS, the European XFEL and so on [1–3]. These X-ray FEL light sources provide much shorter (sub 100 fs) and much brighter pulses than storage rings [4]. Current X-ray FEL facilities are based on pulsed RF linacs with duty factors lower than 1%, which reduces the average electron beam pulse rate (<27000/second) and thus the average X-ray brightness. Operating the superconducting (SC) linacs in CW mode enables both higher average brightness and more flexible timing patterns for X-rays. Two CW X-ray FELs are under construction, one is LCLS-II in the US, and the other is SHINE in China [5,6]. Compared to the pulsed X-ray FEL, the linac energy of CW X-ray FEL is roughly a factor of 2 lower. According to LCLS-II high energy upgrade (LCLS-II-HE) studies, an even brighter electron source (0.1 μm at 100 pC) is needed to extend the lasing energy from 13 keV to 20 keV [7].

Due to the common needs of high brightness CW injectors, both the energy recovery linac (ERL) community and the FEL community are pushing the R&Ds of CW guns. The ERL guns focus more on high average current (~100 mA), while the FEL guns focus more on low emittance beams. Both communities emphasize the developments of high QE cathodes and high gradient guns. R&D is performed on DC guns, normal conducting (NC) RF guns, SC RF gun and hybrid guns [8–11]. Due to the relatively low cathode gradient (<5 MV/m) and low gun voltage (<500 kV), DC guns are mainly developed for the ERL applications to achieve a high average current. The Cornell DC gun also demonstrated

the baseline emittance required by LCLS-II, but the linac bunch compression is compromised according to LCLS-II studies [12, 13]. Therefore in this paper, overview on CW guns is focused on photocathode RF guns for applications in short wavelength FELs.

HIGH BRIGHTNESS INJECTORS FOR FELs

There are two types of photoinjectors for X-ray FELs, one is based on a high gradient RF gun, and the other is based on a medium to low gradient gun. A high gradient gun enables photoemission of both high peak current and low thermal emittance, i.e. ‘pancake’ emission, and the beam is then matched into a booster linac by a gun solenoid for emittance compensation. This type of injector uses high frequency (>1 GHz) pulsed NC guns, and the emission gradient is about 40 to 60 MV/m, which is roughly 50% to 70% of the peak cathode field due to the phase slippage. Such pulsed gun performances cannot be scaled to the CW mode for NC guns due to a few megawatt average RF heating. SC CW guns have the potential to reach similar fields. SC L-band guns are under development at HZDR, HZB, DESY, KEK and PKU. VHF-band quarter wave resonator (QWR) guns are under development at BNL and Wisconsin/SLAC/ANL.

To reach similarly low emittance as achieved in high gradient guns, photoemission in medium to low gradient guns has to start with a longer laser pulse to keep the low thermal emittance, i.e. ‘cigar’ emission. The long beam is compressed by a buncher cavity following the gun to restore the high peak current, and then matched into the booster linac by solenoid focusing for emittance compensation. To host the long beam, the gun cavity should be low frequency, which makes the beam dynamics like DC gun. The phase slippage is negligible in the low frequency gun, hence the emission field is almost equal to the peak cathode field. This type of injector was originally optimized for a DC gun based ERL injector, and was later adapted for the VHF-band NC CW gun developed at LBNL. The NC VHF gun is also under study at SLAC, DESY and SHINE.

APEX Gun and APEX2 Gun at LBNL

Inspired by the Cornell DC gun, a VHF band (185.7 MHz) gun was developed at the Advanced Photoinjector Experiment (APEX) for CW soft X-ray FEL project NGLS. The low frequency and large cavity is good for both the cavity cooling and the vacuum. The reentrant cavity shape not only enhances the cathode field and shunt impedance, but also makes the cavity size compact as compared to a pill-box cavity. The APEX gun concept was demonstrated in three phases. In phase 0, the designed CW RF power and ultra high vacuum was demonstrated [14]. In phase I, the

* h.qian@desy.de
† e.vogel@desy.de

gun demonstrated compatibility with the high QE Cs₂Te cathode and a 300 μ A average current with 1 MHz beam repetition rate [15]. In phase II, the 20 pC beam brightness was demonstrated for LCLS-II [16].

In 2016, LBNL colleagues started to design the AEPX2 gun, which aims to increase the beam brightness at least by a factor of 4 for both LCLS-II-HE and ultrafast electron diffraction and microscopy [17]. To reduce the RF heating, the gun frequency is lowered to 162.5 MHz. The APEX2 gun is a two cell design. The first cell is designed for a higher cathode field above 30 MV/m, and the second cell is for boosting the beam energy above 1 MeV. Simulations show the APEX2 gun can reach 0.1 μ m emittance for 100 pC beam with a 0.6 μ m/mm thermal emittance [18].

The main parameters of the APEX gun and APEX2 gun are summarized in Table 1 together with the other CW normal conducting RF guns.

LCLS-II Gun at SLAC

Simulations show the LCLS-II photoinjector based on the APEX gun meets the baseline requirements [19]. A slightly modified APEX gun is produced for LCLS-II by LBNL. The LCLS-II gun commissioning is ongoing and full RF power is already achieved [20]. Next, they are going to exchange the Mo cathode by the Cs₂Te cathode for 1 MHz beam operation and electron beam optimization.

CW VHF Gun Design for SHINE

SHINE decided to use the VHF gun as the baseline CW gun technology [21]. The SHINE VHF gun frequency is 162.5 MHz with an operation range between 750 kV and 1 MV, corresponding to a RF power of 70 kW and 120 kW respectively. The cathode field reaches 30 MV/m at 1 MV. The prototype gun is now under engineering design and will be produced soon.

DESY – CW Gun for European XFEL

A future upgrade of the European XFEL (EXEL) foresees an additional CW operation mode, which will increase the flexibility in the photon beam time structure [22–25]. One of the challenges of this operation mode is a CW operating photoinjector. For more than a decade DESY, in collaboration with TJNAF, NCBJ, BNL, HZB and HZDR, has performed R&D to develop an all SC RF gun with a lead cathode screwed in a clean room into a hole on the backside of a 1.6 cell L-band cavity [26]. The cavity can be cleaned after the cathode insertion, and possibly lost cathode particles should not heat and quench the cavity, as they are all superconducting. In contrast to setups with cathode loadlock systems, exchanging cathodes requires a complete disassembly of the cryostat and bringing the gun cavity back into the cleanroom. The target parameters of the DESY SC gun can be found in Table 2 together with the other L-band SC guns.

In parallel to the SC gun program, a backup option following the NC VHF gun approach is under physics design study [27]. The DESY VHF gun is a 216.7 MHz single cell

gun with both higher gradient (28 MV/m) and higher voltage (830 kV) than APEX gun. The higher gun frequency reduces the RF breakdown risk and better fits the Eu-XFEL timing system. The acceleration gap is reduced compared to the APEX gun to increase the cathode field and consequently the beam brightness. A 400 kV buncher is also under design to match the higher gun voltage [28].

HZDR – SRF Gun for ELBE (THz FEL)

In the nineties HZDR started the construction of the compact SC L-band linac ELBE as source of different secondary beams which started operation in 2001 [29, 30]. The initial and main injector of ELBE is a thermionic gun. In parallel to the commissioning of the facility R&D for a SC photoinjector started [31]. It includes a 3.5 cell L-band cavity with chock cell and a SC solenoid in a cryostat, and a loadlock system for cathode exchange. The Cs₂Te cathode was successfully tested in the first gun, but has some overheating issues in the second gun [32]. Since 2017, the SC gun started user operations for terahertz beamline with a Mg cathode [33]. Currently, the gun R&D is focused on establishing a Cs₂Te cathode for user operation and a dedicated gun-lab.

HZB – SRF Gun for bERLinPro

BERLinPro is an accelerator facility under development and construction at HZB since 2011 to demonstrate the principle of an energy recovery linac [34, 35]. The first two generations of 1.3 GHz SC guns were tested with SC lead cathode, and a 20 to 30 MV/m peak acceleration gradient was achieved. To achieve the 100 mA average current, the third generation SC gun was designed for a NC high QE CsK₂Sb cathode, including a 1.4 cell cavity with choke cell, a cathode loadlock system and a SC solenoid [36]. In 2011 a first full setup of this injector was tested in the HoBiCaT facility [37]. In 2017 a beam test was performed with a copper cathode. After exchanging the cathode, high field emission was observed limiting the gun performance [38]. The current focus of the R&D work lies on the cathode exchange system to achieve higher gradients with a CsK₂Sb cathode. It is foreseen to move the photoinjector test setup from the HoBiCaT facility to the bERLinPro accelerator hall [39].

KEK – SRF Gun for KEK-ERL

In 2008 the development of the key elements for the compact energy recovery linac (cERL) at KEK started [40]. In 2010 the construction started and in 2014 first beam was transported through the recirculation loop using an injector consisting of a 500 kV photocathode DC gun [41]. Using an SRF gun instead is expected to be advantageous w.r.t. higher bunch charges and low emittances. In 2013 KEK started to develop a 1.5 cell SC gun cavity with a choke cell and performed very successful vertical tests with a record high on axis peak field of about 57 MV/m [42]. In contrast to other SC gun setups the cathode will be illuminated by the cathode laser from the backside using a transparent superconductor as substrate for the CsK₂Sb cathode [43]. Currently the

Table 1: Summary of Normal Conducting VHF Gun Performances

Parameter	APEX	LCLS-II	APEX2	DESY	SHINE	Units
Status	Routine operation	Beam test	Design	Design	Design	N/A
Frequency	185.7		162.5	216.7	162.5	MHz
Cathode field	19.5		34	28	23.5-31	MV/m
Gun voltage	750		1640	830	750-1000	kV
Average RF power	90		176	100	69-120	kW
Shunt impedance	6.3		15.2	6.9	8.2	Mohm
Peak surface field	24.1		37	30.6	28.4-37.5	MV/m
Peak power density	25		32	37	16.9-29.5	W/cm ²
Diameter/Length	69.4/35		78.6/74.7	68/26.8	80/42	cm
Beam parameter	Measurement	Simulation	Simulation	Simulation	Simulation	pC
Bunch charge	20-300	20-300	100	100	100	pC
Bunch rate	1	1	1	1	1	MHz
Dark current	0.1	<400	N/A	N/A	N/A	nA
Projected emittance	<0.2 (20 pC, 6 A)	0.2-0.6 (5-30 A)	0.08 (12 A)	0.2 (11 A)	N/A	µm.rad
Cathode	Cs ₂ Te (CsK ₂ Sb)	Cs ₂ Te	CsK ₂ Sb	N/A	N/A	N/A
Thermal emittance	0.75 (0.6)	N/A	0.6	1.0	N/A	µm.rad/mm
Cathode assembly		Loadlock, RF spring				N/A
Lifetime in operation	8 (2)	N/A	N/A	N/A	N/A	week
Private reference	F. Sannibale	F. Zhou	D. Li	H. Qian	Q. Gu	N/A

Table 2: Summary of L-band SC Gun Performances

Parameter	HZDR	HZB	KEK	DESY	Units
Status	R&D	Routine operation	R&D	R&D	N/A
Frequency	1300	1300	1300	1300	MHz
Cavity type	TESLA 3.5	TESLA 1.4	TESLA 1.5	TESLA 1.5	cell
Gun energy	3-4	2	>3	3-4	MeV
Peak axis field	20.5	7.5	31.5	40	MV/m
Cathode field	12	7.5	23	40	MV/m
Gradient limitation	Field emission	Field emission	N/A	N/A	N/A
Beam parameter	Measurement	Simulation	Simulation	Simulation	N/A
Bunch charge	200	77	80	100	pC
Bunch rate	0.1	1300	1300	0.1	MHz
Dark current	30	100	N/A	N/A	nA
Projected emittance	2-15	<0.5	0.6	N/A	µm.rad
Cathode	Mg (Cs ₂ Te)	Cu (CsK ₂ Sb)	CsK ₂ Sb	Pb	N/A
Cathode assembly	RF choke loadlock	RF choke loadlock	RF choke loadlock	Screw in	N/A
Cathode lifetime	50	N/A	N/A	N/A	week
Private reference	A. Arnold J. Teichert R. Xiang	T. Kamps A. Neumann	T. Konomi	E. Vogel	N/A

R&D focuse is on improving the cathode cooling and the preparation of a horizontal test.

PKU – DC-SRF Gun

Since 2000 work on SRF photo injectors is performed at Peking University [44]. Initially a SC 1.5 cell L-band cavity after a DC voltage gap for the initial acceleration of

the photoelectrons has been used and replaced in 2014 by a 3.5 cell L-band cavity. The DC gap at the entrance of the SC cavity successfully avoided the complication of a NC cathode in the SC cavity, but it also limites the cathode gra-dient. Since 2014 the gun achieved routine operations with a Cs₂Te cathode. The injector is used for the provision of high repetition rate terahertz radiation and ultrafast electron

Table 3: Summary of QWR SC Gun and Hybrid SC Gun Performances

Parameter	BNL	SLAC	PKU	Units
Status	Routine operation	R&D	Routine operation	N/A
Frequency	113	200	1300	MHz
Cavity type	QWR	QWR	TESLA 3.5 (1.5)	cell
Gun energy	1.25	1.1	3-4 (2.8)	MeV
Peak axis field	20	12	22 (26.6)	MV/m
Cathode field	10-20	12	2.6 (6)	MV/m
Gradient limitation	Field emission	N/A	DC	N/A
Beam parameter	Measurement	Measurement	Measurement (simulation)	N/A
Bunch charge	up to 10700	100	20-50 (100)	pC
Bunch rate	0.078	0.001	27 (1)	MHz
Dark current	1	N/A	1 (N/A)	nA
Projected emittance	0.15 (100 pC, <1 A)	1.5	1.5 (0.5-0.3)	$\mu\text{m}\cdot\text{rad}$
Cathode	CsK ₂ Sb	Cu	Cs ₂ Te (CsK ₂ Sb)	N/A
Cathode assembly	RF choke loadlock	RF choke	Screw in loadlock	N/A
Cathode lifetime	4-8	N/A	4-8	week
	V. Litvinenko			
Private reference	E. Wang Q. Wu T. Xin	B. Dunham X. Wang	S. Huang K. Liu	N/A

diffraction (UED) experiments [45]. The next generation DC-SRF gun is optimized for generating high brightness beams for a X-ray FEL with improvements on the cathode gradient and a smaller emittance [46, 47]. The parameters of the existing 3.5 cell gun and the next generation 1.5 cell gun are summarized in Table 3.

BNL – SRF Gun for Cooling Hadrons

In 2001 first plans and proposals were made to add a high energy electron cooling to the Relativistic Heavy Ion Collider (RHIC) [48]. Since 2007 an FEL-based Coherent electron Cooling (CeC) system has been developed and studied [49]. The major installation of the CeC system occurred during RHIC shutdown in 2016 and is in routine operation since then [50]. The electrons are generated by a CW photoinjector using green laser light on a CsK₂Sb cathode. The gun consists of a SC 112 MHz quarter wave resonator (QWR) developed by BNL in collaboration with the company Niowave. The typical cathode lifetime for the high bunch charge (~nC) operation is one to two months and the cathodes can be exchanged via a load lock system [51]. The parameters of the BNL QWR gun are summarized in Table 3.

Wisconsin/SLAC/ANL - SRF Gun for LCLS-II HE & UED/UEM

The University of Wisconsin-Madison presented 2009 a pre-conceptual design for a seeded VUV/soft X-ray FEL, called WiFEL, serving multiple simultaneous users [52].

For the photoinjector a SC 200 MHz QWR gun has been selected, designed and constructed together with the company Niowave [53]. In 2013 first beam was generated and simple beam measurements were made [54]. Afterwards this photoinjector was transported to SLAC as a potential electron source for the LCLS-II-HE and for ultrafast electron microscopy (UED & UEM) experiments. Recommissioning at SLAC took place and first beam were generated in 2018 [55]. Due to the lack of a cryogenics plant for the operation, the R&D activities with this photoinjector will resume at Argonne National Laboratory (ANL) after its transfer from SLAC to ANL [56].

CW GUN VS PULSED GUN

CW RF gun technology is still far from mature, and the peak acceleration gradient of around 20 MV/m is still low w.r.t. the hard X-ray FEL lasing at the shortest wavelength. Besides a higher gun gradient, the beam transverse brightness can also be improved by low emittance cathodes, laser shaping and 'cigar' photoemission instead of 'pancake' photoemission in the low frequency CW guns [12, 57].

Figure 1 is a 100 pC simulation example comparing the PITZ pulsed injector and the LCLS-II CW injector with a thermal emittance of 1 $\mu\text{m}/\text{mm}$. The LCLS-II injector based on the 20 MV/m APEX gun is almost identical to the 40 MV/m PITZ gun in terms of transverse emittance and RMS bunch length. When the beam peak current is around 10 A (RMS bunch length is between 1 mm and 1.3 mm), both the AEPX gun and PITZ gun can deliver the baseline

- [6] Z. Zhu, Z. T. Zhao, D. Wang, Z. H. Yang, and L. Yin, "SCLF: An 8-GeV CW SCRF Linac-Based X-Ray FEL Facility in Shanghai", in *Proc. FEL'17*, Santa Fe, NM, USA, Aug. 2017, pp. 182–184. doi:10.18429/JACoW-FEL2017-MOP055
- [7] T. O. Raubenheimer, "The LCLS-II-HE, A High Energy Upgrade of the LCLS-II", in *Proc. FLS'18*, Shanghai, China, Mar. 2018, pp. 6–11. doi:10.18429/JACoW-FLS2018-MOP1WA02
- [8] A. Arnold and J. Teichert, "Overview on superconducting photoinjectors", *Phys. Rev. ST Accel. Beams*, vol. 14, p. 024801, 2011. doi:10.1103/PhysRevSTAB.14.024801
- [9] J. K. Sekutowicz, "SRF Gun Development Overview", in *Proc. SRF'15*, Whistler, Canada, Sep. 2015, paper THAA02, pp. 994–1000. doi:10.18429/JACoW-SRF2015-THAA02
- [10] F. Sannibale, "Overview of Electron Source Development for High Repetition Rate FEL Facilities", in *Proc. NAPAC'16*, Chicago, IL, USA, Oct. 2016, pp. 445–449. doi:10.18429/JACoW-NAPAC2016-TUB3IO02
- [11] V. Volkov *et al.*, "Latest Results of CW 100 mA Electron RF Gun for Novosibirsk ERL Based FEL", in *Proc. LINAC'18*, Beijing, China, Sep. 2018, pp. 598–600. doi:10.18429/JACoW-LINAC2018-WE1A03
- [12] C. Gulliford *et al.*, "Demonstration of cathode emittance dominated high bunch charge beams in a DC gun-based photoinjector", *Appl. Phys. Lett.*, vol. 106, p. 094101, 2015. doi:10.1063/1.4913678
- [13] F. Zhou, "Review of CW Guns for XFEL", in *Proc. FLS'18*, Shanghai, China, Mar. 2018. http://jacow.org/fls2018/talks/thp1wd01_talk.pdf
- [14] F. Sannibale *et al.*, "Advanced photoinjector experiment photogun commissioning results", *Phys. Rev. ST Accel. Beams*, vol. 15, p. 103501, 2012. doi:10.1103/PhysRevSTAB.15.103501
- [15] D. Filippetto *et al.*, "Cesium telluride cathodes for the next generation of high-average current high-brightness photoinjectors", *Appl. Phys. Lett.*, vol. 107, p. 042104, 2015. doi:10.1063/1.4927700
- [16] F. Sannibale *et al.*, "High-brightness beam tests of the very high frequency gun at the Advanced Photo-injector EXperiment test facility at the Lawrence Berkeley National Laboratory", *Review of Scientific Instruments*, vol. 90, p. 033304, 2019. doi:10.1063/1.5088521
- [17] D. Li *et al.*, "Recent Progress on the Design of Normal Conducting APEX-II VHF CW Electron Gun", in *Proc. IPAC'19*, Melbourne, Australia, May 2019, pp. 1891–1894. doi:10.18429/JACoW-IPAC2019-TUPRB097
- [18] D. Li, personal communication
- [19] C. E. Mitchell *et al.*, "RF Injector Beam Dynamics Optimization and Injected Beam Energy Constraints for LCLS-II", in *Proc. IPAC'16*, Busan, Korea, May 2016, pp. 1699–1702. doi:10.18429/JACoW-IPAC2016-TUPOR019
- [20] F. Zhou *et al.*, "First Commissioning of LCLS-II CW Injector Source", in *Proc. IPAC'19*, Melbourne, Australia, May 2019, pp. 2171–2173. doi:10.18429/JACoW-IPAC2019-TUPTS106
- [21] D. Wang and Q. Gu, personal communication
- [22] J. Sekutowicz *et al.*, "Proposed continuous wave energy recovery operation of an x-ray free electron laser", *Phys. Rev. ST Accel. Beams*, vol. 8, pp. 010701, 2005. doi:10.1103/PhysRevSTAB.8.010701
- [23] J. K. Sekutowicz *et al.*, "Feasibility of CW and LP Operation of the XFEL Linac", in *Proc. FEL'13*, New York, NY, USA, Aug. 2013, paper TUOCNO04, pp. 189–192.
- [24] R. Brinkmann, E. Schneidmiller, J. K. Sekutowicz, and M. V. Yurkov, "Prospects for CW Operation of the European XFEL in Hard X-ray Regime", in *Proc. FEL'14*, Basel, Switzerland, Aug. 2014, paper MOP067, pp. 210–214.
- [25] D. Kostin and J. Sekutowicz, "Progress towards ContinuousWave Operation of the SRF Linac at DESY", in *Proc. SPIE*, vol. 11054, pp. 1105406, 2018. doi:10.1117/12.2524952
- [26] E. Vogel *et al.*, "SRF Gun Development at DESY", in *Proc. LINAC'18*, Beijing, China, Sep. 2018, pp. 105–108. doi:10.18429/JACoW-LINAC2018-MOP0037
- [27] S. Shu, Y. Chen, S. Lal, H. J. Qian, H. Shaker, and F. Stephan, "First Design Studies of a NC CW RF Gun for European XFEL", in *Proc. IPAC'19*, Melbourne, Australia, May 2019, pp. 1698–1701. doi:10.18429/JACoW-IPAC2019-TUPRB010
- [28] S. Lal *et al.*, "RF Design Studies of a 1.3 GHz Normal Conducting CW Buncher for European X-FEL", in *Proc. IPAC'19*, Melbourne, Australia, May 2019, pp. 3109–3111. doi:10.18429/JACoW-IPAC2019-WEPTS012
- [29] F. Gabriel *et al.*, "The Rossendorf radiation source ELBE and its FEL projects", *Nucl. Instrum. Methods Phys. Res., Sect. B*, vols. 161–163, pp. 1143–1147, 2000. doi:10.1016/S0168-583X(99)00909-X
- [30] P. Michel *et al.*, "First Lasing at the ELBE mid-IR FEL", in *Proc. FEL'04*, Trieste, Italy, Aug.-Sep. 2004, paper MOAIS04, pp. 8–13.
- [31] A. Arnold *et al.*, "Development of a superconducting radio frequency photoelectron injector", *Nucl. Instrum. Methods Phys. Res., Sect. A*, vol. 577, pp. 440–454, 2007. doi:10.1016/j.nima.2007.04.171
- [32] R. Xiang *et al.*, "Runing Status of SRF Gun II at the ELBE Radiation Center", in *Proc. LINAC'18*, Beijing, China, Sep. 2018, pp. 952–954. doi:10.18429/JACoW-LINAC2018-THPO125
- [33] J. Teichert *et al.*, "Experiences with the SRF Gun II for User Operation at the ELBE Radiation Source", in *Proc. IPAC'18*, Vancouver, Canada, Apr.-May 2018, pp. 4145–4147. doi:10.18429/JACoW-IPAC2018-THPMF040
- [34] J. Knobloch *et al.*, "BERLinPro - A Compact Demonstrator ERL for High Current and Low Emittance Beams", in *Proc. LINAC'10*, Tsukuba, Japan, Sep. 2010, paper TUP007, pp. 407–409.
- [35] B. Kuske *et al.*, "Conceptual Design Report BERLinPro", HZB, 2012. https://www.helmholtz-berlin.de/media/media/grossgeraete/beschleunigerphysik/berlinpro_MAB/BPro_in_detail/Publications/berlinpro_CDR.pdf
- [36] T. Kamps *et al.*, "Status and perspectives of superconducting radio-frequency gun development for BERLinPro", *J. Phys.: Conf. Ser.*, vol. 298, p. 012009, 2011. doi:10.1088/1742-6596/298/1/012009

- [37] A. Burrill *et al.*, “First Horizontal Test Results of the HZB SRF Photoinjector for BERLinPro”, in *Proc. IPAC’15*, Richmond, VA, USA, May 2015, pp. 2768–2770. doi:10.18429/JACoW-IPAC2015-WEPMA011
- [38] A. Neumann *et al.*, “The BERLinPro SRF Photoinjector System - From First RF Commissioning to First Beam”, in *Proc. IPAC’18*, Vancouver, Canada, Apr.-May 2018, pp. 1660–1663. doi:10.18429/JACoW-IPAC2018-TUPML053
- [39] T. Kamps, personal communication
- [40] R. Hajima *et al.*, “Design Study of the Compact ERL”, KEK Report 2007-7/JAEA-Research 2008-032, 2008.
- [41] N. Nakamura *et al.*, “Present Status of the Compact ERL at KEK”, in *Proc. IPAC’14*, Dresden, Germany, Jun. 2014, pp. 353–355. doi:10.18429/JACoW-IPAC2014-MOPR0110
- [42] T. Konomi *et al.*, “Development of High Intensity, High Brightness, CW SRF Gun with Bi-Alkali Photocathode”, in *Proc. SRF’19*, Dresden, Germany, Jun.-Jul. 2019, pp. 1219–1222. doi:10.18429/JACoW-SRF2019-FRCAB4
- [43] T. Konomi *et al.*, “Development of SRF Gun Applying New Cathode Idea Using a Transparent Superconducting Layer”, in *Proc. ERL’17*, Geneva, Switzerland, Jun. 2017, pp. 1–3. doi:10.18429/JACoW-ERL2017-MOIACC002
- [44] J. Hao *et al.*, “Recent Progresses on DC-SC Photoinjector at Peking University”, in *Proc. SRF’05*, Ithaca, NY, USA, Jul. 2005, paper THP24, pp. 515–517.
- [45] G. Zhao *et al.*, “Tunable High-power Terahertz Free-Electron Laser Amplifier”, in *Proc. FEL’15*, Daejeon, Korea, Aug. 2015, pp. 305–307. doi:10.18429/JACoW-FEL2015-TUB05
- [46] Y. Q. Liu *et al.*, “Engineering Design of Low-Emittance DC-SRF Photocathode Injector”, presented at the FEL’19, Hamburg, Germany, Aug. 2019, paper WEP056, this conference.
- [47] S. Zhao *et al.*, “Performance Optimization of Low-Emittance DC-SRF Injector Using Cs2Te Photocathode”, presented at the 39th Int. Free Electron Laser Conf. (FEL’19), Hamburg, Germany, Aug. 2019, paper WEP057, this conference.
- [48] I. Ben-Zvi *et al.*, “Electron Cooling for RHIC”, in *Proc. PAC’01*, Chicago, IL, USA, Jun. 2001, paper MOPA011, pp. 48–50.
- [49] V. Litvinenko, “Coherent Electron Cooling”, in *Proc. PAC’09*, Vancouver, Canada, May 2009, paper FR1GRI01, pp. 4236–4240.
- [50] I. Pinayev *et al.*, “Performance of CeC PoP Accelerator”, in *Proc. IPAC’19*, Melbourne, Australia, May 2019, pp. 559–561. doi:10.18429/JACoW-IPAC2019-MOPMP050
- [51] S. A. Belomestnykh *et al.*, “Commissioning of the 112 MHz SRF Gun”, in *Proc. SRF’15*, Whistler, Canada, Sep. 2015, pp. 1240–1242. doi:10.18429/JACoW-SRF2015-THPB058
- [52] K. Jacobs *et al.*, “The Wisconsin Free Electron Laser Initiative”, in *Proc. PAC’09*, Vancouver, Canada, May 2009, paper MO4PBC04, pp. 109–111.
- [53] R. Legg *et al.*, “Wisconsin SRF Gun Development”, in *Proc. ERL’09*, Ithaca, NY, USA, Jun. 2009, paper WG118, pp. 45–49.
- [54] J. Bisognano *et al.*, “Wisconsin SRF Electron Gun Commissioning”, in *Proc. NAPAC’13*, Pasadena, CA, USA, Sep.-Oct. 2013, paper TUPMA19, pp. 622–624.
- [55] SLAC Produces First Electron Beam with Superconducting Electron Gun, <https://www6.slac.stanford.edu/news/2018-04-09-slac-produces-first-electron-beam-superconducting-electron-gun.aspx>
- [56] Bruce M. Dunham, personal communication
- [57] H. J. Qian, M. Krasilnikov, and F. Stephan, “Beam Brightness Improvement by Ellipsoidal Laser Shaping for CW Photoinjectors”, in *Proc. FEL’17*, Santa Fe, NM, USA, Aug. 2017, pp. 432–435. doi:10.18429/JACoW-FEL2017-WEP008
- [58] F. Sannibale *et al.*, “Status, Plans and Recent Results from the APEX Project at LBNL”, in *Proc. FEL’15*, Daejeon, Korea, Aug. 2015, pp. 81–84. doi:10.18429/JACoW-FEL2015-MOP024
- [59] ELBE SRF Gun II - New High Gradient SRF Gun, 2009 – Today, <https://www.hzdr.de/db/Cms?pNid=604>
- [60] W. D. Kilpatrick, “Criterion for Vacuum Sparking Designed to Include Both rf and dc”, *Rev. Sci. Instrum.*, vol. 28, p. 824, 1957. doi:10.1063/1.1715731

GROWING AND CHARACTERIZATION OF Cs₂Te PHOTOCATHODES WITH DIFFERENT THICKNESSES AT INFN LASA

L. Monaco*, P. Michelato, D. Sertore, INFN LASA, Segrate, Italy
C. Pagani, G. Guerini Rocco, Università degli Studi di Milano e INFN LASA, Segrate, Italy

Abstract

The INFN LASA group has a long standing experience in the production of cesium telluride photocathodes for high brightness photoinjectors. The well-established recipe relies on the deposition of a typical amount of 10 nm of Te, followed by the Cs deposition until reaching the maximum QE. Nevertheless, for improving the understanding of photocathode properties, we are investigating the effect of Te thickness on the growing process, evaluating photocathode optical properties and quantum efficiency during the growing process and on the final film. These photocathodes will be then operated and analyzed in the real environment of the RF Gun at the PITZ facility in DESY Zeuthen, to estimate their impact on the electron beam properties.

INTRODUCTION

The INFN LASA activities on photocathodes to be used in high brightness photoinjectors started in the '90s in the framework of the TESLA collaboration. After a first phase mainly dedicated to R&D studies, we started the production of Cs₂Te photocathodes and we delivered the first photocathodes in 1998 to the TTF RF Gun at DESY-Hamburg. Since then, we continuously produced photocathodes, reaching now a total delivery of about 150 Cs₂Te films, distributed to several laboratories such DESY-Hamburg for FLASH, DESY-Zeuthen for PITZ, LBNL for APEX and, SLAC for the commissioning of LCLS-II photoinjector.

The need to satisfy requests for usage of our photocathodes in RF guns of accelerators and user facilities guided our activity to develop reproducible and robust recipe, able to furnish the needed Quantum Efficiency (QE) for the operation, a good QE spatial uniformity, a long operative lifetime and a low dark current (DC). All these issues were reached [1] and, as an example, the operative lifetime was increased from few months to few years (24/7) [2]. The development of a multi-wavelength technique for monitoring QE and reflectivity during cathode formation improved further the reproducibility of the final photocathodes [3].

In this paper, we present the results obtained on photocathodes produced with different Te layer thicknesses and we compared them with the properties of our well known standard cathodes. Moreover, these photocathodes have then been used at PITZ for their characterization in the RF Gun, in the framework of the INFN LASA and DESY PITZ collaboration and the results are presented at this conference [4].

* laura.monaco@mi.infn.it

CATHODE DEPOSITION AND DIAGNOSTIC

Photoemissive films are evaporated sequentially on high purity Mo plugs (99.95 %), optically polished (typical roughness $R_a = 10$ nm). The deposition is done in the preparation chamber (base pressure 1×10^{-10} mbar) with a diameter of 5 mm realized with a Mo masking system. After an heating cycle up to 450 °C, the plug is cooled to 120 °C and the Te deposition starts (1 nm/min). When 10 nm of Te are deposited, the Cs deposition starts at 1 nm/min and ends when the QE reaches the typical maximum [5]. For the purpose of this work, we have grown photocathodes with 5 nm and 15 nm of Te besides a standard "10 nm". In all cases, the Cs deposition stopped when the QE reached its maximum.

Reflectivity

During the film growth, the plug is illuminated at different wavelengths, with a spot of approximately 5 mm (corresponding to the active area) to ensure a uniform reaction of the entire film area. The reflected power is extremely useful especially for the control of the real amount of Te deposited on the plug surface. Figure 1 reports the reflectivity variation for three different Te thicknesses and the theoretical predictions based on tabulated values for Mo and Te [6], in the assumption of a formation of a uniform Te layer on top of Mo substrate. The deviation from theory at thicker layers is possibly due to formation of islands of Te on Mo that our model does not take into account.

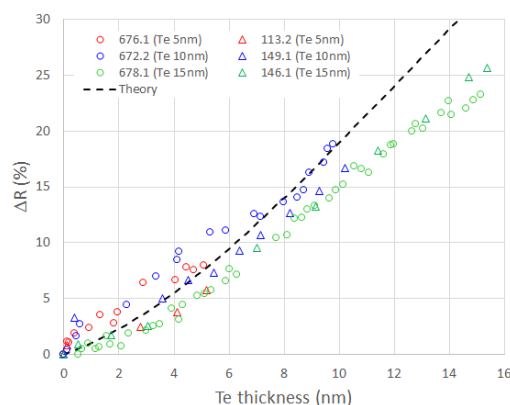


Figure 1: Te reflectivity decrease (ΔR) for three different film thickness and the expectation from tabulated values.

Table 1 reports the average reflectivity variation for the three different types of photocathodes based on all measurements so far available (26 films for "10 nm", 3 films for "5 nm" and "15 nm").

the thinner one shows a slight "shoulder" at low energy probably due to Cs excess during deposition. Indeed, the determination of the "peak" to stop the Cs evaporation is more difficult in this case due to the thin Te layer.

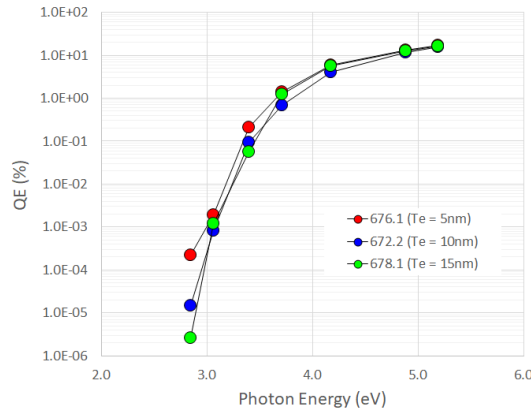


Figure 4: Spectral responses just after the deposition for the three films.

QE maps and Energy Threshold ($E_g + E_a$)

As introduced before, the analysis of the spectral response allows estimating the $E_g + E_a$ (Energy Gap + Electron Affinity) of the Cs_2Te . We have applied this technique to the whole photocathode area. We acquired photocathode maps at different wavelengths and from them we fit the QEs for every single spot and estimate the photocathode $E_g + E_a$ applying the following formula as reported in Kane [10] and adapted for a possible lower energy threshold:

$$QE = A[h\nu - (E_g + E_a)]^m + B[h\nu - (E_{g1} + E_{a1})]^{m1} \quad (1)$$

where A and B are adapting constant, $h\nu$ the photon energy, $E_g + E_a$ and $E_{g1} + E_{a1}$ are the corresponding energy gap and electron affinity and, m and m1 the power coefficients that, in Kane theory, are linked to the transition type in the semiconducting film.

Figure 5 reports the maps for the three photocathodes. The upper row is the $E_g + E_a$ over the photocathode area (the Mo substrate is set top 4.5 eV by default) only for the first term in Eq. 1, middle row is the QE map at 254 nm and the lower row QE map at 365 nm. Besides the QE map uniformity, the maps at 254 nm are not sensitive enough to the $E_g + E_a$ variation. On the contrary, maps at 365 nm show a quite good correlation with the $E_g + E_a$ maps. As expected regions of lower QE correspond to higher $E_g + E_a$ area as clearly shown for the "10 nm" photocathode (middle columns in Fig. 5) where the lower left area shows lower QE in the 365 nm map as well as high $E_g + E_a$ values.

Reflectivity

The final reflectivities of the three cathodes are reported in Fig. 6. These values agree with the one obtained on a similar set of photocathodes produced in the past [8].

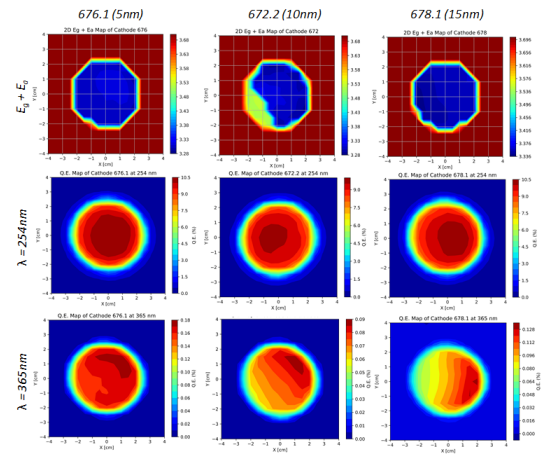


Figure 5: Maps of $E_g + E_a$ (top row), QE at 254 nm (middle row) and 365 nm (bottom row).

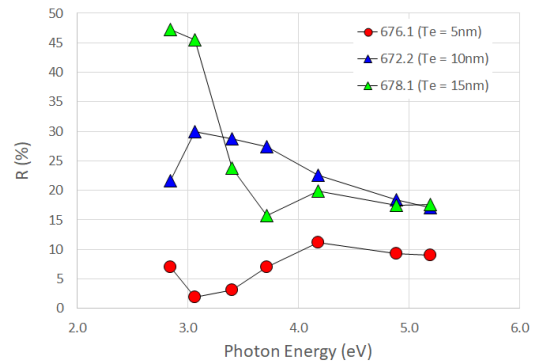


Figure 6: Final reflectivity of the three different films.

Table 3: Photocathode Parameters Summary at 254 nm

	Te [nm]	Cs [nm]	QE [%]	R [%]	$E_g + E_a$ [eV]
676.1	5.1	33.9	12.9	9.3	3.31
672.2	9.8	63.6	11.5	18.4	3.34
678.1	15.1	92.3	12.7	17.5	3.37

CONCLUSION

The photocathodes with different Te thicknesses are quite reproducible and well comparable with films of similar thickness we measured in a previous set. The reflectivity at different wavelengths is a valuable tool for understanding the film growth. To further explore this possibility, we plan to grow even thicker films to have additional information from this optical technique. It will be interesting to learn from measurements at PITZ in the RF Gun environment if any difference will distinguish these three films in terms of lifetime and thermal emittance, having similar properties despite the different Te thicknesses.

REFERENCES

- [1] C. Pagani, P. Michelato, L. Monaco, and D. Sertore, "LASA Cs_2Te Photocathodes: The Electron Source for XFELs", in

- Toward a Science Campus in Milan*, Ed. Springer, 2018, pp. 281-292.
- [2] S. Lederer, S. Schreiber, L. Monaco, and D. Sertore, "Update on the Photocathode Lifetime at FLASH and European XFEL", presented at the 39th Int. Free Electron Laser Conf. (FEL'19), Hamburg, Germany, Aug. 2019, paper WEP047.
- [3] L. Monaco, P. M. Michelato, C. Pagani, and D. Sertore, "On-Line Diagnostic during Cs2Te Photocathodes Formation", in *Proc. 23rd Particle Accelerator Conf. (PAC'09)*, Vancouver, Canada, May 2009, paper MO6RFP072, pp. 536-538.
- [4] P. W. Huang *et al.*, "Test of Cs2Te Thickness on Cathode Performance at PITZ", presented at the 39th Int. Free Electron Laser Conf. (FEL'19), Hamburg, Germany, Aug. 2019, paper WEP062.
- [5] D. Sertore, A. Bonucci, J. H. Han, P. Michelato, L. Monaco, and S. Schreiber, "Review of the Production Process of TTF and PITZ Photocathodes", in *Proc. 21st Particle Accelerator Conf. (PAC'05)*, Knoxville, TN, USA, May 2005, paper MOPB009, pp. 671-673.
- [6] Edward D. Palik, *Handbook of Optical Constants of Solids*, Academic Press, 1985
- [7] A. diBona *et al.*, "Auger and x-ray photoemission spectroscopy study on Cs2Te photocathodes", *J. Appl. Phys.*, vol. 80, p. 3024, 1996. doi:10.1063/1.363161
- [8] L. Monaco, P. M. Michelato, C. Pagani, and D. Sertore, "Multiwavelengths Optical Diagnostic during Cs2Te Photocathodes Deposition", in *Proc. 1st Int. Particle Accelerator Conf. (IPAC'10)*, Kyoto, Japan, May 2010, paper TUPEC006, pp. 1719-1721.
- [9] D. Sertore, P. Michelato, L. Monaco, and C. Pagani, "A Study for the Characterization of High QE Photocathodes", in *Proc. 22nd Particle Accelerator Conf. (PAC'07)*, Albuquerque, NM, USA, Jun. 2007, paper THPMN024, pp. 2760-2762.
- [10] Evan O. Kane, "Theory of photoelectric Emission from Semiconductors", *Phys. Rev.*, vol. 127, p. 131, 1962. doi:10.1103/PhysRev.127.131

IDENTIFICATION AND MITIGATION OF SMOKE-RING EFFECTS IN SCINTILLATOR-BASED ELECTRON BEAM IMAGES AT THE EUROPEAN XFEL

G. Kube, A. Novokshonov, S. Liu, M. Scholz, DESY, Hamburg, Germany

Abstract

Standard transverse beam profile measurements at the European XFEL are based on scintillating screen monitors using LYSO:Ce as scintillator material. While it is possible to resolve beam sizes down to a few micrometers with this material, the experience during the XFEL commissioning showed that the measured emittance values were significantly larger than the expected ones. In addition, beam profiles measured at bunch charges of a few hundred pC showed a 'smoke ring' structure. While coherent OTR emission and beam dynamical influence could be excluded, it is assumed that the profile distortions are caused by effects from the scintillator material itself. Following the experience in high energy physics, a simple model was developed which takes into account quenching effects of excitonic carriers inside the scintillator in a heuristic way. Based on this model, the observed beam profiles can be understood qualitatively. Possible new scintillator materials suitable for beam profile diagnostics are discussed and preliminary test results from beam measurements at the European XFEL are presented.

INTRODUCTION

Transverse beam profile diagnostics in electron linacs is widely based on optical transition radiation (OTR) as standard technique which is observed in backward direction when a charged particle beam crosses the boundary between two media with different dielectric properties. Unfortunately, microbunching instabilities in high-brightness electron beams of modern linac-driven free-electron lasers (FELs) can lead to coherence effects in the emission of OTR, thus rendering it impossible to obtain a direct image of the particle beam and compromising the use of OTR monitors as reliable diagnostics for transverse beam profiles. The observation of coherent OTR (COTR) has been reported by several facilities (see e.g. Ref. [1]), and in the meantime the effect of the microbunching instability is well understood [2].

For the European XFEL it was therefore decided to use scintillation screen monitors because the light emission in a scintillator is a multistage stochastic process from many atoms which is completely insensitive to the longitudinal bunch structure. In a series of test measurements performed in the past few years, the applicability of inorganic scintillators for high resolution electron beam profile measurements was investigated [3, 4]. Most notably, the dependency of the resolution on the scintillator material and on the observation geometry was studied with respect to resolve beam profiles in the order of several tens of micrometers, and it was concluded that $\text{LYSO} (\text{Lu}_{2(1-x)}\text{Y}_{2x}\text{SiO}_5:\text{Ce})$ is a suitable material because it gives the best spatial resolution.

Based on these measurements, screen monitor stations were designed for the European XFEL using 200 μm thick LYSO screens [5]. In a high resolution beam profile measurement using an XFEL-type screen it was demonstrated that it is possible to resolve a vertical beam size of $\sigma_y = 1.44 \mu\text{m}$ [6].

However, the experience during the commissioning of the XFEL showed that the measured emittance values were significantly larger than the expected ones [7, 8]. In addition, beam profiles measured at bunch charges of a few hundreds of pico-Coulomb show a 'smoke ring' shaped structure, see e.g. Fig. 1.

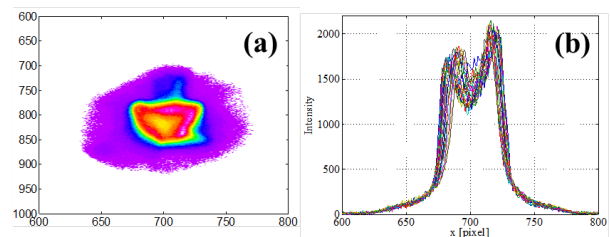


Figure 1: (a) Typical smoke ring shaped beam profile as measured with an XFEL screen monitor based on a 200 μm thick LYSO screen. (b) Various horizontal cuts through the 2D-profile demonstrate the intensity drop in the central part of the beam spot.

While the contribution of COTR emission from the scintillator surface, beam dynamical influence, and camera effects could be excluded to explain this observation, it is assumed that the beam profile distortions are caused by effects from the scintillator material.

In Ref. [9], a simple model was presented which takes into account quenching effects of excitonic carriers inside a scintillator in a heuristic way. Based on this model, the observed beam profiles could be understood qualitatively. In the following, the underlying ideas are briefly summarized with the emphasis on first results from beam measurements at the European XFEL with new scintillator materials suitable for beam profile diagnostics.

SCINTILLATOR MODEL

Degradation effects in scintillator based beam profile measurements are reported in a number of publications, see e.g. Refs. [10–15]. The scintillator influence is mainly interpreted as saturation of the measured profiles, caused e.g. by full excitation of the luminescent centers in some regions inside the scintillator. While inspecting Fig. 1 it is obvious that the XFEL observations cannot simply be described by a saturation effect which would result in a flattening of the

measured beam profiles. It rather leads to the conclusion that luminescent centers may even be quenched in the central part of the beam spot such that the scintillating light intensity is decreased in these regions.

Taking into account the experience of high energy physics, it is known that scintillator based electron calorimeters possess a non-linear energy resolution, and the degree of non-linearity depends on the scintillator material. Following the explanations e.g. in Ref. [16] this effect can be attributed to the ionization density inside the material: if the density is above a critical limit, excitonic states can annihilate in an Auger-like process without creating a scintillating photon. In case of calorimetry the critical ionization density occurs at the end of a particle shower where the particle energy loss is dominated by the kinematical factor β^{-2} ($\beta = v/c$) according to the Bethe–Bloch equation. As a result, the relative light yield in a scintillator typically decreases with decreasing electron energy, see e.g. Ref. [17] and the figures therein. Following Refs. [16, 18], an improvement of the scintillator linearity should in principle correlate with the minimization of the interaction time of excitonic states (electron/hole pairs, excitons, ...) with surrounding traps such that their energy transfer to luminescent centers is unperturbed.

Translating this principle to the case of beam profile diagnostics of ultra-relativistic electron beams, the main idea is that the ionization track density which is responsible for the non-linear scintillator behavior is determined by the primary beam particle density rather than by the secondary energy of shower particles. Following Ref. [9] the ionization tracks inside a scintillator can be modeled as straight tubes, homogeneously filled with electrons and holes. The tube radius is estimated by the Fermi radius $R_\delta \approx c/\omega_p$ with ω_p the plasma frequency of the material. While dynamical processes in scintillators take place in the order of 10^{-12} – 10^{-10} s, the charges inside the ionization tubes can be considered as static with respect to the particle beam dynamics. The situation is schematically depicted in Fig. 2 for the case of a beam with low and with high particle density. Due to the static behavior of the ionization tubes, for the description of the ionization track density a two-dimensional representation

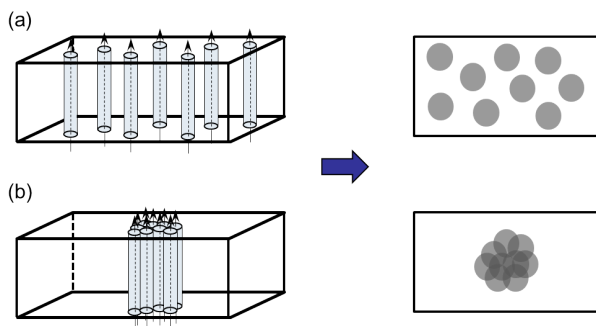


Figure 2: Passage of individual electrons through a scintillator in the case of (a) low and (b) high particle density. Each electron creates a homogeneous ionization tube. Due to the static behavior of the ionization tubes a two-dimensional representation is sufficient.

tion is sufficient as shown on the right side of this figure. In order to estimate particle track densities in cases of a beam with high particle density, a simple geometrical model is used in which the density is estimated as the sum of tube area and track intersections.

Based on these illustrative assumptions, distorted beam profiles are calculated in four consecutive steps. In the first step, the transverse particle beam profile (which is assumed to be Gaussian in the following) is transformed into a 2D surface density profile describing the local particle density. In the second step, the mean distance between the ionization tubes is calculated considering the nearest neighbor distribution. With knowledge of the mean distance, afterwards a regular grid of neighboring tubes is constructed and the density of the local tracks $n_t(x, y)$ is geometrically estimated as described above. Finally, for each point of the beam profile a weighting factor $w(x, y)$ is calculated

$$w(x, y) = \frac{1}{1 + \alpha \frac{dE}{dx}(x, y)}$$

which is similar to the formula of Birks [19] describing the non-linearity in the scintillator light yield. Here it is assumed that $\frac{dE}{dx} \propto n_t^3$ and α is a freely adjustable parameter describing the quenching strength.

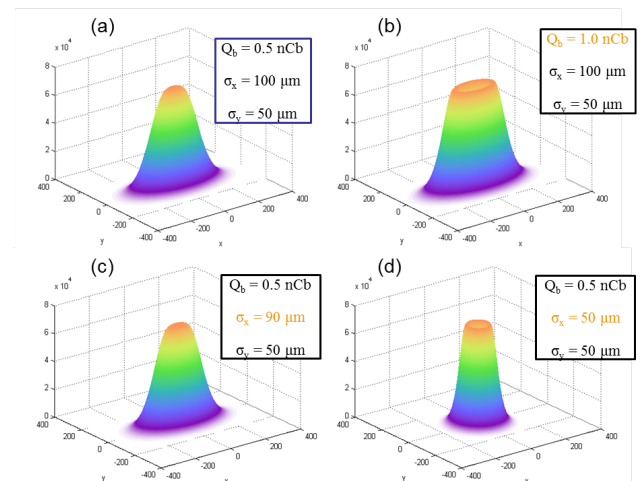


Figure 3: Calculated beam profiles according to the model described in this work. Starting with typical XFEL beam parameters (a) and assuming that $\alpha = 6.4 \times 10^{-5}$, beam profiles for increased bunch charge (b) or decreased horizontal beam size (c,d) are shown.

As an example, Fig. 3 shows calculated beam profiles according to the proposed model presented. Starting with a Gaussian beam profile and typical XFEL beam parameters (a) it can be seen that both increasing the bunch charge (b) and reducing the beam size (c,d) may result in a pronounced beam profile degradation which is caused by an increase in the local ionization track density in the central part of the beam interaction region with the scintillator. Thereby it is possible to produce smoke ring shaped beam profiles as observed at the XFEL.

MITIGATION AND FIRST TEST EXPERIMENTS

Based on to the model described in detail in Ref. [9] and summarized in the previous section, smoke ring shaped beam profiles as observed at the European XFEL can be reproduced. The model takes into account quenching effects of excitonic carriers inside a scintillator in a heuristic way, the level of quenching in the central part of the beam generated spot depends on bunch charge and beam size, i.e. it is controlled by the particle density. However, the model provides no information about suitable scintillator materials for beam profile diagnostic applications because the quenching strength α introduced before is a freely adjustable parameter without direct connection to accessible material properties.

In this context it helps again to refer to the experience of the scintillator community for high energy physics. As shown in Ref. [17], "silicate" based scintillators as LSO, YSO, LPS where the oxygen is intimately bound to the silicon as a SiO_4^{4-} moiety exhibit a strong non-linear behavior, the same holds for LYSO which has similar properties than LSO. In the same reference it is pointed out that exciton-exciton quenching in LuAG doped either with Ce or Pr should be small. However, the resolution study performed in Ref. [4] indicated that the spatial resolution of a LuAG scintillator was worse compared to a LYSO screen. Therefore other materials could be more promising. As previously mentioned, improving the linearity of a scintillator should in principle correlate with the minimization of the interaction time of excitonic states. In this context scintillator materials where gadolinium is stoichiometrically incorporated in the crystal structure seem to be promising [17]. In these materials it is assumed that excitation carriers can rapidly transfer their energy to excited states of gadolinium, and a rapid migration of this energy among the Gd sub-lattice is expected until a Ce doping ion is reached. According to Ref. [20] YAP could also be an interesting material because it exhibits a high mobility of excitonic carriers which may reduce the quenching probability.

In order to test scintillator materials for beam profile diagnostics under realistic conditions, a number of screen stations at the European XFEL was equipped with a LYSO screen together with an additional screen material. Three different materials were selected for first tests, YAG (yttrium aluminium garnet, $\text{Y}_3\text{Al}_5\text{O}_{12}:\text{Ce}$), YAP (yttrium aluminium perovskite, $\text{YAlO}_3:\text{Ce}$), and GAGG (gadolinium aluminium gallium garnet, $\text{Gd}_3\text{Al}_2\text{Ga}_3\text{O}_{12}:\text{Ce}$). While YAG is a material which is widely in use in particle beam diagnostics, YAP has a high mobility of excitonic carriers, and GAGG

is a material containing Gd, thus the latter two materials are of potential interest in view of linearity. In Table 1 the main parameters light yield, maximum emission wavelength λ_{max} , and density ρ for the materials under test are summarized. While YAP emits light in the soft ultraviolet which is not well fitted to the sensitivity of a camera chip, GAGG is a new non-hygroscopic scintillator material on the market with high light yield and well matched to the camera chip sensitivity, thus attracting special attention for various applications.

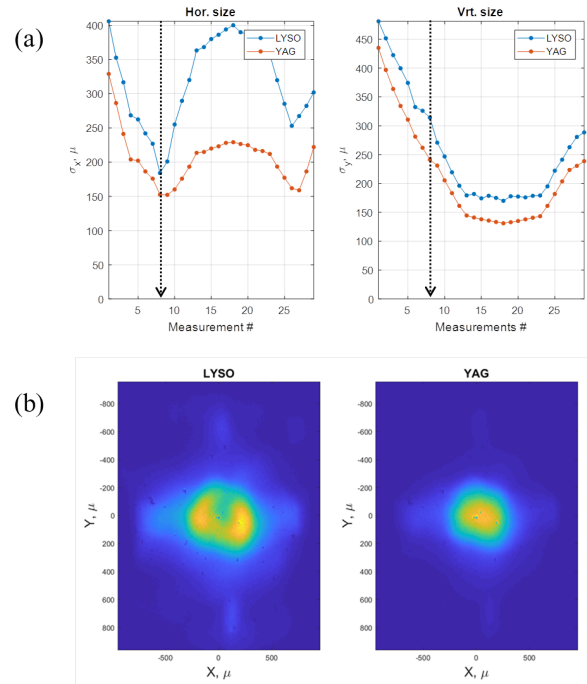


Figure 4: (a) Comparative resolution study using a YAG and a LYSO scintillator at the XFEL. The arrows indicate that measurement where the LYSO beam spot shows the transition to the smoke ring structure. (b) Corresponding beam images at the transition point.

In a first test experiment, profile measurements from a YAG and a LYSO screen were compared for identical beam and camera parameters. Both screens are mounted in the same screen station, and beam images were recorded for individual bunches with charge $Q_b \approx 1$ nC at a beam energy of about 14 GeV. In Fig. 4(a) a series of measurements is shown which was taken while the beam sizes were focused down, thus increasing the ionization track density in the central part of the beam interaction region with the scintillator. As can be seen, the LYSO-based beam size measurements are systematically larger than the ones with the YAG screen. Furthermore, starting from a certain particle density threshold the LYSO measurements show a clear signature of a smoke ring while the YAG measurement is unaffected, c.f. Fig. 4(b).

Keeping in mind that the occurrence of the smoke ring structure is connected with quenching of excitation carriers and causes a decrease of the scintillator light output, it is

Table 1: Scintillating Screen Materials under Test

material	yield [ph/keV]	λ_{max} [nm]	ρ [g/cm ³]
YAG	15 - 35	550	4.53
YAP	25	370	5.37
GAGG	50	530	6.7
LYSO	24	420	7.1

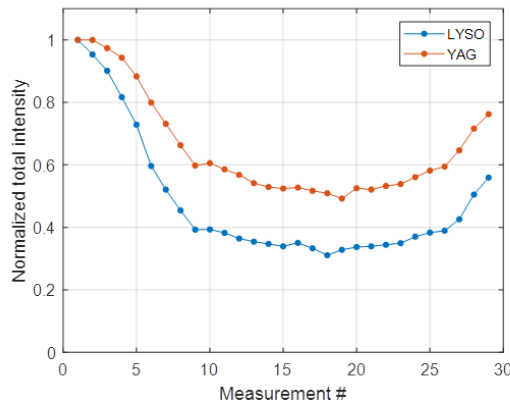


Figure 5: Normalized intensities for the comparative LYSO/YAG measurement series plotted in Fig. 4. The intensity drop is an indication for the onset of scintillator non-linearities.

illustrative to plot this light yield for the individual measurements as shown in Fig. 5. For better comparison, intensities are normalized to the one of the first measurement where no influence of a smoke ring structure is visible. As can be seen from this figure, the light yield of both screens is decreased while focusing the beam, thus indicating that in principle both screen materials are affected by non-linearities. In the case of LYSO this effect seems to be more distinct due to the visibility of the smoke ring structure.

The test experiment was repeated with another screen station where a YAP and a LYSO screen are installed together. While the beam energy was comparable to the previous measurement series, the bunch charge amounted to $Q_b \approx 0.45$ nC. However, as shown in Fig. 6 the beam spot could be focused down to much smaller sizes such that the maximum peak charge density which was roughly estimated

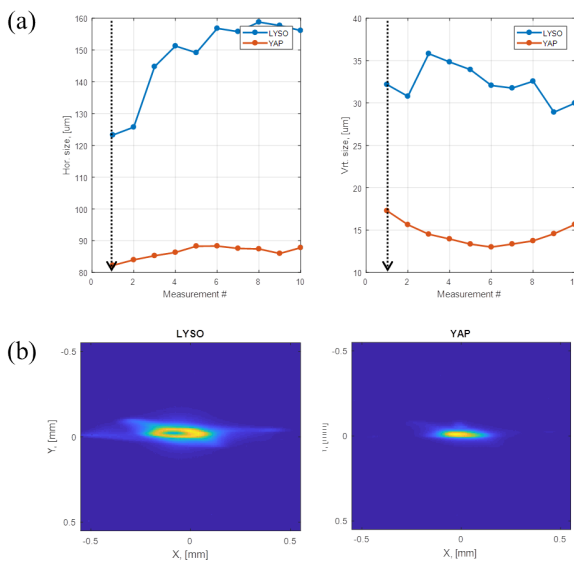


Figure 6: (a) Comparative resolution study using a YAP and a LYSO scintillator. The arrows indicate that measurement for which the beam images in (b) are plotted.

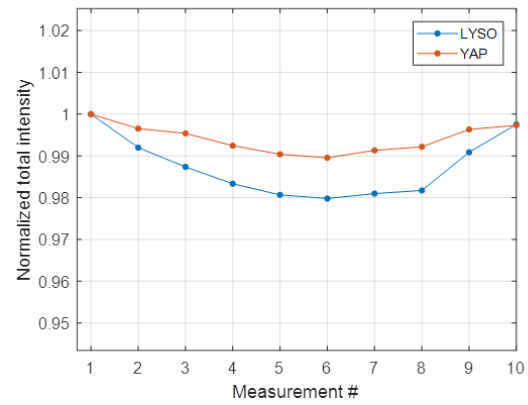


Figure 7: Normalized intensities for the comparative LYSO/YAP measurement series plotted in Fig. 6. The intensity drop for the LYSO screen is much smaller than in the previous measurement because all LYSO based profile measurements showed a smoke ring structure, thus the reference intensity is already affected by non-linearities.

to about $62 \text{ fC}/\mu\text{m}^2$ was significantly higher than in the previous experiment.

As can be seen from Fig. 6(a), the LYSO-based beam size measurements are again systematically larger than the ones with the YAP screen. In this experiment it was even not possible to increase the beam size to a level that no smoke ring structure was measured with the LYSO screen, already the first measurement is affected by this effect, c.f. the measured beam images in Fig. 6(b).

However, even for these large charge densities the YAP based beam images were undisturbed, as shown in Fig. 7 the drop in the normalized intensity is in the order of about 1% over the whole range of measurements.

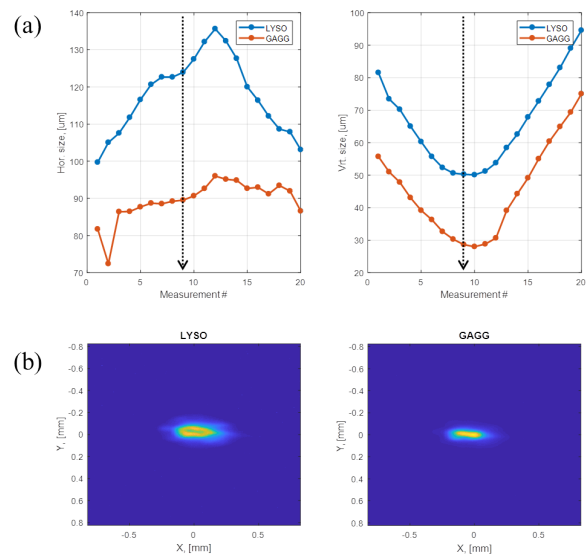


Figure 8: (a) Comparative resolution study using a GAGG and a LYSO scintillator. The arrows indicate that measurement where the LYSO beam spot shows the transition to the smoke ring structure. (b) Corresponding beam images at the transition point.

In the last test experiment, a GAGG screen was compared to LYSO, beam energy and bunch charge were the same Z for the previous YAP measurements. In this experiment, the achievable minimum beam size was slightly larger than before (c.f. Fig. 8(a)), the maximum peak charge density was roughly estimated to about $28 \text{ fC}/\mu\text{m}^2$. Again the LYSO-based beam size measurements are systematically larger than the ones with GAGG, and starting from a certain particle density threshold the LYSO measurements show a clear signature of a smoke ring structure while the GAGG measurements are unaffected, c.f. Fig. 8(b).

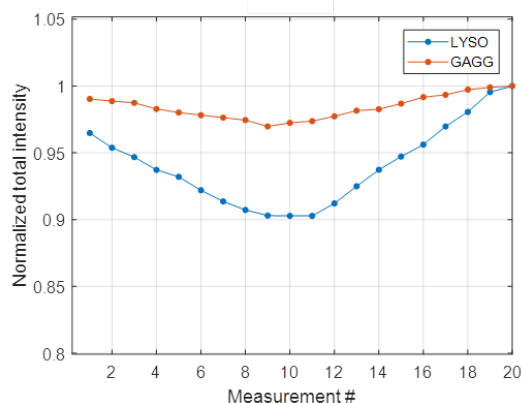


Figure 9: Normalized intensities for the comparative LYSO/GAGG measurement series plotted in Fig. 8.

This behaviour is reflected in the normalized intensity which is depicted in Fig. 9. In this case, the drop for GAGG is in the order of about 2% over the whole range of measurements while the one for LYSO amounts to about 10%.

Compared to the first test experiment with YAG, the drop of the normalized LYSO intensity is much smaller for the GAGG measurement. Presently it is not clear where the difference is coming from, this is a point for future investigations.

SUMMARY AND OUTLOOK

Based on to the observation of smoke ring shaped beam profiles using screen monitor stations at the XFEL which utilize LYSO as standard scintillator material, a simple model is presented which takes into account quenching effects of excitonic carriers inside a scintillator in a heuristic way. With the help of this model, it is possible to reproduce smoke ring shaped beam profiles: the level of quenching in the central part of the beam generated spot in the scintillator depends on bunch charge and beam size, i.e. it is controlled by the particle density.

Improving the linearity of a scintillator should in principle correlate with the minimization of the interaction time of excitonic states. Based on the experience of high energy physics, gadolinium based scintillator materials like GAGG or YAP with its high mobility of the excitation carriers could in principle be interesting for future applications.

A series of test experiments was conducted at the European XFEL. In these experiments, beam images measured

with standard LYSO screens were compared to YAG and to YAP/ GAGG-based measurements. It could be demonstrated that LYSO as scintillator material shows strong non-linearities which render its application difficult in particle beam diagnostics. Even YAG which is widely used for beam profile measurements seems to show non-linear behaviour. However, smoke ring like structures could not be observed with this material. At the other hand, YAP and GAGG demonstrated to have a rather stable behaviour even at highest charge densities. Presently, more detailed studies are in preparation. Nevertheless it is planned already now to replace screens in the XFEL injector by GAGG as scintillator material.

REFERENCES

- [1] S. Wesch and B. Schmidt, "Summary of COTR Effects", in *Proc. DIPAC'11*, Hamburg, Germany, May 2011, paper WEOA01, pp. 539–543.
- [2] G. V. Stupakov, "Control and Application of Beam Microbunching in High Brightness Linac-driven Free Electron Lasers", in *Proc. IPAC'14*, Dresden, Germany, Jun. 2014, pp. 2789–2793. doi:10.18429/JACoW-IPAC2014-THYA01
- [3] G. Kube, C. Behrens, and W. Lauth, "Resolution Studies of Inorganic Scintillation Screens for High Energy and High Brilliance Electron Beams", in *Proc. IPAC'10*, Kyoto, Japan, May 2010, paper MOPD088, pp. 906–908.
- [4] G. Kube, C. Behrens, C. Gerth, B. Schmidt, W. Lauth, and M. Yan, "Inorganic Scintillators for Particle Beam Profile Diagnostics of Highly Brilliant and Highly Energetic Electron Beams", in *Proc. IPAC'12*, New Orleans, LA, USA, May 2012, paper WEOAA02, pp. 2119–2121.
- [5] Ch. Wiebers, M. Holz, G. Kube, D. Noelle, G. Priebe, and H.-Ch. Schroeder, "Scintillating Screen Monitors for Transverse Electron Beam Profile Diagnostics at the European XFEL", in *Proc. IBIC'13*, Oxford, UK, Sep. 2013, paper WEPF03, pp. 807–810.
- [6] G. Kube *et al.*, "Transverse Beam Profile Imaging of Few-Micrometer Beam Sizes Based on a Scintillator Screen", in *Proc. IBIC'15*, Melbourne, Australia, Sep. 2015, pp. 330–334. doi:10.18429/JACoW-IBIC2015-TUPB012
- [7] B. Beutner, "European XFEL Injector Commissioning Results", in *Proc. FEL'17*, Santa Fe, NM, USA, Aug. 2017, pp. 389–393. doi:10.18429/JACoW-FEL2017-WEA01
- [8] D. Nölle, "The Diagnostic System at the European XFEL; Commissioning and First User Operation", in *Proc. IBIC'18*, Shanghai, China, Sep. 2018, pp. 162–168. doi:10.18429/JACoW-IBIC2018-TUOA01
- [9] G. Kube, S. Liu, A. I. Novokshonov, and M. Scholz, "A Simple Model to Describe Smoke Ring Shaped Beam Profile Measurements With Scintillating Screens at the European XFEL", in *Proc. IBIC'18*, Shanghai, China, Sep. 2018, pp. 366–370. doi:10.18429/JACoW-IBIC2018-WEOC03
- [10] A. Murokh, J. Rosenzweig, V. Yakimenko, E. Johnson, and X.J. Wang, "Limitations on the Resolution of Yag:Ce Beam Profile Monitor for High Brightness Electron Beam", *The Physics of High Brightness Beams*, pp. 564–580, 2000. doi:10.1142/9789812792181_0038

- [11] A. Murokh, I. Ben-Zvi, J.B. Rosenzweig, X.J. Wang, and V. Yakimenko, "Limitations on Measuring a Transverse Profile of Ultra-Dense Electron Beams with Scintillators", in *Proc. PAC'01*, Chicago, IL, USA, Jun. 2001, paper TPAH049, p. 1333.
- [12] T. F. Silva, Z.O. Guimarães-Filho, C. Jahnke, and M.N. Martins, "Electron Beam Profile Determination: The Influence of Charge Saturation in Phosphor Screens", in *Proc. PAC'09*, Vancouver, Canada, May 2009, paper TH6REP040, pp. 4039–4041.
- [13] U. Iriso, G. Benedetti, and F. Pérez, "Experience with YAG and OTR Screens at ALBA", in *Proc. DIPAC'09*, Basel, Switzerland, May 2009, paper TUPB15, pp. 200–202.
- [14] F. Miyahara *et al.*, "Response of Scintillating Screens to High Charge Density Electron Beam", in *Proc. IPAC'17*, Copenhagen, Denmark, May 2017, paper MOPAB067, pp. 268–270. doi:10.18429/JACoW-IPAC2017-MOPAB067
- [15] R. Ischebeck *et al.*, "Characterization of High-Brightness Electron Beams at the Frontiers of Temporal and Spatial Resolution", presented at FEL2017, Santa Fe, NM, USA, Aug. 2017, paper WEB01, unpublished.
- [16] W. W. Moses *et al.*, "Scintillator Non-Proportionality: Present Understanding and Future Challenges", *IEEE Trans. Nucl. Sci.*, vol. 55, pp. 1049, 2008. doi:10.1109/tns.2008.922802
- [17] S. A. Payne *et al.*, "Nonproportionality of Scintillator Detectors: Theory and Experiment. II", *IEEE Trans. Nucl. Sci.*, vol. 58, pp. 3392, 2011. doi:10.1109/TNS.2011.2167687
- [18] A. N. Vasil'ev, in *Proc. SCINT'99*, Moscow, Russia, August 1999, p.43, 1999.
- [19] J. B. Birks, "Scintillations from Organic Crystals: Specific Fluorescence and Relative Response to Different Radiations", *Proc. Phys. Soc.*, vol. A64 pp. 874, 1951. doi:10.1088/0370-1298/64/10/303
- [20] Q. Li *et al.*, "A transport-based model of material trends in nonproportionality of scintillators", *J. Appl. Phys.*, vol. 109, pp. 123716, 2011. doi:10.1063/1.3600070

WIRE-SCANNERS WITH SUB-MICROMETER RESOLUTION: DEVELOPMENTS AND MEASUREMENTS

G.L. Orlandi*, S. Borrelli, C. David, E. Ferrari, V. Guzenko,
B. Hermann, O. Huerzeler, R. Ischebeck, C. Lombosi, C. Ozkan-Loch, E. Prat,
Paul Scherrer Institut, Villigen PSI, Switzerland
M. Ferianis, G. Penco, M. Veronese,
Elettra-Sincrotrone Trieste S.C.p.A, Basovizza, Trieste Italy
N. Cefarin, S. Dal Zilio, M. Lazzarino,
IOM-CNR Laboratorio TASC, c/o Area Science Park - Basovizza, Trieste, Italy

Abstract

Monitors of the beam transverse profile with ever more demanding spatial resolution and minimal invasivity are required by the FEL community. In order to improve the spatial resolution towards the sub-micrometer limit as well as to decrease the impact on the lasing process, nano-fabricated wire-scanners have been manufactured independently at PSI and FERMI by means of a lithographic technique. Experimental tests carried out at SwissFEL at a low emittance demonstrated the capability of such innovative wire-scanner solutions to resolve beam transverse profiles with a size of 400-500 nm without being affected by any resolution limit. Status and outlook of nano-fabricated wire-scanners (WS) will be presented.

PREMISE

The present proceeding briefly reports on the recent experimental results obtained in the nano-fabrication and electron beam characterization of free-standing WS with sub-micrometer resolution. The free-standing WS prototypes - independently nano-fabricated at PSI and FERMI by means of lithographic techniques - can measure the transverse profile of an electron beam with a rms geometrical resolution of about 250 nm. The experimental test of the PSI and FERMI WS prototype have been performed at SwissFEL, where electron beams with a vertical size smaller than 500 nm have been successfully and consistently resolved. All information and technical details on the nano-fabrication and experimental tests - carried out at SwissFEL - of the PSI and FERMI free-standing WS with sub-micrometer resolution are reported in a manuscript submitted to a peer-reviewed journal for a publication. For more details on the WS nano-fabrication and characterization, the reader is hence addressed to the archived version of the manuscript, to the paper submitted to the journal and to the slides of the conference talk [1, 2]. In the present proceeding, the authors will summarize the main highlights, achievements and perspectives of the experimental work on free-standing WS with sub-micrometer resolution. In addition, the authors will briefly summarize the background experience of PSI and FERMI on nano-fabrication and test of WS. Results of satellite tests carried out at SwissFEL in parallel with the

characterization of the free-standing WS will be reported as well. The introduction and the conclusion sections are directly derived from [1, 2].

INTRODUCTION

Wire-scanners (WS) constitutes a precious complement to view-screens for monitoring the transverse profile of the electron beam in a linac [3–12]. Because of the multi-shot and mono-dimensional reconstruction of the beam transverse profile, WS are not timewise competitive with view-screens for beam finding and for matching the magnetic optics in an electron linac. WS are inappropriate for slice emittance measurements as well. Nevertheless, WS are a unique and essential diagnostics whenever the beam characterization requires a high spatial resolution along with a minimal invasivity to the beam operation. The spatial resolution of a WS depends on the measurement resolution of the wire positioning, on the possible wire vibrations and, finally, on the geometry of the wire. The geometrical resolution of a WS is inversely proportional to the wire width. This also determines the surface of impact of the wire with the electron beam and hence the wire transparency to the beam (also depending on the wire thickness for non-cylindrical wires). Conventional WS solutions - as normally in operation in several free-electron lasers (FELs) - are realized according to the standard technique to fix and stretch a metallic wire (beam-probe) onto a metallic frame (fork). They are able to attain a spatial resolution at the micrometer scale [12] which is at least an order of magnitude higher than the spatial resolution of a typical view-screen operating in a FEL [13, 14]. Low charge and low emittance machine operation modes - presently under investigation in several FEL facilities - requires the characterization of ever smaller beam profiles. This triggers the community of the electron-beam diagnostics to push forward the resolution limit of the conventional WS beyond the micrometer limit. In order to improve the WS spatial resolution, new fabrication techniques are under investigation at PSI and FERMI. At PSI, a WS prototype with a sub-micrometer resolution nano-fabricated on-a-membrane (250 nm thick Silicon Nitride membrane) was successfully tested [15]; while at FERMI a free-standing nanofabricated WS with a resolution of about $2.9\mu\text{m}$ has been successfully tested [16]. These experiences paved the way to use the

* gianluca.orlandi@psi.ch

nano-lithography technique to fabricate free-standing WS with sub-micrometer resolution, a goal that PSI and FERMI have independently pursued. The PSI and FERMI nano-fabricated WS consist of a free-standing Au stripe fully integrated in a Silicon frame. With a stripe width (w) of 800 nm and 900 nm, respectively, the PSI and FERMI WS attain a geometrical resolution ($\frac{w}{\sqrt{12}}$) of about 250 nm. They have been experimentally tested at SwissFEL at nominal and low bunch charge regime (200 pC and below 1 pC, respectively). The experimental tests carried out at SwissFEL demonstrated the capability of these novel WS solutions to resolve beam profiles with a size of 400 – 500 nm as well as the necessary resilience to the heat-loading at nominal machine operations (200 pC).

NANO-FABRICATED WIRE-SCANNERS AND EXPERIMENTAL TESTS

The research and development on diagnostics of the transverse profile of the electron beam in a Free-Electron-Laser (FEL) is presently aiming at improving the spatial resolution beyond the micrometer scale in order to meet the constraints of low-emittance and low-charge FEL operations. Moreover, in order to preserve radiation sensitive devices as well as the lasing process when monitoring the beam profile, minimally invasive diagnostics of the electron beam is required. In terms of spatial resolution and minimally invasivity, WS are the top-ranked diagnostics. Spatial resolution, beam invasivity and lasing transparency are strictly related features of a WS: the higher the geometrical resolution - i.e., the thinner the wire diameter - the smaller is the surface of impact of the wire with the beam as well as the number of electrons perturbed during a scan. Conventional WS - designed according to the traditional technique to fix and stretch a metallic wire onto a fork - can provide a rms spatial resolution at the micrometer scale, at best. Hence, the necessity to investigate new fabrication techniques. PSI and FERMI independently pursued the way of the nano-lithography to produce WS structures with a sub-micrometer resolution.

At PSI, the first attempt of WS nano-fabrication consisted in a prototype structure made of a 1 μ m wide Au stripe electroplated onto a thin Silicon Nitride membrane (so called *WS on-a-membrane*). After the successful experimental test of this prototype [15], a further progress was achieved at PSI with the nano-fabrication of a WS consisting of a 2 mm long and 800 nm wide Au stripe free-standing over a rigid Silicon frame [1, 2].

FERMI adopted a different approach to the WS nano-fabrication. A first WS prototype consisting of a 10 μ m wide Ag/ Si_3N_4 /Ag stripe free-standing onto a Silicon frame was initially nano-fabricated and tested at FERMI [16]. Finally, an upgrade of the previous free-standing WS solution consisting of a 0.8 mm long and 900 nm wide Au/ Si_3N_4 /Au stripe has been produced at FERMI [1, 2].

The aforementioned free-standing WS structures with a 800 nm and 900 nm wide scanning stripe - nano-fabricated at PSI by LMN and by IOM-CNR for FERMI, respectively

- have been experimental tested at SwissFEL. SwissFEL is a X-ray FEL facility [17–19] in operation at Paul Scherrer Institut. Driven by a rf linac - a S-band injector and a C-band accelerator - in the beam energy range 2.1 – 5.8 GeV, SwissFEL is presently producing tunable and coherent hard X-ray pulses in the wavelength region 0.7–0.1 nm (ARAMIS undulator line) and, by 2021, will also generate soft x-ray radiation in the wavelength region 7 – 0.7 nm (ATHOS undulator line).

The PSI and FERMI free-standing WS were in parallel tested on the electron beam of SwissFEL in two different days at a beam energy of about 300 MeV. In both measurement sessions, SwissFEL was operated according to a low-emittance and low-beta setting [1, 2, 15]. Low-emittance operations at SwissFEL are possible thanks to a low-charge setup (below 1 pC) of the rf gun photo-cathode which allows for a normalized vertical emittance ($\epsilon_{n,y}$) of about 55 nm. Thanks to a suitable magnetic optics (low-beta), at the wire interaction point the beta functions (β_x, β_y) are (0.27, 2.61 $\times 10^{-3}$)m. At the WS position, the vertical beam size ($\sigma_y = \sqrt{\beta_y \epsilon_{n,y} / \gamma}$) is hence about 400 – 500 nm - where γ is the relativistic Lorentz factor at a beam energy of 300 MeV - while the beam horizontal size is about 10 times larger.

The experimental results of the measurements carried out at SwissFEL of the PSI and FERMI free-standing WS with sub-micrometer resolution are summarized in Table 1 where the measured beam size has been obtained by fitting the acquired WS profile by means of an error-function-fit (erf-fit) resulting from the convolution of a Gaussian profile and a rectangular shaped distribution modelling the transverse section of the scanning wire. As reported in Table 1, the two different WS solutions consistently measured a beam profile of about 500 nm which is in agreement with the theoretical prediction.

A beam test of the two WS solutions at the nominal SwissFEL operation mode (200 pC) was also performed in order to check the resilience of the two WS structure to the heat-loading. No damage was observed in the WS structures at 200 pC.

During the experimental test of the free-standing WS a satellite measurement was also performed. This consisted in reconstructing the beam transverse profile from the readout of the beam-loss signal simultaneously detected by a photomultiplier-tube (PMT, standard solution at SwissFEL) and a photodiode during a scan with the free-standing WS. Goal of this test was to verify the signal-to-noise ratio of the photodiode compared to the PMT. The comparative experimental test of the two detectors showed statistically consistent results of the measured beam size. About the quality of the detected signal by the two detectors, the signal-to-noise response of the photodiode was about 10 times worse than the PMT one.

In conclusion, to the best of the authors' knowledge, the experimental results reported in the manuscripts and presented in the FEL2019 conference talk [1, 2] constitute a

Table 1: Results of the erf-fit estimate of the vertical size of the SwissFEL electron beam scanned by the PSI and FERMI free-standing WS in the measurement sessions of December 4, 2018 and March 31, 2019. Beam profile measurements performed at a beam charge less than 1 pC and at a beam energy of 300 MeV. Vertical emittance about 55 nm expected vertical beam size of about 480 nm for a beta function value $\beta_y = 2.61 \times 10^{-3}$ m at the WS position.

WS type	stripe width(nm)	geom. res.(nm)	beam size (nm, Dec 2018)	beam size (nm, Mar 2019)
PSI-WS	800	230	488±20	434±7
FERMI-WS	900	260	477±70	443±33

world record in terms of spatial resolution ever reached by a WS solution made of a free-standing metallic wire. The lithographic nano-fabrication - developed at PSI and FERMI - and the experimental tests carried out at SwissFEL of the free-standing WS with a sub-micrometer resolution paved the way to the development of innovative WS solutions with sub-micrometer resolution to be used as a standard electron beam diagnostics in a FEL.

CONCLUSIONS AND OUTLOOK

PSI and FERMI are independently pursuing a research and development program aiming at improving the spatial resolution of wire-scanners (WS) beyond the standard limit of the micrometer scale as well as the WS transparency to the lasing operations in a FEL. Nano-lithography permits to overcome the bottleneck of the micrometer resolution limit which characterizes the conventional WS design consisting of a metallic wire stretched over a metallic fork. It is indeed possible to nano-fabricate free-standing Au bulk or sandwich $Au/Si_3N_4/Au$ WS stripes with a sub-micrometer width which are fully integrated into a silicon frame. In the present work, the production details and the experimental characterization of two different prototype solutions of nano-fabricated free-standing WS with a geometrical resolution of about 250 nm has been presented. The two free-standing WS prototypes with a stripe width of 800 and 900 nm have been nano-fabricated at PSI and FERMI, respectively. The PSI WS prototype consists of a 2 mm long bulk Au stripe, while the FERMI prototype consists of a 0.8 mm long stripe made of a sandwich of $Au/Si_3N_4/Au$. Both nano-fabricated WS prototypes have been in parallel tested at SwissFEL under a low-charge and low-emittance setting of the machine where a beam size of 400 – 500 nm has been consistently - and without any resolution limit issue - measured by the two WS solutions in two different experimental sessions. Moreover, an experimental test - still performed at SwissFEL under the nominal high charge mode of the machine (200 pC) - demonstrated the resilience to heat-loading of the nano-fabricated WS. The presently nano-fabricated free-standing WS solutions can ensure a beam clearance of about 2 mm. In order to extend the applicability of them as a standard WS solution in a linac driven FEL, the present beam clearance should be increased by a factor 4 – 5, at least. This improvement issue is in the to-do list of the further development program of design and nano-fabrication of free-standing sub-micrometer WS at PSI and FERMI. The hereby experimental campaign of measurement carried out at SwissFEL demonstrated the

excellent performance of the PSI and FERMI free-standing WS in resolving electron beam profile with a sub-micrometer size and the reliability of two independent and different techniques of nano-fabrication. The way to the implementation of nano-fabricated WS with sub-micrometer resolution as a standard WS solution in a FEL is paved.

ACKNOWLEDGEMENTS

The authors wish to thank the Paul Scherrer Institut expert groups, the SwissFEL commissioning and operation team for the support during the measurements. The authors are grateful to Pavle Juranić for his support with the Gas-Detector measurements. This work was also supported by the Gordon and Betty Moore Foundation (ACHIP collaboration).

REFERENCES

- [1] G.L. Orlandi *et al.*, “Nano-Fabricated Free-Standing Wire-Scanners with Sub-Micrometer Resolution”, submitted for publication.
- [2] G.L. Orlandi *et al.*, “Nano-Fabricated Free-Standing Wire-Scanners with Sub-Micrometer Resolution”, <http://arxiv.org/abs/1908.07468>.
- [3] R. Fulton *et al.*, “A high resolution wire scanner for micron-size profile measurements at the SLC”, *Nucl. Instr. Meth. in Phys. Res. A*, vol. 274, pp. 37-44, 1989. doi:10.1016/0168-9002(89)90362-8
- [4] M.C. Ross, J. T. Seeman, E. Bong, L. Hendrickson, D. McCormick, L. Sanchez-Chopitea, “Wire Scanners for Beam Size and Emittance Measurements at the SLC”, in *Proc. PAC’91*. San Francisco, California, USA, p. 1201.
- [5] C. Field, “The wire scanner system of the final focus test beam at SLAC”, *Nucl. Instr. Meth. in Phys. Res. A*, vol. 360, pp. 467-475, 1995. doi:10.1016/0168-9002(95)00077-1
- [6] P. Tenenbaum, T. Shintake, “Measurement of small electron-beam spots”, *Annu. Rev. Nucl. Part. Sci.* vol. 49, p. 12562, 1999. doi:10.1146/annurev.nucl.49.1.125
- [7] H.-D. Nuhn, P.J. Emma, G.L. Gassner, C.M. LeCocq, F. Peters, R.E. Ruland, “Electron Beam Alignment Strategy in the LCLS Undulators”, SLAC-PUB-12098 (2006).
- [8] H. Loos *et al.*, “Operational Performance of LCLS Beam Instrumentation”, SLAC-PUB-14121.
- [9] J. Wu, P. Emma, and R.C. Field, “Electron Signal Detection for the Beam-Finder Wire of the Linac Coherent Light Source Undulator”, SLAC-PUB-12120 LCLS-TN-06-7, April 2006.
- [10] K. Wittenburg, “Conventional wire scanners for TESLA”, Report No. TESLA2000-18 (2000).

- [11] U. Hahn *et al.*, “Wire scanner system for FLASH at DESY”, *Nucl. Inst. Meth. Phys. Res. A*, vol. 592, pp. 189-196, 2008. doi:10.1016/j.nima.2008.04.018
- [12] G.L. Orlandi *et al.*, “Design and experimental tests of free electron laser wire scanners”, *Phys. Rev. Accel. Beams*, vol. 19, p. 092802, 2016. doi:10.1103/PhysRevAccelBeams.19.092802
- [13] M. Veronese *et al.*, “Intra undulator screen diagnostic for the FERMI@Elettra FEL”, in *Proc. IBIC’12*, Tsukuba, Japan, 2012, paper TUPB76, pp. 519-523.
- [14] R. Ischebeck, E. Prat, V. Thominet, C. Ozkan Loch, “Transverse profile imager for ultrabright electron beams”, *Phys. Rev. ST Accel. Beams*, vol. 18, p. 082802, 2015. doi:10.1103/PhysRevSTAB.18.082802
- [15] S. Borrelli *et al.*, “Generation and Measurement of Sub-Micrometer Relativistic Electron Beams”, *Communications Physics-Nature*, vol. 1, p. 52, 2018. doi:10.1038/s42005-018-0048-x
- [16] M. Veronese *et al.*, “A nanofabricated wirescanner with free standing wires: Design, fabrication and experimental results”, *Nucl. Inst. Meth. Phys. Res. Sec. A*, vol. 891, pp. 32-36, 2018. doi:10.1016/j.nima.2018.02.040
- [17] SwissFEL Conceptual Design Report, IAEA, Reference Number 42006326, PSI Bericht Nr. 10-04 April 2012.
- [18] T. Schietinger *et al.*, “Commissioning experience and beam physics measurements at the SwissFEL Injector Test Facility”, *Physical Review Accelerators and Beams*, vol. 19, p. 100702, 2016. doi:10.1103/PhysRevAccelBeams.19.100702
- [19] C. J. Milne *et al.*, “SwissFEL: The Swiss X-ray Free Electron Laser”, *Appl. Sci.*, vol. 7(7), p. 720, 2017. doi:10.3390/app7070720

APPLICATION OF MACHINE LEARNING TO BEAM DIAGNOSTICS

E. Fol^{*1,2}, R. Tomás¹, G. Franchetti^{2,3}, J. Coello de Portugal⁴, ¹CERN, 1211 Geneva 23, Switzerland

²Johann-Wolfgang Goethe University, 60438 Frankfurt am Main, Germany

³GSI Helmholtzzentrum für Schwerionenforschung, 64291, Darmstadt, Germany

⁴Paul Scherrer Institut, 5232, Villigen, Switzerland

Abstract

Machine Learning (ML) techniques are widely used in science and industry to discover relevant information and make predictions from data. The application ranges from face recognition to High Energy Physics experiments. Recently, the application of ML has grown also in accelerator physics and in particular in the domain of diagnostics and control. The target of this paper is to provide an overview of ML techniques and to indicate beam diagnostics tasks where ML based solutions can be efficiently applied to complement or potentially surpass existing methods. Besides, a short summary of recent works will be given demonstrating the great interest for use of ML concepts in beam diagnostics and latest results of incorporating these concepts into accelerator problems, with the focus on beam optics related applications.

MOTIVATION

Traditional optimization tools demonstrate successful performance in applications on linear optics corrections and problems with limited amount of optimization targets [1–6]. Bigger challenges emerge when diagnostics of complex non-linear behavior is required and several variables have to be taken into account as final objective. The amount of time and computational power required by traditional methods might become unacceptable for future accelerator facilities.

ML is well known for surpassing human performance in some specific tasks such fraud detection, forecasting of market trends and risks, online recommendations, recognition of voice and images and in general in discovering correlations in large scale data sets. Most of these tasks can find analogies in beam control and diagnostics. For example, anomaly detection methods applied for fraud detection can be used to detect defects in the instrumentation and forecasting techniques can be transferred to predict beam behavior during operation.

Free Electron Lasers (FEL) problems for optimization and diagnostics have to deal with non-linear, multi-objective functions which depend on thousands of time-varying machine components and settings. These properties meet the limitations of traditional optimization methods and make this problem a perfect candidate for application of ML-based techniques. The main limitation of traditional optimization methods is that the objective function or specific rules and thresholds have to be known. ML methods can learn from given examples without requiring explicit rules.

* elena.fol@cern.ch

RELEVANT MACHINE LEARNING CONCEPTS

ML techniques aim to build computer programs and algorithms that automatically improve with experience by learning from examples with respect to some class of task and performance measure, without being explicitly programmed [7]. Depending on the problem and existence of learning examples, different approaches are preferred. If pairs of input and desired output are available, an algorithm can generalize the problem from the given examples and produce prediction for unknown input. ML algorithms that learn from input/output pairs are called *supervised learning* algorithms. Opposite to supervised learning, *unsupervised learning* algorithms solve the tasks where only input data is available. Unsupervised learning is suitable for the problems such anomaly detection, signal denoising, pattern recognition, dimensionality reduction and feature extraction. In the following a brief overview on significant machine learning concepts that can be used as supervised as well as unsupervised approaches is presented. We also give a short introduction to Reinforcement Learning - ML technique which recently became of great interest especially for control tasks.

Artificial Neural Network

Artificial Neural Networks (ANNs) are well suited for learning tasks, where data is represented by noisy, complex signals and the target output function may consist of several parameters. A basic ANN consists of a single processing unit (*neuron*), that takes the *weighted* inputs and an additional activation function to introduce the nonlinearity in the output. For more complex practical problems, ANNs are composed of several interconnected *hidden layers* with multiple neurons stacked. ANNs can be used for both regression and classification problems. In case of classification the output can be either a class label or a probability of an item belonging to a class. The learning of ANN is performed using *backpropagation* algorithm [8] on a set of examples. For each example the training algorithm computes the derivatives of the output function of the network. The obtained gradients with respect to all weights are then used to adjust the weights in order to achieve a better fit to the target output. In backpropagation *stochastic gradient descent* or one of its improved extensions [9, 10] is applied as optimization method in order to minimize the loss between the network output values and the target values for these outputs by updating the connection weights. ANNs with many hidden layers called *deep neural networks* are able to use fewer neurons per layer and have a better generalization

ability [11], however the optimization of the structure and training of these networks is not trivial. There are no strict rules for building ANN architecture (number of neurons, layers, initial weights) as it usually heavily depends on a particular problem. However, techniques to adjust the architecture parameters exist. A detailed overview on various ANN architectures and training methods and their suitability for different applications can be found in [12–14].

Decision Trees and Ensemble Methods

Decision tree learning is a method for approximating discrete-valued target functions, which are represented by decision trees. Considering the case of classification, decision trees sort down the input instances from the root to leaf nodes. Usually, the splitting is based on one of the input parameters or a specified set of splitting criteria [15, 16]. Each leaf corresponds to one class representing the most appropriate class label. For regression problems the leaf nodes correspond to an approximation of target values.

Using a single tree, a model might not be able to generalize and perform poorly on unexplored sample. One possible solution to overcome this problem is to build ensembles of trees [17]. By training several slightly different models and taking the average prediction, the variance of the model can be reduced.

Compared to ANNs, decision trees are simpler to interpret and to understand its way of obtaining the final results and the underlying process, e.g. through the feature importance analysis. Feature importance analysis helps to understand the contribution of each input parameter to the decision during the training process. The ability of decision trees to evaluate the importance of input parameter is a significant advantage of these algorithms. Knowing the importance of the features we can reduce the model complexity and simplify the data preprocessing steps without significant accuracy loss.

Clustering

Cluster analysis includes methods of grouping or separating data objects into clusters, such that dissimilarity between the objects within each cluster is smaller than between the objects assigned to different clusters [18, 19]. Cluster analysis is used in a wide range of applications. Data clusters can be considered as a summarized representation of the data, such that group labels can describe patterns or similarities and differences in the data. Moreover, clustering can be used for prediction, such that classification of unseen data is performed based on knowledge about the properties of present data and by evaluating their similarity to the incoming data sample. The significant benefit of cluster analysis is the *unsupervised learning* approach, which means that no labeled data is needed to find a solution.

The simplest and the most commonly used clustering algorithm is k-means [20], which is based on centroid search. Another kind of clustering algorithms are the density-based algorithms such DBSCAN [21], that views clusters as areas of high density separated by areas of low density, instead of looking for the centroids. Decision tree based methods also

can be applied for cluster analysis using the data splits based on different features. Most of cluster analysis techniques allow to build clusters in a multidimensional space.

Apart from classification and pattern recognition, cluster analysis can be used as denoising method looking for abnormalities in the signal. Moreover, building clusters combining a large set of different observables can simplify the data visualization and manual analysis, such elimination of outliers in the measurements and detection of anomalies.

Reinforcement Learning

The concept of Reinforcement Learning (RL) is based on environment-agent interaction [22]. The agent takes an action on the environment, and the environment reacts producing a reward, which is used by the agent to learn how to improve its actions. The approach does not require an existing data set consisting of input-output pairs, instead the agent is learning based on the continuous interaction with the environment which is varying depending on the action and its own dynamics. Considering this learning principle, RL can be applied to unstable, time-varying problems since the agent should be able to adjust its action to the changes of the response from the environment. The ability of RL techniques to be applied on time-varying unknown dynamics makes this approach particularly appealing for the control and optimization of accelerator components. Recent advances on RL application on accelerator control tasks can be found in [23].

OVERVIEW ON CURRENT APPLICATIONS

In the following we demonstrate some ML applications currently being used in accelerator technology and ongoing research on potential ML based approaches. An earlier overview on previous works related to beam diagnostics can be found in [24], for a wider overview on opportunities in ML for particle accelerators see [25–27].

Virtual Diagnostics

Various instruments and diagnostics techniques are required in order to monitor the beam itself and variables which affect its parameters. Virtual diagnostics can assist in case a direct measurement would have a destructive impact on the operation or in the locations where no physical instrumentation can be placed. ML can provide techniques to build such virtual beam diagnostics instruments. Simulation studies and experimental demonstrations have been carried out on FACET-II and Linac Coherent Light Source (LCLS) to study ML-based longitudinal phase space (LPS) prediction. Training data for a feed-forward ANN has been acquired from a large number of simulations that represent changes in LPS distribution as response to the change of various accelerator parameters, as well as from the existing measurements at LCLS. ML model demonstrates a good agreement between the prediction and simulated or measured LSP images [28]. Another example is the estimation of

oscillation amplitude and synchrotron damping time based on LPS measurements at Shanghai Synchrotron Radiation Facility (SSRF) [29]. Here, Gradient descent algorithm is used to estimate the fitting parameters which are then used as target variables in a supervised model. ANN is trained to predict these values from longitudinal phase measurements obtained from the Beam Position Monitors (BPM). Another example from SSRF is a study on correlations between the beam size and the images from multi-slit imaging system, aiming to improve the accuracy of BPMs using ANN [30].

A special kind of ANN, *convolutional neural networks* (CNN) [31] have been applied at FAST on image based diagnostic during beam operation [32]. A combination of a CNN and a feed-forward NN yields promising results for the prediction of beam parameters on simulated data sets. The model uses simulated cathode images, solenoid strengths and the gun phase as inputs and produces a prediction for various downstream beam parameters. Application of ANN can be found also in correction of distorted beam profiled measured at ionization profile monitors (IPM) [33]. ANN model has been trained on IPM simulations in order to establish the mapping between measured profiles together with bunch length and bunch intensity to the original beam profile.

Optimization and Operation

ML methods are especially suited for non-linear and time-varying systems with large parameter spaces. Operation of a complex system such as an accelerator, whose beam dynamics exhibits nonlinear response to machine settings can be considered as a typical ML task. Due to the constant increase of machine design complexity and development of new interacting systems, traditional techniques might become insufficient. Reinforcement learning demonstrates a great ability to solve complex control tasks [23]. Recently, its application has been studied on control tasks in the domain of accelerators, e.g. for the control of the micro-bunching instability at the KIT storage ring Karlsruhe Research Accelerator (KARA) [34].

ANN based application has been successfully applied at the LCLS to predict x-ray pulse properties by decoding complex hidden correlations between parameters obtained from slow diagnostics such as photon energy and properties measured by fast diagnostics [35]. Another example is the application of intelligent control techniques to maximize the average pulse energy in FELs. The developed techniques allow to tune up to 105 components simultaneously based only on noisy average bunch energy measurements [36].

Beam Optics Correction

Attempts to build beam diagnostics and beam control systems using ML have been made already in the past decades [37–39]. Despite the early stage of ANN technology at the time, the obtained results have shown the potential of supervised learning solution to be applied in beam control tasks, mainly for linear orbit correction.

Apart from supervised learning, optics correction can be approached from a probabilistic point of view as it was

recently shown in [40]. In this example, the quadrupole error distribution is fitted using Bayesian approach. Degeneracy of error sources is solved by selecting non-correlated BPM signals.

Supervised learning is being under study with two different approaches for optics correction at the LHC aiming to reduce optics errors by finding quadrupolar gradient errors. In order to compute the corrections, measured data have to be compared with the ideal optics design. The deviations from ideal optics introduced by quadrupolar gradient errors have to be compensated by applying corrections [41, 42]. In terms of machine learning, this task can be defined as a regression problem.

In the first approach, simulations of randomly generated errors in the quadrupoles powered in series (circuits) are used as target values and the optics perturbation produced by these errors is the input of the regression model. To correct the perturbed optics, the circuit errors predicted by the trained regression model just have to be applied with the opposite sign. However, under realistic conditions the errors of every single magnet instead of circuits perturb the optics, which has a different effect compared to the strength change in the circuits. In case the objective is to obtain the circuits settings to be implemented in the LHC, the optics functions in the training data have to be perturbed by errors in circuits in order to build input-output pairs required for supervised learning approach. As input we use phase advance, beta and normalized dispersion deviations from the ideal model simulated as measurements at the BPMs, 2560 features in total. The output variables are the values for the strength change in the circuits (193 target variables). The simulated phase advance measurements are given Gaussian noise relative to the $\sqrt{\beta}$ - function at the location of the BPM. In order to assert the ability of the model to correct the optics under realistic conditions, an additional data set is generated for the validation where the optics is perturbed by single quadrupoles instead of circuits. As figures of merit we use β -beating and the deviation of the normalized dispersion to the ideal model after applying the obtained correction values for the circuit strength. The comparison between different algorithms [43], shows that all applied models perform equivalently, therefore we chose Linear Regression implementation of *Scikit-learn* [44] for further studies since the obtained model is easier to interpret and the training can be performed significantly faster. The advantage of regression model against currently used response matrix approach [45] is the ability of extracting an average linear response over the training population instead of only using the unperturbed model and the response of a single observable to a strength change in a single corrector. Despite the fact that the errors of prediction on training and test set are acceptably small, the predicted corrections are less effective on the validation data which is perturbed with individual quadrupole errors. Nevertheless, the ability of such a model to reduce the optics perturbation to the level comparable with traditional response matrix approach is clearly demonstrated and shows the potential of ML-based optics correction.

In the second approach we studied the ability of regression models to address directly the single quadrupole errors. Another simulation dataset is generated in order to train a model to predict the errors of each quadrupole from the phase, beta and dispersion perturbations. The model achieves acceptably high score for R^2 coefficient which is defined as follows:

$$R^2(y, \hat{y}) = 1 - \frac{\sum_{i=1}^n (y_i - \hat{y}_i)^2}{\sum_{i=1}^n (y_i - \bar{y})^2} \quad (1)$$

where \hat{y}_i is the predicted value of the i -th sample, y is the corresponding true value for n total samples and \bar{y} is the mean of true values. The scores of the model are 0.98 and 0.86 for training and test data set respectively, it has to be noted that the resulting difference between training and test scores exhibits slight overfitting of the model. This issue also explains the high relative error between true and predicted values for the validation set ($\sim 20\% \pm 0.23$). Identification of magnet errors in a circular machine is known to be a degenerate problem with multiple solutions. Despite this limitation, the attempt to correct the optics using the ML-model prediction yields impressive results. Figure 1 shows correction results obtained with iterative response matrix approach [46] and ML model using linear regression for 120 LHC simulations. The great correction results achieved with ML model despite the relatively poor performance of the model on the training and test sets can be explained with the fact, that in order to correct the optics, it is sufficient to find one of the multiple solutions which can compensate the introduced optics perturbations fitted into the model.

High R^2 score shows that the model can explain the variance of target values based on all features, but not all of the features are significant to obtain the correct output. Reducing the number of the features by selecting the least correlated BPMs should improve the accuracy of model prediction, prevent overfitting, as well as provide help to deal with the degeneracy. Dimensionality reduction techniques already demonstrated their potential for orbit correction, as well as to be applied to dynamic aperture optimization [47]. Therefore, the next steps of the study is the application of dimensionality reduction techniques, followed by the introduction of non-linear error sources into the data sets and generalization to different optics settings.

Instrumentation Fault Detection

Anomaly detection techniques are suitable for the detection of unusual events that do not conform to expected patterns. They also can be used to identify outliers and remove noise. Anomaly detection can be performed using classification on labeled data (supervised learning), unsupervised learning techniques including clustering or semi-supervised learning methods such as autoencoder, a special ANN representing the model trained on normal data set and then detect the anomalies based on the value of the loss function generated by the representative model on the given test sample [48]. An early example on anomaly detection in beam diagnostics in storage ring is the application of ANN to predict the orbit at particular beam position monitor (BPM)

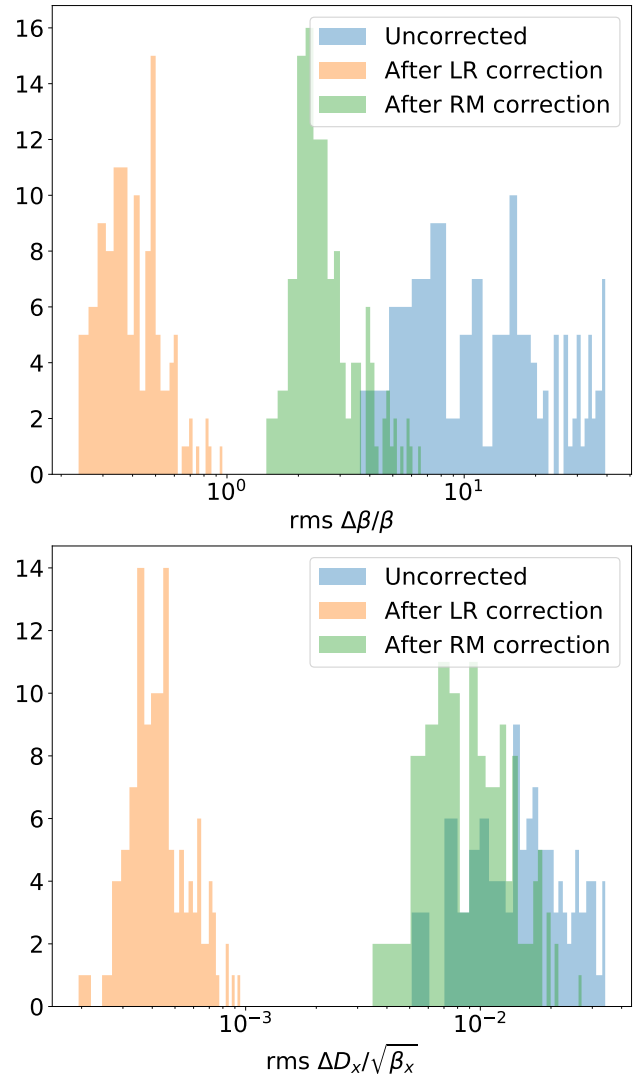


Figure 1: Results on β -beating and normalized dispersion deviation from ideal optics after applying linear regression prediction of individual quadrupole errors (LR) and corrections values for the circuits computed by response matrix (RM). The figure shows rms distribution of 120 simulations.

based on measurements at other BPMs at the Pohang Light Source [49]. A large deviation between measured and predicted orbit should mark malfunctioning BPM.

An example for anomaly detection using unsupervised learning is the detection of faulty BPMs at the LHC [50,51]. This method recently became a standard part of optics measurements at LHC and has been successfully used during beam commissioning and machine developments for different optics settings in 2018. BPMs measure the beam position at several turns around the machine. The optics functions are then calculated from the harmonic analysis of the turn-by-turn BPM readings. Most of the noise and faulty signals can be removed using predefined thresholds, as well as through applying advanced signal-improvement techniques based on SVD [52] to reduce noise in BPM readings. However few nonphysical values are usually observed

in the optics computed from the data cleaned with these techniques. These spikes have to be removed by manually identifying the faulty BPMs, removing them from the harmonic analysis data and repeating the optics analysis, which requires human intervention and loss of valuable machine development time.

Further issue is that the spike does not necessarily appear directly at the location of the faulty BPM, due to the method applied for the optics computation at the LHC [53,54], so identification of actual BPM faults is not trivial. Moreover, not all reasons for the appearance of BPM anomalies are known, therefore we cannot define thresholds which would indicate remaining faulty BPMs. Giving these constraints, unsupervised learning appears as appropriate technique to detect faulty BPMs prior to optics computations. The appearance of outliers is challenging for the application of centroid or distance based clustering methods. Instead, density-based clustering methods such as DBSCAN and LOF [55] have been applied, however Isolation Forest (IF) algorithm which is a decision tree - based method [56] achieves the best results. Figure 2 shows a comparison between the beta-beating reconstructed from the measurements before and after applying IF. It can be clearly observed that most of the remaining outliers have been removed.

Since the knowledge about actual defective BPMs is not available, the assessment of cleaning algorithms has to be performed on simulations where the actual bad BPMs are known and can be used as labeled data to evaluate the performance of the method. The detailed description of this simulations study can be found in [51]. The main challenge of applying any cleaning methods on the measurements data is, that depending on the chosen algorithm parameter, some of the good BPMs can be wrongly identified as faulty. The comparison of different anomaly detection methods applied on the simulated BPM faults is demonstrated in Fig. 3. In case of large machines such as the LHC equipped with hundreds of BPMs, it is important to decrease the number of faulty signal artifacts as much as possible, because a single faulty BPM can affects the optics computation at multiple

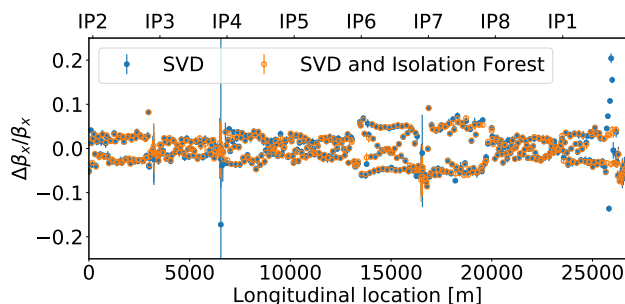


Figure 2: The comparison between beta-beating computed before and after IF cleaning demonstrates that IF anomaly detection significantly reduces the number of nonphysical spikes. The optics is computed for Beam 2 in horizontal plane with $\beta^*=50$ cm.

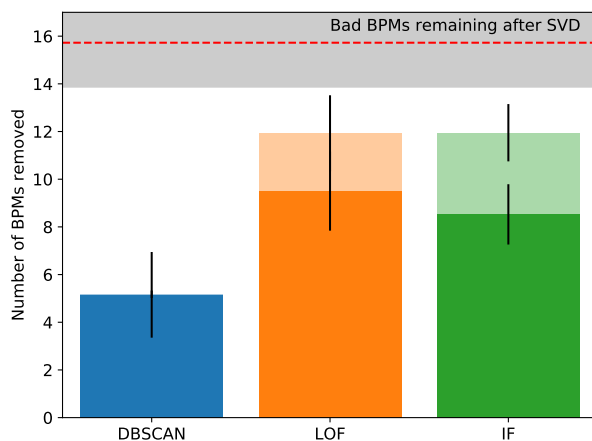


Figure 3: The comparison is carried out on 20 simulations for each plane, the results are averaged. Each bar represents the number of BPMs removed by the method. Dark fraction corresponds to the number of removed BPMs that are actually bad.

locations. The absence of few good BPMs that might be caused by IF algorithm does not have a significant negative effect since the optics computation can be propagated to the next available BPM. Considering smaller machines, it is crucial to keep as much BPM information as possible, removing only critically erroneous signal. In this case, a method such DBSCAN appears to be more appropriate since, as it was shown on simulations [51], the method does not identify any good BPMs as faulty, however a portion of bad BPMs is still remaining in the measurement.

CONCLUSION

Typical characteristic of supervised ML tasks is the ability to deal with large amount of structured data. This leads to the conclusion that the implementation of supervised ML solutions requires large existing training data sets or development of appropriate data acquisition tools in order to provide the data in "machine-understandable" format, which is not necessarily available out-of-the-box since the traditional control systems usually imply human intervention. The effort that has to be put on automation such as building data acquisition infrastructure and training of complex models might be more costly and resources expensive than traditional methods. On the other hand, automation of some particular systems using ML as it was done for example, in collimators alignment at LHC [57] is very effective and can save operational resources.

The ability of unsupervised learning to discover unknown patterns in the data is useful especially for anomaly detection tasks such as detection of instrumentation defects, e.g. using clustering for faulty BPMs signal. Such methods can be performed directly without training in arbitrary accelerator systems. The optics correction results achieved with supervised learning convincingly demonstrate the great potential of this approach opening new opportunities for optics control in current and future accelerators.

REFERENCES

- [1] J. W. Flanagan *et al.*, "A simple real-time beam tuning program for the KEKB injector Linac", in Proceedings of the 1998 International Computational Accelerator Physics Conference, Monterey, CA, KEK Report No. 98-208, 1999.
- [2] N. J. Walker, J. Irwin, and M. Woodley, Report No. SLAC-PUB-6207, 1993.
- [3] Y. Funakoshi *et al.*, "Performance of KEKB with crab cavities", in Proceedings of the 11th European Particle Accelerator Conference, Genoa, 2008, edited by I. Andrian and C. Petit-Jean-Genaz (Ref. [111]), pp. 1893–1895.
- [4] W. Fischer, J. Beebe-Wang, Y. Luo, S. Nemesure, L. K. Rajulapati, "RHIC proton beam lifetime increase with 10- and 12-pole correctors", in Proceedings of IPAC'10, Kyoto, Japan, pp. 4752–4754.
- [5] M. Aiba, M. Boege, N. Milas, A. Streun, "Ultra low vertical emittance at SLS through systematic and random optimization", Nucl. Instrum. Methods Phys. Res., Sect. A, 694, pp.133-139, 2012.
- [6] X. Huang, J. Corbett, J. Safranek, J. Wu, "An algorithm for online optimization of accelerators", Nucl. Instrum. Methods Phys. Res., Sect. A 726, 77 (2013).
- [7] T. Mitchell, "Machine Learning", 1st ed., McGraw-Hill, Inc., New York, USA (1997).
- [8] D. Rumelhart, G. Hinton, R. Williams, "Learning representations by back-propagating errors", Nature 323 (6088), 533–536, (1986).
- [9] D. Kingma and J. Ba, "Adam: A method for stochastic optimization", CoRR abs/1412.6980 (2014).
- [10] J. Duchi, E. Hazan, Y. Singer, "Adaptive subgradient methods for online learning and stochastic optimization", Journal of Machine Learning Research 12 (2010): 2121-2159.
- [11] Y. Bengio, Y. LeCun, G. Hinton, "Deep Learning", Nature. 521 (7553): 436–444, 2015.
- [12] S. Haykin, "Neural Networks: A Comprehensive Foundation", 2nd ed., Prentice Hall PTR Upper Saddle River, NJ, USA (1998).
- [13] J. Schmidhuber, "Deep learning in neural networks: An overview", Neural networks: the official journal of the International Neural Network Society 61 (2015): 85-117.
- [14] F.L. Lewis, "Neural Networks in Feedback Control Systems", Mechanical Engineer's Handbook, John Wiley, New York, USA (2005).
- [15] O. Maimon and L. Rokach, "Data Mining and Knowledge Discovery Handbook", Springer-Verlag New York, Inc., Secaucus, NJ, USA (2005).
- [16] L. Breiman, J. H. Friedman, R. A. Olshen, C. J. Stone, "Classification and Regression Trees", Statistics/Probability Series, Wadsworth Publishing Company, Belmont, USA (1984).
- [17] T.G. Dietterich, "Ensemble Methods in Machine Learning", In Proceedings of the First International Workshop on Multiple Classifier Systems, Springer-Verlag, London, UK (2000).
- [18] T. Hastie, R. Tibshirani, and J. Friedman, "The Elements of Statistical Learning", Springer Series in Statistics, Springer New York Inc., New York, USA (2001).
- [19] A. K. Jain, M. N. Murty, and P. J. Flynn, "Data clustering: a review", ACM computing surveys (CSUR), 31(3) (1999).
- [20] S. P. Lloyd, "Least squares quantization in PCM", IEEE Transactions on Information Theory, 28 (1982).
- [21] M. Ester, H. Kriegel, X. Sander, J. Xu, "A Density-based Algorithm for Discovering Clusters in Large Spatial Databases with Noise", In Proceedings of the Second International Conference on Knowledge Discovery and Data Mining, KDD'96. AAAI Press (1996).
- [22] R.S. Sutton, A. G. Barto, "Reinforcement Learning: An Introduction", MA, USA: MIT Press, 2018.
- [23] T. P. Lillicrap *et al.*, "Continuous control with deep reinforcement learning", arXiv:1509.02971 (2015).
- [24] E. Fol, J. M. Coello de Portugal, and R. Tomás, "Application of Machine Learning to Beam Diagnostics", in Proc. 7th Int. Beam Instrumentation Conf. (IBIC'18), Shanghai, China, Sep. 2018, pp. 169–176. doi:10.18429/JACoW-IBIC2018-TU0A02
- [25] A. L. Edelen, S. G. Biedron, B. E. Chase, D. Edstrom, S. V. Milton, P. Stabile, "Neural Networks for Modeling and Control of Particle Accelerators", IEEE Transaction of Nuclear Science, 63 (2), 2016.
- [26] A. Edelen *et al.*, "Opportunities in Machine Learning for Particle Accelerators", arXiv:1811.03172 (2018).
- [27] S. Biedron, "Adding Data Science and More Intelligence to Our Accelerator Toolbox", in Proc. IPAC'19, Melbourne, Australia, May 2019, pp. 1191–1197, doi:10.18429/JACoW-IPAC2019-TUZPLM1
- [28] C. Emma *et al.* "Machine learning-based longitudinal phase space prediction of particle accelerators", Phys. Rev. Accel. Beams (21), 112802 (2018).
- [29] X.Y. Xu, Y.B. Leng, and Y.M. Zhou, "Machine Learning Application in Bunch Longitudinal Phase Measurement", in Proc. IPAC'19, Melbourne, Australia, May 2019, pp. 2625–2628, doi:10.18429/JACoW-IPAC2019-WEPGW064
- [30] B. Gao, Y.B. Leng, and X.Y. Xu, "Deep Learning Applied for Multi-Slit Imaging Based Beam Size Monitor" in Proc. IPAC'19, Melbourne, Australia, May 2019, pp. 2587–2590, doi:10.18429/JACoW-IPAC2019-WEPGW049
- [31] Y. LeCun, K. Kavukcuoglu, C. Farabet, "Convolutional Networks and Applications in Vision", Proc. International Symposium on Circuits and Systems (ISCAS'10), IEEE, (2010)
- [32] A.L. Edelen *et al.*, "First Steps Toward Incorporating Image Based Diagnostics Into Particle Accelerator Control Systems Using Convolutional Neural Networks", In Proceeding of Proceedings of NAPAC2016, Chicago, IL, USA (2016)
- [33] D. Vilsmeier, M. Sapinski and R. Singh, "Space-charge distortion of transverse profiles measured by electron-based ionization profile monitors and correction methods", Phys. Rev. Accel. Beams (22), 052801 (2019).
- [34] T. Boltz, T. Asfour, M. Brosi, E. Bründermann, B. Härer, P. Kaiser, *et al.*, "Feedback Design for Control of the Micro-Bunching Instability based on Reinforcement Learning", in Proc. IPAC'19, Melbourne, Australia, May 2019, pp. 104–107, doi:10.18429/JACoW-IPAC2019-MOPGW017
- [35] A. Sanchez-Gonzalez *et al.*, "Machine learning applied to single-shot x-ray diagnostics in an XFEL", Nature Communications 8, 15461 (2017).

- [36] A. Scheinker *et al.*, "Model-independent tuning for maximizing free electron laser pulse energy", *Phys. Rev. Accel. Beams* (22), 082802 (2019).
- [37] E. Bozoki, A. Friedman, "Neural network technique for orbit correction in accelerators/storage rings", *AIP Conference Proceedings* 315, 103 (1994).
- [38] E. Meier, G. LeBlanc, and Y. E. Tan, "Orbit Correction Studies using Neural Networks", in *Proc. 3rd Int. Particle Accelerator Conf. (IPAC'12)*, New Orleans, LA, USA, May 2012, paper WEP057, pp. 2837–2839.
- [39] Y. Kijima, M. Mizota, K. Yoshida, K. Suzuki, "A Beam Diagnostic System for Accelerator using Neural Networks", In *Proceedings of 3rd European Particle Accelerator Conference*, Berlin, Germany (1992).
- [40] Y. Li, R. Rainer, W. Cheng, "Bayesian approach for linear optics correction", *Phys. Rev. Accel. Beams* (22), 012804 (2019).
- [41] T. Persson, F. Carlier, J. Coello de Portugal, A. Garcia-Tabares Valdivieso, A. Langner, E.H. Maclean, L. Malina, P. Skowronski, B. Salvant, R. Tomas, and A.C. Garcia Bonilla, "LHC optics commissioning: A journey towards 1% optics control", *Phys. Rev. Accel. Beams* (20), 061002 (2017).
- [42] R. Tomás, M. Aiba, A. Franchi, U. Iriso, "Review of linear optics measurement and correction for charged particle accelerators", *Phys. Rev. Accel. Beams* (20), 054801 (2017).
- [43] E. Fol, J.M. Coello de Portugal, G. Franchetti, and R. Tomás, "Optics Corrections Using Machine Learning in the LHC", in *Proc. IPAC'19*, Melbourne, Australia, May 2019, pp. 3990–3993, doi:10.18429/JACoW-IPAC2019-THPRB077
- [44] F. Pedregosa *et al.*, *Scikit-learn: Machine Learning in Python*, *JMLR* 12, pp. 2825–2830, 2011.
- [45] M. Aiba *et al.*, "First β -beating measurement and optics analysis for the CERN Large Hadron Collider", *Phys. Rev. Accel. Beams* (12), 081002 (2009).
- [46] J. W. Dilly *et al.*, "An Updated Global Optics Correction Scheme", CERN-ACC-NOTE-2018-0056.
- [47] W.F. Bergan, I.V. Bazarov, C.J.R. Duncan, and D. L. Rubin, "Applications of Dimension-Reduction to Various Accelerator Physics Problems", in *Proc. IPAC'19*, Melbourne, Australia, May 2019, pp. 4060–4062, doi:10.18429/JACoW-IPAC2019-THPRB099
- [48] G.E. Hinton, R.R. Salakhutdinov, "Reducing the dimensionality of data with neural networks", *Science*, 313(5786):504 (2006).
- [49] J. W. Leea, S. Chob, M. Yoon, "A neural-network method for diagnosing beam-position monitors in storage ring", *Nucl. Instrum. Methods Phys. Res., Sect. A*, 402 (19), pp. 14-20, 1997.
- [50] E. Fol, "Detection of faulty Beam Position Monitors", presented at ICFA Beam Dynamics Mini-Workshop: Machine Learning Applications for Particle Accelerators, Menlo Park, CA, USA, 2018.
- [51] E. Fol, J.M. Coello de Portugal, and R. Tomás, "Unsupervised Machine Learning for Detection of Faulty Beam Position Monitors", in *Proc. IPAC'19*, Melbourne, Australia, May 2019, pp. 2668–2671, doi:10.18429/JACoW-IPAC2019-WEPGW081
- [52] R. Calaga, R. Tomás, "Statistical analysis of RHIC beam position monitors performance", *Phys. Rev. ST Accel. Beams* 7, 042801 (2004).
- [53] A. Langner, G. Benedetti, M. Carlà, U. Iriso, Z. Martí, J. Coello de Portugal, R. Tomás, "Utilizing the N beam position monitor method for turn-by-turn optics measurements", *Phys. Rev. Accel. Beams* vol. 19, p. 092803, 2016. doi:10.1103/PhysRevAccelBeams.19.092803
- [54] A. Wegscheider, A. Langner, R. Tomás and A. Franchi, "Analytical N beam position monitor method", *Phys. Rev. Accel. Beams* vol. 20, p. 111002, 2017. doi:10.1103/PhysRevAccelBeams.20.111002
- [55] M. Breunig, H. P. Kriegel, R. T. Ng, J. Sander, "LOF: identifying density-based local outliers", in *ACM sigmod record*, vol. 29 no. 2, pp. 93–104, 2002. doi:10.1145/335191.335388
- [56] F. Liu, K.M. Ting, Z. Zhou, "Isolation forest", In *Proceedings of the 2008 Eighth IEEE International Conference on Data Mining*, 413-422 (2008).
- [57] G. Azzopardi, A. Muscat, S. Redaelli, B. Salvachua, and G. Valentino, "Operational Results of LHC Collimator Alignment Using Machine Learning", in *Proc. IPAC'19*, Melbourne, Australia, May 2019, pp. 1208–1211, doi:10.18429/JACoW-IPAC2019-TUZZPLM1

FEW-FEMTOSECOND FACILITY-WIDE SYNCHRONIZATION OF THE EUROPEAN XFEL

S. Schulz*, M. K. Czwalińska, M. Felber, M. Fenner, Ch. Gerth, T. Kozak, T. Lamb, B. Lautenschlager, F. Ludwig, U. Mavric, J. Müller†, S. Pfeiffer, H. Schlarb‡, C. Schmidt, M. Titberidze, F. Zummack, Deutsches Elektronen-Synchrotron (DESY), Hamburg, Germany
C. Sydlo§, Paul Scherrer Institut (PSI), Villigen, Switzerland

Abstract

In this paper, we report on the first facility-wide evaluation of the optical synchronization system at the European XFEL, resulting in excellent arrival time stability of the electron bunches at the end of the 2 km long linac of the machine. It has been measured using two adjacent, individual single-shot femtosecond-resolution bunch arrival time monitors. While each of the monitors is independently connected by a stabilized optical fiber link to a master laser oscillator, with one being installed in the injector building and one in the experimental hall, these two reference lasers are tightly synchronized through another few-km long fiber link and by balanced optical cross-correlation. Thus, our results are not only benchmarking the accelerator performance, but at the same time the optical synchronization infrastructure itself. Femtosecond arrival time stability can only be achieved by also locking the RF reference for cavity field control to the stabilized optical reference and requires an unprecedented synchronization of the master laser oscillator to the accelerator's master RF oscillator, enabled by a novel laser-to-RF phase detection scheme. Finally, with the seed oscillators of the experiment's optical lasers tightly synchronized to the master laser oscillator, first pump-probe experiments at two independent scientific instruments proved a relative X-ray/optical timing jitter in the low tens of femtoseconds.

OVERVIEW

In 2017 the European XFEL officially started operation with early user experiments and has meanwhile been fully commissioned with all three SASE beamlines and six scientific instruments. The machine is capable delivering up to 27,000 hard and soft X-ray pulses per second with a few tens of femtoseconds duration in flexible patterns to the three beamlines, such that three user experiments can be carried out simultaneously. At each beamline, a distinct laser system is available with matching pulse patterns, providing ultrashort optical pulses for exciting samples in pump-probe geometries, and usage in local timing tools. In addition, every scientific instrument is equipped with another optical laser system fulfilling specific requirements of the instrument. One key component for such time-resolved experiments at the instruments and crucial for accelerator stability is the optical synchronization infrastructure, which had been

under commissioning since early 2016 [1–5]. Founded on an ultra-low noise laser oscillator (master laser oscillator, MLO) locked to the facility's master RF oscillator, the synchronization signals are distributed over actively-stabilized optical fiber links, and are used to re-synchronize the reference signal of the accelerator's low-level RF (LLRF) system, the synchronization of the various laser systems, and to provide a reference for longitudinal electron bunch diagnostics. The system evolved from the implementation at the soft X-ray free-electron laser FLASH [6], which showed already 28 fs rms X-ray/optical relative pulse arrival time jitter [7] based on earlier work on electron bunch arrival time stabilization [8]. Since then, significant improvement in all core systems, computing and controls [9, 10] had been made, additional components were developed, and a robust implementation is realized.

TOPOLOGY AND CORE SYSTEMS

At the European XFEL, shown schematically in Fig. 1, the main synchronization laboratory provides precisely controlled environmental conditions with < 0.1 K temperature and < 3% RH (relative humidity) for the core systems of the synchronization infrastructure. The optical timing reference is a commercial, SESAM-based passively mode-locked oscillator at telecom wavelength emitting 200 fs FWHM pulses at a repetition rate of 216.667 MHz. For redundancy, a second identical laser oscillator is operated as hot-spare, such that the system can be switched from one to the other within minutes, with an automated failure detection and switching process under development.

Both laser oscillators are synchronized to the 1.3 GHz main RF oscillator [11] of the facility, which had been realized by a standard heterodyne scheme based on RF generation in a fast photodetector [12] in the first two years of operation. Recently, a Mach-Zehnder-Modulator (MZM)-based laser-to-RF phase detection scheme has been commissioned, resulting in a significant improvement of the timing jitter from 7.2 fs rms (bandwidth 10 Hz to 100 kHz) of the old scheme down to 3.0 fs rms, while also nearly eliminating long-term drifts. This performance is permanently monitored by a second, identical MZM-based laser-to-RF phase detector providing a true out-of-loop measurement (see Fig. 2).

The pulse train of the MLO is then distributed and split by means of polarizing beamsplitters and half-wave plates on a SuperInvar optical table to up to 24 so-called fiber link stabilization units, with presently 18 units in operation.

* corresponding author: seb.schulz@desy.de

† corresponding author: jost.mueller@desy.de

‡ corresponding author: holger.schlarb@desy.de

§ formerly also affiliated with DESY

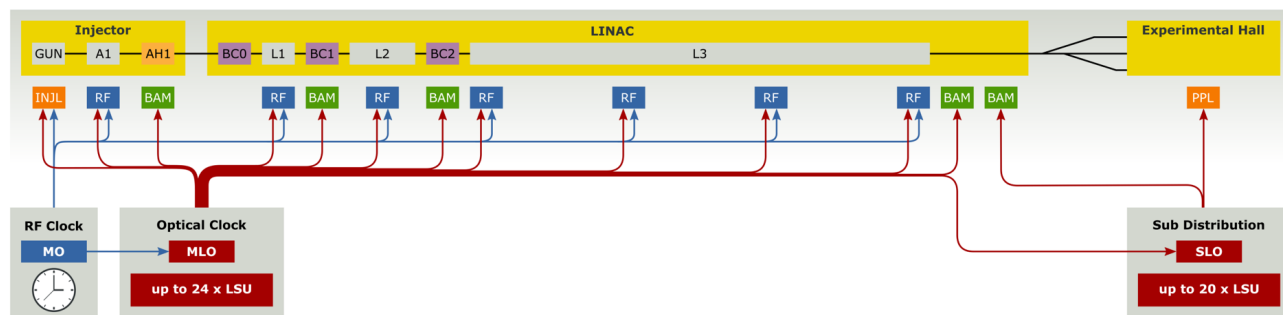


Figure 1: Schematic overview of the main building blocks of the optical synchronization infrastructure installed at the European XFEL.

Special care had been taken in the design of the optical setup such that all beam paths are equally long and thus any residual drift, e.g. by uncontrollable air pressure changes, is common for all connected end-stations.

Polarization-maintaining fiber is used to connect all end-stations in the accelerator tunnel, the photocathode laser and second synchronization laboratory in the experimental hall in Schenefeld. There, another laser oscillator (SLO) of the same type as the MLOs is synchronized to the optical reference by means of balanced optical cross-correlation with a timing jitter of sub-2 fs (Fig. 2). Employing the same free-space distribution scheme as in the main synchronization laboratory, further actively stabilized fiber links are connecting presently seven instrument and pump-probe laser laboratories with capability of further extension. Another fiber link is used to provide the reference for an electron bunch arrival time monitor (BAM) at the end of the linac, such that at this location two adjacent BAMs are connected from both the Hamburg and the Schenefeld synchronization laboratories. The stabilization of each individual fiber link is based on measurement of the round-trip time of pulses traveling forth and back on the optical fiber based on balanced optical cross-correlation. Active feedback on the fiber length using a fast (kHz-bandwidth) piezo-based actuator and a 4 ns-long optical delay line ensure practically long-term drift-free laser pulse arrival time at the link end with sub-femtosecond rms timing jitter. As can be seen in Fig. 2,

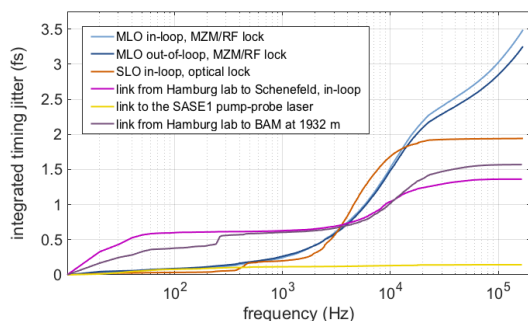


Figure 2: Examples for integrated timing jitter performance of the synchronized master- and slave laser oscillators, and the fiber link stabilization unit from Hamburg to Schenefeld.

the long fiber links to the Schenefeld lab (3.6 km) and to the BAM at the end of the linac (1.6 km) fiber show a significantly higher timing jitter compared to very short links, such as the one at the SASE1 beamline (approx. 100 m fiber). Notably, timing jitter is accumulated in the low-frequency region of the spectrum for long fibers, and this behavior is subject to investigation.

Bunch Arrival Time Monitor

Along the linac, several monitors allow for the non-destructive measurement of the arrival time of every single electron bunch with few-femtosecond resolution. For this, the transient electric field of an electron bunch is exploited to generate an RF pulse in a specifically designed high-bandwidth pickup [13] in the beamline, which then changes the amplitude of the optical reference pulse train in an integrated electro-optical modulator. This amplitude modulation is, within the dynamic range of the monitor of a few hundreds of femtoseconds, proportional to the electron bunch arrival time [14–16]. The signals of the BAMs can be used as inputs for slow and fast feedback loops to stabilize the arrival time of the electron bunches at the end of the accelerator.

Optical Reference Module

The optical reference module (REFM-OPT) is used to re-synchronize the 1.3 GHz RF reference signal distributed throughout the tunnel at distinct locations to fulfill the phase stability requirements of 0.01 deg (approx. 20 fs) of the low-level RF system of the accelerator [17], which cannot be achieved by conventional the RF distribution systems alone. For this, the REFM-OPT employs a drift-free MZM-based phase detection scheme [18] between the optical and the 1.3 GHz electrical reference signals and corrects the phase of the RF signal locally in a PLL. During normal operation of all nine planned and installed REFM-OPTs several picoseconds of drift are corrected to maintain stable RF reference phases for the accelerating field control with a short-term jitter of sub-4 fs rms [19].

External Laser Synchronization

Robust synchronization of all external optical laser oscillators, such as the pump-probe laser systems at the scientific

instruments, as well as the photocathode laser is routinely provided by the conventional heterodyne detection scheme, which had been used at the MLOs in the past [12]. Depending on the specific laser system, where the scheme is individually adapted to, a timing jitter in the order of a few tens of femtoseconds is achieved. Significantly improved timing jitter performance on the single-digit femtosecond level, e.g. required for locking the SLO (Fig. 2), is realized by balanced optical cross-correlation [20]. In addition, such optical cross-correlation schemes can also be applied in slow feedbacks for drift compensation and had recently been used to stabilize the arrival time of the photocathode laser pulses and thus the electron bunch arrival time in the injector. With the feedback active, it was demonstrated that the peak-to-peak drift of the electron bunches measured with an independent BAM could be reduced by a factor of four from around 200 fs down to 45 fs over an period of 8 hours [21]. An integration into the slow feedback systems of the accelerator is under preparation.

PERFORMANCE EVALUATION

Most recently, the two adjacent bunch arrival time monitors, located at the tunnel position “1932 m” with a separation of less than 1 m, have been commissioned together with their corresponding fiber links from the two phase-locked reference laser oscillators in the Hamburg and Schenefeld synchronization labs. Figure 3 shows the correlation of the electron bunch arrival time measured with the two monitors over 600 FEL shots or a period of 1 minute. In this graph,

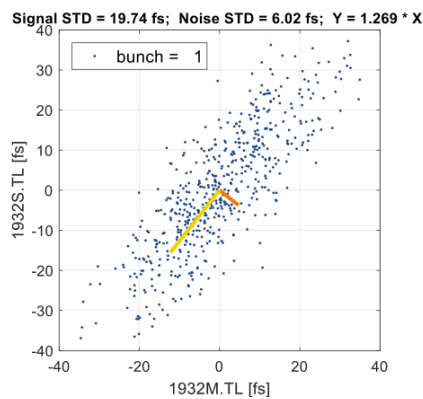


Figure 3: Correlation of the measured electron bunch arrival time with two adjacent BAMs at the end of the linac.

where the first of 195 electron bunches per 10 Hz train is shown, the width along the principal axis of the distribution represents the width of the arrival time distribution (indicated by the yellow line), such that the projection yields an electron bunch arrival time jitter of approx. 12 fs rms at each of the monitors. The width of the correlation in this preliminary analysis in the perpendicular direction (orange line) is approximately 6 fs rms and includes the resolution of the BAMs, the timing stability of the three fiber links to the BAMs and between the two reference lasers, the timing jitter of the synchronization of the SLO to the link, as well as

the high-frequency noise of the lasers themselves. A more rigorous, on-going analysis of the data suggests an even lower timing jitter performance of 2 fs rms for the overall synchronization system on short timescales. A long-term

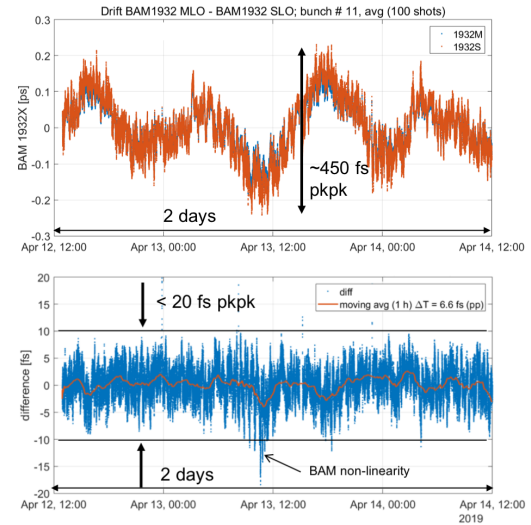


Figure 4: Peak-to-peak (top) and residual long-term drift (bottom) between the two BAMs at the end of the linac.

measurement over two days without any longitudinal feedbacks active revealed a slow arrival time drift of 450 fs peak-to-peak with a characteristic period of approx. 12 h (Fig. 4, upper panel). There are indications that this drift may arise from tidal movement, and consequently more long-term data is presently being acquired and analyzed. The residual drift between the two monitors amounts to 20 fs peak-to-peak over the measurement period (Fig. 4, lower panel). Further investigation on the source of this drift and possible mitigation measures are also presently on-going.

SUMMARY AND OUTLOOK

In conclusion, we demonstrated a performance of the optical synchronization infrastructure at the European XFEL accelerator on the single-digit femtosecond timescale when measured with two independent electron bunch arrival time monitors. Independent measurement campaigns at both scientific instruments at the SASE1 beamline resulted agreeing in an X-ray/optical relative arrival time jitter of approx. 30 fs rms [22], comparable to newest measurements at another hard X-ray facility [23]. In the future, we plan to further improve the stabilization of the photoinjector laser and hence the whole injector section of the linac, and to commission advanced beam-based feedbacks such that long-term low-drift operation with few femtosecond timing jitter can be achieved.

ACKNOWLEDGMENTS

The authors thank the FXE and the SPB/SFX scientific instruments at the European XFEL for providing timing tool data and fruitful discussion.

REFERENCES

- [1] C. Sydlo *et al.*, “Development Status of Optical Synchronization for the European XFEL”, in *Proc. IBIC’13*, Oxford, UK, Sep. 2013, paper MOPC32, pp. 135–138.
- [2] C. Sydlo *et al.*, “Femtosecond Timing Distribution at the European XFEL”, in *Proc. FEL’15*, Daejeon, Korea, Aug. 2015, paper WEP047, pp. 669–671.
- [3] C. Sydlo *et al.*, “Femtosecond Optical Synchronization System for the European XFEL”, in *Proc. IPAC’17*, Copenhagen, Denmark, May 2017, pp. 3969–3971. doi:10.18429/JACoW-IPAC2017-THPAB108
- [4] J. M. Mueller *et al.*, “Large-Scale Optical Synchronization System of the European XFEL”, in *Proc. LINAC’18*, Beijing, China, Sep. 2018, pp. 253–256. doi:10.18429/JACoW-LINAC2018-MOP0121
- [5] T. Lamb *et al.*, “Large-Scale Optical Synchronization System of the European XFEL with Femtosecond Precision”, in *Proc. IPAC’19*, Melbourne, Australia, May 2019, pp. 3835–3838. doi:10.18429/JACoW-IPAC2019-THPRB018
- [6] S. Schulz *et al.*, “Past, Present and Future Aspects of Laser-Based Synchronization at FLASH”, in *Proc. IBIC’13*, Oxford, UK, Sep. 2013, paper WEP32, pp. 753–756.
- [7] S. Schulz, I. Grguraš, C. Behrens, H. Bromberger, J. T. Costello *et al.*, “Femtosecond all-optical synchronization of an X-ray free-electron laser”, *Nat. Commun.*, 6:5938 (2015). doi:10.1038/ncomms6938
- [8] F. Löhl, V. Arsov, M. Felber, K. Hacker, W. Jalmuzna *et al.*, “Electron Bunch Timing with Femtosecond Precision in a Superconducting Free-Electron Laser”, *Phys. Rev. Lett.*, vol. 104, p. 144801 (2010). doi:10.1103/PhysRevLett.104.144801
- [9] M. Felber *et al.*, “Implementation of MTCA.4-based Controls for the Pulsed Optical Synchronization Systems at DESY”, in *Proc. FEL’15*, Daejeon, Korea, Aug. 2015, paper MOP040, pp. 115–117.
- [10] M. Felber, E. P. Felber, M. Fenner, T. Kozak, T. Lamb *et al.*, “Usage of the MicroTCA.4 Electronics Platform for Femtosecond Synchronization Systems”, in *Proc. FEL19*, Hamburg, Germany, Aug. 2019, paper WEB007 (this conference).
- [11] L. Z. Zembala *et al.*, “Master Oscillator for the European XFEL”, in *Proc. IPAC’14*, Dresden, Germany, Jun. 2014, pp. 2771–2773. doi:10.18429/JACoW-IPAC2014-WEPRI116
- [12] M. Felber, M. Hoffmann, U. Mavric, H. Schlarb, S. Schulz, and W. Jalmuzna, “Laser Synchronization at REGAE using Phase Detection at an Intermediate Frequency”, in *Proc. IPAC’12*, New Orleans, LA, USA, May 2012, paper WEPD048, pp. 2624–2626.
- [13] A. Angelovski, A. Kuhl, M. Hansli, A. Penirschke, S. M. Schnepp *et al.*, “High Bandwidth Pickup Design for Bunch Arrival-time Monitors for Free-Electron Laser”, *Phys. Rev.*, 15, 112803 (2012), 8 pages. doi:10.1103/PhysRevSTAB.15.112803
- [14] H. Dinter *et al.*, “Prototype of the Improved Electro-Optical Unit for the Bunch Arrival Time Monitors at FLASH and the European XFEL”, in *Proc. FEL’15*, Daejeon, Korea, Aug. 2015, paper TUP049, pp. 478–482.
- [15] M. K. Czwalinna *et al.*, “New Design of the 40 GHz Bunch Arrival Time Monitor Using MTCA.4 Electronics at FLASH and for the European XFEL”, in *Proc. IBIC’13*, Oxford, UK, Sep. 2013, paper WEP31, pp. 749–752.
- [16] M. Viti *et al.*, “The Bunch Arrival Time Monitor at FLASH and European XFEL”, in *Proc. ICALEPCS’17*, Barcelona, Spain, Oct. 2017, pp. 701–705. doi:10.18429/JACoW-ICALEPCS2017-TUPHA125
- [17] M. Omet *et al.*, “LLRF Operation and Performance at the European XFEL”, in *Proc. IPAC’18*, Vancouver, Canada, Apr.-May 2018, pp. 1934–1936. doi:10.18429/JACoW-IPAC2018-WEPAF051
- [18] T. Lamb, “Laser-to-RF phase detection with femtosecond precision for remote reference phase stabilization in particle accelerators”, Ph.D. thesis, Technische Universität Hamburg-Harburg, 2017. doi:10.3204/PUBDB-2017-02117
- [19] T. Lamb *et al.*, “Laser-to-RF Synchronization with Femtosecond Precision”, in *Proc. FEL’17*, Santa Fe, NM, USA, Aug. 2017, pp. 407–410. doi:10.18429/JACoW-FEL2017-WEB04
- [20] J. M. Mueller *et al.*, “All-Optical Synchronization of Pulsed Laser Systems at FLASH and XFEL”, in *Proc. IPAC’15*, Richmond, VA, USA, May 2015, pp. 854–856. doi:10.18429/JACoW-IPAC2015-MOPHA032
- [21] J. Müller, S. Schulz, L. Winkelmann, M. K. Czwalinna, I. Hartl, and H. Schlarb, “Arrival Time Stabilization of the Photocathode Laser at the European XFEL”, *Conference on Lasers and Electro-Optics*, OSA Technical Digest (Optical Society of America), 2019, paper SF3I.6, doi:10.1364/CLEO_SI.2019.SF3I.6
- [22] T. Sato, R. Letrun, H. J. Kirkwood, J. Liu, P. Vagovic *et al.*, “Femtosecond timing synchronisation at megahertz repetition rates for an X-ray Free-Electron Laser”, *submitted*, 2019.
- [23] M. Kim, C.-K. Min, and I. Eom, “Laser systems for time-resolved experiments at the Pohang Accelerator Laboratory X-ray Free-Electron Laser beamlines”, *J. Synchrotron Rad.*, 26, 868–873 (2019). doi:10.1107/S1600577519003515

BALANCED OPTICAL-MICROWAVE PHASE DETECTOR FOR 800-nm PULSED LASERS WITH SUB-FEMTOSECOND RESOLUTION

K. Şafak[†], H. P. H. Cheng, A. Dai, P. Schiepel, E. Cano, J. Derksen, A. Berlin, M. Neuhaus
Cycle GmbH, Hamburg, Germany

F. X. Kärtner, Deutsches Elektronen Synchrotron and Center for Free Electron Science,
Hamburg, Germany

Abstract

We report a novel optical-to-microwave phase detector designed for 800-nm pulsed laser operation. The detector is based on electro-optic sampling between the microwave and the optical pulse train which is incorporated into a fiber-based Sagnac interferometer containing a phase modulator. The detector has a timing resolution of 0.01 fs RMS for offset frequencies above 100 Hz and a total noise floor of less than 10 fs RMS integrated from 1 Hz to 1 MHz.

INTRODUCTION

Modern light-matter interaction experiments conducted in free-electron lasers, ultrafast electron diffraction instruments and extreme light infrastructures require synchronous operation of microwave sources with femtosecond pulsed lasers [1,2]. In particular, Titanium-sapphire (Ti:Sa) lasers have become the most common near-infrared light source used in these facilities due to their wide gain spectrum, translating into wavelength tunability and ultrashort pulses at around 800-nm optical wavelength [3]. Therefore, a highly sensitive optical-to-microwave phase detector operating at 800 nm is an indispensable tool to synchronize these ubiquitous lasers to the microwave clocks of photon science facilities. Electro-optic sampling is one approach that has proven to be the most precise in extracting the relative phase noise between microwaves and optical pulse trains [4-7]. However, their implementation at 800-nm

wavelength has been so far limited to a few specialized laser laboratories [3,8].

Here, we show a novel optical-microwave phase detector designed for 800-nm operation promising 10-fs level synchronization precision from 1 Hz up to 1 MHz offset frequency.

OPERATION PRINCIPLE

Operation principle of the detector is based on a differentially-biased, fiber-based Sagnac interferometer (SGI) and synchronous detection at half the repetition rate of the optical pulse source. This scheme adopted from the balanced optical-microwave phase detectors (BOMPD) previously demonstrated for 1550-nm operation by our former group members [6,9]. Figure 1 shows the schematic of our 800-nm BOMPD. As inputs, the detector takes an 800-nm pulsed laser (e.g., a Ti:Sa laser) and a microwave signal whose frequency is a higher harmonic of the laser's pulse repetition rate. The optical signal is split into two arms. The first arm (i.e., bias arm) is tapped off by a photodiode to generate a high-frequency (multi GHz) microwave signal which is adjusted in amplitude and phase to achieve quadrature bias. The second arm is sent into a fiber-based SGI containing an optical phase modulator. When both the bias and the microwave signals are applied to the modulator, any phase error between the laser and the microwave source induces an amplitude modulation in the pulse train.

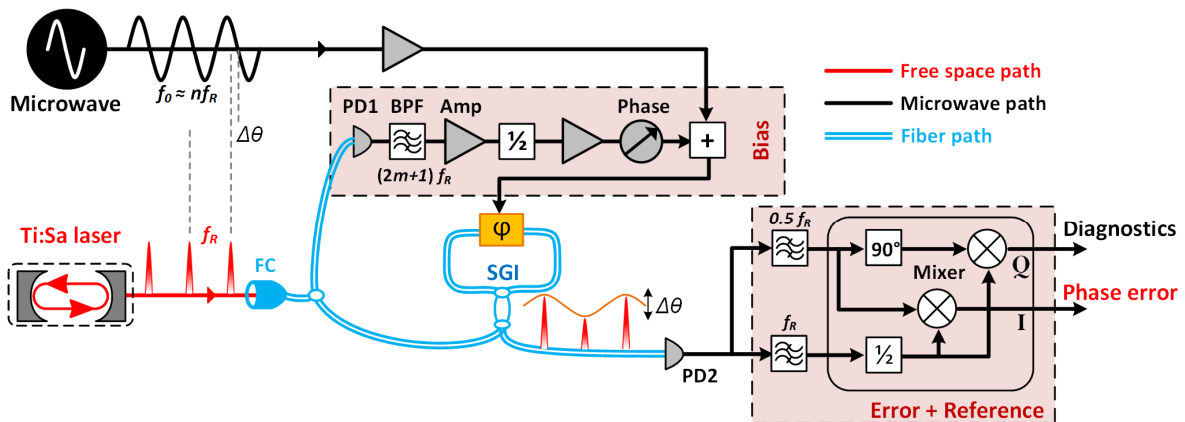


Figure 1: Schematic of the 800-nm BOMPD. $\Delta\theta$: Phase error between the microwave and optical pulse train; PD: photodiode; BPF: bandpass filter; Amp: electronic amplifier; $\frac{1}{2}$: frequency divider; Phase: RF phase shifter; +: microwave diplexer; ϕ : electro-optic phase modulator; SGI: Sagnac-interferometer; FC: fiber collimator, I: in-phase output, Q: in-quadrature output.

[†] kemal.shafak@cyclelasers.com

Upon photodetection, the SGI output contains the phase error information ($\Delta\theta$) at half frequencies of its odd harmonics (i.e., $(m+0.5)f_R$) besides the regular harmonics of the repetition rate (i.e., nf_R) which can serve as a reference signal for down-mixing to baseband. The phase error at $f_R/2$ and the reference signal at f_R are bandpass filtered and sent into an I/Q demodulator. The in-phase output of the demodulator gives the phase error signal of the 800-nm BOMPD at baseband; whereas, the quadrature output can be used as a diagnostic tool, for example, to check and observe the bias signal mismatch.

All detector electronics of the BOMPD (highlighted with red boxes in Figure 1) are designed and integrated into two printed circuit boards (PCB). This allows a compact detector footprint and enhanced environmental insulation which is suitable for accelerator and facility environments. Figure 2 shows the photo of the 800-nm BOMPD containing all the elements in an environmentally insulated enclosure.



Figure 2: Photo of the 800-nm BOMPD.

PERFORMANCE CHARACTERIZATION

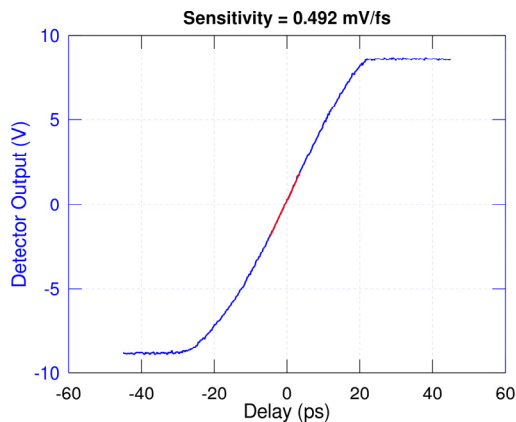


Figure 3: Timing sensitivity of the 800-nm BOMPD.

The performance of the 800-nm BOMPD is characterized using a 79.333 MHz Ti:Sa laser and a 5.712 GHz microwave signal. Figure 3 shows the characteristic BOMPD curve when the optical and microwave inputs are freely

running. The zero-crossing slope shows the timing sensitivity of the detector which is found to be 0.492 mV/fs (± 0.037 mV/fs) after 11 consecutive measurements. As can be inferred from the zero-crossing of the timing sensitivity curve, the detector has a linear detection range of more than 20 ps.

The detector noise floor is measured at the phase error output with a baseband analyzer when the microwave input is turned off and the BOMPD is properly biased with the optical signal. As shown in Figure 4, the integrated noise floor is less than 4 fs RMS for 1 Hz - 100 kHz and less than 10 fs RMS for 1 Hz - 1 MHz.

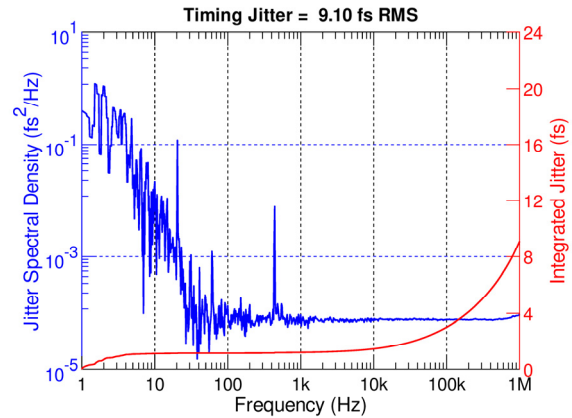


Figure 4: Noise floor of the 800-nm BOMPD.

We define the “timing resolution” of the BOMPD as the minimum timing jitter that can be detected by the detector at a certain offset frequency. This can be calculated from the measured noise floor in Figure 4. Table 1 shows the noise floor (i.e., jitter spectral density in units of fs^2/Hz) and the corresponding timing resolution of the detector at different offset frequencies. The detector has an outstanding timing resolution of ~ 10 attoseconds for offset frequencies above 100 Hz.

We can further define a so-called “dynamic range” for the BOMPD as the ratio of the linear detection range to the timing resolution at a certain offset frequency. As can be seen in Table 1, the 800-nm BOMPD has a dynamic range larger than 45 dB for all offset frequencies above 1 Hz.

Table 1: Timing Resolution and Dynamic Range

Frequency (Hz)	Jitter Spectral Density (fs^2/Hz)	Resolution (fs)	Dynamic range (dB)
1	0.40	0.631	45.009
10	0.02	0.148	51.318
100	1.36×10^{-4}	0.012	62.349
1k	9.41×10^{-5}	0.010	63.142
10k	7.88×10^{-5}	0.009	63.527
100k	7.80×10^{-5}	0.009	63.549
1M	9.59×10^{-5}	0.010	63.100

SUMMARY

In this paper, we have shown a novel optical-to-microwave phase detector designed for 800-nm pulsed laser operation. The detection scheme is adopted from our previous works on 1550-nm BOMPDs [2,6,9] and further developed to be suitable for 800-nm optical input with customized electronics and mechanics. The detector has a noise floor of only 9.1 fs RMS integrated from 1 Hz up to 1 MHz and outstanding timing resolution in the order of few attoseconds for offset frequencies above 100 Hz.

REFERENCES

- [1] M. Xin, K. Şafak, and F. X. Kärtner, “Ultra-precise timing and synchronization for large-scale scientific instruments”, *Optica*, vol. 5, no. 12, pp. 1564-1578, 2018.
doi:10.1364/OPTICA.5.001564
- [2] K. Şafak, “Large-scale laser-microwave synchronization for attosecond photon science facilities”, Doctoral Dissertation, DESY-THESIS-2017-015, Deutsches Elektronen-Synchrotron, Universität Hamburg, Hamburg, 2017.
- [3] H. Yang *et al.*, “10-fs-level synchronization of photocathode laser with RF-oscillator for ultrafast electron and X-ray sources”, *Sci. Rep.*, vol. 7, no. 39966, 2017.
doi:10.1038/srep39966
- [4] J. Kim, F. X. Kärtner, M. H. Perrot, “Femtosecond synchronization of radio frequency signals with optical pulse trains”, *Opt. Lett.*, vol. 29, no. 17, pp. 2076-2078, 2004.
doi:10.1364/OL.29.002076
- [5] K. Jung and J. Kim, “Subfemtosecond synchronization of microwave oscillators with mode-locked Er-fiber lasers”, *Opt. Lett.*, vol. 37., no. 14, pp. 2958-2960, 2012.
doi:10.1364/OL.37.002958
- [6] M. Xin *et al.*, “Attosecond precision multi-kilometer laser microwave network”, *Light Sci. Appl.*, vol. 6, e16187, 2017.
doi:10.1038/lsa.2016.187
- [7] T. Lamb *et al.*, “Femtosecond Stable Laser-to-RF Phase Detection for Optical Synchronization Systems”, in *Proc. IBIC'13*, Oxford, UK, Sep. 2013, paper TUPC33, pp. 447-450.
- [8] M. Titberidze *et al.*, “fs level laser-to-RF synchronization at REGAE”, *J. Phys.: Conf. Ser.*, vol. 874, no. 012085, 2017.
- [9] M. Y. Peng, A. Kalaydzhyan, F. X. Kärtner, “Balanced optical-microwave phase detector for sub-femtosecond optical-RF synchronization”, *Opt. Express*, vol. 22, no. 22, pp. 27102-27111, 2014. doi:10.1364/OE.22.027102

TIMING STABILITY COMPARISON STUDY OF RF SYNTHESIS TECHNIQUES

E. Cano Vargas[†], F. X. Kärtner, Deutsches Elektronen Synchrotron (DESY)
and Center for Free Electron Science (CFEL), Hamburg, Germany
A. Berlin, H. P. H. Cheng, A. Dai, J. Derksen, P. Schiepel, K. Shafak
Cycle GmbH, Hamburg, Germany

Abstract

In this paper, we implement and compare two of the most common techniques used for laser-to-RF synthesis in FEL facilities: (i) microwave signal extraction from the optical pulse train using photodiodes (i.e. direct photodetection), and (ii) voltage-controlled oscillator (VCO)-to-laser synchronization. Test setups are built to measure both the absolute phase noise of the generated RF signal and the relative timing jitter with respect to the mode-locked laser. Short-term timing jitter values varying between 10s and 100s of femtoseconds are achieved for different test setups, while long term timing drift ranging to some hundreds of femtoseconds due to environmental influence are observed.

INTRODUCTION

High-precision and low-noise timing transfer from a master oscillator to different end stations of a free-electron laser (FEL) is a critical requirement. Timing precisions ranging from a few femtoseconds, to sub-femtosecond are required for seeded FELs and attosecond science centers for the generation of shorter x-ray pulses with unmatched brightness [1], which ultimately enables subatomic and attosecond spatiotemporal resolution.

Mode-locked lasers referenced to RF standards are commonly used as master oscillators, due to their superior stability and timing precision, depicting timing jitter in the attosecond range [2]. In this matter, one of the biggest challenges is to transfer the timing stability of mode-locked lasers to RF sources.

Recently, timing distribution systems (TDS) have been demonstrated and implemented, taking advantage of the timing stability of pulsed-optical sources to perform timing distribution along different links, creating a link between different remotely located lasers, through balanced optical cross-correlators (BOCs) and laser-to-microwave synthesis and synchronization based on balanced optical-microwave phase detectors (BOMPDs). These devices can deliver sub-femtosecond precision between remotely synchronized lasers and microwave sources [3,4]. Figure 1 depicts a general overview of the TDS as deployed in [5]. Despite many achievements in these techniques over the last years, laser to microwave synchronization is still one of the bottlenecks of the system by being affected by so many noise sources and perturbations.

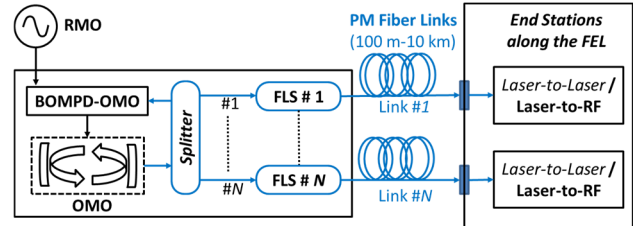


Figure 1: Layout of timing distribution system as deployed in [5]. RMO: RF master oscillator; OMO: optical master oscillator; FLS: fiber link stabilization; BOMPD: balanced optical-microwave phase detector.

Here, we focus on two of the most common techniques used for laser-to-RF synthesis in FEL facilities: (i) RF signal extraction from the optical pulse train using photodiodes, and (ii) VCO-to-laser synchronization. First, we describe the implementation and the test setups. Then, we present measurements of both the absolute phase noise of the generated microwave signal and its relative timing jitter with respect to the mode-locked laser, together with the relative timing drift.

DIRECT PHOTODETECTION

The simplest approach to synthesize microwave signals from an optical source coming from mode-locked lasers is by using a fast response photodiode. Here the optical pulse train envelope is detected by the photodiode and then transduced into an electrical current pulse train, which is limited by the photodiodes response (i.e. bandwidth). A further limitation is the so-called AM-PM conversion which translates amplitude noise, i.e. power fluctuations, from the optical pulse train, into phase noise in the electrical signal [6,7]. Figure 2 illustrates the optical pulse train and the electrical current pulse train after photodetection in time and frequency domain.

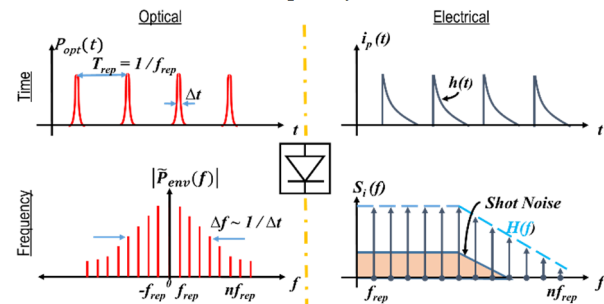


Figure 2: Optical pulse train transduced by fast photodetector in the time and frequency domain.

[†] erwin.cano.vargas@cfel.de

Despite its drawbacks, we wanted to measure the limits of this synthesis technique and its potential for timing stability demanding applications. Following this idea, we built a setup, as depicted in Figure 3. Here, the fast photodiode is followed by a high Q bandpass filter, whose central frequency matches to a harmonic of the repetition frequency of the pulse train, so that a pure sinusoidal signal is obtained. This signal ultimately inherits the timing stability from the optical pulse train, minus the aforementioned disturbances. The bandpass filter is followed by a carefully selected preamplifier stage, which ensures a high gain and minimum added phase noise. The setup is also built in a sealed box to mitigate the influence of environmental factors.

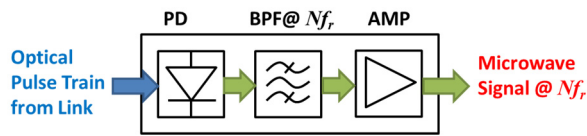


Figure 3: Direct photodetection microwave synthesis setup.

The optical master oscillator (OMO) has a repetition frequency of 238 MHz. The output of the OMO is coupled into a fiber patch cord (i.e. few meters long) and fed to the setup, as shown in Figure 1. The synthesized microwave is then connected to a signal source analyzer (SSA), calibrated for measurements at 5.712 GHz which is the transmitted signal frequency of the band-pass filter. This measurement gives the single-side-band phase noise and absolute timing jitter as shown in Figure 4. An absolute timing jitter of 55.6 fs RMS is obtained integrated from 100 to 100 MHz.

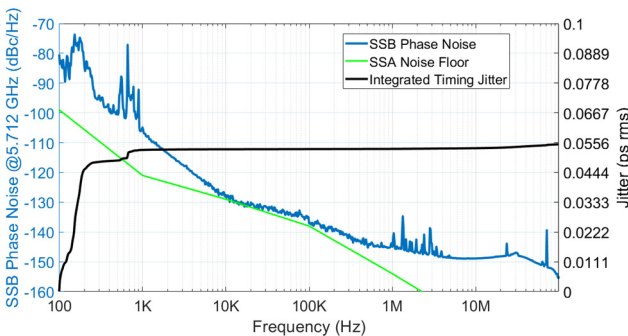


Figure 4: SSB Phase Noise for synthesized microwave from photodetection, Signal Source Analyzer (SSA) noise floor and absolute integrated timing jitter.

VCO-TO- LASER SYNCHRONIZATION

The second technique is the synthesis of a microwave signal of a VCO synchronized to the the optical pulse train by using an opto-electronic phase-locked loop (PLL).

A basic description of this setup is shown in Figure 5. Here, a PLL system is implemented on a standalone board which performs the phase frequency detection and the reverse loop division digitally.

The reference signal is obtained from the optical pulse train using direct photodetection synthesis at the repetition frequency. Then, the microwave signal provided by the VCO is locked to that reference by designing the appropriate integrator (loop filter) in the PLL.

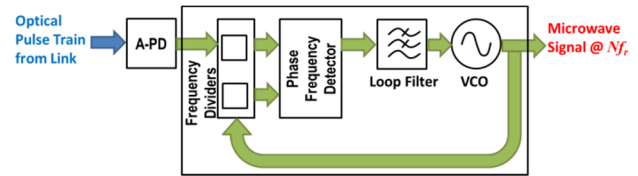


Figure 5: Digital VCO synchronization scheme for microwave synthesis.

As with previous technique, the single side band phase noise and absolute time jitter was measured by calibrating the SSA at 2.856 GHz to match the VCOs frequency. Figure 6 shows the SSB spectrum and the timing jitter integration, which is 90 fs from 100 to 100 MHz.

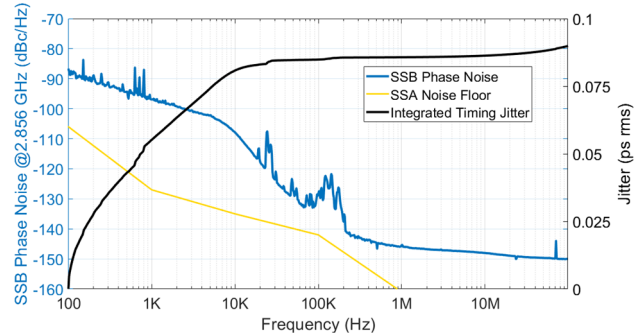


Figure 6: SSB phase noise for locked VCO, signal source analyzer (SSA) noise floor and absolute integrated timing jitter.

RELATIVE TIMING JITTER AND DRIFT MEASUREMENT

Having the two setups ready, we proceed with the characterization of relative timing jitter and drift between the generated microwave and the OMO. Figure 7 shows the experimental setup. Here, a BOMPD is used as a free-running phase detector to compare the optical pulse train from the OMO directly with the microwave synthesis technique under test..

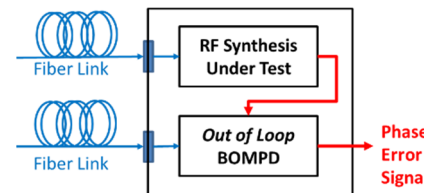


Figure 7: Measurement setup for relative timing jitter between the OMO and the RF synthesized signal using BOMPD as out-of-loop phase detector.

Figure 8 and Figure 9 show both the long term and short term stability measurement results for the direct microwave synthesis and the synchronized VCO, respectively.

The long term measurement is performed by tracking the phase error signal of the BOMPD and measuring its drift. The timing drift over a period of 8 hours was measured for both setups, obtaining 167 fs for direct synthesis and 645 fs for the synchronized VCO. Here, a direct correlation with the environmental fluctuations in the measurement laboratory was observed, which can be mitigated by further temperature control.

The short term stability measurement is calculated from the baseband analysis of the error signal obtained from the BOMPD, taking into account the noise floor of the detector. Here, we obtain an integrated timing jitter of 17 fs for the direct synthesis and 67 fs for the synchronized VCO.

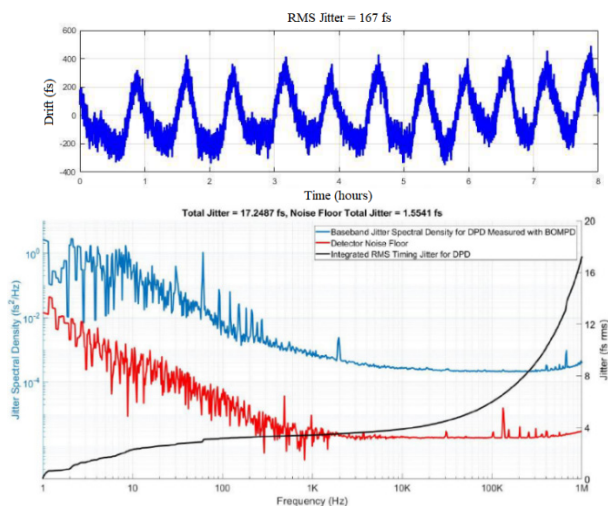


Figure 8: Timing stability of direct photodetected synthesis (a) Long term stability (b) Short term relative jitter given by Jitter Spectral Density.

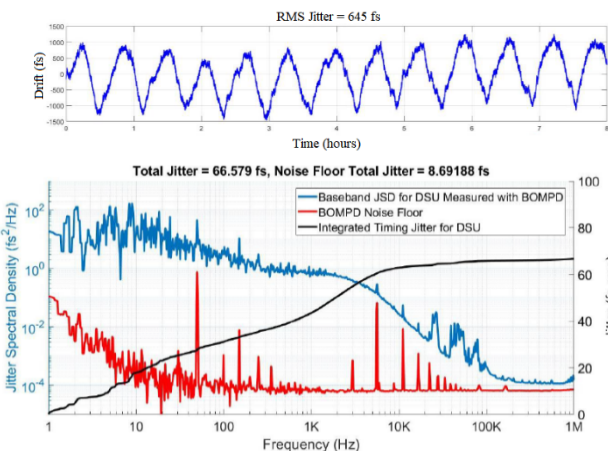


Figure 9: Timing stability of synchronized VCO (a) Long term stability (b) Short term relative jitter given by Jitter Spectral Density.

CONCLUSION

Two synthesis methods were implemented and their timing performance was measured as summarized in Table 1. The absolute timing jitter measured with the SSA gives similar synchronization stability and is limited by

the noise of the SSA. The relative timing jitter measurement with an out-of-loop BOMPD shows that increased stability of the microwave signal synthesis using direct photodetection. The high frequency noise sources are mainly limited by the inherent noise of the VCO and the AM-PM conversion in the photodiode. The high frequency performance could be easily improved to the few-femtosecond regime by employing higher quality VCOs and BOMPDs as RF synthesizer. The main timing drift contribution is due to the susceptibility of fiber and electronic components to the environmental fluctuations. The long-term performance of the remote microwave synchronization could be also improved by more comprehensive temperature/humidity insulation.

Table 1: Summary Timing Stability Measurement Results

	Photodetection Synthesis	VCO Synchron- ization
Abs. Timing Jitter @100 – 100 MHz	56 fs	90 fs
Relative Timing Jitter	17 fs	67 fs
Long Term Drift RMS (8 hrs)	168 fs	645 fs

REFERENCES

- [1] M. Xin, K. Shafak, and F. X. Kärtner, “Ultra-precise timing and synchronization for large-scale scientific instruments”, *Optica*, vol. 5, issue 12, pp. 1564-1578, 2018. doi:10.1364/OPTICA.5.001564
- [2] K. Shafak *et al.*, “Large-Scale Turnkey Timing Distribution System for New Generation Photon Science Facilities”, in *Proc. 38th Int. Free Electron Laser Conf. (FEL'17)*, Santa Fe, NM, USA, Aug. 2017, pp. 485-487. doi:10.18429/JACoW-FEL2017-WEP030
- [3] M. Xin, K. Shafak *et al.*, “Attosecond precision multi-kilometer laser microwave network”, *Light Sci. Appl.*, vol. 6, no. e16187, 2017. doi:10.1038/lsa.2016.187
- [4] M. Xin, K. Shafak, F. X. Kärtner *et al.*, “Breaking the femto-second barrier in multi-km timing synchronization systems”, *IEEE J. Sel. Top. Quantum Electron.*, vol. 23, no. 3, p. 8800212, 2017. doi:10.1109/JSTQE.2016.2614676
- [5] H. P. Cheng, K. Shafak, E. Cano *et al.*, “Commissioning of a Fully-Automated, Pulsed Optical Timing Distribution System at Dalian Coherent Light Source”, *2018 Conference on Lasers and Electro-Optics (CLEO)*, San Jose, CA, 2018, pp. 1-2. doi:10.1364/CLEO_AT.2018.JW2A.138
- [6] J. Kim, F. X. Kärtner, “Sub femtosecond-Drift Microwave Signal Synthesis from Femtosecond Mode-Locked Lasers”. in *Conference on Lasers and Electro-Optics (CLEO) and Quantum Electronics and Laser Science Conference (QELS)*, San Jose, CA, USA, 2010, paper CTuDD4. doi:10.1364/CLEO.2010.CTuDD4
- [7] F. Ludwig, B. Lorbeer, H. Schlarb, A. Winter, “Noise and Drift Characterization of Direct Laser to RF Conversion Scheme for the Laser based Synchronization System for FLASH at DESY”, in *Proc. PAC'07*, Albuquerque, NM, USA, Jun. 2007, paper MOPAN017, pp. 182-184.

A PolariX TDS FOR THE FLASH2 BEAMLINE

F. Christie^{†,*}, J. Rönsch-Schulenburg, M. Vogt
 Deutsches Elektronen-Synchrotron, Hamburg, Germany
[†]also at Universität Hamburg, Hamburg, Germany

Abstract

Transverse Deflecting RF-Structures (TDS) are successfully used for longitudinal diagnostic purposes at many Free-Electron Lasers (FEL) (LCLS, FLASH, EU-XFEL, FERMI). Moreover, by installing a TDS downstream of the FEL undulators and placing the measurement screen in a dispersive section, the temporal photon pulse structure can be estimated, as was demonstrated at LCLS and sFLASH. Here we describe the installation of a variable polarization X-band structure (PolariX TDS) downstream of the FLASH2 undulators. The installation of such a TDS enables longitudinal phase space measurements and photon pulse reconstructions, as well as slice emittance measurements in both planes using the same cavity due to the unique variable polarization of the PolariX TDS.¹

INTRODUCTION

The lasing process in a free-electron laser (FEL) is dominated by the longitudinal parameters of the electron bunches. Hence, the measurement of their longitudinal properties is of utmost importance to control the lasing process. This can, for example, be achieved by means of a Transverse Deflecting Structure (TDS). With this device it is possible to relate the longitudinal coordinate of an electron beam to a transverse one, which then can be imaged using a screen. Additionally, an energy spectrometer, such as a dipole magnet, can be used to relate the beam energy to the other transverse coordinate by deflecting the beam in the plane transverse to the streaking plane of the TDS. By combining both methods, the longitudinal phase space density of the electron bunches can be mapped onto a screen [2]. Additionally, the slice emittance can be measured using a TDS [3, 4]. Such a measurement station is planned as an essential part of the Free-Electron Laser in Hamburg (FLASH) midterm refurbishment and the FLASH2020+ upgrade plans [5]. It will be installed downstream of the FLASH2 undulators to ensure high beam-qualities at FLASH2 as well as brilliant and high-quality photon pulses. The measurement station comprises a novel TDS with a variable polarization feature (PolariX TDS²) [6–8] and will be used as an indispensable diagnostic tool for short electron bunches and photon pulses at FLASH2.

In the following, we will describe the optics for longitudinal phase space density measurements and slice emittance measurements in both planes. In addition, tracking simulations for longitudinal phase space measurements as well as

photon pulse reconstructions and slice emittance measurements are presented.

LAYOUT OF THE TDS DIAGNOSTIC SECTION AT FLASH2

The TDS diagnostic section will be situated directly downstream of the FLASH2 undulators. It will feature two PolariX TDSs [8], which are X-band transverse deflecting structures ($f_{\text{RF}} \approx 12$ GHz) with variable polarization yielding arbitrary streaking directions. A technical drawing of the two cavity supports is displayed in Fig. 1. Additionally, a kicker to deflect the beam onto an off-axis screen station will be installed.

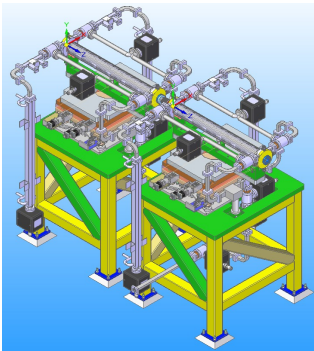


Figure 1: Technical drawing of the supports for the two PolariX TDSs at FLASH2. Courtesy of M. Föse.

The new TDSs at FLASH2 will share their radio frequency (RF) station with the FLASH Forward [9] TDS as both experiments require longitudinal beam diagnostics [7]. The waveguide distribution and RF components can be seen in Fig. 2. The RF source is connected via an RF switch to both experiments. This installation scheme prohibits simultaneous operation, but requires only a single RF station and therefore reduces costs and saves space. The RF source comprises a 6 MW Toshiba E37113A klystron with an Ampegon Type μ , S-Class modulator [8] and is similar to the CERN Xbox3 design [10]. To minimize the attenuation in the waveguides and achieve high deflecting powers, the klystron will be placed as close to the FLASH2 TDSs as possible. Therefore, the klystron will be installed inside the tunnel while the radiation sensitive modulator and low-level RF-rack are placed outside. The klystron and the modulator are connected by pulse cables of 15 m length. The total waveguide length from the klystron to the cavities is about 5 m. In the final stage, an X-band version of the PSI C-band barrel open cavity (BOC) [11] compressor will be installed between the TDSs and the klystron, approximately raising

* florian.christie@desy.de

¹ This article contains excerpts from [1].

² Polarizable X-band TDS

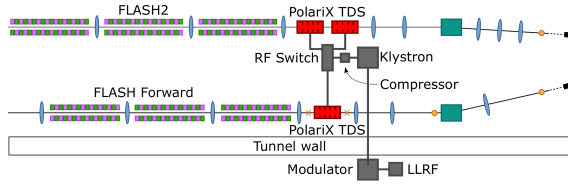


Figure 2: Shared RF system between FLASH2 and FLASH Forward. Courtesy of P. González Caminal.

the input power for the TDSs by a factor of four. The maximum achievable deflecting voltage will then be in the order of 40 MV.

ACCELERATOR OPTICS

The accelerator optics for the longitudinal phase space density measurements can be found in [1]. They are similar to those published in [12]. Temporal resolutions R_t in the order of 1 fs and energy resolutions R_δ in the order of $2 \cdot 10^{-4}$ are expected for low emittance bunches.

Furthermore, the PolariX TDS comprises a variable polarization feature, which allows slice emittance measurements in both transverse planes using the same TDS. This is a unique feature of the PolariX TDS. To fully avail of this feature some design limitations of the beam line have to be considered. As only one screen station is available for the slice emittance measurements, a quadrupole scan has to be performed. Additionally, the screen station should be placed at a point of vanishing M_{16} . Due to space limitations at FLASH2, the screen station can only be placed in the horizontally dispersive section. As a result, the optics have to be matched to achieve $\eta_x = 0$ at the screen

For the optics matching, all quadrupoles between the last FLASH2 SASE undulator and the screen station are used. The emittance reconstruction point is directly upstream of the first quadrupole at s_0 . To increase the accuracy of the measurement, seven different optics covering a total phase advance of $\Delta\Psi_{v,\text{total}} = \frac{3}{5}\pi$ in the slice emittance measurement plane v between the screen and the reconstruction point are matched. In the streak direction a high longitudinal resolution is required. In the horizontal plane, temporal resolutions of 3.8 fs to 4.9 fs are achieved for the seven different optics, whereas in the vertical plane all resolutions are in the order of 4 fs.

TRACKING SIMULATIONS

Various tracking simulations in elegant [13] were carried out to assess the performance of the PolariX TDSs at FLASH2 regarding the longitudinal phase space density measurement, the photon pulse reconstruction, and the slice emittance measurement in both planes. Examples are presented in the following, a much more detailed analysis is found in [1].

Longitudinal Phase Space Density Measurement

For the longitudinal phase space density measurement, a 20 pC bunch [14] is tracked through the TDS at a deflecting voltage of 34 MV and through the downstream beam line.

Figure 3 shows the result of tracking simulations for bunches with a charge of 20 pC [14] and a bunch length of 13.8 fs rms. The mean energy is 1 GeV and its longitudinal phase space density at the undulator exit can be seen in Fig. 3(a). As this bunch is very short, the temporal resolution plays a crucial role. At this deflecting voltage of 34 MV the energy measurement is dominated by the induced energy spread. The longitudinal phase space densities at the TDS exit are shown in Fig. 3(b). The induced energy spread at the TDS exit is clearly visible in comparison to the undulator exit. Additionally, even for a resolutions of 0.8 fs differences between the longitudinal phase space density at the TDS exit and the reconstruction at the screen are visible, c.f. Fig. 3(c). In the core part of the bunch, i.e. between -10 fs and 10 fs, the longitudinal resolution limits the resolving capacity of the measurement. The measurement is blurred when compared to the longitudinal phase space density at the TDS exit.

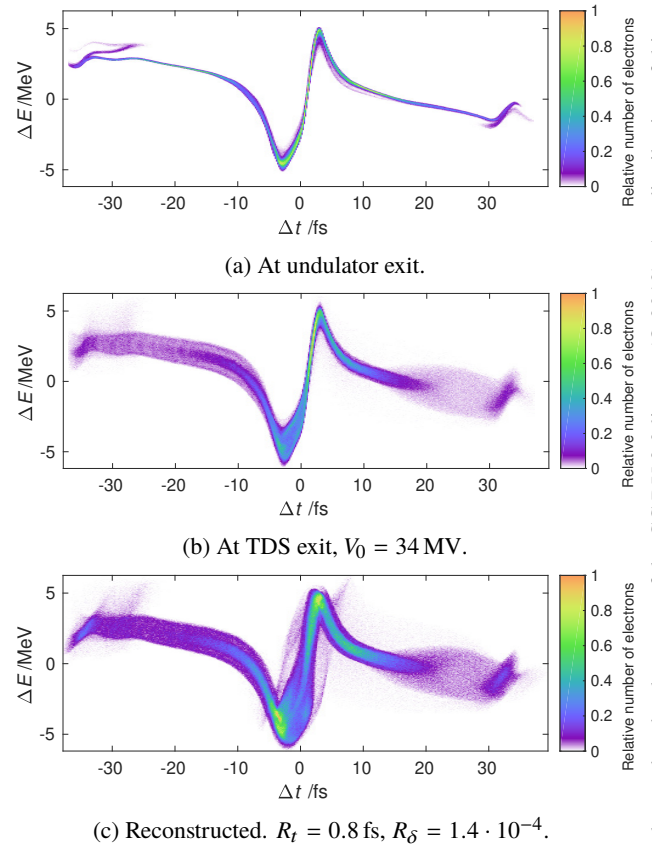


Figure 3: Longitudinal phase space density reconstruction using a 20 pC bunch [14] as input.

Photon Pulse Reconstruction

The FEL process is simulated using Genesis 1.3 [15]. The particle distribution at the end of the exponential regime is

then extracted and used to perform the photon pulse reconstruction following [16]. A lasing bunch (lasing-on) and a bunch where the lasing process is suppressed (lasing-off) are tracked through the TDS and onto the beam screen. The screen image is then analyzed and the photon pulse power P in each slice t_i is calculated from the energy loss in each slice [16]

$$P(t_i) = \Delta E(t_i) \cdot \frac{I(t_i)}{e}, \quad (1)$$

where $\Delta E(t_i) = E_{\text{on}}(t_i) - E_{\text{off}}(t_i)$ is the energy loss, E_{on} and E_{off} are the mean energy for the lasing-on and lasing-off bunch, respectively, and I is the current.

Gaussian bunches with a length of 100 fs and 23 fs at beam energies of 1200 MeV and 700 MeV, respectively, are tracked. The corresponding wavelengths are 6.6 nm and 19.4 nm, respectively.

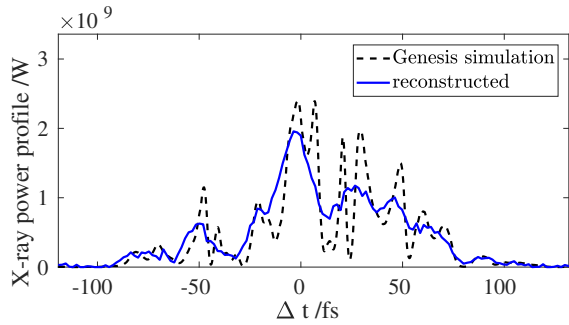


Figure 4: Photon pulse reconstruction of a Gaussian bunch with a bunch length of 100 fs rms at an energy of 1200 MeV using a deflecting voltage of 20 MV. The wavelength is 6.6 nm.

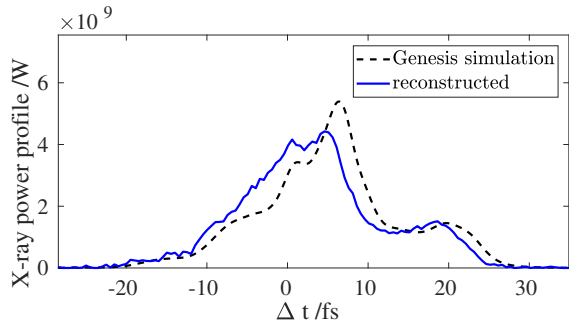


Figure 5: Photon pulse reconstruction of a Gaussian bunch with a bunch length of 23 fs rms at an energy of 700 MeV using a deflecting voltage of 34 MV. The wavelength is 19.4 nm.

For the reconstruction of the 100 fs rms bunch, c.f. Fig. 4, the influence of the limited temporal resolution is visible, although the effect is rather small. Most of the SASE spikes are still visible in the reconstruction, only the separation of spikes that are very close to one another is blurred.

The reconstruction of the shorter pulse of 23 fs rms, c.f. Fig. 5, closely resembles the actual photon pulse. It shows a large single SASE spike with smaller side peaks.

Slice Emittance Measurement

The slice emittance measurement at FLASH2 is performed using a quadrupole scan, the tracking simulations were carried out using elegant [13]. The input distributions are tracked from the emittance reconstruction point directly upstream of the first quadrupole used for the slice emittance measurement to the screen using all of the seven different optics for each transverse plane. The deflecting plane of the TDSs is set to the plane perpendicular to the plane in which the slice emittance is reconstructed. The screen image of each individual measurement is then divided into slices with a fixed width depending of the longitudinal resolution R_L . The central slice is defined as the slice comprising the mean of the distribution at its center [17]. For each individual slice the “rms beam size” is calculated as the square root of the variance of the beam profile [17]. The slices of the tracked bunches are then aligned and for each slice the emittance is calculated according to [18, 19].

The slice emittance reconstruction for a short bunch with a charge of 20 pC is shown in Fig. 6. It reveals, that for the regions of $\Delta t \leq -10$ fs and $\Delta t \geq 10$ fs the reconstructed slice emittances in both planes match very nicely to the original one. Yet, in the region of the current spike, i.e. for -10 fs $< \Delta t < 10$ fs the influence of the limited resolution of this measurement is visible. Particles from adjacent slices mix in the reconstruction and the reconstructed value for the slice emittance is higher than the original one.

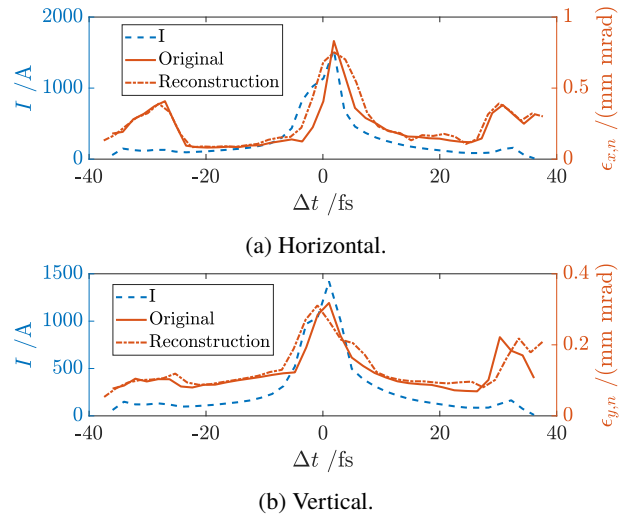


Figure 6: Vertical slice emittance measurement of a 20 pC bunch [14]. The longitudinal resolution is 2.0 fs, the TDS voltage is 34 MV.

CONCLUSION

This paper and the more detailed work in [1] show, that with the installation of two PolariX TDSs downstream of the FLASH2 undulator section meaningful longitudinal phase space density measurements, photon pulse reconstructions as well as slice emittance measurements in both transverse planes can be performed.

REFERENCES

- [1] F. Christie, "Generation of Ultra-Short Electron Bunches and FEL Pulses and Characterization of Their Longitudinal Properties at FLASH2," to be published, PhD thesis, Universität Hamburg, 2019.
- [2] P. Emma, J. Frisch, and P. Krejcik, "A Transverse RF Deflecting Structure for Bunch Length and Phase Space Diagnostics," SLAC National Accelerator Laboratory, California, Tech. Rep. LCLS-TN-00-12, 2000.
- [3] P. Craievich, R. Ischebeck, F. Löhl, G. Orlandi, and E. Prat, "Transverse Deflecting Structures for Bunch Length and Slice Emittance Measurements on SwissFEL," in *Proc. FEL'13*, New York, NY, USA, 2013, pp. 236–241.
- [4] E. Prat *et al.*, "Slice Emittance Optimization at the SwissFEL Injector Test Facility," in *Proc. FEL'13*, New York, NY, USA, 2013, pp. 200–204.
- [5] M. Vogt, K. Honkavaara, J. Rönsch-Schulenburg, S. Schreiber, and J. Zemella, "Upgrade Plans for FLASH for the Years After 2020," in *Proc. IPAC'19*, Melbourne, Australia, 2019, pp. 1748–1751. doi: 10.18429/JACoW-IPAC2019-TUPRB027.
- [6] A. Grudiev, "Design of Compact High Power RF Components at X-Band," CERN, Geneva, Switzerland, CLIC - Note 1067, 2016.
- [7] B. Marchetti *et al.*, "X-Band TDS Project," in *Proc. IPAC2017*, Copenhagen, Denmark, 2017, pp. 184–187, ISBN: 978-3-95450-182-3. doi: 10.18429/JACoW-IPAC2017-MOPAB044.
- [8] P. Craievich *et al.*, "Status of the Polarix-TDS Project," in *Proc. IPAC'18*, Vancouver, BC, Canada, 2018, pp. 3808–3811. doi: 10.18429/JACoW-IPAC2018-THPAL068.
- [9] A. Aschikhin *et al.*, "The FLASHForward facility at DESY," *Nuclear Instruments and Methods in Physics Research Section A: Accelerators, Spectrometers, Detectors and Associated Equipment*, vol. 806, pp. 175–183, 2016. doi: 10.1016/j.nima.2015.10.005.
- [10] N. Catalán Lasheras *et al.*, "Commissioning of XBox-3: A very high capacity X-band test stand," in *Proc. LINAC'16*, East Lansing, MI, USA, 2016, pp. 568–571. doi: 10.18429/JACoW-LINAC2016-TUPLR047.
- [11] R. Zennaro, M. Bopp, A. Citterio, R. Reiser, and T. Stäpf, "C-band RF Pulse Compressor for SwissFEL," in *Proc. IPAC'13*, Shanghai, China, 2013, pp. 2827–2829.
- [12] F. Christie, J. Rönsch-Schulenburg, S. Schreiber, and M. Vogt, "Generation of Ultra-Short Electron Bunches and FEL Pulses and Characterization of Their Longitudinal Properties at FLASH2," in *Proc. IPAC'17*, Copenhagen, Denmark, 2017, pp. 2600–2603. doi: 10.18429/JACoW-IPAC2017-WEPAB017.
- [13] M. Borland, "elegant: A Flexible SDDS-Compliant Code for Accelerator Simulation," *Advanced Photon Source LS-287*, Sep. 2000.
- [14] I. Zagorodnov, *FLASH Beam Dynamics Simulations*, www.desy.de/fe1-beam/s2e/flash.html, 2013.
- [15] S. Reiche, "Numerical Studies for a Single Pass High Gain Free-Electron Laser," PhD thesis, Universität Hamburg, Hamburg, Germany, 1999.
- [16] C. Behrens *et al.*, "Few-femtosecond time-resolved measurements of X-ray free-electron lasers," *Nature Communications*, vol. 5, p. 3762, 2014. doi: 10.1038/ncomms4762.
- [17] M. Yan, "Online diagnostics of time-resolved electron beam properties with femtosecond resolution for X-ray FELs," PhD thesis, Universität Hamburg, 2015.
- [18] J. Zemella, T. Hellert, M. Scholz, and M. Vogt, "Measurements of the Optical Functions at FLASH," in *Proc. IPAC'14*, Dresden, Germany, 2014, pp. 1141–1143. doi: 10.18429/JACoW-IPAC2014-TUPRO050.
- [19] J. Zemella and M. Vogt, "Progress in FLASH Optics Consolidation," in *Proc. IPAC'17*, Copenhagen, Denmark, 2017, pp. 211–214. doi: 10.18429/JACoW-IPAC2017-MOPAB051.

USAGE OF THE MicroTCA.4 ELECTRONICS PLATFORM FOR FEMTO-SECOND SYNCHRONIZATION SYSTEMS

M. Felber[#], E. P. Felber, M. Fenner, T. Kozak, T. Lamb, J. Mueller, K. Przygoda, H. Schlarb, S. Schulz, C. Sydlo, M. Titberidze, F. Zummack, DESY, Hamburg, Germany

Abstract

At the European XFEL and FLASH at DESY optical synchronization systems are installed providing sub-10 femtosecond electron bunch arrival time stability and laser oscillator synchronization to carry out time-resolved pump-probe experiments with high precision. The synchronization system supplies critical RF stations with short- and long-term phase-stable reference signals for precise RF field detection and control while bunch arrival times are processed in beam-based feedbacks to further time-stabilize the FEL pulses. Experimental lasers are tightly locked to the optical reference using balanced optical cross-correlation. In this paper, we describe the electronic hardware for supervision and real-time control of the optical synchronization system. It comprises various MicroTCA.4 modules including fast digitizers, FPGA processor boards, and drivers for piezos and stepper-motors. Advantages of the system are the high-level of integration, state-of-the-art performance, flexibility, and remote maintainability.

INTRODUCING MicroTCA.4

MicroTCA is an electronic framework for signal processing derived from the Advanced Telecommunication Computing Architecture (ATCA). MicroTCA.4 was released as an official standard by the PCI Industrial Manufacturers Group (PICMG) in 2011 and is supported by the xTCA for physics group, a network of physics research institutes and electronics manufacturers. Opposed to other xTCA standards it is also designed for analog processing of low-noise signals. Its main improvements are enhanced rear I/O connectivity and provisions for precision timing. MicroTCA.4 has inherited many of the advantages of ATCA including capabilities for remote monitoring, remote maintenance, hot-swap of components, and the option to duplicate critical components, making the standard highly modular, reliable and flexible. It also made the outstanding digital signal processing performance of ATCA systems more affordable and less demanding in terms of space requirements and energy consumption.

MicroTCA.4 System Architecture

Fundamental components are the chassis which is available in different form factors and sizes, the optionally redundant power supply, an optionally redundant crate management controller (MCH), and CPU with hard drive [1].

For user applications specific analog and digital processing cards are used. From the front, Advanced

Mezzanine Cards (AMC) which can also be used on ATCA carrier cards are inserted to the crate. There are various connections on the backplane which provide e.g. Gigabit Ethernet and PCI Express links between the slots and the MCH, dedicated clock and trigger distribution lines, and point to point links between the slots for fast real time communication between the cards. Additionally, there is the possibility to insert cards from the rear of the crate, so-called Rear Transition Modules (RTM) which connect to the according AMC board via the Zone 3 connector. This connection provides 60 differential pairs for analog or digital signals, which are defined in the standard [1]. Some cards incorporate connectors for additional industrial standard piggy back boards like FPGA Mezzanine Cards (FMC) or IndustryPack (IP) modules.

MicroTCA.4 AT DESY

Meanwhile, for basically all accelerators at DESY the technical groups decided to use the MicroTCA.4 standard. For example at the European XFEL and FLASH this involves the LLRF field control [2], the timing and machine protection systems, standard diagnostics like beam position monitors [3] and camera readouts, and the optical synchronization system [4]. In the course of the developments required for fulfilling the demanding tasks, the standard was further adapted and improved.

In order to facilitate the development of new boards for extending the portfolio of applications and to ensure the availability of spare parts, DESY took the initiative for a better establishment of the MicroTCA.4 standard in industry. With financial support from the Helmholtz Association and industry partners the Helmholtz Validation Fund (HVF) was established in 2012.

Therefore, most board designs are licensed to various industry partners who offer those components as ‘commercial of the shelf’ products. This way it is easy for other institutes and companies to make use of the sophisticated designs (e.g. high speed digital or low noise analog cards) without the need for own developments or additional agreements.

As successor of the HVF the MicroTCA Technology Lab [1] was founded at DESY to help external partners with their MicroTCA related projects. A competent team of engineers offers support for all aspects like hardware and firmware development, or the implementation and commissioning of MicroTCA systems at the facility.

[#]matthias.felber@desy.de

OVERVIEW OF MicroTCA.4 MODULES USED IN THE SYNCHRONIZATION SYSTEM

The hardware modules required for the different tasks in the optical synchronization systems like signal detection, sampling, processing, and actuating are mostly generic and applicable in different setups and configurations. Only for a few very specific tasks individual boards were designed.

In this chapter most of the used modules are introduced with a short description.

SIS8300L2 Versatile FPGA (Virtex 6) AMC board with 10 channel 125 MSPS 16 bit digitizers and 2 fast DACs, available at Struck Innovative Systeme GmbH [5].

FMC25 Versatile FPGA (Virtex 5) AMC board for data processing and FMC carrier with two high pin count FMC slots. The board was developed at DESY and licensed to the company CAEN ELS [6].

FMC20 Low-cost FPGA (Spartan6) AMC board for interfacing with actuator modules and FMC carrier with two FMC slots. The board was developed at DESY and licensed to the company CAEN ELS [6].

AD84 Generic analog IO RTM board with 8 channel 10 MSPS 16 bit digitizers and 4 channel DACs. The board was developed at DESY, not yet licensed to an industry partner [1].

DWC8300 10 channel low-noise down converter RTM board (0.7 GHz – 4 GHz). The board was developed at DESY and licensed to the company Struck GmbH [6].

PZT4 Generic 4 channel piezo driver and piezo sensor RTM board with switchable output range (up to ± 80 V), internal DAC or external input, and internal or external power supply [7]. The board was developed at DESY and licensed to the company Piezotechnics GmbH [8].

MD22 2 channel stepper motor driver FMC board with end-switch and encoder readout. The board is capable of driving up to 1.8 A coil current and supports 256 micro steps. It was developed at DESY and is licensed to the company CAEN ELS [6].

AD16 Generic ADC FMC board with 16 channels up to 200 kSPS and 18 bits resolution. The board was developed at DESY and is not yet licensed to an industry partner [1].

UNIO Versatile, general purpose, low-cost IO FMC board with 48 IO pins. Each pin can be assigned to digital IO, gnd or alternate function like ADC, DAC, power supply, or UART (12 V) via a CPLD. The board was developed at DESY, not yet licensed to an industry partner [1].

SFP4 Generic 2 or 4 channel SFP+ GbE or fiber transmission FMC board. Board was developed at DESY and licensed to the company CAEN ELS [6].

LASY RTM board under development at DESY especially for laser synchronization purposes. Besides down-converter channels with two-tone calibration capabilities it incorporates many laser specific inputs and features.

TOPOLOGY OF THE SYSTEMS

Laser Oscillator Synchronization Electronics

An RF signal (1.3 GHz + laser oscillator repetition rate) generated from the laser pulse train is down-converted on a DWC8300 (later on a LASY board) to an intermediate frequency which is digitized on an SIS8300L2 board [9]. Additionally, the baseband signals from a balanced optical cross-correlator (OXC) [10] or electro-optical detection method (MZM Setup) [11] are fed to other ADC channels on that digitizer AMC. The digital signals contain the phase or timing jitter information with femtosecond precision. The feedback controller output is digitally transferred to the next slot in the crate where it is received by an FMC20 board. From here a PZT4 is addressed to drive the piezo(s) in the laser oscillator cavity. If the required tuning drive exceeds the piezo range a coarse tuning step has to be performed. Depending on the laser oscillator architecture, this is either a temperature step initiated via an UNIO board or a delay stage step driven either by a stepper motor via a MD22 or a piezo motor via another PZT4 channel.

Additional inputs of the down converter and later the LASY are used for bucket detection to set the correct absolute timing and for some other required monitoring and control signals.

As the PZT4 is capable of driving more than one piezo also laser oscillators with two piezos and/or two lasers oscillators can be synchronized with no additional hardware.

Fiber Link Stabilization Electronics

For the stabilization of the numerous up to few km long synchronization fiber links e.g. in the European XFEL [4] MicroTCA.4 offers a very compact and efficient solution because four links can be stabilized using only two slots in the crate. The heart of the link stabilization unit (LSU) is an OXC whose signal is digitized on an AD84 board (2 ADC channels per link). The processing is done on an FMC25 board which computes the feedback controller output and, similar to the laser application, transmits the required actuator stroke to an FMC20 board. Again, this board addresses the piezo driver in the rear which drives a piezo-based fiber stretcher to compensate for the detected timing change in the link fiber by stretching a piece of it. Also here a delay stage is required for coarse tuning when the piezo stretcher reaches its limit. Therefore, also here, a MD22 is used. For a complete set of four LSUs all eight ADC inputs from the AD84, all four piezo driver outputs from the PZT4, and all four motor drivers of two MD22 FMCs mounted on the FMC20 are used.

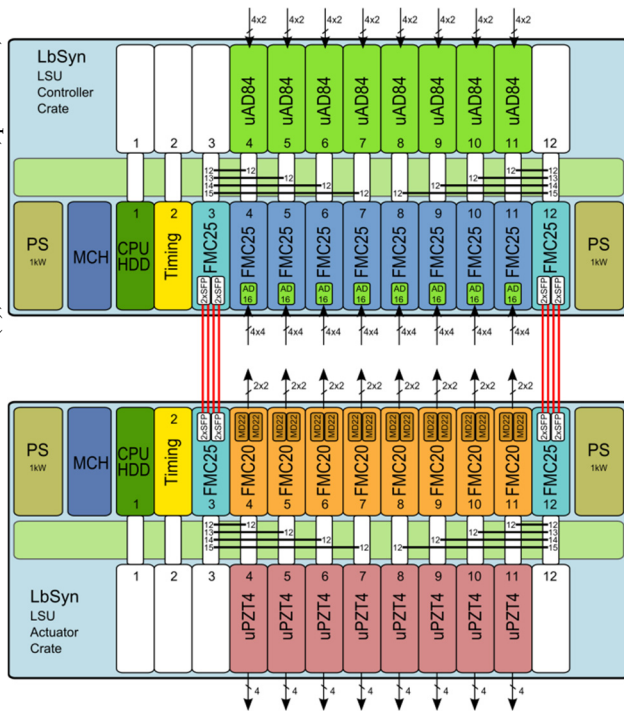


Figure 1: MicroTCA.4 setup for controlling up to 32 Link Stabilization Units.

Additionally, the AD16 FMC mounted on the FMC25 carrier collects slow monitor signals like optical power levels and backup phase detector signals. Four slow ADC channels are available and used for one LSU, again fitting perfectly to the 16 channel ADC when controlling and monitoring four LSUs simultaneously.

In the baseline design of the European XFEL 23 LSUs are foreseen with the possibility for upgrades to more units. Despite the compact design this requires 12 board slots in the crate which are not available since in the 12-slot crate (biggest chassis available) two slots are used by an inevitable timing module and the obligatory CPU board. For this reason and to avoid distortions on the sensitive OXC detector signals by electromagnetic interference from the actuators (piezo = high voltage, stepper motor = sharp current spikes), the detector units comprised of AD84 and FMC25+AD16 are separated from the actuator unit comprised of FMC20+2xMD22 and PZT4 in a different crate. Figure 1 shows a schematic view of the complete setup ready for controlling max. 32 LSUs. The communication between the detector and the actuator crate is done via FMC25 concentrator hubs, collecting the signals from up to four FMC25 controller boards and sending them via SFP4 modules to the corresponding SFP4s on the FMC25 receiver boards. From here the signals are distributed again to the FMC20 boards driving the actuators. To minimize the latency the complete communication happens via low latency point-to-point links on the crate backplane and direct fiber connections between the two SFP4s.

CONCLUSION

The topology of MicroTCA.4 hardware modules used for signal detection, analog/digital processing and actuator driving in the optical synchronization systems was presented.

For example, at the European XFEL, a total number of 25 fiber link stabilization units are in 24/7 operation with this technique, reliably providing femtosecond stable reference signals to the accelerator and experiment lasers.

Up to date, a total number of about 50 different laser oscillators are synchronized at various facilities on the DESY campus and at partner institutes using the described hardware. Still, the demand for further setups is growing as new facilities or sub-systems are continuously being proposed, developed and implemented.

REFERENCES

- [1] MicroTCA, <https://techlab.desy.de>
- [2] J. Branlard *et al.*, “The European XFEL LLRF System”, in *Proc. 3rd Int. Particle Accelerator Conf. (IPAC'12)*, New Orleans, LA, USA, May 2012, paper MOOAC01, pp. 55-57.
- [3] F. Schmidt-Foehre, N. Baboi, G. Kuehn, B. Lorbeer, D. Noelle, and K. Wittenburg, “First Tests with the Self-triggered Mode of the New MicroTCA-based Low-charge Electronics for Button and Stripline BPMs at FLASH”, in *Proc. 5th Int. Particle Accelerator Conf. (IPAC'14)*, Dresden, Germany, Jun. 2014, pp. 3509-3511.
doi:10.18429/JACoW-IPAC2014-THPME117
- [4] S. Schulz *et al.*, “Few-Femtosecond Facility-Wide Synchronization of the European XFEL”, presented at the FEL'19, Hamburg, Germany, Aug. 2019, paper WEB04, this conference.
- [5] Struck Innovative Systeme, <https://www.struck.de>
- [6] CAENels, <https://www.caenels.com>
- [7] K. Przygoda *et al.*, “MTCA.4 Module for Cavity and Laser Piezo Operation”, in *Proc. 5th Int. Particle Accelerator Conf. (IPAC'14)*, Dresden, Germany, Jun. 2014, pp. 3140-3142. doi:10.18429/JACoW-IPAC2014-THPR0105
- [8] Piezotechnics, <https://www.piezotechnics.com>
- [9] M. Felber *et al.*, “Compact MTCA.4 Based Laser Synchronization”, in *Proc. 5th Int. Particle Accelerator Conf. (IPAC'14)*, Dresden, Germany, Jun. 2014, pp. 1823-1825. doi:10.18429/JACoW-IPAC2014-TUPRI107
- [10] J. M. Mueller *et al.*, “All-Optical Synchronization of Pulsed Laser Systems at FLASH and XFEL”, in *Proc. 6th Int. Particle Accelerator Conf. (IPAC'15)*, Richmond, VA, USA, May 2015, pp. 854-856.
doi:10.18429/JACoW-IPAC2015-MOPHA032
- [11] T. Lamb *et al.*, “Large-Scale Optical Synchronization System of the European XFEL with Femtosecond Precision”, in *Proc. 10th Int. Particle Accelerator Conf. (IPAC'19)*, Melbourne, Australia, May 2019, pp. 3835-3838.
doi:10.18429/JACoW-IPAC2019-THPRB018

MULTI-BEAMLINE OPERATION AT THE EUROPEAN XFEL

L. Fröhlich*, A. Aghababian, V. Balandin, B. Beutner, F. Brinker, W. Decking, N. Golubeva, O. Hensler, Y. Janik, R. Kammering, H. Kay, T. Limberg, S. Liu, D. Nölle, F. Obier, M. Omet, M. Scholz, T. Wamsat, T. Wilksen, J. Wortmann, DESY, Hamburg, Germany

Abstract

The European XFEL uses a unique beam distribution scheme to direct electron bunches to its three undulator lines. The accelerator delivers up to 600 microsecond long bunch trains, out of which parts or individual bunches can be selected for photon production in any of the FELs. This contribution gives a brief overview of the kicker-septum scheme facilitating this and highlights how even complex bunch patterns can easily be configured via the timing system.

INTRODUCTION

The European X-ray Free-Electron Laser (XFEL) [1–3] delivers bursts of hard and soft X-ray laser pulses with an unprecedented average power to its experimental end stations. The facility is driven by a superconducting 17.5 GeV pulsed linear accelerator operating at a repetition rate of 10 Hz. Each pulse provides stable accelerating conditions for $\sim 600 \mu\text{s}$, which allows the transport of up to 2700 electron bunches at the maximum rate of 4.5 MHz. Distributing these bunches to the three undulator lines in a reliable and easily configurable way is challenging and requires the interoperation of multiple hard- and software systems. In this paper, we first give an overview of the involved systems before we focus on the high-level software for configuring the bunch distribution.

BEAM DISTRIBUTION SCHEME

The accelerator uses a unique beam distribution scheme to guide the electron bunches to its three undulator lines. This scheme is illustrated in Fig. 1: After the linac, a system of up to 10 in-vacuum stripline kickers [4] can generate pulses of $\sim 30 \text{ ns}$ width, which is short enough to selectively kick individual bunches to the left. A Lambertson septum [5] then deflects these bunches upwards into the transfer line to the linac dump (*TLD*).

The unkicked electrons continue straight to the next system of kickers, which consists of 6 air coils that are mounted on the outside of a ceramic vacuum chamber [6] and deflect upwards. With rise and fall times on the order of $10 \mu\text{s}$, these *beam distribution* kickers are significantly slower than the previous set. This means that they provide better bunch-to-bunch stability, but they can only be used to influence an entire portion of the train, not individual bunches. Again, the kicked bunches are picked up by a Lambertson septum and deflected to the left and into the SASE2 undulator line which ends in the *T5D* dump.

Electrons that are influenced by neither kicker system take the straight path to SASE1 and SASE3 and finally end up

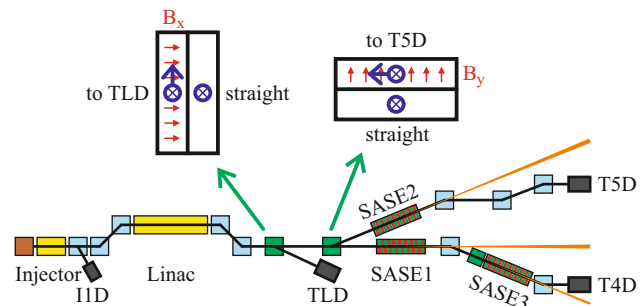


Figure 1: Schematic overview of the European XFEL. Accelerating structures are shown in orange and yellow, major bending magnets in blue, fast kicker systems in green, and beam dumps in dark gray. SASE1–3 are the undulator lines. The drawings above the beamline illustrate the operating direction of the magnetic Lambertson septa.

in the *T4D* dump. A summary of the optics design for the beam distribution system can be found in [7].

The photoinjector is driven by a single laser [8] that can produce a continuous train of pulses at 4.5 MHz, 1.1 MHz, or different rates. While the generated bunch train can be changed in length, it is currently not possible to leave gaps in it. Together with the characteristics of the two main kicker systems, this defines the boundary conditions for bunch distribution:

- From the gun up to the first *TLD* kicker, the beam forms a train of 0–2700 equidistant bunches.
- The *TLD* kickers can send an arbitrary number of the incoming bunches to the linac dump so that they never arrive in any undulator line. This can be decided individually for each bunch.
- Typically once per train the *distribution* kickers can change their state from on to off or vice versa so that a part of the remaining bunches is directed to SASE2 and the other part to SASE1/3. While these kickers are ramping, the incoming bunches must be sent to the linac dump by the *TLD* kickers.
- All of the settings above can be changed from pulse to pulse (i.e. at 10 Hz).

The common electron beamline shared by the SASE1 and SASE3 undulators adds another complication.

SASE1 and SASE3: Fresh Bunch Technique

Bunches destined for the hard X-ray undulator line SASE1 inevitably traverse the soft X-ray undulator line SASE3 and vice versa. This poses a serious problem for the concurrent

* lars.froehlich@desy.de

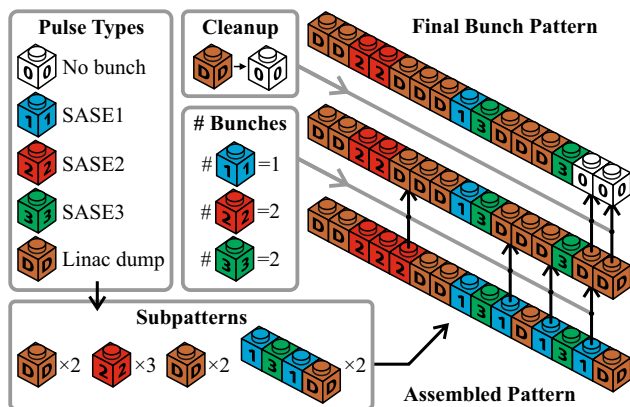


Figure 5: Illustration of the main steps for building a bunch pattern.

2 × 200 two hundred consecutive bunches for SASE2,

D × 120 one hundred and twenty bunches that are dumped during the falling edge of the beam distribution kicker,
131D × 140 one hundred and forty times the interleaved sequence “one bunch to SASE1, one to SASE3, one to SASE1, one to the linac dump”.

As laid out earlier, the native frequency of the timing pattern is 9 MHz. To simplify the definition of patterns for the typically used 4.5 MHz, 2.2 MHz (as in the example above), 1.1 MHz or even lower frequencies, the base frequency for the pattern can be selected. The effect is equivalent to inserting empty timing words (0) between the ones defined in the pattern.

Controlling the Number of Bunches

A pattern defines the maximum number of bunches that are available for each beamline in a single macropulse – in the example, 200 for SASE2, 280 for SASE1, and 140 for SASE3. Both the operators and the beamlines can reduce the number of bunches for a specific beamline through a simple substitution mechanism: If N bunches for SASE1 are desired, only the first N occurrences of 1 in the pattern are retained whereas all of the following ones are replaced by D, which means that these bunches are sent to the linac dump instead. Of course, also this mechanism is fully configurable. If desired, an additional *cleanup* step can automatically truncate unnecessary bunches from the end of the train (e.g. bunches that would only be accelerated to be discarded after the linac). Figure 5 illustrates the way bunch patterns are composed.

Adding Rhythm: Pattern Sequences

The mechanisms outlined above provide a multitude of ways for sharing the bunch train between the three beamlines. Sometimes, however, even more flexibility is required. The coexistence of SASE1 and SASE3 on the same electron beamline implies that the experiments observe spontaneous radiation from the bunches that are destined for the other beamline. This background is greatly reduced through collimation and can in most cases be ignored, but for a few

experiments it may nevertheless become intolerable. Mechanical choppers or similar slow methods for background suppression can help, but they require a bigger temporal separation of FEL pulses and unwanted radiation. For these cases, we added the option to change the bunch pattern from macropulse to macropulse.

Up to 10 bunch patterns can be defined under the symbols [A] to [J], and a *pattern sequence* specifies the order in which they are applied to the machine. These sequences are always repeated periodically, but can be of arbitrary length and complexity. For instance, we might define a pattern [A] which only contains bunches for SASE1 and a pattern [B] with bunches for SASE3 and then define a sequence of “[A] 4 [B]”. This would deliver pattern [A] on every 5th macropulse, followed by 4 shots with pattern [B]. Schemes like this have already found application during user operation.

CONCLUSION AND OUTLOOK

The European XFEL uses a unique beam distribution system to divide its electron bunches among the three undulator lines. The pulsed operation mode and the necessity of beam dynamical schemes such as the *fresh bunch technique* to allow the coexistence of two FELs on the same electron beamline generate extraordinary challenges – not only for hard- and software, but also for the people involved in the operation of the facility.

The flexible configuration of bunch patterns for the machine allows us to cater to the specific needs of our photon experiments. Although the system is capable of generating enormously complex patterns, the chosen abstractions make it manageable for all our operators.

In the future, we are going to add one or more undulator lines in the SASE2 branch. We are also going to commission a set of fast kickers in front of the SASE3 undulators to selectively increase the amplitude of the orbit oscillation that suppresses radiation from passing SASE1 bunches. Both projects can easily be realized with the current timing hard- and software.

ACKNOWLEDGEMENTS

The authors wish to thank their colleagues from the photon beamlines and experiments for many helpful discussions, patience, and support in implementing and testing the beam distribution schemes described in this paper.

REFERENCES

- [1] M. Altarelli *et al.* (editors), “The European X-Ray Free-Electron Laser technical design report”, DESY, Hamburg, Germany, Rep. DESY 2006-097, Jul. 2006.
- [2] E. Cartlidge, “European XFEL to shine as brightest, fastest x-ray source”, *Science*, vol. 354, no. 6308, pp. 22–23, Oct. 2016. doi:10.1126/science.354.6308.22
- [3] W. Decking *et al.*, “Status of the European XFEL”, in *Proc. IPAC’19*, Melbourne, Australia, May 2019, pp. 1721–1723. doi:10.18429/JACoW-IPAC2019-TUPRB020

- [4] F. Obier *et al.*, “Fast kicker system for the European XFEL beam distribution”, presented at FEL’19, Hamburg, Germany, August 2019, paper WEP013, this conference.
- [5] W. Decking and F. Obier, “Layout of the beam switchyard at the European XFEL”, in *Proc. EPAC’08*, Genoa, Italy, June 2008, pp. 2163–2165.
- [6] F. Obier *et al.*, “Long pulse kicker system for the European XFEL beam distribution”, presented at FEL’19, Hamburg, Germany, August 2019, paper WEP014, this conference.
- [7] V. Balandin and N. Golubeva, “Optics for the beam switchyard at the European XFEL”, in *Proc. IPAC’11*, San Sebastián, Spain, September 2011, pp. 2016–2018.
- [8] L. Winkelmann *et al.*, “Compact photo-injector and laser-heater drive laser for the European X-ray Free Electron Laser facility”, in *Conference on lasers and electro-optics, OSA technical digest*, San Jose, USA, May 2018, paper STu4O.5. doi:10.1364/CLEO_SI.2018.STu4O.5
- [9] S. Liu, “Parallel operation of SASE1 and SASE3 at European XFEL”, presented at FEL’19, Hamburg, Germany, August 2019, paper TUA01, this conference.
- [10] A. Aghbabayan *et al.*, “XFEL timing system specifications, short version 2.2”, DESY, Hamburg, Germany, Internal Report, May 2013; <http://ttfinfo2.desy.de/doocs/Timing/CDRv2.2short.pdf>
- [11] P. Geßler, “Synchronization and sequencing of data acquisition and control electronics at the European X-Ray Free Electron Laser”, Ph.D. thesis, Technical University of Hamburg, Germany, 2015. doi:10.15480/882.1262
- [12] E. Sombrowski *et al.*, “jddd: A tool for operators and experts to design control system panels”, in *Proc. ICALEPCS’13*, San Francisco, USA, October 2013, pp. 544–546.

LONG TERM STABILITY AND SLOW FEEDBACK PERFORMANCE AT THE EUROPEAN XFEL

R. Kammering[†], Deutsches Elektronen-Synchrotron DESY, Hamburg, Germany

Abstract

The European XFEL is now routinely running in user operation since more than two years. Up to 8 longitudinal and 9 transversal slow feedback loops are routinely used to keep the accelerators chosen operation conditions. First tests of comparing the machine 'free-floating' state versus fully fixing all relevant monitoring signals have been carried out and show interesting results.

Here we will review the feedback systems in terms of software architecture and conceptual layout but also in respect to feedback and FEL performance.

SOME HISTORY: SLOW FEEDBACKS AT FLASH

Both the transversal and longitudinal feedbacks (FBs) used at the European XFEL have first been introduced at the Free Electron Laser in Hamburg FLASH [1]. The first implementations of a transversal feedback as it is used at the European XFEL [2], date back to 2011. While prior implementations at FLASH where Matlab graphical user interface (GUI) based 'stand-alone' applications, the nowadays used implementation is a DOOCS [3] server based centrally managed application.

While round trip time and also interfacing to monitors and actuators for the stand-alone implementations where acceptable, these architectures hold risk of having multiple instances running at the same time, to name just one of the drawbacks of such an implementation.

THE SLOW TRANSVERSAL FEEDBACK

The server based slow transversal feedback (also called 'orbit feedback') [4] is running on a central server machine hosting the data acquisition system (DAQ) [5]. This system synchronizes all incoming data streams on the level of macro-pulses (this is the repetition rate the machine is triggered with – typically 10 Hz. For details on the structure of beam delivery at the European XFEL see [6]). This ensures that all beam position data served to upstream clients is originating from the same macro-pulse. The general architecture in terms of involved infrastructure and dataflow is shown in Figure 1.

The orbit feedback is using a simple PI controller to correct orbit deviations at the currently active beam position monitors (BPMs). The needed amount of correction is calculated using the theoretically calculated orbit response matrix which is read from the online optics model [7] and doing a singular-value-decomposition (SVD).

All parameters like active actuators (up till now we just use corrector magnets), active monitors (BPMs) as well as SVD parameters etc. can be re-configured on-the-fly. Thereby the orbit feedback offers a lot of flexibility, while

the underlying control algorithm is kept very simple and thereby robust! This has proven to be exactly the combination which was needed to allow for a fast and reliable commissioning of the European XFEL accelerator.

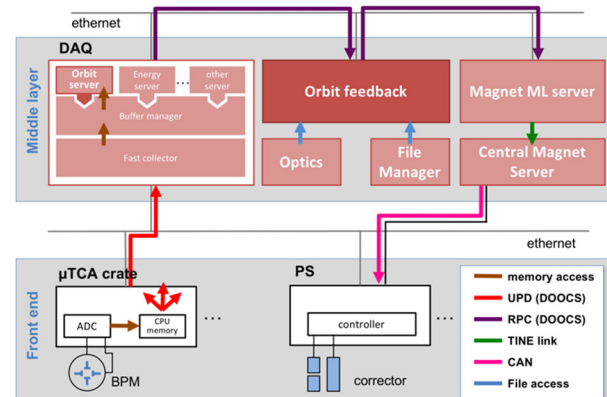


Figure 1: Implementation of the slow transversal feedback within the overall control software architecture.

Layout of Orbit Feedback Along the Linac

First idea has been to run the orbit stabilization as a global feedback. While the software architecture and overall concepts behind the feedback also allow for this, it has shown to be much more practical to use several decoupled instances of the feedback. One global feedback would impose a much more complex architecture in terms of sensitivity and exception handling. Further allows the operation of decoupled feedbacks for more flexibility in terms of the various operation modes of the facility (e.g. only injector operation versus full beam transport to main dumps).

The nowadays used distribution of all orbit feedback instances along the accelerator is shown in Figure 2.

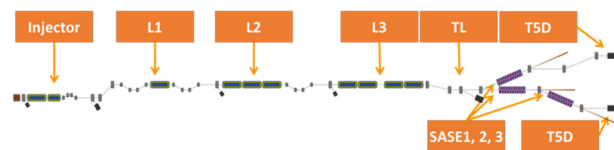


Figure 2: Distribution of orbit feedback instances along the accelerator.

While the single feedback instances are all derived from the same software (and just get configured differently), the demands and targets for the individual instances differ a lot. One can roughly divide the feedbacks into three classes:

- Orbit keeper
 - Here the feedback is aiming for maintaining the orbit over larger sections. Examples are: L2, L3
- Launch stabilization

[†] raikund.kammering@desy.de

- The orbit feedback is aiming to fix position and angle in front of a critical section. Examples are here the undulators (SASE 1, 2, 3) or the collimation section (TL).
- Multi-purpose
 - At these locations the orbit feedback might either be used to keep the launch or in contrast do e.g. larger orbit manipulations. This is the case e.g. for the undulator launch feedbacks (more on this in the following).

In X-ray beam delivery mode, we are typically running 9 instances of the feedback, distributed as shown in Figure 2.

The performance of the feedbacks in terms of targeted maximal allowed orbit deviation depend heavily on the section of the accelerator. Typically, the seen orbit variations in the low energy regions of the linac are much higher compared to the ones in the high energy regions. Table 1 shows a typical set of thresholds of the orbit feedback within it is not reacting – the so-called ‘deadband’.

Table 1: Typical Set of Deadband Settings for All Instances of the Orbit Feedback

Location	FB category	Deadband
Injector	Rarely used	-
Linac 1	Launch	10-20 μm
Linac 2	Orbit keeper	10-20 μm
Linac 3	Orbit keeper	10-20 μm
TL	Launch	5-10 μm
SASE1	Launch/multi-purpose	2-4 μm
SASE2	Launch/multi-purpose	2-4 μm
SASE3	Launch/multi-purpose	2-4 μm
T4D	Launch	40-80 μm
T5D	Launch	40-80 μm

Orbit Feedback Performance and Lessons Learned

The deadbands given in Table 1 present the outcome of the experience made by operating the orbit feedback over the last two years. Excluding the dump lines (where the BPM resolution is the worst one due to e.g. large beam pipe) the empirically chosen deadbands very well reflect the expected beam stability along the machine.

The seen feedback performance and also overall functionality thus very well fits to the current machine operation modes.

While the instances along the linac are usually kept running all the time, the undulator feedbacks are just used in launch configuration if the machine is running in smooth user run. If the machine needs to be tuned to a different setup (e.g. larger wavelength changes), often a so-called

adaptive orbit feedback is used. The details of the concept behind his feedback are described in [8]. Thus, the tuning for optimal SASE performance usually is an iterative process switching back and forth between these different orbit feedbacks. A typical scenario would look like shown in Figure 3.

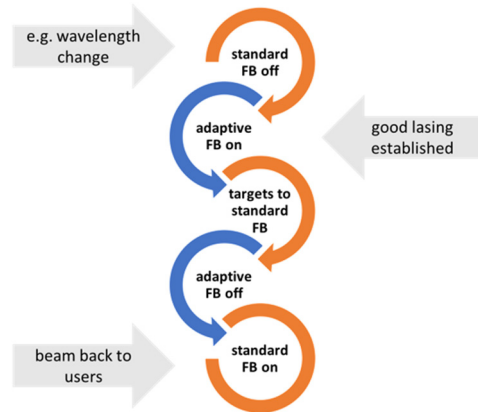


Figure 3: Typical sequence of orbit feedback usage for e.g. wavelength change.

Using the feedbacks in this sequence we are a) able to have an easy way for finding the optimal launch and b) also can rapidly switch to a save state and thereby hand back the beam to the users.

Beside maintaining the launch conditions into the undulators, the SASE orbit feedbacks have also been used to steer the photon beam. The idea arose from the experience that we used ‘some’ correctors within the undulator section to modify the pointing of the photon beam on request of the users. Here we usually just used some few (2-4) correctors per plane. To not apply any drastic kicks to the beam trajectory, the idea was to allow the undulator feedback to use all correctors and just apply a linear slope to the targets along the undulator line.

Figure 4 shows the outcome of applying a linear slope of 200 μm to the vertical plane. Using this approach, we could a) keep the lasing power at the same level, while b) moving the photon beam by roughly 400 μm (as requested by the photon users) and c) did not need to touch any settings of the undulators (which can at least be time consuming).

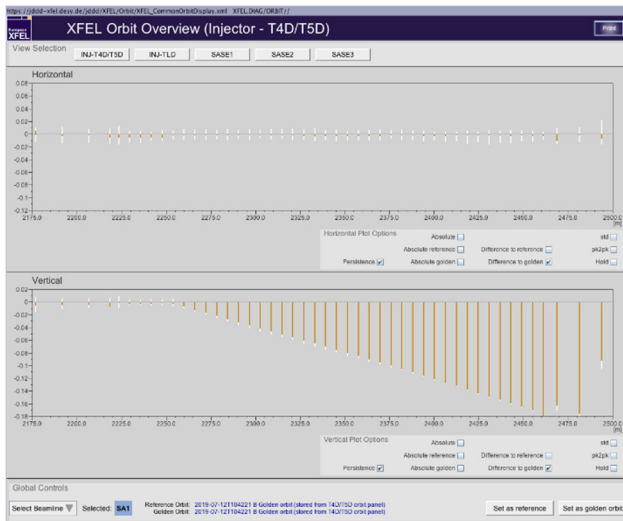


Figure 4: Graphical user interface showing the application of a linear slope of 200 μm in the vertical plane at the SASE1 beam-line. Shown is the difference orbit in respect to the situation before the orbit feedback targets have been modified.

THE SLOW LONGITUDINAL FEEDBACK

Similar as the trajectory feedbacks did the first implementations of the longitudinal feedbacks date back to the early days of the FLASH facility. Also, here first implementations have been realized using stand-alone GUI programs. With the development of the underlying software landscape the implementation as centrally managed server instance has been straight forward.

The architecture and integration into the DAQ system is similar to the one of the orbit feedbacks. The feedback algorithm again uses a simple PI-controller to maintain the desired target for various parameters related to the longitudinal phase space. This feedback has also been designed to run in fully coupled manner, thus allowing to consistently keep machine at a chosen point in the longitudinal phase space.

Table 2: Overview of the Types of Monitors and Corresponding Actuators for the Longitudinal FB

Monitor	Monitor Type	#	Actuator
Toroid		1	Laser attenuator
BCM	Beam compression monitor	3 (6)	RF phase
BAM	Beam arrival time monitor	4 (6)	RF gradient
Energy	Spectrometric energy measurement	4	RF gradient or phase

Table 2 shows an overview of the types of monitors available in the longitudinal feedback. All monitors and actuators can be dis-/enabled on-the-fly. The underlying

architecture does further allow to either run coupled or uncoupled response matrices.

Experience Made with Maintaining the Longitudinal Phase Space

The inherent stability of the European XFEL is already very good due to careful design and engineering providing a stable and contained environment for the electronics and beam-lines. The amount of regulation to keep a certain operation point in longitudinal phase space thus is strongly reduced compared to FLASH. Nonetheless are the visible drifts of the various subsystems having a clearly visible impact on the SASE performance, as shown in Figure 5.

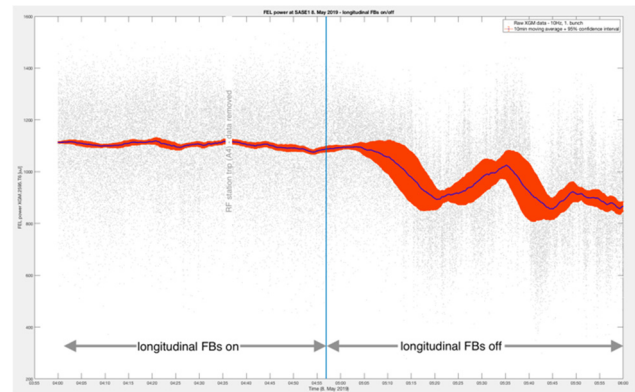


Figure 5: FEL power at SASE2 beam-line over ~ 2 hours. The vertical line marks the time where the longitudinal feedbacks went off. Blue line: 10 minute moving average, red area: 95 % confidence interval.

CONCLUSIONS

The standard orbit feedback has proven to be very appropriate in terms of versatility and robustness. This not only holds true for the commissioning but also for the experience made within the first years of user operation. Even more complex orbit manipulations, like shown for the shifting of the photon beam pointing could easily be accomplished with the feedback as it is.

Even though the longitudinal stability of the European XFEL is inherently very good, did we observe large excursions and degraded FEL performance if run without any feedbacks. The longitudinal feedbacks are very well able to counter fight these drifts and instabilities. So also this feedback provides all needed functionality and performance needed for these days operation modes.

ACKNOWLEDGMENTS

The author would like to thank all people involved in the development and extensions of these DOOCS based feedbacks. Especially I would like to thank J. Carwardine and C. Schmidt for the fruitful initial discussions and ideas.

Further I would like to thank the FLASH team for supporting the essential testing and development of these feedbacks. Without these developments the feedbacks would not have been available at such a mature level for the commissioning of the European XFEL!

REFERENCES

- [1] S. Schreiber *et al.*, “FEL User Facility FLASH”, in *Proc. IPAC'10*, Kyoto, Japan, May 2010, paper TUPE004, pp. 2149-2151.
- [2] M. Altarelli *et al.* (editors), “The European X-Ray Free- Electron Laser technical design report”, DESY, Hamburg, Germany, Rep. DESY 2006-097, Jul. 2006.
- [3] K. Rehlich *et al.*, “DOOCS: an Object Oriented Control System as the integrating part for the TTF Linac”, Proceedings ICALEPCS'97, Beijing China, 1997, paper 97, p.141.
- [4] R. Kammering, John Carwardine, “An Orbit Feedback for the Free Electron Laser in Hamburg (FLASH)”, in *Proc. PCaPAC'10*, Saskatoon, Canada, Oct. 2010, paper WEPL015, pp. 58-60.
- [5] K. Rehlich *et al.*, “Multi-Processor Based Fast Data Acquisition for a Free Electron Laser and Experiments”, *IEEE Transactions on Nuclear Science*, vol. 55, no. 1, pp. 256- 260, February 2008. doi:10.1109/TNS.2007.913936
- [6] L. Froehlich *et al.*, “Multi-Beamline Operation at the European XFEL”, presented at FEL'19, Hamburg, Germany, August 2019, paper WEP008, this conference.
- [7] S. Meykopff, “An Optics-Suite And -Server for the European XFEL”, in *Proc. PCaPAC'14*, Karlsruhe, Germany, Oct. 2014, paper WPO009, pp. 52-54.
- [8] S. Tomin *et al.*, “On-line Optimization of European XFEL with OCELOT”, in *Proc. ICALEPCS'17*, Barcelona, Spain, Oct. 2017, pp. 1038-1042.
doi:10.18429/JACoW-ICALEPCS2017-WEAPL07

FEMTOSECOND LASER-TO-RF SYNCHRONIZATION AND RF REFERENCE DISTRIBUTION AT THE EUROPEAN XFEL

T. Lamb*, M. Felber, T. Kozak, J. Müller, H. Schlarb, S. Schulz, C. Sydlo,
M. Titberidze, F. Zummack, Deutsches Elektronen-Synchrotron (DESY), Hamburg, Germany

Abstract

At the European XFEL, optical pulses from a mode-locked laser are distributed in an optical fiber network providing femtosecond stability throughout the accelerator facility. Due to the large number of RF reference clients and because of the expected higher reliability, the 1.3 GHz RF reference signals are distributed by a conventional coaxial RF distribution system. However, the provided ultra-low phase noise 1.3 GHz RF reference signals may drift over time. To remove these drifts, an optical reference module (REFM-OPT) has been developed to detect and correct environmentally induced phase errors of the RF reference. It uses a femtosecond long-term stable laser-to-RF phase detector, based on an integrated MACH-ZEHNDER amplitude modulator (MZM), to measure and resynchronize the RF phase with respect to the laser pulses from the optical synchronization system with high accuracy. Currently nine REFM-OPTs are permanently operated at the European XFEL, delivering femtosecond stable RF reference signals for critical accelerating field control stations. The operation experience will be reported together with a detailed evaluation of the REFM-OPT performance.

INTRODUCTION

The European X-ray Free-Electron Laser (XFEL) uses a 1.7 km long superconducting linear accelerator (linac) to drive the FEL. A pulsed optical synchronization system has been built and is operated 24/7 at the European XFEL in order to meet various synchronization requirements [1]. For example the synchronization between the FEL and the pump-probe laser systems needs to be in the femtosecond range in order to make time-resolved, ultra-fast pump-probe

experiments possible. This synchronization system also allows to provide RF reference signals with femtosecond stability throughout the linac [2] in order to meet the stability requirement for the accelerating field stability of 0.01° at 1.3 GHz (≈ 20 fs) [3]. See Fig. 1 for a schematic overview of the complete system.

OPTICAL SYNCHRONIZATION SYSTEM

The master laser oscillator (MLO) of the optical synchronization system is a redundant, low jitter, commercial laser system with a repetition rate of 216.66 MHz at a wavelength of 1553 nm. The MLO is precisely phase-locked to the 1.3 GHz RF master oscillator (RF-MO) of the accelerator facility. The laser pulse train from the MLO is split up and distributed in polarization maintaining optical fibers to numerous end stations throughout the accelerator facility. Optical length changes of these fibers are permanently measured and actively corrected. Three different types of end stations are currently supplied by the optical synchronization system and all end stations are synchronized with femtosecond precision [4]. The system is used to precisely synchronize laser systems like the photoinjector laser [5] or the pump-probe laser systems, to operate the bunch arrival time monitors (BAMs) [6, 7], and to provide femtosecond stable RF reference signals to dedicated end stations along the linac via the optical reference module (REFM-OPT).

RF REFERENCE DISTRIBUTION

The conventional RF reference distribution system installed at the European XFEL is a highly reliable system. It is however susceptible to temperature and humidity variations. The RF cables installed along the accelerator tunnel

* Thorsten.Lamb@desy.de

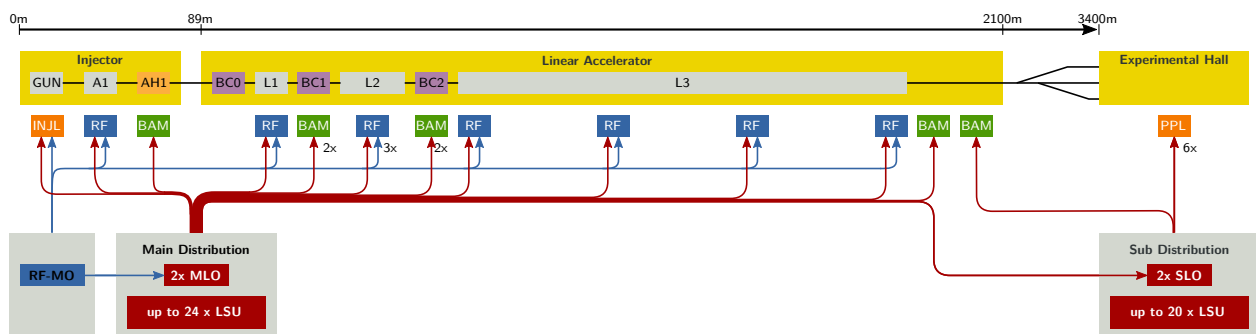


Figure 1: Layout of the RF reference distribution and the pulsed optical synchronization systems of the European XFEL. The RF reference distribution system including the RF-MO and the REFM-OPTs is shown in blue. Stabilized fiber links, MLO/SLO and FSD are presented in red. BAMs are illustrated in green and external laser systems in orange.

suffer mostly from environmental temperature variations. Electronics, like RF amplifiers, which are installed in the tunnel in temperature stabilized racks are additionally susceptible to humidity variations. These effects could regularly cause several tens of picoseconds of RF phase drifts along the linac if they were not measured and directly corrected in a phase-locked-loop (PLL) by the REFM-OPT. The REFM-OPT operates by locally re-synchronizing the 1.3 GHz RF reference signals in order to meet the low-level RF (LLRF) phase stability requirement.

In the L1 and L2 sections of the linac a star topology has been implemented in the RF distribution system in order to achieve the ultimate performance. A dedicated REFM-OPT is installed at each master RF station in these sections. The main linac (L3) is connected by daisy chained modules, where one REFM-OPT supplies several RF stations.

OPTICAL REFERENCE MODULE

A drift-free laser-to-RF phase detector has been specifically developed in order to make use of the femtosecond optical pulse trains provided by the optical synchronization system [8]. It allows to measure the phase drifts and jitter of the 1.3 GHz RF reference signals with respect to the optical reference and correct them up to the locking bandwidth with femtosecond precision in a PLL. The laser-to-RF phase detector is based on a MACH-ZEHNDER amplitude modulator (MZM). The optical pulse train is modulated proportionally to the phase difference between the two signals and the amplitude modulation is used for detection. All nine planned REFM-OPTs are installed and permanently operated. Phase corrections of tens of picoseconds are routinely applied after maintenance days or accelerator operation interruptions in order to maintain stable RF reference phases for the accelerating field control [2].

PERFORMANCE EVALUATION

In order to particularly evaluate the performance of the REFM-OPT in the accelerator tunnel under operation conditions, several of out-of-loop measurements were performed, using a commercial Rohde & Schwarz FSWP phase noise analyzer. A set of absolute phase noise measurements is presented in Fig. 2 to show the overall performance at the RF station A2M in the L1 section of the linac. The phase noise of the RF reference signal at the input of the REFM-OPT is depicted by the green curve. This signal is provided by the RF-MO in the injector building, it is transmitted by RF cables to the accelerator tunnel and amplified in a so-called reference module (REFM) in order to provide the required RF power. The integrated jitter of this signal in a bandwidth of 10 Hz to 1 MHz amounts to 17.3 fs rms with a large contribution from the 50 Hz spike of about 7 fs. This signal is connected to the input of the REFM-OPT.

Two additional measurements were carried out in the same offset frequency range at the output of the REFM-OPT. For the first measurement (red curve) the phase and RF power feedbacks in the REFM-OPT were switched off. The REFM-

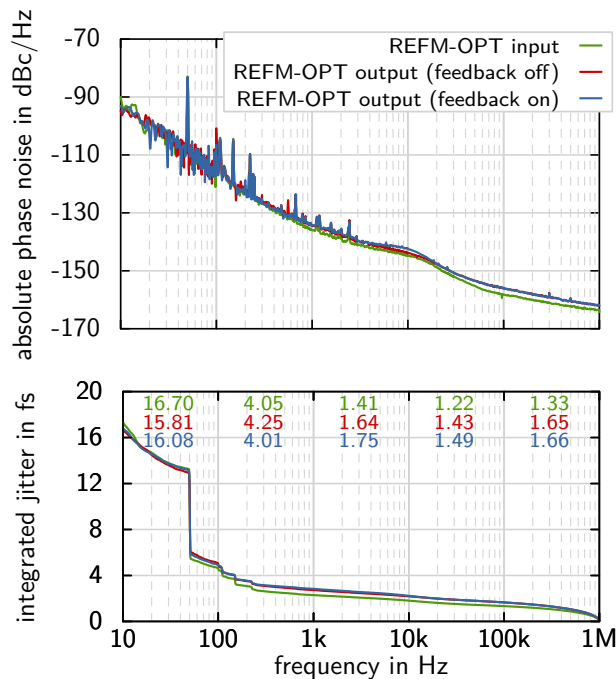


Figure 2: Absolute phase noise measured at the input and the output of the REFM-OPT at the RF station A2M. The measurement was obtained in the accelerator tunnel under operation conditions.

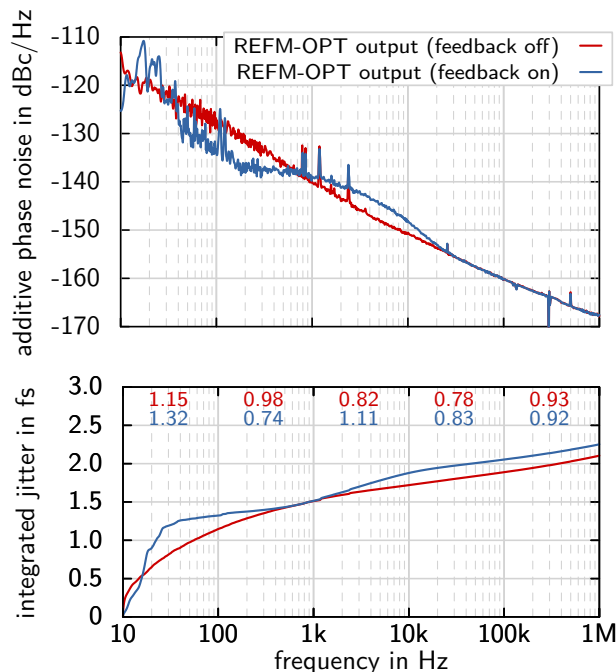


Figure 3: Additive phase noise of the REFM-OPT at the RF station A2M. The measurement was obtained in the accelerator tunnel under operation conditions.

OPT acts in this state like an RF amplifier. For the next measurements the feedbacks were switched on (blue curve) such that the RF signal at the output of the REFM-OPT was actively amplitude and phase stabilized. The curves show two distinct changes. The general phase noise level is slightly elevated by the REFM-OPT in the frequency range of 1 kHz to 1 MHz (from the green to the red curve). One can furthermore see, that the noise bump at 10 kHz is increased when the feedback is switched on (from the red to the blue curve). This noise bump originates from the RF-MO and is transmitted across both the optical and the RF reference distribution system as it is just outside the bandwidth of the involved control loops.

In order to be able to better quantify these effects and to study the actual phase noise contribution of the REFM-OPT, additive phase noise measurements were additionally performed. They are presented in Fig. 3. A reference measurement was carried out, where the REFM-OPT phase and amplitude feedbacks were switched off (blue curve). The integrated additive jitter of the REFM-OPT (without active feedback) in a bandwidth of 10 Hz to 1 MHz amounts to 2.1 fs rms. With active feedbacks the additive jitter is slightly increased (2.3 fs rms) as expected. The REFM-OPT with active feedback is correcting RF phase jitter and drifts which the RF signal accumulated during transmission into the tunnel. One can clearly see low frequency phase drift corrections up to 30 Hz but also how up to the controller bandwidth of 500 Hz the RF amplifier noise is partially suppressed by the phase feedback.

CONCLUSION

Absolute phase noise of the 1.3 GHz RF reference signal amounts to 17.3 fs rms in a bandwidth of 10 Hz to 1 MHz at the input of the REFM-OPT. This measurement was carried out in the accelerator tunnel with no significant contribution from the REFM-OPT when repeated at its output. This measurement shows the low phase noise RF reference signal provided by the RF-MO. It has been shown hereby that the performance of the RF reference signals in the accelerator tunnel fulfill the requirement for the accelerating field stability.

The additive jitter contribution from the REFM-OPT amounts to 2.1 fs rms without active feedback and 2.3 fs with feedback in a bandwidth of 10 Hz to 1 MHz. This out-of-loop measurement proves that there is only little phase noise added by the REFM-OPT while drifts and phase jitter is actively corrected in the same time in the locking bandwidth of up to 500 Hz.

REFERENCES

- [1] J. Müller *et al.*, “Large-scale optical synchronization system of the European XFEL”, in *Proc. 29th Linear Accelerator Conf. (LINAC’18)*, Beijing, China, Sep. 2018, pp. 253–256. doi: 10.18429/JACoW-LINAC2018-MOP0121.
- [2] T. Lamb *et al.*, “Laser-to-RF synchronization with femtosecond precision”, in *Proc. 38th Int. Free Electron Laser Conf. (FEL’17)*, Santa Fe, NM, USA, Aug. 2017, pp. 399–402. doi: 10.18429/JACoW-FEL2017-WEB04.
- [3] M. Omet *et al.*, “LLRF operation and performance at the European XFEL”, in *Proc. 9th Int. Particle Accelerator Conf. (IPAC’18)*, Vancouver, Canada, Apr.–May 2018, pp. 1934–1936. doi: 10.18429/JACoW-IPAC2018-WEPAF051.
- [4] T. Lamb *et al.*, “Large-scale optical synchronization system of the European XFEL with femtosecond precision”, in *Proc. 10th Int. Particle Accelerator Conf. (IPAC’19)*, Melbourne, Australia, May 2019, pp. 3835–3838. doi: 10.18429/JACoW-IPAC2019-THPRB018.
- [5] J. Müller *et al.*, “All-optical synchronization of pulsed laser systems at FLASH and XFEL”, in *Proc. 6th Int. Particle Accelerator Conf. (IPAC’15)*, Richmond, VA, USA, May 2015, pp. 854–857. doi: 10.18429/JACoW-IPAC2015-MOPHA032.
- [6] M. K. Czwalińska *et al.*, “New design of the 40 GHz bunch arrival time monitor using MTCA.4 electronics at FLASH and for the European XFEL”, in *Proc. 2nd Int. Beam Instrumentation Conf. (IBIC’13)*, Oxford, UK, Sep. 2013, paper WEP031, pp. 749–752.
- [7] S. Schulz *et al.*, “Femtosecond all-optical synchronization of an X-ray Free-Electron Laser”, *Nature Communications*, vol. 6, Jan. 2015, paper 5938. doi: 10.1038/ncomms6938.
- [8] T. Lamb, “Laser-to-RF phase detection with femtosecond precision for remote reference phase stabilization in particle accelerators”, Ph.D. thesis, Technische Universität Hamburg-Harburg, Hamburg, Germany, 2016. doi: 10.3204/PUBDB-2017-02117.

LONGITUDINAL INTRA-TRAIN BEAM-BASED FEEDBACK AT FLASH

S. Pfeiffer*, L. Butkowski, M. K. Czwalińska, B. Dursun, Ch. Gerth, B. Lautenschlager,
H. Schlarb, C. Schmidt, Deutsches Elektronen-Synchrotron DESY, Hamburg, Germany

Abstract

The longitudinal intra-train beam-based feedback has been recommissioned after major upgrades on the synchronization system of the FLASH facility. Those upgrades include: new bunch arrival time monitors (BAMs), the optical synchronization system accommodating the latest European XFEL design based on PM fibers, and installation of a small broadband normal conducting RF cavity. The cavity is located prior to the first bunch compressor at FLASH and allows energy modulation bunch-by-bunch (1 μ s spacing) on the per mille range. Through the energy dependent path length of the succeeding magnetic chicane the cavity is used for ultimate bunch arrival time corrections. Recently the RF cavity operated 1 kW pulsed solid-state amplifier was successfully commissioned. First tests have been carried out incorporating the fast cavity as actuator together with SRF stations for larger corrections in our intra-train beam-based feedback pushing now arrival time stabilities towards 5 fs (rms). The latest results and observed residual instabilities are presented.

INTRODUCTION

The free-electron laser in Hamburg (FLASH) at DESY is a research facility which provides laser radiation in the soft X-ray range with tunable wavelengths down to 4.2 nm. The accelerator operates in pulsed mode with a repetition rate of 10 Hz. The laser radiation is generated by the self-amplified spontaneous emission (SASE) process. The electron bunch trains with a variable length and repetition rate are accelerated by superconducting radio frequency (SRF) cavities up to the electron beam energy of 1.25 GeV, with a maximum number of 800 bunches per pulse and a bunch repetition rate of 1 MHz [1].

A high precision synchronization in the range of femtoseconds between an external laser and the free-electron laser (FEL) pulses is required, e.g., for pump-probe experiments. An intra-train beam-based feedback is used to correct arrival time fluctuations of the electron bunches in the magnetic bunch compression chicane in order to improve the bunch arrival time stability, which contributes to the photon beam quality delivered to the experiments. The important signal for the beam-based feedback is provided by the bunch arrival time monitors (BAMs) [2].

The low level radio frequency (LLRF) controller, regulating the 1.3 GHz RF field in amplitude A and phase Φ of the SRF cavities, includes different control strategies like a learning feedforward controller to minimize repetitive amplitude and phase errors from pulse to pulse and a second order multiple-input multiple-output (MIMO) controller to react

within a pulse. The LLRF control system is based on the MicoroTCA.4 standard. The RF field regulation typically reaches an amplitude stability of $\Delta A/A \approx 0.008\%$ and a phase stability of $\Delta \Phi \approx 0.007$ deg for the SRF cavities [3]. In addition, the superposition of the RF field information with beam-based measurements, e.g. the arrival time measured by the BAMs, is included in the control strategy of the RF field [4, 5].

The control strategy with the superposition of the RF-field and the beam-based information is called longitudinal intra-train beam-based feedback. This beam-based feedback control strategy and the controller design is already introduced in [5, 6].

In addition to the recent upgrades of the BAMs [4, 7, 8] and optical synchronization system [9], now using the latest European XFEL design based on PM fibers, a normal conducting cavity has been integrated into the beamline as a fast energy corrector cavity to further improve the arrival time stability to reach the goal of an arrival time stability of about 5 fs (rms). This cavity is called “Bunch Arrival Corrector CAvity” (BACCA). The latest measurement results will be presented in this paper.

SYSTEM DESCRIPTION

Figure 1 shows a scheme of FLASH with the above mentioned diagnostic units and beam-based feedback loops marked with the colored areas. The measured arrival time data of the second BAM (BAM2) after the first bunch compressor (BC2) is transmitted via a high-speed optical link to the LLRF controller and used for the arrival time regulation by adjusting the RF field at the SRF module ACC1. The same arrival time signal is used for the regulation of the fast feedback cavity BACCA. The first BAM (BAM1) is not affected by the beam-based feedbacks and measures the incoming arrival time jitter. After the second bunch compressor the accelerator modules ACC4 to ACC7 increase the beam energy but do not influence the bunch arrival time. Marked in grey and dashed lines are the bunch compression monitors (BCMs) and the additional feedback loop for the regulation of the SRF modules ACC2 and ACC3 by using the arrival time measurements of the third BAM (BAM3). These parts are planned as add-ons in the future for the beam-based control strategy.

Bunch Arrival Time Monitors

The intra-train beam-based control strategy uses the arrival time of every single bunch for the regulation. The bunch arrival time monitors consist of three main parts, the RF unit, the electro-optical unit and the data acquisition (DAQ) unit. The readout electronics according to the MicoroTCA.4 standard are in operation since 2013 [10].

* sven.pfeiffer@desy.de

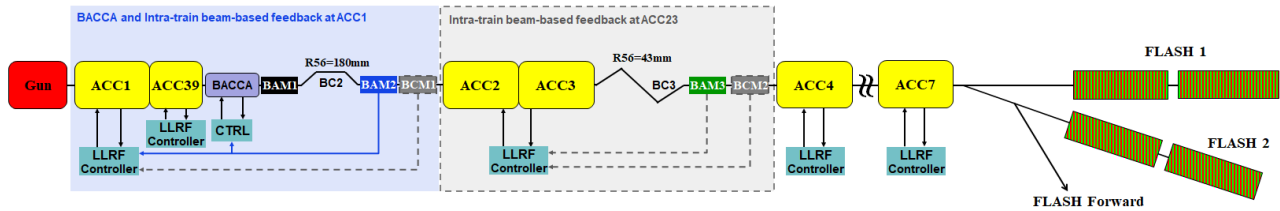


Figure 1: Scheme of FLASH with the superconducting modules ACC1-ACC7, the third harmonic module ACC39, the normal conducting cavity BACCA and the mentioned diagnostic units, as well as the beam-based feedback loops.

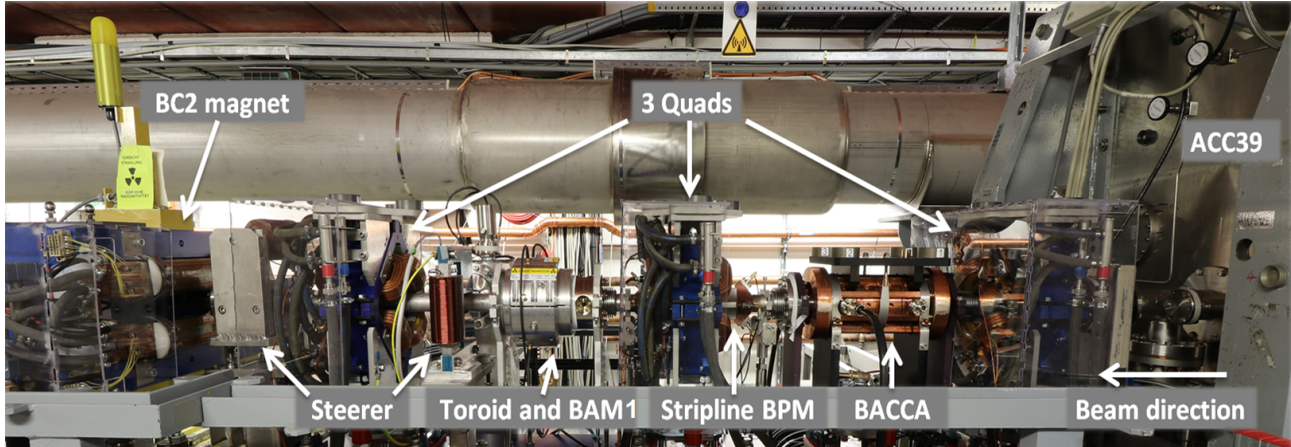


Figure 2: Picture with the part of the beamline where BACCA is located. With the third harmonic module (ACC39) on the right side and the beginning of the first bunch compressor (BC2) on the left side. The beam direction is right to left. [12]

The RF unit includes four pickups to capture the electromagnetic field induced by the electron bunch. For the electro-optical unit timing-stabilized laser pulses are provided as reference signal by the optical synchronization system [9]. The laser pulses are modulated by the signal of the RF unit and these modulations are used to calculate the arrival time. The new designed RF and electro-optic units allow using the full bandwidth of up to 40 GHz and a resolution in the sub-10 femtosecond range which has been evaluated for different FEL facilities [8]. The reference laser pulses are also used as clock for the DAQ system. A more detailed description of the BAM can be found in [2, 4, 7].

BACCA

The normal conducting feedback cavity BACCA with four cells is used as fast energy corrector cavity to improve the arrival time stability. The cavity is located after the third harmonic module (ACC39) and in front of the first bunch compressor (BC2). The specifications and technical design of BACCA are given in [11]. Two important requirements are an energy modulation range of about ± 50 keV and a maximum feedback loop latency of 700 ns. The cavity operates at 2.9972 GHz to keep the cavity length short, due to limited beamline space for the installation. Figure 2 shows a picture of the accelerator part where BACCA is located.

Details about the installation, commissioning and first measurements with and without beam can be found in [12].

The normal conducting cavity is driven by a 1 kW high power RF amplifier. The arrival time variations measured by the BAM (BAM2) behind the first bunch compressor are used to control the driver input of the high power RF amplifier. A MIMO controller similar to a proportional-integral (PI) controller is used.

RESULTS

The presented results are related to the FLASH 1 beamline. The measurements are presented with 340 bunches, due to a limited RF field pulse length of the RF gun, a repetition rate of 1 MHz and a charge of 0.4 nC. The intra-train beam-based feedback at the SRF module ACC1 operates together with the feedback of BACCA. Figure 3 shows the mean free arrival time of BAM2. The grey lines show the measured arrival time for the entire bunch train of 340 bunches and 600 pulses. As an example the measurements of pulse 100 and 550 are highlighted. The blue solid lines represent the standard deviation $\sigma(t_{\text{Arrival}})$ of 600 pulses for each bunch. The beginning of the bunch train illustrates how the beam-based feedback influences the arrival time. The peak-to-peak value of the arrival time is reduced from bunch to bunch in a significant manner (grey lines) and thus, the arrival time jitter is minimized (blue solid lines). It takes $\approx 10 \mu\text{s}$ (10 bunches with a repetition rate of 1 MHz) to reach the steady state value of ≈ 8.5 fs (rms). Figure 4 presents the changes of the arrival time jitter for the same set of data along the accelerator, which means the changes

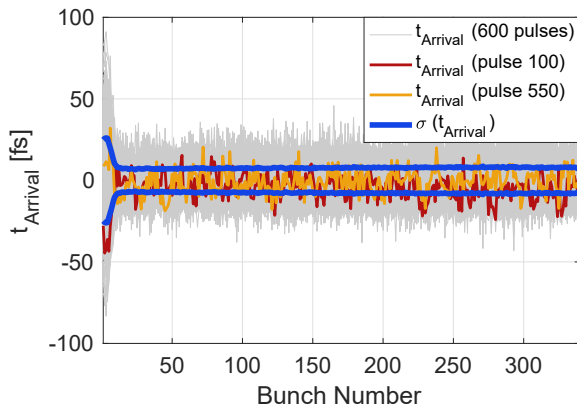


Figure 3: Mean free arrival time of BAM2. The grey lines show the arrival time of 600 pulses and the blue solid line the standard deviation $\sigma(t_{\text{Arrival}})$. The intra-train beam-based feedback at ACC1 runs together with BACCA.

from BAM1 to BAM3. The incoming arrival jitter is ≈ 32 fs (rms) (BAM1 - black solid line). After the first bunch compressor the arrival time jitter starts at around 25 fs (rms) and is pushed down by the beam-based feedbacks at ACC1 and BACCA to ≈ 8.5 fs (rms) (BAM2 - blue solid line). This value increases a little, while the beam passes the accelerator modules ACC2 and ACC3, which results in a jitter of ≈ 14 fs (rms) after the second bunch compressor (BAM3 - green dashed line).

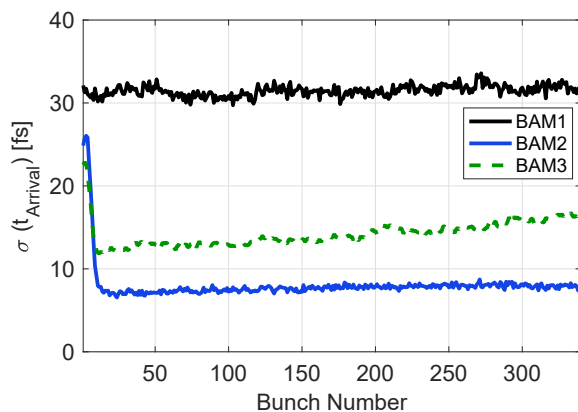


Figure 4: Standard deviation of the arrival time (600 pulses) for all three BAMs (BAM1, BAM2, BAM3). The intra-train beam-based feedback at ACC1 runs together with BACCA.

CONCLUSION AND OUTLOOK

The results show that the arrival time stability can be improved in a significant manner by using the intra-train beam-based feedback at the SRF module ACC1, together with the fast feedback cavity BACCA. The arrival time stability after the first bunch compressor can be improved from 25 fs (rms) for the first bunches to 8.5 fs (rms). The steady state value of the arrival time stability is reached within the first 10 bunches, which corresponds to the time of $10 \mu\text{s}$ for the

repetition rate of 1 MHz. The arrival time jitter increases a little, while the bunch train passes the accelerator modules ACC2 and ACC3, which results in an arrival time stability after the second bunch compressor of ≈ 14 fs (rms).

Next steps: (1) Finding the optimal closed loop bandwidth and optimal gain of ACC1 and BACCA, which is depending on the noise figure of the signals to be controlled. Low frequency distortions should be compensated with ACC1 while the high frequency regulation is done by BACCA. (2) Using the additional intra-train beam-based feedback loop at the SRF modules ACC2 and ACC3 with the arrival time information of BAM3 in order to improve the arrival time stability after the second bunch compressor. Furthermore, it is foreseen to use the bunch compression signals provided by the BCMs as additional beam information for the intra-train beam-based feedback.

REFERENCES

- [1] FLASH, “Free-electron laser FLASH”, (Aug. 12, 2019), <http://flash.desy.de/>
- [2] F. Löhl *et al.*, “Electron Bunch Timing with Femtosecond Precision in a Superconducting Free-Electron Laser”, *Physical Review Letters*, vol. 104, no. 14, p. 144 801, 2010, DOI:10.1103/PhysRevLett.104.144801
- [3] Ch. Schmidt *et al.*, “Recent Developments of the European XFEL LLRF System”, in *Proc. 4th Int. Particle Accelerator Conf. (IPAC'13)*, Shanghai, China, May 2013, paper WEPME009, pp. 2941–2943.
- [4] M. Viti *et al.*, “The Bunch Arrival Time Monitor at FLASH and European XFEL”, in *Proc. of ICALEPCS'17*, Barcelona, Spain, 2017, paper TUPHA125, DOI:10.18429/JACoW-ICALEPCS2017-TUPHA125
- [5] S. Pfeiffer, “Symmetric grey box identification and distributed beam-based controller design for free-electron lasers”, PhD thesis, Hamburg-Harburg, 2014, <https://bib-pubdb1.desy.de/record/205450>
- [6] S. Pfeiffer *et al.*, “Fast Feedback Strategies for Longitudinal Beam Stabilization”, in *Proc. 3rd Int. Particle Accelerator Conf. (IPAC'12)*, New Orleans, LA, USA, May 2012, paper MOOAA03, pp. 26–28.
- [7] H. Dinter *et al.*, “Prototype of the Improved Electro-Optical Unit for the Bunch Arrival Time Monitors at FLASH and the European XFEL”, in *Proc. 37th Int. Free Electron Laser Conf. (FEL'15)*, Daejeon, Korea, Aug. 2015, pp. 478–482. doi:10.18429/JACoW-FEL2015-TUP049
- [8] A. Angelovski *et al.*, “Evaluation of the cone-shaped pickup performance for low charge sub-10 fs arrival-time measurements at free electron laser facilities”, *Phys. Rev. ST Accel. Beams*, vol. 18, no. 1, p. 012 801, 2015, DOI:10.1103/PhysRevSTAB.18.012801
- [9] S. Schulz *et al.*, “Femtosecond all-optical synchronization of an x-ray free-electron laser”, *Nature Communications*, vol. 6, pp. 5938–5949, 2015, DOI:10.1038/ncomms6938
- [10] M. K. Czwalińska *et al.*, “New Design of the 40 GHz Bunch Arrival Time Monitor Using MTCA.4 Electronics at FLASH and for the European XFEL”, in *Proc. 2nd Int. Beam Instrumentation Conf. (IBIC'13)*, Oxford, UK, Sep. 2013, paper WEP31, pp. 749–752.

- [11] S. Pfeiffer, (Aug. 12, 2019), “Technical design report on ultrafast longitudinal feedback for FLASH”, Deliverable: D13.1, EuCARD2, <http://eucard2.web.cern.ch/science/deliverables>
- [12] S. Pfeiffer *et al.*, “Status Update of the Fast Energy Corrector Cavity at FLASH”, in *Proc. 29th Linear Accelerator Conf. (LINAC’18)*, Beijing, China, Sep. 2018, pp. 112–114. doi: 10.18429/JACoW-LINAC2018-MOP0039

THz SPECTROSCOPY WITH MHz REPETITION RATES FOR BUNCH PROFILE RECONSTRUCTIONS AT EUROPEAN XFEL

N. M. Lockmann*, Ch. Gerth, B. Schmidt, S. Wesch
Deutsches Elektronen-Synchrotron DESY, Hamburg, Germany, EU

Abstract

The European X-ray Free-Electron Laser generates most powerful and brilliant X-ray laser pulses. Exact knowledge about the longitudinal electron bunch profile is crucial for the operation of the linear accelerator as well as for photon science experiments. The only longitudinal diagnostic downstream of the main linac is based on spectroscopy of diffraction radiation (DR). The spectral intensity of the DR in the THz and infrared regime is monitored by a four-staged grating spectrometer and allows non-invasive bunch length characterization based on form factor measurements in the range 0.7 – 60 THz. As the readout and signal shaping electronics of the spectrometer allow MHz readout rates, the longitudinal bunch profile of all bunches inside the bunch train can be characterized non-invasively and simultaneously to FEL operation. In this paper, form factor measurements along the bunch train will be described and presented as well as the resulting reconstructed current profiles.

INTRODUCTION

The European XFEL (EuXFEL) generates femtosecond X-ray laser pulses in the wavelength range 0.05 – 6 nm based on Self-Amplified Spontaneous Emission (SASE) at MHz repetition rates [1]. The super-conducting linear accelerator of EuXFEL [2] has recently been operated at a beam energy of 14 GeV, a bunch charge of 250 nC, and with 600 μ s-long trains of up to 675 bunches at a rate of 10 Hz. The femtosecond electron bunches can be distributed into three different SASE undulator beamlines and serve three experimental stations in parallel for which a flexible bunch pattern can be adjusted independently as depicted schematically in Fig. 1.

For a stable operation of the accelerator, e.g. to suppress beam-loading in the accelerator modules, the full bunch train is filled with bunches. Bunches requested by the user experiments, marked as blue, green, and orange bars in Fig. 1, are distributed to the individual undulator beamlines SASE1, SASE2, and SASE3, whereas all other bunches are kicked out by a fast kicker-septum arrangement into a local dump upstream of the SASE undulators (grey bars in Fig. 1). The hard X-ray undulator SASE1 is located in a straight section and followed by the soft X-ray undulator SASE3 downstream of a bending magnet which separates the hard X-rays from the electron beam. A flattop kicker, indicated as a red line in Fig. 1, is used to deflect electron bunches into a septum which deflects the bunches into the undulator beamline SASE2. The radio-frequency (RF) accelerating pulses (solid purple line in Fig. 1) can be split into two flattop regions for which the RF accelerating voltage, i.e. amplitude and

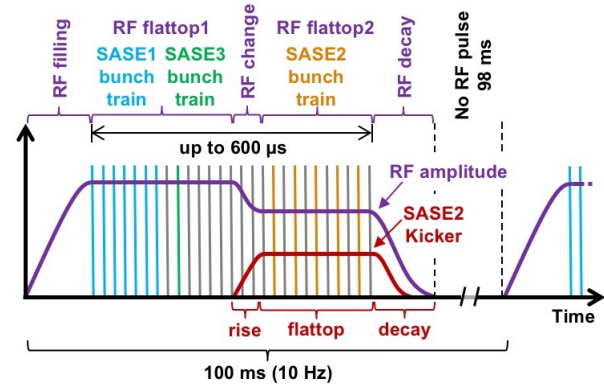


Figure 1: Simplified diagram of the EuXFEL bunch pattern. The RF accelerating pulses (purple line) can be split into two flattops to optimize independently the bunch compression for SASE1/SASE3 and SASE2.

phase, can be adjusted within certain limits for independent optimization of the bunch compression and FEL power of SASE2. The SASE2 bunch train can also be swapped with the SASE1/SASE3 bunch trains to have the SASE2 bunch train in the RF flattop1. The bunches that are accelerated during the time between the RF flattops, required both for adjustment of the accelerating voltage and rise or decay time of the SASE2 flattop kicker, are taken out by the fast kicker-septum arrangement. A layout of the undulator beamlines is shown in Fig. 2.

The exact knowledge of the longitudinal current profile of the individual electron bunches is of high interest for the photon experiments as well as for accelerator operation. At EuXFEL the current profile at final compression is monitored by terahertz (THz) and infrared (IR) spectroscopy of coherent diffraction radiation (DR) just upstream of the undulator beamlines, see also Fig. 2. The spectral content of this coherently emitted radiation is determined by the modulus of the longitudinal form factor, the Fourier transform of the current profile. Therefore, the modulus of the longitudinal form factor $|F_l|$, which is accessible by measurements of the coherently emitted DR [3], yields information about the time structure of the electron bunch.

As the emission of DR does not influence the electron beam quality, it allows for non-invasive bunch length characterization. A four-staged single-shot grating spectrometer [4] has been utilized to measure the spectral intensity of the DR with single bunch resolution. Consequently, the longitudinal form factor of all bunches inside the bunch train can be measured simultaneously during FEL operation.

* nils.maris.lockmann@desy.de

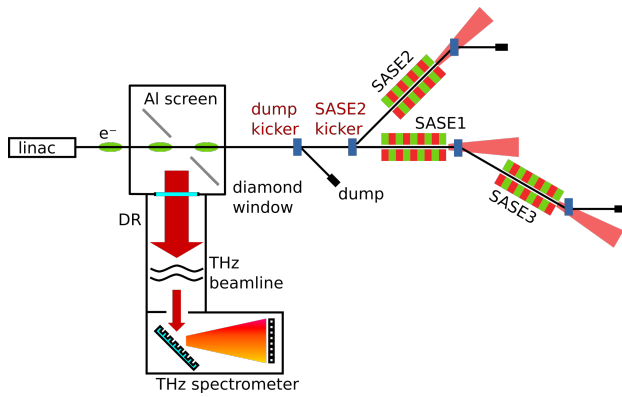


Figure 2: Schematic overview of the coherent radiation diagnostic station and the undulator switchyard at EuXFEL. The coherent radiation emitted at a DR screen is monitored non-invasively by the THz spectrometer.

EXPERIMENTAL SETUP

The aluminum diffraction radiation screen, with a dimension of $80 \text{ mm} \times 32 \text{ mm}$ and 1 mm thickness, has a circular aperture of 5 mm diameter. The screen is mounted under 45° with respect to the incoming electron beam such that the radiation is emitted perpendicular to the electron beam path (indicated by the red arrows in Fig. 2). In order to prevent absorption of the THz radiation in air, the beamline is evacuated and decoupled from the accelerator vacuum by a diamond window, which has an aperture of 20 mm . Four focusing gold mirrors transport the DR to the THz spectrometer. A detailed description of the THz beamline can be found in Ref. [5].

The THz spectrometer consists of four consecutive blazed gratings with decreasing grating constants. Each grating serves as an efficient dispersive device, which will spread a certain frequency range into the first dispersive order. In addition, it also serves as a low-pass filter by efficiently reflecting the radiation below the dispersive frequency range onto the next grating. Focusing ring mirrors focus the dispersive radiation onto the detector planes. The spectral intensity is detected by pyroelectric line array detectors with 30 channels at every grating stage. Together with the possibility to remotely change between two different grating sets, this results in 240 frequency bins covering the range from 0.7 THz to 60 THz . A detailed description of the THz spectrometer can be found in Ref. [4].

After a charge-sensitive preamplifier (Cremat CR-110), the signals of the pyroelectrical detectors are shaped by a Gaussian filter amplifier with selectable shaping times. Finally, the analog signals are converted to digital signals, which are available within the EuXFEL control system. The shaping and analog-to-digital conversion are done by four MicroTCA.4 compliant electronic boards [6]. Each board holds 32 ADCs with a sampling rate of 54 MHz .

SIGNAL PILE-UP AND CORRECTION

The pyroelectrical crystal LiTaO_3 of the detector absorbs the radiation inducing a thermal expansion of the crystal and leading to a surface charge change. The charge sensitive preamplifier converts this charge to an exponential step voltage signal with a decay-time constant of $1.4 \mu\text{s}$. For the purpose of signal sampling and analog-to-digital conversion, these step functions are filtered by Gaussian filter amplifiers leading to pulses with 100 ns RMS duration.

Since the LiTaO_3 crystals are as well piezo-electric, the pyroelectric voltage change leads to mechanical vibrations of the crystal with a characteristic resonance frequency in the MHz range and a decay time of $\sim 20 \mu\text{s}$. These vibrations are in the bandwidth of the shaping amplifier and thereby noticeably in the sampled ADC signals as a ringing following the signal. The dots in the top of Fig. 3 illustrate the amplitude of these oscillations at the positions of subsequent bunches in the ADC signal of one bunch. The decay time of the oscillations is larger than the bunch spacing on a 1.1 MHz pattern. Consequently, the pyrodetector signal of a bunch train is distorted due to signal pile-up. The red curve in the bottom of Fig. 3 shows such a distortion on the signal of a bunch train with 555 bunches. The ringing is reproducible in amplitude and phase and scales linearly with the amplitude of the initial signal. Experimentally determined single bunch patterns can be used to correct for this effect. The result of this correction (green curve in Fig. 3) shows that the baseline after the bunch train is well recovered, which is an indicator for a successful correction of the pile-up. In addition, it can be seen how the different RF phases in the two flattops change the electron bunch compression and thus the height of the pyroelectric signal.

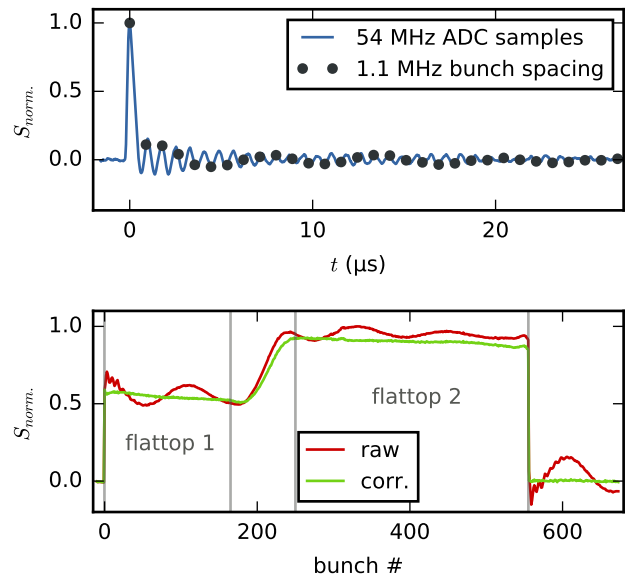


Figure 3: Normalized ADC signal of a pyrodetector for a single bunch against time (top). With this information the pile-up on a bunch train (red) with 555 bunches at a repetition rate of 1.1 MHz can be corrected (green).

EXPERIMENTAL RESULTS

The successful application of the pile-up correction enables form factor measurements for each bunch inside the bunch train. In Fig. 4, the longitudinal form factors of bunch #50 and bunch #500 are shown. The lines represent the averages of 100 RF pulses. The error bands include the RMS fluctuations as well as the influence of any remaining pile-up on the signal. This was estimated by the largest signal deviation from the baseline after the bunch train. This is also the estimate of the detection limit of the spectrometer, which is represented by the gray area.

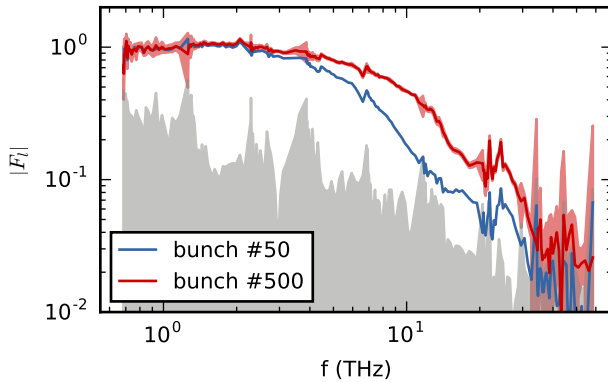


Figure 4: Measured longitudinal form factor modulus $|F_l|$ averaged over 100 RF pulses for bunch #50 and #500 out of a bunch train with 555 bunches at a repetition rate of 1.1 MHz. The gray area indicates the detection limit of the spectrometer. Different bunch compressions for two RF flattops are clearly visible.

The longitudinal form factor of bunch #50, which is part of the first RF flattop, clearly shows a faster fall-off at higher frequencies than bunch #500 of the second RF flattop. This indicates a shorter overall bunch length and thus higher compression of the second RF flattop. It is the result of empirical optimization of the bunch compression for optimum SASE power in the undulator beamlines SASE1 and SASE2.

Based on the algorithm described in Refs. [5, 7], the longitudinal bunch profiles have been reconstructed from the measured spectral intensities, which are depicted in Fig. 5. Here, the different overall bunch compression of the two RF flattops are clearly visible. The RMS bunch length of bunch #50 is 1.3-times larger than the one of bunch #500, while the peak current decreases by a factor of 1.5.

CONCLUSION AND OUTLOOK

The DR beamline at EuXFEL enables non-invasive spectroscopy of the coherently emitted THz and IR radiation simultaneously to FEL operation. The electronics of the THz spectrometer are fast enough to detect each bunch inside the bunch train. The detrimental ringing of the detector signals due to the piezoelectric oscillations of the pyroelectric sensors can be corrected by utilizing a single bunch measurement. The resulting measured longitudinal form factors for

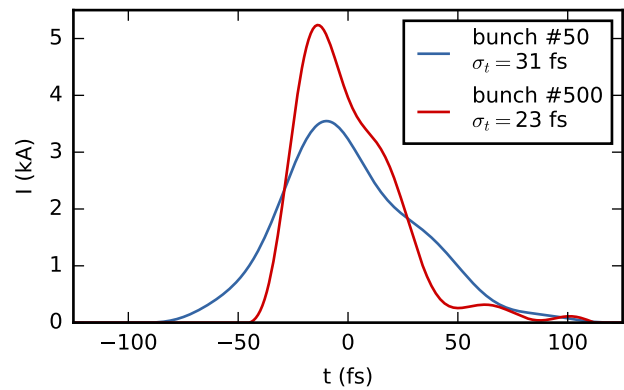


Figure 5: Current profile reconstructions of one bunch of the two respective RF flattops from the form factor measurement shown in Fig. 4.

each RF flattop show clear differences in the bunch compression for an optimal lasing process in the respective SASE beamline. This is also visible in the reconstructed current profiles.

Currently, the pile-up correction is getting implemented in the accelerator control system and will enable a live measurement of the longitudinal form factor for each bunch inside the bunch train with single bunch resolution. This information can then be used as a feedback to optimize and stabilize the accelerator operation.

REFERENCES

- [1] M. O. Wiedorn *et al.*, “Megahertz serial crystallography”, *Nat. Comm.* vol. 9, no. 1, 4025, 2018. doi:10.1038/s41467-018-06156-7
- [2] W. Decking *et al.*, “Status of the European XFEL”, in *Proc. 10th Int. Particle Accelerator Conf. (IPAC'19)*, Melbourne, Australia, May 2019, pp. 1721–1723. doi:10.18429/JACoW-IPAC2019-TUPRB020
- [3] M. Castellano *et al.* “Measurements of coherent diffraction radiation and its application for bunch length diagnostics in particle accelerators”, *Phys. Rev. E* vol. 63, pp. 1–8, 2001. doi:10.1103/PhysRevE.63.056501
- [4] S. Wesch, B. Schmidt, C. Behrens, H. Delsim-Hashemi, P. Schmüser, “A multi-channel THz and infrared spectrometer for femtosecond electron bunch diagnostics by single-shot spectroscopy of coherent radiation”, *Nucl. Instr. Meth. Phys. Res. A*, vol. 665, pp. 40-47, 2011. doi:10.1016/j.nima.2011.11.037
- [5] N. M. Lockmann, Ch. Gerth, B. Schmidt and S. Wesch “A non-invasive THz spectrometer for bunch length characterization at European XFEL”, in *Proc. IPAC'19*, Melbourne, Australia, May 2019, paper WEPGW014, pp. 2495-2497. doi:10.18429/JACoW-IPAC2019-WEPGW014
- [6] TEWS Technologies, TAMC532, 32x12/14 Bit, 50/75 Msps, ADC for MicroTCA.4. <http://www.tews.com>
- [7] B. Schmidt *et al.*, “Longitudinal bunch diagnostics using coherent transition radiation spectroscopy”, arXiv:1803.00608, 2018.

FAST KICKER SYSTEM FOR EUROPEAN XFEL BEAM DISTRIBUTION

F. Obier, W. Decking, M. Hüning, J. Wortmann, DESY, Hamburg, Germany

Abstract

A special feature of the European XFEL [1] X-ray laser is the possibility to distribute the electron bunches of one RF pulse to different free-electron laser (FEL) beamlines. This is achieved through a combination of kickers and a Lambertson DC septum. The integration of a beam abort dump allows a flexible selection of the bunch pattern at the FEL experiment, while the superconducting linear accelerator operates with constant beam loading. The driver linac of the FEL can deliver up to 600 μs long bunch trains with a repetition rate of 10 Hz and a maximum energy of 17.5 GeV. The FEL process poses very strict requirements on the stability of the beam position and hence on all upstream magnets. It was therefore decided to split the beam distribution system into two kicker systems, long pulse kickers (KL) with very stable amplitude (10^{-4}) and a long flat-top ($\sim 300 \mu\text{s}$) with relatively slow rise/fall times ($\sim 20 \mu\text{s}$) and fast stripline kickers (KS) with moderate stability but very fast pulses ($\sim 5 \text{ ns}$).

OVERVIEW

Figure 1 shows a schematic overview of the European XFEL fill pattern and beam distribution system. The six KL flat-top kickers are operated with a rectangular pulse with variable pulse length and switch the beam between the two main FEL beamlines. To create the flexible bunch pattern, a kicker-septum combination including ten KS stripline kickers is installed, with which it is possible to extract individual bunches into the dump beamline (TLD) with the maximum bunch frequency of 4.5 MHz. Pilot bunches for the intra-bunch feedback that is needed to stabilise the beam, bunches during the still-needed gap for rise time of the KL beam distribution kickers and all bunches not needed for lasing are extracted to the dump. Bunches for the SASE3 undulator can be stimulated with a KS kicker so that they do not lase in the SASE1 undulator. All of this requires a sophisticated bunch pattern generator and timing system [2].

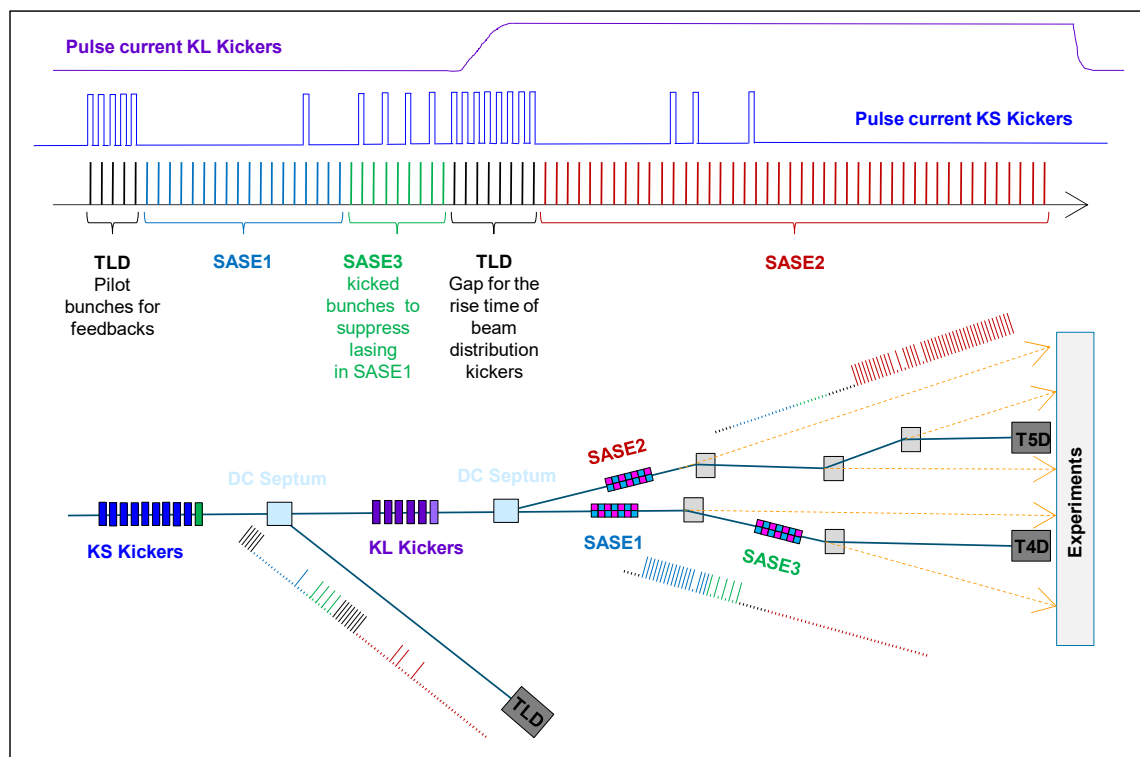


Figure 1: European XFEL fill pattern scheme: The flexible bunch pattern for the FEL lines is created by kicking all bunches that are not used for lasing into the main dump line (TLD) by means of the KS kickers. The bunch train parts for the FEL lines are distributed by the KL kickers. SASE2 bunches are kicked, SASE1/3 bunches are not.

While reducing the bunch repetition rate in the SA1 beamline from 1.1 MHz to 584 kHz by kicking every second bunch into the dump beamline with the KS kickers, a rising displacement of the remaining bunch train in the SA1 beamline was observed (Fig.4). On the vertical axis is the displacement and on the horizontal axis is bunch position number. We see a displacement of 25 μm from the first to the last bunch of train.

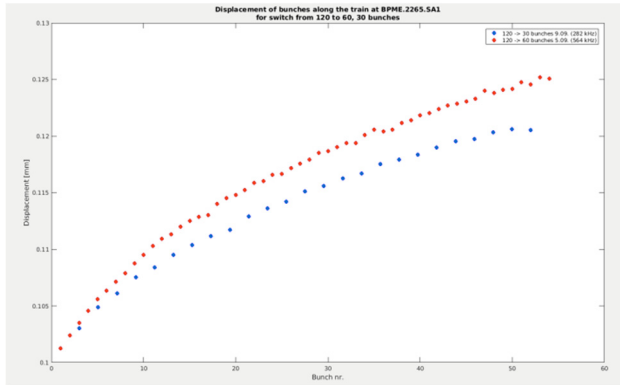


Figure 4: Displacement of bunches along the train at BPME.2265.SA1 for switch from 120 to 60 bunches.

This effect was later re-examined during a 4.5 MHz study period. In the accelerator 500 bunches were generated with a bunch repetition rate of 4.5 MHz. The experiment was started with 100 pre-bunches and 400 bunches in beamline SA1. The offset was measured with a downstream high precision cavity beam position monitor (Fig. 5).

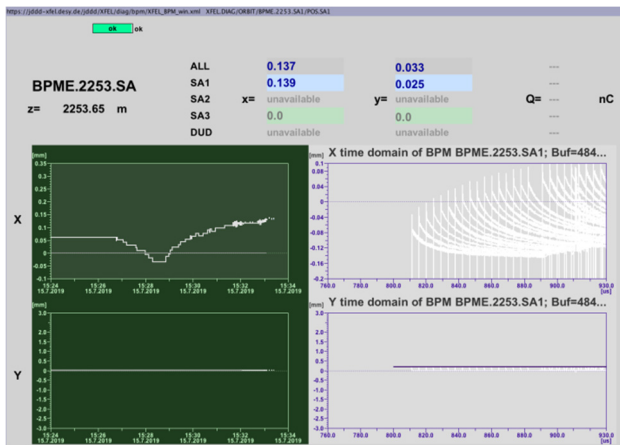


Figure 5: Displacement of bunches along the train at BPM_2253.SA1 with operation of 4.5 MHz.

Then step-by-step the number of pre-bunches was increased by 20 and the number of SA1 bunches was reduced by 20, so that the maximum allowed number of bunches remained the same. An increasing offset with an initial amplitude of up to 200 μm and an exponential decay clearly can be seen. We attribute this effect to eddy currents in the kicker chamber. The eddy currents induced by each kicker pulse (while kicking the pre-bunches into the dump beamline) have not decayed yet when the next pulse occurs, this leads to accumulation of the residual

field up to a saturation level. As the bunches in the SA1 bunch train are not kicked, the residual field induced into the kicker chamber decays.

Figure 6 shows a fit of the rising x-offset with rising number of pre-bunches (blue line) and the decreasing x-offset over the SA1 bunch train (red line). The eddy currents lead to about 2 μm relative kick after 200 ns with a damping time of approximately 20 μs . The nominal kick of the KS kickers is about 18 mm at this position, thus the effect is of the order of 1e-4 .

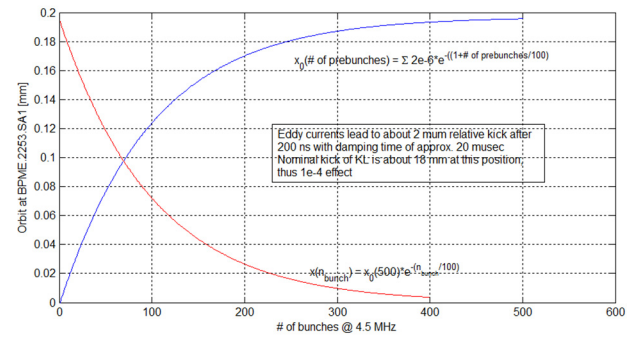


Figure 6: coarse fit of x-offset rising with rising number of pre-bunches (blue) and decreasing over SA1 bunch train (red).

The time constant of the eddy current can be influenced by the choice of chamber material, by its conductivity, or by the pulse shape (rise and fall time). The lower the conductivity of the material, the faster the eddy currents will decay, and the slower the rising and falling edges, the lower the eddy currents will be. This will be studied in the future to reduce the effect.

SUMMARY

The Beam Switchyard of the European XFEL allows fast switching between the various SASE beamlines, which was made possible by the development of a fast kicker system. The residual orbit changes caused by the fast switching should be eliminated by the feedforward capabilities of the intra bunch train feedback.

As the offset due to the eddy currents exceeds the specifications for the existing intra bunch feedback system, a new feedforward system has to be implemented. Most probably one of the KL kickers [6] will be modulated with a correctional signal.

REFERENCES

- [1] M. Altarelli *et al.*, “The Technical Design Report of the European XFEL”, DESY 2006-097.
- [2] L. Fröhlich *et al.*, “Multi-Beamline operation at the European XFEL”, presented at the FEL'19, Hamburg, Germany, Aug. 2019, paper WEP008, this conference.
- [3] A. Xiao, “On-axis injection schema for ultra-low emittance light sources”, in *Proc. NAPAC'13*, Pasadena, CA, USA, Sep.-Oct. 2013, paper WEP013, pp. 1076-1078.

LONG PULSE KICKER FOR EUROPEAN XFEL BEAM DISTRIBUTION

F. Obier, W. Decking, M. Hüning, J. Wortmann, DESY, Hamburg, Germany

Abstract

A special feature of the European XFEL [1] X-ray laser is the possibility to distribute the electron bunches of one RF pulse to different free-electron laser (FEL) beamlines. This is achieved through a combination of kickers and a Lambertson DC septum. The integration of a beam abort dump allows a flexible selection of the bunch pattern at the FEL experiment, while the superconducting linear accelerator operates with constant beam loading. The driver linac of the FEL can deliver up to $600\mu\text{s}$ long bunch trains with a repetition rate of 10Hz and a maximum energy of 17.5GeV. The FEL process poses very strict requirements on the stability of the beam position and hence on all upstream magnets. It was therefore decided to split the beam distribution system into two kicker systems, long pulse kickers (KL) with very stable amplitude (10^{-4} , flat-top) and relatively slow pulses ($\sim 300\mu\text{s}$) and fast stripline kickers (KS) with moderate stability but very fast pulses ($\sim 50\text{ns}$).

OVERVIEW

Figure 1 shows a schematic overview of the European XFEL fill pattern and beam distribution system. The six so-called KL flat-top kickers are operated with a rectangular current pulse with variable pulse length and switch the beam between the two main FEL beamlines. To create the flexible bunch pattern, a kicker-septum combination including ten so-called KS stripline kickers is installed, with which it is possible to extract individual bunches into the dump beamline (TLD) with the maximum bunch repetition frequency of 4.5MHz. Pilot bunches for the intra-bunch feedback that is needed to stabilise the beam, bunches during the still-needed gap for rise time of the KL beam distribution kickers and all bunches not needed for lasing are extracted to the dump. Bunches for the SASE3 undulator can be stimulated with a KS kicker so that they do not lase in the SASE1 undulator. All of this requires a sophisticated bunch pattern generator and timing system [2].

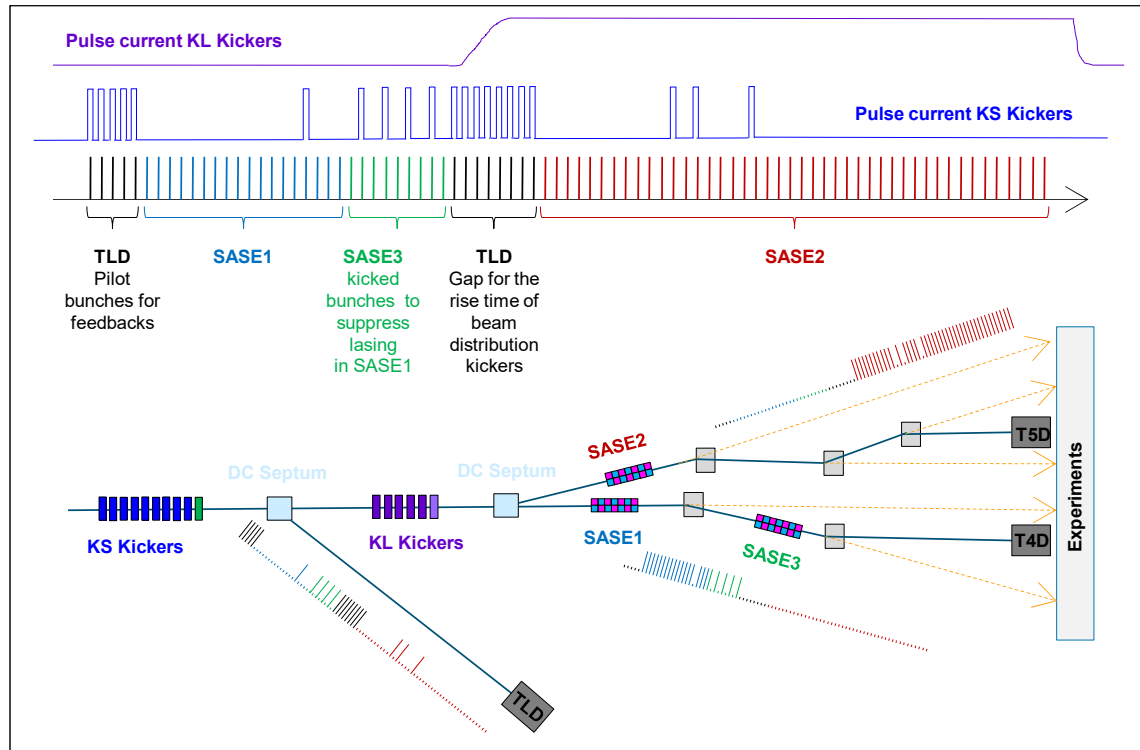


Figure 1: European XFEL fill pattern scheme: The flexible bunch pattern for the FEL lines is created by kicking all bunches that are not used for lasing into the main dump line (TLD) by means of the KS kickers. The bunch train parts for the FEL lines are distributed by the KL kickers. SASE2 bunches are kicked, SASE1/3 bunches are not.

PARAMETERS

The kick angle $\Delta\theta$ from a kicker can be calculated with Energy E and magnetic field B

$$\Delta\theta = \frac{e_0 c}{E} \int B dl = \frac{e_0 c}{E} \cdot \frac{I * N * \mu_0 * l_{eff}}{l_{gap}},$$

with I the current, l_{eff} the length of the kicker, l_{gap} the gap width and N the number of windings.

The maximum energy of European XFEL is 17.5 GeV. The kick angle is calculated about 104 μ rad for one kicker. We need 5 kickers for a kick angle of 0.5 mrad, one kicker is a spare. Table 1 summarizes the KL kicker specification.

Table 1: Specification of the KL Kicker [3]

	Kicker (KL)
Pulse Form	Flat top
Repetition Rate	10 Hz
Max. Pulse Width	300×10^{-6} s
Rise/Fall Time	$\approx 20 \times 10^{-6}$ s
Rel. Amp. Stability	3×10^{-4}
Rel. Residual Ripple	3×10^{-4}
Kick angle	0.5 mrad
Int. Field at 20 GeV	33.4 mTm
Kicker aperture	50 mm
Kicker Type	Strip Line
Kicker active length	936 mm
Number of kickers	6
Pulser Voltage	100 V
Pulse Current	600 A

KICKER MAGNET (KL)

The KL kicker magnets are realised as air coils outside the beam vacuum system (Fig. 2). They use striplines that form a single vertical conductor loop around a ceramic beam chamber, which is sputtered (metal-coated) on the inside. The conductor consists of high-frequency litz wires to reduce eddy current effect, skin effect and proximity effect. The mounting structure of the kickers needs to be non-metallic, as otherwise eddy currents are induced which strongly distort the magnetic field of the current pulses. The thermoplastic PEI was chosen for radiation, heat resistance and mechanical properties.

The design of the kickers requires a metal-coated ceramic chamber. The following aspects of sputtered ceramic chambers are important: Sputtering is necessary in order to transport the mirror current of the beam and to contain the radio frequency (RF) fields from the beam inside the chamber while the magnetic field of the kickers (at lower frequency) penetrates the chamber's wall. The coating material is stainless steel 4.4541 (titanium-stabilised). The thickness of the coating is determined by a compromise between reduction of the magnetic field and heat dissipation due to the mirror current.

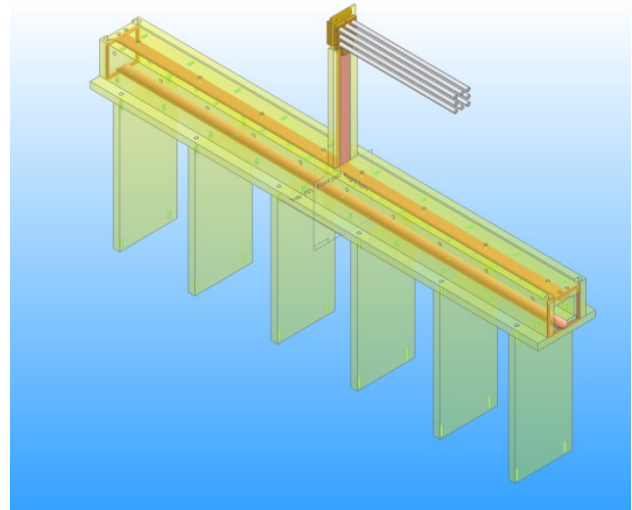


Figure 2: Sketch of the KL beam distribution kicker without ceramic chamber.

PULSER (KL)

For the KL beam distribution kickers, a nearly rectangular current pulse is required, so short rise and fall times of less than 20 μ s and a very stable flat top of the pulse are important. Therefore, a pulse-regulated current source with MOSFET technology is used. The main MOSFET is switched by a push-pull driver providing a fast rise time. While turned on, the current through the kicker magnet is sensed and fed back to the main MOSFET through a high precision controller (operational amplifier circuit), providing a very stable flat top (Fig. 3).

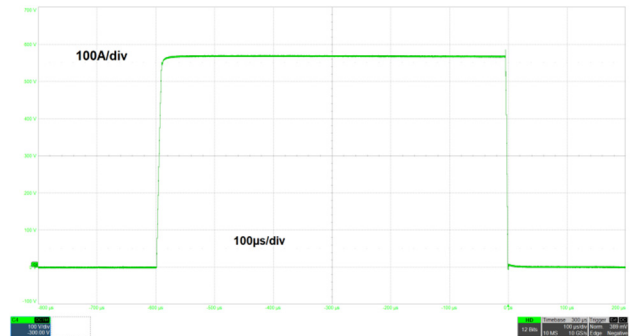


Figure 3: Example of current pulse.

Eight MOSFETs are operated in parallel, generating a pulse current of up to 600 A. Data communications, internal timings, power-up and power-down sequences and some service modes are realised with an FPGA board (Fig. 4). The pulser is triggered with a 5V TTL signal from the MTCA-based main timing system, with the pulse length and trigger start time being controlled by the bunch pattern [2].

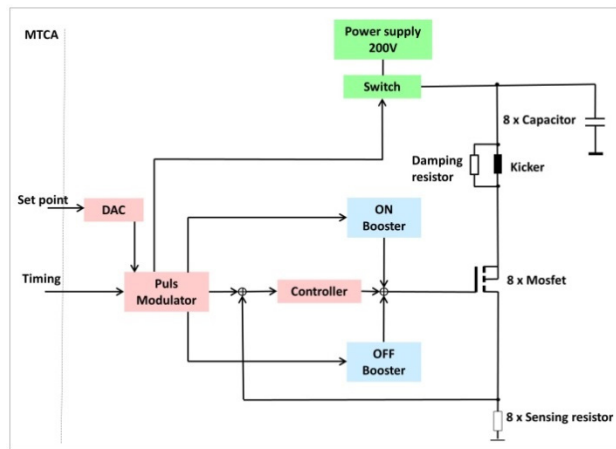


Figure 4: Block diagram of the KL beam distribution pulser.

During commissioning, the pulse flatness (Fig. 5) was also examined with 200 bunches at 1.1 MHz and measuring the SASE intensity in the SASE2 beamline. The beam distribution pulser was set to maximum pulse length of 600 μ s. Then the timing was adjusted so that the 200 bunches were at the beginning of the current pulse flat top. Then the delay was changed in 50us steps until the end of flat top. The shape of the SASE intensity signal did not change over the pulse flat top.

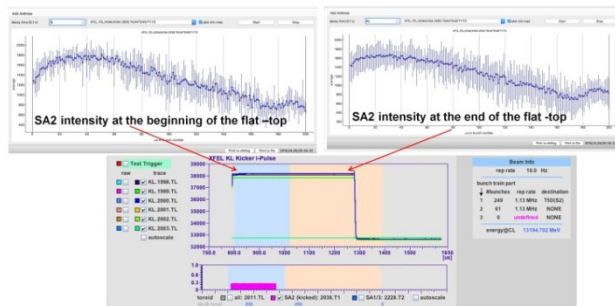


Figure 5: Measurement of KL kicker current pulse amplitude stability. Bottom plot shows kicker pulses (600 μ s) and bunch train (200 bunches). Top plots show SASE2 intensity over bunch train, at beginning (left) and end (right) of pulser flat top (pulser trigger timing was shifted).

The bunches can be distributed into the SASE2 beamline at the beginning or end of the bunch train and so either the falling edge or the rising edge of the KL pulser must be fast, so both were examined. At the falling edge a too long influence on the non-kicked SASE1 bunches (about 50 μ s) was observed. This can be avoided by a modification of the pulser's power circuit. Tests are ongoing and the modification can be installed at the next shutdown in August 2019.

Furthermore, one of the 8 Mosfet stages in one of the pulsers was modified, so it is now possible to generate a variable pulse shape of 80 A, needed to build a feed forward system. A first test (Fig. 6) was carried out at the

FLASH accelerator. A bunch train of 95 bunches was taken to the FLASH 2 beamline. For an energy of 600 MeV two kicker magnets with a current of 245 A are used. In the study, the orbit placement of the bunch train was measured at a BPM and averaged over several iterations. These data were processed using a MATLAB algorithm and passed to the pulser stage via a DAC.

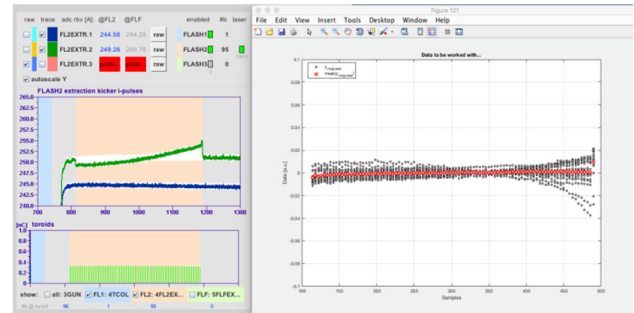


Figure 6: Measurement at FLASH with a modified KL pulser. Left plot shows zoomed current pulses (blue: standard pulser; green: modified pulser with modulated pulse) and bunch train (95 bunches). Right plot shows BPM offset over the pulse train (red: corrected with modulated pulse; dark: history while correction is computed).

SUMMARY

The Beam Switchyard of the European XFEL allows fast switching between the various SASE beamlines.

The pulse flat top stability of the KL kicker system meets the demands for stable SASE operation.

Tests are ongoing to further improve the pulse edges in rise/fall times and ripple.

The orbit changes caused by the offset due to the eddy currents of the fast kickers (KS) [4] exceed the specifications of the existing intra bunch feedback system. A new feedforward system has to be implemented. One of the KL kickers will be prepared to receive a modulated correctional signal.

REFERENCES

- [1] M. Altarelli *et al.*, "The Technical Design Report of the European XFEL", DESY 2006-097.
- [2] L. Fröhlich *et al.*, "Multi-Beamline operation at the European XFEL", presented at the FEL'19, Hamburg, Germany, Aug. 2019, paper WEP008, this conference.
- [3] W. Decking, "Layout of the Beam Switchyard at the European XFEL", in *Proc. EPAC'08*, Genoa, Italy, Jun. 2008, paper WEPC073, pp. 2163-2165.
- [4] F. Obier *et al.*, "Long pulse kicker for European XFEL beam distribution", presented at the FEL'19, Hamburg, Germany, Aug. 2019, paper WEP014, this conference.

ELECTRO-OPTICAL BUNCH LENGTH DETECTION AT THE EUROPEAN XFEL

Bernd Steffen*, Marie Kristin Czwalińska, Christopher Gerth
Deutsches Elektronen-Synchrotron DESY, Hamburg, Germany
Eléonore Roussel, Serge Bielawski, Clément Evain, Christophe Szwaj
Univ. Lille, CNRS, UMR 8523 - PhLAM - Physique des Lasers, Atomes et Molécules,
Centre d'Étude Recherches et Applications (CERLA), Lille, France

Abstract

The electro-optical bunch length detection system based on electro-optic spectral decoding has been installed and is being commissioned at the European XFEL. The system is capable of recording individual longitudinal bunch profiles with sub-picosecond resolution at a bunch repetition rate of 1.13 MHz. Bunch lengths and arrival times of entire bunch trains with single-bunch resolution have been measured as well as jitter and drifts for consecutive bunch trains. In addition, we are testing a second electro-optical detection strategy, the so-called photonic time-stretching, which consists of imprinting the electric field of the bunch onto a chirped laser pulse, and then "stretching" the output pulse by optical means. As a result, we obtain a slowed down "optical replica" of the bunch shape, which can be recorded using a photodiode and GHz-range acquisition. These tests are performed in parallel with the existing spectral decoding technique based on a spectrometer in order to allow a comparative study.

In this paper, we present first results for both detection strategies from electron bunches after the second bunch compressor of the European XFEL.

INTRODUCTION

The accelerator for the European X-ray Free-Electron Laser (EuXFEL) delivers femtosecond electron bunches at an energy of up to 17 GeV at a repetition rate of up to 4.5 MHz in bursts of up to 2700 bunches every 100 ms. The electron bunches can be distributed between three undulator beamlines, and the generated femtosecond X-ray laser pulses at wavelengths between 0.05 nm and 6 nm can serve up to three user experiments in parallel [1].

Short electron bunches with a high peak current are needed to drive the SASE process in the magnetic undulators. To reach these short bunches, the initially long electron bunches created at the photocathode gun are compressed in three magnetic bunch compressor chicane at electron bunch energies of 130 MeV, 700 MeV, and 2.4 GeV, respectively, in between the four accelerating sections.

Electro-optical bunch length detection (EOD) [2] offers the possibility of measuring the longitudinal bunch profile and arrival time in a non-destructive manner with single bunch resolution for every bunch in the bunch train. The measurements presented in this paper were performed at the

EOD system downstream of the second bunch compressor at a beam energy of 700 MeV and with an expected bunch length of around 250 ps.

ELECTRO-OPTICAL BUNCH LENGTH DETECTION AT THE EUROPEAN XFEL

Electro-optically active crystals like gallium phosphide (GaP) become birefringent in the presence of an electric field. The electro-optical detection techniques use this effect to transfer the temporal profile of fast changing electric fields by sampling the change in birefringence with laser pulses. Afterwards, the modulated temporal profile of the laser pulse can be analyzed with classical laser techniques.

For the EOD system at the EuXFEL the spectrally resolved electro-optical detection technique (EOSD) was chosen. It uses a chirped laser pulse, where the frequency components of a broadband laser pulse are sorted in time. The temporal profile of the modulation can be retrieved from its modulated spectrum using the known relationship between wavelength and longitudinal (temporal) position in laser pulse [3]. It has been shown that sub-ps electron bunches of about 100 pC charge can be measured with about 200 fs resolution using EOSD [2, 4].

Temporally [5] and spatially [6] resolved detection offer a higher time resolution as good as 60 fs, but they have higher demands on the imaging system for the laser and need higher laser pulse energies compared to EOSD. For a more comprehensive description of electro-optical detection techniques and theory see [4, 7]. The maximum rate of all techniques is limited by both the repetition rates of the laser system and (line) detector.

To measure single shot laser spectra as needed for EOSD with a high repetition rate, currently two different techniques are available. One can use a spectrometer with a high-speed line camera like the KALYPSO detector [8]. The KALYPSO detector can measure spectra with a repetition rate up to 2.7 MHz and was used previously to measure bunch length in the EOSD systems at the European XFEL [9]. Alternatively one can stretch the picosecond short laser pulse in a fiber of known dispersion to a length of several nanoseconds and measure the temporal profile of the laser pulse with a fast photodiode and gigahertz bandwidth oscilloscope, known as photonic time-stretch [10]. Photonic time-stretch has first been proposed for recording GHz-range RF signals [11]. The principle has been then applied to electro-optic sampling of free-propagating CSR THz pulses at SOLEIL [12], and more

* bernd.steffen@desy.de

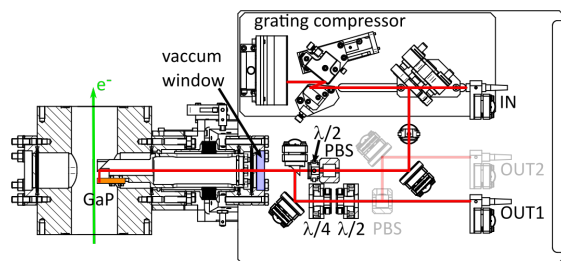


Figure 1: Assembly drawing of the optics set-up at the electron beam line including the vacuum chamber (left). PBS: polarizing beam splitter.

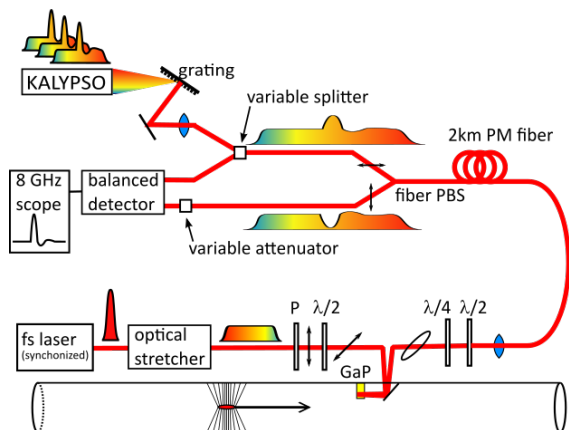


Figure 2: Schematic drawing of a spectrally encoded electro-optical detection setup including the single shot spectrometer and the photonic time-stretch detector. P: polarizer; PBS: polarizing beam splitter.

recently electron bunch near field at KARA [13]. Given the inherent high repetition rate capability of photonic time-stretch, it appears relevant to test the method in the high-repetition rate Free-Electron Laser context, and compare its performances with respect to spectrometer-based electro-optic sampling.

To compare both techniques, the existing EOSD set up was modified to allow applying both techniques in parallel.

MODIFICATIONS OF THE EOSD SYSTEM AT THE EUROPEAN XFEL

Most parts of the EOSD system described earlier [9] remained unchanged, including the Ytterbium fiber laser system and its synchronization, the spectrometer with the KALYPSO MHz line detector, the vacuum chamber with the 2 mm thick GaP crystal, and the MicroTCA.4 [14] crate with the analogue and digital boards for laser synchronization and data readout.

At the optics set-up at the electron beam line vacuum chamber the free-space polarizing beam splitter (PBS) and the following two single-mode fiber couplers were replaced by a fiber coupler (Fig. 1) coupling the laser into a two kilometer long polarization maintaining (PM) fiber. The laser pulse with its polarization modulated in the GaP crystal by

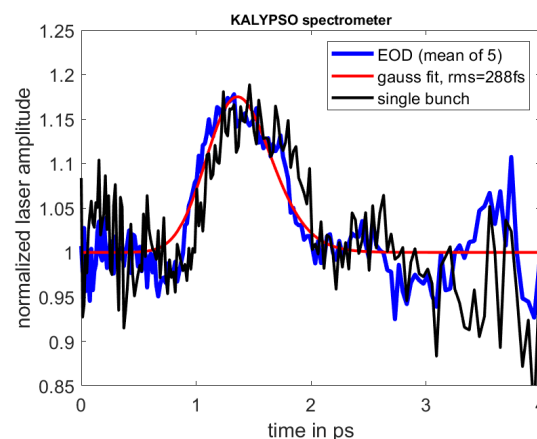


Figure 3: A single-shot EOD measurement from the spectrometer together with an average of five consecutive bunches and a Gaussian fit to the average.

the electric field of the electron bunch is stretched to several nanoseconds in the long fiber and afterwards it is split into its orthogonal polarizations by a fiber PBS. The two polarizations are guided to the two inputs of a balanced photodetector with 20 GHz bandwidth (DSC-R412, Discovery Semiconductors Inc., USA). Both arms hold a variable range of the detector. One of the attenuators is realized as an variable splitter which can also be used to send one polarization to the single shot spectrometer, alternatively (see Fig. 2). The electrical outputs of the balanced photodetector are connected to a 8 GHz Agilent oscilloscope to measure and store the data.

For a given laser chirp, defined by the initial chirp of the pulses from the laser system and the setting of the grating compressor at the beam line, a time calibration can be done by scanning the laser pulse over the electron bunch at stable accelerator conditions. The laser synchronization allows sub-picosecond time steps with high accuracy and the resulting shift of the bunch signal in the laser spectrum allows a detector pixel to time calibration for the spectrometer as well as a measurement of the stretch factor for the photonic time-stretch.

FIRST MEASUREMENTS

Figure 3 shows a single shot measurement from the KALYPSO spectrometer together with an average of five consecutive bunches and a Gaussian fit to the averaged signal. The electron bunch had a charge of 250 pC and was measured to have an approximate bunch length of 290 fs (rms), which is in good agreement with the simulated electron bunch shape for the given accelerator parameters. However the signal-to-noise ratio (SNR) is significantly decreased as compared to measurements done before the modification of the EOSD setup (Fig. 4). We attribute this to the additional attenuation and disturbances in the spectrum from the long PM fiber and other fiber components (especially the fiber PBS) leading to

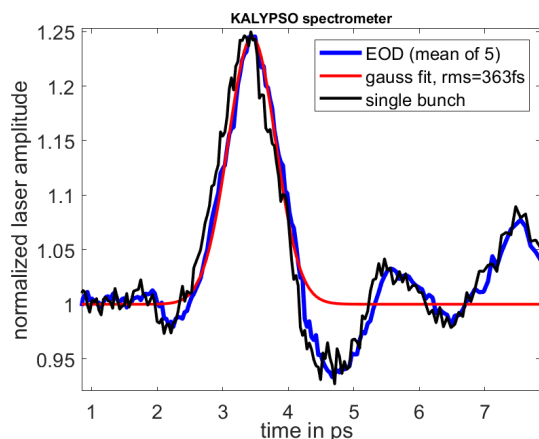


Figure 4: A single-shot EOSD measurement from the spectrometer with the EOSD setup before modification showing a significantly better SNR. Here the bunch charge was 500 pC.

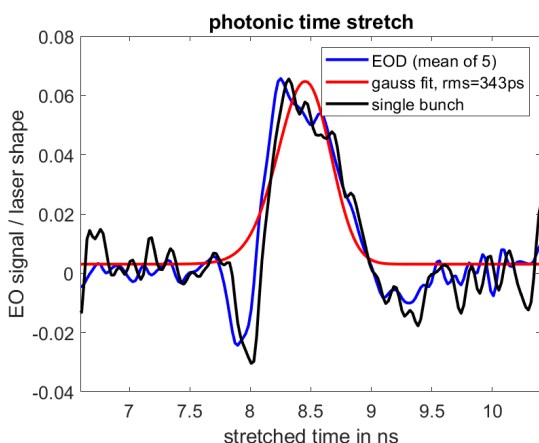


Figure 5: A single-shot EOSD measurement recorded with photonic time-stretch.

a reduced laser power at the line detector and a less stable spectrum with reduced bandwidth.

The corresponding measurement recorded with photonic time-stretch is shown in Fig. 5. The data was measured approx. 30 minutes before the data shown in Fig. 3 at identical accelerator settings. It shows an approximate bunch length of 340 fs (rms), which is slightly longer than measured with the spectrometer measurement.

The laser spectrum recorded with photonic time-stretch without modulation from the electron beam shows significant modulation due to interferences, which are most likely caused by the insufficient performance of the fiber polarizing beam splitter (Fig. 6), leading to some additional artifacts in the reconstructed bunch shape.

CONCLUSION AND OUTLOOK

The EOSD setup at the European XFEL was modified to test two different techniques to capture single shot spectra of the modulated laser pulses with MHz repetition rate, a spectrometer with a MHz line detector and a photonic

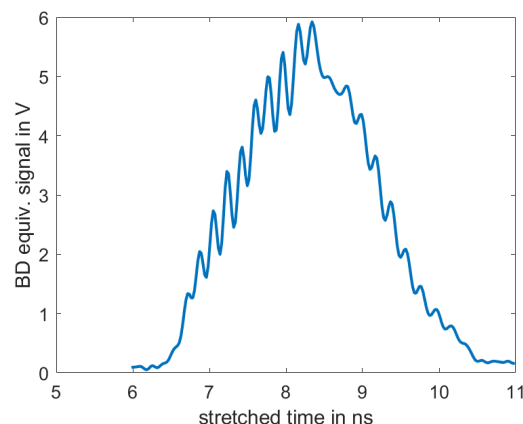


Figure 6: Laser spectrum recorded with photonic time-stretch without modulation from the electron beam.

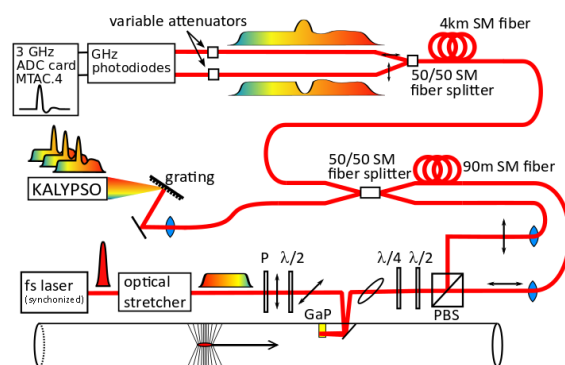


Figure 7: Schematic drawing of a spectrally encoded electro-optical detection setup. P: polarizer; PBS: polarizing beam splitter.

time-stretch technique. Both approaches can measure the bunchlength with the required repetition rate of 1.13 MHz and an estimated resolution of some 10 fs, however both suffer from unwanted distortions and losses due to PM fiber components in the current setup, which limits the possibility to compare the performance of both approaches.

A new setup (Fig. 7) is currently installed which is based purely on SM fiber components. The splitting of the orthogonal polarizations is done by a free-space PBS directly at the beamline again, which has proven to have the better performance. In addition the laser pulse in one polarization is delayed by 440 ns (half of the pulse spacing of the laser) before both polarizations are combined again and sent to the two detectors in parallel. Since both detectors can sample with 2.2 MHz, both polarizations, carrying modulations of opposite sign, can be measured and used for the electron pulse reconstruction.

In addition it is planned to exchange the oscilloscope to an fast MTCA based ADC card (ADQ7DC, Teledyne Signal Processing Devices, Sweden) to integrate the readout into the EuXFEL control system.

REFERENCES

- [1] D. Nölle, "Commissioning of the European XFEL," in *Proceedings of the LINAC'18*, Beijing, China, 2018. doi:10.18429/JACoW-LINAC2018-FR2A02
- [2] B. Steffen *et al.*, "Electro-optic time profile monitors for femtosecond electron bunches at the soft X-ray free-electron laser FLASH," *Physical Review Special Topics - Accelerators and Beams*, vol. 12, no. 3, 2009. doi:10.1103/PhysRevSTAB.12.032802
- [3] I. Wilke, A. M. MacLeod, W. A. Gillespie, G. Berden, G. M. H. Knippels, and A. F. G. van der Meer, "Single-shot electron-beam bunch length measurements," *Phys. Rev. Lett.*, vol. 88, p. 124 801, 12 Mar. 2002. doi:10.1103/PhysRevLett.88.124801
- [4] B. Steffen, "Electro-optic methods for bunch length diagnostics at FLASH," PhD thesis, University of Hamburg, 2007.
- [5] G. Berden, S. P. Jamison, A. M. McLeod, W. A. Gillespie, B. Redlich, and A. F. G. van der Meer, "Electro-optic technique with improved time resolution for real-time, nondestructive, single-shot measurements of femtosecond electron bunch profiles," *Phys. Rev. Lett.*, vol. 93, p. 114 802, 2004. doi:10.1103/PhysRevLett.93.114802
- [6] A. L. Cavalieri *et al.*, "Clocking femtosecond x rays," *Phys. Rev. Lett.*, vol. 94, no. 11, p. 114 801, 2005. doi:10.1103/PhysRevLett.94.114801
- [7] S. Casalbuoni, H. Schlarb, B. Schmidt, P. Schmüser, B. Steffen, and A. Winter, "Numerical studies on the electro-optic detection of femtosecond electron bunches," *Phys. Rev. ST Accel. Beams*, vol. 11, p. 072 802, 7 Jul. 2008. doi:10.1103/PhysRevSTAB.11.072802
- [8] L. Rota *et al.*, "KALYPSO: A Mfaps linear array detector for visible to NIR radiation," in *Proceedings of the IBIC'16*, Barcelona, Spain, 2016. doi:10.18429/JACoW-IBIC2016-WEPG46
- [9] B. Steffen, M. Czwalińska, C. Gerth, and P. Peier, "First electro-optical bunch length measurements at the European XFEL," in *Proceedings of the IBIC'18*, Shanghai, China, 2018. doi:10.18429/JACoW-IBIC2018-WEOA03
- [10] A. Mahjoubfar, D. V. Churkin, S. Barland, N. Broderick, S. K. Turitsyn, and B. Jalali, "Time stretch and its applications," *Nature Photonics*, vol. 11, p. 341, Jun. 2017. doi:10.1038/nphoton.2017.76
- [11] A. Bhushan, F. Copping, and B. Jalali, "Time-stretched analogue-to-digital conversion," *Electronics Letters*, 1998. doi:10.1049/el:19980629
- [12] E. Roussel *et al.*, "Observing microscopic structures of a relativistic object using a time-stretch strategy," *Scientific Reports*, vol. 5, p. 10 330, May 2015. doi:10.1038/srep10330
- [13] S. Bielawski *et al.*, "From self-organization in relativistic electron bunches to coherent synchrotron light: Observation using a photonic time-stretch digitizer," *Scientific Reports*, vol. 9, no. 1, p. 10 391, Jul. 2019, ISSN: 2045-2322. doi:10.1038/s41598-019-45024-2
- [14] T. Wilksen *et al.*, "The control system for the linear accelerator at the European XFEL: Status and first experiences," in *Proceedings of the ICALEPCS'17*, Barcelona, Spain, 2017. doi:10.18429/JACoW-ICALEPCS2017-MOAPL01

PRECISE LASER-TO-RF SYNCHRONIZATION OF PHOTOCATHODE LASERS

M. Titberidze*, M. Felber, T. Kozak, T. Lamb, J. Müller, H. Schlarb, S. Schulz, F. Zummack
Deutsches Elektronen-Synchrotron, DESY, Hamburg, Germany
C. Sydlo, Paul Scherrer Institut, PSI, Villigen, Switzerland

Abstract

RF photo-injectors are used in various large, mid and small-scale accelerator facilities such as X-ray Free Electron Lasers (XFELs), external injection-based laser-driven plasma accelerators (LPAs) and ultrafast electron diffraction (UED) sources. Many of these facilities require a high precision synchronization of the photo-injector laser system, either because of beam dynamics reasons or the photo-injector directly impacting pump-probe experiments carried out to study physical processes on femtosecond timescales. It is thus crucial to achieve synchronization in the order of 10 fs rms or below between the photocathode laser and the RF source driving the RF gun. In this paper, we present the laser-to-RF synchronization setup employed to lock a commercial near-infrared (NIR) photocathode laser oscillator to a 2.998 GHz RF source. Together with the first results achieving ~ 10 fs rms timing jitter in the measurement bandwidth from 10 Hz up to 1 MHz, we describe an advanced synchronization setup as a future upgrade, promising even lower timing jitter and most importantly long-term timing drift stability.

INTRODUCTION

The (short and innovative bunches and accelerators at DESY) SINBAD facility will host several accelerator research and development experiments like ARES [1] and AXISIS [2]. These experiments will mainly focus on the production of ultra-short electron bunches (0.2 fs to 10 fs) and testing novel high gradient acceleration techniques. The (accelerator research experiment at sinbad) ARES is a conventional S-band linear RF accelerator (linac) which is currently in the construction and commissioning phase [3]. It consists of S-band ($f_{\text{RF}} = 2.998$ GHz) normal conducting accelerating structures: 1.5 cell RF gun [4] and two travelling wave structures (TWS1, TWS2) [5]. The electron bunches are produced by impinging ultrashort laser pulses on a photocathode inside the RF gun. The ARES linac is schematically shown in Fig. 1. The final electron beam parameters at ARES are defined in [3] and require an arrival time jitter of < 10 fs rms. In order to meet this requirement it is crucial to achieve a precise laser-to-RF synchronization between the pulsed injector laser and the 2.998 GHz RF reference signal from the RF master oscillator (MO). The injector laser is a commercial system from Light Conversion¹ with a fundamental wavelength of 1030 nm and variable pulse duration of 0.16 ps to 10 ps. The laser oscillator of

this system is designed such that the repetition rate of the optical pulses $f_{\text{rep}} = 83.28$ MHz is the 36th sub-harmonic of the RF reference frequency $f_{\text{RF}} = 2.998$ GHz.

DIRECT CONVERSION BASED LASER-TO-RF SYNCHRONIZATION

General Concept

One of the most common techniques to synchronize a mode-locked laser to an RF signal is using a fast photodetector [6–9]. The pulsed optical signals are converted to electrical pulses which are composed of high spectral purity harmonics of the laser repetition rate. The cutoff frequency of the RF comb is given by the bandwidth of the photodetector. The desired frequency component of the RF comb can be filtered out using an RF band-pass filter (BPF) and amplified until the signal level is sufficient for downconversion. The downconverted signal is digitized using an analog-to-digital converter (ADC) employing so called non-IQ sampling [6, 10, 11]. The amplitude and phase information is extracted in the digital domain. The obtained phase error information is fed back to the piezo actuator of the laser oscillator using a piezo driver to establish the phase locked loop (PLL).

There are several advantages of downconverting the photodetected signal to an intermediate frequency (IF) instead of baseband. Baseband signals are often degraded by undesired DC offsets due to imperfections of the electronics and they are highly susceptible to electromagnetic interference (EMI). Both effects limit the overall PLL performance potentially leading to a poor synchronization performance. These problems are mitigated by direct sampling the IF signal and using digital phase detection.

However, there are still fundamental limitations related to the photodetection process, such as the AM-PM effect, where optical power fluctuations are converted to phase fluctuations of each frequency component of the generated frequency comb [12, 13] while low signal levels from the photodetector together with the intrinsic thermal and shot noise sources lead to a limited signal-to-noise ratio (SNR).

One can estimate the thermal noise limited timing jitter for a 50 Ω terminated photodetector using the following expression [14]:

$$T_{\text{rms}} = \frac{1}{2\pi f_c} \sqrt{\frac{P_{\text{th}}}{P_c} \Delta f}. \quad (1)$$

Here, $P_{\text{th}} = -174$ dBm/Hz is the thermal noise power at room temperature in a 1 Hz bandwidth. P_c and f_c are the

* mikheil.titberidze@desy.de

¹ Pharos SP-06-200-PP

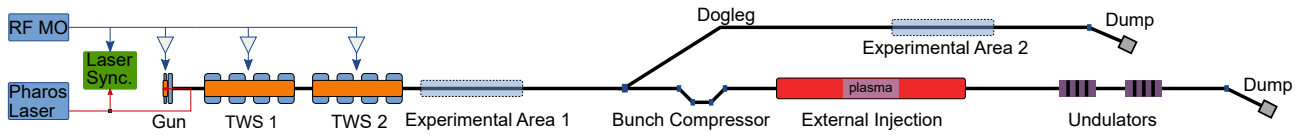


Figure 1: Layout of ARES linac.

carrier power and frequency respectively. Δf is the noise bandwidth. Using a commercial fast photodetector, a carrier power of -25 dBm at 2.998 GHz can be extracted for an average optical power of 5 mW and applied reverse bias voltage of 12 V. This leads to approximately 2 fs thermal noise limited timing jitter in a 1 MHz bandwidth. In addition, the long-term timing drift performance is a major problem in the direct conversion based laser-to-RF synchronization setups. Many RF components involved in the synchronization setup are susceptible to temperature and humidity changes, leading to an unavoidable timing drifts and poor long-term timing stability [15].

Technical Implementation

In this section, technical details of the injector laser synchronization together with the measurement setup (Fig. 2) are discussed. The optical pulse train from the laser oscillator is split by a polarizing beam splitter into two paths. The first path provides the optical pulse train to the direct conversion based laser-to-RF synchronization setup, while the second optical path is reserved for a future upgrade discussed in the next section.

The optical pulse train with an average optical power of ≈ 5 mW is guided to a commercial InGaAs photodetector² via a fiber coupled collimator. The photodetected signal is split by the RF splitter (SPL) providing the signals to in-loop and out-of-loop RF chains. The 37^{th} and 36^{th} harmonics (3.081 GHz, 2.998 GHz) of the laser oscillator repetition rate are filtered using custom built RF bandpass filters for in-loop and out-of-loop setups respectively. The in-loop setup is dedicated to lock the laser oscillator, while the out-of-loop signal is used for performance evaluation.

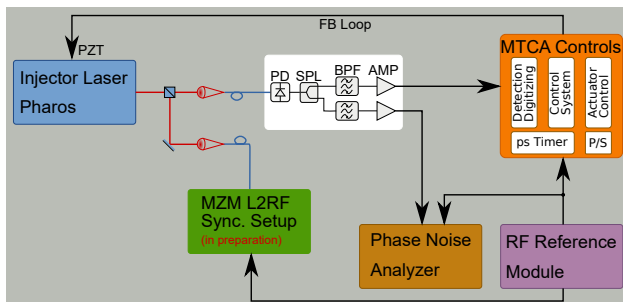


Figure 2: Schematic diagram of the laser oscillator synchronization and out-of-loop measurement setup.

The 3.081 GHz signal is downconverted using the 2.998 GHz RF reference signal resulting in an IF $= f_{\text{rep}} =$

83.28 MHz. The obtained IF is digitized with a sampling rate of $f_s = f_c/24 = 124.92$ MHz. The signal downconversion, digitization and phase feedback is carried out on the MicroTCA.4 electronics platform [16], offering extremely large flexibility for controls compared to conventional analog controllers.

Measurement Results

After successfully locking the laser oscillator to the RF reference signal, the out-of-loop absolute and residual phase-noise measurements have been carried out using a phase-noise analyzer³ with a measurement bandwidth of 10 Hz to 1 MHz. The phase-noise power spectral densities (PSDs) and corresponding integrated jitters are summarized in Fig. 3 and Fig. 4. Here the green curves depict the absolute phase-noise PSD and the corresponding timing jitter of the RF reference signal. The orange curves show the absolute phase-noise PSD and timing jitter of the locked laser oscillator measured at the 36^{th} harmonic (2.998 GHz) of the repetition rate.

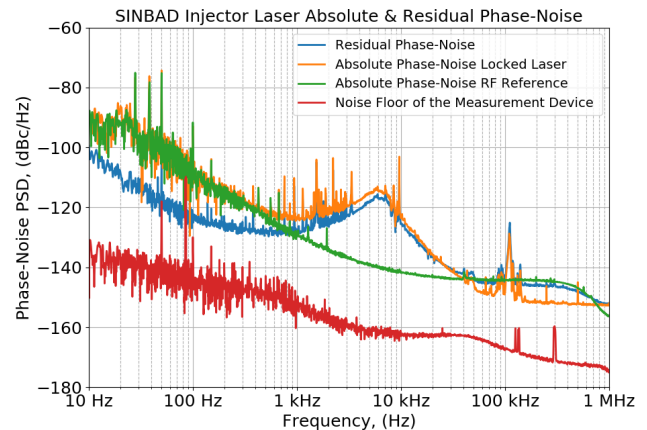


Figure 3: Measured absolute and residual phase-noise power spectral densities.

The overlap of the phase-noise PSD curves (green, orange), indicate that the locking bandwidth of the laser oscillator is about a few kHz. The out-of-loop residual phase-noise measurement between the RF reference and the laser oscillator is depicted by the blue curves in Figs. 3,4. The total integrated timing jitter amounts about 10 fs rms, dominated by the so called "waterbed effect" in the range from 1 kHz to 40 kHz. Beyond 40 kHz the integrated timing jitter is governed by the noise floor of the RF reference. The noise floor of the phase-noise analyzer was measured when both

² <https://www.eotech.com/>, ET3500F

³ R&S FSWP26

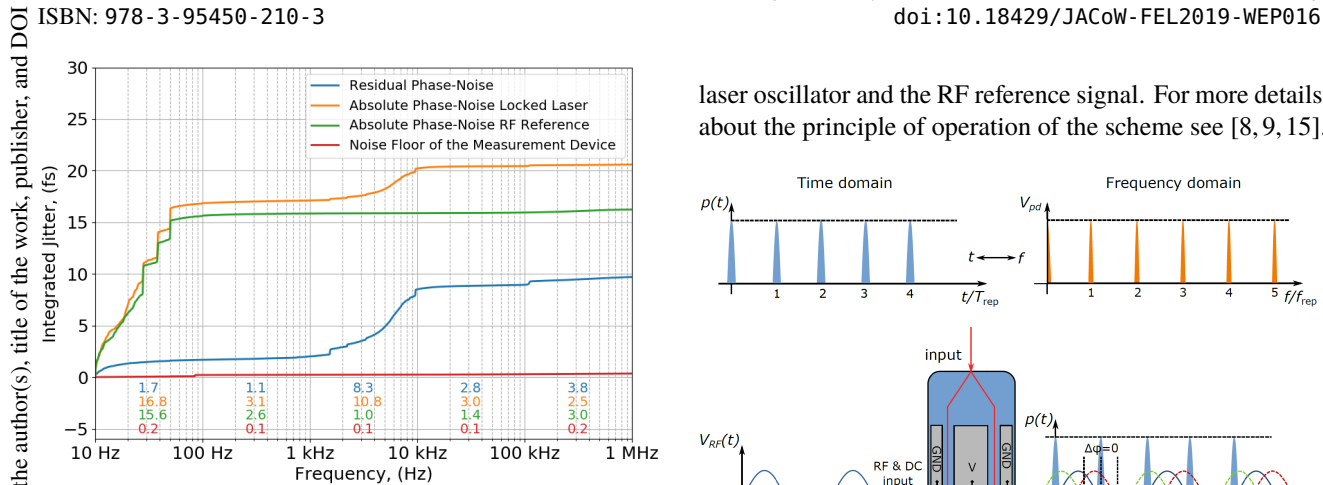


Figure 4: Integrated timing jitter calculated from the phase-noise PSD in Fig 3.

the signal and the external reference were derived from the same source (RF MO). The red curve in Fig. 3 shows the measured noise floor of the phase-noise analyzer amounting 300 as rms in the full measurement bandwidth. The timing jitter contribution added by the measurement device itself is negligible compared to the high frequency noise floors of the RF reference and the laser oscillator.

FUTURE UPGRADE

In order to mitigate the problems associated with the direct conversion based laser-to-RF synchronization setup, it is planned to build a Mach-Zehnder Modulator (MZM) based laser-to-RF synchronization setup [9]. It has been shown in a pilot study that the MZM based laser-to-RF synchronization scheme for S-band frequencies can suppress the AM-PM effect and offer timing jitter and especially drift performance in the order of 10 fs rms [9, 15].

This approach is based on sampling the RF reference signal zero crossings with optical pulses within the integrated MZM. This allows to convert the relative timing error between these two sources into an amplitude modulation of the optical pulses. A sketch for the simplified case is shown in Fig. 5. When the relative timing between the laser oscillator pulse train and the RF reference is zero ($\Delta\phi = 0$), optical pulses arrive at the zero crossings of the RF reference. Hence, an amplitude modulation of the optical pulses does not take place. When the relative timing between the two sources is not zero ($\Delta\phi \neq 0$), the amplitude modulation of the laser pulses will occur. For any $\Delta\phi \neq 0$, each subsequent pair of optical pulses samples opposite slopes of the RF signal. This translates to an amplitude mismatch of the individual laser pulse since they experience positive and negative voltages of the RF signal respectively. The amplitude modulation of the optical pulses in the time domain transfers to the RF spectrum as additional frequency components (orange comb lines in Fig. 5). One can detect the amplitude of one of these modulation frequencies and build a feedback loop in order to establish a PLL between the

laser oscillator and the RF reference signal. For more details about the principle of operation of the scheme see [8, 9, 15].

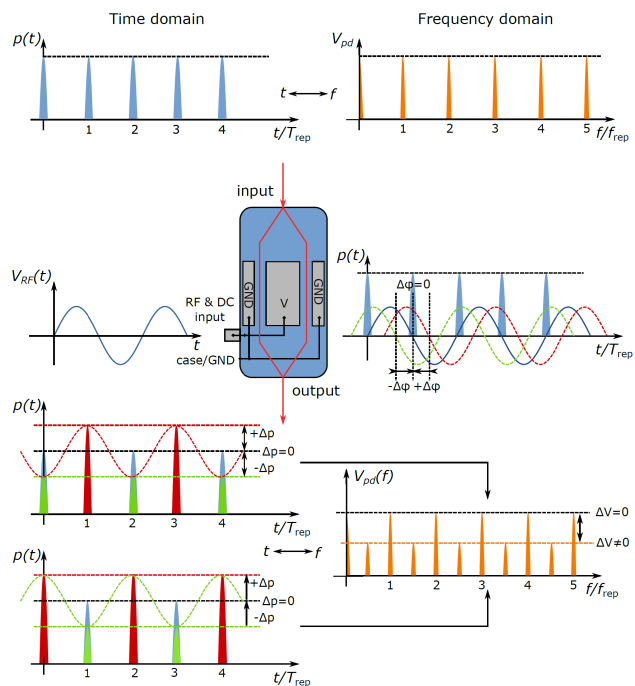


Figure 5: Concept for Mach-Zehnder modulator based laser-to-RF synchronization scheme. Blue pulses indicate the unmodulated optical pulses in time domain, red and green pulses depict the modulated optical pulses in time domain. Orange comb lines show the frequency spectra for both modulated and unmodulated optical pulses.

CONCLUSION

In this paper we have shown the first results of the recently commissioned direct conversion based photo-injector laser-to-RF synchronization setup at the SINBAD facility. The measured timing jitter performance is ≈ 10 fs rms in the bandwidth of 10 Hz to 1 MHz which is sufficient for the initial phase of the experiments planned at ARES and satisfies its design requirements. The MZM based laser-to-RF setup is currently in preperation and commissioning will start in the near future as an upgrade.

REFERENCES

- [1] B. Marchetti *et al.*, "Electron-Beam Manipulation Techniques in the SINBAD Linac for External Injection in Plasma Wake-Field Acceleration", *Nucl. Instr. Meth.*, vol. 829, pp. 278–283, 2016. doi.org/10.1016/j.nima.2016.03.041
- [2] <https://axisis.desy.de/>
- [3] E. Panofski *et al.*, "Status Report of the SINBAD-ARES RF Photoinjector and LINAC Commissioning", in *Proc. 10th Int. Particle Accelerator Conf. (IPAC'19)*, Melbourne, Australia, May 2019, pp. 906–909. doi:10.18429/JACoW-IPAC2019-MOPTS026

- [4] M. Hada *et al.*, "REGAE: New Source for Atomically Resolved Dynamics", in *Proc. 2012 Research in Optical Sciences*, Berlin, Germany, Mar. 2012, paper JT2A.47 DOI:10.1364/HILAS.2012.JT2A.47
- [5] B. Marchetti *et al.*, "Conceptual and Technical Design Aspects of Accelerators for External Injection in LWFA", *Appl. Sci.*, vol. 8, p. 757, May 2018. DOI:10.3390/app8050757
- [6] M. Felber, M. Hoffmann, U. Mavric, H. Schlarb, S. Schulz, and W. Jalmuzna, "Laser Synchronization at REGAE using Phase Detection at an Intermediate Frequency", in *Proc. 3rd Int. Particle Accelerator Conf. (IPAC'12)*, New Orleans, LA, USA, May 2012, paper WEP048, pp. 2624–2626.
- [7] F. B. Kiewiet *et al.*, "Femtosecond synchronization of a 3GHz RF oscillator to a mode-locked Ti:sapphire laser", *Nucl. Instr. Meth.*, vol. 484, pp. 619–624, 2002, DOI:10.1016/S0168-9002(01)01994-5.
- [8] M. Titberidze *et al.*, "Present and Future Optical-to-Microwave Synchronization Systems at REGAE Facility for Electron Diffraction and Plasma Acceleration Experiments", in *Proc. 6th Int. Particle Accelerator Conf. (IPAC'15)*, Richmond, VA, USA, May 2015, pp. 833–836. DOI:10.18429/JACoW-IPAC2015-MOPHA026
- [9] M. Titberidze, M. Felber, T. Lamb, H. Schlarb, C. Sydlo, and R. A. Loch, "Fs Level Laser-to-RF Synchronization at REGAE", in *Proc. 8th Int. Particle Accelerator Conf. (IPAC'17)*, Copenhagen, Denmark, May 2017, pp. 3972–3975. DOI:10.18429/JACoW-IPAC2017-THPAB109
- [10] L. R. Doolittle, M. S. Champion, and H. Ma, "Digital Low-Level RF Control Using Non-IQ Sampling", in *Proc. 23rd Linear Accelerator Conf. (LINAC'06)*, Knoxville, TN, USA, Aug. 2006, paper THP004, pp. 568–570.
- [11] M. Felber *et al.*, "Compact MTCA.4 Based Laser Synchronization", in *Proc. 5th Int. Particle Accelerator Conf. (IPAC'14)*, Dresden, Germany, Jun. 2014, pp. 1823–1825. DOI:10.18429/JACoW-IPAC2014-TUPRI107
- [12] E. Ivanov, S. Diddams and L. Hollberg, "Study of the Excess Noise Associated with Demodulation of Ultra-Short Infrared Pulses", *IEEE Transactions on Ultrasonics, Ferroelectrics, and Frequency Control*, vol. 52, pp. 1068–1074, 2005, DOI:10.1109/TUFFC.2005.1503992.
- [13] W. Zhang, *et al.*, "Amplitude to phase conversion of InGaAs PIN photodiodes for femtosecond lasers microwave signal generation", *Appl. Phys. B. Laser and Optics.*, vol. 106, no. 2, pp. 301–308, 2012, DOI:10.1007/s00340-011-4710-1.
- [14] A. Gliserin, M. Walbran, and P. Baum "Passive optical enhancement of laser-microwave synchronization" *Appl. Phys. Lett.*, vol. 103, p. 031113, 2013. DOI:10.1063/1.4815929
- [15] M. Titberidze, "Pilot Study of Synchronization on a Femtosecond Scale between the Electron Gun REGAE and a Laser-Plasma Accelerator", Ph.D. thesis, Phys. Dept., University of Hamburg, Hamburg, Germany, 2017. DOI:10.3204/PUBDB-2017-11374
- [16] M. Felber *et al.*, "Implementation of MTCA.4-based Controls for the Pulsed Optical Synchronization Systems at DESY", in *Proc. 37th Int. Free Electron Laser Conf. (FEL'15)*, Daejeon, Korea, Aug. 2015, paper MOP040, pp. 115–117, DOI:10.18429/JACoW-FEL2015-MOP040.

CONCEPT OF A NOVEL HIGH-BANDWIDTH ARRIVAL TIME MONITOR FOR VERY LOW CHARGES AS A PART OF THE ALL-OPTICAL SYNCHRONIZATION SYSTEMS AT XFEL AND FLASH*

Andreas Penirschke[†], Technische Hochschule Mittelhessen (THM), Friedberg, Germany

Marie Kristin Czwalińska, Holger Schlarb

Deutsches Elektronen-Synchrotron (DESY), Hamburg, Germany

Wolfgang Ackermann, Technische Universität Darmstadt, Darmstadt, Germany

Abstract

Numerous advanced applications of X-ray free-electron lasers require pulse durations and time resolutions in the order of only a few femtoseconds or better. The generation of these pulses to be used in time-resolved experiments require synchronization techniques that can simultaneously lock all necessary components to a precision in the range of 1fs only. To improve the experimental conditions at existing facilities and enable future development of seeded FELs, a new all-optical synchronization system at FLASH and XFEL was implemented, which is based on pulsed optical signals rather than electronic RF signals. In collaboration with DESY, Hamburg the all-optical synchronization system is used to ensure a timing stability on the 10-fs scale at XFEL.

For a future ultra-low charge operation mode, down to 1 pC at XFEL an overall synchronization of 5+1 fs rms. or better is necessary.

This contribution presents a new concept of an ultra-wideband pickup structure for beam-pipe-diameters down to 10mm for frequencies up to 80 GHz or higher and at the same time providing sufficient output signal for the attached EOMs.

INTRODUCTION

In order to investigate dynamical processes down to the femtosecond (fs) time scale, free electron lasers (FELs) are conducted to deliver ultrashort x-ray pulse for pump-probe experiments [1,2]. These time-resolved measurements require synchronization between an external pumping laser and the FEL pulse for probing lower than the pulse duration, i.e., a few femtoseconds. The FEL pulse timing can be determined by high-resolution arrival-time measurements of electron bunches at the undulators [3].

In recent years, the interest for ultrashort x-ray pulses is continuously rising which requires for the accelerator an ultra-low bunch charge operation down to a few pC only [4,5]. Different schemes for bunch arrival time measurements have been implemented so far allowing for single-shot detection with a resolution of a few fs and below. [6-10].

At the free-electron lasers European XFEL and FLASH in Hamburg, pickup-based arrival-time monitors with electro-optical detection schemes have been implemented.

As part of a laser-based synchronization system, bunch arrival-time monitors (BAMs) measure the arrival time with a sub-10 fs time resolution for bunch charges higher than 500 pC [11]. A beam-induced signal modulates the amplitude of an external laser pulse in a Mach-Zehnder type electro-optic modulator (EOM). This laser pulse is delivered through a stabilized optical fiber link with a drift stability of around 10 fs/day. Thus, as a direct client of this highly stable optical reference, the BAM based on standard telecom EOMs at 1550 nm has an intrinsic low drift feature, in addition to the high resolution. The reference timing is the zero crossing of the pickup signal, where the sampling laser pulse has no modulation. The EOM DC bias is such that without an external rf modulation the amplitude of the sampling laser pulses is halved. Any deviation from the zero crossing of the pickup transient, i.e., bunch arrival-time jitter, results in an amplitude modulation of the reference laser pulse. With a proper calibration with a precession delay line, this amplitude modulation is directly converted to arrival-time information with a dynamic range corresponding to the linear part of the pickup slope. More details are given in [11-12]. The slope steepness at the zero crossing defines the modulation voltage which the laser pulse experiences in the presence of an arrival-time jitter. This determines the time resolution as well as the sensitivity of the BAMs. The slope steepness reduces proportionally with the bunch charge leading to a BAM performance degradation for charges lower than 200 pC [3,13]. In order to achieve sub-10 fs time resolution for a low charge operation mode down to a few pC, the bandwidth of the current BAMs needs to be increased from 40 GHz up to 80 GHz or higher. As a part of the high bandwidth BAM, cone-shaped pickups were introduced in [14]. The cone shaped pickups are part of the synchronization systems at XFEL, FLASH and ELBE (Helmholtz-Zentrum Dresden-Rossendorf) [14-16].

This paper presents a new concept of an ultra-wideband pickup structure for beam-pipe-diameters down to 10mm for frequencies up to 80 GHz or higher with sufficient output signal for driving the attached EOMs.

CONE SHAPED PICKUP DESIGN

The rf properties of the pickup is defined by its shape, the material, the used connectors, and the cables connected to the pickup. However, the pickup shape has the largest influence on the performance of the system.

In [14] a tapered coaxial structure was proposed, which comprises a cone-shaped pickup electrode with the

* This work is supported by the German Federal Ministry of Education and Research (BMBF) under contract no. 05K19RO1.

[†] andreas.penirschke@iem.thm.de

corresponding cut-out, as shown in Figure 1. Unlike the classical button-type pickup, the cone-shaped pickup avoids resonances within the pickup due to the tapered transition from the beam pipe to the connector having a constant line impedance of $50\ \Omega$

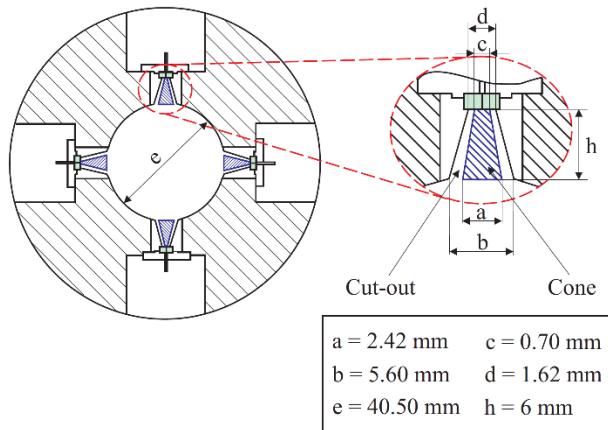


Figure 1: Cross section of the current cone-shaped pickup with dimensions [14].

The cone shaped pickups are installed in XFEL, FLASH which allows for the detection of the arrival time with fs resolution for the low charge operation mode with 20 pC bunch charge in FLASH II and XFEL. Figure 1 shows a sketch of the cross-section of four cone shaped pickups integrated in the housing with corresponding dimensions for FLASH II and XFEL.

The simulation results of one pickup in time domain and the respective normalized frequency spectrum is shown in Figure 2.

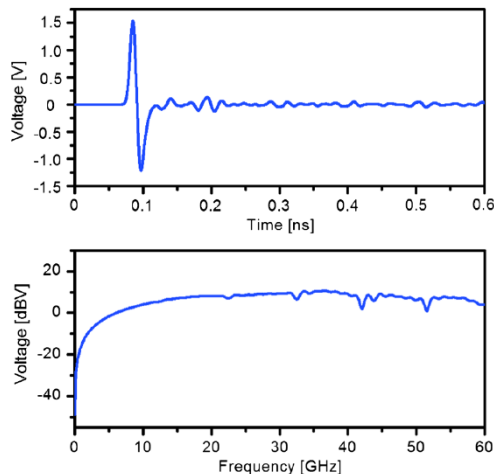


Figure 2: Simulation results of one pickup in time domain (top) and the respective frequency spectrum normalized by the spectrum of the particle beam (bottom) [14].

It can be seen that the spectrum of the voltage is resonance-free up to 40 GHz except small kinks in the spectrum around 23, 33, and 43 GHz.

The ultra-low-charge mode down to 1 pC or less requires a system bandwidth of at least 80 GHz to 100 GHz from the pickup to the attached EOM. In order to increase the

bandwidth of the pickup for a constant line impedance, the pickup dimensions need to be reduced. Figure 3 shows the simulation results of a pickup structure filled with a glass ceramic having a relative permittivity of $\epsilon_r = 3.75$ a radius of the inner conductor $r_{in} = 0.226\text{ mm}$ and the outer conductor radius $r_{out} = 0.5\text{ mm}$ tapered to a outer conductor radius of $r_{out,cone} = 1.13\text{ mm}$.

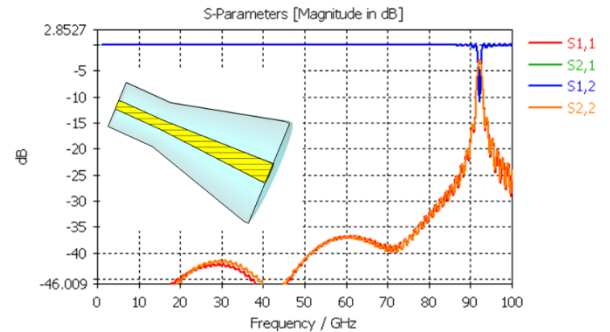


Figure 3: Cross section of the proposed pickup structure and corresponding s-parameter simulation result.

It can be seen, that the pickup structure is resonance free up to 90 GHz. 100 GHz can be reached by further reduction of the pickup diameter.

In order to increase the output voltage at the attached EOM and to reduce the orbit dependency, several pickups need to be arranged in a circle around the beamline. Figure 4 shows a sub-circuit of two pickups and an impedance matched combiner structure.

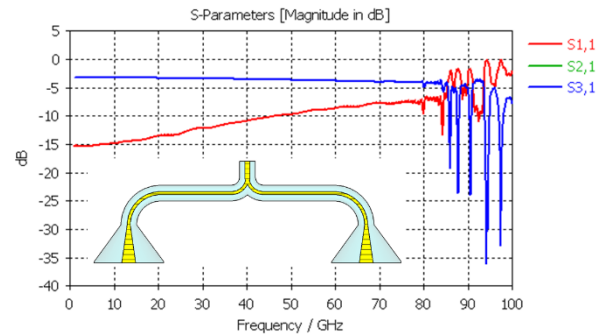


Figure 4: Combination of two pickup structures using an impedance matched combiner structure

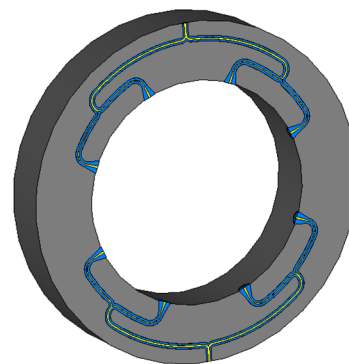


Figure 5: Exemplified pickup arrangement: 8 pickups, 4 pickups each were combined to an integrated sub-circuit with two connectors only.

The simulated s-parameters exhibit resonances above 80 GHz that need to be improved within the project. A further combination is required to connect 4 pickups to s sub-circuit. Figure 5 shows a model of a pickup circuit containing 8 pickups equally spaced around the beamline.

Further research efforts need to be carried out to optimize the pickup circuit for the ultra-low-charge mode down to 1 pC and to provide sufficient output voltage for subsequent EOMs.

CONCLUSION

A high bandwidth cone-shaped pickup for the BAMs for free-electron lasers is introduced. A new concept of an ultra-wideband pickup structure for beam-pipe-diameters down to 10 mm for frequencies up to 80 GHz is presented.

This makes it suitable for enabling a sub-10 fs time resolution for high and low bunch charge operation down to 1 pC of the FELs.

REFERENCES

- [1] A. Azima *et al.*, “Time-resolved pump-probe experiments beyond the jitter limitations at FLASH”, *Appl. Phys. Lett.*, vol. 94, p. 144102, 2009. doi:10.1063/1.3111789
- [2] H. Redlin *et al.*, “The FLASH pump-probe laser system: Setup, characterization and optical beamlines”, *Nucl. Instrum. Methods Phys. Res., Sect. A*, vol. 635, p. S88, 2011. doi:10.1016/j.nima.2010.09.159
- [3] M. K. Bock, “Measuring the Electron Bunch Timing with Femtosecond Resolution at FLASH”, Ph.D. thesis, Universität Hamburg, DESY-THESIS-2013-008, 2012.
- [4] X. Wang and X. Chang, “Femto-seconds kilo-ampere electron beam generation”, in *Proc. of the 24th Int. Free Electron Laser Conference*, Argonne, Illinois, U.S.A., September 9–13, 2002. doi: 10.1016/B978-0-444-51417-2.50074-2
- [5] J. Rosenzweig *et al.*, “Generation of ultra-short, high brightness electron beams for single-spike SASE FEL operation”, *Nucl. Instrum. Methods Phys. Res., Sect. A*, vol. 593, p. 39, 2008. doi:10.1016/j.nima.2008.04.083
- [6] M. Hansli *et al.*, “A Beam Arrival Time Cavity for REGAE at DESY”, in *Proc. IPAC'14*, Dresden, Germany, Jun. 2014, pp. 1820-1822. doi:10.18429/JACoW-IPAC2014-TUPRI104
- [7] M. Felber, M. Hoffmann, U. Mavric, H. Schlarb, S. Schulz, and W. Jalmuzna, “Laser Synchronization at REGAE using Phase Detection at an Intermediate Frequency”, in *Proc. IPAC'12*, New Orleans, LA, USA, May 2012, paper WEP048, pp. 2624-2626.
- [8] F. Tavella, N. Stojanovic, G. Geloni, and M. Gensch, “Few-femtosecond timing at fourth-generation X-ray light sources”, *Nat. Photonics*, vol. 5, p. 162, 2011. doi:10.1038/nphoton.2010.311
- [9] C. Gahl *et al.*, “A femtosecond X-ray/optical cross-correlator”, *Nat. Photonics*, vol. 2, p. 165, 2008. doi: 10.1038/nphoton.2007.298
- [10] I. Grguras *et al.*, “Ultrafast X-ray pulse characterization at free-electron lasers”, *Nat. Photonics*, vol. 6, p. 852, 2012. doi:10.1038/nphoton.2012.276
- [11] F. Löhler *et al.*, “Electron Bunch Timing with Femtosecond Precision in a Superconducting Free-Electron Laser”, *Phys. Rev. Lett.*, vol. 104, p. 144801, 2010. doi:10.1103/PhysRevLett.104.144801
- [12] F. Löhler, “Optical Synchronization of a Free-Electron Laser with Femtosecond Precision”, Ph.D. thesis, Universität Hamburg, 2009. doi:10.3204/DESY-THESIS-2009-031
- [13] K. Hacker, “Measuring the Electron Beam Energy in a Magnetic Bunch Compressor”, Ph.D. thesis, Universität Hamburg, 2010. doi:10.3204/DESY-THESIS-2010-037
- [14] A. Angelovski *et al.*, “High bandwidth pickup design for bunch arrival-time monitors for free-electron laser”, *Phys. Rev. ST Accel. Beams*, vol. 15, p. 112803, 2012. doi: 10.1103/PhysRevSTAB.15.112803
- [15] M. Kuntzsch *et al.*, “Optical Synchronization and Electron Bunch Diagnostic at ELBE”, in *Proc. IPAC'13*, Shanghai, China, May 2013, paper WEPME006, pp. 2932-2934.
- [16] A. Angelovski *et al.*, “Evaluation of the cone-shaped pickup performance for low charge sub-10 fs arrival-time measurements at free electron laser facilities”, *Phys. Rev. ST Accel. Beams*, vol. 18, p. 012801, 2015. doi: 10.1103/PhysRevSTAB.18.012801

1.3 GHz SOLID STATE POWER AMPLIFIER FOR THE BUNCHER IN CTFEL FACILITY*

T. H. He[†], C. L. Lao, P. Li, X. Luo, L. J. Shan, K. Zhou

Institute of Applied Electronics, China Academy of Engineering Physics, Mianyang, China

Abstract

The THz Free Electron Laser facility (CAEP THz FEL, CTFEL) of the China Academy of Engineering Physics uses high-quality electron beams to generate high average power terahertz radiations. A 1.3 GHz RF buncher is used in front of the superconducting linear accelerator of the CTFEL facility to improve the electron beams quality. The RF buncher is driven by a solid state power amplifier (SSPA), and the SSPA is feedback controlled by a low level RF (LLRF) control system to ensure the high stability of the amplitude and phase of the bunching field in the buncher cavity. The SSPA operates at 1.3 GHz and outputs 0 to 5 kW of continuous wave power. This paper mainly introduces the principle and composition of the SSPA, and presents some experiments on the RF buncher driven by the SSPA.

INTRODUCTION

In recent years, with the development of science and technology, high-power terahertz sources have become more and more important in the world. A high average power terahertz radiation facility (CAEP THz FEL, CTFEL) has been developed by the China Academy of Engineering Physics. This is the first THz user facility based on free electron lasers in China [1]. The CTFEL facility is designed to produce 1-3 THz radiation with an average output power beyond 10 W.

The CTFEL facility mainly includes a photocathode high voltage direct current (HV-DC) electron gun [2], an RF buncher, an RF superconducting linear accelerator [3], a high performance undulator [4] and so on. Its general layout is shown in Figure. 1. High quality electron beams are generated by the photocathode HV-DC electron gun. When the electron beams come through the RF buncher cavity, the bunch length of the electron beams will be compressed to 4-8 ps. Then, the electron beams come into the RF superconducting linear accelerator, and will be accelerated to 6-8 MeV, passing through an achromatic section, coming into an undulator with the periodical magnetic field and generate spontaneous THz radiation. The THz radiation oscillates back and forth in the optical cavity. Under resonant conditions, the power of the THz radiation increases rapidly until reaching saturated output state.

The RF buncher is an indispensable component of the CTFEL facility, which provides a longitudinal manipulation of the electron beams and ensures that the bunch length of the electron beams to be compressed to 4-8 ps when com-

ing into the superconducting cavity. In the CTFEL facility, the electron beams are quasi-continuously operated, so the RF buncher needs to be driven by continuous wave. The designed output power of the microwave source is about 2.7 kW. Considering the improvements and upgrades in the future, the CTFEL facility uses an L-band 5 kW continuous wave solid state power amplifier (SSPA). The bunch length and energy spread of the electron beams are directly related to the amplitude and phase of the buncher cavity. In order to ensure that the amplitude and phase stability of the buncher cavity field are less than 0.3% and 0.3°, respectively, the SSPA is cooled by a high precision water cooler and controlled by a low-level RF (LLRF) control system for real-time feedback. This paper mainly introduces the principle and composition of the SSPA, and presents some experiments on the buncher driven by the SSPA.

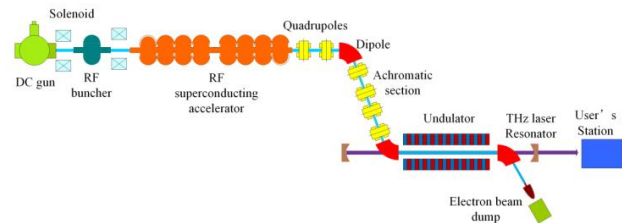


Figure 1: Layout of the CTFEL facility.

SOLID STATE POWER AMPLIFIER

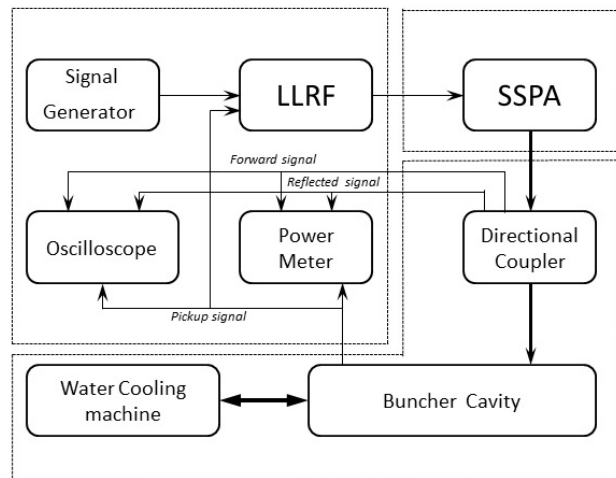
The SSPA is used to drive the RF buncher, its main function is to amplify the input signal and output a continuous wave of high power. And the output power of the SSPA can be adjusted with the change of the input signal.

The SSPA consists of a preamplifier (with one-two splitter, two 3 kW final stage power amplifier arrays, two 3 kW coaxial directional couplers, two waveguide coaxial converters, a two in one waveguide power combiner, a 5 kW waveguide directional coupler, a controller and an embedded computer. The 3 kW final stage power amplifier array consists of a pre-stage power amplifier, ten final stage power amplifier modules, eleven power supply modules, a one-tenth power splitter, a ten in one power combiner and a water cooled board. Board composition. The MCU acquisition unit is integrated in the power supply modules, and the parameters such as voltage, current and temperature are uploaded to the industrial computer through the RS-485 serial ports.

The block diagram of the SSPA is shown in Figure. 2. When a 0 dBm signal is input to the SSPA, it can output a 5 kW continuous wave. The SSPA design targets and test

* Work supported by China National Key Scientific Instrument and Equipment Development Project (2011YQ130018)

[†] hth111@163.com



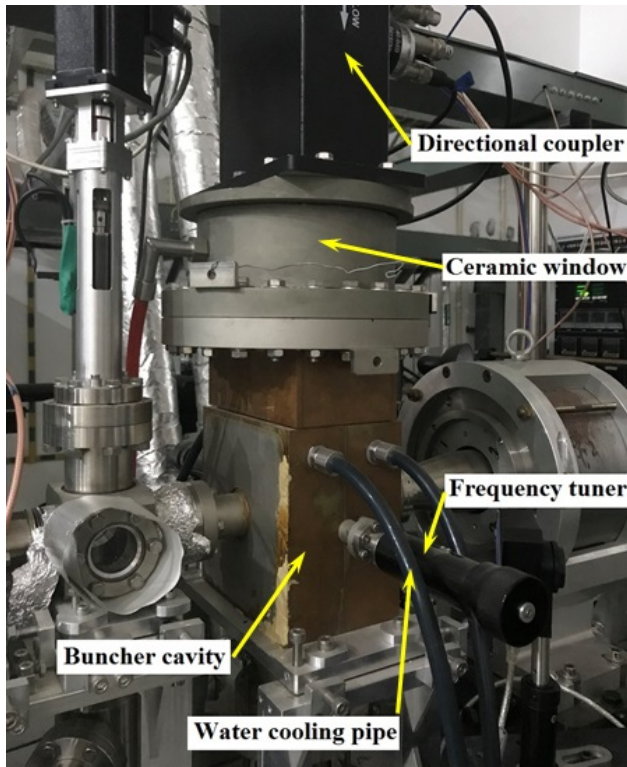


Figure 5: Picture of the buncher cavity.

The buncher conditioning experiment enabled the buncher to withstand high power microwaves without significant temperature rise and gas release. The buncher frequency calibration experiment calibrated the relationship between the buncher cavity resonant frequency and the frequency tuner. The buncher power calibration experiment calibrated the corresponding electric field gradient at different microwave input powers. The bunching phase experiment determines the optimal bunching phase of the buncher cavity when the bunch length of the electron beams is compressed to a minimum. After the beam buncher debugging experiments were completed, the buncher cavity bunching gradient was measured to reach 3 MV/m when the microwave input power was close to 3 kW, and the optimal bunching gradient of the buncher is 1.2 MV/m (corresponding to the microwave input power of about 1.5 kW). The optimal bunching phase of the buncher was at 0° . At this time the bunch length of the electron beams can be compressed from about 19 ps to a minimum.

After the above experiments were completed, the CTFEL facility was debugged and light-extracted. The amplitude and phase stability of the buncher cavity were measured to be 0.05% and 0.09° , respectively, as shown in Figure. 6.

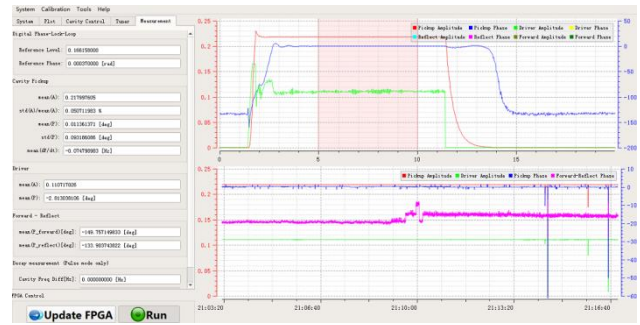


Figure 6: The amplitude and phase stability of the buncher cavity.

The SSPA output a continuous wave power of approximately 1.5 kW. The CTFEL facility received its first saturated light on August 29, 2017.

CONCLUSION

Designed and developed an L-band 5 kW continuous wave solid-state power amplifier, and introduced the experimental platform of the buncher system and related experiments. In the CTFEL facility experiments, when the optimal bunching gradient of the buncher cavity was 1.2 MV/m, the bunch length of the electron beams was compressed to the minimum. The amplitude and phase stability of the bunching field are 0.05% and 0.09° , respectively. The input continuous wave power is 1.5 kW, and the power output range is not exceeded. The experimental results show that the SSPA working index was better than the experimental demand. The CTFEL facility obtained saturated light. In the next step of CTFEL facility improvement and upgrade, the SSPA will play a more important role.

REFERENCES

- [1] Z. Xu *et al.*, "Design of a high average power terahertz fel facility", *Journal of Terahertz Science and Electronic Information Technology*, vol. 11, no. 1, pp. 1-6, 2013.
- [2] H. Wang, K. Li, and M. Li *et al.*, "A GaAs photoemission DC gun for CAEP high-average-power THz FEL," in *Proc. FEL'14*, Basel, Switzerland, Aug. 2014, paper TUA03, pp. 318-321.
- [3] X. Luo X, C. Lao, K. Zhou *et al.*, "Design and fabrication of the 2x4-cell superconducting linac module for the free-electron laser," *Nucl. Instr. and Meth. A*, vol. 871, pp. 30-34, 2017. doi:10.1016/j.nima.2017.06.058
- [4] L. Yan, D. Deng *et al.*, "Physics design of undulator in high average power free electronic laser terahertz source", *High Power Laser and Particle Beams*, vol. 25, pp. 153-157, 2013.

PRELIMINARY GEOMETRY OPTIMIZATION OF A 3.5-CELL SRF GUN CAVITY AT ELBE BASED ON BEAM DYNAMICS *

K. Zhou, Institute of Applied Electronics, CAEP, Mianyang, China
Institute of Radiation Physics, HZDR, Dresden, Germany
P. Li, Institute of Applied Electronics, CAEP, Mianyang, China
A. Arnold, J. Schaber, J. Teichert[†], R. Xiang, S. Ma
Institute of Radiation Physics, HZDR, Dresden, Germany

Abstract

At present, ELBE radiation source at HZDR is optimizing the SRF cavity for the next generation ELBE SRF GUN. This paper presents a preliminary study on the geometry optimization of a 3.5-cell SRF gun cavity based on beam dynamics. By changing the lengths of the half cell and the first TESLA like cell, two new cavity models with higher electric field in the half cell are built and their RF fields are compared with SRF GUN I and SRF GUN II. Through the scanning of the RF phases and the electric fields, the simulation results indicate that new models have smaller transverse emittance at relatively lower electric field gradients and better performance on longitudinal emittance than SRF GUN I and SRF GUN II.

INTRODUCTION

Developing electron sources delivering high quality electron beams is always an active research field for high intensity particle accelerators, such as free electron laser (FEL), energy recovery linacs (ERLs) and electron linear colliders. Superconducting radio-frequency electron gun (SRF gun) is a superior alternative, which is capable to generate high-brightness and low-emittance electron beams when operating in continuous wave (CW) mode. The concept of SRF gun was firstly proposed in 1988 [1], and the first experiments were carried out at the University of Wuppertal four years later [2]. In 2002, world's first electron beams were obtained by the Drossel SRF gun at FZD (now HZDR) [3]. Inspired by this success, SRF gun projects based on different approaches were launched worldwide [4].

In 2004, a SRF photoelectron injector (SRF GUN I) was developed at HZDR in collaboration with DESY, HZB and MBI [5], as shown in Fig. 1. SRF GUN I was the world's first SRF gun with a 3.5-cell niobium cavity operating for a linac and was used to demonstrate the first lasing with the far-infrared FEL at ELBE [6].

After the proof-of-principle demonstration of SRF GUN I, an improved SRF gun (SRF GUN II) was developed as shown in Fig. 2 and has been in operation up to now. Comparing to SRF GUN I, the electric field strength in the first half cell was improved, and a superconducting solenoid was installed in the cryomodule [7]. The influences of RF focus,

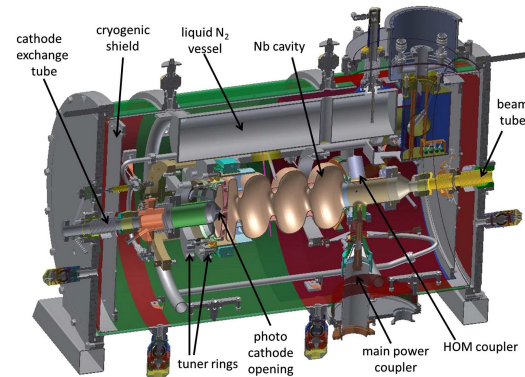


Figure 1: ELBE SRF GUN I.

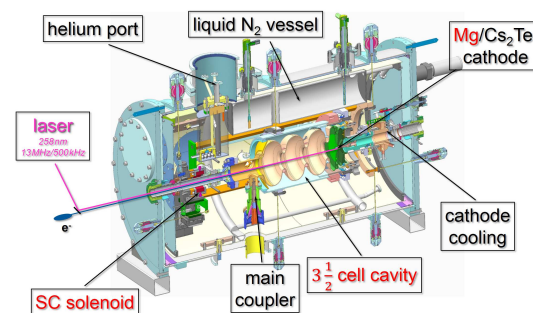


Figure 2: ELBE SRF GUN II.

cathode position and superconducting solenoid on emittance compensation have been investigated in detail [8].

Due to a degradation of available maximum field gradient of SRF GUN II, the construction of the third version, SRF GUN III, was initiated with the same niobium cavity of SRF GUN I refurbished at DESY and a newly built cryomodule with a superconducting solenoid [9].

At present, HZDR is also optimizing the SRF cavity for the next generation ELBE SRF GUN. To optimize the geometry of the 3.5-cell SRF gun cavity, the distributions of the electromagnetic fields and output beam qualities with different geometric models have been investigated and compared [10]. This paper mainly presents an analysis of the output beam parameters of two new models comparing to SRF GUN I and SRF GUN II.

* Work supported by National Natural Science Foundation of China with Grant [11605190 and 11805192].

[†] Email address: j.teichert@hzdr.de

Table 1: Geometry Changes of New Models Comparing to SRF GUN I and SRF GUN II (unit:mm)

Models	SRF GUN I	SRF GUN II	New Model I	New Model II
Z1	25	25.6	25.8	26
Z2	51.89	51.3	51.0	50.8

Table 2: Physical Parameters of New Models Comparing to SRF GUN I and SRF GUN II

Models	Freq. (MHz)	E_{peak1}/E_{peak}	E_{max}/E_0	B_{max}/E_0 mT/(MV/m)	Field Flatness	r/Q
SRF GUN I	1297.67693	64.5%	2.174	4.285	97.8%	336.8
SRF GUN II	1297.66094	81.5%	2.661	5.060	99.0%	330.5
New Model I	1297.62255	88.0%	2.848	5.353	98.8%	327.3
New Model II	1297.67210	97.1%	3.104	5.771	99.1%	323.0

NEW MODELS

The geometry differences between SRF GUN I and SRF GUN II are only located at the first half cell and the first TESLA like cell as shown in Fig. 3. Z1 refers to the length of the right part of the first half cell and Z2 represents the length of the left part of the first TESLA like cell. By appropriately increasing Z1 and decreasing Z2, the electric field gradient in the first half cell can be improved significantly, without changing the electric fields in the TESLA like cells.

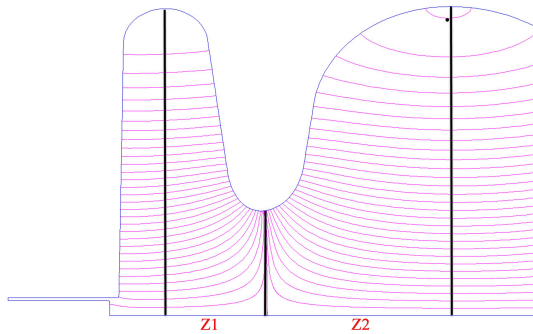


Figure 3: The changing areas of the cavity models.

In this paper, two new cavity models have been built by changing the length of Z1 and Z2 as shown in Table. 1. Figure 4 shows their absolute electric fields on axis normalized to $E_{peak} = 50$ MV/m, where E_{peak} refers to the maximum value of electric field along the central axis. The major differences of their RF fields are located in the half cell. Their physical parameters calculated with Superfish are listed in Table 2, in which E_0 is the average electric field gradient along the central axis; E_{peak1} is the maximum electric field gradient in the first half cell; E_{max} is the maximum electric field of the whole cavity and B_{max} is the maximum magnetic field of the whole cavity. The resonant frequency and field flatness almost remain unchanged. Their field flatnesses are all better than 97.5%. The value of r/Q decreases a little but not much. E_{peak1}/E_{peak} of New Model I and New Model II have been improved to 88% and 97.1%, respectively. Mean-

while, both E_{max}/E_0 and B_{max}/E_0 of New Model I and New Model II also increase obviously.

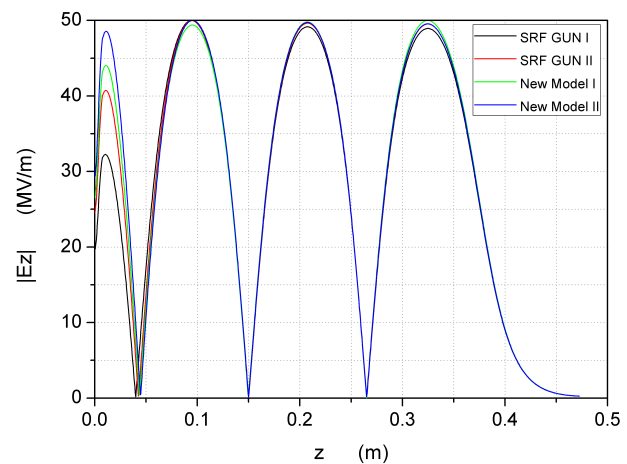


Figure 4: On-axis field profiles of these cavity models normalized to $E_{peak} = 50$ MV/m.

SIMULATION RESULTS

To evaluate how much influence the cavity geometry has on beam dynamics, the RF fields of these models were extracted from Superfish and imported to Astra to calculate their output beam parameters.

In order to compare independently, the simulation did not consider the bias voltage applied on the photocathode and the focus solenoid located at the downstream of the SRF cavity. The initial electron distributions at the photocathode are all the same for these four models. The bunch charge is 100 pC. The laser pulse length is 3 ps, the initial rms radius is 0.5 mm and the initial transverse emittance is 0.05 mm mrad.

Figure 5 and Figure 6 present the output transverse emittance and longitudinal emittance of these models, respectively. They are intensity graphs by scanning the RF phase from 20° to 70° and electric field E_{peak} from 20 MV/m to 50 MV/m. The color of each pixel represents the corresponding

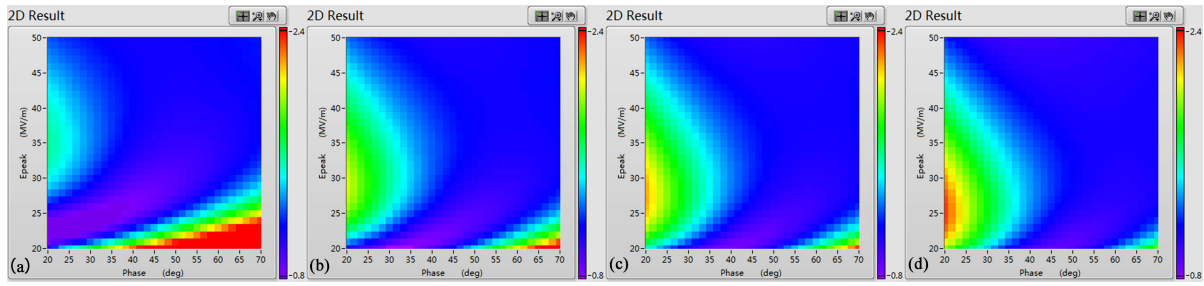


Figure 5: Output transverse emittance (π mm mrad) of (a) SRF GUN I, (b) SRF GUN II, (c) New Model I and (d) New Model II.

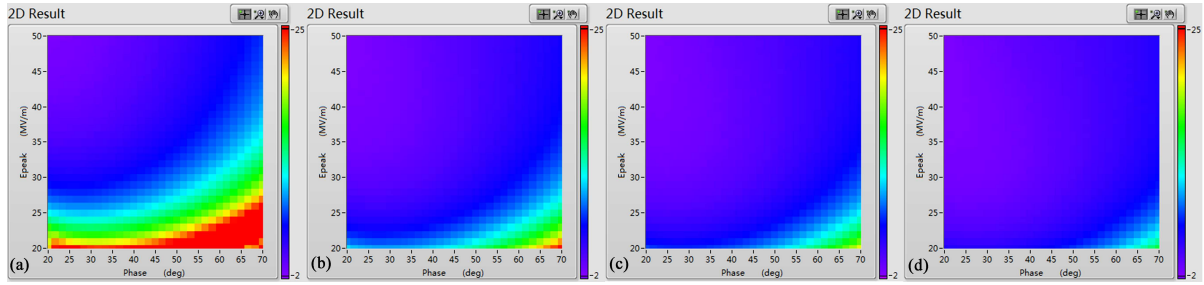


Figure 6: Output longitudinal emittance (π keV mm) of (a) SRF GUN I, (b) SRF GUN II, (c) New Model I and (d) New Model II.

value at the exit of the cryomodule where $z = 1$ m from the photocathode, while the cavity length is about 0.47 m.

In Fig. 5, the variations of the transverse emittance for these four models are similar. With the increase of the electric field gradient, the RF phase corresponding to the minimum transverse emittance will also shift to a larger value. This is reasonable because the RF phase needs to be adjusted to match the electrons acceleration when traveling through the cavity cell under different electric field gradients at low energy. Another interesting variation is that the region of the minimum output transverse emittance (purple area) moves to higher RF phases and lower electric fields from SRF GUN I to New Model II. So New Model I and New Model II have better performance on transverse emittance at relatively low electric fields ($E_{peak} < 20$ MV/m), while in high electric field regions, there are not much differences.

As for the longitudinal direction, in Fig. 6, it is obvious that the longitudinal emittance increases with the RF phase and decreases with the electric field. And New Model I and New Model II offer smaller output longitudinal emittances than SRF GUN I and SRF GUN II, especially at low electric fields.

CONCLUSION

By changing the lengths of the half cell and the first TESLA like cell, we built two new cavity models with higher E_{peak1}/E_{peak} than SRF GUN I and SRF GUN II. Their RF fields were compared and used to calculate their output beam parameters. Through the scanning of the RF phases and the electric fields, the simulation results indicate that New Model I and New Model II have lower transverse emittance

at relatively lower electric fields and better performance on longitudinal emittance than SRF GUN I and SRF GUN II.

ACKNOWLEDGEMENT

The authors would like to thank the SRF group of ELBE team for their great help. This work is supported by State Administration of Foreign Experts Affairs P.R.China and China Academy of Engineering Physics.

REFERENCES

- [1] H. Chaloupka, *et al*, "A proposed superconducting photoemission source of high brightness", *Nuclear Instruments and Methods A*, 285 (1989) 327. doi:10.1016/0168-9002(89)90474-9
- [2] A. Michalke, Ph.D thesis, University of Wuppertal, 1992, WUB-DIS 92-5.
- [3] D. Janssen, *et al*, "First operation of a superconducting RF-gun", *Nuclear Instruments and Methods A*, 507, 314-317, 2003. doi:10.1016/S0168-9002(03)00936-7
- [4] A. Arnold, *et al*, "Overview on superconducting photoinjectors", *Physical Review Special Topics - Accelerators and Beams*, 14 (2011) 024801. doi:10.1103/PhysRevSTAB.14.024801
- [5] A. Arnold, *et al*, "Development of a superconducting radio frequency photoelectron injector", *Nuclear Instruments and Methods A*, 577, p.440, 2007. doi:10.1016/j.nima.2007.04.171
- [6] J. Teichert, *et al*, "Free-electron laser operation with a superconducting radio-frequency photoinjector at ELBE", *Nuclear Instruments and Methods A*, 743 (2014) 114. doi:10.1016/j.nima.2014.01.006

- [7] A. Arnold, *et al*, *LINAC2014*, Geneva, Switzerland, TUPP066, 578. 10.1103/PhysRevAccelBeams.21.093403
- [8] H. Vennekate, *et al*, Emittance compensation schemes for a superconducting rf injector”, *Physical Review Accelerators and Beams*, 21 (2018) 093403. doi:10.1103/PhysRevAccelBeams.21.093403
- [9] H. Vennekate, *et al*, “Building the Third SRF Gun at HZDR”, *IBIC2017*, Grand Rapids, MI, USA, MOPWC01, 98. doi:10.1103/PhysRevAccelBeams.21.093403
- [10] K. Zhou, *et al*, “Geometry Dependent Beam Dynamics of a 3.5-cell SRF Gun Cavity at ELBE”, *SRF2019*, Dresden, Germany, THP082. doi:10.18429/JACoW-SRF2019-THP082

A FAST AND ACCURATE METHOD TO SHIM UNDULATOR USING MULTI-OBJECTIVE GA*

Yan Longgang, Chen Lijun, Deng Derong, Li Peng[†]

Institute of Applied Electronic, China Academy of Engineering and Physics, Mianyang, China

Abstract

GA (Genetic Algorithm) is one of the most excellent methods to search the optimal solution for a problem, which has been applied to solve various problems. It is hard to estimate shim applied on raw undulator precisely. There are many methods have been developed to solve the problem. In this proceeding, we proposed a fast and accurate method to conclude the shim using multi-objective GA. A multi-objective objective function was set, and multi-objective optimization was also implemented. The evolution time is reduced by setting optimal evolution parameters. To demonstrate the method, we also finished some test on a prototype undulator U38. As a result, it can be achieved only by shimming three times that all the parameters of trajectory center deviation, peak-to-peak error and phase error satisfied the requirements.

INTRODUCTION

Light sources based on accelerator, including Synchrotron Radiation (SR) and Free Electron Laser (FEL), use extensively undulators creating a periodic magnetic field for the production of intense of radiation for users [1, 2]. The common-used permanent magnet undulator was invented by K. Halbach in 1980's and contains two magnet and pole arrays [3]. Imperfections and errors are inevitable during design and manufacture of undulators, such as positioning errors of the magnets and poles, small differences of magnetization value and direction from one magnet block to the next, the inhomogeneities of the magnetization inside a volume of a single block. These will introduce magnetic field errors [4, 5]. Uncontrolled magnetic field errors of undulators, including electron trajectory center deviation, peak-to-peak error and phase error, will degrade light sources [6]. There are various shimming methods for correcting them in order to optimize undulator performance. The shimming methods are based on the fact that either moving a magnet or a pole (mechanical shim) or by placing some thin piece of iron at the surface of the magnet (magnetic shim) can make a small local correction of the magnetic field [7]. To shim undulator, it must be concluded that how much to move or how thin piece to place first. Many methods have been developed to solve the problem. In this proceeding, a method based on multi-objective GA to conclude shim fast and accurately was proposed, and in order to demonstrate the method prototype undulator U38 was also shimmed.

* Work supported by National Natural Science Foundation of China under grant of 11505174, 11505173 and 11605190.

[†] burnlife@sina.com

METHOD

Multi-Objective GA

GA was first put forward by professor J. Holland in 1975 and had a prosperous development era in the 90's. Now, GA has been applied in various areas and especially shows many advantages in combination optimization problem.

In an optimization problem based on GA, there is a population consisting of candidate solutions of the problem (individuals). Every candidate solution in population has a set of properties (chromosomes) which can mutate and crossover. An initial population usually contains individuals generated randomly or as required, which is evolved toward better populations. The evolution is an iterative process, and the population in every iteration is a generation. In every generation, the fitness of every individual is evaluated. Portion of individuals is selected from the current population, where fitter individuals decided by fitness are more likely to be selected. Then, chromosome of every individual being selected is modified (crossover and mutation) to form a new generation. The new generation of candidate solutions is then used in the next iteration of the algorithm. Commonly, the algorithm terminates when either a maximum number of generations has been produced, or a satisfactory fitness level has been reached for the population.

In practical optimization problem, there are usually many objectives, and in most cases the objectives are conflicting each other. The weight coefficient transformation method gives the j th sub-objective function $t(p_1, \dots, p_l)$ weight coefficient w_j , and all k sub-objective functions are weighted linearly to form a new objective function T (Eq.1). By this method, the multi-objective optimization problem is transformed into a single-objective optimization problem.

$$T=\sum_{j=1}^kw_jt_j(p_1,\dots,p_l) \tag{1}$$

Model Setup

Model setup includes the following steps:

- $S(z)$, the relation between correction of local magnetic field distribution and minimal shim is built either by calculation or by measurement.
- For undulator with $2N_u$ modules, the correction of local magnetic field distribution for other shim can be concluded by multiplying a coefficient C_n (n is module's number) with $S(z)$. Now, the problem was changed to find optimal C_n for every module.

- The new magnetic field distribution $B_{m+1}(z)$ was generated by adding $C_n * S(z)$ of every module to old magnetic field distribution $B_m(z)$ like Eq. 2.

$$B_{m+1}(z) = B_m(z) + \sum_{n=1}^{2N_u} C_n S(z') \quad (2)$$

- Integer C_n was converted to binary for genetic representation, and all C_n s formed a binary array.

APPLICATION

Prototype Undulator U38

Prototype U38 is a hybrid planar undulator with two antisymmetric Halbach-type magnetic arrays. Each array includes 11 periods made of NdFeB blocks and DT4 blocks. The gap of U38 is fixed at 18 mm. One magnetic module is shown in Fig. 1, where one DT4 block and two half-NdFeB blocks form a sandwich-like structure. So, one period contains two modules. Mechanical shim was implemented by inserting copper pieces with various thicknesses between magnetic modules and beam to modify local field. Besides, to simplify work only magnetic modules of upper magnetic array were adjusted. Correction of local magnetic field after one module displacing of 0.001 mm can be seen in Fig. 2.

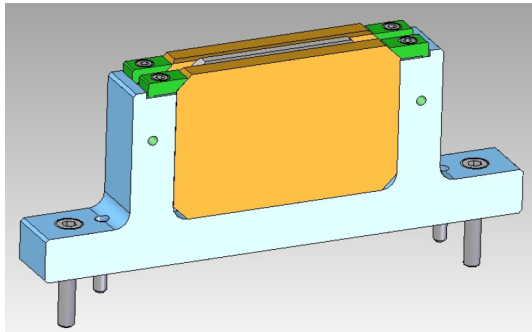


Figure 1: One sandwich-like magnetic module.

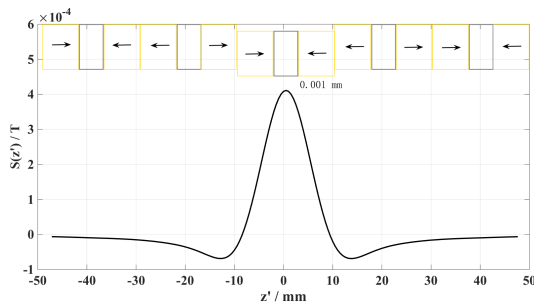


Figure 2: Correction of local magnetic field after displacing of 0.001 mm for one magnetic module.

For U38, there are three specifications must be reached, including trajectory center deviation < 0.2 mm, peak-to-peak error < 0.5%, and phase error < 5°.

Objective Function

As mentioned above, prototype U38 has three specifications must be reached, so it's a multi-objective problem. Objective function was defined as follows:

- Providing the electron energy of 8 MeV, trajectory $x(z)$ was calculated by numerically integrating magnetic field distribution twice like Eq. 3, and then trajectory center deviation Δx_{rms} was concluded.

$$x(z) = -\frac{e}{\gamma m_0 c} \int_{z_{start}}^{z_{stop}} \left(\int_{z_{start}}^{z''_{stop}} B(z) dz \right) dz'' \quad (3)$$

- The peak-to-peak error $(\Delta B/B)_{rms}$ was obtained by root mean square value of peak field dividing mean value of peak field.
- The distribution of phase was calculated using Eq. 4, where $\phi(z)$, λ_u , \bar{K} , c , m_0 and e represented phase, period length, mean value of undulator parameter, light velocity, electron mass in rest frame and electron charge, respectively [8]. Then, phase error $(\Delta \Phi)_{rms}$ equaled phase at poles minus $2n\pi$, where n was pole number.

$$\Phi(z) = \frac{2\pi}{\lambda_u (1 + 0.5 \bar{K}^2)} \cdot \left(z + \left(\frac{e}{m_0 c} \right)^2 \left(\int_{z_{start}}^{z_{stop}} \left(\int_{z_{start}}^{z''_{stop}} B(z) dz \right) dz'' \right) \right) \quad (4)$$

- The linear combination of trajectory center deviation, peak-to-peak error and phase error was defined as the objective function.

$$T(B(z)) = 10\Delta x_{rms} + (\Delta \Phi)_{rms} + 500(\Delta B/B)_{rms} \quad (5)$$

GA Configure

- The chromosome structure is shown in Fig. 3, which is a $6 * 2N_u$ -dimension array.

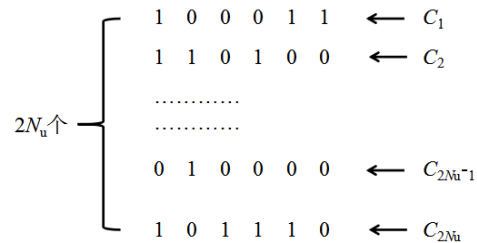


Figure 3: Structure of individual's chromosome.

- Commonly, the initial population is generated randomly, allowing the entire range of possible solutions. But, we filled initial population with zero to limit the number of modules must be moved.

Table 1: Parameters of GA

Parameter	Value
Population size	200
Mutation rate	0.02
Crossover rate	0.8
Elitism	1

- It is commonly accepted that a certain amount of elitism speeds up optimization. So, it was decided to keep the best chromosome to next generation.
- The evolution will terminate when objective function satisfies the requirements.
- GA is a wide diverse group of algorithms, which qualitative working principles vary and our parameters of GA can be seen in Table 1.

Shimming Results

The shimming of prototype U38 was implemented as follows:

- Measuring the magnetic field distribution
- Calculating the optimal C_n for every module using GA
- Shimming U38
- Repeating process of a, b and c until the requirements are satisfied.

We finished three times shimming. The evolution of trajectory, peak-to-peak error and phase error with the shim number are shown in Fig. 4, Fig. 5 and Fig. 6, respectively. It can be seen the performance was improved during evolution. After three times shimming, the requirements were satisfied. The trajectory center deviation, peak-to-peak error and phase error are reduced to 0.15 mm, 0.49% and 1°.

CONCLUSION

In this proceeding, We proposed a fast and accurately method to conclude the shim using multi-objective GA. The method was also applied to shim a prototype U38 to demonstrate. After three times shimming, the performance of U38 satisfied the requirements. The trajectory center deviation, peak-to-peak error and phase error are reduced to 0.15 mm, 0.49% and 1°.

REFERENCES

- [1] Y. Socol, "High-power free-electron lasers—technology and future applications," *Opt. Laser Technol.*, vol. 46, no. 1, pp. 111–126, 2013. doi:10.1016/j.optlastec.2012.06.040
- [2] A. B. Temnykh, "Delta undulator for cornell energy recovery linac," *Phys. Rev. Spec. Top. Accel. Beams*, vol. 11, no. 12, p. 120702, 2008. doi:10.1103/PhysRevSTAB.11.120702

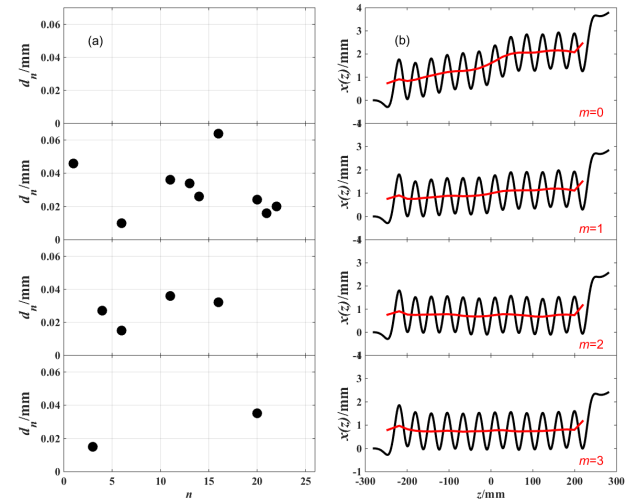


Figure 4: Displacement of one module (a) and evolution of electron trajectory and trajectory center (b).

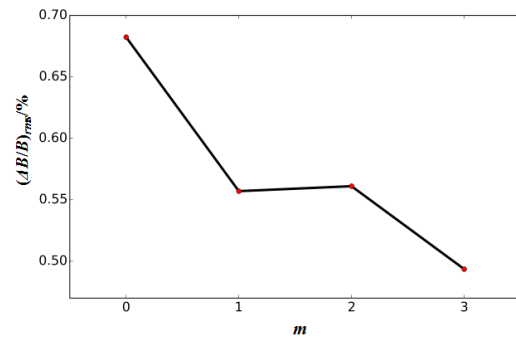


Figure 5: The evolution of peak-to-peak error.

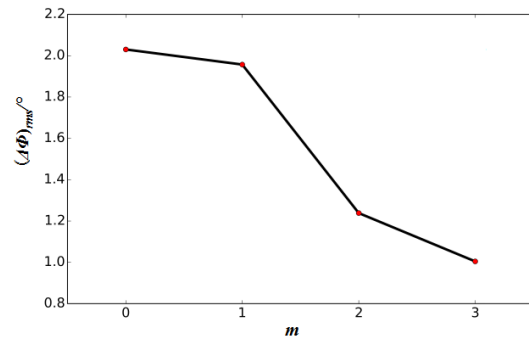


Figure 6: The evolution of phase error.

- [3] K. Halbach, "Physical and optical properties of rare earth cobalt magnets," *Nuclear Instruments & Methods in Physics Research*, vol. 187, no. 1, pp. 109–117, 1981. doi:10.1016/0029-554X(81)90477-8
- [4] Y. Li, B. Faatz, J. Pflueger, "Undulator system tolerance analysis for the european x-ray free-electron laser," *Rev. Mod. Phys.*, vol. 11, no. 10, pp. 320–325, 2008. doi:10.1103/PhysRevSTAB.11.100701
- [5] M. Scheer, B. Kuske, A. Meseck, G. Mishra, M. Abo-Bakr, J. Bahrtdt, "Tolerance studies for the bessy fel undulators," *Nucl. Instrum. Meth. A*, vol. 528, no. 1, pp. 258–262, 2004. doi:10.1016/j.nima.2004.04.059

- [6] R. P. Walker, “Phase errors and their effect on undulator radiation properties,” *Phys. Rev. Spec. Top. Accel. Beams*, vol. 16, no. 1, pp. 122–130, 2013. doi:10.1103/PhysRevSTAB.16.010704
- [7] H. Onuki, P. Elleaume, *Undulators, Wigglers and Their Applications*, USA, CRC Press, 2002.
- [8] P. Li, T. Wei, Y. Li, J. Pflueger, “Magnetic Design of an Apple-X Afterburner for the SASE3 Undulator of the European XFEL,” *Nucl. Instrum. Meth. A*, vol. 870, pp. 103 – 109, 2017. doi:10.1016/j.nima.2017.07.023

ALL-FIBER PHOTONIC, ULTRALOW-NOISE, ROBUST OPTICAL AND MICROWAVE SIGNAL GENERATORS FOR FELs AND UED

D. Kwon, D. Kim, I. Jeon, and J. Kim,

Korea Advanced Institute of Science and Technology, Daejeon, South Korea

Abstract

Optical timing and synchronization is becoming a more important and essential element for future ultrafast X-ray and electron science [1, 2]. As a result, compact, ultralow-noise, mechanically robust and long-term stable optical/microwave signal generators are highly desirable for future XFELs and UEDs. Here we show that the combination of mode-locked fiber laser and fiber delay-based stabilization method enables the generation of ultralow-noise optical and microwave signals. We show that all-PM fiber lasers can provide excellent mechanical robustness: stable laser operation over >1 hour is maintained even in continuous 1.5g vibrations [3]. Using a compactly packaged fiber delay as the timing reference, we could stabilize the repetition-rate phase noise of mode-locked lasers [4, 5] down to -100 dBc/Hz and -160 dBc/Hz at 1-Hz and 10-kHz offset frequency, respectively, at 1-GHz carrier, which corresponds to only 1.4 fs rms absolute timing jitter [1 Hz - 100 kHz]. With DDS-based electronics, low-noise and agile microwave frequency synthesizer was also realized [6]. This new class of photonic signal generator will be suitable for master oscillators in various accelerator-based light sources.

INTRODUCTION

Robust operation of mode-locked lasers is highly desirable for optical timing and synchronization of free electron lasers (FELs) and ultrafast electron diffraction (UED). In accelerator facilities, the environment is often harsher than well controlled optics laboratories due to vibrations, radiation and high voltage and current pulsed signals. Although nonlinear polarization evolution-based mode-locked lasers have been widely used to generate low-noise timing signals, the mode-locking state is sensitive to environment-induced perturbations. In order to operate the mode-locked lasers in a long-term stable way in these facilities, mechanical robustness is important. As a solution, polarization-maintaining fiber-based mode-locked lasers have been investigated because strong birefringence relieves the environment sensitivity.

In addition, for effective optical timing and synchronization, low timing jitter is very important. Mode-locked lasers have shown great short-term timing jitter. Typically, timing jitter (i.e., repetition-rate phase noise) of free-running laser oscillator is fs-level within ~ms time scale. However, it starts diverging over time due to lack of restoring force. Therefore, locking laser oscillator to more longer-term stable reference is highly desirable to maintain great short-term timing jitter over longer time scale. Many microwave reference oscillators and optical references have been used to lock the mode-locked lasers. Among them, an ultra-stable Fabry-Perot cavity-based

locking system has been an effective way to suppress timing jitter over ~10 s time scale. However, it is a high-cost instrument and technically difficult to implement outside of well-controlled laboratories. As an alternative way of timing stabilization, fiber delay line-based technique was developed [4].

In this paper, a simple structured polarization-maintaining fiber-based mode-locked laser is discussed. We examined the mechanical robustness of an all-PM 3 x 3 coupler-based nonlinear amplifying loop mirror (NALM) mode-locked laser under > 1 hour of 1.5g_{rms} vibration condition. Also, a continuous operation of graphene saturable absorber (SA) based mode-locked laser under gamma ray radiation is also discussed [7]. To reduce short-term timing jitter, a compact, robust and all-fiber delay line-based timing jitter suppression technique is introduced. By combining the robust laser with the fiber-based timing jitter stabilization technique and DDS-based electronics, ultralow-noise optical/microwave synthesizer, which can be effectively used for FELs and UED facilities, is demonstrated.

RESULTS

We demonstrated a simple structured, mechanically robust 3 x 3 coupler-based all-PM fiber laser [Schematic shown in Fig. 1(a)]. A 3 x 3 coupler has intrinsic 120 deg phase bias between each port so that it does not require any additional phase shifter to initiate mode-locking in NALM laser. Moreover, mode-locking threshold is reduced compared to 2 x 2 coupler-based PM-NALM laser.

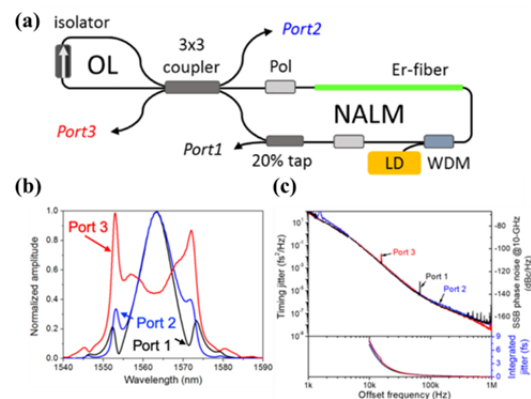


Figure 1: (a) Schematic of an all-PM-fiberized 3 x 3 coupler based NALM laser (b) optical spectra and (c) timing jitter spectra from each port. The data and figures are based on [3].

We can use three fiberized outputs from the 3 x 3 coupler-based PM-NALM laser. Figure 1(b) shows normalized optical spectra of each port, which respectively has

21.6 nm, 15.1 nm, and 14.1 nm bandwidth at 1560-nm center wavelength. Figure 1(c) shows timing jitter power spectral density spectra. The integrated rms jitter from each port is sub-10-fs [10 kHz – 1 MHz]. The mechanical stability of the laser is tested under >1 hour of 1.5g_{rms} vibration on the shaker table (B&K, LDS 721) [Fig. 2(a)]. Note that this level of vibration is above the level in aircrafts, trucks, and boats, which underlines the mechanical robustness of the demonstrated NALM laser. The optical spectra measurement under 1 hour is shown in Figure 2(b). The mode-locked state is maintained robustly even with strong and continuous mechanical perturbation.

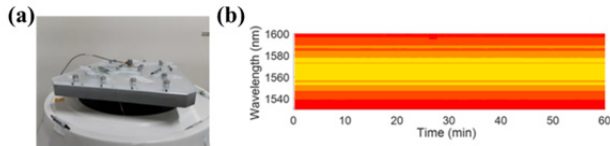


Figure 2: Vibration test of all-PM-fiberized 3 x 3 coupler based NALM laser. (a) The shaker generates 1.5g_{rms} vibration and (b) optical spectrum from the port 1 is recorded for >1 hour. Note that the data and figure are based on [3].

Robust laser operation under radiative environment can be also attractive for the use in accelerator facilities. We examined the use of a graphene saturable absorber in mode-locked fiber lasers [schematic shown in Fig. 3(a)] as a way to achieve robust mode-locking operation in radiative environment. An average irradiation dose rate of 45 Gy/hr and total dose of 2 kGy radiation was applied to the graphene saturable absorber. From the RF pulse train and optical spectrum measurement result under radiation up to 2 kGy in Figure 3(b) and Figure 3(c) respectively, we found that it still maintained the mode-locking operation [7], which is more robust compared to the traditional SESAM-based results.

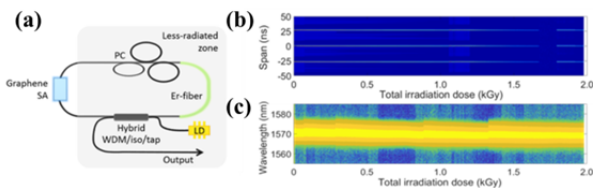


Figure 3: (a) Schematic of a graphene-SA-based mode-locked laser. (b) RF pulse train, and (c) optical spectrum measurement under radiation up to 2 kGy. More detailed information can be found in [7].

Timing jitter of mode-locked lasers diverges over time since there is no restoring force in the laser oscillators. It is highly desirable to stabilize the timing of mode-locked lasers over longer time scales. As a compact and robust timing jitter suppression method, we demonstrate a fiber delay line-based timing jitter suppression technique [4]. The basic principle is to use optical fiber delay as the

timing reference and to detect frequency noise of two optical frequency, $f_m = mf_{rep} + f_{ceo}$ and $f_n = nf_{rep} + f_{ceo}$. Then, common mode f_{ceo} noise is rejected by frequency mixer, resulting in $(m-n)f_{rep}$ (~2.5 THz when $f_m = 194.8$ THz and $f_n = 192.3$ THz) noise detection. Therefore, sensitivity (2.5 THz) of noise detection is much enhanced compared to microwave-based technique (GHz-level). The schematic and photo of compact setup are respectively shown in Figure 4(a) and Figure 4(b). The entire system size is ~30 cm x 30 cm x 15 cm, and we are currently improving the size and performance even further. Figure 4(c) and Figure 4(d) show the suppressed timing jitter power spectral densities with 1-km fiber and 10-km fiber, respectively. As a result, the timing jitter is suppressed down to 20 fs (when 1-km fiber is used is used [4]) and 1.4 fs (when 10-km fiber is used [5]). If it is converted to the equivalent single-sideband phase noise at 1-GHz carrier, it corresponds to -100 dBc/Hz and -160 dBc/Hz at 1-Hz and 10-kHz offset frequency, respectively [5].

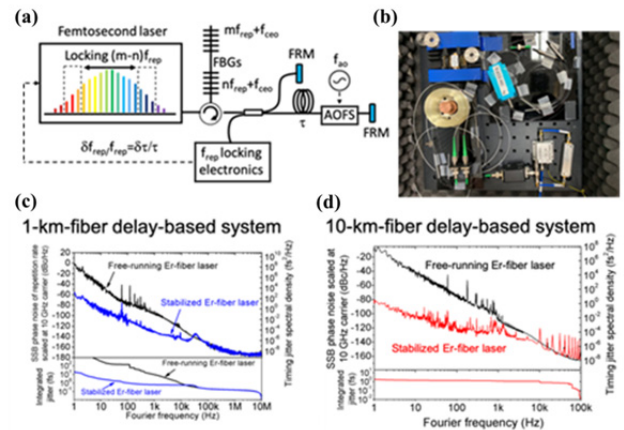


Figure 4: (a) Schematic of fiber delay line-based timing jitter suppression system and (b) setup photo. The suppressed timing jitter power spectral densities when (c) 1-km fiber is used and (d) 10-km fiber is used. Note that the equivalent phase noise is converted for 10-GHz carrier frequency in these plots. More detailed information can be found in refs. [4] and [5].

By adding a fiber-loop optical-microwave phase detector (FLOM-PD, [8]) and DDS electronics, low-noise microwave synthesizer is also demonstrated. Figure 5(a) shows a diagram of it. The repetition rate of mode-locked laser is stabilized by FIRST (Fiber Interferometer based Repetition-rate Stabilization Technique). Then The FLOM-PD (Fiber-Loop Optical-Microwave Phase Detector) is used to generate low-noise microwave using fly-wheel effect between stabilized optical pulse trains with low-timing jitter and a microwave dielectric resonator oscillator (DRO). With commercial DDS electronics, an agile and low-noise 9-11 GHz all-fiber photonic microwave synthesizer is demonstrated [6]. The absolute SSB phase noise and integrated timing jitter of the generated microwave is shown in Figure 5(b). The integrated rms

riming jitter of the 10-GHz signal is 7.6 fs [10 Hz – 10 MHz], which is limited by PNA noise floor indicated in pink curve. The projected phase noise at 10 GHz measured in optical domain by FIRST setup makes lower integrated jitter, which is 2.6 fs [curve blue].

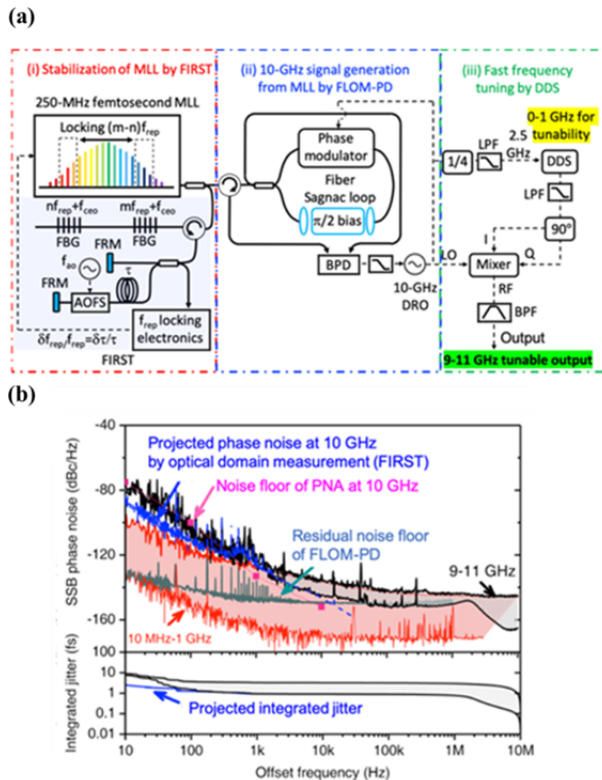


Figure 5: (a) Schematic of the microwave synthesizer. FIRST : Fiber Interferometer based Repetition-rate Stabilization Technique [4,5]. FLOM-PD : Fiber-Loop Optical-Microwave Phase Detector [8]. DDS : Direct Digital Synthesizer. (b) Measured absolute SSB phase noise at 10-GHz and integrated jitter. More detailed information can be found in [6].

CONCLUSION

The all-PM-fiberized 3 x 3 coupler-based NALM laser is demonstrated. The intrinsic 120-degree phase bias decreases system complexity and lowers the mode-locking threshold. Moreover, the all-fiber mode-locked laser shows great mechanical stability, which enables stable operation even under >1 hour of 1.5g_{rms} vibration. The graphene saturable absorber-based mode-locked laser can maintain mode-locked operates up to 2 kGy radiation. These features can be advantageous for the operation in FELs and UED facilities.

Further, to improve precise optical timing, a fiber delay line-based timing jitter suppression is applied. The rms timing jitter can be reduced down to 1-fs-level over 1 s time scale. In phase noise, it is -100 dBc/Hz and -160 dBc/Hz at 1-Hz and 10-kHz offset frequency, respectively, for 1-GHz carrier frequency. By combining the DDS

electronics with the fiber delay line-locked mode-locked laser, ultralow-noise microwave synthesizer is realized. The demonstrated system synthesizes microwave from 9-11 GHz with low-noise and frequency agility. Note that the center frequency and frequency tuning ranges can be easily changed depending on the intended applications.

Currently we are improving the entire system including better packaging. It is expected robust, compact and all-fiber photonics-based ultralow-noise optical and microwave synthesizers can be readily applied for optical timing and synchronization in FELs and UED facilities in the near future.

REFERENCES

- [1] J. Kim, J. A. Cox, J. Chen, and F. X. Kärtner, "Drift-free femtosecond timing synchronization of remote optical and microwave sources," *Nat. Photonics* 2, 733–736, 2008, doi:10.1038/nphoton.2008.225
- [2] S. Schulz *et al.*, "Femtosecond all-optical synchronization of an X-ray free-electron laser," *Nat. Commun.*, vol. 6, 5938, 2015, doi:10.1038/ncomms6938
- [3] D. Kim, D. Kwon, B. Lee, and J. Kim, "Polarization-maintaining nonlinear-amplifying-loop-mirror mode-locked fiber laser based on a 3 x 3 coupler," *Opt. Lett.* 44, 1068–1071, 2019, doi:10.1364/OL.44.001068
- [4] K. Jung and J. Kim, "All-fiber photonic signal generator for attosecond timing and ultralow-noise microwave," *Sci. Rep.* 5, 16250, 2015, doi:10.1038/srep16250
- [5] D. Kwon and J. Kim, "All-fiber interferometer-based repetition-rate stabilization of mode-locked lasers to 10e-14 level frequency instability and 1-fs-level jitter over 1 s," *Opt. Lett.* 42, 5186–5189, 2017, doi:10.1364/OL.42.005186
- [6] J. Wei, D. Kwon, S. Zhang, S. Pan, and J. Kim, "All-fiber-photonics-based ultralow-noise agile frequency synthesizer for X-band radars," *Photon. Res.* 6, 12–17, 2018, doi:10.1364/PRJ.6.000012
- [7] D. Kim, N. Park, H. Lee, J. Lee, D. Yeom, and J. Kim, "Graphene-based saturable absorber and mode-locked laser behaviors under gamma-ray radiation," *Photon. Res.* 7, 742–747, 2019, doi:10.1364/PRJ.7.000742
- [8] K. Jung and J. Kim, "Subfemtosecond synchronization of microwave oscillators with mode-locked Er-fiber lasers," *Opt. Lett.* 37, 2958–2960, 2012, doi:10.1364/OL.37.002958

TIMING SYNCHRONIZATION ACTIVITIES FOR DRIFT-FREE OPERATION OF ULTRAFAST ELECTRON DIFFRACTION SYSTEM AT KAERI

J. Shin, J. Kim[†], Korea Advanced Institute of Science and Technology, Daejeon, Republic of Korea,
I. H. Baek, H. W. Kim, K. Y. Oang, S. Park, Y. U. Jeong, Korea Atomic Energy Research Institute,
Daejeon, Republic of Korea

Abstract

Precise timing synchronization of an ultrafast electron diffraction facility is essential requirement for femtosecond resolution structure analysis. Recent studies of THz-based electron deflectors have enabled the timing drift measurement between ultrafast electrons and an optical pump beam with few femtosecond resolution. In this work, we will introduce timing synchronization activities to suppress the drift of an electron beam. As timing drift of the electron beam originates from every sub-element, each timing drift contribution from RF transfer, RF-to-optical synchronization, and optical amplification is measured. Timing drift of RF transfer through coaxial cable, which exposed to temperature fluctuation, is actively stabilized from 2 ps to 50 fs by active feedback loop. Further additive drift from RF-to-optical synchronization is maintained below 100 fs. Also optical drift due to the regenerative amplifier, measured by optical correlator, is maintained below 20 fs over an hour. This work allows ultrafast electron diffraction system to operate with less drift correction procedure and increased user availability.

INTRODUCTION

Ultrafast electron diffraction allows time-resolved structure analysis at atomic scale [1,2], which enables many potential applications on material science. Note that ultrafast electron offers unique opportunities as a matter, and it takes complementary role with light-based method such as free electron lasers. To further pave the way for ultrafast electron diffraction, it is of importance to optimize the temporal stability of electron sources. High temporal stability of electron sources will flourish not only ultrafast electron diffraction, but also ultrafast electron microscopy [3], and free electron lasers [4]. To generate low noise ultrafast electrons with MeV energy, DC photoguns and RF photoguns could be utilized. DC photogun itself is inherently synchronized with optical gating pulses, while further accelerating stages should be managed properly [5]. RF photogun could provide MeV energy electrons without further acceleration stages due to its intrinsically high electric field strength. Unfortunately, synchronizing RF field with injected optical pulses train could be a challenge [6]. With the recent advancement of THz-driven streak camera [7], jitter-free operation of RF photogun is enabled by optimizing laser injection phase. To fully exploit the jitter-free ultrafast electron sources, suppressing timing drift and maintaining performance over long time are essential. In this

paper, we optimize the timing drift of the ultrafast electron diffraction facility in KAERI, which already achieved jitter-free condition with a RF photogun. To stabilize the timing drift of entire system, all timing contribution from subsystems are investigated. Subsystems are classified into RF distribution, RF-to-optical synchronization, and optical amplification as depicted in Fig. 1. Optimization of each subsystem is described in following sections.

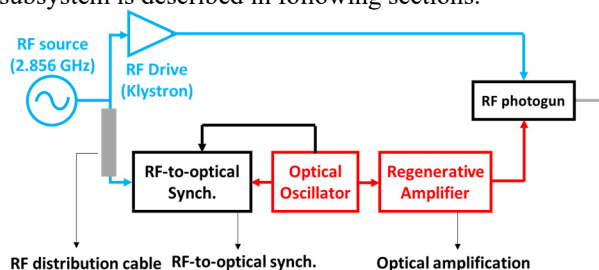


Figure 1: Subsystems contributing timing drift of electron pulses.

RF DISTRIBUTION

To distribute RF carrier from RF oscillator to laser, coaxial cable is installed across the facility. Due to the distance between two locations, cable length of 30 m is required. Note that longer length of coaxial cable is more vulnerable to thermal fluctuation. To mitigate the impact of thermal fluctuation, many previous researches such as stabilizing the cable temperature and measuring thermal sensitivity of cable are reported [4]. In our system, SUCOFLEX404 (H&S) cable is installed for high stability against temperature. Furthermore, active drift compensation system is introduced as shown in Fig. 2. The proposed scheme compares phase between original RF signal and round-trip signal, which reflected from the end of coaxial cable. Detected phase error is feedback controlled by voltage-controlled phase shifter.

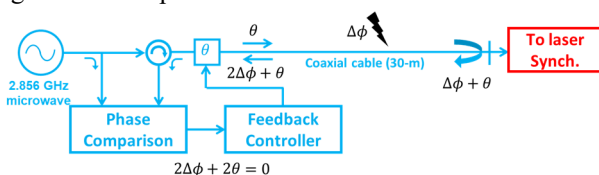


Figure 2: Active drift compensation scheme for the 30-m coaxial cable.

Timing drift of the coaxial cable is stabilized for 60,000 s and recorded with 10 s sampling time. All of stabilization performance, compensated drift amount, and temperature change of cable are recorded and plotted in Fig. 3. Note

[†]jungwon.kim@kaist.ac.kr

that compensated drift amount implies the timing performance without feedback control. The compensated drift shows close relation with temperature. Sharp temperature change near 42,000 s is due to warming up of the entire facility. Large phase shift due to temperature change is about 2 ps. After active stabilization, timing is stabilized in sub-100 fs even under drastic temperature change.

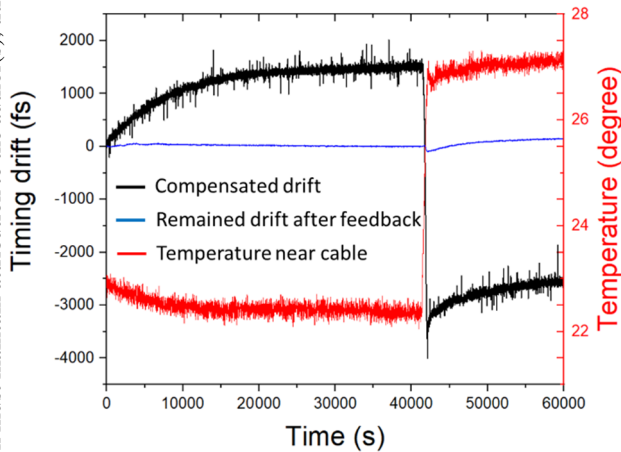


Figure 3: Measurement result of timing drift at coaxial cable after active stabilization.

RF-TO-OPTICAL SYNCHRONIZATION

Synchronization between the optical pulse train and RF carrier has been actively researched over decades. Traditional approach utilizes photodiodes and frequency mixers to compare phase in electrical domain. To overcome the unwanted nonlinearities of mixers and photodiodes, phase detection by electro optic sampling method is actively researched [8]. Electro-optic sampling method is based on the optical interferometer and an electro-optic phase modulator for high precision. In our system, fiber Sagnac loop based interferometer is implemented for RF-to-optical synchronization as shown in Fig. 4. Repetition rate of optical oscillator is 79.3 MHz, and its 36th harmonic is 2.856 GHz. Note that 2.856 GHz is also the operating frequency of RF oscillator. Phase-locked loop is established via modulating repetition rate of optical oscillator.

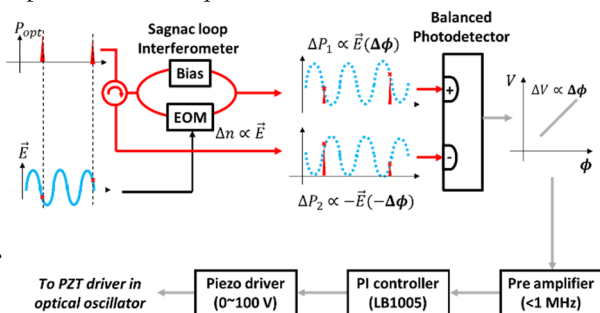


Figure 4: Schematic of fiber Sagnac loop based RF-to-optical phase synchronization. EOM : electro-optic modulator.

To verify the performance of the phase locked loop, additional out-of-loop performance is measured with a secondary phase detector. The measured phase noise by a in-loop phase detector only represents loop performance, while the resolution of the phase detector is not observed. Both in-loop and out-of-loop phase noise are plotted in Fig. 5. In-loop and out-of-loop phase noise follows closely from 100 Hz to 100 kHz offset frequency range. Below 100 Hz offset frequency shows difference due to resolution of the phase detectors. As feedback bandwidth is limited to 2 kHz due to finite bandwidth of the laser actuator, phase noise of the optical oscillator above 2 kHz is not suppressed. This could be mitigated by improvement of the optical oscillator and optimization of the feedback loop with a lead compensator. Integrated timing jitter from 100 kHz to 1 Hz is 17.9 fs (23.14 fs) at in-loop (out-of-loop).

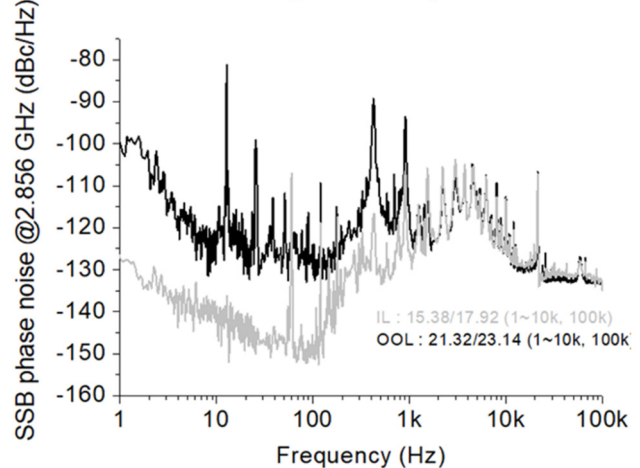


Figure 5: Measured relative phase noise between RF and optical pulse train after synchronization. IL : in-loop, OOL : out-of-loop.

OPTICAL AMPLIFICATION

For optical amplification, a regenerative optical amplifier which operates up to 1 kHz repetition rate is installed. As optical pulses travel repeatedly in the amplifier to build up pulse energy, timing jitter of the regenerative amplifier could be affected by thermal fluctuation. To measure the timing drift between the optical oscillator and the regenerative amplifier, optical correlation method [9] based on second harmonic generation is applied as shown in Fig. 6. By controlling the temporal overlap between optical pulses, second harmonic optical power will be proportional to timing fluctuation.

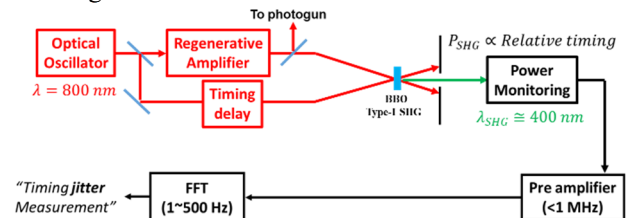


Figure 6: Schematic of optical correlation method to measure timing jitter of the regenerative amplifier. FFT : Fourier Frequency Transform.

Measured timing jitter by optical correlation method and background noise due to instrument is plotted in Fig. 7. Both the background noise and measured timing jitter show strong electrical noise at 60 Hz. The electrical instability is due to the high gain (>1000) applied on baseband. The used photodetector has 100 MHz bandwidth. Note that huge discrepancy between detector bandwidth (100 MHz) and pulse repetition rate (1 kHz) requires very high electrical gain to make signal observable. Regenerative amplifier shows strong fluctuation near 80 Hz. As a future work, measurement of timing drift and improvement of resolution is required.

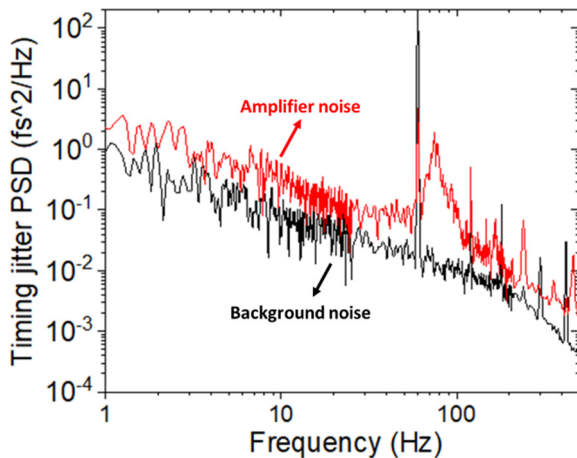


Figure 7: Measured relative timing jitter of optical regenerative amplifier with respect to optical oscillator.

CONCLUSION

In this work, we have implemented timing systems to optimize long-term temporal drift at ultrafast electron diffraction facility in KAERI. To further enhance the long term stability of the electron beam, timing drift of RF signal after Klystron should be handled. Note that optimization of RF drive is within the reach of current technology such as low level RF. This work will could be a foot step to operate the jitter-free ultrafast electron sources over very long time scale. As future work, timing drift of ultrafast electron pulses will be examined by THz-driven streak camera.

REFERENCES

- [1] G. Sciaini, and R. J. Dwayne Miller, "Femtosecond electron diffraction: Heralding the era of atomically resolved dynamics," *Rep. Prog. Phys.*, vol. 74, no. 9, p. 096101, 2011. doi:10.1088/0034-4885/74/9/096101
- [2] S. P. Weathersby *et al.*, "Mega-electron-volt ultrafast electron diffraction at SLAC National Accelerator Laboratory," *Rev. Sci. Instrum.*, vol. 86, p. 073702, 2015. doi:10.1063/1.4926994
- [3] D. J. Flannigan, and A. H. Zewail, "4D Electron Microscopy: Principles and Applications," *Acc. Chem. Res.*, vol. 45, no. 10, p. 1828, 2012. doi:10.1021/ar3001684
- [4] Chang-Ki Min *et al.*, "RF Timing Distribution and Laser Synchronization Commissioning of PAL-XFEL," in *Proc. 7th Int. Particle Accelerator Conf. (IPAC'16)*, Busan, Korea, May 2016, pp. 4234-4236, doi: 10.18429/JACoW-IPAC2016-THP0Y057
- [5] D. Zhang *et al.*, "Segmented terahertz electron accelerator and manipulator (STEAM)," *Nat. Photonics*, vol. 12, pp. 336-342, 2018. doi:10.1038/s41566-018-0138-z
- [6] M. R. Otto, L. P. Rene de Cotret, M. J. Stern, and B. J. Siwick, "Solving the Jitter Problem in Microwave Compressed Ultrafast Electron Diffraction Instruments: Robust Sub-50 fs Cavity-Laser Phase Stabilization," *Struct. Dyn.*, vol. 4, p. 051101, 2017. doi:10.1063/1.4989960
- [7] J. Fabianska, G. Kassier, and T. Feurer, "Split ring resonator based THz-driven electron streak camera featuring femtosecond resolution," *Sci. Rep.*, vol. 4, p. 5645, 2014. doi:10.1038/srep05645
- [8] H. Yang, B. Han, J. Shin, D. Hou, H. Chung, I. H. Baek, Y. U. Jeong, and J. Kim, "10-fs-level synchronization of photocathode laser with RF-oscillator for ultrafast electron and X-ray sources," *Sci. Rep.*, vol. 7, p. 39966, 2017. doi:10.1038/srep39966
- [9] A. Casanova, Q. D'Acremont, G. Santarelli, S. Dilhaire, and A. Courjaud, "Ultrafast amplifier additive timing jitter characterization and control," *Opt. Lett.*, vol. 41, p. 898, 2016. doi:10.1364/OL.41.000898

CHARACTERIZATION OF FEL SPECTRA USING SPECIFIC FIGURES OF MERIT

Mihai Pop*, Francesca Curbis, MAX-IV, Lund University, Lund, Sweden
Enrico Allaria, Elettra Sincrotrone Trieste, Basovizza, Italy

ABSTRACT

There is an increasing demand from the user community for high quality FEL radiation. The spectrum of this radiation can prove to be a useful tool in characterizing the FEL process. Starting from a tool initially developed at FERMI we extend its capabilities to be able to analyze the modal components of the FEL spectrum. In this paper we will describe and compare two different figures of merit and offer initial bench-marking with respect to classic figure of merit for spectra such as FWHM and RMS.

INTRODUCTION

It is a common practice to optimize the setup of the FEL by looking at the spectrum of the radiation. However in order to have any type of automation procedure feeding back on this measurement, a simple figure of merit is needed. This can help not only in automation of the optimization procedure but also in removing biases that a human inevitably has while looking at a spectrum. Important work regarding FEL optimization procedure has been carried out at FERMI FEL as presented in [1].

With this in mind we sought out to create such a figure of merit. The real time acquisition system used at FERMI FEL, REALTA, is capable of using real time scans of numerous hardware components. Along with an offline data analysis software, PyDart, provides a strong tool in characterizing the machine, both software tools are described in [2]. The initial goal of the project was to create a few figures of merit (from here on out referred to as *fom*) that can better characterize the "goodness" of a spectrum. The main addition to the capabilities of PyDart was the decomposition into spectral components by identifying the different peaks in the spectra.

PEAK DETECTION WORK-FLOW AND CAPABILITIES

The peak detection algorithm is a more complex version of scipy's find peaks routine [3] with the added ability to not only detect peaks but also valleys and even find peaks that do not have a prominence but manifest as a shoulder, see Figure 1.

The work-flow is structured as follows:

1. Subtracting a linear background from the Spectrum
2. Evaluate the background in terms of height periodicity and prominence

* mihai.pop@maxiv.lu.se

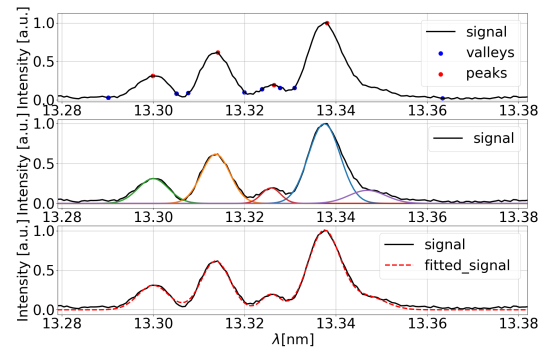


Figure 1: Illustration of work-flow : finding peaks and valleys (top) fitting (mid and bottom). Spectra supplied by Fermi.

3. Find all peaks that Are several times higher than the background, Have a prominence much higher than the background, Are separated from other peaks by n times the peak separation in the background Figure 1 (top).
4. Find the corresponding valleys to the peaks 1 (top).
5. Fit Gaussian functions to the region of interest defined by the peaks and valleys.
6. Calculate goodness of fit Figure 1 (bottom).

For a more comprehensive explanation of the working of the algorithm refer to [4].

FIGURES OF MERIT

In this section we will go through the *fom* to be able to understand their individual strengths and weaknesses. For the present analysis we have chosen a total of 6 *fom* but the list is by no means exhaustive with more work still remaining to be done.

- **Intensity** : the total intensity contained in a spectrum
- **FWHM** : width of the spectrum at half of the maximum intensity
- **Sigma 0** : the weighted RMS of the spectrum with respect to the weighted mean position
- **W of 80 %** : the minimum continuous width over which 80% of the intensity is located
- **A ratio** : the ratio between the area of the highest peak found by gaussian fitting to the total Intensity
- **Multi G sig** : the sigma of the highest peak found by gaussian fit

ANALYSIS

All the spectral analysis was done using PyDart that takes a real time acquisition file as input. This file contains spectral and actuator information and to this file PyDart appends the results of the analysis. The spectra we analyzed were taken among many the spectra acquired during the Echo Enabled Harmonic Generation (EEHG) setup of FEL2. This paper is not meant to give estimates of the performance or quality of the spectra for FERMI FEL2 operating in EEHG mode.

As a first step in the analysis we test the *fom* with a *scanfile*. In this case we use a file where the seed delay line was scanned. This provides a clear trend for the FEL process efficiency and a good baseline to test for our *fom*. In Figure 2 we can see that all the *fom* detect the region where the actuator scan produces the best FEL output. As an observation we could state that among the *fom* plotted **A ratio** shows some sensitivity in the highest intensity region.

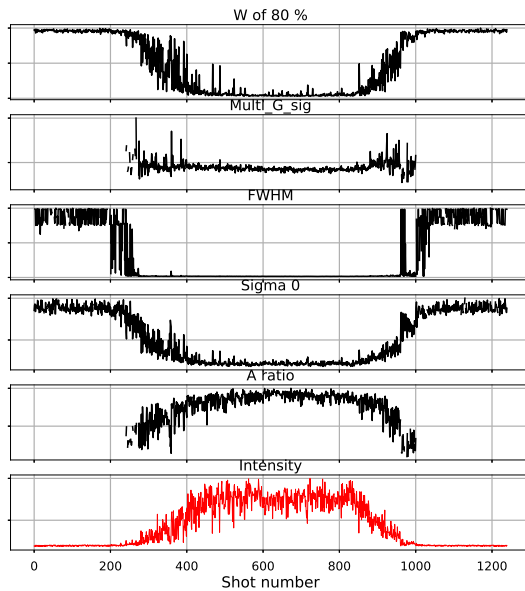


Figure 2: Different *fom* trends for spectra obtained during an actuator scan.

Correlation

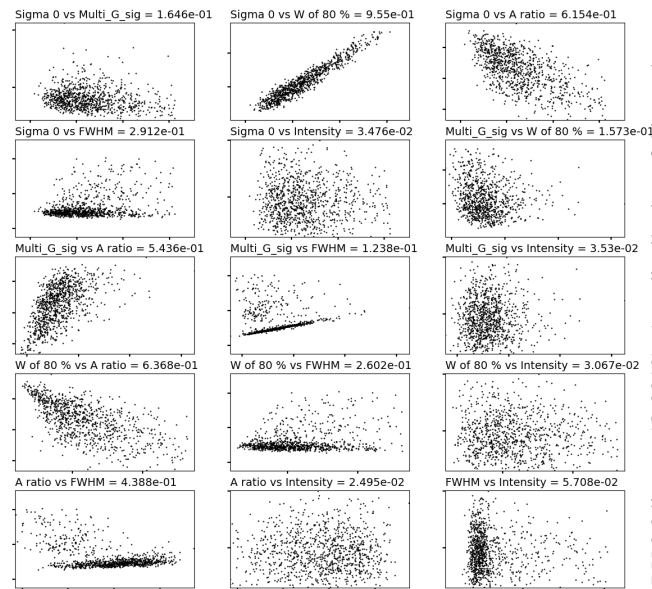
There is no pre-existing, objective way of determining how "good" a spectrum is, so we try to gauge which ones are the best by correlating them with each other so that we have more confidence in *fom* with high degree of correlation. If two *fom* are highly correlated it is probable that they will find the same spectra as being the best. We define the correlation between two *fom* as in equation 1. To be able to compare *fom* fairly, we take the absolute value of the correlation, for single peak clean spectra there should be an inverse correlation between intensity and width related *fom*. Furthermore, for each *fom* we only take values that are within 3 standard

deviations of the mean and for each correlation we use only those shots that both *fom* satisfy this condition.

$$Cor_{x,y} = \frac{(\sum (x_i - \bar{x})(y_i - \bar{y}))}{\sqrt{\sum (x_i - \bar{x})^2} \sqrt{\sum (y_i - \bar{y})^2}} \quad (1)$$

In Figure 3 we plot all the *fom* with respect to each other for another 1000+ shot file with real time acquisition i.e. no parameter was scanned. Several features of this figure stand out :

- The best single correlation is between **Sigma 0** and **W of 80 %**.
- The **Intensity** has the worst correlation with all the other *fom*.
- At a closer look one can find that **A ratio** has the best cumulative correlation with **W of 80 %** a close second.



Cumulative Correlation			
A ratio	0.398	W of 80 %	0.335
Sigma 0	0.312	FWHM	0.2131
Multi G sig	0.144	Intensity	0.0186

Figure 3: Comparison between the different *fom* correlation (top figures) and a cumulative correlation for each one (bottom table).

Sorting Spectra by fom

Having created an initial hierarchy of the *fom* we test the top two (**A ratio** and **W 80 %**) to see how well they sort the spectra. In addition we prepare a compounded *fom*, **mix fom** = $\frac{\text{Multi G sig}}{\text{Intensity}}$ and complete the selection with **Intensity**.

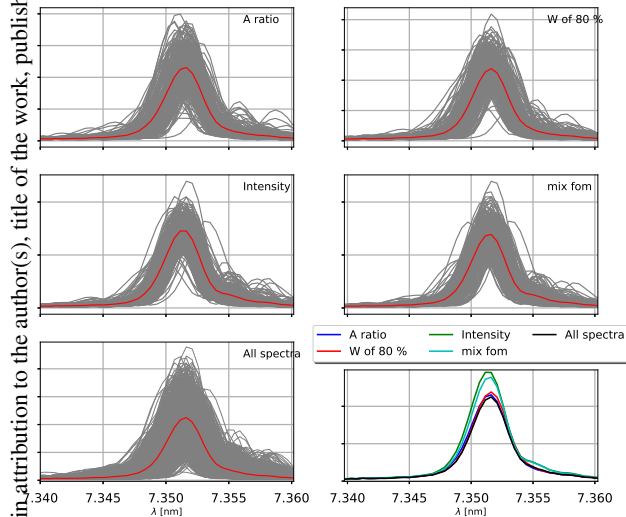


Figure 4: Comparison between the different fom for "not so good" spectra. Top 20 % of spectra as sorted by **A ratio** (top left), **W of 80%** (top right), **Intensity** (middle left), **mix fom** (middle right). 100% of the spectra (bottom left). Average of spectra for each *fom* and for the full selection.

In Figure 4 and 5 we plot the top 20 %, according to each *fom*. Each plot contains the individual top spectra in grey and the average of them in red. The comparison is done in the bottom right plot where the averages are plotted. We use a real time acquisition containing mostly single spike spectra and to show how each *fom* sorts relatively clean spectra (Figure 4). By choosing a file in which the second dispersive section of the EEHG scheme is scanned we illustrate the capabilities of each *fom* to sort though irregular spectra that some have multiple peaks.

The first thing to observe in Figure 4 is that the **Intensity** sorting gives the highest average even though the **mix fom** has a similar height, with a slightly narrower average peak. Secondly, all of the *fom* are better than the total average however the top performing ones in terms of correlation, **A ratio** and **W of 80 %**, are the worst at sorting among the four presented here. In Figure 5 the **Intensity** again shows great results with **A ratio** being only marginally better. The **W of 80 %** being the worst out of the *fom*. One might be inclined to speculate that **A ratio** chooses more narrow spectra, just by eye, but we would need an objective function to estimate this before making any claims.

A peculiar detail that might help in the future development of the code is the fact that even though **Intensity** is the least correlated of the *fom* it performs exceedingly well at sorting. It may be possible to take advantage of this fact and force some dependency of the rest of *fom* with respect to **Intensity** as we have seen with the **mix fom**.

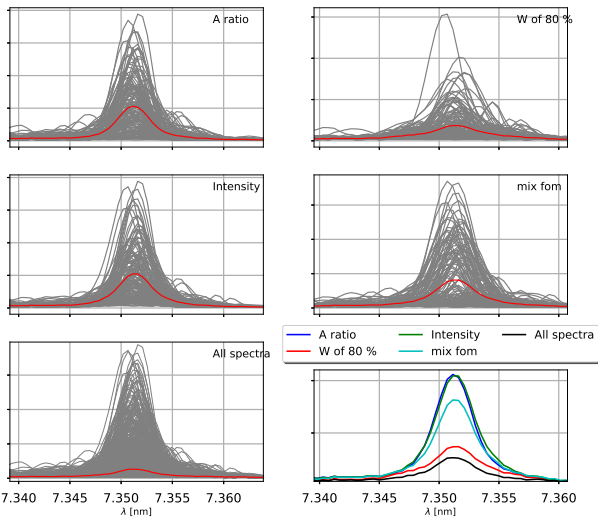


Figure 5: Comparison between the different fom for "not so good" spectra. Top 20 % of spectra as sorted by **A ratio** (top left), **W of 80%** (top right), **Intensity** (middle left), **mix fom** (middle right). 100% of the spectra (bottom left). Average of spectra for each *fom* and for the full selection.

CONCLUSIONS AND OUTLOOK

The *fom* analyzed here manage to find cleaner spectra and show reasonably good correlation among themselves. The **mix fom** performed well I believe largely due to its dependency on **Intensity**. A deeper understanding of the fitting process' efficiency and weaknesses is needed to further optimize *fom* such as **A ratio**.

Speculating, we can infer that among the reasons that **A ratio** and **w of 80 %** are not finding the highest intensity spectra consistently is that they are always scaled with the total intensity. Another improvement might be that in the definition of **A ratio** we should take into account the background level since the total Intensity has a larger contribution from the background than the largest peak.

REFERENCES

- [1] Niky Bruchon, Gianfranco Fenu, Giulio Gaio, Marco Lonza, Felice Andrea Pellegrino, and Lorenzo Saule. Free-electron laser spectrum evaluation and automatic optimization. *Nuclear Instruments and Methods in Physics*, 871:20 – 29, 2017. doi.org/10.1016/j.nima.2017.07.048
- [2] Enrico Allaria, Eugenio Ferrari, Eléonore Roussel, and Luca Vidotto. REALTA and pyDART: A Set of Programs to Perform Real Time Acquisition and On-Line Analysis at the FERMI Free Electron Laser. doi:10.18429/JACoW-ICALEPCS2017-THPHA044

- [3] Eric Jones, Travis Oliphant, Pearu Peterson, et al. SciPy: Open source scientific tools for Python, 2001.
<http://www.scipy.org>
- [4] M.A. Pop and E. Allaria. A Peak Finding Algorithm for FEL Spectra Characterization. 2019.
doi.org/10.18429/JACoW-IPAC2019-TUPRB070

NIR SPECTROMETER FOR BUNCH-RESOLVED, NON-DESTRUCTIVE STUDIES OF MICROBUNCHING AT EUROPEAN XFEL

S. Fahlström, M. Hamberg, Uppsala University, Uppsala, Sweden
Ch. Gerth*, N. M. Lockmann, B. Steffen, DESY, Hamburg, Germany

Abstract

At the European X-ray Free Electron Laser high brilliance femtosecond FEL radiation pulses are generated for user experiments. For this to be achieved, electron bunches must be reliably produced within very tight tolerances. In order to investigate the presence of microbunching, i.e. charge density variation along the electron bunch with features in the micron range, a prism-based NIR spectrometer with an InGaAs sensor, sensitive in the wavelength range 900 nm to 1700 nm was installed. The spectrometer utilizes diffraction radiation (DR) generated at electron beam energies of up to 17.5 GeV. The MHz repetition rate needed for bunch resolved measurements is made possible by the KALYPSO line detector system, providing a read-out rate of up to 2.7 MHz. We present the first findings from commissioning of the NIR spectrometer, and measurements on the impact of the Laser Heater system for various bunch compression settings, in terms of amplitude and bunch-to-bunch variance of the NIR spectra as well as FEL pulse energy.

INTRODUCTION

The European XFEL

In the linear accelerator of the European X-ray Free-Electron Laser (EuXFEL) electron bunches are accelerated to energies of up to 17.5 GeV. The bunches are accelerated in bunch trains of up to 2700 bunches, with an intra-train repetition rate of up to 4.5 MHz (currently 1.1 MHz operation is most common). Trains are generated at 10 Hz, for a total of up to 27 000 bunches per second.[1] After acceleration, the electron bunches are distributed to three undulator sections (designated SASE1, SASE2, and SASE3) where via Self-Amplified Spontaneous Emission (SASE) laser-like X-rays are produced. This enables parallel Free-Electron Laser (FEL) operation of three experimental stations.

Bunch Compression

The peak currents needed for the SASE process demand that the bunches are longitudinally compressed during acceleration. To compress the bunches a longitudinal energy-position correlation called *chirp* is imparted by accelerating them off crest and then leading them through a chicane where energy dependent path length allows the higher energy tail to catch up to the head. At the EuXFEL this is done in 3 stages, for a total compression factor of ~100, and final peak current ~5 kA. [2]

* christopher.gerth@desy.de

Microbunching and Laser Heater

Collective effects during bunch compression can lead to so called *microbunches* developing [3, 4], where random periodic features on the longitudinal charge density from shot noise from the electron-gun can be amplified many orders of magnitude. These features lead to growth of slice emittance, detrimental to the FEL process. Previously similar facilities have implemented Laser Heaters (LH) to inhibit microbunching, with clear improvements to FEL performance.[5–7] In the LH, part of the laser pulse for the photo-cathode electron gun is coupled out and overlapped with the electron bunches in an undulator inside a chicane. This imparts a non-correlated energy spread, which dampens microbunching in the bunch compressor chicanes. A LH was also installed at the EuXFEL.[8–12]

Longitudinal Diagnostics of Short Bunches

For the study of microbunching effects at the EuXFEL a prism based Near Infra-red (NIR) spectrometer was installed.

For longitudinal diagnostics of sub picosecond electron bunches, frequency domain methods using coherent radiation can provide a non-invasive option, important for user facilities. The spectral density of coherent radiation is dependent on the magnitude of the longitudinal form factor, F_L , which is the Fourier transform of the longitudinal charge density of the electron bunch. Coherent Diffraction Radiation (CDR) spanning mm-waves to visible light is generated when the relativistic electron bunches pass through a hole in an aluminum screen. At EuXFEL this CDR is used to non-invasively monitor bunch compression and longitudinal profiles at several stations along the accelerator. [13] Bunch Compression Monitors (BCM) use simple and robust broadband sensors to monitor the overall bunch length. Spectroscopic investigation offer a more complete bunch profile, and at the last CDR station, after full acceleration, a THz spectrometer [14, 15] was previously installed.[16] That spectrometer works in the mid infrared (MIR) to THz spectral range, 5 μm to 450 μm , and can provide complete bunch profiles. However, the smallest features it can resolve is limited by its detection range. Since microbunching is suspected with features in the single μm range, the spectrometer that this paper concerns was installed alongside it, sensitive in the NIR range. Due to the stochastic origins of microbunching great variance from bunch to bunch is expected, which requires bunch-resolved measurements. The development of the KALYPSO detector unit [17–20] has made this possible, with read-out rates up to 2.7 MHz.

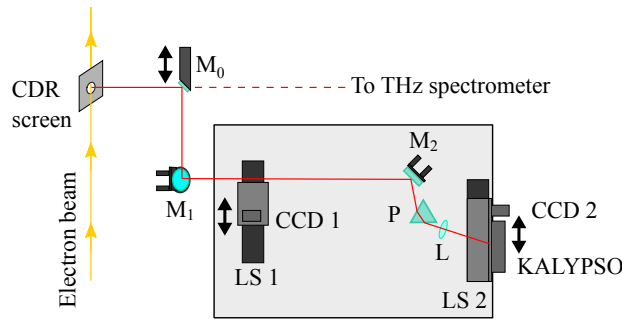


Figure 1: Layout of the NIR spectrometer. Not to scale.

NIR SPECTROMETER

The layout of the NIR spectrometer is shown in Fig. 1. The KALYPSO detector module has a 256 pixel InGaAs line sensor sensitive to $0.9\ \mu\text{m}$ to $1.7\ \mu\text{m}$. The sensor is $12.8\ \text{mm}$ wide, with a pixel pitch of $50\ \mu\text{m}$. The NIR spectrometer also has two Si CCD cameras, CCD1 and CCD2, for alignment and CDR beam profile imaging.

A $60\ \text{mm}$ equilateral n-SF11 prism is used for dispersion. The n-SF11 glass has a relatively flat slope for the sought spectral range. A $2''$ n-BK7, $f = 150\ \text{mm}$ plano-convex lens is used for focusing. To compensate for the shift of focal length due to decreasing refractive index for longer wavelengths, the central wavelength is incident on the sensor at an angle off of the normal.

The NIR spectrometer is assembled on a standard optical breadboard. Two $2''$ mirrors, M1 and M2, mounted on 2-axis Standa motorized mirror mounts, are used for alignment. Two linear stages are mounted on the breadboard, LS1 and LS2. LS1 holds CCD1 and has extra space where e.g. optical filters for calibration purposes can be mounted. LS2 holds the KALYPSO detector module and CCD2.

INITIAL FINDINGS

We present measurements for scans over bunch compression, and LH power from three different measurement runs at different compression settings and FEL operation. Accelerator parameters are presented in Table 1. For the third LH scan run, the accelerator was operated in so-called flattop mode, where two different compression settings can be applied for different ranges of bunches within the same bunch train. Our read-out script was however only able to record the compression settings of the first flattop range. No FEL operation during 3rd run. Points in plots are averages over many bunch trains, and the standard deviation is indicated with error bars or transparent bands.

Changing Compression Settings

Figure 2 shows example spectra from the first readings with the NIR spectrometer. Uncompressed bunches in the left column and bunches at FEL compression settings in the right. The overall intensity decreased by almost 2 orders of magnitude when the bunches were compressed. This is in

Table 1: Accelerator Parameters for LH Measurement Runs

Run	1st acc. section		2nd acc. section	
	ΔE [MeV]	chirp [1/m]	ΔE [MeV]	chirp [1/m]
1	128.9	-9.04	569.8	-10.85
2	128.4	-8.67	579.2	-10.50
3a*	127.6	-8.65	585.4	-10.49

*Accelerator operated in "flattop" mode.

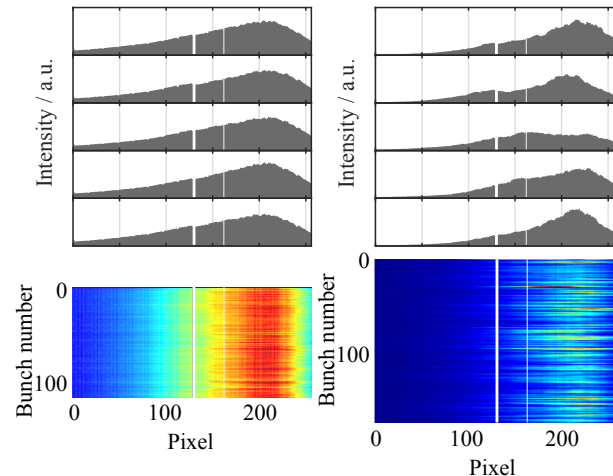


Figure 2: Example spectra from initial measurements with the NIR spectrometer. Longer wavelengths towards higher pixel number (uncalibrated). Left column: uncompressed beam. Right column: FEL compression settings. Top row: Selected spectra. N.B. vertical scales differ: compressed signal ~ 100 times weaker. Bottom row: Whole bunch trains, demonstrates differences in shot-to-shot fluctuations.

line with earlier results from FLASH, where microbunching was observed in the μm range for lower compression settings.[21] With FEL compression the relative bunch-to-bunch variance increased.

Scans over the chirp of the accelerator sections in the first two compression stages were made. The results are shown in Fig. 3. The signal of the NIR spectrometer was split in two halves, integrated and then normalized separately to show the shift of the spectrum during the scan. In black the BCM signal is shown, corresponding to right y-axis. We can see that the decrease in NIR intensity continues after maximum compression is reached. A general dampening occurs of development of features in the μm range in the chicanes.

Changing Laser Heater Power

Figure 4 shows NIR spectrometer and FEL intensities from run 1 and 2. Only SASE1 was operational for run 1. We see an expected behavior, the NIR intensity falls off and the FEL intensity generally sees an initial increase before the induced energy spread from the LH becomes too large. For all except SASE3 during run 2, the increase in intensity is

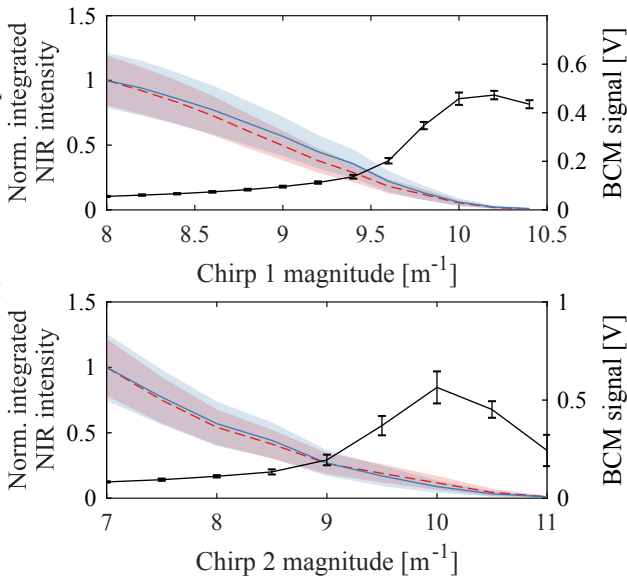


Figure 3: Scans over bunch compression. Left axes: Signal from NIR spectrometer integrated and normalized separately for pixel 0-127 (dashed red line) and 128-255 (solid blue line). Transparent regions indicate the standard deviation. Right axes: Signal from BCM, black line with error bars. Top: Compression adjusted with accelerator chirp before first chicane. Bottom: Adjusted using chirp between first and second chicane.

significant. However, in none of the cases the FEL intensity is higher than what has been achieved without the LH.

Figure 5 shows the NIR intensities for all runs. Run 3 went to higher LH pulse energies, and a difference in behaviour between flattop ranges is seen for these higher energies, with flattop one exhibiting an unexpected increase in intensity and variance.

CONCLUSION

We have shown the first commissioning results from a new NIR spectrometer with bunch-to-bunch read-out capabilities at MHz repetition rates.

The investigations of compression settings show a behaviour in line with previous findings[21] where significant microbunching occurs in the chicanes at lower compression, while with increased chirp microbunching is strongly suppressed, due to longitudinal smearing by the energy distribution inside the bunch. Shot-to-shot variance with high compression suggests that some microbunching could still remain.

LH investigations show some positive effects on the FEL pulse energy for moderate LH pulse energies. The effect is not as significant as in other FEL facilities where the LH is necessary for regular operation, whereas so far at EuXFEL full FEL performance could be achieved without using the LH. Reasons for this could be, for instance, different properties of the photo-cathode material in the electron-gun for

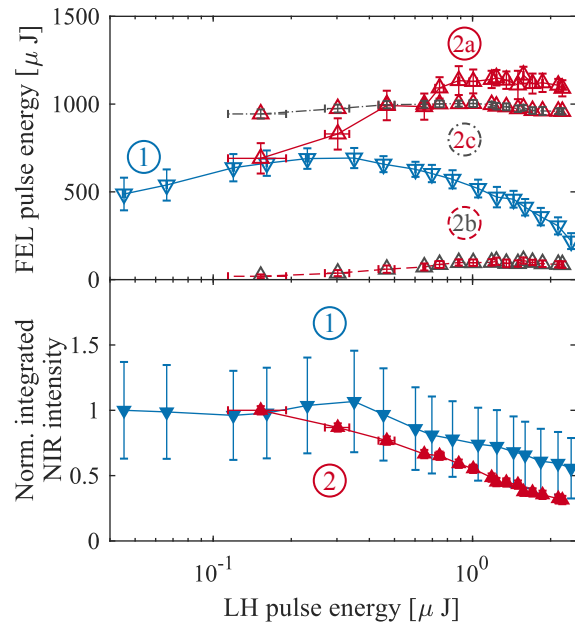


Figure 4: Results from scan of LH pulse energy from Runs 1 and 2. Top: FEL pulse energy. 2a - SASE1, 2b - SASE2, 2c - SASE3. Bottom: Integrated signal across all pixels, normalized with regards to their initial values.

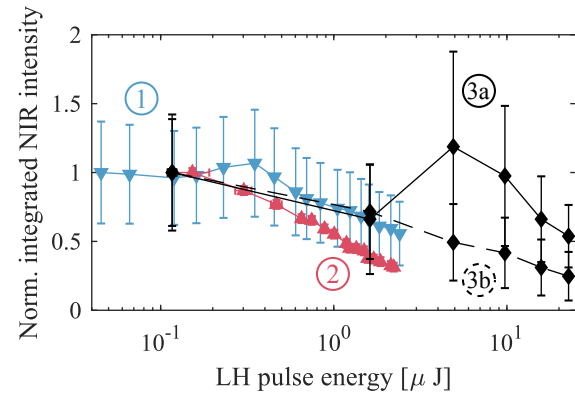


Figure 5: Results from scan of LH pulse energy from all runs. Run 3 was made during "flattop" operation mode, and also to higher LH pulse energies. 3a is flattop 1 (first 100 bunches), 3b is flattop 2 (bunch 160 and onward).

the generation of the electron bunches, or beam dynamics of the entire accelerator not producing microbunching with as high gain for features in the micrometer wavelength range.

ACKNOWLEDGEMENTS

The authors are deeply grateful to all people who contributed to bring European XFEL into successful operation. The authors would also like to thank F. Brinker (DESY) for the support during LH power scans and fruitful discussions, and V. Rybnikov (DESY) for software support with the KALYPSO detector and CCD cameras.

REFERENCES

- [1] M. O. Wiedorn *et al.*, “Megahertz serial crystallography,” *Nat. Commun.*, vol. 9, no. 1, p. 4025, Oct. 2018, ISSN: 2041-1723. DOI: 10.1038/s41467-018-06156-7.
- [2] G. Feng *et al.*, “Beam dynamics simulations for european xfel,” DESY, Tech. Rep., 2013, TELSAs-FEL 2013-04.
- [3] E. L. Saldin, E. A. Schneidmiller, and M. Yurkov, “Klystron instability of a relativistic electron beam in a bunch compressor,” *Nucl. Instrum. Methods Phys. Res., Sect. A*, vol. 490, no. 1-2, pp. 1–8, 2002. DOI: 10.1016/S0168-9002(02)00905-1.
- [4] E. L. Saldin, E. A. Schneidmiller, and M. Yurkov, “Longitudinal space charge-driven microbunching instability in the tesla test facility linac,” in *Free Electron Lasers 2003*, Elsevier, 2004, pp. 355–359. DOI: 10.1016/j.nima.2004.04.067.
- [5] Z. Huang *et al.*, “Suppression of microbunching instability in the linac coherent light source,” *Phys. Rev. Spec. Top. Accel. Beams*, vol. 7, no. 7, p. 074401, 2004. DOI: 10.1103/PhysRevSTAB.7.074401.
- [6] Z. Huang *et al.*, “Measurements of the linac coherent light source laser heater and its impact on the x-ray free-electron laser performance,” *Phys. Rev. Spec. Top. Accel. Beams*, vol. 13, no. 2, pp. 1098–1103, 2010. DOI: 10.1103/PhysRevSTAB.13.020703.
- [7] S. Spampinati *et al.*, “Laser heater commissioning at an externally seeded free-electron laser,” *Phys. Rev. Spec. Top. Accel. Beams*, vol. 17, p. 120705, 12 Dec. 2014. DOI: 10.1103/PhysRevSTAB.17.120705.
- [8] M. Hamberg, V. Ziemann, *et al.*, “Status of the eu-xfel laser heater,” in *Proc. 35th Int. Free Electron Laser Conf. (FEL’13)*, paper TUPSO25, New York, NY, USA, 2013, p. 5.
- [9] M. Hamberg and V. Ziemann, “Progress of the eu-xfel laser heater,” in *Proc. 5th Int. Particle Accelerator Conf. (IPAC’14)*, JACoW, Geneva, Switzerland, Dresden, Germany, 2014, pp. 2912–2913. DOI: 10.18429/JACoW-IPAC2014-THPR0024.
- [10] M. Hamberg and V. Ziemann, “Construction of the EU-XFEL Laser Heater,” in *Proc., 37th Int. Free Electron Laser Conf. (FEL’15)*, Daejeon, Korea, 2015, TUP038. DOI: 10.18429/JACoW-FEL2015-TUP038.
- [11] M. Hamberg, F. Brinker, and M. Scholz, “First Heating with the European XFEL Laser Heater,” in *Proc. 5th Int. Beam Instrumentation Conf. (IBIC’16)*, Barcelona, Spain, 2016, WEPG32. DOI: 10.18429/JACoW-IBIC2016-WEPG32.
- [12] M. Hamberg *et al.*, “Electron beam heating with the european xfel laser heater,” in *Proc. 38th Int. Free Electron Laser Conf.*, Santa Fe, NM, USA, 2017, pp. 458–459. DOI: 10.18429/JACoW-FEL2017-WEP018.
- [13] P. Peier, C. Gerth, and H. Dinter, “Coherent radiation diagnostics for longitudinal bunch characterization at european xfel,” in *Proc. 36th Int. Free Electron Laser Conf. (FEL’14)*, paper THP083, 2014.
- [14] S. Wesch, B. Schmidt, C. Behrens, H. Delsim-Hashemi, and P. Schmüser, “A multi-channel thz and infrared spectrometer for femtosecond electron bunch diagnostics by single-shot spectroscopy of coherent radiation,” *Nucl. Instrum. Methods Phys. Res., Sect. A*, vol. 665, pp. 40–47, 2011. DOI: 10.1016/j.nima.2011.11.037.
- [15] B. Schmidt *et al.*, “Longitudinal bunch diagnostics using coherent transition radiation spectroscopy. physical principles, multichannel spectrometer, experimental results, mathematical methods,” Deutsches Elektronen-Synchrotron (DESY), Tech. Rep., 2018. DOI: 10.3204/PUBDB-2018-01372.
- [16] N. Lockmann, C. Gerth, P. Peier, B. Schmidt, S. Wesch, *et al.*, “A non-invasive thz spectrometer for bunch length characterization at european xfel,” in *Proc. 10th Int. Particle Accelerator Conf. (IPAC’19)*, Melbourne, Australia, 2019, pp. 2495–2497. DOI: 10.18429/JACoW-IPAC2019-WEPGW014.
- [17] L. Rota *et al.*, “A high-throughput readout architecture based on pci-express gen3 and directgma technology,” *J. Instrum.*, vol. 11, no. 02, P02007, 2016. DOI: 10.1088/1748-0221/11/02/P02007.
- [18] L. Rota *et al.*, “Kalypso: A mfps linear array detector for visible to nir radiation,” in *Proc. 5th Int. Beam Instrumentation Conf. (IBIC’16)*, Barcelona, Spain, 2016, pp. 740–743. DOI: 10.18429/JACoW-IBIC2016-WEPG46.
- [19] L. Rota *et al.*, “Kalypso: Linear array detector for high-repetition rate and real-time beam diagnostics,” *Nucl. Instrum. Methods Phys. Res., Sect. A*, 2018. DOI: 10.1016/j.nima.2018.10.093.
- [20] M. Caselle *et al.*, “Ultra-fast detector for wide range spectral measurements,” in *Proc. Real-time Meas., Rogue Phenomena, and Single-Shot Appl. IV*, International Society for Optics and Photonics, vol. 10903, San Francisco, California, United States, 2019, p. 1090306. DOI: 10.1117/12.2511341.
- [21] S. Wesch, C. Behrens, B. Schmidt, and P. Schmüser, “Observation of coherent optical transition radiation and evidence for microbunching in magnetic chicanes,” in *Proc. 31st Int. Free Electron Laser Conf. (FEL’09)*, (Liverpool, UK), paper WEP50, 2009, pp. 619–622.

THE PolariX-TDS PROJECT: BEAD-PULL MEASUREMENTS AND HIGH-POWER TEST ON THE PROTOTYPE

P. Craievich*, M. Bopp, H.-H. Braun, A. Citterio, R. Ganter, F. Marcellini, T. Kleeb, M. Pedrozzi, E. Prat, S. Reiche, PSI, 5232 Villigen, Switzerland
A. Grudiev, W. Lee Millar¹, N. Catalan-Lasheras, G. McMonagle, S. Pitman, V. del Pozo Romano, K. T. Szypula, W. Wuensch, CERN, 1211 Geneva 23, Switzerland
B. Marchetti, R. W. Assmann, F. Christie, R. D'Arcy, U. Dorda, M. Foese, P. Gonzalez Caminal, M. Hoffmann, M. Huening, R. Jonas, O. Krebs, S. Lederer, V. Libov, D. Marx, J. Osterhoff, M. Reukauff, H. Schlarb, S. Schreiber, G. Tews, M. Vogt, A. de Z. Wagner, DESY, 22607 Hamburg, Germany
¹also at Cockcroft Institute, Warrington, Cheshire

Abstract

A collaboration between DESY, PSI and CERN has been established to develop and build an advanced modular X-band transverse deflection structure (TDS) system with the new feature of providing variable polarization of the deflecting force. The prototype of the novel X-band TDS, the Polarizable X-band (PolariX) TDS, was fabricated at PSI following the high-precision tuning-free production process developed for the C-band Linac of the SwissFEL project. Bead-pull RF measurements were also performed at PSI to verify, in particular, that the polarization of the dipole fields does not have any rotation along the structure. The high-power test was performed at CERN and now the TDS is at DESY and has been installed in FLASHForward, where the first streaking experience with beam will be accomplished. We summarize in this paper the status of the project, the results of the bead-pull measurements and the high power test.

INTRODUCTION

Several experiments at DESY (FLASH2, FLASHForward, SINBAD) and PSI (ATHOS at SwissFEL) are interested in the utilization of high gradient X-band TDS systems for high resolution longitudinal diagnostics [1]. In this context, a collaboration between DESY, PSI and CERN has been established to develop and build an advanced modular X-Band TDS system with the new feature of providing variable polarization of the deflecting force [2]. The prototype of the novel X-band TDS, the Polarizable X-band (PolariX) TDS, has been fabricated at PSI following the high-precision tuning-free production process developed for the C-band Linac of the SwissFEL project and already used for the fabrication of the tuning-free X-band structure prototypes for CLIC [3–5]. Bead-pull RF measurements has been performed at PSI between December 2018 and January 2019 in order to verify that the polarization of the dipole fields does not have any rotation along the structure. Figure 1 shows the detail of the input and output couplers (left), the whole TDS prototype (middle) and the basic disk geometry (right). The main RF parameters of the TDS and RF pulse

compressor are summarized in Table 1. High power test on the prototype has been performed at CERN between March and April 2019. In this paper we summarize the status of the collaboration focusing on the results of the bead-pull measurements and the high power tests.

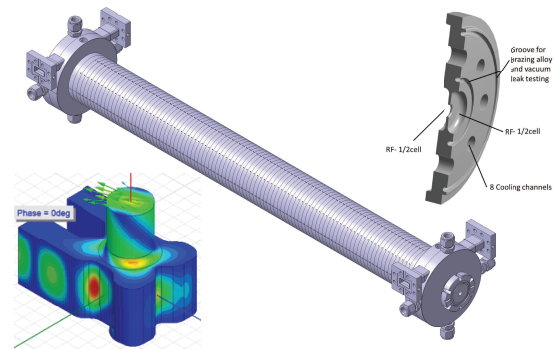


Figure 1: Left: detail of the input/output coupler. Middle: whole TDS prototype. Right: basic disk.

BEAD-PULL MEASUREMENTS

The dipole field flatness and polarization were measured with the bead-pull method. The structure was allocated in a vertical frame and a stepper motor was used to drive along the structure a 2 mm diameter dielectric sphere fixed to a dielectric wire with diameter of 0.16 mm. The bead pulling has been repeated for different offsets, both in the XZ and YZ planes, in ± 2 mm range. The measurements were performed with a 4-port VNA and the reflection coefficient resulted to be less than -35 dB with an insertion loss of -5.5 dB. Figure 2 (upper plot) shows results of the bead-pull measurement with offset 0 mm both in X and Y and phase difference between ports of 0 deg. Cell-to-cell phase advance (lower plot) resulted to be $2\pi/3$ with a dispersion of 0.8° rms at the working frequency of 11995.2 MHz with a temperature of 33.9°C . It is worthwhile noting that same results for the phase advance was obtained varying the relative phase between ports, namely for different polarizations. A spherical and dielectric bead perturbs only the electric field, but cannot distinguish between longitudinal and transverse components. However, since the longitudinal component has the largest

* paolo.craievich@psi.ch

Table 1: RF parameters for short and long X-band TDS. Both structures are constant impedance and backward traveling wave structures. More details on the XBOC designed and fabricated at PSI are in [6]. t_k is the klystron pulse width and the frequency corresponds to an operational temperature of 30° for the ATHOS beamline [7, 8].

Cell parameter		Unit
Frequency	11995.2	MHz
Phase advance/cell	120	°
Iris radius	4	mm
Iris thickness	2.6	mm
Group velocity	-2.666	%c
Quality factor	6490	
Shunt impedance	50	MΩ/m

TDS parameter	Short	Long	Unit
n. cells	96	120	
Filling time	104.5	129.5	ns
Active length	800	1000	mm
Total length	960	1160	mm
Power-to-voltage	5.225	6.124	MV/MW ^{0.5}

TDS + BOC	Short	Long	Unit
BOC Q ₀	145000	145000	
BOC β @ $t_k=1.5\mu s$	7	7	
Power-to-voltage	12.010	13.626	MV/MW ^{0.5}

amplitude in the middle of each cell while the transverse component in the iris region, it is possible to have a separate measurement of both the field components. In the upper plot of Fig. 2 it is shown a measurement performed with the wire centred on the axis structure. With this set up only the transverse component of the electric field E is measured.

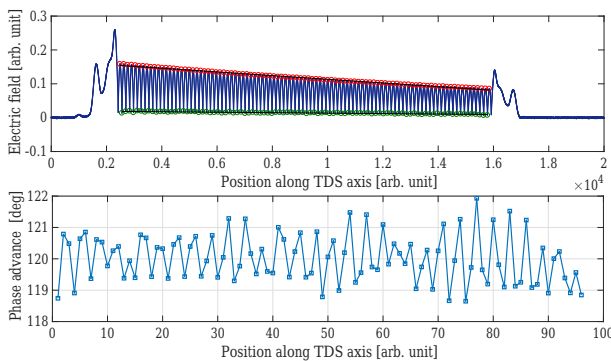


Figure 2: Bead-pull result for an on axis measurement. The green dots identify the points in each cell where the field is minimum and the red dots where it is maximum.

In order to verify if the different polarizations are also well tuned, bead-pull measurements were performed for different offset values and relative phases between ports (polarizations). Figure 3 shows an example of measurement with an offset in one transverse plane of 1 mm with different orientations of the polarization between 0° and 180°. Changing the polarization, the transverse component of E rotates but

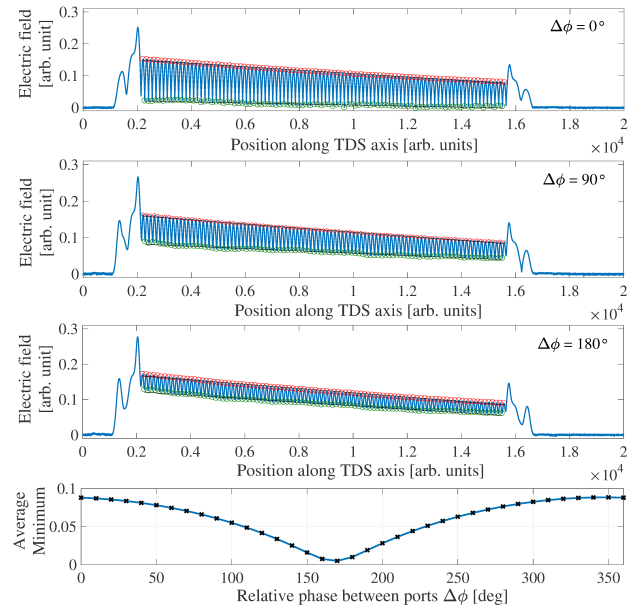


Figure 3: Bead-pull results: first 3 plots on the top: electric field along the TDS axis with offset in one transverse plane of 1 mm for different polarizations. Bottom plot: average minimum (green dots) vs. phase difference between input ports.

its amplitude remains constant. On the contrary, the longitudinal component varies from zero to its maximum when the polarization changes from one plane to its orthogonal one. This behaviour is clearly visible scrolling Fig. 3 from the top. With 0° phase difference between the input coupler ports only the transverse field is measured. Increasing the phase difference, i.e. changing the polarization, also the longitudinal component of E appears and its amplitude reaches the maximum for 180° phase difference (plane of polarization rotated of 90°). Since for a given phase difference the longitudinal component of the electric field (E_z) along the TDS has a linear behaviour (as shown by the green dots in Fig. 3), it is possible to conclude that the polarization of the dipole fields does not have any rotation along the structure. The bottom plot in Fig. 3 shows the mean value of the green dots values as a function of the input port phase difference. More details on the technique and results of the bead-pull measurements will be reported in a future publication.

HIGH POWER TEST

Following low power measurement, the structure was installed in CERN's XBOX2 facility for high power testing [9]. XBOX2 is equipped with a 50MW CPI klystron with a repetition rate of 50Hz and at the time of testing a pulse compression scheme comprised of a prototype BOC (Barrel Open Cavity) [6] and CCC (Correction Cavity Chain) [10]. The high-power variable phase shifter for varying the polarization had been previously conditioned in XBOX3 [11]. As the XBOX2 test stand is a facility without beam capability the polarization during testing was instead inferred via the delta phase measured between two directional couplers connected to the structure output coupler as shown by the

experimental set-up in Fig. 4. Similar to previously tested components an automated conditioning algorithm was used to gradually increase the input power while maintaining a fixed BDR (Breakdown Rate) of 3×10^{-5} bpp (breakdowns per pulse) [12]. Typically, during structure conditioning the pulse length is increased in steps, however due to the short window available for testing it was fixed at 100 ns pulse as this corresponds approximately to the fill time of the structure. With conventional accelerating structures operating in the like-TM₀₁₀ mode the internal field pattern is azimuthally symmetric and so the surface conditions evenly, however in the case of the PolariX-TDS the position of the peak surface fields within the cavity varies with polarization. To ensure the structure is capable of high-power operation in different polarizations the variable phase shifter was moved several times during the conditioning. Figure 5 shows the full conditioning history alongside the polarization for each period. The phase shifter was moved remotely twice during testing

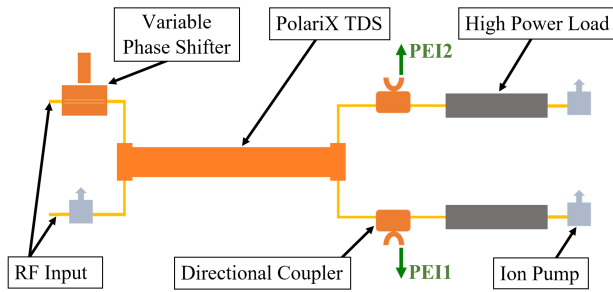


Figure 4: Diagrammatic representation of the experiment setup and signals PEI1 and PEI2 which were used to measure polarization.

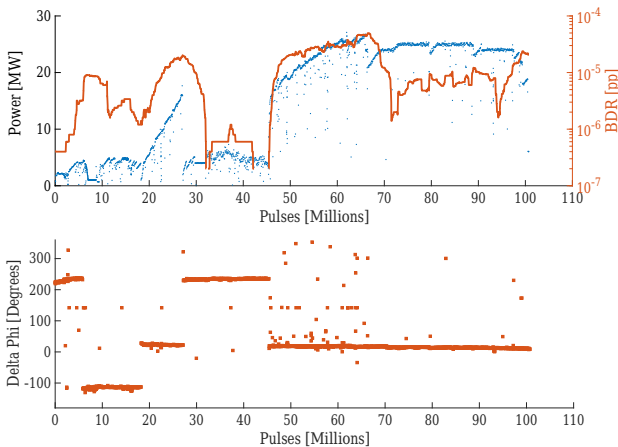


Figure 5: Conditioning history and BDR (top) with phase difference between signals PEI1 and PEI2 (bottom).

after approximately 10 and 30 million pulses. After each of these movements a change in phase was observed however the conditioning immediately following was then limited by high vacuum levels in the region surrounding the phase shifter. Attempts to remotely move the phase shifter back were unsuccessful due to what is believed to be a problem with the magnetic coupling of the mechanical drive system. Interventions to remove and manually reset the phase

shifter were performed at 20 and 45 million pulses. Due to these problems it was decided not to vary the polarization again for the remainder of the testing period. The FLASH-Forward [13] beamline at DESY operates 6MW Toshiba E37113A klystrons with plans to eventually install a pulse compression scheme to increase the peak power by a factor of 4 [14]. The peak input power reached during testing was 26.5 MW at a polarization of ~ 10 degrees however as this exceeds the requirements of the FLASH facility it was then decided to cease ramping and run at a fixed input power and decreased BDR for the remainder of the test to avoid the possibility of damaging the structure. No limit emerged during the test and results indicate that the structure is capable of high-power operation sufficient for installation in the FLASH beamline.

INSTALLATION IN FLASHFORWARD

In July 2019 the prototype-structure has been installed in the FLASHForward [13] beamline at FLASH [15], where the first measurements with electron beam are foreseen to take place. The cavity has been connected to its RF station constituted by a 6 MW Toshiba E37113A klystron and an Ampegon Type- M-class modulator. The klystron has been installed inside the tunnel, whereas the modulator rack is located in an external adjacent corridor. The RF network will be installed in two stages, as already described in [14]. For the PolariX TDS prototype commissioning the maximum deflecting voltage in the TDS will be about 14 MV. It is worthwhile noting that the working frequency is 11988.8 MHz that corresponds to a temperature of 65.9° . In the second stage of the installation an RF pulse compressor will be installed allowing for an increase in peak power by a factor of 4 [14]. The possibility of changing the streaking direction of the beam opens new opportunities for a more complete characterization of the electron bunches to be tested during the commissioning of the structure. Besides the applications in fs-level longitudinal diagnostics of the beam [16, 17], it is planned to perform first experimental measurement of 3D charge density reconstruction of the electron bunch [18]. Simulations performed in preparation to this test [19] have shown the feasibility of the reconstruction of the typical FLASH-beam distribution with the expected longitudinal resolution for the prototype commissioning.

CONCLUSION

In this paper we have summarized the recent results from the bead-pull measurement and high power test performed on the first prototype of the PolariX-TDS system. The results have fully demonstrated the feasibility and the quality of the design and fabrication. In particular, the results in terms of machining, assembly and brazing are excellent. During the first high-power test the prototype performed very well although there were some issues with the phase shifter. Now, the prototype is installed at DESY where the first measurements with electron beam are foreseen to take place in this autumn.

REFERENCES

- [1] B. Marchetti *et al.*, “X-Band TDS project”, in *Proc. IPAC’17*, Copenhagen, Denmark, May 2017, paper MOPAB044, pp. 184-187.
- [2] A. Grudiev, “Design of compact high power RF components at X-band”, CERN, Geneva, Switzerland, Rep. CLIC Note 1067, May 2016; also presented at the *CLIC workshop 2017*, March 2017, Geneva, Switzerland
https://indico.cern.ch/event/577810/contributions/2484990/attachments/1423352/2182280/CLIC17_DesignofXbandTDS.pdf
- [3] P. Craievich *et al.*, “Consolidation and extension of the high-gradient Linac RF technology at PSI”, in *Proc. LINAC’18*, Beijing, China, Sep. 2018, paper THPO115, pp. 937-940.
- [4] U. Ellenberger *et al.*, “Status of the manufacturing process for the SwissFEL C-band accelerating structures”, in *Proc. FEL’13*, New York, USA, paper TUPSO17, pp. 246-249.
- [5] R. Zennaro *et al.*, “High power tests of a prototype X-band accelerating structure for CLIC”, in *Proc. IPAC’17*, Copenhagen, Denmark, May 2017, paper THPIK097, pp. 4318-4320.
- [6] R. Zennaro, “Overview of RF activities at PSI”, presented at the International Workshop on Breakdown Science and High Gradient Technology, Chamonix, France, June 2019,
https://indico.cern.ch/event/766929/contributions/3439426/attachments/1857126/3050744/RZ_HG2019.pdf
- [7] R. Abela *et al.*, “Athos Conceptual Design Report”, Report No. PSI Bericht Nr. 17-02 ISSN 1019-0643, 2017.
- [8] R. Ganter *et al.*, “Status of Athos, the Soft X-Ray FEL line of SwissFEL”, presented at FEL’19, Hamburg, Germany, Aug. 2019, paper THP085, this conference.
- [9] B. J. Woolley, “High Power X-band RF Test Stand Development and High Power Testing of the CLIC Crab Cavity”, Lancaster University, United Kingdom, 2015, <https://eprints.lancs.ac.uk/id/eprint/76926>
- [10] P. Wang, H. Zha, I. Syratchev, J. Shi, H. Chen, “RF design of a pulse compressor with correction cavity chain”, *Phys. Rev. Accel. Beams*, vol. 20, p. 112001, Nov. 2017, doi:10.1103/PhysRevAccelBeams.20.112001
- [11] V. d. P. Romano *et al.*, “High Power Conditioning of X-Band Variable Power Splitter and Phase Shifter”, in *Proc. IPAC’19*, Melbourne, Australia, May 2019, pp. 2964-2967, doi:10.18429/JACoW-IPAC2019-WEPRB064
- [12] N. Catalan-Lasheras *et al.*, “Experience Operating an X-Band High-Power Test Stand At CERN”, in *Proc. IPAC’14*, Dresden, Germany, June 2014, pp. 2288-2290, doi:10.18429/JACoW-IPAC2014-WEPME016
- [13] R. D’Arcy *et al.*, “FLASHForward - A future-oriented wakefield-accelerator research and development facility at FLASH”, in *Proc. IPAC’17*, Copenhagen, Denmark, May 2017, paper TUPIK006, pp. 1692-1695.
- [14] P. Craievich *et al.*, “Status of The Polarix-TDS Project”, in *Proc. IPAC’18*, Vancouver, BC, Canada, May 2018, paper THOAL068, pp. 3808-3811.
- [15] <https://flash.desy.de>
- [16] R. D’Arcy *et al.*, “Longitudinal Phase Space Reconstruction at FLASHForward Using a Novel X-band Transverse Deflection Cavity, PolariX TDS”, in *Proc. IPAC’18*, Vancouver, Canada, May 2018, paper TUPML017.
- [17] F. Christie *et al.*, “Generation of Ultra-Short Electron Bunches and FEL Pulses and Characterization of their Longitudinal Properties at FLASH2”, in *Proc. IPAC’17*, Copenhagen, Denmark, 14-19 May, 2017, paper WEPAB017.
- [18] D. Marx *et al.*, “Reconstruction of the 3D charge distribution of an electron bunch using a novel variable polarization transverse deflecting structure (TDS)”, *Journal of Physics: Conference Series*, 874(1):012077, 2017.
- [19] D. Marx *et al.*, “Simulations of 3D charge density measurements for commissioning of the PolariX-TDS”, *Journal of Physics: Conference Series*, 1067(7):072012, 2018.

RF JITTER AND ELECTRON BEAM STABILITY IN THE SwissFEL LINAC

Z. Geng[#], P. Craievich, R. Kalt, J. Alex, C. H. Gough, T. Lippuner, M. Pedrozzi, F. Löhl,
V. R. Arsov, S. Reiche, E. Prat, Paul Scherrer Institut, Villigen PSI, Switzerland

Abstract

The X-ray FEL machine SwissFEL at the Paul Scherrer Institut in Switzerland is commissioned and transiting to user operation smoothly. FEL operation requires stringent requirements for the beam stability at the linac output, such as the electron bunch arrival time, peak current and energy. Among other things, a highly stable RF system is required to guarantee the beam stability. The SwissFEL RF system is designed based on the state-of-the-art technologies that have allowed achieving excellent RF stability. The propagation of RF amplitude and phase jitter to the electron beam are analyzed theoretically and compared with the measurements performed at SwissFEL.

INTRODUCTION

The layout of SwissFEL is depicted in Figure 1 [1,2]. The accelerator consists of an S-band (2998.8 MHz) RF Gun, two S-band Booster sections, an X-band (11995.2 MHz) RF station and 3 C-band (5712 MHz) Linacs. SwissFEL requires highly stable electron beams for FEL generation. The stability goals reported in [3] require at the exit of Linac 3 the beam energy jitter to be $< 0.05\%$ rms, the peak current fluctuation $< 5\%$ rms and the bunch arrival time jitter < 20 fs rms. In order to meet the stability goals, the RF system must satisfy tight requirements on amplitude and phase stability down to 0.018% RMS in amplitude jitter and 0.018°, 0.036° and 0.072° RMS in phase jitter for S-band, C-band and X-band stations respectively [4].

SwissFEL works in pulsed mode with a repetition rate up to 100 Hz. The pulse-to-pulse jitter of the SwissFEL RF system is dominated by the stability of the klystron driver amplifiers and the high-voltage klystron modulators. The RF pulse width (from 100 ns to 3 μ s) is too short to implement efficient and reliable intra-pulse feedbacks. Pulse-to-pulse feedbacks were implemented in the low-level radio frequency (LLRF) system [5] to compensate for the RF fluctuations at frequencies below 1 Hz. For longer time intervals, the drifts of the LLRF detection chain must be corrected by the beam based feedbacks.

In this paper, the measured RF and beam stability for the operation mode with 200 pC will be presented. In order to

crosscheck the measurements, a beam dynamics model will be used to predict the beam jitter from the measured RF jitter and compare with the direct beam measurements.

RF STABILITY

The pulse-to-pulse phase and amplitude jitter of the RF field used for beam acceleration is measured with the RF detectors. For each pulse, the RF waveforms are averaged within a time window determined by the time constant of the standing wave cavities (e.g. RF Gun) or within the filling time of the traveling wave structures (1000 ns for S-band, 322 ns for C-band, and 105 ns for X-band). This limits the measurements to the RF-beam interaction bandwidth of the cavities or structures: RF Gun 330.8 kHz, S-band structure 475.8 kHz, C-band structure 1346.5 kHz and X-band structure 4219.0 kHz. Because the drifts slower than 1 Hz are suppressed by the RF feedbacks, the jitter given in this section contains the noise power from 1 Hz to the RF-beam interaction bandwidth of the cavities or structures.

The lab tests of the RF detectors promise a phase resolution of 0.0036° rms and an amplitude resolution of 2.6e-5 rms within the noise band. Compared to the overall RF field jitter, the RF detector added jitter can be neglected.

The pulse-to-pulse RF phase and amplitude jitter measured during this campaign at different RF stations is shown in Figure 2. The red lines show the jitter specification mentioned in the last section.

During the test, the beam based feedbacks were switched off, the phase and amplitude feedbacks of the Gun, S-band and X-band stations were on, while for C-band stations, only the phase feedbacks were on but the amplitude feedbacks were off because the C-band klystrons worked in saturation. Some RF stations did not satisfy the stability requirements and the reasons are summarized below:

- The average window of the RF Gun probe signals was much smaller than the cavity time constant, therefore, the measurement contains high frequency noises including the $\pi/2$ -mode signal. Furthermore, the RF Gun modulator was not in good condition during the test resulting in higher amplitude and phase jitter.
- The X-band amplitude jitter was slightly above the specified threshold due mainly to the contribution of

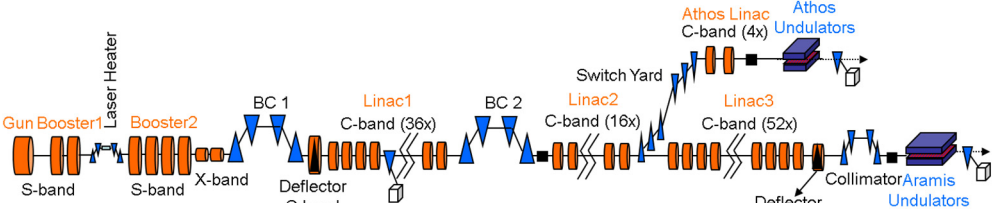


Figure 1: Layout of SwissFEL

[#]zheqiao.geng@psi.ch

the solid-state amplifier and modulator. As the bunch compression jitter is very sensitive to the X-band jitter, an upgrade path is under investigation.

- The C-band stations worked in saturation, which reduced the amplitude jitter, but the RF station “L1 CB06” had larger amplitude fluctuations due to the defected solid-state amplifier.
- Several C-band stations had multipacting in the Barrel Open Cavity (BOC) placed after the klystron to compress the RF pulse to increase the peak RF power. The multipacting happens when the klystron output power is in the range between about 20 MW and 40 MW, and mainly generates wide-band phase jitter that is not controllable by feedbacks. The klystron output power measurement in Figure 3 shows that the powers of the jittering C-band stations are all below 40 MW.

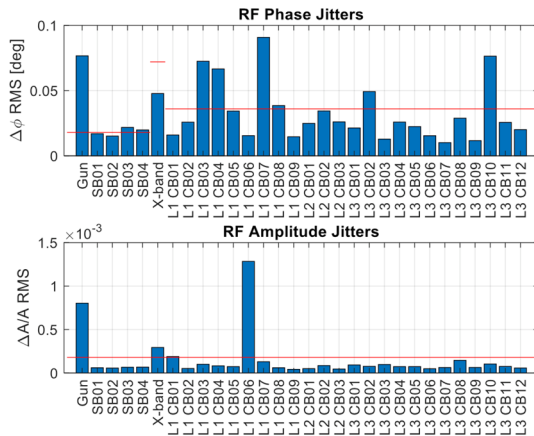


Figure 2: Pulse-to-pulse phase and amplitude jitter of the SwissFEL RF stations.

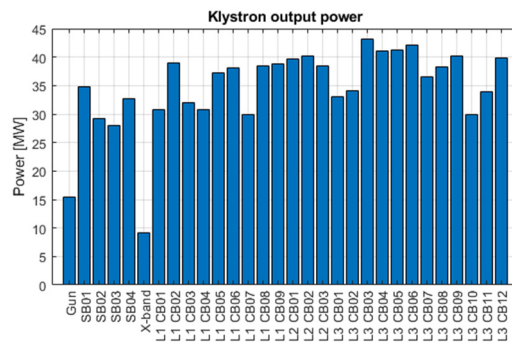


Figure 3: Klystron output powers. The BOCs in C-band RF stations encounter multipacting for powers below 40 MW.

One practical method to mitigate the BOC multipacting is to increase the klystron output power above 40 MW.

As the RF pulse-to-pulse feedbacks can only suppress slow drifts, the fast jitter is dominated by the RF components like the RF actuator (DAC and vector modulator), solid-state amplifier and the klystron modulator. Beside the RF stations with higher jitter mentioned above, the general RF jitter is well within the specifications thanks to the low-noise RF components developed for SwissFEL. The added phase jitter by the RF actuator (S-band and C-band:

< 0.006° rms; X-band: < 0.026° rms) and solid-state amplifier (S-band and C-band: < 0.009° rms; X-band: < 0.03° rms) is small compared to the overall RF stability specification. The high voltage jitter of the klystron modulator is therefore the main source of RF jitter, although the absolute jitter is small due to a voltage jitter below 15 ppm at 100 Hz operation [6].

BEAM STABILITY

The jitter of the beam parameters, including the beam energy, peak current and bunch arrival time are measured at the exit of the two bunch compressors (BC1 and BC2). To verify the correlation between the RF and beam jitter measurements, the beam jitter is also predicted with the measured RF jitter and the beam dynamics model.

Beam Dynamics Model

The sensitivity of the beam parameters at different locations with respect to the RF field errors can be described as a matrix by means of longitudinal beam dynamic simulations. With the sensitivity matrix, the deviations of the beam parameters for each pulse can be predicted from the RF field errors measured at the RF stations. Table 1 shows an example of the sensitivity between the BC2 bunch length (peak current) relative deviation and the upstream RF errors and the initial beam parameter errors at the input to the Booster 2. To simplify the study, here we also view the errors in bunch charge, arrival time (converted to equivalent S-band phase) and beam energy at the input of Booster 2 (after the laser heater (LH) in Figure 1) as inputs to the sensitivity matrix.

Table 1: Sensitivity of the BC2 Relative Bunch Length Deviation ($\Delta L/L$)_{BC2} w.r.t. the Error Sources

Error Source	Notation	Sensitivity
LH Bunch Charge (rel.)	$(\Delta Q/Q)_{LH}$	5.733
LH Bunch Phase (deg)	$(\Delta\phi_b)_{LH}$	68.079
LH Bunch Energy (rel.)	$(\Delta E/E)_{LH}$	-36.768
Booster 2 Amplitude (rel.)	$(\Delta A/A)_{bst2}$	-100.583
Booster 2 Phase (deg)	$\Delta\phi_{bst2}$	94.446
X-band Amplitude (rel.)	$(\Delta A/A)_{xb}$	3.774
X-band Phase (deg)	$\Delta\phi_{xb}$	-56.055
Linac 1 Amplitude (rel.)	$(\Delta A/A)_{L1}$	20.083
Linac 1 Phase (deg)	$\Delta\phi_{L1}$	32.506

The amplitude and phase jitter in Booster 2 and Linac 1 is the averaged jitter of all RF stations in the corresponding accelerator sections. The sensitivity matrix also provides the information about the more critical RF stations to achieve stable beam qualities. In the example as Table 1, the bunch charge, bunch arrival time at LH and the RF phases of the X-band and S-band Booster 2 are the major contributors to the bunch length jitter after BC2.

Beam Stability

The beam energy, bunch length and the bunch arrival time at the exit of BC1 and BC2 were measured with the

beam diagnostics and compared with the predicted jitter from the beam dynamics model (see Figure 4).

The beam energy was measured with the BPMs placed in the dispersion region of BC1 and BC2; the relative bunch length was measured with the bunch compression monitor (BCM) [7] at BC1 and the coherent diffraction radiation (CDR) detector at BC2. At SwissFEL, there is a bunch arrival time monitor (BAM) installed before the BC2, which monitors the bunch arrival time jitter at the exit of BC1 with a resolution about 4 fs.

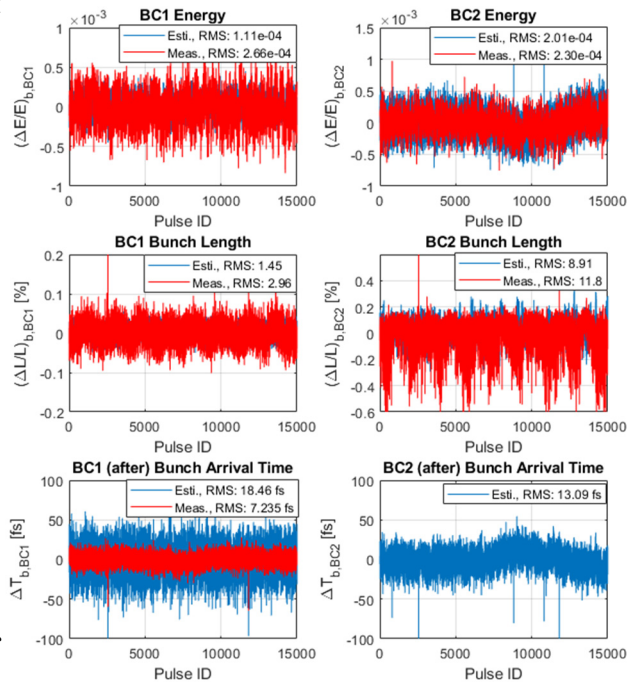


Figure 4: Beam stability measurement (red curve) and prediction (blue curve) at BC1 and BC2. The bunch repetition rate is 25 Hz, bunch charge 200 pC and 10-minute data were collected.

In Figure 4, the measured beam energy jitter and bunch length jitter after BC2 are around 2.3×10^{-4} and 11.8 % respectively. The predicted jitter is slightly smaller than the direct beam measurements, which may be caused by other jitter sources in the machine that are not captured by the sensitivity matrix, or the added noise by the beam diagnostics devices.

The bunch arrival time jitter measurement after BC1 is much smaller than the predicted one. These two results have a good correlation but with different magnitudes. It is planned to measure the sensitivity matrix instead using the theoretical one and make the prediction again. At the exit of Linac 3, the bunch arrival time jitter was measured once with the C-band RF deflectors [8] and the results are shown in Figure 5. The C-band RF deflector is used to measure the absolute bunch length but can also provide the bunch arrival time information. At the exit of Linac 3 and BC2, the bunch arrival time jitter is the same according to the beam dynamics model. Figure 5 indicates a bunch arrival time jitter of 16 fs rms at the exit of BC2. One should be aware that this jitter is a relative value between the actual

bunch arrival time and the RF phase jitter in the RF deflector structures. As the RF phase jitter of the C-band RF deflector was measured to be around 0.02° rms, which corresponds to a time jitter of 10 fs rms for the RF frequency of 5712 MHz, the actual bunch arrival time jitter can be estimated to be 13 fs rms. Here we have assumed the actual bunch arrival time jitter and the RF deflector phase jitter are uncorrelated. This estimation matches pretty well to the predicted bunch arrival time jitter after BC2 from the RF jitter and the sensitivity matrix.

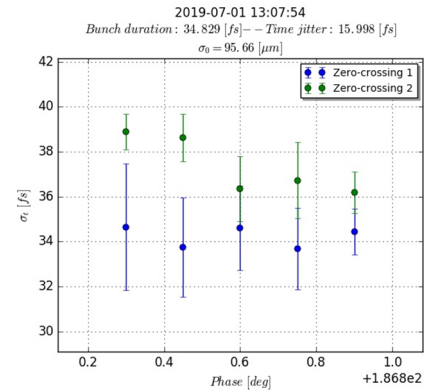


Figure 5: Bunch arrival time measurement with the C-band RF deflector at the exit of Linac 3.

RF-BEAM JITTER CORRELATION

The sensitivity matrix offers the basic information about how significant the RF field jitter contributes to the specific beam parameter jitter. In practice, the measurements of the RF amplitude and phase and the beam parameters can be correlated for each RF pulse. The strength of the correlation shows not only the sensitivity relationship, but also the potential RF stations that have large jitter and require improvements. According to the data in Figure 4, the X-band amplitude and phase jitter shows strongest correlations with the BC2 CDR signal (bunch length) that are shown in Figure 6. Some C-band stations (L1 CB03 and 07) in Linac 1 also have strong correlations (not shown). This information implies the potential improvements that are required for these RF stations.

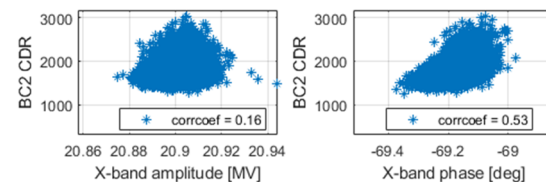


Figure 6: Correlation between the BC2 bunch length jitter and the X-band RF jitter. The X-band jitter has a major contribution to the bunch length jitter.

CONCLUSION

SwissFEL has achieved unprecedented RF and beam stability. The beam energy and bunch arrival time stability meets the requirements, while the bunch length jitter is still over the tolerance. With the systematic RF and beam jitter

study performed in this work, the critical RF stations for the future improvements are identified.

REFERENCES

- [1] SwissFEL, <https://www.psi.ch/en/swissfel/accelerator>
- [2] C. Milne *et al.*, SwissFEL: “The Swiss X-ray Free Electron Laser”, *Applied Sciences*, vol. 7, p. 720, 2017.
doi :10.3390/app7070720
- [3] “SwissFEL Conceptual Design Report”, PSI Report No. 10-04, April 2012.
- [4] B. Beutner and S. Reiche, “Sensitivity and Tolerance Study for the SwissFEL”, in *Proc. FEL'10*, Malmo, Sweden, 2010, paper WEPB17, pp. 437-440.
- [5] Z. Geng *et al.*, “Architecture Design for the SwissFEL LLRF System”, in *Proc. LINAC'14*, Geneva, Switzerland, 2014, paper THPP113 pp. 1114-1116.
- [6] https://ampegon.com/files/poster_ipac_2016_mf.pdf
- [7] V. Schlott *et al.*, “Overview and Status of SwissFEL Diagnostics”, in *Proc. IBIC'15*, Melbourne, Australia, Sep. 2015, pp. 12-16. doi:10.18429/JACoW-IBIC2015-M0BLA03
- [8] P. Craievich *et al.*, “Transverse Deflecting Structures for Bunch Length and Slice Emittance Measurements on SwissFEL”, in *Proc. FEL'13*, New York, NY, USA, Aug. 2013, paper TUPSO14, pp. 236-241.

COMMISSIONING AND STABILITY STUDIES OF THE SwissFEL BUNCH-SEPARATION SYSTEM

M. Paraliev[†], S. Dordevic, R. Ganter, C. Gough, N. Hiller, R. Krempaska, D. Voulot
Paul Scherrer Institute, Villigen PSI, Switzerland

Abstract

SwissFEL is a linear electron accelerator based, X-ray Free Electron Laser at the Paul Scherrer Institute, Switzerland. It is a user oriented facility capable of producing short, high brightness X-ray pulses covering the spectral range from 1 to 50 Å. SwissFEL is designed to run in two electron bunch mode in order to serve simultaneously two experimental beamline stations (hard and soft X-ray one) at its full repetition rate. Two closely spaced (28 ns) electron bunches are accelerated in one RF macro pulse up to 3 GeV. A high stability resonant kicker system and a Lambertson septum magnet are used to separate the bunches and to send them to their respective beamlines. With the advancement of the construction of the second beamline (Athos) the bunch-separation system was successfully commissioned. In order to confirm that the beam separation process is fully transparent a stability study of the electron beam and the free electron laser in the main beamline (Aramis) was done.

INTRODUCTION

The first undulator line of Swiss X-ray Free Electron Laser (SwissFEL) [1], Aramis, was inaugurated in 2016 and the first pilot experiment was conducted in 2017. In 2018 the nominal electron beam energy was achieved and the free electron laser reached its shortest designed X-ray wavelength of 1 Å. The two experimental stations of Aramis (Alvira and Bernina) were commissioned and in the beginning of 2019 Aramis SwissFEL line started regular user operation. In parallel, the second undulator line (Athos) is being constructed [2]. First electron beam to Athos was sent in September 2018 and in December the bunch-separation system was commissioned and the separation of the two bunches was successfully demonstrated. Starting two bunch operation in the early stages of Athos commissioning is very beneficial because it can be done in parallel with regular Aramis user operation.

In order to separate the two electron bunches they both are deflected by a fast resonant kicker system [3] – one up and one down. Compensating dipoles counteract the deflection of the down-kicked bunch and send it straight through the zero-field region of the Lambertson septum to the Aramis beamline. The up-kicked bunch is deflected by the Lambertson field sideways and it is sent to Athos beamline. Since the two bunches are deflected the stability of the kicker system is crucial for the proper operation of both beamlines. To confirm that the bunch-separation is fully transparent and does not affect operation of Aramis beamline several tests were conducted. The results of these tests are discussed below.

[†] martin.paraliev@psi.ch

RESONANT KICKER COMMISSIONING

The two Resonant Kicker (RK) magnets are a key component of SwissFEL electron bunch-separation system. They deflect the two consecutive electron bunches in opposing directions vertically before they are finally separated by a Lambertson septum about 8 m downstream. To work properly RKs need adequate electrical excitation and tight synchronization to the electron beam. To ensure that the deflection amplitude stability down to the ppm level is not dominated by the phase error the RK should be synchronised to a 10s of ps level. A dedicated synchronization module was developed to combine the trigger from the generic accelerator timing system (providing 7 ns resolution) and high stability RF clock in order to generate proper timing with 10 ps programmable delay resolution. High stability RF driver (17.8 MHz) excites the resonant structure to reach the required current, respectively the deflecting magnetic field.

Envelope Synchronization

The RKs were first commissioned in the straight accelerator beamline (Aramis). Using a small deflection amplitude (within the machine acceptance) and detecting the kick with beam position monitors (BPMs) downstream the resonance envelope was located. Figure 1 shows an envelope scan of the RKs excitation. The excitation curve appears backwards because the RKs' delay with respect to the beam arrival time in the scan is increased.

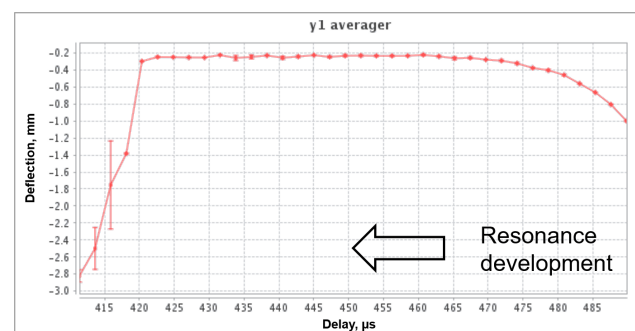


Figure 1: RKs' excitation envelope scan of vertical deflection downstream the kickers.

Phase Synchronization

Once the rough position of the resonance envelope is located the correct phase has to be found. A much finer scan (Fig. 2) was used to probe RKs' deflection and later was used to position the electron bunch at the sine wave crest, where the deflection is maximum and is least sensitive to phase error.

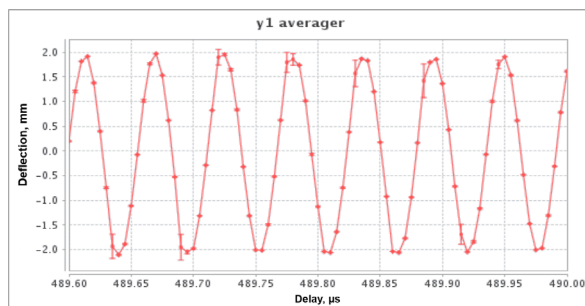


Figure 2: RK phase scan of vertical deflection downstream the kickers.

BUNCH SEPARATION

After the timing setup, the system was tested for phase inversion. It was confirmed that a single bunch can be sent to either Aramis or Athos depending on RKs' phase (180° RKs phase inversion). The proper beam position at the septum location (bunches separation of 10 mm, Fig. 3) depends on all five deflecting elements: two RKs and three compensating dipoles. Since the two bunches are aligned with the positive and negative crest of the RKs' sine deflecting field they experience a deflection and thus a vertical separation. The compensating dipoles act on the two bunches equally, deflecting them up-wards. The amplitude of the RKs and the compensating dipoles is automatically set to provide trajectory compensation for the down-kicked bunch and the required deflection for the up-kicked bunch according to the beam energy.

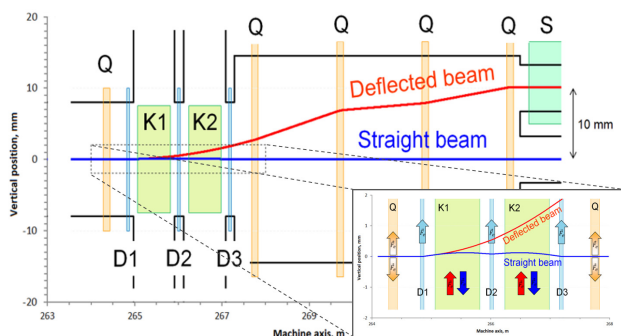


Figure 3: Bunch trajectory in the switchyard region and a zoom into the RKs' region with their corresponding deflecting field regions: Q – quadrupole magnet, K1, K2 – resonant kickers, D1, D2 and D3 – compensating dipoles and S – septum.

SwissFEL BPMs are specially designed to distinguish position and charge of the two 28 ns spaced electron bunches [4] allowing us to track both bunches separately even when they still share the same beam pipe. Figure 4 shows vertical beam position in the two beamlines for the first beam separation test. The RKs-Septum range is indicated. The apparent difference in position is due to the fact that first graph plots the vertical position against machine “Z” axis and the second against BPM number. Bunch two makes large excursion from the beam pipe axis on its way to field gap of the septum 10 mm upwards. Please note the different vertical scale of the two graphs.

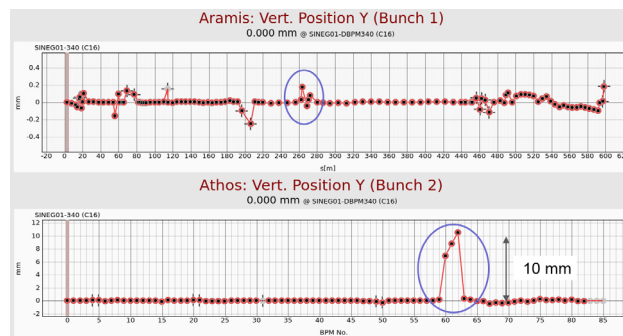


Figure 4: Vertical position of the two bunches during bunch-separation: upper graph – “Bunch 1” through Aramis beamline and lower graph – “Bunch 2” through Athos.

ELECTRICAL STABILITY

The RK system was specially developed to meet high stability pulse-to-pulse beam position requirements necessary for proper Free Electron Laser (FEL) operation. Dedicated RF drivers were designed to excite the resonance with 1 ppm amplitude resolution. To monitor and stabilize the RKs' amplitude two dedicated measurement systems were developed: a Full Range Measurement (FRM) system and Precision Measurement System (PMS). The FRM system measures the overall amplitude of the RKs with measurement noise floor of ~ 5 ppm rms and the phase with ~ 1 millidegree rms. The PMS has much smaller measurement window (~ 1 ppt) but measures with sub ppm resolution level^[3]. The pulse-to-pulse amplitude jitter of the RKs during routine operation is 2 to 3 ppm rms and the phase stability is 2 to 3 millidegree averaged over the macro pulse (the phase noise contribution to the amplitude is negligible). An amplitude feedback (using PMS) and a phase feedback (using FRM system) are controlling the magnets in order to ensure high precision deflection. Motorized mechanical tuner, driven by an iterative algorithm is used to tune RKs' resonator frequency in order to operate at the top of the resonance curve where deflecting current amplitude is maximum and the magnet is least sensitive to mechanical vibrations.

ELECTRON BEAM STABILITY

The bunch-separation system (mainly due to its RKs) is expected to be the most critical element concerning electron beam stability. Since the two bunches are deflected it is possible to check stability using the bunch going straight through Aramis beamline (in single bunch mode). A direct comparison between the bunch going directly through (all deflecting elements off) and when it is deflected (down) and back compensated is done for electron beam trajectory, electron beam shot-to-shot position stability, FEL photon beam shot-to-shot pulse energy and pointing stability. No significant change in horizontal and vertical beam trajectory was found. This indicates proper strength of the RKs and compensating dipoles.

Figure 5 shows shot-to-shot horizontal and vertical electron beam position running standard deviation of 100 consecutive pulses measured by a BPM (SARUN02-DBPM070) right before the FEL undulator section. Note that bunch-separation system is On when the “Kicker mode” shows zero (bottom curve in all following figures). The large jump in vertical standard deviation is due to the turn-Off transient of the deflecting elements. The reprogramming of the RKs and the compensating dipoles is not beam synchronous and up to a couple of bunches could be disturbed during the transient. No notable change in electron beam stability can be seen.

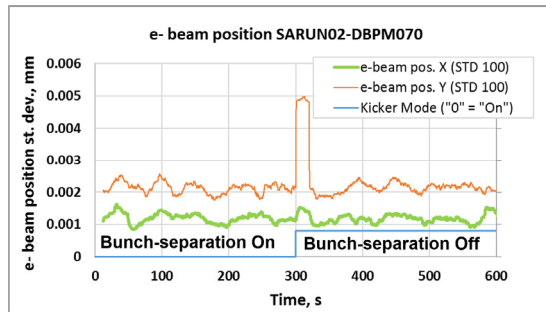


Figure 5: Electron beam position standard deviation of 100 consecutive pulses right before the FEL undulator section with bunch-separation system On and Off.

PHOTON BEAM STABILITY

The effect of bunch-separation system on FEL photon beam pulse-to-pulse stability was checked as well. Measuring the FEL pulse stability should be an even more sensitive way to detect electron beam disturbance and furthermore it serves as ultimate test to determine if the system stability is sufficient.

Amplitude Stability

For FEL photon pulse energy pulse-to-pulse stability two measurement methods were used. The first one was based on the non-destructive gas monitor (SARFE10-PBPG050) and the second (destructive) was based on an integration of photon beam camera image (SARFE10-PPRM064).

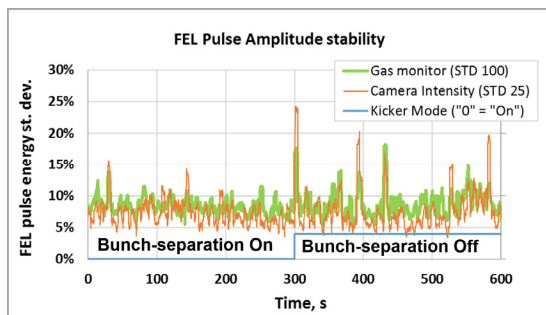


Figure 6: FEL photon beam pulse energy standard deviation of 100 consecutive pulses measured with gas monitor and photon beam image camera with bunch-separation system On and Off.

Since the camera pixels' intensity is proportional to the number of absorbed photons (with FEL wavelength 1.5 Å, within the linearity of the screen conversion) the image intensity integral is proportional to the total absorbed photon pulse energy (not to electromagnetic field intensity). Figure 6 shows standard deviation of the two measurements. Camera image acquisition was about 4 times slower (roughly giving information for each fourth FEL pulse). To match the two results' time structure the running standard deviation calculation for the camera measurement takes 4 times less data points

Pointing Stability

Bunch-separation system effect on the FEL photon beam pointing position was also investigated using the same beam image camera described above. Figure 7 shows horizontal and vertical position running standard deviation of the beams' centre of mass for 100 consecutive pulses. Apparently horizontal stability is much worse than the vertical. This is attributed to the mechanical stability of the screen-camera system (removable screen). The standard deviation peaks around seconds 390 and 580 are due to missing data points and could be associated to the limited bandwidth of the camera server. Thus the peak around turning Off the bunch-separation system might be real. Nonetheless there is no visible change in the FEL pointing position due to the bunch-separation system.

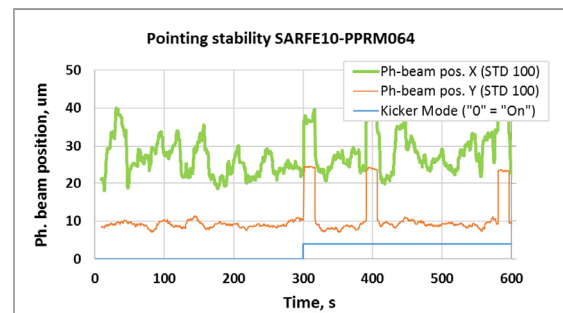


Figure 7: FEL photon beam horizontal and vertical position standard deviation of 100 consecutive pulses with bunch-separation system On and Off.

CONCLUSION

Aramis beamline of SwissFEL is in regular user operation. Commissioning of the second beamline (Athos) is on its way. A fully transparent operation of the bunch-separation system is crucial to the efficient operation of SwissFEL. Number of tests were conducted to check its effect on the electron beam and FEL. It was confirmed that for the level of stability of the Aramis FEL beam present for our measurements, the bunch-separation system did not add any additional jitter to the FEL pointing and pulse energy.

ACKNOWLEDGEMENTS

The authors would like to acknowledge the professional help of many PSI groups and colleagues that made this successful project possible.

REFERENCES

- [1] SwissFEL, <https://www.psi.ch/en/swissfel>
- [2] T. Schietinger, “Towards Full Performance Operation of SwissFEL”, in *Proc. IPAC'18*, Vancouver, Canada, Apr.-May 2018, pp. 24-28.
doi:10.18429/JACoW-IPAC2018-MOZGBD1
- [3] M. Paraliiev, C. Gough, “Resonant Kicker System with Sub-Part-per-Million Amplitude Stability”, in *Proc. IPAC'17*, Copenhagen, Denmark, May 2017, pp. 3174-3177.
- [4] B. Keil, R. Baldinger, R. Ditter, W. Koprek, R. Kramert, F. Marcellini, G. Marinkovic, M. Roggli, M. Rohrer, M. Stadler and D. Treyer, “Design of the SwissFEL BPM System”, in *Proc. IBIC'13*, Oxford, UK, Sep. 2013, paper TUPC25, pp. 427-430.
doi:10.18429/JACoW-IPAC2017-WEPIK098

FEASIBILITY OF SINGLE-SHOT MICROBUNCHING DIAGNOSTICS FOR A PRE-BUNCHED BEAM AT 266 nm*

A. H. Lumpkin^{#1} and D.W. Rule²

¹Argonne Associate, Argonne National Laboratory, Lemont, IL, USA

²Silver Spring, MD, USA

Abstract

We describe potential characterization of microbunched electron beams obtained after a modulator and chicane by using coherent optical transition radiation (COTR) imaging techniques. Beam transverse size (~50 microns), divergence (sub-mrad), trajectory angle (within ~0.1 mrad), spectrum (to a few nm), and pulse length (sub-ps) can be measured. The transverse spatial alignment is provided with near-field imaging, and the angular alignment is done with far-field imaging and two-foil COTR interferometry (COTRI). Analytical model results for a 266-nm wavelength COTRI case with a 10% microbunching fraction will be presented. COTR gains of 7×10^6 were calculated for an initial charge of 300 pC, and this enables splitting the optical signal for single-shot measurements of all the cited parameters.

INTRODUCTION

Co-propagating a relativistic electron beam and a high-power laser pulse through a short undulator (modulator) provides an energy modulation which can be converted to a periodic longitudinal density modulation (or microbunching) via the R56 term of a chicane [1]. Such pre-bunching of a beam at the resonant wavelength and the harmonics of a subsequent free-electron laser (FEL) amplifier seeds the process and results in improved gain. We describe potential characterizations of the resulting microbunched electron beams after the modulator using coherent optical transition radiation (COTR) imaging techniques for transverse size (50 micron), divergence (sub-mrad), trajectory angle (0.1 mrad), spectrum (few nm), and pulse length (sub-ps). The transverse spatial alignment is provided with near-field imaging and the angular alignment is done with far-field imaging and two-foil COTR interferometry (COTRI). Analytical model results for a 266-nm wavelength COTRI case with a 10% microbunching fraction will be presented. COTR gains of 7 million were calculated for an initial charge of 300 pC which enables splitting the optical signal for single-shot measurements of all the cited parameters. Since the beam and laser position jitters may cause some fluctuations in the microbunching spatial distribution, single-shot diagnostics will be beneficial.

*Work supported under Contract No. DE-AC02-07CH11359 with the United States Department of Energy, Basic Energy Sciences.
#lumpkin@anl.gov

EXPERIMENTAL ASPECTS

The APS Linac

The APS linac is based on an S-band rf photocathode (PC) gun which injects beam into an S-band linear accelerator with acceleration capability up to 450 MeV [2]. Beam diagnostics include imaging screens, rf BPMs, and coherent transition radiation (CTR) autocorrelators located before and after the chicane at the 100 MeV point.

The Microbunching Diagnostics

The diagnostics for the microbunching experiments would be located in the linac extension area (LEA) [2]. A schematic of a potential setup is shown in Fig. 1. A seed laser at 266 nm would be injected onto the beamline axis at a chicane to co-propagate with a 375-MeV electron beam micropulse through a modulator section. Immediately after the modulator, a set of 4 magnets would provide a small dispersive, R56 term to convert the energy modulation to the longitudinal density modulation. Such an electron beam would be transported to the COTR diagnostics. As will be shown later, the COTR gain will be significant at 6 orders of magnitude over incoherent OTR so the signal can be split over multiple optical paths for near field (NF) imaging, far-field (FF) imaging, spectral measurements, gain measurements, and a bunch length measurement with a streak camera. A thin laser blocking foil will be inserted before a mirror at 45 degrees to the beam direction as indicated in Fig. 1. A microscope objective will be focused on the back surface of the foil for the forward COTR beam size to provide a NF image in one UV camera. The combination of this source and the backward COTR from the mirror will result in interference fringes when viewed in the far field by a second UV camera. The enhanced light may also be split to provide signals to a UV-visible spectrometer (also readout by a UV camera) and a UV-visible streak camera. We may utilize a C5680 Hamamatsu streak camera with S20 PC operating with the M5675 synchroscan vertical deflection unit phase locked to 119.0 MHz, the 24th subharmonic of the linac S-Band at 2856 MHz. As will be noted in a subsequent section, a unique beam-based alignment technique will be employed using the COTR and COTRI images. The shape and intensity of the images at 266 nm will provide immediate online information on the overlap of the seed laser and e-beam, both spatially and temporally.

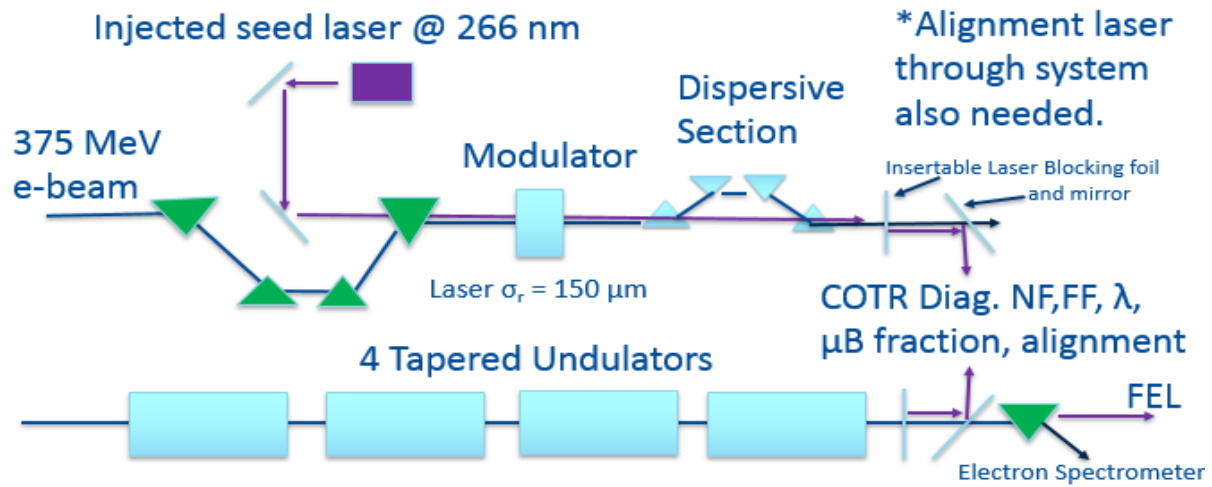


Figure 1: Schematic of the proposed LEA beamline layout showing the chicane, injected seed laser, modulator, COTR screens, undulators, and electron spectrometer.

ANALYTICAL MODEL AND RESULTS

Optical Transition Radiation Basics

When a charged-particle beam transits the interface of two different media, optical transition radiation (OTR) is generated by induced currents at the boundary of those media with different dielectric constants. As schematically shown in Fig. 2, there are forward and backward radiation cones emitted with opening angle of $1/\gamma$ (where γ is the relativistic Lorentz factor) around the angle of specular reflection for the backward OTR and around the beam direction for the forward OTR. For a nominal case of 375 MeV, a foil separation $L = 6.3$ cm, a wavelength of 266 nm, and a beam divergence of 0.1 mrad, one obtains the two-foil angular distribution pattern (red curve) as shown in Fig. 3, which is compared to the single foil pattern (black curve). The fringe visibility decreases with larger divergence values, and this dependence then can be used for a divergence measurement.

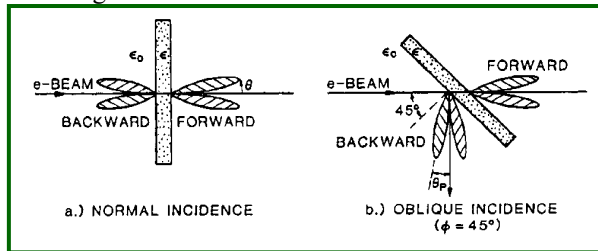


Figure 2: Schematic of OTR generation at boundaries of vacuum and materials for a) normal incidence and b) oblique incidence [3].

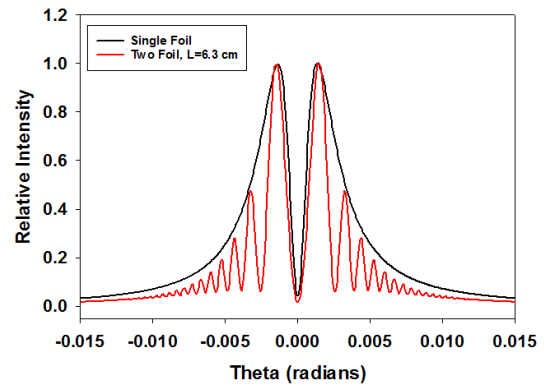


Figure 3: Comparison of far field OTR angular distribution patterns for a single foil and a two-foil interferometer. A beam energy of 375 MeV, wavelength of 266 nm, $L = 6.3$ cm, and a divergence of $\sigma_\theta = 0.1$ mrad were used in the calculations.

The number W_l of OTR photons that a single electron generates per unit frequency ω per unit solid angle Ω is

$$\frac{d^2 W_l}{d\omega d\Omega} = \frac{e^2}{\hbar c} \frac{1}{\pi^2 \omega} \frac{(\theta_x^2 + \theta_y^2)}{(\gamma^{-2} + \theta_x^2 + \theta_y^2)^2} \quad (1)$$

where \hbar is Planck's constant/ 2π , e is the electron charge, c is the speed of light, and θ_x and θ_y are radiation angles [4].

COTRI Model Results at 266 nm

The addition of the interference term $I(\mathbf{k})$ and the coherence function $J(\mathbf{k})$ as shown in Eqs. 2-5 include the effects of the microbunched fraction $f_B = N_B/N$, N_B being the microbunched part of the total N .

$$\frac{d^2 W}{d\omega d\Omega} = |r_{\parallel, \perp}|^2 \frac{d^2 W_l}{d\omega d\Omega} I(\mathbf{k}) J(\mathbf{k}) \quad (2)$$

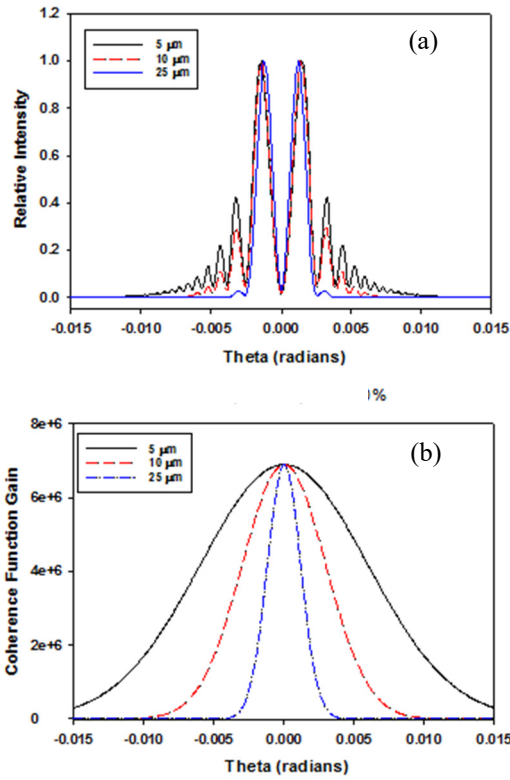


Figure 4: COTRI calculations for a) fringes and b) coherence function for beam sizes of 5, 10, and 25 μm.

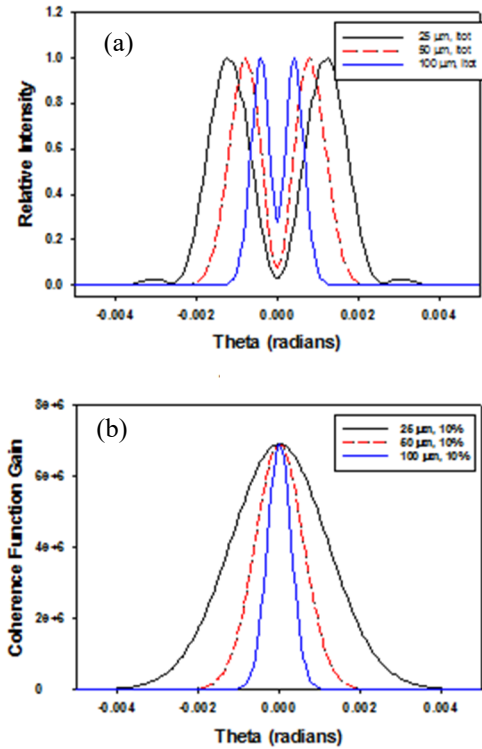


Figure 5: COTRI calculations for (a) fringes and (b) coherence function for beam sizes of 25, 50, and 100 μm.

$$I(\mathbf{k}) = 4 \sin^2 \left[\frac{kL}{4} (\gamma^{-2} + \theta_x^2 + \theta_y^2) \right] \quad (3)$$

$$J(\mathbf{k}) = N + N_B(N_B - 1)|H(\mathbf{k})|^2 \quad (4)$$

$$H(\mathbf{k}) = \frac{\rho(\mathbf{k})}{q} = g_x(k_x) g_y(k_y) F_z(k_z) \quad (5)$$

where $H(\mathbf{k})$ is the Fourier transform of the charge form factors for a single microbunch [4].

The COTRI calculations with the same parameters as Fig. 3 except with $N_B > 0$, for 5, 10 and 25 μm beam sizes show the effect of the microbunched transverse size on the coherence function as a function of angle in Fig 4a. The smallest beams result in the largest angles over which fringes are enhanced. The maximum enhancement is on axis at zero radians in Fig. 4b and shows a gain of 7×10^6 for this case of $f_B = 0.10$ microbunching fraction with 300 pC micropulse charge.

In Figure 5 similar plots are done for 25, 50 and 100 μm, and a noticeable loss of the outer fringe enhancements for these larger beam sizes is observed in Fig. 5a. Note, the angular range plotted is much smaller than that in Fig. 4, but the gain at zero mrad is still 7 million in Fig. 5b.

Angular Alignment Example

These angular distribution patterns can also be used for beam-based angular alignment of the seed laser and the electron beam. The proof of concept is shown in Fig. 6 for the case of the overlap of the SASE FEL beam and the electron beam [5]. Initially, we observed the asymmetric COTRI lobe pattern after undulator 8. By using a steering corrector before undulator 8, we were able to steer for symmetry in the lobes of the image. As a result, we improved the FEL gain by ~ 3.7 times through this one undulator section over the as-found state using rf BPMs and intensities of SASE FEL output as a function of z .

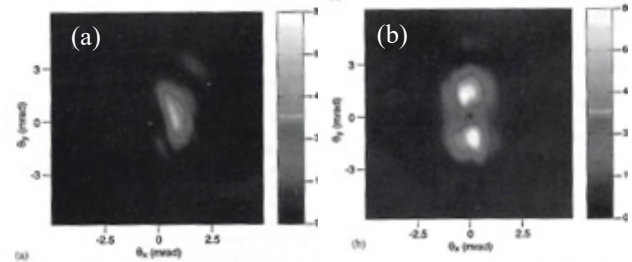


Figure 6: COTRI FF Image at 540 nm obtained after Undulator #8 in previous SASE FEL setup before (a) and after (b) corrected steering [5].

SUMMARY

In summary, we have evaluated the potential of using COTRI-based diagnostics to obtain single-shot characterizations of the transverse beam properties of microbunched electrons from a pre-buncher configuration at 266 nm. The spatial and temporal overlap aspects of the laser pulse and electron micropulse can in principle be addressed as well in an online manner.

ACKNOWLEDGMENTS

The first author acknowledges the support of J. Byrd and discussions with A. Zholents, both at Argonne National Laboratory.

REFERENCES

- [1] L.-H. Yu, “Generation of intense uv radiation by subharmonically seeded single-pass free-electron lasers”, *Phys. Rev. Lett. A*, vol. 44, p. 5178, 1991.
doi: 10.1103/PhysRevA.44.5178
- [2] Y. Sun *et al.*, “APS LINAC Interleaving Operation”, in *Proc. 10th Int. Particle Accelerator Conf. (IPAC'19)*, Melbourne, Australia, May 2019, pp. 1161-1163.
doi:10.18429/JACoW-IPAC2019-MOPTS119
- [3] A. H. Lumpkin, *Accel. Instr. Workshop*, Batavia IL, AIP Conf. Proc., vol. 229, p. 151, 1991.
- [4] D. W. Rule and A. H. Lumpkin, “Analysis of Coherent Optical Transition Radiation Interference Patterns Produced by SASE-Induced Microbunches”, in *Proc. 19th Particle Accelerator Conf. (PAC'01)*, Chicago, IL, USA, Jun. 2001, paper TPAH029, pp. 1288-1290.
- [5] A. H. Lumpkin *et al.*, “On-line SASE FEL gain optimization using COTRI imaging”, *Nuclear Instruments and Methods in Physics Research Section A*, vol. 528, p. 179, 2004.
doi:10.1016/j.nima.2004.04.042

OBSERVATIONS OF SHORT-RANGE WAKEFIELD EFFECTS
IN TESLA-TYPE SUPERCONDUCTING RF CAVITIES*

A.H. Lumpkin[#], R. Thurman-Keup, D. Edstrom Jr., J. Ruan
Fermi National Accelerator Laboratory, Batavia, IL 60510 USA

Abstract

The Fermilab Accelerator Science and Technology (FAST) facility has a unique configuration of a photocathode rf gun beam injecting two TESLA-type single cavities (CC1 and CC2) in series prior to the cryomodule. To investigate short-range wakefield effects, we have steered the beam to minimize the signals in the higher-order mode (HOM) detectors of CC1 and CC2 for a baseline, and then used a vertical corrector between the two cavities to steer the beam off axis at an angle into CC2. A Hamamatsu synchroscan streak camera viewing a downstream OTR screen provided an image of y-t effects within the micropulses with ~10-micron spatial resolution and 2-ps temporal resolution. At 500 pC/b, 50 b, and 4 mrad off-axis steering into CC2, we observed an ~ 100-micron head-tail centroid shift in the streak camera image y(t)-profiles. This centroid shift value is 5 times larger than the observed HOM-driven centroid oscillation within the macropulse and is consistent with a calculated short-range wakefield effect. Additional results for kick-angle compensations will be presented.

INTRODUCTION

The accelerators for high-power x-ray free-electron laser (FEL) facilities such as the European XFEL [1] and planned LCLS-II x-ray FEL [2] are employing TESLA-type SCRF cavities. Beam propagation off axis in these cavities can result in both short-range and long-range transverse wakefields which can lead to emittance dilution within the micropulses and macropulses, respectively. There are limited beam-effects data available, although we recently reported the clear observations of submacropulse beam centroid oscillation effects due to the long-range effects of HOMs [3].

We report here sub-micropulse effects on beam transverse position centroids and sizes correlated with off-axis beam steering in TESLA-type cavities at the Fermilab Accelerator Science and Technology (FAST) Facility [4]. We used a 3-MHz micropulse repetition rate, a unique two separated-single-cavity configuration, and targeted diagnostics for these tests. Our initial data from an optical transition radiation (OTR) imaging source indicated our streak camera can provide ~10-micron spatial resolution with 1-2 ps (σ) temporal resolution depending on the bandpass filter employed. Since the observed bunch lengths were 10-15 ps (σ), we had sufficient resolution for

up to 20 time slices in the 4 σ profile. In this sense we also obtained slice-emittance information. We used the HOM detectors and rf BPMs to assess our off-axis steering to generate and then evaluate the short-range wakefield effects on the beam dynamics.

EXPERIMENTAL ASPECTS

The FAST Injector Linac

The FAST linac is based on the L-band rf photocathode (PC) gun which injects beam into two superconducting rf (SCRF) capture cavities denoted CC1 and CC2, followed by transport to a low-energy electron spectrometer. A Cs₂Te photocathode is irradiated by the UV component of the drive laser system described elsewhere [5]. The basic diagnostics for the studies include the rf BPMs located before, between, and after the two cavities as shown in Fig. 1. These are supplemented by the imaging screens at X107, X108, X121, and X124. The HOM couplers are located at the upstream and downstream ends of each SCRF cavity, and these signals are processed by the HOM detector circuits with the output provided online though ACNET, the Fermilab accelerator controls network. The HOM detectors' bandpass filters were optimized for two dipole passbands from 1.6 to 1.9 GHz, and the 1.3 GHz fundamental was reduced with a notch filter. The rf BPMs electronics were configured for bunch-by-bunch capability with reduced noise. At 2 nC per micropulse, the rms noise was found to be 25 μ m in the horizontal axis (x) and 15 μ m in the vertical axis (y) in B101 in the test with 4.5-MeV beam from the gun. However, for these experiments on short-range transverse wakefields, we relied on a streak camera to provide the sub-micropulse spatial information.

The Streak Camera System

We utilized a C5680 Hamamatsu streak camera with S20 PC operating with the M5675 synchroscan vertical deflection unit that was phase locked to 81.25 MHz. In addition, we used a phase-locked-loop C6878 delay box that stabilizes the streak image positions to about 1 ps temporal jitter over 10s of minutes. These steps enabled the synchronous summing of 50-150 micropulses or bunches (b) generated at 3 MHz by the photoinjector or the offline summing of 10-100 images to improve statistics in the sum images. We applied the principle to optical transition radiation (OTR) generated from an Al-coated Si substrate at the X121 screen location (see Fig.1) with subsequent transport to the beamline streak camera. Commissioning of the streak camera system was facilitated through a suite of

*This manuscript has been authored by Fermi Research Alliance, LLC under Contract No. DE-AC02-07CH11359 with the U.S. Department of Energy, Office of Science, Office of High Energy Physics.

[#]lumpkin@fnal.gov

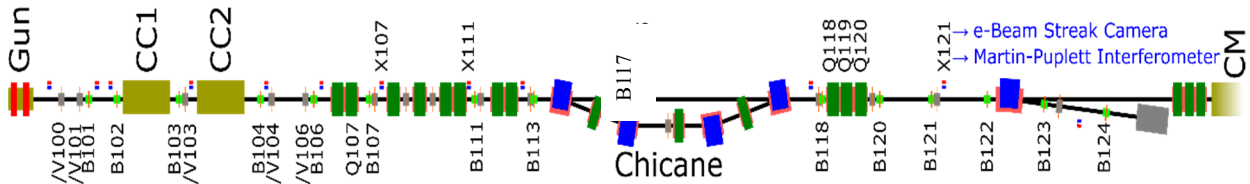


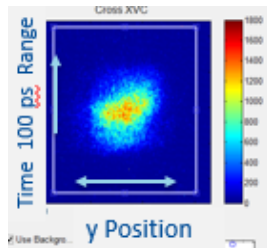
Figure 1: Schematic of the FAST beamline layout showing the capture cavities, correctors, rf BPMs, chicane, X121 OTR screen, spectrometer, and the beginning of the cryomodule (CM).

controls centered around ACNET. This suite includes operational drivers to control and monitor the streak camera as well as Synoptic displays to facilitate interface with the driver. Images are captured from the streak camera using the readout camera, Prosilica 1.3 Mpixel cameras with 2/3" format, and may be analyzed both online with a Java-based ImageTool and an offline MATLAB-based ImageTool processing program [6,7]. Bunch-length measurements using these techniques have been reported previously from the A0 Facility [8] and FAST first system streak camera commissioning at 20 MeV [9].

EXPERIMENTAL RESULTS

Initial Streak Camera Data: As Found Steering

In order to investigate the short-range wakefield driven submicropulse effects, we used the HOM detector signals as a measure of how far off axis the beam was in the cavities. We initially used the beam transport as found with elevated HOM signals in both CC1 and CC2. We identified a y-t effect in the streak camera image shown in Fig. 2. The head of the pulse is lowest in the image so later time is upward. The projected bunch length is 11.2 ps (σ).



HOM Detectors
CC1[8]= -100 mV
CC1[9]= -60 mV
CC2[8]= -100 mV
CC2[9]= -50 mV

Figure 2: OTR streak camera Image at X121 with HOMs as found for Run 1.

The transport optics rotated the image 90° so we observed the y spatial information on the horizontal display axis as indicated. The temporal slices are shown in Fig. 3a for the head and tail of the pulses, and then Fig. 3b shows the Gaussian fits to three such profiles with a clear 343 μm shift of the centroid from head (blue curve) to tail (red curve). Based on the elevated HOM signals, we attribute the effects to a combination of both CC1 and CC2 wakefields.

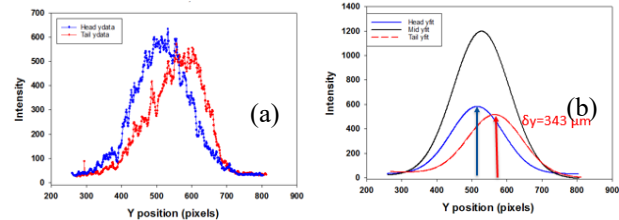


Figure 3: (a) Transverse profiles from the head and tail of the Fig. 2 Image (b) Gaussian fits to the transverse profiles taken at the head, middle, and tail of the longitudinal distribution. A head-to-tail centroid shift of 343 μm was observed.

We next steered the beam with the V103 corrector by ± 2.4 A from the reference or ± 4 mrad to evaluate the effects of CC2's wakefields. Interestingly, the +4 mrad steering almost doubled the head to tail centroid shift to +693 μm in Fig. 4b while the -4 mrad steering seemed to compensate the CC1 kick and reduced the centroid shift to -55 μm as shown in Fig. 4d. The projected beam size was also reduced.

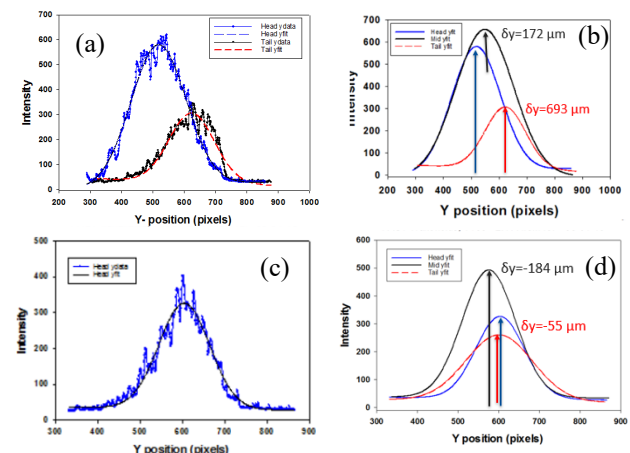


Figure 4: (a) Transverse profiles from the head and tail of the image with V103= +2.4 A. (b) Gaussian fits to the transverse profiles taken at the head, middle, and tail of the longitudinal distribution. A head-to-tail centroid shift of 693 μm was observed. (c) Transverse profiles from the head and tail of the image with V103=-2.4A. (d) Gaussian fits to the transverse profiles taken at the head, middle, and tail of the longitudinal distribution. A head-to-tail centroid shift of only -55 μm was observed for this case.

Wake Fields and HOMs Minimized

The next run we used the H/V 101 correctors before CC1 and H/V 103 correctors before CC2 to minimize the four HOM signals at 500 pC/b and with 150 b. We observed an elliptical beam in y-t space as shown in Figure 5 as would be expected for a space-charge-dominated regime at the PC. In this case the laser spot size was ~ 0.2 mm as in the previous run. Also, we observe almost no y-t tilt during the micropulse so this looks like a preferred way to steer with the four HOM signals low at -13, -10, -5, -7 mV.

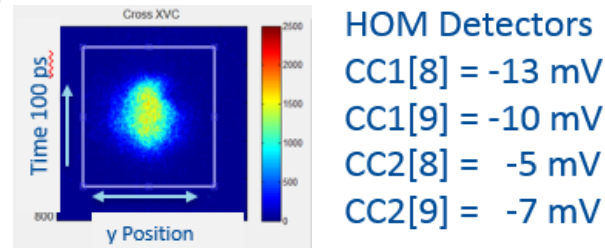


Figure 5: Streak camera y-t image at X121 that exhibits elliptical-shape effect with HOMs minimized.

In Fig. 6 we continued our studies, but we note the laser spot was now 1.2 mm RMS. Our HOM signal minima were not as low as in Fig. 5 with 500 pC/b, but we did observe a somewhat elliptical shape as shown in Fig. 6a. The beam size at the tail is much smaller than at the middle with no head-tail centroid shift. However, when we steered with V103 = -2A from the reference, we observed a clear 106- μ m head-tail centroid shift and significant 139- μ m profile size growth from the initial 224 μ m at the tail. This would indicate significant dilution of slice emittance in that sample.

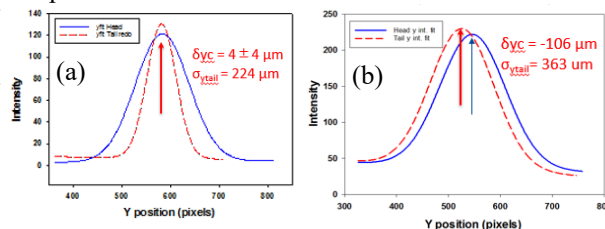


Figure 6: (a) Comparison of the Gaussian fits to the profile taken at the head and the tail of an image with HOMs minimized and laser spot of 1.1 mm RMS. (b) Comparison of the Gaussian fits to the profile taken at the head and the tail of an image with V103 = -2A from reference. A clear centroid shift of -106 μ m is seen, and a > 50 % larger profile at the tail is seen than in (a).

Bunch by Bunch rf BPM Data

We also evaluated the potential long-range wakefield or HOM effects on the beam centroid by using the rf BPM data. An example of the centroid motion within the 50-micropulse train of a macropulse is shown in Fig. 7 with both noise-reduction and bunch-by-bunch capabilities implemented.

The 100-kHz oscillation seen in the B117 data is a difference frequency between HOM mode 14 in CC2 and a beam harmonic [3]. The field oscillations kicked different micropulses varying amounts depending on the amplitude

at that point in time. The quadrupole triplet Q118-120 was used to focus the beam smaller in x while leaving the vertical size about 800 μ m at the X121 station. The beam oscillation amplitude is much reduced to <20 μ m at B121 downstream of these quadrupoles, and thus the main competing mechanism identified does not account for the observed y-t effect in the streak image. Since the numerical model for a TESLA cavity indicated a 100-120 μ m head-tail kick for 500 pC/b and a 4-mm offset at 33 MeV [10], we attribute the 100- μ m head-tail effects seen in Fig. 6 to predominately such short-range wakefields.

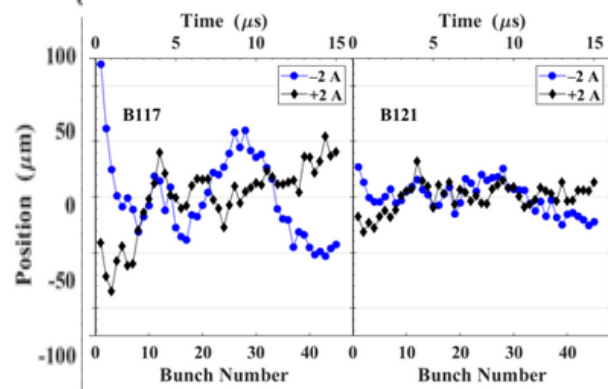


Figure 7: Examples of the variation of the beam vertical centroids bunch by bunch for 50 micropulses at B117 and B121 for V103 settings of ± 2 A from the reference. These were 100-shot averages to show the 100-kHz oscillation effects generated in CC2.

SUMMARY

In summary, a series of preliminary observations of short-range wakefield effects on beam dynamics were made using the streak camera to obtain y-t images at the submicropulse time scale. The HOM detectors and rf BPMs were used to evaluate off-axis steering related to these tests, and the HOM-induced sub-macropulse centroid motion was shown to be much smaller than the observed effects. Moreover, the head-tail centroid kicks were consistent with a short-range wakefield model for the TESLA-type superconducting rf cavity and attributed to that effect.

ACKNOWLEDGMENTS

The authors acknowledge the support of C. Drennan, A. Valishev, D. Broemmelsiek, G. Stancari, and M. Lindgren, all in the Accelerator Division at Fermilab.

REFERENCES

- [1] H. Weise, "Commissioning and First Lasing of the European XFEL", in *Proc. FEL'17*, Santa Fe, NM, USA, Aug. 2017, pp. 9-13. doi:10.18429/JACoW-FEL2017-MOC03
- [2] P. Emma, "Status of the LCLS-II FEL Project at SLAC", presented at *Proc. FEL'17*, MOD01, Santa Fe, NM, Aug. 2017, paper MOD01.
- [3] A. H. Lumpkin *et al.*, "Submacropulse electron-beam dynamics correlated with higher-order modes in Tesla-type superconducting rf cavities", *Phys. Rev. Accel. and Beams*, vol. 21, p. 064401, 2018.

doi:10.1103/PhysRevAccelBeams.21.064401

- [4] The ASTA User Facility Proposal, Fermilab-TM-2568, October 2013.
- [5] J. Ruan, M. Church, D. Edstrom, T. Johnson, and J. Santucci, “Commission of the Drive Laser System for Advanced Superconducting Test Accelerator”, in *Proc. IPAC’13*, Shanghai, China, May 2013, paper WEPME057, pp. 3061-3063.
- [6] J. Diamond, FNAL, online Java-based ImageTool, 2013.
- [7] R. Thurman-Keup, FNAL, off-line MATLAB-based ImageTool, 2011.
- [8] A. H. Lumpkin, J. Ruan, and R. Thurman-Keup, “Synchroscan streak camera imaging at a 15-MeV photoinjector with emittance exchange”, *Nucl. Instr. and Meth. A*, vol. 687, pp. 92-100, 2012.
doi: 10.1016/j.nima.2012.05.068
- [9] A. H. Lumpkin, D. Edstrom, and J. Ruan, “Initial Demonstration of 9-MHz Framing Camera Rates”, in *Proc. NAPAC’16*, Chicago, IL, USA, Oct. 2016, pp. 333-336.
doi:10.18429/JACoW-NAPAC2016-TUP0A25.
- [10] V. Lebedev, private communication, May 2016.

MULTI-ENERGY OPERATION ANALYSIS IN A SUPERCONDUCTING LINAC BASED ON OFF-FREQUENCY DETUNE METHOD*

Z. Zhang[†], Y. Ding, C. Adolphsen, and T. Raubenheimer
SLAC National Accelerator Laboratory, Menlo Park, CA 94025, USA

Abstract

The free-electron laser facilities driven by a superconducting radio-frequency (SRF) linac provide high-repetition-rate electron beam, which makes it feasible to feed multiple undulator lines at the same time. In this paper, we study a method of controlling the beam energy of multiple electron bunches by off-frequency detuning of the SRF linac. Based on the theoretical analysis, we present the optimal solutions of the method and the strategy to allocate linac energy for each possible off-frequency detune. The initial acceleration phases before detuning of the SRF linac can be optimized to reduce the necessary SRF linac energy overhead. We adopt the LCLS-II-HE configuration as an example to discuss possible schemes for two undulator lines.

INTRODUCTION

The successful operation of several hard x-ray free-electron laser (XFEL) facilities [1–4] over the world represents a revolution in the development of light source. Most of the present-day XFELs are driven by copper linac with a repetition rate around 100 Hz. This low repetition rate determines only a modest average brightness, similar to that of the third generation storage ring based sources. Another drawback of these facilities is that they typically only serve one user end-station at a given time.

XFELs driven by a superconducting radio-frequency (SRF) linac are capable to deliver Mega-Hertz (MHz) electron beams, which greatly enhances the photon average brightness and supports multiple beamlines in parallel and/or cascading configurations [5–8]. In this case, the photon energy from different beamlines can be varied by adjusting the undulator gap for a given electron beam energy. To further extend the photon energy range, schemes to control the electron beam energy of every undulator line independently are highly desired.

To provide different beam energies for multiple undulator lines from a SRF linac, different schemes can be applied. For example, one can extract electron beams with a fast kicker at the desired energy point and then send them to the undulator line through a bypass line, as shown in Fig. 1 (a). This scheme is adopted as the baseline design of the present SRF XFEL facilities [6–8]. In this scheme, we can make full use of the energy capability of the SRF linac. However, since the kicker positions are fixed, the beam energy for each undulator line is almost constant. Besides, adding the extraction regions to the SRF linac is lengthy and costly.

Recently, another scheme using achromatic electron delay system is proposed to produce multi-energy beams for the SRF linac-driven XFELs [9].

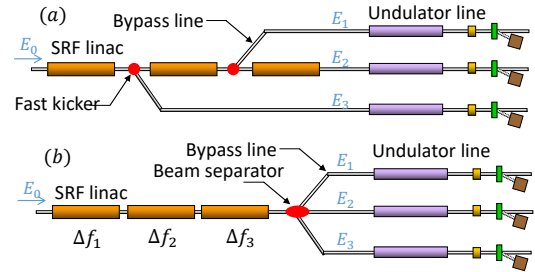


Figure 1: Two schemes of multi-energy operation of a SRF XFEL: (a) kick the beam to bypass line at desired energy point (b) control the beam energy independently by off-frequency detune of SRF cavities.

In this paper, we study a new scheme for multiple-energy operation of a SRF linac based on the off-frequency detune method [10, 11]. The SRF cavities are very sensitive to small mechanical perturbations due to their narrow bandwidth. The resonant frequency can be varied by compressing the cavity. With enough detune range, we can produce periodic energy pattern in CW electron beams. The main advantage is the possibility to control the beam energy independently and extend the XFEL parameter space. In addition, we can adopt the dispersive energy separator, rather than the fast kicker/septum system, to separate beams to different undulator lines.

THEORETICAL ANALYSIS

For CW electron beams, we assume the beam repetition rate f_r and the time separation $T = 1/f_r$. At the nominal resonant frequency of the cavity f_c , all electron beams are accelerated at the same phase ψ_c , as shown in Fig. 2. When the frequency is detuned by Δf and the acceleration phase of the first beam is kept at ψ_c , the acceleration phase of the j -th electron beams is $\psi_c + (j - 1)\Delta\phi$ with phase difference of two neighbouring beams (or we can call it as phase shift)

$$\Delta\phi = 2\pi T \Delta f. \quad (1)$$

In order to reduce the off-frequency detune range, we limit the range of the phase shift to be $\Delta\phi \in [-\pi, \pi]$.

To support M undulator lines, the acceleration phase of the $(M+1)$ -th beam has to be the same with the first one, which can be named as the periodic condition

$$\psi_c + M\Delta\phi = \psi_c + 2\pi k, \quad (2)$$

* Work supported by U.S. Department of Energy Contracts No. DE-AC02-76SF00515 and submitted to *Phys. Rev. Accelerator and Beams*.

[†] zzhang@slac.stanford.edu

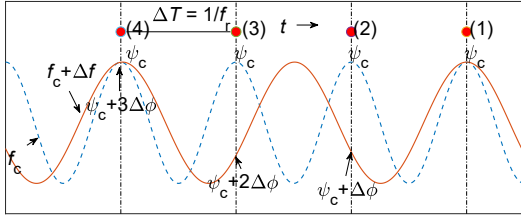


Figure 2: Acceleration phase changes of the CW electron beams by the off-frequency detune of the SRF cavities. Here we use $M = 3$ and acceleration phase of the fourth beam is the same with the first one.

where k is an integer. The possible phase shifts are

$$\Delta\phi_k = \frac{2\pi k}{M}, \quad (3)$$

where $k = 0, \pm 1, \dots, \pm(K-1), \pm K$, $K = \lfloor M/2 \rfloor$ and the function $\lfloor x \rfloor$ returns the largest integer smaller than or equal to x . However, in a SRF cavity with acceleration voltage V_k , acceleration phase ψ_k and phase shift $\Delta\phi_k$, the energy gain of the j -th beam in sequence can be expressed as

$$\begin{aligned} \Delta E_j &= eV_k \cos(\psi_k + (j-1)\Delta\phi_k) \\ &= eV_k \cos(-\psi_k + (j-1)\Delta\phi_{-k}), \end{aligned} \quad (4)$$

with e denoting the electron charge. So the acceleration cavity can be replaced by the one with $-\psi_k$ and $\Delta\phi_{-k}$. In this way, we can further reduce the range of the phase shift to be $\Delta\phi \in [0, \pi]$, and the available k is

$$k = 0, 1, \dots, (K-1), K. \quad (5)$$

The corresponding off-frequency detune can be expressed with the beam repetition rate $\Delta f = \frac{k}{M} f_r$. The full tunable range of the off-frequency detune is

$$\Delta f_{\max} = \begin{cases} \frac{1}{2} f_r, & M \text{ is an even number} \\ \frac{1}{2} (1 - \frac{1}{M}) f_r, & M \text{ is an odd number} \end{cases} \quad (6)$$

$$\begin{cases} eV_0 \cos(\psi_0) + eV_1 \cos(\psi_1) + \dots + eV_K \cos(\psi_K) = \Delta E_1, \\ \dots & \dots & \dots \\ eV_0 \cos(\psi_0) + eV_1 \cos(\psi_1 + \frac{2\pi(j-1)}{M}) + \dots + eV_K \cos(\psi_K + \frac{2\pi K(j-1)}{M}) = \Delta E_j, \\ \dots & \dots & \dots \\ eV_0 \cos(\psi_0) + eV_1 \cos(\psi_1 + \frac{2\pi(M-1)}{M}) + \dots + eV_K \cos(\psi_K + \frac{2\pi K(M-1)}{M}) = \Delta E_M. \end{cases} \quad (10)$$

Here $\Delta E_j = E_j - E_0$ means the energy change of the j -th beam. For $k = 0$, it can be solved by summing over all equations as

$$eV_0 = \frac{1}{M} \sum_{j=1}^M \Delta E_j. \quad (11)$$

The off-frequency detune range for 3 undulator lines is $\frac{1}{3} f_r$, smaller than the cases of 2 and other numbers.

To support M undulator lines, the whole SRF linac is divided into S sections. The maximum total energy gain of the S linac sections, $E_G = \sum_{s=0}^{S-1} eV_s$, is usually larger than the maximum achievable beam energy. In this method, we need more SRF cavities to achieve the designed energy of the facility than usual. We adopt the linac energy overhead factor (η) to evaluate different energy allocation solutions, which can be defined as

$$\eta = \frac{E_G + E_0}{E_{\max}} - 1 \geq 0, \quad (7)$$

where E_{\max} is the largest beam energy among all lines.

When $S > K + 1$, there are at least two sections having the same phase shift. Assuming the s -th and t -th sections have the same phase shift $\Delta\phi$, the energy gain of the j -th beam in sequence is

$$\begin{aligned} \Delta E_j &= eV_s \cos(\psi_s + (j-1)\Delta\phi) \\ &\quad + eV_t \cos(\psi_t + (j-1)\Delta\phi) \\ &= eV_{st} \cos(\psi_{st} + (j-1)\Delta\phi), \end{aligned} \quad (8)$$

with V_{st} , ψ_{st} being the maximum acceleration voltage and initial acceleration phase of the combined section. The acceleration voltage V_{st} can be solved as

$$\begin{aligned} V_{st} &= \sqrt{V_s^2 + V_t^2 + 2V_s V_t \cos(\psi_s - \psi_t)}, \\ &\leq V_s + V_t. \end{aligned} \quad (9)$$

The equality is achieved only when $\psi_s = \psi_t$. So the linac sections with the same phase shift can be combined into one section to obtain lower overhead factor, so we can let $S = K + 1$. In this case, the energy gain of the M lines (E_1, E_2, \dots, E_M) can be written as

Here we already let $\psi_0 = 0$ to reduce the energy overhead factor. The equation above can be rewritten as

$$E_0 + eV_0 = \frac{1}{M} \sum_{j=1}^M E_j, \quad (12)$$

which means that the average energy of all undulator lines determines the beam energy before the off-frequency detune. When $k > 0$ and $2k \neq M$, replacing $\cos(\theta)$ with

$\frac{1}{2}(e^{i\theta} + e^{-i\theta})$ and summing over all equations after multiplying a factor of $e^{\pm i(2\pi k(j-1)/M)}$, we can obtain

$$eV_k M e^{\pm i\psi_k} = 2 \sum_{j=1}^M \Delta E_j e^{\mp i \frac{2\pi k(j-1)}{M}}. \quad (13)$$

The initial acceleration phase ψ_k can be expressed as

$$\psi_k = \arctan 2 \left(- \sum_{j=1}^M \Delta E_j \sin\left(\frac{2\pi k(j-1)}{M}\right), \sum_{j=1}^M \Delta E_j \cos\left(\frac{2\pi k(j-1)}{M}\right) \right). \quad (14)$$

The energy gain of each section eV_k is

$$eV_k = \frac{2}{M} \left(\left(\sum_{j=1}^M \Delta E_j \sin\left(\frac{2\pi k(j-1)}{M}\right) \right)^2 + \left(\sum_{j=1}^M \Delta E_j \cos\left(\frac{2\pi k(j-1)}{M}\right) \right)^2 \right)^{1/2}. \quad (15)$$

When $2k = M$, after multiplying $e^{i\pi(j-1)}$ to each equation we can get

$$eV_K \cos(\psi_K) = \frac{1}{M} \sum_{j=1}^M \Delta E_j e^{i\pi(j-1)}. \quad (16)$$

Similarly with the case of $k = 0$, we can let $\psi_K = 0$ or $\psi_K = \pi$ to reduce energy overhead. So the on-crest energy gain of the section with $f_r/2$ detune ($K = M/2$) is

$$eV_K = \frac{1}{M} \left| \sum_{j=1}^M \Delta E_j e^{i\pi(j-1)} \right|. \quad (17)$$

APPLICATION IN THE LCLS-II-HE

The LCLS-II-HE is a high energy upgrade of the LCLS-II, a superconducting CW XFEL facility at SLAC, which will increase the beam energy from 4 GeV to 8 GeV. It will provide ultrafast X-rays from the soft and hard undulator lines at repetition rate up to 1 MHz. The beam energy range is 3 ~ 4 GeV for soft X-ray undulator line and 3.3 ~ 8 GeV for hard X-ray line. The present baseline design of the LCLS-II-HE adopts the scheme which kicks the beam out of the SRF linac at ~4 GeV.

A compact frequency tuner has been designed for the LCLS-II project, including slow/coarse tuner and fast/fine tuner. The schematic and test performance of the tuner can be found in Refs. [12, 13]. Coarse frequency tuning is achieved with a motor-driven end-lever tuner. When the cavities are cooled to 2K and the frequency is set to 1.3 GHz, there is typically a +/-200 kHz range available over which the tuner can change the cavity frequency. With minor modifications to the tuner design, the low end of the tuning range could likely be extended to -500 kHz, which would

allow two energy operation at about 1 MHz. However multi-beam operation can still be achieved with the current tuner design at lower beam repetition rates.

To support two undulator lines, the first method is the two-beam scheme. The whole linac is divided into two parts and the frequency detune of the second part is half of the beam rates. According to general solutions for $M = 2$, we can produce any set of beam energies without energy overhead in the last 4 GeV SRF linac. For 1 MHz beam, the frequency detune is 500 kHz.

Secondly, we can use the three-beam scheme as well. The first beam is sent to the HXR undulator line and the other two with the same energy are for the SXR. So the beam repetition rates in the two undulator lines are different. In this case, the energy overhead factor is zero for any two energies and the required frequency detune is one third of the total beam repetition rate, i.e. 333 kHz for 1 MHz beam.

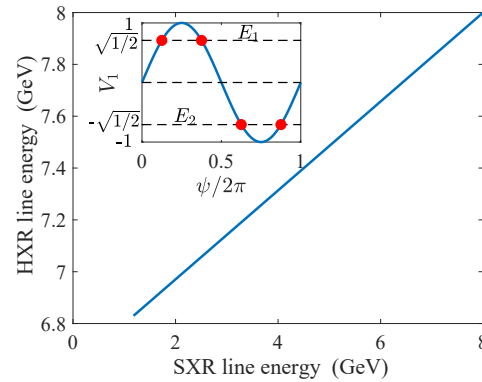


Figure 3: Available beam energies for SXR and HXR lines when using the special solution of four-line scheme.

The third method is to use a special solution of the four-beam scheme. In this scheme, the SRF linac needs to be divided into three sections with frequency detune of 0, $f_r/4$ and $f_r/2$. For a special set of beam energies, the energy gain of the third section can be zero and the maximum off-frequency detune is only $f_r/4$. With the acceleration phases of the four beams in the inserted figure of Fig. 3, we can produce two groups of energy. The final two energies can be varied by changing the fraction of detuned SRF linac. With the parameters of the LCLS-II-HE, the available energies are shown in Fig. 3. The two energies are correlated and the minimum SXR line energy (1.18 GeV) can be achieved when we detune the last 4 GeV linac. When the SXR line energy is 3~6 GeV, the corresponding HXR line energy is 7.14~7.65 GeV, which is smaller than 8 GeV. Despite of these limitations, the small off-frequency detune range (250 kHz for 1 MHz beam) makes it still very promising in practice.

REFERENCES

- [1] P. Emma *et al.*, "First lasing and operation of an ångstrom-wavelength free-electron laser", *Nature Photonics*, vol. 4, p. 641, 2010. doi:10.1038/nphoton.2010.176

- [2] T. Ishikawa *et al.*, “A compact X-ray free-electron laser emitting in the sub-ångström region”, *Nature Photonics*, vol. 6, p. 540, 2012. doi:10.1038/nphoton.2012.141
- [3] H. Kang *et al.*, “Hard X-ray free-electron laser with femtosecond-scale timing jitter”, *Nature Photonics*, vol. 11, p. 708, 2017. doi:10.1038/s41566-017-0029-8
- [4] C. Milne *et al.*, “SwissFEL: The Swiss X-ray Free Electron Laser”, *Applied Sciences*, vol. 7, p. 720, 2017. doi:10.3390/app7070720
- [5] J. Galayda *et al.*, Technical Report. LCLSII-1.1-DR-0251-R0 (SLAC, 2015), 2015.
- [6] M. Altarelli *et al.*, Technical design report, DESY, 97:1-26, 2006.
- [7] Z. Zhu *et al.*, “SCLF: an 8-GeV CW SCRF linac-based X-ray FEL facility in Shanghai”, in *Proc. FEL'17*, Santa Fe, NM, USA, Aug. 2017, pp. 182–184. doi:10.18429/JACoW-FEL2017-MOP055
- [8] T. O. Raubenheimer, “The LCLS-II-HE, a high energy upgrade of the LCLS-II”, in *Proc. FLS'18*, Shanghai, China, Mar. 2018, pp. 6–11. doi:10.18429/JACoW-FLS2018-MOP1WA02
- [9] J. Yan and H. Deng, arXiv preprint arXiv:1907.04176, 2019.
- [10] J. Galayda, private communication, 2017.
- [11] E. Vogel, private communication, 2018.
- [12] Y. M. Pischalnikov *et al.*, “Design and test of the compact tuner for narrow bandwidth SRF cavities”, in *Proc. IPAC'15*, Richmond, VA, USA, May 2015, pp. 3352–3354. doi:10.18429/JACoW-IPAC2015-WEPTY035
- [13] J. P. Holzbauer, Y. M. Pischalnikov, W. Schappert, and J. C. Yun, “Performance of SRF cavity tuners at LCLS II prototype cryomodule at FNAL”, in *Proc. LINAC'16*, East Lansing, MI, USA, Sep. 2016, pp. 808–810. doi:10.18429/JACoW-LINAC2016-THPRC017

STATUS OF THE KLYSTRONS FOR THE EUROPEAN XFEL AFTER COMMISSIONING AND FIRST USER OPERATION PHASE

V. Vogel, M. Bousonville, A. Cherepenko, S. Choroba, H.-J. Eckoldt, T. Grevsmuehl, V. Katalev, K. Machau, P. Morozov, B. Yildirim, DESY, Hamburg, Germany

Abstract

At present 26 RF stations for the European XFEL are in operation. Each of the RF stations consists of a HV modulator located on the DESY campus, up to 1600 m long 10 kV HV cables that connect the modulators and the HV pulse transformers located in the underground tunnel, the horizontal multi-beam klystron (MBK), and an air filled waveguide distribution system (WG) between the klystron and the cavities input couplers. The klystrons can produce RF power up to 10 MW, 1.5 ms RF pulse length and 10 Hz repetition rate. Two RF stations of the injector have already achieved about 30,000 hours of operation, RF stations of the XFEL bunch compressor area have operated up to 20,000 hours and the klystrons in the XFEL main linac already have about 18,000 hours of operation. To increase the lifetime of the klystrons we are using a fast protection system (KLM) that is in routine operation since 2018 in addition to the common interlock system. In this article we will give a summary of the present klystrons operation status including the number of HV and RF arcs in the klystrons and in the WG system and operation statistics for the high power RF part of machine.

INTRODUCTION

The European X-ray Free-Electron Laser (XFEL) [1] can be operated up to energy of 17.5 GeV (July 2018). Currently up to 300 coherent laser pulses per second with duration of less than 100 fs and with photon energy up to 19.1keV are delivered to the experiments. In future the number of pulses will increase to the design value of 27000 per second. For the production of these laser pulses, electrons have to be accelerated using a 2 km long accelerator based on superconducting radio frequency (RF) technology. For the XFEL project for a source of RF power of 26 RF stations were chosen the series horizontal MBKs made by two companies: MBK TH1802 from “Thales” [2, 3] and MBK E3736H from “Toshiba” [4, 5]. Both types of MBKs were equipped with CMs [6, 7] and 3 m long HV cables, and then they were tested on DESY MBK test stands [8]. The test was done with full RF power of 10 MW, full RF pulse length of 1.5 ms and with repetition rate of 10 Hz. Big advantages of using CM and HV cable connection between MBK and HV transformer are that we don't have to work with the oil during MBK installation in the tunnel and that MBK and WGS can be easy connected together. CM has monitors for the measurement of klystron voltage and cathode current. Figure 1 shows the one of 24 RF stations in the XFEL tunnel.



Figure 1: XFEL tunnel view.

Since 2013 the commissioning of the first RF station for XFEL injector has been started. In 2015 the second RF station started operation for the first cold AC module and since 2016 the commissioning of the main part of linac has been started.

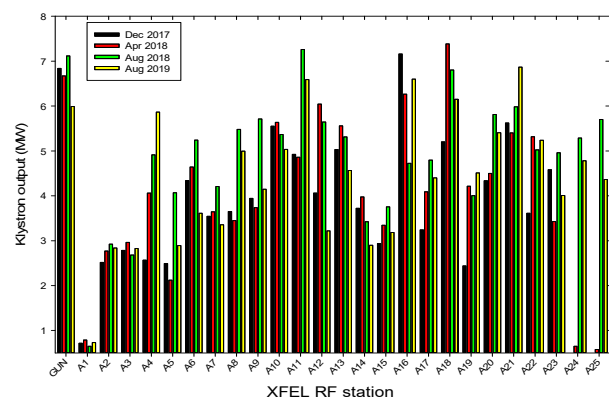


Figure 2: Output power for each of MBK.

In beginning of 2018 the commissioning of last two RF stations was done and in July 2018 the XFEL reached the design energy of 17.5 GeV. Figure 2 shows the output RF power for each of RF station. The average power from one MBK is 4.87 MW, but for several of RF stations the level of output power are more than 7 MW. Figure 3 shows the high voltage level for each of RF stations. In average the high voltage is 104.5 kV. For the moment we don't have any limitation for XFEL operation from RF stations, the level of RF power from each of RF stations are determinates by XFEL longitudinal beam dynamics and bunch compression system.

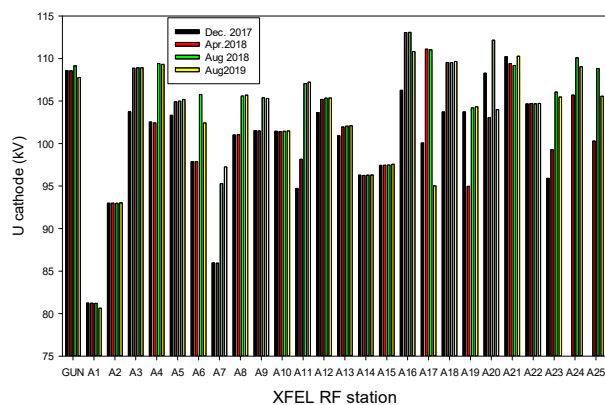


Figure 3: Cathode voltage for each of RF stations.

PROTECTION SYSTEM AND OPERATING STATISTICS

To make the operation of XFEL more reliable and increase the lifetime of the MBKs, in addition to the common interlock system since middle of 2018 we have started to use a fast protection system (KLM) [9 and 10] that was developed and tested during MBKs initial tests. The fast protection system is based on the comparison of the actual RF shape and the expected RF shape. In the case of a difference exceeding a certain margin, for example, in the case of RF breakdown in a klystron or RF breakdown in a waveguide system (WGS), the KLM faster than 800 ns, switches off the input RF signal. Thus, it does prevent the vacuum level in the klystron to worsen too much or it minimizes the RF overvoltage time at the output windows of the klystron in case of breakdown in WGS. The KLM system includes the partial discharge measurement in all of HV parts of RF station. Especially we were worry about life time of enough new HV components which were developed during MBKs test. To be sure that we don't have any degradation in HV system one of HV cable from RF station A19.L3 after 11000 hours of operation on HV level of 104,5 kV, was sent back to factory. The factory test has confirmed the good state of this cable and HV connectors; the level of partial discharge was the same as just after initial cable test. The test of HV quality of CM will be possible to make only after one of MBK will be for some reason removed from XFEL tunnel because CM and MBK can't be separated without working with open transformer oil in the tunnel. Figure 4 shows the number of events that have happened inside of MBKs since beginning of 2017. The most parts of events are the high voltage breakdowns in the gun area of klystrons, usually this type of breakdowns doesn't show the big increasing of vacuum level in the tubes, in contrast with RF breakdown inside of tube, where the vacuum level in the klystron greatly increases and it can provoke the arc in the gun area or, if vacuum level becomes very big, the main interlock system switched off the filament for this tube. For the filament recovery procedure for our type of MBKs it needs at least one hour. In this case it is very important to switch off the drive signal fast. Since the KLM system for MBKs has

been implemented as routine for XFEL operation (08/2018), the number of cases of filament recovery was reduced noticeably.

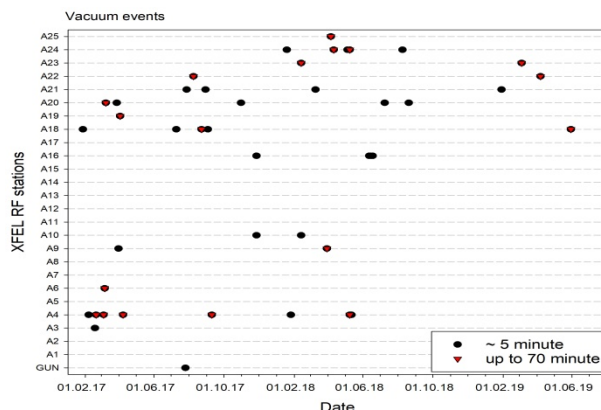


Figure 4: Gun HV arcing and RF breakdowns in XFEL MBKs.

Figure 5 shows the number of events that happened inside MBKs for full 2017 and 2018 years and in comparison the events number for 8 months of 2019, one can see that in the beginning of XFEL operation during the conditioning period the number of events are greater than we have in this year. This is in the good agreement with what was expected. But we also expect that in future the number of events in the klystrons will increase. The good way to reduce the number of events in the future is the reducing the cathode voltage and klystron output power and this is possible using developed in 2010 in DESY the phase modulation procedure [11]. It is the method of changing of the klystron output phase which allows decreasing the required klystron peak power by reducing the reflected power during cavity filling time.

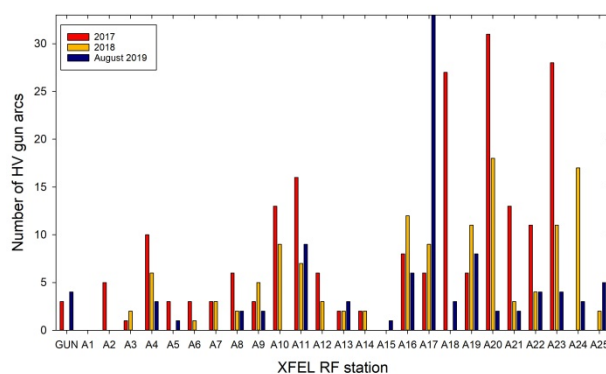


Figure 5: Number of HV arcs in the klystrons guns.

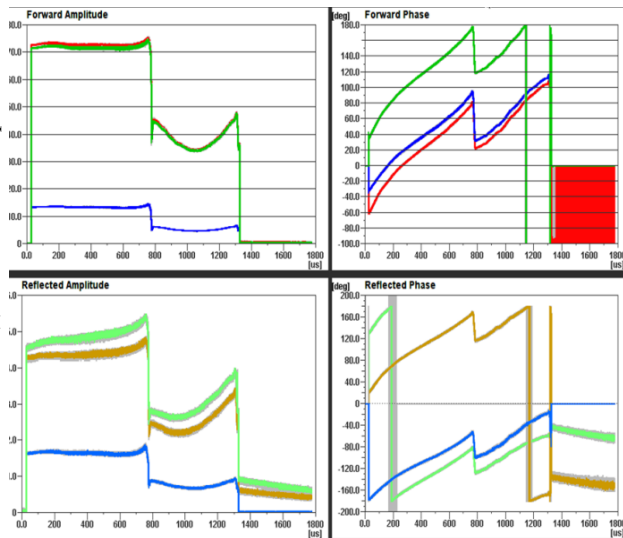


Figure 6: The output RF shapes of MBK in case of using phase modulation.

In case of phase modulation we can get the same gradient in the accelerate cavity but using up to 20% less RF power or, in case of using the same power level, we can reduce cavity filling time. Figure 6 shows RF shapes for amplitude and phase on the klystrons output in case of using phase modulation.

CONCLUSION

In February 2008 the first prototypes of MBK for XFEL had been installed on the MBK test stand DESY. Since August 2012 we have started a test and conditioning of the first one from 27 series MBKs for XFEL. The klystrons were tested together with connection modules (CM) and with different types of HV cables. To increase the lifetime of klystron a special fast protection system (KLM) was designed and tested. In March 2015 we started the installation of MBK to the XFEL tunnel. In July 2018 XFEL reached the design energy of 17.5 GeV. For the moment 26 XFEL RF stations produce 4.87 MW in average, the average cathode voltage is 104.5 kV, RF and HV breakdown rate for the MBK during last 8 months is 0.47 breakdowns per day. For the moment the XFEL operators can get as much RF power from MBKs as it is necessary for current mode of XFEL operation.

REFERENCES

- [1] M. Atarelli *et al.* (Eds.), “XFEL: The European X-Ray “Free-Electron Laser: Technical Design Report”, DESY 2006-097, July 2006.
- [2] A. Beunas, G. Faillon, “10MW/1.5ms, L band multi beam klystron”, *Proc. Conf. Displays and Vacuum Electronics*, Garmisch-Partenkirchen, Germany, April 29-30, 1998.
- [3] V. Vogel *et al.*, “Testing of 10MW Multibeam Klystrons for the European X-Ray FEL at DESY”, in *Proc. PAC07*, Albuquerque, NM, USA, Jun. 2007, paper WEPMN013, pp. 2077-2079.
- [4] A. Yano *et al.*, “The Toshiba E3736 Multi-Beam-Klystron”, in *Proc. LINAC’04*, Lübeck, Germany, Aug. 2004, paper THP45, pp. 706-708.
- [5] V. Vogel and S. Choroba, “Status of Horizontal MBK for XFEL”, http://www.xfel.eu/project/meetings/project_meetings/2009
- [6] V. Vogel *et al.*, “Connection Module for the European X-ray FEL 10MW Horizontal Multibeam Klystron”, in *Proc. IPAC’10*, Kyoto, Japan, May 2010, paper THPEB043, pp. 3978-3980.
- [7] P. Bak, V. Zabrodin, A. Korepanov and V. Vogel, “Klystron Cathode Heater Power Supply System Based on the High-Voltage Gap Transformer”, in *Proc. PAC’09*, Vancouver, Canada, May 2009, paper TU6RFP016, pp. 1562-1564.
- [8] V. Vogel and S. Choroba, “Status of Multi-Beam Klystrons”, presented at 51th ILC DESY General Project Meeting”, Jan. 2007, <https://agenda.linearcollider.org/event/1318>
- [9] V. Vogel, “MBK protection”, LLRF Seminar, 2008, <http://ttfinfo.desy.de/LLRFelog/index.jsp>
- [10] V. Vogel *et al.*, “Summary of the test and installation of 10 MW MBKS for the XFEL project”, in *Proc. LINAC’16*, East Lansing, MI, USA, Sep. 2016, pp. 506-508, doi:10.18429/JACoW-LINAC2016-TUPLR017
- [11] V. Ayvazyan *et al.*, “Optimization of felling procedure for TESLA-type cavities for klystron RF power minimization for European XFEL”, in *Proc. IPAC’10*, Kyoto, Japan, May 2010, paper TUPEA039, pp. 1416-1418.

THE EUROPEAN XFEL PHOTOCATHODE LASER

L. Winkelmann, A. Choudhuri[†], H. Chu, I. Hartl, C. Li, C. Mohr, J. Mueller, F. Peters,
S. Pfeiffer, S. Salman, U. Grosse-Wortmann, ,
Deutsches Elektronen-Synchrotron (DESY), Hamburg, Germany

Abstract

We present the design, performance and long-term stability of the hybrid Yb: fiber, Nd:YVO₄ laser system used to drive the RF photocathode gun and laser heater at the European XFEL facility. The laser system provides deep UV output pulses in 600 μ s long bursts of laser pulses with variable intra-burst repetition rates ranging from 500 kHz to 4.5 MHz. Due to its robust laser architecture, comprised of a mode-locked and synchronized Yb: fiber oscillator, Yb: fiber pre-amplifiers and Nd:YVO₄ power amplifiers, the laser has operated with >99% uptime since January 2017. Using this laser system, the European XFEL reported landmark electron beam energies of 17.5 GeV in July 2018, and simultaneous multi-mJ lasing in its three SASE beamlines. The photocathode laser system offers two parallel outputs, each providing pulses of >100 μ J energy and 11 ps FWHM duration at 1064 nm center wavelength. One output is converted to the deep UV (266 nm) with conversion efficiencies > 25%. The second beam is sent to a laser heater to reduce microbunching instabilities, increasing the SASE efficiency. For efficient XFEL operation several state-of-art laser controls were implemented, such as: feed-forward algorithm to flatten electron charge along the bunch, active beam stabilization with < +/-10 μ m beam pointing jitter at the photocathode, state machines for hands-off operation, temporal pulse synchronization and drift compensation. The latter reduces the timing jitter of the electron bunches to less than 45 fs rms.

INTRODUCTION

The high availability requirements of the photocathode injector laser (>8000 hours of 24/7 operation) [1] for the European XFEL merited the installation of a second laser system, based on high-gain Nd:YVO₄ material to act as a “hot swap” backup in case of failure or temporary downtime of the already existing complex chirped pulse amplifier (CPA) Yb:YAG laser system in 2017. This simpler non-CPA Nd:YVO₄ system was designed for producing all required laser parameters for European XFEL operation with exception of an experimental 3 ps “short pulse” mode with high availability and low jitter. After the integration of the Nd:YVO₄ laser into the XFEL injector, its demonstrated robust performance (>99% uptime for 2018) made the Nd:YVO₄ system the primary driving laser for the XFEL. This paper focuses on key technology developments for the injector laser beamline that enable delivery of laser light to the cathode with high reliability and stability.

THE SYSTEM

Both European XFEL photocathode laser systems offer two outputs, for electron gun (UV) and laser heater (NIR), respectively. Relevant laser parameters are provided in Table 1. The UV and NIR outputs from both lasers are multiplexed; with one laser blocked during normal operation. We also can produce complex bunch trains by simultaneously using both sources. A schematic system overview is provided in Figure 1.

Table 1: Summary of Laser Parameters.

Parameter	Nd:YVO ₄ Laser	Yb:YAG Laser
Oscillator Type	Yb: fiber	Yb:YAG
Amplifier Type	Nd:YVO ₄	Yb:YAG
IR Wavelength	1064 nm	1032 nm
UV Wavelength	266 nm	257 nm
Pulse Width (UV)	8 ps	Short pulse: 3 ps Long pulse: 12 ps
Intra burst repetition rate	500 kHz, 1.13 MHz, 2.25 MHz, 4.5 MHz	
Energy (UV)	>5 μ J / pulse	>3 μ J / pulse
Energy (IR)	50 μ J / pulse	

The Nd:YVO₄ system consist of three modules (see Figure 1): a frontend oscillator module, a pulse picking and amplification module, and a frequency conversion module [2].

The oscillator is a saturable absorber-modelocked polarization maintaining (pm) Yb: fiber linear cavity design, dispersion managed and wavelength stabilized by a chirped fiber Bragg grating centered at 1064 nm. The cavity is synchronized to the main RF timing of the European XFEL using slow and fast PZT actuators. Control circuits monitor the oscillator’s mode-locking state, carrier power and noise levels. A fiber-coupled acousto optic modulator (AOM) after the oscillator is used to pick pulses at the user-selected intra burst repetition rate (see Table 1) out of the 54 MHz repetition rate oscillator signal. The picked pulses are then amplified to ~1.2 μ J/pulse in cascaded pm-Yb: fiber and Nd:YVO₄ amplifiers.

The picked pulses enter the amplification module, where a second AOM is used to cut out 10 Hz bursts from the pulse train (to generate electron bunches with 10Hz burst repetition rate), to further amplify the pulses in the first Nd:YVO₄ power amplifier to ~8.5 μ J.

[†] ara.choudhuri@desy.de

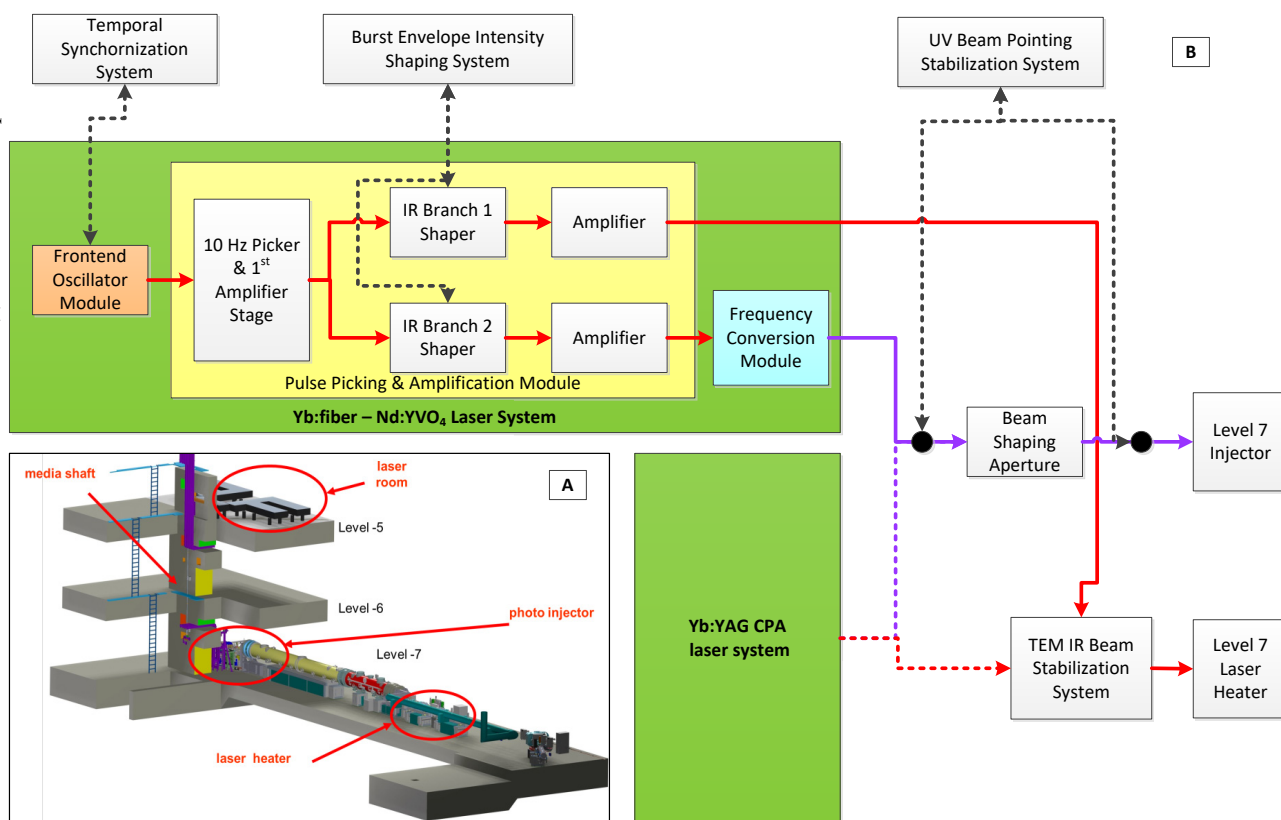


Figure 1A: Injector Building Layout, 1B: Injector Laser System.

The 8.5μJ pulses are split into two parallel arms, additional AOMs shape the burst intensity envelope to a desired profile and a second Nd:YVO₄ power amplifier boosts the pulse energy to the operation point of ~50 μJ/pulse in each arm. All Nd:YVO₄ gain blocks are designed and manufactured by neoLASE GmbH.

One output arm is converted to 266nm via a two-stage second harmonic generation (SHG) process: 1064 → 532nm in 6mm critically phase-matched Lithium Borate (LBO) followed by 532nm → 266nm in 2mm beta Barium Borate (BBO). This process occurs in a purged and sealed, 250x400mm module with motorized linear and rotational stages for remote movement of the nonlinear crystals. Dichroic mirrors are used to filter out remaining 532 nm radiation. The overall 1064 nm → 266 nm conversion efficiency is ~25%.

The UV and NIR beams are then transported from the laser lab in level -5 of the European XFEL injector building to the photo injector & laser heater housed in level -7. The UV beamline consists of multiple beam stabilization stages, variable attenuator, a beam-shaping aperture which cuts the beam profile from a Gaussian to a flat-top beam, shutters controlled by the XFEL Machine Protection System, and shutters controlled by the laser and personnel safety interlock systems.

CHARGE PROFILE SHAPING VIA A FEED-FORWARD ALGORITHM

Electron bunch-to-bunch charge fluctuations are undesirable for XFEL operation. As the burst operation of the injector laser leads to variable inversion efficiency over each pump cycle, and creates a temperature ramp of 100ms within the burst, the intensity of the UV pulses over a burst varies along the burst, despite constant seed pulse energy [3]. A charge feed-forward system is implemented where the electron charge profile over the burst is flattened by controlling the individual pulse intensities after the first main amplifier stage. A FPGA-controlled fast digital to analog (DAC) convertor is used to amplitude-modulate the RF driver of the AOM on the UV branch, which in turn modulates the transparency of the AOM and shapes the intensity profile of the laser pulses over the burst.

A control accuracy of the AOM's diffraction efficiency of better than 0.1% at a maximum diffraction efficiency of 70% has been achieved, with a measured charge stability at the XFEL electron gun of 0.7% rms, (consistent to the measured single pulse stability of 0.6% rms within each laser burst).

TEMPORAL SYNCHRONIZATION

The stability of the arrival time of the laser pulse train at the photocathode is critical for overall FEL synchronization performance. A Phase Locked Loop (PLL)

type scheme is used to lock the Nd:YVO₄ oscillator repetition rate's 25th harmonic (1354 MHz) to the main RF master oscillator running at a RF cavity resonance frequency of 1.3 GHz. In addition, a balanced optical cross-correlation scheme was employed to identify residual timing drifts of the oscillator with respect to an optical reference delivered by a stabilized optical fiber link [4]. The measured drifts are then compensated by acting on the set-point within the oscillator RF synchronization loop resulting in an electron bunch arrival time of 45 fs over 8 hours. (Fig.2)

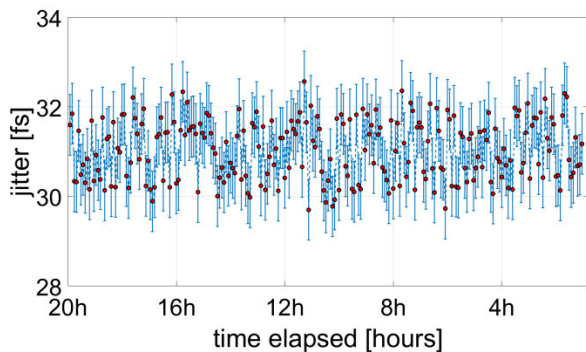


Figure 2: Timing jitter of phase-locked oscillator, mid 2019.

ACTIVE BEAM STABILIZATION

The relay-imaged UV beamline incorporates two active beam pointing stabilization systems at both ends of the beamline. The IR beamline transports a collimated beam and uses a active beam routing and stabilization system.

UV Gun Laser Stabilization

Requirements for the laser spot position on the photocathode are 5% of the beam spot [5], which can vary from 0.1mm to 3mm diameter depending on the aperture settings, with an option to scan the beam over the photocathode. As the laser is relay imaged from the laser room through a non-climate-controlled tunnel shaft in 22m vacuum beam-line, an active beam pointing stabilization system to correct for drifts is essential. The UV wavelength, high robustness, 24/7 uptime and radiation tolerance constrains eliminate most commercial options.

Each stabilization system consists of two actuated mirrors, and two UV cameras in a lead-shielded housing. The image on the cameras is processed (filtered for noise-reduction, binarization, edge-detection and small spot removal) and a first-order moment method is used to determine the centroid, and checks performed to eliminate spurious beam-steering inputs. The mirror-to-camera position transfer matrix was determined during characterization, and is used to drive actuators for a fast-converging steering algorithm. Step-size and error thresholds can be dynamically set to reduce large movements of the beam during the steering process, and to eliminate jerky transitions. The high dynamic range seen by the system during operation (from single bunch operation to bursts consisting of 2700 bunches) requires dynamic

changes to the camera exposure and gain settings to prevent saturation and errors in centroid calculation when switching from a high number to a low number of bunches.

IR Laser Heater Stabilization

The IR laser light is collimated in the level -5 laser lab and transported to injector level -7 over a 46 meter beam-line to the laser heater. System requirements call for less than 10 μ m jitter in spot position at the laser heater.

The stabilization system (ALIGNA, TEM Messtechnik) combines an angle and position detector with seven active mirrors forming a feedback loop to suppress thermal drifts and jitter.

Input rms error of ~ 0.015 mrad results in max 30 μ m rms error at the far end without active beam stabilization. With active stabilization, the same input provides max 7.5 μ m rms error (see Figure 3).

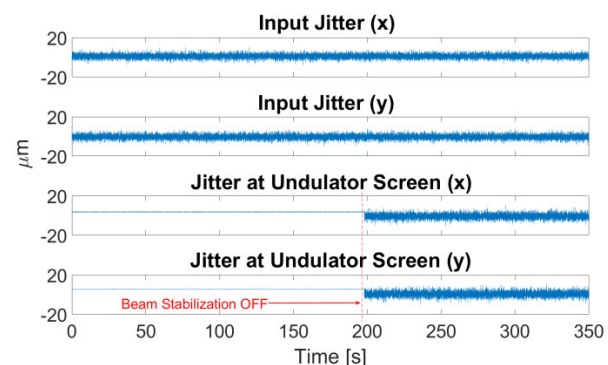


Figure 3: Impact of active stabilization system on laser heater beam.

CONCLUSIONS

We report on a simple and robust hybrid non-CPA Yb: fiber - Nd:YVO₄ laser system, which drives both photocathode and laser heater of the European XFEL facility with 99% availability since 2017. High stability is achieved both by robust design of laser and beam-transport as well as several feedback loops which correct for drifts in pulse energy, timing and pointing. This system is basis for an more complex CPA laser system under current development, which will additionally provide programmable UV pulse durations from 1 – 15 ps FWHM using spectral pulse shaping and larger bandwidth Yb:YAG gain blocks.

REFERENCES

- [1] L. Winkelmann, "Photocathode lasers for free-electron lasers." in *2017 Conference on Lasers and Electro-Optics*, pp. 1-2, IEEE, 2017.
doi:10.1364/CLEO_AT.2017.JTu4L.1
- [2] L. Chen, L. Winkelmann, I. Hartl, "Flexible Pulse-Shape Picosecond Front-End for XFEL Photocathode Lasers." In *CLEO: Science and Innovations*, 2019, pp. SF3I-4.
doi:10.1364/CLEO_SI.2019.SF3I.4
- [3] L. Winkelmann, C. Mohr, S. Pfeiffer, H. Chu, S. Salman, U. Grosse-Wortmann, I. Hartl, "Flexible Pulse-Train Amplitude Shaping for the European XFEL Photoinjector Laser." *8th EPS-QEoD Europhoton Conference*, Barcelona, Spain. September 2018. Talk ThA1.8
- [4] J. Müller, S. Schulz, L. Winkelmann, M. Czwalińska, I. Hartl, H. Schlarb, "Arrival Time Stabilization of the Photocathode Laser at the European XFEL." In *CLEO: Science and Innovations*, pp. SF3I-6, 2019.
doi:10.1364/CLEO_SI.2019.SF3I.6
- [5] F. Kaiser, S. Köhler, F. Peters, L. Winkelmann, I. Hartl, "UV laser beam stabilization system for the European XFEL electron injector laser beamline." In *CLEO: Applications and Technology*, pp. JTh2A-99. Optical Society of America, 2015.
doi:10.1364/CLEO_AT.2015.JTh2A.99

UPDATE ON THE PHOTOCATHODE LIFETIME AT FLASH AND EUROPEAN XFEL

S. Lederer*, F. Brinker, S. Schreiber,
Deutsches Elektronen-Synchrotron, Hamburg, Germany
L. Monaco, D. Sertore,
INFN Milano - LASA, Segrate, Italy

Abstract

The photoinjectors of FLASH and the European XFEL at DESY (Hamburg, Germany) are operated by laser driven RF-guns. In both facilities Cs₂Te photocathodes are successfully used. In this paper we give an update on the lifetime, quantum efficiency (QE), and dark current of the photocathodes used over the last years. At FLASH cathode #73.3 was operated for a record lifetime of 1413 days and was replaced December 2018 by cathode #105.2. At the European XFEL cathode #680.1 is in operation since December 2015, for 1356 days up to now.

INTRODUCTION

At DESY (Hamburg, Germany) two free-electron laser user facilities are operated. Since 2005 FLASH [1–4] delivers successfully high brilliance femtosecond short XUV and soft X-ray SASE to photon experiments. Based on TESLA type superconducting linac technology, FLASH is able to accelerate in burst mode several thousand electron bunches per second. The macro-pulse repetition rate is 10 Hz with a useable length of the RF pulses of maximal 800 μ s. With a micro-bunch frequency of 1 MHz up to 8000 bunches per second can be accelerated at FLASH, limited by the present laser systems. The bunch charge depends on the requirements on the FEL-light and is usually within a span of 20 pC to 1 nC. After acceleration to 1.25 GeV, the electron bunches are distributed into two different undulator beamlines. While the FLASH1 beamline utilizes fixed gap undulators, the FLASH2 beamline is equipped with variable gap undulators.

The second FEL user facility operated at DESY is the European XFEL [5]. It aims for the delivery of high brilliance femtosecond short X-ray pulses in the energy range of 0.25 to 25 keV. As FLASH, the European XFEL uses TESLA type superconducting linac technology with 10 Hz macro-pulse repetition rate. With a micro-bunch frequency of up to 4.5 MHz and an RF-pulse length of 600 μ s, the European XFEL can deliver 27000 bunches per second. Downstream the accelerator the beam can be distributed to three variable gap undulator sections generating the desired SASE light. After the successful commissioning of the accelerator in 2016 [6] and first lasing in May 2017 [7], the first user periods have been successfully accomplished [8].

THE ELECTRON SOURCES

The photoinjectors of FLASH and the European XFEL are very similar. They are both driven by a normal conducting 1.5 cell 1.3 GHz L-band RF-gun, based on the design by [9]. Currently the accelerating field at the photocathode during standard operation at FLASH is 52 MV/m and 54 MV/m for the European XFEL respectively. The complete gun set-ups are dedicated to be interchangeable between both facilities.

Since August 2013 Gun3.1 is operated at FLASH [10]. The first RF-gun operated at the European XFEL was Gun4.3. It was installed in 2013 and operated during the commissioning phase and the first user runs. In December 2017 it was exchanged with Gun4.6 and serves now as hot spare.

In both facilities the electron bunches are generated inside the RF-gun by means of photoemission. The drive lasers at FLASH operate at a wavelength of 262 nm and 257 nm [11], the two lasers at the European XFEL at 257 nm and 266 nm. The vacuum pressure in the RF-guns during operation is in the lower 10^{-9} mbar regime or better. The good vacuum condition allows for the operation of Cs₂Te as photocathode emitting material. The high quantum efficiency (QE) of this material in the UV keeps the required average laser power in a reasonable regime.

The photocathodes are either prepared at INFN-LASA in Milano, Italy, [12] or at DESY. Transfer to the accelerators is done with UHV transport boxes, maintaining a pressure in the low 10^{-10} mbar range. The transport boxes can be equipped with up to four cathodes.

In both facilities a very similar load-lock transfer system is used to insert the Cs₂Te photocathodes under the required UHV conditions into the RF guns [12].

QE AND LIFETIME

QE measurement procedure

To monitor the photocathode performance we perform QE measurements on a regularly bases, if the operational schedules allow. For monitoring purposes the QE is measured always under comparable conditions. The on-crest accelerating field during the measurements is in the order of 52 MV/m. The launch phase is set to 38° w.r.t. zero crossing. This phase was chosen years ago and kept as reference for the QE measurements. It is neither the on-crest phase nor the launch phase during standard operation of the accelerators. On-crest, about 30% more charge is extracted than at 38°.

To determine the QE we measure the charge as function of the laser energy. The charge is measured by means of a toroid

* sven.lederer@desy.de

right after the RF-gun (uncertainty 1%). At FLASH the laser energy is measured by means of a calibrated joulemeter in front of the vacuum window (uncertainty 2%). At the European XFEL the measurement is done by a photo diode which is cross-calibrated with a pyroelectric detector. To obtain the laser energy at the cathode the transmission of the vacuum window and the reflectivity of the in-vacuum mirror are taken into account in the data analysis.

From the linear slope of the charge vs. laser energy data in the not space charge limited regime we calculate the QE [13]. Typical laser spot diameters at the photocathodes during the measurements are 1 to 1.2 mm.

Lifetime at European XFEL

Figure 1 shows the quantum efficiency of cathode #680.1 over time. The cathode is operated at the European XFEL since 2015.

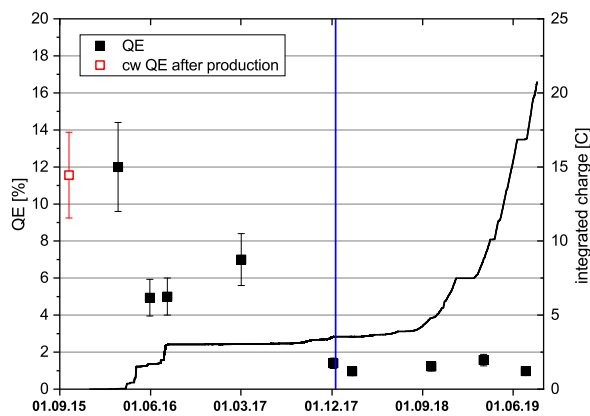


Figure 1: Quantum efficiency (black squares) and integrated charge vs. time for cathode #680.1, operated at European XFEL. The red data point shows the QE right after production in September 2015 measured with Hg-lamp at 254 nm. The vertical blue line marks the change of RF-guns.

Over the first months of operation the quantum efficiency dropped quite a lot but since then is stable. During operation in the first RF-gun of the European XFEL (Gun4.3) around 3.5 C have been extracted from the cathode. Since Gun4.6 is operated up to now 17.2 C have been extracted from cathode #680.1. Overall the cathode is in usage for 1356 days up to now.

Lifetime at FLASH

In the past 4 years at FLASH only two cathodes have been operated. From February 2015 to December 2018 cathode #73.3 was used for a record of 1413 days.

In Fig. 2 the QE of cathode #73.3 as well as the integrated extracted charge are shown over the whole operation time. Even after the 1413 days of usage the QE was still in the order of 4%.

In addition to the regular QE measurements at FLASH, the homogeneity of electron emission from the photocathodes

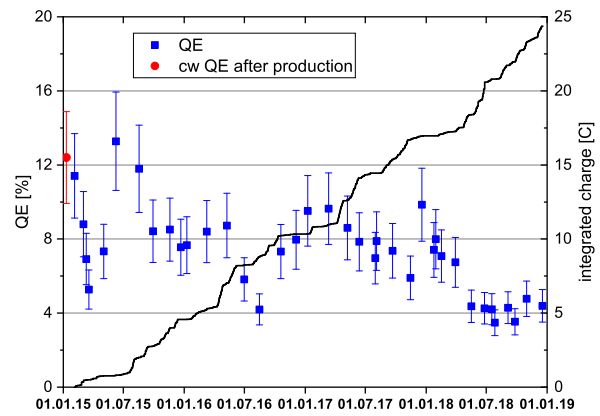


Figure 2: Quantum efficiency (blue squares) and integrated charge vs. time for cathode #73.3, operated at FLASH from February 2015 to December 2018. The red data point shows the QE right after production 23-May-2013, measured with Hg-lamp at 254 nm.

is studied by QE-maps. For this investigations a small spot laser beam (100 μm) is scanned over the cathode and the emitted charge is measured with a high resolution toroid (detection threshold <1 pC). The laser energy is adjusted to generate a maximum charge of 10 to 30 pC.

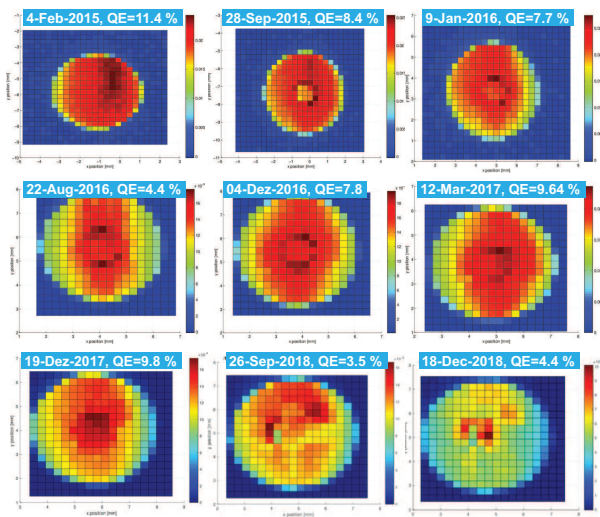


Figure 3: QE-map evolution of cathode #73.3 from February 2015 to December 2018.

In Fig. 3 the evolution of QE-maps of cathode #73.3 is shown. Starting from a homogeneous emission over the whole cathode, over the first months we observe a decrease of QE at the place where the laser hits the cathode. After further operation the picture changes in a way that the point, where the laser impinges, shows higher QE than the rest of the cathodes [10, 14, 15]. In 2018 we observed a severe increase in non-uniformity, resulting in small spots of high QE. This, and not a too low QE, yielded in the decision to exchange the cathode with #105.2 in December 2018.

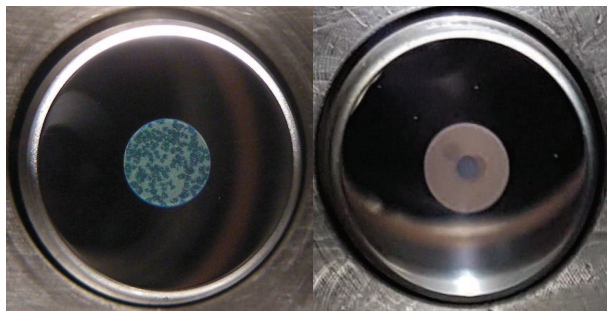


Figure 4: Pictures of cathode #73.3 in the transport box right after deposition in July 2013 (left) and after usage in December 2018 (right).

In Fig. 4 pictures of cathode #73.3 in the transport box are shown. The left one was taken after the production of the cathode in July 2013, the right one after the extraction from Gun3.1 at FLASH in December 2018. The points where the laser usually hits the cathode during operation are clearly visible. But despite of this we can not observe severe irregularities like on other cathodes (see [16]) which could explain the spots in the QE maps.

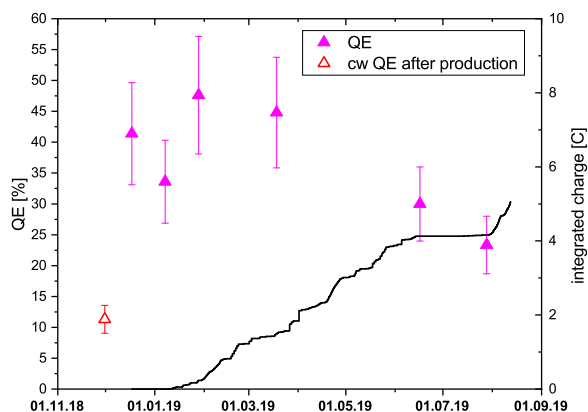


Figure 5: Quantum efficiency (magenta triangles) and integrated charge vs. time for cathode #105.2, operated at FLASH since December 2018. The red data point shows the QE right after production measured 6-Jun-2013 with a Hg-lamp at 254 nm.

Figure 5 shows the QE as well as the integrated charge over time for the new cathode, #105.2. The quantum efficiency obtained for this cathode is remarkable high. Even though it was produced in 2013 the first QE measured in the FLASH RF-gun was about 40%. The big difference between the cw QE and the pulsed QE as well as the high numbers is not understood and under investigation.

SUMMARY

The Cs₂Te photocathodes operated at FLASH and the European XFEL during the last years show a remarkable lifetime. Cathode #680.1 is in use at European XFEL for 1356 days with a total extracted charge of 20.7 C. An even

longer operational time was obtained for cathode #73.3 at FLASH. This cathode was in use for 1413 days and a charge of 24.4 C has been extracted. Since December 2018 cathode #105.2 is operated at FLASH, showing a remarkable high quantum efficiency.

REFERENCES

- [1] W. Ackermann *et al.*, “Operation of a free-electron laser from the extreme ultraviolet to the water window”, *Nature Photonics*, vol. 1, p. 336, 2007. doi:10.1038/nphoton.2007.76
- [2] S. Schreiber, and B. Faatz, “The free-electron Laser FLASH”, *High Power Laser Science and Engineering*, vol. 3, p. e20, 2015. doi:10.1017/hpl.2015.16
- [3] B. Faatz, *et al.*, “Simultaneous operation of two soft x-ray free-electron lasers driven by one linear accelerator”, *New J. Phys.*, vol. 18, p. 062002, 2016. doi:10.1088/1367-2630/18/6/062002
- [4] K. Honkavaara, “Status of the FLASH FEL User Facility at DESY”, in *Proc. FEL’17*, pp. 14–18. doi:10.18429/JACoW-FEL2017-MOD02
- [5] M. Altarelli *et al.* ED., “The European X-Ray Free-Electron Laser - Technical design report”, DESY, Hamburg, Germany, Rep. DESY 2006-097, July 2007.
- [6] W. Decking, and H. Weise, “Commissioning of the European XFEL Accelerator”, in *Proc. IPAC’17*, pp. 1–6. doi:10.18429/JACoW-IPAC2017-MOXA1
- [7] H. Weise and W. Decking, “Commissioning and First Lasing of the European XFEL”, in *Proc. FEL’17*, pp. 9–13. doi:10.18429/JACoW-FEL2017-MOC03
- [8] W. Decking *et al.*, “Status of the European XFEL”, in *Proc. IPAC’19*, pp. 1721–1723. doi:10.18429/JACoW-IPAC2019-TUPRB020
- [9] B. Dwersteg, K. Flöttmann, J. Sekutowicz, and Ch. Stolzenburg, “RF gun design for the TESLA VUV Free Electron Laser”, *NIM A393*, pp. 93–95, 1997. doi:10.1016/S0168-9002(97)00434-8
- [10] S. Lederer and S. Schreiber, “Cs₂Te Photocathode Lifetime at Flash and European XFEL”, in *Proc. IPAC’18*, pp. 2496–2498. doi:10.18429/JACoW-IPAC2018-WEPMF056
- [11] S. Schreiber, C. Gruen, K. Klose, J. Roensch, and B. Steffen, “Simultaneous Operation of Three Laser Systems at the FLASH Photoinjector”, in *Proc. FEL’15*, Daejeon, Korea, Aug. 2015, paper TUP041, pp. 459–463. doi:10.18429/JACoW-FEL2015-TUP041
- [12] S. Schreiber, P. Michelato, L. Monaco, and D. Sertore, “On the Photocathodes Used at the TTF Photoinjector”, in *Proc. PAC’03*, pp. 2071–2073, paper WPAB016.
- [13] S. Lederer *et al.*, “Photocathode Studies at FLASH” in *Proc. EPAC’08*, pp. 232–234, paper MOPC072.
- [14] S. Schreiber and S. Lederer, “Lifetime of Cs₂Te Cathodes Operated at the FLASH Facility”, in *Proc. FEL’15*, pp. 464–467, paper TUP042. doi:10.18429/JACoW-FEL2015-TUP042
- [15] P. Michelato *et al.*, “Cs₂Te Photocathode Robustness Studies”, in *Proc. EPAC’08*, pp. 241–243, paper MOPC075.
- [16] S. Schreiber *et al.*, “Photocathodes at FLASH”, in *Proc. IPAC’12*, pp. 625–627, paper MOPPP029.

FLASH PHOTOINJECTOR LASER SYSTEMS

S. Schreiber*, K. Klose, C. Grün, J. Rönsch-Schulenburg, B. Steffen, DESY, Hamburg, Germany

Abstract

The free-electron laser facility FLASH at DESY (Hamburg, Germany) operates two undulator beamlines simultaneously for FEL operation and a third for plasma acceleration experiments (FLASHForward). The L-band superconducting technology allows accelerating fields of up to 0.8 ms in length at a repetition rate of 10 Hz (burst mode). A fast kicker-septum system picks one part of the electron bunch train and kicks it to the second beamline such that two beamlines are operated simultaneously with the full repetition rate of 10 Hz. The photoinjector operates three laser systems. They have different pulse duration and transverse shapes and are chosen to serve best for the given user experiment in terms of electron bunch charge, bunch compression, and bunch pattern. It is also possible to operate the laser systems on the same beamline to provide specific double pulses for certain type of experiments.

INTRODUCTION

FLASH, the free-electron laser (FEL) user facility at DESY (Hamburg) [1–3] simultaneously operates two undulator beamlines [4,5]. It delivers high brilliance XUV and soft X-ray SASE radiation to photon experiments. FLASH is a user facility since 2005. [6]

A unique feature of FLASH is its superconducting accelerating technology. It allows to accelerate several thousand electron bunches per second. The bunches come in bursts with a duration of 0.8 ms and a repetition rate of 10 Hz. The laser systems of the photoinjector have to produce as many bunches within the burst as possible. For FLASH, the intra-burst repetition rate delivered to user experiments is 1 MHz and lower. Some experiments ask for 100 kHz, photon hungry experiments are able to take higher repetition rates.

An important feature of FLASH is, that one part of the burst is delivered to users at the FLASH1 beamline, the second part to users at the FLASH2 beamline. In order to serve different kind of experiments, the properties of the electron bunches usually differ between the two parts of the burst in charge, duration, and pulse pattern. [7] Therefore, FLASH has three photoinjector lasers running simultaneously on operator chosen beamlines. [8] Two lasers provide bursts of laser pulses with high single pulse energy but fixed single pulse duration. A third system has the feature of short and variable pulse duration optimized for high compression for ultra-short single spike SASE photon pulses, as an example.

THE ELECTRON SOURCE

The electron source of FLASH is a photoinjector based on a normal conducting L-band 1.5 cell RF-gun. The gun

is operated with an RF power of 5 MW at 1.3 GHz, with an RF pulse duration of 650 μ s at a repetition rate of 10 Hz.

Since FLASH can accelerate many thousands of electron bunches per second with a charge of up to 2 nC, the quantum efficiency of the photocathode must be in the order of a few percent in order to keep the average laser power at an acceptable limit. Cesium telluride has been proven to be a reliable and stable cathode material with a quantum efficiency (QE) well above 5 % for a wavelength in the UV (around 260 nm). The lifetime is much longer than 1000 days of continuous operation. [9] To give an idea of the required laser single pulse energy, as an example, for a bunch charge of 1 nC and a QE of 1 % a single pulse energy of 0.5 μ J is required. For 10,000 bunches per second this corresponds to a reasonable intra-train power of 0.5 W (1 ms burst) and an average power of 5 mW in the UV.

The actual challenge for the laser systems is its burst mode structure with 1 ms long flat bursts of laser pulses. Flat in terms of single pulse energy and arrival time at the RF-gun. A feature is implemented to apply a linear slope over the laser pulse train using the phase of the 1.3 GHz synchronization RF. This is used to compensate possible arrival time slopes in respect the the accelerator due to heating of the BBO crystal along the burst (green to UV conversion). The pulse duration of the laser pulses must be in the order of a few degrees in 1.3 GHz RF phase. An optimum duration for longitudinal Gaussian shaped pulses is $\sigma = 5$ to 10 ps and 1 ps for ultra-short pulse operation.

Since FLASH delivers SASE pulses below 100 fs in duration, the required arrival time stability must be better than 50 fs (rms). This is achieved by synchronizing the laser oscillator with an external ultra-stable 1.3 GHz RF-source. The lasers are cross-correlated with the master laser oscillator of the FLASH synchronization system [10, 11] to measure the stability and to realize a slow feedback to compensate slow drifts.

THE LASER SYSTEMS

Laser 1 and Laser 2

The two laser systems [12] described in this section have been installed in 2010 [13] and 2012, and are a substantial upgrade compared to the previous lasers in operation at FLASH and the former TESLA Test facility (TTF) [14, 15]. The lasers have been developed in the Max Born Institute, Germany partially tested at DESY (Zeuthen, PITZ) and finally installed at FLASH.

The layout of both Laser 1 and Laser 2 are very similar. Both systems consist of a pulsed laser oscillator with subsequent amplification stages. A recent description of the laser systems can be found in [8, 16]. The laser material is Nd:YLF lasing at a wavelength of 1047 nm. Nd:YLF has a high gain and a long upper-state lifetime of 480 μ s, and

* siegfried.schreiber@desy.de

exhibits only weak thermal lensing. This makes it suitable to produce pulse trains with milliseconds in duration. After amplification, the wavelength is converted into the UV wavelength of 262 nm in two steps using an LBO and a BBO crystal. Figure 1 shows an example of a scope trace of a laser pulse train (burst). The lasers are equipped with two Pockels cell based pulse pickers before and after the pre-amplification stages. The one before the pre-amplifier is operated at a constant 1 MHz, the second just before the last high power amplifiers are used by the operator to control the number and distance of pulses per train – according to the requirements determined by the experiment of the facility.

The lasers do not apply longitudinal beam shaping, the longitudinal shape is close to a Gaussian. The duration of the UV-pulse as measured with a streak camera [17] is $\sigma = 4.5 \pm 0.1$ ps for Laser 1 and 6.5 ± 0.1 ps for Laser 2. The pulse duration difference is due to their different laser oscillator design.

For details on the pulse train oscillator [15] and amplification stages, the reader is referred to [12, 16]. Table 1 summarizes the pulse parameters for the lasers.

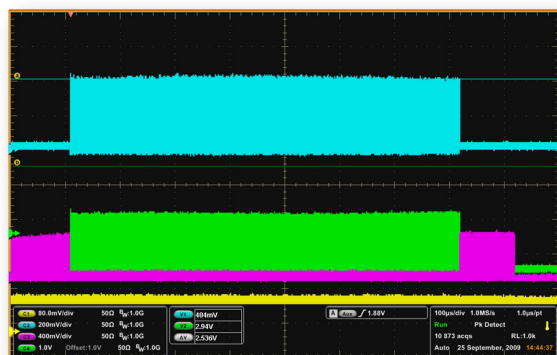


Figure 1: Example of a train of laser pulses taken from [16]. The oscilloscope traces show the pulse train of the 27 MHz oscillator (yellow trace), after pre-amplification (3 MHz, wavelength 1047 nm, magenta), after conversion to 523 nm (green), and to 262 nm (3 MHz, blue). The time scale is 100 μ s per division.

Laser 3

Laser 3 has been installed and commissioned in 2013. [18] The laser oscillator [19] provides 400 fs pulses at 1030 nm with a repetition rate of 54 MHz (cw). An acousto-optic modulator (AOM) picks with 1 MHz before final amplification. The Yb:YAG amplifier [20] is designed to achieve 10 W average power, the single pulse energy is up to 10 μ J at 1030 nm. A second AOM picker before wavelength conversion is used by the operator to adjust the number and distance of pulses (up to 1 ms bursts of 1 MHz or less at 10 Hz). Frequency conversion is again obtained with an LBO/BBO crystal pair into the UV (257.5 nm). Overall, the pulse energy is sufficient for electron bunch charges up to 200 pC.

A special feature of Laser 3 is its adjustable pulse duration. The initial 1 ps long UV pulses are compressed or stretched by two transmission gratings with 4000 lines per cm. A pulse duration between $\sigma = 0.8$ and 1.6 ps is adjustable. The pulses are shorter compared to Laser 1 and Laser 2, because in order to generate ultra-short electron bunches, a very short laser pulse duration is required to ease bunch compression in the subsequent bunch compressors of FLASH.

Energy Control

For each laser, the pulse energy is adjusted by two remote controlled attenuators. One attenuator is used by a feedback system to compensate for slow drifts in pulse energy, the other by the operators of FLASH to adjust the electron bunch charge. The attenuators consist of a remote controlled half-wave plate together with a Brewster angle polarizer plate, which is a thin coated fused silica plate oriented at the Brewster angle of 56° , transmitting 94 % of the p-polarized and reflecting 99.7 % of the s-polarized component. The incoming UV laser pulse is linear polarized. The half-wave plate turns the polarization angle to the desired value while the polarizer transmits the p-polarized state only.

With a similar technique, double pulses by a split and delay technique (21 ns distance) are produced for experiments using THz radiation [21]. These type of polarizer plates are also used to combine the three lasers into one common beamline. [8]

Beamline

Lasers 1 and 2 consequently use relay imaging together with spatial filtering. The UV laser beams are expanded and collimated to overfill a beam shaping aperture (BSA). A set of 15 remotely controlled hard edge apertures of various sizes are available; from 0.05 to 2 mm in diameter. The pulse shaping aperture is imaged onto the cathode of the RF-gun. This method produces a quasi flat truncated Gaussian pulse on the cathode with negligible pointing jitter.

The choice of the appropriate aperture for best beam performance has been evaluated and is predefined depending mainly on the charge, but also on the laser used (pulse duration). The laser spot size needs to balance space-charge effects (better for larger spot sizes, longer pulses) and emittance (better at smaller spot sizes). For normal operation (0.3 - 0.4 nC), usually an aperture size of 1.2 mm is used for Laser 1 and Laser 2. Laser 3 is designed for ultra-short pulse operation. The optimization in this case is different. [18] The laser spot diameter for Laser 3 is usually 0.8 mm.

The laser beamline from the BSA to the cathode has a horizontal geometry with a length of about 5 m. A fused silica vacuum window is used followed by an all metal in-vacuum mirror with an optically polished surface and an enhanced UV-reflectivity. The cathode is hit under a small angle of 3° . Using linear translation stages the laser beam can be moved and aligned on the cathode with a precision of better than 10 μ m. The laser beam can be deflected to a so-called virtual cathode, a Ce:YAG scintillator screen placed at the exact distance as the photo cathode. It is used

to adjust the laser on the beam shaping apertures and to keep the laser beam at the cathode center.

Table 1: Main parameters of the photoinjector laser systems. Some parameters are adjustable and are set according to the requirements of the specific experiment.

Item	Laser 1	Laser 2	Laser 3
Laser material	Nd:YLF	Yb:YAG	
Wavelength	1047 nm	1030 nm	
4th harmonic	261.7 nm	257.5 nm	
Train repetition rate	10 Hz		
Train duration	800 μ s		
Intra-train rate	1 MHz (*)		
Pulses per train (at 1 MHz)	1 – 800		
Pulse energy UV	10 μ J		1 μ J
Average power (IR)	2 W		10 W
Arrival time jitter	<50 fs (rms)		
Longitudinal shape	Gaussian		
Pulse duration (σ)	4.5 \pm 0.1 ps	6.5 \pm 0.1 ps	0.8–1.6 ps
Transverse profile	flat, truncated Gaussian		
Spot size on cathode	1.2 mm diam. (+)		0.8 mm (+)
Charge stability	0.5% rms		1% rms
* also: 500, 250, 200, 100, 50, or 40 kHz; 3 MHz optional			
+ truncated Gaussian; 15 different diameters are available			

Combining the Lasers into One Beamline for Simultaneous Operation

Figure 2 shows how the laser beams of all three lasers are combined to one beamline. Brewster plate polarizers as described in the previous section are used for this purpose. Laser 1 is s-polarized and reflected by combiner 1 into the beamline of Laser 2, which is p-polarized. Laser 3 is injected in a similar way using combiner 2. Since Laser 1 and Laser 2 are cross-polarized (s/p), a half wave plate turns the polarization state of both lasers such that both lasers are equally transmitted by combiner 2. The energy loss due this scheme for Lasers 1 and 2 is acceptable. A second plate compensates the lateral shift of the polarizer plate. Laser 1 and Laser 2 have the same beam shaping aperture (BSA), Laser 3 has its own. A diagnostic beamline features various instruments, a joulemeter, a UV enhanced CCD-camera, a spectrometer, and a streak camera.

SIMULTANEOUS OPERATION FLASH1 AND FLASH2

To allow different photon pulse pattern simultaneously for both FLASH undulator beamlines, two laser systems are used to serve FLASH1 and FLASH2. This is usually Laser 2 for FLASH1, Laser1 or Laser 3 for FLASH2. Laser 3 is used for ultra-short pulse SASE operation. For operational reasons and the realization of different bunch pattern and charge, using three laser systems is a straightforward solution. As discussed above, FLASH operates with 0.8 ms long RF-pulses. The first part of the RF-pulse is used for FLASH1, the second part for FLASH2 (or vice versa). Between the

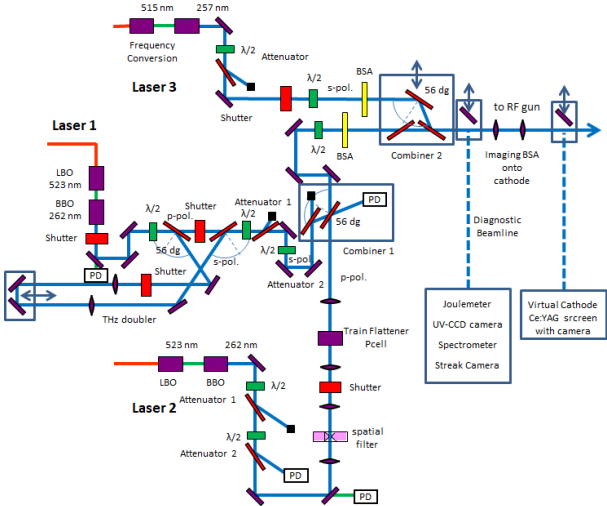


Figure 2: Beamline to combine all three laser systems. See explanations in the text.

sub-trains, a gap of about 50 μ s allows for the transition time of the kicker-septum system and the low level RF system to adjust.

The 3rd FLASH beamline, FLASH3 is used for the development of and experiments with a novel plasma wakefield accelerator, FLASHForward. [22]

SUMMARY AND OUTLOOK

The three photoinjector laser systems are operated simultaneously to produce flexible electron bunch pattern for the FLASH beamlines FLASH1, FLASH2, and also FLASH3. The present laser systems are now in continuous operation for more than 10 years with negligible downtime (a few hours in the last years). Nevertheless, the system is aging and requires a refurbishment. Within the present general refurbishment and upgrade process of FLASH, a new modern laser system is being developed in-house. We expect the new system to be ready for operation in 2021.

ACKNOWLEDGMENT

We like to thank our colleagues from DESY and MBI, Berlin for their valuable and constant support. Thanks to the synchronization team, namely S. Schulz, J. Müller and T. Kozak for their support in synchronizing the lasers to the accelerator.

REFERENCES

- [1] W. Ackermann *et al.*, “Operation of a free-electron laser from the extreme ultraviolet to the water window”, *Nature Photonics*, vol. 1, pp. 336–342, 2007. doi: 10.1038/nphoton.2007.76
- [2] K. Tiedtke *et al.*, “The soft x-ray free-electron laser FLASH at DESY: beamlines, diagnostics and end-stations”, *New J. Phys.*, vol. 11, p. 023029, 2009. doi: 10.1088/1367-2630/11/2/023029

- [3] J. Roensch-Schulenburg, K. Honkavaara, S. Schreiber, R. Treusch, and M. Vogt, "FLASH - Status and Upgrades", presented at the 39th Int. Free Electron Laser Conf. (FEL'19), Hamburg, Germany, Aug. 2019, paper FRA03, this conference.
- [4] B. Faatz *et al.*, "Simultaneous operation of two soft x-ray free-electron lasers driven by one linear accelerator", *New J. Phys.*, vol. 18, p. 062002, 2016. doi:10.1088/1367-2630/18/6/062002
- [5] S. Schreiber and B. Faatz, "The free-electron laser FLASH", *High Power Laser Science and Engineering*, vol. 3, p. e20, 2015. doi:10.1017/hpl.2015.16
- [6] K. Honkavaara and S. Schreiber, "FLASH: The Pioneering XUV and Soft X-Ray User Facility", presented at the 39th Int. Free Electron Laser Conf. (FEL'19), Hamburg, Germany, Aug. 2019, paper THP047, this conference.
- [7] J. Roensch-Schulenburg *et al.*, "Experience with Multi-Beam and Multi-Beamline FEL-Operation", *J. Phys.: Conf. Series*, vol. 874, p. 012023, 2017. doi:10.1088/1742-6596/874/1/012023
- [8] S. Schreiber, C. Gruen, K. Klose, J. Roensch, and B. Steffen, "Simultaneous Operation of Three Laser Systems at the FLASH Photoinjector", in *Proc. 37th Int. Free Electron Laser Conf. (FEL'15)*, Daejeon, Korea, Aug. 2015, paper TUP041, pp. 459–463.
- [9] S. Lederer, F. Brinker, S. Schreiber, L. Monaco and D. Sertore, "Update on the photocathode lifetime at FLASH and European XFEL", presented at the 39th Int. Free Electron Laser Conf. (FEL'19), Hamburg, Germany, Aug. 2019, paper WEP047, this conference.
- [10] S. Schulz *et al.*, "Femtosecond all-optical synchronization of an X-ray free-electron laser", *Nature Comm.*, vol. 6, nb. 5938, 2015. doi:10.1038/ncomms6938
- [11] S. Schulz *et al.*, "Precision Synchronization of the FLASH Photoinjector Laser", in *Proc. 1st Int. Particle Accelerator Conf. (IPAC'10)*, Kyoto, Japan, May 2010, paper WEPEB076, pp. 2875–2877.
- [12] I. Will, H.I. Templin, S. Schreiber, and W. Sandner, "Photoinjector drive laser of the FLASH FEL", *Optics Express*, vol. 19, p. 23770, 2011. doi:10.1364/OE.19.023770
- [13] S. Schreiber *et al.*, "Operation of the FLASH Photoinjector Laser System", in *Proc. 33rd Int. Free Electron Laser Conf. (FEL'11)*, Shanghai, China, Aug. 2011, paper THPA18, pp. 507–510.
- [14] S. Schreiber, D. Sertore, I. Will, A. Liero, and W. Sandner, "Running experience with the laser system for the RF-gun based injector at the TESLA Test Facility linac", *Nucl. Instr. Meth. A*, vol. 445, p. 427, 2000. doi:10.1016/S0168-9002(00)00096-6
- [15] I. Will, G. Koss, and I. Templin, "The upgraded photocathode laser of the TESLA Test Facility", *Nucl. Instr. Meth. A*, vol. 541, p. 467, 2005. doi:10.1016/j.nima.2004.12.007
- [16] S. Schreiber *et al.*, "Upgrades of the Photoinjector Laser System at FLASH", in *Proc. 34th Int. Free Electron Laser Conf. (FEL'12)*, Nara, Japan, Aug. 2012, paper WEPD08, pp. 385–388.
- [17] Femtosecond streak camera C6138 (FESCA-200), Hamamatsu Photonics K.K., Hamamatsu, Japan.
- [18] T. Plath, J. Roensch-Schulenburg, J. Rossbach, H. Schlarb, S. Schreiber, and B. Steffen, "Commissioning and Diagnostics Development for the New Short-Pulse Injector Laser at FLASH", in *Proc. 2nd Int. Beam Instrumentation Conf. (IBIC'13)*, Oxford, UK, Sep. 2013, paper TUPC03, pp. 353–356.
- [19] Origami 10XP by Onefive GmbH, Zurich, Switzerland, <http://www.onefive.com>
- [20] Amplifier by AMPHOS, Aachen, Germany, <http://www.amphos.de>
- [21] O. Grimm, K. Klose, and S. Schreiber, "Double-pulse Generation with the FLASH Injector Laser for Pump/Probe Experiments", in *Proc. 10th European Particle Accelerator Conf. (EPAC'06)*, Edinburgh, UK, Jun. 2006, paper THPCH150, p. 3143.
- [22] R. D'Arcy *et al.*, "FLASHForward: plasma wakefield accelerator science for high-average-power applications", *Phil. Trans. R. Soc. A*, vol. 377, p. 20180392, 2019. doi:10.1098/rsta.2018.0392

RF POWER WAVEGUIDE DISTRIBUTION FOR THE RF GUN OF THE EUROPEAN XFEL AT DESY

B. Yildirim, S. Choroba, V. Katalev, P. Morozov, Y. Nachtigal
DESY, Hamburg, Germany
E. Apostolov, Technical University of Sofia, Bulgaria

Abstract

The first section of the European XFEL provides the 43 m long injector. The injector consists of a 1.3 GHz RF gun, a 1.3 GHz cryomodule, a 3.9 GHz cryomodule and an extensive diagnostic section. The RF gun operates with a maximum RF peak power up to 6.5 MW, 10 Hz repetition rate and up to 650 μ s pulse length. The starting point in the 1.5 cell normal conducting L-Band cavity of the RF gun is a Cs₂Te photocathode, which produces electron bunches, which are injected into the superconducting accelerating section of the European XFEL. The RF power is generated by a 10 MW multi beam klystron and distributed to the RF gun through a RF power waveguide distribution system. In order to enhance the reliability of the distribution system, the peak power is minimized in every section of the system by splitting the power in different branches. The RF power reaches its maximum just in front of the RF gun after combination of all branches. An additional air pressure system decreases the break down level in the waveguides of the distribution.

We present the layout of the waveguide distribution system for the XFEL RF gun at Desy and report on first operation experiences.

REQUIREMENTS FOR THE WAVEGUIDE DISTRIBUTION FOR THE RF GUN

The main requirement is to feed the gun at the 7th underground floor in the XFEL tunnel with a klystron located at the 3rd underground floor with high reliability [1]. Therefore the connecting waveguide distribution has been designed and installed in a narrow shaft with high precision and high accuracy. The connecting waveguide distribution, as shown in Fig. 1, compensates the mechanical misalignment, the thermal expansion and the weight of the waveguide distribution due to flexible waveguides and a customized support system, which consists of several hanging units to stabilize the waveguide system from upper, lateral and lower sides.

To create a system as reliable as possible the two klystron outputs are splitted into four branches, which lead the RF power to unique developed isolators each at the end of the shaft. Through power combiners those branches are connected and the RF power is transferred to the RF gun window.

The Figure 1 shows the Connecting Waveguide Distribution with all four branches, which extend from the 3rd to the 7th underground floor.

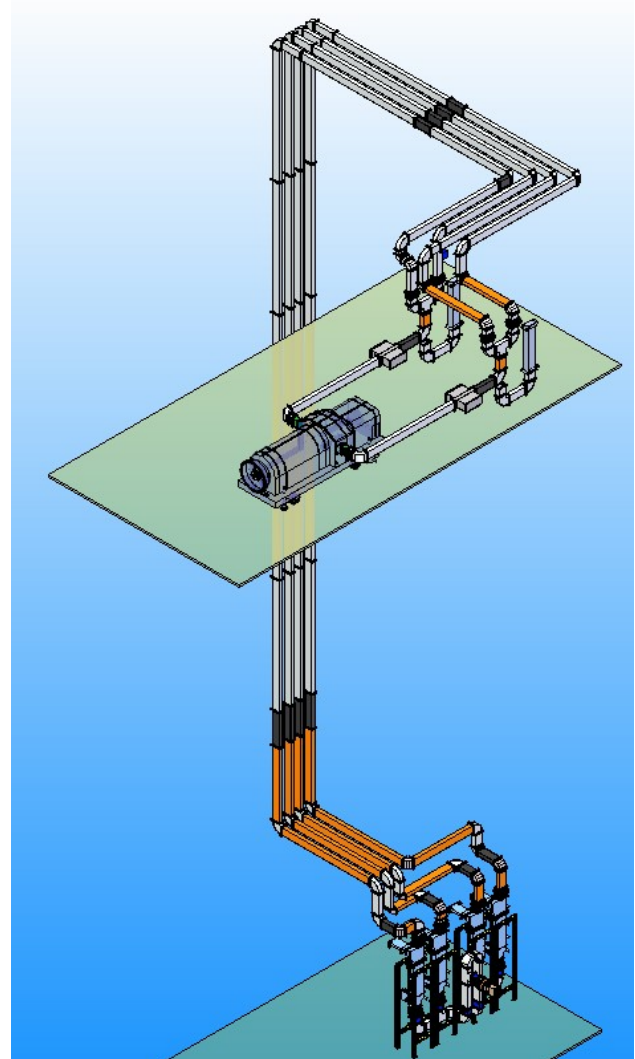


Figure 1: Connecting waveguide distribution for the RF gun.

WAVEGUIDE DISTRIBUTION FOR THE RF GUN

The complex waveguide distribution system for the RF gun consists of 236 parts both standard type WR650 and specific waveguide components [2]. To manage the distance in the injector shaft of approximately 25 m between the 10 MW klystron and the individual gun waveguide distribution, straight waveguides, H – bends as well as flexible waveguides are used and assembled with a support system only developed for this purpose. Several special bearings with springs compensate the waveguide weight over the entire length between the 3rd and 7th

underground floor. To avoid phase changes during the gun operation, the upper and lower ends of the waveguide section in the shaft are fixed and therefore 800 mm flexible waveguides are used to compensate thermal expansions of the waveguide distribution. The installation of such kind long system has completed with a special setup, which provides an adjustment accuracy level of ± 0.1 mm and ± 0.15 degrees. This allows the installation of the waveguide distribution and connection to the gun window without any stress. Monitoring and fastening of the waveguide distribution system in the shaft is carried out regularly.

In order to supply the gun with up to 8 MW RF power with high reliability three sections of different air pressures are realized for the waveguide distribution system.

Four specific 2.5 MW pulse power isolators each with 1.5 bar air pressure were developed by Ferrite, St. Petersburg, and installed in front of the gun window, as shown in Fig. 2. Since non-gas-tight waveguide distributions are used, small air leaks are compensated by the air flow machines. A major benefit of using pressurized waveguides is the resulting change of the waveguide shape, which leads to a phase shift; therefore no movable parts inside the waveguides are necessary.

The installed flanges of the waveguide distribution are standard Desy-type UDR14D flanges, which increase the reliability of the RF contact and decrease air losses caused by small leaks.

To separate the air pressure additionally, ten 5 MW air-air windows are installed at the RF waveguide distribution, four in front of the isolators, two in front of the power combiner and four at the two outputs of the klystron, as shown in Fig. 1 and Fig. 2.

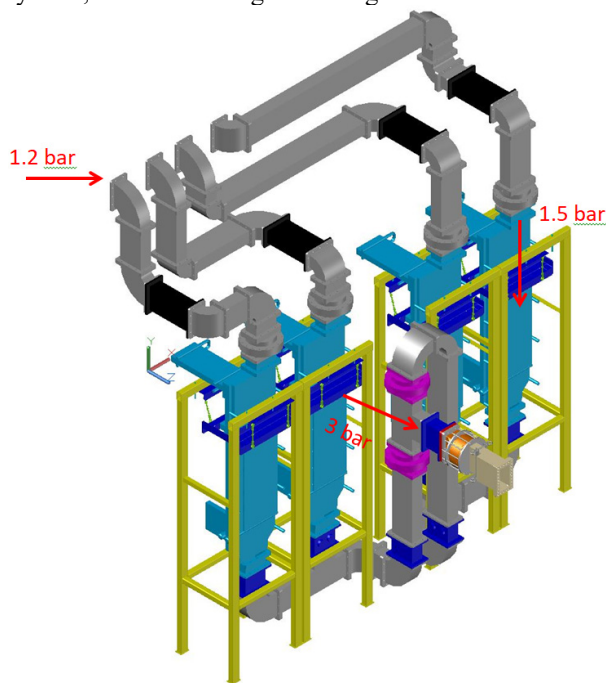


Figure 2: Waveguide distribution for the RF gun with different sections of pressure.

To increase the accuracy of power measurements for the RF gun a specific directional coupler with a high directivity of more than 40 dB is installed in front of the gun window, which is produced by Ferrite St. Petersburg, as shown in Fig. 3. By means of power sensors, which are connected to the directional coupler directly, the power level can be determined precisely without any complicated cable calibration. The power sensors are connected by an USB cable to a computer, which is shielded from radiation, to measure the RF power to the RF gun. From individual power measurements the measurement error is evaluated as ± 0.1 dB both for forward and reflected signal.

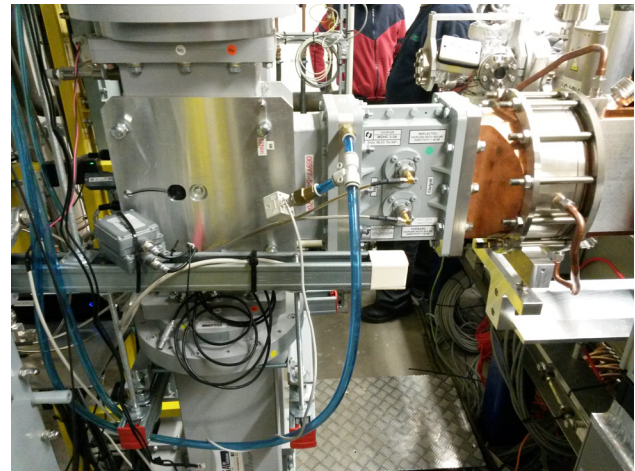


Figure 3: Directional coupler in front of the RF gun window in the XFEL injector.

AIR FLOW SYSTEM FOR THE WAVEGUIDE DISTRIBUTION FOR THE RF GUN

The air flow system for the waveguide distribution for the RF gun consists of two air flow machines, which have been developed to decrease the probability of breakdown and for phase tuning. By changing the air pressure in the waveguides the size of the waveguide changes and therefore the RF phase advance.

Starting at the 3rd underground floor the air flow system supplies an air pressure of 1.2 bar inside the four branches of the waveguides. To set the phase in these four sections independently 5 MW air-air windows have been installed. Each waveguide branch is followed by a 2.5 MW isolator. In order to increase the air spark breakdown limit of these isolators the operating pressure is increased to 1.5 bar. The main reason of using four isolators is to reduce the RF power in each isolator and by this to ensure a highly reliable system.

In order to reach only one waveguide path and thus to supply the maximum RF power to the RF gun with the same phase, all branches are combined by means of three waveguide combiners [3]. To increase the reliability only non-movable waveguide components have been used; any mechanical phase shifters have been avoided. To operate the RF gun as stable as possible an air pressure up to

3 bar is applied in the waveguide section in front of the RF gun.

To control such a complex airflow system, which increases the performance of the waveguide distribution, a Programmable Logic Controller (PLC) with individual software is needed. The installed controller is called BC9000 and the software has been written by Structured Text (ST).

The airflow system is included in the control system of the XFEL. The software enables the operators on the one hand to modify desired parameters quickly and directly, on the other hand it has a feature of an automatic self-diagnosis, which alerts the operator in case of an error.

WAVEGUIDE DISTRIBUTION FOR THE 1.3 GHz INJECTOR CRYOMODULE

The subsequent 1.3 GHz superconducting injector cryomodule, as shown in Fig. 4, is supplied by a klystron and an unique waveguide distribution system, which has a different design in comparison to the other waveguide distributions in the XFEL tunnel.

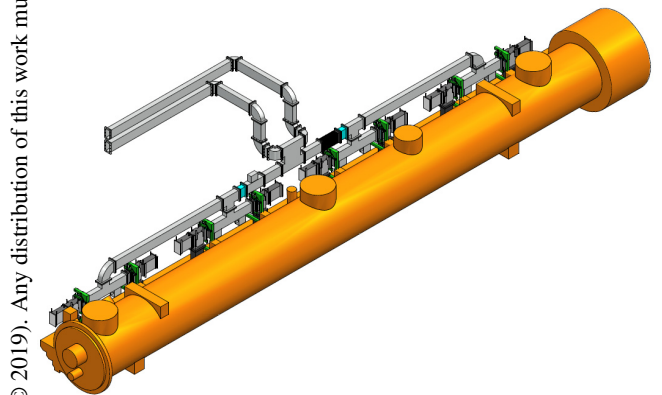


Figure 4: Waveguide distribution for the 1.3 GHz injector cryomodule.

The 10 MW klystron is located in the 3rd underground floor and feeds RF power up to 3 MW with a pulse length of 1.37 ms and a repetition rate of 10 Hz. The RF power between both outputs is tunable due to an additional phase shifter. A connecting waveguide distribution transfers the RF power from the klystron to the waveguide distribution of the cryomodule at 7th underground floor, as shown in Fig. 5.

To operate with the maximum energy for the injector cryomodule, it is necessary to supply individual power to each cavity. Using a 3 dB hybrid each klystron output is feeding four cavities. Due to requirements of beam dynamics the power distribution of the injector cryomodule must be considered as two independent power distributions, since the maximum gradients of the cavities 1-4 and 5-8 show a significant difference. By using specific tuned power splitters and binary cells the power losses are decreased as much as possible [3] [4]. The Fig. 5 shows the waveguide distribution for the injector complex, including the gun waveguide distribution and the connecting waveguide distribution

system.

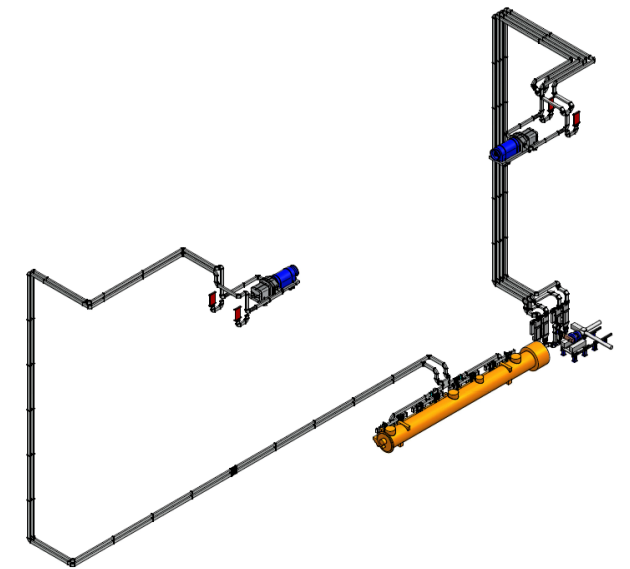


Figure 5: Waveguide distribution for the injector complex.

SUMMARY

The waveguide distribution for the injector of the European XFEL, which consists of several waveguide components, has been successfully installed in the XFEL tunnel. The waveguide distribution for the RF gun has been tuned and tested up to full power. According to experience the RF waveguide distribution shows a high reliable performance.

ACKNOWLEDGEMENTS

The authors are grateful to all the members of the DESY MHF-p teams for the successful tailoring, producing, tuning and installing of the waveguide distribution for the RF gun of the European XFEL at DESY.

REFERENCES

- [1] F. Brinker, "Commissioning the European XFEL injector", in *Proc. IPAC'16*, Busan, Korea, May 2016, pp. 1044-1047. doi:10.18429/JACoW-IPAC2016-TU0CA03.
- [2] V. Katalev, S.Choroba, "Waveguide distribution systems for the European XFEL", in *Proc. EPAC'06*, Edinburgh, UK, Jun. 2006, paper TUPCH116, pp. 1286-1288
- [3] V. Katalev, S. Choroba, "Compact waveguide distribution with asymmetric shunt tees for the European XFEL", in *Proc. PAC'07*, Albuquerque, NM, USA, Jun. 2007, paper MOPAN015, pp. 176-178.
- [4] B. Yildirim, S.Choroba, V.Katalev, P.Morozov, Y.Nachtigal, E.Apostolov, "Series production of the specific Waveguide distribution for the European XFEL at Desy", in *Proc. LINAC'18*, Beijing, China, Sep. 2018, pp. 380-383. doi:10.18429/JACoW-LINAC2018-TUP0027

STATUS OF CHIRPED PULSE LASER SHAPING FOR THE PITZ PHOTOINJECTOR

C. Koschitzki*, J. Good, M. Gross, Y. Chen, G. Loisch,
M. Krasilnikov, R. Niemczyk, F. Stephan, DESY Zeuthen, Germany
L. Winkelmann, T. Lang, DESY Hamburg, Germany
S. Mironov, E. Khazanov, IAP RAS Nischni Nowgorod, Russia

Abstract

In this publication we show the current status on spectral-spatial shaping of laser pulses at the Photo Injector Test facility at DESY-Zeuthen (PITZ) for providing temporally and spatially variable laser pulse intensities at a photo injector cathode. The temporal and spatial distribution of these laser pulses will determine the properties of the emitted electron bunch, which will influence the properties of Free-Electron Laser (FEL) radiation, after these electron bunches are further accelerated in the linac. The presented pulse shaper modulates the spectral amplitude of a chirped pulse with the additional capability to transversely vary the pulse shape, thus allowing a three dimensional pulse shaping. However, these pulses are particularly difficult to convert to shorter wavelength in nonlinear crystals preserving their shape. Shaping components like the spatial light modulator are not available for the required UV radiation and thus a specialized conversion setup had to be built, utilizing angular chirp matching and imaging to achieve shape preservation. In this work we present preliminary results of laser pulses shaped in the infrared and the similarity to their converted ultraviolet counterparts.

INTRODUCTION

Free-Electron Lasers (FEL) are currently the most powerful source for coherent x-rays. They are typically driven by a linear electron accelerator, which as opposed to ring type accelerators, preserves electron bunch properties from its injector source. Thus the performance of photo injectors is studied at PITZ. The initial temporal and spatial distribution of the electron bunch is determined by the shape of the laser pulse used to emit electrons from the photo cathode via the photo electric effect. As laser amplifiers for short-pulse amplification with high average power output are only available for infrared (IR) wavelength, it is necessary to use harmonic generation processes in nonlinear crystals to convert the laser pulses to the ultraviolet (UV) in order to overcome the work function of the photo cathode material. In this case this is a dicaesium telluride (Cs_2Te) with a vacuum threshold energy of 3.5 eV or 354 nm. Two consecutive second harmonic generation (SHG) processes are applied to get to the fourth harmonic of a 1030 nm IR laser and thus 257 nm or 4.8 eV. UV optical components needed for the shaper are either not available, very expensive or inefficient at these wavelength ranges. Thus laser pulse shaping is done in IR

and special care has to be taken to preserve pulse shapes through the conversion process. In particular the conversion from visible (VIS) to UV light is challenging. A laser pulse shaper capable of shaping in three dimensions, i.e. spatially and temporarily, has been developed at PITZ, based on a prior system by Mironov et al. [1]. Preserving such pulses in all three dimensions through the conversion process is a key challenge in order to use the pulse shaper system for the photo injector application. Mironov et al. have proposed and simulated a method for shape preserving conversion [2], using an angular chirp matching with type I phase matching. In this work preliminary experimental results will be shown.

SLM PULSE SHAPER

The most prominent scheme to alter the laser pulses temporal distribution from its typical Gaussian shape is the coherent pulse stacking technique, in which copies of short laser pulses are delayed, attenuated and recombined. The precision depends on the amount of copies produced. Such a system is also operated at PITZ [3]. Spatial shaping is added by masking the transverse distribution typically by a round aperture after the laser pulses have longitudinally been shaped in IR and converted to UV. The dispersive pulse shaper, as proposed and demonstrated by Mironov et al. [1], uses a principle very similar to a spectrograph. The beam is focused into a line onto a spatial light modulator (SLM) by a cylindrical lens, where the spread out spatial dimension can be modulated. Perpendicular to the line focus the beam is dispersed by an optical grating, allowing for a simultaneous modulation of one spatial dimension and the spectrum. The beam path is then reversed to undo the cylindrical focusing and the dispersion (see Figure 1). SLMs can shift the laser phase on each of its pixels between 0 and 2π . The phase shifting of the SLM is polarization dependent, so one can apply quarter $\frac{1}{4}\lambda$ plates and a polarizer in order to turn the phase shift into a spatial-spectral attenuation. Without the $\frac{1}{4}\lambda$ plates the shaper can be operated as variable prism as shown in section . As a single shaper allows only access to one spatial dimension, the beam is rotated by 90 degrees and the shaping process is repeated. Thus the 3D spectral-spatial attenuation function $f_a(x, y, \lambda)$ is not fully arbitrary, but must fulfill the condition

$$f_a(x, y, \lambda) = f_1(x, \lambda) * f_2(y, \lambda). \quad (1)$$

This condition results in 3D shaped pulses consisting of rectangular spatial profiles along the wavelength axis. In order to achieve a targeted attenuation of the laser pulse

* christian.koschitzki@desy.de

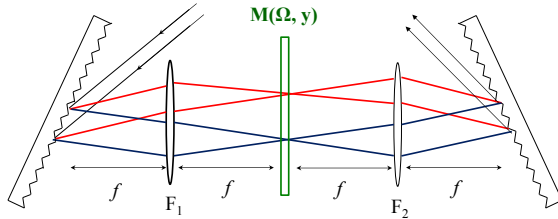


Figure 1: Schematic of an SLM based shaper.

we diagnose the beam using a slit spectrograph. With correct imaging from the SLM to the spectrograph plane we can detect the laser distribution as on the SLM plane and apply a targeted attenuation. Thus we obtained an evenly filled rectangle on the spectrograph as shown in Figure 2 b). This beam moved within 12 hours by less than one pixel on the spectrograph, i.e. shows excellent position stability. Simultaneous shaping by both SLMs can be recovered by scanning the position of the entrance slit of the spectrograph (2) d). The spatial-temporal distribution can be obtained from the spatial-spectral distribution by Fourier transformation along the spectral axis considering the chirp or group delay dispersion (GDD).

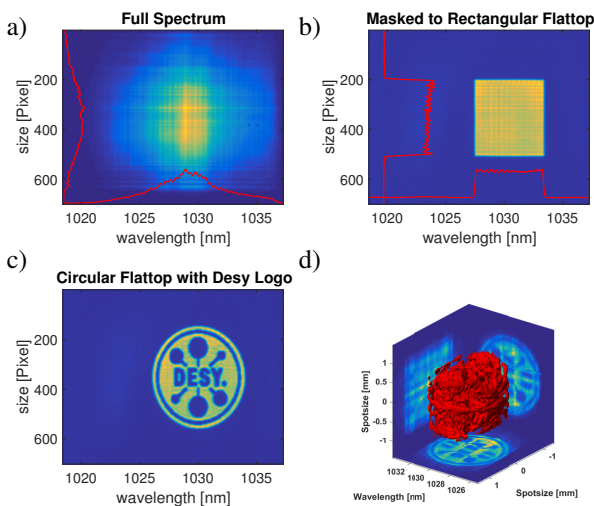


Figure 2: Spectrograph images of the shaped laser pulse. a) unshaped pulse b) Rectangular flattop c) Circular flattop with Desy logo d) Desy logo on both SLMs retrieved by spectrograph slit scan (vertical resolution).

CONVERSION

Second harmonic conversion output of nonlinear crystals depends on the square of the laser pulse intensity. When working with low laser intensities, focusing the laser pulse on the conversion crystal is the typical approach. The focal distribution of a laser pulse corresponds to the Fourier transform of its collimated spatial distribution. High spatial

frequency features, i.e. sharp edges, become low intensity features around the focal spot and will be strongly suppressed due to the non-linearity of the conversion. Thus the conversion acts like a spatial filter. It can be seen that this is also the case for temporal transform limited pulses. Thus the spatially modified laser pulses have to be imaged into the conversion crystal uncompressed. As the intensity is lower than in the focused case, the efficiency will be reduced. Another problem is the phase matching, as for a type I critical phase matching setup only a limited bandwidth is supported in the conversion process. J.P. Torres et al. [4] have proposed a method for broadband phase matching, where an angular chirp (AC) is introduced to match the wavelength dependent phase matching angle. Mironov et al. [2] have shown a numerical method to simulate the nonlinear SHG processes with chirp matching for picosecond laser pulses with high numeric efficiency. The simulation results match those obtained by a more general applicable, but slower tool developed by Lang et. al [5].

The current setup operates with a 4 mm LBO crystal at beam intensities of approximately 2.5 GW cm^{-2} and a 0.5 mm thick BBO crystal at 1.5 GW cm^{-2} . The required AC for broadband matching in the LBO is generated by 2 SF11 prisms with an AC of 0.065 mrad/nm each and magnified by a transport telescope with $M=8.9$ to the required AC of 1.15 mrad/nm for the LBO. The combined origin of dispersion must be aligned to coincide with the image plane of the spatial modulation in order to avoid spatial dispersion in the image plane inside the conversion crystal. To achieve AC matching inside the BBO crystal the existing dispersion from the LBO can be magnified using an intermediate transport telescope between LBO and BBO crystal. Finally, the setup contains a variable three-lens telescope imaging the shaper output to the SF11 prisms in order to vary the beam size on the crystal. Figure 3 shows how a spatial attenuation from the shaper can be retrieved in the UV. In one dimension sharp profiles can be maintained, while in the other direction features are smeared out, owing to the spatial walk-off between fundamental and harmonic beam inside the conversion crystal. This effect is proportional to the crystal thickness. The nonlinear conversion is expected to reduce the width of a gaussian beam by approximately a factor 4, due to nonlinear correlation between input and output profile.

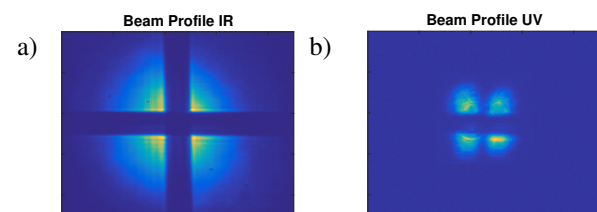


Figure 3: Beam Images in IR. a) and UV b) with spatial line masks from both SLMs. Horizontal smearing is due to spatial walkoff from the BBO crystal.

ANGULAR CHIRP DEPENDENCE

The aforementioned simulation tools ([2], [5]) allows us to simulate the effects of mismatched AC on the conversion efficiency. At the same time the shaper setup can be used to scan this dependence experimentally. For this we have to use the SLM in phase shifting mode without the $\frac{1}{4}\lambda$ plates. By varying the phase shift θ linearly along a spatial dimension x for a given wavelength λ , one applies a deflection angle ϕ to that part of the spectrum

$$\phi = \lambda \frac{\delta\theta}{\delta x}. \quad (2)$$

By also varying this angle along the wavelength axis of the SLM an AC $\delta\phi/\delta\lambda$ is generated. The additional benefit is that the origin of dispersion is at the SLM, which by image transport is moved to the crystal plane, as detailed above. Thus spatial dispersion is minimized and only angular dispersion is generated at the plane of the crystal. The total magnification of the image system from the SLM to the crystal plane has to be considered in order to obtain the AC at the crystal plane from the AC generated at the SLM. In Figure 4 the relative beam energy normalized to the maximum energy and the spectral width are shown as a function of applied angular chirp. The beam energy has been measured using the camera integral of the UV profile camera as in Figure 3. Simulation predicts a conversion efficiency of 0.4 % for this Gaussian beam with 10 ps FWHM pulse duration and 10 μ J pulse Energy, corresponding to a peak intensity of 3.75 GW/cm². In Figure 5 the simulated conversion efficiency is plotted as function of AC for different energies. Absolute pulse energy measurement for the output UV pulses was not available at the time. Spectral width of the output beam has been measured with a UV spectrograph. This experiment demonstrates the importance of the achieved broadband phase matching. As only a fraction of the spectrum, that the shaper is supposed to modulate, would be converted in an unmatched scenario, the temporal structure could not be maintained if no angular chirp is applied to the nonlinear conversion.

CONCLUSION

This paper shows that the SLM shaping approach will provide a stable, versatile and precise method for pulse shaping of infrared laser pulses. The matched angular chirp conversion shows promising results to maintain the pulse shape through the conversion process while reaching satisfying conversion efficiency. In the next step more complex shaping needs to be applied to the infrared pulses, to study the shape preservation and its limitations in detail. In order to get more direct access to the temporal structure, a cross correlator for the IR and a difference frequency cross correlator for the UV pulses are planned. The final goal is to reach homogeneous UV laser intensity distributions of different 3D shapes with as sharp as possible boundaries in all three dimensions.

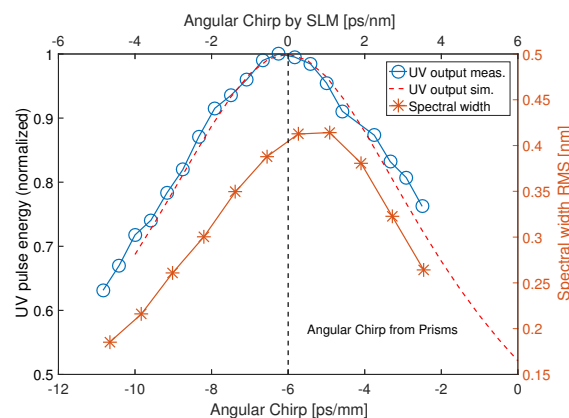


Figure 4: Normalized UV output of conversion section (blue) and spectral width of the UV pulses (orange) as function of applied angular chirp.

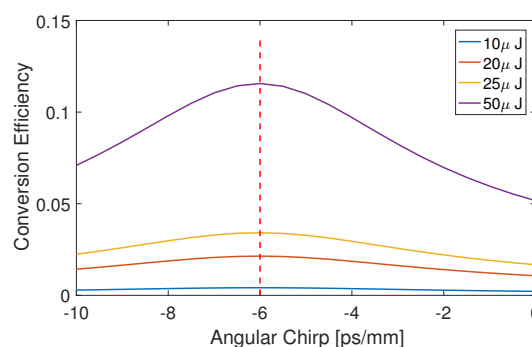


Figure 5: Simulated conversion efficiency for Gaussian beam as function of angular chirp.

REFERENCES

- [1] S. Mironov *et al.*, “Shaping of cylindrical and 3D ellipsoidal beams for electron photoinjector laser drivers”, *Applied Optics*, vol. 55, no. 7, p. 1630-1635, Feb. 2016, doi:10.1364/AO.55.001630
- [2] S. Mironov *et al.*, “Generation of the second and fourth harmonics with retaining the three-dimensional quasi-ellipsoidal distribution of the laser pulse intensity for a photoinjector”, *Radiophysics and Quantum Electronics*, vol. 61, no. 6, p. 456, Nov. 2018, doi:10.1007/s11141-018-9907-2
- [3] I. Will *et al.*, “Generation of flat-top picosecond pulses by coherent pulse stacking in a multicrystal birefringent filter”, *OPTICS EXPRESS*, vol. 16, no. 19, p. 14922-14937, Sep. 2008, doi:10.1364/OE.16.014922
- [4] J. P. Torres *et al.*, “Angular dispersion: an enabling tool in nonlinear and quantum optics”, *Advances in Optics and Photonics*, vol. 2, p. 319-369, May. 2010, doi:10.1364/AOP.2.000319
- [5] T. Lang *et al.*, “Impact of temporal, spatial and cascaded effects on the pulse formation in ultra-broadband parametric amplifiers”, *OPTICS EXPRESS*, vol. 21, no. 1, p. 949-959, Jan. 2013, doi:10.1364/OE.21.000949

PITZ EXPERIMENTAL OPTIMIZATION FOR THE AIMED CATHODE GRADIENT OF A SUPERCONDUCTING CW RF GUN

M. Krasilnikov*, P. Boonpornprasert, Y. Chen, G. Georgiev, J. Good, M. Gross, P. Huang, I. Isaev, C. Koschitzki, S. Lal, X.-K. Li, O. Lishilin, G. Loisch, D. Melkumyan, R. Niemczyk, A. Oppelt, H. Qian, H. Shaker, G. Shu, F. Stephan, G. Vashchenko, DESY, Zeuthen, Germany
M. Dohlus, E. Vogel, DESY, Hamburg, Germany

Abstract

A continuous wave (CW) mode operation of the European X-ray Free-Electron Laser (XFEL) is under considerations for a future upgrade. Therefore, a superconducting radio frequency (SRF) CW gun is under experimental development at DESY in Hamburg. Beam dynamics simulations for this setup have been done assuming 100 pC bunch charge and a maximum electric field at the photocathode of 40 MV/m. Experimental studies for these parameters using a normal conducting RF photogun have been performed at the Photo Injector Test facility at DESY in Zeuthen (PITZ). The beam transverse emittance was minimized by optimizing the main photo injector parameters in order to demonstrate the feasibility of generating electron beams with a beam quality required for successful CW operation of the European XFEL for conditions similar to the SRF gun setup.

INTRODUCTION

For successful CW operation of modern XFEL facilities the electron source should combine high average power and peak beam brightness sufficiently high for proper lasing. A high cathode gradient in the gun is one of the important factors to achieve high phase space density of the generated electron beams. However due to the CW requirements (high average power) on the electron source the peak RF power (gradient) in the RF gun is limited and is typically lower than in the case of pulsed guns. An SRF CW L-band gun is under experimental development at DESY in Hamburg [1]. A maximum electric field at the photocathode of 40 MV/m is considered for the operation of this gun in the CW mode of the European XFEL. Beam dynamics simulations for the SRF photo injector (CW SRF PI) setup have been done for 100 pC bunch charge generated with Gaussian photocathode laser pulses. Optimization of the projected normalized emittance yielded 0.45 mm mrad. In order to demonstrate this brightness the normal conducting PITZ photo injector has been tuned to the proposed conditions, namely 40 MV/m maximum electric field at the cathode and bunch charge of 100 pC. Results of experimental studies at PITZ supplied with corresponding beam dynamics simulations are compared with the optimized SRF CW photo injector setup.

LAYOUTS OF PHOTO INJECTORS

One essential difference between PITZ and the SRF gun setup is the location of the main solenoid. Due to the

superconducting environment a focusing solenoid has to be separated from the SRF gun cavity and located downstream. For the normal conducting PITZ RF gun cavity the main solenoid is located closer to the cathode plane and its field overlaps with RF fields of the L-band PITZ gun cavity. Axial distributions of RF and solenoid fields are shown in Fig. 1 for both setups.

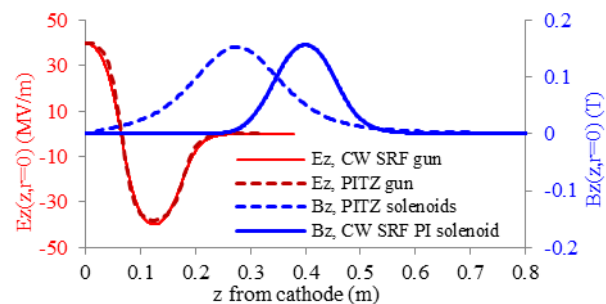


Figure 1: Axial distributions of RF electric fields (amplitudes $E_z(z, r=0)$) and longitudinal magnetic field of solenoids ($B_z(z, r=0)$) for SRF and PITZ guns.

BEAM DYNAMICS SIMULATIONS

Beam dynamics optimization for the CW SRF PI setup were performed using ASTRA [2] for 100 pC bunches applying photocathode laser pulses with a Gaussian temporal profile of 4 ps RMS duration. A module with 8 TESLA cavities (with 14.5 MeV energy gain per cavity) was applied to accelerate the beam up to 120 MeV. RF phase of the gun, strength of the solenoid (corresponding field profiles shown in Fig. 1) and laser transverse spot size were optimized to minimize a transverse emittance at the injector exit. Beam dynamics simulations for the PITZ setup were performed for parameters compromising between assumed CW SRF PI simulations and currently available parameters in experiment. Photocathode pulses with Gaussian temporal profile with 2.6 ps RMS duration (35% shorter than in the CW SRF PI simulations) were applied. The gun with maximum RF field of 40 MV/m at the photocathode and launch phase at the maximum mean momentum gain (MMM) was used. The CDS booster [3] accelerates the beam up to ~17 MeV which is comparable with 1st cavity in cryomodule acceleration in the CW SRF PI case. The photocathode laser spot size and the main solenoid peak field were tuned in order to minimize projected normalized RMS emittance at $z=5.27$ m, the standard location of emittance measurements at PITZ.

Optimized simulated transverse RMS beam size and

* mikhail.kraskilnikov@desy.de

emittance along both photo injectors are shown in Fig. 2 (top plot). Corresponding beam energy and RMS bunch length are shown in the bottom plot. The transverse RMS emittance expected from the PITZ injector is lower mainly due to the optimized position of its main solenoid ($z=0.276$ m in Fig. 1). Because of the above mentioned limitations of the superconducting environment for the CW SRF PI setup the solenoid is separated from the gun cavity and centred at $z=0.4$ m.

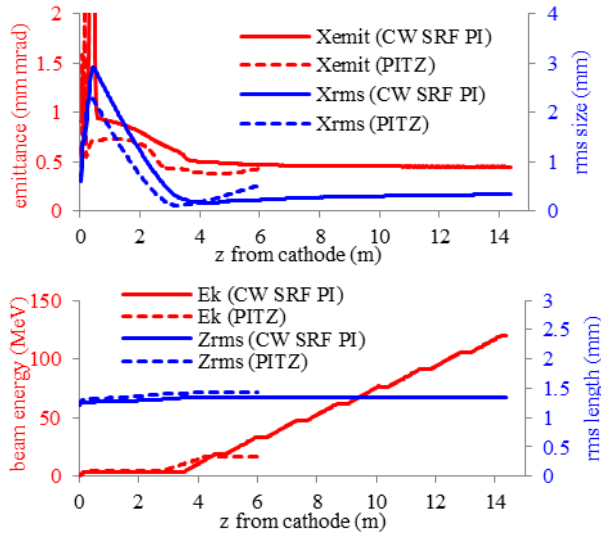


Figure 2: Simulated beam parameters along the beam line. Top: transverse RMS beam size and normalized transverse emittance. Bottom: mean beam energy and RMS bunch length.

Simulated optimized transverse phase space and beam slice parameters at the exit of the injector are shown in Fig. 3 for both setups.

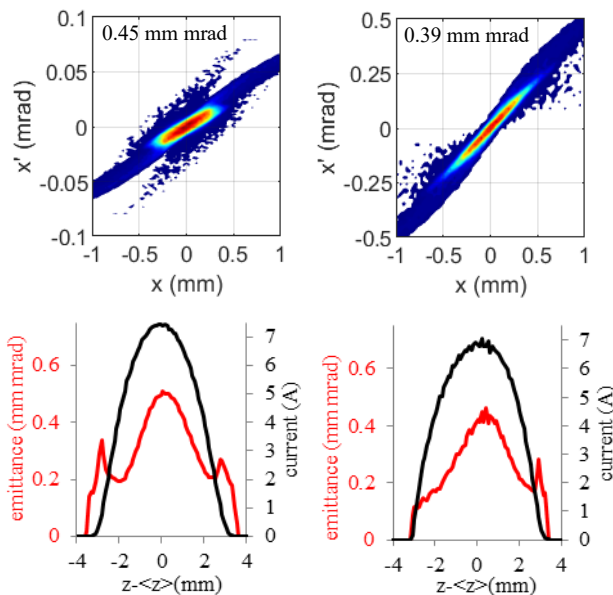


Figure 3: Beam parameters at the photo injector exit: left column – CW SRF PI, right column - PITZ. Top row: transverse phase space; bottom row: slice emittance and beam current profiles.

EXPERIMENTAL PITZ OPTIMIZATION

PITZ has been used to experimentally characterize the electron source performance for a parameter space close to the simulated optimum CW SRF PI setup.

Photocathode Laser

The photocathode laser system was operated with temporal Gaussian pulses with ~ 6 ps FWHM. A corresponding laser pulse temporal profile measurement using a cross-correlator (OSS – Optical Sampling System) is shown in Fig. 4 (left). Transverse shaping of the laser illuminating the photocathode is realized using variable aperture (the so-called Beam Shaping Aperture – BSA). The laser transverse distribution was monitored using a dedicated UV-sensitive CCD camera (Fig. 4, right). Inhomogeneity of the core and presence of radial halo are clearly seen and related to features of the laser system and imperfections of the optical transport beam line.

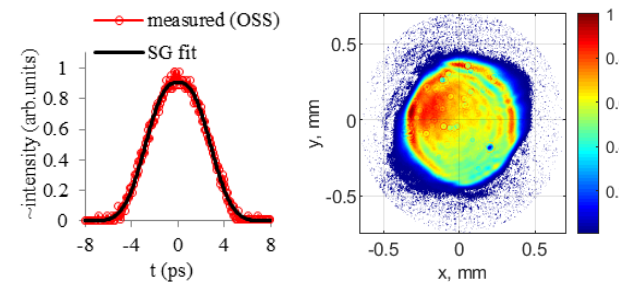


Figure 4: Left: Photocathode laser pulse temporal profile measured with OSS supplied with a Super Gaussian (SG) fit $SG \propto \exp\{-0.5 \cdot |t/2.6|^{2.59}\}$. Right: Transverse distribution of the laser intensity for the BSA diameter of 0.8 mm: laser RMS sizes: $\sigma_{x/y}^{laser} = 0.196/0.200$ mm.

RF Gun

The RF power in the gun (PITZ Gun4.2 prototype) was adjusted to yield a maximum electric field of 40 MV/m at the photocathode. This corresponds to a peak RF power in the gun cavity of 2.78 MW. The launch RF phase was tuned to the MMMG. Corresponding phase scan for the mean momentum and RMS momentum spread is shown in Fig. 5 (left). The momentum distribution for the MMMG phase is shown in the right plot.

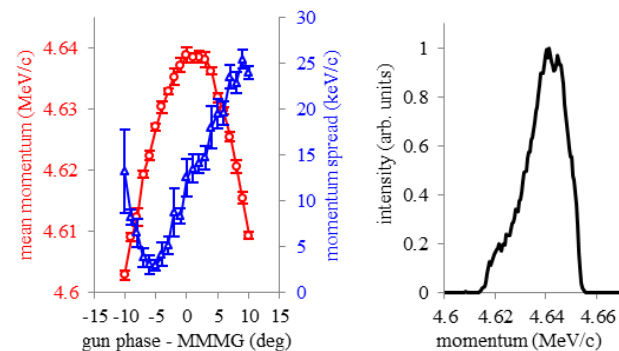


Figure 5: Left: gun RF phase scan for beam momentum. Right: beam momentum distribution after the gun at the MMMG phase, $\langle p_z \rangle = 4.64$ MeV/c, $\sigma_{p_z} = 10$ keV/c.

Further electron beam acceleration was realized using the CDS booster which was operated on-crest at the peak power of ~ 2.3 MW, resulting in a final beam mean momentum of ~ 17.6 MeV/c.

Emittance Measurements

Beam transverse normalized RMS emittance was optimized at the first emittance measurement station (EMSY1) located $z=5.27$ m downstream of the photocathode. The single slit scan technique [3] was applied to measure the horizontal and vertical phase space of the 100 pC electron beam. The laser spot size (BSA diameter) was varied from 0.6 mm to 1.3 mm with a step of 0.1 mm. For each laser spot size, a main solenoid scan was performed to measure horizontal and vertical emittances. For the main solenoid current of 274 A gun quadrupoles [4] were optimized in order to obtain an electron beam distribution at the YAG screen (EMSY1) as round and symmetric as possible. Results of the experimental optimization are presented in Fig. 6 where emittance is shown as a function of the laser spot diameter together with ASTRA simulations. For comparison the results for the CW SRF setup are shown as well. Error bars of the measured curves include estimations on the emittance measurement uncertainty due to the intrinsic charge cut of the slit scan technique. PITZ emittance simulations have been performed with two laser transverse distributions: radially homogeneous and applying core and halo (C+H) model [5] deduced from the measured laser profile (see Fig. 4, right). Simulations for a BSA smaller than 0.7 mm revealed a regime of strong space charge dominated emission from the photocathode. Beam dynamics simulations for this regime show significant discrepancies with experimental observations. This problem is known [5] and under investigations.

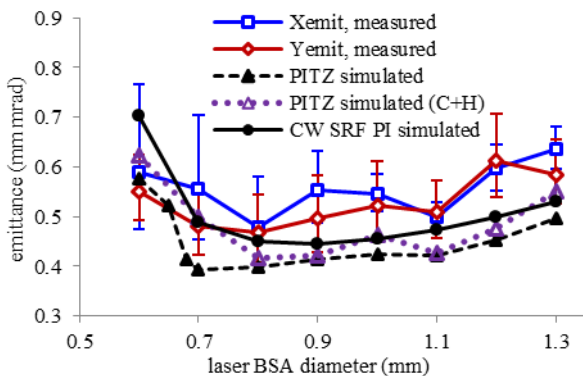


Figure 6: Normalized RMS emittance as a function of the laser Beam Shaping Aperture (BSA) diameter: measured at PITZ and simulated for PITZ and CW SRF PI setups.

Typical results of a basic emittance optimization measurement – emittance as a function of the main solenoid current – are shown in Fig. 7 for BSA=0.8 mm (see right plot in Fig. 4 for the laser transverse distribution). Simulated curves for the PITZ setup are shown as well. Both simulated curves are shifted by +4 A w.r.t. the measured curves for better comparison of the beam size and emittance dependencies on the main solenoid current. This discrepancy as well as vertical regular offset between simulated and measured emittance curves is a part of the above mentioned problem [5]. Measured horizontal and vertical phase spaces for the optimum solenoid current value (274 A) are shown in Fig. 8. Corresponding measured RMS normalized horizontal and vertical emittance values are $\epsilon_{x,n} = (0.479 \pm 0.006_{stat})$ mm mrad and $\epsilon_{y,n} = (0.468 \pm 0.005_{stat})$ mm rad. These values are in a reasonable agreement with simulation results within systematic limitations of emittance measurements.

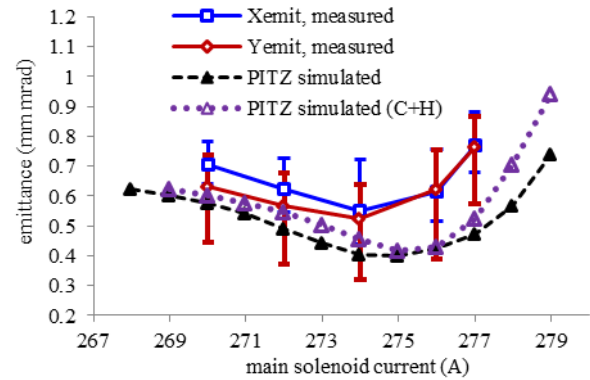


Figure 7: Normalized RMS emittance as a function of the main solenoid current together with ASTRA simulations for the PITZ setup.

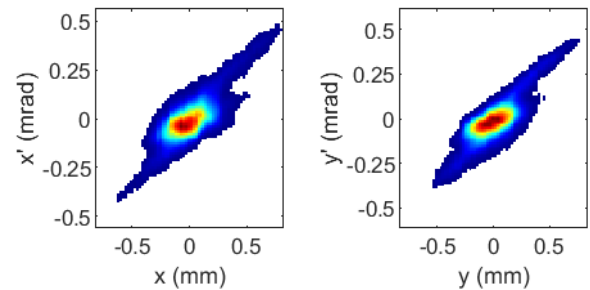


Figure 8: Horizontal (left) and vertical (right) transverse phase space measured for the optimum main solenoid current of 274 A.

CONCLUSION

Beam dynamics simulations for a CW SRF photo injector of the European XFEL have been performed assuming a peak RF electric field of 40 MV/m at the photocathode and 100 pC bunch charge generated by Gaussian photocathode laser pulses with 4 ps RMS duration yielding optimum emittance values of ~ 0.45 mm mrad. Experimental studies for this parameter space have been done at PITZ with Gaussian laser pulses with 2.6 ps RMS duration and yielded measured emittance values of ~ 0.5 mm mrad which is by ~ 0.1 mm mrad higher than the minimum expected from the corresponding PITZ simulations. The difference in optimized emittance between PITZ and CW SRF photo injector setups is mainly related to the main solenoid position w.r.t. the gun cavity and to the difference in the photocathode laser pulse duration.

REFERENCES

- [1] E. Vogel *et al.*, “SRF Gun Development at DESY”, in *Proc. LINAC'18, Beijing, China*, Sep. 2018, pp. 105-108. doi:10.18429/JACoW-LINAC2018-MOP0037
- [2] ASTRA code, <http://www.desy.de/~mpyf1o/>
- [3] M. Krasilnikov *et al.*, “Experimentally minimized beam emittance from an L-band photoinjector”, *Phys. Rev. ST Accel. Beams* 15, 100701, Oct. 2012. doi: 10.1103/PhysRevSTAB.15.100701
- [4] M. Krasilnikov *et al.*, “Electron Beam Asymmetry Compensation with Gun Quadrupoles at PITZ”, in *Proc. 38th Int. Free Electron Laser Conf. (FEL'17)*, Santa Fe, NM, USA, Aug. 2017, paper WEP007, pp. 429-431, doi: 10.18429/JACoW-FEL2017-WEP007
- [5] M. Krasilnikov *et al.*, “Investigations on Electron Beam Imperfections at PITZ”, in *Proc. 28th Linear Accelerator Conf. (LINAC'16)*, East Lansing, MI, USA, Sep. 2016, paper MOPLR013, pp. 165-167, ISBN: 978-3-95450-169-4, doi: 10.18429/JACoW-LINAC2016-MOPLR013

SIMULATION STUDIES ON THE SATURATED EMISSION AT PITZ

X.-K. Li*, P. Boonpornprasert, Y. Chen, J. Good, M. Gross, I. Isaev, C. Koschitzki,
M. Krasilnikov, S. Lal, O. Lishilin, G. Loisch, D. Melkumyan, R. Niemczyk, A. Oppelt,
H. Qian, H. Shaker, G. Shu, F. Stephan, G. Vashchenko, DESY, Zeuthen, Germany

Abstract

In this paper we report our consideration and simulation on the space charge dominated emission in the L-band photocathode RF gun at the Photo Injector Test facility at DESY in Zeuthen (PITZ). It has been found that the emission curve, which relates the extracted and accelerated bunch charge after the gun to the laser energy, doesn't agree very well with Astra simulations when the emission is nearly or fully saturated. Previous studies with a core-halo model for a better fit of the experimentally measured laser transverse profile as well as with an improved transient emission model have resulted in a better agreement between experimental data and simulation. A 3D FFT space charge solver including mirror charge and binned energy/momentum has been built, which also allows more emission mechanisms to be included in the future. In this paper, the energy spread during emission was preliminarily analyzed. Experimentally measured emission curves were compared with simulation, showing the effect of the inhomogeneity of the laser on the emission and beam parameters.

INTRODUCTION

The space charge effect during photo emission in an RF photocathode gun is one of the key factors determining the quality of the accelerated electron beam. For a given bunch charge, it can be optimized, for instance, by tuning gun gradient, injection phase or by cathode laser pulse shaping. According to the magnitude of space charge, the photo emission can be either source dominated or space charge dominated. For the former, the emitted charge depends on the laser energy and the quantum efficiency (QE) of the cathode. For the latter, the space charge is comparable to the accelerating gradient, therefore suppressing the emission. At PITZ [1], the measurement of the emission curve, which gives the relation between the incoming laser energy and the outgoing bunch charge, is a routine task. The modeling of the emission using a particle tracking code such as Astra [2] does not always give satisfying agreement, especially for the space charge dominated emission or saturated emission. Along with the investigation of cathode physics such as Schottky effect [3], a 3D space charge solver has been developed for considerations of effects such as the inhomogeneity of the laser transverse profile and the quantum efficiency over the cathode and the large energy spread of the electron bunch during the emission. Further development will also take into account the physics behind the emission process. In this paper, we report about our 3D space charge solver based on fast Fourier transformation (FFT) [4] and the application of

the solver to study the energy spread effect and to simulate the emission under experimental conditions. The measured laser profile was used to modify a homogeneous distribution generated by Astra for the 3D solver. The simulation results are compared and discussed.

3D SPACE CHARGE SOLVER

In order to calculate the space charge forces, the whole electron bunch of a given distribution is transformed into its rest frame, which turns the problem of space charge into solving the Poisson's equation. The method of solving it in 3D using FFT has been described in detail in Ref. [4]. In this method, the solution of Poisson's equation (or the static potential ϕ) is given by

$$\phi(\vec{r}) = \frac{1}{4\pi\epsilon_0} \times \int G(\vec{r}, \vec{r}') \rho(\vec{r}') d\vec{r}', \quad (1)$$

where $\vec{r} = (x, y, z)$, ρ is the charge density and G is Green's function defined as

$$G(\vec{r}, \vec{r}') = \frac{1}{|\vec{r} - \vec{r}'|}. \quad (2)$$

In Eq. (1) the static potential is written as the convolution of Green's function and the charge density and therefore can be solved efficiently using FFT [5]. After knowing the static potential, the electric fields in the rest frame can be derived by $\vec{E} = -\nabla\phi$ and the fields in the laboratory frame can be obtained by Lorentz transformation.

The mirror charge effect during emission is not negligible and is solved in a similar way by using the shifted Green's function method [4]. In the above, it has been assumed that the bunch has a very small energy spread which makes the bunch static in the Lorentz transformed rest frame. In the case of large energy spread, the bunch should be treated specially, for example, by binning the bunch according to the kinetic energies or momenta of individual electrons or by slicing them longitudinally, if a strong correlation between the kinetic energy and position exists. The fields solved from each bin or slice are then summed together.

EFFECTS OF ENERGY SPREAD ON SPACE CHARGE CALCULATION

As mentioned above, the transformation of the bunch into its rest frame for calculating the static potential is valid when the beam has a small energy spread. In fact, the energy spread during emission is large. For instance, the longitudinal phase space shown in Fig. 1 (left) gives an RMS energy spread ($\Delta E/E$) as high as 140%, when half of the bunch was emitted.

* xiangkun.li@desy.de

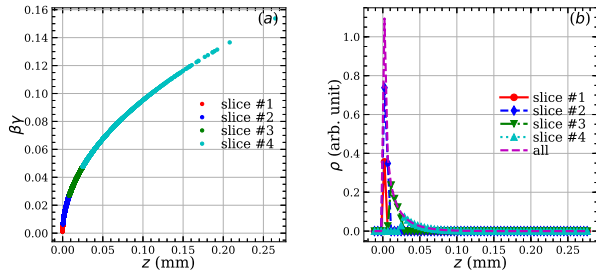


Figure 1: Longitudinal phase space grouped by momentum (a) and charge density profile of each group (b).

In the laboratory frame, the effective transverse space charge field in the horizontal plane is given by $E_x^{\text{eff}} = E_x - vB_y$, where E_x and B_y are the horizontal electric field and vertical magnetic field, respectively, v is the speed of the electron. The components E_x , E_z and B_y are obtained from the static electric field E'_x in the rest frame by Lorentz transformation,

$$E_x = \gamma E'_x, E_z = \gamma E'_z, B_y = \beta \gamma E'_x, \quad (3)$$

where γ is the Lorentz factor. Since $\gamma \sim 1$ during the emission, a large energy spread will affect B_y . In Fig. 2 (a) the B_y fields along the bunch as given in Fig. 1 are plotted. For comparison the space charge forces were solved by either taking the bunch as a whole or by grouping the beam into four slices according to the electrons' momenta (as denoted by colors in Fig. 1 (a)). The longitudinal charge density profile of each bin is shown in Fig. 1 (b). Although the slice #4 has much larger momentum spread, it takes up a much smaller fraction of the whole bunch charge.

In Fig. 2 (a), the difference in B_y between unbinned and binned methods became prominent towards the bunch head (right side) or in the outer part (e.g., $x/\sigma_x = 2$). However, as the B_y component is much smaller than the E_x component (by a factor of β as given in Eq. (3)), the effective focusing field E_x^{eff} turned out to be very insensitive to the momentum spread. As illustrated in Fig. 2 (b), one can hardly see the difference between fields calculated from unbinned and binned methods. The contribution of B_y to the focusing field can be written as $vB_y \sim \beta^2 E_x$. In the case shown here, $\beta \leq 0.14$, thus $vB_y/E_x \ll 1$. As more detailed investigation is still to be performed to study the effect of energy spread on the emission and on the beam dynamics with particle tracking, the unbinned method will be used in the following section to simulate the emission in the RF gun.

EXPERIMENTAL STUDY ON EMISSION

At PITZ, an L-band normal conducting 1.6 cell RF gun with a Cs_2Te photocathode is in operation. A bucking coil and a main solenoid are around the gun cavity for emittance compensation. The gun can provide a gradient as high as 60 MV/m on the cathode [1] for the generation of high-brightness electron bunches for X-ray free-electron

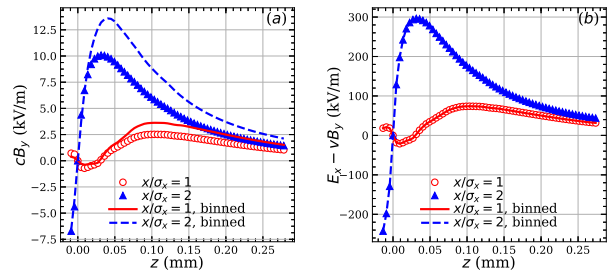


Figure 2: Vertical magnetic field (a) and effective focusing field (b) along the bunch in the laboratory frame.

lasers. The axial field profile in the gun and the accompanying solenoid field profile are given in Fig. 3. In this study, we consider the emission experiments performed at a lower gun gradient of 40 MV/m, which is dedicated to study the emittance optimization for a possible future continuous wave (CW) mode operation condition of the European X-ray Free-Electron Laser (XFEL) with a superconducting RF gun (SCRf) [6].

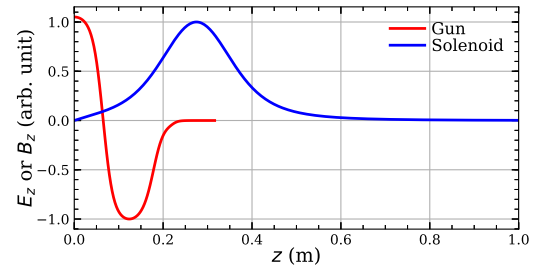


Figure 3: Axial electric and solenoid field profiles in the gun.

The cathode laser passes through a tunable beam shaping aperture (BSA) before hitting the photocathode. By overfilling the BSA with a transversely Gaussian laser, a uniform transverse laser, hence a uniform electron distribution can be generated. The laser can be imaged at a virtual cathode (VC) camera, located at the equivalent distance from the incoming laser as the real cathode inside the RF gun. The measured laser beam deviates from uniform distributions due to optics alignment imperfections or crystal defects, which leaves a core inhomogeneity and non-negligible outer halo surrounding the core. Figure 4 (a) shows the VC image of the laser pulse with a BSA diameter of 1.3 mm. Its radial profile was fitted with a core-halo model [7] in Fig. 4 (b), showing a good uniform core and an apparent tail.

To measure the emission curve, the laser energy was scanned for various BSA diameters. As shown in Fig. 5 (a), the extracted bunch charge increased proportionally with the laser energy when the laser energy was small. As the laser energy increased, the space charge began to dominate the emission, known as emission saturation. When the BSA was

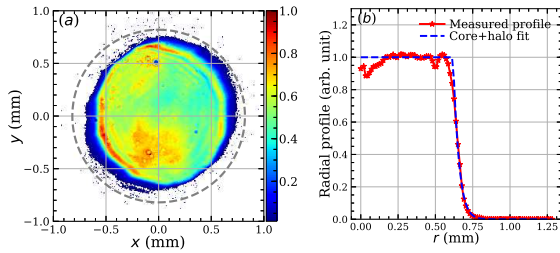


Figure 4: Measured laser transverse profile (a) and core-halo fit (b).

small, the saturation came earlier with respect to the laser energy, as stronger space charge was present.

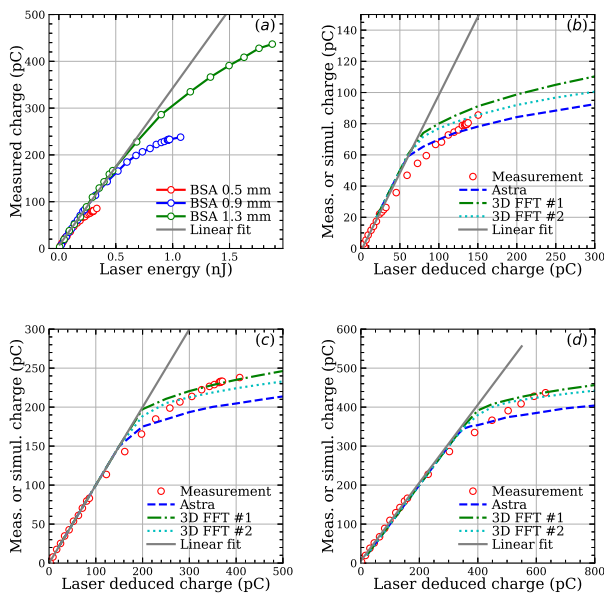


Figure 5: Measurements and simulations on emission curves at various BSA diameters: (a) measurement; (b)-(d) simulations for BSA diameter of 0.5, 0.9 and 1.3 mm.

SIMULATIONS ON EMISSION CURVES

For the simulations, the measured radial profile of the laser pulse was used to modify the initial transverse distribution with 200 k macroparticles generated by Astra for particle tracking using the cylindrical space charge model in Astra. A similar distribution with 10^6 macroparticles was generated for simulations using the 3D space charge solver (referred as 3D FFT #1 later) for comparison with Astra. The 2D laser transverse distribution was also used to generate non-cylindrically symmetric transverse distribution (referred as 3D FFT #2 later) to study the effect of the inhomogeneity on the emission. For the Astra simulation, it has 40 grid cells in radial direction and 50 along the bunch; for the 3D solver, the meshing grids are $N_x \times N_y \times N_z = 32 \times 32 \times 128$.

For three BSA diameters, the input bunch charge was scanned and the extracted bunch charge was collected at the

gun exit. The results are shown in Fig. 5 (b) to (d), where initial transverse distributions are cylindrically symmetric for Astra and 3D FFT #1 and inhomogeneous for #2. For initially cylindrically symmetric distributions, Astra simulations give a lower emission curve in the saturation regime for all the three cases, which may be resulted by the meshing resolution for space charge calculation and will be studied later. For the 3D solver, the inhomogeneity of the initial distribution was found to suppress the emission charge slightly for all the three cases. Still the measured emission curves were not well reproduced. Thus future studies will consider more cathode physics behind the emission process.

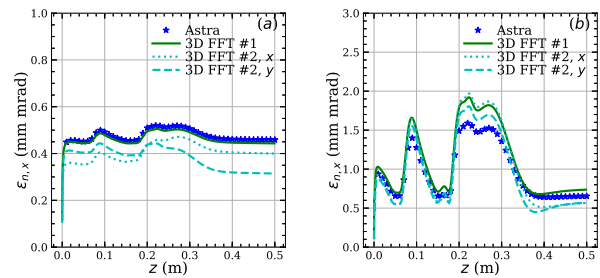


Figure 6: Comparison of simulated RMS emittance in the gun with input charge of 20 pC (a) and 100 pC (b).

In addition, the beam emittance along the gun has been compared for bunch charges of 20 pC and 100 pC at BSA = 0.5 mm, as shown in Fig. 6. For the linear regime (20 pC), good agreement with Astra was found, given the same initial distribution. Meanwhile, the inhomogeneity introduced non-negligible changes to both x and y emittances. For the saturated emission (100 pC), discrepancies appeared after the emission between Astra and the other two, mainly due to the difference in the extracted charges (70 pC for Astra and ~80 pC for the others). The discrepancy implies that the simulated beam parameters in the saturated regime could be unreliable if the emission is not well modelled.

CONCLUSION

A 3D space charge solver using the FFT method has been developed at PITZ for the simulation of the emission curves in the normal conducting RF gun. The large energy spread of the bunch during the emission was analyzed preliminarily and it was found insensitive for space charge calculation. Emission curves were simulated with Astra and tracked with the 3D solver. Discrepancy was found between Astra simulation and the space charge solver, probably due to the meshing solution in the 3D solver. The inhomogeneity of the transverse laser beam distribution could suppress the emission charge slightly. The particle tracking with the 3D solver was also crosschecked with Astra and good agreement was found for the linear regime. The deviation for the saturated regime shows the importance of well modeling the emission.

REFERENCES

- [1] M. Krasilnikov *et al.*, "Experimentally minimized beam emittance from an L-band photoinjector", *Phys. Rev. ST Accel. Beams* 15, Oct. 2012, 100701, doi:10.1103/PhysRevSTAB.15.100701
- [2] K. Flottmann, ASTRA particle tracking code, <http://www.desy.de/~mpyf10/>.
- [3] Y. Chen *et al.*, "Modeling and simulation of RF photoinjectors for coherent light sources", *Nuclear Instruments and Methods in Physics Research Section A: Accelerators, Spectrometers, Detectors and Associated Equipment* 889, 2018, pp. 129-137. doi:10.1016/j.nima.2018.02.017
- [4] J. Qiang *et al.*, "Three-dimensional quasistatic model for high brightness beam dynamics simulation", *Phys. Rev. ST Accel. Beams* 9, 2006, 044204, doi:10.1103/PhysRevSTAB.9.044204
- [5] R.W. Hockney and J.W. Eastwood, *Computer Simulation Using Particles*, Adam Hilger, New York, 1988.
- [6] M. Krasilnikov *et al.*, "PITZ Experimental Optimization for the Aimed Cathode Gradient of a Superconducting CW RF Gun", presented at the 39th Int. Free Electron Laser Conf. (FEL'19), Hamburg, Germany, Aug. 2019, paper WEP051.
- [7] M. Krasilnikov *et al.*, "Investigations on Electron Beam Imperfections at PITZ", in *Proc. 28th Linear Accelerator Conf. (LINAC'16)*, East Lansing, MI, USA, Sep. 2016, pp. 165-167. doi:10.18429/JACoW-LINAC2016-MOPLR013

DEVELOPMENT OF A MULTIALKALI ANTIMONIDE PHOTOCATHODE AT INFN LASA

S. K. Mohanty^{†1}, DESY Zeuthen, Zeuthen, Germany

P. Michelato, L. Monaco, D. Sertore, INFN - LASA, Segrate, Italy

C. Pagani, G. Guerini Rocco, Università degli Studi di Milano & INFN, Segrate, Italy

¹also at INFN-LASA, Segrate, Italy

Abstract

Owing to their excellent properties including high quantum efficiency (QE), low emittance, good lifetime and fast response, alkali antimonides Photocathodes has been considered as one of the eminent candidates for the electron source such as in energy recovery linacs (ERL) and free electron laser (FEL). Along with this fact, our recent projects are aiming for CW operation, where these kinds of material are more suitable for the laser specification. So, by considering this fact and stimulating from former successful development of Cesium Telluride photocathodes, our R&D activity has been started to develop specifically the K-Cs-Sb based multi-alkali photocathodes which are sensitive to the green light at INFN LASA. The primary goal is to develop a stable reproducible alkali antimonide film on INFN plug and test them in the photo injector test facility at DESY in Zeuthen (PITZ). In this report, we present and discuss the different growth procedure and results so far obtained for KCsSb material.

INTRODUCTION

Semiconductor materials belonging to the alkali antimonides family have been widely used for many decades in photon detection application because of their high efficiency in the visible range of the spectrum [1]. But, the reliable growth process for these materials is largely based on recipes obtained by trial and error [2]. So, in order to get highly efficient cathode, a series of different growth procedure and characterization techniques is currently being followed in our R&D activity. Currently our major interest on to develop a reliable and reproducible recipe of K-CS-Sb material, in which we have implemented our past gathered data related on these types of photocathode material [3]. Also, we have included some surface science techniques to investigate the material growth [4].

Information about the film thickness, substrate temperature, thermal treatment and their possible effects on properties of photocathode are discussed in this paper together with a comparison of the performances of the photocathode produced so far.

EXPERIMENTAL LAYOUT

In order to get a stable and reproducible recipe, the current R&D activity has been developed in a dedicated UHV (Ultra High Vacuum) system [5] that consists of two interconnected chambers which are used for cathode growing and storage of samples. The cathode growing chamber is

maintained with based pressure in the 10^{-11} mbar range provided by eight SAES Getters NEG St707[®] modules and a 400 ls⁻¹ ion pump. It is also connected with a μ -metal chamber which hosts a Time Of Flight spectrometer used for thermal emittance measurements [6].

A LDLS (Laser Drive Light Sources) system accompanied by a certain dedicated optical filter (in a range of 239 nm to 436 nm) is used to measure the spectral response of the photocathode. An Ar⁺ and three He-Ne lasers are also used to cover the range from 457 nm to 633 nm.

Photocathode Preparation

To get a better handling, the photo emissive materials are currently being developed on a simplified Mo sample instead of INFN real plug, used in RF guns. These samples are prepared from a thin slab of high purity molybdenum (99.95 %) through machining. Afterwards, these samples are polished to a mirror like finishing (reflectivity > 54 % @ 543 nm w.r.t. 57 % theoretical) to allow reflectivity measurements during and after the photocathode growth. All samples are ultrasonically cleaned before loading then into the UHV system. Afterwards, each sample is heat up to 450 °C for at least one hour to remove the eventual residual on the surface before starting the deposition process.

A custom-made source for Sb and SAES Getters dispensers for Cs and K is used in the operation. Each source is carefully degassed before each deposition and calibrated to have the proper evaporation rate during the cathode growth. The calibration is repeated before each growth process. The usual rate during deposition is 1 nm/min.

FABRICATION RECIPES

Up to now, six photocathodes have been grown and four of them have already been reported in previous papers [5, 7] and summarized in Table 1. The main outcome of this experience was the need for a better temperature control and a diversification of the temperatures for K and Cs. We explored also photocathodes with different Sb thickness to evaluate its influence on the photocathode properties. The details of growth of two successive cathodes including the influence of both temperature and thickness on photocathode's properties has been reported in this report.

KCsSb-5

Since, we recorded a low Quantum Efficiency (QE) for KCsSb-4 (Table 1) where we used 5 nm of Sb, we assumed this was mainly related to the thickness of photocathode material. So, we decided to grow a thicker photocathode. We have grown 10 nm Sb followed by K and Cs at 90 °C

[†] sandeep.mohanty@desy.de.

as for KCsSb-4. The detailed photocurrent (@ 543 nm) and reflected power history is reported in Fig. 1. A very long exposition to Cs is clearly visible without a clear maximum indicating the formation of the photocathode. With this recipe, the QE was recorded 4.6 % at 514 nm.

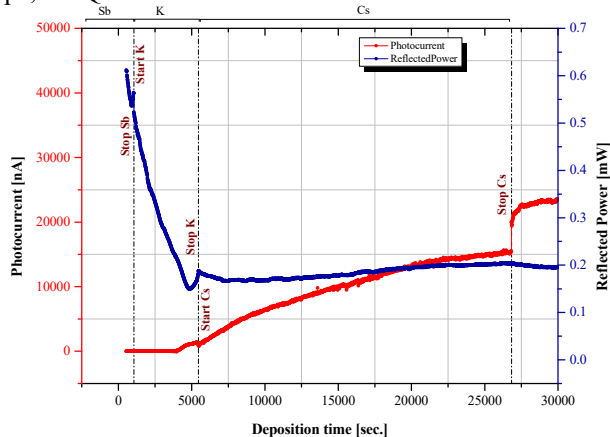


Figure 1: Photocurrent (red) and reflected power (blue) during deposition of cathode KCsSb-5. The incident power @ 543 nm during photocathode growth was 1.9 mW.

KCsSb-6

To further investigate the effect of thickness and temperature, we produced this new cathode with a thin Sb layer by changing the substrate temperature. We have grown 5 nm Sb at 90 °C. Thereafter we increase the substrate temperature up to 120 °C and deposited the K until the maximum photocurrent. During this process we observed a comparatively less amount of K was deposited than the cathode KCsSb-4 as reported in Table 1. Potentially, increase in substrate temperature helps a faster reaction between K and Sb, so that the photocurrent reached to the maximum in less time and required a less amount of K. Thereafter, we decreased the substrate temperature to 90 °C and deposited Cs until the photocurrent reached maximum (see Fig. 2). With this recipe, the final photocathode QE was recorded 4.6 % at 514nm.

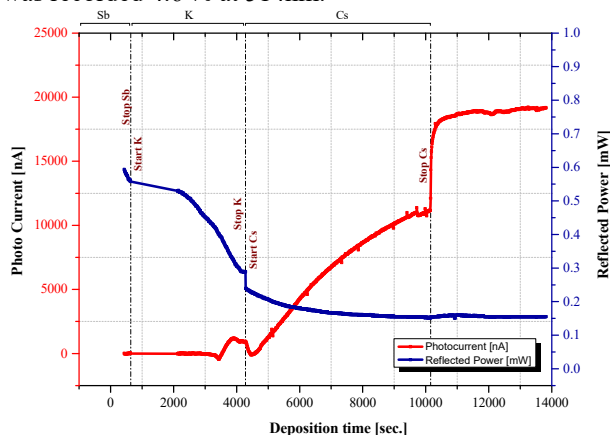


Figure 2: Photocurrent (red) and reflected power (blue) during deposition of cathode KCsSb-6. The incident power @ 543 nm during photocathode growth was 1.9 mW. Notice the much shorter production time with comparable final photocurrent.

CHARACTERIZATION OF THE PHOTO-CATHODES

Since, the QE of cathode 1 and 2 was very low, we did not consider them for the following characterization. Figure 3 shows the comparison of QE @ 543 nm during K deposition for KCsSb-3,4,5,6 cathodes. It clearly shows that the substrate temperature plays a significant role in terms of QE for both thin (5 nm Sb) and thick (10 nm Sb) cathodes. A comparatively higher temperature (120 °C for 5 nm and 90 °C for 10 nm Sb) gives a higher final QE. Moreover, regarding thickness higher temperatures favor less amount of K deposition. All these indications confirm that a higher substrate temperature induces a faster chemical reaction between K and Sb, requiring then less amount of K to reach comparable QEs.

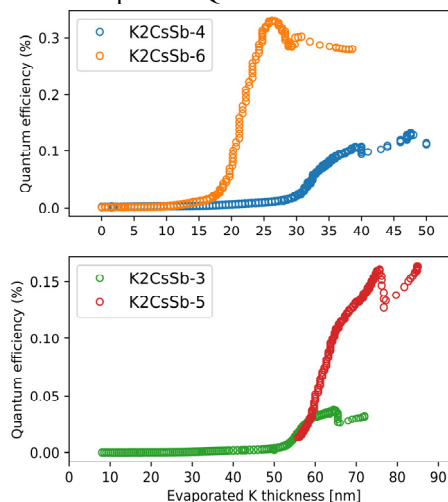


Figure 3: Comparison of QE @ 543 nm during K deposition. Upper plot “5 nm Sb”, lower plot “10 nm Sb”.

Similarly, the QE during the Cs deposition behaves dependently to the substrate temperature for all four cathodes as shown in Fig. 4. For thick cathodes, KCsSb-5 (grown at 90 °C) observed a higher QE slope compare to the KCsSb-3. Similarly, KCsSb-6 cathode observed a higher QE slope compare to KCsSb-4.

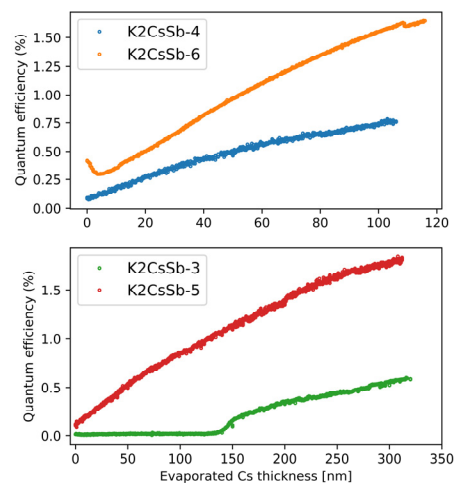


Figure 4: Comparison of QE @ 543 nm during Cs deposition. Upper plot “5 nm Sb”, lower plot “10 nm Sb”.

By comparing the reflected power during the deposition between similar thickness cathodes, we found that the behavior of the reflected power curve is quite reproducible, and it's related to the thickness of the material. This behavior is reported in Fig. 5 for "5 nm Sb" (left) and "10 nm Sb" (right).

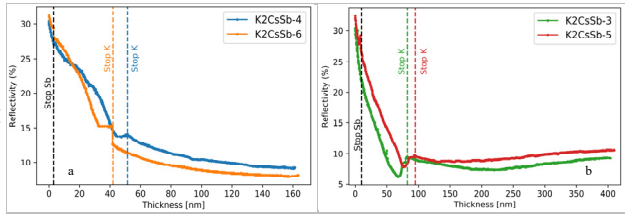


Figure 5: Comparison of reflected power during the photocathodes deposition for 5 nm (a) and 10 nm (b) at 543 nm. The trend is clearly dependent of the Sb layer thickness.

The comparison of final QEs between all four photocathodes is reported in Fig. 6. Due to some technical problem, a spectral response has been limited from 457 nm to 594 nm for KCsSb-3 & 4. Besides this, the behavior of QE at all the wavelengths for all four cathodes is comparable. The maximum QE @ 514 nm recorded 5.2 % for KCsSb-3 and 4 cathodes.

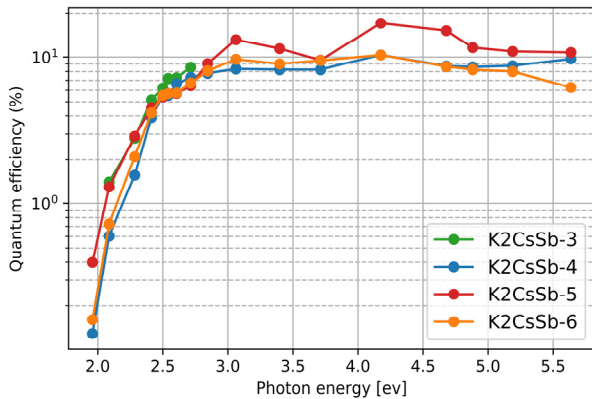


Figure 6: Comparison of QE for KCsSb-3,4,5,6 cathodes.

However, from the comparison of reflectivity behavior between the four cathodes (Fig. 7), shows that thin cathodes (5 nm Sb) at higher wavelength (543 nm, 594 nm) behave completely opposite compare to the thick ones (10 nm Sb).

Table 1: Summary Of Cathode Growing Parameters

Cathode	Sb (nm)	T _{Sb} -T _K -T _{Cs} (°C)	QE (514nm) (%)
KCsSb-1	10	120-150-120	9 · 10 ⁻³
KCsSb-2	5	120-150-120	1.9
KCsSb-3	10	60-60-90*	5.2
KCsSb-4	5	90-90-90	3.9
KCsSb-5	10	90-90-90	4.6
KCsSb-6	5	90-120-90	4.6

*increased from 60 °C to 90 °C during Cs evaporation as reported in [5]

Table 1 summarizes the growing conditions for the KCsSb photocathodes grown so far. All the photocathodes

have been grown monitoring the photocurrent @ 543 nm. The temperature column reports the substrate temperatures during the different element depositions. As already noticed in our previous works, cathode 1 and 2 suffers a too high temperature during K deposition that inhibits the proper cathode formation. Moreover, for thin cathodes 120 °C substrate temperature during K evaporation results in higher QE.

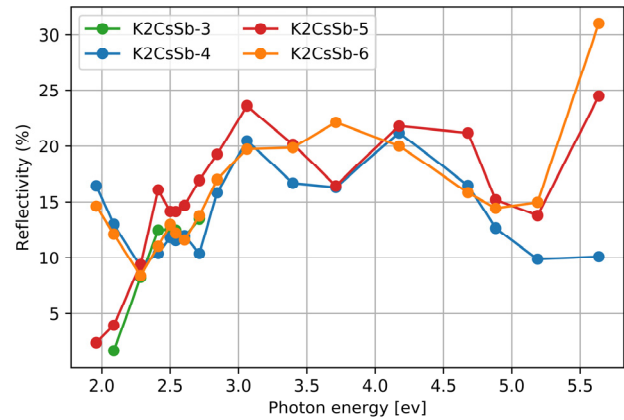


Figure 7: Reflectivity for KCsSb-3,4,5,6 cathodes.

CONCLUSION

The INFN LASA activity on photocathode sensitive to visible light is progressing. A stable recipe is now established, and the R&D activity is exploring influence of Sb thickness and substrate temperatures.

At the same time, we are progressing towards the assembly of a new photocathode production system dedicated to these types of cathodes for growing them on our INFN plugs. This will allow testing them in the environment of RF guns, in particular at the PITZ facility in DESY Zeuthen

ACKNOWLEDGEMENT

We acknowledge DESY Zeuthen for the fruitful collaboration towards the test of these photocathodes in the PITZ RF guns.

REFERENCES

- [1] Photomultiplier Tubes, Hamamatsu Photonics K.K., Electron Tubes Division, 2006.
- [2] A.H. Sommer, *Photoemissive Materials*, 2nd Edition, E. Krieger, New York, 1980.
- [3] P. Michelato, A. di Bona, C. Pagani, D. Sertore, and S. Valeri, "R & D activity on high QE alkali photocathodes for RF guns", in *Proc. 16th Particle Accelerator Conf. (PAC'95)*, Dallas, TX, USA, May 1995, paper WPC23, pp. 1049-1051. doi:10.1109/PAC.1995.505125
- [4] A. di Bona *et al.*, "Development, operation and analysis of bialkali antimonide photocathodes for high-brightness photo-injectors", *Nucl. Instr. Meth. A* 385 (1997), p. 385. doi:10.1016/S0168-9002(96)00809-1
- [5] D. Sertore, P. Michelato, L. Monaco, and C. Pagani, "R&D activity on alkali-antimonide photocathodes at INFN-Lasa", in *Proc. 9th Int. Particle Accelerator Conf. (IPAC'18)*, Vancouver, Canada, Apr.-May 2018, pp. 4284-4286. doi:10.18429/JACoW-IPAC2018-THPMF088

- [6] D. Sertore, D. Favia, P. Michelato, L. Monaco, and P. Pierini, “Cesium telluride and metals photoelectron thermal emittance measurements using a time-of-flight spectrometer”, in *Proc. 9th European Particle Accelerator Conf. (EPAC'04)*, Lucerne, Switzerland, Jul. 2004, paper MOPKF045, pp. 408-410.
- [7] D. Sertore, G. Guerini Rocco, P. Michelato, S. K. Mohanty, L. Monaco and C. Pagani, “Photocathode activities at INFN LASA”, in *Proc. 10th Int. Particle Accelerator Conf. (IPAC'19)*, Melbourne, Australia, May 2019, pp. 2203-2206.
doi:10.18429/JACoW-IPAC2019-TUPTS11

BEAM DYNAMICS OPTIMIZATION OF A NORMAL-CONDUCTING GUN BASED CW INJECTOR FOR THE EUROPEAN XFEL*

H. Shaker[†], H. Qian, S. Lal, G. Shu, F. Stephan, DESY, Zeuthen, Germany

Abstract

The European XFEL is operating up to 17.5 GeV electron energy with maximum 0.65% duty cycle. There is a prospect for continuous wave and long pulse mode (CW/LP) operation of the European XFEL, which enables more flexible bunch pattern time structure for experiments, higher average brightness and better stability. Due to engineering limitations, the maximum electron beam energy in the CW/LP mode is about 8.6/12.8 GeV [1], which puts more pressure on the injector beam quality for lasing at the shortest wavelength. This paper optimizes the beam dynamics of an injector based on a normal-conducting VHF gun.

INTRODUCTION

The European XFEL operates in the pulsed mode at the moment. The duration of each RF pulse is max. 650 μ s and the repetition rate is 10 Hz. The time interval between bunches inside a pulse is 220 ns. This result to 27000 bunches per second and 0.65% duty cycle. For future development, the CW/LP mode operation is considered. Recent study shows a maximum 25 μ A average current capability of SRF cavities in the European XFEL [1]. Based on this, the optimal value for the CW mode is selected to be 100 pC bunch charge with 4 μ s bunch time interval. The maximum achievable energy is about 8.6 GeV for the CW mode. For the LP mode the energy can be increased to about 12.8 GeV [1]. More pressure on the beam quality is at the lower energy of the CW mode for lasing at short wavelengths. This requires better beam quality in comparison to the pulsed mode. The pulsed mode injector is based on a normal-conducting photocathode RF gun which is located in the XTIN1 tunnel [2]. To have the ability to work in dual modes, a new injector is required which will be placed in the XTIN2 tunnel on top of the XTIN1 tunnel. The second injector should have more or less the same energy as the first injector which is above 120 MeV [2,3]. To have a complete superconducting machine, the first choice is a superconducting gun. This kind of injector is under study and test [4]. As a backup solution a normal-conducting gun based CW injector is studied at PITZ [5,6]. CW Normal conducting photo-cathode RF guns were developed at LBNL in last decade based on mature room temperature RF technology [7], and the main limitation is the high average heat loss which limits both the achievable cathode gradient and the gap voltage. From DC to gigahertz frequency range, VHF band frequencies give us a reasonable cathode gradient,

gap voltage and surface heat power. The successful CW APEX gun operates at 187 MHz, 20MV/m cathode gradient and 750KV gap voltage [7]. This gun is used as the electron source for LCLS-II at SLAC [8].

Based on the APEX experience, a 216.6 MHz gun is under physics design at PITZ, and the cathode gradient and gun voltage are increased to 28 MV/m and 830 kV respectively[5, 6]. Besides, a 400 kV normal-conducting 1.3GHz buncher was developed [9]. To validate the gun and buncher design, a new injector dynamics optimization is presented in this paper. A multi-objective optimizer parallel processing code[10] based on the NSGA-II [11] algorithm is used to drive ASTRA [12] simulations for optimizing the injector.

MAIN BEAMLINE ELEMENTS

Figure 1 shows the conceptual beamline layout. To find the right amount of input parameters for the optimization algorithm we will talk about each component in the beamline. The initial laser beam has a flat-top longitudinal distribution with 2ps rise/fall time. The transverse distribution is Gaussian truncated at 1σ . The laser duration and radius are variable in the optimizer. Two cathode thermal emittances are assumed for injector optimizations: 1mm.mrad/mm for conservative case and 0.5mm.mrad/mm for optimistic case. The first case is close to the Cs₂Te cathode [13], and the second case is close to the multi-alkali cathode, such as K₂CsSb and NaKSb [14].

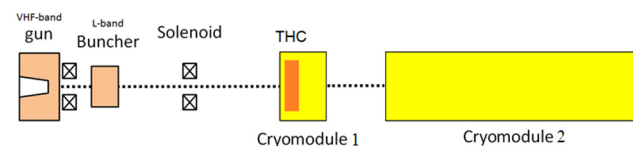


Figure 1: Beamline Layout

Gun and Main Solenoid

To minimize the emittance growth due to space charge, the electrons should be accelerated into the relativistic regime after photoemission as fast as possible. Then the maximum cathode gradient and gap voltage is desirable, but the average heat loss and the peak electric field on cavity surface limits the cathode gradient. Based on APEX gun experience, a maximum 100 kW heat loss and 30 MV/m peak surface field are considered as the baseline parameters. Due to these limitations a gun with 28 MV/m cathode gradient, 832 kV gap voltage and 3cm gap length was designed [5, 6]. Only the gun phase is variable during the beam dynamics optimization. The cathode position is assumed to be zero ($z=0$). The gun solenoid

* Work supported by the European XFEL

[†] hamed.shaker@desy.de

should be as close to the cathode as possible, but without leaking high magnetic field onto the cathode. We fixed the solenoid central position at $z=0.236$ m. We used a solenoid profile designed by HZB, and its spherical aberration is 30% lower than the LCLS-II solenoid [15].

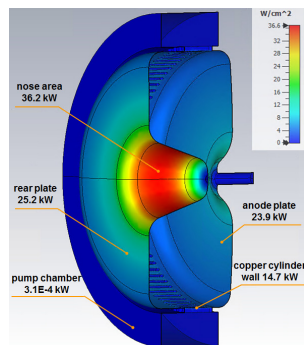


Figure 2: Gun Layout [6]

L-Band Buncher

The 1.3 GHz buncher is mainly for chirping the beam for velocity bunching, meanwhile it also accelerates the beam to reduce the space charge effect and thus reduce emittance growth. Figure 3 shows the current buncher design geometry and its axial electric field, more details of the buncher cavity design can be found in reference [9]. For the optimizer, the parameters we can play with are the RF input phase, total voltage up to 400kV (maximum achievable voltage) and also the buncher longitudinal position. The beam dynamics study shows better results for closer positions to the cathode but because of required components like main solenoid, vacuum valve and BPM, $z=0.73$ m is the closest possible position.

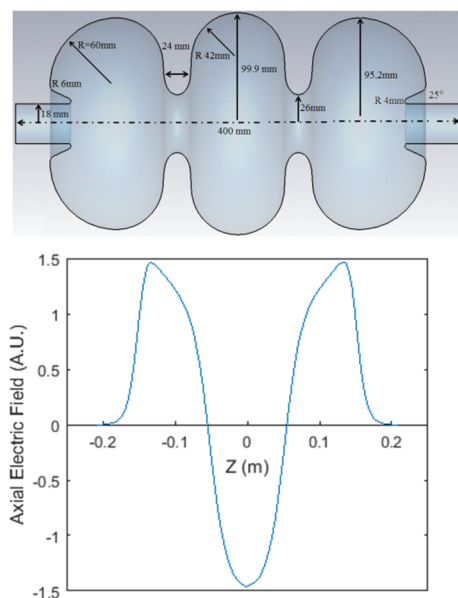


Figure 3: 1.3GHz buncher: geometry and axial field profile

Second Solenoid

The second solenoid is required for the matching of the beam to the following accelerating structure. For the optimizer, the longitudinal position and the current can be used. The result is not so sensitive to the solenoid position due to the preliminary beam dynamic study. Then with considering the required components between buncher and the cryomodule the longitudinal position is fixed to $z=1.6$ m which is about in the center between cathode and the center of first accelerating cavity.

Accelerating Structures

In an initial study we worked with the standard XFEL cryomodule with eight 9-cell TESLA cavities but the result was not satisfying. By turning off the second and third cavities we reached some more satisfying result but the output energy was low (about 90 MeV). To resolve this problem we are using the same number of cavities inside two separate cryomodules for our model. The first cryomodule is smaller and has one or two cavities. The rest cavities are inside the second cryomodule. The distance between the cavity centers is 1.3848 m in each cryomodule. For injector optimization, the amplitudes of the first two cavities are variable. For optimizing the velocity bunching, the phase of the first cavity is also allowed to vary. We put the rest cavities on-crest with maximum conservative amplitude of 32 MV/m. For future development, higher field up to 40 MV/m is planned [1]. Because of required components like laser window, BPM, vacuum valve etc between gun and booster linac, the minimum distance from cathode to the center of the first cavity inside the cryomodule 1 is set to 3 meter in optimizer. The drift between two cryomodules can also be optimized. Two cases are studied separately: 2+6 and 1+7 cavity cryomodules setup. Table 1 shows the best result we found for each case for 100pC bunch charge and 1mm.mrad/mm thermal emittance. Based on these results the 2+6 case is slightly better. To lower the total cost, it is better to use a standard X-FEL cryomodule instead of cryomodule 2 because of its availability. Then our models will be modified to 1+8 and 2+8 cavities with the same parameter values but with higher final energy. In this case we should consider the space availability in XTIN2 tunnel which gives us the 1+8 case as a more practical solution.

Third-Harmonic Cavity

Due to the nonlinear dynamics of velocity bunching in the low energy drift, the beam temporal profile gradually loses the flattop distribution, and develops a long tail at the injector exit. It's found most of the beam longitudinal asymmetry or skewness happens at the entrance of the cryomodule 1, because its RF phase is more close to on-crest phase and the beam gets a high 2nd order energy chirp. Similar to the phase space linearization for optimizing magnetic bunch compression, a harmonic cavity is introduced between buncher and the first cavity in cryomodule 1, as shown in Fig. 1, to symmetrize the beam longitudinal distribution. Figure 4 shows the longitudinal

profile after and before symmetrisation using this cavity. The third case in table 1 shows the final beam parameters when it is longitudinally symmetrized. This cavity will be operated on 3.9 GHz with relatively small dimension and with the peak gradient about 8MV/m. Then it is so difficult to maintain it at resonance temperature in high average power CW operation and therefore it should be a super-conducting cavity. We propose to put this cavity inside the cryomodule 1.

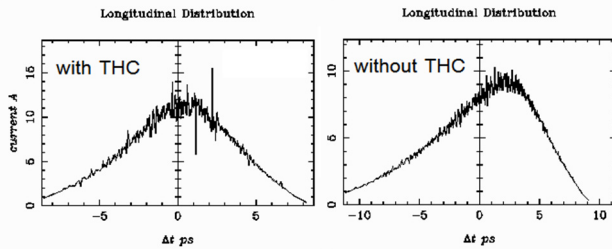


Figure 4: The effect of third-harmonic cavity to symmetrize the longitudinal profile

RESULTS AND SUMMARY

In last section we showed the result for 100pC bunch charge and 1mm.mrad/mm thermal emittance case which is valid for CS₂Te cathode [13]. We used the multi-objective evolutionary optimizer code [10] to minimize the transverse emittance and longitudinal bunch length. The optimizer gives us the Pareto front of optimal solution (see Fig. 5) and afterward in the post-processing we will select the solutions where the peak current is about 10A which is shown by the arrows in the Figure 5. The selected model was simulated again for finer mesh and more particles for more accurate results. We did the same for green cathodes such as K₂CsSb and NaKSb [14] with 0.5 mm.mrad/mm thermal emittance and the result is in the last column of Table 1. In this table just the higher order energy spread is mentioned because the first and second order energy spread will be minimized by the following accelerating structures and the third-harmonic cavity, respectively [16]. The higher order energy spread will remain and will be amplified by the following bunch compressors and reduce the final x-ray radiation brightness. All the rest beamline component parameters are mentioned in the table 2.

Table 1: Final Beam Parameters for Different Cases

Case	2+6	1+7	1+7 With THC	1+7 Green Cathode w/o THC
Emittance (100/95%) (mm.mrad)	0.19/0.13	0.19/0.14	0.18/0.14	0.13/0.09
Average sliced emittance (mm.mrad)	0.13	0.15	0.17	0.09
H.O Energy Spread (KeV)	2.9	2.2	2.7	2.8
Peak current (A)	11.5	10	11.5	10

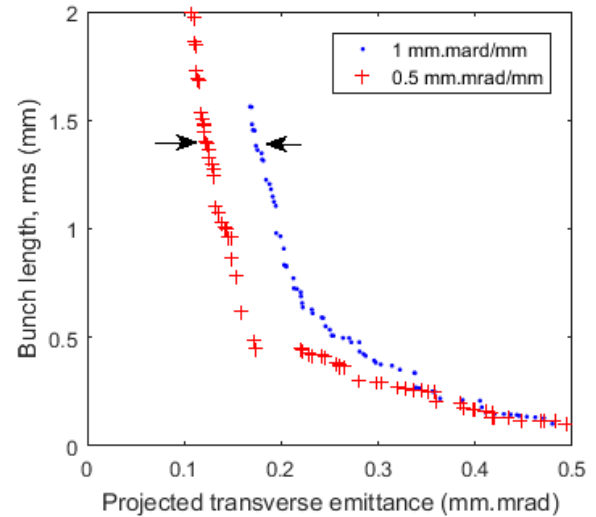


Figure 5: Pareto Front of optimizer for Cs₂Te and green cathode

Table 2: Final Beamline Components Parameters for Different Cases

Case	2+6	1+7	1+7 With THC	1+7 Green Cathode w/o THC
Laser spot size (mm)	0.24	0.26	0.28	0.26
Initial bunch length (ps)	51.5	45.6	40.0	47.8
Gun phase (deg)	3.1	-7.2	-1.1	-5.3
First (Second) Solenoid peak / Integral field (T/T.m)	0.058/ 0.0086 (0.036/ 0.0054)	0.060 /0.0090 (0.037 /0.0055)	0.062/ 0.0080 (0.032/ 0.0042)	0.060 /0.0089 (0.037 /0.0055)
Buncher Voltage (KV)	398	363	380	383
Buncher Phase (Deg)	-26.2	-35.8	-33.1	-32.2
First Cavity center (m) cryomodule 1/2	3.17/ 8.00	3.00 / 6.03	3.36/ 7.51	3.16 / 6.47
First/Second cavity max. field (MV/m)	23.52/ 29.36	23.18/ 3.80	21.14/ 25.11	23.67/ 22.45
First/Second cavity phase (deg)	-58.9/0	-29.7/0	-41.1/0	-36.5/0
Third-Harmonic cavity Max. field (MV/m)	0	0	8.1	0
Third-Harmonic cavity phase (deg)	0	0	180	0
Third-Harmonic cavity center (m)	0	0	1.8	0

REFERENCES

- [1] D. Kostin and J. Sekutowicz, “Ingredients for CW operation of SRF Linacs”, Hamburg Alliance New Beams and Accelerators, DESY, Hamburg, September 2018.
- [2] M. Altarelli *et al.*, “The European X-Ray Free-Electron Laser Technical design report”, DESY 2006-097, July 2007, Ch. 7.
- [3] F. Brinker, “Commissioning of the European XFEL Injector”, in *Proc. 7th Int. Particle Accelerator Conf. (IPAC'16)*, Busan, Korea, May 2016, pp. 1044-1047. doi:10.18429/JACoW-IPAC2016-TU0CA03
- [4] E. Vogel *et al.*, “SRF Gun Development at DESY”, in *Proc. 29th Linear Accelerator Conf. (LINAC'18)*, Beijing, China, Sep. 2018, pp. 105-108. doi:10.18429/JACoW-LINAC2018-MOP0037
- [5] S. Shu, Y. Chen, S. Lal, H. J. Qian, H. Shaker, and F. Stephan, “FIRST DESIGN STUDIES OF A NC CW RF GUN FOR EUROPEAN XFEL”, in *Proc. 10th Int. Particle Accelerator Conf. (IPAC'19)*, Melbourne, Australia, May 2019, pp. 1698-1701. doi:10.18429/JACoW-IPAC2019-TUPRB010
- [6] G. Shu, Y. Chen, S. Lal, H. J. Qian, H. Shaker, and F. Stephan, “Multiphysics Analysis of a CW VHF Gun for European XFEL”, presented at the 39th Int. Free Electron Laser Conf. (FEL'19), Hamburg, Germany, Aug. 2019, paper WEP055.
- [7] F. Sannibale *et al.*, Advanced Photoinjector Experiment Photogun Commissioning Results, PRST AB 15, 103501 (2012), doi.org/10.1103/PhysRevSTAB.15.103501
- [8] LCLS-II Technical Design Report, T.O. Raubenheimer, ed. (2017).
- [9] S. Lal *et al.*, “RF Design Studies of a 1.3 GHz Normal Conducting CW Buncher for European X-FEL”, in *Proc. 10th Int. Particle Accelerator Conf. (IPAC'19)*, Melbourne, Australia, May 2019, pp. 3109-3111. doi:10.18429/JACoW-IPAC2019-WEPTS012
- [10] C. F. Papadopoulos *et al.*, “Longitudinal and Transverse Optimization for a High Repetition Rate Injector”, in *Proc. 36th Int. Free Electron Laser Conf. (FEL'14)*, Basel, Switzerland, Aug. 2014, paper THP057, pp. 864-867.
- [11] K. Deb *et al.*, “A Fast and Elitist Multiobjective Genetic Algorithm: NSGA-II”, *IEEE Transactions on Evolutionary Computation* (Volume: 6, Issue: 2, Apr 2002).
- [12] K. Floettmann. ASTRA code. <https://www.desy.de/~mpyflo/>
- [13] P. W. Huang *et al.*, “Test of Cs₂Te Thickness on Cathode Performance at PITZ”, presented at the 39th Int. Free Electron Laser Conf. (FEL'19), Hamburg, Germany, Aug. 2019, paper WEP062.
- [14] S.S. Karkare *et al.*, “Advances in Photocathode Technology at Cornell University”, in *Proc. North American Particle Accelerator Conf. (NAPAC'13)*, Pasadena, CA, USA, Sep.-Oct. 2013, paper TUOAB1, pp. 391-393.
- [15] Jens Völker, Private communications
- [16] C.F. Papadopoulos *et al.*, “RF Injector Beam Dynamics Optimization for LCLS-II”, in *Proc. 5th Int. Particle Accelerator Conf. (IPAC'14)*, Dresden, Germany, Jun. 2014, pp. 1974-1976. doi:10.18429/JACoW-IPAC2014-WEPRO015

MULTIPHYSICS ANALYSIS OF A CW VHF GUN FOR EUROPEAN XFEL

G. Shu*, H. Qian, S. Lal, H. Shaker, Y. Chen, F. Stephan, DESY, Zeuthen, Germany
*on leave from IHEP/CAS, Beijing, China

Abstract

R&D for a future CW operation mode of the European XFEL (E-XFEL) started after the successful commissioning of the pulsed mode. For the electron source upgrade, a fully superconducting CW gun is under experimental development at DESY in Hamburg, and a normal conducting (NC) CW gun is under physics design at the Photo Injector Test facility at DESY in Zeuthen (PITZ) as a backup option. Based on the experience of the LBNL 185.7 MHz gun, PITZ designed a 216.6 MHz gun with increased the cathode gradient and RF power of 28 MV/m and 100 kW, respectively, to further improve the beam brightness. In this paper, the multiphysics analysis investigating the RF, thermal and mechanical properties of the NC CW gun are presented.

INTRODUCTION

Driven by the user experimental requirements, a future upgrade of the E-XFEL towards to CW operation has been proposed [1-2]. For the electron source upgrade, one option is a superconducting RF gun, which is under experimental verification at DESY Hamburg [3]. The other option is a VHF band NC CW RF gun which has demonstrated high brightness, high repetition rate (MHz-class) beam at LBNL in the APEX project [4]. Based on the APEX gun experience, a VHF band NC CW RF gun resonating at 216.6 MHz is under physical design stage at PITZ as a backup solution for the SRF gun. To further improve the beam brightness the cathode gradient and cavity voltage were pushed to 28 MV/m and 830 kV, respectively, yielding an average power loss of 100 kW.

The aim of this paper is to evaluate the cooling scheme for the PITZ CW gun to avoid excessive structural temperature, stress, and deformation. In addition, the predicted frequency shift due to heat expansion and air pressure can give a hint for the coarse tuning in the machining phase.

METHODOLOGY

The CST Microwave Studio (MWS) [5] in combination with the CST Mphysics Studio (MPS) were used to perform the coupled electromagnetic-thermal-structural finite element analysis to characterize the cooling capability of the water channels. The methodology of multiphysics simulations is described in Fig. 1. We start from the eigenmode solver in the MWS to obtain the RF induced surface heating distribution. Then, the field map is transferred into the MPS thermal module to evaluate the steady-state temperature distribution. Afterwards, the thermal simulation results are imported into the MPS structure module to simulate the heat induced expansion, i.e. the structure deformations and

the von Mises stresses. In the last step, the resonant frequency is calculated again with the deformed shape in the MWS to estimate frequency detuning due to thermal load and vacuum pressure.

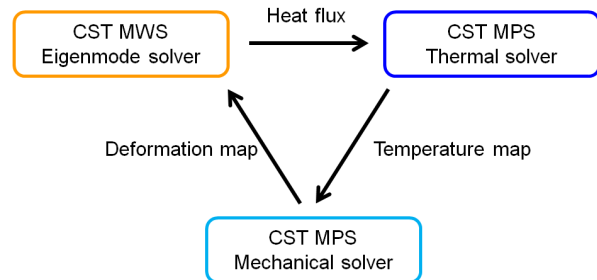


Figure 1: Schematic of the multiphysics simulations.

RF SIMULATION

The 6th sub-harmonic of 1.3 GHz (216.6 MHz), which is higher than the resonant frequency of the APEX gun (185.7 MHz), was selected as resonant frequency for better compatibility with the existing E-XFEL timing system. To improve the beam quality, the cathode gradient and the cavity voltage were enhanced to 28 MV/m and 830 kV, respectively. The cavity shunt impedance was optimized to minimize the heating load to ~100 kW in the gun. By adopting the Rogowski profile, the surface peak electric field was restricted to 2.0 Kilpatrick limit under the consideration of breakdown risk. More details about the RF design can be found in Ref. [6].

Figure 2 shows the RF model in the multiphysics simulations. The vacuum model consists of a re-entrant cavity, 90 vacuum conduction slots and a pump chamber. Figure 2 also indicates the heating distribution on the inner surface and the power dissipation on the sub-assemblies. The total power loss on the cathode nose cone is 36.2 kW with a peak surface loss density of 36.6 W/cm², which can be further reduced by elongating the nose cone. The RF heating on the rear plate, cylinder wall and the anode plate are 25.2 kW, 14.7 kW and 23.9 kW, respectively.

* guan.shu@desy.de

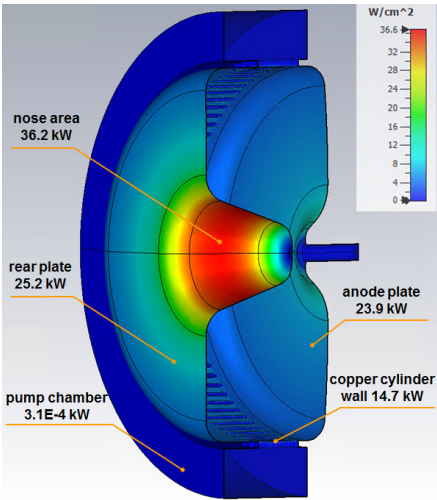


Figure 2: RF heating distribution on the inner surface and the total power dissipation on the sub-assemblies.

THERMAL ANALYSIS

Based on the APEX gun experience [7], the preliminary mechanical design of the PITZ CW gun was conducted to estimate the gun performance at full power operation. The metal body in the mechanical simulations is composed of a stainless steel pump chamber, a copper cavity and four stainless steel tuning rods (see Fig. 3). The inner water channels revealed in Fig. 3 were organized according to the heat flux map. The sub-assemblies are machined individually and jointed together by electron beam welding. All the sub-assemblies of the cavity are made by hard copper except for the cathode nose cone and the rear plate. A vacuum furnace brazing process has to be implemented to embed the cooling channels into the nose cone turning the hard copper to annealed copper.

The RF sealing is realized by a canted spring located between the copper wall and the anode plate. The tight connection surrounding the spring must be maintained by the external reinforcements. Otherwise, a gap might appear to degrade the cavity quality factor thus increasing the heat load and forming a virtual vacuum leak.

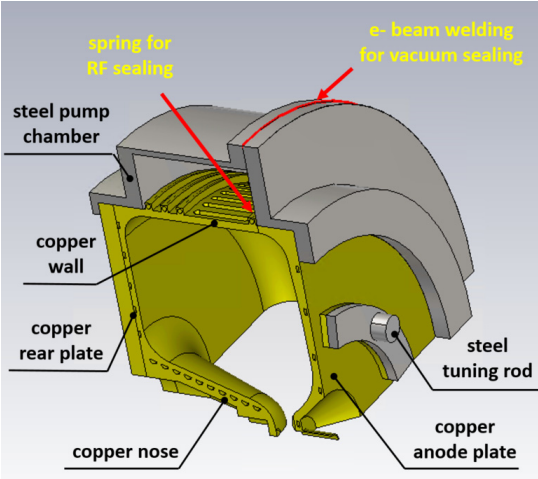


Figure 3: 3D 1/4 model in the mechanical simulations.

In order to simplify the simulation, the non-critical components (e.g. bolts, flanges, supports and external reinforcements) are not included in the model. The nonlinearity of the material properties are not taken into consideration in the thermal simulation. The ambient temperature is considered to be 20°C.

The RF heating is removed by water with a constant temperature of 20°C at a speed of 3 m/s. The water temperature rise distribution in the channel will be complemented in the future work. The cooling parameters used in the thermal simulation are listed in Table 1. The heat convection factors determined by the water velocity, cooling pipe dimensions and water temperature are derived from the empirical formulas [8].

Table 1: Cooling Parameters of the Water Pipes in the Thermal Simulation

Cooling parameters	Water speed [m/s]	Flow rate [L/min]	Heat convection factor [W/(m²K)]
Anode plate	3	7.2	12757.5
Cylinder wall	3	9.0	11927.2
Rear plate	3	7.2	12757.5
Cathode nose cone	3	10.2	12137.0

Figure 4 depicts the steady-state temperature distribution in the cavity body at 100 kW power loss yielding a maximum temperature of 57.2°C located near the center of the anode nose cone. The cathode temperature is 45°C which is compatible with various photocathodes e.g. Cs₂Te and CsK₂Sb [9].

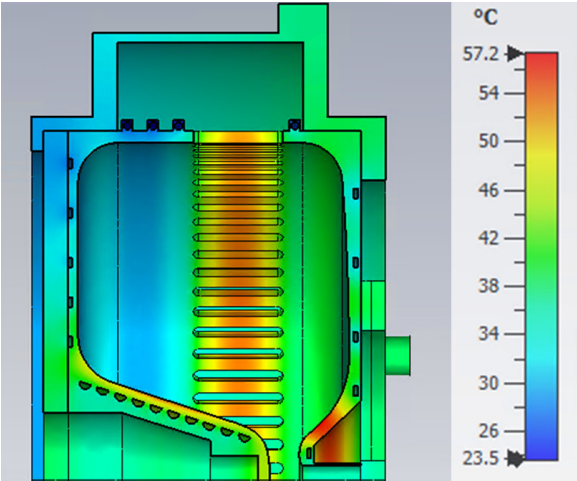


Figure 4: Temperature distribution with 100 kW power dissipation on the cavity wall.

STRUCTURE ANALYSIS

For the structure simulation, the thermal results were imported into the MPS mechanical module. Vacuum pressure was applied to the inner surface as a counteracting force suppressing the thermal expansion. As mentioned in the previous section, the connection between the anode plate and the copper wall is of great importance. Therefore, we fixed the areas related to the electron beam welding line (Fig. 3) in simulations.

The deformation map due to the thermal expansion and inside vacuum pressure is shown in Fig. 5. The maximum displacement is 0.26 mm located at the middle of the anode plate. The equivalent von Mises stress distribution is shown in Fig. 6. The peak stresses in the soft copper, hard copper and the steel chamber are 45.0 MPa, 110 MPa and 114 MPa, respectively. The stresses are much lower than the yield strength of the corresponding materials [10]. In addition, the fixed boundary means the displacement is set to zero mandatorily which overestimates the stress level around the fixed areas.

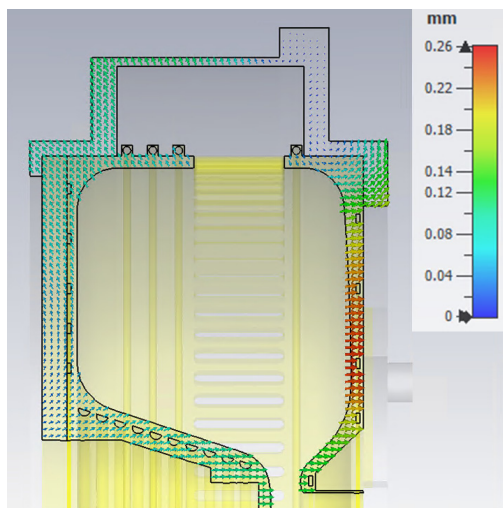


Figure 5: Cavity displacement distribution.

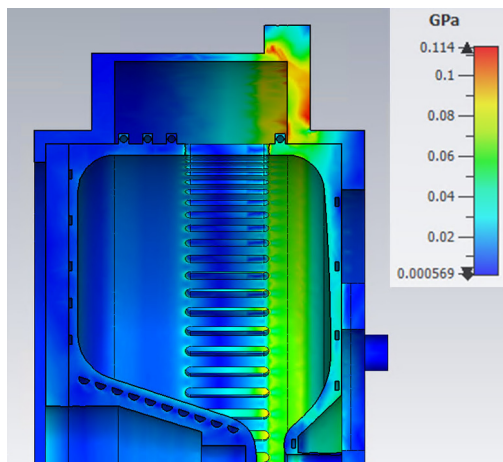


Figure 6: Cavity von Mises stress distribution.

FREQUENCY TUNING APPROACH

Without frequency tuning, the cavity frequency changes under different conditions. From room temperature frequency in the air to the frequency under full power operation, the frequency change is defined by the vacuum pressure induced cavity deformation, air permittivity and thermal expansion. According to the simulations, the frequency is reduced by 262.4 kHz due to the vacuum pressure induced deformation. The 100 kW thermal expansion yields a frequency increase by 206.2 kHz. The frequency is increased by 66.9 kHz due to the air permittivity (here we

assume the air temperature is 20°C, the relative humidity is 40% and the atmospheric pressure is 101 kPa). From the status in the air to the operation condition, the total frequency change is 10.7 kHz. From the cavity off in vacuum to the full operation, the total frequency shift is +206.2 kHz.

It has been found for the APEX gun that the anode temperature has a significant impact on the cavity frequency. Figure 7 shows the dependence of the water heat transfer coefficient and the frequency shift on the anode cooling flow. The frequency can be increased by ~400 kHz with the flow reducing from 9.2 L/min to 1.2 L/min. Simulations indicate the stresses with this anode water flow range are less than the material yield limits. The ‘cut and try’ technique will be used for the coarse tuning in the machining stage. The anode temperature tuning and four external tuners can be used for the fine tuning. The large temperature tuning range can ease the machining precision requirement and reduce the tuner range requirement. The detailed mechanical design of the tuners will be performed in the next stage.

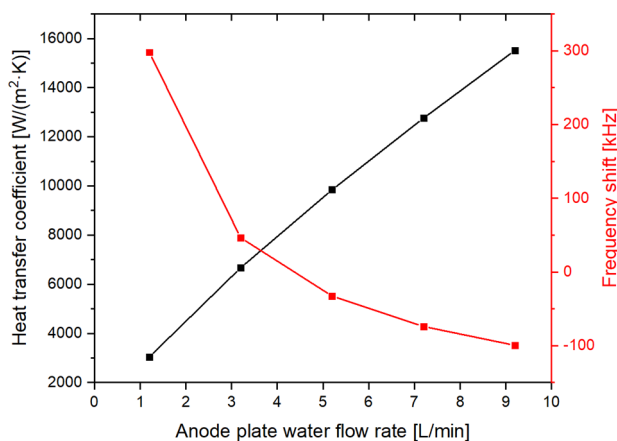


Figure 7: Dependence of the water heat transfer coefficient and the cavity frequency shift on the anode plate water flow rate.

CONCLUSION

A coupled electromagnetic-thermal-structural analysis of a 216.6 MHz NC CW RF gun for the European-XFEL was performed using the CST multiphysics package. The simulated temperature distribution in the nominal operation regime is suitable in respect to the overall physical design. The equivalent stresses are well below the material yield limits. In addition to the CST simulations, the consistent results were also obtained in the ANSYS benchmark analysis. The simulation results indicate that the designed cooling scheme has enough cooling capacity to handle ~100 kW thermal heating.

REFERENCES

- [1] J. K. Sekutowicz *et al.*, “Feasibility of CW and LP Operation of the XFEL Linac”, in *Proc. 35th Int. Free Electron Laser Conf. (FEL’13)*, New York, NY, USA, Aug. 2013, paper TUOCNO04, pp. 189-192.
- [2] R. Brinkmann *et al.*, “Prospects for CW Operation of the European XFEL in Hard X-ray Regime”, in *Proc. 36th Int.*

- Free Electron Laser Conf. (FEL'14)*, Basel, Switzerland, Aug. 2014, paper MOP067, pp. 210-214.
- [3] E. Vogel *et al.*, "SRF Gun Development at DESY", in *Proc. 29th Linear Accelerator Conf. (LINAC'18)*, Beijing, China, Sep. 2018, pp. 105-108.
doi:10.18429/JACoW-LINAC2018-MOP0037
- [4] F. Sannibale *et al.*, *PRST-AB*, 15, 103501 (2012).
doi.org/10.1103/PhysRevSTAB.15.103501
- [5] CST, <http://www.cst.com/>.
- [6] G. Shu *et al.*, "First Design Studies of a NC CW RF Gun for European XFEL", in *Proc. 10th Int. Particle Accelerator Conf. (IPAC'19)*, Melbourne, Australia, May 2019, paper TUPRB010, pp. 1698-1701.
doi:10.18429/JACoW-IPAC2019-TUPRB010
- [7] R. P. Wells *et al.*, "Mechanical design and fabrication of the VHF-gun, the Berkeley normal-conducting continuous-wave high-brightness electron source", *Review of Scientific Instruments*, 87.2 (2016): 023302.
doi:10.1063/1.4941836
- [8] F. Kreith, *The CRC Handbook of Thermal Engineering*, CRC Press, Boca Raton, 2000.
- [9] Z. Ding *et al.*, "Temperature-dependent quantum efficiency degradation of K-Cs-Sb bialkali antimonide photocathodes grown by a triple-element codeposition method", *Physical Review Accelerators and Beams*, 20.11 (2017): 113401.
doi:10.1103/PhysRevAccelBeams.20.113401
- [10] MakeItFrom.com,
<https://www.makeitfrom.com/material-group/Copper-Alloy>

ENGINEERING DESIGN OF LOW-EMITTANCE DC-SRF PHOTOCATHODE INJECTOR

Y. Q. Liu†, M. Chen, S. Huang, L. Lin, K. X. Liu, S. W. Quan, F. Wang, S. Zhao
Institute of Heavy Ion Physics, School of Physics, Peking University, Beijing, China

Abstract

An upgraded version of DC-SRF photocathode injector (DC-SRF-II) is under development at Peking University. The goal is to achieve an emittance below 0.5 mm-mrad at the bunch charge of 100 pC and repetition rate of 1 MHz. The engineering design of the DC-SRF-II photoinjector was accomplished in this May and the fabrication is ongoing now. This paper presents some details of the engineering design.

INTRODUCTION

Superconducting RF (SRF) photocathode injector has the advantage in principle to generate high average current, high-brightness electron beams and has been developed by several laboratories around the world [1-5]. To prevent the contamination of SRF cavity by the semiconductor photocathode materials, at Peking University, we have been developing a DC and SRF combined photocathode injector, known as the DC-SRF injector [6-8]. To meet the requirements of continuous-wave (CW) X-ray FELs, we are developing an upgraded DC-SRF photocathode injector (referred to as DC-SRF-II for short) with the goal to achieve an emittance below 0.5 mm-mrad at the bunch charge of 100 pC and repetition rate of 1 MHz. Recently, the engineering design of the new injector (which is shown in Fig. 1) has been finished and the fabrication is under way. In this paper, we present some results of the engineering design, including the redesign of the DC structure, the evaluation of thermal load for cryomodule, the design of magnetic shielding, and the evaluation of the mechanical property.

NEW DESIGN OF DC STRUCTURE

The DC structure of the injector has been redesigned according to our operation experience with the first-generation DC-SRF injector. The new design reduces the number of ceramics to two and provides a detachable protective electrode for the brazed position of ceramic and metal. Figure 2 shows the new DC structure. An inverted-geometry ceramic insulator approach was adopted. This insulator extends into the vacuum chamber serving as the cathode support structure. The advantage of this design is that it is compact and it helps to reduce field emission [9]. In addition, the shape of the high-voltage electrode was optimized, and the highest surface field has been controlled below 10 MV/m.

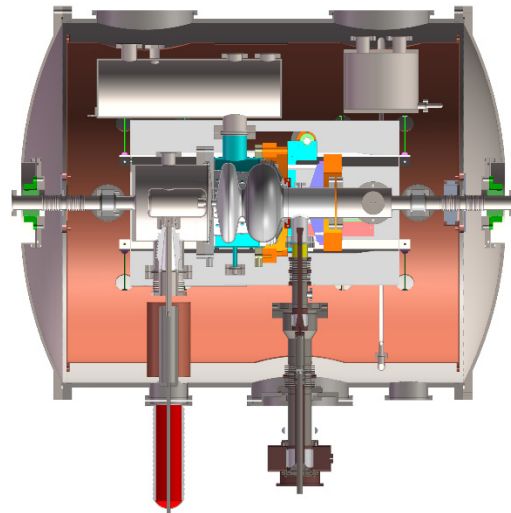


Figure 1: An overview of DC-SRF photocathode injector.

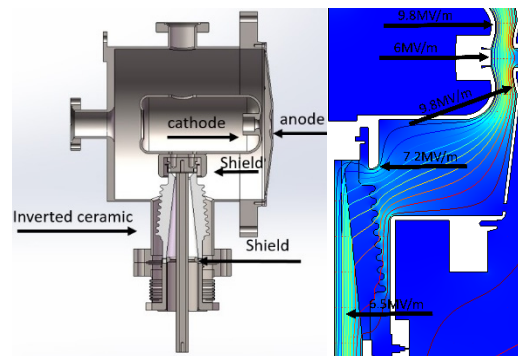


Figure 2: The new design of the DC structure (left) and electric field (right).

THERMAL EVALUATION OF THE CRYO-MODULE

The heat load of the cryomodule has been calculated via COMSOL Multiphysics [10]. Static heat load and dynamic heat load are shown in Table 1 and Table 2. The superconducting cavity surface loss can be estimated from the RF parameters in Table 3. The total heat load of cryomodule is about 12 W at 2 K and about 36 W at 77 K.

In addition, the flow direction of the liquid nitrogen pipe has been redesigned to obtain an optimized temperature distribution on the copper screen. Figure 3 shows that the highest temperature is about 87.5 K.

* Work supported by National Key Research and Development Program of China (Grant No. 2016YFA0401904).

† yqliu17@pku.edu.cn

Table 1: Static Heat Load Evaluation Results

Heat source	2 K / W	77 K / W
Power Coupler	0.4	4.9
Beam Line	0.2	2.1
Supported Rod	1.3	1.7
Tuner Rod	0.1	0.4
Radiation	0.5	10
Total	2.5	19.1

Table 2: Dynamic Heat Load Evaluation Results

Heat source	2 K / W	77 K / W
Power Coupler	1.1	16.2
1.5 Cell Cavity	8	\
Total	9.1	16.2

Table 3: RF Parameters of the Cavity

Parameter	Value	Unit
Frequency	1300	MHz
Q_0	1×10^{10}	\
E_{acc}	14	MV/m
Effective Length	186.6	mm
G-factor	212	Ω
Shunt Impedance r/Q	203	\
E_{peak}/E_{acc}	2.07	\
B_{peak}/E_{acc}	4.86	mT/(MV/m)

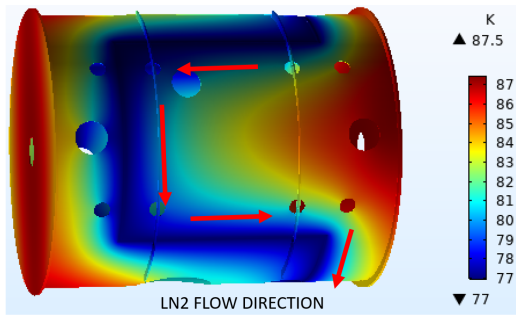


Figure 3: Temperature distribution of the 77 K copper screen.

MAGNETIC SHIELDING

The magnetic shield of the cryomodule consists an outer shell with 304 stainless steel and an inner shield with Permalloy. The goal is to shield the geomagnetic field (~0.5 Gs)

and the leakage field from the orbit corrector located 200 mm outside the Permalloy shield which is shown in Fig. 4. Figure 5 shows that with the shielding of Permalloy, the magnetic field around cavity is controlled below 10 mGs.

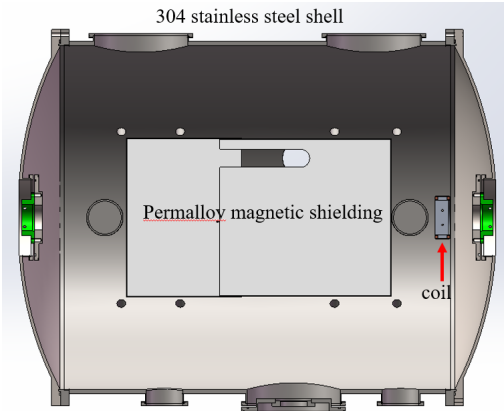


Figure 4: A layout of the magnetic shielding.

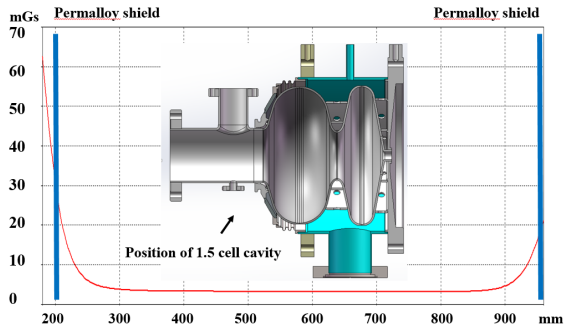


Figure 5: Effect of magnetic shielding.

MECHANICAL PROPERTIES OF THE INJECTOR

The variation of the field distribution and cavity frequency under the tuning forces are shown in Fig. 6. It takes about 35 kN to compress the cavity by 1 mm which leads a frequency change of 1.06 MHz. During the cooling process the frequency is supposed to increase about 2.8 MHz.

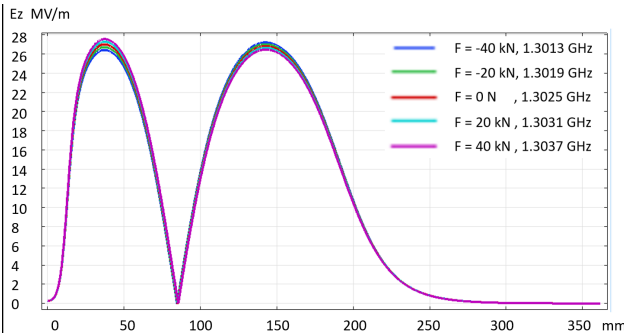


Figure 6: The effect of tuning on field flatness and frequency.

In addition, for gradient $E_{acc} = 14$ MV/m and tuner stiffness 35 kN/mm, the frequency shift due to Lorentz forces is supposed to be 555 Hz. For liquid helium pressure of 30 mbar the frequency shift is supposed to be 1.56 kHz. The evaluation results of mechanical parameters can be seen as Table 4.

Table 4: Mechanical Parameters Evaluation Results of Cavity

Parameter	Value	77 K / W
Frequency	1.3	GHz
Cool down	9.4	kHz/K
df/dp	42.6	Hz/mbar
LFD	-2.47	Hz/(MV/m) ²

CONCLUSION

The major changes include the redesign of the DC structure, the magnetic shielding, the RF coupler, and the cryostat. The engineering design has been accomplished and some results are shown in this paper.

REFERENCES

[1] I. Petrushina *et al.*, “Novel Aspects of Beam Dynamics in CeC SRF Gun and SRF Accelerator”, in *Proc. FEL’17*, Santa Fe, NM, USA, Aug. 2017, pp. 313-316. doi:10.18429/JACoW-FEL2017-TUP034

[2] A. Neumann *et al.*, “The BERlinPro SRF Photoinjector System - From First RF Commissioning to First Beam”, in *Proc. IPAC’18*, Vancouver, Canada, Apr.-May 2018, pp. 1660-1663. doi:10.18429/JACoW-IPAC2018-TUPML053

[3] T. Konomi *et al.*, “Design and Fabrication of KEK Superconducting RF Gun #2”, in *Proc. LINAC’18*, Beijing, China, Sep. 2018, pp. 510-512. doi:10.18429/JACoW-LINAC2018-TUP0074

[4] R. Xiang *et al.*, “Runing Status of SRF Gun II at the ELBE Radiation Center”, in *Proc. LINAC’18*, Beijing, China, Sep. 2018, pp. 952-954. doi:10.18429/JACoW-LINAC2018-THP0125

[5] E. Vogel *et al.*, “SRF Gun Development at DESY”, in *Proc. LINAC’18*, Beijing, China, Sep. 2018, pp. 105-108. doi:10.18429/JACoW-LINAC2018-MOP0037

[6] K. Zhao *et al.*, “Research on DC-RF superconducting photocathode injector for high average power FELs”, *Nucl. Instr. and Meth. A*, vol. 475 (2001), p. 568. doi: 10.1016/S0168-9002(01)01594-7

[7] J. Hao *et al.*, “Primary beam-loading tests on DC-SC photoinjector at Peking University”, *Nucl. Instr. and Meth. A*, vol. 557 (2006), p. 141. doi: 10.1016/j.nima.2005.10.063

[8] S. Quan *et al.*, “Stable operation of the DC-SRF photoinjector”, *Nucl. Instr. and Meth. A*, vol. 798 (2015), p. 117-120. doi: 10.1016/j.nima.2015.07.025

[9] Y. W. Wang *et al.*, “300 kV DC High Voltage Photogun with Inverted Insulator Geometry and CsK2sb Photocathode”, in *Proc. IPAC’18*, Vancouver, Canada, Apr.-May 2018, pp. 4571-4574. doi:10.18429/JACoW-IPAC2018-THPMK110

[10] COMSOL, <http://cn.comsol.com>

PERFORMANCE OPTIMIZATION OF LOW-EMITTANCE DC-SRF INJECTOR USING Cs₂Te PHOTOCATHODE*

Sheng Zhao, Dongming Ouyang, Yunqi Liu, Senlin Huang[†], Kexin Liu
Institute of Heavy Ion Physics & State Key Laboratory of Nuclear Physics and
Technology Physics and Technology, Peking University, Beijing 100871, China

Abstract

A low-emittance DC-SRF injector (DC-SRF-II) is under construction at Peking University, in the earlier design of which K₂CsTe photocathode was chosen. Recently we changed the cathode to Cs₂Te which is more widely used nowadays, and carried out a detailed performance optimization. In this paper, we present our latest simulation results, which show that an emittance under 0.5 mm-mrad can be achieved at the bunch charge of 100 pC.

INTRODUCTION

DC-SRF photocathode injector, which combines a DC gun and a superconducting radio-frequency (SRF) cavity [1, 2], is capable of generating CW electron beams. It was brought into stable operation in 2014 [3] at Peking University. In order to accommodate the requirement of electron beam with higher bunch charge (100 pC) and lower emittance (< 1 μ m), an upgraded version of DC-SRF injector (referred to as “DC-SRF-II” herein) adopting K₂CsTe cathode has been designed and the fabrication is under way now.

In this paper, we present the simulation study of the DC-SRF-II injector with the extensively used Cs₂Te cathode. To investigate its performance as an electron source for CW XFEL, the injector beamline was designed for optimized projected emittance, bunch length, and higher-order energy spread. The multi-objective optimization algorithm was implemented to obtain the global optimal solution.

INJECTOR LAYOUT

A sketch of the DC-SRF-II injector beamline is shown in Fig.1. The photocathode (Cs₂Te) is located at the entrance of the DC gap, soon after which a 1.3 GHz, 1.5-cell SRF cavity boosts the electron beam to a few MeV. Two solenoids downstream the DC-SRF-II injector confine the beam size and compress/compensate the transverse emittance. Following the solenoids is an electron buncher, which is composed of a 1.3 GHz, 2-cell cavity operated around zero crossing phase and a third-harmonic cavity introduced to improve the bunching performance. A standard cryomodule comprising eight 1.3 GHz, 9-cell cavities (referred to as “injection linac” later on) finally accelerates the average energy up to above 100 MeV, followed by a third-harmonic linearizer (four 3.9 GHz, 9-cell cavities) to remove the lower-order energy spread.

The fields of the DC structure, the SRF cavity, and the solenoids are cylindrically symmetric in first order. Our study indicates that the higher-order effects that break the symmetry only have insignificant impact on the emittance, bunch length, and higher-order energy spread herein. Therefore, this paper focuses on the cylindrically symmetric issues. The higher order effects, such as those due to the dipole field of RF coupler and off-axis drive laser, will be discussed elsewhere.

OPTIMIZER DESCRIPTION

Optimization Goals

XFEL operation requires electron beam with low emittance and high peak current. At the exit of injector beamline, the electron beam should have a low emittance and a moderate bunch length ~ 10 picoseconds. The electron beam from the injector beamline will be further accelerated by main linacs and compressed by magnetic compressors to achieve the required energy and peak current. The energy distribution of electrons within a bunch [$E(z) \sim E_0 + c_1 z + c_2 z^2 + O(z^3)$, where z is the position within the bunch] has significant impact on the performance of compression. Its linear and quadratic correlation terms (c_1 and c_2) can be largely eliminated with properly set rf phases and amplitudes of the linac and linearizer (harmonic cavity). The higher-order energy spread $O(z^3)$, however, needs to be suppressed in the injector beamline.

Boundary Conditions

In the optimization, the thermal emittance coefficient of Cs₂Te cathode was assumed to be 1.0 mm-mrad/mm. The drive laser pulse has a plateau distribution with the length of 24 ps and rise time of 2 ps, which can be achieved via coherent pulse stacking [4]. The transverse distribution of the laser is a 2D-Gaussian function truncated at 1 sigma. The initial bunch charge is 100 pC.

The first solenoid downstream the DC-SRF-II injector (see Fig. 1) will be fixed at 1 m, mainly limited by the length of the cryomodule. The position of the second solenoid and the strength of both solenoids need to be optimized. Other knobs used in the optimization, including the amplitude and phase of 1.5-cell cavity field, are given in Table 1. The DC voltage was fixed at 100 kV.

Optimization Process

For the optimization, the MOGA-II algorithm [5] was chosen to drive ASTRA [6] simulations. Since more than one objectives need to be optimized, the result is not a single

* Work supported by National Key Research and Development Program of China (Grant No. 2016YFA0401904).

[†] huangsl@pku.edu.cn

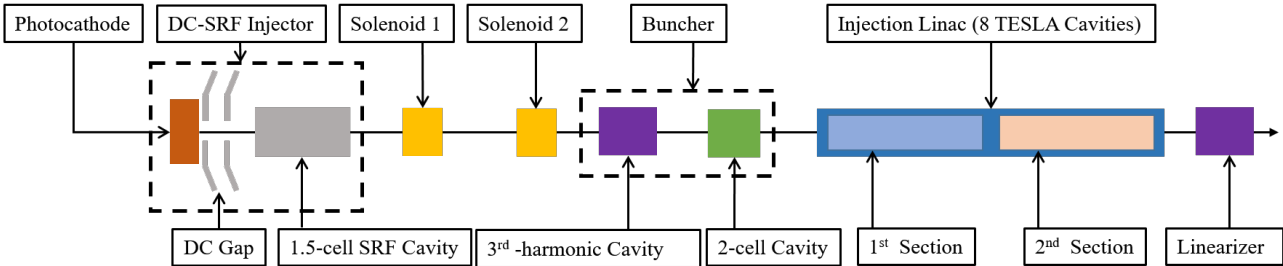


Figure 1: A schematic layout of the DC-SRF-II injector beamline. The drive laser system is not shown.

Table 1: Knobs used for DC-SRF-II injector optimization. All positions refer to the exit of the previous element.

Knob	Range	Unit
1.5-cell phase	$[-30,10]$	degree
1.5-cell amplitude	$[20,28]$	MV/m
Solenoid 1 strength	$[0.01,0.12]$	T
Solenoid 2 strength	$[0.01,0.12]$	T
Solenoid 2 position	$[0,3]$	m
3 rd -harmonic cavity position	$[0,2]$	m
3 rd -harmonic cavity amplitude	$[0,5]$	MV/m
3 rd -harmonic cavity phase	$[-200,-160]$	degree
2-cell position	$[0,2]$	m
2-cell amplitude	$[3,10]$	MV/m
2-cell phase	$[-120,-80]$	degree
1 st section position	$[0,2]$	m
1 st section amplitude	$[20,28]$	MV/m
1 st section phase	$[-6,6]$	degree
2 nd section amplitude	30	MV/m
2 nd section phase	$[-10,10]$	degree
Linearizer position	17	m
Linearizer amplitude	$[5,15]$	MV/m
Linearizer phase	$[-190,-150]$	degree

solution, but a “Pareto front” of a solution set. To accelerate the optimization progress, 5000 macro particles were used in the MOGA-II optimization, and the solutions with emittance higher than 1 mm–mrad, bunch length longer than 1.5 mm, or higher-order energy spread larger than 15 keV were discarded. The optimal solution was finally run with higher accuracy, i.e., 100000 particles.

RESULT AND DISCUSSION

The evolution of electron beam parameters for the optimal case can be found in Fig. 2. We observed significant increase of projected emittance in the DC gap and 1.5-cell cavity, which is due to the slice emittance mismatch caused by space charge effect and time-dependent rf kick. This increase of projected emittance, however, is largely compensated by the solenoids and eventually the emittance gets frozen in the injection linac. The normalized transverse rms emittance at the exit of the injector beamline is 0.49 mm–mrad, as shown in Fig. 2(a). In this case, the initial thermal emittance

(0.43 mm–mrad) is 88% of the projected emittance, which indicates the effectiveness of emittance compensation.

At the exit of the injector beamline, the bunch length is compressed to 1.05 mm and the higher-order energy spread is within 5 keV (rms), as shown in Fig. 2(b) and Fig. 2(c). A detailed investigation of the electron beam evolution shows that the buncher (the 2-cell cavity and third-harmonic cavity) has little influence on the projected emittance, as can be inferred from Fig. 2(a).

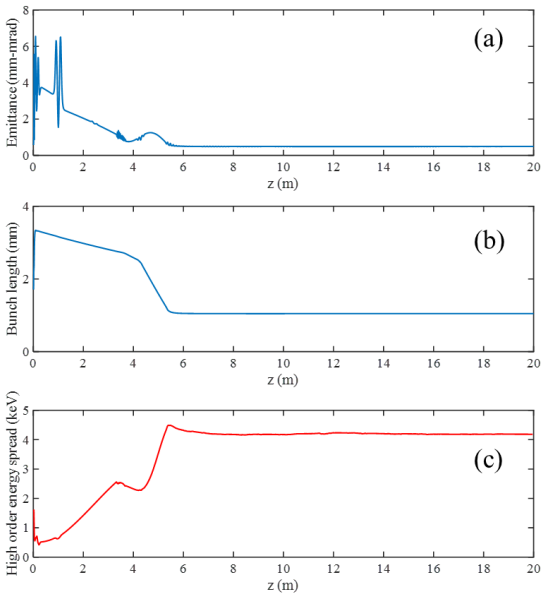


Figure 2: The evolution of electron beam parameters. (a) Emittance. (b) Bunch length. (c) Higher-order energy spread.

Fig. 3 presents more details about the electron beam distribution at the injector beamline exit. As shown in Fig. 3(a), the linear and quadratic correlation energy spread are eliminated by the injection linac and linearizer. The remaining higher-order energy spread is 4.4 keV, while the peak current is 11.3 A. Fig. 3(c) plots the slice energy spread, from which one can see that most slices have an energy spread $\lesssim 1$ keV. The tail part of the beam (on the left side), albeit with larger slice energy spread, has much lower local current. Fig. 3(d) plots the slice emittance and mismatch parameter. As shown in the figure, for most slices, the emittance is under

0.5 mm-mrad and the mismatch parameter is close to the perfectly matched value of 1.

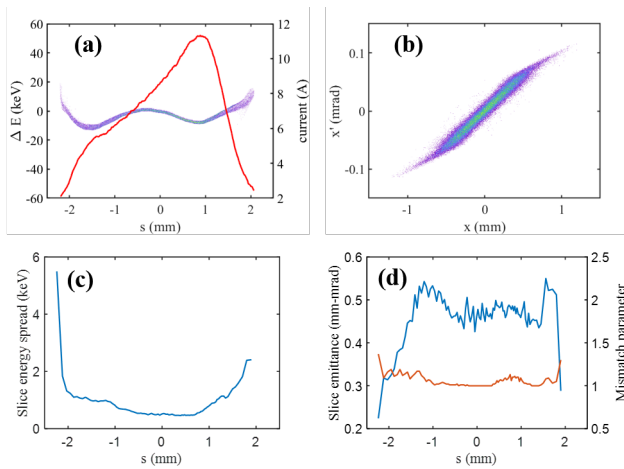


Figure 3: Electron beam distribution at the exit of the injector beamline. (a) Longitudinal phase space and current profile. (b) Transverse phase space. (c) Slice energy spread. (d) Slice emittance and mismatch parameter.

As mentioned earlier, the harmonic cavity in the buncher was introduced to improve the bunching performance. Similar configuration has been used in some recent work [7]. To illustrate its effect, we turned off the harmonic cavity and run the simulation again. The results are shown in Fig. 4. We can find the bunch length almost doubles (increases to 1.9 mm), although the peak current only decreases a little to 9.6 A. This is attributed to the inadequate bunching of the electron beam, as indicated by the long tail in Fig. 4(c). The effect of harmonic cavity will be further studied, and the cavity position, phase, and amplitude may be adjusted for better bunching performance.

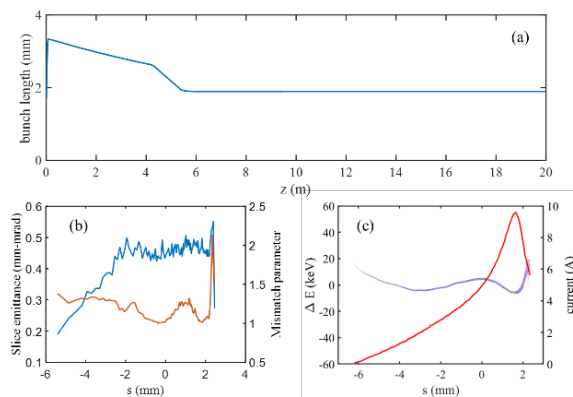


Figure 4: Simulation result of the optimal solution with the harmonic cavity turned off. (a) The evolution of bunch length. (b) Slice emittance and mismatch parameter. (c) Longitudinal phase space and current profile.

We finally investigated the same optimal solution with thermal emittance coefficient reduced to 0.6 and 0.8 mm-mrad/mm. The emittances at the exit of the in-

jector beamline are 0.34 and 0.41 mm-mrad, respectively. The longitudinal distribution almost remains unchanged for all these cases (Fig. 5).

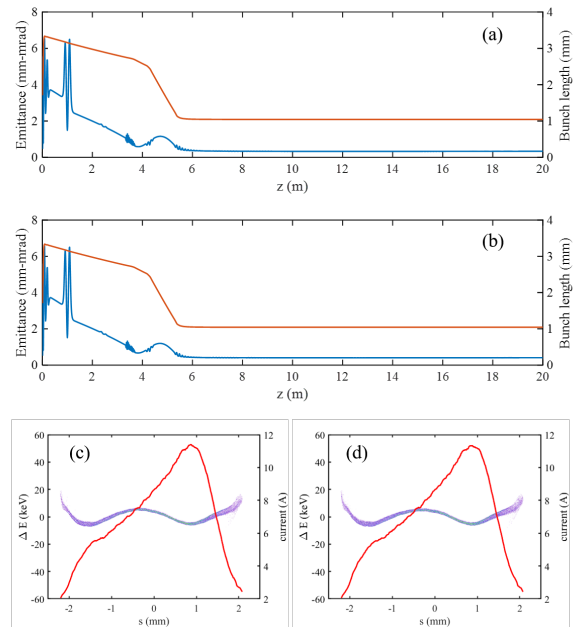


Figure 5: Simulation results of the optimal solution with thermal emittance coefficient of 0.6 and 0.8 mm-mrad/mm. (a-b) Emittance and bunch length. (c-d) Longitudinal phase space and current profile. (a) and (c): 0.6 mm-mrad/mm; (b) and (d): 0.8 mm-mrad/mm.

CONCLUSION

The performance of DC-SRF-II injector with Cs_2Te cathode has been investigated as an electron source for CW XFEL. An injector beamline was designed and optimized. The simulation shows that electron beams with a normalized rms emittance below 0.5 mm-mrad, bunch length ~ 1 mm (rms), peak current of 11.3 A, and higher-order energy spread less than 5 keV (rms) can be obtained at the bunch charge of 100 pC and electron energy of 100 MeV.

We would like to thank Dr. Houjun Qian and Dr. Weilun Qin for helpful discussions.

REFERENCES

- [1] K. Zhao *et al.*, *Nucl. Instr. and Meth. A*, vol. 475, 2001, p. 564-568. doi:10.1016/S0168-9002(01)01594-7
- [2] J. Hao *et al.*, *Nucl. Instr. and Meth. A*, vol. 557, 2006, p. 138-141. doi:10.1016/j.nima.2005.10.063
- [3] S. Quan *et al.*, *Nucl. Instr. and Meth. A*, vol. 798, 2015, p. 117-120. doi:10.1016/j.nima.2015.07.025
- [4] F. Liu *et al.*, *Opt. Express*, vol. 27, 2019, p. 1467-1478. doi:10.1364/OE.27.001467
- [5] K. Deb *et al.*, *IEEE Trans. Evol. Comput.* vol. 6, 2002, p. 182-197. doi:10.1109/4235.996017
- [6] K. Flöttmann, "ASTRA: A Space Charge Tracking Algorithm", <http://www.desy.de/~mpyf10>
- [7] H. Qian *et al.*, in *Proc. SRF 2019*, 2019, THP081.

DRIVE LASER TEMPORAL SHAPING TECHNIQUES FOR SHANGHAI SOFT X-RAY FREE ELECTRON LASER*

Chunlei Li¹, Xingtao Wang[†], Wenyan Zhang, Lie Feng, Taihe Lan, Meng Zhang, Bo Liu¹
Shanghai Advanced Research Institute, Chinese Academy of Science, Shanghai, China
¹also at Shanghai Institute of Applied Physics, Chinese Academy of Science, Shanghai, China

Abstract

The design of Shanghai soft X-ray free electron laser (SXFEL) is based on laser driven photocathode, which can provide normalized emittance <2.5 mm-mrad with 500 pC charge. The temporal shape of drive laser has significant influence on the electron beam brightness. This paper presents the transport line of drive laser system and the temporal shaping techniques for SXFEL. This drive laser produces 8 picosecond 266nm ultraviolet pulses with repetition rate 10Hz. A transverse deflecting cavity was used for indirectly characterizing the laser pulse temporal structure. Here we present the drive laser system with its temporal shaping method, and measurement results.

INTRODUCTION

Drive laser is a crucial component for photo injector producing high density, high brightness electron bunches. The pulse parameters of drive laser determine the properties of electron bunches, such as bunch length, bunch charge, the stability of the produced charge, and its synchronization accuracy to the RF of the photo injector, as well as the emittance of the electron bunches [1-3]. Simulation and experiment indicate that flattop pulse can help photoinjector generate uniform temporal and spatial electron distribution with lower transverse emittance [4-6]. Therefore, effective temporal pulse shaping methods are important to photoinjector laser system. The pulse length required for excitation photocathode are around 260nm, 5~10ps with flattop distribution. Several methods have been explored with their pros and cons, such as α -BBO crystal stacking [7-8], double prism or grating pair stretcher [5]. Presently, Simulation also indicates that quasi ellipsoidal laser pulse can help producing electron bunches with minimized emittance [9].

Table 1 shows the laser parameter requirement of Shanghai soft X ray free electron laser (SXFEL). Currently, no commercial laser system can provide all the requirements. Therefore, an integrated laser system based on α -BBO crystal stacking was developed for producing 8ps ultraviolet (UV) pulse. The temporal structure was characterized by cross correlation method with difference frequency generation (DFG) crystal. By illuminating the UV pulse to copper photocathode RF gun, 10 Hz repetition rate ultra-short electron bunch was produced with emittance less than <2.0 mm-mrad with 500 pC charge.

Table 1: Drive Laser System Requirements

Name	Parameters
Wavelength	260 nm~270 nm
Repetition rate	1~10 Hz
Pulse energy on the photocathode	150 μ J
Energy stability in UV	$<2.0\%$ rms
Spatial profile	Flat top
Laser spot radius on photocathode	0.5~1.5 mm hard edge radius
Laser spot diameter jitter at photocathode	2% rms radius
Pointing jitter	$<2\%$ rms radius
Pulse shape	Flat-top
Pulse duration	Flat-top 10ps edge to edge
Timing stability	<0.25 ps rms

DRIVER LASER SYSTEM

Figure 1 shows the schematic of driver laser system which consists 4 main stages, 1) Oscillator, 2) Amplifier, 3) Frequency tripled modulator, 4) α -BBO crystal stacking. An oscillator (Vitara-T, Coherent Inc.) pumped by 4.88 W Verdi (Coherent Inc.) deliver 800 nm, 0.7 W pulse (79.33 MHz, horizontal polarization) to Ti:sapphire amplifier (Spitfire Ace PA, Spectrum Physics Inc.). The pre-amplified pulses (8.8 nJ) are firstly stretched to 200 ps using grating pair, then amplified to 5 mJ by regenerative amplifier, and further amplified to 10mJ by single pass amplifier. Finally the amplified pulse are compressed to 1ps (10 mJ) and delivered to third harmonic generation (THG).

The compressed pulses was converted from 800 nm to 400nm by second harmonic generation in a β -BBO crystal (type I, $o + o = e$, 0.5 mm, $\theta = 29.2^\circ$), and subsequently sum-frequency generated in a second β -BBO crystal (type I, 0.5 mm, $\theta = 44.4^\circ$). The conversion efficiency from 800 nm to 266 nm was about 2%. As shown in Fig. 1, temporal pulse shaping at 266 nm was conducted by 3 pieces of α -BBO crystals.

The transverse homogenisation shown in Fig. 2 was achieved by selecting the centre part of intensity profile using iris, which was then relay imaging to the photocathode shown in Fig. 1.

* Work supported by Shanghai Sailing Program (18YF1428700)

[†] email address wangxingtao@zjlab.org.cn

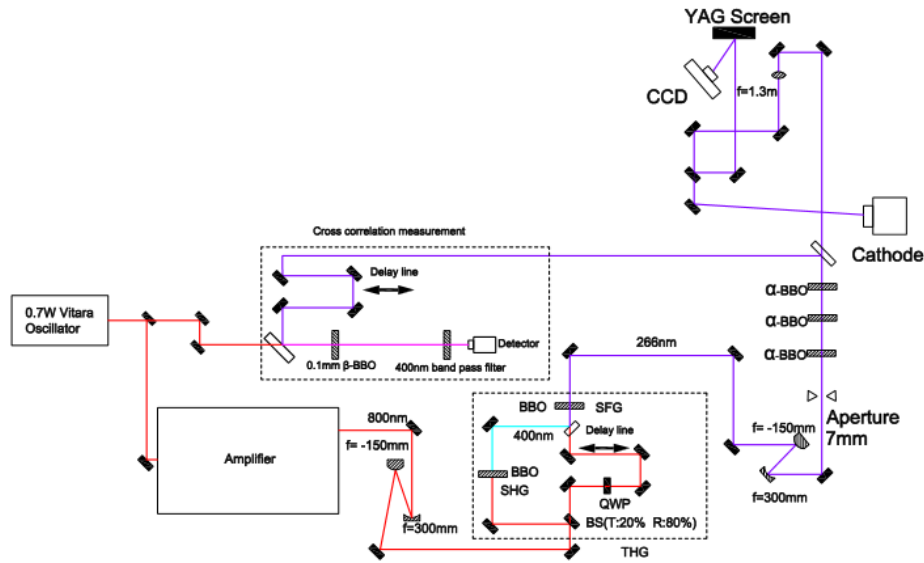


Figure 1: Schematic drawing of SXFEL drive laser system.

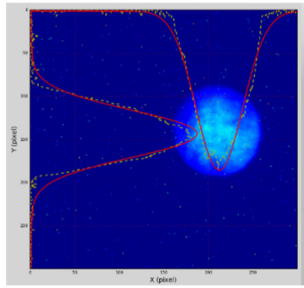


Figure 2: Transverse intensity distribution captured on virtual cathode.

UV PULSE SHAPING WITH BIREFRINGENT CRYSTALS

A brief description of the UV pulse shaping method is presented here. More detailed description can be found in references [7]. α -BBO crystals are anisotropic materials that have different indices of refraction for s , p polarization. Ordinary (o) beam has a polarization perpendicular to the optical axis of crystal, while extraordinary (e) beam has a polarization parallel to the optical axis. For α -BBO crystals, the Sellmeier equations for $n_e(\lambda)$ and $n_o(\lambda)$ are expressed in Eq. (1) and (2) [7-8].

$$n_o(\lambda) = \sqrt{2.7471 + \frac{0.01878}{\lambda^2 - 0.01822} - 0.01354\lambda^2} \quad (1)$$

$$n_e(\lambda) = \sqrt{2.3174 + \frac{0.01224}{\lambda^2 - 0.01667} - 0.01516\lambda^2} \quad (2)$$

Where λ is the wavelength in μm , $n_e(\lambda)$ and $n_o(\lambda)$ are the index of refraction of the o beam and e beam.

The temporal separation (Δt) between o beam and e beam when they propagate through the BBO birefringence crystal is given by Eq. (3).

$$\Delta t = L * \text{GVM} \quad (3)$$

Where L is the thickness of crystal, Group velocity mismatch ($\text{GVM} = (n_e(\lambda) - n_o(\lambda))/c$), c is the speed of light.

Figure 3 shows 3 α -BBO crystals were used for producing 8 ps flat-top 120 μJ UV pulse. The input Gaussian pulse is linearly horizontal polarized while the optical axis of the first BBO crystal with thickness $L_1=4.3306$ mm is oriented at 45° relative to the horizontal direction. For α -BBO, e beam (parallel to the optical axis of crystal) will move ahead of o beam (perpendicular to the optical axis of crystal) by an amount of $\Delta t_1=4$ ps.

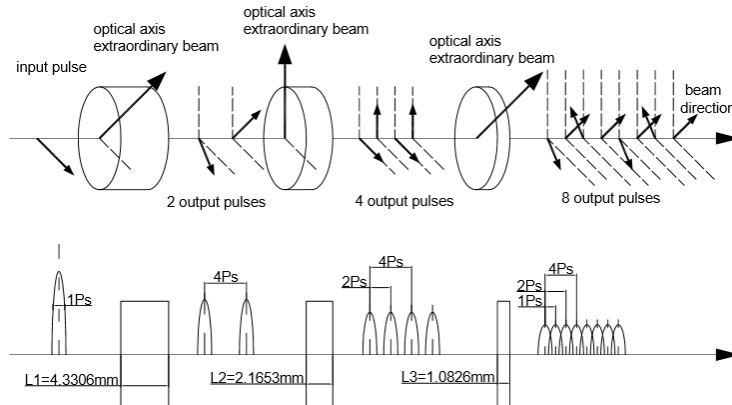


Figure 3: Schematic diagram showing 3 birefringent crystals used to produce 8ps temporal flattop pulse.

According to Eq. (1) and (2), for $\lambda = 266$ nm $n_e = 1.594$, $n_o = 1.761$, the e beam is the fast axis. The 45° orientation creates equal intensity for o beam and e beam. The relative intensity between the two beams can be controlled by a rotation of crystal axis. The two pulses emerging from the first crystal oriented at 45° to the vertical. The optical axis of second BBO crystal oriented in vertical direction. When the two intermediate pulses pass through the second crystal with thickness $L_2 = 2.1653$ mm, each pulse is divided into 2 more pulses separated by Δt_2 , thus producing 4 pulses. Finally, the four pulses pass through the third crystal with thickness $L_3 = 1.0826$ mm, the optical axis of third crystal oriented at 45° relative to vertical direction. When the four pulses pass through it, 8 pulses with separation by Δt_3 are produced. The temporal structure of the UV pulse was indirectly characterized by a transverse deflecting cavity. The measured electron beam temporal structure, as shown in Fig. 4, indicated the stacking procedures and the UV pulse has a good temporal distribution.

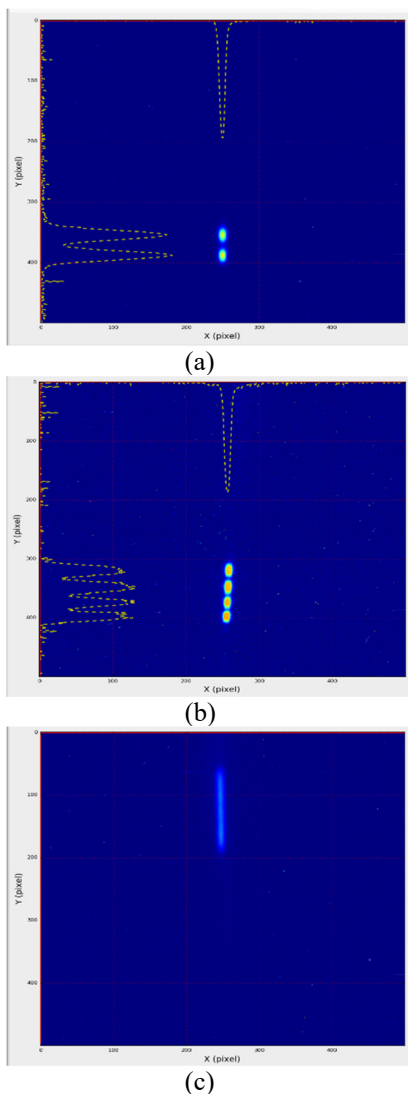


Figure 4: Electron bunch length measurement result from transverse deflecting cavity.

CONCLUSION

We present the design of drive laser system for SXFEL and investigate UV pulse temporal shaping technique based on BBO stacking method. Transverse deflecting cavity measurement results show stacking procedure for producing one 8ps length bunch. Further investigation will attempt to characterize the relationship between the UV pulse temporal structure and corresponding electron beam emittance.

ACKNOWLEDGEMENTS

The work was supported by Shanghai Sailing Program (18YF1428700).

REFERENCES

- [1] Ingo Will *et al.*, “Photoinjector drive laser of the FLASH FEL”, *Optics Express*, vol 19, no.24, pp: 23770. 2011. doi:10.1364/OE.19.023770
- [2] Ingo Will, Guido Klemz, “Drive Lasers for Photoinjectors”, in *Proc. ERL’07*, Daresbury, UK, May 2007, paper 13, pp. 1-5.
- [3] M.B. Danailov *et al.*, “Laser Systems for Next Generation Light Sources”, in *Proc. PAC’09*, Vancouver, Canada, May 2009, paper MO4GRI03, pp. 122-126.
- [4] C. Vicario *et al.*, “Photocathode Drive Laser for SwissFEL”, in *Proc. FEL’10*, Malmö, Sweden, 2010, paper WEPB14, pp. 425-428.
- [5] C. P. Hauri and R. Ganter., “Gun Laser Systems for the SwissFEL Project”, in *Proc. FEL’09*, Liverpool, UK, 2009, paper MOPC63, pp. 157-160.
- [6] LCLS Conceptual Design Report, SLAC-R-593, 2002, pp. 6-24.
- [7] John G. Power and Chunguang Jing, “Temporal Laser Pulse Shaping for RF Photocathode Guns: The Cheap and Easy way using UV Birefringent Crystals”, *Advanced Accelerator Concepts: 13th Workshop*, 2009, pp. 689. doi:10.1063/1.3080991
- [8] Lixin Yan *et al.*, “UV Pulse Trains by α -BBO Crystal Stacking for the production of THz rap rate electron Bunches”, *J. Plasma Physics*, vol. 78, part 4, pp. 429-431, 2012. doi:10.1017/S0022377812000281
- [9] J. Good *et al.*, “Preliminary on-Table and Photoelectron Results from the PITZ Quasi-Ellipsoidal Photocathode Laser System”, in *Proc. FEL’17*, Santa Fe, NM, USA, Aug. 2017, pp. 426-428. doi:10.18429/JACoW-FEL2017-WEP006.

CHARACTERIZING A COHERENT ELECTRON SOURCE EXTRACTED FROM A COLD ATOM TRAP*

Hang Luo, Yanxia Xu, Jie Guo, Peixin Chu, Xi Zhao, Qinghong Zhou, Xiaohong Li, Tao Liu, Kelin Wang, Dept. of Physics, Southwest University of Science and Technology, Mianyang, China

Abstract

In order to generate a fully coherent free electron laser (FEL) within a compact system, one potential approach is to interact a coherent electron bunch with a high power laser operating in the quantum FEL regime. The coherent electron source can be obtained by ionizing the Rydberg atoms in a magneto-optical trap (MOT). The qualities of the electron source will have direct effects on the brightness, coherence, and line width of the free electron laser. A high quality ultra-cold electron source can be obtained by carefully optimizing the extraction electrode structure, the acceleration and focusing system as well as the MOT. Through parameter optimization, a coherent electron source with a temperature lower than 10K is predicted. Details of the optimization and the characteristics of the coherent electron source are reported in this paper.

INTRODUCTION

The planar cathode photoemissive source is simple and stable in performance, and is the most commonly used electron source for time-resolved electron diffraction (TRED) [1], however, the electron source size, effective temperature, the space charge effect, and energy spread [2] factors limit the achievable lateral coherence length [3]; the cutting-edge optoelectronic emission source can be controlled at the sub-femto second time scale [4], which can achieve ultra-short electronic pulse width. It has extremely high coherence and brightness, but the non-uniformity of its initial trajectory and near-field acceleration and the energy spread of electrons lead to the rapid divergence and elongation of the electron beam during propagation [5]. Femtosecond photoemissive sources based on solid cathodes operate well, but lack of coherence [6]. The typical effective field temperature of a conventional field emission or photoemission source is about 5000 K, and the lateral coherence length of an electron pulse has a strong relation with the effective temperature: $L_{\perp} \propto 1/\sqrt{T}$. The lower the temperature, the greater the lateral coherence length. Based on this, we used laser cooling technology to obtain an electron source from a cold atom trap. The electron beam quality will directly affect the brightness, coherence and linewidth of the free electron laser. The electron source transverse temperature obtained by this technology can be as small as 10K or lower, and the atom is very easy to handle, so that coherent electron source can be extracted

from the cold atom. The coherent electron beam can form a very low emittance, coherence temperature. The low emittance of a coherent electron beam results from a high phase space density and a small volume of the coherent electron beam at low temperatures, which is several orders of magnitude lower than conventional electron beam. In addition, the cold electron source can also reach sub-pico-second ultrashort pulse lengths [7]. Thanks to the high coherence and high energy resolution, the cold electron source thus obtained has great applications to various frontier researches.

In order to construct a high-quality ultra-low temperature coherent electron source, a special electrode structure is needed to extract electrons, accelerate and focus. Therefore, we have carried out an optimized design of the electrode structure in the cold atomic trap, and simulated and analyzed the evolution of the three electrode geometries, the position and the influence of the electrode voltage on the electron beam quality.

DEFINITION OF THE QUALITY OF COHERENT ELECTRON

Therefore, our main focus on the coherent electron beam quality factor includes five aspects: energy spread, emittance, electron beam length, beam spot size, and coherent electron beam temperature. Below we give definitions of quality factors:

Energy spread $\frac{\delta}{E}$

Electron beam energy spread has an important impact on the performance of accelerator-based ultrafast scientific devices. The energy spread is closely related to the temperature of the electron, defined as:

$$\frac{\delta}{E} = \frac{\sqrt{\frac{1}{N} \sum_i^N (Ek_i - \langle Ek \rangle)^2}}{\langle Ek \rangle} \times 100\% \quad (1)$$

Emittance

Emittance is the product of the beam size and the opening angle, which is interpreted statistically, that is, using the average of all particles to describe the emittance of the electron beam:

* Work supported by the National Natural Science Foundation of China

$$\varepsilon_{x,rms} = \sqrt{\langle x^2 \rangle \langle x'^2 \rangle - \langle x'x \rangle^2} \quad (2)$$

Electron Beam Length (longitudinal, z-direction)

The length of the particle cluster in the longitudinal direction, which is defined as:

$$length_z = Z_{\max} - Z_{\min} \quad (3)$$

Beam Waist Size (horizontal, x-y plane)

The beam waist radius of the electron beam is a direct reflection of the electron beam focusing effect, as shown in Fig. 1.

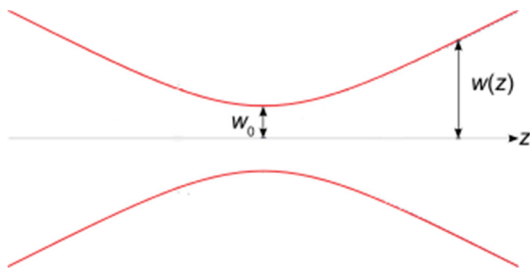


Figure 1: Beam waist $2*w(z)$ as a function of the distance z along the beam. w_0 : beam waist.

Beam width is shown above, we define it as:

$$waist = 2 * \max(\sqrt{x^2 + y^2}) \quad (4)$$

$waist$ is the beam spot size, and x and y are the positions of the electrons in the coordinate system.

Coherent Electron Beam Temperature

We use the effective temperature of the electron under classical conditions. In this design, the electrons have no freedom of rotation and vibration, and we only consider the direction of coherent electron beam transmission, so the coherent electron beam temperature is defined as:

$$T = \frac{mv_{rms}^2}{k} \quad (5)$$

MODELING

The electron beam quality is directly affected by the electric field distribution. We change the electric field distribution by changing the electrode structure and position. In the model, in order to find the appropriate electrode structure and related parameters, we can simulate the electron beam quality. According to the initial requirements, we have established two parallel equal-large electrode plates with aperture, length and spacing $r1 \times L1 \times d1$, $r2 \times L2 \times d2$ respectively. Place a sphere with a spherical radius $r1$ as an electron cluster at a suitable position.

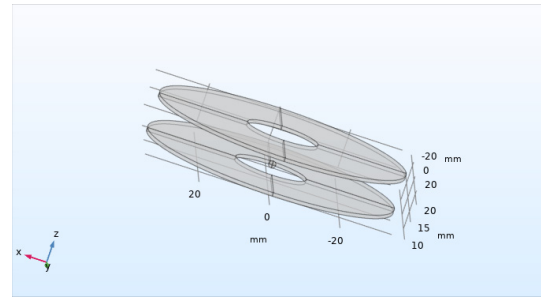


Figure 2: Two electrode plate geometry models.

According to the optimized design, the four pieces design is chosen as the parallel electrode plates. First, in order to make the electrons in the negative electric field, we give priority to the field shielding problem. The first and second boards $V1=V2=-20KV$ are negative voltages, and the two boards have the same voltage, so as to reduce the leakage through the electrode holes. Comparing their potential maps in Fig. 3(c) and (d), we can easily see that. The influence of the positive electric field between $V1$ and the cavity on the electron group; the third plate voltage $V3=-5KV$, which is a variable negative voltage, the purpose is to weaken the complex field leakage at the aperture, and the second is to reduce the kinetic energy loss by adjusting, as shown in Fig. 3(a) to (e). It is the position where the coherence temperature can be controlled when the electronic output is minimum, as shown in Fig. 3(b); the last board is connected to $V4=0V$ for field shielding; the external cavity is grounded to avoid danger.

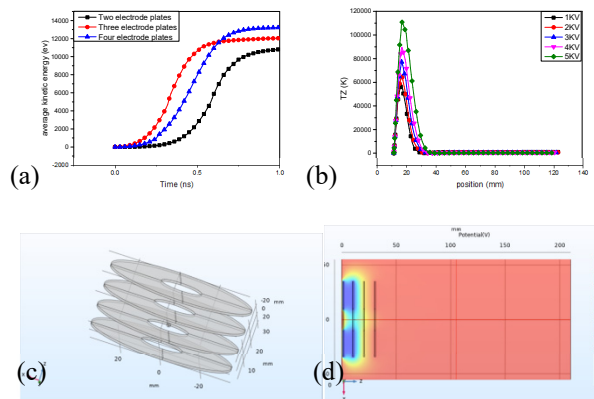


Figure 3: (a) Average kinetic energy obtained by different numbers of parallel plates; (b) The relationship between the coherent electron temperature and the electronic position of the electron moving direction at different voltages of the third electrode plate; (c) Four electrode plate geometry models; (d) potential distribution map.

SIMULATION RESULTS

In the parallel plate electrode model, when the voltages across the parallel plates are the same, the electric field quality is changed by changing the electric field distribution in the cavity by the displacement operation of the parallel plates. At this time, the electrode voltage $V1=V2=-$

20KV, V3=5KV, the hole radius $r1=r2=r3=r4=10\text{mm}$, the length $L1=L2=L3=L4=60\text{mm}$, the distance between plates $d1=d2=d3=10\text{mm}$, currently we show the data obtained when the electrode is displaced. The electron beam quality changes with the electric field distribution. The results are shown in different spatial positions as shown in Fig. 4. It shows a set of optimized results.

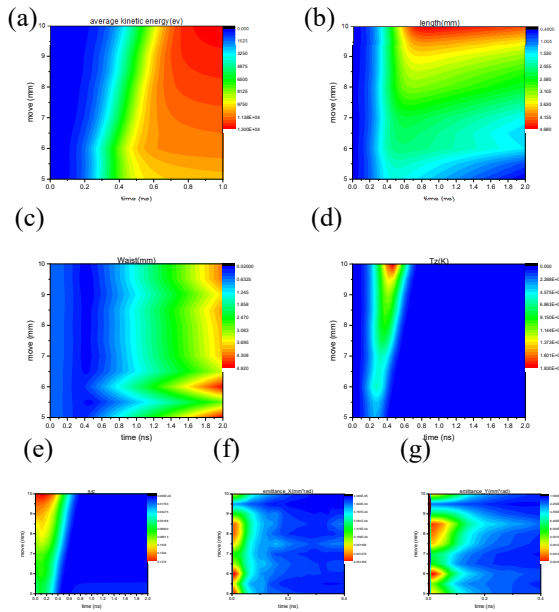


Figure 4: The x-axis is time, y-axis is the moving distance of the electrode plate, the representative color value to: (a) average kinetic energy; (b) electron beam length; (c) electron beam waist; (d) Coherent electron beam temperature; (e) δ/E ; (f) emittance_X; (g) emittance_Y.

When the electron beam moves to the 0.4m position, the electron beam energy spread $\frac{\delta}{E} < 0.032\%$ as shown in Fig. 4(e); At this time, in the direction of electron beam transmission, the coherent electron beam temperature is controlled within 10K, coherent electron beam temperature as shown in Fig. 4(d), which satisfies our initial experimental requirements, and is consistent with M.W. van Mourik and W.J. Engelen in 2014 for ultra-fast electron diffraction experiments at 10K; The electron emittance in the X and Y direction is all $\varepsilon < 0.2 \text{ mm.mrad}$, as shown in Fig. 4(c) and (d); when the electron beam is at this position, the beam length is $\text{length}_z < 3.6\text{mm}$ as shown in Fig. 4(b); The beam waist size is around 1.4 mm, as shown in Fig. 4(c).

DISCUSSIONS

In the continuous simulation analysis, we found that there are at least two problems to be dealt with urgently. First, the large aperture and the spatial position of the electrons cause the kinetic energy loss of the electrons to be excessively large. as shown in Fig. 5(a), (b); Second, we

minimize the positive electric field to the electrons. The influence of the regiment is far from enough to shield, which is also the root cause of the loss of kinetic energy obtained by our electronics. At present, we still need to upgrade the structure and optimize the parameters in order to maintain the quality of other electron beams in the case of kinetic energy loss.

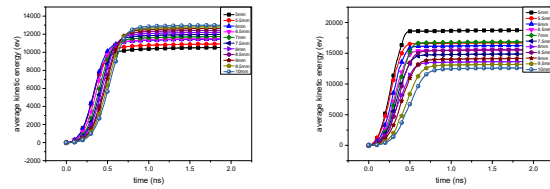


Figure 5: (a) Different moving distances of the electrode plates, the average kinetic energy changes with time. (b) Different hole radii of the electrode plate, the average kinetic energy changes with time.

CONCLUSION

In summary, the more complex the model, the more uncontrollable variables are generated. At present, we can determine the optimization research object as the parallel plate geometry model. The electron beam energy spread $\frac{\delta}{E} < 0.032\%$, and the coherent electron beam temperature is within 10K. The electron emittance in the X and Y direction is all $\varepsilon < 0.2 \text{ mm.mrad}$, and the beam length $\text{length}_z < 3.6 \text{ mm}$. The beam waist size is about 1.4 mm. All of the above are the design of the first stage electrode in the cavity. We will add the electrode to the electron beam for secondary regulation outside the cavity.

REFERENCES

- [1] M.S. Robinson *et al.*, "A compact electron gun for time-resolved electron diffraction", *Review of Scientific Instruments*, 86(1), 013109 (2015). doi:10.1063/1.4905335
- [2] G. Sciaini *et al.*, "Femtosecond electron diffraction: heralding the era of atomically resolved dynamics", *Reports on Progress in Physics*, 74(9), 096101 (2011). doi:10.1088/0034-4885/74/9/096101
- [3] T. van Oudheusden *et al.*, "Electron source concept for single-shot sub-100 fs electron diffraction in the 100 keV range", *Journal of Applied Physics*, 102(9), 93501-0 (2007). doi:10.1063/1.2801027
- [4] K. Krüger *et al.*, "Attosecond control of electrons emitted from a nanoscale metal tip", *Nature*, 475 (7354), 78-81 (2011). doi:10.1038/nature10196
- [5] A. Paarmann *et al.*, "Coherent femtosecond low-energy single-electron pulses for time-resolved diffraction and imaging: A numerical study", *Journal of Applied Physics*, 112(11), 113109 (2012). doi:10.1063/1.4768204.
- [6] S.B. van der Geer *et al.*, "Ultracold Electron Source for Single-Shot, Ultrafast Electron Diffraction", *Microscopy and*

TEST OF Cs₂Te THICKNESS ON CATHODE PERFORMANCE AT PITZ

P. Huang*, H. Qian†, Y. Chen, A. Grigoryan, M. Gross, I. Isaev, P. Kitisri, C. Koschitzki, M. Krasilnikov, S. Lal, X. Li, O. Lishilin, D. Melkumyan, R. Niemczyk, A. Oppelt, H. Shaker, G. Shu, F. Stephan, G. Vashchenko, T. Weilbach, DESY, Platanenallee 6, 15738 Zeuthen, Germany
S. Lederer, DESY, Notkestrasse 85, 22607, Hamburg, Germany
L. Monaco, P. Michelato, D. Sertore, INFN Milano - LASA, Segrate, I-20090, Italy

Abstract

Cesium telluride is a widely used cathode in photo injectors, and its performance is one of the keys for not only emittance but also reliable operation. Over the years lots of experiences with Cs₂Te photocathodes produced with the same recipe and thickness were gained at the DESY photo injectors, but cathode performance dependence on the cathode layer thickness were not investigated. In this paper, we test fresh Cs₂Te cathodes with different thickness at the Photo Injector Test Facility at DESY in Zeuthen (PITZ). The dark current, quantum efficiency (QE) and thermal emittance of these cathodes inside the high gradient RF gun will be compared.

INTRODUCTION

The photocathode is one of the key components of photoinjectors. The performances of the photocathode, including quantum efficiency (QE), thermal emittance, response time, dark current and life time, are closely related to the photoinjector performance and its subsystems, such as the photocathode laser, gun gradient, vacuum, and injector emittance [1]. Even for the same cathode material, different cathode recipes may lead to different cathode performances [2]. Several studies have shown that the thickness of cathodes is one of the parameters to optimize the cathode performance. For transmission mode photocathodes, which are illuminated by laser from the back side, greater thickness would increase electrons possibility to scatter with phonons and reduce thermal emittance [3]. Besides, a fine control of cathode film thickness and substrate can optimize the photon absorption and lead to a higher QE [4]. For K₂CsSb cathodes, a thicker Sb layer has shown improvement in both QE and life time [5]. Among all these studies, a performance dependence test of cathode film thickness in high gradient RF guns is missing.

Cs₂Te cathodes are one of the most widely used cathodes in photoinjectors, especially for applications requiring an average current from 1 μ A to 1 mA. It has a typical high QE of around 10 % in UV and a long life time (months to years [6]), compatible with a gun vacuum of 10⁻⁹ mbar. DESY has been collaborating with INFN-LASA, Milano, on testing and optimizing Cs₂Te cathodes for decades, and Cs₂Te cathodes are reliably used for the user facilities, FLASH and European XFEL, and the Photo Injector Test Facility at DESY in Zeuthen (PITZ). In 2010, INFN-LASA reported the Tel-

lurium thickness effects for Cs₂Te measured in a cathode preparation system [7]. The cathode thickness is specified with the tellurium thickness. They are 5 nm, 10 nm and 15 nm, respectively. The corresponding cesium thickness is determined during the deposition process, where the QE is optimized and the final peak of the QE determines the Cs thickness [7]. At this stage, the cathode is believed to be a complete Cs₂Te film [8]. The three cathodes were maintained in a UHV cathode box after fabrication at Milano and sent to PITZ for testing in the high gradient RF gun [9]. The three fresh Cs₂Te cathodes were tested continuously at PITZ for two weeks in the sequence of 5 nm, 15 nm and 10 nm Te thickness. The testing items include dark current, QE and thermal emittance against electric field, QE and thermal emittance maps. The testing results are reported in this paper.

EXPERIMENTAL SETUP

The experiments were carried out on the PITZ beam line. The simplified layout for the measurements in this paper is shown in Fig. 1. Currently Gun4.2 is installed at PITZ, a 1.5 cell L-band RF-gun operated at high gradient and long pulse train [10]. There are two solenoids around the gun. The main solenoid locates at the gun exit. The other one is the bucking solenoid and it is for compensating the residual magnetic field at the cathode. The dark current is measured with a Faraday cup located at the exit of the gun and the solenoid current is tuned to achieve the strongest signal. The QE is measured by the same Faraday cup and a laser energy meter. For thermal emittance measurement, we use the cathode transverse momentum imaging and the details of this method can be found in [11]. The wavelength of the cathode driving laser is 257 nm. The laser profile is transversely uniform and longitudinally gaussian (6 ~ 7 ps FWHM).

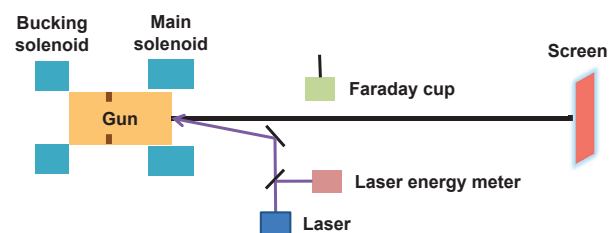


Figure 1: The beam line layout for the experiments. Only the elements related to the experiments are shown.

* hpw17@mails.tsinghua.edu.cn; on leave from Tsinghua University, Beijing 100084, China

† houjun.qian@desy.de

DARK CURRENT

Dark current was measured for every cathode, both at the beginning of their insertion and after some days of operation. The results are presented in Fig. 2. Most of the dark current comes from the gun body, but the differences of the dark current among cathodes are caused by the cathode plug. The dark current results of the 5 nm Te cathode and the 15 nm Te cathode are similar, while the 10 nm Te cathode has more than 40% larger dark current at high gun power. It might be attributed to some imperfections on the cathode plug, which needs further study after the cathode extraction. Several vacuum trip events happened during the conditioning of the 10 nm Te cathode. No significant change of the dark current is found after several days of operation.

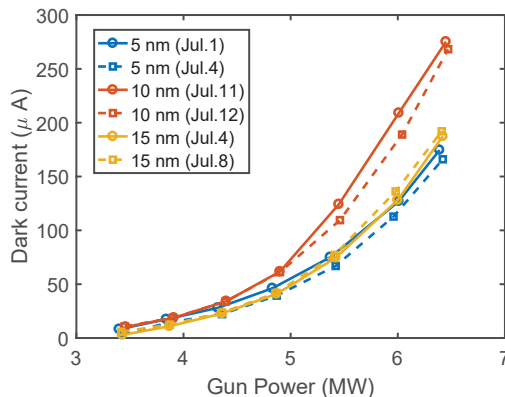


Figure 2: Dark current measurements for different gun power. As a reference, the gun power is 5.65 MW at the working condition of XFEL injector, corresponding to the peak field of 58 MV/m. The solid line is measured with the newly inserted cathode. The corresponding dash line is measured after several days of operation.

QUANTUM EFFICIENCY

The QE is dependent on the laser wavelength and applied electric field. At PITZ, the laser wavelength is 257 nm, corresponding to the photon energy of 4.83 eV. The QE is measured at different emission electric fields by scanning the gun phase. In principle, the QE will increase with the electric field due to the Schottky effect. The results of the QE versus electric field at the cathode center are shown in Fig. 3. All three cathodes show very high QE from 19% to 26%, which is much higher than the typical QE of Cs₂Te [7], and the reasons are still under investigation. Among the three cathodes, the 15 nm Te cathode has the lowest QE, and the QE of the 10 nm Te cathode is the most sensitive to electric field. At the XFEL injector working condition, the emission electric field is 40 MV/m. At this case, the 10 nm Te cathode has the highest QE, around 23.4%.

The QE map was also measured to evaluate the uniformity of the electron emission over the cathode area. The map scan was done with 0.25 mm laser diameter and 0.2 mm step size on the whole surface. Three QE maps are shown

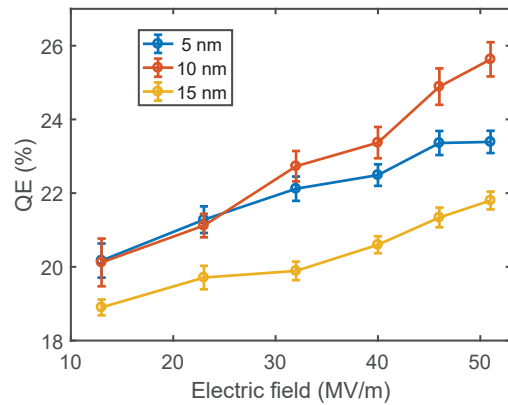


Figure 3: The plot of QE at the center of the cathode against electric field during emission for three cathodes. The error bars are the statistical error.

in Fig. 4 (a)-(c). The rms QE variation over the cathode area are 0.75%, 1.09% and 1.37% for the Te thickness of 5 nm, 10 nm and 15 nm, respectively. Hence, the 5 nm Te cathode has the most homogeneous QE map except for two hot spots. For the other two cathodes, a gradient exists along the horizontal axis and the QE decreases from right to left.

THERMAL EMITTANCE

The thermal emittance determines the lower limit of the beam emittance. Since thermal emittance depends on electric field due to Schottky effect and surface roughness, we took the measurement against electric field during emission. As shown in Fig. 5, although these cathodes have similar thermal emittance at low electric field, the difference becomes larger at high electric field. The thermal emittance of the 5 nm Te cathode is more sensitive to the electric field than the other two cathodes, which may indicate a rougher surface. At XFEL working point, corresponding to the emission field 40 MV/m, the 10 nm Te cathode has the smallest thermal emittance, around 0.97 mm mrad/mm. The transverse momentum profiles of photoelectrons from the three cathodes at 40 MV/m are presented in Fig. 6. From the plot, it is straightforward to find that the 5 nm Te cathode has a broader momentum profile, leading to a higher thermal emittance.

The thermal emittance map was measured for every cathode. The map scan was done with 0.5 mm laser diameter and 0.5 mm step size on the whole surface. Three thermal emittance maps are shown in Fig. 4 (d)-(f). There is a negative correlation between QE map and thermal emittance map, but the discussion is out of the scope of this paper. It should be noted that for all the thermal emittance results, the dominating systematic error comes from the image processing, and we believe the relative changes among all the data points tend to maintain.

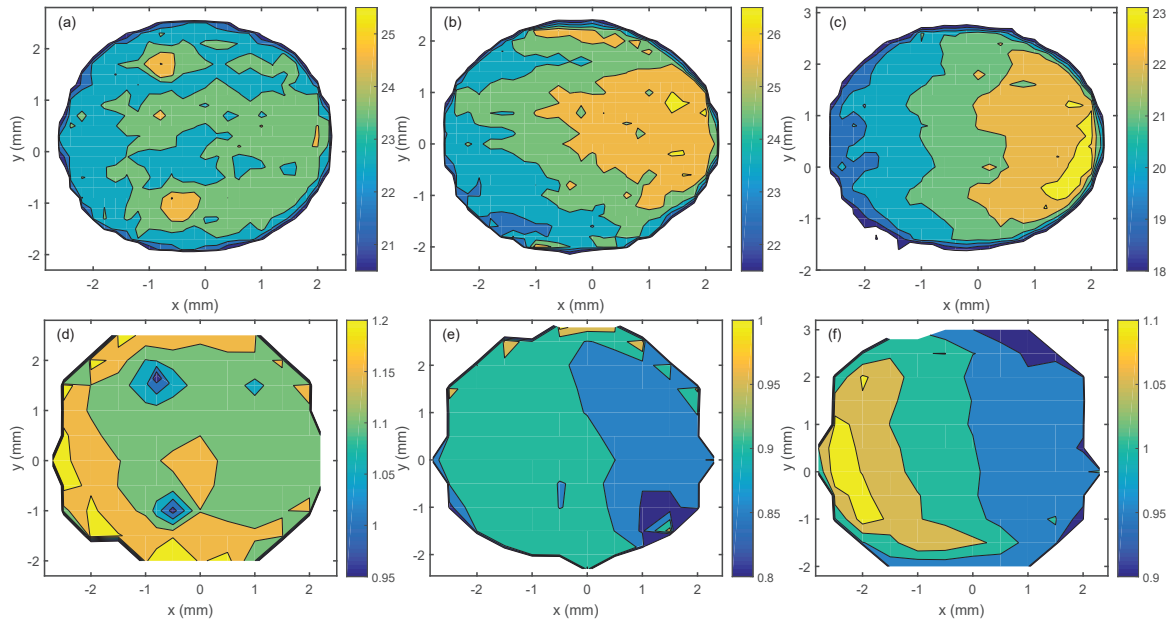


Figure 4: The QE maps (a)-(c) and thermal emittance maps (d)-(f) of three cathodes. The three columns from left to right present the results for 5 nm, 10 nm, and 15 nm Te thickness cathodes, respectively. The number aside the colorbar on the upper row is the corresponding QE with the unit of %. Each color region refers to 1% width of QE within one map. The number aside the colorbar on the lower row is the corresponding thermal emittance with unit mm mrad/mm. Each color region refers to 0.05 mm mrad/mm width of thermal emittance within one map.

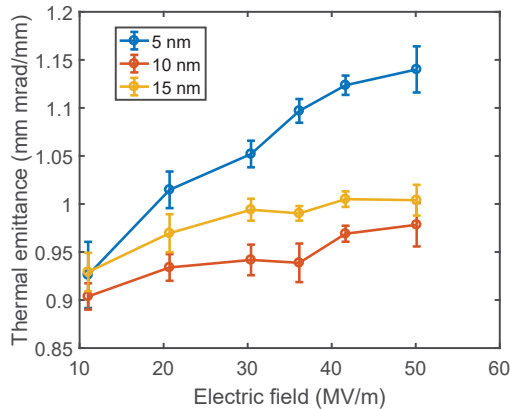


Figure 5: The plot of thermal emittance against electric field for three cathodes. The error bars are the statistical error.

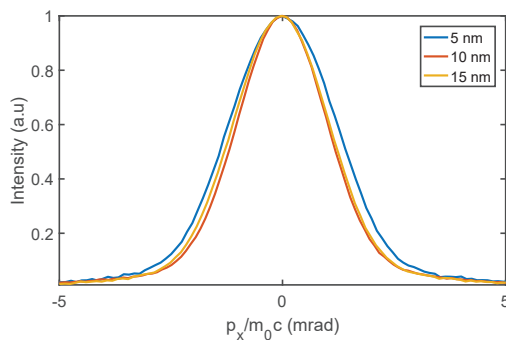


Figure 6: Transverse momentum profile of electrons emitted from different cathodes at 40 MV/m.

CONCLUSION

Three Cs_2Te cathodes from INFN-LASA were tested in the high gradient PITZ gun to study the thickness dependence of cathode performance. The dark current, quantum efficiency and thermal emittance of each cathode have been reported in this paper. More experiments and theoretical analysis are required for a thorough understanding of the thickness effect on the cathode performance.

REFERENCES

- [1] D.H. Dowell *et al.*, “Cathode R&D for future light sources”, *Nuclear Instruments and Methods in Physics Research A*, 622, 2010, 685–697. doi:10.1016/j.nima.2010.03.104
- [2] J. Feng *et al.*, “Near atomically smooth alkali antimonide photocathode thin films”, *J. Appl. Phys.*, 121, 044904, 2017. doi:10.1063/1.4974363
- [3] H. Lee *et al.*, “Intrinsic emittance reduction in transmission mode photocathodes”, *Appl. Phys. Lett.*, 108, 124105, 2016. doi:10.1063/1.4944790
- [4] A. Alexander *et al.*, “Enhanced photocathode performance through optimization of film thickness and substrate”, *J. Vac. Sci. Technol. B* 35(2), Mar/Apr 2017. doi:10.1116/1.4976527
- [5] MAA. Mamun *et al.*, “Effect of Sb thickness on the performance of bialkali-antimonide photocathodes”, *J. Vac. Sci. Technol. A* 34(2), Mar/Apr 2016. doi:10.1116/1.4939563
- [6] S. Lederer and S. Schreiber, “ Cs_2Te photocathode lifetime at Flash and European XFEL”, in *Proc. 9th Int. Particle Accelerator Conf. (IPAC'18)*, Vancouver, Canada. doi:10.18429/JACoW-IPAC2018-WEPMF056

- [7] L. Monaco, P. M. Michelato, C. Pagani, and D. Sertore, “Multiwavelengths optical diagnostic during Cs₂Te photocathodes deposition”, in *Proc. 1st Int. Particle Accelerator Conf. (IPAC'10)*, Kyoto, Japan, May 2010, paper TUPEC006, pp. 1719–1721.
- [8] A. di Bona *et al.*, “Auger and x-ray photoemission spectroscopy study on Cs₂Te photocathodes”, *J. Appl. Phys.* 80 (5), 1 September 1996. doi:10.1063/1.363161
- [9] L. Monaco *et al.*, “Growing and characterization of Cs₂Te photocatodes with different thicknesses at INFN LASA”, presented at FEL'19, Hamburg, Germany, 2019, paper WEA04, this conference.
- [10] S. Rimjaem *et al.*, “Tuning and Conditioning of a New High Gradient Gun Cavity at PITZ”, in *Proc. 11th European Particle Accelerator Conf. (EPAC'08)*, Genoa, Italy, Jun. 2008, paper MOPC078, pp. 244–246.
- [11] P. W. Huang *et al.*, “Single shot cathode transverse momentum imaging in photoinjector”, in *Proc. 10th Int. Particle Accelerator Conf. (IPAC'19)*, Melbourne, Australia, May 2019, pp. 1964–1967. doi:10.18429/JACoW-IPAC2019-TUPTS01

THE PRELIMINARY STUDY OF A PRE-BUNCHED TERAHERTZ FREE ELECTRON LASER BY A VELOCITY BUNCHING SCHEME*

Ruixuan Huang[†], Zhouyu Zhao, Heting Li, Qika Jia
NSRL, University of Science and Technology of China, Hefei, Anhui, 230029, China

Abstract

Terahertz (THz) radiation has broad applications in biological sciences, materials imaging and radar communications and so on. High-power, frequency tunable THz radiation sources are desired. An electron beam, generated in a photoinjector and bunched at THz frequency, can excite a coherent THz radiation in an undulator. The radiation power mainly depends on the particle number and the bunching factor of the electron beam, which is limited by the space charge effect among the microbunches and the total rf phase width the macrobunch occupied. Previously we have designed a pre-bunched THz free electron laser (FEL) with the radiation frequency covering 0.5-5 THz. While the radiation intensity for the lower frequency (below 1 THz) is not very high because of the large energy spread and the low bunching factor. We will report a THz FEL by a velocity bunching scheme, which could realize more highly bunched beam especially in the low THz frequency region. The physical design of the electron source is described in detail.

INTRODUCTION

The undulator-based terahertz (THz) source is a promising way to generate an intense narrow-band THz radiation with a broad frequency tuning range. For instance, a single-pass free electron laser (FEL) driven by a THz-pulse-train photoinjector, in which the electron beam is pre-bunched before entering the undulator and will excite coherent emission during the whole radiation process. The fundamental radiation frequency can be easily tuned by varying the time interval between the electron microbunches (laser micropulses). With the harmonic generation technique, the radiation could be further extended to higher frequency.

Previously, we have introduced a pre-bunched THz FEL by a linear accelerator which is composed of a photocathode rf gun and a short travelling wave (TW) tube [1]. The electron source can launch 16 microbunches with 15 pC charge for each bunch. This project is designed to have a tunable frequency range of 0.5-5 THz. One of the issues is their limited bunching factor at the frequency below 1 THz, since the large pulse width of the whole electron beam. The bunching factor is critical to determine the total radiation power, which will be discussed later. The most straight forward method to achieve a higher bunching factor at a shorter macropulse width is to reduce the microbunch number and increase its charge at the same time.

* Work supported by the National Natural Science Foundation of China
Grant Number 11805200

[†] rxhuang@ustc.edu.cn

BUNCH TRAIN GENERATION BASED ON VELOCITY BUNCHING

It is possible to produce electron pulse trains with several hundreds pC charge within the same accelerating bucket [2]. When each pulse is linearly chirped in energy, it can be longitudinally compressed either by a velocity bunching (VB) scheme, or by a magnetic compression scheme [3, 4]. In the VB procedure, the electron beam performs a rectilinear motion, which is free from the emittance degradation in a magnetic compressor. Moreover, the VB scheme is associated with the emittance compensation by focusing solenoids surrounding the accelerating section and as well as an energy increase. In short, the VB technique may be more suitable to maintain a high-brightness electron pulse train in the low-energy situation. In this section, we investigate the possible VB scheme for the pre-bunched THz FEL.

The scheme is illustrated in Fig. 1, which utilizes a typical setup for an S-band photoinjector. A 51-cell TW accelerator (TWA) is placed about 0.7 meters after a 1.6-cell BNL-type photocathode gun. A femtosecond laser followed by a proper optical system provides the required laser pulse train on the cathode. The TW tube operates at a brake-applied VB mode [5] which is also known as the over-compression regime. The whole compression is served by the TW tube together with a downstream drift segment. Three solenoids and four quadrupoles are used to focus the beam into the undulator. Three solenoids are 0.2 m, 0.5 m and 0.5 m long, respectively. And the quadrupoles are 0.05 m long with a maximum strength of 30 m^{-2} . A short undulator is located approximately 4.5 meters downstream of the TW tube. It should be indicate that the parameter setup is not the optimization result, but just a typical example instead. The designed parameters of this instance are shown in Table 1.

Table 1: Main Parameters of the Beam Line

Parameter	Value
Gradient of the rf gun	115 MV/m
Phase of the rf gun	20°
Gradient of the TWA	$\sim 12 \text{ MV/m}$
Phase of the TWA	$\sim -150^\circ$
Solenoid strength	$\sim 0.2 \text{ T}$ (in the gun) $0.03\sim 0.07 \text{ T}$ (in the TWA)
Quadrupole strength	$\sim 30 \text{ m}^{-2}$
Undulator length	0.432 m for 8 periods
Drift segment length downstream the TWA	4.5 m

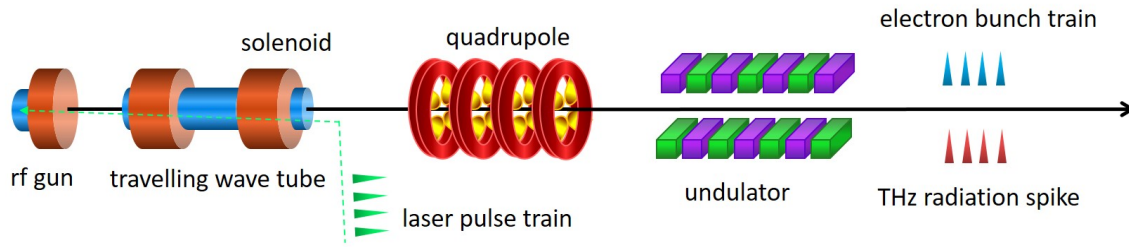


Figure 1: A schematic layout of the pre-bunched THz FEL based on velocity bunching.

A laser pulse train with four Gaussian longitudinal profiles that are 0.1 ps rms long separated by about 7 ps with 2 mm transverse spot size. The extracted charge for each pulse is 200 pC. To avoid a strong destructive force from the space charge, the time interval between the initial pulses is relatively long. The bunch charge and time interval can be adjusted to fine tune the radiation pulse structure.

The rf gun is set to 115 MV/m and a 20° off-crest phase to trade off between a good space charge control and a proper energy chirp. An electron pulse train with an average energy of above 5 MeV is obtained in the gun and then injected into the TW tube at a deep deceleration phase ($\ll -100$ degrees). A strong over-compression regime occurs, the beam energy largely declines and then climbs up along the TW tube (dash line in Fig. 2). The beam length goes through a plunge to a minimal value then a steep rise and finally a gradual decrease which continues in the drift segment (solid line in Fig. 2).

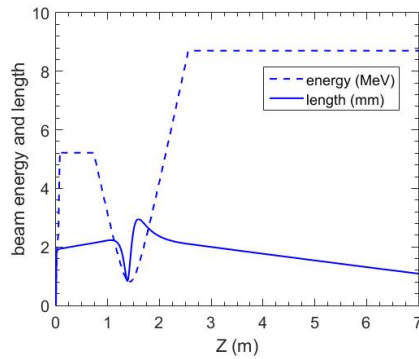


Figure 2: The evolution of the kinatic energy (dash line) and the rms beam length (solid line).

The longitudinal phase space configurations at different location are compared in Fig. 3, as computed by ASTRA code. Each micropulse is labeled with a serial number based on the initial sequence. The corresponding rotation in the longitudinal phase space of the bunch train is clearly visible. The four pulses are rotated clockwise, overlapped in an instant and then flipped over and separated again, which happens in a short section of the TW tube (a distance of about 0.4 m as shown in (c-e) of Fig. 3). A persistent and gradual beam compression occurs after rollover and lasts until the end of the drift segment. At last, the bunch train is shrunk in each micropulse width and shortened in the separation time. The micropulses in average are about 0.15 ps

rms long separated by 3.2 ps with 470 μm of horizontal spot size. A horizontal emittance is about 12 mm mrad which is less important in THz FEL.

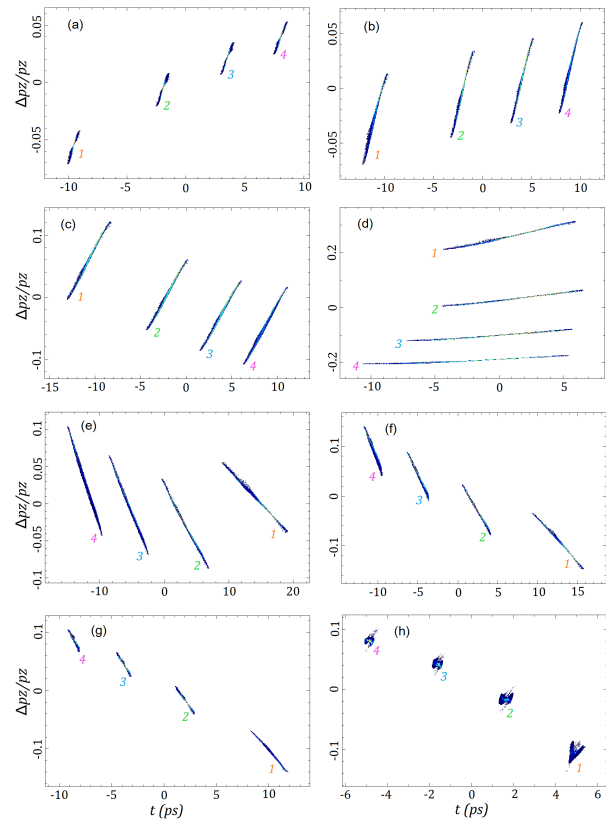


Figure 3: Longitudinal phase space of 4 micropulses. The corresponding locations are gun exit (a), TWA entrance (b), 0.5 m from TWA entrance (c), 0.7 m from TWA entrance (d), 0.9 m from TWA entrance (e), 1.1 m from TWA entrance (f), TWA exit (g), end of drift (h). Each micropulse is labeled with a serial number based on the initial sequence.

It is known that a more highly bunched electron beam could achieve a more intense narrow-band THz radiation in the undulator. The bunching factor b describes the longitudinal density distribution in the electron beam. The bunching factor at a certain frequency ω can be expressed as

$$b(\omega) = \frac{1}{n} \left| \frac{\sin \pi n \omega \Delta t}{\sin \pi \omega \Delta t} \right| e^{-(2\pi \omega \sigma_t)^2/2}. \quad (1)$$

Assumed the electron bunch train is consist of n Gaussian microbunches with rms pulse width of σ_t , spacing by Δt temporal interval. One can find that each micropulse in the bunch train has a narrow width and a quasiequal spacing time, which contributes to a high bunching factor as given in the blue line of Fig. 4. Bunching factor in the previous scheme is also plotted in black line for comparison. In the first five harmonics of the VB scheme, the bunching factor is maintained above 0.4 with a quite narrow bandwidth. It is worth pointing out the initial separation time between each micropulse may be different to provide a uniform space inside the compressed bunch train, which is beneficial to obtain a high bunching factor.

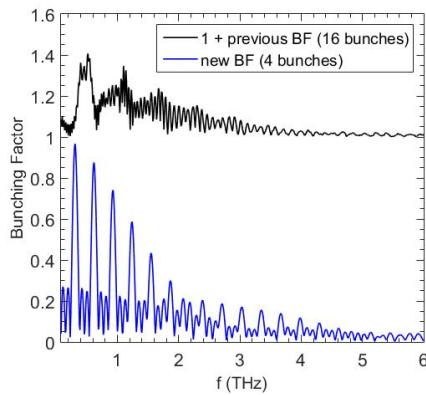


Figure 4: The bunching factor comparison before (black line) and after (blue line) improvement. In previous scheme 16 microbunches with 15 pC charge in each, while 4 microbunches with 200 pC charge in each is assumed in the VB scheme. The black line is entirely raised by 1 to make a legible comparison.

Therefore, it is demonstrated by simulations that electron bunch train with a short micropulse width and a large bunch charge can be generated in a photoinjector, and a good time structure of the beam may be preserved by the VB technique in a deep over-compression regime. Via an optimized compression scheme, a relatively uniform bunch train can be generated, which should have great potential for application in FELs, advanced particle accelerations and THz radiation sources [6].

UNDULATOR RADIATION

After a proper manipulation in the photoinjector, the electron beam passes through a short undulator to generate the coherent radiation. The output wavelength of the undulator radiation is determined by a resonance condition as $\lambda = 0.5\lambda_u(1 + K^2)/\gamma^2$, where γ is the relativistic factor, λ_u and K are the period and the strength parameter of the undulator, respectively. For a certain frequency $\omega = 2\pi c/\lambda$, the total radiation power P can be expressed by [7]

$$\frac{dP}{d\omega} = \frac{dP_0}{d\omega} N_e [1 + (N_e - 1)b^2(\omega)]. \quad (2)$$

N is the total electron number, $dP_0/d\omega$ is the radiation power from a single electron which is considered as incoherent radiation power. It is indicated that the electron beam could be bunched at the fundamental frequency ($\omega = 2\pi/\Delta t$) and the high harmonics ($\omega = 2\pi m/\Delta t$, $m=2,3,\dots$). Thus, a highly bunched electron beam could significantly enhance the total radiation power.

A planar undulator with 8 periods and a period length of 54 mm is preliminarily designed, in which the gap can be tuned from 16 to 48 mm based on different harmonics. At the fundamental frequency, the undulator with a strength of $K=4.33$ can output an FEL pulse with a peak power of 0.46 MW. The time structure of the output FEL pulses at the undulator exit for resonating at 0.31 THz is simulated by GENESIS, as shown in Fig. 5. The full length of the radiation pulse is about 35 ps. The other four harmonics of the FEL pulses also have radiation powers at MW level.

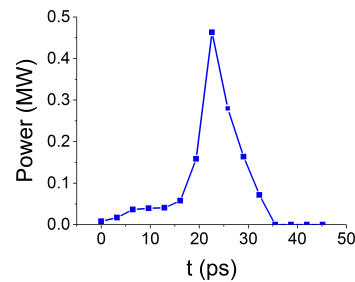


Figure 5: The time structure of the output FEL pulse at the undulator exit for resonating at 0.31 THz.

CONCLUSION

The strong overcompression regime of the velocity bunching scheme is greatly beneficial for bunch train compression due to its relatively large acceptance of longitudinal phase space and its uniformity of compression. The phase space of microbunches are reversed in the TW tube and maintained a linear chirp in energy. A considerable high bunching factor can be achieved especially in the low THz frequency region. With charges of several hundred pC, and a good tunability in time and energy space, the electron bunch train should have great potential for application as FELs and terahertz radiation sources.

REFERENCES

- [1] R. Huang, *et al.*, *Particles* 1, 267 (2018). doi:10.3390/particles1010021
- [2] M. Boscolo, *et al.*, *Nucl. Instrum. Methods Phys. Res., Sect. A* 593, 106 (2008). doi:10.1016/j.nima.2008.04.069
- [3] M. Boscolo *et al.*, "Laser Comb: Simulations of Pre-modulated E- Beams at the Photocathode of a High Brightness RF Photoinjector", in *Proc. 10th European Particle Accelerator Conf. (EPAC'06)*, Edinburgh, UK, Jun. 2006, paper MOPCH025.
- [4] M. Ferrario, *et al.*, *Nucl. Instrum. Methods Phys. Res., Sect. A* 829, 17 (2016). doi:10.1016/j.nima.2016.01.061



- [5] R. Huang, *et al.*, *Nucl. Instrum. Methods Phys. Res., Sect. A* 866, 65 (2017). doi:10.1016/j.nima.2017.05.022
- [6] D. Wang, *et al.*, *Phys. Rev. Accel. Beams* 21, 024403 (2018). doi:10.1103/PhysRevAccelBeams.21.024403
- [7] H. Li, *et al.*, *J. of IRMM and THz Waves* 37: 649 (2016). doi:10.1007/s10762-016-0258-9

PERFORMANCE OF S-BAND PHOTOCATHODE RF GUN WITH COAXIAL COUPLER

J. Hong*, C.-K. Min, J.-H. Han, PAL, Pohang, Kyungbuk 790-784, Korea

Abstract

To improve the characteristics of electron beams, new S-band photocathode RF gun with a coaxial coupler has been developed and fabricated at the Pohang Accelerator Laboratory (PAL). This new RF gun is improved the field symmetry inside the cavity cell by applying the coaxial coupler, and the cooling performance by improving the cooling lines. The RF gun is installed in the injector test facility (ITF) for high power RF test. This paper reports the recent results on the RF conditioning process and the beam tests of the RF gun with high power RF at ITF. We present and discuss the measurement results of the basic beam parameters.

INTRODUCTION

The Pohang Accelerator Laboratory (PAL) has developed two types of S-band photocathode RF guns to generate electron beams for the X-ray free electron laser (PAL-XFEL) [1–3]. The first gun is the four ports side coupled RF gun (GUN-I) and the second one is the coaxial coupled RF gun (GUN-II). Currently we are using GUN-I as an electronic source for PAL-XFEL [4,5]. In the case of GUN-II, an electron gun with a replaceable Cu plug has been fabricated in 2013. In 2015, an electron gun with fixed Cu cathode has been fabricated. Until we were interested again in 2018, GUN2 was out of our memory.

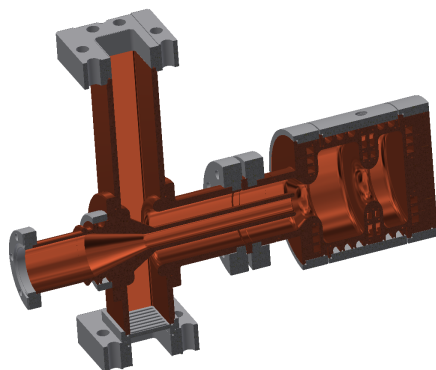


Figure 1: Cutaway view of GUN-II.

The electron gun used in this experiment is an electron gun with fixed Cu cathode. The 3-dimensional cutaway view of GUN-II is shown in Fig. 1. The features of GUN-II are as follows:

- Coaxial coupler is applied for axisymmetric E-field.
- Modified cooling channels to be uniform the RF heating.
- Fixed Cu cathode is applied for easy fabrication and operation.

- Has a narrow (diameter = 14 mm) beam tube. (difficult laser transmission)
- Does not have an gun probe. (can not measure the gun power directly)

The RF parameters of GUN-II are listed in Table 1.

Table 1: RF Parameters

Property	GUN-II	Unit
Operating Frequency	2856	MHz
Mode Separation	20	MHz
Quality Factor	14400	
Coupling coefficient	1.1	
Field Balance	1.02	

TEST SETUP

From August 2015, the important devices in the injector test facility (ITF) were moved to PAL-XFEL. Moved devices are an electron gun, two accelerator columns, a gun energy spectrometer, and a deflector, etc. Until the end of 2018, ITF was shutdown. In April 2019, ITF was restructured to perform the high power beam test for GUN-II. The schematic diagram of the new ITF beam-line for GUN-II is shown in Fig. 2. Electron beams are generated from the new GUN-II.

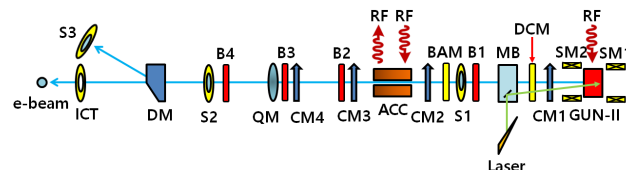


Figure 2: Schematic diagram of the ITF beam-line. Letter abbreviations in the figure are as follows: ACC for accelerating column, SM for solenoid magnet, CM for corrector magnet, DM for dipole magnet, QM for quadrupole magnet, BCM for beam current monitor, MB for laser mirror box, S for screen Monitor, B for beam position monitor, DCM for dark current monitor, BAM for bunch arrival-time monitor.

The main solenoid (SM2 in Fig. 2) and the bucking solenoid (SM1 in Fig. 2) was installed before and after GUN-II to focus the generated electron beams. Downstream of the main solenoid, the dark current monitor (DCM) was installed to measure the dark current. Downstream of the DCM, the laser mirror box for GUN-I (not GUN-II) which permits an UV laser beam to strike the gun cathode was installed. Now we do not have a laser mirror box for GUN-II. If we want laser cleaning and emittance optimization, we need a laser mirror box for GUN-II. The electron beam is accelerated by the new 3-meter dual-feed racetrack-type S-band

* npwinner@postech.ac.kr

accelerating column (ACC in Fig. 2) for which enough to accelerate the beam up to 70 MeV. After acceleration the emittance will be measured using the quadrupole magnet (QM in Fig. 2) and the screen #2 (S2 in Fig. 2). The end of the beam line the integrating current transformer (ICT) was installed to measure the electron bunch charge. To measure the bunch arrival-time, the new bunch arrival-time monitor (BAM, resonance frequency ~ 2826 MHz, loaded quality factor = 760) made of stainless steel was also installed. In the ITF beam-line four beam position monitors and four corrector magnets were installed to align electron beams. More information of ITF can be found in the Ref [6, 7].

RF CONDITIONING

When high gradients are required, RF conditioning of a new RF component is mandatory. The RF network of ITF is sketched in Fig. 3. There are two modules of RF station

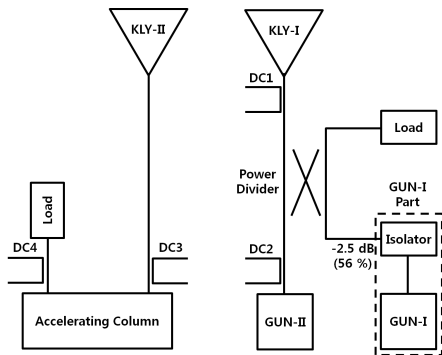


Figure 3: Schematic diagram of the ITF RF network. Letter abbreviations in the figure are as follows: KLY for klystron, DC for directional coupler.

in ITF. The first klystron (KLY-I) feeds GUN-I and GUN-II. GUN-I is a spare gun for PAL-XFEL. Therefore, we will not consider the GUN-I part in this paper. The second klystron feeds only the new accelerating column. GUN-II was conditioned up to 12 MW. In parallel, the accelerating column was conditioned up to 40 MW. The repetition rate was fixed to 10 Hz because of the limiting factor of the RF system. The pulse width is can vary from 0 up to 2.5 μ s for GUN-II and from 0 up to 1.2 μ s for the accelerating column, respectively. These pulses are long enough to fill the RF gun and the accelerating column. The RF conditioning procedure took eight days (eight hours a day) for GUN-II and nine days for the accelerating column. After RF conditioning, the vacuum level is 3×10^{-10} mbar for GUN-II and 2×10^{-8} mbar for the accelerating column, respectively.

The RF power is detected by using the directional couplers and measured by using the low-level RF (LLRF) system. Figure 4 shows measured RF power waveforms from directional couplers. Both klystron input pulses were not very uniform but could be the RF conditioning. In Fig 4 a) and b) the second peaks are the reflections of the RF pulse from the klystron because there is no isolator for GUN-II. Therefor the forward waveform and reflected waveform overlaps heavily.

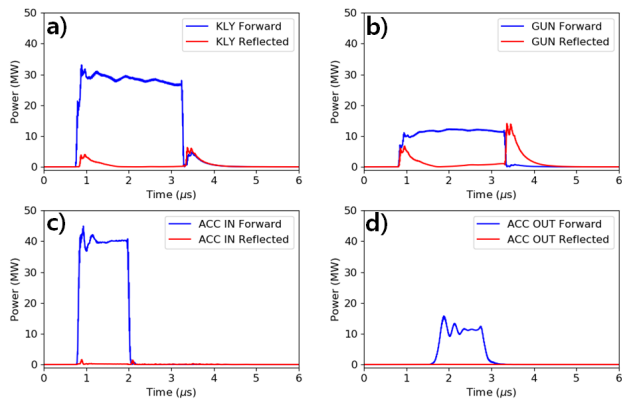


Figure 4: RF power waveforms from directional couplers after RF conditioning. a) DC1, b) DC2, c) DC3, and d) DC4 in Fig 4.

After the conditioning the DCM pickup was connected to the LLRF because the resonance frequency of DCM is equal to the operating RF frequency. The comparison of the measured the GUN-II DCM signal, the GUN-I DCM signal, and the RF induced GUN-I probe pickup signal is shown in Fig. 5. The DCM signals of the two electron guns are almost

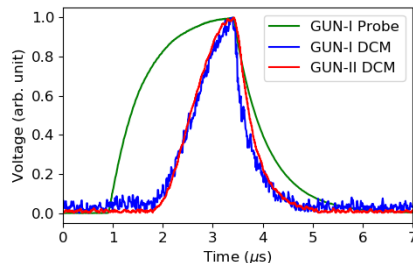


Figure 5: Comparison of the measured dark current induced DCM pickup signal and the RF induced gun probe pickup signal. The DCM and the gun probe signal is compared with two types of electron gun (GUN-I and GUN-II)

similar in shape. In this time, the absolute value could not be measured because DCM has not yet been calibrated.

ELECTRON BEAM MEASUREMENT

After then, GUN-II generated the first electron beams. For the generation of electron beams, the UV laser (see Fig. 6 a), pulse energy = 20 μ J, diameter ~ 1 mm) was used. The beam size and profile are measured using YAG crystals imaged with CCD cameras for image processing. Figure 6 b), c), and d) show typical images of each screen.

The electron beam energy and energy spread, including acceleration in the accelerating column, are measured by using the spectrometer (DM + S3 in Fig 2). The beam energy is about 70 MeV and the energy spread is less than 0.1 %. The gun spectrometer was not installed in this measurement. By analogy to RF power (10 ~ 12 MW), the beam energy of GUN-II will be at least 6 MeV.

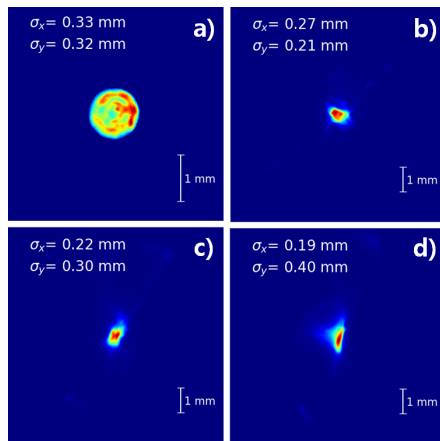


Figure 6: Image of CCD camera. a) UV laser and b) S1, c) S2, d) S3 in Fig 4.

Bunch charge is measured by using ICT. The measured ICT signal is shown in Fig 7. In this measurement, the bunch

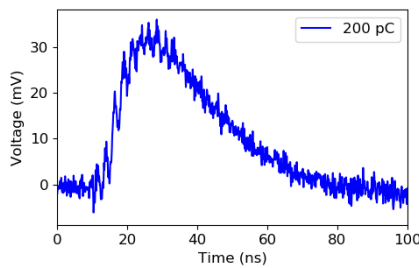


Figure 7: Measured ICT pickup signal for the bunch charge of 200 pC.

charge could occur about 200 pC without IR laser cleaning. This value is 4.5×10^{-5} in the quantum efficiency.

The pickup signal of the new BAM was measured with an oscilloscope under the same electron beam conditions. The measured BAM signal is shown in Fig 8. At the 200 pC

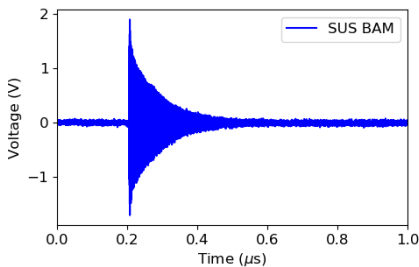


Figure 8: Measured BAM pickup signal for the bunch charge of 200 pC.

bunch charge, the peak voltage is 2 V and the decay time is 40 ns. These values will be used for future R&D of a new BAM electronics.

SUMMARY AND DISCUSSION

GUN-II and the new dual-feed racetrack-type accelerating column were RF conditioned at PAL-ITF. And we generated

the first electron beams. The first electron beams of GUN-II and the ITF system parameters are listed in Table 2.

Table 2: Electron Beams and ITF System Parameters

Parameter	Value	Unit
Electron Beam (GUN / GUN+ACC)		
Energy	6 (estimate) / 70	MeV
Energy Spread	- / 0.1	% (rms)
Charge	200	pC
RF (GUN / ACC)		
Peak power	12 / 40	MW
RF pulse Width	2.5 / 1.2	μs
Repetition Rate	10	Hz
Laser		
Spot size	0.32	mm (rms)
Pulse Length	3	ps (FWHM)
Pulse energy	20	μJ

GUN-II employs the circular waveguide coupler and can reduce the emittance to 0.2 mm-mrad by optimizing the position of the main solenoid. By reinforcing the cooling line, the repetition rate can be increased up to about 1 kHz. Optimization of the laser mirror box for GUN-II will help in the UV laser transmission and the IR laser cleaning. After that, it will be possible to optimize the emittance for various parameters. In this measurement, the repetition rate of GUN2 was fixed to 10 Hz due to the limiting factor of the ITF RF system. In the future, if a high repetition rate RF source is applied, it will be possible to operate at higher repetition rate than GUN-I which is operating at 60 Hz in PAL-XFEL.

REFERENCES

- [1] J. Hong *et al.*, “High-power RF test of an RF gun for PAL-XFEL”, in *Proc. IPAC'12*, New Orleans, Louisiana, USA, May 2012, TUPPD061, <http://www.JACoW.org>
- [2] J. Hong *et al.*, “Development of photocathode RF gun at PAL”, in *Proc. FEL'13*, New York, NY, USA, August 2013, TUPSO28, <http://www.JACoW.org>
- [3] J. Hong *et al.*, “Beam measurement of photocathode RF gun for PAL-XFEL”, in *Proc. FEL'14*, Basel, Switzerland, August 2014, THP011, <http://www.JACoW.org>
- [4] I.-S. Ko *et al.*, *Appl. Sci.* **7**, 479, 2017. doi:10.3390/app7050479
- [5] H.-S. Kang *et al.*, *Nature Photonics* **11**, 708, 2017. doi:10.1038/s41566-017-0029-8
- [6] J.-H. Han *et al.*, “Operation of PAL-XFEL injector test facility”, in *Proc. FEL'14*, Basel, Switzerland, August 2014, WEB02, <http://www.JACoW.org>
- [7] H. Choi *et al.*, “Introduction to beam diagnostics components for PAL-ITF”, in *Proc. IPAC'13*, Shanghai, China, June 2013, MOPME060, <http://www.JACoW.org>

DEVELOPMENT AND COMMISSIONING OF A FLIP COIL SYSTEM FOR MEASURING FIELD INTEGRALS*

J. E. Baader[†], University of Campinas, Campinas, Brazil

Abstract

Many techniques for measuring magnetic fields are available for accelerator magnets. In general, methods based upon moving wires are suitable for characterizing field harmonics, and first and second field integrals. The flip coil moving wire technique stands out due to simplicity, speed, precision, and accuracy. We aimed to develop a reliable, fast and precise flip coil system capable of characterizing field integrals in the two transverse axes. The coil was a single turn loop made of insulated beryllium copper wire. The width of the loop was 5 mm. The approach of measuring second field integrals by changing the coil's width at one of the ends was analyzed and included in the system. High-performance motorized stages performed angular and transverse positioning of the coil, while manual stages were used to stretch the wire, execute fine adjustments in its transverse position, and change coil's geometry. Initial tests with the Earth's field and also with a reference magnet of 126 Gauss-centimeter (G cm) demonstrated that the system achieves repeatability of 0.2 G cm for a 60-cm long coil. This work was carried out for the LCLS-II project at SLAC.

INTRODUCTION AND FLIP COIL SYSTEM OVERVIEW

Various methods are available for the measurement of the magnetic field. The choice of a method depends on many requirements, such as precision, accuracy, speed, geometric constraints, field measurements range, etc [1]. A complete magnetic measurements laboratory would have most of the main available techniques, given that each method offers distinct advantages and the ability to cross-check the results.

The available techniques for characterizing magnetic field at the SLAC Magnetic Measurement Facility (MMF) includes a rotating coil for measuring magnetic center in quadrupoles, a vibrating wire used to fiducialize the quadrupoles, a moving wire for measuring field integrals and Hall probes used to map magnetic fields [2–6]. This paper describes the development of a new flip coil moving wire system to measure field integrals at the SLAC MMF for the LCLS-II project.

In the flip coil technique a long coil is rotated within the magnet by 180° during the measurement, and the induced voltage V is recorded. The flux change $\Delta\phi$ during the measurement is equal to twice the flux ϕ_0 linked with the coil in the initial angular position θ_0 , so $\int V dt = -2N\phi_0$ (N is the

number of turns). If the loop of the coil forms two parallel wires with a small distance of W along the magnet's length, $\phi_0 = WI_1$, where I_1 is the first field integral of the field component perpendicular to the plane θ_0 constant. Therefore, $|I_1| = \int V dt / (2NW)$. If the coil's width is set to zero at one of the ends, it is possible to prove that $\phi_0 = WI_2/L$, where L is the coil's length and I_2 is the second field integral of the field component perpendicular to the plane θ_0 constant. Therefore, $|I_2| = L \int V dt / (2NW)$. For both cases, we assume that the field does not depend on the radial axis of the coil.

SYSTEM DEVELOPMENT

Mechanical Design and Motion

The flip coil is mounted in two towers, each composed of two motorized Newport stages model MTMPP.1 with 250 mm of travel attached at right angles for y (vertical) and x (horizontal) movements. Each tower has one motorized Newport rotation stage model RGV100BL that holds two manual Edmund linear stages with 13 mm of travel for fine adjustments in x -axis and y -axis. All motorized stages are controlled by the Newport Motion Control XPS-Q8. Each end has also one linear stage that moves towards z -axis and is used to stretch the coil. Figure 1 shows the system. A zoomed picture of each end of the system (called End A and End B in Fig. 1) is presented in Fig. 2.

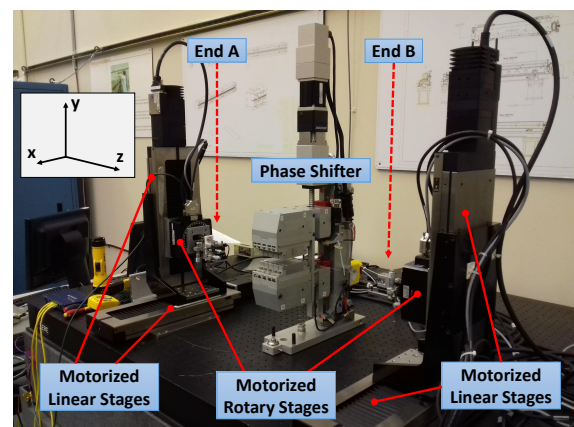
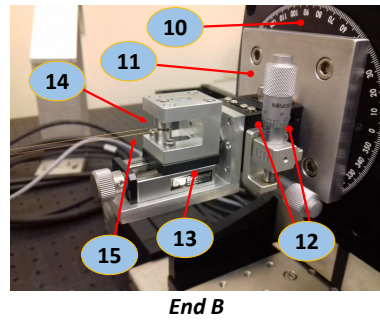
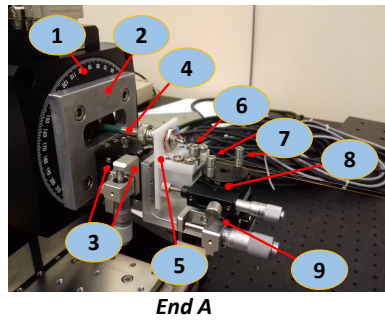


Figure 1: Flip coil system set up at the SLAC MMF.

The coil is a single turn of a 100 μm diameter insulated beryllium copper wire looped between two spools placed on each end, which forms one continuous loop of 5 mm of width (the minimum LCLS-II undulators' gap is 7.2 mm). The coil's length is approximately 60 cm. The End A has one manual Edmund rotary stage with 30 mm of diameter that allows changing the coil's width to measure second field integrals (see details 7 and 8 in Fig. 2). A low noise

* This study was financed in part by the Coordenação de Aperfeiçoamento de Pessoal de Nível Superior - Brasil (CAPES) - Finance Code 001. This work was also supported by FAPESP-UNICAMP and by DOE contract DE-AC02-76SF00515 in support of the LCLS-II project at SLAC.

[†] jebaader@gmail.com



Legend:

- (1) Motorized rotary stage; (2) Bracket;
- (3) Manual linear stages used for fine adjustments in the coil's transverse position; (4) BNC cable;
- (5) Delrin plates; (6) Spool for holding the wire;
- (7) Spools on the manual rotary stage for changing coil's width; (8) Manual rotary stage; (9) Manual linear stage for stretching the wire;
- (10) Motorized rotary stage; (11) Bracket; (12) Manual linear stages used for fine adjustments in the coil's transverse position; (13) Manual linear stage for stretching the wire.
- (14) Spool for holding the wire; (15) Insulated beryllium copper wire.

Figure 2: Zoomed picture of the ends of the flip coil system.

amplifier module model EM DC A22 [7] operating as a low-pass filter with cutoff frequency of 15 Hz is coupled to the wire. The terminals of the amplifier's output are connected to the voltmeter HP3458 to record the voltage signal induced during the coil's rotation and determine the flux change. The angular speed and angular acceleration of the coil are 1,5 turns/s and 1,5 turns/s², respectively. The coil only performs half revolutions (i.e. angular variation of 180°), starting either from the horizontal position in 0° (measures vertical field component) or from the vertical position in 90° (measures horizontal field component). Then, the coil reverses its direction to return to the starting position, during which data is also taken.

Software and Measurement Procedure

LabWindows/CVI-based system software was developed to coordinate the motorized stages and data acquisition. A graphical user interface shows the voltage and flux change samples, with the latter being calculated by numerically integrating the voltage samples by the trapezoidal rule, or

$$\Psi_i = \frac{\Delta t}{2} (V_i + V_{i-1}) + \Psi_{i-1}, i = 2, 3, \dots, n, \quad (1)$$

where $\Psi_1 = 0$ and n is the number of samples for a single flip. The average of the last eight samples of Ψ_i corresponds to the total flux change $-\Delta\phi$ (or $\int V dt$) associated with the flip. Figure 3 shows an example of the voltage and flux change samples taken during the clockwise and counterclockwise movement for a test with a dipole field.

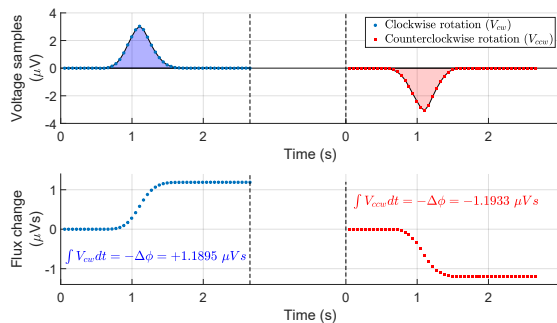


Figure 3: Example of voltage samples, flux change samples (clockwise and counterclockwise rotations) and value of the total flux change for a measurement of a dipole field.

Once the user selects either vertical or horizontal field measurements, the software defines the starting position of the coil as $\theta_0 = 0^\circ$ or $\theta_0 = 90^\circ$, respectively. The system starts the voltage acquisition, waits 0.5 seconds, flips the coil from θ_0 to $\theta_0 + 180^\circ$ (clockwise rotation), waits 1 second, and then stops the voltage acquisition. Integration period of 3 power line cycles (sampling time of 50 ms) is used, which shows good performance since it suppresses 60 Hz noise. One flip takes approximately 3 seconds. The voltage samples taken during the initial and final delay (before and after the angular movement) are used to perform offset corrections, which increases the precision. The software reads all the voltage samples, applies the offset correction, and calculates the flux change samples using Eq. (1). The same procedure is repeated with the coil rotating back to the initial position (counterclockwise rotation). Since the integration is applied for both clockwise and counterclockwise rotations, these integrals have opposite polarity, being subtracted and divided by 2 to determine $\int V dt$. For instance, the example shown in Fig. 3 gives $\int V dt = [1.1895 - (-1.1933)]/2 = 1.1914 \mu Vs$. In addition, due to the short time separation between each rotation, such procedure contributes to cancel voltage offsets. After the coil rotates forth and back and $\int V dt$ is determined, the software calculates the field integral. A few seconds of delay between the flips is required to assure the coil is static. To improve the repeatability, a set of 10 samples of $\int V dt$ is averaged, and the error is expressed as the standard deviation over these samples. The system takes less than three minutes to perform and measure this set of samples.

System Validation and Results

The flip coil system was used to measure the first field integral of a small reference magnet that had its strength estimated as 126 G cm (Gauss-centimeter) by an independent system. We tested both vertical and horizontal field integral measurements by changing the reference magnet's field orientation.

Let I_{yB} and I_{xB} be the first field integral of the background fields on y-axis and x-axis, respectively. Furthermore, let I_{y+} and I_{y-} be the first field integral measured with the flip coil system when a magnet is placed in such a way that its

¹ 10 samples of $\int V dt$ corresponds to 20 flips: 10 repetitions of clockwise and counterclockwise movements.

Table 1: First Field Integral Measurements with a Reference Magnet, the Background Fields and a Phase Shifter

#	Magnet / condition	Field component	With the low noise	Without the low noise
			amp. EM DC A22 Result \pm Error (G cm)	amp. EM DC A22 Result \pm Error (G cm)
1	Reference magnet's field pointing to	positive y-axis	I_{y+}	$+120.75 \pm 0.20$
2		negative y-axis	I_{y-}	-134.48 ± 0.10^2
3		positive x-axis	I_{x+}	$+142.28 \pm 0.13$
4		negative x-axis	I_{x-}	-116.73 ± 0.11
5	Reference magnet first field integral	$(I_{y+} - I_{y-})/2$	$+127.62 \pm 0.11^3$	$+127.22 \pm 1.15^3$
6		$(I_{x+} - I_{x-})/2$	$+129.51 \pm 0.08^3$	$+130.04 \pm 1.28^3$
7	Background first field integral (estimated from the ref. mag. results)	$(I_{y+} + I_{y-})/2$	-6.87 ± 0.11^3	-6.32 ± 1.15^3
8		$(I_{x+} + I_{x-})/2$	$+12.77 \pm 0.08^3$	$+10.95 \pm 1.28^3$
9	Background Fields	I_y	-7.36 ± 0.14	-7.03 ± 2.16
10		I_x	$+11.37 \pm 0.12$	$+12.09 \pm 1.83$
11	Phase Shifter (see Fig. 1)	I_y	-10.93 ± 0.15	—
12		I_x	$+8.88 \pm 0.12$	—

² A similar result was obtained with the long coil and the fluxgate probe, as shown in the technical report [5].

³ Error estimated by propagating the error of the terms I_{y+} , I_{y-} , I_{x+} and I_{x-} .

field points to the positive and negative y-axis, respectively. If the magnet's first field integral is I , then $I_{y+} = I + I_{yB}$ and $I_{y-} = -I + I_{yB}$. Therefore, $(I_{y+} - I_{y-})/2$ is, in theory, equal to I , and may be applied to test the system for vertical field integrals measurements. The same is valid for testing horizontal field integrals by setting the reference magnet's field to point to x-axis.

It is interesting to notice that summing I_{y+} and I_{y-} (or I_{x+} and I_{x-}) and dividing by 2, the reference magnet's field is canceled, and only I_{yB} (or I_{xB}) remains. In this case, I_{yB} and I_{xB} may be compared to the background field obtained directly with the flip coil system without any magnets nearby. The next section presents the measurements we performed with the reference magnet and background fields. We tested the system with and without the amplifier module. An additional set of tests was made with a phase shifter. Table 1 summarizes the results of the measurements performed with the reference magnet (lines 1-8), the background fields (lines 9-10), and a phase shifter (lines 11-12).

DISCUSSION

We designed, built, and commissioned a new flip coil moving wire system for measuring magnetic field integrals. The system is capable of measuring field with a precision of 0.2 G cm for a 60-cm long coil, and takes less than three minutes to perform a complete measurement.

Coupling the EM DC A22 module to the coil reduced the error (standard deviation of the mean) in one order of magnitude—from 2 G cm to 0.2 G cm—, which demonstrates the high stability of the results. Besides, the field strength obtained with and without the EM DC A22 module showed no significant difference. These facts support some of the main features expected from the amplifier module, including high gain stability and low drifts.

Comparing the reference value of 126 G cm obtained by independent measurements and the values calculated in lines

5-6 shows that the measurements performed with the flip coil system agreed at the level of 3%. We believe that the error of the coil's width determination and small displacements of the reference magnet are the main sources of errors that justify the slight disparity. Further studies are necessary to define the optimum coil's width.

We may assume that the most significant influence in the background fields comes from the Earth's magnetic field, which is supposed to induce a very weak signal to the coil. Even so, the background fields measurements exhibited the same order of error observed for the other measurements, as shown in lines 9-10. It is worthy to notice that lines 7-8 present an estimative for background field based on the measurements with the reference magnet—considerable field strength in comparison with the Earth's field strength. The agreement among the results presented in lines 7-8 and 9-10 at the level of 1 G cm confirms that the system detects small field integrals.

A mechanical adaptation was made as an attempt to measure second field integrals by changing the coil's width at one of the ends. The precision of 0.2 G cm for the first field integrals suggests that the precision of second field integrals measurements would be about $0.1 \mu\text{Tm}^2$ for a 60-cm long coil. Still, further tests have to be taken to evaluate the system performance for determining second field integrals. Although the coil's length is suitable for measuring small magnets (e.g. dipoles, quadrupoles, phase shifters, etc.), tests with a longer coil need to be performed with LCLS-II undulators in the future.

ACKNOWLEDGMENT

The author would like to thank the supervisors of this project, Zachary Wolf and Yurii Levashov, for their indispensable advice and support. The author also wish to thank Luis Juarez, Ralph Colon and Scott Anderson for their constant technical support.

REFERENCES

- [1] L. Bottura and K. N. Henrichsen, “Field measurements,” in *Proc. CERN Accelerator School on Superconductivity and Cryogenics for Accelerators and Detectors*, Erice, Italy, May 2002, pp. 118 – 148.
- [2] C. M. Spencer, S. D. Anderson, D. R. Jensen, and Z. R. Wolf, “A rotating coil apparatus with sub-micrometer magnetic center measurement stability,” *IEEE Transactions on Applied Superconductivity*, vol. 16, no. 2, pp. 1334–1337, June 2006. doi:10.1109/TASC.2005.864289
- [3] Z. Wolf, “A vibrating wire system for quadrupole fiducialization,” SLAC, Menlo Park, CA, USA, Tech. Rep. LCLS-TN-05-11, May 2005. doi:10.2172/1000391
- [4] S. Anderson, K. Caban, H.-D. Nuhn, E. Reese, and Z. Wolf, “Magnetic measurement results of the LCLS undulator quadrupoles,” SLAC, Menlo Park, CA, USA, Tech. Rep. LCLS-TN-09-1, Jan. 2010. doi:10.2172/1022518
- [5] Z. Wolf and Y. Levashov, “Undulator long coil measurement system tests,” SLAC, Menlo Park, CA, USA, Tech. Rep. LCLS-TN-07-03, Apr. 2007.
- [6] Y. Levashov, V. Kaplunenko, A. Weidemann, and Z. Wolf, “Magnetic measurements, tuning and fiducialization of LCLS undulators at SLAC,” in *Proc. FEL’07*, Novosibirsk, Russia, Aug. 2007, paper WEBAU05 pp. 314–317.
- [7] “EM Electronics,” <http://www.emelectronics.co.uk/a22.html>

INFLUENCE OF RADIATION EXPOSURE ON THE FEL PERFORMANCE AT FLASH

B. Faatz*, M. Tischer, P. Vagin, DESY, Hamburg, Germany

Abstract

FLASH has been operated as user facility for about 14 years. In this time, the total charge accelerated and transported through the FLASH1 undulator is around 35 Coulomb. Based on detailed monitoring of the radiation loss and reference measurements on degradation of the magnetic field of the undulator, we have performed simulations to study the change in FEL performance and compare the simulations with the changes we observe during operation.

INTRODUCTION

FLASH is the first FEL user facility in the XUV and has been running since 2005 [1]. Continuous upgrades have increased the beam energy from initially about 700 MeV to the present 1.25 GeV, resulting in a wavelength from 13 nm in 2005 to the present 4.2 nm. It is also the only XUV-FEL based on superconducting technology, which produces up to 5000 bunches per second as compared to the typical 50 to 100 for normal conducting machines [2]. And finally, since 4 years FLASH runs two FELs simultaneously from the same accelerator, thus increasing the available beamtime for users [3].

In the foreseeable future, several new facilities will be built with the same superconducting technology, but in this case running in CW mode [4, 5]. Where beam loss in the undulator plays only a minor role for most facilities, for a facility like FLASH or the European XFEL [6], this has resulted in more elaborate systems to detect beam loss and in interlock and machine safety systems that switch off the beam as fast as possible to avoid deterioration of the undulator magnetic field due to radiation damage.

Even after running for 14 years, the accumulated charge produced by FLASH is around 35 C. Had FLASH been running continuously at the highest repetition rate at around 0.3 nC bunch charge, the accumulated charge would have been around 660 C. However, since experiments want different properties and bunch spacing, the machine has been occasionally running 100 kHz or even single bunch and regularly at much lower charge to produce ultra-short pulses with single spikes [7]. Machines running in CW mode at 1 MHz with a charge of 100 pC will produce a similar charge within weeks.

In order to be prepared for this increase in charge and possible damage to the undulators, we have studied the effect of radiation loss on the undulator over the past years [8] and have also gained experience in the magnetic behaviour of radiation-damaged undulators [9, 10]. For this purpose, a one-period, sacrificial undulator is installed in front of the FLASH main undulators. This device is periodically

removed from the beamline and the field re-measured on a magnetic bench. At the same time, both in this undulator and in the main undulator, TLDs are regularly exchanged and the accumulated dose is evaluated. This way, a correlation between integrated dose and magnetic field is determined.

In this paper, we will show the dose which has been accumulated over the years in FLASH1.

ACCUMULATED DOSE IN THE FLASH1 UNDULATOR

A dose is accumulated inside the undulator because of Continuous loss of dark current, continuous loss of beam or because of single events due to operation errors.

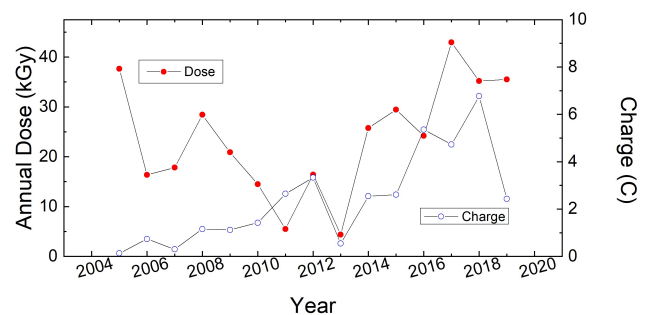


Figure 1: Accumulated annual dose in the sacrificial undulator at two locations since the commissioning of FLASH in 2005 (left scale). Also shown is the charge transmitted through the undulator during the same period (right scale).

As was mentioned, in front of the main undulator a one-period sacrificial undulator is installed. This undulator at FLASH1 has accumulated over the years the largest dose, namely around 350 kGy. As can be seen in Fig. 1, the initial losses are, normalized to the charge, much higher during the first few years. In recent years, the dose is similar to the one in the early years. The transmitted charge has grown by at least an order of magnitude because more users request longer bunch trains. Nevertheless, the increased loss in 2017 can also be observed in the main undulator, as we will see. For 2019, the charge has gone down significantly, but the losses have not. This has not been understood yet.

Losses during the first year of operation (2005) have been exceptionally high. As can be seen in Fig. 2 (top), the loss during the first year has been about half of the total loss, assuming we exclude specific events, that will be discussed below. It becomes even more clear when the data are normalized to the charge, shown in Fig. 2 (bottom). Normalized to the charge the loss in 2005 is up to an order of magnitude more than all of the following years.

Losses during 2006 occurred at the end of the undulator, as can be seen in Fig. 3. The reason was that the beam

* bart.faatz@desy.de

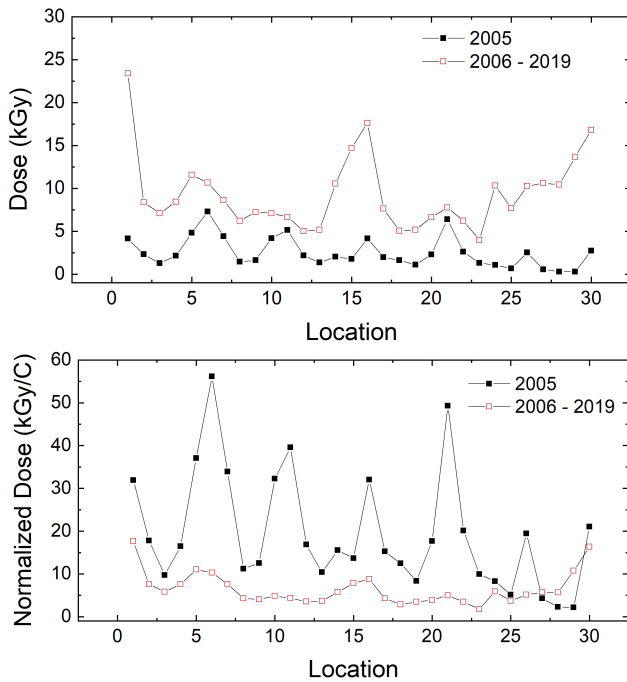


Figure 2: Losses in 2005 (solid black dots) and all following years combined (open red dots) as measured by the TLDs (top) and normalized to produced charge (bottom).

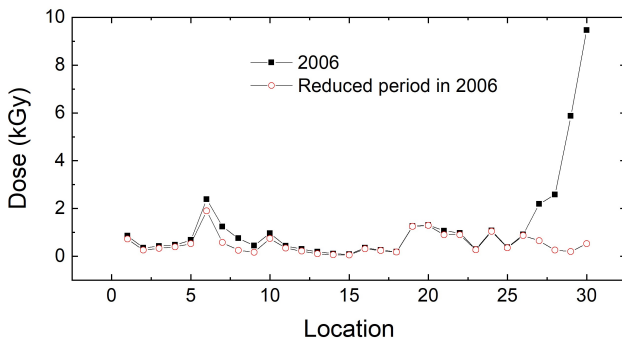


Figure 3: The loss along the undulator in 2006 and during the same period, but excluding 7 weeks of operation from April 11 to June 6.

size was very large at the end of the undulator due to a shortcut in one of the quadrupoles. Since it took several weeks before this was discovered, the accumulated dose was already around 8 kGy. Excluding this 7-week period, the loss along the undulator is more constant (open red dots in Fig. 3).

Fig. 4 shows the losses in 2017 after changing the electronics of the loss system and before the machine protection system thresholds were adjusted. Since also the injector optics was changed, there was for several months a mismatch of the optics, which caused losses in the middle of the undulator. This was only reduced after the thresholds of the machine protection system were changed and the optics was adjusted, as can be seen when the startup period is taken out of the accumulated dose (open red dots compared to

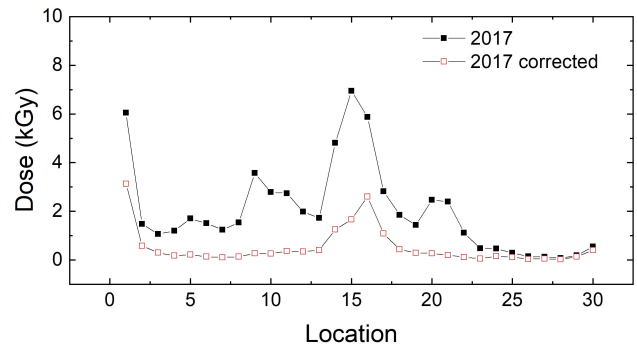


Figure 4: Losses in 2017 (solid black dots) and without startup from July 5 to September 19 (open red dots).

solid black dots in Fig. 4). Since this was only done after a period with long pulse trains, already several kGy were accumulated.

INFLUENCE OF UNDULATOR DAMAGE ON SASE

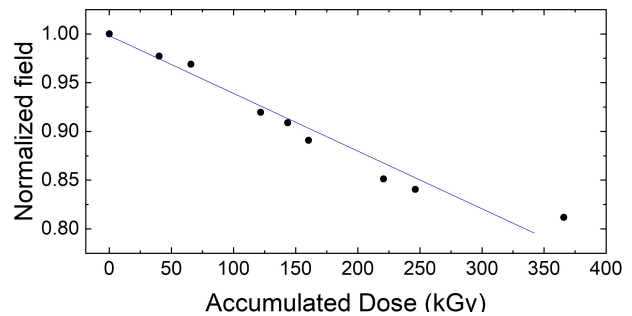


Figure 5: Field degradation due to radiation damage measured by determining at regular time intervals the field of the sacrificial undulator placed in front of the main FLASH1 undulator. Initial absolute field of central pole in 2004 is 0.504T, demagnetization of 1% per 16kGy.

In Fig. 5, the relation between accumulated dose and the reduction of magnetic field is shown. This information was obtained by taking out in regular intervals a one-period sacrificial undulator and measuring the magnetic field on a magnetic bench. The demagnetization rate of 1%/16kGy estimated for this diagnostic undulator can be applied to the accumulated dose in the main FLASH1 undulator. Since the dose is only measured at discrete positions along the undulator, we performed simulations, assuming steps in the magnetic field amplitude between measured TLD-positions or a linear interpolation. The resulting field that is used for the simulation is shown in Fig. 6. As can be seen, the field shows a reduction in amplitude at the beginning, the end and in the middle.

The FEL performance was checked for different field configurations by simulations with Genesis [11]. As can be seen in Fig. 7, the power is around 4 orders of magnitude smaller in case of step errors and almost without power loss in case

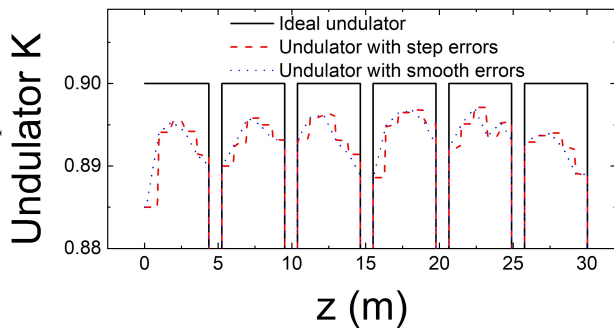


Figure 6: Field along the FLASH1 undulator without errors (black), modeled as a step function (red) and with linear interpolation (blue).

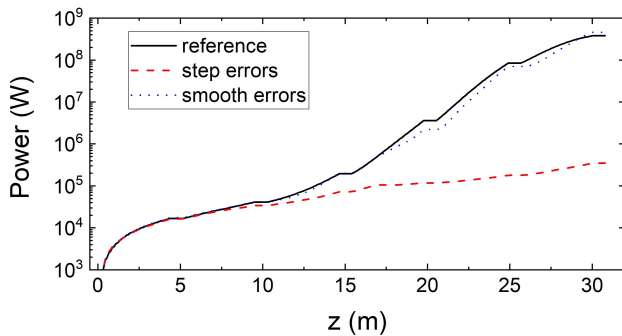


Figure 7: Power growth along the undulator for an error-free undulator and with the errors included as step (red) and smooth interpolation (blue).

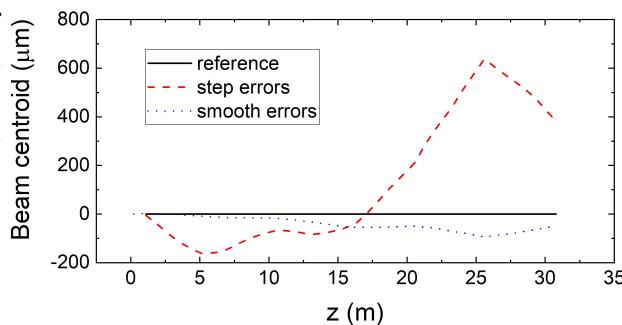


Figure 8: Horizontal orbit along the undulator corresponding to the fields in Fig. 6.

of interpolated errors compared to the case without errors. Although the reduction in pulse energy can be caused by loss of resonance condition and reduced overlap, it is clear from these results that for the assumed fields the dominant effect is a reduction in overlap, as shown in Fig. 8. In case of Genesis, the end fields are not treated correctly. Therefore, it is unclear if the actual orbit is as is described here.

To confirm that the main effect is caused by reduced overlap, we have corrected the orbit with field step-errors. Because the performance with interpolated errors shows very little reduction of the power compared to the ideal case, this is no further optimized. The result of the ideal spectrum is compared with the case of field errors before and after

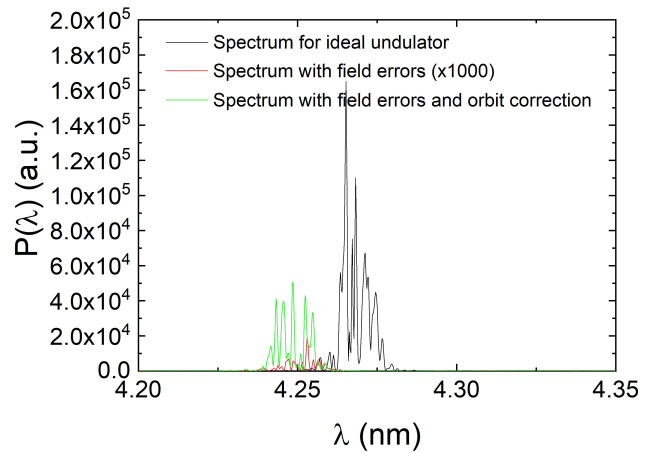


Figure 9: SASE spectrum for an ideal undulator, with step errors, and with step errors and orbit correction.

correction in Fig. 9. Without orbit correction, the spectrum multiplied by 1000 in order to make it visible. As can be seen, after orbit correction the reduction in intensity is only minor. Since the orbit correction is not perfect, even this can still be improved upon.

SUMMARY AND OUTLOOK

As can be seen, most of the beam losses at FLASH1 are produced in single events. With the present TLD readout intervals it is difficult to prove that most of the remaining losses are caused during setup changes for different user experiments. Because FLASH1 has a fixed gap undulator, initial losses cannot be avoided. At FLASH2, where the undulators are closed only after the losses have been reduced, the accumulated dose is much improved. The changed magnetic field has an effect in resonance condition and orbit of the electron beam. For the field profile simulated here, the effect is mainly caused by an orbit deviation, even though the field error exceeds the ρ -parameter.

Extrapolation of these results by two orders of magnitude for FELs running in CW-mode is probably not realistic. In addition, the machines that are planned at the moment or under construction, will run at much higher energies, which probably cause different problems of detecting and avoiding losses. However, based on the results at FLASH, it seems that the undulator lifetime is still at least several years.

ACKNOWLEDGEMENTS

The authors would like to thank Dr. B. Beutner for his useful comments.

REFERENCES

- [1] J. Rossbach, J. Schneider and W. Wurth, "10 years of pioneering X-ray science at the Free-Electron Laser FLASH at DESY", *Physics Reports*, vol. 808, pp. 1-74, 2019. doi: 10.1016/j.physrep.2019.02.002

- [2] P. Neyman *et al.*, “Free Electron Lasers in 2017”, in *Proc. FEL’17*, Santa Fe, NM, USA, Aug. 2017, pp. 204–209. doi:10.18429/JACoW-FEL2017-MOP066
- [3] B. Faatz *et al.*, “The FLASH Facility- Advanced Options for FLASH2 and Future Perspectives”, *Appl. Sci.*, vol. 7, p. 1114, 2017. doi:10.3390/app7111114
- [4] J. N. Galayda, “The New LCLS-II Project : Status and Challenges”, in *Proc. LINAC’14*, Geneva, Switzerland, Aug.-Sep. 2014, paper TUIOA04, pp. 404–408.
- [5] Z. T. Zhao, D. Wang, Z. H. Yang, and L. Yin, “SCLF: An 8-GeV CW SCRF Linac-Based X-Ray FEL Facility in Shanghai”, in *Proc. FEL’17*, Santa Fe, NM, USA, Aug. 2017, pp. 182–184. doi:10.18429/JACoW-FEL2017-MOP055
- [6] W. Decking *et al.*, “Status of the European XFEL”, in *Proc. IPAC’19*, Melbourne, Australia, May 2019, pp. 1721–1723. doi:10.18429/JACoW-IPAC2019-TUPRB020
- [7] V. Balandin *et al.*, “Operation of Free Electron Laser FLASH Driven by Short Electron Pulses”, in *Proc. IPAC’16*, Busan, Korea, May 2016, pp. 732–734. doi:10.18429/JACoW-IPAC2016-MOPOW011
- [8] J. Pflueger, “Radiation exposure and magnetic performance of the undulator system for the VUV FEL at the TESLA Test Facility Phase-1 after 3 years of operation”, *Nucl. Instrum Meth. A*, vol. 507, pp. 186-190, 2003. doi:10.1016/S0168-9002(03)00869-6
- [9] M. Tischer, P. Vagin, “Demagnetization Effects at PETRA III Undulators”, *ICFA Beam Dyn. Newslett.*, vol. 66, p. 37-44, 2015.
- [10] M. Tischer, P. Neumann, A. Schöps, P. Vagin, “Refurbishment of Radiation-Damaged Undulators”, *AIP Conf. Proc.*, vol. 1741, p. 020022, 2016. Dresden, Germany. doi:10.1063/1.4952801
- [11] S. Reiche, “GENESIS 1.3: a fully 3D time-dependent FEL simulation code”, *Nucl. Instrum. Meth. A*, vol. 429, pp. 243-248, 1999. doi:10.1016/S0168-9002(99)00114-X

EXPECTED RADIATION PROPERTIES OF THE HARMONIC AFTERBURNER AT FLASH2

M. Mehrjoo*, B. Faatz, G. Paraskaki, M. Tischer, P. Vagin, DESY, Hamburg, Germany

Abstract

We discuss the afterburner option to upgrade the FLASH2 undulator line, at the FLASH facility at DESY in the Hamburg area, for delivering short wavelengths down to approximately 1.5 nm with variable polarization. This relatively straightforward upgrade enables us to study scientific cases involving the absorption L-edges of 3d metals. The proposed afterburner setting with an energy upgrade to 1.35 GeV will cover many of the community's requests for the short wavelength radiation and circular polarization. We also study the influence of reverse tapering on the radiation output. This contribution presents a series of simulations for the afterburner scheme and some of the technical choices made for implementation.

INTRODUCTION

FLASH delivers radiation in the fundamental wavelength down to 4 nm with the linear polarization [1]. Typical pulse energies that can be delivered are in the order of 100 μ J, depending on the exact parameters required. Many users, however, are interested in much shorter wavelength, and with variable polarization. A typical example are those users aiming at the L-edges of 3d metal metals between 1.3 and 1.6 nm. This clearly beyond the 1st harmonic wavelength range of FLASH. However, because many of these experiments do not require much pulse energy, in many cases less than a microjoule, one could offer to produce this in a harmonic at FLASH. Because the FEL produces bunching at all harmonics, one could use either 2nd or 3rd harmonic radiation. Since the 2nd harmonic is still not in the desired wavelength range, only 3rd and higher harmonics can be used. As the main undulator only delivers linearly polarized light, an afterburner with circular polarization tuned to the 3rd harmonic of the main undulator will be placed behind it.

In the afterburner, the produced circularly polarized radiation is superimposed to the linearly polarized radiation of the main undulator. Because the bunching in the afterburner does not change significantly, the pulse energy of the linear and circular contributions will be of similar magnitude. Because this is not desirable, one can either place the afterburner under an angle, thus separating linear from circular light [2], or use reverse tapering to suppress the radiation from the main undulator while keeping the bunching [3].

In this contribution, we will show results of simulations with the code GENESIS 1.3, version2 [4]. We will study at different beam parameters the wavelength range between 1.3 and 1.6 nm and check the influence of the reverse taper on pulse energy and contrast, defined as the ration between

circular radiation from the afterburner and the linearly polarized light from the main undulator [5].

SIMULATION OF STANDARD CONFIGURATION

The parameters chosen for the simulations are listed in Table 1. It assumes the energy upgrade from the present

Table 1: FLASH2 Parameters Used for the Simulations

Electron beam	
Beam energy	1.35 GeV
Peak current	2.5 kA
Emittance, norm. (x,y)	0.7–1.4 mm mrad
Energy spread	0.2–0.5 MeV
Bunch length	15 μ m
Main Undulator	planar
Period	31.4 mm
K_{rms}	0.87–1.05
Segment length	2.5 m
Number of segments	12
Afterburner	APPLE III, circ.
Period	16 mm
K	0.385–0.61
Segment length	2.5 m
Number of segments	1

1.25 GeV to 1.35 GeV planned in the next years and an additional bunch compressor at final energy, which should enable us to improve the electron beam quality significantly [6]. Therefore, simulations are performed for both a pessimistic set of beam parameters and the expected beam quality after the upgrade.

The main undulator is the one already installed in FLASH2. For the afterburner undulator, we consider an APPLE III device with a K -value that has been obtained from Radia-simulations for the helical mode (see Table 1 and Fig. 1). The minimum undulator gap for the afterburner is 8 mm. This gives us the required tunability from about 1.3 to 1.6 nm as maximum wavelength, where for 1.3 nm, we still have $K = 0.38$.

The first set of simulation has been performed with all 12 undulators set to the same gap and the APPLE undulator to a gap corresponding to the third harmonic. The wavelength in the afterburner undulator is 1.3, 1.45 and 1.6 nm. As can be seen from Fig. 2, the pulse energy that we get from the APPLE undulator increases with increasing K of the undulator, as expected. Furthermore, the dependence on the beam quality is not dramatic, as the pulse energy varies

* masoud.mehrjoo@desy.de

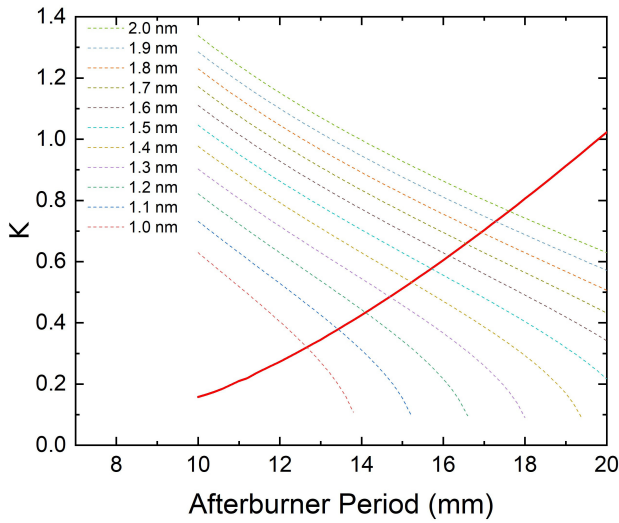


Figure 1: The characteristic radiation parameters of an APPLE III undulator for the different period. Dashed lines indicates minimum K value, required to reach the given wavelength in Table 1.

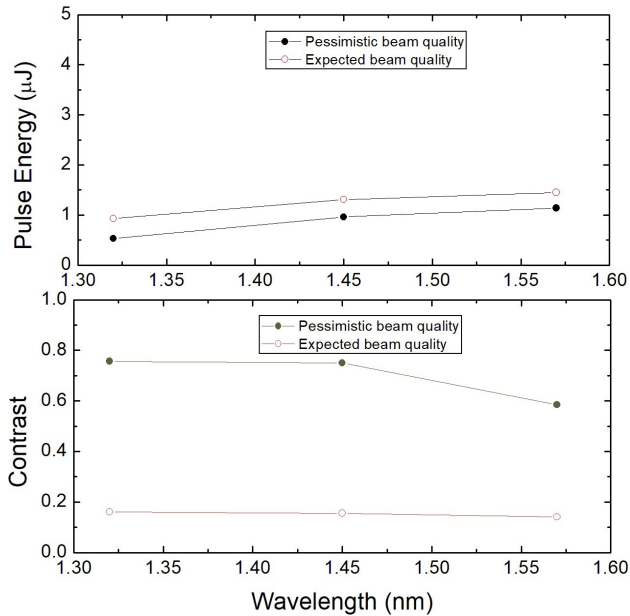


Figure 2: The pulse energy and the contrast of circular polarized radiation from the afterburner and linear radiation coming from the main undulator is shown for 3 different wavelengths and two different beam qualities, as given in Table 1. The afterburner is set to circular polarization and all 12 linear undulators are set to the fundamental.

less than a factor of two for the two parameter sets. However, the linearly polarized radiation emitted in the third harmonic from the main undulator is about an order of magnitude larger for the good beam quality. As a consequence, where the fraction of linear and circular polarization is similar for the pessimistic beam parameters, the ratio becomes around 0.1 to 0.2 for the good electron beam quality. Therefore, the radiation pulse delivered to users is completely dominated by the linear component.

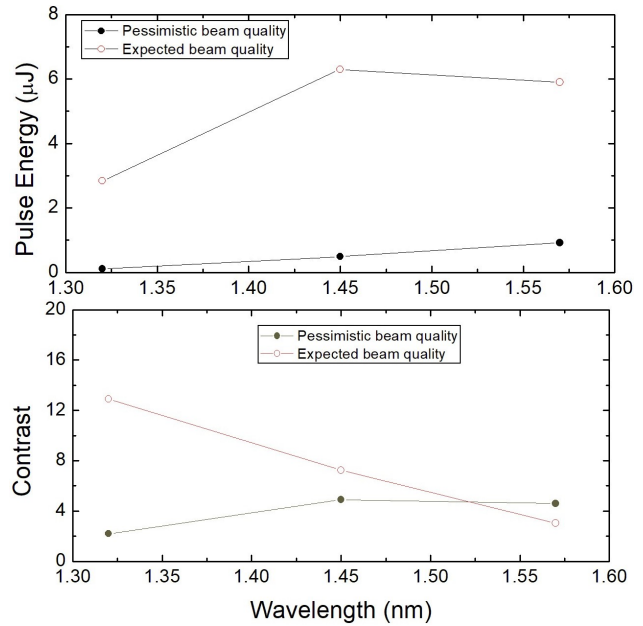


Figure 3: The pulse energy and the contrast of circular and linear coming from the main undulator is shown for 3 different wavelengths and two different beam qualities, as given in Table 1. The afterburner is set to circular polarization and an optimum number of linear undulators are set to the fundamental.

This behaviour changes when we limit the length of the main undulator by opening the gaps for those undulators before maximum bunching has been achieved. In this case, the energy spread is much smaller, the linear component is smaller and the power in the afterburner can still grow. The results are shown in Fig. 3. The pulse energy produced by the afterburner for pessimistic beam parameters is similar. But for the better beam parameters, where in the earlier simulations the energy spread increased beyond saturation in the main undulator, thus avoiding further amplification in the afterburner, now has around an order of magnitude more pulse energy. In addition, because the linearly polarized component from the main undulator is reduced, the contrast is now between 2 and 5 for the pessimistic beam parameters and 8 and 17 for the good beam parameters.

REVERSE TAPER

Although the results with optimized undulator settings seem good, especially when the beam parameters improve, the problem is, that the amplification process in the main undulator did not reach saturation. This means, that the linear background fluctuates, which is highly undesirable for the experiment. The consequence would be that the contrast fluctuates from shot to shot, but also the intensity of the radiation out of the afterburner will fluctuate.

By placing the afterburner under an angle, the linear background can be removed [2]. However, this does not avoid the large intensity fluctuation. Therefore, we study here the possibility to use reverse tapering to keep the energy spread small, but keep the bunching. It has been shown experi-

mentally already at FLASH2 that the reverse tapering keeps bunching while suppressing the radiation intensity. This would improve the stability of the system. However, it is not easy to show experimentally that also the radiation of the harmonic is suppressed as well and therefore, the contrast improves (see Fig. 4). Therefore, we have performed several simulations to study this effect.

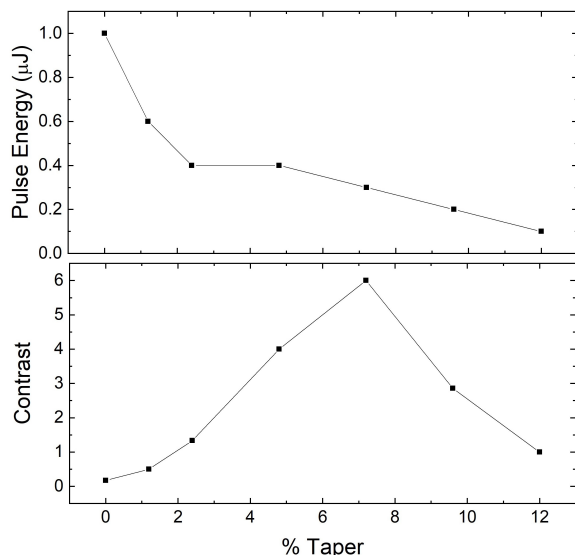


Figure 4: The pulse energy and the contrast of circular and linear coming from the main undulator is shown for 1.3 nm at the expected beam parameters as given in Table 1. The undulator is set to circular polarization and the taper taper is set over the complete undulator length.

As was already shown experimentally at FLASH2, a reverse taper suppresses the radiation of the fundamental. As compared to the 500 μJ for an untapered undulator, it reduces by more than two orders of magnitude when we apply a reverse taper between 5 and 10% over the complete undulator length. We have seen that also the pulse energy at the third harmonic reduces by about the same amount. Unfortunately, also the third harmonic radiation out of the afterburner reduces.

As can be seen in Fig. 5, where the reduction in bunching at the fundamental is much less than the intensity reduction, at the third harmonic these become comparable. As a consequence, the advantage of reverse taper shown in this study is much less at the harmonic.

SUMMARY AND OUTLOOK

It has been shown that we can get between 1 and 8 μJ of circular radiation out of the afterburner undulator with circular radiation, depending on wavelength and electron beam parameters used. By opening the some of the main undulators with linear polarization, the contrast of circular to linear radiation can be optimized to a factor 10 to 60. If this contrast, which will be fluctuating from shot-to-shot, is not sufficient, the afterburner undulator can be placed under an angle or the main undulator can be reversely tapered to

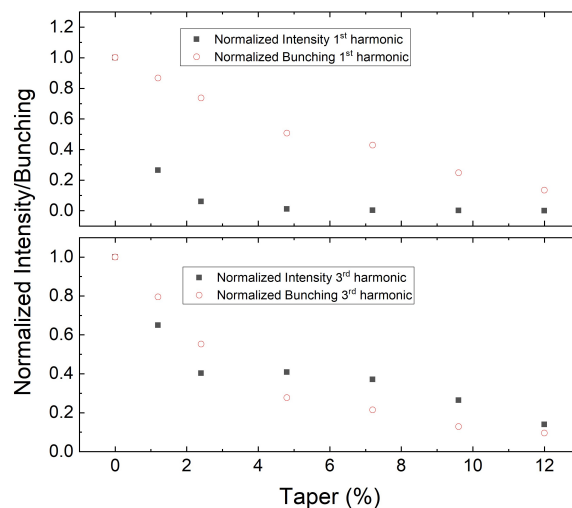


Figure 5: The normalized pulse energy and bunching for different values of tapering at the fundamental of 4 nm (top) and 3rd harmonic of 1.33 nm (bottom) coming from the main undulator at the expected beam parameters as given in Table 1. The taper is set over the complete undulator length.

suppress and stabilize the radiation from this undulator. First simulation results show that this reduces the pulse energy of the circular radiation significantly and further study is needed to optimize the system by adjusting phase shifters and tapering only part of the undulator.

ACKNOWLEDGMENT

This work was supported by the “DESY-Fellowship Photon Science” within the framework of FLASH 2020+ program. We gratefully thank E. Schneidmiller and Y. Yurkov for many stimulating discussions on the reverse tapering concerns and applications.

REFERENCES

- [1] J. Feldhaus *et al.*, “Possible application of X-ray optical elements for reducing the spectral bandwidth of an X-ray SASE FEL”, *Nucl. Instrum. Methods Phys. Res., Sect. A*, vol. 528, pp. 162–166, 2004. doi:10.1016/S0030-4018(97)00163-6
- [2] A. Lutman *et al.*, “Polarization control in an X-ray free-electron laser”, *Nature Photonics*, vol. 10, pp. 468–472, 2016. doi:10.1038/nphoton.2016.79
- [3] E. Schneidmiller and M. Yurkov, “Obtaining high degree of circular polarization at x-ray free electron lasers via a reverse undulator taper”, *Phys. Rev. ST Accel. Beams*, vol. 16, p. 110702, 2013. doi:10.1103/PhysRevSTAB.16.110702
- [4] S. Reiche, “Update on the FEL Code Genesis 1.3”, in *Proc. FEL14*, Basel, Switzerland, Aug. 2014, paper TUP019, pp. 403–407.
- [5] E. Saldin, E.V. Schneidmiller, and M.V. Yurkov, *The Physics of Free Electron Lasers*, Springer, 2000.
- [6] B. Marchetti *et al.*, “X-Band TDS Project”, in *Proc. IPAC’17*, Copenhagen, Denmark, May 2017, pp. 184–187. doi:10.18429/JACoW-IPAC2017-MOPAB044

EXPERIENCE WITH MCP-BASED PHOTON DETECTOR AT FLASH2

S. Grunewald, E. Mueller, E. A. Schneidmiller, K. Tiedtke, M. V. Yurkov, DESY, Hamburg, Germany
O. I. Brovko, A. Grebentsov, E. M. Syresin, JNR, Dubna, Russia

Abstract

We present recent experimental results on statistical measurements of amplification process in FLASH2 SASE FEL. Micro-channel plate (MCP) detector is used for precise measurements of the radiation pulse energy. DAQ based software is used for cross-correlation of the SASE FEL performance and electron beam jitters. Analysis of machine jitters essential for SASE FEL operation has been performed. Application of gating strategy with measured machine parameters allows us to isolate machine jitters from fundamental SASE fluctuations. Subsequent application of statistical techniques for characterization of SASE FEL radiation allows to derive such important quantities as gain length, saturation length, radiation pulse duration, coherence time, and degree of transverse coherence.

INTRODUCTION

VUV and soft x-ray free electron laser FLASH is in operation at DESY since the year 2000 [1–3]. Several upgrades of the facility have been performed, and currently FLASH covers a wavelength range from 3.5 nm to 100 nm in the fundamental. Two beamlines operate in parallel, FLASH1 with fixed gap undulator (period length $\lambda_w = 2.73$ cm), and FLASH2 with variable gap undulator (period length $\lambda_w = 3.14$ cm). FLASH is equipped with a set of detectors for measurements of the energy in the radiation pulse: gas monitor detectors (GMD), micro channel plate (MCP) based detectors, photodiodes, and thermopiles [4, 5]. MCP detectors are installed in front of all other detectors and are used for precise measurements of the radiation pulse energy of single pulses. The MCP detector measures the radiation scattered by a metallic mesh placed behind an aperture. The electronics of MCP-detector has low noise, about 1 mV at the level of signal of 100 mV which provides a 1% relative accuracy of the radiation pulse energy measurement.

Measurements have been performed in the framework of the experimental program at FLASH2 aiming at development of statistical techniques for characterization of SASE FEL process. In February, 2019 we recorded status of FLASH2 operation corresponding to typical conditions of user run during last months. One of the features during user run was sporadic appearance of machine jitters affecting stability of the SASE FEL output. There were several goals of our studies. Main goal was to include MCP detector into the DAQ system recording essential machine parameters. The next step was to measure FEL gain curve and derive essential parameters of the radiation from these measurements. Final step was to analyze correlation data of SASE output and essential parameters of the electron beam (jitters of orbit and beam formation system) and localize origin of the jitters. It turned out that frequency of sporadic machine

jitters during our shift was pretty big, which moved the last planned goal (jitter correlation studies) to the first priority.

Analysis of experimental results shows that the main jitter problem is sporadic orbit jitter which develops from the very beginning of the accelerator. An important feature of this jitter are correlated x-y orbit kicks. Bunch compression system also contributes to the SASE FEL output, but at a smaller level. We also applied gating strategy for cleaning experimental results with subsequent application of statistical techniques for determination of essential parameters of the SASE FEL: gain length, saturation length, coherence time, radiation pulse duration, number of radiation modes in the pulse (longitudinal and transverse), degree of transverse coherence [6–8].

RAW DATA AND MACHINE JITTERS

Measurement of the radiation pulse energy (average and dispersion) provides reliable way for determination of key parameters of the SASE FEL process. In practical situation there are always machine jitters (orbit, beam formation system, sporadic failures of subsystems, etc) which contribute additionally to fluctuations of the SASE FEL output, so relevant technique for gating of the experimental results with measured parameters of the machine has been developed [2, 6–8]. FLASH is modern facility with global computer control of machine operation, electron and photon

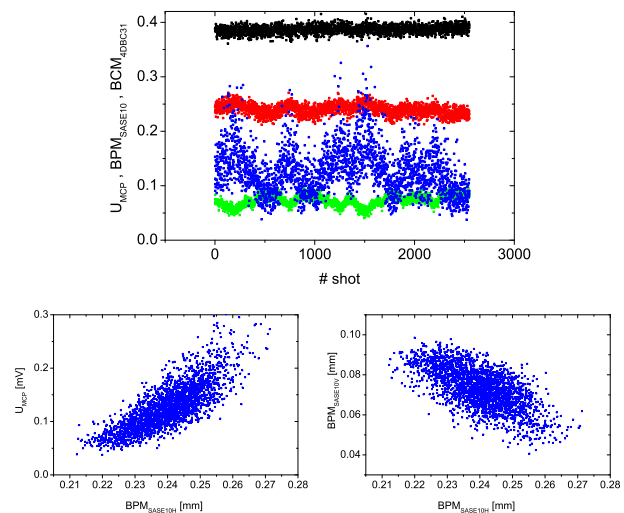


Figure 1: Top: raw signal of MCP detector (blue), BPM 3FL2SASE10 (x - red, y - green), and BCM 4DBC31 (black). Bottom: correlation plots of MCP signal versus BPM 3FL2SASE10H (left), and x and y positions of BPM 3FL2SASE10 (right). Measurements are performed after 7 undulator modules. Radiation wavelength is 10 nm.

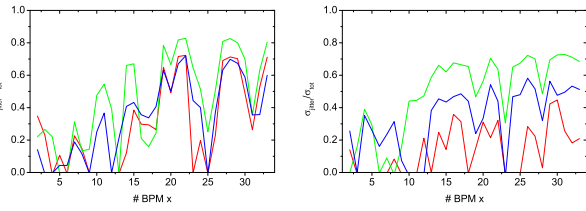


Figure 2: Contribution of the machine jitters seen by BPMs to total fluctuations of the radiation pulse energy. BPMs are numbered according to Table 1. Left: horizontal BPMs, right: vertical BPMs. Red, green, and blue curves refer to measurements after 6, 7, and 8 undulator modules, respectively. Radiation wavelength is 10 nm.

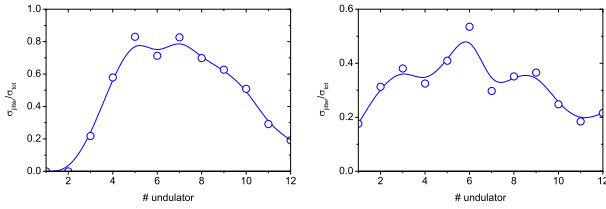


Figure 3: Contribution of machine jitters to total fluctuations of the radiation energy seen by BPM 3FL2SASE10H (left) and BCM 4DBC31 (right) along the undulator. Radiation wavelength is 10 nm.

beam parameters. Each shot of accelerator has unique time stamp, and all essential parameters of the accelerator, electron bunch, and photon pulse related to a specific shot are stored in the data base. For each shot we record signals from MCP and GMD detectors (radiation pulse energy), from the beam position monitors (BPM) along the accelerator and undulator (32 horizontal and 32 vertical listed in Table 1), four signals of beam compression monitors (BCM) installed after BC2 and BC3 compressors, and three signals of bunch charge monitors (gun, FLASH2 extraction section, and undulator entrance). Figure 1 shows data taken for the radiation pulse energy (MCP detector), horizontal beam position in the undulator (3FL2SASE10H), and BCM signal after BC3 stage (4DBC31). Correlation plot in this

Table 1: List of BPMs at FLASH2

1	1GUN	11	3DBC3	21	3FL2SASE3
2	3GUN	12	11ACC7	22	3FL2SASE4
3	2UBC2	13	15ACC7	23	3FL2SASE5
4	1DBC2	14	19ACC7	24	3FL2SASE6
5	3DBC2	15	4FL2EXTR	25	3FL2SASE7
6	5DBC2	16	5FL2EXTR	26	3FL2SASE8
7	7DBC2	17	8FL2EXTR	27	3FL2SASE9
8	11DBC2	18	3FL2SEED1	28	3FL2SASE10
9	1UBC3	19	3FL2SEED4	29	3FL2SASE11
10	2UBC3	20	3FL2SEED7	30	3FL2SASE12
	31	3FL2SASE13	32	3FL2SASE14	

Figure clearly demonstrate sporadic jitter which happened during measurements. Our analysis show that machine jitters, essential for SASE FEL operation, appear at the very beginning of the accelerator, and reach maximum values at the undulator entrance. An important observation is that x-y orbit kicks are correlated (see Fig. 1). This feature is clearly detected already after the first accelerating module ACC1.

It is important to derive figure of merit for quantitative description of an effect of machine jitters on SASE FEL operation. Fundamental SASE fluctuations and machine jitters are statistically independent, so total fluctuations are: $\sigma_{tot}^2 = \sigma_{SASE}^2 + \sigma_{jitter}^2$, and required figure of merit is ratio of machine induced fluctuations to total fluctuations, $\sigma_{jitter}/\sigma_{tot}$. The value of σ_{jitter} is calculated after gating of the experimental results. Application of gating procedure sequentially for each measured machine parameter allows to trace evolution of the jitter along accelerator. Relevant plots for the beam position monitors are presented in Fig. 2. We note that some machine jitters are already detected with BPMs in the gun area, then they become pronouncing after the first accelerating module ACC1, and gradually increase along the accelerator. Influence of machine jitters on SASE FEL output also depends on the stage of amplification process. Maximum contribution of the machine jitters is obtained in the end of the high gain linear regime, and becomes less pronouncing in the saturation regime as it is illustrated in Fig. 3. Correlation signals of MCP-BPM (related to orbit jitters) are clean, but correlation signals MCP-BCMs (reflecting jitters of the beam formation system) are not so clear due to larger noise in BCM devices.

SASE FEL CHARACTERIZATION

Characterization of SASE FEL with statistical methods is based on the analysis of the gain curve with application of basic knowledge on statistical properties of the SASE FEL radiation [1, 2, 6–10]. Radiation from SASE FEL operating in the linear regime holds properties of completely chaotic polarized light, and inverse value of the dispersion of the radiation pulse energy is the number of modes in the radiation pulse, $M = 1/\sigma^2$. Point where fluctuations reach maximum value corresponds to the end of high gain exponential regime with minimum photon pulse length τ_{phot} . Saturation (corresponding to maximum brilliance of the radiation) occurs when fluctuations of the radiation pulse energy fall down by a factor of 3 with respect to the maximum value. Parameter range of SASE FELs operating in the VUV and x-ray wavelength range is such that the number of field gain lengths to saturation is about 10 [9]. Practical estimates for the field gain length L_g , the FEL parameter ρ , radiation pulse duration τ_{phot} , coherence time τ_c , and rms length of the electron beam lasing fraction σ_z are [6–8]:

$$L_g \approx L_{sat}/10, \quad \rho \approx \lambda_w/L_{sat}, \quad \tau_c \approx \lambda L_{sat}/(2\sqrt{\pi}c\lambda_w).$$

$$\tau_{phot} \approx \sigma_z \approx (M\lambda L_{sat})/(5c\lambda_w).$$

Measurements has been performed at FLASH2 at the electron energy of 1130 MeV and bunch charge 280 pC. We tune

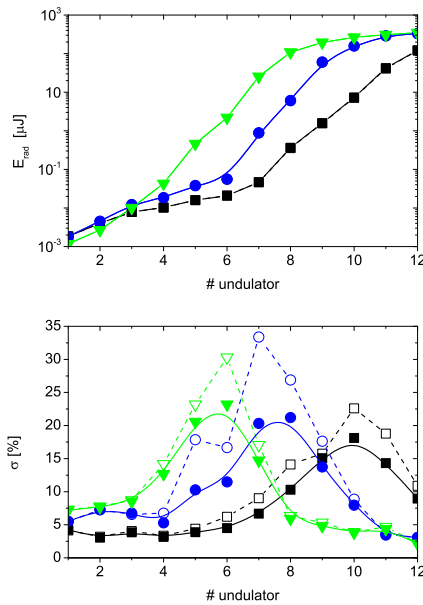


Figure 4: Gain curve of SASE FEL at FLASH2: average energy in the radiation pulse (top) and its fluctuations (bottom). Dashed and solid curves correspond to raw and gated data. Black, blue and green colors correspond to the radiation wavelength 7 nm, 10 nm, and 15 nm.

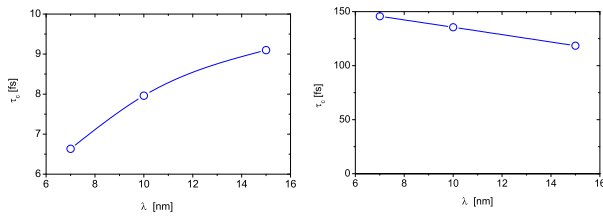


Figure 5: Coherence time (left) and radiation pulse duration (right) derived from the gain curves shown in Fig. 4.

SASE FEL to the maximum signal at full undulator length (12 undulator modules). Then, keeping fixed all machine parameters, we gradually open undulator sections and record all essential machine and photon beam parameters as it has been described in the previous section. Plots in Fig. 4 show experimental results for the gain curve at three radiation wavelengths: 15 nm (closed undulator gap), 10 nm (intermediate gap position), and 7 nm (open undulator gap still providing saturation in the end of the undulator).

In our case sporadic machine jitters contribute significantly to fluctuations, and the next step is to isolate fundamental SASE fluctuations. To do this, we apply gating strategy using measured parameters of the machine. Sensitivity analysis of machine jitters (see previous section) tells us that the most sensitive diagnostics elements are BPM 3FL2SASE10H (orbit) and BCM 4DBC31 (beam compression). Using double discrimination with these parameters we reject 80% of the shots subjected to jitters, and get good quality of the gain curve governed mainly by fundamental SASE FEL fluctuations (see Fig. 4). A strong argument

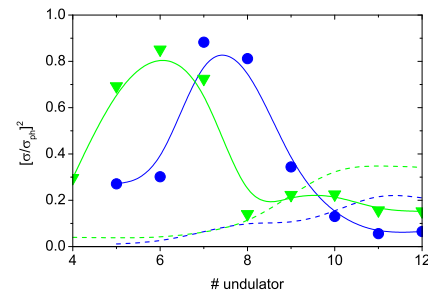


Figure 6: Ratio of dispersions of the full radiation pulse energy to that filtered by a pinhole, σ^2/σ_{ph}^2 (solid lines). Dashed curves show relative fraction of the radiation power passed through a pinhole. Blue and green colors correspond to the radiation wavelength 10 nm and 15 nm.

in favor of this statement is that values of the rms electron pulse duration σ_z derived from gated data agree with good accuracy for all measurements (see Fig. 5).

For the radiation wavelengths 10 nm and 15 nm we performed measurements with a pinhole in order to derive the number of longitudinal modes and degree of transverse coherence. Measurements at 7 nm has not been done due to lack of an appropriate aperture much smaller than photon beam spot. In the linear regime, inverse value of the dispersion of the radiation energy after pinhole gives us the number of longitudinal modes, $M_{long} = 1/\sigma_{ph}^2$. Ratio of dispersions of the full radiation energy to that filtered by a pinhole gives the value of the degree of transverse coherence, $\zeta = \sigma^2/\sigma_{ph}^2$ [7, 8]. We see from Fig. 6 that maximum value of the degree of transverse coherence is about 0.8 which is in agreement with theoretical expectations for FLASH2 SASE FEL [10].

REFERENCES

- [1] V. Ayvazyan *et al.*, “Generation of GW Radiation Pulses from a VUV Free-Electron Laser Operating in the Femtosecond Regime”, *Phys. Rev. Lett.*, vol. 88, p. 104802, 2002. doi:10.1103/PhysRevLett.88.104802
- [2] W. Ackermann *et al.*, “Operation of a free-electron laser from the extreme ultraviolet to the water window”, *Nature Photonics*, vol. 1, p. 336, 2007. doi:10.1038/nphoton.2007.76
- [3] Faatz *et al.*, “Simultaneous operation of two soft x-ray free-electron lasers driven by one linear accelerator”, *New Journal of Physics*, vol. 18, p. 062002, 2016. doi:10.1088/1367-2630/18/6/062002
- [4] K. Tiedtke *et al.*, “The soft x-ray free-electron laser FLASH at DESY: beamlines, diagnostics and end-stations”, *New J. Phys.*, vol. 11, p. 023029, 2009. doi:10.1088/1367-2630/11/2/023029
- [5] A. Bytchkov *et al.*, “Development of MCP-based photon diagnostics at the TESLA Test Facility at DESY”, *Nucl. Instrum. and Methods A*, vol. 528, p. 254, 2004. doi:10.1016/B978-0-444-51727-2.50060-2
- [6] C. Behrens *et al.*, “Constraints on photon pulse duration from longitudinal electron beam diagnostics at a soft x-ray free-

- electron laser”, *Phys. Rev. ST AB*, vol. 15, p. 030707, 2012. doi:10.1103/PhysRevSTAB.15.030707
- [7] E.A. Schneidmiller and M.V. Yurkov, “Application of Statistical Methods for Measurements of the Coherence Properties of the Radiation from SASE FEL”, in *Proc. IPAC’16*, Busan, Korea, May 2016, pp. 738–740. doi:10.18429/JACoW-IPAC2016-MOP0W013
- [8] E.A. Schneidmiller and M.V. Yurkov, *CERN Yellow Reports: School Proceedings*, vol. 1, pp. 539-596, 2018. doi:10.23730/CYRSP-2018-001.539
- [9] E.L. Saldin, E.A. Schneidmiller, and M.V. Yurkov, “Coherence properties of the radiation from X-ray free electron laser”, *Opt. Commun.*, vol. 281, p. 1179, 2008. doi:10.1016/j.optcom.2007.10.044
- [10] E.A. Schneidmiller and M.V. Yurkov, “Coherence properties of the radiation from FLASH”, *J. Mod. Optics*, vol. 63, pp. 293-308, 2015. doi:10.1080/09500340.2015.1066456

A SUPERCONDUCTING UNDULATOR WITH VARIABLE POLARIZATION DIRECTION FOR THE EUROPEAN FEL

Y. Li, European XFEL GmbH, Schenefeld, Germany
R. Rossmanith, DESY, Hamburg, Germany

Abstract

In the SASE3 beam line at the European XFEL a planar undulator produces linearly polarized radiation. In order to obtain a circularly polarized radiation an afterburner will be installed to produce coherent radiation with variable polarization. Recently Argonne National Lab developed a super conductive undulator (called SCAPE) for a storage ring which allows to change polarization direction and field strength without moving mechanically the undulator parts. In this paper it is investigated if a similar device could be useful for an FEL. Such device is also a possible choice for the future undulator beam lines where circular and variable polarization are required.

INTRODUCTION

The magnetic field for undulators is in general produced by permanent magnets at room temperature. During the last years experiments were performed to increase the magnetic field either by cooling the permanent magnets to cryogenic temperatures [1] or by replacing the permanent magnets by superconducting wires.

The magnetic field of cryogenically cooled permanent magnets (CPMUs: cryogenic permanent magnet undulator) is in general higher by only about 15 % but the magnets are less sensitive to radiation. The disadvantage is that the frequency and the polarization of the emitted radiation have to be changed by moving mechanically the undulators gap.

Undulators with superconducting wires (SCU) can produce up to a factor of two higher undulator fields compared with cryogenic undulators and are also almost insensitive to radiation. The SCU technology has in addition the advantage that it is possible to tune the output frequency and the polarization direction electrically without mechanically moving the magnet coils. The disadvantage is that liquid Helium is needed to cool the coils. This problem was recently reduced by using cryocooler. The cryocooler, mechanically attached to the undulator, has a closed helium system. Undulator and cooler together comprise a standalone unit and require therefore not a conventional cryoplant. The cooling time for such a system is about 70 hours. APS and KIT both used such undulators successfully. The advantage is the tunability of the frequency of the produced radiation.

Recently a NbTi undulator was proposed by the Argonne group (SCAPE: Super Conducting Arbitrary Polarization Emitter) [2] was proposed to build an undulator with electrically adjustable photon wavelength and polarization.

The winding technics with NbTi superconducting wires lead to low phase errors (less than 3 degree) and

therefore shimming is not required. NbTi wires are at the moment the used for SCUs. Nb₃Sn wires can produce in general higher fields but are at the moment still difficult to handle. The use of high temperature superconductors are investigated at various institutes.

In this paper first ideas on a program on the development and tests SCUs with the parameters for the European XFEL are presented.

PLANAR SCU

A SCU with the period of 18mm can serve for an ultra-high photon energy SASE beam line up to 100keV at the European XFEL. It also applies the factor of 1.5 to the tenability of the photon energy [3]. Therefore in this section we focus on the field simulations for an 18mm period planar SCU, U18.

Both of the successful examples of planar SCU from APS and KIT take use of so called the vertical winding technique for the magnet coils. It is winding the superconducting coil continuously on a block of iron core with grooves. In this paper we follow it for the undulator design and simulations.

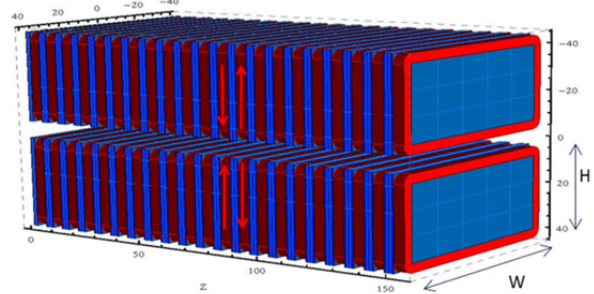


Figure 1: The radia model for the planar SCU.

Figure 1 shows the Radia [4] model for the planar SCU U18. The red coil indicates the NbTi wire and the blue part is the iron core for the wire winding and poles assembling. The arrows indicate the current direction. The wire material is supposed to be NbTi and the iron core is supposed to be normal low carbon steel.

In order to simulate the maximum undulator field it is firstly needed to evaluate the critical current density. It is well known that the superconducting condition is maintained by the nonlinear relations of the temperature, the magnetic field and the current density. We assume the undulator wire is constant in the temperature of the liquid helium which is 4.2K. Following the suggestion of Ref. [5] the critical current density is assumed linearly relates to the magnet field:

$$j_c = j_a \left(1 - \frac{B_m}{B_{c2}}\right), \quad (1)$$

Content from this work may be used under the terms of the CC BY 3.0 licence (© 2019). Any distribution of this work must maintain attribution to the author(s), title of the work, publisher, and DOI

where j_c is the critical current density and B_m is the magnet field at the wires. $j_a = 2.1\text{kA/mm}^2$ and $B_{c2} = 10.4\text{T}$ are the parameters for the superconducting conditions of NbTi. It is seen that the higher the magnet field the lower the maximum current density that the superconducting wire can take.

Figure 2 shows the simulation results for the undulator peak field and the critical current density with respect to the applied current density in the undulator wire. It is seen that as the applied current density increasing the undulator peak field goes up but on the contrary the critical current density goes down. The maximum undulator field is given at the point where the applied current density equals to the critical current density, i.e. the maximum current density the wire can take with the super conducting condition is kept. According to the simulations shown in Fig. 2 the critical current density is 1270A/mm^2 and the maximum peak field is 0.97T .

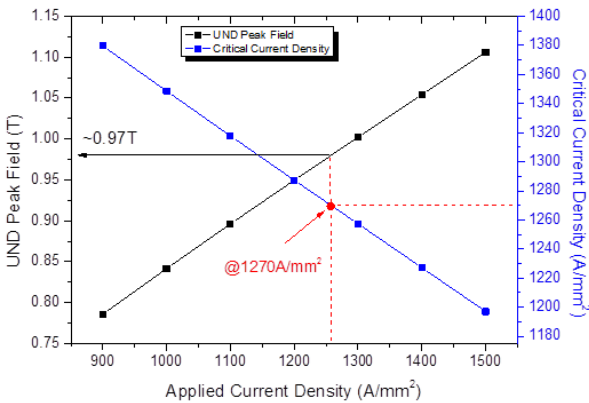


Figure 2: The undulator peak field and the critical current density with respect to the applied current density.

The smaller undulator field can be continuously achieved by reducing the current density. We summarize the parameters of U18 in the Table 1.

Table 1: Parameters for U18

Parameter	Unit	Unit
Period λ_u	18	mm
Coil cross section	5×5	mm
Iron core size W&H	80&40	mm
Pole width	4	mm
Gap g	10	mm
Max. current density	1270	A/mm ²
Max. peak field	0.97	T
Max. K parameter	1.63	--
Long. λ_r @17.5GeV	0.18	Å

HELICAL SCU

The planar undulator only generates the linear polarization SASE, to some users especially to the soft X-ray users the circular and the adjustable polarization is needed. In the European XFEL the permanent helical undulator APPLE-X will be built as the after burner in the soft X-ray beam line SASE3 [6, 7]. In this paper a similar type of APPLE-X undulator in the super conducting version is simulated. Such a superconducting helical undulator is

developed in Argonne lab in the name of SCAPE undulator [2].

The Radia model for a helical super conducting undulator is shown in Fig. 3. It is comprised with four magnet arrays whose cross section is triangle. The pair of horizontal arrays generates the horizontal field and the pair of vertical arrays is for the the vertical field. The red coils indicate the NbTi coil and the blue part indicates the iron core and poles. A round vacuum chamber can be placed in the middle of the undualtor for the beams. Such a undulator is suitable for the small beam size in both horizontal and vertical plane, which is the case in the XFEL facilities and the diffraction-limited SR sources.

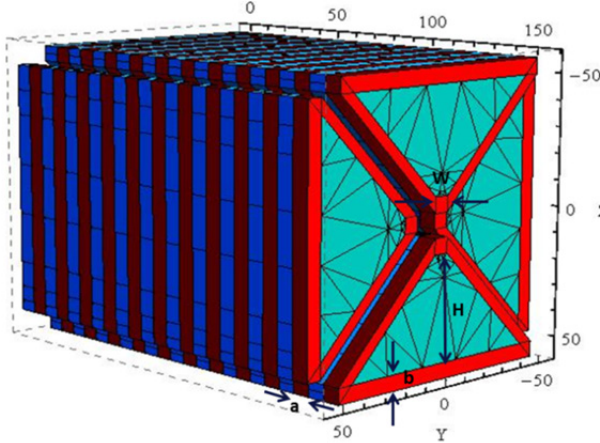


Figure 3: The Radia model for the helical SCU.

Different to the permanent magnet helical undulator APPLE-X whose gap and the longitudinal position of each array are adjustable the SCU helical undulator fixes the positions of all arrays. The pair of the horizontal arrays longitudinally is fixed longitudinally with respect to the pair of vertical arrays by a quarter of period. The polarization status is switched by changing the current in each coil. Therefore the Stokes parameters of such a SCU device are always zero to S_2 : $S_2 = 0$. The other Stokes parameters S_0 , S_1 and S_3 are able to be continuously changed. Both circular and linear polarization and ellipse polarization are achievable.

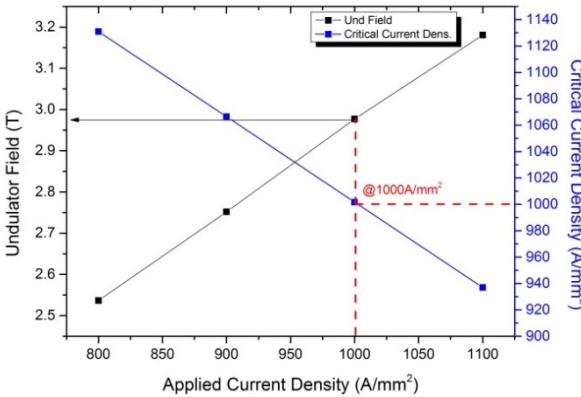


Figure 4: The helical undulator peak field and the critical current density with respect to the applied current density.

Several undulator periods have been simulated and the period 46mm is selected. Even in the linear mode it

matches the maximum K in the soft X-ray beam line SASE3. Similar to the planar undulator we simulate the peak field and critical current density by taking use of Eq. (1) at different applied current densities. Figure 4 shows the results.

As the simulation results shown in Fig. 4 the applied current density equals to the critical current density at the value of 1000A/mm² and accordingly the maximum peak field is 2.98T. To be noticed, here the peak field is from one pair of magnet arrays and it is either vertical or horizontal field. It corresponds to the maximum linear K parameter. The maximum helical K value is therefore the factor of $\sqrt{2}$ larger. We summarize the parameters of the helical super conducting undulator U46 in Table 2.

Table 2: Parameters for the Helical U46

Parameter	Value	Unit
Period λ_u	46	mm
Coil cross section a & b	13 & 9	mm
Iron core size W&H	7 & 40	mm
Pole width	10	mm
Gap g	10	mm
Slit between arrays	2.12	mm
Max. current density	1000	A/mm ²
Max. peak field	2.98	T
Max. linear K, $K_{x,y}$	12.8	--
Max. circular K, $\sqrt{2}K_{x,y}$	18.1	--
Long. λ_r @17.5GeV (Linear)	1.6	nm

CONCLUSION

In this paper we simulated the fields of two types of super conduction undulators, one is the planar undulator with the period of 18mm and the other is the helical undulator with the period 46mm. Both undulators match the parameters for the European XFEL.

The planar undulator U18 can generate high photon energy SASE up to 100 keV with available tunnel length. Since the superconducting undulator is high in the magnet field that the factor of 1.5 of the tunability to the photon energy is achievable. The helical U46 covers the same photon energy range with the existing soft x-ray beam line SASE3 even in the linear mode. It can generate both circular and linear polarization.

REFERENCES

- [1] G. Lebec, J. Chavanne, C. A. Kitegi, C. Penel, and F. Revol, "First Operational Experience with a Cryogenic Permanent Magnet Undulator at the ESRF", in *Proc. 23rd Particle Accelerator Conf. (PAC'09)*, Vancouver, Canada, May 2009, paper WE5RFP067, pp. 2414-2416.
- [2] Y. Ivanyushenkov *et al.*, "Status of the Development of Superconducting Undulators at the Advanced Photon Source", in *Proc. 8th Int. Particle Accelerator Conf. (IPAC'17)*, Copenhagen, Denmark, May 2017, pp. 2499-2502, doi:10.18429/JACoW-IPAC2017-WEOCA3
- [3] Presented at the Workshop on "Shaping the Future of the European XFEL: Options for the SASE4/5 Tunnels", Dec. 2018,
<https://indico.desy.de/indico/event/21806/material/slides/13.pdf>
- [4] Radia,
https://www.esrf.eu/Accelerators/Groups/InsertionDevices/Software/Radia/Radia_env
- [5] S. H. Kim, "A scaling law for the magnetic fields of superconducting undulators", *Nucl. Instr. Meth. A*, 546 (2005) 604-619, doi:10.1016/j.nima.2005.03.150
- [6] M. Altarelli *et al.*, "The European X-ray Free-electron Laser", Technical Design Report, ISBN 3-935702-17-5, 2006.
- [7] P. Li *et al.*, "Magnetic design of an Apple-X afterburner for the SASE3 undulator of the European XFEL", *Nucl. Instrum. Meth. A*, 870 (2017), 103-109,
<http://doi.org/10.1016/j.nima.2017.07.023>

EFFECT OF HEAT LOAD ON CRYO-COOLED MONOCHROMATORS AT THE EUROPEAN X-RAY FREE-ELECTRON LASER: SIMULATIONS AND FIRST EXPERIMENTAL OBSERVATIONS

I. Petrov[†], U. Boesenberg, M. Dommach, J. Eidam, J. Hallmann, K. Kazarian, C. Kim, W. Lu, A. Madsen, J. Moeller, M. Reiser, L. Samoylova, M. Scholz, R. Shayduk, H. Sinn, V. Sleziona, A. Zozulya, European XFEL GmbH, Schenefeld, Germany
X. Dong¹, Shanghai Institute of Applied Physics, Shanghai, China
J. Anton, S. Kearney, D. Shu, ANL, Argonne, Illinois, United States
¹also at Shanghai Advanced Research Institute, Shanghai, China

Abstract

Due to the high intensity of photon pulses generated at the European X-ray Free-Electron Laser facility, the heat load on silicon crystal monochromators becomes an issue. Here, first experimental data of heat load effects on the performance of a cryogenically cooled monochromator are presented. The measurements are compared with a model of X-ray diffraction taking beam absorption and heat deformation into account.

INTRODUCTION

A number of experimental techniques at hard XFELs require monochromators. Such devices reduce the spectral bandwidth, thus improving the temporal coherence of photon pulses. For instance, X-ray Photon Correlation Spectroscopy (XPCS) in wide-angle scattering benefits from increased speckle contrast enabled by a larger coherence time [1,2]. At European X-ray Free-Electron Laser (EuXFEL), several mJ of pulse energy can be reached in every femtosecond-long X-ray pulse. These pulses are arranged into trains containing from one to several hundreds of pulses. Within a train the pulses arrive at MHz repetition rate and ten trains are delivered per second. Currently, the facility operates at 1.1 MHz repetition rate. The planned 4.5 MHz repetition rate has recently been achieved [3]. Such intense radiation renders stable monochromator operation a challenge. Due to absorption and energy deposition in the crystals, the crystal lattice is deformed, which in turn affects the diffraction of X-rays. Here, we experimentally study the performance of cryogenically cooled Si(111) monochromator [4] for various numbers of pulses per train using first experimental data obtained at the Materials Imaging and Dynamics (MID) instrument of EuXFEL. Theoretical simulation results are also shown to estimate the heat load effect on XFEL pulse diffraction in crystals.

ROCKING CURVE MEASUREMENTS

Due to the stochastic nature of Self-Amplified Spontaneous Emission (SASE), the energy spectrum and temporal structure of XFEL pulses are irregular [5]. For example, a characteristic ~40 eV width of the energy spectrum results in ~0.2 fs coherence time.

At the MID instrument of EuXFEL a two-bounce artificial channel cut Si(111) monochromator in vertical scattering geometry has recently been commissioned and is available for user experiments in the range from about 6 to 18 keV. After two consecutive reflections, the spectral bandwidth is reduced from $\sim 5 \cdot 10^{-3}$ to $\sim 10^{-4}$, which significantly increases the temporal coherence of pulses. The optical layout of the MID beamline (Fig. 1) includes offset mirrors, Si(111) and Si(220) monochromators and split-and-delay line (SDL) optics. For instance, the SDL (currently under production) will be used for the generation of pulses with the variable delay time. For the measurements presented in this paper, the Si(111) monochromator has been used.

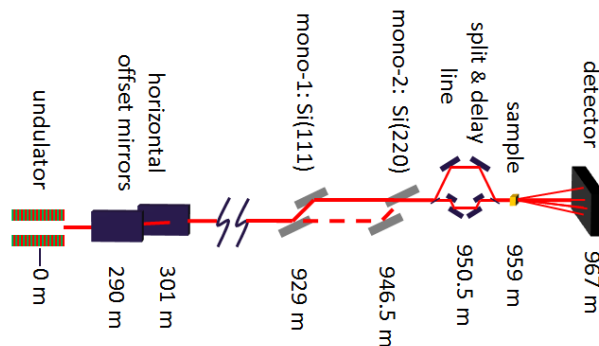


Figure 1: Sketch of MID beamline optical components. Relative positions of each component are shown under elements.

In order to analyse diffraction properties of the monochromator crystals, rocking curves have been measured for various numbers of pulses in the train, while the monochromator crystals have been cryo-cooled to 100 K. The energy of the hard X-rays in a pulse was ~0.25 mJ; the photon energy was 9 keV, the repetition rate 1 MHz, the beam size ~0.5 mm. The bunch charge was 250 pC, the electron energy 14 GeV. Rocking curve measurements were done with the pitch scan of the second crystal of the monochromator.

[†] ilia.petrov@xfel.eu

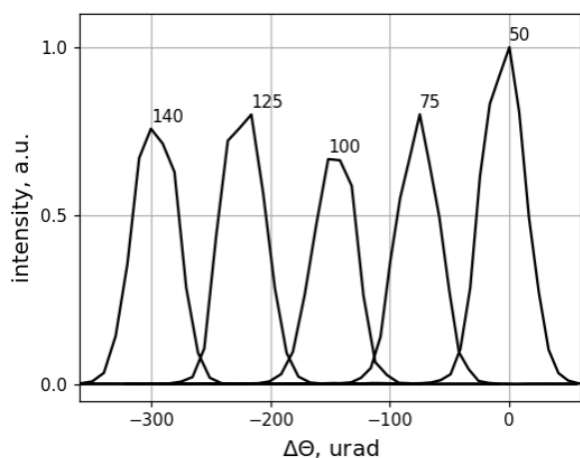


Figure 2: Rocking curves measured for various numbers of pulses per train, $\Delta\Theta$ is the scan angle. Numbers of pulses are shown in the insets. The scan angles are shifted from the measured values for better visibility of the peaks.

The measured curves are shown in Fig. 2. After subtraction of a pedestal, the values are normalized to the numbers of pulses in trains. Due to the uncertainty in the calibration of crystal angle motor, the scan step is normalized to angles such that the width of the measured curve for 50 pulses in a train matches the width of double convolution of Darwin curve for the given reflection.

SIMULATIONS

An in-house developed code [6] has been used to estimate the radial distribution of temperature and deformations at a crystal surface. The used model considers temperature dependence of the specific heat and thermal expansion coefficient. Diffraction is modelled as described in [7], where the reflection amplitude at each point of the wavefront is defined by the local deformation caused by the heating. Rocking curves are considered as double convolution of a curve for one crystal. For the present simulations, heat flow is not considered. The incident beam is Gaussian with 0.5 mm full-width at half-maximum.

Crystal heating in the diffraction region leads to rocking curve widening and a shift towards smaller incidence angles. Figure 3 shows the theoretical rocking curve width widening for 0.25 mJ incident pulses and the measured widths calculated from experimental data in Fig. 2. Theoretical rocking curve width and shift caused by the heating are shown in Fig. 4. Since the initial temperature of the crystal is 100 K, the linear expansion coefficient of silicon changes from negative to positive values during heating. This leads to the peak in the shift curve and the plateau in the width curve. For larger intensities of the pulses, the heating effects are more pronounced. Sample theoretical rocking curves for various numbers of pulses in case of 1 mJ pulses are shown in Fig. 5. Rocking curve width and shift for this case are plotted in Fig. 6. The temperature at the beam center is shown in Fig. 7. For intensities and numbers of pulses considered here, the

deviation from Bragg's law reaches several Darwin widths, as shown by horizontal lines in Fig. 7.

The simulations presented here enable to qualitatively predict the crystal heating under intense hard X-ray FEL pulses and its effect on the diffraction properties. However, for the full-scale modelling, heat flow, inhomogeneous distribution of the deformation and strain waves in three dimensions need to be taken into account and diffraction needs to be modelled using Takagi-Taupin equations. These results will be presented elsewhere.

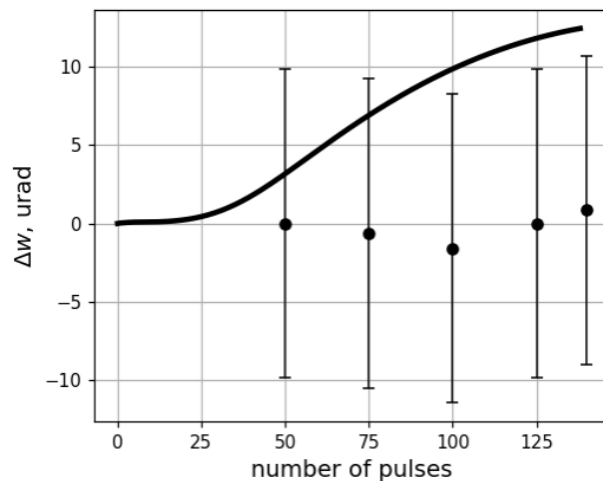


Figure 3: Difference of theoretical double-crystal rocking curve width from the width of double convolution of Darwin curve for a non-deformed crystal (solid line) and the widths calculated from measured data in Fig. 2 (dots). The error bars denote the scan step.

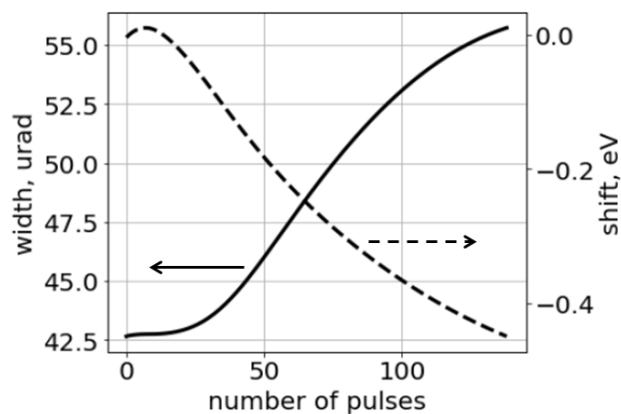


Figure 4: Shift of the center of the theoretical rocking curve for various numbers of pulses (dotted line, right vertical axis) and theoretical rocking curve width (solid line, left vertical axis). Values of the shift are normalized to energies using Bragg's law. Incident pulse energy is 0.25 mJ.

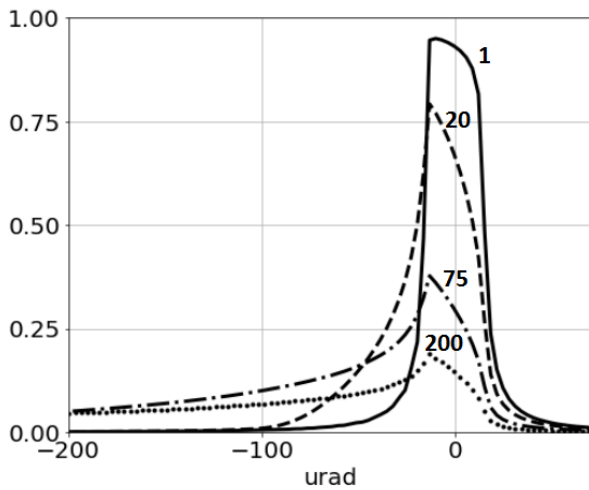


Figure 5: Theoretical rocking curves for various numbers of pulses and 1 mJ incident pulse energy.

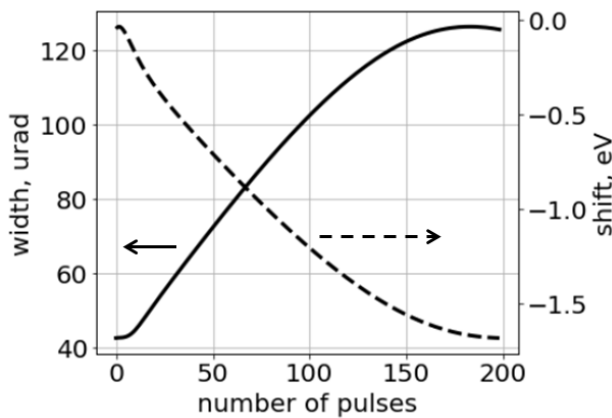


Figure 6: Rocking curve width and position for 1 mJ incident pulse energy.

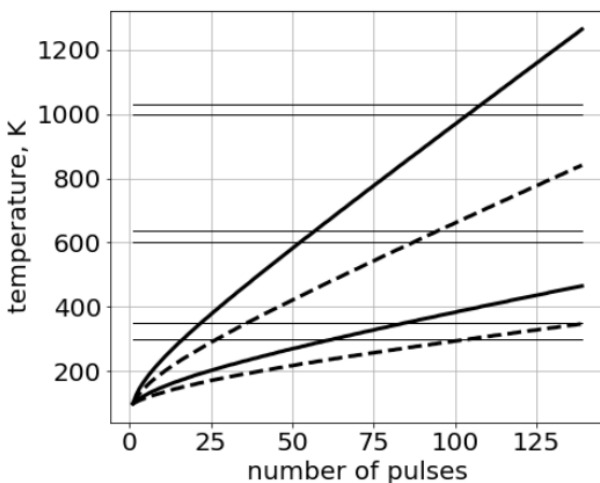


Figure 7: Temperatures at the center of the beam (solid lines) and at the distance corresponding to the σ of the beam profile (dashed lines) for 0.25 mJ pulses (bottom lines) and 1 mJ pulses (top lines). Horizontal lines denote the range of temperatures that cause the deformation within Darwin curve for various temperatures.

CONCLUSION

In conclusion, the monochromator has demonstrated stable operation under cryo-cooling and was tested at the repetition rate of 1 MHz and for up to 140 pulses per train; the energy of individual pulses was 0.25 mJ.

The simulated rocking curve widening during the train has not been observed at experiment. This might be due to losses in the beamline optics upstream of the monochromator, which might have led to an overestimation of the heating in the simulations. The account of the heat flow in the simulations will also lead to a smaller rocking curve widening.

REFERENCES

- [1] A. Madsen, A. Flueraşu, and B. Ruta, “Structural Dynamics of Materials Probed by X-ray Photon Correlation Spectroscopy”, in *Synchrotron Light Sources and Free-Electron Lasers: Accelerator Physics, Instrumentation and Science Applications*, Springer, 2016, pp. 1617-1641.
doi:10.1007/978-3-319-14394-1_29
- [2] F. Lehmkuhler *et al.*, “Dynamics of soft nanoparticle suspensions at hard X-ray FEL sources below the radiation-damage threshold”, *IUCrJ*, vol. 5, pp. 801-807, 2018.
doi:10.1107/S2052252518013696
- [3] W. Decking *et al.*, submitted, 2019.
- [4] H. Sinn *et al.*, “Technical Design Report: X-Ray Optics and Beam Transport”, XFEL.EU T_2012-006. 2012.
- [5] E. Saldin, E. Schneidmiller, and M. Yurkov, “Statistical properties of radiation from VUV and X-ray free electron laser”, *Opt. Comm.*, vol. 148, pp. 383-403, 1998.
doi:10.1016/S0030-4018(97)00670-6
- [6] H. Sinn, “Heat load estimates for XFEL beamline optics”, HASYLAB Annual Report 2007.
- [7] V. A. Bushuev, “Influence of Thermal Self-Action on the Diffraction of High-Power X-ray Pulses”, *J. Surf. Inv.*, vol. 10, no. 6, pp. 1179-1186, 2016.
doi:10.1134/S1027451016050487

ROSA: RECONSTRUCTION OF SPECTROGRAM AUTOCORRELATION FOR SELF-AMPLIFIED SPONTANEOUS EMISSION FREE-ELECTRON LASERS

Svitozar Serkez*, Natalia Gerasimova, Gianluca Geloni, European XFEL, Schenefeld, Germany
 Bohdana Sobko, Lviv National University, Lviv, Ukraine
 Oleg Gorobtsov†, DESY, Hamburg, Germany

Abstract

X-ray Free Electron Lasers (FELs) have opened new avenues in photon science, providing coherent x-ray radiation pulses orders of magnitude brighter and shorter than previously possible. The emerging concept of “beam by design” in FEL accelerator physics aims for accurate manipulation of the electron beam to tailor spectral and temporal properties of radiation for specific experimental purposes, such as x-ray pump/x-ray probe and multiple wavelength experiments. A cost-efficient method to extract information on longitudinal Wigner distribution function of emitted FEL pulses is proposed. It requires only an ensemble of measured FEL spectra.

INTRODUCTION

There has been a rapid growth both in the number of scientific users and in the diversity of new science enabled by Free-Electron laser sources. This growth is possible due to the continuously improving capabilities of FEL facilities. One promising avenue which opens the way to new experiments is the tuning of spectral and temporal properties of radiation for specific experimental purposes, e.g., generating wide bandwidth [1–3], narrow-bandwidth [4] or extremely short [5, 6] radiation pulses. Some information about duration of the typical radiation pulse, hence the length of an electron beam lasing window, can be extracted from radiation spectra of FEL operating in Self-Amplified Spontaneous Emission (SASE) mode. Taking advantage of the radiation statistical properties [7] and assuming a particular temporal profile, spectral correlation analysis gives an estimate of the average duration of the SASE FEL pulse [8, 9]. The close relation between electron phase space and radiation characteristics must be taken into account while trying to performing radiation pulse diagnostics. For example, a chirp in the electron beam energy yields a chirp in radiation frequency [10], it affects the range of spectral coherence [11], and hence the spectrum-based estimation of the SASE pulse duration. We present a fast and efficient method to provide feedback on the temporal and spectral properties of FEL radiation: measurement of the autocorrelation of an ensemble-averaged pulse Wigner distribution. We study an ensemble-averaged Wigner distribution of SASE FEL pulses and its temporal autocorrelation. We discuss how to calculate it based on measured SASE spectra and what

information such reconstruction reveals. We also present results of numerical simulations performed with the code GENESIS [12] and compare calculated Wigner distribution with evaluated reconstructions. It relies entirely on spectrometry of the generated pulses and does not require additional equipment.

THEORY

Consider a scalar field $E(t)$ in the time domain and slowly varying field amplitude $\tilde{E}(\omega) = \bar{E}(\omega) \exp(-i\omega_c z/c)$ of its Fourier transform $\bar{E}(\omega)$, where ω_c is a carrier frequency and z is the direction of propagation.

Measurable single-shot radiation spectra are proportional to the square-modulus of the single-shot scalar field¹

$$\tilde{I}(\omega) \equiv \tilde{E}(\omega)\tilde{E}^*(\omega) . \tag{1}$$

The statistical autocorrelation function of the field $E(t)$ in the time and frequency domains can then be defined as

$$\begin{aligned} \Gamma(t, \Delta t) &= \left\langle E\left(t - \frac{\Delta t}{2}\right) E^*\left(t + \frac{\Delta t}{2}\right) \right\rangle , \\ \tilde{\Gamma}(\omega, \Delta\omega) &= \left\langle \tilde{E}\left(\omega - \frac{\Delta\omega}{2}\right) \tilde{E}^*\left(\omega + \frac{\Delta\omega}{2}\right) \right\rangle , \end{aligned} \tag{2}$$

where angle brackets $\langle \rangle$ denote ensemble average. Note that the autocorrelation function depends on both time t and time separation Δt , allowing to describe non-stationary radiation fields. The intensity autocorrelation function is, instead

$$\begin{aligned} \Gamma_I(t, \Delta t) &= \left\langle I\left(t - \frac{\Delta t}{2}\right) I\left(t + \frac{\Delta t}{2}\right) \right\rangle , \\ \tilde{\Gamma}_I(\omega, \Delta\omega) &= \left\langle \tilde{I}\left(\omega - \frac{\Delta\omega}{2}\right) \tilde{I}\left(\omega + \frac{\Delta\omega}{2}\right) \right\rangle . \end{aligned} \tag{3}$$

The Wigner distribution

$$\begin{aligned} \mathcal{W}(t, \omega) &= \frac{1}{2\pi} \int_{-\infty}^{\infty} d(\Delta t) \Gamma(t, \Delta t) \exp(i\omega \Delta t) \\ &= \int_{-\infty}^{\infty} d(\Delta\omega) \tilde{\Gamma}(\omega, \Delta\omega) \exp(-i\Delta\omega t) \end{aligned} \tag{4}$$

is commonly used to describe properties of FEL radiation [13–17].

Spectrogram of a signal is a two-dimensional convolution of Wigner distribution of that signal with Wigner distribution of the spectrogram window function:

¹ considering cross section perpendicular to the direction of propagation

* svitozar.serkez@xfel.eu

† current address: Cornell University, Ithaca, New York, USA

$$S_f(t, \omega) = \mathcal{W}_f(t, \omega) * \mathcal{W}_h(-t, \omega). \quad (5)$$

RECONSTRUCTION ALGORITHM

The algorithm of reconstruction of the spectrogram autocorrelation consists of the following conceptual steps.

First, sufficiently large (around thousand events) statistics of single shot SASE FEL spectra, in the form of Eq. (1) is acquired. Here we assume that only SASE-related fluctuations are present. Otherwise, the measured data should be filtered since they are prone to additional jitter, unrelated to the SASE process.

Second, we calculate the quantity

$$Q(\omega, \Delta\omega) \equiv \left| \tilde{\Gamma}(\omega, \Delta\omega) \right|^2 = \left\langle \tilde{I}\left(\omega - \frac{\Delta\omega}{2}\right) \tilde{I}\left(\omega + \frac{\Delta\omega}{2}\right) \right\rangle - \left\langle \tilde{I}\left(\omega - \frac{\Delta\omega}{2}\right) \right\rangle \left\langle \tilde{I}\left(\omega + \frac{\Delta\omega}{2}\right) \right\rangle. \quad (6)$$

Finally, third, an inverse Fourier transform yields the reconstruction function $R(t, \omega)$:

$$R(t, \omega) = \int_{-\infty}^{\infty} d(\Delta\omega) Q(\omega, \Delta\omega) \exp(-i\Delta\omega t). \quad (7)$$

It can be shown that $R(t, \omega)$ is the frequency-wise temporal autocorrelation of the Wigner distribution and can be directly calculated based on measured spectra of SASE FEL radiation

$$R(t, \omega) = \mathcal{A}[\mathcal{W}(t, \omega)] = \int_{-\infty}^{\infty} d\tau \mathcal{W}(\tau, \omega) \mathcal{W}(t + \tau, \omega). \quad (8)$$

NUMERICAL SIMULATIONS AND DISCUSSION

In order to illustrate reconstruction capabilities, we simulated several ensembles of FEL spectra with the FEL code GENESIS [12] and analysed them with the OCELOT package [18].

If no energy chirp is present in the electron beam, the undulator resonance condition is constant along the beam and the generated radiation pulse has no frequency chirp (Figure 1). In this special case the Wigner distribution, and hence the reconstruction, are factorisable and the total pulse length can be estimated: the autocorrelation of the flat-top power profile with length Δs would yield an autocorrelation result with triangular shape and full width at half maximum (FWHM) equal to $\Delta s/2$. In the case of a Gaussian radiation pulse with FWHM Δs , the FWHM size of its autocorrelation will be $\sqrt{2}\Delta s$.

When the energy chirp in the electron beam, in terms of the relative difference of electron energy in the head and

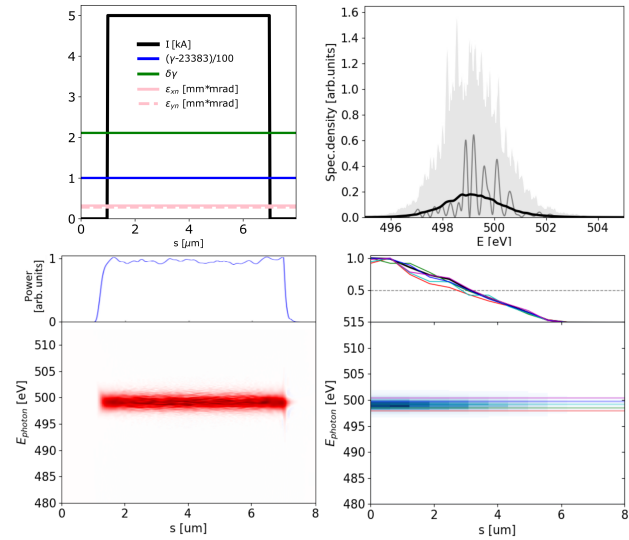


Figure 1: A 6 μm -long flattop model electron beam without energy chirp, see top left plot, used to generate SASE radiation. It is dumped during the exponential growth for 500 statistically independent events. SASE spectra are presented on the top right plot. The ensemble-averaged Wigner distribution of the SASE radiation is presented on the bottom left plot. Hereafter the diverging colormap of a Wigner distribution is normalized to its maximum absolute value, while its zero value is depicted with a white color. The spectrogram autocorrelation reconstruction $R(s, \hbar\omega/e)$ is presented on the bottom right plot. $s = -ct$ is the coordinate along the radiation propagation direction.

tail, exceeds the FEL efficiency parameter $\Delta\gamma/\gamma \gtrsim \rho$, a frequency chirp along the SASE pulse can be observed. As a consequence, it will yield a broader spectrum (which is the integral of the Wigner distribution over time) and typically a shorter pulse length at all photon energies [10] (horizontal line-offs of the Wigner distribution), as presented on Figure 2. These effects are also reflected in the spectral correlation functions, and, if not accounted for, an underestimation of the total pulse duration will take place. Our reconstruction cannot provide information on the group delay of different photon energies, as this information is lost with radiation phases.

In general, the electron beam formation system may yield a highly non-linear energy chirp, as illustrated on Figure 3 (top left plot). If the relative peak-to-valley energy difference in the electron beam is comparable or larger than a Pierce parameter ρ , the electron beam energy chirp will be imprinted into the SASE radiation spectrogram as a radiation frequency chirp. In the given example two distinct pulses of 501 eV photon energy, separated by about 6 μm , are visible on the radiation spectrogram. The separation of these “double pulses” grows with the photon energy, following the separation of the electron beam slices with an equal Lorenz factor γ . Such photon-energy-dependent separation can be straightforwardly observed in the reconstruction function.

CONCLUSION

In this work we show that based on the measureable second order spectral correlation function it is possible to calculate an autocorrelation of the ensemble-averaged Wigner distribution of the radiation. The latter, upon noise filtering via binning, is close in terms of its properties to the well-known spectrogram distribution. Therefore, we call the proposed method ROSA: Reconstruction of Spectrogram Autocorrelation.

It constitutes an extended method to study the time-frequency distribution of X-ray SASE FEL radiation. The method does not require any hardware aside for a high-resolution single-shot spectrometer, which is typically available at XFEL facilities.

The proposed method allows one to characterize the pulse length and approximate temporal shape individually for any photon energy present in the radiation. For instance, it indicates the presence of two temporally separated FEL pulses with overlapping photon energies and provides information about their duration and temporal separation. Comparison of the apriori known Wigner distributions with calculated ROSA distributions for simulation results shows that ROSA distributions provide extensive information about the pulse structure.

The method relies upon the fact that FEL pulses are short, narrow-bandwidth, and follow Gaussian statistics, at least up to saturation. Also, it is statistical in nature and relies upon the assumption that FEL hardware provides a reproducible electron beam along the stable orbit. Otherwise, discrimination of outlier events should take place.

In comparison with the conventional method of fitting the second-order spectral correlation function with a theoretical form-factor [8, 9], the proposed method does not require an initial assumption on the power profile of the SASE pulse. On the contrary: it yields additional information about the time domain of the SASE radiation. We suggest that in many cases, the analysis of a radiation Wigner distribution employing its temporal autocorrelation may be more straightforward and less misleading than fitting, especially when no information about the electron beam longitudinal phase space is available. We expect ROSA to be a valuable tool for XFEL operation and “beam-by-design” applications.

ACKNOWLEDGEMENTS

We would like to thank Guenter Brenner, Stefan Duesterer, Bart Faatz, Jan Gruenert, Vitaly Kocharyan, Naresh Kujala, Jia Liu, Juliane Roensch-Schulenburg, Evgeny Saldin, Takanori Tanikawa, Sergey Tomin, Andrei Trebushinin, Mykola Veremchuk, Mikhail Yurkov for useful discussions and Serguei Molodtsov for his interest in this work.

REFERENCES

- [1] S. Serkez, V. Kocharyan, E. Saldin, I. Zagorodnov, G. Geloni, O. Yefanov, “Extension of SASE Bandwidth up to 2% as a Way to Increase Number of Indexed Images for Protein Struc-

Figure 2: A 6 μm -long flattop model electron beam with linear energy chirp, see top left plot, used to generate SASE radiation. It is dumped during the exponential growth for 500 statistically independent events. Subplots and notations identical to those on Figure 1.

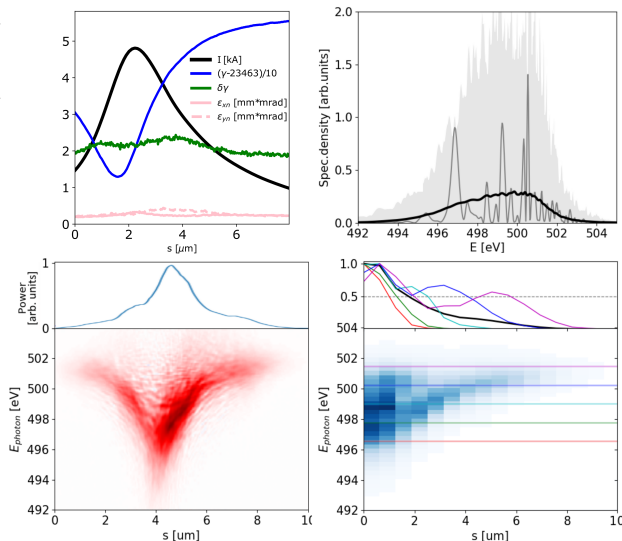


Figure 3: The European XFEL 100 pC electron beam with a non-linear energy chirp produces SASE radiation with different durations at different photon energies. Note the bifurcation in Wigner distribution above 499 eV. Analysis based on 1000 simulated SASE spectra. Subplots and notations identical to those on Figure 1.

- ture Determination by Femtosecond X-Ray Nanocrystallography at the European XFEL”, 2013. [arxiv:1306.4830v1](#)
- [2] I. Zagorodnov, G. Feng and T. Limberg, “Corrugated structure insertion for extending the SASE bandwidth up to 3% at the European XFEL”, *Nucl. Instrum. Methods Phys. Res., Sect. A*, vol. 837, pp. 69–79, 2016. doi:10.1016/j.nima.2016.09.001
- [3] E. Prat, M. Calvi and S. Reiche, “Generation of ultra-large-bandwidth X-ray free-electron-laser pulses with a transverse-gradient undulator”, *J. Synchrotron Radiat.*, vol. 23, no. 4, pp. 874–879, 2016. doi:10.1107/S1600577516007177
- [4] S. Reiche, “Overview of Seeding Methods for FELs”, in *Proc. IPAC’13*, Shanghai, China, May 2013, paper WEZB102, pp. 2063–2067.
- [5] A. Zholents, “Electron-Beam-Based Sources of Ultrashort X-ray Pulses”, *Rev. Accel. Sci. Technol.*, vol. 03, no. 1, pp. 237–259, 2010. doi:10.1142/S1793626810000415
- [6] S. Serkez et al., “Overview of options for generating high-brightness attosecond x-ray pulses at free-electron lasers and applications at the European XFEL”, *J. Opt.*, vol. 20, no. 2, p. 024005, 2018. doi:10.1088/2040-8986/aa9f4f
- [7] E. L. Saldin, E. A. Schneidmiller and M. V. Yurkov, “Statistical properties of radiation from VUV and X-ray free electron laser”, *Opt. Commun.*, vol. 148, pp. 383–403, 1998. doi:10.1016/S0030-4018(97)00670-6
- [8] A. A. Lutman, Y. Ding, Y. Feng, Z. Huang, M. Messerschmidt, J. Wu and J. Krzywinski, “Femtosecond x-ray free electron laser pulse duration measurement from spectral correlation function”, *Phys. Rev. Spec. Top. Accel. Beams*, vol. 15, no. 3, p. 030705, 2012. doi:10.1103/PhysRevSTAB.15.030705
- [9] Y. Inubushi et al., “Determination of the Pulse Duration of an X-Ray Free Electron Laser Using Highly Resolved Single-Shot Spectra”, *Phys. Rev. Lett.*, vol. 109, no. 14, p. 144801, 2012. doi:10.1103/PhysRevLett.109.144801
- [10] S. Krinsky, Z. Huang, “Frequency chirped self-amplified spontaneous-emission free-electron lasers”, *Phys. Rev. Spec. Top. Accel. Beams*, vol. 6, no. 5, pp. 11–17, 2003. doi:10.1103/PhysRevSTAB.6.050702
- [11] O. Y. Gorobtsov et al., “Diffraction based Hanbury Brown and Twiss interferometry at a hard x-ray free-electron laser”, *Sci. Rep.*, vol. 8, no. 1, p. 2219, 2018. doi:10.1038/s41598-018-19793-1
- [12] S. Reiche, Genesis 1.3 manual, 2004. http://genesis.web.psi.ch/download/documentation/genesis_manual.pdf
- [13] J. Wu et al., “Interplay of the chirps and chirped pulse compression in a high-gain seeded free-electron laser”, *J. Opt. Soc. Am. B: Opt. Phys.*, vol. 24, no. 3, p. 484, 2007. doi:10.1364/JOSAB.24.000484
- [14] E. Allaria et al., “The FERMI@Elettra free-electron-laser source for coherent x-ray physics: photon properties, beam transport system and applications”, *New J. Phys.*, vol. 12, no. 7, p. 075002, 2010. doi:10.1088/1367-2630/12/7/075002
- [15] G. Marcus, G. Penn, A. Zholents, “Free-Electron Laser Design for Four-Wave Mixing Experiments with Soft-X-Ray Pulses”, *Phys. Rev. Lett.*, vol. 113, no. 2, p. 024801, 2014. doi:10.1103/PhysRevLett.113.024801
- [16] S. Huang, Y. Ding, Z. Huang, G. Marcus, “Generation of subterawatt-attosecond pulses in a soft x-ray free-electron laser”, *Phys. Rev. Accel. Beams*, vol. 19, no. 8, p. 080702, 2016. doi:10.1103/PhysRevAccelBeams.19.080702
- [17] S. Serkez, “Self-Seeding XFELs: Operation Principle and Challenges”, *Synchrotron Radiation News*, vol. 29, no. 3, pp. 10–14, 2016. doi:10.1080/08940886.2016.1174037
- [18] OCELOT: a versatile computational tool for light sources, 2016–present. <https://github.com/ocelot-collab/ocelot>

DESIGN AND DEVELOPMENT OF HIGH-SPEED DATA ACQUISITION SYSTEM AND ONLINE DATA PROCESSING WITH A HETEROGENEOUS FPGA/GPU ARCHITECTURE

M. Bawatna†, J. Deinert, O. Knodel, S. Kovalev
Helmholtz-Zentrum Dresden-Rossendorf (HZDR), Dresden, Germany
R. Spallek, Institut für Technische Informatik, Technische Universität, Dresden, Germany.

Abstract

The superradiant THz sources at TELBE facility is based on the new class of accelerator-driven terahertz (THz) radiation sources that provide high repetition rates up to 13 MHz, and flexibility of tuning the THz pulse form. The THz pulses are used for the excitation of materials of interest, about two orders of magnitude higher than state-of-the-art tabletop sources. Time-resolved experiments can be performed with a time resolution down to 30 femtoseconds (fs) using the novel pulse-resolved Data Acquisition (DAQ) system. However, the increasing demands in improving the flexibility, data throughput, and speed of the DAQ systems motivate the integration of reconfigurable processing units close to the new detectors to accelerate the processing of tens of GigaBytes of data per second. In this paper, we introduce our online ultrafast DAQ system that uses a GPU platform for real-time image processing, and a custom high-performance FPGA board for interfacing the image sensors and provide a continuous data transfer.

INTRODUCTION

TELBE THz facility is performing ultra-fast pump-probe experiments by providing a unique combination of high pulse energies and high repetition rates. In this type of experiment, the electric or magnetic field in the THz pump pulse acts as the excitation of dynamics in the matter. This dynamic in turn is then probed by ultra-short (light) pulses, typically with the sub THz cycle resolution as in [1]. A pulse resolved DAQ system has been developed at TELBE user facility as in [1] to allow the performance of time-resolved THz spectroscopy measurements with sub 30 fs Full-Width Half Maximum (FWHM) time resolution with excellent dynamic range up to 120 dB as in [2]. However, the high-speed commercial cameras used at TELBE user facility have several drawbacks in terms of data transfer, recording time, and data processing. Currently, most of the operating time is spent on the data transfer, rather than the data acquisition. Images are stored in the camera's internal buffer before being sent further. New data acquisition is only possible when all data is transferred. Therefore the commercial cameras are usually not able to provide online data processing.

The dominant technology used in the visible light detectors is the Charge Coupled Device (CCD) as in [3] due to its sensitivity and low noise performance. However, the high frame rate of the current imaging detectors is limited

by the pixel access time. Therefore, commercially available imaging detectors decrease the number of pixels while increasing the frame rate.

Another drawback is that the firmware that interfaces the visible light detectors is not available to the developers, with a few parameters available for optimization. Therefore optimization of the camera's functionality to the application requirements is not possible.

Recently, there is an increased performance in large-scale real-time data processing using massively parallel architectures such as Graphics Processing Units (GPU) and Field Programmable Gate Arrays (FPGAs).

Accelerating the image processing using FPGAs or GPUs is not a new concept. Although GPUs can provide better performance than the FPGAs for applications where the data processing can be implemented with no inter-dependency in the data flow, the FPGAs are more suitable for applications that require many control operations and parallel processing. FPGAs not only provides flexibility in developing the desired algorithms, but also the ability for parallel data processing.

In this paper, we will present an online DAQ system for applications capable of providing both high data throughput and real-time data processing.

The paper is organized as follows: the first section introduces the requirements for the pulse-resolved DAQ system at TELBE. The second section presents the online pulse-resolved DAQ system, the implemented signal processing techniques, and the implemented firmware. The third section presents the arrival time information measurements. After summarizing the results, foreseeable future development and upgrades are discussed.

REQUIREMENTS FOR THE PULSE RESOLVED DAQ SYSTEM AT TELBE

Femtosecond level diagnostic and control of sub-pico-second electron bunches is an essential topic in modern accelerator research. At the ELBE user facility, there are two available electron injectors in use [4] as in Fig. 1. The thermionic injector, which supports repetition rates up to 13 MHz and bunch charges up to 100 pC, and the Super Radio Frequency (SRF) photo-cathode injector, which is used for experiments that may require lower emittance or higher bunch charges of up to 1 nC as in [4]. Moreover, the SRF injector at ELBE also has a maximum repetition rate of 13 MHz with different macro pulse modes of operation.

† m.bawatna@hzdr.de

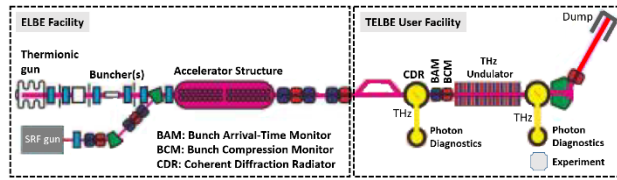


Figure 1: ELBE accelerator beamlines for THz radiation production.

However, the timing jitter of electron bunches as in Fig. 1 is affected by the bunch compression. The measurements of timing jitter for different bunch compression shows that the thermionic injector has a jitter up to 2 picoseconds (ps) and the SRF injector has much lower jitter up to 1 ps as shown in Fig. 2.

Accurate timing of an accelerator to an external laser system can be accomplished in several ways. One method is the Bunch Arrival time Monitor (BAM) system that based on RF pickups installed in the electron beam pipe, and the signal caused by the Coulomb field of the passing bunch can be used to derive an arrival time concerning an external laser. The BAM system is installed between the diffraction radiator and the undulator sources of the TELBE facility, as shown in Fig. 1.

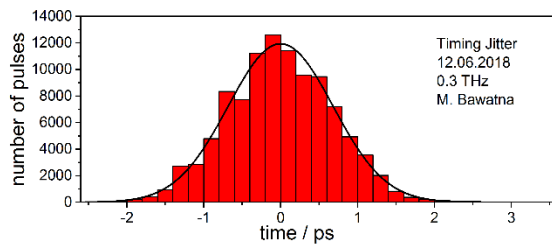


Figure 2: Histogram of the pulse-to-pulse arrival time jitter. Data were taken at the full 101 kHz repetition rate.

However, at TELBE user facility, the more accurate time resolution is required to utilize the transient THz fields as a novel highly selective excitation for non-linear dynamics. These dynamic processes are typically studied using pump-probe experiments as shown in Fig. 3, on few ten fs FWHM timescales involving synchronized external laser systems.

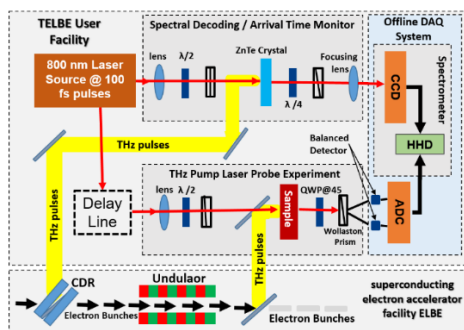


Figure 3: Schematic of the pulse-resolved DAQ system developed in TELBE This diagram shows how the arrival-time monitors are integrated into the experimental setup.

The current DAQ system at TELBE, as shown in Fig. 3, is capable of recording up to eight experimental data channels per pulse at a maximum repetition rate of 100 kHz. After the acquisition, the data is immediately written to disk, where it can be processed later.

Several digital signal processing operations need to be done on the measured arrival time information to achieve an excellent time resolution and performance accuracy of a few ten fs. The three offline signal processing operations as in [5] are: subtracting the pixels from the background noise, then applying the zero-phase filter on these pixels to reduce noise, and then calculating the location of the maximum peak.

Presently no data can be taken while writing to disk and the writing process is slower than the data acquisition by a factor of about 3. The system hence, currently has a duty cycle of about 25%. Therefore, we implemented an FPGA architecture close to the camera to achieve the necessary speed to process data between pulses, as well as improving the transfer rate of data to storage as in [5].

Online Pulse-resolved DAQ System

The online DAQ system enables continuous data acquisition at the highest speed and offers real-time data analysis, which provides opportunities for new experiments. The arrival time information for each THz pulse is recorded as a vector of 256 pixels using a KALYPSO linear array detector [6,7] due to its unprecedented MHz line rate. The measure photon energy at each pixel of the size of 50 μm x 3 mm is converted into a digital value with 12-bit resolution as in Fig. 4.

By applying a threshold level to the recorded vector, only the samples rise above the threshold are processed. If the number of samples above the threshold is below four, then they are considered as glitches. The arrival time information of each THz pulse is calculated based on the location of the maximum value.

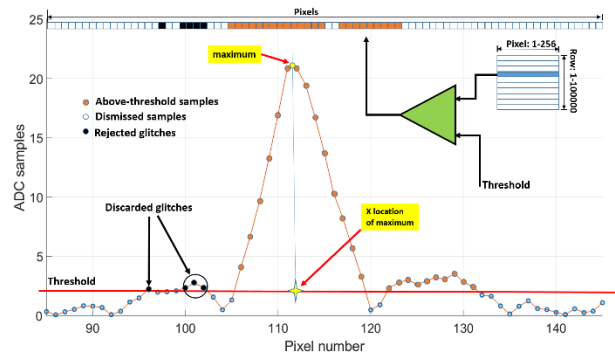


Figure 4: A vector containing the arrival time information of the THz pulse. Data were taken at 100 kHz repetition rate.

Firmware

The architecture of the DAQ system as shown in Fig. 5 is divided into three main parts: KALYPSO front-end, a Xilinx Virtex-6 FPGA ML605 evaluation board and a GUI

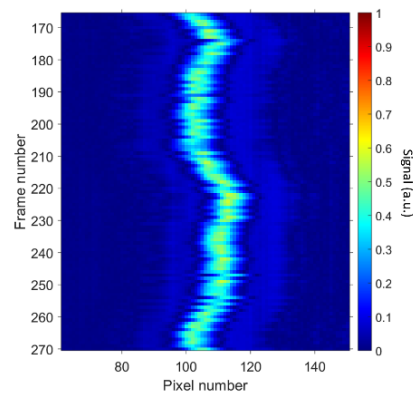
When the exposure or integration time is provided to the sensor, and the FPGA issues a frame request command, the image is stored in the pixel-matrix. The pixel values are digitized. These values are transferred using Low Voltage Differential Signal (LVDS) channels. Each LVDS channel is responsible for a group of adjacent columns of the pixel matrix.

The block diagram illustrates the KALYPSO architecture. A central FPGA block contains several key components: DSP Blocks, DDR Interface, Flash Interface, PC Interface, KALYPSO Interface, Data Buffer, and an Embedded Processor. The KALYPSO Interface and Data Buffer are shown with dashed borders. External components are connected to the FPGA: Timing Input and PLL provide clocking to the DSP Blocks; Sensor, GOTTHARD Readout Chips, and ADC provide data to the KALYPSO Interface; DDR Memories and FLASH provide data to the respective interfaces; System Memory, CPU, PCIe, and GPU are connected to the PC Interface. Bidirectional data flow is shown between the CPU, PCIe, and GPU, and between the CPU and System Memory.

The DDR memory device is used for both temporary frame data storage and image processing algorithms.

The Electro-optic sampling system is most commonly used to measure the time-domain form of THz pulses. They work by altering the polarization of a probe beam that propagates through the electro-optic crystal co-linear with a THz pulse as in [5]. This effect is quasi-simultaneous and can be used to detect signals on femtosecond time-scales.

A raw data of 300 frames at 100 kHz repetition rate, as shown in Fig. 6 has been recorded at TELBE.



CONCLUSION AND FUTURE WORK

REFERENCES

- WEP081**

FIELD INTEGRAL MEASUREMENTS OF DAVV UNDULATORS AND FUTURE MEASUREMENT PLAN

M. Gehlot, S. M. Khan, G. Mishra, R. Khullar

IddA Laboratory, Devi Ahilya University, Indore, India

H. Jeevakhan, Department of Applied Science, NITTTR, Bhopal, India

F. Trillaud, Instituto de Ingeniería, National Autonomous University of Mexico, México

Abstract

The Insertion device development and Application (IddA) laboratory of Devi Ahilya University, Indore, India has ongoing activities on undulator design and development[1-3]. In this paper, we analyze the field integral properties of the two DAVV undulator. The first is the IddA U20 prototype NdFeB-cobalt steel hybrid in house designed device of 20 mm period length with twenty five periods. The uniform gap variable hybrid undulator provides magnetic flux density (in rms) from 2400 G to 500 G in the 10 mm-20 mm gap range. The second is the NdFeB based U50II undulator of 50 mm period length with 20 number of periods. Hall probe results are described. A short description of the measurement plan of the undulator on the pulsed wire bench and stretched wire bench is described.

INTRODUCTION

In the case of an undulator, the magnetic flux density on axis is given by,

$$B_y = \hat{y} B_{peak} \sin(k_u z)$$

Where B_{peak} is the peak magnetic flux density. In case of hybrid undulator, it is given by

$$B_{peak}(T) = a \exp \left[b(g / \lambda_u) + c(g / \lambda_u)^2 \right] \quad (1)$$

where the a, b, c are the empirical coefficients of Eq. (1) and depend on the magnet-pole dimensions, material properties of the NdFeB or SmCo₅ magnets and the poles of the undulator. g, λ_u are the undulator gap and period length respectively. In the case of PPM undulator $c = 0, b = \pi$ Eq. (1) describes the field integral as,

$$I_1 = \int B_y dz \quad I_2 = \int (\int B_y dz) dz \quad (2)$$

Eq. (2) when multiplied by $(e / \gamma mc)$ gives the calculated angular deviation and trajectory offset of the electron respectively. A typical requirement for a good quality undulator is that the value of the measured field integral values should be less than the tolerance limit. A standard procedure to determine the field integrals is the Hall probe measurement. In this method, the field is mapped by the Hall probe point by point along the length of the undulator and the field is integrated by a numerical code over the length of the undulator.

HALL PROBE MEASUREMENT

The undulators specifications are described in Table.1 Fitting the Hall probe data for U20 hybrid undulator to Eq.(1) reads the field coefficients reads $a=3.06$, $b=-5.59$, $c=1.123$ (Fig. 1). The uniform gap variable hybrid undulator provides a magnetic flux density (in rms) from 2400 G to 500 G in the 10 mm-20 mm gap range. Fig. 2 describes the Hall probe data for the PPM undulator. A linear fit of the Hall probe data for reads $a=1.62$ and $b=-3.24$. The magnetic flux density for U50II undulator with variation in the gap range from 10 mm to 35 mm is 1 T to 0.1612 T. Fig. 3 and Fig. 4 are the Hall probe data field mapping for U20 and U50II undulator for the gap of 10 mm. Fig. 5 represents the magnetic field deviation(rms) for the both the undulators. In the operating gap of 10 to 20 mm, the deviation is in 60-140 G range for U50II undulator and 20-50 G for the U20 undulator.

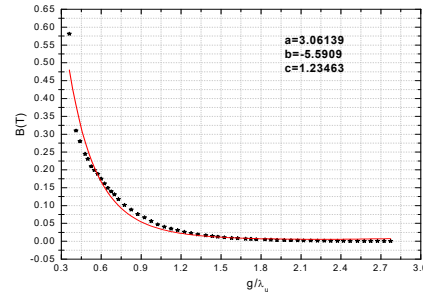


Figure 1: Linear fit to Hall probe data of U20 undulator.

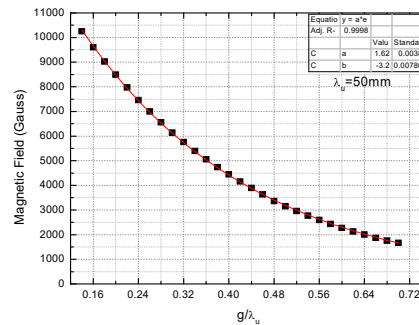


Figure 2: Linear fit to Hall probe data of U50II undulator.

PULSED WIRE MEASUREMENT BENCH

The laboratory has developed[4] and upgraded[5] the pulsed wire bench for the field integral measurements. In this paper we describe the available parameters of the pulsed wire method. In a pulsed wire technique, a thin wire is used along the undulator axis.

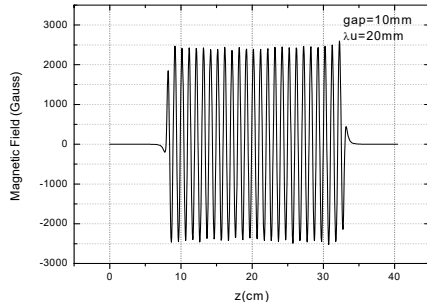


Figure 3: Measured magnetic field of U20.

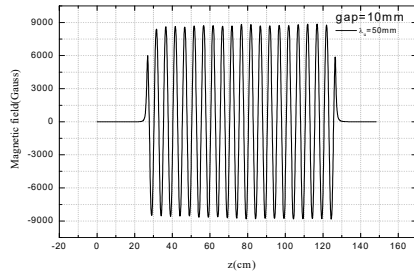


Figure 4: Measured magnetic field of U50.

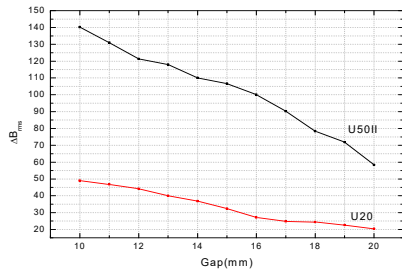


Figure 5: Variations in magnetic field of U50II undulator.

Table 1: Undulators Specification

U20	Undulator type	Hybrid
	Magnet material	NdFeB
	Pole material	Cobalt steel, M35
	Gap	Grade
	Magnetic flux density	10-20 mm
	No. of periods	0.24-0.05 T
	Period length	25
		20 mm
U50II	Undulator type	PPM
	Magnet	NdFeB
	Period length	50 mm
	Number of periods	20
	Gap	10-35 mm
	Magnetic flux density	1T- 0.17 T

One end of the wire is fixed and the other end carries a load over a pulley. Both the ends of the wire is connected to a source of pulse current. A current pulse to the wire produces a force on the wire proportional to the undulator magnetic field. The transverse wire displacement propagates along the wire as a wave longitudinally along both the directions and is detected by a sensor located at the ends of the undulator. The wire displacement at the sensor is given by,

$$x(0,t) = -\frac{I_0 \Delta t}{2v\mu} I_1 \quad (3)$$

I_0 is the amplitude (amp) of the current pulse, v is the velocity of the wave (m/sec) in the wire, Δt is the pulse width (sec), μ (kg/m) is the mass per unit length of the wire. Eq. (3) is evaluated by looking at the wire displacement when a current of short duration is applied to the wire. The short pulse width must satisfy

$$v\Delta t < \lambda_u \quad (4)$$

For U20, $\lambda_u = 0.02$ m , $v = 130.05$ m/sec, Eq. (4) requires a pulse width of $\Delta t < 153$ μ sec for the first field integral measurement. For U50, $\lambda_u = 0.05$ m, $v = 130.05$ m/sec, Eq. (4) requires a pulse width of $\Delta t < 384$ μ sec For $I_1 = 40 \mu T m$, $\mu = 4.04 \times 10^{-4} \text{ kgm}^{-1}$, $I_0 = 12 A$, Eq.(3) predicts a maximum wire displacement of $0.698 \mu m$ and $1.754 \mu m$ for the two undulators. The wire displacement at the sensor for the second field integral is given by for a longer pulse,

$$X(0,t) = -\frac{I_0}{2v^2\mu} I_2 \quad (5)$$

The current pulse must satisfy

$$v\Delta t > N\lambda_u \quad (6)$$

For the U20 and U50-II, the pulse requirements calculated from Eq.(6) are 3.84 msec and 7.689 msec respectively. If $I_0 = 12 A$ and $I_2 = 40 \mu T m^2$, wire of diameter $250 \mu m$, $\mu = 4.04 \times 10^{-4} \text{ kgm}^{-1}$ from Eq.(5) we get the minimum wire displacement as $3.54 \mu m$. Table 2 describes the pulsed wire bench parameters for the DAVV undulator measurements.

Table 2: Pulsed Wire Parameters

Pulse generator	0.2 μ s-200 ms
Maximum current	~ up to 12 amp
Wire material	CuBe
Resistivity(ρ)	$5.4 \times 10^{-8} \Omega \text{ m}$
mass per unit length(μ)	$4.10 \times 10^{-4} \text{ kg/m}$
250 μ m- diameter	
$\mu\rho$	$2.2 \times 10^{-11} \text{ kg } \Omega$
250 μ m- diameter	
Pulse width	U20 1 st integral- $\Delta t < 153 \mu\text{s}$
requirement	2 nd integral - $\Delta t < 3.84 \text{ ms}$
	U50II 1 st integral- $\Delta t < 384 \mu\text{s}$
	2 nd integral- $\Delta t < 7.689 \text{ ms}$
Sensor type	Laser -Photodiode
Sensitivity	8 mV/ μm

STRETCHED WIRE MAGNETIC MEASUREMENT BENCH

A stretched wire bench has been developed at DAVV for magnetic measurement of the two undulators. The components of the system are assembled on a pneumatic vibration isolation table (Holmarc, India make, model No. TTNM 240-120) with honeycomb table top of width 200 mm. The table is 2400 mm in length and 1200 mm wide. Two units of X-Y translation stages are placed at two ends of the table. The distance between these two units is kept at 1860 mm. The translation stages (Holmarc, India make, model No. LMS-100-100) have a travel range of 50 mm, load capacity 15kg. 1 mm pitch and resolution 0.0025 mm each. The physical size of the translation stages measure 100 mm \times 100 mm. The translation stages are driven by stepper motor of Holmarc, India make, model no. 57SH51-4ASM. Motion controller of Holmarc, India make, model No. Ho-HPC-2H and used to interface the stages with the desktop computer system. Both the units of translation stages given a height 355 mm from the table top through which the wire hangs at a height of 275 mm from the table top. Both the units of translation stages sit on a labjack to provide another height adjustment of 60 mm to 115 mm. Litz wire of 100 strands with overall size 1400 μm including enamel coating of the single wires is used for the measurements. The total length of the wire is 5 m. The wire tension plays an important role in controlling sag and thereby the accuracy of the measurement. A digital display unit at the load end reads the tension upto 50 Kg in three digits. Series connections of the 100 strands are made in a PCB located in a terminating box from where the output goes to the integrator through a low pass filter circuit. The input to output length of the wire measures a resistance of 1.13 ohm. The low pass filter circuit has a cutoff frequency of 10 Hz, $f_c = (0.5 * \pi * R_t * C_t)$. Two 15K Ω resistors in series make $R_t = 30K\Omega$. Two capacitors of 1 μf each joined

in series makes $C_t = 0.5\mu\text{f}$. Keithley 2182 A nano voltmeter is used for the voltage integration. A Labview code is written to control the synchronous motion of the positioning stages and the integrator to record the voltage signal induced by the wire movement. The two field integrals are evaluated through,

$$\frac{1}{N\Delta x} \int_0^{\Delta t} V dt = I_1 \quad (7)$$

$$I_2 = \frac{L}{2} \left(\frac{-\int_0^{\Delta t} V dt}{N\Delta x} + I_1 \right) \quad (8)$$

Eq. (7) and Eq. (8) gives the first field integral and second field integral from stretched wire method. Where N the no. of strands in the wire is, Δx is the movement of the wire, L is the length of the wire stretched along the undulator and V is the voltage produced in the wire. The first field integral measurement is completed for the U50II undulator and the stretched wire result is compared with Hall probe data in Fig. 6. for the different undulator gap from 10 mm to 20 mm. The result shows a good agreement between the two methods at wider gaps and differs by $\sim 60 \text{ Gcm}$ at 10 mm. To make a single measurement, the wire is moved in the forward direction by a certain quantity and then moved in the backward direction by the same quantity. The two integrated voltages are averaged and recorded. This procedure eliminates the integrator drift. The sampling distance of the measurement is 2.5 mm and the wire translation velocity is 3.125 mm/sec. The accuracy of the measurement is obtained for a five set of measurements and gives a value better than 2 G cm. The stretched wire measurement is compared with Hall probe results. Table3. describes the starched wire bench parameters.

Table 3: Stretch Wire Parameters

Wire	copper Litz
Number of strands	100
Diameter of single wire including coating	14 μm
Sampling step	2.5 mm
Displacement velocity	1.6 mm/sec
Total length of wire	5.187 m
Stretched Wire length (inside the undulator)	1.8 m
Tension	10.14 kg

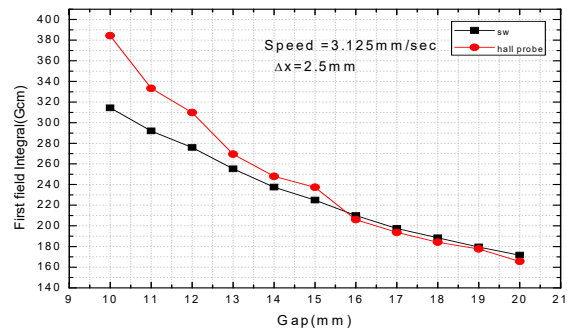


Figure 6: Comparison of first field integral for starched wire and Hall probe measurement.

CONCLUSION

A stretched wire bench and pulsed wire bench has been developed for precision measurement of DAVV undulator system along with Hall probe measurement. A preliminary measurement of U50II in stretched wire bench gives good agreement with Hall probe data. The agreement with Hall probe data is 60 G cm-6 Gcm in the 10 to 20 mm gap

ACKNOWLEDGEMENT

This work is supported by SERB grant CRG/2018/00849 and financial support from UGC [PDFWM-2014-15-GE-MAD-26801(SA-II)], Delhi and DGAPA of UNAM, fund PAPIIT TA100617.

The authors are grateful to Dr. Subrata Das, Ashok Kumar and B. Srinivas of AMTD, RRCAT, Indore for the technical support to develop the stretched wire measurement bench at DAVV, Indore

REFERENCES

- [1] Mona Gehlot *et al.*, "Undulator development activities at DAVV-Indore", in *Proc. FLS'18*, Shanghai, China, Mar. 2018, pp. 133-137. doi:10.18429/JACoW-FLS2018-WEP2PT030.
- [2] G. Mishra *et al.*, "Magnetic field measurement and analysis of prototype hybrid U20 undulator", *IEEE transactions on Plasma Science*, vol. 47, no. 7, p. 3182, 2019.
- [3] G. Mishra *et al.*, "Characterization of hybrid undulator", *IEEE Transactions on Magnetism*, vol. 53, no. 2, p. 7000207, 2017.
- [4] Geetanjali Sharma *et al.*, "Analysis of Pulsed wire measurements on bi-harmonic undulator", *Measurement*, vol. 82, pp. 334-344, 2016.
- [5] Saif Mohd Khan *et al.*, "A measurement plan for the DAVV undulator systems", in *National Symposium on vacuum electronic device and applications*, 22-24th November, IIT Guwahati, India.

CAPABILITIES OF TERAHERTZ SUPER-RADIANCE FROM ELECTRON BUNCHES MOVING IN MICRO-UNDULATORS

N. Balal[†], V.L. Bratman¹, Yu. Lurie, and A. Friedman
Ariel University, Ariel, Israel

¹ also at Institute of Applied Physics, Russian Academy of Sciences, Nizhny Novgorod, Russia

Abstract

An available frequency range of powerful coherent radiation from sub-picosecond and picosecond bunches with high charge and comparatively moderate particle energy of 3 - 6 MeV that are formed in laser-driven linacs significantly extends if one uses a micro-undulator. Such an undulator with a helical symmetry and a high transverse field can be implemented by redistributing a strong uniform magnetic field by a helical ferromagnetic or copper insertion. According to simulations and experiments with prototypes, a steel helix with a period of (8-10) mm and an inner diameter of (2-2.5) mm inserted in the 3T-field of a solenoid can provide a helical undulator field with the same periodicity and an amplitude of about of 0.6 T. Using a more complex hybrid system with a permanently magnetized helical structure can increase this value up to 1.1 T. The necessary helices can be manufactured on the machine, assembled from steel wires, formed from powder placed into a hollow helical shell or 3D - printed. Simulations based on the WB3D code demonstrate that using such undulators with the length of (30-40) cm enable single-mode super-radiance from bunches with charge of 1 nC and duration of 2 ps moving in an over-sized waveguide in frequency range of 3-5 THz. The calculated efficiency of such process many times exceeds efficiency that can be obtained with short bunches of the same initial density.

INTRODUCTION

Advanced laser-driven photo-injectors make possible formation of very dense picosecond and sub-picosecond electron bunches with charge of the order of 1 nC and larger at moderate relativistic energy [1-4]. Such bunches can be attractive for simple production of powerful THz electromagnetic pulses using various mechanisms of the so-called coherent spontaneous radiation and super-radiance [5-16]. In particular, it is planned to use a coherent spontaneous Doppler-upshifted undulator radiation of bunches whose longitudinal size or period of preliminary density modulation is smaller than the wavelength of radiation in first experiments at the Israeli THz source [13]. The modulation can also arise self-consistently in extended bunches during their interaction with the radiated electromagnetic pulses in process of super-radiance (see, e.g., [10-12] and literature cited therein).

At the fixed electron energy, the radiation frequency of the Israeli source can be obviously increased by decreasing of the undulator period. Simple and efficient ways for creation of helical undulators with small periods and strong

amplitudes of a transverse magnetic field were independently proposed in [15-18] and [19-22]. They present modifications of old ideas and based on redistribution of a uniform magnetic field by ferromagnetic [23-25] or conducting bodies placed inside a solenoid.

When using a small-period undulator for implementation of coherent spontaneous radiation it is necessary to provide a very short initial bunch duration. Because of very strong mutual Coulomb repulsion of the particles in the dense bunch this can be only fulfilled at a very limited length of bunch propagation. Other opportunities are opened when one uses radiation of pre-modulated bunches or super-radiance of extended bunches; in the latter case a self-modulation of density and particle bunching in the field of the radiated wave occur [10-12].

HELICAL MICRO-UNDULATORS BASED ON REDISTRIBUTION OF UNIFORM MAGNETIC FIELD

The undulator field with a small period and a large transverse amplitude can be created by redistributing the strong uniform field on a periodic ferromagnetic insertion [15-18, 20-22]. This method was successfully demonstrated many years ago in planar systems with periodic planar ferromagnetic insertions [23-25]. In papers [20-22] and [15-18], it has been proposed to use a helical insertion for creation of a helical undulator field. Experiments with helices including ones with small periods (Fig. 1a) have demonstrated a satisfactory coincidence with calculations [17]. A steel helices with the period of 8-10 mm and inner diameter of 2-2.5 mm placed into a strong uniform field of 3 T can provide a helical undulator field with the amplitude of 0.6 T (Fig. 1). The larger amplitude can be obtained using a hybrid system (Fig. 2). [15] consisting of a steel helix ("bolt") placed inside a permanently magnetized helical block. To avoid changing the direction and value of the magnetic field of the permanent magnet we performed the calculations for the latter system with a low solenoid field of 1.2 T; the rest parameters (Fig. 1a) are as follows: $a=4$ mm, $R_1=0.75$ mm, $R_2=4$ mm, and $d=8$ mm. According to simulations this system can provide the helical undulator field with the amplitude of 1.1 T at the axis.

[†] nezahb@ariel.ac.il

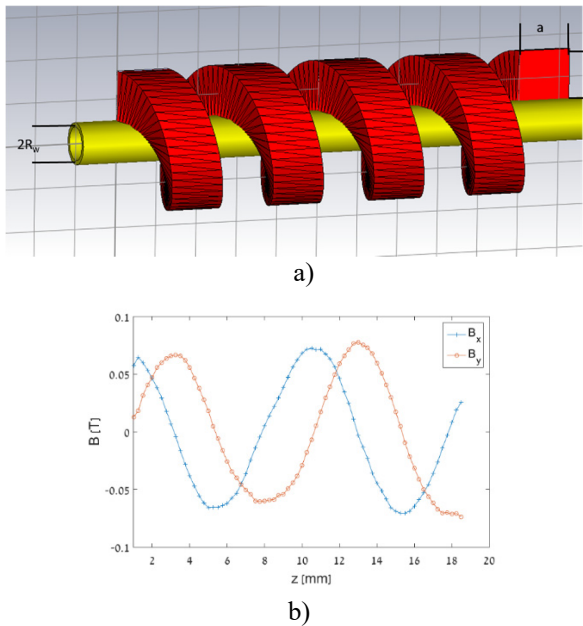


Figure 1: Measured distribution of transverse magnetic field at the axis of the steel helical insertion (a) with the period of 10 mm at a low uniform guiding field of 2 T (b).

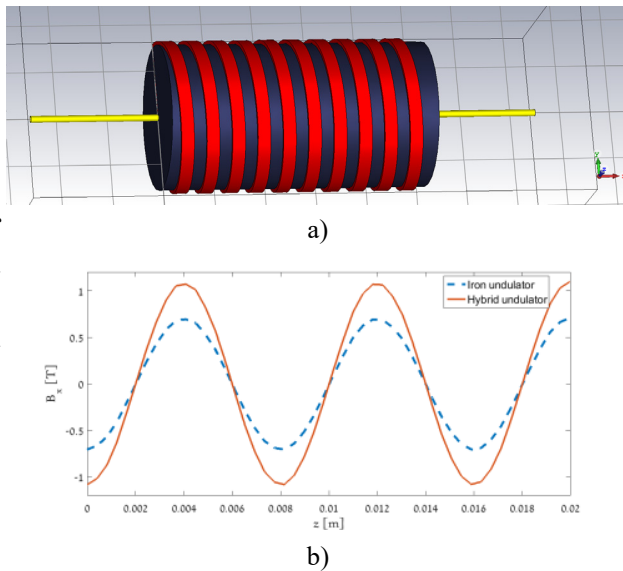


Figure 2: A hybrid insertion (a) consisting of a steel helix (“bolt”, red) placed inside a helical block (“nut”, blue) with permanent magnetization opposite to the direction of the uniform field of a 1.2-T solenoid and CST simulations of distributions for transverse undulator field without and with a permanent magnetized block (b).

RADIATION OF SHORT AND EXTENDED BUNCHES

Let us consider now possibilities of using micro-undulators for production of a high-frequency radiation from dense electron bunches with a certain energy 6 MeV, which are obtained in the photo-injector and then brought to required axial and transverse dimensions in a special forming section. Considering a symmetry of magnetic system and electron bunches it is convenient to use a circular metal

waveguide placed inside the helix as an electrodynamic system of such a THz source. At a relatively small waveguide diameter a selective nearly single-mode generation can be obtained in such the system with predominant high-frequency and following low-frequency radiations. First method for this is based on using very short bunches with duration of the order of (0.08-0.15) ps that are approximately equal to halves radiation periods and provide a coherent spontaneous undulator radiation of particles at the length, which is essentially limited by a longitudinal expansion caused by their mutual Coulomb repulsion [5, 6, 8, 9, 13-17]. Second method supposes using long extended bunches with durations of a few picoseconds that are sufficient in the considered wavelength range for development of a density bunch self-modulation due to its interaction with the radiated wave, which is typical for regimes of super-radiance (see, e.g., [10]).

Consider here the undulators with periods of 10 and 8 mm, for which amplitude of transverse field can be as high as 1 T (see Section 2), and very small (but over-sized) waveguide diameters $D_w = 1.5$ mm and $D_w = 1$ mm, respectively. According to simulations for a point-like small charge moving in these undulators, the high-frequency and low-frequency TE_{11} waveguide modes are basically excited at the fundamental undulator harmonic. At the chosen periods and the same value of undulator field, $B_u = 1$ T, the undulator parameters are $K=0.93$ and $K=0.75$. The radiation frequencies being in synchronism with a 6-MeV particle are 3.7 THz and 6.2 THz, respectively.

When using short and very dense bunches with durations and radii 0.15 ps, 0.3 mm for the first undulator and 0.08 ps, 0.2 mm for the second one the radiation frequency is lower than for a point-like particle even at a low charge of 50 pC. In this case, the electron bunches significantly expand already after $N_u=20$ undulator periods when the radiated energy is 0.32 μ J and 0.45 μ J, respectively.

It is important that the initial length of the electron bunches can be much larger than the radiated wavelength. In this case of dense extended bunches, whose edges can be even very smooth, simulations demonstrate development of a particle self-modulation and super-radiance (Fig. 3a). The effect of super-radiance of the extended bunches was first discovered for longer waves and various radiation mechanisms (see, e.g., [10-12]). It is successfully used for generation of very powerful electromagnetic pulses at millimetre waves. Possibility of undulator super-radiance at THz waves was also studied in [10].

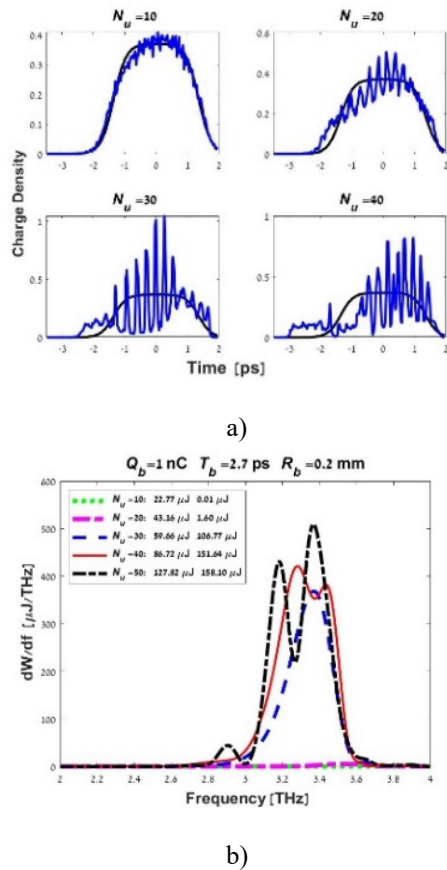


Figure 3: Evolution of bunch density (a) and high-frequency parts of radiation spectra (b) for an extended bunch with charge of 1 nC, radius of 0.3 mm, duration of 2.7 ps, and energy of 6 MeV passing the distance of (10-40) cm in undulator with period of 10 mm and waveguide with diameter of 1.5 mm.

According to our simulations, the undulator super-radiance can be efficient at fairly high frequencies. For example, using of 1-nC bunches with radii (0.2-0.3) mm and initial length of 10 wavelengths moving in the considered waveguides and undulators can provide single-mode generation with energy of 0.15 mJ and 0.24 mJ at the frequencies higher than 3 THz and 5 THz with efficiency (2.5-4)%, respectively (Fig. 3). The energy efficiency of such super-radiance from extended bunches is many times higher than the efficiency of coherent spontaneous radiation from short bunches of the same initial density.

This work was supported by the Israeli Ministry of Science and Technology.

REFERENCES

- [1] J. Power, "Overview of photoinjectors", *AIP Conf. Proc.*, vol. 1299, p. 20, 2010. doi:10.1063/1.3520316
- [2] A. Bartnik, C. Gulliford, I. Bazarov, L. Cultera, and B. Dunham, "Operational experience with nanocoulomb bunch charges in the Cornell photoinjector", *Phys. Rev. ST Accel. Beams*, vol. 18, p. 083401, 2015. doi: 10.1103/PhysRevSTAB.18.083401

- [3] J.B. Rosenzweig, A. Valloni, D. Alesini, G. Andonian, N. Bernard, L. Faillace, L. Ficcadenti, A. Fukusawa, B. Hidding, M. Miglioni, et al., "Design and applications of an x-band hybrid photoinjector", *Nucl. Instrum. and Methods Phys. Res., Sect. A*, vol. 657, p. 107, 2011. doi:10.1016/j.nima.2011.05.046
- [4] K.J. Perez Quintero, S. Antipov, A.V. Sumant, C. Jing, and S.V. Baryshev, "High quantum efficiency ultranano-crystalline diamond photocathode for photoinjector applications", *Appl. Phys. Lett.*, vol. 105, p. 123103, 2014. doi:10.1063/1.4896418
- [5] A. Doria, R. Bartolini, J. Feinstein, G.P. Gallerano, and R.H. Pantell, "Coherent emission and gain from a bunched electron beam", *IEEE J. Quantum Electron.*, vol. 29, p. 1428, 1993. doi:10.1109/3.236158
- [6] A. Gover, F.V. Hartemann, G.P. Le Sage, N.C. Luhmann, Jr, R.S. Zhang, and C. Pellegrini, "Time and Frequency Domain Analysis of Superradiant Coherent Synchrotron Radiation in a Waveguide Free-Electron Laser", *Phys. Rev. Lett.*, vol. 72, p. 1192, 1994. doi:10.1103/PhysRevLett.72.1192
- [7] V.L. Bratman, D.A. Jaroszynski, S.V. Samsonov, and A.V. Savilov, "Generation of ultra-short quasi-unipolar electromagnetic pulses from quasi-planar electron bunches", *Nucl. Instrum. Methods Phys. Res., Sect. A*, vol. 475, p. 436, 2001. doi:10.1016/S0168-9002(01)01633-3
- [8] A. Gover, "Superradiant and stimulated superradiant emission in prebunched electron beam radiators - part I: Formulation". *Phys. Rev. ST Accel. Beams*, vol. 8(3), p. 030701, 2005. doi:10.1103/PhysRevSTAB.8.030701
- [9] Y. Lurie and Y. Pinhasi, "Enhanced super-radiance from energy-modulated short electron bunch free-electron lasers", *Phys. Rev. ST Accel. Beams*, vol. 10, p. 080703, 2007. doi:10.1103/PhysRevSTAB.10.080703
- [10] N.S. Ginzburg, A.A. Golovanov, I.V. Zotova, A.M. Malkin, and V.P. Tarakanov, "Undulator superradiance effect and its applicability for the generation of multimewatt terahertz pulses", *JETP*, vol. 119(4), p. 632, 2014. doi:10.1134/S1063776114100021
- [11] N.S. Ginzburg, I.V. Zotova, I.V. Konoplev, A.S. Sergeev, V.G. Shpak, S.A. Shunailov, M.R. Ul'maskulov, and M.I. Yalandin, "Experimental observation of cyclotron superradiance", *JETP Letters*, vol. 63, No. 5, pp.331-335, 1996. doi:10.1134/1.567026
- [12] N.S. Ginzburg, I.V. Zotova, A.W. Cross, A.D.R. Phelps, M.I. Yalandin, and V.V. Rostov, "Generation, amplification, and nonlinear self-compression of powerful superradiance pulses", *IEEE Trans. on Plasma Science*, vol.41 (4), pp. 646-660, 2013. doi:10.1109/TPS.2013.2252369
- [13] A. Friedman, N. Balal, E. Dyunin, Yu. Lurie, E. Magori, V.L. Bratman, J. Rozenzweig, H. Lay To, A. Gover, "Configuration and Status of the Israeli THz Free Electron Laser", in *Proc. FEL'14*, Basel, Switzerland, Aug. 2014, paper TUP081, pp. 553-555.
- [14] Y. Lurie, A. Friedman, and Y. Pinhasi, "Single pass, THz spectral range free-electron laser driven by a photocathode hybrid rf linear accelerator", *Phys. Rev. ST Accel. Beams*, vol. 18, p. 070701, 2015. doi:10.1103/PhysRevSTAB.18.070701
- [15] N. Balal, V.L. Bratman, and E. Magori, "Efficient electron sources of coherent spontaneous radiation with combined

helical and uniform magnetic fields”, in *Proc. FEL’15*, Daejeon, Korea, Aug. 2015, paper MOP009, pp. 43-45.

[16] N. Balal, I.V. Bandurkin, V.L. Bratman, E. Magory, and A.V. Savilov, “Negative-mass mitigation of Coulomb repulsion for terahertz undulator radiation of electron bunches”, *Appl. Phys. Lett.*, vol. 107, p. 163505, 2015.
doi:10.1063/1.4934495

[17] N. Balal, I.V. Bandurkin, V.L. Bratman, and A.E. Fedotov, “Helical undulator based on partial redistribution of uniform magnetic field”, *Phys. Rev. Accel. Beams*, vol. 20, p. 122401, 2017.
doi:10.1103/PhysRevAccelBeams.20.122401

[18] Y. Lurie, V.L. Bratman, and A.V. Savilov, “Energy enhancement and spectrum narrowing in terahertz electron sources due to negative mass instability”, *Phys. Rev. Accel. Beams*, vol.19, p. 050704, 2016.
doi:10.1103/PhysRevAccelBeams.19.050704

[19] N. Ohigashi, Y. Tsunawaki, M. Fujita, K. Imasaki, K. Mima, and S. Nakai, “Construction of compact fem using solenoid-induced helical wiggler”, *Nucl. Instrum. Methods Phys. Res., Sect. A*, vol. 507, p. 250, 2003.
doi:10.1016/B978-0-444-51417-2.50063-8

[20] R.H. Jackson, M.E. Read, T. Bui, and R.L. Ives, “Performance of Asymmetric Immersed Pole Undulators”, Technical Report 2012, published January 30, 2018.

[21] R.H. Jackson, M.E. Read, T. Bui, and R.L. Ives, “Asymmetric Immersed Pole Undulators”, *IEEE Int. Conference on Plasma Science*, July 2012, Edinburgh, UK.

[22] R.H. Jackson, M.E. Read, and R.L. Ives, “Asymmetric Immersed Pole Undulators for High-Frequency Sources”, *Int. Vacuum Electronics Conference 2013*, 21-23 May 2013, Paris, France.

[23] A. Ho, R. Pantell, J. Feinstein, and B. Tice, “A novel wiggler design for use in a high-efficiency free-electron laser”, *Nucl. Instrum. Methods Phys. Res. Sect. A*, vol. 296, p. 631, 1990.
doi:10.1016/0168-9002(90)91279-K

[24] A.A. Varfolomeev, A.S. Khlebnikov, S.N. Ivanchenkov, N.S. Osmanov, and A.H. Hairtdinov, “Strong magnetic field microundulator with permanent magnets inserted into a solenoid”, *Nucl. Instrum. Methods Phys. Res., Sect. A*, vol. 331, p. 745, 1993.
doi:10.1016/0168-9002(93)90149-C

[25] V.L. Bratman, A.V. Savilov, V.A. Papadichev *et al.*, “FEM with pulsed short-period undulator and low-energy electron beam”, in *Proceedings of 20th International Free Electron Laser Conference*, ed. by G.R. Neil and S.V. Benson (Williamsburg, Virginia, 1998), pp. II–15.

PULSE ENERGY MEASUREMENT AT THE SXFEL

Zipeng Liu ^{1,2}, Luyang Yu ¹, Chao Feng ¹, Haixiao Deng ^{*1}, Bo Liu ^{*1}, Dong Wang ¹

¹Shanghai Institute of Applied Physics, Chinese Academy of Sciences, Shanghai, China

²Chinese Academy of Sciences, Beijing, China

Abstract

The test facility will generate 8.8 nm FEL radiation by using an 840 MeV electron linac passing through the two-stage cascaded HG HG or EEHG-HG HG (high-gain harmonic generation, echo-enabled harmonic generation) scheme. Several methods have been developed to measure the power of pulse. The responsivity of silicon photodiode having no loss in the entrance window. Silicon photodiode reach saturates at the SXFEL. In this work, we simulated the attenuator transmittance for different thicknesses. We also show the preparations of the experiment results at the SXFEL.

INTRODUCTION

The Shanghai soft X-ray Free-Electron Laser Facility (SXFEL) is a phased project, including the SXFEL test facility (SXFEL-TF), and the SXFEL user facility (SXFEL-UF). SXFEL-TF is mainly used for the study of the external seeding FEL operation mode, including High-gain Harmonic Generation (HG HG) and Echo-enabled Harmonic Generation (EEHG) schemes. And various cascade combinations of HG HG and EEHG. The upgrading of the test facility to the water window user facility, SXFEL-UF, has been undertaken by the collaboration between the Shanghai Institute of Applied Physics (SINAP) and Shanghai-Tech University. Shanghai-Tech University is in charge of developing science cases and experimental end-stations, and SINAP is responsible for the remaining parts of facility development, including upgrading the linac energy to 1.5 GeV, building a second undulator line, facility integration, and constructing the utility and SXFEL-UF buildings. The civil construction was started in November 2016.

The SXFEL-TF

The SXFEL-TF is composed of an 840 MeV electron linac and a two-stage cascaded seeding scheme-based undulator system. The initial proposal of the SXFEL-TF project in 2016 was to test the cascaded HG HG scheme [1]. In the following years, it was gradually optimized and more contents of the EEHG were added to the project when the construction started in 2014. A new cascaded EEHG-HG HG operation scheme was incorporated into the SXFEL-TF to further improve the ultra-high harmonic up-conversion efficiency.

The main parameters of SXFEL-TF are shown in Table 1. The first stage uses a seeded laser with a wavelength of 265 nm. The first stage output radiation wavelength is about 44 nm. An 8.8 nm radiation pulse is generated in the second stage based on the HG HG scheme.

Table 1: The Main Parameters of SXFEL-TF [2]

Undulator	Stage 1	Stage 2
Seed laser wavelength	265 nm	*
FEL output wavelength	44 nm	8.8 nm
Modulator undulator period	80 mm	40 mm
Modulator undulator K value	5.81	2.22
Radiator undulator period	40 mm	22.5 mm
Radiator undulator K value	2.22	1.43

Pin Photodiode

The principle of a silicon diode is similar to that of an ionization chamber, absorption of a photon in a silicon crystal creates separations of charge, which are called electron-hole pairs and require an average energy, ϵ , of 3.66 ± 0.03 eV [3,4] Silicon photodiodes (AXUV series) are being used as absolute devices for 50 eV to 1500 eV photons because of their wellknown device parameters, mainly the Internal Quantum Efficiency (IQE). The IQE is 100% from 270 to 800 nm and higher at shorter wavelengths due to the creation of multiple electron-hole pairs by a single high energy photon [5]. IQE is defined as the percentage of internal charge generated in the diode per incident photon. Figure 1 shows the cross-section of the photodiode investigated. The diode is not suitable for high pulse energy measurement at the SXFEL.

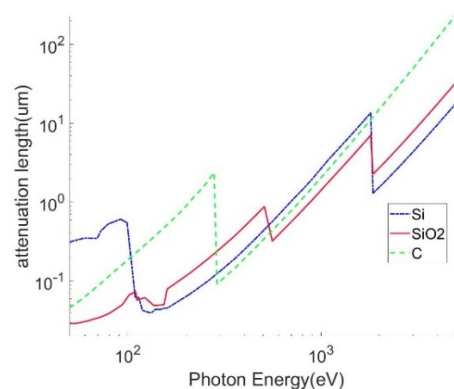


Figure 1: Photodiode absorption attenuation lengths used to calculate soft x-ray responsivity from the model and parameters described in the text. The sources of the data are references [6-8].

Attenuators

A solution to this problem would be to place an absorber in the beam to reduce the flux to a manageable value. Using

REFERENCES

- [1] Z. T. Zhao, "Shanghai Soft X-Ray Free Electron Laser Test Facility", in *Proc. 2nd Int. Particle Accelerator Conf. (IPAC'11)*, San Sebastian, Spain, Sep. 2011, paper THPC053, pp. 3011-3013.
- [2] Zhao, Z.T.; Wang, D.; Yin, L.X.; Gu, Q.; FangG.P.; Liu, B. "The current status of the SXFEL project", AAPPBull. 2016, 26, 12–24. doi:10.3390/app7060607
- [3] F. Scholze, H. Henneken, P. Kuschnerus, H. Rabus, M. Richter, G. Ulm, "Determination of the electron hole pair creation energy for semiconductors from the spectral responsivity of photodiodes", *Nuclear Instruments and Methods in Physics Research A* 439 (2000); 208-215. doi:10.1016/S0168-9002(99)00937-7
- [4] Alig, R. C. and S. Bloom (1975). "Electron-Hole-Pair Creation Energies in Semiconductors." *Physical Review Letters* 35(22): 1522-1525. doi:10.1103/PhysRevLett.35.1522
- [5] F. Scholze, H. Rabus and G. Ulm, "Mean Energy Required to Produce an Electron-Hole Pair in Silicon for Photons of Energies Between 50 and 1500 eV", *Journal of Applied Physics* 84(5), 2926-2939 (1998). doi:10.1063/1.368398
- [6] B. L. Henke, E. M. Gullikson and J. C. Davis, "X-Ray Interactions: Photon Absorption, Scattering, Transmission, and Reflection at $E = 50\text{-}30000$ eV, $Z = 1\text{-}92$," *Atomic Data and Nucl. Data Tables* 54(2), 181 (1993). doi:10.1006/adnd.1993.1013
- [7] CXRO, "X-Ray Interactions With Matter Web Page," http://henke.lbl.gov/optical_constants/.
- [8] J. Rife and J. Osantowski, "Extreme Ultraviolet Optical Properties of Two SiO₂ Based Low-Expansion Materials," *J. Opt. Soc. Am.* 70, 1513 (1980). doi:10.1364/JOSA.70.001513
- [9] Powell, F. R., P. W. Vedder, J. F. Lindblom, and S. F. Powell (1990), "Thin film filter performance for extreme ultraviolet and X-ray applications," *Opt.Eng.*, 26, 614. doi:10.1117/12.55641

SPARE UNDULATOR PRODUCTION FOR PAL-XFEL HX1 BEAMLINE

Jang-Hui Han*, Sojeong Lee, Young Gyu Jung, Dong-Eon Kim,
Pohang Accelerator Laboratory, Pohang, Korea

Abstract

In the PAL-XFEL hard X-ray beamline, 20 undulator segments with a 26 mm period and a 5 m length are installed and operated for XFEL user service. One spare undulator was manufactured in December 2018. The magnetic measurements and tuning was carried out recently. We report the magnet block sorting, the magnetic measurements and the tuning results.

INTRODUCTION

Pohang Accelerator Laboratory X-ray Free Electron Laser (PAL-XFEL) is operational for users since 2017 [1, 2]. PAL-XFEL has two undulator beamlines, one hard X-ray and one soft X-ray. The hard X-ray undulator line is placed at the end of the main linac, where an electron beam is accelerated up to 10 GeV. The soft X-ray line is branched at the 3 GeV point of the main linac and further accelerated up to 3.15 GeV.

The hard X-ray beamline has twenty undulator segments. The undulator is a hybrid type with NdFeB magnets and Vanadium Permendur poles. The period is 26 mm and the segment length is 5 m. The magnet gap is 8.3 mm. At the minimum gap, the effective flux density is 0.812 T and the deflecting parameter K is 1.973. The undulators for the soft X-ray line are similar the hard X-ray ones except for the period, 35 mm [3].

In 2018, a new hard X-ray undulator was built by refurbishing the mechanical frame and control system of a prototype undulator. The prototype undulator was originally constructed in the very early stage of the PAL-XFEL project. The undulator period was different from the present hard or soft X-ray undulators. Even though the magnet structure could not be re-used, the frame was reused for this spare one. During 2020 summer maintenance, this new undulator will be installed upstream of the first undulator segment of the hard X-ray beamline.

MAGNET BLOCK SORTING

The magnetic field through an undulator segment should be as uniform as a tens thousandth to make the phase error within a few degrees. Field errors of the magnet blocks for this undulator production are in one percent range (Fig. 1).

The permanent magnet block has a “hot and cold side effect”. This effect is caused by the magnet block manufacturing process. The magnetization vector of a magnet block has not only M_z component, but also minor M_x and M_y components [4]. Due to the imperfection of magnetization, there is a difference in the B_z field strength between top and bottom sides. The information of the measured magnetic field and moment of the magnet blocks were supplied by

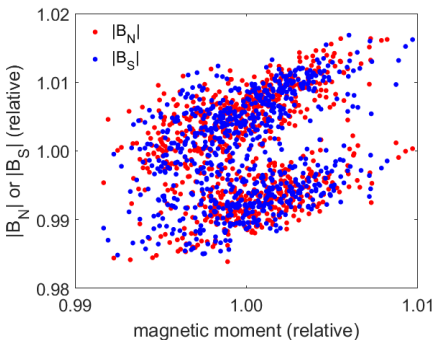


Figure 1: Magnetic field distribution of magnet blocks to magnetic moments.

the vendor. The field of the blocks was measured at a few centimeters from the face.

Figure 2 shows the possible pole field when magnet blocks are distributed randomly. The dotted lines at the middle show the median values of $|B_N|$ and $|B_S|$. The pole fields are placed within about 1%, however a significant pole tuning should be carried out to satisfy the phase error requirement.

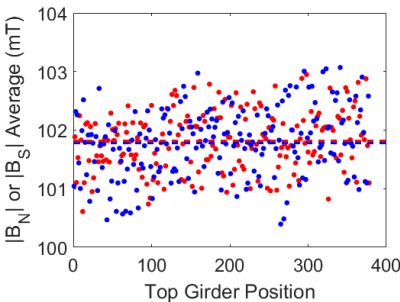


Figure 2: Pole field distribution for randomly installed magnet blocks. The horizontal axis is the pole number in the top magnet structure.

To achieve a field uniformity through an undulator segment, the magnet blocks were sorted and arranged to minimize the field difference among poles as shown in Fig. 3. First, all the magnet blocks were ordered by the $|B_N|$ and $|B_S|$. Then, the magnet block with the median value of $|B_N|$ (or $|B_S|$) is selected to be placed at the first place where an end of the top or bottom magnet structure. In Fig. 3, the block is M1 and the field is $B_{1Z}(s)$. Even though the magnetic field to the end direction (left direction here) is close to the median value, the field of the other side (right direction) of the magnet block ($B_{1Z}(N)$ in Fig. 3) can be far from the median value. After placing a pole (P1), a pair magnet block (M3) is chosen so that the field at the pole is averaged by the

* janghui_han@postech.ac.kr

field ($B_{3z}(N)$) of the block. Such procedures are repeated till the other end of the magnet structure.

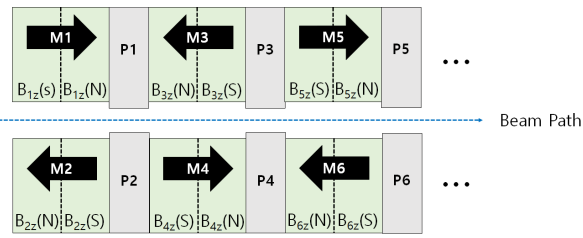


Figure 3: Magnet block pairing.

After pairing the magnet blocks, the pole field was calculated again as shown in Fig. 4. By simple pairing, the pole field can become uniform. Note that enough spare magnet blocks are necessary for this pairing procedure. Field distribution within a magnet block are ignored in this model. Nevertheless, this simple magnet pairing would be a good start of pole tuning for a new undulator segment.

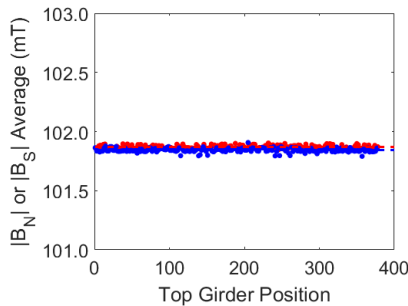


Figure 4: Calculated pole field distribution for magnet blocks sorted by magnetic field pairing.

FIRST MEASUREMENTS

The assembled undulator was measured with a Hall probe. Three FW Bell GH-700 Hall sensors were used for the 3D field measurement. The minimum gap of the magnet structure is 8.3 mm and the tuning gap is 9.5 mm. The vertical field centers of the poles were measured at the 9.5 mm tuning gap as shown in Fig. 5. The colors in the figure displays different magnet structures. The deviation is within $\pm 30 \mu\text{m}$, but there is a drift between magnet structures.

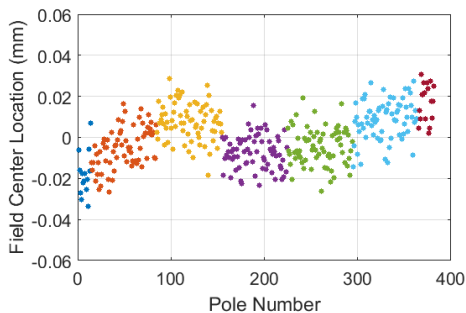


Figure 5: Vertical pole field centers before tuning.

The half gap, the height to be corrected for both top and bottom poles to get an ideal field profile, is plotted in Fig. 6. The four poles near the end are not shown in the figure because the deviations are larger than 0.2 mm. The pole heights in the figure show a drift with linear and quadratic components through the magnet structures.

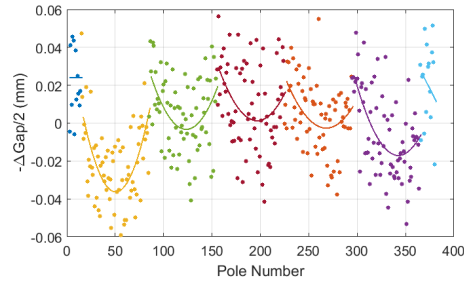


Figure 6: Pole height deviation from ideal position at 9.5 mm gap before tuning. Quadratic fits are applied for each magnet structure.

From the measurements in Fig. 6, a possible magnet structure deformation was estimated as in Fig. 7. The 0.9 m long magnet structures (M1 ~ M5) are fixed to the top or bottom girders. This deformation is larger for narrower gaps.

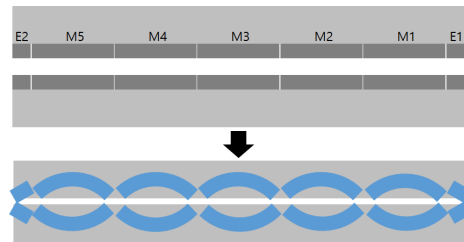


Figure 7: Magnet structure deformation estimated from field measurement.

The phase error distribution before pole tuning is shown in Fig. 8. The short range deviation is small, but there is a long range drift over 80 degree. The rms phase error is 21° .

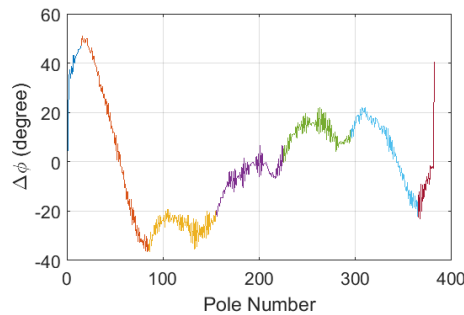


Figure 8: Phase error measured at 9.5 mm gap before tuning.

The poles are assembled to the magnet structure with an accuracy of a few micrometer to the upper face of the structure. The face was carefully machine to have a few tens micrometer flatness, but such a surface roughness can already affect the phase error.

POLE TUNING

The height and roll angle of a pole can be adjusted with four screws independently. The pole tuning was carried out with six times iteration. The vertical pole field center deviation measured at the 9.5 mm gap is shown in Fig. 9.

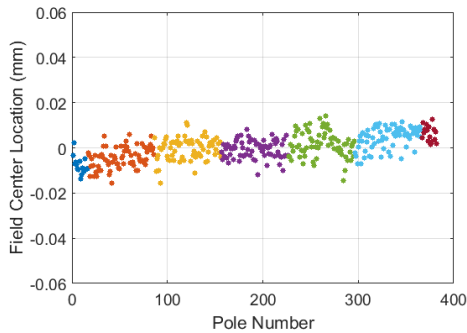


Figure 9: Vertical pole field centers after tuning.

The large long range drift as well as the short range deviation of the pole heights was corrected (Fig. 10). The standard deviation of the pole heights is $2.3 \mu\text{m}$

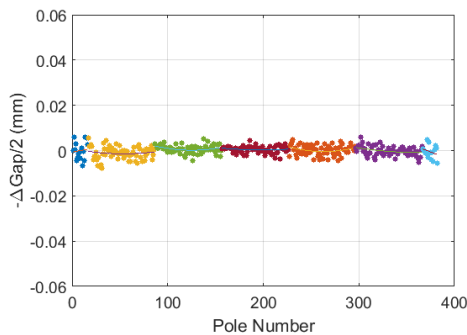


Figure 10: Pole height deviation from ideal position at 9.5 mm gap after tuning.

The phase error distribution before pole tuning is shown in Fig. 11. The rms phase error is 1.78° . The phase errors for the operational gaps were measured and plotted in Fig. 12.

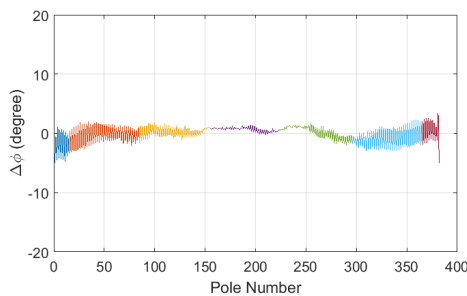


Figure 11: Phase error measured at 9.5 mm gap after tuning.

The black dots are measurements without background field compensation. The red dots are measurements in the magnetic environment where the undulator is to be installed (HX104). The background field in the location in the PAL-XFEL hard X-ray tunnel were measured with a

fluxmeter. The same field was configured with two sets of large Helmholtz coils in the measurement lab. The measured undulator deflection parameters, K , for the operational gaps are shown in Fig. 13.

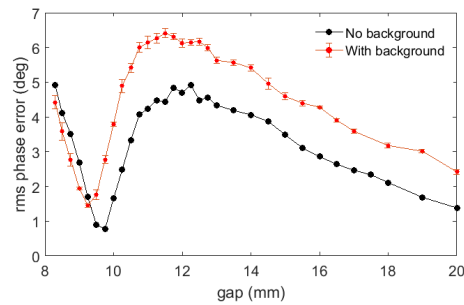


Figure 12: Phase error for various gaps after tuning.

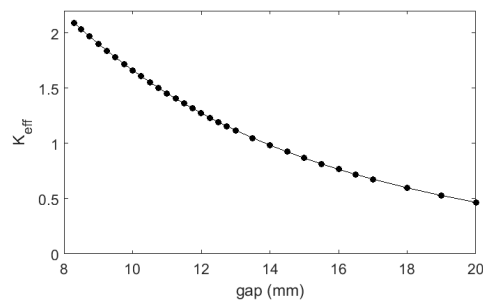


Figure 13: K parameters measured for various gaps.

The entrance and exit kicks for horizontal (x) and vertical (z) directions were analyzed from the measurements and plotted in Fig. 14. The requirement is within 1.5 Gm.

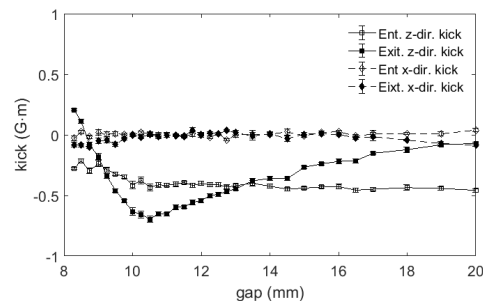


Figure 14: Measured end kicks.

SUMMARY

One additional undulator for the PAL-XFEL hard X-ray beamline was refurbished by using the prototype undulator frame. A new magnet block sorting was tried. The phase error seems mainly come from the magnet structure deformation. The surface roughness of the magnet structure and the magnet sorting may have a minor contribution to the phase error.

REFERENCES

- [1] I. S. Ko *et al.*, “Construction and Commissioning of PAL-XFEL Facility”, *Appl. Sci.* vol. 7, no. 5, p. 479, 2017, DOI: 10.3390/app7050479.
- [2] H.-S. Kang *et al.*, “Hard X-ray free-electron laser with femtosecond-scale timing jitter”, *Nature Photonics* vol. 11, p. 708, 2017, DOI:10.1038/s41566-017-0029-8.
- [3] D. E. Kim *et al.*, “Undulator commissioning experience at PAL-XFEL”, in *Proc. IPAC’17*, Copenhagen, Denmark, May 2017, paper TUPAB087, pp. 1520–1522, DOI:10.18429/JACoW-IPAC2017-TUPAB087.
- [4] F.-J. Börgermann, “Improvements In Production of Permanent Magnets and Pole-Pieces for Undulators”, in *Proc. IPAC’17*, Copenhagen, Denmark, May 2017, paper TUPAB041, pp. 1415–1417, DOI:10.18429/JACoW-IPAC2017-TUPAB041.

RADIATION DAMAGE MONITORING AT PAL-XFEL

Sojeong Lee*, Jang-Hui Han, YoungGyu Jung, Dong Eon Kim and Geonyeong Mun
Pohang Accelerator Laboratory, Pohang, Korea

Abstract

Pohang Accelerator Laboratory X-ray Free Electron Laser (PAL-XFEL) has two undulator beamlines, one hard and one soft X-ray beamlines. These two undulator beamlines are in operation since 2017. To maintain the FEL radiation property, the B-field properties of the PAL-XFEL undulators need to be kept at certain level. Under the beam operation condition up to 10 GeV, the accumulated radiation can affect the permanent magnet properties of the undulators. However, the radiation damage of permanent magnet can be different by the operation environment and the geometry of the undulator. Accumulated radiation sensors and a miniature undulator with a few periods are installed in the PAL-XFEL hard X-ray undulator line to monitor the undulator radiation damage. In this proceeding, the radiation monitoring activities and the recent measurement results are introduced.

PAL-XFEL UNDULATOR SYSTEM

Pohang Accelerator Laboratory X-ray Free Electron Laser (PAL-XFEL) has run user beamtime since 2017. Two undulator beamlines, one hard X-ray and other soft X-ray beamlines provide FEL by using up to 10 GeV for hard X-ray, and 3.15 GeV electron beam for soft X-ray beamline. The maximum repetition rate of electron beams is 60 Hz [1, 2]. The undulators are under radiation environment for about 250 days per year except for shutdown.

The hard X-ray beamline consists of twenty undulator segments, and one additional undulator segment. One additional undulator segment will be installed in the summer maintenance of the next year. For the soft X-ray, beamline consists of the seven undulator segments. The hard and soft X-ray undulator segment have the same magnetic length, 5 m. The undulator period is 26 mm for hard X-ray and 35 mm for soft X-ray beamline undulator. The undulator is hybrid type based on NdFeB magnets and vanadium perme-mur poles [3]. The Vaccumschmelze VAVODYM 776AP, which has $H_{cJ,min} = 1670$ kA/m, was chosen as NdFeB magnets [4].

To maintain the magnetic field strength and the quality of the XFEL facility, the radiation accumulation of undulator needs to be monitored and controlled. The demagnetization of NdFeB base magnets occurs for a kGy level of accumulated radiation dose. The demagnetization of the magnets can lead a undulator kick and K-value change [5, 6].

UNDULATOR RADIATION MONITORING

PAL-XFEL has two different types of radiation damage monitor for the undulator system: on-line dosimeter systems

based on the radFET sensor and a miniature hard X-ray undulator.

RADFET Sensors

As an on-line dosimeter system, the DOSFET-L02 systems from Elettra-Sincrotron Trieste were adopted (Fig. 1). DOSFET-L02 system can monitor the accumulated radiation dose by using the radFET sensors. This system measures the output voltage of the radFET sensors, and accumulated dose level can be estimated using the voltage difference of sensors [7].



Figure 1: DOSFET-L02 controller and sensor mount module from Elettra-Sincrotron Trieste.

After the commissioning of PAL-XFEL, the twelve radFET sensors were installed into the six undulator segments in November 2017, as shown in Fig. 2. Before the radFET sensor installation, the OSLD sensors were installed for every undulator segments from March 2017 to July 2017. Based on the OSLD reading result, the radFET sensor installation points were selected, where the measured dose is high. For the hard X-ray undulator beamline, the first two (HXU105 and HXU106) 11th (HXU116), and 12th (HXU117) undulator segments were selected. For the soft X-ray beamline, the 2nd and 3rd undulator segments (SXU407 and SXU408) were selected. The two radFET sensors were installed into each undulator's upstream and downstream upper magnet structure. The TY1003 radFET sensors from Tyndall were installed for these six undulators segments [8].

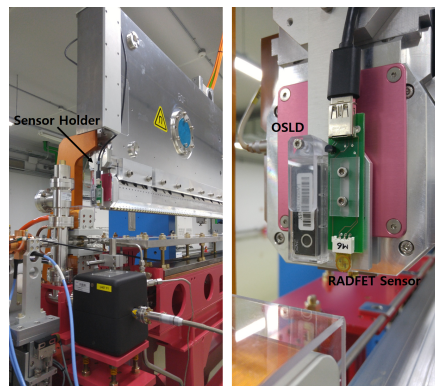


Figure 2: Installation of radFET sensors into undulator. The two sensors were installed into upstream and downstream face of undulator magnet structure [8].

* sojung8681@postech.ac.kr

In November 2018, the additional twelve radFET sensors were installed into other six undulator segments. For this installation, other radFET sensors were used, RFT300-CC10G1 from REM Oxford Ltd. This sensor is known as a good fade aspect, which displays an artificial loss of accumulated radiation. The accumulated radiation dose for total eight of hard X-ray and four of soft X-ray beamline undulator segments are being monitored from 2019 beam time.

Radiation Damage Test Undulator

To estimate the relationship between the accumulated radiation dose and the demagnetization of NdFeB magnets under the hard X-ray beamline environment, the radiation damage test undulator (RTU) was fabricated and installed in winter maintenance 2018. The demagnetization of permanent magnet depends on the electron beam condition, and the undulator magnetic gap. To measure the effect of accumulated radiation dose of electron beams up to 10 GeV, the RTU was fabricated by using the same hard X-ray undulator's magnets and poles. Figure 3 shows the magnet structure of the RTU. The RTU has a 121.6 mm magnet structure length and 12 mm fixed gap. This RTU was designed for easy installation and de-installation for a B-field measurement during every winter maintenance period.

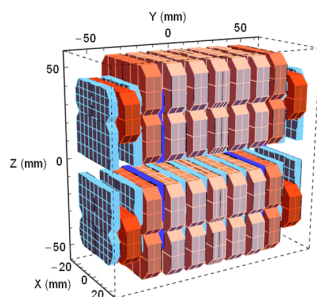


Figure 3: The magnet structure model of RTU. It consists of three period and end magnet sequence.

As shown in Fig. 4, the RTU was installed at the intersection upstream of U104, before the first undulator, HXU105. This U104 space is preserved as drift space now. One additional undulator will be installed at this position in 2020 summer maintenance. Two radFET sensors at the top and bottom positions of magnet structure's upstream face of RTU. Before the installation of the RTU, the B-field was measured by using the Hall probe. Figure 5 shows the measured field. The B-field measurement of the RTU is planned during every winter maintenance to monitor the demagnetization of the magnets. This result together with accumulated radiation dose level will be used as a guide of hard X-ray undulator's re-tuning.

RADIATION DAMAGE MONITORING RESULTS

Figure 6 shows all the radFET sensors readings on 25th July 2019. The maximum dose level was measured at the



Figure 4: RTU in field measurement bench (left) and installation in front of hard X-ray undulator beamline (right).

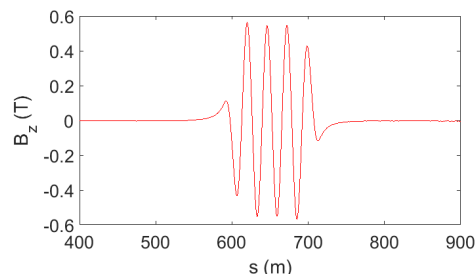


Figure 5: RTU B-field measurement result before installation.

first hard X-ray undulator, HXU105. Considering the exposure day of sensor, the upstream part of HXU105 has been exposed to radiation dose ~ 0.71 Gy/Day in average, and this value is higher than 1.85 times comparing with the second highest accumulated dose undulator segment, HXU106. The total accumulated dose level of HXU105 also has a big difference between the upstream and downstream, as much as ~ 410 Gy.

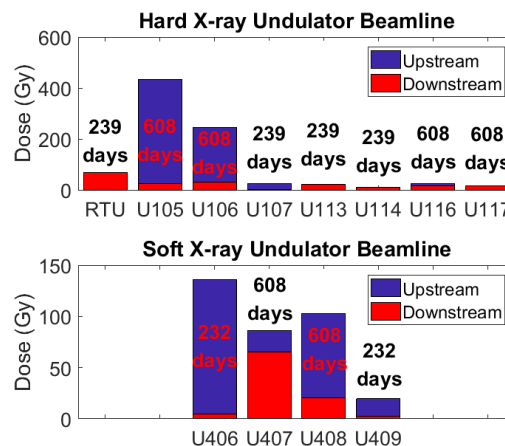


Figure 6: Accumulated radiation dose level of PAL-XFEL undulator segments on July 2019. The undulators with marked 608 days use a Tyndall sensor and other one is REM Oxford Ltd Sensor.

According to these measurement results, the radiation event usually occurs at the front of the undulator beamlines.

The first one or two undulator segments act as radiation shield, protecting the later undulator segments. Also, most radiation dose is absorbed by the upstream part of the magnet structure. From these results, the upstream part of magnets has a higher possibility of demagnetization. However, unlike other cases, the second segment of the soft X-ray beamline has similar dose level between the up and downstream. This case, it looks like that radiation event occurs at the intersection of the undulator segment.

Figure 7 shows the HXU105 monitoring results from November 2017. The dose level is being monitored with Tyndall sensors. Each sensor unit consists of two sub radFET sensors, the one sensor unit gives two reading values, D1 and D2. As shown in Fig. 7, most of HXU105 radiation dose level sharply increased within an hours or day. However, after the sharp increase of dose level, the fade behavior of the radFET sensor was also large. The fade of a sensor decreases artificially actual accumulated dose level. The sensor's fade behavior was corrected so that the reading was kept constant during the voltage drop. The corrected reading is shown in the bottom graph of Fig. 7. Although, the sub sensors reading values are different, the estimated total dose level of HXU105 upstream part is ~ 900 Gy. However, this estimated value does not reflect the accumulated dose level during the PAL-XFEL commissioning period. Usually, it is known as a larger dose level is accumulated during commissioning period than normal operation period. Considering this, the total accumulated dose level of HXU105 upstream part could be estimated over the kGy level, which can lead a demagnetization. On the other hand, there's no clear evidence of demagnetization for HXU105, which can be figured out from the change of the beam trajectory kick angle of the undulator.

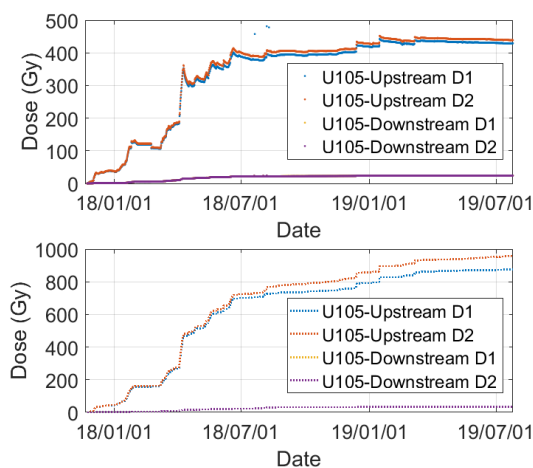


Figure 7: HXU105 radFET sensors reading from November 2017 to July 2019. Top graph shows a raw data from sensor and bottom graph shows a estimated actual accumulated radiation dose level by correcting the loss of sensor reading value.

To protect the HXU105 upper part, 100 mm thickness lead blocks were installed in front of HXU105 in April 2018. After the installation, the amount of stiff incremental of dose level was decreased, however, the RTU, installed in front of HXU105 in November 2018 reading does not shows a sharp incremental behavior. The radiation dose accumulated to the RTU up to now is about 80 Gy. From those measurement results, it looks like that the operational condition was changed to reduce the accumulated dose level.

SUMMARY

For the radiation damage monitoring of the PAL-XFEL undulators, the radFET sensors and the RTU were installed. The radFET sensors are monitoring twelve undulator segments and the monitoring result shows that the first hard X-ray undulator segments has a maximum accumulated radiation dose, ~ 1 kGy. Also, the sensor reading shows that the radiation dose shielded by upstream undulator magnet structures. Based on the measurement result, the lead block was installed to protect the HXU105 upstream magnet structure. The RTU was installed in the hard X-ray undulator hall November 2018. It will be used to study the relationship between the demagnetization of NdFeB magnets under the PAL-XFEL operation condition.

REFERENCES

- [1] I. S. Ko *et al.*, "Construction and Commissioning of PALXFEL Facility", *Appl. Sci.* vol. 7, no. 5, p. 479, 2017, DOI:10.3390/app7050479.
- [2] H.-S. Kang *et al.*, "Hard X-ray free-electron laser with femtosecond-scale timing jitter", *Nature Photonics* vol. 11, p. 708, 2017, doi:10.1038/s41566-017-0029-8.
- [3] D. E. Kim *et al.*, "Undulator commissioning experience at PALXFEL", in *Proc. IPAC'17*, Copenhagen, Denmark, May 2017, paper TUPAB087, pp. 1520–1522, doi:10.18429/JACoW-IPAC2017-TUPAB087.
- [4] Vaccumschmelze, NdFeB magnets VACODYM series data sheet, <https://vacuumschmelze.com/Products/Permanent-Magnets/NdFeB-Magnets---VACODYM>.
- [5] T. Bizen *et al.*, "Radiation-induced magnetization reversal causing a large flux loss in undaultor permanent magnets", *Scientific Reports* vol. 6, p. 37937, 2016, DOI:10.1038/srep37937.
- [6] F. Wolff-Fabris *et al.*, "Status of radiation damage on the European XFEL undulator systems", in *Proc. IPAC'18*, Vancouver, Canada, April 2018, paper WEYGBD2, pp. 1776–1779, doi:10.18429/JACoW-IPAC2018-WEYGBD2.
- [7] DOSFET-L02 reader for MOSFET dosimeters operating instructions, Elettra - Sincrotrone Trieste S.C.p.A., Basovizza, 2014.
- [8] J.-H. Han *et al.*, "RADFET installation at PAL-XFEL undulator", in *Proc. IPAC'18*, Vancouver, Canada, April 2018, paper THPMK032, pp.4366–4368, doi:10.18429/JACoW-IPAC2018-THPMK032.

VARIABLE-PERIOD VARIABLE-POLE NUMBER HYBRID UNDULATOR DESIGN FOR NOVOSIBIRSK THz FEL

I. V. Davidyuk[†], O. A. Shevchenko, V. G. Tcheskidov, N. A. Vinokurov
Budker INP SB RAS, Novosibirsk, Russia

Abstract

The undulator developed for the first FEL of Novosibirsk FEL facility employs variable-period structure based on the hybrid undulator scheme with poles splinted into halves. The design was adapted to deliver optimal performance, estimations were made based on results of three-dimensional field simulations. According to the modeling results, the undulator will not only widen significantly the first FEL tuning range moving the long-wavelength border of the first harmonic from 200 μm to 450 μm but also provide wider aperture and increase efficiency at shorter wavelengths.

INTRODUCTION

Undulators are magnetic devices designed to provide intensive interaction of a monochromatic electromagnetic wave with a relativistic electron beam (see [1]). They are used in both spontaneous and stimulated emission modes. FELs are based on the second one but in both cases, it needs to provide the ability to tune the wavelength of the radiation. The undulator radiation properties depend on the parameters of an electron beam and field distribution in an undulator, but mainly first radiation harmonic properties are determined by following three parameters: electron energy, undulator period, and undulator field amplitude. One way to tune the wavelength is to vary the electron energy. This approach was implemented successfully [2,3] in the first hard x-ray FEL LCLS. Field amplitude variation is the most common way of wavelength tuning. In permanent magnet undulators, it is frequently realized due to change in the gap between the upper and lower halves of undulator [4]. Alternatively, an undulator period may be varied to shift radiation wavelength, some advantages of this approach in comparison with other techniques of radiation tuning are described in [5], where a bellows-like scheme was proposed. A design of electromagnetic variable-period undulators for storage rings was developed in [6]. Recently, a Halbach structure based on an arrangement of rotating cylindrical permanent magnets was proposed, the period of such an undulator may be varied by tuning magnetization rotation angle between adjacent cylinders[7].

A concept of hybrid undulator with freely moving poles was proposed in [8], and a similar helical device was constructed and commissioned at KAERI [9]. Following this concept, a planar undulator with a variable period and a variable pole number was designed for the second FEL of the Novosibirsk FEL facility [10–13]. Results of modeling in [14] show that the new undulator will widen the radiation wavelength tuning range and the gain variation will be

smaller within this range in comparison with existing electromagnetic (EM) undulator and hypothetical optimal variable gap undulator. A prototype of this device has been manufactured; details of tests of its properties can be found in [15].

In this paper authors describe a new permanent magnet variable-period undulator (VPU) that was designed to upgrade the first (terahertz) FEL of the Novosibirsk FEL facility. In order to shift the long-wave limit of the tuning range from 200 μm to 400 μm and beyond, the aperture of the vacuum chamber in the new undulator will be increased, which will reduce the diffraction losses at the ends of the insertion device section. The enlarged gap undulator will be installed on the first track of the energy recovery linac. It will replace the existing two 4-meter long undulators and phase shifter between them. Both old undulators are planar electromagnetic devices with a period of 12 cm, a gap of 8 cm, and the undulator deflecting parameter K varying from zero to 1.1, see Table 1.

Table 1: Basic Undulator Parameters

Parameter	Former EM undulators	VPU
Period, cm	12	10 – 16
Gap (Inner Diameter), cm	8	14
Number of Periods	2 * 32	50 – 80
Radiation Wavelength, μm	90 – 240	82 – 450
Deflection Parameter	0 – 1.1	0.45 – 1.9
Full Length, cm	800	860

DESIGN

Focusing of electron beam due to the undulator field is strong at low electron beam energies (10.5 to 13.3 MeV for the first stage FEL). A concave pole is a common solution to redistribute focusing between the transverse directions. Moreover, it weakens the field dependence on the distance from the undulator axis, which is useful in the case of large aperture. Both the magnet and pole profiles will be segments enveloping the vacuum pipe with different outer diameters; the dimensions are shown in Figure 1.

[†] i.v.davidyuk@inp.nsk.su

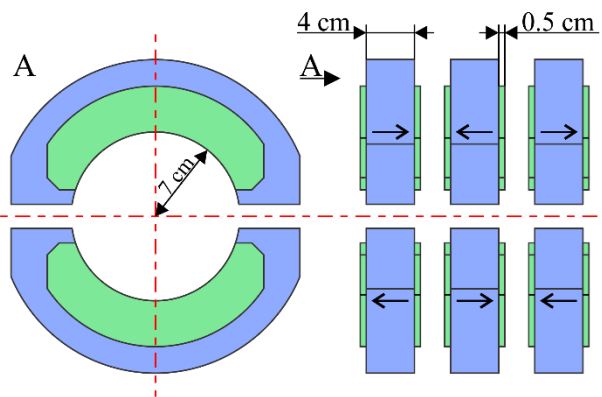


Figure 1: Magnetic design of the undulator. Blue parts are permanent magnets (magnetization is shown with arrows), green parts are iron poles.

At the minimum period $\lambda_{u\min}$, the undulator is a conventional hybrid device with magnets made of NdFeB and poles of low carbon steel. All poles are split into halves, and so the undulator is an array of detachable blocks. Each undulator block has a length of half a minimal undulator period and consists of a magnet embraced by the pole halves and the aluminum frame, as shown in Figure 2. The upper and lower blocks are connected, distances between each pair of upper and lower blocks may be adjusted with help of screws for fine filed tuning (instead of shimming); the whole structure is placed on a carriage that can move freely along undulator axis on two guide rails. Adjacent magnets in a row always have alternating longitudinal magnetizations, and hence they experience repulsion from each other. Due to the strong repulsion force and the low-friction slide guides, the undulator period can be changed by shifting the end blocks, which alters the full undulator length. There will be mechanical pushers that can be operated from the control room. A similar system was described and depicted in [14].

Field adjustment mechanism

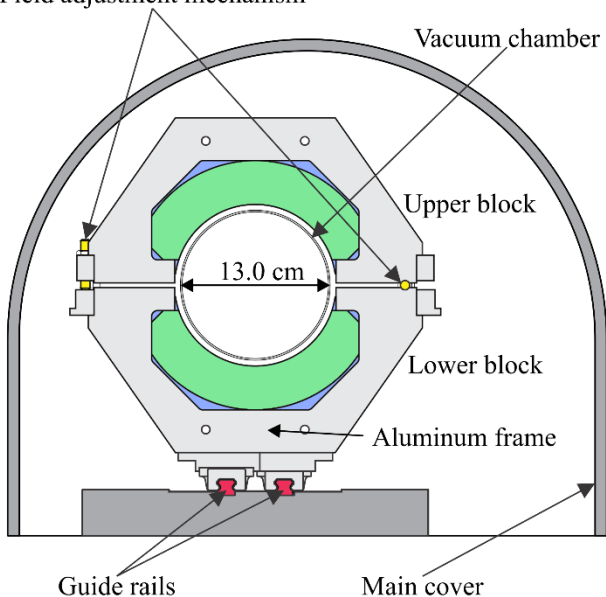


Figure 2: Front view of the undulator.

The undulator will be equipped with a supplementary external device intended for insertion of additional blocks into the undulator. This device slides the two fringe undulator blocks apart so that a period can be placed in the created space. If the desired undulator period is less than the maximum one, it will be possible to add some periods to use the entire space between the pushers.

Beamline Upgrade

The rest of the beamline will also be upgraded. New quadrupole lenses with an enlarged aperture will be installed. The optical resonator will be shortened, which will reduce the radiation beam size at the mirrors. The available space for the new undulator will shrink from 9 m to $L_u = 8.6$ m, but the desired long-wave edge wavelength λ_{\max} will increase two-fold. An eigenmode of the two-mirror optical resonator is Gaussian beam (see, e.g., [16]). To minimize the eigenmode transverse widths at the undulator terminations, one must choose Rayleigh length of the eigenmode to be $L_u/2$. Then the r.m.s (by intensity) size of the Gaussian

radiation beam at the undulator terminations is $\sqrt{\lambda L_u / 4\pi}$.

After doubling the wavelength this width will grow by a factor of $\sqrt{2}$, and thus the aperture should be enlarged too, to avoid significant losses at the undulator edges [17]. The outer vacuum chamber diameter was set to 14 cm, which will enable generation of longwave radiation.

Tolerance Considerations

The main disadvantage of such VPU scheme (with poles moving freely in the longitudinal direction) is some unevenness of their arrangement, which can change significantly the phase shift between the electron transverse velocity and the radiation field. Possible influence of such errors on the radiation spectrum was considered in [14], and a period adjustment procedure was proposed.

Magnetic measurements of the VPU developed for the second FEL of Novosibirsk FEL facility indicated that differences in magnetizations of the magnets in the blocks of undulator affect field regularity in the undulator insignificantly in comparison with blocks position errors. Therefore, shimming was not considered so far. However, magnets will be carefully measured and sorted and installed in blocks to compensate each other's imperfections. Blocks in undulator can be rearranged during magnetic measurements stage to optimize trajectory straightness and minimize phase errors.

MODELLING RESULTS

The dimensions of the magnets and poles were optimized in 3D magnetic field distribution modelings made with help of CST EM Studio. The minimum undulator period was determined in a compromise between a shorter radiation wavelength and a reasonable value of the deflecting parameter. Dependences of the on-axis magnetic field amplitude and the deflecting parameter on the undulator period are shown in Figure 3. The deflecting parameter K was calculated with due account for all field harmonics.

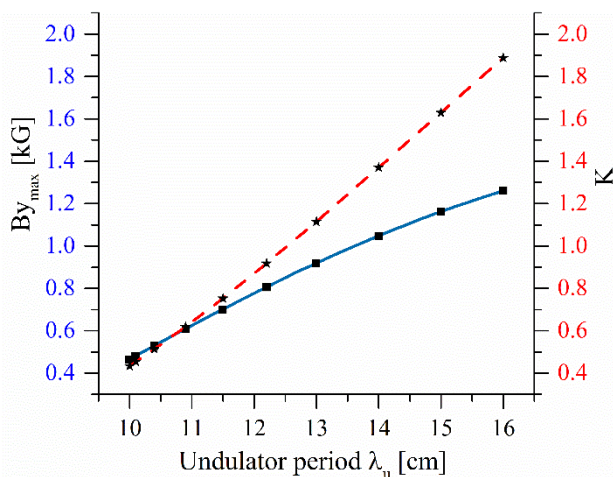


Figure 3: On-axis field amplitude (solid blue line with squares, left vertical axis) and deflection parameter K (dashed red line with stars, right vertical axis) vs. undulator period.

Increase in the undulator period is accompanied by a growth of amplitudes of higher odd field harmonics, however, higher field harmonics are strongly suppressed due to the large undulator gap, so normalized third harmonic amplitude does not exceed 0.3%. The circular pole profile helped to make the field amplitude gradient almost equal for both transverse directions. The undulator thus focuses electron beam in horizontal plane as well. At such a low electrons energy, vertical and horizontal beta functions of an electron beam remain constant along the undulator if initial conditions were matched to minimize average beta function in the undulator [18]. Dependences of the matched beta functions in the undulator on its period are shown in Figure 4.

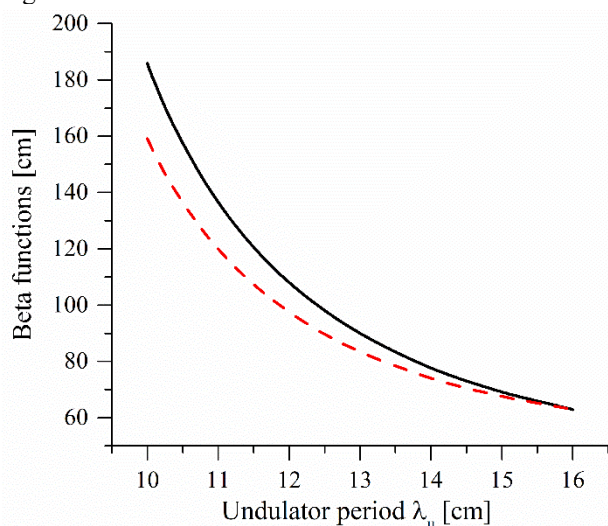


Figure 4: Vertical (dashed) and horizontal (solid) matched beta functions vs. undulator period.

Besides, redistribution of transverse gradients of magnetic field, particularly diminution of the vertical gradient, make the variation in field amplitude between pole tip and undulator axis lower. It worth noting that the arc geometry

used to increase the field on axis is useful for fixed gap only.

Undulator Terminations

The terminations field correction was conducted in several steps. Arc-shaped shields made of soft magnetic steel will be placed at the ends of the undulator to prevent electrons deviations in the field of terminating blocks. In order to weak terminating field peaks thus minimizing first two integrals of the field along the undulator, poles of first two blocks at both ends will be made of aluminum. Moreover, magnets of end blocks will be demagnetized up to 0.3 of their initial magnetization by heating. Aluminum gaskets will be placed after the first two blocks to prevent changing distance between them and the regular part of the undulator. This will make the field integrals minimization scheme independent of the undulator period. Implementation of mentioned above techniques will reduce first and second field integrals along the undulator to tolerable values that can be compensated with the help of dipole correctors in the ends of the undulator.

CONCLUSION

Incorporation of developed undulator will help to upgrade the terahertz FEL of Novosibirsk FEL facility due to advantages of variable-period undulator scheme. Due to the device design based on permanent magnets, the period-to-gap ratio can be made smaller for the minimum period, thus, this scheme allows smaller undulator period for short wavelength radiation and a wider aperture for the long part of the tuning range. Wavelength tuning is accompanied by smaller field amplitude variation for variable-period undulators with free moving blocks, therefore gain length and radiated power vary less across the tuning range. Moreover, this scheme has a remarkable feature of a larger number of periods for the short-wave part of the tuning range, which increases the gain. Besides, permanent magnets need no power supplies and are relatively cheap.

The undulator is now under manufacture. With an obvious size scaling of a permanent magnet structure, one can also use a similar geometry for incertion devices for shorter wavelength FELs.

REFERENCES

- [1] E. Levichev and N. Vinokurov, "Undulators and Other Insertion Devices," *Rev. Accel. Sci. Technol.*, vol. 03, no. 01, pp. 203–220, Jan. 2010.
doi:10.1142/S1793626810000403
- [2] E. Gluskin *et al.*, "Optimization of the design for the LCLS undulator line," *Nucl. Instruments Methods Phys. Res. Sect. A Accel. Spectrometers, Detect. Assoc. Equip.*, vol. 475, no. 1–3, pp. 323–327, Dec. 2001.
doi:10.1016/S0168-9002(01)01612-6
- [3] E. Trakhtenberg, V. Tcheskidov, I. Vasserman, N. Vinokurov, M. Erdmann and J. Pfluger, "Undulator for the LCLS project—from the prototype to the full-scale manufacturing," *Nucl. Instruments Methods Phys. Res. Sect. A Accel. Spectrometers, Detect. Assoc. Equip.*, vol. 543, no. 1, pp. 42–46, May 2005.
doi:10.1016/j.nima.2005.01.110

- 39th Free Electron Laser Conf.
ISBN: 978-3-95450-210-3
- FEL2019, Hamburg, Germany
doi:10.18429/JACoW-FEL2019-WEP094
- JACoW Publishing
- Content from this work may be used under the terms of the CC BY 3.0 licence (© 2019). Any distribution of this work must maintain attribution to the author(s), title of the work, publisher, and DOI
- [4] A. S. Artamonov *et al.*, “The first experiments with an optical klystron installed on the VEPP-3 storage ring,” *Nucl. Instruments Methods*, vol. 177, no. 1, pp. 247–252, Nov. 1980. doi:10.1016/0029-554X(80)90557-1
 - [5] R. Tatchyn, “A universal classification of optimal undulator types and parameters for arbitrary storage ring environments,” *Nucl. Instruments Methods Phys. Res. Sect. A Accel. Spectrometers, Detect. Assoc. Equip.*, vol. 275, no. 2, pp. 430–434, Feb. 1989. doi:10.1016/0168-9002(89)90720-1
 - [6] G. K. Shenoy, J. W. Lewellen, D. Shu, N. A. Vinokurov, “Variable-period undulators as synchrotron radiation sources,” *J. Synchrotron Radiat.*, vol. 10, no. 3, pp. 205–213, May 2003. doi:10.1107/S0909049502023257
 - [7] P. Vagin, A. Schöps, and M. Tischer, “Variable Period Undulator with Tunable Polarization,” *Synchrotron Radiat. News*, vol. 31, no. 3, pp. 48–52, May 2018. doi:10.1080/08940886.2018.1460178
 - [8] N. A. Vinokurov, O. A. Shevchenko, and V. G. Tcheskidov, “Variable-period permanent magnet undulators,” *Phys. Rev. Spec. Top. - Accel. Beams*, vol. 14, no. 4, p. 040701, Apr. 2011. doi:10.1103/PhysRevSTAB.14.040701
 - [9] J. Mun *et al.*, “Variable-period permanent-magnet helical undulator,” *Phys. Rev. Spec. Top. - Accel. Beams*, vol. 17, no. 8, p. 080701, Aug. 2014. doi:10.1103/PhysRevSTAB.17.080701
 - [10] G. N. Kulipanov *et al.*, “Novosibirsk Free Electron Laser—Facility Description and Recent Experiments,” *IEEE Trans. TERAHERTZ Sci. Technol.*, vol. 5, no. 5, 2015. doi:10.1109/TTHZ.2015.2453121
 - [11] O. A. Shevchenko *et al.*, “Current status of the Novosibirsk infrared FEL and the third stage lasing,” *Phys. Part. Nucl. Lett.*, vol. 13, no. 7, pp. 1002–1005, Dec. 2016. doi:10.1134/S1547477116070451
 - [12] O. A. Shevchenko *et al.*, “The Novosibirsk Free Electron Laser – Unique Source of Terahertz and Infrared Coherent Radiation,” *Phys. Procedia*, vol. 84, pp. 13–18, Jan. 2016. doi:10.1016/j.phpro.2016.11.004
 - [13] B. A. Knyazev *et al.*, “Novosibirsk Free Electron Laser as a User Facility,” *Phys. Procedia*, vol. 84, pp. 27–34, Jan. 2016. doi:10.1016/j.phpro.2016.11.006
 - [14] I. Davidyuk, O. A. Shevchenko, V. G. Tcheskidov, and N. A. Vinokurov, “Modeling and designing of variable-period and variable-pole-number undulator,” *Phys. Rev. Accel. Beams*, vol. 19, no. 2, p. 020701, Feb. 2016. doi:10.1103/PhysRevAccelBeams.19.020701
 - [15] I. V. Davidyuk, O. A. Shevchenko, V. G. Tcheskidov, and N. A. Vinokurov, “Results of test of prototype of variable period undulator,” *Nucl. Instruments Methods Phys. Res. Sect. A Accel. Spectrometers, Detect. Assoc. Equip.*, vol. 871, pp. 77–82, Nov. 2017. doi:10.1016/j.nima.2017.07.060
 - [16] A. Yariv, *Quantum electronics*, 3rd Edition John Wiley & Sons, 1989.
 - [17] V. V. Kubarev, B. Z. Persov, N. A. Vinokurov, and A. V. Davidov, “Optical resonator of powerful free-electron laser,” *Nucl. Instruments Methods Phys. Res. Sect. A Accel. Spectrometers, Detect. Assoc. Equip.*, vol. 528, no. 1–2, pp. 199–202, Aug. 2004. doi:10.1016/j.nima.2004.04.046
 - [18] H. P. Freund and T. M. Antonsen, *Principles of Free Electron Lasers*. Cham: Springer International Publishing, 2018. doi:10.1007/978-3-319-7510

THE ATHOS SOFT X-RAY BEAMLINES AT SwissFEL

R. Follath*, U. Flechsig, U. H. Wagner, and L. Patthey
Paul Scherrer Institut, 5232 Villigen PSI, Switzerland

Abstract

SwissFEL is a free electron laser facility for hard and soft X-rays at the Paul Scherrer Institut in Switzerland. The hard X-ray FEL ARAMIS started 2016 with the first experiments and now the soft X-ray FEL named ATHOS is close to completion with the first light being expected in 2019. ATHOS will cover the photon energy range from 250 eV to 1900 eV with pulse energies up to 8 mJ. It will operate with three end stations. Two stations are already defined and are currently in the design and construction phase. MALOJA, the first station, is dedicated to Atomic and Molecular physics as well as nonlinear spectroscopy. It will get first light in mid 2020. The second station, FURKA, is for condensed matter physics and will go online in 2021.

The performance of the beamline was already presented in an earlier paper [1], here we report on the various operation modes and the latest changes in the optical design.

ATHOS SOURCE

In standard operation mode SwissFEL generates double electron bunches with a separation of 28 ns at a repetition rate of 100 Hz and accelerates them in the first part of the main LINAC. Afterwards one of the double bunches stays in the main LINAC and is further accelerated up to 5.9 GeV before entering the ARAMIS undulator. The other bunch is extracted from the main LINAC at beam energies between 2.9 GeV and 3.15 GeV and send to the ATHOS LINAC where the electron energy is modified between 2.65 GeV and 3.4 GeV before it enters the ATHOS undulator. By this, both FELs can operate independently and at a repetition rate of 100 Hz. The ATHOS undulator consist of 2 m long APPLE-X [2] modules in a FODO lattice with 2.8 m period length. Each APPLE-X module is composed of 50 magnet periods with a period length of 38 mm. By tuning the electron beam trajectory it is possible to lase with the tail part of the electron bunch in the first section and with the head part in the second undulator section. The time delay between both pulses can be tuned between -50 fs to +950 fs. The photon wavelength of each undulator section can vary within the tuning range of the undulators ($K = 1 \dots 3.5$) while the working point is determined by the electron beam energy.

The FEL was optimized with the help of GENESIS [3] and foresees several operation modes e.g. high power, low bandwidth or two color modes. The pulse length is about 30 fs (rms), with the ability to reduce it below 1 femtosecond in the attosecond mode.

For the beamline design the high power and two color mode are the most relevant. In the high power mode a maximum pulse energy together with the least photon beam

divergence result in the highest fluence values. This must be considered in the optical layout to avoid single shot damage of the optical elements. In the two color mode the undulator is divided into two sections, each 25.2 m long, with individual k-values where both sections can lase at different wavelengths. The larger photon beam divergence together with the long distance from the first undulator section to the optical elements produce the widest beam cross section at the optical elements and determines the geometrical dimensions of the optical elements. Table 1 summarizes the beam parameters for the largest divergence and the highest fluence.

Table 1: Beam Parameters for the ATHOS Undulator UE38

Photon energy	(eV)	250	250
Mode		power	2 color
Source size*	(μm)	39.6	30.4
Source divergence*	(μrad)	19.8	25.8
Pulse energy	(mJ)	8.1	2.35
Spectr. bandw.*	(%)	0.9	0.57
Source position	(m)	-15.6	-3.9/ -29.1
Beam size* in 73 m (mm)		1.8	1.9/2.6

*rms-values

BEAMLINE

The ATHOS beamline is based on a common grating monochromator and distributes the beam afterwards by means of horizontally steering mirrors to three branches. Its overall scheme is shown in Figure 1. The first, horizontally deflecting mirror separates the FEL-radiation from the Bremsstrahlung that is absorbed in the subsequent radiation shielding. The mirror itself is bendable with a surface profile between flat and a meridional radius of 5000 m. It can either produce an intermediate horizontal focus nearby the exit slit for the MALOJA-branch or set to flat for an undisturbed beam divergence. An intermediate focus allows for a gas based diagnostic unit with small apertures after the monochromator to derive an intensity signal of the monochromatized beam.

The monochromator uses variable line-space gratings on spherical substrates with a variable included angle in a SX-700 geometry [4] and operates without an entrance slit. By mounting the optics in a SX-700 mechanics a vertical beam offset of 9 mm between the incoming and outgoing beam is introduced. The setup of mirror and gratings is reverted with respect to the original setup [5] and the plane mirror is now facing downwards whereas the gratings are oriented face upwards. By this the deflection angle on the plane mirror can be reduced while maintaining a larger deflection angle at the gratings. This results in a slightly upward pointing

* rolf.follath@psi.ch

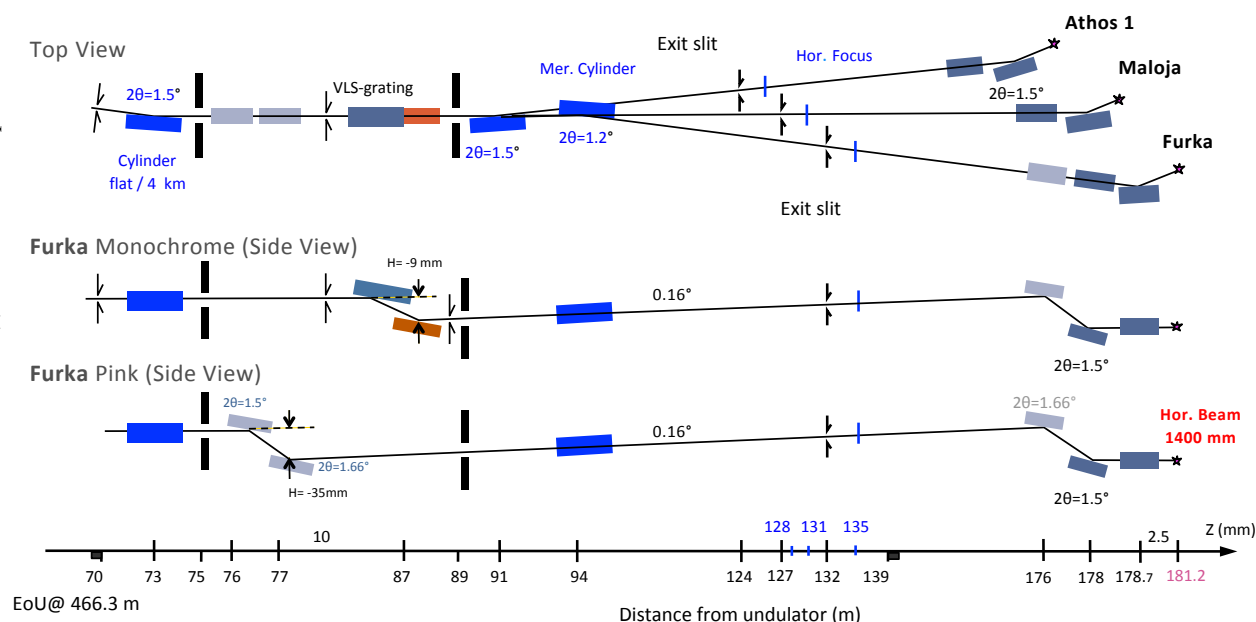


Figure 1: Optical layout of the ATHOS beamlines. Top view of all three branches and side view of the Furka branch in monochrome and pink mode, respectively.

diffracted beam. The upwards pointing diffracted beam is due to a boundary condition set by the FURKA end station, that needs a beam height of 1.4 m while the accelerator has a beam height of 1.2 m. MALOJA does not set this boundary condition and operates with a horizontally diffracted beam.

The gratings and the plane mirror can be moved aside to let the undispersed FEL beam pass towards the end stations.

After the grating chamber the beam is distributed to the branches ATHOS 1 and FURKA by means of two horizontally deflecting and focusing mirrors. The central MALOJA branch omits such a mirror and stays in the direct line. By this a reasonable lateral separation of all three branches is obtained. All three end stations are staggered at different distances from the source in separate enclosed areas of the building.

Each branch has an own exit slit and a dedicated KB-refocusing optics. The KB-systems are modified versions of the KB-system at ARAMIS, mainly with a larger deflection angle. Pink and monochromatic beam operation with the same pointing to the experiment is foreseen for all branches.

Monochromator

The grating chamber hosts two cylindrical gratings with line densities of 50 l/mm and 150 l/mm. The low line density grating has a patterned length of 130 mm, a meridional radius of 8 km and a blaze angle of 0.15° , whereas the high line density grating has a laminar profile, a radius of 10 km and a patterned length of 280 mm. This is due to limitations of the current grating technology that allows blazed gratings only up to a length of 130 mm. Both gratings have a variation in the line density in the order of 10^{-5} l/mm.

Very shallow incidence angles on both gratings are mandatory to reduce the risk of single shot damage. The low line density grating is therefore operated in outside diffraction or-

der, while the high line density grating is operated in inside diffraction order. Both gratings will have the bulk silicon surface for low photon energies and a coating for higher photon energies. The change between both areas is achieved by a lateral translation and does not affect the focal properties.

The gratings disperse the beam and focus it vertically onto the exit slits. The included angle on the gratings can be set by the plane mirror to maintain the focal condition for all photon energies, all three exit slit distances and for the two inclination angles of the diffracted beams in FURKA and MALOJA. Even a – known – variable source distance can be taken into account by the software control.

FURKA

Furka is the right branch of the beamline. Most probably, the monochromatic mode will be the main operation mode. In this mode, the FEL beam deflected from the first mirror enters the grating chamber horizontally. The grating disperses and focuses the dispersed beam vertically onto the exit slit. As the end station is quite large, the beam height must be increased from 1.2 m in the accelerator to 1.4 m at the end station. This can be accomplished by increasing the deflection angle on the grating with respect to the one at the plane mirror by 0.16° . The horizontally steering mirror at 94 m is therefore inclined by the same angle.

In pink mode the grating is retracted and two vertical offset mirrors at 76 m and 77 m bring the beam onto the same trajectory as in the monochromatic mode, at least downstream of the grating. The steering mirror can therefore stay in the same orientation as in pink mode. Between the first offset mirror at 76 m and the grating at 87 m the trajectories in pink and monochromatic mode differ vertically by a value between 0 mm and 35 mm.

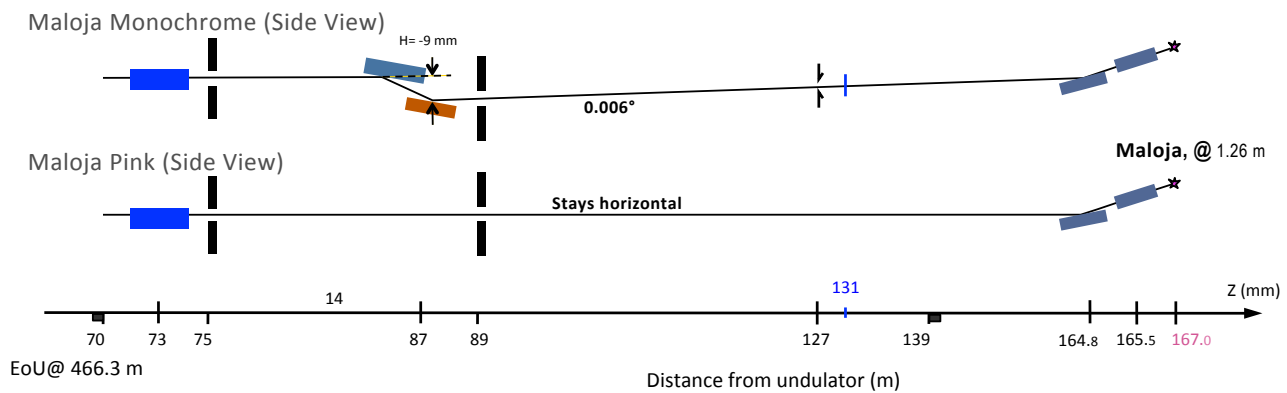


Figure 2: Optical layout of the ATHOS beamlines. Side view of the MALOJA branch in monochrome and pink mode, respectively.

An additional boundary condition set by the FURKA-experiment is a horizontal beam trajectory in the experimental chamber. For this an additional vertical deflecting mirror in front of the KB-mirrors is foreseen. It deflects the beam downward to the KB, which finally brings it back to the horizontal.

Unfortunately, the upcoming angle of the diffracted beam after the grating can not be increased to the deflection angle of 1.5° on the KB-system. This would have been a nice option to omit the deflecting mirror at 176 m.

MALOJA

The central branch with the MALOJA end station (Fig. 2) is optimized for pink beam operation with the least number of optical elements. In pink beam operation the first mirror is set to flat and deflects the beam directly to the KB-system. The exit slits must be opened to pass the unfocused beam. By this configuration the large demagnification ratio allows for a nominal focus size of $1 \mu\text{m}$ in a distance of 1.5 m from the center of the last mirror. In monochrome mode the first mirror can produce an intermediate horizontal focus nearby the exit slit for the gas based intensity monitor with small apertures. The change in source distance of the subsequent KB-system is compensated by a proper bending of the horizontally deflecting KB-mirror.

The beam in this branch stays horizontal at a height of 1200 mm until the KB-system. Afterwards it has an upcoming angle of 1.5° towards the experiment.

In monochrome mode, the grating and plane mirror are introduced and the exit slit closed to $20 \mu\text{m}$ – $200 \mu\text{m}$. To compensate the beam offset within the grating chamber the beam trajectory between grating and the deflecting KB-mirror is different from the pink mode by an angle of 0.006° with a maximum vertical separation of 9 mm. The vertically deflecting KB-mirror stays at the same height, but the deflection angle is slightly changed to guarantee the same pointing as in monochrome mode.

Outlook

The installation of the beamline components started in the front end where first light is expected for December 2019. The first pink beam in MALOJA is expected for April 2020. The mirror mechanics of the first and second mirror chambers are currently assembled in house while the first mirror from Jtec is expected for January 2020. The KB-system for MALOJA from Toyama and Zeiss is expected for the end of the year, while the monochromator and its optical elements, as the most complicated components, are in fabrication at Bestec and Jtec. Their delivery and installation is expected for end of 2020.

REFERENCES

- [1] R. Follath, U. Flechsig, U.H. Wagner, and L. Patthey, "Optical design of the ATHOS beamlines at SwissFEL", *AIP Conference Proceedings*, vol. 2054, pp. 060024, 2019. doi:10.1063/1.5084655
- [2] M. Calvi, C. Camenzuli, E. Prat, and T. Schmidt, "Transverse gradient in Apple-type undulators", *J. Synchrotron Radiat.*, vol. 24, no. 3, pp. 600-608. doi:10.1107/S1600577517004726
- [3] S. Reiche, "GENESIS 1.3: a fully 3D time-dependent FEL simulation code", *Nucl. Instrum. Methods Phys. Res., Sect. A*, vol. 429, no. 1-3, pp. 243-248, Jun. 1999. doi:10.1016/S0168-9002(99)00114-X
- [4] F. Riemer and R. Torge, "Bessy SX 700 UHV monochromator: Design features and kinematic concept", *Nucl. Instrum. Methods Phys. Res.*, vol. 208, no. 1-3, pp. 313-314, Apr. 1983. doi:10.1016/0167-5087(83)91141-9
- [5] H. Petersen, "The plane grating and elliptical mirror: A new optical configuration for monochromators", *Opt. Commun.*, vol. 40, no. 6, pp. 402-406, Feb. 1982. doi:10.1016/0030-4018(82)90040-2

OPERATIONAL MODEL OF THE ATHOS UNDULATOR BEAMLINE

C. Kittel^{*1,2}, M. Calvi¹, X. Liang^{1,3}, T. Schmidt¹, N. J. Sammut²

¹Paul Scherrer Institut, Villigen PSI, Switzerland

²University of Malta, Msida, Malta

³Paris-Sud University, Orsay, France

Abstract

Athos, the new Soft X-ray beamline of SwissFEL, operates 16 Apple X undulators and 15 compact chicanes to implement novel lasing schemes. With the data available after the end of the magnetic measurement campaign (middle 2020), a self-consistent set of equations will be used to summarize all the relevant properties of those devices to start their commissioning. The analytic approach planned will be discussed in great detail and tested with the preliminary experimental data available. Finally, the accuracy of this approach will be evaluated and critically compared to the requirements of the new FEL beamline.

INTRODUCTION

In Apple X undulators [1] synchrotron radiation can be produced with any polarization. Also the deflection parameter K can be changed by radially moving the arrays in and out, defining the gap (pole tip to central axis) of the undulator, also called radius (r). We differentiate between the standard cases: Linear Horizontal (LH), Linear Vertical (LV), Circular plus/minus ($Circ+/-$) and plus/minus 45 degrees ($+/-45^\circ$). Moreover, elliptical polarization angles are possible, but not specifically detailed in this article.

All previous mentioned polarizations but $+/-45^\circ$ can be produced by shifting two opposite magnetic arrays (e.g. No. 1 and No. 3) parallel against their neighboring arrays (e.g. No. 2 and No. 4) [1]. Linear polarization of any angle however can be produced by shifting two opposite magnetic arrays anti-parallel to each other, against their neighboring arrays.

In the following sections we are deducing models from measurement data, in order to predict the undulator positions for any given K and polarization angle α . We are not looking into the Energy mode [1] nor the transverse gradient undulator (TGU) mode in this paper,

In order to allow for a proper set up of the different operational modes, the models should predict K with an error of a few $\frac{\Delta K}{K} = 10^{-4}$.

PARALLEL MODES

Assuming the magnetic field is equal in strength in x and y dimension the parallel modes should be easy to predict. In this case the effective K does not depend on the phase shift of the two moving arrays. However, in the case of a real undulator we have to correct for the slight variation between the magnetic field for the transverse dimensions,

B_x and B_y . When moving the arrays in a parallel way, the K -value varies on a 1% level (see blue points in Fig. 1), which had to be taken into account in order to achieve the requested prediction error. Thus to predict the dependencies of the overall gap and the parallel shift needed for a given K -value a universal model based on the magnetic model was developed. With the magnetic model of sinusoidal form, a variation of K_{eff} (background) can be described by a difference between B_x and B_y , see red line in Fig. 1. For a single gap it can be expressed by Eq. (1), which is discussed in more detail in [2].

$$K(\phi) = 2\sqrt{2}\kappa\sqrt{B_x^2 + B_y^2 - \cos(\phi_p)(B_x^2 - B_y^2)} \quad (1)$$

Here ϕ_p is the shift defined as a relative phase difference of two neighboring arrays and $\kappa = \frac{e\lambda_U}{2\pi m_e c}$. A result can be seen in Fig. 1, where it is fitted for a single gap (red line).

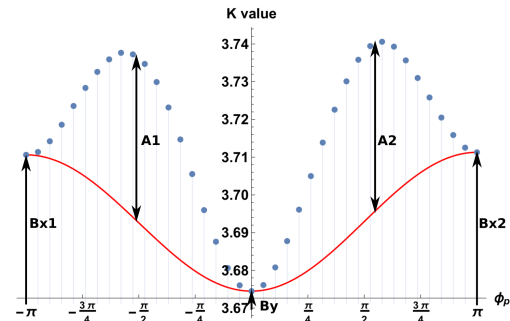


Figure 1: Measured points for a single gap (blue points), background (red line) and model coefficients (black).

Furthermore a second correction has to be added on top to describe the variation probably caused by mechanical deformation due to strong magnetic forces, especially at small gap sizes. It can be described empirically by Eq. (2).

$$K(\phi_p) = A \sin^2(\phi_p) \quad (2)$$

For the data of the same gap as shown in Fig. 1, but with the background removed, the K -correction can now be fitted depending also on the parallel shift ϕ_p (see Fig. 2).

An asymmetry was observed when shifting the arrays in one direction with respect to the opposite direction. Therefore the model coefficients need to be calculated separately for each direction. This helped to minimize the errors at the five points of the dedicated modes ($LH, LV_1, LV_2, Circ+, Circ-$) to below $\frac{\Delta K}{K} = 2 \cdot 10^{-4}$. For all measured gaps the fitting errors can be seen in Fig. 3.

With the above mentioned corrections five coefficients are needed to fit K for each gap ($B_{x1}, A_1, B_y, A_2, B_{x2}$). Doing

* email: christoph.kittel[at]psi.ch

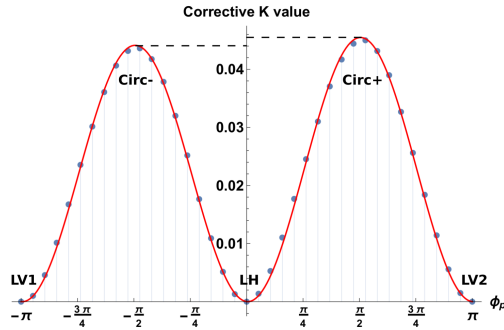


Figure 2: Measured points for a single gap with background subtracted (blue points), fitting their correction (red line) and operational modes indicated (black).

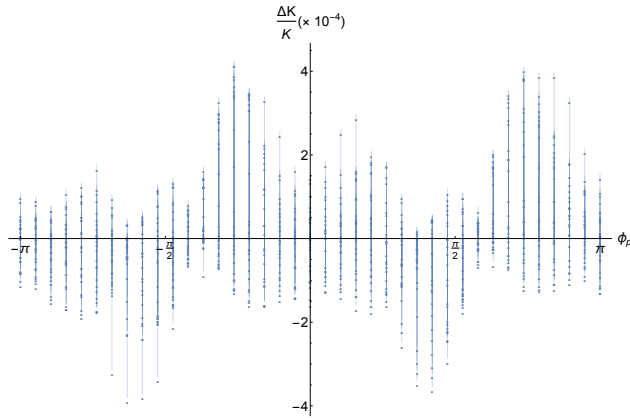


Figure 3: Relative errors when both fits are applied for all measured gaps.

this for all the measured gaps yields a coefficient table. That way each coefficient can be fitted with an exponential gap dependence. For example the resulting expression for B_y is shown in Eq. (3).

$$B_y(g) = \exp(a + bg + cg^2 + dg^3 + eg^4) \quad (3)$$

where all the parameters (a, b, c, d, e) need to be fitted for a particular mode. The same approach can be repeated for the other coefficients, which yields in total five equations. Combining them all into one expression results in the final model. The resulting equation for the case $\phi_p < 0$ is shown in Eq. (4). In case $\phi_p > 0$ two parameters have to be replaced by B_{x2} and A_2 .

$$K(g, \phi_p) = 2\sqrt{2}\kappa [B_{x1}^2(g) + B_y^2(g) - \cos(\phi_p)(B_{x1}^2(g) - B_y^2(g))]^{\frac{1}{2}} + A_1(g) \sin^2(\phi_p) \quad (4)$$

NEW ANTI-PARALLEL MODE

To achieve any given, linear polarization angle, the anti-parallel mode is used. In contrast to the usual, pure anti-parallel shift of two opposing arrays, the Apple X allows also another scheme, which we will describe here. Starting by first opening the two opposing gaps, the polarization angle

starts changing, and only then shift the same two arrays in opposite directions, moving the polarization angle beyond 45° . For polarization angles close to 90 degrees, the gaps can then be closed again. This new mode has in comparison with the legacy mode the advantage of avoiding spurious contribution of longitudinal magnetic forces.

However, there are also certain drawbacks going along with it. The most important ones are:

1. *The partial invalidation of previous shimming campaigns during these movements.* The shimming is currently optimized for the magnetic arrays having equal gap positions. More sophisticated shimming techniques could potentially be developed to comprise also these cases. Though it was not part this study.
2. *The complication of the modeling.* Moving the gap of two out of four arrays adds two new parameters: r_0 the initial gap of all arrays and $r_{1,3}$ the gap of the two arrays which are shifted in anti-parallel directions. This makes it more difficult to use drastic simplifications of the magnetic model. A possible method for mitigation is presented below.

The measurement results for different r_0 are presented in Figs. 4 and 5. The black lines indicate the different domains of movement. Here $gap_{1,3}$ indicates the gap opening of array 1 and 3, respectively closing, while $\uparrow\downarrow shift_{1,3}$ indicates the anti-parallel shift of array 1 and 3.

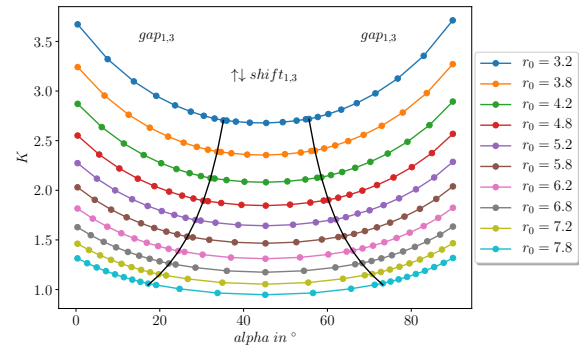


Figure 4: Measurement results of anti-parallel shifts at different r_0 , black lines indicate model domain borders.

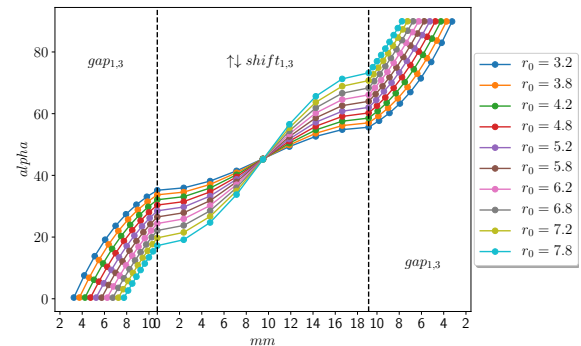


Figure 5: Measurement results of anti-parallel shifts at different r_0 , black lines indicate model domain borders.

One way to fit the measured behavior while mitigating the additional complexity is to split the modeling task into the aforementioned domains of movement. A possible user scenario would be scanning the polarization angle from 0 to 90 degrees while maintaining a constant K . We propose to determine first for each pair of K, α which model is to be used. For that we fit $r_{0\alpha} = f(\alpha, K = \text{const.})$, as well as $r_{0K} = f(\alpha = \text{const.}, K)$ for now with a simple polynomial. Comparing these two initial gaps we can decide which model to use: if $r_{0\alpha} > r_{0K}$ we use the model for $gap_{1,3}$, otherwise the model for $\uparrow\downarrow shift_{1,3}$. However, there are slight asymmetries between the opening and closing of the gap at different shift positions (e.g. LV_3 and LV_4). Thus it is necessary to decide additionally if $\alpha < 45^\circ$ to use the dedicated gap model.

Once a model has been determined. The models themselves have to be broken down into two parts due to the higher number of parameters. First step would be to fit $r_0 = f(\alpha, K)$. Knowing r_0 we can fit $pos = f(\alpha, r_0)$, where pos is the gap or shift depending which model was chosen.

A simple two dimensional, 4th order polynomial fit of the first part to recover r_0 for each domain is shown in Fig. 6. The errors are still rather big and do not satisfy the operational needs of accuracy. Better fit functions need to be found, ideally based in physics.

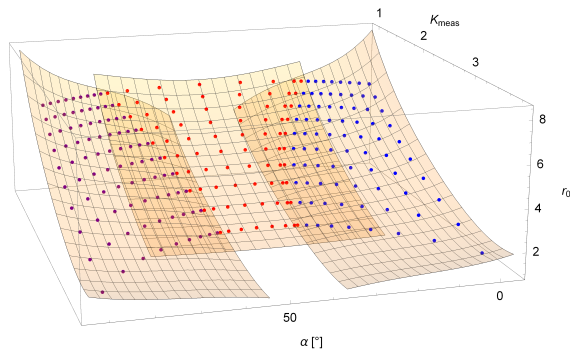


Figure 6: 2D fit results for each model domain.

MECHANICAL HYSTERESIS

We identified the mechanical hysteresis by measuring the magnetic field at 4.75 mm while approaching this value from each side. This was done by repeatedly opening and closing the gap between 3.25 and 10.75 mm, see figure 7 for a visualization.

The measurements were done at different shift positions of the magnetic arrays, representing different operational modes ($LH, LV, Circ +/-, 45^\circ +/-$). The results are shown in Fig. 8. It can be seen, that the mechanical hysteresis of the gap movement is around the level of 10^{-4} for LH, LV and 45° modes, while the hysteresis for circular polarization can be excluded above $2 * 10^{-5}$.

Similarly the magnetic arrays (Top Left and Bottom Right) were shifted in an anti-parallel way repeatedly between ± 19 mm, while the hysteresis was analyzed at ± 9.5 mm.

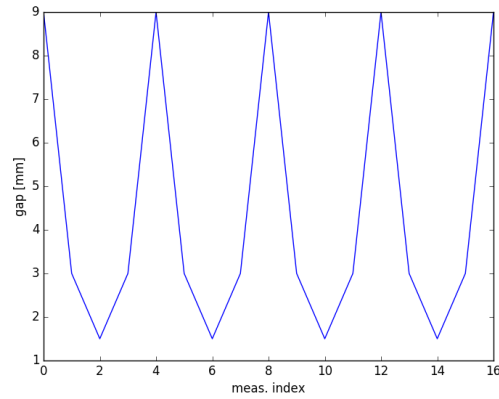


Figure 7: Measurement scheme to investigate hysteresis.

The measurements are not shown here, but yield a slightly bigger error of $2 * 10^{-4}$, which should still cause no problems for the operation.

Mixed gap and shift movements will have to be measured and analyzed next.

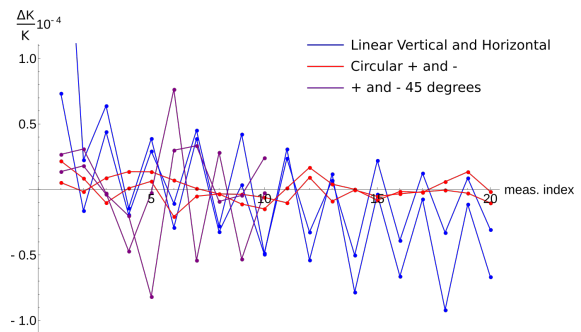


Figure 8: relative K -errors of mechanical hysteresis for different modes.

CONCLUSION

The mechanical hysteresis for gap, respectively shift movements have been investigated and shown to fulfill the required accuracy, with relative errors around 10^{-4} . A complete model to describe distinct parallel operational modes was developed with sufficient accuracy for current operation. Furthermore, a novel anti-parallel operational mode was proposed, which combines opening gaps and shifting arrays. Currently a model split into three domains is under development.

REFERENCES

- [1] M. Calvi, C. Camenzuli, E. Prat, and Th. Schmidt, "Transverse gradient in Apple-type undulators", *J. Synchrotron Rad.*, vol. 24, pp. 600–608, 2017. doi:10.1107/S1600577517004726
- [2] X. Y. Liang, M. Calvi, C. Kittel, T. Schmidt, and N. J. Sammut, "Advanced Operational Models of the Apple X Undulator", presented at the 39th Int. Free Electron Laser Conf. (FEL'19), Hamburg, Germany, Aug. 2019, paper WEP098, this conference.

ADVANCED OPERATIONAL MODELS OF THE APPLE X UNDULATOR

X. Liang^{*1,2}, M. Calvi¹, C. Kittel^{1,3}, T. Schmidt¹ and N. J. Sammut³

¹Paul Scherrer Institut, 5232 Villigen PSI, Switzerland

²Paris-Sud University, 91400 Orsay, France

³University of Malta, Msida, Malta

Abstract

Athos is a new soft X-ray beamline at SwissFEL, where the Apple X type undulators will be equipped. These devices are flexible to produce light in different polarization modes. An adequate magnetic field model is required for the operation of undulator. The undulator deflection parameter K and its gradient are calculated starting from the Fourier series of the magnetic field. In the classical parallel and anti-parallel operational modes - respectively elliptical and linear modes, the variation of the magnetic field as well as its parameters are evaluated by computer modeling. The results are compared to the magnetic measurements of the first Apple X prototype.

INTRODUCTION

16 Apple X undulators will be installed on Athos Beamline. Each one contains 800 magnets distributed in a Halbach configuration in 4 arrays (see Fig. 1 top right). Motors are equipped to move the arrays longitudinally and radially. The different operational modes of the undulator are defined by the way of longitudinal shifting of the arrays.

* xiaoyang.liang@psi.ch, xiaoyang.liang@u-psud.fr

In parallel mode, the opposite arrays are shifted in same direction. The polarization of light changes its elliptical form. While in anti-parallel mode, we move the opposite arrays in different direction, which turns the polarization axes of the photon beam. Moreover, by changing the radial gap between the arrays, we are able to adjust the magnetic strength.

During the parallel mode, the K value variation (see Fig. 2) in the measurement results is not able to be explained with the previous magnetic (single harmonic) model. An updated and adapted physical model with higher harmonics of the Fourier series was proposed. The correction was applied for the non-sinusoidal magnetic field. The analysis of the influence of the high harmonic coefficients are mainly discussed in this contribution. The calculation result indicates that the updated model is not enough to describe the phenomenon. Further discussion about the K value variation will be carried out in the last part.

UPDATED MAGNETIC FIELD MODEL

The convention of the coordinate system of the magnetic field composes a transverse plane (x,y) along with its longitudinal position z . The horizontal and vertical components of the magnetic field are named as B_x and B_y respec-

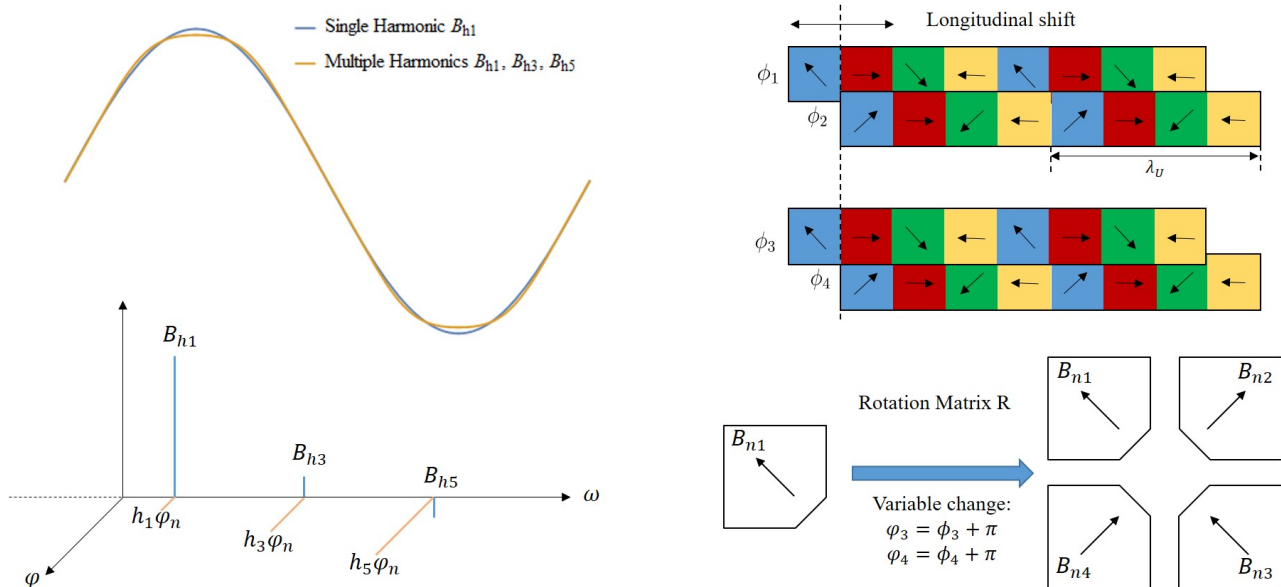


Figure 1: Top left: Example of a non-sinusoidal field correction with multiple harmonics. Top right: Scheme of the longitudinal shift of 4 arrays (Circular mode as an example). Bottom left: Scheme of simplified expression of the magnetic field in Fourier domain. Bottom right: Using the mathematical tools to express 4 arrays as a function of the first array.

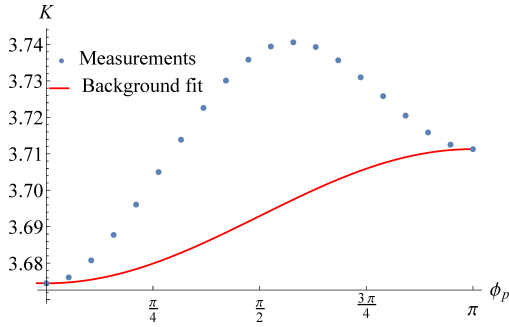


Figure 2: Measurement result of K value variation in parallel mode.

tively. On the reference electron beam orbit, equally speaking $(x, y) = (0, 0)$, the non-sinusoidal and periodical magnetic field of a single array can be expressed with a series. We take the example of B_x component:

$$B_x(z) = \sum_{h=1,3,5} B_{xh} \cos\left(h \frac{2\pi}{\lambda_u} z + \phi_n\right) \quad (1)$$

The different harmonic orders of the series are noted as h . Using only the first 3 odd harmonic orders is enough for the theoretical analysis. λ_u is the undulator period. ϕ_n is the relative longitudinal phase shift of the n^{th} array. (see Fig. 1 top right).

With the simplified expression in the Fourier domain and the rotation matrix [1] (see Fig. 1 bottom left and bottom right), we are able to express the whole field of 4 arrays as a function of harmonic coefficients of one array and longitudinal phase shifts:

$$\hat{B}(\hat{B}_{1h}, \phi_1, \dots) = \sum_{h=1,3,5} \sum_{n=1}^4 \exp(ih\phi_n) R_n \cdot \hat{B}_{1h} \quad (2)$$

where \hat{B}_{1h} is a vector in transverse plan. (\cdot) means that the parameters could be complex due to the expression in the Fourier domain, R_n is the rotation matrix. The advantage of this complex expression is to simplify the calculation of the K value and its gradient. Comparing the previous and the updated model with the measurement results (see Fig. 3 and Fig. 4) show that the updated magnetic model is more reliable.

K VALUE AND ITS GRADIENT

The undulator associated deflection parameter K of a non-sinusoidal magnetic field [2] is expressed:

$$K_{eff} = \kappa \sqrt{\sum_{h=1,3,5} (b_{xh}^2 + b_{yh}^2)} \quad (3)$$

where we define: $\kappa = \frac{e\lambda_u}{2\pi m_e c}$ and $b_h = \frac{B_h}{h}$.
Eq.(3) in complex form is updated as:

$$K_{eff}^2 = \sum_{h=1,3,5} \hat{K}_h \cdot \hat{K}_h^* \quad (4)$$

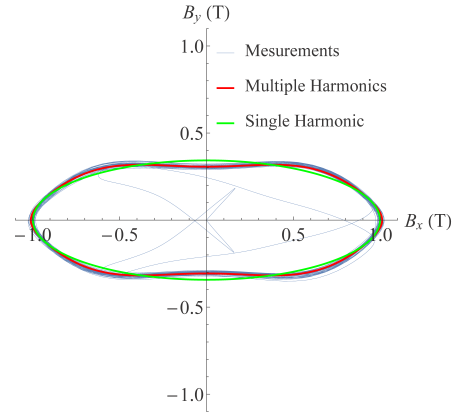


Figure 3: During the parallel mode: Transverse magnetic field distribution along z in elliptical polarization case.

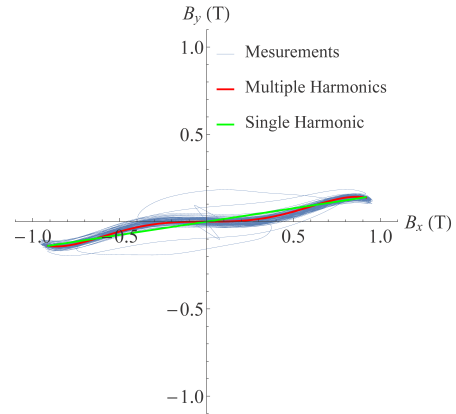


Figure 4: During the anti-parallel mode: Transvers magnetic field distribution along z in the case of linear polarization with certain angle.

where \hat{K}_h is also a vector in transverse plan: $(\hat{K}_{xh}, \hat{K}_{yh}) = \kappa \frac{\hat{B}_h}{h} = \kappa \hat{b}_h$.

For the simplification of the calculation, we define a Z_h matrix as a combination of the rotation matrix R_n and longitudinal phase shifts:

$$\varphi_1 = \phi_1, \quad \varphi_2 = \phi_2, \quad \varphi_3 = \phi_3 + \pi, \quad \varphi_4 = \phi_4 + \pi$$

$$Z_{xh} = e^{ih\varphi_1} - e^{ih\varphi_2} + e^{ih\varphi_3} - e^{ih\varphi_4}$$

$$Z_{yh} = e^{ih\varphi_1} + e^{ih\varphi_2} + e^{ih\varphi_3} + e^{ih\varphi_4}$$

$$Z_h = \begin{bmatrix} Z_{xh} & 0 \\ 0 & Z_{yh} \end{bmatrix}$$

The 4 arrays are in the linear horizontal polarization mode (pure vertical field) when $\varphi_1 = \varphi_2 = \varphi_3 = \varphi_4 = 0$. After the change of variables between ϕ and φ , the magnetic field distribution in the model matches closer the magnetic field of the real undulator.

Then the formula (4) can be expressed as:

$$K_{eff} = \kappa \sqrt{\sum_{h=1,3,5} [(Z_h \cdot \hat{b}_{1h})^T \cdot (Z_h \cdot \hat{b}_{1h})^*]} \quad (5)$$

In parallel mode, we shift relatively arrays No.1 and No.3 in the same direction - the polarization of the photon beam changes its elliptical form. The relative shift phase differences of the arrays vary thus in this way:

$$\varphi_1 = \phi_p, \quad \varphi_2 = 0, \quad \varphi_3 = \phi_p, \quad \varphi_4 = 0$$

With the \mathbf{Z}_h matrix, the number of the array doesn't play a role anymore, we can note b_{1h} as b_h . We obtain then K_{eff} in parallel operational mode:

$$K_{eff}(\phi_p) = 2\sqrt{2}\kappa \sqrt{\sum_{h=1,3,5} (b_{xh}^2 + b_{yh}^2) - \cos(h\phi_p)(b_{xh}^2 - b_{yh}^2)} \quad (6)$$

Implementing the empirical value of b_x and b_y for each harmonic into the Eq. (6), we are able to compare the difference before and after the update with higher harmonics (see Fig. 5). The relative correction is on a level of 10^{-5} .

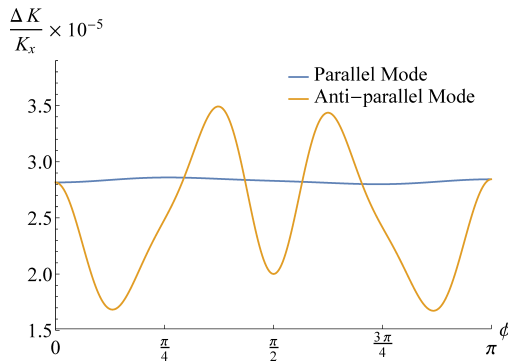


Figure 5: Correction of K value variation with multiple harmonics compared to the single harmonic case.

The anti-parallel mode is able to change the polarization axes of the photon beam. We shift the opposite array No.1 and No.3, or No.2 and No.4, in different direction. The phase shifts vary accordingly:

$$\varphi_1 = \phi_p, \quad \varphi_2 = 0, \quad \varphi_3 = -\phi_p, \quad \varphi_4 = 0$$

The equation of the K variation as a function of ϕ_p in anti-parallel mode is more complicated. Therefore, we only show the simulation result in Fig. 5 together with the result of the parallel mode. The variation in anti-parallel mode is much more important. However, the correction is still on a level of 10^{-5} . The coefficients b_3 and b_5 have not enough influence to create a difference on a level of 1%, which is the case of the measurement (see Fig. 2).

The updated equation of the transverse gradient of K is:

$$\nabla K = \frac{\kappa^2}{K_{eff}} \sum_{h=1,3,5} \Re(\hat{\mathbf{J}}_h \cdot \hat{\mathbf{b}}_h^*) \quad (7)$$

where $\hat{\mathbf{J}}_h$ is the Jacobian: $\hat{\mathbf{J}}_h = \begin{bmatrix} \partial_x \hat{B}_{xh} & \partial_y \hat{B}_{xh} \\ \partial_x \hat{B}_{yh} & \partial_y \hat{B}_{yh} \end{bmatrix}$.

MEASUREMENT AND ANALYSIS

The measurement result in Fig. 2 is reproducible on a level of about 10^{-5} . To operate the undulator for the beamline [3], we need to fit the measurement points to satisfy the precision requirement of 10^{-4} . Based on the analysis of the multiple harmonics update for the physical model, the single harmonic model is enough. The background part can be fitted by the old model. The residual part, called corrective part for fitting, can be well fitted with a model in form of $\sin^2(\phi)$.

This residual part of the K value variation has not yet been fully understood. However, the analysis in Fig. 6 shows that it is strongly related to the magnetic strength. It decreases faster than the magnetic field versus the radial gap between the arrays.

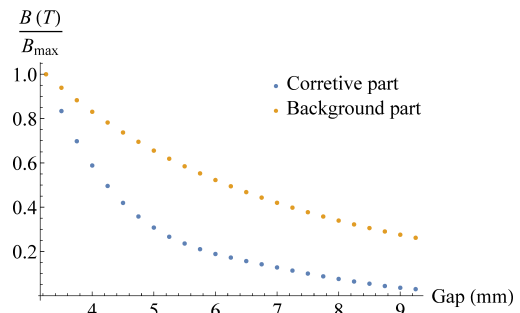


Figure 6: The relative amplitude of the fitted b_1 and the coefficient of the corrective function $\sin^2(\phi)$ versus gap of 4 arrays.

CONCLUSION

The higher harmonics of the magnetic field of the Apple X undulator make a difference on a level of 10^{-5} for the K value variation during different operational modes. These modeling results suggest that the variation of K at a level of 1% is not related to the higher harmonics. We have not fully understood this behavior yet. A further analysis indicates that the mechanical deformation could be the reason of this unknown effect. However, with empirical characterizations and fits, we can handle this problem for operation. The measurements about the mechanical deformation is being carried out in order to find an explanation.

ACKNOWLEDGEMENTS

We would like to thank Romain Ganter for supporting the ID group to finish this research; Marc Brügger for developing the measuring benches and the general explanation about the machine and other colleagues in ID group and PSI who contribute to the project.

REFERENCES

- [1] M. Calvi *et al.*, "Transverse gradient in Apple-type undulators", *J. Synchrotron Rad.*, vol. 24, pp. 600-608, 2017. doi:10.1107/S1600577517004726

CONCEPTUAL DESIGN OF A PERMANENT MAGNET UNDULATOR FOR FAST PULSE-TO-PULSE POLARIZATION SWITCHING IN AN FEL *

Ting-Yi Chung[†] and Ching-Shiang Hwang
National Synchrotron Radiation Research Center, Hsinchu, Taiwan

Abstract

In this paper, we propose the design of an undulator to alter polarization at a fast frequency and the energy spectrum pulse-to-pulse in free-electron lasers (FELs). A fast time varying magnetic field generated in an undulator can alter characteristic light features. An electromagnetic (EM) and permanent magnet (PM) type undulator provides typically a magnetic field switching frequency below 100 Hz. Inductance and heating issues from coils limit the performance for the EM type and favor small magnetic fields and longer periods and for the PM type, strong magnetic forces between magnet arrays create undesired relative motion. In this paper, we discuss these issues and propose an undulator made of Halbach cylinders with rotating magnet arrays to switch the magnetic fields. Concept, magnet structure and performance are discussed in this note.

INTRODUCTION

Polarization control in synchrotron light sources and FELs has many applications in the study of structural, electronic and magnetic properties of materials. Many experiments demand particularly circularly polarized light to probe electronic spin in materials. Several schemes have been implemented at X-ray FELs to fulfil these requirements. There are two important schemes. One is to convert linearly polarized lights to circular polarization based on interference effects [1-3]. The other is to control the motion of the electron beams in helical undulators [4-6].

Polarization switching is another approach to polarization control. The possibility of fast switching would benefit the signal-to-noise ratio for experiments, for instance, for X-ray magnetic circular dichroism (XMCD) [7]. A straightforward method is to switch the helicity using an EM helical undulator by a flip of excitation currents [8,9]. However, the magnetic field strength and the switching frequency of the device is significantly limited by the capacity of power supplies and heating limits generated in coils. A PM helical undulator is compact, promises a shorter period length and is usually arranged linearly according to a Halbach structure [10], as seen in Fig. 1(a). A helical undulator consists of four arrays with a narrow gap between them and can create a helical field by relative linear motion of the arrays to switch the helicity [11,12]. Because of the narrow gap between the arrays, the motion must overpower extremely large magnetic forces, resulting

typically in a low switching frequency of around 1 Hz. Some remedies, such as dedicated force compensation [13] or a driving system [14] have been used to increase the switching frequency.

Except for a superconducting linac, an FEL is normally driven in a pulsed mode by an electron beam from a room temperature linac at a repetition rate of the order of 100 Hz. An undulator with a compatible and tuneable switching frequency would allow multi-polarization and pulse-to-pulse energy changes. This study proposes an undulator consisting of PM cylinders to change the magnetic fields by rotation of magnets, as seen in Fig. 1(b). The switching frequency is tuneable and can exceed 100 Hz.

PM cylinders are useful in many applications, such as particle accelerators [15], motors [16] and for nuclear magnetic resonance (NMR) [17]. A rotatable cylinder structure has been shown to change magnetic fields of focusing quadrupole magnets in Laser Plasma acceleration [18] and the field of steering magnets for modulating the phase between two undulators in a storage ring [19]. A delicate linear configuration of rotatable rods has been developed to modulate the period length of an undulator [20]. These pioneering works inspired us to create a PM cylinder undulator with the ability to switch the polarization quickly. This paper is organized as follows. In Section 2, we discuss operations of polarization changes using a relative rotation of PM cylinders. In Section 3, we study the torque for a practical construction and discuss construction feasibilities. To increase the switching frequency, two types of PM cylinders are studied in Section 4. A discussion for an application in an FEL is given in Section 5.

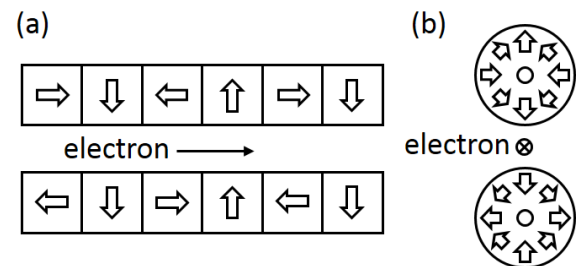


Figure 1: (a) A PM undulator consisting of Halbach arrays. (b) Rotatable Halbach cylinders. The magnetization of the PM is indicated by arrows.

MAGNETIC FIELD CHANGES AND POLARIZATION CONTROL

The magnetic field in our proposed structure is produced by a pair of PM cylinders. Several magnetization configurations in a cylinder are feasible.

* This work was supported in part by the Ministry of Science and Technology under Contract MOST 108-2112-M-213-011

[†]chung.albert@nsrrc.org.tw

for the PM cylinder undulator is given in Fig. 5(a). A Halbach cylinder consists of segments with radial and tangential magnetization. A large number of segments increases the magnetic field but requires a complex technology for construction. Comparing to a delicate Halbach cylinder, dipole rings consists of only radial segments. It can be made by assembly or a superior magnetizing process, e.g. by radial anisotropy or multipole anisotropy, which are both used in motor application. To further understand the magnetic field of Halbach cylinders and dipole rings, simulations with changes of the inside (R_{in}) and outside (R_{out}) radii are shown in Fig. 6. With an increase of the cylinder volume the magnetic field increases after optimization of dimensions. A design with a large n allows a high switching rate but produces a small magnetic field. Compared to a dipole ring, a Halbach cylinder has the advantage of a higher magnetic field but strongly relies on difficult assembly technologies.

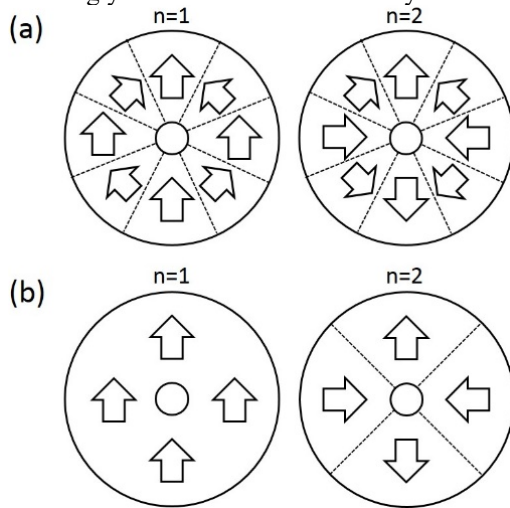


Figure 5: Two practically available designs of the PM cylinder, (a) Halbach cylinders, (b) dipole rings. The index n represents the number of pole-pairs.

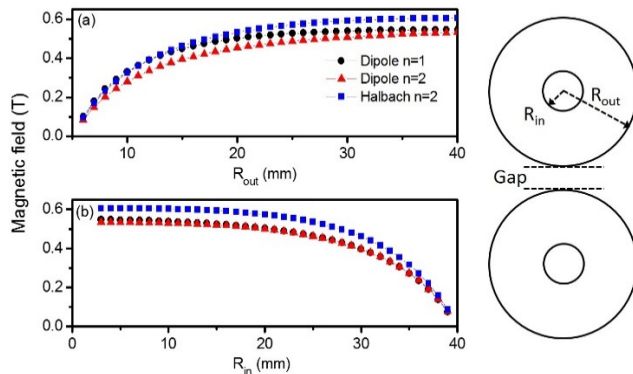


Figure 6: Simulating magnetic fields for the PM cylinder undulator versus dimensions of (a) outside radius and fixed $R_{in} = 5\text{mm}$ and (b) versus inside radius at a fixed $R_{out} = 40\text{mm}$. Other parameters are from Table 1.

DISCUSSIONS

In a PM cylinder undulator the magnetic field is changed by rotation instead of linear motion like in a typical undulator. In addition to a change in the magnetic field by rotation, the polarization can be switched quickly. With delicate matching of the rotating frequency and the beam pulse repetition rate, the device gives a new experience for polarization- or energy-dependent pulse-to-pulse changes. It has potential for applications in a helical afterburner [22] and time-interleaved schemes, which is applicable multi beam lines [23].

Comparing to an EM type undulator, the PM cylinder undulator has better performances for short periods, larger magnetic fields and fast switching rates. It seems to exhibit several technical challenges, though, like demagnetizing effects or torque induced from end fields, which should be discussed to pursue a short period undulator with high magnetic field and desired switching rates for FELs.

We thank D. Ratner and B. Faatz for useful and inspiring discussions.

REFERENCES

- [1] K. J. Kim, "Circular polarization with crossed-planar undulators in high-gain FELs", *Nucl. Instrum. Methods Phys. Res. A*, vol. 445, pp. 329-332, 2000. doi:10.1016/S0168-9002(00)00137-6
- [2] H. Deng *et al.*, "Polarization switching demonstration using crossed-planar undulators in a seeded free-electron laser", *Phys. Rev. ST Accel. Beams*, vol. 17, pp. 020704, 2014. doi:10.1103/PhysRevSTAB.17.020704
- [3] E. Ferrari *et al.*, "Single shot polarization characterization of XUV FEL pulses from crossed polarized undulators", *Sci. Rep.*, vol. 5, pp. 13531, 2015. doi:10.1038/srep13531
- [4] P. Elleaume, "Generation of various polarization states from insertion devices: A review", *Rev. Sci. Instrum.*, vol. 60, pp. 1830-3, 1989. doi :10.1063/1.1140915
- [5] E. Allaria *et al.*, "Highly coherent and stable pulses from the FERMI seeded free-electron laser in the extreme ultraviolet", *Nat. Photon.*, vol. 6, pp. 699-704, 2012. doi.org/10.1038/nphoton.2012.233
- [6] A. A. Lutman *et al.*, "Polarization control in an X-ray free-electron laser", *Nat. Photon.*, vol. 10, pp. 468-472, 2016. doi.org/10.1038/nphoton.2016.79
- [7] C. T. Chen *et al.*, "Experimental confirmation of the X-Ray magnetic circular dichroism sum rules for iron and cobalt", *Phys. Rev. Lett.*, vol. 75, pp. 152-155, 1995. doi:10.1103/PhysRevLett.75.152
- [8] J. Chavanne *et al.*, "A novel fast switching linear/helical undulator", in *Proc. EPAC'98*, Stockholm, Sweden, Jun. 1998, pp. 317-319.
- [9] F. Marteau *et al.*, "Description of an electromagnetic-permanent magnet helical undulator for fast polarization switching", *IEEE Trans. Appl. Supercond.*, vol. 22, pp. 4102004, 2012. doi:10.1109/TASC.2012.2182973

- WEP100**

LINEAR POLARISATION VIA A DELTA AFTERBURNER FOR THE COMPACTLIGHT FACILITY*

H. M. Castañeda Cortés[†], N. R. Thompson, D. J. Dunning

ASTeC and Cockcroft Institute, STFC Daresbury Laboratory, Warrington, United Kingdom

Abstract

We studied the degree of polarisation of the FEL radiation from the diverted-beam scheme [1, 2] using the layout of the CompactLight facility [3], which is in the process of being designed. To satisfy the polarisation requirements defined by the users [4] without compromising the aim of the facility to be compact, we studied a configuration comprising a helical Super Conductive Undulator (SCU) followed by a Delta afterburner (configured to generate linearly polarised light). The trade-offs between the SCU length, afterburner length, degree of polarisation and pulse energy are presented and discussed.

INTRODUCTION

The CompactLight project aims to design next generation light sources which provide competitive FEL performance whilst aiming for a compact design and lower maintenance costs [3]. A study is carried out to characterise a scheme with an afterburner to generate linearly polarised radiation for the CompactLight project. The FEL performance of the undulator line with the afterburner is compared to the case where a variable polarising undulator is considered as stand-alone (set up to generate linearly polarised coherent radiation). The afterburner in the undulator line constrains the beam energy, radiation wavelength and degree of polarisation of the facility. The design choices on the undulator and the afterburner will provide an optimization of the pulse energy without losing sight of the objective of being compact.

AFTERBURNER AND FEL PERFORMANCE (SIMULATION)

A comparison of FEL performance is done for two scenarios:

- I. An undulator line with a stand-alone undulator delta undulator configured to generate linearly polarised light.
- II. Helical SCU as main undulator and delta undulator to generate linearly polarised radiation as afterburner (see Fig. 1).

Both options are tuned up to the same resonant wavelength, corresponding to 16 keV photon energy (list of design parameters for both undulators displayed in Table 1). An electron beam traversing the undulator line with beam parameters listed in Table 2 is simulated in Genesis1.3 [5] to assess the FEL performance of the proposed scenarios. Preliminary es-

* This work has received funding from the H2020 CompactLight Project via the European Union's Horizon 2020 research and innovation programme under grant agreement No 777431.

[†] hector.castaneda@stfc.ac.uk

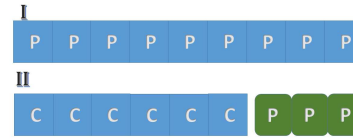


Figure 1: Options to generate linearly polarised radiation.

Table 1: Undulator Parameters Defined for SCU and Delta Undulator

Undulator type	a_w	λ_u (mm)	l_{section} (m)
SCU	0.907	9.85	2.27
Delta (AB)	0.546	13.83	2.28

Table 2: Electron Beam Parameters

Electron beam parameter	Value
Beam Energy	5.5 GeV
Peak Current	5 kA
Normalised $\epsilon_{x,y}$	0.2 mm-mrad
RMS slice energy spread	0.01%
Average β function	9 m

timations of the FEL saturation length and saturation power for the SCU and delta undulators (in stand-alone mode) are calculated and shown in Table 3.

Table 3: FEL Figures of Merits for Both SCU and Delta Undulator in its Configuration to Generate Linearly Polarised Radiation

Undulator type	L_{sat} (m)	P_{sat} (GW)	E_{sat} (μJ)
SCU	15.61	9.53	52.11
Delta	29.13	7.53	41.19

Given that the normal saturation length for the SCU is 15.61 m and the saturation length for the delta undulator is 29.13 m, option II is more compact than option I as long as the length of the afterburner is less than 13 m. Table 4 shows the amount of space saved by different afterburner lengths (with ΔL being the difference between the lengths of both options).

Figure 2 shows the ratio of pulse energies obtained for option II compared to option I. The green dotted line in Fig. 2 corresponds to the maximum pulse energy obtained per number of afterburner sections (from 1 to 5). As shown, the maximum pulse energies for option II take values between 17% up to 68.4% of the pulse energy of the radiation

Table 4: Reduction in Length of the SCU + Afterburner Option Compared to the Delta Undulator Option

AB length (m)	$\Delta L(m)$	$E_{AB}/E_{\text{delta-sat}}$
2.28	10.9	17.2%
4.56	8.7	24.4%
6.84	6.4	31.3%
9.13	4.1	42.6%
11.4	1.8	68.4%

generated for option I. The shortest afterburner will provide a more compact option II layout compared to the option I (saving around 11 m in space), but will also provide the poorest performance in terms of pulse energy obtained at the end of the afterburner (ratio of pulse energies around 17%). On the other hand, the largest afterburner (with 5 sections) provides the closest pulse energy compared to the one generated by option I at saturation (68%). The space saved by adding this afterburner is only 1.8 meters. Thereby, a compromise between the compactness of the undulator line and the FEL performance in terms of pulse energy must be made. A shorter undulator line gives linearly polarized radiation but at the cost of reduced pulse energy.

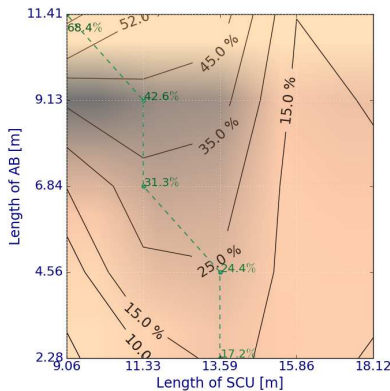


Figure 2: Ratio of the pulse energy for the SCU + afterburner option to the saturation pulse energy from the delta undulator, as a function of the lengths of the SCU and afterburner (green dotted line: maximum pulse energy ratio per afterburner length).

Option II assumes that the radiation coming from the SCU is blocked such that the electron bunch will not interact with it further down the line. Therefore, the degree of polarisation coming out of the afterburner is exactly 100%. In practice, the beam-diverted scheme together with the inverse taper [1] provides a natural solution in order to suppress the background radiation coming from the main undulator before the electrons arrive to the afterburner. In the following, an analysis of the FEL performance of option II, with an inverse tapered helical SCU is performed in accordance to what was proposed in an earlier work by Schneidmiller and Yurkov [1].

IMPACT OF INVERSE TAPER ON FEL PERFORMANCE

For option II, a scan over different linear inverse tapers was done for different SCU and afterburner lengths. To identify the optimal taper, the ratio between bunching parameters and peak power obtained at the end of the tapered undulator and at saturation for the untapered SCU are compared. The growth rate is reduced and the gain length gets longer in the presence of an inverse taper. Therefore, the radiation power at the end of the SCU is noticeably suppressed, whereas the bunching keeps growing [1].

Figure 3 shows the bunching and peak power ratios at the end of the tapered SCU compared to the untapered SCU at saturation. The largest bunching ratio between the tapered and untapered SCU corresponds to a SCU with 8 sections ($L_{SCU}=18.12$ m). For tapers within the range of $\Delta a w_0 \in (-0.006, -0.0045)$, optimal taper range, the bunching ratio is between 75% and 82% (blue contour lines in Fig. 3) The peak power ratio is between 7% and 20% (red contour lines in Fig. 3).

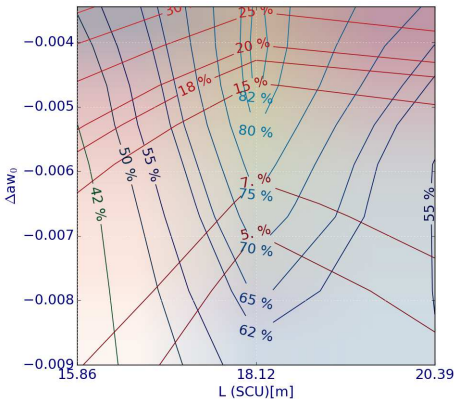


Figure 3: Bunching and peak power ratios obtained at the end of the tapered SCU compared to the untapered SCU (blue contour lines: peak power ratio. Red contour lines: bunching ratio).

Figure 4 shows the ratio of pulse energies obtained for option II compared to option I (for different number of afterburner segments). For afterburners with one to three sections and tapers within the optimal taper range ($-0.045 \geq \Delta a w_0 \geq -0.006$, $L_{SCU} = 18.12$ m), the maximum ratio of pulse energies covers a range between 18% and 62%. Larger afterburners will generate pulses with larger pulse energies for the same taper range (91% of the pulse energy obtained for option I in the case of an afterburner with 4 sections), but will not fulfil the requirement of a compact undulator line. The compromise between total length of option II and FEL performance is still necessary. As shown in Fig. 4, shorter afterburners will have poorer performances in terms of pulse energy (reaching up to 18% of the saturation pulse energy generated via option I).

Following Schneidmiller and Yurkov, the degree of polarisation is defined in terms of the peak power obtained at the

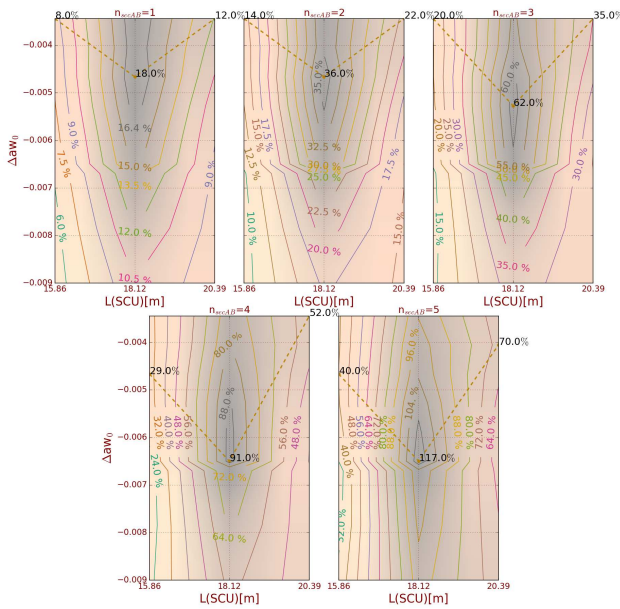


Figure 4: Ratios of pulse energies at the end of the afterburner (option II) compared to the saturation pulse energy obtained for option I (dotted black line: maximum ratio of pulse energies ratio per SCU length).

end of the SCU and the afterburner as follows [1]

$$\text{Deg. Pol.} = 1 - \frac{P_{\text{end-SCU}}}{P_{\text{end-AB}}} \quad (1)$$

The degrees of polarisation for different afterburner lengths are shown in Fig. 5. For the shortest afterburner (one section), the degree of polarisation for the optimal taper is shown to be mainly circular (Deg. Pol. $\ll 1$). The degree of polarisation grows more linear (closer to 100%) as larger afterburners are considered for option II. For an afterburner with 3 sections, the degree of polarisation corresponding to the tapers in the optimal taper range takes values between 55% and 82%. Therefore, a new compromise between the afterburner length and the degree of polarisation needs to be made. A shorter afterburner will defines a more compact option II layout, but the background radiation from the SCU is more prominent. For longer afterburners, the FEL performance improves noticeably (pulse energy ratio of 91% for a four section afterburner within the optimal taper range) and the degree of polarisation shows a suppression of the background radiation from the SCU (around 85%), but the length of the undulator line is less compact.

CONCLUSION

A study was carried out to show the FEL performance of a linearly polarising afterburner for the H2020 CompactLight Project. Comparisons of pulse energy, degree of polarisation and total length of the undulator line (SCU and a delta afterburner to generate linearly polarised radiation) were performed (with and without the installation of an inverse taper in the SCU). For the untapered case, the pulse energy

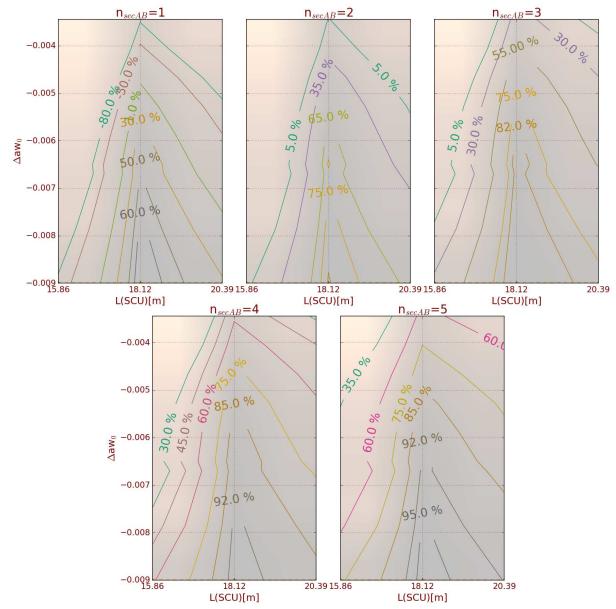


Figure 5: Degree of polarisation, Eq. (1), for different number of afterburner sections.

obtained at the end of the afterburner took values between 17.2% and 68.4% of the saturation pulse energy of the delta undulator as stand-alone. The shortest afterburner had the poorest performance, but saved the largest amount of space in the undulator line (10.9 m). In the case of a inverse tapered SCU, a range of optimal tapers was chosen (corresponding to a tapered SCU with 8 sections, a suppression of the peak power obtained at the end of the tapered SCU between 7% and 20% of the saturation peak power of the untapered SCU and a bunching ratio between 75% and 82%). A shorter afterburner satisfies the main objective of the H2020 CompactLight project to design a compact facility (saving up to 10.9 m), but will provide a poorer FEL performance in pulse energy (around 18% of the saturation pulse energy of the delta undulator as stand-alone for the inverse taper scheme) and a poor degree of polarisation (much less than 1 for the tapered SCU). The degree of polarisation grows and gets closer to 1 as larger afterburners are considered. Generation of variable polarised radiation by changing the configuration of the delta afterburner is a desirable feature and will be studied in the future.

REFERENCES

- [1] E. A. Schneidmiller and M. V. Yurkov, "Obtaining high degree of circular polarization at x-ray free electron lasers via a reverse undulator taper," *Phys. Rev. Spec. Top. - Accel. Beams*, vol. 16, p. 110702, 2013. doi:10.1103/PhysRevSTAB.16.110702
- [2] A. Lutman *et al.*, "Polarization control in an X-ray free-electron laser," *Nat. Photonics*, vol. 10, pp. 468–472, 2016. doi:10.1038/nphoton.2016.79
- [3] G. D'Auria *et al.*, "The CompactLight Design Study Project", in *Proc. IPAC'19*, Melbourne, Australia, May 2019, pp. 1756–1759. doi:10.18429/JACoW-IPAC2019-TUPRB032

A PLASMA ATTENUATOR FOR SOFT X-RAYS IN LCLS-II*

Alan S. Fisher[†], Andrew L. Benwell, Bryce T. Jacobson, and Yiping Feng
SLAC National Accelerator Laboratory, Menlo Park, California, USA

Abstract

LCLS used a gas column to attenuate soft x-ray pulses by factors of up to 10^5 . In LCLS-II, thermal effects from x-ray absorption at high repetition rates will lead to unpredictable attenuation that depends on the spacing and energy of prior pulses. An argon plasma in an RF cavity is presented as an alternative. X-ray absorption then becomes a perturbation compared to the energy deposited from RF excitation. An LCLS-II solid-state RF amplifier, generating up to 5 kW at 1.3 GHz, can provide the drive, and the FPGA-based low-level RF controller can be programmed to track tuning with plasma density. Several diagnostics are planned to monitor plasma properties over a fill-pressure range of 10 to 1000 Pa.

INTRODUCTION

Temporary reduction of the pulse energy of an x-ray FEL beam is often required to prevent damage to critical components, such as highly specialized x-ray detectors, for alignment, or to study x-ray nonlinear effects. An x-ray attenuator allows the user to vary the incident pulse energy in a well-controlled manner without altering other FEL characteristics, unlike other methods such as operating at different points of the FEL gain curve or lowering the electron bunch charge. For soft x-rays, a fully saturated FEL pulse at a typical operating bunch charge of 100 pC would completely damage any solid attenuator located sufficiently close to the FEL source point. Consequently, attenuation in gas has been considered the only viable solution; gas attenuators have been implemented at many facilities around the world, including the Linac Coherent Light Source (LCLS) [1] at SLAC.

At a sufficiently low repetition rate, such as 120 Hz at LCLS, a gas attenuator at room temperature provides an effective attenuation that is simply governed by the Beer-Lambert law [2-4] (relating the gas pressure at a constant temperature to the attenuation length), and is deterministic and independent of the FEL beam parameters. However, LCLS-II will operate at repetition rates up to 1 MHz. With increasing rate, a gas attenuator will begin to exhibit nonlinearities that depend on the FEL pulse rate and energy, along with the thermal diffusivity and absorption cross section of the gas. Even more troubling is the onset of hysteresis: the attenuation of trailing pulses depends on the intensities and arrival times of earlier ones. Such previously unsuspected behavior arises because the energy deposited by an FEL pulse requires a finite time to dissipate, on the order of 1 ms. The original gas density distribution is perturbed, modifying the effective attenuation of the pulses that come during this recovery time.

Here we present the concept of a column of partially ionized plasma in place of the gas, in order to stabilize the attenuation at high repetition rates. The plasma is hotter, and its thermal relaxation is much faster. The energy deposited by a few-mJ FEL pulse would then present only a small perturbation, and the densities of electrons, neutrals, and ions will recover between LCLS-II pulses. The plasma would provide a stable, controllable, and deterministic x-ray attenuator.

ATTENUATION IN A GAS COLUMN

A typical gas-based attenuator for x-ray FEL pulses consists of a few-meter-long gas column, bookended by differential pumping sections to maintain ultra-high vacuum elsewhere along the beamline. Nitrogen and argon are common, inexpensive choices, operating at pressures between 10 and 1000 Pa. Soft x-rays below 1.5 keV can be attenuated by a factor of up to 10^5 .

Early in the planning for LCLS-II, concerns about the effect of its high repetition rate led to thermodynamic and hydrodynamic simulations [5,6] of a gas attenuator. It was found that the x-ray energy deposited by photoabsorption would eventually thermalize into the kinetic degrees of freedom of the gas molecules, raising the temperature on axis and reducing the local density to create a “hole” that lasts for a few ms, during which the attenuation of subsequent pulses is reduced.

When the FEL runs at a high but steady rate and pulse energy, a gas attenuator may stabilize, although at a level different from that prescribed by the Beer-Lambert law. However, the pulse energy fluctuations of a SASE FEL cause each pulse to encounter a different gas density distribution. Instead of a true steady state, the distribution depends on the deposited energy and arrival time of earlier pulses, causing hysteresis in the effective attenuation.

Experimental evidence of the density “hole” induced by an FEL pulse was first demonstrated at LCLS using a two electron bunches separated by 123 ns. Each bunch generated a hard x-ray pulse that passed through a test gas cell. The transmission of the second pulse relative to the first increased by approximately 20% [7].

ATTENUATION IN A PLASMA COLUMN

Concept

The fundamental deficiency of a room-temperature gas attenuator operating at high repetition rate stems from its relatively low energy scale of 25 meV/atom, corresponding to a temperature of 300 K. Thermal equilibrium is destroyed when the gas absorbs a mJ x-ray pulse and recovers after a thermal relaxation time of a few ms, 1000 times too slow for MHz pulse spacing. In contrast, the plasma electron temperature would be 5 eV, or 60 000 K.

* SLAC is supported by the U.S. Department of Energy, Office of Science, under contract DE-AC02-76SF00515.

[†] email address afisher@slac.stanford.edu

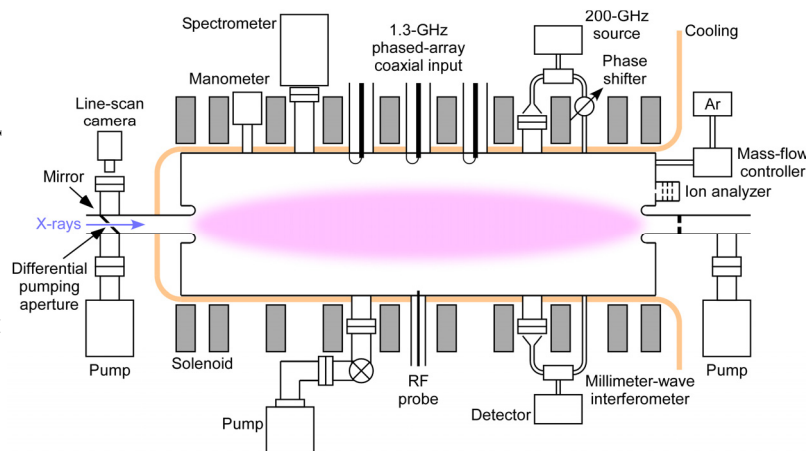


Figure 1: A conceptual design of a plasma-based x-ray attenuator, with the associated pressure controls and plasma diagnostics.

The thermalization of fast photoelectrons generated by the x rays becomes a small perturbation to the plasma with minimal impact on the attenuation of subsequent pulses. The plasma can be created and heated by either RF or a DC discharge [8]. In either case, collisions heat the ions and neutrals. RF heating via certain modes (below) offers the further advantage of direct ion excitation.

Consider partially ionized ($\approx 0.1\%$) argon, with the number density of neutrals n_0 well above that of electrons n_e and ions $n_i = n_e = n$. Compared to ionization, which removes only an outer-shell electron, x-ray absorption ejects a core electron. Because this electron is more tightly bound, ionization should not alter the absorption cross section of an ion compared to a neutral. Consequently, a given attenuation requires the same density for a gas column or for the gas that is ionized to form a plasma column.

Plasma Parameters

In 1889, Paschen found that the minimum electric field to ionize a gas occurs at an optimal pressure [9]. Breakdown requires an avalanche in which the field accelerates a free electron to the ionization energy (15.76 eV for Ar) between collisions. Above the optimal pressure, collisions are too frequent for sufficient energy gain. Below it, in an RF-driven discharge, an electron is unlikely to collide in a period of oscillation. In a DC field, the mean free path exceeds the chamber size, and collisions are again unlikely. This optimal pressure is typically near 100 Pa.

Argon is a relatively easy gas to ionize with RF, requiring a field as low as 400 V/cm at 1 GHz and 130 Pa [10]. Such a field is easily achieved in a resonant cavity of moderate Q . Argon was effective for absorbing x rays in the LCLS gas attenuator and so is well suited for a plasma attenuator. At 100 Pa and 300 K, its mean free path is 70 μm and its density is $2.4 \times 10^{16} \text{ cm}^{-3}$. The collision rate for 5-eV electrons with neutrals is then 13 GHz.

Plasma Diagnostics

Several diagnostics verify the conditions for breakdown and monitor the plasma parameters for suitability and

stability. Figure 1 sketches these, grouped around the chamber.

Since heat from the 5-kW RF drive ultimately flows to the chamber walls, they are water cooled. A solenoid provides an axial (z) magnetic field B_s for better electron confinement. For B_s to be helpful, the electron cyclotron frequency should exceed the collision rate; consequently, a field of at least 0.5 T is desirable. The solenoid is also water cooled.

As in the gas attenuator, differential pumping maintains ultra-high vacuum conditions on either side of the plasma chamber. Inside, a mass-flow controller, a capacitance manometer, and a vacuum pump with a throttling valve operate in a control loop to maintain the desired pressure

on the periphery of the plasma. Confinement of the RF power does not depend on the pumping apertures, since the diameters of the entrance and exit tubes are below cut-off at 1.3 GHz.

The differential-pumping aperture at the upstream end has a mirrored face and is tilted to give a camera an end-on view of the center of the plasma. A density hole would reduce the intensity on axis when high-rate x rays are present. The effect of the plasma can be tested by reducing the RF drive or the solenoidal field. A line-scan (one-dimensional) camera is preferred to a standard 2D camera for the fast readout (up to 200 kHz), which can highlight plasma breakdown and any change in the plasma emission following an x-ray pulse or pulse train.

Optical spectroscopy provides insights into the excitations of plasma ions versus neutrals. X-ray absorption by an argon ion produces doubly ionized argon (Ar^{++}). For a given plasma density, the ratio of the spectral lines of Ar^{++} to lines of single ionized argon (Ar^+) then scales with the energy in the x-ray pulse.

To determine the degree of ionization, a millimeter-wave (200 GHz) interferometer measures the plasma density integrated across the diameter. The phase shift from the plasma's refractive index η is compared to a reference path outside the chamber. Both the interferometer and the camera indicate the stability of the discharge.

The ion analyzer [11], which measures the ion energy distribution, is essentially a Faraday cup with a series of biased grids to reject electrons and to sweep the energy of ions accepted by the cup.

RF Penetration into the Plasma

Consider launching a wave in the y direction at a frequency (see below) $f_{\text{RF}} = \omega_{\text{RF}}/(2\pi) = 1.3 \text{ GHz}$. To heat the center of the plasma, the wave must first propagate inward from the wall through a rising plasma density n that strongly affects RF propagation.

The response of electrons or ions to a z -polarized wave is not affected by B_s , and so the plasma's refractive index is the same as that of an unmagnetized plasma, and depends only on the electron plasma frequency ω_{pe} :

$$\eta^2 = 1 - \frac{\omega_{pe}^2}{\omega_{RF}^2} = 1 - \frac{ne^2}{\epsilon_0 m_e \omega_{RF}^2} \quad (1)$$

The wave penetrates into the plasma until it encounters a cutoff ($\eta^2 < 0$). For 1.3 GHz, this occurs at $n = 2.1 \times 10^{10} \text{ cm}^{-3}$, well below that needed for the desired pressure and ionization fraction. There is no resonance ($\eta \rightarrow \infty$).

An x-polarized wave can excite a resonance at the “lower-hybrid” frequency ω_{LH} [12], which drives both electrons and ions and depends on the ion plasma frequency ω_{pi} :

$$\frac{1}{\omega_{LH}^2} = \frac{1}{\Omega_i^2 + \omega_{pi}^2} + \frac{1}{\Omega_e \Omega_e} \quad (2)$$

Here $\Omega_{e,i} = eB_s/m_{e,i}$ are the electron and ion cyclotron frequencies, respectively above and below ω_{RF} . However, the wave is blocked from the resonance by a cutoff at a density (for $B_s = 0.5 \text{ T}$) of $2.5 \times 10^{11} \text{ cm}^{-3}$, still far too low.

If instead the wave is launched in the yz plane at an angle to y, the cutoff can be avoided [12]. An elliptically polarized wave at an angle of 60° to z can penetrate to a core plasma density exceeding 10^{15} cm^{-3} , where it is strongly resonant. Lower hybrid heating and current drive in fusion experiments launch such angled waves with a phased array of waveguides [13]. The phased array illustrated in Fig. 1 follows this model.

RF Cavity

The plasma chamber will be designed as a resonant cavity that supports the launch of an elliptically polarized 1.3-GHz wave at an appropriate angle to the solenoidal field, to generate and heat the plasma. The cavity will support both the TM_{01} and TE_{11} modes with an electric field on axis of approximately 1.5 kV/cm with 2 kW of applied RF, more than sufficient to ionize 100 Pa of argon [10], with some RF power overhead for cavity control.

The size of a cavity at this frequency is appropriate for an X-ray attenuator, with a length of $\approx 1 \text{ m}$. Because the argon is primarily ionized where the field is high along the axis and where the solenoid confines the plasma, this arrangement is suited to attenuating x rays on axis.

A similar concept, RF-generated plasma in a resonant cavity, is now routinely used to clean niobium accelerator structures. RF at 1.3 GHz ignites 25 Pa of argon, with a small percentage of O_2 added after ignition to aid in removing hydrocarbons [14]. Wall cleaning benefits from using high-order modes to generate a low-temperature plasma throughout the cavity rather than along the axis.

RF Power and Control

The choice of 1.3 GHz allows us to use common LCLS-II RF hardware, including the 5-kW solid state RF amplifier (SSA). The SSA is designed as a transistor array with RF isolators to protect against reflected power at each transistor output. The array can be reconfigured to drive multiple cavity antennas, each at a different phase.

LCLS uses an FPGA-based low-level RF controller with a high closed-loop bandwidth. With a relatively low field gradient in a low-Q wideband cavity, the tuning

range is wide enough to quickly track changes in plasma-loading of the cavity with a self-excited loop algorithm.

SUMMARY AND NEXT STEPS

A gas-based attenuator for a soft x-ray FEL will exhibit unpredictable attenuation and hysteresis at high repetition rates, as the heat deposited by the x rays causes a density depression along the axis. An attenuator based on an RF-driven plasma column can provide a more stable alternative, since the x-ray heat load becomes a perturbation compared to the energy stored in the plasma.

We have proposed a prototype plasma chamber to be built over the next two years, to demonstrate the control of a plasma with the requisite density and stability.

REFERENCES

- [1] D. D. Ryutov *et al.* Technical Report LLNL-TR-421318 (2009). Lawrence Livermore National Laboratory, Livermore, CA 94550, USA.
- [2] J. H. Lambert, *Photometria Sive de Mensural et Gradibus Luminis, Colorum et Umbrae*, Augsburg, Germany: Eberhardt Klett, 1760.
- [3] A. Beer, “Bestimmung der Absorption des rothen Lichts in farbigen Flüssigkeiten”, *Annalen der Physik und Chemie*, vol. 86, p. 78, 1852.
- [4] IUPAC, *Compendium of Chemical Terminology*. doi:10.1351/goldbook.B000626
- [5] Y. Feng *et al.*, “Filamentation effect in a gas attenuator for high-repetition-rate X-ray FELs”, *J. Synchrotron Radiat.*, vol. 23, p. 21, 2016. doi:10.1107/S1600577515018408
- [6] B. Yang *et al.*, “Fluid dynamics analysis of a gas attenuator for X-ray FELs under high-repetition-rate operation”, *J. Synchrotron Radiat.*, vol. 24, p. 547, 2017. doi:10.1107/S1600577517005082
- [7] Y. Feng *et al.*, “Direct experimental observation of the gas density depression effect using a two-bunch X-ray FEL beam”, *J. Synchrotron Radiat.*, vol. 25, p. 145, 2018. doi:10.1107/S1600577517014278
- [8] A. Herscovitch, “Neutralization of multi-MeV light negative ions by plasma neutralizers”, *Rev. Sci. Instrum.*, vol. 55, p. 1744, 1984. doi:10.1063/1.1137669
- [9] F. Paschen, “On the potential difference required for spark initiation in air, hydrogen, and carbon dioxide at different pressures”, *Ann. Physik.*, vol. 273, p. 69, 1889.
- [10] A. D. MacDonald *et al.*, “Microwave Breakdown in Air, Oxygen, and Nitrogen”, *Phys. Rev.*, vol. 130, p. 1841, 1963. Fig. 2. doi:10.1103/PhysRev.130.1841
- [11] A. W. Molvik, “Large acceptance angle retarding-potential analyzers”, *Rev. Sci. Instrum.*, vol. 52, p. 704, 1981. doi:10.1063/1.1136655
- [12] Kenro Miyamoto, *Plasma Physics for Nuclear Fusion*, Cambridge, MA, USA: MIT Press, 1976.
- [13] M. Brambilla, “Slow-wave launching at the lower-hybrid frequency using a phased waveguide array”, *Nucl. Fusion*, vol. 16, p. 47, 1976. doi:10.1088/0029-5515/16/1/005
- [14] P. Berrutti *et al.*, “Plasma ignition and detection for in-situ cleaning of 1.3 GHz 9-cell cavities”, *J. Appl. Phys.*, vol. 126, p. 023302, 2019. doi:10.1063/1.5092235

A HIGH-POWER, HIGH-REPETITION RATE THz SOURCE FOR LCLS-II PUMP-PROBE EXPERIMENTS*

Z. Zhang, A. S. Fisher, M. C. Hoffmann, Z. Huang[†], B. Jacobson,
P. S. Kirchmann, W.-S. Lee, A. Lindenberg, E. Nanni, R. Schoenlein
SLAC National Accelerator Laboratory, Menlo Park, CA, USA
S. Sasaki, J. Xu, Argonne National Laboratory, Lemont, IL, USA

Abstract

Experiments using a THz pump and an x-ray probe at an x-ray free-electron laser (XFEL) facility like LCLS-II require frequency-tunable (3 to 20 THz), narrow bandwidth ($\sim 10\%$), carrier-envelope-phase-stable THz pulses that produce high fields ($> 1\text{ MV/cm}$) at the repetition rate of the x rays and well synchronized with them. In this paper, we study a two-bunch scheme to generate THz radiation at LCLS-II. We describe the two-bunch beam dynamics, the THz wiggler and radiation, as well as the transport system bringing the THz pulses from the wiggler to the experimental hall.

INTRODUCTION

The effective coupling of advanced THz sources with XFEL capabilities will open many new science opportunities. THz oriented workshops at SLAC [1], FERMI, Eu-XFEL [2] and elsewhere in the past eight years have highlighted the demand for the ability to carry out these types of experiments.

The new science opportunities presented by a high-repetition rate FEL such as the LCLS-II create new opportunities, demands, and challenges for THz sources that go beyond what has been considered in previous workshops. Some critical capability gaps can already be identified that appear to be beyond the projected achievable properties of table-top sources. Among them are the intense sources in the well-known THz gap between 3-15 THz. For field driven effects, a broadband, single-cycle THz pulse with a peak electric field strength of 10 MV/cm can approach the atomic bonding strength in matters. For resonant excitation, a tunable, narrow bandwidth ($\sim 10\%$) source with at least $10\text{ }\mu\text{J}$ pulse energies are desired. These required THz characteristics are summarized in Table 1.

Table 1: Required THz Characteristics

Waveform	Single cycle		10 cycles	
E-field	10 MV/m		1 MV/m	
Frequency	5 THz	15 THz	5 THz	15 THz
Spot Size	200 μm	100 μm	200 μm	100 μm
Pulse Duration	100 fs	33 fs	1000 fs	330 fs

Although a dedicated accelerator with tens of MeV beam energy can achieve some of these capabilities [3, 4], it becomes increasingly difficult to reach 10 THz and higher

frequencies with significant pulse energies. In addition, a high-repetition rate stand-alone accelerator with the technical issues of synchronization and the associated machine protections becomes rather complex. Inspired by the pioneering work of the FLASH THz beamline [5], we propose to install a permanent-magnet or electromagnet wiggler after the LCLS-II undulators and to use a two-bunch scheme to produce intense THz pulses for high-rep rate pump-probe experiments. We note that an earlier study of a THz source for Eu-XFEL has a similar two-bunch scheme while employing a high-field superconducting wiggler [6].

TWO-BUNCH SCHEME

Figure 1 shows a schematic of the two-bunch concept at LCLS-II to produce intense THz radiation. Both bunches are generated by the LCLS-II injector with suitable time separation ($\sim 110\text{ ns}$). Because the THz pump must arrive before the X-ray probe, a first bunch is used to produce THz in the wiggler and a second bunch is for FEL lasing. In our design, the THz bunch will be accelerated to 4 GeV and then kicked out to the bypass line. For THz generation, a higher bunch charge and a shorter bunch length are always desirable. The beam parameters of the THz bunch will be optimized to cover the frequency range from 3 to 20 THz. Moreover, stronger compression of the THz bunch results in poorer beam quality and hence suppress its FEL lasing in the SXR undulator.

The accelerator settings of the LCLS-II are optimized to deliver electron bunches for FEL lasing. The control of the THz bunch cannot be allowed to alter the beam dynamics of the FEL bunch. The compression of the THz bunch can be adjusted by the laser injection time, which changes the acceleration phase in the SRF linac (L1) before the first magnetic chicane (BC1). Figure 2 shows that offsetting the laser injection time changes the beam arrival time of 200-pC bunch at the start of L1. The simulations were performed with ASTRA [7]. The change of arrival time at the start of the L1 varies the beam energy chirp and beam compression downstream. An earlier laser pulse shortens the first bunch for better THz generation. Figure 3 shows the final RMS bunch length at the undulator entrance for the 200-pC THz bunch at different offsets of the relative laser injection time.

Figure 4 shows the bunching factors of the THz beam (100 pC and 200 pC) at different frequencies. The bunching factor of the 200-pC bunch damps quickly with increasing frequency. In practice, we can optimize the bunch charge

* Work supported by U.S. Department of Energy Contracts No. DE-AC02-76SF00515.

[†] zrh@slac.stanford.edu

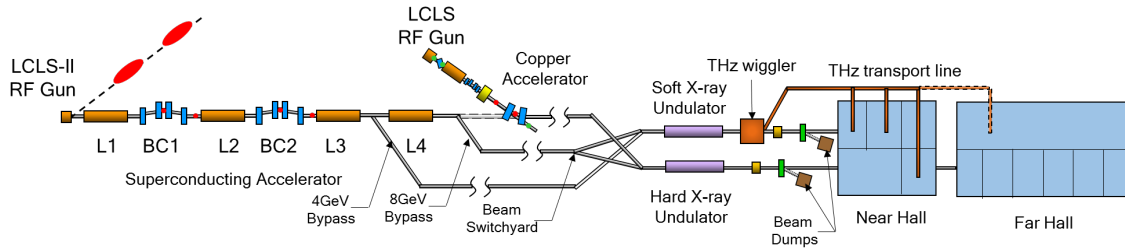


Figure 1: LCLS-II layout showing the linac, soft and hard x-ray undulators, the proposed THz wiggler and transport line, and the Near and Far Experimental Halls.

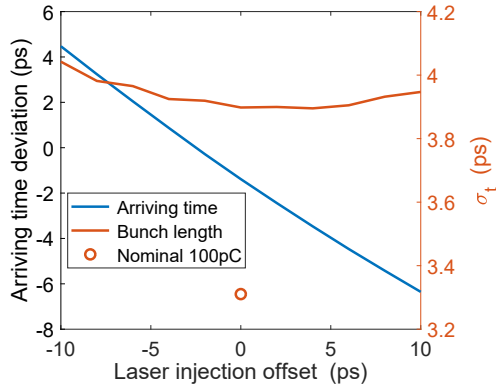


Figure 2: The change in arrival time and RMS bunch length of a 200-pC THz bunch for various laser injection timing offsets at the start of L1 compared with the nominal 100-pC FEL beam. A negative time means arriving the laser pulse arrives earlier in its RF period than does the laser pulse for a nominal 100-pC bunch.

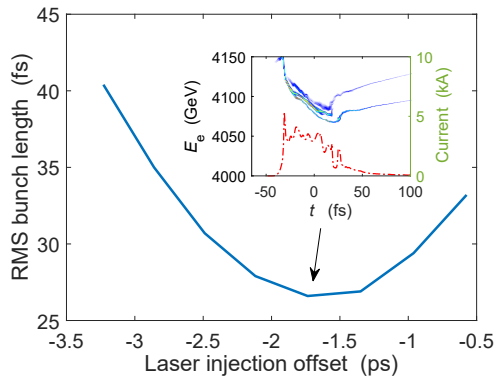


Figure 3: RMS bunch length of the 200-pC THz bunch at the undulator entrance for different laser injection time offset. Insert shows the simulated longitudinal phase space (blue) and the projected peak current (red) for the -1.7 ps laser injection time offset.

to produce THz pulses with high radiated energy at any frequency in the 3- to 20-THz range.

THz WIGGLER AND RADIATION

The parameters of the THz wiggler are optimized for a 4-GeV electron beam energy. We choose 10 wiggler periods to

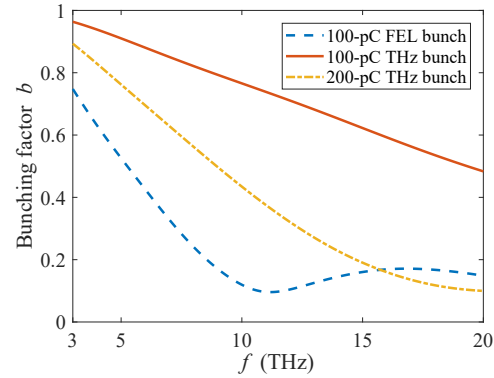


Figure 4: Bunching factors of the nominal LCLS-II 100-pC FEL bunch and the 200-pC THz bunch for 3~20 THz.

produce THz radiation with 10% bandwidth. Figure 5 shows the required peak magnetic field for different wiggler periods. The main limitation in practice is the available magnetic field with a reasonable wiggler gap. We consider two wiggler technologies for THz generation, based on hybrid permanent magnets and electromagnets.

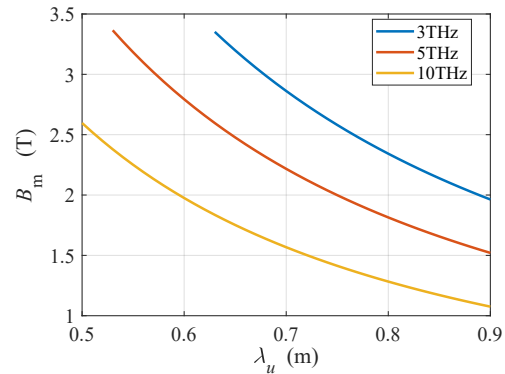


Figure 5: Magnetic field at different wiggler periods when using 4 GeV beam to generate 3, 5 and 10 THz radiation.

In a hybrid permanent-magnet wiggler, the peak field can be numerically fitted as a function of gap g and period λ_u [8]

$$B_0 = a \exp \left(b \frac{g}{\lambda_u} + c \left(\frac{g}{\lambda_u} \right)^2 \right) \quad (1)$$

with $a = 3.381$, $b = -4.730$, $c = 1.198$. Based on this, the wiggler gap is shown in Fig. 6. Note that the equation is

valid in the range $0.1 < g/\lambda_u < 1$. When $\lambda_u = 0.77$ m, the required wiggler gap is ~ 50 mm at 3 THz.

In an electromagnet wiggler, the gap is fixed and the magnetic field is varied by the current in the coils. The conventional electromagnet can reach 2.5 T with a clearance gap of 50 mm. In this case, we can produce 3-THz radiation when the wiggler period is 78 cm. An additional advantage of the electromagnet wiggler is that the magnetic field can be independently controlled by separate power supplies.

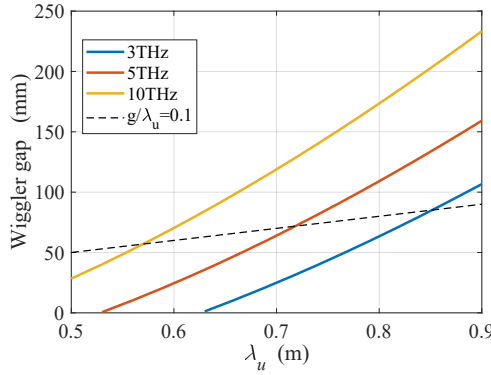


Figure 6: Gap of hybrid-type permanent magnetic wiggler at different wiggler period when using 4 GeV beam to generate 3, 5 and 10 THz radiation.

The transverse distribution can be calculated from angular distribution of undulator radiation. The long wiggler length and small gap limit the THz output due to diffraction, especially at low frequency. Figure 7 shows the transverse distribution of the radiation at 10 THz (with 10% bandwidth from 9.5 to 10.5 THz) for the 77-cm wiggler period. We also present the energy density profiles along the two axis. It can be seen that most of the radiation is emitted within a ~ 4 mrad angle. The collection angle in the wiggler can be estimated by $\theta = g/L_u$ where $L_u = N_u \lambda_u$ is the total wiggler length. With a 50-mm gap in a 10-period wiggler, $\theta = 6.5$ mrad, which is larger than the angular divergence of the 10-THz radiation.

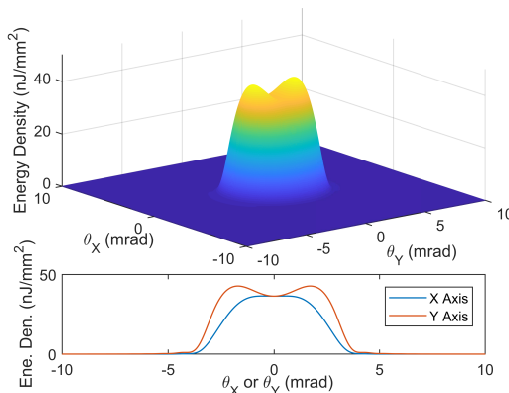


Figure 7: Transverse distribution of 10 THz radiation and the corresponding energy density profiles along two axis.

The total achievable THz pulse energy depends on the specific layout of wiggler and transport system (THz mir-

rors). Here we can estimate the pulse energy by the bunching factor spectra and the simplified equation as [9]

$$\frac{dW}{d\omega/\omega} = 1.43 \times 10^{14} N_u I [A] \frac{h K^2 [JJ]_h^2 \text{ photons}}{1 + K^2/2 \text{ 0.1\% BW}} \quad (2)$$

The pulse energy from the 100-pC and 200-pC THz beam in Fig. 4 is presented in Fig. 8.

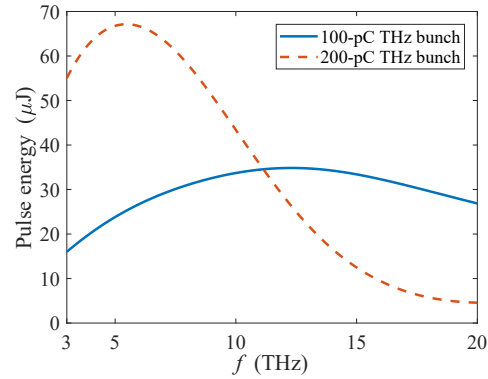


Figure 8: The estimated THz energy of the 100-pC and 200-pC THz bunch for at different radiation frequency.

THz TRANSPORT

Soft X-rays follow a nearly straight path from the undulator to the user hutches in the Near Experimental Hall. The strongly diffracting THz requires optical relay imaging through large-diameter tubing (200 mm) with frequent reimaging (every 12 to 15 m). The imaging uses reflective optics, due to the wide bandwidth and the lack of good refractive materials. Either off-axis paraboloidal (OAP) or toroidal mirrors may be used, with 45° incidence. Imaging is maintained by separating adjacent mirrors by a distance equal to the sum of their focal lengths. Since water vapor absorbs THz, the tubing should be evacuated to 1 Pa or below. Alternatively, the tubing could be filled with nitrogen or another inert gas. A preliminary layout requires a combination of 12 focusing and 22 flat mirrors to reach one of the principal hutches. Fortunately, reflection losses at this frequency are below 1% per surface, which would provide 70% transmission. The time between the two electron bunches is determined by the extra path of the THz compared to the straight x-ray path. The path through the maze requires an additional 108 ns.

REFERENCES

- [1] K. Gaffney, J. Goldstein, P. Kirchmann, A. Lindenberg, and Z.-X. Shen, Workshop *Frontiers of THz Science*, (2012).
- [2] P. Zalden *et al.*, Terahertz Science at European XFEL, XFEL.EU TN-2018-001-01.0 (2018).
- [3] B. Green *et al.*, *Nature Sci. Rep.*, vol. 6, 22256 (2016), doi:10.1038/srep22256(2016).
- [4] J. Schmerge *et al.*, SLAC-R-1049 (2013).

- [5] K. Tiedtke *et al.*, *New Journal of Physics*, vol. 11, 023029 (2009), doi:10.1088/1367-2630/11/2/023029.
- [6] T. Tanikawaa *et al.*, *Journal of Inst.*, vol. 14, P05024 (2019), doi:10.1088/1748-0221/14/05/p05024.
- [7] K. Floettmann, A Space Charge Tracking Algorithm, <http://www.desy.de/~mpyflo/>.
- [8] K. Halbach, *Nucl. Instrum. Methods*, vol. 187, 109 (1981), doi:10.1016/0029-554X(81)90477-8.
- [9] K.-J. Kim, Z. Huang, R. Lindberg, *Synchrotron Radiation and Free-Electron Lasers*, Cambridge University Press, 2017, doi:10.1017/9781316677377.003.

POLARIZING AFTERBURNER FOR THE LCLS-II UNDULATOR LINE*

H.-D. Nuhn[†], SLAC National Accelerator Laboratory, Stanford, USA

Abstract

A fixed-gap polarizing undulator (Delta) has been successfully operated in afterburner mode in the LCLS FEL beamline at the SLAC National Accelerator Laboratory (SLAC) from August 2014 to the end of operations of the LCLS facility in December 2018. The LCLS undulator line is currently being replaced by two new undulator lines (as part of the LCLS-II project) to operate in the hard and soft x-ray wavelength ranges. Polarizing afterburners are planned for the end of the soft x-ray (SXR) line. A new polarizing undulator (Delta-II) is being developed for two reasons: (1) increased maximum K value to be resonant over the entire operational range of the SXR beamline (2) variable gap for K value control. It has been shown that using row phase control to reduce the K value while operating in circular polarizing mode severely degrades the performance of a polarizing undulator in afterburner mode. The device is currently scheduled for installation 2020-2021. The paper will explain the need for the variable gap design backed up by beam based measurements done with the LCLS Delta undulator.

INTRODUCTION

The LCLS Delta polarizing afterburner has been successfully operated [1] with the LCLS FEL for user experiments [2–4] until the shutdown of the facility in December 2018. The SLAC National Accelerator Laboratory (SLAC) is now getting ready to commission a new FEL facility with two undulator lines to produce soft x-ray (SXR) and hard x-ray radiation (HXR). It is planned to install up to three polarizing afterburners at the end of the SXR undulator beamline. It was clear that the 32-mm-period LCLS Delta, which is based on a concept developed by Alexander Temnykh [5], could not be made resonant with the SXR undulators over the high K regime of the operating range because the undulator period of the SXR undulator is 39 mm compared to the 30 mm period length of the LCLS undulators. A new Delta undulator with longer period was required. As work on designing the new device started, the team became aware of a PSI paper by Thomas Schmidt et. al [6]. The PSI group had found that line-width broadening occurred to the undulator radiation under certain operating conditions, when operating a fixed gap APPLE-II undulator, which uses 4 independently movable rows of magnets similar to the Delta undulator and has similar properties. The source of the line-width broadening was found to be a transverse gradient of the undulator parameter, K , that appears when operating the undulator in circular polarizing and at reduced strength. This effect is described in the next section.

TRANSVERSE K GRADIENT

It turns out that polarizing undulators such as the Apple [7] and Delta devices that are basically constructed from 4 rows of permanent magnets, where the longitudinal row positions can be changed during operation to adjust the polarization mode and the undulator parameter, K , will generate a transverse gradient of K for certain combinations of row positions. Such an undulator can be conceptualized as made from two crossed planar pure permanent magnet undulators, each having two rows of permanent magnets in Halbach array [8] configuration mounted on opposite sites of the beam axis. The on-axis field is strongest when north poles at the permanent magnet block end closest the beam axis on one row exactly oppose south poles at the permanent magnet block ends closest to the beam axis on the other row. When the two rows are moved longitudinally with respect to each other by a distance Δz , the on-axis field changes with the cosine of that distance

$$K = K_0 \cos \left(2\pi \frac{\Delta z}{\lambda_u} \right) \quad (1)$$

at constant gap. Here, K_0 is the maximum K value that occurs at $\Delta z = 0$. Such a device is called an Adjustable Phase Undulator [9]. The relative longitudinal position of the two adjustable phase undulators determines the polarization mode, i.e., they will produce planar polarized light when they are aligned and various forms of elliptical, circular or planar light when they are displaced with respect to each other. It turns out that a transverse K gradient occurs in the device when operated in circular mode while $K < K_0$. After the initial observation, this fact was theoretically derived by Zachary Wolf [10] and by Marco Calvi et al. [11]. According to [10], the K gradient can be expressed to first order as

$$\begin{aligned} \left. \frac{\partial K}{\partial x} \right|_{x=y=0} &= \frac{\pm K_{max} k_s^2}{\sqrt{2k_s^2 + 2k_u^2}} \sin \left(\cos^{-1} \left(\frac{K|_{x=y=0}}{K_{max}} \right) \right) \sin \delta, \\ \left. \frac{\partial K}{\partial y} \right|_{x=y=0} &= 0, \end{aligned}$$

where the “+” sign applies when $z_{A,up} > z_{A,dn}$ and $z_{B,up} > z_{B,dn}$ and the “−” sign applies when $z_{A,up} < z_{A,dn}$ and $z_{B,up} < z_{B,dn}$, or

$$\begin{aligned} \left. \frac{\partial K}{\partial x} \right|_{x=y=0} &= 0, \\ \left. \frac{\partial K}{\partial y} \right|_{x=y=0} &= \frac{\pm K_{max} k_s^2}{\sqrt{2k_s^2 + 2k_u^2}} \sin \left(\cos^{-1} \left(\frac{K|_{x=y=0}}{K_{max}} \right) \right) \sin \delta, \end{aligned}$$

where the “+” sign applies when $z_{A,up} > z_{A,dn}$ and $z_{B,up} < z_{B,dn}$ and the “−” sign applies when $z_{A,up} < z_{A,dn}$ and $z_{B,up} > z_{B,dn}$.

* Work was supported by U.S. Department of Energy, Office of Basic Energy Sciences, under Contract DE-AC02-76SF00515.

[†] nuhn@slac.stanford.edu

Here $z_{A,up}$, $z_{A,dn}$, $z_{B,up}$, $z_{B,dn}$ are the z positions of the upper and lower rows of crossed undulators A and B , respectively. The parameter, k_s , depends on the transverse structure of the pole tips. For the SLAC Delta undulator, it has been measured magnetically to $k_s = 186 \text{ m}^{-1}$. Reduction of this parameter is possible to some degree but reducing it to zero seems not to be possible without loosing most of the undulator strength. The parameter $k_u = 2\pi/\lambda_u$ is the undulator wavenumber, with the undulator period $\lambda_u = 32 \text{ mm}$. The parameter, δ , is the polarization control phase, which is $\pm\pi/2$ for the full left or right circular polarization mode and 0 for the linear polarization mode. Thus, in circular polarization mode with $z_{A,up} > z_{A,dn}$ and $z_{B,up} > z_{B,dn}$ the predicted relative on-axis K gradient should be:

$$\frac{1}{K_{\max}} \frac{\partial K}{\partial x} = \frac{k_s^2}{\sqrt{2k_s^2 + 2k_u^2}} \sin\left(\cos^{-1}\left(\frac{K}{K_{\max}}\right)\right) \quad (2)$$

While for individual undulators in a storage ring, this horizontal gradient of the K parameter can cause different parts of the beam to produce different wavelength resulting in linewidth broadening, the situation is quite different when operated as afterburner in an x-ray FEL. When the undulator is operating as afterburner [1], the radiation will be generated from a highly micro-bunched beam modulated by half a dozen undulators just upstream of the afterburner undulator, which causes the electron density to be peaked periodically along the electron bunch. If the K value of the afterburner undulator is set such that the radiation wavelength,

$$\lambda_r = \frac{\lambda_u}{2h\gamma^2} \left(1 + \frac{1}{2}K^2\right), \quad (3)$$

is the same or an integer fraction of the micro-bunching period, the radiation amplitude will be strongly enhanced due to constructive interference. Otherwise, the radiation amplitude will be suppressed. In Eq. 3, γ is the relativistic Lorentz factor and h is the harmonic number. A consequence for the radiation intensity from such a micro-bunched electron beam traveling through an undulator with transverse K gradient is that there is one path line through the device on which radiation is strongest while electrons traveling at a distance to that path line will radiate at a lower amplitude. Therefore, if the transverse beam dimensions are too large or the beam is transversely displaced, the number of electrons contributing to the x-ray intensity can be significantly reduced. This behavior was experimentally tested with the Delta afterburner undulator at the end of the LCLS undulator line in 2015.

MEASUREMENT OF THE EFFECT OF A K GRADIENT ON AFTERBURNER RADIATION

At the last position of the LCLS undulator line, the Delta polarizing afterburner was mounted on a remotely movable girder. Among other modes, the moving mechanism allowed the girder, and thus the Delta undulator, to be moved relative to the incoming electron and x-ray beams in any

transverse direction, while its axis remained parallel to the beams. This capability was used in 2015 to study the effect of the transverse K gradient on radiation produced by the Delta undulator. The experiment made use of the fact that the maximum K value, to which the fixed gap Delta undulator could be set by aligning opposite magnet rows, was larger than the K value needed for resonance with the also fixed gap LCLS undulators.¹ In order to make the Delta afterburner undulator resonant to the LCLS undulators a value of $K/K_0 = 0.942$ was needed. During the experiment, the girder was first moved in horizontal direction across the distance range of -0.5 mm to $+0.5 \text{ mm}$ relative to the beam axis and then in vertical direction across the same distance range. For this scan, the parameter δ (see above) was set to $+\pi/2$ to produce circular polarized radiation. During the scan, the total intensity of the x-ray radiation leaving the Delta afterburner undulator was measured with the LCLS gas detectors (GDET) and recorded.

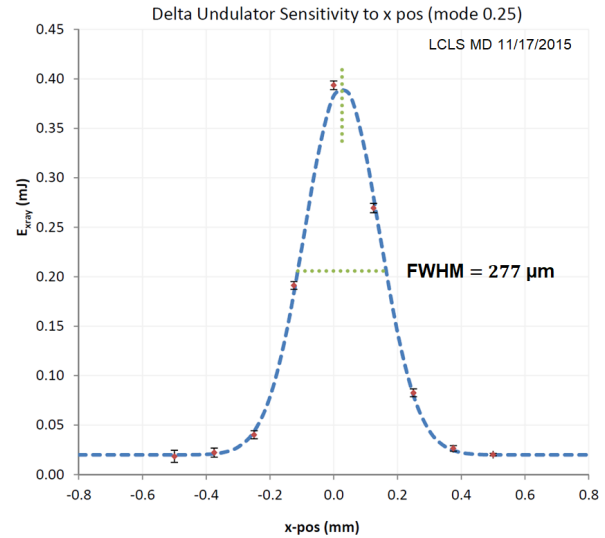


Figure 1: Intensity profile of the x-ray radiation coming from the Delta afterburner undulator at LCLS during a horizontal position scan of the device.

The error bars in Fig. 1 show the results of that scan. For large values of the x position distance, the radiation level is constant. This is mostly the radiation produced by the upstream LCLS undulators. Not much radiation is produced by the Delta afterburner undulator at these large displacements. As the x position is reduced, the total intensity rises, peaking around a position of about 0.023 mm. The dashed line is the result of a Gaussian fit:

$$E_{\text{xray}} = E_{\text{xray},0} e^{-\frac{(x-x_{\text{res}})^2}{2\sigma_x^2}} + E_{\text{xray,bg}} \quad (4)$$

with fit constants: $E_{\text{xray},0} = 0.3667 \text{ mJ}$, $E_{\text{xray,bg}} = 0.0201 \text{ mJ}$, $x_{\text{res}} = 23.1 \mu\text{m}$, $\sigma_x = 117.5 \mu\text{m}$.

¹ The pole planes of the upper and lower jaws of the fixed gap LCLS undulators were slightly canted with respect to each other around the beam axis, which allowed small K adjustments of order 0.1 % by remotely controlling the transverse position of the undulator.

In order to determine the sensitivity of the x-ray intensity to the K value of the Delta afterburner undulator, an independent scan of K was performed over the range $3.29 \leq K \leq 3.40$. For this scan, the transverse position was kept constant at $x_{\text{pos}} = y_{\text{pos}} = 0$ mm and the parameter δ (see above) was set to $+\pi/2$ to produce circular polarized radiation. The total intensity of the x-ray radiation leaving the Delta afterburner undulator was measured with the LCLS gas detectors and recorded.

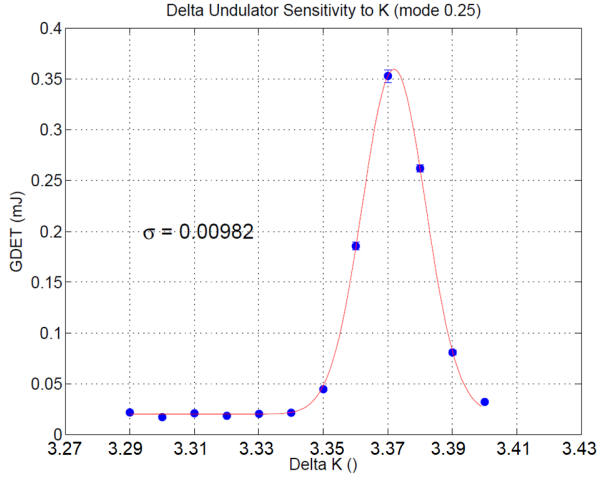


Figure 2: Intensity profile of the x-ray beam coming from the Delta afterburner undulator at LCLS during a scan of the K value ('Delta K ') of the Delta undulator.

The error bars in Fig. 2 show the results of that scan. The curve looks similar to that in Fig. 1. The red line connecting the error bars is the result of a Gaussian fit:

$$GDET = GDET_0 e^{-\frac{(K-K_{\text{res}})^2}{2\sigma_K^2}} + GDET_{\text{bg}}, \quad (5)$$

with fit constants: $GDET_0 = 0.3386$ mJ, $GDET_{\text{bg}} = 0.0201$ mJ, $K_{\text{res}} = 3,3727$, $\sigma_K = 0.00982$.

A comparison of Fig. 1 and Fig. 2 leads to the conclusion that the change in x-ray intensity during the horizontal scan of the device comes from the fact that the K value changes in the device as function of x , such that the electron beam experiences a change in K as the device is moved horizontally with respect to the beam. Also, the similarity of the two curves leads to the conclusion that the $K(x)$ is roughly linear over the width of the resonance. The gradient can then be estimated by

$$\frac{\partial K}{\partial x} \approx \frac{\sigma_K}{\sigma_x} = \frac{0.00982}{117.5 \mu\text{m}} = 0.0000836/\mu\text{m} \quad (6)$$

or

$$\frac{1}{K_{\text{max}}} \frac{\partial K}{\partial x} \approx 2.63 \times 10^{-5}/\mu\text{m}. \quad (7)$$

This is in quite good agreement with Eq. 2, which gives a value of $3.0 \times 10^{-5}/\mu\text{m}$ when evaluated with the parameters given in the text.

According to the equations given on page 1, there should not be a K gradient in y direction if there is one in x direction.

To test this, a scan similar to the one shown in Fig. 1 was done in the y directions. The result is shown as error bars in Fig. 3.

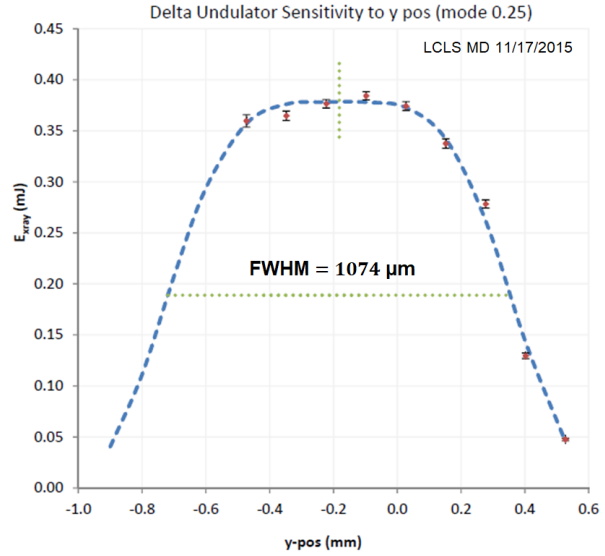


Figure 3: Intensity profile of the x-ray beam coming from the Delta afterburner undulator at LCLS during a vertical position scan of the device.

Figure 3 does look different from Fig. 1 but it is not completely flat, as one might expect at first. The reason is that the magnetic undulator field increases with distance from the beam axis following a hyperbolic cosine function. The dashed line shows a fit to the data points of function:

$$E_{\text{xray}} = E_{\text{xray},0} e^{-\frac{K_{\text{res}}^2 (\cosh(k_y(y-y_{\text{res}}))-1)^2}{2\sigma_x^2}} + E_{\text{xray,bg}}, \quad (8)$$

with fit constants: $E_{\text{xray},0} = 0.3590$ mJ, $k_y = 165 \text{ m}^{-1}$, $y_{\text{res}} = -180 \mu\text{m}$, $E_{\text{xray,bg}} = 0.0201$ mJ. The values of K_{res} and σ_K have been taken from the fit in Fig. 2. When comparing the fits in Fig. 1 and Fig. 2 it appears that the horizontal gain width can be approximated by

$$\sigma_x \approx \frac{5}{4} \frac{\rho_{1D}}{\frac{1}{K_{\text{max}}} \frac{\partial K}{\partial x} \Big|_{x=y=0}}. \quad (9)$$

Equation 9, in which ρ_{1D} is the Pierce parameter, allows a prediction of the afterburner performance for smaller K values introduced by changing the row phases of the two crossed undulators.

Figure 4 illustrates the result of Eq. 9 for the entire LCLS-II SXR operational range as functions of electron energy and photon energy. Only at the lower right hand side corner of the plot, i.e., for large electron energy and low photon energy (at high values of the K parameter) is the gain window wider than the rms of the electron beam (purple to green colors). For photon energies above about 450 eV the gain window is too narrow and is expected to severely reduce afterburner performance. SLAC is now developing a new polarizing undulator, Delta II, which is based on the original

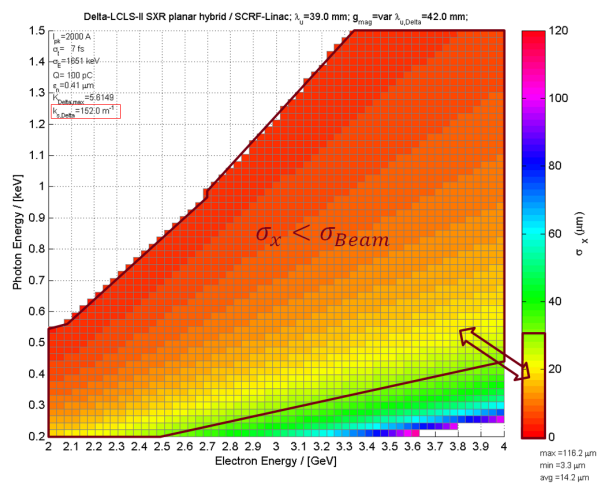


Figure 4: Estimated horizontal gain width for a 42-mm period Delta operating on the LCLS-II SXR line. (The Delta II undulator that is currently under development at SLAC is using a 44 mm period length.) The gain width for most of the operational range is smaller than the rms width of the electron beam, which is expected to significantly reduce the intensity of the radiation from the Delta afterburner undulator.

SLAC Delta undulator but with added variable gap capability, which will be used to set the K value. The row phases will only be used to set the polarization mode.

CONCLUSION

Measurements with the Delta polarizing undulator, operated on the LCLS beamline in afterburner mode, support earlier observations and theoretical work of the occurrence of a transverse variation of the K parameter (K gradient) in 4-row permanent magnet undulators operated in circular or elliptical polarization modes when row phase is used to set the K value of the device. These K gradients will broaden the radiation linewidth in a stand-alone device and limit the generation of radiation and of FEL gain to parts of the electron bunch that falls within a narrow transverse window, thus severely reducing output intensity of the device. While a transverse K gradient might be useful in certain situations to, for instance, combat the effects of a large energy spread, in most situations it is not desirable. Then, it must be avoided by adding variable gap capability to the device, such that gap variations can be used for K adjustments and row phase variations will only be used for adjusting the polarization mode of the radiation.

ACKNOWLEDGMENTS

The author thanks Alberto Lutman and James MacArthur for their support during the data acquisition for this paper.

REFERENCES

- [1] H.-D. Nuhn *et al.*, “Commissioning of the Delta Polarizing Undulator at LCLS”, in *Proc. FEL’15*, Daejeon, Korea, Aug. 2015, paper WED01, pp. 757–763. doi:10.18429/JACoW-FEL2015-WED01
- [2] G. Hartman *et al.*, “Circular Dichroism Measurements at an X-Ray Free-Electron Laser with Polarization Control”, *Rev. Sci. Instrum.*, vol. 87, p. 083113 (2016). doi:10.1063/1.4961470
- [3] D. Higley *et al.*, “Femtosecond X-ray Magnetic Circular Dichroism Absorption Spectroscopy at an X-Ray Free Electron Laser”, *Rev. Sci. Instrum.*, vol. 87, p. 033110 (2016). doi:10.1063/1.4944410
- [4] A.A. Lutman *et al.*, “Polarization Control in an X-Ray Free-Electron Laser”, *Nature Photonics*, vol. 10, p. 468–472 (2016). doi:10.1038/nphoton.2016.79
- [5] A.B. Themnykh, “Delta undulator for Cornell energy recovery linac”, *Phys. Rev. ST Accel. Beams*, vol. 11, p. 120702, 2008. doi:10.1103/PhysRevSTAB.11.120702
- [6] T. Schmidt, M. Calvi, T. Schmitt, V.N. Strocov, D. Zimoch, “Operation experience of the UE44 fixed gap APPLE II at SLS”, *Journal of Physics: Conference Series*, vol. 425, p. 032020, 2013. doi:10.1088/1742-6596/425/3/032020
- [7] S. Sasaki, K. Miyata, T. Takada, “A New Undulator for Generating Variably Polarized Radiation”, *Japanese Journal of Applied Physics*, vol. 31, Part 2, Number 12B. doi:10.1143/JJAP.31.L1794
- [8] K. Halbach, “Design of permanent multipole magnets with oriented rare earth cobalt material”, *Nuclear Instruments and Methods*, vol. 169 (1), p. 1–10, 1980. doi:10.1016/0029-554X(80)90094-4
- [9] R. Carr, “Adjustable phase insertion devices as X-ray sources”, *Nuclear Instruments and Methods*, vol. 306 (1–2), p. 391–396, 1991. doi:10.1016/0168-9002(91)90346-R
- [10] Z. Wolf, “Position Dependence of the K Parameter in the Delta Undulator”, LCLS-TN-16-1, January 2016.
- [11] M. Calvi, C. Camenzuli, E. Oriat, Th. Schmidt, “Transverse gradient in Apple-type undulators”, *J. Synchrotron Radiat.* 2017 May 1, 24(Pt 3), p. 600–608. doi:10.1107/S1600577517004726

EXPERIENCE WITH SHORT-PERIOD, SMALL GAP UNDULATORS AT THE SwissFEL ARAMIS BEAMLINE

T. Schmidt*, M. Calvi, C. Kittel, D. Voulot, N. Hiller, T. Schietinger
E. Prat-Costa, S. Bettoni, S. Reiche, E. Ferrari, M. Aiba, R. Ganter, F. Löhl, A. Alarcon,
U. Wagner, R. Follath, P. Juranic, C. Arrell, , Paul Scherrer Institut, 5232 Villigen, Switzerland
A. Cassar, N.J. Sammut, Univerity of Malta, MSD2080 Msida, Malta

Abstract

The SwissFEL Aramis beamline provides hard X-ray FEL radiation down to 1 Angström with 5.8 GeV and short period, 15mm, in-vacuum undulators (U15). To reach the maximum designed K-value of 1.8 the U15s have to be operated with vacuum gaps down to 3.0 mm. The thirteen-undulator modules are 4m long and each of them is equipped with a pair of permanent magnet quadrupoles at the two ends, aligned magnetically to the undulator axis. Optical systems and dedicated photon diagnostics are used to check the alignment and improve the K-value calibration. In this talk the main steps of the undulator commissioning will be recalled and a systematic comparison between the magnetic results and the electron and photon based measurements will be reported to highlight achievements and open issues.

INTRODUCTION

The hard x-ray Aramis beamline of SwissFEL started operation with first lasing end of 2016, but only in the soft x-ray at 400 eV. This was caused by a delay with the newly developed solid state rf modulators. During 2018, the energy could be successively increased until the full energy with 6 GeV has been reached end of 2018. In March 2018, the working range of the monochromator has been reached, so that a first photon based alignment campaign could be done. Because of the short period length of 15 mm, only 13 undulator modules with 265 periods in 4 m length each are needed for lasing down to 1 Å, as shown in Fig. 1. The gain length is typically between 2 and 3 m, so that every undulator causes a significant increase in power. The undulators are placed on remotely controlled 5-axis cam-shaft mover which allow horizontal and vertical positioning and all 3 angles with µm precision. The mover have a range of up to 3 mm, but are limited by the bellow transverse motion of only 0.5 mm. For the planar U15, height and pitch alignment are the most relevant, but the original design strategy was to use the same support units also for the soft x-ray undulators of APPLE type where in addition horizontal position and yaw angle are of equal importance.

The main issue of the Aramis beamline, like for all the others, is to get the orbit straight at the tolerances of an hard X-ray FEL, align the undulators to this orbit and set the correct *K* - values and phase matching between two successive undulators. For this reason, the first step in setting up the Aramis beamline is the beam based alignment (BBA). While

* thomas.schmidt@psi.ch



Figure 1: SwissFEL hard x-ray Undulator Aramis.

not needed for the commissioning of the fixed gap LCLS, the photon based undulator alignment was essential for the commissioning of SACLA [1]. The strategies for photon based alignment and optimisation have been adapted for SwissFEL, which, however, could start lasing with lower electron energies at longer wavelengths and could successively improve the alignment.

The magnetic field data taken during the magnetic optimisation and characterisation of the undulators in the undulator laboratory are prepared with a bundle of models including the gaps, the corrector settings and the correct phase shifter settings which has been named *SUBLIME* (aramiS Undulator BeamLine Model) [2], see Fig. 2.

In the following, the setup for the alignment of the undulators is discussed with a focus on the photon based diagnostic

on spontaneous synchrotron radiation. The results of two optimisation campaigns will be reported, followed by some examples of the undulator related FEL performance.

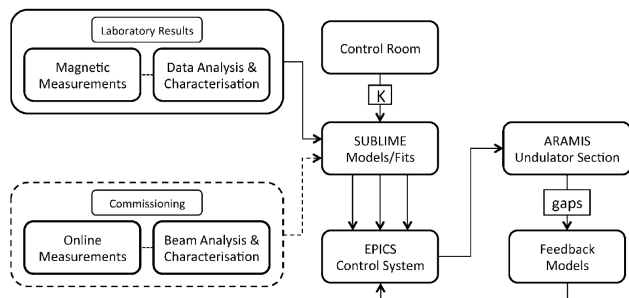


Figure 2: Schematic for the Aramis beamline operation: Magnetic data from the Hall-probe based measurements are fine corrected with photon based commissioning data. The corresponding phase-matcher settings as well as corrector settings from the ends of each undulator and the distributed earth field correction coil are implemented in feed forward mode.

STRAIGHT ELECTRON ORBIT

The pre-condition for a good undulator optimisation is a straight, dispersion-free electron beam orbit through the entire undulator line. At Aramis, different concepts of BBA including a general optimiser tool (PSICO) have been tested: random walk concepts and more recently dispersion free steering [3], which gives the best orbit with zero dispersion in the undulator. Moreover, this *golden orbit* has to be matched with the ideal photon beam axis which is required to pass all optical elements further down the beamline to the sample positions in the endstations. The PSICO optimiser works with the FEL signal and is made for the final tuning on a day to day basis. Undulator related errors are also often caused in orbit errors which can be based i.e in mismatch of the machine optics or dispersion in the undulator. The error source is often not obvious.

All undulators were already installed before the commissioning could start. The undulators can be opened, but not so much that the field and errors in first and second field integrals which causes kicks and offsets are zero. But, of course, all the corrector settings found during the magnetic measurements of the undulators are implemented.

UNDULATOR PRE-ALIGNMENT

The undulators are equipped with a small fixed gap permanent magnet quadrupole at the entrance and exit of each undulator. At the end of the magnetic measurements in the laboratory these alignment quadrupoles (QA) were aligned to the magnetic axis. For this, the Hall probe is positioned at the position of the quadrupoles and with a mechanical flexor system the quadrupoles were aligned to give zero field on axis. A pneumatic system can remotely bring the quadrupoles in and out. The accuracy and reproducibility is about 10 μm . These alignment quadrupoles are designed

to allow an alignment to the electron beam axis, using a beam based alignment algorithm. For that, first the upstream quadrupole will be brought on axis. As the electron beam gets a kick when it goes off-axis through the quadrupole, the center of this quadrupole - and with that the magnetic axis of the undulator - can be detected. The cam-shaft mover settings are corrected remotely and the up-stream QA is extracted from the beam axis. The procedure is repeated with the downstream side of the undulator.

This procedure has a better precision than the laser tracker based installation which has a precision of only 100 μm and, more important, this refers the magnetic axis directly to the beam orbit.

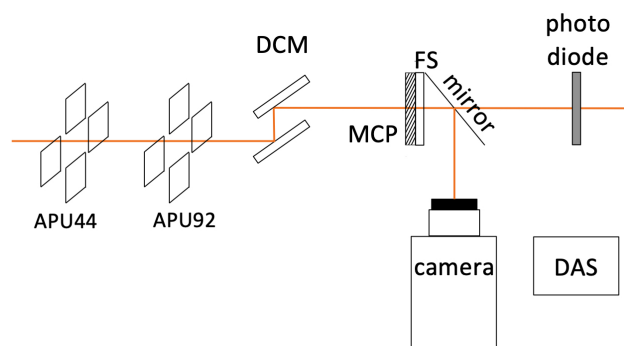


Figure 3: Setup for the photonics instrumentation: the spontaneous radiation cone is shaped with two 2-dim slit units APU, filtered by a double crystal monochromator (DCM) and detected by either a multi channel plate (MCP) for 2-dim pictures or a photodiode for intensity information.

INSTRUMENTATION FOR PHOTON BASED ALIGNMENT

The setup for undulator characterisation using spontaneous undulator radiation is shown in Fig. 3. After a double crystal monochromator two systems are installed for spontaneous synchrotron radiation characterisation. To measure the intensity of the spontaneous synchrotron radiation for alignment and gap scan measurements a Si PIN diode (Hamamatsu S3590 with $10 \times 10\text{mm}^2$) is used. In addition, a multi-channel plate (MCP) in front of a phosphorous screen is viewed by a camera outside of the vacuum chamber (PSRD) up to a rate of 100 Hz. Because of the low intensities the pictures are averaged by the PSRD or in the computer for a reasonable signal to noise ratio. The photon diagnostics for the Aramis beamline was designed and implemented by the photon diagnostic group and is discussed in more detail in [4].

MODELING OF THE ARAMIS UNDULATOR BEAMLINE

The spontaneous undulator radiation is a very important tool to adjust the undulator modules with respect to the correct K respectively gap setting and gives information about the correct alignment of the undulator modules but also of the straightness of the electron trajectory. For systematic

studies special python scripts and EPICS tools have been generated to allow a reasonable fast measurements (see Fig. 4). This work was done in collaboration with students from University of Malta which is highly appreciated.

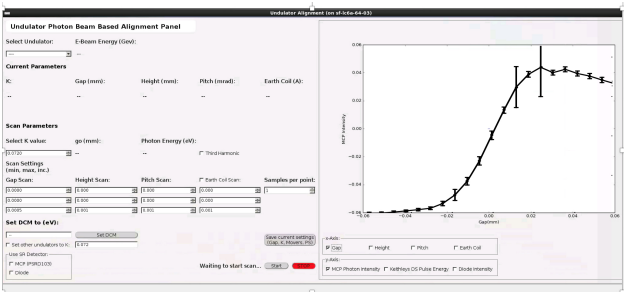


Figure 4: Dedicated panels support a systematic study of the undulators with respect to gap scans, phase matching as well as height and pitch adjustments.

For systematic measurements with spontaneous undulator radiation it is important to reduce the electron beam energy spread by adjusting the compression setup. An example of a gap scan and the corresponding spontaneous radiation distribution distributions are shown in Fig. 5. The 2-dim images allow to control if all undulator modules point in the same direction, Although these rings provide also energy information, at SwissFEL gap scans are used for a K -calibration with higher accuracy.

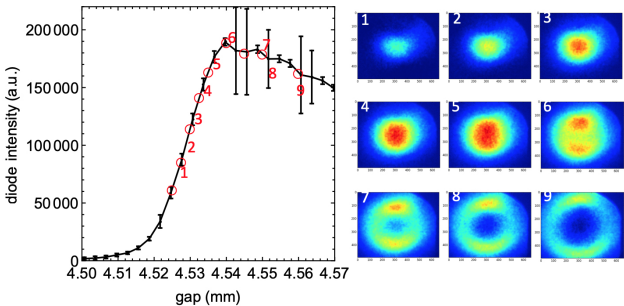


Figure 5: Example of a gap scan at a fixed photon energy of 2.395 keV. On the left side is the diode signal, on the right the corresponding photon distribution measured with the MCP (multi-channel plate).

UNDULATOR SCANS

Height Alignment

Before a fine calibration of the K -value can start the undulator has to be aligned especially in height and pitch. For a planar undulator, the horizontal position as well as the yaw angle does not need further optimisation. The undulator field is also not sensitive to the roll angle which is moreover delicate to adjust because the short bellows which connect the undulator vacuum with the intersections are extremely sensitive in the roll angle. To determine the height of each undulator they are adjusted vertically with the cam-shaft mover by 0.8 mm. The gap scans are done n steps of 20 μm .

As the field in the center of the undulator has a local minimum, the resonant wavelength is at the most blue edge if the undulator is well aligned. The height alignment is carried out at the nominal K -value of 1.2 at a gap of 4.5 mm and not at the minimum gap of 3 mm in order to not provoke beam losses. A height measurement is shown in Fig. 6. When the undulator is centered, the good field region is about 50 μm . The time for one gap scan with 40 data points takes about 1 min, for the entire scan about half an hour.

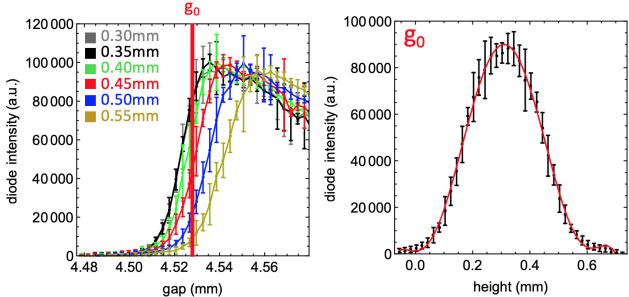


Figure 6: Height alignment of the undulator. Half of the gap scans are plotted on the left side. The field in the vertical center of the undulator gap has a minimum and the resonant wavelength is at its maximum. In a gap scan that means the scan curve is shifted most to the left. On the right, the intensities at a constant gap (g_0) are plotted. The fit delivers the correct height adjustment. This data set was taken at an energy of 2.395 keV.

Pitch Alignment

With a corrected height, the pitch can be adjusted. Again gap scans are done as function of a variation in pitch. The pitch variation shown in Fig. 7 is $\pm 250 \mu\text{rad}$. A tilt smears out the blue edge, so the figure of merit is again that the curve is most left in the gap scan plot and has to be the highest slope. Again a fit gives the correct settings. For best results, first the scan range needs to be defined, which should be large enough to get a high contrast. For such scans the precisely remote controlled mover systems pays off.

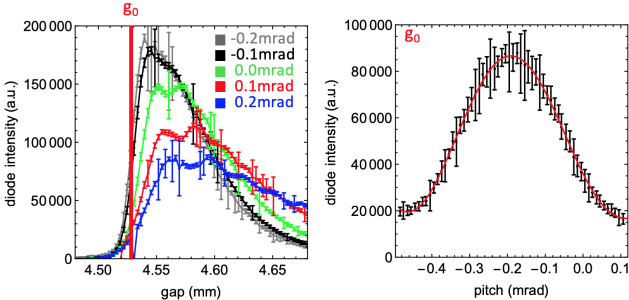


Figure 7: Example of the pitch alignment of the undulator at 2.395 keV. As can be seen is the acceptance in an aligned undulator by 50 μmrad

K Calibration

The K -values have been characterised for the entire working range between $K = 1$ to 1.8 in steps of 0.1, looking at

the spontaneous radiation intensity downstream a monochromator. With K versus gap measurements as illustrated in Fig. 5, all segments can be calibrated in K to give the same photon energy. For any of these K - values gap scans in the range of $\pm 30 \mu\text{m}$ are done. With the data from the magnetic measurements the effective blue edge has a width of $\pm 3 \mu\text{m}$ which corresponds to $\Delta K/K < 8 \cdot 10^{-4}$, see Fig. 8. This calibration is time consuming. Even with prepared experts panels we need two to three shifts for a full characterisation of all 13 undulators.

UNDULATOR ALIGNMENT CAMPAIGNS

So far two major alignment procedures have been carried out with all 13 undulators. During 2018 the electron energy of SwissFEL has been successively increased by commissioning delayed modulators which drive the rf accelerating structures. In March 2018 the maximum electron energy was 2.55 GeV, enough to get into the operating range of the hard x-ray beamline components, so that the first photon based undulator optimisation could be carried out. However, lasing at longer wavelength was achieved already end of 2016 [5, 6].

Campaign March 2018

The first photon based alignment campaign was done in March 2018 at an energy of 2.4 keV. The optimisation was done for a K - value of 1.2 which corresponds to a gap of 4.6 mm. Due to the corrections based on the photodiode measurements of the gain curve, the spread could be reduced by a factor of 2 from $\pm 3 \mu\text{m}$ to $\pm 1.5 \mu\text{m}$ or $\Delta K/K < 4 \cdot 10^{-4}$.

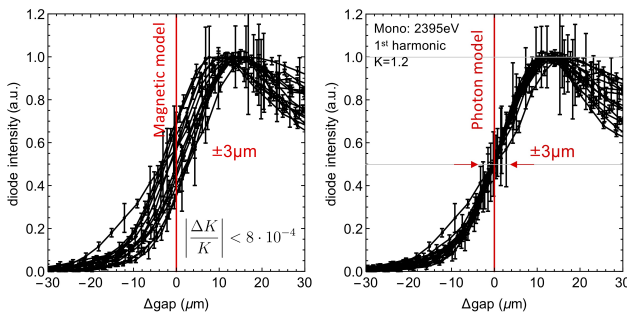


Figure 8: Gap scans with undulators settings based on the magnetic model (top) compared to the results after photon based optimization (bottom). The $\pm 3 \mu\text{m}$ corresponds to $\Delta K/K < 8 \cdot 10^{-4}$. Based on the measurements, the width of the distribution at the nominal gap could be reduced by a factor of 2.

Campaign January 2019

A second measurement campaign was carried out in January 2019 after the winter shutdown. Now with the full electron energy of 6.15 GeV a photon energy of 13.967 keV was reached. The last 8 undulator modules have been tested for K - values of 1.2, 1.4, 1.6 and 1.8. Note, a K -value of 1.8 corresponds to a gap of only 3 mm. Most of the undulator showed the same spread of $\pm 3 \mu\text{m}$ as measure one year

before, based again on the data from the magnet measurements. But it was found that two undulators, SARUN09 and SARUN14 drifted from previous measurements campaign, see Fig. 9. For higher K - values also SARUN7 shows a drift. The reason for this is unclear. But the undulators have been corrected in the same as in the 2018 campaign.

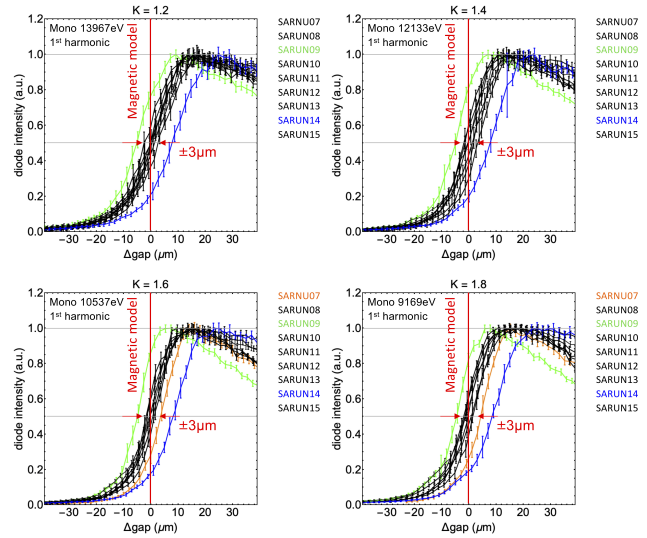


Figure 9: Gap scans for the last 8 out of 13 undulator modules for K - values 1.2, 1.4, 1.6 and 1.8. All measurements are carried out at 6.15 GeV.

The following Fig. 10 shows the resulting corrections:

	SARUN07	SARUN08	SARUN09	SARUN10	SARUN11	SARUN12	SARUN13	SARUN14	SARUN15
K									
	gap setting error								
	(μm)								
1.0	2.4	-2.4	-5.6	-2.1	-1.1	-0.7	1.1	8.4	-0.1
1.1	2.6	-2.2	-5.3	-2.7	-0.8	-1.1	1.4	8.0	0.1
1.2	2.2	0.0	-5.8	-2.4	-0.8	-1.3	1.0	7.2	-0.2
1.3	2.7	0.9	-5.7	-2.5	-1.3	-1.7	1.1	7.2	-0.7
1.4	2.7	1.4	-5.6	-2.0	-1.1	-1.8	0.8	6.7	-1.1
1.5	3.3	0.7	-5.9	-2.1	-0.7	-1.9	0.4	7.4	-1.2
1.6	3.0	0.9	-5.7	-1.8	-1.0	-1.8	0.2	7.5	-1.2
1.7	3.3	0.8	-5.5	-1.7	-1.2	-2.6	0.6	7.6	-1.4
1.8	3.7	1.1	-5.4	-2.0	-1.2	-2.5	0.3	8.1	-2.0
Average:	2.9	0.1	-5.6	-2.2	-1.0	-1.7	0.7	7.6	-0.9
K									
	ΔK/K								
	x10 ⁻⁴								
1.0	-5.9	5.7	13.6	5.2	2.6	1.6	-2.6	-20.3	0.1
1.1	-6.4	5.4	13.2	6.6	2.1	2.7	-3.4	-19.9	-0.3
1.2	-5.7	-0.1	14.7	6.2	2.0	3.2	-2.5	-18.4	0.4
1.3	-7.1	-2.5	15.0	6.6	3.4	4.4	-2.8	-18.8	1.7
1.4	-7.3	-3.7	15.2	5.4	2.9	4.7	-2.2	-18.0	3.0
1.5	-9.0	-1.9	16.2	5.7	1.8	5.2	-1.1	-20.2	3.2
1.6	-8.1	-2.4	15.4	4.9	2.8	5.0	-0.6	-20.3	3.3
1.7	-8.7	-2.1	14.3	4.6	3.0	6.8	-1.5	-19.9	3.6
1.8	-9.5	-2.9	13.9	5.3	3.2	6.3	-0.7	-20.9	5.2
Average:	-7.5	-0.5	14.6	5.6	2.6	4.4	-1.9	-19.6	2.3

Figure 10: Corrections set according to the blue edge scans of the measurement campaign in January 2019. Most undulators required tiny corrections of 1 to 2 μm , but two needed larger corrections between 5 and 2 μm . The values are also given in units of $\Delta K/K$.

FEL PERFORMANCE

The Aramis undulators work reliable in the full expected gap range down to 3 mm. Systematic wakefield studies especially for the small gaps are still pending. The models based on the magnetic measurement data from the magnetic laboratory including individual gap and phase settings as well as feed-forward corrections allow in general reproducible settings. The drive electronics for the gap drive and mover is located at the undulators support. Problems occurred only with locally to high temperature in the cabinets which could be solved by additional small fans.

Figure 11 i.e. shows a gain curve at the nominal electron energy of 5.8 GeV at 1 Å wavelength. A step by step fit to the slope of the gain curve gave the gain length between SARUN8 and SARUN10 to be excellent 2.2 m, which corresponds to about 2 gain length per undulator module. Pulse energies up to 900 μJ at 3.7 keV and 550 μJ at 12 keV have been reached so far, Figure 12 shows a measurement of the

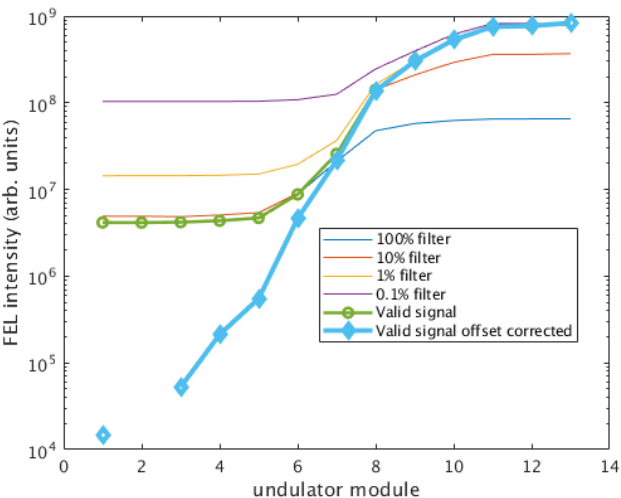


Figure 11: Gain curve measured march 10th 2019 at the nominal electron energy of 5.8 GeV with a charge of 200 pC at 10 Hz. The gain length between SARUN8 and SARUN10 is 2.2 m.

contributions of the individual undulator modules to the FEL signal during setting up the Aramis line for user experiments on July, 15th 2019 at 8 keV with 5.8 GeV electron energy and minimum gap of 3 mm which corresponds to a *K* - value of 1.8.

CONCLUSION

The undulators for the SwissFEL Aramis beamline show a good performance. A beam based alignment for the undulators to the electron beam axis can be done with the integrated alignment quadrupoles. The second step is and with photon based diagnostics using the spontaneous synchrotron radiation Height and pitch are straight forward, The calibration of the *K* - value is more time consuming and suffers from the fact that due to limited optic acceptance not the total

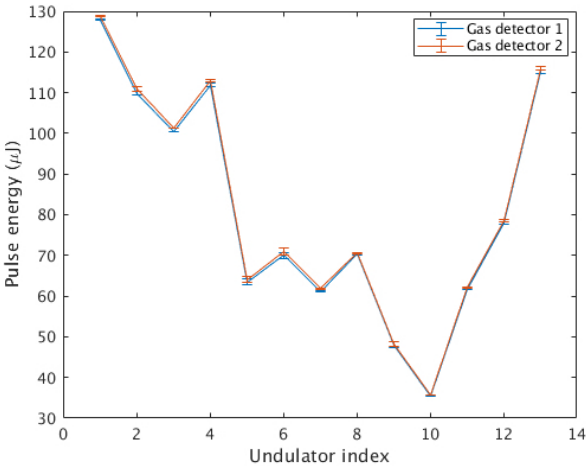


Figure 12: Undulator contribution measured at a pulse energy of 115 μJ only during optimization for user. This plot indicates that the first 4 undulator modules are not contributing.

flux can be collected. The calibration needs to be repeated regularly, at least once a year. For a daily fine tuning of the FEL signal the PSICO system has been implemented.

ACKNOWLEDGEMENTS

Optimisation of the undulators is a common approach of experts from beam dynamics, machine operation, Insertion Devices and photon diagnostics. The authors appreciate also the work of all of those colleagues who are not explicitly in the authors list. And we would like to thank T. Tanaka from RIKEN/SACLA. We followed in many respect his strategies to use the spontaneous light to improve the coherent light.

REFERENCES

- [1] T. Tanaka, T. Hara, T. Hatsui, H. Tanaka, K. Togawa, and M. Yabashi, “X-ray Based Undulator Commissioning in SACLA”, in *Proc. FEL’12*, Nara, Japan, Aug. 2012, paper THOCI01, pp. 543–547.
- [2] M. Calvi *et al.*, “Magnetic assessment and modelling of the Aramis undulator beamline”, *J. Synchrotron Radiat.*, vol. 25, p. 686, 2018. doi:10.1107/S1600577518002205
- [3] H.-D. Nuhn, “LCLS Undulator Commissioning, Alignment, and Performance”, in *Proc. FEL’09*, Liverpool, UK, Aug. 2009, paper THOA02, pp. 714–721.
- [4] P. Juranic *et al.*, “SwissFEL Aramis bemline photon diagnostics”, *J. Synchrotron Radiat.*, vol. 26, p. 906, 2019. doi:10.1107/S1600577519005654
- [5] C. Milne *et al.*, “SwissFEL: The Swiss X-ray Free Electron Laser”, *Appl. Sci.*, vol. 7, p. 720, 2017. doi:10.3390/app7070720
- [6] T. Schietinger, “Towards Full Performance Operation of Swiss-FEL”, in *Proc. IPAC’18*, Vancouver, Canada, Apr.-May 2018, pp. 24–28. doi:10.18429/JACoW-IPAC2018-MOZGBD1

ABSORBED RADIATION DOSES ON THE EUROPEAN XFEL UNDULATOR SYSTEMS DURING EARLY USER EXPERIMENTS

F. Wolff-Fabris[†], H. Sinn, J. Pflüger, European XFEL GmbH, Schenefeld, Germany
F. Hellberg, A. Hedqvist, Stockholm University, Stockholm, Sweden
F. Schmidt-Foehre, D. Noelle, W. Decking, DESY, Hamburg, Germany

Abstract

The European XFEL GmbH (EuXFEL) is a FEL user facility based on a superconducting accelerator with high duty cycle. Three movable gap SASE Undulator Systems using hybrid NdFeB permanent magnet segments are in operation. We observed in a dedicated diagnostic undulator for radiation damage doses up to 4 kGy and 3% demagnetization effect during the commissioning phase. In this work we present characteristics of the absorbed radiation doses in undulators during photon beam delivery for users. Lower absorbed doses are measured since the start of user operation. While ramping up electron beam parameters and repetition rates, individual segments located at the downstream end of the SASE systems show persistent absorbed doses which are proportional to the transmitted charge. In addition, the dose per charge ratio shows photon energy dependence. Portable magnetic flux measurement systems allow in-situ tunnel assessment of undulator magnetic properties in order to estimate radiation dose limits for future user operation.

INTRODUCTION

The European XFEL GmbH is a free-electron laser user facility which started operation in 2017. Its superconducting accelerator is designed to operate at energies up to 17.5 GeV and has the highest duty cycle machine currently in operation with a repetition rate of up to 27000 bunches per second and at 1nC [1]. The EuXFEL operates three separate undulator systems named SASE1, SASE2 and SASE3 to produce FEL radiation with tunable wavelengths from 0.05 to 5.2 nm and pulse lengths of less than 100 fs [2]. These Undulator Systems are built with 91 5-m long undulator segments based on hybrid NdFeB (VA-CODYM 776AP) permanent magnets, which are tuned to optimize the SASE effect [3].

De-magnetization effects of the permanent magnets due to radiation damage have been reported [4-8] in several facilities through the years and have been also observed at EuXFEL [9]. Dedicated passive and active machine protection systems have been designed to minimize such effects and the EuXFEL operates a collimation system [10], an array of on-line readable dosimeters [11], and diagnostic undulators (DU) installed at the upstream extremity of each SASE system. These permit to investigate, reduce and/or minimize the demagnetization effects on the undulator systems.

Table 1 summarizes the starting date of accelerator commissioning, first lasing and start of user program in

each SASE system. The EuXFEL has adopted a ramping up schedule for the beam parameters and the currently used electron and photon parameters available for users are also indicated in Table 1. In this work we consider the commissioning phase for each SASE system stretching from the first beam transmission through the undulators until the start of the early user operation and therefore it also includes the beam delivery for the beamlines commissioning phase. It is important to note that the electron beam transmitted through SASE1 necessarily travels through SASE3 before reaching the nearest dump.

Table 1: Main Event Dates for SASE1-3 and Typical Beam Parameters for User Experiments

System	SASE1	SASE2	SASE3
1 st beam transm.	27.04.2017	13.03.2018	27.04.2017
1 st lasing	02.05.2017	01.05.2018	02.08.2017
1 st Early user exp.	14.09.2017	20.03.2019	28.11.2018
Typical e-beam user par.	14 GeV 250 pC 2000 bps	14 GeV 250 pC 2000 bps	14 GeV 250 pC 2000 bps
Typical photon user par.	6-12keV	6-14keV	0.7-1.6keV

In this manuscript we report on the evolution and characteristics of the absorbed doses during the initial phase of photon beam delivery for users. In particular we discuss time, charge, and photon energy dependences of the absorbed doses. Additionally, we present further enhancement on magnetic measurement capabilities allowed by in-situ tunnel measurements.

ABSORBED DOSES DURING COMMISSIONING AND USER OPERATION

The importance of on-line dosimetry system and diagnostic undulators in the EuXFEL Undulator Systems was demonstrated in the commissioning phase. We have measured de-magnetization effects associated to magnetic field degradation in the diagnostic undulators [9] and to a change in the vertical entrance kick of a 5-m undulator

[†] f.wolff-fabris@xfel.eu

segment [3]. As shown in Figure 1, magnetic degradation higher than 4% for absorbed doses up to 4.8 kGy was observed in the SASE1 and SASE3 DUs. If such levels of magnetic reduction were found in 5-m undulator segments, it may affect the overall quality of the SASE process. We have estimated an initial limit of about 55 Gy for a 4×10^{-4} relative change in magnetic field based in Hall sensor magnetic measurements for K-parameter.

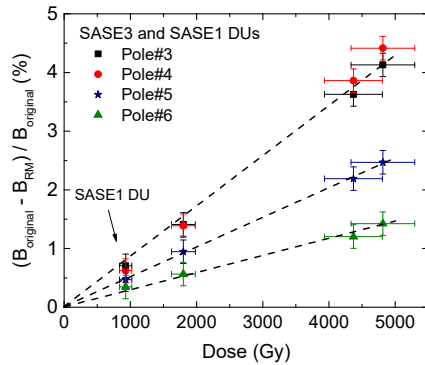


Figure 1: De-magnetization measured on the EuXFEL SASE1 and SASE3 diagnostic undulators.

The absorbed doses in the DUs were mainly generated by localized single e-beam losses and the number of such events could be minimized by extensive commissioning of the collimation system and better understanding and training of operational practices.

Figure 2 presents an overall evolution of the total absorbed doses as function of time for the SASE1-3 Diagnostic Undulators. The time dependence of the total dose increase in DU-SASE1 (black curve) is higher during the commissioning phase between May-17 and September-17 while after the start of user experiments only few single events were mainly responsible for dose increases.

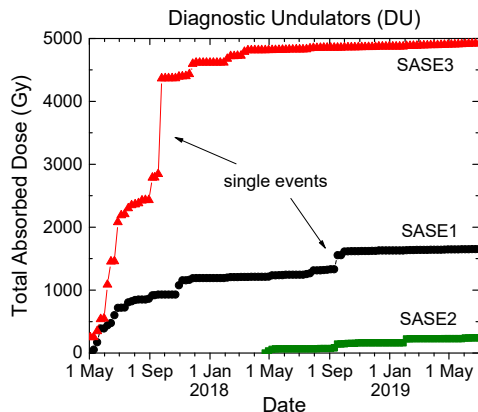


Figure 2: Total absorbed doses in the SASE1-3 Diagnostic Undulators up to July-2019.

The SASE3 Diagnostic Undulator (red curve) shows greater dose increases in 2017 than 2018 or 2019. During the SASE1 commissioning phase the electron beam travels through SASE3 before reaching the dump. Better work practices in beam steering and beam collimation

resulted in fewer single events and consequently lower absorbed doses since the start of 2018. The DU-SASE2 (green curve) shows very low absorbed doses since its first beam transmission. At the present, absorbed doses in the diagnostic undulators are only originated from orbit corrections and/or beam based alignment activities. As the Fig. 2 clearly shows, beam losses deposited in the diagnostic undulator have successfully been minimized.

Figure 3 shows the evolution of the absorbed doses in selected 5-m undulator segments in all 3 SASE systems. It is important to note that the dosimeters are attached to the movable girders and move accordingly to the gap changes. Cell#3 corresponds to segments located at the upstream side of a SASE system, nearly 18 m behind a DU, while SASE1-cell#31, SASE2-cell#29 and SASE3-cell#23 are segments located towards the downstream end.

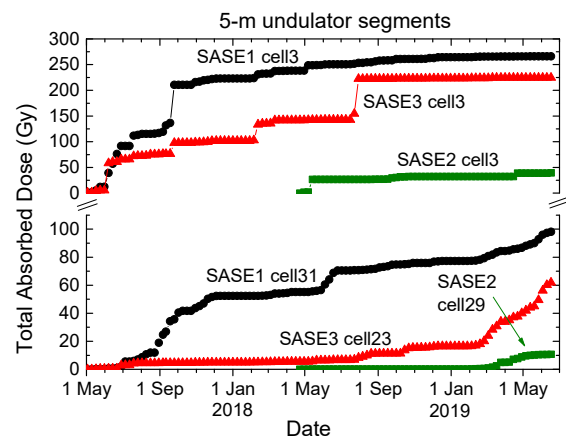


Figure 3: Absorbed doses at upstream (top) and downstream (bottom) 5-m undulator segments.

The absorbed doses in the 5-m undulator segments show different behaviour depending on the segment location along the SASE system. The upstream undulators in cell#3 have similar behaviour as the DUs with higher absorbed doses during the commissioning phase for SASE1 and SASE3. During user operation, the dose increases are mostly seen during eventual singular losses. In contrast, the SASE1-3 downstream undulator segments show an increase of absorbed doses as function of time which nearly coincides with the start of user operation and results from steady dose increases during beam delivery. These findings remain valid for other segments located either at the upstream or at the downstream end of the SASE systems (not shown here).

DOSE PER CHARGE RATIO

We monitor the total transmitted charge through the three undulator systems with the aid of toroids. Figure 4 shows the total transported charge through SASE1-3 since the start of operation.

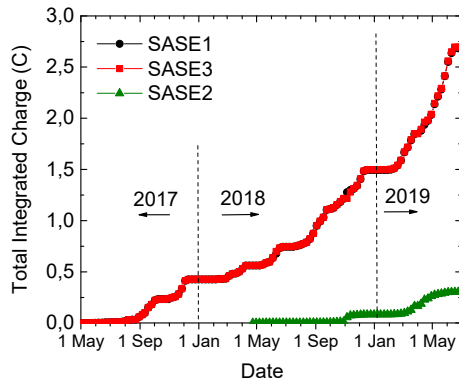


Figure 4: Total transmitted charge in SASE1 and 3 and SASE 2 since start of operation.

SASE1 and 3 have transmitted charge higher than 2.5 C as of July 2019. As comparison, LCLS-I has transmitted a total charge of about 2.5 C during the 10 years of operation [12]. We observe the total transmitted charge rate at EuXFEL has been ramping up as function of time: more than 1 C has passed through SASE1 and SASE3 in 2019 alone. This reflects the experiment and user's demand for higher repetition rates – resulting in higher transmitted charge. Due to safety restrictions the operation is currently limited to 4000 bunches per second and more will be allowed for operation in 2020 after an upgrade in the safety system. As the dose increase as function of time is proportional to the charge rate [9], we expect to observe higher doses associated with higher repetition rates. The SASE2 transmitted charge also has a similar profile resulting in faster increase after the start of beam delivery for user experiments.

The movable gap undulator systems have been operated with fixed gaps corresponding to particular photon energies. The allocated beam time for users at EuXFEL consists of 12 hours shifts for each instrument belonging to a SASE system and typically the photon energy remains constant in a shift. Contrarily, the repetition rate (bunches per second) is frequently changed according to the experiment needs. In order to observe the effects of different operational user modes, we have monitored the transmitted charge (Figure 5a) and the absorbed dose increase (Figure 5b) during a SASE1 user operation period where FXE and SPB/SFX beamlines requested photon energies at 9.3 keV and 6.0 keV, respectively.

As the accelerator operated continuously at 14.5 GeV and 0.25nC, the slope change in the transmitted charge in SASE1 reflects only the beamlines choice of number of bunches. Nevertheless, the linear behavior during a 12 hours shift permits to determine a temporal charge rate. Figure 5b shows the total absorbed doses for undulator segments located at cell#17 and cell#31. These are the segments that showed higher absorbed doses during these user shifts. The steady increase in absorbed doses is seen during user operation mode [9] and its origin will be discussed elsewhere. From these plots we can determine the

temporal absorbed dose rates for both 9.3 and 6.0 keV operational modes.

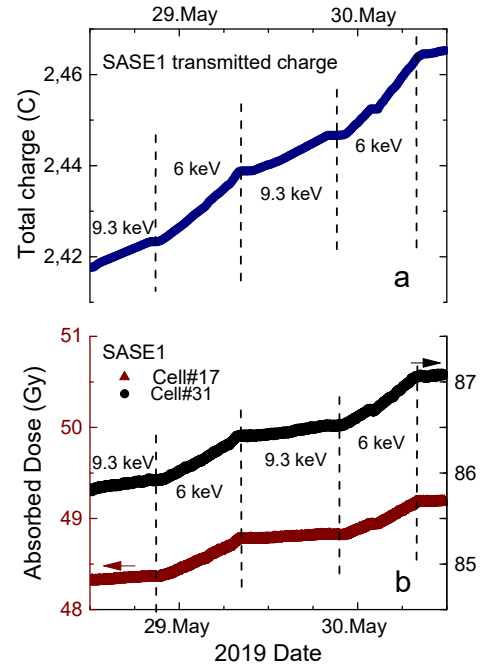


Figure 5: SASE1 total transmitted charge (a) and total absorbed dose in cells #17 and #31 (b) during photon beam delivery for users at 9.3 keV and 6.0 keV.

From the charge and dose rates calculated with linear fits in the plots exemplified in Figure 5 we determined the dose per charge ratio at each individual shift and Table 2 summaries these results.

Table 2: Dose per charge Rate at 9.3 and 6.0 keV in Selected SASE1 Undulator Segments

Photon Energy	SASE1-Cell#17 (Gy/C)	SASE1-Cell#31 (Gy/C)
9.3 keV	8.2	17.4
9.3 keV	6.2	14.9
9.3 keV	4.9	15.9
6.0 keV	27.1	31.7
6.0 keV	21.0	29.0
6.0 keV	21.7	31.8

For cell#17, the dose per charge ratio is between 5 to 8 Gy/C at 9.3 keV (gap \approx 13.7 mm). At this gap, the distance between the outer vacuum chamber surface and the undulator magnetic structure is about 2 mm. When clos-

ing the gap for producing FEL at 6.0 keV (gap \approx 10.7 mm; top and bottom girders are moved closer to the vacuum chamber by 1.5 mm) the ratio is augmented nearly by a factor 4. Further operational modes will provide data for further studies on the dose ratio as function of photon energy/vertical distance between vacuum chamber and magnetic structure.

The cell#31 shows the dose per charge ratio roughly increases a factor 2 between the 9.3 and 6.0 keV photon energy modes. However, during the operation time here discussed, the cell#31 segment was not used for FEL generation and was positioned at the so-called “parking position” at a gap = 210 mm, meaning the magnetic structure and dosimeters were nearly 100 mm distant to the vacuum chamber. So, there is a clear effect on the dose per charge ratio due to the photon energy. This also suggests the measured absorbed doses in cell#31 are originated from low energy radiation. Nevertheless, the reason for the dose ratio change found in an open undulator requires additional studies and could be associated to X-rays or synchrotron radiation emitted in prior segments.

IN-SITU MAGNETIC MEASUREMENTS

Magnetic measurements performed in the laboratory premisses are time consuming in the case of installed components. Typical procedures of de-installation, transport, magnetic measurements, installation and re-alignment range between 4-5 days (for a DU) to a couple of weeks (for a 5-m segment). Therefore, faster in-situ magnetic measurements are of importance when taking into account the constraints imposed due to machine operation for beam delivery to users. Among considered options, we started by developing a measurement setup based in the so-called “flux coil” method, where an integrated voltage signal measured with a coil is proportional to the magnetic flux induced in a pole. If the magnetic flux through the coil changes, e.g., when changing the undulator gap, a voltage is induced. An analog integrator with accuracy of 10^{-6} V.s integrates the induced voltage over from initial time $t1$ to final time $t2$. The magnetic flux through the fluxcoil is therefore given by:

$$\Phi = N \int_{t1}^{t2} V(t) dt \quad , \quad (1)$$

where N is the number of windings.

Figure 6 shows the flux coil placed around a magnetic pole for measurements in tunnel. The coil is mounted in a non-magnetic holder with a hollow in the center which fits the pole dimensions and permit reproducible mounting and alignment. In one working hour we obtain representative data in 15 magnetic poles distributed along the 5-m undulator, allowing measurements to be performed in a temporary tunnel access during maintenance days, for example. On the DU’s fixed gap, measurements are taken by moving the coil from a field free location to the magnetic pole.

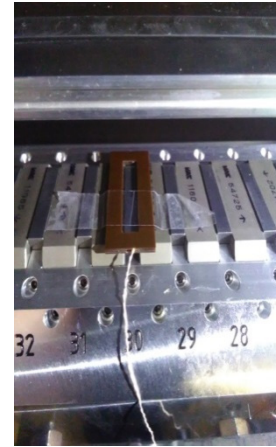


Figure 6: The flux coil is used to perform magnetic measurements on different poles loaded along the 5-m undulator.

The accuracy and reproducibility of the flux coil measurements was tested on reference undulators/DUs located in the magnetic laboratory or in devices installed in the tunnel while performing the same measurement protocol in different days/weeks. The system shows a relative reproducibility better than $\pm 5.10^{-4}$, being in the same order of magnitude as compared to measurements performed with Hall sensor in the magnetic laboratory. This makes it suitable to monitor preliminary de-magnetization effects due to possible radiation damage. To maintain such measurement precision levels, it is important to consider possible temperature effects on the NdFeB magnetic properties at tunnel conditions, in which temperature differences of 0.1 °C will result in 1.10^{-4} change in magnetization. Consequently we compute the undulator temperature during the flux coil measurements and make appropriate corrections.

Magnetic measurements in selected undulators have been performed between Dec.-2018 and July-2019. Figure 7 compares two distinct measurements on the SASE1-DU and SASE3-DU. These diagnostic undulators have absorbed 20 and 50 Gy, respectively, during the operation time between the measurements. The DUs have a total of 4 magnetic periods and the same permanent magnet grade used in the 5-m segments. The temperature in the tunnel was monitored during the measurements and show agreement in the order of 0.1 °C.

The magnetic relative change in the SASE1-DU after absorbing 20 Gy has shown virtually no change in magnetic flux based in the measurement setup accuracy. In contrast, after absorbing 50 Gy, the SASE3-DU has shown a slightly change in the order of 5.10^{-4} on the measured flux of poles #3 and #4. These results obtained with the flux coil in the SASE3-DU have a similar behaviour as previously reported [9] where Hall sensor measurements performed in the magnetic laboratory showed higher de-magnetization effects in poles #3 and #4 and permitted to estimate an initial limit of 55 Gy for relative magnetic field changes of 4.10^{-4} .

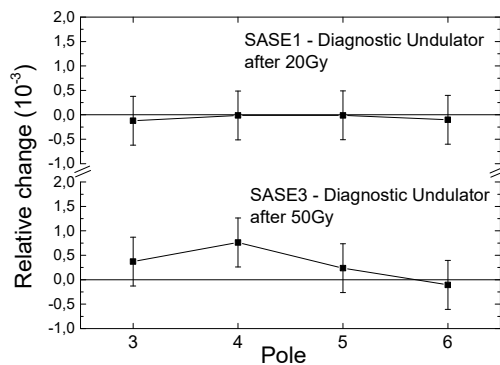


Figure 7: The flux coil is used to perform magnetic measurements on different poles located along the 5-m undulator.

The initial results obtained with the flux coil method reveal the potential of this technique. We have performed measurements on several 5-m long segments. These segments have absorbed doses lower than 20 Gy since the first reference measurements were taken and no relative change in flux have been found for these dose levels. Further developments in data acquisition, signal-to-noise ratio and absolute calibration are ongoing.

CONCLUSION

Since the start of the early user experiments we have measured the total absorbed doses in the undulator segments. The absorbed radiation doses during user experiments are proportional to the transmitted charge. The EuXFEL has transmitted more than 2.5 C in SASE1 and SASE3 in the first two years of operation and the ramping up of beam operational parameters towards the facility design may increase the transmitted charge rate by a factor higher than 10. In addition, operating the undulator systems at lower photon energies will increase the dose rate. Currently dose per charge rates of up to 5-17 Gy/C (at 9.3 keV) and 21-32 Gy/C (at 6 keV) are seen in 5-m segments. The development of in-situ magnetic measurements will permit faster measurements of the magnetic properties of the undulator segments and enable to accurately determine damage thresholds for undulator segments located at any position of a SASE system. Demagnetization effects in the order of $5 \cdot 10^{-4}$ were measured in the SASE1-DU after absorbing 50 Gy.

REFERENCES

- [1] M. Altarelli *et al.*, “The European X-ray Free-electron Laser”, Technical Design Report DESY 2006-097, July 2007.
- [2] E. Schneidmiller *et al.*, “Photon beam properties at the European XFEL”, Technical Design Report DESY 2011-152, Sep. 2011.
- [3] S. Abeghyan *et al.*, “First operation of the SASE1 undulator system of the European X-Ray Free Electron Laser”, *Journal of Synchrotron Radiation*, vol. 26, p. 302, 2019. doi:10.1107/S1600577518017125
- [4] J. Skupin *et al.*, “Undulator demagnetization due to radiation losses at FLASH”, in *Proc. EPAC'08*, Genoa, Italy, Jun.2008, paper WEPC129, pp. 2308-2310.
- [5] H.-D. Nuhn *et al.*, “Undulator radiation damage experience at LCLS”, in *Proc. FEL '14*, Basel, Switzerland, Aug.2014, paper MOP046, pp. 127-130.
- [6] P. Vagin *et al.*, “Radiation damage of undulators at Petralis”, in *Proc. IPAC'14*, Dresden, Germany, Jun. 2014, pp. 2019-2021. doi:10.18429/JACoW-IPAC2014-WEPR0035
- [7] T. Bizen *et al.*, “Radiation-induced magnetization reversal causing a large flux loss in undulator permanent magnets”, *Scientific Reports*, vol. 6, p. 37937, 2016. doi:10.1038/srep37937
- [8] M. Santana Leitner *et al.*, “Life expectancy studies for LCLS-II permanent magnet undulators”, in *Proc. IPAC'17*, Copenhagen, Denmark, May 2017, pp. 1640-1642. doi:10.18429/JACoW-IPAC2017-TUPAB134
- [9] F. Wolff-Fabris *et al.*, “Status of the radiation damage on the European XFEL undulator systems”, *J. of Physics – Conf. Series*, vol. 1067, p. 032025, 2018. doi:10.1088/1742-6596/1067/3/032025
- [10] V. Balandin *et al.*, “Post-Linac Collimation System for the European XFEL”, in *Proc. PAC'09*, Vancouver, Canada, May 2009, paper TH6PFP030, pp. 3763-3765..
- [11] F. Schmidt-Föhre *et al.*, “Commissioning of the New Online-Radiation-Monitoring-System at the New European XFEL Injector with First Tests of the High-Sensitivity-Mode for Intra-Tunnel Rack Surveillance”, in *Proc. IBIC'15*, Melbourne, Australia, Sep. 2015, pp. 585-589. doi:10.18429/JACoW-IBIC2015-WECLA02
- [12] H.-D. Nuhn, “LCLS-I 10 years of undulator operation”, private communication, March 2019.

ULTRAFast MAGNETISATION DYNAMICS AT THE LOW-FLUENCE LIMIT SUPPORTED BY EXTERNAL MAGNETIC FIELDS

M. Riepp[†], L. Müller¹, A. Philippi-Kobs, W. Roseker, R. Rysov, K. Bagschik, M. Walther, T. Golz, N. Stojanovic, G. Grübel¹, DESY, Hamburg, Germany

R. Frömter, H. P. Oepen,

Universität Hamburg, Center for Hybrid Nanostructures, Hamburg, Germany

D. Naumenko, E. Pedersoli, F. Capotondi, M. Kiskinova,

Elettra-Sincrotrone Trieste S.C.p.A., Trieste, Italy

¹also at Universität Hamburg, Department of Physics, Hamburg, Germany

Abstract

We report on ultrafast magnetisation dynamics in ferromagnetic cobalt/platinum multilayers upon pumping by near and mid to far infrared radiation, utilizing sub-100 femtosecond free-electron laser pulses. The evolution of the excited magnetic state is studied on femtosecond timescales with nanometre spatial resolution and element selectivity, employing time-resolved magnetic small-angle X-ray scattering. The obtained results contribute to the ongoing discussion to what extent either coupling of the electromagnetic field or rather quasi-instantaneous heating of the electron-system is the driving force for phenomena like ultrafast demagnetization or all-optical helicity-dependent switching.

INTRODUCTION

Ultrafast demagnetisation on sub-100 femtosecond to picosecond time scales [1] and the related phenomenon of all-optical helicity-dependent switching (AO-HDS) of magnetisation [2] are fascinating effects in fundamental physics with potential for, e.g., energy-efficient future data-storage devices [3,4]. First discovered in amorphous ferrimagnets like GdFeCo [2,5], AO-HDS has also been found recently in various ferromagnets including Co/Pt multilayers [6]. In the latter case, the impact of the laser pulse is controversially debated. Reports on deterministic single-pulse switching in micron-sized magnetic domains [7] contrast with the stochastic nature of a multi-pulse switching mechanism found in different experiments, see, e.g., Ref. [8]. Modelling the deterministic process by means of the magnetic two-temperature model resulted in thresholds for the pump fluence and the duration of the inverse Faraday effect (IFE)-induced magnetic field, set by the length of the pump pulse [9,10]. In that interpretation, the impact of the laser pulse is assumed to be twofold. First, quasi-instantaneous heating of the electron-system above the Curie temperature mediates a transient paramagnetic state (demagnetisation). Second, opto-magnetic coupling of the laser-induced effective magnetic field (H_{IFE}) to the spin system during subsequent cooling down to the paramagnetic phase can result in nucleation and consecutive growth of reversed magnetic domains, depending on the helicity of the laser light. As the spatial

resolution in commonly used Kerr microscopy experiments is limited to the micron range, information on changes in nanoscopic domain systems during demagnetisation is scarce. In this respect, free-electron lasers (FELs), like FERMI and FLASH, providing sub-100 femtosecond extreme ultraviolet (XUV) pulses, allow to explore femtosecond dynamics also in nanometre-sized magnetic domains [11-15]. Tuning the photon energy to resonance with one of the dichroic transitions in the magnetic element, here the $M_{2,3}$ -absorption edge of Co at 59.6 eV, adds element selectivity to studies of magnetisation dynamics [16].

This paper reports on a near-infrared (NIR)-pump-FEL-probe experiment (pump wavelength of 800 nm), in which the pump helicity-dependent response of a magnetic multi-domain state was studied in the presence of an external magnetic field, H_{ext} , following observations in Ref. [17]. The evolution of the domain system was monitored by time resolved resonant magnetic small-angle X-ray scattering (tr-mSAXS). Complementarily, we show the feasibility to study the laser beam's H -field influence on demagnetisation by using polychromatic mid to far-IR pump radiation (wavelength of 30–150 μm) for simplicity denoted in the following as THz-radiation (frequency of 2–10 THz). Since the oscillation periods of the electromagnetic field are slower than for NIR radiation, a direct field-induced response of the magnetic system can be expected [18-20].

EXPERIMENTAL

Cobalt/platinum multilayers with perpendicular magnetic anisotropy were deposited by sputtering techniques on freestanding 50 nm-thin Si_3N_4 membranes [21]. The experiment using NIR-pump wavelength was conducted in tr-mSAXS geometry (Fig. 1) at the DiProI beamline of FERMI at ELETTRA [22]. A multilayer with 6 bilayer repetitions of Co/Pt was used, which is fully remanent with a coercive field of $\mu_0 H_c \approx 15 \text{ mT}$. The global energy minimum, obtained after out-of-plane demagnetization, is a multi-domain state with a characteristic periodicity of 460 nm. A perpendicular magnetic field increases the characteristic length scale as predominantly small domains, oriented oppositely to the field, are erased. The characteristic periodicity at a field of 15 mT is 532 nm.

[†] Matthias.Riepp@desy.de

This rather strong susceptibility enhances the probability to induce features of AO-HDS which might result, e.g., in a second order scattering ring [23]. The *in situ* Helmholtz coil was operated in pulse mode, shaping the driving voltage such that the target field strength was reached well within 200 μ s, kept constant for 250 μ s, before it was switched off and decreased with a time constant of ≈ 1 ms. The field pulses were triggered with a time delay of -250 μ s at the operation frequency of the FEL (50 Hz), ensuring a constant magnetic field at the time of the pump-probe events. A continuous pulse operation of the coils without detectable heating effects was feasible due to the low duty cycle of $\approx 3\%$. Circularly left (CL) or right (CR) polarized pump pulses with a fluence of 3.4 mJ/cm² and a pulse duration of 3.5 ps were utilized, following recent predictions in Refs. [9, 10].

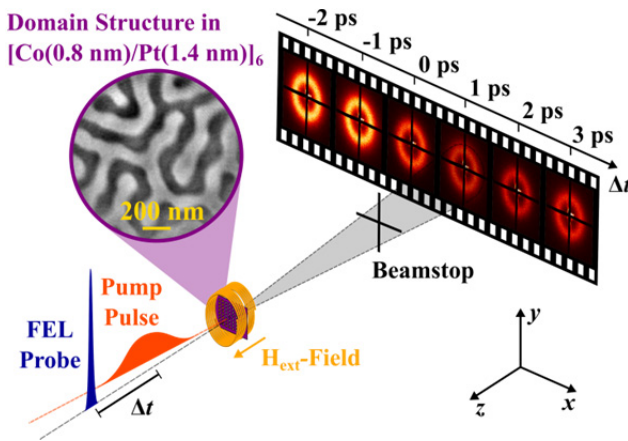


Figure 1: Schematics of the tr-mSAXS experiments. The magnetic multi-domain state was pumped by either circularly polarized NIR or linearly polarized THz pulses. The magnetic response was monitored by a CCD camera detecting scattering of delayed FEL-probe pulses resonantly tuned to the $M_{2,3}$ edge of Co. Magnetic fields were applied normal to the sample surface in the former case.

Complementarily, we used THz radiation to excite the magnetic multi-domain state. Our custom-made endstation allowing for THz-pump-FEL-probe experiments using the tr-mSAXS technique was installed at FLASH's BL3 beamline. A Co/Pt sample with 8 bilayer repetitions and a characteristic periodicity of 440 nm was pumped by polychromatic 10-cycle THz pulses containing wavelengths between 30 μ m and 150 μ m, produced by the additional electromagnetic undulator available at FLASH [24]. The pulses consisted of the fundamental frequency and, predominantly, the third and fifth harmonics. Higher frequency components of the spectrum (wavelengths shorter than 30 μ m) were blocked using a low-pass filter. The actual THz trace as well as the weight of the frequency components could not be measured at the time of the experiment. The pump and probe pulses were geometrically separated and guided along two different beam paths to the endstation where they were focussed quasi-collinearly to the sample.

In both experiments the response of magnetisation was probed by sub-100 femtosecond FEL pulses resonantly tuned to the Co $M_{2,3}$ -absorption edge (photon energy of 59.6 eV \triangleq wavelength of 20.8 nm). The scattered FEL radiation was detected by a CCD camera with 2048 \times 2048 pixels and a pixel size of 13.5 μ m.

RESULTS AND DISCUSSION

Results from tr-mSAXS at FERMI's DiProI beamline are shown in Fig. 2. Scattering from a disordered magnetic maze-domain structure results in an isotropic scattering ring (Fig. 2a) that is azimuthally averaged and fitted with a split Pearson type VII function (Fig. 2b)). Higher order scattering rings are not observed revealing that there is no significant disparity in up and down magnetised domains. The maximum of the scattered intensity $I(Q_c)$ is a measure for the out-of-plane component of the magnetisation $M_z \propto \sqrt{I(Q_c)}$ with Q_c representing the characteristic scattering length. The inset of Fig. 2c) shows the temporal evolution of magnetisation $M_z(\Delta t)$, normalized to the magnetisation $M_{z,0}$ in the unpumped case for CR and CL polarized pump-pulses and external fields of 0 mT and 15 mT. We observe a quenching of magnetisation to 55% during the pulse duration of 3.5 ps. Importantly, a dependence of the strength of demagnetisation on the external field or the pump pulse's helicity is not observed. This is understandable as the disparity in up and down magnetised domains is found to be negligibly small, so that differences in absorption for CR and CL polarized pump pulses average out. Note, that in a homogeneously magnetised Co/Pt sample a small polarization dependent difference in the strength of demagnetisation was assigned to the magnetic circular dichroism effect [17].

The time evolution of the shift in Q_c , $\Delta Q_c(\Delta t)$, normalized to the unpumped $Q_{c,0}$ for both CR and CL polarized pump pulses and different external fields is shown in Fig. 2c) and d), respectively. In the absence of an external bias field $\Delta Q_c(\Delta t)$ remains constant upon NIR-pumping. This behaviour is in line with the results of Ref. [12] where a fluence dependent onset of magneto-structural changes was found for Co/Pt multilayers. However, when applying external bias fields of 5 mT and 15 mT, ΔQ_c temporarily reduces within the pump-pulse duration of 3.5 ps and almost fully recovers within ≈ 100 ps, which is faster than the remagnetisation (inset in Fig. 2c)). For a bias field of $\mu_0 H_{\text{ext}} = 15$ mT a maximum reduction of ΔQ_c by $(2 \pm 0.5)\%$ is found for CR polarization (Fig. 2c)), while for CL polarization the effect is about a factor of 2 stronger, $\Delta Q_c = (5.5 \pm 0.5)\%$ (Fig. 2d)). As speckles are observed (Fig. 2a) even in images averaged over 100 FEL pulses, a significant rearrangement of magnetic domains can be excluded. The observed shift has rather to be interpreted in line with Ref. [12], i.e., as a consequence of superdiffusive spin currents.

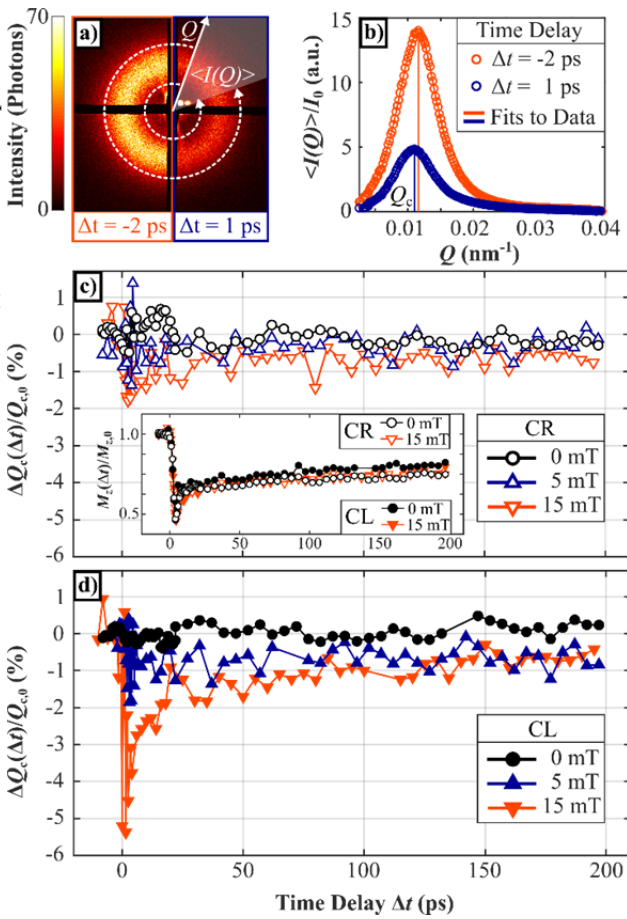


Figure 2: Ultrafast magnetization dynamics using NIR radiation and external magnetic fields. a) Examples of mSAXS images for the unpumped ($\Delta t = -2$ ps) and pumped ($\Delta t = 1$ ps) case (sum of 100 FEL pulses each). b) Respective azimuthally averaged intensities, normalized to the incoming FEL-intensity. The characteristic scattering vector Q_c and the maximum scattering intensity $I(Q_c)$ are obtained from fitting with a split Pearson type VII function. c), d) Time evolution of the relative change of the characteristic scattering length $\Delta Q_c(\Delta t) = Q_c(\Delta t) - Q_{c,0}$ for zero and external fields upon pumping by c) CR and d) CL polarized pump-pulses. The inset in c) shows the corresponding demagnetization for both polarizations and external fields of 0 mT and 15 mT. Lines are guides to the eye.

In that picture, the observed helicity dependence is interpreted to originate from the interplay of the polarization dependent induced magnetic field \mathbf{H}_{IFE} with the external bias field \mathbf{H}_{ext} . The effect of superdiffusive spin transport on the domain-wall is either enhanced or suppressed. A spin-up-polarized current preferentially gets scattered in down-magnetised magnetic domains (and vice versa) in the vicinity of a domain wall, resulting in its transient broadening and the observed shift of Q_c . A quantification of the process using the results of Ref. [25] for the strength of IFE in ferromagnets and heavy paramagnets is planned.

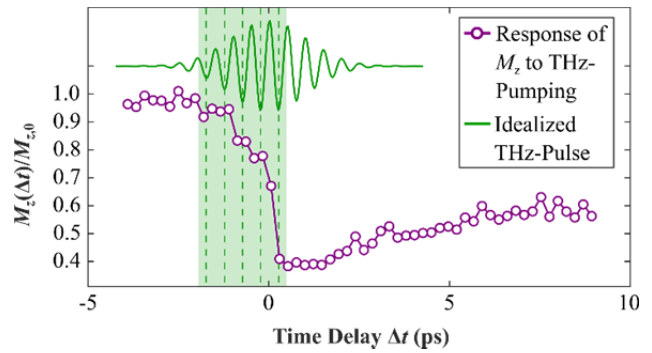


Figure 3: Ultrafast demagnetization using THz radiation (purple). The line is a guide to the eye. The unknown pulse shape is sketched as an ideal 10 cycle 2 THz pulse with Gaussian envelope (green).

Since for Co \mathbf{H}_{IFE} points along the same direction for CR and CL polarized light, the optomagnetic behaviour of Pt might be the driving force as it shows a sign change of \mathbf{H}_{IFE} for CR and CL polarized light [25].

For investigating the direct response of magnetisation to the pump pulse's \mathbf{H} -field, we utilized polychromatic THz radiation, as described above, to pump the magnetic multi-domain state in Co/Pt. Prominently, we observe a strong quenching of the magnetisation to $\approx 40\%$, using a fluence of $\approx 10 \text{ mJ}/\text{cm}^2$ corresponding to a magnetic field component of $\approx 290 \text{ mT}$ (Fig. 3). The falling edge of the demagnetisation curve is not smooth but rather shows a step-like behaviour. We interpret the overall decrease of magnetisation as a result of quasi-instantaneous Joule heating, in line with Ref. [18]. In contrast, the plateaus can be interpreted as the coherent, i.e., directly field-induced, part of the sample's response to the THz magnetic field. It is noted that the demagnetisation effect is large when compared to results in other studies [18-20]. We speculate that the spectral properties, especially the high-frequency part of the pump spectrum, are responsible for this difference.

In conclusion, we studied the influence of optomagnetic fields on demagnetisation dynamics. We found a reduction of the characteristic scattering length already for low-intensity NIR pump-pulses in presence of out-of-plane magnetic fields. The effect evolves on the timescale of the pulse duration and shows strong helicity dependence. A possible explanation lies in a helicity dependent strength of \mathbf{H}_{IFE} in Co and/or sign of \mathbf{H}_{IFE} in Pt. The magnetic response to pumping with THz radiation hints at coherent coupling of the THz magnetic field to the spin system. Recent and planned upgrades of the FLASH facility [26] and the THz beamline [24] will provide strongly improved conditions for further, more quantitative studies of THz-induced magnetisation dynamics.

ACKNOWLEDGMENTS

We acknowledge help from the FLASH and FERMI machine-operator teams and strong support at the beamlines BL3 and DiProI as well as financial support by Deutsche Forschungsgemeinschaft (DFG) within SFB 925.

REFERENCES

- [1] E. Beaurepaire, J.-C. Merle, A. Daunois, and J.-Y. Bigot, "Ultrafast spin dynamics in ferromagnetic nickel", *Phys. Rev. Lett.*, vol. 76, p. 4250, 1996, doi:10.1103/PhysRevLett.76.4250
- [2] C. D. Stanciu *et al.*, "All-optical magnetic recording with circularly polarized light", *Phys. Rev. Lett.*, vol. 99, p. 047601, 2007, doi:10.1103/PhysRevLett.99.047601
- [3] S. N. Piramanayagam, "Perpendicular recording media for hard disk drives", *J. Appl. Phys.*, vol. 102, p. 011301, 2007, doi:10.1063/1.2750414
- [4] A. V. Kimel, and M. Li, "Writing magnetic memory with ultrashort light pulses", *Nat. Rev. Mater.*, vol. 4, p. 189, 2019, doi:10.1038/s41578-019-0086-3
- [5] A. R. Khorsand *et al.*, "Role of magnetic circular dichroism in all-optical magnetic recording", *Phys. Rev. Lett.*, vol. 108, p. 127205, 2012, doi:10.1103/PhysRevLett.108.127205
- [6] C.-H. Lambert *et al.*, "All-optical control of ferromagnetic thin films and nanostructures", *Science*, vol. 345, p. 1337, 2014, doi:10.1126/science.1253493
- [7] M. Vomir, M. Albrecht, and J.-Y. Bigot, "Single shot all optical switching of intrinsic micron size magnetic domains of a Pt/Co/Pt ferromagnetic stack", *Appl. Phys. Lett.*, vol. 111, p. 242404, 2017, doi:10.1063/1.5010915
- [8] R. John *et al.*, "Magnetization switching of FePt nanoparticle recording medium by femtosecond laser pulses", *Sci. Rep.*, vol. 7, p. 4114, 2016, doi:10.1038/s41598-017-04167-w
- [9] T. D. Cornelissen, R. Córdoba, and B. Koopmans, "Microscopic model for all optical switching in ferromagnets", *Appl. Phys. Lett.*, vol. 108, p. 142405, 2016, doi:10.1063/1.4945660
- [10] Z. Du, C. Chen, F. Cheng, Y. Liu, and L. Pan, "Prediction of deterministic switching of ferromagnetic thin film by ultrafast optothermal and optomagnetic couplings", *Sci. Rep.*, vol. 7, p. 13513, 2017, doi:10.1038/s41598-017-13568-w
- [11] C. Gutt *et al.*, "Single-pulse resonant magnetic scattering using a soft x-ray free-electron laser", *Phys. Rev. B*, vol. 81, p. 100401, 2010, doi:10.1103/PhysRevB.81.100401
- [12] B. Pfau *et al.*, "Ultrafast optical demagnetization manipulates nanoscale spin structure in domain walls", *Nat. Commun.*, vol. 3, p. 1100, 2012, doi:10.1038/ncomms2108
- [13] C. E. Graves *et al.*, "Nanoscale spin reversal by non-local angular momentum transfer following ultrafast laser excitation in ferrimagnetic GdFeCo", *Nat. Mater.*, vol. 12, p. 293, 2013, doi:10.1038/NMAT3597
- [14] M. Malvestuto, R. Ciprian, A. Caretta, B. Casarin, F. Parmigiani, "Ultrafast magnetodynamics with free-electron lasers" *J. Phys.: Cond. Matter*, vol. 30, p. 053002, 2018, doi:10.1088/1361-648X/aaa211
- [15] E. Jal *et al.*, "Single-shot time-resolved magnetic x-ray absorption at a free-electron laser", *Phys. Rev. B*, vol. 99, p. 2144305, 2019, doi:10.1103/PhysRevB.99.144305
- [16] D. Weder *et al.*, "Multi-Color Imaging of magnetic Co/Pt multilayers", *IEEE Trans. Magn.*, vol. 53, p. 11, 2017, doi:10.1109/TMAG.2017.2699560
- [17] Yu. Tsema *et al.*, "Helicity and field dependent magnetization dynamics of ferromagnetic Co/Pt multilayers", *Appl. Phys. Lett.*, vol. 109, p. 072405, 2016, doi:10.1063/1.4961246
- [18] S. Bonetti *et al.*, "THz-driven ultrafast spin-lattice scattering in amorphous metallic ferromagnets", *Phys. Rev. Lett.*, vol. 117, p. 087205, 2016, doi:10.1103/PhysRevLett.117.087205
- [19] M. Shalaby, C. Vicario, and C. P. Hauri, "Simultaneous electronic and the magnetic excitation of a ferromagnet by intense THz pulses", *New J. Phys.*, vol. 18, p. 013019, 2016, doi:10.1088/1367-2630/18/1/013019
- [20] M. Shalaby, C. Vicario, and C. P. Hauri, "Low frequency terahertz-induced demagnetization in ferromagnetic nickel", *Appl. Phys. Lett.*, vol. 108, p. 182903, 2016, doi:10.1063/1.4948472
- [21] G. Winkler, A. Kobs, A. Chuvilin, D. Lott, A. Schreyer, and H. P. Oepen, "On the variation of magnetic anisotropy in Co/Pt(111) on silicon oxide", *J. Appl. Phys.*, vol. 117, p. 105306, 2015, doi:10.1063/1.4914039
- [22] F. Capotondi *et al.*, "Invited article: Coherent imaging using seeded free-electron laser pulses with variable polarization: First results and research opportunities", *Rev. Sci. Instrum.*, vol. 84, p. 051301, 2013, doi:10.1063/1.4807157
- [23] O. Hellwig, G. P. Denbeaux, J. B. Kortright, and E. E. Fullerton, "X-ray studies of aligned magnetic stripe domains in perpendicular multilayers", *Physica B: Condensed Matter*, vol. 336, p. 136, 2003, doi:10.1016/S0921-4526(03)00282-5
- [24] R. Pan *et al.*, "Photon Diagnostics at the FLASH THz beamline", *J. Synchrotron Rad.*, vol. 26, p. 700, 2019, doi:10.1107/S1600577519003412
- [25] M. Berritta, R. Mondal, K. Carva, and P. M. Oppeneer, "Ab initio theory of coherent laser-induced magnetization in metals", *Phys. Rev. Lett.*, vol. 117, p. 137203, 2016, doi:10.1103/PhysRevLett.117.137203
- [26] E. A. Schneidmiller, "First operation of a harmonic lasing self-seeded free electron laser", *Phys. Rev. Accel. Beams*, vol. 20, p. 020705, 2017, doi:10.1063/1.49484

UNDERSTANDING 1D TO 3D COHERENT SYNCHROTRON RADIATION EFFECTS

A. D. Brynes*

STFC Daresbury Laboratory & Cockcroft Institute, Warrington, UK

Abstract

Collective effects such as coherent synchrotron radiation (CSR) can have a strong influence of the properties of an electron bunch with respect to the quality of the FEL light that it produces. In particular, CSR experienced by a bunch on a curved trajectory can increase the transverse emittance of a beam. In this contribution, we present an extension to the well-established 1D theory of CSR by accounting fully for the forces experienced in the entrance and exit transients of a bending magnet. A new module of the General Particle Tracer (GPT) tracking code was developed for this study, showing good agreement with theory. In addition to this analysis, we present experimental measurements of the emittance growth experienced in the FERMI bunch compressor chicane as a function of bunch length. When the bunch undergoes extreme compression, the 1D theory breaks down and is no longer valid. A comparison between the 1D theory, experimental measurements and a number of codes which simulate CSR differently are presented, showing better agreement when the transverse properties of the bunch are taken into account.

INTRODUCTION

Synchrotron radiation – the emission of radiation by a charged particle when travelling on a curved trajectory – can become coherent when the length of a particle bunch is shorter than the wavelength of the radiation emitted. This coherent synchrotron radiation (CSR) can degrade the quality of an electron bunch, causing an increase in projected and slice emittance, and energy spread [1–5]. The theoretical explanation of CSR has made significant progress since its initial formulation [6–11], and some experimental studies have demonstrated good agreement between experimental measurements and simulation results [3, 4].

Much of the existing literature on CSR, however, neglects to account for the transverse extent of the electron bunch, however, and this may become increasingly important for future free-electron laser (FEL) facilities and schemes which place increasingly stringent demands on high-brightness, high quality electron bunches. We present some new insights on the theory of the 1D CSR transient field at the edges of dipole magnets, based on the interactions between the velocity and acceleration components of the Liénard-Wiechert field. This work suggests novel compressor designs for the minimization of this instability. A new CSR feature of the General Particle Tracer (GPT) [12] tracking code was developed specifically for this study, which does not use the small-angle or ultrarelativistic approximations.

A number of other codes exist which are capable of simulating the effects of CSR [13, 14], some of which utilise a 1D approximation, based on Refs. [15, 16], and others which extend the model to incorporate 2D and 3D effects [17–19]. While previous studies have shown good agreement between results from some of these simulation codes and experimental data [3, 4], there is a point at which the 1D approximation is no longer valid, as shown in [20], which suggests that projecting the bunch distribution onto a line may overestimate the level of coherent emission, particularly when the bunch has a large transverse-to-longitudinal aspect ratio. There are a number of effects that must be included for a simulation code to fully take account of 3D CSR effects, including (but perhaps not limited to):

1. Taking the transverse extent of the bunch into account for all particles, rather than assuming that all electrons emit and receive on-axis.
2. Self-consistently solving for the trajectory during emission rather than neglecting deviations from the nominal trajectory.
3. Taking the full Liénard-Wiechert field into account rather than only the term which arises during acceleration.
4. Including stochastic effects due to the long-range interaction between a discrete number of radiation cones.

One of the aims of this study is to determine if, during strong bunch compression, or for bunches with a large transverse-to-longitudinal aspect ratio, the limits of the 1D approximation could be found. This is achieved through comparing analytic results with simulation codes that incorporate the transverse bunch distribution, and with experimental data. The projected emittance of the electron beam was measured in parameter scans at the exit of the first bunch length compressor of the FERMI FEL [21, 22].

NUMERICAL VALIDATION

An extension to the 1D theory of CSR was presented in [23], which demonstrated the importance of the so-called ‘velocity’ term of the Liénard-Wiechert field in cases when an electron bunch enters and exits a bending magnet. It was demonstrated that, while the radiation cone from a particle is reduced in volume as the particle becomes ultrarelativistic, there is a small spike in the field experienced by a receiving particle as it enters or exits the curved trajectory which is due to this term. For a full derivation of this effect, see [23]. In order to validate these analytic results, we have

* alexander.brynes@stfc.ac.uk

numerically calculated the electromagnetic field distribution in an electron bunch in both the entrance and exit transient regimes using the GPT code [12]. GPT is a time-domain particle tracking code that integrates the equations of motion of a large number of charged particles in the presence of electromagnetic fields. A dedicated upgrade was made to the code in order to include the computation of the retarded Liénard-Wiechert fields of the tracked particles. Because this involves the storage of the trajectory of the particles and solution of retardation conditions, calculation of Liénard-Wiechert fields is computationally expensive. The cost of these computations can be reduced by approximating the emission of CSR through a longitudinal slicing of the bunch in a discrete number of time steps. From each of these slices, the transverse extent of the bunch is represented by a number of off-axis macroparticle emitters (either four or sixteen per slice), spaced regularly according to the transverse size of the slice. While integrating the equation of motion of a tracked particle, GPT evaluates the Liénard-Wiechert field resulting from the stored history of the past trajectory of each of the representative particles at the longitudinal position of the tracked particle. For more details on the code, see [24].

It is important to note that GPT uses the exact expression for the Liénard-Wiechert fields based on the numerically obtained coordinates of particles in the bunch, and does not apply any analytic approximation or presumed trajectory of the bunch. The parameters used in the simulation are given in [23]. We deliberately chose artificially small energy spread and transverse bunch size, and used hard-edged magnet fringes in the exit transient simulations to match the analytic case as much as possible.

Entrance Transient Effect

The CSR field was initially calculated by GPT at a point 24 cm into the magnet in order to simulate the entrance transient field. This distance is only half that of the steady-state condition D^{SS} [6], and so it is expected that the general expression of the steady-state CSR field will be required to calculate the fields. In this simulation, the drift before the magnet was set to 50 m. The results from the simulation are in good agreement with the expression for the steady-state field, as seen in the right-hand plot of Fig. 1. However, if the simulation is run again, but with the drift before the bend set to 10 cm, the GPT result effectively reduces to the full expression for the entrance transient field, and thereby differs from the usual approximation of Ref. [15]. The approximation of an infinitely long drift before the entrance to a bending magnet is not valid for some cases; as shown in Fig. 1, the GPT simulation reflects this behaviour.

Exit Transient Effect

Next, we numerically validate the analytic results for the CSR forces in the exit transient regime (see [23] for details). Because the net CSR field experienced by the bunch involves cancellations between the radiation and velocity terms, it proves to be of interest to study in turn both the full CSR

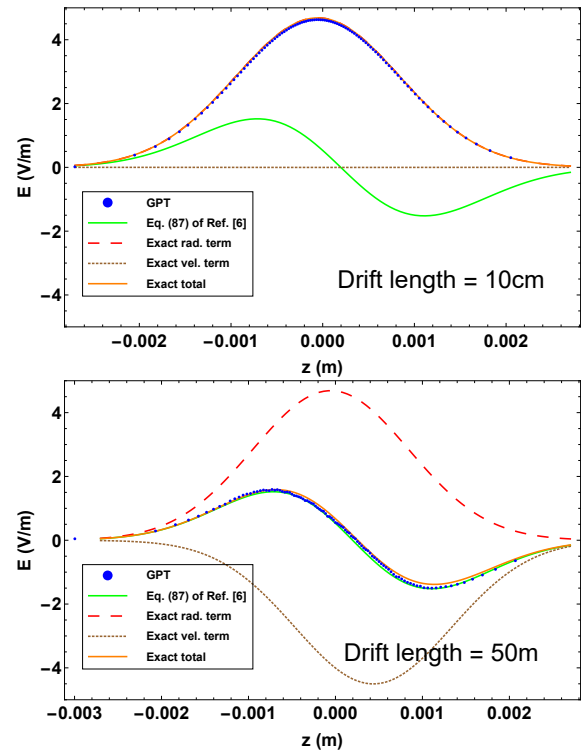


Figure 1: Longitudinal component of CSR electric field as a function of longitudinal position in the bunch and a drift before the magnet of: Above: 10 cm; and Below: 50 m, as simulated by GPT, against both Eq. 87 of Ref. [15] and Eq. 5 of Ref. [23] – both the velocity and radiation terms individually, and combined. Positive values of z refer to the head of the bunch.

field and the radiation term separately. Fig. 2 shows the longitudinal component of the electric field as a function of longitudinal position in the bunch, evaluated at 5 mm past the bending magnet. The full CSR field is represented by the orange line and the blue dots (GPT simulation), and the good agreement between these shows that the 1D, ultrarelativistic and small-angle approximations do not lead to any significant deviations from the exact CSR force.

However, an interesting 3D effect may be observed when studying the radiation term separately. In Fig. 2, this term is plotted according to the analytic result based on the 1D approximation (brown curve) and according to the GPT simulation (black dots). Clearly, the total CSR exit transient field significantly overestimates the magnitude of the radiation term. We found that this overestimation of the radiation field is due to the underestimation of the retarded distances between emitting and observing particles associated with the 1D approximation. Namely, the impact of the finite transverse bunch size could be roughly quantified by including a vertical offset of the emitting electron in the derivation of the CSR force. Due to the offset, the distance σ from emitter to observer is effectively increased.

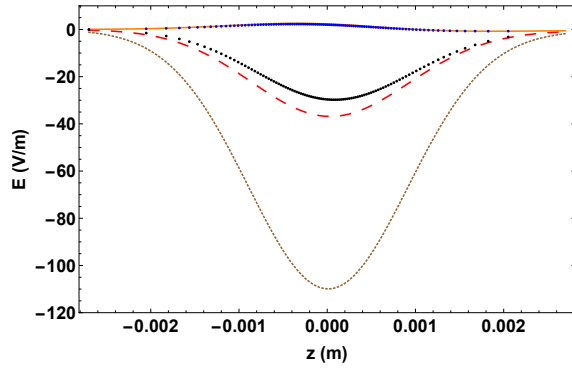


Figure 2: Longitudinal component of electric field as a function of longitudinal position in the bunch, at 5 mm from the exit of the dipole. Blue: GPT simulation of the full field; Black: GPT simulation of the radiation field only; Red: total CSR exit transient field with an offset in the y plane; Brown: radiation term only; Orange: total CSR exit transient field.

In addition, the angles between emitter and receiver are stretched somewhat, such that their cosines become smaller by a factor $\cos \delta = \rho/\sigma$, with ρ the longitudinal distance between the particles. Re-evaluating the Liénard-Wiechert field with these modifications shows that the electric field is still given by the total CSR exit transient field after the substitution $\rho \rightarrow \sigma$. By including this transverse offset, through the substitution $\sqrt{\epsilon_y \beta_y}/\gamma = 4.5 \mu\text{m}$ (with ϵ_y and β_y the vertical geometric emittance and beta function, respectively, and γ the Lorentz factor), the analytic expression for the radiation field is reduced to roughly the magnitude observed in the simulation. This means that the discrepancy between the 1D expression and the simulation can be accounted for by a bunch with a finite transverse extent, meaning that the 1D description cannot fully explain the radiation or velocity terms in the exit transient regime. However, this effect is masked by the fact that the radiation and velocity fields are of opposite sign, and partially cancel each other, resulting in an overall field that is relatively independent of the transverse bunch size.

RESULTS

The emittance was measured at the exit of the first bunch compressor in the FERMI linac, BC1, as a function of Linac 1 RF phase and chicane bending angle, resulting in variations of the bunch compression factor in the range 20 – 64 and 8 – 60 for the two scans, respectively. During the phase scan, the accelerating gradient of Linac 1 was scaled in order to keep the mean bunch energy constant at the entrance to BC1. Measurements were taken using the single quad-scan technique [25], by varying the strength of one quadrupole magnet (Q_BC01.07), located in the section directly after BC1. The machine was operated with a constant bunch charge of 100 pC, and a mean energy of approximately 300 MeV at BC1.

From an injector simulation in GPT, the bunch was then tracked using the ELEGANT code [26] up to the entrance of

BC1. From this point, three particle tracking codes have been used to compare the emittance measurement results with simulation: ELEGANT, CSRTRACK [27] and GPT using the CSR model outlined above in Sec. . In the 1D CSR simulations, ELEGANT applies the calculation of Saldin *et al* [15] to calculate the energy change due to coherent radiation in a bend, and the subsequent transient effect some time after the bunch exits the dipole, based on [16]. At the exit of the bunch compressor (including a drift to account for transient CSR effects), the output is tracked up to Q_BC01.07, the measurement point, in ELEGANT. The relative bunch length was monitored using a pyroelectric detector at the exit of the bunch compressor, and online feedback was used to maintain the compression factor across all sets of measurements.

The emittance was measured by quad scan using the FERMI online emittance tool as a function of bunch compression factor during the experimental run. We compare these measurements of emittance with results from all three simulation codes, as shown in Figs. 3 and 4. The CSR-induced emittance growth in these regimes has also been calculated, based on the analytic theory given in [28], which presented an updated calculation that takes into account the cancellation effect between the transverse CSR and space-charge field in a bunched beam (for further discussion on this cancellation effect see [29–31]). The emittance growth corresponding to the longitudinal and transverse CSR wake with the entire bunch travelling on a circular orbit (i.e. the steady-state regime) are given as:

$$\Delta\epsilon_N^{long} = 7.5 \times 10^{-3} \frac{\beta_x}{\gamma} \left(\frac{r_e N L_b^2}{R^{5/3} \sigma_z^{4/3}} \right)^2 \quad (1a)$$

$$\Delta\epsilon_N^{trans} = 2.5 \times 10^{-2} \frac{\beta_x}{\gamma} \left(\frac{r_e N L_b}{R \sigma_z} \right)^2, \quad (1b)$$

with β_x the horizontal beta function, N the number of particles, L_b the length of the dipole, R the bending radius, σ_z the bunch length, and r_e the classical electron radius. We have also calculated the ratio σ_v [20], indicating the validity of the 1D CSR approximation. For the analytical calculations to be valid, the following condition should be fulfilled:

$$\sigma_v = \sigma_\perp \sigma_z^{-2/3} R^{1/3} < 1, \quad (2)$$

with σ_\perp the transverse beam size. If this condition is not fulfilled, the 1D CSR approximation can be violated approaching maximal compression or in cases where the transverse beam size is large. The values for the σ_\perp and σ_z are taken from ELEGANT simulations with CSR switched off. In order to calculate $\Delta\epsilon_N$, we sum together both terms in Eq. 1 and add them to the initial value of the emittance at the entrance to the bunch compressor. The effect of the emittance from all four dipoles was calculated, but the largest impact by far is expected in the fourth dipole, when the majority of the actual compression takes place.

It can clearly be seen that there is a general agreement between the analytic calculations, the results from simulation

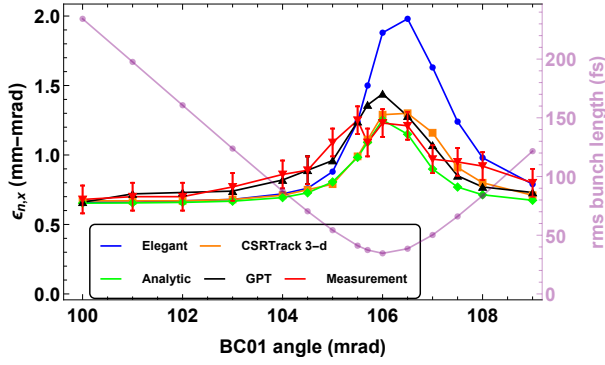


Figure 3: Horizontal emittance as a function of BC01 bending angle, with the corresponding bunch length as simulated by ELEGANT. The analytic results are calculated using Eq. 1.

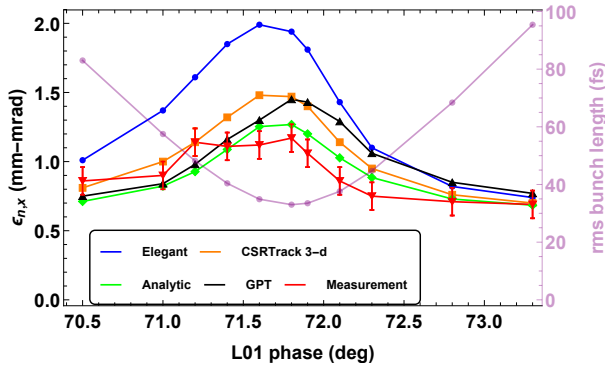


Figure 4: Horizontal emittance as a function of Linac 1 phase, with the corresponding bunch length as simulated by ELEGANT. The analytic results are calculated using Eq. 1.

and the measurement procedure. The discrepancy between simulation and experiment in the peak around 71.6–72.1° in Fig. 4 can be attributed to coherent OTR emission (COTR) [32, 33]. We observe a similar apparent overestimation of emittance growth for the bunch compressor angle scan in Fig. 3 for the ELEGANT simulation. GPT and CSRTRACK 3D are able to capture both the emittance trend and its absolute value more accurately over the entire range of bunch lengths.

By computing σ_v across both sets of compression scans, and comparing the results from simulation and experiment with this value, it is seen that the overestimation of the effect of CSR in the 1D simulation is largest when σ_v is greater than 2.5 at any point in the chicane. For more moderate values of the compression factor, this condition is not violated as strongly, and the agreement between all simulation results and the experimental measurements is good. The analytic estimation manages to reproduce the results generated through simulation and experiment throughout the range of bunch lengths.

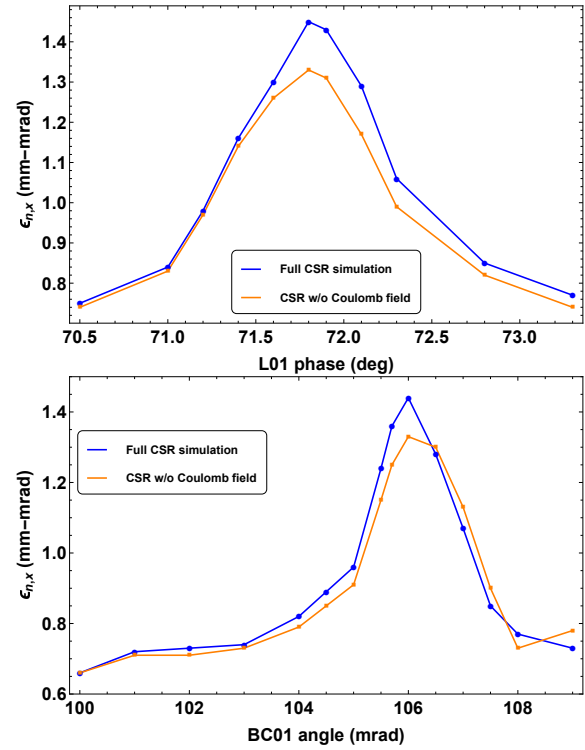


Figure 5: GPT simulation of emittance growth in the Linac 1 phase (top) and bunch compressor angle (bottom) scans with and without the velocity term of the Liénard-Wiechert field.

The differences between the ELEGANT results and those from CSRTRACK and GPT simulations are also noteworthy. It appears that, when the bunch undergoes maximum compression (as seen from the minimal bunch length in Figs. 3 and 4), the discrepancy between the 1D and 3D codes is largest, with ELEGANT returning an emittance value around 40 % larger than CSRTRACK. GPT does return a slightly higher value for the emittance than CSRTRACK and the experimental data around maximal compression. Comparisons between CSR simulations and experimental data have been studied previously [2–4], but only for moderate compression factors (up to around 15 at a given bunch compressor). We also see relatively good agreement between the codes and experimental data to within 10 % in this compression range, but the divergence at large compression suggests that there are limits to the applicability of the 1D CSR approximation when used in simulation.

The GPT code provides the functionality to include or to exclude the Coulomb term in simulation, thus demonstrating the importance of taking account of this term. In Fig. 5 we compare these two CSR simulations for the bunch compressor angle scan and the linac phase scan. It can be seen that, as the bunch approaches maximal compression, the projected emittance increases by around 10 % in the case where the Coulomb field is taken into account as compared with only the simulation of the radiation field. This can be

understood as the relative distance between the Coulomb field and the receiving particle being relatively shorter in the case of a larger bending angle in the dipole, and therefore having a larger effect; analogously, a bunch with a minimal chirp based on the linac phase exhibits the same effect. In machines that have a larger number of compressive bending magnets, this effect will be compounded, and so these results provide further evidence of the importance of taking full account of CSR when designing future accelerators.

CONCLUSIONS

An extension to the 1D theory of CSR has been presented. It was shown that, when considering the longitudinal electric field of a bunch as it enters and exits a bending magnet, it is important to consider the electrostatic term in the Liénard-Wiechert field. This term is sometimes neglected, as it is suppressed under ultrarelativistic conditions. However, since this field is always present, and travels along the direction of motion of the emitting particle, there is a brief crossover point at which the velocity field is able to influence the receiving particle in front of the emitter, and so this field should be taken into account in simulations of CSR. This is more significant when considering an accelerator lattice with multiple bends that are closer together, such as the transport for an ERL, or an FEL spreader line. It is also shown that there is a cancellation effect between these two fields, suggesting that it may be possible to design a magnet or a system of accelerator optics that take advantage of this cancellation, such that the CSR field is suppressed.

After benchmarking these new theoretical expressions using the GPT code, a comparative study between this simulation and two other codes – CSRTRACK and ELEGANT – was conducted. The effect of CSR on the projected emittance of a bunch after compression in the first compressor in the FERMI FEL was studied as a function of compression factor. These results were then compared with experimental measurements and theoretical predictions of the projected emittance. Good agreement was seen between all codes, experiment and theory when the compression factor was relatively low, but as maximum compression was reached, a greater divergence between the 1D simulation and the other results was observed, suggesting that the 1D approximation was no longer applicable. The breakdown of this condition has been studied experimentally; the theory suggested that the condition is valid only in the parameter regime $\sigma_v \ll 1$, whereas it has been demonstrated that up to $\sigma_v \lesssim 2$, the 1D CSR approximation remains valid, and so this condition can be relaxed. A promising result from this study, though, demonstrates that the theory produces good agreement with the other results. This study demonstrates the significance of taking as full an account of CSR as possible when designing future accelerators that place stringent requirements on the beam quality.

ACKNOWLEDGEMENTS

The author would like to acknowledge the support of the Industrial Liason Office of Elettra Sincrotrone Trieste and

the FERMI operations team, Simone Di Mitri in particular, for their support and advice, during and after the experiment. Additional support was also provided by Irwan Setija, Peter Smorenburg and Seth Brussaard of ASML, and Peter Williams of STFC.

REFERENCES

- [1] S. D. Mitri and M. Cornacchia, "Electron beam brightness in linac drivers for free-electron-lasers," *Phys. Rep.*, vol. 539, p. 1, 2014. doi:10.1016/j.physrep.2014.01.005
- [2] S. Bettoni, M. Aiba, B. Beutner, M. Pedrozzi, E. Prat, S. Reiche, and T. Schietinger, "Preservations of low slice emittance in bunch compressors," *Phys. Rev. Accel. Beams*, vol. 19, p. 034402, 2016. doi:10.1103/PhysRevAccelBeams.19.034402
- [3] C. C. e. Hall, "Measurement and simulation of the impact of coherent synchrotron radiation on the Jefferson Laboratory energy recovery linac electron beam," *Phys. Rev. ST Accel. Beams*, vol. 18, p. 030706, 2015. doi:10.1103/PhysRevSTAB.18.030706
- [4] K. L. F. e. Bane, "Measurements and modeling of coherent synchrotron radiation and its impact on the Linac Coherent Light Source electron beam," *Phys. Rev. ST Accel. Beams*, vol. 12, p. 030704, 2009. doi:10.1103/PhysRevSTAB.12.030704
- [5] S. e. Di Mitri, "Transverse emittance preservation during bunch compression in the FERMI free electron laser," *Phys. Rev. ST Accel. Beams*, vol. 15, p. 020701, 2012. doi:10.1103/PhysRevSTAB.15.020701
- [6] E. L. Saldin, E. A. Schneidmiller, and M. V. Yurkov, "On the coherent radiation of an electron bunch moving in an arc of a circle," *Nucl. Instrum. Meth. A*, vol. 398, no. 2, pp. 373 – 394, 1997. doi:10.1016/S0168-9002(97)00822-X
- [7] R. Talman, "Novel relativistic effect important in accelerators," *Phys. Rev. Lett.*, vol. 56, p. 1429, 1986. doi:10.1103/PhysRevLett.56.1429
- [8] M. Dohlus and T. Limberg, "Emittance growth due to wake fields on curved bunch trajectories," *Nucl. Instrum. Meth. A*, vol. 393, no. 2, pp. 494 – 499, 1997. doi:10.1016/S0168-9002(97)00552-4
- [9] C. Mayes and G. Hoffstaetter, "Exact 1D model for coherent synchrotron radiation with shielding and bunch compression," *Phys. Rev. ST Accel. Beams*, vol. 12, p. 024401, 2009. doi:10.1103/PhysRevSTAB.12.040704
- [10] C. Huang, T. J. T. Kwan, and B. E. Carlsten, "Two dimensional model for coherent synchrotron radiation," *Phys. Rev. ST Accel. Beams*, vol. 16, p. 010701, 2013. doi:10.1103/PhysRevSTAB.16.010701
- [11] Y. Cai, "Coherent synchrotron radiation by electrons moving on circular orbits," *Phys. Rev. Accel. Beams*, vol. 20, p. 064402, 2017. doi:10.1103/PhysRevAccelBeams.20.064402
- [12] P. Physics. General Particle Tracer. www.pulsar.n1/gpt
- [13] G. Bassi, T. Agoh, M. Dohlus, L. Giannessi, R. Hajima, A. Kabel, T. Limberg, and M. Quattromini, "Overview of csr codes," *Nucl. Instrum. Meth. A*, vol. 557, no. 1, p. 15, 2006. doi:10.1016/j.nima.2006.10.067

- [14] L. Giannessi, "Simulation codes for high brightness electron beam free-electron laser experiments," *Phys. Rev. ST Accel. Beams*, vol. 6, p. 114802, 2003. doi:10.1103/PhysRevSTAB.6.114802
- [15] E. L. Saldin, E. A. Schneidmiller, and M. V. Yurkov, "On the coherent radiation of an electron bunch moving in an arc of a circle," *Nucl. Instrum. Meth. A*, vol. 398, no. 2, pp. 373 – 394, 1997. doi:10.1016/S0168-9002(97)00822-X
- [16] G. V. Stupakov and P. Emma, "CSR wake for a short magnet in ultrarelativistic limit," *SLAC-PUB-9242*, 2002. doi:10.2172/799089
- [17] R. Li, "Self-consistent simulation of the csr effect on beam emittance," *Nucl. Instrum. Meth. A*, vol. 429, no. 2, p. 310, 1999. doi:10.1016/S0168-9002(99)00135-7
- [18] A. Kabel, M. Dohlus, and T. Limberg, "Using traffic⁴ to calculate and minimize emittance growth due to coherent synchrotron radiation," *Nucl. Instrum. Meth. A*, vol. 455, no. 1, p. 185, 2000. doi:10.1016/S0168-9002(00)00729-4
- [19] L. Giannessi and M. Quattromini, "TREDI simulations for high-brilliance photoinjectors and magnetic chicanes," *Phys. Rev. ST Accel. Beams*, vol. 6, p. 120101, 2003. doi:10.1103/PhysRevSTAB.6.120101
- [20] Y. S. Derbenev, J. Rossbach, E. L. Saldin, and V. D. Shiltsev, "Microbunch radiative head-tail interaction," *TESLA FEL Reports 1995-05*, 1995.
- [21] E. Allaria *et al*, "Highly coherent and stable pulses from the FERMI seeded free-electron laser in the extreme ultraviolet," *Nat. Photon.*, vol. 6, p. 699, 2012. doi:10.1038/nphoton.2012.233
- [22] E. Allaria *et al*, "Two-stage seeded soft-x-ray free-electron laser," *Nat. Photon.*, vol. 7, p. 913, 2013. doi:10.1038/nphoton.2013.277
- [23] A. D. B. *et al*, "Beyond the limits of 1D coherent synchrotron radiation," *New J. Phys.*, vol. 20, no. 7, p. 073035, 2018. doi:10.1088/1367-2630/aad21d
- [24] S. B. van der Geer, M. J. de Loos, I. D. Setija, P. W. Smorenburg, P. H. Williams, and A. D. Brynes, "GPT-CSR: A new simulation code for CSR effects," *Proc. 9th Int. Particle Accelerator Conf. (IPAC'18), Vancouver, Canada*, 2018. doi:10.18429/JACoW-IPAC2018-THPAK078
- [25] M. G. Minty and F. Zimmermann, "Beam techniques - beam control and manipulation," *SLAC-R-621*, 2003. doi:10.2172/813024
- [26] M. Borland, "Elegant: A flexible SDDS-compliant code for accelerator simulation," *Proceedings of ICAP'00, Darmstadt, Germany*, 8 2000. doi:10.2172/761286
- [27] M. Dohlus and T. Limberg, "CSRTrack: Faster calculation of 3-d csr effects," *Proceedings of FEL'04, Trieste, Italy*, 2004, paper MOCOS05.
- [28] G. Stupakov, "Centripetal transverse wakefield in relativistic beam," *arXiv*, vol. 1901, 2019.
- [29] E. P. Lee, "Cancellation of the centrifugal space-charge force," *Part. Accel.*, vol. 25, 1990.
- [30] R. Li and Y. S. Derbenev, "Discussions on the cancellation effect on a circular orbit," *Proceedings of PAC'05, Knoxville, TN, USA*, 2005.
- [31] R. Li and Ya. S. Derbenev, "Canonical formulas and cancellation effect in electrodynamics of relativistic beams on a curved trajectory," *JLAB-TN-02-054*, 2002, unpublished.
- [32] R. e. Akre, "Commissioning the Linac Coherent Light Source injector," *Phys. Rev. ST Accel. Beams*, vol. 11, p. 030703, 2008. doi:10.1103/PhysRevSTAB.11.030703
- [33] A. H. Lumpkin, R. J. Dejus, and N. S. Sereno, "Coherent optical transition radiation and self-amplified spontaneous emission generated by chicane-compressed electron beams," *Phys. Rev. ST Accel. Beams*, vol. 12, p. 040704, 2009. doi:10.1103/PhysRevSTAB.12.040704

LONGITUDINAL PHASE SPACE STUDY ON INJECTOR BEAM OF HIGH REPETITION RATE X-RAY FEL*

Qiang Gu[†], Zhen Wang, Shanghai Advanced Research Institute, Shanghai, China

Abstract

The longitudinal phase space of electron beam from the high repetition rate injector usually twisted and deteriorated by the space charge force. It causes the high order correlated energy spread and the local chirp within the beam, which could not be compensated by the harmonic correction before the compression in the linac. As a consequence of this problem, one could not get ideal beam with a peak current more than kiloamperes. In this paper several approaches have been studied to relieve this effect and get the well compressed beam for the lasing.

INTRODUCTION

Two high repetition rate X-ray free electron laser facilities based on the continuous wave linac are under construction [1-2]. In the early stage of the LCLS-II injector design, people have compared the beam dynamics optimization, as well as the beam performance between the VHF gun and DC gun based injectors. Both of the injectors shown the good transverse emittance, but the longitudinal phase space of the electron beam at the exit of the DC gun based injector had larger high order correlated energy spread which could not be compensated before compression system in main linac. Finally, the VHF gun has been adopted by LCLS-II.

Table 1: Main Parameters of the Electron Beam

Parameter	Value	Unit
Beam energy	8	GeV
Slice emittance, nor.	0.2-0.7	μmrad
Bunch charge	10-300	pC
Repetition rate, max.	1	MHz
Peak current	0.5-1.5	kA

SHINE is a hard X-ray free electron laser facility with a shortest FEL wavelength of 15keV. The main parameters of the electron beam are listed in Table 1. To obtain the FEL with higher energy, LCLS-II HE chose the lower emittance [3], while SHINE chose higher peak current and even higher peak current is preferred for the higher photon energy up to 25keV. LCLS-II and SHINE now has adopted a photo-injector consisting of a VHF gun followed by a velocity bunching and accelerating system to generate the qualified beam. It has shown that even with the VHF gun, the high order correlated energy spread is too large to get a beam current larger than kA. The solution for SHINE is to linearize the global or local high

order correlated energy spread before compression and it is better to complete the correction locally in the injector.

The high repetition rate photo injector usually consists of a photo cathode gun which generates the electron beam, followed by a velocity bunching system to reduce the bunch length which could be accepted by the further acceleration and compression in the linac, and an emittance compensation system with solenoids, drifts and acceleration. Here we show the layout of SHINE injector in Figure 1 for example.

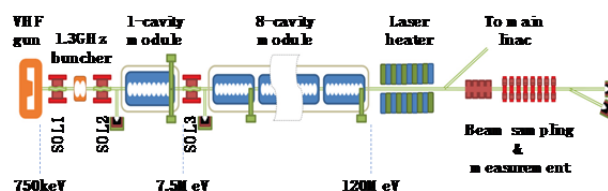


Figure 1: Layout of SHINE injector.

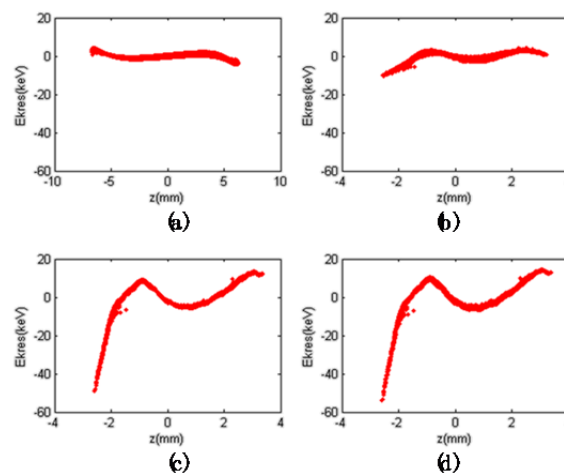


Figure 2: High order energy spread along the injector, (a) at the middle of the buncher; (b) at the entrance of the 1-cavity module; (c) at the entrance of the 8-cavity module; (d) at the end of the injector.

In the injector, the high order correlated energy spread is driven by the space charge force and velocity bunching process. The initial energy modulation is generated from the cathode to the buncher, which contributes the nonlinear chirp during the bunching process. Together with the nonlinear velocity modulation from the buncher, the non-uniform longitudinal density distribution of the bunched beam is produced. After bunching, this distribution enhances the energy modulation when the electron beam goes through the accelerating and drifting. Growth of the energy modulation almost stops at the end of the injector,

* Work supported by SHINE project

[†] guqiang@sinap.ac.cn

but this is too large to get the higher current at the linac. The high order energy spread along the injector is shown in Figure 2.

METHOD ON HIGH ORDER ENERGY MODULATION COMPENSATION

To cure this problem, one should linearize the energy modulation driven by the space charge force during accelerating and drifting, as well as the velocity modulation from the buncher. As noted, the all the steps of the high order term in longitudinal density and energy distribution mix up in the injector, so divide-and-rule for each cause and result is not practical. We hope to introduce simple corrector to resolve most of the problem.

The 3D-ellipsoid distribution of the electron beam is used to minimize the longitudinal mismatch of the transverse sliced emittance and reduce the projected emittance [4]. There are several methods to get the 3D-ellipsoid distribution electron beam based on laser pulse shaping or self-evolving by space charge [5-8]. Here, it is used to linearize the space charge force directly, while the nonlinear velocity modulation is left uncompensated.

Harmonic cavity is widely used to correct the nonlinear energy modulation before compression in free electron laser facilities [9]. In velocity bunching system, the nonlinear velocity modulation also could be compensated by a harmonic cavity [10]. In high repetition rate injector, the harmonic cavity could play the same role to correct the nonlinear velocity modulation introduced by the fundamental bunching cavity. In the layout of SHINE injector, there are no extra place to put an individual harmonic cavity near the buncher, so a dual mode cavity is designed for the beam dynamics study. The field distribution of the two modes is shown in Figure 3.

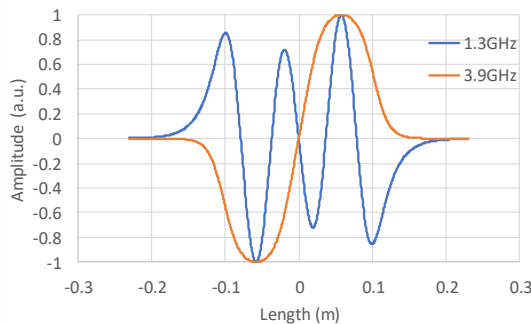


Figure 3: Fundamental and Harmonic electric field along the axis of the buncher.

Another idea has come out when we look at the electron bunch length at the buncher. It is long enough to feel the nonlinear field of the harmonic cavity, which means one can use the harmonic cavity to correct the high order energy modulation along the beam. The principle of this scheme is shown in Figure 4, in which only the correction is shown and the bunching voltage is not applied.

All the methods noted has been studied through injector to the linac with Astra [11] and LiTrack [12]. In the 2D tracking in linac, the longitudinal distribution will be

affected by lots of parameter and nonlinear terms [13]. We hope to use the genetic algorithm [14] to optimize the whole accelerator, but it turns out that this scheme was time-consuming and error-prone. Finally, we optimize the injector beam and linac beam separately. In linac optimization, we stop the tracking after the last compressor, because the longitudinal density distribution does not charge through the last acceleration section.

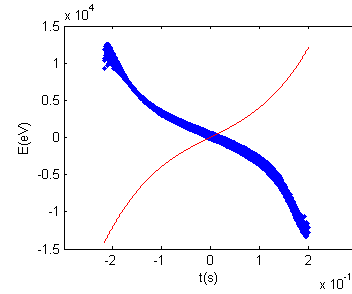


Figure 4: Correction of the high order energy modulation by harmonic cavity. Blue dots represent the longitudinal distribution at the entrance of the buncher. Red line is the combined electric field of two modes.

RESULTS AND DISCUSSION

We used the same bunch length as the beer-can distribution for the 3D-ellipsoid distribution. There are a lot of solutions on the pareto front with GA optimizer, but only the solution of the highest current is shown in Figure 5.

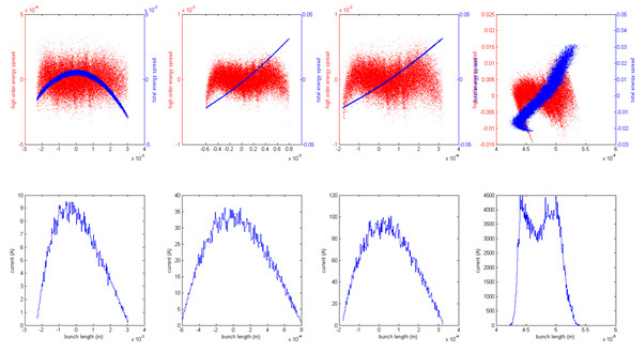


Figure 5: Longitudinal phase space along the linac (method 1). The figures from the left to right in columns are the longitudinal phase space at the end of injector, at the end of the 1st compressor, at the end of the 2nd compressor and at the end of the 3rd compressor. In the up row of the figures, the red dots represent the high order energy spread, while the blue dots represent the total energy spread.

From the figures, the bunch has an almost linear energy spread at the end of the injector, while the centre of current profile is shift to the head of the bunch. The nonlinear chirp of the energy spread is observed with the compression, which introduces the double-horn current profile at the final compression. As a whole, this method could let the beam compressed to much higher current than the original request [1].

To correct the nonlinear velocity modulation of the fundamental mode, a harmonic mode is applied with amplitude around 10% to the fundamentals. The linac optimization result is shown in Figure 6. It shows that the peak of the current profile shifts to the centre of the bunch with the correction. At the same time, the high order energy modulation is compensated slightly, and the double-horn current profile at the end of the linac improved. If the bunch length at the linac exit increases, the core of the current could be improved much.

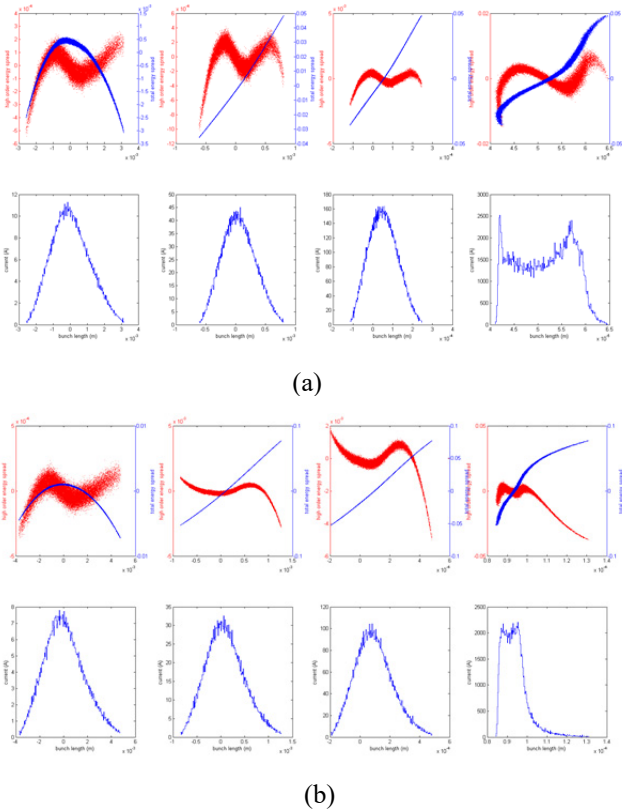


Figure 6: Longitudinal phase space along the linac (method 2). (a) bunch length is 1.1 mm (original design) at the injector exit; (b) bunch length is 1.6 mm at the injector exit.

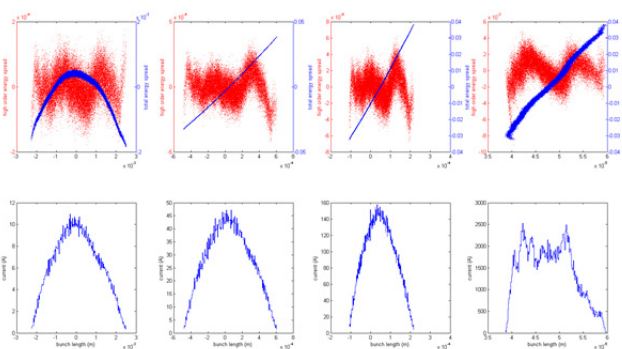


Figure 7: Longitudinal phase space along the linac (method 3).

The fundamental and harmonic field is set to another working point to compensate the high order energy modulation by space charge force. The result is shown in Figure 7. Most of the high order energy modulation is reduced to about 1/2 of the original amplitude and the double-horn like current profile is removed at the linac exit.

CONCLUSION AND EXPECTATION

To manipulate the longitudinal phase space with harmonic field is effective, but with drawbacks. The velocity linearizing with longer beam at injector exit could improve the core current of beam at linac exit, while the beam tails are lengthened. The long beam tail may cause the beam loss in the successive components. The high order energy spread could be compensated almost as good as using the 3D ellipsoid distribution, but the cavity voltage is about 1MV for fundamental field and 0.4MV for the harmonic field which could not be supported by the normal conducting structure. With the higher energy gun, optimized injector optics, and SRF technology, this method could be realizable and flexible.

Including the pulse stacking method, most of 3D ellipsoid distribution generation methods have been demonstrated with beam. So far, there are some limitations to apply to the high repetition rate photo injector, but the 3D-ellipsoid distribution electron beam is considered as an upgrade path in the future.

REFERENCES

- [1] SHINE CDR, 2018.
- [2] Linac Coherent Light Source at SLAC, <https://lcls.slac.stanford.edu/lcls-i>
- [3] Report of the Basic Energy Sciences Workshop on the Future of Electron Sources, 8-9 September 2016, SLAC National Accelerator Laboratory, Menlo Park, CA, USA.
- [4] C. Limborg-Deprey, P. R. Bolton, "Optimum electron distributions for space charge dominated beams in photoinjectors", *Nuclear Instruments and Methods in Physics Research A*, vol. 557 (2006) 106–116, doi:10.1016/j.nima.2005.10.061
- [5] P. Musumeci *et al.*, "Experimental Generation and Characterization of Uniformly Filled Ellipsoidal Electron-Beam Distributions", *Phys Rev Lett.*, 100, 244801 (2008), doi:10.1103/PhysRevLett.100.244801
- [6] Y. Li and J. W. Lewellen, "Generating a Quasi ellipsoidal Electron Beam by 3D Laser-Pulse Shaping", *Phys. Rev. Lett.*, 100, 078401 (2008), doi:10.1103/PhysRevLett.100.078401
- [7] S. Yu. Mironov *et al.*, "Generation of 3D ellipsoidal laser beams by means of a profiled volume chirped Bragg grating", *Laser Physics Letters*, vol. 13, number 5 (2016), doi:10.1088/1612-2011/13/5/055003
- [8] S. Yu. Mironov *et al.*, "Shaping of cylindrical and 3D ellipsoidal beams for electron photoinjector laser drivers," *Applied Optics.*, vol. 55, 1630-1635 (2016), doi:10.1364/AO.55.001630
- [9] P. Emma, "X-Band RF Harmonic Compensation for Linear Bunch Compression in the LCLS", LCLS-TN-01-1, 2001.
- [10] L. Serafini and M. Ferrario, "Velocity bunching in photoinjectors", *AIP Conference Proceedings*, vol. 581, 87 (2001), doi:10.1063/1.1401564

- [11] ASTRA, <http://www.desy.de/~mpyflo/>.
- [12] P. Emma and K. L. F. Bane, “LiTrack: A Fast Longitudinal Phase Space Tracking Code with Graphical User Interface”, in *Proc. 21st Particle Accelerator Conf. (PAC'05)*, Knoxville, TN, USA, May 2005, paper FPAT091.
- [13] I. Zagorodnov and M. Dohlus, “Semi-analytical modeling of multistage bunch compression with collective effects”, *Phys. Rev. ST Accel. Beams*, 14.014403 (2011), doi:10.1103/PhysRevSTAB.14.014403
- [14] MathWorks, NGPM -- A NSGA-II Program in Matlab v1.4, <https://www.mathworks.com/matlabcentral/fileexchange/31166-ngpm-a-nsga-ii-program-in-matlab-v1-4>

STEFFEN HARD-EDGE MODEL FOR QUADRUPOLES WITH EXTENDED FRINGE-FIELDS AT THE EUROPEAN XFEL

N. Golubeva*, V. Balandin, W. Decking, L. Fröhlich, M. Scholz,
DESY, Hamburg, Germany

Abstract

For modeling of linear focusing properties of quadrupole magnets the conventional rectangular model is commonly used for the design and calculations of the linear beam optics for accelerators. At the European XFEL the quadrupole magnets are described using a more accurate Steffen hard-edge model. In this paper we discuss the application of the Steffen approach for the European XFEL quadrupoles and present the examination of the model with the orbit response matrix technique.

INTRODUCTION

The 3.4 km long European XFEL facility is in operation since 2017 and currently serves three FEL beamlines simultaneously for user experiments [1, 2]. The facility is based on superconducting accelerator technology. After the injector which contains one standard superconducting accelerating module and a 3rd harmonic module, the beam is accelerated in the superconducting linear accelerator. To achieve a high peak current, the bunches are longitudinally compressed in three magnetic chicanes which are located in the injector and after the first (Linac 1) and second (Linac 2) parts of the accelerator. Diagnostic sections are placed in the injector and after the second and third compression stages. After the final acceleration in Linac 3 the beam passes a collimation section, and then the bunches of one bunch train are distributed between two electron beamlines leading to the SASE1 and SASE3 undulators and to the SASE2 undulator. Individual bunches can be selectively directed to the linac dump.

In such complicated machine the design linear optics incorporates many constraints on the behaviour of optical functions. For example, in the bunch compressors a special choice of Twiss function reduces the emittance growth due to coherent synchrotron radiation, diagnostic sections have to provide the special conditions for measurements of beam parameters, the optical functions in the collimation section have to be suitable for collimation purposes, the distribution system based on the kicker-septum scheme presents challenges for the dispersion suppression in both planes.

To provide a good performance of such sophisticated design optics, a good knowledge of optical properties of all magnetic elements is required. Before the commissioning, on the stage of the manufacturing of magnets we have arranged the comprehensive set of magnetic measurements. The accurate measurements of longitudinal field and field-gradient profiles have been made for all types of the European XFEL magnets. But an analysis of measured data

for quadrupole magnets has shown that for all quadrupoles the conventional hard-edge model does not provide a sufficient accuracy. For example, for the QI quadrupole type the conventional model can not provide more than two correct decimal digits in the transfer matrix elements (see Figure 1), that does not seem to be very satisfactory. This motivated us to consider other models for quadrupole magnets.

In general, having the field gradient profiles one may develop a special code calculating the focusing of quadrupoles with extended fringe-fields, but for practical purposes and especially for online optics calculations it is desirable to employ more practicable model. We have considered a Steffen approach [3] to quadrupole modeling. As it has been shown in the paper [4], for the European XFEL quadrupoles the Steffen parameters exist, and with sufficient for our purposes accuracy can be approximated using low order polynomials in the variable k_0 (m th-order Steffen model). And, for our luck, already the zeroth-order Steffen model can essentially improve the accuracy in comparison with the conventional hard-edge model (see Figure 1). In this paper we discuss the application of the zeroth-order Steffen model for the European XFEL quadrupoles. One should note that although the Steffen approach is not yet widely known, the interest seems to grow during last time (for example, see references in [4]).

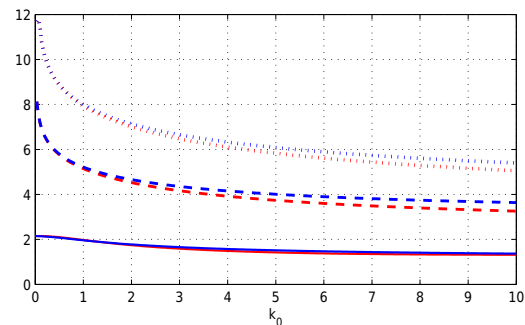


Figure 1: Quadrupole QI. The number of correct decimal digits in the approximation of the transport matrices $M^\pm(k_0)$ by conventional rectangular model (solid curves), and by zeroth (dashed curves) and first (dotted curves) order Steffen models. Red and blue colors refer to the focusing and defocusing matrices, respectively.

CONVENTIONAL AND STEFFEN HARD-EDGE MODELS

Optical linear properties of quadrupoles are determined by the quadrupole focusing strength k_0 and by the field gradient shape function $k(s)$ (the longitudinal field gradient profile). Figure 2 shows an example of the function $k(s)$

* nina.golubeva@desy.de

for one of the European XFEL quadrupoles. Here we use the notation from the paper [4], and assume that the maximum value of $k(s)$ is equal to one, and it is zero outside the interval $[-l_f/2, l_f/2]$ of the longitudinal s -axis.

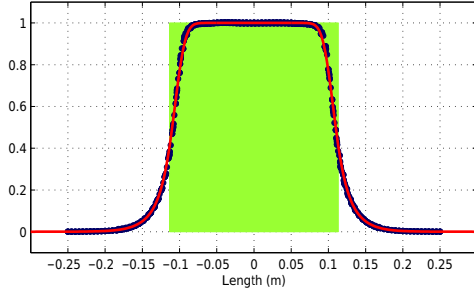


Figure 2: Quadrupole QI. Red curve shows its gradient shape function $k(s)$, which was obtained (in the form of some combination of the Enge functions) as a fit to the measured data represented in this figure by the blue dots. Green rectangle shows effective field boundary l_e .

Conventional Rectangular Model

In the conventional rectangular model the function $k(s)$ is approximated by the rectangular function which is unity inside and zero outside of an effective quadrupole length

$$l_e = \int_{-l_f/2}^{l_f/2} k(s) ds. \quad (1)$$

The linear beam transport through quadrupole can be described by 2×2 focusing and defocusing matrices $M^\pm(k_0)$ using the approximation

$$M^\pm(k_0) \approx D\left(\frac{l_f - l_e}{2}\right) Q^\pm(l_e, k_0) D\left(\frac{l_f - l_e}{2}\right), \quad (2)$$

where D is the 2×2 drift matrix, and Q^+ and Q^- are the usual focusing and defocusing matrices of the hard-edge quadrupole model, respectively. Parameters l_e and k_0 are usually named as effective quadrupole parameters.

Steffen Hard-Edge Model

A basis of the Steffen approach is to find a rectangular type model with different effective parameters for focusing and defocusing planes whose transfer matrices are exactly equal to the matrices $M^\pm(k_0)$. As the Steffen quadrupole parameters, Steffen effective lengths l^\pm and Steffen gradient reduction coefficients r^\pm are introduced such that the following equations have to be hold

$$M^\pm(k_0) = D\left(\frac{l_f - l^\pm}{2}\right) Q^\pm(l^\pm, r^\pm k_0) D\left(\frac{l_f - l^\pm}{2}\right). \quad (3)$$

As mentioned in [4], the functional dependence $l^\pm = l^\pm(k_0)$ and $r^\pm = r^\pm(k_0)$ can be found only once at the stage of the analysis of magnetic measurement data and then stored as a property for each quadrupole magnet. For

the European XFEL quadrupoles it is sufficient to approximate the effective parameters using low order polynomials in the variable k_0 and, as it has been shown in [4], already the zeroth-order Steffen model can essentially improve the accuracy in comparison with the conventional rectangular model. In this case as the Steffen quadrupole parameters the zeroth-order Steffen coefficients l_0 and r_0 can be used, which are given by the formulas [4]

$$l^\pm \approx l_0 = \left(\frac{12}{l_e} \int_{-l_f/2}^{l_f/2} s^2 k(s) ds \right)^{\frac{1}{2}}, \quad r^\pm \approx r_0 = \frac{l_e}{l_0}. \quad (4)$$

One should note that the zeroth-order Steffen model can be used in any standard beam dynamics program (for example, MAD and *Elegant*) because it is the same as conventional model but with modified effective parameters.

At the European XFEL there are in total about 500 quadrupole magnets which are grouped in 10 types, as reported in Table 1 (B_r is the quadrupole bore radius).

Table 1: European XFEL Quadrupole Types

Type	l_e (m)	l_0 (m)	r_0 (m)	B_r (m)	Count
Q	0.1973	0.2136	0.9240	0.040	98
QA	0.1098	0.1137	0.9655	0.008	103
QI	0.2268	0.2377	0.9541	0.025	58
QD	0.2252	0.2367	0.9516	0.025	34
QE	0.2254	0.2400	0.9393	0.025	42
QF	0.5261	0.5321	0.9887	0.025	89
QH	1.0262	1.0291	0.9972	0.025	34
QM	1.0515	1.0597	0.9923	0.050	12
QK	1.0450	1.0552	0.9903	0.050	21
QB	0.3215	0.3289	0.9775	0.025	2

It can be seen from Table 1 that for short quadrupoles (for example, the QI and QD types which are used in the injector and in the sections with chicanes for bunch compression, and the QA quadrupoles used in all three SASE undulator systems) the effective lengths in the conventional model and zeroth-order Steffen models differ for 3% – 5%. For long quadrupoles this difference becomes smaller.

MODEL PREDICTIONS AND MEASUREMENTS

To examine the optics model a precise setup of the beam optics is needed, for that a good knowledge of the beam energy and a calibration of magnets are essential. As concerning the beam energy, for sections where the beam energy is not changed the pre-defined energy is used for the setting of magnets, and the real beam energy is adjusted relying on beam-based energy measurements in dispersive sections of the machine.

An issue of importance is the calibration function between the field gradient and the power supply current. For

all quadrupole types the accurate measurements of full magnetic excitation curves have been made according the cycling procedures used in the machine operations, and two different calibration functions (in a form of a lookup table or a fifth-order polynomial) for the upward and downward current ramp are used. Using the Steffen quadrupole model the calibration functions are defined taking into account the Steffen gradient reduction coefficients r_0 .

For the examination of quadrupole model, the measurements of orbit response matrices - which are widely employed to find and correct linear optics errors in accelerators - have been performed. The actual measurements from the machine, which are provided by an orbit response tool [5], have been compared with the prediction of online optics model [6]. To check the model for different types of quadrupoles and exclude other focusing contributions the measurements are performed locally in different sections.

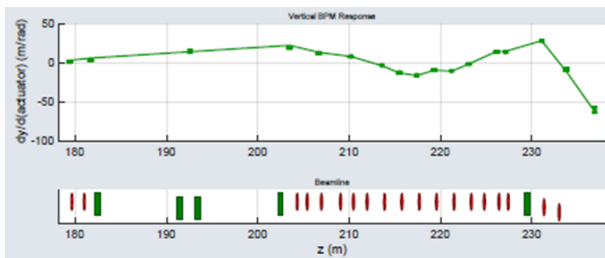


Figure 3: Section B1. Measured (solid curve) and predicted by model (dots) orbit response in the vertical plane. Rectangles mark dipole (green) and quadrupole (red) magnets.

Figures 3-5 present examples demonstrating the level of agreement between the model and measurements. The first example is for the section equipped with 20 short quadrupoles of the QI and QD types. The second example presents the post-linac collimation section which contains two types of quadrupoles (QF and QH), and dipole and sextupole magnets. For sextupole modeling the hard-edge model using the effective length is applied, but they are usually switched off for checking the quadrupole model.

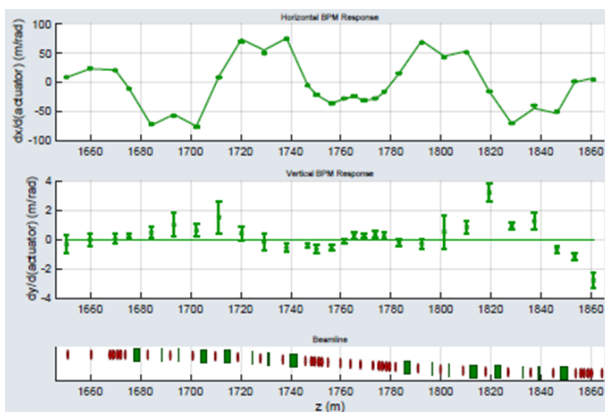


Figure 4: Collimation section. Measured (solid curve) and predicted by model (dots) orbit response in the horizontal plane (top). Response in other plane is also shown.

The Steffen model for superconducting quadrupoles also shows a good performance. Figure 5 shows the part of the accelerator (Linac 2) where the RF cavity focusing is negligible small.

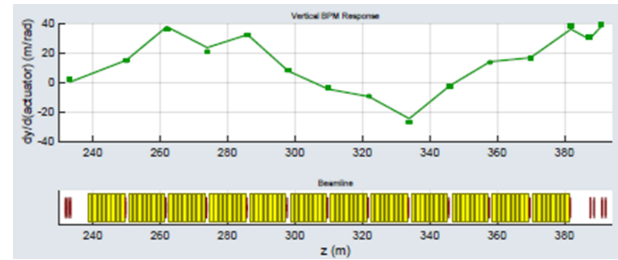


Figure 5: Linac 2. Acceleration from 700 MeV to 2.4 GeV. Measured (solid curve) and predicted by model (dots) orbit response in the vertical plane. Yellow rectangles mark the RF modules.

As can be seen, the agreement between measurements and model predictions is surprisingly good. About the same level of agreement is observed in all beamlines equipped with quadrupoles. We find that the zeroth-order Steffen model for quadrupoles is acceptably good, and currently we do not apply any corrections to the quadrupole model, neither to the quadrupole strengths nor to the calibration functions. Different design optics have been successfully used for the commissioning and for beam optics studies.

CONCLUSION

The zeroth-order Steffen model is used for the description of optical linear properties of all quadrupoles at the European XFEL from the beginning of operations and, together with the precise calibration of magnets, demonstrates a good accuracy for the application in the linear beam optics. Presently no any corrections based on beam-based measurements are applied to optical linear properties of quadrupoles.

REFERENCES

- [1] W. Decking *et al.*, "Status of the European XFEL", in *Proc. 10th Int. Particle Accelerator Conf. (IPAC'19)*, Melbourne, Australia, May 2019, pp. 1721–1723. doi:10.18429/JACoW-IPAC2019-TUPRB020
- [2] L. Froehlich *et al.*, "Multi-Beamline Operation at the European XFEL", presented at the 39th Int. Free Electron Laser Conf. (FEL'19), Hamburg, Germany, Aug. 2019, paper WEP008.
- [3] K. Steffen, *High Energy Beam Optics*, New York, 1965.
- [4] V. Balandin, W. Decking, and N. Golubeva, "Notes on Steffen Parameters of Extended Fringe-Field Quadrupoles", in *Proc. 7th Int. Particle Accelerator Conf. (IPAC'16)*, Busan, Korea, May 2016, pp. 3226–3228. doi:10.18429/JACoW-IPAC2016-THPMB005
- [5] L. Froehlich *et al.*, "High Level Software for the Commissioning of the European XFEL", in *Proc. 11th Int. Work-*

shop on Personal Computers and Particle Accelerator Controls (PCaPAC'16), Campinas, Brazil, Oct. 2016, pp. 110–113. doi:10.18429/JACoW-PCAPAC2016-THPOPRP013

puters and Particle Accelerator Controls (PCaPAC'14), Karlsruhe, Germany, Oct. 2014, paper WPO009, pp. 52–54.

- [6] S. M. Meykopff, “An Optics-Suite and -Server for the European XFEL”, in *Proc. 10th Int. Workshop on Personal Com-*

BEAM BASED ALIGNMENT IN ALL UNDULATOR BEAMLINES AT EUROPEAN XFEL

M. Scholz*, W. Decking, DESY, Hamburg, Germany
Y. Li, European XFEL, Hamburg, Germany

Abstract

The Free Electron Laser European XFEL aims at delivering X-rays from 0.25 keV up to 25 keV out of three SASE undulators. A good overlap of photon and electron beams is indispensable to obtain good lasing performance, especially for the higher photon energies. Thus the quadrupole magnets in the undulators must be aligned as good as possible on a straight line. This can only be realized with a beam based alignment procedure. In this paper we will report on the method that was performed at the European XFEL. We will also discuss our results.

INTRODUCTION

The European XFEL aims at delivering X-rays from 0.25 to up to 25 keV out of 3 SASE undulators [1,2]. The radiators are driven by a superconducting linear accelerator based on TESLA technology [3]. A schematic layout of the European XFEL is shown in Fig. 1. The linac operates in 10 Hz pulsed mode and can deliver up to 2700 bunches per pulse. The electron beam can be distributed to three different undulator beamlines within a pulse [4,5]. The European XFEL is being realized as a joint effort by 12 European countries. European XFEL's accelerator and major parts of the infrastructure are contributed by the accelerator construction consortium, coordinated by DESY.

The alignment of the magnets in FELs, especially in the undulator beamlines is crucial for top performance in the sense of maximum SASE pulse energy. This is especially the case with hard X-ray beamlines, which are extraordinarily sensitive to misalignments. In order to provide an efficient overlap between the electron and photon beams inside the undulator, the electron beam has to go through the undulators on a straight line with displacements below 10 μm . This alignment precision cannot be achieved by traditional optical alignment procedures thus beam based alignment (BBA) becomes necessary. The BBA procedure has been regularly carried out for all undulator beamlines at European XFEL. The method is well tested at other facilities [6,7] and it was also studied theoretically for European XFEL [8] before the start of the commissioning. We will report on the BBA activities at European XFEL as well as on some results we have achieved so far.

UNDULATOR SECTIONS

The two hard X-ray undulator beamlines SASE1 and SASE2 (see Fig. 1) are build up with 35 undulator cells. SASE3, the soft X-ray undulator consists of 21 undulator cells [9]. Each cell is 6.1 meters long and is composed of the

5 m long undulator itself and a 1.1 m long intersection. The elements of the intersections are, inter alia, a beam position monitor (BPM) as well as a quadrupole magnet. The magnet is mounted on a mover that allow adjusting its position in both transverse directions. The undulator period length is 40 mm for the hard X-ray undulators and 68 mm for the soft X-ray undulator. Figure 2 shows a technical drawing of an undulator cell including the intersection. The beam position monitors in the intersections are cavity BPMs with a sub μm resolution [10]. This is crucial because the alignment has to be accomplished in the μm range.

BEAM BASED ALIGNMENT METHOD

The BBA method has been described in previously published papers and reports e.g. [6–8]. We will refrain from a further description in detail in order to leave room for the presentation of the BBA results. In summary: The goal is to find the offsets of all BPMs as well as of all quadrupole magnets. The concept is to measure the electrons' trajectory for different beam energies while the magnetic field of the quadrupoles is kept constant. This allows to distinguish between BPM offsets, which are not depending on the beam energy, and the quadrupole offsets which lead to an energy depending kick when they are aligned off axis. The greater the energy difference between the measurement steps, the better the distinction between BPM and magnet offsets. The alignment procedure has to be carried out in several iterations until the final precision can be reached. BBA at European XFEL is carried out with four different electron beam energies, namely 10, 12, 14 and 17 GeV. 5-10 iteration are typically necessary to accomplish the BBA's goal. The whole procedure takes about 4-8 hours depending on the initial beamline setup. A significant part of the time is used to prepare all three undulator beamlines for beam transport with all four electron energies. The electron beam's energy is precisely determined for each energy step. This can be done most efficiently using the highly chromatic beam optics in the collimation section. Comparisons of measured and design trajectory responses to a horizontal kick upstream the collimations section allows to determine the beam energy to a precision in the per mille level. This ensures that the transfer matrices in the undulator, which are necessary to calculate the BPM and magnet offsets, are as precise as possible. For each energy, a machine setup is saved to a dedicated file, which can then be loaded during the BBA iterations within minutes. The fast kicker distribution system of European XFEL [4,5] allows to do BBA for all three beamlines at the same time. The BBA iterations are always carried out from low to high beam energies.

* matthias.scholz@desy.de

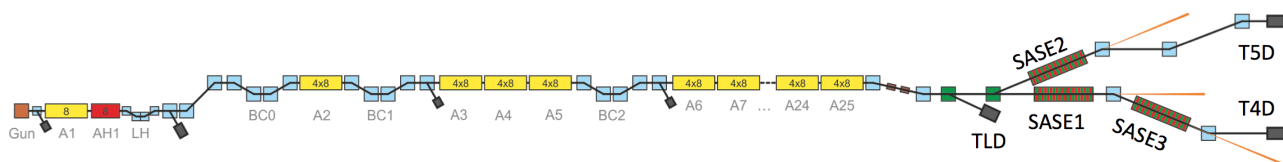


Figure 1: Schematic overview of the European XFEL. The injector including the electron gun, the first cryogenic 1,3 GHz acceleration module as well as the third harmonic RF-module are depicted on the left hand side. The next section contains the linac as well as the bunch compressors, followed by the collimation part and the beam distribution section. Finally the undulator beamlines are presented on right hand side.

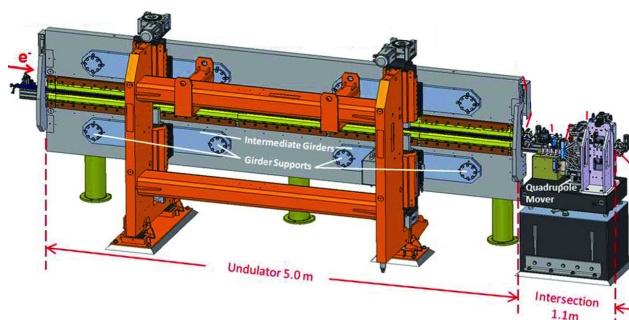


Figure 2: An undulator cell as used for European XFEL including the 5 m long variable gap undulator as well as a 1.1 m long intersection consisting, inter alia, of a beam position monitor and a quadrupole magnet.

RESULTS FROM BEAM BASED ALIGNMENT AT EUROPEAN XFEL

We will focus on some results from beam based alignment carried out at European XFEL that have been essential for FEL operation. These results are related to the hard X-ray beamlines SASE1 and SASE2, which are more sensitive to quadrupole magnet misalignments than SASE3. All undulator and photon beamlines were aligned initially with respect to a laser based straight line reference system. The expected alignment precision with respect to the straight line was in the range $\pm 100 \mu\text{m}$. However, due to systematic problems with the reference system the alignment of the beamlines was not as good as expected. Figure 3 shows the BPM and quadrupole offsets of SASE2 in both planes determined with beam based alignment. Two curves in each plot represent the BPM and quadrupole data from a measurement in February 2018 while the other two graphs show the data from a BBA in August 2019. The first BBA carried out in 2018 showed clearly that the intersection elements of the beamline carrying the BPMs and quadrupoles were misaligned. The offsets followed a sinusoidal curve with about one period over the undulator lengths and amplitude of about 1 mm. Realignment was arranged based on the data from the first BBA. Later measurements, e.g. the presented data from August 2019, showed that the new alignment was significantly better. Figure 4 and Fig. 5 show the offsets of 10 selected quadrupole magnets determined with BBA since the end of 2017. All offsets are plotted with respect to the current machine setup (August 2019). The first plot shows data from

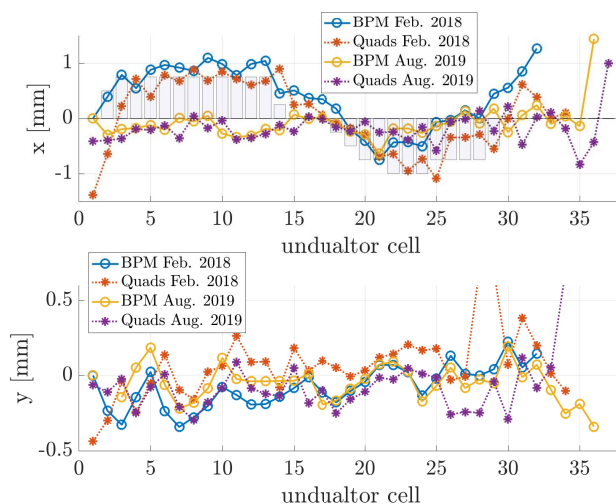


Figure 3: BBA result for quadrupole and BPM offsets from February 2018 and August 2019. The results from 2018 revealed a strong misalignment of the beamlines in the horizontal plane. This misalignment was correct. The correction offsets are depicted as bars in the upper plot. The BBA results from 2019 show that the realignment was successful.

SASE1 and the second plot depicts the same information for SASE2. Our BBA learning curve can be reconstructed from these plots. It is clearly visible that the relative offsets were constantly large or did even oscillate with large amplitudes around the current value. However, we converged to solutions that are close to what we use right now. This could be achieved with the BBA carried out in January 2019 for SASE1 and with the BBA carried out in April 2019 for SASE2. The major changes were: The electron beam energies were determined more precisely for each energy step. And all iterations started with the lowest and ended with the highest beam energy. Before that the beam energy was changed in one iteration from lowest to highest energy and in the next iteration in the opposite direction. Furthermore, more time was spent to keep the launch trajectory to the undulator the same for all measurements within one iteration. The SASE pulse energy could be increased with these BBAs in the respective beamlines. The pulse energy development over the last year for SASE1 and SASE2 can be found in Fig. 6. The maximum SASE level in SASE1 was in the range of 1.5 mJ in 2018. The BBA carried out in January 2019

helped to achieve up to 3 mJ at 9.3 keV photon energy and 4 mJ at 7 keV in the following months. Operation of SASE2 was difficult until April 2019. The SASE pulse energy was typically in a range of 300–400 μ J. The BBA carried out on April 3, 2019 changed the situation completely. SASE2 pulse energies are since that alignment typically close to the pulse energies of SASE1.

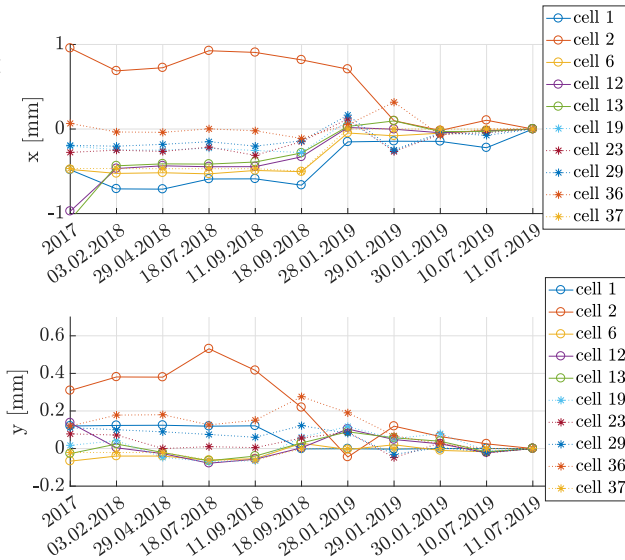


Figure 4: Relative quadrupole offsets of 10 selected magnets in the SASE1 beamline. All offsets are plotted with respect to the current machine settings (August 2019). The offsets' variation from one BBA to the next became smaller with the measurement carried out at the beginning of 2019.

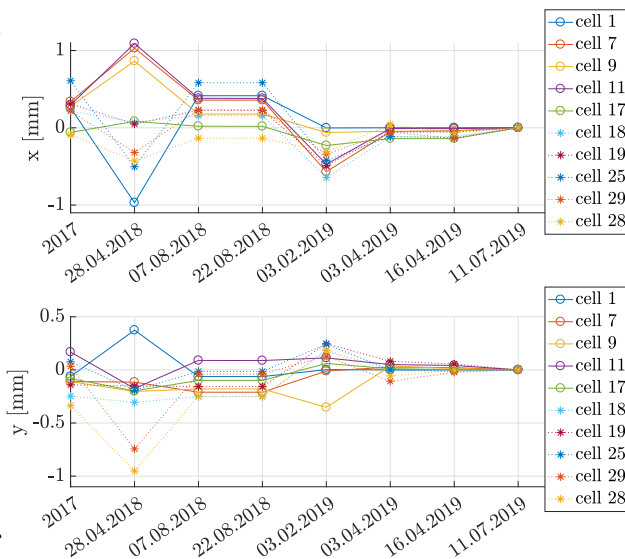


Figure 5: Relative quadrupole offsets of 10 selected magnets in the SASE2 beamline. All offsets are plotted with respect to the current machine settings (August 2019). The offsets' variation from one BBA to the next became smaller with the measurement carried out in April 3, 2019.

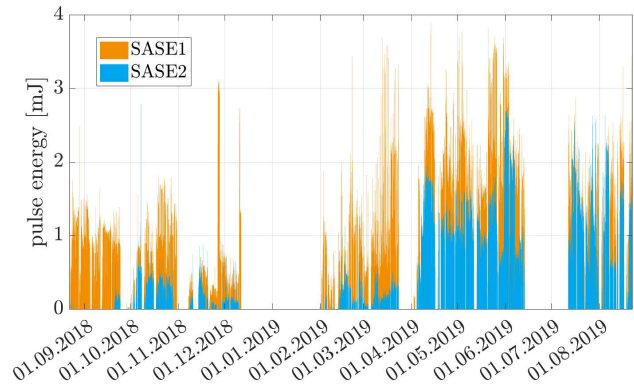


Figure 6: SASE pulse energy development for the hard x-ray undulator beamlines SASE1 and SASE2 during the last year. The BBA carried out at the beginning of February 2019 helped to increase the pulse energy of SASE1 significantly. The improvement due to the BBA in SASE2 carried out at the beginning of April 2019 is even more significant.

CONCLUSIONS AND OUTLOOK

We improved the BBA procedure during the last months and could achieve a significant increase of the SASE pulse intensities in both hard X-ray beamlines of European XFEL, SASE1 and SASE2. A strong misalignment of the SASE2 beamline could be found due to the BBA procedure. The realignment was carried out successfully based on the BBA data, which was confirmed by the results of the next BBA. We will continue to work on the procedure in order to improve the result even further. The goal is to align all undulator beamlines with offsets below 10 μ m which could not yet been achieved.

ACKNOWLEDGMENT

We like to thank all colleagues who have been involved the operation of the European XFEL.

REFERENCES

- [1] M. Altarelli *et al.*, “The European X-Ray Free-Electron Laser, Technical design report”, DESY-06-097, July 2007. doi: 10.3204/DESY_06-097
- [2] R. Brinkmann *et al.*, “TESLA XFEL: First stage of the X-ray laser laboratory. Technical design report, supplement”, DESY 02-167, March 2002.
- [3] R. Brinkmann *et al.*, “TESLA Technical Design Report – Part II: The Accelerator”, DESY 01-011, March 2001.
- [4] S. Liu *et al.*, “Parallel Operation of SASE1 and SASE3 at European XFEL”, presented at FEL'19, Hamburg, Germany, 2019, paper TUA01, this conference.
- [5] L. Fröhlich *et al.*, “Multi-Beamline Operation at the European XFEL”, presented at FEL'19, Hamburg, Germany, 2019, paper WEP008, this conference.
- [6] P. Emma, R. Carr, H.-D. Nuhn, “Beam-based alignment for the LCLS FEL undulator”, *Nuclear Instruments and Methods*

- in *Physics Research A*, vol. 429, pp. 407-413, 1999. doi:10.1016/S0168-9002(99)00117-5
- [7] Y. Woon *et al.*, “Automation of beam based alignment for the PAL-XFEL undulator line”, *Nuclear Instruments and Methods in Physics Research A*, vol. 782, pp. 120-125, May 2015. doi:10.1016/j.nima.2015.02.009
- [8] H. Jin, W. Decking, T Limberg, “Beam-based alignment in the European XFEL SASE1”, TESLA-FEL 2013-03, 2013.
- [9] S. Abeghyan *et al.*, “First operation of the SASE1 undulator system of the European X-ray Free-Electron Laser”, *J. Synchrotron Rad.*, vol. 26, pp. 302-310, 2019. doi:10.1107/S1600577518017125
- [10] D. Lipka, “Very First Experience with the Standard Diagnostics at the European XFEL”, in *Proc. IPAC’17*, Copenhagen, Denmark, May 2017, pp. 180-183. doi:10.18429/JACoW-IPAC2017-MOPAB043

ARBITRARY ORDER PERTURBATION THEORY FOR A TIME-DISCRETE MODEL OF MICRO-BUNCHING DRIVEN BY LONGITUDINAL SPACE CHARGE

Ph. Amstutz*, Lawrence Berkeley National Lab, Berkeley, USA
M. Vogt, Deutsches Elektronen-Synchrotron DESY, Hamburg, Germany

Abstract

A well established model for studying the micro-bunching instability driven by longitudinal space charge in ultra-relativistic bunches in FEL-like beamlines can be identified as a time-discrete Vlasov system with general drift maps and Poisson type collective kick maps. Here we present an arbitrary order perturbative approach for the general system and the complete all-orders solution for a special example. For this example we benchmark our theory against our Perron-Frobenius tree-code.

INTRODUCTION

Longitudinal dynamics in the magnetic bunch-compressors of free-electron laser injectors can drive a micro-bunching instability, deteriorating the electron bunch quality [1, 2]. As established in References [3, 4] the space-charge driven micro-bunching effect – in the ultra-relativistic limit – be investigated by means of a time-discrete model. In this model the longitudinal dynamics of the system are exactly captured by a combination of drift maps $D[\lambda]: \mathbb{R}^2 \rightarrow \mathbb{R}^2$

$$D[\lambda]: z = (q, p) \mapsto (q + \lambda(p), p)$$

with a dispersion function $\lambda \in C^1(\mathbb{R}, \mathbb{R})$ and kick maps $K[k]: \mathbb{R}^2 \rightarrow \mathbb{R}^2$

$$K[k]: (q, p) \mapsto (q, p + k(q))$$

with a kick function $k \in C^1(\mathbb{R}, \mathbb{R})$. The collective nature of the micro-bunching is accounted for by adopting the Vlasov-picture, where the electron bunch is described by its probability density in phase space $\Psi: \mathbb{R}^2 \rightarrow \mathbb{R}$. A remarkable property of the model is the fact that it remains exactly solvable in terms of time-discrete maps, even in presence of *collective* kick functions $k[\Psi]$. It can be shown that a phase-space density (PSD) evolves as

$$\Psi(x) \mapsto \Psi(M^{-1}(x))$$

where M is the solution of the equations of motion of the system. A PSD is therefore propagated by objects defined by

$$\mathcal{M}\Psi := \Psi \circ M^{-1}$$

called Perron-Frobenius operators (PFO). The overall effect of a single bunch-compressor stage is then given by

$$\mathcal{M}[\Psi] = \mathcal{D}_{\text{Chic}} \mathcal{K}_{\text{Cav}} \mathcal{K}[\Psi]_{\text{SC}}$$

* amstutz@lbl.gov

where $\mathcal{D}_{\text{Chic}}$ is the PFO associated to the drift map describing the dispersive magnetic chicane. \mathcal{K}_{Cav} and \mathcal{K}_{SC} are the PFOs of the kick maps describing the impact of the accelerating cavity and the collective self-interaction of the bunch in the field-free region upstream of the chicane, respectively. Thus the complete time-discrete Vlasov system is defined by

$$\Psi \mapsto \mathcal{M}[\Psi] \Psi.$$

PERTURBATION THEORY

The effect that initially small perturbations $\varepsilon\phi$ of an otherwise homogeneous charge distribution Ψ amplify themselves by virtue of a collective self-interaction

$$\mathcal{M}\Psi + \varepsilon\phi \quad (1)$$

is generally referred to as *Micro-bunching*. While PFOs are linear operators in the sense that $\mathcal{M}(c_1\Psi_1 + c_2\Psi_2) = c_1\mathcal{M}\Psi_1 + c_2\mathcal{M}\Psi_2$, collective PFOs are generally not linear in their *internal* dependence on the PSD $\mathcal{M}[c_1\Psi_1 + c_2\Psi_2] \neq c_1\mathcal{M}[\Psi_1] + c_2\mathcal{M}[\Psi_2]$. This drives the need for a perturbation theory to investigate Equation (1), as derived in [4, 5]. It has been shown that Equation (1) for a general collective PFO $\mathcal{M}[\Psi]$ can be expanded in ε

$$\begin{aligned} \mathcal{M}[\Psi_0 + \varepsilon\phi_0](\Psi + \varepsilon\phi_0) &= \mathcal{M}[\Psi_0]\Psi_0 + o(\varepsilon^{N+1}) \\ &+ \sum_{n=1}^N \varepsilon^n \left(\mathcal{M}^{(n)}[\Psi_0]\phi_0^n\Psi_0 + \mathcal{M}^{(n-1)}[\Psi_0]\phi_0^n \right) \\ &\equiv \Psi_1 + \sum_{n=1}^N \varepsilon^n \phi_{1,n} + o(\varepsilon^{N+1}), \end{aligned} \quad (2)$$

where $\mathcal{M}^{(n)}$ is the n -th Frechet derivative of \mathcal{M} . $\Psi_1 \equiv \mathcal{M}[\Psi_0]\Psi_0$ is the solution of the unperturbed system.

For a collective PFO of the form

$$\mathcal{M}[\Psi] = \mathcal{L}\mathcal{K}[k[\Psi]] \quad (3)$$

with an arbitrary non-collective PFO \mathcal{L} it can be shown that the n -th order propagated perturbations take the form

$$\begin{aligned} \phi_{1,n} &= (-1)^n \mathcal{M}[\Psi_0] \left(\frac{k[\phi_0]^n \circ Q}{n!} \partial_p^n \Psi_0 \right. \\ &\quad \left. - \frac{k[\phi_0]^{n-1} \circ Q}{(n-1)!} \partial_p^{n-1} \phi_0 \right), \end{aligned} \quad (4)$$

where the projection operator $Q: \mathbb{R}^2 \rightarrow \mathbb{R}$

$$Q: (q, p) \mapsto q$$

has been introduced. For a detailed derivation see References [4, 5].

EXAMPLE: LONG BUNCH, HARMONIC MODULATION

Consider an long bunch with undisturbed PSD $\Psi_0(q, p) = \Lambda(\alpha; q)\xi(0, \sigma; p)$, where $\xi(\mu, \sigma; \cdot)$ is a Gaussian distribution and

$$\Lambda(\alpha; q) \equiv \begin{cases} 1/\alpha & -\alpha/2 \leq q \leq \alpha/2 \\ 0 & |q| \geq \alpha/2 + d \\ \text{smooth} & \alpha/2 \leq |q| \leq \alpha/2 + d \end{cases} \quad (5)$$

with $d \ll \alpha$ and α large enough to make edge-effects negligible. Let

$$\mathcal{M}[\Psi] = \mathcal{D}[q \mapsto \beta q] \mathcal{K}[k[\Psi]], \quad (6)$$

$k[\Psi] = \mathcal{G} * \int_{\mathbb{R}} \Psi dp$ being a Poisson-type collective kick with Greens function \mathcal{G} . This setup corresponds to a single bunch compressor stage with vanishing RF-Voltage and therefore no actual compression. For disturbances of the form $\varepsilon\phi_0(q, p) = \Psi_0(q, p)S(q)$ it can be shown that the propagated disturbances (4) take the form

$$\begin{aligned} \phi_{1,n} = & (-1)^n \Lambda(\alpha; q) \xi(0, \sigma; p) \\ & \left(\frac{k[\phi_0]^n (q - \beta p)}{n!} \tilde{H}_n(\sigma; p) \right. \\ & \left. - \frac{k[\phi_0]^{n-1} (q - \beta p)}{(n-1)!} S(q - \beta p) \tilde{H}_{n-1}(\sigma; p) \right), \end{aligned} \quad (7)$$

where $\tilde{H}_n(\sigma; p) \equiv H_n(p/\sqrt{2\sigma^2})(-\sqrt{2\sigma^2})^{-n}$ the modified n -th Hermite polynomial.

For a sinusoidal modulation $S(q) \equiv \mu \sin(\kappa q)$ the collective kick function can be solved explicitly

$$k[\phi_0](q) = \hat{\mu}_\kappa \cos(\kappa q),$$

with $\hat{\mu}_\kappa \equiv \tau \mu \mathfrak{I} \tilde{\mathcal{G}}(\kappa)/\alpha$, where τ is proportional to the length of the chicane and $\tilde{\mathcal{G}}(\kappa)$ is the Fourier transform of the Greens function (impedance). Of particular interest for the investigation of microbunching effects is the evolution of the spatial charge densities of the propagated disturbance terms $\rho_{1,n}(q) = \int_{\mathbb{R}} \phi_{1,n}$, which for the example at hand can be calculated explicitly, albeit with significant algebraic effort as carried out in [5]. Depending on the evenness of n two different terms are obtained

$$\begin{aligned} \rho_{1,n,\text{even}} = & \frac{(-1)^{\frac{n}{2}} \hat{\mu}_\kappa^n \beta^n \kappa^n}{n! 2^{n-1} \alpha} \left\{ \sum_{k=1}^{\frac{n}{2}} \left(\binom{n}{\frac{n}{2}-k} \cos(2k\kappa q) (2k)^n e^{-\frac{1}{2}(2k\sigma\beta\kappa)^2} \right. \right. \\ & + \frac{n\mu}{\hat{\mu}_\kappa \beta \kappa} \binom{n-1}{\frac{n}{2}-k} \left[\cos(2k\kappa q) (2k)^{n-1} e^{-\frac{1}{2}(2k\sigma\beta\kappa)^2} \right. \\ & \left. \left. - \cos([2k-2]\kappa q) (2k-2)^{n-1} e^{-\frac{1}{2}(\sigma\beta\kappa[2k-2])^2} \right] \right\}. \end{aligned} \quad (8)$$

$$\begin{aligned} \rho_{1,n,\text{odd}} = & \frac{(-1)^{\frac{n-1}{2}} \hat{\mu}_\kappa^n \beta^n \kappa^n}{n! 2^{n-1} \alpha} \left\{ \sum_{k=0}^{\frac{n-1}{2}} \left(\binom{n}{\frac{n-1}{2}-k} \sin(\kappa q [2k+1]) (2k+1)^n e^{-\frac{1}{2}(\sigma\beta\kappa[2k+1])^2} \right. \right. \\ & + \frac{n\mu}{\hat{\mu}_\kappa \beta \kappa} \binom{n-1}{\frac{n-1}{2}-k} \left[\sin(\kappa q [2k+1]) (2k+1)^{n-1} e^{-\frac{1}{2}(\sigma\beta\kappa[2k+1])^2} \right. \\ & \left. \left. - \sin(\kappa q [2k-1]) (2k-1)^{n-1} e^{-\frac{1}{2}(\sigma\beta\kappa[2k-1])^2} \right] \right) \\ & \left. - \frac{n\mu}{\hat{\mu}_\kappa \beta \kappa} \binom{n-1}{\frac{n-1}{2}} \sin(\kappa q) e^{-\frac{1}{2}(\sigma\beta\kappa)^2} \right\}. \end{aligned} \quad (9)$$

While we can report that direct numerical evaluation has shown that the sum $\sum_{n=1}^N \rho_{1,n}$ does converge (albeit slowly) for $N \rightarrow \infty$ over a wide range of parameters, a formal investigation of its convergence properties is still outstanding.

SIMULATION

In order to verify the presented analytical results we compare them to simulations using our tree-based Perron Frobenius code [6]. The lower plots in Figures 1 show the propagated PSDs

$$\Psi_1 = \mathcal{D}[q \mapsto \beta q] \mathcal{K}[k[\Psi_0]] \Psi_0,$$

where the initial density – as above – is given by

$$\Psi_0(q, p) = \Lambda(\alpha; q) \xi(0, \sigma; p) [1 + \mu \sin(\kappa q)].$$

For the impedance term, we chose a model that treats the longitudinal space-charge force as the force that a cylindrical bunch with radius a exerts on an electron on its axis

$$\mathfrak{I} \tilde{\mathcal{G}}(\kappa) = \frac{2}{a^2 \kappa} [1 - a |\kappa| K_1(a |\kappa|)], \quad (10)$$

with the first-order modified Bessel-Function K_1 . In the upper plots the spatial charge densities obtained from simulation (black) is compared to the analytical result (red) given by $\rho = \int_{\mathbb{R}} \Psi_1 + \sum_{n=1}^{N=128} \phi_{1,n} dp$. All parameters are the same in both cases; their explicit value is not meaningful in the framework of this dimensionless benchmark. In the left plot the case of vanishing chicane strength $\beta = 0$ is depicted whereas in the right plot β is set to a positive value. It can be seen that in both cases the analytical and numerical results are in very good agreement.

The right plot shows the formation of “double horns” in the spatial charge density: Around this particular chicane setting β^* , the crests of the momentum-modulated PSD overlap in such a way to form *two* maxima. For $\beta \ll \beta^*$ only a single maximum resulting from the erecting falling edge of the modulation is formed. For $\beta \gg \beta^*$ the bunching washes out and is much less pronounced. Investigation of this effect will be the subject of future work.

CONCLUSION

We have summarized recent advancements of our Perron-Frobenius-Vlasov perturbation-theory. For a specific, yet

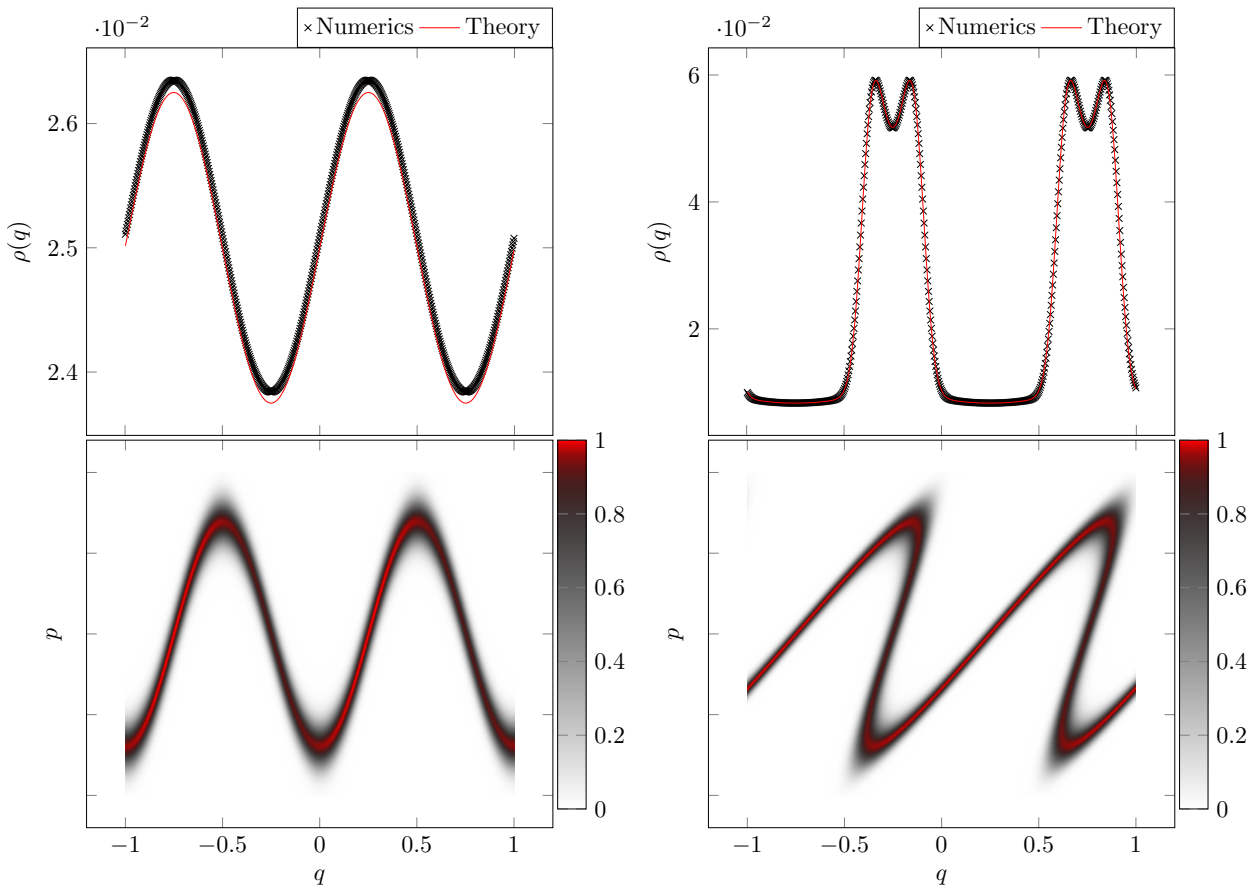


Figure 1: Comparison of the charge densities obtained from simulation with our Perron-Frobenius code and the analytical result (top plots), for vanishing (left) and a positive (right) chicane strength. The lower plots depict the PSD calculated by the code.

practically relevant example the theory is analytically tractable to arbitrary order and yields predictions for both, PSD and charge density of the propagated bunch, which have been presented. A cross-check between analytical and numerical results has been performed, showing good agreement.

REFERENCES

- [1] E. L. Saldin, E. A. Schneidmiller, M. V. Yurkov, “Longitudinal Space Charge Driven Microbunching Instability in TTF2 Linac”, *Proceedings of the ICFA Future Light Sources Sub-Panel Mini Workshop on Start-to-End Simulations of X-RAY FELs, Zeuthen* (2003), http://www.desy.de/s2e/Talks/Monday/Talk_schneidmiller.pdf
- [2] M. Venturini, M. Migliorati, C. Ronsivalle, M. Ferrario, and C. Vaccarezza. “Dynamics of longitudinal phase-space modulations in an rf compressor for electron beams” *Phys. Rev. ST Accel. Beams*, vol. 13, p. 080703, 2010. doi:10.1103/PhysRevSTAB.13.080703
- [3] M. Dohlus, “Space Charge Instability in XFEL”, *talk given at the DESY XFEL Beam Dynamics Seminar* (21.11.2005), http://www.desy.de/xfel-beam/data/talks/talks/dohlus_-_sc_gain_500mev_20x5_20051121.pdf
- [4] M. Vogt, Ph. Amstutz, “Arbitrary Order Perturbation Theory for Time-Discrete Vlasov Systems with Drift Maps and Poisson Type Collective Kick Maps”, in *Nonlinear Dynamics and Collective Effects in Particle Beam Physics*, World Scientific, 2019, pp. 169–181.
- [5] Ph. Amstutz, “Vlasov Simulation of Exotic Phase-Space Densities via Tree-Based Domain-Decomposition”, Verlag Deutsches Elektronen-Synchrotron, DESY-THESIS-2018-022, 2018.
- [6] Ph. Amstutz, M. Vogt, “Time-Discrete Vlasov Approach to LSC Driven Microbunching in FEL-like Beam Lines”, in *Nonlinear Dynamics and Collective Effects in Particle Beam Physics*, World Scientific, 2019, pp. 182–191. .

FREQUENCY-DETUNING DEPENDENT TRANSIENT COAXIAL RF COUPLER KICK

Y. Chen^{*1,2}, H. Qian¹, M. Krasilnikov¹, F. Brinker², W. Decking², J. Good¹, M. Gross¹, P. Huang¹, I. Isaev¹, C. Koschitzki¹, S. Lal¹, X. Li¹, O. Lishilin¹, G. Loisch¹, D. Melkumyan¹, R. Niemczyk¹, A. Oppelt¹, H. Shaker¹, G. Shu¹, F. Stephan¹, G. Vashchenko¹
¹DESY, 15738 Zeuthen, Germany; ²DESY, 22603 Hamburg, Germany

Abstract

A transverse kick which results from the coaxial RF coupler in the L-band RF gun at the Photo Injector Test facility at DESY in Zeuthen (PITZ) has been modeled and characterized. The used RF pulse is typically 600 μ s long and used to produce a train of up to 2700 electron bunches. The kick is transient and found to be dependent on the detuning of the resonance frequency of the gun cavity. The frequency-detuning within the RF macro-pulse results in a variation in the kick strength along the pulse. This leads to a downstream orbit and size change of individual bunches within the train. Using 3D RF field distributions, calculated at detuned frequencies of the cavity, particle tracking simulations are performed to simulate the behavior of the transient kick onto the electron bunch. The temperature of the cooling water for the gun is tuned, allowing detailed characterization of the frequency-detuning within the RF pulse and thereby measurements of the kick which are of practical interest. Systematic measurements of the kick along the bunch train have meanwhile been carried out. The results will be presented and discussed.

INTRODUCTION

The European X-ray Free-Electron Laser (XFEL) provides excellent opportunities in pursuing excellence in physics and advanced applications of coherent x-ray radiation [1]. The photoelectron source in use at the European XFEL is a photocathode RF gun developed at the Photo Injector Test facility at DESY in Zeuthen (PITZ) [2,3]. The key component of the PITZ gun is a 1.6-cell 1.3 GHz copper resonator. The gun can be operated with a high electric field gradient of about 60 MV/m on the cathode surface with long RF pulses of up to 650 μ s at a repetition rate of 10 Hz. This allows the production of a maximum number of 27000 bunches per second at the XFEL and results in a high peak RF power of about 6.5 MW in the cavity while a high average RF power of about 42 kW dissipates in a rather short cavity length of about 20 cm and a cavity radius of about 9 cm. The RF power in the gun is supplied by a 10 MW multi-beam klystron. The power is coupled from the input waveguide via a door-knob transition into the rotationally symmetric coaxial coupler and the gun cavity.

A transient transverse kick, due to the disturbed RF fields of rotational symmetry by the transition from the input rectangular waveguide to the coaxial power coupler of the PITZ

gun, has been simulated and quantified in [4]. In this paper, we present the dependency of the kick on the detuning of the resonance frequency of the gun cavity within the RF pulse. The effect is then demonstrated in both simulation and experiment. Consequently, measurements of the resulting downstream orbit and size change of individual bunches along the train are reported.

KICK VS. FREQUENCY-DETUNING

The reflection coefficient (S_{11}) is defined as the ratio of the reflected power over the forward power for a resonant cavity with a resonance frequency f_0 (~ 1.3 GHz for the PITZ case) fed by the RF with a frequency f . In order to protect the microwave source (klystron), the reflected power from the cavity must be low (typically $\ll 2$ MW). This requires a resonant frequency kept close to the RF frequency. The frequency-detuning, $\Delta f = f - f_0$ is then used to describe how much the cavity is detuned from its resonance.

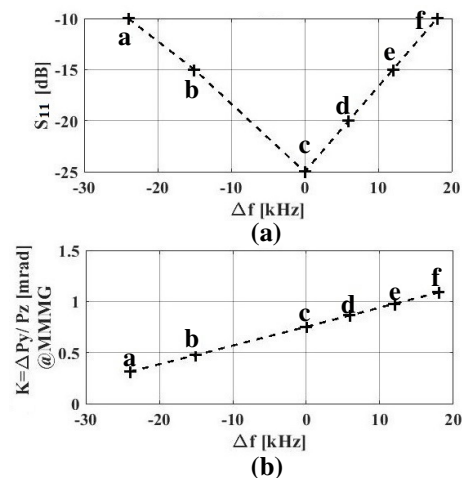


Figure 1: Simulated reflection coefficient and kick dependency on frequency-detuning.

Simulation

To simulate the kick behavior in response to the frequency-detuning, a simplification is made in the simulations: the RF frequency is varied at the port position of the input waveguide (see Fig. 1 in Ref. [4]) for defining the detuned frequency w.r.t. the cavity resonance. This allows computing 3D RF field distributions of the gun cavity at the detuned frequencies in frequency domain calculation. Using the obtained field distributions, particle tracking simulations using CST Particle Studio [5] are enabled and the kick strength

* ye.lining.chen@desy.de

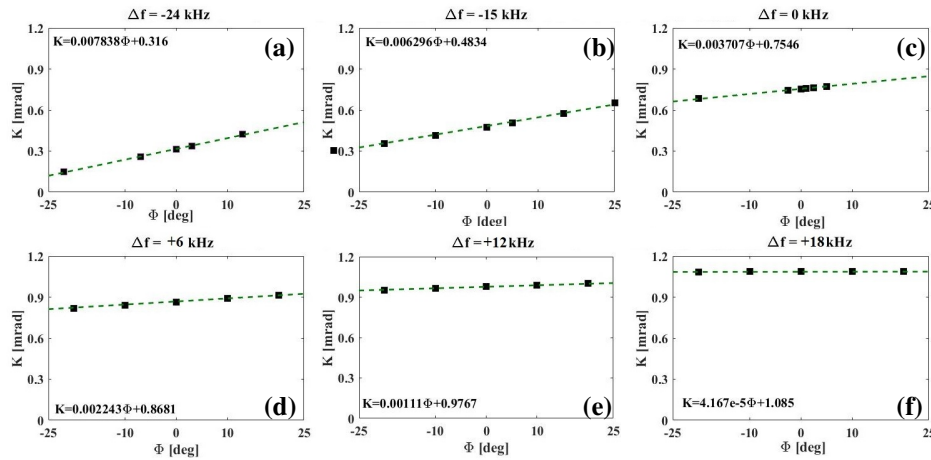


Figure 2: Simulated phase slopes of the kick vs. Δf . Green lines: linear fits to the simulation results. Φ : gun phase w.r.t. MMMG.

(K , the ratio of transverse beam momentum change over longitudinal momentum) can thus be computed at the detuned frequencies.

Figure 1 (a) shows the simulated S_{11} as a function of Δf with points $a - f$ as the set-points for frequency-detuning. Figure 1 (b) illustrates the change of the kick strength over the detuned frequencies at the maximum mean momentum gain (MMMG) phase of the gun for the individual cases $a - f$. The beam momentum at the MMMG phase is kept the same (~ 6.8 MeV/c) for all cases by adjusting the amplitudes of the applied RF field distributions in the simulations. As shown, the kick strength varies with the frequency-detuning, and for the chosen set-points, this shows a nearly linear behavior.

In Fig. 2, the phase dependency of the kick is shown for each case defined in Fig. 1 at the specified Δf , respectively. It is important to note, that the phase slope of the kick varies with the change of the frequency-detuning. An overheating state ($\Delta f > 0$) of the gun cavity renders smaller phase slopes than in the overcooled cases ($\Delta f < 0$). More specifically, the effect leads to a flattened phase slope in the overheated case (f) while resulting in the most significant slope (or curvature) for the overcooled case (a). Since a phase slope of the kick can result in the mismatch of slices within the bunch, an emittance growth on the order of $0.02 \sim 0.04 \mu\text{m}$ can be expected for a 20 ps bunch based on preliminary studies. This also suggests, that operating the gun at its overheated state can effectively reduce (and even avoid) the emittance growth caused by the phase-dependent kick for single bunch operation.

Experiment

Measurements of the kick dependencies on the frequency-detuning have been carried out. Due to thermal expansion, the resonant frequency of a cavity is linearly proportional to the temperature of the cavity. The latter is controlled by adjusting the cooling water temperature of the cavity. The frequency-detuning (w.r.t. the timing of the electron bunch) within the RF pulse can thus be adjusted by tuning the temperature of the cavity cooling water. Figure 3 (a)

shows the measured S_{11} versus the cavity temperature with cases A, B and C denoting the cooling states of the gun as overcooled, at resonance and overheated, respectively. For each case, the kick strength is measured in terms of the bunch position change (Δr). This is conducted at a downstream observation screen (~ 5.27 meters from cathode) as the gun phase is scanned. As shown, the phase slope of the kick is reduced as evolving from overcooling to overheating. Case A ($\Delta r_{p2p} \sim 0.9\text{mm}$) shows the strongest linear slope while case C ($\Delta r_{p2p} \sim 0.4\text{mm}$) delivers the smallest phase slope, particularly for the phase range of MMMG ± 5 degrees ($\Delta r_{p2p} < 0.05\text{mm}$). This is in fairly good consistency with the simulated kick behavior, as shown in Fig. 2. Figure 3 (e) shows the measured kick strength varies as the cavity temperature (frequency-detuning) changes. The resonance temperature of the gun cavity is at $\sim 73.2^\circ\text{C}$. The green line shows a linear fit to the measurement data (black dots with error bars).

IMPACTS ON BUNCH TRAINS

For the operation with long RF pulses of several hundred microseconds, the impacts of the characterized kick onto the properties of electron bunch trains are experimentally investigated. The position and size change of the bunches along the train are measured. This is done through measuring transverse properties of a single witness bunch moving along the long RF pulse by varying the cathode laser timing. The frequency-detuning seen by the witness bunch and thus the frequency-detuning dependent kick strength can be varied and measured. Note that the bunch charge and momentum are kept the same for all measurements. Figure 4 shows the bunch position change along a $240 \mu\text{s}$ train for a fixed beam momentum of ~ 6.35 MeV/c at the MMMG phase of the gun. A peak to peak (P2P) position change of $\sim 650 \mu\text{m}$ is obtained, which corresponds to roughly a P2P kick difference of 0.13 mrad between the head and tail of the bunch train. Experimentally operating such a bunch train within a $300 \mu\text{s}$ long RF pulse results in roughly a 6 dB

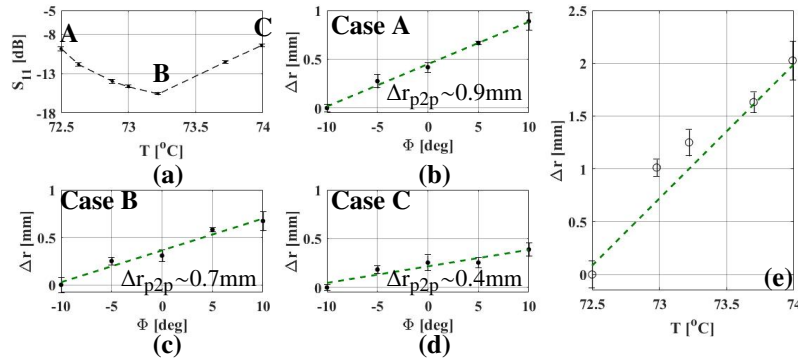


Figure 3: Measured kick dependencies on gun phase and frequency-detuning (or cavity temperature). Green lines: linear fits to the data. Φ : gun phase w.r.t. MMMG.

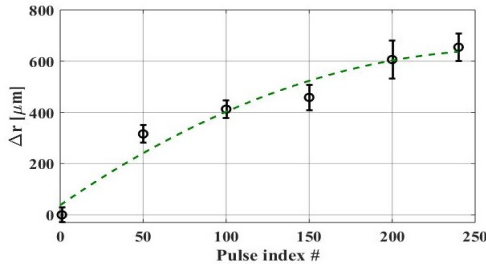


Figure 4: Measured bunch position change along a 240 μ s train at ~ 5.27 meters downstream from cathode. The solenoid current is fixed. Green curve: a fit to the data.

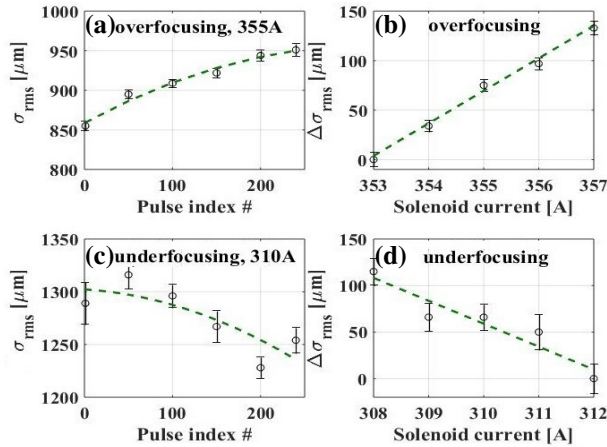


Figure 5: Measured RMS bunch size and size change along a 240 μ s train for both the over- and under-focusing case.

difference in the measured S_{11} between the head and tail of the train. This is in correspondence to the simulation results as shown in Fig. 1 (a) for emulating the bunch train operation in between case c and case d in the overheated state of the gun. As shown in Fig. 1 (b), the difference in the simulated kick strength along the train can be estimated as 0.11 mrad, which is in fairly good consistency with the experimental findings although the simulated curvature of S_{11} is not yet optimized to precisely match the measured S_{11} at exactly the same beam momentum. Furthermore, an

RMS bunch size change has been measured for both the overfocusing and underfocusing case when the gun solenoid is set to 355 A and 310 A, respectively. As shown in Fig. 5 (a) and (c), a size change of ~ 90 μ m is obtained for the overfocusing case while ~ 65 μ m is measured for the case of underfocusing. Since the bunch size change is equivalent to the change of solenoid focusing, the effect can also be evaluated by means of solenoid focusing change which is more relevant for the SASE tuning at FEL facilities. In Fig. 5 (b), a solenoid scan around 355 A leads to a change of ~ 33.8 μ m per ampere (overfocusing case). Likewise, ~ 28.8 μ m per ampere is given for the underfocusing case (Fig. 5 (d)). This defines roughly a 2.7 A focusing change along the 240 μ s bunch train for the overfocusing case and a 2.3 A change for the case of underfocusing. These effects should be more prominent for longer RF pulses. The change of the orbit and size degrades the quality of the bunch train and may disturb the overall tuning for the SASE lasing in FELs.

CONCLUSION

A frequency-detuning dependent RF coupler kick is analyzed in both simulation and experiment, where the transient behavior of the identified kick is consistent. The resulting orbit and size change along the electron bunch train are exemplarily quantified for a 240 μ s train along a 300 μ s RF pulse. The beam momentum is kept at ~ 6.35 MeV/c, which corresponds to gun operation at ~ 5.7 MW at the MMMG phase. A P2P difference in the kick strength between the head and tail of the bunch train is estimated as 0.13 mrad, which is consistent with the simulation results. A P2P focusing change along the same train is quantified as ~ 2.7 A and ~ 2.3 A for the case of overfocusing and underfocusing, respectively. Schemes for the correction and compensation of the kick effects onto the bunch train operation are currently under discussions.

ACKNOWLEDGMENTS

The authors would like to thank Dr. Holger Schlarb from DESY for useful discussions and instructive guidance.

REFERENCES

- [1] W. Decking and H. Weise, “Commissioning of the European XFEL Accelerator”, in *Proc. IPAC’17*, Copenhagen, Denmark, May 2017, paper MOXAA1, pp. 1-6.
- [2] F. Stephan, C. H. Boulware, M. Krasilnikov *et al.*, “Detailed characterization of electron sources yielding first demonstration of European X-ray Free-Electron Laser beam quality”, *Phys. Rev. ST Accel. Beams*, vol. 13, p. 020704, 2010. doi:10.1103/PhysRevSTAB.13.020704
- [3] M. Krasilnikov, F. Stephan *et al.*, “Experimentally minimized beam emittance from an L-band photoinjector”, *Phys. Rev. ST Accel. Beams*, vol. 15, p.100701, 2012. doi:10.1103/PhysRevSTAB.15.100701
- [4] Y. Chen, W. Ackermann, P. Boonpornprasert, H. De Gerssem, M. Dohlus, J. Good *et al.*, “Coaxial Coupler RF Kick in the PITZ RF Gun”, in *Proc. FEL2017*, Santa Fe, NM, USA, Aug. 2017, paper WEP005, pp. 422–425.
- [5] Computer Simulation Technology CST, <http://www.cst.de>

DESIGN OF A MULTI-CELL SRF REDUCED-BETA CAVITY FOR THE ACCELERATION OF LOW ENERGY ELECTRON BEAMS

D. Bazyl, H. De Gersem, W.F.O. Müller, TEMF, TU Darmstadt, Darmstadt, Germany
J. Enders, S. Weih, Institut für Kernphysik, TU Darmstadt, Darmstadt, Germany

Abstract

A recent upgrade of the superconducting Darmstadt linear accelerator (S-DALINAC) allowed the operation in the energy recovery linac (ERL) regime. The ERL mode provides significant benefits for free electron laser (FEL) experiments. At the same time, it imposes strict requirements for the quality of the accelerated beams. Presently, an increased longitudinal energy spread is observed at the S-DALINAC due to the mismatch in phase in the first accelerating structure, which is a superconducting radio-frequency (SRF) 5-cell $\beta = 1$ cavity. In this work we discuss an alternative design for accelerating low-energy electron beams using an SRF multi-cell cavity with a constant geometric β .

INTRODUCTION

Historically, the S-DALINAC is the third superconducting particle accelerator in the world [1]. Recently, the accelerator has been commissioned for ERL operation [2]. High currents available at ERLs prove beneficial for driving FELs or other radiation sources, and, hence, investigating ERL beam dynamics at the S-DALINAC is expected to provide insight into FEL operation in multiturn ERLs. Historically, the S-DALINAC has been the driver of the first German FEL [3].

There are several projects aimed at improving the performance of the S-DALINAC. This work deals with finding a solution for the problem of the significantly increased energy spread of the beam that has been observed at the S-DALINAC. The increased energy spread originates from the capture section which is a part of the injector linac.

Two electron guns are available at the S-DALINAC: a spin polarised gun (SPG) and a thermionic gun (TG), which produce electron beams with initial energies of 200 keV (after upgrade [4]) and 250 keV, respectively. The purpose of the injector linac is to accelerate these low-energy electron beams. Presently, it consists of a 3 GHz 5-cell SRF $\beta = 1$ cavity and two 3 GHz 20-cell SRF $\beta = 1$ cavities. Initially, in addition to the 5-cell structure a 2-cell cavity with a reduced value of geometric β has been implemented in order to preaccelerate the beam. Figure 1 shows the cooling cryostat (red) which hosts the 2-cell and the 5-cell cavity and the RF power input system (green). Nowadays, the 2-cell cavity is permanently out of operation and cannot be replaced without a new cryostat. This situation necessitates to accelerate electron beams with relative velocities β of 0.69 in the 5-cell $\beta = 1$ cavity. A significant mismatch in phase results in an inefficient acceleration (see Fig. 2) and an increased energy spread of 27 keV for the output beam.

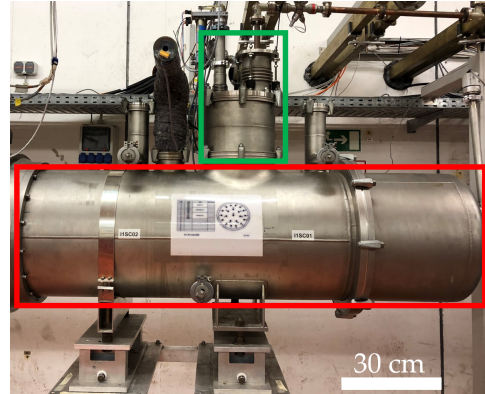


Figure 1: Cryostat.

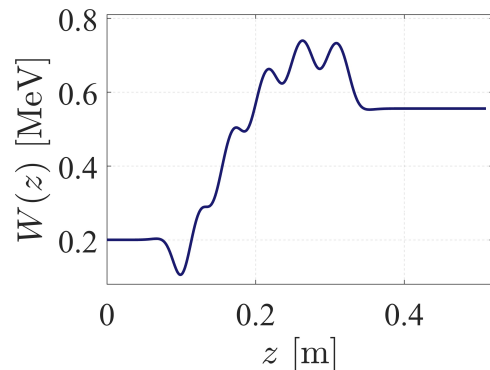


Figure 2: Energy gain of the beam in the 5-cell cavity.

UPGRADE OF THE CAPTURE SECTION

In order to reduce the energy spread of the beam at the S-DALINAC, the 5-cell cavity must be replaced with a new cavity. The new cavity must be capable of accelerating the electron beam up to an energy of at least 1 MeV while keeping the energy spread minimal. Other important requirements for the new structure are mechanical reliability and minimal investment costs.

The most commonly used methods for the acceleration of low energy electron beams are normal conducting β -graded cavities and SRF 1-cell or 2-cell independently driven structures. At the S-DALINAC spatial restrictions exclude a possibility of implementation of a normal conducting cavity for the injector linac. The implementation of independently driven SRF cavities would require a new cryostat, thereby failing to satisfy the minimal investment-cost requirement.

Hence, a cavity that can be operated with the existing cooling cryostat and the existing RF input power system was developed. As result of a quantitative and qualitative analysis, a 6-cell reduced- β cavity has been designed and will replace the 5-cell cavity [5]. The 6-cell cavity is now

being manufactured. In the next chapters we discuss the RF design, beam-dynamics, mechanical characteristics and current state of production of the 6-cell cavity.

RF DESIGN

The cell shape of the 6-cell cavity is based on the 1.3 GHz TESLA cavity type, dimensions of which have been scaled such that the resonant frequency of the fundamental mode is 3 GHz. The cell shape was additionally optimised in order to match a reduced value of geometric beta ($\beta < 1$). The choice of the geometric beta and the number of cells for the 6-cell $\beta = 0.86$ cavity has been discussed in [6]. The RF design and optimisation has been carried out in CST MWS® [7]. The RF parameters of the 6-cell $\beta = 0.86$ cavity (see Fig. 3) are collected in Table 1.

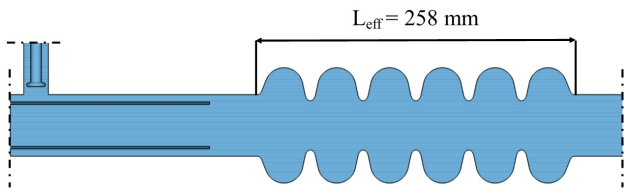


Figure 3: Layout of the 3 GHz 6-cell $\beta = 0.86$ cavity.

Table 1: RF Parameters of the 6-cell Cavity

Parameter	Value
Mode	TM ₀₁₀
Frequency	2.997 GHz
Operation regime	CW
Operation temperature	2 K
Accelerating gradient	4.8 MV/m
R-over-Q	308 Ω

The 6-cell cavity is planned to be operated at a moderate accelerating gradient of 4.8 MV/m. This allowed to make design decisions in favour of the mechanical rigidity of the cavity. In particular, the iris radius was increased in order to increase the longitudinal rigidity of the structure despite the disadvantageous effect on the R-over-Q value.

Analytic calculations have shown that approximately 100 W of the forward RF power from the generator is required in order to operate the 6-cell cavity at the specified accelerating gradient. The existing RF amplifier at the S-DALINAC can deliver up to 500 W of RF power. In addition, numerical calculations in CST MWS® have shown that the 6-cell cavity is fully compatible with the existing RF input power coupler. The coupling coefficient between the generator and the cavity can be adjusted over a wide range.

BEAM DYNAMICS

The 6-cell cavity is capable of accelerating electron beams injected from the TG and the SPG up to energies of up to 1.5 MeV with a minimised energy spread growth. Figure

4 illustrates results of the particle tracking simulation in ASTRA [8] for the 200 keV and the 250 keV beam in the 6-cell cavity.

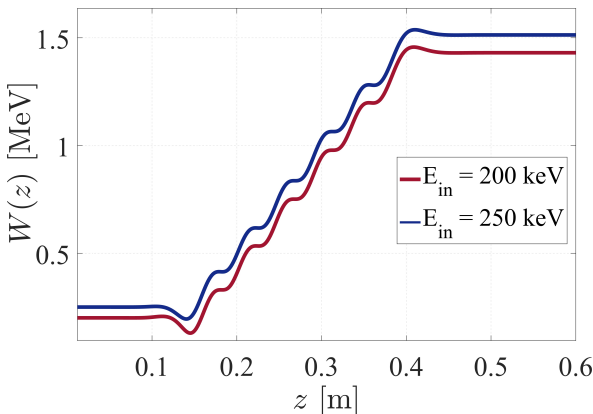


Figure 4: Energy gain of the beam in the 6-cell cavity.

Figure 5 shows the longitudinal phase space of the output beam from the 6-cell cavity injected from the SPG. The resulting bunch tail is due to the constant length of the cavity cells. However, the tail is located beyond 95% of the distribution of particles. Thus, its effect is negligible in our case. The energy spread could be further reduced by shortening the length of the left end-cell and by increasing the length of the right end-cell. The obtained results for the 6-cell cavity indicate an eight-times-lower energy spread and three-times-higher energy gain of the beam in comparison to the 5-cell $\beta = 1$ cavity for the same electric field on axis of the cavity of 10 MV/m .

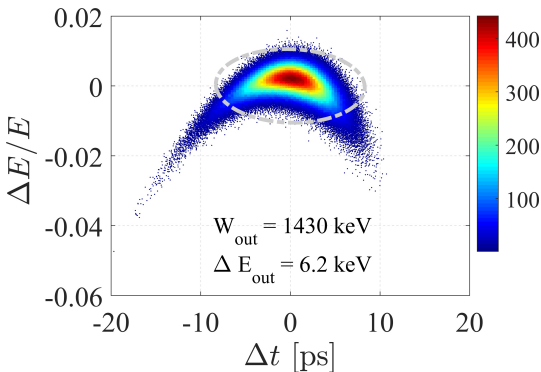


Figure 5: Longitudinal phase space of the output beam (grey dashed ellipsoid enclosing 95 % of particles in the distribution).

In order to minimise the energy spread of the accelerated low energy electron beams in a multi-cell cavity with cells of constant length, bunches must be short compared to the full RF cycle. In case of the S-DALINAC the bunch length is expected to be 5 ps, while the full RF cycle of the 6-cell cavity is 333 ps. An increase of the input bunch length will lead to an increase of the energy spread of the output beam. In order to effectively control the bunch length at the entrance of the 6-cell cavity a beam diagnostic tool is under development and will be used for the commissioning of the 6-cell cavity [9].

MECHANICAL CHARACTERISTICS

The mechanical stability of the 6-cell cavity was one of the priorities during the optimisation of its geometry. A mechanical model of the 6-cell cavity with a wall thickness of 2.5 mm has been studied and optimised using finite element analysis in ANSYS [10]. A smooth transition from the end-cells to the drift tubes allowed to increase the longitudinal rigidity K of the cavity by 1 kN/mm. The key mechanical parameters of the 6-cell cavity are collected in Table 2.

Table 2: Mechanical Characteristics of the 6-cell Cavity

Parameter	Value
Material	Nb
Wall thickness, mm	2.5
K , kN/mm	5.6
df/dl , kHz/ μ m	2.1
df/dp , Hz/mbar	26

From the experimental data it is known that the average pressure fluctuations in the cryostat of the capture section during operation is approximately 1.5 mbar. Thus, a frequency detuning of 39 Hz is expected, which can be easily compensated by the tuning system. The existing tuning system now implemented for tuning the existing 5-cell cavity will be used for the 6-cell cavity as well. To enable that, the existing tuner frame and piezo tuners will be modified.

CAVITY MANUFACTURING

The production of the new 6-cell cavity has started end of 2018. Prior to the manufacturing of the single components, the expected cool-down and BCP frequency shifts of the cavity were estimated in order to correct the inner dimensions accordingly for the mechanical processing. The half-cells were then deep-drawn from 2.8 mm thick niobium sheets (RRR=300). After that, the dumbbells and endgroups were welded from the single components. Currently, these parts are trimmed in order to reach the desired target frequencies which correspond to the correct resonance frequency of the cavity after assembly. Target frequencies and trimming sensitivities df/dl were obtained through CST simulations taking into account the increased half-cell length of the components compared to the assembled cavity which is necessary for the preparation of the welds. After finishing the trimming of the components, the cavity will be welded and a first BCP will be conducted. Afterwards, a tuning and cold test is planned at the S-DALINAC vertical test cryostat [11] to verify the cool-down and BCP frequency shifts. The final amount of material to be removed through the second BCP treatment can then be determined from the measurements to ensure that the correct operational frequency will be achieved. Expected cavity delivery is end of 2019. Final field-flatness tuning, heat treatment and HPR are planned before the cavity could be ready for installation around spring 2020.

ACKNOWLEDGEMENTS

The authors acknowledge financial support through DFG Research Training Group 2129 "AccelencE".

CONCLUSION

The need for a non-standard method for the acceleration of the low-energy electron beam is motivated by limitations in space and investment costs at the S-DALINAC. In absence of practical constraints the suggested method can be improved further on by optimising the lengths of the first cell and the last cell of the cavity. The implementation of the 6-cell cavity at the injector of the S-DALINAC will improve the overall beam quality. The cavity is expected to be delivered to the S-DALINAC facility in end of 2019.

REFERENCES

- [1] A. Richter, "Operational Experience at the S-DALINAC", in *Proc. 5th European Particle Accelerator Conf. (EPAC'96)*, Sitges, Spain, Jun. 1996, paper WEX02A.
- [2] M. Arnold *et al.*, "First ERL Operation of S-DALINAC and Commissioning of a Path Length Adjustment System", in *Proc. 9th Int. Particle Accelerator Conf. (IPAC'18)*, Vancouver, Canada, Apr.-May 2018, pp. 4859–4862. DOI:10.18429/JACoW-IPAC2018-THPML087
- [3] M. Brunken *et al.*, "First lasing of the Darmstadt cw free electron laser", in *Nucl. Instr. Meth.*, vol. 429, pp. 21-26, 1999. doi:10.1016/S0168-9002(99)00060-1
- [4] M. Herbert, J. Enders, Y. Fritzsche, N. Kurichyanil, and V. Wende, "Inverted Geometry Photo-Electron Gun Research and Development at TU Darmstadt", in *Proc. 9th Int. Particle Accelerator Conf. (IPAC'18)*, Vancouver, Canada, Apr.-May 2018, pp. 4545–4547. DOI:10.18429/JACoW-IPAC2018-THPMK101
- [5] D. B. Bazyl, H. De Gersem, W. F. O. Müller, J. Enders, and S. Weih, "A 3 GHz SRF Reduced-beta Cavity for the S-DALINAC", in *Proc. 9th Int. Particle Accelerator Conf. (IPAC'18)*, Vancouver, Canada, Apr.-May 2018, pp. 3838–3840. DOI:10.18429/JACoW-IPAC2018-THPAL081
- [6] D. B. Bazyl, H. De Gersem, and W. F. O. Müller, "Upgrade of the Capture Section of the S-DALINAC Injector", in *Proc. 8th Int. Particle Accelerator Conf. (IPAC'17)*, Copenhagen, Denmark, May 2017, pp. 993–995. DOI:10.18429/JACoW-IPAC2017-MOPVA055
- [7] CST Studio, <https://www.cst.com>.
- [8] ASTRA, <http://www.desy.de/~mpyflo/>
- [9] S. Weih *et al.*, "Upgrade of the S-DALINAC Injector Capture Section", presented at the 19th Int. Conf. RF Superconductivity (SRF'19), Dresden, Germany, Jun.-Jul. 2019, paper MOP065, DOI:10.18429/JACoW-SRF2019-MOP065.
- [10] ANSYS, <https://www.ansys.com>.
- [11] R. Grewe *et al.*, "Superconducting RF Cavity Materials Research at the S-DALINAC", presented at the 19th Int. Conf. RF Superconductivity (SRF'19), Dresden, Germany, Jun.-Jul. 2019, paper MOP022, DOI:10.18429/JACoW-SRF2019-MOP022.

SPACE CHARGE FIELD BEAM DYNAMICS SIMULATIONS FOR THE THz SASE FEL AT PITZ*

S. A. Schmid[†], E. Gjonaj, and H. De Gersm, TU Darmstadt, TEMF, Darmstadt, Germany
M. Krasilnikov, DESY, Zeuthen, Germany
M. Dohlus, DESY, Hamburg, Germany

Abstract

A proof-of-principle experiment on a THz SASE FEL is under consideration at the Photo Injector Test facility at DESY in Zeuthen (PITZ). One of its options assumes utilization of 4.0 nC bunches at 16.7 MeV [1]. In this operation mode, space charge interaction strongly influences the dynamics of the electron beam inside the undulator. In this contribution, we investigate the beam dynamics in the THz undulator of PITZ using a particle-particle interaction model based on a Liénard-Wiechert approach. We analyze the influence of retardation and radiation fields on the beam dynamics resulting in the microbunching effect. Furthermore, we compute the radiation field and estimate the radiation power at the exit of the undulator. The validity of the underlying numerical models is discussed.

INTRODUCTION

The photoinjector test facility at DESY in Zeuthen (PITZ) is currently developing a high power, tunable THz radiation source for pump and probe experiments at the European XFEL [1]. The source design uses SASE-FEL to generate THz pulses with 100 μm center wavelength and up to ~ 40 MW peak power [1]. Reaching the design specifications requires a 16.7 MeV electron beam with up to 4.0 nC bunch charge. Due to the moderate energy, space charge induced beam divergence along the 3.4 m long FEL undulator is extremely critical. In the following, we use a 3D, fully relativistic Liénard-Wiechert simulation code [2] to analyze the beam dynamics inside the undulator. Furthermore, we evaluate the particle fields at the exit of the undulator and investigate the generation of THz radiation.

MODELING APPROACH

The undulator field is modeled as,

$$\vec{B}(\vec{r}) = -B_0 \cdot \vec{\nabla} \phi(y, z), \quad (1)$$

$$\phi(y, z) = \sinh(k_u y) \sin(k_u z) / k_u \quad (2)$$

using a periodic 2D potential of an idealized planar undulator [3]. In addition to the oscillatory motion of the particles in the x-direction, this model allows to reproduce the undulator focusing effect in the y-direction. The parameter values for the field amplitude $B_0 = 1.28$ T and the undulator wavelength $\lambda_u = 2\pi/k_u = 3.0$ cm reflect the experimental setup described in [1]. Figure 1 shows the magnetic field map for a 3.6 m long undulator with 120 periods as used in

the simulations. We use a linearly increasing or decreasing amplitude, $B_0 = B_0(z)$, towards the entrance or exit of the undulator, respectively, to guarantee a smooth transition of the particle beam at both undulator ends.

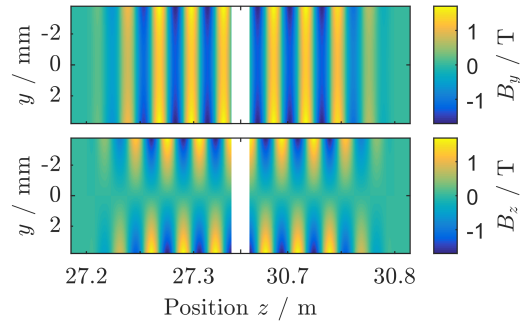


Figure 1: Magnetic field map used in the simulations. Only a small section including the entrance and exit of the 3.6 m long undulator model is shown.

A complete electromagnetic field model for relativistic particles undergoing oscillatory motion has to take retardation and radiation effects into account. Our simulation code [2] models the space charge interaction based on the Liénard-Wiechert (LW) fields of a charged particle moving along a trajectory $r_s = r_s(t)$:

$$\vec{E}(\vec{r}, t) = \frac{q_s \left\{ \underbrace{\frac{(\vec{n}_s - \vec{\beta}_s)}{\gamma_s^2 |\vec{r} - \vec{r}_s|^2}}_{\text{static}} + \underbrace{\frac{\vec{n}_s \times [(\vec{n}_s - \vec{\beta}_s) \times \dot{\vec{\beta}}_s]}{c_0 |\vec{r} - \vec{r}_s|}}_{\text{radiation}} \right\}}{(1 - \vec{n}_s \vec{\beta}_s)^3}, \quad (3)$$

$$\vec{B}(\vec{r}, t) = \frac{\vec{n}_s \times \vec{E}(\vec{r}, t)}{c_0}, \quad (4)$$

where q_s is the charge of the particle, c_0 the speed of light, γ_s the Lorentz factor, $\beta_s = \dot{r}_s/c$, and $\vec{n}_s \equiv (\vec{r} - \vec{r}_s)/|\vec{r} - \vec{r}_s|$. All s-indexed expressions in (3) have to be evaluated at the retarded time t_s such that

$$c_0(t - t_s) = |\vec{r} - \vec{r}_s| \quad (5)$$

holds. Equations (3) and (4) need to be evaluated for every particle pair. This implies, first, that the calculation of space charge forces in this simulation model scales with N^2 , where N is the number of particles. Second, the full history of

* This work is supported by the DFG in the framework of GRK 2128.

[†] schmid@temf.tu-darmstadt.de

particle previous positions and velocities needs to be stored in memory. Therefore, LW simulations are computationally expensive and require parallel cluster computing to achieve a reasonable runtime.

Conventional space charge codes like ASTRA [4] or KRACK [5] use rest frame (RF) approximations. In this approach, a purely electrostatic field is computed in the rest frame of the bunch. Assuming this frame to be inertial, the space charge fields in the laboratory frame are determined by Lorentz transformation. However, for the particle's oscillatory motion in the undulator, the rest frame is clearly non-inertial. Furthermore, synchrotron radiation cannot be modeled properly. In the following section we compare simulation results for both space charge field models.

SIMULATION RESULTS

Figure 2 compares the simulated growth of the transverse rms bunch size σ_x along the undulator for three different space charge field models. The LW model includes both, time retarded static as well as acceleration radiation fields. The Radiation Off (RO) model uses time retardation, but neglects the radiation term (cf. (3)). A comparison of the simulation results for the LW model (dashed line) and the RO model (dotted line) provides an estimation on the relative contribution of radiation fields in the undulator. The RF model (solid line), KRACK (plus), and ASTRA (cross) simulations correspond to different implementations of the rest frame space charge field model. These latter simulations, agree perfectly with each other. Compared to the LW model,

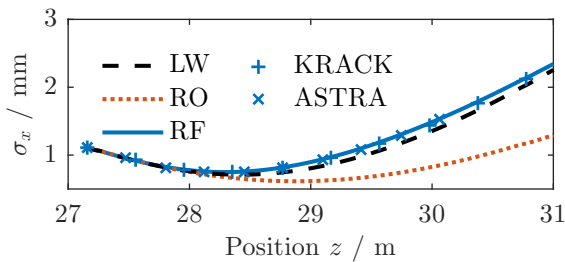


Figure 2: Transversal rms bunch size σ_x inside the undulator computed with three different space charge field models.

the RO model significantly underestimates the transversal space charge effects. This shows that radiation fields are important for the beam dynamics. The RF approximation seemingly provides reasonable values for the bunch rms size σ_x even if it does not include radiation field effects. This behavior is related to the effectively reduced mean longitudinal momentum of a particle bunch undergoing oscillatory motion. This increases the effective space charge field of the bunch artificially and, thus, leads to some sort of compensation for the missing radiation field contribution to the transverse size growth of the bunch. On the other hand, the reference frame EM field model introduces non-negligible errors, especially, in the longitudinal phase space. The energy spread σ_E shown in Fig. 3 demonstrates the significant error induced by the RF approach in the longitudinal beam

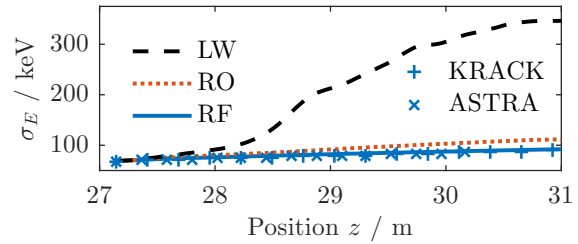


Figure 3: Energy spread σ_E inside the undulator computed with three different space charge field models.

dynamics. Table 1 gives an overview of the beam properties at the undulator exit. For the investigated simulation parameters, the simulated beam dimensions $\sigma_{x,y,z}$ of the RF model are in reasonable agreement with the results of the LW approach. Hence, the RF approximation provides a quick and reasonable estimate for the size of the electron bunch within the undulator for this particular configuration. In the general case, however, the discrepancy induced by the deficiency of the RF space charge field model may be larger for other beam and undulator configurations. The huge deviation between LW and RF resulting for the rest of phase space parameters (cf. Table 1) indicates that the RF model is not appropriate for the simulation of THz SASE radiation effects. Figure 4 compares the longitudinal phase

Table 1: Beam Properties at Undulator Exit

Qty.	LW-model	RF-model	Rel. Dev.
σ_x	3.1 mm	3.1 mm	+0.5%
σ_y	2.6 mm	2.6 mm	-0.9%
σ_z	2.2 mm	2.2 mm	-2.3%
σ_E	347.4 keV	95.7 keV	-72.5%
ε_x	17π mrad mm	13π mrad mm	-24.6%
ε_y	10π mrad mm	7π mrad mm	-30.5%
ε_z	1366π mrad mm	282π mrad mm	-79.4%

spaces at the undulator exit computed by RF and LW simulations, respectively. From FEL theory it is known that shot noise in the particle bunch distribution gives rise to coherent microbunching instability [3]. This effect is present in the simulation results for the LW model. The mean longitudinal periodicity $\Delta \sim 119 \mu\text{m}$ fits quite well to the THz radiation wavelength $\lambda_{\text{THz}} \sim 107 \mu\text{m}$ of the simulated setup. Furthermore, simulating the beam dynamics for different magnetic field amplitudes B_0 consistently reproduces the analytically known correlation $\lambda_{\text{THz}} \propto B_0^2$. The phase space profile obtained by RF simulations features a substantially smaller energy spread. Furthermore, microbunching cannot be reproduced. This is expected as this effect is intrinsically due to radiation fields. For the investigation of THz radiation field, we record EM field samples with $\Delta x = 20 \mu\text{m}$, $\Delta y = 200 \mu\text{m}$, $\Delta z = 1 \mu\text{m}$ spatial and $\Delta t = 0.02$ ps temporal resolution at the undulator exit, $z_0 = 30.8$ m. Figure 5 shows the THz radiation spectra of four different initial particle bunches consisting of 50 k particles each. At the en-

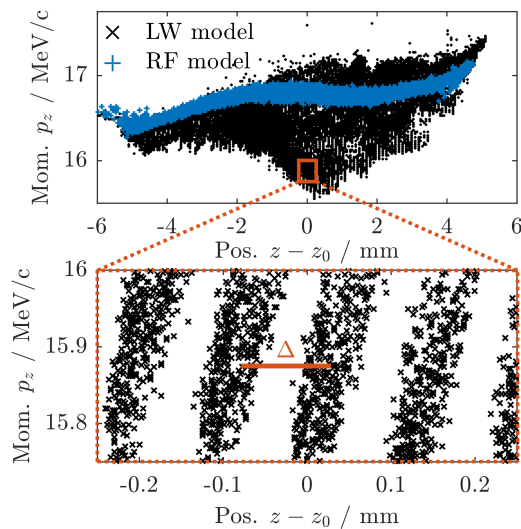


Figure 4: Longitudinal phase space at the undulator exit (top). Magnified view of the microbunching effect simulated by the LW approach (bottom).

trance of the undulator, all four bunches describe the phase space of the beam after passing through the electron gun and booster section. However, each of the four particle distributions correspond to different random realizations. Thus, the simulation results for the THz radiation spectra are slightly different depending on the shot noise characterizing the initial distribution. The averaged spectrum of all samples is centered at $\lambda_{THz} = 108.5 \mu\text{m}$ and has a spectral width of $\delta\lambda_{FWHM} = 4.7 \mu\text{m}$. For comparison, GENESIS 1.3 simulations in [1] based on a non-idealized magnetic field map find $\lambda_{THz} = 106.8 \mu\text{m}$ and $\delta\lambda_{FWHM} = 4.8 \mu\text{m}$. Considering the differences in the field map model, the results agree very well. Figure 6 shows the corresponding intensity profiles of the generated THz radiation pulses at the undulator exit. Beam matching studies have shown that optimum beam transport through the undulator requires a transversally asymmetric particle distribution [1]. This is reflected in the asymmetric radiation pattern generated by this distribution as depicted in Fig. 6. Compared to a real electron beam, the initial shot noise of a 50 k macroparticles bunch is larger. We plan to conduct simulations using larger particle numbers N to investigate the influence of macroparticle shot noise in the LW approach. A more detailed investigation of space charge effects in the paraxial approximation as used, e.g., in GENESIS 1.3 will be presented in future work.

CONCLUSION

We present space charge beam dynamics simulations for the full undulator length of the THz SASE FEL experiment at PITZ. The simulations use a relativistic, three dimensional Liénard-Wiechert field model that takes radiation and retardation effects into account. We show that the conventional rest frame approximation provides reasonable results for the bunch size inside the PITZ undulator, however, it cannot properly reproduce the longitudinal phase space dynamics.

THP009

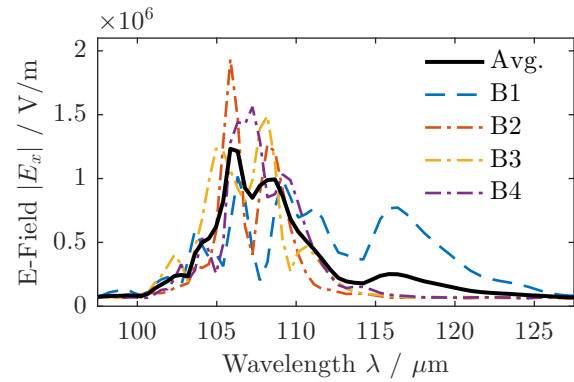


Figure 5: THz radiation spectrum of four different initial particle distributions and their average spectrum as simulated at the undulator exit.

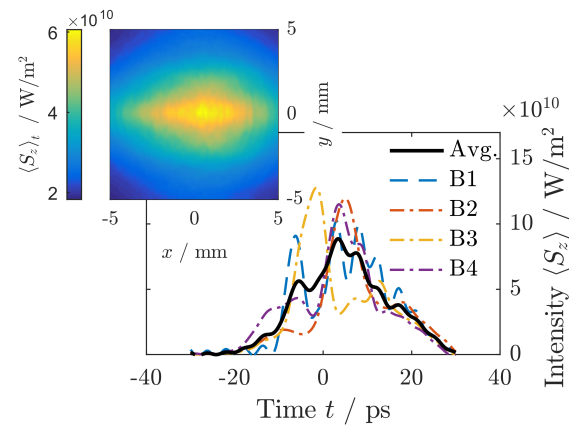


Figure 6: Temporal profile of the THz radiation pulse at the undulator exit. Spatial pattern of radiation intensity at the undulator exit (contour plot).

On the other hand, the LW approach can predict the microbunching effect that is in the core of the SASE process. The simulations clearly show the expected radiation amplification at the undulator exit and the computed THz spectra are in good agreement with previously reported results.

REFERENCES

- [1] M. Krasilnikov *et al.*, “Start-to-end simulations of THz SASE FEL proof-of-principle experiment at PITZ”, in *Proc. ICAP'18*, Key West, FL, USA, Oct. 2018, pp. 246-252. doi:10.18429/JACoW-ICAP2018-TUPAF23
- [2] Y. Chen *et al.*, “Modeling and simulation of RF photoinjectors for coherent light sources”, *NIMA*, vol. 889, pp. 129-137, May 2018. doi:10.1016/j.nima.2018.02.017
- [3] P. Schmüser *et al.*, *Free-Electron Lasers in the Ultraviolet and X-Ray Regime*. Heidelberg, BW, Germany: Springer, 2014.
- [4] K. Floettmann, “ASTRA: A space charge tracking algorithm”, <http://www.desy.de/~mpyf1o/>
- [5] M. Dohlus, “Krack 3”, <https://www.desy.de/~dohlus/Krack3/>

SIMPLE AND ROBUST FREE ELECTRON LASER DOUBLER*

S. Di Mitri[†], G. De Ninno¹, R. Fabris, S. Spampinati, Elettra Sincrotrone Trieste, 34149, Italy
N. R. Thompson², ASTeC, STFC Daresbury Laboratory, Warrington, WA44AD Cheshire, UK
¹also at Laboratory of Quantum Optics, University of Nova Gorica, Nova Gorica 5001, Slovenia
²also at Cockcroft Institute, Sci-Tech Daresbury, Warrington, WA44AD, UK

Abstract

We present the design of a Free-Electron Laser (FEL) doubler suitable for the simultaneous operation of two FEL lines. The doubler relies on the physical selection of two longitudinal portions of an electron bunch at low energy, and on their spatial separation at high energy. Since the two electron beamlets are naturally synchronized, FEL pump-FEL probe experiments are enabled when the two photon pulses are sent to the same experimental station. The proposed solution offers improved flexibility of operation w.r.t. existing two-pulse, two-color FEL schemes, and allows for independent control of the color, timing, intensity and angle of incidence of the radiation pulses at the user end station. Detailed numerical simulations demonstrate its feasibility at the FERMI FEL facility.

INTRODUCTION

We propose a scheme in which two longitudinal portions of the electron bunch (beamlets) are physically selected with a thick mask at low energy in the linac (beam scraping), and spatially separated with a septum magnet at high energy. Each beamlet is then sent to a distinct undulator line. Unlike any of the preceding schemes, ours allows the simultaneous operation of two FEL lines, naturally synchronized at (sub-)fs level, with continuously tuneable relative delay from few fs to ps. Since two undulator lines are used, full and independent control of color, timing, intensity and angle of incidence of the individual radiation pulses on the sample is ensured. If the two FEL pulses are directed to the same user end station, FEL-pump FEL-probe experiments can be done with unprecedented flexibility, either in self-amplified spontaneous emission (SASE) [1,2] or in seeded configurations [3,4].

ELECTRON BEAM MANIPULATION

The scheme is sketched in Fig. 1, and typical parameters at FERMI [5,6] are considered in the following as a case study. A high brightness electron bunch is generated in a photo-injector (gun) and time-compressed in a magnetic chicane (BC1). The bunch length compression factor is $C \equiv \frac{\sigma_{t,i}}{\sigma_{t,f}} \cong \left(1 - \frac{R_{56}\sigma_\delta}{c\sigma_{t,i}}\right)^{-1}$, with $\sigma_\delta = 2\%$ the relative energy spread linearly correlated to the initial bunch duration $\sigma_{t,i} = 2.8$ ps. A mask with two apertures is installed in the middle of BC1, where the particles horizontal position w.r.t. the reference trajectory is $x(s) \cong \eta_x(s)\delta$, and betatron oscillations can be neglected. The mask, made of

~ 10 mm thick copper, physically selects two transversally displaced beamlets, the rest of the bunch being scattered at large angles and absorbed in the chamber. Since the chicane is achromatic, the two beamlets exit BC1 separated both in energy and in time, but spatially aligned. With V-shape geometry, the vertical position of the mask determines both the width of the two apertures and their transverse separation. The beamlets duration at the exit of BC1, as well as their time separation, is estimated by [7] $\Delta t_{FWHM} \approx \frac{2\Delta x}{\eta_x} \frac{\sigma_{t,i}}{C\sigma_\delta}$, with Δx either the apertures width or the width of the central slit, respectively. For example, with $C = 10$ and $\Delta x = 3$ mm, $\Delta t_{FWHM} \approx 320$ fs.

Downstream of BC1, the linac RF phases are adjusted to ensure both a large relative energy offset of the beamlets (δ_f), which is suitable for their spatial separation in the switchyard, and a small energy spread in each beamlet ($\sigma_{\delta,f}$), as required for efficient lasing. The RF phasing takes into account the effect of the longitudinal wakefields excited by the leading beamlet on the trailing one. For example, we obtain in simulation $\delta_f = 0.9\%$ and $\sigma_{\delta,f} = 0.04\%$. Doing so, the final mean energy is lowered from 1.40 GeV for the standard whole bunch preparation, to 1.25 GeV (see Fig. 2).

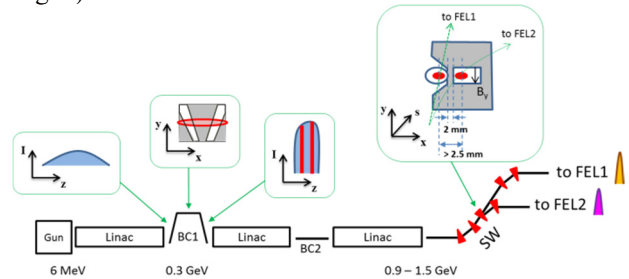


Figure 1: FEL doubler applied to FERMI (not to scale): selection of electron beamlets in BC1 with a mask (red slices), and separation in the switchyard (SW) with a septum magnet.

The FERMI switchyard (SW in Fig. 1) is a ~ 40 m long line working in the energy range 0.9-1.5 GeV. It comprises two branches, each including two modified double bend achromatic cells. The first cell is in common, and the dipoles bending angle is 3 deg. The two branches lead to the FEL1 and FEL2 undulator lines; these are parallel and separated by 1 m. Depending on the electron beam energy and on the resonant harmonic jump set by the variable gap undulators, FERMI covers the fundamental wavelength range 20–100 nm with FEL1, and 4–20 nm with FEL2, in high gain harmonic generation (HGHG) mode of operation [3].

For the purpose of separating the beamlets in the bending plane, the SW optics was modified. A dispersion function

* Work supported by European Union's Horizon2020 research and innovation programme under Grant Agreement No. 777431

[†] simone.dimitri@elettra.eu

as large as -0.3 m is generated at the location of the third dipole magnet, i.e., at the entrance to the FEL2 branch line (see Fig. 1). The dipole magnet would be replaced by a thin septum magnet, having similar length of 0.5 m and the same bending angle. The beamlet at low energy-positive x coordinate is bent by the septum magnetic field and directed to-wards FEL2. The other beamlet continues its straight path towards the next double bend cell, and is eventually directed to FEL1. In order for the two beamlets to safely reach the present common dump at the end of the undulators, the FERMI dump line would be modified. This modification is not required in facilities where multiple dumps downstream of distinct undulators are already available.

Figure 2 shows the beamlets longitudinal phase spaces at the entrance of the septum magnet, for different separations of the apertures in the mask. Particle tracking was carried out with the elegant code [8], including all major collective effects from the injector exit to the undulator. The main beam and mask parameters are listed in Table 1. In this simulation, the outer borders of the mask apertures are kept fixed, so that a larger apertures separation (larger energy offset of the two beamlets) implies a smaller apertures width (shorter beamlets duration). Figure 2 also shows the corresponding horizontal separation of the beamlets at the septum entrance, and their current profile.

Table 1: Electron Beam Parameters at the Entrance of BC1 (Whole Bunch) and of the Undulator (Each Beamlet) as from Tracking Tun. The mask geometry is also reported.

Quantity	@ BC1	@ UND	Units
Charge	0.7	~0.2	nC
Mean energy	0.27	1.25	GeV
Relative energy spread, rms	2.0	< 0.03	%
Duration, fwhm	10.8	0.3	ps
Peak current (core)	650	650	A
Horizontal normalized emittance, projected rms	0.6	0.7	μm
Vertical normalized emittance, projected rms	0.6	0.6	μm
Mask slit width	1		mm
Mask apertures width	3		mm

The horizontal separation of the beamlets at the septum entrance is $\eta_x \delta_f \geq 2.5$ mm, and much larger than their individual betatron beam size. We thus consider a minimum septum thickness of 2 mm, which can be provided by an in-vacuum eddy-current septum magnet. We developed a septum design of 15×25 mm² transversal acceptance. A maximum electric power of ~100 W is expected to be safely dissipated, which translates into a repetition rate of 25 Hz at the beamlets' mean energy of 1.25 GeV. The beamlets' rms position jitter at the septum must be much smaller, say one-tenth, of 2 mm, which implies a relative rms energy jitter of 0.07%, and an overall trajectory jitter ≤ 50 μm. This error budget is well within reach of x-ray FEL facilities [9].

The optics of the switchyard branches is achromatic. Although it is not isochronous ($R_{56} = -0.3$ mm for FEL1, +2.9 mm for FEL2), the beamlets' duration is almost unchanged by virtue of their negligible correlated energy spread, i.e., $\Delta\sigma_t \cong R_{56}\sigma_{\delta,f}/c \leq 4$ fs. The minimum relative delay of the beamlets at the undulator is determined by the difference in the transfer matrix of the two branches: $\Delta t \cong (R_{51}\Delta x + R_{52}\Delta x' + R_{56}\delta)/c \cong (R_{51}\eta_x\delta + R_{52}\eta'_x\delta + R_{56}\delta)/c = (67 + 5 + 75)$ fs = 147 fs in our case.

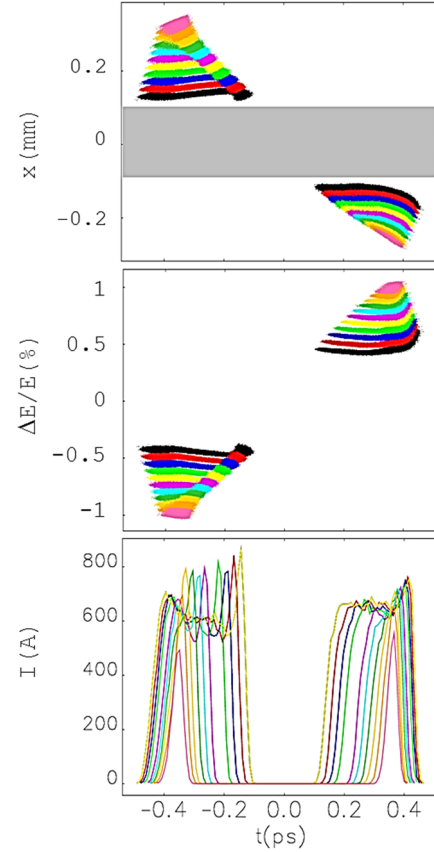


Figure 2: From top to bottom, longitudinal phase space, top view (with shadow of the 2 mm septum thickness) and current profile of the two beamlets at the undulator entrance, for a mask slit width in the range 3–8 mm, and apertures width of 1–6 mm. Bunch head is on the left. The linac RF phases were optimized for one beamlet's duration only (black).

LASING

Figure 3 shows the result of time-dependent FEL1 and FEL2 simulations done with the Genesis 1.3 code [10], for the mask geometry and beam parameters in Table 1. The mask was chosen so as to make the beamlets long enough, approximately 300 fs full width, to accommodate an external seeding laser of 50 fs. The FEL input and output parameters are summarized in Table 2.

We also conducted an experiment with beam and mask parameters close to those in Table 1, but a single mask aperture as due to available hardware. Figure 4 shows the measured spectrum of the first HGHG stage of FERMI

FEL2, tuned at the 8th harmonic of the seed laser wavelength. The seed laser duration was about 50 fs. The spectrum is measured as a function of the delay of the seed laser relative to the electron bunch arrival time. The top plot is without beam scraping; the bottom plot is for scraping in BC1 set to generate beamlet duration of approximately 330 fs. The extension of the lasing region as a function of the seed laser-electron bunch delay confirms the expected beamlet duration, and it highlights a region of efficient lasing in the beamlet as long as ~ 150 fs. The spectrum intensity is normalized to the peak value in both plots: the average FEL pulse energy was 35 μ J for the whole beam, 15 μ J for the selected beamlet without further optimization of the spatial and temporal overlap of seed laser and electron beamlet.

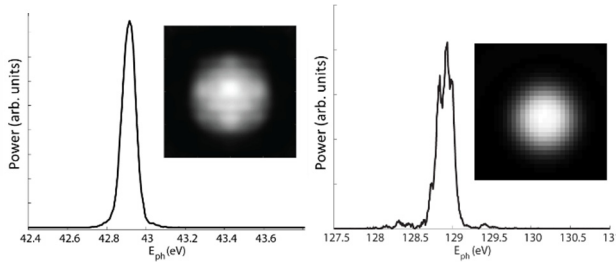


Figure 3: Spectral power and transverse intensity distribution (inset) at the end of the FEL1 (left) and FEL2 undulator line (Genesis 1.3 simulation). Electron beamlets parameters as in Table 1.

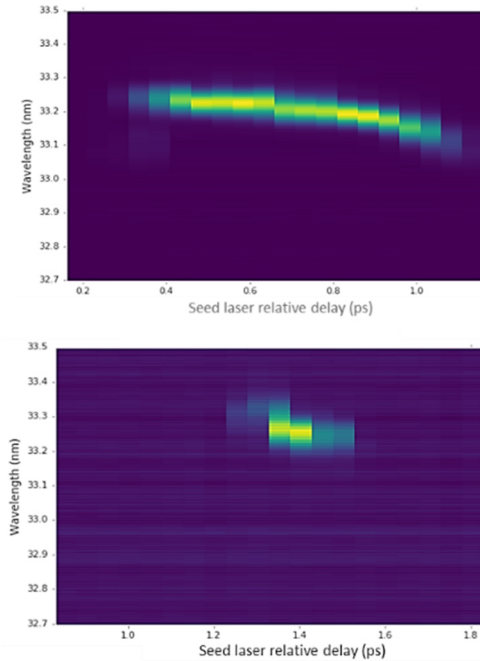


Figure 4: Spectrum of the first stage of FERMI HGHG FEL2 vs. seed laser delay. The seed laser is superimposed to the whole electron beam (top), and to a single beamlet produced with scraping in BC1 (bottom). The spectrum intensity is normalized in both plots to the peak value. The seed is time-shifted in steps of 50 fs, 20 shots are consecutively recorded for each delay value.

Table 2: FEL1 and FEL2 Input and Output Parameters. Electron beamlets parameters as in Table 1.

Quantity	FEL1	FEL2	Units
Seed laser pulse energy	5	10	μ J
Seed laser duration, fwhm	50	50	fs
Harmonic jump	9	27	
Central wavelength	28.8	9.6	nm
Relative bandwidth, fwhm	0.20	0.18	%
Pulse energy	60	13	μ J
Pulse duration, fwhm	30	37	fs
Peak power	2.0	0.4	GW

CONCLUSIONS

In conclusion, we have demonstrated with detailed numerical simulations that two-pulse, two-color FEL emission synchronized at sub-fs level can be generated by splitting the electron bunch in two beamlets, and that these can be safely sent to distinct undulator lines. The scheme is suitable for the simultaneous operation of experimental beamlines receiving FEL pulses generated by very similar *electron* beam parameters, and can be implemented at existing facilities with limited cost and reduced impact on the infrastructure.

Unlike any HGHG option, the proposed scheme has no color limitation due to the harmonic up-conversion of the seed laser wavelength. Accordingly, this study is expected not only to pave the way to simultaneous operation of two synchronized FEL lines, but also to more flexible, robust and reliable two-color, two pulse schemes for, e.g., four wave mixing spectroscopy as well as a broader variety of FEL-pump FEL-probe experiments, including transient grating spectroscopic methods. Since pump and probe are generated with two different undulators, and for relative time separation of the two pulses up to 1 ps or so, there is no need of a large split-and-delay system for the photon beam, which can be costly, difficult to operate, and reducing the photon flux at the sample.

For future facilities with freedom of parameter choice, the two beamlets could be created using a double photo-injector laser pulse, accelerated at the same phase on different RF cycles, before being given small energy offsets in a subharmonic cavity so that they can be separated into two FEL beamlines by the septum with the same scheme presented above. Such double pulse option may offer some more flexibility in beam compression, and avoids relatively large beam power losses induced by scraping at high repetition rates.

REFERENCES

- [1] A.M. Kondratenko and E.L. Saldin, "Generation of coherent radiation by a relativistic electron beam in an undulator", *Part. Accel.*, vol. 10, pp. 207–216, Aug. 1980.
- [2] R. Bonifacio, C. Pellegrini, and L. Narducci, "Collective instabilities and high-gain regime in a free electron laser", *Opt. Commun.* vol. 50, pp. 373–378, Jul. 1984.
doi:10.1016/0030-4018(84)90105-6

- [3] L.-H. Yu, “Generation of intense uv radiation by subharmonically seeded single-pass free-electron lasers”, *Phys. Rev. A*, vol. 44, pp. 5178–5193, Oct. 1991.
doi:10.1103/PhysRevA.44.5178
- [4] G. Stupakov, “Using the Beam-Echo Effect for Generation of Short-Wavelength Radiation”, *Phys. Rev. Lett.*, vol. 102, pp. 074801, Feb. 2009.
doi:10.1103/PhysRevLett.102.074801
- [5] E. Allaria *et al.*, “Highly coherent and stable pulses from the FERMI seeded free-electron laser in the extreme ultraviolet”, *Nat. Phot.* vol. 1, pp. 699-704, 2012.
doi:10.1038/nphoton.2012.233
- [6] E. Allaria *et al.*, “Two-stage seeded soft-X-ray free-electron laser”, *Nat. Phot.*, vol. 7, pp. 913-918, Oct. 2013.
doi:10.1038/nphoton.2013.277
- [7] W. Qin, Y. Ding, A. A. Lutman, and Y.-C. Chao, “Matching based fresh-slice method for generating two-color x-ray free-electron lasers”, *Phys. Rev. Accel. Beams*, vol. 20, pp. 090701, 2017.
doi.org/10.1103/PhysRevAccelBeams.20.090701
- [8] M. Borland, “elegant: A Flexible SDDS-Compliant Code for Accelerator Simulation”, Advanced Photon Source Technical Note LS-287, Aug. 2000.
doi:10.2172/761286
- [9] L. Wang *et al.*, “Energy Jitter Minimization at LCLS”, in *Proc. FEL'15*, Daejeon, Korea, Aug. 2015, paper TUP070, pp. 523-529.
- [10] S. Reiche, “GENESIS 1.3: a fully 3D time-dependent FEL simulation code”, *Nucl. Instrum. Methods Phys. Res., Sect. A*, vol. 429, no. 1-3, pp. 243-248, Jun. 1999.
doi:10.1016/S0168-9002(99)00114-X

EXPERIMENTAL BENCHMARKING OF WAKEFIELDS AT THE FERMI FEL LINAC AND UNDULATOR LINE

S. Di Mitri^{†,1,2}, L. Sturari¹, Elettra Sincrotrone Trieste, Trieste, Italy
C. Venier, R. Vescovo, University of Trieste, Dept. of Engineering, Trieste, Italy
²also at University of Trieste, Dept. of Physics, Trieste, Italy

Abstract

Collective effects such as wakefields affect the dynamics of high brightness electron beams in linear accelerators (linacs), and can degrade the performance of short wavelength free-electron lasers (FELs). If a reliable model of wakefields is made available, the accelerator can be designed and configured with parameters that minimize their disrupting effect. In this work, the simulated effect of geometric (diffractive) wakefields and of coherent synchrotron radiation on the electron beam energy distribution at the FERMI FEL is benchmarked with measurements, so quantifying the accuracy of the model. Wakefields modelling is then extended to the undulator line, where particle tracking confirms the limited impact of the resistive wall wakefield on the lasing process. The study reveals an overall good understanding of collective effects in the facility.

INTRODUCTION

At the FERMI FEL [1,2], a systematic study of collective effects has been carried out since the early stage of machine design [3–7]. In the last decade, numerical predictions were benchmarked with experimental results to demonstrate the interplay of longitudinal geometric wakefields and beam current profile [8,9], to quantify the effect of transverse wakefields on the beam projected emittance [10,11], and to compare 1- vs. 3-dimensional CSR effects on the beam emittance [12–14]. They all confirm, on top of the routine operation of the facility, that the electron beam dynamics is strongly affected by geometric (diffractive) wakefields in the linac sections (L0–L4 in Fig.1), and by CSR emission in the magnetic chicane devoted to bunch length compression (BC1). In addition to this, a semi-analytical formulation of the resistive wall wakefield in the undulator elliptical vacuum chamber was provided [15]. Still, a systematic characterization of the longitudinal wakefields acting in the linac, as well as a start-to-end particle tracking run in the presence of resistive wall wakefield in the undulator line, is lacking. The present work targets these two points.

After a theoretical introduction to wakefields, we complement the aforementioned studies by investigating the effect of linac geometric wakefields and of CSR on the beam energy distribution. The effect is quantified by measuring the beam mean energy and energy spread in a spectrometer line installed at the linac end, as function of bunch length and bunch charge. The final bunch length is determined by magnetic compression, and it was varied by scanning the RF phase of the upstream linac. The bunch charge was varied by changing the intensity of the laser pulse that drives

the photoelectron emission at the Gun cathode. The study is extended to the computation and simulation of resistive wall wakefields in the FERMI FEL-2 undulator vacuum chamber. This is the second and longer undulator line of the two currently installed at FERMI. It is devoted to the emission of the shortest FEL wavelengths, in the range 4–20 nm, and it is expected to be more sensitive to the degradation of electron beam brightness.

The FERMI layout is sketched in Fig.1. The electron beam is generated in the RF Gun by photoelectron emission from a Copper cathode illuminated by a UV laser. Electrons are accelerated up to 1.5 GeV in the L0–L4 S-band linac sections. It is time-compressed, nominally by a factor ~ 10 , in the BC1 bunch compressor, at the energy of 0.3 GeV (BC2 is not used routinely). Each linac section includes different travelling wave accelerating structures, which are grouped by length and inner geometry. They are of type “INJ” (3.2 m-long each; 9 mm average radius), “LIL” (4.5 m-long each; 10 mm average radius), “BTW” (6.1 m-long each; 5 mm average radius), and “X-band” (0.75 m-long; 5 mm average radius). “LH” stays for laser heater. The whole linac is 175 m long. The Spreader transfer line is ~ 30 m long. The FEL-1 and FEL-2 undulator lines are, respectively, 30 m and 44 m long.

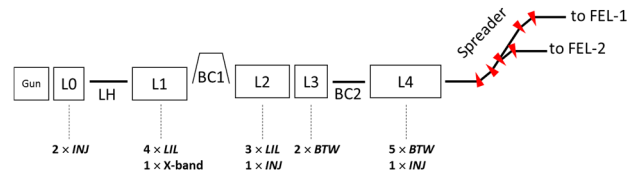


Figure 1: Sketch (not to scale) of the FERMI electron beam delivery system. Published in [16].

WAKEFIELDS MODEL

Geometric Wakefield in RF Cavities

The analytical expressions of the FERMI linac wake functions, in unit of V/(pC m), are given in Eq.1, and are plotted in Fig.2. They well represent the e.m. field pattern established along the whole multi-cell accelerating structure, and apply to bunch lengths shorter than 5 mm [3,5]. The upper-case label of each wake function refers to the structures naming in Fig.1. Please note that the numerical coefficients are consistent with the s-coordinate expressed in units of meter.

$$\begin{aligned} w_l^{INJ}(s) &= 380 \cdot e^{-\sqrt{\frac{s}{1.28 \cdot 10^{-3}}}} \\ w_l^{LIL}(s) &= 311 \cdot e^{-\sqrt{\frac{s}{1.38 \cdot 10^{-3}}}} \end{aligned} \quad (1)$$

[†] simone.dimitri@elettra.eu

$$w_i^{BTW}(s) = 1226 \cdot e^{-\sqrt{\frac{s}{3 \cdot 10^{-4}}}} + \frac{0.494}{\sqrt{s}} + 494 \cdot \sqrt{s}$$

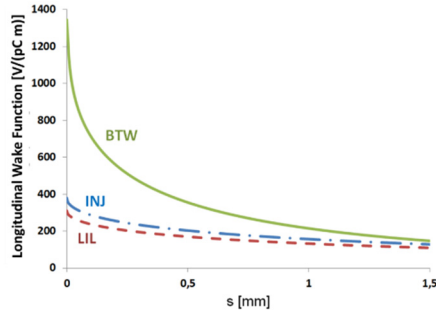


Figure 2: Geometric longitudinal wake functions per unit length associated to the diverse inner geometries of the FERMI S-band accelerating structures, see Eq.1. Labels refer to the structures naming adopted in Fig.1. Published in [16].

Resistive Wall Wakefield in Undulator Chamber

The FERMI undulator vacuum chamber is made of 1.1 m-long sections in Stainless Steel 304LN, of cylindrical cross section and 11 mm inner radius. These are interleaved by 3.2 m-long elliptical chambers in Aluminum, of inner diameters 7 mm \times 22 mm. Since the ellipticity of the elliptical chambers is larger than 3, the wake function can be approximated to that of parallel plates at a gap equal to the shortest (vertical) diameter [15].

The longitudinal resistive wall impedance of a cylindrical metallic vacuum chamber of inner radius b and conductivity σ_{AC} is [17]:

$$Z_{AC}^{cyl}(k) = \frac{Z_0}{2\pi b} \left(\frac{f(k)}{k} - i \frac{kb}{2} \right)^{-1} \quad (2)$$

The wake function is calculated as the inverse-Fourier transform of Eq.2:

$$G_{LAC}(z) = \frac{2c}{\pi} \int_0^\infty \text{Re}[Z_{AC}(k)] \cos(kz) dk \quad (3)$$

The analytical expression of the longitudinal resistive wall impedance of parallel plates is known from the Bane and Stupakov model in the limit $s_1 \ll b$, where $s_1 = \sqrt{\frac{2b^2}{Z_0 \sigma_{DC}}}$ estimates the distance at which the wakefield associated to σ_{AC} in a cylindrical pipe of inner radius b is damped [18,19]. That condition is satisfied at FERMI, and the wake function is calculated as the inverse-Fourier transform of the following impedance:

$$Z_{AC}^{pp}(k) = \frac{Z_0}{4\pi} \int_{-\infty}^{+\infty} \left(\frac{f(k)}{k} (\cosh(bx))^2 - i \frac{k}{x} \cosh(bx) \sinh(bx) \right)^{-1} dx \quad (4)$$

Coherent Synchrotron Radiation

In the FERMI BC1, most of the CSR physics is described by the steady-state emission [12,14], which is represented by the impedance per unit length [20]:

$$Z_{CSR}(k) = \frac{Z_0 k^{1/3}}{\pi R^{2/3}} (0.41 + i0.23) \quad (5)$$

The 1-D approximation is expected to fail for bunches approaching full compression, *i.e.*, upright longitudinal phase space. In this case, CSR direct transverse forces and the dependence of the longitudinal electric field on the transverse coordinates become important. Since the elegant code, used in the following, projects the charge distribution onto a line-charge, an artificially stronger CSR interaction is expected to be simulated, whereas the actual interaction is somehow “diluted” in the transverse plane [14].

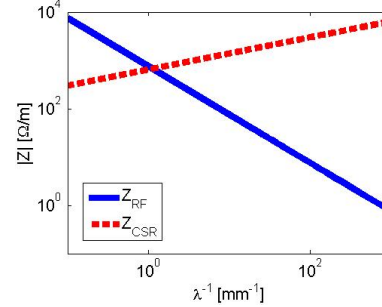


Figure 3: Spectral behaviour of the RF geometric (Eq.1) and CSR impedance (Eq.5) per unit length. Z_{RF} is calculated for an iris radius of 5 mm (average value in the FERMI BTW structures), Z_{CSR} is calculated for a curvature radius of 4 m (typical of FERMI BC1). Published in [16].

WAKEFIELDS BENCHMARKING

Linac

The effect of wakefields on the particle dynamics in FERMI was simulated with elegant. The code convolutes the charge distribution produced by tracking with geometric wake functions provided as external text files. CSR is simulated in the 1-D approximation, including entrance and exit transient effects. The quantities in Eq.2 predicted by the code at the linac end were compared with the corresponding measured quantities. Table 1 summarizes the main linac and electron beam parameters adopted in the experiment and used in the simulations.

Table 1: FERMI Electron Beam and Linac Parameters for the Nominal Bunch Length Compression Factor. Asterisk marks simulated-only parameters.

Parameter	Value	Units
Charge	0.35, 0.70	nC
Peak Current at Injector Exit	35*, 70*	A
Linac-1 RF Phase	116.5	deg
Energy at BC1	0.28	GeV
BC1 Dipole Bending Angle	85	mrad
BC1 Compression Factor	10*, 11	
Final Peak Current (bunch core)	400*, 750	A
Final Bunch Duration, fwhm	0.3*, 0.8	ps
Energy Spread at Linac End, rms	1.2, 1.9	MeV
Mean Energy at Linac End	1.45	GeV

The RF phase of L1 was varied in the code in order to scan the final bunch length. Finally, the mean energy and energy spread predicted by the code were compared with

measured quantities, as illustrated in Fig.4. The comparison was repeated at the bunch charge of 0.35 nC and 0.70 nC. In both cases the largest discrepancy between experiment and simulation is in correspondence of 117.5 deg RF phase, *i.e.*, at the point of full compression. Left plot suggests that the 1-D CSR modeling in elegant overestimates the strength of the interaction for full compression (compare red dashed line with solid blue line). In the right plot, the discrepancy at the phase of full compression is due to the discrepancy in the energy spread induced by CSR, which sums to that one determined by the RF curvature and longitudinal geometric wakefields. In other words, Instead, an excellent agreement is obtained both in mean energy and energy spread for all other RF phases. In addition to this, Fig.4 confirms that the longitudinal effect of CSR is negligible w.r.t. the linac geometric impedance for bunch lengths longer than $\sim 50 \mu\text{m}$.

The successful benchmarking of simulation and experiment results for RF phases far from the point of full compression confirms the reliability of the model adopted for the linac geometric wakefields. Moreover, one is allowed to infer that the linac geometric wakefields dominate the beam dynamics over other collective effects not considered here, such as space charge forces in the main linac, geometric wakefields associated to discontinuities of the beam pipe outside the accelerating structures, and linac resistive wall wakefield.

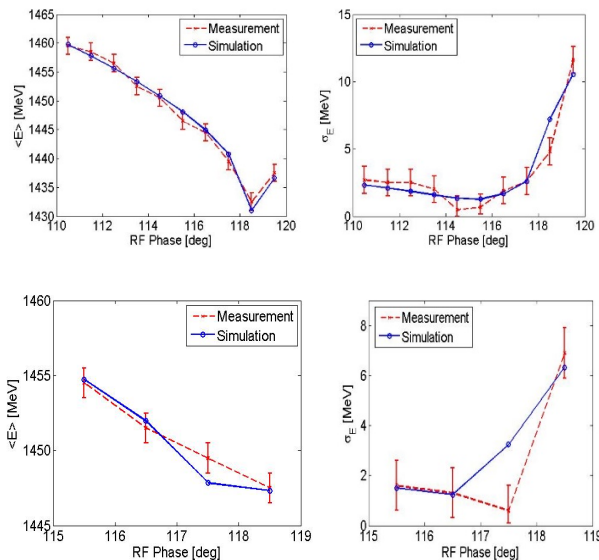


Figure 4: Simulated and measured beam mean energy (left) and rms energy spread (right) at the linac end as function of the L1 RF phase, for 0.7 nC (top) and 0.35 nC bunch charge (bottom). Each measured data is the average of 10 consecutive measurements. Published in [16].

Undulator

The FERMI FEL-2 undulator vacuum chamber is made of Aluminum elliptical sections, surrounded by undulators, alternated with Stainless Steel cylindrical sections, surrounded by other magnetic and diagnostic elements. The longitudinal resistive wall wake function was calculated as

the inverse-Fourier transform of Eq.2 for the cylindrical sections, and of Eq.4 for the elliptical sections. Figure 5 compares the simulated electron beam longitudinal phase space at the end of the undulator line, with and without resistive wall wakefields. Particle tracking reveals that only a ~ 100 fs-long portion of the bunch head is affected by resistive wall wakefields; even in that region, the energy spread is weakly affected, at the level of 0.1%. Owing to the fact that the VUV seed laser that initiates the FEL process at FERMI is typically ~ 70 fs long or shorter, that it is superimposed to the central portion of the bunch and with relative arrival time jitter smaller than 50 fs, we can reasonably conclude that the resistive wall wakefield is predicted to have no impact on the lasing efficiency.

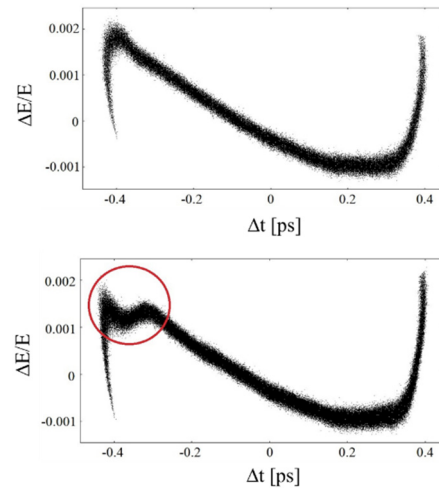


Figure 5: Simulated longitudinal phase space at the end of the FERMI FEL-2 undulator line, without (top) and with (bottom) resistive wall wakefields. The red circle highlights the region of the bunch head in which wakefields have most effect. Published in [16].

CONCLUSIONS

The study confirms that the linac geometric wakefields dominate the longitudinal beam dynamics at the FERMI nominal working point, together with the RF curvature. CSR plays an important role only at rms bunch lengths shorter than $50 \mu\text{m}$, whereas nominal bunch durations at FERMI are longer than $70 \mu\text{m}$. Particle tracking through the undulator line in the presence of resistive wall wakefields confirms the limited impact of that impedance on the beam quality, thus on the lasing process.

REFERENCES

- [1] E. Allaria, R. Appio, L. Badano, W.A. Barletta, S. Basanese, S.G. Biedron, A. Borgia, E. Busetto, D. Castronovo, P. Cinquegrana, et al., “Highly coherent and stable pulses from the FERMI seeded free-electron laser in the extreme ultraviolet”, *Nature Photon.*, Vol. 6 (2012) 699–704. doi:10.1038/nphoton.2012.233
- [2] E. Allaria, D. Castronovo, P. Cinquegrana, P. Craievich, M. Dal Forno, M. Danailov, G. D’Auria, A. Demidovich, G. De Ninno, S. Di Mitri, et al., “Two-stage seeded soft-X-ray

- free-electron laser”, *Nature Photon.* Vol 7 (2013), 913–918. doi:10.1038/nphoton.2013.277
- [3] P. Craievich, T. Weiland, and I. Zagorodnov, “The short-range wakefields in the BTW accelerating structure of the ELETTRA LINAC”, *Nucl. Instr. Meth. Phys. Research A*, vol. 558 (2006), 58–61. doi:10.1016/j.nima.2005.11.069
- [4] P. Craievich, S. Di Mitri and A. A. Zholents, “Single-bunch emittance preservation in the presence of trajectory jitter for FERMI@elettra-seeded FEL”, *Nucl. Instr. and Methods in Phys. Res. A*, vol. 604, (2009) 457–465. doi:10.1016/j.nima.2009.03.106
- [5] P. Craievich, *Short-range longitudinal and transverse wake-field effects in FERMI@Elettra FEL project*, Ph.D. thesis, Technische Universiteit Eindhoven, Department of Applied Physics, Eindhoven, The Netherlands, ISBN 978-90-386-2294-1 (2010).
- [6] S. Di Mitri et al., “Design and simulation challenges for FERMI@elettra”, *Nucl. Instr. and Methods in Phys. Res. A*, vol. 608, (2009) 19–27. doi:10.1016/j.nima.2009.06.028
- [7] S. Di Mitri, “Machine Design and Electron Beam Control of a Single-Pass Linac for Free Electron Laser: the FERMI@Elettra Case Study”, Ph.D. Thesis, *University of Groningen, Zernike Institute for Advanced Materials*, ISBN 978-90-367-5176-6 (2011).
- [8] M. Cornacchia, S. Di Mitri, G. Penco and A. A. Zholents, “Formation of electron bunches for harmonic cascade x-ray free electron lasers”, *Phys. Rev. Special Topics – Accel. and Beams*, vol. 9, 120701 (2006). doi:10.1103/PhysRevSTAB.9.120701
- [9] G. Penco, M. Danailov, A. Demidovich, E. Allaria, G. De Ninno, S. Di Mitri, W.M. Fawley, E. Ferrari, L. Giannessi, and M. Trovo’, “Experimental Demonstration of Electron Longitudinal-Phase-Space Linearization by Shaping the Photoinjector Laser Pulse”, *Phys. Rev. Letters*, vol. 112, 044801 (2014). doi:10.1103/PhysRevLett.112.044801
- [10] S. Di Mitri, “Maximum brightness of linac-driven electron beams in the presence of collective effects”, *Phys. Rev. Special Topics – Accel. and Beams*, vol. 16, 050701 (2013). doi:10.1103/PhysRevSTAB.16.050701
- [11] S. Di Mitri, L. Froehlich and E. Karantzoulis, “Influence of longitudinally tapered collimators on a high brightness electron beam”, *Phys. Rev. Special Topics – Accel. and Beams*, vol. 15, 061001 (2012). doi:10.1103/PhysRevSTAB.15.061001
- [12] S. Di Mitri, E. M. Allaria, P. Craievich, W. Fwaley, L. Giannessi, A. Lutman, G. Penco, S. Spampinati and M. Trovo’, “Transverse emittance preservation during bunch compression in the Fermi free electron laser”, *Phys. Rev. Special Topics – Accel. and Beams*, vol. 15, 020701 (2012). doi:10.1103/PhysRevSTAB.15.029901
- [13] S. Di Mitri, M. Cornacchia, and S. Spampinati, “Cancellation of Coherent Synchrotron Radiation Kicks with Optics Balance”, *Phys. Rev. Letters*, vol. 110, 014801 (2013). doi:10.1103/PhysRevLett.110.014801
- [14] A. Brynes, et al., “Beyond the limits of 1D coherent synchrotron radiation”, *New J. Phys.*, vol. 20, 073035 (2018). doi:10.1088/1367-2630/aad21d
- [15] A. Lutman, R. Vescovo, P. Craievich, “Electromagnetic field and short-range wake function in a beam pipe of elliptical cross section”, *Phys. Rev. Special Topics – Accel. and Beams*, vol. 11, 074401 (2008). doi:10.1103/PhysRevSTAB.11.074401
- [16] S. Di Mitri, L. Sturari, C. Venier, Ro. Vescovo, “Wakefield benchmarking at a single-pass high brightness electron linac”, *Phys. Rev. Accel. and Beams*, vol. 22, 014401 (2019). doi:10.1103/PhysRevAccelBeams.22.014401
- [17] B. W. Zotter, S. A. Kheifets, “Impedances and Wakes in High-Energy Particle Accelerators”, *World Scientific Publishing Co. Pte. Ltd.*, Singapore (1998). doi:10.1142/3068
- [18] K. L. F. Bane and G. Stupakov, “Resistive Wall Wakefield in the LCLS undulator”, in *Proc. PAC2005.*, Knoxville, Tennessee, USA (2005) 3391. doi:10.1109/PAC.2005.1591481
- [19] H. Henke and O. Napoly, “Wake fields between two parallel resistive plates”, in *Proc. 2nd EPAC 90.*, Nice, France (1990), p. 1046–1048.
- [20] J. B. Murphy, S. Krinsky, and R. L. Gluckstern, “Longitudinal Wakefield for Synchrotron Radiation”, in *Proc. PAC 95*, Dallas, TX, USA, (1995). doi:10.1109/PAC.1995.505757

COMPACT FEL-DRIVEN INVERSE COMPTON SCATTERING GAMMA-RAY SOURCE

M. Placidi¹, G. Penn, Lawrence Berkeley National Laboratory, Berkeley, CA 94720, USA
S. Di Mitri[†], Elettra - Sincrotrone Trieste S.C.p.A., 34149 Basovizza, Trieste, Italy
C. Pellegrini², Stanford Linear Accelerator Center, Menlo Park, CA 94025, USA

¹on leave

²also at University of California, Los Angeles, CA 90095, USA

Abstract

We explore the feasibility of a compact source of quasi-monochromatic, multi-MeV gamma-rays based on Inverse Compton Scattering (ICS) from a high intensity ultra-violet (UV) beam generated in a free-electron laser by the electron beam itself [1]. This scheme introduces a stronger relationship between the energy of the scattered photons and that of the electron beam, resulting in a device much more compact than a classic ICS for a given scattered energy. The same electron beam is used to produce gamma-rays in the 10-20 MeV range and UV radiation in the 10-15 eV range, in a ~4x22 m² footprint system.

INTRODUCTION

We discuss the feasibility and the performance of an Inverse Compton Scattering (ICS)-based scheme where the electron beam interacts with its own radiation emitted in a Free Electron Laser (FEL). The energy of the outgoing radiation has a steeper dependence on the electron energy than a classical ICS scheme, thus providing a relatively compact layout.

Methods of X-ray production presently include ICS facilities and synchrotron radiation sources from insertion devices in electron storage rings. Contrast imaging of massive sculptures would profit [2] from radiation sources more powerful than the X-ray CT industrial instruments operating in the 450 keV range. Specific case studies can be identified, for example, on the basis of the energy content of the scattered light. At low photon energy (up to few MeV), contrast imaging of massive objects in Geo-archeology [2] would greatly benefit from such an intense and compact source, and this was actually the driving case of this work. At photon energies in the 1–10 MeV range, photons propagating through dense materials prompt nuclear reactions, generating *e.g.* alpha particles and neutrons, which can be easily identified and used for isotope separation [3]. At photon energies higher than 10 MeV, the proposed scheme would approach the specifications for an elastic photon-photon scattering source for frontier experiments in QED [4]. As a by-product of the proposed scheme, a naturally synchronized UV beam with large fraction of coherent photons at 100 fs duration level, ideal for pump-probe experiments, would be provided by the FEL. High-flux multi-MeV gamma-ray beams and UV radiation can be simultaneously available for applications in Nuclear Physics, Security Inspections, Cultural

Heritage and UV Science.

FEL-ICS CONCEPT

In a classical ICS process a relativistic electron transfers a fraction of its energy to an incoming laser photon which is scattered in the electron direction of flight with a Doppler-upshifted frequency. The scattered radiation energy

$$E_s = \frac{a_c}{1+X} \gamma^2 \hbar \omega_{ph} \quad (1)$$

exhibits a quadratic energy dependence on the electron energy as the incoming photon energy is constant. The kinematic factor

$$a_c \approx \frac{2(1+\cos\varphi)}{1+(\gamma\theta)^2} \leq 4 \quad (2)$$

modulates the scattered energy via the collision angle φ within the semi-aperture θ of the emission cone, while the term

$$X = 4\gamma \frac{\hbar \omega_{ph}}{m_e} \quad (3)$$

accounts for the recoil of the electron [5].

The FEL-ICS scheme introduces a stronger γ -dependence by making the relativistic electron beam interact with its own UV radiation produced in an FEL [6]. The on-axis FEL radiation wavelength is related to the axial electron velocity β_z and the undulator period λ_u as [7]:

$$\lambda_r = \lambda_u \frac{1-\beta_z}{\beta_z} \approx \frac{\lambda_u}{2\gamma^2} (1 + a_u^2) \quad (4)$$

Here $a_u = K_u = eB_0\lambda_u/2\pi m_e c = 93.4 B_0[T] \lambda_u[m]$ is the helical undulator parameter, B_0 the undulator central magnetic field, e the electron charge. The energy of the FEL photons in terms of the electron energy reads:

$$E_r \equiv \frac{hc}{\lambda_r} = a_{FEL} hc \frac{\gamma^2}{\lambda_u} \quad (5)$$

where we define $a_{FEL} = 2/(1 + a_u^2)$ for on axis undulator radiation. When the FEL photon energy (5) replaces that from the laser in (1), the scattered photon energy can be written as:

$$E_s = a_c E_r \gamma^2 = a_c a_{FEL} hc \frac{\gamma^4}{\lambda_u}. \quad (1')$$

The term (3), of the order of 10^{-2} , has been neglected in this kinematic scaling. Introducing the Compton wavelength $\lambda_c = hc/m_e c^2 = 2.426 \times 10^{-3}$ nm, the scattering efficiency, *i.e.* the fraction of the electron energy transferred to the scattered photons, reads

[†] simone.dimitri@elettra.eu

$$\eta \equiv \frac{E_s}{E} = a_c a_{FEL} \frac{\lambda_c}{\lambda_u} \gamma^3 \quad (6)$$

The cubic energy dependence of the scattering efficiency (6) provides compactness to the system, as lower electron energy is required to produce a given upshifted radiation. The UV and the FEL-ICS radiation energies are tunable via the undulator parameter K_u , typically ranging from 1 to 5 in an out-of-vacuum APPLE-II type device [8] or Delta undulator [9].

A conservative figure $\varphi = 25^\circ$ has been assumed for interaction angle resulting from the optimization of different competing requirements, like the scattering efficiency, via the impact parameter a_c , the ICS luminosity and the loop in Fig. 1. The dependence of the incoming (5) and scattered photon energy (1') on the electron beam energy is shown in Fig. 2. It can be gathered that:

- The ~ 16 MeV outgoing radiation energy for the 300 MeV electron energy considered in the present study compares with the ~ 3 MeV obtainable in the classical ICS case.
- The scattering efficiencies E_s/E are larger than in the ICS case by one order of magnitude or more in the present energy range, and the comparison dramatically improves with the electron energy.

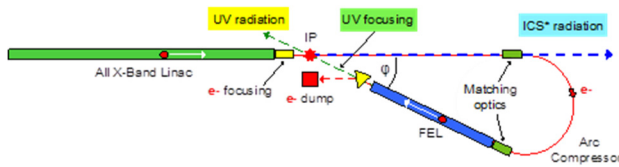


Figure 1: Sketch, not to scale, of the FEL-ICS scheme.

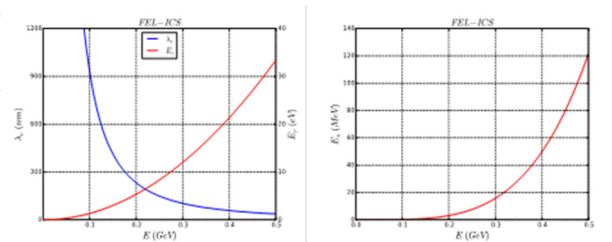


Figure 2: Wavelength of the incoming radiation from undulator with $\lambda_u = 20$ mm (left), and scattered radiation energy (right).

FEL-ICS LAYOUT

Facility Footprint

A single-pass conceptual layout of the FEL-ICS scheme is shown in Fig. 1. The main characteristics of the system are summarized in Table 1 and discussed in the following. Trains of electron bunches are produced in an X-Band Linac at 1 kHz repetition rate. A return arc acting as a bunch length compressor [10,11] rises the bunches peak current from 35 A to 500 A and guides them into an FEL undulator operating in the high-gain SASE regime [7,12], long enough to reach saturation. The emerging UV radiation produced by the leading bunches in the train is focused at the IP, where high-energy gamma-rays are produced via Compton interaction with the trailing bunches.

The low value of the Thomson cross section preserves the electron bunch quality for the FEL performance and allows a simultaneous use of the UV radiation for additional applications. The 180° original arc deflection [10] is extended to 205° to comply with the 25° design interaction angle.

The large FEL power compensates for the low Thomson cross-section. The electron bunches and UV radiation are focused to similar transverse spot sizes at the IP to optimize the scattered flux. The electron focusing, bunch compression, and UV optics are all crucial for providing the desired compactness and gamma-ray flux. The short undulator length allowed by bunch compression; an arc compressor length of about 6.5 m and the associated matching optics leave about 2 m for the UV focusing drift downstream the undulator.

Linac and ICS Repetition Rate

We consider a room temperature operation in the original spirit of keeping the photon source within cost-effective limits. Compactness requirements suggest the adoption of high-gradient X-Band technology [13], both for the photo-injector and the accelerating structure. Power dissipation issues associated to the acceleration of electron beams with kHz time structures can be mitigated by choosing operating frequencies in the 11.4–12.0 GHz range in order to increase the RF power transfer efficiency with a higher specific shunt impedance of the structure, proportional to its frequency [14]. Warm X-Band RF technology operating at the above-mentioned repetition rates with a 35 MV/m gradient [15], considerably lower than the 100 MV/m reached at the CTF [16] in laboratory operating conditions, is adopted in this design.

An X-Band photo-injector has been built and commissioned at the X-Band Test Area (XTA) at SLAC with good beam quality. Complementing this injector with a 9 m long, 35 MV/m X-Band accelerating structure sets up an “all X-Band Linac” [17] capable of delivering a 300 MeV electron beam within a ~ 10 m total length. The 1 kHz repetition rate of the ~ 1 μ s long RF pulse containing 100 electron bunches gives an average beam current of about 30 μ A and a 9 kW beam power to the dump. Operation of the X-band linac at the high gradient of 100 MV/m can only be envisioned at a repetition rate lower than 100 Hz, and in single pulse mode. This scenario would therefore shrink the linac length to approximately 3 m for a final beam energy of 300 MeV. However, the average electron beam current, as well as the average FEL-ICS photon flux would be lowered by a factor 1000 with respect to the low-gradient, high pulse rate option, which therefore remains our basic design.

Return Arc Compressor

The bunch final peak current of 0.5 kA is important to obtain a high average FEL photon flux and reduce the undulator gain length. So, electron bunch length compression is critical for the flux of UV FEL photons interacting at the interaction point (IP). The return arc compressor in Fig. 1 gives a 205° beam deflection via a modified dou-

ble-bend achromatic cell magnetic structure characterized by a 3.58 Tm integrated bending field at $E=300$ MeV. The 6.5 m central arc trajectory length yields a bunch length compression factor $C \approx 15$ for 300 pC bunches, while limiting the growth of the transverse projected normalized emittances – here weakly affected by the emission of coherent synchrotron radiation (CSR) – to about 0.3 μm .

The outgoing bunch has 0.5 kA peak current, 1 μm normalized projected emittances and $\sim 0.2\%$ correlated rms energy and energy distribution. Particle tracking indicates that CSR emission in the arc dipoles leads to some modulation in the bunch current profile FEL parameter threshold, and no relevant impact on the FEL performance is anticipated.

UV FEL

After bunch length compression the beam is injected into the undulator. In the 1-D approximation the FEL gain length is given in terms of the ‘FEL parameter’ ρ_{FEL} [12] by

$$L_G = \frac{\lambda_u}{4\pi\sqrt{3}\rho_{\text{FEL}}}. \quad (7)$$

The radiation bandwidth and the saturation power to electron beam power ratio scale linearly with the FEL parameter.

In the scenario depicted in Fig. 1 a helical undulator is proposed to maximize the output power of the UV FEL, reduce the gain length and provide transverse focusing. A compact design based on Permanent Magnet technology [8,18] can provide the desired field amplitude, such as $B_0=0.86$ T at $\lambda_u=20$ mm, and eventually an undulator parameter $a_u=1.60$. A ~ 5 m long undulator allows the FEL to reach saturation at the fundamental wavelength of 103 nm (12 eV photon energy). The analytical evaluation of the undulator length needed to reach saturation is shown in Fig. 3 as a function of the beam peak current, along with the final average gamma-ray photon flux. The FEL parameter is about 5.5×10^{-3} , the gain length 0.22 m and the FEL peak power at saturation 0.77 GW. The corresponding photon peak rate is 4×10^{26} UV ph/s.

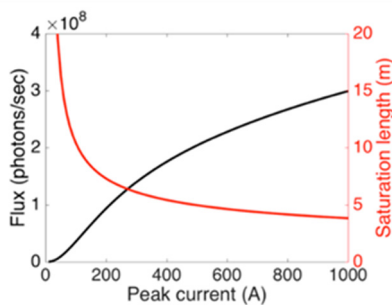


Figure 3: FEL-ICS performance in terms of scattered photon flux and FEL saturation length vs. the electron bunch peak current, for an undulator period length $\lambda_u=20$ mm.

Table 1: Electron beam parameters of the THz experimental sessions. (*) means “at the linac end”.

Parameter	Value	Units
Electron Beam Energy	300	MeV
Bunch Charge	300	pC
Bunch Duration, rms	2.5	ps
Bunch Peak Current	35	A
UV Photon Energy	12.0	eV
UV Peak Flux	2×10^{19}	photons/s
UV Duration, rms	0.16	ps
UV and e- rms beam sizes at IP (x / y)	60 / 15	μm
Interaction Angle	25	deg
Interacting e- Bunches per Train	90	
Interaction Rate	90	kHz
ICS Duty Factor	7.7×10^{-7}	
Scattered Photon Maximum Energy	~ 16	MeV
Scattered Photon Average Flux	1.1×10^8	photons/s mW
Scattered Photon Average Power	0.14	
Scattered Photon Average Intensity	1.8×10^7	photons/s/ mrad ²
Scattered Photon Peak Flux	1.4×10^{14}	photons/s mW
Scattered Photon Peak Power	1.8×10^5	
Scattered Photon Peak Intensity	2.3×10^{13}	photons/s/ mrad ²

CONCLUSIONS

By interacting with its own FEL radiation through an Inverse Compton Scattering process, a relatively low energy electron beam can simultaneously produce UV photons in the 10 to 12 eV range, and high-energy gamma-rays in the 6-16 MeV range. These photon beams can be used for Cultural Heritage, Nuclear Physics and UV science. A compact ~ 5 m long undulator is sufficient to simultaneously produce an UV flux of $\sim 2 \times 10^{19}$ ph/s and a high-energy photon flux in excess of 2×10^8 ph/s, within a system footprint of about 4×21 m². The scheme can be considered as an alternative to neutrons for the analysis of soil blocks of a certain volume containing archaeological findings like prehistoric teeth and old jewelry in the Geo-archaeology and Cultural Asset field. Moreover, it offers options for a wide range of multi-MeV photons applications in the Industry and Defense environments.

ACKNOWLEDGEMENT

Valuable contributions from G. D’Auria, L. Doolittle and F. Sannibale on Linac technical aspects are acknowledged and from D. Cocco for a feasibility estimate of a UV focusing system. This publication was funded by the Accelerators Group of Elettra Sincrotrone Trieste and by the Director, Office of Science, of the U.S. Department of Energy under Contract No. DE-AC02-05CH1123.

REFERENCES

- [1] M. Placidi *et al.*, NIM A 855 (2017) 55-60.
- [2] F. Casali *et al.*, “X-ray computed tomography for damage assessment of cultural heritage assets”, Protection of Historical Buildings, PROHITECH 09, Mazzolani (ed), 2009 Taylor & Francis Group, London, ISBN 978-0-415-55803-7.
- [3] C. P. J. Barty, “Nuclear photonics with laser-based gamma rays”, *SPIE Opt. Optoelectron.* Paper 8080B-30 (2011), doi: 10.1117/2.1201110.003681.
- [4] D. Micieli *et al.*, PRST-AB 19, 093401 (2016).
- [5] A. Curatolo *et al.*, “Analytical description of photon beam phase spaces in Inverse Compton Scattering sources”, arXiv:1705.07740v1 [physics.acc-ph], 22 May 2017.
- [6] H. Motz, W. Thon and R.N. Whitehurst, “Experiments on Radiation by Fast Electron Beams”, *J. Appl. Phys.* **24**, No. 7, (1953) 826, doi:10.1063/1.1721389.
- [7] C. Pellegrini, A. Marinelli and S. Reiche, “The physics of free-electron lasers”, *Reviews of Modern Physics* **88** (2016) 015006, doi:10.1103/RevModPhys.88.015006.
- [8] A. B. Temnykh, “Delta undulator for Cornell energy recovery linac”, *Phys. Rev. ST Accel. Beams* **11** (2008) 120702, doi:10.1103/PhysRevSTAB.11.120702.
- [9] S. Sasaki, “Analyses for a planar variably-polarizing undulator”, *Nucl. Instr. Meth. A* **347** (1994) 83-86, doi:10.1016/0168-9002(94)91859-7.
- [10] S. Di Mitri and M. Cornacchia, “Transverse emittance-preserving arc compressor for high-brightness electron beam-based light sources and colliders”, *EPL* **109** (2015) 62002, doi:10.1209/0295-5075/109/62002.
- [11] S. Di Mitri, “Feasibility study of a periodic arc compressor in the presence of coherent synchrotron radiation” *Nucl. Instr. Meth. A* **806** (2015) 184-192, doi:10.1016/j.nima.2015.10.015.
- [12] R. Bonifacio, C. Pellegrini and L. M. Narducci, “Collective instabilities and high-gain regime in a free electron laser”, *Opt. Commun.* **50** (1984) 373, doi:10.1016/0030-4018(84)90105-6.
- [13] G. D’Auria, “Application of X-Band Linacs”, *Proc. LINAC2012*, Tel-Aviv, Israel (2012) 724-728, ISBN 978-3-95450-122-9.
- [14] C. Christou, “X-band linac technology for a high repetition rate light source”, *Nucl. Instr. Meth. A* **657** (2011) 13, doi:10.1016/j.nima.2011.06.050.
- [15] C. Limborg-Deprey *et al.*, “Achieved Performance of an All X-Band Photo-Injector”, *Proc. IPAC2016*, Busan, Korea. (2016) 4253, ISBN 978-3-95450-147-2.
- [16] R. Bartolini, “Beam dynamics optimisation of an X-band Linac driven soft X-ray FEL”, *Nucl. Instr. Meth. A* **657** (2011) 177, doi:10.1016/j.nima.2011.06.046.
- [17] C. Limborg-Deprey *et al.*, “Achieved Performance of an All X-Band Photo-Injector”, *Proc. IPAC2016*, Busan, Korea. (2016) 4253, ISBN 978-3-95450-147-2.
- [18] H.-D. Nuhn *et al.*, “Commissioning of the Delta Polarizing Undulator at LCLS”, *Proc. FEL2015*, Daejeon, Korea (2015) 757-763, ISBN 978-3-95450-134-2.

USER OPERATION OF SUB-PICOSECOND THz COHERENT TRANSITION RADIATION PARASITIC TO A VUV FEL

S. Di Mitri^{†,1}, N. Adhlakha, E. Allaria, L. Badano, G. De Ninno², P. Di Pietro, G. Gaio, L. Giannessi³, G. Penco, A. Perucchi, P. Rebernik Ribic, S. Spampinati, C. Spezzani, M. Trovo', M. Veronese, Elettra - Sincrotrone Trieste S.C.p.A., Basovizza, Trieste, Italy

S. Lupi, Sapienza University of Rome, Italy

E. Roussel, PhLAM/CERCLA, Villeneuve d'Ascq Cedex, France

Federica Piccirilli, IOM-CNR, Trieste, Italy

²also at University of Nova Gorica, Slovenia

³also at ENEA C.R. Frascati, Rome, Italy

Abstract

Coherent transition radiation is enhanced in intensity and extended in frequency spectral range by the electron beam manipulation in the beam dump beam line of the FERMI FEL, by exploiting the interplay of coherent synchrotron radiation instability and electron beam optics [1]. Experimental observations at the TeraFERMI beamline [2] confirm intensity peaks at around 1 THz and extending up to 8.5 THz, for up to 80 μ J pulse energy integrated over the full bandwidth. By virtue of its implementation in an FEL beam dump line, this work might stimulate the development of user-oriented multi-THz beamlines parasitic and self-synchronized to VUV and X-ray FELs.

INTRODUCTION

This study demonstrates that coherent transition radiation (CTR) with sub-picosecond duration, up to nearly 80- μ J pulse energy in the THz gap, was produced by exploiting the electrons' interaction with coherent synchrotron radiation (CSR) emitted in the post-undulator dispersive region of the VUV FERMI free electron laser (FEL) [3,4]. THz radiation with those characteristics finds application in experiments involving, for example, resonantly exciting collective modes as phonons, polarons, charge/spin-density-wave gaps, superconducting gaps in high-temperature superconductors and plasmons.

A sketch of the FERMI electron beam delivery system is shown in Fig. 1. Only the first magnetic bunch length compressor (BC1) is routinely active for lasing. Start-to-end simulations of the electron beam dynamics were carried out, for diverse linac settings, from the Gun (G) through the linac sections (L0–L4) until the Main Beam Dump (MBD), where the Al target for CTR emission is installed. The bottom plot is a 3-D rendering of the MBD, from the FEL post-undulator region to the dump. The active dipole magnets, named “Dipole 1” and “Dipole 2” in the figure, are long 1.12 m and 2.44 m, with bending angles of 15.7 deg and 31.4 deg respectively. Three quadrupoles between “Dipole 1” and “Dipole 2” tune the momentum compaction (R_{56}) of the beam line. CTR is emitted at the 1 μ m-thick Al target. Four quadrupoles installed upstream of the first dipole control the beam envelope along the line without affecting the R_{56} value. The transverse RMS beam sizes at

the CTR target are kept smaller than 0.5 mm. Steering magnets and beam position monitors (not shown) allow control of beam trajectory. While electrons are bent and eventually dumped, FEL propagates straight to the downstream experimental hall (EH).

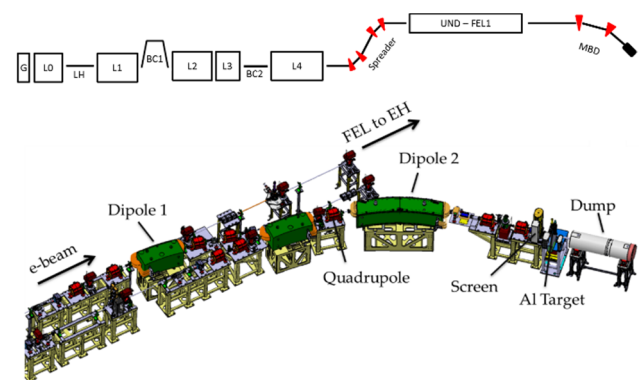


Figure 1: Sketch (not to scale) of the FERMI electron beam delivery system (top) and MBD line. Published in [1].

CSR-DRIVEN BUNCH COMPRESSION

The full width duration of the electron bunch prepared for lasing, thus entering the MBD line, is approximately 1 picosecond full width. In order to maximize transition radiation intensity at frequencies of 1 THz and above, a sub-picosecond charge density structure, *i.e.*, a kA-level current spike has to be generated in the bunch passing through the MBD, before reaching the Al target. Doing so, radiation can be emitted coherently in the multi-THz range at several tens of μ J-energy per pulse.

The FERMI dump line was designed to enhance the CSR wakefield by adopting relatively long and large angle dipole magnets, and for producing a tuneable but yet relatively large and positive R_{56} . This term couples with the CSR-induced negative energy chirp [5,6] and, as shown in the following, generates a ~ 100 fs-long leading current spike that radiates coherently in the THz range. The CSR-induced single particle energy deviation is actually correlated with z and, in particular, a negative linear chirp $h_1 < 0$ is produced at the bunch head, *i.e.*, leading particles are moved to higher energy with respect to trailing ones.

At the linac exit, the linear energy chirp in the head of the bunch was approximately -2 MeV/ps (see Fig.2). The

energy chirp induced by the CSR wakefield in the two dipole magnets shown in Fig.1, and according to beam parameters reported in Tab.1, is predicted to be -6 MeV/ps or $h_{1,CSR} \approx -23$ m⁻¹, and therefore it dominates the time-compression of the bunch head through the dump line. An optics setting which provides $R_{56} = 20$ mm, for instance, is expected to increase the bunch head peak current by a factor ~ 2 , thus reaching the kA-level at the target.

Table 1: Electron Beam Parameters of the THz Experimental Sessions; (*) Means “at the Linac End”

Parameter	Value	Units
Bunch Charge	0.7	nC
Initial Duration	2.8	ps
Mean Energy*	1308 / 871	MeV
Hor. Emittance*	2.1 / 1.8	μm
Vert. Emittance*	1.7 / 1.5	μm
Compr. Factor*	8 / 8, 11	
Bunch Duration*	0.35 / 0.35, 0.25	ps
Peak Current*	560 / 560, 750	A
R_{56} of the Dump Line	5, 19 / 37	mm

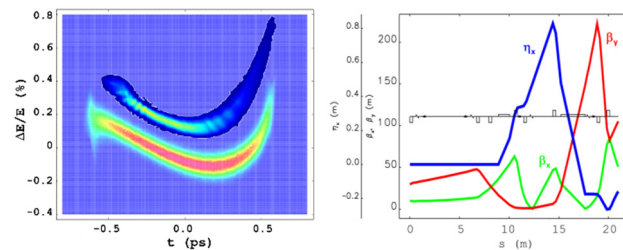


Figure 2: Left: simulated and measured electron beam longitudinal phase space at the end of the FERMI linac, at the beam energy of 1308 MeV; bunch head is at negative time coordinates. The current profile is approximately flat at the level of ~ 600 A (the measured phase space is upper-shifted w.r.t. the simulation for visualization). Right: betatron functions ($\beta_{x,y}$) and horizontal energy-dispersion function (η_x) from the exit of the FERMI undulator to the Al target, calculated starting from Twiss parameters measured in front of the undulator, and for the actual quadrupoles setting. ($R_{56} = 19$ mm). Published in [1].

CHARACTERIZATION OF CTR

Table 1 summarizes the electron beam parameters and the accelerator setting discussed so far. Two additional linac configurations at lower beam energy are also shown, and discussed below. For each configuration, the aforementioned control of longitudinal phase space and optics was accomplished.

CTR pulse energy and spectrum were calculated by applying the generalized Ginzburg-Frank formula, corrected by the prescription for far-field emission [7], to the electron bunch distribution simulated at the Al target. The expected value of the photon pulse energy was compared with the one measured by means of a pyroelectric detector installed after a Diamond window, in proximity of the target.

In order to demonstrate that, as predicted by the model, a larger R_{56} increases the bunch head peak current and

therefore the THz radiation intensity, pulse energies were measured for two optics settings of the dump line, named “OS1” ($R_{56}=5$ mm) and “OS2” ($R_{56}=19$ mm), at fixed CF in the linac (beam and linac parameters in Tab. 1, $E=1308$ MeV). Figure 3a shows the electron beam current profiles corresponding to OS1 and OS2, simulated at the target starting from the measurement shown in Fig.2-left plot, plus an unphysical case *without* CSR. A 3 kA, 100 fs-long current spike is obtained for OS2. In this case, the CTR calculation in Fig. 3b reveals that a significant frequency content is present up to 8.5 THz. Namely, at 8.5 THz the emission still contains 0.5 μJ energy over a 10% bandwidth, a value which is plausibly high enough to induce nonlinear effects in matter. The theoretical pulse energies integrated over the bandwidth 0.01–10 THz and represented by solid lines in Fig. 3c, are compared with the measured ones (dots with error bar). A striking agreement is achieved only when CSR is included in the simulations. It is worth mentioning that the multi-THz frequency content predicted in Figs. 3b and 4b reflects typical spectral measurements [8] collected during TeraFERMI operation, as shown in Fig.5.

To additional highlight the relevance of the CSR wake-field for the production of THz radiation, another series of measurements was carried out with a fixed R_{56} in the dump line (beam and linac parameters in Tab. 1, $E=871$ MeV), and for two values of the linac CF, named “CF1” ($CF=8$) and “CF2” ($CF=11$). A shorter bunch at the entrance of the dump line is expected to emit stronger CSR field. This produces a larger negative chirp and therefore a higher leading current spike, thus more intense THz emission. Figure 4a shows two current profiles simulated at the Al target for the two values of the linac CF, plus an unphysical case *without* CSR. Similarly to Fig. 3c, the measured pulse energies in Fig.4c confirm the expectations only when CSR is included in the simulations.

A summary of the experimental settings of the dump line, of the simulated and of the measured THz-pulse energy is given in Table 2. The uncertainty on the pulse energy value is dominated by the RMS fluctuation of the THz signal collected by the detector, which is typically smaller than 10%. The striking agreement of measured and predicted pulse energies for all the cases considered, and the energy reduction found in the simulation when CSR is not included, are a conclusive demonstration of the validity of our modelling.

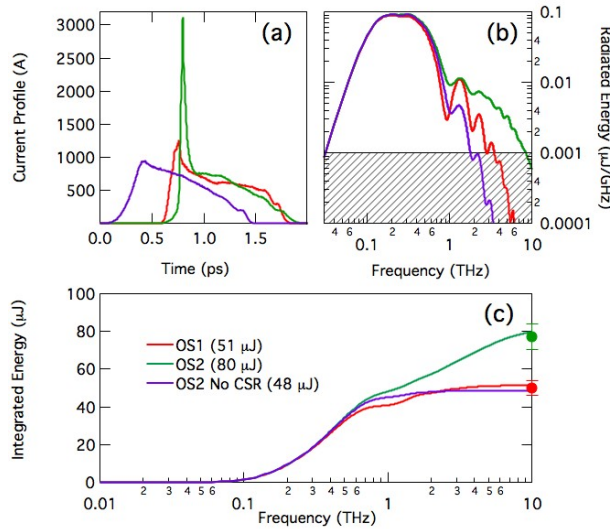


Figure 3: Simulated electron bunch current profiles at the Al target for two optics settings of the dump line (OS1-red and OS2-green). For comparison, a case without CSR in the dump line dipole magnets is shown (violet), see also Tab.2. (b) Calculated CTR spectra. A threshold of 20 dB from the main intensity peak is indicated by the gray area. (c) Solid lines: CTR pulse energy integrated over the frequency range 0.01–10 THz and calculated from the above current profiles. Dots with error bars: measured pulse energy, see also Tab.2. Published in [1].

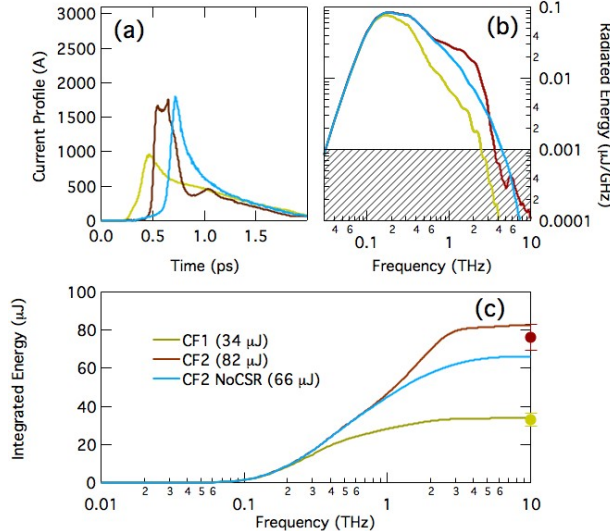


Figure 4: (a) Simulated electron bunch current profiles at the Al target for two compression factors in the linac (CF1-yellow and CF2-brown) and fixed R_{56} in the dump line. For comparison, a case without CSR in the dump line dipole magnets is shown (cyan), see also Tab.2. (b) Calculated CTR spectra. A threshold of 20 dB from the main intensity peak is indicated by the gray area. (c) Solid lines: CTR pulse energy integrated over the frequency range 0.01–10 THz and calculated from the above current profiles. Dots with error bars: measured pulse energy, see also Tab.2. Published in [1].

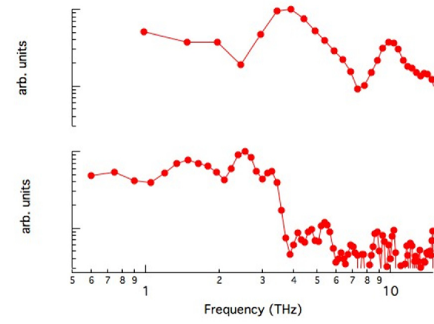


Figure 5: Two examples of experimental FTIR spectra acquired with different machine settings at the TeraFERMI laboratory. Published in [8].

Table 2: Momentum Compaction of the Beam Dump Line (R_{56} , Bunch Duration at Its Entrance ($\sigma_{t,i}$, Measured and Simu-Lated Pulse Energies in the 0.01–10 THz Range

Configura- tion	R_{56} [mm]	$\sigma_{t,i}$ [ps]	E [μJ] simul.	E [μJ] meas.
OS1	5	0.35	51	50 ± 4
OS2	19	0.35	80	77 ± 7
OS2 No CSR	19	0.35	48	
CF1	37	0.35	34	33 ± 3
CF2	37	0.25	82	76 ± 7
CF2 No CSR	37	0.25	66	

CONCLUSIONS

The enhancement of the CTR pulse energy as a function of the momentum compaction of the FERMI dump line and of the incoming bunch length was verified experimentally. The systematic agreement of measured and calculated pulse energy for different accelerator and dump line optics settings confirms the fundamental role played by the CSR wakefield in generating a ~ 0.1 ps long, \sim kA level-current spike in the bunch head, when a positive linear momentum compaction is established. Since the electron beam manipulation for CTR emission occurs after lasing, the scheme allows the TeraFERMI photon beamline to run in parasitic mode to the FEL. The THz pulse is self-synchronized to the FEL emission thus opening, in principle, a wide range of scientific applications in pump-probe configurations. By virtue of the relatively simple set up, the scheme promises dissemination of user-oriented multi-THz beamlines at existing and planned FEL infrastructures.

REFERENCES

- [1] S. Di Mitri et al., “Coherent THz Emission Enhanced by Coherent Synchrotron Radiation Wakefield”, *Scientific Reports*, vol. 8, p. 11661, 2018. doi:10.1038/s41598-018-30125-1
- [2] A. Perucchi et al., “TeraFERMI: a superradiant beamline for THz nonlinear studies at the FERMI free electron laser facility”, *Synch. Rad. News* 4, vol. 30, 2017. doi:10.1080/08940886.2017.1338423

- THP013**

THE X-BAND LINEAR COMPRESSION SYSTEM IN DALIAN COHERENT LIGHT SOURCE

Yong Yu, Qinming Li, Jiayue Yang, Hongli Ding, Kai Tao, Lei Shi, Zongbin Li, Long Huang, Guanglei Wang, Gongkui Cheng, Jitao Sun, Zequn Wang, Zhigang He, Yuhuan Tian, Zhichao Chen, Guorong Wu, Dongxu Dai, Weiqing Zhang[†], Xueming Yang[†]

State Key Laboratory of Molecular Reaction Dynamics, Dalian Institute of Chemical Physics, Chinese Academy of Sciences, Dalian, P. R. China

Abstract

Dalian Coherent Light Source (DCLS) is a free-electron laser (FEL) user facility working in the extreme ultraviolet (EUV) wavelength region from 50 to 150 nm. It mainly operates on the High Gain Harmonic Generation (HGHG) mode with the seed laser, although it can also run in the Self Amplified Spontaneous Emission (SASE) mode. The brightness and bandwidth of FEL radiation strongly depends on electron bunch quality, such as normalized transverse emittance, electron bunch energy, energy spread, peak current, etc. The high peak current with uniform longitudinal distribution is especially helpful for high peak power and narrow bandwidth of FEL, although it is not easy to achieve, due to the nonlinearity of sinusoidal accelerating radio frequency (RF) field and the 2nd-order momentum compaction coefficient T_{566} of bunch compressor. An X-band linearizer will be installed before the bunch compressor in order to correct this nonlinearity properly. In this paper, the beam dynamics design of the X-band linear compression system in DCLS is focused, and the simulation results with Elegant are presented and discussed.

INTRODUCTION

As shown in Fig. 1, DCLS is composed of linear accelerator (LINAC) and FEL Amplifier, and its main parameters are listed in Table 1 [1]. The high-quality electron bunch is produced, accelerated and compressed in the LINAC, and then delivered into the FEL Amplifier to generate the desired FEL radiation. In this process, bunch compression plays a vital role in the generation of intense FEL radiation, because the brightness of the radiation is closely related to the peak current and longitudinal distribution of electron bunch. In order to achieve high peak current, the longitudinal phase space of electron bunch is compressed in the bunch compressor. For DCLS, the compression ratio is 3-5 indicating the peak current up to 300 Amperes. Furthermore, the flat longitudinal current distribution is critical to increase the pulse energy of FEL radiation, and the flat longitudinal energy distribution is essential to improve the bandwidth of FEL spectrum when the FEL facility operates on HGHG mode [2]. Hence, the linear compression system is usually a standard configuration for the HGHG-mode FEL facility with narrow bandwidth and high brightness.

Table 1: Main Parameters of DCLS

Parameter	Nominal Value
Electron Bunch	
Energy	300 MeV
Slice Energy Spread	<20 keV
Normalized Emittance	1-2 mm·mrad
Charge	500 pC
Peak Current	≥300 Amp
Repetition Rate	50 Hz
FEL Radiation	
Wavelength	50-150 nm
Pulse Energy@1ps	≥100 μJ
Pulse Duration (FWHM)	130fs / 1ps

The configuration of X-band linear compression system is shown in Fig. 1. L1 provides a positive chirp for the electron bunch, and then the chirped bunch can be compressed in the chicane with negative (1st-order) momentum compaction coefficient R_{56} . In order to eliminate the nonlinear longitudinal part imposed by sinusoidal curve of L1 and 2nd-order momentum compaction coefficient T_{566} of Chicane, an X-band RF structure is employed following L1. The theoretical description of X-band linear compression system has been illustrated in detail by P. Emma [3]. According to the theory, the X-band RF structure works on the maximal decelerating RF phase π , and the linear compression can be achieved when the following condition is satisfied

$$eV_x = \frac{E_0 \left\{ 1 + \frac{1}{2\pi^2} \frac{\lambda_s^2 T_{566}}{|R_{56}|^3} (1 - \sigma_z / \sigma_{z0})^2 \right\} - E_i}{(\lambda_s / \lambda_x)^2 - 1}, \quad (1)$$

where e is elementary charge, V_x is the desired decelerating voltage of X-band, E_i and E_0 are the electron bunch energy at the exit of L0 and at the exit of Chicane, σ_z and σ_{z0} denote the rms bunch length at the entrance of L1 and at the exit of Chicane, λ_s and λ_x represent the wavelength of S-band and X-band RF field, and $\lambda_s = 4\lambda_x$. For the Chicane of DCLS, the approximate relation $T_{566} = -\frac{3}{2}R_{56}$ can be used.

[†] weiqingzhang@dicp.ac.cn, xmyang@dicp.ac.cn

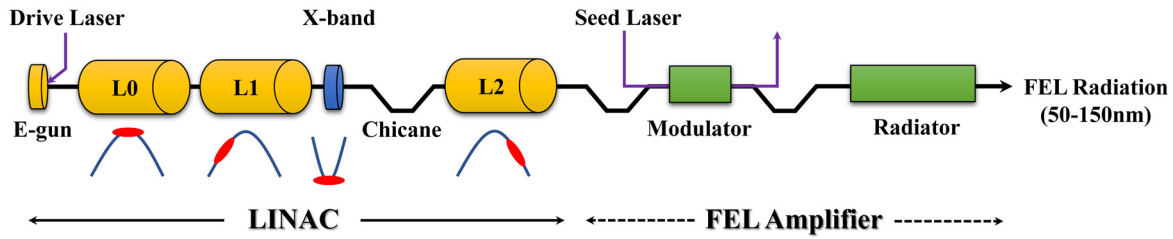


Figure 1: Layout of DCLS. The X-band linear compression system is composed of L1, X-band and Chicane. L0, L1 and L2 are the S-band RF structure. L0 works on the maximum RF acceleration phase. L1 provides a positive chirp which means the head of electron bunch suffers a lower accelerating RF field than the tail (the head is in the left), and then, the electron bunch with positive chirp comes into the negative chicane and is compressed. Because the accelerating field is sinusoidal, the longitudinal energy distribution is not linear actually but with a broad convex curve. However, the X-band RF structure could provide a narrow concave curve which happens to remove the convex curve from L0~L1 and also compensates the 2nd-order momentum compaction coefficient of Chicane. After the linear compression, the electron bunch undergoes a negative chirp to eliminate the positive chirp imprinted by L1. Finally, at the exit of LINAC, the linearly compressed electron bunch is of a high peak current and flat longitudinal distribution. Then it is delivered into the HGHG-mode FEL Amplifier to generate FEL radiation of high intensity and narrow bandwidth.

Table 2: Main Parameters of Linear Compression System in DCLS

Parameter	Nominal Value
Accelerator (S-band, 2856MHz)	
L0 Voltage V_0	50 MV
L0 Phase ϕ_0 (peak phase)	0°
L1 Voltage V_1	86 MV
L1 Phase ϕ_1	-23°
L2 Voltage V_2	96 MV
L2 Phase ϕ_2	26°
Linearizer (X-band, 11.424GHz)	
Voltage V_x	7.8 MV
Phase ϕ_x	180°
Chicane	
1 st -order Momentum Compaction Coefficient R_{56}	-50 mm
2 nd -order Momentum Compaction Coefficient T_{566}	75 mm
Electron Bunch Energy	
At the Entrance of L1 E_i	4.5 MeV
At the Exit of Chicane E_0	128 MeV
Before/After Compression	
Peak Current I_p	72 / 305 Amp
Bunch Length (rms) σ_t	2.26 / 0.58 ps
Normalized Equivalent Charge Ratio C_e (with X-band)	0.32 / 0.35
Normalized Equivalent Charge Ratio C_e (without X-band)	0.32 / 0.44

SIMULATION RESULTS

When the X-band RF structure works on the RF phase π , its desired voltage can be calculated via Eq. (1). And using the parameters of accelerator, linearizer and Chicane listed

in Table 2, the S2E simulation results via Elegant [4] were obtained, as shown in Fig. 2. The initial current distribution (a2, b2, c2 in Fig. 2) before compression is approximately flat, but after compression without X-band, a large number of electrons move towards the head of electron bunch and the current distribution becomes distorted (Fig. 2-e2). It is the reason that the longitudinal energy distribution at the exit of L1 holds a convex curve (Fig. 2-b1) and the Chicane with negative R_{56} and positive T_{566} will enhance the convexity (Fig. 2-e1). In order to compensate this convex curve imposed by L1 and Chicane, a concave curve is required and the radius of curvature should be larger than that of convex curve to ensure the little energy loss of electron bunch. According to these constraints, the X-band RF structure which is of larger radius of curvature and works on the decelerating RF phase (concave curve) is selected as a linearizer, but not the S-band RF structure. In comparison with the results without X-band RF structure (e1 and e2 in Fig. 2), X-band linearizer makes the electron bunch of much flatter longitudinal energy distribution (Fig. 2-d1) and current distribution (Fig. 2-d2).

DISCUSSION

The simulation results under the nominal peak current 300A have been presented. In addition, more works have been done when the compression ratio σ_z/σ_{z0} is not at the nominal point, and the relationship of the linear compression ratio and the desired voltage of X-band RF structure is shown in Fig. 3. The simulation result was obtained by Elegant tracking (blue star) and was well fitted (orange curve) via Eq. (1). The goodness of fit is 0.999, which indicates that the quadratic relation between V_x and σ_z/σ_{z0} in Eq. (1) is valid.

In order to estimate the flat level of current distribution and linearized level of compression, a parameter is defined as normalized Equivalent Charge Ratio C_e

$$C_e = \frac{I_p \cdot \sigma_t}{Q_0}, \quad (2)$$

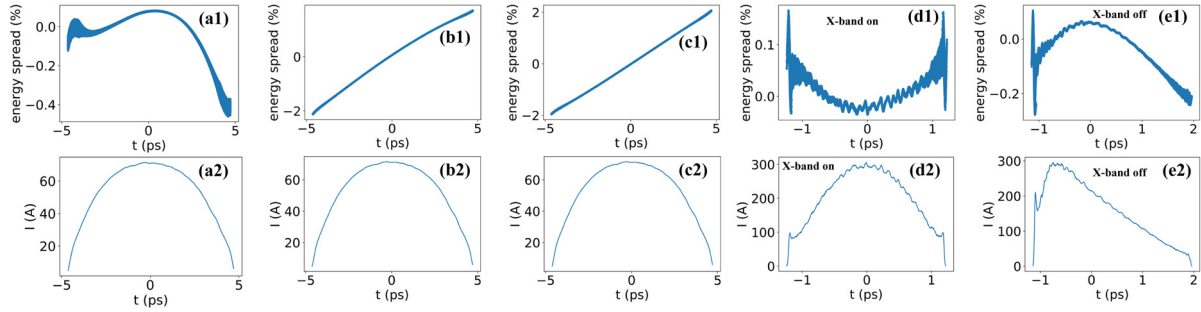


Figure 2: Simulation results of the longitudinal phase space (upper) and current distribution (lower) at the exit of L0 (a1, a2), at the exit of L1 (b1, b2) and X-band (c1, c2), and at the exit of LINAC with X-band on (d1, d2) and off (e1, e2). When the X-band is on, the longitudinal energy distribution (d1) and current distribution (d2) at the exit of LINAC is flatter than that when the X-band is off (e1, e2).

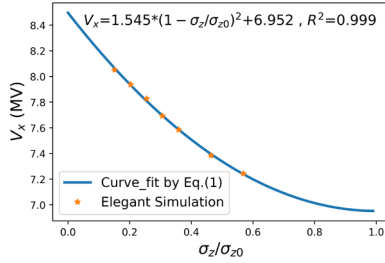


Figure 3: The relationship of the linear compression ratio and the desired voltage of X-band. The blue star represents the results from Elegant simulation. The orange line is the fitting result of the simulation via Eq. (1), and the goodness of fit is 0.999.

where I_p and σ_t are the peak current and the rms bunch length in time scale respectively, and Q_0 is the total charge of electron bunch.

As an illustration, we discuss the Gaussian distribution and uniform distribution (shown in Fig. 4). The former is usually used to describe the current distribution of electron bunch actually and the latter is the ideal current distribution for FEL lasing. The basic Gaussian current distribution can be expressed as

$$I(t) = \frac{Q_0}{\sqrt{2\pi}\sigma_t} e^{-\frac{t^2}{2\sigma_t^2}}, \quad (3)$$

where t is the longitudinal position in electron bunch. According to Eq. (3), it can be derived that $I_{p,G} = \frac{Q_0}{\sqrt{2\pi}\sigma_t}$ and $C_{e,G} = \frac{1}{\sqrt{2\pi}} = 0.399$. On the other hand, uniform current distribution can be expressed as

$$I(t) = \begin{cases} \frac{Q_0}{t_{FWHM}}, & |t| \leq \frac{t_{FWHM}}{2} \\ 0, & |t| > \frac{t_{FWHM}}{2} \end{cases}, \quad (4)$$

where t_{FWHM} is the full width at half maximum and $\sigma_t = \frac{t_{FWHM}}{2\sqrt{3}}$. Similarly, it is shown that $I_{p,u} = Q_0$ and $C_{e,u} = \frac{1}{2\sqrt{3}} = 0.289$. In comparison with these results, it suggests

that the smaller of the normalized Equivalent Charge Ratio C_e , the flatter of the current distribution.

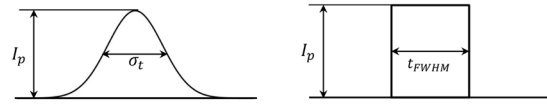


Figure 4: The gaussian distribution (left) and uniform distribution (right).

According to the simulation results of linear compression listed in Table 2, the initial (at the exit of L0) and final (at the exit of LINAC) normalized Equivalent Charge Ratios in DCLS are $C_{e,0} = 0.32$ and $C_{e,w} = 0.35$ respectively. It indicates that the compression is almost linear. In addition, the normalized Equivalent Charge Ratio is $C_{e,w0} = 0.44$ when compression without X-band. It is clear that $C_{e,u} < C_{e,w} < C_{e,G} < C_{e,w0}$, which implies that although both the flat levels of compression with and without X-band are not better than uniform distribution, compression with X-band is better than Gaussian distribution while compression without X-band is worse. In a word, the X-band makes C_e better in the electron bunch compression system.

In contrast to DCLS, the normalized Equivalent Charge Ratio of SXFEL test facility [5] is also calculated at the exit of its LINAC, where $I_p = 727A$, $\sigma_t = 235fs$, $Q_0 = 500pC$, thus $C_e = 0.34$. It can be found easily that the normalized Equivalent Charge Ratio of DCLS ($C_e = 0.35$) and SXFEL test facility ($C_e = 0.34$) is almost same. Although both of them don't reach the C_e value of uniform distribution ($C_{e,u} = 0.289$), they are better than that of Gaussian distribution ($C_{e,G} = 0.399$).

CONCLUSION

The X-band linear compression system in DCLS is described in this paper, including the layout and simulation results. The relationship of the linear compression ratio and the desired voltage of X-band is discussed, and the normalized Equivalent Charge Ratio C_e is defined to estimate the flat level of current distribution and linearized level of compression.

ACKNOWLEDGEMENTS

The authors are grateful to the useful discussion with M. Zhang and D. Gu in Shanghai Advanced Research Institute. This work was supported by the National Natural Science Foundation of China (21127902, 21688102) and the “Strategic Priority Research Program (B)” of the Chinese Academy of Sciences, Grant No. XDB17000000.

REFERENCES

- [1] X.M. Yang *et al.*, “Conceptual Design Report of Dalian Coherence Light Source”, Dec. 30, 2013.
- [2] L.H. Yu *et al.*, “High-gain harmonic-generation free-electron laser”, *Science*, vol. 289, no. 5481, pp. 932-934, Aug 11, 2000. doi:10.1126/science.289.5481.932
- [3] E. Paul. “X-band RF harmonic compensation for linear bunch compression in the LCLS”, No. SLAC-TN-01-1, Stanford Linear Accelerator Center (SLAC), Menlo Park, CA, November 14, 2001.
- [4] M. Borland, “Elegant: A flexible SDDS-compliant code for accelerator simulation”, ANL/APS Rep. LS-287, Sep. 2000.
- [5] Z. Zhao *et al.* “Status of the SXFEL Facility”, *Applied Sciences*, vol. 7, no. 6, p. 607, 2017. doi:10.3390/app7060607

STUDY OF MICROBUNCHING INSTABILITY IN SHINE LINAC*

Dazhang Huang[†], Duan Gu, Meng Zhang, Shanghai Advanced Research Institute, Shanghai, China

Abstract

Microbunching instability usually exists in the linear accelerator (linac) of a free electron laser (FEL) facility. If it is not controlled effectively, the beam quality will be damaged seriously and the machine will not operate properly. As a typical example, the microbunching instability in the linac of the proposed Shanghai high repetition rate XFEL and extreme light facility (SHINE) is investigated in detail by means of both analytical formulae and simulation tools.

INTRODUCTION

As the beam passes through a bunch compressor, for example, a magnetic chicane, the energy modulation introduced by those effects is transformed into density modulation and may thus introduce the so-called microbunching effects. In certain situations, the microbunching effects can be so large that the microbunching instability can also take effects, and the final gain of the instability can become significant. On the other hand, the FEL process has a high demand for electron beam quality in terms of peak current, emittance, energy spread, etc. Therefore to preserve the beam quality, the microbunching effects must be studied in the design stage of the machine. In this paper, the study of microbunching instability in the linear accelerator (linac) of Shanghai high repetition rate XFEL and extreme light facility (SHINE) is reported, the comparison between numerical and analytical results shows very good consistency, given the gain curve of the instability. Meanwhile, the preliminary study of the laser heater to suppress the instability is also illustrated. The paper is organized as the following: first the basic methods to study the microbunching instability is introduced and the results are shown, followed by the study of the laser heater including its effect on the instability and the transverse matching. The conclusion is drawn as the last part.

METHODS

The recently approved SHINE project is a high repetition rate hard X-ray free electron laser (XFEL) facility based on the superconducting radio-frequency (SCRF) technology. In order to fulfil the goal of the project, a high energy, high peak current and low emittance electron beam is required as an output of linac. The main design parameters are illustrated in Table 1, and the schematic layout of the whole facility is shown in Figure 1 as well.

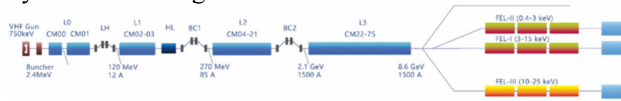


Figure 1: Layout of SHINE facility.

Table 1: Main Design Parameters of SHINE Linac

Parameter	Value
Beam energy (GeV)	4 - 8.6
Bunch charge (pC)	10 - 300
Peak current (kA)	1.5 - 3
Repetition rate (MHz)	Up to 1
Pulse length (fs)	5 - 200

The microbunching instability starts from the initial beam current/density modulation, turned into the energy modulation by a variety of impedances such as linac wake, longitudinal space charge (LSC), coherent synchrotron radiation (CSR), and gets amplified by the dispersion in a bunch compressor (chicane). As usual, the SHINE linac includes multiple stage of bunch compression. In the physical design, two bunch compressors are employed and the third one is reserved as a spare to compress the bunch current up to 3 kA. The main parameters of the bunch compressors are listed in Table 2.

Table 2: Main Parameters of Bunch Compressors in SHINE Linac

Parameter	BC1	BC2
Beam energy (MeV)	269	2156
Compression ratio	7	15
R_{56} (mm)	-60.8	-34.6
Total length (m)	12.2	24

The microbunching is modelled with the simulation code ELEGANT [1], which is commonly considered as a high-fidelity code in accelerator and beam physics. Due to the computing power, 20 million macro-particles are used to simulate 100 pC charge in the simulation. However, referring to [2], this number of macro-particle are nearly enough for this amount of charge.

To study the microbunching effects, equation (1) [3] is used to estimate the wavelength of the microbunching at the peak. Or in other words, the smearing of microbunching from the uncorrelated energy spread across the chicane is not effective until

$$\lambda_0 \leq \left| \frac{2\pi R_{56}}{1+hR_{56}} \right| \sigma_\delta \equiv \lambda_c, \quad (1)$$

Where h is the energy chirp, R_{56} is the momentum compaction of the chicane, and σ_δ is the uncorrelated energy spread of the beam before compression. With the magnetic chicane parameters in Table 1 and the corresponding beam parameters, we have $\lambda_c = 70.9 \mu\text{m}$ for BC1, and $\lambda_c = 15.1 \mu\text{m}$ for BC2 which corresponds to the initial density modulation of $\lambda_c \approx 106 \mu\text{m}$ before BC1. Therefore, one

* Work supported by National Natural Science Foundation of China, Grant No. 1675248

[†] email address: huangdazhang@zjlab.org.cn

may conclude that the peak of the overall microbunching gain shall locate in the vicinity of 72.7 μm and 106 μm in wavelength.

The analytical estimation above is reasonably consisted with the numerical simulation. Figure 2 and Figure 3 shows the final gain curve which peaks around 110 μm , and the longitudinal phase spaces of the beam with various initial density modulations, respectively. The gain curve in Figure 1 is computed from the Fast Fourier Transform (FFT) of the residual current amplitude obtained through the polynomial fit to the current profile in the middle part of the beam [3] at the linac exit.

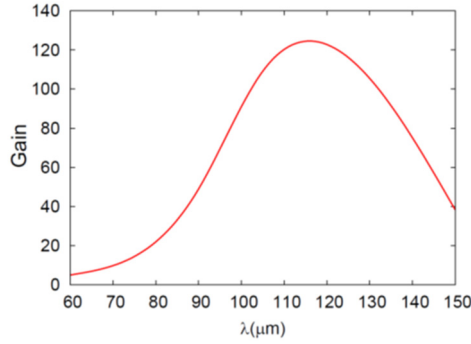
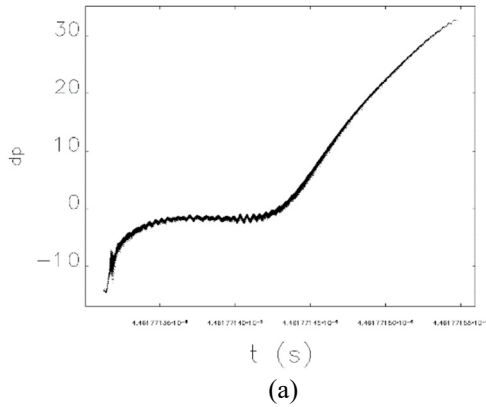
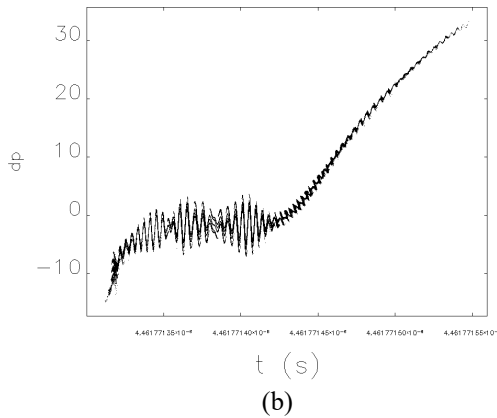


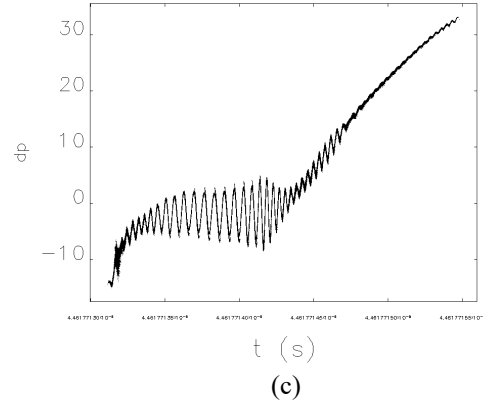
Figure 2: Final gain curve computed from the residual current of FFT of beam current obtained by ELEGANT.



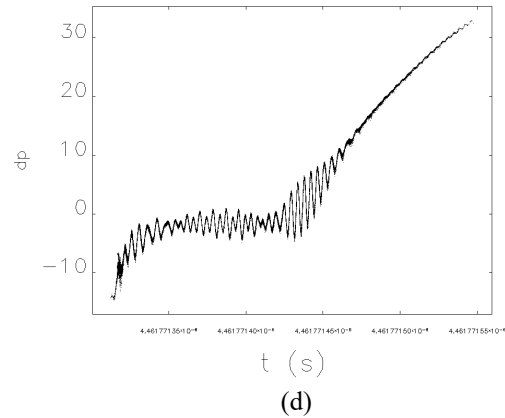
(a)



(b)



(c)



(d)

Figure 3: Longitudinal phase space of the beam at the exit of SHINE linac, with (a) 60 μm , (b) 90 μm , (c) 120 μm , (d) 150 μm initial density modulation.

LASER HEATER

The gain (growth rate) of the microbunching instability for the case of linear compression has been discussed by Saldin et al. [4] phenomenologically by comparing the energy distributions before and after the compression. Consider a density modulation at wavenumber k , without higher harmonic of beam current taken into account, the gain of the instability driven by the wakefields upstream of the compressor reads (2) [4]

$$G = Ck|R_{56}|\frac{I_0}{\gamma I_A}\frac{|Z_{tot}(k)|}{Z_0}\exp\left(-\frac{1}{2}C^2k^2R_{56}^2\frac{\sigma_Y^2}{\gamma^2}\right), \quad (2)$$

where γ is the nominal relativistic factor of the electron beam with rms local energy spread σ_Y in front of the bunch compressor, $C = 1/(1 + hR_{56})$ is the compression ratio, h is the linear energy chirp, R_{56} is the 5-6 element of the transport matrix, I_0 is the initial peak current of the beam, $Z_0 = 377 \Omega$ is the free-space impedance, Z_{tot} is the overall impedance upstream of the compressor including those of the LSC, linac wake, etc., and $I_A = 17 \text{ kA}$ is the Alfven current.

From equation (2) one can see that the most effective way to suppress the microbunching instability is to increase the uncorrelated energy spread σ_Y . For the purpose of that, the device called laser heater has been designed.

The layout of a typical laser heater is shown in Figure 4, which consists of an injection laser, an undulator and a chicane-type bunch compressor.

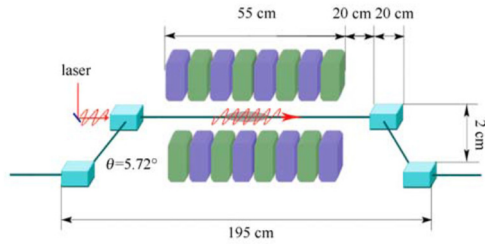


Figure 4: Layout of a typical laser heater.

A laser heater increases the uncorrelated energy spread of the beam by introducing the interaction between beam and laser. The detailed study of the laser heater can be found in [4]. Besides introducing the extra uncorrelated energy spread, there is also focusing effect on the vertical plane in the undulator, therefore we also have to rematch the beam twiss parameters to recover the optics.

Figure 5 shows the longitudinal phase space of the beam at the exit of SHINE linac with the laser heater on and off. In the figure one can see that microbunching is significantly suppressed by the laser heater.

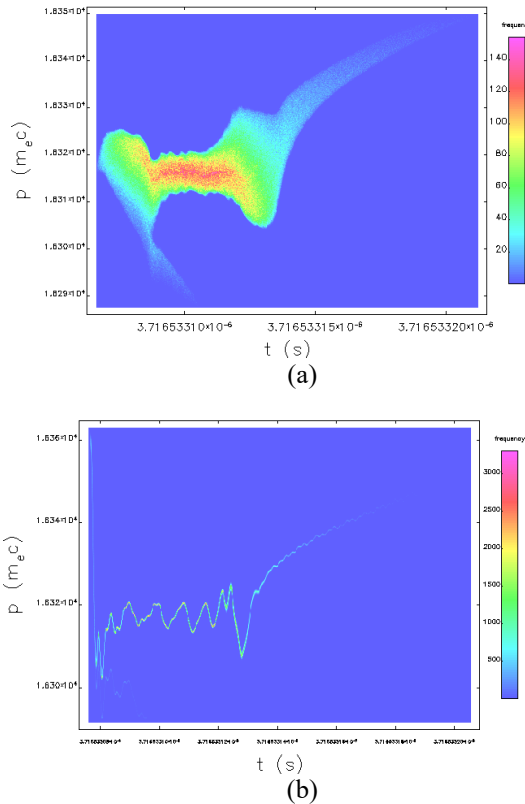


Figure 5: Longitudinal phase space of the beam at the linac exit, with laser heater on (a) and off (b)

The β function in the laser heater and throughout the whole linac are also illustrated in Figure 6. In the figure we can see that the variations of the β functions on both horizontal and vertical plane along the undulator in the laser heater are very small, which is requested by the interaction

condition of the beam and laser in the undulator, whereas the β functions still need to be optimized throughout the linac globally.

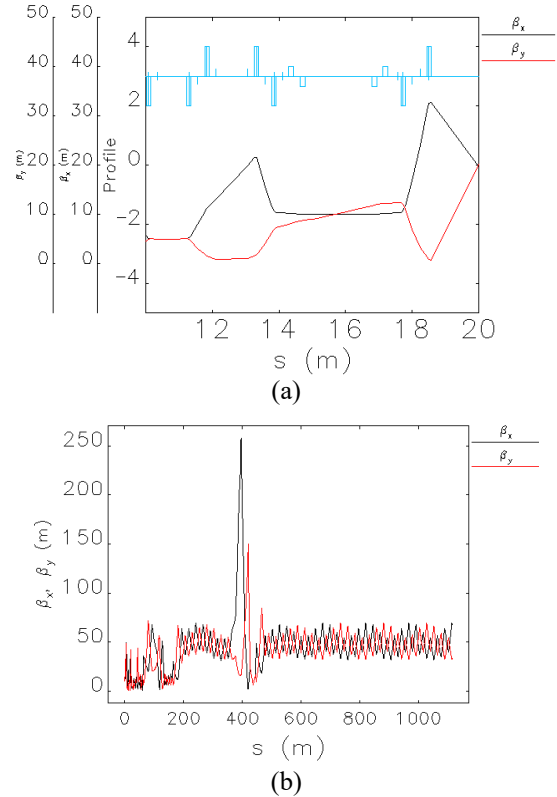


Figure 6: β function in the laser heater and throughout the whole linac.

CONCLUSIONS

The study of microbunching instability of SHINE linac has been carried out with the lattice design up-to-date. The results show that the analytical estimation is reasonably consisted with the numerical simulation, which provides us the information about the range of the initial modulation wavelength that should be avoided when operating the machine. The preliminary study of the laser heater for the suppression of the instability is done, and further investigations of the laser heater is needed to reveal the suppression effects for various modulation wavelength.

REFERENCES

- [1] Y. Wang and M. Borland, "Pelegant: A Parallel Accelerator Simulation Code for Electron Generation and Tracking", *AIP Conf. Proc.*, vol. 877, p. 241, 2006.
doi:10.1063/1.2409141
- [2] M. Borland, "Modeling of the microbunching instability", *Phys. Rev. ST Accel. Beams*, vol. 11, p. 030701, 2008.
doi: 10.1103/PhysRevSTAB.11.030701
- [3] Z. Huang, M. Borland, P. Emma *et al.*, "Suppression of microbunching instability in the linac coherent light source", *Phys. Rev. ST Accel. Beams*, vol. 7, p. 074401, 2004.
doi:10.1103/PhysRevSTAB.7.074401
- [4] Z. Huang *et al.*, "Insightful D-branes", SLAC, USA, Rep. SLAC-PUB-13584, 2009.

TRANSVERSE DEFLECTING STRUCTURE DYNAMICS FOR TIME-RESOLVED MACHINE STUDIES OF SHINE

J. W. Yan^{1,2}, H. X. Deng^{1,3*}, B. Liu^{1,3}, D. Wang^{1,3}

¹Shanghai Institute of Applied Physics, Chinese Academy of Sciences, Shanghai, China

²University of Chinese Academy of Sciences, Beijing, China

³Shanghai Advanced Research Institute, Chinese Academy of Sciences, Shanghai, China

Abstract

The transverse deflecting structure (TDS) has been widely used in modern free electron laser facilities for the longitudinal phase space diagnostics of electron beams. As the first hard x-ray free electron laser in China, the SHINE is designed to deliver photons with a repetition rate up to 1 MHz. In this paper, we present the beam dynamics study of the X-band TDS behind the undulator of SHINE. In order to prevent the screen from being damaged by electron bunches with a high repetition rate, the phase of the transverse deflecting cavity is designed to deviate from zero, and only those electron bunches that are kicked by the transverse deflecting cavity are sent to the screen. In addition, the evolutionary algorithm is introduced to optimize the lattice of the TDS line to reach the highest possible resolution.

INTRODUCTION

Due to characteristics of high peak brightness, short pulse duration, and coherence, X-ray free electron lasers (XFELs) play an important role in many research fields. In recent years, the high-repetition-rate XFEL based on superconducting linac attracts increasing attention because of its ability to produce radiation with higher average brightness. SHINE [1] is designed to be a continuous-wave x-ray free electron laser generating photons between 0.5 keV and 30 keV with a repetition rate up to 1 MHz. The high resolution measurement of the longitudinal phase space of the electron bunch is critical for the XFEL operation.

In recent years, the transverse deflecting structure (TDS) has been widely used in the measurement of the length of electron bunch [2,3]. The transverse kick induced by the cavity translates the time coordinate into a transverse coordinate of the downstream screen. Therefore, the longitudinal properties of the electron beam can be probed. Combined with dipoles, the TDS can be used to reconstruct the longitudinal phase space of the electron beam. Moreover, the x-ray FEL temporal shape can be reconstructed through measuring the difference in the electron beam longitudinal phase space between FEL-on and FEL-off [4]. The TDS will be equipped after each undulator line of SHINE. However, the electron bunches with high-repetition-rate will easily damage the screen used for measurement.

In this paper, to separate the kicked electron bunches from the electron bunches that are not kicked by the TDS, we propose to provide an additional transverse kick to the

electron beam by letting the phase of the TDS deviate from zero. In addition, the lattice of the TDS line are optimized to achieve the highest possible resolution.

LAYOUT OF THE TDS LINE

Since the design of TDS lines behind the undulator lines of SHINE is similar, the TDS line after FEL-III will be taken as an example in this paper. The schematic layout of the TDS line behind FEL-III is shown in Fig. 1. There are six quadrupoles before the transverse deflecting cavity to match the electron beams coming from the undulator to achieve a high temporal resolution of the TDS. Two X-band transverse deflecting cavities with a length of 2 m and a voltage of 20 MV are used to kick the electron bunch in the horizontal direction. Behind the transverse deflecting cavities, there are a bend that gently deflects the beams without generating significant synchrotron radiation in the forward direction and three strong bending magnets that deflect the beams to the screen or beam dump.

In general, the phase of the TDS is set to 0° to obtain the maximum deflection force. However, in this case, those electron bunches that are not kicked by the TDS are also sent to the screen. This causes the screen to be easily damaged when the machine is operated at a high repetition rate. In order to separate the kicked and un-kicked electron bunches, we set the phase of the TDS to -3°. Due to the extra transverse kicking force, those electron beams that are kicked by the TDS will be horizontally offset. As shown in Fig. 2, those electron bunches that have been kicked by the TDS can be offset in the horizontal direction by about 10 mm from the un-kicked electron bunches. Therefore, those two kinds of electron beams can be sent to the screen and dump, respectively. According to the basic theory of TDS [2], the temporal resolution can be calculated as:

$$\Delta_s = \frac{c(E/e)}{\omega V_0} \frac{\sqrt{\epsilon_x}}{\sqrt{\beta_d \sin \Delta\psi \cdot \gamma}}, \quad (1)$$

where β_d is β functions at the centre of the TDS, $\sin \Delta\psi$ is the phase advance between the TDS and screen. According to the Eq. (1), a high temporal resolution of the TDS can be achieved with high voltage of the deflecting cavity, large beta function at the deflecting cavity, and appropriate phase advance between the deflecting cavity and monitor. The optimal beta function and phase advance can be obtained by optimizing the lattice of the TDS line. Therefore, the strength of the twelve quadrupoles of the TDS line are

* denghaixiao@zjlab.org.cn

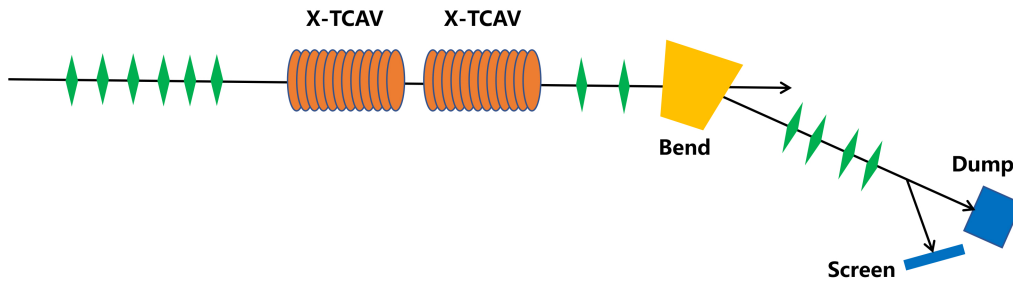


Figure 1: Schematic layout of the TDS beamline downstream the undulator section.

optimized with evolutionary algorithm [5] to achieve high temporal resolution. The optimization objectives consist of maximizing the horizontal β function at the TDS and the phase advance between the deflecting cavity and the screen being as close as possible to $\pi/2$, while the β function along the entire line and the vertical dispersion after the bending magnets are controllable.

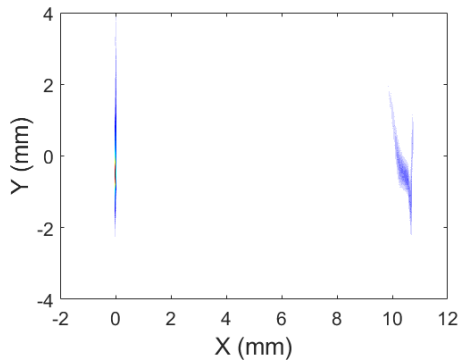


Figure 2: The un-kicked (left) and kicked (right) electron beams by the TDS when the phase of TDS is set to -3° .

OPTIMIZATION RESULTS OF THE TDS LINE

The optimized beam optics of the TDS line are presented in Fig. 3. As shown in Fig. 3 (left), the β_x at the TDS is larger than 400 m. And the phase advance between the TDS and the screen is about $\pi/2$. According to the Eq. (1), the calculated temporal resolution is about 1 fs. To further verify the temporal resolution, the relationship between the horizontal electron beam size on the screen and electron beam length is analyzed based on the ELEGANT simulation. As presented in Fig. 4, based on the optimized lattice, the horizontal RMS beam size on the screen decreases linearly as the electron bunch length decreases. When the bunch length is shorter than 1 fs, the beam size on the screen is almost unchanged.

As mentioned previously, the TDS in combination with the dipole magnet can be used to reconstruct the longitudinal phase space of the electron bunch. Fig. 5 (top left) shows the beam image on the observation screen when the deflecting cavities switched off. While Fig. 5 (top right)

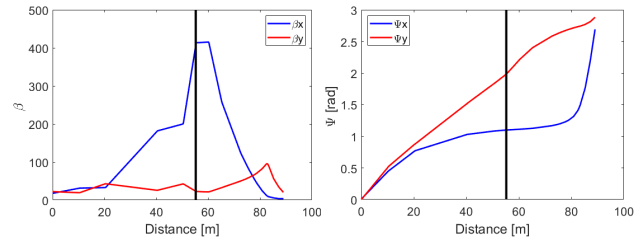


Figure 3: The beta functions (left) and phase advance (right) along the TDS line (to the screen). The vertical black line indicates the entrance of the TDS.

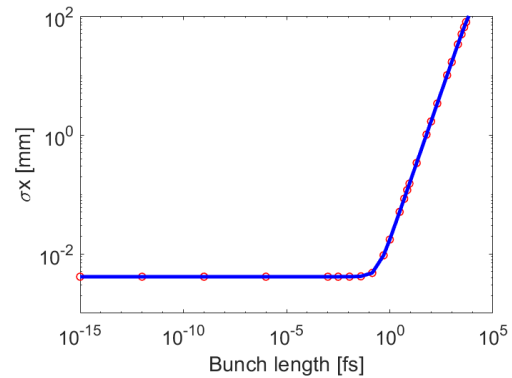


Figure 4: The relationship between the horizontal RMS beam size on the screen and the RMS bunch length.

presents beam image with TDS switched on and this will give a longitudinal resolution of 1 fs. Figure Fig. 5 (middle left) represents the original electron bunch longitudinal phase space at the entrance of the dump line. Fig. 5 (middle right) is presented in the reconstructed longitudinal phase space located at the observation screen, which derived from Fig. 5 (top right). It can be seen from the two figures that there are some differences between the reconstructed phase space and the original phase space. The main reason is that TDS introduces additional energy spread. The simulation results containing FEL lasing is presented in Fig. 5 (bottom). Besides, the tracked current profile and the reconstructed current profile is presented in Fig. 6, which shows a good agreement between the reconstructed profile and the original one.

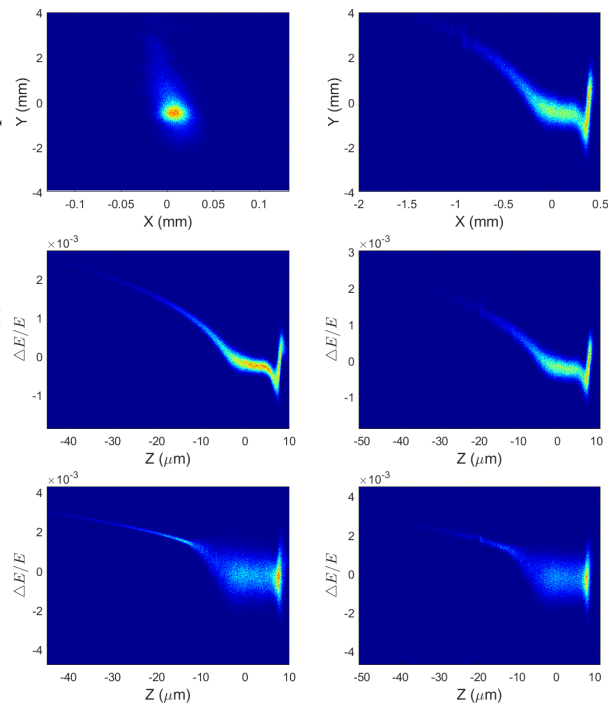


Figure 5: Simulated screen beam images with TDS off (top left) and TDS on (top right). Simulated longitudinal phase spaces of the FEL-off (middle) and FEL-on (bottom) including the original phase spaces (left) and the reconstructed phase spaces (right).

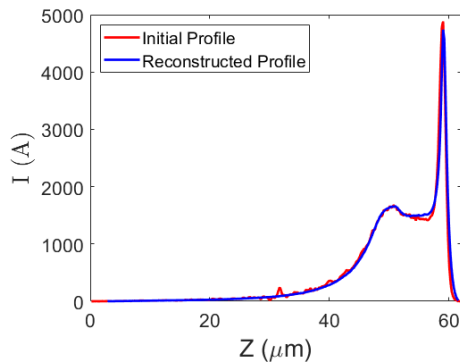


Figure 6: Comparison between the tracked current profile and the reconstructed current profile.

CONCLUSION

In this paper, the schematic layout and lattice of the TDS line of the SHINE are described and optimized. To separate the electron beams that kicked by the TDS from those un-kicked electron beams, the phase of the TDS is designed to deviate from zero. The strength of the twelve quadrupoles of the TDS line is optimized to achieve high temporal resolution. More research about the influence of the collective effects and timing jitter will be studied in future work.

ACKNOWLEDGEMENTS

This work was partially supported by the National Key Research and Development Program of China (2018YFE0103100, 2016YFA0401900) and the National Natural Science Foundation of China (11935020, 11775293).

REFERENCES

- [1] Z.T. Zhao, D. Wang, Z.H. Yang, and L. Yin, “SCLF: An 8-GeV CW SCRF Linac-Based X-Ray FEL facility in Shanghai”, in *Proc. FEL2017*, <https://doi.org/10.18429/JACoW-FEL2017-MOP055>, 2018.
- [2] Emma P J., “A Transverse RF deflecting structure for bunch length and phase space diagnostics”, Stanford Linear Accelerator Center Menlo Park, CA (US), 2001.
- [3] M. Song, H.X. Deng, B. Liu, and D. Wang, “Deflecting cavity dynamics for time-resolved machine studies of SXFEL user facility”, in *Proc. 5th Int. Beam Instrumentation Conf. (IBIC'16)*, Barcelona, Spain, Sep. 2016, paper MOPG50, pp. 169–172, <http://jacow.org/ibic2016/papers/mopg50.pdf>, doi:10.18429/JACoW-IBIC2016-MOPG50, 2017.
- [4] Ding Y, Behrens C, Emma P, *et al.*, “Femtosecond x-ray pulse temporal characterization in free-electron lasers using a transverse deflector”, *Physical Review Special Topics-Accelerators and Beams*, 2011, vol. 14(12): page 120701. doi:10.1103/PhysRevSTAB.14.120701
- [5] Yan J, Deng H., “Generation of large-bandwidth x-ray free electron laser with evolutionary many-objective optimization algorithm”, *Physical Review Accelerators and Beams*, 2019, vol. 22(2): page 020703. doi:10.1103/PhysRevAccelBeams.22.020703

MICROBUNCHING ENHANCEMENT BY ADIABATIC TRAPPING

Xiujie Deng*, Alex Chao¹, Wenhui Huang, Chuanxiang Tang,
Tsinghua University, Beijing, China
¹ also at SLAC, Menlo Park, USA

Abstract

Storage ring based concept called steady-state microbunching (SSMB) was proposed years ago for generating high average power narrowband coherent radiation. There are now active efforts on-going by the SSMB collaboration established among Tsinghua University and several other institutes. In this paper we study the particle trap and filamentation process of beam in RF or Micro Bucket which is useful for understanding the injection beam dynamics of SSMB. One remarkable result is the steady-state current distribution after full filamentation has little dependence on the bucket height as long as it is several times larger than the energy spread. A discrete increase of bucket height after filamentation can boost the bunching, with the sacrifice of emittance growth. An adiabatic change of bucket height from a smaller value to the final desired value is then proposed to boost the bunching while preserving the longitudinal emittance.

INTRODUCTION

Microbunching is and will continue to be in the coming years one of the accelerator physics research focus. Storage ring based concept called steady-state microbunching (SSMB) [1] was proposed years ago for high average power narrowband coherent radiation generation, digging the potential of longitudinal coherence of beam which is parallel to the efforts on diffraction limited rings emphasizing on the transverse dimension. The idea of SSMB is using laser modulator to play the role of RF focusing in traditional rings as shown in Fig. 1 and 2. By precise longitudinal phase space manipulations (laser modulator cooperated with dedicated lattice), microbunching is formed and maintained turn-by-turn each time passing through the radiator. The high peak power coherent radiation from microbunches and high repetition rate from storage ring combined lead to a high average power facility.

There are now active research efforts on-going for different issues of SSMB by a collaboration established among Tsinghua University and several other institutes [2–5]. In this paper we investigate the particle trap and filamentation process of beams in RF or Micro Bucket which is useful for understanding the dynamics of SSMB beam injection.

PARTICLE TRAP AND FILAMENTATION IN RF OR MICRO BUCKET

To simplify the analysis, we restrict ourselves to longitudinal dimension only and ignore the various noises from laser and lattice. Quantum excitation and radiation damping

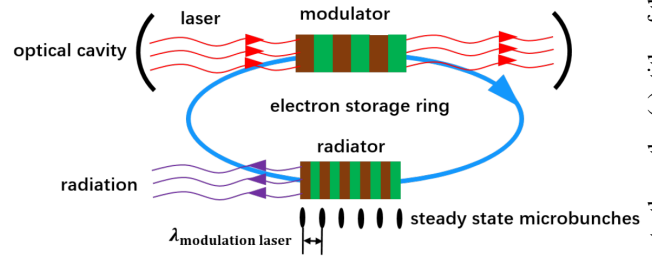


Figure 1: Schematic layout of SSMB.

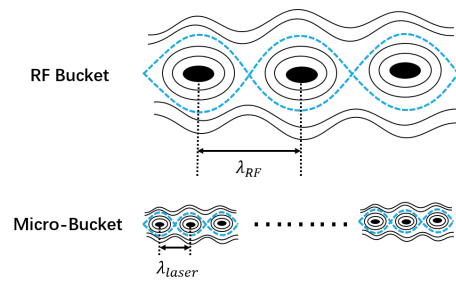


Figure 2: From RF Bucket to Micro-Bucket.

is also neglected as this paper focus on the first stage after the beam injection. The symplectic longitudinal dynamics of a particle in a storage ring with a single RF cavity (laser modulator) can be modeled by the well-known “standard map” [6]

$$\begin{aligned} I_1 &= I_0 + K \sin \theta_0, \\ \theta_1 &= \theta_0 + I_1, \end{aligned} \quad (1)$$

in which

$$\theta = kz, I = R_{56}k\delta, K = VR_{56}k. \quad (2)$$

Equation 1 can be described with the pendulum Hamiltonian driven by a periodic perturbation

$$H(I, \theta, t) = \frac{1}{2}I^2 + K \cos \theta \sum_{n=-\infty}^{\infty} \cos(2\pi nt). \quad (3)$$

For small K and I , which is the case for usual storage rings, the differences in Eq. 1 can be replaced approximately by derivatives and the Hamiltonian by a pendulum Hamiltonian

$$H = \frac{1}{2}I^2 + K \cos \theta. \quad (4)$$

The separatrix is $H = K$ with a bucket half-height of $2\sqrt{K}$. Chaos is beyond the discussion of this paper.

The longitudinal phase space evolution of a monoenergetic beam after injection into RF bucket described by Eq. 1 is shown in Fig 3. As can be seen in Fig. 4, there is

* dxj11@tsinghua.org.cn

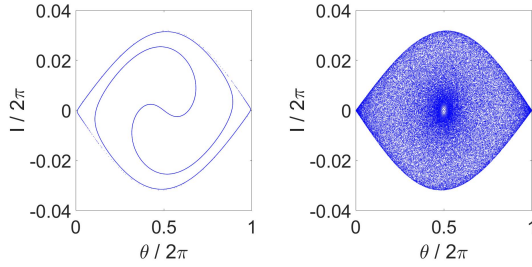


Figure 3: Filamentation in RF or Micro Bucket.

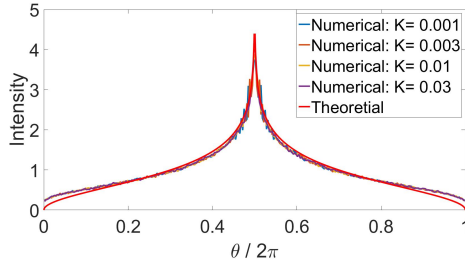


Figure 4: Steady-state current distribution of different K (bucket height) after full filamentation.

a steady-state current distribution due to filamentation (phase mixing). One thing remarkable is that the steady-state distribution has little dependence on the bucket height which is count-intuitive at the first sight. Now we try to give some semi-rigorous analysis.

In the following derivations, the pendulum approximation described above is made. For convenience, we shift the center of bucket to the origin, which means $\theta - \pi \rightarrow \theta$. Since the electron bunch is usually much longer than the laser wavelength and to get the main physics, we assume an initial bunch with uniform distribution of θ in $[0, \pi]$ and $I = 0$ (mono-energetic beam). What we want to know is the steady-state distribution $f(\theta, I, t \rightarrow \infty)$.

In action-angle coordinates (ϕ, J) , the distribution function evolves according to

$$f(\phi, J, t) = f(\phi - \omega(J)t, J, 0). \quad (5)$$

When there is a tune dependence $\omega(J)$ on J and in the limit of $t \rightarrow \infty$, the steady-state distribution depends only on the initial action distribution as a result of phase mixing

$$f(\phi, J, t \rightarrow \infty) = \frac{1}{2\pi} \int_0^{2\pi} f(\phi, J, 0) d\phi = \frac{1}{2\pi} f(J, 0). \quad (6)$$

For $0 < x < \pi$, the probability of $\theta \leq x$ is

$$P(\theta \leq x) = \frac{x}{\pi} + \int_x^\pi \left(1 - \frac{\phi(x, I(x, \beta))}{\pi}\right) \frac{1}{\pi} d\beta, \quad (7)$$

in which $I(x, \beta)$ represents the I coordinate of a point on the phase space trajectory traversing $(\beta, 0)$ with a θ coordinate of x . The current distribution can then be got according to

$$f(\theta) = \frac{\partial P}{\partial x} \Big|_{x=\theta}. \quad (8)$$

However, $\phi(x, I(x, \beta))$ has a complex form, so it is hard to get a simple analytical expression for $f(\theta)$. Below we made a great simplification by approximating all the phase space trajectories in the bucket by ellipses to arrive at an analytical formula of $f(\theta)$.

For ellipse, we have

$$\phi(x, I(x, \beta)) = \arccos \frac{x}{\beta} \quad (9)$$

Note the result has no dependence on K . For a real RF bucket, there is a dependence of $\phi(x, I(x, \beta))$ on K . The dependence is however weak, especially for trajectories close to the origin. Substituting Eq. 9 into Eq. 7 and 8, we have

$$f(\theta) = \frac{1}{\pi^2} \ln \left| \frac{\pi + \sqrt{\pi^2 - \theta^2}}{\theta} \right| \quad (10)$$

Note the steady-state current distribution is independent of K . It is actually the ellipse approximation of phase space trajectory leading to this result. The simplified theoretically calculated current distribution $f(\theta)$ and its comparison with “standard-map” numerical simulation is shown in Fig. 4. As can be seen the theory agrees well with numerical results close to the stable fixed point while deviate more closer to the unstable fixed point, which fits with our expectation as the ellipse approximation is more valid around the stable fixed point.

The simulation and analysis presented in this section reveals a remarkable feature of filamentation in RF or Micro Bucket: the steady-state current distribution after full filamentation has little dependence on bucket height as long as most of the particles can be trapped in the bucket. This is helpful for the Quasi-SSMB [7] experiment focusing on the period after beam injection and before arriving at the true steady-state as it means the requirement on laser power is not that demanding. Other interesting ideas could also be invented by taking advantage of this characteristic.

VARIATION OF BUCKET HEIGHT

Discrete Change of K

Although the steady-state current distribution has little dependence on the bucket height, it can be anticipated that more particles will bunch closer to the stable fixed point phase when we increase K after the beam reach its steady-state distribution after filamentation as shown in the numerical simulation in Fig. 5. A similar steps to the above section can be performed for calculating the new steady-state current distribution. A transformation of action when K changed is all that extra needed.

Adiabatic Trapping

An discrete change of K can boost bunching (Fig. 5). However, it is not without sacrifice, the filamentation process will result in beam emittance growth. This emittance increase may be harmful in some cases. As well-studied in RF gymnastics [8], an adiabatic change of RF voltage or

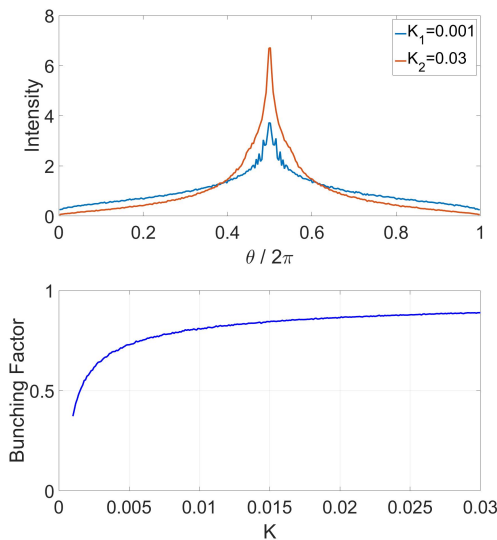


Figure 5: UP: steady-state current distribution with increase of K from 0.001 to 0.03 in 2 steps. Down: bunching factor on the modulation wavelength evolution with K increased from 0.001 to 0.03 in 300 steps. 10^6 particles simulated, 10^5 kicks for each step.

lattice parameters can manipulate the bunch length while preserving the longitudinal emittance. Similar ideas can also be applied to microbunching. The adiabatic trapping of microbunch simulation is shown in Fig. 6. Note the dramatic difference between Fig. 6 and Fig. 3. The spirit of adiabatic buncher [9, 10] is the same with adiabatic trapping for enhancing microbunching while causing as little emittance growth which is useful for FEL and IFEL.

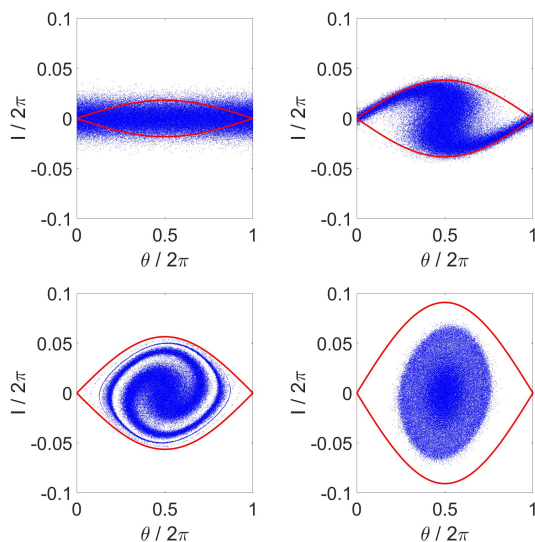


Figure 6: Adiabatic trapping. Red line: separatrix.

SUMMARY

In this paper, we study the particle trap and filamentation process after beam injected into an SSMB storage ring with modulation laser. One remarkable result is the steady-state current distribution after full filamentation has little dependence on bucket height as long as it is several times larger than the energy spread. Discrete and adiabatic change of bucket height is proposed for microbunching enhancement.

ACKNOWLEDGMENT

This work is supported by Tsinghua University Initiative Scientific Research Program.

REFERENCES

- [1] D. F. Ratner and A. W. Chao., “Steady-state microbunching in a storage ring for generating coherent radiation”, *Physical review letters* 105.15 (2010): 154801. doi:10.1103/PhysRevLett.105.154801
- [2] C.-X. Tang *et al.*, “An Overview of the Progress on SSMB”, in *Proc. 60th ICFA Advanced Beam Dynamics Workshop on Future Light Sources (FLS’18)*, Shanghai, China, Mar. 2018, pp. 166–170. doi:10.18429/JACoW-FLS2018-THP2WB02
- [3] X. J. Deng *et al.*, “From Coherent Harmonic Generation to Steady State Microbunching”, in *Proc. 9th Int. Particle Accelerator Conf. (IPAC’18)*, Vancouver, Canada, Apr.-May 2018, pp. 4583–4586. doi:10.18429/JACoW-IPAC2018-THPMK113
- [4] C. L. Li, A. Chao, C. Feng, and B. C. Jiang, “Lattice Design for the Reversible SSMB”, in *Proc. 10th Int. Particle Accelerator Conf. (IPAC’19)*, Melbourne, Australia, May 2019, pp. 1507–1509. doi:10.18429/JACoW-IPAC2019-TUPGW045
- [5] Z. Pan *et al.*, “A Storage Ring Design for Steady-State Microbunching to Generate Coherent EUV Light Source”, presented at the 39th Int. Free Electron Laser Conf. (FEL’19), Hamburg, Germany, Aug. 2019, paper THP055.
- [6] B. V. Chirikov “A universal instability of many-dimensional oscillator systems”, *Physics reports* 52.5 (1979): 263-379. doi:10.1016/0370-1573(79)90023-1
- [7] Xiujie Deng, Alex Chao, Wenhui Huang and Chuanxiang Tang, unpublished.
- [8] R. Garoby, *RF Gymnastics in Synchrotrons* No. CERN-PS-2000-022-RF, CERN, 2000. doi:10.5170/CERN-2005-003.290
- [9] E. Hemsing and X. Dao, “Cascaded modulator-chicane modules for optical manipulation of relativistic electron beams”, *Physical Review Special Topics-Accelerators and Beams* 16.1 (2013): 010706. doi:10.1103/PhysRevSTAB.16.010706
- [10] N. Sudar, *et al.*, “Demonstration of cascaded modulator-chicane microbunching of a relativistic electron beam”, *Physical review letters* 120.11 (2018): 114802. doi:10.1103/PhysRevLett.120.114802

A GENERAL OPTIMIZATION METHOD FOR HIGH HARMONIC GENERATION BEAMLINE

Yao Zhang*, Xiujie Deng, Zhilong Pan, Wenhui Huang, Chuanxiang Tang
Tsinghua University, Beijing 100084, China

Abstract

Shorter bunches produce a more coherent radiation and contain higher harmonic components. Here, based on transverse and longitudinal phase space coupling, a general method for analyzing the production of very short beam and searching for compression beamline is presented. With this method, several beamlines are found and optimized. The electron beam can be compressed to tens of nanometers, generating coherent high harmonic radiation.

INTRODUCTION

The coherence of synchrotron radiation depends strongly on beam length and has been enormously demanded by many applications. Generally, a beam will radiate coherently while its length is comparable to the radiation wavelength [1]. For this reason, shortening bunch length in storage ring has been studied widely, but the length is still on the order of tens femtoseconds [1–4]. On the other hand, free electron laser (FEL), benefiting from the natural microbunching process, holds the shortest length achieved. Combining these short bunches with storage rings, and uniting the high brightness of FEL with the high repetition rate of synchrotron radiation will create a new light source with excellent properties. However, this combination requires to compress the beam to a very short length before injecting it into the undulator. Several compression methods and beamlines have been proposed [5–12]. But the optimization methods vary. In this paper, we present a general method for analyzing the production of very short beam and searching for compression beamlines. Based on this method, several beamlines are found and optimized. The electron beam can be compressed to tens of nanometers, and very coherent high harmonic radiation can be generated.

GENERAL METHOD

Transfer matrix is used to analyze the compression problem. For simplicity, the electron six-dimensional phase space is shortened to four, $(x, x', z, \delta)^T$. Here, the symbol x can be either horizontal or vertical direction. Under this simplification, a general matrix form for both dipole and quadrupole magnets is

$$a = \begin{pmatrix} a_{11} & a_{12} & 0 & a_{14} \\ a_{21} & a_{22} & 0 & a_{24} \\ a_{31} & a_{32} & 1 & a_{34} \\ 0 & 0 & 0 & 1 \end{pmatrix}. \quad (1)$$

The symplectic condition tells that only six elements in the matrix are free. Besides, it can be proved that the product of any number of matrix in this type has the same form. Hence, this matrix is actually a general expression for an arbitrary beamline consisting of only dipoles and/or quadrupoles. Now, we use symbols A (with elements A_{ij}), B (with elements B_{ij}) to express two such beamlines.

Another critical component is the modulator, where an undulator and a laser cooperate to act like a radio frequency (RF) cavity. Considering the case that laser incidents with a small angle t , the beam energy modulation can be expressed as

$$\delta = \delta_0 + \tilde{\delta} \sin(kz + tkx), \quad (2)$$

with $\tilde{\delta} = \frac{\Delta\gamma}{\gamma_c}$ the maximum absorbed energy, and γ_c the beam central energy. k is laser wave number. Panofsky-Wentzel theorem [13] indicates that this energy modulation will be accompanied by an angular modulation

$$x' = x_0 + t\tilde{\delta} \sin(kz + tkx). \quad (3)$$

Thus, the linearized transfer matrix for a modulator is

$$M = \begin{pmatrix} 1 & 0 & 0 & 0 \\ ht^2 & 1 & ht & 0 \\ 0 & 0 & 1 & 0 \\ ht & 0 & h & 1 \end{pmatrix}. \quad (4)$$

Here, $h = k\tilde{\delta}$, is a parameter representing modulation strength. With $t = 0$, M degenerates into a standard modulator, which changes electron energy only.

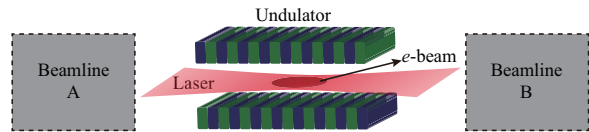


Figure 1: Structure of a compression beamline.

Generally, a full compression cell is a modulator sandwiched by two beamlines, assuming the upstream one A and downstream one B , shown as Fig. 1. The complete transfer matrix can be written into

$$T = BMA \quad (5)$$

Hence, the final longitudinal position of an electron is

$$z = T_{31}x_0 + T_{32}x'_0 + T_{33}z_0 + T_{34}\delta_0, \quad (6)$$

with

$$T_{31} = A_{21}B_{32} + A_{31}(1 + B_{34}h + B_{32}ht)$$

$$+ A_{11}[B_{31} + ht(B_{34} + B_{32}t)]$$

$$T_{32} = A_{22}B_{32} + A_{32}(1 + B_{34}h + B_{32}ht)$$

$$+ A_{12}[B_{31} + ht(B_{34} + B_{32}t)]$$

$$T_{33} = 1 + B_{34}h + B_{32}ht$$

$$T_{34} = A_{24}B_{32} + B_{34} + A_{34}(1 + B_{34}h + B_{32}ht)$$

$$+ A_{14}[B_{31} + ht(B_{34} + B_{32}t)].$$

* zhangyao18@mails.tsinghua.edu.cn

This equation gives the bunch length after passing through copression beamline, $\sigma_s^2 = T_{31}^2 \sigma_{x0}^2 + T_{32}^2 \sigma_{x'0}^2 + T_{33}^2 \sigma_{s0}^2 + T_{34}^2 \sigma_{s0}^2$. The size in each dimension will contribute to final beam length. A straightforward way to realize bunch compression is keeping only one contribution while evanishing others.

THREE CASES OF BEAM COMPRESSION

Based on this method, three cases of beam compression will be discussed in this section.

Pure Dispersive Compression

Pure dispersive compression has the longest and most successful history. It only utilizes a dispersive section to change energy modulation into density distribution. Perfect examples are the coherent harmonic generation (CHG) or high gain harmonic generation (HG) [6, 14–21], where by increasing the modulation amplitude h , a small B_{34} , hence T_{34} , is achieved, leading to a compression ratio of $R = \frac{\sigma_{s0}}{\sigma_s} = \frac{h\sigma_{s0}}{\sigma_{s0}}$. With a small energy spread $\sigma_{x'0}$, the beam can be compressed at a significant ratio. However, it is of great difficulty to minify σ_{s0} down to 10^{-4} . Thus, a large compression requires a very great modulation amplitude, which indicates a powerful laser.

T_{33} indicates an alternative way for pure dispersive compression, which may ease the requirements of laser power. The idea is to use an obliquely incoming laser.

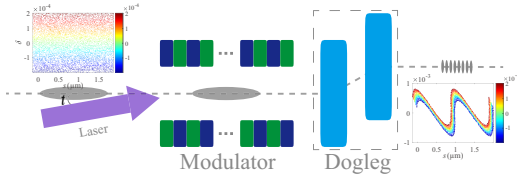


Figure 2: A variant of CHG.

When laser incidents with an angle, the energy and divergence modulation will be generated. With an x' and z coupling in beamline, the extra term $B_{32}ht$ will contribute to a smaller B_{34} . This means a shorter bunch. Figure 2 presents a simple beamline arrangement of this idea, a modulator followed by a dogleg. The two subfigures at upper-left and bottom-right corners are the initial and final beam longitudinal phase space respectively, with both colorbars representing initial energy deviation. The initially uniform distributed beam is micro-bunched after passing through the whole beamline. And final length of a microbunch is determined by initial energy spread and modulation amplitude.

The compression ratio of this idea is

$$R = \frac{h\sigma_{s0}}{(1 - |B_{32}ht|)\sigma_{s0}}. \quad (7)$$

It is of great similarity with the CHG case. But under the same energy modulation amplitude, the final length will be $|B_{32}ht|$ times shorter in this case. However, at fixed laser power, h shrinks with the growth of t , as Fig. 3 shows. This fact restricts the compression of bunch length greatly.

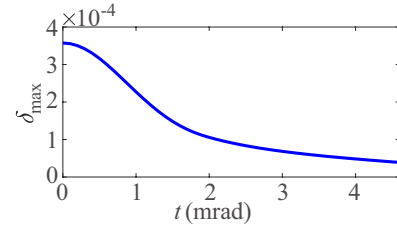


Figure 3: Modulation amplitude at various incident angle. Laser parameter: $P = 5$ MW, $w_0 = 398$ μ m, $\lambda_l = 1.0$ μ m.

For both CHG and its variant, limited by laser power, the modulation depth $D = \frac{\delta}{\sigma_{s0}}$ is typically below 10. And the harmonic bunching factor

$$b_n = e^{-\frac{1}{2}(nkT_{34}\sigma_{s0})^2} J_n[-nk(B_{32}t + B_{34})\tilde{\delta}] \quad (8)$$

is also hard to improve for a significant σ_{s0} . To reach a higher harmonic, one more complicated cascaded scheme, putting two or more beamlines in sequence, is proposed. But this one is beyond bunch compression, readers interested can refer to [22–30].

x - z Coupling Compression

To get a larger R with a moderate laser power, taking advantages of some beam properties helps. For example, under the absence of vertical dispersion and horizontal-vertical coupling, the vertical beam size in storage ring may be extremely small [31].

Utilizing this small-size feature means to keep only T_{31} nonzero in Eq. 6. Then, the final beam length will be $\sigma_s = T_{31}\sigma_{x0}$. A small T_{31} results to a good compression. Combining $T_{32} = T_{33} = T_{34} = 0$ with the symplectic condition, we get

$$T_{31} = 1/(A_{32}h + A_{12}ht). \quad (9)$$

It is obvious that bunch stretching caused by A_{32} contradicts with compressing. By inclining the incident laser, this contradiction can be alleviated.

Equation 9 indicates a compression ratio of $R = (A_{32}h + A_{12}ht)\frac{\sigma_{s0}}{\sigma_{x0}}$. And final beam bunching factor

$$b_n = e^{-\frac{1}{2}(nkT_{31}\sigma_{x0})^2} J_n[-nk(B_{32}t + B_{34})\tilde{\delta}]. \quad (10)$$

A small transverse size contributes to a large compression ratio and a high harmonic number.

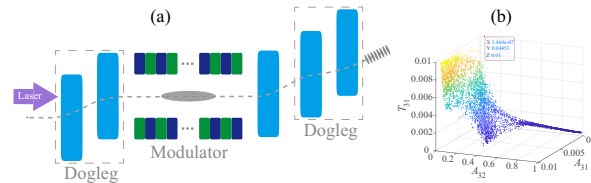


Figure 4: Compression beamline using x - z coupling.

Figure 4(a) presents a compression beamline making use of x - z coupling. The normally incoming laser means an inversely proportional relation between T_{31} and $A_{32}h$. Optimized result of a multi-objective genetic algorithm (MOGA) code, given in Fig. 4(b), shows clear, too. Great compression and little bunch stretching require huge dipoles and long drifts.

One working point (red dot in Fig. 4(b)) is selected for test, where beam stretching is well controlled, while well compression is sacrificed. Figure 5 is the final electron distribution. The significant difference of beam length results from various initial horizontal beam size. The left one is 100 times greater than the right.

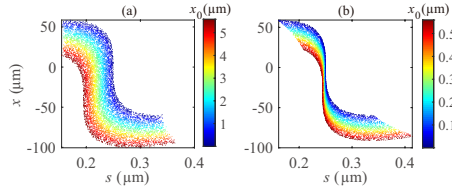


Figure 5: Electron distribution after compression.

When laser incidents with an angle, the co-work with a transversely dispersion section can also compress beam well [7]. Besides, another effective method called the Off-Resonance Laser Modulation or Phase-merging Enhanced Harmonic Generation [8,9], where an undulator with a transverse gradient (called TGU) [10] is used, also takes advantage of small transverse size.

$x'-z$ Coupling Compression

If the beam angular spread is orders smaller than beam size, one alternative coupling — $x'-z$ — can be much better for beam compression.

To get a full analysis of this idea, we follow the path in Sec . Again, utilizing $x'-z$ coupling means to keep only T_{32} in Eq. 6. And the coupling coefficient is

$$T_{32} = -1/(A_{31}h + A_{11}ht). \quad (11)$$

Upon this, the simplest design is given by X. F. Wang, which uses the tilt term along [11]. The beamline is shown in Fig. 6(a). Because upstream beamline does not exits, there is also no bunch stretching. For a long beam, and considering a sinusoidal energy modulation, the bunching factor of this case is

$$b_n = e^{-\frac{(nk_l\eta_b\sigma_{x'})^2}{2}} J_n(nh\xi_b), \quad (12)$$

where $\eta_b = -\frac{1+\xi_b h}{ht}$ is the dispersion of dipole, with ξ_b dipole momentum compaction. Owing to the tiny angular spread $\sigma_{x'}$, the bunching factor at harmonic number n still has a significant value.

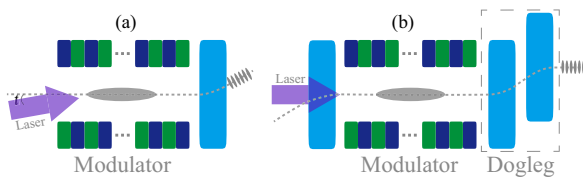


Figure 6: Two beamlines using $x'-z$ coupling.

Another ingenious design reported by C. Feng is presented in Fig. 6(b) [12]. The idea lies in using a dipole to create a $x'-z$ or $y'-z$ coupling, and then utilizing energy modulation and momentum compaction to neutralize original z value, during which the dispersion introduced by first dipole is also canceled by the dogleg.

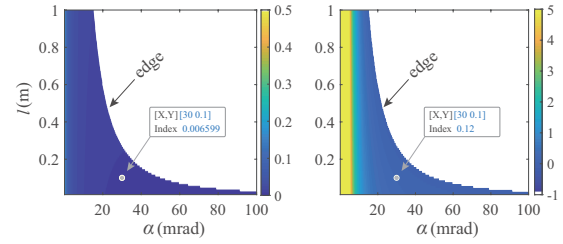


Figure 7: Matched η_d (left) and L (right) of dogleg at various bending angle α and length l .

Here, a well compression requires a smaller η_d . But achieving this needs to increase bending angle of the upstream dipole, which will cause a significant beam stretching. Figure 7 shows the parameter space of dogleg. At a fixed modulator, a smaller η_d means the working point moves closer to the edge in Fig. 7, which corresponds to smaller distance between the two dipoles of dogleg. With the working point chosen in Fig. 7, one beam can be greatly compressed, and up to 35th harmonic can be achieved. Figure 8 gives this result.

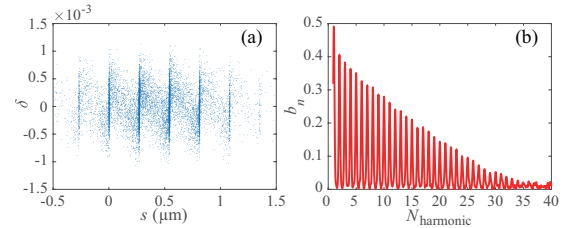


Figure 8: (a) Beam final phase space and (b) bunching factor.

Typically, the angular spread is over ten times smaller than the corresponding beam size. Thus it is very helpful to take advantage of angular spread, and the beam can be greatly compressed, leading to a very slow decreasing of high harmonic bunching factor.

SUMMARY

In this paper, based on transverse-longitudinal coupling, a general method for optimizing and searching for compression beamline is presented. With the optimized result, electron beam can be compressed at large ratio and up to 35th harmonic can be generated. However, only a beam with initial length smaller than $\lambda_l/2$ works, longer one will be splitted into several bunches. And only a linear modulation can be well compressed, but the energy modulated is sinusoidal. This may be relieved by using a two-color-laser modulator.

ACKNOWLEDGEMENTS

The authors thank Alexander Wu Chao and Chao Feng for discussions which do help to this paper. This work is supported by Tsinghua University Initiative Scientific Research Program.

REFERENCES

- [1] M. Abo-Bakr, J. Feikes *et al.*, “Brilliant, Coherent Far-Infrared (THz) Synchrotron Radiation”, *Phys. Rev. Lett.* **90**, 094801 (2003). doi:10.1103/PhysRevLett.90.094801
- [2] H. Hama, S. Takano *et al.*, “Control of the bunch length on an electron storage ring”, *Nucl. Instrum. Methods Phys. Research A* **329**, 29 (1993). doi:10.1016/0168-9002(93)90919-9
- [3] R. W. Schoenlein, S. Chattopadhyay *et al.*, “Generation of Femtosecond Pulses of Synchrotron Radiation”, *Science* **287**, 2237 (2000). doi:10.1126/science.287.5461.2237
- [4] P. Beaud, S. L. Johnson *et al.*, “Spatiotemporal Stability of a Femtosecond Hard-X-Ray Undulator Source Studied by Control of Coherent Optical Phonons”, *Phys. Rev. Lett.* **99**, 174801 (2007). doi:10.1103/PhysRevLett.99.174801
- [5] P. L. Csonka, “Enhancement of Synchrotron Radiation by Beam Modulation”, *Part. Accel.* **8**, 225 (1978).
- [6] L. H. Yu, “Generation of intense uv radiation by subharmonically seeded single-pass free-electron lasers”, *Phys. Rev. A* **44**, 5178 (1991). doi:10.1103/PhysRevA.44.5178
- [7] C. Feng and T. Zhang *et al.*, “Design of a 4.8m ring for inverse Compton scattering x-ray source”, *Phys. Rev. ST Accel. Beams* **17**, 070701 (2014). doi:10.1103/PhysRevSTAB.17.070701
- [8] H. X. Deng and C. Feng, “Using Off-Resonance Laser Modulation for Beam-Energy-Spread Cooling in Generation of Short-Wavelength Radiation”, *Phys. Rev. Lett.* **111**, 084801 (2013). doi:10.1103/PhysRevLett.111.084801
- [9] C. Feng and H. X. Deng *et al.*, “Phase-merging enhanced harmonic generation free-electron laser”, *New J. of Phys.* **16**, 043021 (2014). doi:10.1088/1367-2630/16/4/043021
- [10] Z. R. Huang, Y. T. Ding *et al.*, “Compact X-ray Free-Electron Laser from a Laser-Plasma Accelerator Using a Transverse-Gradient Undulator”, *Phys. Rev. Lett.* **109**, 204801 (2012). doi:10.1103/PhysRevLett.109.204801
- [11] X. F. Wang, C. Feng *et al.*, “Angular dispersion enhanced prebunch for seeding ultrashort and coherent EUV and soft X-ray free-electron laser in storage rings”, *J. Synchrotron Rad.* **26**, 677 (2019). doi:10.1107/S1600577519002674
- [12] C. Feng and Z. T. Zhao, “A Storage Ring Based Free-Electron Laser for Generating Ultrashort Coherent EUV and X-ray Radiation”, *Sci. Rep.* **7**, 4724 (2017). doi:10.1038/s41598-017-04962-5
- [13] W. Panofsky and W. Wenzel, “Some considerations concerning the transverse deflection of charged particles in radiofrequency fields”, *Rev. Sci. Instrum.* **27**, 967 (1956). doi:10.1063/1.1715427
- [14] B. Girard, Y. Lapierre *et al.*, “3D simulation of high gain FELs in an optical klystron configuration”, *Phys. Rev. Lett.* **53**, 2405 (1984). doi:10.1016/0168-9002(92)91138-Y
- [15] M. Labat, M. Hosaka *et al.*, “Coherent harmonic generation on UVSOR-II storage ring”, *Eur. Phys. J. D* **44**, 187 (2007). DOI:10.1140/epjd/e2007-00177-6
- [16] G. De Ninno, E. Allaria *et al.*, “Generation of Ultra-short Coherent Vacuum Ultraviolet Pulses Using Electron Storage Rings: A New Bright Light Source for Experiments”, *Phys. Rev. Lett.* **101**, 053902 (2008). doi:10.1103/PhysRevLett.101.053902
- [17] G. De Ninno, E. Allaria *et al.*, “Self-Induced Harmonic Generation in a Storage-Ring Free-Electron Laser”, *Phys. Rev. Lett.* **100**, 104801 (2008). doi:10.1103/PhysRevLett.100.104801
- [18] D. Xiang and W. Wan, “Generating Ultrashort Coherent Soft X-Ray Radiation in Storage Rings Using Angular-Modulated Electron Beams”, *Phys. Rev. Lett.* **104**, 084803 (2010). doi:10.1103/PhysRevLett.104.084803
- [19] L. H. Yu, M. Babzien *et al.*, “Ultrafast Electron Localization Dynamics Following Photo-Induced Charge Transfer”, *Science* **289**, 932 (2000). doi:10.1126/science.289.5481.93
- [20] L. H. Yu, L. DiMauro *et al.*, “First Ultraviolet High-Gain Harmonic-Generation Free-Electron Laser”, *Phys. Rev. Lett.* **91**, 074801 (2003). doi:10.1103/PhysRevLett.91.074801
- [21] E. Allaria, R. Appio *et al.*, “Highly coherent and stable pulses from the FERMI seeded free-electron laser in the extreme ultraviolet”, *Nature Photon.* **6**, 699 (2012). doi:10.1038/nphoton.2012.233
- [22] J. H. Wu, L. H. Yu, “Coherent hard X-ray production by cascading stages of High Gain Harmonic Generation”, *Nucl. Instrum. Methods Phys. Research A* **475**, 104 (2001). doi:10.1016/S0168-9002(01)01552-2
- [23] B. Liu, W. B. Li *et al.*, “Demonstration of a widely-tunable and fully-coherent high-gain harmonic-generation free-electron laser”, *Phys. Rev. ST Accel. Beams* **16**, 020704 (2013). doi:10.1103/PhysRevSTAB.16.020704
- [24] E. Allaria, D. Castronovo *et al.*, “Two-stage seeded soft-X-ray free-electron laser”, *Nature Photon.* **7**, 913 (2013). doi:10.1038/nphoton.2013.277
- [25] D. Xiang and G. Stupakov, “Echo-enabled harmonic generation free electron laser”, *Phys. Rev. ST Accel. Beams* **12**, 030702 (2009). doi:10.1103/PhysRevSTAB.12.030702
- [26] G. Stupakov, “Using the Beam-Echo Effect for Generation of Short-Wavelength Radiation”, *Phys. Rev. Lett.* **102**, 074801 (2009). doi:10.1103/PhysRevLett.102.074801

- [27] D. Xiang, E. Colby *et al.*, “Demonstration of the Echo-Enabled Harmonic Generation Technique for Short-Wavelength Seeded Free Electron Lasers”, *Phys. Rev. Lett.* **105**, 114801 (2010). doi:10.1103/PhysRevLett.105.114801
- [28] D. Xiang, E. Colby *et al.*, “Evidence of High Harmonics from Echo-Enabled Harmonic Generation for Seeding X-Ray Free Electron Lasers”, *Phys. Rev. Lett.* **108**, 024802 (2012). doi:10.1103/PhysRevLett.108.024802
- [29] Z. T. Zhao, D. Wang *et al.*, “First lasing of an echo-enabled harmonic generation free-electron laser”, *Nature Photon.* **6**, 360 (2012). doi:10.1038/nphoton.2012.105
- [30] E. Hemsing, M. Dunning *et al.*, “Echo-enabled harmonics up to the 75th order from precisely tailored electron beams”, *Nature Photon.* **10**, 512 (2016). doi:10.1038/nphoton.2016.101
- [31] J. B. Murphy, C. Pellegrini, “Generation of high-intensity coherent radiation in the soft-x-ray and vacuum-ultraviolet region”, *J. Opt. Soc. Am. B* **2**, 259 (1985). doi:10.1364/JOSAB.2.000259

SPONTANEOUS COHERENT RADIATION OF STABILIZED DENSE ELECTRON BUNCHES*

Yu. S. Oparina[†], A. V. Savilov, Institute of Applied Physics, Nizhny Novgorod, Russia
V. L. Bratman, Yu. Lurie, N. Balal, Ariel University, Ariel, Israel

Abstract

Modern electron sources allow formation of dense bunches with energies of 3–6 MeV, ps pulse durations, and charges of up to 1 nC. Such bunches can be used for the realization of relatively simple terahertz sources based on spontaneous coherent radiation. This regime is realized when the effective bunch phase size doesn't exceed 2π . Power and duration of the process of such type of emission are limited due to an increase in the bunch length under the Coulomb repulsion. This complicates the effective implementation of the regime of spontaneous coherent radiation for dense bunches. Therefore, special methods for stabilization of the length of the bunch should be used. We describe several methods of the stabilization used in different systems (cyclotron radiation, emission in the traditional undulator system, and emission in the "negative-mass" undulator system).

CYCLOTRON RADIATION

We consider particles motion in a waveguide immersed in a uniform longitudinal magnetic field (Fig. 1a). There are two characteristic regimes of radiation for electrons moving in a waveguide depending on the value of the magnetic field (Fig. 1b): group synchronism, regime of the "grazing" of dispersion characteristics (G), at which the group velocity of the wave is close to the initial longitudinal velocity of particles, and intersection of the dispersion characteristics, at which high-frequency (H) and low-frequency (L) waves are simultaneously excited. In the case of grazing of dispersion characteristics, the total compensation of Coulomb repulsion takes place [1]. In the case of two waves excitation low-frequency spontaneous radiation provides the bunch forming respect to high-frequency wave [2-4].

The change in electron energy is the sum of the changes in energy due to the Coulomb interaction and the wave effect: $\Delta\gamma = \Delta\gamma_c + \Delta\gamma_w$. Evolution of the cyclotron electron phase is described as follows

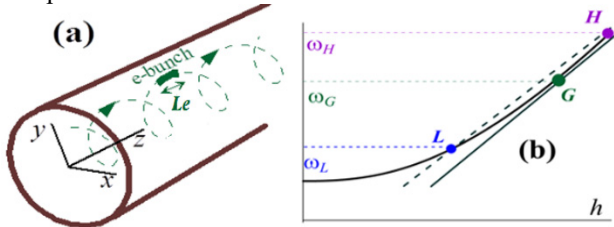


Figure 1. (a) Electron bunch moving along a helical undulator. (b) Dispersion diagram of the operating mode.

* Work supported by Russian Foundation for Fundamental Research, projects 18-32-00351 and 18-02-00765, as well as by the IAP RAS Project 0035-2019-0001.

[†]oparina@appl.sci-nnov.ru

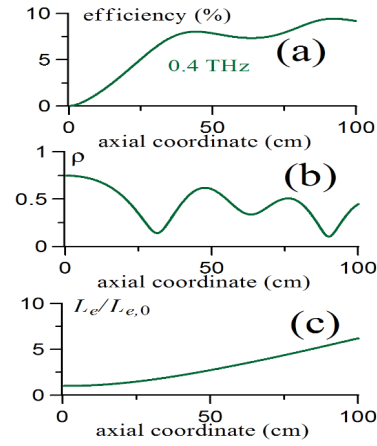


Figure 2: (a) Efficiency of the electron-wave interaction $\langle\gamma_0 - \gamma\rangle/(\gamma_0 - 1)$. (b) Electron bunching efficiency $\rho = \langle\exp(-i\vartheta)\rangle$. (c) Effective normalized bunch length $L_e/L_{e,0}$ versus the axial coordinate.

$$\frac{d\vartheta}{d(\omega t)} = \frac{\Delta\gamma_c}{\gamma_0}(\beta_{z,0} - \beta_{gr})\left(\beta_{z,0} + \frac{1}{\gamma_{z,0}^2}\right) + \frac{\Delta\gamma_w}{\gamma_0}(1 - \beta_{gr}^2). \quad (1)$$

here $\vartheta = \omega t - k_{zz} - \int \omega_c dt$ is the electron resonance phase change, ω is the frequency of the radiated wave, which is described by the Doppler up-conversion of non-relativistic cyclotron frequency

$$\omega = \frac{\Omega_c}{\gamma(1 - \beta_{gr}\beta_z)}, \quad (2)$$

$\gamma = \sqrt{1 - \beta^2}$ is the relativistic gamma-factor, $\beta = V/c$ is the normalized electron velocity, β_z is the normalized longitudinal velocity, β_{gr} is the normalized wave group velocity; $\Delta = 1 - \beta_{gr}\beta_{z,0} - b/\gamma_0$ is the mismatch of the electron-cyclotron resonance (here, $b = \Omega_c/\omega$).

Approximate equation (1) makes it obvious, that the Coulomb interaction of the particles does not change the phase of the electron relative to the wave in the regime of group synchronism, $\beta_{z,0} = \beta_{gr}$, despite change in bunch length. This is due to the electron bunch spreads along the helix of the constant phase [1].

We consider the spontaneous radiation of a cylindrical bunch with a diameter of 1 mm, a charge of 0.2 nC, a duration of 0.5 ps, a particle energy of 6 MeV, and initial transverse velocities $\beta_{\perp 0} = 1/\gamma_0$ in a waveguide with a diameter of 4 mm. The particles are in group synchronism with the TE₁₁ mode at the field $H_0 = 2.2$ T. The frequency of radiation is 0.4 THz, and efficiency of about 8% (Fig. 2a). In the process of motion of the bunch along the operating waveguide, the bunch length increases (Fig. 2c). However, such an increase in the bunch length doesn't lead to a significant increase in the bunch phase size, described by the bunching efficiency $\rho = \langle\exp(-i\vartheta)\rangle$, which remains at a level $\rho \sim 0.5$ (Fig. 2b).

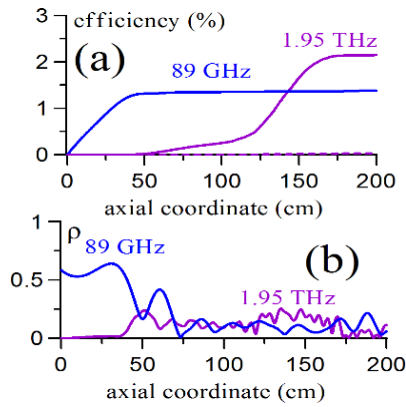


Figure 3: Numerical simulation for emission from the 1 nC / 3 ps bunch in the regime of the highly Doppler up conversion. Efficiency of the electron-wave interaction (a), electron bunching efficiency ρ (b).

In the regime of the highly Doppler up-conversion the group velocity of high-frequency wave is still close to the longitudinal electron velocity, and simultaneously is close to the speed of light (Fig 1b, H), so electron energy changes weak influence the electron phase change [5]. Therefore, an additional stabilization of the particle phase size is necessary, if an electron bunch initially is not phased respect to the high-frequency wave. Such stabilization can be provided by a low-frequency wave L (Fig. 1b) due to the simultaneous bunching by Coulomb [2,3] fields and by fields of the radiated wave fields [4]. At magnetic field of 5.5 T, the bunch emits in the same waveguide simultaneously at frequencies of about 89 GHz and 1.95 THz. The efficiency of high-frequency radiation is close to 2% (Fig. 3). This relatively low efficiency is caused by non-sufficient bunching with respect to the high-frequency wave.

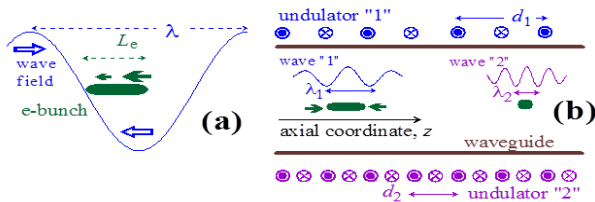


Figure 4: (a) Self-compression of the bunch in the radiated wave field. (b) Bicolor rf source: spontaneous radiation of the long-wavelength wave "1" leads to the compression of the bunch and spontaneous radiation of the short-wavelength wave "2".

UNDULATOR RADIATION

A possible way to provide stabilization of the axial size of a dense electron bunch is super-radiative self-compression of the bunch [6] that occurs in the process of spontaneous undulator emission in the regime of "grazing" of the dispersion characteristics. In this regime, the bunch is shifted to $\pi/4$ relative to the maximum of the decelerating wave phase (Fig. 4a). If the bunch length is close to a quarter of the wavelength, then the front of the bunch is decelerated by the wave, whereas the tail is placed in the wave "zero" and, therefore, does not lose the

energy. This results in compression of the bunch by its own radiated field.

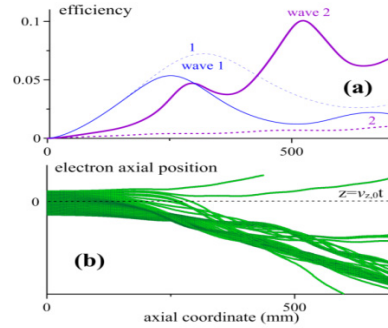


Figure 5: (a) Efficiencies of interaction of the electron bunch with waves "1" and "2" in the two-wave regime (solid curves) versus the axial coordinate, as well as efficiencies of excitation of each wave in the single-wave regime (dashed curves). (b) Axial positions of electrons with respect to the unperturbed coordinate of the bunch center in the two-wave regime.

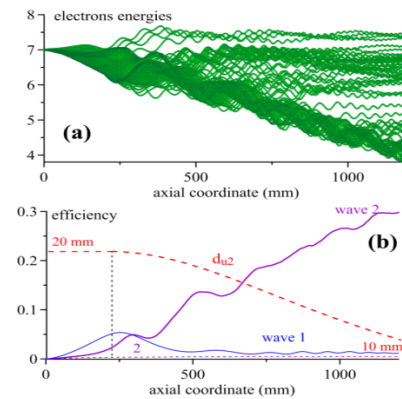


Figure 6: Two-wave radiation process in the sectioned profiled system. (a) Energies of electrons versus the axial coordinate of the bunch. (b) Efficiencies of interaction of the electron bunch with waves "1" and "2" versus the axial coordinate, as well as profiling of the period of the second undulator. The dashed curve corresponding wave "2" in Fig. 4b illustrates interaction of electrons with this wave in the single-wave process.

We propose to use this mechanism of self-compression in the field of relatively long-wavelength ($\lambda_1 > L_e$) wave to provide spontaneous emission of a wave with shorter wavelength ($\lambda_2 \sim L_e$). Figure 4 b illustrates a bicolor source based on the cascade two-wave super-radiative undulator radiation. Two undulators with different periods provide the "grazing" regimes of the electron-wave resonance (Fig. 1a) for two waveguide waves having the same transverse structures.

In simulations we consider an electron bunch with an electron energy of 3 MeV, a total charge of 0.3 nC, the diameter 1 mm, and a pulse duration of 3 ps ($L_e = 0.9$ mm), $\lambda_1 = 2L_e = 1.8$ mm. For the both undulators, the undulator factors $K_{u1,2} = \gamma\beta_{u1,2}$ are assumed to be equal to 0.8. In this case, the grazing regime for wave "1" is provided when the waveguide diameter is 4.2 mm and the period of the first undulator is $d_1 = 31$ mm. The last step

is to choose the frequency of wave “2” and the period of the second undulator. We consider a possibility to excite a 0.5 THz high-frequency wave ($\lambda_2 = 0.6$ mm). For this wave, the grazing regime is provided when $d_2 = 20$ mm. Figure 5a illustrates the result of simulations for the bunching: the compression by the radiated wave “1” makes the spontaneous radiation of wave “2” possible. The efficiency of this process is relatively high 10%. Thus, it is possible to obtain radiated pulses having a duration of ~ 0.1 ns and a power of ~ 3 MW. Note that the dashed curve in Fig. 5a describes the situation without stabilization by the wave “1”.

The use of the trapping regime [7-10] ensures the enhancement of the saturated efficiency of excitation of the high-frequency wave (2) from $\sim 10\%$ up to 30% at a length of the electron-wave interaction ~ 1 m, due to decrease of the short-period undulator from $d_2 = 20$ mm to $d_1 = 10$ mm (see Fig. 6b).

NEGATIVE-MASS REGIME

The negative-mass regime of the electron motion is realized in a combination of periodic undulator field and relatively strong homogeneous axial magnetic field (Fig. 7 a). The cyclotron frequency corresponding to the axial field should be slightly higher than the undulator bounce-frequency of the particle. In this case, the Coulomb field inside the bunch leads not to repulsion of electrons but to their mutual attraction [11]. This effect is a result of an abnormal dependence of the velocity of undulator oscillations of electrons on the cyclotron frequency (Fig. 7 b).

Generation at high frequencies in two-waves regimes, such as described above (Fig. 1b) is more efficient in the negative-mass regime. The resonance phase $\vartheta = \omega t - (h + h_u)z$ (here $h_u = 2\pi/d$) change in the case of undulator radiation

$$\frac{d\vartheta}{d(\omega t)} \approx \frac{\Delta\gamma}{\gamma_0^3} - \delta, \quad (3)$$

δ – the mismatch of resonance. In this case the parameter of bunching doesn't depend on the group velocity, moreover the coulomb interaction and the radiated wave effect have equally contributions [compare with (1)]. It is important to note, that the group synchronism mismatch is necessary condition to provide conditions for the bunching by the wave field (the superradiative self-compression opposite effect described above).

Let's consider the radiation of the bunch with pulse duration of 1 ps, with a diameter 1mm, with a charge 1. nC at frequencies of 0.12 THz and 1.35 THz (an undulator period of 3.5 cm, an undulator parameter 0.1, and guiding field of 4.4 T) in a waveguide with diameter 4 mm. The efficiency of high-frequency radiation of 20% at the length ~ 1 m, the low-frequency wave generation efficiency by half. Initially, the bunch compressed by Coulomb fields inside a bunch [12], thereafter by the high-frequency wave field [4] (Fig. 8). Centers of compression are slightly shifted relative to each other.

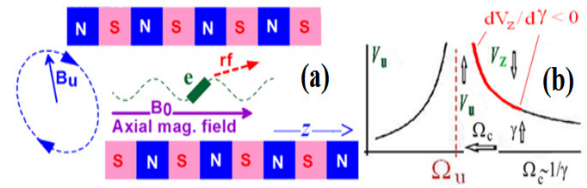


Figure 7: Electron motion in the combined helical undulator and uniform axial fields. Characteristic dependence of the transverse electron velocity on the cyclotron frequency.

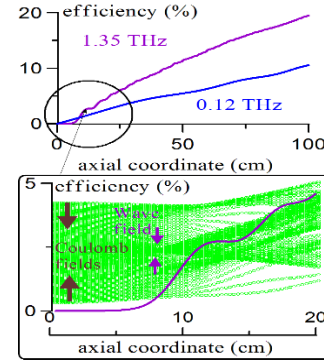


Figure 8: The efficiency of two-frequency generation in the negative-mass regime and the bunching process.

REFERENCES

- [1] Yu. S. Oparina and A. V. Savilov, “Spontaneous superradiant sub-THz coherent cyclotron emission from a short dense electron bunch”, *Phys. Rev. Accel. Beams*, vol. 22, p. 030701, 2019, doi:10.1103/PhysRevAccelBeams.22.030701
- [2] V. L. Bratman, A. V. Savilov, “Phase mixing of bunches and decrease of negative-mass instability increments in cyclotron resonance masers”, *Phys. Plasmas*, vol. 2, p. 557, 1995, doi:10.1063/1.870981
- [3] A. V. Savilov, “Negative-mass instability in magnetron injection guns”, *Phys. Plasmas*, vol. 4, p. 2276, 1997, doi:10.1063/1.872391
- [4] I. V. Bandurkin et al., “Self-compression of dense photo-injector electron bunches”, *J. Phys.: Conf. Ser.*, vol. 1135, p. 012018, 2018, doi:10.1088/1742-6596/1135/1/012018
- [5] V. L. Bratman, N. S. Ginzburg, G. S. Nusinovich, M. I. Petelin, P. S. Strelkov, “Relativistic gyrotrons and cyclotron autoresonance masers”, *Int. J. Electronics*, vol. 51, p. 541, 1981, doi:10.1080/00207218108901356
- [6] I. V. Bandurkin, Yu. S. Oparina, and A. V. Savilov, “Superradiative self-compression of photo-injector electron bunches”, *Appl. Phys. Lett.*, vol. 110, p. 263508, 2017, doi:10.1063/1.4990972
- [7] P. Sprangle, C. M. Tang, and W. M. Manheimer, “Nonlinear formulation and efficiency enhancement of free-electron lasers”, *Phys. Rev. Lett.*, vol. 43, pp. 1932-1936, 1979, doi:10.1103/PhysRevLett.43.1932
- [8] N. M. Kroll, P. L. Morton, and M. N. Rosenbluth, “Free-electron lasers with variable parameter wigglers”, *IEEE J. Quantum Electron.*, vol. 17, p. 1436, 1981, doi:10.1109/JQE.1981.1071285

- [9] A. V. Savilov, "Cyclotron resonance maser with a tapered magnetic field in the regime of "nonresonant" trapping of the electron beam", *Phys. Rev. E*, vol. 64, p. 066501, 2001, doi:10.1103/PhysRevE.64.066501
- [10] A. V. Savilov, I. V. Bandurkin, N. Yu. Peskov, "Regime of non-resonant trapping in a FEM," *Nucl. Instr. Meth. Phys. Res. A*, vol, 507, p. 158, 2003, doi:10.1016/S0168-9002(03)00862-3
- [11] N. Balal, I. V. Bandurkin, V. L. Bratman, E. Magory, A. V. Savilov, "Negative-mass mitigation of Coulomb repulsion for terahertz undulator radiation of electron bunches" *Appl. Phys. Lett.*, v. 107. p. 163505, 2015, doi:10.1063/1.4934495
- [12] I. V. Bandurkin, I. S. Kurakin, A. V. Savilov, "Compression of a photoinjector electron bunch in the negative mass undulator", *Phys. Rev. AB.*, vol. 20. p. 020704, 2017, doi:10.1103/PhysRevAccelBeams.20.020704

SIMULATION AND OPTIMIZATION OF THE TRANSPORT BEAMLINE FOR THE NOVOFEL RF GUN

A. S. Matveev^{1†}, I. V. Davidyuk¹, O. A. Shevchenko, V. G. Tcheskidov, N. A. Vinokurov¹,
V. N. Volkov, BINP, Novosibirsk, Russia
¹also at Novosibirsk State University, Russia

Abstract

A new low-frequency CW RF gun was developed and tested at Budker Institute of Nuclear Physics recently. We plan to use it to upgrade the ERL of the Novosibirsk FEL facility. It will allow increasing the average beam current (due to higher beam repetition rate) and thus increasing the average radiation power. The transport beamline for the RF gun uses the ninety-degree achromatic bend. It is designed in a way that keeps an option to operate with the old electrostatic gun as well. Due to the low beam energy (290 keV) the beam dynamics is strongly influenced by space-charge forces. The paper describes results of simulation and optimization of the RF gun transport beamline. Space-charge forces were taken into account with the code ASTRA. Main sources of emittance degradation were considered in order to decrease their influence during the optimization. In addition, the RF gun output beam parameters were measured for various RF gun emission phases. These experiments were simulated, and the results were compared. The resulting beam parameters meets requirements of the Novosibirsk FEL facility ERL.

INTRODUCTION

Injector of the Novosibirsk FEL [1] now uses static electron gun. In near future it is planned to be supplemented with new low-frequency CW RF gun [2]. It will allow increasing the maximum of the average beam current from 30 mA to 100 mA and more due to higher beam repetition rate. The cathode grid assembly of the RF gun is the same as the static gun one. Basic RF gun parameters are listed in Table 1.

Increasing of the average beam current should lead to increasing of the average radiation power. It requires accurate simulation and optimization of beamline magnetic optics in order to reduce losses of high current beam, and consequently to prevent vacuum chamber heating and vacuum breakdown.

Table 1: Basic RF Gun Parameters

Parameter	Value	Unit
Average Current	≤ 100	mA
Electron Energy	240-300	keV
Bunch Charge	≤ 2.0	nC
Bunch Length (FWHM)	1.0	ns
Peak Current	15	A
Beam repetition rate	0.002 – 90.2	MHz

[†] matveev.a.s@yandex.ru

TRANSPORT BEAMLINE FOR THE RF GUN

Beamline Scheme

The scheme of the Novosibirsk FEL injector is illustrated in Fig. 1. A 300 kV static electron gun, a bunching RF resonator and two RF cavities are in operation now. A beam is generated in the static electron gun. Then it is bunched and accelerated up to an electron energy of 1.8 MeV. At the injector output the beam normalized emittance is 30 mm·mrad.

The RF gun will be connected to the injector by the ninety-degree achromatic bend (as shown in Fig. 1) in order to keep an option to operate it with the static gun. The working regime of the RF gun is around 40° from the phase of the maximum beam acceleration. So, the bunching resonator is not required for the RF gun beamline.

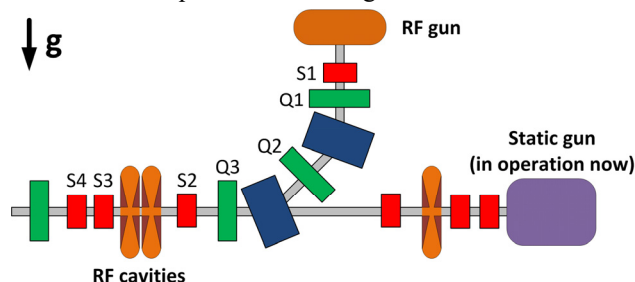


Figure 1: A scheme of the NovoFEL injector with the new RF gun: red – solenoids, green – quadrupoles.

Simulation

Simulations of beam dynamics in the injector are performed with the code ASTRA [3] by the following reasons: taking into account space-charge forces and a possibility of defining 1D and 3D electromagnetic field distribution of magnet and accelerator elements.

The simulation starts from the cathode. The cathode grid assembly and anode focusing is considered.

Optimization

The program package ASTRA has a lack of optimization features, except scanning or optimizing by one parameter in predefined value range. Thus, it has been decided to write a script for automatic calculations of beamline regimes with ASTRA that would be easily used with external optimization modules. The program language Python was chosen due to powerful open-source mathematical libraries.

Two Python scripts AstraTools.py and AstraProc.py were written that make the simulation as a calculation of

fitness function. It works the following way as it described in Fig. 2. Module AstraTools.py takes a vector of parameters (any parameters defining by ASTRA input file), changes values of corresponding parameters in the pattern input file and saves this as a new one. Then the module launches the simulation in Astra.exe with modified file. When the simulation finishes AstraProc.py script starts processing output data and calculating fitness function. It is possible to define the function as any combination of ASTRA parameters.

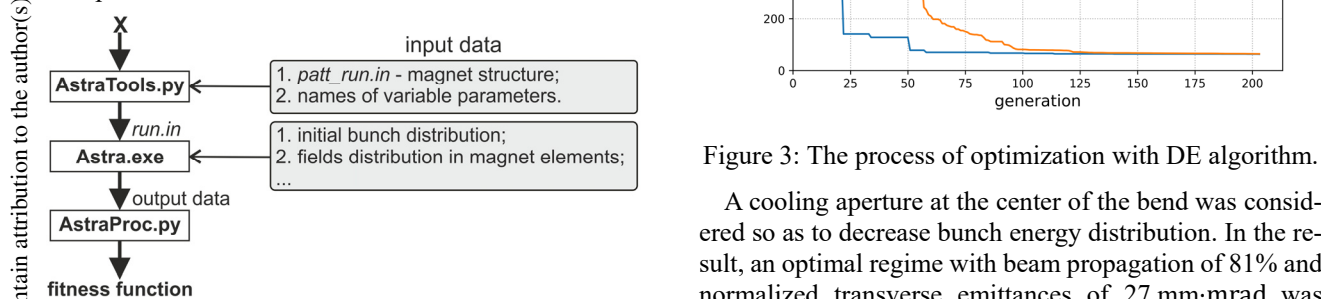


Figure 2: Python scripts make a simulation of magnet optics regime as a calculation fitness function.

Using these scripts, the RF gun beamline regime was optimized. Figure 1 demonstrates free parameters for optimization: currents in elements S1-S4 and Q1-Q3. However, the strength of quadrupole Q2 is determined so as to get an achromatic bend. The bunch is not round after the bend so currents in solenoids S2-S4 are defined by Eq. (1) in order to suppress coupling of transverse betatron oscillations

$$\phi(S2)+\phi(S3)+\phi(S4)=0 \tag{1}$$

where ϕ is an angle of beam rotation in the plane XY in solenoid

$$\phi=\frac{e}{2pc}\int_{-\infty}^{\infty}B_z(z)dz \tag{2}$$

where B_z is the longitudinal magnet field of solenoid on its axis. Solenoid S3 and S4 currents are chosen equally to decrease their focusing strength. Thus, there are only four variable parameters boundary constrained: currents of Q1 and Q3 are in range -3...3 A, and S1 and S2 are in range 0...10 A.

In this paper two algorithms of optimization were used: differential evolution (DE) algorithm [4] and Nelder-Mead method [5]. The first one is for global optimization of a function that satisfies boundary constraints (in our case: currents in magnet elements), and the second one is for further faster but local optimum solution search.

In order to minimize transverse emittances and to keep beta function to around 1 m the fitness function was defined by the relation

$$f=0.5\left[10^6\left(\varepsilon_x+\varepsilon_y\right)+10^3\left(\sigma_x+\sigma_y\right)\right] \tag{3}$$

where $\varepsilon_{x,y}$ – normalized emittance and $\sigma_{x,y}$ – rms beam size (both in meters).

The process of global optimization with DE algorithm is illustrated in Fig. 3. A size of the population is 45, maximum number of iterations is 450.

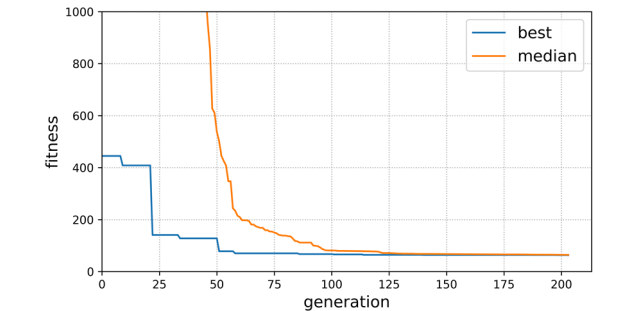


Figure 3: The process of optimization with DE algorithm.

A cooling aperture at the center of the bend was considered so as to decrease bunch energy distribution. In the result, an optimal regime with beam propagation of 81% and normalized transverse emittances of 27 mm·mrad was achieved. A distribution of beam transverse rms sizes along the beamline is shown in Fig. 4. More output beam parameters are listed in Table 2.

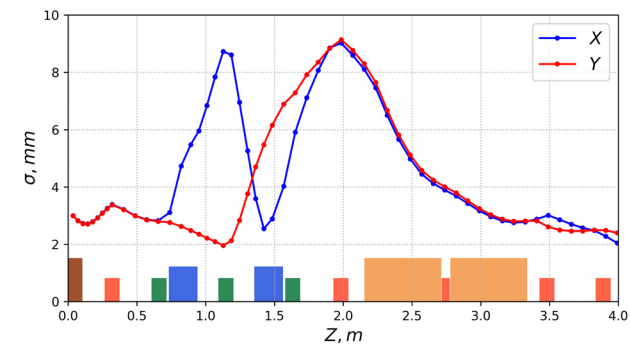


Figure 4: The optimized beam sizes for the RF gun beamline.

Table 2: Optimized Regime: Electron Beam Parameters at the Output of RF Gun Beamline Bend

Parameter	X	Y
Propagation	0.81	
Normalized Emittance, mm·mrad	27.6	27.0
Average Local Norm. Emittance, mm·mrad	13	20
Beta Function (β), m	0.39	0.82
Alpha Function (α)	-0.092	0.017
Longitudinal Size, ps	42	
Kinetic Energy of Electrons, MeV	1.356	
Energy distribution, σ _p /p ₀	0.008	

MEASUREMENTS OF THE RF GUN BEAM PARAMETERS

In order to verify a model of the RF gun measurements of beam parameters were performed. The RF gun is testing at the stand now. The scheme of the test stand is shown in Fig. 5. It consists the RF gun, a solenoid, a quadrupole lens,

a bend dipole magnet and an optical transition radiation (OTR) monitor.

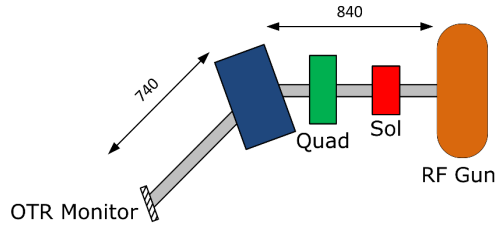


Figure 5: The scheme of the RF gun test stand.

A bend magnet in the scheme allows measuring an energy distribution of the beam from the RF gun. The experiment was conducted in the following way: the solenoid was turned off and the quadrupole strength was chosen so that the horizontal beta function was a minimal. Thus, the best energy resolution is achieved

$$\frac{\delta p}{p_0} \approx \frac{\sqrt{\varepsilon\beta}}{\eta} \quad (4)$$

where p_0 and δp is an average of electron impulse and its deviation, ε is the emittance, η and β – are the dispersion and the beta function at the OTR monitor position. The result of measurements of transverse horizontal beam density is shown in Fig. 6, which demonstrates good agreement between the simulation with ASTRA code and the experimental data. However, the deviation is more as the RF gun phase is far from the phase of maximum acceleration (0°). We assume that it is the result of less the peak current in the simulation than in the experiment, which we can see because of the acceleration at the slope and a time-longitude dependence.

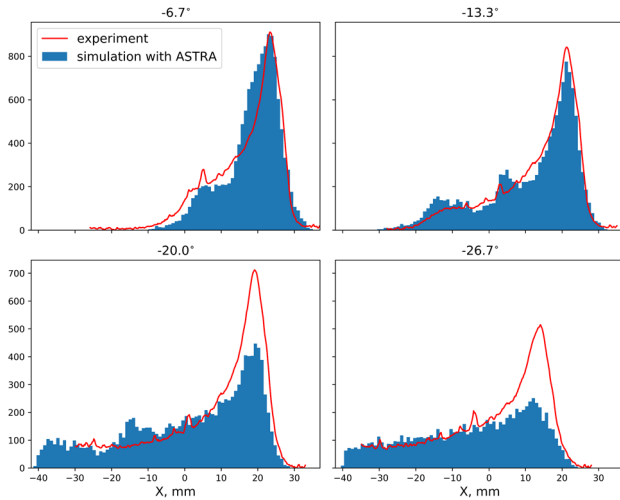


Figure 6: Transverse horizontal beam density distribution at the monitor for several RF gun injection phases (0° - the phase of the maximum acceleration).

Also, dependence of vertical beam size at the monitor on the strength of the quadrupole focusing was measured and compared with the simulation. The result is demonstrated in Fig. 7. The simulation and the experimental data are equivalent to a shear along the abscissa axis. Possibly,

some focusing (e.g. the anode one) is calculated wrong or is not taken into account.

The vertical normalized emittance in the simulations is 18.5 and 16.0 mm-mrad for the solenoid current of 0.0 and 4.0 A, respectively. Figure 8 illustrates typical beam image and its vertical distribution fitting during the experiment.

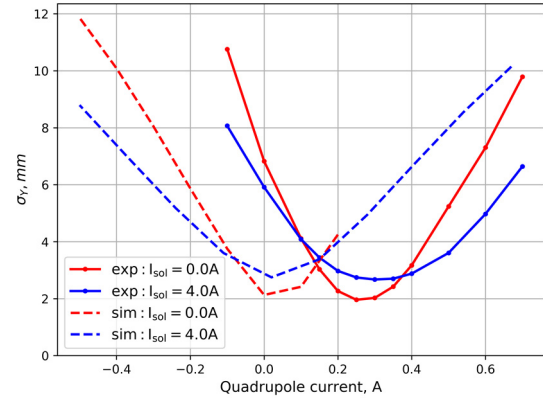


Figure 7: Dependence of vertical beam size at the monitor on quadrupole strength for two currents of solenoid (measurements and simulation).

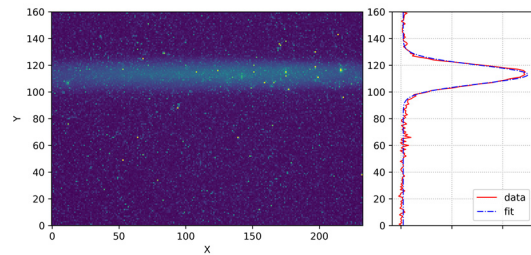


Figure 8: The example of beam image in a quadrupole strength variation experiment.

CONCLUSION

The simulation model of the RF gun is in a good agreement with the experimental data. The regime for the new RF gun beamline was optimized. Results will be applied when the beamline is commissioned.

REFERENCES

- [1] O. A. Shevchenko *et al.*, “Novosibirsk Free Electron Laser: Recent Achievements and Future Prospects,” *Radiophys. Quantum Electron.*, vol. 59, no. 8–9, pp. 605–612, Jan. 2017. doi:10.1007/s11141-017-9727-9
- [2] V. Volkov *et al.*, “Thermocathode radio-frequency gun for the Budker Institute of Nuclear Physics free-electron laser,” *Phys. Part. Nucl. Lett.*, vol. 13, no. 7, pp. 796–799, Dec. 2016. doi:10.1134/S1547477116070517
- [3] K. Floettmann, ASTRA – A Space Charge Tracking Algorithm, <http://www.desy.de/~mpyf10>
- [4] K. Price, R. M. Storn, and J. A. Lampinen, *Differential Evolution*, Springer-Verlag Berlin Heidelberg, 2005.

- [5] J. A. Nelder and R. Mead, "A Simplex Method for Function Minimization," *Comput. J.*, vol. 7, no. 4, pp. 308–313, Jan. 1965. doi:10.1093/comjnl/7.4.308

AN UPDATED DESIGN OF THE NSRRC SEEDED VUV FREE ELECTRON LASER TEST FACILITY

W.K. Lau¹, C.K. Chan¹, C.C. Chang¹, C.H. Chang¹, L.H. Chang¹, C.H. Chen¹, M.C. Chou¹, P.J. Chou¹, F.Z. Hsiao¹, H.P. Hsueh¹, K.T. Hsu¹, K.H. Hu¹, C.S. Hwang¹, J.Y. Hwang¹, J.C. Jan¹, C.K. Kuan¹, A.P. Lee¹, M.C. Lin¹, G.H. Luo¹, S.Y. Teng², K.L. Tsai¹, J. Wu³, A.W. Chao³

¹ NSRRC, Hsinchu, Taiwan

² Department of Physics, NTHU, Hsinchu, Taiwan

³ SLAC National Accelerator Laboratory, Menlo Park, USA

Abstract

In this report, we present an updated design of the facility which is a 200 nm seeded, HGHG FEL driven by a 250 MeV high brightness electron linac system with dogleg bunch compressor for generation of ultrashort intense coherent radiation in the vacuum ultraviolet region. It employs a 10-periods helical undulator for enhancement of beam energy modulation and a helical undulator of 20 mm period length as the radiator (i.e. THU20) to produce hundreds of megawatts radiation with wavelength as short as 66.7 nm. An optional planar undulator can be added to generate odd harmonics (e.g. 22.2 nm, 13.3 nm etc.) of the fundamental. The facility layout and expected FEL output performance is reported.

INTRODUCTION

The Baseline design of the test facility is a VUV high-gain harmonic generation (HGFG) FEL seeded by a 200 nm laser. The seed laser is injected to a 10-periods helical undulator of 24 mm period length (i.e. THU24) for beam energy modulation. A small chicane located at downstream of THU24 provides the required dispersion for microbunching. In the first phase of the project, a THU20 undulator of length at about twice of gain length will be used as the radiator which allows generation of MW-level coherent radiation at 66.7 nm wavelength (i.e. the third harmonic of the seed). If the more segmented THU20 undulators are used, the radiation grows and saturates in ~6 m. In the initial stage, the facility has to be fitted into the existing 38 m × 5 m tunnel in the Accelerator Test Area (ATA). Since the total length of the accelerator system from the gun to beam modulator entrance is about 25.5 m, the length of the FEL section and its output diagnostics station is limited to 12.5 m. Future extension of the laboratory building will be necessary if more

THU20 undulators are installed for FEL operation at saturation. Extra space will also be needed for photon beamlines and experimental stations if a practical user facility is under consideration. Nevertheless, a 1.5 m long THU20 undulator prototype will be used to demonstrate the concepts in the initial stage. A schematic of the overall layout is shown in Fig. 1.

Broad tunability of radiation wavelength of the VUV FEL can be achieved by using tunable seed laser. The klystron systems operate at 10 Hz pulse-prepetition-rate rate, and can be increased up to 50 Hz if demand arises.

ACCELERATOR SYSTEM

The facility is based on a recently built 2998 MHz laser driven photoinjector which delivers low emittance electron beam for the 250 MeV drive linac system. Since the beam brightness required for the seeded VUV FEL system located at downstream of the linac system is as high as 5×10^{13} A/m², bunch compressor with capability to linearize electron distribution in longitudinal phase space is therefore essential. Conventional four-dipole chicanes are usually equipped with harmonic rf linearizers to compensate the nonlinearities introduced into beam distribution by the rf curvature of chirper linac. However, harmonic rf linac as well as the corresponding pulsed klystron system do not fit into our budget plan, we therefore consider to exploit the concept of dogleg bunch compressor with linearization optics. After bunch compression, the sub-100 fs beam is then accelerated to designed beam energy by two rf linac sections that are powered by a single klystron with standard SLED cavity for rf pulse compression. A linear achromatic beam transport system delivers the beam to the FEL system and allows coupling seed laser collinearly with the beam in the beam energy modulator unit. Beam parameters are listed in Table 1.

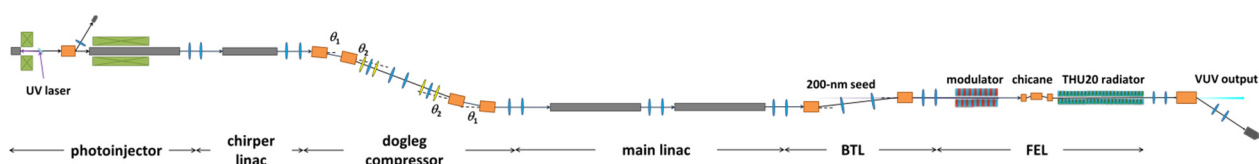


Figure 1: Layout of the NSRRC VUV FEL test facility.

Photoinjector

Operation of the 2998 MHz photo-cathode rf gun system (Fig. 2) has been successful in 2013 after high power microwave processing of the gun cavity up to ~ 70 MV/m. A 266 nm, 300 μ J laser system that consists of an ultrafast Ti:Sapphire regenerative amplifier and nonlinear optics has been used to drive the Cu photo-cathode. The system delivers regularly an electron beam with energy of 3.3 MeV at 250 pC bunch charge [1]. Beam transverse emittance of 2-3 mm-mrad is achievable. With a 5.2 m long rf linac section, the beam energy will be boosted to ~ 70 MeV. For operation at higher field gradient and 50 Hz pulse repetition rate, a new rf gun cavity is under development [2].



Figure 2: The NSRRC 2998 MHz photoinjector system.

Dogleg Bunch Compressor

A single stage nonlinear bunch compressor designed for the proposed facility is a double dog-leg configuration that provides a first order longitudinal dispersion function (i.e. R_{56}) with a sign opposite to that of a conventional four-dipole chicane. Variation in the bunch length or the peak current for various operation conditions can be done by tuning R_{56} . This can be realized by changing the longitudinal positions of the outside dipoles and by adjusting the quadrupoles and sextupoles settings for desired bunch compression [3].

Main Linac

After bunch compression, the beam is accelerated to higher energy by two 5.2 m rf linac sections. They are powered by a 35 MW pulsed klystron with standard SLED cavity for rf pulse compression. We expect a beam energy gain of 140 MeV from these two rf linac sections.

Dechirper

As revealed from ELEGANT simulation, a residual energy chirp of 41.7 keV/ μ m is left after bunch compression. It can be corrected by a capacitive dechirper structure when the bunch is slightly over-compressed. We tentatively use a 1 m long corrugated pipe to remove the residual energy chirp in our previous study [3]. However, we considered using dielectric-lined waveguide structures to simplify the mechanical design of the dechirper system and to save space [4,5].

Table 1: Nominal Beam Parameters of the Drive Linac used in Design Study

Beam energy [MeV]	250
Beam current [A]	500
Bunch length [fsec]	~ 50
Normalized sliced emittance [mm-mrad]	3
Sliced energy spread [keV]	200
Repetition rate [Hz]	10

FEL SYSTEM

The 200 nm seed laser is coupled into a 10-period helical undulator of 24 mm period length for beam energy modulation (see Fig. 3). With the dispersion provided by a small chicane after the modulator, the beam is slightly bunched at 200 nm spacing and radiate coherently at its harmonics when some resonant condition is met. In our case, we employ a THU20 helical undulator of 20 mm period length which is tuned to resonance at third harmonics as radiator which allows generation of intense coherent radiation at 66.7 nm wavelength. If the more segmented THU20 undulators are available, as can be shown from start-to-end simulation, the coherent undulator radiation grows exponentially and saturates within a few meters [6]. In the initial stage, the facility has to be fitted into the existing 38m x 5m tunnel in the Accelerator Test Area (ATA). Future extension of the laboratory building will be necessary if more THU20 undulators are installed for FEL operation at saturation. Extra space will also be needed for photon beamlines and experimental stations if a practical user facility is under consideration. Nevertheless, a 1.5 m long THU20 undulator prototype can be used to demonstrate the concepts in the initial stage. Design FEL parameters are listed in Table 2. An optional planar undulator can be added to generate odd harmonics of the fundamental.

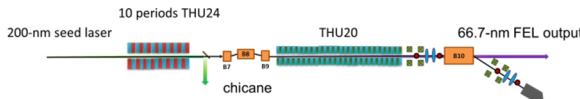


Figure 3: The VUV FEL system.

Table 2: Design Parameters of the NSRRC VUV FEL

Modulator	
Period length [mm]	24
Length [m]	0.24
Strength parameter K	1.73
Seed laser wavelength [nm]	200
Laser power [MW]	300
Energy modulation [%]	0.14
Radiator	
Period length [mm]	20
Strength parameter K	0.78
VUV radiation	
Wavelength [nm]	66.7
Peak power [MW]	200
Gain length [m]	0.69

Seed Laser

The 200 nm seed (Fig. 4) is produced from a fourth harmonic generator (FHG) which is driven by a 800 nm laser amplifier. This 800 nm laser amplifier shares the same master oscillator with the photo-cathode rf gun drive laser system. The seed laser will be coupled to the THU24 helical undulator via the achromatic beam transport section located upstream. Broad tunability of radiation wavelength of the VUV FEL can be achieved by using tunable seed laser.

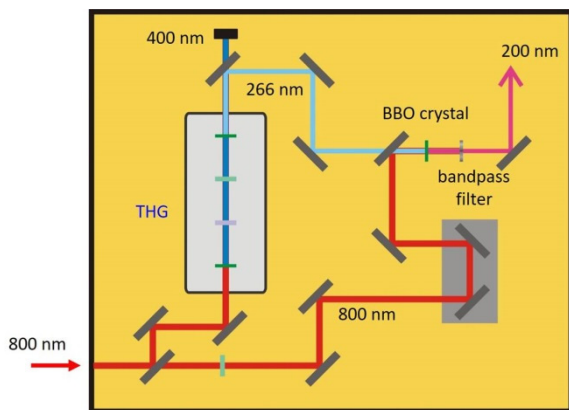


Figure 4: Schematic diagram of the 200-nm seed driven by a 800 nm laser.

Helical Undulators

A novel type twin-helix undulator (THU) with a short period length of 20 mm has been designed for the NSRRC VUV free electron laser test facility [7]. This undulator consists of two helical magnet arrays symmetrically arranged along a 1.5 m beam axis. The NdFeB permanent magnet with helical shaped poles is designed and optimized to generate a high helical field of 1.05 T in a 5.6 mm round gap along its axis. End pole design and shimming methods are considered to achieve a wider and very precise field performance in the small-bore diameter. Moreover, with a 0.5 mm space between two helical arrays, weak magnetic forces of only 1500 kgf are expected for the 1.5 meter long undulator. A simple and low-cost mechanical structure was designed for this horizontal open gap undulator. The modulator is a 10-period helical undulator of the same type except period length is 24 mm.

CONCLUSION

We presented a new design of the facility which is a 200 nm seeded, HGHG FEL driven by a 250 MeV high brightness electron linac system with dogleg bunch compressor for generation of ultrashort intense coherent radiation in the vacuum ultraviolet region. It employs novel helical undulator for enhancement of beam-wave interactions in modulator as well as the radiator. It is capable of producing 200 MW coherent VUV radiation with wavelength as short as 66.7 nm.

REFERENCES

- [1] A. P. Lee *et al.*, “First beam test of the high brightness photo-injector at NSRRC”, in *Proc. 7th Int. Particle Accelerator Conf. (IPAC’16)*, Busan, Korea, May 2016, pp. 1800–1802.
doi:10.18429/JACoW-IPAC2016-TUP0W025
- [2] W. T. Chiu, “Design of a 2998 MHz laser-driven photo-cathode rf gun for EUV free electron laser operation at high repetition rate”, National Tsing Hua University master thesis, 2019.
- [3] W. K. Lau *et al.*, “Design of a dogleg bunch compressor with tunable first-order longitudinal dispersion”, in *Proc. FEL’17*, Santa Fe, NM, USA, Aug. 2017, pp. 309-312.
doi.org/10.18429/JACoW-FEL2017-TUP031
- [4] L. Xiao, W. Gai and X. Sun, “Field analysis of a dielectric-loaded rectangular waveguide accelerating structure”, *Phys. Rev. E*, vol. 65, p. 016505, 2001.
doi:10.1103/PhysRevE.65.016505
- [5] S. Antipov *et al.*, “Experimental observation of energy modulation in electron beams passing through terahertz dielectric wakefield structures”, *Phys. Rev. Lett.*, vol. 112, p. 114801, 2014.
doi:10.1103/PhysRevLett.112.114801
- [6] S. Y. Teng *et al.*, “Start-to-end simulation of the NSRRC seeded VUV FEL”, presented in the *39th Int. Free-Electron Laser Conf. (FEL’19)*, Hamburg, Germany, Aug. 2019, TUP091, this conference.
- [7] T. Y. Chung *et al.*, “Twin-helix undulator for round beam-related light sources”, *Synch. Rad. News*, vol. 31, no. 3, p. 14-17, 2018.
doi:10.1080/08940886.2018.1460169

SIMULATION AND OPTIMIZATION OF INJECTOR SYSTEM FOR THE PRE-BUNCHED THz FEL

N. Chaisueb^{a,b,†}, S. Rimjaem^{a,c,††}

^aPlasma and Beam Physics Research Facility (PBP), Department of Physics and Materials Science,
Faculty of Science, Chiang Mai University, Chiang Mai, Thailand

^bDoctor of Philosophy Program in Physics (International Program), Department of Physics and
Materials Science, Faculty of Science, Chiang Mai University, Chiang Mai, Thailand

^cThailand Center of Excellence in Physics, CHE, Bangkok, Thailand

Abstract

A linac-based light source for generation of infrared free-electron laser is under the development at the Plasma and Beam Physics (PBP) Research Facility, Chiang Mai University, Thailand. The injector system of the facility consists mainly of an S-band thermionic cathode RF electron gun, a pre-bunch compressor in a form of an alpha magnet and a travelling-wave linac structure. Two 180-degree magnetic bunch compressors, which each system has 4 dipole magnets, quadrupoles and steering magnets, are installed downstream the injector system. Two separate radiation beamlines for mid-infrared (MIR) and terahertz (THz) free-electron laser (FEL) are located following the bunch compressor systems. In this contribution, we focus only on the coherent and high-power pre-bunch THz FEL that is generated from electron bunches with a femtosecond length. Electron beam dynamic simulations with program ASTRA were performed to obtain optimal electron beam properties. Optimization of the injector system for the THz FEL is thus presented. The simulated results show that the beam at the linac exit has a bunch length of 282 fs with a charge of 200 pC when the linac RF phase is 90° and the alpha gradient is 300 G/cm. This optimal condition will be used as an input for simulation in the 180-degree bunch compressor system and in the THz undulator magnet.

INTRODUCTION

Nowadays, the THz radiation has been used in many applications due to its unique features. Since the THz wave can pass through non-metallic materials, reflected by metal and absorbed by liquid, it is suitably used in THz imaging for non-destructive analysis of different density materials e.g. investigation of chemical structures of pharmaceutical materials or imperfection observation of integrated circuits, semiconductor devices or electronic cards [1].

The frequency ranges of the THz radiation also correspond well with rotational and vibration modes of many bio-molecules. Therefore, it can be used to study the characteristics of intermolecular bonds such as hydrogen bonding, Van der Waals forces, and molecule-ion attractions by using the THz spectroscopy technique. Various applications of THz radiation lead to broad studies on development of THz light sources, detectors, and experimental techniques. An accelerator-based light source is one of the most powerful sources for producing the THz

radiation. Many accelerator centers and laboratories develop the THz light sources worldwide including free-electron lasers.

In typical FELs, the radiation emits when an electron bunch moving through magnetic field of an undulator magnet interacts with the radiation, which is produced in the first section of a long undulator or inserted from external seed laser. The co-propagating radiation modulates the longitudinal velocity of electrons and eventually the electrons are bunched, which is called the micro bunching process. Contradictory, in case of pre-bunched FELs, ultrashort and high-charged electron bunches are produced before injecting the beam into the undulator. When the electron bunches with a length of equal or shorter than the radiation wavelength travelling in the undulator magnetic field, the radiation will be coherently emitted. In this case, the radiation emitted from different undulator poles along the beam trajectory overlaps and interferes constructively. This leads to properly add up of the radiation in the forward direction and results in the enhancement of the radiation intensity that is proportional to the electron number squared.

The construction of the pre-bunched THz FELs from femtosecond electron bunches and the typical MIR FEL oscillator (as shown in Fig. 1) are underway at our laboratory. The accelerator system includes the injector part, the 180-degree bunch compressors, and radiation stations. However, this paper focuses only on optimization of the injector system for generation of the femtosecond electron bunches at the entrance of the THz undulator magnet. This system consists of a thermionic cathode RF electron gun, an alpha magnet and a travelling-wave linac structure. The optimization was divided into three parts; in the RF-gun, from the gun exit to the alpha magnet and from the alpha magnet to the linac. The optimal electron beam with small emittance, low energy spread, short bunch length, and high beam current is expected to achieve downstream the linac.

METHOD

Properties of the radiation from charged particle beam depend significantly on the beam qualities. Numerical optimization of electron beam properties has to be done before installation of the accelerator components. Electron beam dynamic simulations throughout the injector system by using program ASTRA [2] were performed to determine the appropriate operational parameters of the

[†]natthawut_chai@cmu.ac.th, ^{††}sakhorn.rimjaem@cmu.ac.th

pre-bunched THz FELs beamline. Considered parameters for the simulation are an RF gun electric field amplitude, a gradient of alpha magnet and a linac RF phase. These parameters were optimized to obtain shortest electron bunch length, maximum charge per bunch, lowest energy spread, and small transverse emittance at the linac exit.

Firstly, the electric field amplitude inside the gun was varied to achieve the electron bunch with the maximum kinetic energy of 2.5 MeV according to the designed performance of the RF gun [3]. After that, the electron

beam is properly guided to the alpha magnet by adjusting the fields of steering and quadrupole magnets. The gradient of the alpha magnet was then optimized from 200 G/cm to 400 G/cm. The beam exiting the alpha magnet moves forward to the linac that has an RF phase of 90° for maximum acceleration condition. Quadrupoles' and steerers' field were adjusted to achieve small emittance and low energy spread. For all magnets, three-dimensional (3D) magnetic field distributions are obtained from simulations with program CST EM Studio 2018 [4].

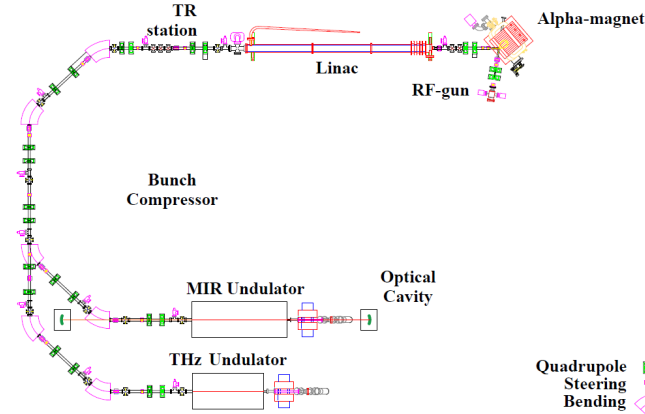


Figure 1: Schematic drawing of the infrared free-electron laser sources at the PBP Facility.

RESULTS AND DISCUSSION

Simulation in RF-gun

Electrons with no energy spread and non-zero emittance are emitted uniformly from the cathode surface with the average current of 2.6 A over an RF period. An initial kinetic energy of 0.165 eV was defined for a cathode temperature of 1000°C. An initial number of macro-particles is 350,000 with a total charge of 910 pC. We applied the 3D RF field distribution of the RF-gun obtained from the program CST EM Studio 2012 in the simulation [3]. The electric field amplitude inside the gun was optimized to obtain the electron bunch with the kinetic energy of 2.5 MeV.

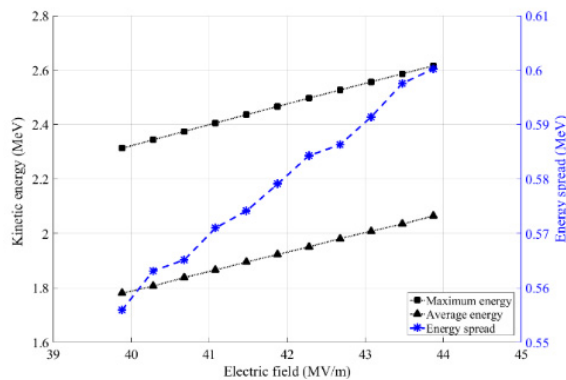


Figure 2: Dependency of maximum energy, average energy and energy spread of electron bunch at the gun exit as a function of electric field at the center of the full cell.

Results of electric field variation shown in Fig. 2 obviously indicate that the electrons gain higher energy for

higher electric field. The energy spread of the beam is large at high electric field due to time-varying feature of the RF field. The maximum electron energy of 2.5 MeV is achieved at the field amplitude of 42.3 MV/m. About 75% of the particles are lost inside the RF-gun. An electron bunch exiting the RF-gun has a charge of 224 pC, an average energy of 2 MeV and an energy spread of 0.62 MeV.

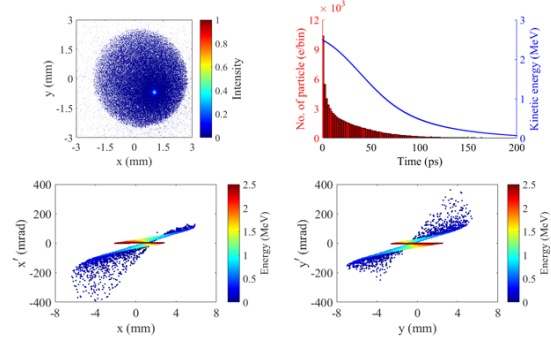


Figure 3: Transverse beam distribution, longitudinal distribution and transverse phase spaces of electron bunch at the gun exit for the field amplitude of 42.3 MV/m.

The transverse beam distributions in Fig. 3 show that the beam centroid is off-axis due to the influence of the asymmetric field distribution inside the gun cavities [3]. Electrons with high kinetic energy are accommodated at the head of the bunch and have nearly zero divergence.

Simulation from RF-gun Exit to Alpha Magnet

After leaving the gun, the beam was directed to the alpha magnet by using steering magnets. Two quadrupoles were used to minimize the transverse size and divergence of the

to obtain the proper beam properties at the entrance of the THz undulator magnet.

ACKNOWLEDGEMENTS

This research work was partially supported by Chiang Mai University and the Thailand Center of Excellence in Physics (ThEP-61-EQP-CMU1). The authors would like to express our essential gratitude to the Graduate School of Chiang Mai University, the Science Achievement Scholarship of Thailand and the Photo Injector Test Facility at DESY, Location Zeuthen (PITZ) for collaboration work with the CST EM Studio simulation.

REFERENCES

- [1] G. P. Gallerano *et al.*, “Phase-Sensitive Reflective Imaging Device in the mm-wave and Terahertz Regions”, *J. Infrared. Milli. Terhz Waves*, vol. 30, pp. 1351-1361, 2009.
doi:10.1007/s10762-009-9560-0
- [2] K. Floettmann, A Space Charge Tracking Algorithm (AS-TRA). www.desy.de/mpyf10
- [3] S. Rimjaem, K. Kusoljariyakut, C. Thongbai, “RF study and 3-D simulations of a side-coupling thermionic RF-gun”, *Nucl. Instrum. Methods A*, vol. 736, pp. 10-21, 2014.
doi:10.1016/j.nima.2013.10.057
- [4] Computer Simulation Technology, CST EM Studio 2018. <http://www.cst.com/>
- [5] K. Kusoljariyakul, Master thesis, Chiang Mai University, Thailand, 2008.

XFEL ISOCHRONOUS CHICANES: FEASIBILITY STUDY

N. R. Thompson*

ASTeC and Cockcroft Institute, STFC Daresbury Laboratory, Warrington, United Kingdom

Abstract

FEL schemes such as High-Brightness SASE [1] and Mode-Locking [2] require electron beam delays inserted between undulator sections. These schemes have been shown in simulations to perform most effectively when the electron beam delays are very close to isochronous, i.e. the first order longitudinal dispersion is very small. To minimise the disruption to the FEL process in the inter-undulator gaps, these delays must also be as compact as possible. In this paper we study the maximum longitudinal space that a delay chicane could occupy in an XFEL operating at 6 GeV before the peak power drops below a defined threshold, and we present a limit for the maximum longitudinal dispersion of the delay chicanes. We then present the optical designs of two chicanes that satisfy the requirements of length and isochronicity and show how these designs could be realised practically using small-aperture high-field quadrupoles.

ISOCHRONOUS CHICANES

A number of related schemes have been proposed in which electron beam delay chicanes are used to manipulate the electron/radiation interaction within the FEL, for example Mode-Locking [2], the Mode-Locked Afterburner [3] and High-Brightness SASE (HB-SASE) [1]. For all of these schemes, the performance has been shown to be better if the delays are isochronous [4], meaning that the first order dispersion $R_{56} = 0$. For HB-SASE, simulation studies have been done in 1D and 3D codes, and in two different wavelength regimes, to assess the performance as a function of the level of isochronicity. These studies showed that for performance very close to that obtained with purely isochronous chicanes, the normalised chicane dispersion D , defined here as the ratio of the R_{56} to that of a standard 3 dipole chicane imparting the same delay, must satisfy $D \leq 0.01$.

SPACE CONSTRAINTS FOR AN XFEL

In any FEL it is normal practice to make the inter-undulator gaps as compact as possible to minimise the total length of the FEL and to mitigate the degradation to the FEL performance caused by debunching and radiation diffraction. Some initial chicane design work indicated that the minimum length would be several meters. To investigate the impact of a chicane length of this order, two FEL lattices were set up using typical XFEL parameters, with $E = 6$ GeV, $Q = 50$ pC, $\varepsilon_n = 0.5$ mm-mrad, $\sigma_\gamma/\gamma_0 = 10^{-4}$, $I_{pk} = 2$ kA, $\lambda_r = 0.124$ nm and $\lambda_w = 25$ mm. The nominal SASE lattice comprised 4 m undulator modules within a FODO focussing structure with half period 5 m. This meant the gap between undulators was 1m. An alternative lattice was

set up in which every other undulator was removed to allow delay chicanes up to several metres long to be inserted. In this lattice the gap between undulator modules is therefore 6 m.

In SASE mode, for the nominal lattice with 1m gaps, the saturation power of 5 GW was reached after 17 undulator modules. For the alternative lattice, with the gap length increased to 6m, the saturation power of 2.2 GW was reached after 18 undulator modules. For the 6m gaps the rms radiation size stabilises at a level about double that of the case with 1m gaps. These results indicate that a 5 m chicane is acceptable in terms of FEL performance, assuming a 50% reduction in output power and 100% increase in floor length are viable.

DELAY CHICANE DESIGNS

The first consideration is the magnitude of the required electron beam delay. For the generic XFEL parameters of a gaussian electron bunch of peak current $I_{pk} = 2$ kA and charge $Q = 50$ pC, the bunch duration is 3 μ m. For HB-SASE it is assumed the largest delay ever required would be $\delta = 2.5$ μ m. In fact the required delay turns out not to be the limiting factor in making the chicanes as compact as possible. For a three-dipole chicane the beam delay, found from simple geometry, is given by $\delta = (L_m^3/2 + 2L_dL_m^2)(Bc/E[\text{eV}])^2$ where L_m is the dipole length, L_d is the drift length between dipoles and B is the dipole field. For $L_m = L_d$, $\delta = 2.5$ μ m, $B = 1$ T and $E = 6$ GeV the minimum total chicane length of a dipole-only chicane is $L_c \simeq 0.4$ m. However, to obtain an isochronous solution, space must be left for quadrupoles to control dispersion. It is assumed that the aperture is $d = 10$ mm, and the minimum dipole length is $L_m = 3d = 30$ mm. The bend angle is then $\theta = BL_m c/E = 1.5$ mrad and the drift length $L_d = 0.5$ m.

To obtain an isochronous chicane the R_{56} of the chicane transfer matrix must be set to zero. The R_{56} is defined as the integral of the dispersion over the bend radius, i.e. $R_{56} = \int \eta(s)/\rho(s)ds$ so can be minimised by balancing positive and negative dispersion within the dipoles using quadrupoles. Two chicane options are considered. Option 1 is a three-dipole chicane with four quads which are inserted 1/4 and 3/4 of the way along the drifts between the dipoles. Option 2 is a four dipole chicane with three quads inserted midway between the dipoles. Both options are shown in Fig. 1 with properties summarised in Table 1.

Option 1

Option 1 is shown in Fig. 1 (top). The quadrupoles set the dispersion to zero at the midpoints between the dipoles and at the dipoles themselves. This means the effect of the quadrupole is to invert the sign of the dispersion gradient

* neil.thompson@stfc.ac.uk

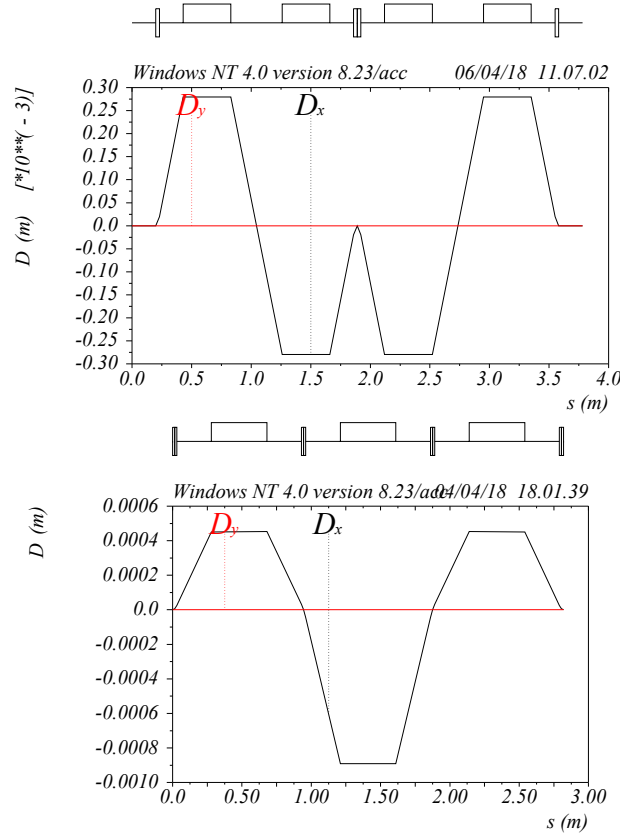


Figure 1: Top: Chicane Option 1, a three-dipole chicane with four quads. Bottom: Option 2, a four dipole chicane with three quads.

η_{px} [5]. This condition is achieved if the quadrupole focal length is $f = \eta_x / (2\eta_{px})$ where η_x and η_{px} depend on the dipole bend angle θ , bend radius ρ and drift length from dipole to quad L_d as $\eta_x = \rho(1 - \cos \theta) + L_d \sin \theta \approx L_d \theta$ and $\eta_{px} = \sin \theta \approx \theta$ where the approximations are valid for small θ . Using $k = 1/fL_q$ the required quadrupole k to invert the sign of the dispersion gradient is $k = 2/(L_d L_q)$ then also using $k = 300G[\text{T/m}]/E[\text{MeV}]$ the required integrated quadrupole gradient is $GL_q[\text{T}] = 2E[\text{MeV}]/300L_d$. This shows that for small angles the quadrupole integrated gradient only depends on the drift length and the beam energy, and is independent of the electron beam delay. It also shows that the quadrupole gradient needs to be high. For example, for drift length and quadrupole length 0.5 m and beam energy 6 GeV the required gradient is $G = 160 \text{ T/m}$.

The obtainable gradient from a Halbach quadrupole is given by $G = 2B_r K(1/r_i - 1/r_e)$ with B_r the permanent magnet remanent field, K a geometric factor which depends on the number of radial elements, and r_i and r_e internal and external radii [6]. Using $B_r = 1.35 \text{ T}$, $K = 0.94$ (which assumes 16 radial elements), $r_i = 5 \text{ mm}$ and $r_e = 30 \text{ mm}$, the maximum achievable gradient is 430 T/m and hence the maximum achievable k for a 6 GeV beam is $k = 21.5 \text{ m}^{-2}$. For a electromagnetic quadrupole the maximum gradient is limited by the pole-tip field B_0 . Assuming $B_0 = 1 \text{ T}$ and

Table 1: Summary of Option 1 and Option 2 Parameters

	Option 1	Option 2
Length (m) (Halbach quads)	3.75	2.8
Length (m) (EM quads)	5.35	4.0
Delay (μm)	2.7	2.5
R_{56}	33 nm	3.0 nm
T_{566}	-7.3 μm	-18.0 μm
Scaled dispersion D	0.006	0.0006

$r = 5 \text{ mm}$ then the maximum gradient is 200 T/m and the maximum achievable k for a 6 GeV beam is $k = 10 \text{ m}^{-2}$.

An optimisation was therefore done to achieve the required quadrupole k in the minimum total chicane length. This was done for the design shown in Fig. 1, incorporating Halbach quadrupoles and then EM quadrupoles. The results are shown in Fig. 2. The left plot is the required quadrupole k for reversing the gradient of the dispersion, vs the quadrupole and drift space lengths. The bold contours indicate the maximum achievable k for Halbach and electromagnetic quadrupoles. The right plot shows the total chicane length $L(\text{chicane}) = 4L_m + 8L_d + 4L_q$ vs L_q and L_d . It is clear that a high quadrupole k enables a more compact chicane. The red dot indicates combination of L_q and L_d that gives the *minimum* chicane length that provides sufficient quadrupole k , assuming Halbach quads. The blue dot indicates the same but assuming EM quadrupoles. The minimum chicane length if using Halbach quadrupoles is therefore 3.75 m, and if using EM quads it is 5.35 m.

Figure 1 (top), calculated in MAD, corresponds to the parameters of this minimum length chicane. In fact in MAD the quadrupole k value turns out to be $k = 17.5 \text{ m}^{-2}$. It is seen that the dispersion is close to zero at each dipole allowing a small R_{56} . For a 6 GeV beam the delay given by the chicane is $\delta = 2.7 \mu\text{m}$ and the R_{56} , after subtraction of the drift R_{56} over the chicane length is $R_{56} = 33 \text{ nm}$. For the equivalent chicane without quadrupoles, a standard four-dipole chicane, then $R_{56} = 5.57 \mu\text{m}$. This means that the scaled chicane dispersion is $D = 0.006$, within the required value of $D \lesssim 0.01$. The second order dispersion term is found to be $T_{566} = -7.3 \mu\text{m}$, compared to $T_{566} = -9.8 \mu\text{m}$ for a dipole-only chicane.

Option 2

Option 2 is a more simple, and slightly more compact design, as shown in Fig. 1 (bottom). The same optimisation and analysis was done as for Option 1. The minimum chicane length if using Halbach quadrupoles is 2.8 m, and if using EM quads it is 4 m. For a 6 GeV beam the delay given by the chicane is $\delta = 2.5 \mu\text{m}$ and $D = 0.0006$, a factor of ten lower than for Option 1 and again within the required value of $D \lesssim 0.01$. The second order dispersion term is $T_{566} = -18.0 \mu\text{m}$, compared to $T_{566} = -8.6 \mu\text{m}$ for a dipole-only chicane. This is three times larger than for Option 1.

As yet, the designs do not include transverse focussing. Option 1 would allow insertion of 2 matching quadrupoles

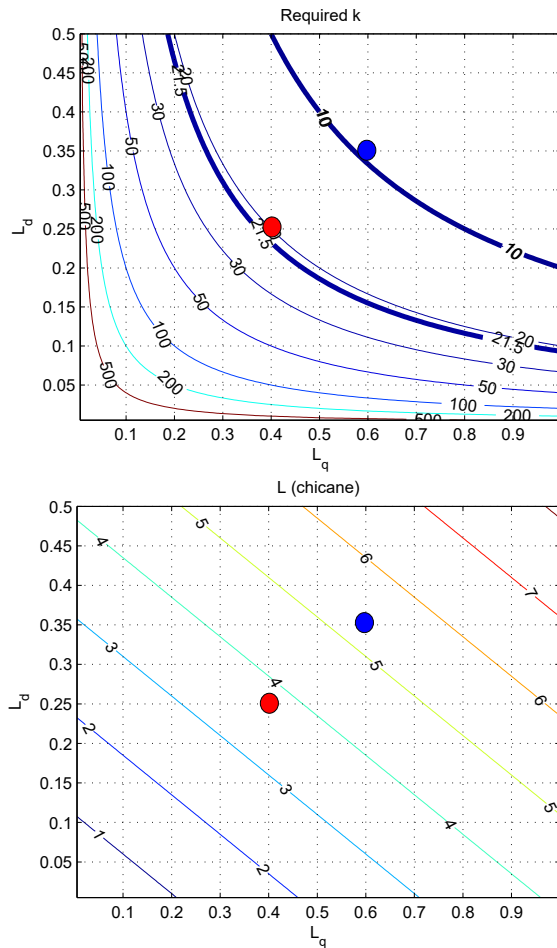


Figure 2: Chicane Option 1 optimisation. Top: Required quadrupole k vs L_d and L_q , with bold contours indicating the maximum achievable k for Halbach and EM quadrupoles. Bottom: total chicane length vs L_q and L_d . The red and blue dots indicate the combinations of L_q and L_d giving the minimum chicane length that provides sufficient k for Halbach and EM quadrupoles respectively.

at the midpoints between the dipoles and the central dipole could be split to add a third matching quad. These positions all have zero dispersion so the quadrupoles for dispersion control would change little and the design would allow the transverse matching and dispersion cancellation to be approximately independent. The extra length would then be a minimum of $3L_q$, approximately 1.2 m taking the total length (using Halbach quadrupoles) to approximately 5 m, i.e. just within the space assumed to be feasible in terms of FEL performance. For Option 2 there are no obvious locations to add matching quadrupoles. One possibility would be for dipoles 2 and 3 to be replaced by offset quadrupoles, then an extra quadrupole either side of the chicane. The total length increase would then be $2L_q + 2L_d$, approximately 1.3 m, taking the total length to about 4.1 m (if using Halbach quadrupoles). Further considerations should be the tolerances to errors in magnet position, beam trajectory, beam energy and magnet field quality.

CONCLUSION

For High-Brightness SASE the performance is close to ideal if the chicane scaled dispersion factor $D \lesssim 0.01$. With generic XFEL parameters, the acceptable delay chicane length could be as long as 5 m which would allow the saturation power to be nearly 50% of that of normal SASE with a saturation length, in terms of the number of undulator periods, only increased by 6% (although the total floor length is more than doubled). Two candidate designs for chicanes have been investigated and shown to have a level of isochronicity satisfying $D \lesssim 0.01$. The length of the chicanes is determined by the available integrated gradient of the quadrupoles used for dispersion control and does not depend on the required delay. The quadrupole field does not need to be changed depending on the delay. The designs shown here are not suitable for the Mode-Locked Afterburner schemes because the fact that these schemes require much smaller delays does not mean that the chicanes can be more compact. The fact that the quadrupole field does not need to vary with delay but only with beam energy implies that only a small range of tuning is required for a fixed beam energy (in fact a prototype of a tunable hybrid quadrupole with inscribed radius 4.125 mm, peak gradient 500 T/m and tuning range of 20% has previously been demonstrated [7]). The candidate designs do not yet include transverse focussing but it is anticipated that the inclusion of extra quadrupoles to achieve this can be done while keeping the overall chicane length within 5 m—this has yet to be confirmed. The effect of higher order dispersion on the FEL performance has not been studied but the value of the T_{566} term has been determined and is of the same order as that for a dipole only chicane with the same delay.

REFERENCES

- [1] B. W. J. McNeil and N. R. Thompson, "Transform-Limited X-Ray Pulse Generation from a High-Brightness Self-Amplified Spontaneous-Emission Free-Electron Laser", *Phys. Rev. Lett.* **110**, 134802, 2013, doi:10.1103/PhysRevLett.110.134802
- [2] N. R. Thompson and B. W. J. McNeil, "Mode Locking in a Free-Electron Laser Amplifier", *Phys. Rev. Lett.* **100**, 203901, 2008, doi:10.1103/PhysRevLett.100.203901
- [3] D. J. Dunning, B. W. J. McNeil and N. R. Thompson, "Few-Cycle Pulse Generation in an X-Ray Free-Electron Laser", *Phys. Rev. Lett.* **110**, 104801, 2013, doi:10.1103/PhysRevLett.110.104801
- [4] N. R. Thompson, PhD Thesis, University of Strathclyde, 2013
- [5] A. Wolski, *Beam Dynamics in High Energy Particle Accelerators*, Imperial College Press, 2014.
- [6] K. Halbach, "Design of permanent multipole magnets with oriented rare earth cobalt material", *Nucl. Inst. & Meth.* **169**, p1-10, 1980. doi:10.1063/1.1435248
- [7] M. Modena *et al.*, "Design, Assembly and First Measurements of a Short Model for CLIC Final Focus Hybrid Quadrupole QD0", in *Proc. 3rd Int. Particle Accelerator Conf. (IPAC'12)*, New Orleans, LA, USA, May 2012, paper THPPD010, pp. 3515–3517.

BEAM SHAPING FOR HIGH-REPETITION-RATE X-RAY FELS*

Y. Ding[†], K. Bane, Y. Nosochkov, SLAC National Accelerator Laboratory, Menlo Park, USA

Abstract

Beam shaping at normal-conducting, accelerator-based FELs, such as LCLS, plays an important role for improving lasing performance and for supporting special operating modes, such as the self-seeding scheme. Beam shaping methods include horn-collimation and dechirper manipulation. Applying the beam shaping concept to high-repetition-rate FELs driven by a superconducting linac, such as LCLS-II, beam invasive methods are not preferred due to concerns about high power deposition. We have recently studied a few shaping options for LCLS-II, such as manipulating the beam chirp before compression using corrugated devices, and modifying higher order optics terms in a chicane using octupoles. In this report we will discuss the results.

INTRODUCTION

In LCLS-II x-ray FEL pulses will be generated that have high average brightness at a megahertz-level repetition rate, opening up remarkable, new capabilities for various scientific research fields. The electron beam quality is the most important factor affecting the FEL performance; typically what is required is an electron beam with low emittance and high current. While the (slice) emittance is determined at the gun, high peak current can be achieved by longitudinal compression of the bunch.

For the LCLS-II driven by superconducting linacs, the electron bunch, coming from a very-high-frequency (VHF) gun, has a lower peak current and a lower energy than what is achieved at the present (normal conducting) S-band RF gun of LCLS. To achieve a final peak current at the kA-level, stronger compression is required. However, the achievable peak current is limited by strong nonlinearities in single particle and collective effects in the linacs and bunch compressors. For example, according to the present LCLS-II design, at 100 pC bunch charge, the peak current is about 800 A [1]. For some operating scheme such as the self-seeding mode, electron beam longitudinal phase space distribution is also critical for seeded FEL lasing performance.

Beam shaping schemes typically include electron beam phase space manipulation for achieving higher beam current, lower transverse emittance, and uniform longitudinal phase space. This type of beam phase space manipulation can be realized by direct interaction on the electron beam phase space, or by machine configuration optimization. For example, at the LCLS, beam shaping methods such as horn collimation [2] and emittance spoiling by foil [3, 4] have greatly improved the FEL performance and operating flexibility. Unfortunately, such beam invasive methods are not preferred for high-repetition rate FELs and new schemes

have to be developed. We summarize two beam shaping methods for the high-repetition rate FELs in this paper. The LCLS-II machine layout is shown in Fig. 1.

MANIPULATION OF BEAM CHIRP BEFORE FINAL COMPRESSION

In a technical note [5], manipulation of electron beam high-order time-energy chirp has been studied. The idea is to add a dechirper-like corrugated structure in the low energy region of the LCLS-II linac, where it can function as a passive phase space linearizer and help customize the beam energy chirp before it enters the second bunch compressor. After optimizing the parameters of the system, it is possible to enhance the compression factor in the final bunch compressor and thus to achieve a higher final peak current. Note also that, with this method, the current profile can be shaped to avoid large spikes at the head and tail of the distribution. Details of this scheme can be found in [5], and in Fig. 2 we show one result of the final beam before the undulator with using a 0.25-m long corrugated structure (diameter of the structure is 1 mm). Comparing to standard LCLS-II simulation results, we found that the current horn at the bunch head is suppressed, and the core beam current is improved to above 1 kA.

MANIPULATION OF HIGH ORDER OPTICS TERMS IN COMPRESSOR CHICANE

To shape the beam current profile after compression, besides manipulation of the electron beam chirp as discussed above, one can also modify the high-order (nonlinear) terms of the compressor optics. We investigated a scheme recently reported in [6], where an octupole magnet has been adopted in the chicane for U5666 control. Following the methods in [6], we studied the requirement of the U5666 for a given electron beam at the LCLS-II before final compression, developed an optimization procedure using LiTrack code [7], derived formulas to calculate the corresponding octupole strength from U5666, and verified the solutions by Elegant [8] tracking simulations. We discuss these results in the following subsections.

Required U5666 for Current Horn Suppression

With a known beam longitudinal chirp before compression and the chicane R56, to avoid current spikes, one can solve the required high-order term U5666 following the method developed in [6]. But for the overall machine setup, the system should be optimized with also including the machine parameters such as linac phase and amplitude, harmonic linearizer amplitude and phase, BC1 chicane R56, BC2 chicane R56, etc. LiTrack tracking is fast and can be

* Work supported by US Department of Energy under Contract DE-AC02-76SF00515.

[†] email: ding@slac.stanford.edu

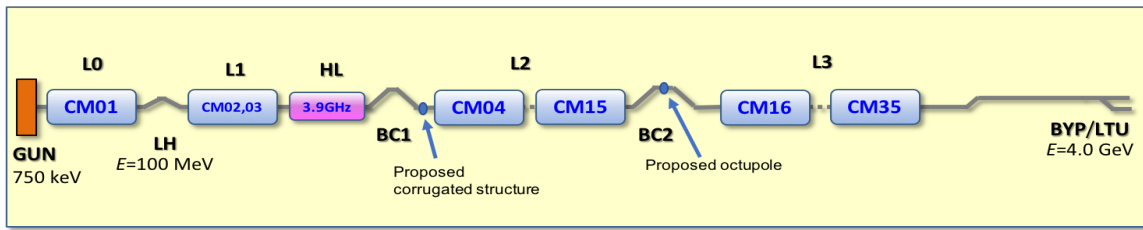


Figure 1: A schematic of the LCLS-II machine layout. The two locations for proposed corrugated structure and octupole are marked in the figure.

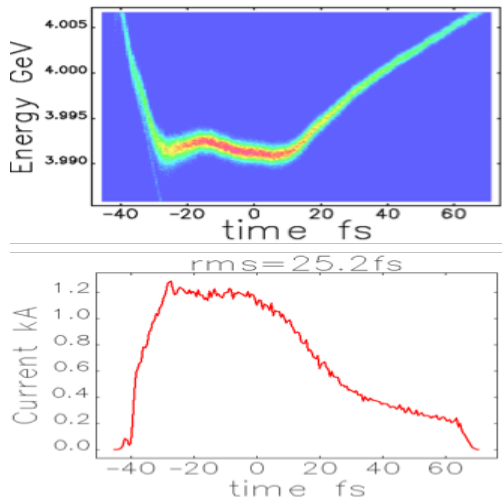


Figure 2: Electron beam phase space and current profile with adding a corrugated structure after BC1, from Elegant simulations. Bunch head is to the left. Same as in the following plots.

Table 1: Main Parameters for Machine Setup with U5666

Parameter	value	unit
Energy out of injector	100	MeV
Bunch charge	100	pC
Final beam energy	4	GeV
L1 phase	-22	deg
L1H phase	-160	deg
BC1 energy	232	MeV
BC1 R56	-60	mm
L2 phase	-25	deg
BC2 energy	1.63	GeV
BC2 R56	-60	mm
BC2 U5666	45	m

combined with multi-objective optimization. We adopted the Non-dominated Sorting Genetic Algorithm (NSGA) in the optimization process for this purpose, with the variables of the linac and chicane parameters. The BC2 chicane is treated as a general compressor in LiTrack with providing two variables: R56 (with fixed T566 = -1.5 R56) and U5666. The optimization target includes higher core current, uniform current shape and small energy spread right after compressor. We show one example of the solutions from LiTrack optimizer with a good current profile in Fig. 3. The optimized machine configuration for this example is summarized in Table 1. We will discuss further in the following subsections using this example.

U5666 and Octupole Strength

Once we know the required U5666 based on LiTrack optimization, we still need to solve the corresponding octupole strength. In this configuration, the octupole is located at the center of a symmetric 4-dipole chicane. In a note by Nosochkov [9] the path length difference through the chicane due to octupole kick is calculated, from which the U5666 from the octupole can be derived as:

$$U_{5666} \approx -\frac{1}{6} K_3 L_0 \theta^4 (L_B + L_D)^4, \quad (1)$$

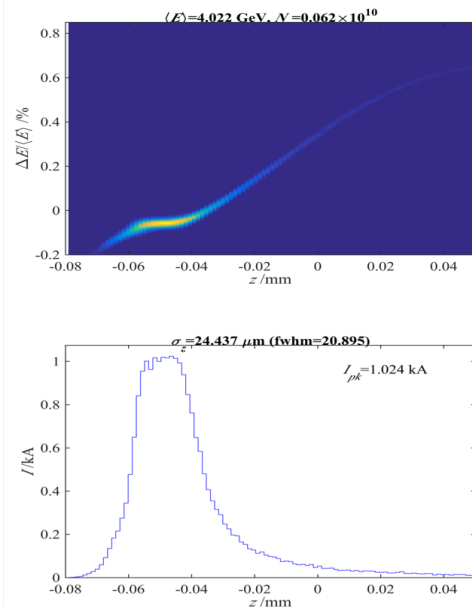


Figure 3: Electron beam phase space and current profile with U5666 = 45 m from LiTrack simulations.

where K_3 is the octupole strength ($K_3 = \frac{B'''}{B\rho}$), L_0 is the octupole length, θ is the chicane single dipole bending angle, L_B is the chicane dipole straight length, and L_D is the drift length between the first (third) and second (fourth) dipole. For the example in Table.1, the LCLS-II BC2 chicane R56

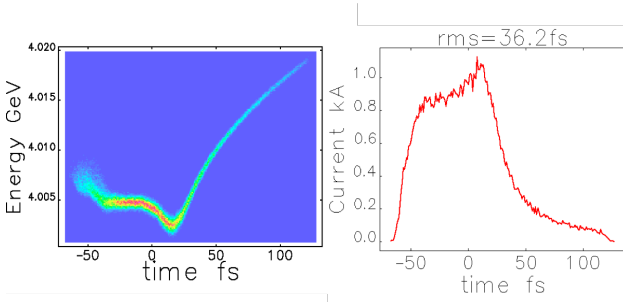


Figure 4: Electron beam phase space and current profile at the undulator entrance with octupole $K_3L_0 = -2700 \text{ m}^{-3}$ from Elegant simulations, other parameters are used from Table 1.

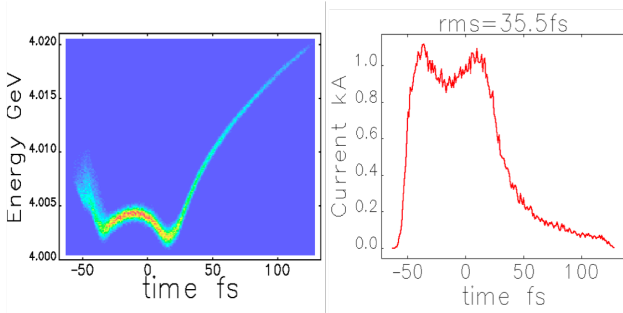


Figure 5: Electron beam phase space and current profile at the undulator entrance with octupole $K_3L_0 = -2200 \text{ m}^{-3}$ from Elegant simulations, other parameters are used from Table 1.

is -60 mm, $L_B = 0.549 \text{ m}$, $L_D = 9.86 \text{ m}$, and $\theta = 0.0541 \text{ rad}$, so Eq. (1) can be written as:

$$U_{5666} \approx -0.0167 K_3 L_0 \quad (2)$$

According to the LCLS-II BC2 chicane vacuum chamber size (full horizontal width 50 mm), with assuming the maximum allowed octupole pole-tip field $B = 5 \text{ kG}$ and octupole length $L_0 = 0.2 \text{ m}$, at an energy of 1.6 GeV, the maximum achievable $K_3L_0 = 7195 \text{ m}^{-3}$, which corresponds to a maximum achievable U_{5666} of 120 m from Eq. (2).

Elegant Tracking

We use Elegant code [8] to verify the solution that was found from LiTrack optimizer, and check transverse effects such as emittance growth. The machine configuration is set up using the same parameters as listed in Table 1 and the octupole strength is calculated using Eq. (2), which is $K_3L_0 = -2700 \text{ m}^{-3}$ here. The final phase space and current profile at the undulator entrance are shown in Fig. 4.

We see from Fig. 4 that the core part current profile has a small ramp. We can tweak the strength of the octupole to correct it. With reducing the K_3L_0 to be -2200 m^{-3} , we have a more balanced current shape, as shown in Fig. 5.

One major concern about using an octupole is the emittance growth. The octupole at the center of the chicane will mainly modify the bunch head and tail, increasing the

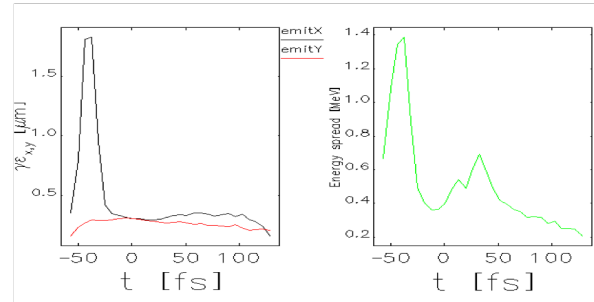


Figure 6: Electron beam sliced emittance and energy spread at the undulator entrance with octupole $K_3L_0 = -2200 \text{ m}^{-3}$ from Elegant simulations, other parameters are used from Table 1.

head/tail emittance and mismatch. We checked the slice emittance and energy spread for the case with $K_3L_0 = -2200 \text{ m}^{-3}$, and show the results in Fig. 6. We see the slice emittance and energy spread at the core part in the bunch center are preserved, with head and tail showing emittance and energy spread growth. We also observed an obvious mismatching at the bunch head and tail. If we send this beam to undulator, only the core part of the bunch will lase efficiently. So this method actually provides a way for x-ray pulse length control, similar to the slotted foil scheme that selectively spoils the beam emittance.

Due to emittance growth at the bunch head and tail, it might cause particle loss along the downstream beamline. A small fraction of particle loss is typically fine for a copper-linac based FEL facility, since the average beam power is low, but it could cause damage and radiation protection issues for a high-repetition rate, superconducting linac with average beam power up to a few hundred kilowatts. With our present setup, we see about 6% particle loss at the halo collimators in the bypass beamline section. Reduction of particle loss needs further study.

DISCUSSION

Electron beam shaping is helpful to improve the FEL lasing performance and increase the operating flexibility of an x-ray FEL. Such shaping at the LCLS copper-linac based accelerator has been very successful. However, in a superconducting linac with high average power, invasive methods should be avoided. In this paper we investigated two schemes: modifying the beam chirp with a corrugated structure or the chicane higher order optics terms using an octupole. Both methods showed improvement on the current profile and beam phase space. The octupole method induces emittance growth on the bunch head and tail, resulting in particle loss in downstream collimator sections; these needs further investigation. Note this also provides a new way of controlling the lasing part along the electron bunch hence generating shorter x-ray pulse. These methods can also be applied in the copper-linac based FELs, where particle loss should not be a problem.

REFERENCES

- [1] LCLS-II Final Design Report, 2014.
- [2] Y. Ding *et al.*, “Beam shaping to improve the FEL performance at the LCLS”, *Physical Review Accelerator and Beams*, vol. 19, p. 100703, 2016. doi:10.1103/PhysRevAccelBeams.19.100703
- [3] P. Emma, K. Bane, M. Cornacchia, Z. Huang, H. Schlarb, G. Stupakov, and D. Walz, “Femtosecond and Subfemtosecond X-Ray Pulses from a Self-Amplified Spontaneous-Emission-Based Free-Electron Laser”, *Phys. Rev. Lett.*, vol. 92, p. 074801, 2004. doi:10.1103/PhysRevLett.92.074801
- [4] Y. Ding *et al.*, “Generating femtosecond X-ray pulses using an emittance-spoiling foil in free-electron lasers”, *Appl. Phys. Lett.*, vol. 107, p. 191104, 2015. doi:10.1063/1.4935429
- [5] Y. Ding *et al.*, “Beam shaping with a passive linearizer at the LCLS-II for high-current operation”, LCLS-II technical note, LCLS-II-TN-18-02.
- [6] T. K. Charles *et al.*, “Current-horn suppression for reduced coherent-synchrotron-radiation-induced emittance growth in strong bunch compression”, *Physical Review Accelerator and Beams*, vol. 20, p. 030705, 2017. doi:10.1103/PhysRevAccelBeams.20.030705
- [7] K. Bane and P. Emma, “LiTrack: A Fast Longitudinal Phase Space Tracking Code with Graphical User Interface”, in *Proc. PAC’05*, Knoxville, TN, USA, May 2005, paper FPAT091, p. 4266.
- [8] M. Borland, “elegant: A Flexible SDDS-Compliant Code for Accelerator Simulation”, Advanced. Photon Source LS-287, September 2000.
- [9] Y. Nosochkov, technical note (not published yet).

MICROBUNCH ROTATION FOR HARD X-RAY BEAM MULTIPLEXING*

R. A. Margraf^{†1}, Z. Huang¹, J. MacArthur, G. Marcus, SLAC National Laboratory, 94025 Menlo Park, USA
X. Deng, Tsinghua University, Beijing, China
¹also at Stanford University, Stanford, USA

Abstract

Electron bunches in an undulator develop periodic density modulations, or microbunches, which enable the exponential gain of X-ray power in a SASE FEL. Many FEL applications could from the ability to preserve microbunching through a dipole kick. For example, X-ray beam multiplexing can be achieved if electron bunches are kicked into separate beamlines and allowed to lase in a undulator. The microbunches developed in upstream undulators, if properly rotated, will lase axis, producing radiation at an angle from the initial beam axis. Microbunch rotation with soft X-rays was previously published and demonstrated experimentally [1], multiplexing LCLS into three X-ray beams. Additional 2018 data demonstrated multiplexing of hard X-rays. Here we describe ts to reproduce these hard X-ray experiments using an analytical model and Genesis simulations. Our goal is to apply microbunch rotation to out-coupling from a cavity-based XFEL, (RAFEL/XFEL0) [2].

ANALYTICAL MODEL

Microbunch rotation can be accomplished by providing a dipole kick to a bunch as it travels through a defocusing quadrupole. This dipole kick can be provided by either a dipole magnet or a transversely quadrupole. An analytical model for microbunch rotation within a defocusing quadrupole was developed previously by MacArthur et al. [1]. Here, we introduce a new analytical method for describing microbunch rotation using matrices, which is more intuitive to use with multiple quadrupoles.

Microbunch Rotation by Offset Thin Quadrupole

We begin by a thin quadrupole in 4D phase space (y, y', z, δ) . The quadrupole has focal length f , and is in y by a distance o_1 , producing a kick $\theta = -\frac{1}{f}(y_0 + o_1)$, where y_0 is the transverse beam position before the quadrupole. We treat an quadrupole as an on-axis quadrupole which also rotates the coordinate system in the y - z plane by θ to follow the beam trajectory. We assume a small kick angle ($\sin(\theta) \approx \theta$, $\cos(\theta) \approx 1$), and neglect order terms, ($\theta z \approx 0$, $-\theta y' \approx 0$) to simplify the rotation matrix.

$$M_\theta \approx \begin{bmatrix} 1 & 0 & 0 & 0 \\ 0 & 1 & 0 & \theta \\ -\theta & 0 & 1 & 0 \\ 0 & 0 & 0 & 1 \end{bmatrix} \quad (1)$$

our initial microbunch size and divergence in the center of the quadrupole, we an quadrupole matrix with double the focal length of our full quadrupole

$$M_{Q\theta} = M_Q + M_\theta = \begin{bmatrix} 1 & 0 & 0 & 0 \\ -\frac{1}{2f} & 1 & 0 & \theta \\ -\theta & 0 & 1 & 0 \\ 0 & 0 & 0 & 1 \end{bmatrix}. \quad (2)$$

Note that we still rotate the coordinate system by the full kick, θ , produced by the quadrupole. This is because the y - z plane (which we must rotate) is initially at the angle of the beam entering the quadrupole, $y'_0 = 0$, but our microbunch rotation analysis begins with particles at the center of the quadrupole, $(y_1, y'_1, z_1, \delta_1)$.

We apply a drift of length L to get our transfer matrix,

$$M = M_L M_{Q\theta} = \begin{bmatrix} 1 - \frac{L}{2f} & L & 0 & L\theta \\ -\frac{1}{2f} & 1 & 0 & \theta \\ -\theta & 0 & 1 & 0 \\ 0 & 0 & 0 & 1 \end{bmatrix}. \quad (3)$$

We assume a single Gaussian microbunch, with a sigma matrix that is uncorrelated in the center of the quadrupole,

$$\Sigma_1 = \begin{bmatrix} \sigma_{y_1}^2 & 0 & 0 & 0 \\ 0 & \sigma_{y'_1}^2 & 0 & 0 \\ 0 & 0 & \sigma_{z_1}^2 & 0 \\ 0 & 0 & 0 & \sigma_{\delta_1}^2 \end{bmatrix}. \quad (4)$$

We then evolve the microbunch envelope using the transfer matrix, and obtain the second moments.

$$\Sigma = M \Sigma_1 M^T \quad (5)$$

$$\begin{aligned} \langle y^2 \rangle &= \left(1 - \frac{L}{2f}\right)^2 \sigma_{y_1}^2 + L^2 \sigma_{y'_1}^2 + L^2 \theta^2 \sigma_{\delta_1}^2 \\ \langle z^2 \rangle &= \sigma_{z_1}^2 + \theta^2 \sigma_{y_1}^2 \\ \langle yz \rangle &= -\left(1 - \frac{L}{2f}\right) \theta \sigma_{y_1}^2 \end{aligned} \quad (6)$$

The tilt in the rotated coordinate system, t_{yz} , can then be geometrically found from,

$$\tan(2t_{yz}) = \frac{2\langle yz \rangle}{\langle y^2 \rangle - \langle z^2 \rangle}, \quad (7)$$

$$t_{yz} \approx \frac{\langle yz \rangle}{\langle y^2 \rangle - \langle z^2 \rangle}. \quad (8)$$

In the limit of pancake microbunches, $\langle z^2 \rangle \ll \langle y^2 \rangle$ and if $\theta^2 \approx 0$, we write the tilt in terms of the Beta function, β_1 .

$$t_{yz} \approx \frac{\langle yz \rangle}{\langle y^2 \rangle} = \frac{-\left(1 - \frac{L}{2f}\right) \theta}{\left(1 - \frac{L}{2f}\right)^2 + \frac{L^2}{\beta_1^2}} \quad (9)$$

* This work was supported by the Department of Energy, Laboratory Directed Research and Development program at SLAC National Accelerator Laboratory, under contract DE-AC02-76SF00515.

[†] rmargraf@stanford.edu

For relatively large kick angles and energy spread, we found $\theta^2 \approx 0$ was not always a safe assumption, and used Eq. (8) for our analysis. However, Eq. (9) is useful for building intuition that the microbunch rotation direction is determined by the sign of f . Eq. (9) we

$$\left. \frac{\partial t_{yz}}{\partial L} \right|_{L=0} = -\frac{\theta}{2f} \quad (10)$$

This result shows that a defocusing quadrupole ($f < 0$) will rotate the microbunch in the direction of the kick, θ .

Microbunch Rotation by Thin Quadrupole Triplet

Next, we want to analyze the rotation of a microbunch through three quadrupoles with focal lengths f_1, f_2, f_3 ; in y by distances o_1, o_2, o_3 ; separated by drifts L_1, L_2 ; and followed by a drift L_3 . Subsequent simulations will consider a defocusing-focusing-defocusing triplet, $f_1 < 0, f_2 > 0, f_3 < 0$, as this triplet achieves a given rotation with the smallest kick angles, but the analytical method can be applied to quadrupoles of arbitrary focal length.

We the transfer matrix for each quadrupole,

$$M_{Q\theta 1} = \begin{bmatrix} 1 & 0 & 0 & 0 \\ -\frac{1}{2f_1} & 1 & 0 & \theta_1 \\ -\theta_1 & 0 & 1 & 0 \\ 0 & 0 & 0 & 1 \end{bmatrix}, M_{Q\theta 2,3} = \begin{bmatrix} 1 & 0 & 0 & 0 \\ -\frac{1}{f_{2,3}} & 1 & 0 & \theta_{2,3} \\ -\theta_{2,3} & 0 & 1 & 0 \\ 0 & 0 & 0 & 1 \end{bmatrix} \quad (11)$$

The kick angles can be readily solved using a matrix method. If $\langle y_0 \rangle = \langle y'_0 \rangle = 0$, the kick angles are,

$$\begin{aligned} \theta_1 &= -\frac{o_1}{f_1}, \\ \theta_2 &= -\frac{1}{f_1 f_2} (f_1 o_2 - L_1 o_1), \\ \theta_3 &= -\frac{1}{f_1 f_2 f_3} (f_1 f_2 o_3 + f_2 f_3 o_1 - f_2 L_1 o_1 - f_1 L_2 o_2 \\ &\quad - f_2 L_2 o_1 - L_1 L_2 o_1). \end{aligned} \quad (12)$$

Using these, we build our transfer matrix,

$$M = M_{L3} M_{Q\theta 3} M_{L2} M_{Q\theta 2} M_{L1} M_{Q\theta 1}. \quad (13)$$

To the tilt, one can propagate a sigma matrix at the center of the triplet quadrupole, Σ_1 , through this transfer matrix using Eq. (5). An expression for the microbunch tilt, too long to write out here, can be obtained using Eq. (8).

For arbitrary quadrupole the microbunch tilt will continue to evolve with additional drift distance, L_3 . To achieve microbunch rotation, we need to lock the microbunch tilt into the direction of beam travel, eg. $t_{yz} = 0$ and $\frac{\partial t_{yz}}{\partial L_3} = 0$. We found this is equivalent to requiring the matrix be achromatic, eg. $D = 0$ and $D' = 0$. D and D' are the dispersion and change in dispersion (R36 and R46) of M , read directly from the transfer matrix. For a given beam trajectory angle α , we solve this system of equations,

$$\begin{aligned} D &= 0, \\ D' &= 0, \\ \alpha &= \langle y'_0 \rangle + \theta_1 + \theta_2 + \theta_3. \end{aligned} \quad (14)$$

We obtain the ideal for microbunch rotation through three thin quadrupoles. For $\langle y_0 \rangle = \langle y'_0 \rangle = 0$,

$$\begin{aligned} o_1 &= \frac{-\alpha f_1 f_2}{L_1}, \\ o_2 &= \frac{-\alpha f_1 (f_2 L_1 + f_2 L_2 - L_1 L_2)}{L_1 L_2}, \\ o_3 &= \frac{-\alpha f_1 (L_2^2 + f_2 f_3)}{L_2}. \end{aligned} \quad (15)$$

Microbunch Rotation by Thick Quadrupole

We also pursued a thick lens approach, with quadrupole length L_Q and $k^2 = \frac{1}{|f_{thickens}|L_Q}$. A shifted defocusing and focusing quadrupole can be respectively,

$$\begin{aligned} M_{Q_D \theta} &= \begin{bmatrix} \cosh(kL_Q) & \frac{1}{k} \sinh(kL_Q) & 0 & 0 \\ k \sinh(kL_Q) & \cosh(kL_Q) & 0 & \theta \\ -\theta & 0 & 1 & 0 \\ 0 & 0 & 0 & 1 \end{bmatrix}, \\ M_{Q_F \theta} &= \begin{bmatrix} \cos(kL_Q) & \frac{1}{k} \sin(kL_Q) & 0 & 0 \\ -k \sin(kL_Q) & \cos(kL_Q) & 0 & \theta \\ -\theta & 0 & 1 & 0 \\ 0 & 0 & 0 & 1 \end{bmatrix}. \end{aligned} \quad (16)$$

For the defocusing-focusing-defocusing case, we again build our transfer matrix similarly to Eq. (13), shortening L_Q by half in the triplet quadrupole and using the full L_Q in the second two. $\theta_1, \theta_2, \theta_3$ are also recalculated using thick quadrupoles. We solve for the optimal using the system of equations in Eq. (14), obtaining a lengthy analytical solution for the optimal used in subsequent sections.

COMPARISON OF ANALYTICAL MODEL TO GENESIS SIMULATIONS

We supported our analytical model with Genesis [3] simulations, summarized in Fig. 1 and Table 1.

Table 1: Genesis Simulation Parameters

Parameters Common to All Triplets					
B'_1	-65.267 T/m	L_1	4.05 m		
B'_2	65.600 T/m	L_2	3.9 m		
B'_3	-65.267 T/m	L_Q	6 cm		
a_w	2.4749	$L_{Undulator}$	3.3 m		
$E_{electron}$	14.535 GeV	E_{λ_r}	9.3858 keV		
σ_{y_1}	1.745×10^{-5} m	$\sigma_{y'_1}$	8.059×10^{-7} rad		
σ_{z_1}	3.457×10^{-11} m	σ_{δ_1}	2.378×10^{-4}		
Triplet Quadrupole Offsets (μ m)					
α	-5 μ rad		-10 μ rad		Exp
Model:	Thin	Thick	Thin	Thick	
o_1	-190.94	-193.84	-381.89	-387.68	-150
o_2	-258.23	-262.66	-516.46	-525.33	-263
o_3	-178.79	-180.54	-357.58	-361.08	-206

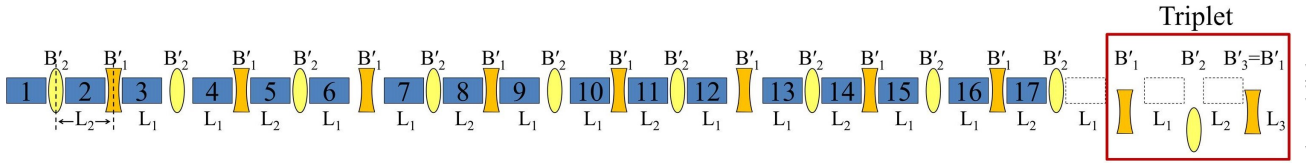


Figure 1: Genesis lattice. The beam was pre-bunched in 17 undulators (blue), then sent through an quadrupole triplet.

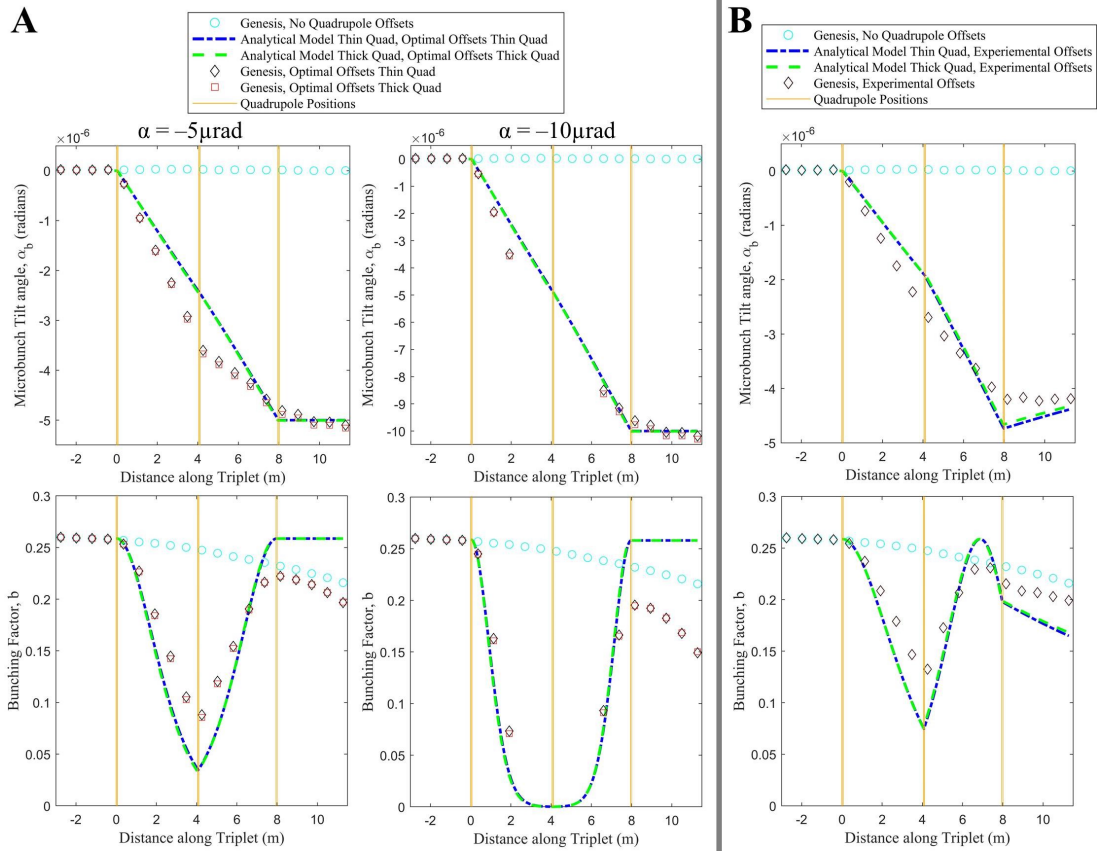


Figure 2: Microbunch tilt angle in nonrotated frame, α_b and bunching factor, b , through an quadrupole triplet. are A) analytical model optimal using thin or thick quadrupoles, or B) replicating a 2018 experiment.

We calculated optimal for $\alpha = -5 \mu\text{rad}$ and $\alpha = -10 \mu\text{rad}$ using thin and thick quadrupole models, and simulated each. As shown in Fig. 2A, both models achieved similar results. The analytical models predict 99.98% or 99.7% recovery of b after a $-5 \mu\text{rad}$ or $-10 \mu\text{rad}$ rotation. For these angles at $L_3 = 15 \text{ cm}$, Genesis predicts 85.9% or 75% recovery. Some loss can be explained by the degradation of b to 89.7% over the long length of the triplet. While this recovery is sizable, we suspect there are still unaccounted for in our matrix model which limit our ability to choose optimal. Genesis shows the microbunch angle continues to evolve slowly with distance, instead of locking into the beam travel angle. We suspect this is due to second-order (microbunch smearing) [1] which Genesis accounts for, or $\langle yz \rangle$ correlations in the quadrupole center caused by imperfect lattice matching.

We would like to use Genesis and our analytical model to explain the microbunch rotation observed in an experiment

at LCLS in 2018. A successful microbunch rotation, which lased at angles between -2 to $-7 \mu\text{rad}$ was achieved through a combination of quadrupole and corrector dipole magnets, producing e quadrupole given in Table 1. For these our analytical model and Genesis give results shown in Fig. 2B.

The analytical model predicts only a 76% recovery, while Genesis shows 83.2% recovery of b . Interestingly, Genesis shows these lock the microbunch rotation into an average angle of $-4.19 \mu\text{rad}$, close to $\alpha = -4.11 \mu\text{rad}$. While these generally behave better than the analytical model would predict, the model does correctly predict a maximum in bunching between the last two quadrupoles.

CONCLUSION

We have developed an analytical model for microbunch rotation using matrices which gives a t-order estimate of microbunch rotation through an quadrupole triplet.

REFERENCES

- [1] J. P. MacArthur, A. A. Lutman, J. Krzywinski, and Z. Huang, "Microbunch Rotation and Coherent Undulator Radiation from a Kicked Electron Beam," *Physical Review X*, vol. 8, no. 4, Nov. 2018. doi:10.1103/PhysRevX.8.041036
- [2] G. Marcus, F.-J. Decker, Z. Huang, Y. Liu, J. MacArthur, R. Margraf, T. Raubenheimer, A. Sakdinawat, T.-F. Tan, D. Zhu, L. K.-J. Kim, R. Lindberg, X. Shi, D. Shu, Y. Shvyd'ko, M. White. 'Cavity-Based Free-Electron Laser Research and Development: A Joint Argonne National Laboratory and SLAC National Laboratory Collaboration.' *Presented at FEL2019*, TUD04, Hamburg, Germany, 2019.
- [3] Genesis. Version 1.3. S. Reiche. Available: <http://genesis.web.psi.ch/index.html>

A NOVEL ONE-DIMENSIONAL MODEL FOR CSR WAKEFIELDS*

Gennady Stupakov[†], SLAC National Accelerator Laboratory, Menlo Park, CA, USA

Abstract

The existing 1D models of the coherent synchrotron radiation (CSR) wakefield in free space assume that the longitudinal bunch distribution remains constant when the beam propagates through a magnetic lattice. In this paper, we derive a formula for a 1D CSR wake that takes into account variation of the bunch length along the orbit. The formula is valid for arbitrary curvilinear beam trajectory. We analyze the validity of the 1D model in a typical implementation of an FEL bunch compressor.

INTRODUCTION

When the trajectory of a relativistic beam is bent by magnetic field, the beam radiates electromagnetic field and experiences a radiation reaction force. A popular 1D model for this force in the case of a circular motion, often called the coherent synchrotron radiation (CSR) wake, was first developed in Refs. [1–3]. A generalization of this model for the case of a bending magnet of finite length is described in Refs. [4, 5] and is implemented in several computer codes¹. These models assume a constant bunch length, σ_z , along the orbit. Their applicability becomes questionable in a bunch compressor where $\sigma_z(s)$ is a function of the beam position s . In practice, one usually substitutes a local bunch length $\sigma_z(s)$ into the formulas derived with the assumption $\sigma_z = \text{const}$. Such a substitution, strictly speaking, is not justified because it ignores the fact that the wake is formed by the beam radiation emitted at previous times, when the bunch length is different from the value of σ_z at the moment when the wake interacts with the beam. More recently, in Ref. [6], a 1D CSR model was derived from Jefimenko's form for the electric field of a relativistic beam with an attempt to include a time dependent bunch length by heuristically introducing $\sigma_z(t)$ into equations derived with the assumption of constant bunch length.

In this paper, we derive a 1D CSR wake that takes into account the variation of the bunch length along the orbit. Our derivation is based on the 3D formulas from Ref. [7].

We use the CGS system of units throughout this paper.

FORMULA FOR THE LONGITUDINAL WAKE IN 3D

We begin from the formulation of general 3D wake from Ref. [7]. In 3D, the beam is represented by its charge density $\rho(\mathbf{r}, t)$ that depends on time t and the position vector \mathbf{r} , and its velocity $\mathbf{v}(\mathbf{r}, t)$, with the beam current density \mathbf{j} given

by the product $\mathbf{j} = \rho\mathbf{v}$. Note that in this model assigning a particular value of \mathbf{v} at each point we neglect the uncorrelated velocity spread in the beam due to the angular and energy spread — an approximation that is typically well satisfied for relativistic beams. For given functions $\rho(\mathbf{r}, t)$ and $\mathbf{j}(\mathbf{r}, t)$, one can derive an equation for the electric field in the beam, $\mathbf{E}(\mathbf{r}, t)$, and calculate the instantaneous energy change per unit time and *per unit charge*, \mathcal{P} ,

$$\mathcal{P}(\mathbf{r}, t) = \mathbf{v}(\mathbf{r}, t) \cdot \mathbf{E}(\mathbf{r}, t). \quad (1)$$

We will loosely call \mathcal{P} the *longitudinal wake*, although the classical wake fields are typically associated with the energy loss integrated over the beam path and the transverse cross section of the beam.

A general expression for the quantity \mathcal{P} is given in Ref. [7]. It consists of three terms two of which in many cases are much smaller than the third one. We neglect these terms in our analysis leaving only the dominant one:

$$\mathcal{P}(\mathbf{r}, t) = -c \int \frac{d^3\mathbf{r}'}{|\mathbf{r}' - \mathbf{r}|} [\boldsymbol{\beta}(\mathbf{r}, t) - (\boldsymbol{\beta}(\mathbf{r}, t) \cdot \boldsymbol{\beta}(\mathbf{r}', t_{\text{ret}}))\boldsymbol{\beta}(\mathbf{r}', t_{\text{ret}})] \cdot \partial_{\mathbf{r}'} \rho(\mathbf{r}', t_{\text{ret}}), \quad (2)$$

where $\boldsymbol{\beta} = \mathbf{v}/c$, $t_{\text{ret}}(\mathbf{r}, \mathbf{r}', t) = t - |\mathbf{r}' - \mathbf{r}|/c$, and we use the notation $\partial_{\mathbf{r}'} \rho(\mathbf{r}', t_{\text{ret}})$ to indicate differentiation with respect to the space coordinates in function $\rho(\mathbf{r}', t_{\text{ret}})$ with a fixed t_{ret} (in other words, the operator $\partial_{\mathbf{r}'}$ ignores the fact that t_{ret} also depends on \mathbf{r}'). Note that due to the factor $|\mathbf{r}' - \mathbf{r}|^{-1}$ the integrand has a singularity at $\mathbf{r}' \rightarrow \mathbf{r}$, however, this singularity is integrable². The singularity disappears in the ultra-relativistic limit $|\boldsymbol{\beta}| = 1$ because the factor in square brackets vanishes when $\mathbf{r} \rightarrow \mathbf{r}'$. As one can see, the integral (2) is taken over the volume around the beam trajectory at preceding times $t_{\text{ret}} < t$.

1D MODEL

It is known that the transverse size of the beam, σ_{\perp} , does not affect the CSR wake if $\sigma_{\perp} \lesssim (\sigma_z^2 R)^{1/3}$, where R is the bending radius [3] (see, however, discussion below). Assuming that this is the case, we can simplify integral (2) and derive a 1D model for the wake \mathcal{P} . In 1D all particles in the beam move along a curve given by the radius-vector $\mathbf{r}_0(s)$, where s is the path length measured along the orbit. Positions in the vicinity of this orbit are represented in a Frenet–Serret coordinate system as $\mathbf{r}_0(s) + \hat{\mathbf{x}}(s)x + \hat{\mathbf{y}}(s)y$, where $\hat{\mathbf{x}}(s)$ and $\hat{\mathbf{y}}(s)$ are the unit vectors perpendicular to the tangential vector, $\boldsymbol{\tau}(s) \equiv d\mathbf{r}_0/ds$, and each other so that x , y and s constitute a local orthogonal coordinate system. In what follows we will assume an ultra-relativistic beam

* Work supported by the Department of Energy, contract DE-AC03-76SF00515

[†] stupakov@slac.stanford.edu

¹ Here, we only deal with the longitudinal part of the forces in the bunch that changes particles' energy in the beam; for the effect of the transverse force, see a recent study [8].

² It is also integrable in a 2D model when the three dimensional integration $\int d^3\mathbf{r}'$ is replaced by $\int d^2\mathbf{r}'$. It is not integrable in 1D.

with $|\boldsymbol{\beta}| = 1$. The velocity is everywhere directed along the trajectory, so we can identify $\boldsymbol{\beta}$ with the tangential vector, $\boldsymbol{\beta} = \boldsymbol{\tau}(s)$. We then write Eq. (2) as

$$\mathcal{P}(s, t) = -c \int \frac{ds' dx' dy'}{|\mathbf{r}_0(s') - \mathbf{r}_0(s)|} [\boldsymbol{\tau}(s) - (\boldsymbol{\tau}(s) \cdot \boldsymbol{\tau}(s')) \boldsymbol{\tau}(s')] \cdot \partial_{\mathbf{r}'} \rho(x', y', s', t_{\text{ret}}), \quad (3)$$

where we have associated the observation vector \mathbf{r} with $\mathbf{r}_0(s)$ (the wake is calculated on the beam orbit) and replaced \mathbf{r}' by $\mathbf{r}_0(s')$ ³. We note that $\boldsymbol{\tau}(s) \cdot \boldsymbol{\tau}(s')$ is the projection of vector $\boldsymbol{\tau}(s)$ onto the vector $\boldsymbol{\tau}(s')$ and subtracting $(\boldsymbol{\tau}(s) \cdot \boldsymbol{\tau}(s')) \boldsymbol{\tau}(s')$ from $\boldsymbol{\tau}(s)$ gives a part of the vector $\boldsymbol{\tau}(s)$ that is perpendicular to $\boldsymbol{\tau}(s')$. Denoting this difference by $\mathbf{m}(s, s')$,

$$\mathbf{m}(s, s') = \boldsymbol{\tau}(s) - (\boldsymbol{\tau}(s) \cdot \boldsymbol{\tau}(s')) \boldsymbol{\tau}(s'), \quad (4)$$

we have $\mathbf{m}(s, s') \cdot \boldsymbol{\tau}(s') = 0$, and hence this vector has only x' and y' components at s' . Using this vector, we can re-write Eq. (3) as

$$\begin{aligned} \mathcal{P}(s, t) &= -c \int \frac{ds' dx' dy'}{|\mathbf{r}_0(s') - \mathbf{r}_0(s)|} \mathbf{m}(s, s') \cdot \partial_{\mathbf{r}'} \rho(x', y', s', t_{\text{ret}}) \\ &= -c \int \frac{ds' dx' dy'}{|\mathbf{r}_0(s') - \mathbf{r}_0(s)|} [m_{x'}(s, s') \partial_{x'} \rho(x', y', s', t_{\text{ret}}) \\ &\quad + m_{y'}(s, s') \partial_{y'} \rho(x', y', s', t_{\text{ret}})]. \end{aligned} \quad (5)$$

At a first glance, it seems that this integral is equal to zero because we integrate partial derivatives of ρ with respect to x' and y' over x' and y' from minus to plus infinity, and, of course, the distribution function goes to zero at $|x'|, |y'| \rightarrow \infty$. However, at this point we need to take into account the dependence of $t_{\text{ret}} = t - |\mathbf{r} - \mathbf{r}'|/c$ versus x' and y' . In our curvilinear coordinate system, vector $\mathbf{r} - \mathbf{r}'$ can be written in the following way:

$$\mathbf{r} - \mathbf{r}' = \mathbf{r}_0(s) + (\hat{\mathbf{x}}x' + \hat{\mathbf{y}}y') - \mathbf{r}_0(s') - (\hat{\mathbf{x}}'x' + \hat{\mathbf{y}}'y'), \quad (6)$$

where we use the notations: $\hat{\mathbf{x}} = \hat{\mathbf{x}}(s)$, $\hat{\mathbf{x}}' = \hat{\mathbf{x}}(s')$, and similar abbreviations for the y components. Given the assumed smallness of the transverse size of the beam, we will use the Taylor expansion of t_{ret} , keeping only linear terms in x' and y' (the linear terms in x and y will be annihilated by the integration by parts below, so we ignore them),

$$\begin{aligned} t_{\text{ret}} &\approx t - \frac{1}{c} |\mathbf{r}_0(s) - \mathbf{r}_0(s')| \\ &\quad + \frac{1}{c} \frac{\mathbf{r}_0(s) - \mathbf{r}_0(s')}{|\mathbf{r}_0(s) - \mathbf{r}_0(s')|} \cdot (\hat{\mathbf{x}}'x' + \hat{\mathbf{y}}'y'). \end{aligned} \quad (7)$$

We then expand function ρ ,

$$\begin{aligned} \rho(x', y', s', t_{\text{ret}}) &\approx \rho\left(x', y', s', t - \frac{1}{c} |\mathbf{r}_0(s) - \mathbf{r}_0(s')|\right) \\ &\quad + \partial_t \rho\left(x', y', s', t - \frac{1}{c} |\mathbf{r}_0(s) - \mathbf{r}_0(s')|\right) \\ &\quad \times \frac{1}{c} \frac{\mathbf{r}_0(s) - \mathbf{r}_0(s')}{|\mathbf{r}_0(s) - \mathbf{r}_0(s')|} \cdot (\hat{\mathbf{x}}'x' + \hat{\mathbf{y}}'y'). \end{aligned} \quad (8)$$

³ Replacing d^3r by $ds' dx' dy'$ we ignore the Lamé coefficients in the curvilinear coordinate system x, y, s . The account of these coefficients would add only small corrections to our results.

Substituting this expression into (5) we note that the first term in ρ vanishes after the integration over x' and y' , and the second term, after integration by parts, gives

$$\begin{aligned} \mathcal{P}(s, t) &= \int ds' \frac{(\mathbf{r}_0(s) - \mathbf{r}_0(s')) \cdot \mathbf{m}(s, s')}{|\mathbf{r}_0(s') - \mathbf{r}_0(s)|^2} \\ &\quad \times \partial_t \lambda\left(s', t - \frac{1}{c} |\mathbf{r}_0(s) - \mathbf{r}_0(s')|\right), \end{aligned} \quad (9)$$

where λ is the longitudinal distribution function of the beam

$$\lambda(s, t) = \int dx' dy' \rho(x', y', s', t). \quad (10)$$

Note that the integrand in the 1D integral (9) does not have a singularity at $s' \rightarrow s$ because both terms in the numerator, $\mathbf{r}_0(s) - \mathbf{r}_0(s')$ and $\mathbf{m}(s, s')$, vanish when $s' = s$.

Using the method of images, Eq. (9) can be also generalized for the case when a plane beam orbit lies between two parallel conducting plates.

TRANSIENT CSR WAKE IN A BEND MAGNET

To benchmark Eq. (9) against known solutions of 1D CSR problems, we first calculated the steady-state wake for a short Gaussian bunch, $\sigma_z \ll R$, moving in a circular orbit of constant radius R . Our result (not shown here) agrees very well with the wake profile which can be found in the literature.

Another benchmark problem, that of a bending magnet of finite length L was studied in Refs. [4, 5]. In this problem, the beam travels on an arc of radius R inside the magnet, $-\frac{1}{2}L < s < \frac{1}{2}L$. Outside of the magnet, the beam moves with $v = c$ along straight lines tangential to the circular orbit at the points of entrance and exit, respectively. For the sake of comparison, we have chosen the same set of parameters as in Ref. [5]: $R = 1.5$ m, $\sigma_z = 50$ μm , $Q = 1$ nC and $L = 25$ cm.

We first calculated the wake inside the bunch when it enters the bend from a straight line. The plot of this wake at various distances from the magnet entrance edge is shown in Fig. 1 by solid lines. For comparison, the dashed green lines show the result of 1D model computed in Ref. [5].

We have also calculated the wake in the bunch after it exits the bend magnet and continues to travel along a straight line, and found an excellent agreement of our theory with the 1D model of Ref. [5].

CSR WAKE IN A BUNCH COMPRESSOR

A much more difficult problem is presented by a chicane bunch compressor consisting of four dipole magnets. To illustrate how Eq. (9) can be used in a situation when σ_z varies with s , we calculated the CSR wake in a configuration studied at the CSR workshop at DESY-Zeuthen in 2002 [9]. The four magnets have the length $L = 0.5$ m with the bending radius $R = 10.35$ m resulting in the momentum compaction factor $R_{56} = 2.5$ cm. In our simulations, the beam with

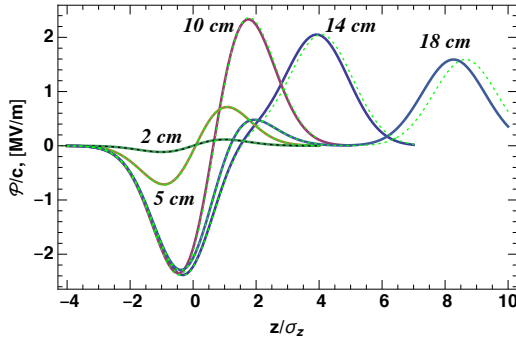


Figure 1: Longitudinal wake in the bunch as a function of distance from the entrance edge of the bend shown by a number near each curve. The longitudinal coordinate z in each case is measured from the center of the bunch.

the energy of 5.0 GeV and Gaussian distributions in energy and coordinates is compressed from the initial rms length of $200 \mu\text{m}$ to the final length of $150 \mu\text{m}$, as shown in Fig. 2⁴. The beam charge is 1 nC, the slice energy spread is 10^{-4} , and the energy chirp is -10 m^{-1} . We calculated the CSR wake in the middle of the second and third magnets as well as at the center of the chicane, see Fig. 2.

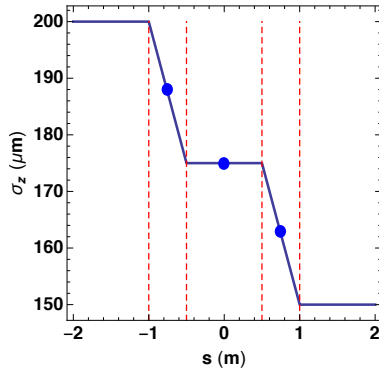


Figure 2: Variation of the bunch length $\sigma_z(s)$ through the second and third magnets of the chicane (the magnet edges are shown by red dashed lines). The coordinate $s = 0$ corresponds to the center of the chicane. The blue dots show three positions in the chicane where the CSR wake was calculated.

The wake calculated in the 1D model with the help of Eq. (9) is shown in Fig. 3 by solid lines. These wakes are compared with the wakes calculated with a 2D version of Eq. (2) (shown by dashed lines). The 2D wakes plotted as a function of z are actually calculated along the axis of the tilted beam, that is at $x = z \tan \alpha$, where α is the tilt angle ($\alpha = 72^\circ$ at the center of the chicane). The plots show a considerable difference between the 1D and 2D wakes. We discuss the origin of this difference in the next section.

⁴ We have intentionally chosen a small compression factor in an attempt to improve the applicability of the 1D model for the CSR wake.

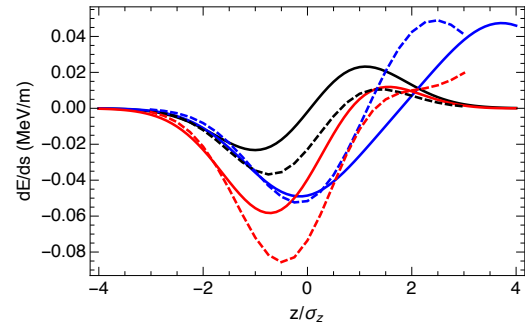


Figure 3: Wakes calculated in 1D model are shown by solid lines: black — in the middle of the second magnet ($s = -0.75 \text{ m}$), blue — at the center of the chicane ($s = 0$), and red — in the middle of the third magnet ($s = 0.75 \text{ m}$). Dashed lines (with the corresponding color) are calculated for the same locations using a 2D version of Eq. (2). The coordinate z is normalized by the rms bunch length, $\sigma_z(s)$.

DISCUSSION

The simple 1D models [2–4, 6] of the CSR wake have two important limitations when applied to bunch compressors. First, they assume a constant bunch length, and, second, they ignore the tilt of the bunch with an energy chirp when it passes through the region of large dispersion. In contrast to the previous theories, our Eq. (9), takes the variation of the bunch length into account but it still misses the bunch tilt. This is the reason of noticeable discrepancy between our 1D and 2D calculations in Fig. 3.

It is often assumed that a 1D model that ignores the transverse size of the beam is supposed to work when the following condition [3] is met: $\sigma_\perp \lesssim (\sigma_z^2 R)^{1/3}$. This is well satisfied for the parameters of the chicane studied in the preceding section: at the center of the chicane $\sigma_\perp = 0.54 \text{ mm}$, $\sigma_z = 175 \mu\text{m}$, and $(\sigma_z^2 R)^{1/3} = 6.8 \text{ mm}$; however, as Fig. 3 shows, our 1D model does not agree with the more accurate 2D one. One can argue that a more accurate estimate should use not the total bunch length σ_z , but the lengths of a longitudinal slice of the beam (say, for $x = 0$), $\sigma_{z,x=0} = 16 \mu\text{m}$, which makes $(\sigma_{z,x=0}^2 R)^{1/3} = 1.3 \text{ mm}$, but even this estimate apparently underestimate the effect of the beam tilt, as our results demonstrate.

We note that our choice of a relatively small energy chirp in the beam, and hence a small compression, was motivated by the desire to minimize the effect of the beam tilt when it passes through the second and third magnets. For the compression factor of 10 originally studied in [9], the tilt is much stronger, and the 1D model even less likely to work near the center of the chicane. It should work, though, in the last magnet of the chicane where the bunch is already compressed longitudinally and the tilt gradually vanishes together with the dispersion. Our results indicate that one has to be very careful when simulating the beam dynamics in chicanes using a 1D model of the CSR wakefields.

REFERENCES

- [1] J. B. Murphy, S. Krinsky, and R. L. Gluckstern, “Longitudinal wakefield for synchrotron radiation”, in *Proc. IEEE Particle Accelerator Conference and International Conference on High-Energy Accelerators, Dallas, 1995*, Piscataway, NJ, 1996. IEEE. (IEEE Conference Record 95CH35843).
- [2] J. B. Murphy, S. Krinsky, and R. L. Gluckstern, “Longitudinal wakefield for an electron moving on a circular orbit”, *Part. Accel.*, 57:9–64, 1997.
- [3] Ya. S. Derbenev, J. Rossbach, E. L. Saldin, and V. D. Shiltsev, “Microbunch radiative tail-head interaction”, DESY FEL Report TESLA-FEL 95-05, Deutsches Elektronen-Synchrotron, Hamburg, Germany, September 1995.
- [4] E. L. Saldin, E. A. Schneidmiller, and M. V. Yurkov, “On the coherent radiation of an electron bunch moving in an arc of a circle”, *Nuclear Instruments and Methods*, A398:373, 1997. doi:10.1016/S0168-9002(97)00822-X
- [5] G. Stupakov and P. Emma, “CSR wake for a short magnet in ultrarelativistic limit”, in *Proceedings of 8th European Particle Accelerator Conference*, page 1479, Paris, France, 2002.
- [6] David Sagan, Georg Hoffstaetter, Christopher Mayes, and Udom Sae-Ueng, “Extended one-dimensional method for coherent synchrotron radiation including shielding”, *Phys. Rev. ST Accel. Beams*, 12:040703, 2009. doi:10.1103/PhysRevSTAB.12.040703
- [7] G. Stupakov, “New Method of Calculation of the Wake due to Radiation and Space Charge Forces in Relativistic Beams”, in *Proceedings, 10th International Particle Accelerator Conference: Melbourne, Australia, May 19-24, 2019*, page 1223, 2019. doi:10.18429/JACoW-IPAC2019-TUZZPLS3
- [8] Gennady Stupakov, “Centripetal Transverse Wakefield in Relativistic Beam”, arXiv 1901.10745, 2019.
- [9] P. Emma, “CSR Benchmark Test-Case Results”, presentation at the ICFA Beam Dynamics mini workshop *Coherent Synchrotron Radiation and its impact on the dynamics of high brightness electron beams: January 14-18, 2002 at DESY-Zeuthen (Berlin, GERMANY)*, http://www.desy.de/csr/csr_workshop_2002/csr_workshop_2002_index.html.

INTERACTION OF POWERFUL ELECTRO-MAGNETIC FIELDS WITH BRAGG REFLECTORS*

I. Bahns[†], W. Hillert, P. Rauer, J. Rossbach, Universität Hamburg, Hamburg, Germany
H. Sinn, European XFEL GmbH, Schenefeld, Germany

Abstract

The interaction of an X-ray free electron laser (XFEL) with a Bragg Reflector can cause a change of the lattice constant, which has a direct influence on the stability of the reflection conditions [1] and can also excite modes of vibration [2]. The dynamical thermoelastic effects of the photon-matter-interaction are simulated with a finite-element-method (FEM) using the assumptions of continuum mechanics. To compare the simulation results with measured signals, a Michelson interferometer with ultra-fast photodiodes (risetime < 175 ps bandwidth > 2 GHz) has been built up. To test the experimental setup in an in-house environment a pulsed UV laser is used to introduce a temporal displacement field in a silicon crystal created by about 0.26 μJ of absorbed energy. The measured signal is in agreement with the FEM simulation and has shown that if averaging over thousands of pulses is applied a resolution < 0.5 pm is feasible. This makes this experimental setup useful to investigate the X-ray-matter-interaction of Bragg reflectors at modern X-ray facilities.

INTRODUCTION

When electro-magnetic fields are interacting with an X-ray Bragg reflector, the absorbed part of the energy will cause a change of the local thermal energy of the crystal. Due to thermal expansion this also affects the value of the local lattice parameter, and due to Bragg's law this has a direct influence on the reflection conditions. To investigate such effects one method is to directly observe the temporal change of the lattice by using X-ray radiation [1]. However, for this experimental method a modern X-ray facility is needed where the beam time for experiments is mostly limited. An alternative method could be to use optical methods like thermorefectance [3], the knife-edge method or interferometry [4]. In the present work a Michelson interferometer is tested in terms of the requirements for such a measurement. For the first test measurement, a pulsed UV laser introduced temporal change of the displacement on the backside of a silicon crystal was detected (Fig. 1). The temporal development of the displacement can be simulated with numerical methods like the finite-element-method (FEM), which can solve the coupled partial differential equations of thermoelasticity using the assumption of continuum mechanics. These results can be compared with measured displacements such as presented in the present paper. This is useful to investigate the stability of an X-ray free electron laser oscillator [5].

* Work supported by BMBF (FKZ 05K16GU4)

[†] immo.bahns@desy.de

EXPERIMENTAL SETUP

To build up a Michelson interferometer a linear polarized continuous wave laser operating at a wavelength of 532 nm is used. As illustrated in Fig. 1 polarizing beamsplitters (PBS) in combination with rotatable wave plates ($\lambda/2$ and $\lambda/4$) give control over the intensity, which is transmitted or reflected by the PBS. Film polarizers (FP) reduce the amount of intensity, which reaches the photo detector areas to the desired value. A PID controller stabilizes the working point of the interferometer by controlling the position of the mirror in the reference arm of the interferometer. Spherical lenses are used to collimate and focus the beam in a way that the focal plane lies on the surface of the silicon crystal and at the detector areas. Also the focal spot at the detector area is reduced to a size which is smaller than the area of the detector. The $\lambda/4$ wave plates are adjusted such that the total amount of the reflected beam of both interferometer arms goes into the direction of PBS3. The setup is adjusted in a way that the beam waists coming from each interferometer are equal. The beam size at the focal spot lying on the surface of the crystal and the reference mirror is $\omega_0 = 25 \mu\text{m}$.

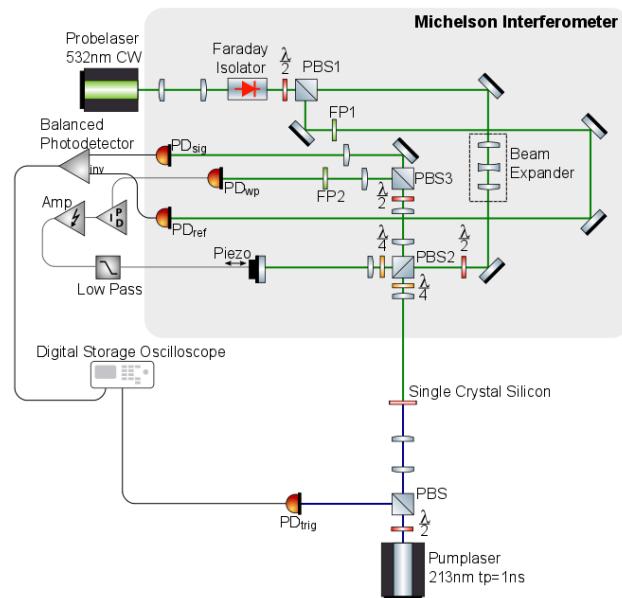


Figure 1: Pump-probe setup with Michelson interferometer. For a detailed description see the text.

The electric field amplitude and phase of the probe laser is described by using the Jones calculus:

$$\vec{J} = \begin{pmatrix} E_{0x}e^{i\varphi_x} \\ E_{0y}e^{i\varphi_y} \end{pmatrix}. \quad (1)$$

Following Maxwell's equations the intensity in this case is proportional to $I \sim \mathbf{E}^\dagger \cdot \mathbf{E}$. With the $\lambda/2$ plate before the PBS2 the intensities coming from each interferometer arm are adjusted to be the same. Therefore the Jones vectors for the beams become:

$$\vec{J}_1 = \begin{pmatrix} E_0 e^{i\varphi_1} \\ 0 \end{pmatrix}, \quad \vec{J}_2 = \begin{pmatrix} 0 \\ E_0 e^{i\varphi_2} \end{pmatrix}. \quad (2)$$

Because the polarization states are perpendicular the beams won't interfere with each other. The intensity at this point is $I \sim 2E_0^2$. The fast axis of the $\lambda/2$ plate before PBS3 makes an angle of $\varphi = \pi/8$ with respect to the horizontal axis (x-direction), which gives considering the Jones Matrix [6], the following change of \vec{J}_1 and \vec{J}_2 :

$$\vec{J}_1 = E_0 e^{i\varphi_1} \frac{1}{\sqrt{2}} \begin{pmatrix} -i \\ -i \end{pmatrix}, \quad \vec{J}_2 = E_0 e^{i\varphi_1} \frac{1}{\sqrt{2}} \begin{pmatrix} -i \\ i \end{pmatrix}. \quad (3)$$

The PBS3 transmits the vertical (y-direction) and reflects the horizontal (x-direction). So the transmitted intensity becomes $I_{tr} \sim E_0^2(1 - \cos(\varphi_2 - \varphi_1))$ and the reflected $I_{ref} \sim E_0^2(1 + \cos(\varphi_2 - \varphi_1))$. The phase difference $\phi = \varphi_2 - \varphi_1$ can be calibrated by changing the position Δz of one interferometer arm while holding the position of the other constant: $\phi = \frac{4\pi\Delta z}{\lambda}$. To achieve the optimal amplification performance of the balanced photo detector (BPD) both channels needs an input signal of 600 mV. This demands that the intensity of working point as well as the intensity reaching PD_{ref} must be adjusted with the help of the $\lambda/2$ plate before PBS1 and FD1 in a way that 600 mV reaches each channel of the BPD. This calibration results in an output signal of 0 mV if no pump signal is present. The reflected part of PBS3 is used to adjust the working point at the value between constructive and destructive interference. The considered displacements to be measured with this setup are below 1 nm, so the relation between voltage and displacement can be considered linear. The UV laser operates at a wavelength of 213 nm and emits pulses with a repetition of 1 kHz and a pulse duration of ≈ 1.5 ns. With a thermal power meter an average power of 0.8 mW has been measured, and the pulse energy therefore is 0.8 μ J. Each pulse sends a trigger signal to a digital storage oscilloscope. The measured signal has been averaged over thousands of sweeps. The beam profile can be expressed with by a multi-Gaussian radial symmetric distribution and has been measured with an UV converter in combination with a beam profiler. The displacement signals created by the UV laser is measured with an ultrafast photodiode with a risetime < 175 ps. In this work the first 60 ns after the arrival of the UV laser pulse are measured. The results can be seen in Fig. 2 (a) The sub-plot shows the first 10 ns before the trigger signal, where the displacement should be zero, indicating that the accuracy of the interferometer is below 0.5 pm. The silicon crystal has a area of 4 mm x 10 mm and a thickness of 100 μ m

NUMERICAL SIMULATION OF DISPLACEMENT

The coupled non-linear¹ partial differential equations of thermoelasticity considering the infinitesimal strain theory under assumption of continuum mechanics and the Fourier heat law are used to simulate the displacement field of the above described measurement. Thermal losses by convection and radiation of the material surface are neglected. The simulations were carried out with the FEM software COMSOL Multiphysics[®] using the coupled *solid mechanics* and *heat transfer in solids* module. The absorption coefficient at 213 nm has a value of $1.7884 \times 10^6 \text{ cm}^{-1}$ for silicon [7]. Due to the high value of the absorption coefficient the temporal and spatial function of the UV laser pulse is considered as a boundary heat flux:

$$Q(r, t) = \frac{E_{abs}}{2\pi(A\sigma_1^2 + B\sigma_2^2)} \left[Ae^{-\frac{r^2}{2\sigma_1^2}} + Be^{-\frac{r^2}{2\sigma_2^2}} \right] f(t). \quad (4)$$

The choice of multi-Gaussian function was necessary considering the measurement of the beam profiler. The data has been fitted to Eq. (4) using the software Origin[®] giving the values $A=0.00544$, $B=0.01059$, $\sigma_1=57.634 \mu\text{m}$, $\sigma_2=18.748 \mu\text{m}$. The function $f(t)$ in Eq. (4) is the temporal profile of the laser pulse. The integral of this function is normed to unity and contains discrete values, which have been measured with a fast photo diode. The interpolation between the values is piecewise cubic. Due to the refractive index 1.1222 and extinction coefficient 3.0314 [7] of silicon the reflectance is 0.67218 and therefore only $E_{abs}=0.26 \mu\text{J}$ are absorbed in the crystal. The temperature dependent values of thermal conductivity [8], thermal expansion coefficient [9] and the heat capacity [10] of silicon were taken from the cited publications. The following material parameters are considered temperature independent and taken from the COMSOL material library: Poisson's ratio $\nu=0.28$ Young's modulus $Y=170 \text{ GPa}$, ρ =density 2329 kg/m^3 . A radial symmetric simulation is considered with a mesh covering $z=100 \mu\text{m}$ and $r=700 \mu\text{m}$. The mesh has quad elements of size $=2 \mu\text{m}$ and a distributed boundary layer mesh at side where the heat source is applied.

The results of the simulation have shows that the strain σ_{zz} is about 10^{-5} and the strain σ_{rr} in the range of 10^{-6} . This shows that even small energy amounts (0.26 μJ) could have a significant effects considering the stability criteria for Bragg reflection because even strain of 10^{-7} can have noticeable effects on a Bragg reflection [1]. The dips in Fig. 2 (a), which occur in the measurement as well as in the simulations around 33 ns and 56 ns, give a time distance of 23 ns, which matches the time 23.5 ns observed by dividing twice the crystal thickness 100 μm by the longitudinal speed of sound $v_s = \sqrt{Y/\rho}$. The cause for this periodical dips are longitudinal ultrasonic waves, which are created by the dynamical thermal expansion due to the absorption of short laser pulse radiation. The ultrasonics are propagating with

¹ Temperature dependence of material parameters is considered

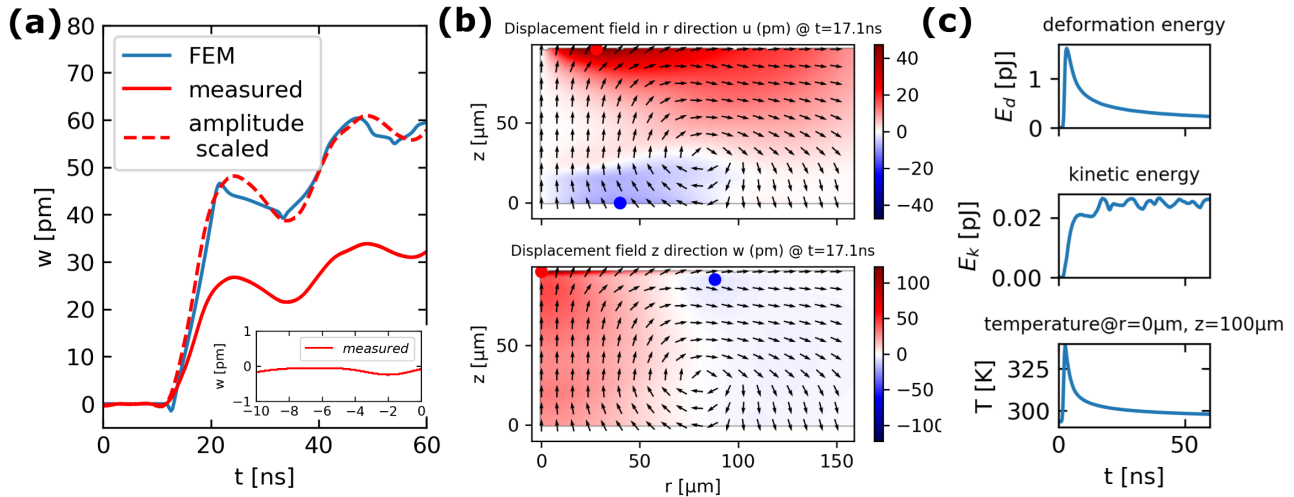


Figure 2: (a) Comparison of the measured signal with FEM simulations. The broken line is the measured amplitude scaled to fit the simulation results. (b) Simulated displacement field inside the silicon crystal 17.1 ns after the photon matter interaction. The UV laser pulse arrives at $z=100\text{ }\mu\text{m}$ with center (maximum intensity) at $r=0\text{ }\mu\text{m}$. The arrows are normed to a fixed value indicating the direction of the total displacement. The color code is set symmetric with white being the zero value. Maximum and minimum values are marked $u_{max}=47.43\text{ pm}$ (red dot), $u_{min}=-9\text{ pm}$ (blue dot), $w_{max}=122.2\text{ pm}$ (red dot), $w_{min}=-5.4\text{ pm}$ (blue dot). (c) Temporal evolution of the deformation energy, kinetic energy and the temperature value at $r=0\text{ pm}$, $z=100\text{ pm}$.

the speed of sound and are reflected at the boundaries of the crystal [11]. The simulated displacement at the backside illustrated in Fig. 2 (a) shows a similar form as the measured. However, the amplitude of the measurement is significantly smaller compared with the simulations. The reason could be that the used UV laser, after operating for some time, shows an intensity jitter, which lowers the mean energy per pulse. The general rise of the over all displacement, which is observed in the measurements as well as in the simulation can be explained by considering Fig. 2 (b). It shows the displacement field in the r and z direction at a time step 17 ns after the UV laser arrival at the top surface (at $z=100\text{ }\mu\text{m}$). The absorbed laser energy causes a rise in the temperature at the top of the crystal. Due to the spatial profile (Eq. (4)) of the laser the maximum temperature will occur at $r=0\text{ }\mu\text{m}$ (Fig. 2 (c)). Due to thermal expansion, this causes a displacement field illustrated in Fig 2 (b). Because of the boundary conditions at the top ($z=100\text{ }\mu\text{m}$), the displacement w (in z -direction) will move upwards (positive z direction) and the displacement u (r direction) will move away from the center. However at the bottom ($z=0\text{ }\mu\text{m}$) the temperature is nearly the one of the initial value. This causes the backside of the crystal at $r=0\text{ }\mu\text{m}$, $z=0\text{ }\mu\text{m}$ to move upwards. This is the area where the interferometer measures the displacement.

Considering the deformation energy and the kinetic energy² in Fig. 2 (c) it is seen that most of the deformation energy is caused by the thermal strain. The kinetic energy is about 0.025 pJ. The repetition rate of the laser is 1 kHz. Considering the crystal as a cantilever the first mode would be $f=1.38\text{ kHz}$. To have a rough estimation, which mean displacement u_m amplitude the crystal might have, the formula

for kinetic energy is considered: $0.5M(2\pi f)^2 u_m^2$. With the mass of the crystal $M=9.3\text{ mg}$, u_m is some tens of nanometre. However, in this estimation passive damping is not considered. An observation of the measurement is, that at the start the displacement is nearly zero, which shows at least that the signal is not affected by vibrations. However, the measured signal is averaged and therefore further investigations considering mechanical vibration have to be carried out.

DISCUSSION AND OUTLOOK

Some of the assumptions made for the simulation like the Fourier heat law might not be not fully valid for the investigated system, e.g diffusion of the excess electrons and holes have to be considered. However, except for the modest amplitude scaling factor, the quantitative and the very good qualitative agreement between measurements and simulations indicate that the present results are a good starting point for more detailed investigations of Bragg reflectors with interferometer techniques.

REFERENCES

- [1] S. Stoupin, A. M. March, H. Wen, D. A. Walko, Y. Li, E. M. Dufresne, S. A. Stepanov, *et al.*, "Direct observation of dynamics of thermal expansion using pump-probe high-energy-resolution x-ray diffraction," *Phys. Rev. B*, vol. 86, no. 5, p. 054301, 2012. doi:10.1103/PhysRevB.86.054301
- [2] B. Yang, S. Wang, and J. Wu, "Transient thermal stress wave and vibrational analyses of a thin diamond crystal for X-ray free-electron lasers under high-repetition-rate operation," *J. Synchrotron Radiat.*, vol. 25, no. 1, pp. 166-176, 2018. doi:10.1107/S1600577517015466

² For definition of the deformation energy and kinetic energy see [2]

- [3] Puqing Jiang, Xin Qian, and Ronggui Yang, "Tutorial: Time-domain thermoreflectance (TDTR) for thermal property characterization of bulk and thin film materials," *J. Appl. Phys.*, vol. 124, no. 16, p. 161103, 2018. doi:10.1063/1.5046944
- [4] J-P. Monchalin, "Optical Detection of Ultrasound," *IEEE Trans. Ultrasonics Ferroelectrics and Frequency Control*, vol. 33, pp. 485-499, 1986. doi:10.1109/T-UFFC.1986.26860
- [5] P. Rauer, I. Bahns, W. Hillert, J. Rossbach, W. Decking, and H. Sinn, "Integration of an XFEL at the European XFEL Facility," presented at the 39th Int. Free Electron Laser Conf. (FEL 19), Hamburg, Germany, Aug. 2019, paper TUP009, this conference.
- [6] E. Hecht, in *Hecht optics*, Addison Wesley, 1998, pp. 213-214.
- [7] D. E. Aspnes and A. A. Studna, "Dielectric functions and optical parameters of Si, Ge, GaP, GaAs, GaSb, InP, InAs, and InSb from 1.5 to 6.0 eV," *Phys. Rev. B*, vol. 27, no. 2, p. 985, 1983. doi:10.1103/PhysRevB.27.985
- [8] C. J. Glassbrenner and Glen A. Slack, "Thermal Conductivity of Silicon and Germanium from 3°K to the Melting Point," *Phys. Rev.*, vol. 134, p. A1058, 1964. doi:10.1103/PhysRev.134.A1058
- [9] Y. Okada and Y. Tokumaru, "Precise determination of lattice parameter and thermal expansion coefficient of silicon between 300 and 1500 K," *J. Appl. Phys.*, vol. 56, no. 2, pp. 314-320, 1984. doi:10.1063/1.333965
- [10] H. R. Shanks, P. D. Maycock, P. H. Sidles, and G. C. Danielson, "Thermal Conductivity of Silicon from 300 to 1400°K," *Phys. Rev.*, vol. 130, p. 1743, 1963. doi:/10.1103/PhysRev.130.1743
- [11] C. Thomsen, H. T. Grahn, J. M. Humphrey, and J. Tauc, "Surface generation and detection of phonons by picosecond light pulses," *Phys. Rev. B*, vol. 34, p. 4129, 1986. doi:10.1103/PhysRevB.34.4129

THE SIMULATION STUDY FOR SINGLE AND MULTI TURN ERL BASED EUV FEL

K. M. Nam and G. S. Yun, Department of Advanced Nuclear Engineering, POSTECH, Pohang, Korea
Y. W. Parc[†], Pohang Accelerator Laboratory, Pohang, Korea

Abstract

Photolithography technology is the core part of the semiconductor manufacturing process. It has required that the power of EUV light should be higher about ~ kW for higher throughput. ERL based EUV FEL is emerging as a next generation EUV source which can produce over 10 kW EUV power. In this simulation study, EUV-FEL design with single turn is presented. An electron beam with 40 pC beam charge is accelerated to 600 MeV and produces EUV light with 37 kW power. Secondly, multi-turn based design is also presented. Multi-turn design improved compactness for industrial application. Simulation study shows that the multi-turn design can also generate about 15.5 kW average power. This study is expected to increase the practical industrialization potential of ERL-based photolithography.

INTRODUCTION

Photolithography process means microfabrication to pattern certain circuit into wafer. It is the core part of semiconductor manufacturing process and has been evolved from I-line, Krypton Fluoride Lasers (248 nm), Argon Fluoride Lasers to Laser-Produced Plasma (LPP, 13.5 nm). However, semiconductor industries have demanded new light source with high average power over 1 kW and high repetition rate in order to produce much-integrated semiconductor [1-5]. Thus, new EUV source has been studied and Energy Recovery Linac (ERL) based Free Electron Laser (FEL) has been received attention, which is believed that can replace the LPP source. ERL is a new type of accelerator, which can reuse kinetic energy of accelerated electron beams in order to accelerate other electron beam. ERL-based FEL can supply high current over 500 A to generate high power over 10 kW per second. This field faced many beam dynamics issues such as longitudinal phase space manipulation, bunch compressing, high order effect control, energy recovery [6], and space charge effect [7]. Therefore, it is vital to consider many collective effects and beam dynamics to produce high quality EUV.

In this paper, single and multi-turn ERL simulation study was performed by using ASTRA [8], ELEGANT [9] and GENESIS simulation [10]. It includes generation of electron from dc gun, bending, compression, acceleration, bending, compression and EUV generation. Most of simulations were performed through ELEGANT code, but we used ASTRA code to optimize injector part and

GENESIS 1.3 code for simulation of FEL.

OVERVIEW

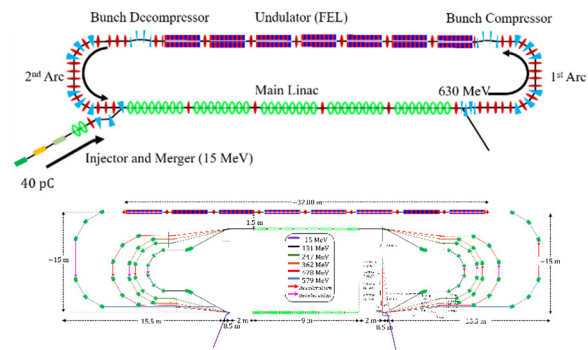


Figure 1: Layout of Single turn(Upper part) and multi-turn design(Lower part) used in the simulation study.

In Fig.1, two designs of the EUV-FEL used in the simulation are shown. For the both designs, an electron beam with 40 pC beam charge is generated from the injector, accelerated to 15 MeV at superconducting RF cavity and transmitted to a merger. The merger compresses the beam, and transports it to linac simultaneously for both designs. However, they have different structural concept. At single turn design, electron beam circulates only one time. Thus, it requires multiple number of rf modules in the linac part as it cannot pass same linac before deceleration. Thus, the single turn design (upper part of Fig. 1) has larger size than multi turn case. Multi-turn design concept, suggested in 2011 [11], means circulating the electron beams to improve the compactness of facility. In multi-turn design (lower part of Fig. 1), electron beam circulates several times and it passes the same linac two or three times during acceleration process. This point can improve the compactness of a EUV facility.

SINGLE TURN SIMULATION RESULT

Injector in Fig. 2 consists of high average current DC photocathode gun, two solenoids, buncher cavity, superconducting RF cavities and merger that transfers the beam to main linac. DC photocathode gun produces 40 pC bunch charge and accelerates it to 960 kV with 1.3 GHz repetition rates.

In single turn design, superconducting RF cavities In Fig. 3 accelerate the beam from 15 MeV to 638 MeV while it makes chirp of electron beam linearly. It also recovers the kinetic energy of the used beam down to 15 MeV. Dump magnets separate high and low energy electron beam to dump the low energy beam. After the electron beam passes matching section that consists of 4

* Work supported by Max Planck POSTECH/KOREA Research Initiative Program [Grant No 2016K1A4A4A01922028] through the National Research Foundation of Korea (NRF) funded by Ministry of Science, ICT & Future Planning.

[†] young1@postech.ac.kr

quadrupoles, a path of electron beam is turned around 180° by isochronous arc as shown in Fig. 4.

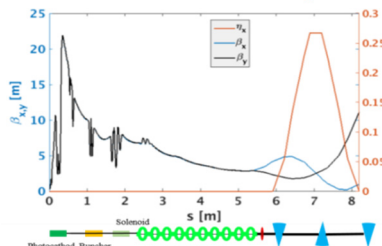


Figure 2: Injector layout and betatron function.

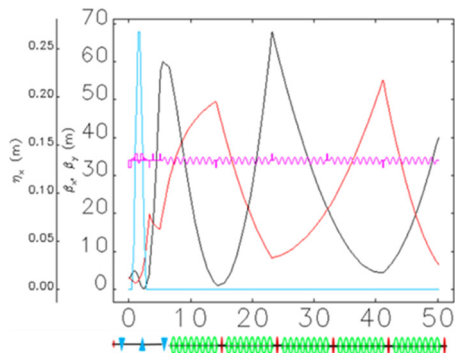


Figure 3: Linac layout and betatron function.

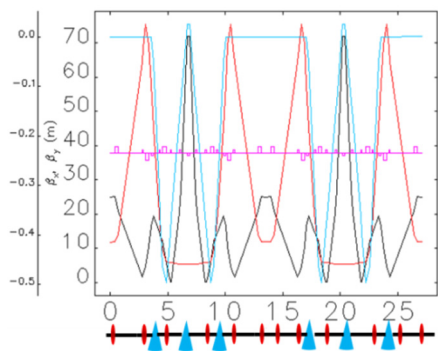


Figure 4: Isochronous Arc betatron function.

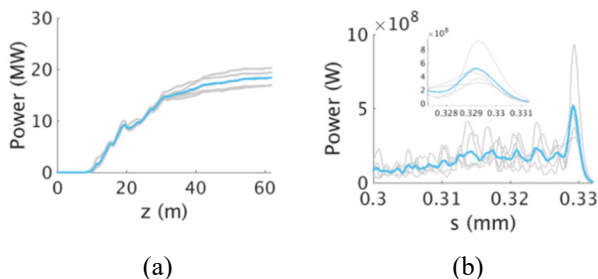


Figure 5: Single turn FEL Simulation. (a) Growing of mean power in the undulator line. (b) Shape of the photon pulse.

Arc has symmetric TBA structure to make it achromatic for the 90 degree bending. One 90° bending arc includes 6 quadrupole magnets and 3 bending magnets which has 30° bending angle. Four quadrupole magnets are added at the beginning part and end part to keep the horizontal and vertical beta function as periodic and symmetric. Two quadrupole magnets are added at the

front of the arc and the other two are added at the end of the arc. Simulation result shows that R_{56} of the arc is only 0.15 μm . At bunch compressor, current of the beam is increased to 600 A to generate high power EUV.

FEL simulation results with GENESIS 1.3 code are shown in Fig. 5. Mean power of pulse is growing up 20 MW, which are averaged over 5 simulation results with different seeding number. From this result, average power of facility is calculated as 37 KW. It shows that ERL FEL can produce EUV with extremely high average power for the lithography process.

MULTI TURN SIMULATION RESULT

To decrease the size of whole machine, we did study about the multi-turn design as shown in Fig. 1 (lower part). Multi-turn design has same injector with single turn case. After injection, electron beam encounters two rf modules. Phase of rf cavity is designed to minimize the chirp to decrease the nonlinear transverse kick at the arc. We used 85° for the one cavity and 95° for the another. It makes the electron beam have almost zero chirps, so it can avoid to increasing the emittance when the beam is passing the arcs.

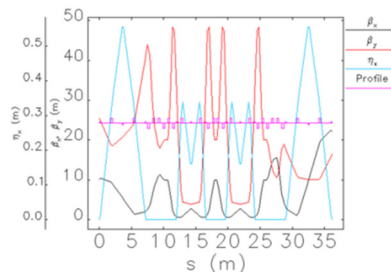


Figure 6: Example of isochronous Arc of multiturn ERL.

Core of multi-turn design is 180 bending arc. It should bend the electron beam without reducing emittance and keep the betatron function proper. Good example of arc is shown in Fig. 6. It is designed to have two symmetric parts. First part consists of 3 bending magnet and 2 quadrupoles. It starts from spreader (a bending magnet which spread out the electron beam for different energy) which is located at the end of each RF module. Second part consists of two TBAs which is similar for the single turn case. The whole arc is isochronous, even though second part itself is not isochronous. Maximum arc size for completed design is about 15 m which improves compactness of the EUV facility.

FEL simulation results for multi-turn design are shown in Fig. 7. It shows that peak power of pulse about 0.3 GW and mean power about 5 MW, which are averaged over 5 simulations with different seeding number. The pulse of the photon beam is about 81 μm . From this result, average power of facility is calculated as 15.5 KW. Compared with single turn design result, it decreases almost as half, however, there are still enough number of photons for the lithography.

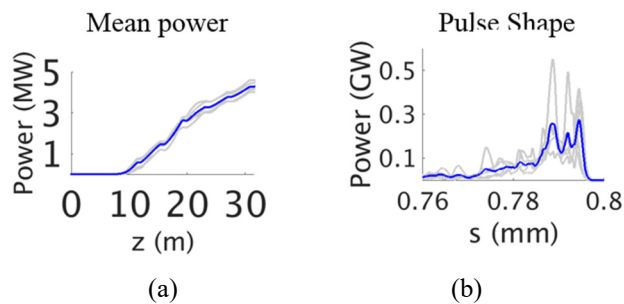


Figure 7: Multi turn FEL Simulation results. (a) Growing of mean power. (b) Pulse shape of the photon beam.

CONCLUSION

Single and multi-turn ERL based EUV-FELs are designed. It accelerates electron beam to about 600 MeV and FEL power exceeds 10 KW for the both cases and its wavelength is 13.5 nm. We expect that these designs can be helpful to realize the industrial application of accelerator.

REFERENCES

- [1] ASML presentation at 2010 International Workshop on Extreme Ultraviolet Sources (2010)
- [2] N. Nakamura, R. Kato, T. Miyajima, M. Shimada, R. Hajima, and T. Hotei, "S2E Simulation of an ERL-Based High-Power EUV-FEL Source for Lithography", in *Proc. 8th Int. Particle Accelerator Conf. (IPAC'17)*, Copenhagen, Denmark, May 2017, pp. 894-897. doi:10.18429/JACoW-IPAC2017-MOPVA020
- [3] Akira Endo, "Optimization of high average power FEL beam for EUV lithography", in *Proc. SPIE 9512, Advanc*
- es in X-ray Free-Electron Lasers Instrumentation III*, 95121O, 12 May 2015. doi:10.1117/12.2182239
- [4] T. Hotei, R. Kato, T. Miyajima, N. Nakamura, and M. Shimada, "Optics Design of the Compact ERL Injector for 60 pC Bunch Charge Operation", in *Proc. 8th Int. Particle Accelerator Conf. (IPAC'17)*, Copenhagen, Denmark, May 2017, pp. 898-901. doi:10.18429/JACoW-IPAC2017-MOPVA021
- [5] Christian Wagner & Noreen Harned, "EUV lithography: Lithography gets extreme", *Nature Photonics*, vol.4, pp 24-26, January 2010. doi:10.1038/nphoton.2009.251
- [6] Rick Merritt, "Samsung Ramps 7nm EUV Chips Multiple tapeouts race toward 2019 announcements", *EETimes*, 10.17.18. https://www.eetimes.com/document.asp?doc_id=1333881
- [7] R. Courtland, "The molten tin solution", *IEEE Spectrum*, Vol. 53, No. 11, pp. 28-41, November 2016. doi:10.1109/MSPEC.2016.7607024
- [8] ASTRA: A Space Charge Tracking Algorithm, <http://www.desy.de/~mpyf10>
- [9] M. Borland, "elegant: A Flexible SDDS-Compliant Code for Accelerator Simulation", presented at the *6th International Computational Accelerator Physics Conference, ICAP2000*, September 11-14, 2000, Darmstadt, Germany.
- [10] S. Reiche, "GENESIS 1.3: a fully 3D Time-Dependent FEL Simulation Code", *Nucl. Instrum. and Methods Phys. Res. A*, vol. 429, p. 243, 1999. doi:10.1016/S0168-9002(99)00114-X
- [11] Y. Socol, "Compact 13.5-nm free-electron laser for extreme ultraviolet lithography", *Phys. Rev. ST Accel. Beams* 14, 040702, 2011. doi:10.1103/PhysRevSTAB.14.040702

LASER-DRIVEN COMPACT FREE ELECTRON LASER DEVELOPMENT AT ELI-BEAMLINES

A.Molodozhentsev*, G.Korn, K.Kruchinin, J.Hawke, D.Kocon, T.Green, M.Kaur
ELI-BL, Institute of Physics of CAS, Prague, Czech Republic
A. R. Maier, University of Hamburg and CFEL, Hamburg, Germany

Abstract

ELI-Beamlines Centre, located near Prague (Czech Republic) is an international user facility for fundamental and applied research using ultra-intense lasers and ultra-short high-energy electron beams. Using the optical parametric chirped-pulse amplification (OPCPA) technique, the ELI-Beamlines laser system will provide the laser pulse energy up to 10 Joules with the repetition rate up to 25 Hz. Combination of new laser development with constant improvement of the LWFA electron beam parameters has great potential in future development of a next generation of the compact high repetition rate Free Electron Laser, which is extremely demanded by the X-ray community.

The LWFA-driven FEL project, called 'LUIS', is currently under preparation at ELI-Beamlines in collaboration with University of Hamburg. The goal of the project is improvement of the electron beam parameters in order to demonstrate the amplification and saturation of the SASE-FEL photon power in a single unit of a FEL undulator.

An overview of the LUIS project including design features and a description of all instrumentations used to characterize the laser, plasma, electron beam, photon generation is presented in frame of this report.

INTRODUCTION

Extreme Light Infrastructure (ELI) [1] was heralded by the European Community to develop in Europe a new type of large-scale laser infrastructure specifically designed to provide high peak power and focused intensity ultrashort pulses. ELI should be the world's first international laser research infrastructure implemented as a distributed research infrastructure based on 3 specialized and complementary facilities located in the Czech Republic, Hungary and Romania. ELI-Beamlines (located in Dolni Brezany, near Prague, the Czech Republic) will be the high-energy beam facility responsible for development and use of ultra-short pulses of high-energy particles and radiation stemming from the ultra-relativistic interaction. In particular, using laser systems in ELI-Beamlines it will be possible to accelerate electrons up to a few GeV.

The principle of the 'laser-wake-field-acceleration' (LWFA) [2] is based on an ultra-high longitudinal electric gradient, created by the high-intensity laser pulse focused in underdense plasma (in a gas-jet, gas-cell or capillary discharge targets). A travelling longitudinal electric field can reach several hundreds of GV/m, which is much larger than the accelerating field achievable in conventional accelerators, making LWFA extremely attractive as a compact ac-

celerator to provide high-energy beams for different applications. During last decades, a remarkable progress has been made in the field of electron acceleration based on the LWFA concept. Electron beams with peak energies of multi-GeV in a short plasma channel (a few cm) have been obtained experimentally [3].

Using these achievements [4] one can define the parameters of the LWFA electron beam at the exit of the plasma channel as following: the electron beam energy is in the range of 300÷1000 MeV; the RMS transverse beam size in the horizontal and vertical plane is less than 1µm; the RMS transverse beam divergence in the horizontal and vertical planes is less than 1 mrad; the RMS bunch length is about 1µm; the RMS relative (total) energy spread is less than 1 %; the normalized RMS transverse beam emittance in the horizontal and vertical planes is 0.2 π mm.mrad and the bunch charge is about 50 pC.

The novel acceleration methods open a new way to develop a compact "laser-based" SASE [5] free electron laser (FEL) with the 'fsec' photon pulse length. We present the laser-driven 'demo'-FEL setup, which is under development at ELI-Beamlines. After commissioning this setup will deliver to users a photon peak brightness up to 10³⁰ photons/pulse/mm²/mrad²/0.1%BW using a single undulator. The 'laser-driven' FEL at ELI-Beamlines can operate with high repetition rate (up to 50Hz), which is limited by the current 'state-of-art' of the laser technology. Successful realization of the 'demo'-FEL research program at ELI-Beamlines will open a new perspective in development of compact soft and hard X-ray FELs with few or even sub-femtosecond photon bunches for a very wide user community.

LASER-DRIVEN 'DEMO'-FEL

The goal of the 'demo'-FEL setup at ELI-Beamlines is experimental demonstration of the laser-driven FEL in a single unit FEL undulator. For this purpose, a commercial-available 'in-vacuum' planar undulator, based on the hybrid permanent magnets [6], can be used. Such undulator has the undulator period of 15 mm with the variable gap (3 ÷ 6 mm).. The undulator parameter (K_0) is in the range of 0.8÷1.6 depending on the gap size. In order to simplify the 'matching' condition the total length of such undulator should be 2.5 m. The average beta-function is 1.6 m. The saturation length ($L_{\text{sat}} \sim 20L_{\text{g,3D}}$), estimated by using the Xie parametrization of the gain length [7] and checked by using the fitting formula for free-electron lasers with strong space charge effects [8], does not exceed such undulator length for the electron beam summarized in Table 1.

*Alexander.Molodozhentsev@eli-beams.eu

Table 1: Main Parameters of the ‘Demo’-FEL

<i>Electron beam in Undulator ($K_0=1.4$)</i>		
Beam energy	MeV	350
Bunch charge	pC	30
RMS bunch duration	fs	3
Peak current	kA	4
Matched beam size	μm	25
Normalized emittance	$\pi \text{ mm.mrad}$	0.24
‘Slice’ energy spread	%	0.3
<i>Photon coherent radiation at saturation</i>		
Radiation wavelength	nm	32
Pierce parameter, ρ	$\times 10^{-2}$	0.8
Coherent normalized RMS emittance, $\epsilon_{n,\text{coh}}$	$\pi \text{ mm.mrad}$	1.7
Cooperation length (3D), L_{coop}	μm	0.26
Gain length (3D), $L_{g,3D}$	m	0.12
Saturation length (3D)	m	2.4
Radiation bandwidth	%	0.65
Photon flux per 0.1%bw	$\times 10^{12} \#$	2.2
Photon brilliance	$\times 10^{30} \#$	1
Photon pulse power	GW	8.2
Photon pulse energy	μJ	63

corresponding units are shown in the text

LASER SYSTEM FOR THE LASER-DRIVEN FEL AT ELI-BEAMLINES

A high repetition rate ‘100TW’-class laser is currently under development at ELI-Beamlines, which will be used to produce a stable electron beam with required parameters for the laser driven compact ‘demo’-FEL. The laser system is designed to produce the laser pulse with extraordinary energy and pointing stability. The laser system is based on a diode pumped solid state laser (DPSSL) with optical parametric chirped pulse amplification (OPCPA). The central wavelength of the laser is 820 nm and the pulse duration is less than 25 fs. The ultimate goal of the laser system is to reach the energy of 5 Joules for the 50 Hz operation. As the result of the first phase of the laser development the energy should be 2.5 Joules at 20 Hz. In addition, the laser system will be able to produce a synchronized, high repetition rate mid-IR auxiliary output. Because it is synchronized with the main output pulse, it can be used to generate X-ray pulses via the high harmonic generation (HHG) which will be synchronized with the driver laser of the electron acceleration. In the frame of the ‘demo’-FEL development at ELI-Beamlines the ‘seeded’ FEL is planned.

Laser Diagnostics

The laser diagnostic will be integrated into the ‘setup’, which is under development at ELI-Beamlines in order to measure the laser properties before and after the laser-plasma interaction. It will allow to optimize the interaction process and guiding acceleration of electrons to get required parameters of the electron beam. The prototype of such setup has been developed and tested for the LUX setup at DESY in the frame of the collaboration between University of Hamburg and ELI-Beamlines [9].

GUIDED LWFA FOR ‘DEMO’-FEL

We aim to use a plasma channel guide of the laser beam in order to produce the required electron beams with the energy of 300 ÷ 500 MeV by using the laser power of 50 TW ($\lambda_{\text{Laser}} \sim 820 \text{ nm}$) [10,11]. The discharge capillary should be 20 mm or smaller. For the laser pulse duration of 25 fsec the corresponding laser energy is 2 Joules assuming 80% of the total laser energy in the spot. Such requirements on the laser parameters open the way for the high repetition rate laser operation (up to 50 Hz).

The on-axis plasma density in the preformed plasma channel should be around $1 \times 10^{18} \text{ cm}^{-3}$. The laser intensity on the target is $\sim 1 \times 10^{18} \text{ W/cm}^2$. In order to optimize the plasma parameters for the capillary-discharge setup, the plasma characterization will be measured by using the Stark broadening of the H_α , H_β and H_γ Balmer emission lines. The plasma discharge setup with the proper plasma diagnostics is under preparation at ELI-Beamlines. The continuous operation of the setup with the gas-filled capillary has been tested for the LUX setup in Hamburg with the laser repetition rate up to 5 Hz [9], producing stable electron beam with the energy of 450 MeV.

ELECTRON BEAM TRANSPORT

The electron beam transport has to be developed to minimize growth of the RMS normalized transverse emittance, provide required energy spread of the electron beam and to have sufficient laser beam and electron beam diagnostics. Initial electron beam parameters from the LWFA source are quite different from typical parameters reachable in conventional linear accelerators. Significant relative energy spread and transverse divergence of the LWFA electron beam in combination with strong space charge effect require a dedicated design of the electron beam transport [12] to capture, transport and match the electron beam to the FEL undulator. It was shown that by using the permanent quadrupole magnets at the beginning of the beamline, the transverse normalized RMS emittance can be kept at the level, acceptable for the FEL lasing [13-16]. The control of the slice energy spread can be performed by using the magnetic chicane (so called ‘decompressor’, which can be the ‘C-type’ chicane) [17]. The performed study of the electron beam dynamics in the beam transport including the space charge and the magnetic chicane shows that the average slice energy spread of 0.25 % can be obtained, if the initial bunch charge is 40 pC and the bending angle in the decompression chicane is 0.4 degree. In this case after the chicane the particle distribution in the bunch becomes semi-uniform with the bunch length of 6 μm (the peak current is 2 kA).

Finally, using the matching triplet of the quadrupole magnets it is possible to provide required average size of the electron beam along the undulator $\sim 25 \mu\text{m}$ along the 2.5 m undulator. The total length of the proposed electron beam transport from the LWFA source till the exit from the undulator is 14 m. The electron and photon beams will be separated by using the dipole magnet of the electron beam spectrometer. Conceptual design of the photon beam

transport from the undulator up to the user chamber is in progress.

Electron Beam Diagnostics

Electron beam diagnostics are absolutely crucial for achievement the aim of the ‘laser-driven’ FEL development. Specific properties of the beam produced nowadays by LWFA, such as low charge, poor beam stability, large beam divergence and energy spread, require re-evaluation of the conventional diagnostic tools or development of completely new ones. The electron beam diagnostic for the ‘laser-driven’ FEL should be compact, stable, non-invasive allowing the measurements in a single-shot operational mode. For this purpose, a comprehensive set of diagnostic instruments has been designed at ELI-Beamlines [18].

LASER-DRIVEN ‘DEMO’-FEL

The photon beam parameters for the ‘demo’-FEL setup has been simulated for different cases: (1) without the ‘decompression’ chicane; (2) including the optimized ‘decompression’ chicane and (3) including the ‘decompression’ chicane and the external seeding. The aim of this study was establishing the SASE-FEL regime with amplification of the photon beam power along the undulator. The photon pulse energy along the undulator for all these cases is presented in Figure 1. The energy of the electron beam is 350 MeV and the undulator parameter is $K_0=1.4$. The simulations have been performed by using SIMPLEX [19] for different parameters of the electron beam, obtained from the multi-particle tracking through the whole beamline taking into account the space charge effects [20]. The other collective effects, such as the coherent synchrotron radiation (CSR) in the magnetic chicane, has been studied by using ELEGANT [21]. It was shown, that CSR will lead to significant degradation of the transverse RMS normalized emittance of the 350 MeV electron beam, if the bunch charge exceeds 50 pC and the bending angle of the chicane dipole magnets exceeds 1 degree. Any beam or beam-transport imperfections, which will lead to additional degradation of the electron beam quality, were not included into the analysis.

The saturation of the photon beam power starts if the bending angle of the chicane magnets is 0.4 degree (Figure 1: the ‘black’ line). The ‘blue’ line represents the case without the chicane. The external seeding reduces the saturation length for the same electron beam parameters (Figure 1: the ‘red’ line). In this case the seeding signal with the following parameters has been used: the seeding wave-length is 32 nm and the seeding power is 2 kW. The simulations indicate that without the external ‘seeding’ the saturation can be reached in the 2.5 m-long undulator. The external seeding allows to get the saturation even at 2.2 m.

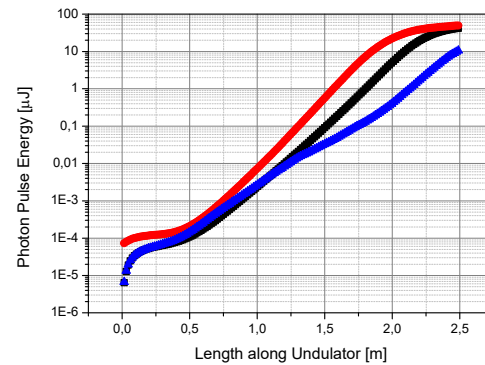


Figure 1: The saturation of the photon pulse energy in the case different ‘demo’-FEL setups.

CONCLUSION

The laser-driven ‘demo’-FEL program at ELI-Beamlines is based on combination of new laser development, novel LWFA acceleration approaches and development of the dedicated electron beam transport. Successful demonstration of the laser-driven FEL operation at ELI-Beamlines will open the way to compact laser-driven soft and hard X-ray FELs, which are extremely demanding by the X-ray community.

ACKNOWLEDGEMENTS

This work is partially supported by the project Advanced research using high intensity laser produced photons and particles (CZ.02.1.01/0.0/16.019/0000789) from European Development Fund.

REFERENCES

- [1] ELI beamlines ‘White’ book: <https://www.eli-beams.eu/en/projects/eli-white-book/>.
- [2] T. Tajima and J. M. Dawson, “Laser Electron Accelerator”, *Phys. Rev. Lett.*, vol. 43, p. 267, 1979.
doi:10.1103/PhysRevLett.43.267
- [3] W. Leemans *et al.*, “Multi-GeV Electron Beams from Capillary-Discharge-Guided Subpetawatt Laser Pulses in the Self-Trapping Regime”, *Phys. Rev. Lett.*, vol. 113, p. 245002, 2014.
doi: 10.1103/PhysRevLett.113.245002
- [4] W. T. Wang *et al.*, “High-Brightness High-Energy Electron Beams from a Laser Wakefield Accelerator via Energy Chirp Control”, *Phys. Rev. Lett.*, vol. 117, p. 124801, 2016.
doi:10.1103/PhysRevLett.117.124801
- [5] E. Saldin *et al.*, “Design formulas for short-wavelength FELs”, DESY 03-012, 2004.
- [6] T. Schmidt, S. Reiche, “Undulators for the SwissFEL”, in *Proc. FEL’09*, Liverpool, UK, Aug. 2009, paper THOA01, pp. 706-713.
- [7] M. Xie, LBNL-44381, CBP Note-323, 1999.
- [8] G. Marcus *et al.*, “Gain length fitting formula for free-electron lasers with strong space-charge effects”, *Phys. Rev. ST-AB*, vol. 14, p. 080702, 2011.
doi:10.1103/PhysRevSTAB.14.080702

- [9] N. Delbos *et al*, “Lux – A laser-plasma driven undulator beamline”, *NIMA*, vol. 909, pp. 318-322, 2018.
doi:10.1016/j.nima.2018.01.082
- [10] W. P. Leemans *et al*, “GeV electron beams from a centimetre-scale accelerator”, *Nature Physics*, vol. 2, p. 696, Sep. 2006.
doi.org/10.1038/nphys418
- [11] Nakamura *et al*, “GeV electron beams from a centimeter-scale channel guided laser wakefield accelerator”, *Physics of Plasma*, vol. 14, p. 056708, 2007.
doi:10.1063/1.2718524
- [12] A. Molodozhentsev *et al*, “LWFA-driven” Free Electron Laser for ELI-Beamlines”, in *Proc. FLS'18*, Shanghai, China, Mar. 2018, pp. 62-67. doi:10.18429/JACoW-FLS2018-TUA2WC02
- [13] M. Migliorati *et al*, “Intrinsic normalized emittance growth in laser-driven electron accelerators”, *Phys. Rev. ST-AB*, vol. 16, p. 011302, 2013.
doi/10.1103/PhysRevSTAB.16.011302
- [14] P. Winkler *et al*, “Measurements of High-Order Magnetic Field Components of Permanent Quadrupole Magnets for a Laser-Plasma-Driven Undulator X-Ray Source”, in *Proc. IPAC'17*, Copenhagen, Denmark, May 2017, pp. 4145-4146. doi:10.18429/JACoW-IPAC2017-THPIK022
- [15] I. Hofmann, “Performance of solenoids versus quadrupoles in focusing and energy selection of laser accelerated protons”, *Phys.Rev.ST-AB*, vol. 16, p. 041302, 2013.
doi/10.1103/PhysRevSTAB.16.041302
- [16] A. Molodozhentsev *et al*, “ELI Electron Beam Line for Laser-plasma-driven Undulator X-ray Source”, in *Proc. IPAC'16*, Busan, Korea, May 2016, pp. 4005-4007.
doi:10.18429/JACoW-IPAC2016-THPOW030
- [17] A. Maier *et al*, “Demonstration Scheme for a Laser-Plasma-Driven Free-Electron Laser”, *Phys. Rev. X*, vol. 2, p. 031019, 2012. doi/10.1103/PhysRevX.2.031019
- [18] K. Kruchinin *et al*, “Electron Beam Diagnostics Concept for the ELI LUX Project”, in *Proc. IPAC'18*, Vancouver, Canada, Apr.-May 2018, pp. 1954-1957.
doi:10.18429/JACoW-IPAC2018-WEPAF057
- [19] T. Takana, “SIMPLEX: simulator and postprocessor for free-electron laser experiments”, *J. Synchrotron Rad.*, vol. 22, p. 1319-1326, 2015.
doi:10.1107/S1600577515012850
- [20] D. Uriot, R. Duperrier and N. Pichoff, TraceWin, CEA Saclay, 2015.
- [21] M. Borland, User's manual for Elegant, 2016.

PROGRESS TOWARDS LASER PLASMA ELECTRON BASED FREE ELECTRON LASER ON COXINEL

M. E. Couprie *, T. André, F. Blache, F. Bouvet, F. Briquez, Y. Dietrich, J. P. Duval, M. El-Ajjouri, A. Ghaith, C. Herbeaux, M. Khojoyan, N. Hubert, C. Kitégi, M. Labat, N. Leclercq, A. Lestrade, A. Loulergue, O. Marcouillé, F. Marteau, D. Oumbarek Espinos, P. Rommeluère, M. Sebdaoui, K. Tavakoli, M. Valléau, Synchrotron SOLEIL, GIF-sur-YVETTE, France
C. Benabderrahmane, ESRF, Grenoble, France
S. Corde, J. Gautier, J. P. Goddet, O. Kononenko, G. Lambert, A. Tafzi, K. Ta Phuoc, C. Thauray, Laboratoire d'Optique Appliquée, Palaiseau, France
S. Bielawski, C. Evain, E. Roussel, C. Szwaj, Laboratoire PhLAM, Villeneuve d'Ascq, France
I. Andriyash, V. Malka, S. Smartzev, Weizmann Institute, Rehovot, Israel

Abstract

Laser plasma acceleration (LPA) [1] with up to several GeV beam in very short distance appears very promising. The Free Electron Laser (FEL), though very challenging, can be viewed as a qualifying application of these new emerging LPAs. The energy spread and divergence, larger than from conventional accelerators used for FEL, have to be manipulated to answer the FEL requirements. On the test COXINEL experiment [2–4] line, "QUAPEVA" permanent magnet quadrupoles of variable strength [5, 6] handle the emittance growth and a decompression chicane reduces the slice energy spread, enabling FEL amplification for baseline reference parameters [2]. A beam pointing alignment compensation method enables to properly transport the electrons along the line, with independent adjustments of position and dispersion [7]. The measured undulator spontaneous emission radiated exhibits the typical undulator radiation pattern, and usual features (gap tunability, small linewidth...).

INTRODUCTION

Accelerator based light sources presently know a very wide development [8], with the FEL [9] advent in the X-ray domain [10] coming along with an increase of the peak brightness by several orders of magnitude, enabling fifty years after the laser invention [11] to decipher the matter structure in unexplored areas and dynamics on ultra-fast time scales unraveling the processes involved various domains [12]... Following the laser invention, alternately of developing FELs relying on non bounded relativistic electrons in an undulator periodic permanent magnetic field as a gain medium [9], laser have been considered to generate and accelerate electrons in plasmas [1]. An intense laser focused onto a gas target ionizes the gas and creates a plasma. As the laser pulse propagates, the ponderomotive force expels electrons from the optical axis, forming a cavity free of electrons in the laser wake with large amplitude electric fields where electrons can be trapped and accelerated. With the growth of ultra high power laser making advantage of Chirped Pulse Amplification techniques [13],

electrons can be accelerated with plasma up to several GeV within ultra-short distances [14–16] with kA peak current, ultra-short bunches, 1π mm.mrad normalized emittance beams, enabling to consider LPA to drive an FEL [3, 17]. Even though some LPA features such as peak current and emittance seem to be quite suitable for the FEL application, energy spread and divergence do not meet conventional accelerator μ rad divergence and per mille of energy spread beams. They should be handled to mitigate chromatic effects [18, 19], that can lead to a dramatic emittance growth and afferent beam quality degradation in the transfer lines. Large divergence requires strong focusing right after the electron source, with for instance high gradient permanent magnet quadrupoles [20]. Large energy spread can be managed by a decompression chicane [3, 21] or a transverse gradient undulator [22, 23]. The energy-position correlation introduced by the chicane [2] can be turned into an advantage. There are still very few experiments with LPA electron beam transport towards an undulator [24] and preliminary observation of undulator radiation [25–28]. The COXINEL program [29] aiming at demonstrating FEL amplification using a dedicated manipulation line is developed in the frame of the LUNEX5 project of advanced compact free electron laser demonstrator [30, 31]. We report here the progress on the COXINEL experimental program.

THE COXINEL LINE DESIGN

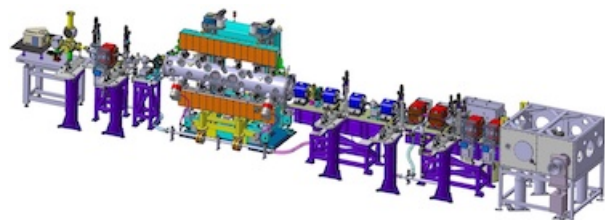


Figure 1: COXINEL line CATIA sketch.

The COXINEL line (see Fig. 1) has been designed and built at Synchrotron SOLEIL [4, 32] (ERC Advanced COXINEL 340015) using the baseline reference parameters given in Table 1 for the 180 MeV case, for being installed at Labora-

* couprie@synchrotron-soleil.fr

toire d'Optique Appliquée (LOA). The divergence is rapidly mitigated (5 cm away from the source) via strong focusing with a triplet of QUAPEVA permanent magnet based quadrupoles of variable strength (with rotating cylindrical magnet surrounding a central Halbach ring quadrupole [33]) and adjustable magnetic center position (with translation tables) [5,6]. A magnetic chicane then longitudinally stretches the beam, sorts electrons in energy and selects the energy range of interest via a removable and adjustable slit mounted in the middle of the chicane. A second set of quadrupoles matches the beam inside an in-vacuum undulator. Electron diagnostics include current transformers, cavity beam position monitors and removable scintillator screens for electron profile imaging [34]. The "200 MeV" corresponds to radiation in the UV with a 2 m long cryo-ready undulator U18 (period 18 mm) [35], while the 400 MeV case associated to the U15 cryogenic undulator enables to reach the VUV spectral range. The line equipments have been characterized [4, 32].

The electron transport [36] images the electron source in the undulator. The total emittance growth is frozen at the QUAPEVA triplet exit. The "supermatching optics" focuses each electron beam slice in synchronisation with the progression of the amplified synchrotron radiation along the undulator, taking advantage of the energy - position correlation introduced in the chicane, and enables to achieve FEL amplification with the baseline reference parameters [2]. The sensitivity study of the FEL versus different parameters has been carried out [37]. Other optics (focusing on the screens for transport tuning, focusing vertically in the chicane equipped to select the energy of interest with a slit) are also available.

Table 1: COXINEL baseline reference case at the source and undulator (Und.), measured (Meas.) beam at the source.

Parameter (unit)	Baseline Source	Und.	Meas. Source
Vert. divergence (mrad)	1	0.1	1.2-5
Hor. divergence (mrad)	1	0.1	1.8-7.5
Beam size (μm)	1	50	
Bunch length (fs RMS)	3.3	33	
Charge (pC)	34	34	
Charge density (pC/MeV)	5	0.5	0.2-0.5
Peak Current (kA)	4.4	0.44	
Energy spread RMS %	1	0.1	>10
Norm. emittance ϵ_N (mm.mrad)	1	1.7	

COXINEL MEASUREMENTS

LPA is operated in ionisation injection [38] for robustness with the LOA 1.5 J, 30 FWHM fs pulse laser is focused into a supersonic jet of $\text{He} - \text{N}_2$ gas mixture. Electron energy distribution (see Fig. 2 (left)) is broad and ranges up to 250

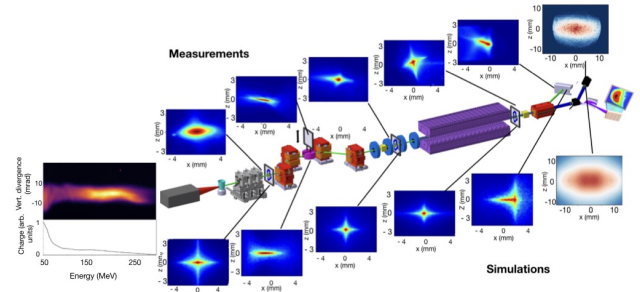


Figure 2: COXINEL electron and photon beam measurements compared to simulations using measured electron beam distribution as an input. Left : electron beam spectrometer measurements and transverse distributions along the line. Right : undulator radiation transverse pattern.

MeV, with a much lower charge density at the energy of interest and larger divergences than expected (see Table 1).

Besides prior alignment of the line components within $\pm 100 \mu\text{m}$ on the same axis with a laser tracker, and optics daily alignment with a green reference laser, the LPA electron beam pointing (of the order of 1.5 mrad RMS) makes critical the electron beam transport along the line. Thus, a matrix response beam pointing alignment compensation method taking advantage of the "QUAPEVA" adjustable magnetic center and gradient is applied : the electron position and dispersion are independently adjusted [7] step by step along the screens enabling a proper transport along the line. The QUAPEVA strength is slightly adjusted to optimize the focusing thanks to the rotation of the QUAPEVA cylindrical magnets. The matched transported beam measurements are well reproduced with simulations for measured beam characteristics (see Fig. 2), with cross-like shaped focused beam due to chromatic effects and measured tilted beams due to skew quadrupolar terms, that have been further corrected [39].

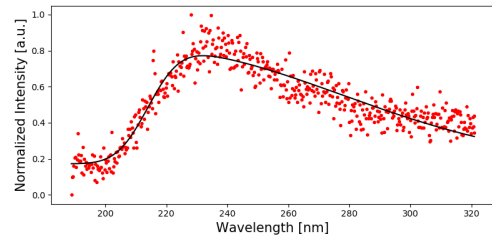


Figure 3: Undulator spectral flux measured with the Horiba iHR 320 spectrometer at 5 mm gap (3 mm electron slit).

The radiation from the 2 m long 107 x 18.16 mm periods U18 is then characterized while applying an optics enabling to select a small energy range centered onto the energy of interest with the slit inserted in the magnetic chicane. A typical spectrum is presented Fig. 3, and 2D measured and simulated transverse patterns are displayed in Fig. 2. The undulator radiation (resonant wavelength, intensity) has been tuned by changing the gap. The radiation linewidth can be

controlled using the electron beam energy selection via the slit in the chicane. The estimated full number of photons per beam charge N_{ph} is $\approx 3.10^7$ pC⁻¹.

CONCLUSION

We have demonstrated a proper LPA electron beam transport on COXINEL, handling its performance for a FEL application. We have then observed at the end of the line undulator radiation exhibiting the usual characteristics in terms of spatio-spectral distribution, wavelength dependance with gap, spectral purity. The observation of an FEL effect seems possible, provided electron beam measured parameters get closer to the baseline reference case ones [40].

ACKNOWLEDGMENTS

The authors thank European Research Council (ERC) for COXINEL (340015, P. I. M. E. Couprie), X-Five (339128, PI: V.Malka), the EuPRAXIA design study (653782), the Fondation de la Cooperation Scientifique (QUAPEVA-2012-058T) and for the support of SOLEIL and LOA staff.

REFERENCES

- [1] T. Tajima and J. M. Dawson, "Laser electron accelerator", *Phys. Rev. Lett.*, vol. 43, p. 267–270, Jul 1979. doi:10.1103/PhysRevLett.43.267
- [2] A. Loulergue *et al.*, "Beam manipulation for compact laser wakefield accelerator based free-electron lasers", *New Journal of Physics*, vol. 17, no. 2, p. 023028, 2015. doi:10.1088/1367-2630/17/2/023028
- [3] M. E. Couprie *et al.*, "Towards a free electron laser based on laser plasma accelerators", *J. Phys. B: Atomic, Molecular and Optical Physics*, vol. 47, no. 23, p. 234001, 2014. doi:10.1088/0953-4075/47/23/234001
- [4] M. E. Couprie *et al.*, "An application of laser-plasma acceleration: towards a free-electron laser amplification," *Plasma Phys. Cont. Fusion*, vol. 58, no. 3, p. 034020, 2016. doi:10.1088/0741-3335/58/3/034020
- [5] F. Marteau *et al.*, "Variable high gradient permanent magnet quadrupole (QUAPEVA)", *Applied Physics Letters*, vol. 111, p. 253503, 2017. doi:10.1063/1.4986856
- [6] A. Ghaith *et al.*, "Tunable high gradient quadrupoles for a laser plasma acceleration based FEL", *Nucl. Instrum. Meth. A*, vol. 909, p. 290-293, 2018. doi:10.1016/j.nima.2018.02.098
- [7] T. André, T. *et al.* "Control of laser plasma accelerated electrons for light sources", *Nat. Comm.*, vol. 9, pp. 1334, 2018. doi:10.1038/s41467-018-03776-x
- [8] M. E. Couprie, J. M. Filhol, "X radiation sources based on accelerators", *Comptes Rendus Phys.*, vol. 9:487–506, 2008. doi:10.1016/j.crhy.2008.04.001
- [9] J. M. Madey, "Stimulated emission of Bremsstrahlung in a periodic magnetic field", *Jour. Appl. Phys.*, vol. 42, p. 1906–1913, 1971. doi:10.1063/1.1660466
- [10] P. Emma *et al.*, "First lasing and operation of an Ångström-wavelength free-electron laser", *Nature Photonics*, vol. 4, p. 641, 2010. doi:10.1038/nphoton.2010.176
- [11] A. L. Schawlow and C. H. Townes, "Infrared and optical masers", *Physical Review*, vol. 112, no. 6, p. 1940, 1958. doi:10.1103/PhysRev.112.1940
- [12] C. Bostedt *et al.*, "Linac Coherent Light Source: The first five years", *Rev. Mod. Phys.*, vol. 88 (1), p. 015007, 2016. doi:10.1103/RevModPhys.88.015007
- [13] D. Strickland and G. Mourou, "Compression of amplified chirped optical pulses", *Optics communications*, vol. 55, no. 6, p. 447-449, 1985. doi:10.1016/0030-4018(85)90120-8
- [14] E. Esarey, C. Schroeder, and W. Leemans, "Physics of laser-driven plasma-based electron accelerators", *Reviews of Modern Physics*, vol. 81, no. 3, p. 1229, 2009. doi:10.1103/RevModPhys.81.1229
- [15] V. Malka *et al.*, "Laser-driven accelerators by colliding pulses injection: A review of simulation and experimental results", *Physics of Plasmas*, vol. 16, no. 5, p. 056703, 2009. doi:10.1063/1.3079486
- [16] W. P. Leemans *et al.*, "Multi-GeV electron beams from capillary-discharge-guided subPetaWatt laser pulses in the self-trapping regime", *Phys. Rev. Lett.*, vol. 113, p. 245002, 2014. doi:10.1103/PhysRevLett.113.245002
- [17] F. Gruner *et al.*, "Design considerations for table-top, laser-based VUV and X-ray free electron lasers", *Appl. Phys. B*, vol. 86, p. 431-435, 2007. doi:10.1007/s00340-006-2565-7
- [18] K. Floettmann, "Some basic features of the beam emittance", *Phys. Rev. ST Accel. Beams*, vol. 6, p. 034202, 2003. doi:10.1103/PhysRevSTAB.6.034202
- [19] M. Migliorati *et al.*, "Intrinsic normalized emittance growth in laser-driven electron accelerators", *Phys. Rev. ST Accel. Beams*, vol. 16, p. 011302, 2013. doi:10.1103/PhysRevSTAB.16.011302
- [20] A. Ghaith *et al.*, "Permanent Magnet-Based Quadrupoles for Plasma Acceleration Sources", *Instruments*, vol. 3, no. 2, pp. 27, 2019. doi:10.3390/instruments3020027
- [21] A. Maier *et al.*, "Demonstration scheme for a laser-plasma-driven free-electron laser", *Physical Review X*, vol. 2, no. 3, p. 031019, 2012. doi:10.1103/PhysRevX.2.031019
- [22] T. I. Smith *et al.*, "Reducing the sensitivity of a free-electron laser to electron energy", *Journal of Applied Physics*, vol. 50, no. 7, pp. 4580–4583, 1979. doi:10.1063/1.326564
- [23] Z. Huang, Y. Ding, C. B. Schroeder, "Compact X-ray free-electron laser from a laser-plasma accelerator using a transverse-gradient undulator", *Phys. Rev. Lett.*, vol. 109, no. 20, pp. 204801, 2012. doi:10.1103/PhysRevLett.109.204801
- [24] C. Widmann *et al.*, "Beam transport system from a laser wakefield accelerator to a transverse gradient undulator", *Proceed. IPAC conf., Dresden, Germany*, p. 2803, 2014. doi:10.18429/JACoW-IPAC2014-TH0BA03
- [25] H. P. Schlenvoigt *et al.*, "A compact synchrotron radiation source driven by a laser-plasma wakefield accelerator", *Nature Physics*, vol. 4, no. 2, pp. 130–133, 2008. doi:10.1038/nphys811
- [26] M. Fuchs *et al.*, "Laser-driven soft-X-ray undulator source," *Nature physics*, vol. 5, no. 11, pp. 826–829, 2009. doi:10.1038/nphys1404

- [27] G. Lambert *et al.*, "Progress on the generation of undulator radiation in the UV from a plasma-based electron beam", *Proceed. FEL conf., Nara, Japan*, Aug. 2012, paper THPD47, pp. 638-641.
- [28] M.P. Anania *et al.*, "An ultrashort pulse ultra-violet radiation undulator source driven by a laser plasma wakefield accelerator", *Appl. Phys. Lett.*, vol. 104, no. 26, pp. 264102, 2014. doi:10.1063/1.4886997
- [29] M. Couprie *et al.*, "Experiment preparation towards a demonstration of laser plasma based free electron laser amplification", in *Proc. 36th Int. Free Electron Laser Conf. (FEL'14)*, Basel, Switzerland, Aug. 2014, paper TUP086, pp. 569-573.
- [30] M.-E. Couprie *et al.*, "The LUNEX5 project in France", *Jour. of Physics: Conf. Series*, vol. 425, no. 7, pp. 072001, 2013. doi:10.1088/1742-6596/425/7/072001
- [31] M. Couprie *et al.*, "Strategies towards a compact XUV free electron laser adopted for the LUNEX5 project", *Journal of Modern Optics*, vol. 63, no. 4, pp. 1-13, 2015. doi:10.1080/09500340.2015.1075617
- [32] M. E. Couprie *et al.*, "Towards free electron laser amplification to qualify laser plasma acceleration", *The review of laser engineering*, vol. 45, no. 2, pp. 94-98, 2017.
- [33] K. Halbach *et al.*, "Design of permanent multipole magnets with oriented rare earth cobalt material," *Nucl. Instrum. Meth.*, vol. 169, p. 1-10, 1980. doi:10.1016/0029-554X(80)90094-4
- [34] M. Labat *et al.*, "Electron and photon diagnostics for plasma acceleration-based FELs", *Journal of synchrotron radiation*, vol. 25, no. 1, p. 59-67, 2018. doi:10.1107/S1600577517011742
- [35] C. Benabderrahmane *et al.*, "Development and operation of a $Pr_2Fe_{14}B$ based cryogenic permanent magnet undulator for a high spatial resolution x-ray beam line", *Phys. Rev. Acc. Beams*, vol. 20, no. 3, p. 033201, 2017. doi:10.1103/PhysRevAccelBeams.20.033201
- [36] M. Khojayan *et al.*, "Transport studies of LPA electron beam towards the FEL amplification at COXINEL", *Nucl. Instrum. Meth. A*, vol. 829, no. 2, pp. 260-264, 2016. doi:10.1016/j.nima.2016.02.030
- [37] M. Labat *et al.*, "Robustness of a plasma acceleration based Free Electron Laser", *Phys. Rev. Acc. Beams*, vol. 21, no. 11, pp. 114802, 2018. doi:10.1103/PhysRevAccelBeams.21.114802
- [38] C. McGuffey *et al.*, "Ionization induced trapping in a laser wakefield accelerator", *Phys. Rev. Lett.*, vol. 104, no. 2, p. 025004, 2010. doi:10.1103/PhysRevLett.104.025004
- [39] D. Oumbarek-Espinos *et al.*, "Skew quadrupole effect of laser plasma electron beam transport", *Applied Science*, vol. 9, no. 12, p. 2447, 2019. doi:10.3390/app9122447
- [40] M. Labat *et al.*, "Interferometry for full temporal reconstruction of laser-plasma accelerator-based seeded free electron lasers", *ArXiv 1906.11140v2*, 2019.

A VERSATILE THz SOURCE FOR HIGH-REPTITION RATE XFELS

F. Lemery^{1*}, K. Floettmann¹, M. Dohlus¹, M. Marx¹, M. Ivanyan², V. Tsakanov²

¹ DESY, Hamburg, Germany

² Center for the Advancement of Natural Discoveries using Light Emission, Yerevan, Armenia

Abstract

The development of high-repetition rate XFELs brings an exciting time for novel fundamental science exploration via pump-probe interactions. Laser-based pump sources can provide a wide range of wavelengths (200-10000 nm) via various gain media. These sources can also be extended with optical parametric amplifiers to cover a largely versatile spectral and bandwidth range. However beyond 10 μm , toward the THz regime, there exists no suitable gain media, and optical-to-THz efficiencies are limited below 1%. In this paper we discuss the use of Cherenkov-based radiators with conventional electron bunches to generate high-power THz radiation over a wide range of parameters for existing and future XFEL facilities.

INTRODUCTION

The last decades of accelerator physics flourished, the development of superconducting radio frequency (SRF) machines has provided a surge toward unparalleled efficiencies, leading to incredible beam powers $O(1 \text{ MW})$ at MHz repetition rates for a plethora of applications. These machines are very suitable candidates for colliders as in the proposal of the International Linear Collider (ILC), but the limited (but increasing) accelerating gradients of SRF cavities has limited such TeV-frontier facilities to 10s of kilometers.

Other fundamental sciences desire X-rays to explore life sciences, chemistry and more, which require more modest beam energies $O(10 \text{ GeV})$ to provide X-ray energies $O(10 \text{ keV})$ using conventional undulators. While a large portion of users are interested in direct-imaging of their samples, pump-probe spectroscopy has gained significant interest, where generally a pump-laser of specific wavelength and bandwidth is shone onto the sample to e.g. excite it, subsequently an X-ray pulse then measures the developing effects. This technique provides a way to diagnose electromagnetic responses of samples of interest.

Unfortunately the limited optical-to-THz conversion efficiencies below 1% has left an electromagnetic hole of research opportunities in various sciences [1]. Alternatively electron beam based THz sources can in principle cope with the high power, repetition rate, and frequency requirements. The freely available spent beam after a SASE undulator is an attractive option for this purpose, as it still has a high beam power. Moreover it is naturally synchronized to the X-ray pulses and can fulfill all repetition rate requirements. (For a detailed discussion on the compensation of path length differences between THz and X-ray pulses see [2])

At the XUV FEL FLASH, for example, a 9 period electromagnetic undulator with 40 cm period length is installed behind the SASE undulator [3,4]. The generated THz radiation in the range of 1.5 – 30 THz is transported through a 65 m long evacuated beam line to the experimental chamber where it meets the XUV pulse on the sample [5,6]. Six refocusing mirrors in combination with planar mirrors keep the beam size under control and direct the beam to the experiment. A variable delay line allows for adjusting the relative timing of pump and probe beam.

Following the design ideas of FLASH the installation of a special undulator for the generation of THz radiation behind a SASE undulator at XFEL-facilities is discussed in [7]. However, the high beam energy of XFEL facilities ($>10 \text{ GeV}$) requires a total undulator length of 10 m with peak fields of up to 7.3 T and a period length of 1 m to comply with the requested THz parameters. While such an undulator appears to be technically feasible with state-of-the-art superconducting technology the cost and complexity of such a device is unattractive. Another conceivable option is the installation of a separate accelerator near the experimental hutch, because THz radiation can be generated with conventional undulator parameters already at modest $\sim 10 \text{ MeV}$ beam energies. While the SASE process in the THz range is possible at these low electron beam energies [8,9], this option is complex and expensive. Finally, compact accelerators based on advanced concepts like e.g. plasma acceleration are not yet able to deal with the beam quality, charge and repetition rate requirements.

In this paper we consider an alternative method which has not yet been proposed in the context of pump-probe sources at XFEL user facilities: the usage of Cherenkov-type waveguides to produce high-power, superradiant THz radiation in a wide range of desired parameters [10–13]. There are various types of radiating structures which include dielectric-lined waveguides (DLW), corrugated structures, and bimetallic waveguides [14, 15]. We provide a brief introduction to various suitable radiation waveguides before discussing the wakefield generation process in arbitrary waveguides. This is followed by a section on radiation extraction and finally, a case for the European XFEL is presented.

SUITABLE RADIATORS

There are many existing candidate structures which have come forward for e.g. beam-driven acceleration and radiation generation with phase velocities of the speed of light. Of these there exists the dielectric-lined waveguide (DLW), the corrugated waveguide, a bimetallic waveguide, and others e.g. photonic bandgap structures, see Fig 1. We give a

* francois.lemery@desy.de

brief introduction to each structure and provide a summary discussion on their relations below.

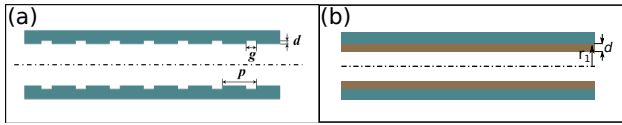


Figure 1: A corrugated structure is shown in (a), in (b) a bimetal or dielectric-lined waveguide is shown, where the thin layer with thickness d is interchanged; generally dielectric-lined waveguides have much larger layers than bimetal structures.

The DLW consists of a dielectric capillary with the outside surface coated with an appropriately thick conductor to cover the skin depth of the particular frequency. The DLW is very easy to manufacture, generally capillaries can be drawn and the coating process is rather trivial, using an e.g. sputtering machine. However, dielectrics do have drawbacks including charging, multipacting, and limited heat conduction.

The corrugated structure consists of periodic grooves along the longitudinal length of the structure. The groove periods are generally much shorter than the wavelength which avoids spatial harmonics. Corrugated structures can be manufactured with high precision CNC machines, for the case of a cylindrical corrugated pipe, generally two hemispheres are manufactured and attached together. The corrugated pipe can be represented as a DLW with the relation, $\frac{\epsilon'}{\epsilon'-1} = \frac{p}{g}$.

Recently, bimetallic structures have been proposed and developed [14, 15]. Here a thin-layer of conducting material is deposited upon another conductor. The properties of bimetallic structures are very similar to DLWs, exhibiting a large range of possible operation parameters.

The various structures have been compared in detail in [16] and exhibit a very similar range of characteristics along the properly scaled dimensions. The following section discusses the generalized radiation characteristics of these structures.

SUPERRADIANT WAKEFIELD GENERATION IN ARBITRARY WAVEGUIDES

For a lossless single-mode structure, a charged particle traveling through the structure will produce a wakefield potential, which is equivalent to the Green's function,

$$G(z) = \kappa \cos(kz), \quad (1)$$

where κ is the loss factor. For a charged bunch, the wakefield is given by the convolution of the Green's function and the current profile of the bunch $I(z)$,

$$W(z) = \kappa \int_{-\infty}^z dz' G(z') I(z - z'). \quad (2)$$

Equivalently we can express this equation as,

$$W(z) = qF\kappa \cos(kz), \quad (3)$$

where q is the charge, and F is the usual bunch form factor. The total possible extraction energy is then given by

$$\mathcal{E} = q^2 F^2 \kappa L = q^2 F^2 L \frac{Z_0 c}{\pi r_1^2}, \quad (4)$$

where L is the structure length, r_1 is the inner radius of the structure, and Z_0 is the impedance of free space, and we have used the identity $\kappa = \frac{Z_0 c}{\pi r_1^2}$. Now, specifying to a dielectric-lined waveguide, it can be shown that the resonance condition is given by [17],

$$k_0^2 = \frac{2}{r_1 d} \frac{\epsilon'}{\epsilon' - 1}, \quad (5)$$

where the dielectric permittivity is given by $\epsilon_1 = \epsilon_0(\epsilon' + i\epsilon'')$, and here we assume $\epsilon'' \ll \epsilon'$.

The pulse length of the radiation is related to the group velocity via

$$\tau = \frac{L}{c} (1 - \beta_g) = L \frac{\epsilon' - 1}{\epsilon'} \frac{4d_1}{r_1 c} = \frac{8}{(k_0 f_1)^2} \frac{L}{c} \quad (6)$$

By taking the ratio between the energy and the pulse length, the radiated power is given by,

$$P = (qFk_0)^2 \frac{Z_0 c}{8\pi} \propto \frac{q^2 F^2}{r_1 d_1}. \quad (7)$$

There are practical considerations to the range of applicable waveguides, generally determined by the Twiss parameters of the driving beam since we should avoid beam losses on the structure, therefore one may impose a condition on the beam sizes at the structure edges e.g. $N\sigma_r < r_1$. We can then find the limitations on the Twiss parameters, beginning with the envelope equation,

$$\beta(s) = \beta^* + \frac{s^2}{\beta^*}, \quad (8)$$

where β^* is the minimum betatron value at $s = 0$ corresponding to the center of the waveguide, and from the beam size relation,

$$\sigma = \sqrt{\frac{\beta(L/2)\epsilon^*}{\gamma}} \quad (9)$$

where ϵ^* is the normalized emittance and γ is the Lorentz factor. We can reexpress the condition as

$$r_1 > N \sqrt{\frac{\epsilon^*}{\gamma} \beta^* + \frac{L^2}{4\beta^*}}. \quad (10)$$

Then if we are interested in maximizing the energy extracted from a drive beam through such a waveguide, following Eq. 4 above, $V \propto L/r_1^2$, then

$$V \propto \frac{4\gamma\beta^*}{N^2\epsilon^*} \frac{L}{4\beta^{*2} + L^2}. \quad (11)$$

Maximizing this equality,

$$\frac{\partial V}{\partial L} = 0 = \frac{4\beta^{*2} - L^2}{(4\beta^{*2} + L^2)^2} \frac{4\gamma\beta^*}{N^2\epsilon^*}, \quad (12)$$

and rearranging terms for minimum rms beam size σ_0 corresponding to β^* ,

$$a > N\sqrt{2}\sigma_0, \quad (13)$$

which in correspondence to,

$$L = \frac{2\sigma_0^2\gamma}{\epsilon^*}, \quad (14)$$

gives the optimum structure length to the inner radius,

$$\frac{L}{r_1} = \frac{\sqrt{2}\sigma_0\gamma}{N\epsilon^*}. \quad (15)$$

For the sub-ultrarelativistic regime, these conditions should be considered and optimized for specific applications. However in the ultrarelativistic regime which is the case at XFELs, these conditions are significantly relaxed, allowing for structures with larger aspect ratios, i.e. toward high-frequency structures.

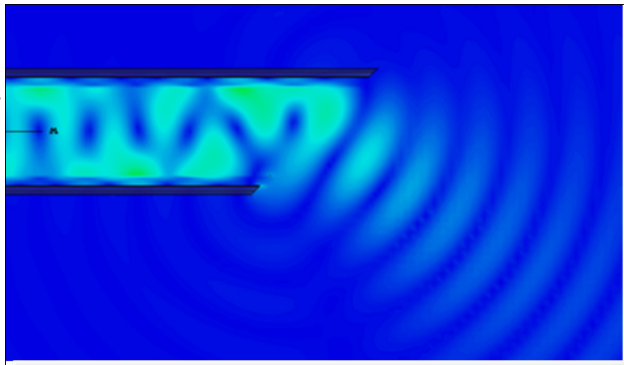


Figure 2: A CST simulation result is shown for the absolute longitudinal component of the electric field for a launched TM mode at 300 GHz. The cut is at 45 degree.

EXTRACTION

It is worthwhile to briefly discuss power extraction. In a conventional undulator, radiation travels with the radiating bunch and a bending magnet is used to separate the two. Alternatively a significant advantage of radiating waveguides is the opportunity to configure the waveguide as a Vlasov antenna [18]. In such a configuration the end of the waveguide is usually cut at an angle which allows the radiation to exit at a similar angle to the cut. A simulation was carried out in CST and is shown in Fig. 2. The simulations show that output coupling efficiencies above 90% can be achieved with various angle cuts.

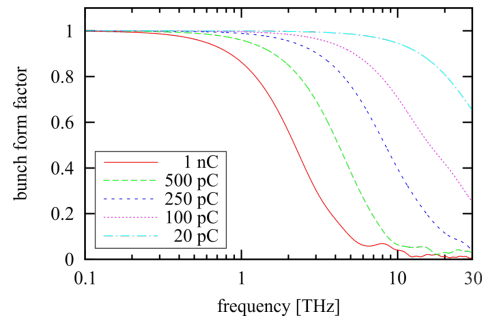


Figure 3: Bunch form factor as a function of frequency for various charge modes of the EuXFEL.

EXAMPLE FOR EUROPEAN XFEL

The European XFEL is designed to operate in a wide range of modes with various bunch charges which covers different user applications. The bunch form factor for the different modes of the Eu-XFEL is shown in Fig. 3. Below 1 THz the bunch form factor is close to 1 even for a high bunch charge of 1 nC. To generate an energy of 3 mJ at 0.1 THz would require for example a structure of only 33 cm length when the structure radius is 2 mm and the bunch charge is 1 nC. The temporal length of the radiation pulse would be 500 ps (50 cycles). And the power reached in this case is 6 MW.

At higher frequencies the bunch form factor shrinks considerably. Lower bunch charges achieve higher form factors so that it can become advantageous to reduce the bunch charge when radiation above 3 THz shall be generated. On the other hand the higher bunch charge of 1 nC is preferable for the lower frequency range but it is not mandatory as longer structures and/or smaller radii are not excluded.

The reduced energy requirements still allow generating sufficient amounts of energy also at higher frequencies. At 6.6 THz only 0.7 μ J radiation energy are requested which requires less than a centimeter structure length (1 mm radius) at charges between 1 nC and 100 pC. Beyond 10 THz, the 20 pC operational mode of XFEL is appealing; however, the usage of bimetallic and corrugated structures becomes challenging due to manufacturing constraints. Fortunately, drawing procedures for e.g. hollowcore optic fibers can produce DLW capillaries to with radii below 1 μ m and wall thickness of \sim 100 nm [19].

CONCLUSION

We have presented a versatile THz source for high-repetition rate XFELs. Our beam-based approach uses radiating or Cherenkov waveguides and can cover a wide range of parameters which are desired by users. The waveguide approach is significantly easier and less expensive than undulator-based approaches which have been previously proposed. Moreover, the flexibility to outcouple radiation without disrupting the beam path is largely appealing to reduce required modifications to beamlines and for its capability to generate multiple THz beamlines with different parameters.

REFERENCES

- [1] P. Zalden, R. Carley, T. Tschentscher, C. Bressler, S. Molodtsov, G. Geloni, A. Scherz, A. Perucchi, S. Bonetti, A. Cavalieri, K. Holldack, D. Turchinovich, A. Lindenberg, K. Nelson, L. DiMauro, M. Lederer, M. Hoffmann, F. Kärtner, A. Cavalleri, M. Krasilnikov, M. Gensch, N. Stojanovic, C. Hauri, A. Savilov, Z. Huang, “Terahertz Science at European XFEL”, European XFEL Report XFEL.EU TN-2018-001-01.0, 2018. <https://xfel.tind.io/record/1564>
- [2] Tanikawa, T., Karabekyan, S., Kovalev, S., Casalbuoni, S., Asgekar, V., Gensch, M., Geloni, G., “Superradiant Undulator Radiation for Selective THz Control Experiments at XFELs”, European XFEL Report XFEL.EU TN-2018-002, 2018. <https://xfel.tind.io/record/1563>
- [3] E. Syresin *et al.*, “Simulations of Electromagnetic Undulator for Far Infrared Coherent Source of TTF at DESY”, in *Proc. 10th European Particle Accelerator Conf. (EPAC'06)*, Edinburgh, UK, Jun. 2006, paper THPLS133.
- [4] A. Chesnov *et al.*, “Magnetic Measurements of the FLASH Infrared Undulator”, in *Proc. 29th Int. Free Electron Laser Conf. (FEL'07)*, Novosibirsk, Russia, Aug. 2007, paper WEPH003, pp. 318–321.
- [5] M. Gensch *et al.*, “New Infrared Undulator Beamline at FLASH”, *Infrared Physics & Technology*, 51, 5 (2008). doi:10.1016/j.infrared.2007.12.032
- [6] A. Willner, “Investigations into the FLASH Infrared Undulator as an Electron Beam Diagnostic Tool”, Diploma Thesis, TESLA-FEL 2008-04, (2008). https://flash.desy.de/sites2009/site_vuvfel/content/e403/e1642/e2308/e2310/infoboxContent2
- [7] T. Tanikawa *et al.*, “Superradiant Undulator Radiation for Selective THz Control Experiments at XFELs”, submitted to *Struct. Dyn.* 2018. <https://arxiv.org/abs/1803.05323>
- [8] M. Krasilnikov, F. Stephan, E. Schneidmiller, and M. V. Yurkov, “Tunable IR/THz Source for Pump Probe Experiments at the European XFEL”, in *Proc. 34th Int. Free Electron Laser Conf. (FEL'12)*, Nara, Japan, Aug. 2012, paper WEPD55, pp. 503–506.
- [9] T. L. Vardanyan *et al.*, “ALPHA – The THz Radiation Source based on AREAL”, in *Proc. 36th Int. Free Electron Laser Conf. (FEL'14)*, Basel, Switzerland, Aug. 2014, paper TUP083, pp. 561–563.
- [10] B. M. Bolotovskii, “Theory of Cherenkov Radiation (III)”, *Soviet Physics Uspekhi* 4, 781 (1962). doi:10.1070/PU1962v004n05ABEH003380
- [11] K.-Y. Ng, “Wake fields in a dielectric-lined waveguide”, *Physical Review D* 42, 5, (1990) doi:10.1103/PhysRevD.42.1819
- [12] M. Hüning, H. Schlarb, P. Schmüser, M. Timm, “Measurements of Harmonic Wake Fields Excited by Rough Surfaces”, *Phys. Rev. Lett.* 88, 074802 (2002). doi:10.1103/PhysRevLett.88.074802
- [13] A. M. Cook *et al.*, “Observation of Narrow-Band Terahertz Coherent Cherenkov Radiation from a Cylindrical Dielectric-Lined Waveguide”, *Physical Review Letters* 103, 095003 (2009). doi:10.1103/PhysRevLett.103.095003
- [14] M. Ivanyan, V. Tsakanov, “Longitudinal impedance of two-layer tube”, *Phys. Rev. ST Accel. Beams* 7, 114402 (2004). doi:10.1103/PhysRevSTAB.7.114402
- [15] M. Ivanyan, E. Laziev, V. Tsakanov, A. Vardanyan, S. Heifets, A. Tsakanian, “Multilayer tube impedance and external radiation”, *Phys. Rev. ST Accel. Beams* 11, 084001 (2008). doi:10.1103/PhysRevSTAB.11.084001
- [16] Paper in preparation.
- [17] M. Hüning, “Analysis of Surface Roughness Wake Fields and Longitudinal Phase Space in a Linear Electron Accelerator”, DESY-Thesis-2002-029 (2002). <http://www-library.desy.de/cgi-bin/showprep.pl?desy-thesis-02-029>
- [18] Vlasov, S.N. & Orlova, “Quasioptical transformer which transforms the waves in a waveguide having a circular cross section into a highly directional wave beam”, *I.M. Radiophys Quantum Electron* (1974) 17: 115. doi:10.1007/BF01037072
- [19] RF Cregan, BJ Mangan, JC Knight, TA Birks, P St J Russell, PJ Roberts, DC Allan, “Single-mode photonic band gap guidance of light in air”, *Science* 285, 5433 (1537-1539), 1999. <https://pdfs.semanticscholar.org/9f51/bfedab35926d03fdd3e7c13013a0600a4394.pdf>

GENERATING TRAINS OF ATTOWECOND PULSES WITH A FREE-ELECTRON LASER

Svitozar Serkez*, Gianluca Geloni, European XFEL, Schenefeld, Germany
MyungHoon Cho, Inhyuk Nam, Heung-Sik Kang, Gyujin Kim,
Chang-Ki Min, Jun Ho Ko, Chi Hyun Shim, PAL, Pohang, Korea
Franz-Josef Decker, SLAC, Menlo Park, California, USA
Yuri Shvyd'ko, ANL, Argonne, Illinois, USA

Abstract

Recently, a Hard X-ray Self-Seeding setup was commissioned at PAL XFEL. Its main purpose is to actively increase the temporal coherence of FEL radiation. We report another application of this setup, namely - to generate trains of short sub-femtosecond pulses with linked phases. We discuss the preliminary results of both experiment and corresponding simulations as well as indirect diagnostics of the radiation properties.

INTRODUCTION

Hard X-ray Self-Seeding (HXRSS) based on a single crystal monochromator [1–4] allows for an increased spectral density and longitudinal coherence at hard X-ray SASE FELs through active spectral filtering. It was originally proposed to use a single Bragg or Laue reflection from a thin diamond to generate a series of trailing maxima following SASE pulse. The electron beam is delayed to temporally overlap with one of these maxima, which is then amplified in a downstream undulator up to saturation and beyond. Later it was proposed to use two crystals [5], or several reflections of a single crystal simultaneously [6, 7], to generate a seed that contains more than one frequency within the FEL amplification bandwidth. Then, the final FEL section amplifies such multi-frequency seed radiation and due to non-linear intermodulation yields satellites – “beat waves” – observable at saturation [8].

One easy way to understand the emergence of satellite frequencies is to consider the amplification process of two spectral lines in the time domain. Combination of two overlapped seed beams with frequencies different by $\Delta\omega$ yields sinusoidal “beating” of the resulting seed power in the time domain at that difference frequency. Upon amplification of this seed to saturation, the now-increased radiation slip-page distorts the shape of that sinusoidal modulation. Such distortion manifests itself in the frequency domain via the emergence of the additional equidistant “satellites”. The resulting train of short pulses will allow studies of ultrafast phenomena [9–11].

SELF-SEEDING WITH “PHANTOM LINES”

PAL-XFEL at Pohang accelerator laboratory is the world’s third hard X-ray free-electron laser facility starting its user

* svitozar.serkez@xfel.eu

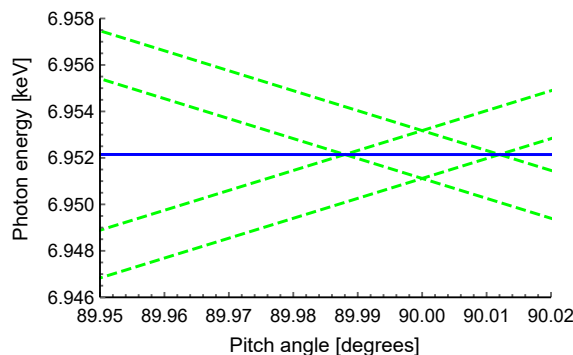


Figure 1: Seeding lines for Bragg reflections from diamond with photon energy versus crystal pitch angle for [004] reflection and four reflections from the [022] family assuming 0.012° yaw angle.

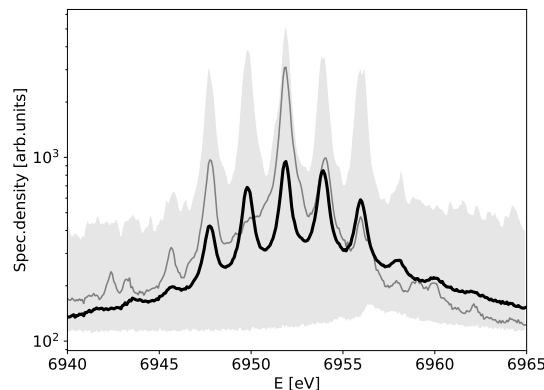


Figure 2: Radiation power spectrum as a function of photon energy for the case of seeding with 5 equidistant reflections. Also we can already see non-linear effects as additional maxima on both sides. Black line depicts the ensemble average over the ensemble of 10000 events, dark grey line shows a single-shot spectrum, light grey band represents the range of maximum and minimum values in the ensemble.

service operation in June 2017, and since then it has proven to be one of the most stable XFEL with a FEL timing jitter of 18 fs and a mJ-class hard X-ray FEL up to 14.4 keV [12, 13]. And a HXRSS for PAL-XFEL was successfully commissioned in 2018 to be able to provide users with a high spectral intensity FEL three times more than SASE [14].

The self-seeding operation mode was established using the diamond crystal with (001) lattice orientation. The FEL was tuned to generate SASE with photon energy around 6952 eV, that corresponds to a [004] Bragg reflection at 90° pitch angle.

If the crystal is not perfectly aligned, four additional reflections appear around the [004] line, namely [022], [0-22], [202] and [-202]. Tuning the crystal pitch and yaw angles, to approximately 89.965° and 0.012° respectively, see Figure 1, allowed us to arrange the reflection lines at equal separation of $\hbar\Delta\omega = 2$ eV. Upon FEL amplification, four satellite “beat waves” with the same spacing were observed, as presented on Figure 2.

Therefore, FEL radiation pulses with 9 discrete equidistant frequency components were generated, 4 of which do not have a crystallographic origin.

The spectral properties of the emitted radiation were measured with a single-shot spectrometer installed at the beam-line which is equipped with Si(111), Si(220), and Si(333) crystals [14].

OPTIMISING FOR TRAINS OF SHORT PULSES

Seeding simultaneously at n discrete equidistant frequencies yields, depending on the combination of crystal reflections, up to n^2 times higher peak power of the seed. Nevertheless, the temporal structure of such combined seed depends on phase differences between those frequencies and can be quite complex, see Figure 3.

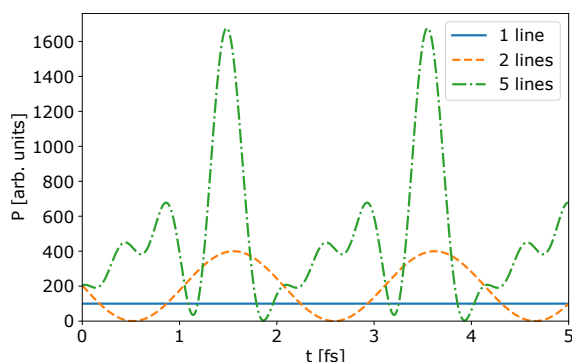


Figure 3: Illustration of the power distribution along the seed for the different number of the contributing resonance lines, separated by 2 eV, each providing radiation with random phases and equal intensities.

The seed is effectively generated via bandpass-filtering the SASE radiation spectrum. The latter is stochastic, therefore the intensity and phase of each transmitted frequency component vary randomly shot-to-shot.

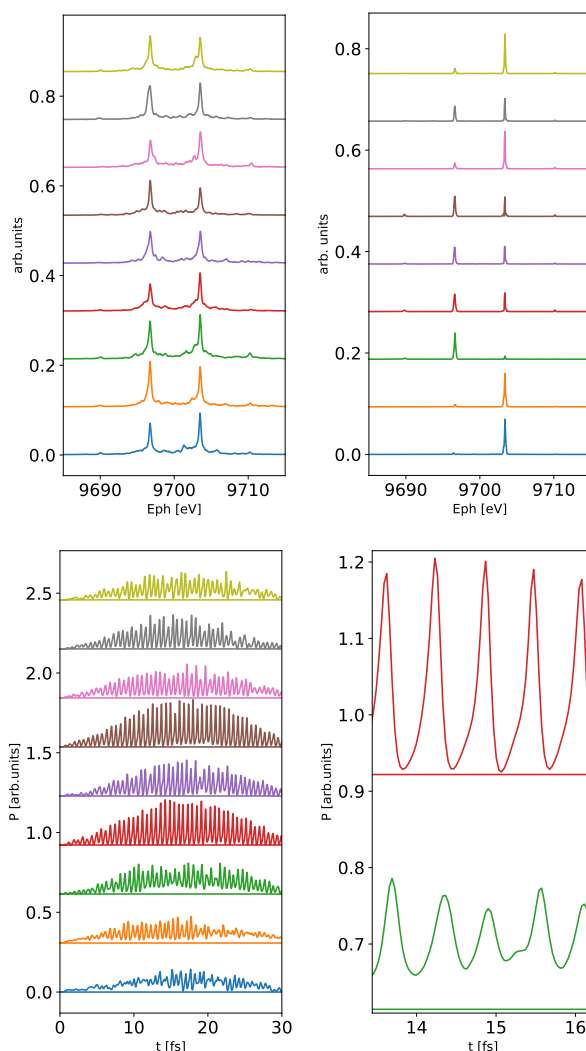


Figure 4: Measured FEL spectra (top left subplot with filtered subset representing best 1% of events in terms of peaks ratio and pulse energy) and simulated spectra (top right plot) with corresponding power profiles (bottom left plot). The bottom right plot depicts an enlarged part of the left plot, illustrating events with good and poor contrast.

If only two seed frequencies are chosen, the phase difference between them determines the temporal shift of the sinusoidally modulated seed- and, consequently, the amplified pulse. The phase of such modulation may, in principal, be measured, by examining the optical replica from the spent electron beam before reaching saturation [15]. The maximum contrast of the modulated seed is achieved when the intensities of both seed components are comparable. Such condition can be diagnosed using a non-invasive online spectrometer with subsequent filtering of the undesired events.

Such seed radiation with sinusoidally modulated power can be considered as a comb of pulses with durations equal to their temporal separation. The emergence of the satellite peaks in the spectrum at saturation would indicate a decrease of their duration.

This scenario was studied experimentally and numerically: the 9700 eV SASE radiation was filtered using [1-15] and [1-15] forward Bragg reflections, separated by 6.76 eV and consecutively amplified beyond saturation. On Figure 4 we present the acquired single-shot FEL spectra with emerging satellites as well as the simulation results in both time and frequency domains using Genesis numerical code [16] and Ocelot package [17]. Simulation results indicate that trains of the 180 as-long pulses (FWHM value) with 610 as separation can be generated.

Separation between the seeding frequencies ΔE allows one to control the temporal separation of the pulses in the trains: Δt [fs] $\approx 4.135/\Delta E$ [eV].

The proposed method to generate trains of attosecond pulses has the relaxed hardware requirements compared to the method proposed in [10], especially for the facilities that have already installed a HXRSS monochromator setup. Nevertheless, both methods may potentially be combined to achieve the best results.

CONCLUSIONS

We proposed a cost-effective method to generate a series of ultrashort pulses with a Hard X-ray Self-Seeded FEL and demonstrated it at PAL XFEL.

The seed radiation is produced using two adjacent crystal reflections. The seed radiation, modulated in time, is amplified beyond saturation. The emergence of the satellite frequencies indicates that the duration of the resulting pulses within the train decreases. The expected duration of a single pulse in such train is in order of 200 attoseconds.

The usage of only two reflections allows to discriminate the events with a poor contrast in the time domain by examining the single-shot FEL spectra. Otherwise, FEL pulses containing up to 9 discrete equidistant frequencies can be delivered.

REFERENCES

- [1] G. Geloni, V. Kocharyan and E. Saldin “A novel self-seeding scheme for hard X-ray FELs”, *J. Mod. Opt.*, vol. 58, no. 16, pp. 1391–1403, 2011; <https://doi.org/10.1080/09500340.2011.586473>
- [2] J. Amann *et al.*, “Demonstration of self-seeding in a hard-X-ray free-electron laser”, *Nat. Photonics*, vol. 6, pp. 693–698, 2012; <https://doi.org/10.1038/nphoton.2012.180>
- [3] Yu. Shvyd’ko, R. Lindberg, “Spatiotemporal response of crystals in x-ray Bragg diffraction”, *Phys. Rev. Spec. Top. Accel Beams*, vol. 15, no. 10, p. 100702, 2012; <https://doi.org/10.1103/PhysRevSTAB.15.100702>
- [4] R. R. Lindberg, and Yu. V. Shvyd’ko, “Time dependence of Bragg forward scattering and self-seeding

- of hard x-ray free-electron lasers”, *Phys. Rev. Spec. Top. Accel Beams*, vol. 15, no. 5, p. 050706, 2012; <https://doi.org/10.1103/PhysRevSTAB.15.050706>
- [5] G. Geloni, V. Kocharyan and E. Saldin, “Generation of doublet spectral lines at self-seeded X-ray FELs”, *Opt. Commun.*, vol. 284, no. 13, pp. 3348–3356, 2011; <https://doi.org/10.1016/j.optcom.2011.02.082>
- [6] F.-J. Decker *et al.*, “Two-color self-seeding and scanning the energy of seeded beams at LCLS” in Proc. 35th Int. Free-Electron Laser Conf. (FEL’13), New York, NY, USA, Aug. 2013, paper WEP009, pp. 514–517.
- [7] A. A. Lutman *et al.*, “Demonstration of Single-Crystal Self-Seeded Two-Color X-Ray Free-Electron Lasers”, *Phys. Rev. Lett.*, vol. 113, p. 254801, December 2014. <https://doi.org/10.1103/PhysRevLett.113.254801>
- [8] H. P. Freund, and P. G. O’Shea, “Two-Color Operation in High-Gain Free-Electron Lasers”, *Phys. Rev. Lett.*, vol. 84, no. 13, pp. 2861–2864, 2000; <https://doi.org/10.1103/PhysRevLett.84.2861>
- [9] A. Zholents, “Attosecond X-Ray Pulses from Free-Electron Lasers”, *Laser Phys.*, vol. 15, no. 6, p. 855, 2005.
- [10] N. R. Thompson and B. W. J. McNeil, “Mode Locking in a Free-Electron Laser Amplifier”, *Phys. Rev. Lett.*, vol. 100, no. 20, p. 203901, 2008.
- [11] S. Serkez *et al.*, “Overview of options for generating high-brightness attosecond x-ray pulses at free-electron lasers and applications at the European XFEL”, *J. Opt.*, vol. 20, no. 2, p. 024005, 2018.
- [12] H.-S. Kang *et al.*, “Hard X-ray free-electron laser with femtosecond scale timing jitter”, *Nat. Photon.*, vol. 11, no. 11, pp. 708–713, 2017.
- [13] H.-S. Kang *et al.*, “FEL performance achieved at PAL-XFEL using a three-chicane bunch compression scheme”, *J. Synchrotron Rad.*, vol. 26, no. 4, pp. 1127–1138, 2019.
- [14] C.-K. Min *et al.*, “Hard X-ray self-seeding commissioning at PAL-XFEL”, *J. Synchrotron Rad.*, vol. 26, no. 4, pp. 1101–1109, 2019.
- [15] E. L. Saldin, E. A. Schneidmiller, M. V. & Yurkov, “Optical afterburner for an x-ray free electron laser as a tool for pump-probe experiments”, *Phys. Rev. Spec. Top. Accel Beams*, vol. 13, no. 3, p. 030701, 2010; <https://doi.org/10.1103/PhysRevSTAB.13.030701>
- [16] S. Reiche, “GENESIS 1.3: A fully 3D time-dependent FEL simulation code”, *Nucl. Instrum. Methods Phys. Res., Sect. A*, vol. 429, no. 1, pp. 243–248, 1999; [https://doi.org/10.1016/S0168-9002\(99\)00114-X](https://doi.org/10.1016/S0168-9002(99)00114-X)
- [17] OCELOT: a versatile computational tool for light sources, 2016–present; <https://github.com/ocelot-collab/ocelot>

NANOSECOND PULSE ENHANCEMENT IN NARROW LINEWIDTH CAVITY FOR STEADY-STATE MICROBUNCHING

Qinghong Zhou[†], Science School, Southwest University of Science and Technology, Mianyang, China

Abstract

In steady-state microbunching (SSMB), nanosecond laser pulse with megawatt average power is required. We build up a theoretic model to simulate the enhancement process of such pulse in narrow linewidth (e.g. kHz level) cavity for this demand, which shows that a mode-locked mechanism in frequency domain should be considered. Simulations indicate that such pulse can be enhanced sufficiently under this condition. And we also propose some experimental schematics to realize it.

INTRODUCTION

In SSMB, nanosecond pulse laser field with megawatt average power is required [1]. To our knowledge, such power level is difficult and expensive to achieve with direct generation methods. In another hand, power enhancement by an optical cavity has been studied intensively in both cw and ultrashort pulse case last few decades, and 7.5kW [2] and 670kW [3] intracavity average power has been realized respectively. Also, enhancement of nanosecond laser pulse [4] has been studied theoretically and experimentally, which illustrate that such pulse can be sufficiently enhanced with the condition that the pulse linewidth is narrower than or comparable to that of the cavity. However, the linewidth of the cavity used for SSMB is narrower than ordinary one under same finesse because of its larger round trip length, which indicate that a nanosecond pulse hardly can be enhanced by such cavity.

In this paper, we propose a kind of nanosecond pulse with comb structure in frequency domain, which can be sufficiently enhanced in such narrow linewidth cavity. Using the model of pulsed multi-beam interference we numerically analyze the enhancement process of a nanosecond pulse in a travelling wave narrow linewidth cavity, which indicate that the pulse with any time duration can be sufficiently enhanced by this method. We also propose some schemes to generate such pulse.

MODEL OF NANOSECOND PULSE ENHANCEMENT FOR SSMB

Figure 1 shows the schematic of the enhancement cavity for SSMB. Here, a standard bowtie travelling wave ring cavity is chosen, whose advantages have been discussed already in detail [5].

To quantify the enhancement process, pulsed multi-beam interference model should be considered. However, two differentials should be noticed here. First, the transmis-

sions occur at every mirror. Second, the reflectivity and transmission of input coupler should be different from other mirrors because of the requirement for impedance matching.

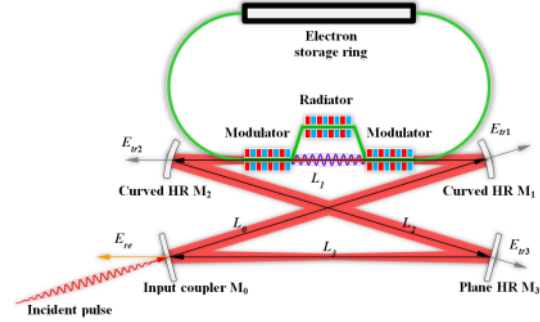


Figure 1: Schematic of SSMB with standard bowtie ring cavity.

To quantify the enhancement process, pulsed multi-beam interference model should be considered. However, two differentials should be noticed here. First, the transmissions occur at M_1 , M_2 and M_3 . Second, the reflectivity and transmission of input coupler M_0 should be different from M_1 - M_3 because of the requirement for impedance matching. Then, the model is modified as follow,

$$E_{re} = \left[\sqrt{R_0} \cdot E(t) + T_0 \sum_{n=1}^{\infty} (-\sqrt{R_0})^{n-1} (-\sqrt{R})^{3n} E \left(t - \frac{nL}{c} \right) e^{in\delta} \right] e^{i(\omega t - kz)} \quad (1)$$

$$E_{tr1} = \left[\sqrt{T_0 T} \sum_{n=0}^{\infty} (-\sqrt{R_0})^n (-\sqrt{R})^{3n} E \left(t - \frac{nL+L_0}{c} \right) e^{in\delta} \right] e^{i(\omega t - kz)} \quad (2)$$

$$E_{tr2} = \left[\sqrt{T_0 T} \sum_{n=0}^{\infty} (-\sqrt{R_0})^n (-\sqrt{R})^{3n+1} E \left(t - \frac{(2n+1)L}{2c} \right) e^{in\delta} \right] e^{i(\omega t - kz)} \quad (3)$$

$$E_{tr3} = \left[\sqrt{T_0 T} \sum_{n=0}^{\infty} (-\sqrt{R_0})^n (-\sqrt{R})^{3n+2} E \left(t - \frac{(n+1)L-L_3}{c} \right) e^{in\delta} \right] e^{i(\omega t - kz)} \quad (4)$$

$$E_{in} = \sqrt{T_0} \sum_{n=0}^{\infty} (-\sqrt{R_0})^n (-\sqrt{R})^{3n} E \left(t - \frac{z}{c} - \frac{nL}{c} \right) e^{i \left(\omega \left(t - \frac{z}{c} - \frac{nL}{c} \right) - kz - n\delta \right)} \quad (5)$$

Where, E_{re} , E_{in} represent reflection and intracavity field. E_{tr1} , E_{tr2} and E_{tr3} are the transmission fields from M_1 to M_3 . c and z is the speed of light and the position in the cavity along the direction of the beam propagation, and the origin of z is set at M_0 . L_0 - L_3 is the distance between two mirrors. $L=L_0+L_1+L_2+L_3$, is the round trip length of the cavity and δ is the corresponding phase shift. R_0 , T_0 is the reflectivity and transmittance of M_0 , and R , T is that of

[†] email address: nanguaa51@163.com

M_1 , M_2 and M_3 . k , ω is the wave vector and frequency of incident pulse. Then the electric field can be expressed as $E(t, z) = E(t)e^{i(\omega t - kz)}$.

SIMULATION OF THE TRADITIONAL NANOSECOND PULSE ENHANCEMENT

Nanosecond pulse is generated by Q switching method usually, which have transform limited linewidth of megahertz level. Such pulse can't be enhanced in high Q cavity obviously, because this kind of cavities always has linewidth of kilohertz level or even narrower.

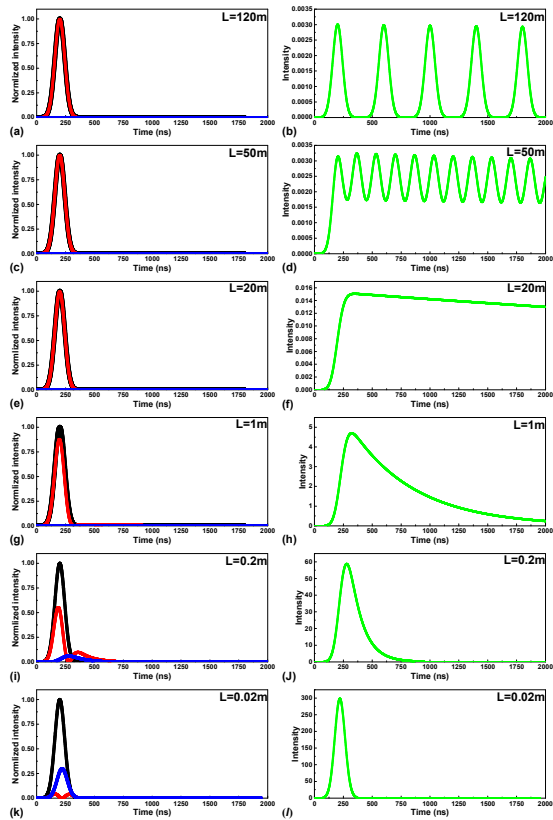


Figure 2: Simulation of traditional nanosecond pulse enhancement in different cavity length.

Assume that the incident pulse is the gaussian and the duration is 100ns with normalized amplitude. The simulation conditions are chosen as following: laser wavelength λ is set to 1064nm, mirror reflectivity R and transmittance T are set to 0.999 and 0.001, and for impedance matching the condition of $T_0 = 3T$ has been used. Cavity lengths L are set to 120m, 50m, 20m, 1m, 0.2m, and 0.02m respectively, we calculate the intensity of E_{re} , E_{tr} , and E_{in} for revealing the enhancement process.

Figure 2 shows the results. We can understand the process in time domain: when the cavity length is long (e. g. 120m and 50m, which is longer than the pulse length $c\tau \approx 30m$), the different part of laser filed can't overlap. When the cavity length gets shorter than the pulse length (e. g. 20m, 1m, 0.2m and 0.02m), the laser filed superposition occurs. The shorter the cavity length is, the more the superposition times are, and then we get the stronger enhancement. In addition, the longer cavity length (e. g.

20m, 1m and 0.2m) induce the broaden of pulse duration, which can be understood as the superposition of the pulse end to end.

In another hand, this process also can be understood with a simple picture in frequency domain. First, the linewidth of the Gaussian pulse is always transform limited because no chirp arises, for 100ns duration the ideal linewidth $\Delta\nu_p$ is 4.4MHz. Following above simulation parameters, the different cavity length lead to different free spectral range (FSR) and cavity linewidth ($\Delta\nu$), Table 1 shows these results. Comparing $\Delta\nu$ with $\Delta\nu_p$ we can see that when the cavity linewidth is bigger than the pulse the sufficient enhancement occurs, which can be seem as the cavity has enough capacity to hold the pulse in frequency domain.

Table 1: FSR and $\Delta\nu$ with Different Cavity Length Comparing the Pulse Linewidth.

	120 m	50m	20m	1m	0.2m	0.02m
FSR (MHz)	2.49	5.99	14.9	299.7	1498.9	17989.
$\Delta\nu$ (kHz)	8	6	90	90	62	623
$\Delta\nu/\Delta\nu_p$	2.38	5.73	14.3	286.5	1432.8	14328.
	8	1	28	67	38	379
	0.00	0.00	0.00	0.065	0.3256	3.2564
	05	13	33	1		

SIMULATION OF MODE-LOCKED NANOSECOND PULSE ENHANCEMENT

Comb structure in frequency domain has been used to generate ultrashort pulse with duration down to femtosecond. For realizing such ultrashort pulse millions of discrete lines have been used. On the other hand, a few lines produce the pulse with duration much longer. This physical picture can be easily understood by Fourier transform mechanism. We choose appropriate quantity of the discrete lines, besides the linewidth of single line is equal to or narrower than the cavity and the spacing between each other is equal to the cavity FSR. Such pulse train should be able to be enhancement in the cavity.

Here, the round trip cavity length is set to 120m, leading 2.5MHz in FSR. And other conditions are same as above, which bring the cavity linewidth of 2.39kHz. We assume that a pulse with 39 discrete lines, whose spacing and linewidth match the cavity's. The envelope and line shape are Gaussian and Lorentzian respectively. The pulse train structure in frequency and time domain are shown in Figs. 3 (a) and (b). Using the enhancement model above we obtain the reflection, transmission and intracavity field intensity, which are shown in Figs. 3 (c) and (d). We can see that the reflection is almost vanished, which means the impedance matching achieve, and the enhancement factor is about 332. These results indicate such kind of pulse can be enhancement sufficiently.

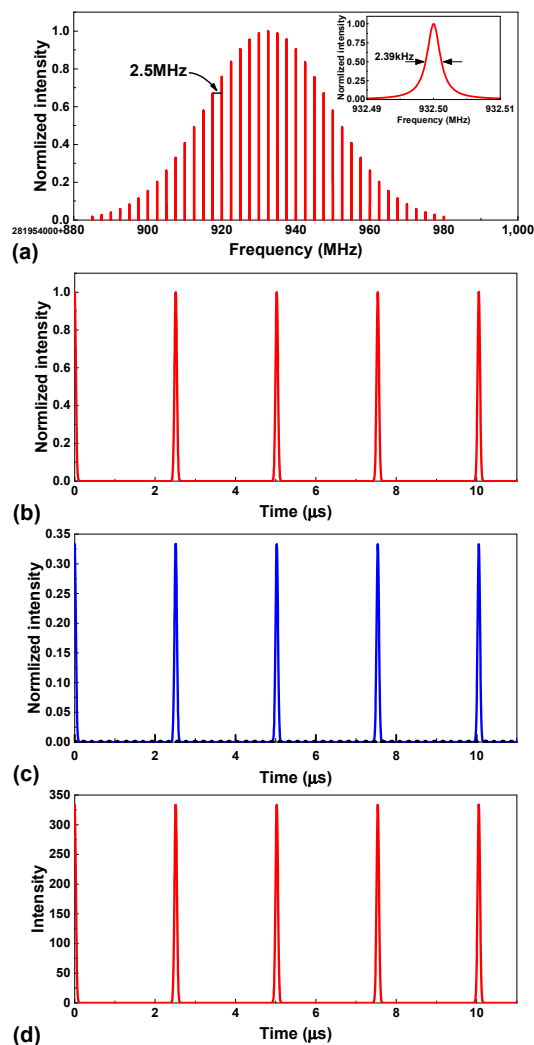


Figure 3: Simulation of mode-locked ns pulse enhancement. The structure of (a) frequency and (b) time domain of the pulse; (c) the reflection (black dot line) and transmission (blue solid line) intensity of the cavity; (d) intracavity intensity.

GENERATION OF THE MODE-LOCKED NANOSECOND PULSE

To realize the enhancement of mode-locked nanosecond pulse two aspects should be considered carefully. First, in the given narrow linewidth cavity the pulse which can be sufficiently enhanced has a certain structure in frequency and time domain, which means for generation of such a pulse one should obtain the cavity structure firstly. And such a cavity structure may be decided by other requirements, e.g. the dimensions of the modulator and radiator for the electron beam. Second, the number of discrete lines (or modes) decides the pulse duration directly, so the technique which can generate lines with a given number has to be developed.

Two candidate methods based on narrow linewidth cw laser may be feasible. The first one is based on coherent combination. The second one produces many sidebands and then filters out the superfluous lines to obtain such

a pulse. The phase locking technique (e.g. PDH method) is required in both methods for locking the cavity and laser source.

CONCLUSIONS

We propose a kind of nanosecond pulse generated by the mode locking process, which can be sufficiently enhanced in a high Q long (narrow linewidth) cavity. Comparing with traditional nanosecond pulses, e.g. generated by Q switching, such a pulse is fully coherent, which is just suitable for the application in SSMB.

REFERENCES

- [1] J. Wu, A. W. Chao, "Accelerator-based compact extreme ultraviolet (EUV) sources for lithography", *International Conference on Extreme Ultraviolet Lithography 2018*, 1080907, doi: 10.1117/12.2501900
- [2] O. Schwartz, J. J. Axelrod, D. R. Tuthill, P. Haslinger, C. Ophus, R. M. Glaeser, and H. Muller, "Near-concentric Fabry-Pérot cavity for continuous-wave laser control of electron waves", *Optics Express* 25, 14453, 2017, doi:10.1364/OE.25.014453
- [3] H. Carstens, N. Lilienfein, S. Holzberger, C. Jocher, T. Eidam, J. Limpert, A. Tünnermann, J. Weitenberg, D. C. Yost, A. Alghamdi, Z. Alahmed, A. Azeer, A. Apolonski, E. Fill, F. Krausz, and I. Pupeza, "Megawatt-scale average-power ultrashort pulses in an enhancement cavity", *Optics Letters* 39, 2595, 2014, doi:10.1364/OL.39.002595
- [4] R. Tanaka, T. Matsuzawa, H. Yokota, T. Suzuki, Y. Fujii, A. Mio, and M. Katsuragawa, "Stable confinement of nanosecond laser pulse in an enhancement cavity", *Optics Express* 16, 18667, 2008, doi:10.1364/OE.16.018667
- [5] H. Carstens, S. Holzberger, J. Kaster, J. Weitenberg, V. Pervak, A. Apolonski, E. Fill, F. Krausz, and I. Pupeza, "Large-mode enhancement cavities", *Optics Express* 21, 11606, 2013, doi:10.1364/OE.21.011606

A STORAGE RING DESIGN FOR STEADY-STATE MICROBUNCHING TO GENERATE COHERENT EUV LIGHT SOURCE

Zhilong Pan^{*1}, Tenghui Rui¹, Weishi Wan², Alex Chao³,

Xiujie Deng¹, Yao Zhang¹, Wenhui Huang¹, Chuanxiang Tang¹

¹Department of Engineering Physics, Tsinghua University, Beijing, China

²School of Physical Science and Technology, Shanghai Tech University, Shanghai, China

³SLAC, Menlo Park, CA, USA

Abstract

The proposal of Steady State Microbunching (SSMB) makes it available to generate high average power coherent radiation, especially has the potential to generate kW level of EUV source for lithography. In order to achieve and maintain SSMB, we propose several concepts. One is that a very short electron bunch below 100 nm is stored in the ring, inserting a strong focusing part to compress the bunch to ~3 nm, then radiating coherently, which is called longitudinal strong focusing (LSF) scheme. We have optimized the candidate lattice to achieve the very short electron bunch storage and microbunching for electron beam. The tracking results show the equilibrium length of the electron bunch is about 400 nm and no particles lose after 4.3 damping time while only single-particle effect is considered. More optimization and some new design based on the simulation results are still implementing.

INTRODUCTION

Because of the limitation of electron beam size in the traditional storage ring based synchrotron facilities, the average power of the incoherent radiation from this kind of facility will still be low although with extremely high repetition rate. On the other hand, the linac based FEL facilities can't generate high average power radiation due to the low repetition rate. The SSMB makes it achievable to radiate coherently in storage ring with high repetition rate, in other words, high average power radiation is available.

To achieve SSMB, several schemes have been proposed and pushed by our collaboration team in recent time, including longitudinal strong focusing (LSF) [1], reversible seeding[2], and hybrid scheme. Among those schemes, the LSF scheme requires that the storage ring can stably store the electron beam with a bunch length under 100 nm.

Based on the conventional formula by Sands[3], the length of electron bunch is determined by momentum compaction factor of the storage ring and RF parameters.

$$\sigma_s = \sigma_\delta L \frac{\alpha_c}{2\pi\nu_s}, \quad (1)$$

where α_c is momentum compaction factor, L is the circumference of the storage ring, σ_δ is equilibrium rms energy spread, ν_s is synchrotron tune.

According to eq.1, a storage ring with low momentum compaction factor on the magnitude of 1×10^{-6} or lower

is needed to match our requirements. On the other hand, the second order momentum compaction factor may dominate the longitudinal dynamics and reduce the RF bucket area if not been optimized properly in the low momentum compaction factor storage ring [4].

The bunch length formula from Sands neglects the part of path length fluctuation from photon emission, which associates with local momentum compaction factor, or partial alpha [1]. The bunch length formula by taking account this effect in is [5]

$$\sigma_s = \sigma_\delta L \sqrt{\left(\frac{\alpha_c}{2\pi\nu_s}\right)^2 + I_{\bar{\alpha}}}, \quad (2)$$

where $I_{\bar{\alpha}}$ is the variance of partial alpha. So the partial alpha of the storage ring should also be minimized to prevent the bunch length increasing.

The isochronous cell scheme has been proposed by our team to design the SSMB lattice [6]. We adopt that lattice in this paper and make some improvement in terms of slight adjustment of momentum compaction factor, minimizing second order momentum compaction factor, and dynamic aperture optimization. Then we do some single-particle simulation based on this lattice. The simulation results will show some direction for further lattice optimization.

LATTICE PARAMETERS

The lattice layout can refer to [6]. There are two dispersion free straight sections and two arc sections, and 6 isochronous cells in per arc section. The twiss function of one isochronous cell is shown in Fig.1. The integration of $\int_0^{L_b} \frac{\eta_x(s)}{\rho} ds$ will be 0 through the dipole in the isochronous cell, where L_b is the dipole length. So the momentum compaction factor of the whole ring could be very small. Three families of sextupoles named S1, S2, S3 are introduced to minimize the chromaticity and second order momentum compaction factor. The ring parameters are listed in Table.1.

The second order compaction factor has been optimized and the relation $\alpha_c > 10\alpha_{c2}\sigma_\delta$ is satisfied by referring to Table.1, so the longitudinal dynamics is still dominant by α_c . The bunch length induced by partial alpha is related with $\sqrt{I_{\bar{\alpha}}}$, the value will be ~ 300 nm. The equilibrium bunch length of this lattice will not be shorter than 300 nm, we will do some single-particle simulation based on this lattice later to check the partial alpha theory and get some guideline on the next step optimization.

* pzl15@mails.tsinghua.edu.cn

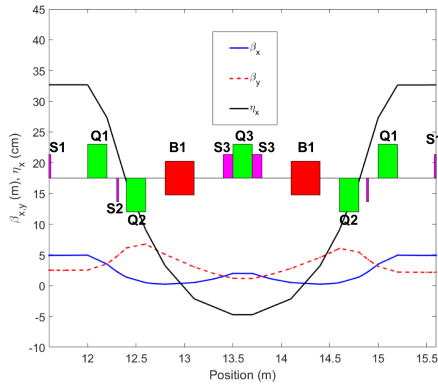


Figure 1: Twiss function of one isochronous cell in the lattice.

Table 1: Ring Parameters

Ring Parameters	Values
Circumference	94.4 m
Tunes(x/y)	13.22/3.48
Chrom.(x/y)	0.657/0.987
α_c	2.73×10^{-7}
α_{c2}	3.45×10^{-5}
$\sqrt{I_{\bar{a}}}$	1.1×10^{-5}
Energy Spread σ_δ	2.97×10^{-4}
Energy Loss Per Turn	1.736 keV
Natural emittance	1.67 nm
Hor./Ver Damping Time	145/145 ms
Long. Damping Time	72.5 ms

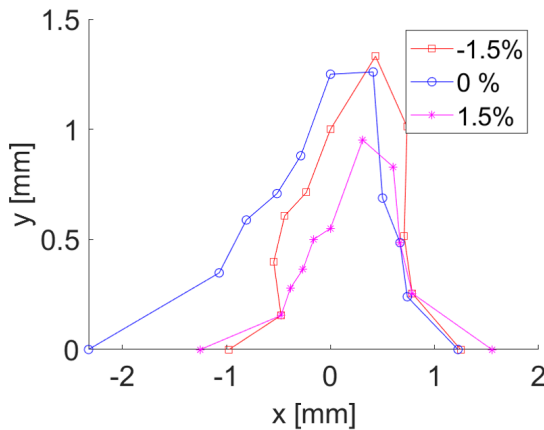


Figure 2: Dynamic aperture of the lattice.

DYNAMIC APERTURE

The dynamic aperture is optimized by inserting two families of harmonic sextupoles at the dispersion free locations. Taking the diffusion rate as objective, we scan the strengths of the two families sextupoles to get an optimal solution. Dynamic aperture is about 2 mm in horizontal direction and 1 mm in vertical direction as shown in Fig.2.

Table 2: RF Settings for Tracking in the Lattice

RF wavelength	$\lambda = 3 \mu\text{m}$	$\lambda = 5 \mu\text{m}$
RF Voltage V	120 kV	100 kV
Half bucket height δ_{rf}	2.09×10^{-3}	2.45×10^{-3}
Synchrotron tune ν_s	0.045	0.032
Bunch length $\sigma_{s,sands}$	134.48 nm	190.21 nm
RF Voltage V	250 kV	150 kV
Half bucket height δ_{rf}	3.03×10^{-3}	3.02×10^{-3}
Synchrotron tune ν_s	0.065	0.039
Bunch length $\sigma_{s,sands}$	93.17 nm	155.29 nm

SIMULATION

We have set up several simulations for this lattice, while only single-particle effects are considered in terms of synchrotron radiation, quantum excitation, and the nonlinear effects in this lattice. We choose different RF cavity wavelength and voltage to study the effects that dominant the particle loss for single particle. Four sets of parameters are chosen and listed in Table.2.

The four settings are labeled as C1 through C4: i) RF wavelength and voltage are $3 \mu\text{m}$ and 120 kV respectively (C1); ii) RF wavelength and voltage are $3 \mu\text{m}$ and 250 kV respectively (C2); iii) RF wavelength and voltage are $5 \mu\text{m}$ and 100 kV respectively (C3); iv) RF wavelength and voltage are $5 \mu\text{m}$ and 150 kV respectively (C4).

The Pelegant[7] will track 200 macro-particles for 1 million turns (4.3 damping time) for all the four different settings based on the lattice. It is single particle tracking so there is no space charge effect, no coherent synchrotron radiation effect, and no intra-beam scattering effect. The lattice error is not included in this simulation too.

We record the phase space coordinates of electrons every 1000 turns during simulation, and collect the data from latest 50 recording points (the latest 50 thousands turns, if no particle lose, there will be 10000 particles in total) to calculate the rms bunch length, energy spread, and horizontal emittance for electron bunch.

Simulation Results

After tracking for 1 million turns, the survived particles are collected in a file, the lost conditions are summarized in Table.3. It is obvious that the particles can't be stored in the ring if we set the RF wavelength at $3 \mu\text{m}$, because the rms bunch length induced by the partial alpha is larger than 300 nm , which means the distribution length will be larger than $1.8 \mu\text{m}$, while the phase stable area of the $3 \mu\text{m}$ RF is smaller than $1.5 \mu\text{m}$, so most particles will lose during tracking. As for $5 \mu\text{m}$ RF, all the particles can stay in the phase stable area and simulation results show that no particle lose for RF settings C3 and C4.

Comparing the lost conditions for C1 and C2, the particles can survive more with the setting of C1. That is because the larger RF voltage in setting C2 will give a larger kick to the

particle while it go through the RF cavity. The larger kick make it more likely to escape from the RF bucket.

Table 3: Lost Conditions for All the Four Settings

RF settings	lost condition
C1	79 survived over 200 particles
C2	5 survived over 200 particles
C3	200 survived over 200 particles
C4	200 survived over 200 particles

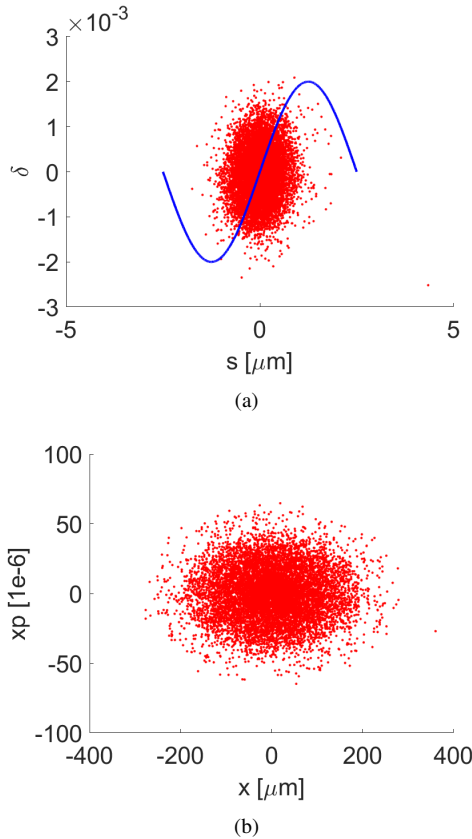


Figure 3: Longitudinal and horizontal distributions of the survived particles for setting C3. (a) is longitudinal distribution and (b) is horizontal distribution.

The longitudinal and horizontal distribution of the survived particles in setting C3 and C4 have been plotted in Fig.3 and Fig.4. As mentioned above, the data from latest 50 thousands turns with the interval of 1000 turns are used in the plot. The rms bunch length and energy spread calculated from the data in the plot for setting C3 is $\sigma_s = 400.7 \text{ nm}$ and $\sigma_\delta = 5.92 \times 10^{-4}$, as for the bunch length from Sands formula is $\sigma_{s,sands} = 190.21 \text{ nm}$, so the bunch length from partial alpha is $\sigma_{s,\sqrt{I_a}} = 352.67 \text{ nm}$. For setting C4, $\sigma_s = 373.3 \text{ nm}$ and $\sigma_\delta = 6.83 \times 10^{-4}$, as for the bunch length from Sands formula is $\sigma_{s,sands} = 155.29 \text{ nm}$, so $\sigma_{s,\sqrt{I_a}} = 339.46 \text{ nm}$. The difference of $\sigma_{s,\sqrt{I_a}}$ between the two settings C3 and C4 is about 3%.

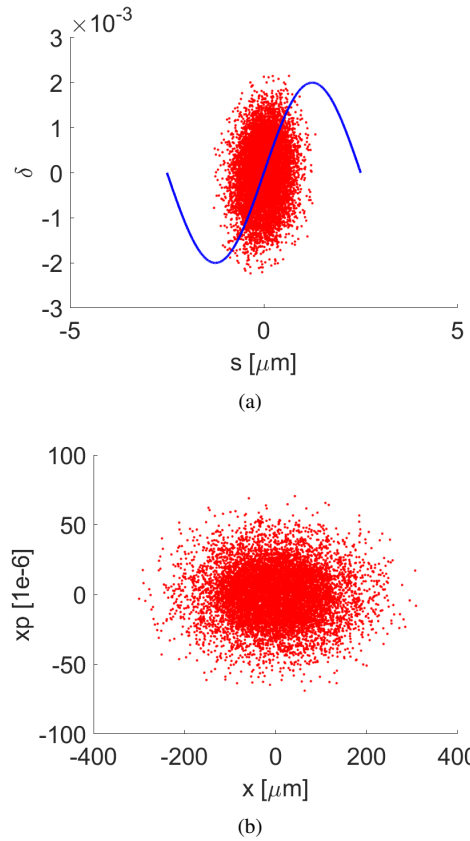


Figure 4: Longitudinal and horizontal distributions of the survived particles for setting C4. (a) is longitudinal distribution and (b) is horizontal distribution.

CONCLUSION

The lattice based on isochronous cell has been optimized for SSMB project. The second order compaction factor and dynamic aperture are optimized within requirements. The simulation of single particle tracking has shown that the bunch length of electron stored in this lattice will be $\sim 400 \text{ nm}$ due to the limitation of large partial alpha. A new lattice with designed value of $\sqrt{I_a}$ to 1×10^{-6} has also been designed and the single particle tracking is performing. The new lattice will store the electron bunch with rms bunch length of $\sim 40 \text{ nm}$.

REFERENCES

- [1] C. Tang *et al.*, “An Overview of the Progress on SSMB”, in *Proc. 60th ICFA Advanced Beam Dynamics Workshop on Future Light Sources*, paper THP2WB02, 2018. doi:10.18429/JACoW-FLS2018-THP2WB02
- [2] D. Ratner and A. Chao, “Reversible Seeding in Storage Rings”, No. *SLAC-PUB-14718*, 2011.
- [3] M. Sands, “The physics of electron storage rings: an introduction”, in *Conf. Proc. Vol. 6906161. No. SLAC-121*, 1970.

- [4] E.-S. Kim, “Compact Storage Ring for Far-Infrared Coherent Synchrotron Radiation Source”, *Japanese Journal of Applied Physics*, Vol. 46, No. 12, 2007, pp. 7952–7958.
doi:10.1143/JJAP.46.7952
- [5] A. Chao, “Evaluation of beam distribution parameters in an electron storage ring”, *Journal of Applied Physics*.50.2 (1979): 595-598.
doi:10.1063/1.326070
- [6] T. Rui *et al.*, “Strong focusing lattice design for SSMB” in *Proc. 60th ICFA Advanced Beam Dynamics Workshop on Future Light Sources*, paper WEP2PT014, 2018.
doi:10.18429/JACoW-FLS2018-WEP2PT014
- [7] M. Borland, “elegant: A Flexible SDDS-Compliant Code for Accelerator Simulation”, *Advanced Photon Source LS-287*, September 2000.
doi:10.2172/761286

DEVELOPMENT OF RF-UNDULATORS AND POWERING SOURCES FOR COMPACT EFFICIENT COMPTON FEL-SCATTRONS*

A.V. Savilov[†], E.B. Abubakirov, N. S. Ginzburg, S.V. Kuzikov, N. Yu. Peskov, A.A. Vikharev,
V. Yu. Zaslavsky, Institute of Applied Physics, Nizhny Novgorod, Russian Federation

Abstract

Conception of Compton-type FELs operating up to X-ray band is under development currently at IAP RAS. This concept is aimed at reducing energy of a driving relativistic electron beam and thereby increasing efficiency of the electron-wave interaction in FEL, as well as achieving relative compactness of the generator. The basis of this concept is RF-undulators of a new type - the so-called 'flying' undulators. Results of current research of these RF-undulators, their simulations and 'cold' tests in the Ka-band are presented. For powering RF-undulators spatially-extended narrow-band Cerenkov masers are developed in the specified frequency range. In order to achieve the required sub-gigawatt power level of the pumping wave in a strongly oversized oscillator, we exploit the original idea of using two-dimensional distributed feedback implemented in the 2D doubly-periodical slow-wave structures. The design parameters of Ka-band surface-wave oscillator intended for powering RF-undulators, results of its simulation and initial experimental studies are discussed.

INTRODUCTION

Free electron lasers (FELs) are the most powerful sources of coherent radiation in the ranges up to X-rays and are being actively developed around the world. However, the main challenge of these projects are related currently with the gigantic size of the facilities, low efficiency of the electron-wave interaction and strong requirements to the quality of driving beams. As a way to solve these problems, development of Compton FELs can be considered. The use of the counter-propagating pumping wave (so-called RF-undulator) of the mm- wavelength band (instead of "traditional" magnetostatic undulators, the period of which is limited to several centimeters) makes it possible significantly reduce the energy of driving electron beam required for operation in the X-ray range, resulting in a decrease in the length of both the accelerator and the FEL interaction region (by increasing the FEL electron-wave interaction parameter), and enhance the efficiency of radiation generation.

The conception of Compton FEL-scatteron has been developing in recent years at IAP RAS. The basis of this concept is a novel scheme of RF-undulator - the so-called "flying" undulator [1]. Simulations of various schemes of

such undulators, including the ones with profiled parameters were conducted currently. It is shown that the use of these undulators allows realization of a non-resonant multi-pulse trapping regime [2], which leads to a decrease in sensitivity to the quality (i.e. energy and velocity spread) of the driving beam and, thus, to a further increase in the efficiency of this type FEL [3].

Experimental studies of the prototype of pumping system (including RF-undulators and RF-power sources) for FEL-scatteron were started at IAP RAS in the Ka-band. The required high power level in powering pulsed relativistic masers is planned to be achieved by extending their transverse size and exploiting novel two-dimensional (2D) distributed feedback mechanism to maintain narrow-band operation in strongly oversized systems. Operation principles, design parameters and results of simulation of Ka-band Surface-Wave Oscillator (SWO) intended for the experiments on powering "flying" rf undulator are discussed in this work.

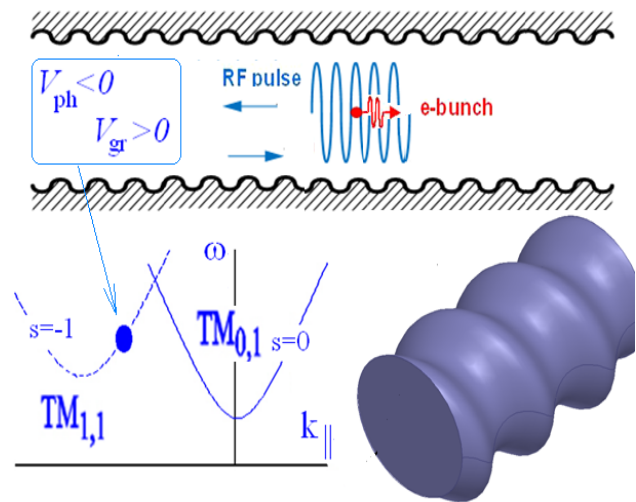


Figure 1: Flying RF-undulator. Microwave system and dispersion diagram of the operating undulator wave.

FLYING RF UNDULATOR

The "flying" RF-undulator [1] represents a powerful short pulse of coherent microwave radiation propagating synchronously with the electron bunch (Fig. 1). The microwave system of this RF-undulator consists of a cylindrical waveguide section with helical corrugation, which ensures the presence in the microwave pulse of a wave component with a backward (with respect to the direction of the electron bunch propagation) phase velocity but, simultaneously, with a group velocity close to the speed of light. Thus, the proximity of the group velocity of the microwave pulse wave and the electron bunch velocity realizes a long-time electron-wave interaction, while the

* Work is partially supported by the Russian Foundation for Basic Research (grant # 18-02-40009). Experimental facilities are developed and exploited in the frame of the Russian State Task Program (project #0035-2019-0001) and the RAS Presidium Project no.10 (#0035-2018-0022).

[†] savilov@appl.sci.nnov.ru

presence of a counter-propagating partial wave provides the stimulated scattering of the RF pulse into the short-wavelength radiation with a high Doppler frequency up-conversion factor.

At present, a prototype model of a “flying” RF-undulator (Fig. 2 a) with an operating frequency of around 33.5 GHz was made in the form of a cylindrical waveguide section with a diameter of 12.2 mm having a single-turn helical corrugation of a period of 6 mm and an amplitude of 3 mm, providing coupling and mutual scattering of partial waves $TM_{0,1}$ (zero spatial harmonic) and $TM_{1,1}$ - type (-1 harmonic).

According to the 3D simulations, this corrugation under the operating parameters forms a normal wave with a group velocity close to the speed of light ($\sim 0.7c$), which possesses a weak frequency dispersion. It is important that this normal wave contains about 50% of the partial wave $TM_{1,1}$, counter-propagating with respect to the electrons. The wave-number of the counter-propagating component of the RF-wave in this prototype model corresponds to the effective undulator period $d_u \approx 5.4$ mm, and the calculated undulation factor under the design parameters is $\sim 0.1 - 0.15$ when the RF-pulse power is ~ 0.5 GW. Circular polarization of operating wave gives twice the factor of electron-wave interaction (in comparison with the planar undulator). Note, that near the waveguide center (where the electron beam is transported) “parasitic” transverse field of the forward-propagating partial wave $TM_{0,1}$ is absent. Results of the “cold” tests of the undulator prototype model are shown in Fig. 2 b and coincide well with the simulations.

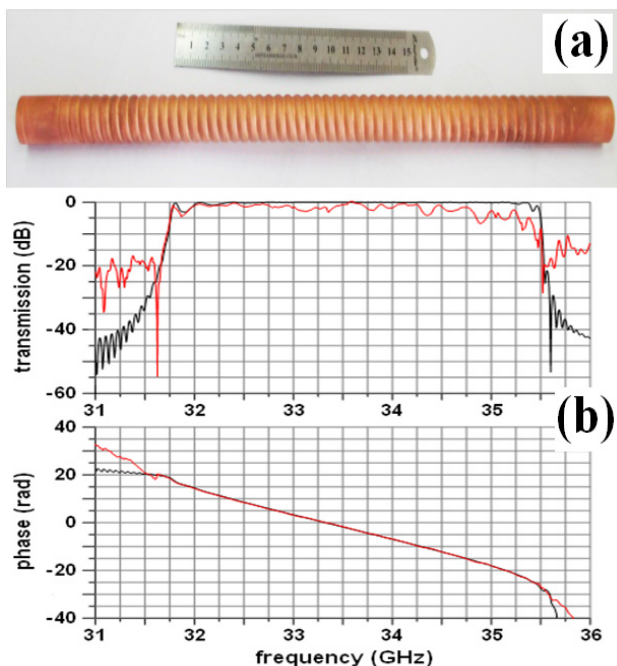


Figure 2: (a) Photograph of the prototype model of “flying” RF-undulator and (b) results of the 3D simulations (black curves) and “cold” tests (red curves) of transmission of the $TM_{0,1}$ wave (top) through this undulator and phase of the transmission (bottom).

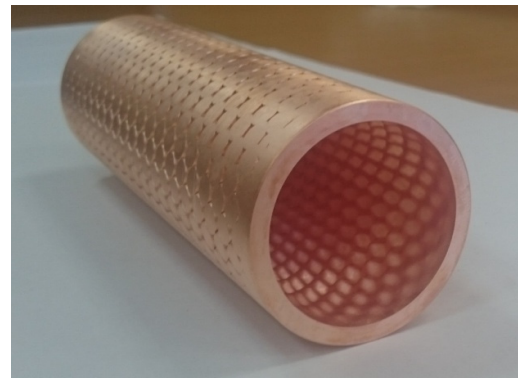


Figure 3: Photograph of cylindrical slow-wave structure with the inner 2D sinusoidal corrugation (oversize parameter $\varnothing/\lambda \sim 5$) for operation at Ka-band.

POWERFUL KA-BAND 2D SURFACE-WAVE OSCILLATOR

Powerful spatially-extended Ka-band SWO is constructed based on the high-current explosive-emission accelerator «Sinus-6» 0.5 MeV / 5 kA / 25 ns. Oscillators of such type are preferable among the relativistic Cherenkov masers due to the larger values of the electron-wave coupling impedance. This project is a promising development of our original concept of the radiation power enhancement in relativistic masers by extending the cross-section of their interaction space while maintaining the beam current density and the electromagnetic fluxes densities at a moderate level.

The radiation power enhancement in relativistic Cherenkov masers is intended by extending cross-section of the interaction space while keeping the beam current density and the electromagnetic fluxes densities at the moderate level. The use of large-size electron beams and strongly oversized (in the wavelength scale) electrodynamic systems (Fig. 3) is aimed on advance of the oscillators into the short-wavelengths up to submillimeter band and achievement of the record power levels. To ensure high coherence of the radiation (necessary for pumping resonant structures of RF-undulators) we proposed to exploit two-dimensional distributed feedback [4, 5] realized (in the case of Cherenkov masers) by two-dimensional (2D) double-periodical slow-wave structures. This novel feedback mechanism is a universal method for obtaining coherent radiation in spatially-extended relativistic masers of different types [6 - 8].

For the generator operating at Ka-band, the 2D slow-wave structure of cylindrical geometry was designed with an average diameter $\varnothing = 4.6$ cm (perimeter of about 16 wavelengths), length of 8.4 cm having 2D sinusoidal corrugation of 7 mm period, 2.5 mm amplitude and 16 azimuthal turns (Fig.3). In the 2D SWO slow-wave structure combines the properties of a slow-wave system realizing conditions for an effective Cherenkov interaction with a high-current rectilinear sheet REB, and a high-Q resonator utilizing the mechanism of 2D distributed feedback and providing selective excitation of the operating mode in the strongly oversized system. Considered

scheme of the oscillator is characterized by the presence of the four electromagnetic (e.m.) energy fluxes propagating in the axial $\pm z$ and the transverse (azimuthal) $\pm\phi$ directions. To provide single-output of radiation from the 2D SWO, additional coaxial reflector was designed for installation at the up-stream side (cathode-side) of the generator.

Simulations of 2D SWO based on the “Sinus-6” accelerator were carried out using PIC code CST Studio Suite. Parameters for the simulations were taken close to the experimental conditions. In the preliminary electron-optical experiments, hollow electron beam of the mean diameter 4.4 mm was realized and guided through the interaction space by the solenoidal axial magnetic field of about 1.4 T. Results of simulations are presented in Fig. 4 and demonstrate establishment of narrow-band oscillation regime under the design parameters. The output power reaches 0.5 GW under the electron efficiency of $\sim 25\%$. In this case, mode pattern of the operating synchronous slow wave demonstrates azimuthally symmetric distribution (Fig. 5) and contains of the waveguide modes of the $TM_{0,n}$ type (see Fig. 4 a). Experiments on realization and experimental studies of the 2D SWO are in progress currently based on the “Sinus-6” accelerator.

REFERENCES

- [1] S.V. Kuzikov, A.V. Savilov, A.A.Vikharev, “Short-pulse “flying” RF undulator”, *Appl. Phys. Lett.*, vol.105, p.033504, 2014.
- [2] S.V. Kuzikov, A.V. Savilov “Regime of “multi-stage” trapping in electron masers”, *Phys. Plasmas*, vol.25, p.113114, 2018.
- [3] S. V. Kuzikov, S. P. Antipov, A. Liu, A. V. Savilov, and A. A. Vikharev, “Tapered Flying Radiofrequency Undulator”, in *Proc. 38th Int. Free Electron Laser Conf. (FEL'17)*, Santa Fe, NM, USA, Aug. 2017, pp. 525-528. doi:10.18429/JACoW-FEL2017-WEP055
- [4] N.S. Ginzburg, N.Yu. Peskov, A.S. Sergeev, “Use of two-dimensional distributed feedback in free-electron lasers”, *Pisma v Zhurnal Tekhnicheskoi Fiziki*, vol.18, no.9, pp.23-28, 1992 (in Russian).
- [5] N.S. Ginzburg, N.Yu. Peskov, A.S. Sergeev, A.V. Arzhannikov, S.L. Sinitsky, “Super-power free-electron lasers with two-dimension distributed feedback”, *Nucl. Instr. and Meth. in Phys. Research A*, vol.A358, pp.189-192, 1995.
- [6] A.V. Arzhannikov, A.W. Cross, N.S. Ginzburg, W. He, P.V. Kalinin, I.V. Konoplev, S.A. Kuznetsov, N.Yu. Peskov, A.D.R. Phelps, C.W. Robertson, K. Ronald, A.S. Sergeev, S.L. Sinitsky, V.D. Stepanov, M. Thumm, C.G. Whyte, V.Yu. Zaslavsky, “Production of powerful spatially coherent radiation in planar and coaxial FEM exploiting two-dimensional distributed feedback”, *IEEE Trans. on Plasma Sci.*, vol.37, no.9, pp.1792-1800, 2009.
- [7] A.V. Arzhannikov, N.S. Ginzburg, P.V. Kalinin, S.A. Kuznetsov, A.M. Malkin, N.Yu. Peskov, A.S. Sergeev, S.L. Sinitsky, V.D. Stepanov, M. Thumm, V.Yu. Zaslavsky, “Using two-dimensional distributed feedback for synchronization of radiation from two parallel-sheet electron beams in a Free-Electron Maser”, *Phys. Rev. Lett.*, vol.117, p.114801, 2016.
- [8] N.S. Ginzburg, E.V. Ilyakov, I.S. Kulagin, A.M. Malkin, N.Yu. Peskov, A.S. Sergeev, V.Yu. Zaslavsky, “Theoretical and experimental studies of relativistic oversized Ka-band surface-wave oscillator based on 2D periodical corrugated structure”, *Phys. Rev. Accel. and*

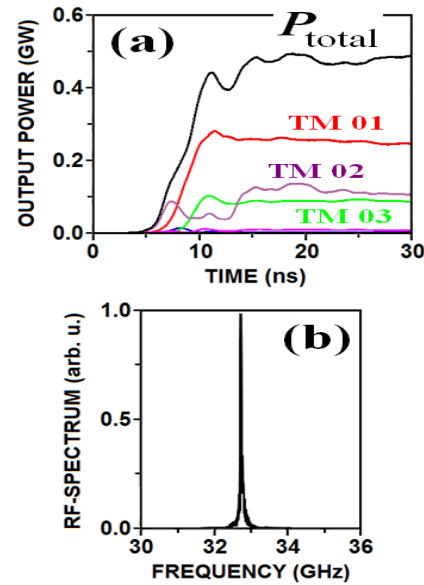


Figure 4: Results of 3D PIC simulations of sub-GW Ka-band 2D SWO. (a) Time dependence of the total output power and partial powers associated with different waveguide modes. (b) Radiation spectrum in the steady-state generation regime.

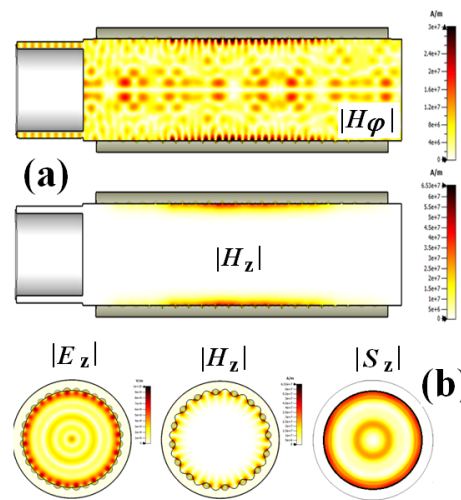


Figure 5: Spatial instantaneous structure of the RF-field in the sub-GW Ka-band 2D SWO (simulations): (a) H_ϕ and H_z components in the longitudinal cross-section and (b) E_z and H_z components in the transverse cross-section inside the interaction region, as well as the axial component of the Poynting vector S_z of the output radiation. Components H_ϕ and E_z correspond to interference of the axially propagating wave beams (interacting with the electrons partial waves) and H_z to interference of transversely (azimuthally) propagating partial wave beams (“waves of synchronization”).

BAYESIAN OPTIMISATION FOR FAST AND SAFE PARAMETER TUNING OF SWISSFEL

J. Kirschner, M. Nonnenmacher, M. Mutný, A. Krause, Dept. of Computer Science, ETH Zurich
N. Hiller, R. Ischebeck, A. Adelman, Paul Scherrer Institute

Abstract

Parameter tuning is a notoriously time-consuming task in accelerator facilities. As tool for global optimization with noisy evaluations, Bayesian optimization was recently shown to outperform alternative methods. By learning a model of the underlying function using all available data, the next evaluation can be chosen carefully to find the optimum with as few steps as possible and without violating any safety constraints. However, the per-step computation time increases significantly with the number of parameters and the generality of the approach can lead to slow convergence on functions that are easier to optimize. To overcome these limitations, we divide the global problem into sequential subproblems that can be solved efficiently using safe Bayesian optimization. This allows us to trade off local and global convergence and to adapt to additional structure in the objective function. Further, we provide slice-plots of the function as user feedback during the optimization. We showcase how we use our algorithm to tune up the FEL output of SwissFEL with up to 40 parameters simultaneously, and reach convergence within reasonable tuning times in the order of 30 minutes (< 2000 steps).

INTRODUCTION

Empirical parameter tuning is an important and reoccurring task of the FEL setup. Common tuning objectives include the pulse energy or spectrum of the FEL signal and loss minimization, or a combination of multiple criteria. A recent effort started to use optimization methods to automate the tuning process [1–6], and significant speedups compared to manual operator tuning have been obtained. As only point evaluations of the objective function are available, one has to rely on *zero-order or blackbox optimization methods*. Due to their simplicity, the Nelder-Mead (Simplex) [7] algorithm and random walk optimizers have become popular choices to assist operator tuning in some facilities. As an alternative, Bayesian optimization (BO) [8, 9] has recently gained interest also in the accelerator community [1, 2]. Bayesian optimization deals with observation noise in a principled way, allows to leverage prior data and comes with theoretical convergence guarantees in some cases [10]. A variant (SafeOPT) has been proposed [11], that takes additional safety constraints into account. This is of importance for tuning FEL parameters, for instance to avoid electron losses or to maintain a minimum level of the FEL signal during optimization. However, these benefits come at the expense of increased computational requirements as well as additional complexity in the choice and sensitivity of BO hyperparameters. We believe that these issues constitute the main

reasons that prevent a more wide-spread use of Bayesian optimization in this context beyond an academic setup. Moving forward with this, we present the following contributions.

- We implement the LineBO [12] algorithm at SwissFEL. The algorithm is designed to be computationally efficient when used with a large number of parameters and allows to take safety critical constraints into account.
- On SwissFEL we compare our methods to a simple parameter scan and the Nelder-Mead method, and obtain promising results when tuning up to 40 parameters.

Mathematical Setting

Let d denote the number of tuning parameters. The parameter space is $\mathcal{X} = [a_1; b_1] \times \dots \times [a_d; b_d] \subset \mathbb{R}^d$, where $a_i \leq x_i \leq b_i$ defines the allowed range for each parameter $i = 1, \dots, d$. The objective function (e.g. the FEL pulse energy) is an unknown function $f : \mathcal{X} \rightarrow \mathbb{R}$. The constraints are modelled by some unknown $g : \mathcal{X} \rightarrow \mathbb{R}$. A parameter $x \in \mathcal{X}$ is said to satisfy the safety constraint if $g(x) \leq \tau$ for a user-specified threshold level $\tau \in \mathbb{R}$. For simplicity, we use the formulation with a single constraint but multiple constraints are possible by choosing g vector valued. The only way to access f and g is to measure at any $x \in \mathcal{X}$, which yields noisy point observations of the objective and the constraint, $y = f(x) + \epsilon$ and $s = g(x) + \eta$. We refer to this process as *evaluating at x* , which in our case includes averaging the FEL signal over multiple shots. Formally, the tuning objective is

$$x^* = \arg \max_{x \in \mathcal{X}; g(x) \leq \tau} f(x). \quad (1)$$

An optimization algorithm iteratively chooses a sequence of parameters x_1, \dots, x_T and obtains evaluations of f and g for each point. After T steps (when the user stops the optimization), a final solution x_T is returned. A tuning method is called *safe* if all the iterates $(x_t)_{t=1}^T$ satisfy $g(x_t) \leq \tau$. In the unconstrained case the requirement $g(x) \leq \tau$ is dropped.

BAYESIAN OPTIMIZATION

Bayesian optimization is a method for global optimization. The idea is to learn a model of the objective function based on the data collected during the optimization (and possibly any available prior data). The decision where to place the next evaluation is then based on the model's predictions of plausible locations of the optimum x^* and also takes the model uncertainty into account. More formally, in the unconstrained case, Bayesian optimization uses the following steps.

Step 0) Initialize step counter $t = 0$, data $\mathcal{D}_0 = \{\}$.

Step 1) Compute a Gaussian Process (GP) estimate \hat{f}_t of f using data \mathcal{D}_t . Gaussian processes are probabilistic regression models that provide confidence intervals $\hat{f}_t \pm \beta_t \sigma_t(x)$. Here $\sigma_t(x)$ quantifies the model uncertainty at x , and β_t is a scaling factor that controls the coverage probability.

Step 2) Evaluate at $x_t = \arg \max_{x \in \mathcal{X}} \alpha_t(x)$. Here, $\alpha_t(x)$ is a so-called acquisition function based on \hat{f}_t and the model uncertainty, which captures the utility of choosing a point x_t . One of the most common acquisition functions is the upper confidence bound (UCB) $\alpha_t(x) = \hat{f}_t(x) + \beta_t \sigma_t(x)$. In this case the point with the largest plausible value according to the confidence intervals is chosen.

Step 3) The point x_t is evaluated and the outcome $y_t = f(x) + \epsilon$ is added to the data set \mathcal{D}_{t+1} . Increase $t := t + 1$, go to *Step 1*).

The interested reader may consult the excellent tutorials [8,9] for a more detailed introduction to Gaussian processes and Bayesian optimization. For the constrained case, a safe BO method has been proposed (SafeOPT) [11]. The above outline is then modified to construct estimates \hat{f}_t and \hat{g}_t of f and the constraint function g in *Step 1*), and the acquisition function in *Step 2*) is re-defined to ensure that a) all evaluations are safe b) the set of safe parameter settings is explored sufficiently and c) the optimum within the set of safe parameters is identified. We describe this approach in more detail below.

Our Approach: SafeLineBO

Bayesian optimization as defined above has been successfully used in many applications, and was shown to outperform alternative approaches on some domains [13]. When applied to high-dimensional settings, the major challenge is to scale *Step 2*), which itself defines an optimization problem over the parameter space \mathcal{X} . The reasoning behind replacing the main objective (1) by the acquisition *Step 2* is that α_t can be optimized offline (without taking evaluations on the machine) and with enough computational power a solution can be obtained in reasonable time. Still, *Step 2* becomes prohibitive as the number of parameters increases. For the case of safe optimization already $d \geq 5$ parameters are problematic, because the SafeOPT method requires a discretization of the domain, hence requires to iterate over exponentially (in d) many points in each step.

To address this short-coming, we use Bayesian optimization combined with a linesearch technique as we previously proposed in [12]. Below we give the algorithmic outline.

Step 0) Initialize $t = 0$, $\mathcal{D}_0 = \{\}$, $\epsilon > 0$, safe starting point x_0 .

Step 1) Query f and g at $\sim d$ local perturbations of x_t , and add the evaluations to the data set \mathcal{D}_t .

Step 2) Update the Gaussian Process (GP) estimates $\hat{f}_t(x) \pm \beta_t \sigma_t(x)$, $\hat{g}_t(x) \pm \beta_t \rho_t(x)$ of f and g with \mathcal{D}_t .

Step 3) Compute the estimated gradient $l_t := \nabla \hat{f}_t(x_t)$.

Step 4) Define 1d subspace $\mathcal{L}_t = \{\lambda \cdot l_t + x_t : \lambda \in \mathbb{R}\} \cap \mathcal{X}$.

Step 5) Use SafeOPT to solve the objective (1) on \mathcal{L}_t :

- i) Define safe subset of \mathcal{L}_t ,
 $\mathcal{L}_s = \{x \in \mathcal{L}_t : \hat{g}_t(x) + \beta_t \rho_t(x) \leq \tau\}$.
- ii) Compute a candidate expander point $x_e \in \mathcal{X}_s$ that is predicted to enlarge the estimated safe set.
- iii) Compute a candidate optimizer $x_o \in \mathcal{X}_s$ that reduces uncertainty about the optimum on \mathcal{L}_t .
- iv) Among $\{x_e, x_o\}$ choose the point where the prediction of \hat{f} is more uncertain, ie $x = \arg \max_{\tilde{x} \in \{x_e, x_o\}} \sigma_t(\tilde{x})$.
- v) Evaluate at x , update data \mathcal{D}_t and estimates \hat{f}_t , \hat{g}_t .
- vi) As long as error is larger than ϵ , go to i).

Step 6) Until user stops optimization, increase $t := t + 1$, go to *Step 1*).

A fully formal description as well as a more extensive empirical evaluation of this approach is given in [12]. Importantly, *Step 4-5*) circumvent the expensive maximization of the acquisition function by restricting the global problem to iteratively chosen 1-dimensional subsets of the domain, while keeping all data in a global model. Nevertheless, this approach satisfies strong convergence guarantees [12]. We present the evaluation of this approach on SwissFEL in the next section.

PARAMETER TUNING AT SWISSFEL

We implemented a python interface for optimizers based on pyepics. The optimization framework runs on a server and can be controlled via an application interface. We have beam checks in place, that pause the optimization in case the signal is lost. Further, we have a configurable settling time and we check for feedback error signal to fall below a threshold before we evaluate a point.

Objective: Per shot pulse energy measured with a gas detector [14], averaged over 10 measurements at 25-50 Hz. With the settling and computation time, we are able to run 1-2 optimization steps per second.

Tuning parameters:

- 24 (horizontal & vertical) beam position monitor (BPM) target values of the orbit feedback through the undulators (maintaining 2 fixed points in each plane).
- 5 matching quadrupoles before the undulators.
- 11 gap settings of the undulators.

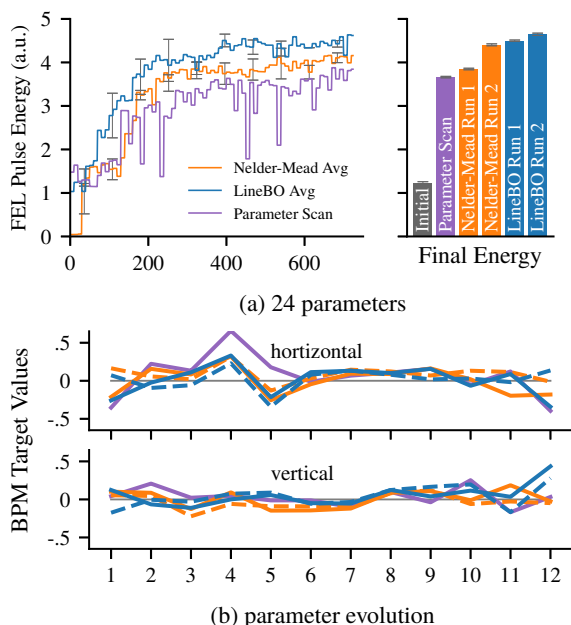


Figure 1: *Top*: Performance of parameter scan, Nelder-Mead and LineBO without safety constraints in terms of number of evaluations on the machine, using the 24 BPM target values. *Bottom*: Corresponding final BPM target values relative to the starting parameter in the allowed range ($\pm 80 \mu\text{m}$). Note that the algorithms converge to different solutions, which likely is due to local optima or insensitive parameters.

Constraints: As a constraint we used a lower bound on the FEL signal (Fig. 2a). A possible use-case is parasitical tuning during user operation, where a minimum signal is required. Losses were not a major concern with these parameters, but could be included for other parameters or for optimization on other accelerators (e.g. proton accelerators).

EMPIRICAL RESULTS

We did multiple test runs comparing LineBO and SafeLineBO (with the constraint) to Nelder-Mead and a simple parameter scan baseline, using the 24 BPM target values as tuning parameters. For the parameter scan baseline, we consecutively optimized each parameter with a single scan. For each test run, we manually detuned the machine to a fixed starting point with a low signal value. Additionally, we conducted an experiment with 40 parameters, including BPM target values, matching quadrupoles and gap settings of the undulators. Our findings are presented in Fig. 1 and 2. Note that the figures show results from different tuning sessions. We found that the Bayesian optimization method was able to consistently outperform our baselines, however our method required setting GP hyperparameters such as lengthscales, which we have not fully automatized yet.

OUTLOOK

The ultimate goal is to establish a well-performing optimization method to assist operators with tuning FEL param-

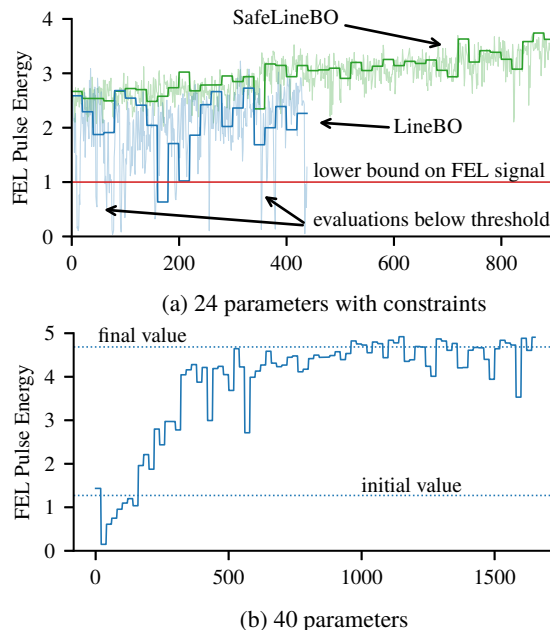


Figure 2: *Top*: Comparing LineBO and SafeLineBO (with and without safety constraint). In this case SafeLineBO performs significantly better because the search space is more constrained: parameter that yield very low values (<1) are never explored whereas LineBO also evaluates points below this threshold. *Bottom*: Tuning with 40 parameters where we obtain good values with 800 steps (15 minutes).

eters, in particular those that need regular adjustments. For such a method to be practical, the method itself should have at most 1-2 hyper-parameters that need adjustment, where ideally the best setting is relatively robust or obtained with a guiding principle. In our current implementation we explore learning some of the GP hyper-parameters such as lengthscales from initial scans (a process that needs to be done only once); however the results are not yet fully satisfying. An additional advantage of the LineBO method is that one can obtain slice plots of the model predictions on the current line as feedback of the current optimization progress, which can also guide the setting of GP hyper-parameters.

We also think that a more systematic comparison to other methods should be conducted. Another candidate that to the best of our knowledge has not yet been tested substantially for FEL tuning is CMA-ES [15], which however does not directly deal with safety constraints.

ACKNOWLEDGEMENTS

The authors would like to acknowledge the support of the entire SwissFEL team. This research was supported by SNSF grant 200020_159557 and 407540_167212 through the NRP 75 Big Data program. Further, this project has received funding from the European Research Council (ERC) under the European Union's Horizon 2020 research and innovation programme grant agreement No 815943.

REFERENCES

- [1] M. W. McIntire, T. M. Cope, D. F. Ratner, and S. Ermon, "Bayesian Optimization of FEL Performance at LCLS", in *Proc. 7th Int. Particle Accelerator Conf. (IPAC'16)*, Busan, Korea, May 2016, pp. 2972–2975. doi:10.18429/JACoW-IPAC2016-WEPOW055
- [2] S. I. Tomin, G. Geloni, I. V. Agapov, W. Decking, M. Scholz, and I. Zagorodnov, "On-line Optimization of European XFEL with OCELOT", in *Proc. 16th Int. Conf. on Accelerator and Large Experimental Control Systems (ICALEPCS'17)*, Barcelona, Spain, Oct. 2017, pp. 1038–1042. doi:10.18429/JACoW-ICALEPCS2017-WEAPL07
- [3] E. Schuster, C. K. Allen, and M. Krstic, "Optimized Beam Matching Using Extremum Seeking", in *Proc. 21st Particle Accelerator Conf. (PAC'05)*, Knoxville, TN, USA, May 2005, paper FPAT092, pp. 4269–4271.
- [4] A. Scheinker, R. W. Garnett, D. Rees, D. K. Bohler, A. L. Ede- len, and S. V. Milton, "Applying Artificial Intelligence to Accelerators", in *Proc. 9th Int. Particle Accelerator Conf. (IPAC'18)*, Vancouver, Canada, Apr.-May 2018, pp. 2925–2928. doi: 10.18429/JACoW-IPAC2018-THYGBE1
- [5] X. Huang, "Robust simplex algorithm for online optimization," *Phys. Rev. Accel. Beams*, vol. 21, p. 104601, Oct 2018. doi: 10.1103/PhysRevAccelBeams.21.104601
- [6] X. Huang and J. Safranek, "Online optimization of storage ring nonlinear beam dynamics," *Phys. Rev. ST Accel. Beams*, vol. 18, p. 084001, Aug 2015. doi:10.1103/PhysRevSTAB.18.084001
- [7] J. A. Nelder and R. Mead, "A simplex method for function minimization," *The computer journal*, vol. 7, no. 4, pp. 308–313, 1965. doi:10.1093/comjnl/7.4.308
- [8] B. Shahriari, K. Swersky, Z. Wang, R. P. Adams, and N. De Fre- itas, "Taking the human out of the loop: A review of bayesian optimization," *Proceedings of the IEEE*, vol. 104, no. 1, pp. 148–175, 2015. doi:10.1109/JPROC.2015.2494218
- [9] P. I. Frazier, "A tutorial on bayesian optimization," *arXiv preprint arXiv:1807.02811*, 2018.
- [10] N. Srinivas, A. Krause, S. M. Kakade, and M. Seeger, "Gaus- sian process optimization in the bandit setting: No regret and experimental design," *International Conference on Machine Learning*, 2010.
- [11] Y. Sui, A. Gotovos, J. Burdick, and A. Krause, "Safe ex- ploration for optimization with gaussian processes," in *Pro- ceedings of the 32nd International Conference on Machine Learning*, vol. 37, pp. 997–1005, PMLR, 2015.
- [12] J. Kirschner, M. Mutny, N. Hiller, R. Ischebeck, and A. Krause, "Adaptive and safe Bayesian optimization in high dimensions via one-dimensional subspaces," in *Proceedings of the 36th International Conference on Machine Learning*, vol. 97, pp. 3429–3438, PMLR, 2019.
- [13] P.-I. Schneider, X. Garcia Santiago, V. Soltwisch, M. Ham- merschmidt, S. Burger, and C. Rockstuhl, "Benchmarking five global optimization approaches for nano-optical shape optimization and parameter reconstruction," *arXiv preprint arXiv:1809.06674*, 2018.
- [14] P. Juranić, J. Rehanek, C. A. Arrell, C. Pradervand, R. Is- chebeck, C. Erny, P. Heimgartner, I. Gorgisyan, V. Thominet, K. Tiedtke, A. Sorokin, R. Follath, M. Makita, G. Seniutinas, C. David, C. J. Milne, H. Lemke, M. Radovic, C. P. Hauri, and L. Patthey, "SwissFEL Aramis beamline photon diagnostics," *Journal of Synchrotron Radiation*, vol. 25, pp. 1238–1248, Jul 2018. doi:10.1107/S1600577518005775
- [15] N. Hansen, S. D. Müller, and P. Koumoutsakos, "Reducing the time complexity of the derandomized evolution strategy with covariance matrix adaptation (cma-es)," *Evolutionary computation*, vol. 11, no. 1, pp. 1–18, 2003. doi:10.1162/106365603321828970

MULTI-OBJECTIVE FEL DESIGN OPTIMISATION USING GENETIC ALGORITHMS

D. J. Dunning*, J. K. Jones, H. M. Castañeda Cortés, N. R. Thompson
STFC Daresbury Laboratory and Cockcroft Institute, Daresbury, UK

Abstract

Simulation studies were carried out to optimise the performance of various FEL designs, with examples including longitudinal current profile shaping for a seeded FEL, and selection of the chicane delays for the High-Brightness SASE technique. In these examples multi-objective genetic algorithms were applied to a single section of the overall facility simulation, i.e. the undulator, as is the common approach. Further studies are also reported in which a full start-to-end simulation chain was optimised, with the aim of delivering a more holistic facility design optimisation.

INTRODUCTION

Simulations are a key component in the design and operation of modern FEL facilities. The full machine is often modelled with a ‘start-to-end’ (S2E) chain of different simulation codes, each developed for specific sections of the facility (e.g. gun, accelerator, FEL, photon beamline), shown schematically in Fig. 1 (a). Optimisation within this simulation chain is often segmented in the same way, e.g. the accelerator section is often optimised to meet a set of target electron beam properties, which themselves are specified to allow the FEL section to deliver the target photon output, see Fig. 1 (b).

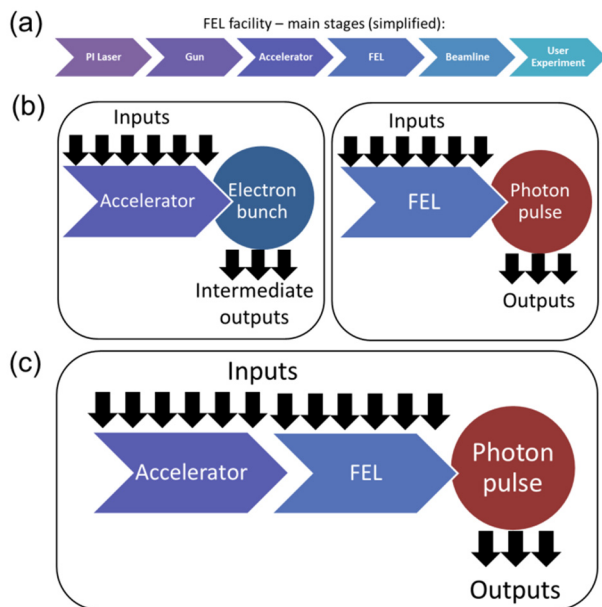


Figure 1: (a) Example of the main stages in a FEL facility, (b) a segmented optimisation approach requires specification of intermediate parameters, (c) joining up stages allows optimisation on the final outputs.

* david.dunning@stfc.ac.uk

A problem with this method is that mapping from electron bunch properties to photon output is a complex non-linear process. Intermediate parameters such as emittance and bunch length are often overly reductive as a predictor of FEL performance when applied to realistic – sometimes highly non-Gaussian – distributions. One solution is to develop more prescriptive specifications of the intermediate parameters; however this can become increasingly elaborate, as illustrated in the first section of this paper.

An alternative approach, considered in the second section, is to combine multiple stages of the simulation chain into a single optimisation problem, Fig. 1 (c). This allows, e.g. the accelerator parameters to be directly optimised on the FEL output, without the need to specify intermediate targets. Previous studies have combined accelerator simulation codes with FEL analytical models, however not all effects are included [1]. Here we present a combined accelerator + FEL simulation framework with examples.

In the final section a more advanced FEL scheme is considered. In each case multi-objective genetic algorithms (MOGA) are used as the optimisation technique.

SINGLE-STAGE OPTIMISATION

This section considers an example of optimising a single stage of the S2E chain, as shown in Fig 1 (b).

At the interface between the accelerator and FEL sections a common starting point is to specify the longitudinal profile in terms of peak current and electron bunch length. For non-Gaussian distributions these measures can be poor predictors of FEL performance, such that more refined targets (e.g. bunch shape) are required. A simple case was set up to optimise the current profile for a seeded FEL, using parameters of the CLARA project [2,3]. 3D FEL simulations were carried out using the Genesis 1.3 FEL code [4] (version 2, utilising the OCELOT framework [5]), in which the current profile was described by a 36-element array, entered via the ‘beamfile’ method (with all other properties kept constant). Optimisation was carried out using the NSGA-II [6] MOGA method, inside DEAP [7] and FEL performance was optimised on peak power and bandwidth at the end of the undulator (further refinement is discussed later).

In the first instance the system started from random current distributions. The mutation effect was to randomly modify a randomly selected subset of the current array elements. The crossover effect was to interleave elements from two existing current profiles. In both cases a further step to maintain constant charge was applied. Figure 2 shows the results of the optimisation. Some effects were expected – concentrating charge into a high current region in order to increase pulse energy: indeed surpassing the pulse energy of a Gaussian but with larger bandwidth.

However an unexpected alternative solution concentrated charge into a series of high current regions. This is probably not desirable for users but it is an interesting finding. Individual Genesis runs took ~1 minute with 24 processors, Figure 2 took ~2 days to complete 38 generations.

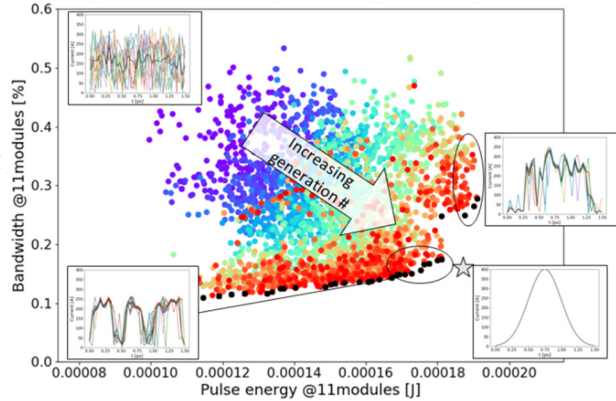


Figure 2: MOGA optimisation of FEL current profile starting from noise (top left) to an approximately flat-top solution (right) or a series of peaks (bottom left). The black points are the Pareto front after 38 generations. The result for a Gaussian profile (star, bottom right) is shown.

Further cases were performed to investigate current profile evolution beyond a Gaussian or a flat-top, as shown in Fig. 3. Some findings are obvious: a long, smooth bunch gives narrow bandwidth/low power; and vice versa. Some are less so, e.g. spiking at the bunch tail.

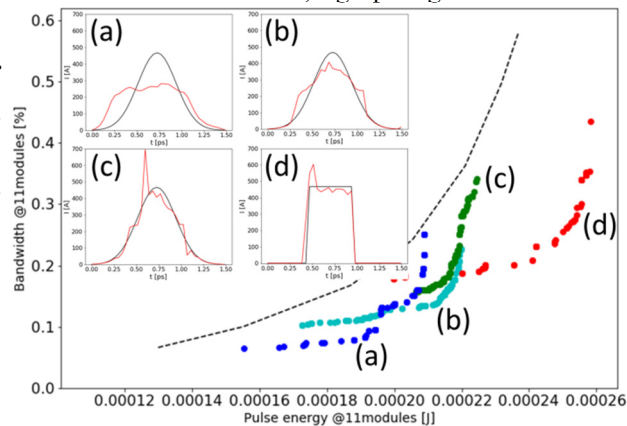


Figure 3: Pareto fronts and example profiles (inset – red) vs starting profiles (inset – black) for four different MOGA optimisations of FEL current profile. The black dashed line shows results for a range of Gaussian profiles.

The benefit of the approach taken in this section is that it helps to understand one property of the bunch in isolation. However the degree of complexity possible in specifying a single property also illustrates the difficulty in specifying a set of intermediate parameters.

INTEGRATED S2E OPTIMISATION

This section describes combining multiple S2E stages into a single optimisation problem, as shown in Fig. 1 (c), thereby avoiding the issue of intermediate parameters.

The optimisation framework comprises ASTeC's in-house S2E framework (SimFrame) [8] in combination with OCELOT and DEAP as shown in Fig. 4.

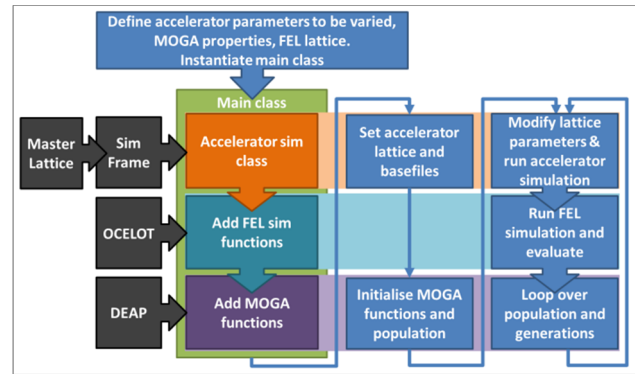


Figure 4: Schematic of S2E optimisation framework.

The Simulation Framework (SimFrame) is a python-based framework for performing accelerator simulations using a transparent interface to multiple tracking codes (ASTRA [9], Elegant [10], CSRTrack [11] and GPT [12]). It interfaces with the Master Lattice [13, 14] (written in YAML [15]), which is the central repository for machine and element information (mechanical and magnetic properties, errors, control system names etc.). SimFrame doesn't interface to a dedicated FEL code, relying instead on OCELOT's python interface to Genesis. Integration between the frameworks was relatively straightforward, allowing S2E from the cathode to the end of the FEL.

As shown in Fig. 4, the main class inherits from the accelerator simulation class (SimFrame functionality), OCELOT (FEL simulation functions) and DEAP (MOGA functions). A python script defines the MOGA parameters, FEL lattice and the accelerator parameters to be varied. Once the main class is instantiated, the accelerator lattice and a set of starting beam files is specified, allowing the simulation to start from a previously simulated location, thereby minimising duplication. DEAP functions are used to generate a population, which is evaluated and modified over a number of generations, with accelerator and FEL simulations performed for each individual.

The MOGA framework was used to optimise the performance of a S2E simulation of the proposed XARA [16] upgrade to CLARA. A key factor to achieving a successful outcome was establishing a simulation method that was suitably detailed while also suitably fast in order to perform the many hundreds of simulations required in a reasonable time. The 'distfile' method of input to Genesis was chosen since it retains the 6D information more completely than the 'beamfile' method, however it requires more macroparticles ($2^{15}=32k$). The baseline injector modelling (up to the exit of linac 1) was performed in ASTRA with 2^{18} (262k) particles and then sampled to create the 32k macro-particles used in Elegant/Genesis. The input parameters varied were: phase and amplitude of linacs 2-6 and the 4th harmonic cavity; bunch compressor angle; de-chirper gap; and laser heater interaction strength (modelled as momentum scattering). For simplicity the

FEL mode was SASE rather than seeded and the target FEL parameters were maximum pulse energy and minimum bandwidth, evaluated at the position of maximum brightness to allow for different saturation lengths. Fig. 5 shows the Pareto front in the pulse energy-bandwidth space, with a clear trade-off evident between the two. Fig. 6 shows two individuals at different parts of the front – examples of the range of different radiation pulse durations, and corresponding electron bunch properties.

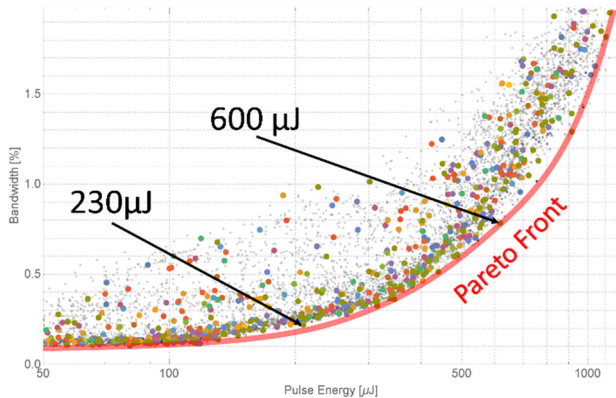


Figure 5: Final Pareto front and solutions for each generation of the S2E MOGA run. Individual points are shown in grey. The two example solutions are highlighted.

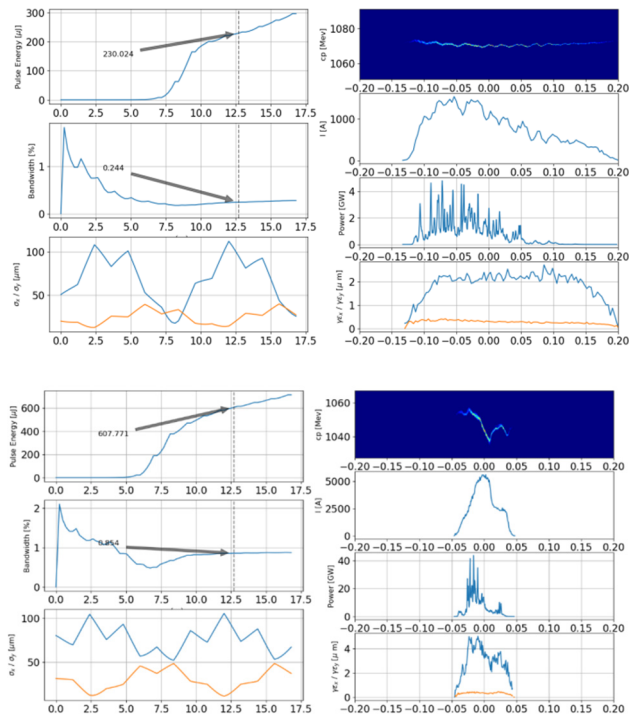


Figure 6: FEL output and bunch parameters (*left*: pulse energy, bandwidth and beam-size, *right*: longitudinal phase space, current, power, emittance) for example solutions at 230 μJ (top) and 600 μJ (bottom).

STABILISED HB-SASE

The MOGA framework was applied to the simultaneous optimisation of two FEL schemes which utilise the same configuration of delay chicanes inserted between undulator modules. In the first scheme, HB-SASE [17], the delay chicanes increase slippage and hence coherence length. Here we use dipole-only chicanes as these are more compact than isochronous chicanes. Studies using such chicanes in monotonically increasing or decreasing delay sequences show an increase in coherence length limited to a factor of 5-10. In this implementation the first fitness value (Figure 7, horizontal) is the FEL pulse energy multiplied by the coherence length, representing scaled brightness. We average over 9 shot noise seeds per data point. The second scheme aims to improve the shot-to-shot stability of the SASE FEL by varying the chicane dispersion to manipulate the electron bunching, and introduce a passive, negative feedback into the FEL mechanism [18]. The second fitness value (Figure 7, vertical) is the rms. of the scaled brightness over the shot noise seeds.

Figure 7 shows initial results, with the fitness values calculated at 13 m along the undulator, and tuned to 100 nm at 250 MeV/c. The points are colour coded from dark blue to light green as the generations increase. The ‘Hall of Fame’ (HOF) points are shown along with the Pareto front, indicated with the dotted red line. The equivalent SASE scaled brightness and rms. brightness variation are shown as green diamonds, for undulator lengths from 11–17 m. The delays corresponding to maximum brightness and minimum fluctuation are shown.

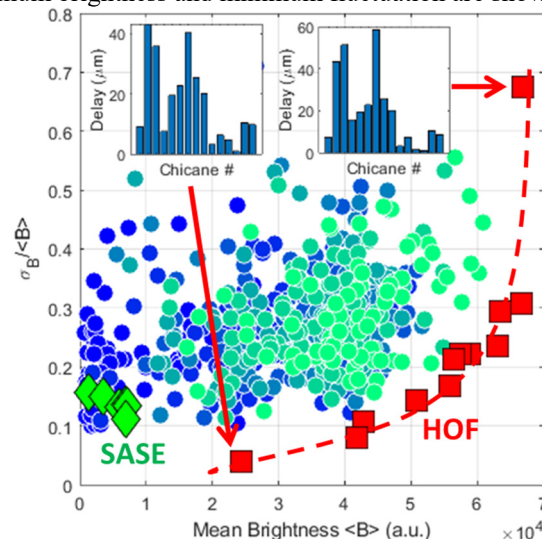


Figure 7: Initial results of optimisation to maximise $\langle B \rangle$, HB-SASE output brightness averaged over an ensemble of shot noise seeds, and minimise $\sigma_B / \langle B \rangle$, rms shot-to-shot brightness fluctuation within the ensemble.

These results show solutions with brightness increased by an order of magnitude but with increased fluctuations, and solutions with slightly less brightness increase but with fluctuations damped compared to SASE. It should be noted that in regular SASE the fluctuations should scale

approximately as $\sigma_B/\langle B \rangle \propto \langle B \rangle$ so the results favourably violate this scaling. The chicane settings for maximum brightness and minimum fluctuations appear qualitatively similar to each other, while very different to the monotonically varying sequences employed in previous studies. These are interesting findings for further investigation.

REFERENCES

- [1] R. Bartolini, M. Apollonio and I. P. S. Martin, "Multi-objective genetic algorithm optimization of the beam dynamics in linac drivers for free electron lasers", *Phys. Rev. ST Accel. Beams*, vol. 15, no. 3, p. 030701, 2012. doi:10.1103/PhysRevSTAB.15.030701
- [2] J. A. Clarke *et al.*, "CLARA conceptual design report," *Journal of Instrumentation*, vol. 9, no. 05, p. T05001, 2014. doi:10.1088/1748-0221/9/05/T05001
- [3] D. J. Dunning *et al.*, "Start-to-End Simulations of the CLARA FEL Test Facility", in *Proc. 9th Int. Particle Accelerator Conf. (IPAC'18)*, Vancouver, Canada, Apr.-May 2018, pp. 4430-4433. doi:10.18429/JACoW-IPAC2018-THPMK060
- [4] S. Reiche, "GENESIS 1.3: a fully 3D time-dependent FEL simulation code," *Nucl. Instr. Meth. Phys. Res. Sect. A*, vol. 429, p. 243, 1999. doi:10.1016/S0168-9002(99)00114-X
- [5] I. Agapov, G. Geloni, S. Tomin, and I. Zagorodnov, "OC-ELOT: A software framework for synchrotron light source and FEL studies," *Nuclear Instruments and Methods in Physics Research Section A: Accelerators, Spectrometers, Detectors and Associated Equipment*, vol. 768, pp. 151-156, 2014. doi:10.1016/j.nima.2014.09.057
- [6] K. Deb, A. Pratap, S. Agarwal and T. Meyarivan, "A fast and elitist multiobjective genetic algorithm: NSGA-II," in *IEEE Transactions on Evolutionary Computation*, vol. 6, no. 2, pp. 182-197, April 2002.
- [7] Félix-Antoine Fortin, François-Michel De Rainville, Marc-André Gardner, Marc Parizeau and Christian Gagné, "DEAP: Evolutionary Algorithms Made Easy", *Journal of Machine Learning Research*, pp. 2171-2175, no 13, July 2012.
- [8] ASTeC, <https://github.com/VELA-CLARA-software/OnlineModel/tree/master/SimulationFramework>
- [9] K. Flöttmann, "ASTRA - A Space Charge Tracking Algorithm," 2000. <http://www.desy.de/~mpyf10>
- [10] M. Borland, "User's Manual for elegant," APS-ANL, Chicago, IL, 2017.
- [11] M. Dohlus, "CSRtrack code", <http://www.desy.de/fel-beam/csrtrack/>
- [12] Pulsar Physics, "General Particle Tracer.", <http://www.pulsar.nl/gpt/>
- [13] T. J. Price *et al.*, "Virtual VELA-CLARA: The Development of a Virtual Accelerator", in *Proc. 9th Int. Particle Accelerator Conf. (IPAC'18)*, Vancouver, Canada, Apr.-May 2018, pp. 4773-4776. doi:10.18429/JACoW-IPAC2018-THPML060
- [14] ASTeC, <https://github.com/VELA-CLARA-software/OnlineModel/tree/master/MasterLattice>
- [15] K. Simonov, <https://github.com/yaml/pyyaml>
- [16] D. J. Dunning, J. K. Jones, and L. S. Cowie, "XARA: X-Band Accelerator for Research and Applications", presented at the 39th Int. Free Electron Laser Conf. (FEL'19), Hamburg, Germany, Aug. 2019, paper THP066, this conference.
- [17] B. W. J. McNeil, N. R. Thompson, and D. J. Dunning, "Transform-Limited X-Ray Pulse Generation from a High-Brightness Self-Amplified Spontaneous-Emission Free-Electron Laser", *Phys. Rev. Lett.*, vol. 110, p. 134802, 2013. doi:10.1103/PhysRevLett.110.134802
- [18] N. Thompson, "Possible Method for the Control of SASE Fluctuations", in *Proc. 38th Int. Free Electron Laser Conf. (FEL'17)*, Santa Fe, NM, USA, Aug. 2017, pp. 129-131. doi:10.18429/JACoW-FEL2017-MOP039

XARA: X-BAND ACCELERATOR FOR RESEARCH AND APPLICATIONS

D. J. Dunning*, L. S. Cowie¹, J. K. Jones

STFC Daresbury Laboratory and Cockcroft Institute, Daresbury, UK,

¹also at University of Lancaster, Lancaster, UK

Abstract

XARA (X-band Accelerator for Research and Applications) is a proposal for a compact ~ 1 GeV/c accelerator to produce attosecond light pulses in the EUV to soft X-ray region. It is under consideration as a potential future upgrade to the CLARA facility at Daresbury Laboratory, utilising high-performance X-band RF technology to increase the electron beam momentum from 250 MeV/c. Emerging techniques for generating single-cycle undulator light would give access to attosecond timescales, enabling studies of ultra-fast dynamics, while also being very compact. XARA would also enhance the existing capabilities for accelerator science R&D by incorporating X-band development and increasing the electron beam momentum for novel acceleration studies.

INTRODUCTION

We propose a high-energy upgrade of the CLARA facility [1], utilising high-gradient X-band RF technology to achieve a maximum beam momentum of around 1 GeV/c, with FEL light output in the extreme-ultra-violet (EUV) to soft X-ray (SX) regime, including the ‘water window’ wavelength region between 2.3-4.4 nm. In addition to its inherent scientific interest due to the presence of important K-edges and transparency of water, this wavelength region coincides with state-of-the-art technological developments in temporally coherent FEL output [2] and attosecond pulse generation [3, 4].

The aim of the proposal is therefore to deliver a photon source that is attractive to both FEL and HHG users, and to do so through developing advanced accelerator technologies. XARA represents an opportunity to implement the developments in X-band technology and innovative short-period undulators coming from the Horizon 2020-funded project ‘CompactLight’ [5], of which STFC is a member. STFC is also involved with EuPRAXIA [6] and XARA would be synergistic with EuPRAXIA@SPARC_LAB [7]. Another key feature is the potential to utilise emerging techniques for single-cycle undulator light, as developed by the LUSIA consortium [8].

CLARA is presently supported to phase 2 (250 MeV/c plus full energy beam extraction (FEBE) line and user station). The UK is developing a science case for its XFEL project, due to report in May 2020, which will inform thinking regarding CLARA phase 3 (the FEL line – to demonstrate novel FEL schemes for use in an XFEL [9]). XARA is therefore considered as an alternative or future upgrade option for the straight-ahead line, which would utilise the existing CLARA front-end and building. XARA is currently aiming to fit inside the existing

CLARA building footprint, however extension of the building by several tens of meters is feasible, if required.

SCIENCE CASE

The science case for XARA comprises photon science, particle accelerator R&D and electron beam exploitation.

Photon Science

The science case for XARA is centred on the opportunity to study ultra-fast dynamics [10] in e.g. photosynthesis, photo-induced catalysis and light-wave electronics, and to influence such effects e.g. through coherent control [11]. To do so requires pulse durations on the scale of tens to hundreds of attoseconds. Figure 1 shows the parameter space for relevant existing sources in this area. HHG provides the shortest pulses but with relatively low number of photons per pulse compared to FELs, particularly at higher photon energy. The target for XARA (also shown in Fig. 1) would extend EUV-SX FELs to shorter pulse duration, aiming for higher pulse energies than HHG.

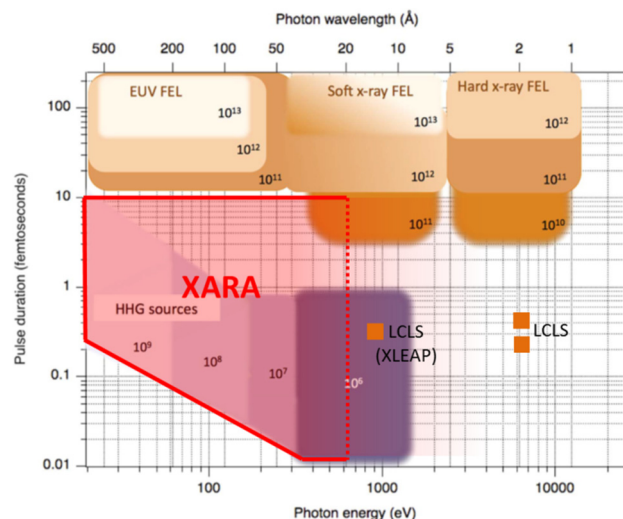


Figure 1: XARA target parameter space relative to the ultrafast science landscape, adapted from [10].

Accelerator R&D/Electron Beam Exploitation

XARA would enhance CLARA’s existing function as a centre for accelerator R&D and electron beam exploitation. At present the beam from the CLARA front-end (~ 35 MeV/c) is used for topics that include novel acceleration, medical applications and basic accelerator R&D [12]. Novel acceleration is a particular focus of the Cockcroft Institute, which is co-located at Daresbury Laboratory (dielectric WFA, PWFA). Medical studies on CLARA include VHEE dose and damage studies, and there are strong links with nearby universities and hospitals. Accelerator R&D includes commissioning of the 400 Hz 1.5

* david.dunning@stfc.ac.uk

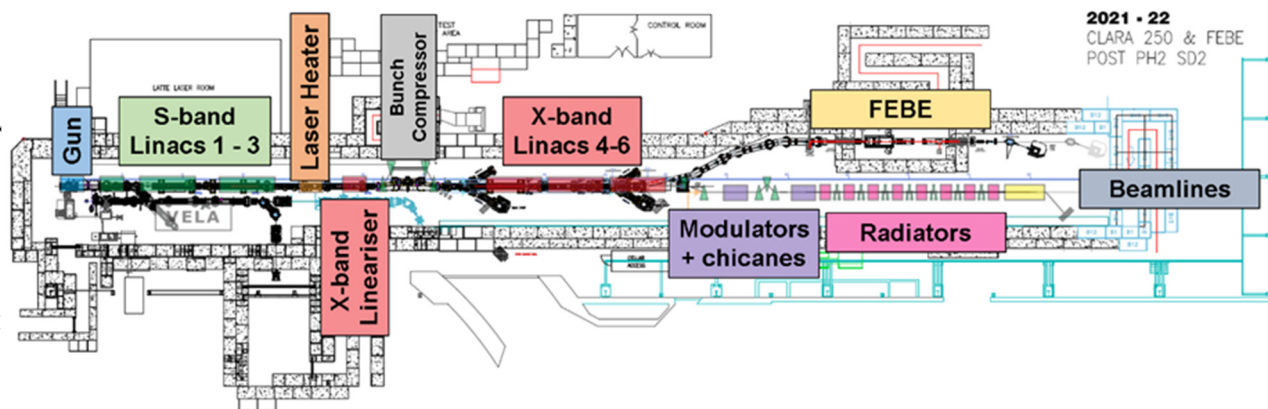


Figure 2: Layout of CLARA phase 2 showing the potential XARA layout overlaid. CLARA linac 4 (S-band) is replaced with 3-4 X-band linacs to achieve ~ 1 GeV/c beam momentum. The FEL and beamlines section is indicative and could extend beyond the present building if required.

cell RF gun [13, 14], beam studies with superconducting undulators [15, 16], and dielectric de-chirpers [17-19]. Along with cavity BPMs and other diagnostic developments, such as electro-optic bunch length monitors and passive longitudinal streakers, these developments are also relevant for XARA. The present phase of CLARA installation takes the beam to 250 MeV/c with a dedicated experimental user station on the FEBE line (Fig. 2). XARA would increase the momentum for electron beam exploitation in FEBE to ~ 600 MeV/c, limited by the physical machine layout. New accelerator R&D would focus on X-band linac development and novel undulator light production, whilst providing a new energy regime for existing studies.

ACCELERATOR

This section describes the main components of the XARA accelerator, utilising the CLARA front-end.

S-Band Injector

The CLARA Phase 2 machine (sans linac 4) will act as the S-band injector for XARA. This will provide a ~ 180 MeV/c, sub-ps FWHM, 250 pC electron bunch, compatible with injection into the X-band linacs. The injector will consist of an S-band 1.5 cell RF photo-injector [13, 14] operating at up to 400 Hz, and up to 120 MV/m in 100 Hz mode, with a dual feed H-coupler to eliminate dipole components in the coaxial input coupler which can lead to transverse beam asymmetry [20], as well as a load-lock in-vacuum cathode exchange system. The front end of CLARA (gun and first linac) has recently been commissioned with a low rep-rate, 2.5 cell, 10 Hz gun, whilst the 1.5 cell cavity will be commissioned in the coming months. The phase 2 machine (incl. linacs 2, 3 and 4, X-band lineariser [21] and variable bunch compressor) will be commissioned in 2021. Significant advances have already been made in both commissioning and experimental running procedures for CLARA, including advances in high level software capabilities [22], such as implementation of a new C++/python API interface to EPICS. This allows for automated accelerator controls, improving reliability and repeatability, such as unmanned

cavity conditioning, cavity cresting, BPM calibration, and beam-based alignment, as well as improvements in machine development studies such as fast, reproducible measurements of transverse emittance, longitudinal bunch length and momentum spread. An online model and virtual accelerator have also been implemented [23].

X-Band Linac

The X-band linac section will comprise of 3 or 4 modules similar to those proposed for the CompactLight and EuPRAXIA@SPARC_LAB projects [24], which can be seen in Fig. 3. Each module comprises a high-power RF source of one or two 50 MW X-band klystrons, low loss waveguide and a SLED type pulse compressor, feeding into 4 m of X-band RF cavities. The module will be re-optimised for XARA for two options. The first option is a single bunch, very high gradient option, where the gradient must be greater than 70 MV/m to ensure a beam momentum of 1 GeV/c can be reached with only 3 modules. In this option, because of the limited space for XARA and the relatively low number of modules required, gradient will be prioritised, even at the expense of requiring two klystrons over one. The second option is for a multi-bunch regime, which will require a longer RF pulse or shorter cavities to minimise the filling time (this option is under consideration for drive/witness plasma acceleration or a regenerative amplifier FEL, and would need associated photo-injector upgrades).

Due to the short bunch lengths, short range wake-fields in the X-band cavities have a strong impact on the beam dynamics. If these are found to be deleterious to the beam it may necessitate changes to the X-band cavity design, specifically to widen the iris.

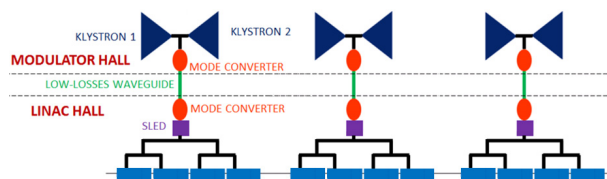


Figure 3: Schematic of the proposed X-band linac section, adapted from [24].

FEL OPTIONS

CLARA at 250 MeV/c was designed for a shortest wavelength of 100 nm (12.4 eV photon energy). Increasing the beam momentum to 1 GeV/c would provide a factor of 16 reduction to 6 nm (200 eV). Utilising more ambitious undulator technology [5, 15, 16] would allow a significant further reduction, potentially to 2.3 nm (540 eV), covering the ‘water-window’ region of particular scientific interest (Fig. 4).

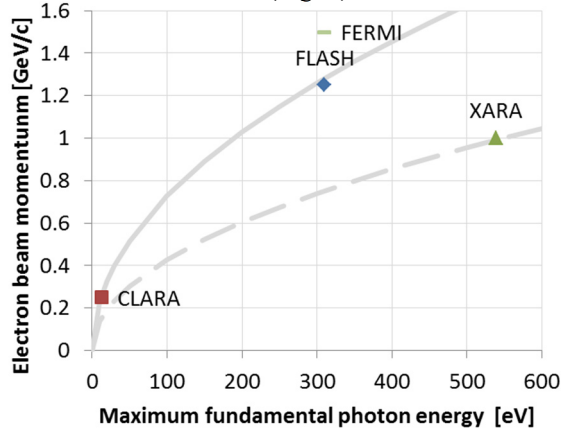


Figure 4: Maximum photon energy at the fundamental against electron beam momentum for relevant facilities. The dashed line indicates the use of advanced short-period undulators to reach higher photon energy compared to presently installed technologies (solid line).

Single-Cycle Undulator Light

A key feature of the XARA proposal is the potential to utilise emerging new FEL techniques for single-cycle undulator light [8]. Application of such methods at XARA wavelengths would deliver attosecond pulses with > 100 nJ pulse energies (Fig. 5), while also being extremely compact (a few metres). There is potential for particular synergy between novel acceleration and light source development, with the former potentially extending the scope of the latter to higher photon energies, and both requiring similar hardware, e.g. high-power lasers.

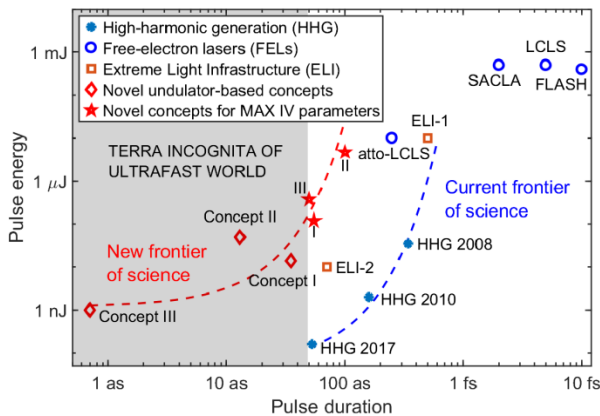


Figure 5: State-of-the-art methods of generating short pulses of light [24], XARA output would be expected to be reasonably close to the red stars, which were modelled at 1.5 GeV/c.

SASE and Seeding

A longer undulator (~ 15 m) would allow access to a larger parameter space, including longer pulses with significantly higher pulse energy (> 100 μ J). Figure 6 shows SASE simulation results. Seeding and associated advanced FEL schemes [2] could also be implemented.

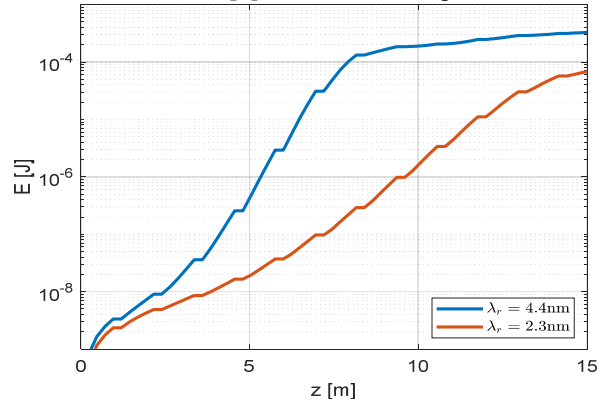


Figure 6: Simulated FEL pulse energy vs distance along the undulator for XARA at water-window wavelengths.

START-TO-END SIMULATIONS

Start-to-End (S2E) simulations of XARA with best-guess models of X-band linac structures and associated wakefields have been performed using a python-based framework, integrated with the Genesis FEL code. A full MOGA optimisation was undertaken to ascertain feasible FEL light properties and is more fully described in [25]. Initial results are encouraging: Figure 7 shows the Pareto front after optimising on maximising pulse energy and minimising bandwidth for a XARA simulation utilising ASTRA, Elegant and Genesis with 32k macro-particles.

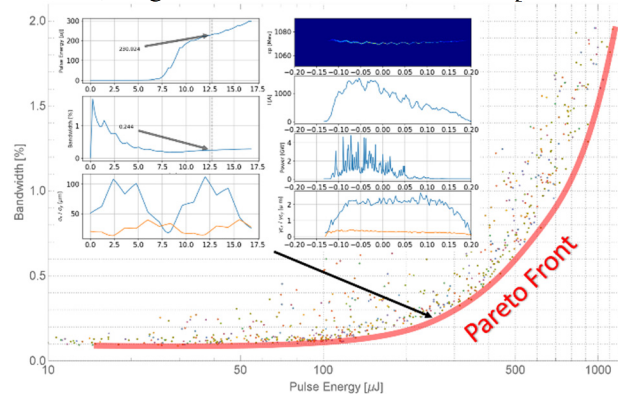


Figure 7: Pareto front in Pulse energy – Bandwidth space for a S2E model of XARA, using Genesis in SASE mode. A 230 μ J representative point on the Pareto front is shown.

SUMMARY AND NEXT STEPS

XARA would be a medium-scale national light-source facility and a centre for particle accelerator R&D, using existing infrastructure to significantly reduce cost. The next steps are to consult the UK user base to determine the benefits of short pulses vs higher pulse energy; optimise the RF module design; and investigate wake-fields, compact optical beamlines and detailed FEL designs.

REFERENCES

- [1] J. A. Clarke *et al.*, “CLARA conceptual design report,” *Journal of Instrumentation*, vol. 9, no. 05, p. T05001, 2014. doi:10.1088/1748-0221/9/05/T05001
- [2] L. Giannessi and C. Masciovecchio, “FERMI: Present and Future Challenges”, *Appl. Sci.*, vol. 7, p. 640, 2017. doi:10.3390/app7060640
- [3] P. B. Corkum and F. Krausz, “Attosecond science”, *Nat. Phys.*, vol. 3, pp. 381–387, 2007. doi: 10.1038/nphys620
- [4] F. Calegari *et al.*, “Advances in attosecond science”, *J. Phys. B: At. Mol. Opt. Phys.*, vol. 49, p. 062001, 2016. doi:10.1088/0953-4075/49/6/062001
- [5] G. D'Auria, “Status of the CompactLight Design Study”, presented at the 39th Int. Free Electron Laser Conf. (FEL'19), Hamburg, Germany, Aug. 2019, paper THP078, this conference.
- [6] P. A. Walker *et al.*, “Horizon 2020 EuPRAXIA design study”, *J. Phys.: Conf. Ser.*, vol. 874, p. 012029, 2017. Doi:10.1088/1742-6596/874/1/012029
- [7] M. Ferrario, “EuPRAXIA@SPARC LAB Design study towards a compact FEL facility at LNF”, in *Nucl. Instrum. Methods Phys., Sect. A*, vol. 909, p. 134, 2018. doi:10.1016/j.nima.2018.01.094
- [8] A. Mak *et al.*, “Attosecond single-cycle undulator light: a review”, *Rep. Prog. Phys.*, vol. 82, p. 025901, 2019. doi:10.1088/1361-6633/aafa35
- [9] D. J. Dunning, “CLARA Facility Layout and FEL Schemes”, in *Proc. 38th Int. Free Electron Laser Conf. (FEL'17)*, Santa Fe, NM, USA, Aug. 2017, pp. 178-181. doi:10.18429/JACoW-FEL2017-MOP054
- [10] L. Young *et al.*, “Roadmap of ultrafast x-ray atomic and molecular physics”, in *J. Phys. B: At. Mol. Opt. Phys.*, vol. 51, p. 032003, 2018. doi:10.1088/1361-6455/aa9735
- [11] K. C. Prince *et al.*, “Coherent control with a short-wavelength free-electron laser”, in *Nat. Photonics*, vol. 10, pp. 176-179, 2016. doi: 10.1038/nphoton.2016.13
- [12] D. Angal-Kalinin *et al.*, “Status of Clara Front End Commissioning and First User Experiments”, in *Proc. IPAC'19*, Melbourne, Australia, May 2019, pp. 1851-1854. doi:10.18429/JACoW-IPAC2019-TUPRB083
- [13] J. W. McKenzie *et al.*, “High Repetition Rate S-band Photoinjector Design for the CLARA FEL”, in *Proc. 36th Int. Free Electron Laser Conf. (FEL'14)*, Basel, Switzerland, Aug. 2014, paper THP064, pp. 889-892.
- [14] L. S. Cowie and D. J. Scott, “RF Conditioning of the CLARA 400 Hz Photoinjector”, in *Proc. IPAC'19*, Melbourne, Australia, May 2019, pp. 2067-2070. doi:10.18429/JACoW-IPAC2019-TUPTS065
- [15] B. J. A. Shepherd, J. A. Clarke, V. Bayliss, T. W. Bradshaw, and E. C. Longhi, “Modelling of a Short-period Superconducting Undulator”, in *Proc. IPAC'14*, Dresden, Germany, Jun. 2014, pp. 2716-2718. doi:10.18429/JACoW-IPAC2014-WEPRI095
- [16] J. A. Clarke *et al.*, “Optimization of Superconducting Undulators for Low Repetition Rate FELs”, in *Proc. FEL'17*, Santa Fe, NM, USA, Aug. 2017, pp. 411-414. doi:10.18429/JACoW-FEL2017-WEC02
- [17] T. H. Pacey, G. X. Xia, D. J. Dunning, and Y. M. Saveliev, “Phase Space Manipulation of Sub-Picosecond Electron Bunches Using Dielectric Wakefield Structures”, in *Proc. IPAC'17*, Copenhagen, Denmark, May 2017, pp. 3302-3304. doi:10.18429/JACoW-IPAC2017-WEPVA021
- [18] Y. Nie, G. Xia and T. H. Pacey, “Simulations of an energy dechirper based on dielectric waveguides”, in *Nucl. Instrum. Methods Phys., Sect. A*, vol. 909, p. 271, 2018. doi:10.1016/j.nima.2017.11.050
- [19] M. Colling, D. J. Dunning, B. D. Fell, T. H. Pacey, and Y. M. Saveliev, “Mechanical Design of a Dielectric Wake-field Dechirper System for CLARA”, in *Proc. IPAC'19*, Melbourne, Australia, May 2019, pp. 1912-1915. doi:10.18429/JACoW-IPAC2019-TUPRB108
- [20] I. Isaev, “Stability and performance studies of the PITZ photoelectron gun”, PhD Thesis, University of Hamburg, 2018.
- [21] L. S. Cowie *et al.*, “An X-Band Lineariser for the CLARA FEL”, in *Proc. IPAC'18*, Vancouver, Canada, Apr.-May 2018, pp. 3848-3851. doi:10.18429/JACoW-IPAC2018-THPAL084
- [22] D. J. Scott, A. D. Brynes, and M. P. King, “High Level Software Development Framework and Activities on VELA/CLARA”, in *Proc. IPAC'19*, Melbourne, Australia, May 2019, pp. 1855-1858. doi:10.18429/JACoW-IPAC2019-TUPRB084
- [23] T. J. Price *et al.*, “Virtual VELA-CLARA: The Development of a Virtual Accelerator”, in *Proc. IPAC'18*, Vancouver, Canada, Apr.-May 2018, pp. 4773-4776. doi:10.18429/JACoW-IPAC2018-THPML060
- [24] M. Diomedede, “Preliminary RF design of an X-band linac for the EuPRAXIA@SPARC LAB project”, in *Nucl. Instrum. Methods Phys., Sect. A*, vol. 909, p. 243, 2018. doi:10.1016/j.nima.2018.01.032
- [25] D. J. Dunning, H. M. Castaneda Cortes, J. K. Jones, and N. Thompson, “Multi-Objective FEL Design Optimisation Using Genetic Algorithms”, presented at the 39th Int. Free Electron Laser Conf. (FEL'19), Hamburg, Germany, Aug. 2019, paper THP065, this conference.

LCLS-II EXTRUDED ALUMINUM UNDULATOR VACUUM CHAMBERS—NEW APPROACHES TO AN IMPROVED APERTURE SURFACE FINISH*

Greg Wiemerslage†, Patric Den Hartog, Jun Qian, Marion M. White
Argonne National Laboratory, 9700 South Cass Ave., Lemont, IL 60439, USA

Abstract

The Linac Coherent Light Source (LCLS), the world's first x-ray free-electron laser (FEL), became operational in 2009. The Advanced Photon Source (APS) contributed to the original project by designing and building the undulator line. Two slightly different variations of these chambers were required for LCLS-II: one for a soft x-ray (SXR) undulator line and one for a hard x-ray (HXR) undulator line. Because of the extremely short electron bunch length, a key physics requirement was to achieve the best possible surface finish within the chamber aperture. Improvements to our earlier fabrication methods allowed us to meet the critical surface roughness finish defined by rf impedance requirements. We were able to improve the surface finish from an average of 812 nm rms to 238 nm rms. The average longitudinal surface roughness slope of all chambers was to be less than 20 mrad. We achieved an average longitudinal surface roughness slope of 8.5 mrad with no chamber exceeding 20 mrad. In the end, sixty-four undulator vacuum chambers and alignment systems were delivered to SLAC National Accelerator Laboratory for the LCLS-II Upgrade project. Here we will report on the process improvements for the fabrication of these chambers.

NEW APPROACHES TO AN IMPROVED APERTURE SURFACE FINISH

The Linac Coherent Light Source (LCLS) at the SLAC National Accelerator Laboratory was the world's first x-ray free-electron laser (FEL) when it became operational in 2009 [1]. The Advanced Photon Source (APS) contributed to the project by designing and building the undulator line, including 41 undulator vacuum chambers [2]. The chamber's thin wall, small aperture, and aperture surface finish presented new production challenges. Although the aperture surface finish met requirements, schedule constraints at that time prevented us from further improving the polishing method beyond what was needed for the project. When presented with the opportunity to produce new undulator vacuum chambers for the new undulator lines of the LCLS-II upgrade, we were eager to improve the process and meet the technical requirements of the LCLS-II FEL.

Because of the extremely short electron bunch length, one of the key requirements from the LCLS-II physics specification was to achieve the best possible surface finish within the chamber aperture. The highly-polished aperture

was achieved through a renewed collaboration with Engineered Finishing Corporation [2], the abrasive-flow machining vendor that polished the original LCLS vacuum chambers. Normally, the maximum aspect ratio for this process is 8/1, length/aperture. In this case, the process was modified to enable polishing of a small oval aperture extrusion (5 vertical mm × 11 horizontal mm × 4000 mm deep) with an aspect ratio ~700/1. The improved process permitted simultaneous polishing of two 4-m-long extrusions to meet the critical surface roughness finish defined by the radio-frequency impedance requirements—and with more consistent polishing results than before. The surface finish was improved from an average of 812-nm rms for an unpolished extrusion to an average surface finish of 238-nm rms after polishing. More importantly for the success of the project, the average longitudinal rms surface roughness slope (dh/dz, where h is the height of the peak) rms of all chambers was to be less than 20 mrad [3]; in fact, an average longitudinal surface roughness slope of 8.50 mrad was achieved, with no chamber exceeding 20 mrad. An example of the effects of polishing are best seen in comparing the unpolished samples and the after polishing samples of the same extrusion (shown in Fig. 1).

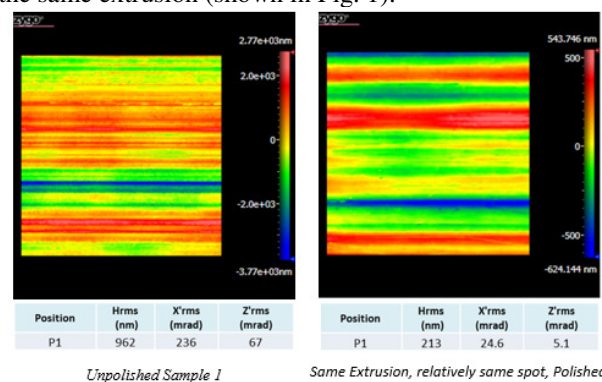


Figure 1: A comparison of unpolished (left) vs. polished surface roughness profiles (right).

To achieve these surface finish requirements, we modified our previously invented ninety-degree diverter. Our original polishing process only utilized one of the pistons of the abrasive flow machining equipment to push the polishing paste through the right angle diverter, through the extrusion aperture from one end, and allowed it to flow into a bucket at the other end. The paste was reloaded periodically as needed, which required constant attention from the operator, and the pressure of the paste on the aperture walls decreased down the length of the aperture [2]. The new diverter was built so that it now serves both the upper and lower pistons at the same time (see Fig. 2.) Second, we

* Work supported by the U.S. Department of Energy, Office of Science under Contract No. DE-AC02-06CH11357.

† wiemer@anl.gov

added a manifold that is attached to the opposite end of the extrusions being polished (see Fig. 3.) This combination of the new diverter and opposite end manifold allows two extrusions to be connected to the polishing machine at the same time (see Fig. 4), thereby reducing the production time by a factor of two. The polishing paste now slides back and forth through the extrusions as it should when the pistons move up and down. In addition, now that the pressure is consistent throughout both extrusions and the polishing machine is being utilized more as it was designed to be, the finish is more consistent down the entire length.



Figure 2: The right angle diverter showing flow direction.



Figure 3: The return end manifold.



Figure 4: Photo of the setup. Behind this setup is a second identical setup under an insulating blanket during processing. Also shown here are the roller brackets that also hold the heaters in place.

We still polish using three different grits and step down in coarseness to achieve the desired finish just as before [2]. The temperature of the extrusions being polished is elevated to 32°C to maintain a consistent and predictable viscosity each time. A fixture was developed that holds the heaters neatly in place over the apertures being polished and allows the extrusions to be rolled (see Fig. 4.) In the past, the extrusions were flipped end-for-end to equalize the head pressure at each end and flipped over to counter the effects of gravity on the polishing process. While still concerned about the potential effects of gravity on the polishing process, the equalized pressure no longer requires us to flip end-for-end. The rolling fixture allows the polishing operator to more easily reposition the extrusions half way through the grit cycle without disconnecting the manifold. As an improvement to the process, we finish the polishing with a cycle of gritless polishing paste to help clean out the remaining grit to reduce the possibility of residual grit left in the aperture and then rinse with a cleanser (Ensolve) to help remove any residue from the polishing paste before further processing of the extrusion takes place. In the past, the residual polishing paste sometimes proved difficult to clean from the aperture. These two additional steps helped minimize the number of extrusions that needed additional cleaning.

Final machining was performed after the abrasive flow polishing. The pressure of the media on the aperture walls is about 430 psi, and it would deform the thin 0.5-mm wall of the vacuum chamber that exists after machining. The thick un-machined extrusions provide ample strength to withstand the polishing pressure. Each extrusion was longer than the actual chamber length in order to have extra material from both ends for sampling to check the polishing quality. The Metrology Laboratory at the APS performed the surface finish measurements and calculated the slope error at three spots on each sample along and across the extrusion direction. Six extrusions of each type were cut to verify the surface finish in the center of the extrusion. The measurements of the center of the sacrificed chambers were also consistent with our average results.

For the LCLS-II upgrade, two slightly different variations of chambers were required: one version for the soft x-ray (SXR) undulator line (Fig. 5) and one for the hard x-ray (HXR) undulator line (Fig. 6). The HXR chambers are mounted and aligned in a vertical orientation because the HXR undulators are horizontal-gap, vertically-polarized undulators.

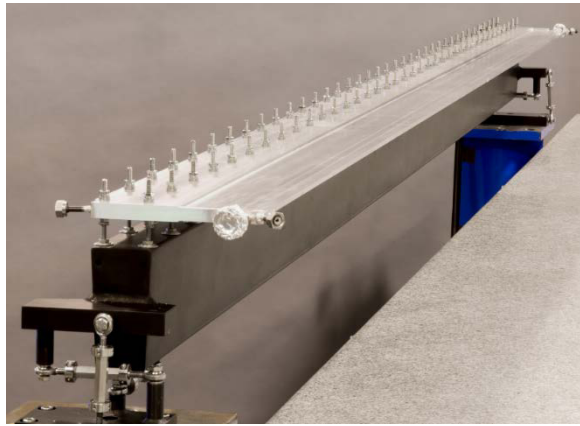


Figure 5: SXR chamber on alignment beam before installation of Earth-field coils.



Figure 6: Five HXR chambers assembled in alignment fixtures with water fittings and Earth-field coils.

Among the many requirements were that all chambers would maintain a finished nominal wall thickness of 0.5 mm, achieve a vacuum of less than 1×10^{-6} Torr, and a maximum outgassing rate after bake-out of less than 2×10^{-10} Torr*L/sec/cm². Chambers for both undulator lines are capable of being aligned to within $\pm 100 \mu\text{m}$ straightness along their entire length. For this upgrade, all chambers are water cooled so that an operating temperature of 20°C , $\pm 1^\circ\text{C}$ can be maintained. All chambers have coils installed within the surface of the chamber to allow correcting for the Earth's magnetic field (without violating the space constraints; that is, the chamber thickness may not exceed 6 mm $+0.15/0.05\text{mm}$).

Sixty-four chambers (26 SXR chambers and 38 HXR chambers) and their alignment systems were delivered to SLAC for the LCLS-II upgrade.

REFERENCES

- [1] G. Pile *et al.*, "Design and construction of the Linac Coherent Light Source (LCLS) undulator system," in *Proc. FEL'08*, Gyeongju, Korea, Aug. 2008, paper THAAU01, pp. 460-466.
- [2] E. Trakhtenberg, P. Den Hartog, M. Erdmann, and G. Wiemerslage, "LCLS extruded aluminum vacuum chamber – new approaches," in *Proc. MEDSI 2008*, Saskatoon, Canada, 2008.
- [3] H.-D. Nuhn, "LCLS-II undulator vacuum chamber surface roughness evaluation," LCLS-II, LCLSII-TN-17-08, March 2017.

OBSERVATIONS ON MICROBUNCHING OF ELECTRONS IN LASER-DRIVEN PLASMA ACCELERATORS AND FREE-ELECTRON LASERS*

A.H. Lumpkin^{#1}, D.W. Rule², M. LaBerge³, and M.C. Downer³
¹Fermi National Accelerator Laboratory, Batavia, IL 60510 USA

²Silver Spring, MD 20904 USA

³Physics Department, University of Texas at Austin, Austin, TX 78712 USA

Abstract

We provide observations on the visible-wavelength microbunching of relativistic electrons at beam energies >200 MeV in both laser-driven plasma accelerators (LPAs) and a self-amplified spontaneous emission (SASE) free-electron laser (FEL). An analytical model for coherent optical transition radiation interferometry (COTRI) addresses both cases. It is noted that the COTR/OTR gain observed in the LPA rivals that of the SASE FEL at saturation, although the few micron transverse sizes of the microbunched beamlets are much smaller than in the FEL. The broadband microbunching observed in the LPA case could act as a seed for a SASE FEL experiment with tunability over the visible regime, in principle.

INTRODUCTION

The periodic longitudinal density modulation of relativistic electrons at the resonant wavelength (microbunching) is a well-known, fundamental aspect of free-electron lasers (FELs) [1]. In one classic case, microbunching fractions reached 20% at saturation of a self-amplified spontaneous emission (SASE) FEL resulting in gains of 10⁶ at 530 nm [2]. In that experiment the concomitant z-dependent gain of coherent optical transition radiation (COTR) was also measured at the >10⁵ level. Microbunching at visible wavelengths in laser-driven plasma accelerators (LPAs) had been reported previously [3,4], but it has only recently been measured in near-field and far-field images on a single shot for the first time with significant COTR enhancements involved [5-7].

We reintroduce an analytical model for COTR interferometry (COTRI) first developed for the SASE-FEL-induced microbunching case [8] to evaluate the LPA case. The coherence function was treated in this analytical model that addresses both cases and the expected fringe patterns. In the FEL, one identified microbunched transverse cores of 25-100 microns in extent while in the LPA the recently reported transverse sizes at the exit of the LPA were a few microns [5-7]. In the latter case, signal enhancements >10⁵ and extensive fringes out to 30 mrad in angle space were recorded. We suggest the broadband microbunching observed in the LPA case could act as a seed for a SASE FEL experiment with tunability in principle over the visible regime.

* This manuscript has been authored by Fermi Research Alliance, LLC under Contract No. DE-AC02-07CH11359 with the U.S. Department of Energy, Office of Science, Office of High Energy Physics.

EXPERIMENTAL ASPECTS

The APS Linac and Previous SASE FEL Setup

The APS linac is based on an S-band rf photocathode (PC) gun which injects beam into an S-band linear accelerator with acceleration capability currently up to 450 MeV as shown in Fig. 1 [9]. The drive laser is a Nd:Glass-based chirped pulse amplifier (CPA) operating at an IR wavelength of 1053 nm, twice frequency doubled to obtain UV output at 100 μJ per pulse which irradiated the Cu photocathode of the gun [10]. Beam diagnostics in the linac include imaging screens, rf BPMs, and coherent transition radiation (CTR) autocorrelators located before and after the chicane at the 150-MeV point.

The previous SASE FEL configuration is also seen in Fig. 1 and included up to 9 undulators (~21 m of magnetic structure) with a period of 3.3 cm and appropriate undulator parameter, K, of value 3.1 resulting in lasing at 530-540 nm at a beam energy of 217 MeV. The FEL gain saturated at about z=15 m, or ~20 gain lengths. Diagnostic imaging stations were located before the first undulator and after each undulator to provide assessment of both the optical gain and uniquely the COTR gain. These are described in more detail in Ref. [11]. This experiment motivated the development of the COTRI model which is now being applied to the recent LPA results.

The LPA at HZDR

The LPA is based on the DRACO laser with a peak power of 150 TW at a central wavelength 800 nm interacting with a He gas jet (with 3% Nitrogen) at the Helmholtz-Zentrum Dresden-Rossendorf (HZDR) facility [12]. The LPA was operated with a plasma electron density n_e ~3 x 10¹⁸ cm⁻³ in the self-truncated ionization-injection mode. Beam energies of ~215 MeV in a quasi-monoenergetic peak were observed in a downstream spectrometer. After the LPA, a 75-μm thin Al foil blocked the laser pulse and was followed by an Al-coated Kapton foil as shown in Fig. 2. The latter's back surface provided the source point of the near field (NF) COTR imaging, and a polished Si mirror at 45° to the beam direction redirected this light to the microscope objective. The configuration provided a magnification factor of 42 at the camera and a calibration factor of 0.09 μm/pixel. This mirror was located 18.5 mm downstream of the Al-coated Kapton and also generated backward COTR that combined with the first source to provide COTRI in the far-field (FF) imaging

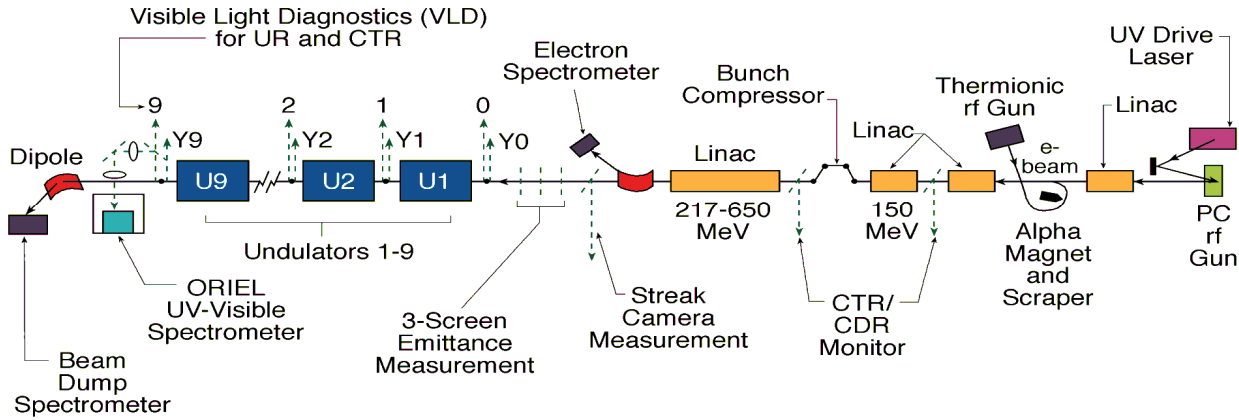


Figure 1: Schematic of the APS linac and SASE FEL beamline layout showing the UV drive laser, PC rf gun, linac, and SASE FEL undulators with diagnostic station locations circa 2002 [2].

camera. The significantly enhanced signal allowed the splitting of the signal into two NF cameras as well as a FF camera with a 633 ± 5 nm bandpass filter (BPF) as in Fig. 3.

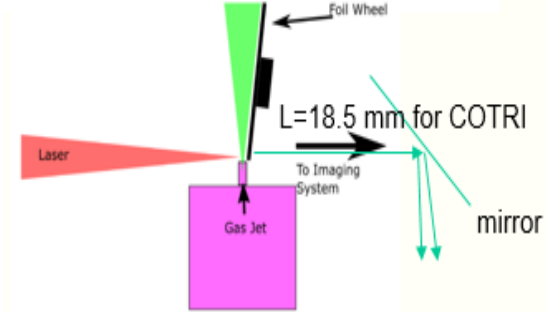


Figure 2: Schematic of the LPA showing the laser, gas jet, and foil geometry at HZDR with a foil separation $L = 18.5$ mm for COTRI [5,6].

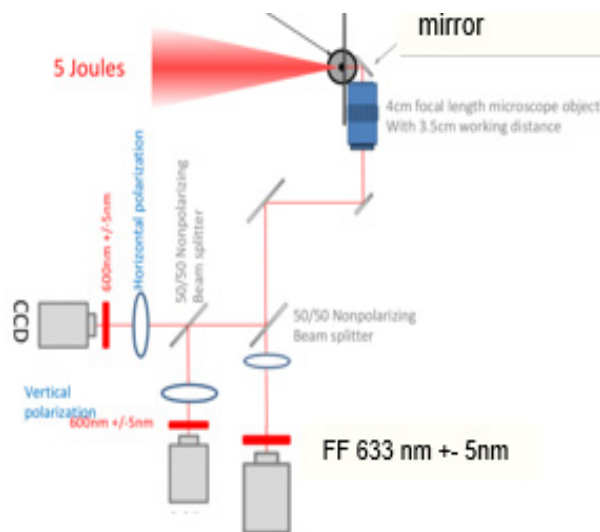


Figure 3: Schematic of the LPA and an early version of the NF and FF imaging setup using the beam splitters to redirect the optical signals to the different cameras [5,6].

ANALYTICAL MODEL RESULTS

Space precludes a full description of the COTRI analytical model which is being applied to the LPA case. The base equation includes the reflection coefficients, single electron spectral angular distribution $d^2W_1/d\omega d\Omega$, the interference term $I(k)$, and the coherence function $J(k)$.

$$\frac{d^2W}{d\omega d\Omega} = |r_{\parallel, \perp}|^2 \frac{d^2W_1}{d\omega d\Omega} I(k) J(k) \quad (1)$$

This has been presented in detail in Ref. [8] and more recently in [7]. However, relevant model results are shown in Fig. 4 illustrating the divergence effect on fringe visibility (negative angles) and the beam size effect on the enhancement of fringes (positive angles). One can see the fringe visibility is reduced for the 1.0 mrad case vs the 0.5 mrad case at the left. On the right, the coherence function is shown to be dramatically reduced at larger angles for the larger beam sizes. This means the FEL data only had a few visible fringes while the LPA fringe data extend out to 30 mrad. The foil separation was 18.5 mm and $\lambda = 633 \pm 5$ nm.

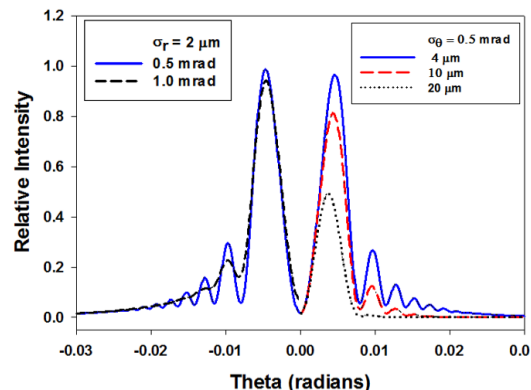


Figure 4: COTRI calculations for the effects of beam divergence in negative angles for a fixed beam size and the effects of microbunched beam size on fringe intensity for a fixed beam divergence of 0.5 mrad for the positive angles.

EXPERIMENTAL RESULTS

Previous SASE FEL Data

Fig. 4 illustrated how the transverse charge form factors determine the COTR gain as a function of angle. Previously the effect was evaluated for 0.2% microbunched beams of 25-, 50-, and 100- μm radius as shown in Fig. 5a [13]. This figure compares the COTR fringes to the incoherent OTRI pattern. Three fringes are enhanced for the 25- μm beam, but only one for the 100- μm case. Former COTRI results from a SASE FEL operating at 537 nm as shown in Fig. 5b graphically illustrate this principle [2]. Here, azimuthally asymmetric fringes (one x-fringe spanning $0 < \theta_x < 2$ mrad, 3 y-fringes spanning $0 < \theta_y < 6$ mrad) from post saturated gain regions of the FEL pointed to a microbunched core of radii $\sigma_x=100$ μm and $\sigma_y=25$ μm , embedded within a total electron beam of radii $\sigma_x=200$ μm and $\sigma_y=100$ μm . However, at saturation both fringe patterns were single fringes indicating more extensive microbunching transversely in the core and with a $\sim 20\%$ microbunching fraction.

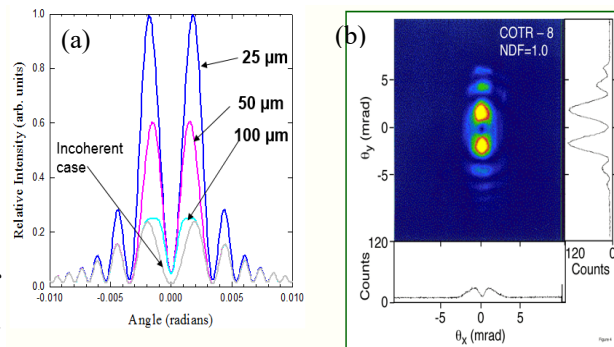


Figure 5: a) COTRI calculations for three beam sizes of 25, 50, and 100 μm indicating the effects on fringe intensity for a fixed divergence of 0.2 mrad [13]. b) Example COTRI image obtained post saturation after undulator 8 in the SASE FEL showing the results of the spatially asymmetric microbunched distribution at that z location [2].

Recent LPA Data

Examples of the NF and FF images from the same LPA shot at 215 MeV are shown in Figs. 6 and 7, respectively. In Fig. 6a we see the vertically polarized COTR point spread function (PSF) lobes for two beamlets separated on the x axis (laser polarization axis) by about 6 μm . A sample of the analysis technique which used the measured PSF lobe separation of 5.0 μm in y to determine the vertical beam size of about $\sigma = 2.0$ μm is shown in Fig. 6b. In Fig. 7a, the FF COTRI pattern is shown whose fringe number and visibility are compared to Fig. 4 model results as well as nearby model results to obtain a sub-mrad divergence of 0.5 ± 0.2 mrad and a beam size less than 4 μm . In addition, the analysis of the intensity of the FF image referenced to a calibrated laser source at 633 nm led to an estimated COTR gain $>10^5$ [7]. This is surprisingly similar to the SASE FEL COTR result at saturation,

although the number of microbunched electrons in the LPA case is 30-50 times smaller, as is the beam distribution.

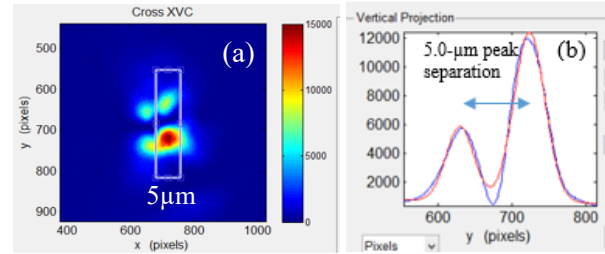


Figure 6: a) Vertically polarized NF image showing two pairs of coherent PSF lobes for two beamlets separated by about 6 μm . b) vertical profile of right hand beamlet with a 5- μm lobe separation which is mapped to 4.6 μm (FWHM) or 2.0 μm (σ).

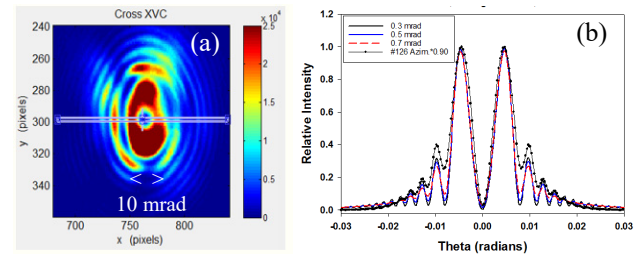


Figure 7: (a) Example of a FF COTRI image at 633 ± 5 nm from the same shot as Fig. 5. (b) Comparison of the azimuthally averaged fringe data and the COTRI model for 0.3, 0.5, and 0.7 mrad divergence. The fringe peak positions are well matched, but the relative intensities of some outer fringes are higher in the data. The best match is 0.5 mrad.

SUMMARY

In summary, we have revisited a classic SASE FEL case where the electron microbunching was tracked as a function of z , and a COTRI model was applied. We have compared that observed COTR gain seen at saturation to a recent LPA experiment that obtained single shot NF and FF images to determine beam size and divergence. We have noted the similar COTR gain in the two experiments, although there is a marked difference in the transverse size of the microbunched portion. In the case of the LPA, this microbunching appears to be a fundamental aspect of the LPA process and merits further investigation. We also suggest that the LPA microbunching at the 1% level in a narrow band might be used to seed a visible light SASE FEL experiment by adding an undulator(s) downstream of the LPA.

ACKNOWLEDGMENTS

The first author acknowledges the support of C. Drennan and M. Lindgren of the Accelerator Division at Fermilab. The University of Texas authors acknowledge support from DoE grant DE-SC0011617, and M.C.D. from the Alexander von Humboldt Foundation.

REFERENCES

- [1] See for example, Kwang-Je Kim, Zhirong Huang, Ryan Lindberg, *Synchrotron Radiation and Free-Electron Lasers: Principles of Coherent X-ray Generation*, Cambridge University Press, 2017.
- [2] A. H. Lumpkin *et al.*, “Evidence for Microbunching Sidebands in a Saturated Free-electron Laser Using Coherent Optical Transition Radiation”, *Phys. Rev. Lett.*, vol. 88, no.23, p. 234801, 2002.
doi:10.1103/PhysRevLett.88.234801
- [3] Y. Glinec, J. Faure, A. Norlin, A. Pukhov, and V. Malka, “Observation of Fine structures in Laser-driven Electron beams Using Coherent Transition Radiation”, *Phys. Rev. Lett.*, vol. 98, p. 194801, 2007.
doi.org/10.1103/PhysRevLett.98.194801
- [4] C. Lin *et al.*, “Long-Range Persistence of Femtosecond Modulations on Laser-Plasma-Accelerated Electron Beams”, *Phys. Rev. Lett.*, vol. 108, p. 094801, 2012.
doi.org/10.1103/PhysRevLett.108.094801
- [5] M. LaBerge *et al.*, Talk presented, EAAC17, Sept. 2017, Elba, Italy.
- [6] A. H. Lumpkin *et al.*, “Observations of Coherent Optical Transition Radiation Interference Fringes Generated by Laser Plasma Accelerator Electron Beamlets” in *Proc. AAC18*, Breckenridge CO, USA, Aug. 2018, (IEEE) 2019.
doi:10.1109/AAC.2018.8659381
- [7] A. H. Lumpkin, M. LaBerge, D.W. Rule *et al.*, submitted to *Phys. Rev. Lett.*, July 2019.
- [8] D. W. Rule and A. H. Lumpkin, “Analysis of Coherent Optical Transition Radiation Interference Patterns Produced by SASE-Induced Microbunches”, in *Proc. PAC'01*, Chicago, IL, USA, Jun. 2001, paper TPAH029, pp. 1288-1290.
- [9] N. D. Arnold *et al.*, “Observation and analysis of self-amplified spontaneous emission at the APS low-energy undulator test line”, *Nucl. Instr. and Meth. in Phys. Res. A*, vol. 475, pp. 28-37, 2001.
Doi:10.1016/S0168-9002(01)01530-3
- [10] J.C. Dooling and A.H. Lumpkin, “Streak Camera Measurements of the APS PC Gun Drive Laser”, in *Proc. NAPAC'16*, Chicago, IL, USA, Oct. 2016, pp. 85-88.
doi:10.18429/JACoW-NAPAC2016-M0POB08.
- [11] A. H. Lumpkin *et al.*, “Evidence for transverse dependencies in COTR and microbunching in a SASE FEL”, *Nucl. Instr. and Meth. A*, vol. 507, p. 200, 2003.
doi:10.1016/S0168-9002(03)00874-X
- [12] M. Mirzaie *et al.*, “Demonstration of self-truncated ionization injection for GeV electron beams”, *Sci. Rpts.*, vol. 5, p. 14659, 2015. doi:10.1038/srep14659
- [13] A. H. Lumpkin, R. J. Dejus, and D. W. Rule, 519-522, “First Direct Comparisons of a COTRI Analytical Model to Data from a SASE FEL at 540, 265, and 157 nm”, in *Proc. FEL'04*, Trieste, Italy, Aug.-Sep. 2004, paper TUPOS49, pp. 519-522.

PROGRESS IN HIGH POWER HIGH BRIGHTNESS DOUBLE BUNCH SELF-SEEDING AT LCLS-II

A. Halavanau, F.-J. Decker, C. Emma, A. Krasnykh, G. Marcus, A.A. Lutman, Z. Huang, Y. Ding, D. Zhu, J. Krzywinski, A. Ratti, A. Marinelli, C. Pellegrini¹

¹ SLAC National Accelerator Laboratory, Stanford University, Menlo Park CA 94025, USA

Abstract

We have previously shown that we can generate near TW, 15 fs duration, near transform limited X-ray pulses in the 4 to 8 keV photon energy range using the LCLS-II copper linac, two electron bunches, a 4-crystal monochromator/delay line and a fast transverse bunch kicker. The first bunch generates a strong seeding X-ray signal, and the second bunch, initially propagating off-axis, interacts with the seed in a tapered amplifier undulator, where it propagates on axis. In this paper, we investigate the design of the 4-crystal monochromator, acting also as an X-ray delay system, and of the fast kicker, in preparation of the implementation of the system in LCLS-II.

INTRODUCTION

The Double-Bunch FEL (DBFEL) is a method to generate high power and brightness in an X-ray FEL. In this scheme, shown in Fig. 1, the first bunch generates a high power SASE signal, near to saturation value, in the first undulator section and is not used in the second undulator section. The second bunch is seeded at the entrance of the second tapered undulator section by the high power SASE signal, filtered by a four crystals monochromator, also acting as a delay line. A transverse kicker is used to put the second bunch in oscillations around the undulator axis in the first section to avoid lasing. The kick is compensated to propagate the second bunch on axis in the second tapered section.

This concept was first considered to improve the performance of European XFEL and LCLS in Refs [1–3]. The overall design of the DBFEL at LCLS-II has been outlined in [4, 5]. A similar configuration using the second bunch as a fresh bunch with an ultra-fast kicker has been analyzed in the context of self-seeding and harmonic lasing in Ref. [6]. The experimental demonstration of fresh bunch self-seeding in a single bunch was also reported in Ref. [7].

Over the years of LCLS operations, electron beams containing multiple bunches separated by a few RF-buckets have been routinely created in LCLS CuRF linac [8–11]. It was previously demonstrated the DBFEL configuration of LCLS-II HXR undulator gives high peak power and high brightness X-rays in the photon range of 4 to 8 keV [4]. In this proceeding, we provide an update on DBFEL four crystal monochromator design, ultra-fast kicker and XFEL performance.

DBFEL NUMERICAL SIMULATIONS

The LCLS CuRF beamline is simulated using the code elegant [12], to evaluate the effects of the wakefields in the linac and bunch compressors. The particle distribution is

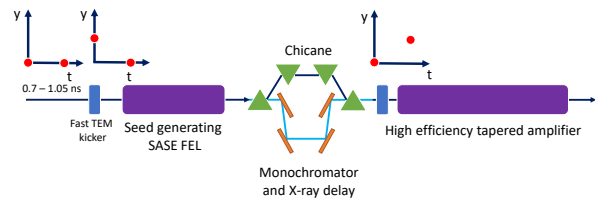


Figure 1: DBFEL schematics: two bunches with 0.7 - 1.05 ns separation are used to generate a high power seed on the second cold bunch at the entrance of the tapered amplifier.

then converted and passed to the FEL code genesis [13] running in time-dependent mode. For tapering studies, we utilize the technique described in [4]. In our simulations, the two bunches are considered to be identical, with 4 kA peak current and 15 fs quasi-flat top profile. We note that optimizing start-to-end beam and optimum taper profile for the amplifier section is a subject of an ongoing study.

FOUR CRYSTAL MONOCHROMATOR

An important part of the DBFEL system is the four crystal monochromator, presented in Fig. 2, that provides narrow bandwidth for double bunch seeding, and matches the delay $\Delta\tau$ between the two bunches. Currently, the monochromator is planned to be installed in the same chicane with the proposed LCLS-II RAFEL project, limiting its horizontal size to $L = 0.67$ cm.

In order to proceed with the design of the four bounce monochromator, let us discuss a few salient parameters of this device. We first start with the location of the monochromator in the undulator beamline. LCLS-II HXR undulator is built with 33 sections, each 3.6 m long, separated by a 0.4 m of free space. Two empty slots at U8 and U15 are available for self-seeding chicane installation.

LCLS-II HXR undulator currently has two empty slots at U8 and U15 locations available for self-seeding chicanes installation. Figure 3 displays gain curves of different photon energies in the SASE section. 4 keV case saturates after 8 undulators, while 8 keV case continues to grow exponentially until U12 location. At the next empty slot at U15 both 4 keV and 8 keV photon energies are saturated. Thus, we conclude that a SASE section of 8 undulators provides more seeding power for DBFEL. We note, that ultimately, experimental electron beam parameters and HXR gain length should be the key factors that determine the location of the DBFEL four crystal monochromator. These measurements are planned shortly after LCLS-II HXR undulator commissioning.

Table 1: C*(111) Parameters in 4-8 keV Photon Energy Range

Parameter	Units	Photon energy	Value
Bragg angle	deg.	4 keV	48.8
Darwin width	μrad	4 keV	69.4
Extinction length	μm	4 keV	2.9
Bandwidth	$\cdot 10^{-5}$	4 keV	6.1
Bragg angle	deg.	8 keV	22.1
Darwin width	μrad	8 keV	24.3
Extinction length	μm	8 keV	5.8
Bandwidth	$\cdot 10^{-5}$	8 keV	6.0

The monochromator uses diamond crystals to provide a narrow bandwidth and avoid complex thermal management [4]. We opt to select C*(111) diamond crystals as the best option for 4-8 keV energy range. C*(111) parameters are given in Tab. 1. The monochromator bandwidth is determined by the Darwin width, which is plotted in Fig. 4. Darwin curves were produced in XOP program [14].

The choice of diamond reflection also defines the geometry of the monochromator via the value of Bragg angle θ . Simple kinematic calculations yield the following equations for monochromator crystals' coordinates. Let us denote the distance between two upper crystals by L . Then the separation between two lower crystals is determined by $\Delta_z = L - c\Delta\tau(\cot^2\theta - 1)/2$, and the lateral displacement by $h = c\Delta\tau/2\tan\theta$. In addition, the bandwidth is defined by $\Delta\omega/\omega = -\Delta\theta/\tan\theta$, where $\Delta\theta$ is the Darwin width. See Fig. 2.

Thus, driven by the space limitations and four crystal geometry, we determine the optimum double bunch separation

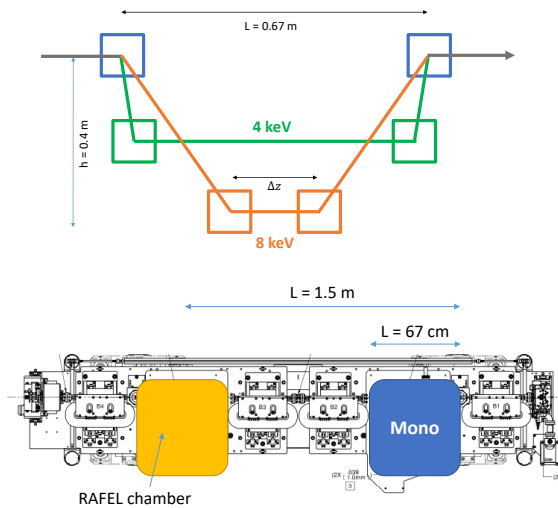


Figure 2: Four crystal monochromator layout (top) and location in the chicane (bottom). Two upper crystals stay fixed, while two lower crystals move in XY plane. See Ref. [15, 16] for the description of the RAFEL project.

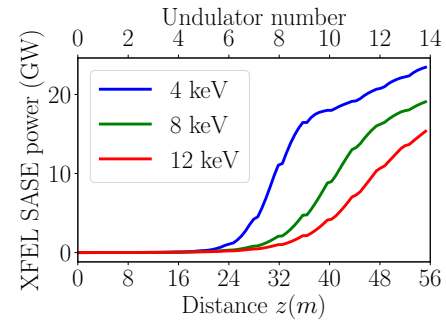


Figure 3: Start-to-end simulation of the SASE section XFEL power as a function of distance for different photon energies.

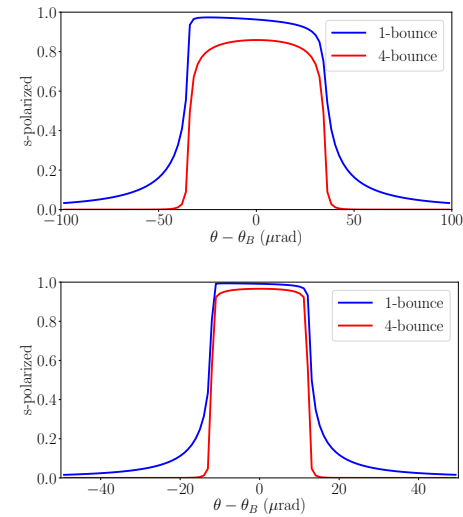


Figure 4: Darwin width of C*(111) 4 keV (top) and 8 keV (bottom) reflections for single and four bounces.

to be 2 RF buckets or $\Delta\tau=0.7$ ns, compared to previously reported number of 3 RF buckets or $\Delta\tau=1.05$ ns. This calculation is summarized in Fig. 5. Alternatively, one can consider the next diamond Bragg reflection of C*(220) to operate at higher photon energies, e.g. up to 12 keV, while reducing the footprint of the monochromator. However, to access 4 keV photons, we consider C*(111) as our primary choice. C*(111) will be procured from Sumitomo Electric and tested at Spring-8 facility in Japan.

We also note the existing nanopositioning stages have a precision of about 20 nm, which translates into about ± 0.2 fs error in total delay time $\Delta\tau$. We estimate the effect of the angular pointing error via $\Delta\tau \sim \Delta\theta/\cos\theta^2$ to be of the order of 1 fs.

ULTRA-FAST KICKER

The performance of the DBFEL system is critically dependent on the ability to control the orbits of two bunches. Initially, first bunch has to propagate on axis in order to provide high power seeding signal. The second bunch has to be put off axis before the SASE section enough to suppress lasing. This will be done with an ultra-fast transverse electromag-

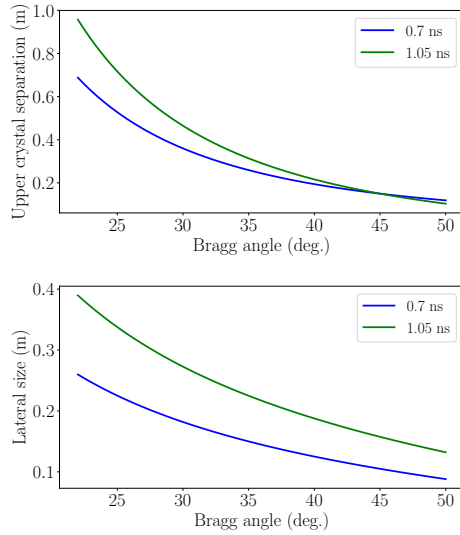


Figure 5: Four crystal monochromator size as a function of Bragg angle for 2 and 3 RF buckets double bunch separation and $\Delta z = 0.15$ m.

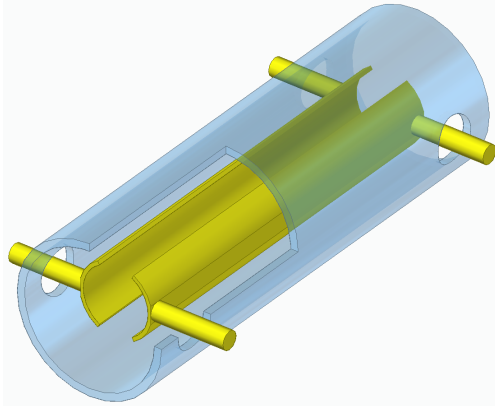


Figure 6: A schematic view of vertical TEM kicker.

netic (TEM) kicker system. Similar kickers were designed for high energy electron beams, including LCLS-II, albeit at larger bunch separations. In the case of DBFEL, bunch separation is about 0.7 ns, approaching the rise time limit of ultra-fast high voltage power supplies. As discussed above, DBFEL can also operate with 1.05 ns or three RF-buckets separation, in case practical implementation of the kicker device does not provide required rise time stability.

The transverse kick required to suppress lasing in the undulators is given by $\theta_C = \sqrt{\lambda/L_g}$, where λ is the radiation wavelength and L_g is the gain length [17]. This value is in the order of $10 \mu\text{rad}$ and is translated into about 60 keV/c of transverse momentum at 6 GeV beam energy, thereby determining the required TEM kicker strength. For a TEM structure, kicker strength is given by

$$\alpha = \frac{2VL}{r} \frac{4}{\pi} \sin \frac{\psi}{2}, \quad (1)$$

Table 2: TEM Kicker Specifications

Parameter	Units	Value
Voltage	kV	± 10
Rise time	ns	<0.3
Flat top	ns	3.5 ± 0.5
Pre-pulse	-	$<2\%$
Impedance	Ohm	50

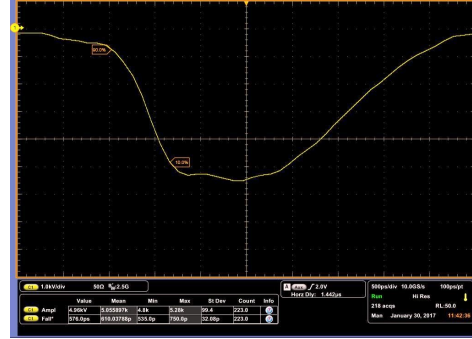


Figure 7: TEM kicker voltage as a function of time.

where $\psi = \pi/3$, V is the voltage, L is the length of the TEM structure, r is the structure radius and ψ is the opening angle [18]. Assuming TEM structure length of about 0.1 m with aperture of 0.01 m, we obtain 3 kV of required voltage.

We then consider a TEM structure, as shown in Fig. 6, with the specifications listed in Tab. 2. In this configuration, high voltage pulse is applied on two vertical plates, filling up TEM structure with EM field collinear with the beam direction. Our initial experiments with pulser prototypes show promising results for 5 kV peak voltage, 0.7 nsec rise time on a 50 Ohm resistive load; see Fig. 7. Pulser power supply design will be based on an employment of drift step recovery processes in semiconductors.

SUMMARY

We have presented the design of two critically DBFEL components: four crystal monochromator and ultra-fast TEM kicker. We concluded that given the limitations of the existing chicane design and CuRF wakefields, the separation of 0.7 ns or two RF-buckets is optimal. This, however, poses a strict constraint on the ultra-fast kicker's rise time. To solve the problem, we consider TEM structure, compatible with existing ultra-fast high voltage power supplies.

ACKNOWLEDGEMENTS

This work was supported by the U.S. Department of Energy Contract No. DE-AC02-76SF00515. The authors are grateful to Y. Feng, H.-D. Nuhn, J. Wu, C. Mayes (SLAC), K.-J. Kim, Y. Shvydko (ANL) for useful discussions.

REFERENCES

- [1] G. Geloni, V. Kocharyan, and E. Saldin, *arXiv, physics.acc-ph:1003.2548*, (2010).

- [2] G. Geloni, V. Kocharyan, and E. Saldin, *arXiv, physics.acc-ph:1207.1981*, (2012).
- [3] Y. Ding, Z. Huang, and R. D. Ruth, *Phys. Rev. ST Accel. Beams*, 13:060703, (2010). doi:10.1103/PhysRevSTAB.13.060703
- [4] A. Halavanau, F.-J. Decker, C. Emma, J. Sheppard, and C. Pellegrini, *Journal of Synchrotron Radiation*, 26(3), (2019). doi:10.1107/S1600577519002492
- [5] A. Halavanau, F.-J. Decker, Y. Ding, C. Emma, Z. Huang, J. Krzywinski, A. A. Lutman, G. Marcus, C. Pellegrini, and D. Zhu, In *Proc. 10th International Particle Accelerator Conference (IPAC2019), Melbourne, Australia, May 19-24, 2019*, paper TUPRB088, 2019. doi:10.18429/JACoW-IPAC2019-TUPRB088
- [6] C. Emma, Y. Feng, D. C. Nguyen, A. Ratti, and C. Pellegrini, *Phys. Rev. Acc. and Beams*, 20:030701–10, (2017). doi:10.1103/PhysRevAccelBeams.20.030701
- [7] C. Emma, A. Lutman, M. W. Guetg, J. Krzywinski, A. Marinelli, J. Wu, and C. Pellegrini, *Applied Physics Letters*, 110(15):154101, (2017). doi:10.1063/1.4980092
- [8] F.-J. Decker *et al.*, “A Demonstration of Multi-bunch Operation in the LCLS”, in *Proc. 32nd Int. Free Electron Laser Conf. (FEL’10)*, Malmö, Sweden, Aug. 2010, paper WEPB33, pp. 467–470.
- [9] F.-J. Decker *et al.*, “Two Bunches with ns-Separation with LCLS”, in *Proc. 37th Int. Free Electron Laser Conf. (FEL’15)*, Daejeon, Korea, Aug. 2015, paper WEP023, pp. 634–638.
- [10] F.-J. Decker, K. L. F. Bane, W. S. Colucho, A. A. Lutman, and J. C. Sheppard, “Recent Developments and Plans for Two Bunch Operation with up to 1 μ s Separation at LCLS”, in *Proc. 38th Int. Free Electron Laser Conf. (FEL’17)*, Santa Fe, NM, USA, Aug. 2017, pp. 288–291. doi:10.18429/JACoW-FEL2017-TUP023
- [11] F.-J. Decker *et al.*, “Four X-ray Pulses within 10 ns at LCLS”, in *Proc. 10th Int. Particle Accelerator Conf. (IPAC’19)*, Melbourne, Australia, May 2019, pp. 1859–1862. doi:10.18429/JACoW-IPAC2019-TUPRB086
- [12] M. Borland, “elegant: A Flexible SDDS-Compliant Code for Accelerator Simulation”, APS, LS-287, (2000). doi:10.2172/761286
- [13] S. Reiche, “GENESIS 1.3: a fully 3D time-dependent FEL simulation code”. *Nuclear Instruments and Methods in Physics Research A*, 429:243–248, (1999). doi:10.1016/S0168-9002(99)00114-X
- [14] M. Sanchez del Rio and R. J. Dejus, “Xop v2.4: recent developments of the x-ray optics software toolkit”, *Proc.SPIE*, 8141:8141 – 8141 – 5, (2011). doi:10.1117/12.893911
- [15] G. Marcus *et al.*, Regenerative Amplification for a Hard X-ray Free-Electron Laser. presented at FEL19, Hamburg, Germany, paper TUP032, 2019.
- [16] G. Marcus *et al.*, Regenerative Amplification for a Hard X-ray Free-Electron Laser. presented at FEL19, Hamburg, Germany, paper TUD04, 2019.
- [17] T. Tanaka, H. Kitamura, and T. Shintake, *NIM:A*, 528(1), pp. 172– 178, (2004). doi:10.1016/j.nima.2004.04.040
- [18] D. A. Goldberg and G. R. Lambertson, “Dynamic devices. a primer on pickups and kickers”, *AIP Conference Proceedings*, 249(1):537–600, 1992. doi:10.1063/1.41979

STATUS UPDATE FOR THE HIGH GAIN HIGH EFFICIENCY TESSA-266 EXPERIMENT

Youna Park, Pietro Musumeci, Paul Denham, David Dang, Nick Sudar, UCLA, Los Angeles, USA
Alexander Zholents, Yine Sun, ANL, Argonne, USA

Tara Campese, Ivan Gadjev, Ronald Agustsson, Alex Murokh, RadiaBeam, Los Angeles, USA
Stephen Webb, Chris Hall, RadiaSoft, Boulder, USA

Abstract

This paper will provide a status report on the high gain high efficiency TESSA-266 experiment planned at the Linac Extension Area (LEA) facility at Argonne Photon Source (APS). The goal of this project which is carried forward by a multi-institutional collaboration between university (UCLA), national laboratory (ANL) and small industries (Radiabeam and Radiasoft) is to demonstrate very high efficiency electron beam energy extraction in a 4-meter long strongly tapered helical undulator seeded by an ultraviolet 1 GW peak power laser seed pulse, and to study the spatial and spectral properties of the amplified radiation. We focus here on the discussion of the break-section area in between the undulators which has been designed to maximize the efficiency, and show the results of the numerical simulations for the system.

INTRODUCTION

Free-Electron-Lasers enjoy many unique properties as radiation sources, including high power, coherence and tunability and have been at the forefront of scientific research for decades. Especially in the short wavelength region of the electromagnetic spectrum, FELs have enabled a novel generation of radiation sources opening new frontiers in scientific research. On the other hand a characteristic drawback for conventional Free-Electron-Lasers amplifiers is that the energy efficiency is actually relatively poor, limited by the Pierce parameter [1] which at short wavelength (ultraviolet and below) is typically below 1 percent and often below 0.1 percent.

Following up earlier work on Inverse Free Electron Laser acceleration [2], few years ago a novel regime of operation has been proposed to greatly increase the FEL efficiency using prebunched electron beams, intense seed laser, and strongly tapered undulators (so called TESSA scheme) [3]. An experimental demonstration of the TESSA concept in the mid-infrared was carried out at BNL [4] where using a 200 GW seed laser at 10 μm wavelength, an energy extraction efficiency as high as 30 % was demonstrated. The intense seed laser pulse used for this experiment hindered measurements of the spatial and spectral properties of the newly generated radiation (i.e. the experiment was carried out in the low-gain TESSA regime).

The current TESSA-266 project aims at pushing the performances of the proof-of-principle BNL experiment and explore this interaction in the high gain regime (using a less intense seed laser pulse) and extending the scheme to shorter

wavelengths where high efficiency radiation sources would be extremely attractive (EUVL). The experimental design is based on a tapered gap-tunable helical Halbach [5] undulator which will be installed in the Linac Extension Area (LEA) at the end of the Argonne Photon Source injection linac. The APS linac will provide 375 MeV and up to 1 kA e-beam at 1-10 Hz pulse repetition rate in the interleaving mode that makes the beam available for this experiment 75 % of time. A seed laser of 1 GW and pulse length 0.6 ps will then be used first to bunch, extract energy and quickly decelerate the electron beam, yielding high gain TESSA amplification and an extraction efficiency which in the ideal simulation case reaches values as high as 10 percent (see Table 1 for a summary of the experiment parameters).

EXPERIMENT DESIGN

The tapered helical undulator for TESSA-266 is designed to maintain the resonant condition as the electrons lose their energy to the radiation along the interaction varying the undulator K factor while keeping the undulator period constant [6]:

$$\gamma_r^2 = \frac{\lambda_u}{2\lambda}(1 + K^2) \quad (1)$$

where λ_u is the undulator period, λ is the laser wavelength, and K the normalized undulator vector potential.

The undulator period is chosen to be at 3.2 cm in order to satisfy the resonance condition with e-beam energy of 375 MeV and wavelength of 266 nm with a gap of sufficient size to hose the vacuum pipe (> 5.5 mm).

Table 1: TESSA266 Nominal Parameters

Element	
Beam Energy	375 MeV
Peak Current	1 kA
Emittance	2 μm
Energy Spread	0.1 %
RMS Mean Spot Size	47 μm
Undulator Period	32 mm
Undulator K Parameters	2.8 - 2.4
Radiation wavelength	266 nm
Seed Power	1 GW

A number of considerations entered the final choice on the length of the undulator sections in the design of the experiment. There is enough space in the LEA tunnel to house

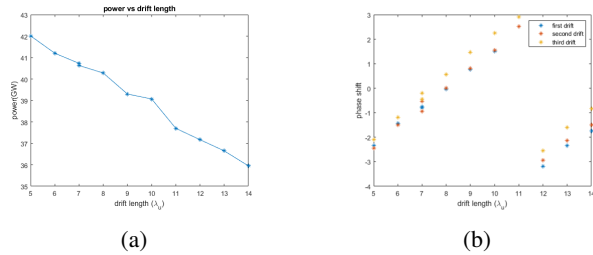


Figure 1: Optimized power output of time-independent simulation obtained from parameters in Table 2. (a) Output power vs. Drift length. A linear fit indicates that increasing the drift length of the break-sections, the output power decreases by around .5 % per centimeter, (b) Optimized phase shift vs. drift length in each break section.

a very long undulator, but it has been shown that high gradient deceleration is particularly important in order to avoid excessive growth of the synchrotron side-band instability which is the main limit to the radiation extraction efficiency. In order to leave open the possibility to reach the ambitious goal of 10 % efficiency we then set the undulator length to 4 m. A compromise is then made between i) using one long undulator which would enable continuous energy exchange and ii) breaking up the interaction using multiple undulator sections. The latter option leaves the opportunity to add focusing elements that can squeeze the beam transversely and maximize energy extraction efficiency [7]. In addition, a maximum undulator section length of 1 m is set by the length of the mill workplane at Radiabeam where the undulator is going to be built. In the final design of the experiment the THESEUS (Tapered HELical SEGmented Undulator System) undulator will comprise four 990 mm long sections.

An integral part of the THESEUS design are the break-sections in between the undulators. The radiation in these regions freely diffracts quickly reducing the on-axis intensity at the restart of the interaction and degrading the energy exchange. With our parameters we simulated that the output power would decrease as much as 0.5% per centimeter of break section length (Figure 1a) putting a strong request on keeping the break sections as short as possible.

At the same time, a large number of elements needs to fit within this section, transforming the design of this part of the experiment in a unique engineering feat. The focusing schemes for TESSA266 includes a doublet of permanent magnet quadrupoles to minimize the e-beam size along the interaction. [8]. Furthermore, simulations indicate that a tunable phase shifter would be highly beneficial in order to maximize the energy extraction. Vacuum pumps, undulator and laser diagnostic station add their own level of complexity to the challenge. The final design includes an extremely dense 17 cm long break section, hosting doublet quadrupoles, a phase shifter, a diagnostic station, and built-in bellows for correcting misalignments as shown in Figure 2.

Using Genesis simulations, we determined that the optimal phase shift in this configuration will be close to a full 2π

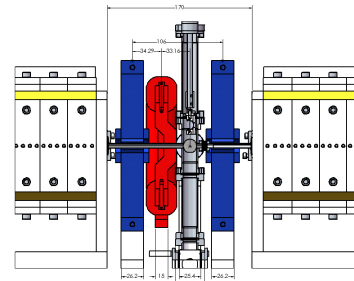


Figure 2: Break Section Design with the two permanent quadrupoles (blue), electromagnetic dipole (red), and diagnostic station (grey).

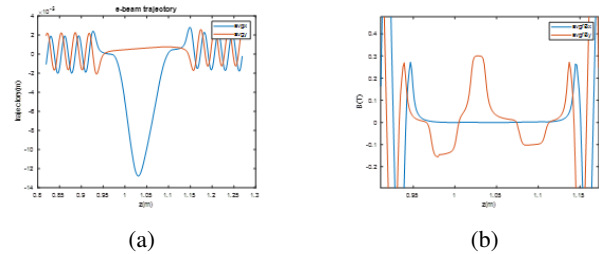


Figure 3: GPT Simulation of the break section with two transversely shifted quadrupoles and an electromagnetic dipole. (a) e-beam trajectory (b) magnetic field.

shift (Figure 1b). To obtain a phase-shifter in the very limited space available, we took advantage of the quadrupole pair already included in the focusing lattice. When a quadrupole is shifted in the transverse direction it behaves as a dipole and can be used to deflect the beam. The phase shift is then based on the use of remotely controllable translation stages for the PMQs (which effectively double as dipoles for this) and the addition of a small electromagnetic dipole (EMD) in between, to form a very short 3-dipole mini-chicane (Figure 3b). The chicane lengthens e-beam trajectory (Figure 3a) so that the phase of the electron beam micro-bunches is shifted relative to the photons that travels in a straight trajectory.

The transverse shift in the quadrupole position required to correct the trajectory for a given dipole field is:

$$\Delta x_{1,2} = \frac{L_D B_D}{L_Q g_Q} \frac{z_{2,1}}{z_1 + z_2} \quad (2)$$

where L_D and B_D are the length and field strength of the EMD respectively, L_Q and g_Q are the length and gradient of quadrupole, z_1 and z_2 the center-to-center displacements from each quadrupole to the EMD. The shift would then be minimized if the dipole was placed in the center of the break section equidistant from the two quadrupoles. However because of the diagnostic cross, it is not feasible to place the EMD in the center. In addition, due to the very tight boundaries around the diagnostic station and the quadrupoles, only 28-mm space in the longitudinal direction and 38-mm transverse was available for the dipole. This required maximizing the coil volume and bending the pole to redirect the field

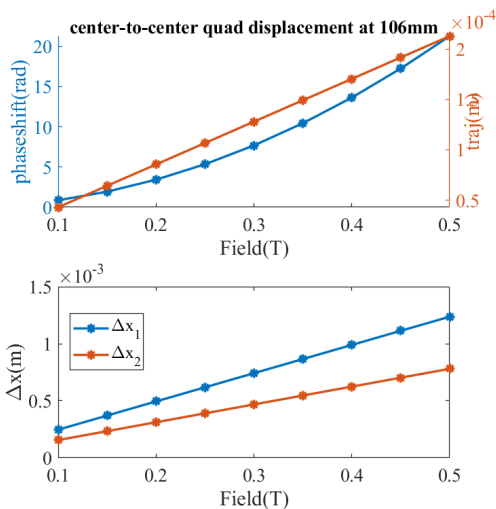


Figure 5: phase shift and quadrupole shift vs. dipole magnetic field strength. For a full phase shift the dipole field is 0.25 T, for which the first quadrupole needs to be shifted by 0.7 mm to straighten the electron trajectory.

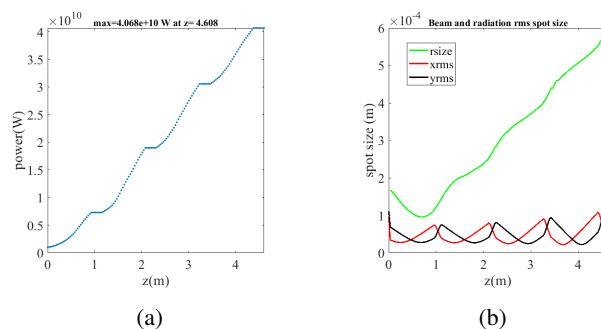
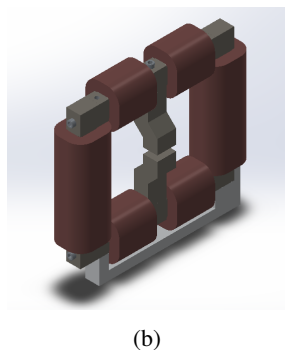


Figure 6: FEL Time-Independent Genesis Simulation Result. (a) radiation power at the end of the 4th undulator, (b) radiation (green) and e-beam size (red and black).

SIMULATION RESULTS

The optimal tapering for the experiment is finally determined using a period-by-period Genesis simulation as discussed in [3]

$$\frac{dK}{dz} = -2k_u K_l \sin \psi_r \quad (3)$$

where k_u is the undulator wavenumber, K_l is the normalized laser vector potential and ψ_r the design resonant phase.

The time-independent simulation result for four undulator sections of 29 undulator periods, the nominal drift length, and quadrupoles of 195 T/m gradient, along with optimal phase shifts in between undulator sections shows an extraction efficiency near ten percent (Figure 6).

Table 2: TESSA266 Distances

Element	Physical Length
THESEUS section length	989.4 mm
Physical break section length	170 mm
Total Sys. Length with pre-buncher	6610 mm
Quadrupole Effective Length	26.2 mm
EMD Effective Length	15.0 mm

ACKNOWLEDGEMENT

This project has been funded by DOE SBIR Grant No. DE-SC0013749.

REFERENCES

- [1] C. Pellegrini, A. Marinelli, and S. Reiche, "The physics of x-ray free-electron lasers," *Rev. Mod. Phys.*, vol. 88, p. 015006, Mar 2016. doi:10.1103/RevModPhys.88.015006
- [2] J. Duris, P. Musumeci, and R. Li, "Inverse free electron laser accelerator for advanced light sources," *Physical Review Special Topics-Accelerators and Beams*, vol. 15, no. 6, p. 061301, 2012. doi:10.1103/PhysRevSTAB.15.061301
- [3] J. Duris, A. Murokh, and P. Musumeci, "Tapering enhanced stimulated superradiant amplification," *New Journal of Physics*, vol. 17, no. 6, p. 063036. doi:10.1088/1367-2630/17/6/063036

- [4] N. Sudar, P. Musumeci, J. Duris, I. Gadjev, M. Polyanskiy, I. Pogorelsky, M. Fedurin, C. Swinson, K. Kusche, M. Babzien, and A. Gover, “High efficiency energy extraction from a relativistic electron beam in a strongly tapered undulator,” *Phys. Rev. Lett.*, vol. 117, p. 174801, Oct 2016. doi:10.1103/PhysRevLett.117.174801
- [5] K. Halbach, “Physical and optical properties of rare earth cobalt magnets,” *Nuclear Instruments and Methods in Physics Research*, vol. 187, no. 1, pp. 109 – 117, 1981. doi:10.1016/0029-554X(81)90477-8
- [6] N. Kroll, P. Morton, and M. Rosenbluth, “Free-electron lasers with variable parameter wigglers,” *IEEE Journal of Quantum Electronics*, vol. 17, pp. 1436–1468, August 1981. doi:10.1109/JQE.1981.1071285
- [7] C. Emma, K. Fang, J. Wu, and C. Pellegrini, “High efficiency, multiterawatt x-ray free electron lasers,” *Phys. Rev. Accel. Beams*, vol. 19, no. 2, p. 020705, 2016. doi:10.1103/PhysRevAccelBeams.19.020705
- [8] Y. Park, P. Musumeci, N. Sudar, A. Zholents, A. Murokh, Y. Sun, S. Webb, C. Hall, and D. Bruhwiler, “Strongly Tapered Undulator Design for High Efficiency and High Gain Amplification at 266 nm,” in *Proc. FEL’17*, Santa Fe, NM, USA, Aug. 2017, pp. 49–52. doi:10.18429/JACoW-FEL2017-MOP011

FLASH: THE PIONEERING XUV AND SOFT X-RAY FEL USER FACILITY

K. Honkavaara*, S. Schreiber, DESY, Hamburg, Germany†

Abstract

FLASH, the free-electron laser (FEL) at DESY (Hamburg), started user operation in summer 2005. It delivers high peak and average brilliance XUV and soft X-ray FEL radiation to photon experiments. Nowadays, FLASH has a 1.25 GeV superconducting linac, and two undulator beamlines, which are operated simultaneously. This paper provides an overview of its evolution from a test facility for superconducting accelerator technology to a full-scale FEL user facility.

INTRODUCTION

FLASH [1–6] at DESY (Hamburg, Germany) is an FEL user facility. It started user operation in summer 2005, and it was the first user facility worldwide delivering FEL radiation in XUV wavelengths to photon experiments.

Presently, FLASH consists of a photoinjector, a superconducting linac, two undulator beamlines (FLASH1 and FLASH2), and two experimental halls. The schematic layout is shown in Fig. 1. In addition, FLASH hosts a seeding experiment sFLASH [7], and a plasma wakefield acceleration experiment FLASHForward [8].

Electron bunches are generated by a photoinjector consisting of a normal conducting RF-gun with an exchangeable Cs₂Te photocathode, and three injector lasers. The linac has seven TESLA type 1.3 GHz superconducting accelerator modules, and two magnetic chicane bunch compressors. The maximum electron beam energy is 1.25 GeV. The use of superconducting RF cavities allows operation with long RF-pulses (800 μs), and thus with long electron bunch trains. FLASH1 and FLASH2 beamlines are operated simultaneously with a bunch train repetition rate of 10 Hz [9]. The separation of the bunch trains is realized by a kicker-septum system downstream of the last accelerator module.

The production of FEL radiation is based on the SASE (Self Amplified Spontaneous Emission) process. The FLASH1 undulator beamline consists of six 4.5 m long fixed gap (12 mm) undulator modules, which are the original ones and in use since 2004. FLASH2 has twelve 2.5 m long variable gap undulators. A planar electromagnetic undulator, installed downstream of the FLASH1 SASE undulators, provides, on request, THz radiation for user experiments.

The photon wavelength of FLASH1, due to fixed gap undulators, is defined by the electron beam energy. The minimum wavelength (fundamental), which FLASH1 can provide for user experiments is 4.2 nm, the maximum one slightly above 50 nm. FLASH2 with variable gap undulators provides FEL radiation at wavelengths between 4 nm and 90 nm.

Part of the material presented here has been discussed also in previous conferences, for example in [10–14].

TESLA TEST FACILITY (TTF) LINAC

The origin of FLASH is the TESLA Test Facility (TTF) Linac [15], constructed at DESY in mid 1990's. TTF was originally dedicated to test the feasibility of high gradient superconducting accelerator technology in the framework of the TESLA linear collider project [16].

The TTF injector I [17], operated in 1996–1998, consisted of a thermionic gun, a subharmonic buncher, a capture cavity (one superconducting TESLA type 9-cell cavity), and a diagnostics section. The first electron beam was produced in April 1996. The first complete TESLA type accelerator module with eight 9-cell superconducting niobium cavities was installed into the TTF Linac in spring 1997. Successful beam tests were carried out in 1997–1998 [18].

In autumn 1998, the injector was replaced by a photoinjector (Injector II) consisting of a laser-driven RF-gun with a Cs₂Te photocathode, a capture cavity (the same one as used in Injector I), a bunch compressor, and a diagnostic section [19]. In addition, a second bunch compressor [20] and a second accelerator module [21] were installed. The bunch compressor was located between the two accelerator modules.

Moreover, the TTF Linac was used to drive the SASE free-electron laser pilot facility TTF-FEL [22]. Three fixed gap undulator modules, similar to those still in use at FLASH1, were installed in 1999. In addition, the first accelerator module was replaced by a new one. The first SASE lasing in VUV worldwide (109 nm) was achieved in February 2000 [23]. TTF-FEL was successfully operated at photon wavelengths from 80 nm to 120 nm [24, 25] to demonstrate the feasibility of SASE FELs in the VUV range for photon experiments. The operation of the TTF Linac finished in November 2002.

FEL USER FACILITY FLASH

FLASH – originally called VUV-FEL at TTF2 – was constructed in 2003–2004. The first stage consisted of a photoinjector, a superconducting linac of five TESLA type accelerator modules, two bunch compressors, and an undulator beamline of six fixed gap undulator modules. The injector and the first part of the linac were located in the former place of TTF-FEL. An extension tunnel was built to host the undulator beamline, and a new experimental hall was constructed for the photon beamlines and user experiments.

The first lasing (32 nm) was achieved in January 2005 [26]. The user operation started in summer 2005, opening new possibilities for photon science, for example diffractive imaging [27]. During 2005–2007, FLASH delivered FEL radiation in wavelengths from 13 nm to 47 nm (fundamental),

* katja.honkavaara@desy.de

† for the FLASH team

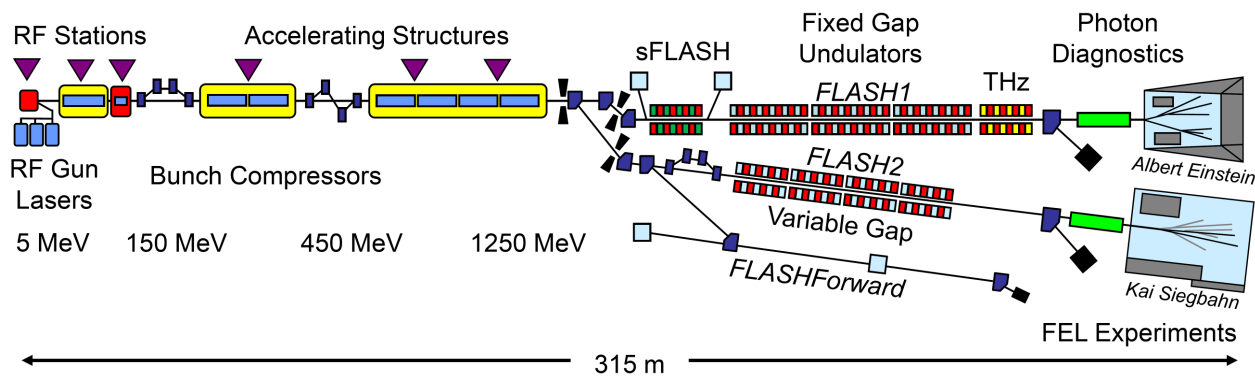


Figure 1: Schematic layout of the FLASH facility in 2019 (not to scale).

entering the water window with the third and fifth harmonics [1].

The sixth accelerator module was installed in 2007 to reach the design energy of 1 GeV. The photon wavelength range was extended to the soft X-rays with wavelengths down to 6.5 nm [28].

In 2009-2010, the last upgrade of the FLASH linac was accomplished [29]. Installation of the seventh accelerator module increased the electron beam energy up to 1.25 GeV. This allows lasing with wavelengths down to 4.1 nm [30], entering thus the water window also with fundamental wavelengths. In addition, a module with four third harmonic (3.9 GHz) superconducting RF cavities was installed to linearize the longitudinal phase space. In parallel, a seeding experiment sFLASH [31] was installed upstream of the SASE undulators.

In 2013, a second undulator beamline, located in a new building, was connected to the FLASH linac. Since then the original FLASH undulator beamline with fixed gap undulators has been called FLASH1, the new one with variable gap ones FLASH2.

FLASH2

In order to fulfill the continuously increasing demands on the beam time and on the photon beam properties, a second undulator beamline FLASH2, was constructed in 2011-2014. FLASH2 consists of an extraction beamline to connect it to the FLASH linac, an undulator beamline of twelve variable gap undulators, and a sophisticated photon diagnostics section. Photon beamlines are located in a new experimental hall [32].

The connection of FLASH2 to the FLASH linac was accomplished in 2013 within a 6 months shutdown. In winter 2013/2014, the FLASH2 beamline installation continued in parallel to the FLASH1 operation. The beam commissioning of FLASH2 started in spring 2014, and the first lasing was achieved in August 2014 [33]. Since April 2016, FLASH2 is in user operation.

The installation and instrumentation of photon beamlines has continued during the last years, allowing an increasing number of user experiments to take place at FLASH2. For example, a pump-probe laser has been available since autumn

2018. Thanks to variable gap undulators, fast wavelength scans are feasible and routinely performed by FLASH2 experiments.

FLASH2 provides also a possibility to test novel lasing schemes, like HLSS (harmonic lasing self-seeded FEL) [34] and two-color lasing [35].

A third electron beamline, located in the same building as FLASH2, hosts a plasma wakefield acceleration experiment FLASHForward [8]. Its experimental program started in 2018 [36].

PRESENT STATUS

FLASH is nowadays a full-scale of user facility with two undulator beamlines. More than 300 papers on photon science at FLASH has been published in scientific journals [37].

FLASH has two user periods per year. 60% of the available beam time is dedicated to user operation (4500 h per year), 30% to developments to improve the performance as a user facility, and 10% to general accelerator physics developments, like seeding (sFLASH) and plasma wakefield acceleration (FLASHForward). The beam time is organized with an alternating pattern of user blocks (4-5 weeks) and study blocks (2-3 weeks). Shutdown periods are scheduled twice per year: typically 4 weeks in summer and 2 weeks over Christmas.

OUTLOOK

In order to keep FLASH a state-of-the-art FEL user facility, a refurbishment and upgrade program is on-going [38].

In summer 2019, a third bunch compressor was installed at FLASH2 downstream of the extraction beamline. An installation of a transverse deflecting structure "PolariX-TDS" [39] downstream of the FLASH2 undulators is foreseen in 2020. The two oldest and weakest accelerator modules (module 2 and module 3) will be replaced in 2021 by refurbished modules with high gradient cavities. This, together with an optimization of the waveguide distribution system, will provide an energy upgrade to 1.35 GeV. In addition, several other refurbishments are on-going, concerning, for example, the injector laser system, the optical synchronization system, and electron beam diagnostics.

As part of the DESY strategy process, an upgrade project “FLASH 2020+” has been proposed. The key aspects of the proposal are replacement of the FLASH1 undulators with variable gap ones, establishment of a high repetition rate seeding (goal 1 MHz) at FLASH1, extension of the wavelength (fundamental) range at FLASH2 down to the oxygen K-edge (2.3 nm), and exploration of possibilities for novel lasing schemes towards attosecond physics.

SUMMARY

In the last 20 years, FLASH has been a pioneer for SASE FELs. Already TTF-FEL demonstrated the feasibility of FELs in the VUV range, and in 2005 FLASH was the first facility providing SASE XUV radiation for user experiments, encouraging several other FEL user facilities, like the European XFEL, to be constructed. With several upgrades, FLASH has extended its wavelength range to soft x-rays. Since 2014, FLASH has operated simultaneously two undulator beamlines, being the first worldwide also in this aspect. We believe that with the on-going refurbishment and the planned upgrades, FLASH will stay an state-of-the-art FEL also for the coming years.

ACKNOWLEDGMENT

We acknowledge B. H. Wiik for his dedication on the TESLA project. We thank all the colleagues at DESY and in collaborating institutes worldwide, who have provided over the years their indispensable contribution to the success of TTF and FLASH.

REFERENCES

- [1] W. Ackermann *et al.*, “Operation of a free-electron laser from the extreme ultraviolet to the water window”, *Nature Photonics*, vol. 1, pp. 336–342, 2007. doi:10.1038/nphoton.2007.76
- [2] K. Tiedtke *et al.*, “The soft x-ray free-electron laser FLASH at DESY: beamlines, diagnostics and end-stations”, *New J. Phys.*, vol. 11, p. 023029, 2009. doi:10.1088/1367-2630/11/2/023029
- [3] S. Schreiber and B. Faatz, “The free-electron laser FLASH”, *High Power Laser Science and Engineering*, vol. 3, p. e20, 2015. doi:10.1017/hpl.2015.16
- [4] B. Faatz *et al.*, “Simultaneous operation of two soft x-ray free-electron lasers driven by one linear accelerator”, *New J. Phys.*, vol. 18, p. 062002, 2016. doi:10.1088/1367-2630/18/6/062002
- [5] J. Rossbach, J. R. Schneider, and W. Wurth, “10 years of pioneering X-ray science at the free-electron laser FLASH at DESY”, *Physics Reports*, vol. 808, pp. 1–74, 2019. doi:10.1016/j.physrep.2019.02.002
- [6] J. Roensch-Schulenburg, K. Honkavaara, S. Schreiber, R. Treusch, and M. Vogt, “FLASH - Status and Upgrades”, presented at the 39th Int. Free Electron Laser Conf. (FEL’19), Hamburg, Germany, Aug. 2019, paper FRA03, this conference.
- [7] C. Lechner *et al.*, “Seeding R&D at sFLASH”, presented at the 39th Int. Free Electron Laser Conf. (FEL’19), Hamburg, Germany, Aug. 2019, paper TUP076, this conference.
- [8] R. D’Arcy *et al.*, “FLASHForward: plasma wakefield accelerator science for high-average-power applications”, *Phil. Trans. R. Soc. A*, vol. 377, p. 20180392, 2019. doi:10.1098/rsta.2018.0392
- [9] J. Roensch-Schulenburg *et al.*, “Experience with Multi-Beam and Multi-Beamline FEL-Operation”, *J. Phys.: Conf. Series*, vol. 874, p. 012023, 2017. doi:10.1088/1742-6596/874/1/012023
- [10] K. Honkavaara, B. Faatz, J. Feldhaus, S. Schreiber, R. Treusch, and M. Vogt, “FLASH: First Soft X-ray FEL Operating Two Undulator Beamlines Simultaneously”, in *Proc. 36th Int. Free Electron Laser Conf. (FEL’14)*, Basel, Switzerland, Aug. 2014, paper WEB05, pp. 635–639.
- [11] K. Honkavaara, B. Faatz, J. Feldhaus, S. Schreiber, R. Treusch, and M. Vogt, “Status of the Soft X-Ray FEL User Facility FLASH”, in *Proc. 37th Int. Free Electron Laser Conf. (FEL’15)*, Daejeon, Korea, Aug. 2015, paper MOP014, pp. 61–65.
- [12] K. Honkavaara, “Status of the FLASH FEL User Facility at DESY”, in *Proc. 38th Int. Free Electron Laser Conf. (FEL’17)*, Santa Fe, NM, USA, Aug. 2017, pp. 14–18. doi:10.18429/JACoW-FEL2017-MOD02
- [13] M. Vogt, K. Honkavaara, M. Kuhlmann, J. Roensch-Schulenburg, S. Schreiber, and R. Treusch, “Status of the Superconducting Soft X-Ray Free-Electron Laser FLASH at DESY”, in *Proc. 9th Int. Particle Accelerator Conf. (IPAC’18)*, Vancouver, Canada, Apr.-May 2018, pp. 1481–1484. doi:10.18429/JACoW-IPAC2018-TUPMF090
- [14] J. Roensch-Schulenburg, K. Honkavaara, M. Kuhlmann, S. Schreiber, R. Treusch, and M. Vogt, “Status of the Superconducting Soft X-Ray Free-Electron Laser User Facility FLASH at DESY”, in *Proc. 10th Int. Particle Accelerator Conf. (IPAC’19)*, Melbourne, Australia, May 2019, pp. 1909–1911. doi:10.18429/JACoW-IPAC2019-TUPRB106
- [15] D. A. Edwards, Ed., “TESLA Test Facility Linac, Design Report”, DESY, Hamburg, Rep. TESLA-1995-01, March 1995.
- [16] R. Brinkmann, K. Floettmann, J. Rossbach, P. Schmueser, N. Walker, and H. Weise, Eds., “TESLA Technical Design Report. Part II: The Accelerator”, DESY, Hamburg, Rep. DESY-2001-011, March 2001.
- [17] T. Garvey *et al.*, “First Beam Tests of the TTF Injector”, in *Proc. 17th Particle Accelerator Conf. (PAC’97)*, Vancouver, Canada, May 1997, paper 4W003, pp. 2823–2825.
- [18] S. Schreiber, “The Tesla Test Facility Linac - Status Report”, in *Proc. 6th European Particle Accelerator Conf. (EPAC’98)*, Stockholm, Sweden, Jun. 1998, paper MOP14F, pp. 475–477.
- [19] S. Schreiber, “First Experiments with the RF Gun Based Injector for the TESLA Test Facility Linac”, in *Proc. 18th Particle Accelerator Conf. (PAC’99)*, New York, NY, USA, Mar. 1999, paper MOCR6, pp. 84–86.
- [20] M. Geitz, A. Kabel, G. Schmidt, and H. Weise, “Bunch Compressor II at the TESLA Test Facility”, in *Proc. 18th Particle Accelerator Conf. (PAC’99)*, New York, NY, USA, Mar. 1999, paper WEP110, pp. 2507–2509.

- [21] D. Proch, “Activities with Superconducting Cavities at DESY”, in *Proc. 9th Int. Conf. RF Superconductivity (SRF’99)*, Santa Fe, NM, USA, Nov. 1999, paper MOA005, pp. 19–23.
- [22] J. Rossbach, “A VUV free electron laser at the TESLA test facility at DESY”, *Nucl. Instrum. Meth. A*, vol. 375, pp. 269–273, 1996. doi:10.1016/0168-9002(95)01332-6
- [23] J. Andruszkow *et al.*, “First Observation of Self-Amplified Spontaneous Emission in a Free-Electron Laser at 109 nm Wavelength”, *Phys. Rev. Lett.*, vol. 85, p. 3825, 2000. doi:10.1103/PhysRevLett.85.3825
- [24] V. Ayvazyan *et al.*, “Generation of GW Radiation Pulses from a VUV Free-Electron Laser Operating in the Femtosecond Regime”, *Phys. Rev. Lett.*, vol. 88, p. 104802, 2002. doi:10.1103/PhysRevLett.88.104802
- [25] V. Ayvazyan *et al.*, “A new powerful source for coherent VUV radiation: Demonstration of exponential growth and saturation at the TTF free-electron laser”, *Eur. Phys. J. D*, vol. 20, pp. 149–156, 2002. doi:10.1140/epjd/e2002-00121-4
- [26] V. Ayvazyan *et al.*, “First operation of a free-electron laser generating GW power radiation at 32 nm wavelength”, *Eur. Phys. J. D*, vol. 37, pp. 297–303, 2006. doi:10.1140/epjd/e2005-00308-1
- [27] H. N. Chapman *et al.*, “Femtosecond diffractive imaging with a soft-X-ray free-electron laser”, *Nature Physics*, vol. 2, pp. 839–843, 2006. doi:10.1038/nphys461
- [28] S. Schreiber, B. Faatz, and K. Honkavaara, “Operation of FLASH at 6.5 nm Wavelength”, in *Proc. 11th European Particle Accelerator Conf. (EPAC’08)*, Genoa, Italy, Jun. 2008, paper MOPC030, pp. 133–135.
- [29] S. Schreiber, B. Faatz, J. Feldhaus, K. Honkavaara, R. Treusch, and M. Vogt, “Status of the FEL User Facility FLASH”, in *Proc. 33rd Int. Free Electron Laser Conf. (FEL’11)*, Shanghai, China, Aug. 2011, paper TUPB04, pp. 267–270.
- [30] S. Schreiber, “First Lasing in the Water Window with 4.1 nm at FLASH”, in *Proc. 33rd Int. Free Electron Laser Conf. (FEL’11)*, Shanghai, China, Aug. 2011, paper TUOBI2, pp. 164–165.
- [31] S. Ackermann *et al.*, “Generation of Coherent 19- and 38-nm Radiation at a Free-Electron Laser Directly Seeded at 38 nm”, *Phys. Rev. Lett.*, vol. 111, p. 114801, 2013. doi:10.1103/PhysRevLett.111.114801
- [32] E. Ploenjes, B. Faatz, M. Kuhlmann, and R. Treusch, “FLASH2: Operation, beamlines, and photon diagnostics”, *AIP Conference Proceedings*, vol. 1741, p. 020008, 2016. doi:10.1063/1.4952787
- [33] S. Schreiber and B. Faatz, “First Lasing at FLASH2”, in *Proc. 36th Int. Free Electron Laser Conf. (FEL’14)*, Basel, Switzerland, Aug. 2014, paper MOA03, pp. 7–8.
- [34] E. A. Schneidmiller *et al.*, “First operation of a harmonic lasing self-seeded free electron laser”, *Phys. Rev. Accel. Beams*, vol. 20, p. 020705, 2017. doi:10.1103/PhysRevAccelBeams.20.020705
- [35] E. Schneidmiller *et al.*, “Two-Color Operation of FLASH2 Undulator”, presented at the 39th Int. Free Electron Laser Conf. (FEL’19), Hamburg, Germany, Aug. 2019, paper TUP055, this conference.
- [36] R. D’Arcy *et al.*, “Tunable Plasma-Based Energy Dechirper”, *Phys. Rev. Lett.*, vol. 122, p. 034801, 2019. doi:10.1103/PhysRevLett.122.034801
- [37] http://photon-science.desy.de/facilities/flash/publications/scientific_publications
- [38] M. Vogt, K. Honkavaara, J. Roensch-Schulenburg, S. Schreiber, and J. Zemella, “Upgrade Plans for FLASH for the Years After 2020”, in *Proc. 10th Int. Particle Accelerator Conf. (IPAC’19)*, Melbourne, Australia, May 2019, pp. 1748–1751. doi:10.18429/JACoW-IPAC2019-TUPRB027
- [39] F. Christie, J. Roensch-Schulenburg, and M. Vogt, “A PolariX TDS for the FLASH2 Beamline”, presented at the 39th Int. Free Electron Laser Conf. (FEL’19), Hamburg, Germany, Aug. 2019, paper WEP006, this conference.

STATUS OF THE COMPACTLIGHT DESIGN STUDY*

G. D'Auria[†], S. Di Mitri, R. Rochow, Elettra Sincrotrone Trieste, 34149 Basovizza, Italy
A. Latina, X. Liu, C. Rossi, D. Schulte, S. Stappes, X. Wu, W. Wuensch, CERN, 1211 Geneva, CH
H. M. Castañeda Cortes, J. Clarke, D. Dunning, N. Thompson, STFC Daresbury Lab., Warrington, UK
W. Fang, Shanghai Institute of Applied Physics, Shanghai 201800, P. R. China
E. Gazis, N. Gazis[‡], E. Tanke[‡], E. Trachnas[‡], IASA, Athens, Greece
V. Goryashko, M. Jacewicz, R. Ruber, Uppsala University, Uppsala, Sweden
G. Taylor, Melbourne University, Melbourne, Australia
R. Dowd, D. Zhu, Australian Synchrotron, ANSTO, Australia
A. Aksoy, Z. Nergiz, Ankara University, Ankara, Turkey
R. Apsimon, G. Burt, A. Castilla, Lancaster University, Lancaster, UK
H. Priem, X. Janssen, VDL Enabling Technology Group, Eindhoven, Netherlands
J. Luiten, P. Mutsaers, X. Stragier, Tech. University of Eindhoven, Netherlands
D. Alesini, M. Bellaveglia, B. Buonomo, F. Cardelli[§], M. Croia, M. Diomedea, M. Ferrario,
A. Gallo, A. Giribono[§], L. Piersanti[§], J. Scifo, B. Spataro, C. Vaccarezza, INFN-LNF, Frascati, Italy
R. Geometrante, M. Kokole, Kyma S.r.l., Trieste, Italy
J. Arnesano, F. Bosco, L. Ficcadenti, A. Mostacci, L. Palumbo, Sapienza University, Rome, Italy
G. Dattoli, F. Nguyen, A. Petralia, ENEA, Frascati, Italy
J. Marcos, E. Marin, R. Munoz Horta, F. Perez, ALBA Synchrotron, Barcelona, Spain
A. Faus-Golfe, Y. Han, CNRS, Paris, France
A. Bernhard, J. Gethmann, Karlsruher Institut für Technologie, Karlsruhe, Germany
M. Calvi, T. Schmidt, K. Zhang, Paul Scherrer Institut, 5232 Villigen, Switzerland
D. Esperante, J. Fuster, B. Gimeno, D. Gonzalez-Iglesias, IFIC (CSIC-University of Valencia), Spain
M. Aicheler, Helsinki University, Helsinki, Finland
R. Hoekstra, ARC NL, Amsterdam, Netherlands
A. W. Cross, L. Nix, L. Zhang, Strathclyde University, Glasgow, UK

Abstract

CompactLight (XLS) is an International Collaboration of 24 partners and 5 third parties, funded by the European Union through the Horizon 2020 Research and Innovation Programme. The main goal of the project, which started in January 2018 with a duration of 36 months, is the design of an hard X-ray FEL facility beyond today's state of the art, using the latest concepts for bright electron photo-injectors, high-gradient accelerating structures, and innovative short-period undulators. The specifications of the facility and the parameters of the future FEL are driven by the demands of potential users and the associated science cases. In this paper we will give an overview on the ongoing activities and the major results achieved until now.

INTRODUCTION

The CompactLight project aims to design a hard X-ray FEL facility beyond today's state of the art, combining the

latest and most innovative technologies for the major components of the FEL system, very high gradient accelerating structures at X-band (12 GHz), the most advanced concepts for high brightness electron photo injectors, and innovative compact short-period undulators. Compared to existing facilities, the proposed facility will have a smaller footprint due to the high gradient and will require a lower electron beam energy, owing to the enhanced undulator performance. The whole infrastructure will have lower electrical power demand, construction and operation costs. The user require-

Table 1: Baseline Parameters of the CompactLight FEL

Parameter	Unit	SXR	HXR
Photon Energy	keV	0.25-2.0	2.0-16.0
Repetition rate	Hz	250	100
Pulse duration	fs	0.1-50	1-50
Polarization		Variable, selectable	
Two-pulse delay	fs	± 100	± 100
Two-colour separation	%	20	10
Synchronization	fs	< 10	< 10

ments have been identified by existing and potential FEL users via discussions at several workshops, meetings, and surveys. They are summarised in Table 1 and in [1].

* This project has received funding from the European Union's Horizon2020 research and innovation programme under grant agreement No 777431.

[†] gerardo.dauria@elettra.eu

[‡] Now at ESS-ERIC, Lund, Sweden

[§] Now at ENEA, Frascati, Italy

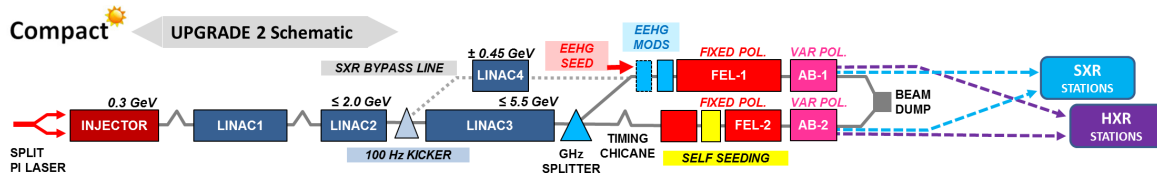


Figure 1: Schematic of CompactLight with Upgrade 2 applied.

FACILITY OVERVIEW

A key user request is double FEL pulses separated in wavelength and time. We propose to generate a double electron bunch at the photo-injector (PI) using a split and delayed PI laser pulse. Each bunch will be accelerated on a separate cycle of the RF then given a small energy separation in a short linac section operating at a sub-harmonic of the main linac. A DC magnet and septum system will then separate the two bunches and send them into two parallel undulator sections one of which may contain a electron beam delay chicane. This parallel option is more compact than using two undulators in series and allows the two FEL pulses to have independently controllable wavelength and timing separation and to be combined into a single experiment or sent to two independent experiments, doubling the capacity of the facility. Several advanced undulator technologies are being assessed [2] and it has been found that a maximum beam energy of 5.5 GeV is sufficient for a number of technologies to deliver the required FEL performance, with the final choice to be made at a later date in combination with a cost and risk analysis. The summary of electron beam parameters is shown in Table 2.

Table 2: Baseline Electron Beam Parameters

Parameter	Unit	SXR	HXR
Beam Energy	GeV	1-2	2.75-5.5
Bunch Charge	pC	75	75
Normalized Emittance	mm-mrad	0.2	0.2
Max Peak Current	kA	5	5
Min Bunch Length	fs	2	2
RMS slice energy spread	%	0.03	0.01

Both CompactLight FEL beamlines will operate over the full wavelength range. In HXR mode the electron energy will be up to 5.5 GeV at 100 Hz. In SXR mode the energy will be up to 2.0 GeV and, since the linac gradient will be reduced, it will be possible to increase the repetition rate to 250 Hz for the baseline configuration.

The baseline configuration satisfies all the essential output requirements identified by the users. Two upgrades beyond the baseline configuration are envisaged. Upgrade Option 1 will enable the SXR repetition rate to increase to 1 kHz by adding further RF klystrons. Upgrade Option 2 will add seeding to both FEL lines (currently we are investigating EEHG for FEL1 and self-seeding for FEL2) and a SXR bypass line with a extra linac section, this will allow simultaneous independent HXR/SXR output to two independent

experiments. Figure 1 shows a schematic of CompactLight with Upgrade Option 2 applied.

Injector

The XLS injector must generate and accelerate the electron beam up to 300 MeV with charge, emittance, bunch length and energy spread suitable for acceleration in the X-band linac. The target injector parameters are reported in Table 3. To achieve these parameters, the injector integrates various components: the gun, the capture section to boost the energy to 300 MeV, including the possibility to operate in the velocity bunching configuration [3], the solenoids for beam emittance compensation, and higher harmonics RF structures for longitudinal phase space linearization. Different schemes have been investigated including RF gun injectors at different operating frequencies (S, C and X band) and a DC gun based design aiming to achieve the target parameters. One of the most promising injectors is the C-band one.

Table 3: Target CompactLight Injector Parameters

Parameters	Units	Value
Beam Energy	MeV	300
rms Bunch Length σ_t	fs	350
Peak current $Q/\sqrt{12}\sigma_t$	A	60
rms Energy Spread	%	0.5
Projected norm. emittance	mm-mrad	0.2
Repetition Rate	Hz	100-1000

The gun is followed by two C-band TW structures [4] and the solenoids after the gun and around the TW structures control the beam emittance increase also in case of longitudinal compression by velocity bunching. The gun, the most critical component of the injector, will operate at very high cathode peak field (>200 MV/m) and will be powered with extremely short RF pulses (<200 ns) to allow operation up to the kHz regime [4]. Different types of RF gun couplers have been studied to control the pulsed heating. They are represented in Fig. 2. The first type is a mode launcher-type [5] while the second one is a proposed new coupler that operates on the TM_{020} mode on the full cell. This permits to couple the field in the waveguide, electrically, strongly reducing the pulsed heating. The main gun parameters are reported in Table 4.

RF Systems

The CompactLight linacs, which accelerate from 300 MeV to 5.5 GeV, are based on X-band, high-gradient technology. The linac is highly modular with repeated ≈ 4 m long units.

Table 4: Main Parameters of the C-Band Gun

Parameter	Unit	Value
Resonant frequency	GHz	5.712
$E_{\text{cath}}/\sqrt{P_{\text{diss}}}$	MV/(m.MW ^{0.5})	65 (55)
RF input power	MW	40 (70)
Cathode peak field	MV/m	200–240
Rep rate	Hz	100 ^(*)
Filling time	ns	150
RF pulse length	ns	180
$E_{\text{surf}}/E_{\text{cath}}$		0.9
Pulsed heating	K	<40
Average diss. power	W	200

^(*) Upgrade Options 1 and 2, respectively at 250 Hz and 1 kHz rep rate, are being studied.

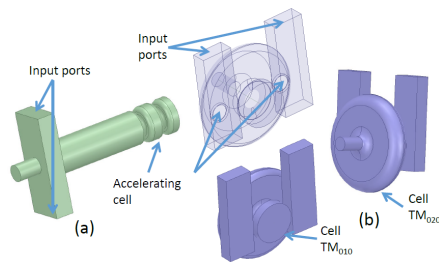


Figure 2: Proposed input couplers: (a) mode launcher type; (b) new coupler with TM₀₂₀ cell.

Each so-called rf unit consists of a modulator, klystron pulse compressor and wave guide network which feeds four 1 m long accelerating structures. The klystron of the baseline rf unit is a 50 MW klystron running at 100 Hz. It is available commercially from CPI and is used at more than four laboratories. With an rf pulse compressor, it can deliver 44 MW to each of the four accelerating structures. The accelerating structures have an average beam aperture of 3.5 mm, which is determined in an optimization which balances short-range wakefields (large aperture) against the number of klystrons needed for the final energy (small aperture). The accelerating gradient with the 44 MW input pulse is 65 MV/m giving a total energy gain of 234 MV/rf unit.

The linac can be upgraded (Upgrade Option 1) to enable a repetition rate up to 1 kHz at 2 GeV energy operation. This is accomplished by adding a 6 MW klystron and a power switch to each rf unit. The rest of the rf unit remains the same. The 6 MW klystron is available commercially, manufactured by Canon, and is also operational at over four laboratories. In this mode the input power to each structure is 5.4 MW, the gradient is 22.7 MV/m and the total energy gain across each rf unit is 81.7 MeV.

START-TO-END (S2E) SIMULATIONS

Particle tracking runs have been done assuming a 65 MV/m accelerating gradient in the main X-Band linac at 100 Hz. Injector optimisation studies have addressed the minimisation of the transverse projected and sliced emittances. Two stage magnetic bunch compressors (BC1 + BC2) are employed to reach a peak current of 5 kA at the end of the

linac. Table 2 lists the main electron beam parameters at the FEL for the 100 Hz repetition rate scenario.

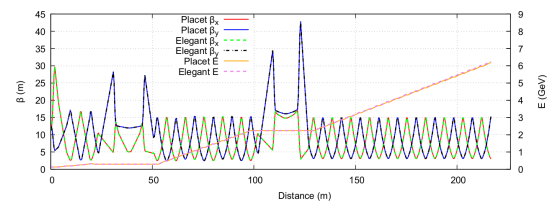


Figure 3: Beta Functions and beam energy along the linacs.

Full 6-D Tracking simulations have been performed using both Placet [6] and Elegant [7] codes. The simulation of the linac starts at 60 MeV using the distribution created by ASTRA [8]. The s2e first order optics are illustrated in Fig. 3. The final bunch distribution and its parameters are shown in Fig. 4. It is seen that the bunch is compressed down to 9 μm and the RMS energy spread of the bunch at the end of linac is 0.03%, which is acceptable for FEL generation.

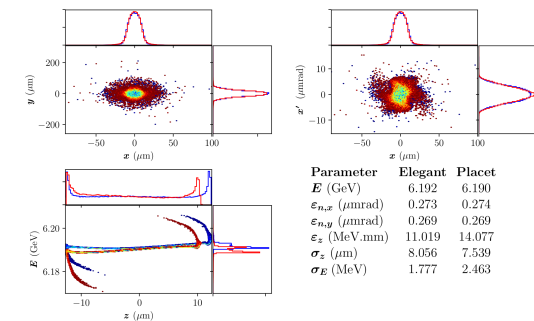


Figure 4: Beam parameters, phase spaces and transverse distribution of bunch at the end of linac with associated histograms.

To benchmark the FEL codes and semi-analytic approximations a study case has been carried out to determine the performance of a FEL tuned to 16 keV based on a cryogenic permanent magnet undulator (CPMU), one of the candidate technologies. The electron beam has a flat-top charge distribution and length 1.64 μm , which corresponds to 5kA peak current for 27 pC bunch charge. The other parameters are listed in Table 2. The optimised average β function of 9 m minimised the gain length. Figure 5 shows the results

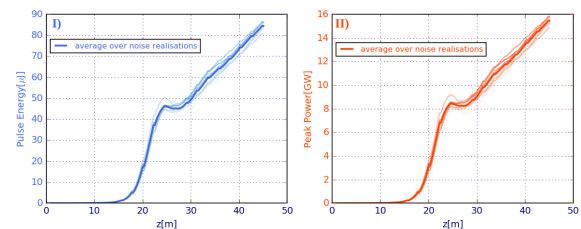


Figure 5: a) Evolution of pulse energy along the undulators, b) average of peak power over all electron beam slices.

using Genesis 1.3 [9] code. As shown, the FEL saturates at a distance of about 25 m and the peak power reaches 5 GW in SASE operation.

REFERENCES

- [1] A. Mak, P. Salen, V. Goryashko, and J. Clarke, "Science requirements and performance specification for the compact-light x-ray free-electron laser," Uppsala University, Tech. Rep. 2019/01, 2019.
- [2] F. Nguyen *et al.*, "XLS D5.1: Technologies for the CompactLight undulator," Tech. Rep., 2019. http://www.compactlight.eu/uploads/Main/D5.1_XLS_Final.pdf
- [3] M. Ferrario *et al.*, "Experimental demonstration of emittance compensation with velocity bunching," *Physical Review Letters*, vol. 104, no. 5, p. 054801, 2010. doi: 10.1103/PhysRevLett.104.054801.
- [4] D. Alesini *et al.*, "Design of a Full C-Band Injector for Ultra-High Brightness Electron Beam," in *Proc. of IPAC'19*, 2019. doi: 10.18429/JACoW-IPAC2019-TUPTS024.
- [5] C. Nantista *et al.*, "Low-field accelerator structure couplers and design techniques," *Phys. Rev. ST Accel. Beams*, vol. 7, p. 072001, 2004. doi: 10.1103/PhysRevSTAB.7.072001.
- [6] A. Latina *et al.*, "Recent Improvements in the Tracking Code Placet," in *Proc. of EPAC'08*, 2008, paper TUPP094.
- [7] M. Borland, "ELEGANT: A flexible SDDS-compliant code for accelerator simulation," Tech. Rep., 2000. doi: 10.2172/761286.
- [8] K. Flöttmann, *Astra: A space charge tracking algorithm*, 2011. <http://www.desy.de/~mpyflo/>
- [9] S. Reiche, "GENESIS 1.3: a fully 3D time-dependent FEL simulation code," *Nucl. Instruments Methods Phys. Res. Sect. A Accel. Spectrometers, Detect. Assoc. Equip.*, vol. 429, no. 1-3, pp. 243-248, Jun. 1999, ISSN: 0168-9002. doi: 10.1016/S0168-9002(99)00114-X.

STATUS AND PERSPECTIVES OF THE FERMI FEL FACILITY (2019)

L. Giannessi[†], E. Allaria, L. Badano, S. Bassanese, F. Bencivenga, C. Callegari, F. Capotondi, D. Castronovo, F. Cilento, P. Cinquegrana, M. Coreno, I. Cudin, M. B. Danailov, G. D'Auria, R. De Monte, G. De Ninno, P. Delgiusto, A. Demidovich, M. Di Fraia, S. Di Mitri, B. Diviacco, A. Fabris, R. Fabris, W. M. Fawley, L. Foglia, M. Ferianis, P. Furlan Radivo, G. Gaio, F. Gelmetti, F. Iazzourene, S. Krecic, M. Lonza, G. Kurdi, N. Mahne, M. Malvestuto, M. Manfredda, C. Masciovecchio, M. Milloch, R. Mincigrucci, N. Mirian, I. Nikolov, F. H. O Shea, G. Penco, A. Perucchi, O. Plekan, M. Predonzani, K. C. Prince, E. Principi, L. Raimondi, P. Rebernik Ribič, F. Rossi, L. Rumiz, C. Scafuri, C. Serpico, N. Shafqat, P. Sigalotti, A. Simoncig, S. Spampinati, C. Spezzani, M. Svandrlik, M. Trovò, A. Vascotto, M. Veronese, R. Visintini, D. Zangrando, M. Zangrando
Elettra Sincrotrone Trieste S.C.p.A., Basovizza, Italy

Abstract

FERMI is the seeded Free Electron Laser (FEL) user facility at the Elettra laboratory in Trieste, operating in the VUV to EUV and soft X-rays spectral range; the radiation produced by the seeded FEL is characterized by wavelength stability, low temporal jitter and longitudinal coherence in the range 100-4 nm. During 2018 a dedicated experiment has shown the potential of an Echo Enabled Harmonic Generation (EEHG) scheme to cover most of this spectral range with a single stage cascade [1]. Such a scheme, combined with an increment of the beam energy and of the accelerator performances, could extend the FERMI operating range up to the oxygen K-edge. With this future perspective, we present the development plans under consideration for the next 3 to 5 years. These include an upgrade of the linac and of the existing FEL lines, consisting in the conversion of FEL-1 first, and FEL-2 in a second moment, into EEHG seeded FELs.

INTRODUCTION

FERMI is located at the Elettra laboratory in Trieste. The FEL facility covers the VUV to soft X-ray photon energy range with two seeded FELs, FEL-1 [2] and FEL-2 [3], both based on the High Gain Harmonic Generation seeded mode (HGHG) [4-6] to operate in the range 100-4 nm, producing radiation characterized by wavelength stability, low temporal jitter and longitudinal coherence [7-10].

The FELs are in operation with users since 2010. During the commissioning phase “with users”, concluded in December 2018, seven calls for experiments (see Fig.1) contributed to establish and consolidate the various modes of operation. In January 2019 the facility entered into standard operation mode, with two calls for experiments every year and more than 4k hours per year of user operation regularly scheduled.

Strategic development goals for FERMI are the reduction of the pulse duration, which is typically in the range 30-100 fs depending on the duration of the seed and on the harmonic order [11], and the extension of the photon energy range of operation; there is indeed significant interest and there are important science opportunities in extending

the photon energy range to include the K-edges of nitrogen (410 eV) and oxygen (543 eV) [12-14].

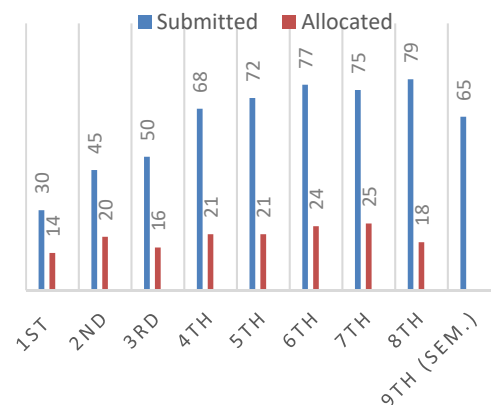


Figure 1: User proposal statistics at FERMI

As to the reduction of the pulse duration, an upgrade of the laser system to start with a shorter seed is under development. This, combined with nonlinear dynamics in the FEL amplifier [15] has shown the potential to reduce to sub 10-fs the FEL pulse duration. As to the extension of the photon energy range, the amplitude of the energy modulation necessary to initiate the HGHG process grows with the order of the harmonic conversion, and the induced energy dispersion has a detrimental effect on the high gain amplification in the final radiator. This fact limits the harmonic multiplication factor of FERMI FEL-1 to 13-15. Substantially higher orders can be reached with FEL-2 with the double stage HGHG cascade, where the harmonic conversion is performed with the fresh bunch injection technique [6]. This scheme was implemented for the first time on FERMI FEL-2 [3] and was used to demonstrate the seeded FEL coherent emission in the soft-X rays, up to harmonic orders of 65, and higher [7].

An alternative method to increase the order of the harmonic conversion in a single stage is the Echo Enabled Harmonic Generation (EEHG) scheme proposed in [16-17]. During 2018 a dedicated experiment has shown the potential of EEHG to cover at FERMI most of this spectral

range with a single stage cascade [1]. The experiment consisted in a modification of the FEL-2 layout to accommodate the installation of dedicated systems necessary for the EEHG. Main changes included a new undulator to replace the second modulator allowing seeding with a UV laser after the delay line chicane that provides the large dispersion necessary for EEHG. The strength of the delay line chicane was increased to reach a maximum of 2 mm dispersion required for the EEHG experiment.

The experiment demonstrated high-gain and high-quality lasing using the EEHG scheme down to wavelengths as short as 5.9 nm with narrow and clean spectra with low shot-to-shot central wavelength jitter [1]. Coherent emission was observed at harmonics up to 101 indicating the potential to extend the lasing region to the oxygen K-edge either by using EEHG directly, or with a cascade employing both EEHG and HGHG techniques.

Regardless of the selected approach, a prerequisite for the extension of the spectral range to the oxygen K-edge is the upgrade of the linac/final amplifier performances, in terms of beam energy, undulator parameters and phase space quality. The first will ensure sufficient gain at 2 nm, the second will preserve as much as possible the longitudinal coherence and wavelength stability that are distinguishing features of FERMI.

LINAC UPGRADE

The high energy part of the FERMI linac is presently equipped with seven Backward Traveling Wave (BTW) structures with small beam apertures and nose cone geometries for high gradient operation. Nevertheless, those structures have been suffering from increased breakdown rates when operated at 25-26 MV/m and 50 Hz repetition rate. A plan for the replacement of the seven BTW structures is under development. A new accelerating module for operation up to 30 MV/m (at 50 Hz) and low wake-fields contribution has thus been designed [18-20] and the first prototype module is under development in collaboration with the Paul Scherrer Institut (PSI). The modules consist of two newly designed three meters long accelerating structures to replace each single 6.1 m long BTW structure. The new structures are designed to guarantee reliable operation at 30 MV/m, a short (0.5 m) prototype was realized according to the PSI recipe and tested at Elettra during the last few months, showing a fault rate of only $3.9 \cdot 10^{-8}$ breakdowns per pulse at 35 MV/m.

The installation of the first full-length module replacing the horizontal deflector at the end of the present linac should already ensure a beam energy close to 1.7 GeV (at 10 Hz repetition rate). The replacement of all the BTW structures with new modules will allow a final energy of 1.8 GeV at 50 Hz, with sufficient margin for compression and phase space manipulation.

The reduced transverse/longitudinal wake-fields of the new structures will also allow an improved beam phase space, both transverse and longitudinal, increased stability and higher compression. In the following analysis we assume the parameters in Table 1 for the electron beam generated by the upgraded linac.

Table 1: Linac Parameters

e-beam	
Energy (GeV)	1.8
Peak Current (kA)	1.0
Norm. emitt. (slice – mm-mrad)	1
Relative energy spread (slice)	10^{-4}
β -Twiss parameter (m)	12
undulator	
Period (cm)	2.8
Module length (m)	2.2
Number of modules	8

FEL-2 UPGRADE

We have analysed the performances of the FERMI FELs in both HGHG and EEHG modes of operation using the model developed in [21]. This method implements the Xie scaling relations on an FEL operating with a pre-modulated beam and provides an estimate of the FEL performance, as a function of the undulator parameters (period, UM length ...), beam parameters (energy, emittance, energy spread ...) and of the scheme used to generate the initial modulation, e.g. EEHG vs HGHG with fresh bunch. The Xie power scaling [22] predicts the output power and the model provides the maximum harmonic order at which saturation should be reached. The power can be converted in pulse energy using the theory in [11] to estimate the expected pulse duration. It can be used to optimize the set of input parameters of a given configuration (seed intensity, amplitude of dispersions ...)

As an example, in Fig. 2 we show the dependence of the FEL peak power in comparable configurations EEHG and HGHG with fresh bunch vs. the harmonic order. The two configurations share the same amplifier and electron beam parameters, as listed in Table 1.

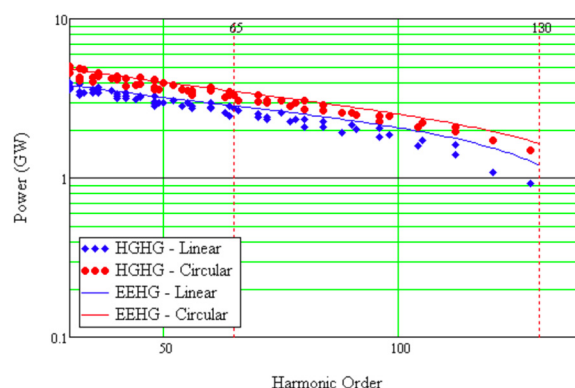


Figure 2: Output peak power for FEL peak power in comparable EEHG (red-blue continuous lines for circular (C) and linear (L) polarizations) and HGHG with fresh bunch configurations vs. the harmonic order; markers: red-blue for C and L polarizations respectively.

The EEHG configuration shows a better behavior at high harmonic orders, but requires a large dispersion in the first chicane. The behavior of the maximum harmonic order reaching saturation vs. the first chicane dispersion in EEHG configuration is shown in Fig. 3. A seed wavelength of 260 nm was assumed; the dispersion required to reach

saturation at 2.0 nm, corresponding to harmonic 130 is about 15 mm.

The model assumes an ideal dispersion and does not include debunching effects due to intrabeam scattering or other effects associated with CSR or non-linear dynamics in the chicane which may degrade the beam emittance or energy spread. Further work is required to determine which configuration is the best suited to reach the 2 nm wavelength or shorter. The final configuration could be HHG or EEHG, or a hybrid configuration where fresh bunch HHG at harmonics 4-5 is seeded by a first stage in EEHG operating at a relatively modest harmonic order ~30-35. In this case the first dispersion could be limited to 3-5 mm and would have a lower impact on the beam quality.

FEL-1 UPGRADE

While we may question the operation of EEHG at harmonic orders higher than 100, we already have convincing experimental evidence that EEHG is a real breakthrough with respect to a single stage HHG configuration. FERMI FEL-1 may operate in HHG up to harmonic 15-17, while the EEHG experiment carried out at FERMI [1] has shown convincing FEL performances up to harmonic ~50. This strongly supports a plan of upgrade of FERMI FEL-1 to an EEHG configuration. The spectral range of FEL-1 would be extended to 100-10 nm and the FEL in the new layout would be an ideal test bed for further EEHG studies. New experimental opportunities would be available for the users, such as the operation at the Fourier limit with longer seed pulses and the possibility of operating multi-pulse multi-colour configurations, presently not available in the range 10-20 nm. A second aspect is connected to the FEL-2 future upgrade, as FEL-1 covering the range 100-10 nm would allow an optimized design of FEL-2 focused on the reduced range 10 - 2 nm.

We are planning the upgrade of FEL-1 preserving the possibility to extend the first dispersive chicane of EEHG up to 15 mm, even if this value exceeds by a factor three the required value, in order to have a test result, aims to

explore beam dynamics of a modulated beam in the chicane.

The upgrade of FEL-1 requires an additional laser system for a second, independent seed. The refurbished modulator performed well during the EEHG experiment and will be used as the additional modulator for FEL-1. In Fig. 4 we show the maximum harmonic reaching saturation in the FEL-1 configuration, with a dispersive section of 10 mm.

Highest harmonics reaching saturation are 34 (7.6nm) and 26 (10 nm) in circular and linear polarization respectively.

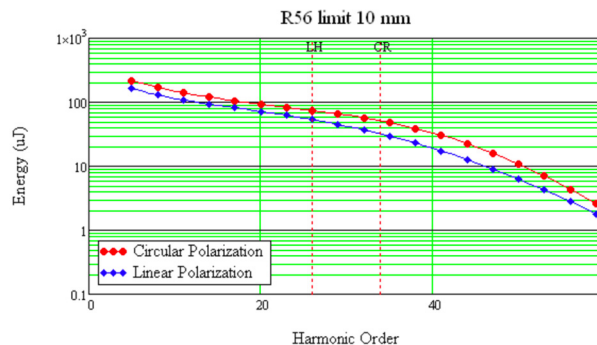


Figure 4: Output pulse energy for FEL-1 in EEHG operation mode (red-blue for circular (C) and linear (L) polarizations) . FEL-1 present configuration: six undulator modules, 2.2 m long, 5 cm of period length.

FEL-1 will operate as a conventional HHG at low harmonics and in EEHG at intermediate harmonics (h15-h30). These figures support the fact that the present FEL-1 is limited by the configuration (HHG vs. EEHG) and in EEHG mode can cover the range 100 nm to sub 10 nm wavelengths. Once the linac upgrade will be completed the beam energy will increase to 1.8 GeV and FEL-1 could in principle cover most of the present FEL-2 range.

CONCLUSIONS

A first upgrade phase of FERMI has allowed us to achieve reliable, intense and stable user operation over the whole spectral region 100-4 nm. Further upgrades are presently being considered to extend the spectral range to higher photon energies, and increase the FEL flexibility for the generation of multiple pulses also in the spectral range of FEL-2.

REFERENCES

- [1] Primož Rebernik Ribič *et al.*, “Coherent soft X-ray pulses from an echo-enabled harmonic generation free-electron laser”, *Nature Photonics*, vol. 13, pp. 555–561, 2019. doi: 10.1038/s41566-019-0427-1
- [2] E. Allaria *et al.*, “Highly coherent and stable pulses from the fermi seeded free-electron laser in the extreme ultraviolet”, *Nat. Photonics*, vol. 6, pp. 699–704, 2012. doi: 10.1038/nphoton.2012.233
- [3] E. Allaria *et al.*, “Two-stage seeded soft-X-ray free-electron laser”, *Nat. Photonics*, vol. 7, pp. 913–918, 2013. doi: 10.1038/nphoton.2013.277

- [4] I. Boscolo, V. Stagno, “The converter and the transverse optical klystron”, *Nuovo Cimento B*, vol. 58(2), pp. 267–285, 1980. doi:10.1007/BF02874012
- [5] L. H. Yu, “Generation of intense uv radiation by subharmonically seeded single-pass free-electron lasers”, *Phys. Rev. A*, vol. 44, pp. 5178–5193, 1991. doi:10.1103/PhysRevA.44.5178
- [6] L.-H. Yu, I. Ben-Zvi, “High-gain harmonic generation of soft X-rays with the “fresh bunch” technique”, *Nucl. Instrum. Methods Phys. Res. A*, vol. 393, pp. 96–99, 1997. doi:10.1016/S0168-9002(97)00435-X
- [7] E. Allaria *et al.*, “The FERMI free-electron lasers”, *J. Synchrotron Radiat.*, vol. 22, pp. 485–491, 2015. doi:10.1107/S1600577515005366
- [8] E. Allaria *et al.*, “Tunability experiments at the FERMI@Elettra free-electron laser”, *New J. Phys.*, vol. 14, p. 113009, 2012. doi:10.1088/1367-2630/14/11/113009
- [9] D. Gauthier *et al.*, “Spectrotemporal Shaping of Seeded Free-Electron Laser Pulses”, *Phys. Rev. Lett.*, vol. 115, p. 114801, 2015. doi:10.1103/PhysRevLett.115.114801
- [10] O. Yu. Gorobtsov *et al.*, “Seeded X-ray free-electron laser generating radiation with laser statistical properties”, *Nature Communications*, vol. 9, p. 4498, 2018. doi:10.1038/s41467-018-06743-8
- [11] P. Finetti *et al.*, “Pulse duration of seeded Free Electron Lasers”, *Phys. Rev. X*, vol. 7, p. 021043, 2017. doi:10.1103/PhysRevX.7.021043
- [12] L. Giannessi and C. Masciovecchio, “FERMI: Present and future challenges”, *Applied Sciences*, vol. 7, p. 640, 2017. doi:10.3390/app7060640
- [13] F. Bencivenga, L. Giannessi, C. Masciovecchio, “Perspective: Free Electron Lasers—Future Challenges”, *Synchrotron Radiation News*, vol. 30(6), pp. 17–20, 2017. doi:10.1080/08940886.2017.1386994
- [14] L. Foglia *et al.*, “Exploring the multiparameter nature of EUV-visible wave mixing at the FERMI FEL”, *Structural Dynamics*, vol. 7, p. 040901, 2019. doi:10.1063/1.5111501
- [15] N. Mirian *et al.*, in preparation.
- [16] G. Stupakov, “Using the beam-echo effect for generation of short-wavelength radiation”, *Phys. Rev. Lett.*, vol. 102, p. 74801, 2009. doi:10.1103/PhysRevLett.102.074801
- [17] D. Xiang, D. and G. Stupakov, “Echo-enabled harmonic generation free electron laser”, *Phys. Rev. Spec. Top. Accel. Beams*, vol. 12, p. 30702, 2009. doi:10.1103/PhysRevSTAB.12.030702
- [18] C. Serpico *et al.*, “Analysis and comparison between electric and magnetic power couplers for accelerators in Free Electron Lasers (FEL)”, *Nucl. Instr. Meth. A*, vol. 833, p. 8–14, 2016. doi:10.1016/j.nima.2016.06.131
- [19] C. Serpico *et al.*, “Development of an High Gradient, S-band, Accelerating Structure for the FERMI Linac”, in *Proc. LINAC’16*, East Lansing, MI, USA, Sep. 2016, pp. 136–138. doi:10.18429/JACoW-LINAC2016-MOPLR004.
- [20] N. Shafqat *et al.*, “Design study of high gradient, low impedance accelerating structures for the FERMI Free Electron Laser linac upgrade”, *Nucl. Instrum. Methods A*, vol. 867, pp. 78–87, 2017. doi:10.1016/j.nima.2017.04.018
- [21] L. Giannessi, in “Synchrotron Light Sources and Free-Electron Lasers Accelerators Physics, Instrumentation and Science Applications”, edited by E. Jaeschke, S. Khan, J. R. Schneider, and J. B. Hastings, Springer International Publishing, Switzerland, 2015.
- [22] M. Xie, “Design optimization for an X-ray free electron laser driven by slac linac”, in *Proc. Particle Accelerator Conference*, Knoxville, vol. 1, pp. 183–185, 1995. doi:10.1109/PAC.1995.504603

PolFEL - NEW FACILITY IN POLAND*

K. Szamota-Leandersson[†], R. Nietubyć, P. Czuma, P. Krawczyk, J. Krzywiński, J. Sekutowicz¹,
M. Staszczak, J. Szewiński, National Centre for Nuclear Research, Otwock-Świerk, Poland
W. Bał, J. Poznański, Institute of Biochemistry and Biophysics, PAS, Warsaw, Poland

A. Bartnik, H. Fiedorowicz, K. Janulewicz, N. Pałka

Institute of Optoelectronics, Military University of Technology, Warsaw, Poland

¹DESY, Hamburg Germany

Abstract

PolFEL will be first free electron laser in the part of eastern Europe, Poland. The source of low energy linac will be superconducting photocathode. PolFEL will operate in CW and long pulse (lp) mode. PolFEL will generate THz, IR and VIS-VUV radiation. PolFEL is going to prepare number of end-stations for user activities. The most unique end-station base on Inverse Compton Scattering phenomena will allow to perform measurements with X-ray photons with time resolution in fs range.

PolFEL DESCRIPTION

In this short document the main parameters of PolFEL are mentioned. In last three decades Polish scientists and engineers participated in and contributed to many projects related to Free Electron Laser- and High Energy Physics facilities worldwide, not having any of these facilities in the country. Therefore, group of Polish scientific institutes interested in the modern research with coherent radiation was very pleased receiving in 2018 funds for the free electron laser PolFEL project from the Smart Growth Operational Programme, Measure 4.2: Development of modern research infrastructure of the science sector.

A PolFEL consortium was established with NCBJ as project leader and eight Polish research institutes and universities as members. PolFEL will be driven by cw operating superconducting linac with SRF electron source developed in collaboration with DESY and 8 superconducting TESLA cavities housed in 4 Rossendorf type cryomodules. Moreover, accessibility of new superconducting technology enabled us to designed state-of-art linear accelerator operating both in the continuous wave (cw) mode and long pulse (lp) mode. The cw mode allows for full flexibility of electron beam time structure and hence photon beams. Time structure (max repetition rate 50 KHz) is defined by laser beam irradiating the cathode in a superconducting injector (SRF injector). The injector cryomodule for PolFEL contains one 1.3 GHz SRF 1.5-cell cavity made of niobium. Designing of this cryomodule base on the conceptual design from DESY is a part of project and cryomodule will be made at NCBJ. Cavity is housed in a titanium helium vessel in temperature range 1,8 – 2,0 K. Thermal shielding is the most crucial system, will include two lines of the helium (2 K, 5 K) and Liq-

uid Nitrogen. The PolFEL project has received already significant hardware support from the STFC Daresbury Laboratory, e.g. components of a 120 W@2K cryogenic plant, many beam optics components and RF-components. The cryogenic system design is in charge of specialist from Wroclaw University of Science and Technology. PolFEL will generate THz, IR radiation and VIS-VUV radiation in two beam lines, respectively. In the first one, with electron beam below 80 MeV, the THz/IR radiation source will be generated in permanent magnet super-radiant undulator, delivering THz radiation in 0.5–3 THz range. IR undulators will be positioned upstream THz undulators. In the second beam line with up to 180 MeV electrons, the VIS/VUV radiation will be generated in the SASE undulator delivering coherent radiation down to 55 nm in the third harmonic. Both undulators will be based on the modified Bazin design shared by the STFC Daresbury Lab and assisting the NCBJ team in the modification effort. Both undulators are going to be made in NCBJ.

PolFEL parameters are written in Table 1 and Table 2.

Table 1: PolFEL Electron Beam Parameters

	Unit	Gun	VUV /electron line	THz line
Bunch charge	pC	20-250	max 100	250
Bunch repetition rate	kHz	50	50	50
Transvers normalized 80% slice emittance	μm·rad	0.1-0.4	< 0.5	<0.75
Bunch duration at the electron line exit	ps	2-10	0.4	up to 10
Beam energy at the line exit: cw mode lp mode @ duty factor of 40%	MeV	4	90-154 up to 187	up to 65
Maximal beam current	μA	12.5	5	12.5
Beam power at dump: cw lp @ duty factor of 40%	W	-	650 374	813

* Work supported by Smart Growth Operational Programme, Measure 4.2: Development of modern research infrastructure of the science sector.

[†] Karolina.Szamota-Leandersson@ncbj.gov.pl

Table 2: PolFEL Photon Beam Parameters

	Unit	VUV (1 st Harm.)	VUV (3 rd Harm.)	THz line
Min wave length: cw lp @ DF=40%	nm	210 165	70 55	(0.5 - 6)·10 ⁵ (0.5-6 THz)
Energy per pulse, E _y : cw lp @ DF=40%	μJ	75.0 19.6	0.22 0.03	30
Radiation power: cw lp @ DF=40%	W	3.75 0.40	0.01 0.0006	1.5
Pulse duration	ps	0.35	0.35	30
ΔE _y / E _y	-	0.008	0.008	0.05

The construction of the experimental end-stations receives much attention in the project. At the moment, four end-stations are planned based on the scientific case developed during meetings with potential users. PolFel will give opportunity to adopt time parameters on user demands. Photons parameters will be monitored during run time with diagnostic systems. The experimental setup will allow for studies of physical and chemical properties of solid states, gases, and liquid samples facility is going to provide a infrastructure for studies of life samples. The facility will be equipped with optical laser system with OPA, which parameters will allow for repetition rate from single shot to max. 50 kHz. The three wavelengths 1030 nm, 515 nm and 257 nm and OPA tuneable range from 190 nm to 16 μm will be available. Users will have access to experiments equipped with dedicated Pump-Probe spectrometer in whole range of photon radiation. The end-stations are designed in cooperation with experimental groups from Institute of Biochemistry and Biophysics Polish Academy of Sciences and Military University of Technology. For The UV beamline beam leaving the SASE undulator is going to contain two spectral components - the fundamental wavelength of 255/165 nm and its third harmonic at 85/55 nm, depending on the working regime (CW/pulsed). The output photon beam diameter from source is calculated as 0.1 mm and the estimated divergence equal to 0.5 mrad. Giving estimated beam diameter in the first steering mirror chamber (~10 m) of about 5 mm. One of proposed solution for diagnostic purpose is separating the fundamental and third harmonics by a thin foil filter, however most likely of customized diffraction grating out-coupling a few percent of the incident energy is going to be used. The main part of energy (more than 90 %) will be directed in the zeroth order along the path determined by the axis. It is assumed that the grating designed for the 3rd harmonic will not distort the wavefront of the beam at the fundamental frequency. The second method even if more expensive and complicated has the advantage that the wavefronts of the sepa-

rated waves will be influenced in a very limited degree. There are no pellicle beam-splitter of nanometer thickness and flatness conserving the wavefront quality at reflection. The final diameter of the beam spot on the sample in experimental chamber will be of 20 μm. Beam spectrum will be monitored on the shot-to-shot basis even in the case of assumed reproducibility of the energetically stable emission. The measurement of the temporal shape requires very specific tools and here it is planned to develop such a method based on secondary effects of interaction, e.g. ionization. The energy level or the photon flux delivered in the beam will be monitored by GDM together with the support for controlling the beam positioning relative to the assumed optical path. GMD is going to be designed with help of FLASH /DESY advisory.

In addition to already known application of VUV like ablation or desorption, in the spectral range of the Pol-FEL most of the solid materials show very short attenuation, in extreme cases going down to significantly less than 100 nm. Combination of moderate focusing and the minimum absorption depth make density of the absorbed energy to be higher than the high energy density limit (HED), recently redefined as 104 J/cm³. This would open an unexpected field of interest and very attractive research branch. The beamlines in the terahertz photon energies region starting from 0.5 THz allows for examination of matter properties not observed so far. End-stations will be equipped to perform experiments in the magnetic field of low temperature samples, (absorption and emission spectroscopy in wide sample temperature range (LHe-HT), gases, liquids, molecules, solids). Experience from specialist of the MUT in the THz imaging technology is going to be important factor to design THz imaging end-station (2D or 3D) in PolFEL. Separated experimental station will be devoted to Life Science experiments. This station will operate in the whole radiation range provided by PolFEL.

Specially designed system will conduct IR, UV and THz radiation to entrance of Life Science beamline. In addition the pump-probe experiment will be available. At present the main experimental method offered to the user will be based on the commercially provided stopped-flow apparatus (Fig.1).

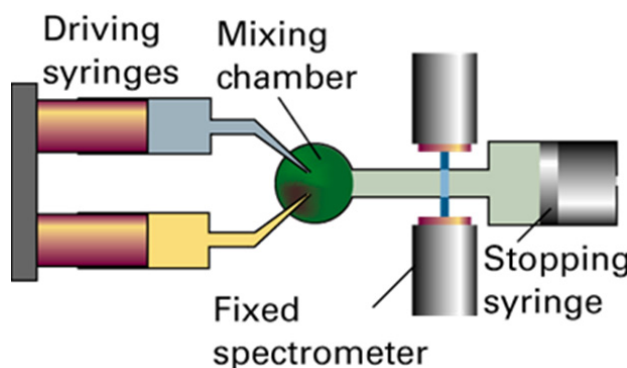


Figure 1: Geometry of the stopped flow apparatus.

STATUS OF THE SOFT X-RAY LASER (SXL) PROJECT AT THE MAX IV LABORATORY*

F. Curbis[†], J. Andersson, F. Lindau, L. Isaksson, M. Kotur, E. Mansten, M. Pop, W. Qin,
H. Tarawneh, P. Tavares, S. Thorin, S. Werin[‡], MAX IV laboratory, Lund, Sweden
A. Nilsson, M. Larsson, P. Salen, S. Bonetti, Stockholm University, Stockholm, Sweden
J. A. Sellberg, KTH Royal Institute of Technology, Stockholm, Sweden
V. Goryashko, Uppsala University, Uppsala, Sweden
P. Johnsson, Lund University, Lund, Sweden

Abstract

A Soft X-ray Laser project (the SXL) aiming to produce FEL radiation in the range of 1 to 5 nm is currently in a conceptual design phase and a report on the design is expected to be delivered by March 2021. The FEL will be driven by the existing 3 GeV linac at MAX IV laboratory, which also serves as injector for the two storage rings. The science case has been pushed by a large group of mainly Swedish users and consists of experiments ranging from AMO physics to condensed matter, chemistry and imaging in life science. In this contribution, we will present the current conceptual design of the accelerator and the FEL operation modes together with a general overview of the beamline and experimental station. In particular design options for the FEL will be discussed in conjunction with the features of the electron beam from the MAX IV linac and the connection with the proposed experiments.

INTRODUCTION

The linear accelerator, which serves as injector for the two storage rings and the Short Pulse Facility (SPF) at the MAX IV laboratory in Sweden, can also drive a soft X-ray FEL with minor modifications. The SXL project has been proposed by Swedish users interested in exploiting FEL radiation in the range between 1 and 5 nm.

The linac will for the SXL project run at its maximum energy of 3 GeV with 100 Hz repetition rate and an upgraded photo cathode gun [1].

Several Swedish universities are engaged in this project: Stockholm university, Royal Institute of technology (KTH), Uppsala University and Lund University.

The project timeline sees now a three years period to work on a Conceptual Design Report (CDR) with final delivery in March 2021. The CDR work is divided in six work packages; Science Case, Accelerator, FEL, Insertion Devices, Beamline and Experimental Station.

GENERAL LAYOUT

A schematic layout of the SXL is shown in Fig. 1. The 3 GeV linac is followed by the undulator modules (currently 3 m long, with 4.0 cm period). A long drift space, where

photon diagnostics will be placed and the power density allowed to drop until reaching the first mirror, will be followed by the monochromator. The experimental station will also include a laser for pump-probe experiments. Different options for the timing/synchronization system are now under discussion to make sure the best stability can be achieved with very short pulses. The data handling and collection will prove a challenge and is envisaged to be integrated into the existing capabilities and future capacity upgrades of MAX IV laboratory.

THE SCIENCE CASE

Following a successful workshop in March 2016 where more than 100 Swedish (mostly but not only) users gathered in Stockholm to contribute to the science case [2] for the SXL, a set of representative experiments has been selected in the following categories: AMO, Condensed matter, chemistry and imaging in life science. The AMO experiments will explore processes from charge migration to charge transfer thanks to ultrashort pulses and the possibility to have two pulses with different colors in order to implement pump-probe schemes. For the chemistry applications the main focus is in understanding the dynamics of heterogeneous catalysis and probing transition states in surface reactions, and for these variable polarization is desired. In condensed matter the goal is to create new phases in quantum materials (like strontium titanate) with THz radiation and probe the emergent order with the SXL beam. Also experiments on coherence control in the attosecond frontier are foreseen, and they will require sub-fs pulses, besides the full control of the FEL polarization. Pumping with an HHG (High Harmonic Generation) source will also be beneficial. In Life Science the combination of THz or other pump lasers with the FEL radiation will allow to probe conformational changes in solution for the scattering experiments. Relatively long (50 fs) pulses with two colors will be required together with a split-and-delay line for dynamics between 100 fs and 10 ms.

LINAC

The SXL will use the 3 GeV S-band linac currently serving the MAX IV 1.5 and 3 GeV storage rings and Short Pulse Facility (SPF). As of today a photo cathode gun and two bunch compressors provide 100 fs long pulses for the

* Work supported by KAW foundation.

[†] francesca.curbis@maxiv.lu.se

[‡] sverker.werin@maxiv.lu.se

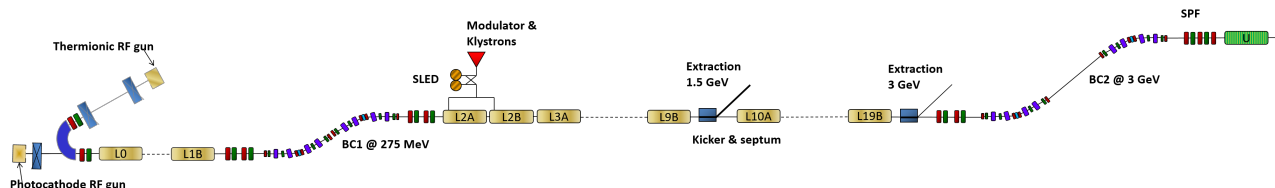


Figure 1: Schematic layout of the SXL at MAX IV (not-to-scale).

SPF with a normalised emittance below $1 \mu\text{m}$. The bunch compressors are two achromats placed at 250 and 3 GeV respectively. Together they can in simulations compress the electron pulse to a few fs without the double horn features of chicane compressors. The compressors are also able to passively linearize the longitudinal phase space, removing the need for a higher harmonic cavity. The compressors work with negative R56 and the energy chirp has a higher energy at the head of the pulse. While the final compression is at full energy a remaining energy chirp will be present in the beam. As the chirp is positive it provides some complexity to remove, as standard de-compressors will increase the chirp. An ongoing study is exploring different possibilities, including; reversing the R56 of the bunch compressors by additional optics, over compression and adding a traditional chicane compressors combined with a harmonic cavity and de-chirper.

THE SXL BASELINE

Given the circumstances of being based on an existing and running linac, at present two main phases are foreseen for the SXL beamline, based on the linac operating with the current energy chirp or with the chirp removed.

Initially a baseline design has been defined using three linac modes. In phase 1 two modes using the chirped beam in a long pulse and a short pulse respectively, and in Phase 2 an un-chirped beam (Tab. 1). These modes were checked for consistency in time-independent SASE simulations and the followed up by time-dependent SASE simulations based on the defined parameter space. This information was then fed to the beamline and experimental stations design.

The simulations are now moving into full Start-to-end simulations of the system and analysis of advanced concepts for the SXL. Additional FEL modes are also added into the portfolio, such as a mode for higher flux, with 200-300 pC bunch.

Table 1: Basic Operation Modes of the MAX IV linac for the SXL

Phase	1	1	2
Linac mode	A	B	
Charge	100 pC	10 pC	100 pC
Bunch length (rms)	16 fs	2 fs	16 fs
Emittance (norm)	$0.5 \mu\text{m}$	$0.25 \mu\text{m}$	$0.5 \mu\text{m}$
Energy chirp	0.5 MeV/m	1 MeV/m	no chirp

INSERTION DEVICES

The insertion devices for the SXL project will are being designed to allow compactness, flexibility and polarisation control. A concept for an APPLE-X type undulator in a very compact frame has been elaborated [3]. The K-value adjustment is done by radial magnetic motion. The tuning range will cover 250-1000 eV ($K=1.51-3.9$). A drawing of the undulator is shown in Fig. 2.

Initially 3 m long undulator sections with 0.75 m intrasections are envisaged, but studies of advanced concepts, such as HB-SASE, may point towards a shortening the undulator sections.

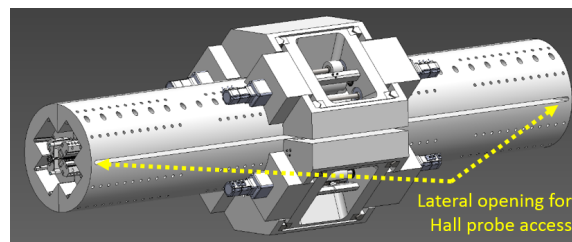


Figure 2: The compact APPLE-X type undulator for the SXL project.

FEL

The FEL operation modes for SXL should accommodate different requirements from the science case in terms of spectral brightness, synchronization, coherence and power enhancement, very short pulses, two-color and two-pulses.

The current strategy is based on initially operating the SXL in SASE mode, which will cover a large set of requirements in the Science Case, and using the positively chirped electron pulses. This is complemented by linac modes with ultra strong compression, reaching the "few fs pulse" length range. To enhance the photon pulse flux tapering is anticipated. To reduce the bandwidth and increase the wavelength stability, and thus increase the throughput in the monochromator systems, HB-SASE type techniques [4] are being studied if possible to include already before phase 2. This concept incorporates short undulators and multiple chicanes which also open for as-pulse techniques [5]. While seeding most likely will require a non-chirped pulse it is investigated but not defined for the initial phase of the SXL. Alternatively seeding will, in addition to coherence enhancement, also provide improved timing and synchronization, which might be of high user interest. The system will thus be prepared

for external seeding, both ECHO and self-seeding. While an ECHO station [6] preceding the undulator chain also provides hardware for as-pulse generation, the self-seeding chicane is also a tool for two-pulse two-color operation.

How this is supposed to be implemented is shown in Fig. 3.



Figure 3: Implementing various FEL modes in the SXL.

FEL Simulations

The baseline design has been simulated first in time-independent mode using Genesis 1.3 [7] using average parameters from the current linac followed by time dependent simulations allowing us to compile a table with baseline parameters for the FEL performance (Tab. 2) which also guided the second phase with start-to-end simulations. First time-dependent start-to-end simulations have been carried out (Fig. 4) with an electron beam that has been tracked in Astra [8] (for the pre-injector part) and Elegant [9] for the linac and bunch compressors [10]. In the following work focus will be put in enhanced modeling of the pre-injector, tolerances and stability and advanced concepts [11].

Table 2: Baseline FEL Performance in SASE Mode (time-dependent, parameter based, no taper)

Linac mode (Tab. 1)	1A	1B
Power (1/5 nm)	9/22 GW	10/18 GW
Saturation length (1/5 nm)	41/22 m	34/19 m
Pulse energy (1/5 nm)	0.18/0.49 mJ	0.03/0.04 mJ

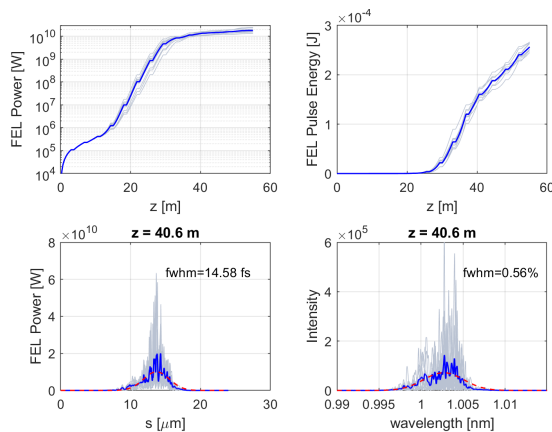


Figure 4: Start-to-end simulation in SASE mode at 1 nm (100 pC, no tapering, multiple shots & average).

BEAMLINES AND EXPERIMENTAL STATIONS

Two beamlines are foreseen for the first phase of the SXL, a pink beamline and a monochromator beamline. Both beamlines will target the full photon energy range, 250-1000 eV, and share the same undulator line as radiation source. These two beamlines will allow most of the experiments put forward in the user case to be realized. The beamlines will define a substantial part of the length budget of the facility. By reducing the incidence angle on the first element to 0.5 deg this element can be placed closer than 40 m from the source also when operating in high-flux mode using tapering. While the monochromator beamline should operate at resolutions of 5000, the pink beamline will provide a resolution of 100.

The experimental stations should be flexible, allowing for sample changing systems and environment systems, which can also directly be used in complementary studies at the storage ring stations on the MAX IV 3 GeV and 1.5 GeV rings. Sample systems should be transportable within the building between the different photon sources. Currently two instruments are envisaged: one X-ray spectroscopy instrument for surface science, and one low density matter end station with a CCD and spectrometer.

The laser system is assumed to be a commercial solution and will be located near the end-station, it will be used for HHG and for low-harmonics/visible radiation.

Different options are under investigation for the synchronization, in particular the stability of the main drive line for the linac RF will be analysed if it is sufficient to reach sub 10 fs arrival jitter. Another option is exchanging the existing RF synchronisation system for an optical system, currently used in many other FEL facilities.

Initially optical synchronization of about 10 fs is required, while for the second phase 5 fs or better, while to reach 1 fs post-experiment methods will be needed.

CONCLUSION

In this paper we presented the current status of the SXL project, which is in conceptual design phase. The performance of the linac, the undulator design and the beamline/experimental station concepts are described as well as the foreseen FEL operation modes. A glimpse of the science cases has been also presented. The work for the conceptual design report is supposed to deliver a document by March 2021.

ACKNOWLEDGEMENTS

The SXL Design study is partly financed by the Knut and Alice Wallenberg foundation (<https://kaw.wallenberg.org/>). The main simulations are supported by the Center for scientific and technical computing at Lund University (LUNARC: <http://www.lunarc.lu.se/>).

REFERENCES

- [1] J. Andersson, *et al.*, "The Pre-Injector and Photocathode Gun Design for the MAX IV SXL", in *Proc. IPAC2019*, Melbourne, Australia (2019). doi:10.18429/JACoW-IPAC2019-TUPTS061
- [2] "Science case for the SXL", http://frielektronlaser.se/onewebmedia/SXL_science_case_161102.pdf
- [3] H. Tarawneh, P. N'gotta, L.K. Roslund, A. Thiel, K. Åhnberg, "Compact APPLE X for Future SXL FEL and 3 GeV Ring at MAX IV Laboratory", in *Proc. IPAC2019*, Melbourne, Australia (2019), doi:10.18429/JACoW-IPAC2019-TUPRB024
- [4] N.R. Thompson, B.W.J. McNeil, "Mode locking in a free-electron laser amplifier", *PRL* 100, 203901 (2008). doi:10.1103/PhysRevLett.100.203901
- [5] D.J. Dunning, B.W.J. McNeil, N.R. Thompson, "Few-cycle pulse generation in an X-ray free-electron laser", *PRL* 110, 104801 (2013). doi:10.1103/PhysRevLett.110.104801
- [6] M. Pop, F. Curbis, S. Werin, "Considerations on implementing EEHG with a linear chirp", FEL2019, Hamburg, Germany (2019), paper TUP090, this conference.
- [7] S. Reiche, "GENESIS 1.3: a fully 3D time-dependent FEL simulation code", *Nucl. Instr. Meth. Phys. Res. Sect. A*, vol. 429, no. 1–3, pp. 243–248, 1999. doi:10.1016/S0168-9002(99)00114-X
- [8] K. Flöttmann, "ASTRA: A space charge tracking algorithm", Manual, Version, vol. 3, p. 2014, 2011.
- [9] M. Borland, "Elegant: A flexible SDDS-compliant code for accelerator simulation", *ICAP 2000*, report number: LS-287
- [10] W. Qin, *et al.* "Start-to-end simulations for the soft X-ray FEL at the MAX IV laboratory", *FEL2019*, Hamburg, Germany (2019), paper TUP066, this conference.
- [11] W. Qin, F. Curbis, M. Pop and S. Werin, *Advanced concepts for the design for the soft X-ray FEL at MAX IV*, FEL2019, Hamburg, Germany (2019), paper TUP067, this conference.

STATUS OF Athos, THE SOFT X-RAY FEL LINE OF SwissFEL

R. Ganter[†], G. Aeppli, J. Alex, A. Al Haddad, C. Arrell, V. Arsov, C. Bostedt, S. Bettoni, H.H. Braun, M. Calvi, T. Celcer, P. Craievich, R. Follath, F. Frei, N. Gaiffi, Z. Geng, C. Gough, M. Huppert, R. Ischebeck, H. Jöhri, P. Juranic, B. Keil, F. Loehl, F. Marcellini, G. Marinkovic, G. L. Orlandi, C. Ozkan Loch, M. Paraliev, L. Patthey, M. Pedrozzi, C. Pradervand, E. Prat, S. Reiche, T. Schietinger, T. Schmidt, K. Schnorr, C. Svetina, A. Trisorio, C. Vicario, D. Voulot, U. Wagner, A. Zandonella, PSI, Villigen, Switzerland

Abstract

The Athos line will cover the photon energy range from 250 to 1900 eV and will operate in parallel to the hard X-ray line Aramis of SwissFEL. The Athos FEL line starts with a fast kicker magnet followed by a dogleg transfer line, a small linac and 16 APPLE undulators. From there the photon beam passes through the photonics front end and the beamline optics before reaching the experimental stations Maloja and Furka. This contribution summarizes the two-bunch operation commissioning (two bunches in the same RF macropulse), which started in 2018, and the characterization of key components like the APPLE X undulator UE38. The Athos installation inside the tunnel is alternating with Aramis FEL user operation, and the first lasing is planned for winter 2019 / 2020.

Athos FEL LAYOUT

Athos [1] is the soft X-ray FEL line of SwissFEL (Fig. 1). Athos is currently under assembly and will deliver first FEL beam to the Maloja experimental station in 2020. This second branch of SwissFEL (Aramis being the hard X-ray FEL) starts at meter 270 (distance to the photocathode) with a resonant kicker [2,3]. This fast kicker separates the two bunches: one going to Aramis and the second one going to the Athos FEL line. The electron beamline portion between the resonant kicker ($z=265$ m) and the beam stopper ($z=383$ m) just upstream the 1st undulator is already installed and currently under beam commissioning. The undulator line consists of 16 APPLE X undulator [4] segments of 2 m length (Fig. 2). The inter-undulator section will have the usual quadrupole / BPM combination and also a small magnetic chicane made of permanent magnets. This chicane can be operated as an intra-undulator phase shifter or used to delay (5 fs max.) or shift transversally the bunch (250 μ m max.). This chicane is the essential tool to provide a large variety of operation schemes [5]. In addition, a delay line chicane (500 fs max. delay) with four

electro magnets splits the FEL line in two halves (Fig. 2). Each half can be tuned to a different K value to produce two different colors. The main diagnostic of the Athos FEL line will be an X band RF Transverse Deflecting Structure (Polarix –TDS [6, 7]) positioned downstream the last undulator to allow on line monitoring of the lasing portion of the electron bunch. The variable polarization of the deflecting force will allow measurements of the bunch length, energy and of the transverse slice emittances (vertical and horizontal). Downstream the beam dump, starts the X-ray front end which will include a gas monitor to measure the FEL pulse energy and position. The mirrors to deflect the FEL beam to the different end stations are located in a separate room outside the tunnel [8]. Athos will have three experimental stations, where two (Maloja and Furka) are already under construction. Maloja will start commissioning tests in 2020 and will focus on very short FEL pulses (few fs and below). After first SASE lasing, the next goal will be to operate Athos in the optical klystron regime using the inter-undulator chicane. This scheme will speed up the SASE process so that lasing with only half of the undulator line becomes possible. This will then allow the test of the two color mode of operation.

TWO BUNCH OPERATION

Two distinct lasers are illuminating the photocathode to produce two electron bunches separated by 28 ns. The repetition rate and also the machine protection system logic can be set independently for bunch 1 and bunch 2. This independence of both timing event systems is important for parallel operation of Aramis and Athos FEL lines. Both bunches are accelerated simultaneously up to 3.15 GeV. The radio-frequency macropulses of the injector S band and X band modulator have an extra step of about 28 ns length in order to control the phase and amplitude of the bunch 2 independently of bunch 1.

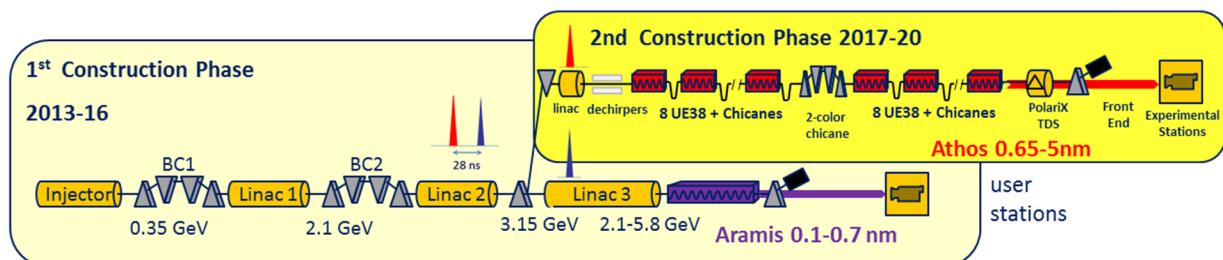


Figure 1: Layout of SwissFEL showing the extraction of second bunch at 3.15 GeV which is then transported along the Athos branch of SwissFEL.

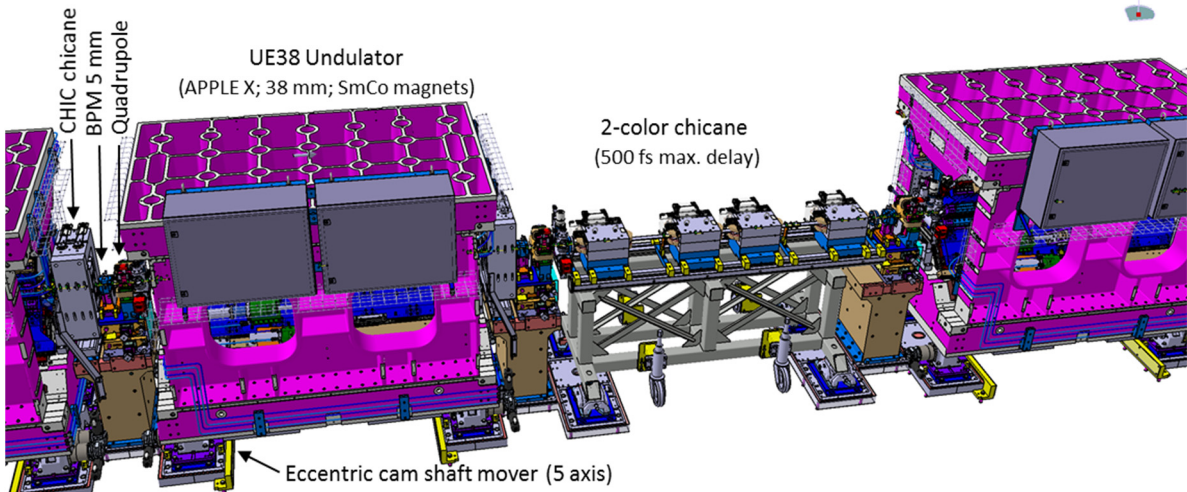


Figure 2: Layout of the Athos FEL line with the inter-undulator section (CHIC chicane, BPM, quadrupole), the APPLE X undulator and the two-color chicane.

This is important for fine tuning the compression of bunch 2. The C band Linac 1 and 2 are just delayed by 14 ns in order to have same acceleration for both bunches. The demonstration of two bunch transport from the RF gun to the extraction point has been achieved in 2018. The different feedback systems (orbit and energy) prepared for bunch 1 are also correcting bunch 2 as illustrated in Fig. 3.

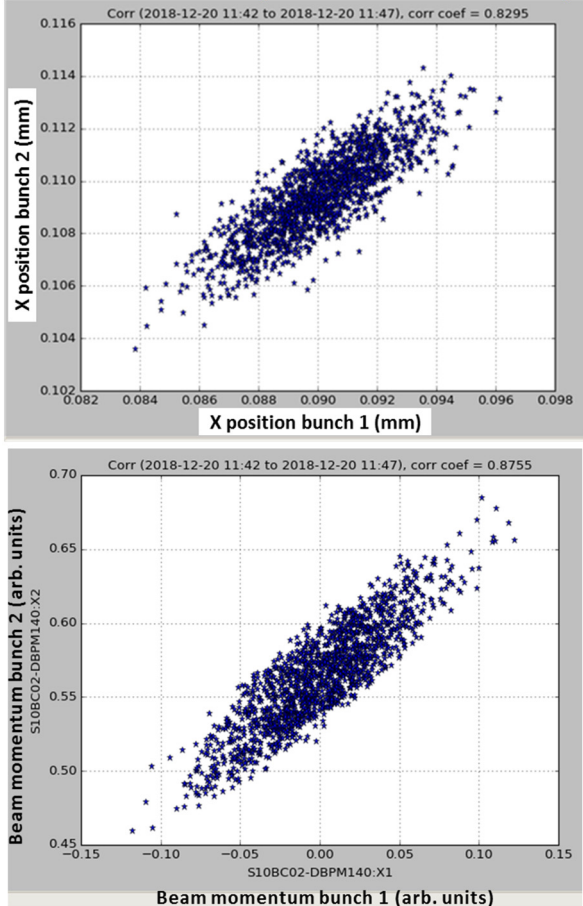


Figure 3: Correlation plot measurements of the BPM position of bunch 2 against bunch 1 (Top) and beam momentum of bunch 2 against bunch 1.

Transmission of the two bunches through the Aramis FEL line resulted in the lasing of both bunches simultaneously. This confirms that the quality of the second bunch was good enough for hard X-ray lasing. More important, the FEL pointing stability, 100 m downstream last undulator, was not affected by the fast kicker [3]. Keeping the beam emittance of second bunch when going through the dogleg section is however more difficult. This so called “dogleg” section requires very precise optic tuning in order to avoid deterioration of the emittance. An emittance of about 900 nm in both planes has been obtained (Fig. 4) during preliminary measurements. Magnet optic tuning should further reduce the emittance by about a factor two in order to support lasing of the second bunch in the Athos FEL line.

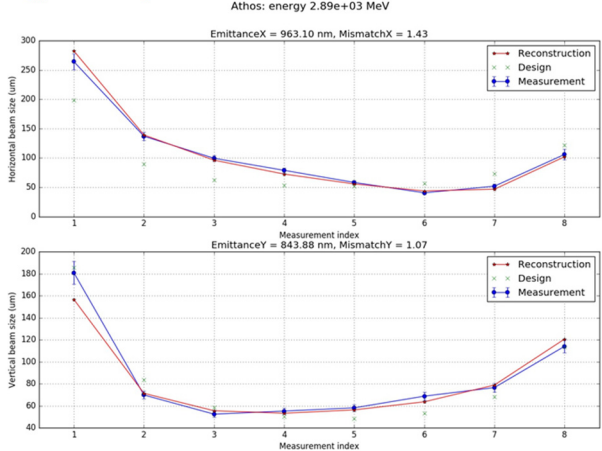


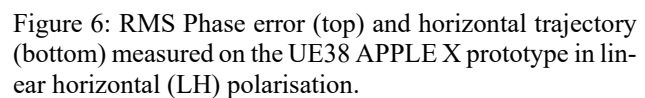
Figure 4: Projected emittance of second bunch measured downstream the dogleg at Athos undulator entrance (2.89 GeV, 200 pC).

APPLE X UNDULATOR

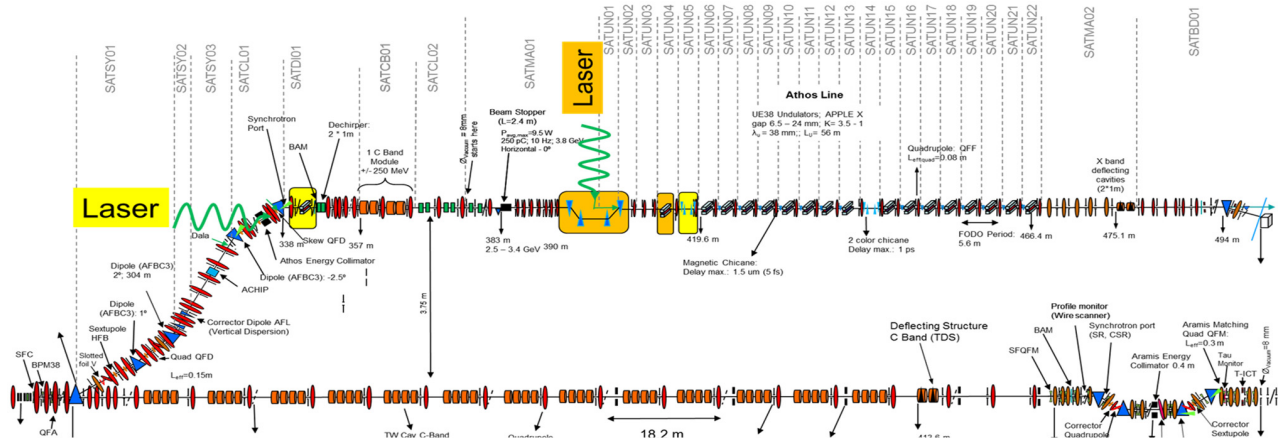
The 16 undulators segments of the Athos FEL lines are APPLE type undulators where the polarisation can be varied from linear to circular. One special characteristic of these APPLE “X” undulators is that the four magnets arrays can move radially and longitudinally (Fig. 5) [4].



Thorough tests of the prototype undulator mechanics, of the hall probe measurements and shimming procedures have been recently completed. A rms phase error of 1.5° and an orbit envelope straightness within $1\mu\text{m}$ was finally obtained (Figure 6). The mechanical position reproducibility (mechanical hysteresis) produces less than 10^{-4} dK/K variation.



Recently the construction of a seeding / slicing option for the Athos FEL line was initiated. It consists in two external lasers, two modulators and two compression chicanes as depicted in Figure 7. The first stage of this seeding scheme (yellow highlighted) will allow the generation of ultra-short sub fs pulses synchronized to the external seeding laser. The second stage (orange highlighted) will offer the possibility to apply echo enable harmonic generation (EEHG) to produce high brightness beam up to 500 eV.

**THP085**

REFERENCES

- [1] R. Abela *et al.*, Athos Conceptual Design Report, Report No. PSI Bericht Nr. 17-02, ISSN 1019-0643, 2017.
- [2] M. Paraliiev and C. H. Gough, “Resonant Kicker System With Sub-part-per-million Amplitude Stability”, in *Proc. 8th Int. Particle Accelerator Conf. (IPAC'17)*, Copenhagen, Denmark, May 2017, pp. 3174-3177.
doi:10.18429/JACoW-IPAC2017-WEPIK098
- [3] M. Paraliiev *et al.*, “Commissioning and Stability Studies of the SwissFEL Bunch-Separation System”, presented at the 39th Int. Free Electron Laser Conf. (FEL'19), Hamburg, Germany, Aug. 2019, paper WEP038.
- [4] T. Schmidt and M. Calvi, *Synchrotron Radiation News*, vol. 31, pp. 35-40, (2018).
doi.org/10.1080/08940886.2018.1460174
- [5] R. Abela *et al.*, *Journal of Synchrotron Radiation*, vol. 26, part 4, pp. 1073-1084, (2019).
- [6] P. Craievich *et al.*, “The PolariX-TDS Project: Bead-Pull Measurements and High-Power Test on the Prototype”, presented at the 39th Int. Free Electron Laser Conf. (FEL'19), Hamburg, Germany, Aug. 2019, paper WEP036.
- [7] P. Craievich *et al.*, “Status of the PolariX-TDS Project”, in *Proc. 9th Int. Particle Accelerator Conf. (IPAC'18)*, Vancouver, Canada, Apr.-May 2018, pp. 3808-3811.
doi:10.18429/JACoW-IPAC2018-THPAL068
- [8] R. Follath, U. Flechsig, L. Patthey, and U. H. Wagner, “The Athos Soft X-Ray Beamlines at SwissFEL”, presented at the 39th Int. Free Electron Laser Conf. (FEL'19), Hamburg, Germany, Aug. 2019, paper WEP095.

OPERATION MODES OF THE SwissFEL SOFT X-RAY BEAMLINE ATHOS

S. Reiche*, E. Ferrari, E. Prat, T. Schietinger, Paul Scherrer Institut, Villigen PSI, Switzerland

Abstract

The SwissFEL linac drives the two FEL beamlines Aramis and Athos, a hard and soft X-ray FEL, respectively. The layout of Athos extends from a simple SASE FEL beamline with the addition of delaying chicanes, external seeding and beam manipulation with wakefield sources (dechirper). It also reserves space for a possible upgrade to self-seeding. This presentation gives an overview on the detailed layout enabling the unique operation modes of the Athos facility.

INTRODUCTION

Since the first demonstration of Free-electron Lasers (FEL) [1], based on SASE [2] – the amplification of the spontaneous undulator radiation – several user facilities became operational worldwide [3–7] to extend the wavelength down to the hard X-rays. While there has been significant progress to overcome the limited longitudinal coherence of the SASE pulse or to control the pulse length and peak power, only FERMI [8] can be considered a user facility, which deviates significantly from basic SASE operation by providing a fully seeded signal with an external seed laser.

The soft X-ray beamline Athos of SwissFEL [9], which is currently realized as a second step after the commissioning of the hard X-ray beamline Aramis, features a layout optimized away from basic SASE operation at the cost of shorter undulator modules, more focusing quadrupoles and delaying chicanes about 1000 times stronger than phase shifters. It has also sufficient space to host additional hardware such as external seeding.

So far simulations have shown better performances than SASE in terms of saturation length or brilliance but also a more direct control on the FEL output pulse characteristics. This leads to a catalog of various operation modes, depending on the specific needs of user experiments. In the following we give a very brief description of the capabilities of the Athos soft X-ray FEL beamline.

DESIGN AND LAYOUT CONSIDERATIONS

The aim to operate the soft X-ray beamline Athos at SwissFEL independently of the hard X-ray beamline Aramis, whose wavelength is mostly tuned by the electron beam energy between 2.1 GeV and 5.8 GeV, resulted in an optimum solution to extract a second bunch at the intermediate energy of 3 GeV to drive Athos. Up to that point the machine is fixed in its energy profile and only the succeeding linac changes the beam energy for Aramis. The two FEL beamlines share the same infrastructure, they are installed parallel to each

other with a shift of 50 m to accommodate the layout of the end stations, see Fig. 1. Also the experimental stations are in the same building. The Athos undulator modules are 2 m long and interlined with dispersive chicanes, thereby offering new modes of operation, as explained in more detail in the next section. A re-optimization of the undulator length resulted in a reduction from 4 m to 2 m [10]. This change did not compromise the baseline SASE operation of Athos, but it allowed for a reduction of the total undulator length since the optical klystron (OK) effect [11] reduces the saturation length. Currently there are 16 modules of 2 m each in the baseline layout with a chicane of 2 m length and a delay of 500 fs in the middle, splitting the undulator beamline in two halves for two-color operation based on tilted beams [12].

An additional grant now allows financing the interaction of the electron beam with a laser. This will be realized in two stages. The first is an energy modulation and conversion into a current modulation (ESASE) [13] by means of a chicane identical to that of the two-color operation. The second phase adds another modulator and a larger chicane for an Echo-Enabled Harmonic Generation (EEHG) [14] set-up to provide seeded pulses to the users at least for the low photon energy range of Athos. The required infrastructure is placed directly in front of the main undulator with the exception of the first modulator, which is located all the way upstream at the end of the out-coupling switchyard to eliminate the need for an additional chicane. The modulator is resonant in the wavelength range between 250 to 1500 nm.

Self-seeding [15] was considered a possible upgrade option for Athos but the decision for shorter undulator modules makes a simple implementation difficult, since the filtering of the FEL signal by a monochromator does not fit into the 2.8 m periodicity of the Athos lattice, much shorter than the implementation at LCLS [16]. Also, self-seeding requires a rather uneven split of the 16 undulator modules for best performance, which is not compatible with two-color operation. Therefore, self-seeding is no longer part of the baseline design. However, the large chicane in the first stage of EEHG is upgradable to include a spectrometer, and the available space before can host up to 5 undulator modules, providing the SASE signal for self-seeding.

Figure 1 shows the final layout with a total length of about 80 m for the FEL beamline, split into 50 m for the main undulator line, 15 m for the EEHG chicanes and modulator and another 15 m for the first stage in a possible self-seeding upgrade. In addition to the standard SASE operation, this arrangement allows control of the bandwidth via either external seeding, self-seeding or HB-SASE [17], as well as the possibility to achieve extremely short pulses. A summary of the Athos parameters are given in Table 1.

* sven.reiche@psi.ch

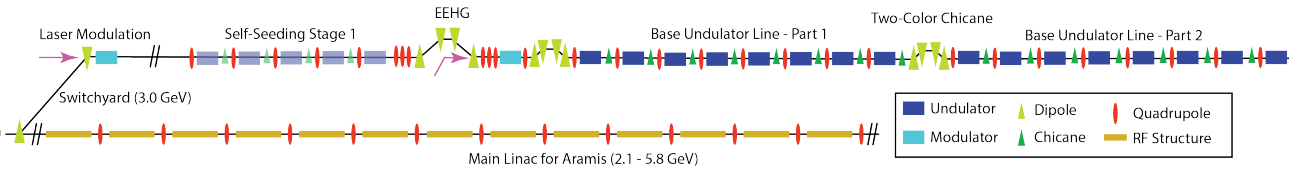


Figure 1: Layout of the Athos beamline.

Table 1: Athos Design Parameters

Parameter	Value	Unit
Photon Energy Range	250–1900	eV
Beam Energy	2.9–3.4	GeV
Current	2–6	kA
Charge	10–200	pC
Emittance	100–430	nm
Energy Spread	500	keV
Undulator K-Value	1.1–3.4	
Undulator Period	38	mm
Undulator Module Length	2	m
Number of Modules	16	

OPERATION MODES

The majority of the operation modes for Athos are based on SASE amplification, using the 16 undulator modules interlined with delaying chicanes. To achieve the maximum pulse energy, we plan to operate at the maximum possible K value giving the required resonance at a beam energy of 3.4 GeV. To cover the full tunability range of the beamline, see Table 1, we will have to lower the K value from its maximum above 400 eV final emission. If the optical klystron scheme is not utilized the total length of the undulator is sufficient to reach saturation at 1900 eV photon energy with a K value of 1.1 and the nominal electron beam parameters. This leaves us some safety margin.

Given the limited scope of this conference proceedings, not all modes can be presented in detail. For a summary, see Table 2 where we list the expected performance of the most prominent modes at the reference wavelength of 1 nm.

Chic Modes

Dispersive chicanes of 20 cm length are installed between the undulators. They can act both as phase shifters and/or an electron beam line up to 5 femtoseconds. The longitudinal position of the magnetic arrays of the undulators can also be adapted to compensate for small phasing errors between successive modules. This is particularly important since for large delays the chicanes do not need to have a sub-wavelength tuning precision. The chicanes are also more robust against fluctuations as they are based on permanent magnets. Unavoidable fluctuations in the beam energies are taken into account in the simulations.

A straight-forward application is the distributed optical klystron (OK) [11], where the growth in the micro-bunching is enhanced by the longitudinal dispersion of the chicanes.

This is particularly effective in the linear amplification regime. The benefit is a significant reduction in the saturation length of about 30%. The OK effect can also be used to measure the slice energy spread of the electron beam with high precision [18].

The chicanes can also act as small delay lines, retarding the electrons with respect to the radiation field. If the imposed delay is larger than the slippage in one module, the spectro-temporal profile of the output radiation will exhibit mode-coupling. In the case of the Athos undulators, the maximum slippage occurs for emission at the lowest photon energies and is on the order of 200 nm per module, while the maximum delay from the chicanes is 1.5 μ m. Another possible approach is to distribute different delays over the entire undulator to increase the slippage. This suppresses the appearance of the modal structure, while at the same time increasing the longitudinal coherence, in the so-called “high-brightness SASE” scheme [17]. In this configuration it is in principle possible to achieve bandwidths comparable to self-seeding, with the only drawback that the electron beam energy jitter causes a jitter in the central wavelength of the FEL radiation. In the original proposal for high-brightness SASE, the delays were supposed to be non-dispersive. Yet, this is very difficult to achieve in a compact design. Therefore, Athos features a compromise between the high-brightness SASE operation and the optical klystron effects, which on the one hand reduces the total saturation length, but on the other hand limits the overall achievable delay before overbunching occurs. We refer to it as the compact high-brightness mode [19]. Its performance is better than standard SASE, as the saturation length is reduced, the power levels are similar to SASE and the final radiation bandwidth is reduced by a factor 7 to 10 depending on the wavelength.

The chicanes can also be used to implement the fresh slice technique [20], in which the radiation is superimposed with different parts of the electron beam that were not involved in the FEL process in previous undulator modules. In this mode, the radiation growth can be superradiant [21] and the FEL amplification can overcome the SASE saturation, while the pulse duration is reduced. Preventing the beam from lasing before it overlaps with the radiation field is achieved by tilt generation [22]. Transversally misaligned slices undergo betatron oscillation disrupting the overlap between electron beam and radiation field, effectively preventing lasing of all slices except the aligned one. The final requirement for achieving superradiant growth is the realignment of the fresh slice. To this end the initial and final magnets of the chicanes are independently tunable, giving control of the transverse

Table 2: Expected Performances for the Athos Operation Modes at 1 nm

Mode	Pulse Energy	Pulse Duration (r.m.s)	Bandwidth (r.m.s)	Comment
SASE	>1 mJ	30 fs	0.1–0.4 %	
HB-SASE	>1 mJ	30 fs	0.01–0.06 %	
High-power short-pulse	~ 300 μ J	~ 250 as	1% FWHM	20 modules assumed
Large-bandwidth	~ 100 μ J	30 fs	>10% FW	
Slicing	1 μ J per pulse	< 1 fs per pulse	0.1–0.4%	Number of pulses defined by laser pulse length
Self-seeding	~1 mJ	30 fs	< 10 ⁻⁴	

offset of the electron beam. The corrector coils installed on the quadrupoles, also located between each undulator modules, allow for further angular correction. The transverse tilt can be generated either by leaking dispersion from the upstream electron beam transport line or the transverse wake of the dechirpers, which are placed in front of the undulator with the primary reason to remove the residual energy chirp needed for compression. The dechirpers are not indispensable for this mode as each undulator can be retuned for the corrected resonance condition.

The delaying chicanes allow Athos to provide either FEL pulses close to the TW level in the high-power short-pulse mode or with improved temporal coherence in the compact high-brightness configuration. We refer to these modes as “CHIC”, which stands for “Compact, High power and Improved Coherence” [10]. They can be also used in combination with laser-manipulated electron beams as discussed below.

Transverse-Gradient Undulator Modes

Athos also introduces a new type of undulator called APPLE-X [23] and derived from the APPLE-II/III layout. Here the 4-quarter arrays of permanent magnets can be moved longitudinally and radially. This avoids the problem of DELTA undulators reducing the effective K value of the undulator by guiding the magnetic field longitudinally and thus reducing the magnetic flux transversely. Since all four motions are controlled independently, two adjacent arrays can be moved out further resulting in a transverse gradient of the undulator field. This feature enables two operation modes. First, a transverse gradient together with a tilted beam, injected into the undulator beamline without external focusing, yields a spatially frequency-chirped pulse [24]. In comparison to alternative methods, such as over-compression, the direction and the amount of chirp can be easily controlled and FEL pulses with full-width spectra up to 20% are achievable. Second, a transverse gradient, together with a rotation of the undulator module around its yaw axis, converts effectively the transverse gradient into a longitudinal intra-module taper. This is needed when a very strong taper is required and the module-wise taper is not sufficiently smooth to maintain the FEL resonance condition within a single undulator module [25].

External Laser Manipulation Modes

With additional funding available, a manipulation of the electron beam by means of a laser field is currently under consideration. Starting with a modulator and a chicane, operation modes such as ESASE and slicing can be obtained, in particular for the case when the laser seed is shorter than the bunch length. This case results in a passive stabilization in the longitudinal arrival time of the FEL pulse with the laser pulse, if the same laser is used also as the pump for the experiments. While ESASE is preferred at shorter wavelengths due to the negative impact of the slippage, the preferred method for short pulses at longer wavelengths is slicing [25]. Here the resonance condition is adapted, while the field slips along the energy modulation. Because the required energy modulation amplitude is larger for slicing, the use of an intra-module taper, as described in the previous subsection, is beneficial.

A very attractive option unique to Athos is the combination of energy modulation with the delay of the intra-undulator chicanes to achieve mode-locked lasing [26]. This configuration is comparable to ESASE with the exception that the radiation spikes are correlated in phase, exhibiting a strong modal structure in radiation spectrum. Besides an energy modulation, we are currently studying also other means of modulation, for instance by current or energy spread.

A further extension of laser-based electron manipulation is echo-enabled harmonic generation, which seems promising for the low photon energy range of Athos. For this, a second modulator and a larger chicane of up to 10 mm R_{56} and a length of 7 m are foreseen. Finally, a possible extension to shorter wavelengths is under study, using either fresh-bunch techniques or staging.

Upgrade Options

Beside the above-mentioned modes, which are funded and currently planned, further upgrades will be still possible. One is self-seeding to provide a stable seed signal in the high photon-energy range, which cannot be covered easily by EEHG. As mentioned above, the large chicane of EEHG can be used to host the monochromator, while the 6 m distance between the end of the chicane and the beginning of the main SASE/CHIC undulator will enhance the resolution as the electron beam will act as an “aperture” for the monochromatized radiation. There is sufficient space

to place up to 5 modules before the chicane to provide the initial SASE signal to the monochromator. To enhance the resolution, we plan to operate the self-seeding at a subharmonic and then tune to the final wavelength once the seed has introduced a sufficiently high coherent signal at higher harmonics [27].

CONCLUSION

The design of the soft X-ray beamline Athos goes beyond a simple SASE operation. It embeds small chicanes for delaying the electron bunch and the radiation, enhancing the induced bunching or shifting the radiation to a fresh part of the bunch. Together with the flexibility of the APPLE-X undulator design it offers many options to tailor the FEL pulse towards the user needs. This will be complemented by external seeding or slicing to provide narrow bandwidth or trains of attosecond pulses. In the upcoming months the beamline will be commissioned and, if these additional modes will resonate well with users' requests, it will demonstrate the next step in the design of X-ray facilities towards more individual control on pulse characteristics such as length, peak power and bandwidth.

REFERENCES

- [1] J. M. J. Madey, "Stimulated emission of bremsstrahlung in a periodic magnetic field," *Journal of Applied Physics*, vol. 42, no. 5, pp. 1906–1908, 1971. doi: 10.1063/1.1660466.
- [2] R. Bonifacio, C. Pellegrini, and L. M. Narducci, "Collective instabilities and high-gain regime in a free-electron laser," *Optics Communications*, vol. 50, no. 6, pp. 373–378, 1984. doi: 10.1016/0030-4018(84)90105-6.
- [3] P. Emma *et al.*, "First lasing and operation of an angstrom-wavelength free-electron laser," *Nature Photonics*, vol. 4, no. 9, pp. 641–647, 2010. doi: 10.1038/nphoton.2010.176.
- [4] T. Ishikawa *et al.*, "A compact x-ray free-electron laser emitting in the sub-angstrom region," *Nature Photonics*, vol. 6, no. 8, pp. 540–544, 2012. doi: 10.1038/nphoton.2012.141.
- [5] H. S. Kang *et al.*, "Hard x-ray free-electron laser with femtosecond-scale timing jitter," *Nature Photonics*, vol. 11, no. 11, p. 708, 2017. doi: 10.1038/s41566-017-0029-8.
- [6] H. Weise and W. Decking, "Commissioning and first lasing of the european XFEL," *38th International Free-Electron Laser Conference, FEL 2017, Santa Fe, USA*, pp. 9–13, 2017. doi: 10.18429/JACoW-FEL2017-MOC03.
- [7] C. J. Milne *et al.*, "Swissfel: The swiss x-ray free electron laser," *Applied Sciences-Basel*, vol. 7, no. 7, 2017. doi: 10.3390/app7070720.
- [8] E. Allaria *et al.*, "Highly coherent and stable pulses from the fermi seeded free-electron laser in the extreme ultraviolet," *Nature Photonics*, vol. 6, no. 10, pp. 699–704, 2012. doi: 10.1038/nphoton.2012.233.
- [9] R. Abela *et al.*, "The swissfel soft x-ray free-electron laser beamline: Athos," *Journal of Synchrotron Radiation*, vol. 26, pp. 1073–1084, 2019. doi: 10.1107/S1600577519003928.
- [10] E. Prat, M. Calvi, R. Ganter, S. Reiche, T. Schietinger, and T. Schmidt, "Undulator beamline optimization with integrated chicanes for x-ray free-electron-laser facilities," *Journal of Synchrotron Radiation*, vol. 23, pp. 861–868, 2016. doi: 10.1107/S1600577516007165.
- [11] R. Bonifacio, R. Corsini, and P. Pierini, "Theory of the high-gain optical klystron," *Physical Review A*, vol. 45, no. 6, pp. 4091–4096, 1992. doi: 10.1103/physreva.45.4091.
- [12] E. Prat, S. Bettoni, and S. Reiche, "Enhanced x-ray free-electron-laser performance from tilted electron beams," *Nuclear Instruments and Methods in Physics Research Section a-Accelerators Spectrometers Detectors and Associated Equipment*, vol. 865, pp. 1–8, 2017. doi: 10.1016/j.nima.2016.06.135.
- [13] A. A. Zholents, "Method of an enhanced self-amplified spontaneous emission for x-ray free electron lasers," *Physical Review Special Topics-Accelerators and Beams*, vol. 8, no. 4, 2005. doi: 10.1103/PhysRevSTAB.8.040701.
- [14] D. Xiang and G. Stupakov, "Echo-enabled harmonic generation free electron laser," *Physical Review Special Topics-Accelerators and Beams*, vol. 12, no. 3, 2009. doi: 10.1103/PhysRevSTAB.12.030702.
- [15] J. Feldhaus, E. L. Saldin, J. R. Schneider, E. A. Schneidmiller, and M. V. Yurkov, "Possible application of x-ray optical elements for reducing the spectral bandwidth of an x-ray sase fel," *Optics Communications*, vol. 140, no. 4-6, pp. 341–352, 1997. doi: 10.1016/S0030-4018(97)00163-6.
- [16] D. Ratner *et al.*, "Experimental demonstration of a soft x-ray self-seeded free-electron laser," *Physical Review Letters*, vol. 114, no. 5, 2015. doi: 10.1103/PhysRevLett.114.054801.
- [17] B. W. J. McNeil, N. R. Thompson, and D. J. Dunning, "Transform-limited x-ray pulse generation from a high-brightness self-amplified spontaneous-emission free-electron laser," *Physical Review Letters*, vol. 110, no. 13, 2013. doi: 10.1103/PhysRevLett.110.134802.
- [18] E. Prat, E. Ferrari, S. Reiche, and T. Schietinger, "Using the optical-klystron effect to increase and measure the intrinsic beam energy spread in free-electron-laser facilities," *Physical Review Accelerators and Beams*, vol. 20, no. 4, 2017. doi: 10.1103/PhysRevAccelBeams.20.040702.
- [19] E. Prat and S. Reiche, "A simple and compact scheme to enhance the brightness of self-amplified spontaneous emission free-electron-lasers," *Journal of Synchrotron Radiation*, vol. 26, pp. 1085–1091, 2019. doi: 10.1107/S1600577519005435.
- [20] A. A. Lutman *et al.*, "High-power femtosecond soft x rays from fresh-slice multistage free-electron lasers," *Physical Review Letters*, vol. 120, no. 26, 2018. doi: 10.1103/PhysRevLett.120.264801.
- [21] E. Prat and S. Reiche, "Simple method to generate terawatt-attosecond x-ray free-electron-laser pulses," *Physical Review Letters*, vol. 114, no. 24, 2015. doi: 10.1103/PhysRevLett.114.244801.
- [22] E. Prat, F. Lohl, and S. Reiche, "Efficient generation of short and high-power x-ray free-electron-laser pulses based on superradiance with a transversely tilted beam," *Physical Review Special Topics-Accelerators and Beams*, vol. 18, no. 10, 2015. doi: 10.1103/PhysRevSTAB.18.100701.
- [23] M. Calvi, C. Camenzuli, E. Prat, and T. Schmidt, "Transverse gradient in apple-type undulators," *Journal of Synchrotron Radiation*, vol. 24, pp. 600–608, 2017. doi: 10.

1107/S1600577517004726.

- [24] E. Prat, M. Calvi, and S. Reiche, "Generation of ultra-large-bandwidth x-ray free-electron-laser pulses with a transverse-gradient undulator," *Journal of Synchrotron Radiation*, vol. 23, pp. 874–879, 2016. doi: 10.1107/S1600577516007177.
- [25] E. Prat and S. Reiche, "Time locking options for the soft x-ray beamline of swissfel," *37th International Free-Electron Laser Conference, FEL 2015, Daejeon, South Korea, paper TUP019*, pp. 388–392, 2015.
- [26] N. R. Thompson and B. W. J. McNeil, "Mode locking in a free-electron laser amplifier," *Physical Review Letters*, vol. 100, no. 20, 2008. doi: 10.1103/PhysRevLett.100.203901.
- [27] E. Prat and S. Reiche, "Compact coherence enhancement by subharmonic self-seeding in x-ray free-electron laser facilities," *Journal of Synchrotron Radiation*, vol. 25, pp. 329–335, 2018. doi: 10.1107/S1600577518000395.

FEL OPTIMIZATION: FROM MODEL-FREE TO MODEL-DEPENDENT APPROACHES AND ML PROSPECTS

S. Tomin[†], G. Geloni, The European XFEL, Schenefeld, Germany
 M. Scholz, DESY, Hamburg, Germany

Abstract

Users beam-time at modern FEL sources is an extremely valuable commodity. Moreover, maximization of FEL up-time must always be performed accounting for stringent requirements on the photon pulse characteristics. These may vary widely depending on the Users requests, which poses challenges to parallel operation of high-repetition rate facilities like the European XFEL. Therefore, both model free or model-dependent optimization schemes, where the model might be given, or provided by machine-learning approaches, are of high importance for the overall efficiency of FEL facilities. In this contribution we review our previous activities and we report on current efforts and progress in FEL optimization schemes at the European XFEL. Finally, we provide an outlook of future developments.

INTRODUCTION

Automatic optimization of accelerator performance is part of the daily operation procedures at the European XFEL [1,2] and other FEL facilities, e.g. [3-5]. The dedicated tools help to tune machines performance faster and more efficient (multidimensional optimization) in comparison to manual tuning. However, the tuning of the large-scale facilities as the European XFEL remains a time-consuming procedure. Moreover, the best machine performance is usually achieved for the most explored operation modes, see Fig. 1, which also points to the importance of optimization procedures. Figure 1 shows dependence of the photon energy against the photon pulse energy for the hard X-Ray undulator SASE1. The colour shows number of machine files – a snapshot of the machine in a stable state. As it can be seen, one of the most frequently used photon energy is around 9–9.3 keV, where the maximum photon pulse energy was around 2.7 mJ. At longer wavelengths, for example 8 keV the maximum photon pulse energy was half as much.

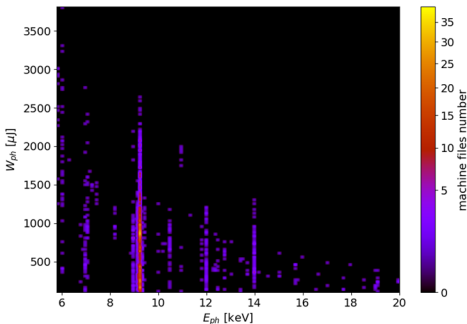


Figure 1: EuXFEL SASE1 performance statistics.

[†] sergey.tomin@xfel.eu

Taking into account high pressure on the machine availability for parallel multi-user operation, the European XFEL is looking for more automation of optimization procedures and new effective approaches to speed up the machine performance tuning.

The analysis of the collected optimization logs performed by OCELOT Optimizer [6] shows that one of the problems is the high dimensionality of parameter space that needs to be explored in the optimization process. For example, 446 unique devices have been used in optimizations at the European XFEL to maximize the SASE pulse energy within the last 2.5 years [2]. Although the frequency of use of a particular set of devices varies. It can still give an indication of how complex the tuning is. Another obstacle to fast and efficient machine tuning is that hyperparameters of optimization algorithms and set of devices which need to tune specific physical parameters, e.g. beam matching, are not always optimally selected, which also affect efficiency. In this paper we will consider the current state of optimization methods used in the European XFEL, and possible ways to overcome the problems discussed.

MODEL-FREE OPTIMIZATION

The main tool for a model-free SASE optimization in the European XFEL is the OCELOT Optimizer. It is the next generation of the SASE optimizer developed for FLASH [6] but with the possibility of creating/modifying an objective function by the operator. Each optimization is logged including an objective function and actuator changes during optimization and can be analyzed afterwards. The tool was deployed in the EuXFEL control room at the beginning of 2017. Since then we collected experience of more than 6000 optimizations (Fig. 2). More details of OCELOT optimizer statistics analysis can be found in [2].

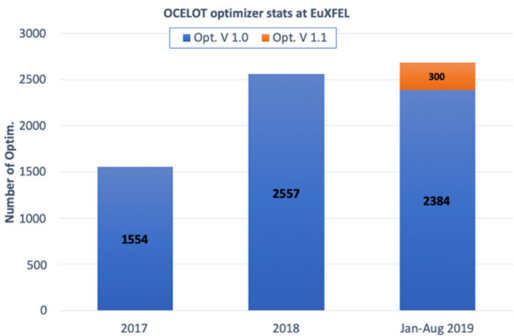


Figure 2: OCELOT optimizer statistics.

As it was mentioned above high dimensionality of the parameter space is one of the problems for fast FEL ma-

chine tuning. Recently, the Extremum Seeking method [7, 8] was added to a family of other optimization algorithms in the OCELOT optimization toolbox [9]. One of the features of the algorithm from the optimizing point of view is the smooth change of actuator's parameters (this can be an essential advantage for tuning of mechanical devices) and the ability to find an extremum in parameter space with many (>10) dimensions, one of the examples of such an optimization is SASE maximization with 16 simultaneously tweaked phase-shifters (Fig. 3). More details and examples of optimizations at European XFEL can be found in [9].

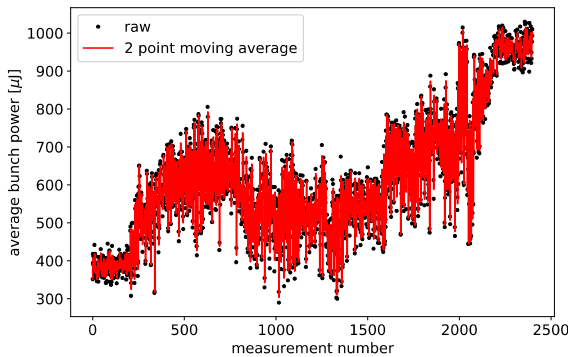


Figure 3: Extremum Seeking simultaneous optimization of 16 phase-shifters gaps [9].

A new version (v1.1) of the optimization toolbox was developed and deployed to the control room in June 2019, taking into account the proposals outlined in [2]. One of the main changes is the extension of command line interface (CLI) capabilities of the tool. The CLI offers a flexible way of using all the functions of the Optimizer without GUI restrictions. For example, the ability to connect a physical accelerator model to an optimization algorithm or run an optimization sequence. Also, the number of logged control channels in the new version was considerably increased mainly by adding channels about machine conditions to allow in the future to use ML methods for choosing the most effective optimization setups for particular machine condition.

Use of a Physics Model in Optimizations

FEL performance maximization in the European XFEL usually includes tuning of the orbit with correctors and optimizing bunch compression by tweaking RF settings as well as beam matching with quadrupoles in dedicated sections. One of the advantages of the model-independent optimization is the flexibility when an operator can apply optimization for any set of devices and any objective function. However, the flexibility has drawbacks: often chosen actuators as well as hyperparameters for the optimization algorithm (e.g. initial step size, number of iterations etc) to tune in particular the accelerator section is nearly random. In general, that affects the effectiveness of the optimization. From another side, a physical model of an accelerator can be used to define the most effective

setup for the optimization, e.g. hyperparameters and/or most effective sets of actuators.

One example is the beam matching with help of the beta mismatch parameters [10] and mismatch phases tuning instead of tweaking quadrupoles directly. The advantage of this approach is that only 4 parameters with well-defined boundaries are required to tune a certain matching accelerator section with several quadrupoles. In this case, the optimization procedure looks as shown in Fig. 4. To convert the mismatch parameters into quadrupole strengths and vice versa, a physical accelerator model based on the OCELOT beam dynamics module is used [11, 12]. We tested this approach to tune a matching section in front of the SASE1 undulator. The result of such an optimization is shown on Fig. 5. The set of quadrupoles was chosen to cover a range of beta mismatch parameters $M_{x/y} = [1, 2]$ and phases $\psi_{x/y} = [-90, 90]$.

A similar approach can be applied for orbit tuning using the amplitude and angle of the orbit distortion instead of tweaking corrector's strengths.

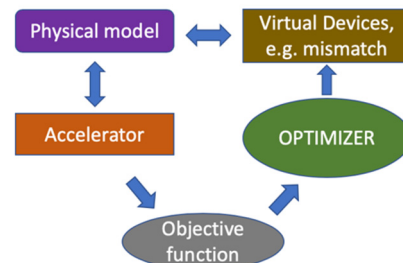


Figure 4: Optimization procedure for tuning beta mismatch parameters and phases.

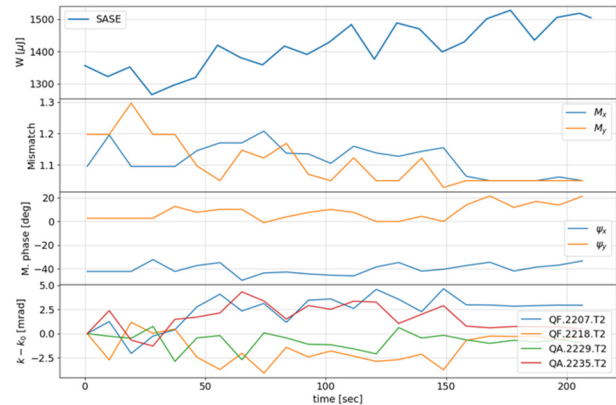


Figure 5: Optimization SASE pulse energy with beta-mismatch parameters $M_{x/y}$ and mismatch phases $\psi_{x/y}$ in matching section in front of SASE1 undulator, number iteration is 25.

Sequence of Optimizations

The ability to launch a sequence of optimizations (*Actions*) was proposed for the first time in [6]. But due to technical reasons it was not implemented but the efforts were aimed at a single optimization that affects the existing capabilities of the OCELOT graphical interface.

Reliability and efficiency of the model-free optimizations have raised the question of applying optimization sequences without an operator intervention, increasing the level of automation of optimization procedures. As a first step we tested the capability of a new software to run predefined optimization sequence. One of the preliminary results is shown in Fig. 6, where two optimizations in a row were used to optimize the SASE pulse energy by aircoils. In addition, the software monitors the status of the machine, and in the event of a beam shutdown, the optimization is paused.

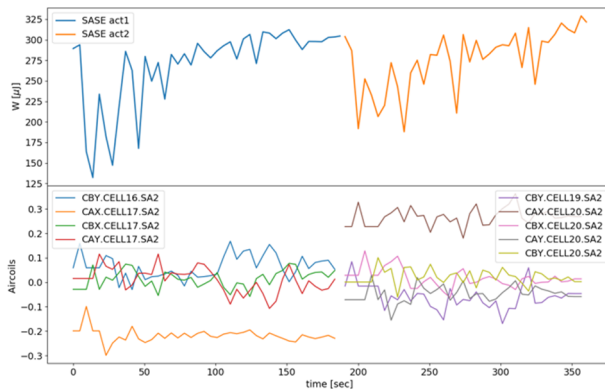


Figure 6: Sequence of optimization with aircoils in SASE2 undulator.

MODEL-DEPENDENT OPTIMIZATION

Model-based optimization methods use/build a regression model that predicts performance. The regression model may be provided, for example, either by a physical/mathematical model or by fitting the previously collected data, for example, with help of ML methods.

If the construction of a mathematical model to predict FEL performance on the real FEL facility with hundreds of free parameters - the task is extremely difficult, then a physical model of the multi-stage bunch formation system can be mathematically described [13]. This algorithm was implemented in OCELOT and was used in simulations to optimize compression scenarios with taking into account collective effects for the European XFEL accelerator [14]. The peculiarity of the algorithm is its fast convergence. Only a few iterations (<10) are required to obtain a compression scenario with the desired beam parameters. It is also planned to implement and test this approach on the accelerator.

Another example of a model-dependent optimization which is in operation at the European XFEL is a statistical optimization of the launch orbit to the SASE1 undulator. The method proposed in [15] was implemented in OCELOT under the name 'Adaptive Feedback'. Details can be found in [1]. Here, the regression model is not provided by physics or ML methods but rather by simple statistical analysis of synchronously collected data of the orbit and the SASE pulse energy. The best trajectories in terms of maximum pulse energy are averaged and used as a golden orbit by the orbit feedback. That moves the beam quickly

to its best trajectory and thus it pushes the pulse energy to its maximum.

OUTLOOK AND ML METHODS

Model-free optimization methods were widely used during commissioning and further in daily operation of the European XFEL. A model-based method such as the adaptive orbit feedback proved to be extremely useful and more advantageous compared to purely empirical methods.

Recently, new approaches have been developed with the aim to reduce tuning time. One of them is the Bayesian optimization utilizing Gaussian process [4, 16, 17] that allows to find the extremum of an objective function faster than, for example, the Nelder-Mead algorithm [18]. The version of the Bayesian optimization described in [4] was included to a family of optimization methods of the Optimizer but not yet tested at the European XFEL.

The other approach uses a combination of two methods: a machine learning technique, which suggests a working point close to the global minimum based on the previously collected data, and a model-independent optimization, which explores the proposed area and makes final optimization [19].

A third approach, which we can note, is virtual diagnostics, which is not directly related to the optimization, but can be used to get additional information about the electron and/or photon beams properties, which in turn can be used for machine or experiment performance optimization [20,21].

The approaches described are promising, but the lack of infrastructure to collect, process, cleanse and analyse these large volumes of data is one of the main obstacles to integrating these methods into the accelerator control systems for daily use. The importance of the problem has been recognized and the high level control teams are making efforts to create a more user-friendly control room environment for machine learning applications, for example, see [22].

CONCLUSION

We present the status of the existing optimization procedures used at the European XFEL accelerator, as well as new approaches including test results.

A new version of the OCELOT Optimizer was recently launched. The main difference are the advanced features of the command line interface, which allow us to perform various types of optimizations in script mode. Thus, we are now able to run an optimization sequence without operator intervention and use the physical accelerator model to determine hyperparameters in some types of optimizations.

ACKNOWLEDGEMENTS

The authors wish to thank the European XFEL accelerator team for help and support. Also, the authors thank V. Balandin and I. Zagorodnov for many fruitful discussions.

REFERENCES

- [1] S. Tomin *et al.*, “On-line Optimization of European XFEL with OCELOT”, in *Proc. ICALEPCS’17*, Barcelona, Spain, Oct. 2017, pp. 1038-1042. doi:10.18429/JACoW-ICALEPCS2017-WEAPL07
- [2] S. Tomin *et al.*, “Status of Automated Optimization Procedures at the European XFEL Accelerator”, in *Proc. IPAC’19*, Melbourne, Australia, May 2019, pp. 1212-1215. doi:10.18429/JACoW-IPAC2019-TUZZPLM2
- [3] F. Löhl, “SwissFEL feedbacks and automated machine optimization”, 10th Hard X-ray Collaboration Meeting, Monterey, CA, USA, 2019.
- [4] M. McIntire *et al.*, “Bayesian Optimization of FEL Performance at LCLS”, in *Proc. IPAC’16*, Busan, Korea, May 2016. doi:10.18429/JACoW-IPAC2016-WEPOW055
- [5] G. Gaio *et al.*, “Advances in Automatic Performance Optimization at FERMI”, in *Proc. ICALEPCS’17*, Barcelona, Spain, Oct. 2017, pp. 352-356. doi:10.18429/JACoW-ICALEPCS2017-TUMPA07
- [6] I. Agapov, G. Geloni, S. Tomin, and I. Zagorodnov, “Automatic tuning of Free Electron Lasers”, Apr 2017. arXiv:1704.02335
- [7] A. Scheinker, “Model Independent Beam Tuning”, in *Proc. IPAC’13*, Shanghai, China, May 2013, pp. 1862-1864, paper TUPWA068.
- [8] A. Scheinker and D. Scheinker, “Bounded extremum seeking with discontinuous dithers”, *Automatica*, vol. 69, pp. 250, 2016. doi:10.1016/j.automatica.2016.02.023
- [9] A. Scheinker *et al.*, “Model-independent tuning for maximizing free electron laser pulse energy”, *Phys. Rev. Accel. Beams*, vol. 22, pp. 082802, August 2019. doi:10.1103/PhysRevAccelBeams.22.082802
- [10] M. Sands, “A Beta mismatch parameter”, SLAC-AP-85, 1991. <https://lib-extopc.kek.jp/preprints/PDF/1991/9105/9105527.pdf>
- [11] I. Agapov, G. Geloni, S. Tomin, and I. Zagorodnov, “OCELOT: A software framework for synchrotron light source and FEL studies”, *Nucl. Instr. Meth A*, 768, pp. 151-156, 2014. doi:10.1016/j.nima.2014.09.057
- [12] S. Tomin *et al.*, “Ocelot as a framework for beam dynamics simulations of X-Ray sources”, in *Proc. IPAC’17*, Copenhagen, Denmark, May 2017, pp. 2642-2645. doi:10.18429/JACoW-IPAC2017-WEPAB031
- [13] I. Zagorodnov and M. Dohlus, “Semianalytical modeling of multistage bunch compression with collective effects”, *Phys. Rev. ST Accel. Beams*, vol. 14, pp. 014403, 2011. doi:10.1103/PhysRevSTAB.14.014403
- [14] I. Zagorodnov, M. Dohlus, and S. Tomin, “Accelerator beam dynamics at the European X-ray Free Electron Laser”, *Phys. Rev. Accel. Beams*, vol. 22, pp. 024401, 2019. doi:10.1103/PhysRevAccelBeams.22.024401
- [15] G. Gaio, M. Lonza, “Automatic FEL Optimization at FERMI”, in *Proc. ICALEPCS’15*, Melbourne, Australia, Oct. 2015. doi:10.18429/JACoW-ICALEPCS2015-MOC3003
- [16] J. Kirschner *et al.*, “Adaptive and Safe Bayesian Optimization in High Dimensions via One-Dimensional Subspaces”, Feb. 2019. arXiv:1902.03229
- [17] J. Duris, “Bayesian Optimization for Online FEL Tuning at LCLS”, presented at the 2nd ICFA Mini-Workshop on Machine Learning for Charged Particle Accelerators, PSI, Villigen, Switzerland, 2019. <https://indico.psi.ch/event/6698/contributions/16607/>
- [18] J.A. Nelder and R. Mead, “A Simplex Method for Function Minimization”, *The Computer Journal*, vol. 7, no. 4, Apr. 1965, pp. 308-313. doi:10.1093/comjnl/7.4.308
- [19] A. Scheinker *et al.*, “Demonstration of Model-Independent Control of the Longitudinal Phase Space of Electron Beams in the Linac-Coherent Light Source with Femtosecond Resolution”, *Phys. Rev. Lett.*, vol. 121, pp. 044801. doi:10.1103/PhysRevLett.121.044801
- [20] C. Emma *et al.*, “Machine learning-based longitudinal phase space prediction of particle accelerators”, *Phys. Rev. Accel. Beams*, vol. 21, pp. 112802, Sep. 2018. doi:10.1103/PhysRevAccelBeams.21.112802
- [21] A. Sanchez-Gonzalez *et al.*, “Accurate prediction of Xray pulse properties from a free-electron laser using machine learning”, *Nat. Commun.*, vol. 8, pp. 15461, 2017. doi:10.1038/ncomms15461
- [22] G.R. White *et al.*, “The EPICS Software Framework Moves from Controls to Physics”, in *Proc. IPAC’19*, Melbourne, Australia, May 2019, pp. 1216-1218. doi:10.18429/JACoW-IPAC2019-TUZZPLM3

FEL OPERATION AT THE EUROPEAN XFEL FACILITY*

D. Nölle†, Deutsches Elektronen-Synchrotron DESY, Hamburg, Germany
on behalf of the European XFEL Operation Team

Abstract

The European XFEL is a SASE FEL based user facility in the metropole region of Hamburg providing hard and soft X-ray photons with extremely high brilliance. The three FEL lines are operated simultaneously and are powered by a superconducting LINAC based on TESLA technology. Average power levels of up to several W have been demonstrated as well for soft and hard X-rays and can be requested by user experiments on day by day basis. This paper will report on the operation within the last two years. Typical operation conditions for parallel operation of 3 SASE lines will be discussed. The perspective for the operation with an extended photon energy range, as well as for full power operation with up to 27000 pulses per second will be presented.

2009. Commissioning of the facility began end of 2015 with a ½ year long injector run [4]. End of 2016 the commissioning of the superconducting accelerator started. 9 month later in Sept. 2017 the instruments at SASE1 started with photon energies of 9.3 keV. In spring 2018 within one year from the first lasing of SASE1 parallel lasing in all 3 FELs was established [5, 6]. Distribution of the electron beam to the different sources with almost arbitrary bunch pattern is done by the flexible beam switchyard [7]. While SASE1 is in operation since fall 2017 SASE3 and SASE2 served first users at the end of 2018 and beginning of 2019. All experiments are far advanced on their way from first to standard user operation.

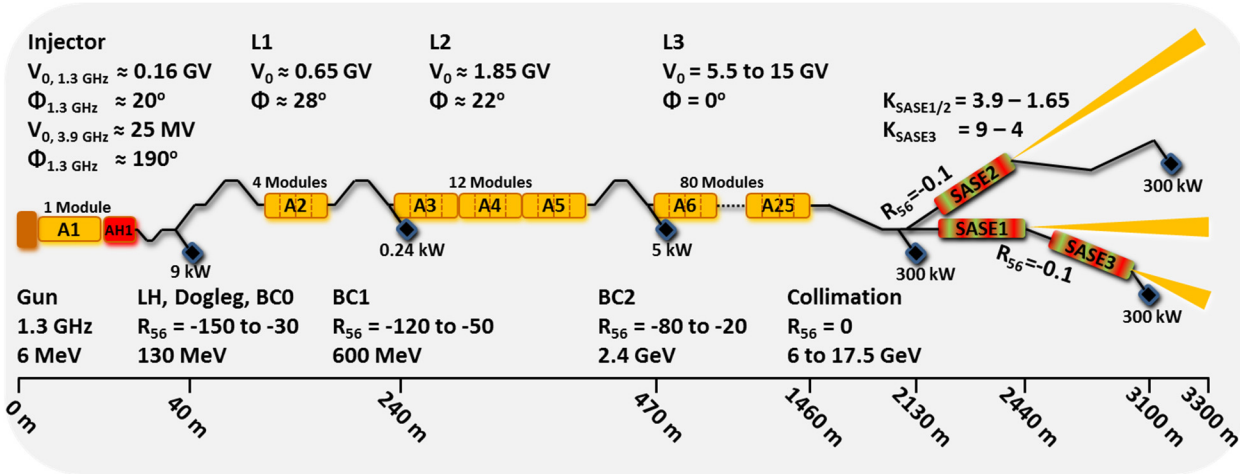


Figure 1: Schematic overview of the European XFEL accelerator. Single RF stations are named An and feed either one module (A1) or 4 accelerating modules (A2-A25). R56 ranges for the bunch compressors are given in mm, and the phases of the different linac sections refer to typical compression set-ups. The maximum allowed beam power of the three commissioning dumps after the injector and the 2nd and 3rd bunch compressor (BC1 and BC2) as well as of the main dumps after the linac and each beam distribution line is given.

INTRODUCTION

The European XFEL aims at delivering X-rays from 0.25 to up to 25 keV out of three SASE FEL lines [1, 2]. The FELs are driven by a superconducting linear accelerator based on TESLA technology [3]. The accelerator operates in 10 Hz pulsed mode and can deliver up to 2,700 bunches per RF-pulse. Electron beams can be distributed to three different beamlines: the two FEL branches and a dump line. The switching is done within the RF-pulse allowing for simultaneous operation of three FELs.

Construction of the European XFEL started in early

FACILITY LAYOUT

The complete facility is constructed in an underground tunnel up to 30 m below surface level. Access to the tunnels is possible in the injector area as well as through shaft buildings at the bifurcation points, where one tunnel splits up into two. The longest tunnel is the main accelerator tunnel with about 2 km length. Total length of the entire tunnel system is about 6 km. The distance of injector to experimental hall is 3.3 km. Besides of the three already installed FEL lines, the tunnels provide space for two more FEL sources [8]. The schematic layout of the accelerator is shown in Fig. 1.

The injector consists of the normal conducting gun, one TESLA type accelerating module and a 3.9 GHz module

* Work supported by the respective funding agencies of the contributing institutes; for details please see <http://www.xfel.eu>
† dirk.noelle@desy.de

[9] for phase space linearization, a laser heater system [10], followed by a diagnostic section [11,12].

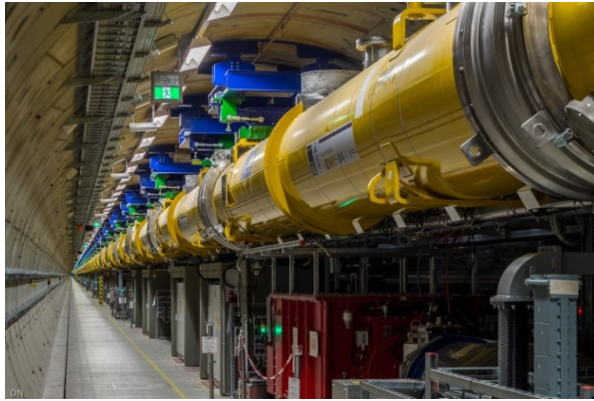


Figure 2: View into the linac tunnel with the accelerator modules suspended from the ceiling and the RF infrastructure placed below, on the floor.

From the injector the beam is fed to the main accelerator tunnel. The superconducting linear accelerator consists of 96 TESLA type accelerator modules [13] grouped into 3 sections, intercepted by the 3 stage bunch compression. The first section is named L1, consisting of 4 modules, the second is L2 with 12 modules and the main linac L3 consists of 80 modules. The cryogenic installation is built as one continuous cryostat. Always 4 modules are fed by one 10 MW multi-beam klystron. The accelerator modules are suspended from the ceiling (see Fig. 2), while the complete infrastructure, except the modulator is installed below. The modulators are placed in one single hall above ground, and the high-voltage pulse is fed to the pulse transformer by up to 2 km long special pulse cables.



Figure 3: First bunch compression chicane.

The bunch compressor B0 is located in front of L1 at 130 MeV and B1 before L2 at 700 MeV (Fig. 3). The last stage B2 at 2.4 GeV is located between L2 and tL3. All magnetic chicanes are tuneable within a wide range of R56 allowing for flexible compression scenarios. Diagnostic stations are placed after the second and third compression stage. The later is equipped with a transverse deflecting system (TDS) for longitudinal phase space diagnostics [14].

After bunch compression to a few 10 fs, the beam is accelerated in the main linac L3 to energies up to 17.5 GeV. After the main linac a collimation section is providing cleanup of transverse phase space to about 60σ and energy collimation for particles exceeding 2% relative energy deviation [15].

Between collimation and beam distribution section the Intra-Bunch-Train-Feedback System (IBFB) [16] for fast trajectory feedback within the bunch train is located.

The beam distribution system is built from two switchyards [17] based on a combination of kicker and DC Lambertson septum. The first makes use of a fast kicker system to send selected bunches out of the train into the 300 kW dump line (TLD) at the end of the accelerator tunnel. The bandwidth of the kicker system allows removing single bunches even at 4.5 MHz bunch repetition rate.

The second switchyard is based on a high precision kicker with about 20 μ s rise time and a precise flat top. This system is used to split the bunch train into two parts, one going straight to the SASE1/3 branch, and the other being kicked into the SASE2 branch. The beam dumps at the end of both beam lines are also capable for 300 kW electron beam power, each. In the SASE1/3 branch, the electron beam first passes the hard X-ray FEL SASE1 followed by the soft X-ray FEL SASE3. The other branch currently contains the hard X-ray FEL SASE2 only, but the tunnel system has space for up to 2 more FELs. The beam distribution system allows not only providing beam to all FELs within the same RF pulse, but also – obeying some constraints - arbitrary bunch pattern. Thus experiments are served with beam for real parallel operation [7].

OPERATION OF THE XFEL FACILITY

With the transition from commissioning to operation phase the FEL operation is rapidly approaching the specified delivery time for X-rays of 4800 h/y. The annual operation time is about 6000 -7000 h/y, depending on the required shutdown periods for upgrade programs. In the following several aspects of the operation will be highlighted.

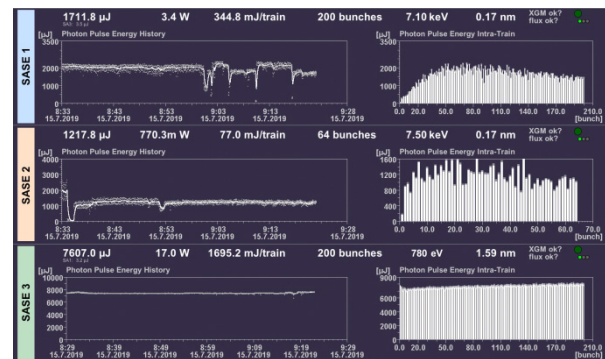


Figure 4: Screenshot of the FEL status panel, taken during a 4.5 MHz run with parallel multibunch operation in all 3 beamlines. Note the 2000 pulses/s produced in SASE1 and SASE3 correspond to 4000 bunches in the north branch of EXFEL.

At European XFEL variable gap undulators are used to tune photon energies within a given range. Overlapping photon energy ranges are realized by operating the machine at different energy working points. Up to now energy points at 11.5 GeV for low photon energy operation and 14 GeV for standard photon energy range are established. A 16.5 GeV working point easily reaching photon energies in the 20 keV range will be established soon. Nevertheless, the design energy of E-XFEL of 17.5 GeV was demonstrated up to the first dump in the TLD line [5].

The superconducting accelerator offers the possibility to run long bunch trains within an RF pulse compared to single or few bunch operation typical for conventional warm copper linacs. With a bunch repetition rate of up to 4.5 MHz and a 600 μ s flat top of the RF pulse, 2700 electron bunches per RF pulse, or with 10 Hz operation 27000 electron bunches per second can be provided. Operation of the full train up to the first main dump has already been demonstrated [18]; as well a FEL operation with up to 200 bunches per FEL, or up to 6000 lasing pulses per second. (Fig. 4). The limit on the bunch numbers of 6000 bunches is a temporary limit due to safety constraints, since intense FEL radiation drills to almost all absorbing materials. Plans to update the safety system will be presented [19].

Since the high bunch repetition rate of 4.5 MHz is still demanding for the instrumentation of the experiments, the machine usually runs with 1.13 MHz bunch repetition rate and 500 to 600 bunches per RF train. A typical bunch distribution within the train reflects the properties of the distribution system. At 1.13 MHz bunch rep rate a train starts with 10 pre bunches. These bunches are foreseen for fast feedbacks to catch and start stabilizing the entire train. Currently only the fast orbit feedback is active. It provides orbit stabilization within the bunch train to about 2 μ m RMS [16]. The pre bunches are kicked by the fast kicker system in to the TLD dump line. The remaining bunch train is split into 2 parts of configurable length (within the limits of the flattop length), one directed straight on to the SASE1/3 FEL lines or by means of the slow kicker to the SASE2 line. The kicker fall time needs a gap in the bunch train of about 20 μ s, realized using the fast kickers sending the corresponding bunches to the TLD dump line. In order to decouple the lasing of SASE1 and SASE3, using a common electron beam path, one of the dump kickers operated at low kick strength is used to suppress lasing of “SASE3” bunches in SASE1 and vice versa. The so called soft kick drives a betatron oscillation of kicked bunches in SASE1, suppressing lasing. In front of SASE3 a DC steerer compensates the kick for “SASE3” and send “SASE1” bunches to a non lasing betatron oscillation [19].

Due to the high bandwidth of the fast dump kickers, arbitrary bunch patterns can be realized by kicking all bunches not requested by users to the TLD dump line. Within a predefined number for the maximum number of bunches, users can change the bunch numbers by themselves. With support of the operators also complex bunch

pattern can be “programmed”. This includes reduction of bunch rep rates to 560 or other subharmonics of the bunch rep rate, interleaved operation of SASE1 and SASE3, up to programming bit pattern into the bunch train. Even a complete bunch pattern can be swapped in and out at a 10 Hz rate [7]. This provides maximum flexibility for the experiments. On the other hand many not requested bunches are dumped in the TLD region. Therefore, currently only a little less than 20% of the 18 C charge accelerated was used to produce photons (Fig. 5). It shows that there is still a large of potential for increasing the number of photons at the experiments.

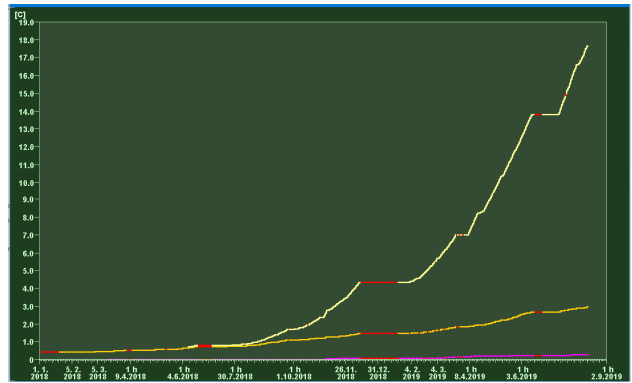


Figure 5: Integrated charge transported in the EXFEL. The bright yellow line shows the charge provided by the accelerator; dark yellow and pink give the amount of charge send through SASE1/3 and SASE2 respectively.

The SASE lines for E-XFEL are designed for different photon energy ranges. SASE1 and SASE2 are hard X-ray sources with design photon energies from 3 to 25 keV for electron beam energies between 8.5 and 17.5 GeV. SASE3 the soft X-ray line is able cover 0.4 to 3 keV at the corresponding electron beam energies.

The delivered photon energy range is driven by request of the experiments. Their demand is mostly 9.3 keV for hard X-rays and around 1 keV for soft X-rays. Both photon energy ranges are covered well at 14 GeV electron beam energy, making this energy the current standard working point of the facility. On user request the photon energies of the hard X-ray lines can be routinely tuned to energies between 6 and 14 keV at power levels of a least 1 mJ. With careful tuning up to 4 mJ in regime of 6-7 keV and 2-3 mJ at 9-10 keV are obtainable.

During machine development times an extended range of photon energies was checked for the hard X-ray regime. By simple gap changing and slight tuning of beam parameters and undulator orbit photon energies up to 20 keV could be demonstrated for SASE1 and SASE2.

SASE3 photon intensities turned out to be rather insensitive to gap changes. Without any further tuning changes within from 700 eV up to 2.5 keV show only a variation in pulse energy of about a factor of 2. Therefore, gap control on request is handed over to the experiments, allowing for precise tuning of resonances and scanning techniques.

In fall 2019 the 16.5 GeV working point will be established, allowing for exploring the potential of EXFEL for high photon energies. In addition several weeks of beam-time are scheduled at 11.5 GeV to allow of experiments in the soft X-ray regime, e.g. at the oxygen edge.

CHALLENGES AND IMPROVEMENTS

While extending the operational range of the facility, some issues and problems have been found and are now going to be tackled.

As mentioned before, some initial bunches of the train, those sitting in kicker gaps and RF transition times and the parts of the bunch train not required in the FEL lines are removed with the fast kicker system. I turned out; that extensive use of these kicker had an influence even on bunches going straight. Investigation of the orbit showed, time dependent kick are present depending on the pulse pattern of the kicker magnets. These effects are expected to be due to eddy currents generated in the kicker. Since the observed shapes of the kick are highly repetitive, a feed forward system using spare kickers from the slow kicker system should be able to cope with this effect. Meanwhile a model to predict the effects of the fast kicker system was established and the preparation to run wave fronts instead of flat top current profiles was prepared. Tests in order to compensate the effect of the eddy currents will take place in near future [20].

More serious restrictions in the ramp up of the facility performance are given by safety restrictions. Intense FEL radiation focused to tiny spots easily creates plasmas, when hitting material. With the complex optics of an X-ray beamline the risk cannot be fully excluded, that focused beams can hit and thus can penetrate absorbers or shutters. Therefore, very shortly after first FEL light, tests were done, to verify the actual photon safety systems. This included not only testing the absorber materials under extreme conditions, but also investigating the beamline, determining potential critical settings. In order to ensure safe operation, operation restrictions were set to prevent performance levels of the machine, not safely within a tested envelope. With improving FEL performance the tested envelope was extended, so that currently, in the hard X-ray regime depending on photon energy between 0.8 and 8 W, average power, can safely be delivered. SASE3 is allowed to provide 30 W below 1.2 keV and 9 W higher than 1.2 keV. With typical values of the FEL performance these limits can be reached with between 40 to 400 bunches per train. From these results, it becomes clear, that a pure passive confinement system for FEL radiation will not be able to cover the full performance of EXFEL with up to 27000 pulses per second.

Therefore an upgrade of the safety system is being implemented. Besides of the improvement of X-ray absorbers with a combination of diamond and B4C ceramics, active sensors of appropriate safety level, will be the major change. The so called burn through monitors will be located in the beam shutter system, between the radiation absorber and the main beam shutter. A sketch and a picture of the system are shown in Fig. 6. As soon as

these monitors detect X-rays, meaning the absorber gets penetrated, they will trigger an emergency stop of the accelerator by means of the PPS system. Therefore, the main shutter has to persist the FEL beam only for the latency of the PPS system, being less or on the order of a second. Large area versions of this these detectors, also connected with the PPS system will be placed at critical places within the experimental hutches to ensure the integrity of the instruments area. The update will get active after the winter shutdown 2019/2020. Therefore, after restart in 2020 XFEL operation without limitations on the bunch numbers will be possible.

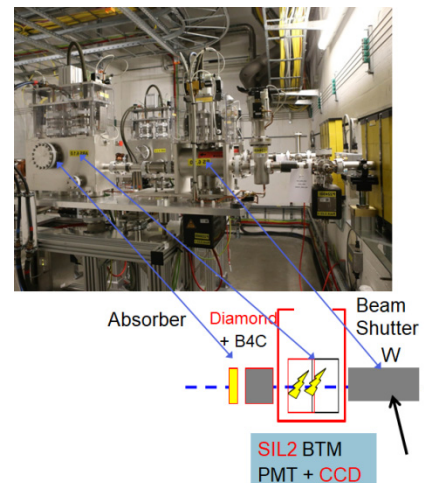


Figure 6: Layout of the beam shutter system with an absorber in front, followed by the active burn through monitor and the main beam shutter.

UPGRADES

While the machine in baseline setup is still ramping up performance, upgrade programs have already started. Both hard X-Ray FELs SASE1 and SASE2 will get self-seeding options; the corresponding chicanes are already available and installed in SASE2. Just recently the beam commissioning in SASE2 has started [21].

Other projects cover extending the photon properties in the soft X-ray regime. The installation of an afterburner system with variable polarization undulators [22] as well as a chicane system for two color operation modes [23] is being prepared, and will start installation within the winter shutdown 2019/2020.

A rather long term project is the extension of the facility with two more FEL sources. In the south branch there are still to sections available, capable for installation of recently long undulator systems. Technical possibilities and the science case for these additional sources is currently being explored [8].

The current operation parameters of EUROPEAN XFEL as well as the design parameters are summarized in Table 1.

Table 1: Parameter Set of EUROPEAN XFEL, comparing project goals, with parameters already demonstrated and routinely delivered.

Quantity	Unit	Project Goal	Achieved	Routine
Beam energy	GeV	8-17.5	6 - 17.6	14
Rep Rate (intra train)	MHz	4.5	.14 – 4.5	0.14-4.5
Charge	pC	10-1000	10-500	250
Beam power	kW	500	95	35
Pulses/s	1/s	27000	27000	<13000
SASE1				
Photon Energy	keV	3-25	6-20	6-14
Pulse Energy	mJ		< 4	1-2.5
SASE2				
Photon Energy	keV	3-25	5.8-20	5.8 – 14
Pulse Energy	mJ		< 3	1-2
SASE3				
Photon Energy	keV	0.25 - 3	0.65–4.5	0.65-2.4
Pulse Power	mJ		10	4-8

CONCLUSION AND OUTLOOK

The European XFEL entered the operation phase. All major design parameters were demonstrated. Ramping up the facility performance to full range is well advancing. All 3 FEL sources have started the experimental program and the fraction of beam time with X-Ray delivery is continuously increasing. Unexpected issues compromising the performance envelope are tacked and removed. With the beginning of 2020 operation modes with up 27000/s can be provided on user request.

ACKNOWLEDGEMENT

The European XFEL is a joint achievement of many colleagues from the participating labs working in different parts of the project. The Author wishes to thank all of them for their long lasting devotion and enthusiasm. In addition the author would like to acknowledge the strong commitment of the DESY and European XFEL staff for the operation of the facility. Collaboration is the key to success!

REFERENCES

- [1] M. Altarelli *et al.* Ed., “The European X-Ray Free-Electron Laser–Technical Design Report”, DESY, Hamburg, Germany, Rep. DESY 2006-097, July 2007.
- [2] R. Brinkmann *et al.* Ed., “TESLA XFEL Technical Design Report Supplement”, DESY, Hamburg, Germany, Rep. DESY 2002-167, March 2002.
- [3] R. Brinkmann *et al.* Ed., “TESLA Technical Design Report – Part II: The Accelerator”, DESY, Hamburg, Germany, Rep. DESY 2001-011, March 2001.
- [4] F. Brinker, “Commissioning of the European XFEL Injector”, in *Proc. 7th Int. Particle Accelerator Conf. (IPAC'16)*, Busan, Korea, May 2016, pp. 1044-1047. doi:10.18429/JACoW-IPAC2016-TU0CA03

- [5] D. Noelle, “Commissioning of the European XFEL”, in *Proc. 29th Linear Accelerator Conf. (LINAC'18)*, Beijing, China, Sep. 2018, pp. 994-999. doi:10.18429/JACoW-LINAC2018-FR2A02
- [6] M. Scholz, “First Lasing at the SASE2 and SASE3 FELs of European XFEL”, presented at the 39th Int. Free Electron Laser Conf. (FEL'19), Hamburg, Germany, Aug. 2019, paper MOA04, this conference.
- [7] L. Froehlich *et al.*, “Multi-Beamline Operation at the European XFEL”, presented at the 39th Int. Free Electron Laser Conf. (FEL'19), Hamburg, Germany, Aug. 2019, paper WEP008, this conference.
- [8] “Shaping the Future of the European XFEL: Options for the SASE4/5 Tunnels”, workshop held in December 2019, Schenefeld, Germany, slides available at <https://indico.desy.de/indico/event/21806/>.
- [9] C. G. Maiano *et al.*, “Commissioning and Operation Experience of the 3.9 GHz System in the EXFEL Linac”, in *Proc. 8th Int. Particle Accelerator Conf. (IPAC'17)*, Copenhagen, Denmark, May 2017, pp. 999-1002. doi:10.18429/JACoW-IPAC2017-MOPVA058
- [10] M. Hamberg *et al.*, “Electron Beam Heating with the European XFEL Laser Heater”, in *Proc. 38th Int. Free Electron Laser Conf. (FEL'17)*, Santa Fe, NM, USA, Aug. 2017, pp. 458-459. doi:10.18429/JACoW-FEL2017-WEP018
- [11] C. Gerth, B. Beutner, O. Hensler, F. Obier, M. Scholz, and M. Yan, “Online Longitudinal Bunch Profile and Slice Emittance Diagnostics at the European XFEL”, in *Proc. 6th Int. Beam Instrumentation Conf. (IBIC'17)*, Grand Rapids, MI, USA, Aug. 2017, pp. 153-156. doi:10.18429/JACoW-IBIC2017-TUPCC03
- [12] D. Lipka *et al.*, “First Experience with the Standard Diagnostics at the European XFEL Injector”, in *Proc. 5th Int. Beam Instrumentation Conf. (IBIC'16)*, Barcelona, Spain, Sep. 2016, pp. 14-19. doi:10.18429/JACoW-IBIC2016-MOBL02
- [13] H. Weise, “How To Produce 100 Superconducting Modules for the European XFEL in Collaboration and with Industry”, in *Proc. 5th Int. Particle Accelerator Conf. (IPAC'14)*, Dresden, Germany, Jun. 2014, pp. 1923-1928. doi:10.18429/JACoW-IPAC2014-WEIB03
- [14] M. Huening, “Bunch Length Measurements using Transverse Deflecting Systems”, in *Proc. 29th Linear Accelerator Conf. (LINAC'18)*, Beijing, China, Sep. 2018, pp. 972-976. doi:10.18429/JACoW-LINAC2018-FR1A02
- [15] V. Balandin, R. Brinkmann, W. Decking, and N. Golubeva, “Post-linac collimation system for the European XFEL”, presented at *PAC'09*, Vancouver, Canada, May 2009, paper TH6PFP030, pp. 3763-3765.
- [16] B. Keil *et al.*, “Status of The European XFEL Transverse Intra Bunch Train Feedback System”, in *Proc. 4th Int. Beam Instrumentation Conf. (IBIC'15)*, Melbourne, Australia, Sep. 2015, pp. 492-496. doi:10.18429/JACoW-IBIC2015-TUPB064
- [17] W. Decking, F. Obier, “Layout of the Beam Switchyard at the European XFEL”, presented at *EPAC'08*, Genoa, Italy, WEP073, pp. 2163-2165.
- [18] W. Decking *et al.*, “Status of the European XFEL”, in *Proc. 10th Int. Particle Accelerator Conf. (IPAC'19)*, Melbourne, Australia, May 2019, pp. 1721-1723. doi:10.18429/JACoW-IPAC2019-TUPRB020

- [19] S. Liu, “Parallel Operation of SASE1 and SASE3 at European XFEL”, presented at the 39th Int. Free Electron Laser Conf. (FEL'19), Hamburg, Germany, Aug. 2019, paper TUA01, this conference.
- [20] F. Obier, W. Decking, and M. Huening, “Long Pulse Kicker System for European XFEL Beam Distribution”, presented at the 39th Int. Free Electron Laser Conf. (FEL'19), Hamburg, Germany, Aug. 2019, paper WEP014, this conference.
- [21] G. Geloni *et al.*, “Status of the Hard X-Ray Self-Seeding Setup at the European XFEL”, presented at the 39th Int. Free Electron Laser Conf. (FEL'19), Hamburg, Germany, Aug. 2019, paper TUP079, this conference.
- [22] S. Serkez, G. Geloni, V. Kocharyan, T. Mazza, M. Meyer, and E. Saldin, “Opportunities for Two-Color Experiments at the SASE3 Undulator Line of the European XFEL”, in *Proc. 38th Int. Free Electron Laser Conf. (FEL'17)*, Santa Fe, NM, USA, Aug. 2017, pp. 121-124. doi:10.18429/JACoW-FEL2017-MOP03
- [23] P. Li, T. Wei, Y. Li, J. Pflueger, “Magnetic design of an Apple-X afterburner for the SASE3 undulator of the European XFEL”, *Nucl. Instr. Meth. A*, vol. 870 (2017), 10.

LCLS-II – STATUS AND UPGRADES*

Brachmann[†], B. Dunham, J. Schmerge for the LCLS-II Collaboration,
SLAC National Accelerator Laboratory, Menlo Park, CA, USA

Abstract

LCLS-II is a major project to build and operate a 1 MHz, continuous-wave Free Electron Laser covering a wide photon energy range from ~ 200 eV up to 25 keV. A superconducting accelerator, providing beams up to 4 GeV, drives two variable gap undulator systems, one providing soft energy X-rays (SXR) up to ~ 2 keV, the other hard energy X-rays (HXR) up to 25 keV. In addition, the normal conducting accelerator used for LCLS-I will remain in operation, primarily driving the hard X-ray undulator beam line delivering photon energies up to 25 keV. We will summarize the project goals, current status of construction of the main sub-systems and future plans. The focus of this contribution will be the FEL itself. We will mention the X-ray instrumentation for context.

LCLS-II PROJECT OVERVIEW

A detailed overview of the LCLS-II facility is given in the Technical Design Report [1]. A schematic layout of the facility is shown in Figure 1. The project is supported by the United States Department of Energy and is a collaboration of several National Laboratories and Cornell University. The cryomodules are built by the Thomas Jefferson National Accelerator Facility (JLab) and Fermilab (FNAL). The undulator systems for the hard and soft X-ray energy ranges are provided by Argonne National Laboratory (ANL) and Keller Technology Corporation, New York, USA (KTC), respectively. The electron gun is a contribution of the Lawrence Berkeley National Laboratory (LBNL). This system is already fully installed, and commissioning activities are in progress. A key system is the cryo-plant. It is based on the 2K plant in operation at JLAB. The entire cryogenic system was designed and constructed collaboratively by SLAC, JLab, FNAL and several industrial partners. A ‘dual’ plant is installed to provide headroom for capacity and future extension of the cryogenic linac.

The goal of the project is to construct and operate an FEL user facility for advanced X-ray science that will be available to the international user community. Scientific motivation and opportunities have been summarized in [2]. The existing normal conducting (NC) accelerator will continue to operate and primarily provide beams in the HXR energy range but will also be used to assist commissioning of the new SXR beamlines and instrumentation.

The main construction activities will be completed in 2021. User operation based on the NC accelerator will

commence in the spring of 2020. ‘First light’, generated by SC accelerator beams is anticipated in 2021, followed by a ramp-up period to full performance, over 3-4 years. A set of Design Parameters is given in table 1. Figure 2 shows the X-ray energy range and average beam brightness.

Table 1: Design Parameters

KPP	SC linac	NC linac
Linac Energy	4 GeV	15 GeV
Repetition Rate	1 MHz	120 Hz
Nominal Bunch Charge	0.1 nC	0.125 nC
Photon Energy Range	0.2-5 keV	0.2 - 25 keV
Photon Pulse Energy	0.5 mJ	~ 2 mJ

Approximately half of the cryomodules are now installed in the first kilometre of SLAC’s linac tunnel. The undulators both for SXR and HXR systems are in the process of magnetic measurement and calibration. Installation is imminent and we expect completion of commissioning in the early part of 2020, enabling the restart of the facility and user operation based on the NC linac. Many other systems are currently installed, for example the RF systems, cryogenic plant and cryogenic distribution system, beam transport and switching systems, beam dumps, controls and safety systems. In parallel, a major upgrade of the X-ray instrumentation is taking place: 3 new end stations will be added, high repetition rate capabilities will be implemented, and appropriate data processing technology is being developed and installed. A comprehensive description of photon and experimental system development is summarized in a strategic development plan [3].

LCLS-II Injector

The LCLS-II Injector uses a normal conducting VHF electron gun. The gun has been developed at LBNL and a prototype has been in operation for several years, also known as the ‘APEX gun.’ The injector design and gun are described in references [4, 5]. Beam is generated by a Cs₂Te cathode driven by a 257 nm laser system. The LCLS-II electron gun is installed in its final location. We succeeded to generate first beam, including a measurement of the electron beam energy, confirming specified performance (Figures 3 and 4).

* Work supported by the U.S. Department of Energy, Office of Basic Energy Sciences, Contract No. DE-AC02-76SF00515.

[†]brachman@slac.stanford.edu

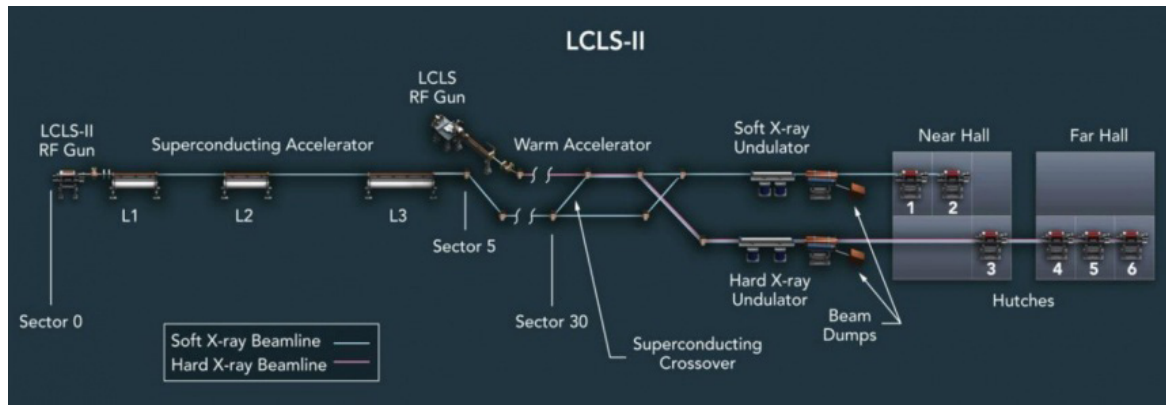


Figure 1: Schematic layout of the LCLS-II Facility.

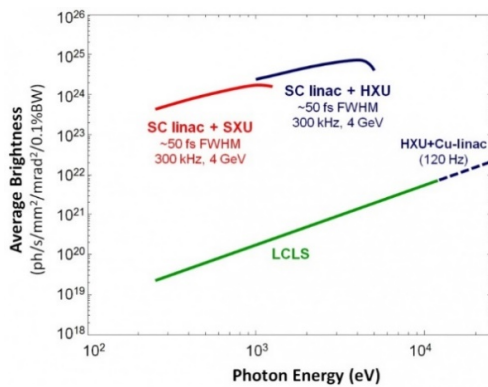


Figure 2: Photon energy and brightness of the LCLS FEL.

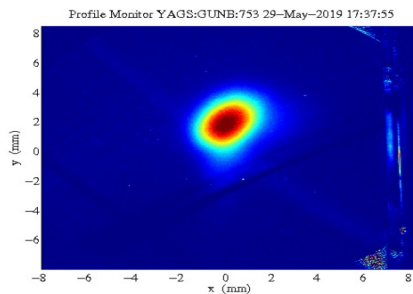


Figure 3: Profile of first LCLS-II electron beam.

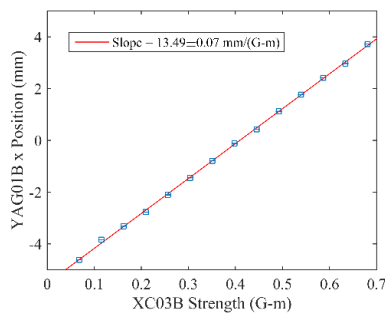


Figure 4: Gun electron beam kinetic energy 766 keV as determined from calibrated corrector scan.

SC Linac and Cryomodule Installation

The LCLS-II linac consists of 37 cryomodules, each containing eight 9 cell niobium cavities. The SC linac is arranged into 3 sections, L1, L2 and L3. The spaces between L1 / L2 and L2 / L3 provide room for bunch compressors (BC1 and BC2). Otherwise the linac forms a continuous cryogenic system with welded connections between the cryomodules. Approximately half of the cryomodules arrived from JLab and FNAL and are installed in SLAC's linac tunnel. At this time, the cryomodule connections are being welded, using automated orbital welding technology.

Early in the CM shipping phase, we experienced a technical issue with excessive vibrations during transport, leading to a failure of bellows, which caused the venting of the vacuum system. This problem was mitigated by temporary constraints implemented for the road journey of the CM's across the American continent. A related problem occurred during installation, leading to damage of the fragile bellow convolutions. An appropriate investigation and failure analysis lead to improved processes, techniques and procedures. Installation continues at approximately one unit per week in a routine manner. We expect to have the full compliment of CM's installed and connected by early summer of 2020 and plan to begin the cooldown process in the summer of 2020.

Cryoplant

The cryoplant for LCLS-II will provide the liquid Helium required to operate the cryogenic linac at temperatures of 2K. A dual interconnected plant provides capacity and room for future expansion. A complex distribution system transfers cryogens to the modules installed in the linac tunnel. Plant construction is currently underway with completion of commissioning of plant #1 in mid-2020 and about a year later for plant #2. Operation of the SC linac will begin with only one operational plant.

now unused LCLS fixed gap undulators. Availability of sub-femtosecond pulses in the HXR range will remain by continued use of non-linear compression techniques developed with the LCLS NC linac [9].

X-ray beams with up to 99% circular polarization have been available for the LCLS (DELTA undulator [10]). A new design appropriate for high repetition rate beams is currently in the engineering phase [11] and will be installed shortly after the initial commissioning phase of the LCLS-II. It is anticipated to be operational in 2022.

LCLS-II-HE

The LCLS-II-HE project will continue to extend the energy reach of the LCLS facility up to 12 keV at a 1 Mhz repetition rate [12]. This will be achieved by addition of 19 cryomodules, using improved cavities, doubling the electron beam energy of the superconducting accelerator up to 8 GeV. It is necessary to install a new cryogenic distribution box and transfer line between the cryoplat and new L4 linac. A system of beam switching devices and bypass lines will allow to run multiple CW beams at different energies, further extending the flexibility of the LCLS facility. The full range of energy reach is illustrated in Figure 8.

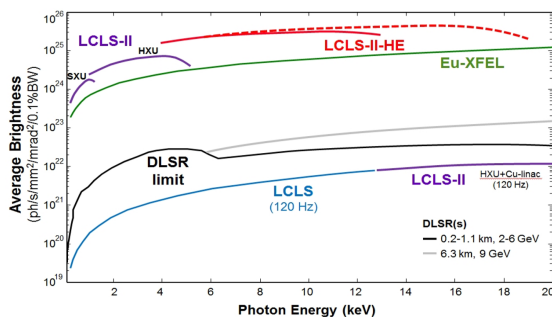


Figure 8: Energy reach and brightness of the LCLS FEL complex.

CONCLUSION

The LCLS-II project is well underway, approximately >85% complete. User operation will commence in 2020 driven by the NC linac, followed in 2021 by first SC beam operation. Undulator performance will be initially established using the NC linac followed in 2021 by first SC beam operation. Many advanced capabilities such as self-seeding, sub-femtosecond pulses and polarized beams will be available for early user operation. A major extension, doubling the SC linac energy is planned for the near future, further extending the reach of the LCLS FEL facility.

ACKNOWLEDGEMENTS

We wish to thank the staff of SLAC and our partner labs in the US that contribute to the LCLS-II project

(JLab, FNAL, ANL, LBNL and Cornell University). The team's dedication is tremendous and sustained over many years. A multi-laboratory collaboration is crucial to have access to a large amount of expertise, talent and resources. We also thank our funding agency, the US Department of Energy, Office of Science, Office of Basic Energy Science for their guidance and trust with this large project. Finally, we must acknowledge and thank our colleagues internationally, especially the accelerator physics and technical teams of DESY and the European XFEL for their advice, collaboration, sharing of knowledge and expertise with many aspects of superconducting accelerator technology.

REFERENCES

- [1] LCLS-II Final Design Report, SLAC, Menlo Park, CA, USA, LCLSII-1.1-DR-0251-R0, Nov. 2015
- [2] New Science Opportunities Enabled by LCLS-II X-Ray Lasers, SLAC, Menlo Park, CA, USA, SLAC-R-1053, June 2015.
- [3] LCLS Strategic Facility Development Plan, 2018. 2. Published by: SLAC National Accelerator Laboratory. 2575 Sand Hill Road. Menlo Park, CA 94025.
- [4] J. F. Schmerge *et al.*, "The LCLS-II Injector Design", in *Proc. 36th Int. Free Electron Laser Conf. (FEL'14)*, Basel, Switzerland, Aug. 2014, paper THP042, pp. 815-819.
- [5] F. Sannibale *et al.*, "Status of the APEX Project at LBNL", in *Proc. 3rd Int. Particle Accelerator Conf. (IPAC'12)*, New Orleans, LA, USA, May 2012, paper WEEPPB004, pp. 2173-2175.
- [6] J. Amann *et al.*, "Demonstration of self-seeding in a hard-X-ray free-electron laser", *Nature Photonics*, vol. 6, 2012, pp. 693-698. doi:10.1038/nphoton.2012.180
- [7] D. Ratner *et al.*, "Experimental Demonstration of a Soft X-Ray Self-Seeded Free-Electron Laser", *Phys. Rev. Lett.*, vol. 114, 2015, p. 054801. doi:10.1103/PhysRevLett.114.054801
- [8] A. Marinelli *et al.*, "Experimental demonstration of a single-spike hard-X-ray free-electron laser starting from noise". *Appl. Phys. Lett.*, vol. 111, 2017, p. 151101. doi:10.1063/1.4990716
- [9] Huang S *et al.*, "Generating single-spike hard X-ray pulses with nonlinear bunch compression in free-electron lasers" *Phys. Rev. Lett.*, vol. 119, 2017, p. 154801. doi:10.1103/PhysRevLett.119.154801
- [10] A. Lutman *et al.*, "Polarization control in an X-ray free-electron laser", *Nature Photonics*, vol. 10, 468-472 (2016). doi:10.1038/nphoton.2016.79
- [11] K. Tian and H.-D. Nuhn, "Numerical Study of the Delta II Polarizing Undulator for LCLS II", in *Proc. 10th Int. Particle Accelerator Conf. (IPAC'19)*, Melbourne, Australia, May 2019, pp. 1899-1902. doi:10.18429/JACoW-IPAC2019-TUPRB102
- [12] T.O. Raubenheimer, "The LCLS-II-HE, A High Energy Upgrade of the LCLS-II", in *Proc. FLS2018 Shanghai*, China, 2018. doi:10.18429/JACoW-FLS2018-MOP1WA0

FLASH - STATUS AND UPGRADES

J. Rönsch-Schulenburg*, K. Honkavaara, S. Schreiber, R. Treusch, M. Vogt,
DESY, Hamburg, Germany

Abstract

FLASH, the Free-Electron Laser at DESY in Hamburg was the first FEL user facility in the XUV and soft X-ray range [1–5]. The superconducting RF technology allows to produce several thousand SASE pulses per second with a high peak and average brilliance. It developed to a user facility with a 1.25 GeV linear accelerator, two undulator beamlines running in parallel, and a third electron beamline containing the FLASHForward plasma wakefield experiment. Actual user operation and FEL research are discussed. New concepts and a redesign of the facility are developed to ensure that also in future FLASH will allow cutting-edge research. Upgrade plans are discussed in the contribution.

FLASH FACILITY

FLASH, the Free-Electron Laser at DESY in Hamburg is a user facility which delivers FEL pulses based on the self-amplified spontaneous emission (SASE) in the wavelength range from 4 to 90 nm for user experiments. The extension of the FLASH facility by a second undulator beamline allows multi-user operation [6, 7]. Both FLASH undulator-beamlines are driven by a common linear accelerator consisting of a laser driven radio-frequency (RF) gun with a photocathode, seven superconducting accelerating modules, a third-harmonic accelerating module, and two bunch compressors. The superconducting technology allows the acceleration of electron bunch trains of several hundred bunches with a spacing of a microsecond or more and a repetition rate of 10 Hz for both beamlines. An electron beam energy of up to 1.25 GeV can be reached. A fast kicker system and a Lambertson septum are used to extract one part to FLASH1 and the other part of the bunch train into the FLASH2 beamline.

The FLASH1 beamline has six fixed-gap undulators, with a length of 4.5 m each. The SASE wavelength of FLASH1 is determined by the electron beam energy. Additionally a planar electromagnetic undulator is installed downstream of the FLASH1 SASE undulators providing THz radiation. The FLASH1 beamline also contains a seeding experiment called sFLASH [8–10].

In the FLASH2 beamline a third bunch compressor was installed in June 2019 to increase the compression flexibility, reduce the effects of space charge and of coherent synchrotron radiation (CSR). The new bunch compressor in the FLASH2 beamline has been commissioned and is now a part of the standard operation. FLASH2 contains twelve variable-gap undulators with a length of 2.5 m each, which allow choosing the wavelength to a certain extend independently from FLASH1 by varying the gap width of the undulators. In order to operate FLASH2 almost independently of

FLASH1, a second injector laser and a flexible low level RF system are used. First lasing of FLASH2 was achieved in August 2014 simultaneous to FLASH1 SASE operation. In April 2016, two user experiments, one at FLASH1 and the other at FLASH2, were running in parallel for the first time. Two experiments, requiring different beam parameters, can run simultaneously, since the bunch pattern and compression scheme can be chosen almost independently for FLASH1 and FLASH2 beamlines, allowing to tune the SASE properties specifically for each of the experiments [11].

Figure 1 shows a schematic layout of the FLASH facility with its common accelerator and the two undulator beamlines with their own experimental halls. In addition, a third electron beamline, FLASH3, hosts a pioneering beam driven plasma-wakefield acceleration experiment, FLASH-Forward [12, 13].

An overview of the photon science at FLASH and the evolution of the FLASH facility over the years can be found in [4, 5, 14]. For more details of the facility and its parameters we refer to [6, 7, 15, 16].

FLASH OPERATION

FLASH has two user periods per year. In 2018, FLASH1 was operated a total of 7103 hours, of which 59% (4189 h) was devoted to FEL user operation, 30% for studies and user preparation, and 11% for general accelerator R&D. FLASH2 was operated 6831 hours, of which 33% (2269 h) was FEL user operation. In 2018 FLASH served beam time for 38 experiments; many wavelengths in the XUV and soft X-ray range from 52 down to 4.4 nm have been realized. In 2018, two photon beamlines have been completed in the FLASH2 Kai Siegbahn experimental hall. This led to an increase of scheduled user experiments in FLASH2, a plus of 50% compared to 2017.

FLASH2 Pump-Probe Laser

The new FLASH2 pump-probe laser system [17] was commissioned in September 2018 with a successful pilot experiment, and is now in routine use. Since most experiments at FLASH1 are indeed pump-probe experiments with optical lasers, for example 58% in the first half of 2018, and 71% in the second half of 2018, the availability of the new pump-probe laser system at FLASH2 significantly increases the number of possible experiments.

New Photon Diagnostics

Another new improvement is a fast line detector for intra-train spectrum measurements named KALYPSO [18] which has been installed in the FLASH1 photon beamline. It offers an online single shot measurement of the SASE wavelength spectrum along the whole bunch train for several hundreds of

* juliane.roensch@desy.de

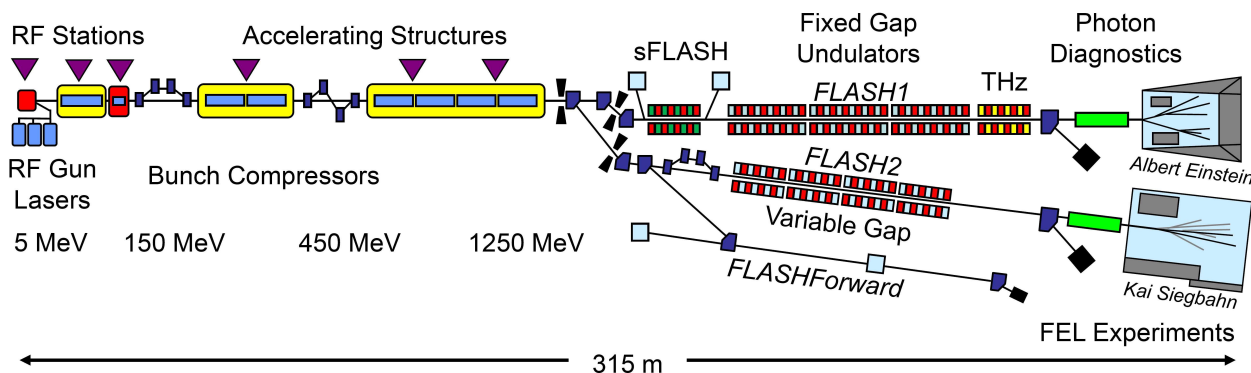


Figure 1: Layout of the FLASH facility (not to scale). Downstream the FLASH2 extraction a bunch compressor was installed in June 2019.

bunches. This optimizes the tuning procedure and monitors the spectral properties of SASE pulses along bunch trains in real time.

Additionally a THz-streaking system is under commissioning at FLASH2 which will allow measure the photon pulse duration.

FLASH Photo Injector

The present RF gun of the FLASH photo injector is in operation since August 2013. In summer 2018, its RF window developed a small vacuum leak in the order of 7×10^{-8} mbar l/s and has been replaced. The window was in operation for two years. The cathodes for the FLASH gun have a thin film of caesium tellurite with a diameter of 5 mm on a molybdenum plug [19]. "The previous photocathode was continuously operated at FLASH for 1413 days with 25 C total charge extracted from the cathode [20].

FLASH's superconducting linac can produce bunch trains of up to 800 bunches within a 0.8 ms RF flat top at a repetition rate of 10 Hz. In standard operation during 2018, FLASH supplied up to 500 bunches divided into two bunch trains with independent fill patterns and compression schemes to each of the two beamlines.

SASE

The variability of the undulators gaps at FLASH2 is an important feature allowing to vary the SASE wavelength within a few minutes per wavelengths step. However, a change of the undulator gap requires adaption of optics, correction magnets, and phase shifters. These parameters have been automatized such that users can control the wavelengths by themselves and can now be incorporated the wavelength into automated scanning scripts. Figure 2 shows an example for a beam energy of 1.1 GeV. FLASH1 was running stable while in FLASH2 SASE was tuned and measurements were taken for 3 different wavelengths: 5 nm, 9 nm and 15.3 nm. For a wavelength of 5 nm the undulator gap is opened to 18.4 mm, while for 15.3 nm SASE radiation the gap width is reduced to 9.3 mm (very close to the minimum). For 15.3 nm a single pulse energy of 1250 uJ has been produced. This corresponds to about 10^{14} photons per pulse.

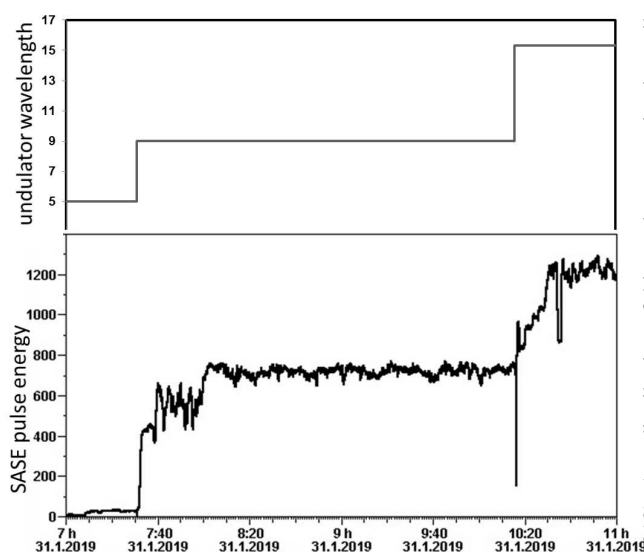


Figure 2: Example of single SASE pulse energy measured at FLASH2 (bottom) as a function of time and the FLASH2 undulator wavelength (top) used. Here the wavelength was increased from 5 to 9 and 15.3 nm while FLASH1 running stable with 5 nm (beam energy: 1.1 GeV).

New Lasing Schemes

Beside the standard SASE operation different lasing schemes have been tested using variable gap undulators at FLASH2. Frequency doubler divides the undulator section into two parts, where the second has the double frequency of the first one. This allows operation with two wavelengths and one of them at shorter wavelengths with respect to standard SASE scheme. Harmonic lasing self seeding (HLSS) amplifies higher odd harmonics and allows to improve spectral brightness of the FEL [21]. Reverse tapering in combination with an afterburner for harmonics of the fundamental has been demonstrated with an enhancement of SASE intensity by several order of magnitude [22]. Using two color lasing, two different arbitrary wavelengths are generated using alternating undulator gap widths [23].

REFURBISHMENTS

FLASH has been user facility since summer 2005. A refurbishment and upgrade program is in progress to keep FLASH a state-of-the-art FEL [24]. The refurbishment comprises the replace of aged and outdated equipment, but also to adapt the hardware and diagnostics to changed requirements over the years. As an example, the electron beam diagnostics was designed for bunch charges of >1 nC, but FLASH is nowadays routinely operated with 20 to 600 pC. High charge is applied very rarely. Therefore the diagnostics has been upgraded for operation down to 20 pC.

The synchronization system at FLASH has three aspects: Electron Bunch Timing (measured by the bunch arrival time monitors (BAMs)), Laser-to-Laser Synchronization, and the Phase Drift Compensation of the RF-Reference used for Acceleration. The synchronization has been completely refurbished, for the BAM new pick-ups and electro-optical front-ends have been developed. In order to enhance the gain of the intra train bunch arrival time feedback, a normal-conducting S-band cavity was installed. It has a larger bandwidth to improve the arrival time stability below 5 fs. Latest measurements show an improvement of the arrival time stability from 25 fs (rms) to 8.5 fs (rms). The steady state value of the arrival time stability is reached within the first 10 bunches (10 μ s for 1 MHz). For details see [25].

For the characterization of the longitudinal properties of the electron bunch and the slice emittance of the FLASH2 bunch a newly designed transversely deflecting X-band structure “PolariX” [26] is foreseen to be installed downstream of FLASH2 undulators in 2020. In June 2019, a prototype of the TDS cavity has been installed in the FLASH3 (FLASH-Forward) beamline.

The two oldest and weakest accelerator modules (module 2 and module 3) will be replaced in 2021 by refurbished modern modules designed as prototypes for the European XFEL, with high gradient cavities. This, together with an optimization of the waveguide distribution system, will provide an energy upgrade from 1.25 GeV to 1.35 GeV.

FLASH 2020+

As part of the DESY strategy process, an upgrade project “FLASH 2020+” has been proposed. The FLASH 2020+ proposal is motivated by the requests of the FEL users, taking into account the technological and beam physics requirements and constraints. The key aspects of the proposal are:

- The replacement of the FLASH1 undulators with variable gap ones, in order to operate both beamlines more independent from each other and thus reduce setup times by minimizing the required beam energy changes.
- The establishment of a high repetition rate seeding at FLASH1, with the goal of 1 MHz.
- The extension of the wavelength (fundamental) range at FLASH2 down to the oxygen K-edge (2.3 nm) to cover the whole water window.
- The exploration of possibilities for novel lasing schemes towards attosecond physics [27].

For more details see [24].

CONCLUSION

FLASH started as the first XUV-FEL user facility. In 2014, with the extension by a second undulator beamline, it became a multi-user facility. To keep FLASH a state-of-the-art FEL, a refurbishment and upgrade program is on-going.

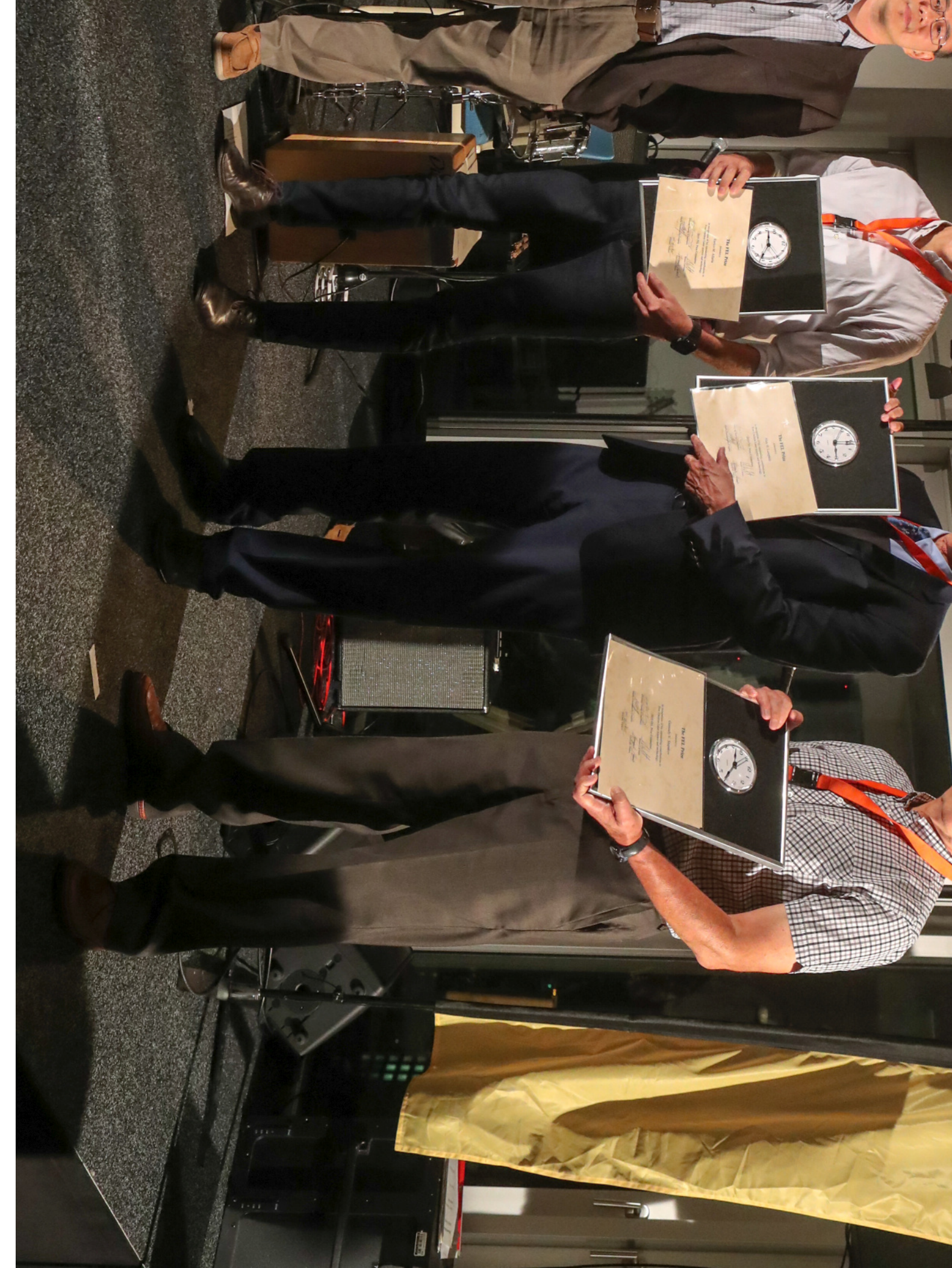
ACKNOWLEDGEMENTS

We would like to thank all our colleagues at DESY for their continuous dedication in operation, maintenance and upgrade of the FLASH facility.

REFERENCES

- [1] W. Ackermann *et al.*, “Operation of a free-electron laser from the extreme ultraviolet to the water window”, *Nature Photonics*, vol. 1, pp. 336–342, 2007. doi:10.1038/nphoton.2007.76
- [2] K. Tiedtke *et al.*, “The soft x-ray free-electron laser FLASH at DESY: beamlines, diagnostics and end-stations”, *New J. Phys.*, vol. 11, p. 023029, 2009. doi:10.1088/1367-2630/11/2/023029
- [3] S. Schreiber, “First Lasing in the Water Window with 4.1 nm at FLASH”, in *Proc. 33rd Int. Free Electron Laser Conf. (FEL'11)*, Shanghai, China, Aug. 2011, paper TUOB12, pp. 164–165.
- [4] J. Rossbach, J. R. Schneider, and W. Wurth, “10 years of pioneering X-ray science at the free-electron laser FLASH at DESY”, *Physics Reports*, vol. 808, pp. 1–74, 2019. doi:10.1016/j.physrep.2019.02.002
- [5] K. Honkavaara and S. Schreiber, “FLASH: The pioneering XUV and soft X-ray FEL user facility”, presented at the 39th Int. Free Electron Laser Conf. (FEL'19), Hamburg, Germany, Aug. 2019, paper THP074, this conference.
- [6] S. Schreiber and B. Faatz, “The free-electron laser FLASH”, *High Power Laser Science and Engineering*, vol. 3, p. e20, 2015. doi:10.1017/hpl.2015.16
- [7] B. Faatz *et al.*, “Simultaneous operation of two soft x-ray free-electron lasers driven by one linear accelerator”, *New J. Phys.*, vol. 18, p. 062002, 2016. doi:10.1088/1367-2630/18/6/062002
- [8] S. Ackermann *et al.*, “Generation of Coherent 19- and 38-nm Radiation at a Free-Electron Laser Directly Seeded at 38 nm”, *Phys. Rev. Lett.*, vol. 111, p. 114801, 2013. doi:10.1103/PhysRevLett.111.114801
- [9] C. Lechner *et al.*, “Seeding R&D at sFLASH”, presented at the 39th Int. Free Electron Laser Conf. (FEL'19), Hamburg, Germany, Aug. 2019, paper TUP076, this conference.
- [10] C. Lechner *et al.*, “Status of the sFLASH Experiment”, in *Proc. IPAC'18*, Vancouver, Canada, Apr.-May 2018, pp. 1471–1473. doi:10.18429/JACoW-IPAC2018-TUPMF085
- [11] J. Roensch-Schulenburg *et al.*, “Experience with Multi-Beam and Multi-Beamline FEL-Operation”, *J. Phys.: Conf. Series*, vol. 874, p. 012023, 2017. doi:10.1088/1742-6596/874/1/012023

- [12] R. D'Arcy *et al.*, "FLASHForward: plasma wakefield accelerator science for high-average-power applications", *Phil. Trans. R. Soc. A*, vol. 377, p. 20180392, 2019. doi:10.1098/rsta.2018.0392
- [13] R. D'Arcy *et al.*, "Tunable Plasma-Based Energy Dechirper", *Phys. Rev. Lett.*, vol. 122, p. 034801, 2019. doi.org/10.1103/PhysRevLett.122.034801
- [14] K. Honkavaara, B. Faatz, J. Feldhaus, S. Schreiber, R. Treusch, and M. Vogt, "FLASH: First Soft X-ray FEL Operating Two Undulator Beamlines Simultaneously", in *Proc. 36th Int. Free Electron Laser Conf. (FEL'14)*, Basel, Switzerland, Aug. 2014, paper WEB05, pp. 635–639.
- [15] M. Vogt, K. Honkavaara, M. Kuhlmann, J. Roensch-Schulenburg, S. Schreiber, and R. Treusch, "Status of the Superconducting Soft X-Ray Free-Electron Laser FLASH at DESY", in *Proc. 9th Int. Particle Accelerator Conf. (IPAC'18)*, Vancouver, Canada, Apr.-May 2018, pp. 1481–1484. doi:10.18429/JACoW-IPAC2018-TUPMF090
- [16] J. Roensch-Schulenburg, K. Honkavaara, M. Kuhlmann, S. Schreiber, R. Treusch, and M. Vogt, "Status of the Superconducting Soft X-Ray Free-Electron Laser User Facility FLASH at DESY", in *Proc. 10th Int. Particle Accelerator Conf. (IPAC'19)*, Melbourne, Australia, May 2019, pp. 1909–1911. doi:10.18429/JACoW-IPAC2019-TUPRB106
- [17] N. Schirmel *et al.*, "Long-Term Stabilization of Temporal and Spectral Drifts of a Burst-Mode OPCPA System", in *Conference on Lasers and Electro-Optics*, OSA Technical Digest (Optical Society of America), 2019, paper STu4E.4. doi:10.23919/CLEO.2019.8749414
- [18] L. Rota *et al.*, "KALYPSO: Linear array detector for high-repetition rate and real-time beam diagnostics", *Nucl. Instr. Meth A*, 2018, in press. doi:10.1016/j.nima.2018.10.093
- [19] S. Lederer and S. Schreiber, "Cs2Te Photocathode Lifetime at Flash and European XFEL", in *Proc. IPAC'18*, Vancouver, Canada, Apr.-May 2018, pp. 2496–2498. doi:10.18429/JACoW-IPAC2018-WEPMF056
- [20] S. Lederer and S. Schreiber, "Update on the Photocathode Lifetime at FLASH and European XFEL", presented at the 39th Int. Free Electron Laser Conf. (FEL'19), Hamburg, Germany, Aug. 2019, paper WEP047, this conference.
- [21] E.A. Schneidmiller *et al.*, "First operation of a harmonic lasing self-seeded free electron laser", *Phys. Rev. Accel. Beams*, vol. 20, p. 020705, 2017. doi.org/10.1103/PhysRevAccelBeams.20.020705
- [22] E. Schneidmiller *et al.*, "Background-Free Harmonic Production in XFELs via a Reverse Undulator Taper", in *Proc. 8th Int. Particle Accelerator Conf. (IPAC'17)*, Copenhagen, Denmark, May 2019, pp. 2618–2520. doi:10.18429/JACoW-IPAC2017-WEPAB022
- [23] E. Schneidmiller *et al.*, "Two-Color Operation of FLASH2 Undulator", presented at the 39th Int. Free Electron Laser Conf. (FEL'19), Hamburg, Germany, Aug. 2019, paper TUP055, this conference.
- [24] M. Vogt, K. Honkavaara, J. Roensch-Schulenburg, S. Schreiber, and J. Zemella, "Upgrade Plans for FLASH for the Years After 2020", in *Proc. 10th Int. Particle Accelerator Conf. (IPAC'19)*, Melbourne, Australia, May 2019, pp. 1748–1751. doi:10.18429/JACoW-IPAC2019-TUPRB027
- [25] B. Lautenschlager *et al.*, "Longitudinal Intra-Train Beam-Based Feedback at FLASH", presented at the 39th Int. Free Electron Laser Conf. (FEL'19), Hamburg, Germany, Aug. 2019, paper WEP011, this conference.
- [26] F. Christie, J. Roensch-Schulenburg, and M. Vogt, "A PolariX TDS for the FLASH2 Beamline", presented at the 39th Int. Free Electron Laser Conf. (FEL'19), Hamburg, Germany, Aug. 2019, paper WEP006, this conference.
- [27] E. Schneidmiller *et al.*, "A Concept for Upgrade of FLASH2 Undulator Line", in *Proc. 10th Int. Particle Accelerator Conf. (IPAC'19)*, Melbourne, Australia, May 2019, TUPRB024. doi:10.18429/JACoW-IPAC2019-TUPRB024



List of Authors

Bold papercodes indicate primary authors; ~~crossed-out~~ papercodes indicate 'no submission'

— A —

Abrami, A. **MOA02**
Abubakirov, E.D. **THP060**
Ackermann, S. **TUP073**, **TUP074**, **TUP076**,
TUP077, **TUP078**
Ackermann, W. **WEP019**
Adelmann, A. **THP061**
Adhlakha, N. **THP013**
Adolphsen, C. **WEP043**
Aeppli, G. **THP085**
Aghababayan, A. **WEP008**
Agustsson, R.B. **THP073**
Aiba, M. **WED01**, **THB03**
Aicheler, M. **THP078**
Aksoy, A. **THP078**, **TUP025**
Al Haddad, A. **THP085**
Alarcon, A.D. **WED01**
Alesini, D. **THP078**
Alex, J. **WEP037**, **THP085**
Allaria, E. **MOA02**, **TUB04**, **TUP083**,
WEP034, **THP013**, **THP079**

Alotaibi, B.M. **TUP051**
Altuijri, R. **TUP051**
Amann-Winkel, K. ~~**THA02**~~
Amirkhanyan, Z.G. **TUP001**
Amstutz, Ph. **THP003**
Andersson, J. **TUP066**, **THP084**
André, T. **THP048**
Andriyash, I.A. **THP048**
Anisimov, P.M. **MOC01**, **THB01**
Anton, J.W.J. **TUP079**, **TUD04**, **WEP079**
Apostolov, E.M. **WEP049**
Apsimon, R. **THP078**
Arbelo, Y.P. ~~**TUA03**~~
Arnesano, J.M. **THP078**
Arnold, A. **WEP026**
Arrell, C. **WED01**, **THP085**
Arsov, V.R. **WEP037**, **THP085**
Arzhannikov, A.V. **TUP021**
Asakawa, M.R. **TUP012**
Asgekar, V.B. **TUP004**
ASSmann, R.W. **TUP076**, **WEP036**
Assoufid, L. **TUD04**
Azima, A. **TUP076**

— B —

Baader, J.E. **WEP067**
Badano, L. **MOA02**, **TUB04**, **THP013**,
THP079

Bae, S. **TUD03**
Baek, I.H. **WEP031**
Bagschik, K. **THA04**
Bahns, I. **TUP009**, **THP041**

Bal, W. **THP081**
Balal, N. **WEP086**, **THP024**
Balandin, V. **TUP056**, **TUP058**, **WEP008**,
THP001
Bandurkin, I.V. **TUP019**
Bane, K.L.F. **THP035**
Bartnik, A. **THP081**
Bassanese, S. **THP079**
Bawatna, M. **TUP007**, **WEP081**
Bazyl, D.B. **THP008**
Büsing, B. **TUP080**
Bellaveglia, M. **THP078**
Benabderrahmane, C. **THP048**
Bencivenga, F. **THP079**
Benson, S.V. ~~**TUD01**~~
Benwell, A.L. **WEP103**
Berlin, A. **WEP003**, **WEP004**
Bernhard, A. **THP078**
Bettoni, S. ~~**TUA03**~~, **WED01**, **THB03**,
THP085
Beutner, B. **TUP058**, **WEP008**
Bielawski, S. **WEP015**, **THP048**
Biss, H. **TUP076**
Blache, F. **THP048**
Blank, V.D. **TUP079**
Boesenberg, U. **TUP058**, **WEP079**
Boffo, C. **TUP061**
Bohler, D.K. **TUP035**
Boll, R. **TUA01**
Bonetti, S. **THP084**
Boonpornprasert, P. **TUP001**, **TUP002**, **TUP003**,
WEP051, **WEP052**

Bopp, M. **WEP036**
Borrelli, S. **WEP02**
Bosco, F. **THP078**
Bossi, M. **MOA02**
Bostedt, C. **THP085**
Bousonville, M. **WEP045**
Bouvet, F. **THP048**
Brachmann, A. **FRA02**
Bratman, V.L. **WEP086**, **THP024**
Braun, H.-H. **MOA02**, **WEP036**, **THP085**
Braune, M. **TUP055**
Brinker, F. **TUA01**, **TUA04**, **TUP058**,
WEP008, **WEP047**, **THP007**

Briquez, F. **THP048**
Brovko, O.I. **WEP073**
Bruchon, N. **MOA02**
Brynes, A.D. **THB02**
Buaphad, P. **TUP065**
Bucksbaum, P.H. ~~**THD02**~~
Buechler, C.E. **MOC01**
Buonomo, B. **THP078**

Content from this work may be used under the terms of the CC BY 3.0 licence (© 2019). Any distribution of this work must maintain attribution to the author(s), title of the work, publisher, and DOI

Burt, G.	THP078
Butkowski, Ł.	WEP011
Bykov, E.V.	TUP024
— C —	
Callegari, C.	TUB04, THP079
Calvi, M.	WEP097, WEP098, WED01, THP078, THP085
Campbell, L.T.	TUP049, TUP050
Campese, T.J.	THP073
Cano Vargas, E.	WEP003, WEP004
Capotondi, F.	MOA02, THA04, THP079
Cardelli, F.	THP078
Carlsten, B.E.	MOC04
Casalbuoni, S.	TUP004, TUP061
Cassar, A.	WED01
Castañeda Cortés, H.M.	WEP101, THP065, THP078
Castilla, A.	THP078
Castronovo, D.	MOA02, THP079
Catalán Lasheras, N.	WEP036
Cautero, M.	MOA02
Cefarin, N.	WEB02
Celcer, T.	THP085
Chaisueb, N.	THP031
Champenois, E.	THD02
Chan, C.K.	THP030
Chang, C.-C.	THP030
Chang, C.-H.	THP030
Chang, L.-H.	THP030
Chao, A.	THP020, THP030, THP055
Chen, C.H.	TUP091, THP030
Chen, L.J.	WEP027
Chen, M.	WEP056
Chen, Y.	TUP002, WEA03, WEP050, WEP051, WEP052, WEP055, WEP062, THP007
Chen, Z.	THP015
Cheng, G.K.	THP015
Cheng, H.P.H.	WEP003, WEP004
Cherepenko, A.	WEP045
Cho, M.H.	TUB03, TUP064, THP051
Choroba, S.	WEP045, WEP049
Chou, M.C.	THP030
Chou, P.J.	THP030
Choudhuri, A.	WEP046
Christie, F.	WEP006, WEP036
Chu, P.X.	WEP059
Chung, T.Y.	WEP100
Cilento, F.	THP079
Cinquegrana, P.	MOA02, THP079
Citterio, A.	WEP036
Clarke, J.A.	THP078
Coello de Portugal, J.M.	WEB03
Colson, W.B.	TUP006
Corde, S.	THP048
Coreno, M.	MOA02, THP079
Couprrie, M.-E.	MOA01, MOA02, THP048

Cowan, T.E.	TUP008
Cowie, L.S.	THP066
Craievich, P.	TUA03, WEP036, WEP037, THB03, THP085
Croia, M.	THP078
Cross, A.W.	THP078
Cryan, J.	THD02
Cudin, I.	MOA02, THP079
Curbis, F.	TUP066, TUP067, TUP090, WEP034, THP084
Czuma, P.J.	THP081
Czwalinna, M.K.	WEB04, WEP011, WEP015, WEP019
— D —	
D'Arcy, R.T.P.	WEP036
D'Auria, G.	THP078, THP079
Dai, A.	WEP003, WEP004
Dai, D.X.	THP015
Dal Zilio, S.	WEB02
Danailov, M.B.	MOA02, THP079
Dang, D.K.	THP073
Dattoli, G.	MOA01, THP078
David, Ch.	WEB02
Davidyuk, I.V.	WEP094, THP027
De Gersem, H.	THP008, THP009
De Monte, R.	THP079
De Ninno, G.	MOA02, TUB04, THP010, THP013, THP079
De Pas, M.	TUP006
Decker, F.-J.	TUD04, THP051, THP071
Decking, W.	TUA01, TUA04, TUP009, TUP056, TUP058, TUP062, TUP079, WEP008, WEP013, WEP014, WED02, THP001, THP002, THP007
Deinert, J.-C.	WEP081
del Pozo Romano, V.	WEP036
Delgiusto, P.	THP079
Demidovich, A.A.	MOA02, THP079
Den Hartog, P.K.	THP068
Deng, D.R.	WEP027
Deng, H.X.	MOA05, TUP063, TUP088, THP018, WEP089
Deng, X.J.	THP020, THP022, THP036, THP055
Denham, P.E.	THP073
Derksen, J.	WEP003, WEP004
Di Fraia, M.	TUB04, THP079
Di Mitri, S.	MOA02, TUB04, THP010, THP011, THP012, THP013, THP078, THP079
Di Pietro, P.	THP013
Dietrich, F.	WED03
Dietrich, Y.	THP048
Dijkstal, P.	TUA03, THB03
Ding, H.L.	THP015

Ding, Y. TUP032, TUP035, WEP043, THP035, THP071
Diomede, M. THP078
Diviacco, B. MOA02, THP079
Dohlus, M. TUP056, TUP058, TUP060, TUP061, WEP051, THP009, THP049
Dommach, M. WEP079
Dong, X. TUP079, TUP087, WEP079
Dorda, U. WEP036
Dordevic, S. WEP038
Dowd, R.T. THP078
Dowell, D. TUP006
Downer, M. THP069
Drescher, M. TUP076
Driver, T.D.C. THD02
Dunham, M. FRA02
Dunning, D.J. WEP101, THP065, THP066, THP078
Duris, J.P. THD02
Dursun, B. WEP011
Duval, J.P. THP048
Dyunin, E. THP052

— E —

Eckoldt, H.-J. WEP045
Edstrom, D.R. WEP042
Eidam, J. WEP079
El Ajjour, M. THP048
Elçim, Ö.F. TUP025
Emma, C. TUP092, THP071, TUT01
Enders, J. THP008
Esperante Pereira, D. THP078
Evain, C. WEP015, THP048
Evtushenko, P.E. TUP008

— F —

Faatz, B. TUP055, TUP073, TUP074, TUP076, TUP077, TUP078, WEP070, WEP072
Fabris, A. THP079
Fabris, R. THP010, THP079
Fahlström, S. WEP035
Fang, G.P. MOA05
Fang, W. THP078
Faus-Golfe, A. THP078
Fawley, W.M. MOA02, THP079, TUP035
Fedin, M.V. TUP024
Feifel, R. TUB04
Felber, E.P. WEP007
Felber, M. WEB04, WEP007, WEP010, WEP016
Feng, C. MOA02, TUP087, WEP089
Feng, L. WEP058
Feng, Y. TUP032, TUP033, TUP035, WEP103
Fenner, M. WEB04, WEP007
Ferianis, M. MOA02, WEB02, THP079

Ferrari, E. MOA02, MOC02, MOC03, TUA03, WEB02, WED01, THB03, THP086
Ferrario, M. THP078
Fiadonu, V. TUP032
Ficcadenti, L. THP078
Fiedorowicz, H. THP081
Fisher, A.C. TUP036
Fisher, A.S. WEP103, WEP104
Flehsig, U. WEP095
Flöttmann, K. THP049
Foese, M. WEP036
Foglia, L. MOA02, THP079
Fol, E. WEB03
Follath, R. WEP095, WED01, THP085
Franchetti, G. WEB03
Frassetto, F. MOA02
Frömter, R. THA04
Frei, F. THP085
Freund, H. TUP050
Freund, W. TUP058, WED03, WED04
Friedman, A. TUT01, WEP086, THP052
Fröhlich, L. TUA01, TUP058, TUP062, WEP008, WED04, THP001
Furlan Radivo, P. THP079
Fuster, J. THP078

— G —

Gadjev, I.I. THP073
Gaiffi, N. THP085
Gaio, G. MOA02, THP013, THP079
Gallo, A. THP078
Ganter, R. WEP036, WEP038, WED01, THP085
Garzella, D. MOA02
Gassner, G.L. TUD04
Gautier, J. THP048
Gazis, E.N. THP078
Gazis, N. THP078
Gehlot, M. WEP085
Gelmetti, F. THP079
Geloni, G. TUA04, TUP004, TUP056, TUP061, TUP062, TUP073, TUP077, TUP079, WEP080, THP051, THD03
Geng, Z.G. WEP037, THP085
Gensch, M. TUP004
Geometrante, R. THP078
Georgiev, G.Z. TUP001, TUP002, TUP003, WEP051
Gerasimov, M.G. THP052
Gerasimova, N. TUA01, TUA04, TUP062, WEP080
Gerth, C. WEB04, WEP011, WEP012, WEP015, WEP035
Gethmann, J. THP078
Getmanov, Ya.V. TUP024, TUD03

lazzourene, F. **MOA02, THP079**
Inoue, I. **TUB02**
Isaev, I.I. **TUP002, WEP051, WEP052, WEP062, THP007**
Isaksson, L. **TUP066, THP084**
Ischebeck, R. **WEB02, THB03, THP061, THP085**
Ivanov, R. **TUP076**
Ivanyan, M. **THP049**

— J —

Jacewicz, M. **THP078**
Jacobson, B.T. **WEP103, WEP104**
Jan, J.C. **THP030**
Janik, Y. **WEP008**
Jansma, W.G. **TUD04**
Janssen, X.J.A. **THP078**
Janulewicz, K. **THP081**
Jastrow, U. **TUP055, TUP058**
Jeevakhan, H. **TUP041, TUP042**
Jeon, I.J. **WEP030**
Jeong, I.G. **TUP065**
Jeong, Y.U. **TUD03, WEP031**
Jia, Q.K. **MOA07, TUP047, WEP063**
Jöhri, H. **THP085**
Johnsson, P. **THP084**
Jonas, R. **WEP036**
Jones, J.K. **THP065, THP066**
Joo, Y.J. **TUP065**
Jung, Y.G. **WEP092, WEP093**
Junkes, H. **TUP006**
Juranič, P.N. **TUA03, WED01, THP085**

— K —

Kärtner, F.X. **WEP003, WEP004**
Kalt, R. **WEP037**
Kammering, R. **TUA01, TUP058, WEP008, WEP009**
Kang, H.-S. **TUB03, TUP017, TUP064, THP051**
Karabekyan, S. **TUA04, TUP004, TUP061, TUP062, TUP079, WED04**
Karsli, Ö. **TUP025**
Kashiwagi, S. **TUP014**
Katalev, V.V. **WEP045, WEP049**
Kato, R. **THA03**
Kaur, M. **THP047**
Kawase, K. **TUD02**
Kawata, H. **THA03**
Kay, H. **WEP008**
Kaya, Ç. **TUP025**
Kazarian, K. **WEP079**
Kearney, S.P. **TUP079, TUD04, WEP079**
Keil, B. **THP085**
Khan, S. **TUP076, TUP080**
Khan, S.M. **WEP085**
Khazanov, E. **WEP050**
Khojayan, M. **THP048**

Khullar, R. **WEP085**
Kim, C. **TUB03**
Kim, C. **WEP079**
Kim, D. **WEP030**
Kim, D.E. **WEP092, WEP093**
Kim, G. **TUB03, TUP064, THP051**
Kim, H.W. **WEP031**
Kim, J. **WEP030, WEP031**
Kim, K. **TUB03, TUP028, TUP037, TUP038, TUD04**

TUP053, TUP054
THA02
TUB03
TUP065
WEP104
THP061
THA04
TUP033
THP048
WEP062
WEP097, WEP098, WED01
WEP036
THD02
WEP048
WEP081
TUB03, TUP017, THP051
TUP025
TUP058, TUP062, WED03, WED04

TUP062, TUP079
THP047
THP078
THP048
THP047
TUP002, WEP050, WEP051, WEP052, WEP062, THP007
TUP001, TUP003
TUP062
TUP066, THP084
TUP004, WEP081
WEB04, WEP007, WEP010, WEP016

TUP001, TUP002, TUP003, WEA03, WEP050, WEP051, WEP052, WEP062, THP007, THP009
THP071
THP061
THP081
WEP036
THP079
WEP038
TUP080
THP047
THP081, TUP032, TUP033, TUP035, THP071

39th Free Electron Laser Conf. ISBN: 978-3-95450-210-3		FEL2019, Hamburg, Germany		JACoW Publishing	
Content from this work may be used under the terms of the CC BY 3.0 licence (© 2019). Any distribution of this work must maintain attribution to the author(s), title of the work, publisher, and DOI	Kuan, C.K.	THP030	Li, X.H.	WEP059	
	Kubarev, V.V.	TUD03	Li, Y.	TUA04, TUP056, TUP061,	
	Kube, G.	WEB01		WEP076, THP002	
	Kuhlmann, M.	TUP055	Li, Y.S.	TUP037, TUP038	
	Kujala, N.G.	TUA04, TUP058, WED03	Li, Z.B.	THP015	
	Kukk, E.	TUP062	Liang, X.	WEP097, WEP098	
	Kurdi, G.	MOA02, THP079	Libov, V.	WEP036	
	Kuzikov, S.V.	THP060	Limberg, T.	TUP058, WEP008	
	Kwon, D.	WEP030	Lin, L.	WEP056	
	— L —		Lin, M.-C.	THP030	
	La Civita, D.	TUP079	Lindau, F.	THP084	
	Laarmann, T.	TUP076	Lindberg, R.R.	TUP027, TUP028, TUP037,	
	Labat, M.	THP048		TUP038, TUP053, TUP054,	
	LaBerge, M.	THP069		TUD04	
	Laksman, J.	TUA04, TUP062, WED03	Lindenberg, A.	WEP104	
	Lal, S.	TUP002, WEP051, WEP052,	Lippuner, T.	WEP037	
		WEP054, WEP055, WEP062,	Lishilin, O.	TUP002, WEP051, WEP052,	
		THP007		WEP062, THP007	
	Lamb, T.	WEB04, WEP007, WEP010,	Litvinenko, V.	MOA06	
		WEP016	Liu, B.	MOA05, TUP063, TUP088,	
	Lambert, G.	THP048		WEP058, THP018, WEP089	
	Lan, T.	WEP058	Liu, J.	TUA04, TUP058, WED03,	
	Lang, T.	TUP074, TUP076, WEP050		WED04	
	Lantz, B.	TUD04	Liu, J.	MOA03	
	Lao, C.L.	WEP024	Liu, K.X.	WEP056, WEP057	
	Larsson, M.	THP084	Liu, P.	TUD01	
	Latina, A.	THP078	Liu, S.	TUA01, TUA04, TUP079,	
	Lau, W.K.	TUP091, THP030		WEB01, WEP008	
	Lautenschlager, B.	WEB04, WEP011	Liu, T.	TUP087	
	Lazzarino, M.	WEB02	Liu, T.	WEP059	
	Lechner, C.	TUP073, TUP074, TUP076,	Liu, W.	THD04	
		TUP077, TUP078	Liu, X.	THP078	
	Leclercq, N.	THP048	Liu, Y.	MOA03	
	Lederer, S.	WEP036, WEP047, WEP062	Liu, Y.	TUD04	
	Lee, A.P.	TUP091, THP030	Liu, Y.Q.	WEP056, WEP057	
	Lee, H.R.	TUP065	Liu, Z.P.	WEP089	
	Lee, J.Y.	TUP065	Lockmann, N.M.	WEP012, WEP035	
	Lee, S.H.	TUP065	Löhl, F.	WEP037, WED01, THB03,	
	Lee, S.J.	WEP092, WEP093		THP085	
	Lee, W.S.	WEP104	Loisch, G.	TUP002, WEP050, WEP051,	
	Lehnert, U.	TUP008		WEP052, THP007	
	Lemery, F.	THP049	Lombosi, C.	WEB02	
	Leng, Y.B.	MOA05	Lonza, M.	MOA02, THP079	
	Lestrade, A.	THP048	Loulergue, A.	THP048	
	Li, C.	WEP046	Lu, W.	WEP079	
	Li, C.L.	WEP058	Ludwig, F.	WEB04	
	Li, H.T.	MOA07, WEP063	Lueangaramwong, A.	TUP003	
	Li, L.B.	TUP015	Luiten, O.J.	THP078	
	Li, M.	MOA03, TUP015	Lumpkin, A.H.	WEP041, WEP042, THP069	
	Li, P.	MOA03, TUP015, WEP024,	Luo, G.-H.	THP030	
		WEP026, WEP027	Luo, H.	WEP059	
	Li, Q.M.	THP015	Luo, X.	MOA03, TUP015, WEP024	
	Li, S.	THD02	Lupi, S.	THP013	
	Li, X.	TUP002, WEP051, WEP052	Lurie, Yu.	WEP086, THP024	
	Li, X.	TUP001, TUP003, WEP062,	Lutman, A.A.	TUA02, TUP035, TUP092,	
		THP007		THP071, THD02	

— M —	
Ma, S.	WEP026
MacArthur, J.P.	MOD02 , TUP032, TUP033, TUD04, THP036, THD02
Machau, K.	WEP045
Madsen, A.	WEP079
Mahne, N.	MOA02, TUB04, THP079
Mai, C.	TUP080
Maier, A.R.	THP047
Malka, V.	THP048
Malkin, A.	TUP018, TUP021
Maltezopoulos, Th.	TUA04, TUP058, TUP062, WED03
Malvestuto, M.	MOA02, THP079
Malyzhenkov, A.	TUA03, THB03
Manfreda, M.	MOA02, TUB04, THP079
Mansten, E.	TUP066, THP084
Marcellini, F.	WEP036, THP085
Marchetti, B.	WEP036
Marcos, J.	THP078
Marcouillé, O.	THP048
Marcus, G.	TUP032, TUP033, TUP035, TUP092, TUD04, THP036, THP071
Margraf, R.A.	TUP032, TUD04, THP036
Marín, E.	THP078
Marinelli, A.	THP071, THD02
Marinkovic, G.	THP085
Marksteiner, Q.R.	MOC01
Marteau, F.	THP048
Marx, D.	WEP036
Marx, M.	THP049
Masciovecchio, C.	MOA02, THP079
Matveev, A.S.	THP027
Mavrič, U.	WEB04
Mazza, T.	TUA01, TUB04, TUP062
Müller, L.	THA04
Müller, W.F.O.	THP008
McMonagle, G.	WEP036
McNeil, B.W.J.	TUP026, TUP049, TUP050, TUP051, TUP072
Mehrjoo, M.	TUP077, WEP072
Meijer, G.	TUP006
Melkumyan, D.	TUP002, WEP051, WEP052, WEP062, THP007
Melnikov, A.R.	TUP024
Messerschmidt, M.	TUP058
Meyer auf der Heide, A.	TUP080
Meyer, M.	TUA01, TUP062
Miceli, A.	TUD04
Michel, P.	TUP008
Michelato, P.	WEA04, WEP053, WEP062
Mikhailov, S.F.	TUD01
Millar, W.L.	WEP036
Millich, M.	THP079
Miltchev, V.	TUP076

Min, C.-K.	TUB03, WEP064, THP051
Mincigrucci, R.	THP079
Miotti, P.	MOA02
Mirian, N.S.	MOA02, MOD04, TUB04, THP079
Mironov, S.	WEP050
Mishra, G.	TUP041, TUP042, WEP085
Miyajima, T.	TUD02, THA03
Möller, J.	WEP079
Mohammad Kazemi, M.M.	TUP074, TUP076
Mohanty, S.K.	WEP053
Mohr, C.	WEP046
Molodzhentsev, A.Y.	THP047
Molodtsov, S.	TUP056
Monaco, L.	WEA04, WEP047, WEP053, WEP062
Moody, N.A.	WEA02
Morgan, J.F.	TUP072
Morita, N.M.	TUP014
Morozov, P.	WEP045, WEP049
Mostacci, A.	THP078
Muñoz Horta, R.	THP078
Mueller, F.	TUP001, TUP003
Müller, J.	WEB04, WEP007, WEP010, WEP016, WEP046
Muller, E.	WEP073
Mun, G.	WEP093
Muratori, B.D.	TUP072
Murokh, A.Y.	THP073
Musumeci, P.	TUP036, TUT01, THP073
Mutný, M.	THP061
Muto, T.	TUP014
Mutsaers, P.H.A.	THP078

— N —	
Na, D.H.	TUB03
Nachtigal, Y.	WEP049
Nagai, R.	TUD02
Nakamura, N.	THA03
Nam, I.H.	TUB03, THP051
Nam, K.M.	THP044
Nanbu, K.	TUP014
Nanni, E.A.	TUP036, WEP104
Naumenko, D.	THA04
Negodin, E.	TUP079
Nergiz, Z.	THP078
Neuhaus, M.	WEP003
Nguyen, D.C.	MOC01
Nguyen, F.	THP078
Niemczyk, R.	TUP002, WEP050, WEP051, WEP052, WEP062, THP007
Nietubyc, R.	THP081
Nikolov, I.	MOA02, THP079
Nilsson, A.	THA02, THP084
Nix, L.J.R.	THP078
Nölle, D.	TUA01, TUA04, TUP056, TUP058, WEP008, WED02,

Nonnenmacher, M.	WED04, FRA01
Nosochkov, Y.M.	THP061
Novokshonov, A.I.	THP035
Nuhn, H.-D.	WEB01
	WEP107
— O —	
O'Shea, F.H.	THP079
Oang, K.	WEP031
Obier, F.	TUA01, WEP008, WEP013 , WEP014
Oepen, H.P.	THA04
Oh, B.G.	TUB03
Ohgaki, H.	TUD02
Omet, M.	WEP008
Oparina, Yu.S.	TUP019, TUP020, THP024
Oppelt, A.	TUP001, TUP002, TUP003, WEP051, WEP052, WEP062, THP007
Orlandi, G.L.	WEB02 , THB03, THP085
Osterhoff, J.	WEP036
Oumbarek Espinos, D.	THP048
Ouyang, D.M.	WEP057
Ozkan Loch, C.	WEB02, THP085
— P —	
Pagani, C.	WEA04, WEP053
Palka, N.	THP081
Palumbo, L.	THP078
Pan, Q.	MOA03, TUP015
Pan, Z.	THP022, THP055
Paraliev, M.	WEP038 , THP085
Paraskaki, G.	TUP073, TUP074, TUP076, TUP077 , TUP078 , WEP072
Parc, Y.W.	THP044
Park, J.-W.	TUP053 , TUP054
Park, S.	WEP031
Park, Y.	THP073
Patthey, L.	WEP095, THP085
Pedersoli, E.	THA04
Pedrozzi, M.	WEP036, WEP037, THP085
Pellegrini, C.	MOA01, TUP092, THP012, TUT01, THP071
Penco, G.	MOA02, TUB04, WEB02, THP013, THP079
Penirschke, A.	WEP019
Penn, G.	MOA02, THP012
Pérez, F.	THP078
Perucchi, A.	THP013, THP079
Peskov, N.Yu.	TUP019, TUP020, TUP021, THP060
Peters, F.	WEP046
Petralia, A.	THP078
Petrov, I.	TUA04, TUP058, WEP079
Pfeiffer, S.	WEB04, WEP011 , WEP046
Pflüger, J.	TUP056, WED02
Philipp, S.	TUP001, TUP003
Philippi-Kobs, A.	THA04

Piccirilli, F.	THP013
Piersanti, L.	THP078
Pitman, S.	WEP036
Placidi, M.	THP012
Planas, M.P.	WED03
Plekan, O.	TUB04, THP079
Poletto, L.P.	MOA02
Pongchalee, P.	TUP026
Pop, M.A.	MOA02, TUP066, TUP067, TUP090 , WEP034 , THP084
Popov, V.	TUD01
Poznański, J.	THP081
Pradervand, C.	THP085
Prat, E.	MOA02, TUA03, WEB02, WEP036, WEP037, WED01, THB03 , THP085, THP086
Predonzani, M.	THP079
Priem, J.M.A.	THP078
Prince, K.C.	TUB04, THP079
Principi, E.	MOA02, THP079
Przygoda, K.P.	WEP007
Przystawik, A.	TUP076
— Q —	
Qian, H.J.	TUP002, WEA01 , WEA03, WEP051, WEP052, WEP054, WEP055, WEP062, THP007
Qian, J.	THP068
Qin, W.	TUP090, THP084, TUP066 , TUP067
Quan, S.W.	WEP056
— R —	
Rah, S.Y.	TUB03
Raimondi, L.	MOA02, TUB04, THP079
Rathke, J.	TUP006
Ratner, D.F.	TUP035
Ratti, A.	THP071
Raubenheimer, T.O.	TUP032, TUD04, WEP043
Rauer, P.	TUP009 , THP041
Rebernik Ribič, P.	MOA02, TUB01 , TUB04, TUP083, THP013, THP079
Reiche, S.	MOA02, TUA03, WEP036, WEP037, WED01, THB03, THP085, THP086
Reiser, M.	WEP079
Reukauff, M.	WEP036
Riepp, M.	THA04
Rimjaem, S.	THP031
Rochow, R.A.	THP078
Rönsch-Schulenburg, J.	WEP006, WEP048, FRA03
Rommelure, P.	THP048
Roseker, W.R.	THA04
Rosenberger, P.	THD02
RoSSbach, J.	TUP009, TUP076, THP041
Rossi, C.	THP078
Rossi, F.	THP079
Rossmanith, R.	WEP076

Roussel, E. THP013, MOA02, MOC03, WEP015, MOC02, THP048

Ruan, J. WEP042

Ruber, R.J.M.Y. THP078

Rui, T. THP055

Rule, D.W. WEP041, THP069

Rumiz, L. THP079

Rysov, R. THA04

— S —

Saito, H. TUP014

Sakai, H. THA03

Sakai, T. TUD02

Sakdinawat, A. TUD04

Saldin, E. TUP062, TUP079

Salén, P.M. THP084, THD01

Salman, S.H. WEP046

Sammur, N.J. WED01, WEP097, WEP098

Samoylova, L. TUA04, TUP058, TUP079, WEP079

Sandalov, E.S. TUP021

Sasaki, S. WEP104

Sato, T. TUP033

Sauro, R. MOA02

Savilov, A.V. TUP019, TUP020, THP024, THP060

Scafuri, C. MOA02, THP079

Schaber, J. WEP026

Schöllkopf, W. TUP006

Scherz, A. TUA01

Schiepel, P. WEP003, WEP004

Schietinger, T. WED01, THB03, THP085, THP086

Schlarb, H. WEB04, WEP007, WEP010, WEP011, WEP016, WEP019, WEP036

Schmerge, J.F. FRA02

Schmid, S.A. THP009

Schmidt, B. WEP012

Schmidt, Ch. WEB04, WEP011

Schmidt, T. WEP097, WEP098, WED01, THP078, THP085

Schmidt-Föhre, F. WED02

Schneidmiller, E. TUA01, TUA04, TUP055, TUP056, TUP057, TUP059, TUP060, TUP061, TUP062, WEP073

Schnorr, K. THP085

Schoenlein, R.W. WEP104

Scholz, M. MOA04, TUA01, TUA04, TUP058, TUP062, WEB01, WEP008, THP001, THP002, THD03

Schreiber, S. WEP036, WEP047, WEP048, THP074, FRA03

Schulte, D. THP078

Schultheiss, T. TUP006

Schulz, S. WEB04, WEP007, WEP010, WEP016

Scifo, J. THP078

Sebdaoui, M. THP048

Sekutowicz, J.K. THP081

Sellberg, J.A. THP084

Serednyakov, S.S. TUP024

Sergeev, A. TUP018, TUP021

Serkez, S. TUA04, TUP004, TUP056, TUP061, TUP062, TUP073, TUP077, TUP079, WEP080, THP051

Serpico, C. THP079

Sertore, D. WEA04, WEP047, WEP053, WEP062

afak, K. WEP003, WEP004

Shafqat, N. THP079

Shaker, H. TUP001, TUP002, TUP003, WEP051, WEP052, WEP054, WEP055, WEP062, THP007

Shamuilov, G.K. THD01

Shan, L.J. MOA03, TUP015, WEP024

Shayduk, R. TUP079, WEP079

Sheffield, R.L. MOC01

Shen, X. MOA03, TUP015

Shevchenko, O.A. TUP023, TUP024, TUD03, WEP094, THP027

Shi, L. THP015

Shi, X. TUD04

Shim, C.H. TUB03, TUP064, THP051

Shimada, M. TUD02, THA03

Shin, J. WEP031

Shu, D. TUB03, TUP079, TUD04, WEP079

Shu, G. TUP002, WEP051, WEP052, WEP054, WEP055, WEP062, THP007

Shvyd'ko, Yu. TUB03, TUD04, THP051

Sigalotti, P. MOA02, THP079

Simoncig, A. THP079

Sinitsky, S.L. TUP021

Sinn, H. TUA01, TUA04, TUP009, TUP056, TUP058, TUP079, WEP079, WED02, WET01, THP041

Skovorodin, D.I. TUP021

Sleziona, V. TUP079, WEP079

Smartzev, S. THP048

Smedley, J. WEA02

Snively, E.J. TUP036

Sobko, B. WEP080

Sorokin, A.A. TUP055, TUP058

Spallek, R.G. WEP081

Spampinati, S. MOA02, TUB04, TUP083, THP010, THP013, THP079

Spataro, B. THP078

39th Free Electron Laser Conf. ISBN: 978-3-95450-210-3		FEL2019, Hamburg, Germany		JACoW Publishing	
Content from this work may be used under the terms of the CC BY 3.0 licence (© 2019). Any distribution of this work must maintain attribution to the author(s), title of the work, publisher, and DOI	Spezzani, C.	MOA02, TUB04, THP013, THP079	Tian, Y.H.	THP015	
	Squibb, R.	TUB04	Tiedtke, K.I.	TUP055, TUP058, WEP073	
	Stapnes, S.	THP078	Tischer, M.	WEP070, WEP072	
	Starostenko, A.A.	TUP021	Titberidze, M.	WEB04, WEP007, WEP010, WEP016	
	Staszczak, M.	THP081	Todd, A.M.M.	TUP006	
	Steffen, B.	WEP015, WEP035, WEP048	Tomás, R.	WEB03	
	Stephan, F.	TUP001, TUP002, TUP003, WEA03, WEP050, WEP051, WEP052, WEP054, WEP055, WEP062, THP007	Tomin, S.	TUP056, TUP061, TUP062, THD03	
	Stojanovic, N.	THA04	Trachnas, E.	THP078	
	Stragier, X.F.D.	THP078	Traczykowski, P.	TUP049, TUP050, TUP051	
	Stupakov, G.	THP037	Trebushinin, A.	TUP061	
	Sturari, L.	MOA02, THP011	Treusch, R.	FRA03	
	Sudar, N.S.	TUT01, THP073	Trillaud, F.	WEP085	
	Suh, Y.J.	TUB03	Trisorio, A.	THP085	
	Sullivan, J.P.	TUD04	Trovò, M.	MOA02, TUB04, THP013, THP079	
	Sumitomo, Y.	TUD02	Tsai, C.-Y.	MOD01	
	Sun, J.T.	THP015	Tsai, K.L.	THP030	
	Sun, Y.	THP073	Tsakanov, V.M.	THP049	
	Svandrlík, M.	MOA02, THP079	Tsuchiya, K.	THA03	
	Svetina, C.	THP085	— V —		
	Sydlo, C.	WEB04, WEP007, WEP010, WEP016	Vaccarezza, C.	THP078	
	Syresin, E.	WEP073	Vagin, P.	WEP070, WEP072	
	Szamota-Leandersson, K.	THP081	Valléau, M.	THP048	
	Szewiński, J.	THP081	van der Geer, S.B.	TUP036	
	Szwaj, C.	WEP015, THP048	van der Slot, P.J.M.	TUP050	
	Szypula, K.T.	WEP036	Vannoni, M.	TUP079	
	— T —		Vartaniants, I.	MOD03	
	Ta Phuoc, K.	THP048	Vascotto, A.	THP079	
	Tafzi, A.	THP048	Vashchenko, G.	TUP002, TUP003, WEP051, WEP052, WEP062, THP007	
	Tan, T.-F.	TUD04	Veber, S.L.	TUP024	
	Tanaka, H.	MOD01	Venier, C.	THP011	
	Tang, C.-X.	THP020, THP022, THP055	Veronese, M.	MOA02, WEB02, THP013, THP079	
	Tanikawa, T.	MOA02, TUP004, TUP056, TUP061, TUP073, TUP077	Vescovo, R.	THP011	
	Tanimoto, Y.	THA03	Vicario, C.	THP085	
	Tanke, E.	THP078	Vikharev, A.A.	THP060	
	Tao, K.	THP015	Vinokurov, N.A.	TUP023, WEP094, THP027	
	Tararyshkin, S.V.	TUP024	Visintini, R.	THP079	
	Tarawneh, H.	THP084	Vivoda, D.	MOA02	
	Tavakoli, K.T.	THP048	Vogel (Fogel), V.	WEP045	
	Tavares, P.F.	THP084	Vogel, E.	WEA01, WEP051	
	Taylor, G.	THP078	Vogt, M.	WEP006, WEP036, THP003, FRA03	
	Tcheskidov, V.G.	WEP094, THP027	Volkov, V.	THP027	
	Teichert, J.	WEP026	von Helden, G.	TUP006	
	Teng, S.Y.	TUP091, THP030	Voulot, D.	WEP038, WED01, THP085	
	Terentiev, S.	TUP079	— W —		
	Tews, G.	WEP036	Wagner, A.	WEP036	
	Thaury, C.	THP048	Wagner, U.H.	WEP095, WED01, THP085	
	Thompson, N.	THP010, THP065, WEP101, THP033, THP078	Walther, M.	THA04	
	Thorin, S.	TUP066, THP084	Wamsat, T.	WEP008	
	Thurman-Keup, R.M.	WEP042	Wan, W.	THP055	
			Wang, D.	MOA05, TUP063, TUP088,	

Wang, F. THP018, WEP089
Wang, G.L. WEP056
Wang, H. THP015
Wang, H. MOA03, TUP015
Wang, J. MOA03, TUP015
Wang, K. WEP059
Wang, X.T. WEP058
Wang, Z. THB04
Wang, Z.Q. THP015
Webb, S.D. THP073
Weih, S. THP008
Weilbach, T. TUP001, TUP003, WEP062
Weise, H. M0B02
Werin, S. TUP066, TUP067, TUP090, THP084
Wesch, S. WEP012
White, M. TUD04, THP068
Wiemerslage, G.E. THP068
Wilgen, J. WED04
Wilksen, T. TUA01, WEP008
Williams, P.H. TUP072
Winkelmann, L. WEP046, WEP050
Wohlenberg, T. TUP079
Wolff-Fabris, F. TUA04, TUP061, WED02
Wolski, A. TUP072
Wortmann, J. WEP008, WEP013, WEP014
Wu, D. MOA03, TUP015
Wu, G.R. THP015
Wu, J. THP030
Wu, X.W. THP078
Wu, Y.K. THD01
Wuensch, W. WEP036, THP078

— X —

Xiang, D. MOA02
Xiang, R. WEP026
Xiao, D.X. MOA03, TUP015
Xu, J.Z. WEP104
Xu, Y. MOA03
Xu, Y.X. WEP059

— Y —

Yakopov, M. TUP079
Yalandin, M.I. TUP018
Yamada, H. TUP014
Yamaguchi, S. TUP012
Yan, J. THD01
Yan, J.W. THP018
Yan, L.G. MOA03, TUP015, WEP027
Yang, H. THB03, TUP064
Yang, J.Y. THP015

Yang, X. M0B04, TUB04
Yang, X.M. THP015
Yildirim, B. WEP045, WEP049
Yin, L. MOA05
Young, L.M. TUP006
Yu, L.Y. WEP089
Yu, Y. THP015
Yun, G.S. THP044
Yurkov, M.V. TUA01, TUA04, TUP055, TUP056, TUP057, TUP058, TUP059, TUP060, TUP061, TUP062, WEP073

— Z —

Zaccaria, M. MOA02
Zagorodnov, I. TUA04, TUP056, TUP058, TUP060, TUP061, TUP062
Zandonella, A.C. THP085
Zangrando, D. MOA02, THP079
Zangrando, M. MOA02, TUB04, THP079
Zaslavsky, V.Yu. TUP021, THP060, TUP018
Zemella, J. TUP078
Zen, H. TUD02
Zhang, K. THP078
Zhang, L. THP078
Zhang, M. THP016, MOA05, WEP058
Zhang, P. MOA03, TUP015
Zhang, W.Q. THP015
Zhang, W.Y. WEP058
Zhang, Y. THP022, THP055
Zhang, Z. WEP043, WEP104, THD02
Zhao, S. WEP057, WEP056
Zhao, X. WEP059
Zhao, Z. WEP063
Zhao, Z.T. MOA05, FRA04
Zheleznov, I.V. TUP018
Zheng, J. TUP076
Zholents, A. THP073, THD02
Zhou, K. MOA03, TUP015, WEP024, WEP026
Zhou, K.S. TUP088
Zhou, Q.H. WEP059, THP054
Zhu, D. THP078
Zhu, D. TUP032, TUP033, TUD04, THP071
Zotova, I.V. TUP018
Zozulya, A. WEP079
Zummack, F. WEB04, WEP007, WEP010, WEP016

Institutes List

AAI/ANL

Lemont, Illinois, USA

- [Lumpkin, A.H.](#)

AES

Medford, New York, USA

- [Rathke, J.](#)
- [Schultheiss, T.](#)

ALBA-CELLS Synchrotron

Cerdanyola del Vallès, Spain

- [Marcos, J.](#)
- [Marín, E.](#)
- [Muñoz Horta, R.](#)
- [Pérez, F.](#)

AMMTodd Consulting

Princeton Junction, New Jersey, USA

- [Todd, A.M.M.](#)

Ankara University Institute of Accelerator Technologies

Golbasi, Turkey

- [Aksoy, A.](#)
- [Elçim, Ö.F.](#)

Ankara University, Accelerator Technologies Institute

Golbasi, Turkey

- [Aksoy, A.](#)
- [Karsli, Ö.](#)
- [Kaya, Ç.](#)
- [Koç, .B.](#)

Ankara University, Faculty of Sciences

Ankara, Turkey

- [Nergiz, Z.](#)

ANL

Lemont, Illinois, USA

- [Anton, J.W.J.](#)
- [Assoufid, L.](#)
- [Den Hartog, P.K.](#)
- [Goetze, K.](#)
- [Jansma, W.G.](#)
- [Kearney, S.P.](#)
- [Kim, K.-J.](#)
- [Kim, K.](#)
- [Lindberg, R.R.](#)
- [Miceli, A.](#)
- [Qian, J.](#)
- [Sasaki, S.](#)
- [Shi, X.](#)
- [Shu, D.](#)
- [Shvyd'ko, Yu.](#)

- [Sullivan, J.P.](#)

- [Sun, Y.](#)
- [White, M.](#)
- [Wiemerslage, G.E.](#)
- [Xu, J.Z.](#)
- [Zholents, A.](#)

ARCNL

Amsterdam, The Netherlands

- [Hoekstra, R.](#)

Ariel University

Ariel, Israel

- [Balal, N.](#)
- [Bratman, V.L.](#)
- [Dyunin, E.](#)
- [Friedman, A.](#)
- [Gerasimov, M.G.](#)
- [Lurie, Yu.](#)

AS - ANSTO

Clayton, Australia

- [Dowd, R.T.](#)
- [Zhu, D.](#)

Bilfinger Noell GmbH

Wuerzburg, Germany

- [Boffo, C.](#)

BINP

Novosibirsk, Russia

- [Trebushinin, A.](#)

BINP SB RAS

Novosibirsk, Russia

- [Arzhannikov, A.V.](#)
- [Bykov, E.V.](#)
- [Davidyuk, I.V.](#)
- [Getmanov, Ya.V.](#)
- [Kubarev, V.V.](#)
- [Matveev, A.S.](#)
- [Sandalov, E.S.](#)
- [Serednyakov, S.S.](#)
- [Shevchenko, O.A.](#)
- [Sinitsky, S.L.](#)
- [Skovorodin, D.I.](#)
- [Starostenko, A.A.](#)
- [Tararyshkin, S.V.](#)
- [Tcheskidov, V.G.](#)
- [Vinokurov, N.A.](#)
- [Volkov, V.](#)

Upton, New York, USA

- Rossi, C.
- Schulte, D.
- Stapnes, S.
- Szypula, K.T.
- Tomás, R.
- Wu, X.W.
- Wuensch, W.

Mianyang, Sichuan, People's Republic of China

- Chiang Mai University

Chiang Mai, Thailand

- CNR-IFN**

Padova, Italy

- Miotti, P.

Trieste, Italy

- Coreno, M.

Warrington, Cheshire, United Kingdom

- Campbell, L. T.
- Cowie, L.S.
- Habib, A.F.
- Hidding, B.
- Jones, J.K.
- M^CNeil, B.W.J.
- Millar, W.L.
- Morgan, J.F.
- Muratori, B.D.
- Thompson, N.
- Traczykowski, P.
- Williams, P.H.
- Wolski, A.

Lancaster, United Kingdom

- Apsimon, R.
- Burt, G.
- Castilla, A.
- Cowie, L.S.

Naples, Italy

- Lupi, S.

Ithaca, New York, USA

- Gorobtsov, O.

Hamburg, Germany

- Berlin, A.
- Cano Vargas, E.
- Cheng, H.P.H.

Mainyang, Sichuan, People's Republic of China

- Liu, Y.

Yerevan, Armenia

- Grigoryan, A.
- Ivanyan, M.
- Tsakanov, V.M.

Yerevan, Armenia

- Amirkhanyan, Z.G.

Gif-sur-Yvette, France

- Garzella, D.

Meyrin, Switzerland

- Catalán Lasheras, N.
- del Pozo Romano, V.
- Fol, E.
- Grudiev, A.
- Latina, A.
- Liu, X.
- McMonagle, G.
- Millar, W.L.
- Pitman, S.

- Dai, A.
- Derksen, J.
- Neuhaus, M.
- Schiepel, P.
- afak, K.

Czech Republic Academy of Sciences, Institute of Physics

Prague, Czech Republic

- Molodozhentsev, A.Y.

DELTA

Dortmund, Germany

- Büsing, B.
- Khan, S.
- Krieg, D.
- Mai, C.
- Meyer auf der Heide, A.

Department of Applied Physics, UIT

Bhopal, India

- Hussain, J.

DESY

Hamburg, Germany

- Ackermann, S.
- Aghababayan, A.
- ASSmann, R.W.
- Bagschik, K.
- Balandin, V.
- Beutner, B.
- Bousonville, M.
- Braune, M.
- Brinker, F.
- Butkowski, Ł.
- Cherepenko, A.
- Choroba, S.
- Choudhuri, A.
- Christie, F.
- Czwalińska, M.K.
- D'Arcy, R.T.P.
- Decking, W.
- Dohlus, M.
- Dorda, U.
- Dursun, B.
- Eckoldt, H.-J.
- Faatz, B.
- Felber, E.P.
- Felber, M.
- Fenner, M.
- Flöttmann, K.
- Foese, M.
- Fröhlich, L.
- Gerth, C.
- Golubeva, N.
- Golz, T.
- Gonzalez Caminal, P.
- Grattoni, V.
- Grevsmühl, T.

- Grosse-Wortmann, U.
- Grün, C.
- Grunewald, S.
- Grübel, G.
- Guetg, M.W.
- Hartl, I.
- Hartwell, S.D.
- Hensler, O.
- Hoffmann, M.
- Honkavaara, K.
- Hüning, M.
- Ivanov, R.
- Janik, Y.
- Jastrow, U.
- Jonas, R.
- Kammering, R.
- Katalev, V.V.
- Kay, H.
- Klose, K.
- Kocharyan, V.
- Kot, Y.A.
- Kozak, T.
- Krebs, O.
- Kube, G.
- Kuhlmann, M.
- Laarmann, T.
- Lamb, T.
- Lang, T.
- Lautenschlager, B.
- Lechner, C.
- Lederer, S.
- Lemery, F.
- Li, C.
- Libov, V.
- Limberg, T.
- Liu, S.
- Lockmann, N.M.
- Ludwig, F.
- Machau, K.
- Marchetti, B.
- Marx, D.
- Marx, M.
- Mavrič, U.
- Mehrjoo, M.
- Mohammad Kazemi, M.M.
- Mohr, C.
- Morozov, P.
- Müller, J.
- Muller, E.
- Müller, L.
- Nachtigal, Y.
- Negodin, E.
- Nölle, D.
- Novokshonov, A.I.
- Obier, F.
- Omet, M.
- Osterhoff, J.
- Paraskaki, G.
- Peters, F.
- Pfeiffer, S.
- Philippi-Kobs, A.

- Koss, G.
- Krasilnikov, M.
- Lal, S.
- Li, X.
- Lishilin, O.
- Loisch, G.
- Lueangaramwong, A.
- Melkumyan, D.
- Mohanty, S.K.
- Mueller, F.
- Niemczyk, R.
- Oppelt, A.
- Philipp, S.
- Qian, H.J.
- Shaker, H.
- Shu, G.
- Stephan, F.
- Vashchenko, G.
- Weilbach, T.

Hamburg, Germany

- Devi Ahilya University

Indore, India

- Gehlot, M.
- Khan, S.M.
- Khullar, R.
- Mishra, G.

DICP

Dalian, People's Republic of China

- Chen, Z.
- Cheng, G.K.
- Dai, D.X.
- Ding, H.L.
- He, Z.G.
- Huang, L.
- Li, Q.M.
- Li, Z.B.
- Shi, L.
- Sun, J.T.
- Tao, K.
- Tian, Y.H.
- Wang, G.L.
- Wang, Z.Q.
- Wu, G.R.
- Yang, J.Y.
- Yang, X.M.
- Yu, Y.
- Zhang, W.Q.

DESY Zeuthen

Zeuthen, Germany

- DLR**

Berlin, Germany

- Gensch. M.

Elettra-Sincrotrone Trieste S.C.p.A.

Basovizza, Italy

- Abrami, A.
- Adhlakha, N.
- Allaria, E.
- Badano, L.
- Bassanese, S.
- Bencivenga, F.
- Bossi, M.
- Bruchon, N.
- Callegari, C.
- Capotondi, F.
- Castronovo, D.
- Cautero, M.
- Cilento, F.
- Cinquegrana, P.
- Coreno, M.
- Cudin, I.
- D'Auria, G.
- Danailov, M.B.
- De Monte, R.
- De Ninno, G.
- Delgiusto, P.
- Demidovich, A.A.
- Di Fraia, M.
- Di Mitri, S.
- Di Pietro, P.
- Diviacco, B.
- Fabris, A.
- Fabris, R.
- Fawley, W.M.
- Ferianis, M.
- Foglia, L.
- Furlan Radivo, P.
- Gaio, G.
- Gelmetti, F.
- Giacuzzo, F.
- Giannessi, L.
- Grulja, S.
- Iazzourene, F.
- Kiskinova, M.
- Krecic, S.
- Kurdi, G.
- Lonza, M.
- Mahne, N.
- Malvestuto, M.
- Manfreda, M.
- Masciovecchio, C.
- Milloch, M.
- Mincigrucci, R.
- Mirian, N.S.
- Naumenko, D.
- Nikolov, I.
- O'Shea, F.H.
- Pedersoli, E.
- Penco, G.
- Perucchi, A.
- Plekan, O.
- Predonzani, M.
- Prince, K.C.
- Principi, E.

- Raimondi, L.
- Rebernik Ribič, P.
- Rochow, R.A.
- Rossi, F.
- Roussel, E.
- Rumiz, L.
- Sauro, R.
- Scafuri, C.
- Serpico, C.
- Shafqat, N.
- Sigalotti, P.
- Simoncig, A.
- Spampinati, S.
- Spezzani, C.
- Sturari, L.
- Svandrlík, M.
- Trovò, M.
- Vascotto, A.
- Veronese, M.
- Visintini, R.
- Vivoda, D.
- Zaccaria, M.
- Zangrando, D.
- Zangrando, M.

ELI-BEAMS

Prague, Czech Republic

- Green, J.T.
- Hawke, J.
- Kaur, M.
- Kocon, D.
- Korn, G.
- Kruchinin, K.O.

ENEA C.R. Frascati

Frascati (Roma), Italy

- Dattoli, G.
- Giannessi, L.
- Nguyen, F.
- Petralia, A.

ESRF

Grenoble, France

- Benabderrahmane, C.

ESS

Lund, Sweden

- Tanke, E.
- Trachnas, E.

ETH

Zurich, Switzerland

- Kirschner, J.
- Krause, A.
- Mutný, M.
- Nonnenmacher, M.

- Khazanov, E.
- Kuzikov, S.V.
- Malkin, A.
- Mironov, S.
- Oparina, Yu.S.
- Peskov, N.Yu.
- Savilov, A.V.
- Sergeev, A.
- Vikharev, A.A.
- Zaslavsky, V.Yu.
- Zheleznov, I.V.
- Zotova, I.V.

IBB

Warsaw, Poland

- Bal, W.
- Poznański, J.

IFIC

Valencia, Spain

- Esperante Pereira, D.
- Fuster, J.
- Gonzalez-Iglesias, D.

INFN/LASA

Segrate (MI), Italy

- Michelato, P.
- Monaco, L.
- Sertore, D.

INFN/LNF

Frascati, Italy

- Alesini, D.
- Bellaveglia, M.
- Buonomo, B.
- Cardelli, F.
- Croia, M.
- Diomedede, M.
- Ferrario, M.
- Gallo, A.
- Giribono, A.
- Piersanti, L.
- Scifo, J.
- Spataro, B.
- Vaccarezza, C.

International Tomography Center, SB RAS

Novosibirsk, Russia

- Fedin, M.V.
- Melnikov, A.R.
- Veber, S.L.

IOM-CNR

Trieste, Italy

- Cefarin, N.
- Dal Zilio, S.
- Lazzarino, M.

- Piccirilli, F.

JINR

Dubna, Moscow Region, Russia

- Brovko, O.I.
- Grebentsov, A.Yu.
- Syresin, E.

JLab

Newport News, Virginia, USA

- Benson, S.V.

KAERI

Daejeon, Republic of Korea

- Bae, S.
- Baek, I.H.
- Buaphad, P.
- Jeong, Y.U.
- Joo, Y.J.
- Kim, H.W.
- Kim, Y.
- Lee, H.R.
- Oang, K.
- Park, S.

KAIST

Daejeon, Republic of Korea

- Jeon, I.J.
- Kim, D.
- Kim, J.
- Kwon, D.
- Shin, J.

Kansai University

Osaka, Japan

- Asakawa, M.R.
- Yamaguchi, S.

KEK

Ibaraki, Japan

- Honda, Y.
- Kato, R.
- Kawata, H.
- Miyajima, T.
- Nakamura, N.
- Sakai, H.
- Shimada, M.
- Tanimoto, Y.
- Tsuchiya, K.

KIT

Karlsruhe, Germany

- Bernhard, A.
- Casalbuoni, S.
- Gethmann, J.

- Fiedorowicz, H.
- Janulewicz, K.
- Palka, N.

National Technical University of Athens

Athens, Greece

- Gazis, E.N.
- Gazis, N.

NCBJ

Świerk/Otwock, Poland

- Czuma, P.J.
- Krawczyk, P.
- Krzywiński, J.
- Nietubyć, R.
- Staszczak, M.
- Szamota-Leandersson, K.
- Szewiński, J.

NITTTR

Bhopal, India

- Jeevakhan, H.

NPS

Monterey, California, USA

- Colson, W.B.

NSRRC

Hsinchu, Taiwan

- Chan, C.K.
- Chang, C.-C.
- Chang, C.-H.
- Chang, L.-H.
- Chen, C.H.
- Chou, M.C.
- Chou, P.J.
- Chung, T.Y.
- Hsiao, F.Z.
- Hsu, K.T.
- Hsueh, H.P.
- Hu, K.H.
- Hwang, C.-S.
- Hwang, J.-Y.
- Jan, J.C.
- Kuan, C.K.
- Lau, W.K.
- Lee, A.P.
- Lin, M.-C.
- Luo, G.-H.
- Tsai, K.L.

NSU

Novosibirsk, Russia

- Davidyuk, I.V.
- Getmanov, Ya.V.
- Matveev, A.S.
- Serednyakov, S.S.

- Vinokurov, N.A.

NTHU

Hsinchu, Taiwan

- Teng, S.Y.

PAL

Pohang, Republic of Korea

- Cho, M.H.
- Han, J.H.
- Heo, H.
- Hong, J.H.
- Jung, Y.G.
- Kang, H.-S.
- Kim, C.
- Kim, D.E.
- Kim, G.
- Kim, M.J.
- Ko, J.H.
- Lee, S.J.
- Min, C.-K.
- Mun, G.
- Na, D.H.
- Nam, I.H.
- Oh, B.G.
- Parc, Y.W.
- Rah, S.Y.
- Shim, C.H.
- Suh, Y.J.
- Yang, H.

Peking University

Beijing, People's Republic of China

- Zhao, S.

PhLAM/CERCLA

Villeneuve d'Ascq Cedex, France

- Bielawski, S.
- Evain, C.
- Roussel, E.
- Sz waj, C.

PhLAM/CERLA

Villeneuve d'Ascq, France

- Bielawski, S.
- Evain, C.
- Roussel, E.
- Sz waj, C.

PKU

Beijing, People's Republic of China

- Chen, M.
- Huang, S.
- Lin, L.
- Liu, K.X.
- Liu, Y.Q.
- Ouyang, D.M.

- Huppert, M.
- Ischebeck, R.
- Jöhri, H.
- Juranič, P.N.
- Kalt, R.
- Keil, B.
- Kittel, C.
- Kleeb, T.
- Krempaská, R.A.
- Liang, X.
- Lippuner, T.
- Löhl, F.
- Lombosi, C.
- Malyzhenkov, A.
- Marcellini, F.
- Marinkovic, G.
- Orlandi, G.L.
- Ozkan Loch, C.
- Paraliev, M.
- Patthey, L.
- Pedrozzi, M.
- Pradervand, C.
- Prat, E.
- Reiche, S.
- Schietinger, T.
- Schmidt, T.
- Schnorr, K.
- Svetina, C.
- Trisorio, A.
- Vicario, C.
- Voulot, D.
- Wagner, U.H.
- Zandonella, A.C.
- Zhang, K.

Riyadh, Kingdom of Saudi Arabia

- van der Geer, S.B.

Pohang, Kyungbuk, Republic of Korea

- ## QST

Tokai, Japan

- Hajima, R.
- Kawase, K.
- Nagai, R.

Silver Spring, USA

- Rule, D.W.

Villigen PSI, Switzerland

- Adelmann, A.
- Aeppli, G.
- Aiba, M.
- Al Haddad, A.
- Alarcon, A.D.
- Alex, J.
- Arbelo, Y.P.
- Arrell, C.
- Arsov, V.R.
- Bettoni, S.
- Bopp, M.
- Borrelli, S.
- Bostedt, C.
- Braun, H.-H.
- Calvi, M.
- Cassar, A.
- Celcer, T.
- Citterio, A.
- Coello de Portugal, J.M.
- Craievich, P.
- David, Ch.
- Dijkstal, P.
- Dordevic, S.
- Ferrari, E.
- Flechsig, U.
- Follath, R.
- Frei, F.
- Gaiffi, N.
- Ganter, R.
- Geng, Z.G.
- Gough, C.H.
- Guzenko, V.
- Hermann, B.
- Hiller, N.
- Huerzeler, O.

RadiaBeam

Los Angeles, California, USA

- Agustsson, R.B.
- Campese, T.J.
- Gadjev, I.I.
- Murokh, A.Y.

RadiaSoft LLC

Boulder, Colorado, USA

- Hall, C.C.
- Webb, S.D.

RAS/IEP

Ekaterinburg, Russia

- [Yalandin, M.I.](#)

RIKEN SPring-8 Center

Hyogo, Japan

- [Hara, T.](#)
- [Inoue, I.](#)
- [Tanaka, H.](#)

Santa Clara University

Santa Clara, California, USA

- [Fiadonu, V.](#)

Sapienza University of Rome

Rome, Italy

- [Arnesano, J.M.](#)
- [Bosco, F.](#)
- [Ficcadenti, L.](#)
- [Lupi, S.](#)
- [Mostacci, A.](#)
- [Palumbo, L.](#)

SARI-CAS

Pudong, Shanghai, People's Republic of China

- [Deng, H.X.](#)
- [Dong, X.](#)
- [Feng, C.](#)
- [Feng, L.](#)
- [Gu, D.](#)
- [Liu, B.](#)
- [Liu, T.](#)
- [Wang, D.](#)
- [Wang, Z.](#)
- [Zhou, K.S.](#)

Shanghai Advanced Research Institute

Pudong, Shanghai, People's Republic of China

- [Li, C.L.](#)
- [Zhang, M.](#)

Shanghai Jiao Tong University

Shanghai, People's Republic of China

- [Xiang, D.](#)

ShanghaiTech University

Shanghai, People's Republic of China

- [Wan, W.](#)

Shenkar College of Engineering and Design

Ramat Gan, Israel

- [Ianculescu, R.](#)

SINAP

Shanghai, People's Republic of China

- [Deng, H.X.](#)
- [Dong, X.](#)
- [Fang, G.P.](#)
- [Fang, W.](#)
- [Feng, C.](#)
- [Huang, D.](#)
- [Huang, N.](#)
- [Lan, T.](#)
- [Liu, B.](#)
- [Liu, Z.P.](#)
- [Wang, D.](#)
- [Wang, X.T.](#)
- [Yan, J.W.](#)
- [Yin, L.](#)
- [Yu, L.Y.](#)
- [Zhang, M.](#)
- [Zhang, W.Y.](#)

SLAC

Menlo Park, California, USA

- [Adolphsen, C.](#)
- [Bane, K.L.F.](#)
- [Benwell, A.L.](#)
- [Bohler, D.K.](#)
- [Brachmann, A.](#)
- [Bucksbaum, P.H.](#)
- [Champenois, E.](#)
- [Chao, A.](#)
- [Cryan, J.](#)
- [Decker, F.-J.](#)
- [Ding, Y.](#)
- [Driver, T.D.C.](#)
- [Dunham, M.](#)
- [Duris, J.P.](#)
- [Emma, C.](#)
- [Fawley, W.M.](#)
- [Feng, Y.](#)
- [Fisher, A.S.](#)
- [Gassner, G.L.](#)
- [Halavanau, A.](#)
- [Hastings, J.B.](#)
- [Hemsing, E.](#)
- [Hoffmann, M.C.](#)
- [Huang, Z.](#)
- [Jacobson, B.T.](#)
- [Kirchmann, P.S.](#)
- [Kiss, A.M.](#)
- [Krasnykh, A.K.](#)
- [Krzywiński, J.](#)
- [Lee, W.S.](#)
- [Lindenberg, A.](#)
- [Liu, Y.](#)
- [Lutman, A.A.](#)
- [MacArthur, J.P.](#)
- [Marcus, G.](#)
- [Magraf, R.A.](#)
- [Marinelli, A.](#)
- [Nanni, E.A.](#)
- [Nosochkov, Y.M.](#)

TEMF, TU Darmstadt

Darmstadt, Germany

- Ackermann, W.
- Bazyl, D.B.
- De Gersem, H.
- Gjonaj, E.
- Müller, W.F.O.
- Schmid, S.A.

The University of Liverpool

Liverpool, United Kingdom

- Wolski, A.

The University of Melbourne

Melbourne, Victoria, Australia

- Taylor, G.

The University of Texas at Austin

Austin, Texas, USA

- Downer, M.
- LaBerge, M.

ThEP Center, Commission on Higher Education

Bangkok, Thailand

- Rimjaem, S.

THM

Friedberg, Germany

- Penirschke, A.

TISNCM

Troitsk, Russia

- Blank, V.D.
- Terentiev, S.

Tohoku University, Research Center for Electron Photon Science

Sendai, Japan

- Hama, H.
- Kashiwagi, S.
- Morita, N.M.
- Muto, T.
- Nanbu, K.
- Saito, H.
- Yamada, H.

TU Darmstadt

Darmstadt, Germany

- Enders, J.
- Weih, S.

TUB

Beijing, People's Republic of China

- Deng, X.J.

- Huang, P.W.
- Huang, W.-H.
- Pan, Z.
- Rui, T.
- Tang, C.-X.
- Zhang, Y.

TUE

Eindhoven, The Netherlands

- Luiten, O.J.
- Mutsaers, P.H.A.
- Stragier, X.F.D.

UCLA

Los Angeles, USA

- Dang, D.K.
- Denham, P.E.
- Emma, C.
- Fisher, A.C.
- Musumeci, P.
- Park, Y.
- Pellegrini, C.
- Sudar, N.S.

UNAM

México, D.F., Mexico

- Trillaud, F.

UNICAMP

Campinas, São Paulo, Brazil

- Baader, J.E.

University of Chicago

Chicago, Illinois, USA

- Kim, K.-J.
- Li, Y.S.

University of Hamburg

Hamburg, Germany

- Maier, A.R.

University of Hamburg, Institut für Experimentalphysik

Hamburg, Germany

- Azima, A.
- Bahns, I.
- Biss, H.
- Drescher, M.
- Frömter, R.
- Hillert, W.
- Miltchev, V.
- Oepen, H.P.
- Rauer, P.
- RoSSbach, J.

University of Hawaii

Honolulu, USA

- Park, J.-W.

Università degli Studi di Milano & INFN

Segrate, Italy

- Guerini Rocco, G.
- Pagani, C.

UNN

Nizhny Novgorod, Russia

- Zaslavsky, V.Yu.

Uppsala University

Uppsala, Sweden

- Fahlström, S.
- Feifel, R.
- Goryashko, V.A.
- Hamberg, M.
- Jacewicz, M.
- Ruber, R.J.M.Y.
- Salén, P.M.
- Shamuilov, G.K.
- Squibb, R.

USTC

Hefei, Anhui, People's Republic of China

- Wang, K.

USTC/NSRL

Hefei, Anhui, People's Republic of China

- Huang, R.
- Jia, Q.K.
- Li, H.T.
- Liu, W.
- Zhao, Z.

USTRAT/SUPA

Glasgow, United Kingdom

- Alotaibi, B.M.
- Altuijri, R.
- Campbell, L.T.
- Cross, A.W.
- Habib, A.F.
- Henderson, J.
- Hidding, B.
- M^CNeil, B.W.
- Morgan, J.F.
- Pongchalee, I.
- Traczykowski
- Zhang, L.

USTRAT/SUPA

Glasgow, United Kingdom

- Buaphad, P.
- Jeong, I.G.
- Joo, Y.J.
- Kim, Y.
- Lee, H.R.

- Altunji, R.
- Campbell

- Cross A W

- Nix, L.J.R.

- Hidding, E
- McNeil, R

- M-Nell, B.W.J.
- Morrison, J.F.

- Gover, A.
- Ianconescu, R.

UVEG

Burjasot (Valencia), Spain

- Bruchon, N.
- Venier, C.
- Vescovo, R.

VDL ETG

Eindhoven, The Netherlands

- Kukk, E.

- Janssen, X.J.A.
- Priem, J.M.A.

Weizmann Institute of Science, Physics

Rehovot, Israel

- Andriyash, I.A.
- Malka, V.
- Smartzev, S.

